WILEY-VCH

Edited by
Günter Gauglitz and David S. Moore

Handbook of Spectroscopy

Second, Completely Revised and Enlarged Edition

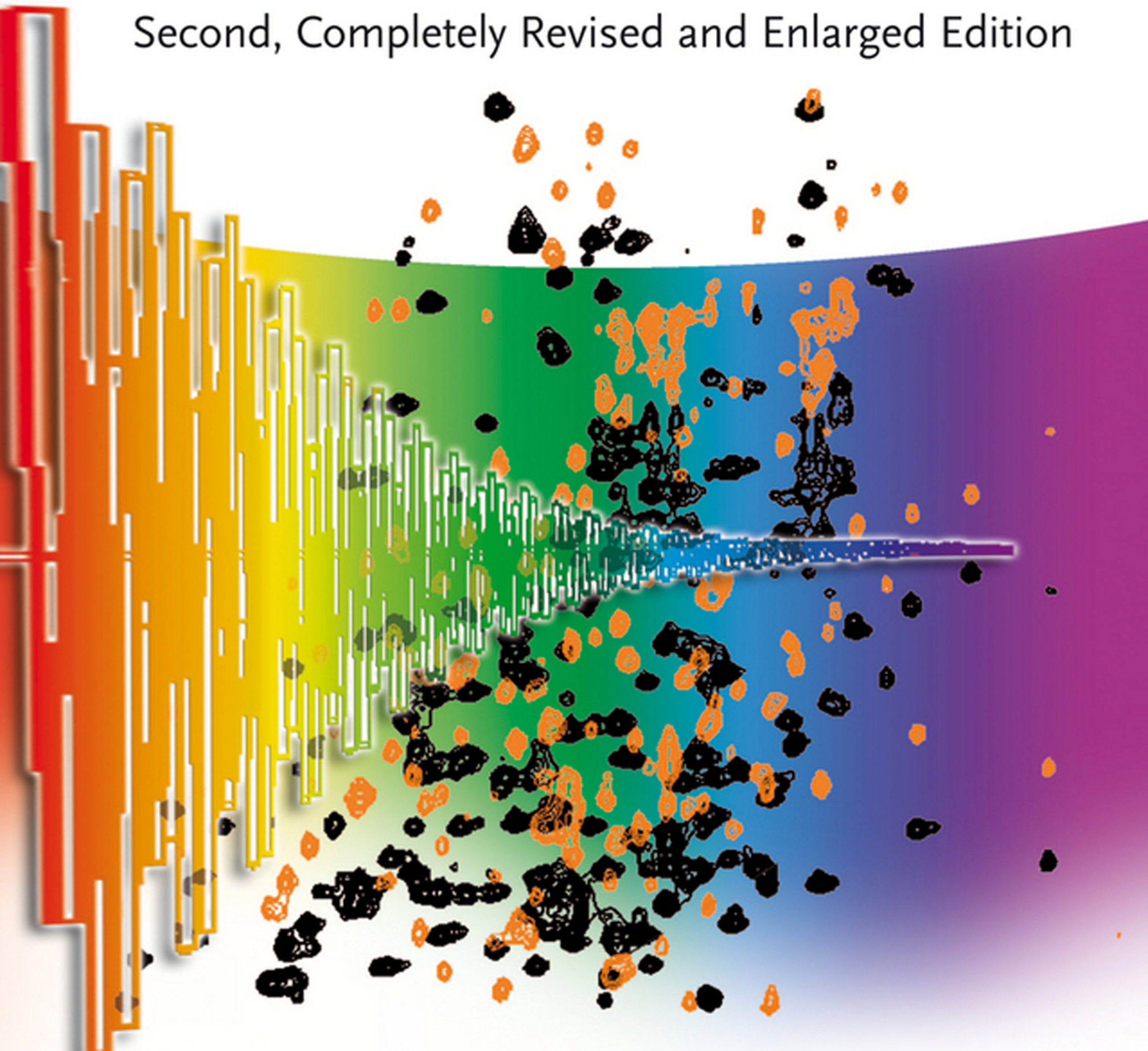

Edited by
Günter Gauglitz and David S. Moore

Handbook of Spectroscopy

Related Titles

Gunther, H.

NMR Spectroscopy
Basic Principles, Concepts and Applications in Chemistry
Third, Completely Revised and Updated Edition

2013
ISBN: 978-3-527-33004-1

Zerbe, O., Jurt, S.

Applied NMR Spectroscopy for Chemists and Life Scientists

2013
ISBN: 978-3-527-32774-4

Friebolin, H.

Basic One- and Two-Dimensional NMR Spectroscopy
Fifth, Completely Revised and Enlarged Edition

2010
ISBN: 978-3-527-32782-9

Berger, S., Sicker, D.

Classics in Spectroscopy
Isolation and Structure Elucidation of Natural Products

2009
ISBN: 978-3-527-32617-4

Andrews, D. L. (ed.)

Encyclopedia of Applied Spectroscopy
Series: Encyclopedia of Applied Physics

2009
ISBN: 978-3-527-40773-6

Edited by
Günter Gauglitz and David S. Moore

Handbook of Spectroscopy

Second, Enlarged Edition

Volume 1

WILEY-VCH
Verlag GmbH & Co. KGaA

Edited by
Günter Gauglitz and David S. Moore

Handbook of Spectroscopy

Second, Enlarged Edition

Volume 2

WILEY-VCH
Verlag GmbH & Co. KGaA

Edited by
Günter Gauglitz and David S. Moore

Handbook of Spectroscopy

Second, Enlarged Edition

Volume 3

WILEY-VCH
Verlag GmbH & Co. KGaA

Edited by
Günter Gauglitz and David S. Moore

Handbook of Spectroscopy

Second, Enlarged Edition

Volume 4

WILEY-VCH
Verlag GmbH & Co. KGaA

The Editors

Prof. Dr. Günter Gauglitz
University of Tübingen
Institute for Physical and Theoretical Chemistry
Auf der Morgenstelle 18
72076 Tübingen
Germany

Dr. David S. Moore
Shock and Detonation Physics
Los Alamos National Laboratory
MS-P952, Los Alamos, NM 87545
USA

Library of Congress Card No.: applied for

British Library Cataloguing-in-Publication Data
A catalogue record for this book is available from the British Library.

Bibliographic information published by the Deutsche Nationalbibliothek
The Deutsche Nationalbibliothek lists this publication in the Deutsche Nationalbibliografie; detailed bibliographic data are available on the Internet at <http://dnb.d-nb.de>.

Print ISBN: 978-3-527-32150-6
ePDF ISBN: 978-3-527-65473-4
ePub ISBN: 978-3-527-65472-7
mobi ISBN: 978-3-527-65471-0
oBook ISBN: 978-3-527-65470-3

Cover-Design Bernd Adam Design, Weinheim, Germany
Typesetting Laserwords Private Limited, Chennai, India
Printing and Binding Markono Print Media Pte Ltd, Singapore

Printed on acid-free paper

Contents

Section III Methods 2: NMR *183*

Section IV Methods 3: Mass Spectrometry *355*

Volume 2

Volume 3

Volume 4

Section XII Applications 6: Spectroscopy at Surfaces *1439*

Contents

Volume 1

Volume 2

Section VII Methods 6: Spectroscopy in Nano Dimensions 821

Volume 3

Volume 4

Contents

Volume 1

Volume 2

Volume 3

Volume 4

Contents

Volume 2

Volume 3

Volume 4

List of Contributors

Rigoberto Advincula
Case Western Reserve University
Department of Macromolecular Science and Engineering
2100 Adelbert Road
Cleveland, OH 44106
USA

Willem M. Albers
VTT Technical Research Centre of Finland
Bio and Process Technology
Functional Plastics
Sinitaival 6
FI-33720 Tampere
Finland

Klaus Albert
University of Tuebingen
Department of Chemistry
Institute of Organic Chemistry
Auf der Morgenstelle 18
D-72076 Tübingen
Germany

Akira Baba
Niigata University
Center for Transdisciplinary Research
Department of Electronics and Electrical Engineering
8050 Ikarashi 2-nocho
Nishi-ku
Niigata 950-2181
Japan

Garfield Beckford
Georgia State University
Department of Chemistry
38 Peachtree Ctr Ave
Suite 540
Atlanta, GA 30303
USA

Christian Blum
University of Twente
Nanobiophysics, MESA +
Institute for Nanotechnology
PO Box 217
7500AE
Enschede
The Netherlands

Sophie Bourcier
Ecole Polytechnique
Laboratoire des Mécanismes
Réactionnels
CNRS
route de Saclay
91128
Palaiseau cedex
France

Marc Brecht
University of Tuebingen
Institute of Physical and
Theoretical Chemistry
Auf der Morgenstelle 8
72076 Tuebingen
Germany

José Alfons Clement Broekaert
University of Hamburg
Department of Chemistry
Institute for Inorganic and
Applied Chemistry
Martin-Luther-King-Platz 6
D 20146 Hamburg
Germany

Steven P. Brown
Laboratoire de Stereochimie
et des Interactions Moleculaires
Ecole Normale Superieure de
Lyon
46 Allee d'Italie
69364 Lyon
Cedex 07
France

Michael Brudel
InProcess Instruments GmbH
Sophie-Germain-Str. 1
28201 Bremen
Germany

Leslie G. Butler
Lousiana State University
Department of Chemistry
Baton Rouge, LA 70803-1804
USA

Pengfei Cao
Case Western Reserve University
Department of Macromolecular
Science and Engineering
2100 Adelbert Road
Cleveland, OH 44106
USA

Maria Benedetta Casu
University of Tuebingen
Institute of Physical and
Theoretical Chemistry
Auf der Morgenstelle 18
72076 Tuebingen
Germany

Thomas Chassé
University of Tuebingen
Institute of Physical and
Theoretical Chemistry
Auf der Morgenstelle 18
72076 Tuebingen
Germany

Brian M. Cullum
University of Maryland Baltimore
County
Department of Chemistry and
Biochemistry
1000 Hilltop Circle
Baltimore, MD 21250
USA

Allan Cyago
Case Western Reserve University
Department of Macromolecular
Science and Engineering
2100 Adelbert Road
Cleveland, OH 44106
USA

Tuan Vo-Dinh
Duke University
Department of Biomedical
Engineering
Fitzpatrick Institute for Photonics
Durham, NC 27708
USA

Markus Ehni
University of Tuebingen
Institute of Physical and
Theoretical Chemistry
Auf der Morgenstelle 18
72076 Tuebingen
Germany

Lyndon Emsley
Laboratoire de Stereochimie
et des Interactions Moleculaires
Ecole Normale Superieure de
Lyon
46 Allee d'Italie
69364 Lyon
Cedex 07
France

John C. Fetzer
Fetzpahs Consulting
PO Box 942
Pinole, CA 94564
USA

Dieter Fischer
Leibniz Institute of Polymer
Research Dresden, Analytics
Hohe Str. 6
01069 Dresden
Germany

Toshihiro Fujii
Meisei University
Department of Chemistry
Faculty of Sciences and
Engineering
Hodokubo 2-1-1
Hino
Tokyo 191-8506
Japan

Detlef Günther
ETH Zurich
Department of Chemistry and
Applied Biosciences
Laboratory for Inorganic
Chemistry
HCI G105, Wolfgang Pauli Str. 10
CH-8093
Zurich
Switzerland

Günter Gauglitz
University of Tuebingen
Institute of Physical and
Theoretical Chemistry
Auf der Morgenstelle 8
72076 Tuebingen
Germany

Alexander Gerlach
Universität Tübingen, Institut für
Angewandte Physik
Auf der Morgenstelle 10
72076 Tübingen
Germany

Michael O. Glocker
University of Rostock
Proteome Center Rostock
Schillingallee 69
18057 Rostock
Germany

Nicholas J. Goddard
University of Manchester
School of Chemical Engineering
and Analytical Science (SCEAS)
PO Box 88
Manchester
M60 1QD
UK

Igor Gornushkin
BAM Federal Institute for
Materials Research and Testing
Department 1 Analytical
Chemistry
Reference Materials
Division 1.4 Process Analytical
Technology
Richard-Willstaetter-Str. 11
D-12489 Berlin
Germany

Pekka Hänninen
University of Turku
Department of Biophysics
Cell Biology and Anatomy
Tykistökatu 6
20520 Turku
Finland

Chad E. Hadden
Rapid Structure Characterization
Group
Pharmaceutical Development
Pharmacia Corporation
Kalamazoo
MI 49001-0199
USA

Achim Hartschuh
LMU Muenchen
Department Chemie & CeNS
81377 Muenchen
Germany

Bodo Hattendorf
ETH Zurich
Department of Chemistry and
Applied Biosciences
Laboratory for Inorganic
Chemistry
HCI G105, Wolfgang Pauli Str. 10
CH-8093
Zurich
Switzerland

Martin Hof
J. Heyrovský Institute of Physical
Chemistry of ASCR
v.v.i., Dolejškova 2155/3
Prague
CZ-182 23
Czech Republic

Koen Janssens
University of Antwerp, Campus
Groenenborger
G.V.144, Groenenborgerlaan 171
2020 Antwerpen
Belgium

Peter Uhd Jepsen
Technical University of Denmark
Department of Photonics
Engineering
DK-2800
Kongens Lyngby
Denmark

Rudolf W. Kessler
Reutlingen University
Prozessanalytik
Fakultät Angewandte Chemie
Reutlingen Research Institute
Alteburgstr. 150
72762 Reutlingen
Germany

Waltraud Kessler
Steinbeis-Transferzentrum
Prozesskontrolle und
Datenanalyse
Herderstr. 47
72762 Reutlingen
Germany

Seong-Soo Kim
University of Ulm
Institute for Analytical and
Bioanalytical Chemistry
Albert-Einstein-Allee 11
89081 Ulm
Germany

Yuki Kitahara
Meisei University
Department of Chemistry
Faculty of Sciences and
Engineering
Hodokubo 2-1-1
Hino
Tokyo 191-8506
Japan

Cornelia Koy
University of Rostock
Proteome Center Rostock
Schillingallee 69
18057 Rostock
Germany

Markus Kramer
Rapid Structure Characterization
Group
Pharmaceutical Development
Pharmacia Corporation
Kalamazoo
MI 49001-0199
USA

Georg Kurz
Roche Diagnostics Deutschland
GmbH
Nonnenwald 2
82377 Penzberg
Germany

Stephan Küppers
Forschungszentrum Jülich
GmbH ZEA-3: Analytics
Leo-Brandt-Str.
52425 Jülich
Germany

Al de Leon
Case Western Reserve University
Department of Macromolecular
Science and Engineering
2100 Adelbert Road
Cleveland, OH 44106
USA

Hong Peter Lu
Bowling Green State University
Center for Photochemical
Sciences
Department of Chemistry
Bowling Green, OH 43403
USA

Peter B. Luppa
Technische Universität München
Institut für Klinische Chemie und Pathobiochemie
Klinikum rechts der Isar
Ismaninger Str. 22
81675 München
Germany

Juhász Márta
Meisei University
Department of Chemistry
Faculty of Sciences and Engineering
Hodokubo 2-1-1
Hino
Tokyo 191-8506
Japan

Radek Macháň
J. Heyrovský Institute of Physical Chemistry of ASCR
v.v.i., Dolejškova 2155/3
Prague
CZ-182 23
Czech Republic

and

Czech Technical University in Prague
Faculty of Biomedical Engineering
Sítná 3105
Kladno
CZ-272 01
Czech Republic

Anna Macková
Nuclear Physics Institute of Academy of Sciences of the Czech Republic
Rez near Prague
250 68
Czech Republic

and

J.E. Purkinje University
Department of Physics, Faculty of Science
Ceske mladeze 8
Usti nad Labem
400 96
Czech Republic

Michael Maiwald
BAM Federal Institute for Materials Research and Testing
Department 1 Analytical Chemistry
Reference Materials
Division 1.4 Process Analytical Technology
Richard-Willstaetter-Str. 11
D-12489 Berlin
Germany

Joey Mangadlao
Case Western Reserve University
Department of Macromolecular Science and Engineering
2100 Adelbert Road
Cleveland, OH 44106
USA

Gary E. Martin
Rapid Structure Characterization Group
Pharmaceutical Development
Pharmacia Corporation
Kalamazoo
MI 49001-0199
USA

Alfred J. Meixner
University of Tuebingen
Institute of Physical and
Theoretical Chemistry
Auf der Morgenstelle 18
72076 Tuebingen
Germany

Boris Mizaikoff
University of Ulm
Institute for Analytical and
Bioanalytical Chemistry
Albert-Einstein-Allee 11
89081 Ulm
Germany

David S. Moore
Los Alamos National Laboratory
Shock and Detonation Physics
Group
MS-P952
Los Alamos, NM 87545
USA

Simon Morton
Lawrence Berkeley National
Laboratory
Advanced Light Source
MS 7–222, 1 Cyclotron Road
Berkeley, CA 94607
USA

Holger Mueller
BlueSens Gas Sensor GmbH
Snirgelskamp 25
45699 Herten
Germany

Markus Ostermann
BAM Federal Institute for
Materials Research and Testing
Department 1 Analytical
Chemistry
Reference Materials
Division 1.4 Process Analytical
Technology
Richard-Willstaetter-Str. 11
D-12489 Berlin
Germany

Katrina Pangilinan
Case Western Reserve University
Department of Macromolecular
Science and Engineering
2100 Adelbert Road
Cleveland, OH 44106
USA

Ulrich Panne
BAM Federal Institute for
Materials Research and Testing
Department I; Analytical
Chemistry; Reference Materials
Unter den Eichen 87
D-12205 Berlin
Germany

Gabor Patonay
Georgia State University
Department of Chemistry
38 Peachtree Ctr Ave
Suite 540
Atlanta, GA 30303
USA

Ulrich Pecks
University Hospital of the RWTH
Department of Obstetrics and
Gynecology
Pauwelsstraße 30
52074 Aachen
Germany

Perttu Permi
University of Helsinki
The Finnish Biological NMR
Center
Program in Structural Biology
and Biophysics
Institute of Biotechnology
Biocenter 3, Viikinkaari 1
FI-00014 Helsinki
Finland

Andrew Pratt
J.E. Purkinje University
Department of Physics, Faculty of
Science
Ceske mladeze 8
Usti nad Labem
400 96
Czech Republic

Günther Proll
University of Tuebingen
Institute of Physical and
Theoretical Chemistry
Auf der Morgenstelle 18
72076 Tuebingen
Germany

Michael Przybylski
University of Konstanz
Department of Chemistry
Laboratory of Analytical
Chemistry and Biopolymer
Structure
Universitätsstraße 10
78457 Konstanz
Germany

Claudia Röwer
University of Rostock
Proteome Center Rostock
Schillingallee 69
18057 Rostock
Germany

Toralf Reimer
University of Rostock
Department of Obstetrics and
Gynecology
Suedring 81
18059 Rostock
Germany

Wolfgang Robien
University of Vienna
Department for Organic
Chemistry
Währinger Straße 38
A-1090
Vienna
Austria

Erwin Rosenberg
Vienna University of Technology
Institute of Chemical
Technologies and Analytics
Getreidemarkt 9/164 AC
A-1060 Vienna
Austria

J. Ray Runyon
Laboratory for Advanced
Separations Technologies
Department of Chemistry and
Geochemistry
Colorado School of Mines
Golden, CO 80401
USA

David J. Russell
Rapid Structure Characterization
Group
Pharmaceutical Development
Pharmacia Corporation
Kalamazoo
MI 49001-0199
USA

Michel Sablier
Ecole Polytechnique
Laboratoire des Mécanismes
Réactionnels
CNRS
route de Saclay
91128
Palaiseau cedex
France

Valdas Sablinskas
Vilnius University
Faculty of Physics
Sauletekio av. 9 bl 3
Vilnius-10222
Lithuania

Georgeta Salvan
Chemnitz University of
Technology
Semiconductor Physics
Reichenhainer Strasse 70
D-09107 Chemnitz
Germany

Reiner Salzer
Dresden University of Technology
Institute of Bioanalytical
Chemistry
01062 Dresden
Germany

Frank Schleifenbaum
University of Tuebingen
Center of Plant Molecular Biology
(ZMBP)
Biophysical Chemistry
Auf der Morgenstelle 8
72076 Tuebingen
Germany

Uwe Schmidt
Hüttlin GmbH
Hohe-Flum-Str. 42
79650 Schopfheim
Germany

Heike Schneider
Technische Universität München
Institut für Klinische Chemie und
Pathobiochemie
Klinikum rechts der Isar
Ismaninger Str. 22
81675 München
Germany

Frank Schreiber
Universität Tübingen, Institut für
Angewandte Physik
Auf der Morgenstelle 10
72076 Tübingen
Germany

Gerald Steiner
Dresden University of Technology
Carl Gustav Carus Faculty of
Medicine
Clinical Sensoring and
Monitoring
Fetscher Str. 74
01307 Dresden
Germany

Stefan Stieler
BIS Prozesstechnik GmbH
Industriepark Höchst
65926 Frankfurt/Main
Germany

Seiji Takahashi
Meisei University
Department of Chemistry
Faculty of Sciences and
Engineering
Hodokubo 2-1-1
Hino
Tokyo 191-8506
Japan

Steffen Thiele
Dresden University of Technology
Institute of Bioanalytical
Chemistry
01062 Dresden
Germany

Brylee Tiu
Case Western Reserve University
Department of Macromolecular
Science and Engineering
2100 Adelbert Road
Cleveland, OH 44106
USA

David Touboul
Centre de recherche de Gif
Institut de Chimie des
Substances Naturelles, CNRS
Avenue de la Terrasse
91198
Gif-sur-Yvette Cedex
France

Masamichi Tsukagosi
Meisei University
Department of Chemistry
Faculty of Sciences and
Engineering
Hodokubo 2-1-1
Hino
Tokyo 191-8506
Japan

Karel Volka
Vysoká škola
chemicko-technologická v Praze
Ústav analytické chemie
Technická 5, 16628
Praha 6 –Dejvice
Czech Republic

Manja Wölter
University of Rostock
Proteome Center Rostock
Schillingallee 69
18057 Rostock
Germany

Christopher George Havelock Walker
University of York
Department of Electronics
Heslington
York
North Yorkshire
YO10 5DD
UK

Wolfgang Werther
University of Vienna
Institute of Analytical Chemistry
Alserbachstraße 8/6
A-1090, Vienna
Austria

James S. Wilkinson
University of Southampton
Department of Optoelectronics
Research Centre
Highfield
Southampton
Hampshire SO17 1BJ
UK

Kim Ratanathanawongs Williams
Laboratory for Advanced
Separations Technologies
Department of Chemistry and
Geochemistry
Colorado School of Mines
Golden, CO 80401
USA

Dietrich R. T. Zahn
Chemnitz University of
Technology
Semiconductor Physics
Reichenhainer Strasse 70
D-09107 Chemnitz
Germany

Renato Zenobi
ETH Zurich
Department of Chemistry and
Applied Biosciences
CH-8093, Zurich
Switzerland

Dai Zhang
University of Tuebingen
Institute of Physical and
Theoretical Chemistry
Auf der Morgenstelle 18
72076 Tuebingen
Germany

Paolo de Zorzi
ISPRA Istituto Superiore per la
Protezione e la Ricerca
Ambientale
Servizio Metrologia Ambientale
Via Castel Romano
100 - 00128
Roma (Italia)

Preface

Since the first edition of the *Handbook of Spectroscopy*, there have been many fantastic developments in instrumentation and great research progress in spectroscopy. In addition, many new applications have been published. This second version of the *Handbook* therefore covers new fields of spectroscopy, provides an update on the status in the various fields, and includes an enlarged applications section; two further volumes have been added to accommodate this new information. However, although this second version of the *Handbook of Spectroscopy* is intended to serve as an authoritative reference source for a broad audience involved in the research, teaching, learning, and practice of spectroscopic technologies, it also takes into account that spectroscopy is defined as a science that deals with interaction between electromagnetic radiation and matter. This field of research has experienced a continuous growth as a result of innovations in methodologies and instrumentation, which offer opportunities for new applications and novel methods of analysis to solve common analytical problems and to address new challenges. Accordingly, research scientists, analytical scientists, environmental investigators, and industrial engineers who are often confronted with the ever-increasing complexity of real-life sample analysis, need a readily accessible source of information and an authoritative guidance on how best to apply currently available spectroscopic techniques to their particular fields of interest and to their specific applications.

Like the first edition, this second edition of the *Handbook of Spectroscopy* is designed to provide a straightforward introduction to spectroscopy, what this field can do, and how an investigator can use it effectively. The Handbook also provides a clear, integrated, and objective account of the wealth of information that can be derived from spectra. The sequence of chapters covers the range of the electromagnetic spectrum and the physical mechanisms involved, from rotation processes in molecules to phenomena in the nucleus.

Following the success of the first edition, the second edition of the Handbook is also not designed to be just another treatise on the theory of spectroscopy, but rather a practical day-to-day laboratory guide. It is intended to help the newcomer in the various fields of spectroscopy, and the academic level is based on the standard level of a graduate student in the physical or life sciences.

The Handbook represents the work of over ***60*** leading scientists and engineers in their field of research. The Handbook contains ***56*** chapters, which are grouped into ***15*** sections.

Seven sections cover the state-of-the-art practices in major fields of spectroscopy. The treatment of each field of spectroscopy presents the most up-to-date developments in methodologies, techniques, instrumentation, and data treatment. These sections are:

(I) Sample Preparation and Sample Pretreatment
(II) Methods 1: Optical Spectroscopy
(III) Methods 2: Nuclear Magnetic Resonance Spectroscopy
(IV) Methods 3: Mass Spectrometry
(V) Methods 4: Elemental Analysis
(VI) Methods 5: Surface Analysis
(VII) Methods 6: Spectroscopy in Nano Dimensions

Section VII has been added to cover also the growing interest in using spectroscopy in the nanosciences.

To enlarge the essential part of applications, further applications have been added. This application part comprises the following sections:

(VIII) Applications 1: Bioanalysis
(IX) Applications 2: Polymer Analysis
(X) Applications 3: Environmental Analysis
(XI) Applications 4: Process control
(XII) Applications 5: Spectroscopy at Surfaces
(XIII) Applications 6: Nano-Optics

Section XIV: Hyphenated Techniques and Section XV General Data Treatment has been updated.

The goal of this Handbook is to provide a comprehensive forum that integrates interdisciplinary research and development of interest to scientists, engineers, manufacturers, teachers, and students. The Handbook is designed to present, in a single source, the most recent advances in instrumentation and methods. Light has become an important diagnostic tool; therefore, the range of applications has been enlarged, and it is our hope that this Handbook will be a valuable companion to the practicing spectroscopist and will stimulate a greater appreciation of the usefulness, efficiency, and potential of spectroscopy.

Guenter Gauglitz
University of Tuebingen
Tuebingen
Germany

and

David Moore
Los Alamos National Laboratory
Los Alamos
NM 87545
USA

Section I
Sample Preparation and Sample Pretreatment

Handbook of Spectroscopy, Second Edition. Edited by Günter Gauglitz and David S. Moore.

1

Preparation of Liquid and Solid Samples

Brian M. Cullum and Tuan Vo-Dinh

1.1

Introduction

Sampling and sample preparation of liquids and solids often present significant challenges for real-world quantitative analyses using spectrometric techniques (e.g., UV–vis and infrared absorption, luminescence and Raman spectroscopies). Very often, the native form of a sample is unsuitable for analysis. This could be due to (i) the complex nature of the object, which could provide false measurements due to interferences or masking agents; (ii) the size of the object being too large to analyze in its entirety (e.g., laboratory sample of contaminated soil); or (iii) the awkward shape of the object, preventing it from fitting within the instrument in which the measurement is to be made. To overcome these problems, some sort of sample preparation must be performed. In many cases, sample preparation is required before any quantitative analysis, and both can have dramatic impacts on the measured results and their accuracy.

The previous chapter presented the main criteria to be followed for solid and liquid sample collection. This chapter presents a general overview of various methods for sample preparation. This general topic has been described extensively in a variety of research papers and review chapters in the literature [1–6], with specific variations for particular applications often being necessary. This chapter deals with the sample preparation required to provide a material suitable for spectrometric analysis.

1.2

Preparation of Samples for Analysis

1.2.1

Measurement Process

Samples collected for spectral analysis can generally be classified into three categories based on their state: (i) solids, (ii) liquids, and (iii) gases. Samples

Handbook of Spectroscopy, Second Edition. Edited by Günter Gauglitz and David S. Moore.

are typically classified on the basis of their state as a method of providing an initial means of handling/treating them. A general flow diagram depicting the measurement process for various samples is shown in Figure 1.1.

1.2.2
Preparation of Samples for Analysis

Once a representative sample has been obtained from the object of interest, the next step is to prepare the sample for analysis. Since sample preparation depends upon both the analyte (e.g., iron in water, polycyclic aromatic compounds in benzene, etc.) and the instrumentation used to perform the spectroscopic measurement (e.g., UV–vis or IR absorption, luminescence, Raman, HPLC-fluorescence, GC–MS, etc.), details of the preparation process will vary from analysis to analysis. Many general procedures have been developed over the years for the preparation of various types of samples prior to analysis. Most of these procedures can be classified depending upon the type of samples that are to be analyzed, either solid or liquid. Within each of these categories exist several subcategories based upon the type of analyte to be measured.

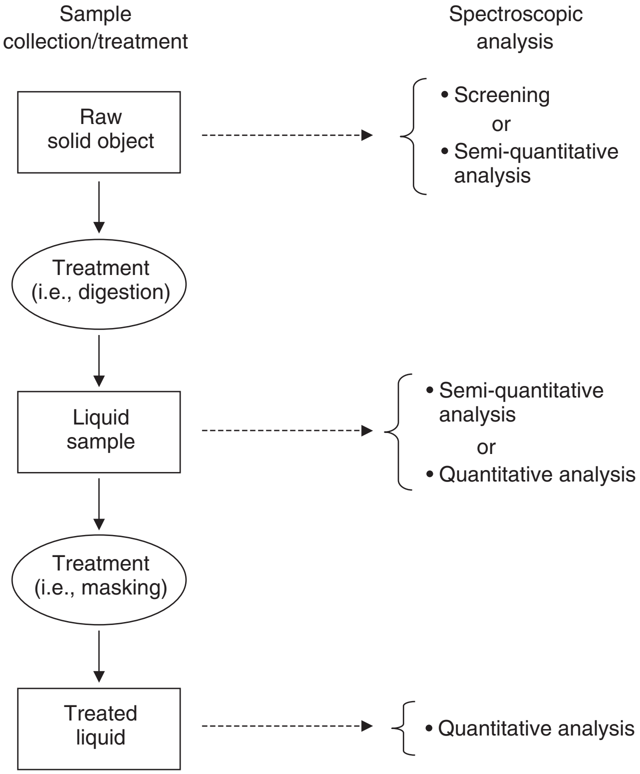

Figure 1.1 Schematic diagram depicting generalized sample preparation and analysis steps.

1.2.3
Solid Samples

The first of the two categories that we will discuss is solid samples. The various types of solid samples that are most often encountered have been discussed elsewhere in the sampling section of this chapter (i.e., powders, chunks, or cores). In the case of the latter two sample types (chunks and cores), the first preparation step involves grinding the larger pieces into a powder, which is much easier to deal with, and introduce it into the measuring instrument. The most common method for obtaining powders from these samples involves grinding a solid sample into a powder using either a mortar and pestle or a ball mill. Mortars typically come in two different types: the agate version (or ceramic) for relatively soft solid materials (e.g., large crystalline substances) that must be ground into a fine powder; or steel mortars, which are used for crushing much harder materials. In agate mortars, the material to be ground is placed in the depression of the mortar and then the sample is pressed down with the pestle in a rotating movement. When using agate or ceramic mortars and pestles, it is important to clean them thoroughly to avoid sample contamination. Less expensive mortars are typically softer and hence can be scratched more easily than more expensive ones. This is especially the case for ceramic mortars. Once scratched, they are much more difficult to clean, and may require the use of an abrasive or even a strong HCl solution. Steel mortars, also known as *percussion mortars*, have a hardened steel sleeve and pestle that fit snuggly into the mortar, and a hammer is then used to strike the pestle and subsequently crush the sample.

Another grinding tool that is often used to grind solid samples is the ball mill. A ball mill is a ceramic drum within which are placed the sample and many small balls made of hard ceramic. To grind the sample, the drum is rotated, producing a very fine powder. Ball mills are often used on softer solids, as the time taken for grinding is directly proportional to the hardness of the material. To ensure that none of the material that is being ground sticks to the walls of the mill during the grinding process, thereby producing larger pieces, the samples are typically dried to 100–110 °C prior to grinding to expel any water.

1.2.3.1 Sample Preparation for Inorganic Analysis

Most commercially available instruments for quantitative analyses in chemical and biological sciences are designed for the analysis of liquid samples. Because of this, solid samples that are to be analyzed are typically dissolved in a suitable solvent, usually following conversion to a powder by one of the previously described methods. The solvent chosen for this dissolution process may be either polar (e.g., water) or nonpolar (e.g., benzene) depending on the polarity and reactivity of the sample. In order to ensure that the entire analyte has been dissolved in the solution of interest, a solvent is chosen that can dissolve the entire solid sample (analyte as well as other materials). If the sample cannot be readily dissolved in these mild conditions, many other techniques are available for dissolution. As inorganic materials often present the greatest difficulty in dissolution, this section will deal primarily with these materials.

1.2.3.1.1 **Acid Digestion** Acid digestion of inorganic materials is a common alternative to the mild solvents used for dissolution, as described above. When using acids to digest metallic materials, great care should be taken not to change the speciation of the metal or metallic species to be analyzed. When analyzing a reduced state of a metal or metallic species, several nonoxidizing acids can be used. These include HF, HCl, HBr, H_3PO_4, dilute H_2SO_4, and dilute $HClO_4$. These acids dissolve most metals with negative reduction potentials. However, in some cases (i.e., aluminum), a protective oxide layer is formed that prevents the metal from being dissolved, which must be removed prior to dissolution. Substances that cannot be dissolved in the nonoxidizing acids described above are often soluble in the oxidizing acids: HNO_3, hot and concentrated H_2SO_4, and hot and concentrated $HClO_4$.

In most cases, the solubility of a metal dramatically increases by heating the acid. To improve the dissolution of samples in hot acids, a device often referred to as a *digestion bomb* has been developed. This device is comprised of a Teflon™-lined sample container that can be sealed and placed in a microwave oven for heating. An alternative to using the digestion bomb is to heat the acids in an open container, thereby allowing volatile species created during the reaction (e.g., H_2S, H_3BO_3, etc.) to escape. However, in rare cases, some metal halides (e.g., $SnCl_4$, $HgCl_2$, OsO_4, and RuO_4) are volatile and can escape as gases.

1.2.3.1.2 **Nonoxidizing Acids** HCl and HBr are typically used for the dissolution of most metals, oxides, sulfides, phosphates, and carbonates. HCl and HBr digestions are typically performed with a concentration of 37% and 48–65%, respectively. When using hot acids, HCl has a constant boiling composition of 20% at 109 °C, and HBr has a constant boiling composition of 48% at 124 °C. H_2SO_4 is an excellent solvent for most materials when used at its boiling point, which is 338 °C. The composition of H_2SO_4 for digestion purposes is typically 95–98%. Heating H_2SO_4 causes the sample to become dehydrated while dissolving the metals and, in addition, causes any organic material to become oxidized. To dissolve refractory oxides that are insoluble in other acids, hot H_3PO_4 can be used at a concentration of 85%. As the temperature of the acid is increased, it dehydrates. At temperatures above 150 °C, it becomes anhydrous; at temperatures greater than 200 °C, it dehydrates to pyrophosphoric acid; and, finally, at temperatures greater than 300 °C, it is converted to meta-phosphoric acid. A 50% HF solution is often used for the dissolution of silicates. Since glass is comprised primarily of silica, HF must be used in Teflon, silver, or platinum containers. At 112 °C, HF has a constant boiling composition of 38%.

1.2.3.1.3 **Oxidizing Acids** HNO_3 is capable of dissolving most metals, with the exception of gold and platinum. To dissolve these two metals, a 3 : 1 volumetric mixture of HCl and HNO_3 (also known as *aqua regia*) can be used. As described above, H_2SO_4 is typically considered a nonoxidizing acid with respect to metals; however, it provides a useful means of oxidizing organic material in the sample. When the organic material in the sample cannot be oxidized by either HNO_3 or H_2SO_4, a 60–72% solution of hot $HClO_4$ can be used. In either cold or dilute conditions, $HClO_4$ is not oxidizing. However, at high temperatures, $HClO_4$ becomes an explosive oxidizer. Because of this extreme oxidizing potential, it is important to evaporate and destroy as much organic material as possible with hot HNO_3 prior to using $HClO_4$.

It should be noted that mineral acids used to digest solid samples may contain a large number of metals in different concentration ranges (usually parts per million or subparts per million levels) themselves. This could provide a source of contamination, especially significant for trace analysis work. One way to account for this contamination source is to include a blank preparation with the digestion procedure. This involves exposing an extra beaker or flask, identical to the one containing the sample, to the same digestion treatment (added acids, thermal treatment, dilutions, etc.) to which the sample was exposed. The blank solution prepared this way will contain an approximately equal amount of contaminants introduced to the sample by the acid digestion.

1.2.3.1.4 **Fusion Reactions** Fusion is a process by which a finely powdered sample is mixed with 5–10 times its mass of inorganic material (flux) and heated in a platinum crucible to temperatures of 300–1200 °C, thereby melting the flux and the sample. While in the molten state, chemical reactions between the flux and the sample produce new species which are more soluble. After the sample has been thoroughly melted, the molten solution is allowed to cool slowly. During this cooling process, the crucible is swirled to create a thin layer of solidified material on the walls of the container. The newly solidified material is then dissolved in a dilute acid. Many different flux materials have been used over the years, with Na_2CO_3, $Li_2B_4O_7$, $LiBO_2$, $Na_2B_4O_7$, NaOH, KOH, Na_2O_2, $K_2S_2O_7$, B_2O_3, and a 2 : 1 mixture (w/w) of $Li_2B_4O_7$ and Li_2SO_4 being the most common. Fluxes are typically classified as acidic, basic, or amphoteric, with basic fluxes being best suited to dissolve acidic oxides of silicon and phosphorus and acidic fluxes being best suited to the dissolution of basic oxides, alkali metals, alkaline earths, lanthanides, and aluminum. The basic fluxes listed above include Na_2CO_3, $LiBO_2$, NaOH, KOH, and Na_2O_2. The acidic fluxes include $Li_2B_4O_7$, $K_2S_2O_7$, B_2O_3, and $Na_2B_4O_7$.

Na_2CO_3 is one of the most common fluxes, and is typically used for dissolving silicates (e.g., clays, rocks, minerals, glasses, etc.) as well as refractory oxides and insoluble sulfates and phosphates. To dissolve aluminosilicates, carbonates, and samples with high concentrations of basic oxides, $Li_2B_4O_7$, $LiBO_2$, or $Na_2B_4O_7$ is typically used. Analysis of both silicates and SiC-based materials can be performed using a flux of either NaOH or KOH. When using these two fluxes, however, frothing may occur in the absence of water. Therefore, best results are often achieved by first melting the flux and then adding the sample. It is also important to note that, when using NaOH and KOH as fluxes, either a gold or silver crucible should be used for the reaction. For silicates that cannot be dissolved using

Na_2CO_3, a more powerful oxidant such as Na_2O_2 can be used. This flux is good for dissolving iron and chromium alloys and should be used in a nickel crucible. Owing to the strong oxidizing and basic properties of Na_2O_2, the crucible used for this reaction should be coated with a thin layer of Na_2CO_3, which melts at a higher temperature than the peroxide and therefore protects the crucible. To dissolve refractory oxides and not silicates, $K_2S_2O_7$ is the flux of choice. $K_2S_2O_7$ is prepared by either heating $KHSO_4$ until all the water is driven off and all the foaming has stopped or decomposing $K_2S_2O_8$ with heat. B_2O_3 is a very useful flux for the dissolution of oxides and silicates. Its main advantage over the other fluxes listed previously is that the flux can be removed from the crucible completely, following reaction with the sample, as a volatile methyl borate, by simply washing several times with HCl in methanol. For relatively fast dissolution of refractory silicates and oxides (10–20 min at 1000 °C), a 2 : 1 mixture (w/w) of $Li_2B_4O_7$ and Li_2SO_4 works well. One gram of this flux can dissolve 0.1 g of sample, and the resulting material can be easily dissolved in hot HCl. While fusion has proven to be a necessary method for the dissolution of many compounds, it should be used only as a last resort, because of the possibility of introducing impurities into the sample as well as being a very time-consuming process.

1.2.3.2 **Decomposition of Organics**

1.2.3.2.1 **Ashing** When elemental analysis of an organic sample or quantitative analysis of inorganic species complexed with organic species is desired, the first step of the process is to decompose the organic material. This process of decomposition of organic matter is often termed *ashing*. Ashing is typically subdivided into two different categories: those processes that do not require the use of a liquid, that is, dry ashing; and those processes that rely on liquids for the decomposition, that is, wet ashing. Fusion can be used as a type of ashing, with the most common fluxes used in these processes being Na_2O_2 and alkali metals, but the simplest and most common form of dry ashing is via combustion. In this procedure, the organic material is burned in a stream of oxygen gas, with catalysts added for more complete combustion. The released CO_2 and H_2O are then trapped and analyzed quantitatively. Variations of this procedure are also used to perform quantitative analyses of nitrogen, sulfur, and halogens in organic matter.

Wet ashing methods have existed for over several hundred years. One such method, which has been used since 1883, is known as the *Kjeldahl procedure*. This procedure is one of the most accurate and widely applicable methods for determining the nitrogen composition of organic matter. The first step in this procedure is to digest the organic matter in boiling H_2SO_4, which converts the nitrogen atoms in the sample to NH_4^+ while oxidizing other elements such as carbon and hydrogen. To speed up the process, K_2SO_4 can be added, which increases the boiling point of the H_2SO_4 to 338 °C.

Another common procedure that has been developed is known as the *Carius method*. This procedure, which involves the digestion of organics in fuming HNO_3, is carried out in a heavy-walled, sealed glass container that is heated to 200–300 °C.

A very powerful technique that can be widely applied to the decomposition of organic matter is refluxing the sample in a mixture of HNO_3 and $HClO_4$. However, perchloric acid is a strong explosive, and great care should be taken by the experimentalist to shield himself/herself from the digestion process. In this procedure, the sample is first heated in boiling HNO_3, and the solution is then evaporated until almost dry. This process is repeated several times to remove any easily oxidized material that might explode in the presence of $HClO_4$. The sample is then collected and the process repeated with $HClO_4$.

One of the fastest and easiest methods of wet ashing organic matter involves the use of a Teflon-lined digestion bomb (described earlier in the section on dissolution) and a microwave oven for heating. While many different procedures have been developed for various analyses, they all generally involve the addition of the sample and a liquid into the digestion bomb, which is then placed in the microwave oven and heated. An example of such a procedure is the decomposition of animal tissue using a 1 : 1 mixture of HNO_3 and H_2SO_4 and heating it in a microwave oven for 1 min. Another example is a modified version of the Kjeldahl reaction in which H_2SO_4 and H_2O_2 are mixed in a Teflon-lined bomb and heated, thereby reducing the digestion time to approximately 15 min.

In contrast to these wet ashing procedures that rely on concentrated acids, a mild form of wet ashing has also been developed. This procedure uses hydroxyl radicals that are produced using Fenton's reagent, a combination of H_2O_2 and $Fe(NH_4)_2(SO_4)_2$, to oxidize the organic materials. The mixture is then heated to 50 °C with the organic material present, allowing the radicals to oxidize the sample (Table 1.1).

Table 1.1 Various sample preparation methods for solid samples.

Dissolution of solids

Acid digestion
- Nonoxidizing acids
  - HF, HCl, HBr, H_3PO_4, dilute H_2SO_4, dilute $HClO_4$
- Oxidizing acids
  - HNO_3, hot and concentrated H_2SO_4, hot and concentrated $HClO_4$

Fusion reactions
- Basic fluxes
  - Na_2CO_3, $LiBO_2$, NaOH, KOH, Na_2O_2
- Acidic fluxes
  - $Li_2B_4O_7$, $K_2S_2O_7$, B_2O_3, $Na_2B_4O_7$

Decomposition of organics

Ashing methods
- Dry ashing
  - Combustion in O_2, and fusion with Na_2O_2 or alkali metals
- Wet ashing reagents
  - Hot H_2SO_4, fuming HNO_3, $HClO_4$, hydroxyl radicals (H_2O_2 and $Fe(NH_4)_2(SO_4)_2$)

1.2.4
Liquid Samples

1.2.4.1 Extraction/Separation and Preconcentration

Once a liquid sample has been obtained, either from an original liquid object or from the dissolution of a solid object, the various species of interest must be isolated for analysis. In the case of a liquid suspension, filtration or centrifugation is often performed prior to analysis to remove any solid particles. In the case of a solution, there are many methods available for isolating analytes, including complexation, separation, or extraction. These procedures are performed prior to analysis, for many reasons. Most often, these procedures are performed either to remove any species that may cause interferences in the particular analysis or to provide a means of concentrating the analyte prior to analysis.

1.2.4.1.1 **Extraction** Extraction has historically been one of the most common means of isolating a particular species from a solution. Several different types of extraction are commonly used for analyte isolation, including liquid/liquid extraction and solid-phase extraction. In any extraction procedure, the isolation of particular components is based upon the affinity of the particular species for two different phases. In liquid/liquid extractions, the two phases are both liquid and are immiscible in each other (e.g., an aqueous phase and an organic phase), creating two layers with a distinct boundary. The affinity of the various components within the sample for each of the two layers is used to separate them. The distribution of the analyte or solute between the two different phases is described as the partition coefficient (the ratio of the solute's concentration in one solvent to its concentration in the second). Therefore, the ideal extraction would happen with either a very large or a very small partition coefficient. When this is not the case, and the solute is only slightly more soluble in one solvent than the other, multiple extractions may have to be performed to remove most of the solute. In addition, as this extraction is based on fractional partitioning of the solute, it is impossible to extract 100% into any one phase. Therefore, to determine the amount of analyte that has been extracted, one needs to keep track of the number of extractions that were performed and the partition coefficient of the process.

Another type of extraction commonly used on liquid samples is based upon the partitioning of an analyte between the liquid in which it is dissolved and a solid support. Such extractions are typically based upon adsorption of the solute onto the solid. An example of such an extraction is in the adsorption of hydrocarbons in an aqueous solution onto activated charcoal. This process has long been used in such areas as pollution control (e.g., oil spills in water) and much more recently is beginning to be implemented more in trace analysis procedures as a technique called *solid-phase microextraction*. The main disadvantage of extraction techniques is typically the time that is required to recover most of the solute. Because of this problem, extraction in quantitative analyses is typically performed as a last choice.

1.2.4.1.2 **Complexation** To increase the specificity of a particular analysis, it is often necessary to remove components from the solution that could produce erroneous results. One means of performing this task is through complexation reactions. One such procedure, known as *masking*, involves the complexation of an interfering species with a chelating agent. The reaction between the two species forms a stable complex which cannot undergo certain chemical reactions that are essential for quantification of the analyte. Therefore, by complexing possible interferents, a more selective measurement can be obtained. Another form of complexation that is often employed for the removal of interferences is precipitation. In precipitation reactions, an insoluble complex is selectively formed with either the interfering species or the analyte itself. Once the precipitate is formed, it can be removed and discarded in the case of an interfering species or analyzed in the case of the analyte. Complexation reactions typically involve elaborate procedures, and depend upon many parameters such as the chemical composition of the solution, its pH, and the temperature. When these factors are considered, complexation procedures can provide excellent results. For example, uranium can be isolated from associated metals in solution with the addition of carbonates. Carbonates form a soluble complex with uranium, while most other metals form insoluble carbonate of hydroxide precipitates. The complexation of a particular species is dependent on the chemical equilibria of the various species involved. Table 1.2 provides a general list of the most common complexing agents and the species with which they react.

Using Table 1.2 and the particular formation constants and solubility constants of the involved species, at the correct pHs and temperatures, determination of the best complexing agents for a liquid sample should be possible. In the case where two agents form complexes with the same elements, the particular solution parameters (e.g., pH) should be used to determine which is the most suitable. For

Table 1.2 Common masking agents.

Masking agent	Ions of elements complexed
1. Carbonate	Be, Th, U
2. Citrates and tartrates	Be, Mg, Ca, Sc, Ti, Cr, Mn, Fe, Ga, Sr, Y, Zr, Nb, Mo, In, Sb, Ba, La, Hf, Ta, W, Re, Tl, Pb, Bi, Ce, Th, U
3. Cyanide and amine	Co, Ni, Cu, Zn, Ru, Rh, Pd, Ag, Cd, Os, Ir, Pt, Au, Hg
4. EDTA	Mg, Al, Ca, Sc, Mn, Fe, Co, Ni, Cu, Zn, Ga, Sr, Y, Cd, In, acetic Ba, La, Pb, Bi, Ce, Th
5. Fluoro (F^-) agents	B, Al, Si, Ti, Zr, Nb, Mo, Hf, Ta, W
6. Halides (Cl^-, Br^-, I^-)	Ge, As, Ru, Rh, Pd, Cd, Sn, Os, Ir, Pt, Au, Hg, Tl
7. Oxalate	V, Cr, Fe, Co, Ni, Ge, In, Re, Tl, Bi
8. Oxo and hydride	Be, B, Al, P, V, Cr, Mn, Zn, Ga, Ge, As, Se, Mo, Ru, Sn, Sb, Te, W, Re, Os, Pb
9. Peroxo agents	Ti, V, Zr, Nb, Hf, Ta, U
10. Sulfide	As, Sn, Sb

EDTA, ethylenediaminetetraacetic acid.

instance, citrates usually form more stable complexes in acidic solutions, whereas tartrates are typically more stable in alkaline solutions.

1.2.4.2 Chromatographic Separation

With continued developments in chromatographic columns and equipment, separation of various analytes from a sample via chromatography has become the most common pretreatment to complex liquid samples [7]. The combination of chromatography and spectroscopy is described in detail later in the chapter on Hyphenated Techniques in this Handbook. This section only provides a brief discussion of the separation methods used in sample treatment prior to spectrochemical analysis. As with solid extraction procedures, chromatographic separation is based upon the partitioning of the various solutes between two different phases, namely a liquid phase and a solid phase. However, unlike extractions, the two different phases are not separated to allow removal of the component of interest. Instead, the liquid containing the solute is flowed across the solid phase, and the partitioning of the various components in the liquid between the two phases causes them to be retained temporarily and eluted from the solid matrix at different times. The time of elution from the solid matrix, or the retention time, is determined by the partitioning coefficient of the particular component between the solid and the liquid. Many chromatographic techniques exist for separating various solutes in liquids. These techniques are generally classified by the types of interactions that occur between the analytes and the solid phase, or matrix. These categories include (i) adsorption, (ii) ion exchange, (iii) partition, (iv) thin layer, and (v) size exclusion. In adsorption chromatography, the separation is based upon the polarity of the solid matrix and the solutes. Solid matrices for adsorption chromatography can include alumina, charcoal, clay, diatomaceous earth, silica, silica gels, cellulose, or starch, which are packed into a glass column. In the case of alumina, which is a polar matrix, the sample would be flowed down the column, with the nonpolar solutes eluting first and the polar solutes eluting later because of their stronger interactions with the matrix.

Ion-exchange chromatography is similar to adsorption chromatography, with the exception that elution of the various components is based upon the affinity of ions for the solid matrix. The solid support matrix for such separations is some form of ion-exchange resin, depending upon the materials to be separated. The mobile, or liquid phase, in ion-exchange chromatography is generally an aqueous solution. Ion-exchange chromatography is used to separate solute molecules based upon their charge. Under optimum conditions, ions of equal charge, such as the alkali metals, can even be separated in an ion-exchange column. In particular separations, the effectiveness of ion-exchange chromatography can be enhanced by the addition of chelating agents to the mobile phase, thus reducing the ionic interactions of particular species and making them elute earlier in time.

The third type of liquid chromatography, partition chromatography, is performed by placing the sample on a column of solid support that has been impregnated with a liquid. The sample is then flowed down the column, with a second liquid as the mobile phase and immiscible in the liquid used to moisten the column. Therefore, as the sample flows down the column, the various components are partitioned between the solid and liquid phases based upon their solubility in the two solvents, and thus elute at different times.

Thin-layer chromatography is performed using a glass plate that has been evenly coated with an absorbent such as alumina or silica gel. To ensure binding of the adsorbent to the glass, starch, plaster of paris, collodion, or a plastic dispersion is often added. The coated plates are then dried in an oven prior to use. Once dried, the sample is spotted on one end of the plate, which is then placed in a dish containing a solvent. The solvent then travels up the plate via capillary action, and the various components in the sample travel at a different rates and therefore different distances during a specific time depending upon their solubility in the solvent. Therefore, by changing the solvent used, the separation of the components can be varied until the particular analyte of interest is separated out from other components.

Another form of liquid chromatography that can be used for separation of components in a solution is known as *size-exclusion chromatography*. In this technique, the solid matrix, which has well defined pore sizes, is placed in a column through which the liquid sample is flowed. The size of the pores varies from matrix to matrix, and it is these pore sizes that are used to separate the compounds. As the components travel down the column, their elution times are based upon their size, with the larger unretained species eluting first and the smaller species being held up in the pores and eluting later. This technique typically works best for larger molecules such as biomolecules or polymers.

Another more recently developed means of separating components in a solution is known as *electrophoresis*. This technique is used for the separation of components based upon their ability to travel in an electric field. Many different matrices have been used for electrophoretic separations, including buffered solutions and gels (e.g., agarose gel). Gel electrophoresis has been used extensively for the separation of biomolecules; however, it is often slow and irreproducible. A faster and more reliable form of electrophoretic separation is known as *capillary electrophoresis*. In this technique, a buffer-filled capillary is used to span the distance between two containers of the same buffer solution. A potential of 20–30 kV is typically applied between the two containers, and a small amount of sample is injected into the capillary. The individual components of the sample are then separated, which is based on the combination of their overall charge and their friction within the solvent. The individual components can then either be collected or detected upon elution from the column.

References

1. Ayres, G.H. (1968) *Quantitative Chemical Analysis*, 2nd edn, Harper and Row, New York.
2. Harris, D.C. (1991) *Quantitative Chemical Analysis*, 3rd edn, W. H. Freeman and Company, New York.

3. Minczewski, J., Chwastowska, J., and Dybczynski, R. (1982) *Separation and Preconcentration Methods in Inorganic Trace Analysis*, New York, John Wiley & Sons, Inc.
4. Miller, J.C. and Miller, J.N. (1992) *Statistics for Analytical Chemistry*, 2nd edn, Ellis Horwood, New York.
5. Phipps, C.R. (2010) *Laser Ablation and its Applications*, 1st edn, Springer, New York.
6. Pickering, W.F. (1966) *Fundamental Principles of Chemical Analysis*, Elsevier, New York.
7. Skoog, D.A. and Leary, J.J. (1992) *Principles of Instrumental Analysis*, Harcourt Brace Jovanovich, Fort Worth, TX.

2
Liquid and Solid Sample Collection

Paolo de Zorzi

2.1
Introduction

A variety of terms are used in the practice of sampling. However, many terms identify a specific (single) operation, and, in some cases, different terms are used to describe the same concept. Furthermore, it is quite usual in the scientific literature for different authors use different terms to describe the same operation or concept. Also, in works produced by standardization bodies, it is possible to find different terms for sampling operations as well as for the definition of sampling strategy. Depending on the matrix of interest, the definition related to the same term may be slightly different. The International Union of Pure and Applied Chemistry (IUPAC) recommendations, ''Nomenclature for sampling in analytical chemistry,'' published in 1990 [1], and the ISO standard 11074:2005 [2], are the most widely used terminology documents related to soil sampling. The IUPAC Recommendations ''Terminology in soil sampling'' [3] recently updated the terminology on soil sampling, which may be partly applicable for solid sampling. The IUPAC defines a sample as a portion of material selected from a larger quantity of material and sample preparation as the set of material conditions that may be necessary to transform an aggregate or bulk sample into a laboratory or test sample. With reference to liquid sampling, ISO standard 6107-2 ''Water quality-Vocabulary-Part 2'' [4] reports a different definition for the term *sample* as the portion, ideally representative, removed from a specified body of water, either discretely or continuously, for the purpose of examination of various defined characteristics. Therefore, it is important that, within a stated context, the terms used are intended by all in the same precise way, without any possible ambiguity.

A correct sampling requires, before starting, a plan of the activity based on clear objectives (general and specific) prepared by the person responsible of the whole process (sampling and measurement). Historically, the sampler, defined as the person or group of persons carrying out the sampling procedures, operates separately from the one responsible of the measurement. The latter knows exactly what the purposes of the measurement are, the quality of the data to be assured, and all aspects that may interfere (chemically, biologically, or simply operatively)

Handbook of Spectroscopy, Second Edition. Edited by Günter Gauglitz and David S. Moore.

in the instrumental analysis. But on the other hand, the sampler should have the competence to perform the sampling in different contexts, know the criteria to be followed to implement a suitable sampling strategy and technique, and be aware of the factors potentially influencing the sample collection as well as the quality of the sample, including also aspects such as health and safety.

When the measurement result is used to assess the properties of a large batch of materials (be solid or liquid), such as from a contaminated soil area or a wide water basin (from which the samples analyzed are collected and prepared), the measurement process includes sampling. In this case, sampling, sample preparation (physical and chemical), and instrumental analysis can influence measurement results and their reliability. In this case, it is necessary to establish a good communication between the analytical scientist and the sampler in all phases of the measurement process.

However, a third party must be considered in the process: the ‘‘end user.’’ A measurement may be requested by many different subjects, such as a private individual (e.g., owner of a factory monitoring the industrial process), or by a public authority (e.g., responsible for controlling or authorizing a wastewater discharge), or maybe by the analytical scientist himself interested in studying the behavior (in time or space) of the property of interest in the environment. All of them will take decisions or will make evaluations on the basis of the measurement results that are unavoidably affected by the quality of the samples collected.

This chapter presents an overview of the sampling process, focusing on the collection of solid and liquid materials and on the implementation of quality assurance (QA)/quality control (QC) procedures for sampling.

2.2
Sampling Process

A typical sampling process, designed by Ramsey and Ellison [5] and shown in Figure 2.1, requires the definition of the measurand, that is, the quantity intended to be measured [6], before any other subsequent step. With reference to sampling, this means a clear statement about the following:

- the sampling target (the portion of material, at a particular time, that the sample is intended to represent [5]);
- the matrix to be sampled;
- the quantity (property of a phenomenon, body, or substances, where the property has a magnitude that can be expressed as a number and a reference [6]).

The critical definition of the sampling target may be given by a regulator body or by the experience and competence of the interested parties. For example, in the case of solid sampling, the measurand may be the hydrocarbon mass fraction (on dry mass basis), determined by infrared spectroscopy and expressed in milligram per kilogram, within a batch of 5000 kg of, say, contaminated soil; whereas, for a liquid sample, a measurand may be the copper mass concentration, determined by

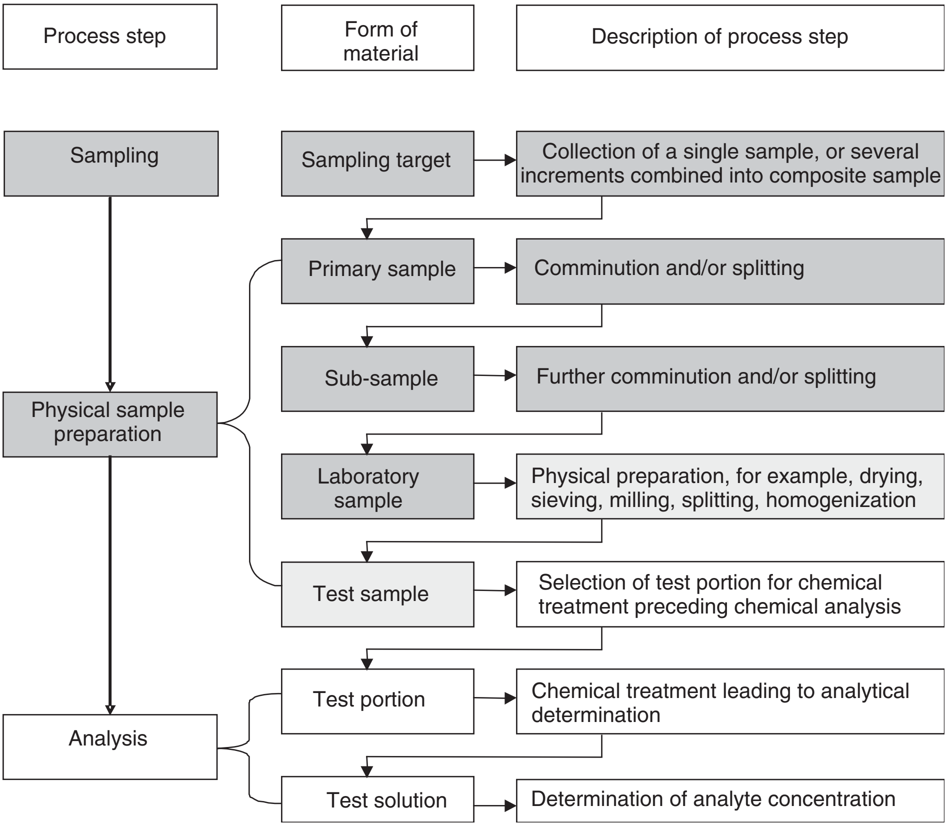

Figure 2.1 Schematic outline of the measurement process including sampling. (Scheme taken from 5.)

inductively coupled plasma mass spectrometry (ICP-MS) expressed as microgram per liter, within a batch of 10 000 l of, say, wine. The measurement results and the associated uncertainty (including the contribution arising from sampling) will be referred to the sampling target defined. In both the cases mentioned above, the final objective of the analyst is to measure the quantity of a substance contained in the test portion of few milligrams or aliquot of few microliters representing the whole batch from which it has been collected and then prepared.

The first operative step of sampling is the collection of samples at the sampling target. Depending on the objective stated in the sampling plan and on the sampling strategy chosen, the sampler will collect the primary samples as a single sample or composite samples (obtained pooling several increments). The size of the primary samples, in terms of volume and/or mass, and the overall amount of primary samples collected are parts of the strategy driving the sampling activity.

Commonly, it will be required to reduce the size (mass/volume) of the primary sample and, for the solid samples, its particle size, in order to obtain the laboratory sample. The operator may comminute the sample (reducing the particle size), mix, homogenize, split, and/or quarter in order to reduce the volume and the mass of the primary sample. All these operations, commonly carried out at the site and in different hierarchical order, produce subsamples till obtaining a laboratory sample of suitable size. The laboratory sample is delivered to the laboratory and stored under suitable conditions previously fixed.

The physical sample preparation, including some of the operations already carried out at the site, continues at the laboratory in order to obtain a test sample from which the final test portion or aliquot is taken. The general aim of the operation carried out in the laboratory is to condition a sample to a state that will allow subsequent analysis or long-term storage.

2.3
Sampling Strategy and Collection

The definition of the sampling strategy is aimed at giving possible answers to specific questions such as the type and the number of samples to be collected, the size of the sample, the sampling techniques, the pattern to apply, and the selection of the sampling points. In general, the sampling strategies consider patterns falling into the following four categories with possible variations depending on the situation encountered:

- random sampling
- systematic sampling
- stratified random sampling
- judgmental sampling.

The first three sampling patterns belong to the common class of probabilistic sampling, that is, based on the principle that each element of a (statistical) population intended to be assessed has an equal chance to be selected. In random sampling, the selection of the sampling point is done independent of other sampling points. Stratified random sampling is based on the principle that the sampling target is better represented by strata in which the property of interest (e.g., the trace element content) is supposed to be homogeneously distributed. The strata are randomly sampled. The systematic method is based on sampling performed by some logical and organized way which means collecting samples, for example, at regular temporal intervals or spatial distances. The two ways of applying systematic sampling are referred to properties of a population that vary in space or change over time within the sampling target. The fourth category is represented by the judgmental sampling. In some cases, the specific knowledge of the sampling target, combined with expert and professional judgment of the sampler, allows the application of this strategy which is not based on probabilistic assumptions.

The different strategies have to be applied properly, considering the objectives given. Commonly, the measurement results obtained by analyzing the samples collected are subjected to statistical assessment (e.g., statistical distribution, mean, median, variance, etc.). To this end, all the probabilistic sampling strategies are suitable, while any statistical assessment is applicable using judgmental sampling. Other criteria must be followed in the selection of the most suitable strategy: the budget available to perform the sampling and the subsequent measurements; the time needed to collect the samples; the need to obtain information about the variability of the property of interest (over space or time) in the sampling target (or even more in each stratum in the case of stratified sampling); the request of specific quality objectives for sampling; and the possibility to modify easily the sampling design.

Type of samples. Each measurement process (including sampling), based on a stated sampling strategy, is characterized by the constitution of different types of samples. The related terms and typology reflect the stage of the sampling process.

The main classes are

1) Primary sample – increment – single sample;
2) Composite sample;
3) Subsample;
4) Laboratory sample;
5) Test sample or test portion.

The primary sample is related to one or more increments or units initially taken for a population and refers to the first stage of the sampling process. When more increments are pooled together, a composite sample is obtained. IUPAC [3] defines the composite sample as the collection of more increments/subsamples mixed together in appropriate portions, either discretely or continuously, from which the average value of a desired characteristic may be obtained. Composite samples might be of both large and small size (it depends on the increments) and they are normally split and/or comminuted to obtain subsamples. The choice of collecting composite samples is useful when detailed information about the distribution of the property (in space and time) are not of interest; otherwise, it is necessary to collect and process single samples. With certain limitation, composite samples are useful to increase the amount of material available for the analyses if the limit of detection of the method is an issue. The compositing is considered also the way by which it is possible to reduce the analytical costs, reducing the number of single samples to be measured; for this reason, this approach is commonly appreciated. A sampling target may be characterized by analyzing five single samples and averaging the measurement results. A similar result may be obtained by pooling the five single samples (increments) into one composite sample to be homogenized, processed, and then analyzed once. In the first case, information about the heterogeneity (variance) of the sampling target is known; in the second one, such information, together with information on possible contamination due to a specific increment, is not available. Subsamples obtained from the primary samples (composite or single) are obtained, by definition, from a population. They may be formed using the same method applied for forming the primary sample or by using appropriate devices aimed at reducing the sample size (mass, volume, etc.). The sample sent to the laboratory and intended for inspection or testing is the laboratory sample. It may be directly a primary sample or the result of an *in situ* sample preparation from a primary sample. For example, within the context of the environmental analysis, typical laboratory samples may be

- 1 l of groundwater bottle potentially contaminated by polychlorinated biphenyls (PCBs);
- grams of soil contaminated by trace elements;
- kilograms of vegetation harvested containing unknown activity concentration of radionuclides.

The test sample is prepared from the laboratory sample. The test portion is formed for testing or analysis. Test sample represents the last stage of sampling, even though it is obtained within the laboratory, and may be considered the ‘‘object of desire’’ for the analyst who is not interested in sampling.

2.3.1
Liquid Sampling

Regardless the context in which the sampler has to operate (environment, food, industry, etc.), liquid sampling means having to deal with at least three different categories of materials:

- homogeneous solutions
- liquids in a flowing sample
- immiscible mixtures.

Homogeneous solutions (or reasonably considered homogeneous with reference to the property of interest) are the simplest type of liquids to be collected. For example, a sampling target represented by a basin of water solution, containing anions and cations, may be sampled by taking few single samples from any point of the basin to represent the whole sampling target. However, this is only a general consideration. In the real world, such as in environmental sampling, a typical situation of water sampling may be from a lake or a reservoir. As the water may be considered a homogeneous system, the water column, at different depths or positions, constantly shows relevant variability in composition. In these cases, it might be necessary to collect single samples at different depths (stratum) and maintain them separately if one is looking at the variability of the concentrations with depth, or to collect composite samples if looking at the mean value along the whole water column.

The second category of liquid that is often encountered is a flowing sample that is constantly changing (e.g., a polluted river, a process stream at a plant, etc.). The material to be sampled may vary over a given time period, both in terms of flow rate and/or quality (e.g., mass concentration of the property to be measured). To account for this constantly changing composition of the sampling target, increments of the same size (volume) can be taken at regular time intervals (time-weighted sampling). In some cases, when the flow of a stream varies with time, is useful to apply a flow-weighted sampling: (i) increments of different volume depending on the flow and collected at regular intervals and (ii) increments of the same volume collected at irregular time intervals depending on the flow.

For all these types of sampling, manual systems are widely used but sometimes they may not be cost effective. In most cases (e.g., monitoring the discharge at a manufacturing facility), a large number of primary samples must be taken over an extended period, such as sampling once every hour through the day, and manual sampling is not practical or impossible. For these reasons, automatic samplers are commonly considered the most suitable systems. A wide variety of automatic sampling equipment are today available with different designs and accessories, depending on the sampling purposes, which are able to be programed and operated without the constant control of the operator. The use of an automatic sampler, however, does not solve all the problems. The correct application of the automatic procedures, with respect to the sampling objectives, needs always skilled and experienced operators and a planned sampling strategy fitting the purposes. Moreover, with the advent of faster and more sensitive detectors and analysis systems, the possibility of real-time analyses being performed on samples has dramatically improved. To obtain samples for such analyses, short bypasses are often introduced into flow lines. These can divert a small amount of the total liquid into the particular instrument being used for analysis (e.g., spectrophotometers, etc.). When such bypasses are inserted into the overall flow of the reaction process, it is important to ensure that they do not change the flow of the original system, possibly skewing the sample that is being analyzed [7].

The last type of liquid specimen that can be encountered in the real world is an immiscible mixture (e.g., a mixture of organic compounds or lubricants and water). In such cases, the sampler must take into account the evident differences in the layer composition and in the proportion between the two phases. The strategy may require the collection of single increments from each layer and the subsequent constitution of composite samples. Subsampling of the primary samples (composite), if needed, may require a preliminary homogenization in order to minimize any loss of representativeness.

Owing to the chemically dynamic state of the samples collected, the preservation and the storage conditions present a critical issue. An incorrect application of the fundamental principles aimed at preserving the sample's integrity/stability over the time will nullify any subsequent measurement and assessment about the property investigated. Any decision taken on the basis of measurement results obtained by analyzing an incorrect sample will be misleading. Hopefully, this issue will be always tackled by the responsible analyst, together with the responsible sampling that is involved in the first stage after the sample collection. The main elements to be taken into accounts are

- the property of interest (e.g., trace element, organic substances)
- the suitability of the containers
- preservatives
- storage condition (temperature, light, time).

The analytical method will guide the sampler in the correct selection of the containers. The volume capacity should be appropriate to perform all the measurements requested (independent replicates commonly are necessary), and there may be differences between volumes sampled for inorganic and organic analyses. The latter, for example, not only in the case of very low mass concentration, may require laboratory samples higher than 1 l in order to apply the extraction phase needed. In this phase, the aspects to be considered are as follows:

- reducing the contamination of the container (including the cap) due to the release of inorganic interferences from the glass or organic and trace elements (metals) from plastics;
- the chance to clean easily the inner surface (decontamination);
- biological and chemical inactivity of the container to prevent cross-contamination between sample and container;
- avoiding adsorption phenomena with the container surface (e.g., metals are easily adsorbed on glass surfaces, whereas organics, such as oils or pesticides, are likely adsorbed on to the sides of plastic containers);
- shock resistance;
- ease in opening and closing.

Most of the above-mentioned aspects may be solved by using inert containers in Teflon and or glass for the organics. Inert plastic containers are used for storing liquids for inorganic analyses. The use of suitable preservatives (e.g., adding nitric acid until a pH less than 2 to a sample to be analyzed for trace inorganic element content) allows the prevention of chemical degradation of the sample collected before the analyses and increase the time within which the analysis may be carried out. Containers with dark colored walls could minimize the photodegradation of samples. Recommendations about the correct combination containers and the property of interest are commonly listed in the ISO standard related to the preservation and handling conditions (e.g., ISO 5667-3 [8]).

2.3.2
Solid Sampling

The way to perform the sampling of solid material is strongly dependent on the heterogeneity of the material itself. Homogeneity, even of the finest powder observed, is an illusion, and heterogeneity is considered the only state in which a set of material units (fragments) can be observed in practice [9]. Nevertheless, the measurand, as already reported, will allow the sampler to select the best sampling technique and sample preservation methods. The knowledge about the behavior of the property of interest in respect of the matrix sampled is mandatory to reduce the risk of biased samples. For example, a trace element (such as a metal) is uniformly associated with fine particles of a soil (e.g., silt), or an organic substance (such as hydrocarbons) may be distributed on the surface of solid fractions (e.g., above 1 cm). In these cases, the sampler must operate appropriately, and avoid discarding the fractions of interest and thus losing important information about the composition of the whole sampling target from which the sample was collected.

The general criteria to be followed in solid sampling must be stated in the sampling strategy. Variability of a property over time and space (also three dimensional) requires that single samples are collected in different sampling points or at different times and analyzed separately. Statistical analyses (classical statistics and/or kriging interpolation) allow the assessment of such spatial and temporal variability. In other cases, compositing several increments (e.g., in waste pile analyses, product lot characterization, or food analyses) may be the most appropriate method; the average composition of the sampling target, possibly highly heterogeneous, is known and the variance effects between the increments collected is minimized. In any case, depending on the objectives of the measurements and the specific context investigated, it is possible to combine single samples and composite samples. To assess the variability of a property on a large scale, ruling out small space/time variability of the sampling target, the constitution of several composites samples and polling increments collected at short time/distance may be pursued.

The sampling techniques and devices differ from one sampled material to another, reflecting their different characteristics. A wide set of corers, augers (hand and motor-powered), scoops and spatulas, and other devices are available on the market to sample under different conditions. The devices are designed (shape, dimension, material, etc.) in order to respond to the different problems to be solved.

Solid materials may be sampled to determine the content of both inorganic elements and organic substances. Their behavior will force the sampler to adopt any cautions and procedures that may reduce the risk of an artificial change in the composition of the sample collected till its analysis. As in the case of liquid samples, even solid samples are affected by degradation phenomena (biological and chemical). Once the primary (solid) sample has been obtained, it is important to select the appropriate container for its storage. For example, in environmental analysis, trace elements (metals) are quite stable within the matrix, and plastic containers are suitable for storage. Organic substances, because of adsorption phenomena, commonly require the use glass containers with inert caps (such as Teflon) and dark containers to prevent the risk of photodegradation (e.g., dioxins). For other samples of different composition and reactivity, various other precautions should be observed during storage to ensure that the sample does not change from its original composition.

2.4
QA/QC in Sampling

It is commonly accepted that an analytical laboratory aimed at obtaining reliable measurements results and comparable all over the world and at maintaining the measurement system under statistical control has to implement quality assurance/quality control procedures. These include the validation of measurement methods, routine internal QC procedures, and independent external QC procedures. The importance of QA/QC in sampling activity, mainly when it is considered part of the overall measurement process, is also recognized now. Whatever the objectives of the sampling, it is recommended to apply sampling procedures validated and follow sampling quality control procedures. Validation allows the evaluation of the sampling quality under stated (routine) conditions and provides an estimation of the contribution of sampling to the measurement uncertainty (including the analysis). In 2005, with reference to the quality management system practices, the ISO/IEC standard 17025 [10] on the competence of testing laboratories reported sampling as a factor to be considered in the total uncertainty of measurement. In 2007, the Eurachem/CITAC (The Cooperation on International Traceability in Analytical Chemistry) Guide on measurement uncertainty arising from sampling [5] provided a guide to the methods and approaches for the estimation of the contribution of sampling (and sample preparation) to the requested measurement uncertainty, as an independent component from the analytical uncertainty. Through the application of the proposed approaches to tackle this issue, a basis for the validation of sampling procedures was defined, regardless the field of investigation (industry, food, environment, etc.)

In the field of environmental sampling, for example, sampling validation include replicate (duplicates) samples (not less than eight) collected at the same site differing as little as possible from each other over space and time, or running a sampling interlaboratory comparison exercise.

The simplest way to assess the component of uncertainty arising from sampling is the quantification of the random component of uncertainty (repeatability). By replicating the analyses on each duplicate collected (and prepared), the contribution due to the analytical phase is also evaluated. Generally, sampling is performed to determine the content of a very wide range of substances in a sampling target, and it is not practicable to validate all the properties of interest. For this reason and for minimizing the additional costs (more samples, more analyses), in this kind of QC activity request the sampling quality performance may be assessed only for the selected measurand (e.g., chromium). Once a sampling quality requirement is fixed (by a regulator organization or by the laboratory itself), the sampling procedure performance may be maintained under control during routine sampling activity, applying on the same sampling target the same sampling procedure previously validated. Replicates samples, as in the validation, should be collected and a quality control chart should be implemented.

By following the examples provided by the Eurachem/CITAC Guide, it is possible to estimate the contribution of sampling to the overall measurement uncertainty within the framework of the characterization of a contaminated soil area of about $10\,000\,\text{m}^2$. The experimental design proposed, the so-called balanced empirical duplicate, is based on the duplication of sampling and analysis. The area is divided into 100 sampling targets. Two duplicate primary samples (Sample 1 and Sample 2) are taken at the sampling target, repeating the same sampling procedure. One test sample is obtained from each primary sample. On each test sample, analyses of the duplicate test portion are performed. This is followed for a fixed ratio (10%) of all the sampling targets (Figure 2.2). The application of the two-way robust

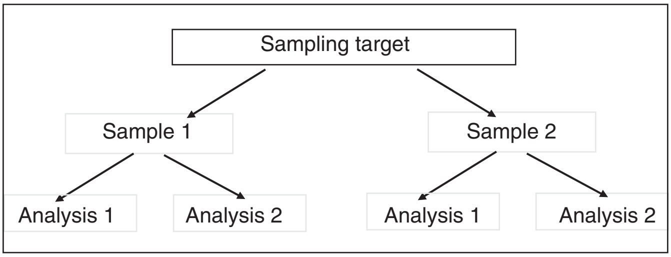

Figure 2.2 Design outline of the (balanced) empirical-duplicate approach. *Note*: the "*duplicate design*" is based on the duplication of sampling and analysis. Sample 1 and Sample 2 are duplicate primary samples taken at one sampling target repeating the same sampling procedure. One test sample is obtained from each primary sample. Analysis 1 and Analysis 2 represent the duplication of the analysis of the test portion taken from each test sample. This scheme is followed for all the sampling targets randomly selected (10%).

analysis of variance (RANOVA) allows the separation of the variability due to spatial distribution of the property of interest (e.g., lead), sampling, and measurements.

The evaluation of the performances of different sampling strategies, through sampling interlaboratory comparison exercises, is a challenging task and requires tools well characterized and stable over time, in analogy with the reference materials used for interlaboratory exercise for analytical laboratories, called *reference sites*. The IUPAC [3] recently defined the reference site for soil sampling as an area, one or more of whose element concentrations are well characterized in terms of spatial and temporal variability.

A number of soil sampling intercomparisons in the field of environmental analysis have been realized at the international level for various aims: comparison among soil sampling guidelines; estimation of bias and measurement uncertainty due to the sampling process; evaluation of sampler performance and their ability to delineate spatially a contaminated area; harmonization of the sampling strategies used at the national level [11].

QA/QC is not limited to the implementation of the above-mentioned practices and procedures, but should include a list of other elements, such as the following:

- basic knowledge on sampling
- availability of appropriate sampling equipment
- competence of the samplers (continuous training and practice)
- written sampling procedures and documentation
- use of QC samples.

Quality is to be pursued not only in the laboratory but also in the field. To this end, the sampler must operate according to a well-defined sampling plan, and any deviation from it and any observed aspects potentially affecting the final result have to be reported (e.g., the laboratory samples must be transported and stored as defined and documented in the plan). Field sampling documentation and sample chain-of-custody procedures are mandatory in a sampling QA/QC system. The correct application of sampling procedures as well as the attitude of not overlooking them can be reached through continuous training of the samplers. In some cases, as a quality objective, it may be requested that the sampler be certified according to ISO standard 17024:2012. Furthermore, the correct application of specific health and safety procedures may reduce the risks for the operator and ensure an improvement of the sampling activity.

An important role in controlling the quality of the sampling operation and assessing data quality is played by the regular use of QC samples. Besides the already mentioned replicate (duplicate) samples used to estimate the variance due to sampling, other QC samples may control some specific aspects (cross-contamination, transportation, storage, etc.). Blank samples, that is, clean matrix samples processed to detect artifacts in the measurement process, and trip blanks, that is, clean matrix sample transported to the field (sampling site) and returned to the laboratory without being exposed to sampling procedures, allow the identification of the contamination (e.g., due to the containers). In addition, field blanks (clean samples transported to the field and exposed to the sampling location) and equipment blanks (clean samples collected by using the same device used in the field and delivered to the laboratory) may be used, for example, to detect the correct application of decontamination on the sampling tools [12].

References

1. IUPAC, Analytical Chemistry Division, Commission on Analytical Nomenclature (1990) Nomenclature for sampling in analytical chemistry (Recommendations 1990). *Pure Appl. Chem.*, **62**, 1193–1208.
2. ISO (2005) 11074:2005. *Soil quality – Vocabulary*. International Organization for Standardization (ISO), Geneva.
3. IUPAC, Analytical Chemistry Division (2005) Terminology in soil sampling (IUPAC Recommendation 2005). *Pure Appl. Chem.*, **77** (5), 827–841.
4. ISO 6107-2. *Water Quality-Vocabulary-Part 2*, International Organization for Standardization (ISO), Geneva.
5. Ramsey, M.H. and Ellison, S.L.R. (eds) (2007) *Eurachem/EUROLAB/CITAC/Nordtest/AMC Guide: Measurement Uncertainty Arising from Sampling a Guide to Methods and Approaches*, Eurachem, ISBN: 978 0 948926 26 6.
6. ISO Guide (2007) 99:2007. *International Vocabulary of Metrology – Basic and General Concepts and Associated Terms VIM – First Edition*, International Organization for Standardization (ISO), Geneva.
7. Cullum, M.C. and Vo-Dinh, T. (2005) *Handbook of Spectroscopy*, John Wiley & Sons, Ltd, Chichester, pp. 17–35.
8. ISO (2012) 5667-3:2012. *Water Quality – Preservation and handling of water samples – Part 3*, International Organization for Standardization (ISO), Geneva.
9. Gy, P. (1998) *Sampling for Analytical Purposes*, John Wiley & Sons, Ltd, Chichester.
10. ISO/IEC (2005) 17025:2005. *General Requirements for the Competence of Testing and Calibration Laboratories*, International Organization for Standardization (ISO), Geneva.
11. de Zorzi, P., Barbizzi, S., Belli, M., Mufato, R., Sartori, G., and Stocchero, G. (2008) Soil sampling strategies: evaluation of different approaches. *Appl. Radiat. Isot.*, **65**, 1691–1694.
12. Kulkarni, S.V. and Bertoni, M.J. (1996) in *Principles of Environmental Sampling*, 2nd edn (ed. L.H. Keith), American Chemical Society, Washington, DC, pp. 111–137.

Section II
Methods 1: Optical Spectroscopy

Handbook of Spectroscopy, Second Edition. Edited by Günter Gauglitz and David S. Moore.

Introduction

Optical spectroscopy techniques have become customary in day-to-day laboratory work, and routine procedures often dominate the actual image of optical spectroscopy. The enormous development during recent years is often underestimated.

Optical spectroscopy, nowadays, refers to all techniques that use nonionizing radiation. This covers the region from the far ultraviolet (UV) to the far infrared (IR). The latter is now often called the *terahertz region* [1]. Sometimes X-ray spectroscopy is also (or still) considered as part of optical spectroscopy, but the current rise of the field of biophotonics has contributed greatly to the restriction to nonionizing radiation. Analytical (bio-)photonics may now be seen as the contemporary term for optical (bio-)spectroscopy.

While there is a wide range of energies between the UV and the far IR, all these spectroscopic techniques share a common theoretical background. Certain types of spectrometers are used at all wavelength ranges, and there are common requirements for basic operations, from sample preparation to data evaluation, that exist for all techniques. For this reason, the subsequent chapters are not organized according to wavelength ranges, but according to the universal topics: (i) basics of optical spectroscopy, (ii) instrumentation, and (iii) measurement techniques. Dedicated applications for the distinct measurement techniques are collected in the final chapter of this section, starting at the low-energy side with the mid IR, and going up to the energy-rich fluorescence. Typical experimental parameters for all major techniques are compiled in tables.

Compared to the previous edition, all chapters of the Optical Spectroscopy Section are expanded. This section now includes the terahertz region, spectroscopic imaging, nonlinear techniques of optical spectroscopy, as well as the utilization of nanoparticles and quantum dots for spectroscopic purposes. Owing to the required abandonment of solvents, various reflection methods and microscopic techniques are increasingly used. This is reflected in the subsequent chapters on optical spectroscopy as well.

A particular potential of optical molecular spectroscopy – the unique combination of high structural sensitivity and excellent time resolution – has attracted great interest. This combination permits analyzing and understanding of biological processes on the molecular level. The range of applications extends from investigations of the fastest molecular processes to single molecule analytics. Proteins exert their biological functions via a sequence of structural changes, with

Handbook of Spectroscopy, Second Edition. Edited by Günter Gauglitz and David S. Moore.

movements occurring in the range between picoseconds and seconds or even beyond. Spectroscopic techniques can be used to record processes such as electron transfer, proton transfer, hydrogen bonding, and chromophore isomerization at excellent sensitivity and rate. All these processes are crucially important in many functional molecules. Molecular imaging and fluorescence spectroscopy techniques have made particularly vast accomplishments here. The complicated situation of a fluorescing chromophore in interacting solvents can now be handled much more easily. Technical developments now permit the investigation of particularly sensitive proteins, label-free, and in their native environment [2]. In particular, nonlinear spectroscopic methods have the potential to provide the required information very fast without impacting the investigated system [3]. Even novel procedures for *in vivo* diagnosis based on optical fibers are expected.

Current imaging spectrometers may provide several thousands of complete spectra within seconds. Nobody is able to manually inspect the quality of this huge amount of spectra, but spectra of border regions of the sample or even of regions outside the sample shall inevitably be collected. Such spectra of inferior quality in the data set may even preclude chemometric evaluation procedures from achieving useful results. This is a standard problem in spectroscopic imaging, as homogeneous sample areas are normally not imaged. Thus, in spectroscopic imaging, approximately 10% of the required time is used for sample preparation and measuring the spectra, and the remaining 90% for thorough chemometric evaluation of images. The basics for these elaborate evaluations are given both within this Optical Spectroscopy Section as well as in Chapter 53 General Data Treatment/Optical Spectroscopy.

References

1. Mantsch, H.H. and Naumann, D. (2010) *J. Mol. Struct.*, **964**, 1–4.
2. Freudiger, C.W., Min, W., Saar, B.G., Lu, S., Holtom, G.R., He, C., Tsai, J.C., Kang, J.X., and Xie, X.S. (2008) *Science*, **322**, 1857–1861.
3. Therien, M.J. (2009) *Nature*, **458**, 716–717.

3

Basics of Optical Spectroscopy

Martin Hof and Radek Macháň

3.1

Absorption of Light

The theoretical description of light can be performed in two ways: light can be regarded as a stream of corpuscles (photons) or as an electromagnetic wave. In case of corpuscle description, the behavior of the photons, and in particular the interaction between photons and molecules, might be described by the laws of quantum optics. In case of electromagnetic description, the interaction of the electromagnetic wave with a medium is described by the electromagnetic theory comprising *Maxwell*'s equations [1].

In the first case – corpuscle description – the energy of the photons is

$$E = h\nu \tag{3.1}$$

where h is the Planck constant ($h = 6.626 \times 10^{-34}$ J s) and ν the frequency of light. The light velocity in vacuum c and the wavelength λ are related to each other by

$$\nu = \frac{c}{\lambda} \tag{3.2}$$

Thus, the energy of electromagnetic waves is directly proportional to the reciprocal wavelength. In particular, in vibrational spectroscopy, the reciprocal wavelength is used and denoted as wavenumber k

$$E = hck \tag{3.3}$$

Usually, the wavenumber k is written in the form

$$k\ (\text{cm}^{-1}) = \frac{10\,000}{\lambda\ (\mu\text{m})} \tag{3.4}$$

In the second case – describing light as electromagnetic wave – its propagation may be written as

$$A(\phi) = A_0(\phi)\mathrm{e}^{i(\omega t - \delta)} \tag{3.5}$$

where A is the amplitude, ω the circular frequency, t the time, δ the phase angle, and ϕ the polarization angle. The circular frequency may be expressed by the

Handbook of Spectroscopy, Second Edition. Edited by Günter Gauglitz and David S. Moore.

wavelength λ and the refractive index n

$$\omega = \frac{c}{\lambda n} \tag{3.6}$$

Equation (3.5) applies for the propagation of light in a nonabsorbing medium. In case of an absorbing medium, Eq. (3.5) has to be modified by replacing the refractive index n by its complex form n^*

$$n^* = n + i\kappa \tag{3.7}$$

where n and κ are always nonnegative. In case of an absorbing medium, the absorption coefficient α is often used

$$\alpha = \frac{4\pi\kappa}{\lambda} \tag{3.8}$$

On the basis of Eq. (3.5), the light intensity I can now be described as

$$I = I_0 \mathrm{e}^{-\alpha l} \tag{3.9}$$

where l is the path length of light within the absorbing medium. The Beer–Lambert law results directly from Eq. (3.9)

$$I = I_0 \mathrm{e}^{-\varepsilon c l} \tag{3.10}$$

with ε as molar absorption coefficient and c as concentration of the absorbing compound. The Beer–Lambert law is usually expressed in its logarithmic form

$$\log\left(\frac{I0}{I}\right) = A = \varepsilon c l \tag{3.11}$$

Note that the absolute value of ε changes by a factor of 2.303 if "ln" is used instead of "log."

In the medium, absorption of light causes a transition from an energetic ground state to a particular excited state. Depending on the energy of light and on the chemical nature of the interacting compound, the excited states may differ very much in nature (cf. Figure 3.1). Rotations and vibrations are excited in the infrared spectral range. In the UV–vis range, absorption of light causes electronic and vibrational excitations. Relaxation of excited states back to the ground state may cause emission or luminescence, which are also evaluated spectroscopically. Electronic and vibrational transition can be excited simultaneously (vibronic transitions), but owing to the large differences in their transition energies, the different types of optical excitation (electronic transitions, vibrational, and rotational motions) can be discussed separately (Born–Oppenheimer approximation). Spectral band parameters are the position of the band maximum (wavenumber k or wavelength λ), the intensity of the band (height or area above the baseline), and the band shape (influenced by the environment of the vibrating group) [2].

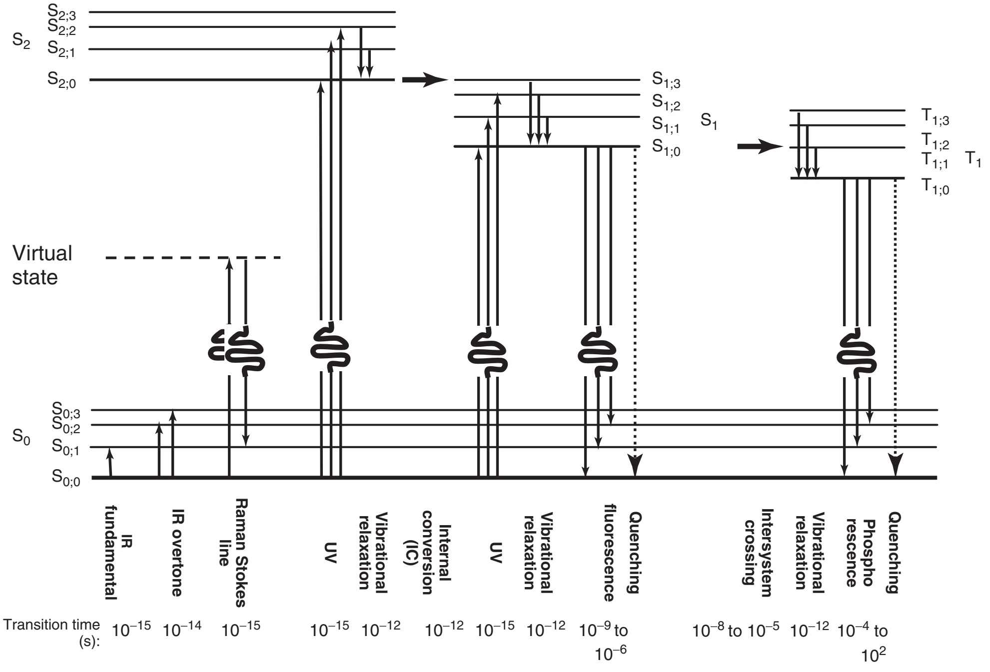

Figure 3.1 Schematic depiction of vibrational and electronic transitions described in this chapter. The distance between electronic states has been compressed by a factor of at least 10 compared to the distance of vibrational states.

3.2
Infrared Spectroscopy

The mid (fundamental) infrared (IR or MIR) region extends from 4000 cm^{-1} ($\lambda = 2.5\,\mu$m) to 400 cm^{-1} (25 μm). It is surrounded by the far infrared (FIR) region from 400 cm^{-1} (25 μm) to 10 cm^{-1} (1 mm) and the very important near infrared (NIR) region from 12 500 cm^{-1} (800 nm) to 4000 cm^{-1} (2.5 μm). Infrared spectroscopy is the most used spectroscopic technique. There are a number of reasons for its great success and dissemination. The method is rapid, sensitive, easy to handle, and provides many different sampling techniques for gases, liquids, and solids. Important aspects are the convenient qualitative and quantitative evaluation of the spectra.

The standard format of an IR spectrum is transmittance T (%) versus wavenumber (cm^{-1}). According to IUPAC recommendations, the values of the wavenumber axis diminish toward its right end [3]. This recommendation is, however, not always obeyed because of limitations in commonly used computer programs for spectra processing. The features of an IR spectrum (number of infrared absorption bands, their intensities, and their shapes) are directly related to the molecular structure of a compound. The IR spectrum is a unique physical property of an individual compound; it is its molecular fingerprint [4].

The IR region comprises fundamental vibrations of bound atoms. Whenever such bound atoms vibrate, they absorb infrared energy, that is, they exhibit IR absorption bands. The condition for a normal vibration j to be IR active is a change in molecular dipole moment μ during vibration

$$\mu_j = \mu_0 + \left(\frac{\delta\mu}{\delta q_j}\right) q_j + \frac{1}{2}\left(\frac{\delta^2\mu}{\delta q_j{}^2}\right) q_j{}^2 + \cdots \tag{3.12}$$

q stands for the normal coordinate describing the motion of atoms during a normal vibration.

With respect to the direction of the vibrational movement, we may distinguish between stretching vibrations (changes of bond lengths) and deformation vibrations (changes of bond angles). Deformation vibrations may be subdivided into bending modes, twisting or torsion modes, wagging modes, and rocking modes. Further subdivisions refer to the symmetry of the vibration (e.g., symmetric or antisymmetric, in-plane or out-of-plane) [5].

Complications in evaluation of IR spectra are the overlapping of individual bands and the appearance of additional bands, for example, overtone and combination bands, which may be caused by anharmonicity of some vibrations. In the NIR region, all bands are overtone and combination bands. They are always weaker in intensity than the corresponding fundamental bands. Originally considered as a drawback, the weak intensity of the NIR bands turned out to be the background for the large success of NIR spectroscopy in process analysis [6, 7].

The concept of characteristic vibrations is used for qualitative analysis of polyatomic molecules [8]. In organic compounds, characteristic vibrations occur usually between 4000 and 1500 cm^{-1}. Inorganic compounds containing heavy atoms may exhibit characteristic vibrations at much lower frequencies [9]. Characteristic vibrations are based on motions, mostly stretching vibrations, that are localized in and characteristic of typical functional groups. While individual bands are not sufficient in confirming the identity of a molecule, they provide useful information about the type and abundance of substructures that make up a molecule. All frequencies of organic compounds below 1500 cm^{-1} involve molecular vibrations, usually bending motions that represent a characteristic fingerprint of the entire molecule or large fragments of the molecule. The comparison of the spectrum of an unknown compound with spectra stored in spectra libraries together with corresponding search programs are an excellent possibility for qualitative analysis. Currently, these programs offer search routines based on complete spectra, compound information, molecular structures, and substructures (see Chapter 53).

The intensities of the bands in pure components and in mixtures are proportional to the concentrations of the components. The relation between measured intensities and concentration is expressed in the Lambert–Beer law (Eq. (3.11)). Thus, it is possible to carry out quantitative investigations by methods based on band heights or preferably by methods based on integrated intensities. Both single-component analysis and multicomponent analysis by multivariate methods (see Chapter 53.3.3) can be performed.

3.3
Raman Spectroscopy

The Raman effect is a light-scattering effect. The exciting monochromatic beam has to be of high intensity (laser beam) in order to induce in the molecule a virtual energy state (cf. Figure 3.1). Most of the molecules relax directly back to the $S_{0;0}$ state, whereby light of the same wavelength as the exciting light is emitted (Rayleigh scattering). Only a very small percentage of the excited molecules relax back to a vibrationally excited state, hence the emitted photons have smaller energy than the exciting photons (Stokes lines). Because only a very small percentage of molecules uses this relaxation pathway, Raman scattering is always of very low intensity, its investigation requires high-quality instrumentation. Molecules, which were originally in a vibrationally excited state, can after excitation relax to the ground state emitting photons of higher energy than the exciting ones (anti-Stokes lines). The fraction of molecules residing initially in the vibrationally excited state is given by factor $\exp(-E/bT)$, where E is the energy difference between ground and excited state, b is Boltzmann's constant, and T is temperature. The intensity of anti-Stokes lines is, therefore, much smaller than that of Stokes lines and the ratio of their intensities can be used for *in situ* monitoring of temperature [10]. The Raman effect can be excited in the UV region, in the visible region, or in the NIR region.

The condition for a molecule to be Raman active is a change in the polarization (deformation) of the electron cloud during the interaction with the incident radiation. In case of Raman scattered radiation, the magnitude of the field vector E of the exciting radiation is modulated by the molecular vibrations. The induced dipole moment μ' is

$$\mu' = \chi_1 E + \frac{1}{2}\chi_2 E^2 + \frac{1}{6}\chi_3 E^3 + \cdots \tag{3.13}$$

χ_i is the molecular polarizability, a three-dimensional (tensor) term, whereas the dipole moment (Eq. (3.12)) is a two-dimensional (vector) term. At commonly employed field strength values (laser output up to 1 kW per line), Eq. (3.13) can be reduced to its linear term. Nonlinear terms have to be taken into account only in case of very high intensity of the exciting light (above 1 MW per line). On the basis of this situation, the conventional Raman effect is often denoted "linear Raman effect," in contrast to "nonlinear Raman effects" observed with very strong laser excitation [11]. χ_2 contributions lead to the hyper-Raman effect, χ_3 contributions to the stimulated Raman scattering (SRS), and the coherent anti-Stokes Raman spectroscopy (CARS), cf. Section 4.8.

SRS is described as a two-photon stimulated process. Only Raman modes with the highest gain factors give rise to stimulated Stokes emissions. All active Raman modes can, in principle, be observed if the molecular system is provided with an intense external Stokes field by using a second laser beam for excitation (three-wave mixing). The superposition of two electromagnetic waves of the frequencies ω_1 and ω_2 generates a third electromagnetic wave at the difference frequency (difference frequency generation, DFG, $\omega_1 - \omega_2$), the second harmonic in case of

$\omega_1 = \omega_2$ (second harmonic generation, SHG, $\omega_1 + \omega_2$), or the sum frequency in case of arbitrary ω_i (sum frequency generation, SFG, $\omega_1 + \omega_2$). The intensities of harmonics emitted by oscillating dipoles depend on the square of the vibrational amplitudes.

The Raman method is the complementary method to IR spectroscopy, where the excited vibrational state is directly approached. The Raman spectrum is the plot of Raman intensity versus Raman shift. Raman band parameters are band position in the spectrum (Raman shift), intensity of the band, and band shape. As in case of the IR spectrum, the features of a Raman spectrum (number of Raman bands, their intensities, and their shapes) are directly related to the molecular structure of a compound [11, 12].

The complementarity of IR and Raman spectra is based on the different excitation conditions: change of dipole moment (vector quantity) in case of IR spectrum, change of polarization (tensor quantity) in case of Raman spectrum. Because a tensor is a three-dimensional quantity, the depolarization ratio ρ can be obtained by measuring Raman spectra with polarized light (polarization directions parallel and perpendicular to the optical plane)

$$\rho = \frac{I_{||}}{I_{\perp}} \tag{3.14}$$

The qualitative analysis by group frequencies and the quantitative analysis procedures for single and multicomponent analysis are, in principle, the same as in IR. A severe limitation in application of Raman is the fluorescence phenomenon. Fluorescence can be up to 10^7 times stronger than Raman scattering. Fluorescence of trace impurities may, therefore, render observation of the Raman spectrum of the analyte impossible. In order to avoid the masking of Raman scattering by fluorescence, the gap between the virtual energy state and the electronically excited state S_1 has to be sufficiently large (choice of excitation wavelength between UV, MIR, and NIR). NIR excitation is often preferred because there are very few electronic transitions in the NIR. The drawback of NIR excitation is the severely reduced Raman scattering intensity (proportional to $\lambda_{\text{exc}}^{-4}$).

3.4
UV–vis Absorption and Luminescence

UV–vis absorption and luminescence spectra are related to electronic and vibrational transitions. The term *luminescence* summarizes a combination of basic processes such as fluorescence and phosphorescence, which are described subsequently. Transitions occur between energy levels described as in $S_{n,v}$, where S points to an electronic singlet state and n,v to the corresponding electronic (n) and vibrational (v) excitation levels. The intensity of a transition from an electronic and vibrational ground state $S_{0,0}$ to a corresponding excited state $S_{n,v}$ is proportional to the square of the transition dipole moment $\boldsymbol{M}$, which itself can be separated in an electronic part $M_{0;n}$ and the vibrational contribution $F_{0,0;n,\nu}$

$$\boldsymbol{M} = M_{0;n} F_{0,0;n,\nu} \tag{3.15}$$

$F_{0,0;n,\nu}$ represents the so-called vibrational overlap integral of the vibronic wavefunctions $\chi_{0,0}$ and $\chi_{n,\nu}$, given by

$$F_{0,0;n,\nu} = \int \chi_{0,0}\chi_{n,\nu}\mathrm{d}r \tag{3.16}$$

where r is the internuclear distance. The square of $F_{0,0;n,\nu}$ is known as the *Franck Condon factor*, which is a measure of the transition probability between the vibrational ground state of S_0 and a vibrational excited state of $S_{n.}$ Individual Franck Condon factors are directly related to the intensity of the vibrational bands and thus determine the vibrational fine structure of the absorption spectrum. The electronic transition dipole moment $M_{0;n}$ is defined as

$$M_{0;n} = \int \psi_0 \boldsymbol{\mu} \psi_n dq_{\mathrm{e}} \tag{3.17}$$

where ψ_0 and ψ_n are the electronic wavefunctions of ground and excited states, respectively, $\boldsymbol{\mu}$ is the electric dipole moment operator, and q_{e} are the electron coordinates. The probability of an electronic transition is directly related to the square of the value of cos ζ, where ζ is the angle between the plane of oscillation of the electrical vector of light and the direction of the electronic transition dipole moment $M_{0;n}$.

After the creation of the so-called "Franck Condon state" $S_{n,\nu}$ by "ultrafast" absorption of light (10^{-15} s), the molecule usually relaxes within 10^{-12} s into the lowest excited state ($S_{1,0}$). Although some rare examples of direct fluorescence from the $S_{2,0}$ exist, they are considered as curiosities and do not find application in material or life sciences [13]. The photophysical processes populating the $S_{1,0}$ are vibrational relaxation and internal conversion (e.g., $S_{2,0} \rightarrow S_{1,\nu}$). Subsequently, the molecule can return back to the ground state $S_{0,\nu}$ by fluorescence (typically between 10^{-9} and 10^{-6} s). As the vibrational fine structure of the fluorescence spectrum is again determined by the Franck Condon factors for the possible $S_{1,0} \rightarrow S_{0,\nu}$ transitions, the emission is for most chromophores the mirror image of the $S_{0,0} \rightarrow S_{1,\nu}$ transition. Alternatives to the light emission are several radiationless deactivation pathways from the $S_{1,0}$ state. The most fundamental processes are the intramolecular processes internal conversion ($S_{1,0} \rightarrow S_{0,\nu}$) and intersystem crossing ($S_{1,0} \rightarrow T_{n,\nu}$), as well as intermolecular interactions such as collisional quenching or resonance energy transfer. After the population of an excited triplet level $T_{n,\nu}$ by intersystem crossing, vibrational relaxation and internal conversion lead again to the population of the lowest triplet excited state $T_{1,0}$. The luminescence from the $T_{1,0}$ state is called *phosphorescence* and is spin forbidden, hence relatively low in intensity and relatively slow (typically between 10^{-4} and 10^{2} s). It is quite common at temperatures of liquid nitrogen or helium, but rare at room temperature and even rarer at physiological temperatures. Thus, phosphorescence as well as the rare process of delayed fluorescence will be skipped when further discussing practical limits and possibilities of luminescence. It has to be stressed that the described picture (summarized in Figure 3.1) does hold only for measurements in the gas phase and in nonpolar solvents as well as in the absence of special intramolecular photochemical processes. The real situation of a chromophore in interacting solvents is much more complicated. One must include interaction with the surrounding molecules, transfer of the excitation energy from one molecule to another, variety of photochemical processes, effects of polarized excitation and detection, different mechanisms of quenching, and relaxation of the solvent [13, 14]. Those processes that yield information when applied in material and life sciences are discussed in Section 6.5.

References

1. Born, M. and Wolf, E. (2002) *Principles of Optics*, 7th edn, Cambridge University Press, Cambridge.
2. Chalmers, J. and Griffiths, P. (eds) (2001) *Handbook of Vibrational Spectroscopy*, Vol. 1, John Wiley & Sons, Inc., New York.
3. Becker, E.D. (1978) *Pure Appl. Chem.*, **50**, 231–236.
4. Silverstein, R.M., Bassler, G.C., and Morrill, T.C. (1998) *Spectrometric Identification of Organic Compounds*, 5th edn, John Wiley & Sons, Ltd, Chichester.
5. Bunker, P.R. and Jensen, P. (1998) *Molecular Symmetry and Spectroscopy*, 2nd edn, NRC Press, Ottawa.
6. Hollas, J.M. (2004) *Modern Spectroscopy*, 4th edn, John Wiley & Sons, Ltd, Chichester.
7. Siesler, H., Ozaki, Y., Kawata, S. *et al.* (eds) (2002) *Near-Infrared Spectroscopy*, Wiley-VCH Verlag GmbH, Weinheim.
8. Griffiths, P.R. and Haseth, J.A. (2007) *Fourier Transform Infrared Spectrometry*, 2nd edn, John Wiley & Sons, Inc., Hoboken.
9. Nakamoto, K. (2009) *Infrared and Raman Spectra of Inorganic and Coordination Compounds*, 6th edn, John Wiley & Sons, Inc., Hoboken.
10. Maher, R.C., Cohen, L.F., Le Ru, E.C., and Etchegoin, P.G. (2006) *Faraday Discuss.*, **132**, 77–83.
11. Schrader, B. (ed.) (1995) *Infrared and Raman Spectroscopy*, Wiley-VCH Verlag GmbH, Weineim.
12. Larkin, P. (2011) *Infrared and Raman Spectroscopy: Principles and Spectral Interpretation*, Elsevier, Amsterdam.
13. Lakowicz, J.R. (2006) *Principles of Fluorescence Spectroscopy*, 3rd edn, Springer, New York.
14. Valeur, B. and Berberan-Santos, M.N. (2012) *Molecular Fluorescence*, 2nd edn, Wiley-VCH Verlag GmbH, Weinheim.

4
Instrumentation

Valdas Sablinskas

There are a few basic types of instruments that are used in optical spectroscopy for the determination of absorption, fluorescence, or Raman spectra of condensed and gaseous samples. These basic types are monochromators, interferometers, and polychromators. The wavelength range of conventional optical spectroscopy extends from 200 nm (UV) to 500 μm far infrared (FIR). In very modern applications, the long wavelength region is even reaching 1 cm (or 0.03 terahertz (THz)). This region is called *terahertz spectral region*. It is impossible to build one single spectral instrument capable of covering the region completely and to provide information about the different processes of absorption, emission, and scattering of light. Light sources, detectors, and other optical components have limited operational ranges, caused by the underlying physical work principles. The choice of the appropriate instrument type depends on the application. The interaction process of light with the material and the spectral interval of interest have to be taken into account. Traditionally, spectrometers for absorption measurements are optimized for UV/vis (175–750 nm), near-infrared (NIR) (0.75–2.5 μm), mid-infrared (MIR) (2.5–50 μm), FIR (50–1000 μm), and THz (1–10 mm) ranges. Some commercial spectrometers are capable of covering neighboring spectral regions (for instance, UV/vis/NIR or MIR/FIR).

Spectrometers for investigation of scattering and emission of light belong to a second class of instruments. Some recently developed spectral instruments for studying the emission of light as a result of nonlinear interaction of radiation with matter, such as sum frequency generation (SFG) spectrometers, also belong to this second class.

Spectrometers can be combined with appropriate microscopes and collect spectral information from selected small areas of the sample. This combination is sometimes called *microspectrometer*. A motorized x,y stage or an array detector may be added to the microscope in order to produce detailed chemical maps of the sample. Such spectrometers are often described as spectral imaging devices.

Handbook of Spectroscopy, Second Edition. Edited by Günter Gauglitz and David S. Moore.

4.1
MIR Spectrometers

There are two types of MIR spectrometers, dispersive and Fourier transform (FT) spectrometers. Currently, the predominantly used spectrometers are FT spectrometers. The most significant advantage of FT spectrometers is that radiation from all wavelengths can be measured simultaneously, whereas in dispersive spectrometers all wavelengths are measured consecutively. Therefore, an FT spectrometer is much faster and more sensitive. Nowadays, dispersive MIR spectrometers are not anymore available on the market, but they still are in use in laboratories.

Information about absorption of infrared (IR) radiation in the sample is obtained by measuring the intensity ratio of the radiation before and after the sample. In order to obtain this ratio with sufficient accuracy, IR absorption spectrometers should be double channel instruments.

4.1.1
Dispersive Spectrometers

Basically, dispersive instruments are much simpler than FT ones, as they measure the spectrum directly (Figure 4.1). The IR beam from the source of IR radiation is directed both to a sample and a reference position inside the sample chamber (double-beam principle). After passing the sample chamber, both beams are combined into one common path by means of a rotating chopper mirror. The combined beams enter the grating monochromator and, finally, reach the detector. By turning the grating, all spectral elements are eventually directed to the detector. The spectrum is recorded in real time as ratio of the sample beam intensity (I) to the reference beam intensity (I_0). Usually, one grating is not sufficient to cover the complete MIR spectral range. Up to four different gratings are subsequently used for the region 4000–400 cm^{-1}.

The great advantage of the double-beam principle is the automatic compensation in the spectra of most of the external disturbances, such as contributions by optical components or absorptions due to solvents or atmospheric water and CO$_2$. Regardless of this automatic compensation, no meaningful results are obtained

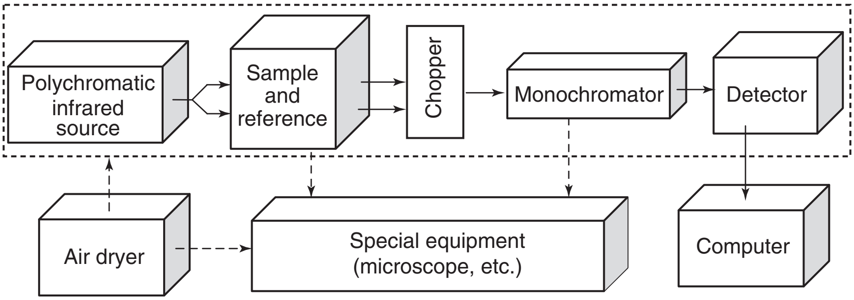

Figure 4.1 Block diagram of a dispersive IR spectrometer.

if the absorption due to these disturbances is too strong. Such regions are called *dead spectral regions*. For instance, because of the strong absorption of CO_2 around $2450\,cm^{-1}$, this region may be blocked in conventional MIR spectrometers. The problem of dead spectral regions can be overcome by purging of the spectrometer with dry and CO_2-free air or evacuating it. An air dryer can be installed to any MIR spectrometer as an option. Vacuum spectrometers are usually more expensive than purged ones. Moreover, vacuum-tight sample cells may be needed.

The most common source in MIR spectrometers is a glowing ceramic bar, a so-called glowbar (or globar). More intense emission is provided by the Nernst glower because of its higher operation temperature (black body radiator). A thermocouple or a thermopile is commonly used as detector. The response behavior of such detectors is slow, what prevents rapid scanning by dispersive MIR spectrometers.

4.1.2
Fourier-Transform Spectrometers

FT-IR spectrometers cannot be built as double-beam instruments. Unlike dispersive instruments, FT-IR spectrometers acquire single-channel spectra of sample and reference, their ratio is calculated afterwards (Figure 4.2). Sample and reference may automatically be replaced by a sample slider, or the IR beam may be switched between sample and reference by flip mirrors. In case of higher accumulation numbers, the instrument switches repeatedly between sample and reference scan.

The heart of any FT-IR spectrometer is an interferometer. The Michelson interferometer consists basically of a beamsplitter and two flat mirrors. One of the mirrors is fixed in one interferometer arm, and the other mirror is movable in the second interferometer arm. Most common MIR beamsplitters are made of KBr with a multilayer coating. The beamsplitter should have a reflectivity of 50% and no absorption across its range of use.

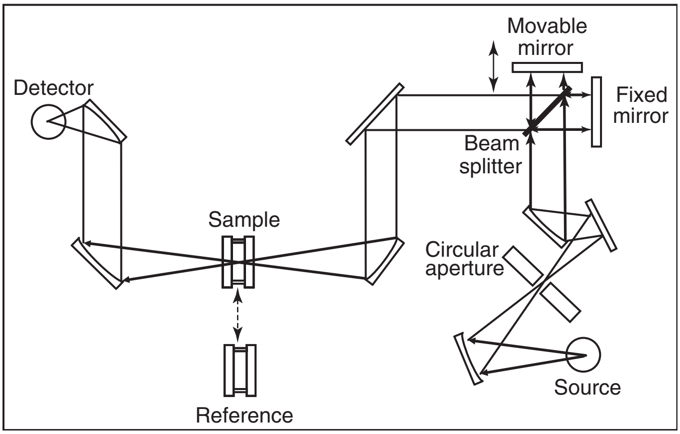

Figure 4.2 Diagram of an FT-IR spectrometer with a Michelson interferometer.

The operation of a Michelson interferometer is based on a collimated IR beam. The latter is directed to the beamsplitter, which divides the beam into two parts of equal intensity (in the ideal case). The divided beams are reflected by the fixed and the movable mirrors back to the beamsplitter, where they recombine and interfere. The displacement of the movable mirror causes changes in the optical pathlength between the two beams, so that the conditions for constructive and destructive interference as well as all intermediate states between the two are consecutively met. The recombined IR beam passes the sample (or the reference) and reaches the detector. Position and movement of the movable mirror are controlled by a helium–neon laser ($\lambda_{\mathrm{HeNe}} = 632.8\,\mathrm{nm}$). The interferogram of the helium–neon laser is used to control the sampling of the IR interferograms in steps down to $\lambda_{\mathrm{HeNe}}/2 = 316.4\,\mathrm{nm}$.

The mathematical procedure, which is employed to convert the IR interferogram (intensity vs time, also called *time domain*) to an IR spectrum (intensity vs frequency, also called *frequency domain*), is called *Fourier transformation*. Sample and reference interferograms are separately transformed. Afterwards, the ratio of both is automatically calculated and displayed as instrument-independent IR transmittance spectrum (Figure 4.3).

Resolution in an FT-IR spectrometer is mainly defined by the maximum path difference between the interferometer arms. It is crucial to maintain the optical

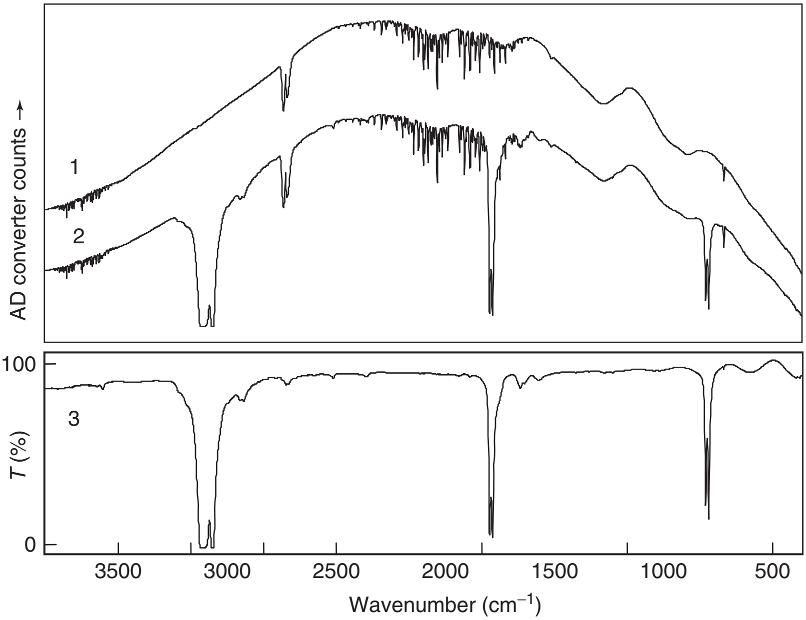

Figure 4.3 IR absorption spectrum of polyethylene: (1) single-eam reference spectrum (without sample); (2) single-beam sample spectrum; and (3) ratioed transmittance spectrum.

alignment of the interferometer during mirror movement; hence, the efficiency of the device for moving the mirror (the so-called scanner) is very important. Most interferometers employ either a mechanical pivot bearing, a mechanical slide bearing, or an air bearing to translate the mirror along a linear path. Alternatively, an optical retardation can be introduced by rotating a pair of planar mirrors instead of translating one mirror. The larger the angle of the mirror rotation, the greater is the achieved optical retardation. Regardless of the type of mirror drive, it moves continuously and does not stop during data collection at each interferogram sampling point (continuous-scan operation). In order to correct for alignment errors during mirror movement, newer interferometers employ fast-response piezoelectric crystals to align the position of the fixed mirror during the scan. Moving mirror tilt may also be eliminated optically by using the so-called corner cube mirrors. This method is preferable for high-resolution instruments, where the moving mirror displacement may be as large as a few meters.

Traditionally, FT-IR spectrometers used to be divided into two groups, routine and research spectrometers. Both have an affiliated PC for data processing and handling. Routine spectrometers usually have a resolution limit at about 1 cm^{-1}. Research spectrometers can achieve resolution as high as 0.001 cm^{-1}. Sources, beamsplitters, and detectors are exchangeable in research spectrometers, so one could use these spectrometers from 40 000 down to 20 cm^{-1} (from UV to FIR). In some spectrometers, different sources and detectors are installed permanently. They can be switched on or off by means of flip mirrors. Nowadays there are no designated limits anymore between routine and research instruments.

The high efficiency of FT-IR spectrometers is mainly attributed to the so-called Jacquinot advantage, that is, the optical throughput is not anymore limited by a relatively narrow monochromator slit. Interferometers have circular apertures, whose diameter depends only on the desired spectral resolution. In general, the beam cross section of an FT instrument is usually 75–100 times larger than the slit opening of a dispersive instrument. Correspondingly, a much larger amount of IR radiation reaches the detector of an FT instrument. The diameter of the aperture in FT instruments is limited by the chosen spectral resolution. The better the needed resolution, the smaller the computer-controlled diameter of the aperture and eventually the signal at the detector.

Another important advantage of FT-IR spectrometers is their outstanding frequency accuracy (Connes advantage), the basis for all achievements in difference spectroscopy. This accuracy of spectral frequencies is due to the precise and stable collection of the interferogram signal, triggered by the helium–neon laser. An accuracy in wavenumber of better than 0.01 cm^{-1} can be achieved.

The third advantage is high speed and/or high sensitivity (Fellgett advantage). The time needed by the movable mirror for one scan cycle varies between 0.01 and 1 s, depending on the spectral resolution as well as the detector response. Typically, 20–200 scans are accumulated in one measurement to acquire a sufficient signal-to-noise ratio. The number of accumulations depends on the experimental condition and can be much higher if least spectral effects have to be studied.

4.1.2.1 **Detectors**

The standard detector in routine FT-IR instruments is the pyroelectric DTGS (deuterated triglycine sulfate) detector, whose response in the MIR range is wavelength independent. The detector operates at ambient temperature and shows good linearity across the whole transmittance scale. The DTGS detector responds to signal frequencies of up to several thousand hertz, and hence the time needed to scan one spectrum at a resolution of 4 cm^{-1} is in the order of 1 s.

The MCT (mercury cadmium telluride) detector is much more sensitive and faster than the DTGS detector. Operation of the MCT detectors is based on an internal photo effect. Each IR radiation quantum excites one bound electron of the detector material to a free state, that is, the electrical conductivity of the MCT detector element increases. A serious drawback of the MCT detector is its spectral working range. Low-energy photons are not able to promote the bound electrons to the free state (low wavenumber cut-off of MCT detector at 600 cm^{-1}). In some MCTs, this cut-off is even higher (750 cm^{-1}) because of absorption in the detector optical window. Owing to its low operating temperature, the detector element is covered by a vacuum enclosure with an optical window in front of the detector element. The vacuum housing makes the MCT detector rather expensive. Furthermore, the MCT detector shows a nonlinear response, which can be minimized by special electronics and software. The time needed to scan one spectrum is only 0.01 s; that is, rates of 100 scans per second are achieved. The MCT is the detector of choice for experiments in conditions of low radiation levels.

FT-IR spectrometers with array detectors can be considered a new class of IR instruments. The size of an array detector chip with its sensitive elements placed in one plane (because of this arrangement called *focal plane array* (FPA)) is usually about 4 mm × 4 mm and, depending on the number of individual MCT detector pixels in the array, a large number of interferograms is collected simultaneously. In case of an FPA detector with 64 × 64 individual pixels, 4096 interferograms are collected simultaneously and the spectral imaging of a sample area of 4 mm × 4 mm can be completed in a few seconds. Images from areas as small as 250 μm × 250 μm can be acquired by combining the FT-IR imaging spectrometer with an IR microscope. As the read-out electronics needs some time to collect signals from all MCT elements of the FPA detector, the scanner speed has to be reduced substantially. For this reason, interferometers in imaging instruments are commonly operated in the step-scan mode.

4.1.2.2 **Step-Scan Operation**

In the step-scan mode, the moving mirror of the interferometer is stopped at each data acquisition point and held for some time (seconds to minutes), during which data are acquired. Interferograms collected in the step-scan mode contain the same information as those collected in the continuous-scan mode, only the time required to complete an experiment is much longer. Under stroboscopic measuring conditions, a time resolution of 100 ns can be achieved. This technique can be applied to processes, which can repeatedly be started under highly reproducible conditions. The step-scan technique can also be applied for the acquisition of voluminous data. This is the case for FPA detectors, where data points from a vast number of individual detector elements have to be collected.

4.1.2.3 **Combined Techniques**

Many FT-IR spectrometers have external ports for optical coupling to dedicated accessories. The IR radiation is conveniently directed to/from the external ports by computer-controlled flip mirrors. A large variety of accessories such as IR microscopes, interfaces for gas chromatography (GC/FT-IR), high-performance liquid chromatography (HPLC/FT-IR), thin layer chromatography FT-IR (TLC/FT-IR), and so on, is commercially available. This type of method combination is usually called *hyphenated techniques*. FT-IR spectrometers can even be supplemented by an FT-Raman accessory. The versatile combination of FT-IR spectrometers with other instruments have substantially contributed to their abundance in most analytical laboratories.

4.2
NIR Spectrometers

Absorption of electromagnetic radiation in the NIR region is caused by overtone and combination vibrations. Polyatomic molecules exhibit many overtone and combination vibrations, their spectral bands overlap and make typical NIR bands look very broad and featureless. Nevertheless, NIR spectra comprise molecular information about the sample, and this information can be extracted by means of chemometric methods (cf. Chapter 53). The prerequisite for chemometric evaluations is a high quality of the collected spectral data. Therefore, wavelength validity (accurate and precise) resolution, photometric validity, and signal-to-noise ratio are important criteria for the selection of an NIR spectrometer.

Among all optical spectroscopic methods, NIR offers the greatest diversity of instrumentation principles, and the market for commercially available instruments is in continuous change and growth. NIR has an enormous variety of applications, for example, in agriculture, in food processing, in medical and in pharmaceutical applications, in polymer and plastics processing, in environmental analysis, in material recycling, and in satellites or aircrafts for remote sensing. Commercial NIR spectrometers vary remarkably with respect to cost, to size and portability, to measurement time, and to environmental conditions for in-line applications in industry. According to their measurement principles, NIR spectrometers fall into one of the six categories:

1) Fourier transform spectrometers
2) Scanning-grating spectrometers
3) Diode array spectrometers (fixed-grating spectrometers)
4) Filter spectrometers
5) LED (light-emitting diode) spectrometers
6) AOTF (acousto-optical tunable filter) spectrometers.

4.2.1
FT-NIR Spectrometers

These are identical to FT spectrometers already described in Section 4.1.2. The most used light source for the FT-NIR spectrometer is the tungsten-halogen lamp. Such a lamp delivers high and constant energy throughout the NIR range, is very stable, and has a long lifetime. Beamsplitters for FT-NIR spectrometers are usually made from CaF_2 with working range 10 000–1600 cm^{-1} (1000–6000 nm). There is no detector available to cover the complete NIR range or to suit all types of NIR spectrometers. A list of detectors and their application ranges is given in Table 4.1. Most used detectors in the range 1100–2500 nm are PbS and PbSe detectors, whereas Si diodes are preferred in the range 400–1100 nm.

4.2.2
Scanning-Grating Spectrometers

These spectrometers and their basic construction have already been described in Section 4.1.1. Scanning-grating NIR spectrometers often permit continuous scans from the UV through vis to the NIR region; therefore, they have two detectors, one for the UV/vis (Si) and one for the NIR regions (mostly PbS). Because NIR spectral bands of solid or liquid samples are rather broad, NIR spectrometers usually do not provide high spectral resolution. For many NIR applications, a resolution of 10 nm is sufficient. This allows rapid scans across the entire NIR range in only 0.1–1 s. The broad spectral range of such spectrometers, their speed, and accuracy are great advantages of these instruments. Full-range spectrometers are rather expensive; hence, they are mainly found in research laboratories.

Table 4.1 NIR detectors and their application ranges.

Detector	Working temperature (K)	Application range (nm)
Ge detector	77	From 600 to 1800
Si detector	300	From 400 to 1100
InGaAs detector	300	From 900 to 1700
PbS detector	196	From 1100 to 3500
InAs detector	77	From 1500 to 3500
Extended InGaAs detector	300	From 1100 to 2800
Ge detector	300	From 600 to 1900
InSb detector	77	From 2000 to 4000
PbS detector	300	From 1000 to 3000
PbSe detector	300	From 1100 to 4000

4.2.3
Diode Array Spectrometers

These have no moving parts. NIR radiation is spread by a fixed grating across the diode array detector, so that a definite wavelength range is directed toward each detector element. Diode arrays usually consist of 256 or 512 InGaAs and InSb detector elements. The spectral resolution depends on the number of elements in the array and the wavelength range. The great advantage of these spectrometers is the possibility of miniaturization. Such spectrometers can fit on a PC plug-in card. NIR radiation is delivered from the lamp via sample to the detector by optical fiber cables (single fiber of 50–1000 μm diameter or bundles of up to 80 single fibers). If the wavelengths to be investigated are known in advance, one may use a set of bandpass filters to send radiation of only discrete wavelengths through the sample to the detector array.

4.2.4
Filter Spectrometers

These may have several filters mounted on a rotating wheel. The wheel has either a set of filters with predefined wavelength regions for a specific application or a customary set of filters for the NIR region of interest. The advantages of these spectrometers are their robustness and low cost.

4.2.5
LED Spectrometers

These work at predefined wavelengths, they have no moving parts. Because LEDs emit radiation of discrete wavelengths, these instruments do not need any wavelength selector (filter, monochromator, etc.). Additional interference filters can be used in order to limit the spectral bandwidth (SBW). Advantages are the possibility of miniaturization and the high stability of these light sources.

4.2.6
AOTF Spectrometers

These are built around a birefringent crystal, which is used for rapid and precise wavelength selection. Usually it is a TeO_2 crystal with one or more piezoelectric transducers. The working principle is based on a phonon–photon scattering mechanism. Broadband randomly polarized light is incident on the AOTF crystal, where it is separated into ordinary and extraordinary polarized components. When radio frequency acoustic waves are coupled into the crystal via a piezoelectric transducer, the refractive index is spatially modulated, producing a phase grating that diffracts one specific wavelength of the incident light. This light is symmetrically deflected into two orthogonal polarized beams on exit from the crystal, one of which is imaged on to the detector; all other wavelengths travel through the crystal without being diffracted along the incident ray. By changing the frequency of acoustic waves, the wavelength of diffracted light is changed. Spectral resolution depends on the size of the crystal. Advantages of such a spectrometer over a filter wheel or a grating monochromator include high resolution, high speed, random or sequential wavelength access, no moving parts, compact size, and imaging capabilities. A disadvantage is the high cost of the instrument.

Some types of the described spectrometers can be applied for NIR imaging purposes. FT-NIR and AOTF imaging spectrometers are already available on the market.

4.3
Terahertz Spectrometers

THz spectral instruments differ significantly from those for NIR, IR, and FIR spectroscopy. Figure 4.4 shows a typical schematic setup for coherent THz time-domain spectroscopy. The major components of a THz time-domain spectrometer are a femtosecond laser, a THz emitter, and a THz detector. Additionally needed are focusing and collimating optics for laser and THz radiation, a motorized delay line,

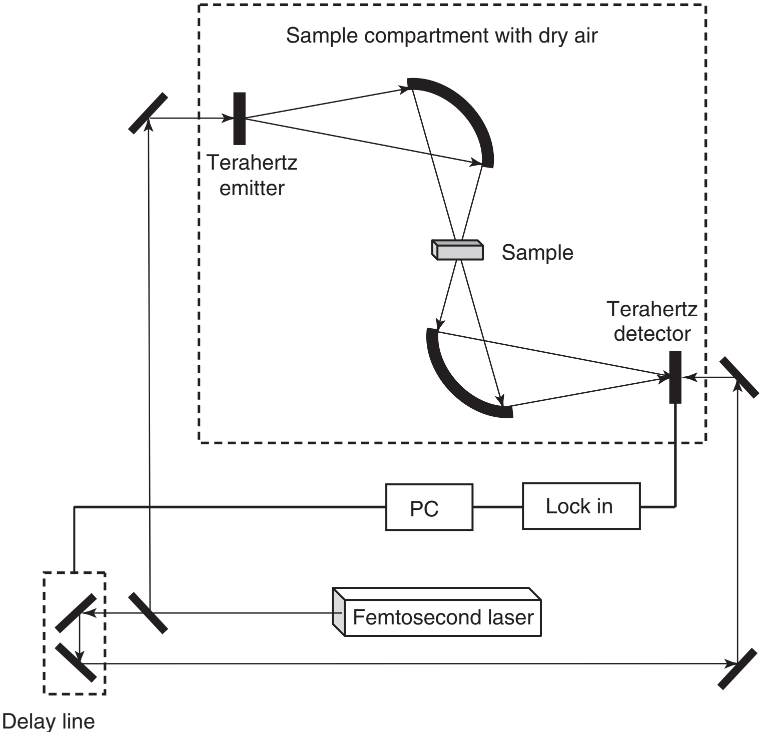

Figure 4.4 Setup of a terahertz spectrometer.

a lock-in amplifier, and a data acquisition system (PC). In contrast to conventional IR spectroscopy, THz radiation sources generate pulsed and coherent radiation. The THz source works like a photoconductive semiconductor antenna. When a femtosecond laser pulse is absorbed at the surface of a semiconductor, a single cycle THz transient is emitted. The surface of some semiconductors (for instance, InAs crystals) is a very efficient generator of THz radiation.

Neither a monochromator nor an interferometer is needed to obtain a THz spectrum. After Fourier transformation of the signal before the sample (reference) and after sample (reflection or transmission), the THz absorbance spectrum is obtained. Measured quantities are amplitude and phase of the THz pulse reflected by or transmitted through the sample. Therefore, both the absorption coefficient and the refractive index of the sample are measured directly.

4.4
Raman Spectrometers

Raman spectrometers are used to analyze light scattered by molecules. A major advantage of Raman spectroscopy is the high spatial resolution that can be obtained, typically in the order of 1 μm (compared to approximately 10 μm in case of IR).

In conventional Raman experiments, the sample is illuminated by monochromatic light. The registration of low-intensity Raman scattering in the presence of strong Tyndall and Rayleigh scattering implies special requirements to Raman spectrometers. A Raman spectrometer has to combine very good filter characteristics for eliminating Rayleigh and Tyndall scattering with high sensitivity for detecting very weak Raman bands. Currently, there are three types of Raman instruments available on the market:

1) Raman grating spectrometer with single channel detector
2) FT-Raman spectrometer with NIR excitation
3) Raman grating polychromator with multichannel detector.

All three types of the instruments have particular advantages and disadvantages for a given analytical task.

4.4.1
Raman Grating Spectrometer with Single Channel Detector

The Raman grating spectrometer with single channel detector is the conventional type of Raman instruments. It consists of three main parts: a monochromatic light source, a grating monochromator, and a single-channel detection system. Light sources in Raman spectrometers are lasers. The laser power impinging on the sample may vary between 10 and 1000 mW depending on the thermal stability of the latter. The laser may be continuous or quasi-continuous. The longer the wavelength of the laser the lower is the probability of generating fluorescence. On the other hand, the Raman scattering intensity diminishes proportional to the

Table 4.2 Lasers used with dispersive Raman instruments.

Laser	Type	Type of radiation	Wavelength (nm)	Maximum power (W)	Beam diameter (mm)	Price; comments
Ar^+	Gas	CW	488.0 514.5	4 4	1.5	Medium; standard source
Kr^+	Gas	CW	647.1 725.5	4	1.8	Medium; standard source
He–Ne	Gas	CW	632.8	0.05	1.1	Low; not intense
Liquid dye	Liquid	CW, pulsed, tunable	Depends on dye	0.1		Low; used mainly for RRS
Ti-sapphire	Solid	CW, pulsed, tunable	720–980	2	0.95	High; used mainly for RRS
Diode	Solid	CW	700–900	0.5		Very low; modern source

RRS, resonance Raman scattering.

fourth power of the laser wavelength. A list of most frequently used lasers in dispersive Raman instruments is given in Table 4.2.

Lasers with short pulses are not used in Raman spectrometers, mainly because detectors in Raman spectrometers are tuned to high sensitivity. Such detectors are very easy to saturate and this is a case when short and intense laser pulses are employed for excitation of Raman scattering. It must be noted, that gas lasers are not perfect sources of monochromatic radiation. Together with intense coherent radiation such lasers produce weak incoherent radiation, caused by different transitions between electronic energy levels of the gas. The intensity of this incoherent and noncollimated radiation can be suppressed by increasing the distance between the laser and the sample, by placing a spatial filter (consisting of two lenses and a pinhole) or a narrow-band filter (usually an interference filter) in to the laser beam.

The monochromator is the main part of a grating Raman instrument. Single monochromators should not be used in Raman spectrometers because of their insufficient performance in eliminating Rayleigh and Tyndall scattering. Instead, double or even triple monochromator systems are well suited. The common configuration for double monochromator systems is the so-called Czerny–Turner arrangement (Figure 4.5). Two identical monochromators are placed in such a way that their angular dispersions are coadded (additive mode). The slit between monochromators (intermediate slit) acts as a filter to prevent stray light from the first monochromator to enter the second one. In general, entrance, intermediate, and exit slit widths in a double monochromator Raman spectrometer are of the same size. A triple monochromator is preferred when very low-frequency Raman bands (frequency range close to laser frequency) have to be recorded. In addition

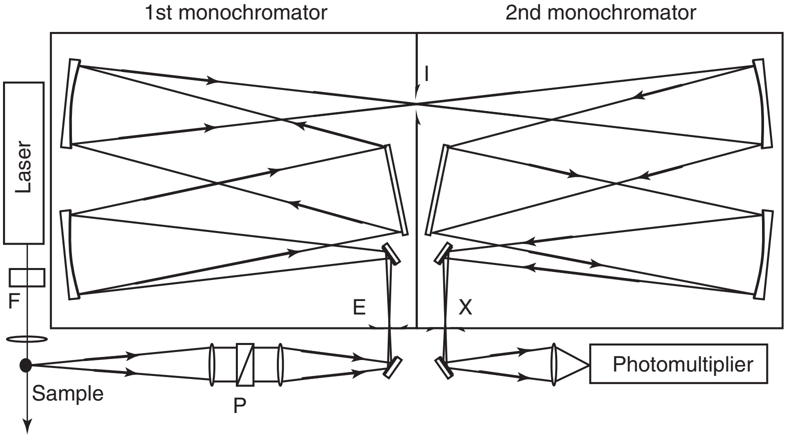

Figure 4.5 Dispersive grating Raman spectrometer with a single channel detector and double monochromator in Czerny-Turner configuration. F, narrow band filter; P, polarizer; E, entrance slit; I, intermediate slit; X, exit slit.

to their very low stray light level, triple monochromators in additive mode have high angular dispersion and permit the recording of Raman spectra with very good resolution.

4.4.1.1 **Detectors**

Detectors are crucial parts of Raman spectrometers because of the low intensity of Raman bands. Photomultipliers have excellent characteristics in ultraviolet and visible spectral regions; hence, they are preferred detectors in single-channel dispersive Raman spectrometer. The sensitivity of photomultipliers is limited by their dark current (residual electrical detector signal observed in the absence of any light). Dark current increases with temperature, that is, cooling increases the signal-to-noise ratio of photomultipliers. Liquid N_2 cooling provides the best performance, but for routine Raman experiments Peltier cooling often is sufficient.

4.4.1.2 **Calibration**

In case of dispersive instruments, the Raman spectrum is obtained as a function of the rotation of the dispersive element (prism or grating). In modern dispersive Raman instruments, a cosecant drive mechanism is used (usually, stepping motor), which provides a nearly linear relation between grating angle and Raman shift scale. In all cases, a calibration of the Raman shift scale by recording a well-known spectrum with narrow spectral bands is necessary. Atomic emission spectra are well suited as well. Very often an ordinary neon lamp is used, whose emission lines are narrow, intense, and distributed over a wide range in the visible. The line positions can be found in any catalog of atomic emission spectra. A frequently used calibration is the use of plasma lines of the Raman excitation laser itself: after setting up the Raman experiment, the laser resonator mirrors are slightly deadjusted. Under

Table 4.3 Intensities and positions of plasma lines of the Ar^+ laser.

Relative intensity (a.u.)	Wavelength, λ (nm) (in air)	Wavenumber, $\tilde{\nu}$ (cm^{-1})	Raman shift, $\Delta\tilde{\nu}$ (cm^{-1}) ($\lambda_{exc} = 488.0$ nm)	Raman shift, $\Delta\tilde{\nu}$ (cm^{-1}) ($\lambda_{exc} = 514.5$ nm)
1120	487.9860	20 486.67	0	
25	488.9033	20 448.23	38.4	
16	490.4753	20 382.70	104.0	
121	493.3206	20 265.13	221.5	
14	494.2915	20 225.33	261.3	
1	495.5111	20 175.53	311.1	
120	496.5073	20 135.07	351.6	
41	497.2157	20 106.39	380.3	
190	500.9334	19 957.16	529.5	
77	501.7160	19 926.03	560.6	
155	506.2036	19 749.39	737.3	
1	509.0496	19 638.98	847.7	
45	514.1790	19 443.06	1043.6	
125	514.5319	19 429.73	1056.9	0
1	516.2745	19 364.14	1122.5	65.6
4	516.5774	19 352.79	1133.9	76.9
5	517.6233	19 313.69	1173.0	116.0
3	521.6816	19 163.44	1323.2	266.3
18	528.6895	18 909.43	1577.2	520.3
2	530.5690	18 842.45	1644.2	587.3
2	539.7522	18 521.87	1964.8	907.9
1	540.2604	18 504.45	1982.2	925.3
1	540.7348	18 488.21	1998.5	941.5
2	545.4307	18 329.04	2157.6	1 100.7
2	549.5876	18 190.47	2296.2	1 239.3
2	549.8185	18 182.76	2303.9	1 247.0
2	550.0334	18 175.66	2311.0	1 254.1
3	555.4050	17 999.88	2486.8	1 429.8
3	555.87031	17 984.81	2501.9	1 444.9

such conditions, the laser emits weak atomic radiation, whose intensity is usually strong enough to obtain an atomic calibration spectrum. Intensities and positions of plasma spectral lines of the Ar^+ laser are listed in Table 4.3.

4.4.2
FT-Raman Spectrometers with Near-Infrared Excitation

Interferometers are superior to monochromators in obtaining spectra of electromagnetic radiation, but technical problems prevent interferometers from being used in routine spectrometers at wavelengths shorter than NIR. Fortunately, Raman excitation by NIR radiation is just possible (λ^{-4} law, cf. Section 3.3).

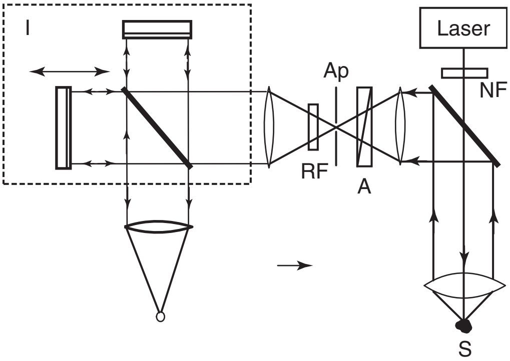

Figure 4.6 Basic diagram of an FT-Raman spectrometer. S, sample; NF, notch filter for rejecting not lasing radiation from laser; A, analyzer; RF, Rayleigh filter for rejecting radiation at laser frequency; Ap, aperture wheel; I, interferometer.

The laser in FT-Raman spectrometers (Figure 4.6) is the continuous wave Nd^{3+}/YAG system operating at 1064 nm with output power up to 2000 mW. The laser is optically pumped by either a lamp or a diode system. In both cases, nonlasing lines are generated. They have to be removed by very effective notch filters (NFs); otherwise, they get mixed up with the Raman spectrum and produce the so-called laser line artifacts.

The scattered radiation in an FT-Raman spectrometer contains Rayleigh and Tyndall radiation at laser frequency. Usually, scattered radiation at laser frequency is up to eight orders of magnitude more intense than the Raman scattering; hence, it can cause satusration or even damage of the detector. A so-called Rayleigh filter (RF) for filtering out radiation at laser frequency is an obligatory part of any FT-Raman spectrometer. The best RFs have a cut-off frequency closer than 50–40 cm^{-1} to the exciting laser frequency. RFs remain the main limiting factor, preventing application of FT-Raman spectrometers in low-frequency Raman spectroscopy.

4.4.3
Raman Grating Polychromator with Multichannel Detector

Conventional multichannel Raman instruments consist of a double monochromator working in the subtractive mode and a polychromator (Figure 4.7). The double monochromator acts as a filter for rejection of stray light at laser frequency. Common detectors in such instruments are nitrogen-cooled charge-coupled device (CCD) cameras with up to 1024 pixels in a row. This limited number of the pixels in a row does not allow to fully exploit the spectral resolution power of the polychromator in only one measurement. In order to obtain a complete Raman spectrum with spectral resolution 1 cm^{-1}, the spectrum should be measured with the above-mentioned configuration in at least four steps by measuring spectral intervals up to 1000 cm^{-1} and mechanically rotating the monochromator grating between measurements. After completion of the successive measurements, the

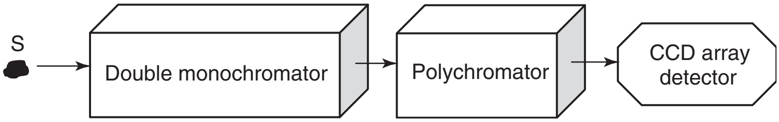

Figure 4.7 Block diagram of a conventional multichannel Raman spectrometer. S, sample. *Note*: the double monochromator is operating in subtractive mode.

spectra from different spectral regions are merged together by the instrument's software. In this kind of multichannel Raman instruments, rather sophisticated mechanical systems for rotating of gratings and changing opening of the slits of monochromators and spectrograph are used.

Recent achievements in the design of NIR diode lasers, of volume-phase transmission multiplexed holographic gratings and of sensitive CCD arrays allow to build very efficient multichannel Raman grating spectrometers, which can be considered as a new class of Raman instruments. In such modern spectrometers, a small holographic NF is used to reject the stray light at laser frequency instead of a large double monochromator (Figure 4.8). The reflectivity of the NF is very high and its bandwidth very narrow. The transmission at the center of the notch is less than 0.0001% and half maximum of the notch corresponds to 175 cm^{-1}. An NF is usually operated at normal incidence. Tilting the filter at a small angle (typically 15°) shifts the rejection band to lower frequencies. This allows one to use the NF line for low-frequency Raman applications as close as 40 cm^{-1} to the exciting laser. The conventional spectrograph is replaced by holographic transmission gratings. Several of such gratings may be assembled in order to extend the operating range of the system. Each grating may deflect the light to different areas on the CCD array detector. In such a way, modern multichannel Raman instruments permit the acquisition of complete Raman spectra at a spectral resolution of 2 cm^{-1} at once without rotating any grating.

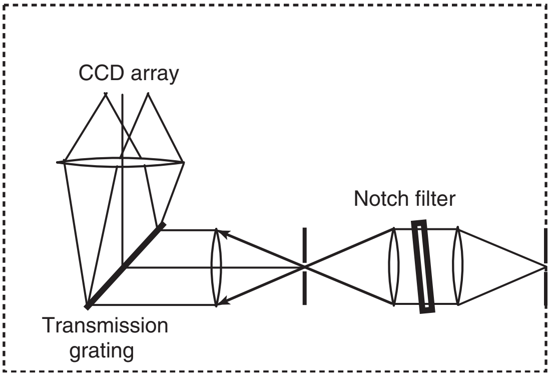

Figure 4.8 Basic diagram of an axial transmissive multichannel Raman instrument.

4.4.4
Handheld Raman Spectrometers

Recently, a new class of portable Raman instruments – the so-called handheld Raman spectrometers – was introduced to the market. The development of handheld Raman spectrometers has drastically changed the way (i) industry conducts quality control for incoming raw materials and (ii) security scans are performed. Such spectrometers permit tests of samples directly through transparent packing material such as glass or plastic. This approach minimizes risks of exposure and contamination of the material under study.

Handheld Raman spectrometers are based on grating polychromators equipped with CCD detectors. These spectrometers usually have no moving parts and the whole spectrum can be acquired at once. Their technical parameters are comparable to bench top Raman spectrometers, and they perform sufficiently well for express analysis of chemical materials. Typical parameters of handheld Raman spectrometers are summarized in Table 4.4.

The general layout of handheld Raman spectrometers is presented in Figure 4.9. The Raman signal is collected from the focal point of the microscope objective (located at working distance of the spectrometer), which focuses the laser beam on the surface of the sample under investigation. A long-wave pass (LWP) filter insures that only Stokes-Raman scattered light enters the grating polychromator. If the sample is packed, usually the packing material does not touch the sample surface and the laser beam remains unfocused across the packing material, which ensures only very weak Raman signals of the packing material. This signal does not disturb the Raman signal of the sample under investigation. When packed samples have to be analyzed with the handheld Raman spectrometer, the main requirement is the transparency of the packing material to the laser light at 785 nm.

Handheld Raman spectrometers are usually equipped with various accessories – sample holders, fibers, and probes – for measuring Raman spectra of samples in liquid, amorphous, and crystalline states.

Table 4.4 Typical parameters of handheld Raman spectrometers.

Raman spectral range (Raman shift)	170–2900 cm^{-1}
Spectral resolution	From 7 to 11 cm^{-1}
Excitation laser	Diode laser at 785 nm
Laser power	Up to 300 mW
Working distance	116–200 mm
Laser spot diameter	0.2–2.5 mm
Detector	Thermoelectrically cooled linear CCD array
Weight	1–2 kg
Maximal working time on battery	Up to 5 h

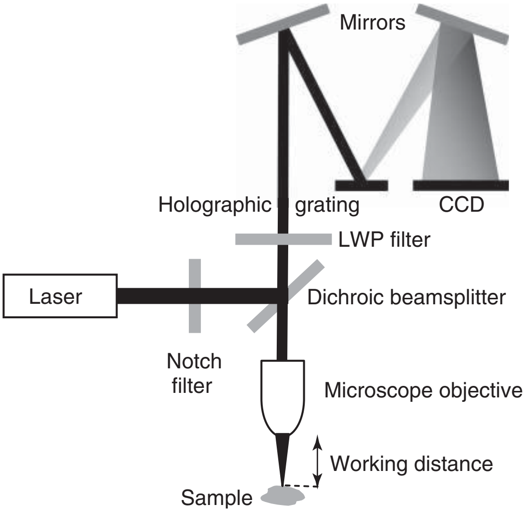

Figure 4.9 General schematics of a handheld Raman spectrometer.

4.5
UV/vis Spectrometers

The UV/vis spectral region extends from 190 to 400 nm (UV range) and from 400 to 780 (visible range). In order to obtain complete spectra in the UV/vis range, dual beam dispersive scanning instruments or dispersive multichannel instruments are employed. UV/vis scanning spectrometers consist of a light source, a monochromator, a chopper (rotating sector mirror or rotating sector disk) to generate a sample and a reference beam as well as to recombine them, a sample and reference compartment, and a detector (Figure 4.10). Spectrometers, which permit a synchronous measurement of sample and reference beams, are denoted double-beam instruments (cf. Section 4.1.1). Note the position of sample and reference after the monochromator in this type of UV/vis spectrometer. There they are substantially less exposed to the high-energy UV radiation than directly after the source. The disadvantage of this optical layout is its sensitivity to ambient stray light, which may directly reach the detector if the sample chamber is not fully covered.

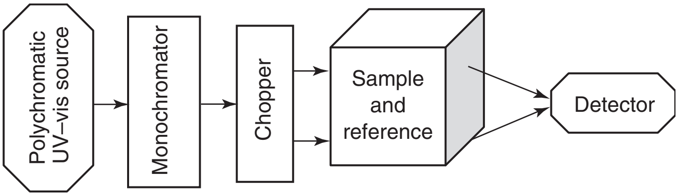

Figure 4.10 Block diagram of a UV/vis scanning spectrometer.

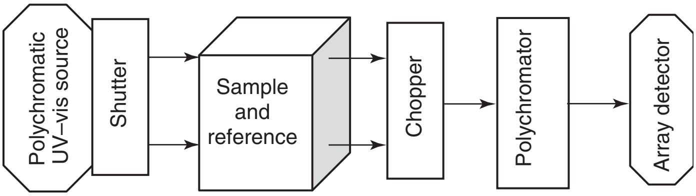

Figure 4.11 Block diagram of a UV/vis multichannel spectrometer.

A multichannel spectrometer has a light source with shutter, a sample and reference compartment, a grating polychromator, and a diode array detector (Figure 4.11). All spectral elements are recorded simultaneously by the array detector, that is, the measuring time with the shutter in its open position is very short. The short illumination time permits the sample and reference positions immediately after the light source. Multichannel spectrometers may also be constructed as double-beam instruments. For special measurements, for example, rapid kinetic investigations, when the chopper frequency is too low with respect to the speed of the process under investigation, double-beam instruments with two separate detectors are used.

UV/vis absorption spectra may be obtained with single-beam instruments as well. In single-beam spectrometers, the background and sample spectra are measured one after the other. As chopper and reference chamber are not needed, single-beam instruments are usually cheaper than double-beam instruments.

4.5.1
Sources

The most used light sources are deuterium lamps in the region from 180 to 350 nm and tungsten filament and halogen lamps in the region from 330 to 900 nm. A light source for the complete range is the xenon arc from 175 to 1000 nm. Furthermore, for special applications such as high-resolution studies, tunable lasers can be used. For time-resolved measurements, pulsed arc lamps can be used.

4.5.2
Monochromators

The cheapest versions for dedicated applications are filter monochromators. Monochromators in routine spectrometers usually have a prism or diffraction grating. The complete spectrum can be measured by turning the prism or grating. The slit width and the dispersion of the monochromator determine the SBW. The SBW of single monochromators does not extend below 5 nm. For applications that require higher resolution, the use of double monochromators with SBWs down to 1 nm is necessary. In addition, double monochromators improve the stray light rejection and allow measurement of samples with high optical density. The drawback of double monochromator systems is their lower optical throughput, which deteriorates the signal-to-noise ratio.

4.5.3
Detectors

Standard UV/vis detectors are photomultipliers and silicon diodes. Silicon diodes are smaller and cheaper, whereas photomultipliers have a higher sensitivity. Most research instruments are based on photomultipliers. The recent development is the use of photomultiplier arrays and CCD cameras as in all other spectroscopic methods.

An important consideration for all types of instruments is the linear absorption range, that is, maximum absorption measured at a predetermined accuracy. The photometric accuracy depends on the instrument's electronics, which may be sensitive to ambient temperature and humidity. Spectrometers should be calibrated from time to time. Commonly used for absorbance calibration are neutral density filters of well-defined absorbance. Solutions of potassium chromate and potassium dichromate are also widely used as reference standards for validating the photometric scale. Current estimations for linear absorption limits are 1 absorption unit for multichannel instruments or scanning dispersive instruments with single monochromator, and 2.5 absorption units for dispersive instruments with double monochromator.

The exit beam from the monochromator includes some amount of unwanted stray radiation. This is partly caused by imperfections in the diffraction grating (or prism) and partly by undesired reflections at optical surfaces. For accurate results of the measurements, it is vital to use a spectrometer with stray light levels as low as possible. Hence it is desired to have a method for measuring such levels. The usual method for the measurement of stray light in a spectrometer is to insert into the optical path a blocking filter that absorbs nearly completely at the wavelength of interest while passing radiation at other frequencies unattenuatedly. A signal observed by the detector under these conditions at the wavelength of interest is due to stray radiation. Materials for checking and calibration of UV/vis spectrometers recommended by the U.S. National Bureau of Standards are listed in Table 4.5.

As in case of dispersive Raman spectrometers (cf. Section 4.4.1), it is necessary to calibrate the wavelength scale of dispersive UV/vis spectrometers. The most accurate standards for checking the UV/vis wavelengths are lasers of various types. The inexpensive helium–neon laser can be used to check at 632.8 nm. For spectrometers with a deuterium source, spectral lines at 486.6 and 656.1 nm can be used for calibration. A common method for wavelength calibration is the use of optical filters. A filter of didymium glass has many sharp absorption peaks, which can be used as a second wavelength standard (precision within 0.5 nm).

If measurements have to be done in the UV region below 240 nm, it is necessary to purge the spectrometer with dry nitrogen gas in order to remove oxygen. Oxygen absorbs at wavelengths shorter that 240 nm and is transformed into ozone. Absorption by oxygen molecules inside an instrument can make measurements

Table 4.5 Standard reference materials (SRMs) for UV/vis spectrophotometry used at the National Bureau of Standards (NBS).[a]

SRM number	Type	Parameter checked	Wavelength range (nm)
930Dmm	Glass filters	Transmittance	440–635
931d	Liquid filters	Absorbance	302–678
932	Quartz cuvette	Pathlength	—
935	Potassium dichromate	UV absorbance	235–350
2009	Didymium-oxide glass	Wavelength	400–760
2031	Metal-on-quartz filters	Transmittance	250–635
2032	Potassium iodide	Stray light	240–280
2034	Holmium oxide solution	Wavelength	240–650
936	Quinine sulfate dihydrate	Fluorescence	375–675

[a] A more complete description can be found in R. Mavrodineanu, J.I. Schultz, and O. Menis, *Accuracy in Spectrophotometry and Luminescence Measurements*, National Bureau of Standards Special Publication 378, National Bureau of Standards, Washington, DC, 1973.

below 240 nm meaningless. Moreover, ozone is very reactive and can cause damage to optical and mechanical components of the spectrometer.

4.6
Fluorescence Spectrometers

Basically, instruments for measuring fluorescence and phosphorescence spectra have similar construction and should be called *luminescence spectrometers*. But the group of molecules that exhibit fluorescence is by far larger than that exhibiting phosphorescence; hence, the term *fluorescence spectrometer* is used. The main spectral features of luminescence are spectral distribution, polarization, and radiation lifetime. For analytical purposes, mainly spectral distribution and polarization are used. Measuring of the lifetimes requires rather sophisticated time-resolved spectroscopic techniques. The latter is very seldom used for analytical purposes and will not be discussed in this chapter.

Two basic types of spectra can be produced by a conventional fluorescence spectrometer. In the emission spectrum, the wavelength of the exciting radiation is held constant (at an absorption wavelength of the analyte) and the spectral distribution of the emitted radiation is measured. In the excitation spectrum, the fluorescence signal is measured at a fixed wavelength of the emission selector, as the wavelength of the exciting radiation is varied. An analyte can fluoresce only after it has absorbed radiation, and an excitation spectrum identifies the wavelengths of light that the analyte is able to absorb. Thus, the excitation spectrum of a molecule should be the same as its UV/vis absorption spectrum.

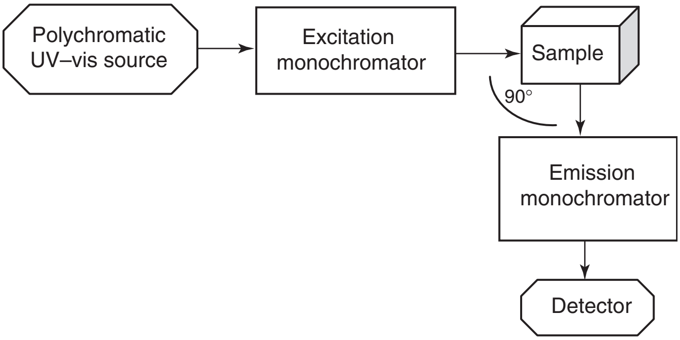

Figure 4.12 Block diagram of a fluorescence spectrometer.

A general layout of a fluorescent spectrometer is shown in Figure 4.12. The instrument contains the source of UV/vis radiation, an excitation wavelength selector, an emission wavelength selector, a sample chamber, and a detector. Basically this is a single beam instrument. The fluorescence emitted by the sample is usually measured at 90° in order to avoid disturbances by nonabsorbed excitation radiation.

The excitation wavelength selector can be either a filter or a monochromator. Filters offer better detection limits, but do not provide spectral scanning capabilities. Often, a filter is used in the excitation beam along with a monochromator in the emission beam to allow emission spectra to be acquired. Full emission and excitation spectral information can be acquired only if monochromators are used in both the excitation and emission beams. In modern instruments with array detectors, a polychromator is used in the emission beam instead of a monochromator. Recent research instruments are able to scan both excitation and emission automatically and combine all data into a 2D excitation–emission spectrum. In lifetime spectrometers, a pulsed light source and a gated detector are synchronized in order to measure the time dependence of the luminescence emission.

The luminescence intensity is directly proportional to the intensity of the light source, and a high-intensity light source can therefore be used to increase the sensitivity and to lower the detection limits for luminescence analyses. The xenon arc lamp is a commonly used source. The Xe lamp emits continuously over a broad wavelength range and is therefore well suited for spectral scanning. Another common source is the high-pressure mercury arc lamp. Its output is a continuum with a line spectrum superimposed, making the mercury lamp better suited to nonscanning filter instruments. Other sources include halogen lamps and combined xenon-mercury lamps. Lasers are also used in luminescence experiments, in which continuous scanning of excitation is not required. Tunable lasers can be used to provide multiwavelength excitation capabilities. The excitation laser beam must often be greatly attenuated in order to avoid photodecomposition of the sample.

Pulsed sources, including both lamps and lasers, are used for special applications such as dynamic measurements of luminescence lifetimes and time-resolved elimination of background signals.

Photomultiplier tubes (PMTs) are the most commonly used detectors, and various types are available for different applications. In general, they are sensitive in the range from 200 to 600 nm, with maximum sensitivity obtained in the 300–500 nm range. Red-sensitive PMTs are also available for investigations beyond 600 nm. The PMT housings are sometimes cooled to temperatures as low as −40 °C to minimize temperature-dependent noise.

Among the more commonly used multichannel detectors are diode arrays, vidicons, silicon intensified target vidicons, CCD and charge-injection devices, and numerous other devices made available by recent technological advances. The use of multichannel detectors in fluorescent spectrometers has increased the range of applications of luminescence experiments to include real-time experiments, kinetic measurements, and on-line detection for chromatography and other flow systems. The ability to acquire complete spectral information nearly instantaneously has also greatly facilitated qualitative analysis by reducing the time required per analysis.

Fluorescence spectrometers can be used to measure fluorescence polarization by placing polarizers in the excitation and emission beams. High-quality instrumentation for polarized fluorescence measurements is commercially available.

As most fluorescence spectrometers are single-beam instruments, different kinds of distortions may be found in excitation and emission spectra. These distortions are mainly due to variations of source power or detector sensitivity with wavelength. Spectra of the same sample obtained using two different fluorescence spectrometers may therefore be quite different. Even changing the source or detector in a spectrometer may alter the apparent fluorescence or excitation spectrum of a compound. These artifacts can be eliminated instrumentally, and several instruments that can produce corrected spectra are commercially available. Unfortunately, most published spectra are uncorrected; they cannot be fully reproduced by other investigators. There exist only few extensive and broadly used databases of fluorescence spectra.

4.7
Spectral Imaging Devices

A spectral image of some area of a sample can be obtained using one of two experimental approaches: (i) only a very small sample area is illuminated by the light beam and the light-response from the sample is collected by a single detector and (ii) the whole area of interest is illuminated by the light beam and the light-response from the sample is collected by a two-dimensional detector array (FPA). In the former case, a spectral image can be composed after measuring at one point and subsequently moving the sample step by step by a motorized x,y stage. The point-by-point measurement of a spectral image is correctly called *spectral mapping* (Figure 4.13a). In the latter case, a complete spectral image is directly delivered by the detector array (Figure 4.13b). If small samples or small areas of interest are to be imaged, a microscope is necessary in order to focus the sensing light beam precisely and to select the sample area for imaging exactly. Usually, commercial IR

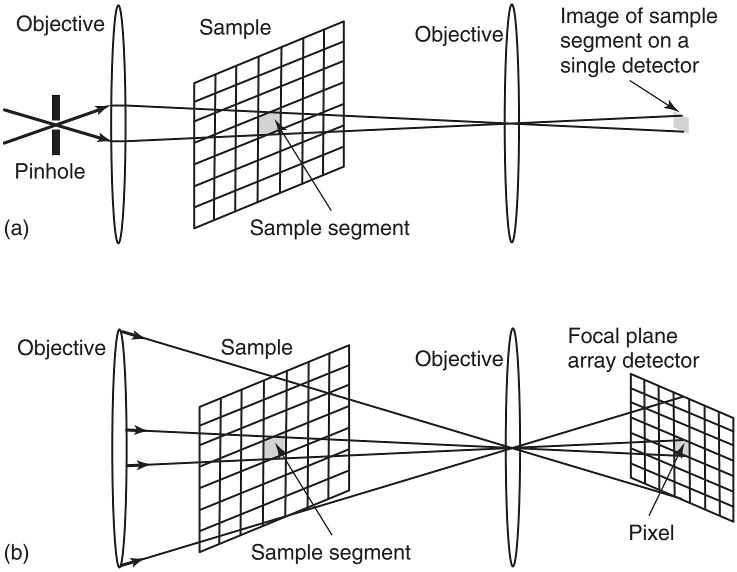

Figure 4.13 Simplified drawing of the concepts of (a) spectral mapping with a single detector and (b) spectral imaging with a focal plane array detector.

microscopes can be used in both modes – mapping and imaging. Larger samples can either be placed in the usual position in the sample chamber and imaged at a relatively low spatial resolution or they can be placed under the microscope, and the area of interest can be covered by a sequence of small images at high spatial resolution. This procedure is often called *tiling*.

The layout of the required microscope strongly depends on the spectral experiment. An example of an experimental setup for the imaging in NIR and MIR spectral regions is presented in Figure 4.14. This setup is rather common nowadays.

The instrument consists of a commercially available IR Michelson-type step-scan interferometer coupled to an IR microscope. Two identical IR objectives are used to illuminate the sample and to collect the signal. The IR objectives consist of mirrors in Cassegrainian configuration in order to reduce the required focal length and to maintain perfect focusing throughout the whole IR spectral region. Moreover, Cassegrainian objectives in comparison to conventional ones do not suffer from absorption within the objective material. The signal is detected either by an MCT detector for the MIR spectral region or by an indium antimonide detector for the NIR spectral region.

FT-IR imaging simultaneously collects full IR spectral data from a wide sample area. The FPA detector is an IR camera consisting of many single detectors. Typical array sizes of the FPA detectors are 32 × 32, 64 × 64, 128 × 128 detector elements. An IR spectroscopic image can also be obtained with a linear array of individual detectors (16 × 1 up to 256 × 1 detector elements) in combination with an x,y scanner to produce a spectroscopic map. Linear array detectors may be advantageous in case of small sample areas, which can be captured rapidly.

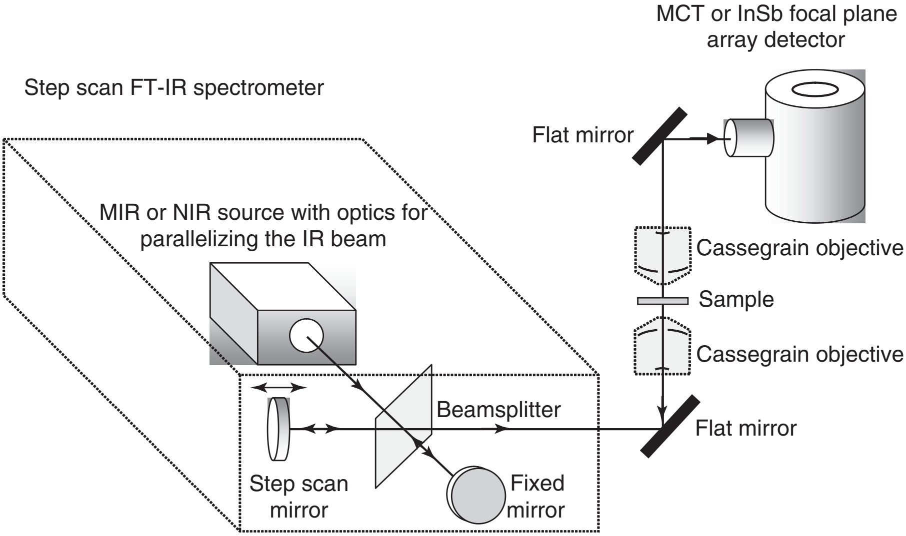

Figure 4.14 Block diagram of an FT-IR imaging spectrometer.

In standard IR microscope configurations, the array detector comes as 64 × 64 pixel array, but higher resolution FPA detectors are already available on the market. Each of the 4096 pixels of a 64 × 64 FPA detector provides a full FT-IR spectrum. In case of standard 15× Cassegrainian objectives, each pixel covers approximately a 7–8 μm^2 sample area. Consequently, 4096 spectra are recorded simultaneously from a 170 μm × 170 μm sample area at a diffraction limited spatial resolution of 10 μm at a wavenumber of 1500 cm^{-1} or at correspondingly higher resolution at higher wavenumbers.

Reading data from a 64 × 64 or larger FPA array is a time-consuming process, because frame rates (time to read one complete image) do not exceed a couple of kilohertz. This is much too slow to capture the interferogram produced by a continuously scanning interferometer with sufficient precision. For this reason, a step-scan interferometer has to be used. The step-scan process involves data collection at exact time intervals during the cycle of mirror displacement. Unlike the continuous process that collects frequency data continuously as a function of time and mirror displacement, frequency data are collected on a step-scan optical bench at each step for a fixed time through the displacement sequence.

There are a couple of sample handling modes available in IR imaging. This includes specular reflection, attenuated total reflection, and grazing angle reflection. A special objective is required for each imaging mode. The objectives can be obtained from manufacturers of IR microscopes. The imaged area of the sample can be increased either by tiling (see preceding text) or by using objectives with lower magnification together with a so-called macrochamber – a special compartment that accommodates the sample and the objectives.

4.8
Instrumentation for Nonlinear Vibrational Spectroscopy

Recent advances in laser technology made high-power tunable lasers available at moderate prices. This development provides easier access to investigation of various spectroscopic multiwave mixing processes. Hyper Raman scattering (HRS), stimulated Raman scattering (SRS), second harmonic generation (SHG), SFG, and coherent anti-Stokes Raman scattering (CARS) are typical examples of such experiments. Some of them already found application in spectroscopic and spectromicroscopic structural studies of biological samples. Compared to conventional (linear) methods such as IR absorption and spontaneous Raman scattering (cf. Section 3.3), the main advantage of nonlinear methods of vibrational spectroscopy is their extremely high sensitivity. This enhanced sensitivity enables the investigation of smallest amounts of substance (low concentrated solutions, ultrathin films, interfaces) or permits mapping of chemical images. Some nonlinear spectroscopic setups are already commercially available. This is particularly true for SRS, SFG, and CARS spectrometers. General features of their setups are presented in subsequent text.

4.8.1
Stimulated Raman Scattering (SRS) Spectrometers

SRS is quantum mechanically described as a two-photon stimulated process where one pump photon at ν_p is annihilated (stimulated Raman loss (SRL)) and one Stokes photon at ν_t is created (stimulated Raman gain (SRG)), while the Raman medium makes a transition from the lowest vibrational state to the vibrationally excited state. SRS then appears in the form of a gain or a loss of the Stokes and pump laser beams on the sample, when the difference in laser frequencies matches a particular molecular frequency. An energy-level diagram for the SRS four-wave mixing process is presented in Figure 4.15a. When the difference frequency does not match any molecular frequency, no signal is generated. Thus, the SRS spectrum is essentially identical to a conventional Raman spectrum, making spectral assignment much easier than in CARS. Similar to CARS microscopy, SRS microscopy allows three-dimensional imaging of specific molecular species to a depth of about 0.3 mm.

The general experimental layout of an SRS microscope is schematically depicted in Figure 4.15b. The pump and Stokes pulse trains are provided by two electronically synchronized lasers (usually Ti:sapphire lasers). The wavelengths of both lasers are independently tunable. Both the pump and Stokes beams are expanded to fill the back aperture of the microscope objective before being combined on a dichroicbeam combiner (BC) and directed into a microscope. A microscope objective is used to focus the collimated and collinear pump and Stokes beams into the sample. The transmitted pump beam is collected in the forward direction by a second objective and spectrally isolated from the Stokes beam by a stack of short-pass filters.

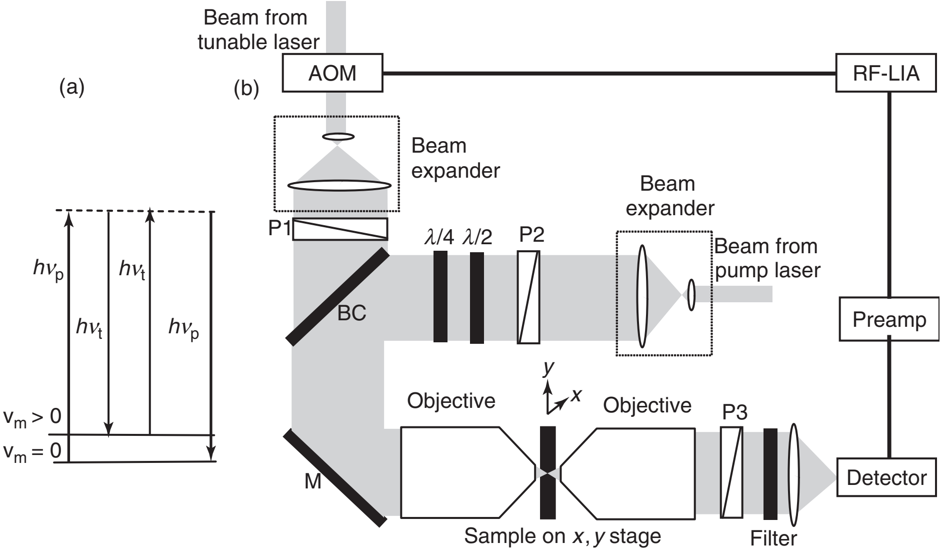

Figure 4.15 (a) Transitions between molecular energy levels during SRS: ν_p, frequency of high-power pump laser; ν_t, frequency of tunable laser; ν_m, quantum number of *m*-vibrational mode; (b) Layout of an SRS microscope: BC, dichroic beam combiner; P, polarizer; M, mirror; λ/2 and λ/4, phase plates; AOM, acousto-optical modulator; Preamp, preamplifier; RF-LIA, radiofrequency lock-in amplifier.

It is crucial to modulate the Stokes beam in the SRL experiment. The SRL (or SRG) in an SRS experiment is very small in comparison to the laser intensity. Therefore, the SRS signal cannot be measured directly. High-frequency modulation of tunable laser modulation has to be used. In the modulated signal, the AC component is proportional to SRS signal while the DC component is proportional to the tunable laser intensity. For the modulation, an acousto-optical modulator (AOM) operating at a frequency of a couple of megahertz is used. The modulation of the pump intensity due to SRL is detected by a diode detector, a current preamplifier, and a radiofrequency lock-in amplifier (RF-LIA). The SRS images can be collected by raster scanning the sample, using an *x,y,z* piezo-driven scanner, which limits pixel dwell times to a few milliseconds. The scanning can be significantly speeded up when laser beam-scanning schemes are used instead.

4.8.2
Sum Frequency Generation (SFG) Spectrometers

SFG spectroscopy is based on the fact that for most materials the second-order nonlinear susceptibility is nonzero only at the surface. Overlapping irradiation of a particular sample region by IR (ν_{IR}) and visible (ν_{vis}) laser beams may result in the generation of sum frequency (SF) radiation ($\nu_{SF} = \nu_{IR} + \nu_{vis}$). This excitation mechanism makes SFG spectroscopy an ideal method for studying molecules at

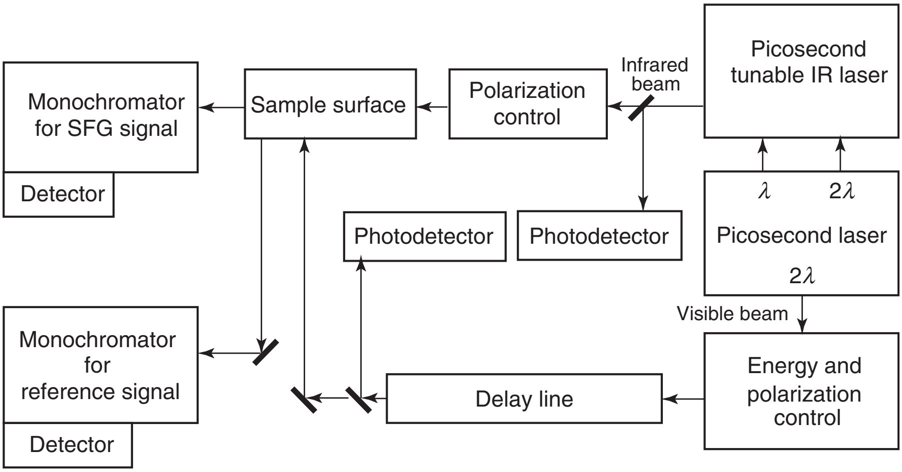

Figure 4.16 Block diagram of an SFG spectrometer.

surfaces and even at buried interfaces because of its selectivity to surface regions and its higher degree of molecular specificity.

At present, two basic SFG setups are used for the tunable radiation: (i) a picosecond system with tunable IR wavelength and (ii) a femtosecond system with large SBW. An example of a picosecond system is presented in Figure 4.16. In its standard configuration, a picosecond tunable laser (optical parametric generator) is used to generate IR light in the spectral region of about 4300–1000 cm^{-1}. This region is considered the easily accessible IR region for the SFG technique. Manufacturers of SFG spectrometers claim that this region can be extended down to 600 cm^{-1}.

Most of the SFG experiments are time resolved and employ a variable delay between the laser pulses. Initially, the system is brought out of equilibrium by an excitation (pump) pulse, afterwards the return to equilibrium is monitored by a delay (probe) pulse or a pair of probe pulses at different times after the pump pulse. The three scenarios of time-resolved SFG experiments are (i) two pulses – IR and vis – are slightly delayed with respect to each other but an overlap of the pulses in the time domain persists; (ii) two pulses – IR and vis – do not overlap in the time domain, the delay time between them may vary; and (iii) three pulses – one intense IR and an IR/vis pair – do not overlap in the time domain, the delay time between them may vary.

SFG spectrometers are still a state-of-the-art technique in nonlinear optics; hence, SFG spectroscopy cannot yet be considered a routine technique. Knowledge of basic and nonlinear optics is needed for running an SFG spectrometer.

4.8.3
Coherent Anti-Stokes Raman Scattering (CARS) Systems

CARS is a nonlinear Raman technique in which two lasers (a pump pulse and an anti-Stokes pulse from a tunable laser) interact with the sample. When the

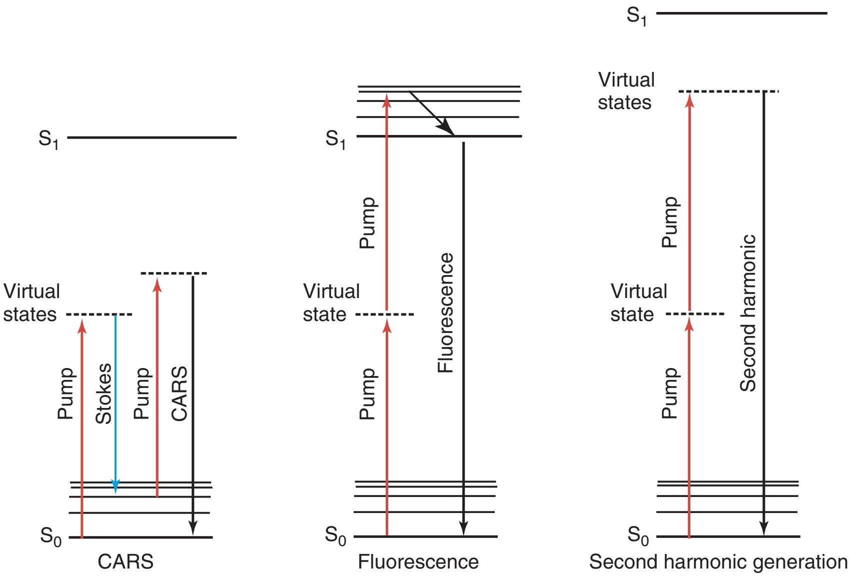

Figure 4.17 Jablonski diagrams of imaging techniques that can be used with a single setup.

difference in frequency between the two pulses matches a molecular vibrational transition, the anti-Stokes field will be resonantly enhanced. Because of its coherent nature, in which the molecular bonds oscillate in phase and interfere constructively, and its active pumping of the vibrational states, the CARS signal is at least five orders of magnitude more sensitive than spontaneous Raman scattering. One important exception in CARS is the symmetric CH_2 stretching mode at 2850 cm^{-1}. A limiting factor of CARS is the nonresonant background. The nonresonant background signal originates from instantaneous four-photon mixing processes. As the linewidth of most Raman active transitions is typically around 10–20 cm^{-1}, picosecond pulses are the optimum for a CARS setup. With spectrally broader femtosecond pulses, other multiphoton processes such as fluorescence or SHG can be used with the same setup. Figure 4.17 shows the Jablonski diagram of the CARS, fluorescence, and SHG processes.

The basic configuration of a CARS spectrometer is presented in Figure 4.18. Two lasers are used to excite the CARS signal. A powerful pump laser at the frequency ν_p excites the molecule to a virtual energy level. Lower energy (anti-Stokes) photons from the tunable laser ν_t initiate stimulated emission, when it is tuned to a frequency equivalent to the energy difference between the virtual and some excited vibrational ($\nu_m > 0$) state of the molecule under investigation. A second ν_p photon brings the molecule to another virtual state and finally the molecule returns to its initial vibrational state by emitting a photon in the anti-Stokes region. This secondary emission is coherent. Four wave vectors are involved in this process and the phase matching conditions has to be fulfilled. Therefore, the collinear beam

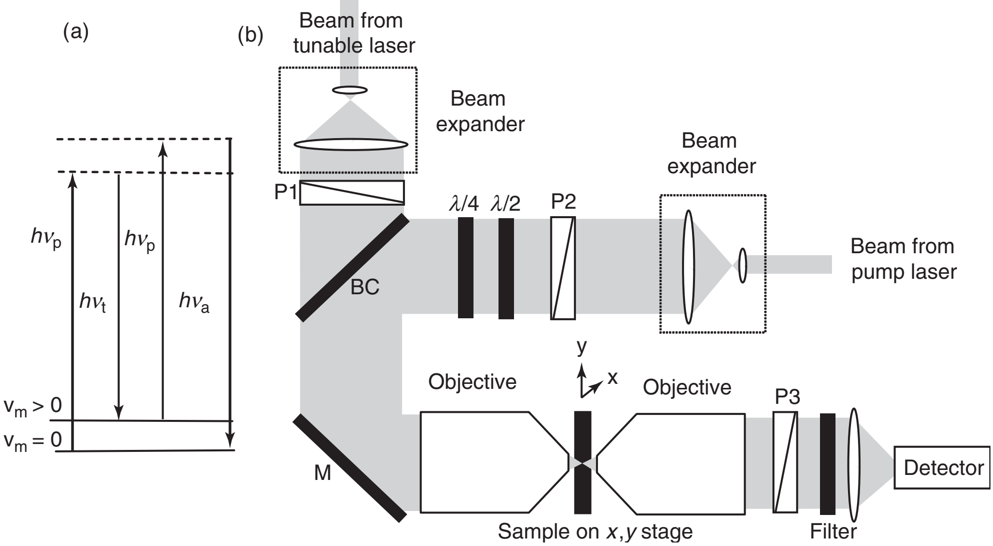

Figure 4.18 (a) Transitions between molecular energy levels during CARS: ν_p, frequency of high-power pump laser; ν_t, frequency of tunable laser; ν_a, frequency of coherent anti-Stokes Raman scattering band; ν_m, quantum number of *m*-vibrational mode; (b) Layout of a CARS spectrometer: BC, dichroic beam combiner; P, polarizer; M, mirror; λ/2 and λ/4, phase plates.

geometry became the configuration of choice in CARS microscopy. The CARS signal can be observed either in forward direction (depicted in Figure 4.18) or backward direction. For investigation of a backscattered CARS signal, the mirror M in the spectrometer setup has to be replaced by some dichroic beamsplitter. The CARS signal emitted by the sample is accompanied by radiations from pump and tunable lasers. These radiations are usually removed by placing a high-pass filter between sample and detector. The filter transmits only CARS radiation owing to its higher frequency.

Very important issues in the construction of CARS spectrometers are the large diameters of both parallel laser beams and the very short focal length of the objective used to focus the beams on the sample. The phase-matching conditions in collinear CARS microscopy can only be fulfilled by tight focusing: a small dimension of the excitation volume and a large cone angle of wave vectors compensate the wave vector mismatch induced by the spectral dispersion of the refractive index of the sample. Beam expanders are used to condition the beams. Expanded beams from pump and tunable lasers are combined by means of the BC. Another important issue concerning the CARS signal is the strong background. Electronic contributions to the third-order susceptibility of sample and solvent cause a nonresonant background signal, which provides no vibrational contrast. In addition, the solvent water has strong resonant signals of broad spectral width. Both background signals often overwhelm the CARS signal from small objects and limit the sensitivity. Polarizers P and phase plates $\lambda/2$ and $\lambda/4$ are used to diminish the level of this background and to increase the signal-to-noise ratio of the CARS signal. Another way to suppress the background involves a slight rearrangement of the experimental setup in order to observe the SRS (see preceding text) instead of the CARS signal. The CARS signal from an area of the sample as small as $0.5\,\mu m \times 0.5\,\mu m$, defined by the size of the focused laser beams on the sample, can be measured in a fraction of milliseconds. This makes CARS very attractive for chemical imaging.

CARS imaging has emerged in recent years as a new imaging technique. In CARS microscopy, both laser beams are collinearly directed into a microscope so that the pulses overlap in space and time. As they are raster scanned across the sample, the intensity of the anti-Stokes signal is captured point by point and transferred into a two-dimensional image. The scanning rate is often in the range of video rates. A CARS image of a sample area equal to $100\,\mu m \times 100\,\mu m$ using a high-speed x,y piezo stage can be obtained in a couple of minutes. 3D CARS images can be obtained by adding the third coordinate to the sample stage. CARS spectra can be measured over a wide frequency range. The low-frequency limit is usually located at $400-500\,cm^{-1}$. This limit is related to the insufficient steepness of the filter used to prevent the lasers beams from reaching the detector.

Further Reading

4.1 MIR Spectrometers

Ewing, G.W. (ed.) (1990) *Analytical Instrumentation Handbook*, Marcel Dekker.

Griffiths, P.R. and Haseth, J.A. (1986) *Fourier Transform Infrared Spectrometry*, John Wiley & Sons, Inc..

Henry, C. (1998) *Rev. Anal. Chem.*, **70**, 273A–276A.

Kellner, R., Mermet, J.M., Otto, M., and Widmer, H.M. (eds) (1998) *Analytical Chemistry*, Wiley-VCH Verlag GmbH.

Meyers, R.A. (ed.) (2000) *Encyclopedia of Analytical Chemistry. Applications, Theory and Instrumentation*, John Wiley & Sons, Ltd.

Noble, D. (1995) *Rev. Anal. Chem.*, **67**, 381A–385A.

Settle, F. (ed.) (1997) *Handbook of Instrumental Techniques for Analytical Chemistry*, Prentice Hall.

4.2 NIR Spectrometers

Burns, D.A. and Ciurczak, E.W. (1992) *Handbook of Near-Infrared Analysis*, Marcel Dekker, New York.

Murray, I. and Cowe, I.A. (1992) *Making Light Work. Advances in Near Infrared Spectroscopy*, Wiley-VCH Verlag GmbH.

Siesler, H.W. *et al.* (eds) (2001) *Near-Infrared Spectroscopy. Principles, Instruments, Applications*, Wiley-VCH Verlag GmbH.

William, P. and Norris, K. (1998) *Near Infrared Technology in the Agriculture and Food Industries*, The American Association of Cereal Chemists, St. Paul.

4.3 Terahertz Spectrometers

Dexheimer, S.L. (ed.) (2007) *Terahertz Spectroscopy: Principles and Applications*, CRC Press.

Sakai, K. (ed.) (2005) *Terahertz Optoelectronics*, Springer.

Tkachenko, N.V. (2006) *Optical Spectroscopy: Methods and Instrumentations*, Elsevier Science.

Wegener, M. (2004) *Extreme Nonlinear Optics: An Introduction*, Advanced Texts in Physics, Springer.

4.4 Raman Spectrometers

Chang, R.K. and Furtak, T.E. (1982) *Surface Enhanced Raman Scattering*, Plenum Press, New York.

Laserna, J.J. (ed.) (1996) *Modern Techniques in Raman Spectroscopy*, John Wiley & Sons, Ltd.

Long, D.A. (1977) *Raman Spectroscopy*, McGraw-Hill, New York.

Mukamel, S. (1995) *Principles of Nonlinear Optical Spectroscopy*, Oxford University Press, New York.

Schrader, B. (ed.) (1995) *Infrared and Raman Spectroscopy. Methods and Applications*, Wiley-VCH Verlag GmbH.

4.5 UV/vis Spectrometers and
4.6 Fluorescence Spectrometers

Burgess, C. and Knowles, A. (1981) *Techniques in Visible and Ultraviolet Spectrometry*, Standards in Absorption Spectrometry, Vol. 1, Chapman & Hall, London.

Clark, B.J., Frost, T., and Russell, M.A. (1993) *Techniques in Visible and Ultraviolet Spectrometry*, UV Spectroscopy, Vol. 4, Chapman & Hall, London.

Knowles, A. and Burgess, C. (1984) *Techniques in Visible and Ultraviolet Spectrometry*, Practical Absorption Spectrometry, Vol. 3, Chapman & Hall, London.

Lakowicz, J.R. (2006) *Principles of Fluorescence Spectroscopy*, 3rd edn, Springer.

Miller, J.N. (1981) *Techniques in Visible and Ultraviolet Spectrometry*, Vol. 2 Standards in Fluorescence Spectrometry, Chapman & Hall, London.

4.7 Spectral Imaging Devices

Cheng, J.X. and Xie, X.S. (2004) Coherent anti-Stokes Raman scattering microscopy: instrumentation, theory, and applications. *J. Phys. Chem. B*, **108**, 827.

Freudiger, C.W. *et al.* (2008) Label-free biomedical imaging with high sensitivity by stimulated Raman scattering microscopy. *Science*, **322**, 1857–1861.

Koffas, T.S., Amitay-Sadovsky, E., Kim, J., and Somorjai, G.A. (2004) Molecular composition and mechanical properties of biopolymer interfaces studied by sum frequency generation vibrational spectroscopy and atomic force microscopy. *J. Biomater. Sci. Polym. Ed.*, **15**, 475–509.

Kukura, P., McCamant, D.W., and Mathies, R.A. (2007) Femtosecond stimulated Raman spectroscopy. *Annu. Rev. Phys. Chem.*, **58**, 461.

Ploetz, E., Laimgruber, S., Berner, S., Zinth, W., and Gilch, P. (2007) Femtosecond stimulated Raman microscopy. *Appl. Phys. B*, **87**, 389.

Richmond, G.L. (2002) Molecular bonding and interactions at aqueous surfaces as probed by vibrational sum frequency spectroscopy. *Chem. Rev.*, **102**, 2693–2724.

Shultz, M.J., Schnitzer, C., Simonelli, D., and Baldelli, S. (2000) Sum frequency generation spectroscopy of the aqueous interface: ionic and soluble molecular solutions. *Int. Rev. Phys. Chem.*, **19**, 123–153.

Volkmer, A. (2005) Vibrational imaging and microspectroscopies based on coherent anti-Stokes Raman scattering microscopy. *J. Phys. D: Appl. Phys.*, **38**, R59–R81.

Wang, H.F., Gan, W., Lu, R., Rao, Y., and Wu, B.H. (2005) Quantitative spectral and orientational analysis in surface sum frequency generation vibrational spectroscopy (SFG-VS). *Int. Rev. Phys. Chem.*, **24**, 191–256.

Williams, C.T. and Beattie, D.A. (2002) Probing buried interfaces with nonlinear optical spectroscopy. *Surf. Sci.*, **500**, 545–576.

4.8 Instrumentation for Nonlinear Vibrational Spectroscopy

Salzer, R. and Siesler, H.W. (eds) (2009) *Infrared and Raman Spectroscopic Imaging*, Wiley-VCH Verlag GmbH, Weinheim ISBN: 13: 978-3-527-31993-0.

Smith, E. and Dent, G. (2005) *Modern Raman Spectroscopy: A Practical Approach* Kindle Edition, John Wiley & Sons, Ltd.

5
Measurement Techniques

Gerald Steiner

Upon interacting with a sample, incident light of intensity I_0 may partly be reflected at optical interfaces (I_R), it may be scattered (I_S) and absorbed in the sample (I_A), the remaining part will be transmitted (I_T) (Figure 5.1).

According to the law of conservation of energy, the energy balance for the incident light may be written as

$$I_0 = I_A + I_T + I_R + I_S \tag{5.1}$$

The light intensities I_0, I_T, I_R, and I_s can easily be measured by placing a detector at the corresponding position. All chemical information about the sample goes into I_A, but this value cannot directly be measured. I_A can only be accessed by evaluating Eq. (5.1). In all commercial spectrometers, only one detector is used to measure a particular couple of intensity values (I_0 and either I_T, I_R, or I_S; cf. Table 5.1). It is the goal of sample preparation to bring the remaining intensities to zero (or at least very close to it). Neglecting these basic considerations will result in measurement errors, which can never be eliminated by subsequent digital data treatment.

5.1
Transmission Measurements

Transmission spectroscopy is the most widely used measurement technique. It is simple and can be applied to characterize gases, liquids, and solids. Quantitative evaluations are based on the Beer–Lambert law as described in Chapter 3. Typical sample cells for gases and liquids are shown in Figure 5.2. Note the polished windows in the light path, while the other cell walls may be opaque. Polished windows must not be touched or even scratched. Fingerprints in the light path cause light scattering, and hence deteriorate the accuracy of the measurement. Normal incidence of the incoming light is required in order to minimize reflection.

The range of use of a particular cell depends on the window material. Most common materials for optical windows or fibers are summarized in Table 5.2. The refractive index of the window material should be very close to that of the sample in order to avoid reflection or scattering contributions.

Handbook of Spectroscopy, Second Edition. Edited by Günter Gauglitz and David S. Moore.

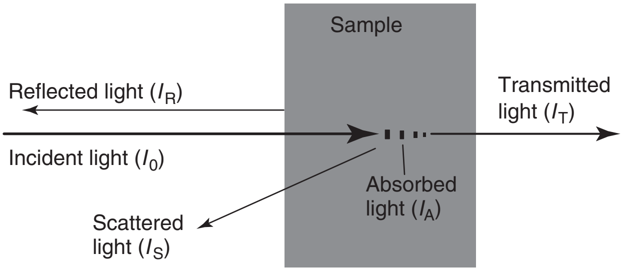

Figure 5.1 Energy balance of incident light on interaction with a sample.

Table 5.1 Measured and illicit contributions of light.

Measured	Aim of sample preparation	Evaluation	Experimental technique
I_0, I_T	$I_R = I_S = 0$	$I_A = I_0 - I_T$	Transmission measurement
I_0, I_R	$I_T = I_S = 0$	$I_A = I_0 - I_R$	Reflection measurements
I_0, I_S	$I_T = I_R = 0$	$I_A = I_0 - I_S$	Diffuse reflection measurements

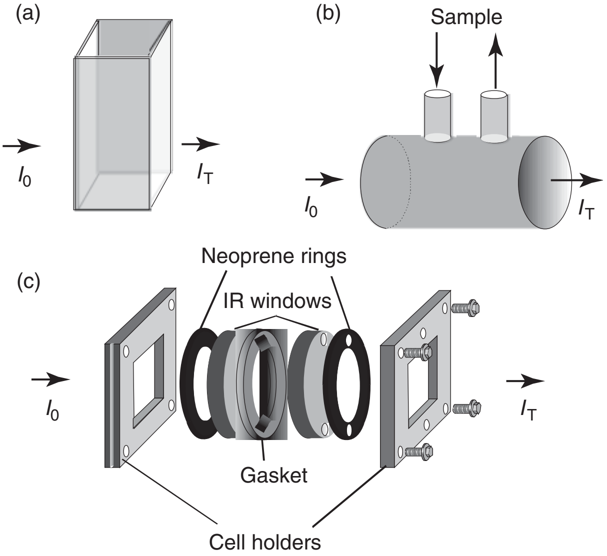

Figure 5.2 Cells for transmission measurements: (a) UV/vis liquid cell, (b) flow cell for gases and liquids, and (c) demountable IR liquid cell.

Table 5.2 Window or fiber material for optical spectroscopy.

Material	Transmission range (μm)	Refractive index (@ 20 °C)	Used for	Solubility
Optical glasses (SiO_2) Quartz	0.2–2.2	1.6 @ 0.2 μm 1.5 @ 2 μm	Windows, fibers	High resistance to acids (except hydrofluoric acid)
Fused silica	0.2–2.5	1.55 @ 0.2 μm 1.44 @ 2 μm		
Sapphire (single crystal Al_2O_3)	0.2–4.5	1.73 @ vis, 1.65 @ 4 μm	Fibers, ATR crystals	High resistance to acids and alkali at temperatures up to 1000 °C very hard
KBr	0.25–25	1.5	Windows, pellets	Soluble in water (53 g/100 ml H_2O) and alcohol
KRS-5 (TlBr/TlI)	0.3–40	2.4	Windows	Slightly soluble in water (0.02 g/100 ml H_2O), vulnerable to organic solvents, toxic
CsI	0.3–60		Windows	Soluble in water (44 g/100 ml H_2O) and alcohol
NaCl	0.3–16	1.55	Windows	Soluble in water (36 g/100 ml H_2O), slightly soluble in alcohol
CaF_2	0.2–10	1.4	Windows	Soluble in solutions of ammonium salts
Silicon (Si)	1.5–10	3.5 @ 1.5 μm 3.4 @ 10 μm	ATR crystals	Hard
Germanium (Ge)	2.0–15	4.1 @ 2 μm 3.9 @ 15 μm	ATR crystals	Soluble in mixtures of HCl and HNO_3 and H_2O_2
Zinc selenide (ZnSe, Irtran-4)	0.6–15	2.5 @ 0.6 μm 2.3 @ 15 μm	ATR crystals, windows	Soluble in acids, solubility in water @296 K: 0.001 g/100 H_2O
Zinc sulfide (ZnS, Irtran-2)	0.5–18	2.3 @ 0.5 μm 2.0 @ 18 μm	ATR crystals, windows	Soluble in acids, slightly soluble in water
AMTIR-1 $Ge_{33}As_{12}Se_{55}$)	1–14	2.5–2.6	ATR crystals, windows	High homogeneity, not soluble in water
Polyethylene	to 1000	1.5	Windows	Not soluble in water, organic solvents, and acids; used for far infrared
Silver halides	1–15	1.6	Fibers, windows	Soluble in NH_3, sensitive to UV and visible light
Chalcogenides (e.g., As_2S_3, $As_{40}Se_{35}S_{25}$)	0.8–10	1.56	Fibers	Sensitive to water
Diamond (C)	0.2 to >20	2.4	ATR crystals, windows	Extremely hard, high resistance to acids and alkalis at temperatures up to 1200 °C

5.2
Reflection Measurements

Reflection measurements at *optically flat interfaces* can be performed in two basic configurations, external and internal reflection. In case of external reflection (also called *specular reflection*), light propagates within the optically rare medium (e.g., air), whereas in the case of internal reflection (usually employed as attenuated total reflection (ATR)) light propagates within the optically dense medium (Figure 5.3).

5.2.1
External Reflection

The intensity distribution between reflected and transmitted light at plane optical interfaces is based on *Maxwell's* theory and *Fresnel's* equations. The reflectivity R relates the intensity I_R of the reflected light to the intensity I_0 of the incident light

$$R = |r|^2 = \frac{I_R}{I_0} \tag{5.2}$$

where r denotes the amplitude of the reflected wave.

The measured reflectivity R is polarization dependent, the amplitude coefficients for parallel polarization $r_{||}$ and perpendicular polarization $r_\perp$ are

$$r_{||} = \frac{n_2 \cos\alpha - n_1 \cos\beta}{n_2 \cos\alpha + n_1 \cos\beta} \tag{5.3}$$

$$r_\perp = -\frac{n_2 \cos\beta - n_1 \cos\alpha}{n_2 \cos\beta + n_1 \cos\alpha} \tag{5.4}$$

At the *Brewster angle* or polarizing angle α_B, no parallel polarized light is reflected ($r_{||} = 0$). Beyond the critical angle α_C, the incident light undergoes total reflection

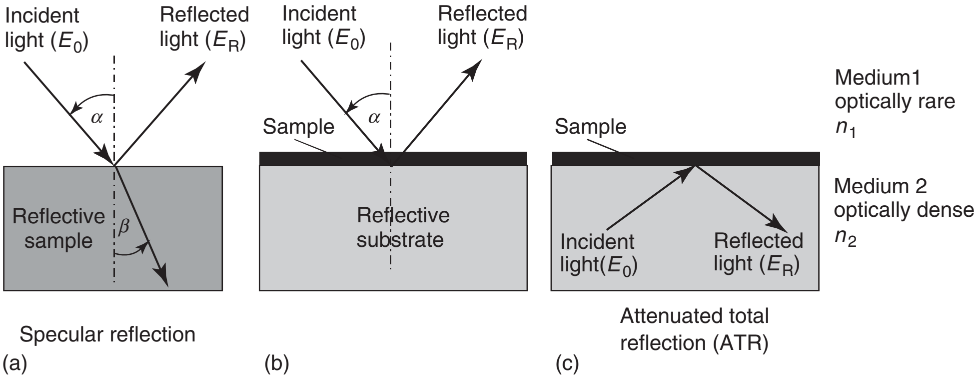

Figure 5.3 Measurement of (a) external reflection, (b) reflection absorption, and (c) internal reflection. Reflection and transmission of light at a plane optical interface with $n_2 > n_1$ (α, angle of incidence; β, angle of refraction). Parallel polarized light has its electric vector parallel to the plane of incidence.

at the interface

$$\alpha_C = \arcsin\left(\frac{n_1}{n_2}\right) \tag{5.5}$$

In order to calculate the transmitted intensity $T = (1 - R)$ immediately after the interface in a manner similar to that in Eq. (5.2), the intensity in the different media has to be taken into account

$$I_T = (1 - R)I_0 \tag{5.6}$$

In the usual case of absorbing media, the refractive index n has to be replaced by its complex form

$$n^* = n(1 - i\kappa) \tag{5.7}$$

where κ denotes the absorption index, which is related to the absorption coefficient a (cm^{-1}) and the decadic molar absorptivity ε ($\mathrm{l\,mol^{-1}\,cm^{-1}}$) in the *Beer–Lambert* law $A = \varepsilon c d$

$$a = 4\pi k\kappa = \frac{\varepsilon c}{\ln 10} \tag{5.8}$$

In an absorption region, the real part n of the complex refractive index n^* exhibits an anomaly, as schematically shown in Figure 5.4.

This effect occurs especially in the infrared range because narrower absorption bands affect a stronger anomaly of n. As a consequence, band shapes in IR reflection spectra differ severely from those in corresponding transmission spectra (Christiansen effect). The *Kramers–Kronig* relation can be used to analyze reflection spectra and to relate them to transmittance data.

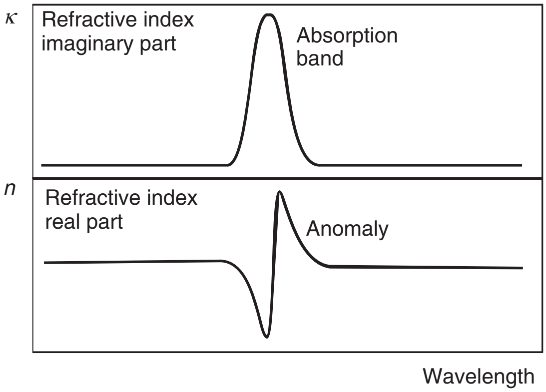

Figure 5.4 Anomaly in the real part of the complex refractive index within an absorption region.

5.2.2
Reflection Absorption

Reflection absorption measurements are performed by placing the analyte on a reflective substrate (Figure 5.3). The reflective substrate might be either optically flat or diffusely reflecting. Incident light passes the analyte twice, and a sort of transmission spectrum is obtained (sometimes called the *transflection spectrum*). The greater the angle of incidence, the larger is the effective path length in the analyte. The technique is known under the acronyms IRRAS (infrared reflection absorption spectroscopy) and RAIRS (reflection absorption infrared spectroscopy). The extreme case is the so-called grazing incidence technique, where the area illuminated by the incident beam is maximized (maximum number of molecules in the beam).

Reflection absorption experiments on samples with a thickness larger than the wavelength used give absorbance values corresponding to the enlarged effective pathlength described earlier. In case of sample thickness in the order of the wavelength or even below, the Beer–Lambert law is not anymore valid, because the field amplitude of the standing wave emerging during reflection varies regularly. In case of a very thin sample layer, its transmission is not only dependent on its optical properties but on the regular field variations in the vicinity of the reflecting surface as well. Additional enhancement factors may occur, which could provide submonolayer sensitivity. As the light of different polarization behaves differently upon reflection, a very complex situation results. In particular, in case of grazing incidence, only absorptions with components of the transition moments normal to the reflecting surface can be observed. Main application areas are surface coatings, very thin films, and adhesives on reflective surfaces as well as molecular orientation studies.

5.2.3
Attenuated Total Reflection (ATR)

A beam propagating in an optically dense medium with the refractive index n_2 undergoes total reflection at the interface with the optically rare medium (n_1) when the angle of incidence exceeds the critical angle α_C (cf. Eq. (5.5)). Upon total reflection, the electromagnetic wave propagates through the optical interface and generates an evanescent field, which penetrates the rare medium (Figure 5.5).

The evanescent field is a nontransverse wave along the optical surface, whose amplitude can be expressed as an exponential function along the z-axis into the rare medium

$$E_z = E_0 \mathrm{e}^{-z \frac{2\pi n_2}{\lambda_0} \sqrt{\sin^2\alpha - \left(\frac{n_1}{n_2}\right)^2}} \tag{5.9}$$

where E_z is the amplitude of the evanescent field at distance z, λ_0 the vacuum wavelength of the light used. The penetration depth z_p is defined as distance where

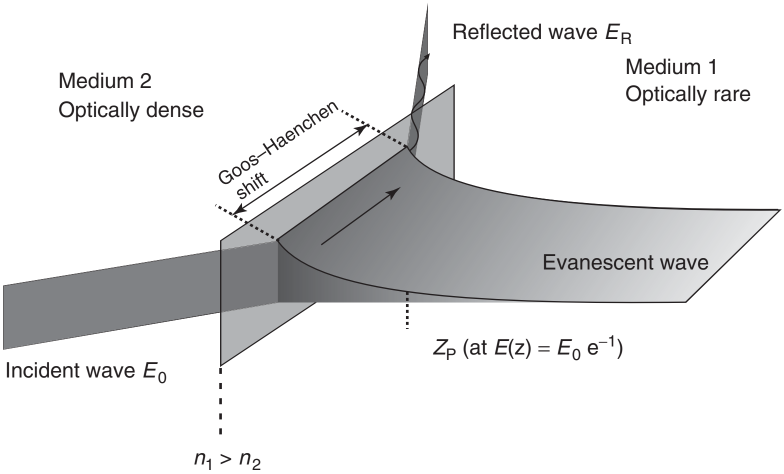

Figure 5.5 Strength and penetration of the evanescent field.

the exponent is equal to one

$$z_p = \frac{\lambda_0}{2\pi n_2\sqrt{\sin^2\alpha - \left(\frac{n_1}{n_2}\right)^2}} \tag{5.10}$$

If medium 1 is absorbing, the evanescent field will be absorbed and less intensity can be reflected (ATR). ATRs are similar to the conventional absorption spectrum except the band intensities at longer wavelengths. At longer wavelengths, the evanescent penetrates ever deeper into the sample, equivalent to an increasing sample thickness. Sometimes an empirical so-called ATR correction is applied in order to compensate across the spectrum for the linear wavelength increase in Eq. (5.10)

$$R_{\text{corr}} \sim R\frac{1}{\lambda} \tag{5.11}$$

Other differences may occur because of surface effects between the sample and the optical crystal or absorption changes across the sample. A single-reflection or a multireflection crystal may be used. The measured reflectivity depends on the number of reflections as well as on the efficiency of contact between sample and substrate surface.

An important advantage of the ATR technique is its applicability to turbid solutions, aqueous solutions included. Suspended particles are surrounded by a thin liquid film (hydrating shell). This shell forms also the phase boundary to the ATR crystal surface so that evanescent field will not be scattered by the particle.

ATR crystals for the UV, vis, and NIR ranges are usually made of quartz glass. Sapphire is used for special UV and NIR applications; it is one of the hardest of all optical materials so the surface is more resistant to scratches (Table 5.2). In the mid infrared (MIR), zinc selenide, silicon, germanium, and diamond are used. Zinc selenide is currently the most popular material for ATR crystals. Its most important advantage is its low absorbance at wavelengths over 10 μm, but zinc selenide scratches easier than germanium and silicon, and it is toxic. Amorphous material transmitting infrared radiation (AMTIR-1) is a glasslike amorphous material with a high homogeneity. The low thermal change refractive index of $7 \times 10^{-6}\,^{\circ}\mathrm{C}^{-1}$ is of advantage in optical systems.

5.2.4
Reflection at Thin Films

Thin films can be investigated either by reflection absorption or by a sort of internal reflection measurement using the occurrence of multiple reflections. In case of plane, parallel-sided, homogeneous, and isotropic thin films (Figure 5.6), the amplitude of the reflected light can be expressed in the form

$$r \sim \frac{r_{12} + r_{23}\mathrm{e}^{-2i\delta}}{1 + r_{12}r_{23}\mathrm{e}^{-2i\delta}} \tag{5.12}$$

where r_{12} is the reflection coefficient for the interface 1–2 and r_{23} for the 2–3 interface (cf. Eq. (5.3) and Eq. (5.4)). The term δ is given by

$$\delta = \frac{2\pi}{\lambda} n_2 d \cos(\beta) \tag{5.13}$$

where d is the layer thickness of the sample. For nonnormal incidence, the amplitude of the reflected light depends on the state of polarization of the incident light. If the film itself, or the surrounding medium, is absorbing, the reflection coefficients r_{ij} become complex (cf. Eq. (5.7)).

Spectral features arise from two properties: (i) the intrinsic absorption strength and (ii) the orientation of the transition dipole with respect to the wave vector of the incident light. In samples with random distribution, an averaged spectrum will be recorded. In highly ordered films, the absorption depends on the ordering within the film and the orientation of the sample. Therefore, the angle of incidence and polarization of the light have to be chosen carefully.

The analysis of thin films is often performed by infrared spectroscopy. Compared to reflection absorption measurements on metal surfaces using p-polarized light at grazing incidence, investigation of self-supported thin films or of thin films on

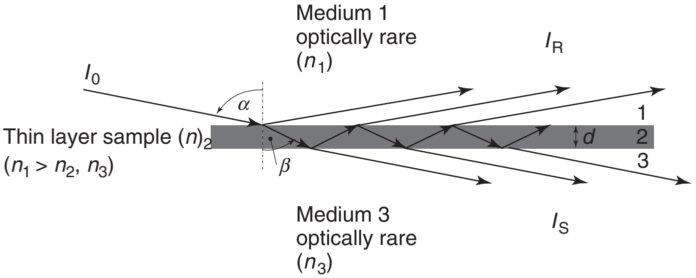

Figure 5.6 Reflection and transmission of light in a thin film.

transparent substrates shows weaker infrared absorption bands. Weaker absorption bands are caused by the absence of the surface enhancement mechanism and the poorer reflectivity. On the other hand – owing to the absence of the metal selection rule – spectra of p- and s-polarization can be recorded in case of free-standing films or of transparent substrates. Complex spectral features may arise from optical features of the substrate or in case of optical dispersion within the sample film.

5.2.5
Diffuse Reflection

Light incident at *optically scattering interfaces* (inhomogeneous samples such as powders) with roughness down to the range of the wavelength may partly be reflected regularly, partly scattered diffusely, partly entering the substrate. The latter part may undergo absorption within particles, diffraction at grain boundaries, reemerge at the sample surface, and intermingle with reflected parts. The measured reflectivity includes contributions from all mechanisms (Figure 5.7).

Quantitative evaluation of diffuse reflectance spectra requires "optically indefinitely thick" samples ($I_T = 0$; cf. Table 5.1). The reflectivity R_∞ of such a sample (in the IR, its thickness does normally not exceed a few millimeters) is

$$R_\infty = \frac{R_{\infty\,\text{(sample)}}}{R_{\infty\,\text{(reference)}}} \tag{5.14}$$

R_∞ is transformed by the empirical *Kubelka–Munk* relation into an absorption-proportional parameter $f(R_\infty)$

$$f(R_\infty) = \frac{1 - R_\infty}{2R_\infty} = \frac{k}{s} \tag{5.15}$$

where k describes the absorbing and s the scattering properties. The parameters k and s vary with particle size and packing density. It is assumed that s does not depend on wavelength and the sample is weakly absorbing. The former assumption has to be ensured by proper sample preparation, the latter by dilution of strong absorbers

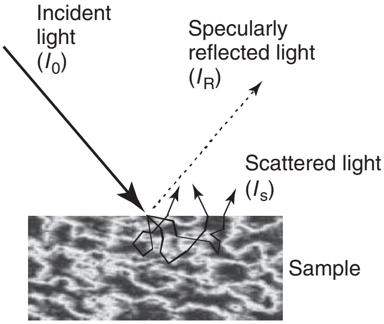

Figure 5.7 Schematic illustration of light trajectories in a scattering sample.

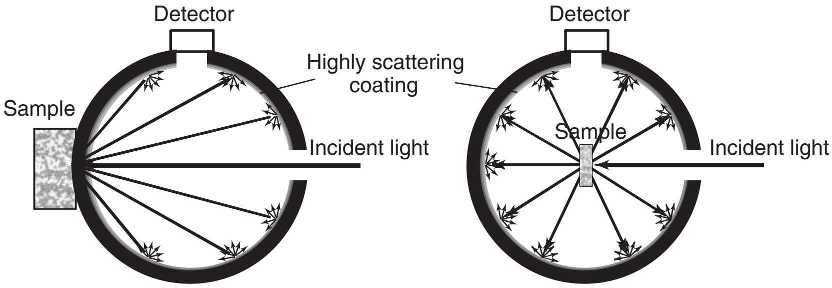

Figure 5.8 Two configurations of Ulbricht spheres for diffuse reflectance measurement. Large or thick samples are usually positioned at a sphere port, and small samples are mounted in the center.

with nonabsorbing substrate powder. In case of $R_\infty < 0.01$, the transformation is often done by the simpler functions $-\log R_\infty$ or simply by $1/R_\infty$. Such small R_∞ values are usually found in the NIR region.

Measurement of diffuse reflection spectra has a much longer tradition in UV/vis than in IR because (i) the scattering is much more efficient at shorter wavelengths and (ii) an ideal nonabsorbing scattering substrate is missing in the MIR.

UV/vis and NIR diffuse reflection spectra are usually measured by an integrating sphere. The inner surface of the so-called ‘‘Ulbricht sphere’’ (Figure 5.8) is coated with a strongly scattering, nonabsorbing powder. After repeated reflections at the inside of the sphere, all radiation will eventually reach the detector.

Of practical importance is the sphere factor K

$$K = \frac{\rho}{1 - \rho(1 - a)} \tag{5.16}$$

where ρ is the reflectivity of the cover and a the ratio between the area of all holes and the total sphere area. If the factor a does not exceed a range of 5–10%, K will essentially remain independent of sample properties.

Barium-sulfate-based coatings are mainly used in the UV/vis range; it is characterized by a reflectivity of up to 80% and an almost constant factor K throughout the vis range. Poly(tetrafluoroethylene) (PTFE) is suitable throughout the whole range from UV to NIR. In the NIR, a rough gold surface can be used as well.

In the MIR, diffuse reflectance is very weak and could only be measured after routine FT-IR spectrometers became available (DRIFT spectroscopy, diffuse reflectance infrared Fourier-transform spectroscopy). Owing to the lack of ideal nonabsorbing scattering substrates in the MIR, the diffusely reflected MIR radiation is generally collected by large ellipsoidal mirrors, which cover as much area above the sample as possible. Two optical configurations are commercially available, on-axis and off-axis designs (Figure 5.9).

In the on-axis configuration, the ellipsoidal mirror collects both diffusely and regularly reflected light. In the off-axis configuration, the ellipsoidal mirror is positioned off the plane of regular reflection; the latter influences the measurement

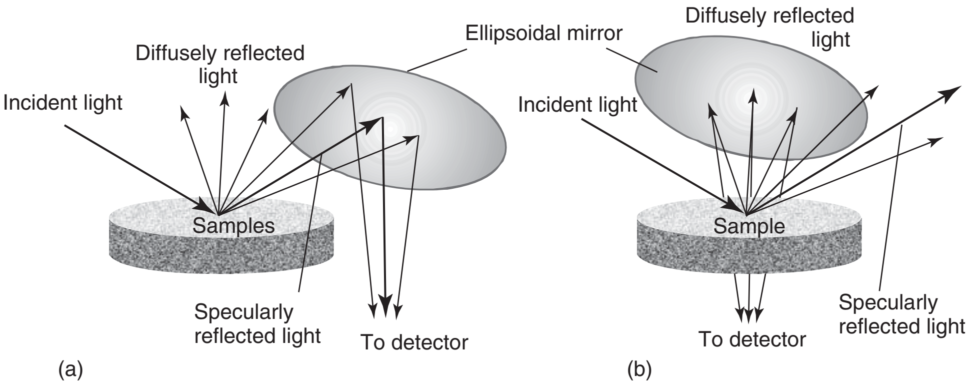

Figure 5.9 Optical layout for measurements of diffuse reflection in the infrared range: (a) on-axis arrangement with the collecting mirror in the optical plane of incident and specularly reflected light and (b) off-axis arrangement with the collecting mirror out of the optical plane of incident and specularly reflected light.

much less. While the on-axis design has the advantage of much simpler alignment in the interferometer, superposition of regular and diffuse reflection leads to both inferior sensitivity and reduced accuracy in quantitative analysis. Off-axis models provide superior sensitivity and accuracy at the expense of acquisition costs and laboratory experience. KBr or KCl powders are used as reference as well as dilutant for strong absorbers.

5.3
Spectroscopy with Polarized Light

Chiral molecules occur in pairs related by a symmetry plane; their mirror images cannot be superimposed (enantiomers). Such molecules exhibit optical activity, that is, they transmit left and right circularly polarized light in a different manner. The difference in the refraction indices for left and right circularly polarized light and is called *optical rotatory dispersion* (*ORD*), the corresponding difference in absorption coefficients is called *circular dichroism* (*CD*). ORD and CD can be related to each other by *Kramers–Kronig* transformation.

5.3.1
Optical Rotatory Dispersion (ORD)

Pairs of chiral molecules transmit left and right circularly polarized light by a different velocity. The two forms of chiral molecules have an asymmetric distribution of electrons, and hence they interact with right and left polarized light in opposite ways. If the index of refraction for right polarized light is larger than for left polarized light, the plane of polarization will be rotated toward left, and vice versa (Figure 5.10).

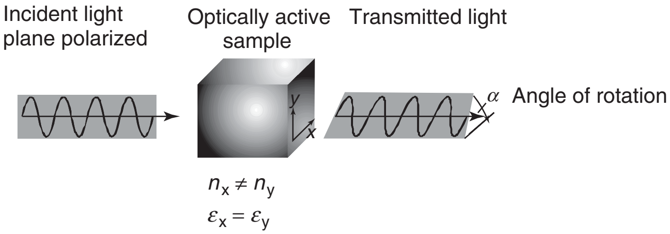

Figure 5.10 Optical rotatory dispersion: linearly polarized light can be considered as superposition of opposite circularly polarized light of equal amplitude and phase. Different velocities of left and right circularly polarized light lead to optical rotation of the polarization plane of the transmitted light.

The angle of rotation α at the wavelength λ is directly proportional to the concentration c

$$\alpha = [\alpha]_{\lambda}^{T} lc \tag{5.17}$$

where l is the path length of the sample cell. $[\alpha]_{\lambda}^{T}$ is the specific angle of rotation ($\mathrm{grd\,cm^{-3}}$), and it depends on wavelength and temperature. In polymer chemistry and biochemistry, the rotation is related to the molar mass, for example, to the average mass of all amino acids of the protein (mean residue weight, M_0)

$$[\mathrm{m}] = \frac{\alpha M_0}{10lc} \tag{5.18}$$

The obtained molar rotation [m] may be influenced by the refractive index n of the solvent. The corrected molar rotation is defined by

$$[\mathrm{m}]_{\lambda} = \frac{3}{n_{\lambda}^{2} + 2} \frac{\alpha M_0}{10cl} \tag{5.19}$$

5.3.2
Circular Dichroism (CD)

CD is observed when refraction indices as well as absorption coefficients are different for light and right circularly polarized light (Figure 5.11).

CD is measured by passing left circularly polarized light ($I_{\mathrm{T}}^{\mathrm{L}}$) and right circularly polarized light ($I_{\mathrm{T}}^{\mathrm{R}}$) consecutively through the sample and subtracting the observed intensities

$$\Delta I_{\mathrm{T}}(\lambda) = I_{\mathrm{T}}^{\mathrm{L}}(\lambda) - I_{\mathrm{T}}^{\mathrm{R}}(\lambda) \tag{5.20}$$

The difference in left and right polarized absorbance is usually in the range of 0.0001, corresponding to an ellipticity of approximately 0.01°. The molar ellipticity is defined as

$$[\Phi] = \frac{M\Phi}{10cl} \tag{5.21}$$

Φ is the measured ellipticity, c is the concentration, and l the path length of the sample cell.

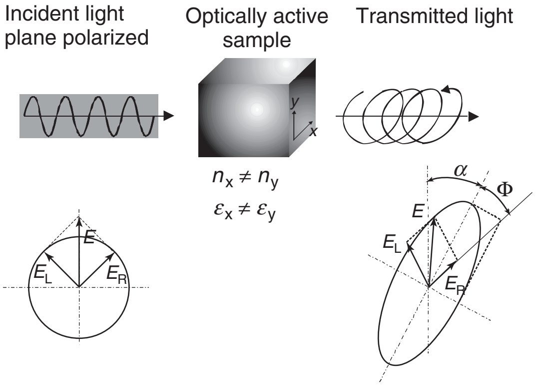

Figure 5.11 Principles of CD: similar to that in ORD, linearly polarized light can be considered as superposition of circularly polarized light of opposite direction of rotation but equal amplitude and phase. Differences in absorption of left and right polarized light lead to elliptic polarization of the transmitted light.

CD is a very sensitive method to study molecular conformation, in particular for analyzing secondary structures of proteins and nucleic acids in solution. Because different conformations have their characteristic CD spectra, the CD spectrum of a protein gives quantitative information about each kind of secondary structure. Moreover, CD is suited to study the rate of structural changes, and it can probe interactions such as protein–ligand, protein–protein, or protein–nucleic acid.

5.4
Photoacoustic Measurements

After selective absorption of radiation, excited molecules may relax either by emission of radiation or by nonradiative processes (cf. Chapter 3, Figure 3.1). In photoacoustic measurements, the conversion of absorbed radiation into thermal energy is utilized. This type of conversion results in changes of the sample's thermodynamic parameters such as temperature or pressure. Changes in pressure generate acoustic waves, which eventually will be transferred to the surroundings of the sample (Figure 5.12) where they can be measured by a sensitive microphone; see Figure 5.13 (photoacoustic spectroscopy (PAS)).

Acoustic waves are exclusively generated by the process of light absorption and subsequent relaxation; neither reflection nor scattering do produce PAS signals. For this reason, optical absorption in high-scattering samples and at optical interfaces can more accurately be measured by PAS. Moreover, the indirect measurement in PAS being more sensitive than optical transmission measurements, samples with low absorbance can well be investigated. Concentrations below 10^{-10} M or microsamples may even be measured. Some other key features are PAS is nondestructive, noncontactive, and macro as well as micro samples can be

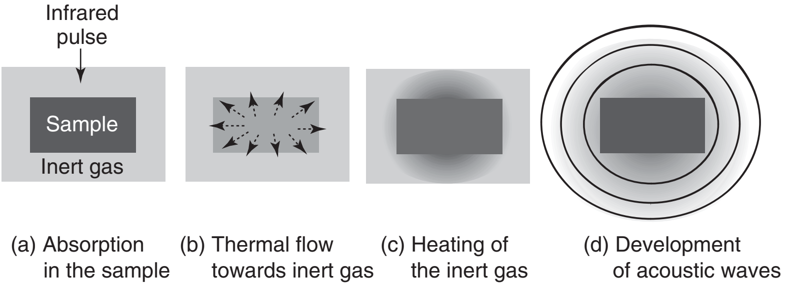

Figure 5.12 Photoacoustic signal generation: (a) IR pulses are absorbed by the sample, (b) the sample is heated and thermal pulses are generated, (c) thermal pulses are transferred from the sample to the surrounding gas, and (d) thermal pulses cause pressure waves (acoustic waves) within the surrounding gas. The PAS cell does not need to be closed for the measurement of the acoustic signal.

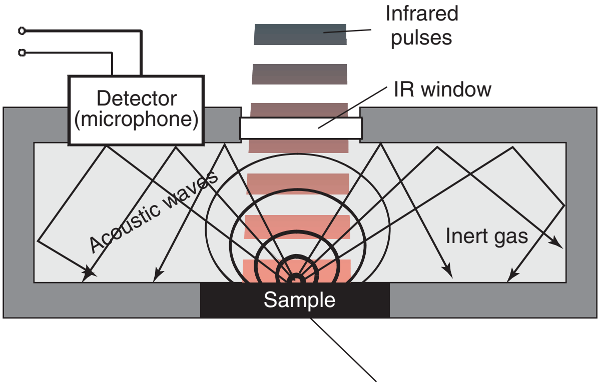

Figure 5.13 Schematic of photoacoustic cell.

investigated. The application range of PAS extends from the UV to the far IR. Because PA signals depend directly on light absorption, a PA spectrum looks like a conventional absorption spectrum. However, additional processes such as internal conversion, thermal diffusion, and other thermal effects may occur and render the spectrum more or less distorted.

One important application of PAS is the depth-resolved measurement of layered samples. As the thermal waves propagate from the point where absorption occurred to the sample surface, they decay rapidly. The intensity of thermal pulse is a square root function of the frequency at which the light is modulated (pulse repetition rate). The photoacoustic sampling depth l_{PA} is controlled by the modulation frequency

$$l_{PA} = \sqrt{\frac{D}{\pi f}} \tag{5.22}$$

where f is the modulation frequency and D the sample's thermal diffusion parameter. Typical values of l_{PA} are between 0.5 and 500 μm, depending on sample and wavelength.

5.5
Microscopic Measurements

Microscopes focus the light beam at the sample position to a very small area. Microsamples may fully fit this small area. The minimal diameter of the light spot in a conventional microscope may reach the order of the wavelength of this light (diffraction limit), but the optical conductance of microscopes is usually considerably lower than that of the spectrometer alone.

Every microscope is characterized by its numerical aperture NA, which describes the angle between the optical axis and the most remote point of the sample that can be observed. NA is directly proportional to the energy throughput. Objectives with infinity correction provide advantages such as sharper images and better signal–noise ratio. Infinity corrected objectives are increasingly used, especially in microscopic imaging with array detectors.

Because of the different capabilities of the various optical spectroscopic techniques as well as because of their distinct demands, special types of microscopes have been developed.

5.5.1
Infrared Microscopes

In contrast to vis microscopes with a system of glass lenses, IR microscopes are built around reflecting components. The heart of most infrared microscopes is a Cassegrainian or Schwarzschild objective (Figure 5.14).

Common IR objectives have NA values between 0.5 and 0.7, and typical magnification is 15 ×. Higher magnification objectives up to 36 × are available. IR microscopic measurements can be done in transmission, in external reflection, and in internal reflection. The latter requires a so-called ATR objective. ATR

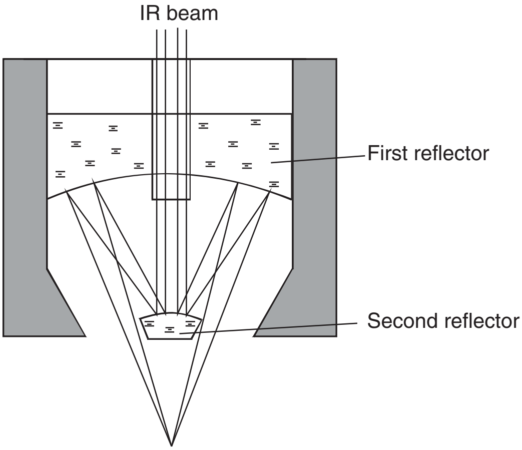

Figure 5.14 Optical setup of a Cassegrainian objective.

objectives permit *in situ* investigations of highly absorbing samples even without sample preparation.

The sample position is controlled by visible light. Thus, IR microscopes must transmit both IR and vis light; only small differences in coverage between IR and the vis images remain unavoidable because of aberration effects. Typical sample thickness in transmission is 5–50 μm. Investigations of strongly absorption or opaque samples are carried out in reflection mode. The latter has the disadvantages of lower signals due to the splitting between incident and reflected beams.

5.5.2
Confocal Microscopes

Confocal microscopes provide a particular good spatial resolution. They are mainly used in Raman and fluorescence measurements. The basic idea of a confocal microscope is that all structures being out of focus are suppressed at the detector. This is achieved by point illumination and a pinhole in front of the detector, as shown in Figure 5.15.

In contrast to a conventional microscope, the object is not being illuminated as a whole at the same time. The image will be reconstructed by stepwise moving the sample. Scanning in the plane as well as along the optical axis allows

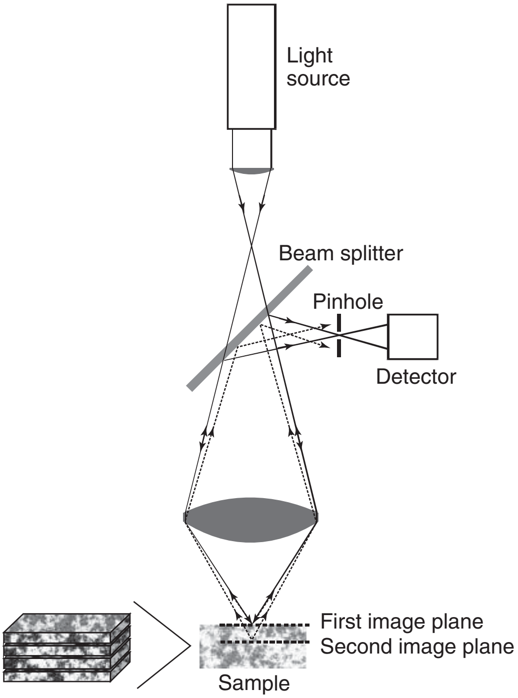

Figure 5.15 Optical layout of a confocal microscope.

three-dimensional investigations. Defocusing does not lead to blurring but it cuts out a part of the sample image as they move away from the focal plane so that these parts become darker or even disappear. This feature is also known as *optical sectioning*. The depth of the focus is determined by the objective's NA, the diameter of the pinhole, and by the wavelength.

5.5.3
Near-Field Microscopes

Near-field scanning optical microscopes (NSOM or SNOM) are mainly used in fluorescence and vis measurements. They provide optical images with spatial resolution less than the *Abbe's* limit of $\lambda/2$. The high lateral resolution is commonly achieved by using the optical near field, for example, in close vicinity of a very narrow fiber tip. Figure 5.16 illustrates the design of a near-field microscope.

Light can leave the extremely narrow orifice of the fiber tip only by a tunneling mechanism, which results in the generation of an evanescent field (or near field) outside the tip. The fiber tip must be positioned merely a few nanometers away from the sample surface by a device as is used in atomic force microscopy (AFM). A spatial resolution of approximately $\lambda/10$ can currently be achieved, limited by

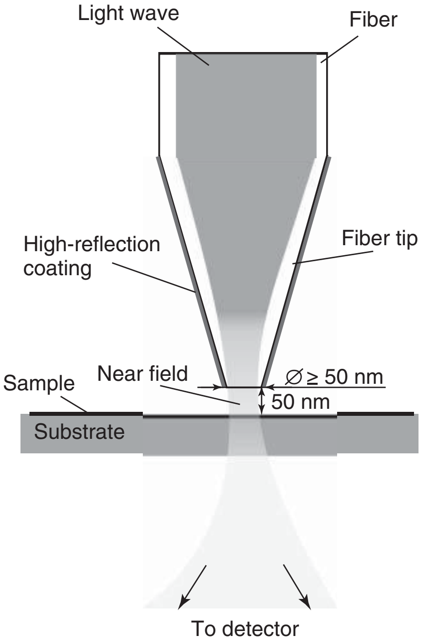

Figure 5.16 Scheme of a near-field microscope. Light is emerging from a fiber tip with the diameter of the orifice below the refraction limit. The configuration shown employs near-field excitation/far-field detection. The alternative configuration is far-field excitation/near-field detection.

the signal/noise ratio obtained at the detector and the distance of the fiber tip from the sample. Because of the extreme damping of the fiber tip, lasers are commonly used as light sources. The development of new powerful NIR and IR lasers makes near-field IR microscopy feasible for the near future.

Near-field microscopy was successfully applied in investigations of polymer surfaces, of biological samples, and of advanced inorganic film materials. No special sample preparation is required.

5.6
Infrared Spectroscopic Imaging

Spectroscopic imaging gained particular importance in the infrared spectral region. It can be done without a microscope (macrospectroscopic imaging) or with a microscope (microspectroscopic imaging). All detector elements of a focal plane array (FPA) detector (cf. Section 4.1.2.1) are read out simultaneously to provide a 3D data set (x and y dimensions of the sample plus IR intensities) from which spectroscopic images can be constructed. Typical array sizes of FPA detectors are 32 × 32, 64 × 64, 128 × 128 detector elements [Bhargava *et al.*]. Linear array detectors (cf. Section 4.7) may be advantageous in case of small sample areas, which can be captured rapidly.

Infrared spectroscopic imaging can be performed in transmission, reflection, transflection, or ATR mode. For microscopic investigations, the user can currently choose between four types of Cassegrainian objectives:

	Magnification	**NA**
	15×	0.4
	32×	0.65
	36×	0.5
Grazing angle	15×	0.99

NA, numerical aperture.

Because the spatial resolution (s_{res}) is determined by

$$s_{\mathrm{res}} = \frac{0.61\lambda}{\mathrm{NA}} \tag{5.23}$$

a microscopic objective with an NA of 0.65 allows a spatial resolution in the range of the used wavelength (λ). The sample area (a) can be calculated as

$$a = \frac{d_{\mathrm{FPA}} s_{\mathrm{D}}}{f_{\mathrm{obj}}} \tag{5.24}$$

where d_{FPA} is the number of the FPA elements in a row (e.g., 64, 128), s_{D} is the size of the detector elements (usually 40 μm), and f_{obj} is the magnification of the Cassegrainian objective. The registration time for one image ranges between few seconds and several minutes. ATR diamond objectives are also available for imaging purposes. An advantage of FT-IR ATR microimaging is the improvement in spatial resolution due to the high refractive index of the ATR crystal. The high refractive index causes a high NA and, in turn, a higher spatial resolution. Alternatively, FT-IR ATR macroimaging allows the investigation of larger samples under *in situ* conditions.

5.6.1
Analysis of Spectroscopic Images

A spectroscopic image may consist of thousands of individual spectra. Some or even many of those spectra may be of inferior quality (sample defects, sample edge, exterior areas). Spectra of inferior quality in the data set may preclude chemometric evaluation procedures from achieving useful results. This is a standard problem in spectroscopic imaging as homogeneous sample areas are normally not imaged. In consequence, the large imaging data set has to be subject to a sequence of processing steps.

Chemometric imaging is a term that encompasses a wide range of mathematical methods for evaluation of three-dimensional spectroscopic data sets. Advanced multivariate methods of data analysis are used in vibrational spectroscopic imaging to extract and to quantify relevant constituents, variations in the chemical structure, or composition. The common approach involves four steps (Figure 5.17): (i) detection and elimination of outliers, (ii) data preprocessing, (iii) feature selection and classification, and (iv) image processing.

During detection and elimination of outliers, all spectra of inferior quality or those that are not directly related to the sample are removed. The outlier spectra can be either removed from the data set or substituted by the spectral information from surrounding pixel. Table 5.3 summarizes some useful criteria for the detection of outlier spectra.

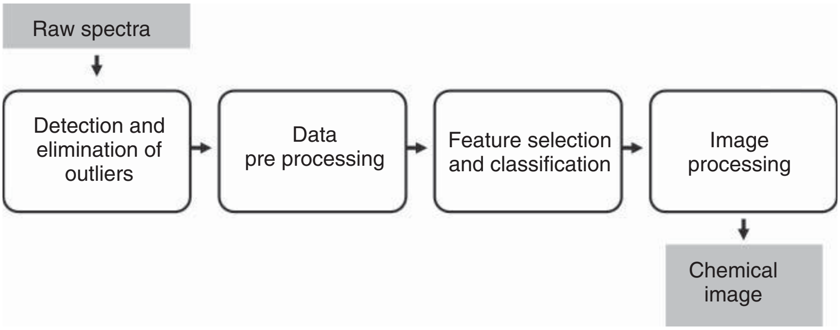

Figure 5.17 Recommended sequence of data treatment from spectroscopic raw data to a chemical image.

Table 5.3 Recommended criteria for the identification of outlier spectra.

Criterion	Comments and recommendations
Highest absorbance > 2	Useful, should always be used
Lowest absorbance < −0.5	Useful, should be used
Slope of the baseline > 0.5	Depends on the sample, can be corrected
Signal to noise ratio < 2	Useful, should be used when more than 10% of the spectra exhibit an SNR < 2
No characteristic bands	Useful when the sample spectrum is well known
Strong absorption bands of water and CO_2	Not recommended, can be compensated for
Oscillations (arise from the FPA electronics or from interferences of thin films)	Useful; however, hard to detect

Table 5.4 Selection of methods for data preprocessing.

Method	Comments and recommendations
Off-set correction	Should always be performed
Linear baseline correction	Should be used with care
Quadratic or higher degree baseline correction	Not recommended; should be used with care when a strong scattering occurs
Derivation	Can be used when spectra have good SNR
Normalization and centering	Recommended; optimized method has to be tested
Smoothing	Sometimes helpful when spectra have low SNR, usually in imaging spectroscopy not necessary
Extended multiplicative scatter correction	Recommended when scattering artifacts affect spectra

Data preprocessing is necessary to compensate for variations such as sample thickness or so-called dispersion artifacts. The latter are due to local variations in the sample refractive index. In general, data preprocessing includes routines that do not alter the information content of the spectra (cf. Table 53.1, Basic operations) and those that do (cf. Table 53.1, Manipulations). Improper manipulations cannot be compensated for anymore in later processing steps. Common manipulations are nonlinear background corrections, smoothing, derivation, or the removal of multiplicative and additive effects by extended multiplicative scatter correction (EMSC) [Gallagher *et al.*]. Common and often applied methods for data preprocessing are listed in Table 5.4. The best strategy for preprocessing is strongly depended on the quality of the data set. The outcome of preprocessing has to be evaluated carefully.

Feature selection and classification are used to extract the molecular information hidden in large spectral data sets. By feature selection those spectral regions

Table 5.5 Selection of multivariate pattern recognition methods.

Method	Basic function
PLS	Finds a linear model describing selected predicted variables
PCA	Calculates variances within the data set, identifies structure, and redundance
Wavelets	Extracts certain information from the data set
FA	Calculates variability of spectral information (linear combination)
Hierarchical CA	Assigns spectra into groups, represented as dendrogram
Partition cluster analysis	Assigns spectra to the cluster or computes a degree belonging to clusters whose center is nearest
Artificial neuronal networks	Finds patterns in the spectra set and shows relationships between spectra and additional information
SVM	Calculates and maximizes margin between the two or more classes
Discriminant analysis	Separates two or more classes by linear or function with higher degree

PLS, partial least-squares; PCA, principal components analysis; FA, factor analysis; CA, cluster analysis; SVM, support vector machines.

are identified that will best express the required molecular information in a most optimal way and at the same time at high specificity. Spectral information that is either redundant or irrelevant to the subsequent classification step is removed from the data set. Also, the noise level is reduced during the feature selection step. Multivariate methods for feature selection and classification can be roughly divided into classification and regression techniques. The family of classification techniques can be further divided into supervised and unsupervised methods. Supervised methods use prior knowledge of the data (training set), whereas unsupervised methods do not require additional information about the data. Supervised methods are often used for classification of spectra. Unsupervised methods are preferred to investigate similarities and/or variations between spectra. Table 5.5 summarizes important multivariate methods for the classification of spectra. Multivariate regression is applied to determine one or multiple constituents in a sample. Frequently used multivariate regressions are principle component regression (PCR) and partial least-squares regression (PLS).

Classification aims at assigning individual objects (spectra) to known classes. A class is defined by the similarity of the selected spectral features. Objects belonging to one class should be most similar with respect to the selected features, whereas objects belonging to different classes should show the largest differences. Classification methods can be divided into methods for class discovery (supervised) and methods for class prediction (nonsupervised) (Chapter 53.1). Supervised classification is based on a training set of previously labeled spectra, that is, spectra of known origin. Unsupervised classification requires no a priori information. Various classification algorithms are in use. Some do not yield confidence or class

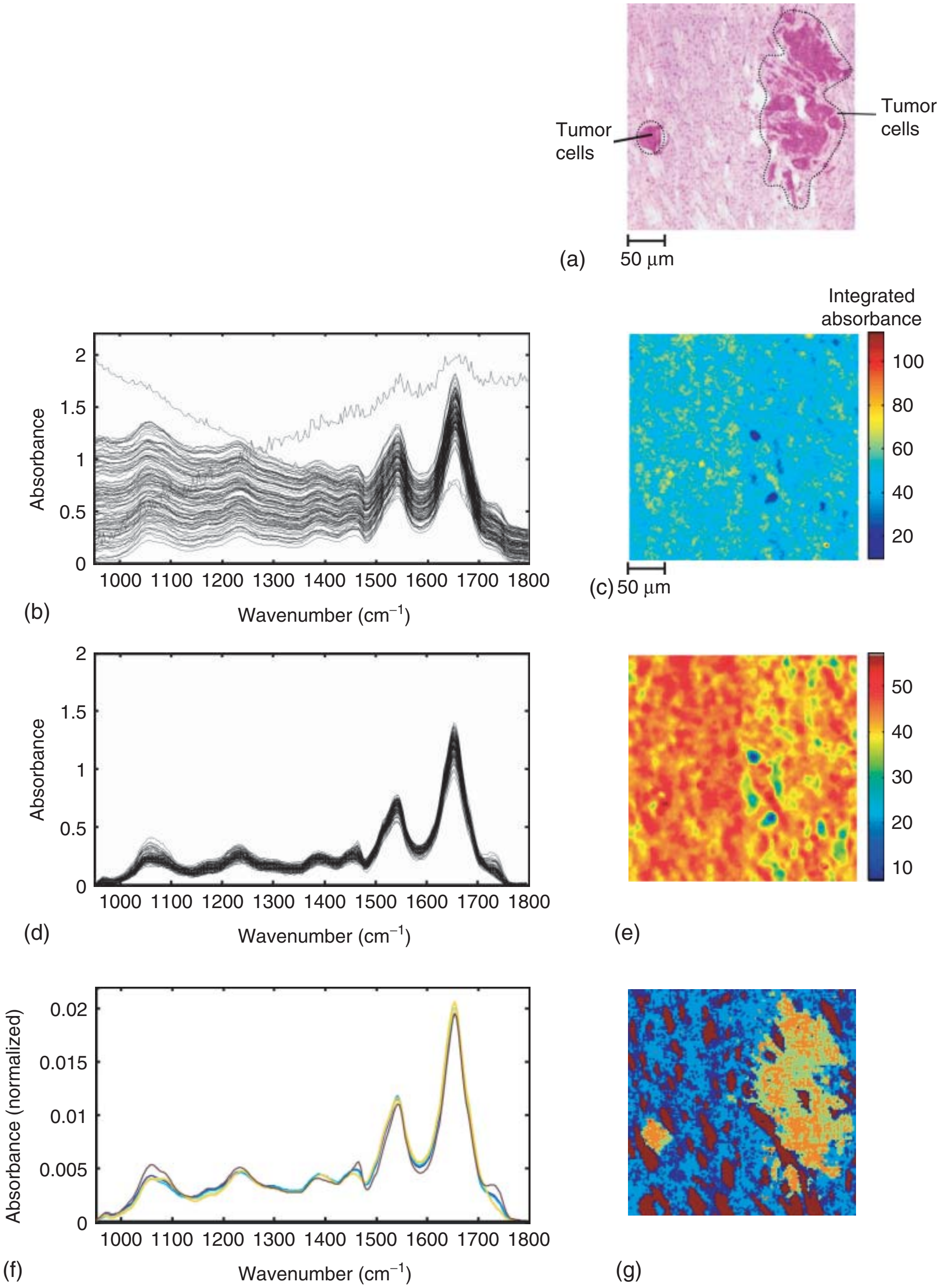
Tumor cells
Tumor cells
(a)
50 µm
Integrated absorbance
100
80
60
40
20
(c)
50 µm
2
1.5
1
0.5
0
Absorbance
1000 1100 1200 1300 1400 1500 1600 1700 1800
Wavenumber (cm^{-1})
(b)
2
1.5
1
0.5
0
Absorbance
1000 1100 1200 1300 1400 1500 1600 1700 1800
Wavenumber (cm^{-1})
(d)
50
40
30
20
10
(e)
0.02
0.015
0.01
0.005
0
Absorbance (normalized)
1000 1100 1200 1300 1400 1500 1600 1700 1800
Wavenumber (cm^{-1})
(f)
(g)

probabilities; others first apply unsupervised classification and attempt to label each of the classes afterwards.

Image processing is the final step that visualizes the classified spectra. Commonly different colors are assigned to the classified spectra. The latter are subsequently reassembled into a false color image. Methods of rendering can be used to eliminate noise and to highlight areas of equal or similar features. Pattern recognition techniques may be used to visualize particular features in spectral images.

An example of the work flow of multivariate data processing is given for a thin tissue section of a mouse tumor sample (Figure 5.18). A stained thin section of the tissue was visually diagnosed by a histologist. Identified tumor areas are surrounded by a dotted line (Figure 5.18a). The adjacent thin section was imaged under the FT-IR microscope. A randomly selected subset of the raw spectra is shown in Figure 5.18b. Some are typically affected by distortions such as scattering (spectrum in the upper left part) or noise (spectrum in the upper right part). The spectroscopic image in Figure 5.18c was calculated from the raw spectra by integrating the absorbance values between 950 and 1800 cm^{-1}. The contrast in the image is deteriorated by one prominent outlier spectrum. The corresponding red dot is indicated by arrows in the lower right part of Figure 5.18c. All outlier spectra, which contain little or no information about the sample, were subsequently eliminated, the accepted spectra were scattering corrected, and background removed (Figure 5.18d). Figure 5.18e shows the spectroscopic image after elimination of outlier spectra. Normal and tumor tissue cannot be distinguished yet. Finally, a fuzzy *k*-means cluster analysis (nonsupervised multivariate data analysis; cf. Table 53.10) was carried out. Normalization to the area was performed in order to compensate for variation in the thickness of the tissue section. The five centroid spectra of the resulting clusters (Figure 5.18f) indicate different types of tissue. Figure 5.18g reveals the lateral distribution of the cluster spectra of Figure 5.18f. The clusters can be assigned to the following tissue types: red and green tumor tissue, blue and brown normal tissue. These areas correspond very well with the hematoxylin–eosin (HE)-stained histological microscopic image in Figure 5.18a.

For a more detailed description of the data analysis techniques the reader is referred to Chapter 53.1 and to the relevant literature.

Figure 5.18 Multivariate analysis of a 128×128 spectroscopic image of a tumor. (a) Microscopic image of the tissue section after histological HE staining. The tumor area is surrounded by a dotted line. (b) A subset of 100 accidentally selected raw spectra. (c) Spectroscopic image of the raw spectra. The integrated absorbance between 950 and 1800 cm^{-1} is shown by color codes. (d) The spectra subset after elimination of 24 outlier spectra and data preprocessing. (e) Spectroscopic image using the preprocessed spectra. The integrated absorbance between 950 and 1800 cm^{-1} is again shown by color codes. (f) The four centroid spectra obtained by fuzzy *k*-means cluster analysis. The centroid spectra can be assigned to the following tissue types: red and green tumor tissue, blue and brown normal tissue. (g) The lateral distribution of the clusters (color code as in (f)) corresponds very well with the histological image above and clearly reveals the diseased tissue region.

Further Reading

Barker, J.R. and Toselli, B.M. (1998) in *Photothermal Investigations in Solids and Fluids* (ed. J.A. Sell), Academic Press, New York.

Betzig, E. and Trautman, J.K. (1992) Near-field optics: microscopy, spectroscopy and surface modification beyond the diffraction limit. *Science*, **257**, 189–195.

Bhargava, R. and Levin, I.W. (2005) *Spectrochemical Analysis Using Infrared Multichannel Detectors*, John Wiley & Sons, Inc., Hoboken.

Bordo, V.G. and Rubahn, H.G. (2005) *Optics and Spectroscopy at Surfaces and Interfaces*, Wiley-VCH Verlag GmbH, Weinheim.

Buffeteau, T., Desbat, B., and Turlet, J.M. (1991) Polarization modulation FT-IR spectroscopy of surfaces and ultra-thin films: experimental procedure and quantitative analysis. *Appl. Spectrosc.*, **45** (3), 380–389.

Clark, R.J.H. and Hester, R.E. (eds) (1998) *Spectroscopy for Surface Science*, John Wiley & Sons, Ltd, Chichester.

Fischer, U.C., Koglin, J., Naber, A., Raschewski, A., Thiemann, R., and Fuchs, H. (1996) Near field optics and scanning near field optical microscopy, in *Quantum Optics of Confined Systems* (eds M. Ducloy and D. Bloch), Kluwer Academic Publishers, Dordrecht.

Gallagher, N.B., Blake, T.A., and Gassman, P.L. (2005) *J. Chemometr.*, **19**, 271–281.

Gobrecht, H. (1987) *Lehrbuch der Experimentalphysik*, Optik, Bd., Vol. III, Walter de Gruyter, Berlin, New York.

Grittiths, P.R. (1995) *Chemical Infrared Fourier Transform Spectroscopy*, John Wiley & Sons, Inc., New Nork.

Griffiths, P.R. and de Haseth, J.A. (2007) *Fourier Transform Infrared Spectroscopy*, John Wiley & Sons, Inc., Hoboken.

Günzler, H. and Gremlich, H.U. (2002) *IR Spectroscopy: An Introduction*, Wiley-VCH Verlag GmbH, Weinheim.

Harrick, N.J. (1986) *Internal Reflection Spectroscopy*, John Wiley & Sons, Inc., New York.

Hollas, J.M. (2003) *Modern Spectroscopy*, 4th edn, Wiley-VCH Verlag GmbH, Weinheim.

Hollas, J.M. (1987) *Modern Spectroscopy*, John Wiley & Sons, Inc., New York.

Kortüm, G. (1969) *Reflexions Spektroskopie*, Springer, Berlin.

Maeder, M. and De Juan, A. (2009) *Compr. Chemom.*, **2**, 261–274.

Michaelian, K.H. (2003) *Photoacoustic Infrared Spectroscopy*, Wiley-VCH Verlag GmbH, Weinheim.

Michl, J. and Thulstrub, E.W. (1986) *Spectroscopy with Polarized Light*, VCH Publishers, New York.

Milosevic, M., Milosevic, V., and Berets, S.L. (2007) *Appl. Spectrosc.*, **61**, 94A–102A and 459–569.

Mirabella, F.M. (ed.) (1992) *Internal Reflection Spectroscopy, Theory and Applications*, Marcel Decker, New York.

Mirabella, F.M. (1998) *Modern Techniques in Applied Molecular Spectroscopy*, John Wiley & Sons, Inc., New York.

Nascimento, J.M.P. and Dias, J.M.B. (2005) *IEEE Trans. Geosci. Remote Sens.*, **43**, 898–910.

Paesler, M.A. and Moyer, P.J. (1996) *Near-Field Optics: Theory, Instrumentation, and Applications*, John Wiley & Sons, Inc., New York.

Prats-Montalban, J.M., de Juan, A., and Ferrer, A. (2011) *Chemom. Intell. Lab. Syst.*, **1**, 1–23.

Schilling, H. (1980) *Optik und Spektroskopie*, Fachbuchverl, Leipzig.

Schmidt, W. (1994) *Optische Spektroskopie*, Wiley-VCH Verlag GmbH, Weinheim.

Schmidt, W. (2005) *Optical Spectroscopy in Chemistry and Life Sciences: An Introduction*, Wiley-VCH Verlag GmbH, Weinheim.

Schrader, B. (ed.) (1995) *Infrared and Raman Spectroscopy*, Wiley-VCH Verlag GmbH, Weinheim.

Shinzawa, H., Awa, K., Kanematsu, W., and Ozaki, Y. (2009) *J. Raman Spectrosc.*, **40**, 1720–1725.

Stuart, B.H. (2004) *Infrared Spectroscopy: Fundamentals and Applications*, Wiley-VCH Verlag GmbH, Weinheim.

Suetaka, W. (1995) *Surface Infrared and Raman Spectroscopy: Methods and Applications*, Plenum Press, New York.

Wang, L. and Mizaikoff, B. (2008) *Anal. Bioanal. Chem.*, **391**, 1641–1654.

6

Applications

Valdas Sablinskas, Gerald Steiner, Martin Hof, and Radek Macháň

6.1

Mid-Infrared (MIR) Spectroscopy

In the mid-infrared (MIR) spectral region, we are dealing with transitions between various vibrational energy levels of molecules. Gaseous samples are a special case, because rotational fine-splitting of spectral bands can be observed. Fine-splitting is caused by simultaneous excitation of rotational and vibrational transitions.

The MIR spectral range extends from 4000 to 400 cm^{-1}. Transitions can be observed by absorption or emission measurements. For analytical purposes, absorption measurements are usually preferred. The decision about an optimal sampling technique is very much dependent on the aggregate state of the sample under investigation.

6.1.1

Sample Preparation and Measurement

According to the Beer–Lambert law, the density of the analyte (or concentration of it in case of mixtures or solutions) and the infrared (IR) pathlength in the sample are crucial. These parameters have to be chosen in such a way that good measurable optical signals are obtained in contemporary spectrometers between 20% and 60%T for band maxima. In order to minimize the background in the spectrum, care should be taken about the homogeneity of the sample, the level of impurities, and about absorptions in the solvent. The quality of spectral data acquired depends very much on the sampling technique chosen. Detailed descriptions of sampling techniques can be found in [1–3]. A summary of common sampling techniques is given in Figure 6.1.

6.1.1.1 **Gases**

Gas cells are essentially gas-tight containers fitted with IR transparent windows to enable the radiation to enter and exit the container. Gas cells should be equipped with inlets for introducing, pressurizing, and evacuating the gas. Cell sizes vary from a cylinder of a few centimeter pathlength, typically 10–20 cm and constructed

Handbook of Spectroscopy, Second Edition. Edited by Günter Gauglitz and David S. Moore.

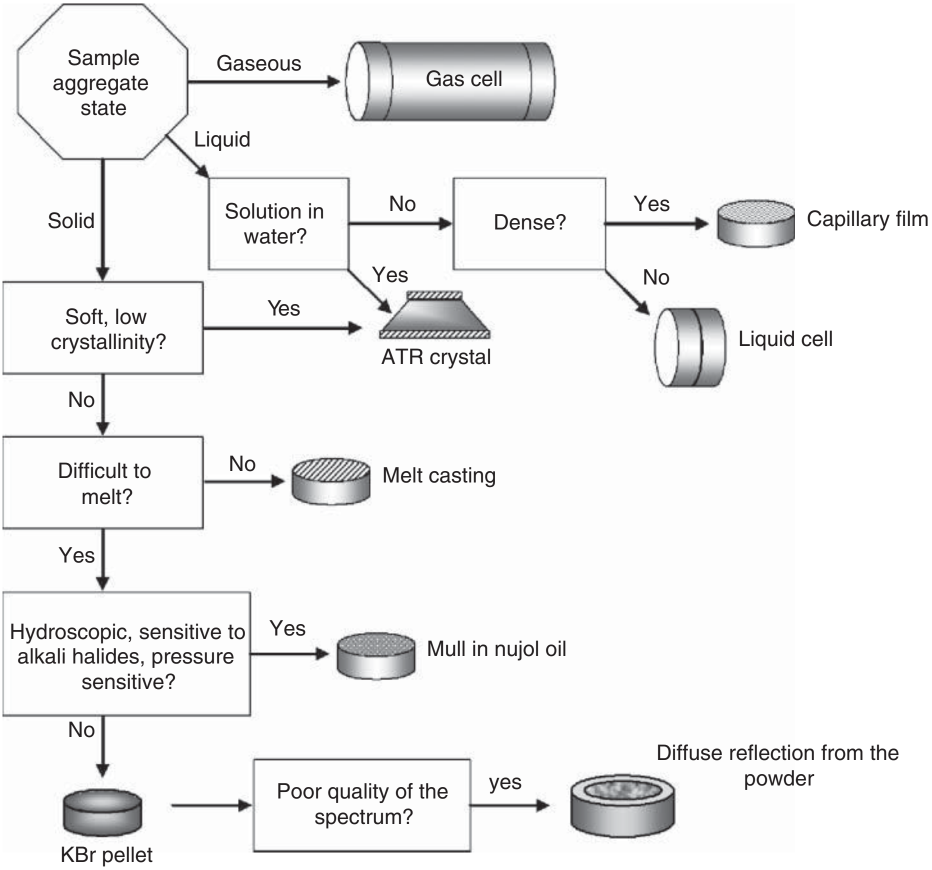

Figure 6.1 Summary of common IR sampling techniques.

from glass or stainless steel, with windows at each end, to compact long-pathlength cells, which have internal gold mirrors (multipass gas cells) in order to provide effective pathlength of many meters within the gas sample. At a pressure up to 50 Torr, many gases yield useful spectra in a standard 10 cm pathlength cell. Unfortunately, many molecular species have much lower saturated vapor pressure at room temperature, that is, a longer pathlength is required for meaningful measurements.

A sketch of a gas cell with multipass optics in the so-called White arrangement is given in Figure 6.2. It comprises three spherical mirrors, which can be adjusted for the desired number of passes. Four passes (as shown in Figure 6.2a) is the minimal number of passes in such an arrangement. The achievable maximum number of passes depends on the reflectivity of the mirrors and on the quality of the incoming beam. The latter is partly defined by the size of the IR source. Commercial cells with White optics have an outer length of about 30–100 cm and provide a folded optical with total path of up to 100 m. Measurements with the multipass gas cells

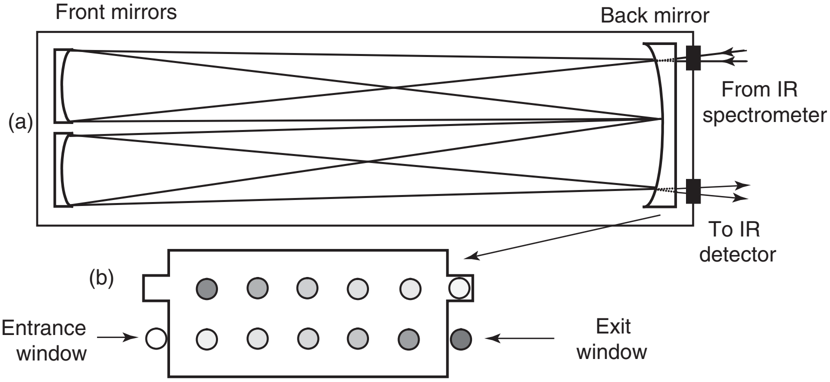

Figure 6.2 Multipass gas cell with White optics. (a) Ray diagram for four optical passes and (b) front view of the back mirror with images of the IR source on it in case of 24 passes.

should be carried out in a single beam mode. A restriction of multipass gas cells concerns cooling. It is very difficult to ensure stable alignment and prevention of atmospheric water condensation on the windows in low temperature experiments with such type of a cell.

High-resolution MIR spectrometers are required in order to resolve the rotational fine structure of vibrational bands. MIR instruments providing resolution down to 0.001 cm^{-1} are commercially available. The width of rotational spectral lines of a gaseous analyte depends not only on its partial pressure, but is a function of total pressure and temperature as well. Molecular collisions will broaden the rotational spectral lines, a phenomenon known as *pressure broadening*. The statistical distribution of velocities of the molecules causes the so-called Doppler broadening of the rotational lines. This broadening effect can be partly eliminated by cooling the gaseous sample.

Spectra of compounds with vapor pressure down to 0.001 Torr can be obtained using multipass gas cells. This technique proved very useful for the detection of atmospheric impurities or trace components in waste and combustion gases.

6.1.1.2 **Solutions and Neat Liquids**

Every solvent has its own absorption bands in the MIR region. For this reason, the most appropriate solvent for the given situation has to be chosen from a whole selection. Unfortunately this selection does not include water and alcohols, which exhibit broad and strong bands in their MIR spectra. Moreover, many optical materials used as MIR windows for liquid cells (alkali halides, such as KBr) are soluble in water and alcohol. The solvents with the largest absorption free areas in the MIR are carbon tetrachloride and carbon disulfide. As both solvents are quite toxic, they must be handled carefully. A list of most common MIR solvents is given in Chapter 5. A comprehensive review of the spectral transmission of all solvents is found in [1].

Windows for liquid cells typically consist in case of nonaqueous samples of NaCl or KBr or in case of aqueous solutions of CaF_2. A list of common MIR window material is given in Chapter 5.

For the selection of optical windows – besides such parameters as useful spectral range, mechanical resistance, and solubility – the refractive index has to be taken into account as well. The refractive index of the windows should match that of the liquid sample in order to minimize reflection losses, stray light, and distortions of band shapes (Christiansen effect). NaCl and KBr are very well suited for organic analytes. Inorganic analytes may have much higher refractive indices. The higher the refractive index, the greater the reflection losses result for the incident IR radiation.

For solutions, the typical thickness of liquid cells is in the 0.05–1 mm range, which is provided by a Teflon gasket placed between the two windows. Both fixed thickness and variable thickness liquid cells are available commercially. Typically, solutions of 0.05–10% in concentration are handled in IR cells. In double beam spectrometers, a reference cell is filled with pure solvent and placed in the reference beam in order to compensate for solvent bands and other background effects. In single beam instruments, solvent bands and background effects are usually removed by computing the difference of sample and solvent spectra. Both cell thickness and analyte concentration can be calculated from the measurements with high accuracy. This renders MIR spectroscopy well suited for quantitative measurements.

Neat liquids require a film thickness in the 10 μm range. As it would be difficult to fill a cell of such low thickness and even more difficult to clean it, capillary films of such samples are usually formed by squeezing few drops of compound between two windows.

In case of relatively low-melting solids, it is also possible to prepare a thin film by melting and squeezing the sample between two windows. Thin films of nonvolatile liquids or solids can be deposited on the window by solvent evaporation. The sample is first dissolved in a volatile solvent. A few drops of the solution are placed on the window. After evaporation of the solvent, a thin film of sample on the window is obtained. Windows can usually be cleaned using carefully dried methylene chloride or acetone. Preparing a thin film from solution or solidification from the melt are methods well suited to examine amorphous materials, such as waxes or soft resins.

6.1.1.3 **Pellets and Mulls**

Pellets are used for solid samples that are difficult to melt or dissolve in any suitable solvent, or which have to be measured in their native solid state. The sample is finely ground and mixed with dry potassium bromide (or other alkali halide) powder. The usual analyte/KBr ratio is approximately 1 : 100. An agate mortar and pestle or a vibrating mill can be used for grinding and mixing. The mixture then is pressed into a transparent disk in an evacuable die for 2 min at a pressure of 0.6 GPa (6 tons cm^{-2}). Without evacuation (e.g., when moist air is present during pressing) it is impossible to obtain highly transparent pellets. The ground particles should not exceed 2 μm in diameter, otherwise scattering losses may result. IR spectra

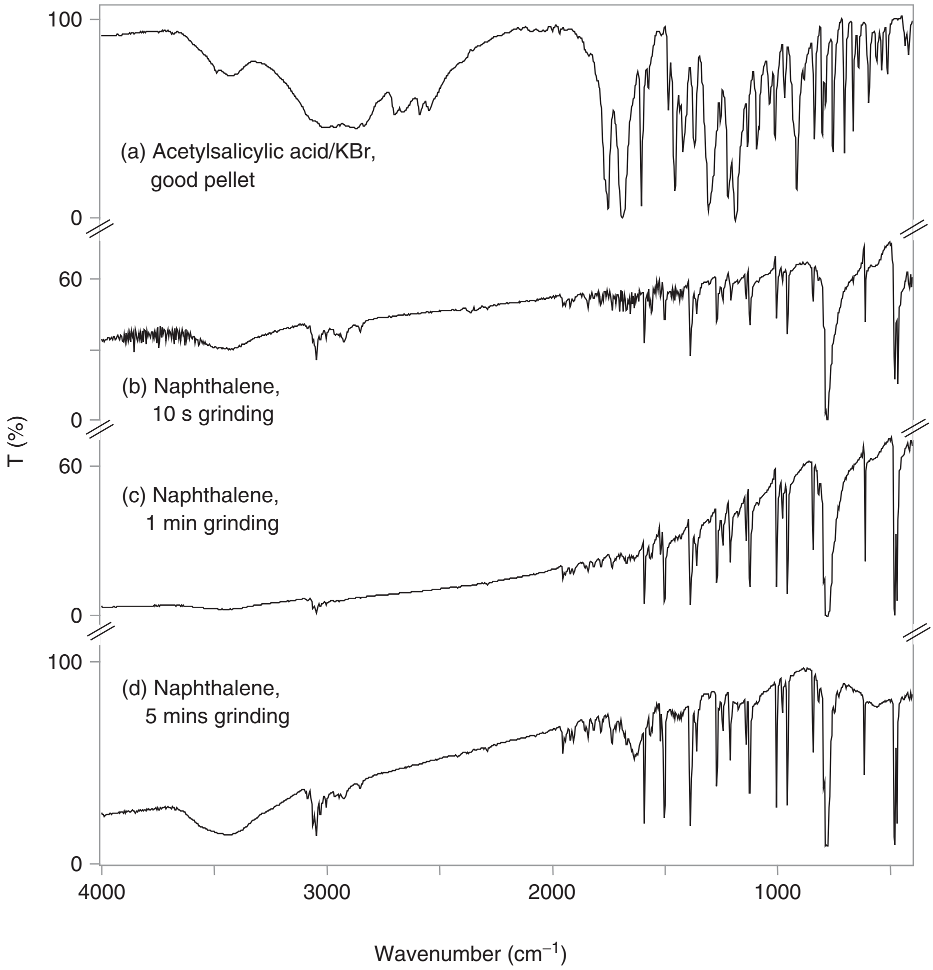

Figure 6.3 Examples of possible errors in the KBr pellet technique: (a) good spectrum of acetylsalicylic acid in a KBr pellet; (b) insufficient grinding results in light scattering (background slope) and small absorption bands; (c) longer, but still insufficient grinding improves size and shape of absorption bands; and (d) too long grinding results in good size and shape of absorption bands but causes adsorption of larger amounts of water in the pellet (broad band at 3450 cm^{-1}).

obtained by the pellet technique often exhibit bands at 3450 and 1640 cm^{-1} because of adsorbed moisture. Without internal standard added, the pellet technique is not suitable for quantitative measurements because the thickness is not precisely reproducible and the size of IR bands depends on dispersion of the sample (see Figure 6.3).

Mulls are used as alternatives for pellets. The sample (1–5 mg) is carefully ground into a suspension using a couple of drops of a mulling agent. This mull is pressed between two IR transmitting windows to form a thin film. Common mulling agents are Nujol (liquid paraffin), Fluorolube (a chlorofluorocarbon polymer), and hexachlorobutadiene. To obtain a complete IR spectrum that is free of mulling agent bands, experiments with various mulls are generally required. The mull technique is recommended for water-sensitive samples and for samples that interact with alkali halides.

A detailed description of all techniques can be found in [1].

6.1.1.4 **Neat Solid Samples**

Pellet or mull techniques cannot usually be applied to polymeric samples because of their softness. Samples of thermoplastic polymers can be prepared by using a so-called press tool for melt films. This tool consists of two heatable metal plates, which can be placed in a hydraulic press. The thickness of the squeezed film is defined by the thickness of a metal spacer placed between the heated plates. Metal plates may be wrapped by aluminum foil in order to prevent adhesion of the sample to the plates. The foils can be easily removed by dissolution in dilute HCl.

If the compound under investigation is both insoluble and nonmeltable, it can be cut into slices of appropriate thickness using a microtome. Conventional sampling techniques require sample areas of a few square centimeters, which might hardly be achievable for slices between 20 and 50 μm thickness. Samples of smaller area may advantageously be investigated by micro-attenuated total reflectance (microATR) (see below).

6.1.1.5 **Reflection–Absorption Sampling Technique**

This technique is used to study thin (down to submonolayer) films adsorbed on reflective substrates such as metals. Experimentally it involves measuring the change in the reflectance spectrum of the substrate that accompanies thin film formation. Various acronyms for the technique are used – infrared reflection–absorption spectroscopy (IRRAS, IRAS) and reflection–absorption infrared spectroscopy (RAIRS). Basics of IRRA spectra are described in Section 5.2.2.

According to theory, the maximum sensitivity in reflection–absorption measurements should be achieved at grazing incidence angle (between 65° and 85°). Various accessories are available, either with fixed angle of incidence or variable angle of incidence. It is necessary to record the reflectance spectrum of the substrate with a high signal-to-noise ratio both before and after formation of the thin film. The IRRA spectrum is then computed as a ratio of both former spectra. The range of incidence angles that can be effectively utilized is rather limited. The experiment has to be designed carefully, particularly in terms of source and detector types.

The depth of penetration of the electrical field from the surface of the metal substrate into the adsorbed sample is between 5 and 500 nm. This enables investigation of submonolayers. IRRA spectra differ from conventional transmission spectra of bulk compounds, because only vibrations with transition dipole moments perpendicular to the surface will be excited. As the evanescent field decays rapidly, vibrating groups closer to the surface yield larger absorption bands. Moreover, the polarization status of incident radiation is crucial – only p-polarized light will interact.

Another practical consideration is film thickness. In case of IRRAS of thick films, one observes a superposition of two spectra – a spectrum caused by molecules close to the surface (with some enhanced spectral bands) and a spectrum caused by the bulk sample (conventional transmission spectrum). In case of very thick samples, the bulk spectrum dominates and the angle of incidence is not so important. In case of thickness between 0.1 and 1 μm, both types of the spectra have to be taken into consideration.

Compared to other sampling technique for surface investigations, a great advantage of IRRAS results from propagation of the probe photon in a nonvacuum environment. This enables the spectrometer to be set up outside a ultra-high vacuum chamber, which considerably simplifies operation.

6.1.1.6 **Sampling by ATR**

ATR accessories are especially useful for obtaining IR spectra of samples that cannot be readily examined by common transmission methods. Such accessories are suitable for studying thick or highly absorbing solid and liquid samples, including films, coatings, powders, threads, adhesives, polymers, and aqueous samples. ATR requires only little sample preparation for most samples. It is one of the most versatile sampling techniques.

The basics of ATR have been described in Section 5.2.3. The sample has to be brought into good optical contact to the ATR crystal as shown in Figure 6.4. The IR beam is directed toward the bevel edge of the ATR crystal and undergoes single or multiple internal reflections. ATR multireflection crystals may be trapezoidal or rod-shaped. The number of reflections as well as the penetration depth decreases with increasing angle of incidence. The resulting IR-ATR spectrum is similar to a conventional IR spectrum, but the intensities of bands at longer wavelengths are higher because of the larger penetration depth at longer wavelengths. ATR accessories fit easily into the sample compartment of any grating or FT-IR spectrometer, but high-quality spectra can only be obtained by FT-IR spectrometers because of the energy limited condition.

ATR is a surface and interface investigation method. The penetration depth is in the order of a few tenths of the wavelength of investigation, in the IR between 0.5 and 10 μm (cf. Eq. (10) in Section 5.2.3). A variety of ATR accessories including various kinds of liquid cells or even horizontal units for cell-less investigation of liquids is available. Heatable ATR cells are commercially available as well. A special

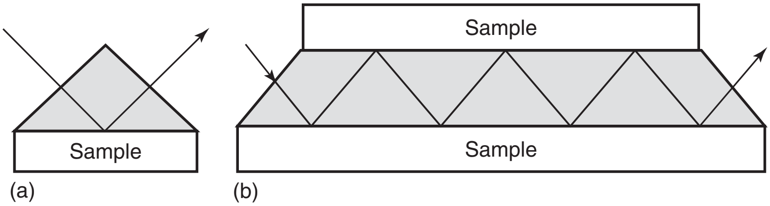

Figure 6.4 ATR sampling technique. (a) ATR crystal for single reflection measurement and (b) ATR crystal for multi reflection measurements.

and meanwhile widespread ATR variety uses a single reflection diamond. The fields of application of ATR are metals, polymers, lacquers, rubbers, coatings, laminates, papers, textiles, fibers, jelly-like samples, and interfaces of liquids and solids.

6.1.1.7 **Thin Samples**

Parts of the incident beam are reflected at each optical boundary (air-sample boundary in case of a free-standing thin sample or air-window/window-sample boundaries in case of a liquid cell), even at normal incidence. Of particular importance is that part of radiation, which undergoes multiple reflections at the two opposite surfaces of a plan-parallel sample. The double-reflected beam can interfere with the original beam, which results in sinus type periodical features in the background of the spectrum (Figure 6.5). Such features usually cause difficulties during evaluation of spectra. On the other hand, the interference provides access to the effective thickness of the sample as well as optical quality of its boundaries (deviations from plan-parallelity cause reduced amplitudes of interference fringes). The effective sample thickness can be calculated according to

$$d = \frac{N \times 10\,000}{2 \times n_\mathrm{D} \times (\tilde{\nu}_1 - \tilde{\nu}_2)}\ (\mu\mathrm{m})$$

where N is the number of interference fringes between $\tilde{\nu}_1$ and $\tilde{\nu}_2$, n_D is the refractive index of medium inside of the cell ($n_\mathrm{D} = 1$ in case of empty cell), 10 000 is the conversion factor between wavenumber (cm^{-1}) and thickness (μm). Usually, pathlengths of liquid cells of thickness up to 1 mm are determined by evaluation of their interference fringes (cf. Figure 6.5).

6.1.1.8 **Diffuse Reflection Sampling Technique**

There is a large group of solid samples (such as powders, pastes, pellets with rough and scattering sample surface) that do not give good-quality spectra by any of the above described sampling techniques. In these cases, measurement of the diffuse reflection may be an alternative. Diffuse reflection means scattering of a large part of radiation in all directions. The penetration depth of incident IR radiation into

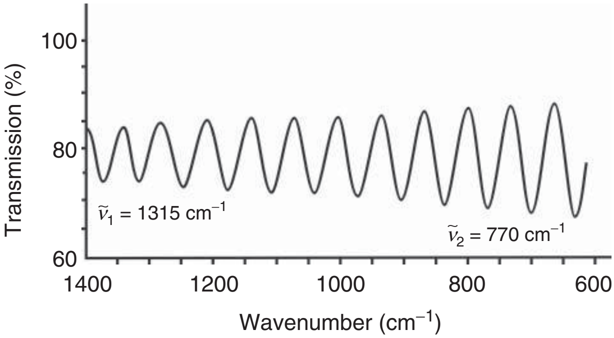

Figure 6.5 Interference fringes in an IR spectrum of an empty KBr cell. Eight fringes between 1315 and 770 cm^{-1} correspond to a cell thickness of 73 μm.

the scattering sample is usually between 10 and 500 μm. Even in case of rough surfaces, a small contribution of specularly reflected radiation always persists. Specularly reflected IR radiation does not contain much information about the sample (very short path within the sample); it mainly deteriorates the accuracy of the quantitative measurement and increases detector noise.

Diffuse reflection accessories are commercially available. They collect the diffusely scattered IR radiation by means of large ellipsoid mirrors. Even the largest mirrors only permit the collection of a part of the scattered radiation; therefore, the use of diffuse reflection accessories is restricted to FT-IR spectrometers (diffuse reflection in infrared by Fourier Transform spectrometer – DRIFT). The Kubelka–Munk transformation has to be performed in order to linearize the ordinate of the obtained spectra. Integrating spheres (the so-called Ulbricht spheres) are not any longer used in MIR because of the lack of nonabsorbing and uniformly high-scattering coatings for the inside of the sphere.

DRIFT spectra depend on both the scattering and the absorbing properties of the sample (Kubelka–Munk theory). DRIFT spectra are considerably complex. They are influenced by particle size, crystallite orientation, sample homogeneity, and analyte concentration. The bigger the particle size, the larger the contribution of specular reflection and absorption. Both contributions have to be minimized for quantitative evaluation. The ideal particle size is between 2 and 10 μm. Bigger particles have to be ground before measurement. Low absorbance is achieved by dilution in a nonabsorbing matrix, usually KBr powder in a ratio from 1 : 3 to 1 : 100. A special variation for compact materials is the abrasion technique. Nickel–diamond abrasive pads are used to rub off a part of the sample, for example, a varnish. The pad is then inserted into the DRIFT accessory and directly measured.

An excellent description of all aspects of diffuse reflectance can be found in [4].

6.1.1.9 **Sampling by Photoacoustic Detection**

The basics of photoacoustic spectroscopy (PAS) are described in Section 5.4. PAS is useful for examining highly absorbing samples that are difficult to analyze by other IR techniques. Minor or even no sample preparation is required here. Size and shape of the sample are not critical. PA spectra can be obtained from a wide variety of samples such as powders, polymer pellets, viscous glues, single crystals, and single fibers.

PA spectra are generally similar to conventional IR spectra except that strong spectral bands will often be saturated (truncated). However, the presence of such truncated bands does not much limit the practical use of PAS. Depth resolved measurements are an important feature of the FT-IR PAS technique. Depth resolution can be varied from 1 to 20 μm simply be changing the velocity of the moving mirror inside the interferometer. Multilayer samples such as polymer composites can easily be studied by PA spectroscopy.

6.1.1.10 **Microsampling**

Microsampling techniques have to be applied when either small amounts or small sizes of analytes have to be investigated. Microsampling techniques may be derived from conventional techniques by miniaturization. For all such miniaturized sampling techniques, a beam condenser (micro illuminator) is needed. Standard beam condensers are made of a pair of ellipsoidal mirrors. Micropellets for solids have a diameter of 0.5 and 1.5 mm with sample amounts of 5–10 μg in 4 mg KBr. For liquids and solutions, microcells with volume down to 0.3 μl are commercially available. A special case of microsampling is the so-called diamond anvil cell, where a tiny drop of liquid analyte is squeezed between two diamond crystals. Even solidification of the sample between the diamonds can be achieved by applying pressure up to 100 bar. Usual dimensions of the diamond surfaces are below 1 mm. This technique is very useful for conformational analysis.

Nowadays, microsampling is performed by using IR microscopes (see also Section 5.5). They permit easy access to spectra from small sample areas down to about 10 μm × 10 μm. This size limit results from the basic diffraction theory. Spectral information from smaller areas can be obtained only by investigating wavelengths closer to near infrared (NIR) spectral range. IR microscopes equipped with a x,x-motorized stage permit the 2D mapping of chemical properties with good lateral resolution (e.g., distribution of impurities). Several years ago, MIR instrument with array detectors became commercially available. Such instruments permit the collection of IR images in only a few seconds by direct imaging.

All microsampling techniques require very thorough sample preparation. For obtaining meaningful results in either transmission or reflection mode of an IR microscope, sufficient skills in microscopic sample preparation are required.

A wide range of compounds can be investigated by IR microscopy. The broad scale of sampling accessories for IR microspectroscopy includes even objectives for ATR or grazing angle measurements.

6.1.2
Structural Analysis

Every chemical compound has its own characteristic IR spectrum. The IR spectrum contains the entire information about the molecular structure of the investigated sample. The main problem is the assignment of experimental spectral bands. In addition to fundamental vibration bands, very often the so-called combination and overtone bands are present. Fermi resonance can cause intensity changes and frequency shifts of the bands involved. Intermolecular interactions (such as hydrogen bonding) can cause additional bands. Furthermore, influences of solvents, temperature, and pressure have to be considered. There are two different approaches for the assignment of vibrational bands.

The most convenient tool for identification of molecules from their vibrational spectrum are spectral databases (cf. Chapter 53). The matching process gets very much accelerated by computerized search programs. If an exact match cannot be found, these programs usually list the reference compounds that numerically match the unknown spectrum much closely. Attention: close proximity in a search hitlist does not guarantee close similarity of molecular structures.

A more chemical approach is the evaluation of characteristic or group frequencies. Some chemical groups exhibit highly characteristic bands no matter in what kind of molecule they are included. The group frequency approach is very useful for structural analysis. From frequencies and intensities of some spectral bands, it is possible to predict what kind of chemical groups are present in the molecule, how they are connected to other groups and, finally, the structure of the molecule under investigation may be guessed.

According to the theory of molecular vibrations in any N-atomic molecule, there are $3N - 6$ ($3N - 5$ in case of linear molecules) fundamental vibrations. By the group frequency approach, one takes into account only movements of atoms with largest amplitude but neglects atoms with much smaller vibration amplitude. Vibrations can be subdivided in two groups – stretching vibrations (when bond lengths are

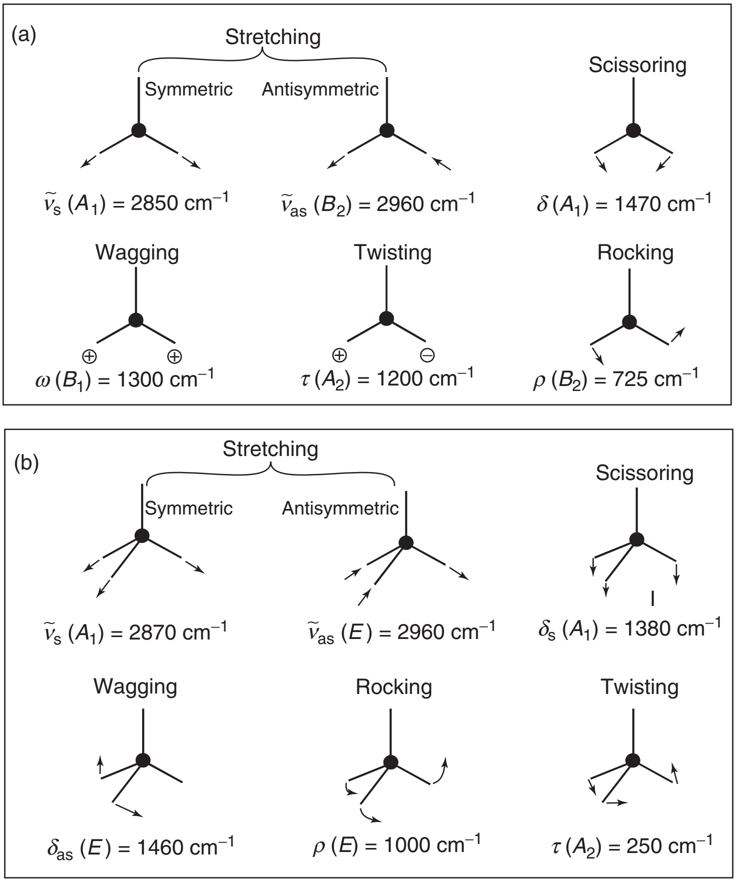

Figure 6.6 Group frequencies of (a) CH_2 and (b) CH_3 groups. The name of each type of vibration (abbreviated by a Greek letter) reflects the kind of movement. The italic letters given in parenthesis are used to fully describe the symmetry properties of the oscillator.

changing during vibration, also called *valence vibrations*) and deformation vibrations (when bond angles are changing). Deformation vibrations are subdivided further into scissoring, wagging, rocking, and twisting modes. Vibrations of CH_2 and CH_3 groups are summarized in Figure 6.6.

Each normal vibration has particular symmetry properties, described by symmetry elements of the point group to which the molecule under investigation belongs. Symmetry considerations are very useful for the assignment of the spectral bands. The so-called character tables may be used to derive the symmetry of each normal vibration and to deduce the IR and Raman activity of a given vibration. A vibration is IR active, if the total molecular dipole moment changes during vibration. It is Raman active, if the molecular polarizability changes during vibration. It can be deduced from symmetry considerations, whether dipole moment or polarizability changes occur during vibration. IR or Raman activity merely indicates the appearance of a particular band in the spectrum. In order to further predict the intensity of vibrational bands, detailed information about the magnitude of the transition moment is needed.

Not all vibrations exhibit characteristic frequencies. For instance, vibrational frequencies of the various C–C bonds in the carbon backbone of aliphatic molecules are very much coupled between each other (the so-called skeleton modes), and they depend very much on chemical groups connected to this aliphatic chain. This behavior can also be used for spectrum interpretation. A short list of group frequencies of some chemical groups is given in Table 6.1 and Table 6.2. A more comprehensive list of characteristic bands can be found in spectral correlation tables and charts, for example, in [4, 5].

For practical evaluation, the IR spectrum is often divided into three regions: (i) from 4000 to 1400 cm^{-1}, (ii) from 1400 to 900 cm^{-1}, and (iii) from 900 to 400 cm^{-1}.

6.1.2.1 **The Region from 4000 to 1400 cm^{-1}**

This region comprises stretching vibrations involving movements of light atoms (molar mass below 20 g mol^{-1}). O–H and N–H stretching bands are located in the region from 3700 to 2500 cm^{-1}. These groups very often participate in the formation of hydrogen bond complexes. The formation of such complexes results in red shifted and very broad spectral bands. C–H stretching bands are found in the 3300–2800 cm^{-1} spectral range. Bands in the 2700–1850 cm^{-1} spectral region usually belong to C≡C, C≡N, N≡N, or some groups containing hydrogen and a heavier atom (S–H, P–H, and Si–H). The 1950–1450 cm^{-1} region exhibits IR absorption from a wide variety of double-bonded chemical groups, in particular C=O. This region is of particular importance for investigations of biological molecules. Conjugation, ring size, hydrogen bonding, steric and electronic effects often result in significant shifts in absorption frequencies.

6.1.2.2 **The Region from 1400 to 900 cm^{-1}**

This is called the *fingerprint region*. Many chemical groups with single bonds have group frequencies in this region. These vibrations usually couple very strongly, that is, particular bands in this region can hardly be attributed to a single chemical

Table 6.1 Selection of characteristic group frequencies of organic compounds.

Spectral range (cm^{-1})	Chemical group	Group vibration
3700–3200	−OH	OH stretching
3400–3330	$-NH_2$	Antisymmetric stretching
3300–3250	$-NH_2$	Symmetric stretching
3065–3050	$-C-H_{aromat}$	C−H stretching
3020–2950	$-CH_3$	Antisymmetric stretching
2960–2910	$-CH_2$	Antisymmetric stretching
2970–2860	$-CH_3$	Symmetric stretching
2860–2840	$-CH_2$	Symmetric stretching
2590–2560	−SH	S−H stretching
2600–2350	−B−H	B−H stretching
2450–2275	−P−H	P−H stretching
2300–2230	$-C{\equiv}C-$	$C{\equiv}C-$ stretching
2260–2230	$-C{\equiv}N$	$C{\equiv}N$ stretching
2250–2100	−Si−H	Si−H stretching
2250–2100	−C−D	CD, CD_2, CD_3 stretching
1760–1720	−C=O	In organic acids
1740–1700	N−C=O	In ketones
1660–1650	−C=O	In amides
1660–1640	−C=N	Stretching
1700–1625	−C=O	Amide I
1660–1640	$-C{=}C^-$	Stretching
1600–1595	$-COO^-$	Antisymmetric $-COO^-$ stretching
1600–1450	−N=O	N=O stretching in organic nitrates
1470–1440	$-CH_3$	Antisymmetric deformation
1470–1440	$-CH_2$	Symmetric and antisymmetric deformation
1430–1420	−CO−OH	CO stretching in organic acids
1410–1390	$-COO^-$	Symmetric $-COO^-$ stretching
1400–1310	$-S{=}O_2^{\ -}$	Antisymmetric stretching
1390–1370	$-CH_3$	Symmetric deformation
1380–1300	$-CF_3$	Stretching
1340–1250	−CO−NH	Amide III
1330–1250	−CH	Deformation
1265–1250	−CO−OH	CO−OH deformation in organic acids
1280–1250		Oxirane, breathing of the ring
1300–1140	−P=O	Stretching
1300–1120	$-CF_2$	Stretching
1200–1120	$-S{=}O_2^{\ -}$	Symmetric stretching
1120–1060	−C−F	Stretching
1300–1100	−C−O−	Stretching
1150–950	−C−C−	Stretching
1070–1040	−S=O	Stretching
1040–980	$-C_6H_5$	In-plane deformations of benzene rings
900–670	$-CCH_{aromat}$	Aromatic C−H out-of-plane bend

(continued overleaf)

Table 6.1 (*Continued*)

Spectral range (cm^{-1})	**Chemical group**	**Group vibration**
930–830	–COC–	Symmetric stretching in ethers
760–680	–C–Cl	Stretching
780–720	$-CCl_2$	Symmetric stretching
700–660	$-CCl_3$	Symmetric stretching
650–600	–C–Br	Stretching
620–600	$-CBr_2$	Symmetric stretching
560–540	$-CBr_3$	Symmetric stretching
560–500	–C–I	Stretching

Table 6.2 Selection of characteristic group frequencies of inorganic compounds.

Spectral range (cm^{-1})	**Chemical group**	**Group vibration**
3300–3030	Ammonium NH_4^+	NH stretching
2200–2000	Cyanide, thiocyanate, cyanate, complex ions	CN stretching
1450–1410	Carbonates CO_3^-	CO stretching
1430–1390	Ammonium NH_4^+	NH_4 bending
1380–1350	Nitrates NO_3^-	NO stretching
1250–1230	Nitrites NO_2^-	NO stretching
1130–1080	Sulfates SO_4^-	SO stretching
1100–1000	Phosphates PO_4^-, HPO_4^-, $H_2PO_4^-$	PO stretching
1100–900	Silicates	SiO stretching
880–860	Carbonates CO_3^-	OCO bending
840–815	Nitrates NO_3^-	ONO bending
840–800	Nitrites NO_2^-	ONO bending
680 to 610	Sulfates SO_4^-	OSO bending

bond or group. On the other hand, bands caused by complex interacting vibrations constitute a unique fingerprint for each compound. If two spectra exhibit identical fingerprint patterns in this region, the corresponding samples are generally considered to be identical.

6.1.2.3 The Region from 900 to 400 cm^{-1}

Some characteristic bands of aromatics occur in this region. These bands are due to aromatic C–H out-of-plane bending vibrations. The absence of absorption bands in the 900–650 cm^{-1} region usually indicates the absence of aromatic rings in the molecule under investigation. Some organic molecules containing halogen atoms can also contribute in this region. In the case of inorganic molecules, the bands due to bending vibrations of the molecular fragments OXO type, where X = C, N, or S are present in this region.

On the basis of extensive experience, the following scheme for interpretation of IR spectra based on group frequencies was worked out. No systematic procedure of general validity exists, and a reasonable way to proceed is as follows:

1. Carbon backbone:	Evaluation of C−H str, C−H def, C−C str Presence of aromatics −C−C−, −C=C−, −C≡C− groups Compare with NMR data!
2. O-containing compounds:	Evaluation of C=O str, O−H str Interactions with −C−H− str, −N−H− str, −O−H str
3. N-containing compounds:	Evaluation of N−H str, C≡N str Compare with MS data!
4. S-, P-, Hal-containing compounds:	Evaluation of S−H str, S=O str, $-SO_2$ str, P=O str, C−Hal str Compare with chemical analysis and MS data!

It should always be remembered that the aim of structural analysis based on characteristic IR frequencies is to identify structural groups, not to ascertain the total molecular structure of the analyte. Even the identification of structural groups should be based on different chemical and physical data, not just on a single IR spectrum. In general, it is impossible to deduce the total molecular structure solely by interpretation of IR spectra by means of correlation tables. Sometimes, the absence of a particular absorption may be more informative than its presence.

A very general approach is the comparison of experimental spectra with calculated spectra. For small molecules (up to 40–60 atoms), it is possible to predict their structure and IR and Raman spectra with reasonable precision by quantum chemical (*ab initio*) methods. By comparing theoretical and experimental spectra, the bands can be assigned. If calculated and the experimental spectra fit each other, the structure used for calculation should be the correct one.

Nowadays, the spectra of polymers and other large molecules can only be computed by semiempirical or molecular mechanics calculations. Such calculations allow one to predict the molecular structures, but do not give (or give too little) information about the vibrational frequencies and cannot be used for the interpretation of spectra.

6.1.3
Special Applications

Various modern accessories (ATR crystals, acoustic detectors, IR microscopes, polarization modulation technique) as well as hyphenation techniques substantially expanded the field of applications of IR spectroscopy. Applications of IR spectroscopy to surface investigations (characterization of the surface, physisorption and chemisorption studies, catalytic properties) are reviewed in [6–8]. Applications of hyphenated techniques, in particular combinations with chromatography, are given in [7].

IR spectroscopy retains its importance in the field of *industrial applications*, Raman spectroscopy regains attraction. A detailed summary of applications can be found in [9]. The industrial environment requires special conditions for the instruments such as rapid measurements, the high degree of automation and reliability, robustness, and special software. Of importance are the sampling methods, the data transfer to computer networks, and the software for quantitative analysis. A major field is quality assurance, for example, in the pharmaceutical and semiconductor industry. A very new field is the use of IR for industrial combinatorial chemistry. The most rapidly growing area is the on- and in-line process control in almost all industrial applications. For the investigation of inorganic substances and coordination and organometallic compounds, IR techniques also are suitable. An excellent survey of the experimental aspects and the applications with many examples is given in [10].

In recent years, the use of IR spectroscopy for *medical applications* such as in the analysis of human tissues and body fluids such as blood has substantially increased. In such kinds of measurements, all modern spectroscopic methods such as mapping and ATR microscopy, the data need to be evaluated by statistical and multivariate analysis. IR spectroscopy is very sensitive to structure and concentration changes of biological macromolecules such as nucleic acids, proteins, and lipids. A summary of this field is given in [11]. Examples of successful applications of IR are the monitoring of cellular metabolism and the identification of tumors. PAS applications in life sciences studies as well as on solids, liquids, and gases are described in [12]. A new method for applications in biology, medicine, and industry (semiconductors) is IR imaging spectroscopy, a combination of IR microscopy with a focal plane array detector. Another new method is 2D spectroscopy where the spectral intensity is obtained as a function of two independent spectral variables. A short description of the method is given in [13] and the literature cited therein.

The *analysis of polymers* is one of the most important application fields for IR spectroscopy. This kind of spectroscopy can be successfully used for the determination of chemical structures such as stereoregularity, chain conformation, orientation, and crystallinity, for the identification of complex polymeric systems, for monitoring the reaction processes, and for the study of dynamic properties such as diffusion. All these applications are discussed in [14].

For *forensic analysis*, IR spectroscopy is a commonly used method. A description of all application fields with many samples is described in [15]. Specific analyses are the analysis of paints, paper, inks, gemstones, polymers, fibers, food, and the analysis of physiological samples, and environmental samples. The main methods of investigation are the ATR diamond cell and all reflectance techniques as well as the GC-IR technique.

An excellent summary about the use of the IR spectroscopy in the *study of works of art* is given by Edwards [8]. So it is possible to investigate plastics, glass, faience, biomaterials, paintings, medieval manuscripts, and wall paintings to determine the origin and the age of all these art objects (see Reference Data Table 6.1).

Reference Data Table 6.1 Method parameter reference sheet.

Method	IR spectroscopy
Characterized parameter	Absorbance
Type of information	Functional groups, structure, concentration, identity
Required user skills	Unskilled for routine measurements

Sample

	Excellent	Good	Fair	Poor	Problems
Pure compound	+				
Multi-analyte	+				
Gaseous		+			
Liquid	+				
Solid	+				
Matrix effects/matrix assisted			+		
Size		+			
Trace			+		
Cross sensitivity	+				
Identification	+				
Quantification	+				

Equipment (typical data)

CW/Fourier	Fourier
Internal/external reference	External reference
Single/double beam	Single and dual beam
Destroying sample	Noninvasive
Sequential/simultaneous	Simultaneous
Source	Glowbar
Dispersion by	
Filter/monochromator	
Nondispersive	Nondispersive
Absorption/emission/scattering	Absorption
Ratio recording	Yes

Spectrometer (typical parameter)

Frequency/wave number/wavelength range	4000–400 cm^{-1} (2.5–25 μm)
Time per spectrum	0.5–10 min
Noise	
Signal/noise	1000 : 1 at high concentration
At high/low concentration limit	5 : 1 at low concentration
Reproducibility (wavelength, signal)	$\pm 1\ cm^{-1}$
Spectra overlay (single/multi)	Multi

(*continued overleaf*)

Reference Data Table 6.1 (*Continued*)

Sampling (number of times)	64–1024
Resolution (nm, s^{-1}, cm^{-1}, molecular weight)	$1\,cm^{-1}$
Limit of detection	mM
Time required for analysis	
Preparation	0–10 min
Measurement	0.5–10 min
Evaluation	10–30 min
Cost per sample (€)	10 (estimated)

CW, continuous wave.

Techniques yielding similar information: Raman spectroscopy.

Typical features of attached computers: computers (not built-in) are part of modern MIR spectrometer. The supplied software manages data acquisition and analysis. Additional software for chemometric evaluation is available.

Typical application (*as demonstrated in chapter*): qualitative and quantitative analysis, *in situ* measurements, process control.

Preferable samples: solutions in percent concentration.

Problematic samples: water as solvent, weakly absorbing samples.

6.1.4
Infrared and Raman Spectroscopic Imaging

Applications of IR and Raman spectroscopic imaging are nowadays found in all areas from bioanalytical chemistry of cells and tissue via food and polymers to homeland security [16].

The identification of relevant molecular processes and the distribution of biochemical features now provide the potential for an early detection of diseases and

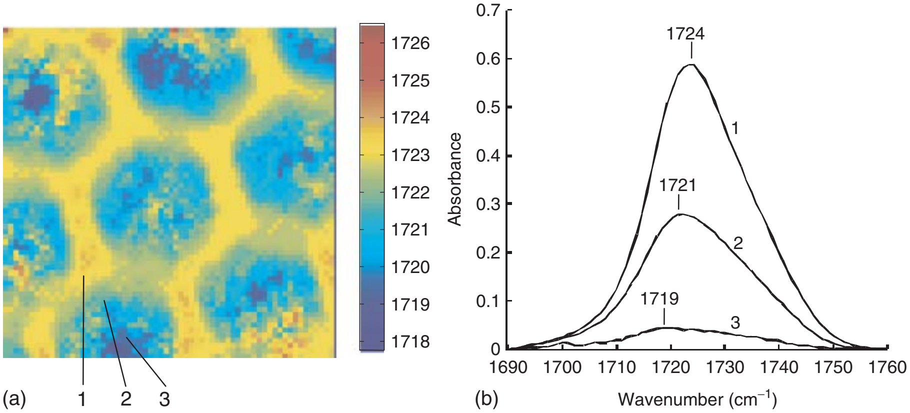

Figure 6.7 (a) Color-coded image, indicating the distribution of PMMA molecules in a microstructured 350 nm thick PMMA layer on gold substrate. Intensity and position of ν(C=O) infrared spectral band is taken as an indicator of concentration and type of adsorption of PMMA. (b) ν(C=O) bands that represent web region (1), pore wall (2), and pore center (3).

their optimized treatment. Therefore, the majority of the FTIR imaging activities are aimed at biochemical and medical questions. Most of these applications have been performed on thin tissue sections with the use of an IR microscope. The characterization of polymer samples based on FTIR imaging has emerged rapidly during the past 5 years. Chemical image of poly(methyl methacrylate) (PMMA) microstructured layer on gold substrate obtained by means of IR spectroscopic imaging is presented in Figure 6.7.

Other applications are focused on the identification and visualization of components in polymer blends and copolymers. The chemical images allow to identify the spatial distribution of polymers, the crystallinity, or the degree of orientation. Relatively new applications of FTIR imaging are the forensic analysis and the chemical monitoring of finger marks. Another growing field of spectroscopic imaging covers investigations of plant tissue (Figure 6.8). IR spectroscopic imaging is also an ideal tool for the high-throughput analysis.

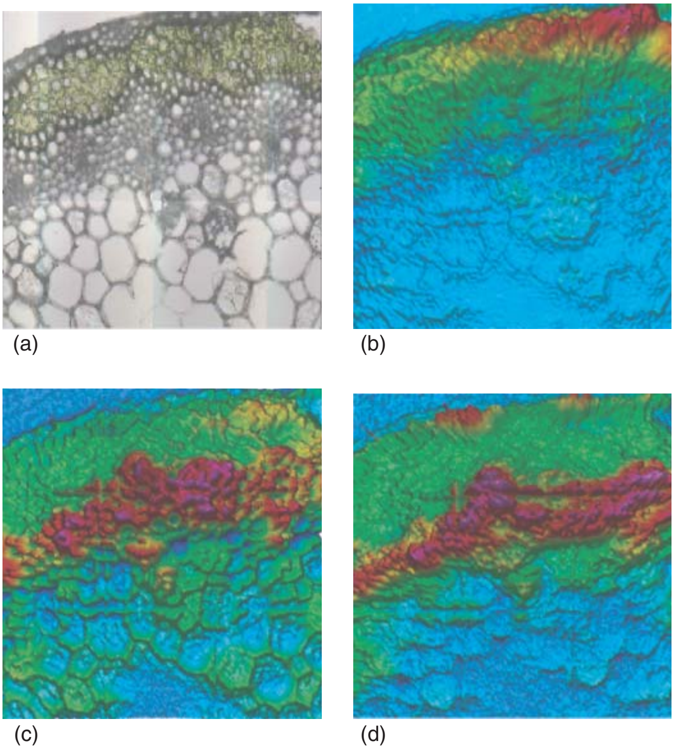

Figure 6.8 (a) Microscopic video image of a thin section of wheat stalk. The dimension of the image is approximately 500 µm × 500 µm. (b–d) The false color images representing the distribution of the three main components. The contrast is calculated from the intensity of the absorption in representative spectral ranges: proteins 1480–1710 cm^{-1}, carbon hydrates 900–1140 cm^{-1}, and lipids 1700–1770 cm^{-1}.

6.2
Near Infrared Spectroscopy

The NIR spans the range from 12 500 to 4000 cm^{-1} (800–2500 nm) and is dominated by overtones and combinations of O–H, N–H, C–H, and C=O vibrations. Overtone and combination bands are rather weak. Band intensities usually drop by a factor between 10 and 100 from excitation level to excitation level. The low absorbance of overtones and combinations restricts the application range of NIR spectroscopy usually to liquids and solids. Absorption regions for some important groups and vibrations are given in Table 6.3. In addition, the short wavelength NIR range covers lowest-energy electronic transitions. Fermi and other resonances occur in the region as well [17].

NIR is increasingly used in process and environmental analysis, food industry, agriculture, pharmaceutical industry, and polymer analysis. In-line measurement with fiber optics and rapid multicomponent quantification are the most important advantages of NIR spectroscopy. In comparison to MIR, NIR analysis is much faster and more versatile. Most samples are analyzed in 1 min or less. Often chemometric methods must be applied to determine the parameter of interest.

6.2.1
Sample Preparation and Measurement

One of the greatest advantages of NIR spectroscopy is the ease of sample handling. Often, common transmission and reflection techniques can be used for nondestructive analysis. Thus, NIR analysis eliminates the sampling errors caused by manual handling and reagent or solvent contamination.

Table 6.3 NIR absorption regions of important groups and vibrations.

Group	Type of vibration (ν, stretching, δ, bending)	Wavenumber (cm^{-1})	Wavelength (nm)
Free OH	3ν (second overtone)	10 400–10 200	960–980
Bound OH	3ν (second overtone)	10 000–8 850	1000–1130
C–H (CH_3, CH_2)	3ν (second overtone) and	8 700–8 200	1150–1220
	combination $2\nu + 2\delta$	7 350–7 200	1360–1390
Free OH	2ν (first overtone)	7 140–7 040	1400–1420
C–H (CH_3, CH_2)	Combination $2\nu + \delta$	7 090–6 900	1410–1450
Hydrogen-bonded OH	2ν (first overtone)	7 140–6 170	1420–1620
Free NH	2ν (first overtone)	6 710–6 500	1490–1540
Hydrogen-bonded NH	2ν (first overtone)	6 620–6 250	1510–1600
S–H	2ν (first overtone)	5 780–5 710	1730–1750
CH_3 and CH_2	2ν (first overtone)	6 020–5 550	1660–1800
C=O	3ν (second overtone)	5 230–5 130	1910–1950
Free OH	Combination $\nu + 2\delta$ and 3δ	5 210–5 050	1920–1980
C–H (CH_3, CH_2)	Combination $\nu + \delta$	4 440–4 200	2250–2380

For liquids, quartz cells similar to those used in UV/vis can be used. Because of the weak absorption coefficients, most samples need not be diluted, and cell of large pathlength up to some centimeters are possible. NIR spectra of some common solvents are shown in Figure 6.9. Tetrachloromethane is well suitable because all C–Cl vibrations occur far away from the NIR range. In contrast, water and ethanol are not suitable because of their strong O–H absorption bands. For the same reason, drying may be necessary for native samples (agriculture and food analysis) (Table 6.4).

Weakly scattering solids can be investigated by transmission techniques. For strongly scattering samples, diffuse reflection accessories must be used.

Slight temperature variations may lead to a shift of band positions and to changes in absorbance. This is of particular importance for quantitative evaluation of NIR spectra. The NIR spectra of water at several temperatures, shown in Figure 6.10, reveal band shifts toward shorter wavelengths, which arise from changes in average size of molecular clusters and from weakening of strongly H-bonded states [18]. Temperature effects of this size in aqueous samples can easily overlap weak absorption signals from weakly concentrated analyte.

The availability of low-cost, highly transmitting NIR fibers led to wide spread application of NIR fiber sensors. Fibers may simply be used as light guide between the NIR spectrometer and the measuring point, or they may serve as sensor by using the evanescent field of light totally reflected inside the fiber. NIR fiber optic sensors combined with statistical data evaluation are increasingly used for in-line monitoring of chemical compounds or reactions.

6.2.2
Application of NIR Spectroscopy

Fiber optic sensors provide access to real-time reaction profiles and to careful controlling of reactions. The need to measure product quality during the production process has driven the development of NIR fiber optic sensors. Gas, liquid, and solid material can be analyzed. An important field is *environmental monitoring*. NIR in combination with fiber optics is applied to acquire information about volatile organic compounds in water and waste water, sediments, mud, and solid samples. The polymer cladding (e.g., silicone) of optical fibers may act as a hydrophobic membrane that enriches nonpolar compounds in water. Chlorinated hydrocarbons and aromatic substances in water can be detected by using the evanescent field absorption of fiber guided light up to the subparts per million concentration range [17].

NIR spectroscopy has been used for more than 30 years in the *food industry and agriculture*. Main applications are in the determination of moisture and characterization of other compounds, for example, protein content in grain and milk products. Usually, diffuse reflection is measured, because samples need not be prepared extensively. Compared to wet chemical analysis or other instrumental methods of analysis, NIR in particular allows rapid detection even under field conditions. Some basic characteristic wavelengths are listed in Table 6.3.

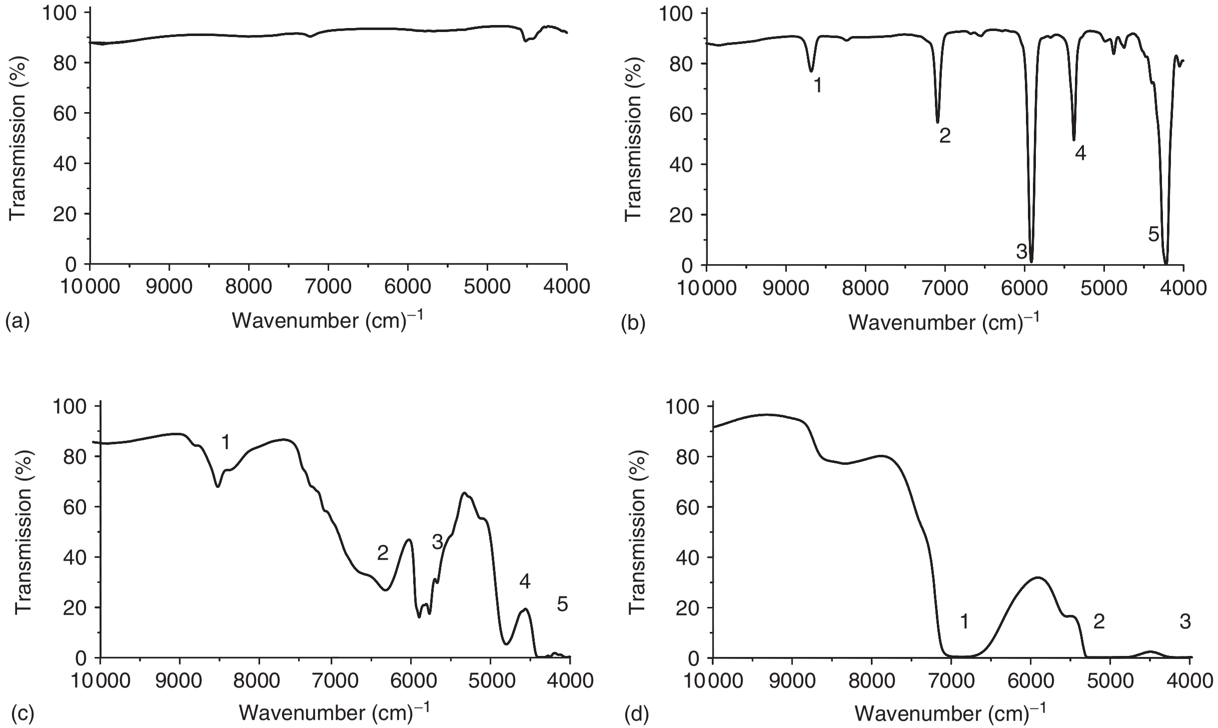

Figure 6.9 NIR spectra of some typical solvents such as (a) tetrachloromethane, (b) trichloromethane, (c) ethanol, and (d) water, recorded in 2 mm quartz cells. For band assignments see Table 6.4.

Table 6.4 Assignments of the most pronounced NIR absorption bands of solvents shown in Figure 6.9.

Water		Ethanol		Trichloromethane	
#		#		#	
1	2ν O–H	1	Second overtone ν C–H, combination C–H	1	Second overtone ν C–H
2	Combination	2	First overtone ν O–H, combination CH_2/CH_3	2	Combination C–H
3	ν O–H	3	First overtone ν C–H	3	First overtone ν C–H
		4	Combination O–H, ν C–O fourth overtone	4	Combination C–H
		5	Combination CH_2/CH_3, νO–H	5	Combination C–H

Bands are numbered as in the figure.

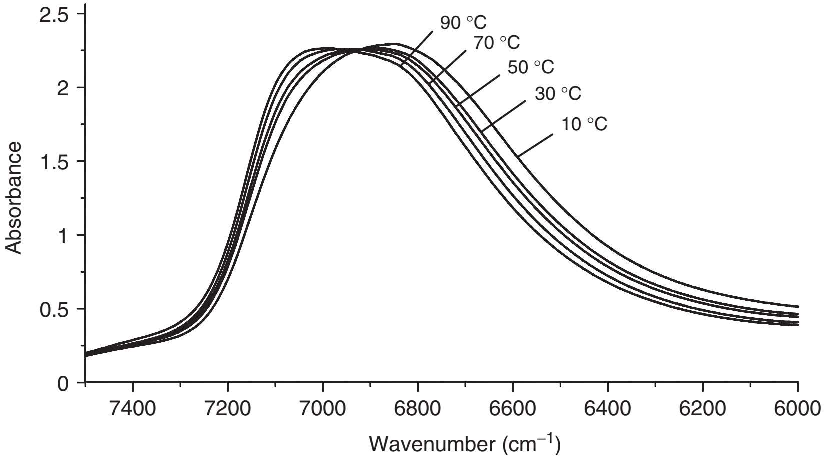

Figure 6.10 NIR spectra of water at different temperatures, recorded in a 2 mm quartz cell.

Table 6.5 Typical wavelengths for characterizing of food by NIR measurements [19].

Wavenumber (cm^{-1})	Compound
4400	Lignin
4330	Oil
4280	Cellulose
4590	Protein
4760	Carbohydrate
5150	Moisture

Moisture and hydroxyl number are important parameters, which are determined by measuring either the first overtone at 6890 cm^{-1} or the combination band at 5180 cm^{-1}. A few details about chemical structure are accessibly by interpretation of these bands. Changes in hydrogen bonding lead to changes in band shape and band location. Difference spectra or second derivatives must be calculated in order to detect minor chemical interactions of OH with other molecular species in the sample. The content of double bounds is another important parameter to describe properties of fats and oils, for example, their degree of unsaturation.

NIR spectroscopy can also be used to identify different makes or different charges of the same product. Chemometric evaluation even of very similar looking spectra provides access to the parameter of interest or to distinguish between similar samples. Spectra of different edible oils are shown in Figure 6.11. Despite the similarity of their spectra, samples can be well discriminated by statistical data analysis.

In the food industry, NIR spectroscopy is the most common in-line method to monitor moisture, oil, fat, and analyze grains, feeds, meat dairy, and other products for protein content. Metabolites in the leaves of spice plants can be determined by using NIR reflection measurements [20]. Accuracy and precision achieved are better than ±0.2% [21]. On-line measurements are also made in diverse snack food products.

NIR spectroscopy is applied in the *pharmaceutical industry* to analyze raw material, drugs, and to identify packing materials. The effect of drugs – among other things – depends on the crystalline form in which the drug exists. While structural information is available in MIR, secondary interactions between several groups are often seen in NIR. Thus, polymorphism of drugs as well as isomeric purity of optically active substances can be monitored by NIR.

In *polymer industry*, packing material, laminates including multilayer films, pellets, or molded products can be analyzed by NIR. Even polymer latex particles with up to 99% water content may be analyzed. NIR provides information about reaction mechanism, polymerization, crystallinity, orientation, water content, and hydrogen bonding, even during the process of polymers manufacturing. For example, the disappearance of the double bonds in polyethylene and polypropylene can be monitored. In their NIR spectrum, C=C bonds lead to a combination band at about

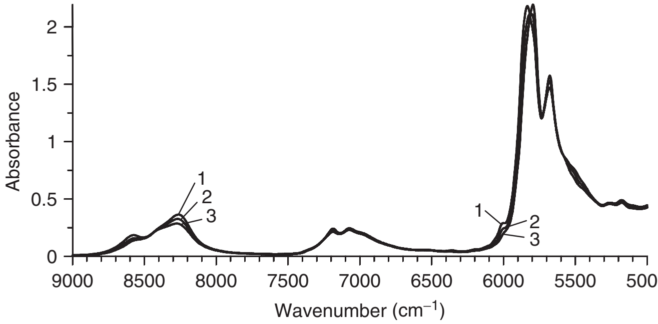

Figure 6.11 NIR spectra of three different edible oils: (1) flax oil, (2) sunflower oil, and (3) olive oil. The spectra are dominated by C–H and O–H bands.

$4740\,\mathrm{cm}^{-1}$ and a first overtone at about $6170\,\mathrm{cm}^{-1}$. NIR spectroscopy is applied to characterize ester-, nitrile-, or amide-based acrylic and methacrylic polymers. Other examples are the identification of poly(vinyl chloride), poly(vinyl alcohol), and poly(vinyl acetate) or the analysis of polymerization in epoxy and phenolic resins.

NIR is applied in many areas of *medicine*, *biology*, and *biotechnology*. Optical fibers for the NIR and new fiber optic compact process spectrometer as well as NIR light emitting diodes (LEDs) permit new applications in medical diagnosis [22]. Proteins [23], blood glucose [24], cholesterol, and fatty acids have been subjected to the investigations. Although *in vivo* NIR is connected with many problems such as high water absorbance in tissue, light scattering, band shift caused by temperature changes, and band overlap, the advantages of NIR are evident in the application in living tissues and cells [25]. Optical tomography systems use NIR spectroscopy to image the cerebral cortex and the level of oxygenated blood in the tissue [26]. In biotechnology, NIR spectroscopy is mainly used to monitor fermentation processes and to measure biomass, nutrient products, or the concentration of byproducts in real time.

NIR spectroscopy is an important method for rapid on-line monitoring of oil *and petrol production* processes. It has become an essential component in hydrocarbon processing. NIR reflection spectrometers are also used to analyze oil sand in petrol industry. NIR spectroscopy is used for *in situ* quantification of liquid natural gas. Feed streams can be monitored as well. Finally, NIR reflection spectroscopy is also used to determine pollution and contamination of oil and other petrol chemical products in sand and earth [27] (see Reference Data Table 6.2).

Reference Data Table 6.2 Method parameter reference sheet.

Method	NIR spectroscopy
Characterized parameter	Absorbance
Type of information	Concentration, structure
Required user skills	Skilled in preparation of samples

sample

	Excellent	Good	Fair	Poor	Problems
Pure compound	+				
Multi-analyte	+				
Gaseous				+	
Liquid		+			
Solid			+		
Matrix effects/matrix assisted			+		
Size			+		
Trace				+	
Cross sensitivity				+	
Identification		+			
Quantification		+			

(*continued overleaf*)

Reference Data Table 6.2 (*Continued*)

Equipment (typical data)	
CW/Fourier	CW
Internal/external reference	External reference
Single/double beam	Single and double beam
Destroying sample	Noninvasive
Sequential/simultaneous	Sequential
Source	Tungsten lamp, NIR diodes
Dispersion by	
Filter/monochromator	Filter, monochromator, interferometer
Nondispersive	
Absorption/emission/scattering	Absorption
Ratio recording	Yes

Spectrometer (typical parameter)	
Frequency/wave number/wavelength range	12 500–4 000 cm^{-1} (800–2 500 nm)
Time per decay curve	0.5 till 5 min
Noise	
Signal/noise	500 : 1 at high concentration
At high/low concentration limit	5 : 1 at low concentration
Reproducibility (wavelength, signal)	$\pm 1\ cm^{-1}$
Spectra overlay (single/multi)	Single
Sampling (number of times)	Once
Resolution (nm, s^{-1}, cm^{-1}, molecular weight)	1.5 cm^{-1} typically
Limit of detection	mM
Time required for analysis	
Preparation	0 till 10 min
Measurement	0.5 till 5 min
Evaluation	10 till 30 min
Cost per sample (€)	10 (estimated)

CW, continuous wave.
Techniques yielding similar information: infrared spectroscopy.
Typical features of built-in computers: built-in computers are not part of modern NIR spectrometer. The supplied software manages data acquisition and analysis. Additional software for chemometric evaluation is also available.
Typical application (*as demonstrated in chapter*): in-line measurements, process control, quantitative analysis.
Preferable samples: molar till micro molar solutions.
Problematic samples: water as solvent, gaseous samples, weak absorbing samples.

6.3
Raman Spectroscopy

Raman spectroscopy is a technique, which is complementary to IR spectroscopy. It offers particular advantages over MIR and NIR spectroscopy. As water is a weak scatter medium in the vis range, no special accessories are needed for measuring aqueous solutions. Furthermore, atmospheric gases are very weak scatterers, and therefore purging of the Raman instrument is not needed. Ordinary glass is transparent in visible and NIR spectral regions, where Raman spectra are excited, hence inexpensive liquid sample cells made from glass can be used in most Raman measurements. For remote analysis, glass fiber optics can be used. The standard Raman spectral range extends down to $10\,\mathrm{cm}^{-1}$, the technique is ideal for both organic and inorganic samples.

Limitations of Raman spectroscopy in comparison to IR are sensitivity and undesired fluorescence. Relatively expensive and sophisticated instrumentation also should be taken into account.

6.3.1
Sample Preparation and Measurements

The alignment of optics used for delivering the laser beam to the sample and for collecting Raman scattered radiation toward the spectrometer entrance slit is very important for the effective application of Raman spectroscopy, as Raman scattering is very weak. In conventional Raman instruments, this procedure is rather tedious and requires some experience. In FT-Raman instruments, this is more a routine task, because the alignment is based on the observation of the Raman interferogram. Various setups can be used to collect Raman scattering. The most common ones are 90° collection and 180° collection (back scattering) geometries (Figure 6.12). Zero degree scattering geometry is also possible but rarely used.

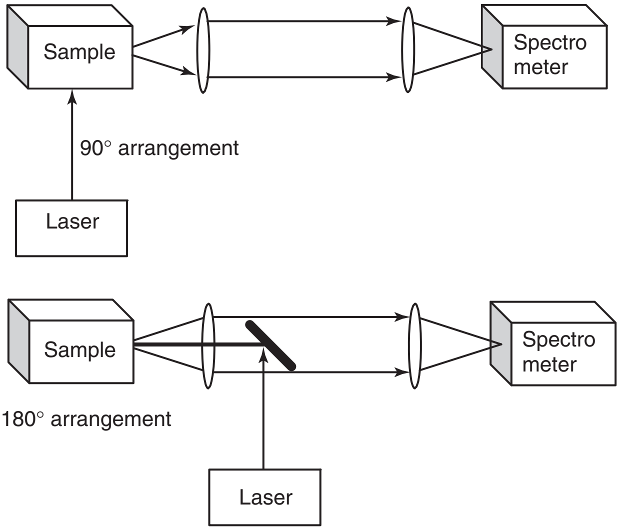

Figure 6.12 Most common sampling geometrics in Raman spectroscopy.

6.3.1.1 Sample Illumination and Light Collection

Sample illumination and methods for collecting Raman scattered light can be subdivided into three groups: by the use of conventional optics such as lenses and mirrors, by the use of fiber optics, and by optical microscopes.

A comprehensive overview of cells and sample illumination methods in Raman spectroscopy is given in [3]. Rectangular cells, spherical cells, NMR tubes, or light pipes may be used. Most popular arrangements for sample illumination are shown in Figure 6.13.

Optical fibers are increasingly used for remote Raman probing, for example, to monitor chemical processes in-line or inside a reactor. The laser beam is guided to the probe head by an excitation fiber, and the Raman signal is returned to the detector by a collection fiber. Probe heads usually work in the 180° arrangement. There are two different types of fiber probes for common use in Raman spectroscopy: the concentric unfiltered fiber bundle and the filtered probe. The fiber bundle is less expensive, while the filtered probe offers better signal-to-background ratio in certain applications.

Usually, fiber bundles consist of fibers of 100 μm core diameter. The fibers are cemented into a cylindrical holder and then polished. The central fiber (excitation fiber) delivers laser light to the sample, while the surrounding fibers collect Raman radiation. The laser beam is focused into the excitation fiber by a microscope objective. For coupling to the entrance slit of dispersive spectrometer, the output

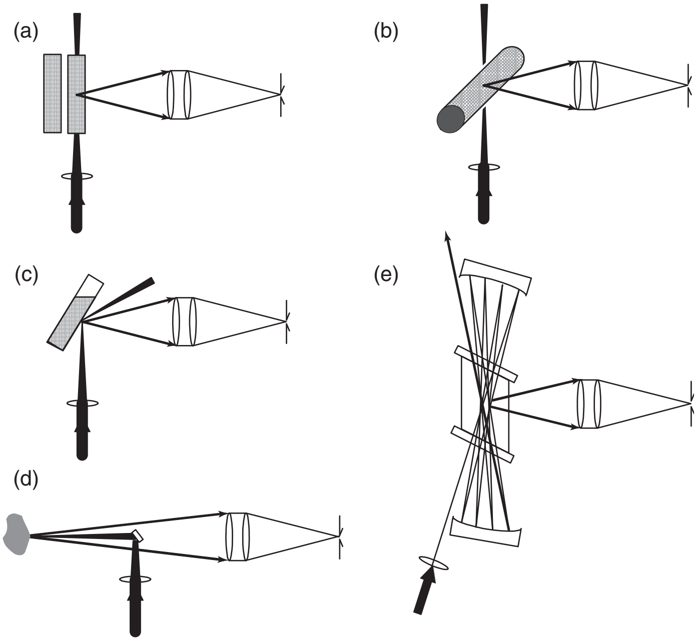

Figure 6.13 Sample illumination in Raman spectroscopy: (a,b) liquid sample; (c) liquid or solid sample; (d) solid sample; and (e) gaseous sample by multipath excitation.

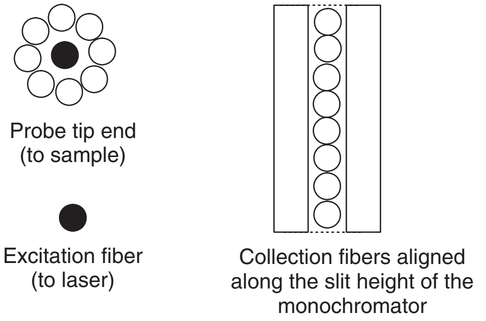

Figure 6.14 Sketch of an eight-around-one fiber probe, showing both ends of the fiber probe.

ends of the collection fibers are arranged in a row, as shown in Figure 6.14. Matching optics are only needed in case of a difference in f/numbers between fiber and spectrometer. The fiber bundle can be immersed into liquid samples or held at a short distance from the surface of a solid sample. Fibers are usually made from silica, which itself generates Raman as well as fluorescence signals. In most cases, fiber signals can be eliminated, but some noise may be introduced and weak Raman signals may be obscured. These problems are avoided by filtered probes. The basic diagram of such a probe is given in Figure 6.15. Light emerging from the excitation fiber is collimated and diffracted by a transmission grating. All signals except the laser light are blocked by the pin hole. Afterward, the laser light is reflected from the first filter of the notch filter pair toward the sample. The excited Raman and Rayleigh scattering as well as reflected laser light are passed back to the notch filters. These filters remove reflected laser light in order to avoid any fiber background generation as the collected Raman light travels to the spectrometer. The use of lenses allows efficient delivery and collection with single fiber. The advantage of such an arrangement is that once the coupling between the fibers, the laser, and the spectrometer has been optimized, the fiber probe will permit

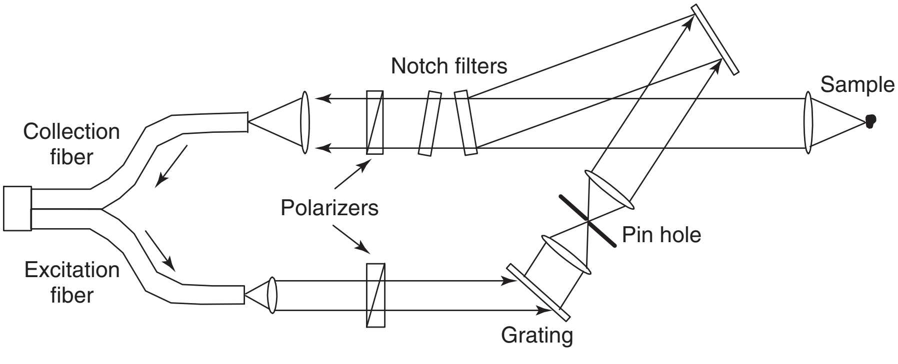

Figure 6.15 Basic diagram of a filtered Raman fiber probe.

spectral acquisition from a variety of liquid or solid samples without any optical realignment. Advanced fiber optics are available in particular in the NIR region.

A sampling technique of distinctly growing importance is the Raman microprobe by using a microscope. It permits the collection of Raman images by mapping or imaging. These techniques allow investigation of samples or sample regions at 1 µm in lateral resolution and 2 µm depth resolution. Depth resolution usually depends on the sample, and in the case of transparent samples, it is worse than the lateral resolution. Depth resolution can be enhanced by decreasing the depth of the focus by using a confocal Raman microscope (cf. Section 5.5.2).

The lateral step size in Raman mapping experiments can be as small as 100 nm. In case of imaging, the Raman signal from the observed sample area is directed by the microscope to a charge-coupled device (CCD) array detector. The wavelength range for investigation has to be selected by a tunable or a set of changeable filters.

6.3.1.2 Polarization Measurements

The depolarization ratio ρ is usually measured in 90° geometry. The experimental setup for Raman polarization measurements is shown in Figure 6.16. Four different spectra can be measured: I_{VV}, I_{VH}, I_{HV}, and I_{HH}, with the first index denoting the polarization of laser radiation and second one the polarization of the Raman scattered light. Actually, the last three polarized Raman spectra contain the same information ($I_{VH} = I_{HV} = I_{HH}$) and the depolarization ratio is defined as $\rho = I_{VH}/I_{VV}$ (cf. Eq. (14) in Section 3.3). These two spectra are usually measured one after the other with the corresponding positions of the analyzer. Polarization measurements have significant value for chemical analysis. They can give important information about the molecular symmetry of an unknown (symmetry of molecular packing in the crystal cell in case of monocrystalline samples) or give additional arguments for assignment of Raman bands.

In the case of highly symmetrical molecules (e.g., molecules with symmetry axes higher than second order), the depolarization factor ρ is equal to zero for total symmetric normal vibrations. In case of molecules of low symmetry, ρ can vary between 0 and ¾ for the corresponding Raman bands. For non-fully symmetric

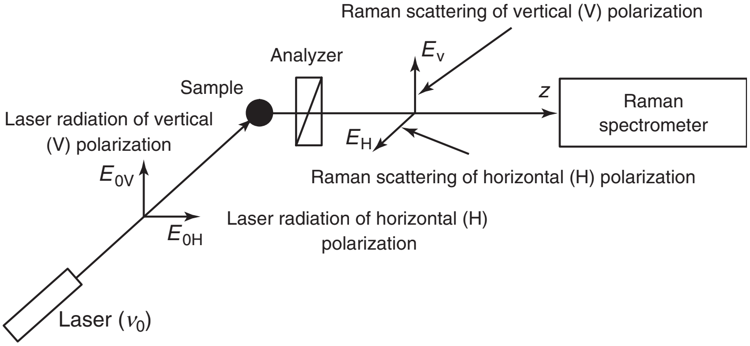

Figure 6.16 Setup for measuring depolarization ratios of Raman bands in 90° geometry.

vibrations of any molecule, ρ is equal to ¾ (or to 6/7 in case of excitation with nonpolarized light). This polarization rule is valid for liquids and gases, that is, for samples with chaotically oriented molecules. In solids, the situation is more complex. The spectral intensities I_{VV} and I_{VH} of crystalline samples depend on the orientation of the crystal axis with respect to the polarization of the incident light. In polycrystalline samples consisting of many small crystallites of different orientation, the scattered light undergoes multireflection at the crystallites, and the polarization information of Raman bands is lost.

In any anisotropic system, the depolarization factor may be used as a valuable source of information about the orientation of molecules, for example, about the orientation of polymer chains in fibers or the orientation of adsorbed molecules on surfaces.

6.3.1.3 **Enhanced Raman Scattering**

The quantum yield of the classical (or so-called linear) Raman effect is rather poor. Only a fraction of 10^{-6} to 10^{-8} of the exciting photons are converted into Raman photons. This excludes low concentrated analytes from being detected. Moreover, Owing to the very high quantum yield of fluorescence, even traces of fluorescent impurities may mask the Raman signal by their fluorescence. Therefore, there are many scientific efforts in developing Raman based methods, which allows one to overcome the problem. Such methods are resonance Raman scattering (RRS) and surface enhanced Raman scattering (SERS).

6.3.1.3.1 **Resonance Raman Scattering (RRS)** In linear Raman spectroscopy, the energy of the exciting photon is assumed to be much smaller than the energy of the lowest electronic transition. If the energy of the exciting photon approaches the energy of the electronic transition, the intensity of some Raman spectral bands increases by a factor of 10^2–10^4 because of resonance between electronic and vibrational excitation. The selection rules RRS are completely different from those in linear Raman scattering. Overtones of normal vibrations with $\Delta\nu = 1, 2, 3, 4, \ldots$ can be observed in RRS spectra. Figure 6.17 shows the RRS of I_2, whose spontaneous Raman spectrum has only one spectral band at 211 cm^{-1} with a low intensity of about 100 photon counts per second.

There are two physical reasons for the enhancement in RRS, the Franck–Condon (FC) enhancement and the vibronic enhancement. Both mechanisms are complicated, a detailed description of which is given in [28]. An application of RRS is the investigation of biological molecules such as metalloporphyrins and carotenoids. These molecules have very strong electronic transitions in the vis. The vibrations of the chromophoric part become resonance enhanced, whereas the vibrations of the surrounding protein matrix do not. This allows observation of the chromophoric site without spectral interference from the surrounding protein. RRS is suitable for molecules with strong vis absorptions such as fullerenes or polydiacetylenes. RRS can also be exploited in the UV, where many molecules absorb. However, the high costs of the equipment (lasers, optics, spectrometers) have limited the use of UV-RRS spectroscopy to a small number of specialists.

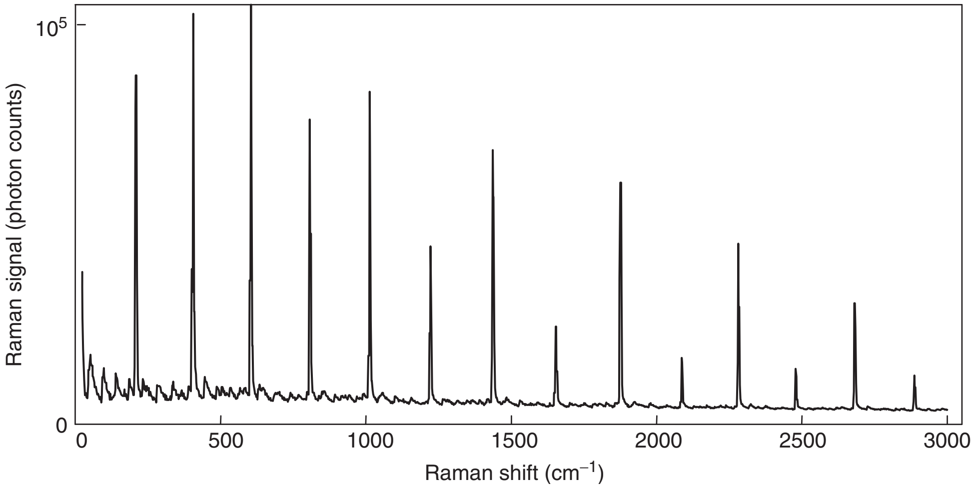

Figure 6.17 Resonance Raman spectrum of gaseous iodine. The argon ion laser line at $\lambda = 514.5$ nm was used for excitation.

6.3.1.3.2 **Surface Enhanced Raman Scattering (SERS)** This effect gives rise to an enhancement of the Raman signal up to six (or even more) orders of magnitude. As yet there is no complete theoretical understanding of this type of enhancement. Two mechanisms are taken into account to explain the SERS effect.

The first is an enhanced electromagnetic field formed at the surface of the metal. Molecules adsorbed on the metal surface experience a large increase in electromagnetic field strength compared to the strength of the incident radiation. The extent of the electromagnetic enhancement depends on a number of factors, including the electric properties of the metal, the distance of the molecule from the surface, the orientation of the molecule with respect to the normal of the surface, the energy of the incident radiation, the morphology of the surface, size, and geometry of surface roughness. Of particular importance is the surface roughness, which can be tailored electrochemically or by the use of solid or island films. The best morphologies are small particles of less than 100 nm in size or atomic rough surfaces. Only particular metals such as silver, copper, or gold can be used as substrate in SERS technology.

The second mechanism of SERS enhancement consists in the formation of a charge-transfer complex between the metal surface and the molecule. Molecules with lone pair electrons or π clouds such as aromatic amines or phenols show the strongest SERS effect. The effect can also be seen in other electron-rich compounds such as carboxylic acids.

The selection rules for SERS are essentially the same as those for the linear Raman effect. However, because of the fact that the local electrical field at the surface is highest in the direction normal to the surface, only vibrations perpendicular to the surface are strongly enhanced. In order to optimize the surface enhancement effect, the laser frequency has to match the frequency of a plasma resonance.

A large variety of SERS substrates is reported in the literature. The most common substrates are electrodes, colloids, metal films, and silver island metal films.

Because of the huge signal enhancement, SERS is particularly useful for trace analysis as well as for *in situ* investigations of various interfacial processes or of monolayers adsorbed on metals. However, sample preparation is a rather tedious procedure. For this reason, SERS is still more an academic tool rather than a routine analytical instrument. Some applications of SERS are given in [29].

6.3.1.4 Applications of Nonlinear Spectroscopic Techniques

Sum frequency generation (SFG) spectroscopy (cf. Section 3.3 and Section 4.8.2) is a technique very well suited for the investigation of surfaces. The method can be applied under normal conditions, at high pressure, on electrodes of electrochemical systems and at interfaces between solid and liquid phases. Various combinations of polarizations and incidence angles of laser beams can be used. SFG spectra contain information about orientation of molecules at the surface, about their conformations, about composition and structure of the surface layer [30]. Some applications of SFG spectroscopy are described below.

Self-assembled monolayers are perfect objects for SFG spectroscopy – the intensity of the SFG signal usually depends on the degree of ordering of the surface layer. Monolayers can be studied not only on metal surfaces, but also on dielectrics, semiconductors, and even on liquids. A typical SFG study is the investigation of an octadecanethiol (ODT) $SH{-}(CH_2)_{17}{-}CH_3$ monolayer on a gold surface. The CH stretching region of a SFG spectrum of ODT is shown in Figure 6.18. The most intense spectral bands are 2880 cm^{-1} ($\nu_s CH_3$), 2932 cm^{-1} (Fermi resonance duplet), and 2963 cm^{-1} ($\nu_{as} CH_3$). The CH_2 vibrations are inactive in SFG spectra because of the symmetry of the $(CH_2)_{17}$ chain.

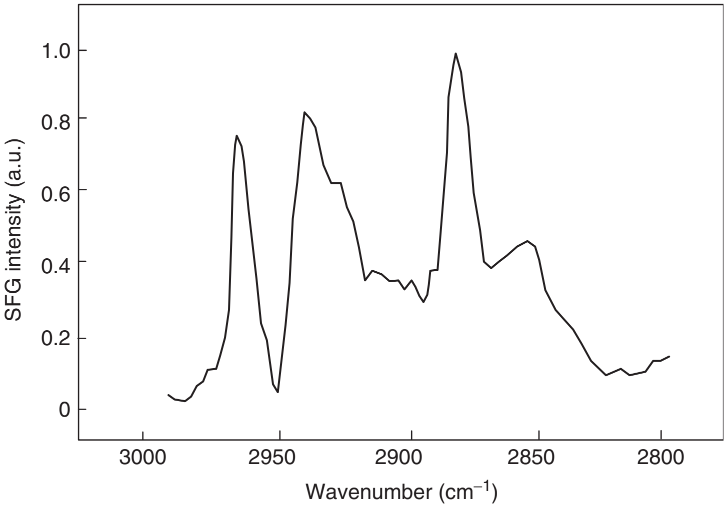

Figure 6.18 SFG spectrum of an octadecanethiol monolayer on gold.

SFG spectroscopy enables the study of *in situ modified polymer surfaces*. SFG was already applied to such technically important polymers as polyethylene, polyimide, poly(ethylene glycol). It was also applied to polymers chemically tuned to be biocompatible such as polymethacrylate and electricity conducting polymers such as polyaniline [3, 30].

Liquid surfaces are very important for processes such as biological functions, electrochemical reactions, wetting chemistry. The asymmetry of the surface layer causes properties of the surface which differ from those in the bulk phase. Investigations by conventional spectroscopic techniques are usually hampered by overlapping of spectral signals from the surface and from the bulk phase. SFG does not suffer from this problem because of the fact that signals from the centrosymmetric bulk phase are usually very weak. An SFG spectrum of a liquid surface is shown in Figure 6.19. The SFG spectrum of methanol consists of intense spectral band of the CH_3 symmetrical stretch at 2832 cm^{-1} and two less intense bands at 2925 and 1951 cm^{-1} because of Fermi resonance between the CH_3 symmetrical stretch and the overtone $2\rho(CH_3)$. This spectrum reveals that the methanol molecules are oriented at the surface with alkyl groups sticking out of the surface.

For Raman studies of biomolecules, which are often not available in large amounts, nonlinear techniques such as stimulated Raman spectroscopy (SRS) and coherent anti-Stokes Raman spectroscopy (CARS) (cf. Section 3.3 and Section 4.8.3) can be used. The particular advantage of CARS is its intense signal in the anti-Stokes spectral region, which enables investigations of fluorescent and luminescent samples. A wide application field for nonlinear Raman techniques is the study of gases and their temperature dependence. Applications of nonlinear Raman techniques (hyper-Raman spectroscopy, SRS, CARS) are described in [31, 32].

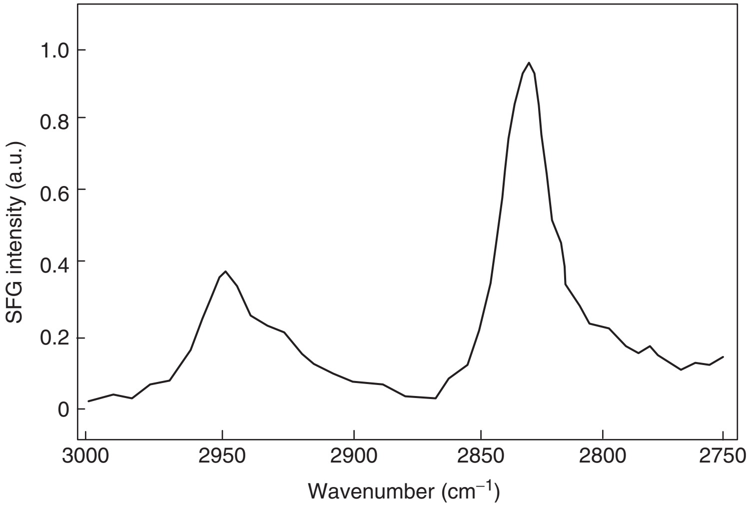

Figure 6.19 SFG spectrum of methanol.

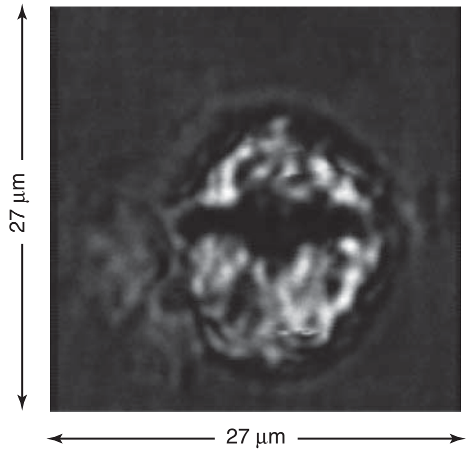

Figure 6.20 CARS image of the nucleus of a T lymphocyte from human blood. The image was obtained by mapping. The CARS microscope was tuned to the CH_2 stretching band at $2850\,cm^{-1}$. Light areas denote higher concentrations of chromatan.

All nonlinear Raman techniques as well as linear Raman enhancement techniques such as RRS and SERS have very high importance in Raman imaging. Owing to the fact that only one Raman spectrum from a very small area of the sample (defined by the size of the focused laser beam) can be captured at a time using a Raman microscope, Raman images of larger sample areas can only be obtained by the mapping technique. In order to ensure a reasonably low measuring time (in the range of minutes) for a mapping experiment at a reasonable lateral resolution, the Raman spectrum of one mapping point should be captured in a couple of milliseconds. This is only possible using one of the enhancement methods for the Raman signal. An example is the CARS image in Figure 6.20. It was obtained by using a Nd:YAG laser at 1.065 µm and an optical parametric oscillator with tunable wavelength for the excitation. The lateral resolution in the image is 0.4 µm. It consists of 270 × 270 mapping points. This CARS image was captured in 5 min (4 ms for one mapping point). A comprehensive review of various Raman imaging applications is given in [33].

6.3.2
Special Applications

The traditional application field of Raman spectroscopy as a complementary method to IR spectroscopy is structural analysis. In the case of molecules featuring a center of inversion, the combined evaluation of Raman and IR spectra is vital because of the so-called mutual exclusion rule: in such molecules, while one part of fundamental vibrations is IR active, the other part is Raman active only. The basics of structural analysis are described in Section 6.1.2 and will not be repeated here.

In a number of experimental situations, Raman spectroscopy is superior to IR spectroscopy, that is, the vibrational fingerprints obtained by Raman spectroscopy are more informative:

1) A Raman spectrum from 4000 to 10 cm^{-1} can be acquired in one scan, unlike the IR experiment.
2) In the case of hydrogen-bonded or wet samples, IR bands are often diffuse and broad, whereas Raman equivalents are sharp.

A survey of the advantages and special applications of FT-Raman spectroscopy is given in [34]. FT-Raman has widespread applications in biology, medicine, pharmacy, art, forensic science, inorganic materials, geology, and polymers.

Water is an ideal solvent for Raman studies; and this is reflected in the large volume of published work on organic and inorganic compounds in *aqueous solutions*. Both identification of species present and evaluation of their concentration are feasible, thus providing information on chemical processes in aqueous solution and their rate constants, often as a function of temperature and pressure. Raman spectroscopy is an appropriate method to analyze hydrogen bonding in aqueous solutions. Intramolecular interactions caused by hydrogen bond formation, or very weak intermolecular forces indicated by very low frequency vibrations (down to 10 cm^{-1}) can be investigated directly.

Rapid advances in *semiconductor technology*, including thin film formation by deposition, interface preparation, or microstructuring, demand characterization techniques that provide understanding of the fundamental processes involved, including information on structural order–disorder and spatial inhomogeneity. Raman spectroscopy is used both in process control and quality assessment [35]. Typical examples for semiconductor applications are composition determination, analysis of crystal structure, surface and interface analysis, phase determination, doping, point defects, temperature influence, and mechanical stress.

The most commonly used material in semiconductor industry is silicon. The Raman spectra of crystalline and amorphous silicon differ quite markedly in the region $\Delta\nu = 600\text{–}100\,\mathrm{cm}^{-1}$ (region of the phonon bands), the two phases can well be characterized. For other semiconductors, this difference is smaller. One should keep in mind that Raman bands from polycrystalline sample areas are similar to those from monocrystalline areas. The effect of strain can also be assessed, local stress can be studied via a Raman microscope. Silicon–metal interfaces are amenable to examination. For instance, it is possible to identify the PtSi layer, estimate its thickness and describe its crystallographic order. Zinc blende type semiconductors, particularly gallium arsenide (GaAs) and related materials such as GaAlAs, can be studied. Concentrations of free carrier may be determined, together with the width of the space charge layer. The effect of an amorphous phosphorous overlayer on n-type GaAs can be studied. The spectroscopic information usefully complements what has been deducted from the electric properties of the material. Alloy semiconductors can effectively be studied by Raman spectroscopy, for example, in a system like $\mathrm{Ga}_{1-x}\mathrm{Al}_x\mathrm{As}$, the value of x can be determined. As with the zinc blende type semiconductors, it is possible to determine carrier concentrations and assess the effect of ion implantation and annealing. Similarly, in the case of $Hg_{1-x}Cd_xTe$, the value of x may be determined.

Important targets for *biochemical and biomedical investigations* are proteins, nucleic acids, and biomembranes. It is also possible to investigate the dynamics of biological systems such as living cells or to study biological interfaces. Tissue differentiation has a great potential for clinical usage in the near future. The most promising medical areas for Raman applications are angiology, lithiasis, orthopedics, dentistry, ophthalmology, dermatology, and pathology.

Spectra obtained with a Raman microscope can be used to investigate nerve cells containing a one-layer membrane composed mainly of proteins and long-chain phospholipids. A field, where Raman microscopy may make major contributions, is characterization of tumors. The Raman spectra of carcinomas are dissimilar from those of the surrounding normal tissue.

Raman spectra of molecules with a solubility even lower than 5×10^{-4} g per 100 g H_2O can be obtained by means of SERS. In the case of biopolymers with chromophoric groups, Raman bands are both resonance and surface enhanced and high-resolution Raman spectra from very dilute solutions down to $10^{-8}\,\text{mol}\,\text{l}^{-1}$ can be measured. Summaries about biochemical and biomedical applications of Raman spectroscopy are given in [3, 34]. A review of pharmaceutical applications of Raman spectroscopy is given in [8].

When using the SERS technique for large molecules, one has to keep in mind that SERS activity decays very fast with increasing distance from the surface. In small molecules of an approximate size of 0.6 nm (benzene), all vibrations are enhanced. In large biomolecules with approximate size around 5 nm (hemoglobin protein), only groups which are attached directly to the surface will yield surface enhancement. Native DNA in solution exhibits some 30–40 Raman bands. The most intense bands are caused by vibrations of the base residues, adenine, guanine, cytosine, and thymine. DNA consists of a double-stranded helix with weak Raman scattering groups (sugar–phosphate groups) at the outside of the helix and strong Raman scattering groups (nucleic basis) located at the center of the helix. The distance from the center of DNA to the phosphate group is about 1 nm. These building blocks of DNA, when adsorbed on a silver surface, exhibit strong SERS bands. The interaction of DNA with other molecules, for example, antitumor anthracyclines, can also be investigated by means of SERS.

There are many Raman applications in the *pharmaceutical industry* varying from structural testing to chemical imaging. The ability to analyze samples without sample preparation leads to fast and specific identification tests for raw materials, finished products, package components, and packaged products. In the *food industry*, the degree of hydrogenation of fats (number of C=C bonds in the skeletal backbone of fat molecules) can be measured in seconds. No sample preparation is needed, in contrast to the chromatographic techniques still employed for this type of analysis.

Raman spectroscopy can be useful in the synthesis and characterization of *catalytic materials*, and in examining adsorbates and their reactivity on metals, metal oxide surfaces, and zeolites. Thin films can be characterized using the waveguide technique. SERS in combination with RRS and microRaman spectroscopy offer the possibility of detecting amounts of substance in the nanogram range. The sensitivity can reach detection limits at the level of highly sensitive fluorescence spectroscopy, maintaining the high structural sensitivity of Raman spectroscopy. Small metallic particles with a diameter of 10 nm, for example, Raney nickel or platinum black, can be used for Raman enhancement. Silica- and alumina-supported particles, consisting of 10 nm particles covered with 3 nm diameter metallic islands, can be used as well. An enhancement of 10^3–10^4 was observed for molecules such as CO, C_2H_4, and C_6H_6. The spectra consist of a series of sharp lines of the excited vibrational modes of the adsorbed molecules superimposed on a broad, enhanced background. Ethylene has been used to study the formation of intermediates on catalytic surfaces. Ethylene is chemisorbed dissociatively as acetylene at room temperature. This is revealed by the appearance of the C=C stretching vibration at 1204 cm^{-1} and was confirmed by inelastic electron loss spectroscopy applied to acetylene chemisorbed on Ni(111) surfaces. The strongest line in the spectrum of benzene chemisorbed at room temperature is the totally symmetric ring-breathing mode at 990 cm^{-1}. All molecules with ring systems exhibit this characteristic band, as it is the most strongly enhanced mode.

One important catalytic reaction cycle which starts from a primary gas mixture of carbon monoxide and hydrogen is the Fischer–Tropsch synthesis. Depending on the reaction parameters (temperature of the catalytic surface, gas pressure, and composition of the gas mixture), a great variety of aliphatic, aromatic, and even oxygen-containing compounds can be obtained. The understanding of reaction mechanisms in terms of the appearance of intermediates on the surface, their structure and symmetry, is of fundamental interest for the development of well-defined reaction pathways. The frequency of the C–H stretching Raman band is a measure for the state of hybridization of the adsorbed molecule.

The fact that Raman measurements can usually be made through glass and plastic packaging, eliminating the need to prepare samples prior to analysis, makes it very attractive for *forensic science*. The availability of commercial portable instrumentation and extended fiber optic probes makes Raman suitable for on-site forensic use, minimizing the risk of investigating personnel to potentially hazardous chemicals. For identification of explosives, SERS method has proved to be very useful. A tiny amount of explosive, diluted in colloid solution with silver particles, is enough to produce a SERS spectrum sufficient for analysis.

Raman spectra of drugs are full of information and are unique to each substance. Very similar chemicals, for example, amphetamine × HCl and amphetamine sulfate or heroin and morphine, yield very different spectra. Usually such samples consist of many constituents; hence, multivariate analysis (cf. Chapter 53) should be used to obtain quantitative models of drug concentrations in solid mixtures. The ability to correctly identify unknowns also depends on the availability of high-quality reference spectra.

Raman spectroscopy has proven useful also in areas such as identification of *gems and artworks*. A summary of the use of Raman spectroscopy for studies of artworks is given in [36]. Investigations of paintings, medieval manuscripts, and wall paintings of glass, pottery, plastics, biomaterials are working fields of Raman spectroscopy. The origin and the age of such objects can be determined.

Polymer science is an area, where Raman methods have found their widest application. Progress has been reported across the field from synthetic thermoplastics through elastomers, including vulcanizates and biopolymers. Virtually any polymer, degraded or loaded with filter, will give a superb Raman spectra. Liquid crystalline polymers change their structure as they are heated, which in turn gives rise to changes in their Raman spectra. A review of Raman applications in polymer science is given in [9]. Applications include polymer identification, multivariate quantitative analysis of composition, analysis of polymer microstructure such as isomers, chain sequence, and endgroups, analysis of morphology such as conformation, crystallinity, and molecular orientation. Furthermore, it is possible to investigate curing and degradation. Polymeric reactions (kinetics and degree of polymerization) can even be characterized in-line.

Sulfur or sulfur-containing organic compounds produce particularly intense Raman bands. This fact is employed in monitoring the reaction occurring during mastication of elastomers with vulcanization agents (sulfur, ZnO, and accelerators). Isomerization frequently occurs during vulcanization. As cis–trans and vinylic moieties of C=C groups oscillate at distinctly different frequencies, they can conveniently be kept apart by Raman spectroscopy. A serious limitation for Raman investigations of polymeric samples is set by carbon black. Already 1% content of carbon black renders Raman spectroscopy impossible. If it is attempted, the sample starts burning because of strong absorption of laser light and no spectra are obtained.

Further *industrial applications* of Raman spectroscopy include identification, quality assurance, reaction monitoring and on-line process control, and the analysis of gases. These applications require special conditions for the instruments such as rapid measurements, high degree of automation, reliability, and robustness. Raman spectrometers equipped with multiple-fiber optics can simultaneously record data collected at several remote locations, even in chemically hazardous environment for on-site monitoring in chemical plants. Advantages and disadvantages of Raman applications for industrial use are described in [32] (see Reference Data Table 6.3).

Reference Data Table 6.3 Method parameter reference sheet.

Method	Raman spectroscopy
Characterized parameter	Intensity of Raman scattering
Type of information	Functional groups, structure, concentration, identity
Required user skills	Skilled in preparation of samples and carrying out the measurements

(*continued overleaf*)

Reference Data Table 6.3 (*Continued*)

Sample

	Excellent	Good	Fair	Poor	Problems
Pure compound	+				
Multi-analyte	+				
Gaseous				+	
Liquid		+			
Solid		+			
Matrix effects/matrix assisted			+		
Size	+				
Trace				+	
Cross sensitivity	+				
Identification	+				
Quantification		+			

Equipment (typical data)

CW/Fourier	CW
Internal/external reference	Internal reference
Single/double beam	Single beam
Destroying sample	Noninvasive, can be destructive for absorbing samples
Sequential/simultaneous	Simultaneous
Source	Laser
Dispersion by	
Filter/monochromator	Polychromator
Nondispersive	
Absorption/emission/scattering	Scattering
Ratio recording	No

Spectrometer (typical parameter)

Frequency/wave number/wavelength range	Raman shift from 50–4000 cm^{-1}
Time per spectrum	0.5–10 min
Noise	
Signal/noise	500 : 1 at high concentration
At high/low concentration limit	5 : 1 at low concentration
Reproducibility (wavelength, signal)	$\pm 1\ \text{cm}^{-1}$
Spectra overlay (single/multi)	Multi
Sampling (number of times)	64–1024
Resolution (nm, s^{-1}, cm^{-1}, molecular weight)	$1\ \text{cm}^{-1}$
Limit of detection	mM
Time required for analysis	
Preparation	0–10 min
Measurement	0.5–10 min

Reference Data Table 6.3 (*Continued*)

Evaluation	10–30 min
Cost per sample (€)	30 (estimated)

CW, continuous wave.
Techniques yielding similar information: IR spectroscopy.
Typical features of attached computers: computers (not built-in) are part of modern Raman spectrometers. The supplied software manages data acquisition and analysis. Additional software for chemometric evaluation is available.
Typical application (*as demonstrated in chapter*): qualitative and quantitative analysis, *in situ* and *in vivo* measurements, process control, stand-off measurements.
Preferable samples: neat liquids and solids.
Problematic samples: fluorescent and totally absorbing (black or umbra) compounds.

6.4
UV/vis Spectroscopy

Absorptions in UV/vis are caused by electronic transitions from the ground level to an excited state. The strongest transitions are $\sigma \rightarrow \sigma^*$, they are observed below 200 nm (vacuum UV). Typical examples are C–C and C–H bonds. Because all molecules include σ electrons, $\sigma \rightarrow \sigma^*$ transitions constitute the short wavelength cutoff of the routine UV/vis range. Saturated compound with pairs of free electrons exhibit $\mathrm{n} \rightarrow \sigma^*$ transitions in a wavelength range from 150 to 250 nm, their absorption coefficients do not exceed $1000\,\mathrm{l\,cm^{-1}\,mol^{-1}}$. Most UV/vis investigations are based on $\mathrm{n} \rightarrow \pi^*$ or $\pi \rightarrow \pi^*$ transitions, which occur across the UV/vis range and result from unsaturated groups. Typical absorption coefficients of $\mathrm{n} \rightarrow \pi^*$ transitions are below $100\,\mathrm{l\,cm^{-1}\,mol^{-1}}$, while absorption coefficients of $\pi \rightarrow \pi^*$ transitions exceed $1000\,\mathrm{l\,cm^{-1}\,mol^{-1}}$. Absorptions of transition metal ions are caused by their 3d and 4d electrons, whereas 4f and 5f electrons are excited in lanthanide and actinide ions. Absorption bands of d and f electrons are sharper than those of most chromophores because inner orbitals are largely shielded from external influences. Transitions of donor electrons to an acceptor orbital (charge-transfer complexes) originate in inorganic as well as organic compounds, their absorptions coefficients usually exceed $10\,000\,\mathrm{l\,cm^{-1}\,mol^{-1}}$. Band transitions in solids lead to UV/vis absorptions as well. Such transition may occur between valence and conduction bands or between a band and a localized energy level in the forbidden zone. Such condition may occur for instance in case of lattice defects or point defects.

A number of historic terms are still used in UV/vis spectroscopy:

Chromophore: system which is responsible for the absorption.
Auxochrome: substituent which leads to shift of the absorption maximum.
Bathochromic effect: red-shift (toward longer wavelength) of an absorption maximum.
Hypsochromic effect: blue-shift (toward shorter wavelength) of an absorption maximum.

Hyperchromic effect: increasing absorption intensity.
Hypochromic effect: decreasing absorption intensity.

6.4.1
Sample Preparation

Samples are prepared as described in the preceding chapters, mostly by dilution with a suitable solvent. The application range of solvents is given by their short wavelength cutoff (Table 6.6).

Water and ethanol are good solvents for most samples. Both are cheap and transparent down to about 210 nm. Hexane and other hydrocarbons are more suitable for less polar samples. The latter solvents interact only weakly with the solute, so that the fine structure of the absorption band may be revealed much better.

All solvents influence the position of absorption bands. $n \rightarrow \pi^*$ absorption bands are shifted toward shorter wavelengths on increasing solvent polarity, whereas $\pi \rightarrow \pi^*$ transitions become red shifted on increasing solvent polarity. Forces between the solvent and the sample lead to a lower energy level of both the excited and unexcited levels. The effect also influences $n \rightarrow \pi^*$ transitions but the stronger blue-shift resulting from solvation of lone pairs may cover the weaker red-shift (Figure 6.21).

6.4.2
Structural Analysis

Locations of the typical UV absorption bands of representative chromophores are listed in Table 6.7. Substitution leads to a bathochromic shift of the band maximum. Conjugation of π electrons leads to lower π^* energy levels. As the

Table 6.6 Cutoff wavelengths of common solvents.

Solvent	Cutoff wavelength (nm)
Hexane	200
Ethanol	210
Water	210
Methanol	210
Acetonitrile	215
Cyclohexane	215
Chloroform	250
Carbon tetrachloride	280
Benzene	280
Pyridine	310

At the cutoff, transmission drops below 60% at an optical path of 1 cm.

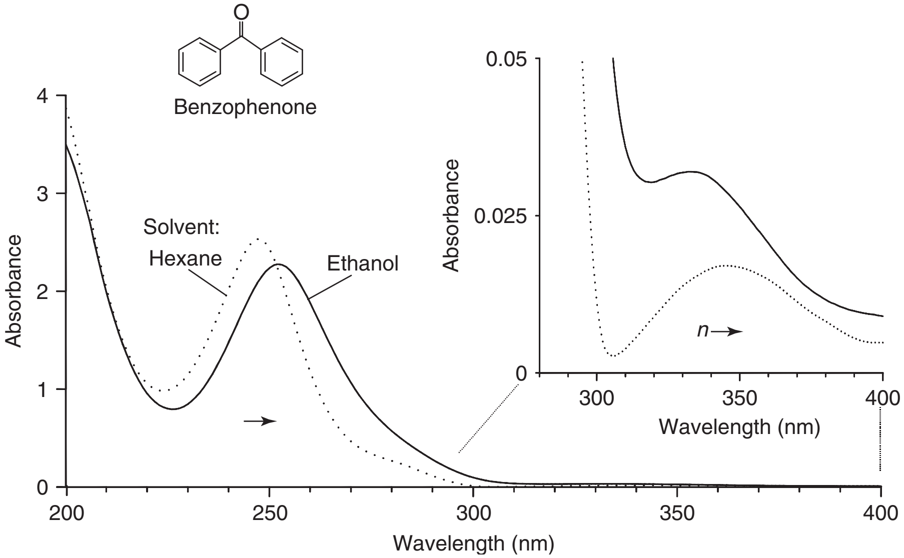

Figure 6.21 Shift in absorption bands of benzophenone dissolved in either ethanol or in hexane. The more polar ethanol leads to a red-shift of $\pi \rightarrow \pi^*$ and to a blue-shift of $n \rightarrow \pi^*$ transitions.

Table 6.7 Absorption of representative chromophores.

Chromophore	**Band maxima (nm)**
$-C \equiv C-$	175
	195
	225
$> C = C <$	175
$> C = O$	160
	185
	280
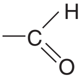	210
	280
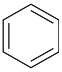	184
	205
	255
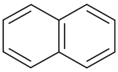	220
	275
	310
R-NO_2	205
R-ONO	225

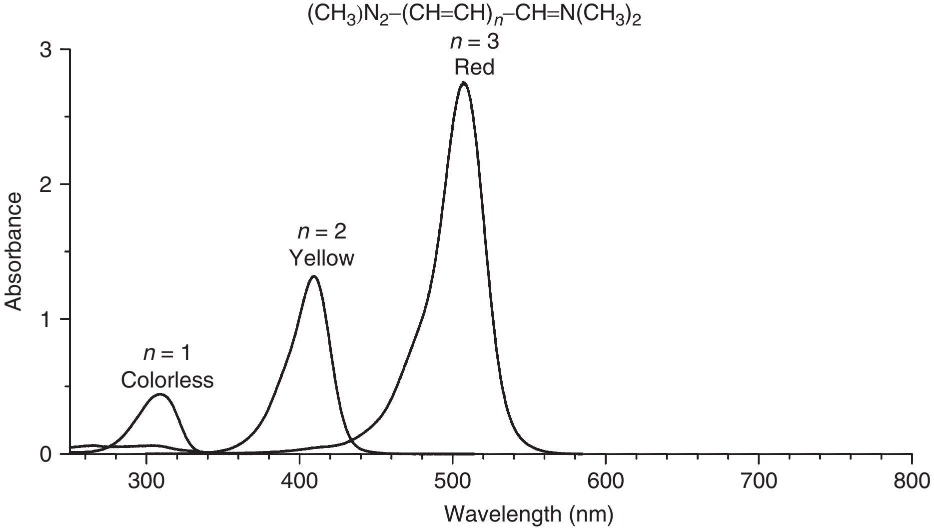

Figure 6.22 UV/vis spectra of polymethines. The absorption maximum shifts toward longer wavelengths and the absorbance increases because of the increasing number of double bonds.

number of double bonds in conjugation increases, the absorption maximum will shift toward longer wavelengths. In coincidence with the spectral shift also, the absorption coefficient will increase (Figure 6.22). Besides the number of double bonds in long-chain polyenes, changes from cis- to trans-configuration may lead to red-shift and increasing absorbance as well.

The Woodward rules provide values for estimation of positions of absorption bands for dienes. The calculation is based on typical parent compounds and takes into account the red-shift increments by additional conjugated double bonds and by further auxochromes:

Parent diene:	Acyclic	217 nm
	Heteroannular	214 nm
	Homoannular	253 nm
	α, β unsaturated carbonyl	222 nm
Additions for each substituent:	Double bond extending the conjugation	30 nm
	Exocyclic double bond	5 nm
	Each alkyl group or ring residue	5 nm
	$-OR$	6 nm
	$-SR$	30 nm
	$-NR_2$	60 nm
	$-Cl$, $-Br$	5 nm

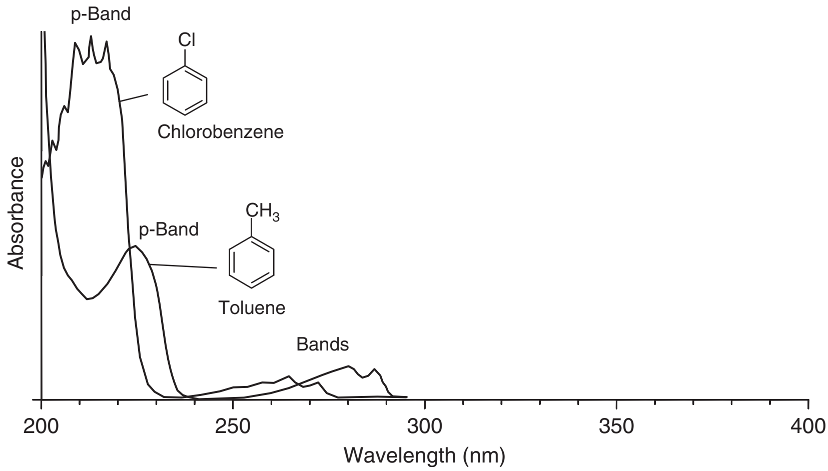

Figure 6.23 UV/vis absorption spectra of chlorobenzene and toluene. Both p- and α-bands show vibrational fine structure. Toluene was fivefold less concentrated than chlorobenzene. Solvent: *n*-hexane.

A weak band in the 275–300 nm range is an indicator of a ketone or aldehyde carbonyl group. Substituents such as OH, NH_2, NHR, or halogen shift the $n \rightarrow \pi^*$ transition toward shorter wavelengths. Conjugation of a C=O group with C=C bonds shifts the $\pi \rightarrow \pi^*$ transition toward the vis range.

The $\pi \rightarrow \pi^*$ transitions in *benzene* and *benzene derivates* lead to absorption bands in the range 160–270 nm. Although four transition $\pi_{2/3} \rightarrow \pi_{4/5}{}^*$ are expected in benzene, only three bands can be observed because of a degenerate state. The band at 250 nm shows vibrational fine structure (Figure 6.23).

In *disubstituted benzenes*, p-substitution causes red-shift of main absorption bands, whereas o- or m-substitution does bands not much shift (Figure 6.24).

Spectra of *polycyclic aromatic hydrocarbons* may be used as fingerprints for identification of the compounds. Highest and lowest orbitals are not degenerate so that four transitions may occur. On increasing annulation, bands shift toward longer wavelengths. *Heteroaromatic compounds* show roughly the same effects as their corresponding hydrocarbons. Spectroscopic effects caused by the heteroatom depend on the electronic properties and on the orientation of the substituent.

Proteins show typical absorptions in the 190–350 nm range. Peptide bonds have an intense $\pi \rightarrow \pi^*$ transition between 190 and 210 nm. The $n \rightarrow \pi^*$ transition at 210–220 nm is weak as it is forbidden and forms a shoulder on the $\pi \rightarrow \pi^*$ absorption band.

Aromatic amino acids have bands between 210 and 280 nm. These bands are commonly used to determine the total protein concentration in solutions. Proteins may have colored prosthetic groups, such as heme, Cu complexes, and covalently bound coenzymes. Some proteins show absorption because of changes of the pH. For example, the chromophore of tyrosine is the phenolic group. On decreasing pH, the maximum absorption is shifted from 275 to 295 nm. Proteins show a slight

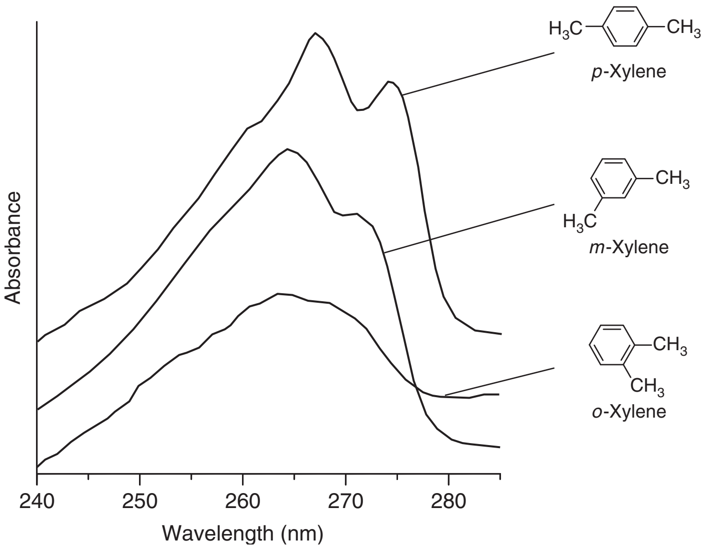

Figure 6.24 UV/vis spectra of xylenes. The red-shift increases from o- via m- to p-substitution.

sensitivity to the polarity of the environment; they arise from the aromatic side chains and indicate their interaction with polar groups. An increase in nonpolar constituents leads to a red-shift of the absorption maximum. Especially tyrosine and tryptophan show such environmental sensitivity which can be used to detect conformational differences in different states of a protein (Table 6.8).

The aromatic L-amino-acids tryptophan, tyrosine, and phenylalanine are responsible for protein absorption in the UV. The aromatic side chains of amino acids have often characteristic spectra. UV/vis spectroscopy offers the advantages of being nondegrading to the sample.

6.4.3
Metal Complexes and Semiconductors

The color appearance of *metal complexes* is basically controlled by three kinds of transition: charge-transfer, $\pi \rightarrow \pi^*$, and $n \rightarrow \pi^*$ transitions in complexes with organic ligands, d–d transitions within the metal ion. The latter are usually weaker than the former two, nevertheless the color of aqueous solutions of transition metals is caused by d–d transitions. Owing to splitting of d-orbitals in ligand field or crystal field (Figure 6.25), absorptions at longer wavelengths may occur. UV/vis spectra of Ti ions with and without ligand field splitting are shown in Figure 6.26.

The degree of splitting depends on several factors: the charge on the metal, the size of the metal, and the nature of the ligand. It is possible to correlate empirically the various ligands in a sequence according to their ability to split the orbital. The

Table 6.8 Absorption maxima of some amino acids.

Amino acid		Band maxima (nm)
Histidine	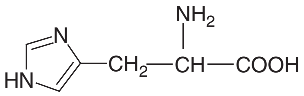	210
Tryptophan	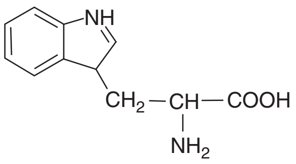	220, 280
Tyrosine	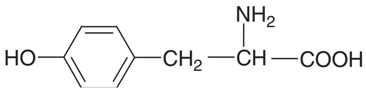	195, 222, 275
L-Cysteine	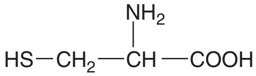 $HS-CH_2-CH(NH_2)-COOH$	235
L-Cystine	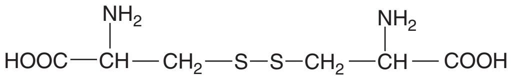 $HOOC-CH(NH_2)-CH_2-S-S-CH_2-CH(NH_2)-COOH$	250
Phenylalanine	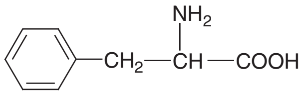	190, 205, 255

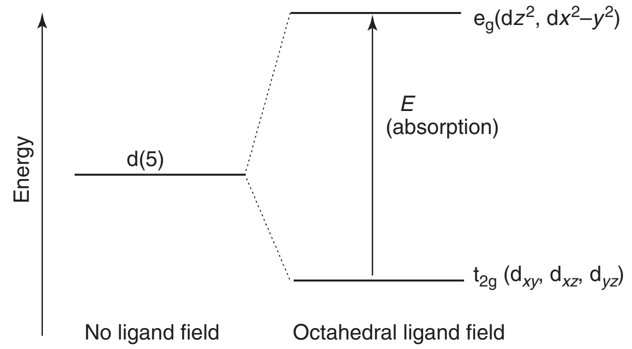

Figure 6.25 The octahedral ligand field splits the d orbital into two levels, which give rise to a new absorption band.

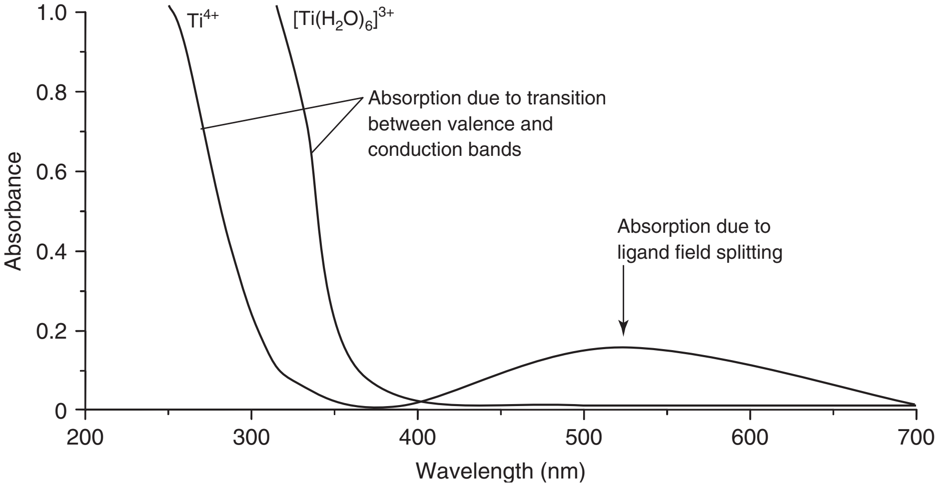

Figure 6.26 UV/vis spectra of Ti^{4+} and Ti^{3+} complexes. Ti^{3+} has an octahedral ligand field where the d-level is split into two levels. Transitions between the latter cause an additional absorption band at 510 nm. The absorption edges around 300 nm arise from transition between valence and conduction band.

cyanide anion has the strongest ligand field in the so-called spectrochemical series:

$$\text{halides} < OH^- < H_2O < NCS^- < NO_2{}^- < CO, CN^-$$

Metal complexes with organic ligands show different spectroscopic effects, dependent whether the metal–ligand bonds are covalent or ionic. If the metal–ligand bond is essentially ionic, only small changes occur. The spectrum of the complex is similar to that of the protonated ligand. On the other hand, the spectrum gets significantly changed for complexes with strong covalent metal–ligand bonds, and such complexes are highly colored.

Charge-transfer transitions may occur in case of covalently bound ligand orbitals and empty or antibonding metal orbitals. Organic ligands forming charged transfer complexes are often used in the analysis of ions such as Fe, Cu, Cd, or Zn.

The porphyrin dyes hemoglobin and chlorophyll are biologically important. Both belong to octahedral metal complexes, as proteins are bound to the central atom. In the hemoglobin molecule are five ligand positions occupied by histidine.

In most *semiconductors*, the gap between valence and conduction bands gives rise to a transition in the UV/vis range. Such transitions produce an UV/vis absorption edge (Figure 6.27).

The absorption edge λ_{gap} may be expressed by

$$\lambda_{\text{gap}} = \frac{h}{W_0} c$$

where W_0 is the binding energy, h is the Planck constant, and c is the speed of light in vacuum. If $W_0 > 3.1$ eV, the semiconductor is transparent whereas crystals with $W_0 < 1.5$ eV are absorbing across the whole UV/vis range and look like metals. Gap

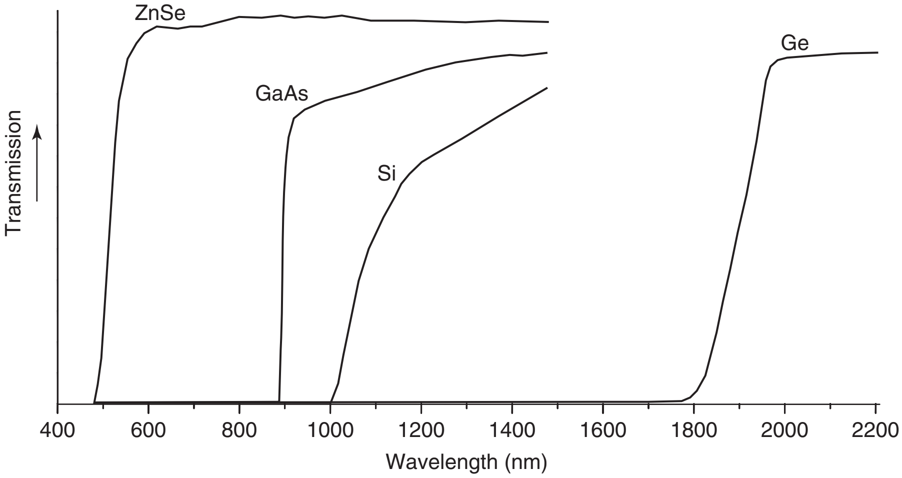

Figure 6.27 UV/vis absorption edges of selected semiconductors.

Table 6.9 Gap transition energies of relevant semiconductors.

Semiconductor	**λ_{gap} (eV)**	**(nm)**
ZnO	3.44	360
SiC	3.0	413
CuO	2.15	576
GaAs	1.40	885
Si	1.17	1059
ZnS	0.91	1362
GaSb	0.81	1530
Ge	0.66	1875
InAs	0.36	3443
PbS	0.29	4274
InSb	0.23	5390

transition energies and corresponding wavelengths for a range of semiconductors are given in Table 6.9.

In UV/vis spectra of semiconductors with an indirect band transition (photon–phonon excitation), the absorption band edge may indicate a higher binding energy W_0. Additional energy levels may occur in imperfect semiconductor crystals. These energy levels are often placed between valence and conduction band and lead to absorption at greater wavelengths. Other processes such as electronic interaction between excited electron and hole may lead to intrinsic band changes. A well-known example is the absorption band edge of CuO where additional narrow absorption bands occur.

Band structure details of *insulators* can be determined by their UV/vis spectra. Defects in the crystal produce electronic levels within the gap between conduction and valence bands. Spectroscopic measurements at low temperature allow the investigation of the phonon structure of a crystal. Owing to lattice or point defects, absorptions can be used to describe the optical and electronic properties of the insulator. For example, Cr in Al_2O_3 crystals introduces an intensive color change of the crystal. Many so-called *color centers* are based on lattice defects caused by intercalation of atoms in the crystal lattice.

For further reading please see [37, 38] (see Reference Data Table 6.4).

Reference Data Table 6.4 Method parameter reference sheet.

Method	UV/vis spectroscopy
Characterized parameter	Absorbance
Type of information	Concentration, structure
Required user skills	Skilled in preparation of samples

Sample

	Excellent	Good	Fair	Poor	Problems
Pure compound	+				
Multi-analyte		+			
Gaseous					+
Liquid		+			
Solid		+			
Matrix effects/matrix assisted			+		
Size		+			
Trace		+			
Cross sensitivity				+	
Identification				+	
Quantification		+			

Equipment (typical data)

CW/Fourier	CW
Internal/external reference	External reference
Single/double beam	Single and double beam
Destroying sample	Noninvasive
Sequential/simultaneous	Sequential
Source	W lamp, D_2 lamp
Dispersion by	
Filter/monochromator	Filter or monochromator
Nondispersive	
Absorption/emission/scattering	Absorption
Ratio recording	Yes

(*continued overleaf*)

Reference Data Table 6.4 (*Continued*)

Spectrometer (typical parameter)	
Frequency/wave number/wavelength range	200–800 nm
Time per decay curve	0.5 till 5 min
Noise	
Signal/noise	1000 : 1 at high concentration
At high/low concentration limit	5 : 1 at low concentration
Reproducibility (wavelength, signal)	±0.1 nm
Spectra overlay (single/multi)	Single
Sampling (number of times)	Once
Resolution (nm, s^{-1}, cm^{-1}, molecular weight)	1 nm typically
Limit of detection	μM
Time required for analysis	
Preparation	1–10 min
Measurement	0.5–5 min
Evaluation	20–60 min
Cost per sample (€)	10 (estimated)

CW, continuous wave.
Techniques yielding similar information:
Typical features of built-in computers: built-in computers are not part of modern UV/vis spectrometer. The supplied software manages data acquisition and analysis.
Typical application (*as demonstrated in chapter*): characterization of organic compounds, biological samples, semiconductors, quantitative analysis.
Preferable samples: molar till micro molar solutions.
Problematic samples: gaseous samples, highly absorbing samples, scattering samples.

6.4.4
UV/vis Spectroscopic Imaging

UV/vis spectroscopic imaging is a technique which combines spectroscopy, high-resolution CCD imaging, and computing. The key to achieving high sensitivity in the UV/vis spectral range (0.2–0.8 µm) is the use of silicon based low-light-level CCD cameras. Commercial systems are either filter-wheel multiple exposure systems, or full spectral capture systems based on interferometers. The advantages of the filter multiplex system are high sensitive measurements at the selected wavelengths and a robust optical system. Typical systems are available in a turnkey format completed with up to eight interchangeable filters. The CCD camera has more than 4 MP. Images can be recorded continuously at one wavelength or at different wavelengths (changing filters) with frame rates of 1 s.

The principle of full spectral systems is the simultaneous recording of an entire spectrum for each pixel of the CCD camera. Spectral imaging systems are used to obtain brightfield images, or imaging data sets of fluorescence, absorption, transmission, or reflection spectra. Acquisition times range from few seconds to several minutes. A Sagnac interferometer mounted on a rotatable disk provides a spectral resolution as good as 2 nm at short wavelengths increasing to approximately

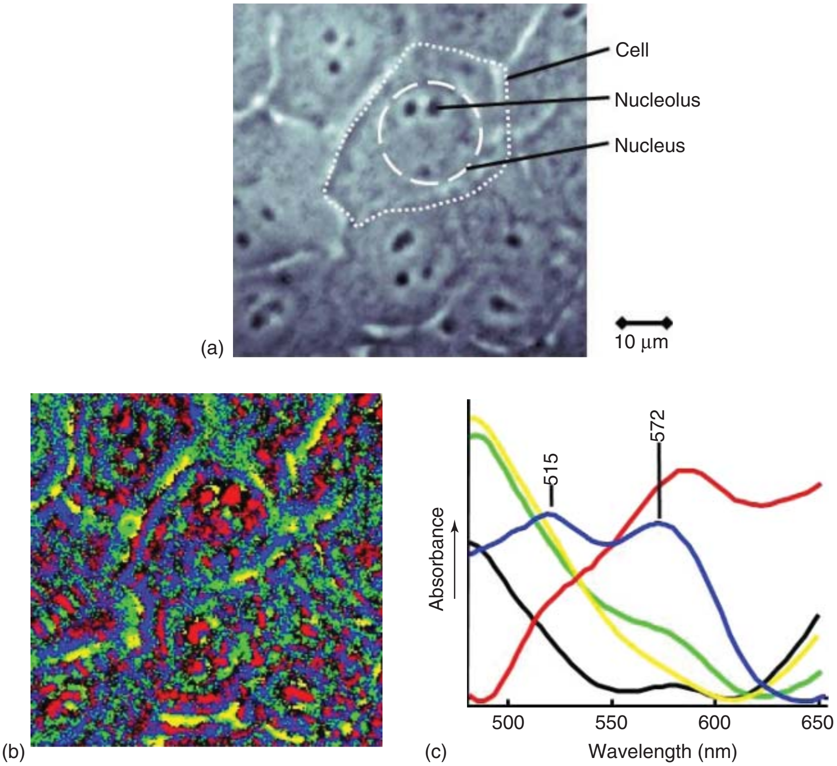

Figure 6.28 Vis spectroscopic image of retinal ganglion cells. (a) Microscopic image; (b) spectroscopic image evaluated with *k*-means cluster analysis; and (c) cluster centroid spectra.

25 nm toward the NIR range. Figure 6.28 shows the spectroscopic image of retinal ganglion cells. Contrast in the unstained cells in the brightfield image (a) is mainly based on light scattering on the cell membrane and on nucleoli. Each pixel of the spectroscopic image contains an entire vis spectrum. The spectral data set is analyzed by *k*-means cluster analysis and reassembled to the image (b). The corresponding cluster centroid spectra are shown in (c). Red and black pixels indicate mainly nuclei and nucleoli. Green and yellow pixels can be assigned to membrane structures. Blue pixels indicate cytochrome *c*. The two spectral bands at 515 and 572 nm are assigned to the β-band and to the α-band, respectively.

6.4.5
Metal Nanoparticles

Some recent applications involve the characterization of *metal nanoparticles*. Because of their unique chemical, electronic, and optical properties, metal nanoparticles are of interest for a variety of applications in chemistry, material science,

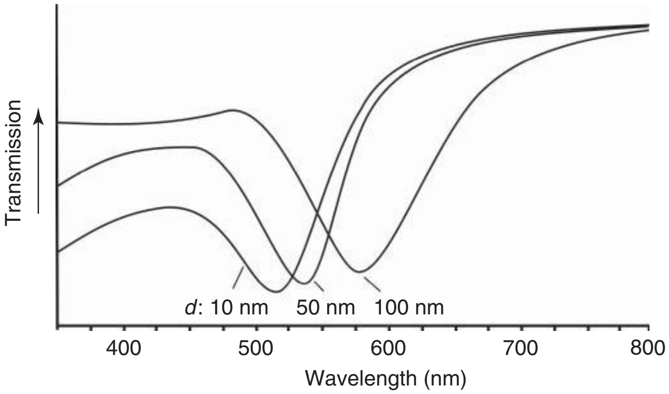

Figure 6.29 Calculated plasmon resonance spectra for single gold nanoparticles of spherical shape at different diameters (*d*).

medicine, biology, and environmental science. Typical sizes and shapes of the nanoparticles range from spheres with few nanometers in diameter up to nanorods with more than 1000 nm in length. Such small particles are known to act as strong light scatterers, if the wavelength of the incoming light and the particle's plasmon resonance are in the same range. This may happen in the visible spectral region. Plasmon resonance causes an intense absorption. Position, shape, and intensity of the absorption band give information about size, shape, and chemical nature of the nanoparticles as well as about their interactions with the surrounding medium. A detailed description is given in [39, 40]. Figure 6.29 illustrates the effect of the size of nanoparticles on the spectral position of the plasmon resonance for gold nanoparticles deposited on a glass slide.

Fluorescent nanoparticles, called *quantum dots* (*QDs*), emit up to 3000 times brighter light than conventional nanoparticles. QDs are very small semiconductor crystals between 1 and 5 nm in size that generate light when stimulated by electrons or photons. Owing to the small dimension of QDs, electrical charges within the dots are confined in all directions. Thus, behavior and properties of QDs are controlled by quantum mechanical effects. QDs are becoming increasingly popular in optical spectroscopy and biosensing. QDs are being used for cellular labeling because of their lower toxicity in addition to their brighter fluorescence.

6.5
Fluorescence Spectroscopy

After the appearance of the first book on fluorescence in 1951 [41], fluorescence spectroscopy became a widely used scientific tool in biochemistry, biophysics, as well as in material science. Within the last years, however, several new applications based on fluorescence have been developed, promoting fluorescence spectroscopy from a primarily scientific to a more routine method. The phenomena of fluorescence is, for example, exploited in simple analytical assays in environmental science and clinical chemistry, in cell identification and sorting in flow cytometry, and in imaging of single cells in medicine. The analyte, whose light emission is investigated, is often called a *dye*. Fluorescence measurements give information about the photophysical properties of the dye as well as about the chemical and physical nature of the surroundings of the dye.

6.5.1
Sample Preparation and Measurements

Beside the classical sampling techniques using different types of cuvettes, there are several advanced ways of detecting the fluorescence signal. The use of fiber optics allows for measuring fluorescence in whole organs *in vivo*. When looking to cells, one can use cell culture plates or flow cytometry. Selected spots within a cell can be monitored using classical, confocal, or multiphoton microscopy (cf. Section 5.5).

As each of the measurement techniques is providing different information based on different ways of detecting the fluorescence signal, the data evaluation is different for each method. Table 6.10 provides the references, dealing with the mathematical data treatment and evaluation of the basic fluorescence techniques. Some details of fluorescence data treatment are outlined in Chapter 53 "General Data Treatment."

6.5.1.1 Fluorescence Quantum Yield and Lifetime

In the gas phase or noninteracting solvents and in the absence of other photophysical processes (cf. Figure 6.30), the fluorescence intensity F detected over a certain emission wavelength range decays following a monoexponential decay law with an average lifetime τ. The rate constant of this fluorescence decay k $(=1/\tau)$ represents the sum of the emissive rate of the fluorophore k_0 $(=1/\tau_0)$ and the rate constants of the two radiationless processes, internal conversion, and intersystem crossing, k_{ic} and k_{isc}, respectively. The radiative lifetime τ_0 can be correlated to the transition

Table 6.10 References for fluorescence data evaluation.

Spectroscopic method	Basic parameter characterized	References
Steady-state fluorescence	Quantum yield	[4]
Time-resolved fluorescence	Lifetime	[3, 42]
Fluorescence correlation spectroscopy	Particle number, diffusion time	[43]
Fluorescence recovery after photobleaching	Rate and extent of recovery	[44]
Application of total internal reflection fluorescence	Depending on the combined method	[45]

dipole moment **M** by

$$\tau_0 \approx \frac{1}{k_{\text{ave}}^3 n^2 |\mathbf{M}|^2} \tag{6.1}$$

where n is the refractive index of the solvent and k_{ave} is the average wavenumber of the center of gravity of the fluorescence emission spectrum. The natural lifetime τ_0 can be considered as a photophysical constant of a chromophore surrounded by a defined solvent shell. In the case of planar aromatic systems, it appears to be temperature-independent [46]. As the internal conversion and intersystem crossing processes compete with fluorescence for deactivation of the lowest excited singlet-state, not all will return to the ground state by fluorescence (Figure 6.30). The fraction of excited molecules that do fluoresce is called the *quantum yield* ϕ. In terms of the above defined rate constants and lifetimes, ϕ is given by Eq. (6.2)

$$\phi = \frac{k_0}{k_0 + k_{\text{ic}} + k_{\text{isc}}} = \frac{\tau}{\tau_0} \tag{6.2}$$

The fluorescence lifetime τ can be determined directly by monitoring the decay curve of fluorescence intensity following a brief excitation pulse [47] or by detecting the emission delay of intensity modulated excitation light [48]. Using a standard

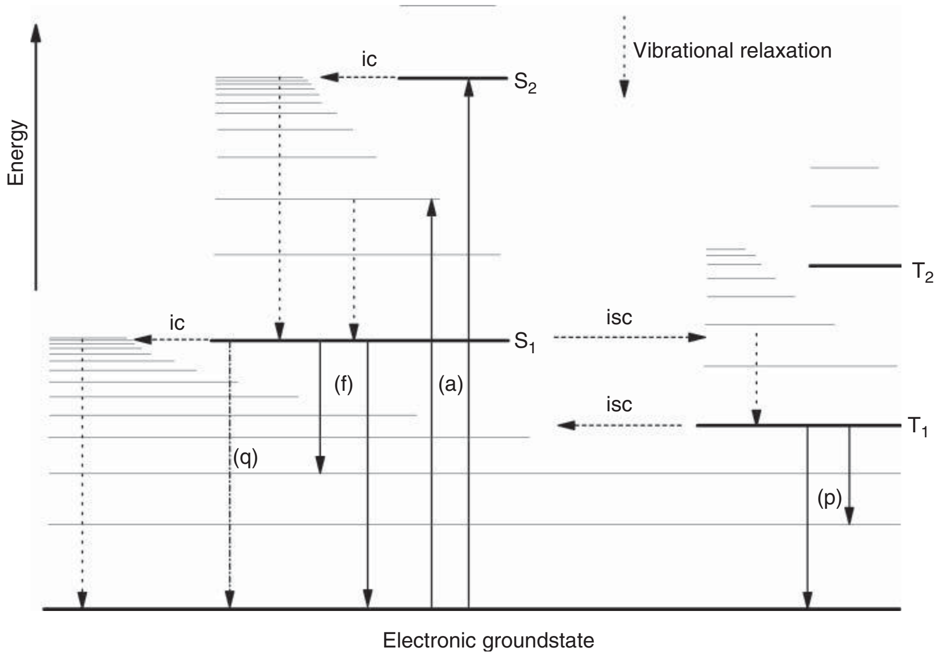

Figure 6.30 Jablonski diagram illustrating the creation and fate of an excited singlet-state, including absorption (a), fluorescence (f), internal conversion (ic), intersystem crossing (isc), phosphorescence (p), vibrational relaxation, and collisional quenching (q). Not included are processes such as solvent relaxation, energy transfer, and photochemical reactions.

steady-state fluorometer, the quantum yield ϕ is determined, usually by comparison with standard compounds of known quantum yield [49].

6.5.1.2 Fluorescence Quencher

A fluorescence quencher is a compound, the presence of which leads to a decrease of the fluorescence quantum yield or lifetime of the examined chromophore. The quenching system can be molecules or ions added to the solution, which come into molecular contact with the chromophore introducing new or promoting already existing nonradiative pathways (solute quenching). Further possibilities are the self-quenching by other molecules of the same dye type and the quenching by solvent molecules. In any case, the quenching term k_Q [Q] has to be added to Eq. (6.2), yielding

$$\phi = \frac{k_0}{k_0 + k_{ic} + k_{isc} + k_Q[Q]} \tag{6.3}$$

where k_Q is the bimolecular quenching constant and [Q] is the concentration of the quencher.

6.5.1.2.1 Solute Quenching Solute quenching reactions are a very valuable tool for studies of proteins, membranes, and other supra- or macromolecular assemblies and can provide information about the location of fluorescent groups in the examined molecular structure. A fluorophore that is located on the surface of such a structure will be relatively accessible to a solute quencher (for a list of quenchers see Table 6.11). The quenching agent will quench a chromophore that is buried in the core of the molecular assembly to a lesser degree. Thus, the quenching experiment can be used to probe topographical features of the examined structure and to detect structural changes that may be caused by addition of external compounds or changed physical conditions. In usual quenching experiments, the

Table 6.11 List of selected solute quenchers.

Type of fluorophore	Used quenchers	References
Indole	Carboxy groups, chlorinated compounds, dimethylformamide	[6–8]
Tyrosine	Disulfides	[9]
Tryptophan	Acrylamide, histidine, succinimide, trifluoroacetamide, iodide, disulfides	[10–15]
Naphthalene	Halogens, nitroxides	[16, 17]
Anthracene	Amines, halogens, thiocyanate	[18–20]
Anthranoyloxy probes	Tetracaine	[21]
Quinolinium ions and their betains	Chloride, bromide, iodide	[22–24]
Pyrene	Halothane	[25]
Carbazole	Amines, chlorinated compounds, halogens	[26, 27, 3, 28]
Common quencher for almost all dyes	Oxygen	[29, 50]

solute is added successively to the probe. The analysis of the dependence of the fluorescence intensity, F, quantum yield, Φ, or lifetime, τ, yields quantitative information about the accessibility of the chromophore within the macro- or supramolecular structure.

Depending on the chemical nature of the quenching agent as well as that of the chromophore, one has to distinguish between two forms of quenching, the dynamic and the static quenching. Static quenching results from the formation of a nonfluorescent complex between a quencher and a fluorophore already in the ground state. Characteristic of that type of quenching is that the increasing quencher concentration decreases the fluorescence intensity or quantum yield, but does not affect the fluorescence lifetime. A further characteristic feature of static quenching is its decrease with increasing temperature, as the stability of the complexes between the fluorophore in the electronic ground state and the quencher is generally lower at higher temperatures. If quenchers act by competing with the radiative process (see Eq. (6.3) and Figure 6.30), the ratio of the quantum yield in the absence, ϕ_a, and the presence, ϕ, of the quencher will be equal to the ratio of the corresponding lifetimes, τ_a/τ (see Eq. (6.2)). The concentration dependence of this so-called dynamic or collisional quenching is described by the Stern–Volmer equation, where the Stern–Volmer constant K_{SV} is equal to $k_Q \tau_a$

$$\frac{\phi_a}{\phi} = \frac{\tau_a}{\tau} = \frac{F_a}{F} = 1 + K_{SV}[Q] = 1 + k_Q \tau_a [Q] \tag{6.4}$$

Thus from the plot of one of those ratios versus the quencher concentration and by knowing τ_a separately, the bimolecular quenching constant, k_Q, can be determined. The magnitude of k_Q is given by the following factors

$$k_Q = 4\gamma \pi D r N' \tag{6.5}$$

where γ is the efficiency of the quenching reaction, D and r are the sum of the diffusion coefficients and molecular radii, respectively, for the quencher and chromophore, and $N' = 6.02 \times 10^{20}$. The diffusion coefficient for a single species i can be calculated by using the Stokes–Einstein relationship to be

$$D_i = \frac{bT}{6\pi \eta r_i} \tag{6.6}$$

where b is Boltzmann's constant and η is viscosity. Thus the quenching constant increases with increasing temperature T because of the diffusion control of dynamic quenching. The molecular mechanism of the fluorescence quenching depends on the chemical nature of the chromophore and solute. Quenchers that possess halogens or heavy atoms quench by increasing the intersystem crossing rate induced by spin orbital coupling mechanism. Acrylamide quenching of tryptophans in proteins is probably due to excited state electron transfer from the indole to acrylamide. Paramagnetic species are believed to quench aromatic fluorophores by an electron spin exchange process. In many instances, the fluorophore can be quenched both by dynamic and static quenching. The characteristic feature for mixed quenching is that the plot of the concentration dependence of the quantum yield or intensity ratios (see Eq. (6.4)) shows an upward curvature. In this case, the Stern–Volmer equation has to be modified resulting in an equation, which is second order in [Q]. More details on theory and applications of solute quenching can be found in [51]. Table 6.11 gives an overview of characterized fluorophore-quencher pairs [52–77].

6.5.1.2.2 **Example for Application of Solute Quenching in Protein Studies** One of the main aims in biophysical studies of the structure and function of proteins is to identify the protein domains, which are responsible for the interaction of the entire protein with physiologically relevant binding partners. Proteins usually contain several tryptophan residues, which might be distributed among the different protein domains. As each of these tryptophan residues is located in a distinct environment, each residue might exhibit different fluorescence lifetime profile as well as different accessibilities to quenching molecules. Using picosecond time-resolved fluorescence spectroscopy, the tryptophan fluorescence lifetime profile of proteins containing up to three tryptophan residues can be determined with high accuracy [56]. A picosecond tryptophan study of prothrombin fragment 1 (BF1), which is the 1–156 N-terminal peptide of prothrombin, a key blood coagulation protein, may serve as an example here. It is believed to be the region predominantly responsible for the metal ion and membrane binding properties of prothrombin. An important question has been as to what extent the conformation of the two protein domains, the so-called Gla and kringle domain, are altered by the interaction with calcium ions and negatively charged phospholipid surfaces (see Figure 6.31).

The analysis of the fluorescence decays of the three tryptophan residues (Trp42, Trp90, Trp126) in apo-BF1 resulted in a five exponential decay model, where the five fluorescence lifetimes are wavelength independent. As structural data show a huge difference in solvent accessibilities for the kringle tryptophans ($4 \times 10^{-20}\,\mathrm{m}^2$ for Trp90 and Trp126) and the Gla tryptophan ($133 \times 10^{-20}\,\mathrm{m}^2$ for Trp42), acrylamide quenching studies were performed to assign the five lifetimes to the two types

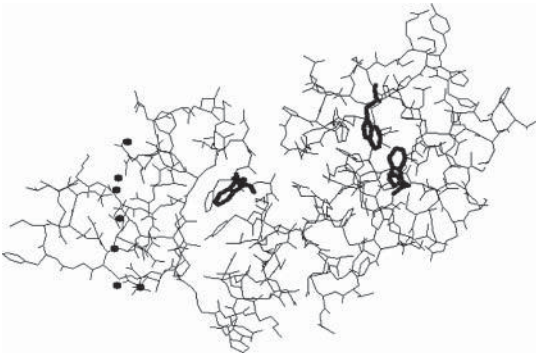

Figure 6.31 A depiction of the X-ray structure of Ca-BF1. The right part of the protein is the kringle domain, where the solvent inaccessible tryptophan residues Trp90 and Trp126 are located. The Gla domain is the left part of the protein, containing the solvent and quencher accessible Trp42 and seven calcium ions (dots).

of tryptophans. Acrylamide was added successively up to a concentration of 0.7 M. The Stern–Volmer analysis of the fluorescence decays showed that the five lifetimes are basically due to two different types of tryptophans characterized by two different k_Q values ($0.2 \pm 0.2 \times 10^9$ and $1.1 \pm 0.3 \times 10^9\,\mathrm{M}^{-1}\,\mathrm{s}^{-1}$ for the kringle and Gla tryptophan components, respectively). Note that the theoretical k_Q value for a fully exposed polypeptide-tryptophan is about $3 \times 10^9\,\mathrm{M}^{-1}\,\mathrm{s}^{-1}$. The resulting assignment of the lifetime compounds to the two types of tryptophans allowed for a separate investigation of conformational changes in the two protein domains without cleaving BF1 into the isolated Gla (containing Trp42) and kringle domains (containing Trp90 and Trp126) or modifying the protein by site-directed mutagenesis. On the basis of the assignment of the lifetimes to the two tryptophan types in BF1, further experiments led to the conclusion that the Gla domain is exclusively responsible for the interaction with calcium ions and negatively charged phospholipids. Moreover, the first experimental evidence for a lipid specific conformational change in the Gla domain of prothrombin was found, indicating an important role of this domain in the regulation of blood coagulation [78].

6.5.1.2.3 **Solvent Quenching** The influence of solvent molecules on the fluorescence characteristic of a dye is certainly one of the most complex issues in fluorescence measurement. Eventually, every chromophore shows some dependence of its quantum yield on the chemical structure of the surrounding solvent. This observation is to some extent due to fluorescence quenching by the solvent. One possibility is that the interaction of the chromophore with its solvent shell can promote nonradiative pathways, by changing the energy levels of the S_0, S_1, and T_1 states. The transition probabilities for the internal conversion and intersystem crossing processes are governed by the energy-gap law [79]. This law states that the rate constants k_{ic} or k_{isc} increase exponentially as the energy gaps between the S_1 and S_0 or S_1 and T_1 states, respectively, decrease [79]. Thus any change in those energy levels will strongly influence the fluorescence lifetime and quantum yield (see Eq. (6.2)). Some of the so-called hemicyanine dyes represent special cases for the promotion of nonradiative pathways by increasing solvent polarity [80]. These dyes undergo an intramolecular twist in the excited state. The intramolecular twist leads to an increase of the polarity and the twisted form of the S_1 states is very effectively deactivated by fast internal conversion. Increasing solvent polarity promotes the intramolecular twist and, therefore, the nonradiative deactivation by internal conversion [80]. Moreover, evidence has been accumulated that quenching by interaction with solvent molecules can proceed by a vibrational mechanism. It has been speculated that the collision between dye and solvent molecules results in vibrational coupling that favors efficient internal conversion [81]. In this connection, the solvent deuterium effect on the fluorescence lifetime, which has been observed for a variety of chromophores should be mentioned [82–84]. It has been found that the quantum yield is substantially increased when using D_2O instead of H_2O as the solvent. Interestingly, this effect appears to be independent of the chemical nature of the dye. It is conceivable that the different energies of the OH versus OD stretching vibrations (3657 and $2670\,\mathrm{cm}^{-1}$, respectively) are responsible for more effective solvent quenching by H_2O versus D_2O. Independent of the physical nature, this heavy atom effect in solvent quenching has been shown to be a smart tool for the characterization of water accessibilities in supra- and macromolecular assemblies [82].

6.5.1.2.4 **Self-Quenching**

Self-quenching is the quenching of one fluorophore by another. It is a widespread phenomenon in fluorescence, but it requires high loading concentrations or labeling densities. The general physical treatment of self-quenching processes involves a combination of trap-site formation and energy transfer among fluorophores, with the possibility of migration of trap-sites, which results in quenching. Trap-sites may be formal fluorophore complexes or aggregates, or may result from fluorophore proximity at sufficiently high concentrations. A mathematical modeling of such processes is given in [85]. Self-quenching experiments are frequently exploited, by simply monitoring the increase in the fluorescence intensity F because of decrease of local dye concentrations. One example represents a self-quenching assay for the characterization of leakage of aqueous contents from cells or vesicles as a result of lysis, fusion, or physiological permeability. This assay is based on the fact that carboxyfluorescein is $>95\%$ self-quenched at concentrations >100 mM [86]. Concentrated solutions of these water-soluble dyes are encapsulated in liposomes. On addition of a fusogen or other permeabilizing agent, dye release is accompanied by an increase in fluorescence. Other chromophores, the self-quenching properties of which are exploited in biochemical assays are NBD (derivatives of 7-nitrobenz-2-oxa-1,3-diazol-4-yl) [87, 88], Bodipy (derivatives of 4,4-difluoro-4-bora-3a,4a-diaza-s-indacene) [89], and DPH (derivatives of 1,6-diphenyl-1,3,5-hexatriene) [90].

6.5.1.2.5 **Trivial Quenching**

Trivial quenching arises from attenuation of the exciting beam and/or the inability of fluorescence photon to reach the detector. It occurs mainly when compounds are added that strongly absorb in the UV range. Although the added concentration may be small, they might block the excitation light completely. Turbidity of the sample can be another reason for trivial quenching. True and trivial quenching, however, are easily differentiated, as in trivial quenching lifetime and quantum yield remain constant.

6.5.1.3 Solvent Relaxation

Any electronic excitation from the ground state S_0 to the excited state S_1 is paralleled by a change in the dipole moment $\Delta\mu_c$ ($\Delta\mu_c = \mu(S_1) - \mu(S_0)$). As the timescale of the electronic transition is much shorter than that of nuclear motion, the excitation causes an ultrafast change of the probes charge distribution but does not affect the position or orientation of the surrounding solvent molecules. The solvent molecules are, thus, forced to adapt to the new situation, and start to reorient themselves in order to find an energetically favored position with respect to the excited dye. The dynamic process starting from the originally created nonequilibrium FC state and gradually establishing a new equilibrium in the excited state (R) is called *solvent relaxation* (SR). This relaxation red-shifts the probe's emission spectrum continuously from the emission maximum frequency of the FC state ($\upsilon(0)$ for $t = 0$) to the emission maximum of the fully relaxed R-state ($\upsilon(\infty)$ for $t = \infty$). As a more polar solvent leads typically to a stronger stabilization of the polar R-state, the overall shift $\Delta\upsilon$ ($\Delta\upsilon = \upsilon(0) - \upsilon(\infty)$) increases with increasing solvent polarity for a given change of the solute's dipole moment $\Delta\mu_c$. The accurate mathematical description of this relationship depends on the choice of the dielectric solvation theories [91–96]. The fundamental ''dielectric continuum solvation model'' [94–96] predicts a linear proportionality between $\Delta\upsilon$ and a dielectric measure of solvent polarity for a large variety of solvents [97]. According to this model, changes in $\Delta\upsilon$ directly reflect polarity changes in the dye environment, giving the first major information accessible by studies of the SR process. The second information obtainable from the investigation of SR processes is based on the fact that the SR kinetics is determined by the mobility of the dye environment. The response of solvent molecules to the electronic rearrangement of the dye is the fastest in the case of water: more than half of its overall solvation response occurs within 55 fs [98]. If the dye is located in a viscous medium, the SR takes place on the nanosecond (ns) timescale [99]. In vitrified solutions, on the other hand, the dye may fluoresce before SR toward the R-state is completed [100].

6.5.1.3.1 **Steady-State Spectra** Nonviscous solvents at ambient temperature respond with a fast inertial (vibrational) motion in the range between 50 and 500 fs to the ultrafast change in the dipole moment because of electronic excitation. After this initial period of solvation response, the diffusion of the solvent molecules, occurring on the pico- to subnanosecond timescale leads to further solvation energy relaxation toward the R-state [97, 98, 101, 102]. The fluorescence decay time τ of chromophores is usually 1 ns or longer. Thus, almost the entire fluorescence in a steady-state experiment occurs from the equilibrium state R. Considering the above described connections between $\Delta\upsilon$ and the dipole moments of the solute, $\Delta\mu_c$, and the polarity of the solvent, there are two basic consequences for the spectral position of the steady-state fluorescence spectrum: (i) increased solvent polarity leads generally to a red-shift of the emission spectrum. For illustration, the influence of the solvent on the emission maximum of Prodan (6-propionyl-2-(dimethylamino)-naphthalene) is depicted in Figure 6.32. (ii) The larger $\Delta\mu_c$, the more pronounced the effect of solvent polarity on the position of the emission spectrum. Moreover, as SR is much faster than fluorescence, the wavelength of the maximum emission and the fluorescence lifetimes are independent of the excitation wavelength.

If the dye is located in a viscous medium, the SR might take place on the nanosecond (ns) timescale. Thus, emission occurs to a substantial extent during SR, and the emission spectrum represents an average of the partially relaxed emission. In this case, the maximum of emission spectrum is no longer directly correlated with the polarity of the solvent. An increase of the temperature leads to a faster solvent reorientation process and, thus, to a red-shift of the maximum of the emission spectrum. Moreover, the wavelength of the emission band maximum of polar fluorophores in motionally restricted media, such as in very viscous solutions

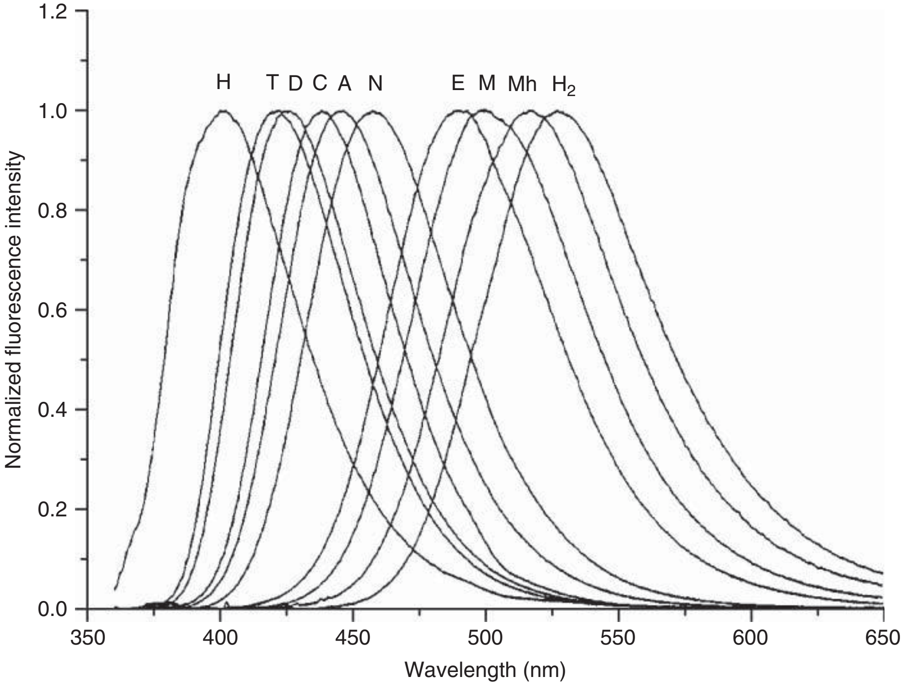

Figure 6.32 Fluorescence spectra of Prodan in different solvents at ambient temperature; $\lambda_{ex} = 337$ nm; H, heptane; T, toluene; D, dioxane; C, chloroform; A, acetone; N, acetonitrile; E, ethanol; M, methanol; Mh, methanol/water 1 : 1; H_2, water.

[103, 104] or membranes [99], shifts to longer wavelength by shifting the excitation wavelength toward the red-edge of the absorption band [105]. The observed shift should be maximal if the SR is much slower than the fluorescence, and it should be zero if SR is fast and independent of the excitation wavelength the entire fluorescence origins from the relaxed R-state. Thus, the red-edge excitation shift can serve as an indicator of the mobility of the probe surrounding [103, 104, 106]. Usually, red-edge excitation shift values range from several up to 40 nm depending on the chosen solute and solvent system. The red-edge excitation shift is especially useful when using dyes, the absorption and fluorescence maxima of which hold linear correlations with the polarity of low-viscosity solvents [100, 107], because then the probed polarity as well as the hypothetical emission maximum of the fully relaxed R-state can be estimated from the absorption maximum. In vitrified solutions such as sol–gel matrices [100], SR becomes much slower than fluorescence and it arises from states close to the FC state.

6.5.1.3.2 **Time-Resolved Emission Spectra** Although there have been several attempts to simplify the characterization of the SR process, the determination of time-resolved emission spectra (TRES) is certainly the most general and most precise way to quantitatively describe the solvent response. The TRES are usually

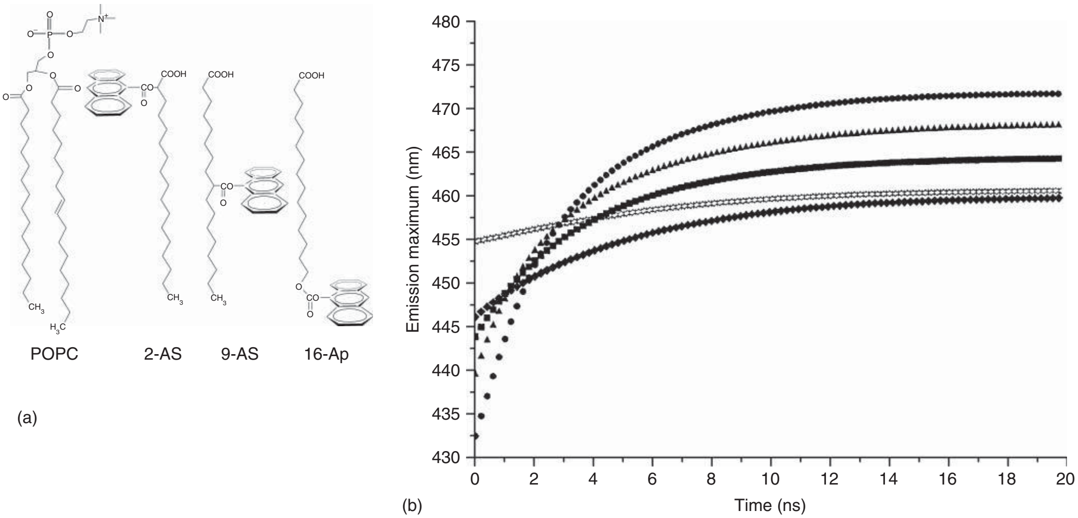

Figure 6.33 (a) Schematic structures of 2-AS, 9-AS, and 16-AP and their relative position within phospholipid bilayers with respect to a phospholipids molecule (1-palmitoyl-2-oleoyl-*sn*-glycero-3-phosphocholine, POPC). (b) Time course of the emission maximum wavelength λ (in nanometer) as a function of time after excitation of the *n*-AS in PC-SUV at 25 °C. Circles, 2-AS; triangles, 6-AS; boxes, 9-AS; diamonds, 12-AS; asterisks, 16-AP recorded with a time resolution of approximately 200 ps. For a fully quantitative description of the solvent relaxation process of those *n*-AS dyes see [109].

determined by "spectral reconstruction" [97, 98, 107]. The TRES at a given time t is calculated from the wavelength dependent time-resolved decays by relative normalization to the steady-state spectrum [108]. By fitting the TRES at different times t by the empirical "log-normal" function, the emission maximum frequencies $\upsilon(t)$ (or emission maximum wavelengths $\lambda(t)$: see Figure 6.33b) and the total Stokes-shift $\Delta\upsilon$ (or $\Delta\lambda$) are usually derived [107]. As $\upsilon(t)$ contains both information about polarity ($\Delta\upsilon$) and viscosity of the reported environment, the spectral shift $\upsilon(t)$ may be normalized to the total shift $\Delta\upsilon$. The resulting "correlation functions" $C(t)$ (Eq. (6.7)) describe the time course of the solvent response and allow for comparison of the SR-kinetic and, thus, of relative microviscosities, reported from environments of different polarities [97, 98, 103, 109, 110].

$$C(t) = \frac{\upsilon(t) - \upsilon(\infty)}{\Delta\upsilon} \tag{6.7}$$

SR probes used for the characterization of microviscosities and polarities are listed in Table 6.12 [111–121]. They are characterized by a large change in the dipole moment $\Delta\mu_c$ on electronic excitation.

6.5.1.3.3 **Example for Using Solvent Relaxation for Probing Micropolarities** The benefit of the SR techniques in probing micropolarities might be demonstrated

Table 6.12 List of solvent relaxation probes.

Dye or chromophore	References
1,8-ANS	[68]
2,6-ANS	[68]
2,6-TNS	[69, 122]
NPN	[71]
Dansyl Lysin	[72]
Prodan	[73, 74, 79]
Laurdan	[75]
Patman	[73, 74, 79]
NBD	[55]
Coumarin 153	[53, 123, 63]
Nile red	[76]
Hemicyanine dyes	[62, 77]
Piperidine-bridged electron donor acceptor systems	[77]

1,8-ANS, 1-anilinonaphthalene-8-sulfonate; 2,6-ANS, 2-anilinonaphthalene-6-sulfonate; 2,6-TNS, 2-(*p*-toluidinylnaphthalene)-6-sulfonate; NPN, *N*-phenyl-1-naphthylamine; Dansyl Lysin, *N*-e-(5-dimethylaminonaphthalene-1-sulfonyl)-L-lysine; Prodan, 6-propionyl-2-(dimethylamino)-naphthalene; Laurdan, 2-dimethylamino-6-lauroylnaphthalene; Patman, 6-palmitoyl-2-[[2-(triethylammonium)ethyl]methylamino]naphthalene chloride; NBD, 7-nitrobenz-2-oxa-1,3-diazol-4-yl.

by the TRES of the *n*-anthroyloxy fatty acids (*n*-AS) in small unilamellar vesicles (SUVs) [109]. These compounds constitute a unique set of fluorescent dyes with the advantage of using a common chromophore, which is covalently attached at different positions ($n = 2, 9, 16$) along the acyl chain of the fatty acid (stearic acid for $n = 2, 9$; palmitic acid for $n = 16$; see Figure 6.33a). The *n*-AS probes are believed to insert into the membrane with the stearoyl chains parallel to the phospholipid acyl chains. While the total Stokes-shifts $\Delta\upsilon$ in highly viscous, nonpolar solvents such as paraffin oil evoking from an intramolecular relaxation process are small and independent of the fluorophore position ($\Delta\lambda = 1630\,\text{cm}^{-1}$), the *n*-AS dyes show much larger $\Delta\upsilon$ values increasing within the series 16-AP < 9-AS < 2-AS (i.e., 2950, 2450, 2300 cm^{-1}, respectively), when incorporated in phosphatidylcholine small unilamellar vesicles (PC-SUVs). Apparently, 2-AS, which is located closest to the membrane/water interface probes the most hydrated, polar environment, while 16-AP residues in much more hydrophobic environment, although still seeing some water molecules. The presented trends illustrate the $\Delta\upsilon$/solvent polarity relationship and show that the SR is an excellent direct method for detecting externally induced polarity and fluidity changes within the bilayer and other self-organizing systems. Recent examples of the application of the SR technique in membrane science have been highlighted in publications [110, 116]. In both contributions, it is shown how the headgroup mobility and hydration in liposomes used in drug [116] and DNA [110] carrier systems are controlled by small variations in the composition of those liposomes.

6.5.1.4 **Polarized Fluorescence**

Excitation with linear polarized or to lesser extent even unpolarized light leads to an anisotropic spatial distribution of excited state molecules. As this selection persists also in emission, the emitted light is also polarized. The degree of fluorescence polarization is largest when linear polarized excitation is used and depends on how well the effect of photoselection has been kept in the emission. The polarization can be diminished by excitation energy transfer and by rotational diffusion of the excited molecule. The latter process depends on the viscosity of the dye environment and on the size of the diffusing species. This connection represents the basis for the applications of fluorescence polarization studies. The depolarization by excitation energy transfer [124] is usually an undesirable process. Resonance energy transfer, however, occurs only in concentrated solution where the average distance between the dyes is typically near 5 nm (see Section 6.5.1.5). Thus, this depolarization mechanism can be avoided by the use of dilute solutions.

The polarization is conventionally characterized with reference to a system of laboratory coordinates defined by the directions of linear polarized excitation ($E_{||}$) and of the fluorescence beam. It is customary to observe the fluorescence beam resolved in directions parallel ($F_{||}$) and perpendicular ($F_{\perp}$) to the direction of the excitation light ($E_{||}$). The degree of fluorescence polarization P is defined as

$$P = \frac{F_{||} - F_{\perp}}{F_{||} + F_{\perp}} \tag{6.8}$$

An equivalent parameter used for the description of polarization of fluorescence is the anisotropy a

$$a = \frac{F_{||} - F_{\perp}}{F_{||} + 2F_{\perp}} \tag{6.9}$$

Although both parameters are equivalent for the description of polarized light, anisotropy is usually preferred. Following pulse excitation, the anisotropy of spherical particles in homogeneous isotropic medium decays exponentially, given by

$$a = a_0 \exp\left(\frac{-t}{\tau_\mathrm{p}}\right) \tag{6.10}$$

where τ_p is the rotational correlation time of a sphere and a_0 is the anisotropy at $t = 0$. The initial value of the anisotropy a_0 is constant if the fluorophore is fixed in space. Thus, it can be experimentally determined by measuring the steady-state anisotropy of the dye in a rigid and homogeneous medium, such as a vitrified solution. It depends on the angle between the absorption and transition moment of the dye, β. As the orientations of absorption and transition moments are characteristic for the corresponding electronic transitions, the angle β is a constant for a pair of electronic transitions of a dye. Fluorescence usually arises from a single transition. Thus a_0 is supposed to be invariant to the emission wavelength. The presence of SR occurring on the nanosecond timescale, however, can result in a wavelength dependent change of the emitting S_1 state (see Section 6.5.1.3.1), and thus to a substantial decrease in anisotropy across the emission spectrum. As the excitation spectrum might be composed of several absorption bands corresponding to several transition moments, the polarization of fluorescence might change with the exciting light wavelength. Thus, polarization excitation spectra can be used to identify different overlapping electronic transitions. Using linear polarized light under one-photon excitation conditions (for multiphoton excitation see [125]) a_0 for a randomly orientated molecule is

$$a_0 = 0.6\ \cos^2\beta - 0.2 \tag{6.11}$$

For collinear transition dipole moment, the theoretical maximum value a_0 is equal 0.4.

6.5.1.4.1 **Steady-State Fluorescence Anisotropy**

In low-viscosity solvents, the rotational depolarization of low molecular weight compounds occurs on the picosecond timescale [126]. As in this case, the rotation is much faster than the fluorescence, the steady-state emission is nonpolarized. If the rotational motion of the fluorophore is on the same scale as the fluorescence, a steady-state polarization is observed. In the simplest case for a spherical rotor and single-exponential fluorescence intensity decay (τ), the measured anisotropy is given by

$$a = \frac{a_0}{1 + \tau/\tau_\mathrm{p}} \tag{6.12}$$

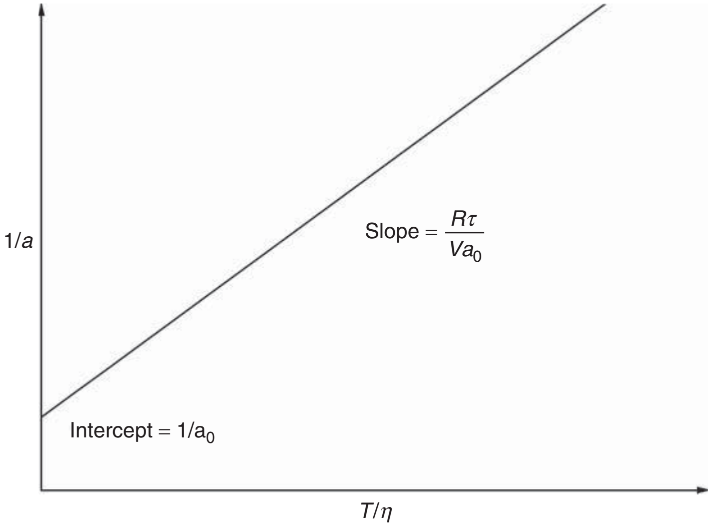

Figure 6.34 Illustration of a Perrin plot for the determination of the apparent hydrodynamic volume V by steady-state fluorescence anisotropy measurements.

The rotational correlation time of a sphere τ_p is given by

$$\tau_\mathrm{p} = \frac{\eta V}{RT} \tag{6.13}$$

where η is the viscosity, T the temperature, R the gas constant, and V the volume of the rotating unit. It is important to note that these connections hold only for spherically symmetrical molecules. A formal description of these connections for spherically unsymmetrical and ellipsoidal molecules can be found in the literature [124, 127–129]. By combining Eq. (6.12) and Eq. (6.13), it can be seen that a plot of $1/a$ versus T/η should be linear, with intercept equal to $1/a_0$ and with a slope/intercept that is directly proportional to τ and indirectly proportional to V (see Figure 6.34). If one of the latter two parameters is known, the other can be calculated from such data. The absence of viscosity dependence indicates that some other depolarizing process dominates. A nonlinear plot of $1/a$ versus T/η indicates the existence of more than one rotational mode.

Prior to the availability of time-resolved measurements, such so-called Perrin plots have been extensively used to determine the apparent hydrodynamic volume of proteins [130, 44, 131]. As protein association reactions usually affect the rotational correlation time of the protein label, such reactions have been characterized by steady-state anisotropy measurements [132, 133].

6.5.1.4.2 **Time-Resolved Fluorescence Polarization** As described by Eq. (6.10), the anisotropy of spherical particles in homogeneous isotropic medium decays exponentially. Anisotropy decays, however, can be more complex. The three most important origins for nonmonoexponential decays are described in the following:

1) *Nonspherical particles in homogeneous isotropic medium*
   The theory for rotational diffusion of nonspherical particles is complex. In theory, the anisotropy decay of such a molecule can be composed of a sum of up to five exponentials [134]. The ellipsoids of revolution represent a smooth and symmetrical figure, which is often used for the description of the hydrodynamic properties of proteins. They are three-dimensional bodies generated by rotating an ellipse about one of its characteristic axes. In this case, the anisotropy decay displays only three rotational correlation times, which are correlated to the rotational diffusion coefficients $D_{||}$ and $D_{\perp}$. In this case, the indices || and ⊥ denote the rotation around the main and side axis, respectively [129]. The preexponential factors of the three exponentials depend on the angle between the emission transition moment and the main axis of the rotational ellipsoid. In practice, owing to the limited time resolution, one rarely resolves more than two exponentials [129].
2) *Segmental mobility of the chromophore*
   A more important factor is that the chromophore is not rigidly fixed to the biopolymer and, thus, rotates about the bond linking it to the biopolymer. Consequently, the anisotropy decay kinetics is found to be double or triple exponential, because of the contributions from internal and global rotation of the macromolecule. The same concept applies for the rotational wobble of that portion of the biopolymer in proximity to the fluorophore or in the more defined case for the rotation of a molecular domain [45].
3) *Hindered rotors: fluorescent dyes in biological membranes.*
   If isotropic rotors are imbedded in an anisotropic environment, such as phospholipid bilayers, the decay of fluorescence anisotropy can be complex. Let us consider a dye, such as 1-(4-trimethylammonium-phenyl)-6-phenyl-1,3,5-hexatriene (TMA-DPH) or DPH, intercalated inside the bilayer. The polarization of its fluorescence depends on the resistance to its motion, exerted by its molecular environment. In the case of a fixed hindrance to rotational relaxation motion, the value of anisotropy decreases exponentially, not to zero, but to a finite value a_∞, yielding Eq. (6.14)

$$a = (a_0 - a_\infty)\exp\left(\frac{-t}{\tau_\mathrm{p}}\right) + a_\infty \tag{6.14}$$

Thus, the time-resolved measurement of such membrane probes contains information on the dynamics of the hindered probe rotation, often interpreted as the microviscosity, and about the hindrance of this rotation, usually interpreted as the static packing arrangement of the lipids or the so-called membrane order [135, 136]. Fluorescence polarization studies in membranes, however, exhibit some major limitations: the experimentally determined steady-state and time-resolved anisotropies characterize the motional restrictions of the ‘‘reporter’’ molecule itself and give therefore only *indirect* information about the dye environment, with the consequence that, if the probe is bound covalently to the lipid (TMA-DPH), this attachment may dominate the recorded depolarization behavior. The membrane order parameters obtained from freely mobile probes such as (DPH) result from a broad distribution of localizations within the hydrophobic interior, the detailed characterization of which reveals inherent ambiguities [137].

Among the fluorescence techniques employed, the determination of fluorescence anisotropy has certainly been the dominating fluorescence method in studies of biological systems. For a detailed description of the theory and several examples of its application, readers are referred to two review articles [129, 136].

6.5.1.5 **Förster Resonance Energy Transfer**

The Förster (often called *fluorescence*) resonance energy transfer (FRET) is a nonradiative transfer of the excitation energy from a donor to an acceptor chromophore. It is governed by a long-range interaction between the emission and absorption transition dipole moments of the donor and acceptor, respectively. The rate of energy transfer depends on the extent of the spectral overlap of the emission and absorption spectra of the donor and acceptor, respectively, on the quantum yield of the donor, the relative orientation of the transition dipole moments, and the distance between donor and acceptor molecules. The distance dependence has resulted in its widespread use to measure distances between donors and acceptors in macromolecular systems. The quality of a *donor/acceptor* pair is usually characterized by the parameter R_0, which is typically in the range between 2 and 9 nm. It is defined as the distance at which the rate of resonance energy transfer is equal to what would be the decay rate of the donor on the absence of an acceptor and can be estimated, as follows

$$R_0(\mathrm{nm}) = 979(\kappa^2 n^{-4} \phi_0 J)^{\frac{1}{6}} \tag{6.15}$$

where n is the refractive index of the medium, ϕ_0 is the fluorescence quantum yield of the donor, J the spectral overlap integral, and κ an orientation factor. The rate of energy transfer k_{ET} is given by

$$k_{\mathrm{ET}} = \frac{1}{\tau_{\mathrm{d}}} \left(\frac{R_0}{r} \right)^6 \tag{6.16}$$

where τ_{d} is the decay time of the donor in absence of the acceptor and r is the distance between donor and acceptor. Thus the rate depends strongly on distance, providing a spectroscopic ruler for determining distances in macromolecular assemblies.

The magnitude of k_{ET} can be determined from the efficiency of energy transfer, ET, via

$$k_{\mathrm{ET}} = \frac{1}{\tau_{\mathrm{d}}} \frac{\mathrm{ET}}{1 - \mathrm{ET}} \tag{6.17}$$

and ET, in turn, can be experimentally evaluated by the measurements of the decrease in the intensity F or lifetime τ of the donor in the presence of the acceptor

$$\mathrm{ET} = 1 - \frac{F}{F_{\mathrm{d}}} = 1 - \frac{\tau}{\tau_{\mathrm{d}}} \tag{6.18}$$

Thus, determining ET and knowing R_0, the separation distance r can be calculated. In such distance measurements, there is often a concern about the effects of the orientation factor κ^2, which depends on the relative orientation of the emission oscillator of the donor and the absorption oscillator of the acceptor. The value of κ^2 varies from 4 (parallel orientation of the oscillators) to 0 (perpendicular orientation). Often a value of $\kappa^2 = 2/3$ is assumed, which corresponds to the situation when there is rapid, isotropic rotation of the donor and acceptor molecules. Randomly oriented dipoles that remain fixed during the singlet lifetime give $\kappa^2 = 0.476$. When required, the range of values for κ^2 can be estimated by polarization measurements [138]. A comprehensive discussion on the theory and effects of the orientation factor is given in [139].

When assuming the simplest case of a monoexponentially decaying donor τ_{d}, a fixed distance r and a dynamically random orientation factor $\kappa^2 = 0.476$, k_{ET} will be added to Eq. (6.3) and thus the energy transfer will simply result in a shortened, monoexponential decay of the donor τ_{d}. In homogeneous solution, however, at low donor concentrations and without diffusion of the donor and acceptor within the fluorescence lifetime, the intensity decay is given by [140–143]

$$F = F_0 \exp\left(\frac{-t}{\tau_{\mathrm{d}}}\right) \exp\left[-\gamma\left(\frac{t}{\tau_{\mathrm{d}}}\right)^{\delta}\right]; \quad \delta = \frac{\mathrm{dim}}{6} \tag{6.19}$$

For randomly distributed donor and acceptor molecules the value for the dimension dim is equal 3 and γ is

$$\gamma = \frac{4}{3} g \pi^{\frac{3}{2}} c_{\mathrm{a}} R_0, \quad \text{where } g = \sqrt{\frac{3}{2}\kappa^2} \tag{6.20}$$

with c_{a} as the acceptor concentration. With knowledge of the acceptor concentration and on the condition that the donor fluorescence decays monoexponentially in the absence of the acceptor, the R_0 value and the dimension of the medium in which donor and acceptors are imbedded can be determined. Two-dimensional or the so-called fractal energy transfer is of interest, if the dye molecules are bound to phospholipid membranes [43, 144] or imbedded in silicate networks [145]. One-dimensional energy transfer has been considered for dyes bound to DNA [146].

FRET is widely used in biosciences as a molecular ruler to characterize the topography of macromolecules and supramolecular structures in cells and model systems [147–150]. The method is usually combined with microscopic imaging in case of living cells studies. A variety of experimental approaches exist for microscopic FRET studies [151]. The simplest approach is to perform two-color ratio imaging of donor and acceptor emission. Overlap of excitation and emission spectra of donor and acceptor can result in problems with cross-talk, making control experiments needed to establish the presence of FRET [148]. A more rigorous, although experimentally more complicated approach, is fluorescence lifetime imaging (FLIM) of the donor. This method is less prone to cross-talk artifacts and allows also the use of nonfluorescent acceptors [148]. Fluorescence anisotropy can be also used to measure FRET. This approach is convenient in cases where the mobility of the donor is strongly restricted and its fluorescence, thus, strongly anisotropic. If the transition moment of the acceptor is oriented randomly or differently than that of the donor, energy transfer results in depolarization of fluorescence of the sample. This method can easily detect the presence of FRET, however, it is not good for estimating the strength of the effect [148].

Studies of protein conformation and folding represent an important field of FRET applications [147, 152, 153]. Green fluorescent protein (GFP) and its analogs are the main tools of fluorescence spectroscopy in protein science and FRET assays are no exception. Cyan fluorescent peptide (CFP) as the donor and yellow one (yellow fluorescent peptide, YFP) as the acceptor are the most widely used FRET pair; other possible pairs include GFP or YFP as the donor and orange or red proteins like mCherry as the acceptor [148, 153]. Assays for the characterization of fusion of cells or vesicles represent another application field of FRET. Usually such membrane systems are labeled either by a donor or an acceptor molecule. Fusion leads to an intermixing of these membrane labels in the same bilayer, allowing resonance energy transfer to occur. Examples can be found in the literature [154–158]. Another membrane application of energy transfer has been the demonstration of lipid asymmetry in human red blood cells [159]. Moreover, energy transfer has been shown to be a very useful tool in elucidating the subunit structure of oligomeric assemblies in membranes. Examples are studies on the oligomerization of ATPase of sarcoplasmic reticulum in phospholipid vesicles [160], on gramicidin A transmembrane channels [161], and on the aggregation state of bacteriorhodopsin [162]. Finally, the combination of energy transfer with flow cytometry [163] and its use in immunoassays should be mentioned [164]. More detailed information on theory and applications of energy transfer can be found in [139, 165, 164].

6.5.1.6 **Excimer Fluorescence**

The term *excimer* is used when the excited dye forms a transient fluorescent dimeric complex with another fluorophore of the same kind. The excimer fluorescence is usually red shifted with respect to that of monomers (see Figure 6.35). The most widely used types of *excimer-forming probes* are pyrene (see Figure 6.35) and perylene and their derivatives. The ratio of the maxima of the excimer to the monomer spectra can be used to judge the efficiency of excimer formation. This (Ex/Mo)-ratio depends on the concentration of the dye and is controlled by the diffusion properties. When using pyrene or perylene labeled fatty acids or phospholipids (see Figure 6.35), it allows for the estimation of the probe's lateral diffusion coefficients in lipid bilayer membranes. Thus, membrane fluidity can be measured by monitoring the fluorescence spectra of such an excimer probe.

As increasing temperature leads to increased fluidity and thereby to a faster probe diffusion, pyrene lipids have been frequently used to study phase transition in membranes [166, 167]. Phospholipid phase separation increases the local concentration of dye labeled lipids and can be, therefore, investigated via the characterization of excimer formation. The binding of proteins or ions, however, might induce phase separation as well as decrease lateral lipid diffusion. As these two effects are opposing in terms of excimer formation, the binding of such proteins or ions cannot be studied by the (Ex/Mo)-ratio. The time-resolved analysis of the monomer fluorescence of the labeled lipid, however, allows for the separation of

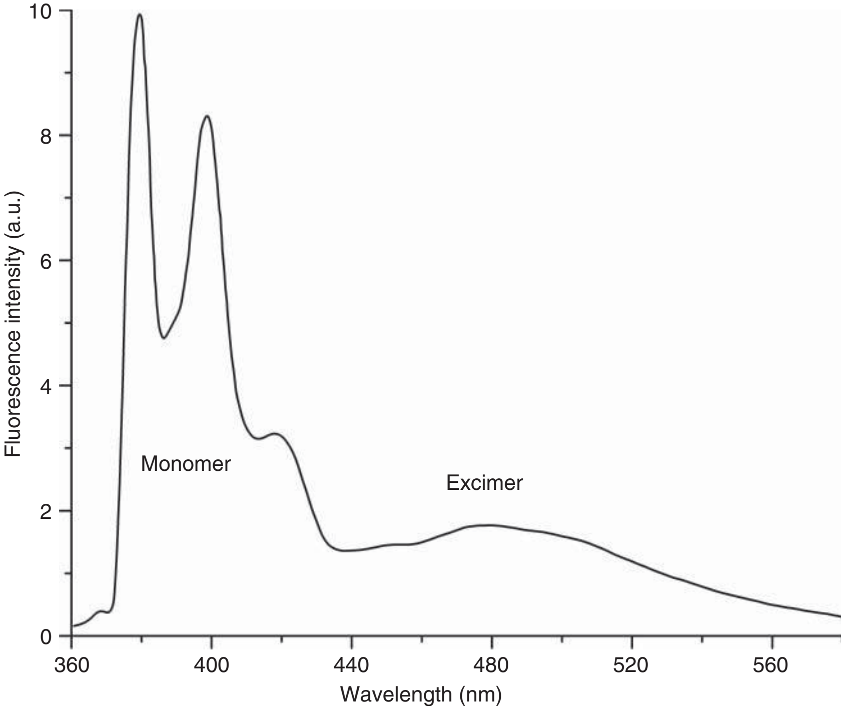

Figure 6.35 Fluorescence spectrum of pyrene-labeled phosphatidylglycerol (5 mol%) in phosphatidylcholine small unilamellar vesicles at ambient temperature; $\lambda_{ex} = 337$ nm.

both effects [168]. A comprehensive treatise of theory and application of excimer probes in membrane research can be found in [169, 170].

6.5.2
Special Applications

6.5.2.1 Fluorescence Recovery after Photobleaching (FRAP)

Fluorescence recovery after photobleaching (FRAP) was introduced as a method to measure the local mobility of fluorescently labeled particles bound to the plasma membrane of living cells [171–173]. It has been used to study transport phenomena in a wide variety of biological membrane-bound systems, as well as to probe the photobleaching properties of fluorescent molecules [174]. FRAP is based on the principle of observing the rate of recovery of fluorescence, because of the movement of a fluorescent marker into an area of the membrane which contains this same marker but which has been rendered nonfluorescent via an intense photobleaching pulse of laser light. The two-dimensional diffusion coefficient of the fluorophore is related to both its rate and extent of recovery. For a discussion of the photophysical mechanism of photobleaching see Ref. [175]. In order to create a finite observation area, both laser beams, the single short pulse with rather

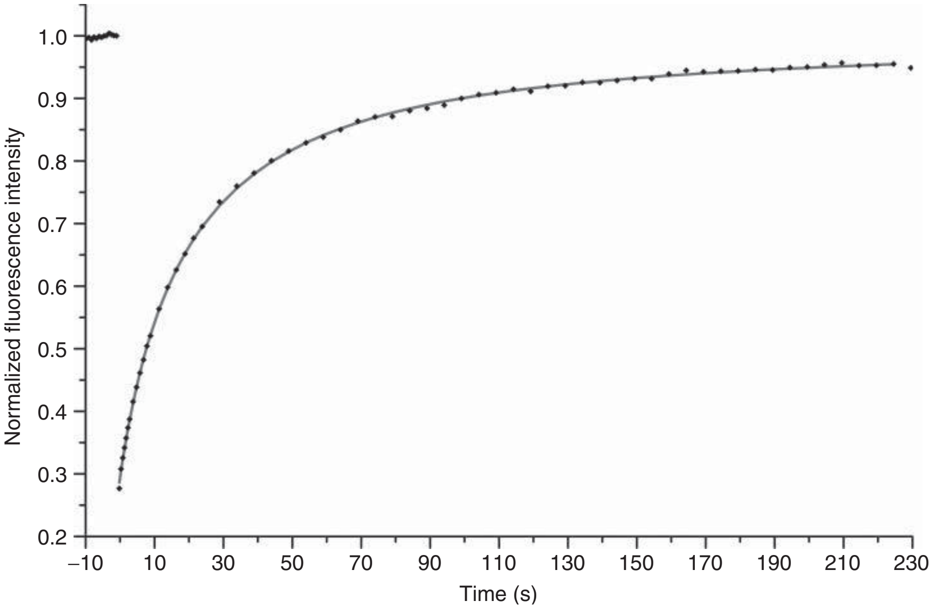

Figure 6.36 Representative TIR–FRAP curve for splicing regulator Brd2 tagged with GFP in the nucleoplasm of HeLa cells. Note that the fluorescence intensity does not recover fully. This effect is generally observed in photobleaching experiments and is one of the major drawbacks of this method. (Data courtesy of Dr David Staněk and Eva Šimková, Institute of Molecular Genetics of ASCR, Prague, Czech Republic.)

high intensity leading to photobleaching and the less intensive pulse monitoring the fluorescence recovery, are usually focused by an epifluorescence or confocal microscope. A very elegant variation is to combine FRAP with total internal reflection fluorescence (TIRF) [176]. Here, a laser beam totally internally reflects at a solid/liquid interface, creating an evanescent field, which penetrates only a fraction of the wavelength into the liquid domain. When using planar phospholipid bilayer and fluorescently labeled proteins, this method allows for the determination of adsorption/desorption rate constants and surface diffusion constants [177, 178]. Figure 6.36 shows a representative FRAP curve for splicing regulator Brd2 tagged with GFP in the nucleoplasm of HeLa cells. It should be mentioned that, similar to other applications of fluorescence microscopy, two and three photon excitation might be combined with FRAP as well [179].

6.5.2.2 **Fluorescence Correlation Spectroscopy (FCS)**

Since its first introduction in the early 1970s [180–183], the method has developed significantly and has become a standard tool in many scientific disciplines. The typical setup contains a laser with high temporal stability, a single photon detector with low noise (usually a single photon counting photomultiplier tube or a single photon avalanche diode), and a confocal or multiphoton fluorescence microscope with a high-quality objective [184, 185]. In such a setup, fluorescence emission is collected only from a very small volume of the sample, which is typically about 1 μm^3 or smaller. Its radius within the focal plane is diffraction limited and about 200–300 nm, while its characteristic dimension along the optical axis of the microscope is a few micrometers [184, 185]. The method is based on recording time traces of fluorescence intensity $I(t)$ with high temporal resolution and calculating their normalized autocorrelation function $G(\tau)$, which measures probability of detecting a photon at time $t+\tau$ if a photon was detected at time t

$$G(\tau) = \frac{\langle I(t)I(t+\tau)\rangle}{\langle I(t)\rangle^2} \tag{6.21}$$

where pointed brackets represent averaging over all values of t. The shape of the autocorrelation function reflects the timescale of fluorescence intensity fluctuations. On a nanosecond timescale, within the lifetime of fluorescence, it rises steeply from zero to a maximum. This effect, called *photon antibunching*, is related to the time delay between two consecutive photon emissions by a single fluorophore [184] and it can be used to determine the number of independent fluorophores per molecule or molecular complex [186]. Intensity fluctuations on a microsecond timescale result mainly from photophysical and photochemical processes such as intersystem crossing to nonfluorescent triplet state and, in case of polarized detection, rotational diffusion of molecules also contributes. On longer timescales, translational diffusion of molecules in and out of the detection volume dominates the autocorrelation function. In cases of reactions, where a product has much higher fluorescence quantum yield than the reactants, concentration fluctuations around equilibrium can be also detected and used to determine reaction kinetics [182]. If more processes happen on comparable timescale, it is difficult to distinguish their contributions to the autocorrelation function.

The detection volume is usually approximated by a three-dimensional Gaussian volume element [184]. The autocorrelation function $G(\tau)$ for a three-dimensional Brownian diffusion is then given by Eq. (6.22) [187]

$$G(\tau) = 1 + \frac{1}{N}\frac{1}{1+(\tau/\tau_\mathrm{D})}\left(\frac{1}{1+\left(\tau/\tau_\mathrm{D}\right)(\omega_0/\omega_\mathrm{z})}\right)^{\frac{1}{2}} \tag{6.22}$$

where ω_0 and ω_z are characteristic dimensions of the detection volume in the focal plane and along the optical axis respectively defined as distances at which the intensity drops by the factor e^{-2}. τ_D is the diffusion time and N is the particle number (number of fluorescent particles within the detection volume). The dimension of the detection volume can be determined by a measurement of diffusion of a molecule with known diffusion coefficient.

To account for intersystem crossing, an average fraction of fluorophores in triplet state T and intersystem crossing relaxation time τ_T need to be induced into

Eq. (6.22) [187]

$$G(\tau) = 1 + \left[1 - T + T\exp\left(\frac{-\tau}{\tau_T}\right)\right] \frac{1}{N(1-T)}\frac{1}{1+(\tau/\tau_D)}\left(\frac{1}{1+(\tau/\tau_D)(\omega_0/\omega_z)}\right)^{\frac{1}{2}} \tag{6.23}$$

If more fluorescent species are present in the sample, a multicomponent autocorrelation function (Eq. (6.24)) is used [187]

$$G_M(\tau) = 1 + \frac{\sum_{i=1}^{M}\left(\frac{Q_i}{Q_1}\right)^2 F_i g_i(\tau)}{N\left[\sum_{i=1}^{M}\frac{Q_i}{Q_1}F_i\right]^2},$$
$$g_i(\tau) = \frac{1}{1+(\tau/\tau_{Di})}\left(\frac{1}{1+(\tau/\tau_{Di})(\omega_0/\omega_z)}\right)^{\frac{1}{2}} \tag{6.24}$$

where Q_i is the detection efficiency of ith species and F_i its fraction. When the diffusion is confined only to two dimensions, as in the cases of supported phospholipid bilayers (SPBs) [188], giant unilamellar vesicles (GUVs) [189], or monolayers on air–water interfaces [188], Eq. (6.22) is reduced to the following form

$$G_{2D}(\tau) = 1 + \frac{1}{N}\frac{1}{1+(\tau/\tau_D)} \tag{6.25}$$

The physically relevant parameters τ_D and N can be, then, extracted from the experimentally obtained autocorrelation function $G(\tau)$ via nonlinear fitting with an appropriate theoretical model (Eq. (6.22), Eq. (6.23), Eq. (6.24), and Eq. (6.25)). Owing to the highly nonlinear connection between the physically relevant parameters and the measured autocorrelation function, it is very difficult to analyze the accuracy of their estimation. The standard deviation of the fit of the autocorrelation curve can be obtained using the method described by Wohland *et al.* [190]. Knowing the size of the detection volume, it is possible to easily calculate diffusion coefficient D and concentration c of the fluorescent molecule from the measured parameters τ_D and N respectively.

The signal-to-noise ratio is the highest when there is on average about one fluorescent molecule within the detection volume [188, 191], which means very low (nM) concentrations are optimal. For that reason, FCS (fluorescence correlation spectroscopy) is often included among *single molecule* techniques; it is based on detection of fluctuations caused by single molecules, but extracts from them ensemble-averaged kinetic data. High excitation intensities can lead to artifacts because of photobleaching and optical saturation, when an increased number of molecules within the detection volume are not in the ground state but in an excited or triplet state leading to loss of proportionality between excitation and fluorescence intensities [184, 185]. Other artifacts, which can influence the results of FCS, are caused by deviations of the real shape of the detection volume from the Gaussian one assumed in Eq. (6.22), Eq. (6.23), Eq. (6.24), and Eq. (6.25).

A detailed discussion of the artifacts of FCS can be found in the works of Enderlein and his group [184, 185, 192]. The most important source of artifacts in the case of two-dimensional systems is the problem with exact positioning of the sample along the optical axis of the microscope (z axis). There exist several methods to overcome this problem: two-focus scanning fluorescence correlation spectroscopy (SFCS) [193] or two-focus FCS with overlapping foci, which uses two alternatively pulsed polarized lasers [192] and a single-focus technique called *z-scan FCS*, which can be performed with most standard FCS setups [188].

z-Scan FCS is based on measuring fluorescence autocorrelation functions $G(\tau)$ at different positions of the sample along the z axis (with step size typically 200 nm), thus changing the distance Δz between the sample and the focus. Diffusion time τ_D and particle number N depend quadratically on Δz (Eq. (6.26)) [194]

$$\tau_D(\Delta z) = \frac{\omega_0^2}{4D}\left(1 + \frac{\lambda^2 \Delta z^2}{\pi^2 \omega_0^4}\right), \quad N(\Delta z) = \pi c_S \omega_0^2 \left(1 + \frac{\lambda^2 \Delta z^2}{\pi^2 \omega_0^4}\right) \tag{6.26}$$

where D is the lateral diffusion coefficient of the fluorescent molecule, c_S its surface concentration, ω_0 is the radius of the excitation beam in the plane of focus, and λ is the wavelength of the excitation light in the medium of the sample. Diffusion coefficients obtained by this method are independent of external calibration and free of most artifacts of standard FCS [192].

FCS is widely used in biological sciences to study diffusion of lipids and proteins in cellular membranes or their models. The high spatial resolution of FCS allows for the characterization of diffusion processes in different compartments of cell [195–199]. In many applications, the diffusion properties of two species with different molecular weight are analyzed. In case that the fluorescently labeled low molecular weight compound binds to the high molecular weight compound, titration of the latter allows for the determination of equilibrium binding constants. This principle can be used, for example, for the characterization of interactions between different proteins [200–203], proteins and membranes [204], xenobiotics and proteins [205], or polynucleotides and DNA [206]. Moreover, any chemical or biochemical reactions leading to a marked change of the molecular weight can be analyzed in real time [195, 196, 207]. However, when the change in molecular weight and, thus, diffusion coefficient is not a big one, as for example, in case of dimerization of relatively small molecules, FCS may not be able to resolve the contributions from the two populations. In some cases, photon counting histograms (PCHs) may be a useful tool to extract the concentrations of different components of the mixture using the difference in their molecular brightness ϵ defined as average number of photons per molecule per sampling time. The PCH of a mixture is the convolution of PCHs of the individual components [208].

Signals from two fluorophores of different emission wavelengths can be separated by means of optical filters and their diffusions measured independently by dual-color FCS. Cross-correlation of their signals reveals whether the two fluorophores move independently or not [209]. Cross-correlation dual-color FCS is also suitable to study kinetics in changes of FRET efficiency; for example, a CFP and YFP bound to different domains of a protein can provide information on internal protein dynamics [210]. Different lifetimes of fluorescence can also serve to identify signal from different fluorophores. The method called *lifetime FCS* may even separate signal coming from the same fluorophore located in different environments [211]; this approach has been applied successfully to elucidate the mechanism of DNA compaction by multivalent cations [212].

Determination by FCS of diffusion coefficient of very slowly diffusing molecules, such as proteins or protein complexes in cellular membranes, may require impractically long measurement times which are connected with an increased risk of artifacts caused by photobleaching and photoinduced degradation of the biological samples. For that reason, several variations of FCS have been developed, which are better suited for such range of applications. In SFCS, the microscope focus is constantly moving along a certain trajectory within the sample (a line or a circle usually). The exposure time of each individual point in the sample is, thus, considerably reduced [193, 123]. FCS measurements in a small number of individual points may not yield representative values of molecular diffusion in as inhomogeneous systems as cellular membranes and other biological structures. That issue is addressed by camera-based FCS, which probes diffusion in many points simultaneously providing a map of molecular mobility [214, 215]. Apart from the possibility of obtaining FCS data from each individual point of an image, whole images may be analyzed by image correlation spectroscopy (ICS), a variant of FCS in which spatial correlations between individual pixels of the image are calculated with interpixel distance playing the role of lag-time τ in standard FCS. Spatial correlations are employed, for example, in spatiotemporal image correlation spectroscopy (STICS), which is efficient in the characterization of directed flows and enables construction of complete transport maps of proteins within regions of cellular membrane [216]; similar information is provided by a related technique *k*-space image correlation spectroscopy (kICS), which uses transformation to the reciprocal space [217]. Raster image correlation spectroscopy (RICS) is based on spatial correlations of images recorded by laser scanning microscopes. Its main advantages include easy implementation using standard laser scanning microscopes as well as broad dynamic range provided by two distinct timescales of scanning (pixels in the same row and pixels in adjacent rows respectively) [218].

6.5.2.3 **Single Molecule Fluorescence**

Following the advances in ultrasensitive instrumentation, the number of works using single molecule experiments has grown rapidly in recent years and some of the techniques have already become well-established experimental procedures. Thanks to its high sensitivity, fluorescence spectroscopy using laser-induced fluorescence is a leading method of single molecule detection. Several optical methods have been used to study single molecule fluorescence; their principles and application can be found, for example, in the reviews [219, 220]. These methods are listed in Table 6.13 [221–241]. Almost any type standard fluorescence spectroscopic measurement can be performed at single molecule level, such as measurements of excitation spectra [242, 243], fluorescent lifetimes by time-correlated single photon counting (TCSPC) [228, 244], or correlation measurements of kinetics of fluorophore’s transition to

Table 6.13 Methods for studying single molecules using laser-induced fluorescence.

Method for studying single molecules	References
Solid matrices at low temperatures	[219, 221]
Liquid streams	[222–225]
Microdroplets	[225, 227]
Near-field scanning optical microscopy	[229, 230, 232, 247]
Far-field confocal microscopy, including fluorescence correlation spectroscopy	[233, 234]
Microscopy combined with multiphoton excitation	[235–237]
Wide-field epi-illumination	[238, 239]
Evanescent wave excitation	[240]

a dark state [245]. The photostability of the single fluorophores is in many cases a limiting factor [245] and for that reason QDs are sometimes used in single molecule studies. These luminescent nanocrystals have supreme brightness and photostability; however, their main drawbacks are larger size, which can interfere more with the investigated system, and their cytotoxicity [246].

One of the motivations for single molecule studies is the development of ultrasensitive analytical assays [220, 248]; a very perspective example is single molecule DNA sequencing [249]. But the most important motivation for single molecule experiments is undoubtedly the possibility of collecting detailed information, including complete statistical distributions, about processes on the level of individual molecules, which cannot be extracted from ensemble-averaged data provided by other techniques. This approach has yielded much deeper insight into several phenomena in many scientific disciplines, such as chemistry, molecular biology, molecular medicine, and material science. Single molecule excitation spectra of fluorophores embedded in crystals revealed, for example, time-dependent spectral shifts related to motions of surrounding molecules [242]. Single molecule fluorescence has also proved to be an efficient tool for gaining deeper insight into intracellular processes such as the mechanism of function of various enzymes. A well-known example is the elucidating of the step-wise movement of molecular motors and the importance of thermal fluctuations for their function [250].

6.5.2.3.1 **Single Particle Tracking** This is a well-established method for studying diffusion of molecules in cells, cellular membranes, and model systems [251–253]. The position of the fluorescently labeled molecule is recorded with a given time interval Δt and the mean square displacement (MSD) (Δt) of the molecule is calculated. Equation (6.27) relates the MSD (Δt) to the lateral diffusion coefficient D

$$\mathrm{MSD}(\Delta t) = \langle \boldsymbol{r}^2 \rangle = 4D\Delta t^{\alpha} \tag{6.27}$$

where $\boldsymbol{r}$ is the particle position and α is the scaling exponent. α equals 1 for free Brownian diffusion and $\alpha < 1$ for anomalous diffusion [253]. Concentration of fluorescent molecules is a crucial parameter in single particle tracking experiments; it has to be sufficiently low to minimize the probability of detecting two closely neighboring fluorophores, but high enough that the fraction of observed trajectories of fluorescent impurities is negligible [245]. More information on the single particle tracking experiments and their applications in investigations of cellular processes can be found, for example, in a recent review [254]. As the position of single molecules in tracking experiments is determined with precision from 10 to 30 nm [255], investigating movement of molecules confined to a certain structure, for example, cytoskeletal filaments, can determine the dimensions and morphology of the structure with a precision superior to imaging by confocal fluorescence microscope [251].

Other possibilities of reaching sub-diffraction-limited resolution in single molecule fluorescence microscopy are the use of near-field scanning optical microscope (NSOM) [228, 231] or tip-enhanced near-field optical spectroscopy, which is discussed in more detail in Chapter 23.

6.5.2.4 **Fluorescence Sensors**

Thanks to the high sensitivity, selectivity, and versatility of fluorescence spectroscopy, fluorescence based sensors are the most highly developed ones. They are not only very easy to use and cost-efficient, but usually also among the most sensitive methods for sensing given analytes and, thus, opening new possibilities in analytical chemistry. For example, FRET based sensors for metal ions have reached single ion sensitivity [256]. In many cases, the sensing probe is placed on a carrier material and the analyte can be either in gas phase or in solution. Interaction between the sensing probe and the analyte leads to a fluorescence change. The use of fiber optics allows one to perform fluorescence measurements on remote objects, which is especially useful in clinical applications. The required fluorescence change, monitoring, for example, the pH, O_2 pressure, or the concentration of ions in blood, can occur in the intensity, emission spectrum, anisotropy, or lifetime of the sensing probe. The mechanism for a change in the listed fluorescence parameters can be collisional quenching, resonance energy transfer, photoinduced electron transfer, or analyte induced change of the state of sensing chromophore. Table 6.14 gives some examples for analyte, sensing probe, and sensing mechanism [70, 257–263]. As intensity measurements are dependent on

Table 6.14 Examples of fluorescence sensing.

Analyte	Sensing dye	Sensing mechanism	References
Oxygen	Several Ru-complexes (e.g., $[Ru(Ph_2phen)_3]^{2+}$	Collisional quenching	[266]
Chloride	Sultons (betains) of quinolinium and acridinium ions	Collisional quenching	[24, 259]
Calcium	Blue and green fluorescent proteins	Resonance energy transfer	[260]
pH	Fluoresceins	pH-dependent ionization	[261, 263]
Glucose	Fluorescein and rhodamine	Resonance energy transfer	[267]

the concentration of the fluorophore, they are often not usable and they might be inaccurate if photobleaching occurs. Moreover, intensity-based systems suffer from other problems including turbidity, limited range of detection, low signal-to-noise ratios, and optical losses. Fluorescence lifetime-based sensing, on the other hand, does not suffer from these problems and are much more promising for the future. An overview of this topic is given in the chapter ''Fluorescence sensing'' in Ref. [264], and more information on the design of fluorescent sensors can be found in review [265].

Acknowledgments

The authors MH and RM acknowledge the financial support provided by the Ministry of Education, Youth, and Sports of the Czech Republic (via CZ.1.07/2.3.00/20.0092) and by Czech Science Foundation (via grant P208/12/G016). Further, MH acknowledges the Praemium Academiae Award (Academy of Sciences of the Czech Republic).

References

1. Gremlich, H.U. (2002) *IR Spectroscopy*, Wiley-VCH Verlag GmbH, Weinheim.
2. Siesler, H.W. and Holland-Moritz, K. (1980) *Infrared and: Raman Spectroscopy of Polymers*, Marcel Dekker, New York and Basel.
3. Schrader, B. (1995) *Infrared and Raman Spectroscopy*, Wiley-VCH Verlag GmbH, Weinheim.
4. Socrates, G. (1994) *Infrared Characteristic Group Frequencies*, John Wiley & Sons, Ltd, Chichester.
5. Bellamy, L.J. (1975 and 1980) *The Infrared Spectra of Complex Molecules*, Vol. 1 and 2, Chapman & Hall, London.
6. Sheppard, N. (2000) *Encyclopedia of Spectroscopy and Spectrometry*, Vol. 3, Academic Press, San Diego, CA, pp. 2320–2328.
7. White, R.L. (2000) *Encyclopedia of Spectroscopy and Spectrometry*, Vol. 1, Academic Press, San Diego, CA, pp. 288–293.
8. Edwards, H.G.M. (2000) *Encyclopedia of Spectroscopy and Spectrometry*, Vol. 1, Academic Press, San Diego, CA, pp. 2–17.
9. Gilbert, A.S. and Lancaster, R.W. (2000) *Encyclopedia of Spectroscopy and Spectrometry*, Vol. 2, Academic Press, San Diego, CA, pp. 881–893.
10. Pettinari, C. and Santini, C. (2000) *Encyclopedia of Spectroscopy and Spectrometry*, Vol. 2, Academic Press, San Diego, CA, pp. 1021–1034.
11. Jackson, M. and Mantsch, H.H. (2000) *Encyclopedia of Spectroscopy and Spectrometry*, Vol. 2, Academic Press, San Diego, CA, pp. 1271–1281.
12. Sigrist, M.W. (2000) *Encyclopedia of Spectroscopy and Spectrometry*, Vol. 3, Academic Press, San Diego, CA, pp. 1800–1809.
13. Noda, I. *et al.* (1999) International Conference on Fourier Transform Spectroscopy: Proceedings of the 12th ICOFTS, Tokyo, Japan, pp. 57–60.
14. Snively, C.M. and Koenig, J.L. (2000) *Encyclopedia of Spectroscopy and Spectrometry*, Vol. 3, Academic Press, San Diego, CA, pp. 1858–1864.
15. Lindon, J.C. (2000) *Encyclopedia of Spectroscopy and Spectrometry*, Vol. 1, Academic Press, San Diego, CA, pp. 603–615.

16. Salzer, R. and Siesler, H.W. (2009) *Infrared and Raman Spectroscopic Imaging*, Wiley-VCH Verlag GmbH, Weinheim.

17. Siesler, H.W., Ozaki, Y., Kawata, S., and Heise, H.M. (2002) *Near –Infrared Spectroscopy*, Wiley-VCH Verlag GmbH, Weinheim.

18. Libnau, F.O., Kvalheim, O.M., Christy, A.A., and Toft, J. (1994) Spectra of water in the near- and mid-infrared region. *Vib. Spectrosc.*, **7**, 243–254.

19. Burns, D.A. and Ciurczak, E.W. (1992) *Handbook of Near-Infrared Analysis*, Marcel Dekker, New York.

20. Schulz, H., Drews, H.H., and Krüger, H. (1999) Rapid NIRS determination of quality parameters in leaves and isolated essential oils of mentha species. *J. Essent. Oil Res.*, **11**, 185–190.

21. Baldwin, E. (1992) Prozeß- und qualitätskontrolle mit on-line-NIR-spektroskopie. *Z. Lebensmitteltech.*, **43**, 502–508.

22. Dempsey, R.J., Davis, D.G., Buice, R.G. Jr., and Lodder, R.A. (1996) Biological and medical applications of near-infrared spectrometry. *Appl. Spectrosc.*, **50**, 18A–33A.

23. Bittner, A., Marbach, R., and Heise, H.M. (1995) Multivariate calibration for protein, cholesterol and triglycerides in human plasma using short-wave near infrared spectrometry. *J. Mol. Struct.*, **349**, 341–344.

24. Marbach, R., Koschinska, T.H., Gries, F.A., and Heise, H.M. (1993) Noninvasive blood glucose assay by near-infrared diffuse reflectance spectroscopy of the human inner lip. *Appl. Spectrosc.*, **47**, 875–881.

25. Jöbsis-vanderVliet, F.F. and Jöbsis, P. (1999) Biochemical and physiological basis of medical near-infrared spectroscopy. *J. Biomed. Opt.*, **4**, 397–402.

26. Yamashita, Y., Maki, A., and Koizumi, H. (1999) Measurement system for noninvasive dynamic optical topography. *J. Biomed. Opt.*, **4**, 414–417.

27. Zwanziger, H.W. and Förster, H. (1998) Near infrared spectroscopy of fuel contaminated sand and soil. I preliminary results and calibration study. *J. Near Infrared Spectrosc.*, **6**, 189–197.

28. Myers, A.B. and Mathies, R.A. (1987) *Biological Applications of Raman Spectroscopy*, Resonance Raman Spectra of Polyenes and Aromatics, Vol. 2, John Wiley & Sons, Ltd, New York.

29. Smith, W.E. and Rodger, C. (2000) *Encyclopedia of Spectroscopy and Spectrometry*, Vol. 3, Academic Press, San Diego, CA, pp. 2329–2334.

30. Kiefer, W. (2000) *Encyclopedia of Spectroscopy and Spectrometry*, Vol. 2, Academic Press, San Diego, CA, pp. 1609–1623.

31. De Wolf, I.D. (1999) *Analytical Applications of Raman Spectroscopy*, Blackwell Science Ltd, London, pp. 435–472.

32. Hildebrandt, P. and Lecomte, S. (2000) *Encyclopedia of Spectroscopy and Spectrometry*, Vol. 1, Academic Press, San Diego, CA, pp. 88–97.

33. Guan, Y., Lewis, E.N., and Levin, I.W. (1999) *Analytical Applications of Raman Spectroscopy*, Blackwell Science, London, pp. 276–327.

34. Frank, C.J. (1999) *Analytical Applications of Raman spectroscopy*, Blackwell Science, London, pp. 224–275.

35. Ortins, N.J., Kruger, T.A., and Dutta, P.K. (1999) *Analytical Applications of Raman Spectroscopy*, Blackwell Science, London, pp. 328–366.

36. Everall, N. (1999) *Analytical Applications of Raman Spectroscopy*, Blackwell Science, London, pp. 127–192.

37. Perkampus, H.H. (1992) *UV–VIS-Atlas of Organic Compounds*, VCH Verlagsgesellschaft mbH, Weinheim.

38. Williams, D.H. and Flemming, I. (1995) *Spectroscopic Methods in Organic Chemistry*, McGraw-Hill, London.

39. Brongersma, M.L. and Kik, P.G. (eds) (2007) *Surface Plasmon Nanophotonics*, Springer Series in Optical Science, Vol. 131, Springer, Dordrecht.

40. Kreibig, U. and Vollmer, M. (1995) *Optical Properties of Metal Clusters*, Springer Series in Material Science, Vol. 25, Springer, Berlin, Heidelberg, New York.

41. Foerster, T. (1951) *Fluoreszenz organischer Verbindungen*, VandenHoech und Ruprecht, Goettingen.

42. Korte, E.-H. (1990) *Infrarot-Spektroskopie diffus reflektierender Proben*

(Infrared spectroscopy of diffusely reflecting samples), Analytiker Taschenbuch, Vol. 9, Springer, Berlin.

43. Lianos, P. and Duportail, G. (1993) *Biophys. Chem.*, **48**, 293–299.

44. Gorovits, B.M. and Horowitz, P.M. (1995) *J. Biol. Chem.*, **270**, 13057–13062.

45. Lipari, G. and Szabo, A. (1980) *Biophys. J.*, **30**, 489.

46. Lanig, H., Hof, M., Bringmann, G., and Schneider, F.W. (1997) *Chem. Phys. Lett.*, **272**, 478–483.

47. Becker, W. (2005) *Advanced Time-Correlated Single Photon Counting*, Springer, Berlin.

48. Lakowicz, J.R. and Gryczynski, I. (1991) in *Topics in Fluorescence Spectroscopy: Techniques* (ed. J.R. Lakowicz), Plenum Press, New York, pp. 293–336.

49. Parker, C.A. and Rees, W.T. (1960) *Analyst (London)*, **85**, 587.

50. Brody, R.H., Carter, E.A., Edwards, H.G.M., and Pollard, A.M. (2000) *Encyclopedia of Spectroscopy and Spectrometry*, Vol. 1, Academic Press, San Diego, CA, pp. 649–657.

51. Eftink, M.R. (1991) in *Topics in Fluorescence Spectroscopy: Principles* (ed. J.R. Lakowicz), Plenum Press, New York, pp. 53–126.

52. James, D.R. and Ware, W.R. (1985) *J. Phys. Chem.*, **89**, 5450–5458.

53. Namiki, A., Nakashima, N., and Yoshihara, K. (1979) *J. Chem. Phys.*, **71**, 925–930.

54. Fucaloro, A.F., Forster, L.S., and Campbell, M.K. (1984) *Photochem. Photobiol.*, **39**, 503–506.

55. Swadesh, J.K., Mui, P.W., and Scheraga, H.A. (1987) *Biochemistry*, **26**, 5761–5769.

56. Hof, M., Fleming, G.R., and Fidler, V. (1996) *Proteins Struct. Funct. Genet.*, **24**, 485–494.

57. Vos, R. and Engelborghs, Y. (1994) *Photochem. Photobiol.*, **60**, 24–32.

58. Eftink, M.R. and Ghiron, C.A. (1984) *Biochemistry*, **23**, 3891–3899.

59. Midoux, P., Wahl, P., Auchet, J.C., and Munsigny, M. (1984) *Biochim. Biophys. Acta*, **801**, 16–25.

60. Lehrer, S.S. (1971) *Biochemistry*, **10**, 3254–3263.

61. Sanyal, G., Kim, E., Thompson, F.M., and Brady, K.E. (1989) *Biochem. Biophys. Res. Commun.*, **165**, 772–781.

62. Behera, P.K., Mukherjee, T., and Mishra, A.K. (1995) *J. Lumin.*, **65**, 131–136.

63. Green, S.A., Simpson, D.J., Zhou, G., Ho, P.S., and Blough, N.V. (1990) *J. Am. Chem. Soc.*, **112**, 7337–7346.

64. Obyknovennaya, I.E., Vasileva, I.M., and Cherkasov, A.S. (1986) *Opt. Spectrosc.*, **60**, 169–171.

65. Bowen, E.J. and Metcalf, W.S. (1951) *Proc. R. Soc. London*, **206A**, 437–447.

66. Mac, M., Najbar, J., Phillipis, D., and Smith, T.A. (1992) *J. Chem. Soc., Faraday Trans.*, **88**, 3001–3005.

67. Hutterer, R., Krämer, K., Schneider, F.W., and Hof, M. (1997) *Chem. Phys. Lipids*, **90**, 11–23.

68. Chao, S.C., Tretzel, J., and Schneider, F.W. (1979) *J. Am. Chem. Soc.*, **101**, 134.

69. Urbano, E., Offenbacher, H., and Wolfbeis, O.S. (1984) *Anal. Chem.*, **56**, 427–429.

70. Wolfbeis, O.S. and Urbano, E. (1983) *Fresenius J. Anal. Chem.*, **314**, 577–581.

71. Washington, K., Sarasua, M.M., Koehler, L.S., Koehler, K.A., Schultz, J.A., Pedersen, L.G., and Hiskey, R.G. (1984) *Photochem. Photobiol.*, **40**, 693–701.

72. Bisht, P.B. and Tripathi, H.B. (1993) *J. Lumin.*, **55**, 153–158.

73. Johnson, G.E. (1980) *J. Phys. Chem.*, **84**, 2940–2946.

74. Daems, D., Boens, N., and Schryver, F.C. (1989) *Eur. Biophys. J.*, **17**, 25–36.

75. Ahmed, A. and Durocher, G. (1981) *Photochem. Photobiol.*, **34**, 573–578.

76. Kikuchi, K., Sato, C., Watebe, M., Ikeda, H., Takahashi, Y., and Miyashi, T. (1993) *J. Am. Chem. Soc.*, **115**, 5180–5184.

77. Subczynski, W.K., Hyde, J.S., and Kusumi, A. (1989) *Proc. Natl. Acad. Sci. U.S.A.*, **86**, 4474–4478.

78. Hof, M. (1998) *Biochim. Biophys. Acta*, **1388**, 143–153.

79. Schlag, E.W., Schneider, S., and Fischer, S. (1971) *Annu. Rev. Phys. Chem.*, **22**, 465.

80. Fromherz, P. (1995) *J. Phys. Chem.*, **99**, 7188–7192.

81. Schulman, S.G. (1977) *Fluorescence and Phosphorescence Spectroscopy: Physicochemical Principles and Practice*, Pergamon Press, New York.

82. Brand, K., Hof, M., and Schneider, F.W. (1991) *Ber. Bunsen Ges. Phys. Chem.*, **95**, 1511–1514.

83. Foerster, T. and Rokos, K. (1967) *Chem. Phys. Lett.*, **1**, 279.

84. Sriram, R. and Hoffman, M.Z. (1982) *Chem. Phys. Lett.*, **85**, 572.

85. Baumann, J. and Fayer, M.D. (1986) *J. Chem. Phys.*, **85**, 4087.

86. Chen, R.F. and Knutson, J.R. (1988) *Anal. Biochem.*, **198**, 119.

87. Brown, R.S., Brennan, J.D., and Krull, U.J. (1994) *J. Chem. Phys.*, **100**, 6019–6021.

88. Chattopadhyay, A. (1990) *Chem. Phys. Lipids*, **53**, 1.

89. Hendrickson, H.S., Hendrickson, E.K., Johnson, I.D., and Farber, S.A. (1999) *Anal. Biochem.*, **276**, 27–35.

90. Massenburg, D. and Lentz, B.R. (1993) *Biochemistry*, **32**, 9172.

91. Bagchi, B., Oxtoby, S.D., and Fleming, G.R. (1984) *Chem. Phys.*, **86**, 257.

92. Rips, I., Klafter, J., and Jortner, J. (1988) *J. Chem. Phys.*, **89**, 4288.

93. Friedman, H.L., Raineri, F.O., Hirata, F., and Perng, P.C. (1995) *J. Stat. Phys.*, **78**, 239.

94. Bakshiev, N.G. (1964) *Opt. Spectrosc. (USSR)*, **16**, 446.

95. Mazurenko, Y.T. and Bakshiev, N.G. (1970) *Opt. Spectrosc. (USSR)*, **28**, 490.

96. Liptay, W. (1974) in *Excited States*, Vol. 1 (ed. E.C. Lim), Academic Press, New York, p. 129.

97. Horng, M.L., Gardecki, J.A., Papazyan, A., and Maroncelli, M. (1995) *J. Phys. Chem.*, **99**, 17320.

98. Jimenez, R., Fleming, G.R., Kumar, P.V., and Maroncelli, M. (1994) *Nature*, **369**, 471.

99. Mukherje, S. and Chattopadhyay, A. (1995) *J. Fluorescence*, **5**, 237.

100. Hof, M. and Lianos, P. (1997) *Langmuir*, **13**, 290.

101. Zhang, H., Jonkman, A.M., van der Meulen, P., and Glasbeek, M. (1994) *Chem. Phys. Lett.*, **236**, 587.

102. Bingemann, D. and Ernsting, N.P. (1995) *J. Chem. Phys.*, **102**, 2691.

103. Demchenko, A.P. (1991) in *Topics in Fluorescence Spectroscopy: Biochemical Applications* (ed. J.R. Lakowicz), Plenum Press, New York, p. 65.

104. Demchenko, A.P. (1994) *Biochim. Biophys. Acta*, **1209**, 149.

105. Galley, W.C. and Purkey, R.M. (1970) *Proc. Natl. Acad. Sci. U.S.A.*, **67**, 1116.

106. Hof, M., Lianos, P., and Laschewsky, A. (1997) *Langmuir*, **13**, 2181.

107. Maroncelli, M. and Fleming, G.R. (1987) *J. Chem. Phys.*, **86**, 6221.

108. Hof, M., Schleicher, J., and Schneider, F.W. (1989) *Ber. Bunsen Ges. Phys. Chem.*, **93**, 1377.

109. Sýkora, J., Slavíček, P., Jungwirth, P., Barucha, J., and Hof, M. (2007) *J. Phys. Chem. B*, **111**, 5869–5877.

110. Jurkiewicz, P., Olzynska, A., Langner, M., and Hof, M. (2007) *Langmuir*, **111**, 6869–5877.

111. Slavik, J. (1982) *Biochim. Biophys. Acta*, **694**, 1.

112. Lakowicz, J.R., Thompson, R.B., and Cherek, H. (1983) *Biochim. Biophys. Acta*, **815**, 295.

113. Hof, M., Hutterer, R., Perez, N., Ruf, H., and Schneider, F.W. (1994) *Biophys. Chem.*, **52**, 165.

114. Matayoshi, E.D. and Kleinfeld, A.M. (1981) *Biochim. Biophys. Acta*, **644**, 233.

115. Epand, R.M. and Leon, B.T.C. (1992) *Biochemistry*, **31**, 1550.

116. Rieber, K., Sýkora, J., Olzynska, A., Jelinek, R., Cevc, G., and Hof, M. (2007) *Biochim. Biophys. Acta*, **1768**, 1050–1058.

117. Hutterer, R., Schneider, F.W., Hermens, W.T., Wagenvoord, R., and Hof, M. (1998) *Biochim. Biophys. Acta*, **1414**, 155–164.

118. Sýkora, J., Kapusta, P., Fidler, V., and Hof, M. (2002) *Langmuir*, **18** (3), 571–574.

119. Parasassi, T., Di Stefano, M., Loiero, M., Ravagnan, G., and Gratton, E. (1994) *Biophys. J.*, **66**, 763.

120. Deye, J.F., Berger, T.A., and Anderson, A.G. (1990) *Anal. Chem.*, **62**, 615.

121. Fromherz, P. (1995) *J. Phys. Chem.*, **99**, 7185.

122. Wolfbeis, O.S. and Urbano, E. (1983) *Fresenius Z. Anal. Chem.*, **314**, 577–581.

123. Hof, M., Fleming, G.R., and Fidler, V. (1996) *Proteins Struct. Funct. Genet.*, **24**, 485–494.

124. Perrin, F. (1926) *J. Phys. Radium*, **7**, 390.

125. Callis, P.R. (1997) *Annu. Rev. Phys. Chem.*, **48**, 271–297.

126. Hansen, J.E., Rosenthal, S.J., and Fleming, G.R. (1992) *J. Phys. Chem.*, **96**, 3034–3029.

127. Jablonski, A. (1960) *Bull. Acad. Pol. Sci.*, **8**, 529.

128. Kawski, A. (1993) *Crit. Rev. Anal. Chem.*, **23**, 459–529.

129. Steiner, R.F. (1991) in *Topics in Fluorescence Spectroscopy: Principles* (ed. J.R. Lakowicz), Plenum Press, New York, pp. 1–52.

130. Ferguson, B.Q. and Yang, D.C.H. (1986) *Biochemistry*, **25**, 529–539.

131. Lim, K., Jameson, D.M., Gentry, C.A., and Herron, J.N. (1995) *Biochemistry*, **34**, 6975–6984.

132. Lukas, T.J., Burgess, E.H., Prendergast, F.G., Lau, W., and Watterson, D.M. (1986) *Biochemistry*, **25**, 1458–1464.

133. LeTilly, V. and Royer, C. (1993) *Biochemistry*, **31**, 7753–7758.

134. Tao, T. (1969) *Biopolymers*, **8**, 609.

135. Jaehnig, F. (1980) *Proc. Natl. Acad. Sci. U.S.A.*, **76**, 6361.

136. Lentz, B.R. (1989) *Chem. Phys. Lipids*, **50**, 171.

137. Van der Heide, U.A., van Ginkel, G., and Levine, Y.K. (1996) *Chem. Phys. Lett.*, **253**, 118.

138. Dale, R.E., Eisinger, J., and Blumberg, W.E. (1979) *Biophys. J.*, **26**, 161.

139. Van der Meer, B.W., Coker, G., and Chen, S.Y.S. (1994) *Resonance Energy Transfer Theory and Data*, Wiley-VCH Verlag GmbH, Weinheim.

140. Foerster, T. (1959) *Discuss. Faraday Soc.*, **27**, 7–17.

141. Goesele, U. (1978) *Spectrosc. Lett.*, **11**, 445.

142. Hauser, M., Klein, U.K.A., and Goesele, U. (1976) *Z. Phys. Chem.*, **101**, 255.

143. Klafter, J. and Blumen, A. (1984) *J. Phys. Chem.*, **80**, 875.

144. Loura, L.M.M., Fedorov, A., and Prieto, M. (1996) *Biophys. J.*, **71**, 1823–1836.

145. Schleicher, J., Hof, M., and Schneider, F.W. (1993) *Ber. Bunsen Ges. Phys. Chem.*, **97**, 172–176.

146. Mergny, J.L., Slama-Schwok, A., Monteney-Garestier, T., Rougee, M., and Helene, C. (1991) *Photochem. Photobiol.*, **53**, 555–558.

147. Ciruela, F. (2008) *Curr. Opin. Biotechnol.*, **19**, 338–343.

148. Piston, D.W. and Kremers, G.J. (2007) *Trends Biochem. Sci.*, **32**, 407–414.

149. Wang, Y.X., Shyy, J.Y.J., and Chien, S. (2008) *Annu. Rev. Biomed. Eng.*, **10**, 1–38.

150. Krishnan, R.V., Varma, R., and Mayor, S. (2001) *J. Fluorescence*, **11**, 211–226.

151. Jares-Erijman, E.A. and Jovin, T.M. (2003) *Nat. Biotechnol.*, **21**, 1387–1395.

152. Chen, H.M. and Rhoades, E. (2008) *Curr. Opin. Struct. Biol.*, **18**, 516–524.

153. Shimozono, S. and Miyawaki, A. (2008) *Fluorescent Proteins*, Elsevier, San Diego, CA.

154. MacDonald, R.I. (1987) *J. Biol. Chem.*, 10392–10397.

155. Keller, P.M., Person, S., and Snipes, W. (1968) *J. Cell Sci.*, **28**, 167–177.

156. Gibson, G.A. and Loew, L.M. (1979) *Biochem. Biophys. Res. Commun.*, **88**, 135–140.

157. Struck, D.K., Hoekstra, D., and Pagano, R.E. (1981) *Biochemistry*, **20**, 4093–4099.

158. Morris, S.J. and Bradley, D. (1984) *Biochemistry*, **23**, 4642–4650.

159. Connor, J. and Schroit, A.J. (1987) *Biochemistry*, **26**, 5099–5105.

160. Vanderkoi, J.M., Ierokomas, A., Nakamura, H., and Martonosi, A. (1977) *Biochemistry*, **16**, 1262–1267.

161. Veatch, W. and Stryer, L. (1977) *J. Mol. Biol.*, **113**, 89–102.

162. Hasselbacher, C.A., Street, T.L., and Dewey, T.G. (1984) *Biochemistry*, **23**, 6445–6565.

163. Tron, L., Szoelloesi, J., Damjanovich, S., Helliwell, S.H., Arndt-Jovin, D.J., and Jovin, T.M. (1984) *Biophys. J.*, **45**, 939–946.

164. Andrews, D.L. (2008) *Can. J. Chem.*, **86**, 855–870.

165. Cheung, H.C. (1991) in *Topics in Fluorescence Spectroscopy: Principles* (ed. J.R. Lakowicz), Plenum Press, New York, pp. 127–176.

166. Galla, H.J. and Hartmann, W. (1980) *Chem. Phys. Lipids*, **27**, 199.

167. Chen, S.Y., Cheng, K.H., and Ortalano, D.M. (1990) *Chem. Phys. Lipids*, **53**, 321.

168. Hutterer, R., Haefner, A., Schneider, F.W., and Hof, M. (1998) in *Fluorescence Microscopy and Fluorescence Probes*, Vol. 2 (ed. J. Slavik), Plenum Press, New York, pp. 93–98.

169. Kinnunen, P.K.J., Koiv, A., and Mustonen, P. (1993) in *Fluorescence Spectroscopy* (ed. O.S. Wolfbeis), Springer-Verlag, Berlin, pp. 159–171.

170. Duportail, G. and Lianos, P. (1996) in *Vesicles* (ed. M. Rosoff), Marcel Dekker, New York, pp. 296–372.

171. Axelrod, D. (2008) in *Biophysical Tools for Biologists*, Vol. 2: In Vivo Techniques, Vol. 89 (eds J. Correia and H. Detrich), Elsevier, San Diego, CA, pp. 169–221.

172. Edidin, M., Zagyansky, M., and Lardner, T. (1976) *Science*, **191**, 466.

173. Peters, R., Peters, J., Tews, K., and Bahr, W. (1974) *Biochim. Biophys. Acta*, **367**, 282–294.

174. Periasamy, N., Bicknese, S., and Verkman, A. (1996) *Photochem. Photobiol.*, **63**, 265.

175. Eggeling, C., Widengren, J., Rigler, R., and Seidel, C.A.M. (1999) in *Applied Fluorescence in Chemistry, Biology and Medicine* (eds W. Rettig, B. Strehmel, S. Schrader, and H. Seifert), Springer-Verlag, Berlin, pp. 193–240.

176. Thompson, N.L., Burghardt, T.P., and Axelrod, D. (1981) *Biophys. J.*, **33**, 435–454.

177. Huang, Z.P., Pearce, K.H., and Thompson, N.L. (1994) *Biophys. J.*, **67**, 1754–1766.

178. Pearce, K.H., Hof, M., Lentz, B.R., and Thompson, N.L. (1993) *J. Biol. Chem.*, **268**, 22984–22991.

179. Schnell, E.A., Eikenes, L., Tufto, I., Erikson, A., Juthajan, A., Lindgren, M., and Davies, C.D. (2008) *J. Biomed. Opt.*, **13**, 064037.

180. Elson, E. and Magde, D. (1974) *Biopolymers*, **13**, 1–27.

181. Magde, D. and Elson, E. (1974) *Biopolymers*, **13**, 29–61.

182. Magde, D. and Elson, E. (1972) *Phys. Rev. Lett.*, **29**, 705–708.

183. Ehrnber, M. and Rigler, R. (1974) *Chem. Phys.*, **4**, 390–401.

184. Enderlein, J., Gregor, I., Patra, D., Dertinger, T., and Kaupp, U.B. (2005) *ChemPhysChem.*, **6**, 2324–2336.

185. Enderlein, J., Gregor, I., Patra, D., and Fitter, J. (2004) *Curr. Pharm. Biotechnol.*, **5**, 155–161.

186. Sýkora, J., Kaiser, K., Gregor, I., Bonigk, W., Schmalzing, G., and Enderlein, J. (2007) *Anal. Chem.*, **79**, 4040–4049.

187. Ries, J., Weidemann, T., and Schwille, P. (2012) in *Biophysical Techniques for Characterization of Cells* (ed P. Schwille), Academic Press, Oxford, pp. 210–245.

188. Benda, A., Beneš, M., Mareček, V., Lhotský, A., Heremens, W.T., and Hof, M. (2003) *Langmuir*, **19**, 4120–4126.

189. Kahya, N., Scherfeld, D., Bacia, K., and Schwille, P. (2004) *J. Struct. Biol.*, **147**, 77–89.

190. Wohland, T., Rigler, R., and Vogel, H. (2001) *Biophys. J.*, **80**, 2987–2999.

191. Kask, P., Gunther, R., and Axhausen, P. (1997) *Eur. Biophys. J. Biophys.*, **25**, 163–169.

192. Dertinger, T., Pacheco, V., von der Hocht, I., Hartman, R., Gregor, I., and Enderlein, J. (2005) *ChemPhysChem.*, **6**, 164–170.

193. Ries, J. and Schwille, P. (2006) *Biophys. J.*, **91**, 1915–1924.

194. Palmer, A.G. and Thompson, N.L. (1989) *Appl. Opt.*, **28**, 1214–1220.

195. Widengren, J. and Rigler, R. (1998) *Cell. Mol. Biol.*, **44**, 857–879.

196. Földes-Papp, Z., Thyberg, P., Björling, S., Holmgren, A., and Rigler, R. (1997) *Nucleosides Nucleotides Nucleic Acids*, **16**, 781–787.

197. Berland, K.M., So, P.T., and Gratton, E. (1995) *Biophys. J.*, **68**, 694–701.

198. Politz, J.C., Browne, E.S., Wolf, D.E., and Pederson, T. (1998) *Proc. Natl. Acad. Sci. U.S.A.*, **95**, 6043–6048.

199. Brock, R., Hink, M.A., and Jovin, T.M. (1998) *Biophys. J.*, **75**, 2547–2557.

200. Rauer, B., Neumann, E., Widengren, J., and Rigler, R. (1996) *Biophys. Chem.*, **58**, 3–12.

201. Tjernberg, L.O., Pramanik, A., Björling, S., Thyberg, P., Thyberg, J., Nordstedt, C., Berndt, K.D., Terenius, L., and Rigler, R. (1999) *Chem. Biol.*, **6**, 53–62.

202. Van Cranenbroeck, E. and Engelborghs, Y. (1999) *Biochemistry*, **38**, 5082–5088.

203. Pitschke, M., Prior, R., Haupt, M., and Riesner, D. (1998) *Nat. Med.*, **4**, 832–834.

204. Bastiens, P.I.H., Pap, E.H.W., Widengren, J., Rigler, R., and Visser, A.J.W.G. (1994) *J. Fluorescence*, **4**, 377–383.

205. Beneš, M., Hudeček, J., Anzenbacher, P., and Hof, M. (2001) *Collect. Czech. Chem. Commun.*, **66**, 855–869.

206. Björling, S., Kinjo, M., Foldes-Papp, Z., Hagman, E., Thyberg, P., and Rigler, R. (1998) *Biochemistry*, **15**, 12971–12978.

207. Kettling, U., Koltermann, A., Schwille, P., and Eigen, M. (1998) *Proc. Natl. Acad. Sci. U.S.A.*, **95**, 1416–1420.

208. Chen, Y., Müller, J.D., So, P.T.C., and Gratton, E. (1999) *Biophys. J.*, **77**, 553–567.

209. Heinze, K.G., Koltermann, A., and Schwille, P. (2000) *Proc. Natl. Acad. Sci. U.S.A.*, **97**, 10377–10382.

210. Gratton, E., Breusegem, S., Barry, N., Ruan, Q., and Eid, J. (2005) in *Biophotonics: Optical Science and Engineering for the 21st Century* (eds X. Shen and R. VanWijk), Springer, New York, pp. 1–14.

211. Kapusta, P., Wahl, M., Benda, A., Hof, M., and Enderlein, J. (2007) *J. Fluorescence*, **17**, 43–48.

212. Humpolíčková, J., Štěpánek, M., Kral, T., Benda, A., Procházka, K., and Hof, M. (2008) *J. Fluorescence*, **18**, 679–684.

213. Ruan, Q., Cheng, M.A., Levi, M., Gratton, E., and Mantulin, W.W. (2004) *Biophys. J.*, **87**, 1260–1267.

214. Kannan, B., Guo, L., Sudhaharan, T., Ahmed, S., Maruyama, I., and Wohland, T. (2007) *Anal. Chem.*, **79**, 4463–4470.

215. Bag, N., Sankaran, J., Paul, A., Kraut, R.S., and Wohland, T. (2012) *ChemPhysChem.*, **13**, 2784–2794.

216. Hebert, B., Constantino, S., and Wiseman, P.W. (2005) *Biophys. J.*, **88**, 3601–3614.

217. Kolin, D.L., Ronis, D., and Wiseman, P.W. (2006) *Biophys. J.*, **91**, 3061–3075.

218. Brown, C.M., Dalal, R.B., Hebert, B., Digman, M.A., Horwitz, A.R., and Gratton, E. (2008) *J. Microsc. (Oxford)*, **229**, 78–91.

219. Nie, S. and Zare, R.N. (1997) *Annu. Rev. Biophys. Biomol. Struct.*, **26**, 567–596.

220. Ambrose, W.P., Goodwin, P.M., Jett, J.H., Van Orden, A., Werner, J.H., and Keller, R.A. (1999) *Chem. Rev.*, **99**, 2929–2956.

221. Orrie, M. and Bernard, J. (1990) *Phys. Rev. Lett.*, **65**, 2716–2719.

222. Moerner, W.E., Plakhonik, T., Irngartinger, T., Croci, M., Palm, V., and Wild, U.P.J. (1994) *J. Phys. Chem.*, **98**, 7382–7389.

223. Dovichi, N.J., Martin, J.C., Jett, J.H., and Keller, R.A. (1983) *Science*, **219**, 845–847.

224. Chen, D. and Dovichi, N.J. (1996) *Anal. Chem.*, **68**, 690–696.

225. Shopa, S.A., Davis, L.M., and Shera, E.B. (1992) *J. Opt. Soc. Am. B*, **9**, 1761–1769.

226. Barnes, M.D., Kung, C.Y., Whitten, W.B., and Ramsey, J.M. (1997) *Anal. Chem.*, **69**, 2115.

227. Barnes, M.D., Ramsay, W.B., and Whitten, W.B. (1995) *Anal. Chem.*, **67**, 418–423.

228. Xie, X.S. and Dunn, R.C. (1994) *Science*, **265**, 361.

229. Dunn, R.C., Holton, G.R., Mets, L., and Xie, X.S. (1994) *J. Phys. Chem.*, **98**, 3094–3098.

230. Betzig, E. and Trautmann, J.K. (1992) *Science*, **257**, 189–195.

231. Betzig, E. and Chichester, R.J. (1993) *Science*, **262**, 1422.

232. Trautmann, J.K., Macklin, J.J., Bruns, L.E., and Betzig, E. (1994) *Nature*, **369**, 40–42.

233. Eigen, M. and Rigler, R. (1994) *Proc. Natl. Acad. Sci. U.S.A.*, **91**, 5740–5747.

234. Nie, S., Chiu, D.T., and Zare, R.N. (1995) *Anal. Chem.*, **67**, 2849–2857.

235. Mertz, J., Xu, C., and Webb, W.W. (1995) *Opt. Lett.*, **20**, 2532–2534.

236. Brown, E.B., Shear, J.B., Adams, S.R., Tsien, R.Y., and Webb, W.W. (1999) *Biophys. J.*, **76**, 489–499.

237. Schwille, P., Haupts, U., Maiti, S., and Webb, W.W. (1999) *Biophys. J.*, **77**, 2251–2265.

238. Schmidt, T., Schultz, G.J., Baumgartner, W., Gruber, H.J., and Schindler, H. (1996) *Proc. Natl. Acad. Sci. U.S.A.*, **9**, 2926–2929.

239. Gosh, R.N. and Webb, W.W. (1994) *Biophys. J.*, **66**, 1301–1318.

240. Vale, R.D., Funatsu, T., Pierce, D.W., Romberg, L., Harada, Y., and Yanagida, T. (1996) *Nature*, **380**, 451–453.

241. Moerner, W.E. and Fromm, D.P. (2003) *Rev. Sci. Instrum.*, **74**, 3597–3619.

242. Ambrose, W.P. and Moerner, W.E. (1991) *Nature*, **349**, 225.

243. Plakhotnik, T., Walser, D., Pirotta, M., Renn, A., and Wild, U.P. (1994) *Science*, **265**, 364.

244. Enderlein, J., Goodwin, P.M., Van Orden, A., and Ambrose, W.P. (1997) *Chem. Phys. Lett.*, **270**, 164–470.

245. Xiao, Y., Buschmann, V., and Weston, K.D. (2005) *Anal. Chem.*, **77**, 36–46.

246. Kaji, N., Tokeski, M., and Baba, Y. (2007) *Chem. Rec.*, **7**, 295–304.

247. Ambrose, W.P., Affleck, R.L., Goodwin, P.M., Keller, R.A., and Martin, J.C. (1995) *Exp. Tech. Phys.*, **41**, 1–12.

248. Lermer, N., Barnes, M.D., Kung, C.Y., Whitten, W.B., and Ramsey, J.M. (1997) *Anal. Chem.*, **69**, 2115.

249. Werner, J.H., Cai, H., Jett, J.H., Reha-Karntz, L., Keller, R.A., and Goodwin, P.M. (2003) *J. Biotechnol.*, **102**, 1–14.

250. Yanagida, T., Iwaki, M., and Ishii, Y. (2008) *Philos. Trans. R. Soc. Lond. B: Biol. Sci.*, **363**, 2123–2134.

251. Schütz, G.J., Axman, M., Freudenthaler, S., Schindler, H., Kadror, K., Roder, J.C., and Jeromin, A. (2004) *Microsc. Res. Tech.*, **63**, 159–167.

252. Kusumi, A., Ike, H., Nakada, C., Murase, K., and Fujiwara, T. (2005) *Semin. Immunol.*, **17**, 3–21.

253. Selle, C., Rückerl, F., Martin, D.S., Forstner, M.B., and Käs, J. (2004) *Phys. Chem. Chem. Phys.*, **6**, 5535–5542.

254. Levi, V. and Gratton, E. (2007) *Cell. Biochem. Biophys.*, **48**, 1–15.

255. Murcia, M.J., Garg, S., and Naumann, C.A. (2007) *Methods Mol. Biol.*, **400**, 277–294.

256. Sutter, J.U., Macmillan, A.M., Birch, D.J., and Rolinski, O.J. (2008) *Ann. N. Y. Acad. Sci.*, **1130**, 62–67.

257. Wolfbeis, O.S. (1991) *Fiber Optic Chemical Sensors and Biosensors*, CRC Press, Boca Raton, FL.

258. Verkman, A.S. (1990) *Am. J. Physiol.*, **253**, C375–C388.

259. Miyawaki, A., Llopis, J., Heim, R., NcCaffery, J.M., Adams, J.A., Ikura, M., and Tsien, R.Y. (1997) *Nature*, **388**, 882–887.

260. Thomas, J.A., Buchsbaum, R.N., Zimniak, A., and Racker, E. (1979) *Biochemistry*, **18**, 2210–2218.

261. Rink, T.J., Tsien, R.Y., and Pozzan, T. (1982) *J. Cell Biol.*, **95**, 189–196.

262. Miesenbock, G., de Angelis, D.A., and Rothman, J.E. (1998) *Nature*, **394**, 192–195.

263. Szmacinski, H. and Lakowicz, J.R. (1994) in *Topics in Fluorescence Spectroscopy: Probe Design and Chemical Sensing* (ed. J.R. Lakowicz), Plenum Press, New York, pp. 295–334.

264. Lakowicz, J.R. (2006) *Principles of Fluorescence Spectrosopy*, 3rd edn, Springer, New York, pp. 623–674.

265. Basabe-Desmonts, L., Reinhoudt, D.N., and Crego-Calama, M. (2007) *Chem. Soc. Rev.*, **36**, 993–1017.

266. Thompson, N.L. (1991) in *Topics in Fluorescence Spectroscopy: Techniques* (ed. J.R. Lakowicz), Plenum Press, New York, pp. 337–378.

267. Lakowicz, J.R. (1999) *Principles of Fluorescence Spectroscopy*, Plenum Press, New York, pp. 531–572.

Section III
Methods 2: NMR

Handbook of Spectroscopy, Second Edition. Edited by Günter Gauglitz and David S. Moore.

Introduction

The nuclei of all elements possess mass and charge. One or more isotopes of most nuclei also have spin, that is, angular momentum. As spinning charge creates a magnetic field, there is a magnetic moment, μ, associated with the angular momentum. It is this property of matter that is exploited in nuclear magnetic resonance (NMR) spectroscopy. The magnetic moment, a vector quantity, can be aligned in the presence of an intense static magnetic field, B_0, then manipulated in space, that is, caused to evolve in time under the influence of specific interactions and, finally, observed. The detected response can provide information about (i) the specific nuclear isotope present, (ii) the local structure around the nucleus, and (iii) the motional dynamics of the matter containing the nuclei. As will be apparent in the following three chapters, the environment reported on by nuclear magnetization extends far beyond the immediate nuclear horizon, giving information on the bonding arrangement of neighboring nuclei, many angstroms removed. Each magnetic nucleus in a molecule reports on itself and on its relationship with its neighboring nuclei such that the sum of the overlapping connectivity information from all nuclei redundantly determines a unique structure for the molecule. The goal of much of the research activity in NMR over the past 25 years has been the development of multi-dimensional NMR techniques that makes it possible to extract the needed information from NMR spectra. With the current, routine solution state ^{1}H NMR capabilities it is possible to assign essentially every proton resonance in modest molecular weight proteins to a specific proton in a specific amino acid residue, determine the amino acid sequence, and determine the three-dimensional (3D) structure of the folded protein. Such a *tour de force* requires high static magnetic field strengths (today's state-of-the-art magnets have $B_0 = 21.15$ T, i.e., 900 MHz proton frequency) and modern multi-dimensional correlation pulse sequences replete with their editing, filtering, and solvent-suppression schemes. This stunning accomplishment represents one marker on the path of NMR progress that, 55 years after the birth of this spectroscopy, is still a healthy, burgeoning research that provides one of the most exciting areas of science to work in.

The quantum mechanical description of the NMR experiment tells us that the maximum observable component of the angular momentum is $Ih/2\pi$, where I is the nuclear spin quantum number, or simply, the spin, and h is Planck's constant. The magnetic moment is quantized along $2I + 1$ orientations with respect to the

Handbook of Spectroscopy, Second Edition. Edited by Günter Gauglitz and David S. Moore.

static field. The magnitude of the moment vector is a measure of the strength of the nuclear magnet. It depends on the angular momentum and on the internal structure of the nucleus, that is, the distribution of protons and neutrons and their associated angular momenta, according to Eq. (1):

$$\mu = \gamma Ih/2\pi \tag{1}$$

where γ, the gyromagnetic ratio, is the proportionality factor between the magnetic moment and the angular momentum.

For $I = 1/2$ nuclei such as ^{1}H, ^{13}C, or ^{15}N, there are two orientations of the moment in the applied field, aligned parallel and anti-parallel to the field. The force exerted by the static field on the moments causes them to precess about the static field direction. This motion is analogous to that of a toy top: the top spins with its angular momentum along its spinning axis and wobbles (precesses) about the Earth's gravitational field. Nuclei with spin $I > 0$ have isotope-specific nuclear magnetic moments and field dependent addresses, ω_0 or ν_0, the precession frequency, given by the Larmor relation:

$$\omega_0 = \gamma B_0 \rightarrow \nu_0 = \frac{\gamma B_0}{2\pi} \tag{2}$$

For typical magnetic field strengths, the Larmor frequency is in the radio frequency region of the electromagnetic spectrum. For protons in an 18.8 T field, $\nu_0 = 800$ MHz; for ^{13}C in the same field $\nu_0 = 201.6$ MHz.

The NMR experiment consists of inducing transitions between the states of quantized magnetization. This is accomplished by irradiating the sample with radio frequency (RF) energy. The frequency of the RF must exactly match the precession frequency of the nuclei in order to cause the transition. This specificity is the resonance phenomenon, analogous to the tuned circuit in a radio receiver. The tuned receiver (the spin system composed of a specific nuclear isotope) is only capable of interacting with the broadcast signal whose frequency matches the Larmor frequency of the nuclei.

It is our good fortune that NMR has layers of complexity that are not explicitly revealed in Eqs. (1) and (2). Unraveling this complexity (shielding, coupling, and relaxation) has been the preoccupation of NMR spectroscopists for more than half a century, and is the topic of this section of the Handbook. Three chapters on NMR spectroscopy are assembled. They are authored by outstanding experimentalists working at the forefront of NMR research.

In Chapter 7, Leslie Butler (Louisiana State University) introduces the fundamental structure parameters in the NMR experiment through a discussion on solution state ^{1}H NMR. The shielding of nuclei by core and valence electrons, gives rise to those structure-pregnant numbers called *chemical shifts*, δ, that have been accrued and correlated since the earliest days of NMR. Scalar coupling, J, is the through-bond transmission of spin state orientation that historically has been the avenue through which chemists have established bonded atom relationships, configuration, and conformation in molecules. This section is followed by a discussion of properties commonly studied through solid state NMR, namely, chemical shift anisotropy (CSA), dipolar coupling, and quadrupolar interactions. A section on spin–lattice relaxation precedes a discussion of the use of NMR to measure the dynamics of molecular motion. A short introduction to NMR imaging follows to acquaint the reader with spin density mapping using linear gradients. The chapter ends with a description of a 3D NMR experiment used to establish atom connectivity and provides an appropriate segue into the next chapter.

Chapter 8 by Gary Martin, Chad Hadden, and David Russell (Pharmacia Corporation) begins with an exposition of the uses of scalar coupling in the context of one-dimensional (1D) experiments. Homonuclear decoupling experiments and nuclear Overhauser effect (NOE) difference spectroscopy are illustrated before moving on to heteronuclear coupling and the selective population transfer (SPT) experiment. SPT is the basis for enhanced signal intensity in the non-selective polarization transfer experiments, insensitive nuclei enhanced by polarization transfer (INEPT) and distortionless enhancement by polarization transfer (DEPT), J-modulated experiments that sort ^{13}C spectra into resonance subsets based on carbon multiplicity groups, for example, C, CH, CH_2, and CH_3 groups. The principles of two-dimensional (2D) NMR are introduced and illustrated in the context of 2D J-resolved spectroscopy in which the 2D spectrum correlates chemical shifts on one axis with scalar coupling on the second frequency axis. Homonuclear 2D NMR experiments in which both frequency axes are chemical shift and that reveal J-coupling partners (correlation spectroscopy (COSY), total correlation spectroscopy (TOCSY)) or NOE connected partners (nuclear Overhauser spectroscopy (NOESY), rotating-frame Overhauser spectroscopy (ROESY)) as off-diagonal elements are illustrated. The focus then shifts to heteronuclear chemical shift correlation and treats experiments based on one-bond coupling (heteronuclear multiple-quantum correlation (HMQC), heteronuclear single-quantum correlation (HSQC)). Heteronuclear chemical shift correlation via long-range coupling (heteronuclear multiple bond correlation (HMBC)) is described in turn along with multiplicity-edited versions of these experiments. In current practice, most 2D NMR experiments are implemented using pulsed field gradients (PFGs) to select coherence transfer pathways in lieu of using phase cycling routines, as originally conceived, to successively add desired magnetization components and cancel unwanted magnetization components. Thus, gradient correlation spectroscopy (GCOSY), gradient heteronuclear multiple-quantum correlation (GHMQC), and gradient heteronuclear multiple bond correlation (GHMBC), for example, are the modern experiments in use, giving the same experimental correlations, but with excellent artifact cancellation and time savings, in instances where sample size is not limiting. Pulse sequence modifications which optimize the HMBC experiment over a range of J-coupling amplitudes are discussed and end with a description of ^2J, ^3J HMBC, an experiment which makes possible the detection *and* differentiation of two-bond and three-bond proton couplings to protonated carbon and nitrogen centers. It is worth reflecting for a moment on the evolution in the use of three-bond coupling that has occurred since the early discovery of scalar coupling. Correlations of unambiguous ^3J with structure, that is, Karplus relations, dihedral angle dependence of three-bond coupling, were established in many molecular fragments. Karplus relationships have been used to make structural and conformational predictions in applicable systems, it being necessary to establish independently the correct designation of similar magnitude two- and three-bond long-range couplings. ^2J, ^3J HMBC now provides the long-range assignment capability, experimentally distinguishing ^2J from ^3J.

The chapter continues with an overview of inverse (proton-detected) ‘‘hyphenated’’ 2D NMR techniques which join together two correlation experiments. HSQC–TOCSY, for example, first labels protons with the chemical shift of the directly bound heteronuclide, ^{13}C say, in the HSQC part of the experiment, and after the magnetization is transferred back to the proton, homonuclear vicinal coupling is propagated between contiguous protons in the homonuclear TOCSY segment of the experiment. The proton magnetization ultimately acquired provides homonuclear correlated spin systems sorted by the chemical shift of the directly bound carbon(s) in question.

In cases in which just a select coupling or correlation is needed from a spectrum to complete an assignment or structure determination, a complete 2D analysis may not be required. There are 1D analogs of 2D NMR experiments which can provide the specific information in a more time-efficient manner than performing a full 2D NMR analysis. Examples of 1D analogs for NOESY and heteronuclear correlation experiment (HETCOR) experiments are described that use field gradients to select the resonance of interest.

The chapter concludes with a discussion of NMR sensitivity using probes designed for small samples. 2D NMR data are presented for a submicro inverse-detection gradient (SMIDG) probe that demonstrate the current performance (10s of micrograms) for sample limited NMR analysis. The future in the area of small sample NMR studies is in the development of cold metal NMR probes, that is, cryogenic probes, which have the potential to reduce analysis time by nearly one order of magnitude. A COSY spectrum on a 2.9 μg sample of Taxol and an HSQC spectrum of the aliphatic region of strychnine (40 μg), recorded in 45 min and <2 h, respectively, illustrate the state of the art in sensitivity using cryogenic probe technology.

A short description of DOSY and how NMR can be used to determine diffusion constants with the aid of pulsed field gradients is presented next.

For the structural analysis of molecules residual dipolar couplings have proved to be a powerful tool. Its determination and usage in gaining structural information makes up the last part of this chapter.

Chapter 9 the authors briefly introduce the concept of magic angle spinning and its ability to produce high resolution NMR spectra from suspensions and emulsions.

Chapter 10 by Lyndon Emsley and Steven Brown (EcoleNormaleSupériere de Lyon) begins with sketches of the major interactions that lead to spectral broadening in the solid state. The motionally averaged spectrum observed in solution NMR is replaced in the solid phase with a more complex spectrum reflecting the tensor character of the CSA, dipolar coupling (D), and quadrupolar coupling (C_q). Each of these anisotropic interactions can broaden the NMR resonance beyond the normal limits of the isotropic chemical shift distribution. This, in and of itself, does not prevent analysis of the spectrum. The theoretical description of the spectrum is well known for each interaction and the appropriate parameters can be extracted, in principle, by fitting the experimental and calculated spectrum. However, this method fails for materials where many resonances overlap.

In typical applications, say of organic solids by ^{13}C NMR, microcrystalline solids or amorphous samples are studied in which all orientations of molecules are present. Each ^{13}C in a molecule is represented by a distribution of resonances, a powder pattern, which reflects the orientation dependence of the chemical shift and ^{1}H$-$^{13}C dipolar interactions. The experimental spectrum is the sum of powder patterns from all the resonances in the spectrum, and as such usually presents a nearly featureless and uninterpretable solid state NMR spectrum. The authors present the principal line narrowing method used in solid state NMR, namely, magic angle spinning (MAS), in which the sample is mechanically spun along a unique axis, inclined at angle $\theta = 54.74^\circ$ with respect to the static field axis. This coherent motion narrows the orientation dependent CSA and D interactions by the factor $(1 - 3\cos^2\theta)$. At the magic angle, the chemical shift tensor reduces to the isotropic chemical shift and the dipolar interaction vanishes, yielding a high-resolution spectrum. In practice, the sample cannot be spun fast enough using current technology to completely remove the broadening from dipolar interactions. MAS is used in concert with high power decoupling (dipolar decoupling) to eliminate the dipolar broadening.

Having demonstrated the achievement of high-resolution solid state NMR capability, the authors describe experiments that combine the high-resolution aspect of MAS NMR with methods that retain the structure and/or dynamic information inherent in the anisotropic interactions. Rotational-echo double resonance (REDOR) allows the determination of D between isolated heteronuclear spin pairs. D is related simply and without approximation to internuclear separation. Hence, REDOR makes possible the unambiguous direct determination of internuclear distance between the labeled spin pair, independent of pair orientation, that is, in *amorphous* and/or *microcrystalline* solids, and extends our ability to quantitatively explore complex materials. It is also possible to extract internuclear distance from homonuclear dipolar coupled spin pairs, and these experiments are also reviewed.

As in solution state NMR, the extension of experiments into two or more dimensions is the path used to gain the resolution required to measure multiple, large anisotropic interactions (dipolar coupling, CSA) that are accessible in solids. Experiments that focus on homonuclear multi-dimensional experiments include J-mediated ^{13}C$-$^{13}C correlation and dipolar-mediated ^{1}H 2D double quantum (DQ) MAS spectroscopy. The authors give an example of the state of the art in solid state ^{1}H NMR line narrowing experiments using combined rotation and multiple pulse decoupling (CRAMPS), and indicate that the newest variants of this experiment have yielded line widths as low as 60 Hz for the aliphatic protons resonances of the amino acid L-alanine.

The correlations of anisotropic and isotropic interactions in 2D NMR are illustrated with experiments that measure the CSA of spin 1/2 nuclei. Results using the elegant magic angle turning (MAT) experiment are illustrated for the monoterpene verbenol that show the determination of the CSA tensor quantities for all carbons in this polymorphic substance. The usefulness of 2D NMR methods for characterizing chemical exchange processes is illustrated using static ^{2}H NMR and MAS ^{13}C NMR. In contrast to the rotor synchronized ^{1}H$-$^{1}H double quantum magic angle spinning (DQ-MAS) experiment referred to above, this experiment can also be performed using a large spectral width in the isotropic dimension, reintroducing the spinning sideband patterns in the spectrum. From their intensities, it is possible to calculate D directly and, hence, inter-proton distances. The applications of this experiment and others allow the measurement of proton–heteroatom distances position NMR as a powerful method to quantitatively study hydrogen bonding.

The focus of the chapter then shifts to heteronuclear 2D correlation (HETCOR) experiments. The evolution of single quantum coherence (SQC) of two different nuclei in these experiments with a coherence transfer step provides the basic formula for these correlations. In ^{1}H$-$^{13}C wide line separation (WISE), a wide dipolar broadened ^{1}H resonance is correlated with narrow ^{13}C resonances in the isotropic ^{13}C dimension. These experiments are used to distinguish rigid and mobile components of mixtures as the width of the ^{1}H dipolar coupling in the ^{1}H dimension is partially averaged by molecular motion. ^{1}H$-$^{13}C correlation with high resolution in both dimensions is useful for establishing one bond correlations using the dipolar coupling. In contrast to using D, experiments that use the isotropic J-coupling for the coherence transfer are complementary signal assignment methods that only detect intra-molecular contributions to the correlations.

Experiments that allow the measurement of multiple heteronuclear dipolar couplings in a single experiment and, hence, the simultaneous measurement of multiple internuclear distances, are reviewed. Variations of these experiments are also reported that allow the determination of bond angles, for example, the H–N–H bond angle in the NH_2 group, and torsion angles in fragments like $H^{N}-N-C^{\alpha}-H^{\alpha}$. The application of heteronuclear 2D correlation experiments using ^{15}N chemical shift and ^{15}N$-$^{1}H dipolar coupling in oriented samples, that is, uniformly ^{15}N-labeled membrane proteins in an oriented lipid bilayer, allows the determination of the tilt angle of a polypeptide helix with respect to the bilayer normal.

This chapter concludes with a section on measuring spectra of half-integer quadrupolar nuclei. For such nuclei, the central transition, $m_{\mathrm{I}} = +1/2 > \leftrightarrow m_{\mathrm{I}} = -1/2>$, is not broadened by the quadrupolar coupling to first order, and is observable. The resonance is broadened to second order by a fourth rank tensor contribution that is not removed by MAS. This broadening often confuses the recognition of chemically or crystallographically distinct sites. Mechanical methods to eliminate this broadening, that is, dynamic-angle spinning (DAS) and double rotation (DOR) are summarized. The 2D multiple quantum magic angle spinning (MQ/MAS) technique is an echo experiment that refocuses the second order quadrupolar broadening and yields 2D spectra from which both quadrupolar and chemical shift parameters can be extracted. The MQ/MAS experiment extends the effective domain of solid state NMR to dozens of half-integer quadrupolar nuclei using conventional MAS technology. This robust experiment has already proven itself capable of providing new insight into many inorganic systems.

It is an understatement to say that the manipulation of nuclear magnetization in physical and spin space described in the three chapters of this section on NMR constitutes one of the most powerful spectroscopic approaches to the study of matter in solution and solid phases. NMR continues to evolve in delightful ways that keeps this spectroscopy fresh and applicable in solving structure and dynamics problems in complex materials.

7
An Introduction to Solution, Solid-State, and Imaging NMR Spectroscopy

Leslie G. Butler

7.1
Introduction

Nuclear magnetic resonance (NMR) is a flexible technique with many applications [1, 2]. For substances dissolved in solution, NMR observation of ^{1}H, ^{13}C, ^{15}N, and ^{31}P yields structures of organic molecules, organometallic complexes, proteins, and nucleic acid oligomers. For solid materials, ^{2}H and ^{13}C NMR yields polymer structure, ^{27}Al and ^{29}Si NMR spectra yield zeolite and cement structures, and ^{17}O and $^{63/65}$Cu NMR yield properties of high-T_c superconductors. For solids containing fluid inclusions, ^{1}H NMR yields porosity and diffusivity information, even from thousands of meters below ground with *in situ* NMR instruments lowered through boreholes into petroleum formations. NMR is a fast, sensitive measure of magnetic fields; based on this, airborne NMR was used to detect submarines, and satellite-mounted NMR mapped the Earth's magnetic field. Adding a magnetic field gradient yields an imaging experiment: ^{1}H and ^{31}P magnetic resonance imaging (MRI) provide three-dimensional views of the human body, even showing specific brain activity. Even our breathing can be visualized with ^{129}Xe MRI.

In synthetic organic and organometallic chemistry, solution-state NMR means a 300–500 MHz NMR spectrometer, high-precision glass sample tubes, 2 ml of deuterated solvent (typically fully deuterated chloroform, acetone, benzene, or dichlorobenzene), several milligrams of pure sample, and a basic suite of ^{1}H and ^{13}C NMR experiments [3–7]. With several hours of spectrometer time and data interpretation, the structures of new compounds with molecular weights up to 2000 Da can be determined, especially when analyzed along with results from NMR databases and mass spectroscopy.

The structure of a protein in solution usually compares well with a crystallographic determination. However, not all proteins crystallize, and crystals of membrane-bound proteins are especially rare. Hence, the 600–950 MHz and newly constructed 1000 MHz NMR spectrometers are largely allocated for biological samples [8, 9]. Although most proteins are studied in solution, membrane-bound proteins may be studied in assembled bilayers. Currently, the greater part of NMR

Handbook of Spectroscopy, Second Edition. Edited by Günter Gauglitz and David S. Moore.

technology research and development efforts is directed toward new techniques in biological NMR, especially magnet development and software for data analysis.

In material science applications, solid-state NMR often employs a 200–750 MHz NMR spectrometer (Table 7.1) with a wide-bore magnet and high-power radio frequency (RF) amplifiers and matching NMR probes [10–12]. This equipment is especially useful for analysis of polymer structures with ^{2}H and ^{13}C NMR and for analysis of zeolites with ^{27}Al and ^{29}Si NMR. In polymers, local dynamics can be studied with time scales ranging from seconds to picoseconds; phase separations can be studied with domain sizes from nanometers to micrometers. For zeolites, the structures are characterized in terms of silicon/aluminum ratios, aluminum–hydrogen distances, and the chemistry of catalytic sites.

Why is NMR so widely used? In brief, NMR gives detailed information on selected nuclei, information about the chemical bonding, the local electronic structure, and the local site dynamics. For example, in protein NMR, each of the 20 amino acids has a distinctive set of resonances. Also, these resonances shift slightly with a twist of the amide bond, and other interactions yield the distance between one amino acid and its neighbors, provided that the distance is less than about 8 Å.

What makes NMR such a unique analytical technique? NMR uses the very weak interaction between a nucleus and the rest of the universe. The interaction between the magnetic moment of a nucleus and the RF field of an NMR pulse/receiver circuit is extremely weak: of the order hundreds of megahertz versus several electronvolts for optical spectroscopy (500 MHz corresponds to about 2 μeV). At first glance, this seems to be an enormous disadvantage as, for an equivalent sample mass, NMR has a much lower signal-to-noise ratio relative to many other spectroscopic techniques. However, the weak interaction also yields extremely high resolution. The weak interaction isolates the nucleus from external perturbation for long periods; relaxation times of the order of seconds are common and, conversely, line widths can be <1 Hz. Small changes to the environment at an NMR-active nucleus can be detected and identified. Most other analytical techniques are burdened with broad line widths.

How sensitive is an NMR resonance to the environment at the nucleus? Consider these observations:

Table 7.1 NMR spectrometers and applications.

^{1}H resonance (MHz)	Magnet	Applications
600–1000	Narrow-bore superconducting	Biological NMR
100–500	Narrow-bore superconducting	Organic chemistry
200–750	Wide-bore superconducting	Materials science
40–100	Benchtop permanent magnet	Quality control
40	1 m open-access permanent magnet	Whole body imaging
200	1 m bore superconducting	Whole body imaging and spectroscopy
About 50	Permanent magnet fringe field	Borehole logging

- In a material such as diamond, the NMR signal can be saturated, and it will be nearly a day before the signal is regained; the spin–lattice relaxation time for ^{13}C in diamond is hours as the rare (1.08 atom%) ^{13}C nuclei in diamond individually have weak interactions with the rest of the universe.
- Following pulse excitation, a coherent signal can typically be observed for 10–100 ms (solid) and 1–10 s (liquid samples). The natural line widths are roughly the inverse of these decay times.
- NMR spectroscopy of organic molecules relies on shifts and couplings between nuclei separated by several chemical bonds. The couplings between nuclei separated by two and three chemical bonds is especially important in protein NMR, even though the coupling is 10 Hz or less.

NMR theory is extensive: a working knowledge for materials science applications requires an understanding of these models and concepts:

- The rotating frame is used for simple descriptions of spin–lattice (T_1) and spin–spin (T_2) relaxation and some basic pulse sequences.
- Time-independent quantum mechanics gives transition frequencies and intensities for static systems (solids) or systems in the fast motion limit (solutions) subject to J-coupling, chemical shift, and quadrupolar coupling interactions.
- Motional averaging, for example, a two-site exchange, will affect both solution and solid-state spectra.
- Time-dependent quantum mechanics can be used to describe the spin system evolution in multiple pulse experiments.

In this short introduction to NMR spectroscopy, a discussion of important NMR parameters will be presented through experiments that cover solution-state ^{1}H NMR, solid-state NMR, and MRI.

7.2
Solution-State ^{1}H NMR

Consider the molecule in 1-chloroethene (vinyl chloride), $ClCHCH_2$, a carcinogenic gas (*http://toxnet.nlm.nih.gov/*) and a precursor for polyvinylchloride. If we study the most common isotopomer, all hydrogens are ^{1}H (nuclear spin (I) = 1/2), both carbons are ^{12}C ($I = 0$), and the chlorine is either ^{35}Cl or ^{37}Cl (both $I = 3/2$).

1-Chloroethene will dissolve in chloroform; thus, the solvent of choice is deuterated chloroform, $CDCl_3$, commonly available in solution-state NMR labs. The typical NMR tube is a thin-walled glass tube and too likely to break to risk a hazardous, volatile sample. A better choice is a thick-walled NMR tube sealed with an attached O-ring valve; flame sealing is sometimes used. As detailed toxicological studies often use isotopic labels to follow the metabolic pathways of a toxin, let us note in the following discussion the ability of NMR to monitor the position of a label, either ^{2}H or ^{13}C, in the 1-chloroethene molecule. In the following discussion, it should become obvious that NMR is an effective method for deducing subtle details of molecular structure and has distinct advantages over mass spectrometry or vibrational spectroscopy.

A typical solution-state ^{1}H NMR spectrum of 1-chloroethene is shown in Figure 7.1. We are first shocked by 11 peaks as we expected only three, one for each hydrogen. The physicist Murray Gell-Mann said at the discovery of the subatomic particle, the quark, ''Who ordered this?'' In general, spectroscopy should yield sufficient, but not overwhelming, information. Here, we will examine the 1-chloroethene spectrum and learn for ourselves if the 11 peaks are overwhelming or just what we might have ordered. A few general questions:

- Can chemical structure be used to predict the spectrum? Conversely, can the spectrum be used to predict the chemical structure?
- Can the spectrum be generated from a few parameters?
- Experimentally, can the adjustment of a few parameters modify the spectrum in a predictable manner?
- Do experimental procedures exist to simplify the spectrum?
- How does the spectrum change with deuteration or ^{13}C labeling?
- How does the spectrum change with chemical modification, for example, fluorine for chlorine?

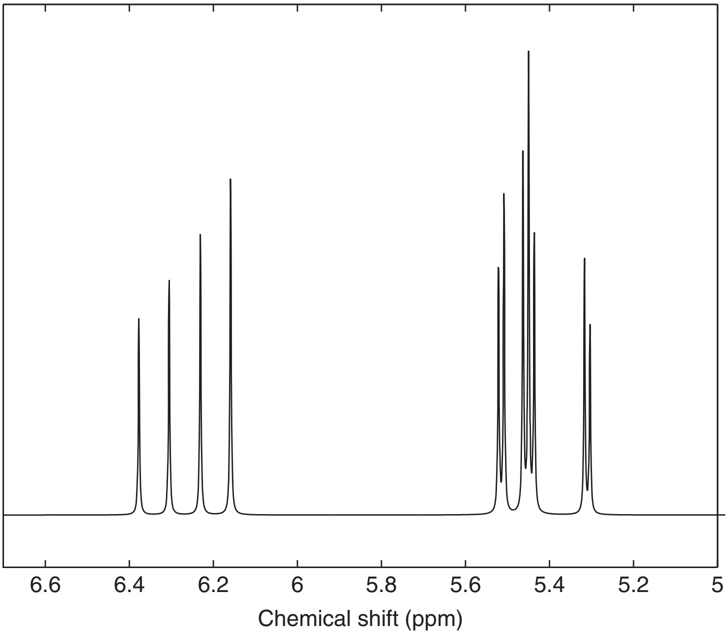

Figure 7.1 Solution-state ^{1}H NMR spectrum (simulated) of 1-chloroethene for $B_0 = 2.3488$ T, $\nu_{RF} = (1-6 \times 10^{-6}) \times 100$ MHz, $T_2 = 1$ s, spectral width = 300 Hz (digitization rate = 3.33 ms per complex data point) and 212 complex data points. At this resolution, 11 distinct peaks are observed.

The parameters that determine the 1-chloroethene spectrum are magnetic field (B_0), detection frequency (ν_{RF}), nuclear spin, gyromagnetic ratio, chemical shift, and J-coupling constants.

Briefly, a ^{1}H nucleus in a magnetic field of 2.3488 T will typically resonate within 1 kHz of 100 MHz. Because of the response of the molecule's core and valence electrons to the magnetic field, the actual field at the nucleus will be slightly different, that is, it will be "shifted" from 2.3488 T, hence the label "chemical shift," with the symbol δ and in units of parts per million. Based on the asymmetric structure of 1-chloroethene, all three hydrogens will have slightly different chemical shifts, as shown in Figure 7.2. For example, in 1-chloroethene, H_a has a chemical shift of 6.26 ppm, while for the analogous vinyl fluoride, the shift for the H_a is reduced to 6.17 ppm. On the basis of years of experience with NMR spectroscopy, chemical shift databases are available for ^{1}H, ^{13}C, ^{15}N, ^{29}Si, ^{19}F, and most other $I = 1/2$ nuclei. In many cases, approximate correlations are noted between chemical bonds, such as carbon–carbon single, double, and triple bonds; the electronegativity of substituents, such as F, Cl, and NO_3; and other molecular features in organic and organometallic compounds. In practice, a synthetic chemist or structural biochemist may become a walking database of ^{1}H, ^{13}C, and ^{15}N chemical shifts. The definition of chemical shift is

$$\delta = \frac{\nu - \nu_{\text{reference}}}{\nu_{\text{reference}}} \times 10^6 \text{ ppm} \tag{7.1}$$

where ν is the observed NMR frequency and $\nu_{\text{reference}}$ is the frequency at which a reference molecule has $\delta = 0$ ppm in that magnetic field.

The J-coupling constants describe short-range, through-bond (as opposed to through-space) interactions that connect the spins of neighboring nuclei. An immensely positive result is connectivity information. A minor negative result is a visually complicated spectrum. However, there are experimental methods that simplify the spectrum: one method is to increase the magnetic field from 2.3488 T by a factor of 4 or 8, as will be discussed shortly.

The solution-state ^{1}H NMR spectrum of 1-chloroethene (Figure 7.1) is easily described by time-independent quantum mechanics using an uncoupled basis set

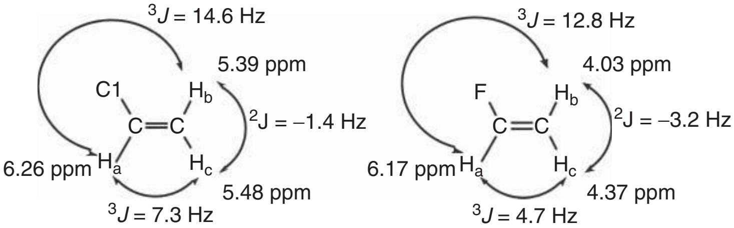

Figure 7.2 ^{1}H NMR parameters, chemical shifts, and J-coupling constants, for 1-chloroethene and 1-fluoroethene.

of spin functions. The total Hamiltonian is

$$\begin{aligned} H_{\text{total}}(\text{Hz}) = & -\frac{\gamma_{\text{H}} B_0}{2\pi}(1+\delta_{\text{A}})S_{z\text{A}} - \frac{\gamma_{\text{H}} B_0}{2\pi}(1+\delta_{\text{B}})S_{z\text{B}} - \frac{\gamma_{\text{H}} B_0}{2\pi}(1+\delta_{\text{c}})S_{z\text{C}} + \cdots \\ & J_{\text{AB}}[S_{x\text{A}} \times S_{x\text{B}} + S_{y\text{A}} \times S_{y\text{B}} + S_{z\text{A}} \times S_{z\text{B}}] + \cdots \\ & J_{\text{AC}}[S_{x\text{A}} \times S_{x\text{C}} + S_{y\text{A}} \times S_{y\text{C}} + S_{z\text{A}} \times S_{z\text{C}}] + \cdots \\ & J_{\text{BC}}[S_{x\text{B}} \times S_{x\text{C}} + S_{y\text{B}} \times S_{y\text{C}} + S_{z\text{B}} \times S_{z\text{C}}] \end{aligned} \tag{7.2}$$

where γ_{H} is the gyromagnetic ratio for hydrogen, B_0 is the applied magnetic field, and $S_{z\text{A}}$, and so on, are the spin functions for $I = 1/2$. The chemical shifts and J-coupling constants are as defined in the line structure above. Evaluation of Eq. (7.2) in matrix form yields an 8×8 matrix in bracket notation:

$$\langle \Psi | H_{\text{total}} | \Psi \rangle = \begin{pmatrix} -150\,000\,851 & 0 & 0 & 0 & 0 & 0 & 0 & 0 \\ 0 & -50\,000\,306 & -0.7 & 0 & 3.65 & 0 & 0 & 0 \\ 0 & -0.7 & -50\,000\,319 & 0 & 7.3 & 0 & 0 & 0 \\ 0 & 0 & 0 & 50\,000\,225 & 0 & 7.3 & 3.65 & 0 \\ 0 & 3.65 & 7.3 & 0 & -50\,000\,236 & 0 & 0 & 0 \\ 0 & 0 & 0 & 7.3 & 0 & 50\,000\,316 & -0.7 & 0 \\ 0 & 0 & 0 & 3.65 & 0 & -0.7 & 50\,000\,311 & 0 \\ 0 & 0 & 0 & 0 & 0 & 0 & 0 & 150\,000\,862 \end{pmatrix}_{\text{Hz}} \tag{7.3}$$

The off-diagonal elements from the J-coupling interaction are small and scarcely perturb the energy levels defined by the chemical shift and Zeeman interaction. On the other hand, the experimental resolution is frequently better than 1 Hz, so even small interactions can be observed. The allowed transitions are single quantum; for example, spin H_A will absorb a single quantum of energy near 100 MHz while H_B and H_C stay in one of four possible quantum configurations. Diagonalization of Eq. (7) yields the energy levels; the unitary matrix that performs the matrix diagonalization yields the relative transition probabilities. Listed in Table 7.2 are the 12 allowed transitions.

Of the 12 transitions listed, two are overlapping at the resolution of the spectrum shown in Figure 7.1. The peaks have Lorenztian lineshapes. The full width at half of the maximum peak height (full width at half maximum, FWHM) is given by

$$\Delta\nu = 1/\pi T_2 \tag{7.4}$$

In Figure 7.1, T_2 is set at 1 s, hence the peak widths are 0.3 Hz.

In Figure 7.1, four peaks appear at frequencies just slightly greater than the detection frequency ($\nu_{\text{RF}} = 100\,\text{MHz} + 6\,\text{ppm} = (1 + 6 \times 10^{-6}) \times 100\,\text{MHz}$) and seven resolved peaks occur at lower frequencies. The NMR parameters, chemical shifts, and J-coupling constants, are given in Figure 7.2 and cannot be determined precisely by inspection of the spectrum in Figure 7.1. Basically, the spectrum in Figure 7.1 is difficult to interpret because the off-diagonal elements (Eq. (7.3)) are large with respect to the differences between diagonal elements. As we can increase B_0, which then increases the magnitude of the diagonal elements, spectra acquired at higher magnetic field will show a closer, more obvious relationship with the NMR

Table 7.2 Calculated ^{1}H NMR transitions for 1-chloroethene at $B_0 = 2.3488$ T.

|abc>	*E*(*i*) (MHz)	<abc|	*E*(*f*) (MHz)	$\nu - \nu_{RF}$ (Hz)[a]	Amplitude	Nucleus[b]	δ (ppm)
$+--$	$-50\,000\,224$	$---$	$-150\,000\,862$	-37.7	0.764	H_A	6.38
$+-+$	$-50\,000\,320$	$--+$	$-50\,000\,311$	-30.5	0.902	H_A	6.31
$++-$	$-50\,000\,306$	$-+-$	$-50\,000\,317$	-23.1	1.052	H_A	6.23
$+++$	$-150\,000\,851$	$-++$	$-50\,000\,236$	-15.9	1.281	H_A	6.16
$-++$	$-50\,000\,236$	$-+-$	$-50\,000\,317$	-47.9	0.949	H_C	5.52
$--+$	$-50\,000\,311$	$---$	$-150\,000\,862$	-49.2	1.235	H_C	5.51
$-++$	$-50\,000\,236$	$--+$	$-50\,000\,311$	-53.7	1.332	H_B	5.46
$-+-$	$-50\,000\,317$	$---$	$-150\,000\,862$	-55.0	1.001	H_B	5.45
$+++$	$-150\,000\,851$	$++-$	$-50\,000\,306$	-55.1	0.760	H_C	5.45
$+-+$	$-50\,000\,320$	$+--$	$-50\,000\,224$	-56.4	1.057	H_C	5.44
$+++$	$-150\,000\,851$	$+-+$	$-50\,000\,320$	-68.3	0.959	H_B	5.32
$++-$	$-50\,000\,306$	$+--$	$-50\,000\,224$	-69.6	0.707	H_B	5.30

[a] $\nu_{RF} = 100\,\text{MHz} + 6\,\text{ppm} = (1 + 6 \times 10^{-6}) \times 100\,\text{MHz}$.

[b] Transition dominated by spin function at this site.

parameters such as chemical shifts and *J*-coupling constants. The NMR spectra of 1-chloroethene at increasing magnetic fields is shown in Figure 7.3.

Here, the linear dependence of the diagonal components of H_{total}, terms such as $-\gamma B_0(1 + \delta_A)S_{zA}$, causes the increased dispersion of peaks at higher magnetic fields. To observe the subtle effects of the *J*-coupling constants, it is convenient to replot the spectra on the chemical shift scale, Eq. (7.1), as shown in Figure 7.4.

When solution-state NMR spectra are plotted on a chemical shift scale, the center-of-mass of a group of peaks defines the chemical shift for that nucleus, provided that the field is large enough to diminish the effect of the off-diagonal *J*-coupling terms. We can see above that good estimates of $\delta(H_A)$ can be read from the plots at all magnetic fields but that values for $\delta(H_B)$ and $\delta(H_C)$ require a 400 MHz or larger NMR spectrometer. Thus, increasing the magnetic field is one experimental method for simplifying the NMR spectrum.

In addition to magnetic field, the two other experimental methods frequently used for spectral simplification and/or modification are selective decoupling and chemical modification. Selective decoupling can be done in a variety of ways; one method is the application of low power RF over a narrow frequency range during the time of NMR signal acquisition. Within a selected, narrow frequency range, low power RF causes the nuclei to undergo rapid absorption and stimulated emission. In simple terms, a nucleus, such as H_B, will flip rapidly between spin up and spin down states. If the flip-rate is fast enough, the *J*-coupling terms involving nucleus H_B in Eq. (7.2) average to zero; the NMR jargon is H_B is "decoupled" from the other spins. The effect of H_B decoupling is shown in Figure 7.5b. Compared to the original 200 MHz spectrum for 1-chloroethene (Figure 7.5a), the decoupled spectrum is quite simple, a four-line pattern that clearly shows two hydrogens with

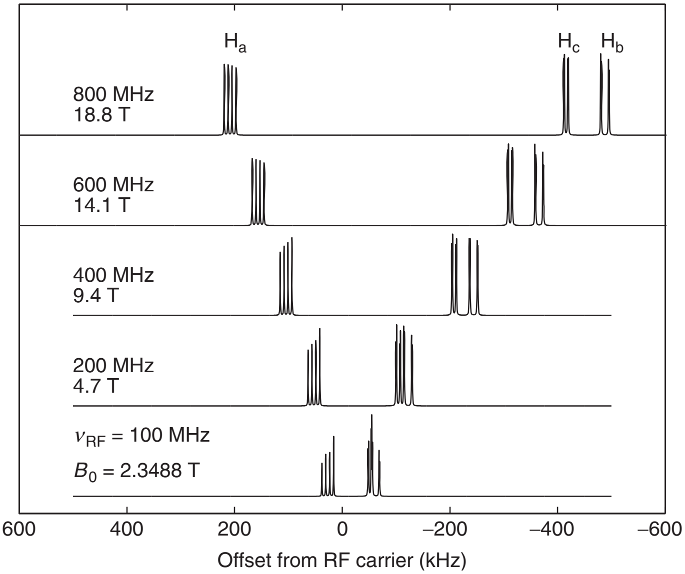

Figure 7.3 Solution-state ^{1}H NMR spectrum of 1-chloroethene, plotted on the frequency scale. For each spectrum, the RF carrier, ν_{RF}, is set to $(1 + 6 \times 10^{-6}) \times 100$ MHz, 200 MHz, and so on.

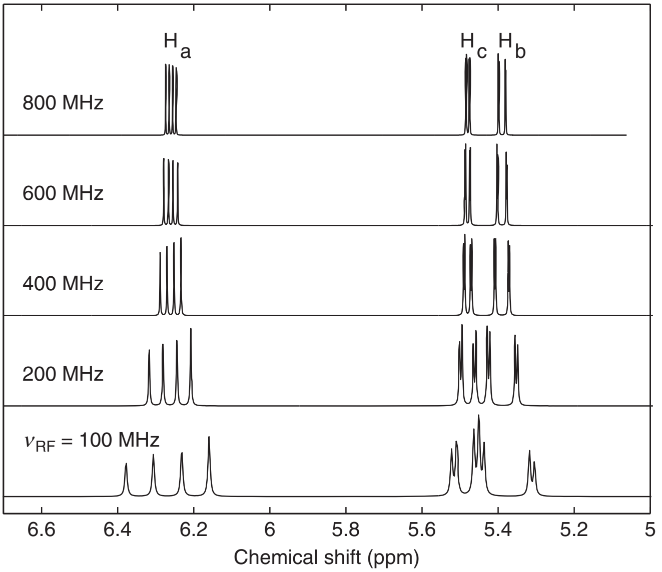

Figure 7.4 Solution-state ^{1}H NMR spectrum of 1-chloroethene, plotted on the chemical shift scale. Here, the zero, 0 ppm, is set by $\nu_{\text{reference}}$, the frequency at which hydrogens of a chemical shift standard are resonant at B_0.

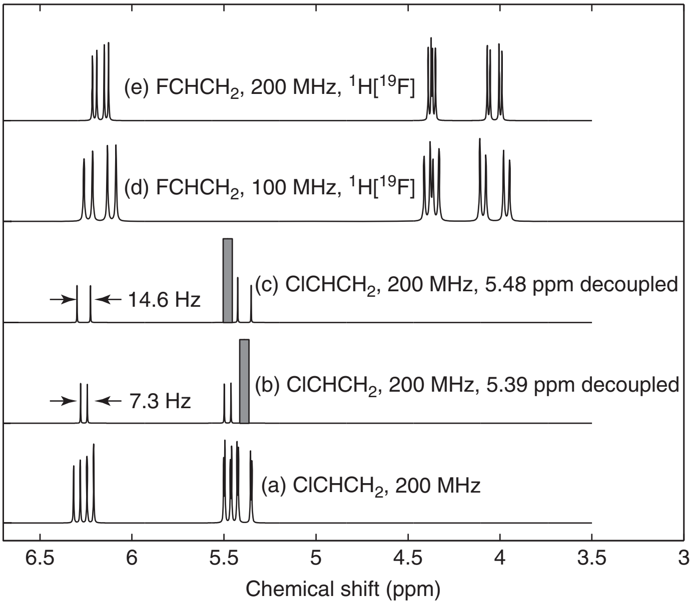

Figure 7.5 (a–e) Solution-state ^{1}H NMR spectrum of 1-chloroethene and 1-fluoroethene. The results of selective homonuclear decoupling are shown in (b,c). The results of heteronuclear decoupling are shown in (d,e). Not shown is the simple, ^{19}F coupled ^{1}H NMR spectrum (or the double negative "^{19}F undecoupled") of 1-fluoroethene, which has twice as many ^{1}H transitions as shown in (d,e) (each line is then a doublet from $^nJ(^1H-^{19}F)$, $n = 2, 3$).

chemical shifts of 6.26 and 5.48 ppm and a J-coupling of 1.3 Hz. Similarly, the decoupling of H_C yields another four-line pattern (Figure 7.5c) showing resonances centered at 6.26 and 5.39 ppm, and a J-coupling of 14.6 Hz.

To explore the relationship between structure and NMR parameters, a series of similar molecules should be studied. Shown in Figure 7.5d,e is 100 and 200 MHz ^{1}H NMR spectra for the analogous 1-fluoroethene. To suppress the effect of $J(^1H-^{19}F)$ coupling, this spectrum is shown as acquired with ^{19}F decoupling. That is, during the experiment, RF power is applied to all ^{19}F resonances. In NMR nomenclature, $^1H\{^{19}F\}$ means ^{1}H observation with ^{19}F decoupling.

A few more details about the ^{1}H NMR spectrum of 1-chloroethene are worthy of discussion. First, the J-coupling from ^{35,37}Cl is averaged to zero because, in solution, the chlorine nucleus has a very short T_1; in effect, the ^{35,37}Cl nuclei are self-decoupled from the hydrogen spins. Second, selective deuteration of 1-chloroethene will yield spectra very similar to Figure 7.5b,c for deuteration at the B and C sites, respectively. The values of $J(^1H-^2H)$ are about one-sixth (=15.351/100 MHz) of the $J(^1H-^1H)$ values shown in Figure 7.2 and the $I = 1$ ^{2}H nucleus creates triplets instead of doublets. The net results are slightly line-broadened versions of the spectra shown in Figure 7.5b,c. Third, ^{13}C labeling at one site will add coupling with the $I = 1/2$ ^{13}C nucleus to the ^{1}H spectrum.

The one-bond coupling, $^1J(^1\text{H}-^{13}\text{C})$, is about 150 Hz and the two-bond coupling, $^2J(^1\text{H}-^{13}\text{C})$, is about 10 Hz. So, the ^{13}C-labeled site will cause a great change, due to $^1J(^1\text{H}-^{13}\text{C})$ coupling, in either the H_A resonances or in both H_B and H_C resonances, depending on which carbon site is labeled.

Almost all NMR spectra are acquired with pulse methods. The ^{1}H NMR spin system is excited with a short duration RF pulse, and the response of the spin system is measured, both the in-phase and out-of-phase components. Based on the terminology of complex numbers, these two components are referred to as the *real and imaginary components*. This NMR signal is called the free-induction decay, FID, a name which harks back to a classical viewpoint of a freely moving magnet precessing within a solenoidal coil, thus inducing a current. In fact, a current is measured in the NMR probe, which is often a coil of wire, and then digitized. When the raw data is viewed, it shows an exponentially decaying set of sinusoidal signals. Figure 7.6 shows the FID for 1-chloroethene, acquired under the conditions leading to the spectrum shown in Figure 7.1.

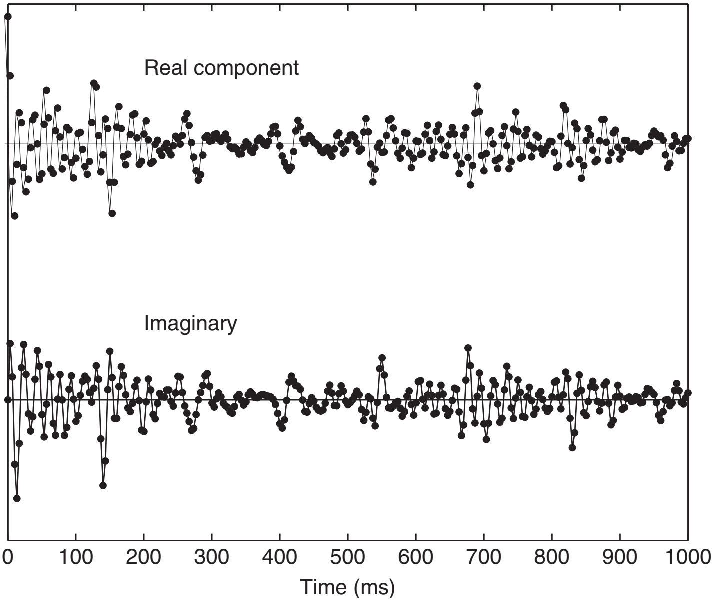

Figure 7.6 The first 1000 ms of the FID corresponding to the spectrum shown in Figure 7.1. The digitization interval is 3.33 ms per complex data point, yielding a spectral width of 300 Hz, an unusually small spectral window. At 9.4 T, ^{1}H NMR is usually done with a 10 kHz spectral window, ^{13}C with 25–50 kHz, and solid-state ^{2}H with 1 MHz (and a corresponding 1 μs digitization rate). While $\nu_{\text{reference}}$ is fixed by the nucleus and the magnetic field, ν_{RF} is adjustable, and usually set near the middle of the peaks of interest. The absolute values of the vertical scale are not used except to note whether or not the first data point is "clipped" by the NMR receiver system; clipping leads to unacceptable spectral distortion.

The data processing usually involves four user-intervention steps: (i) applying a smoothing function to the FID, (ii) Fourier transformation, (iii) phasing the frequency domain data into pure real and imaginary components, and (iv) setting the 0 ppm point for the chemical shift axis. A common smoothing function is a Lorentzian line-broadening function, equivalent to point by point multiplication of the FID by an exponentially damped function. Phasing removes linear changes in phase within the spectrum, producing uniform absorption line shapes for all signals.

To summarize, solution NMR spectra of small organic, organometallic, and biological materials show well-resolved ^{1}H NMR spectra. The two major interactions affecting the spectra are chemical shift and *J*-coupling; extensive databases of interactions aid the identification of the molecule and the assignment of the spectrum. Both low and high magnetic fields are functional, though there is a preference for higher fields that yield greater resolution between peaks and spectra which are easier to interpret.

7.3
Solid-State NMR

Consider hypothetical studies of the orientations and dynamics of a self-assembled monolayer (SAM) of organic thiols chemisorbed on a gold surface. Aside from the chemical information that comes from chemical shifts and *J*-coupling, NMR can also provide orientation information for selected sites within a molecule. Consider a related series of organic thiols and their ^{13}C, ^{2}H, and ^{1}H NMR spectra. The alkyne thiol derivatives shown in Figure 7.7 will be used to demonstrate how to obtain orientation and dynamic information. We will first consider static samples, then samples in which the molecule is executing one of several modes of motion. For static samples, we seek information about the angle between the magnetic

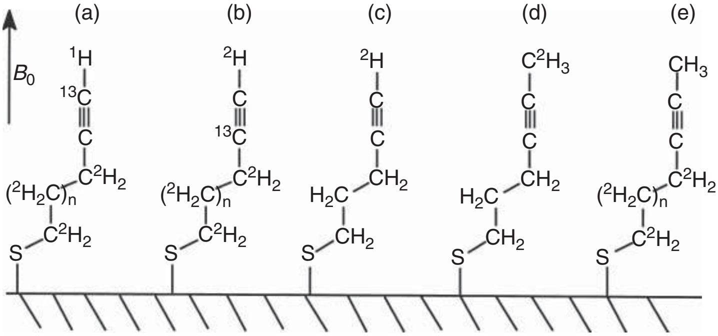

Figure 7.7 Alkyne thiol derivatives illustrating (a) ^{13}C–^{1}H dipolar interaction, (b) ^{13}C chemical shift anisotropy, (c) ^{2}H quadrupolar interaction, (d) dynamics of a deuterated methyl site, and (e) ^{1}H $T_{1\rho}$ relaxation times. Assume a gold-coated glass slide that is uniformly covered with one of these molecules. Because of signal-to-noise considerations, a number of these slides may be stacked together in the NMR sample coil.

field and a labeled portion of the molecule. For molecules that are in motion, we seek the rate of motion, the activation energy, and the mode of motion. The mode of motion can be random, isotropic molecular motion; thermally activated motion about a molecular axis; or rapid motion of the entire sample about a magic angle, a special angle with respect to the magnetic field.

NMR of solids differs from solution-state NMR in several important ways. First, the solution-state ‘‘tumbling’’ of molecules is, of course, restricted in the solid phase. In the absence of rapid isotropic motion, magnetic dipolar interaction between neighboring spins affects the NMR line shape. Second, the chemical shift interaction is not just a simple scalar, but a tensor quantity. In solution-state NMR, only the scalar average is seen, while in solid-state NMR, the tensor elements are observed. In the solid-state, the chemical shift tensor yields a variety of possible NMR line shapes. Likewise, the quadrupolar interaction also creates a variety of line shapes. Third, a single molecular motion can dominate the process of thermal equilibration of the NMR spin system with its environment.

7.3.1
Dipolar Interaction

The alkyne thiol, $\mathrm{R{-}C{\equiv}{}^{13}C{-}{}^{1}H}$, has two neighboring magnetic spins, both aligned with the large magnetic field, B_0. From the viewpoint of the ^{13}C site, the magnetic field is a sum of B_0 and the small magnetic field generated by the ^{1}H nucleus. The magnetic field at ^{13}C varies with the orientation of the ^{13}C–^{1}H unit with respect to B_0 and with the nuclear spin quantum state (m_s) of the ^{1}H site. When the ^{13}C–^{1}H unit is parallel with B_0 ($\theta = 0^\circ$) and $m_s(^{1}\mathrm{H}) = +1/2$, the total magnetic field at ^{13}C is a maximum, yielding an absorption about 24 kHz above the isotropic ^{13}C chemical shift, as shown in Figure 7.8 by the leftmost vertical line to the dashed line. The dashed line represents the subspectrum for all ^{13}C spins dipolar coupled to a ^{1}H in the $m_s = +1/2$ spin state. As the ^{13}C–^{1}H unit is rotated to a perpendicular position, the dipolar magnetic field from ^{1}H ($m_s = +1/2$) decreases until the ^{13}C peak is at -12 kHz (vertical bar to dashed line) relative to the ^{13}C chemical shift. The ^{13}C–^{1}H dipolar interaction is described by

$$H_{\mathrm{dipolar}}(\mathrm{J}) = \left(\frac{\mu_0}{4\pi}\right)\hbar^2\gamma_s\gamma_I\left[\frac{\mathbf{S}\times\mathbf{I}}{r^3} - 3\frac{\mathbf{S}\times\mathbf{r}\mathbf{I}\times\mathbf{r}}{r^5}\right] \tag{7.5}$$

$$\omega[^{13}\mathrm{C}{-}^{1}\mathrm{H}] = \left(\frac{\mu_0}{4\pi}\right)\hbar\frac{\gamma_{^{13}\mathrm{C}}\gamma_{^{1}\mathrm{H}}}{r^3} = (2\pi)(23.6\,\mathrm{kHz}) \quad \{\text{for } r = 108.5\,\mathrm{pm}\} \tag{7.6}$$

The NMR signal amplitude is larger for $\theta = 90^\circ$ than $\theta = 0^\circ$. In a powder, there are many possible orientations of the molecule. For this axially-symmetric ^{13}C–^{1}H unit, one can imagine the range of possible orientations as the Earth with an arrow pointing from the center to the surface. Only one arrow orientation points to the North Pole, but an infinite number of orientations point to the equator (fortunately, the NMR sample has a finite number of molecules). Thus, relatively few ^{13}C–^{1}H

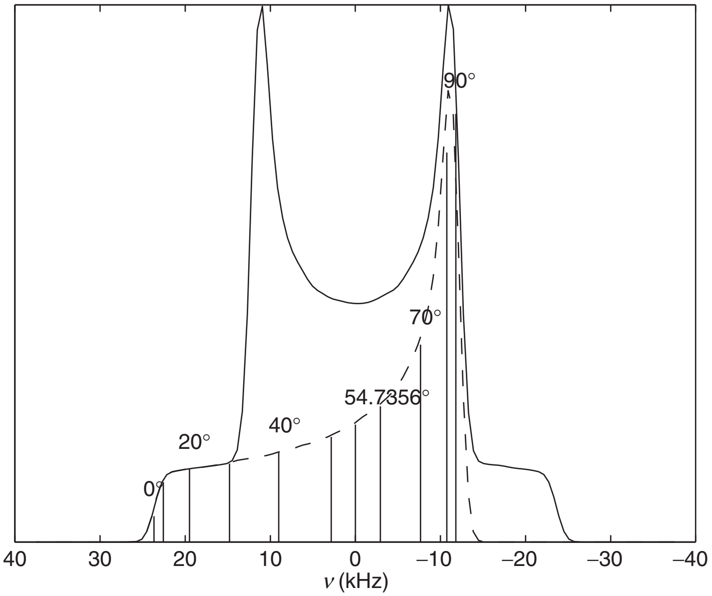

Figure 7.8 Solid-state ^{13}C NMR "powder pattern" line shape for the case of ^{13}C−^{1}H dipolar interaction and an ensemble of randomly oriented ^{13}C−^{1}H units. The frequency axis is centered on the ^{13}C resonance. The upper trace (—) is the observed line shape while the lower trace (— — —) is a subspectrum from ^{13}C sites adjacent to a ^{1}H site in the $m_s = +1/2$ spin state. Not shown is the corresponding subspectrum for ^{1}H $m_s = -1/2$. Vertical bars show the ^{13}C resonance frequency at $\theta = 0°$, $10°$, ..., $90°$, including $\theta = 54.7356°$, an orientation of the ^{13}C−^{1}H unit for which the dipolar interaction is zero.

sites are oriented at $\theta = 0°$ and contribute to the absorption at +24 kHz; many more molecules contribute to the −12 kHz absorption corresponding to the $\theta = 90°$ orientation.

The ^{13}C−^{1}H dipolar powder pattern has features that affect other NMR experiments. First, this is an inhomogeneously broadened line composed of many, narrow but homogenously broadened peaks. Second, the two subspectra generated by $m_s(^{1}H) = \pm 1/2$ are mirror images of each other. Third, powder pattern averages of axially-symmetric units, such as C≡^{13}C−^{1}H, give the characteristic "Pake doublet" [1, 10–12]. The "Pake doublet" is obscured by interactions between three or more spins, hence the deuteration of the methylene chain in molecule A (Figure 7.7). Fourth, the orientation at which the dipolar interaction is zero, $\theta = 54.7356°$, is a critical feature of the "magic angle spinning experiment," to be discussed later.

Finally, ^{13}C NMR of a stack of gold-coated glass slides will likely yield information about the orientation of the R−C≡^{13}C−^{1}H molecules. This experiment is easier at moderate fields than at high fields. If the R−C≡^{13}C−^{1}H molecules are uniformly tilted with respect to the gold-coated glass slide, and the surface is perpendicular to B_0, then a pair of peaks should be seen in the ^{13}C NMR spectrum, one for each spin state of ^{1}H, and the peak separation will yield the tilt angle. The experimental problems are surface roughness, low signal-to-noise ratio because of the small number of ^{13}C spins in the NMR sample volume, and the range of magnetic fields at the ^{13}C nuclei due to the difference between the magnetic susceptibility of gold versus air, especially near the sides of the gold layers. This line-broadening effect increases linearly with the magnetic field strength; thus, the optimum field strength is a field sufficient to obtain a signal.

For simplicity, the spectrum in Figure 7.8 assumes an isotropic ^{13}C chemical shift. As it turns out, all known ^{13}C alkyne sites have highly anisotropic chemical shifts, which are best described by tensors. This is a nice lead-in to a discussion of chemical shift anisotropy.

7.3.2
Chemical Shift Anisotropy

The chemical shift at a nucleus is due to the core and valence electrons near that nucleus. The bonding electrons in the axially-symmetric $-^{13}\mathrm{C}{\equiv}\mathrm{C}$ unit (Figure 7.7b) increase the field at the $\theta = 0^\circ$ orientation, causing the ^{13}C resonance to occur at lower frequency than expected; on the chemical shift scale, the resonance is at -69 ppm. When the $-^{13}\mathrm{C}{\equiv}\mathrm{C}$ unit has the more probable orientation of $\theta = 90^\circ$, the magnetic field is less at ^{13}C than for the chemical shift standard, tetramethylsilane

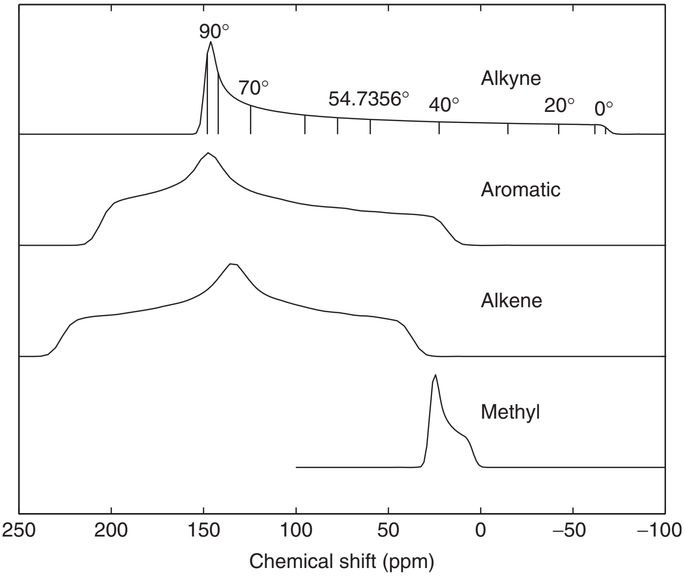

Figure 7.9 Solid-state ^{13}C{^{1}H} NMR "powder pattern" line shape for ^{13}C chemical shift anisotropy and an ensemble of randomly oriented $-^{13}\mathrm{C}{\equiv}\mathrm{C}$ (alkyne) units. Vertical bars show the ^{13}C resonance frequency at $\theta = 0^\circ$, 10°, …, 90°, including $\theta = 54.7356^\circ$, an orientation of the $-^{13}\mathrm{C}{\equiv}\mathrm{C}$ unit for which the peak position corresponds to the isotropic chemical shift observed in solution-state NMR. Also shown are the typical chemical shift anisotropy powder patterns for ^{13}C aromatic, alkene, and methyl sites.

(TMS), yielding a peak near 148 ppm, as shown in Figure 7.9. The chemical shift anisotropy depends upon the bonding at carbon, as can be seen in the other traces in Figure 7.9 which shows the predicted $^{13}C\{^1H\}$ NMR powder pattern line shapes for aromatic, olefinic, and methyl sites. As can be seen, the extraction of molecular orientation from the line shape is particularly straightforward for the alkyne.

The chemical shift anisotropy is usually described in a principal axis system, which is usually not the molecular axis system. In the principal axis system, the chemical shift tensor is diagonal. The elements of this tensor contribute to the NMR spectrum via these two equations:

$$\delta^{\text{lab}} = R^{-1}(\phi,\theta,\psi)\begin{vmatrix} \delta_{xx}^{\text{PAS}} & 0 & 0 \\ 0 & \delta_{yy}^{\text{PAS}} & 0 \\ 0 & 0 & \delta_{zz}^{\text{PAS}} \end{vmatrix} R(\phi,\theta,\psi) \tag{7.7}$$

$$H_{\text{total}}(\text{Hz}) = H_{\text{Zeeman}} + H_{\text{chemical shift}} = -\frac{\gamma B_0}{2\pi}(1+\delta_{zz}^{\text{lab}})S_z \tag{7.8}$$

In summary, orientation of $R{-}^{13}C{\equiv}C{-}^1H$ molecules (Figure 7.7b) chemisorbed on gold surfaces can be obtained from $^{13}C\{^1H\}$ NMR of a stack of gold-coated glass slides. The same issues of signal-to-noise and magnetic susceptibility line-broadening discussed earlier will also apply to the $^{13}C[^1H]$ NMR experiment.

7.3.3
Quadrupolar Interaction

The quadrupolar interaction occurs for nuclei with $I \geq 1$ and tends to align the nucleus with the electric charge distribution near the nucleus. While there are many more $I \geq 1$ nuclei than $I = 1/2$ nuclei, the typical NMR spectrometer is equipped to observe with ease only ^2H ($I = 1$), ^{27}Al (5/2), and maybe ^{17}O (5/2), ^{11}B (3/2), ^7Li (3/2), and ^{23}Na (3/2). Less common are experiments for $^{63,65}Cu$ (both 3/2), ^{91}Zr (5/2), ^{93}Nb (9/2), $^{35,37}Cl$ (3/2), $^{79,81}Br$ (3/2), and ^{127}I (5/2).

In short, the electric charge asymmetry of the nucleus and asymmetry of the charge distribution around the nucleus causes the electric quadrupolar interaction. In electrostatics, magnetic and electric interactions can be described in a progression of moments: monopole, dipole, quadrupole, and so on. For an $I = 1/2$ nucleus such as ^1H, the relevant moments are: a non-zero electric monopole moment (+1 charge), a small magnetic dipole moment, and zero values for nuclear magnetic monopole, nuclear magnetic quadrupole, and nuclear electric dipole moments. As more protons and neutrons are added to the nucleus, the nuclear electric quadrupole moment can become non-zero. In much the same way that the magnetic dipole aligns with a magnetic field, an electric quadrupole moment aligns with the electric field gradient (EFG). The quadrupolar interaction can be small, about 170 kHz for many ^2H sites, to over 1 GHz for some ^{127}I sites. The EFG can be computed from the positions of all charges, both electrons and neighboring nuclei, near the quadrupolar nucleus. In practice, most molecular orbital programs can calculate accurate EFGs for ^2H, ^{14}N, ^{17}O, and other nuclei in medium size molecules such as nitrobenzene. Thus, the observation of quadrupolar spectra and comparison with calculated EFGs can aid investigations of many different structural questions.

The quadrupolar interaction is described by a tensor. The EFG is described with size, shape, and orientation parameters: The size of the EFG tensor is given by the quadrupolar coupling constant in Hertz, variously labeled as C_q, $e^2q_{zz}Q/h$, and QCC (not recommended). The shape of the EFG tensor is given by the asymmetry parameter, η. The EFG tensor has a well-defined orientation with respect to the molecular or crystal structure. For the quadrupolar nucleus, the important nuclear properties are spin and quadrupole moment: $I = 1$, 3/2, 5/2, 3, 7/2, and 9/2 are frequently encountered. The nuclear electric quadrupole moment is given by Q in units of m^2. So, for a given materials science study, one generally selects a nucleus (I, Q), and then measures C_q and η as a function of structure with frequent comparisons to calculated EFG tensors from molecular orbital calculations (C_q, η, orientation). The quadrupolar hamiltonian is

$$H_{\text{quadrupolar}}(\text{Hz}) = \frac{1}{6I(2I-1)} \sum_{\alpha\beta}^{x,y,z}{}' \quad Q_{\alpha\beta}^{\text{lab}} \left[\frac{3}{2} \left(I_\alpha I_\beta + I_\beta I_\alpha - \delta_{\alpha\beta} I^2 \right) \right] \tag{7.9}$$

$$Q^{\text{lab}} = R^{-1}(\phi,\theta,\psi) C_q \begin{vmatrix} \frac{\eta-1}{2} & 0 & 0 \\ 0 & -\frac{\eta-1}{2} & 0 \\ 0 & 0 & 1 \end{vmatrix} R(\phi,\theta,\psi) \tag{7.10}$$

Representative quadrupolar nuclei and some quadrupolar interaction data are listed in Table 7.3. Simulated spectra for several of these sites are shown in Figure 7.10 as if the spectra were acquired on a 9.4 T (400 MHz) NMR spectrometer with a probe having a fantastically wide spectral width. In practice, the α-alumina spectrum can barely be acquired and the andalusite and nitro spectra are essentially unobservable. Even the ^{2}H spectrum can be difficult to acquire without distortion from probe ringdown effects.

The deuterated alkyne thiol, Figure 7.7c, is a relatively easy molecule to prepare at levels of >80% deuteration and, in general, the ^{2}H NMR experiment yields spectra with good signal-to-noise ratios. Thus, it is reasonable to expect a ^{2}H quadrupolar powder pattern NMR spectrum showing a combination of the features of the ^{2}H NMR (Figure 7.10) with the orientational aspects of the Pake doublet (Figure 7.8). If a SAM has high orientational order and an oriented sample is studied (stacks

Table 7.3 Representative C_q and η for ^{2}H in some sites [13].

Site	C_q (kHz)	η
C(sp^3)–^{2}H	170–175	~0
C(aromatic)–^{2}H	180–185	~0.1
C(sp)–^{2}H	200–210	0
O–^{2}H	50–320	0–1
N–^{2}H	50–280	0–1

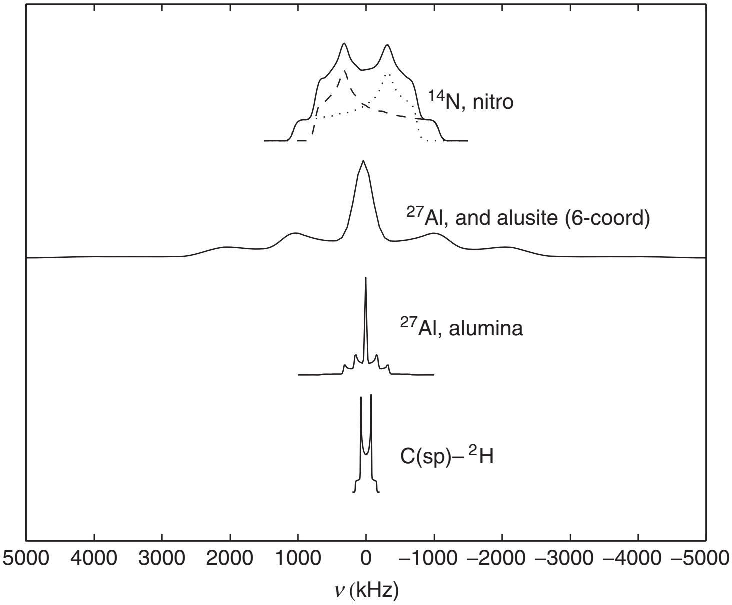

Figure 7.10 Static, solid-state quadrupolar NMR line shapes for some ^{2}H, ^{27}Al, and ^{14}N sites in powder (non-oriented) samples at a field of 9.4 T (400 MHz for ^{1}H). The useful bandwidth of a solid-state NMR spectrometer is typically 1 MHz; thus, spectra cannot be acquired for the andalusite or nitro sites. Also shown for ^{14}N are subspectra making up the total line shape: the transition $|+1\rangle \rightarrow |0\rangle$ yields the subspectrum (— — —) and the transition $|0\rangle \rightarrow |-1\rangle$ yields the subspectrum (. . .).

of glass slides), then the ^{2}H spectrum could show two peaks corresponding to the $|+1\rangle \rightarrow |0\rangle$ and $|0\rangle \rightarrow |-1\rangle$ transitions. The frequency difference between the two peaks would then give the angle between the C–^{2}H bond and B_0 (Figure 7.8). Conversely, a random orientation between the C–^{2}H bonds and B_0 yields a line shape like the Pake doublet (Figures 7.8 and 7.10).

7.3.4
Magic Angle Spinning (MAS) NMR

The quadrupolar powder patterns of Figure 7.10 and the chemical shift powder patterns of Figure 7.9 provide much insight into local chemical structure and dynamics. However, if the sample contains two or more different ^{2}H or ^{13}C sites, say, then overlapping patterns can be difficult to interpret. Therefore, we seek a method which can “turn off” the quadrupolar interaction and the chemical shift tensor effects. A clue is obtained from solution NMR; the line widths are much narrower because the rapid molecular tumbling averages the interactions. For the chemical shift tensor, the average is the isotropic chemical shift, δ_{iso}, as introduced in the solution NMR section. For the quadrupolar interaction, the average is zero. Given a solid sample, the question is how to quickly average the orientation of each nuclear site with respect to B_0, and to do so with a simple instrument modification. A clue comes from the orientations of sites detailed in Figure 7.8 and Figure 7.9. At an orientation of 54.7356°, the dipolar and quadrupolar interactions are zero and the chemical shift tensor average is δ_{iso}.

Magic angle spinning (MAS) NMR of solids consists of rapid rotation of the sample about an axis set at 54.7356° relative to B_0. The rotational velocity should be greater than the static (non-spinning) line width. For ^{13}C and $B_0 = 9.4$ T, typical rotation rates are about 10 kHz, that is, 600 000 rpm. At these high rotation rates, the strength of the sample holder (the rotor) is critical, with zirconia a common material. To further reduce stress, the maximum diameter of the rotor is often reduced to 5 mm or less. The drive mechanism is compressed air, and compressed air is also used for all of the bearing surfaces. Obviously, failure of the bearing air supply is very likely to cause destruction of the zirconia rotor and perhaps the rest of the MAS probe.

When the MAS experiment is applied to $I = 1/2$ nuclei such as ^{13}C, ^{29}Si, and ^{31}P, advantage is taken of the ^{1}H spin system, assuming the sample also contains abundant ^{1}H sites. A pulse sequence incorporating dipolar decoupling and cross polarization is used for two reasons: (i) to reduce the ^{13}C, ^{29}Si, and ^{31}P line width because the MAS rotational rate is usually not fast with respect to dipolar coupling (see Figure 7.8 for an example of ^{1}H–^{13}C dipolar coupling) and (ii) to increase the signal-to-noise ratio. More details and examples of the cross polarization-magic angle spinning (CP/MAS) experiment are given in a following chapter.

When the MAS experiment is applied to quadrupolar nuclei such as ^{27}Al, the quality of the NMR spectrum depends dramatically on the magnitude of C_q compared with both the MAS spin rate and the magnetic field, B_0. Excellent spectra are obtained for small C_q sites when studied with high-speed MAS spin rates at high B_0. Conversely, ^{27}Al sites can be "invisible" for high C_q values and modest MAS spin rates and B_0; note the evolution in line shapes for the ^{27}Al MAS NMR spectra in Figure 7.11. Likewise, the four-coordinate AlO_4 sites in an aluminum isoproxide complex, with $C_q = 12.3$ MHz, are observable at 20 kHz and 19.6 T while three-coordinate aluminum sites in related complexes, with $C_q > 30$ MHz, are not observable [14].

7.3.5
T_1 and $T_{1\rho}$ Relaxation

Whenever we talk about spins aligning with B_0, we know that the spin system must release energy. For the ^{1}H spins in a $-CH_3$ group in a 400 MHz NMR spectrometer, the alignment of each ^{1}H will release a 400 MHz quantum of energy. At 400 MHz, the spontaneous release of energy by photon emission is extremely slow; for comparison, the emission of a visible photon from an excited rhodamine dye molecule is much faster. Instead, at 400 MHz, energy release is stimulated by the motion of neighboring magnetic dipole moments, that is, the three ^{1}H spins in a methyl group contribute to the relaxation of each other, provided the methyl group is moving. In most $R-CH_3$ groups, the methyl group rotates quite

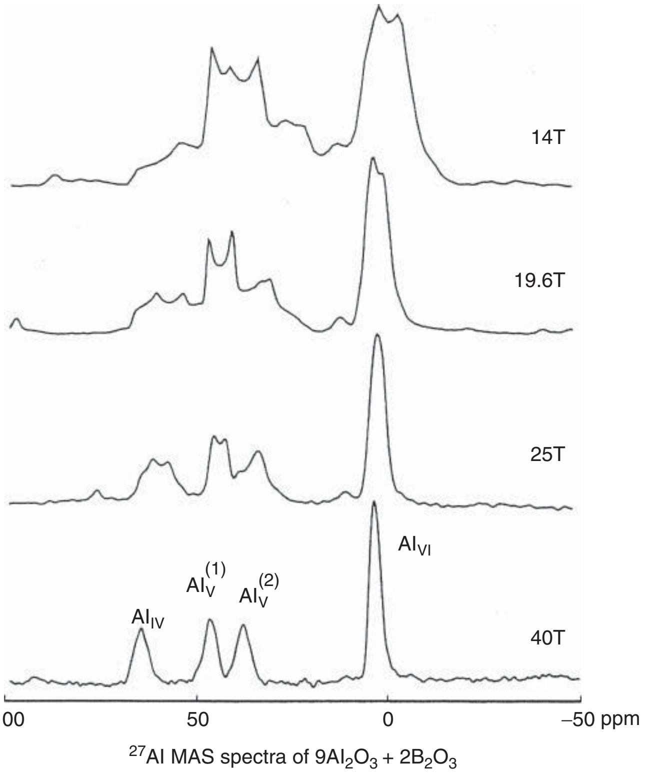

Figure 7.11 ^{27}Al MAS NMR line shapes as a function of magnetic field. The spectra of the ceramic $9Al_2O_3 + 2B_2O_3$ have been acquired with a spin rate of 35 kHz. (Figure courtesy of Dr. Zhehong Gan, National High Magnetic Field Laboratory [15]. Reprinted with permission.)

fast, with rotation rates of the order of gigahertz, and correlation times of the order of picoseconds, at room temperature. At very low temperature, ^{1}H NMR of methyl groups can provide detailed information of motional processes, both classical motion and quantum-mechanical tunneling. In the more common room temperature and -100 to 200 °C experiments, relaxation experiments will probe motions with thermal activation energies of about 5–30 kJ mol^{-1}.

There are many relaxation paths and experiments to measure the relaxation kinetics. Three common relaxation pathways are

- T_1, spin–lattice relaxation. Measures the rate of energy exchange between the spin system and the vibrational and phonon modes of the lattice. Has B_0 dependence.
- T_2, spin–spin relaxation. Measures the loss of coherence of the NMR signal during a FID.
- $T_{1\rho}$, spin–lattice in the rotating frame relaxation. While an on-resonance RF pulse is applied, this parameter is a measure of the rate of energy exchange

between the spin system and the vibrational and phonon modes of the lattice. $T_{1\rho}$ depends upon the magnitude of both B_0 and B_1, where B_1 is the amplitude of the RF pulse.

For common experiments in the solid state, T_1 is critical to determining the length of the experiment. It is possible that raising or lowering the sample temperature can dramatically improve the experimental set-up. Also, in some cases, measurement of T_1 or $T_{1\rho}$ values can yield insight into molecular motion. Shown in Figure 7.12 are idealized T_1 and $T_{1\rho}$ values for three different thermal activation energies. There are several obvious features. The most efficient spin–lattice relaxation, that is, shortest T_1 value, occurs when the correlation time is approximately equal to the inverse of the resonance frequency, $\tau\omega_0 \sim 1$, as listed in Table 7.4. Second, the slopes of the T_1 and $T_{1\rho}$ curves are determined by the activation energy; the plot shows relaxation times for activation energies of 5, 15, and 30 kJ mol^{-1}. Third, when slow frequency motions are suspected, that is, moderate temperatures and high activation energies, then $T_{1\rho}$ experiments at variable B_1 fields are more convenient than switching from magnet to magnet to access T_1 data.

The correlation times shown in Figure 7.13 range from 1 ps to 10 s. The corresponding T_1 and $T_{1\rho}$ values are all accessible given a range of magnets, variable temperature probes, and appropriate RF pulse sequences. Thus, the ability

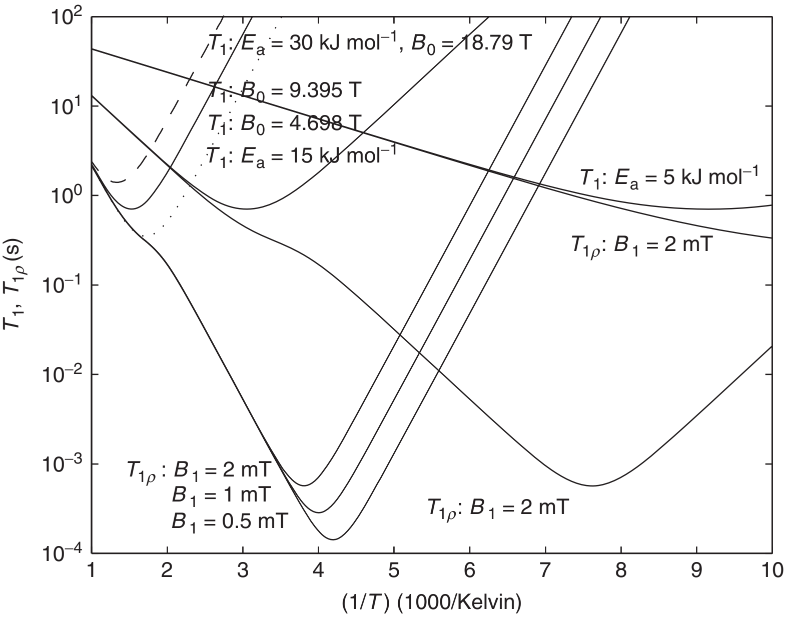

Figure 7.12 Simulated spin–lattice (T_1) and spin–lattice in the rotating frame ($T_{1\rho}$) relaxation times for a ^{1}H moving with respect to the molecular structure, for example, methyl group rotation. Shown here, from left to right, are three sets of curves corresponding to $E_a = 30$, 15, and 5 kJ mol^{-1}. $B_0 = 9.395$ T (^{1}H = 400 MHz) except for T_1 at $B_0 = 4.698$ T (. . .) and 18.79 T (— — —) corresponding to 200 and 800 MHz, respectively.

Table 7.4 Activation energies and temperatures of T_1 minima, correlation times, and magnetic field (given as the resonant frequency in radians per second).

E_a (kJ mol^{-1})	T_{min} (K)	τ_{min} (ps)	ω_0 (10^9 rad s^{-1})
30	750	120	5.0265
30	660	240	2.5133
30	580	500	1.2566
15	330	240	2.5133
5	110	240	2.5133

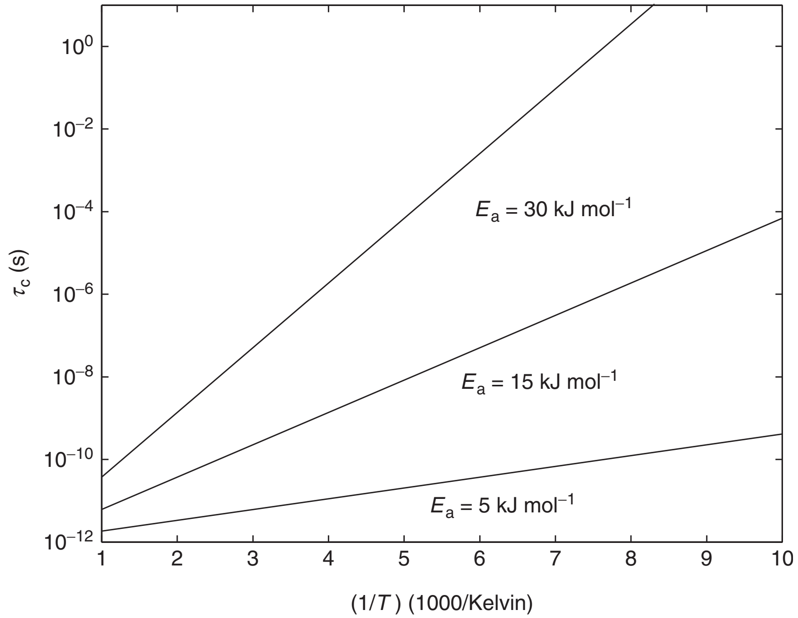

Figure 7.13 Correlation times used to generate the T_1 and $T_{1\rho}$ values of the previous figure from the Arrhenius relationship $\tau = \tau_0 \exp(-E_a/RT)$ where $\tau_0 = 10\text{–}12$ s.

of NMR to measure dynamic processes is quite powerful; quick survey experiments can be done with any NMR signal and more detailed studies can be done with specifically labeled samples. To return to the SAM samples, compound *E* of Figure 7.7 may be expected to show two T_1 minima, the first in the range of 10–50 K corresponding to thermal activation of methyl group rotation and a second minimum at higher temperature due to a larger motion of the alkyl chain. There is one significant problem with the use of relaxation methods to monitor kinetic processes: while the rate constants and activation energies can be measured, often the mode of motion is not clearly determined. In the case of compound *E*, the higher temperature minimum could be assigned to a simple motion at the end of the alkyl chain or to a cooperative motion of all of the alkyl chains. With only relaxation methods, the mode of motion remains ambiguous.

7.3.6
Dynamics

In solid-state NMR, a common technique for measuring the rate of molecular motion, and the mode of motion, is ^{2}H NMR. For C–^{2}H bonds, the value of C_q is usually known, and for a static system yields a predictable powder pattern. Recall that each orientation of the C–^{2}H bond with respect to B_0 yields a discrete pair of transition frequencies. If the C–^{2}H bond orientation should change, then the transition frequencies may change. For modes of motion such as methyl group rotation, the transition frequencies average to new values, but still offset from the Zeeman frequency. With increasing rate of methyl group rotation, the ^{2}H NMR evolves smoothing to a new, motionally averaged, line shape, as shown in Figure 7.14. For compound D (Figure 7.7), this experiment could show the onset of fast methyl group rotation and then the onset of more complex molecular motions such as chain motion or migration of the chain across the surface.

Solid-state ^{2}H NMR is, among techniques that measure molecular motion, capable of measuring an extremely wide range of motional rates. When ^{2}H T_1 measurements are included, rate constants of more than 10 orders of magnitude are accessible. In addition to methyl group rotation, the combination of deuteration

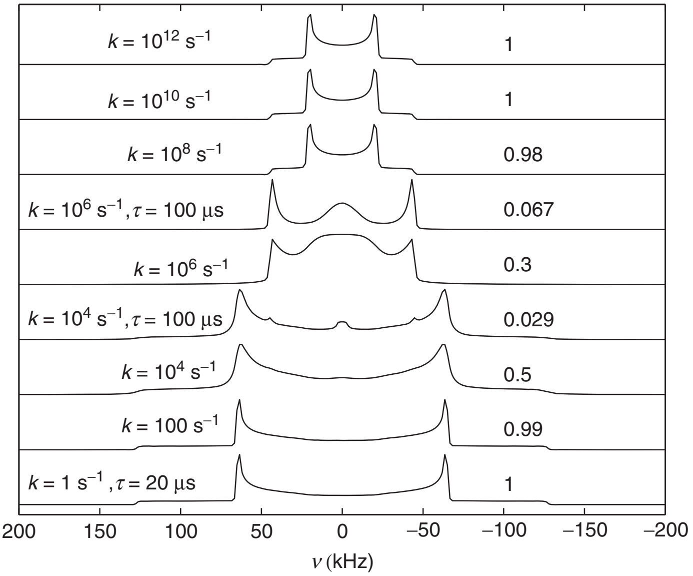

Figure 7.14 Simulated ^{2}H NMR line shapes of a methyl group as a function of methyl group rotation rate, k. The interpulse spacing, τ, is 20 μs, unless otherwise specified. The relative amplitudes of each spectrum are given on the right.

and solid-state ^{2}H NMR has yielded molecular dynamic information on phenyl groups, aliphatic chains, and ethene bound to transition metal centers.

7.4
Imaging

MRI is NMR spectroscopy with magnetic field gradients applied to the sample. Thus, every volume element within a sample can be exposed to a specific magnetic field. As RF and magnetic fields can penetrate many samples, NMR is a widely applicable imaging technique. However, the most convenient NMR imaging methods work only with narrow NMR resonances, such as the ^{1}H NMR resonances of water and lipids or the ^{3}He and ^{129}Xe resonances of helium and xenon [8].

In any imaging experiment, the critical issues are sample preparation, image contrast, spatial resolution, field of view, and total time of the experiment. Relative to other imaging techniques, the NMR spectroscopists's control over the image contrast mechanisms is exceptional. Of course, MRI images are affected by the number of nuclei in each volume element. In addition, the NMR relaxation dynamics, T_1 and T_2, can be used to control image contrast, especially for the soft tissues in the human body. Sample preparation is perfectly simple for the patient: remove metal objects and lie still. For inanimate objects, sample preparation of this simplicity enables many unique experiments: variable temperature, variable pressure and/or flow, and measurements as a function of time. The other NMR interactions discussed earlier find modest applications in MRI. The chemical shift interaction is used in ^{31}P MRI of muscle tissue to monitor metabolism via phosphocreatine/ATP concentrations.

An MRI pulse sequence, spin–warp, is shown here as a 2D imaging sequence (Figure 7.15). An initial ^{1}H 90_x pulse converts ^{1}H z-magnetization to magnetization aligned with the y'-axis of the rotating frame. In this chapter, this is the first NMR pulse sequence to be described with the rotating frame concept. The description

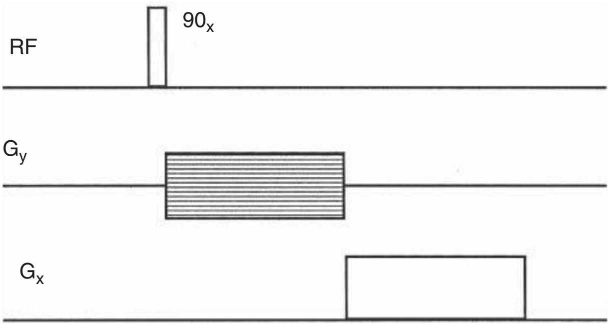

Figure 7.15 Spin–warp pulse sequence for 2D imaging. In successive experiments, the amplitude of G_y is varied while the amplitude of G_x is fixed. The NMR signal is acquired during the application of G_x.

of other pulse sequences, such as two pulse sequences used for T_1 and T_2 measurement are given in many textbooks. We chose the rotating coordinate system to have B_0 parellel to the z-axis; the x' and y' axes are chosen to be synchronized with the RF frequency of the initial pulse in a pulse sequence. The primes denote the two moving axes; primes are generally omitted from labels such as "90_x" because it is understood that the RF pulse is referenced to the rotating coordinate system.

To visualize the effect of a pulse sequence with the rotating frame description, one makes the following assumptions:

- The magnetization vector, $\boldsymbol{M}$, represents the vector sum of all the magnetic moments in the sample.
- The coordinate system chosen is rotating about an axis parallel to B_0 at a rate equal to the ^{1}H resonance frequency.
- In the rotating frame, the initial orientation of $\boldsymbol{M}$ is along the $+z$ axis (denoted as $\boldsymbol{M}_z$) and a 90_x pulse results from the application of a magnetic field along the x'-axis (denoted as B_{1x}).
- The motion of $\boldsymbol{M}_z$ in response to B_{1x} is a torque which causes $\boldsymbol{M}$ to precess toward the y'-axis. Of course, when $\boldsymbol{M}$ is aligned with the y'-axis, the RF pulse is terminated. Then, $\boldsymbol{M}'_y$ will stay aligned with the y-axis until: (i) its resonance frequency changes or (ii) another RF pulse is applied to the sample.
- The detected NMR signal is described with complex numbers. M'_y is positive, real, and magnetization along the x-axis, M'_x, is imaginary. Note: when pulse sequences are analyzed in greater detail, and with more regard to sign conventions, the axis labels will change. Nevertheless, the rotating frame model remains quite useful.

A hypothetical sample is shown in Figure 7.16. This sample has five spins at $x = -3$, $y = +2\,\text{cm}$ and one spin at $x = 1$, $y = 0\,\text{cm}$. We assume that all spins will, in the absence of any magnetic field gradients, have exactly the same resonance frequency. The evolution of the magnetization in the rotating frame illustrates how the sample spin density distribution is imaged.

Shown in Figure 7.17 are plots of $\boldsymbol{M}_x$ and $\boldsymbol{M}_y$, starting immediately after the 90_x pulse of the spin–warp 2D imaging pulse sequence. For $G_y = 0\,\text{mT}\,\text{m}^{-1}$ (Figure 7.17a), magnetization stays aligned with the $+y$ axis for 10 ms; the resonant frequency is exactly equal to the rotating frame frequency. Then, with the application of the G_x gradient, the resonant frequency changes for spins at sample sites with nonzero x-coordinates. For $G_y = +0.1175\,\text{mT}\,\text{m}^{-1}$ and $y = +2\,\text{cm}$, the change in resonant frequency is $+100\,\text{Hz}$,

$$\Delta\nu = \frac{\gamma}{2\pi}\Delta^{\chi} G_y = (42.57\,\text{MHz}\,\text{T}^{-1})(+0.02\,\text{m})(+0.1175\,\text{mT}\,\text{m}^{-1}) = +100\,\text{Hz} \tag{7.11}$$

creating the sinusoidal dependence in the magnetization along the y-axis (rotating frame) in Figure 7.17b, and, separated in phase by ±90°, a component along the x-axis. An even larger gradient increases the offset frequency. The phase of the

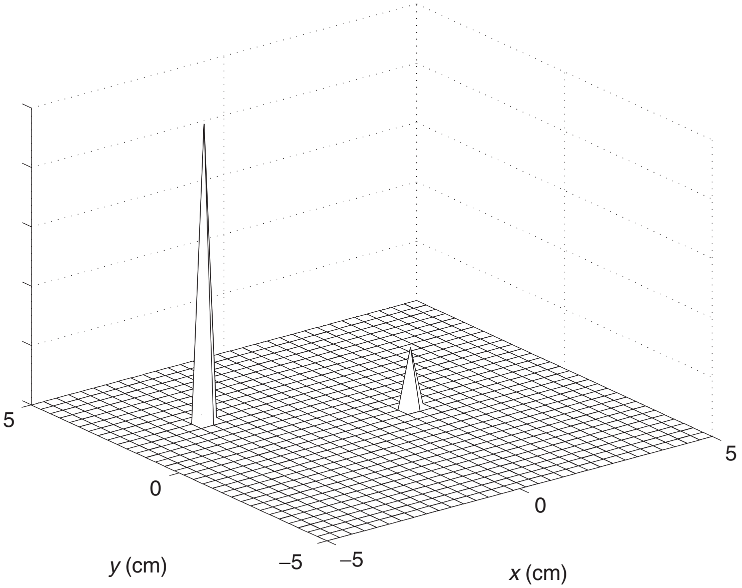

Figure 7.16 Hypothetical sample with five ^{1}H nuclei at $x = -3$, $y = 2$ cm, and one ^{1}H nucleus at $x = 1$, $y = 0$ cm.

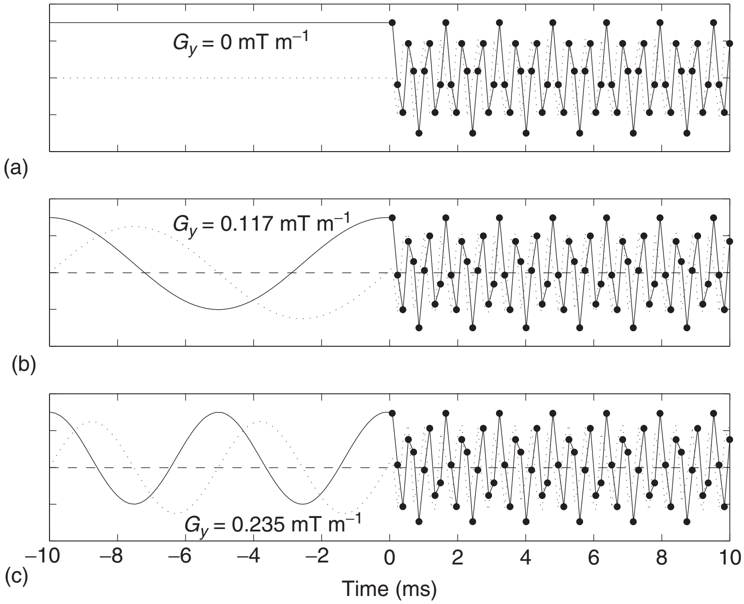

Figure 7.17 (a–c) Magnetization in the rotating frame: $\boldsymbol{M}_y$ (—) and $\boldsymbol{M}_x$ (. . .). The acquired data (●) is taken during the application of the G_x gradient.

imaginary component changes by 180° for $G_y < 0\,\mathrm{T\,m^{-1}}$ or sample position <0 cm. The digitized values are indicated (•) in Figure 7.17 and again, the frequency of the signal depends upon G_x and the location of the spins in the sample. A complete 2D spin–warp experiment consists of 2^n different values of G_y and, for each G_y value, a digitized FID with 2^n data points.

For the purpose of image filtering, a smoothing function is often applied to the 2D FID data set. Shown in Figure 7.18 is the smoothed 2D FID data array (real component). This surface plot shows both the oscillation set by G_x and the variable phase of that oscillation set by G_y. This last point, the phase encoding by a pulse or gradient, is a key feature of multidimensional NMR experiments.

Lastly, 2D Fourier transformation of the smoothed 2D FID data set yields the image (Figure 7.19), which corresponds quite well to the original distribution of spin density through the field of view.

Besides the spin–warp sequence, the echo planar sequence is widely used in biomedical applications. Figure 7.20 shows an image recently acquired of a young girl's sprained knee. The instrument used a permanent magnet system configured to reduce the claustrophobic feeling of a more traditional solenodial magnet.

Besides imaging, pulsed magnetic field gradients are also used to study self-diffusion of solutes and solvents. Basically, the pulsed field gradients ''encode'' a structure on the spin system, and the evolution of this structure yields the rate of translational motion in the solution. Since magnetic field gradients can be quite large and the time of application can be of the order of milliseconds,

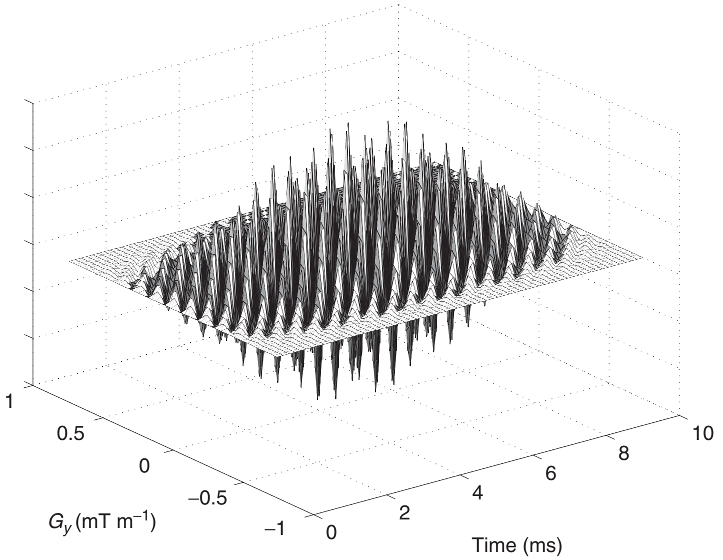

Figure 7.18 The real (M_y) component 2D FID data set after smoothing with a sine function. The oscillation frequency along the time axis is set by G_x and the initial phase of each oscillation is set by G_y.

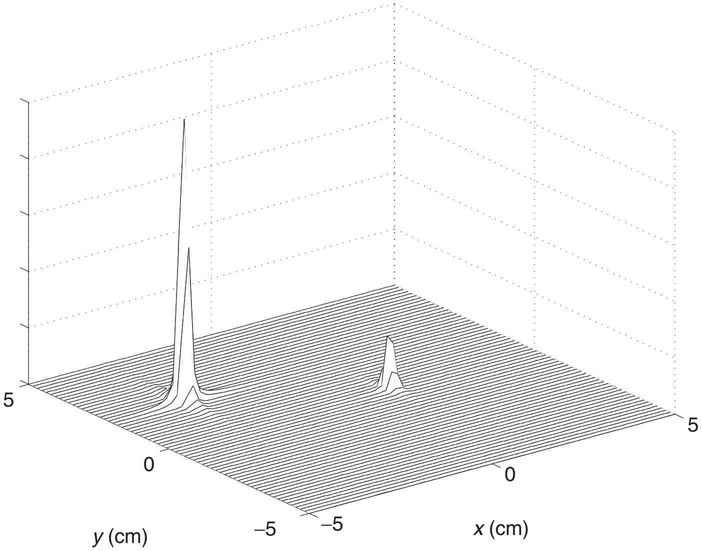

Figure 7.19 The MRI image, obtained by 2D FFT of the smoothed 2D FID array.

Figure 7.20 An MRI image of a knee. The high-intensity region shows a small amount of fluid concentration following a sprain.

the structure can be created at sub-micron resolution. Therefore, quite small translational motions are measured.

7.5
3D NMR: The HNCA Pulse Sequence

Multiple pulse NMR sequences for the solution state can be modeled with either product operator or density matrix calculations. Here, we use the latter for analyzing a pulse sequence for three-dimensional NMR, the HNCA pulse sequence. The HNCA pulse sequence is used to establish connectivity between the amide hydrogen, the amide nitrogen, and the α-carbon in an amino acid in a polypeptide sequence. The detected ^{1}H NMR signal shows a modulation that is dependent upon $^1J(^1\mathrm{H}{-}^{15}\mathrm{N})$ and $^2J(^1\mathrm{H}{-}^{13}\mathrm{C})$, a modulation thay will be simulated with density matrix calculations. Because a polypeptide has many amide hydrogens, amide nitrogens, and α-carbons, a necessary step for assigning the NMR spectra is identifying neighboring atoms. Fortunately, these three nuclei are coupled by unique and nearly uniform *J*-coupling constants (Figure 7.21).

The HNCA pulse sequence has groups of three pulse sequences optimized for the *J*-coupling constants. The rotating frame description can be applied to parts of the pulse sequence (Figure 7.22), but is insufficient to describe the entire sequence. With tools such as Mathematica or Matlab, it is straightforward to simulate the pulse sequence (Figure 7.23). These tools allow for the evaluation of the exponent of a Hermitian matrix, a common step in time-dependent quantum mechanics.

In this 3D NMR pulse sequence, two time increments, t_1 and t_2, are successively incremented. Because of the *J*-coupling, each time increment leads to a modulation of the detected ^{1}H NMR signal. Shown here (Figure 7.24) are simulated ^{1}H NMR spectra acquired at various time increments. A large array of these spectra, processed in total by 3D FFT (fast Fourier transform), will lead to a cube of data, which is typically analyzed slice by slice.

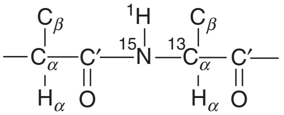

$^1J(^1\mathrm{H}{-}^{15}\mathrm{N}) = +90$ Hz

$^2J(^1\mathrm{H}{-}^{13}\mathrm{C}_\alpha) = +11$ Hz

Figure 7.21 A portion of a polypeptide structure focusing on the amide hydrogen and α-carbon.

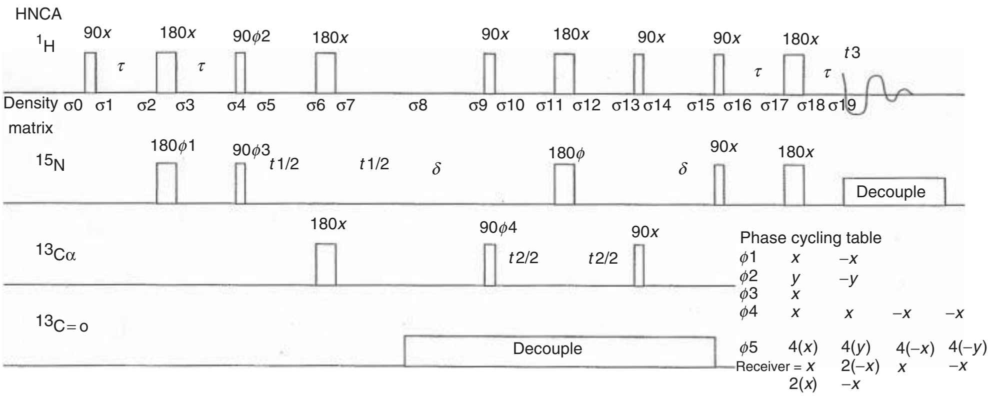

Figure 7.22 The HNCA 3D NMR pulse sequence. The objective is to correlate the detected ^{1}H NMR signal of an amide hydrogen with adjacent ^{15}N and $^{13}\mathrm{C}_\alpha$ sites. The labels below the ^{1}H RF pulses refer to density matrices used in the pulse sequence simulation.

$U = \text{MatrixExp}\,[\frac{-\pi}{2}\,\mathrm{i} \times S_{xH}]\;;$

$\sigma 1 = U.\ \sigma 0\ .\ \text{Transpose [Conjugate [U]]}\;;$

$\text{Hinteraction} = -\,(V_{H} - V_{HRef})\,S_{zH} - (V_{N} - V_{NRef})\,S_{zN} - (V_{c}\ \text{-}\ V_{CRef})\,S_{zC}$
$+\,J_{HN}\,(S_{zH}\,.\,S_{zN}) + J_{NC}\,(S_{zN}\,.\,S_{zC})\;;$
$U = \text{MatrixExp}\,[-\mathrm{i} \times (2\,\pi\,\tau) \times \text{Hinteraction}\ ]\;;$
$\sigma 2 = U\ .\ \sigma 1\ .\ \text{Transpose [Conjugate [U]]}\;;$

$\text{Hpulse} = -\pi\,\mathrm{i} \times S_{xH} + -\pi\,\mathrm{i} \times \phi 1;$
$U = \text{MatrixExp [Hpulse]}\;;$
$\sigma 3 = U\ .\ \sigma 2\ .\ \text{Transpose [Conjugate [U]]}\;;$

$U = \text{MatrixExp}\,[-\,\mathrm{i} \times (2\,\pi\,\tau) \times \text{Hinteraction}]\;;$
$\sigma 4 = U\ .\ \sigma 3\ .\ \text{Transpose [Conjugate [U]]}\;;$

Figure 7.23 A brief portion of a Mathematica program used to simulate the HNCA pulse sequence. With an analysis such as this, it is possible to follow the basic features of a complex pulse sequence, in particular, how the detected signal changes with the magnitude of the *J*-coupling constants. The complete program is long, but repetitive, with commands as shown above repeated from the first pulse to the last pulse.

NMR of proteins uses a suite of 2D and 3D NMR pulse sequences like HNCA with the objective of acquiring connectivity information. Besides the signal-to-noise ratio for the detected signal, other issues are the separation of one ^{15}N resonance from another, and likewise, the separation of one $^{13}C_{\alpha}$ resonance from another. The S/N and resolution issues both push the experiment to higher and higher magnetic fields.

7.6
Conclusion

NMR spectroscopy is a very effective method to examine the interactions between nuclei and their environments. NMR spectra yield information that can be used to determine the structure of complex organic, organometallic, and biological molecules as these structures exist in solution. For similar molecules in the solid state, the hierarchy of dominant NMR interactions changes, and other information becomes available, yielding more emphasis on chemical bonding and molecular dynamics. The application of magnetic field gradients enables imaging experiments such as MRI and self-diffusion measurements. The NMR interactions are well-described by time-independent and time-dependent quantum mechanics.

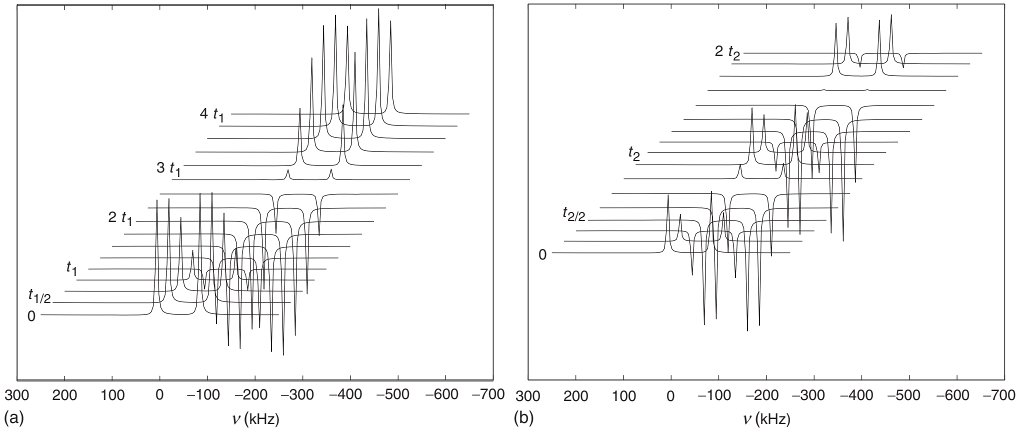

Figure 7.24 Simulated amide ^1H NMR spectra from an HNCA pulse sequence, shown here without ^{15}N decoupling. (a) The ^1H NMR signal as a function of t_1 evolution, and (b) t_2 evolution. These evolutions will only be seen for ^1H *J*-coupled to ^{15}N and ^{13}C.

References

1. Abragam, A. (1961) *The Principles of Nuclear Magnetism*, Oxford University Press, Oxford.
2. Grant, D.M. and Harris, R.K. (eds) (1996) *Encyclopedia of Nuclear Magnetic Resonance*, John Wiley & Sons, Ltd, Chichester.
3. Becker, E.D. (1999) *High Resolution NMR: Theory and Chemical Applications*, 3rd edn, Academic Press, New York.
4. Evans, J.N.S. (1995) *Biomolecular NMR Spectroscopy*, Oxford University Press, Oxford.
5. Friebolin, H. (1998) *Basic One- and Two-Dimensional NMR Spectroscopy*, 3rd edn, John Wiley & Sons, Ltd, Chichester.
6. Braun, S., Kalinowski, H.-O., and Berger, S. (1998) *150 And More Basic NMR Experiments: A Practical Course*, 2nd edn, John Wiley & Sons, Ltd, Chichester.
7. Sanders, J.K.M. and Hunter, B.K. (1993) *Modern NMR Spectroscopy: A Guide for Chemists*, Oxford University Press, Oxford.
8. Ernst, R.R., Bodenhausen, G., and Wokaun, A. (1987) *Principles of Nuclear Magnetic Resonance in One and Two Dimensions*, Oxford Science Publications, Oxford.
9. Croasmun, W.R. and Carlson, R.M.K. (eds) (1994) *Two-Dimensional NMR Spectroscopy: Applications for Chemists and Biochemists*, 2nd edn, John Wiley & Sons, Ltd, Chichester.
10. Fukushima, E. and Roeder, S.B.W. (1981) *Experimental Pulse NMR a Nuts and Bolts Approach*, Addison-Wesley, Reading, MA.
11. Stejskal, E.O. and Memory, J.D. (1994) *High Resolution NMR in the Solid State: Fundamentals of CP/MAS*, Oxford University Press, Oxford.
12. Schmidt-Rohr, K. and Spiess, H.W. (1997) *Multidimensional Solid-State NMR and Polymers*, Academic Press, New York.
13. Butler, L.G. and Keiter, E.A. (1994) *J. Coord. Chem.*, **32**, 121–134. (Note: Eq. (4) is missing plus signs.).
14. Bryant, P.L., Harwell, C.R., Mrse, A.A. *et al.* (2001) *J. Am. Chem. Soc.*, **123**, 12009–12017.
15. Cron, Z., Gorikov, P., Cross, T.A., Samoson, A., and Massiot, O. (2002) *J. Am. Chem. Soc.*, **124**, 5634–5635.

8

Solution NMR Spectroscopy

Gary E. Martin, Chad E. Hadden, and David J. Russell

8.1

Introduction

NMR, or nuclear magnetic resonance spectroscopy, affords one of the richest sources of molecular connectivity information available to the structural chemist. Since the inception of NMR, which originated as a curiosity of the physicist when the principle was first discovered just over 50 years ago [1, 2], the discipline has gone on to become universally recognized for its unique capability to precisely define molecular structures through a variety of fundamental parameters. It is entirely safe to say that NMR has become the cornerstone technique for the elucidation of chemical structure.

The fundamental parameters of the NMR experiment have been covered in a previous chapter and will be mentioned here only briefly. Structure elucidation by NMR at the simplest level may simply entail a comparison of the chemical shifts of the molecule of interest with a database library of chemical shift information. Commonly studied nuclides include, ^{1}H, ^{13}C, ^{19}F, and ^{31}P for organic molecules; less commonly, for reasons of sensitivity, other nuclides such as ^{15}N may be investigated. In addition to the nuclides just cited, which are of primary interest to investigators working with organic and bio-organic molecules, studies of the diverse array of metallic nuclides that comprise the periodic table are also possible [3–12]. The assumption will be made that individuals reading this chapter have the ability to utilize NMR chemical shift data bases and we will thus focus our attention on the utilization of experiments that ‘‘exploit’’ fundamental NMR parameters. At the next level of complexity, an investigator is likely to take an interest in scalar (J) spin coupling interactions between appropriate nuclide pairs, which may include ^{1}H–^{1}H, ^{1}H–^{13}C, or more recently ^{1}H–^{15}N. Homo- or heteronuclear scalar (through bond) couplings may either be directly observable, probed by decoupling techniques, or alternatively, they may provide the basis for performing homo- or heteronuclear chemical shift correlation experiments. On a similar plane are through-space connectivity and molecular motion measurements such as the nuclear Overhauser effect (NOE), molecular diffusion measurements, and others.

Handbook of Spectroscopy, Second Edition. Edited by Günter Gauglitz and David S. Moore.

A convenient collection of explanations of some of the terminology of NMR spectroscopy to which some may wish to refer is the monograph, *A Handbook of Nuclear Magnetic Resonance*, by Freeman [13]. In addition, there are also numerous monographs dealing with various aspects of NMR that have appeared over the last 10–15 years that are worthy of note [14–32]. Those cited are by no means intended to be an exhaustive compilation, but rather are those volumes that the authors have found useful.

Beyond simple one-dimensional (1D) NMR spectra, users will generally begin to consider multidimensional NMR experiments. Such experiments allow the segregation of information between two discrete frequency domains. The earliest two-dimensional (2D) NMR experiments were homonuclear experiments in which both frequency domains were used for proton chemical shift information. Here, the scalar coupling between two protons in a chemical structure is exploited to generate off-diagonal responses in a diagonally symmetric data matrix (spectrum) to correlate protons to one another in a fashion analogous to correlating proton resonances with homonuclear decoupling. These experiments are called COSY experiments, which is an acronym for correlated spectroscopy. A diverse array of 2D NMR experiments exist in which proton chemical shift information may be relegated to one axis while ^{13}C or even ^{15}N chemical shift information may be on the other axis of the experiment, to give just two examples. These techniques will be treated following the presentation of simpler, 1D NMR methods.

8.2
1D (One-Dimensional) NMR Methods

The simplest 1D NMR experiments involve the application of a pulse followed by observation of the resulting signal in the time domain, with subsequent Fourier transformation of the data to the frequency domain for presentation in a format that we, as chemists, can understand. Pulsed NMR methods had their inception in 1966 [33] and have almost completely supplanted earlier continuous wave (CW) methods. For reasons of sensitivity, only ^{1}H 1D NMR spectra were typically acquired prior to the 1970s. The advent of pulsed Fourier transform NMR instruments made it possible to acquire natural abundance ^{13}C NMR spectra on a routine basis in the early 1970s. With the routine availability of ^{13}C NMR data came the compilation of chemical shift data bases and a very different way of approaching chemical structure elucidation.

We will briefly consider in this section various aspects of homonuclear spin-decoupling experiments and nuclear Overhauser effect (NOE) difference spectra. Obviously any detailed treatment is far beyond the size limitations of this chapter. Moving next to 1D ^{13}C NMR techniques, we will briefly consider the utilization of selective population transfer (SPT) and experiments which rely on these principles such as insensitive nuclei enhanced by polarization transfer (INEPT) and distortionless enhancement by polarization transfer (DEPT), off-resonance proton decoupling techniques, decoupler gating experiments, and finally spin–lattice or T_1 relaxation techniques, which also have application to proton NMR spectroscopy in many instances to establish acquisition parameters for 2D NMR experiments, and so on.

8.2.1
Proton Spin Decoupling Experiments

Proton spins interact with one another through scalar (J) coupling mechanisms. These processes give rise to the familiar multiplets seen in proton spectra, for example, the quartet for the methylene and a triplet for the methyl signal of an ethyl group. In the case of simple molecules, spin multiplets are likely to be well separated. Alphabetically, a system of two sets of spins that are widely separated, that is, $\Delta\nu \gg J$ (where $\Delta\nu$ is the difference in the chemical shifts of the two spin-coupled nuclides) will be referred to as an *AX spin system*. Such a system is also referred to as a *first order spectrum*. As molecular complexity increases, spectral congestion generally increases in parallel. With increasing spectral congestion, chemical shift differences between coupled spins frequently decrease. As $\Delta\nu$ begins to become comparable to J, spin systems become less first order in nature, making spectral interpretation by visual inspection progressively more difficult.

Prior to the advent of 2D NMR methods in the mid-1970s, it was common to use spin decoupling as a method of deciphering which proton was coupled to another, the second located perhaps in a congested region of a spectrum. This experiment uses radiofrequency (RF) irradiation, at a frequency coinciding with a proton resonance of interest, to alter the spectral response of the protons coupled to the target resonance. As a function of the strength of the RF field applied, a range of phenomena can be observed. In order of increasing RF field strength, one begins from selective population transfer (SPT) in which a single resonance line of a multiplet, or a ^{13}C satellite resonance for that matter, is selectively irradiated without perturbing other resonance lines of the same multiplet. A more intense field will give a result known as *spin tickling*. The interested reader is referred to the monograph of Freeman [13] for a discussion of this phenomenon. At higher RF field strength complete spin-decoupling occurs. Applying RF irradiation at this field strength to a proton that is resolved will collapse the scalar coupling(s) of the proton(s) to which the irradiated proton is J-coupled. Spin decoupling is well documented in any of the monographs cited above, and the interested reader is referred to these sources for further discussion. If an investigator can see the collapsed spin multiplets by simple visual inspection of the resulting spectrum, he or she is finished and can move on with the investigation of the structure. In more complex spectra, the location of the protons affected by the irradiation of one proton may not be easily discerned. In such cases, one may wish to resort to decoupled difference spectra.

8.2.2
Proton Decoupled Difference Spectroscopy

Difference spectroscopy, as the name implies, requires spectral subtraction. Two spectra are acquired. One in which the proton of interest is decoupled and a second reference spectrum in which the irradiation is applied in an isolated region far from the nearest proton resonance. The two spectra are then subtracted from one another, the resulting difference spectrum highlighting protons that were affected by the decoupling process [34]. Several excellent examples of applications of this technique are found in the monograph by Nakanishi [24].

8.2.3
Nuclear Overhauser Effect (NOE) Difference Spectroscopy

The nuclear Overhauser effect or NOE is a spatial phenomenon involving two magnetically active nuclides in close proximity. Generally, we think of these experiments in terms of $^1H-^1H$ interactions, but heteronuclide pairs also exhibit these effects. In the $^1H-^1H$ homonuclear case, given two protons in spatial proximity that are not coupled to one another through bonds, the irradiation of one proton (saturation) will lead to an observable enhancement in the signal of the neighboring proton through dipolar cross-relaxation mechanisms. Simplified in the extreme, this is the nuclear Overhauser effect or an NOE. Two excellent monographs treat these experiments in considerable detail. The aging volume by Noggle and Schrimer [35], while dated, is still an excellent reference. The more recent and comprehensive monograph by Neuhaus and Williamson [36] is probably the best source of information on the NOE currently available.

While homonuclear NOEs may range to as great as 50% enhancements of signal intensity, it is much more common to observe NOEs of only a small percentage. Visually observing perhaps what may only be a 2–3% enhancement of the intensity of a signal is very difficult. In contrast, by using a difference approach, in which only signals enhanced by a given irradiation remain in the spectrum, it is a facile process to determine which protons exhibit a NOE when a neighbor is irradiated. The principle is the same as that used in preparing difference-decoupled spectra. Two spectra are acquired, one in which the proton of interest is irradiated and a second in which the irradiation is in an isolated region of the spectrum. The reference spectrum is subtracted and the difference spectrum is examined. Applications for the use of NOEs are widely varied. NOEs may be used to determine stereochemical relationships, to measure distances between a pair of protons, and for many other purposes. The interested reader is referred to the monographs cited above for further information and examples.

8.2.4
Selective Population Transfer (SPT)

Applying RF fields of lower intensity to selectively perturb a single resonance or satellite line is the basis of the SPT or selective population transfer experiment. Perhaps the most interesting example of the utilization of SPT experiments, which form the basis for the INEPT, DEPT, and other spectral editing experiments that have been developed, is found in the consideration of an AX heteronuclear spin system, for example, $^1H-^{13}C$ or $^1H-^{15}N$ where the heteronuclear spin is insensitive relative to the proton. The energy level diagram for such a spin system will have four transition lines corresponding to the four resonance lines in the spectra of the two nuclides; the proton resonance will be a doublet due to $^{n}J_{CH}$. The observed ^{1}H spectrum will consist of three lines, actually, the central line comprising ~98.9% of the total resonance intensity will arise from $^{1}H{-}^{12}C$; the ^{13}C satellite lines will be separated from the central resonance by $\pm ^{n}J_{CH}/2$, and will have an aggregate intensity of ~1.1%. Based on the gyromagnetic ratios of the heteronuclides, γ_H and γ_C in this case, the four transitions associated with the energy level diagram of this heteronuclear AX spin system can be assigned numerical values. In the case of the Boltzmann equilibrium state, the two resonance lines for ^{13}C will each have an intensity of +1. By selectively inverting one of the proton transitions, and then sampling the perturbed system, the ^{13}C resonance can be observed with transition intensities of +5 and −3 (this special case is termed spin population inversion (SPI)). This signal enhancement is the basis for the sensitivity improvements obtained with the INEPT and DEPT experiments. SPT has also been employed as a means of making resonance assignments. Nagel *et al.* [37] have reported an excellent example in the course of determining the structure of the complex alkaloid oxaline. When this technique is applied to ^{15}N, even larger enhancement of the involved resonances is observed because of the greater difference between the gyromagnetic ratios of ^{1}H and ^{15}N.

8.2.5
J-Modulated Spin Echo Experiments

While the SPT experiment has obvious utility, it is cumbersome to use unless the selective nature of the experiment is specifically being exploited for structure elucidation purposes. A group of experiments that may be categorized as *J*-modulated spin echo experiments allows the simultaneous investigation of the entire spectrum. As the name of this group of experiments implies, they utilize a spin echo of the type shown in Eq. (8.1), over which a scalar coupling driven process (using $^{1}J_{CH}$ most commonly) is superimposed:

$$\tau - 180^{\circ} - \tau \tag{8.1}$$

Experiments that fall into this category include INEPT, DEPT, and APT (attached proton test). These experiments are discussed in considerable detail in any of the monographs cited in the Introduction to this chapter to which the interested reader is referred. Below, we will focus briefly on the INEPT and DEPT experiments since these are conceptually useful for the development of 2D heteronuclear shift correlation spectroscopy.

8.2.5.1 INEPT (Insensitive Nucleus Enhancement by Polarization Transfer)

While the SPT method, as the name indicates, is a selective experiment, techniques derived from the principle of population transfer of a non-selective nature are also available. The first of these to appear was the INEPT experiment [38]. The pulse sequence schematics for INEPT and refocused INEPT are shown in Figure 8.1.

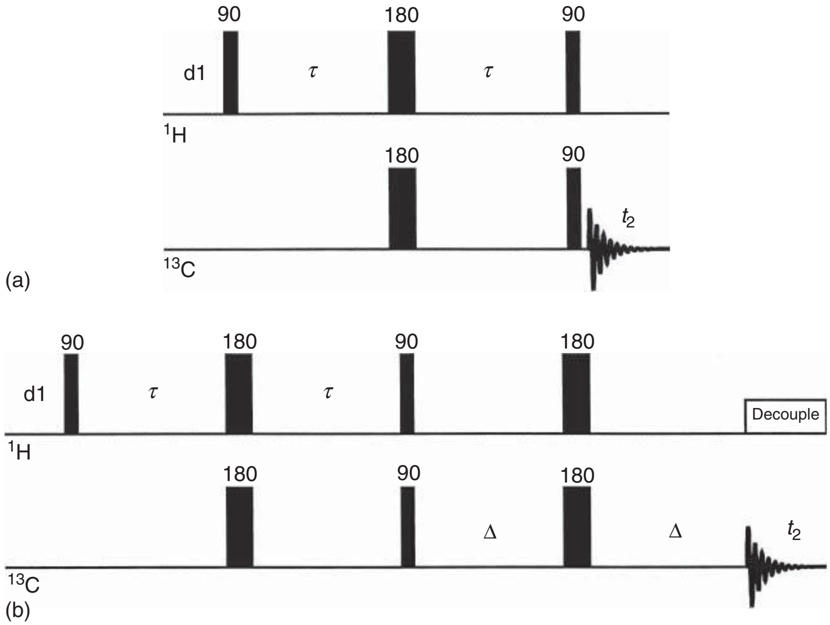

Figure 8.1 (a,b) Pulse sequences for the INEPT and INEPT-R experiments [38–40]. These experiments rely on spin population transfer (SPT) and provide the means of detecting ^{13}C or other insensitive nuclides with enhanced sensitivity.

As with the SPT experiment described above, INEPT and its successor, the DEPT experiment, both operate with enhanced sensitivity through the perturbation of the Boltzmann populations. This prototypical non-selective experiment is now relatively seldom used as more refined variants have been developed. The INEPT experiment ($\tau = (4J)^{-1}$, Figure 8.1a) generates antiphase responses analogous to those observed with SPT experiments. The antiphase components of magnetization can, however, be refocused by adding a delay of 2Δ with a ^{1}H/^{13}C 180° pulse sandwich in the center of the interval where $\Delta = 1/x^{n}J_{\mathrm{CH}}$ ($x = 4$–8) [39, 40]. This modification, since the antiphase components of magnetization are refocused, also allows the utilization of broadband decoupling during acquisition.

8.2.5.2 **DEPT (Distortionless Enhancement Polarization Transfer)**

The next level of refinement in non-selective polarization transfer experiments was the DEPT experiment developed by Doddrell and co-workers [41, 42]. The DEPT pulse sequence schematic shown in Figure 8.2 employs a variable flip angle read pulse, θ, as the last proton pulse of the sequence. By varying the flip angle of this pulse, edited subspectra based on resonance multiplicity (CH, CH_2, and CH_3) can be readily generated. When $\theta = 45^\circ$, a spectrum in which all protonated carbons have positive intensity is produced; quaternary carbons are suppressed and absent. When $\theta = 90^\circ$, only methine carbons are observed and have positive intensity. Finally, when $\theta = 135^\circ$, a spectrum in which methine

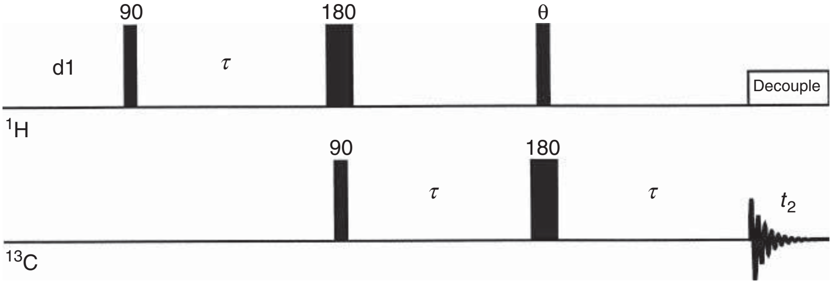

Figure 8.2 Pulse sequence for the DEPT experiment [41, 42]. By adjusting the variable flip angle read pulse, θ, it is possible to generate edited subspectra based on resonance multiplicity (CH, CH_2, and CH_3). When $\theta = 45°$, all protonated carbons will exhibit positive intensity. When $\theta = 90°$, only methine carbons are observed and have positive intensity. When $\theta = 135°$ a spectrum is produced in which methine and methyl resonances have positive intensity while methylene resonances have negative intensity. Plotting the $\theta = 90°$ spectrum gives a methane-only subspectrum; the difference spectrum obtained by subtracting the $\theta = 135°$ spectrum from the $\theta = 45°$ spectrum gives a methylene-only spectrum; finally, a methyl-only spectrum can be generated by adding the experimental results of the $\theta = 45°$ and 135° experiments. An example of the edited subspectra of a model compound are shown in Figure 8.3.

and methyl resonances have positive intensity while methylenes are negative is obtained. Given these three spectra, plotting the result with $\theta = 90°$ gives a CH-only spectrum. Plotting the difference spectrum obtained by subtracting the $\theta = 135°$ spectrum from the $\theta = 45°$ spectrum gives a methylene-only spectrum. A methyl-only spectrum can be generated by adding the results of the $\theta = 45°$ and 135° experiments and subtracting the result of the $\theta = 90°$ experiment. Simple subtraction will give residual responses in the edited subspectra, which can be eliminated by using multiplication coefficients if necessary. Residual responses, however, rarely confuse the sorting of carbon resonance by multiplicity. Examples of DEPT-edited subspectra are shown in Figure 8.3.

8.2.6
Off-Resonance Decoupling

If a low power RF field is selectively applied to a specific proton resonance and a ^{13}C spectrum is subsequently recorded, the resulting spectrum will nominally be proton coupled, with the exception of the carbon associated with the selected proton. In this fashion, by performing a series of such experiments, it is possible to correlate carbon resonances with their directly attached protons. As the decoupling frequency is moved off-resonance, residual coupling, J_R, will be observed in the carbon spectrum with J_R a function of the strength of the applied RF field and how far off resonance it is applied. By preparing a series of such experiments, various carbon multiplets will successively collapse and reappear as the frequency of the applied proton decoupling field is systematically varied from one experiment to the next. Such experiments were an early forerunner of 2D heteronuclear shift

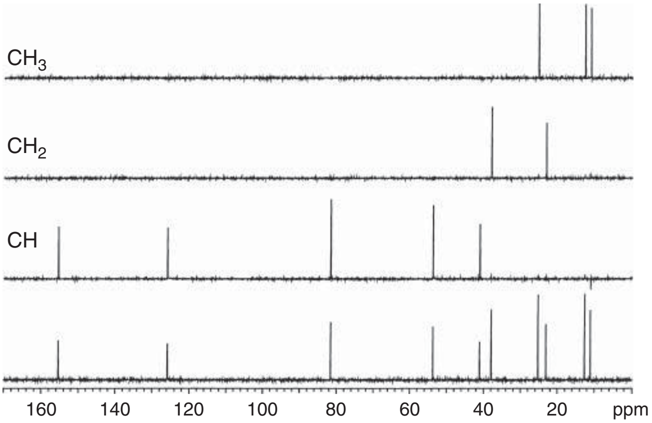

Figure 8.3 Multiplicity-edited DEPT spectra recorded at 125 MHz for a sample of santonin (**1**).

correlation experiments. Perhaps it is worthy of note that a whole qualitative dimension of spectral information is available from inspecting multiplicity shape as a function of J_R. Such information frequently allows specific assignment of resonances within multiplicity groups. This information is lost, however, in spectral editing sequences like INEPT and DEPT that rely on sign and intensity variation of the coupled or decoupled resonance [43].

8.2.7
Relaxation Measurements

Following the application of a pulse or pulses to an NMR sample and the acquisition of whatever data are of interest, time is required for the system to return to some level of equilibrium. Two fundamental relaxation processes govern the return of a perturbed spin system to equilibrium. These processes are spin–lattice or T_1 relaxation, and spin–spin or T_2 relaxation. A variety of means are available to measure both of these fundamental processes [27, 29, 31]. We will limit the discussion here to the former.

Spin–lattice relaxation is the time constant for the recovery of magnetization along the z-axis in a NMR experiment. Various methods are available for the measurement of spin–lattice relaxation times. The interested reader is referred to the series of monographs edited by Levy on carbon-13 NMR spectroscopy [44, 45] for more details. The energy transfer between nuclear moments and the "lattice," the three-dimensional (3D) system containing the nuclei, provides the mechanism to study molecular motion, for example, rotations and translations, with correlation times of the order of the nuclear Larmour frequencies, tens to hundreds of megahertz. We will limit our discussion here to the simple inversion recovery T_1 relaxation time measurement experiment, which, in addition to providing a convenient means for the quick estimation of T_1 to establish the necessary interpulse delay in 2D NMR experiments, also provides a useful entry point into the discussion of multi-dimensional NMR experiments.

The inversion recovery experiment, applies a 180° pulse to align the magnetization along the $-z$-axis using the pulse sequence shown in Figure 8.4. A variable delay, τ, follows, which is adjusted across a range of values in a series of experiments, generally beginning with periods much shorter than the actual relaxation time through delays which are several times longer than the relaxation time to be measured. Following the τ interval, the evolved state of the magnetization is sampled using a 90° pulse. The intensity of the observed response can range from fully negative intensity, when τ is much shorter than T_1, through full positive responses when $\tau > 5T_1$, as shown in Figure 8.5. The signal intensity will be zero at the crossover point when $\tau = 0.69T_1$. Each data point represents a separate experiment differing from the other experiments in the series by the duration of τ. The T_1 relaxation time is encoded in the signal intensity in this series of

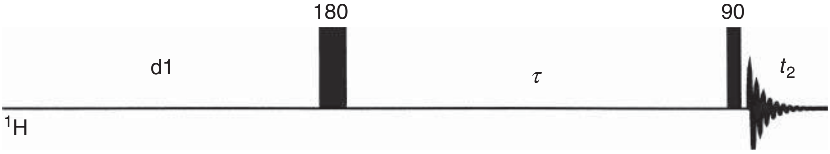

Figure 8.4 Spin–lattice (T_1) inversion recovery pulse sequence. The 180° pulse inverts magnetization, allowing it to recover along the z-axis. The duration of the delay, τ, is varied from $\ll T_1$ to several times the longest expected T_1 relaxation time in the molecule. The resulting, varying states of relaxation are sampled by the 90° pulse. The "null point," when there is essentially no signal intensity corresponds to 0.69 T_1. The results of an inversion recovery experiment applied to ^{1}H for strychnine (**2**) are shown in Figure 8.5.

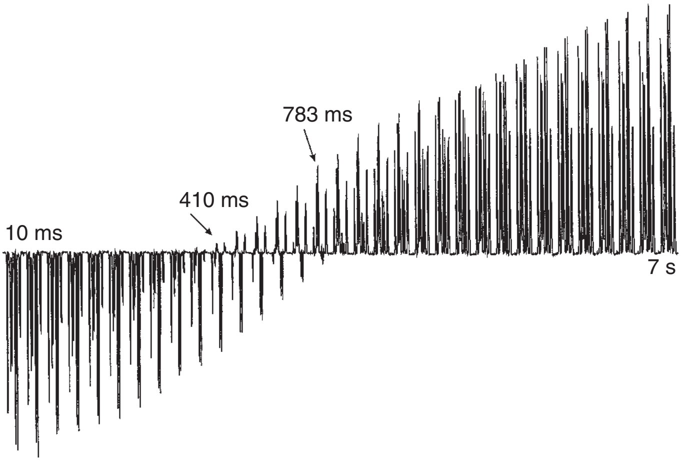

Figure 8.5 Inversion recovery experiment results for strychnine (**2**) shown as a horizontal stack plot where the duration of the delay, τ, between the 180° and 90° pulses is increased from right to left.

experiments through the successive variation of the duration of τ. This process is exactly analogous to the encoding of chemical shift information, or other spectral parametric information, in a 2D NMR experiment.

To establish interpulse delays for 2D NMR experiments, it is frequently convenient to run a very quick proton T_1 relaxation measurement. Given the sensitivity of modern spectrometers, this can usually be done with only a single or a few transients for each of the τ values in the series, and typically requires 10 min or less. By visual inspection, the T_1 relaxation time can be estimated from the τ value at which response intensity is zero. A knowledge of the T_1 relaxation time is also useful for establishing mixing times for nuclear Overhauser enhancement spectroscopy (NOESY) and rotating frame Overhauser enhanced spectroscopy (ROESY) experiments, which empirically can generally be performed by setting the mixing time to $\sim 0.7T_1$ and $\sim 0.5T_1$, respectively.

8.3
Two-Dimensional NMR Experiments

Two-dimensional NMR spectroscopy has been the topic of numerous monographs [14–17, 23–27, 29–31]. It is the intent here to provide the reader with a brief introduction and the means of accessing key aspects of what has become a voluminous literature on the subject. Briefly, 2D NMR experiments are comprised of several fundamental segments or building blocks. Three periods are obligatory in a 2D NMR experiment. These consist of a preparation period, the evolution period, t_1, which corresponds to what will be the indirectly digitized time domain, and a detection period, t_2, which is the directly detected time domain. In addition, some 2D NMR experiments contain a fourth period for "mixing" that is inserted between evolution and detection. Double Fourier transformation of the resulting data matrix affords a 2D frequency matrix in which responses are a function of two frequencies as shown by Eq. (8.2):

$$S(t_1, t_2) \longrightarrow s(F_1, F_2) \tag{8.2}$$

The two frequency axes may consist of a diverse assortment of pairs of fundamental NMR parameters. Examples might include chemical shift on one axis and a frequency axis for scalar couplings on the second as in the 2D *J*-resolved NMR experiments. Both axes may be proton chemical shift, in which responses may be correlated by scalar (*J*) coupling as in the COSY experiment [46–48], by dipolar relaxation pathways as in the NOESY [35, 36, 49–51] and ROESY [35, 36, 52, 53] experiments, or by chemical exchange pathways as in the exchange spectroscopy (EXSY) experiment [54–59]. Other examples may involve chemical shift on one axis and a multiple quantum frequency on the second axis. Examples here would include proton double [60–62] and zero quantum spectroscopy [63–67], ^{13}C–^{13}C INADEQUATE [68, 69], and so on. The available axes in a 2D NMR experiment may also be used for heteronuclear chemical shift correlation, for example, ^{1}H–^{13}C or

^1H–^{15}N, where the respective nuclide pairs are correlated via their one-bond ($^1J_{XH}$) or multiple bond ($^nJ_{XN}$) heteronuclear couplings [14, 16, 17, 23–27, 29–31, 70–72].

While the subject of 2D NMR spectroscopy may initially appear a daunting one, the simplest point of entry into 2D NMR is undoubtedly via *J*-resolved experiments [73, 74]. From a fundamental understanding of the segregation of spectral parameter information between frequency domains in a 2D *J* experiment, the reader can successfully begin to delve into homo- and heteronuclear 2D NMR techniques.

8.3.1
2D *J*-Resolved NMR Experiments

2D *J*-resolved NMR experiments are a conceptual amalgamation of two topics discussed above, the *J*-modulated spin echo and the 2D characteristic of the spin–lattice relaxation experiments. As the name of these experiments implies, scalar coupling information, *J*, will be displayed in the one frequency domain; chemical shift information will be presented in the second frequency domain. The simplest 2D *J* experiments sort ^{13}C chemical shift information in the detected time domain, labeled t_2 by convention, while the heteronuclear scalar couplings of each carbon are sorted into the indirectly determined time domain, t_1 (do not confuse lower case t_1 with the spin–lattice relaxation time, T_1).

The pulse sequence for an amplitude modulated heteronuclear 2D *J* experiment is shown in Figure 8.6 [75]. The experiment consists of a 90° ^{13}C pulse to rotate magnetization into the *xy*-plane where it begins to evolve with the decoupler turned on. After the first half of the evolution time has elapsed, $t_1/2$, a 180° ^{13}C pulse is applied and the decoupler is gated off for the second half of the evolution period. As might be expected at this point, two processes are ongoing in the second half of the evolution period. First, having applied a 180° ^{13}C pulse at $t_1/2$, we should expect

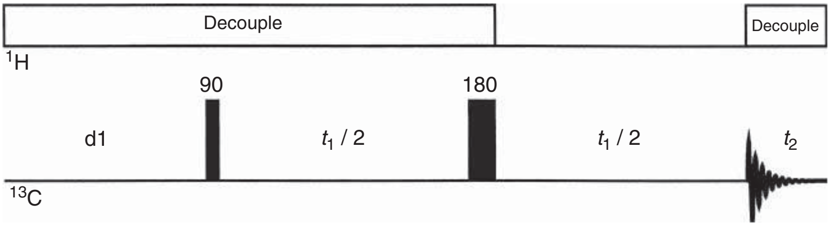

Figure 8.6 Pulse sequence for the amplitude modulated 2D *J*-resolved NMR experiment. The experiment is based on a *J*-modulated spin echo. The first 90° pulse tips magnetization into the *xy*-plane where it evolves during the first half of the evolution period, $t_1/2$. The 180° pulse is applied and the decoupler is simultaneously gated off for the second half of evolution. Decoupling is resumed when acquisition is started. The evolution of magnetization under the influence of the heteronuclear coupling during the second half of the evolution period leads to a 2D spectrum in which heteronuclear couplings are scaled by a factor of 2 and sorted as a function of the ^{13}C chemical shift as shown by the contour plot presented in Figure 8.9.

that magnetization will be refocused in a spin echo at time $= t_1$. Second, since the decoupler has been gated off for the second half of the evolution period, the spin echo will be *J*-modulated by the evolution of heteronuclear couplings during the second $t_1/2$ interval.

A 2D *J* experiment, or any 2D NMR experiment for that matter, consists of a series of 1D experiments in which the duration of the evolution time, t_1, is systematically incremented in some fashion from one experiment to the next. In the specific case of a 2D *J* experiment, the incremented parameter is the dwell time, which corresponds to 1/sw1, where sw1 is the desired spectral width of the second frequency domain, F_1, in hertz. Typical one-bond heteronuclear couplings range from about 125–160 Hz for aliphatic to aromatic compounds, respectively, with some heteroaromatics having one-bond couplings ranging up to about 210 Hz. In most cases, the spectral width in the second frequency domain of a 2D *J* experiment can be set to a total of 100 Hz, keeping in mind that couplings will be scaled by $J/2$ since *J*-modulation occurs for only half of the evolution time.

Experimentally, the results of performing a 2D *J* experiment such as that shown in Figure 8.6 are represented by the following several figures. First, as shown in Figure 8.7, response intensity is amplitude modulated for a given carbon from one experiment to the next as the evolution time, t_1 is incremented. The amplitude modulated resonance corresponds to the data arising from the first Fourier transformation as defined by Eq. (8.3):

$$S(t_1, t_2) \longrightarrow s(t_1, F_2) \tag{8.3}$$

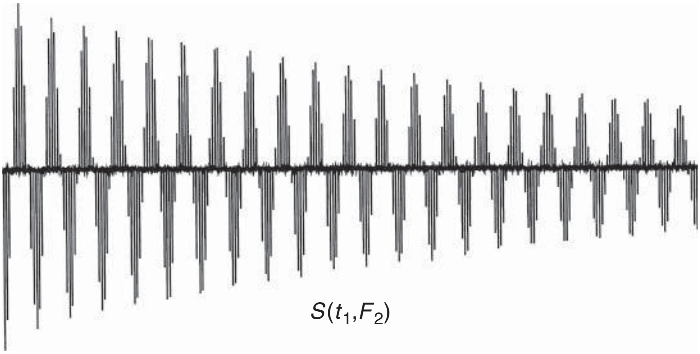

Figure 8.7 Amplitude modulation of a single ^{13}C resonance extracted from a partially processed amplitude modulated 2D *J*-resolved experiment. The data set was subjected to the first Fourier transform to give a data set of the form $S[t_1, F_2]$ from which the data shown were extracted. Successive incrementation of the duration of the evolution period, t_1, leads to the amplitude modulation of the ^{13}C signal observed. The heteronuclear coupling information is encoded into the modulation frequency. Each peak in this horizontal stack plot is obtained for a different value of the evolution time, t_1. Generally, these data would be shown in a stack plot of the type shown in Figure 8.8. They are shown here as a simple horizontally plotted series of 256 spectra to emphasize the amplitude modulation of the carbon resonance.

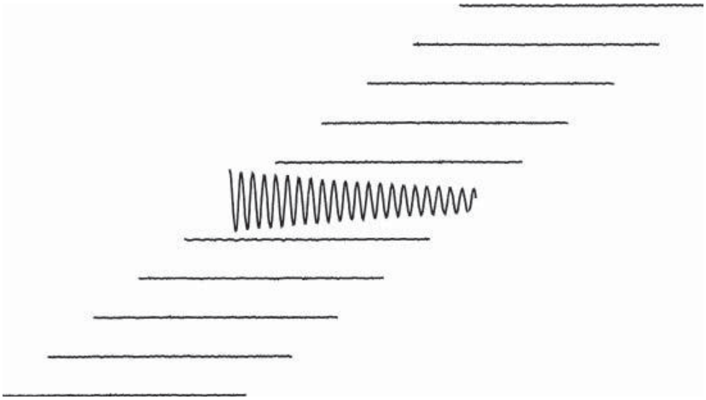

Figure 8.8 Interferograms from the region surrounding the amplitude modulated resonance shown in Figure 8.7. These data would correspond to transposition of the $S[t_1, F_2]$ data set to the form $S[F_2, t_1]$. Fourier transformation of the interferograms extracts the heteronuclear coupling information encoded into the amplitude modulation of the resonance, sorted by ^{13}C chemical shift. The final, Fourier transformed result of the amplitude modulated 2D *J*-resolved experiment is shown in Figure 8.9.

Transposition of the 2D data matrix, as defined by Eq. (8.4) allows us to look at the modulation of response intensity in the time domain, which is analogous to looking at a free induction decay (FID). These data are shown in Figure 8.8:

$$S(t_1, F_2) \longrightarrow s(F_2, t_1) \tag{8.4}$$

Completion of the second Fourier transform Eq. (8.5) gives the resulting 2D *J* spectrum, which is shown as a contour plot in Figure 8.9:

$$S(F_2, t_1) \longrightarrow s(F_2, F_1) \tag{8.5}$$

The data shown in Figure 8.9 were acquired for santonin (**1**). The ^{13}C chemical spectrum of the sesquiterpene is shown plotted along the F_2 axis. If a projection were done through the F_1 or second frequency domain, a so-called *J* spectrum would be obtained, which in this case is not especially useful. Each of the carbons contains, at its respective chemical shift in F_2, responses due to the scalar (*J*) couplings of that carbon. For protonated carbons, the larger spacing arises from the $^1J_{CH}$ coupling; the smaller spacings, when clearly resolved in this presentation, for example, the carbon near 80 ppm just downfield of the chloroform response, are a result of the $^nJ_{CH}$ coupling, where $n = 2$ or 3. The non-protonated carbons, for example, the two non-protonated vinyl carbons, exhibit responses centered on the axis $F_1 = 0$ Hz due to $^nJ_{CH}$ couplings but do not have larger $^1J_{CH}$ responses.

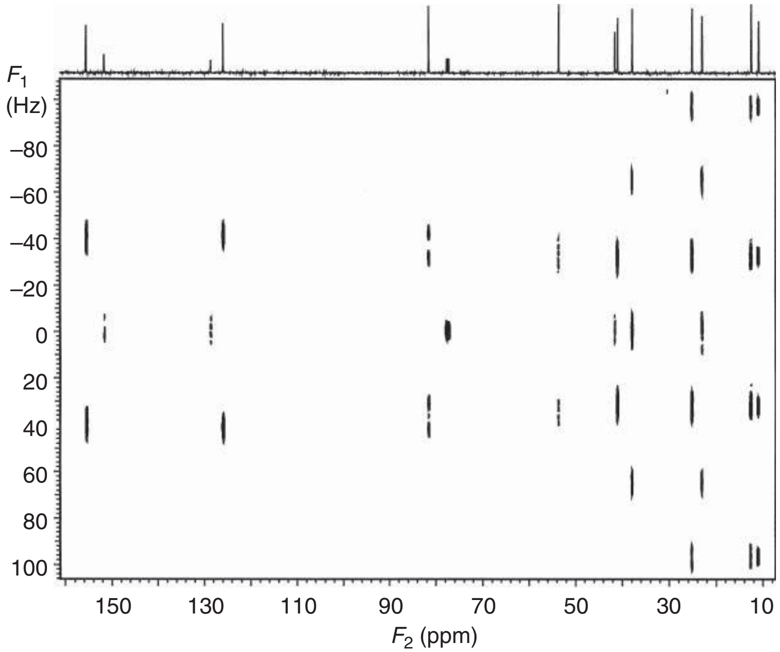

Figure 8.9 Contour plot of the amplitude modulated 2D *J*-resolved NMR spectrum of the simple alkaloid santonin (**1**) recorded at 400 MHz. The ^{13}C reference spectrum is plotted along the horizontal axis; the so-called *J* spectrum (not shown) is obtained by projection through the data matrix. Heteronuclear couplings are scaled by a factor of 2 since they evolve without decoupling for only half of the evolution period, t_1.

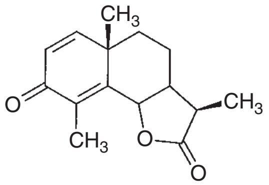

1

In addition to the use of *J* spectroscopy for $^1H-^{13}C$ heteronuclear coupling, there are also homonuclear variants of the experiment [76]. For the most part, however, the 2D *J*-resolved experiments have fallen into disuse as there are more efficient means of deriving the same spectral information.

8.3.2
Homonuclear 2D NMR Spectroscopy

There are probably, at present, about four homonuclear 2D NMR experiments in common usage for small molecules. These include COSY [46–48], TOCSY (total correlation spectroscopy) [77–79], NOESY [35, 36, 49–51], and ROESY

[35, 36, 52, 53], the latter two corresponding to nuclear Overhauser and spin-locked Overhauser correlated experiments, respectively. Several less frequently employed homonuclear 2D experiments are also possible and include: $^{13}C-^{13}C$ [68, 69]; ^{1}H double quantum spectroscopy [60–62], ^{1}H zero quantum spectroscopy [63–67], and others ^{H}H. We will discuss the primary experiments in the category briefly in turn, and we will direct the reader interested in other homonuclear 2D variants to the appropriate literature.

8.3.2.1 COSY, Homonuclear Correlated Spectroscopy

The COSY experiment was developed early in the history of 2D NMR [46–48]. Both frequency axes in the experiment are used to display proton chemical shift information in most cases. The actual proton spectrum of these experiments resides along the diagonal in the 2D spectrum. Individual proton resonances in the experiment are correlated to one another via scalar (*J*) coupling through off-diagonal correlation responses. Geminal ($^{2}J_{HH}$) and vicinal ($^{3}J_{HH}$) correlations will almost always be observed if the scalar coupling between the protons in question is of a reasonable size. Depending on the extent of digitization in the second frequency domain, weak vicinal couplings (those for protons whose couplings are weak because of Karplus considerations) and longer-range couplings may or may not be observed. The observation of weaker responses is also, in part, a function of the mathematical weighting functions used in processing the data. It is entirely possible through data processing procedures to retain or eliminate weak vicinal and longer-range proton–proton correlation responses.

The pulse sequence used for the COSY experiment is extremely simple, consisting of a pair of 90° pulses separated by the incremented evolution period, t_1, as shown in Figure 8.10. The incrementation of the evolution time is generally set to afford

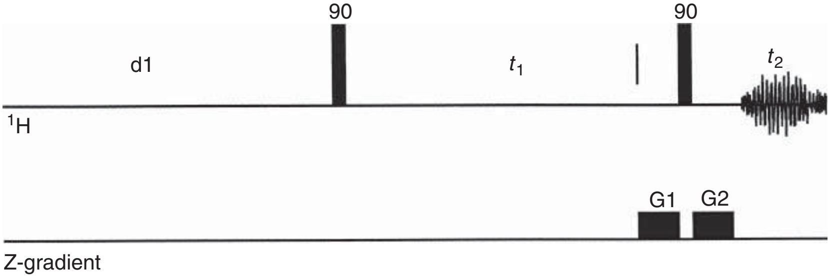

Figure 8.10 Pulse sequence for homonuclear correlation spectroscopy, COSY/GCCOSY [46–48]. Although the gradient version of the experiment is shown, the pulse sequences are the same except for the two gradients and their associated delays. The non-gradient experiment employs a four-step phase cycle; the gradient experiment allows the acquisition of data with a single transient/t_1 increment since the coherence transfer pathway is selected by the gradients. The proton spectrum appears along the diagonal of the diagonally symmetric data matrix. Correlations between scalar (*J*) coupled resonances are denoted by off-diagonal elements in the spectrum, as shown in Figure 8.11.

a square data matrix since it is desirable to have both frequency axes identical in homonuclear correlation experiments. In the case of macro-driven modern NMR instruments, setting the spectral width in the second frequency domain of an experiment like COSY is usually transparent. In general, for a survey experiment, it is useful to acquire perhaps 2K points in the observed time domain (t_2; 1K points after Fourier transformation) and similar to one-sixth as many points in the second time domain, t_1, as the transformed result in F_2. Generally, for a survey COSY experiment we find it convenient to acquire 128–160 files in the second time domain. After processing, these data will yield a spectrum in which geminal and most vicinal correlation responses will be observed. When weaker or long-range homonuclear correlation responses are sought, higher levels of digitization of t_1 are necessary, up to a maximum of half the number of points acquired in t_2.

Processing COSY data usually employs sinebell multiplication, with zero filling in the second frequency domain to yield a square data matrix. As an example, consider the COSY spectrum of the aliphatic region of strychnine (**2**) shown in Figure 8.11. The COSY data shown were acquired using the general survey conditions suggested above. The data are presented as a contour plot, which is analogous to a topographic map. *Peaks* are defined by contours; weak responses in the spectrum may be represented by one or only a few contour levels while stronger peaks may require numerous contours for representation. The diagonal in this presentation corresponds to the proton reference spectrum that is plotted above the contour plot. Protons in the molecular structure that are scalar coupled to one another are correlated in the experimental spectrum by the off-diagonal responses. Several correlation pathways are shown in Figure 8.11. A full discussion of the interpretation and or utilization of COSY data is beyond the scope of this treatment and the interested reader is referred to any of the monographs on the subject of 2D NMR cited in the introduction to this chapter. Briefly, however, referring to the H11α/β geminal proton resonances at 3.11 and 2.6 ppm, we note that these protons are correlated to one another in the spectrum with correlations also observed to the H12 proton resonating at 4.23 ppm. If one were to continue from the H12 correlation on the diagonal, in a step-wise fashion, the H13 methine resonance at 1.3 ppm could next be assigned, as shown in Figure 8.11. Continuing in this fashion, the contiguous proton spin system can be constructed as far as it is possible to follow correlations from one proton to the next, in principle to the H16 resonance.

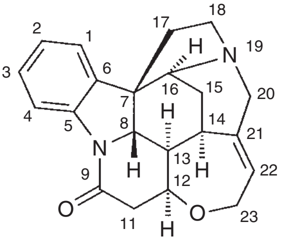

2

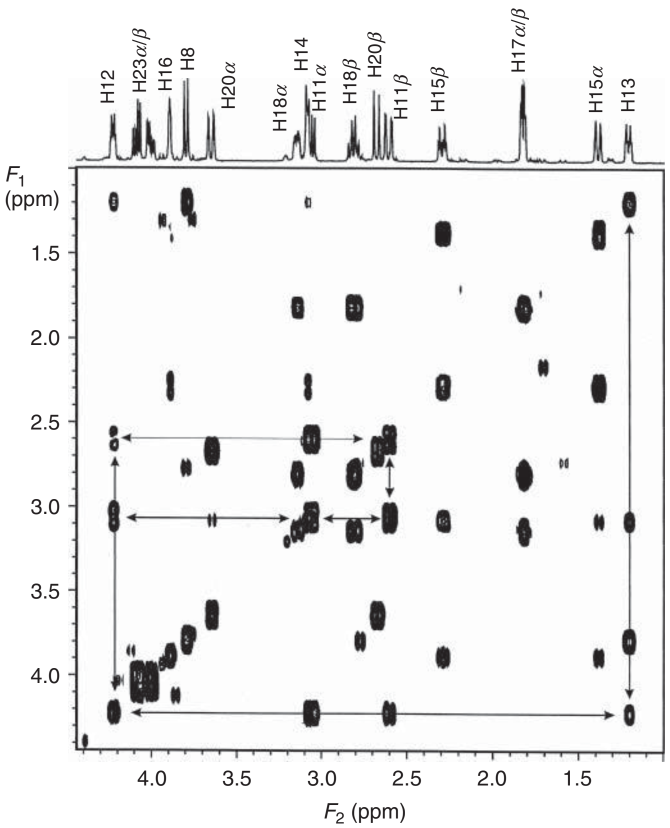

Figure 8.11 COSY spectrum of the aliphatic region of the strychnine (**2**) ^{1}H spectrum. Connectivities are shown from the anisochronous, geminal H11 resonances to H12, and in turn to the H13 resonance. The COSY spectrum is essentially the equivalent to the simultaneous acquisition of all possible selective homonuclear spin decoupling experiments. The COSY experiment has become one of the fundamental cornerstone experiments used in the determination of natural product structures and for many related structural studies.

8.3.2.2 **Homonuclear TOCSY, Total Correlated Spectroscopy**

In an effort to extend the correlation ability of the COSY experiment just described, the relayed-correlated spectroscopy or R-COSY experiment [80, 81] was developed. While the COSY experiment correlates $H_A \rightarrow H_B$ in the hypothetical structural fragment shown by **3**, the R-COSY experiment ideally extends the correlation a step further $H_A \rightarrow H_B \rightarrow H_C$ via an additional delay following the evolution period and a 90° pulse. Double relayed-correlated spectroscopy or 2R-COSY is a trivial extension of the R-COSY experiment that repeats the relay process, giving correlation from H_A ultimately to H_D, assuming that the delays were set appropriately for the intervening homonuclear couplings. Likewise, the so-called long-range correlated spectroscopy or LR-COSY experiment [82] used a fixed delay to emphasize long-range homonuclear couplings in much the same sense as in long-range heteronuclear shift correlation experiments which are described below. The assemblage of experiments has been largely supplanted by a single experiment known as *homonuclear TOCSY*, which is the experimental amalgamation of the series of ideas just advanced.

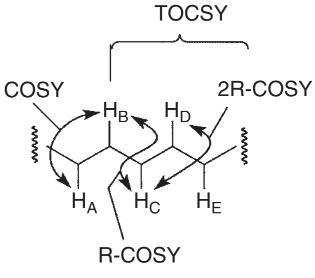

3

The homonuclear TOCSY experiment [77, 79] utilizes the fundamental COSY pulse sequence and evolution time followed by a delay and then an isotropic mixing period; the pulse sequence is shown in Figure 8.12. Homonuclear vicinal coupling coherence is established during the evolution period; magnetization is propagated from the vicinal neighbor to its vicinal neighbor, and so on. The extent to which magnetization is propagated is a function of the mixing time and the size of the homonuclear coupling constants between the vicinally coupled protons in question. The longer the mixing time, the further magnetization is propagated through the contiguous homonuclear vicinal coupling network. Shorter mixing times, for example, ~12 ms for aromatic systems and 18–24 ms for aliphatic or alicyclic systems will establish correlations to protons one or two bonds removed from the starting resonance. In the case of **3**, shorter mixing times will establish correlations from H_A to protons as far removed as H_C or H_D depending on the size of the intervening homonuclear couplings. Longer mixing times, for example, 18–24 ms for aromatic compounds and 24–36 ms for aliphatic/alicyclic molecules will transfer magnetization still further. It should be remembered, however, that these are only approximations.

Returning to the example of strychnine (**2**), a 30 ms TOCSY spectrum of the aliphatic region of the proton spectrum at 500 MHz is shown in Figure 8.13. Again,

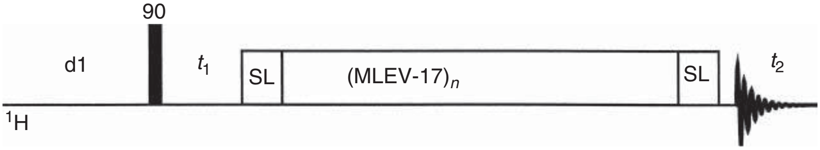

Figure 8.12 Homonuclear TOCSY pulse sequence [77–79]. Isotropic mixing is provided by a pulse train, and serves to propagate magnetization from a given proton to its scalar coupled neighbor. The extent to which coherence will be transferred along a series of coupled, homonuclear spins, is a function of the duration of the mixing time.

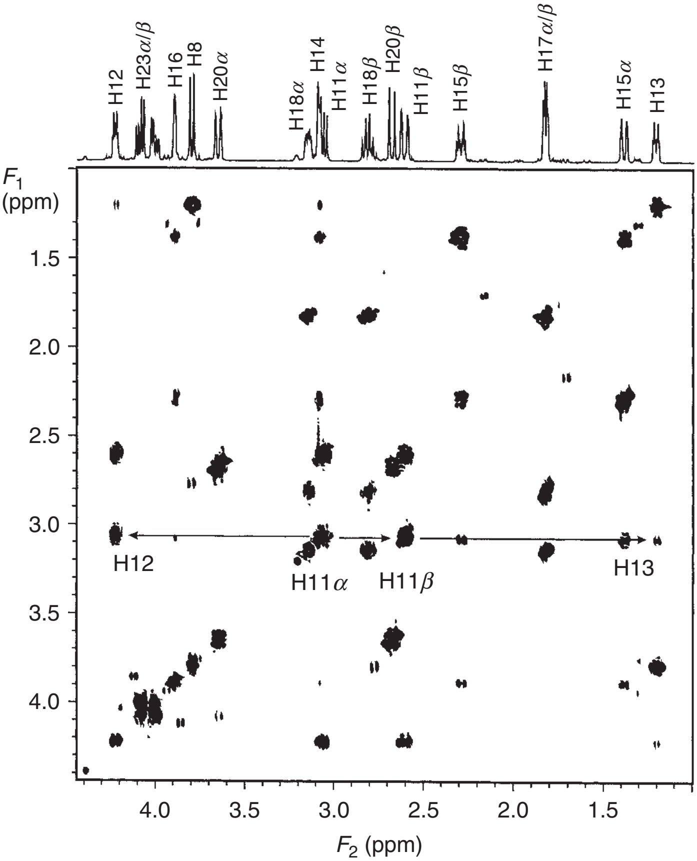

Figure 8.13 TOCSY spectrum of the aliphatic region of the strychnine (**2**) proton spectrum recorded with a mixing time of 30 ms. Correlations from the H11 protons are shown as in the COSY spectrum shown in Figure 8.11. The off-diagonal elements from the H11 resonances correlate them to each other (geminally) and to the H12 resonance as in the COSY spectrum. However, in addition, the 30 ms mixing time is long enough to propagate magnetization from the H11 resonances to H12 and then on to the H13 resonance.

starting from the H11 geminal methylene pair, correlations are established as far as H13 through the intervening protons.

8.3.2.3 NOESY, Nuclear Overhauser Enhancement Spectroscopy

The NOESY experiment is another of the homonuclear autocorrelated experiments in which both frequency axes display chemical shift information (usually ^{1}H, although ^{19}F experiments are certainly possible in perfluorinated compounds, and possibly ^{13}C for molecules biosynthesized using 1,2-^{13}C acetate). The experiment begins in a fashion analogous to the COSY experiment and again employs a

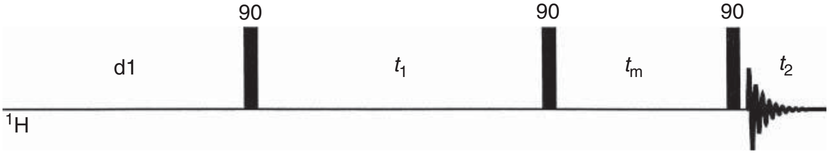

Figure 8.14 NOESY pulse sequence. The NOESY experiment is one which uses a mixing period, τ_m, in addition to the obligatory preparation, evolution, and detection periods. Protons are labeled with the individual chemical shifts during the evolution period, t_1. The mixing period, τ_m, allows dipolar cross relaxation to occur, which is detected with the final 90° pulse of the sequence. The duration of the mixing time is usually set to about $0.7T_1$, which corresponds to the null point when an inversion recovery T_1 relaxation measurement is done.

mixing period to permit the dipolar relaxation processes to occur, which are being sampled to correlate resonances (Figure 8.14) [35, 36, 49–51]. As noted above, a convenient means of establishing the duration of the mixing period is afforded from a simple spin–lattice (T_1) inversion–recovery relaxation experiment. The "null" point in the inversion–recovery experiment is $\sim 0.69T_1$, which is a useful rule-of-thumb for setting the duration of the mixing time in a NOESY experiment. The NOESY spectrum of strychnine (**2**) recorded with a 350 ms mixing time, is shown in Figure 8.15. Several brief observations concerning the spectrum shown are warranted. First, the relative orientation of the H12 resonance relative to the H11α and H11β protons is readily established from the data. In addition, it is also possible to establish a correlation across the oxepin ether linkage from the 11- to 23-position in the molecule. This affords new structural connectivity information, which is probably very difficult to obtain via a homonuclear scalar coupling, if it is observable at all.

8.3.2.4 **ROESY, Rotating Frame Overhauser Enhanced Spectroscopy**

The ROESY experiment combines ideas drawn from the TOCSY and NOESY experiments. Protons are correlated to one another via ROEs (rotating frame Overhauser effects) [35, 36, 52, 53]. ROEs are developed in the ROESY experiment through the use of a spin-locking field in a manner analogous to the propagation of magnetization in the homonuclear TOCSY experiment (Figure 8.16). The duration of the mixing time in a ROESY experiment can also be conveniently set from a simple inversion–recovery experiment. Recalling that the "null" point in the inversion recovery experiment is $\sim 0.69T_1$, the rough approximation of the average T_1 relaxation time for the proton(s) of interest can be easily determined. As a general rule of thumb, setting the mixing time in a ROESY experiment to $\sim 0.5T_1$ will generally provide usable data.

Again returning to strychnine (**2**) as a structural model, the ROESY spectrum with a mixing time of 250 ms is shown in Figure 8.17. Comparison of the correlations observed in the ROESY spectrum shows them to be qualitatively similar to those seen in the NOESY experiment shown in Figure 8.15.

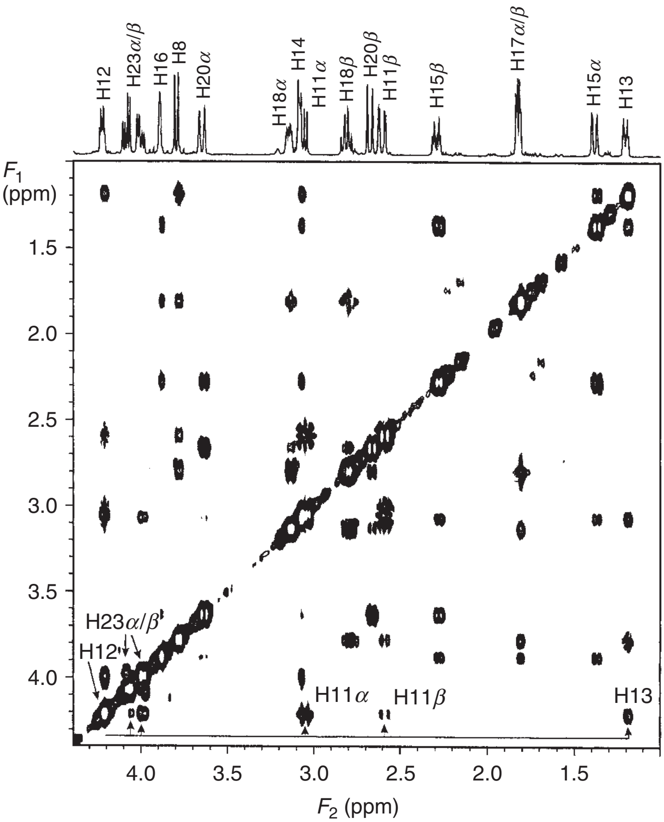

Figure 8.15 NOESY spectrum of the aliphatic region of the strychnine (**2**) proton spectrum recorded with a 350 ms mixing time. These data are useful, in establishing correlations between protons that are not scalar coupled, for example, the correlation between the 23- and 12-methine proton, as shown by the labeled connectivities in the spectrum. In addition, these data also show that the H12 methine and H13 methine resonance are located on the same side of the molecule. The more intense response of the 23- and 11-anisochronous methylene resonances are also located on the same side of the molecule, α, as the H12 resonance, providing a convenient means of differentiating and assigning these resonances.

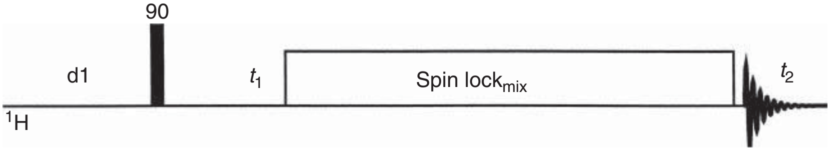

Figure 8.16 ROESY pulse sequence [35, 36, 52, 53]. Protons are labeled with their respective chemical shifts during the evolution time, t_1, as with the COSY and NOESY experiments. ROEs are developed by the isotropic mixing sequence applied during the mixing time, τ_m, which is generally set to about $0.5T_1$.

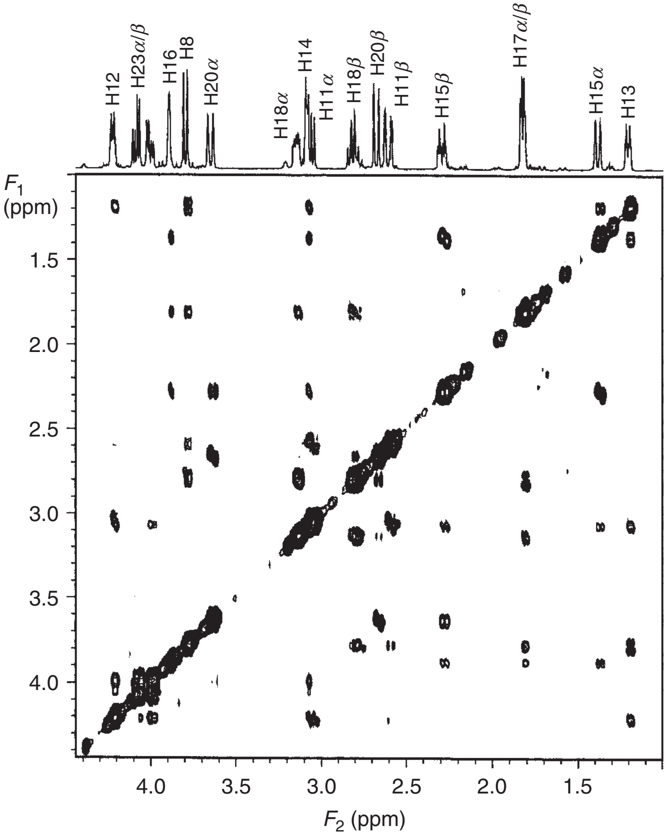

Figure 8.17 ROESY spectrum of the aliphatic region of strychnine (**2**) recorded with a 250 ms mixing time. The correlations observed and the assignment information which can be derived from them is the same as for the NOESY experiment presented in Figure 8.15.

8.3.2.5 **NOESY Versus ROESY**

The comparable responses in the NOESY and ROESY experiment obviously beg the question of which experiment is preferable? Dipolar relaxation processes are dependent on molecular motion (tumbling), as defined by the reorientational correlation time, τ_c. Very small molecules will generally afford quite usable NOESY spectra as they tumble quite rapidly in solution. Larger "small" molecules will generally reorient in solution more slowly; dipolar relaxation processes are consequently less efficient. Correspondingly, the size of the NOE response diminishes, making them more difficult to observe. Eventually, when molecules are large enough, they are tumbling slowly enough that the sign of the NOE is reversed and they begin again to exhibit progressively larger but negative NOEs. As a general guideline, when the molecular weight is approximately the same as the spectrometer observation frequency, NOEs will generally be weaker and more difficult to observed. In the intermediate condition, ROESY experiments, which rely on a spin-lock rather than being dependent on molecular tumbling, will still give reliable data. Fundamentally, there is no reason why ROESY experiments cannot be performed on very small molecules as well. The choice becomes one of preference and perhaps the prior experience of the spectroscopist doing the work.

8.3.2.6 **Other Homonuclear Autocorrelation Experiments**

In addition to the homonuclear autocorrelated experiments just described, there are numerous additional autocorrelated experiments, the description of which is beyond the scope of this chapter. What follows is a brief, non-exhaustive listing of some of these experiments that will provide the interested reader with some entry points into the literature.

Previous sections have exploited the scalar coupling, J, and dipolar relaxation mechanisms for purposes of autocorrelation. It is certainly possible, however, to correlate resonances via other fundamental processes. Some examples include exchange processes. As a group, these experiments are sometimes collectively referred to as *EXSY* experiments [54–59].

Resonances can also be correlated via multiple quantum frequencies. One seminal example is found in the work of Müller [83] in which heteronuclear multiple quantum coherence (HMQC) was used for heteronuclear shift correlation. We will discuss this further in the sections on heteronuclear shift correlation experiments later in this chapter. For homonuclear correlation of resonances via multiple quantum coherence, Freeman and co-workers pioneered the development of the $^{13}C-^{13}C$ INADEQUATE experiment [68, 69]. Remarkably, the INADEQUATE experiment allows an investigator to trace out the carbon skeleton of a molecule using adjacent $^{13}C-^{13}C$ resonant pairs at natural abundance. Unfortunately the statistical probability of such molecules in a sample is about 1 molecule in 10 000 at the natural abundance of ^{13}C which is $\sim 1.1\%$. Thus, $^{13}C-^{13}C$ INADEQUATE requires very large samples, frequently making the experiment inappropriate for natural product structure elucidation when sample sizes are limited.

Applying the idea of using multiple quantum coherence to correlate protons has also been explored. Mareci and Freeman [60] reported the first experimental demonstration of proton double quantum correlated spectroscopy. The F_2 axis in these experiments is used to present ^1H chemical shift in the usual fashion. In contrast, the F_1 axis is used for the double quantum frequency axis. Protons correlated to one another via double quantum coherence will exhibit a response in F_1 at the algebraic sum of the offsets of the coupled resonances relative to the transmitter frequency. A scant few applications have been reported including an exploratory study of strychnine (**2**) [61] and the structural characterization of the marine natural product plumericin [62].

Correlation in the second frequency domain using zero quantum coherence has also been described by Müller [63] and in work by Hall and co-workers [84–87]. Unlike higher quantum coherence experiments, zero quantum spectroscopy is insensitive to magnetic field inhomogeneities. Responses in the second frequency domain are observed at the zero quantum frequency, which is the algebraic difference of the coupled resonances relative to the transmitter. Again, only a scant few examples appear in the literature, including an exploratory study of strychnine (**2**) [64] and the characterization of several marine natural products [65]. One area of potential utility for zero quantum correlated spectroscopy is in the characterization of molecules with heavily congested proton spectra, for example, polynuclear aromatics [66, 67] although this area has yet to receive much attention from investigators.

8.3.3
Gradient Homonuclear 2D NMR Experiments

Traditionally, coherence transfer pathway selection has been accomplished by phase cycling routines. The desired components of magnetization are successively added to the memory storage location while undesired components are alternately added and then subtracted on subsequent scans such that at the end of the phase cycle they are ideally eliminated [88, 89]. The two most common phase cycling prescriptions are probably the CYCLOPS [90] and EXORCYCLE [91] routines. As an alternative to phase cycling, coherence transfer pathways can also be selected through the use of pulsed field gradients (PFGs) [92–94]. The gradient-selection procedure allows the selected coherence to remain in phase and the signal for it to thus be acquired while unwanted coherences are dephased and not detected. Essentially no, or minimal, phase cycling is required to generate largely artifact-free spectra. The spectral quality of gradient-selected experiments is not, however, without penalty. Since only one coherence transfer pathway is selected, other comparable pathways are not selected and thus do not contribute to the detected signal, resulting in a sensitivity loss when compared to phase cycle-based experiments [95]. This shortcoming of using gradients can be partially circumvented by using PEPs (preservation of equivalent pathways) methods as suggested in the work of Cavanaugh and co-workers [96–98]. When not severely sample limited (D.J. Russell, C.E. Hadden, and G.E. Martin, 1999, unpublished results) [99], the use of gradient NMR experiments is strongly recommended.

Gradient homonuclear 2D NMR experiments give results (albeit with the exception of noise) that are indistinguishable from phase-cycled experiments. Experiments such as GCOSY [100, 101] can be performed by accumulating a single transient per t_1 increment when not sample limited rather than using the obligatory four-step phase cycle of the conventional COSY experiment. A comparison of the COSY and GCOSY spectra of the aliphatic region of strychnine (**2**) recorded by accumulating 4 and 1 transient per t_1 increment, respectively, are shown in Figure 8.18. GTOCSY (gradient total correlation spectroscopy) [101–103], GNOESY (gradient nuclear Overhauser enhancement spectroscopy (also known as *GOESY*) [101, 104], and GROESY (gradient rotating frame Overhauser enhanced spectroscopy) [101–103] experiments can be performed with similar minimal phase cycling and corresponding time savings and reduced artifact response intensity. Gradient heteronuclear and gradient selective 1D NMR experiments are discussed below.

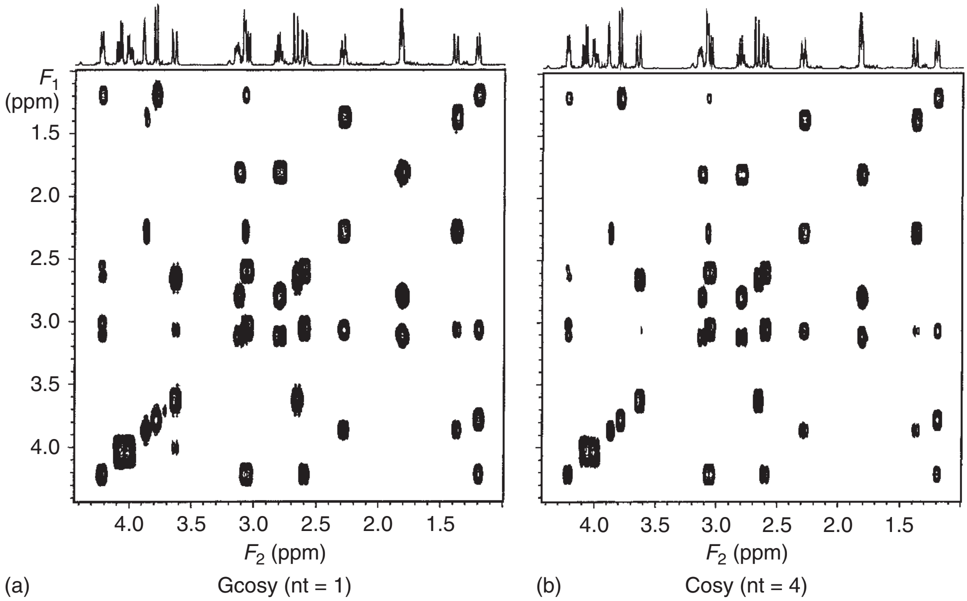

Figure 8.18 Comparative presentation of the GCOSY (nt = 1) (a) and COSY (nt = 4) (b) spectra of the aliphatic region of strychnine (**2**). The spectra differ only in that the former data were acquired by accumulating a single transient/t_1 increment while the latter required the acquisition of four transients/t_1 increment to satisfy phase cycling requirements.

8.3.4
Heteronuclear Shift Correlation

The development of heteronuclear 2D shift correlated spectroscopy began, indirectly, with the idea of "walking" the decoupler through the ^{1}H spectrum with the decoupler operating to collapse a single frequency while acquiring ^{13}C spectra. As successive experiments are recorded, each with the decoupler repositioned, resonances will begin to collapse from multiplets, will appear as a singlet when the decoupler is on resonance, and will then resume multiplet structures as the decoupler moves away again. The SPT (spin population transfer) experiments discussed above represented the next level of sophistication in this development saga. Finally, heteronucleus-detected 2D heteronuclear shift correlation experiments evolved through a series of steps that are discussed in chronological detail in the monograph by Martin and Zektzer [16].

Initially, heteronuclear shift correlation experiments exploited the large one-bond ($^1J_{CH}$) heteronuclear coupling to afford direct correlation spectra. Long-range heteronuclear shift correlation, via $^nJ_{CH}$ couplings was proposed but not experimentally realized in the visionary communication of Hallenga and van Binst [105]. It remained for Reynolds andco-workers in 1984 [106] to report the first experimental demonstration of this important experiment. Reynold's seminal report sparked a flurry of activity to develop new heteronucleus-detected long-range heteronuclear shift correlation experiments which were the topic of a 1986 review by one of the authors [107].

Heteronucleus-detected shift correlation experiments have now been largely supplanted by far more sensitive proton- or ''inverse''-detected methods. The heteronucleus-detected experiments are now largely reserved, in laboratories with modern NMR spectrometers, for those occasions when very high digital resolution is needed in the carbon frequency domain because of high spectral congestion [108, 109]. The remainder of this section will focus on the now widely utilized proton-detected heteronuclear shift correlation methods.

8.3.5
Direct Heteronuclear Chemical Shift Correlation Methods

The ''direct'' heteronuclear shift correlation experiments exploit the one-bond ($^1J_{CH}$) heteronuclear coupling as the basis of establishing chemical shift correlations. The concept of using multiple quantum coherence was developed by Müller in 1979 [83]; that of using single quantum coherence came out of the work of Bodenhausen and Ruben in 1980 [110].

8.3.5.1 HMQC, Heteronuclear Multiple Quantum Coherence

From the standpoint of experimental complexity, the HMQC experiment for direct correlation purposes is much simpler than the heteronuclear single quantum coherence (HSQC) experiment described below. The HMQC experiment has its origins in the work of Bax *et al.* in 1983 [111], which was directed at establishing $^1H-^{15}N$ correlations. The version of the experiment that came into common usage was that described by Bax and Subramanian in 1986 [112]. The gradient version of this experiment shown in Figure 8.19 was reported in 1991 by Hurd and John [115]. In general, the gradient version of the heteronuclear shift correlation experiment will be the preferred method, with the exception of very small samples, when it will be preferable to revert to the non-gradient version of the experiment to avoid signal losses associated with the use of the gradient methods [95, 99]. The topic of gradient heteronuclear shift correlation experiments was the topic of an early benchmark paper by Ruiz-Cabello and co-workers [113] and also of a more recent review by Parella [114]. The interested reader is referred to these excellent reports, to the various monographs cited in Section 8.1, or to the reviews cited in the section dealing with selective 1D experiments below.

Figure 8.19 shows the gradient version of the HMQC experiment since in most cases users will want to opt for the improved performance of the gradient experiment. Following a preparation period, HMQC (zero and double) is created by the 90° X-nucleus pulse applied at the initiation of the evolution period, t_1. Evolution occurs and the 180° ^1H pulse serves to refocus proton chemical shift evolution and interchanges zero and double quantum coherence terms. At the end of the evolution period, unobservable HMQC is reconverted to observable, antiphase single quantum coherence by the 90° X-nucleus pulse the ends the evolution

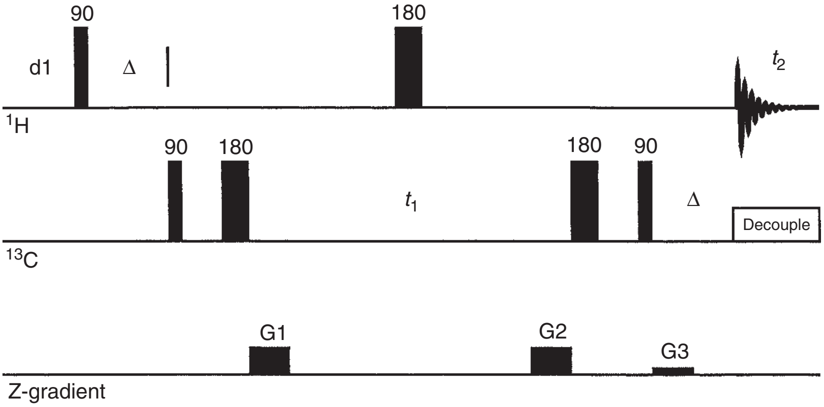

Figure 8.19 Schematic representation of the gradient heteronuclear multiple quantum coherence or GHMQC pulse sequence. The gradient version of this experiment now in use [115] is derived from the earlier non-gradient experiment described by Bax and Subramanian [112]. Coherence pathway selection is obtained by the application of gradients in a ratio of 2 : 2 : 1 as shown. Other ratios are also possible, as considered in the reports of Ruiz-Cabello *et al.* [113] and Parella [114]. The experiment creates heteronuclear multiple quantum coherence with the 90° ^{13}C pulse that precedes evolution. Both zero and double quantum coherences are created and begin to evolve through the first half of the evolution period. The 180° ^{1}H pulse midway through evolution interchanges zero and double quantum coherence terms in addition to "decoupling" proton chemical shift evolution during evolution. Antiphase proton single quantum coherence is recreated by the final 90° ^{13}C pulse which is then allowed to refocus before acquisition and the application of broadband heteronuclear decoupling. The GHMQC experiment is infrequently used in the author's laboratory relative to the GHSQC experiment which gives substantially better resolution in the second frequency domain [70, 116–118] (Figure 8.20, Figure 8.21, and Figure 8.22).

period. The three coherence pathway selection gradients are nominally applied in a 2 : 2 : ±1 ratio for ^{1}H–^{13}C heteronuclear shift correlation measurements and in a 5 : 5 : ±1 for ^{1}H–^{15}N correlation. (Note: other gradient ratios are possible, for example, 5 : 3 : 4 for ^{1}H–^{13}C, and so on. See the work of Ruiz-Cabello *et al.* [113] or that of Parella [114] for a further discussion on this point.) At this point, the antiphase proton single quantum coherence is labeled with the chemical shift of the directly bound ^{13}C. Magnetization is refocused and acquisition and broadband heteronuclear decoupling are initiated simultaneously.

The HMQC/GHMQC (gradient heteronuclear multiple quantum coherence) experiments are quite useful and were treated in an early review by Martin and Crouch [71]. Relative to the single quantum variant of the experiment discussed below, the effective F_1 resolution of the multiple quantum experiment suffers due to homonuclear coupling modulation during the evolution period, which leads to broadened responses being observed in the F_1 dimension. The difference in the effective resolution of the HMQC versus HSQC experiments was noted in a review on applications of inverse-detection in alkaloid chemistry by Martin and Crouch [70] and has since been treated in more detail by Reynolds and others [116–118]. On this basis, the HSQC/GHSQC (gradient heteronuclear single quantum coherence) experiments discussed in the following section should be preferentially used on a routine basis in the opinion of the authors.

8.3.6
HSQC, Heteronuclear Single Quantum Coherence Chemical Shift Correlation Techniques

The idea of heteronuclear single quantum coherence experiments derives from the early work of Bodenhausen and Ruben [110]. The contemporary variant of their experiment is shown in Figure 8.20. The fundamental concept of the experiment, regardless of refinements to augment the performance of the experiment, is unchanged. The experiment utilizes an INEPT step to transfer single quantum magnetization from proton to the heteronuclide immediately prior to the beginning of the evolution time. During evolution chemical shift labeling for the heteronuclide occurs; proton chemical shift evolution is reversed by the 180° ^{1}H pulse applied midway through the evolution period. Following evolution, magnetization is transferred back to the protons and refocused to allow data acquisition with broadband decoupling.

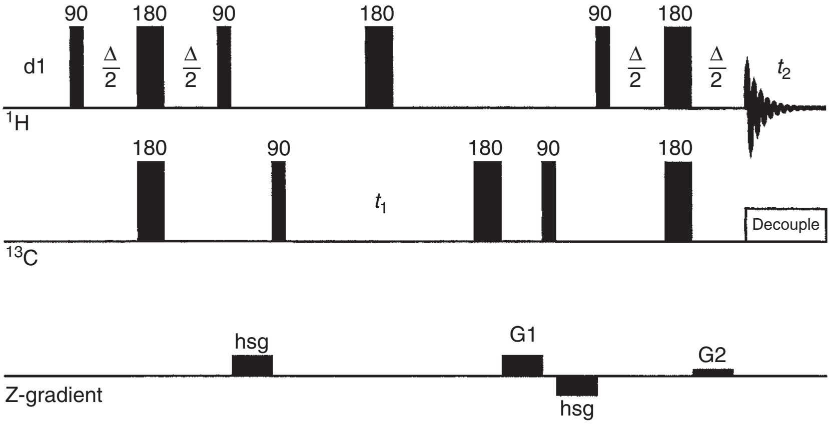

Figure 8.20 Schematic representation of the gradient heteronuclear single quantum coherence or GHSQC pulse sequence. The non-gradient version of this experiment was described originally by Bodenhausen and Ruben [110]. Heteronuclear single quantum coherence is created by the first INEPT segment of the experiment which evolves during the evolution period, t_1. The reverse INEPT step following evolution converts the heteronuclear single quantum coherence to proton single quantum coherence which is then detected. The gradient version of the experiment currently in use in the author's laboratory is shown. While phase-sensitive, the experiment offers only about half the sensitivity of the non-gradient variant since only one of the two equivalent coherence pathways is selected by the simple gradient version of the experiment [95]. More complex variants of the experiment developed by Cavanaugh and co-workers [96–98] utilize a technique known as *preservation of equivalent pathways* or PEP to recover both coherence pathways giving a $\sqrt{2}$ improvement in signal-to-noise for methine resonances.

The gradient or GHSQC version of the experiment applies a pair of gradients rather than the three gradients used in the GHMQC experiment (Figure 8.19). Gradients are applied in the ratio of 4 : 1 for $^1H-^{13}C$ heteronuclear correlation. The first gradient, G1, is applied during the evolution period while the second gradient, G2, is applied during the final refocusing delay following the 180° pulse sandwich just prior to acquisition. More sophisticated variants of the experiment use a process known as *PEPs* [96–98] to record high sensitivity, phase-sensitive 2D HSQC spectra. The PEP variant of the experiment employs a second reverse INEPT "block" to reclaim both orthogonal components of magnetization thereby giving a $\sqrt{2}$ improvement in signal-to-noise. The phase of one of the 90° X-pulses and that of the G2 gradient are inverted on alternate scans and the data are stored separately to provide a phase-sensitive final result.

The phase-sensitive GHSQC spectrum of strychnine is shown in Figure 8.21a.

8.3.6.1 Multiplicity-Edited Heteronuclear Shift Correlation Experiments

Heteronuclear chemical shift correlation methods establish the direct link between protons and the respective, directly attached carbons (or nitrogens). In the case of methylenes with inequivalent (anisochronous) protons, the "multiplicity" of the carbon in question is irrefutably obvious. For isotropic methylenes and other resonances, the multiplicity of the resonance (CH, CH_2, or CH_3) in question may be less obvious. Early work by Kessler and co-workers [119] addressed this issue via the development of the DEPT–HMQC experiment. Multiplicity editing is also available for experiments such as GHSQC. An extra pair of delays and pulses, with the flip angle of the proton pulse being adjustable, allow the acquisition of data in which the response phase is indicative of resonance multiplicity [120–122]. The multiplicity-edited GHSQC sequence presently in use in the author's laboratory is shown in Figure 8.22; the framed segment of the pulse sequence provides the multiplicity editing. Adjusting the flip angle α of the proton pulse to 180° affords a spectrum in which the phase of the methine/methyl resonances is opposite to that of the methylenes. By setting the "adjustable" pulse to $\alpha = 90^\circ$ a spectrum containing only methine resonances is obtained. The multiplicity-edited GHSQC spectrum of the aliphatic region of the spectrum of strychnine (**2**) is shown in Figure 8.21b; responses plotted in red denote inverted methylene resonances while black responses denote positive methine resonances (there are no methyl groups in strychnine).

8.3.6.2 Accordion-Optimized Direct Heteronuclear Shift Correlation Experiments

Following the development of accordion-optimized long-range heteronuclear shift correlation experiments (Section 8.3.7.3), Hadden and Angwin [123] have recently reported the development of an accordion-optimized direct correlation experiment, accordion-optimized direct correlation single quantum coherence (ADSQC). Additionally, Zannger and Armitage [124] also reported the accordion-HMQC experiment. These experiments provide a convenient means of circumventing the choice of optimization in the direct correlation experiments. Under most

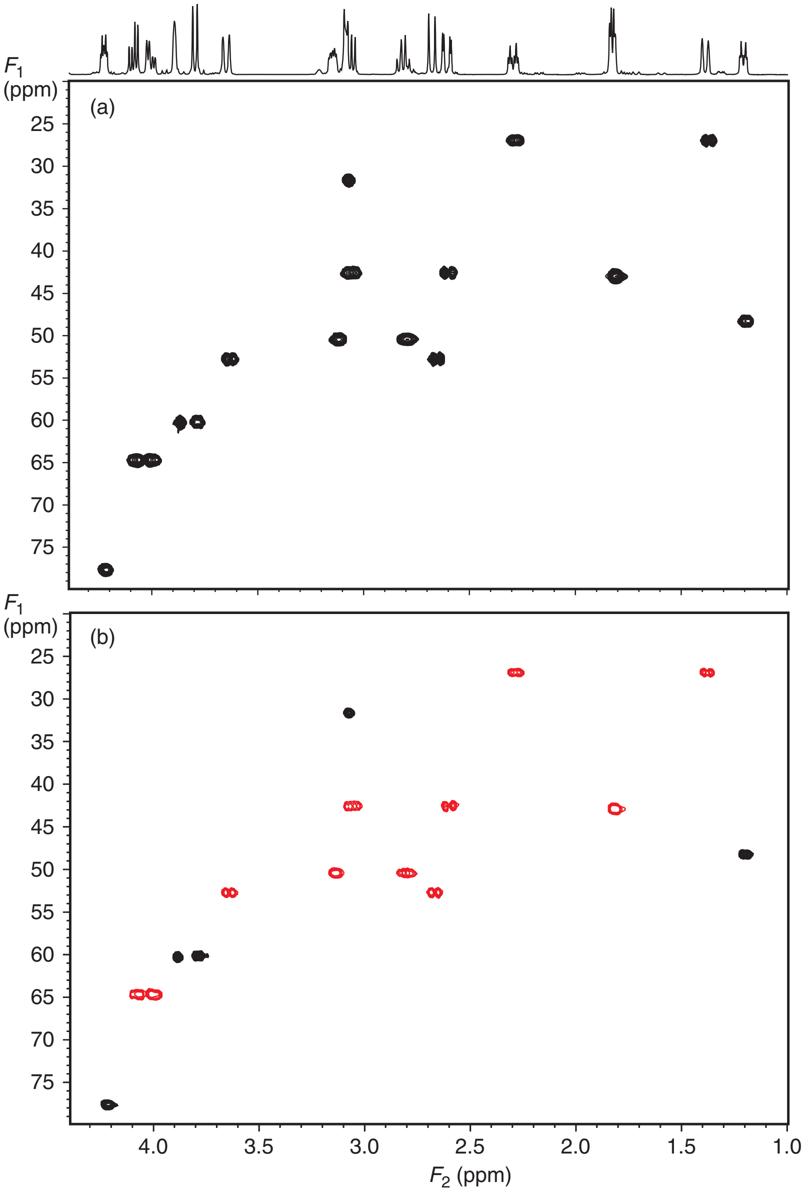

Figure 8.21 (a) GHSQC spectrum of the aliphatic region of the strychnine (**2**) spectrum recorded using the pulse sequence shown in (b). Multiplicity-edited GHSQC [119–122] spectrum of strychnine showing methylene resonances in red and opposite in phase from methine and methyl resonances that are shown in black (no methyls are in the strychnine structure). These data were acquired using the pulse sequence shown in Figure 8.22 with the multiplicity editing step following the reverse INEPT portion of the experiment.

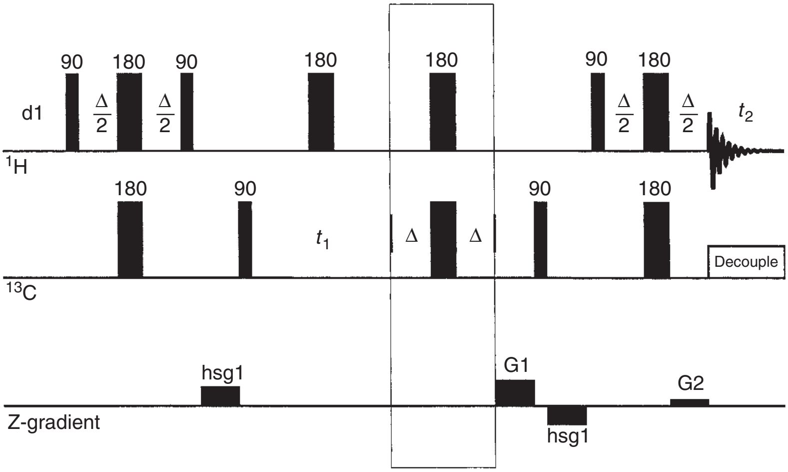

Figure 8.22 Schematic representation of the multiplicity-edited GHSQC pulse sequence in use in the author's laboratory with the multiplicity editing step following the evolution period [119–122].

circumstances a one-bond correlation experiment is not problematic; survey optimization of the one-bond delays for ∼140 Hz provides quite reliable results. However, molecules containing some heterocyclic moieties, for example, furans and other species having proton–carbon pairs with exceptionally large one-bond coupling constants may fail to give direct correlation responses under standard survey conditions. As an example, the two-position of furan has a 208 Hz $^1J_{CH}$ coupling that reproducibly fails to give a direct correlation response under standard survey conditions. By optimizing the ADSQC or accordion-HMQC over a range of one-bond couplings, for example, 120–210 Hz, this problem can be avoided.

8.3.7
Long-Range Heteronuclear Chemical Shift Correlation

Successful exploitation of the use of one-bond ($^1J_{CH}$) heteronuclear coupling constants in the development of direct heteronuclear shift correlation experiments in the late 1970s prompted the visionary suggestion of Hallenga and van Binst [105] in 1980 of doing the same experiment using instead the long-range heteronuclear coupling, $^nJ_{CH}$. Unfortunately, the long-range heteronuclear chemical shift correlation experiment was not realized in their seminal work. Rather, it remained for Reynolds and co-workers [106] in 1984 to demonstrate experimentally the viability of long-range heteronuclear chemical shift correlation experiments.

Reynolds' initial report sparked the development of numerous long-range heteronuclear shift correlation experiments that continued through about 1986. Experiments developed included the constant time correlation by long-range coupling (COLOC) experiment [125, 126], experiments designed to decouple one-bond modulation effects [127, 128], and the XCORFE experiment of Reynolds and co-workers

[129] that allowed the differentiation of $^{2}J_{CH}$ from $^{3}J_{CH}$ long-range couplings to protonated carbon resonances (**4**). The heteronucleus-detected long-range shift correlation experiments are the topic of a 1986 review by Martin and Zektzer [107].

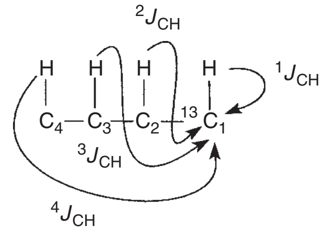

4

Bax and Summers [130] 1986 report of the proton-detected heteronuclear multiple bond correlation (HMBC) experiment essentially ushered to a close the development of new, heteronuclide-detected long-range chemical shift correlation experiments. Aside from the development of a gradient-enhanced heteronuclear multiple bond correlation (GHMBC) experiment [131, 132] there was a nearly decade-long hiatus in the development of new, inverse-detected, long-range heteronuclear shift correlation methods. More recently, the reported development of new proton-detected long-range experiments has resumed and is treated briefly in the following sections of this chapter.

The increase in sensitivity afforded by the proton-detected HMBC experiment revolutionized structure elucidation studies. The utilization of HMBC data in the characterization of alkaloid structures has been reviewed [70] and is also treated in a more general review of the application of inverse-detected methods in natural products structure elucidation [71]. Other applications of the experiment are quite numerous and any complete survey is beyond the scope of this chapter. It should also be noted here that within the past five years it has become feasible to perform long-range $^{1}H-^{15}N$ heteronuclear shift correlation experiments at natural abundance, which is the subject of a recent review by two of the authors [72].

8.3.7.1 **HMBC, Heteronuclear Multiple Bond Correlation**

The original pulse sequence for the HMBC experiment, as reported in 1986 by Bax and Summers [130] is shown in Figure 8.23a. The sequence begins with a pulse sequence operator known as a *low-pass J-filter*. Alternatively, dual stage gradient low-pass *J*-filters [133, 134] or double pulsed field gradient spin echoes (DPGSEs) [135] can be substituted for the low-pass *J*-filter and afford substantially better suppression of residual direct response signals. This component of the experiment is designed to remove unwanted direct correlation responses. While the 90° X-pulse in the low-pass *J*-filter is phase cycled as 0022, the receiver phase is cycled 0202, which effectively adds and subtracts the unwanted direct response component of magnetization. The first delay, Δ, is optimized as a function of $1/2(^{1}J_{CH})$. The second 90° X-pulse, which is applied after a delay, δ, of $1/2(^{n}J_{CH})$, where $n = 2$ or 3 and corresponds to an optimization in the range of 6–10 Hz, creates heteronuclear zero and double quantum coherence that begins to evolve through the evolution

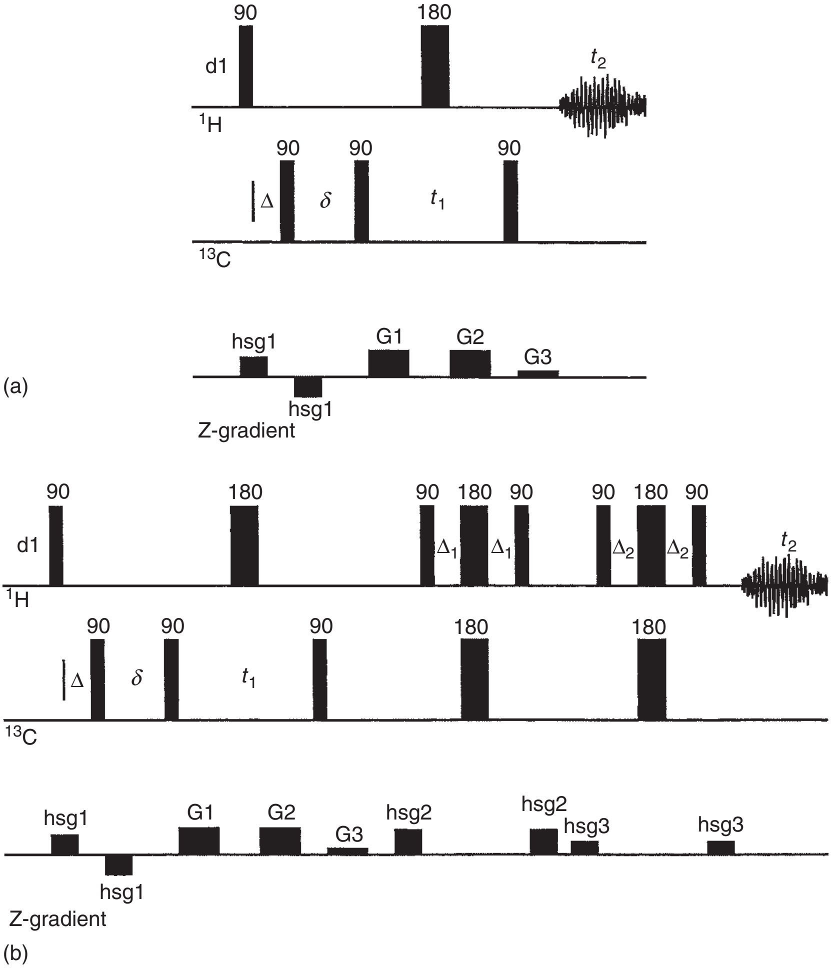

Figure 8.23 (a) Schematic representation of the original HMBC experiment of Bax and Summers [130]. The experiment begins with a low-pass *J*-filter. The phase of the first 90° ^{13}C pulse is alternated 0202 while the receiver phase is cycled as 0022. In this fashion, the magnetization arising from the direct correlation responses is alternately added and subtracted in memory and ultimately canceled. Much like the HMQC experiment, HMBC creates zero and double quantum coherences but does so for the long-range couplings rather than the direct couplings. Given that long-range couplings are typically in the range of about 6–10 Hz, delays in the range from 83 to 50 s, respectively, are typical. The HMBC experiment has been largely replaced by the gradient or GHMBC experiment [125, 126] in many NMR laboratories. (b) The version of the GHMBC experiment currently in use in the author's laboratories is shown here and employs a double pulsed field gradient spin echo (DPFGSE) [135] to suppress the residual, unwanted direct correlation responses. For very weak samples, recent work has shown that it is actually preferable to utilize the non-gradient phase cycled version of the HMBC experiment rather than the newer gradient versions of the experiment [99].

period, t_1. The 180° ^{1}H pulse interchanges zero and double quantum coherence terms and simultaneously removes proton chemical shift evolution. The last 90° X-pulse pulse converts the HMQCs back into observable single quantum coherence, which is then detected. Gradient versions of the experiment were developed in the early 1990s by Willker and co-workers [131] and by Rinaldi and Keifer [132] and are now generally used *in lieu* of the original, non-gradient version of the experiment (Figure 8.23b).

The aliphatic region of the 6 Hz optimized GHMBC spectrum of strychnine is shown in Figure 8.24a. In the specific case of the H-12 resonance of strychnine, only a single long-range correlation of the several possible long-range couplings (shown in **5**) is observed in the spectrum. We will use the H12 correlations as a performance comparison for several of the more recently developed, accordion-optimized long-range experiments described below. Correlations which predominate in HMBC/GHMBC spectra are $^2J_{CH}$ and $^3J_{CH}$ with $^4J_{CH}$ long-range correlations observed only occasionally. In the specific case of strychnine, four $^4J_{CH}$ couplings are typically observed in the 10 Hz optimized GHMBC spectrum.

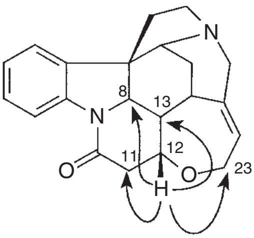

5

Structure elucidation strategies that employ long-range heteronuclear shift correlation experiments generally use the correlations observed to position quaternary atoms relative to protonated carbon fragments, for example, in the case of a correlation from H-12 to the C-8 quaternary carbon, or to bridge heteroatoms, for example, the correlation from H-12 to C-23 across the oxepin ether linkage, as shown above.

Figure 8.24 (a) GHMBC experiment recorded using the gradient variant of the pulse sequence shown in Figure 8.23a. The spectrum shown is the aliphatic region of the strychnine (**2**) spectrum; the long-range delays in the GHMBC sequence delays in the experiment were optimized for 6 Hz. Note that for the H12 resonance (furthest downfield at 4.27 ppm) only one response is observed in the data shown, which correlates H12 to C8. Care must be exercised when interpreting weak responses in HMBC/GHMBC experiment such as that denoted with the arrow that correlates the H18a resonance via two bonds to C17. (b) Data from a 6–10 Hz optimized ACCORD-HMBC (Figure 8.25) experiment [136, 134] for the same region of the strychnine (**2**) spectrum. The ability to sample a broad range of potential long-range couplings in a single experiment is well demonstrated by these data. When compared to the GHMBC spectrum shown in Figure 8.24a, the H12 resonance, for instance, shows four correlation responses. While the H18a–C17 correlation response was weak in the GHMBC data, it is now quite strong. Furthermore, the characteristic F_1 "skew" of the ACCORD-HMBC data provides a convenient means of response authentication: legitimate long-range correlations will be skewed, making them readily distinguishable from weak noise peaks. (Reproduced with permission – Wiley-VCH.)

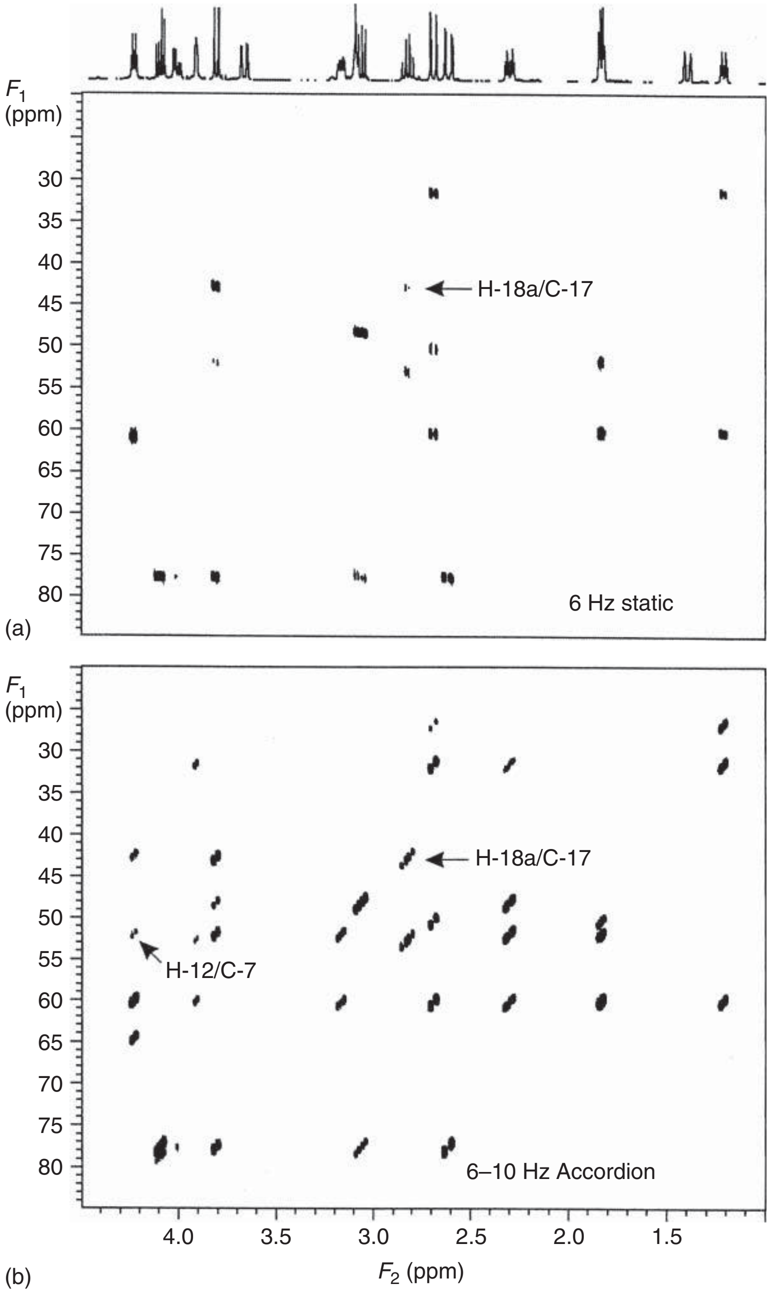
F_1 (ppm)
30
35
40
45
50
55
60
65
70
75
80
H-18a/C-17
6 Hz static
(a)
F_1 (ppm)
30
35
40
45
50
55
60
65
70
75
80
H-18a/C-17
H-12/C-7
6–10 Hz Accordion
4.0
3.5
3.0
2.5
2.0
1.5
F_2 (ppm)
(b)

8.3.7.2 Variants of the Basic HMBC Experiment

Beginning in 1995, a number of reports of variants of the HMBC/GHMBC experiment began to appear. The inclusion of a refocusing delay to allow broadband decoupling during acquisition was described by Bermel *et al.* [137]; Furihata and Seto [138] subsequently described this experiment giving it the acronym D-HMBC experiment, apparently unaware of the prior work by Bermel *et al.* A report of a pseudo-3D variant followed, each plane of the third dimension having a different long-range optimization [139]. Projection of the F_2/F_3 plane gave, albeit rather inefficiently, the equivalent of an accordion-optimized spectrum. Marek and coworkers [140] described a phase-sensitive single quantum long-range experiment, GSQMBC, that allowed in the case of some multiplets, the measurement of long-range heteronuclear couplings. Another phase-sensitive method was reported in 1998 by Sheng and van Halbeek [141] for the purpose of extracting long-range heteronuclear couplings. Later in 1998, Furihata and Seto [142] described several constant time variants of the basic HMBC experiment in an effort to suppress homonuclear coupling modulations that arise during the incrementation of the evolution time, t_1. These experiments set the stage for the subsequent development of accordion-optimized long-range experiments.

8.3.7.3 Accordion-Optimized Long-Range Heteronuclear Shift Correlation Methods

The idea of accordion-optimization is by no means new [143]. The idea of applying this method to the optimization of the long-range delay of HMBC-type experiments, however, was only reported in 1998 by Wagner and Berger [136] in their description of the ACCORD-HMBC experiment. The ACCORD-HMBC pulse sequence is shown in Figure 8.25. Quite simply, the ACCORD-HMBC experiment is governed by the limits $1/2^nJ_{\text{min}}$ to $1/2^nJ_{\text{max}}$, which correspond to τ_{max} to τ_{min}, respectively. As the evolution time, t_1, is systematically incremented, the duration of the variable delay, Vd, is decremented from τ_{max} to τ_{min} in increments of $(\tau_{\text{max}} - \tau_{\text{min}})/n_{\text{i}}$, where n_{i} is the number of increments of the evolution period. In this fashion, the ACCORD-HMBC experiment essentially integrates across a range of potential long-range couplings, allowing the complete range to be sampled in a single experiment.

A drawback of accordion-optimization of the long-range delay in the ACCORD-HMBC experiment is F_1 "skew" caused by homonuclear coupling modulation occurring during the variable delay, which serves as a pseudo-evolution period for these processes [134]. Conversely, F_1 skew also serves as a determinant of response authenticity for weak long-range responses since noise or other random signals cannot exhibit F_1 skew.

Comparison of the performance of a statically optimized GHMBC (i.e., optimized for a single value of the long-range delay) experiment with ACCORD-HMBC is shown by comparing the spectral segments shown in Figure 8.24. The 6 Hz optimized GHMBC results are shown in Figure 8.24a. A single correlation from the H12 resonance is observed in this data. In contrast, for the 6–10 Hz optimized ACCORD-HMBC spectrum presented in Figure 8.24b, four correlations, those shown by **5**, are observed from the H12 resonance. In addition, some correlations, such as the H18a–C17 correlation, which is observed with weak response intensity

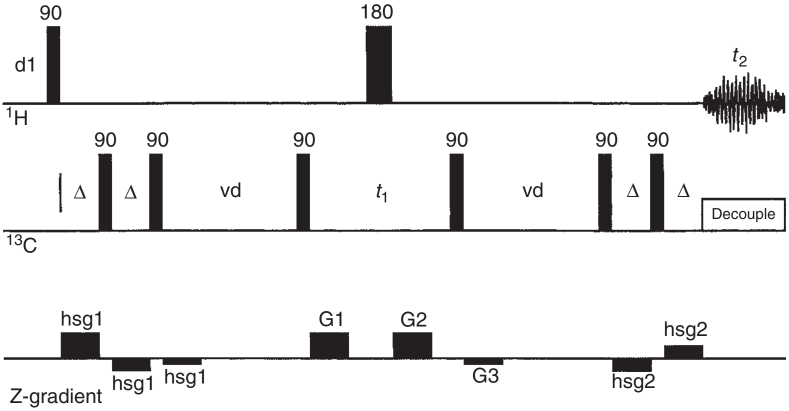

Figure 8.25 Pulse sequence schematic for the ACCORD-HMBC experiment pioneered by Wagner and Berger [136]. The experiment begins with a gradient dual-stage low-pass *J*-filter to suppress unwanted direct correlation responses. A variable duration delay, Vd, follows, the duration of which is decremented from $1/2^nJ_{\text{min}}$ to $1/2^nJ_{\text{max}}$ (τ_{max} and τ_{min}, respectively) in successive increments of the evolution time, t_1. In this fashion, all possible long-range couplings in the user-selected range are sampled in a single experiment. The 90° ^{13}C pulse following the variable delay functions in the usual fashion to create heteronuclear zero and double quantum coherences which are manipulated as in the HMBC/GHMBC experiment (Figure 8.23). To allow broadband heteronuclear decoupling during acquisition, Wagner and Berger originally proposed a symmetric experiment so that all long-range couplings are refocused immediately prior to acquisition. In practice, we have found that it is actually desirable to initiate acquisition following the final coherence pathway selection gradient to avoid potential signal losses due to the long, variable delay.

in the 6 Hz optimized GHMBC spectrum, are observed with much better response intensity in the accordion-optimized experiment.

An ACCORD-HMBC spectrum of the aliphatic region of strychnine optimized over the range 2–25 Hz is shown in Figure 8.26. It is interesting to note that while only four $^4J_{\text{CH}}$ long-range couplings are observed in the 10 Hz GHMBC spectrum of strychnine, 17 such couplings are observable in this very aggressively optimized ACCORD-HMBC spectrum, as shown in **6** [134].

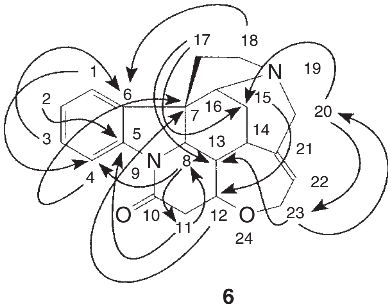

6

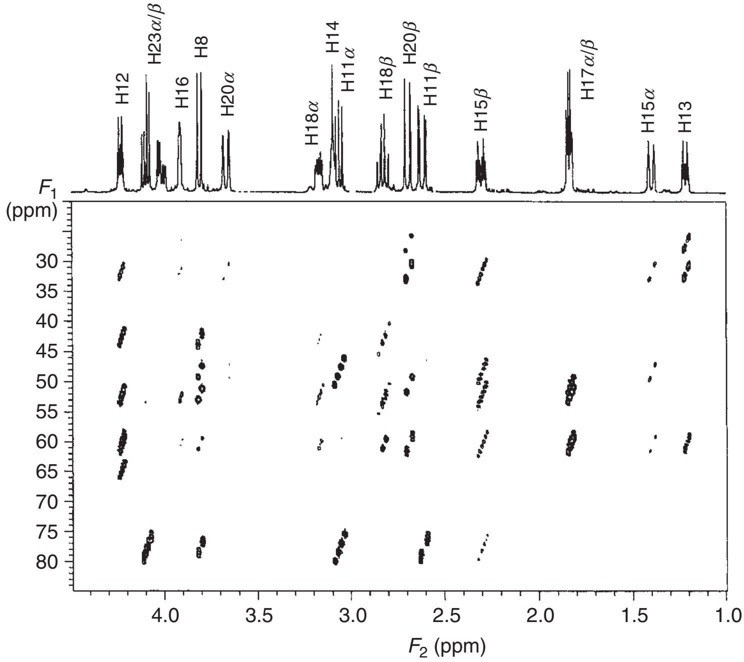

Figure 8.26 Results of an aggressively optimized 2–25 Hz ACCORD-HMBC experiment performed on strychnine (**2**) are presented here. Such data might be used when it becomes necessary to resort to relatively uncommon four-bond (${}^{4}J_{\mathrm{CH}}$) long-range couplings to solve a structural problem. In the 10 Hz optimized GHMBC spectrum of strychnine (**2**) a total of four four-bond long-range couplings are observed. In contrast, the 2–25 Hz ACCORD-HMBC experimental data shown identified 17 four-bond long-range couplings as shown by **6**. (Reproduced with permission – Wiley-VCH.)

Homonuclear coupling modulation during the variable delay in the ACCORD-HMBC experiment prompted the development of a constant time variable delay to replace the simple variable delay in the ACCORD-HMBC experiment. This pulse sequence element was incorporated into the IMPEACH-MBC (improved performance accordion heteronuclear multiple bond correlation) experiment [144]. The constant time variable delay segregates the manipulation of homo- and heteronuclear components of magnetization. First, by keeping the overall duration of this pulse sequence operator constant, homonuclear coupling modulation can be made to occur in constant time, thereby rendering the effect of this modulation unobservable. This then requires a modification of the delay to maintain its variable character for long-range heteronuclear couplings. This task is accomplished by adding a second variable delay, D, within the overall constant time variable delay which contains the following element:

$$\begin{array}{l} D/2 - 180^{\circ}\,{}^{13}\mathrm{C} - D/2 - \mathrm{Vd} \\ |\longleftarrow\ {}^{n}J_{\mathrm{CH}}\ \text{refocused}\ \longrightarrow|\longleftarrow\ {}^{n}J_{\mathrm{CH}}\ \text{evolves}\ \longrightarrow| \end{array} \tag{8.6}$$

The variable delay, D, is halved about a 180° ^{13}C pulse which serves to refocus $^{n}J_{CH}$ components of magnetization at D. These same components of magnetization then experience a variable delay, Vd, during which they are sampled. The accordion range is determined as in the ACCORD-HMBC experiment. However, as the duration of Vd is decremented from τ_{max} by $(\tau_{max} - \tau_{min})/n_i$, rather than allowing the overall duration of the delay to be decremented, the interval $[(\tau_{max} - \tau_{min})/n_i]/2$ is instead added to each of the $D/2$ intervals keeping the total duration constant. Thus, while homonuclear coupling processes evolve in a constant time, $^{n}J_{CH}$ components of magnetization are refocused at D and evolve only during the variable delay, Vd, thereby eliminating F_1 skew with the exception of that which arises due to the incrementation of the evolution period, t_1, which is identical to what one observes in the HMBC/GHMBC experiments.

While uncontrolled F_1 response skew of the type encountered in the ACCORD-HMBC experiment is undesirable [134], user-defined F_1 skew can be a useful determinant of response authenticity. A further generation accordion-optimized long-range experiment, CIGAR-HMBC (constant time inverse-detected gradient accordion rescaled long-range heteronuclear multiple bond correlation), was developed to provide this flexibility. The constant time variable delay from the IMPEACH-MBC experiment was further modified as follows:

$$(D/2 + \Delta2/2) - 180^{\circ}\,{}^{13}\mathrm{C} - (D/2 + \Delta2/2) - \mathrm{Vd} \qquad (8.7)$$

The range of optimization is defined as in the previous experiments; Vd is decremented and D is incremented as in the IMPEACH-MBC experiment [144]. The interval $\Delta2$ is used to provide user-defined F_1 skew. The CIGAR-HMBC experiment uses a new parameter J_{scale} to control the extent of F_1 skew introduced [145]. The duration of $\Delta2$ is incremented by the interval $(J_{scale} - 1)t_1$. There are three possible conditions: $J_{scale} = 0$, 1, >1. When $J_{scale} = 0$, the interval $\Delta2$ will actually be decremented as the evolution time, t_1 is incremented, keeping the total duration of the experiment completely constant. This results in the suppression of homonuclear coupling modulation occurring during the incremented evolution period and gives the highest possible F_1 resolution as in the CT-HMBC experiment described by Furihata and Seto [142]. When $J_{scale} = 1$, results identical to an IMPEACH-MBC experiment are obtained. Finally, and most interestingly, when $J_{scale} > 1$, the overall duration of the modified constant time variable delay becomes ''non-constant'' in a user-defined manner. Incrementation of the $\Delta2/2$ intervals in the experiment reintroduces F_1 skew to a user-determined extent. The degree of F_1 skew is determined by the setting of the parameter J_{scale} as illustrated in Figure 8.27.

8.3.7.4 ^{2}J,^{3}J-HMBC

The most sophisticated accordion-optimized long-range shift correlation experiment to be developed to date is the ^{2}J,^{3}J-HMBC experiment [146]. For the first time in an inverse-detected experiment, it is possible to differentiate two-bond from three-bond long-range correlations to protonated carbon or nitrogen resonances. This

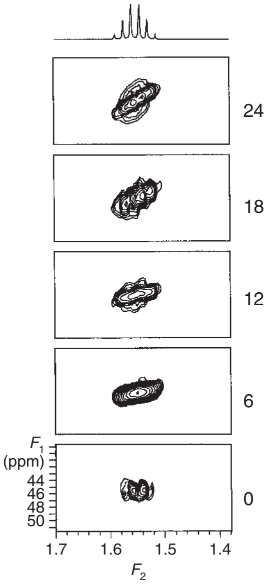

Figure 8.27 F_1 skew inherent to responses in ACCORD-HMBC spectra is only partially user controllable. These properties prompted the development of the IMPEACH-MBC experiment [144], which suppresses F_1 skew. Further modification to re-introduce user-controlled F_1 skew was incorporated into the CIGAR-HMBC experiment using a parameter called J_{scale} [145]. The effect of adjusting the J_{scale} parameter in the CIGAR-HMBC experiment is shown for the 3-methylene group of 2-pentanone over a range of J_{scale} settings from 0 to 24.

capability was last available for protonated carbons *via* the heteronucleus-detected XCORFE sequence pioneered by Reynolds and co-workers in 1985 [129].

Selective manipulation of the various components of magnetization to allow the differentiation of two-bond from three-bond long-range correlations is through the application of a new pulse sequence operator given the acronym STAR (selectively tailored accordion F_1 refocusing) shown schematically in Figure 8.28a while the full ${}^2J,{}^3J$-HMBC pulse sequence is shown in Figure 8.28b. Homonuclear couplings evolve through the D interval, while heteronuclear couplings are refocused by the 180° ^{13}C pulse prior to the second $D/2$ segment. The interval $\Delta 1$ is incremented from zero by $J_{\mathrm{scale}} \times t_1$ $J_{\mathrm{scale}} \times t_{1\mathrm{max}}$ while conversely, the $\Delta 2$ delay is decremented from $J_{\mathrm{scale}} \times t_{1\mathrm{max}}$ to zero. Hence, the sum of the $\Delta 1 + \Delta 2$ intervals is constant. All homonuclear couplings evolve through $\Delta 1$; all long-range heteronuclear couplings

Figure 8.28 The ${}^2J,{}^3J$-HMBC experiment is the most sophisticated accordion-optimized long-range heteronuclear shift correlation experiment reported to date [146]. The experiment uses a pulse sequence operator known as a STAR (selectively tailored F_1 accordion refocusing) to selectively manipulate two-bond and three-bond long-range correlations to protonated carbon or nitrogen resonances. (a) STAR operator used in the ${}^2J,{}^3J$-HMBC experiment. The experiment takes advantage of the ability of a BIRD(*x*, *x*, *x*) pulse to refocus the one-bond heteronuclear coupling of a protonated carbon. By doing this, the ${}^2J_{\mathrm{CH}}$ coupling to this proton labeled "A" in **7** is effectively decoupled. Within the STAR operator, the consequence of this event is to cause the ${}^2J_{\mathrm{CH}}$ long-range coupling to evolve in variable time (see evolution bars above the operator schematic), leading this response to selectively exhibit F_1 skew. (b) Incorporation of the STAR operator into the ${}^2J,{}^3J$-HMBC pulse sequence. Some of the detail in the expansion of the operator in (a) is eliminated for clarity. The schematic representation of the expectation of the results of using the STAR operator in the ${}^2J,{}^3J$-HMBC experiment are shown in Figure 8.29.

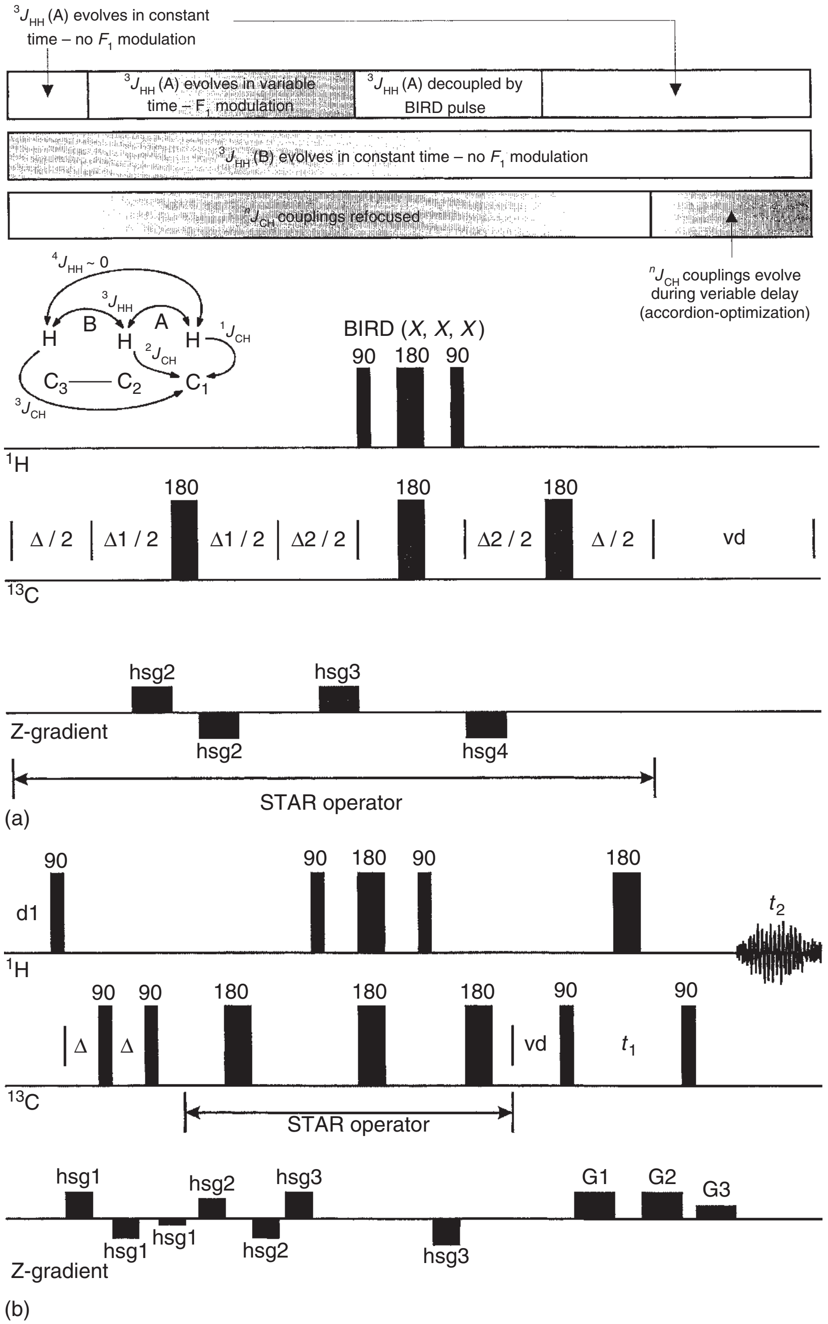
$^3J_{HH}$ (A) evolves in constant time – no F_1 modulation
$^3J_{HH}$ (A) evolves in variable time – F_1 modulation
$^3J_{HH}$ (A) decoupled by BIRD pulse
$^3J_{HH}$ (B) evolves in constant time – no F_1 modulation
$^nJ_{CH}$ couplings refocused
$^nJ_{CH}$ couplings evolve during veriable delay (accordion-optimization)
$^4J_{HH}$ ~ 0
$^3J_{HH}$
B
A
H
H
H
$^1J_{CH}$
$^2J_{CH}$
C_3
C_2
C_1
$^3J_{CH}$
BIRD (X, X, X)
90
180
90
^1H
180
180
180
Δ / 2
Δ1 / 2
Δ1 / 2
Δ2 / 2
Δ2 / 2
Δ / 2
vd
^{13}C
hsg2
hsg3
Z-gradient
hsg2
hsg4
STAR operator
(a)
90
90
180
90
180
d1
t_2
^1H
90
90
180
180
180
90
90
Δ
Δ
vd
t_1
^{13}C
STAR operator
hsg1
hsg2
hsg3
G1
G2
G3
hsg1
hsg1
hsg2
hsg3
Z-gradient
(b)

are refocused by the 180° ^{13}C pulse at $\Delta1/2$. The BIRD pulse located at $\Delta2/2$ serves as a 180° pulse for ^{1}H–^{13}C$_1$ and as a 360° pulse for other couplings. This results in a selective refocusing of the $^{3}J_{HH}$ coupling between H_2–$H_1{}^{13}C$. As a consequence of the incrementation of $\Delta1$ and the decrementation of $\Delta2$, the sum of the two intervals serves as a variable delay for this homonuclear coupling, causing the $^{2}J_{C1H2}$ coupling response to be selectively skewed in F_1 while other long-range correlations have the appearance of what would be the corresponding response in the IMPEACH-MBC experiment with $J_{scale} = 1$. The appearance of the long-range couplings from H11α–C12 ($^{2}J_{CH}$) and from H11α–C13 ($^{3}J_{CH}$) are shown schematically in Figure 8.29; experimental results are presented in Figure 8.30. The "staggered skew" exhibited by the two-bond H11α–C12 correlation response is typical of two-bond long-range correlations in the $^{2}J,^{3}J$-HMBC experiment. The setting for the parameter J_{scale} as in the predecessor CIGAR-HMBC experiment, [145] allows user control over the degree of staggered F_1 skew of two-bond responses in the experiment.

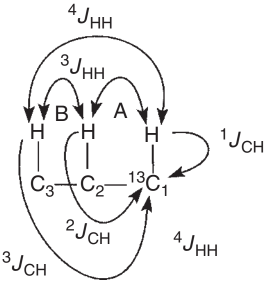

7

8.3.7.5 **Relative Sensitivity of Long-Range Heteronuclear Shift Correlation Experiments**

Relative to direct correlation experiments, the various long-range correlation experiments now available are all lower in sensitivity. It is generally accepted that the HMBC experiment ranges from one-fourth to one-eighth the sensitivity of a direct correlation experiment. While comparative data are not available for all of

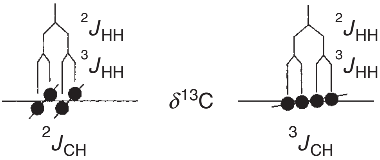

Figure 8.29 Schematic representation of expectations for two-bond (left, e.g., the H11α–C12) and three-bond long-range couplings (right, e.g., the H11α–C13) long-range couplings in strychnine (**2**). The staggered F_1 skew is typical of what would be expected from the function of the STAR operator. Experimental verification of these anticipated results is shown in Figure 8.30. (Reproduced with permission – Academic Press.)

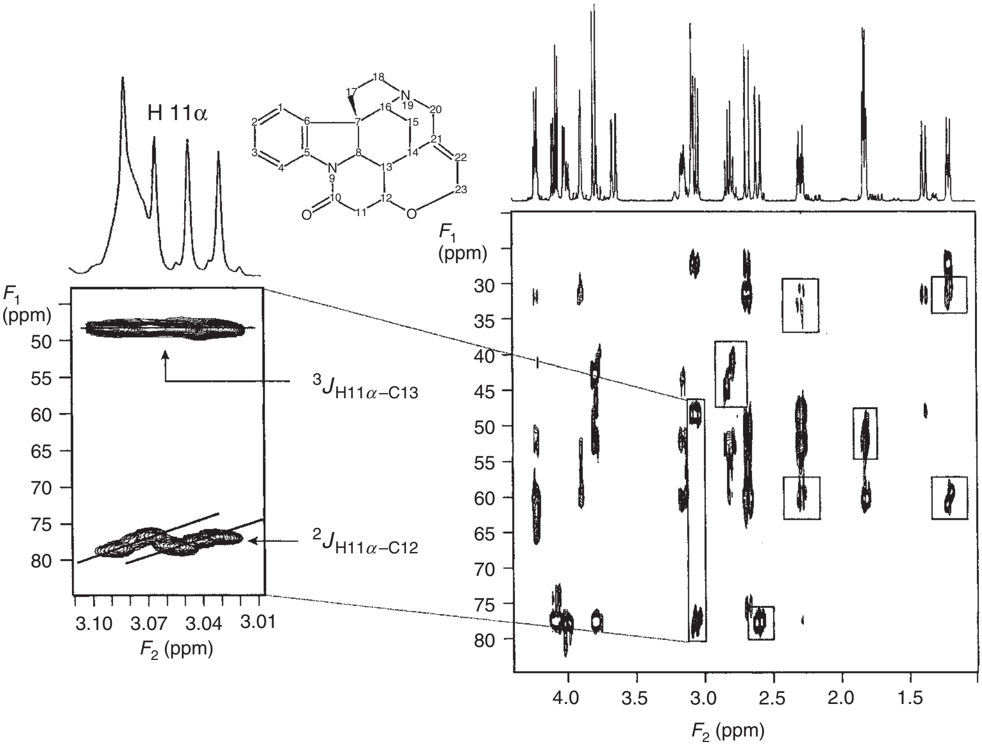

Figure 8.30 Results obtained with the $^2J,^3J$-HMBC using strychnine (**2**) as a model compound [146]. The aliphatic region is shown. The expanded region shows the two- and three-bond correlations from H11α to C12 and C13. The staggered F_1 skew exhibited for the H11α–C12 two-bond correlation is consistent with the schematic shown in Figure 8.29. The experiment utilizes an accordion-optimization range (6–10 Hz) as in predecessor experiments. The parameter J_{scale} is also employed to allow a user-selected degree of F_1 skew to be introduced into the two-bond correlation responses ($J_{scale} = 16$). (Reproduced with permission – Academic Press.)

the available long-range experiments, all of the accordion-optimized long-range experiments have been directly compared to the HMBC experiment in the recent description of the $^2J,^3J$-HMBC experiment [146]. It is likely that the other available experiments will range in sensitivity from that of HMBC downward, with the 3D-HMBC experiment of Furihata and Seto [139] likely to have the lowest sensitivity of any of the available experiments.

8.3.7.6 **Applications of Accordion-Optimized Long-Range Heteronuclear Shift Correlation Experiments**

To date, aside from the papers reporting the development of the accordion-optimized long-range experiments there have only been two reported applications, although more will doubtless follow. Two of the authors have reported a comparison of accordion-optimized experiments for long-range $^1H-^{15}N$ heteronuclear shift correlation at natural abundance to avoid problems inherent to the optimization of these experiments with more conventional experiments [147]. Zannger and Armitage [124] have also reported the utilization of an accordion-optimized HMQC experiment for the observation of the possible long-range $^1H-^{113}Cd$ couplings in a metalloprotein. Most recently, Sørensen and co-workers [148] have reported a method for measuring long-range $^1H-^{31}P$ coupling constants in nucleic acids which utilizes the accordion methods just described.

8.3.8
Hyphenated-2D NMR Experiments

The inverse-detected 2D NMR experiments that have been discussed to this point have all been discrete, single-purpose experiments, for example, correlating protons with their directly bound heteronuclide (typically ^{13}C or ^{15}N). There are another class of inverse-detected 2D NMR experiments that are generally referred to as *hyphenated* 2D experiments. These are experiments that first establish one type of correlation, followed by an additional experiment segment that then pursues a further spectroscopic task. Predecessors of the inverse-detected variants of these experiments were the HC-RELAY (proton–carbon heteronuclear relayed coherence transfer) experiments pioneered by Bolton [149–153]. Examples of these include, but are by no means limited to HSQC–COSY and –TOCSY [154–156], –NOESY [157], –ROESY [158], and more recent gradient variants [159], and so on, where X = S (single) or M (multiple) quantum variants of the experiments.

Hyphenated 2D NMR experiments utilize the obligatory three fundamental experiment segments (preparation, evolution, and detection) with a fourth period, for example, a mixing period, inserted between evolution and detection. Probably the most commonly encountered member of this class of experiments is HSQC– or HMQC–TOCSY (there are, of course, non-gradient predecessor versions of these experiments) [154–156]. Using the modern GHSQC–TOCSY experiment as an example, the experiment begins with the usual preparation period followed by an evolution period which labels amenable protons (the experiment does not work for protons on oxygen, or nitrogen, for example, if a proton–carbon correlation experiment is being performed) with the chemical shift of the directly bound heteronuclide. After magnetization is transferred back to the proton in question, homonuclear vicinal coupling is propagated between contiguous protons as in a homonuclear TOCSY experiment. The proton magnetization ultimately acquired provides homonuclear TOCSY correlated proton spin systems sorted by the chemical shift of the directly bound carbon(s) in question. In similar fashion, the –COSY, –NOESY, and –ROESY related experiments provide the corresponding homonuclear correlation data sorted by heteronuclide chemical shift.

Direct response-edited variants of the HSQC– and HMQC–TOCSY experiments and their gradient analogs have been developed following the initial, pioneering report of the HSQC–TOCSY experiment by Domke [160]. Possible choices include inverted direct response (IDR) and suppressed direct response (SDR) variants

[161] and gradient variants of the experiment [162], which can be quite useful when dealing with homonuclear spin systems that contain direct and relayed correlation responses with AB character. In the case of molecules with AB spin systems, the ability to either IDR or SDR increases the certainty of observing the relayed correlation response, which is not always true in the original version of the heteronuclear relayed coherence experiments. The GHSQC–TOCSY pulse sequence with multiplicity editing capability is presented in Figure 8.31.

Unfortunately, the relative sensitivity of the hyphenated 2D NMR experiments, as a group, is not high. The more sensitive experiments, for example, GHSQC–TOCSY, are lower in sensitivity than the long-range experiments such as GHMBC by at least a factor of 2 in the experience of the authors. The–NOESY and –ROESY hyphenated variants are much lower in sensitivity since the S/N ratio in the data set must be high enough to allow the observation of NOE or ROE responses with intensities of only a small percentage of the direct responses to be observed. Despite the inherent insensitivity of these techniques they have still found a number of useful applications. Examples include the application of IDR GHSQC–TOCSY in the total assignment of the proton and carbon NMR spectra of complex marine polyether toxins such as brevetoxin-2 (**8**) [163] (Figure 8.32); the observation of couplings between overlapped protons [164]; ROEs between "equivalent" protons in C2 symmetric molecules [158, 165–168]; and the unequivocal determination of the structure of complex polynuclear heteroaromatics [166, 167] to list a few of the applications contained in the literature.

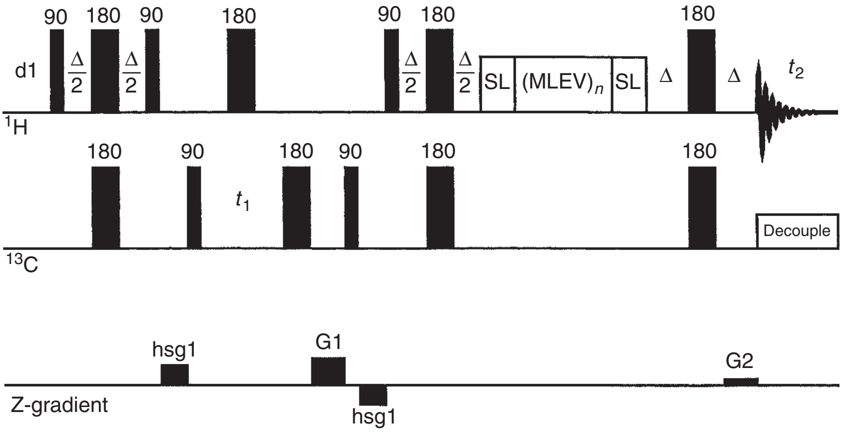

Figure 8.31 Pulse sequence schematic for the inverted direct response GHSQC–TOCSY experiment. After labeling protons with the respective, directly bound carbon chemical shifts, magnetization is propagated from a given proton to its vicinal and further removed neighboring protons through the isotropic mixing period. The number of bonds through which magnetization is propagated is a function of the duration of the mixing time.

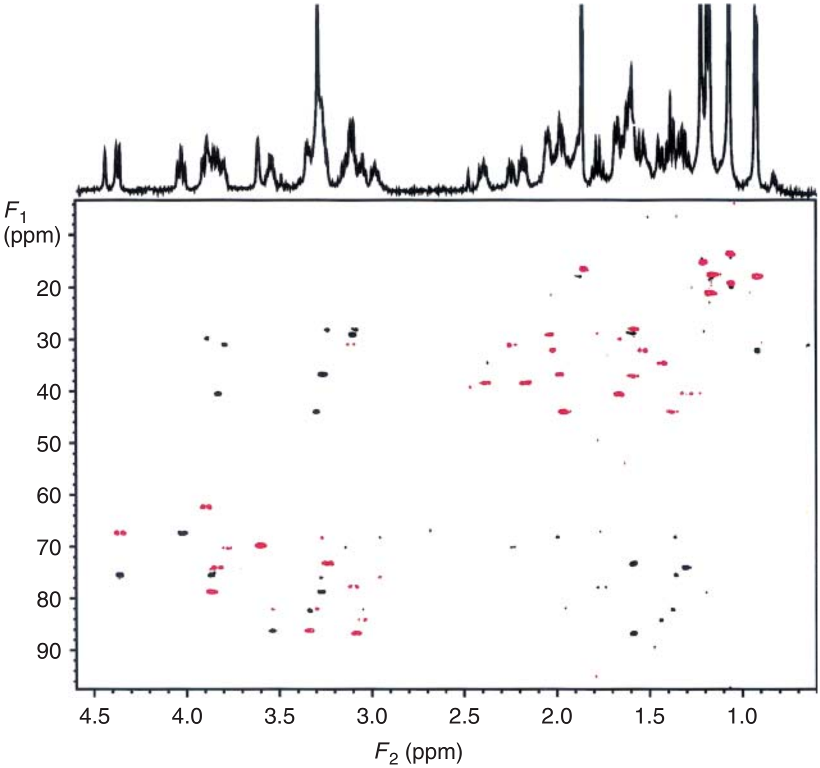

Figure 8.32 IDR GHSQC–TOCSY spectrum of a 500 µg sample of brevetoxin-2 (**8**) in 30 µl of d_6-benzene. Data were acquired at 600 MHz using a Varian INOVA spectrometer equipped with a Nalorac SMIDG-600-1.7 submicro gradient inverse detection probe. Data were acquired overnight. Direct responses are inverted and plotted in red; relayed responses have positive intensity and are denoted by black responses.

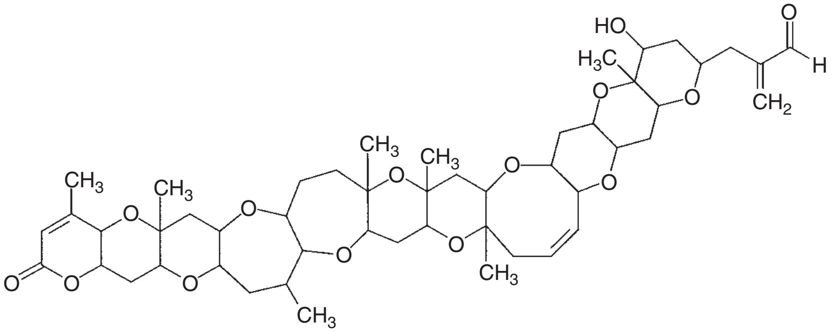

8

8.3.9
One-Dimensional Analogs of 2D NMR Experiments

Frequently, a single piece of correlation data such as an NOE or ROE, or a long-range heteronuclear coupling is sufficient to complete the structural characterization of a molecule. To provide these data, a number of selective, 1D analogs of 2D NMR experiments have been devised. Early work in this area has been reviewed by Kessler and co-workers in 1991 [169]. More recently, Parella [170] in 1996 and Berger [171] in 1997 have reviewed the combined use of selective pulses and gradients in NMR experiments. Specialized, shaped RF pulses frequently used in selective 1D NMR experiments have also been reviewed by Freeman [172]. At present, in the author's experience, the most frequently employed selective 1D NMR experiments are the gradient 1D NOESY experiment and selective 1D analogs of the HMBC experiment. These techniques are discussed in the following sections of this chapter.

8.3.9.1 **Gradient 1D NOESY**

Gradient selected experiments [104, 135, 173] are finding increased use in structural characterization. The gradient 1D NOESY experiment [173], in particular, is robust and has been very useful in the author's laboratory. The pulse sequence employs a DPFGSE (double pulsed field gradient spin echo) element to select the resonance for which NOEs will be developed and sampled in the experiment. The gradient 1D NOESY pulse sequence is shown in Figure 8.33. The selected resonance is refocused by the selective 180° pulses while other resonances are left in random orientations in the *xy*-plane. The resonance of interest is ultimately rotated to the $-z$-axis by the second 90° pulse. The NOE develops during the ensuing mixing delay, τ_m, and is sampled by the final 90° pulse. Results that can be obtained with the gradient 1D NOESY experiment are shown in Figure 8.34 and are compared to results from a conventional NOE difference experiment. Gradient 1D NOESY

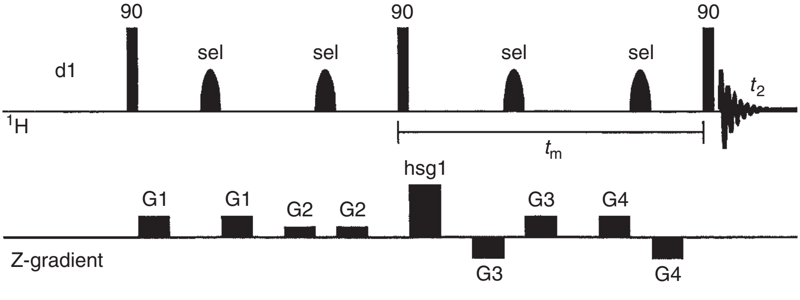

Figure 8.33 Pulse sequence schematic for the gradient 1D NOESY experiment. The double pulsed field gradient spin echo (DPFGSE) refocuses only for that resonance subject to the selective pulse. All other magnetization is left defocused in the *xy*-plane. Ultimately, a NOESY spectrum is recorded only for the selected resonance. In general 1D gradient NOESY data are substantially freer of subtraction artifacts, and so on, than the older 1D NOE difference experiment data (Figure 8.34). In essence, 1D gradient NOESY represents a selected "slice" of what would otherwise be a normal 2D NOESY experiment.

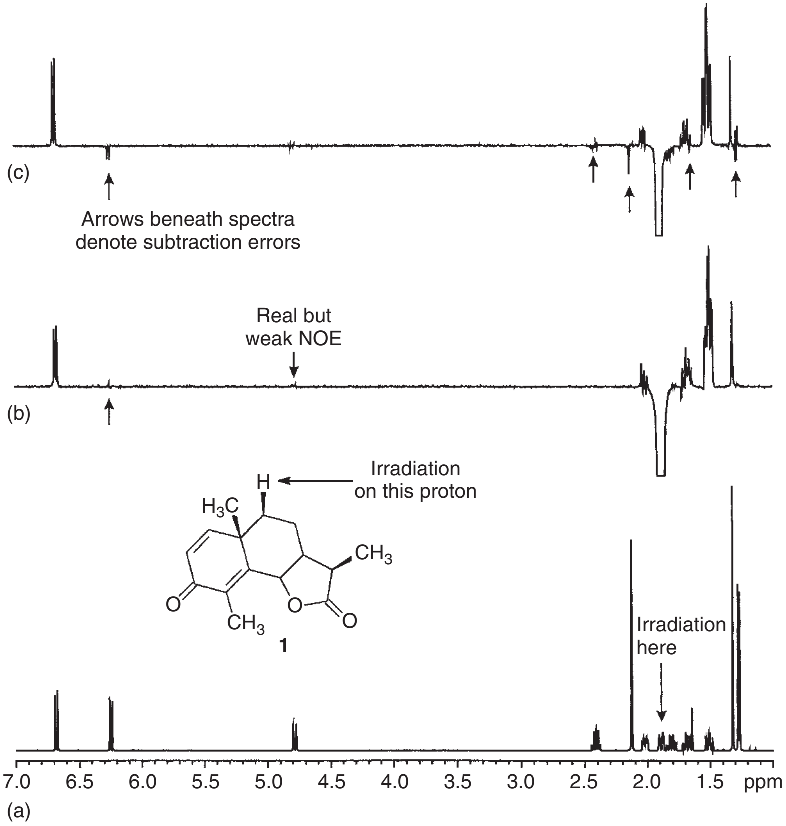

Figure 8.34 Application of the 1D gradient NOESY experiment to santonin (**1**). Comparison reference spectrum (a), 1D gradient NOESY (b), and 1D NOE difference (c) spectra. The proton shown on the structure inset was selected for both the 1D gradient NOESY data shown in trace (b) and the 1D NOE difference data shown in trace (c). The gradient 1D NOESY data shown in trace (b) is substantially free of artifacts with the exception of the one response denoted by an arrow below the trace and potential strong coupling effects for the geminal coupling partner of the selected resonance. In comparison, the 1D NOE difference data shown in trace (c) have a substantial number of subtraction artifacts, as denoted by arrows below the trace.

experiments are particularly useful in that they do not require the calculation of difference spectra to observe the NOE being sought and they cleanly remove signals not arising from NOEs making them more readily interpretable. These data are very useful for qualitative determinations of stereochemical orientation.

Unlike steady-state NOEs calculated from difference spectra, the transient NOEs determined using the 1D gradient NOESY technique have some attributes associated with responses that are worthy of mention. Responses are sensitive to mixing time choices and may vary markedly as a function of this parameter choice. The NOE enhancement will depend on the degree of inversion, which can be influenced by pulse calibration. This can lead to the absolute percentage enhancement that is observed being smaller than in a NOE difference experiment, necessitating a ''recalibration'' of what the spectroscopist may consider to be a reliable response. Despite the potential shortcomings just noted, gradient 1D NOESY experiments are extremely useful and will probably see more widespread use with time.

8.3.9.2 **Selective 1D Long-Range Heteronuclear Shift Correlation Experiments**

Situations frequently arise where one or a few heteronuclear correlations are all that is needed to complete the elucidation of a given structure. Often this missing information is a consequence of an inappropriate choice for the optimization of the long-range delay if HMBC/GHMBC experiments are being employed. In such situations, rather than acquiring another full, long-range 2D experiment, it is far more expedient to consider the acquisition of a selective long-range heteronuclear correlation experiment.

Following the description of the non-gradient SIMBA (selective inverse multiple bond analysis) experiment by one of the authors in 1991 [174], a number of reports describing related methods appeared [175–181]. There have been a few successful applications of SIMBA experiments reported in the literature [70, 182–184] used to establish specific correlations to complete structure assignments.

With the advent of gradient NMR methods, there have been several reports of gradient analogs of the SIMBA method [185–188]. Most recently, a double-selective *J*-HMBC method has been reported [189] and used to extract long-range couplings to the selectively excited resonances of the alkaloid harmane. Given the potential utility of SIMBA-type experiments augmented by PFGs, it is probable that this class of experiments will see expanded use in the future.

8.3.9.3 **Pulsed Field Gradients and Diffusion Ordered NMR Spectroscopy (DOSY)**

8.3.9.3.1 **Pulsed Field Gradients (PFGs)**

Markus Kramer

Many modern NMR experiments utilize PFGs to create or eliminate coherence. Field gradients are a defined linear disturbance of the static magnetic field and a function of the position. This disturbance can be applied to each direction, whereas most PFGs are applied along the B_0 field, that is, the z-direction. The resulting magnetic field (B_{res}) then consists of the B_0 field and the magnetic field of the gradient (B_{g}), which depends on the gradient strength (G_z) and its position along the z-axis:

$$B_{\text{res}}(z) = B_0 + B_{\text{g}} = B_0 + G_z \times z \tag{8.8}$$

For the sake of clarity one can imagine the sample to be cut in microscopically small slices along B_0. After application of a 90° pulse without succeeding z-gradient the magnetization vectors in every slice are aligned parallel in the xy-plane (Figure 8.35a). A field gradient along the z axis immediately after this excitation pulse results in a helical arrangement of the magnetization vectors because every

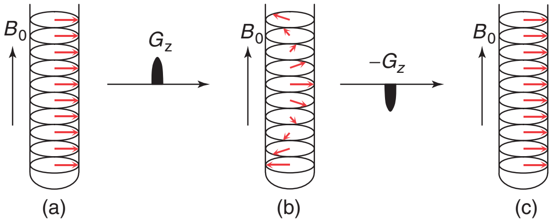

Figure 8.35 (a,b,c) The effect of a pulsed field gradient on the magnetization.

slice experiences a different magnetic field as a linear function of its position (Figure 8.35b). This change in the strength of the B_0-field causes a change of the Larmor frequency of the spins in each slice and thus a fanning out along the z axis.

$$\nu_L = \frac{\gamma \cdot B_{res}(z)}{2\pi} = \frac{\gamma \cdot (B_0 + G_z \times z)}{2\pi} \tag{8.9}$$

Starting the acquisition right now will result in a very low or no signal intensity, because all spin vectors of the sample will add up to zero. A second field gradient of the same strength and duration as the first one but of opposite sign will neutralize the effect of the first field gradient and the original magnetization is re-established (Figure 8.35c).

The field gradient causes the magnetization vector in a particular slice to be rotated about an angle Φ_z, which is a function of the coherence order (p), the gyromagnetic ratio of the observed nucleus (γ), the gradient field (B_g), and the duration of the field gradient (τ_g) [190]

$$\Phi_z = p \cdot \gamma \cdot B_g(z) \cdot \tau_g \tag{8.10}$$

Thus, for the same gradient strength the rotation angle of double quantum coherence is twice as large as that of single quantum coherence, while zero quantum coherence is not influenced by a field gradient. Consequently, with a combination of several field gradients and the correct choice of B_g and τ_g it is possible to select desired and to destroy unwanted coherence.

8.3.9.3.2 **Diffusion Ordered NMR Spectroscopy (DOSY)**

Diffusion ordered NMR spectroscopy (DOSY) [191, 192] is an NMR spectroscopic method which was developed to separate the signal sets of the substances in a mixture. This method is therefore often called *chromatographic NMR spectroscopy*. The separation is carried out by the different diffusion coefficients (D) of the single components. According to the Stokes Einstein equation (Eq. (8.11)) for spherical particles D is dependent upon the temperature (T), the viscosity of the mixture (η), and the hydrodynamic radius of the examined particle (r_H):

$$D = \frac{k_B \cdot T}{6\pi \cdot \eta \cdot r_H} \tag{8.11}$$

DOSY spectra are acquired utilizing NMR spectroscopic methods applying PFGs. The simplest pulse sequence for that purpose is called the *Carr–Purcell spin echo* (Figure 8.36).

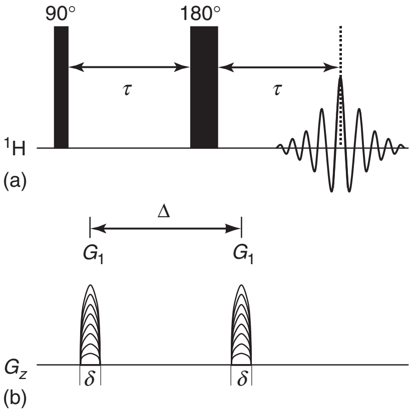

Figure 8.36 (a,b) The pulse sequence of the Carr–Purcell spin echo experiment.

The phase coherence of the individual spins produced by the initial 90° ^{1}H pulse is destroyed by the subsequent *z*-gradient G_1 leading to the same helical arrangement of the spins as shown in Figure 8.35b. During the diffusion time Δ the spins move owing to the self-diffusion of the molecules, while the 180° ^{1}H pulse causes an inversion of all spins. The following second *z*-gradient of the same strength and duration as the first one rephases all spins. In the absence of self-diffusion during the delay Δ the sequence $G_1{-}180^\circ{-}G_1$ would have no effect on the magnetization, because all dephased spins are rephased in the same way (without considering relaxation). Self-diffusion along the *z* axis of the sample during Δ leads to incomplete rephasing of the spins by the second gradient pulse, thus the overall sample magnetization is reduced. According to the following equation the resulting signal intensity is dependent on the diffusion coefficient D and the gradient strength

$$I = I_0 \cdot e^{-D\gamma^2 g^2 \delta^2 \left(\Delta - \frac{\delta}{3}\right)} \tag{8.12}$$

with D, diffusion coefficient; γ, gyromagnetic ratio; g, gradient strength; δ, gradient pulse duration; and Δ, diffusion time.

The two parameters δ and Δ have to be optimized at the beginning of the experiment and are then held constant, resulting in D being the only variable in the above mentioned equation. Repeating the experiment with linearly increasing gradient strength and plotting the signal intensity against g will result in a diagram as shown in Figure 8.37. Curve fitting with the aid of Eq. (8.12) finally yields in the diffusion coefficient D.

Performing this procedure for every signal in the spectrum and plotting the D values against the chemical shift results in a DOSY spectrum (Figure 8.38). For the calculation of these spectra several algorithms which are implemented in every established NMR processing software are employed.

For studying the diffusion behavior of larger molecules, very strong gradients (up to 30 T m^{-1}) are necessary. Strong gradient pulses of this order cause eddy currents

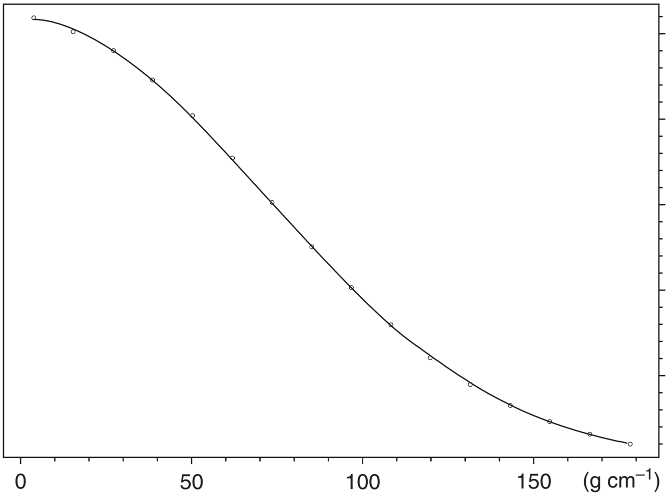

Figure 8.37 Attenuation of the signal intensity with increasing gradient strength.

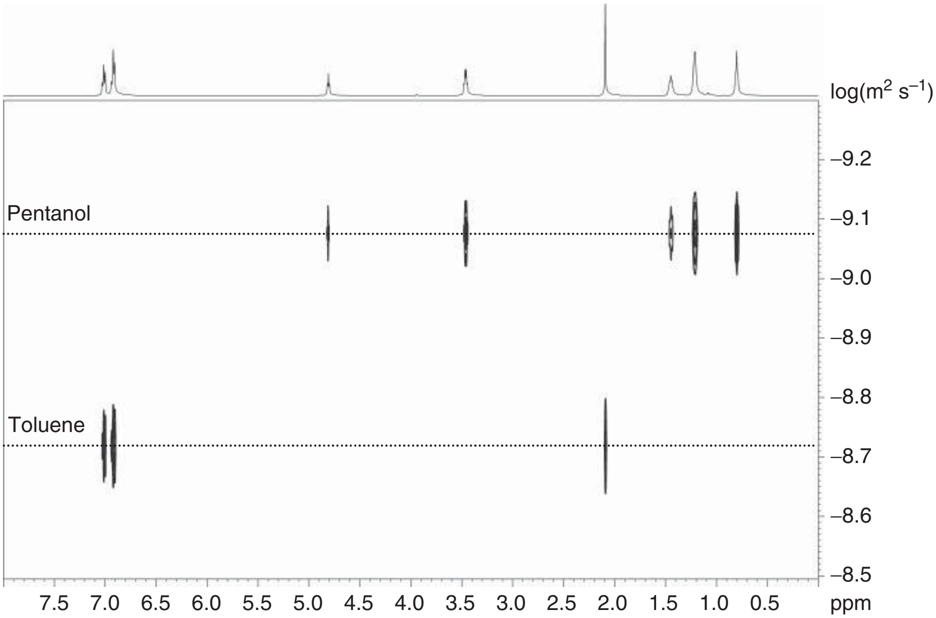

Figure 8.38 DOSY spectrum of a mixture of pentanol and toluene.

in the probehead which furthermore cause signal distortions. To minimize these eddy currents, nowadays alternatives of the presented pulse sequence are used. These modern sequences incorporate bipolar gradient pulses and contain a short delay, which allows the eddy currents to decay before the acquisition is started [192].

8.3.9.4 **Residual Dipolar Couplings (RDC) in Structural Analysis**

Markus Kramer

The dipolar or direct coupling between two spins I and S is mathematically given by the following equation (Eq. (8.13)) [193]:

$$D_{\mathrm{IS}} = -\left(\frac{\mu_0}{4\pi}\right)\frac{\gamma_{\mathrm{I}}\gamma_{\mathrm{S}}h}{2\pi^2\langle r_{\mathrm{IS}}^3\rangle}\left\langle\frac{3\cos^2\theta_{\mathrm{IS}}-1}{2}\right\rangle \tag{8.13}$$

with μ_0, magnetic field constant; γ_{I},γ_{S}, gyromagnetic ratio of the nuclei I and S; h, Planck's constant; r_{IS}, distance between the investigated nuclei; θ, angle formed by the internuclear vector and the static magnetic field B_0 (Figure 8.39).

The arrow brackets depict an ensemble average over all existing molecular motions. In solution, the dipolar interaction of two nuclei is only indirectly measurable via cross relaxation processes as nuclear Overhauser effect because the θ-dependent term averages to zero.

The molecular alignment in the static magnetic field leads to a measurable direct interaction. In perfect oriented samples, the absolute values of the dipolar couplings are much greater than that of the scalar couplings (e.g., 60.42 kHz compared to ~150 Hz for a CH group with $r = 1$Å and $\theta_{\mathrm{IS}} = 0°$). By lowering the degree of order, the dipolar interaction can be reduced to a value that is usually smaller than the scalar interaction and, in addition, the high resolution of the NMR spectra is retained. For that purpose, different liquid crystalline alignment media or gels have been investigated, which only align about 0.05% of the solute molecules at the same time. For a detailed description of several alignment media and suitable solvents refer to [194, 195].

Owing to the unknown molecular orientation of partially oriented samples, the Eq. (8.13) given in that form as shown above is not useful for the structural analysis. To allow an evaluation of the measurable dipolar couplings, an arbitrary molecular frame (M_x, M_y, M_z in Figure 8.40) is chosen, where the position of the internuclear vector of two spins (here: C–H) can be described by the three angles ϕ_x, ϕ_y, and ϕ_z.

The orientation of the molecular frame toward the static magnetic field can then be determined by calculating an order matrix S_{kl} [197]. Therefore, the equation is

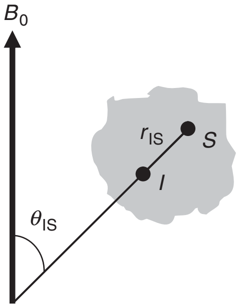

Figure 8.39 Graphical representation of the variables used in Eq. (8.13).

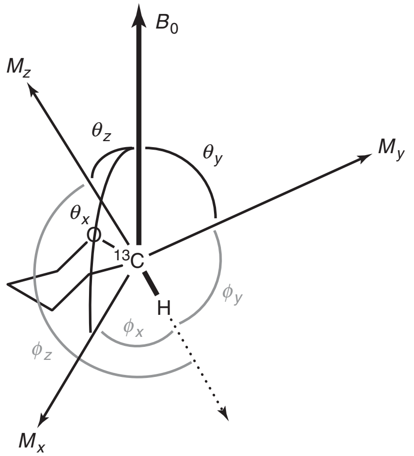

Figure 8.40 The position of a CH group in the arbitrary molecular frame and its orientation in the external magnetic field (after [196]).

recasted in a matrix form resulting in the following equation [198]

$$D_{\mathrm{IS}} = \frac{D_{\max \mathrm{IS}}}{r_{\mathrm{IS}}^3} \sum_{k,l} S_{kl} \cos \phi_k \cos \phi_l \tag{8.14}$$

with $D_{\max \mathrm{IS}}$, maximum possible D_{IS}-value at a distance of I and S (r_{IS}) of 1 Å and the internuclear vector oriented along B_0; k, l, x, y, z; $s_{kl} = \begin{bmatrix} s_{xx} & s_{yx} & s_{zx} \\ s_{xy} & s_{yy} & s_{zy} \\ s_{xz} & s_{yz} & s_{zz} \end{bmatrix}$; and ϕ_k, ϕ_l, angle between the internuclear vector and the k- and l-axis, respectively, of the arbitrary molecular frame.

The elements of the order matrix S_{kl} are given by Eq. (8.15)

$$S_{kl} = \left\langle \frac{3 \cos \theta_k \cos \theta_l - \delta_{kl}}{2} \right\rangle \tag{8.15}$$

where θ_k, θ_l, angle between the k- and l-axis, respectively, of the arbitrary molecular frame and the B_0 field; δ_{kl}, 0 if $k \neq l$, otherwise 1 (Kronecker delta).

For each D_{IS} value the order matrix has five linear-independent elements, because it is symmetric and has a zero trace. With at least five independent D_{IS} values the resulting system of equations can be solved and thus the elements of the order matrix can be determined. For additional structural information six independent D_{IS} values are necessary. The correctness of a calculated structure can now be confirmed by comparing experimental residual dipolar couplings (RDC) values with those obtained theoretically by back-calculation with the aid of the order matrix. The structure has to be evaluated as correct if the theoretical and experimental D values lie in between a certain error range. In flexible molecules the D values are averaged due to several possible conformers present in solution. Modern programs for the analysis of D values allow a consideration of intramolecular dynamic during the calculations.

8.3.9.4.1 **The Experimental Determination of RDC Values** By far, the most used RDCs are the $^1D_{C,H}$ or $^1D_{N,H}$ values, that is, the one-bond heteronuclear residual dipolar coupling constant for a CH or NH group (henceforth referred to as $^1D_{X,H}$). Depending on the degree of order these residual dipolar couplings are usually much smaller than the scalar couplings and lead to an additional splitting of the corresponding signals. The heteronuclear scalar interaction of two spins is usually detected by the HSQC experiment. Owing to decoupling the hetero-nucleus during the data acquisition and refocusing the proton scalar couplings by a 180° pulse it is impossible to extract a coupling constant from the standard HSQC experiment. Removing either this decoupling sequence or the refocusing pulse will result in a signal splitting in the direct (ω_2, t_2, F_2) and indirect (ω_1, t_1, F_1) dimension, respectively (Figure 8.41). Performing an coupled HQSC experiment on an oriented sample (with alignment medium) results in a signal splitting that is produced by the sum of $^1J_{X,H}$ and $^1D_{X,H}$. For the isotropic case (without alignment medium) the contribution of $^1D_{X,H}$ is missing. The difference in the splitting of corresponding signals for the anisotropic and isotropic case reveals the $^1D_{X,H}$ value for a certain CH and NH group, respectively.

Enthart *et al.* [199] showed, that the presence of antiphase magnetization during the data acquisition in an F_2-coupled HSQC experiment leads to a phase distortion

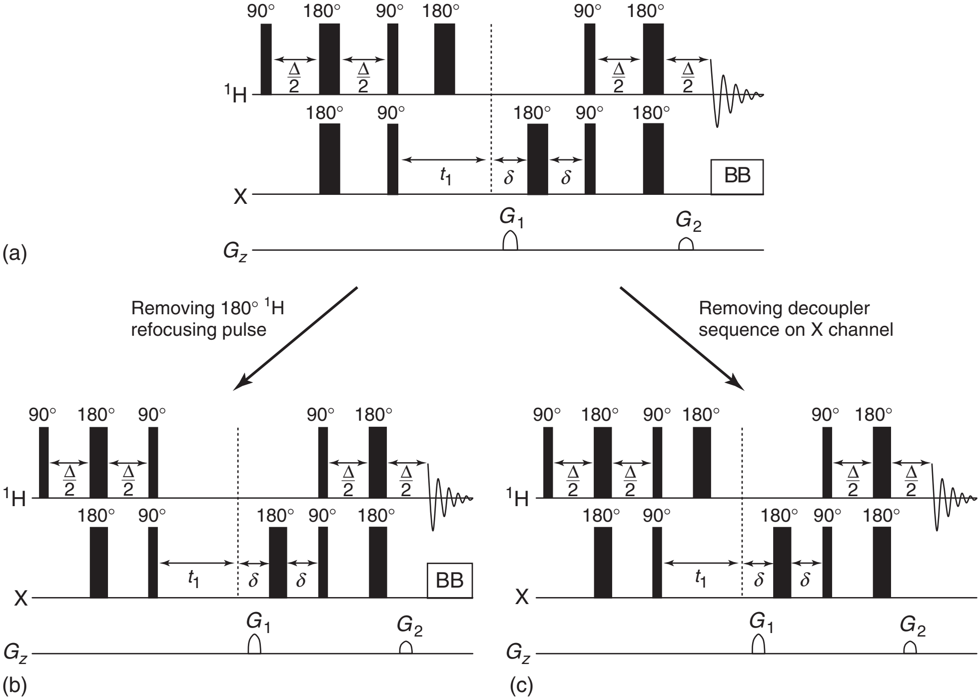

Figure 8.41 Modification of a standard HSQC sequence (a) to obtain either the F_1-coupled (b) or the F_2-coupled (c) HSQC pulse sequence. BB, broad band decoupling.

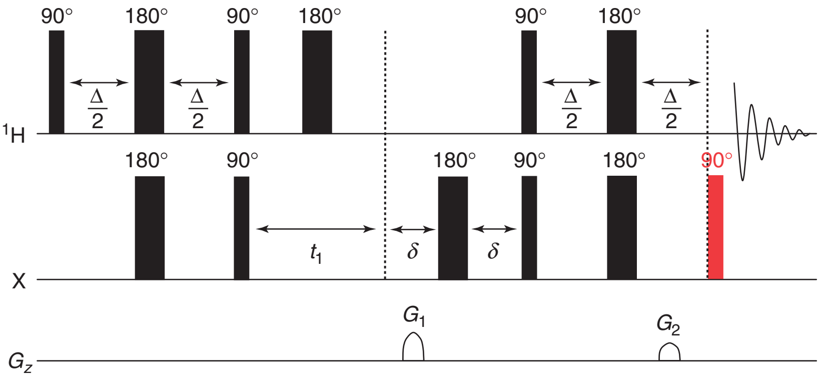

Figure 8.42 One of three possible pulse sequences for the CLIP-HSQC experiment.

of the signals and therefore presents erroneous RDC values. To remove this antiphase magnetization they proposed a modified version of the HSQC experiment, which they called CLIP-HSQC (clean in-phase heteronuclear single quantum coherence). This modification is made up of additional pulses inserted in the pulse sequence on the ^{1}H or X channel right before the acquisition is started. One of these modified pulse sequences is shown in Figure 8.42. Here, the inserted 90° pulse (red bar in Figure 8.42) on the X channel converts the antiphase magnetization to double quantum coherence, which cannot be detected directly and consequently produces pure in-phase signals.

Other RDC values often used for structural analysis are the $^nD_{\mathrm{H,H}}$, $^nD_{\mathrm{C,H}}$, $^1D_{\mathrm{C,C}}$, and $^nD_{\mathrm{C,C}}$ coupling constants [194, 195].

8.3.9.5 Small Sample NMR Studies

All NMR experiments detect signals from the sample being studied using some form of probe. Conventionally, NMR spectrometers have generally utilized 5 mm probes. There have, however, been a number of early reports of studies utilizing small sample NMR probes. A number of pioneering reports by Shoolery [200–202] using 1.7 mm probe designs were reported in the late 1970s. Following these studies, there was a hiatus of more than a decade before interest in small volume NMR probes was rekindled. In 1992, the collaborative development of 3 mm “micro” NMR probes was reported by one of the authors; comparative evaluation of 3 mm probes relative to 5 mm probes with identical quantities of material showed that the former achieved a given S/N ratio in roughly a quarter the time required for a conventional 5 mm probe [203, 204]. There followed a number of natural product studies utilizing 3 mm probes through the mid 1990s [204–213].

The development of the magic angle, liquid Nano-probe™ by Varian was reported in the mid 1990s [214–217]. A number of studies utilizing this probe technology have been reported and there have been a few comparative comments made regarding 3 mm micro-probes versus the nano-probe design [209, 210]. At about the same time, Sweedler and colleagues [218] began to report the results of their development of what they referred to as *μ-coil NMR probes* [219]. A number of subsequent studies have been reported by these authors including the development of μ-coil inverse probe designs [220, 221] and probes with multiple μ-coils contained in a single probehead [222]. The 1.7 mm probe format was revisited in 1998 by one of the authors when the development of the submicro inverse-detection gradient or SMIDG probe design was reported [223, 224]. A number of small sample $^1H-^{13}C$ and $^1H-^{15}N$ studies utilizing this probe design have also been reported [224–230]. To illustrate the capabilities of the 1.7 mm submicro NMR probe, GHSQC spectra of a 750 μg sample of the alkaloid cryptospirolepine (**9**) (MW 505 Da) recorded in 34 s and <5 min are shown in Figure 8.43a,b, respectively [218]. The trace

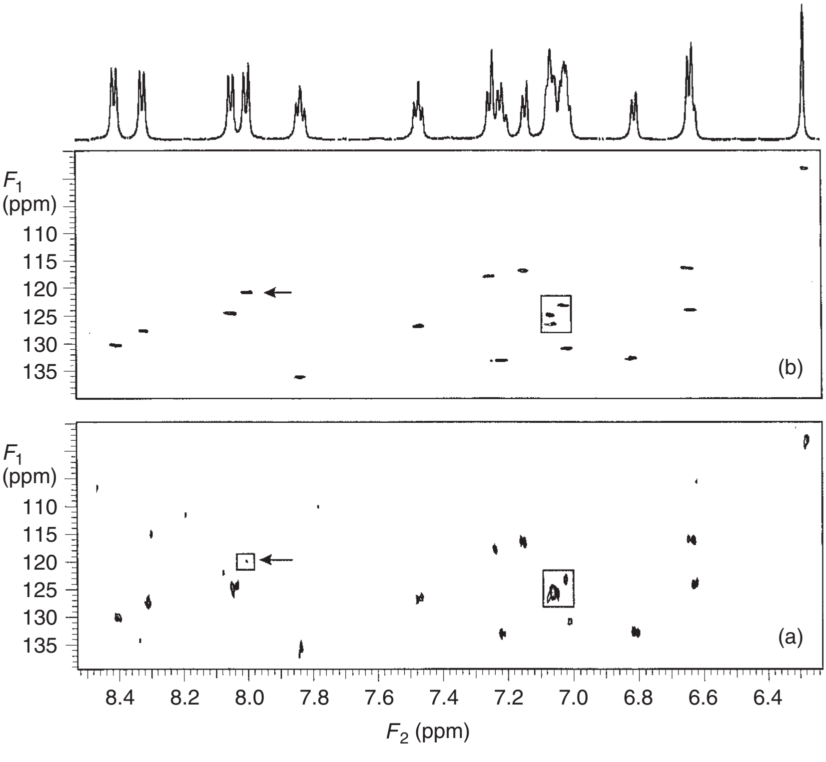

Figure 8.43 GHSQC spectra obtained using a 750 μg sample (~1.5 μmol) of cryptospirolepine (**9**) in 30 μl of DMSO-d_6 [229]. The data shown in (a) were acquired in a scant 34 s as 16 × 2 hypercomplex files with one transient accumulated/t_1 increment. The weak, boxed response denoted by the arrow is the weakest correlation in the spectrum (Figure 8.44). The other boxed region of the spectrum that is not well resolved under the data acquisitions used to acquire the 34 s spectrum shown should contain responses for three correlations. (b) GHSQC spectrum acquired in approximately 5 min with 48 × 2 hypercomplex files with two transients accumulated/t_1 increment. The weak boxed response in (a) is now clearly identifiable as a legitimate correlation and the three responses in the boxed region of (a) are now clearly resolved. (Reproduced with permission – HeteroCorp.)

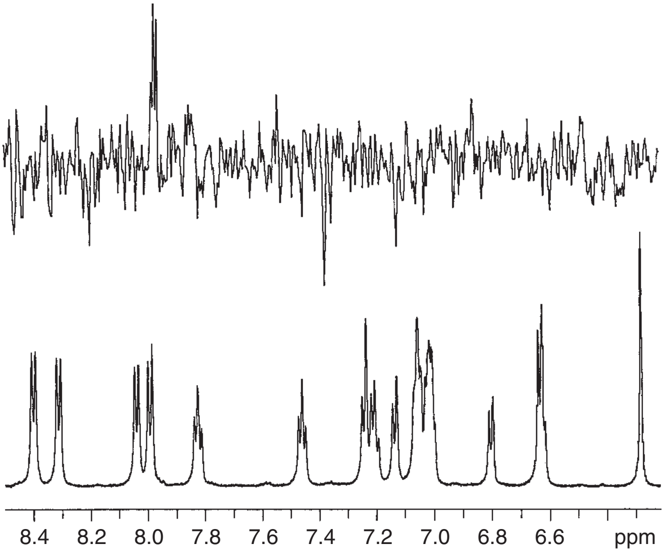

Figure 8.44 Proton reference spectrum and trace from the 2D GHSQC spectrum shown in Figure 8.34a of the weakest response in the 34 s spectrum of **9**. Despite the extremely short acquisition time for the GHSQC spectrum, the S/N ratio of the weakest peak is still ~3 : 1, which when coupled with the multiplet appearance, makes it easy to validate this as a real response from the examination of the slice. (Reproduced with permission – HeteroCorp.)

containing weakest response in the 34 s GHSQC spectrum of the alkaloid is plotted above a proton reference spectrum in Figure 8.44. Despite the extremely short acquisition time, the S/N ratio even for the weakest response is adequate. Work in the area of small sample NMR is the subject of a recent review by Sweedler and co-workers [231].

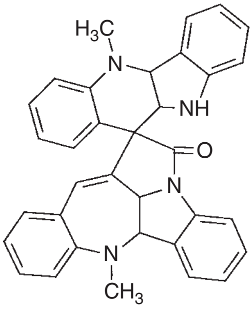

9

What will undoubtedly have the greatest impact on small sample NMR studies will be the development of small volume cold metal NMR probes. Probes of this type have RF coils designed to operate in the range of about 8–25 K [232–235]. Efforts in this area have only begun to be reported within the past year [236], but the initial results are quite promising. Sensitivity for 2.5 or 3 mm versions of these probes have reported gains of as much as fourfold relative to conventional probes operating at ambient magnet bore temperatures [237, 228]. To illustrate the potential of cold metal NMR probes, two examples are shown. The 45 min COSY spectrum of a 2.9 μg sample of paclitaxel (**10**, Taxol™) acquired using a 3 mm cryogenic NMR probe is shown in Figure 8.45 (D.J. Russell *et al.*, unpublished results). An HSQC spectrum of the aliphatic region of strychnine (**2**) acquired using a 3 mm cryogenic NMR probe is shown for a 40 μg (0.12 μmol) sample. The data, shown in Figure 8.46 were acquired in <2 h [239]. Comparable data acquired in a conventional 3 mm micro NMR probe required a 17 h acquisition. Full characterization of a sample of this size, if it required the acquisition of an HMBC or GHMBC spectrum in addition to the HSQC spectrum, would consume approximately 100 h of spectrometer time. In contrast, using a 3 mm cryogenic NMR probe, it should be possible to acquire all of the necessary data in approximately 10 h. Consequently, it is likely that the use of small volume cryogenic NMR probes will be an area of intense research in the coming years.

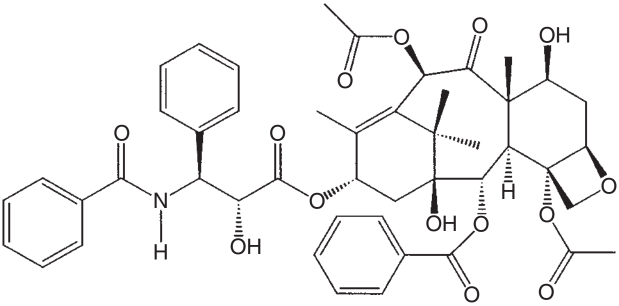

10

8.4
Conclusions

NMR experiments performed in the solution state are capable of providing a wealth of chemical structure information both through bonds and through space. The array of experiments available to the spectroscopist with which to probe chemical structure is vast. Many of the issues relating to the inherent insensitivity of the NMR experiment have been addressed through increases in magnetic field strength, with 600 MHz instruments now frequently available for the determination of small molecule structures. Sample limitations have been largely circumvented by small volume NMR probes, specialized NMR cells, and by the very recent availability of 3 mm cryogenic NMR probes. When the available technology is used in concert and in conjunction with data from other analytical spectroscopic techniques such as mass spectrometry and vibrational methods, most chemical structures can be

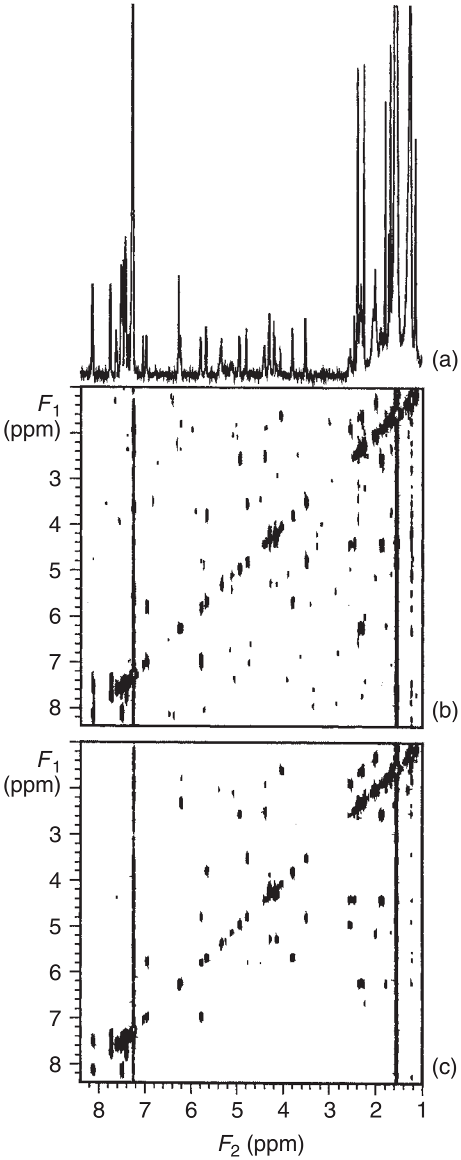

Figure 8.45 Spectra recorded with a 2.9 μg sample of paclitaxel (Taxol™, **10**, ~3.4 nmol) dissolved in 165 μl $CDCl_3$ [227]. (a) Proton reference spectrum recorded in 32 transients. (b) COSY spectrum recorded in 46 min as a 2048 × 128 point file accumulating 12 transients/t_1 increment. All of the expected correlations are observable in the spectrum and are discernible from the noise. (c) COSY spectrum recorded in 3 h 4 min as a 2048 × 192 point file accumulating 32 transients/t_1 increment. The spectrum is essentially noise-free.

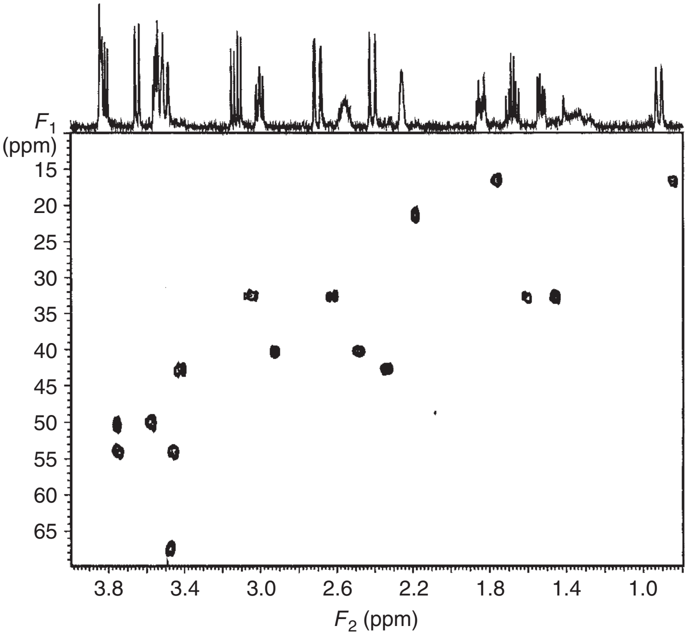

Figure 8.46 HSQC spectrum of a 40 µg sample (120 nmol) of strychnine (**2**) dissolved in 160 µl benzene-d_6 in a 3 mm NMR tube. The data were acquired in 90 min using a Varian INOVA 500 MHz instrument equipped with a Nalorac 3 mm Cryo•Spec® NMR probe. The acquisition of an HSQC spectrum with comparable signal-to-noise using a conventional 3 mm NMR probe required 17 h [239].

solved in reasonable periods of time even if only submicromole quantities of material are available for analysis.

References

1. Purcell, E.M., Torrey, H.C., and Pound, R.V. (1946) *Phys. Rev.*, **69**, 37–38.
2. Bloch, F., Hansen, W.W., and Packard, M.E. (1946) *Phys. Rev.*, **69**, 127.
3. Harris, R.K. and Mann, B.E. (1981) *NMR and the Periodic Table*, Academic Press, New York.
4. Brevard, C. and Granger, P. (1986) *Handbook of High Resolution Multinuclear NMR*, John Wiley & Sons, Inc., New York.
5. Harris, R.K. (1986) *Nuclear Magnetic Resonance Spectroscopy*, John Wiley & Sons, Inc., New York.
6. Mason, J. (1987) *Multinuclear NMR*, Plenum Press, New York.
7. Pregosin, P. (ed.) (1991) *Transition Metal Nuclear Magnetic Resonance*, Elsevier, Amsterdam.
8. Fäcke, T., Wagner, R., and Berger, S. (1994) *Concepts Magn. Reson.*, **6**, 293–306.
9. Günther, H. (1996) in *Advanced Applications of NMR to Organometallic Chemistry* (eds M. Gielen, R. Willem, and B. Wrackmeyer), John Wiley & Sons, Inc., New York, pp. 247–290.
10. van der Klink, J.J. and Brom, H.B. (1999) *Annu. Rep. NMR Spectrosc.*, **36**, 89–201.
11. Orrell, K.G. (1999) *Annu. Rep. NMR Spectrosc.*, **37**, 1–74.

12. Gudat, D. (1999) *Annu. Rep. NMR Spectrosc.*, **38**, 139–202.

13. Freeman, R. (1987) *A Handbook of Nuclear Magnetic Resonance Spectroscopy*, John Wiley & Sons, Inc., NewYork.

14. Bax, A. (1982) *Two-Dimensional Nuclear Magnetic Resonance in Liquids*, D. Reidel, Boston, MA.

15. Brey, W.S. (ed.) (1988) *Pulse Methods in 1D and 2D Liquid-Phase NMR*, Academic Press, New York.

16. Martin, G.E. and Zektzer, A.S. (1989) *Two-Dimensional NMR Methods for Establishing Molecular Connectivity: A Chemist's Guide to Experiment Selection, Performance, and Interpretation*, Wiley-VCH Verlag GmbH, Weinheim.

17. Croasmun, W.R. and Carlson, R.M.K. (eds) (1994) *Two-Dimensional NMR Spectroscopy, Applications for Chemists and Biochemists*, 2nd edn, Wiley-VCH Verlag GmbH, Weinheim.

18. Farrar, T.C. and Becker, E.D. (eds) (1971) *Pulse and Fourier Transform NMR*, Academic Press, New York.

19. Fukushima, E. and Roeder, S.B.W. (1981) *Experimental Pulse NMR: A Nuts and Bolts Approach*, Addison-Wesley, New York.

20. Farrar, T.C. (1997) *Introduction to Pulse NMR Spectroscopy*, Farragut Press, Madison, WI.

21. Breitmaier, E. and Voelter, W. (1987) *Carbon-13 NMR Spectroscopy*, 3rd edn, Wiley-VCH Verlag GmbH, Weinheim.

22. Fehrli, F.W., Marchand, A.P., and Wehrli, S. (1983) *Interpretation of Carbon-13 NMR Spectra*, 2nd edn, John Wiley & Sons, Inc., New York.

23. Macomber, R.S. (1998) *A Complete Introduction to Modern NMR Spectroscopy*, John Wiley & Sons, Inc., New York.

24. Nakanishi, K. (1990) *One-Dimensional and Two-Dimensional NMR Spectra by Modern Pulse Techniques*, University Science Books, Mill Valley, CA.

25. Friebolin, H. (1998) *Basic One- and Two-Dimensional NMR Spectroscopy*, 3rd edn, Wiley-VCH Verlag GmbH, Weinheim.

26. Braun, S., Kalinowski, H.-O., and Berger, S. (1998) *150 and More Basic NMR Experiments–A Practical Course*, 2nd edn, Wiley-VCH Verlag GmbH, Weinheim.

27. DeRome, A.E. (1987) *Modern NMR Techniques for Chemistry Research*, Pergamon Press, New York.

28. Berger, S., Braun, S., and Kalinowski, H.-O. (1997) *NMR Spectroscpy of the Non-Metallic Elements*, John Wiley & Sons, Inc., New York.

29. Günther, H. (1992) *NMR Spectroscopy*, 2nd edn, John Wiley & Sons, Inc., NewYork.

30. Ernst, R.R., Bodenhausen, G., and Wokaun, A. (1987) *Principles of Nuclear Magnetic Resonance in One and Two Dimensions*, Clarendon Press, Oxford.

31. Claridge, T.D.W. (1999) *High-Resolution NMR Techniques in Organic Chemistry*, Pergamon, Amsterdam.

32. Freeman, R. (1998) *Spin Choreography*, Oxford University Press, Oxford.

33. Ernst, R.R. and Anderson, W.A. (1966) *Rev. Sci. Instrum.*, **37**, 93–102.

34. Sanders, J.K.M. and Mersh, J.D. (1982) *Prog. Nucl. Magn. Reson.*, **13**, 355–361.

35. Noggle, J.H. and Schrimer, R.E. (1971) *The Nuclear Overhauser Effect–Chemical Applications*, Academic Press, New York.

36. Neuhaus, D. and Williamson, M. (1989) *The Nuclear Overhauser Effect in Structural and Conformational Analysis*, Wiley-VCH Verlag GmbH, Weinheim.

37. Nagel, D.W., Pachler, K.G., Steyn, P.S. *et al.* (1976) *Tetrahedron*, **32**, 2625–2631.

38. Morris, G.A. and Freeman, R. (1979) *J. Am. Chem. Soc.*, **101**, 760–762.

39. Morris, G.A. (1980) *J. Am. Chem. Soc.*, **102**, 428–429.

40. Doddrell, D.M. and Pegg, D.T. (1980) *J. Am. Chem. Soc.*, **102**, 6388–6390.

41. Doddrell, D.M., Pegg, D.T., and Bendall, M.R. (1982) *J. Magn. Reson.*, **48**, 323–327.

42. Doddrell, D.M., Pegg, D.T., and Bendall, M.R. (1982) *J. Chem. Phys.*, **77**, 2745–2752.

43. Hagaman, E.W. (1976) *Org. Magn. Res.*, **8**, 389–398.

44. Lyerla, J.R. Jr., and Levy, G.C. (1974) in *Topics in Carbon-13 NMR Spectroscopy*, Vol. 1 (ed. G.C. Levy), Wiley-Interscience, New York, pp. 79–149.

45. Wehrli, F.W. (1976) in *Topics in Carbon-13 NMR Spectroscopy*, Vol. 2 (ed. G.C. Levy), Wiley-Interscience, New York, pp. 343–391.

46. Jenner, J. (1971) Ampere International Summer School, Basko Polje, Jugoslavia.

47. Aue, W.P., Bartholdi, E., and Ernst, R.R. (1976) *J. Chem. Phys.*, **64**, 2229–2246.

48. Bax, A., Freeman, R., and Morris, G.A. (1981) *J. Magn. Reson.*, **42**, 164–168.

49. Macura, S., Huang, Y., Suter, D., and Ernst, R.R. (1981) *J. Magn. Reson.*, **43**, 259–281.

50. Olejniczak, E.T., Hoch, J.C., Dobson, C.M. *et al.* (1985) *J. Magn. Reson.*, **64**, 199–206.

51. Andersen, N.H., Nguyen, K.T., Hartze, C.J. *et al.* (1987) *J. Magn. Reson.*, **74**, 195–211.

52. Bothner-By, A.A., Stephens, R.L., Lee, J. *et al.* (1984) *J. Am. Chem. Soc.*, **106**, 811–813.

53. Bax, A. and Davis, D.G. (1985) *J. Magn. Reson.*, **63**, 207–213.

54. Jeener, J., Beier, B.H., Bachmann, P. *et al.* (1979) *J. Chem. Phys.*, **71**, 4546–4553.

55. Orrell, K.G., Šik, V., and Stephenson, D. (1990) *Prog. Nucl. Magn. Reson. Spectrosc.*, **22**, 141–208.

56. Perrin, C.L. and Dwyer, T.J. (1990) *Chem. Rev.*, **90**, 935–967.

57. Orrell, K.G. and Šik, V. (1993) *Annu. Rep. NMR Spectrosc.*, **27**, 103–171.

58. Sandström, J. (1982) *Dynamic NMR Spectroscpy*, Academic Press, London.

59. Oki, M. (1985) *Applications of Dynamic NMR Spectroscopy to Organic Chemistry*, Wiley-VCH Verlag GmbH, Weinheim.

60. Mareci, T.H. and Freeman, R. (1983) *J. Magn. Reson.*, **51**, 531–535.

61. Craig, D.A. and Martin, G.E. (1986) *J. Nat. Prod.*, **49**, 456–465.

62. Martin, G.E., Sandjua, R., and Alam, M. (1985) *J. Org. Chem.*, **50**, 2383–2387.

63. Müller, L. (1984) *J. Magn. Reson.*, **59**, 326–331.

64. Zektzer, A.S. and Martin, G.E. (1987), *J. Nat. Prod.*, **50**, 455–462.

65. Barnekow, D.E., Cardellina, J.H. II,, Zektzer, A.S. *et al.* (1989) *J. Am. Chem. Soc.*, **110**, 3511–3517.

66. Zektzer, A.S., Martin, G.E., and Castle, R.N. (1987) *J. Heterocycl. Chem.*, **24**, 879–884.

67. Zekzter, A.S., Stuart, J.G., Martin, G.E. *et al.* (1986) *J. Heterocycl. Chem.*, **23**, 1587–1593.

68. Bax, A., Freeman, R., and Kempsell, S.P. (1980) *J. Am. Chem. Soc.*, **102**, 4849–4851.

69. Bax, A., Freeman, R., and Frenkiel, T.A. (1980) *J. Am. Chem. Soc.*, **102**, 2102–2104.

70. Martin, G.E. and Crouch, R.C. (1994) in *Modern Methods of Plant Analysis*, Vol. 15 (eds H.F. Linskens and J.F. Jackson), Springer-Verlag, Berlin, pp. 25–89.

71. Martin, G.E. and Crouch, R.C. (1991) *J. Nat. Prod.*, **54**, 1–70.

72. Martin, G.E. and Hadden, C.E. (2000) *J. Nat. Prod.*, **63**, 543–585.

73. Martin, G.E. and Zektzer, A.S. (1989) *Two-Dimensional NMR Methods for Establishing Molecular Connectivity: A Chemist's Guide to Experiment Selection, Performance, and Interpretation*, Wiley-VCH Verlag GmbH, Weinheim, pp. 19–29.

74. Claridge, T.D.W. (1999) *High-Resolution NMR Techniques in Organic Chemistry*, Pergamon, Amsterdam, pp. 259–276.

75. Freeman, R., Morris, G.A., and Turner, D.L. (1977) *J. Magn. Reson.*, **26**, 373–378.

76. Aue, W.P., Karhan, J., and Ernst, R.R. (1976) *J. Chem. Phys.*, **64**, 4226–4227.

77. Bax, A. and Davis, D.G. (1985) *J. Magn. Reson.*, **63**, 207–213.

78. Bax, A. and Davis, D.G. (1985) *J. Magn. Reson.*, **65**, 355–360.

79. Braunschweiler, L. and Ernst, R.R. (1983) *J. Magn. Reson.*, **53**, 521–528.

80. Eich, G., Bodenhausen, G., and Ernst, R.R. (1982) *J. Am. Chem. Soc.*, **104**, 3731–3732.

81. Bax, A. and Drobny, G. (1985) *J. Magn. Reson.*, **61**, 306–320.

82. Bax, A. and Freeman, R. (1981) *J. Magn. Reson.*, **44**, 542–561.

83. Müller, L. (1979) *J. Am. Chem. Soc.*, **101**, 4481–4484.

84. Hall, L.D. and Norwood, T.J. (1986) *J. Chem. Soc., Chem. Commun.*, 44–46.

85. Hall, L.D. and Norwood, T.J. (1986) *J. Magn. Reson.*, **69**, 391–396.

86. Hall, L.D. and Norwood, T.J. (1986) *J. Magn. Reson.*, **69**, 585–590.

87. Hall, L.D. and Norwood, T.J. (1987) *J. Magn. Reson.*, **74**, 171–176.

88. Bain, A. (1984) *J. Magn. Reson.*, **56**, 418–427.

89. Bodenhausen, G., Kogler, H., and Ernst, R.R. (1984) *J. Magn. Reson.*, **58**, 370–388.

90. Hoult, D.I. and Richards, R.E. (1975) *Proc. R. Soc. London, Ser. A*, **344**, 311.

91. Bodenhausen, G., Freeman, R., and Turner, D.L. (1977) *J. Magn. Reson.*, **27**, 511–514.

92. Maudsley, A.A., Wokaun, A., and Ernst, R.R. (1978) *Chem. Phys. Lett.*, **55**, 9–14.

93. Bax, A., De Jong, P.G., Mehlkopf, A.F. *et al.* (1980) *Chem. Phys. Lett.*, **69**, 567–570.

94. Baker, P.B. and Freeman, R. (1985) *J. Magn. Reson.*, **64**, 334–338.

95. Kontaxis, G., Stonehouse, J., Laue, E.D., and Keeler, J. (1994) *J. Magn. Reson., A*, **111**, 70–76.

96. Cavanaugh, J., Palmer, A.G. III,, Wright, P.E. *et al.* (1991) *J. Magn. Reson.*, **91**, 429–436.

97. Palmer, A.G. III,, Cavanaugh, J., Wright, P.E., and Rance, M. (1991) *J. Magn. Reson.*, **93**, 151–170.

98. Cavanaugh, J. and Rance, M. (1993) *Annu. Rep. NMR Spectrosc.*, **27**, 1–58.

99. Reynolds, W.F. and Enriquez, R.G. (2001) *Magn. Reson. Chem.*, **39**, 531–538.

100. Bernstein, M.A. and Trimble, L.A. (1994) *Magn. Reson. Chem.*, **32**, 107–110.

101. Dalvit, C. (1995) *J. Magn. Reson., A*, **113**, 120–123.

102. Adell, P., Parella, T., Sánchez-Ferrando, F. *et al.* (1995) *J. Magn. Reson., B*, **108**, 77–80.

103. Dalvit, C. and Bovermann, G. (1995) *Magn. Reson. Chem.*, **33**, 156–159.

104. Stonehouse, J., Adell, P., Keele, J. *et al.* (1994) *J. Am. Chem. Soc.*, **116**, 6037–6038.

105. Hallenga, K. and van Binst, G. (1980) *Bull. Magn. Reson.*, **2**, 343.

106. Reynolds, W.F., Enriquez, R.G., Escobar, L.I. *et al.* (1984) *Can. J. Chem.*, **62**, 2421–2425.

107. Martin, G.E. and Zektzer, A.S. (1988) *Magn. Reson. Chem.*, **26**, 631–652.

108. Reynolds, W.F., McLean, S., Jacobs, H. *et al.* (1999) *Can. J. Chem.*, **77**, 1922–1930.

109. Reynolds, W.F., Yu, M., and Enriquez, R.G. (1997) *Magn. Reson. Chem.*, **35**, 614–618.

110. Bodenhausen, G. and Ruben, D.J. (1980) *Chem. Phys. Lett.*, **69**, 185–188.

111. Bax, A., Griffey, R.H., and Hawkins, B.L. (1983) *J. Magn. Reson.*, **55**, 3301–315.

112. Bax, A. and Subramanian, S. (1986) *J. Magn. Reson.*, **67**, 565–569.

113. Ruiz-Cabello, J., Vuister, G.W., Moonen, C.T.W. *et al.* (1992) *J. Magn. Reson.*, **100**, 282–302.

114. Parella, T. (1998) *Magn. Reson. Chem.*, **36**, 467–495.

115. Hurd, R.E. and John, B.K. (1991) *J. Magn. Reson.*, **91**, 648–653.

116. Reynolds, W.F., Mclean, S., Tay, L.L. *et al.* (1997) *Magn. Reson. Chem.*, **35**, 455–462.

117. Eastwick, D.M. and Pascoe, K.O. (1997) *Magn. Reson. Chem.*, **35**, 455–462.

118. Claridge, T.D.W. (1999) *High-Resolution NMR Techniques in Organic Chemistry*, Pergammon, Amterdam, pp. 229–230.

119. Kessler, H., Schmeider, P., and Kurz, M. (1989) *J. Magn. Reson.*, **85**, 400–405.

120. Parella, T., Belloc, J., Sánchez-Ferrando, F. *et al.* (1998) *Magn. Reson. Chem.*, **36**, 715–519.

121. Parella, T., Sánchez-Ferrando, F., and Virgili, A. (1997) *J. Magn. Reson.*, **126**, 274–277.

122. Claridge, T.D.W. (1999) *High-Resolution NMR Techniques in Organic Chemistry*, Pergamon, Amsterdam, pp. 239–240.

123. Hadden, C.E. and Angwin, D.T. (2001) *Magn. Reson. Chem.*, **39**, 1–8.

124. Zannger, K. and Armitage, I.M. (2000) *Magn. Reson. Chem.*, **38**, 452–458.

125. Kessler, H., Griesinger, C., Zarbock, J. *et al.* (1984) *J. Magn. Reson.*, **37**, 331–336.

126. Kessler, H., Criesinger, C., and Lautz, J. (1984) *Angew. Chem., Int. Ed. Engl.*, **23**, 444–445.

127. Krishnamurthy, V.V. and Casida, J.E. (1987) *Magn. Reson. Chem.*, **25**, 837–842.

128. Quast, M.J., Zektzer, A.S., Martin, G.E. *et al.* (1987) *J. Magn. Reson.*, **71**, 554–560.

129. Reynolds, W.F., McLean, S., Perpick-Dumont, M. *et al.* (1989) *Magn. Reson. Chem.*, **27**, 162–169.

130. Bax, A. and Summers, M.F. (1986) *J. Am. Chem. Soc.*, **108**, 2093–2094.

131. Willker, W., Leibfritz, D., Kerssebaum, R. *et al.* (1993) *Magn. Reson. Chem.*, **31**, 287–292.

132. Rinaldi, P.L. and Keifer, P.A. (1994) *J. Magn. Reson., A*, **108**, 259–262.

133. Sørensen, O.W., Nielsen, N.C., Bildso, H. *et al.* (1986) *J. Magn. Reson.*, **70**, 54–70.

134. Martin, G.E., Hadden, C.E., Crouch, R.C. *et al.* (1999) *Magn. Reson. Chem.*, **37**, 517–528.

135. Stott, K., Stonehouse, J., Keeler, J. *et al.* (1995) *J. Am. Chem. Soc.*, **117**, 4199–4200.

136. Wagner, R. and Berger, S. (1998) *Magn. Reson. Chem.*, **36**, S44–S46.

137. Bermel, W., Wagner, G., and Griesinger, C. (1989) *J. Magn. Reson.*, **83**, 223–232.

138. Furihata, K. and Seto, H. (1995) *Tetrahedron Lett.*, **36**, 2817–2820.

139. Furihata, K. and Seto, H. (1996) *Tetrahedron Lett.*, **37**, 8901–8904.

140. Marek, R., Králík, L., and Sklenář, V. (1997) *Tetrahedron Lett.*, **38**, 6654–558.

141. Sheng, S. and van Halbeek, H. (1998) *J. Magn. Reson.*, **130**, 296–299.

142. Furihata, K. and Seto, H. (1998) *Tetrahedron Lett.*, **39**, 7337–7340.

143. Bodenhausen, G. and Ernst, R.R. (1982) *J. Am. Chem. Soc.*, **104**, 1304–1309.

144. Hadden, C.E., Martin, G.E., and Krishnamurthy, V.V. (1999) *J. Magn. Reson.*, **140**, 274–280.

145. Hadden, C.E., Martin, G.E., and Krishnamurthy, V.V. (2000) *Magn. Reson. Chem.*, **38**, 143–147.

146. Krishnamurthy, V.V., Russell, D.J., Hadden, C.E. *et al.* (2000) *J. Magn. Reson.*, **146**, 232–239.

147. Martin, G.E. and Hadden, C.E. (2000) *Magn. Reson. Chem.*, **38**, 251–256.

148. Gotfredsen, C.H., Meissner, A., Duus, J.O. *et al.* (2000) *Magn. Reson. Chem.*, **38**, 692–695.

149. Bolton, P.H. (1982) *J. Magn. Reson.*, **48**, 336–340.

150. Bolton, P.H. and Bodenhausen, G. (1982) *Chem. Phys. Lett.*, **89**, 139–144.

151. Bax, A. (1983) *J. Magn. Reson.*, **53**, 149–153.

152. Kessler, H., Bernd, M., Kogler, H. *et al.* (1983) *J. Am. Chem. Soc.*, **105**, 6944–6952.

153. Bigler, P., Ammann, W., and Richarz, R. (1984) *Org. Magn. Reson.*, **22**, 109–113.

154. Bolton, P.H. (1985) *J. Magn. Reson.*, **62**, 143–146.

155. Lerner, L. and Bax, A. (1986) *J. Magn. Reson.*, **69**, 375–380.

156. Brühwiler, D. and Wagner, G. (1986) *J. Magn. Reson.*, **69**, 546–551.

157. Sohn, K. and Opella, S.J. (1989) *J. Magn. Reson.*, **82**, 193–197.

158. Kawabata, J., Fukushi, E., and Mizutami, J. (1992) *J. Am. Chem. Soc.*, **114**, 1115–1117.

159. Hoffman, R.E., Shenhar, R., Willner, I. *et al.* (2000) *Magn. Reson. Chem.*, **38**, 311–314.

160. Domke, T. (1991) *J. Magn. Reson.*, **95**, 174–177.

161. Crouch, R.C., Spitzer, T.D., and Martin, G.E. (1992) *Magn. Reson. Chem.*, **30**, S71–73.

162. Crouch, R.C., Davis, A.O., and Martin, G.E. (1995) *Magn. Reson. Chem.*, **33**, 889–892.

163. Crouch, R.C., Martin, G.E., Dicke, R.W. *et al.* (1995) *Tetrahedron*, **51**, 8409–8422.

164. Crouch, R.C., McFadyen, R.B., Daluge, S.M. *et al.* (1990) *Magn. Reson. Chem.*, **28**, 792–796.

165. Kawabata, J., Fukushi, E., Hara, M. *et al.* (1992) *Magn. Reson. Chem.*, **30**, 6–10.

166. Castle, L.W., Johnston, M.D., Camoutsis, C.L. *et al.* (1992) *J. Heterocycl. Chem.*, **29**, 1869–1871.

167. Hoffman, R.E., Shenhar, R., Willner, I. *et al.* (2000) *Magn. Reson. Chem.*, **38**, 311–314.
168. Kawabata, J., Fukushi, E., and Mizutani, J. (1993) *Phytochemistry*, **32**, 1347–1349.
169. Kessler, H., Mronga, S., and Gemmecher, G. (1991) *Magn. Reson. Chem.*, **29**, 527–557.
170. Parella, T. (1996) *Magn. Reson. Chem.*, **34**, 329–347.
171. Berger, S. (1997) *Prog. Nucl. Magn. Reson. Spectrosc.*, **30**, 137–156.
172. Freeman, R. (1998) *Prog. Nucl. Magn. Reson. Spectrosc.*, **32**, 59–106.
173. Stott, K., Keeler, J., Van, Q.N. *et al.* (1997) *J. Magn. Reson.*, **125**, 302–324.
174. Crouch, R.C. and Martin, G.E. (1991) *J. Magn. Reson.*, **92**, 189–192.
175. Keniry, M.A. and Poulton, G.A. (1991) *Magn. Reson. Chem.*, **29**, 46–48.
176. Poppe, L. and van Halbeek, H. (1991) *J. Magn. Reson.*, **92**, 636–641.
177. Poppe, L. and van Halbeek, H. (1991) *Magn. Reson. Chem.*, **29**, 848–851.
178. Nuzillard, J.M. and Bernassau, J.M. (1994) *J. Magn. Reson., B*, **103**, 284–287.
179. Poppe, L., Sheng, S., and van Halbeek, H. (1994) *J. Magn. Reson., A*, **111**, 104–107.
180. Poppe, L., Sheng, S., and van Halbeek, H. (1994) *Magn. Reson. Chem.*, **32**, 97–100.
181. Uhrín, D., Mele, A., Köver, K.E. *et al.* (1994) *J. Magn. Reson., A*, **108**, 160–170.
182. Morris, S.A., Schwartz, R.E., Sesin, D.F. *et al.* (1994) *J. Antibiotics*, **47**, 755–764.
183. Hensens, D.O., Goetz, M.A., Liesch, J.M. *et al.* (1995) *Tetrahedron Lett.*, **36**, 2005–2008.
184. Horn, W.S., Simmonds, M.S.J., Schwartz, R.E. *et al.* (1995) *Tetrahedron*, **51**, 3969–3978.
185. Parella, T., Sánchez-Ferrando, F., and Virgili, A. (1995) *J. Magn. Reson., A*, **112**, 106–108.
186. Parella, T., Sánchez-Ferrando, F., and Virgili, A. (1995) *J. Magn. Reson., A*, **114**, 32–38.
187. Stelten, S. and Leibfritz, D. (1995) *Magn. Reson. Chem.*, **33**, 827–830.
188. Vogt, F.G. and Benesi, A.J. (1998) *J. Magn. Reson.*, **132**, 214–219.
189. Seki, H., Tokunaga, T., Utsumi, H. *et al.* (2000) *Tetrahedron*, **56**, 2935–2939.
190. Claridge, T.D.W. *High Resolution NMR Techniques in Organic Chemistry*, 2nd edn, 2009, Elsevier.
191. Morris, K.F. and Johnson, C.S. (1992) *J. Am. Chem. Soc.*, **114**, 3139.
192. Wu, D., Chen, A., and Johnson, C.S. (1995) *J. Magn. Reson. A*, **115**, 260.
193. Losonczi, J.A., Andrec, M., Fischer, M.W.F., and Prestegard, J.H. (1999) *J. Magn. Reson.*, **138**, 334–342.
194. Kummerlöwe, G. and Luy, B. (2009) *Annu. Rep. NMR Spectro.*, **68**, 193–230.
195. Thiele, C.M. (2008) *Eur. J. Org. Chem.*, **14**, 5673–5685.
196. Jiménez-Barbero, J. and Peters, T. (2003) *NMR Spectroscopy of Glycoconjugates*, Wiley-VCH Verlag GmbH, Weinheim.
197. Saupe, A. (1968) *Angew. Chem. Int. Ed.*, **7**, 97.
198. Prestegard, J.H. and Yi, X. (2006) in *NMR Spectroscopy and Computer Modeling of Carbohydrates*, ACS Symposium Series, Vol. 930 (eds J.F.G. Vliegenthart and R.J. Woods), Oxford University Press, pp. 40–59.
199. Enthart, A., Freudenberger, J.C., Furrer, J., Kessler, H., and Luy, B. (2008) *J. Magn. Reson.*, **192**, 314–322.
200. Shoolery, J.N. (1977) *Varian Instrum. Applic.*, **10**, 19–20.
201. Shoolery, J.N. and Majors, R.E. (1977) *Am. Lab.*, **9**, 51–61.
202. Shoolery, J.N. (1979) in *Topics in Carbon-13 NMR Spectroscopy*, Vol. 3 (ed. G.C. Levy), Wiley-Interscience, New York, pp. 28–38.
203. Crouch, R.C. and Martin, G.E. (1992) *J. Nat. Prod.*, **55**, 1343–1347.
204. Crouch, R.C. and Martin, G.E. (1992) *Magn. Reson. Chem.*, **30**, S66–S70.
205. Shockcor, J.P., Wurm, R.M., Silver, I.S. *et al.* (1994) *Tetrahedron Lett.*, **35**, 4919–4922.
206. Crouch, R.C., Davis, A.O., Spitzer, T.D. *et al.* (1995) *Heterocycl. Chem.*, **32**, 1077–1080.
207. Kawabata, J. and Fukushi, E. (1995) *J. Magn. Reson., A*, **117**, 88–90.

208. Sharaf, M.H.M., Schiff, P.L. Jr.,, Tackie, A.N. *et al.* (1995) *Magn. Reson. Chem.*, **33**, 767–778.

209. Crouch, R.C., Martin, G.E., Musser, S.M. *et al.* (1995) *Tetrahedron Lett.*, **36**, 6827–6830.

210. Musser, S.M., Eppley, R.M., Mazzola, E.P. *et al.* (1995) *J. Nat. Prod.*, **58**, 1392–1397.

211. Reynolds, W.F., Yu, M., and Enriquez, R.G. (1997) *Magn. Reson. Chem.*, **35**, 614–618.

212. Kolehmainen, E., Voivisto, J., Laihia, K. *et al.* (1999) *Magn. Reson. Chem.*, **37**, 359–364.

213. Logusch, S.J., Feng, P.C.C., Fujiwara, H. *et al.* (1999) *J. Agric. Food Chem.*, **47**, 2125–2129.

214. Barbara, T. (1994) *J. Magn. Reson., A*, **109**, 265–269.

215. Fitch, W.L., Degre, G., Holmes, C.P. *et al.* (1994) *J. Org. Chem.*, **59**, 7955–7956.

216. Shoolery, J.N. (1995) *Prog. Nucl. Magn. Reson. Spectrosc.*, **28**, 37–52.

217. Keifer, P.A., Baltusis, L., Rice, D.M. *et al.* (1996) *J. Magn. Reson.*, **119**, 65–75.

218. Olson, D.L., Peck, T.L., Webb, A.G. *et al.* (1995) *Science*, **270**, 1967–1970.

219. Olson, D.L., Lacey, M.E., and Sweedler, J.V. (1998) *Anal. Chem.*, **70**, A257–A264.

220. Olson, D.L., Lacey, M.E., and Sweedler, J.V. (1998) *Anal. Chem.*, **70**, 645–650.

221. Subramanian, R., Sweedler, J.V., and Webb, A.G. (1999) *J. Am. Chem. Soc.*, **121**, 2333–2334.

222. Li, Y., Wolters, A.M., Malawy, P.V. *et al.* (1999) *Anal. Chem.*, **71**, 4815–4820.

223. Martin, G.E., Crouch, R.C., and Zens, A.P. (1998) *Magn. Reson. Chem.*, **36**, 551–557.

224. Martin, G.E., Guido, J.E., Robins, R.H. *et al.* (1998) *J. Nat. Prod.*, **61**, 555–559.

225. Hadden, C.E. and Martin, G.E. (1998) *J. Nat. Prod.*, **61**, 969–972.

226. Hadden, C.E. and Martin, G.E. (1999) *Magn. Reson. Chem.*, **37**, 385–388.

227. Hadden, C.E., Martin, G.E., Tackie, A.N. *et al.* (1999) *J. Heterocycl. Chem.*, **36**, 1115–1117.

228. Hadden, C.E. and Martin, G.E. (1999) *Magn. Reson. Chem.*, **37**, 721–729.

229. Hadden, C.E., Martin, G.E., Tackie, A.N. *et al.* (1999) *Magn. Reson. Chem.*, **37**, 529–537.

230. Hadden, C.E., Sharaf, M.H.M., Guido, J.E. *et al.* (1999) *J. Nat. Prod.*, **62**, 238–240.

231. Lacey, M.E., Subramanian, R., Olson, D.L. *et al.* (1999) *Chem. Rev.*, **99**, 3133–3152.

232. Styles, P., Soffe, N.F., Scott, C.A. *et al.* (1983) *J. Magn. Reson.*, **60**, 397–404.

233. Styles, P., Soffe, N.F., and Scott, C.A. (1989) *J. Magn. Reson.*, **84**, 376–378.

234. Anderson, W.A., Brey, W.W., Brooke, A.L. *et al.* (1995) *Bull. Magn. Reson.*, **17**, 98–102.

235. Hill, H.D.W. (1997) *IEEE Trans. Appl. Supercond.*, **7**, 3750–3755.

236. Logan, T.M., Murali, N., Want, G. *et al.* (1999) *J. Magn. Reson.*, **37**, 762–765.

237. Pease, J., Withers, R., Nast, R. *et al.* (1999) 40th Experimental NMR Conference, Orlando, Florida, February 28–March 5, 1999, Abstract W&Th P202.

238. Liu, Y., Pease, J., Potts, B. *et al.* (2000) SMASH Small Molecule NMR Conference, Argonne, Illinois, July 16–19, 2000, Poster 21.

239. Russell, D.J., Hadden, C.E., Martin, G.E. *et al.* (2000) *J. Nat. Prod.*, **63**, 1047–1049.

9

Suspended-State NMR Spectroscopy (High-Resolution Magic Angle Spinning (HR-MAS) NMR Spectroscopy)

Markus Kramer and Klaus Albert

Structural assignment and ligand–receptor interactions [1, 2] have been studied recently in solution and also in suspension using methods of high-resolution (HR) nuclear magnetic resonance (NMR) spectroscopy, employing routine 5 mm NMR tubes.

Suspended solid- or gel-like samples cannot be investigated with conventional HR NMR spectroscopy. Owing to the inhomogeneity of the sample strong susceptibility distortions are present, leading to severe signal broadening. These susceptibility distortions can be eliminated by the application of high-resolution magic-angle spinning (HR-MAS) NMR spectroscopy. Here, the sample is rotated in a 4 mm ZrO_2 rotor at the "magic angle" of 54.7° at a rotation speed between 3000 and 5000 Hz. Under MAS conditions, spectral resolution can approach the typical values obtainable in the liquid state. Thus, an insoluble sample swollen in an appropriate solvent can be rapidly characterized by HR-MAS ^1H NMR spectroscopy [3–5].

Figure 9.1 shows the ^1H NMR spectrum of a cosmetic emulsion recorded in a conventional 5 mm NMR tube. The same sample is recorded under MAS conditions. The effect of MAS is clearly visible. Because of the increased resolution, coupling constants can be depicted and all essential information characterizing a ^1H NMR spectrum can be obtained [6].

Other examples of the application of HR-MAS NMR spectroscopy deal with the characterization of other emulsions such as milk, the reaction monitoring of peptide synthesis on a polymeric support [7] and the investigation of interactions between analytes and chromatographic supports in the presence of a mobile phase [8–21].

Handbook of Spectroscopy, Second Edition. Edited by Günter Gauglitz and David S. Moore.

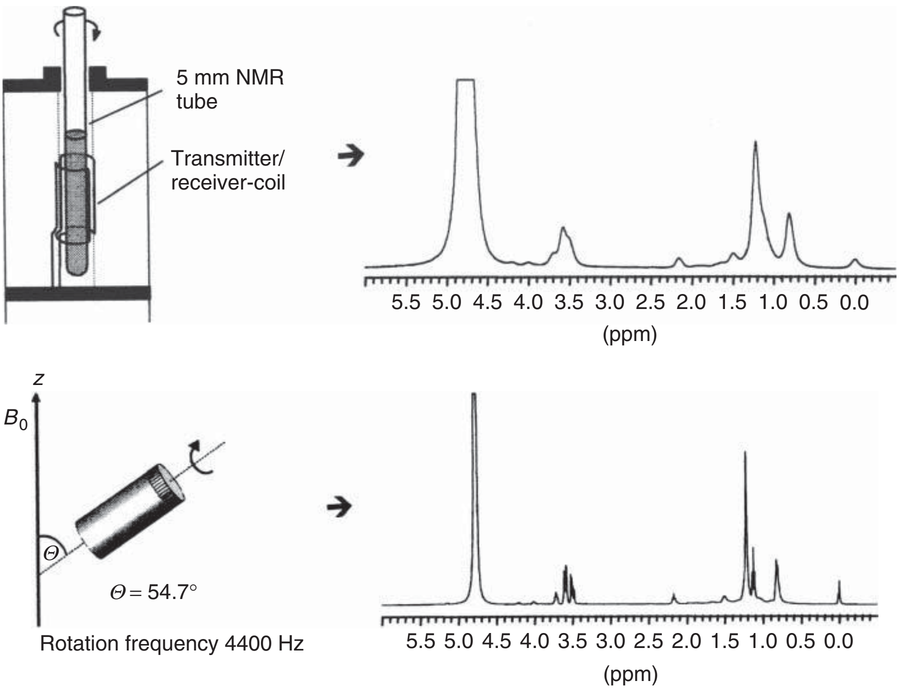

Figure 9.1 ^{1}H NMR spectrum of a cosmetic emulsion recorded under conventional and HR-MAS conditions.

References

1. Henrichson, D., Ernst, B., Magnani, J.L., Wang, W.-T., Meyer, B., and Peters, T. (1999) Bioaffinity NMR spectroscopy—identification of an E-selectin antagonist in a substance mixture by transfer NOE. *Angew. Chem. Int. Ed.*, **111**, 106–110. 1999) *Angew. Chem. Int. Ed.*, **38**, 98–102.
2. Klein, J., Meinecke, R., Mayer, M., and Meyer, B. (1999) Detecting binding affinity to immobilized receptor proteins in compound libraries by HR-MAS STD NMR. *J. Am. Chem. Soc.*, **121**, 5336–5337.
3. Anderson, P.C., Jarema, M.A., Shapiro, M.J., Stokes, J.P., and Ziliox, M. (1995) Analytical techniques in combinatorial chemistry—Mas Ch correlation in solvent-swollen resin. *J. Org. Chem.*, **60**, 2650–2651.
4. Keifer, P.A., Baltusis, L., Rice, D.M., Tymiak, A.A., and Shoolery, J.N. (1996) A comparison of NMR spectra obtained for solid-phase-synthesis resins using conventional high-resolution, MAS, and HR-MAS probes. *J. Magn. Reson.*, **119**, 65–75.
5. Keifer, P.A. (1996) Influence of resin structure, tether length, and solvent upon the high-resolution ^{1}H NMR spectra of solid-phase-synthesis resins. *J. Org. Chem.*, **61**, 1558–1559.
6. Tseng, L.-H., Emeis, D., Raitza, M., Händel, H., and Albert, K. (2000) Application of high-resolution—magic-angle-spinning (HR-MAS) NMR spectroscopy to cosmetic emulsions. *Z. Naturforsch.*, **55b**, 651–656.
7. Pursch, M., Schlotterbeck, G., Tseng, L.-H., Albert, K., and Rapp, W. (1996) *Angew. Chem., Int. Ed. Engl.*, **108**,

3034–3036. 1996) Monitoring the reaction progress in combinatorial chemistry: ^{1}H MAS NMR investigations on single macro beads in the suspended state. *Angew. Chem., Int. Ed. Engl.*, **35**, 2867–2869.

8. Strohschein, S., Pursch, M., Lubda, D., and Albert, K. (1998) Shape selectivity of C_{30} phases for RP-HPLC separation of tocopherol isomers and correlation with MAS NMR data from suspended stationary phases. *Anal. Chem.*, **70**, 13–18.

9. Albert, K., Lacker, T., Raitza, M., Pursch, M., Egelhaaf, H.-J., and Oelkrug, D. (1998) Investigating the selectivity of triacontyl interphases. *Angew. Chem., Int. Ed. Engl.*, **37**, 778–780.

10. Bachmann, S., Hellriegel, C., Wegmann, J., Händel, H., and Albert, K. (2000) Characterization of polyalkylvinyl ether phases by solid-state and suspended-state NMR investigations. *Solid State Nucl. Magn. Reson.*, **17**, 39–51.

11. Wegmann, J., Krucker, M., Bachmann, S., Fischer, G., Zeeb, D., Lienau, A., Glaser, T., Runge, F., Lüddecke, E., and Albert, K. (2002) Characterization of lycopene nanoparticles combining solid-state and suspended-state NMR spectroscopy. *J. Agric. Food Chem.*, **50**, 7510–7514.

12. Händel, H., Gesele, E., Gottschall, K., and Albert, K. (2003) Application of HRMAS ^{1}H NMR spectroscopy to investigate interactions between ligands and synthetic receptors. *Angew. Chem. Int. Ed.*, **42**, 438–442.

13. Skogsberg, H., Händel, H., Gesele, E., Sokoließ, T., Menyes, U., Jira, T., Roth, U., and Albert, K. (2003) Investigation of the retention behaviour of calixarene-based stationary phases by modern NMR spectroscopy. *J. Sep. Sci.*, **26**, 1119–1124.

14. Skogsberg, U., Händel, H., Sanchez, D., and Albert, K. (2004) Comparison of the interactions between two analytes and two structurally similar chiral stationary phases using high-performance liquid chromatography, suspended-state high-resolution magic angle spinning nuclear magnetic resonance and solid-state nuclear magnetic resonance spectroscopy. *J. Chromatogr. A*, **1023**, 215–223.

15. Hellriegel, C., Skogsberg, U., Albert, K., Lämmerhofer, M., Maier, N.M., and Lindner, W. (2004) Characterization of a chiral stationary phase by HR/MAS NMR spectroscopy and investigation of enantioselective interaction with chiral ligates by transferred NOE. *J. Am. Chem. Soc.*, **126**, 3809–3816.

16. Coutois, J., Fischer, G., Schauff, S., Albert, K., and Irgum, K. (2006) Interactions of bupivacaine with a molecularly imprinted polymer in a monolithic format studied by NMR. *Anal. Chem.*, **78**, 580–584.

17. Skogsberg, U., Händel, H., Welsch, N., Albert, K., and Kromidas, S. (2006) *HPLC Made to Measure*, Wiley-VCH Verlag GmbH, Weinheim, pp. 334–347.

18. Skogsberg, U., Meyer, C., Rehbein, J., Fischer, G., Schauff, S., Welsch, N., Albert, K., Hall, A.J., and Sellergren, B. (2007) A solid-state and suspended-state magic angle spinning nuclear magnetic resonance spectroscopic investigation of a 9-ethyladenine molecularly imprinted polymer. *Polymer*, **48**, 229–238.

19. Schauff, S., Friebolin, V., Grynbaum, M.D., Mayer, C., and Albert, K. (2007) Monitoring the interactions of tocopherol homologues with reversed-phase stationary HPLC Phases by ^{1}H suspended-state saturation transfer difference high-resolution/magic angle spinning NMR spectroscopy. *Anal. Chem.*, **79**, 8323–8326.

20. Friebolin, V., Bayer, M.P., Matyska, M.T., Pesek, J.J., and Albert, K. (2009) ^{1}H HR/MAS NMR in the suspended state: molecular recognition processes in liquid chromatography between steroids and a silica hydride-based cholesterol phase. *J. Sep. Sci.*, **32**, 1722–1728.

21. Friebolin, V., Marten, S., and Albert, K. (2009) Characterization of binding affinities in a chromatographic system by suspended state HR/MAS NMR spectroscopy. *Magn. Reson. Chem.*, **48**, 111–116.

10
Solid-State NMR

Steven P. Brown and Lyndon Emsley

10.1
Introduction

For the chemist today, the importance of solution-state NMR is well established. Individual nuclei within a molecule are differentiated on account of their chemical shift, while connectivities, which permit spectral assignment, are identified by through-bond *J*-couplings. Through-space proximities, which yield information about three-dimensional structure, are accessible by experiments which exploit the nuclear Overhauser effect (NOE). Moreover, a host of multidimensional experiments have been developed which further enhance the information content [1, 2]. In many cases, however, the most appropriate sample to study molecular structure and dynamics is the solid. The purpose of this chapter is to give an overview of the different solid-state NMR methods which are available in such cases. Our focus is on the structural and dynamic information which a particular method can deliver, and, at most, only a simple qualitative explanation of how the experiment works will be given, although the relevant literature will always be cited, such that the interested reader can find details about, for example, the experimental implementation.

Firstly, it is necessary to consider how and why NMR of solid samples differs from the solution-state case. High-resolution solution-state spectra are a result of fast isotropic molecular tumbling. In the solid-state, this motion is (usually) absent, and anisotropic interactions, that is, the chemical shift anisotropy (CSA), and the dipolar and quadrupolar couplings, lead to a broadening, see Section 10.2, of the resonances [3–5] These anisotropic interactions, on the one hand, have the significant disadvantage of hindering the resolution of distinct sites, but, on the other hand, contain valuable structural and dynamic information. Specifically, the CSA and quadrupolar interactions provide insight into electronic structure and bonding, while the dipolar coupling offers direct access to internuclear distances. Moreover, all three anisotropic interactions are formidable probes of dynamics. As is demonstrated in this chapter, a number of ingenious experimental approaches have been developed which provide access to the information inherent to the anisotropic

Handbook of Spectroscopy, Second Edition. Edited by Günter Gauglitz and David S. Moore.

Table 10.1 The properties of the NMR-active nuclei of most relevance for organic solids [6].

Nucleus	I	γ (10^7 rad T^{-1} s^{-1})	Natural abundance (%)
^1H	1/2	26.8	99.99
^2H	1	4.1	0.02
^{13}C	1/2	6.7	1.10
^{14}N	1	1.9	99.63
^{15}N	1/2	−2.7	0.37
^{17}O	5/2	−3.6	0.04
^{19}F	1/2	25.2	100.00

interactions particular to the solid state, while retaining the site specificity associated with high-resolution NMR.

Tables 10.1 and 10.2 list the NMR-active nuclei (i.e., those with $I > 0$) of most relevance for organic and inorganic solids, respectively, together with their nuclear spin quantum numbers, their magnetogyric ratios (γ), and natural abundances. (For a comprehensive listing of all NMR-active nuclei, the reader is referred to [6].) For spin $I = 1/2$ nuclei, the two most important anisotropic interactions are the anisotropy of the chemical shielding interaction and the dipolar coupling between the dipole moments of two or more spins. This is to be compared to the case of nuclei with $I \geq 1$, which possesses a quadrupole moment and whose spectra are dominated by the interaction of the quadrupole moment with the electric field gradient at the nucleus. Thus, a separate methodology exists for quadrupolar nuclei. Moreover, it is further necessary to distinguish between quadrupolar nuclei with integer (only $I = 1$) and half-integer ($I = 3/2$, $5/2$, $7/2$, $9/2$) spin, because in the latter case the presence of a "central transition," which is not broadened by the quadrupolar interaction to a first-order approximation, modifies the experimental approach. Solid-state NMR methods suitable for half-integer quadrupolar nuclei, for example, ^{17}O, ^{23}Na, and ^{27}Al, which are of much importance in inorganic systems, are therefore discussed separately in Section 10.7.

Nuclei can be further classified as to their natural abundance: nuclei with 99+% natural abundance, for example, ^1H, ^{19}F, and ^{31}P, are referred to as *being abundant*, while nuclei with low natural abundances, for example, ^2H, ^{13}C, and ^{15}N, are termed *dilute* or *rare*. For dilute nuclei, there exists the possibility of achieving site selectivity by means of selective isotopic labeling. In an NMR experiment, the sensitivity, that is, the signal-to-noise ratio (S/N), depends on the natural abundance, that is, the number of NMR-active nuclei in the sample, as well as the magnetogyric ratio, which determines the Larmor frequency of the nucleus at a particular magnetic field. Of all the naturally occurring nuclei, the proton, ^1H, thus, has the best sensitivity. However, unlike in solution-state NMR where ^1H NMR is of central importance, in the solid-state, there exists a major complication with ^1H NMR primarily due to its high natural abundance; namely, the abundance of protons in organic solids means that there exist strongly dipolar-coupled proton networks,

Table 10.2 The properties of the NMR-active nuclei of most relevance for inorganic solids [6].

Nucleus	I	γ (10^7 rad T^{-1} s^{-1})	Natural abundance (%)
^{6}Li	1	3.9	7.50
^{7}Li	3/2	10.4	92.50
^{11}B	3/2	8.6	80.10
^{17}O	5/2	−3.6	0.04
^{23}Na	3/2	7.1	100.00
^{25}Mg	5/2	−1.6	10.00
^{27}Al	5/2	7.0	100.00
^{29}Si	1/2	−5.3	4.67
^{31}P	1/2	10.8	100.00
^{33}S	3/2	2.1	0.75
^{45}Sc	7/2	6.5	100.00
^{47}Ti	5/2	−1.5	7.30
^{49}Ti	7/2	−1.5	5.50
^{51}V	7/2	7.0	99.75
^{55}Mn	5/2	6.6	100.00
^{59}Co	7/2	6.3	100.00
^{67}Zn	5/2	1.7	4.10
^{71}Ga	3/2	8.2	39.89
^{87}Rb	3/2	8.8	27.83
^{93}Nb	9/2	6.6	100.00
^{113}Cd	1/2	−6.0	12.22
^{119}Sn	1/2	−10.0	8.59
^{133}Cs	7/2	3.5	100.00
^{195}Pt	1/2	5.8	33.80
^{207}Pb	1/2	5.6	22.10

which lead to static line broadenings of the order of 50 kHz. As a consequence, as far as organic solids are concerned, attention has rather focused on dilute spin $I = 1/2$ nuclei, for example, ^{13}C and ^{15}N. However, as will be discussed briefly in this chapter, new high-resolution ^{1}H solid-state NMR methods have recently been developed [7], such that the importance of ^{1}H solid-state NMR is expected to increase significantly in the coming years.

In this chapter, we will first illustrate how anisotropic interactions lead to a broadening of the NMR resonances (Section 10.2), and then describe the principal line-narrowing method in solid-state NMR, namely magic-angle spinning (MAS), in Section 10.3. As stated above, achieving high-resolution is not the only goal in solid-state NMR, and ideally the spectroscopist would like to combine this with the retention of the structural and dynamic information inherent to the anisotropic interactions responsible for the line broadening. Recoupling methods [8, 9] are the subject of Section 10.4. As in solution-state NMR, the extension of the experiment to a second (and higher) dimension is of much importance in solid-state NMR;

homonuclear and heteronuclear multidimensional experiments are discussed in Sections 10.5 and 10.6, respectively. Finally, methods applicable to half-integer quadrupolar nuclei are introduced in Section 10.7.

10.2
Solid-State NMR Lineshapes

10.2.1
The Orientational Dependence of the NMR Resonance Frequency

In solid-state NMR, a very important concept is that *the resonance frequency of a given nucleus within a particular crystallite depends on the orientation of the crystallite* [3–5]. Considering the example of the CSA of a ^{13}C nucleus in a carboxyl group, Figure 10.1 illustrates how the resonance frequency varies for three particular orientations of the molecule with respect to the static magnetic field, B_0. At this point, we note that the orientation dependence of the CSA, dipolar, and first-order quadrupolar interactions can all be represented by what are referred

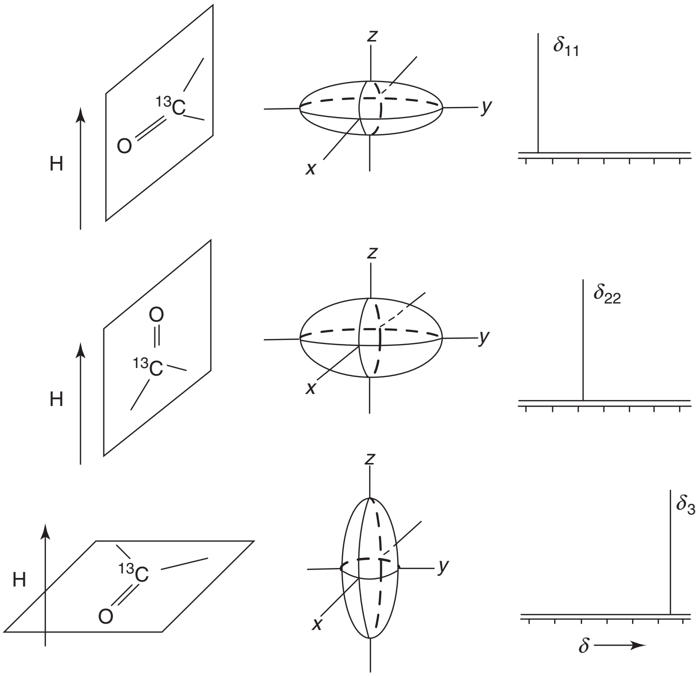

Figure 10.1 The dependence of the resonance frequency upon orientation for an anisotropic interaction, namely the CSA of a ^{13}C nucleus in a carboxyl group. The orientations illustrated correspond to the alignment of the three principal axes of the chemical shift tensor with the axis defined by B_0. (Reproduced by permission of the Società Italiana di Fisica from [5].)

to as *second-rank tensors*. This simply means that the interaction can be described mathematically in Cartesian space by a 3×3 matrix (this is to be compared with scalar and vector quantities, which are actually zero- and first-rank tensors, and are specified by a single element and a 3×1 matrix, respectively). For such a second-rank tensor, there exists a principal axes system (PAS) in which only the diagonal elements of the matrix are nonzero. Indeed, the orientations illustrated in Figure 10.1 correspond to the orientation of the three principal axes of the chemical shift tensor with respect to the axis defined by B_0.

To fully characterize the CSA and the first-order quadrupolar coupling, it is necessary to determine the three principal values (corresponding to the diagonal elements in the PAS) as well as the two angles (referred to as *Euler angles*) which describe the rotation of the PAS onto a fixed reference frame, for example, that are specified by B_0. The mathematical expression for the dependence of the resonance frequency of a given nucleus in a crystallite on these parameters is given in Appendix. It should be noted that the dipolar coupling between a pair of spins is always axially symmetric, and is fully specified by a single principal value and a single angle (see also Appendix). As the principal values and Euler angles for a given anisotropic interaction contain valuable chemical information, for example, about the electronic environment, one of the principal aims of solid-state NMR is the development of methods by which these parameters can be determined.

10.2.2
Single-Crystal NMR

One approach by means of which the principal values and orientations of the different anisotropic interactions can be determined involves the measurement of the change in the observed resonance frequencies upon rotating a single crystal in a well-defined fashion [10]. This is illustrated in Figure 10.2 for the case of ^{2}H NMR of a single crystal of the peptide *N*-acetyl-D,L-valine (NAV) for which the exchangeable amide and carboxyl hydrogens were deuterated [11]. The quadrupolar coupling leads to an inequivalence of the two single-quantum (SQ) transitions associated with a spin $I = 1$ nucleus such that a doublet is observed for each distinct deuterium. There are two molecules in the unit cell of NAV, and thus two crystallographically distinct hydrogen positions for both the amide and carboxyl groups, yielding four different deuterons, and therefore eight separate lines are observed (Figure 10.2a).

The change in the resonance frequencies of these eight lines upon rotating the crystal in 10° steps around two orthogonal axes is shown in Figure 10.2b,c. These results can then be analyzed to yield the principal values and orientations of both the ^{2}H CSA and quadrupolar tensors for both the amide and carboxyl hydrogens in NAV. As described in [11], it was found that, while the eigenvectors corresponding to the largest and intermediate principal values of the quadrupolar interaction are aligned (within experimental error) with the NH bond direction and the normal to the peptide plane, respectively, small but significant deviations are observed for the orientation of the CSA tensor.

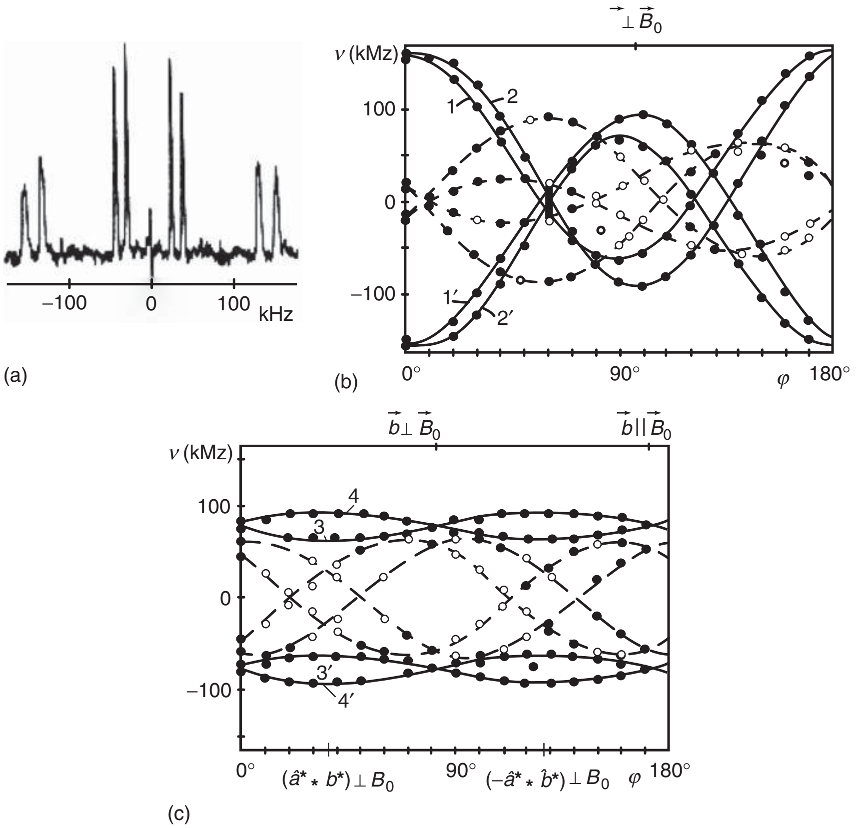

Figure 10.2 (a) ^{2}H NMR spectrum for a particular orientation of a single crystal of the peptide *N*-acetyl-D,L-valine (NAV) for which the exchangeable amide and carboxyl hydrogens were deuterated. (b,c) The change in the resonance frequencies of the eight lines upon rotating the crystal in 10° steps around two orthogonal axes. (Reproduced by permission of the American Chemical Society from [11].)

Although the power of the single-crystal method is evident, it suffers from a couple of significant limitations. First, a single crystal of sufficient size, several mm in each dimension, with a typical volume of $50\,\text{mm}^3$, is necessary. Second, a specialized NMR probe incorporating a goniometer is required for the well-defined rotation of the sample, and such equipment is available in only a handful of laboratories worldwide. If, however, both the crystal and the equipment are available, this kind of study yields very precise measurements of parameters that are not available from diffraction techniques.

At this point, we mention a related class of sample, namely oriented samples. In the case of a perfect macroscopic ordering, each equivalent nucleus is oriented identically, and the situation is the same as that in a single crystal. Specific oriented samples of relevance (with varying degrees of ordering) include polymer fibers [4], liquid crystals (LCs) [12, 13], and membrane proteins in oriented lipid bilayers [14].

We will return to the latter two cases in the discussion of two-dimensional experiments in Sections 10.5 and 10.6.

10.2.3
Powder Spectra

In solid-state NMR, it is more usual to deal with a powdered sample, where there is a uniform distribution of molecular orientations over three-dimensional space. The NMR spectrum for a powdered sample, therefore, consists of a superposition of many lines, corresponding to all the possible resonance frequencies, where each line originates from a given nucleus in a particular crystallite. Examples of powder spectra are shown in Figures 10.3 and 10.4. In Figure 10.3, the anisotropic

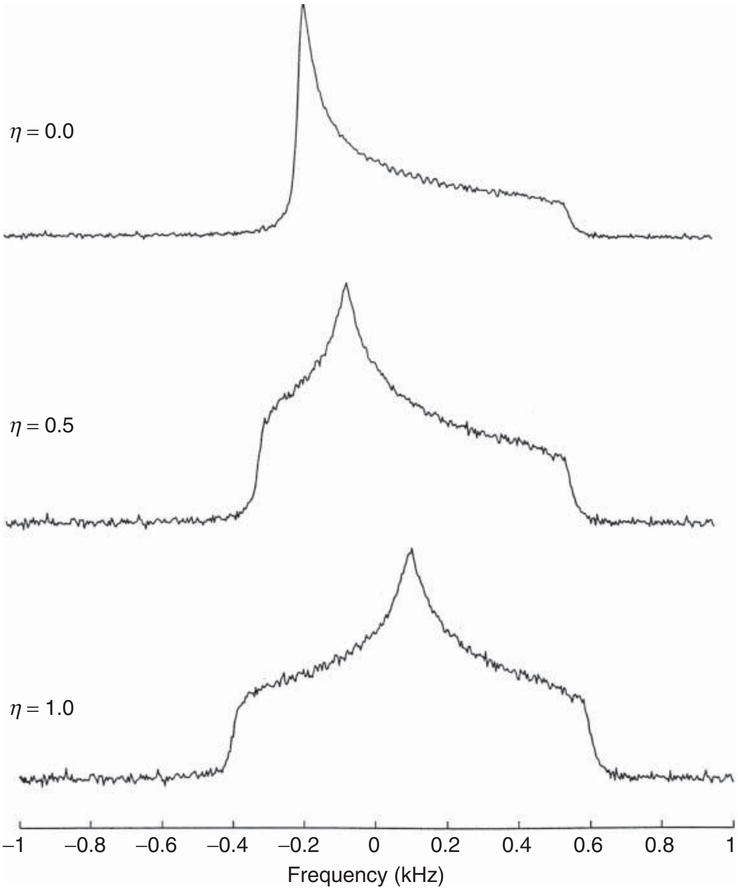

Figure 10.3 Simulated static powder spectra (with added noise) for the anisotropic broadening due to the CSA of a spin $I = 1/2$ nucleus, for example, ^{13}C. Spectra are shown for three different values of the asymmetry parameter, η (Appendix). (Reproduced by permission of the Società Italiana di Fisica from [5].)

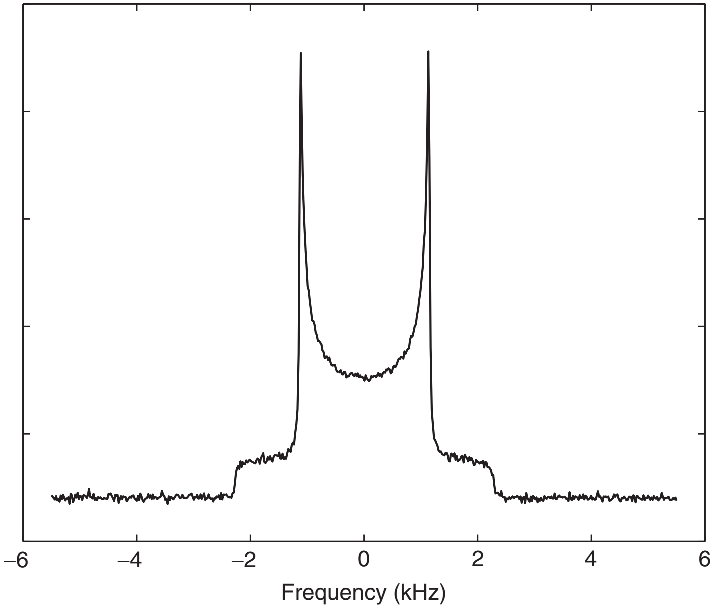

Figure 10.4 Simulated static powder spectrum (with added noise) for the anisotropic broadening due either to a dipolar coupling between an isolated pair of spin $I = 1/2$ nuclei or to the first-order quadrupolar coupling of a spin $I = 1$ nucleus, for example, ^{2}H. (Reproduced by permission of the Società Italiana di Fisica from [5].)

broadening is due to the CSA of a spin $I = 1/2$ nucleus, for example, ^{13}C (for three different values of the asymmetry parameter, η (Appendix)) while Figure 10.4 corresponds either to a dipolar coupling between an isolated pair of spin $I = 1/2$ nuclei or to the first-order quadrupolar coupling of a spin $I = 1$ nucleus, for example, ^{2}H.

If powder spectra of the type shown in Figure 10.3 and Figure 10.4 can be obtained experimentally, the principal values of the anisotropic interaction in question (though *not* the orientation of the PAS with respect to a fixed frame) can be obtained by a straightforward lineshape analysis. However, to obtain such spectra, it is necessary that there is only one distinct nucleus, and that one anisotropic interaction dominates. Usually, the static NMR lineshape is a ''broad featureless hump'' due to the overlapping of many powder patterns as well as the interplay of the different broadening mechanisms. As an example of this, Figure 10.5 presents a ^{1}H NMR spectrum of a representative organic solid, together with, for comparison, the corresponding solution-state ^{1}H spectrum. It is to be noted that the problem in such a case is not a lack of information, but rather there is essentially an overload, such that the net effect is the virtual loss of all information. In the remainder of this chapter, solid-state NMR approaches by which this information can be recovered will be demonstrated.

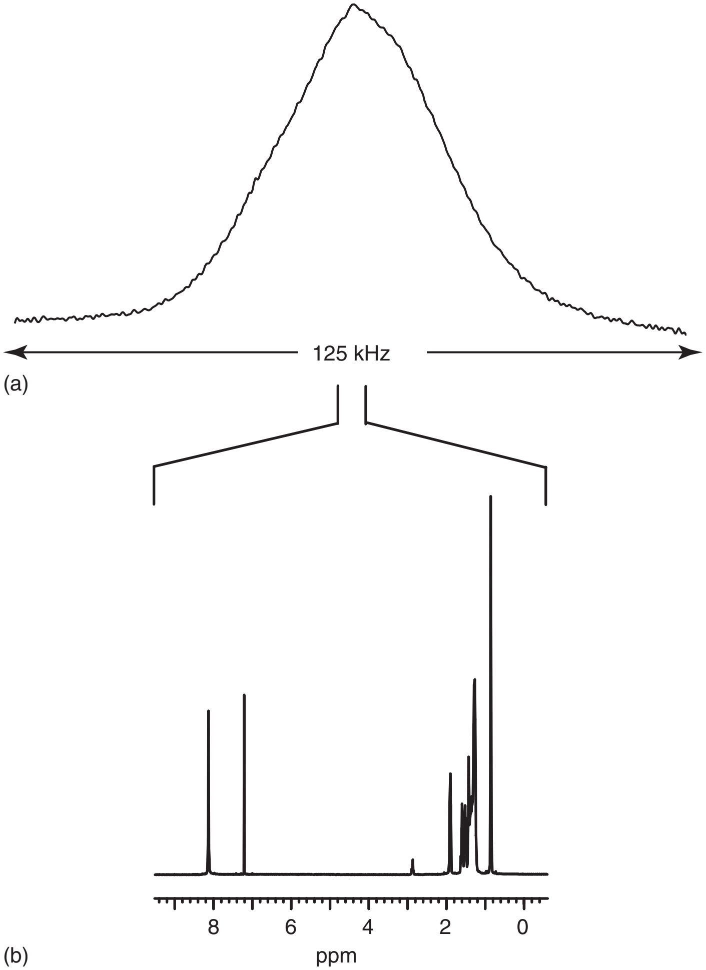

Figure 10.5 A comparison of the (a) static solid-state and (b) solution-state ^{1}H NMR spectra of a typical organic compound. (Reproduced by permission of the American Chemical Society from [7].)

10.2.4
One-Dimensional ^{2}H NMR

One notable case where it is possible to obtain powder spectra due to a single resonance for the case where one broadening mechanism dominates is ^{2}H NMR. As the natural abundance of deuterium is very low (Table 10.1), the ^{2}H NMR spectrum of a sample which has been selectively deuterated at a particular hydrogen position contains, to an extremely good approximation, only the response of that particular ^{2}H nucleus. Moreover, ^{2}H is a spin $I = 1$ nucleus, and it, therefore, possesses a quadrupole moment. Although the ^{2}H quadrupolar coupling ($\sim$200 kHz) is relatively small compared to other quadrupolar nuclei, it still dominates the other anisotropic interactions in diamagnetic compounds, for example, the CSA and the dipolar coupling.

The applications of ^{2}H NMR usually relate to the investigation of dynamic processes [4]. Indeed, one of the most important facets of solid-state NMR, in general, is its ability to probe molecular dynamics with atomic site selectively. This ability to probe dynamics is a direct consequence of the orientational dependence of the NMR resonance frequency: a given motional process leads to a particular crystallite experiencing a range of different orientations and hence a range of different frequencies. The motion is thus reflected in a marked change in the NMR spectrum as compared to the static case, with an extreme example of this phenomenon being the complete removal of anisotropic broadening as a consequence of isotropic molecular tumbling in solution. Notably, solid-state NMR spectra are not only sensitive to the *rates* of dynamic processes but also the *geometry*.

In ^{2}H NMR of a selectively labeled molecule, the one-dimensional (1D) powder spectrum depends only on the quadrupolar interaction for a single resonance. Moreover, the quadrupolar interaction for a deuteron bonded to a carbon atom is invariably axially symmetric and aligned with the bond direction. By recording a series of spectra at different temperatures, it is therefore possible, by means of a relatively straightforward lineshape analysis based on computer simulations, to determine the kinetic parameters, that is, the rate constants and the activation energy, as well as the motional mechanism for the dynamic process under investigation. Moreover, such investigations are aided by the fact that the experiment can be performed over a very wide temperature range, because the sample is static and in the solid-state (i.e., there is no problem with a solvent freezing or evaporating). It should be noted that it is usual practice to record ^{2}H powder spectra using the quadrupolar (or solid) echo technique [15].

As a specific example, consider the ^{2}H NMR spectra shown in Figure 10.6, which were recorded for a sample of [18-CD_3]-6-*s*-*cis*-retinoic acid, such that the motion of the methyl hydrogens could be investigated [16]. Marked changes in the spectra are apparent on increasing the temperature. In particular, as well as changing its shape, the linewidth is observed to narrow by approximately a factor of 2, when comparing the spectra for the lowest (top) and highest (bottom) temperatures. The rate constant for a model invoking a three-site jump motion was determined at each temperature by means of a lineshape analysis, and in Figure 10.6, the best-fit simulated spectra are shown to the right of the corresponding experimental spectra. For the lowest (top) and highest (bottom) temperatures investigated, the rate constant was determined to be 2.3×10^4 and $1.5 \times 10^{10}\,s^{-1}$, respectively. These two temperatures, therefore, correspond to a motion which is, respectively, ‘‘slow’’ and ‘‘fast’’ compared to the relevant timescale of this NMR experiment (corresponding, in this case, to the time required to record the free-induction decay (FID)). From the knowledge of the rate constant for each temperature, it was possible to determine an activation energy of $14.5\,kJ\,mol^{-1}$. By additionally investigating the methyl group jump motion in the corresponding trans model

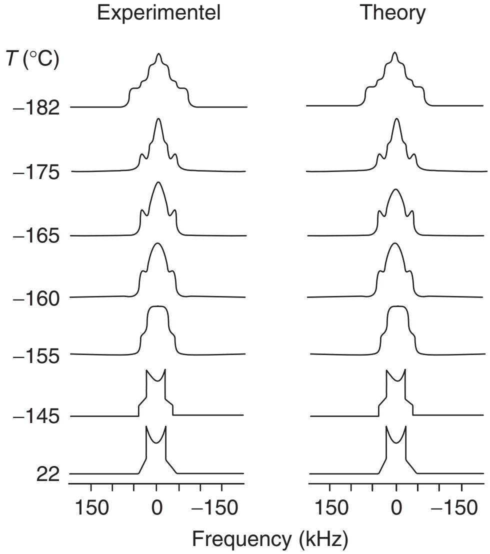

Figure 10.6 Variable-temperature ^{2}H NMR spectra recorded for a sample of [18-CD$_3$]-6-*s*-*cis*-retinoic acid. Best-fit spectra simulated for a model invoking a three-site jump motion are shown to the right of the corresponding experimental spectra. (Reproduced by permission of the American Chemical Society from [16].)

compound as well as in the membrane protein bacteriorhodopsin, Copié *et al.* [16] were able to postulate the existence of a 6-*s*-*trans* chromophore in the protein.

10.3
Magic-Angle Spinning

The above example of the effect of dynamics on a ^{2}H NMR powder spectrum illustrates that motion leads to line narrowing. Moreover, as noted above, in solution, fast isotropic tumbling of the molecules causes the averaging *to zero* of the line broadening due to the anisotropic interactions. To achieve high resolution, the solid-state NMR spectroscopist would like to mimic this averaging process. Rather than requiring random isotropic motion of each molecule, it can be shown that a physical rotation of the whole sample around an axis inclined at an angle of $\arctan(\surd 2) = 54.7^\circ$ (referred to as the *magic angle*) to B_0 suffices to average any second-rank tensor interaction to zero [17, 18].

To understand why so-called magic-angle spinning (MAS) is so successful as a means of line narrowing, it is first necessary to recognize that the CSA, dipolar, and first-order quadrupolar interaction all have basically the same orientational dependence: for an axially symmetric tensor (this is always the case for the dipolar interaction, and corresponds to a CSA or first-order quadrupolar interaction with a zero asymmetry parameter), the orientationally dependent part of the frequency of a particular crystallite can be expressed in the form

$$\omega \propto \frac{1}{2}(3\cos^2\theta - 1) \tag{10.1}$$

where θ denotes the angle between the tensor PAS direction and B_0 (see Appendix for the full mathematical expressions). For a static sample, there is thus no anisotropic frequency shift for those crystallites with $\theta = 54.7^\circ$.

To illustrate the effect of MAS, we consider in Figure 10.7 the specific example of a dipolar coupling between two spins. The four cones represent the range of positions adopted over the course of one rotor period for four different orientations of the internuclear vector relative to the rotor axis. In each case, the sample rotation leads to those components *perpendicular* to the rotation axis being zero on average, and only the component *parallel* to the rotation axis remains nonzero on average. Thus, for any original orientation, rotation around an axis yields an ‘‘average orientation’’ parallel to the axis of rotation. If the rotation axis is inclined at the magic angle to B_0, this parallel component has an anisotropic frequency shift equal to zero for all cases. Thus, under MAS, the anisotropic broadening is averaged to zero by the sample rotation for all crystallite orientations.

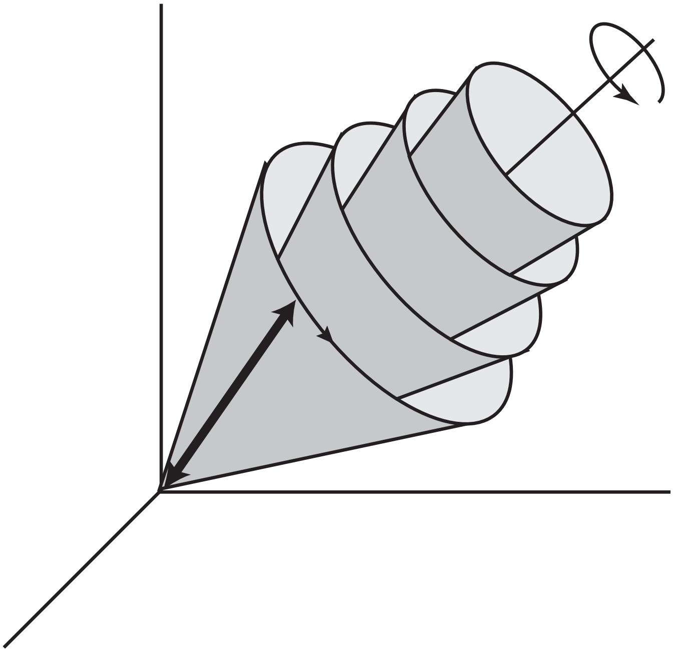

Figure 10.7 The effect of MAS for the specific example of a dipolar coupling between two spins. The four cones represent the range of positions adopted over the course of one rotor period for four different orientations of the internuclear vector relative to the rotor axis. The double-headed arrow represents an arbitrary position of one of the internuclear vectors.

10.3.1
Cross Polarization Magic-Angle Spinning Nuclear Magnetic Resonance CP MAS NMR

For solid-state NMR of a dilute spin $I = 1/2$ nucleus, for example, ^{13}C or ^{29}Si, MAS is usually combined with the method of cross polarization (CP) [19, 20], whereby a sensitivity enhancement results as a consequence of the transfer of polarization from an abundant nucleus with a high magnetogyric ratio, usually ^{1}H; the approach is referred to as *CP MAS NMR* [21]. High-power proton decoupling is normally applied during the acquisition of the FID to remove broadenings due to dipolar couplings involving the protons, such that the dominant anisotropic broadening is the CSA.

The simulated spectra in Figure 10.8 illustrate the effect of MAS for the case of a CSA interaction. On rotating the sample, the static lineshape is seen to break up into a centerband and spinning sidebands, separated by the rotor frequency. At a low MAS frequency, ν_R, the sideband manifold is observed to map out the shape of the static pattern. As the ν_R is increased, the signal intensity is increasingly concentrated at the centerband position, which corresponds to the isotropic chemical shift. It is to be noted that the linewidths are narrow and independent of ν_R [22].

In principle, it is possible to extract the anisotropy and asymmetry of the CSA by fitting the observed MAS sideband intensities. This is referred to as a *Herzfeld–Berger analysis* [24]. Such an approach is restricted to relatively small molecules, as it is necessary to be able to resolve, at a low ν_R, the sidebands of different resonances. As the number of distinct resonances increases, the 1D spectrum becomes increasingly more crowded; the advantage of extending the experiment to a second dimension in such cases will be discussed in Section 10.5.

The main interest of the CP MAS technique is that it can provide high-resolution purely isotropic spectra. As is apparent from Figure 10.8, as ν_R is increased such that it becomes large as compared to the static linewidth, the signal is increasingly concentrated in the centerband position. The spectrum is obviously much simplified if there is only one narrow resonance line, at the isotropic chemical shift, for each distinct nucleus. As an example, Figure 10.9 presents a ^{13}C CP MAS spectrum of powdered cyclosporin A, a cyclic 11-residue peptide. In this case, the isotropic spectrum is obtained by employing a ν_R of 33.3 kHz, and there are virtually no spinning sidebands. (MAS probes capable of supporting such a ν_R have only become available in the past 2–3 years. It is to be noted that at such a fast ν_R, it is necessary to employ a modified CP procedure, which is referred to as *ramped CP* [25, 26].) An alternative means by which a purely isotropic spectrum without spinning sidebands can be achieved for the case of a moderate ν_R is to employ a specially designed sequence of radio frequency (RF) pulses to suppress the spinning sidebands; the classic example is the TOSS (total suppression of sidebands) sequence [27, 28] which involves the application of four (or $2n + 2$) appropriately spaced 180° pulses before the start of acquisition.

In solid-state NMR experiments, a central theme is that of resolution. For ^{13}C CP MAS NMR, a critical factor in this respect is the efficiency of ^{1}H decoupling.

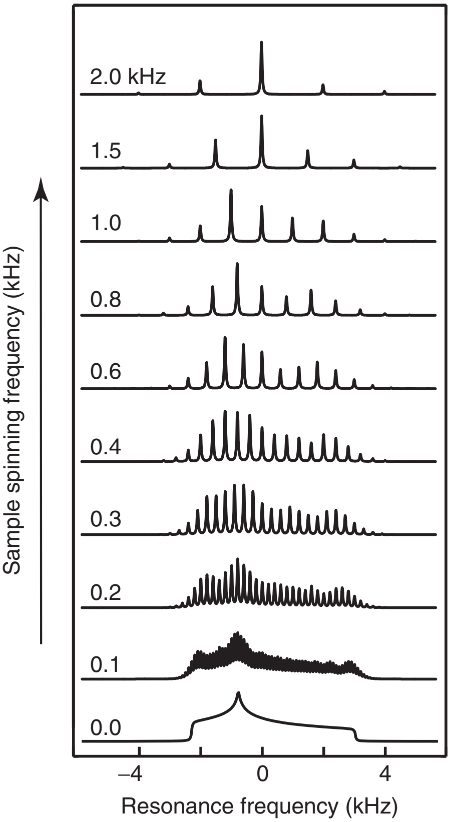

Figure 10.8 Simulated spectra showing the effect of MAS on the anisotropic lineshape due to a CSA interaction. (Reproduced by permission of the American Institute of Physics from [23].)

The simplest method, which is termed continuous wave (CW) decoupling, involves the application of a continuous RF pulse of fixed phase for the duration of the acquisition of the FID [29]. Recently, more sophisticated decoupling methods, such as two-pulse phase-modulation TPPM [30] or other sequences possessing a RN_n^ν symmetry [31], have been introduced; an explanation of why these methods yield narrower ^{13}C linewidths than conventional CW decoupling is given in [31, 32]. In simple terms, the efficiency of ^{1}H decoupling increases as the RF field strength increases (note that NMR literature usually refers to the inherent nutation frequency of the pulse, $|\omega_1| = |\gamma B_1|$, where B_1 is the RF field strength). Experimentally, care must of course be taken to find the power level which gives the optimum decoupling performance without damaging the probe. In Figure 10.9, it is shown that current state of the art ^{1}H decoupling, namely TPPM at a ω_1 of 200 kHz, yields a ^{13}C linewidth (full-width at half-maximum height, FWHMH) of 14 Hz (see the inset for a methyl carbon in cyclosporin A). The spectrum in Figure 10.9 was recorded at a B_0 of 11.8 T (corresponding to ^{1}H and ^{13}C Larmor frequencies of 500 and

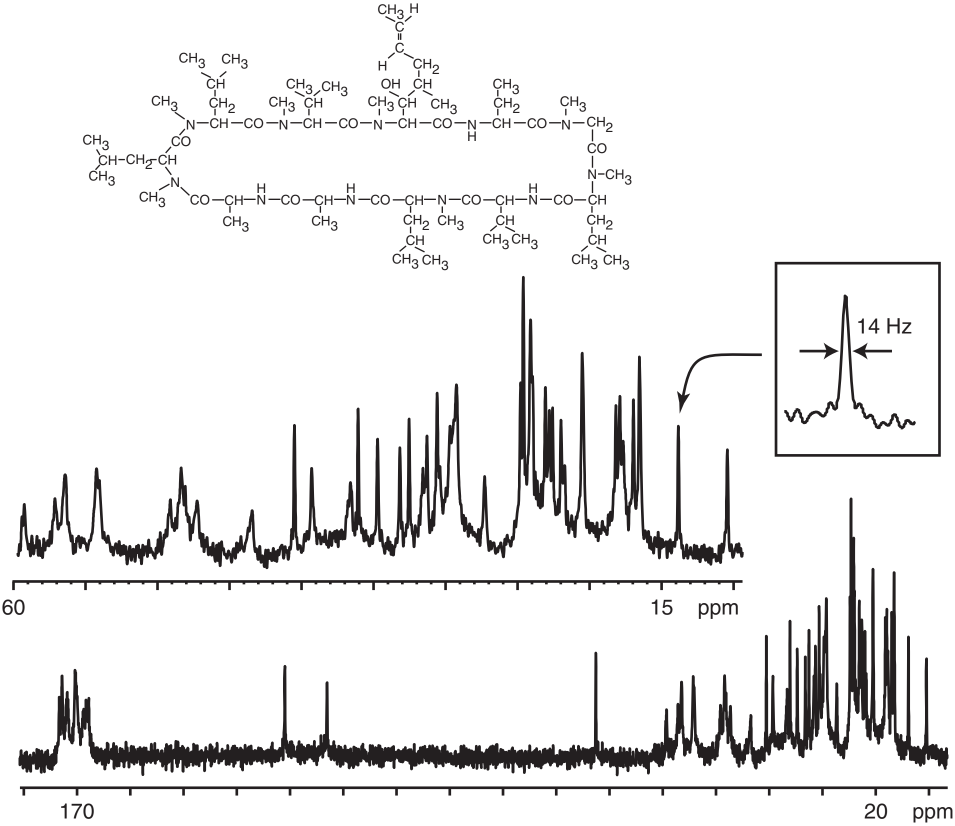

Figure 10.9 A ^{13}C CP MAS ($\nu_R = 33.3$ kHz) spectrum of powdered cyclosporin A, a cyclic 11-residue peptide, at natural abundance. (Courtesy of A. Lesage and P. Charmont.)

125 MHz). Today, solid-state NMR is being performed at B_0 fields approaching 20 T; provided that the same or narrower linewidths (in Hertz) can be achieved at the higher B_0, and this can certainly not be taken for granted in solid-state NMR, the resolution of resonances with different chemical shifts will be further improved at higher B_0.

For small molecules, some of the ^{13}C resonances can usually be assigned by reference to an assigned solution-state spectrum, as ^{13}C chemical shifts are relatively insensitive to the through-space effects of importance in the solid phase. As the molecular size increases, however, this is no longer the case. To assign a complicated ^{13}C CP MAS spectrum, such as that in Figure 10.9, spectral editing methods which can distinguish between CH_3, CH_2, CH, and quaternary carbons are of much help [33–36]. As a specific example, Figure 10.10 shows a 1D ^{13}C spectrum of L-histidine monohydrochloride monohydrate recorded using the SS-APT (solid-state attached proton test) method [34]: resonances due to carbons with an even (i.e., quaternary and CH_2 moieties) or odd (i.e., CH and CH_3 moieties)

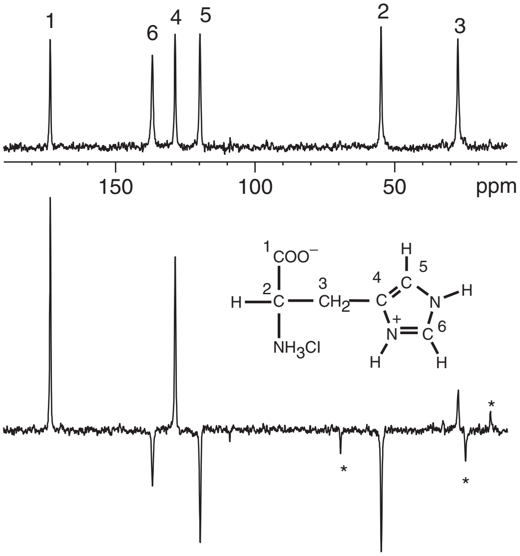

Figure 10.10 One-dimensional ^{13}C spectrum of L-histidine monohydrochloride monohydrate recorded using the SS-APT method. Resonances due to carbons with an even (i.e., quaternary and CH_2 moieties) or odd (i.e., CH and CH_3 moieties) number of attached protons are positive or negative, respectively. Spinning sidebands are labeled by asterisks. For comparison, the ^{13}C CP MAS spectrum is shown at the top. (Reproduced by permission of the American Chemical Society from [34].)

number of attached protons are positive or negative, respectively. It is to be noted that the SS-APT method is based on through-bond *J*-couplings, and thus has the advantage of being unaffected by molecular motion, which can lead to the erroneous interpretation of spectra obtained with the other spectral editing methods which exploit through-space dipolar couplings.

1D CP MAS is the workhorse solid-state NMR experiment, a fact which is apparent from the very wide range of applications, with specific examples including fossil fuels [37], that is, coals [38], and cokes [39], food science, for example, polysaccharides [40], pharmaceuticals [41], polymer blends [42], and soil science [43]. In addition to ^{13}C and, to a lesser extent, ^{15}N, another much investigated nucleus is ^{29}Si, with ^{29}Si solid-state NMR being of much importance in materials science and geology [44, 45]. Although ^{31}P has a 100% natural abundance, the relatively large separation between phosphorus atoms in a typical solid means that ^{31}P often has the characteristics of a rare spin. ^{31}P CP MAS NMR is of importance in, for example, the investigation of glasses [46].

Valuable information can often be obtained by simple experiments which determine the relaxation times, in particular the spin–lattice (or longitudinal) relaxation times in the laboratory or rotating frame, namely the ^{13}C T_1 and the ^{1}H $T_{1\rho}$, respectively, for the different resolved resonances in a 1D CP MAS spectrum. In simple terms, a faster relaxation time is due to an increase in molecular mobility.

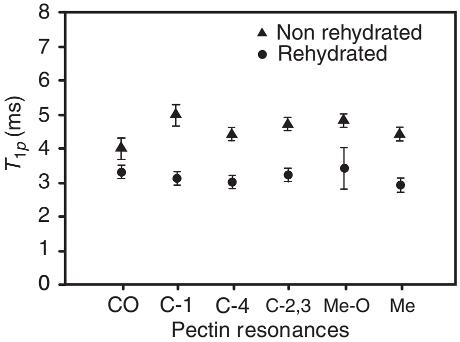

Figure 10.11 Fitted ^{1}H $T_{1\rho}$ relaxation time constants as read out at the various assigned ^{13}C resonances for 10% hydrated (triangles) and 35% hydrated (circles) onion cell-wall material. The difference directly reflects the increased mobility in the hydrated sample. (Reproduced by permission of Elsevier Science Publishers from [47].)

As a specific example, Figure 10.11 shows the ^{1}H $T_{1\rho}$ relaxation time constants, as read out at the ^{13}C resonances, for the pectin resonances in onion cell-wall material [47]. It is apparent that increasing the sample hydration from 10% to 35% leads to a clearly faster relaxation.

10.3.2
^{1}H Solid-State NMR

In the discussion of Figure 10.8, it was noted that the linewidths of the centerband and spinning sidebands are narrow and independent of ν_R. This is a general feature of *rare spin* spectra. A different situation is usually encountered in ^{1}H solid-state NMR. Figure 10.12 shows the effect of increasing ν_R upon the centerband in the ^{1}H MAS NMR spectrum of a medium-sized organic solid. In particular, it is apparent that the linewidth is dependent on ν_R, with a line narrowing being observed on increasing ν_R. Even at 35 kHz, the linewidths (FWHMH ≈ 750 Hz) are, however, much larger than those observed in ^{13}C MAS spectra.

The different effect of MAS in ^{1}H and ^{13}C NMR is a consequence of the central importance and relative insignificance of homonuclear (i.e., between like spins) dipolar couplings in the respective two cases. The homonuclear dipolar coupling between a pair of protons is approximately 16 times larger than that between two ^{13}C nuclei at the same internuclear separation. Moreover, the natural abundance of ^{13}C is only 1% as opposed to nearly 100% for ^{1}H, such that (except for the case of isotopically enriched samples) very few ^{13}C nuclei have a nearby ^{13}C neighbor.

For a typical organic solid, there exists a strongly dipolar-coupled multiproton network, and the effect of MAS is quite different as compared to the case of the CSA interaction. This difference is explained in a classic paper by Maricq and Waugh [22]. The CSA is an example of an interaction where the anisotropic broadening is perfectly refocused at the end of each rotor period, τ_R, (in the language of quantum mechanics, the corresponding Hamiltonian for a given

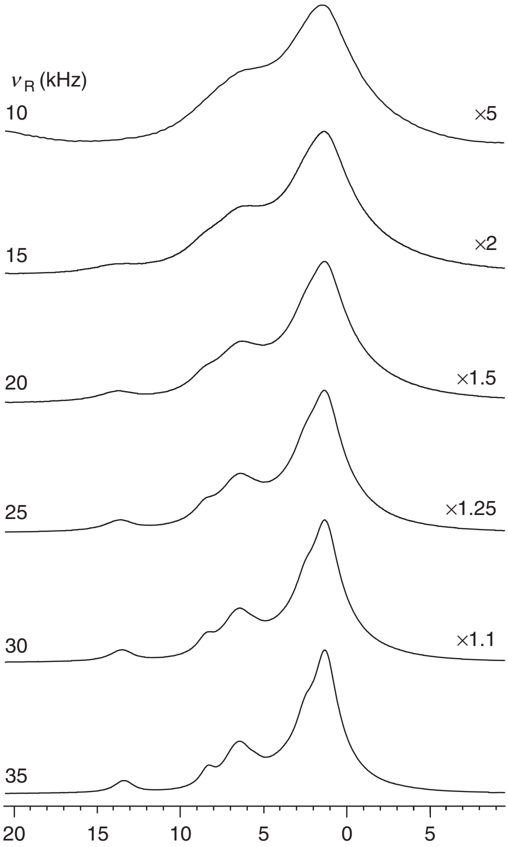

Figure 10.12 The effect of increasing the MAS frequency, ν_R, on the centerband of a ^{1}H MAS spectrum of a typical organic compound. (Reproduced by permission of the American Chemical Society from [48].)

crystallite commutes with itself at all times). By comparison, when there are three or more dipolar-coupled protons, the perturbing influence of the other dipolar-coupled protons on a particular dipolar-coupled pair means that the Hamiltonian does not commute with itself at all times, and the evolution under the dipolar coupling of a particular pair is no longer refocused at the end of each τ_R.

It was noted in the previous section, that a ν_R in excess of 20 kHz has only become possible in the past 2–3 years. The advantage in terms of the enhanced line narrowing in a ^{1}H MAS NMR spectrum is evident in Figure 10.12. Indeed, it has been shown that a ν_R of 30+ kHz at a ^{1}H Larmor frequency of 500+ MHz is sufficient to allow some ^{1}H resonances due to particular chemically distinct protons to be resolved in ^{1}H MAS NMR spectra of small to moderately sized organic solids [48–51]. The line narrowing achieved by MAS alone at a ν_R equal to 30 kHz is, however, still far from the limiting case, where all residual dipolar broadening has been removed.

Brute-force fast MAS is not the only means by which line narrowing can be achieved in solid-state NMR. A particularly ingenious alternative approach, first presented over 30 years ago by Waugh and coworkers [52, 53], involves the removal of the dipolar broadening by specific multiple-pulse techniques, where RF pulses achieve rotations in spin space. These rotations can complement the effect of the physical rotation of the sample; combined rotation and multiple-pulse spectroscopy (CRAMPS) [54–56] yields well-resolved ^{1}H spectra [57]. We will discuss the CRAMPS approach in more detail in Section 10.5.3.

An inspection of Table 10.1 reveals that ^{19}F has similar NMR properties to ^{1}H. Thus, methods which deal with the residual broadening owing to homonuclear dipolar couplings are also of much relevance in ^{19}F solid-state NMR [58]. Although fluorine is much less commonly encountered in chemistry than the omnipresent hydrogen, ^{19}F solid-state NMR has found a number of important applications, with recent examples including fluoropolymers [59] and biomembranes [60].

10.4
Recoupling Methods

Anisotropic interactions present both problems and opportunities. On the one hand, there is the significant disadvantage of hindering the resolution of distinct sites, and methods, such as MAS, which remove the line broadening due to the anisotropic interactions are essential to allow the recovery of the isotropic chemical shift information. On the other hand, they contain valuable structural and dynamic information. This information can be accessed while maintaining high resolution by employing the so-called recoupling method [8, 9] to recover the anisotropic interaction during part of the NMR experiment. In simple terms, recoupling involves the application of RF pulses to counteract the effect of the physical rotation. The conceptually most simple technique to illustrate the principle is rotational-echo double resonance (REDOR).

10.4.1
Heteronuclear Dipolar-Coupled Spins: REDOR

In the REDOR [61–63] technique, the distance between two heteronuclei is determined by comparing the signal intensity in two closely related experiments. The interpretation of the experimental results assumes the existence of isolated spin pairs, and there is thus usually a requirement for selective isotopic labeling at the two sites, the distance between which is of interest.

In a reference experiment, an echo corresponding to the refocusing of the evolution under both the chemical shift and the heteronuclear dipolar coupling is formed. The echo intensity in the reference experiment, S_0, is then compared to that in a second experiment where the application of 180° pulses at intervals of $\tau_R/2$ on the channel where there is no transverse magnetization interferes with the refocusing by MAS of the evolution due to the heteronuclear dipolar coupling,

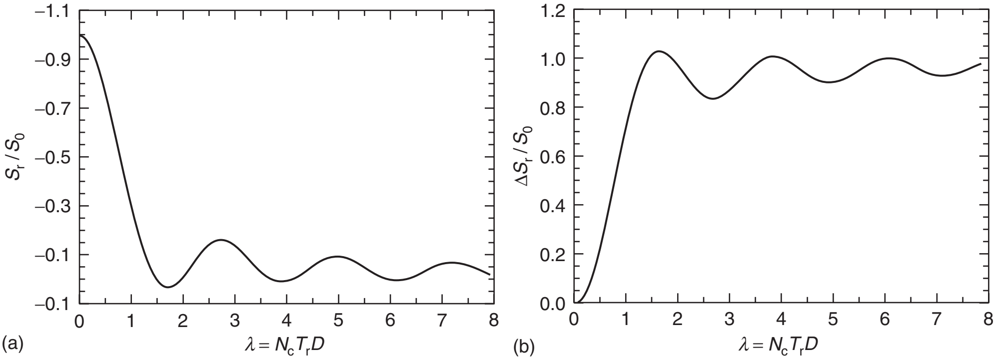

Figure 10.13 (a,b) REDOR master curves for an isolated dipolar-coupled spin pair showing the dependence of the ratios S_r/S_0 and $\Delta S/S_0$ upon the product of the evolution time and the heteronuclear dipolar coupling. (Reproduced from [63].)

and hence results in a reduced signal intensity, S_r. For an isolated spin pair, the ratio S_r/S_0 depends solely and in a straightforward manner on the product of the evolution time and the heteronuclear dipolar coupling. The REDOR master curve applicable to all heteronuclear spin pairs is plotted in Figure 10.13. Note that it is common to see the REDOR literature referring to the difference, $\Delta S = S_0 - S_r$. By simple reference to this master curve, it is possible to determine the heteronuclear dipolar coupling between the spin pair under consideration. It is of course advisable to determine two or more S_r values to ensure the reliability of the analysis. As the dipolar coupling depends on the internuclear distance to the inverse cubed power (Appendix), this method allows the determination of internuclear distances for heteronuclear spin pairs.

A number of interesting applications of the REDOR method have been presented (see Table 10.1 of [9]), with a particular emphasis on samples of biological relevance. A specific example is shown in Figure 10.14, where the distance between the specific spin labels in [1-^{13}C,^{15}N]acetyl-L-carnitine is determined to be 0.496 nm [63]. In this particular case, a distance determination was possible even though the C1 resonance is not resolved from that of the indicated C8 carbon. As well as ^{13}C and ^{15}N, other spin $I = 1/2$ nuclei studied by REDOR include ^{19}F, ^{29}Si, and ^{31}P. For example, Holl *et al.* [64] have demonstrated the measurement of a 0.8 nm ^{13}C–^{19}F internuclear distance in a nine-residue fragment of the peptide antibiotic emerimicin. Extensions of the REDOR method to measure distances where one or even both of the nuclei are quadrupolar have also been proposed. For quadrupolar nuclei, the large quadrupolar interactions present significant problems, in particular a simple 180° pulse does not achieve a uniform inversion for all crystallites for the case of a broad quadrupolar lineshape. Various methods, for example, TRAPDOR [65] and rotational-echo adiabatic passage double resonance (REAPDOR) [66], have been introduced which attempt to address this problem.

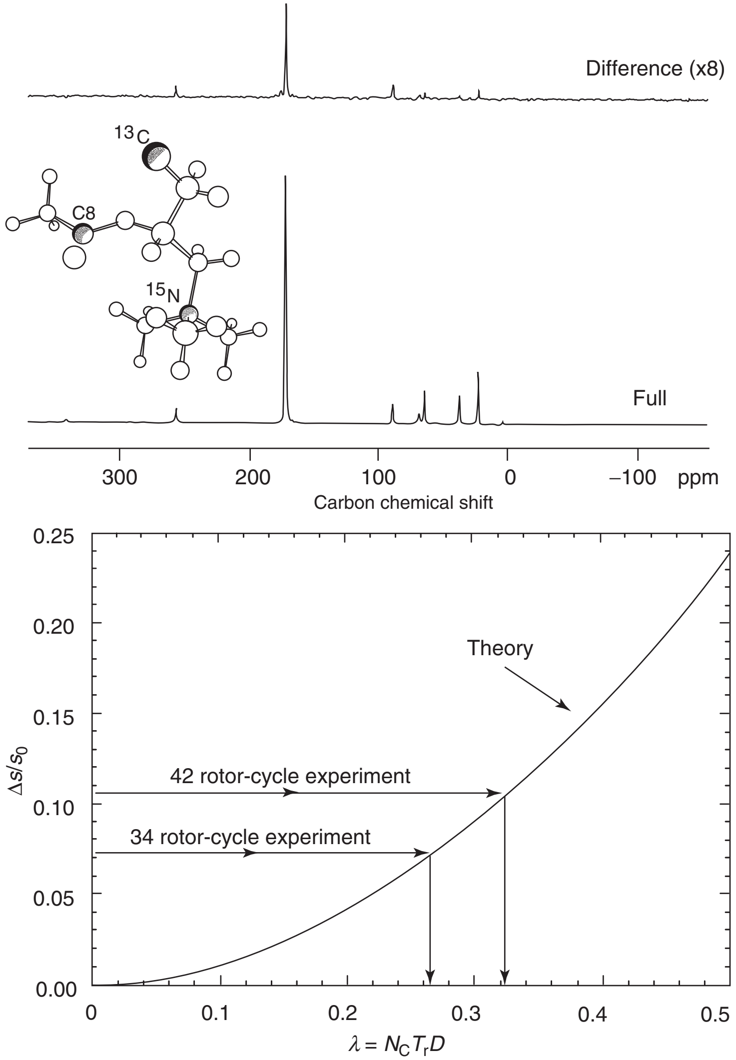

Figure 10.14 The determination of the distance between the specific spin labels in [1-^{13}C, ^{15}N]acetyl-L-carnitine by the REDOR technique. The difference, ΔS, and reference, S_0, REDOR spectra are shown for the 34-τ_R experiment. (Reproduced from [63].)

10.4.2
Homonuclear Dipolar-Coupled Spins

There are small but important differences between the evolution of a given spin under a homonuclear as opposed to a heteronuclear dipolar coupling [3–5]. As a consequence, a different methodology is required for the determination of the internuclear distance between a homonuclear dipolar-coupled pair of spins.

Rotational resonance (RR) is an intriguing phenomenon which is observed when ν_R is equal to a small integer multiple of the difference in the isotropic chemical shift frequencies of two resonances in the spectrum [67, 68]. The most apparent effect of RR is that the normally narrow spectral peaks acquire splittings and broadenings, the nature of which depends on the dipolar coupling between the two spins. As a specific example, experimental spectra (together with best-fit simulations) corresponding to the $n = 1$, 2, and 3 RR conditions for all-E-[11,20-$^{13}C_2$]-retinal are shown in Figure 10.15 [69]. In this case, it was possible to determine that the internuclear distance between the two ^{13}C labels is 0.301 ± 0.008 nm.

In the last decade, a large number of methods for recoupling the homonuclear dipolar coupling have been developed, with specific examples including DRAMA

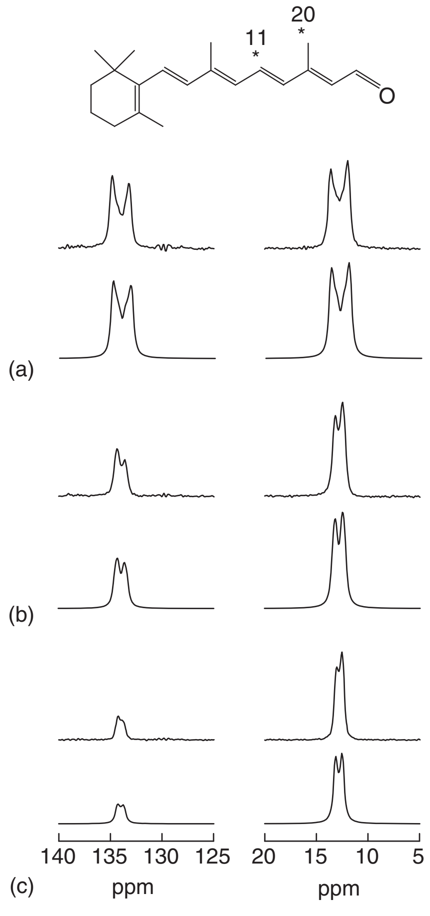

Figure 10.15 ^{13}C rotational-resonance experimental spectra (top), together with best-fit simulations (bottom), corresponding to the $n =$ (a) 1, (b) 2, and (c) 3 RR conditions for all-E-[11,20-$^{13}C_2$]-retinal. (Reproduced by permission of Elsevier Science Publishers from [69].)

[70], radio-frequency-driven recoupling (RFDR) [71], HORROR [72], C7 [73], BABA [74], DRAWS [75], and DREAM [76] (for a comprehensive account, see [8, 9]). We note that Levitt and coworkers have recently introduced a very helpful classification system, based on symmetry principles, which explains how many of these sequences work and provides a framework for generating other sequences [31, 77]. Rather than allowing the accurate determination of internuclear distances, these sequences, as will be illustrated in Section 10.5, are usually employed to establish correlations or to select dipolar-coupled spin pairs in multidimensional homonuclear experiments.

10.4.3

The CSA: CODEX

It was stated above that MAS causes the evolution under the CSA to be refocused at the end of each τ_R. If a 180° pulse is applied every $\tau_R/2$, the refocusing of the CSA evolution is prevented (the same principle applies for the case of the heteronuclear dipolar coupling in the REDOR experiment (Section 10.4.1) or the homonuclear dipolar coupling in the RFDR [71] sequence). Recently, de Azevedo *et al.* [78, 79] have shown how an experiment incorporating two periods of such CSA recoupling separated by a mixing time, τ_m, allows the detection of slow dynamic processes. The method is applicable at fast MAS, and is termed centerband-only detection of exchange (CODEX). The principle of the experiment is that a loss of signal intensity is observed if the orientation of the CSA tensor for a particular carbon changes during τ_m. By subtracting the signal intensity from that measured in a reference experiment, a pure-exchange CODEX spectrum is obtained.

As a specific example, Figure 10.16 shows pure-exchange CODEX ^{13}C NMR spectra, recorded for a sample of amorphous poly(methyl methacrylate), PMMA (at natural abundance in ^{13}C), at 300 K with different τ_m [78]. For the very small mixing time, τ_m, of 1 ms, no intensity is observed, indicating the absence of dynamics on this timescale. For a longer τ_m, intensity is seen to build up at the COO and OCH_3 positions as well at the quaternary C position due to side group and backbone motion, respectively, in the polymer. From a series of CODEX experiments, it is possible to determine the reorientation angle, the correlation time, as well as the fraction of mobile segments.

10.5

Homonuclear Two-Dimensional Experiments

The importance of solution-state NMR today owes much to the extension of the experiment to a second (and higher) dimension [1]. Two-dimensional (2D) NMR spectroscopy is also of much significance in solid-state NMR. In attempting to classify the many important different 2D solid-state NMR experiments which have been proposed to date, we make, in this chapter, a distinction between homonuclear (i.e., those involving only one kind of nucleus) and heteronuclear experiments.

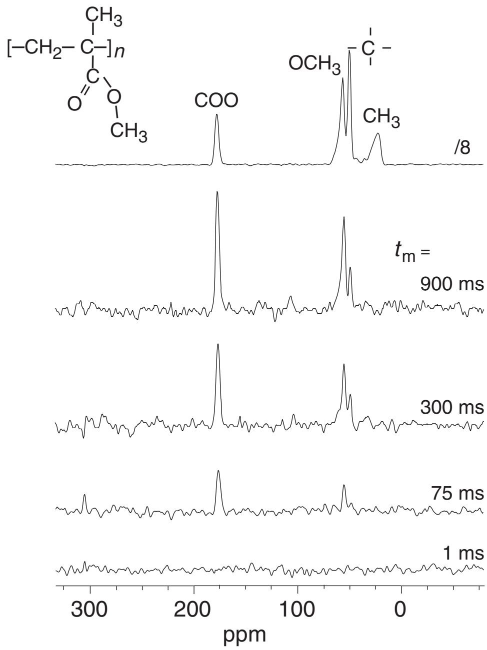

Figure 10.16 Pure-exchange CODEX ^{13}C NMR spectra, recorded for a sample of amorphous PMMA, (at natural abundance in ^{13}C) at 300 K with different τ_m. A ^{13}C CP MAS spectrum is shown at the top. (Reproduced by permission of the American Chemical Society from [78].)

10.5.1
Establishing the Backbone Connectivity in an Organic Molecule

In Section 10.3.1, the problem of assigning the many resolved ^{13}C resonances in a 1D MAS spectrum was mentioned, and 1D spectral editing methods were introduced. In this section, we describe homonuclear ^{13}C–^{13}C 2D correlation experiments in which a selection is usually made such that 2D peaks are only observed for pairs of directly bonded carbons (or at least these peaks are significantly more intense). In this way, it is possible to trace out the connectivity along the backbone of the organic molecule, and thus assign the ^{13}C resonances. As a consequence of the significant sensitivity problems associated with the very low probability of finding a pair of directly bonded ^{13}C nuclei in a sample at natural abundance, these experiments are usually performed on fully or partially ^{13}C-enriched (normally globally, i.e., at all carbon positions) samples.

In the first class of ^{13}C–^{13}C 2D correlation experiments described here, single-quantum coherence (SQC), that which is detected in a conventional 1D NMR experiment, evolves in both dimensions of the NMR experiment. A mixing time is inserted between the two evolution periods during which a pulse sequence is applied which recouples the homonuclear dipolar coupling (Section 10.4.2), such that coherence transfer occurs between ^{13}C nuclei which are close together in space. As a specific example, Figure 10.17 shows the region corresponding to the C_α and aliphatic side-chain carbons of a ^{13}C–^{13}C SQ–SQ correlation spectrum of ^{13}C globally labeled antanamide (a cyclic decapeptide), recorded using the DREAM [76] recoupling sequence. The indicated negative off-diagonal peaks are due to one-bond correlations among the aliphatic side-chains.

By using very high magnetic fields, even larger biopolymers are becoming accessible to solid-state NMR. As an example, Figure 10.18 presents a ^{13}C–^{13}C SQ–SQ correlation spectrum of a solid 62 residue ^{13}C and ^{15}N globally labeled protein containing the α-spectrin SH3 domain, recorded at 17.6 T [80]. In this case, mixing was achieved using proton-driven spin diffusion; a long mixing time of 15 ms was employed such that longer-range correlations are also observed. Using this and other experiments, it was possible to assign all the ^{13}C and ^{15}N resonances.

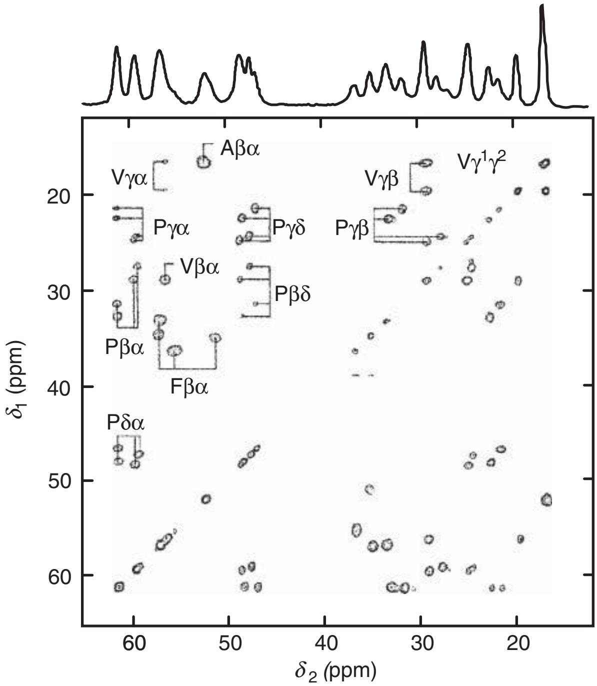

Figure 10.17 The region corresponding to the C_α and aliphatic side-chain carbons of a ^{13}C–^{13}C SQ–SQ correlation spectrum of ^{13}C globally labeled antanamide (Val-Pro-Pro-Ala-Phe-Phe-Pro-Pro-Phe-Phe), recorded at a magnetic field of 14.1 T and $\nu_R = 30$ kHz. Mixing was achieved using a DREAM [76] recoupling sequence of duration 7 ms. Positive and negative peaks are shown as dark- and light-shaded lines, respectively. The indicated negative off-diagonal peaks are due to one-bond correlations among the aliphatic side-chains. (Courtesy of B.H. Meier.)

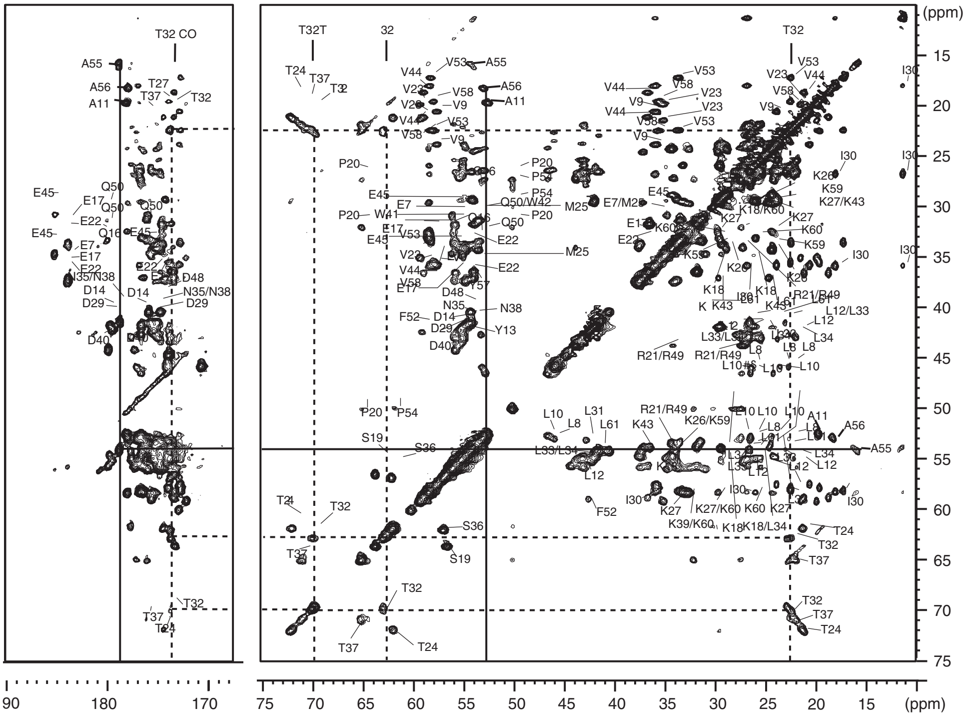

Figure 10.18 A 2D ^{13}C–^{13}C SQ–SQ correlation spectrum of a solid 62 residue ^{13}C and ^{15}N globally labeled protein containing the α-spectrin SH3 domain, recorded at 17.6 T. Mixing was achieved using proton-driven spin diffusion; a long mixing time of 15 ms was employed such that longer-range correlations are also observed. (Reproduced from [80].)

Emsley and coworkers have recently suggested an alternative approach for establishing carbon–carbon connectivities, namely the solid-state INADEQUATE experiment [81]. It is so termed because of the analogy to the solution-state experiment of the same name [82]. Unlike the experiments described above which utilize through-space dipolar couplings, this approach is based on the through-bond *J*-coupling. A further important difference is that double-quantum coherence (DQC) as opposed to SQC evolves during the t_1 (or indirect) dimension of the experiment. Experiments involving the creation of DQC and multiple-quantum coherence (MQC) in general are of much importance in both solution-state and solid-state NMR. For example, in pioneering work, Pines and coworkers have shown that the analysis by so-called spin-counting experiments of the very high MQC orders excitable in static ^{1}H solid-state NMR provides valuable information about large clusters (often up to 100 nuclei) of dipolar-coupled protons [83, 84].

For a detailed discussion of the concept of MQC, the reader is referred to, for example, [1, 85]. Here, we simply note two relevant features: first, a MQC cannot be directly detected in an NMR experiment, that is, an experiment involving a multiple-quantum (MQ) evolution period is inherently at least 2D, since the MQC must be converted into detectable SQC; and, second, for spin $I = 1/2$ nuclei, MQC can only be created for coupled nuclei. As illustrated by the specific example of L-tyrosine in Figure 10.19, an advantage over the SQ–SQ correlation spectra in Figure 10.17 and Figure 10.18 is the absence of signal along the diagonal. Furthermore, by using the *J*-coupling, the observation of a pair of correlated peaks can only be due to directly bonded ^{13}C nuclei. However, S/N of the *J*-coupled INADEQUATE experiment is invariably worse than that of the dipolar-based experiments used for Figure 10.17 and Figure 10.18, although refocused INADEQUATE experiments [86, 87] reduce the signal loss and are applicable to disordered systems.

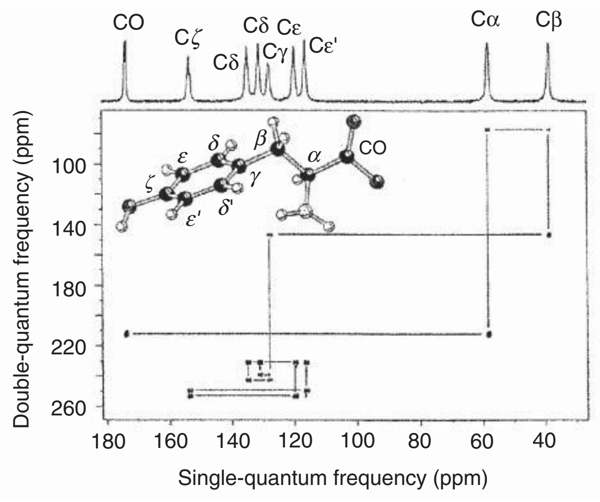

Figure 10.19 A 2D ^{13}C–^{13}C INADEQUATE spectrum of L-tyrosine.

10.5.2
Dipolar-Mediated Double-Quantum Spectroscopy

Double-quantum (DQ) spectroscopy is not only useful for homonuclear ^{13}C–^{13}C correlation experiments which allow the identification of the backbone connectivity. In this section, the utility of other 2D DQ experiments which provide insight into, for example, through-space proximities will be illustrated. As opposed to the solid-state INADEQUATE experiment introduced in the previous section, the experiments described in this section are based on the dipolar as opposed to the *J*-coupling of spins.

A ^{1}H 2D DQ MAS spectrum [88] recorded in a rotor-synchronized fashion in t_1 (i.e., the t_1 increment is set equal to one rotor period such that all spinning sidebands in the DQ dimension (F_1) fold back onto the centerband position) is shown in Figure 10.20a. To create DQC as well as to allow its conversion into

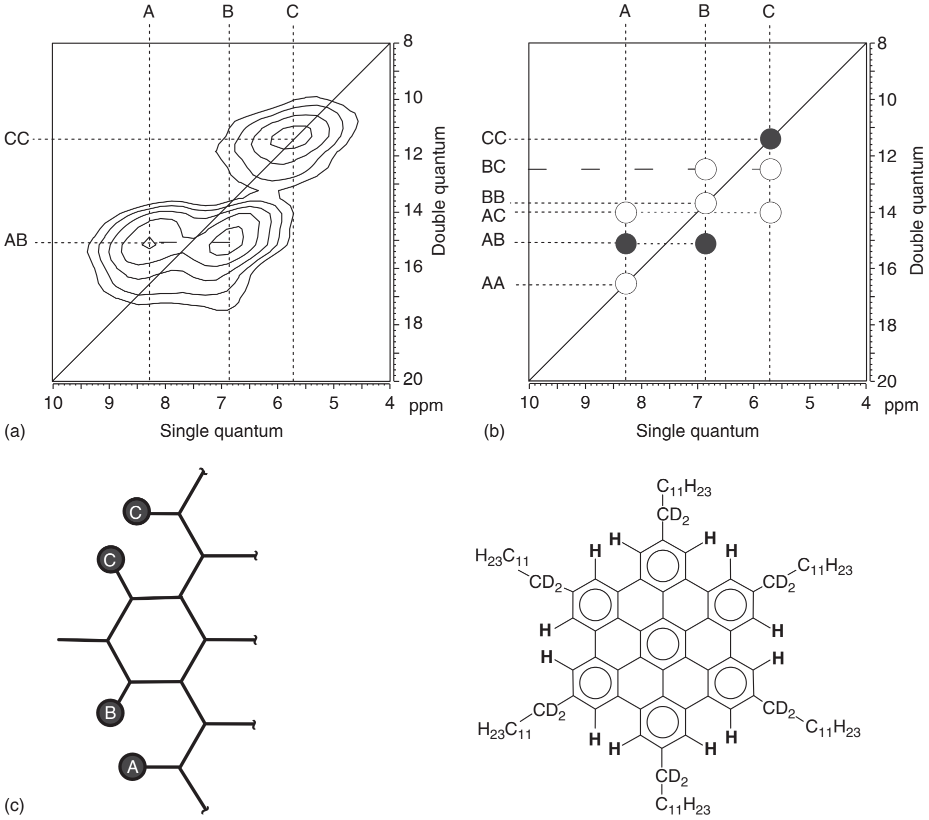

Figure 10.20 (a) A representative rotor-synchronized ^{1}H DQ MAS spectrum, corresponding to the aromatic protons in HBC-C_{12}. (b) A schematic representation showing the positions of the six possible DQ peaks; the observed AB and CC peaks (filled circles) imply the proton–proton proximities indicated in (c). (Reproduced by permission of Elsevier Science Publishers from [50].)

observable SQC, the BABA [74] recoupling sequence (Section 10.4.2) was used. This is a robust sequence which is suitable for the fast ν_R of 35 kHz employed. The ability of the ^{1}H DQ MAS experiment to identify proton–proton proximities lies in the fact that both the excitation and subsequent reconversion of DQC relies on the presence of a dipolar coupling between a particular two spins. As the dipolar coupling is proportional to the internuclear distance to the inverse cubed power, a peak is, hence, only observed in the DQ MAS spectrum if the corresponding two protons are close together in space. As a rule of thumb, the presence of a peak in a ^{1}H DQ MAS spectrum implies a proton–proton proximity of under 0.35 nm.

For this particular example, which corresponds to the aromatic protons of an alkyl-substituted polycyclic aromatic system (HBC-C_{12}) [49], three resonances (labeled A, B, and C) can be identified in the corresponding 1D ^{1}H (500 MHz) MAS spectrum, which is shown at the top of Figure 10.20a. The six possible DQ peaks in this case are shown in Figure 10.20b. As the DQ frequency corresponding to a given DQC is simply the sum of the two SQ frequencies, DQCs between like (AA), and unlike (AB) spins can, in general, be distinguished in that, in the former case, a single peak at $(2\nu_A, \nu_A)$ is observed, while, in the latter case, two peaks at $(\nu_A + \nu_B, \nu_A)$ and $(\nu_A + \nu_B, \nu_B)$ are observed. (The notation (ν_1, ν_2) refers to a DQ peak centered at ν_1 and ν_2 in the F_1 and F_2 dimensions, respectively.) Note that for the anisotropic dipolar coupling, it is, unlike for the isotropic J-coupling, possible to observe an auto peak for a DQC between two like spins. It should be noted that an advantage of the DQ approach over a spin diffusion experiment [4, 89] in which a mixing time is inserted between two SQ evolution periods is that an auto peak is only observed if there is a close proximity of two protons. By contrast, in the spin diffusion experiment, strong auto peaks are seen for all resonances, regardless of whether there is a close proximity.

Of the six possible DQ peaks, only two, namely AB and CC, are observed in the experimental spectrum in Figure 10.20a. For this system, the aromatic protons are arranged into well-isolated pairs of "bay protons;" the observed DQ peaks thus correspond to these bay protons pairs. As discussed in [49], the implied presence of only two types of pairs of aromatic protons, H_A–H_B and H_C–H_C (Figure 10.20c) is a consequence of intermolecular ring current effects; for an isolated molecule, the sixfold symmetry leads to all aromatic protons being equivalent. Using quantum-chemical calculations of ^{1}H chemical shifts, the experimental data could be assigned in a fully quantitative manner to a particular structural model [90]. Such effects of ring currents on NMR chemical shifts are, of course, well established [91]; however, it is only recently, with the development of solid-state NMR methods allowing the resolution of ^{1}H resonances, that the widespread importance of these effects in organic solids is gaining attention; other clear examples of the phenomenon can be found in, for example, [92, 93]. It is to be noted that, although the absolute shifts due to ring currents are similar for both ^{1}H and ^{13}C, the much smaller range of chemical shifts ($\sim$20 ppm as opposed to 200 ppm) means that the influence is much more evident in ^{1}H NMR. In addition, protons are normally located at the more exposed parts of the structure.

^{1}H NMR is well suited for the investigation of hydrogen bonding, with it being well-known that hydrogen bonding leads to a marked lowfield (to a high parts per million value) chemical shift. For example, for a general hydrogen bond O–H$\cdots$O, a clear correlation between the ^{1}H isotropic chemical shift and the hydrogen-bond strength as given by the O$\cdots$H and O$\cdots$O distances determined by single-crystal diffraction studies has been established [94–96]. By identifying specific proton–proton proximities, rotor-synchronized 2D ^{1}H DQ MAS spectra have been shown to differentiate between distinct hydrogen-bonded structures [48].

Applications of dipolar-mediated DQ spectroscopy are not limited to ^{1}H NMR. For example, ^{31}P–^{31}P DQ MAS spectra have provided valuable insight into the structure of inorganic phosphates [97] and glasses [98]. In addition, Nielsen *et al.* [99] and Hong [100] have presented dipolar analogs of the *J*-coupled ^{13}C–^{13}C DQ MAS correlation experiment described in Section 10.5.1. Finally, we note that Schmidt-Rohr and coworkers [101] have elegantly demonstrated that 2D ^{13}C–^{13}C DQ spectra recorded for static samples can identify the chain conformation statistics for ^{13}C-labeled polymer samples. Remembering that the frequency of a given ^{13}C resonance depends on the orientation of the CSA tensor (Section 10.2.1), the method relies on the fact that the adoption of a particular torsional angle along the chain results in DQ peaks for only specific pairs of ^{13}C frequencies. As illustrated in Figure 10.21, trans and gauche conformations lead to very different 2D DQ powder

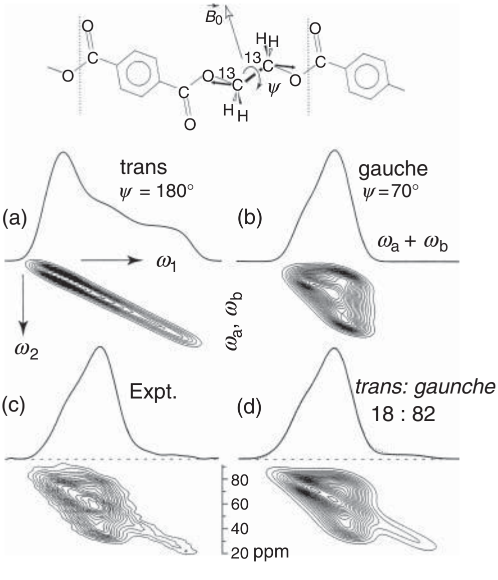

Figure 10.21 Two-dimensional ^{13}C–^{13}C DQ static spectra allow the determination of the chain conformation statistics for ^{13}C-labeled polymer samples. The simulated spectra show that (a) trans and (b) gauche conformations lead to very different 2D DQ powder spectra. For the experimental spectrum (c) obtained for amorphous PET, a best-fit simulation (d) revealed a 18 : 82 trans : gauche distribution. (Reproduced by permission of the American Association for the Advancement of Science from [101].)

spectra, and it was thus possible to quantitatively determine the conformation statistics for a sample of amorphous poly(ethylene terephthalate) (PET).

10.5.3
High-Resolution ^{1}H Solid-State NMR

The previous section has illustrated that the resolution in a ^{1}H DQ MAS spectrum provided by a combination of very-fast MAS and a high magnetic field as well as the extension to a second frequency dimension is sufficient to allow the differentiation of some particular ^{1}H resonances. However, as noted in Section 10.3.2, the line narrowing achieved by MAS alone at a ν_R equal to 30 kHz is still far from the limiting case, where all residual dipolar broadening has been removed. Section 10.3.2 also briefly introduced experiments which provide homonuclear ^{1}H decoupling by combining multiple (RF) pulse sequences with MAS. In this section, we demonstrate that a marked line narrowing as compared to MAS alone can be achieved by this CRAMPS approach.

In this section, we consider ‘‘windowless’’ homonuclear decoupling sequences. Specific examples are the Lee–Goldburg (LG) technique [102] and refinements, namely the frequency switched and phase-modulated LG (frequency switched Lee–Goldburg, FSLG [103, 104] and phase-modulated Lee–Goldburg, PMLG [105]) sequences, as well as the computer-optimized sequence, DUMBO-1 [106]. For a discussion of these different decoupling sequences, the interested reader is referred to, for example, [7]. Such sequences are so-called because no windows during which acquisition of the FID would be possible are built into the sequence. NMR experiments incorporating evolution under the application of a windowless homonuclear decoupling are thus inherently multidimensional. For example, Vinogradov, *et al.* [105] have presented a 2D experiment in which a high-resolution ^{1}H dimension, incorporating PMLG homonuclear decoupling, is correlated with ^{1}H acquisition, with only moderate MAS (10–15 kHz) providing line narrowing in the direct dimension.

Using LG-based decoupling methods, a FWHMH of 150–170 Hz has been reported for the aliphatic ^{1}H resonances in L-alanine [107]; this is demonstrated in Figure 10.22c, where, for comparison, the Figure 10.22a static and Figure 10.22b MAS ($\nu_R = 30$ kHz) spectra are also shown. Lesage *et al.* [107] have further shown that the frontiers of high-resolution ^{1}H solid-state NMR can be pushed back yet further; using the constant-time (CT) CRAMPS experiment a FWHMH as low as 60 Hz can be obtained for the aliphatic resonances in L-alanine (Figure 10.22d).

10.5.4
Anisotropic–Isotropic Correlation: the Measurement of CSAs

In Section 10.3.1, it was stated that it is possible to extract the anisotropy and asymmetry of the CSA by fitting the observed MAS sideband intensities. It is, however, necessary to be able to resolve, at a low ν_R, the sidebands of the different resonances. The problem of the 1D spectrum becoming increasingly more crowded

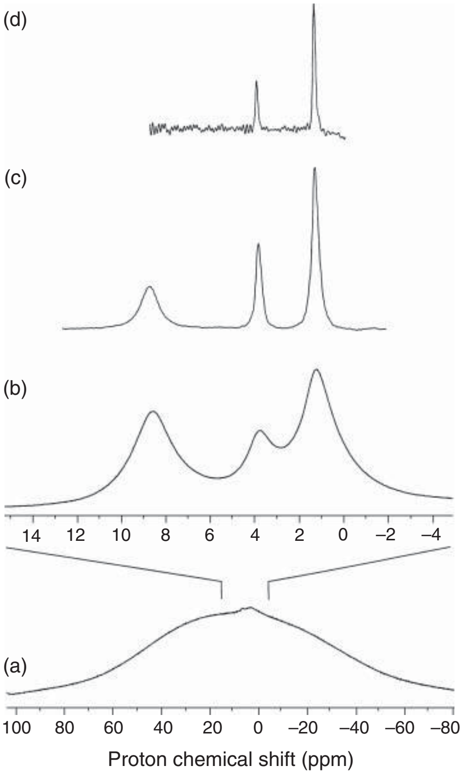

Figure 10.22 ^{1}H (500 MHz) NMR spectra of natural abundance powdered L-alanine, recorded with (a and b) a one-pulse experiment for (a) a static sample and (b) under MAS at a $\nu_R = 30$ kHz, (c) the 2D FSLG ($\nu_R = 12.5$ kHz) experiment, and (d) the CT-CRAMPS ($\nu_R = 12.5$ kHz) experiment using FSLG decoupling. (Reproduced by permission of the American Chemical Society from [107].)

as the number of distinct resonances increases can be overcome by extending the NMR experiment to a second dimension.

In a first class of experiment, a 2D spectrum is obtained in which a separate anisotropic powder lineshape (corresponding to either the static case or a slow spinning frequency) is associated with each resolved resonance in an isotropic dimension. Two elegant approaches have been presented by which this can be achieved, namely magic-angle hopping (MAH) [108] and magic-angle turning (MAT) [109]. In the MAH experiment, t_1 consists of the sample making three hops of 120° about an axis inclined at the magic angle to B_0, with a period of evolution of the same incremented duration (during which the sample is static) before each hop. In this way, the evolution periods correspond to each crystallite adopting three orthogonal positions relative to B_0; for this case, it can be shown that the average chemical shift evolution equates to the isotropic chemical shift. The same effect is achieved in the MAT experiment under conditions of very slow (typically <100 Hz) continuous sample rotation by rotations in spin space, that is, by the application of RF pulses. Moreover, related experiments such as switched angle sample spinning (SASS) [110, 111] and variable angle correlation spectroscopy (VACSY) [112], which involve a change in the orientation of the rotor axis with respect to B_0, have also been presented.

For the original MAH and MAT techniques, a significant drawback was the long measuring time (1–2 days) that was required even when up to 5 g of sample was used. However, modified versions of the MAT approach employing 180° rather than 90° pulses and using a faster ν_R have been presented, which offer a better experimental sensitivity [113, 114] For example, Figure 10.23 shows the anisotropic CSA patterns for each resolved resonance in a selected region of the isotropic ^{13}C spectrum of the terpene verbenol [115]. Six resonance lines are resolved for both the C2 and C3 carbons, with the CSA tensor spinning-sideband patterns being remarkably similar. Supported by quantum-chemical calculations of the ^{13}C CSA tensors, the solid-state NMR analysis demonstrated that verbenol exhibits polymorphism, with, however, only minor conformational variations in the distinct solid-state environments. It is to be noted that single crystals suitable for an X-ray diffraction analysis could only be obtained for the major crystalline form.

An alternative means by which the isotropic and anisotropic chemical shift interactions can be separated is the 2D PASSs (phase-adjusted spinning-sidebands) experiment due to Levitt and coworkers [116]. By changing the timings of the application of five π pulses in the t_1 dimension, it is possible to separate the spinning sidebands by order. As a specific example, Figure 10.24 shows the 2D ^{13}C PASS spectrum for the antibiotic, penicillin-V [117]. An analysis of this spectrum allowed the determination of the CSA principal values for all the ^{13}C resonances. A distinct advantage of this approach is that only very few (typically 16) increments must be made in the indirect dimension.

10.5.5
The Investigation of Slow Dynamics: 2D Exchange

The basic principle of 2D exchange NMR involves the measurement of the frequency of the same molecular segment at two different times. A slow dynamic process is detected on account of the change, during a mixing time between the two evolution periods, in the NMR frequency caused by a reorientation of the molecular segment. In this section, we describe ^{2}H static and ^{13}C MAS 2D exchange experiments [4].

In static ^{2}H 2D exchange NMR, advantage is taken of the simplification resulting from both the presence of a single ^{2}H resonance and the fact that the quadrupolar interaction dominates (Section 10.2.4). Without any slow dynamics in the mixing time, the frequency of each molecular segment remains unchanged, and the intensity in the 2D frequency-domain spectrum is restricted to a ridge along the $\nu_1 = \nu_2$ diagonal. If a reorientation occurs, off-diagonal intensity is observed as a consequence of the frequency change. In particular, a

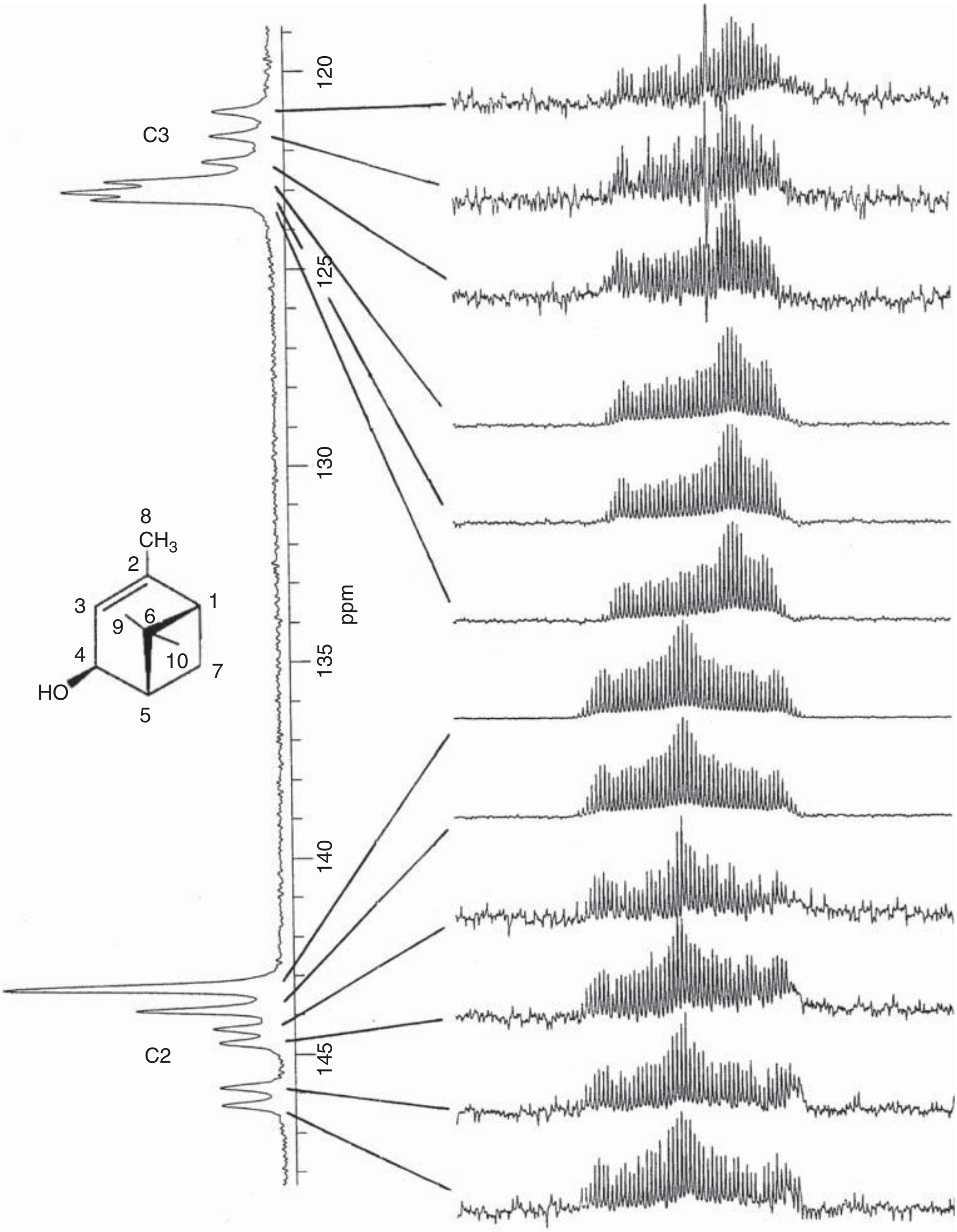

Figure 10.23 The anisotropic CSA patterns for each resolved resonance in a selected region of the isotropic ^{13}C spectrum as obtained from a FIREMAT (five π replicated magic-angle turning) experiment recorded for a sample of the terpene verbenol. (Reproduced by permission of the American Chemical Society from [115].)

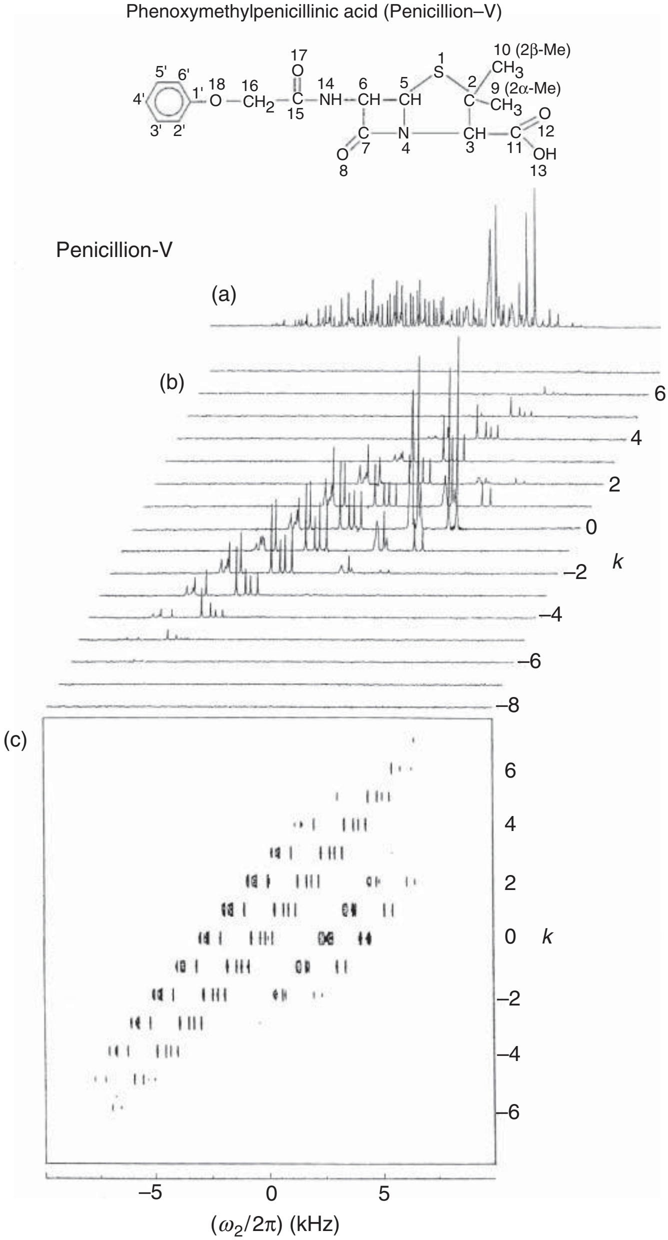

Figure 10.24 A 2D ^{13}C PASS spectrum recorded for the antibiotic, penicillin-V. The 1D CP MAS spectrum is shown in (a). (Reproduced by permission of Academic Press from [117].)

well-defined motion yields an elliptical off-diagonal pattern which is characteristic of the reorientation angle. The beauty of the static ^{2}H exchange experiment is illustrated in Figure 10.25, which shows a spectrum recorded for a sample of methyl-deuterated isotactic polypropylene (iPP) [118]. The observed elliptical ridges are characteristic of the helical chain reorientation illustrated in the inset.

A 2D exchange experiment can also be recorded under MAS, although care must be taken to ensure that pure absorption-mode spinning sidebands are obtained. As compared to a static experiment, both the resolution and sensitivity are improved, which is of much importance for ^{13}C NMR. These gains are, however, at the expense of the ease with which information about the reorientation process can be accessed. As in the static case, a reorientation is associated with the observation of off-diagonal intensity. As a specific example, Figure 10.26 presents a ^{13}C 2D MAS exchange spectrum recorded for polyoxymethylene (POM) [119]. In addition to

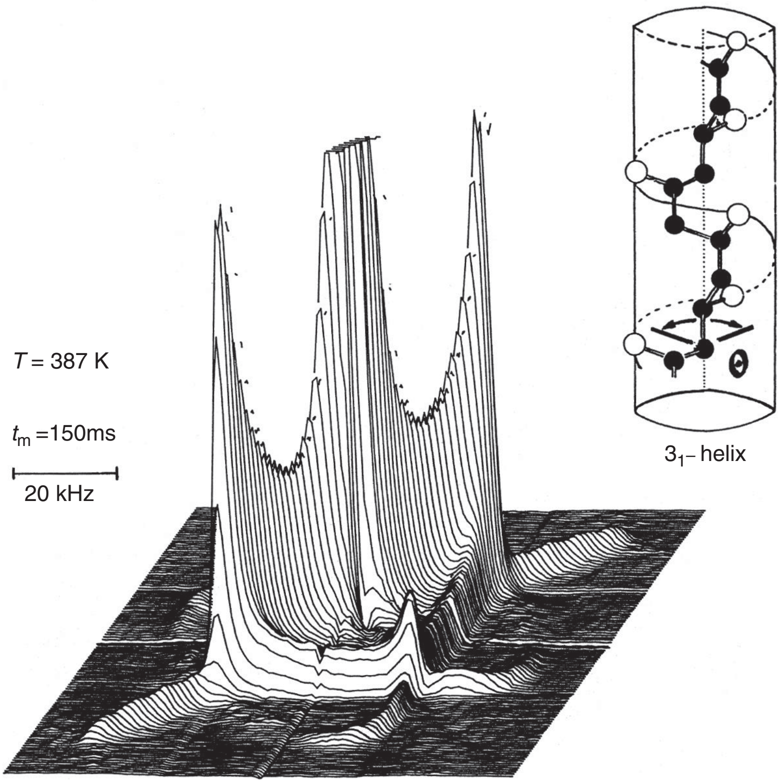

Figure 10.25 A static ^{2}H exchange experiment recorded for a sample of methyl-deuterated isotactic polypropylene (iPP) at $T = 387$ K. The observed elliptical ridges are characteristic of the helical chain reorientation illustrated in the inset. (Reproduced by permission of the American Chemical Society from [118].)

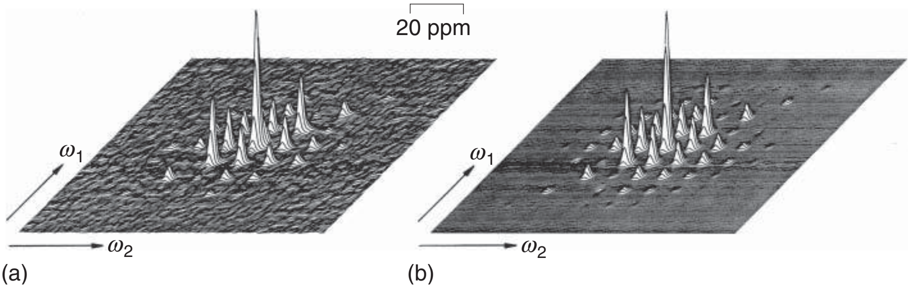

Figure 10.26 (a) Experimental and (b) theoretical ^{13}C 2D MAS pure absorption-mode exchange spectra recorded for polyoxymethylene (POM). The experimental spectrum corresponded to $T = 360$ K and a mixing time of 1.5 s. (Reproduced by permission of Academic Press from [119].)

probing the motion of a particular molecular moiety, 2D exchange experiments are well suited to the investigation of slow chemical exchange processes; for example, Titman *et al.* have studied the hydrogen shift and/or π flip which occurs in solid tropolone.

10.5.6
^{1}H–^{1}H DQ MAS Spinning-Sideband Patterns

In Section 10.5.2, a rotor-synchronized ^{1}H–^{1}H DQ MAS spectrum was presented (Figure 10.20). The 2D DQ MAS can be performed in an alternative fashion; if the t_1 increment is reduced, which corresponds to an increase in the DQ spectral width, a DQ MAS spinning-sideband pattern is observed [121, 122]. Such DQ MAS sideband patterns exhibit characteristic unusual features. In particular, the observed patterns are very sensitive to the product of the dipolar coupling constant, D, and the recoupling time, τ_{rcpl}, with an increase in this product leading to the appearance of higher-order spinning sidebands.

Importantly, since τ_{rcpl} is known, the absolute value of D can be extracted by an analysis of DQ MAS spinning-sideband patterns. As a specific example, Figure 10.27 presents experimental ^{1}H–^{1}H DQ MAS spinning-sideband patterns for the aromatic protons in (i) the crystalline and (ii) the LC phases of the same alkyl-substituted polycyclic aromatic system, HBC-C$_{12}$, discussed in Section 10.5.2 [49]. The dotted lines represent best-fit spectra simulated using the analytical time-domain expression for an isolated spin pair. As is evident from the insets on the right of Figure 10.27, the DQ MAS spinning-sideband patterns are very sensitive to the product of D and τ_{rcpl}. The best-fit spectra for the solid and LC phases then correspond to $D/(2\pi)$s equal to 15.0 ± 0.9 and 6.0 ± 0.5 kHz, respectively.

Comparing the evaluated D values for the crystalline and LC phases, a reduction of D by a factor of 0.40 ± 0.04 is observed, corresponding to an order parameter [123] of 0.80 ± 0.08. This could be explained by postulating the presence of out-of-plane motion in addition to the axial rotation of the molecule about an axis perpendicular

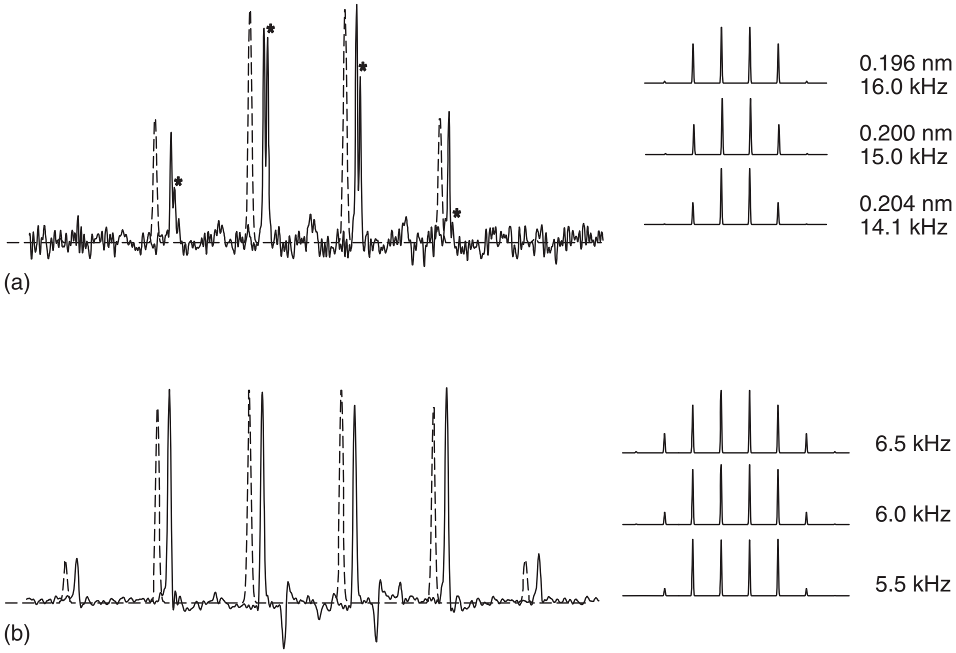

Figure 10.27 Extracted columns from ^{1}H (500.1 MHz) DQ MAS spectra of HBC-C_{12}, showing the DQ spinning-sideband patterns for (a) the aromatic protons at 8.3 ppm in the solid phase ($T = 333$ K) and (b) the aromatic protons at 6.2 ppm in the LC phase ($T = 386$ K). In each case, best-fit spectra, generated according to the analytical expression for a spin pair, are shown (shifted to the left to allow a better comparison) as dotted lines. A spinning frequency, ν_R, equal to 35 and 10 kHz was used for the solid and LC phases, respectively, with the two rotor period compensated BABA recoupling sequence being used for the excitation and reconversion of DQCs in both cases. In (a), additional peaks corresponding to DQCs between aromatic and residual undeuterated α-carbon protons are marked by *. The insets to the right of the experimental spectra show the sensitivity of the spinning-sideband patterns to the product $D\tau_{\mathrm{rcpl}}$. (Reproduced by permission of the American Chemical Society from [49].)

to the ring. The good agreement with the value of 0.84 obtained from an analysis of ^{2}H 1D NMR lineshapes is to be noted [124]. It is to be emphasized, however, that the ^{1}H DQ MAS method is applicable to as-synthesized samples, that is, there is no reliance on isotopic labeling.

As well as the investigation of dynamics, an analysis of ^{1}H DQ MAS spinning-sideband patterns can be used to determine proton–proton distances. For example, it was possible to determine that the distance between the lactam and pyrrole NH protons in the complex hydrogen-bonding arrangement in the biologically important molecule bilirubin is 0.186 ± 0.002 nm [125]. In this respect, it is to be noted that structure determination by single-crystal X-ray diffraction methods, being based on the diffraction of X-rays by electrons, is not well suited to the localization of lighter atoms. This is of particular relevance with regards to the localization of hydrogen-bonded protons, in which case a neutron diffraction study is to be preferred [126]. Moreover, neutron diffraction is not the perfect solution: as well as the requirement for both larger crystals and very expensive facilities, the investigation of protons is complicated by their large incoherent cross section, such that deuteration, which may cause a change in the hydrogen-bonding arrangement, is often required. Thus, solid-state NMR methods which can provide interproton and proton–heteroatom distance constraints, by means of which the localization of the important protons in the single crystal structure can be refined, are of much value.

Finally, we note that 1D DQ-filtered MAS experiments (corresponding to setting $t_1 = 0$) can also provide insight into dynamic processes. The principle, in this case, is that signal is only observed for pairs of protons which remain dipolar-coupled for the timescale of the experiment, which in this case is the time required to excite and reconvert the DQC. For example, in [127], the kinetics of hydrogen-bond breaking and formation is quantitatively analyzed for a carboxylic acid dimer on the basis of the fall off in the DQ intensity with increasing temperature.

10.6
Heteronuclear Two-Dimensional Experiments

10.6.1
Heteronuclear Correlation

In a 2D heteronuclear correlation (HETCOR) experiment, the t_1 and t_2 periods correspond to the evolution of SQC of two different nuclei, for example, ^{1}H and ^{13}C. A number of different HETCOR experiments have been proposed which differ with respect to, for example, the means by which coherence transfer is achieved, the type of coherence which evolves during t_1, as well as the application of homonuclear decoupling sequences.

One of the simplest HETCOR experiments is the ^{1}H–^{13}C WISE (wideline separation) experiment [128]. After the t_1 period, during which ^{1}H transverse magnetization created by a 90° pulse evolves, coherence transfer to ^{13}C SQC, which is detected in t_2, is achieved by a simple CP step. The experiment is performed under MAS. At a low to moderate ν_R, a wide dipolar-broadened ^{1}H lineshape in F_1 (Section 10.3.2) is correlated with a narrow resonance line in a well-resolved isotropic ^{13}C dimension (F_2). Remembering that motion leads to a narrowing of the ^{1}H resonance due to the reduction in the dipolar broadening, the WISE experiment has found a number of applications in polymer chemistry on account of its ability to distinguish between rigid and mobile chemical moieties [4]. For example, in Figure 10.28, narrow and broad lines in the ^{1}H dimension are observed for the resonances due to the mobile spoly(butyl methacrylate) (PbuA) and the rigid PMMA, respectively, in a core–shell system [129]. Furthermore, as illustrated by the investigation of onion cell-wall material in Ref. [47], the information provided

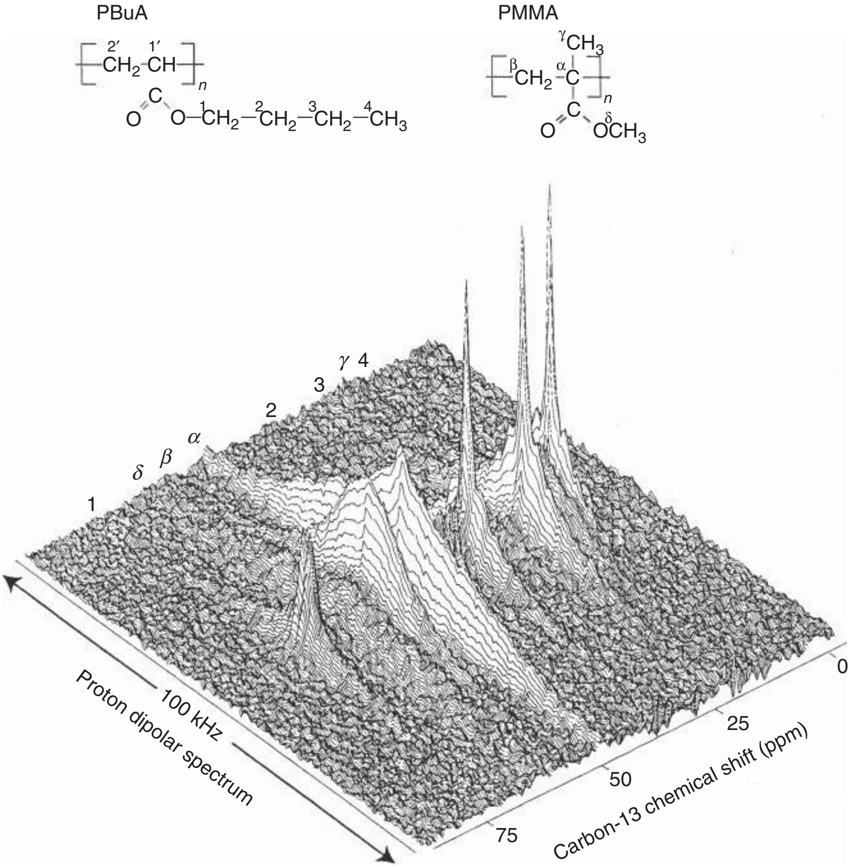

Figure 10.28 A ^{1}H–^{13}C WISE experiment recorded for a core–shell system comprising mobile poly(butyl methacrylate) (PbuA) and rigid PMMA. (Reproduced by permission of the American Chemical Society from [129].)

by WISE spectra complements that yielded by an analysis of ^{13}C T_1 and the ^{1}H $T_{1\rho}$ relaxation times.

^{1}H–^{13}C HETCOR spectra incorporating a high-resolution ^{1}H dimension can be achieved. As early as 1982, Caravatti *et al.* presented an experiment which employed a multiple-pulse sequence at a low ν_R (as in the conventional CRAMPS approach) to achieve homonuclear decoupling in t_1 [130, 131]. Recently, various alternative high-resolution HETCOR experiments applicable at a fast or a very-fast ν_R have been proposed. Two methods which utilize the through-space dipolar coupling to achieve coherence transfer are those due to van Rossum *et al.* [132] and Saalwächter, *et al.* [133, 134]. In the former case, coherence transfer occurs via CP, while FSLG ^{1}H homonuclear decoupling (Section 10.5.3) is applied during the evolution of transverse ^{1}H magnetization in t_1. This is to be compared with the latter recoupled polarization transfer (REPT) methods, which employ REDOR recoupling under very-fast MAS (Section 10.4.1) to create a heteronuclear single-quantum coherence (HSQC) or a heteronuclear multiple-quantum coherence (HMQC), the evolution of which is followed during t_1. The analogy to the well-known solution-state HSQC [135] and HMQC [136] experiments (dilute spin, e.g., ^{13}C, detected) is to be noted.

Alternatively, the MAS-*J*-HMQC [137, 138] and MAS-*J*-HSQC experiments [139] utilize the isotropic through-bond *J*-coupling. The primary aim of recording a ^{1}H–^{13}C correlation spectrum is usually the establishing of one-bond correlations, such that the ^{1}H chemical shifts can be identified. For correlation methods based on the dipolar coupling, it is necessary to ensure that the observed peaks are then not due to close through-space proximities. This problem is obviously avoided by utilizing through-bond *J*-couplings. As an example, Figure 10.29 presents ^{1}H–^{13}C and ^{1}H–^{15}N MAS-*J*-HMQC spectra recorded for 20 mg of a tripeptide sample at natural abundance [138]. The recording of ^{1}H–^{13}C MAS-*J*-HMQC spectra which reveal one- and multiple-bond connectivities allowed the complete assignment of the ^{1}H, ^{13}C, and ^{15}N resonances for the tripeptide.

It should be noted that the existence of methods based on both dipolar and *J*-couplings opens up the possibility of distinguishing through-bond connectivities and through-space proximities on a medium to long range, such that insight into intermolecular packing arrangements is provided. In this way, the two approaches are complimentary in a similar way to the case of the correlation spectroscopy (COSY) and nuclear Overhauser spectroscopy (NOESY) [1, 2] solution-state NMR experiments.

10.6.2
The Quantitative Determination of Heteronuclear Dipolar Couplings

As described in Section 10.4.1, the REDOR experiment, by allowing the quantitative determination of dipolar couplings, accurately yields the distance between two heteronuclei. Indeed, REDOR is currently the workhorse experiment for structure determination. The method does, however, rely on selective isotopic labeling. As well as measuring internuclear distances, Section 10.5.6 showed how probing the change in the dipolar coupling provides insight into a dynamic process. In this section, 2D experiments which have the aim of measuring multiple heteronuclear dipolar couplings (as opposed to only one in the REDOR experiment) are described.

In a separated local field (SLF) experiment [140–143] the basic principle is that a spinning-sideband pattern, from which the heteronuclear dipolar coupling can be extracted, is obtained in the indirect dimension for each resolved resonance in the direct dimension, that is, the dipolar interaction is separated from the chemical shift interaction (the experiment is sometimes referred to as the *DIPSHIFT experiment*). In the original SLF articles, a homonuclear decoupling method is applied in t_1, but recently McElheny *et al.* [144] have shown that fast MAS alone at a ν_R of at least 12 kHz (much faster MAS should be avoided as the higher-order spinning sidebands become too weak to allow a reliable fitting) provides sufficient proton

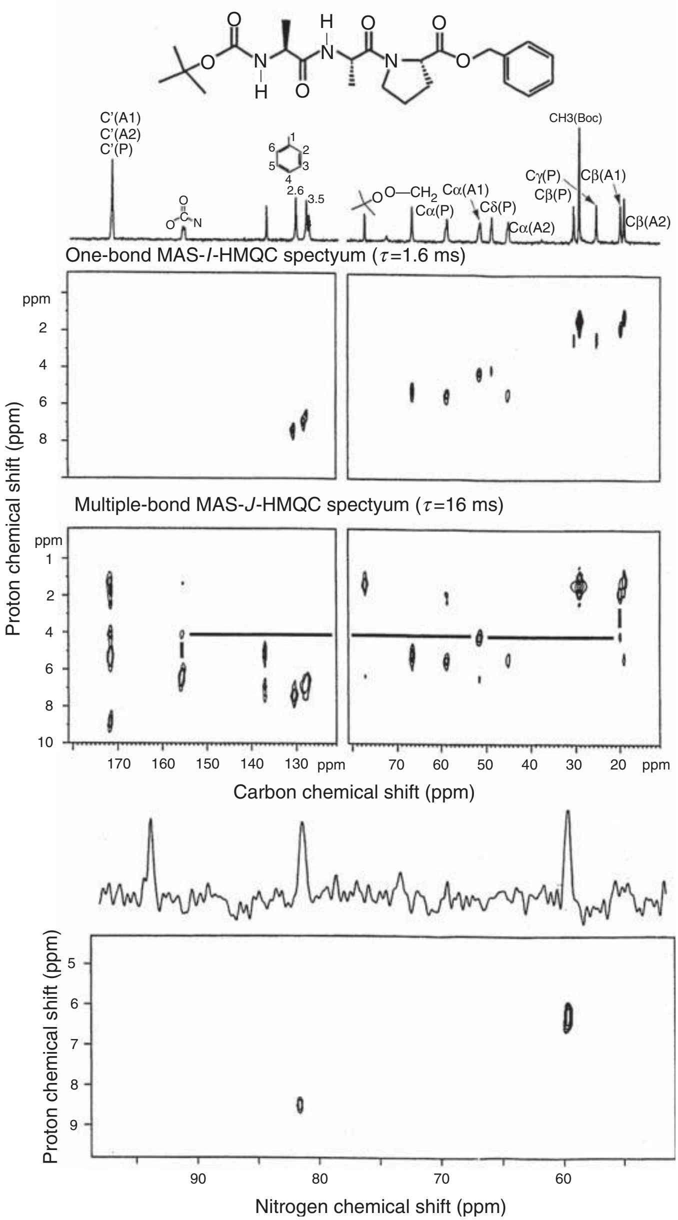

Figure 10.29 $^1H-^{13}C$ and $^1H-^{15}N$ MAS-*J*-HMQC spectra recorded for a tripeptide sample at natural abundance. Two different $^1H-^{13}C$ experiments were performed, with the use of a short ($\tau = 1.6$ ms) and a long ($\tau = 16$ ms) evolution period selecting in the former case one-bond correlations, while the latter case allowed the identification of multiple-bond correlations. ^{13}C and ^{15}N CP MAS spectra are presented above the relevant 2D spectra. (Reproduced by permission of the American Chemical Society from [138].)

dipolar decoupling such that relatively reliable $^1H-^{13}C$ dipolar couplings can be extracted.

Alternatively, in a modification of the original SLF method, Hohwy *et al.* [145] have presented a sophisticated experiment in which a pulse sequence is applied during t_1 which actively recouples the weak heteronuclear dipolar coupling while decoupling the homonuclear $^1H-^1H$ dipolar coupling. Instead of giving a spinning-sideband pattern, a powder line shape is obtained in the indirect dimension. It is shown that this experimental approach allows the accurate determination of both N–H distances as well as the H–N–H bond angle in an NH_2 group. Another state-of-the-art method which has recently been proposed involves performing CP from ^1H to ^{13}C with the RF pulse on the ^1H channel fulfiling the LG condition mentioned in Section 10.5.3 [146]. The suppression of the homonuclear ^1H dipolar couplings means that a LG–CP signal builds up in an oscillatory manner, reflecting coherent heteronuclear transfer. The Fourier transformation of such build-up curves yields powder spectra with marked singularities from the separation of which the heteronuclear dipolar coupling can be determined. Alternatively, it is to be noted that an analysis of a standard CP build-up curve under fast MAS can, in some cases, allow the determination of the heteronuclear dipolar coupling [147].

In direct analogy to the homonuclear DQ MAS experiment (Section 10.5.6), if the t_1 increment in the REPT pulse sequences (Section 10.6.1) is not set equal to τ_R, a spinning-sideband pattern rotor-encoded by the heteronuclear dipolar coupling is obtained [133, 134, 148]. An advantage of the heteronuclear $^1H-^{13}C$ approach is that it benefits from the better resolution in a ^{13}C SQ dimension. An example of this is provided by the hexa(*para*-*n*-dodecylphenyl)-substituted HBC (henceforth referred to as *HBC-PhC$_{12}$*) [148]. In this case, ^1H solid-state NMR is unable to distinguish the core and *exo*-phenyl protons. By comparison, as shown in the ^{13}C CP MAS spectrum at the top right of Figure 10.30, the corresponding ^{13}C resonances are well resolved. It is, thus, possible to use the heteronuclear approach to probe separately the dynamics of the core and the outer phenyl rings. For example, the right-hand side of Figure 10.30 presents $^1H-^{13}C$ spinning-sideband patterns obtained at the core aromatic CH ^{13}C resonance for the solid and LC phases of HBC-PhC$_{12}$, using the REPT–HMQC experiment.

A comparison of the spinning-sideband patterns obtained for the LC phases of HBC-C$_{12}$ and HBC-PhC$_{12}$ reveals that the third-order spinning sidebands are significantly higher in the latter case; they are of the same height as the first-order spinning sidebands for HBC-PhC$_{12}$. As the same experimental conditions were used in both cases, this result immediately indicates a larger dipolar coupling and, hence, a larger order parameter for HBC-PhC$_{12}$. Indeed, the order parameter is determined to be 0.93 ± 0.09, indicating less out-of-plane mesogen mobility. It is interesting that this NMR result is correlated with an improved intra- and inter-columnar packing as evidenced by powder X-ray diffraction patterns [148].

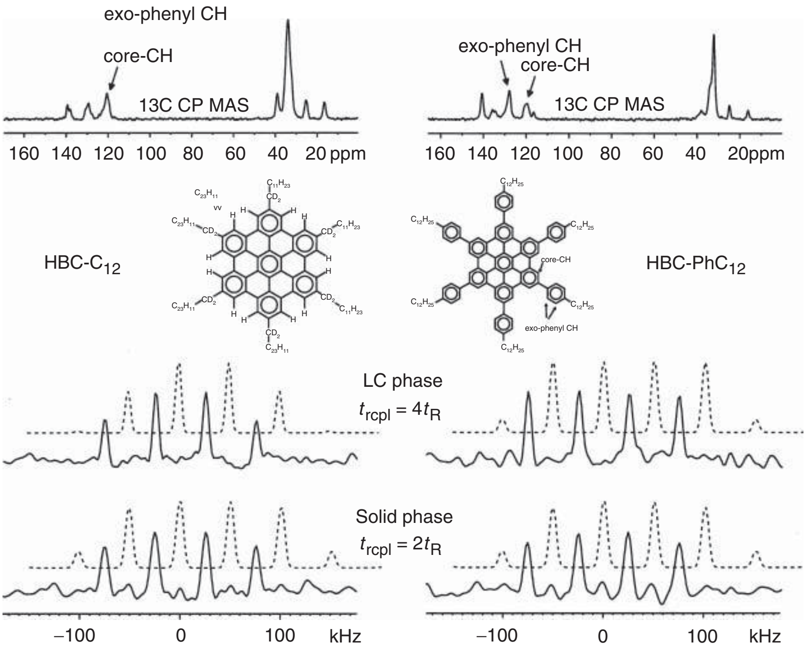

Figure 10.30 $^1H-^{13}C$ heteronuclear MQ MAS spinning-sideband patterns, obtained at a $\nu_R = 25$ kHz, using the REPT–HMQC experiment. The patterns correspond to the sum projections over the ^{13}C resonance due to the aromatic core CH in the 2D spectra of HBC-C_{12}, and HBC-PhC_{12}. The spectra for the room temperature (solid) and high temperature LC phases were recorded at 35 and 120 °C, respectively. The dashed traces represent simulated spectra, obtained by taking into account the best-fit *D*s for the CH groups. At the top, ^{13}C CP MAS ($\nu_R = 15$ kHz) spectra are presented, with the signal positions of the aromatic CH resonances being identified. (Reproduced from [148].

10.6.3
Torsional Angles

In an extension to experiments which measure internuclear distances, Levitt and coworkers and Griffin and coworkers have presented ingenious methods which allow the measurement of torsional angles [149, 150]. The methods involve the creation of MQC between a pair of nuclei (selective isotopic labeling is required), which may be homonuclear, for example, $^{13}C-^{13}C$, or heteronuclear, for example, $^{13}C-^{15}N$. A spinning-sideband pattern is observed as a result of the evolution of the two spins which make up the MQC under the dipolar couplings to the directly attached nuclei. As a specific example, consider the $H^N-N-C^{\alpha}-H^{\alpha}$ moiety in ^{15}N-labeled NAV [150]. By incrementing a period of ^1H homonuclear decoupling, a t_1 FID (Figure 10.31a) is obtained which depends on the evolution under the $N-H^N$ and $C^{\alpha}-H^{\alpha}$ dipolar coupling, and in particular the relative orientation of the two bonds. From the best-fit simulation (Figure 10.31c) of the experimental

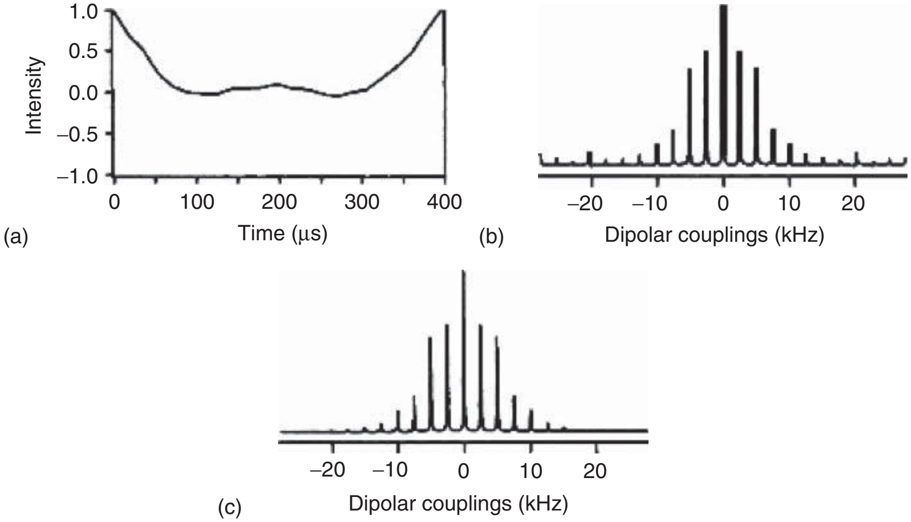

Figure 10.31 The measurement of the H^N–N–C^α–H^α torsional angle in ^{15}N-labeled NAV. The (a) t_1 FID and (b) frequency-domain spinning-sideband pattern depend on the evolution under the N–H^N and C^α–H^α dipolar coupling, and in particular the relative orientation of the two bonds. The (c) best-fit simulation corresponds to a torsional angle of -135°. (Reproduced by permission of the American Chemical Society from [150].)

frequency-domain spinning-sideband pattern (Figure 10.31b), the torsional angle was determined to be -135°.

10.6.4
Oriented Samples

The difficulties associated with the preparation of samples suitable for diffraction studies has led to much interest in the application of solid-state NMR to the investigation of the three-dimensional structure adopted by membrane proteins in their functional environment of phospholipid bilayers [14]. As an oriented sample, the NMR spectrum of a membrane protein is much simplified as compared to the case of a powder sample; for perfect ordering, all structurally equivalent nuclei have the same orientation with respect to B_0, and hence the same anisotropic resonance frequency (Section 10.2.1). This phenomenon is taken advantage of in the PISEMA (polarization inversion with spin exchange at the magic-angle) experiment [151]. This technique is closely related to the experiments described in Section 10.6.2, although it is to be noted that it is applied to static samples.

Figure 10.32a presents a 2D PISEMA spectrum of a uniformly ^{15}N-labeled polypeptide in an oriented lipid bilayer [152]. For each ^{15}N resonance, the ^{15}N chemical shift (horizontal axis) is correlated with the corresponding ^{15}N–^{1}H dipolar coupling, with both the chemical shift and the dipolar coupling depending on the orientation of the particular nitrogen containing moiety. Making the

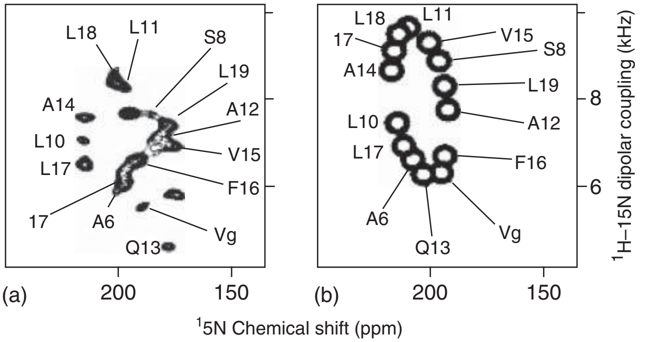

Figure 10.32 (a) A 2D PISEMA spectrum of a uniformly ^{15}N-labeled polypeptide in an oriented lipid bilayer. (b) The best-fit simulated spectrum corresponds to a helix tilt angle of 12°. (Reproduced by permission of Academic Press from [152].)

assumption that the local chemical environment leads to only slight variations in the principal values and orientations of the CSA and dipolar tensors, the observed PISEMA pattern allows the tilt angle of the polypeptide helix with respect to the bilayer normal to be determined. For example, the best-fit simulated spectrum in Figure 10.32b corresponds to a helix tilt angle of 12°.

PISEMA experiments yield the local dipolar field experienced by the ^{13}C or ^{15}N nucleus. Perhaps counter intuitively, it has been shown that better resolution is obtained by using experiments which detect the local dipolar field on protons [130, 153–155]. As specific examples, the ^{1}H detected local field experiment has recently successfully been applied to the characterization of LCs [156, 157] and membranes [158]. As illustrated by Figure 10.33, this approach has even been shown to yield sufficient resolution in 3D versions to allow the direct measurement of internuclear dipolar couplings between nuclei separated by up to five bonds in LCs, thereby providing very strong conformational constraints [159].

10.7
Half-Integer Quadrupole Nuclei

An inspection of Table 10.2 displays that many nuclei of relevance in inorganic systems, for example, ^{23}Na (spin $I = 3/2$), ^{27}Al (spin $I = 5/2$), and ^{17}O (spin $I = 5/2$), are quadrupolar with a half-integer nuclear spin. For such nuclei, an important result is that the $|m_I = +s\rangle \leftrightarrow |m_I = -s\rangle$ transitions are not broadened by the quadrupolar coupling to first-order (for a spin $I = 3/2$ nucleus, the energy levels are labeled −3/2, −1/2, +1/2, and +3/2). As a consequence, for the usual case that the quadrupolar coupling is large (typically of the order of megahertz), only the central transition, $|m_I = +1/2\rangle \leftrightarrow |m_I = -1/2\rangle$, is observed in the normal spectrum, because the broadened satellite transitions ($|m_I = +3/2\rangle \leftrightarrow |m_I = +1/2\rangle$ and $|m_I = -1/2\rangle \leftrightarrow |m_I = -3/2\rangle$ for a spin $I = 3/2$ nucleus) are lost in the baseline. It should be noted that various groups have presented ingenious methods which

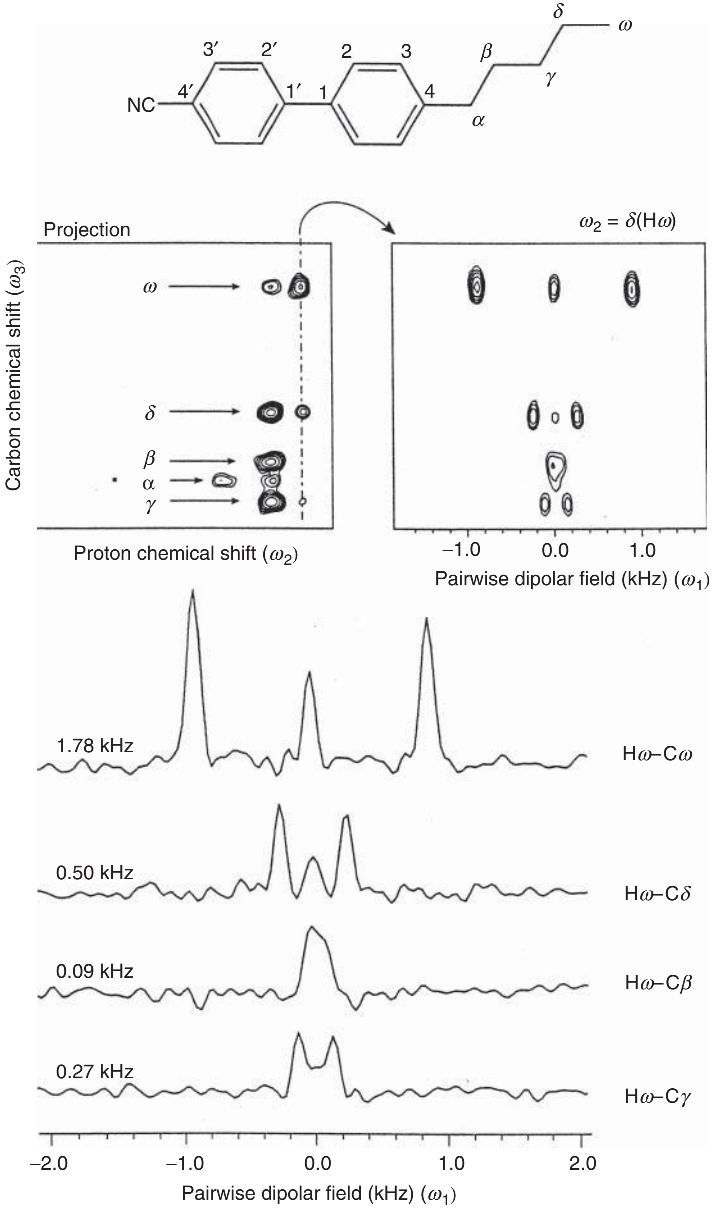

Figure 10.33 The aliphatic region of the 3D pairwise local field spectrum of the nematic LC, 5CB. A projection onto the $\omega_2 - \omega_3$ plane yields a $^1H-^{13}C$ correlation spectrum (upper left), and a plane taken perpendicular to this at a particular ^1H chemical shift yields a $\omega_3 - \omega_1$ slice (upper right) that contains a series of pairwise local fields for each carbon atom. The pairwise local fields obtained for H^{ω} are shown, which demonstrate that couplings to carbons all the way down the chain to C^{β} can be measured. (Reproduced by permission of the American Chemical Society from [159].)

use the satellite transitions to enhance the sensitivity of the central transition spectrum [160–162].

The central transition of a half-integer quadrupolar nucleus is, however, broadened to second order. In contrast to the CSA, and dipolar and first-order quadrupolar couplings, the orientation dependence of the broadening associated with second-order quadrupolar coupling is no longer purely a second-rank tensor. In particular, there is a fourth-rank tensor contribution, which is not fully removed by MAS (regardless of what ν_R is used). The residual second-order quadrupolar broadening of the central transition often prevents the resolution of resonances due to chemically or crystallographically distinct sites [163]. For example, Figure 10.34b shows the ^{87}Rb (spin $I = 3/2$) MAS spectrum of $RbNO_3$; the presence of residual second-order quadrupolar broadening precludes the resolution of the three crystallographically distinct sites.

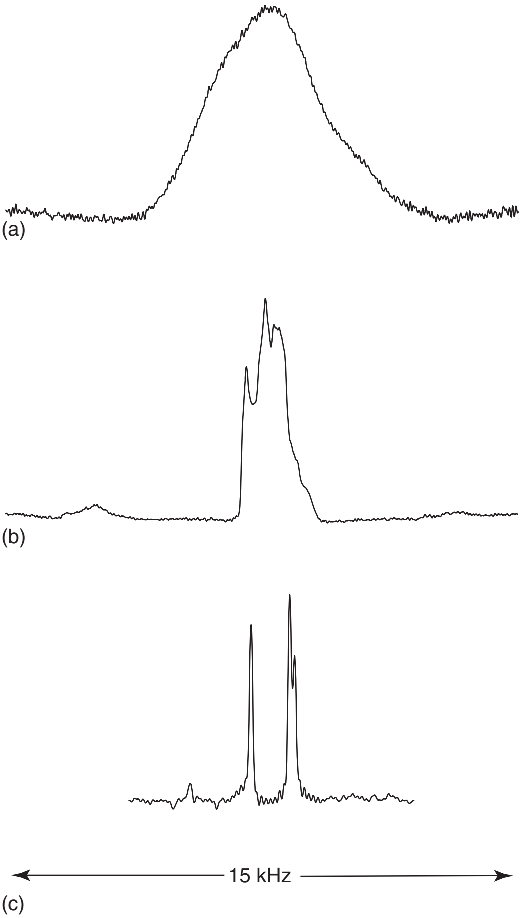

Figure 10.34 ^{87}Rb (130.9 MHz) (spin $I = 3/2$) (a) static, (b) MAS, and (c) isotropic MQ MAS spectra of $RbNO_3$.

As the fourth-rank anisotropic broadening can be removed by sample rotation at an angle of 30.6° or 70.1° with respect to B_0, high-resolution spectra corresponding to the removal of the residual second-rank quadrupolar broadening can be achieved by the methods of double rotation (DOR) [164] and dynamic-angle spinning (DAS) [165], which, respectively, involve the simultaneous and sequential rotation of the sample about two axes [166]. As a specific example, Figure 10.35a presents a ^{17}O

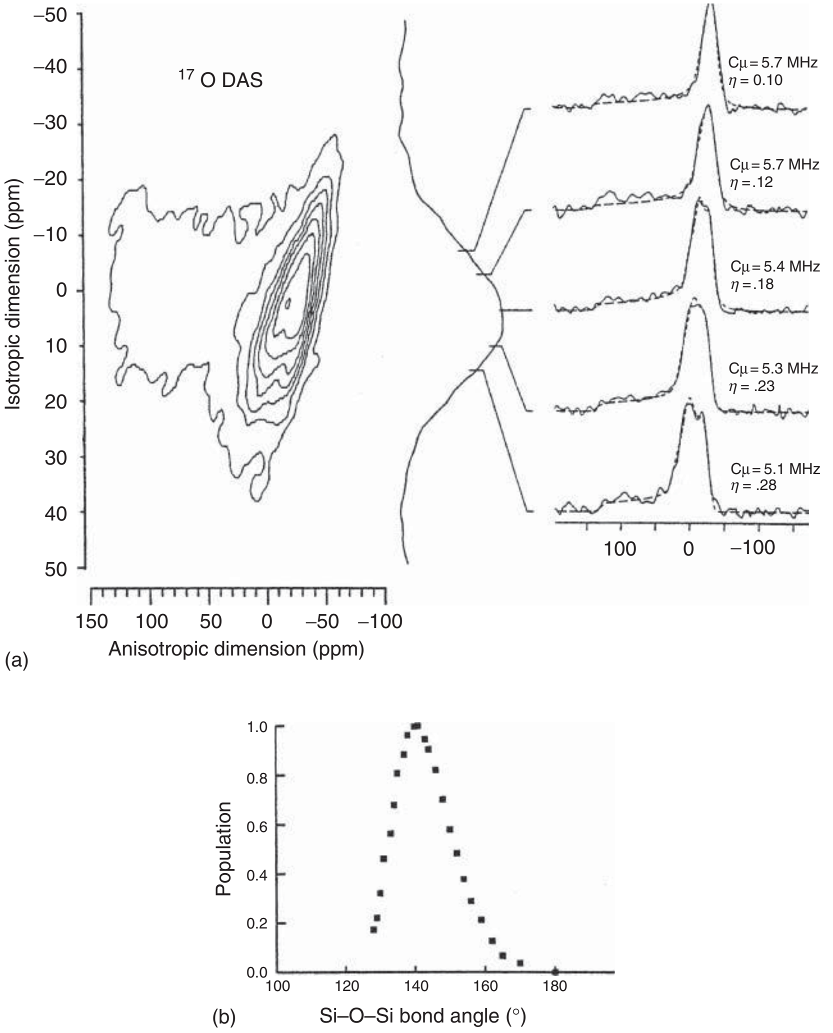

Figure 10.35 (a) A ^{17}O 2D DAS spectrum of the bridging oxygen (Si–O–Si) resonances in a $K_2Si_4O_9$ glass. Selected anisotropic cross sections corresponding to different ^{17}O isotropic frequencies are shown. (b) The Si–O–Si bond angle distribution in the glass, as determined by the use of quantum-chemical calculations to interpret the experimental information about the ^{17}O quadrupolar interactions. (Reproduced from [168].)

2D DAS spectrum of the bridging oxygen (Si–O–Si) resonances in a $K_2Si_4O_9$ glass [167, 168]. Residual second-order quadrupolar broadening is removed from the isotropic dimension such that the broadness of the isotropic lineshape reflects a continuous variation in the ^{17}O isotropic frequency. The selected anisotropic cross sections demonstrate that the quadrupolar coupling parameters vary as the isotropic frequency changes. In combination with quantum-chemical calculations, the information about the ^{17}O quadrupolar interactions allows the determination of the Si–O–Si bond angle distribution in the glass (Figure 10.35b). Although a number of impressive applications of both the DAS and DOR methods have been presented, the technical complexity of both experiments has meant that their use is not widespread.

In 1995, Frydman and Harwood [169] presented a 2D MQ MAS experiment, which, by means of the formation of an echo corresponding to the refocusing of the fourth-rank second-order quadrupolar broadening, yields 2D spectra in which anisotropically broadened ridges are resolved on the basis of their different isotropic shifts. The resolution of the three distinct Rb sites in $RbNO_3$ in an isotropic MQ MAS spectrum is demonstrated in Figure 10.34c. It is to be noted that the experiment is only applicable for odd MQ orders (e.g., 3Q or 5Q), for which there is no first-order quadrupolar broadening. Moreover, as compared to the spin $I = 1/2$ MQ methods described earlier in this chapter, MQC can be excited for a single isolated nucleus.

The MQ MAS technique has the big advantage of requiring only conventional MAS hardware. In the last five years, much attention has been devoted to the optimization of the technique, with respect to, for example, obtaining pure absorption-mode lineshapes, improving the sensitivity, and extending the applicability to nuclei with ever greater quadrupolar couplings; various groups have carried out studies to compare the different variants which have been proposed [170–172]. The development has been so rapid that MQ MAS NMR of nuclei such as ^{23}Na, ^{27}Al, and ^{17}O can now be considered to be routine, with many applications having been presented, which encompass, for example, glasses, minerals, and microporous materials [173–178].

As a specific example, Figure 10.36 shows ^{27}Al 5Q MAS spectra corresponding to the tetrahedral aluminum sites in the microporous aluminum methylphosphonates Figure 10.36a AlMePO-α and Figure 10.36b AlMePO-β [176]. In Figure 10.36b, three distinct sites can be distinguished in the isotropic (F_1) dimension. In a MAS experiment (this corresponds to the projection onto the F_2 dimension), only a single peak is observed in the tetrahedral region. AlMePO-β can be converted by a thermal transformation into AlMePO-α. As discussed in [176], insight into this process is provided by the subtle but significant differences between the 5Q MAS spectra for a physical mixture of the two forms (Figure 10.36c) and for a sample in which the thermal transformation was interrupted (Figure 10.36d).

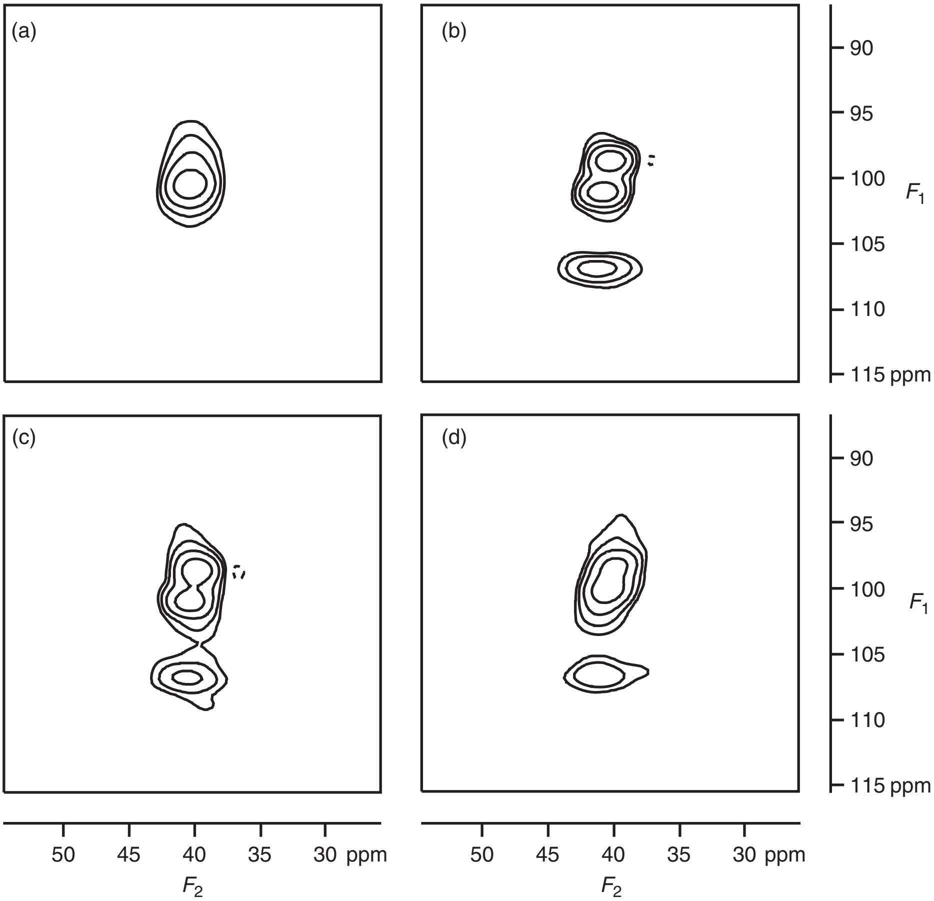

Figure 10.36 ^{27}Al (104.3 MHz) 5Q MAS spectra corresponding to the tetrahedral aluminum sites in the microporous aluminum methylphosphonates (a) AlMePO-α and (b) AlMePO-β, as well as (c) a physical mixture of the two forms, and (d) a sample in which the thermal transformation between the two forms was interrupted. (Reproduced by permission of the American Chemical Society from [176].)

10.8
Summary

This chapter has given an overview of the wide range of solid-state NMR experiments available today. The central role of anisotropic interactions, for example, the CSA and the dipolar and quadrupolar couplings, has become evident. Through the orientation dependence imparted to the resonance frequency, access is made available to valuable structural and dynamic information. However, for a powder sample, the associated line broadening hinders the resolution of distinct sites. Achieving high-resolution NMR while retaining access to the information inherent to the anisotropic interactions particular to the solid state is a key aim of many of the described experimental methods.

A number of NMR methods applicable to small amounts (10–20 mg) of a powdered sample at natural abundance have been presented. In particular, recent advances in both NMR hardware and the development of new pulse sequences means that ^{1}H solid-state NMR is becoming routinely feasible. In this way, insight into the structure and dynamics of, in particular, hydrogen-bonded systems as well as aromatic π–π interactions can be provided. A further important new class of experiments are those which exploit the *J*-coupling to establish through-bond connectivities. As a general strategy, as much information as possible should be first gleaned for the sample at natural abundance (for large biological systems, global isotopic labeling is unavoidable). If pertinent questions remain unanswered, a strategy involving the synthesis of a sample incorporating selective isotopic labeling can be considered.

Solid-state NMR spectroscopy should certainly not be used in isolation. For example, the assignment of solid-state spectra is aided by the existence of solution-state NMR spectra, while if dynamic processes are to be investigated, it is very useful if differential scanning calorometry (DSC) curves can be first obtained, so that the temperatures at which phase transitions occur are known in advance. In addition, the advances in computing power as well as the development of methodology means that the use of quantum-chemical calculations of NMR parameters in the interpretation of experimental results will become ever more popular.

Solid-state NMR should not be considered as a replacement for the established diffraction methods. Instead, the two methods should be thought of as being complementary, as they have much to offer each other. For example, the existence of a single-crystal X-ray structure for a related system aids the interpretation of NMR spectra obtained for a system, where it is not possible to obtain a single crystal suitable for an X-ray analysis. In addition, solid-state NMR is of use when an X-ray single-crystal structure is available. For example, as structure determination by single-crystal X-ray diffraction methods, being based on the diffraction of X-rays by electrons, is not well suited to the localization of lighter atoms, the ability of solid-state NMR to provide distance constraints, which can be used in the optimization of a crystal structure, in particular the very relevant hydrogen-bonded part, is of much importance. Furthermore, solid-state NMR is extremely well suited to the investigation of dynamic processes. It can also detect polymorphic forms, which may be overlooked when selecting single crystals for X-ray diffraction analysis. Finally, by probing the CSA and quadrupolar interactions, solid-state NMR provides electronic information which is not accessible to X-ray studies.

Acknowledgments

SPB is supported by a Marie Curie Fellowship of the European Community program ‘‘Improving Human Research Potential and the Socio-economic Knowledge Base’’ under contract number ‘‘HPMFCT-2000-00525.’’ The information published does

not represent the opinion of the Community, and the Community is not responsible for any use that might be made of data appearing therein.

Appendix

Anisotropic Interactions: The Orientation Dependence of the Resonance Frequency

For the CSA,

$$\omega_{\mathrm{CS}} = \omega_0(\sigma_{xx}^{\mathrm{PAS}}\cos^2\phi\,\sin^2\theta + \sigma_{yy}^{\mathrm{PAS}}\,\sin^2\phi\,\sin^2\theta + \sigma_{zz}^{\mathrm{PAS}}\cos^2\theta) \tag{A1}$$

where ω_0 is the Larmor frequency, $\sigma_{xx}^{\mathrm{PAS}}$, $\sigma_{yy}^{\mathrm{PAS}}$, and $\sigma_{zz}^{\mathrm{PAS}}$ are the principal values (eigenvalues) in the PAS, and φ and θ are polar angles defining the transformation of the PAS onto the laboratory frame defined by B_0 [4].

The CSA is more commonly expressed as a sum of an isotropic and an anisotropic part. The isotropic chemical shift is given by

$$\sigma_{\mathrm{iso}} = \frac{1}{3}(\sigma_{xx}^{\mathrm{PAS}} + \sigma_{yy}^{\mathrm{PAS}} + \sigma_{zz}^{\mathrm{PAS}}) \tag{A2}$$

while the anisotropic frequency is

$$\omega_{\mathrm{aniso}} = \frac{\delta}{2}(3\cos^2\theta - 1 - \eta\sin^2\theta\cos 2\phi) \tag{A3}$$

where δ and η describe the anisotropy and the asymmetry of the interaction, respectively.

An important feature of solid-state NMR is that the orientation dependence of the CSA, dipolar, and first-order quadrupolar interactions can all be represented by what are referred to as *second-rank tensors*. As a consequence, Eq. (A3) can be considered as a general expression which applies to all three interactions. It should be noted that the isotropic part is zero for both the dipolar coupling and the first-order quadrupolar interaction.

For the dipolar coupling between a pair of spins, the interaction is always axially symmetric and thus $\eta = 0$. It is necessary to distinguish between a heteronuclear and a homonuclear dipolar coupling. For the heteronuclear case,

$$\delta = D \tag{A4}$$

while for the homonuclear case,

$$\delta = \frac{3D}{2} \tag{A5}$$

where D is the dipolar coupling constant:

$$D = \frac{\mu_0 \eta \gamma_{\mathrm{I}} \gamma_{\mathrm{S}}}{4\pi r^3} \tag{A6}$$

r denotes the internuclear distance, while γ corresponds to the magnetogyric ratio.

For the first-order quadrupolar interaction,

$$\delta = \frac{3\pi C_{\mathrm{Q}}}{2I(2I-1)} \tag{A7}$$

where the quadrupolar coupling constant, C_Q (in units of Hz), is given by

$$C_Q = \frac{e^2qQ}{h} \tag{A8}$$

eq corresponds to the electric field gradient at the nucleus and Q to the nuclear quadrupole moment.

References

1. Ernst, R.R., Bodenhausen, G., and Wokaun, A. (1987) *Principles of Nuclear Magnetic Resonance in One and Two Dimensions*, Clarendon Press, Oxford.
2. Claridge, T.D.W. (1999) *High-Resolution NMR Techniques in Organic Chemistry*, Pergamon Press, Amsterdam.
3. Mehring, M. (1983) *Principles of High Resolution NMR in Solids*, Springer, Berlin.
4. Schmidt-Rohr, K. and Spiess, H.W. (1994) *Multidimensional Solid-State NMR and Polymers*, Academic Press, New York.
5. Emsley, L., Laws, D.D., and Pines, A. (1999) in *The Proceedings of the International School of Physics "Enrico Fermi", Course CXXXIX*, 3rd edn (ed B. Maraviglia), IOS Press, Amsterdam, p. 45.
6. Harris, R.K. (1996) in *Encyclopedia of Nuclear Magnetic Resonance*, Vol. 5 (eds D.M. Grant and R.K. Harris), John Wiley & Sons, Ltd, Chichester, p. 3301.
7. Brown, S.P. and Spiess, H.W. (2001) *Chem. Rev.*, **101**, 4125.
8. Bennett, A.E., Griffin, R.G., and Vega, S. (1994) *NMR Basic Principles and Progress*, Vol. 33, Springer-Verlag, Berlin, p. 1.
9. Dusold, S. and Sebald, A. (2000) *Annu. Rep. NMR Spectrosc.*, **41**, 185.
10. Sherwood, M.H. (1996) in *Encyclopedia of Nuclear Magnetic Resonance*, Vol. 2 (eds D.M. Grant and R.K. Harris), John Wiley & Sons, Ltd, Chichester, p. 1322.
11. Gerald, R. II,, Bernhard, T., Haeberlen, U. *et al.* (1993) *J. Am. Chem. Soc.*, **115**, 777.
12. Dong, R.Y. (1994) *Nuclear Magnetic Resonance of Liquid Crystals*, Springer, New York.
13. Emsley, J.W. (1996) in *Encyclopedia of Nuclear Magnetic Resonance*, Vol. 4 (eds D.M. Grant and R.K. Harris), John Wiley & Sons, Ltd, Chichester, p. 2788.
14. Davis, J.H. and Auger, M. (1999) *Prog. NMR Spectrosc.*, **35**, 1.
15. Davis, J.H., Jeffrey, K.R., Bloom, M. *et al.* (1976) *Chem. Phys. Lett.*, **42**, 390.
16. Copié, V., McDermott, A.E., Beshah, K. *et al.* (1994) *Biochemistry*, **33**, 3280.
17. Andrew, E.R., Bradbury, A., and Eades, R.G. (1958) *Nature*, **182**, 1659.
18. Lowe, I. (1959) *Phys. Rev. Lett.*, **2**, 285.
19. Hartmann, S.R. and Hahn, E.L. (1962) *Phys. Rev.*, **128**, 2042.
20. Pines, A., Gibby, M.G., and Waugh, J.S. (1972) *J. Chem. Phys.*, **56**, 1776.
21. Schaefer, J. and Stejskal, E.O. (1976) *J. Am. Chem. Soc.*, **98**, 1031.
22. Maricq, M.M. and Waugh, J.S. (1979) *J. Chem. Phys.*, **70**, 3300.
23. Hodgkinson, P. and Emsley, L. (1997) *J. Chem. Phys.*, **107**, 4808.
24. Herzfeld, J. and Berger, A.E. (1980) *J. Chem. Phys.*, **73**, 6021.
25. Metz, G., Wu, X., and Smith, S.O. (1994) *J. Magn. Reson., Ser. A*, **110**, 219.
26. Hediger, S., Meier, B.H. *et al.* (1994) *Chem. Phys. Lett.*, **223**, 283.
27. Dixon, W.T. (1981) *J. Magn. Reson.*, **44**, 220.
28. Dixon, W.T. (1982) *J. Chem. Phys.*, **77**, 1800.
29. Bloch, F. (1958) *Phys. Rev.*, **111**, 841.
30. Bennett, A.E., Rienstra, C.M. *et al.* (1995) *J. Chem. Phys.*, **103**, 6951.
31. Carravetta, M., Edén, M., Zhao, X. *et al.* (2000) *Chem. Phys. Lett.*, **321**, 205.
32. Ernst, M., Zimmermann, H., and Meier, B.H. (2000) *Chem. Phys. Lett.*, **317**, 581.
33. Wu, X., Burns, S.T., and Zilm, K.W. (1994) *J. Magn. Reson., Ser. A*, **111**, 29.

34. Lesage, A., Steuernagel, S., and Emsley, L. (1998) *J. Am. Chem. Soc.*, **120**, 7095.

35. Hu, J.Z., Harper, J.K., Taylor, C. *et al.* (2000) *J. Magn. Reson.*, **142**, 326.

36. Sakellariou, D., Lesage, A., and Emsley, L. (2001) *J. Magn. Reson.*, **151**, 40.

37. Botto, R.E. (1996) in *Encyclopedia of Nuclear Magnetic Resonance*, Vol. 3 (eds D.M. Grant and R.K. Harris), John Wiley & Sons, Ltd, Chichester, p. 2101.

38. Pugmire, R.J. (1996) in *Encyclopedia of Nuclear Magnetic Resonance*, Vol. 2 (eds D.M. Grant and R.K. Harris), John Wiley & Sons, Ltd, Chichester, p. 1355.

39. Pruski, M. (1996) in *Encyclopedia of Nuclear Magnetic Resonance*, Vol. 2 (eds D.M. Grant and R.K. Harris), John Wiley & Sons, Ltd, Chichester, p. 1378.

40. Saitô, H. (1996) in *Encyclopedia of Nuclear Magnetic Resonance*, Vol. 6 (eds D.M. Grant and R.K. Harris), John Wiley & Sons, Ltd, Chichester, p. 3740.

41. Harris, R.K. (1996) in *Encyclopedia of Nuclear Magnetic Resonance*, Vol. 6 (eds D.M. Grant and R.K. Harris), John Wiley & Sons, Ltd, Chichester, p. 3734.

42. Veeman, W.S. (1996) in *Encyclopedia of Nuclear Magnetic Resonance*, Vol. 6 (eds D.M. Grant and R.K. Harris), John Wiley & Sons, Ltd, Chichester, p. 3655.

43. Newman, R.H. (1996) in *Encyclopedia of Nuclear Magnetic Resonance*, Vol. 2 (eds D.M. Grant and R.K. Harris), John Wiley & Sons, Ltd, Chichester, p. 738.

44. Marsmann, H.C. (1996) in *Encyclopedia of Nuclear Magnetic Resonance*, Vol. 7 (eds D.M. Grant and R.K. Harris), John Wiley & Sons, Ltd, Chichester, p. 4386.

45. Engelhardt, G. (1996) in *Encyclopedia of Nuclear Magnetic Resonance*, Vol. 7 (eds D.M. Grant and R.K. Harris), John Wiley & Sons, Ltd, Chichester, p. 4398.

46. Eckert, H. (1994) *NMR Basic Principles and Progress*, Vol. 33, Springer-Verlag, Berlin, Heidelberg, p. 125.

47. Hediger, S., Emsley, L., and Fisher, M. (1999) *Carbohydr. Res.*, **322**, 102.

48. Schnell, I., Brown, S.P., Low, H.Y. *et al.* (1998) *J. Am. Chem. Soc.*, **120**, 11784.

49. Brown, S.P., Schnell, I., Brand, J.D. *et al.* (1999) *J. Am. Chem. Soc.*, **121**, 6712.

50. Brown, S.P., Schnell, I., Brand, J.D. *et al.* (2000) *J. Mol. Struct.*, **521**, 179.

51. Yamauchi, K., Kuroki, S., Fujii, K. *et al.* (2000) *Chem. Phys. Lett.*, **324**, 435.

52. Waugh, J.S., Huber, L.M., and Haeberlen, U. (1968) *Phys. Rev. Lett.*, **20**, 180.

53. Haeberlen, U. and Waugh, J.S. (1968) *Phys. Rev.*, **175**, 453.

54. Gerstein, B.C., Pembleton, R.G., Wilson, R.C. *et al.* (1977) *J. Chem. Phys.*, **66**, 361.

55. Scheler, G., Haubenreisser, U., and Rosenberger, H. (1981) *J. Magn. Reson.*, **44**, 134.

56. Maciel, G.E., Bronnimann, C.E., and Hawkins, B. (1990) *Adv. Magn. Reson.*, **14**, 125.

57. Dec, S.F., Bronnimann, C.E., Wind, R.A. *et al.* (1989) *J. Magn. Reson.*, **82**, 454.

58. Miller, J.M. (1996) *Prog. NMR Spectrosc.*, **28**, 255.

59. Ando, S., Harris, R.K., Hirschinger, J. *et al.* (2001) *Macromolecules*, **34**, 66.

60. Grage, S.L. and Ulrich, A.S. (2000) *J. Magn. Reson.*, **146**, 81.

61. Gullion, T. and Schaefer, J. (1989) *J. Magn. Reson.*, **81**, 196.

62. Gullion, T. and Schaefer, J. (1989) *Adv. Magn. Reson.*, **13**, 57.

63. Gullion, T. (1998) *Concepts Magn. Reson.*, **10**, 277.

64. Holl, S.M., Marshall, G.R., Beusen, D.D. *et al.* (1992) *J. Am. Chem. Soc.*, **114**, 4830.

65. Grey, C.P., Veeman, W.S., and Vega, A.J. (1993) *J. Chem. Phys.*, **98**, 7711.

66. Gullion, T. (1995) *Chem. Phys. Lett.*, **246**, 325.

67. Raleigh, D.P., Levitt, M.H., and Griffin, R.G. (1988) *Chem. Phys. Lett.*, **146**, 71.

68. Levitt, M.H., Raleigh, D.P., Creuzet, F. *et al.* (1990) *J. Chem. Phys.*, **92**, 6347.

69. Feng, X., Verdegem, P.J.E., Lee, Y.K. *et al.* (1999) *Solid State Nucl. Magn. Reson.*, **14**, 81.

70. Tycko, R. and Dabbagh, G. (1991) *J. Am. Chem. Soc.*, **113**, 9444.

71. Bennett, A.E., Ok, J.H., Griffin, R.G. *et al.* (1992) *J. Chem. Phys.*, **96**, 8624.

72. Nielsen, N.C., Bildsøe, H., Jakobsen, H.J. *et al.* (1994) *J. Chem. Phys.*, **101**, 1805.

73. Lee, Y.K., Kurur, N.D., Helmle, M. *et al.* (1995) *Chem. Phys. Lett.*, **242**, 304.

74. Sommer, W., Gottwald, J., Demco, D.E. *et al.* (1995) *J. Magn. Reson., Ser. A*, **113**, 131.

75. Gregory, D.M., Wolfe, G., Jarvie, T. *et al.* (1996) *Mol. Phys.*, **89**, 1835.

76. Verel, R., Baldus, M., Ernst, M. *et al.* (1998) *Chem. Phys. Lett.*, **287**, 421.

77. Brinkmann, A., Edén, M., and Levitt, M.H. (2000) *J. Chem. Phys.*, **112**, 8539.

78. de Azevedo, E.R., Hu, W.-G., Bonagamba, T.J. *et al.* (1999) *J. Am. Chem. Soc.*, **121**, 8411.

79. de Azevedo, E.R., Hu, W.-G., Bonagamba, T.J. *et al.* (2000) *J. Chem. Phys.*, **112**, 8988.

80. Pauli, J., Baldus, M., van Rossum, B. *et al.* (2001) *Chem. Biochem.*, **2**, 272.

81. Lesage, A., Auger, C., Caldarelli, S. *et al.* (1997) *J. Am. Chem. Soc.*, **119**, 7867.

82. Bax, A., Freeman, R., and Frenkiel, T.A. (1981) *J. Am. Chem. Soc.*, **103**, 2102.

83. Yen, Y.-S. and Pines, A. (1983) *J. Chem. Phys.*, **78**, 3579.

84. Baum, J., Munowitz, M., Garroway, A.N. *et al.* (1985) *J. Chem. Phys.*, **83**, 2015.

85. Hore, P.J., Jones, J.A., and Wimperis, S. (2000) *NMR . . . : The Toolokit*, Oxford University Press, Oxford.

86. Lesage, A., Bardet, M., and Emsley, L. (1999) *J. Am. Chem. Soc.*, **121**, 10987.

87. Verel, R., van Beek, J.D., and Meier, B.H. (1999) *J. Magn. Reson.*, **140**, 300.

88. Geen, H., Titman, J.J., Gottwald, J. *et al.* (1994) *Chem. Phys. Lett.*, **227**, 79.

89. Caravetti, P., Neuenschwander, P., and Ernst, R.R. (1985) *Macromolecules*, **18**, 119.

90. Ochsenfeld, C., Brown, S.P., Schnell, I. *et al.* (2001) *J. Am. Chem. Soc.*, **123**, 2597.

91. Lazzeretti, P. (2000) *Prog. NMR Spectrosc.*, **36**, 1.

92. van Rossum, B.-J., Boender, G.J., Mulder, F.M. *et al.* (1998) *Spectrochim. Acta, Part A*, **54**, 1167.

93. Brown, S.P., Schaller, T., Seelbach, U.P. *et al.* (2001) *Angew. Chem. Int. Ed.*, **40**, 717.

94. Berglund, B. and Vaughan, R.W. (1980) *J. Chem. Phys.*, **73**, 2037.

95. Jeffrey, G.A. and Yeon, Y. (1986) *Acta Crystallogr., Sect. B*, **42**, 410.

96. Harris, R.K., Jackson, P., Merwin, L.H. *et al.* (1988) *J. Chem. Soc., Faraday Trans.*, **84**, 3649.

97. Feike, M., Graf, R., Schnell, I., Jäger, C. *et al.* (1996) *J. Am. Chem. Soc.*, **118**, 9631.

98. Witter, R., Hartmann, P., Vogel, J. *et al.* (1998) *Solid State Nucl. Magn. Reson.*, **13**, 189.

99. Nielsen, N.C., Creuzet, F., Griffin, R.G. *et al.* (1992) *J. Chem. Phys.*, **96**, 5668.

100. Hong, M. (1999) *J. Magn. Reson.*, **136**, 86.

101. Schmidt-Rohr, K., Hu, W., and Zumbulyadis, N. (1998) *Science*, **280**, 714.

102. Lee, M. and Goldburg, W.I. (1965) *Phys. Rev. A*, **140**, 1261.

103. Bielecki, A., Kolbert, A.C., and Levitt, M.H. (1989) *Chem. Phys. Lett.*, **155**, 341.

104. Bielecki, A., Kolbert, A.C., de Groot, H.J.M. *et al.* (1990) *Adv. Magn. Reson.*, **14**, 111.

105. Vinogradov, E., Madhu, P.K., and Vega, S. (1999) *Chem. Phys. Lett.*, **314**, 443.

106. Sakellariou, D., Lesage, A., Hodgkinson, P. *et al.* (2000) *Chem. Phys. Lett.*, **319**, 253.

107. Lesage, A., Duma, L., Sakellariou, D. *et al.* (2001) *J. Am. Chem. Soc.*, **123**, 5747.

108. Bax, A., Szeverenyi, N.M., and Maciel, G.E. (1983) *J. Magn. Reson.*, **52**, 147.

109. Gan, Z. (1992) *J. Am. Chem. Soc.*, **114**, 8307.

110. Bax, A., Szeverenyi, N.M., and Maciel, G.E. (1983) *J. Magn. Reson.*, **55**, 494.

111. Terao, T., Fujii, T., Onodera, T. *et al.* (1984) *Chem. Phys. Lett.*, **107**, 145.

112. Frydman, L., Chingas, G.C., Lee, Y.K. *et al.* (1992) *J. Chem. Phys.*, **97**, 4800.

113. Gann, S.L., Baltisberger, J.H., and Pines, A. (1994) *Chem. Phys. Lett.*, **210**, 405.

114. Alderman, D.W., McGeorge, G., Hu, J.Z. *et al.* (1998) *Mol. Phys.*, **95**, 1113.

115. Harper, J.K. and Grant, D.M. (2000) *J. Am. Chem. Soc.*, **122**, 3708.

116. Antzutkin, O.N., Shekar, S.C., and Levitt, M.H. (1995) *J. Magn. Reson., Ser. A*, **115**, 7.

117. Antzutkin, O.N., Lee, Y.K., and Levitt, M.H. (1998) *J. Magn. Reson.*, **135**, 144.

118. Schaefer, D., Spiess, H.W., Suter, U.W. *et al.* (1990) *Macromolecules*, **23**, 3431.

119. Hagemeyer, A., Schmidt-Rohr, K., and Spiess, H.W. (1989) *Adv. Magn. Reson.*, **13**, 85.

120. Titman, J.J., Luz, Z., and Spiess, H.W. (1992) *J. Am. Chem. Soc.*, **114**, 3756.

121. Geen, H., Titman, J.J., Gottwald, J. *et al.* (1995) *J. Magn. Reson., Ser. A*, **114**, 264.

122. Gottwald, J., Demco, D.E., Graf, R. *et al.* (1995) *Chem. Phys. Lett.*, **243**, 314.

123. Demus, D., Goodby, J.W., Gray, G.W. *et al.* (eds) (1998) *Handbook of Liquid Crystals*, Wiley-VCH Verlag GmbH, Weinheim.

124. Herwig, P., Kayser, C.W., Müllen, K. *et al.* (1996) *Adv. Mater.*, **8**, 510.

125. Brown, S.P., Zhu, X.X., Saalwächter, K. *et al.* (2001) *J. Am. Chem. Soc.*, **123**, 4275.

126. Jeffrey, G.A. and Saenger, W. (1991) *Hydrogen Bonding in Biological Structures*, Springer-Verlag, New York.

127. Brown, S.P., Schnell, I., Brand, J.D. *et al.* (2000) *Phys. Chem. Chem. Phys.*, **2**, 1735.

128. Schmidt-Rohr, K., Clauss, J., and Spiess, H.W. (1992) *Macromolecules*, **25**, 3273.

129. Landfester, K., Boeffel, C., Lambla, M. *et al.* (1996) *Macromolecules*, **29**, 5972.

130. Caravatti, P., Bodenhausen, G., and Ernst, R.R. (1982) *Chem. Phys. Lett.*, **89**, 363.

131. Caravatti, P., Braunschweiler, L., and Ernst, R.R. (1983) *Chem. Phys. Lett.*, **100**, 305.

132. van Rossum, B.-J., Förster, H., and De Groot, H.J.M. (1997) *J. Magn. Reson.*, **124**, 516.

133. Saalwächter, K., Graf, R., and Spiess, H.W. (1999) *J. Magn. Reson.*, **140**, 471.

134. Saalwächter, K., Graf, R., and Spiess, H.W. (2001) *J. Magn. Reson.*, **148**, 398.

135. Bodenhausen, G. and Ruben, D.J. (1980) *Chem. Phys. Lett.*, **69**, 185.

136. Müller, L. (1979) *J. Am. Chem. Soc.*, **101**, 4481.

137. Lesage, A., Sakellariou, D., Steuernagel, S. *et al.* (1998) *J. Am. Chem. Soc.*, **120**, 13194.

138. Lesage, A., Charmont, P., Steuernagel, S. *et al.* (2000) *J. Am. Chem. Soc.*, **122**, 9739.

139. Lesage, A. and Emsley, L. (2001) *J. Magn. Reson.*, **148**, 449.

140. Hester, R.K., Ackerman, J.L., Neff, B.L. *et al.* (1976) *Phys. Rev. Lett.*, **36**, 1081.

141. Munowitz, M.G., Griffin, R.G., Bodenhausen, G. *et al.* (1981) *J. Am. Chem. Soc.*, **103**, 2529.

142. Munowitz, M.G. and Griffin, R.G. (1982) *J. Chem. Phys.*, **76**, 2848.

143. Roberts, J.E., Harbison, G.S., Munowitz, M.G. *et al.* (1987) *J. Am. Chem. Soc.*, **109**, 4163.

144. McElheny, D., DeVita, E., and Frydman, L. (2000) *J. Magn. Reson.*, **143**, 321.

145. Hohwy, M., Jaroniec, C.P., Reif, B. *et al.* (2000) *J. Am. Chem. Soc.*, **122**, 3218.

146. van Rossum, B.-J., de Groot, C.P., Ladizhansky, V. *et al.* (2000) *J. Am. Chem. Soc.*, **122**, 3465.

147. Hediger, S. (1997) Improvement of heteronuclear polarization transfer in solid-state NMR. PhD thesis. ETH, Zurich.

148. Fechtenkötter, A., Saalwächter, K., Harbison, M.A. *et al.* (1999) *Angew. Chem. Int. Ed.*, **38**, 3039.

149. Feng, X., Lee, Y.K., Sandstrom, D. *et al.* (1996) *Chem. Phys. Lett.*, **257**, 314.

150. Hong, M., Gross, J.D., and Griffin, R.G. (1997) *J. Phys. Chem. B*, **101**, 5869.

151. Wu, C.H., Ramamoorthy, A., and Opella, S.J. (1994) *J. Magn. Reson., Ser. A*, **109**, 270.

152. Marassi, F.M. and Opella, S.J. (2000) *J. Magn. Reson.*, **144**, 150.

153. Weitekamp, D.P., Garbow, J.R., and Pines, A. (1982) *J. Chem. Phys.*, **77**, 2870.

154. Schmidt-Rohr, K., Nanz, D., Emsley, L. *et al.* (1994) *J. Phys. Chem.*, **98**, 6668.

155. Caldarelli, S., Hong, M., Emsley, L. *et al.* (1996) *J. Phys. Chem.*, **100**, 18696.

156. Fung, B.M., Ermolaev, K., and Yu, Y. (1999) *J. Magn. Reson.*, **138**, 28.

157. Sun, H. and Fung, B.M. (2000) *Liq. Cryst.*, **27**, 755.

158. Massou, S., Tropis, M., and Milon, A. (1999) *J. Chim. Phys. Phys.-Chim. Biol.*, **96**, 1595.

159. Caldarelli, S., Lesage, A., and Emsley, L. (1996) *J. Am. Chem. Soc.*, **118**, 12224.

160. Haase, J. and Conradi, M.S. (1993) *Chem. Phys. Lett.*, **287**, 209.

161. Kentgens, A.P.M. and Verhagen, R. (1999) *Chem. Phys. Lett.*, **300**, 435.

162. Yao, Z., Kwak, H.-T., Sakellariou, D. *et al.* (2000) *Chem. Phys. Lett.*, **327**, 85.

163. Ganapathy, S., Schramm, S., and Oldfield, E. (1982) *J. Chem. Phys.*, **77**, 4360.

164. Samoson, A., Lippmaa, E., and Pines, A. (1988) *Mol. Phys.*, **65**, 1013.

165. Mueller, K.T., Sun, B.Q., Chingas, G.C. *et al.* (1990) *J. Magn. Reson.*, **86**, 470.

166. Llor, A. and Virlet, J. (1988) *Chem. Phys. Lett.*, **152**, 248.

167. Farnan, I., Grandinetti, P.J., Baltisberger, J.H. *et al.* (1992) *Nature*, **358**, 31.

168. Grandinetti, P.J. (1996) in *Encyclopedia of Nuclear Magnetic Resonance*, Vol. 3 (eds D.M. Grant and R.K. Harris), John Wiley & Sons, Ltd, Chichester, p. 1768.

169. Frydman, L. and Harwood, J.S. (1995) *J. Am. Chem. Soc.*, **117**, 5367.

170. Brown, S.P. and Wimperis, S. (1997) *J. Magn. Reson.*, **128**, 42.

171. Vosegaard, T., Florian, P., Grandinetti, P.J. *et al.* (2000) *J. Magn. Reson.*, **143**, 217.

172. Pruski, M., Wiench, J.W., and Amoureux, J.-P. (2000) *J. Magn. Reson.*, **147**, 286.

173. Rocha, J., Esculas, A.P., Fernandez, C. *et al.* (1996) *J. Phys. Chem.*, **100**, 17889.

174. Dirken, P.J., Kohn, S.C., Smith, M.E. *et al.* (1997) *Chem. Phys. Lett.*, **266**, 568.

175. Xu, Z., Maekawa, H., Oglesby, J.V., and Stebbins, J.F. (1998) *J. Am. Chem. Soc.*, **120**, 9894.

176. Brown, S.P., Ashbrook, S.E., and Wimperis, S. (1999) *J. Phys. Chem. B*, **103**, 812.

177. Caldarelli, S. and Ziarelli, F. (2000) *J. Am. Chem. Soc.*, **122**, 12015.

178. Alemany, L.B., Callender, R.L., Barron, A.R. *et al.* (2000) *J. Phys. Chem. B*, **104**, 11612.

Section IV
Methods 3: Mass Spectrometry

Handbook of Spectroscopy, Second Edition. Edited by Günter Gauglitz and David S. Moore.

11
Mass Spectrometry

Michael Przybylski

11.1
Introduction: Principles of Mass Spectrometry

Mass spectrometry (MS) is an analytical method in which gaseous ions are produced and subsequently subjected to magnetic and electric fields in a high vacuum for analysis of mass/charge ratios. Although initially developed predominantly for physicochemical investigations, MS now has broad application areas for more than three decades in the analysis of complex organic, bioorganic, and nearly all classes of biochemical molecules [1–3]. Initial applications of MS in the study of biological processes using stable isotope ratio measurements date back to the 1940s. Using gas phase ionization, complex mixtures of compounds that either were volatile or could be derivatized to enhance volatility could be analyzed by combined gas chromatography–mass spectrometry (GC-MS). However, the use of MS in applications in life sciences was possible only on solving one of the central problems, the generation and gas-phase transfer of intact, structurally relevant ions of biomacromolecules [4–6]. In recent years, dramatic analytical developments and advancements in instrumentation have rendered MS central to many problems in modern biopolymer chemistry and biochemistry. These advances have made it possible to determine the molecular masses of large biomacromolecules to isotopic accuracy (Section 11.2.4); this opened new possibilities and approaches in identifying, for example, small – yet functionally critical – posttranslational modifications of proteins, supramolecular interactions in biopolymers, and biomolecular recognition processes, using small sample amounts with low purity and even mixtures, unrivaled by classical methods of structure determination [6, 7].

Since the 1980s, a revolution in the utility of MS for biological analyses has occurred, and continues to date. A major reason for this development was the introduction of a first set of ‘‘soft’’ ionization techniques such as fast atom bombardment (FAB), 252Cf-plasma desorption Parkinson’s Disease (PD), and thermospray (TSP), which permitted the production of gas phase ions from charged and polar biopolymers [6–10]. It reached culmination with the award of the 2002 Nobel prize in chemistry to two scientists pioneering the development of electrospray ionization mass spectrometry (ESI-MS) and matrix-assisted laser

Handbook of Spectroscopy, Second Edition. Edited by Günter Gauglitz and David S. Moore.

desorption/ionization mass spectrometry (MALDI-MS), John Fenn *et al.* [11] and Koichi Tanaka *et al.* [12]. Today, ESI-MS and MALDI-MS are the two central standard ionization methods in the analysis of biopolymers.

11.1.1
Application Areas of Mass Spectrometry to Biopolymer Analysis

The development of efficient ''soft'' ionization methods has led to a breakthrough in the direct molecular characterization of biopolymers, such as proteins and nucleic acids [5–7]. While FAB and 252Cf-plasma desorption (PD) have enabled accurate mass determinations of polypeptides and small proteins, biopolymers considerably beyond 100 kDa have become feasible by ESI-MS and MALDI-MS [11, 12]. In addition to molecular weight determinations, ''soft'' desorption–ionization MS methods are now used in *primary structure* analysis of proteins; characterization of *intracellular processing* pathways; and the identification of *posttranslational structure* modifications. Beyond these, recent approaches to the characterization of *higher order* (secondary and tertiary) structures, *structure–function* studies, *noncovalent interactions* of proteins, and even *specific biomolecular recognition* of structures have been emerging as exciting new areas of MS [13–15]. Moreover, the feasibility of the use of soft ionization MS methods in the analysis of multicomponent proteolytic mixtures (peptide mapping) has been applied successfully to the molecular characterization of chemical modification sites in proteins, providing useful structural information, for example, on surface topology, tertiary structure microenvironment, and specific antigenic binding sites (epitopes) to antibodies [15–19]. More recently, conformation- and topology-specific approaches of biopolymer analysis have become amenable through the development of new hybrid MS systems, notably ion mobility mass spectrometry (IM-MS) [20–22].

In this chapter, classical and modern ionization techniques and instrumental development of MS are described in the first part in order to provide an overview and understanding of its current feasibility and application in life sciences. In a subsequent part (Section 11.2.5), an overview of important sample preparation and handling techniques for bioanalytical applications is given. Today, amounts of samples down to the attomole (10^{-11} M) range and molecular masses of proteins and biopolymer complexes over the mega dalton range can be analyzed with accuracies many thousand times greater than those with classical gel electrophoresis; moreover, today's analyzers and electronics developments enable some of these powerful mass spectrometers to be relatively small and easy to use. This performance has recently experienced further unrivaled breakthroughs with the development of Fourier transform ion cyclotron resonance mass spectrometry (FTICR-MS), and orbitrap-MS (Section 11.2.4). In the final part (Section 11.3), selected application examples are then described to illustrate the feasibility and perspectives of the application of mass spectrometric methods in biopolymer analysis; the most recent offsprings, *proteome analysis* and application to protein *''misfolding''-aggregation* pathways, have been included as two final parts to illustrate new exciting areas emerging from advances in instrumentation and technology developments [22, 23]. This part is by no means intended to provide a comprehensive review of the field of bioanalytical MS application; rather, it should provide perspectives on today's MS instrumentation and the applications of a highly dynamic area for biomolecular analysis.

11.2
Techniques and Instrumentation of Mass Spectrometry

11.2.1
Sample Introduction and Ionization Methods

11.2.1.1 Preconditions

In MS, ions are subjected to magnetic and electric fields in vacuum. For this purpose, a compound has to be in a charged state or must be ionized prior to mass spectrometric analysis. Moreover, the ions have to be transferred to the gas phase in the vacuum system of a mass spectrometer. MS, in general, is used to analyze free ions in high vacuum. The main challenge in its biochemical application during the past decades has been the nondestructive transfer of polar and thermally labile molecules into the gas phase, especially in the presence of suitable matrices. Gaseous or heat-volatile samples can be easily handled but many compounds cannot be heated without decomposition.

Therefore, specific ionization methods capable of providing desolvation and/or desorption of the analyte out of different matrices and simultaneous ionization had to be developed. The choice of an ionization method depends on the characteristics of the analyte and the required type of analytical information. Classically, ''hard ionization'' methods such as *electron ionization* (EI) or *chemical ionization* (CI) make use of their fragmentation capabilities to gain structural information, typically of small organic molecules. In contrast, ''soft ionization'' techniques such as ESI or laser desorption are used to obtain mass spectra of intact molecules with little or no fragmentation, being capable of analyzing complex multicomponent mixtures.

11.2.1.2 Gas Phase (''Hard'') Ionization Methods

11.2.1.2.1 Electron Impact Ionization (EI) This classical ''hard'' ionization method employs an electron beam passing through the sample in the gas phase [24]. When colliding with neutral analyte molecules, another electron can be knocked off either resulting in a positively charged molecular ion of the intact analyte molecule or more often producing fragment ions corresponding to a certain molecular substructure. Typically, electron beams of 70 eV are used for EI (Figure 11.1). Decreasing this energy may result in reduced fragmentation, but it also causes reduced sensitivity.

The samples are usually introduced through a heated direct insertion probe or, for extremely volatile samples, through a gas chromatograph. EI is the oldest and best characterized ionization method and can be applied to all volatile and thermally stable compounds. EI mass spectra show a high reproducibility (''fingerprinting''),

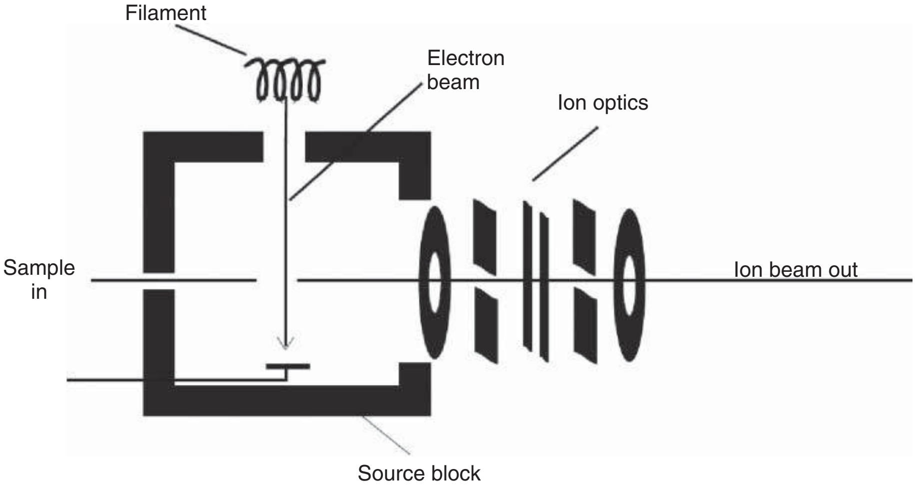

Figure 11.1 Scheme of an ion source for electron ionisation (EI). The analyte sample has to be available in gaseous state within the ion source. Sample admission may be performed by gaseous and liquid inlet systems or with a heatable solid insertion probe.

often used in combination with mass spectral libraries [25]. Additionally, structural information can be obtained from the fragmentation pattern produced.

11.2.1.2.2 **Chemical Ionization (CI)** In CI, a reagent gas such as ammonia or methane is ionized by electron impact [26]. Ion–molecule reactions between ions and neutral molecules of the reagent gas occur because of a high reagent gas pressure within the source. Some of these ions can react with analyte molecules to form analyte ions. The reagent gas is an energy mediator reducing the energy transfer to the sample molecules. Therefore, compared to EI, fragmentation is reduced and molecular ions such as $[M + H]^+$ are obtained.

Samples can be introduced into the ion source through a heated direct insertion probe or by a gas chromatograph. As a variation on CI, the analyte can be placed on a filament and rapidly heated in the CI plasma in the presence of a reagent gas. This so-called desorption CI reduces fragmentation and is applicable to samples that cannot be thermally desorbed without decomposition.

11.2.1.3 “Soft” Ionization Techniques

Targeting the detection and analysis of intact molecular ions of biopolymers, “soft” ionization techniques had to be developed. Field desorption (FD) was the first ionization technique established to produce mass spectra with little or no fragment ion content. FD is based on electron tunneling from an emitter biased at a high electrical potential [27]. The filament of the emitter is heated and the sample is evaporated into the gas phase. Typically, intact molecular ions are detected. This method is limited to relatively low-molecular-weight compounds, which additionally have to be thermally stable to some extent.

A further soft ionization method 252Cf-plasma desorption (PD) has been developed and has been successfully applied to a range of polypeptides [28]. The nuclear decay of ^{252}Cf results in two 100 MeV products that desorb the analyte molecules from a nitrocellulose-coated film and give the start signal for the pulsed time-of-flight (TOF) detection as well.

11.2.1.3.1 **Fast Atom Bombardment (FAB)**

FAB is particularly capable of analyzing polar molecules, and has been applied to biomolecules, typically with molecular weights up to about 10–15 kDa [29]. The sample is dissolved in a liquid matrix with low volatility such as glycerol or *m*-nitrobenzyl alcohol and deposited on a target. The target is then bombarded with a continuous beam of fast atoms (e.g., Xe) or ions (e.g., $^{131}Cs^+$). In the latter case, this ionization method is also referred to as secondary ion mass spectrometry (SIMS). Molecular ions and fragments of the analyte are desorbed together with cluster ions from the liquid matrix. The latter are responsible for some chemical background in the mass spectra.

Besides the direct insertion probe, liquid chromatography (LC) has been interfaced to FAB-MS [30]. This rapid and simple ionization method is relatively tolerant of variations in sampling and is suitable for a large variety of compounds. It is limited by a high chemical background and the consequent difficulty in distinguishing low molecular weight components from the background.

11.2.1.3.2 **Electrospray Ionization (ESI)**

Electrospray ionization (ESI) is a method in which the analyte is sprayed at atmospheric pressure into an interface to the vacuum of the mass spectrometer ion source [31]. The sample solution is sprayed across a high potential difference (1–4 kV) from a needle tip into an orifice of the mass spectrometer. Heat and gas flows (e.g., a countercurrent gas) may assist in the desolvation of the charged droplets containing the analyte molecular ions. Finally, ion emission (Taylor cone model) leads to the formation of multiply protonated or deprotonated ions (Figure 11.2).

The extremely soft desolvation and ionization in ESI allow the detection of tertiary structure-related biopolymer ions, and even intact noncovalent complexes comprising specific interactions (Section 11.3.3). Typically, multiply charged molecular ions are produced. The number of charges increases with increasing molecular weight and surface structure (or extended topology) [6, 13, 17, 23]. Furthermore, ion compositions correlate well with, for example, the presence of a basic or acidic analyte structure. Results of several model studies and applications have provided evidence for a correlation of the *charge structures* of ions, and the solution structures of biopolymers [13, 31]. This feasibility for characterization of higher order biopolymer structures is one of the outstanding features of ESI-MS, among other ‘‘soft’’ ionization methods [6, 15–17].

Solution flow rates can range from nano/microliters to several milliliters, making this ionization method well suited for interfacing it to chromatographic and other microseparation methods. During the past few years, several microflow devices have been developed to meet the needs in protein analysis caused by low amounts of available sample [32, 33]. Especially, nanoelectrospray has been shown to be

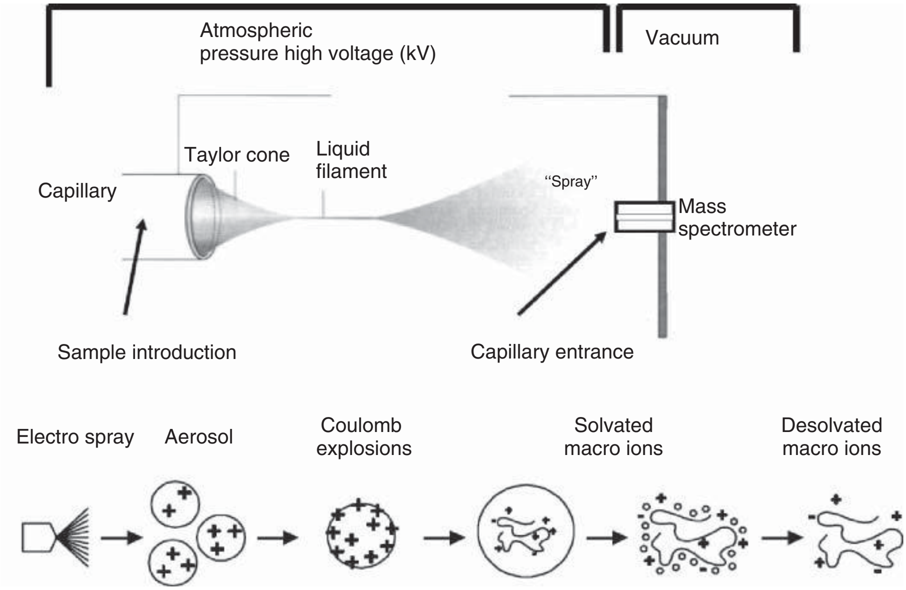

Figure 11.2 Principle of ionisation source and mechanism of gaseous ion formation in ESI MS. The sample solution is admitted through a small capillary from which the spray is formed at atmospheric pressure condition. The charged aerosol is evaporated due to Coulomb explosions to smaller droplets which finally result in desolvated macro-ions.

feasible for protein analysis and also for the characterization of noncovalent complexes [6, 13]. The small nanospray droplets enable a higher ionization efficacy at significantly reduced spray potentials. The low flow rates provide enhanced experimental variation, which is especially useful for MS/MS experiments and for multiple reaction monitoring (MRM) [34, 35].

In atmospheric pressure chemical ionization (APCI), a corona discharge is used to ionize the analyte in the source of the mass spectrometer [32]. Complementary to ESI, which is especially suitable for charged basic or polar analytes, APCI can be used for analysis of uncharged or low-polarity compounds (e.g., steroids).

11.2.1.3.3 **Matrix-Assisted Laser Desorption/Ionization (MALDI)** For laser desorption–ionization methods, a pulsed laser is typically used to desorb species from a target surface. Therefore, a mass analyzer compatible with pulsed ionization methods has to be used. Typically, TOF analyzers are employed, but several hybrid systems [quadrupole time-of-flight (Q-TOF)] and, recently, high-resolution FTICR analyzers have been successfully adapted (Section 11.2.4). Direct laser desorption relies on the very rapid heating of the sample or sample substrate to vaporize molecules without decomposition. The more recent development of MALDI relies on the absorption of laser energy by a solid, microcrystalline matrix compound such as α-cyano-4-hydroxy cinnamic acid or sinapinic acid [8, 36]. MALDI has become the most widely used method for the rapid and sensitive analysis of high-molecular-weight biomolecules [4].

The analyte is typically dissolved in a solution containing an excess of the matrix that contains a chromophore absorbing at the laser wavelength. Mainly, UV lasers are used for protein analysis, but for certain biopolymer classes such as polynucleotides IR lasers are also employed [8, 36]. Several sample preparation techniques have been developed to place a small amount of solution on the target. The MALDI process is schematically depicted in Figure 11.3. Although details of the mechanism are still unknown at present, it is generally accepted that the matrix absorbs energy from the laser pulse and produces a plasma, resulting in the desorption of matrix–analyte clusters and also in the ionization of analyte molecules [37]. Notably, low charges are generally produced even for large biopolymers (e.g., singly and doubly protonated ions) in contrast to the multiply charged ion structure series in ESI-MS [31].

11.2.2
Mass Spectrometric Analyzers

In a mass spectrometer, ion formation, mass analysis, and ion detection are combined. Various mass analyzers have been developed to separate ions according to their mass-to-charge ratio. Each analyzer has its own special characteristics and field of application, and no single mass analyzer can meet all possible requirements. The choice of the analyzer generally should be based on the application, the desired performance, and the cost.

All commonly used mass analyzers employ electric and/or magnetic fields to apply a force on charged molecules. The acceleration force is dependent on the mass as well as on the ionic charge. With the general understanding that mass spectrometers separate ions according to their mass-to-charge ratio (m/z), all principles of m/z analyzers depend on ion energies, with the exception of FTICR. Since kinetic energy differences are crucial for biopolymer ions and are limiting

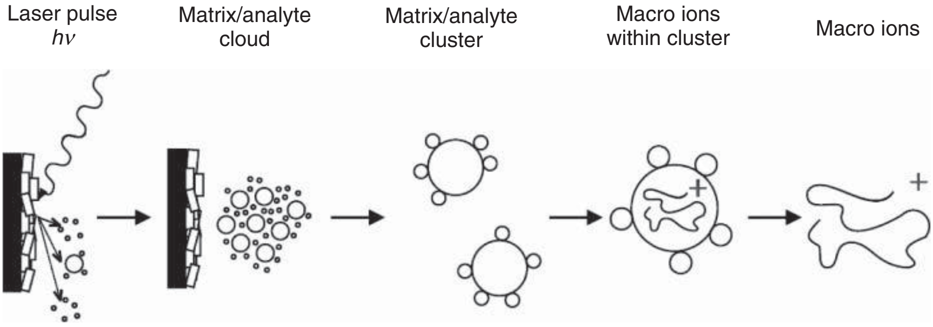

Figure 11.3 Principle of ionisation/desorption in MALDI MS. A matrix/analyte-cloud is desorbed from the microcrystalline matrix/sample preparation by a laser-pulse. Proton-transfer from matrix ions is thought to be primarily responsible to subsequently generate analyte ions.

analyzer performance, this renders FTICR-MS a prominent tool for high-resolution analysis of biopolymers (Section 11.2.4).

11.2.2.1 **Magnetic Sector Mass Analyzers**

In a magnetic deflection mass spectrometer, ions leave the ion source and are accelerated to high velocity. The ions subsequently pass through a magnetic sector in which the magnetic field is applied in a direction perpendicular to the direction of ion motion. Applying an acceleration perpendicular to the direction of motion of an object, the object's velocity remains constant, but the object travels in a circular path. Therefore, the magnetic sector follows an arc, the radius and angle of which vary with different ion optical designs.

A magnetic sector alone will separate ions according to their mass-to-charge ratio, but the resolution is limited by the fact that ions leaving the ion source do not all have exactly the same energy and therefore do not have identical velocity. To focus ions according to their kinetic energy, an additional electric sector is necessary to achieve higher resolution. Similar to the magnetic sector, the electric sector applies a force perpendicular to the direction of ion motion, and therefore has the form of an arc.

A schematic representation of a double-focusing mass spectrometer is shown in Figure 11.4. For historical reasons, this setup is referred to as a *reverse-geometry magnetic sector mass spectrometer*, which means that the magnetic sector precedes the electric sector [1]. The simplest mode of operation of a magnetic sector mass spectrometer keeps the accelerating potential and the electric sector potential constant and varies the magnetic field. Ions that have a constant kinetic energy, but different mass-to-charge ratio are brought into focus at the detector slit at different magnetic field strengths. The working equation of a magnetic sector mass

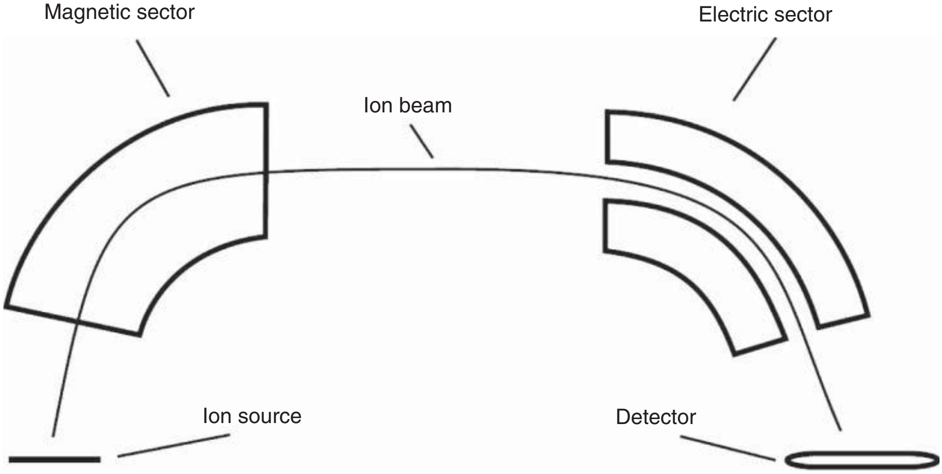

Figure 11.4 Scheme of a double-focusing magnetic sector instrument with BE configuration. Dependant on the mass-to-charge ratio the ions are distracted by the magnetic field to a circular arch with different radii.

spectrometer shows the dependency of m/z from the magnetic field B and the kinetic energy of the ions resulting from a certain acceleration voltage V:

$$\frac{m}{z} = \frac{B^2r^2}{2V}$$

Typically, the electric sector is held constant at a value that passes only ions having a specific kinetic energy. Therefore, the parameter that is most commonly varied is the magnetic field strength B. A magnetic field scan can be used to cover a wide range of mass-to-charge ratios with a sensitivity that is essentially independent of the mass-to-charge ratio. The maximum ion transmission and sensitivity occur at the maximum working accelerating voltage for a given magnetic sector mass spectrometer, whereas the effective mass range of the mass spectrometer can be increased by decreasing the accelerating voltage. The resolving power of a magnetic sector mass spectrometer is determined by the slit widths. Higher resolution is obtained by decreasing the slit widths, thereby decreasing the number of ions that reach the detector.

Linked scans, in which the magnetic and electric fields are scanned together, can be used to perform MS/MS experiments (product, precursor, and neutral loss) with a double focusing mass spectrometer.

Focal plane (array) detectors can detect a range of masses simultaneously. This provides a multichannel advantage that can improve the sensitivity for magnetic sectors, and detection limits can be improved if the analysis is limited by the analyte ion current instead of the chemical background level. This is the case for experiments such as MS/MS, ESI, and FD. Array detectors can be used with pulsed ionization methods, but the array detectors for commercial magnetic sector mass spectrometers can only detect a portion of the entire mass range at any given instant.

Double focusing magnetic sector mass analyzers provide very high reproducibility, high resolution, and a high dynamic range. However, their use is limited by their size and higher cost compared to other mass analyzers.

11.2.2.2 **Quadrupole Mass Analyzers**

The quadrupole mass analyzer is a ‘‘mass filter.’’ Combined DC and RF potentials on the quadrupole rods can be set to pass only ions of a selected mass-to-charge ratio [38]. All other ions do not have a stable trajectory through the quadrupole mass analyzer and will collide with the quadrupole rods, never reaching the detector. The operation of a quadrupole mass analyzer is usually treated in terms of a stability diagram that relates the applied DC potential and the applied RF potential, and the RF frequency to a stable versus unstable ion trajectory through the quadrupole rods. A schematic diagram of a quadrupole mass filter is shown in Figure 11.5.

Increasing the resolution decreases the number of ions that reach the detector. Good resolution also depends on the quality of the machining for the quadrupole rods. Quadrupole rods can have other functions besides their use as a mass filter. An RF-only quadrupole will act as an ion guide for ions within a broad mass range. For example, the collision region of a triple quadrupole mass spectrometer uses an RF ion guide. A DC-only quadrupole is used as a lens element in some ion optical systems.

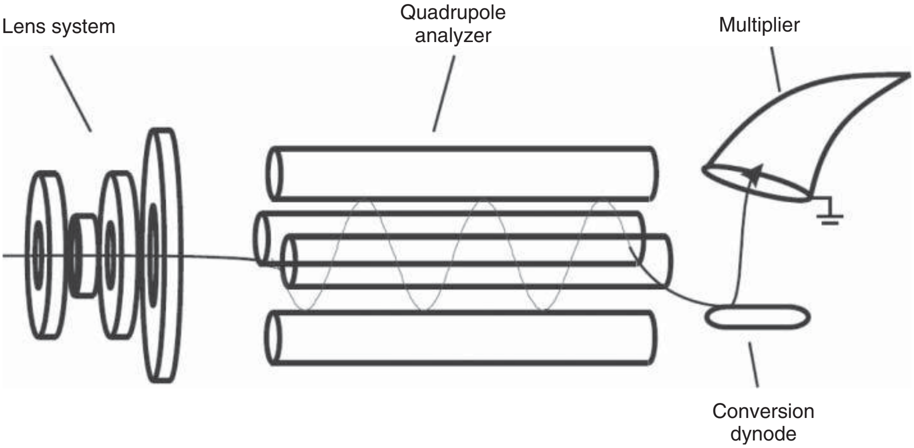

Figure 11.5 Scheme of a quadrupole mass analyser. Only ions with selected mass-to-charge ratio pass the combined DC and RF potentials on the quadrupole rods to reach the detector.

Quadrupole mass analyzers provide good reproducibility and represent a relatively small and low-cost system. Low-energy collision-induced dissociation collision-induced dissociation (CID) MS/MS experiments are feasible with triple quadrupole and hybrid mass spectrometers and have efficient conversion of precursors to products. These spectra strongly depend on energy, collision gas, pressure, and other factors. The use of quadrupole mass analyzers alone has limitations because of their comparatively low resolution. In addition, they are not well suited for pulsed ionization methods. Quadrupole mass analyzers are employed in the majority of benchtop GC/MS and LC/MS systems because of their low cost and stable operation. Moreover, they are gaining increasing importance as components in new hybrid-type mass spectrometers, as illustrated in Section 11.2.6.4.

11.2.2.3 **Time-of-Flight Mass Analyzers**

A TOF mass spectrometer measures the mass-dependent time it takes ions of different masses to move from the ion source to the detector. This requires that the start time (the time at which the ions leave the ion source) be well defined. Therefore, ions are formed by a pulsed ionization method (typically MALDI-MS), or various kinds of rapid electric field switching are used as a ‘‘gate’’ to release the ions from the ion source in a very short time.

The working equation for the TOF mass spectrometer is

$$\frac{m}{z} = \frac{2 \times V \times t^2}{L^2}$$

The ions leaving the ion source of a TOF mass spectrometer do not have exactly the same starting times or exactly the same kinetic energies. Various types of TOF mass spectrometers have been developed to compensate for these differences. A linear-field reflectron allows ions with greater kinetic energies to penetrate deeper into the reflectron than ions with smaller kinetic energies. The ions that penetrate deeper will take longer to return to the detector. If a packet of ions of a given mass-to-charge ratio contains ions with varying kinetic energies, then the reflectron will decrease the spread in the ion flight times, and therefore improve the resolution of the TOF mass spectrometer. A curved-field reflectron ensures that the ideal detector position for the TOF mass spectrometer does not vary with mass-to-charge ratio. This also results in improved resolution for TOF mass spectrometers.

TOF analyzers are the fastest MS analyzers making them especially suitable for application in high-performance LC/MS. They are well suited for pulsed ionization methods (method of choice for the majority of MALDI-MS systems). MS/MS information can be obtained from post-source decay. TOF analyzers also provide the highest practical mass range of all MS analyzers, but require pulsed ionization or ion beam switching. Furthermore, for most MS/MS experiments, ion selectivity is limited.

11.2.2.4 **Trapped-Ion Mass Analyzers**

There are two principal trapped-ion mass analyzers: three-dimensional quadrupole ion traps (“dynamic” traps) and ion cyclotron resonance mass spectrometers (“static” traps, see Section 11.2.3.1). Both operate by storing ions in the trap and manipulating the ions by using DC and RF electric fields in a series of carefully timed events. This provides several unique capabilities, such as extended MS/MS experiments, very high resolution, and high sensitivity. The trade-off is that trapping the ions for long periods (milliseconds to hours) provides sufficient time for the ions to degrade spontaneously (unimolecular decomposition), to experience unwanted interactions with other ions (space charge effects), neutral molecules (ion–molecule reactions), or perturbations in the ion motion due to imperfect electric fields [38]. This can lead to artifacts and unexpected changes in the mass spectrum (the so called “nonclassical mass spectra”).

In quadrupole ion traps, ions are dynamically stored in a three-dimensional quadrupole ion storage device (Figure 11.6) [39]. The RF and DC potentials can be scanned to eject successive mass-to-charge ratios from the trap into the detector (mass-selective ejection). Ions are formed within the ion trap or injected into an ion trap from an external source. The ions are dynamically trapped by the applied RF potentials (a common trap design also makes use of a “bath gas” to help contain the ions in the trap). The trapped ions can be manipulated by RF events to perform ion ejection, ion excitation, and mass-selective ejection. This provides MS/MS and MS^n experiments, which are eminently suited for structure determination of biopolymers [40] (Section 11.2.4).

Space-charge effects (ion–ion repulsion) limit the inherent dynamic range of the ion trap. This is usually handled by autoranging: a pre-scan is performed to determine the ion current and the ionizing electron current is then adjusted to reduce the number of ions formed to within the working range. This can be done wherever the ion formation event can be manipulated to control the number of ions formed.

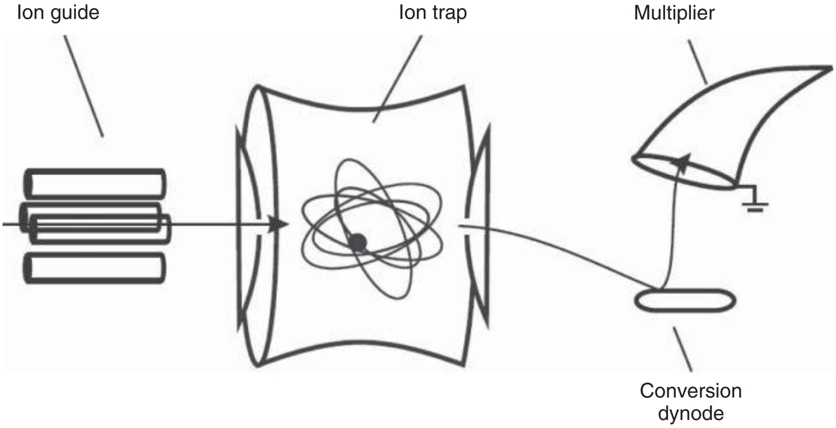

Figure 11.6 Scheme of an ion trap mass spectrometer. A defined ion beam is admitted into the trap through a focusing ion guide, e.g. a quadrupole.

11.2.2.5 Hybrid Analyzers

Hybrid TOF mass spectrometers make use of a TOF analyzer placed orthogonal to a beam of ions. Ions are deflected at right angles into the TOF analyzer by a pulsed electrical potential from an electrode placed alongside the beam.

By having a quadrupole analyzer as a gate in conjunction with an orthogonal TOF analyzer (Q-TOF analyzer) [41], a full mass spectrum may be obtained of all ions from an ion source if the ‘‘gate’’ is open. Alternatively, precursor ions can be selected for MS/MS so as to give the fragment ion spectrum characteristics of the precursor ions chosen, which gives structural information [42].

Combining an ion trap instrument with an orthogonal TOF instrument leads to a hybrid with high sensitivity in both MS and MS/MS modes and rapid switching between both modes [43]. The combination is particularly useful for biochemical analyses because of its high sensitivity and the ease of obtaining MS/MS structural information from small amounts of material. In either case, the TOF analyzer is used to obtain the mass spectrum. Furthermore, this hybrid provides high sensitivity and a linear mass scale to 10 000 at full sensitivity. The digitized accumulation of spectra provides a better signal-to-noise ratio than can be obtained from one spectrum alone.

11.2.3
High-Resolution Mass Spectrometers

11.2.3.1 Fourier Transform Ion Cyclotron Resonance Mass Spectrometry

Ions move in a circular path in a magnetic field. The cyclotron frequency of the ion’s circular motion is mass dependent. By measuring the cyclotron frequency, one can determine an ion’s mass [44].

The working equation for ion cyclotron resonance (ICR) can be quickly derived by equating the centripetal force and the Lorentz force experienced by an ion in a magnetic field:

$$\frac{m}{z} = \frac{B}{\omega_z}$$

A group of ions of the same mass-to-charge ratio will have the same cyclotron frequency f_c, but they will be moving independently and out of phase at roughly thermal energy ranges. If an excitation pulse is applied at the cyclotron frequency, the ''resonant'' ions will absorb energy and be brought into phase with the excitation pulse. As ions absorb energy, the size of their orbit also increases.

The packet of ions passes close to the receiver plates in the ICR cell and induces image currents that can be amplified and digitized. The signal induced in the receiver plates depends on the number of ions and their distance from the receiver plates.

If several different masses are present, one must apply an excitation pulse that contains components at all cyclotron frequencies. This is carried out by using a rapid frequency sweep (''chirp''), an ''impulse'' excitation, or a tailored waveform. The image currents induced in the receiver plates will contain frequency components from all mass-to-charge ratios. The various frequencies and their relative abundances can be extracted mathematically by using a Fourier transformation that converts a time-domain signal (the image currents) to a frequency-domain spectrum (the mass spectrum).

A cubic ICR cell consists of three pairs of parallel plates (Figure 11.7). The functions of the excitation and receiver plates are apparent from the preceding discussion. A small potential is applied to the trapping plates to keep the ions contained within the ICR cell because the magnetic field does not constrain the ion motion along the direction of the applied magnetic field. Besides the cubic cell, many other ICR cell designs have been evaluated and used in FTICR instruments, each having its own special characteristics. A new cylindrical FTICR cell with dynamic harmonization that provides ultrahigh resolution has been recently developed by Nikolaev *et al.* [45].

Excitation events can be used to increase the kinetic energy of ions or to eject ions of a given mass-to-charge ratio from the cell by increasing the orbital radius until ions are lost by collisions with the cell plates. The background pressure of an FTICR should be very low to minimize ion–molecule reactions and ion–neutral collisions that damp the coherent ion motion. A variety of external ion source designs have been developed to deal with this problem, and each design has its own performance characteristics [46].

Most FTICR mass spectrometers use superconducting magnets that provide a stable calibration over a long period. Although some mass accuracy can be obtained without internal calibrant, mass accuracy and resolution are inversely proportional to m/z, and the best accurate mass measurements require an internal calibrant. Unlike the quadrupole ion trap, the FTICR mass spectrometer is not operated as a scanning device.

The above working equation of FTICR shows that the m/z measurement is only dependant on the external magnetic field, and – in contrast to all other mass spectrometric analyzer systems – independent of the ion's kinetic energy [44]. This feature provides the basis for the intrinsic high-resolution capability of the FTICR method for the analysis of biopolymers.

FTICR-MS has recently enabled a breakthrough in the ultra-high-resolution mass spectrometric analysis of biopolymers using both ESI and MALDI ionization. A unique attribute of FTICR-MS in comparison to other MS methods is its ability to simultaneously provide high mass resolution ($>10^7$), mass determination accuracy (<0.1 ppm), and sensitivity. A schematic diagram of a commercial FTICR mass spectrometer (Bruker Apex II/III with ESI and MALDI ionization sources) is shown in Figure 11.7. Of particular interest is the versatility of FTICR-MS^n techniques for structure determination using fragmentation by CID or IR laser irradiation [infrared multiphoton dissociation (IRMPD)] [47], and the coupling with micro/nano-ESI. As an example of the ESI-FTICR performance, the spectrum of the protein ubiquitin (Figure 11.8) provides a mass determination accuracy of about 1 ppm at a mass resolution of about 80 000 [48]. The charge states of the multiply protonated ions are readily defined from the mass difference of two adjacent isotopes, without the necessity of deconvolution techniques. This is of importance, for example, for the ESI-MS analysis of noncovalent complexes where a low charge distribution may yield only few peaks that are difficult to deconvolute [6, 13].

11.2.3.2 **Orbitrap Mass Spectrometry**

Orbitrap-MS has been recently emerging as a second high-resolution, high-performance mass analyzer, and has been established with an astounding pace in the last few years [49, 50]. The key features of the orbitrap analyzer are accurate

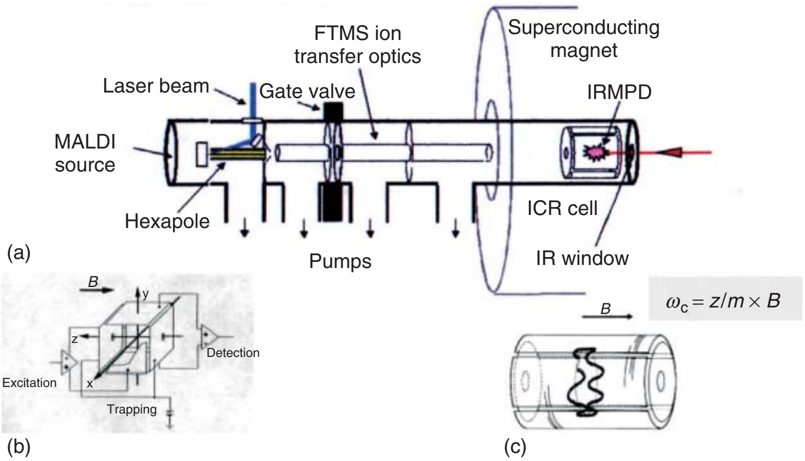

Figure 11.7 Scheme of the Bruker Apex-II/III FT-ICR mass spectrometer (a) with MALDI ionisation source and subsequent hexapole ion retardation, ion transfer optics/high vacuum system, and ICR cell with IRMPD system through a rear exit IR window. (b), (c) schematic illustration of cubic and cylindrical ICR cell configurations with excitation, trapping and detection plates.

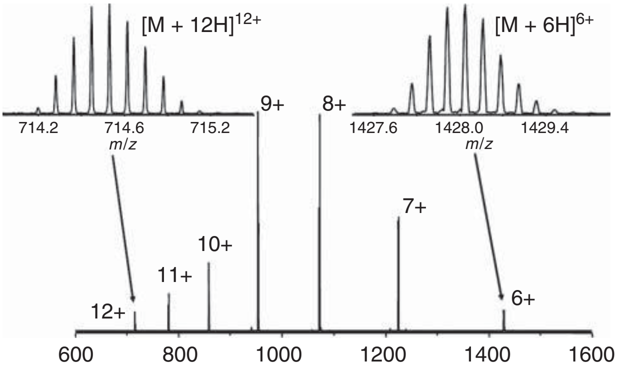

Figure 11.8 ESI-FT-ICR ESI-FTICR mass spectrum of bovine ubiquitin. A sample solution of c. 0.01 mg/ml in 3% aqueous acetic acid:methanol (4:1) was employed. The inserts show isotopic separations of the 6- and 12-fold protonated ions (monoisotopic molecular weight, determined: 8559,5912; calculated: 8559, 6162; Δm: 3 ppm).

mass determination and high resolution, similar to that achievable with FTICR instrumentation. The orbitrap can be applied to the identification, structural characterization, and quantification of a large variety of biomolecules and components in biological systems [50]. With its ability to deliver low-parts-per-million mass accuracy and extremely high resolution within a timescale compatible with nano-LC separations, the orbitrap has become a powerful instrument for many bioanalytical and proteomics applications.

The orbitrap mass analyzer consists of an inner (central) and an outer electrode that are suitable to trap ions in a quadrologarithmic electrostatic potential (Figure 11.9). Ions revolve about the central electrode and oscillate harmonically along its axis (the z-direction) with a frequency characteristic of their m/z values. Image current signal of these oscillations is converted to a frequency using Fourier transformation in a manner similar to that employed in FTICR. The orbitrap mass analyzer has demonstrated high resolving power, mass accuracy, and high space charge capacity with pulsed ion sources [51].

Although it may be possible to fragment ions in the orbitrap, it is more practical and faster to manipulate them in another mass analyzer to which the orbitrap can be linked as a detector. Recently, a linear ion trap was interfaced to the orbitrap to combine the tandem MS capability of the ion trap mass spectrometer with the high resolution and mass accuracy capability of the orbitrap. It was shown that a linear ion trap is an ideal partner for the orbitrap – it is exquisitely sensitive, fast, and capable of multiple levels of fragmentation. Ions accumulated in the linear ion trap can be transferred into an RF-only quadrupole called a *C-trap*, which accumulates and stores the ions. This additional storage improves the analytical capabilities of the instrument. The last part of the system is the orbitrap itself, which is filled by a pulse of ions accumulated in the C-trap. Therefore, this hybrid system contains two complete mass analyzers capable of detecting ions and recording spectra: the

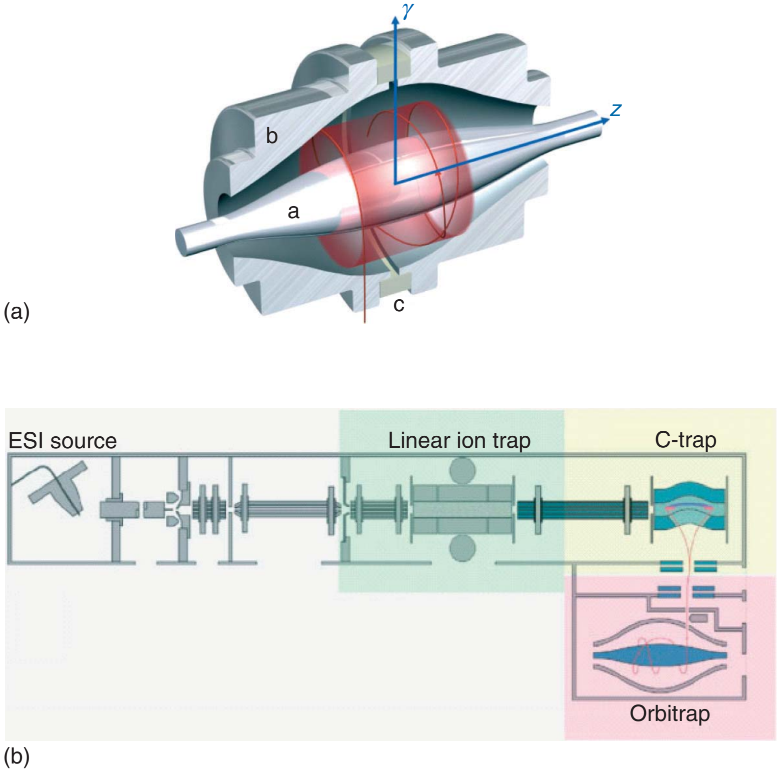

Figure 11.9 Schematic representation of the orbitrap mass analyzer (A) and of the LTQ Orbitrap (B). Ions are moving in spirals around a central electrode (a). An outer electrode (b) is split in half by an insulating ceramic ring (c). An image current induced by moving ions is detected via a differential amplifier between the two halves of the outer orbitrap electrode. The m/z if different ions in the orbitrap can be determined from respective frequencies of oscillation after a Fourier transformation.

linear ion trap and the orbitrap. Depending on the requirements for analysis, the two analyzers can be used independently or in concert [51].

11.2.4
Ion Detection and Spectra Acquisition

After the mass analyzer has dispersed the ions in space or in time according to their m/z values, they may be collected by a detector. In modern MS, a detector consists of a planar assembly of small electron multipliers, called an *array* in one case (spatial separation) and a *microchannel plate* in the other (temporal separation). Collectors can either detect the arrival of all ions sequentially at a point (point ion collector) or detect the arrival of all ions simultaneously (array or multipoint collector).

Quadrupole mass spectrometers (mass filters) allow ions at each m/z value to pass through the analyzer sequentially. Therefore, the ion collector at the end of the quadrupole unit needs only to cover one point or focus in space and thus can be placed immediately behind the analyzer. A complete mass spectrum is recorded over a period of time, which is set by the voltages on the quadrupole analyzer. The resolution of m/z values is entirely dependent on the analyzer and not on the detector.

A multipoint ion collector (also called *detector*) consists of a large number of miniature electron multiplier elements assembled side by side over a plane. A multipoint collector may be an array detecting a dispersed beam of ions simultaneously over a range of m/z values, and is frequently used with a sector type mass spectrometer. Alternatively, a microchannel plate collector detects all ions of one m/z value. When combined with a TOF analyzer, the microchannel plate affords an almost instantaneous mass spectrum. Because of their construction and operation, microchannel plate detectors are cheaper to fit and maintain.

Other types of mass spectrometer may use point or array detectors, or both types of ion detection. Ion trap mass spectrometers may detect ions sequentially or simultaneously and, in some cases, may not use a formal electron multiplier type of ion collector at all; the ions can be detected by their different electric field frequencies in flight, according to their m/z values.

11.2.5
Sample Preparation and Handling in Bioanalytical Applications

Most biological samples analyzed by GC/MS or LC/MS need sample preparation, depending on the matrix content and concentration of the analyte. In clinical chemistry and forensic toxicology, for example, body fluids such as blood/serum and urine have to be analyzed as well as tissue samples (organs, muscle), stomach contents, and hair [52]. In environmental toxicology, sewage sludge, sediments, wastewater, or plant material may contain only traces of the analytes of interest; thus, concentration and clean-up steps are necessary prior to analysis.

For the determination of drugs in plasma, extraction and concentration are also necessary in most cases. Matrix effects can influence the chromatographic separation in GC/MS or LC/MS and also the ionization process in ESI-MS [52, 53].

11.2.5.1 Liquid–Liquid Extraction (LLE)

Liquid–liquid extraction (LLE) of organic, nonpolar analytes for subsequent mass spectrometric analysis is still a common method in clinical, pharmaceutical, and environmental analysis, especially for the analysis of aqueous phases such as plasma and urine, but also for tissue samples. Major goals of methodology development in the past few years have been miniaturization, automation [54], and the removal of solvents with high toxicity (e.g., benzene and halogenated solvents). LLE is usually a robust method because only two natural constants are relevant for the extraction efficiency, the distribution constant between organic and aqueous phase, and the dissociation constant of the acidic or basic analyte; moreover, pH and temperature can be easily optimized and controlled. LLE can provide high selectivity for the analytes of interest. Considerable efforts in automation have been made for high-throughput pharmacokinetic analysis of human plasma samples, by using deep-well 96-well plates for extraction (e.g., in the determination of the anticancer drug methotrexate [55]), or an automated liquid handling system customized with integrated mechanical shaker and valve systems [54].

For systematic clinical toxicological analysis – also known as ''*general unknown screening*'' – Pfleger *et al.* [56] have developed extraction and derivatization methods for GC/MS analysis with subsequent electron impact mass spectral library searching. In this procedure, urine (plasma or gastric content) is extracted either directly or after acidic hydrolysis (for cleavage of phase II metabolites) with solvent mixtures containing ethyl acetate, diethylether, and dichloromethane. The hydrolyzed fraction is acetylated prior to GC/MS to convert amines and hydroxides into volatile derivatives. Other derivatization methods employed include alkylation with phase-transfer catalysis and silylation, for example, for the detection of carboxylic acids. In LLE procedures for drugs from plasma or urine, 1-chlorobutane has been used for subsequent GC/MS or high-performance liquid chromatography (HPLC) analysis [57, 58].

11.2.5.2 **Solid-Phase Extraction (SPE)**

In contrast to LLE, solid-phase extraction (SPE) is considerably more complex and is based on a sorbent with specific affinity for the analyte. Several sorbents have been developed, most being silica-based with different modifications (reversed phase, ion exchange, diol and amino phases) or polymer based (e.g., polystyrene–divinylbenzene copolymer). SPE methods for toxicological screening have been reviewed by Franke and De Zeeuw [59] with the conclusion that although silica-bonded phases (especially mixed-bonded phases with reversed-phase C8 or ion-exchange functions) were favorably used for screening analysis, no single extraction procedure provides optimum results for different sample types and detection techniques. Sample pretreatment is highly dependent on the sample type: For example, whole blood or tissue homogenate cannot be applied directly on SPE columns, whereas plasma or urine can be applied directly or after simple dilution.

Using SPE disks or small bead-volume cartridges for miniaturization of sample volumes, and robotics with 96-well plates, automation is facilitated for large numbers of plasma and urine samples – especially in combination with LC/MS/MS detection [60, 61]. Online sample concentration by trapping columns for automated LC/MS analysis will be discussed in Chapter 11.2.6.1.

11.2.5.3 **Immunoaffinity Extraction (IAE)**

Immunoaffinity extraction (IAE) is probably the most effective way for the extraction of trace amounts of analytes from biological samples, especially if coupled directly to LC/MS/MS. Henion *et al.* [62, 63] reported a method for automated IAE-LC/LC-MS/MS-analysis for detection of lysergic acid diethylamide (LSD) metabolites and β-agonists in urine and benzodiazepines from chemical libraries, whereas Maurer *et al.* [64] used IAE for the determination of amanitines in urine. Approximately

20-fold higher sensitivity was obtained in these studies by IAE compared to a standard SPE method. However, a disadvantage of IAE is the narrow linear range because antibodies may be easily overloaded.

11.2.5.4 Solid-Phase Microextraction

Solid-phase microextraction (SPME) is currently under investigation in many laboratories for its usefulness for a large variety of bioanalytical applications. SPME involves extraction and preconcentration with a fused silica fiber or tubing coated with a polymeric stationary phase. SPME can be performed in two-phase (sample–fiber coating) and three-phase (sample–headspace–fiber coating) systems [65].

Desorption for GC analysis is performed directly in the GC injector by elevated temperature. For HPLC analysis, an interface has been constructed for solvent extraction of the analyte from the fiber, followed by introduction of the solvent into the LC injector [66, 67]. Besides applications to volatiles from solid samples, liquids, and gaseous samples, polar and less volatile compounds are increasingly under study as analytical targets, and difficulties with small partition coefficients and long equilibration times have been identified. Headspace methods minimize interactions between sample and fiber and have proved useful for semivolatile analytes such as amphetamines from urine, and free volatile fatty acids in wastewater [68]. Several experimental concepts have been pursued for optimization of the method, including matrix modification by heating, addition of salt, and pH buffering.

Automated ‘‘in-tube’’ SPME has recently been coupled with LC/ESI-MS, for example, for the determination of drugs in urine [69]. In-tube SPME is an extraction technique in which analytes are extracted from the sample directly into an open tubular capillary by repeated draw/eject cycles of sample solution. The analyte is then desorbed with methanol and transferred to an analytical HPLC column.

The SPME device has been also employed as a time-weighted average (TWA) sampler for gas phase analytes [70]. This was performed by retracting the coated fiber for a known distance into its needle housing during the sampling period. Unlike in conventional spot sampling with SPME, the TWA sampling approach does not allow the analytes to reach equilibrium with the fiber coating, but rather they diffuse through the opening in the needle to the location of the sorbent. The amount of analytes accumulated over time gives the average concentration to which the device was exposed. Depending on the sorbent used, TWA sampling is possible for durations from 15 min to 12 h.

11.2.5.5 Supercritical Fluid Extraction (SFE)

Supercritical fluid extraction (SFE) has been automated for serial extraction of samples. Fields of application of SFE with supercritical carbon dioxide and additional modifiers have been environmental (sewage sludge [71]) and forensic toxicology (drugs [72, 73]), as well as food and plant analysis [74]. Online coupling to different analytical methods (IR, NMR, fluorescence detection, MS) has recently been reviewed [75], but most bioanalytical applications are based on the off-line extraction with subsequent analysis by GC/MS or LC/MS.

11.2.6
Combination of Mass Spectrometry with Microseparation Methods and New Mass Spectrometric Hybrid Systems

A detailed review on interfacing microseparation methods with MS has been published by Tomer [76], which covers the development of interfaces for micro- and nano-LC, capillary electrophoresis (CE), capillary electrochromatography (CEC), micellar electrokinetic chromatography (MEKC), and capillary isotachophoresis (ITP) MS. Furthermore, multidimensional chromatography-MS, microfabricated microfluidic devices (microchip)/MS, LC/MALDI-MS, affinity chromatography/MS, and supercritical fluid chromatography/MS have been discussed in this chapter. Although GC-MS is often considered a mature field, new developments in GC-MS have been covered including fast GC-MS using TOF-MS and supersonic molecular beam GC-MS. In the following, overviews are given about new developments in the combination of (i) electrophoresis with MS and (ii) the miniaturization of LC-MS, since both combinations are key tools in proteomics and have become routine techniques in many bioanalytical laboratories, as well as for the structural identification of biopolymers. In addition, perspectives for bioanalytical applications are briefly discussed for two new hybrid MS, online bioaffinity/biosensor-MS [77] and IM-MS [20–22], both of which are presently emerging with promising future application potential as microseparation-MS tools from complex biological mixtures.

11.2.6.1 *Liquid Chromatography-Mass Spectrometry Coupling (LC-MS)*

GC/MS with capillary columns has been the gold standard for more than 20 years, but LC/MS has become a complementary method because of the remarkable success in interface development with atmospheric pressure ionization (API) for low-molecular-weight compounds, as well as the application to biopolymers. For many areas of analytical chemistry and biochemistry, LC/MS has become indispensible because of its advantages over GC/MS for polar and thermolabile analytes. A limiting factor for LC/MS has been the incompatibility between the liquid eluting from the LC and the mass spectrometer vacuum. However, this has been overcome in ESI with the use of a nebulizer gas (“ion spray”) or additional heated drying gas (“turbo ion spray”) [78, 79]. Because of its high sensitivity and selectivity, API-MS has become a standard tool for the structure elucidation of analytes from many complex mixtures.

Standard electrospray is limited to flow rates below 10 µl min^{-1}, while nebulizer-assisted ESI can handle up to 100 µl (ion spray); turbo ion spray, orthogonal, or Z-spray (from different instrument manufacturers) can handle flow rates up to 2 ml min^{-1} without split. APCI is normally used with flow rates of 0.2–1 ml min^{-1} and can be used with normal- and narrow-bore columns without splitting the eluent, while ESI can also be used with microseparation methods. Microseparation methods such as nanocapillary-HPLC, CE, and CEC have the advantage that higher separation efficiencies are achieved, yielding narrow analytes peaks and high peak concentrations. Drawbacks of the microseparation approaches are that only low sample amounts are applicable [80] and only a short path length can be used for detection. The advantage of low flow rates is that the complete effluent can be transferred to the mass spectrometer thus yielding high detection sensitivity. Several ESI parameters such as the diameter of the spray tip and position relative to the sampling orifice can be optimized to improve ionization efficiency and ion sampling. As noted in Section 11.2.1.3, the use of microsprays systems enhances sampling efficiency. Another way to increase the number of ions fed to the mass spectrometer is the use of larger entrance skimmers or capillaries; however, this requires a higher gas flow entering the mass spectrometer. The relationship between flow rate and sensitivity has been investigated by Hopfgartner *et al.* [81] and Oosterkamp *et al.* [82], showing that optimum flow rates for conventional ESI range from 1 to 10 $\mu l\,min^{-1}$, while rates for ion sprays range from 50 to 1000 $\mu l\,min^{-1}$ using a heated drying gas. Micro-LC/ESI-MS can be performed with conventional ESI sources with ESI emitters of small internal diameter [83], whereas for nano-LC (flow rates $<2\,\mu l\,min^{-1}$), micro-ESI interfaces with custom-made ESI emitters have been used [84]. Low diameter ESI emitters have been produced by different techniques, for example, by electropolishing of metal needles, treatment of silica capillaries with HF, or drawing with a laser puller with subsequent surface coating (gold sputtering) [85]. However, most promising is the coupling of nanoscale capillary-LC with nanospray-MS using a coaxial sheath flow interface. Flow rates below 200 $nl\,min^{-1}$ [33] can be achieved, yielding high sensitivity, for example, for peptide mixture analysis. With the downscaling of LC-separation and ESI interfaces, detection limits down to the low femtomole range have been obtained; however, online separations with flow rates $>100\,nl\,min^{-1}$ are still less sensitive compared to continuous sample flow from nanoelectrospray tips [86, 87], which have typical flow rates of 1–20 $nl\,min^{-1}$. Furthermore, online preconcentration by column-switching prior to micro- or nano-LC/MS has been shown to improve detection limits [88] and can be used to overcome limited sample volumes. During the last few years, ESI emitters for nano-flow LC or CE separations have become commercially available. A major drawback of nano-LC/MS is still its lack of robustness due to capillary plugging; however, miniaturized LC/MS systems will likely be further optimized in the near future.

11.2.6.2 **Combination of Mass Spectrometry with Electrophoresis**

The combination of desorption–ionization methods of MS (ESI-; MALDI-MS) with gel electrophoresis has developed in the last few years to one of the most successful microseparation-MS combinations, and has been widely employed in the analysis of biopolymers from biological samples, particularly in proteomics [89, 90]. For microseparation using both polyacrylamide sodium dodecyl sulfate gel electrophoresis sodium dodecyl sulfate- polyacrylamide gel electrophoresis (SDS-PAGE) under denaturation conditions, or native electrophoresis, a variety of detection and visualization techniques for protein bands or spots from one- and two-dimensional electrophoretic separations have been employed in mass spectrometric proteomics (Section 11.3.5). Well-established staining procedures for visualization of proteins have used dyes such as Coomassie Brilliant Blue, silver salts, and fluorescent dyes (Flamingo, Sypro® Ruby) [91]. Although several of these approaches provide high detection sensitivities for proteins, major problems are frequently encountered with the compatibility of staining procedures with mass spectrometric analysis because of the high background arising from polar staining materials and the need for applying destaining procedures for isolated proteins [91].

Recently, alternative procedures are being explored to overcome these problems, using unstained gels in electrophoretic separations [92–95]. In fluorescence labeling studies of glycoproteins, Zhao *et al*. observed a fluorescent signal for non-glycosylated proteins such as hen lysozyme, which was attributed to intrinsic (native) protein fluorescence [92]. Fluorescence detection of proteins has been evaluated with pre- or post-electrophoretic incorporation of halogenated compounds such as trichloromethane, trichloroethanol, and trichloroacetic acid, which react with tryptophane residues upon UV light exposure, yielding products with emission in the visible light range, suitable for visualization of protein bands [93]. A direct UV fluorescence detection method for unstained proteins, first reported by Roegener *et al*. [93] showed the visualization of proteins in both 1D- and 2D-gel separations with low detection limits (1–5 ng).

A commercial gel bioanalyzer based on native fluorescence has been recently developed (LaVision-BioTec; Bielefeld, Germany) [94], and applied in a recent study for the development of native fluorescence detection in one- and two-dimensional gel electrophoretic separations in mass spectrometric proteome analysis. The sensitivity of the stain-free native fluorescence detection with the gel–bioanalyzer was evaluated in comparison with standard staining procedures by Coomassie and silver visualization, showing comparable sensitivities for the fluorescence detection and silver staining (detection limits 1–5 ng), while Coomassie-stained gel bands were not detectable at this concentration range [94]. Moreover, it was shown that in stain-free visualization, no fixation step is needed following gel electrophoretic separation, and protein spots can be directly analyzed after scanning, providing proteomics data with high sensitivity and nearly complete lack of background, for example, in bacterial proteomics [94, 95]. These results, providing unequivocal protein identifications at low detection limits, indicate broad applicability of the stain-free gel separation and visualization approach as an efficient and sensitive tool in mass spectrometric proteomics, as illustrated in a study of bacterial proteins from *Desulfotignum phosphitoxidans* by the identification of a new NAD(P)-dependent epimerase/dehydratase, and its different phosphorylated forms (Figure 11.10) [95].

11.2.6.2.1 **Capillary Electrophoresis (CE)-Mass Spectrometry** In contrast to HPLC, flow rates of capillary zone electrophoresis (CE) are in the low nanoliter-per-minute range. Migration of analytes between the buffer reservoirs at both ends of a fused-silica capillary is effected by electromigration and electroosmosis [96]. Electrophoretic migration occurs with positively charged species from the anode (high positive potential) to the cathode (low or ground potential) or vice versa. Electroosmotic flow (EOF) occurs with an electrical potential applied across a liquid-filled porous medium; it acts to sweep all solutes through the capillary and does not promote separation. Surface deactivation can lead to suppression of the EOF so that the flow of solvent from the capillary is minimized.

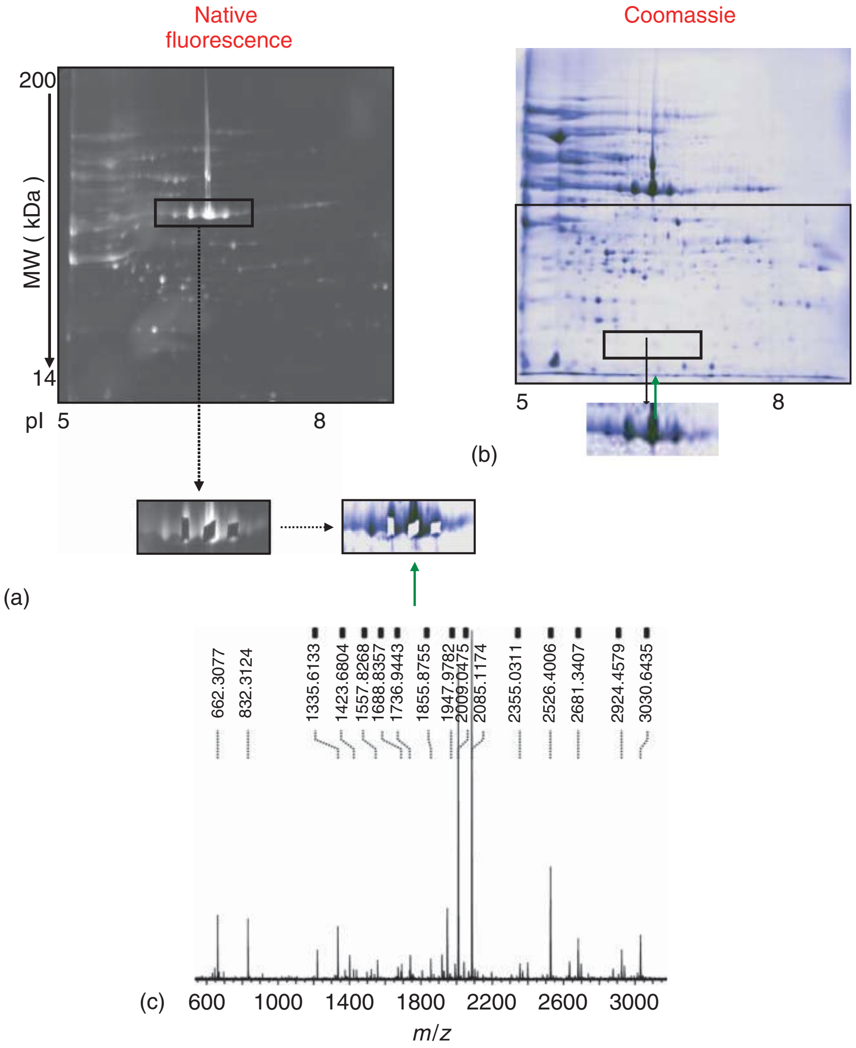

Figure 11.10 Detection and localisation of protein spots in 2D-gels by native fluorescence using precise spot localization and picking tools. Separation gels were prepared with protein extracts from Desulfotignum phosphitoxidans (grown with phosphite/fumarate/sulfate; approximately 0.4 mg total protein were applied onto 17 cm IPG strips 5–8). Spot picking tools were used to cut spots from unstained gels. (a), Unstained gel with native fluorescence detection. (b), 2D gel stained with Coomassie, prepared in identical manner with the Bio-Analyzer gel. (c), MALDI-TOF mass spectrometric identification of NAD(P)-dependent epimerase/dehydratase from Desulfotignum phosphitoxidans. Spot 3 was excised from the native fluorescence gel, digested with trypsin and analysed by MS. Masses of peptide ions for protein spot 3 were compared with the calculated masses for fragment ions of the open reading frame obtained from genomic DNA amplification.

For CE-MS coupling, different sheath-flow interfaces have been designed [97–99] in addition to a liquid-junction interface (using a liquid reservoir for electrical contact without a make-up flow of liquid). Furthermore, off-line coupling devices have been developed for the coupling of MALDI to CE, basically by means of sheath-flow interfaces for sample collection and subsequent target preparation [100, 101]. To overcome the low amounts of analyte in CE, capillary transient isotachophoresis (tITP) has been used for analyte concentration [102, 103]. The high separation efficiency of CE makes it attractive for the analysis of complex mixtures after sample clean-up and concentration; a main drawback still is the limited amount of sample load onto the CE capillary.

In CEC, a liquid flow through a packed capillary is created by application of an electric field. Several interfaces have been designed for coupling to ESI-MS, and current applications have been reviewed [104, 105]. CEC is a good alternative for neutral analytes in combination with mass spectrometric detection, since no interferences with micellular matrix can occur [106]. The combination with LC, resulting in an electrically and pneumatically driven flow of solvent, has been called *pressurized CEC*. This combination offers new opportunities for the separation of complex mixtures.

11.2.6.3 **Online Bioaffinity–Mass Spectrometry**

Although a number of affinity techniques have become established approaches over the last decades for the analysis of biomolecular interactions, their combination with MS is only recently developing as a new hybrid methodology for structure identification and quantification of bioaffinity ligands and in the molecular characterization of biopolymer interactions [77]. Methods widely used for characterization of protein–ligand interactions include immunoaffinity analysis such as ELISA and Western blot, isothermal titration calorimetry (ITC), and biosensor technologies, such as surface plasmon resonance (SPR), surface-acoustic wave (SAW), and quartz-crystal microbalance (QCM) [77]. For example, SPR has already developed into a highly efficient, standard tool for the analysis of biomolecular recognition processes at a biosensor surface, and has been successfully applied as a quantitative probe to a variety of biopolymer interactions, such as protein–peptide, protein–nucleotide, and –antibody complexes [6, 7, 13, 77]. However, while providing sensitive and accurate determinations of binding/dissociation constants (K_i or K_D), a major limitation of all bioaffinity methods is the lack of chemical structure information of affinity-bound ligands. In contrast, the direct, online combination of biosensor detection and MS provides access to both structural identification and quantification of bioaffinity interactions and the involved biomolecular ligands.

One of the newest methods of affinity-MS is the recently developed online coupling of biosensor to ESI-MS, which allows simultaneous detection and quantification of affinity interactions and chemical structure identification of the ligand [77]. The SAW technology, which employs a piezoelectric detection of mass differences according to the ‘‘love-wave’’ principle [107], was first employed for online bioaffinity-MS; however, most recently alternative biosensors such as the QCM have also been successfully employed. The use of ESI to this combination provides two important advantages; (i) the possibility to implement the online analysis within a continuous microfluidic system that provides direct structural characterization of the ligand molecules involved in the affinity interaction and (ii) the generation of multiply charged ions whose m/z values are easy to determine. In order to effectively obtain the coupling of biosensor and MS, several preconditions must be met, particularly to remove or reduce the high salt content from the biosensor sample, and to adjust the different flow rates used for the biosensor and into the ESI-MS ion source. Both preconditions have been effectively solved by the development of a biosensor–MS interface [77] consisting of two electrical multiport valves that connect the biosensor and the mass spectrometer (Figure 11.11). The interface is capable of (i) transferring the sample from the biosensor outlet to the ESI ion source; (ii) desalting the sample by trapping the ligand on a guard column, and removing the salts for subsequent transfer of the ligand into the ESI source; and (iii) providing a flow rate equilibration, typically between 15 and 40 μl min^{-1} (optimal flow rate of the ESI ion source). A suitable software has also been developed (Biosensor2MS; [77]) for the automation of the transfer procedure.

First bioanalytical applications of the online bioaffinity–MS combination include the identification of calmodulin–polypeptide complexes, and the structural characterization and differentiation of β-amyloid (Aβ) peptide epitopes upon binding to Aβ-specific antibodies, and the identification of bioaffinity-specific posttranslational protein modifications [77, 108, 109]. An example of the latter application

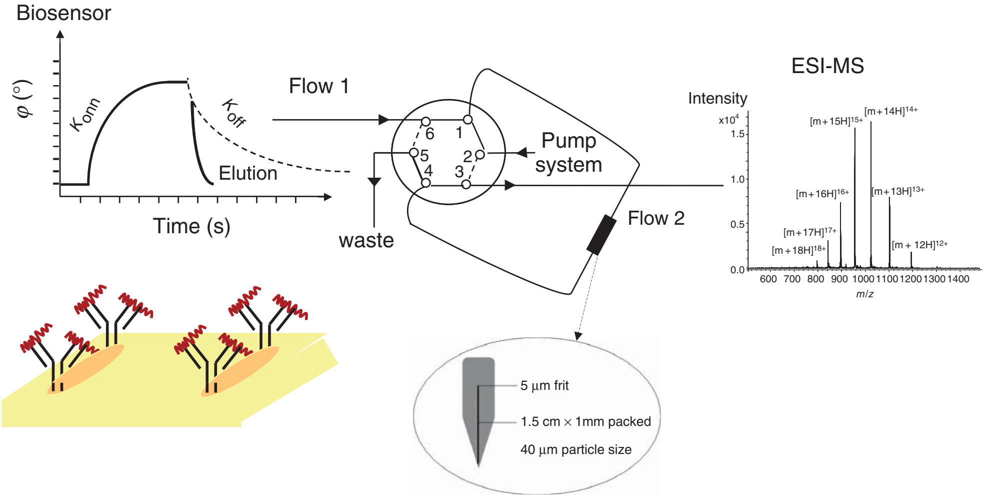

Figure 11.11 Schematic of the on-line SAW-ESI-MS combination using an SSens/K5-SAW biosensor and a six-port-valve micro-column interface. (a) The biosensor exit capillary is connected to the interface in position 6, with the ESI-MS inlet capillary in position 3. Dissociation of the ligand from the SAM-Chip is performed by eluting with acidic glycine buffer or hydrochloric acid into the micro-column interface (flow 1). (b), Removal of buffer salt solution and transfer of the eluate into the ESI source by switching the interface valve to position inject, and elution with aqueous acetonitrile/HCOOH as described in the Experimental section (flow 2).

is the direct identification of a tyrosine nitration in physiological proteins in eosinophils by the bioaffinity-isolated 3-nitrotyrosine-modified peptide bound to a nitrotyrosine-specific antibody [110]. In all cases, accurate determinations of dissociation constants of the protein– and antibody–peptide complexes in the micro- to nanomolar concentration range were obtained from the biosensor signal. These initial results indicate broad bioanalytical application potential of the online biosensor–MS combination for the simultaneous label-free structure determination and quantification of biopolymer–ligand interactions, as diverse as antigen–antibody and lectin–carbohydrate complexes.

11.2.6.4 **Ion Mobility Mass Spectrometry**

Among the range of hybrid systems of MS suitable for combining microseparation and molecular characterization by MS, IM-MS has recently emerged as the most successful new MS system [21]. Ion mobility spectrometry (IMS) was introduced in the 1970s as a portable, economical alternative to MS for the detection of airborne volatiles, for example, environmental and industrial process contaminants, explosives, chemical warfare agents, and drugs [20, 21, 111]. Over the past decade, two major technical developments decisively broadened the analytical range of IMS: (i) the effective coupling of IMS to MS, especially the advent of IMS-TOF instrumentation that enables a parallel dispersion of ion mixtures in mobility and mass/charge (m/z) dimensions [23] and (ii) interfacing of ESI and MALDI ionization sources to IMS and IMS/MS [112], which enabled access to many bioanalytical applications.

IMS and MS share a similar theoretical background, the historical development of which was presented by Uetrecht *et al.* [22]. Mass spectrometric methods are limited to the separation of ions measured by mass-to-charge (m/z) ratios and ion intensities, while IM separates ions based on their mobility and measures the time it takes an ion to migrate through a buffer gas in the presence of a low electric field (drift time) (Figure 11.12). The ion velocity, v (drift velocity) is directly proportional to E with the proportionality constant K called *ion mobility* and is determined by measuring the time (t_D) required to traverse a drift cell of known dimensions, d:

$$v = KE = \frac{d}{t_D}$$

The development of ‘‘soft-ionization’’ methods of MS in the last years, such as ESI-MS, has enabled substantial progress in the characterization of chemical structures and their modifications, for example, in proteome analysis; however, applications of HPLC-MS methods are unsuitable to direct ‘‘in situ’’ analysis of conformational states and reaction intermediates in protein assemblies. Most recently, IM-MS is emerging as a new tool to probe protein complex structures from solution phase structures, owing to the potential of IM-MS for the separation of mixtures of protein complexes by conformation state and spatial shape and topology. A first commercial quadrupole-TOF IM-MS instrument has been developed, which is suitable for the analysis of large biopolymers (Waters-Synapt IM-Q-TOF-MS). In this IM-MS system, ions produced by ESI and preselected by a quadrupole are

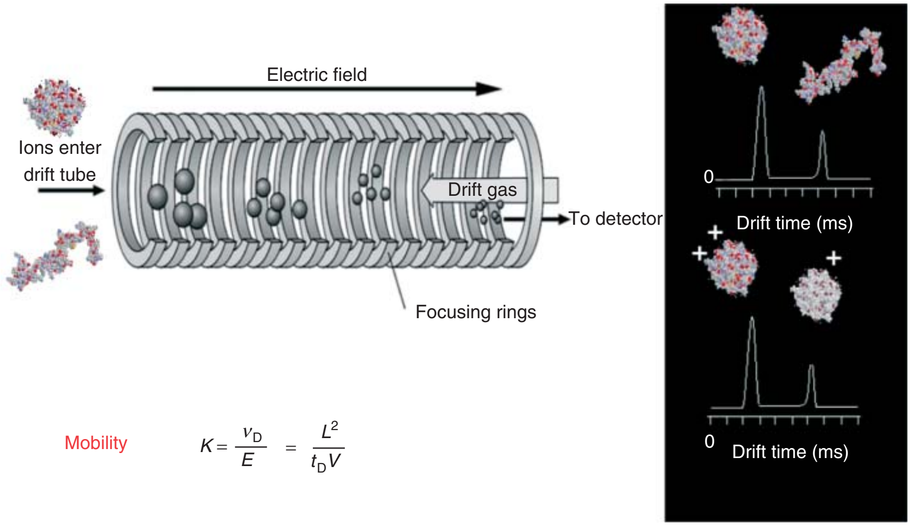

Figure 11.12 Principle of ion mobility-MS. Ion mobility separates ions based on their mobility and the drift time to migrate through a buffer gas in the presence of a low electric field. The ion velocity is proportional to E and is determined by measuring the time required to traverse a drift cell of known dimensions. IMS-MS separates species according to their collisional cross section (CCS) which represents the orientationally averaged area of the ion capable to interact with a buffer gas. For macromolecular ions Ω is approximated computationally. IMS-MS enables the differentiation of protein conformational states, protein folding and unfolding, as schematically shown.

separated according to their conformation/topography-dependent cross sections upon passing an electric drift field, and MS-MS-generated product ions are identified by a TOF-MS. First successful applications include the characterization of large protein complexes, structural differentiation of isomers, and conformational studies [113–115], clearly indicating the broad application potential of IM-MS. Applications of IM-MS to the structure identification of reaction intermediates in the oligomerization–aggregation of target proteins of neurodegenerative diseases are described in Section 11.3.7.

11.3
Applications of Mass Spectrometry to Biopolymer Analysis

11.3.1
Introduction

As pointed out in the introductory chapter (cf. 11.1.1), the development of "soft"-ionization MS has caused a revolution both in the range of bioanalytical application areas and, particularly, in the possibilities for molecular structure–function analysis of biopolymers. The two currently dominant techniques, ESI-MS and MALDI-MS have driven the refinement and perfection of several high-resolution separation techniques, particularly 2D-gel electrophoresis and HPLC, for mass spectrometric applications. Combinations of these MS approaches with suitable protein-chemical and biochemical procedures have become feasible for molecular studies of even complex mixtures and heterogeneous forms of biopolymers [6, 13]. Thus, mass spectrometric approaches are now suitable for the identification of low levels of specific sequence mutations, posttranslational modifications, and other subtle covalent structural changes, frequently hitherto undetectable [5–7]. Moreover, MS approaches have been recently developed for new applications with great demand, owing to a lack of conventional molecular-biochemical techniques, for example, in the characterization of tertiary structures and conformational states, specific *non-covalent* biopolymer complexes, and *molecular recognition* structures (epitopes) [31].

In the following paragraphs, illustrations of *some* of these applications are presented, including an outline of mass spectrometric *proteome* analysis as an area that has recently been exerting a dramatic impact on biotechnology and biomedical research. Furthermore, the particular role of high-resolution MS as a molecular tool in biopolymer analysis will be illustrated. Within these bioanalytical applications, studies employing a combination of specific protein-chemical modification reactions and mass spectrometric peptide mapping have been included [15, 16] to illustrate the wide variety of useful structural information amenable to biopolymer MS, such as on surface topology and tertiary structure microenvironment.

11.3.2
Analysis of Peptide and Protein Primary Structures and Posttranslational Structure Modifications

Mass spectrometric methods have been effectively developed in the last years for the sequence determination (partial or complete) of polypeptides and even *de-novo* sequencing of proteins [7, 116, 117]. The two general strategies for peptide sequencing, (i) mass spectrometric fragmentation of a peptide backbone using tandem-MS methodologies and (ii) specific enzymatic or chemical cleavage and subsequent mass spectrometric analysis of truncated peptide mixtures, are complementary to each other. Different types of MS/MS instrumentation with triple quadrupole and tandem magnetic sector spectrometers have been successfully employed and have been summarized in reviews [117, 118]. Fragmentations at the peptide backbone produce major types of sequence-specific ions from both the N- and C-terminal ends (e.g., ‘‘b’’- and ‘‘y’’-ions, Figure 11.13), which have been termed according to a nomenclature first proposed by Roepstorff and Fohlman [119]. Such fragmentations can occur as a result of the ionization method directly, such as capillary-skimmer voltage-induced dissociation of molecular ions in ESI-MS (ΔCS), or by collision-induced decomposition (CID) with a neutral gas; they are, in principle, suitable both for sequence determinations and the identification of posttranslational modifications.

Sequence determinations have been performed by FAB-MS/MS fragmentations of $[M + H]^+$ ions both with magnetic sector and triple-quadrupole instruments.

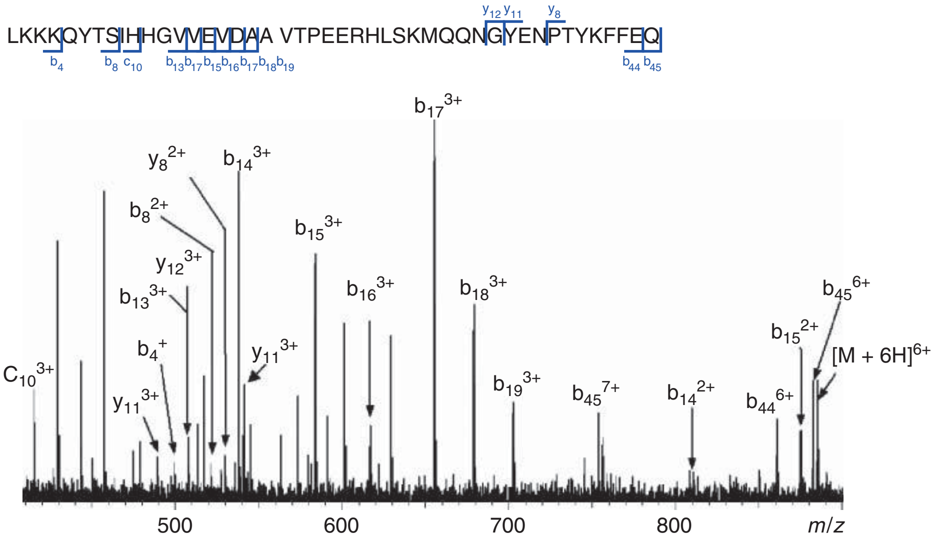

Figure 11.13 ESI-FTICR spectrum showing capillary-skimmer fragmentation of the cytosolic polypeptide domain of Alzheimer-amyloid-precursor protein, APP(723–767). Sequence-specific b- and y-ions are indicated with sequence positions and charge states in the spectrum, and partially in the sequence. Capillary exit voltage, 130 V; sample concentration ca. 0.01 µg/µl.

A major disadvantage of the tandem magnetic sector is the relatively large and expensive instrumentation, while triple-quadrupole MS/MS as smaller, low-resolution instruments have been shown to be effective for rapid sequencing of peptides [7, 32, 117]. ESI has been also used effectively for peptide sequencing, both with triple-quadrupole MS/MS and ion trap systems [116, 119]. More recently, FTICR- and orbitrap-MS have been shown to provide substantial advances by the high mass determination accuracy and high sensitivity over a wide mass range; the possibility of simultaneous excitation and detection of *in-source* fragment ions of all mass-to-charge ratios and of collision-induced dissociation (CID) in the ICR ion cell enables the acquisition of detailed primary structure data [44, 47, 48, 120–122]. This is illustrated in Figure 11.13 by the capillary-skimmer fragmentation in the ESI-FTICR spectrum of a cytoplasmic polypeptide of Alzheimer-amyloid precursor protein, APP(723–767). It has been shown that the cleavage of APP to amyloidogenic products involves a complex pathway that is mediated by intracellular targeting sequences located in the cytoplasmic tail; hence, knowledge of the cytoplasmic APP structure is important for understanding the amyloid formation at the molecular level [123, 124]. The accuracy of fragment ion mass determinations (Figure 11.13) yields detailed structural information by b- and y-sequence ions [125]. In addition, fragmentation by ESI-FTICR using collision-induced dissociation [sustained off-resonance irradiation collision-induced dissociation (SORI-CID)] in the ICR cell provides fragment ions covering the complete sequence.

A second general approach consists of the successive chemical and/or enzymatic exopeptidolytic cleavage, in combination with mass spectrometric analysis of the truncated peptide mixture [7]. This approach has been quite successful in obtaining *partial* sequence determinations with a variety of carboxypeptidases and aminopeptidases of broad specificity (such as carboxypeptidase Y) by using ESI-MS and MALDI-MS, and is suitable for identifying modified amino acids in peptides [126–128]. The limitations of this approach are that (i) isobaric residues cannot be determined (Leu/Ile), (ii) Gln/Lys require high-resolution MS with isotopic mass accuracy [129], and (iii) it is difficult to produce a homogeneous truncated peptide series. For the last reason, techniques employing N-terminal Edman degradation and mass spectrometric analysis of the stepwise shortened peptide have been successfully employed [130, 131]; for example, the addition of a small amount of reaction-terminating phenyl isocyanate in Edman degradation to produce a homogeneous truncation series (''ladder sequencing'') has been successful in determining shorter peptide sequences [132].

Mass spectrometric sequencing and specific fragmentation methods have been developed with considerable success (in some cases as key techniques) for the identification of covalent posttranslational modifications in proteins, such as glycosylation, acylation, intramolecular disulfide linkages, and phosphorylations [133–138]. Using suitable chemical procedures for (i) selective cleavage of the modification group from the peptide backbone and (ii) partial sequencing, in conjunction with MS, the modification position within the polypeptide chain can be often identified even in cases where a complete structure determination is not feasible [137, 138]. Such approaches include the mass spectrometric analysis of the intact protein before and after removal of a modification group, and/or Edman degradation and MS analysis of the modified sequence. While these methods have been successful in the identification of single-site modifications such as alkylated or fatty acylated residues [139, 140], more complex modification structures such as glycosylations [141–143] require a specific setup of chemical reactions in combination with MS. For the analysis of glycosylations, the identification of carbohydrate attachment sites (N- and O-linked) is a tedious task, aided by the consensus Asn-tripeptide motif for possible N- (but not O-) glycosylation. However, the considerable heterogeneity and structural complexity (e.g., branched, multiantennary) of glycosylations make it frequently necessary to use separate analytical strategies for the carbohydrate analysis. Mass spectrometric determination of carbohydrate structures in glycosylated proteins have been summarized in reviews [144].

The characterization of phosphorylated protein structures is discussed in the following to illustrate the use of specific mass spectrometric strategies for posttranslational modifications. Phosphorylation is a key modification not only for replication control but also for regulation of gene expression and protein synthesis controlling cell growth, division, and differentiation; hence, the identification of the specific phosphorylation site is essential in order to understand the molecular basis of these regulatory mechanisms. Owing to the low level and complexity (multiplicity) of many phosphorylations, the use of immobilized metal ion affinity (IMAC) enrichment of phosphopeptides from proteolytic mixtures has been shown to be essential for their identification by MALDI-MS and ESI-MS [145, 146]. The adsorption in IMAC is based on a reversible complex between the phosphate and Ga-III under acidic conditions, which dissociates at slightly alkaline pH. Enzymatic cleavage by alkaline phosphatase, in combination with Ga-III-IMAC and MALDI-MS, provides the identification of phosphopeptides based on 80 amu mass shifts, and by analysis of metastable fragmentations (loss of HPO_3 and H_3PO_4) [147].

The selectivity of Ga-III-IMAC for phosphopeptides, combined with the specificity of mass determination by MALDI-MS, often enables the identification of phosphopeptide candidates by comparing the predicted proteolytic peptide masses with experimental mass values. However, the high mass determination accuracy of FTICR-MS or orbitrap-MS may enable the *direct* (without enrichment) characterization of phosphorylation structures, as shown in a study of the multi-phosphorylated Tau protein [48, 148]. Tau is a microtubule-associated protein involved in promoting microtubule assembly that has recently gained widespread interest as a target protein for neurofibrillary tangle formation in Alzheimer's disease [149]; the pathophysiological aggregation of tau in brain tissue has been shown to be associated to hyperphosphorylation. In the ESI-FTICR spectrum of a tryptic peptide mixture of human neurofibrillary tau, the complete primary structure including a total of 18 serine and threonine phosphorylations could be identified, illustrating the high efficiency of high-resolution MS; for the tryptic peptides 7 and 5, phosphorylation sites could be directly identified as multiphosphorylation domains (512–538) and (382–398), respectively (Figure 11.14).

11.3.3
Tertiary Structure Characterization by Chemical Modification and Mass Spectrometry

Chemical modification reactions have long been employed in structure–function studies of proteins, for example, for modifying enzymatic properties and immunological reactivity [15, 150]. Although a number of specific reactions for amino acid residues have been evaluated ([13, 15] for reviews), their full development has long been impeded by the lack of specific methods for characterizing multiple reaction products [150]. In contrast to conventional methods based on electrophoretic or chromatographic procedures, mass spectrometric peptide mapping of proteolytic digest mixtures has been found highly suitable for the rapid and sensitive identification of multiple chemical modification sites [151, 152]. A general analytical scheme has been developed for the characterization of ''native-like'' chemically modified proteins [15], which involves the determination of the extent of modification (i.e., number and distribution of modified residues) by direct mass spectrometric molecular weight determination, as a first step. Here, an additional level of information is provided by ESI-MS by the distribution of multiply charged ions (''charge structures'' [13, 31]) due to their correlation with conformation states in solution [13]. In a second step, proteolytic digestion is performed, and the sites of modifications are identified by mass spectrometric peptide mapping [129]. Moreover, assignments of relative reactivities at specific residues can be obtained from a series of partially modified proteins [128].

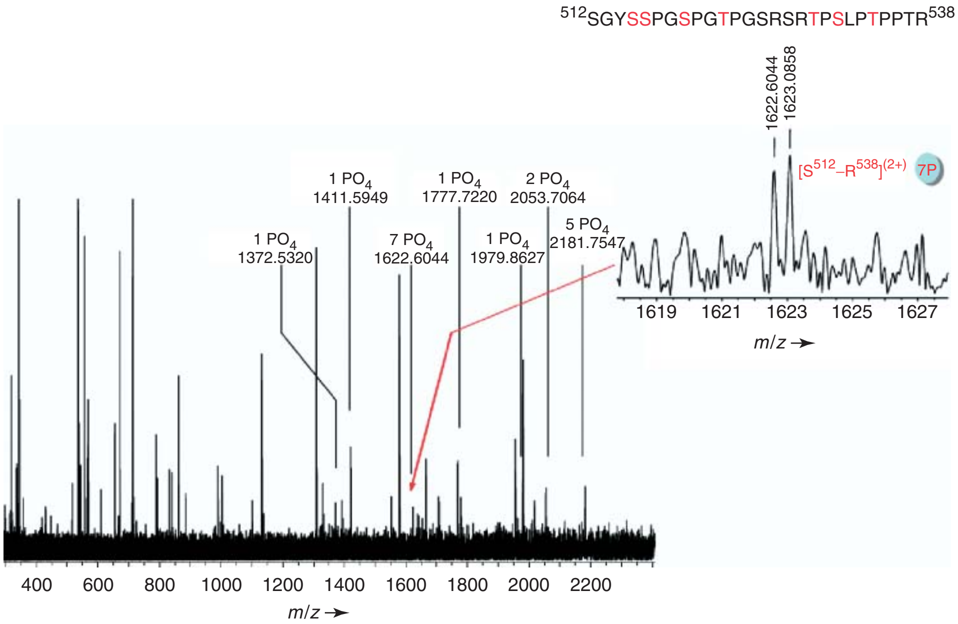

Figure 11.14 ESI-FTICR mass spectrum of tryptic digest mixture of multi- phosphorylated human neurofibrillary tau protein. Peak assignments within the m/z detection range, 200–2500, are shown for phosphorylated peptides. The insert shows the peptide fragment of the phosphorylation domain (512–538); the seven phosphorylation sites, identified using information of NiceProt View of Swiss Prot database (primary accession number P10636), are indicated in red (C_{113}, H_{191}, N_{36}, P_7, doubly protonated; calc. 1622.55513, found 1622.60435, $\Delta = 30$ ppm).

Using this approach, mass spectrometric determinations of reactive sites in intact protein structures by chemical modifications in proteins have been found highly useful in structure–function studies of proteins [15], for example, for ion-channel proteins (porins; Figure 11.15). The structures of several bacterial porins have been determined by X-ray crystallography; for example, the porin from *Rhodobacter capsulatus* (R.c.-porin) [153] forms a trimeric complex of 16- or 18-stranded β-barrels. A characteristic structure element of R.c.-porin is a central constriction loop inside the β-barrel, which has been suggested as the central site determining cation/anion permeability and transport selectivity [15]. The R.c.-porin was succinylated at conditions that provide native-like acylation of amino groups [154]. The structure of the succinylated porin was identified by X-ray crystallography at 2.4 Å resolution (*i 15*); however, the electron density maps did not permit an assignment of the succinylated groups, although ion transport experiments revealed substantial single channel conductance. The precise extent and sites of succinylations were determined by MALDI-MS, which revealed the formation of a specifically tetra-succinylated protein (Mw 31 941 Da; Figure 11.15) [154]. The identification of the succinylation sites by MALDI-MS peptide mapping showed

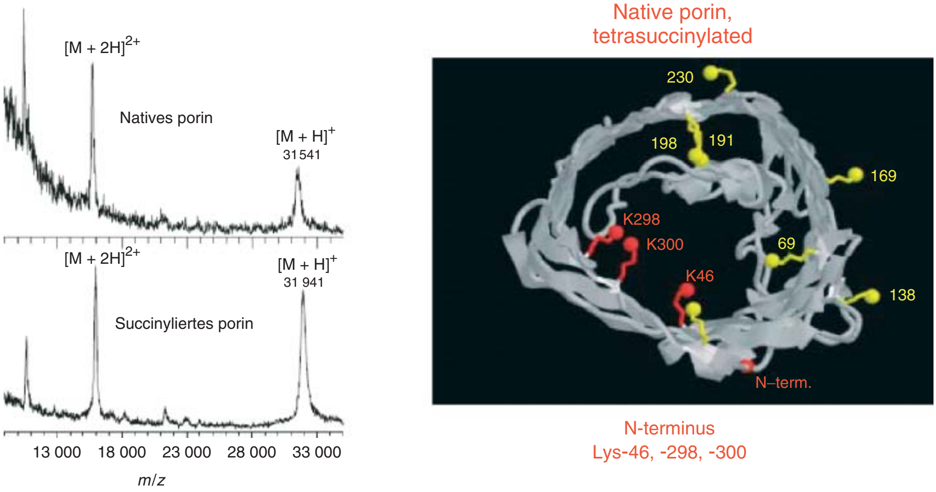

Figure 11.15 MALDI mass spectra (left) of native and tetra-succininylated Rhodobacter capsulatus porin, and x-ray structure (right) of the succinylated porin. The modified residues Lys-46, −298 and −300 and the N-termin are indicated in red; unmodified Lys residues are shown in yellow.

selective modification of three Lys-amino groups at the inner channel surface (K-46, K-298, K-300), and of Lys-46 at the channel constriction loop. This pattern was in agreement with a point charge model explaining the concomitant increase of single-channel conductance *and* cation selectivity.

11.3.4
Characterization of Noncovalent Supramolecular Complexes

Beyond the characterization of primary structures, the direct analysis of tertiary structure states and even noncovalent supramolecular complexes by MS has not been considered feasible in initial biopolymer-MS work. In a few cases, structure correlations were found, for example, specific fragmentations in FAB mass spectra of α-helical polypeptides and some MALDI and PD mass spectra of proteins, suggesting the formation of "native-like" macromolecular ions [126, 127]. This situation has changed substantially in the past few years with the analytical development of ESI-MS. A large number of ESI-MS studies have demonstrated the identification of supramolecular complexes of biopolymers, as well as specific noncovalent complexes with low-molecular-weight constituents [15–18, 31]. In contrast to other ionization methods in which predominantly *singly charged* ions are produced (FAB, MALDI), the continuous series of *multiply charged* macroions in ESI-MS reflects charge states and distributions characteristic of the solution structure (charge structure; cf. 11.2.1.3.2) [31]. Moreover, ESI-MS can be readily carried out with aqueous solutions at physiological conditions, enabling comparative studies with other structure determination methods such as NMR [155]. This feasibility of the direct mass spectrometric characterization of noncovalent complexes has clearly opened new analytical perspectives for supramolecular chemistry and biochemistry (“native mass spectrometry”) [6, 156–158].

Although the mechanism of ion formation in ESI-MS has not yet been elucidated in detail, a large variety of noncovalent interactions (e.g., ionic, hydrophobic) have been successfully characterized. Experimental parameters and criteria employed for the identification of noncovalent complexes based on chemical conditions of complex formation, and their effects on the ion formation in ESI-MS have been summarized [31]. These include the identification of the specific stoichiometry of complexes by modification of the stoichiometry of solution components and modification of the ESI-MS conditions (interface temperature; declustering potential). Further evidence is provided by competition experiments between complex components and analysis of the specificity of pH or concentration changes. An illustrative example demonstrating the close correlation between solution structures and charge structures of molecular ions are the pH-dependent ESI spectra of myoglobin [13]. The high-resolution ESI-FTICR spectrum in aqueous solution at pH 6 reveals a most abundant $[M+9H]^{9+}$ ion of the intact hem-protein complex, while under acidic conditions (pH 2) complete dissociation is observed showing the apoprotein molecular ions of high charge states (up to 20+) and the ion of the free heme group (Figure 11.16). A particularly attractive feature of high-resolution MS analysis is the complete isotopic resolution and direct characterization of charge states [48, 159].

Thus, although the quantitative characterization of equilibria of complex formation has not yet been established, the large number of already successful

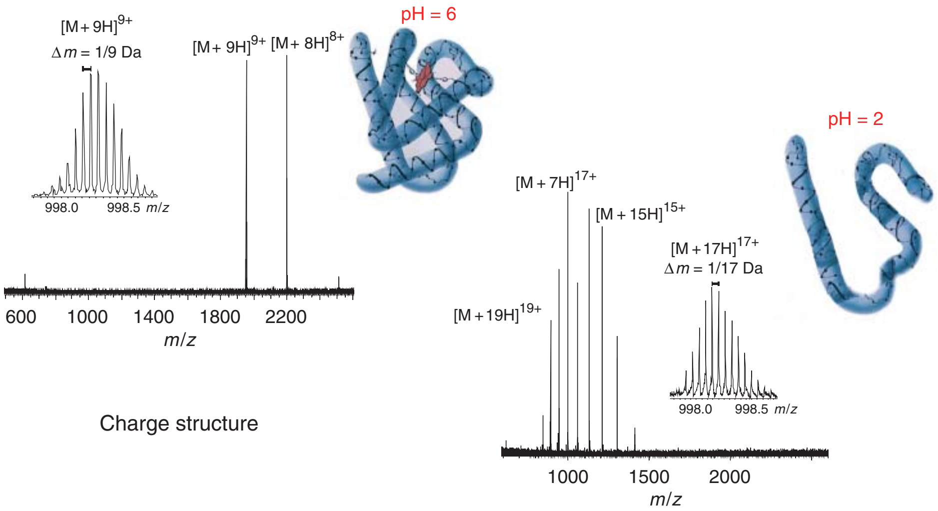

Figure 11.16 ESI-FT-ICR mass spectra of (a) the native intact hem-protein complex of horse heart myoglobin; (b) spectrum of the denatured apoprotein upon dissociation of hem in trifluoroacetic acid, pH 3. The inserts show isotopic resolutions for the 9- and 17-fold protonated molecular ions.

applications indicates broad potential for the analysis of noncovalent complexes by ESI-MS.

11.3.5
Mass Spectrometric Proteome Analysis

During the past decade, large amounts of protein sequence data have been deposited in a number of databases as a result of different genome projects [160]. Only a minor part of these sequence data has been from expressed proteins, whereas a major portion has been deduced from the corresponding gene sequences. Sequence determination of several genomes in the past few years has reached a first culmination point in the completion of the human genome in 2001 [161]. It has become clear that functions from such protein sequences are frequently only predicted and remain undefined for a substantial part of structural genes, for example, due to processes such as alternative splicing, RNA editing, and posttranslational protein modifications [160, 162]. With this consideration, *proteomics*, using the term *proteome* to define the PROTE in complement of the genOME [160], has created an explosion of interest with the use of MS as a key technology for the large-scale identification of proteins from cellular expression material [163]; the reader is referred to recent reviews in this area [162–164]).

Within the past few years, several combinations of high-performance separation techniques with mass spectrometric peptide mapping have been developed and employed for the identification of proteins from complex biological systems, such as cell lysates [164]. At present, one of the most efficient techniques is the proteolytic degradation of proteins, separated by 2D-gel electrophoresis, within the gel matrix and subsequent mass spectrometric analysis of eluted peptide fragments. Both MALDI-MS and ESI-MS have been extensively employed for these studies [164]. The unequivocal identification of proteins from sequence databases using peptide mass fingerprint data without any additional sequence information such as sequence tags and MS/MS data [164, 165] requires typically a set of 10–20 peptide masses with high mass determination accuracy (<200 ppm mass error) [166]. Furthermore, a high sequence coverage by the observed peptide molecular ions is an important criteria for the certainty of protein identification.

In recent proteome studies, the combination of 2D-gel electrophoresis with high-resolution MS has been widely employed as a powerful tool [167, 168]; the high (low parts per million) mass determination accuracy and isotopic fine structure obtained by high-resolution MS provide particular advantages for the identification of cellular proteins expressed with minor or very low abundance. Accurate masses obtained by high-resolution MS allow the use of low tolerance thresholds in database searches and greatly improve the selectivity of protein identification, compared to standard techniques, for example, using MALDI-TOF-MS [164]. The identification of a protein component, TNFα-IgG, in a serum cryoprecipitate from a patient with cryogobulinemia by MALDI-FTICR-MS is illustrated in Figure 11.17, requiring only a minimum number of peptides [144]. Cryoglobulins are cold-precipitated serum immunoglobulins associated with a number of infectious,

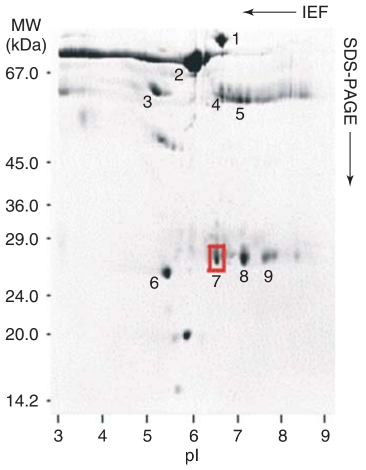

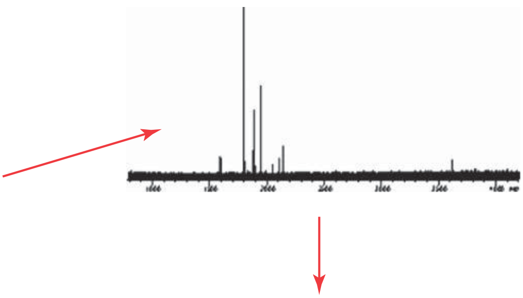

MS-fit search results

Parameters used in search

Nr. of peptide masses	Peptide Mass accuracy	Peptide mass	Digestion	Nr. of missed cleavages	Covalently Modified by	Peptide N-terminus	Peptide C-terminus
7	7.000 ppm	Monoisotopic	Trypsin	2	Carbamidomethylation	Hydrogen (H)	Free acid (HO)

Result summary

Rank	MASCOT score	# Mached peptides	Protein mass (Da)/ pI	Species	Accession #	Protein name
1	2e + 003	712 (5641)	23323.94 /69	HOMO SAPIENS	AB027440.1	AB027438 TNF-α antibody light chain fab fragment

1-Transferrrin
2-Serum albumin
3-α-1-antitrypsin
4, 5 -Ig γ-chain
6-Apolipoprotein A-I
7, 8, 9 - Anti TNF- α antibody light chain fab fragment

Figure 11.17 2D-PAGE Separation of a cryoglobulin isolated from serum of a patient with glomerulonephritis (left) and MALDI-FT-ICR-MS of tryptic in-gel digest mixture of spot 7 (right). The MS-fit search using SwissProt data base yielded identification of anti-TNF-alpha-light chain fragment.

autoimmune, and neoplastic disorders such as hepatitis C [169, 170]; therefore, their characterization using high-performance proteomics tools has become of considerable interest. The main protein components in a serum cryoprecipitate from a patient with type II cryogobulinemia were identified by MALDI-FTICR-MS as IgG and IgM μ- and γ-heavy chains, κ- and λ-light chains, and j-chains [171].

One major shortcoming in applications of the combination of 2D-gel electrophoresis with MS is the loss of information about specific protein–protein interactions and molecular recognition processes due to the denaturing electrophoretic conditions. At present, only a few – yet promising – attempts have been made to directly analyze interactions in proteome studies [19, 164, 172]. More recently, a new approach for the identification of affinity-bound proteins by proteolytic generation and mass spectrometric analysis of its antibody-bound epitope peptides has been described [173]. The selectivity of identification of antibody-bound proteins using the combination of antigen–antibody specificity, and the redundancy of epitope peptide sequences render this ''affinity-proteomics'' approach a powerful tool for the mass spectrometric identification of proteins from complex biological material [173].

11.3.6
Application of Affinity-Mass Spectrometry to the Analysis of Biomolecular Recognition Structures

Although the application of affinity techniques in the analysis of biopolymers by MS has become an established approach over the last decade, it is re-emerging as new methodology combinations and tools for the structure identification and quantification of biopolymer interactions become available. Affinity MS techniques can be productively used for the identification of proteins and protein complexes from biological material and for the enrichment and analysis of protein structure modifications. These approaches may be viewed as examples of ''affinity MS''; they are presently emerging as valuable tools for a variety of important research areas, from identification of the epitopes involved in biomolecular interactions and quantitative determination of their interactions to utilizing them in personalized medicine.

A recent focus issue of the *Journal of the American Society for Mass Spectrometry* gives an assessment of the current state of affinity MS by presenting a number of studies that illustrate both methods and applications [174]. Applications include approaches for studying antibody–peptide epitopes and quantifying their affinities; identifying posttranslational modifications; mapping epitopes using chemical modification reactions; utilizing and improving the specificity of proteomics; and applications to problems in personalized medicine [108, 175–178]. Thus, the ''marriage'' of affinity techniques with the structure determination capability of MS has opened new applications in biochemistry, immunology, and biomedicine. These developments also show that the combination provides information that cannot be provided by other methods, and not by any single methodology.

A new approach for the analysis of protein–carbohydrate interactions is described in the following as an example for methodology and application of affinity MS. The interaction of carbohydrates with proteins is one of the most important types of biological interactions in cell differentiation, fertilization, pathogen infection, signal transduction, inflammation processes, and cancer cell metastasis. The characterization of such interactions is of crucial importance in understanding the mechanisms by which lectins, anticarbohydrate antibodies, and carbohydrate-processing enzymes exert their functions. Although X-ray and NMR are capable of revealing details of carbohydrate recognition structures and binding, their application is limited by the large amounts of high purity material needed [179]. Recently, a new molecular method for identifying carbohydrate recognition structures with high sensitivity, specificity, and low requirements in sample purity has been described, based on the combination of MS and proteolytic excision of

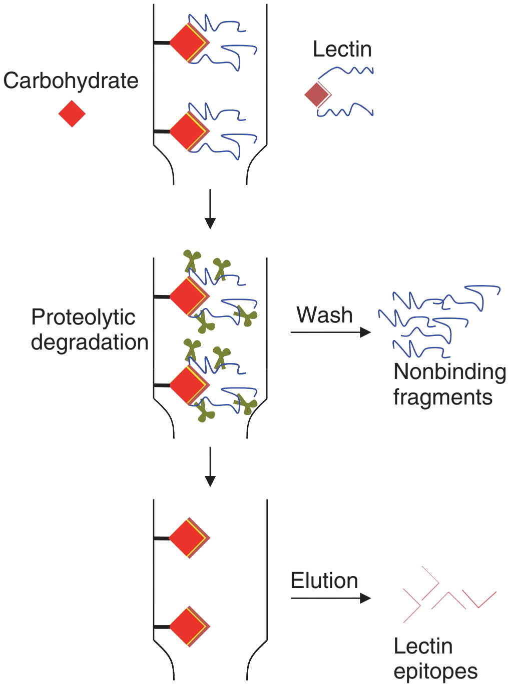

Figure 11.18 Analytical concept of proteolytic-excision mass spectrometric identification of CRD sequences. The carbohydrate binding protein (lectin, antibody, etc) is bound on a column with immobilised carbohydrate and the complex digested with proteases. The protein fragments not binding to the carbohydrate are washed from the column and analysed by mass spectrometry. The remaining bound fragments are eluted and analyzed by mass spectrometry. Competitive elution of remaining bound CRD peptides is performed with the carbohydrate, or with a substitute mixture of organic solvents (acetonitrile, acetic acid, etc.). The native conformation of the bound protein is kept by physiological conditions maintained during the binding experiment.

protein–carbohydrate complexes: carbohydrate recognition domain excision-mass spectrometry (CREDEX-MS) [180, 181]. This new method has been initially demonstrated by the carbohydrate recognition structure determination of galectin-1 and galectin-3 (Gal-3), which were selected owing to the known crystal structures of their carbohydrate complexes. The CREDEX-MS approach consists of immobilizing the carbohydrate on an affinity column, adding the binding protein and allowing formation of the complex, which is then digested with proteases, followed by washing away nonbinding protein fragments (Figure 11.18). The remaining affinity-bound epitope peptides are then isolated for mass spectrometric analysis, employing competitive elution with the carbohydrate or, alternatively, by a supplementing aqueous organic solvent mixture [180]. Galectin-1 and Gal-3 are intimately involved in tumor growth and progression, as well as in inflammatory diseases such as rheumatic arthritis. The Gal-3 complexes with lactose and *N*-acetyl lactosamine have been determined by X-ray crystallography at 2.1 Å resolution [179] (Figure 11.19), showing that the C-4 hydroxyl group of galactose is central for binding by interacting with the highly conserved Gal-3 residues His-158, Asn-160, and Arg-162, while the galactose C-6 hydroxyl group interacts with Glu-184 and Asn-174, and the planar C-3 to C-6 carbon atoms of galactose are in van der Waals contact with the side chain of Trp-181 [179].

Human Gal-3 was bound to lactosyl-Sepharose (prepared by covalent binding of lactose to epoxy-activated Sepharose 6B) and digested using trypsin. When the last washing fraction did not show any ion signals, elution was performed with 0.3 M lactose. MALDI-MS of the elution fractions identified two Gal-3 peptides, (152–162) and (177–183) (Figure 11.19b); in contrast, MALDI-MS of a control digestion mixture showed all expected peptides. When galectin 3 was digested in solution and the digest mixture added to the lactosyl-Sepharose column, identical peptides, (152–162) and (177–183) were identified in the elution fraction, providing evidence for these sequences as the lactose-binding site. The peptide (152–162) contains H-158, N-160, R-162, all of which are essential residues for the carbohydrate binding in the crystal structure. The peptide (177–183) comprises a single residue, W-181 interacting with the carbohydrate. These results were in complete accordance with the X-ray crystallographic data (Fig. 11.19a, c).

The same approach was applied to identify the Gal-3 CRD peptides for blood group A-trisaccharide (Tri-A). Peptides remaining affinity-bound upon trypsin digestion were isolated by competitive elution using a high lactose concentration, as supplement to the more expensive Tri-A. MALDI-MS of the elution fraction identified two specific peptides, (152–162) and (130–144). Despite the lack of X-ray crystal structure data for the orientation of the trisaccharide, the presence of the Gal-3 (130–144) peptide is well explained by the binding of *N*-acetylgalactosamine or fucose ring in an extended binding site comprising the Arg-144 residue. The specificity of all CRD peptides was ascertained by functional binding assays of two carcinoma cell lines, showing specific inhibition of intact Gal-3 [180].

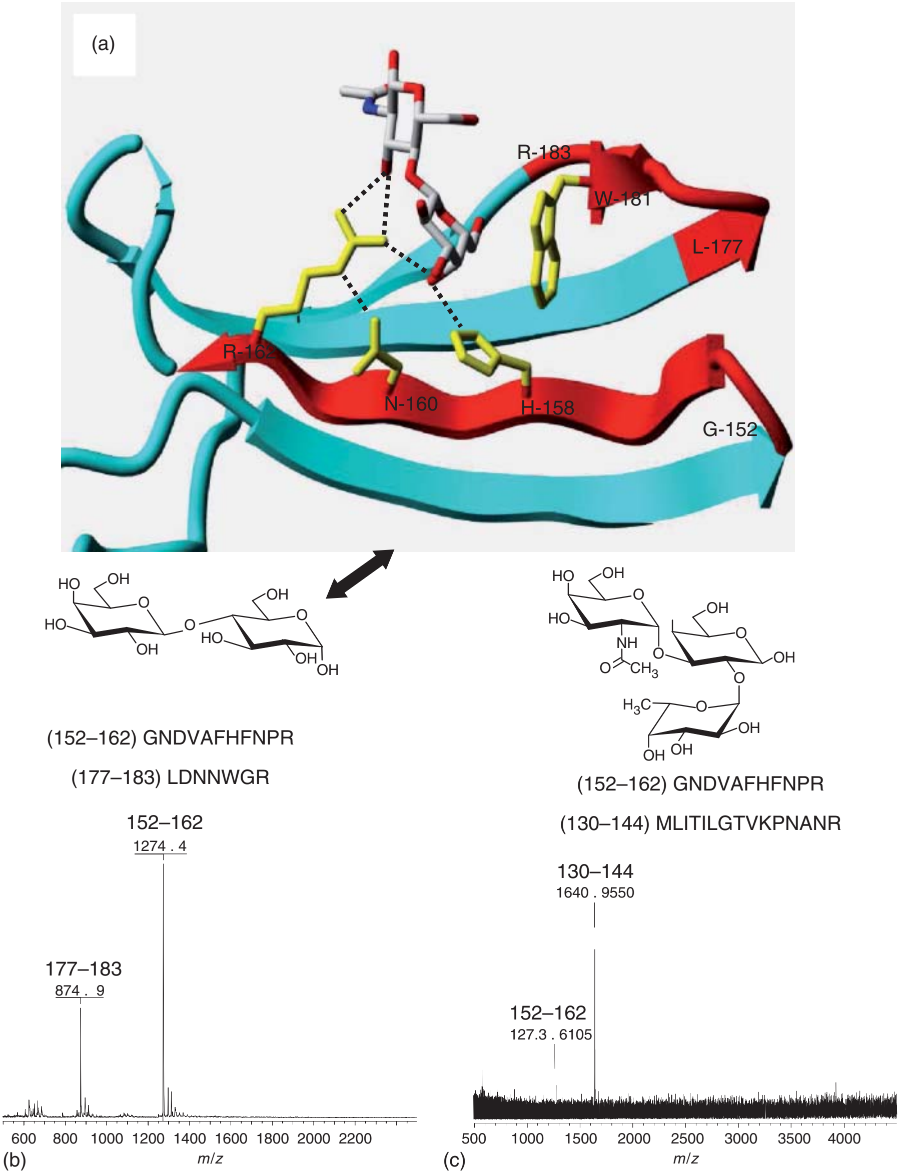

Figure 11.19 Topology of galectin-3 CRD peptides identified by CREDEX-MS (152–162) and (177–183) (in red) in the crystal structure of galectin-3. Representation of the crystal structure is described by PDB file 1A3K (Brookhaven Laboratory). Amino acid side chains involved in direct interaction with the carbohydrate are shown in yellow (H158, N160, R162, W181). The structures of lactose and Tri-A are given in the lower part of the Figure. (B), MALDI-FTICR-MS of the elution fraction for the galectin-3/lactose complex reveals two CRD peptides (152–162) and (177–183) with the sequences given. (C), MALDI-FTICR-MS of the elution fraction for the galectin-3/blood group Tri-A complex reveals two CRD peptides (152–162) and (130–144).

11.3.7

Identification of Oligomerization – Aggregation Structures and Pathways of Neurodegenerative Proteins by Ion Mobility Mass Spectrometry

A large variety of cellular processes are based on the formation and dynamics of multi- and supramolecular protein assemblies, and several diseases, previously thought to be unrelated, such as cancer and neurodegenerative diseases, are characterized by "misfolded" protein aggregates. Several neurodegenerative diseases are associated with the formation and accumulation of different types of "misfolding-aggregation" products [182–184]. The formation of neurotoxic oligomers is generally thought to precede aggregation, as shown for Aβ polypeptide, Tau protein, and the key protein in Parkinson's disease (PD), α-Synuclein (αSyn) [185]. Chemical structures and reaction pathways of pathophysiological aggregates are only poorly characterized and understood at present. "Soft-ionization" MS, such as HPLC-ESI-MS, is frequently unsuitable for the direct analysis of reaction pathways involved in aggregation, particularly because of the low concentrations of intermediates. IM-MS has been recently emerging as a new, powerful tool for the analysis of protein oligomerization–aggregation reactions, owing to the concentration-independent gas phase separation capability of IM-MS.

Direct, *in situ* applications of IM-MS are illustrated in the following for the *in vitro* oligomerization of αSyn, a key protein of Parkinson's disease (PD) [113, 186]. αSyn, a 140-aa protein occurring in the presynaptic terminals of neurons, is strongly correlated with PD. αSyn is natively unfolded but adopts an α-helical structure when it binds to lipid vesicles, and forms a β-sheet that facilitates the formation of aggregated morphologies [186]. Intracellular accumulation of αSyn aggregates has been recognized at conditions inducing PD. Although oligomeric intermediates may represent major neurotoxic species [185], chemical structures of αSyn oligomers and possible intermediates have not been previously identified. The slow rates of formation and low concentrations of aggregating intermediates may be major reasons for the failure of conventional MS methods to detect and identify oligomers. IM-MS studies of the time-dependent *in vitro* oligomerization–aggregation of αSyn provided the first identification of specific autoproteolytic fragments, which were previously observed by gel electrophoresis but not identified [113], particularly a highly reactive C-terminal fragment, αSyn(72–140), formed by cleavage within the central aggregation-prone domain of the protein (Figure 11.20). The αSyn(72–140) polypeptide, synthesized both by chemical solid-phase peptide synthesis (SPPS) and by recombinant expression, showed rapid formation of oligomers and substantially faster aggregation and increased neurotoxicity, compared to the intact protein. Most recently, further IM-MS studies of drift time profiles ascertained the formation of conformationally different forms of αSyn upon incubation *in vitro* [186]. Moreover, first studies of αSyn *in vivo* by online affinity MS using an αSyn-antibody with C-terminal epitope specificity enabled the direct structure identification of αSyn polypeptides from mouse brain material [187]. These results suggest IM-MS as a powerful tool for the molecular elucidation of structures involved in oligomerization–aggregation of neurodegenerative proteins, providing a

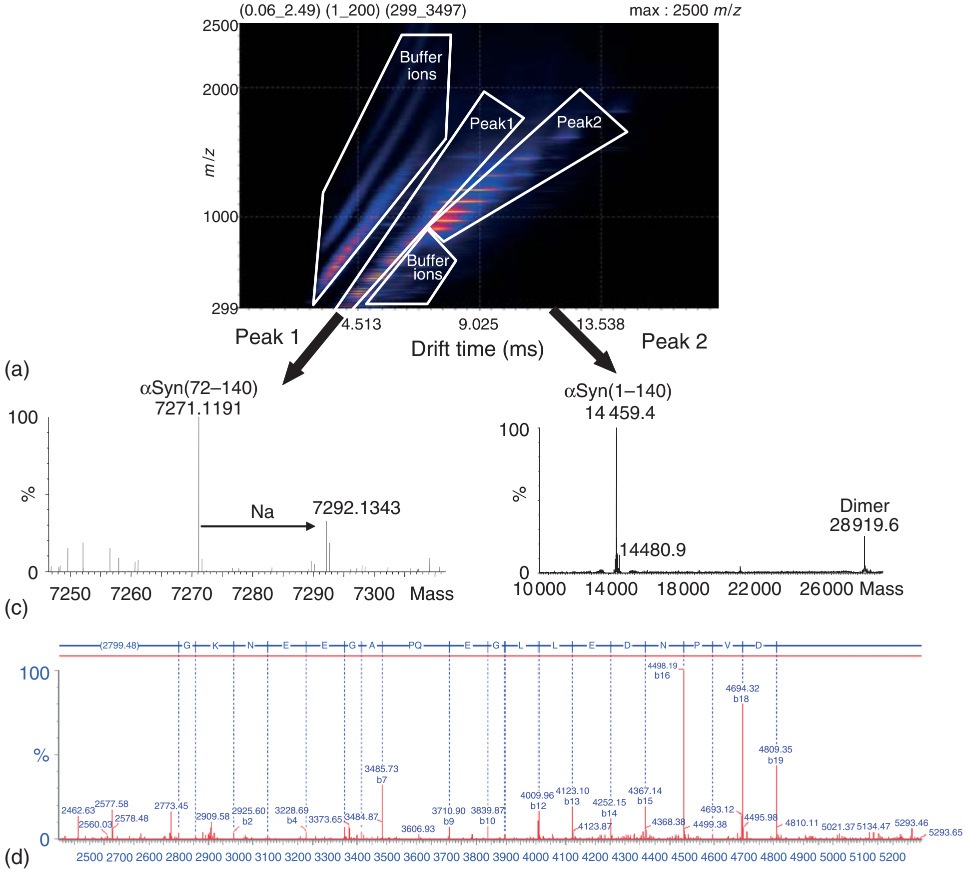

Figure 11.20 Identification of autoproteolytic truncation products of αSyn by ion-mobility mass spectrometry: (a), HDMS analysis (driftscope data view) of oligomerization-aggregation products of αSyn incubated in PBS for 7 d at 37 °C. Signals corresponding to monomers, dimers and truncated peptide sequences are observed. Each pixel represents one ion with color representing intensity from low (blue) to high (yellow); (b), Extracted deconvoluted spectrum of peak 1 is the truncated peptide sequence αSyn(72–140); (c), Extracted deconvoluted spectrum of peak 2 showing monomer plus dimer of αSyn; (d) MS/MS fragmentation of 1455.6 (+5) m/z precursor ion using elevated collision energy in the transfer region provides identification of the proteolytic product, αSyn(72–140).

basis for the detailed study of reaction pathways and intermediates, and the design of peptides capable of inhibiting or modifying aggregation.

Acknowledgments

The author gratefully acknowledges a number of present and previous coworkers for their enthusiasm, help, and many fruitful discussions throughout the studies

reported here, particularly Dr. Marilena Manea; Adrian Moise; Claudia Cozma; Marius Iurascu; Dr. Gabriela Paraschiv; Kathrin Lindner; Dr. Camelia Vlad; Dr. Andreas Marquardt; Dr. Dmitry Galetskiy; Dr. Alina Petre; Stefan Slamnoiu; Frederike Eggers; Dr. Irina Perdivara; Prof. Dr. Christoph Borchers; Dr. Jürgen Kast; Dr. Marcus Bantscheff; Dr. Delev Suckau; Dr. Marcus Macht; Prof. Dr. Martin Kussmann; Dr. Jenny Albanese; Dr. Thilo Fligge; Dr. Stefan Bühler; Dr. Reinhold Weber; Prof. Dr. Wolfgang Weinmann. We are also grateful to several colleagues for their stimulating collaboration, helpful discussions and advice, and for making available unpublished studies: Professors M. Glocker, K.P. Schäfer; M. Gross; D. Clemmer; B. Hengerer; S. Muyldermans; U. Pecks; W. Welte; M. Ehrmann; K. Tomer; F. Hudecz; B. Penke; P. Roepstorff; M. Scheffner; M. Leist; Dr. S. Maeser; Dr. J. Hörnschemeyer. The author's own research work described herein was partially supported by the Deutsche Forschungsgemeinschaft; Bundesministerium für Forschung und Technologie, and Bundesministerium für Wirtschaft; the European Union; Genzyme GmbH; Centogene GmbH; and Boehringer Ingelheim.

References

1. Nier, O. (1991) *J. Am. Soc. Mass Spectrom.*, **2**, 447–452.
2. Amy, J.W., Baitinger, W., and Cooks, R.G. (1990) *J. Am. Soc. Mass Spectrom.*, **1**, 119–128.
3. Gohlke, R.S. and McLafferty, F.W. (1993) *J. Am. Soc. Mass Spectrom.*, **4**, 367–371.
4. Burlingame, A.L. and Carr, S.A. (1996) *Mass Spectrometry in the Biological Sciences*, Humana Press, Totowa, NJ.
5. Siuzdak, G. (1994) *Proc. Natl. Acad. Sci. U.S.A.*, **91**, 11290–11297.
6. Przybylski, M. and Glocker, M.O. (1996) *Angew. Chem., Int. Ed. Engl.*, **35**, 806–826.
7. Matsuo, T., Caprioli, R., and Gross, M. (1994) *Biological Mass Spectrometry: Present and Future*, John Wiley & Sons, Inc., New York.
8. Karas, M., Bahr, U., and Giessmann, U. (1991) *Mass Spectrom. Rev.*, **19**, 335–381.
9. Przybylski, M. (1983) *Fresenius' Z. Anal. Chem.*, **315**, 402.
10. Sundquist, R. and McFarlane, R.D. (1985) *Mass Spectrom. Rev.*, **4**, 421.
11. Fenn, J.B., Mann, M., Meng, C.K., and Wong, S.F. (1989) *Science*, **246**, 46–49.
12. Tanaka, K., Waki, H., Ido, Y., Akita, S., and Yoshida, Y. (1988) *Rapid Commun. Mass Spectrom.*, **2**, 151–153.
13. Przybylski, M. (1995) *Adv. Mass Spectrom.*, **13**, 257–283.
14. Jensen, O.N., Larsen, M.R., and Roepstorff, P. (1998) *Proteins*, **2** (Suppl. 2), 74–89.
15. Przybylski, M., Schnaible, V., Kast, J., Bühler, S., Michels, J., Wattenberg, A., Fligge, T.A., Forst, D., Diederichs, K., Zeth, C., Glocker, M.O., and Welte, W. (1998) in *New Methods for the Study of Biomolecular Complexes* (eds W. Ens, K.G. Standing, and I.V. Chernushevich), Kluwer Academic Publishers, Amsterdam, pp. 17–43.
16. Aplin, R.T. (1998) in *New Methods for the Study of Biomolecular Complexes* (eds W. Ens and K.G. Standing), Kluwer Academic Publishers, Amsterdam.
17. Loo, J.A. (1997) *Mass Spectrom. Rev.*, **16**, 1–23.
18. Smith, R.D., Bruce, J.E., Wu, Q., and Lei, Q.P. (1997) *Chem. Soc. Rev.*, **26**, 191–202.
19. Suckau, D., Kohl, J., Karwath, G., Schneider, K., Casaretto, M., Bitter-Suermann, D., and Przybylski,

M. (1990) *Proc. Natl. Acad. Sci. U.S.A.*, **87**, 9848–9852.

20. Trimpin, S. and Clemmer, D.E. (2008) *Anal. Chem.*, **80**, 9073–9083.
21. Kanu, A.B., Dwivedi, P., Tam, M., Matz, L., and Hill, H.H. (2008) *J. Mass Spectrom.*, **43**, 1–22.
22. Uetrecht, C., Rose, R.J., van Duijn, E., Lorenzen, K., and Heck, A.J. (2010) *Chem. Soc. Rev.*, **39**, 1633–1655.
23. Ruotolo, B.T., Benesch, J.L., Sandercock, A.M., Hyung, S.J., and Robinson, C.V. (2008) *Nat. Protoc.*, **3**, 1139–1152.
24. Budzikiewicz, H., Djerassi, C., and Williams, D.H. (1967) *Mass Spectrometry of Organic Compounds*, Holden Day, San Francisco, CA.
25. McLafferty, F.W. (1989) *The Wiley/NBS Registry of Mass Spectral Data*, Wiley-Interscience, New York.
26. Munson, M.S.B. and Field, F.H. (1966) *J. Am. Chem. Soc.*, **88**, 2621–2630.
27. Beckey, H.D. (1969) *Int. J. Mass Spectrom. Ion Phys.*, **2**, 500–503.
28. Macfarlane, R.D. and Torgerson, D.F. (1976) *Science*, **191**, 920–925.
29. Barber, M., Bordoli, R.S., Sedgwick, R.D., and Tyler, A.N. (1981) *J. Chem. Soc., Chem. Commun.*, 325–327.
30. Ito, Y., Takeuchi, T., Ishi, D., and Goto, M. (1985) *J. Chromatogr.*, **346**, 161–166.
31. Fenn, J.B., Mann, M., Meng, C.K., Wong, S.F., and Whitehouse, C.M. (1989) *Science*, **246**, 64–71.
32. Emmett, M.R. and Caprioli, R.M. (1994) *J. Am. Soc. Mass Spectrom.*, **5**, 605–613.
33. Wilm, M.S. and Mann, M. (1994) *Int. J. Mass Spectrom. Ion Processes*, **136**, 167–180.
34. Körner, R., Wilm, M., Morand, K., Schubert, M., and Mann, M. (1996) *J. Am. Soc. Mass Spectrom.*, **7**, 150–156.
35. Fligge, T.A., Kast, J., Bruns, K., and Przybylski, M. (1999) *J. Am. Soc. Mass Spectrom.*, **10**, 112–118.
36. Karas, M. and Hillenkamp, F. (1988) *Anal. Chem.*, **60**, 2299–2301.
37. Dey, M. and Grotemeyer, J. (1995) *Eur. Mass Spectrom.*, **1**, 95–103.
38. Dawson, P.H. (1976) *Quadrupole Mass Spectrometry and Its Applications*, Elsevier, New York.
39. Cooks, R.G. and Kaiser, R.E. (1990) *Acc. Chem. Res.*, **23**, 213–219.
40. Bahr, U., Pfenninger, A., Karas, M., and Stahl, B. (1997) *Anal. Chem.*, **69**, 4530–4535.
41. Pringle, S.D., Giles, K., Wildgoose, J.L., Williams, J.P., Slade, S.E., Thalassinos, K., Bateman, R.H., Bowers, M.T., and Scrivens, J.H. (2007) *Int. J. Mass Spectrom.*, **261**, 1–12.
42. Morris, H.R., Paxton, T., Dell, A., Langhorne, J., Berg, M., Bordoli, R.S., Hoyes, J., and Bateman, R.H. (1996) *Rapid Commun. Mass Spectrom.*, **10**, 889–896.
43. Qian, M.G. and Lubman, D.M. (1996) *Rapid Commun. Mass Spectrom.*, **10**, 1911–1920.
44. Marshall, A.G., Hendrickson, C.L., and Jackson, G.S. (1998) *Mass Spectrom. Rev.*, **17**, 1–35.
45. Belov, M.E., Nikolaev, E.N., Anderson, G.A., Auberry, K.J., Harkewicz, R., and Smith, R.D. (2001) *J. Am. Soc. Mass Spectrom.*, **12**, 38–48.
46. Baykut, G., Jertz, R., and Witt, M. (2000) *Rapid Commun. Mass Spectrom.*, **14**, 1238–1247.
47. Rossier, J.S., Youhnovski, N., Lion, N., Damoc, E., Reymond, F., Girault, H.H., and Przybylski, M. (2003) *Angew. Chem. Int. Ed.*, **42**, 53–58.
48. Yates, R.J., Cociorva, D., Liao, L., and Zabrouskov, V. (2006) *Anal. Chem.*, **78**, 493–500.
49. Perry, R.H., Cooks, R.G., and Noll, R.J. (2008) *Mass Spectrom. Rev.*, **27**, 661–699.
50. Fornelli, L., Damoc, E., Thomas, P.M., Kelleher, N.L., Aizikov, K., Denisov, E., Makarov, A., and Tsybin, Y.O. (2012) *Mol. Cell. Proteomics*. doi: 0.1074/mcp.M112.019620
51. Rose, R.J., Damoc, E., Denisov, E., Makarov, A., and Heck, A.J.R. (2012) *Nat. Methods*. doi: 10.1038/nmeth.2208
52. Bonfiglio, R., King, R.C., Olah, T.V., and Merkle, K. (1999) *Rapid Commun. Mass Spectrom.*, **13**, 1175–1185.
53. King, R.C., Bonfiglio, R., Fernandez-Metzler, C., Miller-Stein,

C., and Olah, T.V. (2000) *J. Am. Soc. Mass Spectrom.*, **11**, 942–950.

54. Mueck, W., Leitner, D., Marter, W., Ponnet, T., and Schuettler, C. (1999) *Am. Biotechnol. Lab.*, **27**, 78–91.
55. Steinborner, S. and Henion, J. (1999) *Anal. Chem.*, **71**, 2340–2345.
56. Pfleger, K., Maurer, H.H., and Weber, A. (1999) *Mass Spectral and GC Data on Drugs, Posons, Pesticides, and Pollutants and Their Metagbolites, Part 3*, 2nd edn, Verlag Chemie, Weinheim.
57. Cairns, E.R., Dent, B.R., Ouwerkerk, J.C., and Porter, L.J. (1994) *J. Anal. Toxicol.*, **18**, 1–6.
58. Kabra, P.M., Mar, N.A., and Marton, L.J. (1981) *Clin. Chim. Acta*, **111**, 123–132.
59. Franke, J.P. and De Zeeuw, R.A. (1998) *J. Chromatogr., B*, **713**, 51–59.
60. Simpson, H., Berthemy, A., Buhrmann, D. *et al.* (1998) *Rapid Commun. Mass Spectrom.*, **12**, 75–82.
61. Zweigenbaum, J., Heinig, K., Steinborner, S., Wachs, T., and Henion, J. (1999) *Anal. Chem.*, **71**, 2294–2300.
62. Cai, J. and Henion, J. (1996) *Anal. Chem.*, **68**, 72–78.
63. Nedved, M.L., Habibi-Goudarzi, S., Ganem, B., and Henion, J.D. (1996) *Anal. Chem.*, **68**, 4228–4236.
64. Maurer, H.H., Kraemer, T., Ledvinka, O., Schmitt, C.J., and Weber, A.A. (1997) *J. Chromatogr., B*, **689**, 81–89.
65. Pawliszyn, J. (1997) *Solid Phase Microextraction – Theory and Practice*, Wiley-VCH Verlag GmbH, Weinheim.
66. Jinno, K., Muramatsu, T., Saito, Y., Kiso, Y., Magdic, S., and Pawliszyn, J. (1996) *J. Chromatogr., A*, **754**, 137–144.
67. Lord, H.L. and Pawliszyn, J. (1997) *Anal. Chem.*, **69**, 3899–3906.
68. Abalos, M., Bayon, J.M., and Pawliszyn, J. (2000) *J. Chromatogr., A*, **873**, 107–115.
69. Kataoka, H., Narimatsu, S., Lord, H.L., and Pawliszyn, J. (1999) *Anal. Chem.*, **71**, 4237–4244.
70. Martos, P.A. and Pawliszyn, J. (1999) *Anal. Chem.*, **71**, 1513–1520.
71. Berset, J.D. and Holzer, R. (1999) *J. Chromatogr., A*, **852**, 545–558.
72. Staub, C. (1997) *Forensic Sci. Int.*, **84**, 295–304.
73. Spell, J.C., Srinivasan, K., Stewart, J.T., and Bartlett, M.G. (1998) *Rapid Commun. Mass Spectrom.*, **12**, 890–894.
74. Senorans, F.J., Ibanez, E., Cavero, S., Tabera, J., and Reglero, G. (2000) *J. Chromatogr., A*, **870**, 491–499.
75. Amador-Hernandez, J. and Luque De Castro, M.D. (2000) *J. Biochem. Biophys. Methods*, **43**, 329–343.
76. Tomer, K.B. (2001) *Chem. Rev.*, **101**, 297–328.
77. Dragusanu, M., Petre, B.A., Slamnoiu, S., Vlad, C., Tu, T., and Przybylski, M. (2010) *J. Am. Soc. Mass Spectrom.*, **21**, 1643–1648.
78. Bruins, A.P. (1994) *Trends Anal. Chem.*, **13**, 37–43.
79. Bruins, A.P. (1998) *J. Chromatogr., A*, **794**, 345–357.
80. Tomer, K., Moseley, M.A., Deterding, L.J., and Parker, C.E. (1994) *Mass Spectrom. Rev.*, **13**, 431–457.
81. Hopfgartner, G., Wachs, T., Bean, K., and Henion, J. (1993) *Anal. Chem.*, **65**, 439–446.
82. Oosterkamp, A.J., Gelpi, E., and Abian, J. (1998) *J. Mass Spectrom.*, **33**, 976–983.
83. Vanhoutte, K., van Dongen, W., and Esmans, E.L. (1998) *Rapid Commun. Mass Spectrom.*, **12**, 15–24.
84. Abian, J., Oosterkamp, A.J., and Gelpi, E. (1999) *J. Mass Spectrom.*, **34**, 244–254.
85. Moseley, M.A. (2000) *Mass Spectrometry in Biology and Medicine*, Humana Press, Totowa, NJ, pp. 179–196.
86. Mann, M. and Wilm, M. (1994) *Anal. Chem.*, **66**, 4390–4399.
87. Zell, M., Husser, C., and Hopfgartner, G. (1997) *Rapid Commun. Mass Spectrom.*, **11**, 1107–1114.
88. Smith, R.D., Barinaga, C.J., and Udseth, H.R. (1988) *Anal. Chem.*, **60**, 1948–1952.
89. Eckerskorn, C., Strupat, K., Schleuder, D., Hochstrasser, D., Sanchez, J.-C., Lottspeich, F., and Hillenkamp, F. (1997) *Anal. Chem.*, **69**, 2888–2892.

90. Baltz-Knorr, M., Ermer, D.R., Schriver, K.E., and Haglund, R.F. Jr., (2002) *J. Mass Spectrom.*, **37**, 254–258.

91. Sluszny, C. and Yeung, E.S. (2004) *Anal. Chem.*, **76**, 1359–1365.

92. Xu, Y., Little, M.W., Rousell, D.J., Laboy, J.L., and Murray, K.K. (2004) *Anal. Chem.*, **76**, 1078–1082.

93. Roegener, J., Lutter, P., Reinhardt, R., Blueggel, M., Meyer, H.E., and Anselmetti, D. (2003) *Anal. Chem.*, **75**, 157–159.

94. Susnea, I., Bernevic, B., Svobodova, E., Simeonova, D.D., Wicke, M., Werner, C., Schink, B., and Przybylski, M. (2011) *Int. J. Mass Spectrom.*, **301**, 22–28.

95. Susnea, I., Bernevic, B., Wicke, M., Ma, L., Liu, S., Schellander, K., and Przybylski, M. (2013) in *Topics in Current Chemistry* (eds M. Cai and S. Liu). Applications of MALDI-TOF Spectroscopy. Vol. 331, Springer Berlin Heidelberg, pp. 37–54.

96. Tomer, K.B. and Moseley, M.A. (1990) in *Continuous-Flow Fast Atom Bombardment Mass Spectrometry* (ed. R.M. Caprioli), John Wiley & Sons, Inc., New York, pp. 121–136.

97. Parker, E., Perkins, J.R., Tomer, K.B., Shida, Y., O'Hara, K., and Kono, M. (1992) *J. Am. Soc. Mass Spectrom.*, 563–574.

98. Wachs, T., Sheppard, R.L., and Henion, J. (1996) *J. Chromatogr., B*, **685**, 335–342.

99. Settlage, R.E., Russo, P.S., Shabanowitz, J., and Hunt, D.F. (1998) *J. Microcolumn Sep.*, **10**, 281–285.

100. Weinmann, W., Parker, C.E., Baumeister, K., Maier, C., Tomer, K.B., and Przybylski, M. (1994) *Electrophoresis*, **15**, 228–233.

101. Weinmann, W., Parker, C.E., Deterding, L.J., Papac, D., Hoyes, J., Przybylski, M., and Tomer, K.B. (1994) *J. Chromatogr., A*, **680**, 353–361.

102. Javerfalk-Hoyes, E.M., Bondesson, U., Westerlund, D., and Andren, P.E. (1999) *Electrophoresis*, **20**, 1527–1532.

103. Tang, Q., Harrata, A.K., and Lee, C.S. (1995) *Anal. Chem.*, **65**, 3515–3519.

104. Lane, S.J. and Tucker, M.G. (1998) *Rapid Commun. Mass Spectrom.*, **12**, 947–954.

105. Apffel, A., Yin, H., Hancock, W.S., McManigill, D., Frenz, J., and Wu, S.-L. (1999) *J. Chromatogr., A*, **832**, 149–163.

106. Ding, J., Barlow, T., Dipple, A., and Vouros, P. (1998) *J. Am. Soc. Mass Spectrom.*, **9**, 823–829.

107. Gronewold, T.M. (2007) *Anal. Chim. Acta*, **603**, 119–128.

108. Paraschiv, G., Vincke, C., Czaplewskac, P., Manea, M., Muyldermans, S., and Przybylski, M. (2012) *J. Mol. Recognit.* doi: 10.1002/jmr.2210

109. Juszczyk, P., Paraschiv, G., Szymanska, A., Kolodziejczyk, A.S., Rodziewicz-Motowidlo, S., Grzonka, Z., and Przybylski, M. (2009) *J. Med. Chem.*, **52**, 2420–2428.

110. Petre, B.A., Ulrich, M., Stumbaum, M., Bernevic, B., Moise, A., Döring, G., and Przybylski, M. (2012) *J. Am. Soc. Mass Spectrom.* doi: 10.1007/s13361-012-0461-4

111. Hoaglund, C.S., Valentine, S.J., Sporleder, C.R., Reilly, J.P., and Clemmer, D.E. (1998) *Anal. Chem.*, **70**, 2236–2242.

112. Iurascu, M.I., Cozma, C., Langridge, J., Tomczyk, N., Desor, M., and Przybylski, M. (2010) in *Ion Mobility Spectrometry – Mass Spectrometry: Theory and Applications* (eds C.I. Wilkins and S. Trimpin), CRC Press, pp. 313–326.

113. Vlad, C., Lindner, K., Karreman, C., Schildknecht, S., Leist, M., Tomczyk, N., Rontree, J., Langridge, J., Danzer, K., Ciossek, T., Petre, A., Gross, M.L., Hengerer, B., and Przybylski, M. (2011) *ChemBioChem*, **12**, 2740–2744.

114. Jung, J.E., Pierson, N.A., Marquardt, A., Scheffner, M., Przybylski, M., and Clemmer, D.E. (2011) *J. Am. Soc. Mass Spectrom.*, **22**, 1463–1471.

115. Vlad, C., Iurascu, M.I., Slamnoiu, S., Hengerer, B., and Przybylski, M. (2012) *Characterization of Oligomerization-Aggregation Products of Neurodegenerative Target Proteins by Ion Mobility Mass Spectrometry*, Intrinsically Disordered Protein Analysis, Vol. 896 (eds V.N.

Uversky and A.K. Dunker) Springer New York. pp. 399–412.

116. Hunt, D.F., Krishnamurthy, T., Shabanowitz, J., Griffin, P.R., Yates, J.R. III,, Martino, P.A., McCormack, A.L., and Hauer, C.R. (1991) in *Mass Spectrometry of Peptides* (ed. D.M. Desiderio), CRC Press, Boca Raton, FL, pp. 139–158.

117. Biemann, K. (1991) in *Methods in Enzymology: Mass Spectrometry* (ed. J.A. McCloskey), Academic Press, San Diego, CA, pp. 455–479.

118. Imahori, K. and Sakiyama, F. (eds) (1993) *Methods in Protein Sequence Analysis*, Plenum Press, New York, pp. 167–171.

119. Roepstorff, P. and Fohlman, J. (1984) *Biomed. Mass Spectrom.*, **11**, 601.

120. Belov, M.E., Gorshkov, M.V., Udseth, H.R., Anderson, G.A., Tolmachev, A.V., Prior, D.C., Harkewicz, R., and Smith, R.D. (2000) *J. Am. Soc. Mass Spectrom.*, **11**, 19–23.

121. Emmett, M.R., White, F.M., Hendrickson, C.L., Shi, S.D., and Marshall, A.G. (1998) *J. Am. Soc. Mass Spectrom.*, **9**, 333–340.

122. Bauer, S.H., Wiechers, M.F., Bruns, K., Przybylski, M., and Stuermer, C.A.O. (2001) *Anal. Biochem.*, **298**, 25–31.

123. Ramelot, T.A., Gentile, L.N., and Nicholsen, L.K.J. (2000) *Biochemistry*, **39**, 2714–2718.

124. Steiner, H., Capell, A., and Haass, C. (1999) *Biochem. Soc. Trans.*, **27**, 234–242.

125. Tian, X., Cecal, R., Amstalden, E., Kohlmann, K., Bruns, K., Buehler, S., and Przybylski, M. (2002) *J. Pept. Sci.*, **8**, 182–186.

126. Roepstorff, P., Nielsen, P.F., Klarskov, B., and Hojrup, P. (1988) *Biomed. Environ. Mass Spectrom.*, **16**, 9–24.

127. Przybylski, M., Manz, I., Fonrobert, P., Dietrich, I., and Brueckner, H. (1986) *Adv. Mass Spectrom.*, **10**, 1519–1521.

128. Caprioli, R.M. and Fan, T. (1986) *Anal. Biochem.*, **154**, 596–603.

129. Windberg, E., Hudecz, F., Marquardt, A., Sebestyen, F., Kiss, A., Bosze, S., Medzihradszky-Schweiger, H., and Przybylski, M. (2002) *Rapid Commun. Mass Spectrom.*, **16**, 834–839.

130. Biemann, K. (1989) in *Protein Sequencing – A Practical Approach* (eds J.B.C. Findley and M.J. Geisow), IRL, Oxford, pp. 99–121.

131. Nielsen, P.F., Landis, B., Svoboda, M., Schneider, K., and Przybylski, M. (1990) *Anal. Biochem.*, **191**, 202–312.

132. Chait, B.T., Wang, R., Beavis, R.C., and Kent, S.B.H. (1993) *Science*, **262**, 89–92.

133. Krishna, R.G. and Wold, F. (1993) in *Methods in Protein Sequence Analysis* (eds K. Imahori and F. Sakiyama), Plenum Press, New York, pp. 167–171.

134. Martin, S.A., Vath, J.E., Yu, W., and Scoble, H. (1993) in *Biological Mass Spectrometry: Present and Future* (eds T. Matsuo, R. Caprioli, M. Gross, and Y. Seyama), John Wiley & Sons, Inc., New York, pp. 313–330.

135. Smith, D.L. and Zhou, Z. (1990) in *Methods in Enzymology: Mass Spectrometry*, Vol. 193 (ed. J.A. McCloskey), Academic Press, San Diego, CA, pp. 374–389.

136. Kinumi, T., Niwa, H., and Matsumoto, H. (2000) *Anal. Biochem.*, **277**, 177–186.

137. Jaffe, H. and Veeranna, P.H.C. (1998) *Biochemistry*, **37**, 16211–16234.

138. Lennon, J.J. and Walsh, K.A. (1999) *Protein Sci.*, **8**, 2487–2493.

139. Przybylski, M., Maier, C., Haegele, K., Bauer, E., Hannappel, E., Nave, R., Melchers, K., Krueger, U., and Schäfer, K.P. (1994) in *Peptides – Chemistry, Structure and Biology* (eds R.S. Hodges and J.A. Smith), Escom, Leiden, pp. 338–340.

140. Voss, T., Schäfer, K.P., Nielsen, P.F., Schäfer, A., Maier, C., Hannappel, E., Maassen, J., Landis, B., Klemm, K., and Przybylski, M. (1992) *Biochim. Biophys. Acta*, **1138**, 261–270.

141. Albach, C., Klein, R.A., and Schmitz, B. (2001) *Biol. Chem.*, **382**, 187–194.

142. Perdivara, I., Petrovich, R., Allinquant, B., Deterding, L.J., Tomer, K.B., and Przybylski, M. (2009) *J. Proteome Res.*, **8**, 631–642.

143. Zachara, N.E., Cole, R.N., Hart, G.W., and Gao, Y. (2002) *Curr. Protoc. Mol. Biol.*, **3**, 1761–1762.

144. Wuhrer, M., Deelder, A.M., and Hokke, C.H. (2005) *J. Chromatogr. B: Anal. Technol. Biomed. Life Sci.*, **825**, 124–133.

145. Posewitz, M.C. and Tempst, P. (1999) *Anal. Chem.*, **71**, 2883–2892.

146. Cao, P. and Stults, J.T. (1999) *J. Chromatogr., A*, **853**, 225–235.

147. Wind, M., Wesch, H., and Lehmann, W.D. (2001) *Anal. Chem.*, **73**, 3006–3011.

148. Becker, J.S., Boulyga, S.F., Damoc, N., and Przybylski, M. (2003) *Int. J. Mass Spectrom.* **228**, 985–997.

149. Goetz, J., Chen, S., van Dorpe, J., and Nitsch, R.M. (2001) *Science*, **293**, 1491–1495.

150. Glazer, A.N. (1976) in *The Proteins*, Vol. 2 (eds H. Neurath and R.L. Hill), Academic Press, New York, pp. 1–103.

151. Suckau, D., Mak, M., and Przybylski, M. (1992) *Proc. Natl. Acad. Sci. U.S.A.*, **89**, 5630–5634.

152. Glocker, M.O., Borchers, C., Fiedler, W., Suckau, D., and Przybylski, M. (1994) *Bioconjugate Chem.*, **5**, 583–590.

153. Welte, W., Nestel, U., Wacker, T., and Diederichs, K. (1995) *Kidney Int.*, **48**, 930–940.

154. Przybylski, M., Glocker, M.O., Nestl, U., Schnaible, V., Blüggel, M., Diederichs, K., Weckesser, J., Schad, M., Schmid, A., Welte, W., and Benz, R. (1996) *Protein Sci.*, **5**, 1477–1489.

155. Smith, L.J., Sutcliff, M.J., Refield, C., and Dobson, C.M. (1991) *Biochemistry*, **30**, 986–994.

156. Rostom, A.A. and Robinson, C.V. (1999) *Curr. Opin. Struct. Biol.*, **9**, 135–141.

157. van Duijn, E., Bakkes, P., Heeren, R., van den Heuvel, R., van Heerikhuizen, H., van der Vies, S.M., and Heck, A.J.R. (2005) *Nat. Methods*, **2**, 371–376.

158. Mallick, P. and Kuster, B. (2010) *Nat. Biotechnol.*, **28**, 695–709.

159. Fligge, T.A., Reinhard, C., Harter, C., Wieland, F.T., and Przybylski, M. (2000) *Biochemistry*, **39**, 8491–8496.

160. Wilkins, M.R. and Williams, K.L. (1997) *Proteome Research: New Frontiers in Functional Genomics*, Springer, Berlin.

161. NCBI (2013) The National Center for Biotechnology Information Advances Science and Health by Providing Access to Biomedical and Genomic Information, *http://www.ncbi.nlm.nih.gov./genome/seq/* (accessed 14 March 2013).

162. Godovac-Zimmermann, J. and Brown, L.R. (2001) *Mass Spectrom. Rev.*, **20**, 1–57.

163. Anderson, N.G., Matheson, A., and Anderson, N.L. (2001) *Proteomics*, **1**, 3–12.

164. Lottspeich, F. (1999) *Angew. Chem. Int. Ed.*, **38**, 2476–2492.

165. Wilm, M., Shevchenko, A., Honthaeve, T., Breit, S., Schweigerer, L., Fotsis, T., and Mann, M. (1996) *Nature*, **379**, 466–469.

166. Jungblut, P. and Thiede, B. (1997) *Mass Spectrom. Rev.*, **16**, 145–162.

167. Goodlett, D.R., Bruce, J.E., Anderson, G.A., Rist, B., Pasa-Tolic, L., Fiehn, O., Smith, R.D., and Aebersold, R. (2000) *Anal. Chem.*, **72**, 1112–1118.

168. Lion, N., Rohner, T.C., Dayon, L., Arnaud, I.L., Damoc, E., Youhnovski, N., Wu, Z.Y., Roussel, C., Josserand, J., Jensen, H., Rossier, J., Przybylski, M., and Girault, H. (2003) *Electrophoresis*, **24**, 3533–3562.

169. Tissot, J.D., Vu, D.H., Aubert, V., Schneider, P., Vuadens, F., Crettaz, D., and Duchosal, M.A. (2002) *Proteomics*, **2**, 813–824.

170. Tissot, J.D., Sanchez, J.C., Vuadens, F., Scherl, A., Schifferli, J.A., Hochstrasser, D.F., Schneider, P., and Duchosal, M.A. (2002) *Electrophoresis*, **23**, 1203–1206.

171. Damoc, E., Youhnovski, N., Crettaz, D., Tissot, J.D., and Przybylski, M. (2003) *Proteomics*, **3**, 1425–1433.

172. McCormack, A.L. (1997) *Anal. Chem.*, **69**, 767–776.

173. Macht, M., Marquardt, A., Deininger, S.O., Damoc, E., Kohlmann, M., and Przybylski, M. (2004) *Anal. Bioanal. Chem.*, **378**, 1102–1111.

174. Gross, M.L. and Przybylski, M. (2010) *J. Am. Soc. Mass Spectrom.*, **21**, 1–2.

175. Reid, J., Holmes, D.T., Mason, D.R., Shah, B., and Borchers, C. (2010)

J. Am. Soc. Mass Spectrom., **21**, 1680–1686.

176. Savitski, M., Fischer, F., Mathieson, T., Sweetman, G., Lang, M., and Bantscheff, M. (2010) *J. Am. Soc. Mass Spectrom.*, **21**, 1668–1679.

177. Dragusanu, M., Petre, B.A., and Przybylski, M. (2011) *J. Pept. Sci.*, **17**, 184–191.

178. Susnea, I., Bunk, S., Wendel, A., Hermann, C., and Przybylski, M. (2011) *J. Am. Soc. Mass Spectrom.*, **22**, 784–788.

179. Gabius, H.-J. (2009) *The Sugar Code: Fundamentals of Glycosciences*, Wiley-VCH Verlag GmbH, Weinheim.

180. Moise, A., Andre, S., Eggers, F., Krzeminski, M., Przybylski, M., and Gabius, H.-J. (2011) *J. Am. Chem. Soc.*, **133**, 14844–14847.

181. Jimeénez-Castells, C., Defaus, S., Moise, A., Przbylski, M., Andreu, D., and Gutierrez-Gallego, R. (2012) *Anal. Chem.*, **84**, 6515–6520.

182. Forman, M.S., Lee, V.M., and Trojanowski, J.Q. (2005) *Neuron*, **47**, 479–486.

183. Olzscha, H., Schermann, S.M., Woerner, A.C., Pinkert, S., Hecht, M.H., Tartaglia, G.G., Vendruscolo, M., Hayer-Hartl, M., Hartl, F.U., and Vabulas, R.M. (2011) *Cell*, **144**, 67.

184. Dunker, A.K., Silman, I., Uversky, V.N., and Sussman, J.L. (2008) *Curr. Opin. Struct. Biol.*, **18**, 756.

185. Crews, L., Tsigelny, I., Hashimoto, M., and Masliah, E. (2009) *Neurotoxic. Res.*, **16**, 306.

186. Przybylski, M., Lindner, K., Vlad, C., Pierson, N., Karreman, C., Schildknecht, S., Leist, M., Tomczyk, N., Langridge, J., Ciossek, T., Petre, A., Gross, M., Hengerer, B., and Clemmer, D. (2013) Ion Mobility- and Affinity- Mass Spectrometry: New tools for elucidating structures and pathways of ''misfolding'' – aggregating proteins, (eds G. Kokotos, V. Constantinou– Kokotou and J. Matsoukas), Proceedings of the 32nd European Peptide Symposium. University of Athens, Athens, pp. 12–13.

187. Slamnoiu, S., Vlad, C., Moise, A., Stumbaum, M., Engel, N., Cozma, A., and Przybylski, M. (2012) Determination of antibody- epitopes and binding affinities of β-amyloid and α-synuclein polypeptides from biological material using online SAW-biosensor-FTICR mass spectrometry. *Int. J. Mass Spectrom.* in press.

12

Multiparametric Analysis of Mass Spectrometry-Based Proteome Profiling in Gestation-Related Diseases

Michael O. Glocker, Claudia Röwer, Manja Wölter, Cornelia Koy, Toralf Reimer, and Ulrich Pecks

12.1

Introduction on Gestational Diseases

Physiological pregnancy leads to distinct alterations in maternal organ functionalities. The cardiovascular, hematologic, metabolic, renal, and respiratory systems, all are affected in order to assist fetal survival as well as in preparation for labor [1]. Failures in any of the involved systems to respond adequately to pregnancy-associated physiological changes consequently result in pregnancy-related disorders, such as gestational diabetes or pregnancy-induced hypertension, and ultimately lead to poor maternal and/or fetal outcome. Moreover, women suffering from gestation-related disorders are at an increased risk of developing diabetes mellitus or cardiovascular diseases later in their lives. As such, pregnancy itself might be regarded as a ‘‘stress test’’ for maternal metabolic and vascular functions [2, 3].

In this chapter, we focus on mass spectrometric profiling of severe forms of hypertension that complicate pregnancy. Clinically manifested gestation-related diseases, such as preeclampsia (PE) and associated conditions, such as HELLP syndrome (hemolysis, elevated liver enzymes, and low platelets), as well as intrauterine growth restriction (IUGR), are of major concern, as it is of utmost importance to learn about their molecular pathogenesis processes. Such knowledge may hopefully lead to novel therapy and clinical care options.

12.1.1

Preeclampsia

Preeclampsia is defined as new onset of hypertension $\geq$140/90 mm Hg and proteinuria of more than 300 mg day^{-1} that, according to definition, manifests after the twentieth week of gestation. From a more clinical point of view PE is also defined as a combination of new onset hypertension and further complications that affect at least one more organ system. Hence, PE may be diagnosed even in the absence of proteinuria. Regardless of its definition, PE is recognized as a multisystemic disorder that may lead to renal insufficiency, liver disease (potentially leading to HELLP),

Handbook of Spectroscopy, Second Edition. Edited by Günter Gauglitz and David S. Moore.

hematological disturbances, placental insufficiency (likely causing IUGR), and/or neurological problems including convulsions (which is then called *eclampsia*) [4].

Despite more than 100 years of excessive research, the pathogenesis of PE still remains unclear. Two main reasons might be responsible for this phenomenon. First, PE is a specific disease in humans and does not exist in animal mammals. Therefore, no adequate animal model can be developed with which one might be able to study the disease in a laboratory setting. Second, it is likely that the disease initiates early in pregnancy, weeks to months before the onset of symptoms. For obvious practical and ethical reasons, most of the biological samples obtained for studying the disease are taken earliest at appearance of disease symptoms or even later, for example, at delivery–very likely a long time after the condition had been initiated. Hence, early events of cellular or molecular changes that lead to the disease are not accessible.

However, it is generally accepted that rather than the fetus' or the mother's physiology, the placenta triggers the disease. This is evidenced by several known associations. (i) PE is a pregnancy-specific disease. No similar pathology exists outside of pregnancy. (ii) The risk increases with placental size. For example, women with twin pregnancies have a fourfold increased risk for developing PE. (iii) PE occurs even without a fetus, that is, in hydatidiform moles. (iv) The symptoms disappear after removal of the placenta (delivery) [5].

Current hypothesis states a two-stage pathophysiological model. The first stage is characterized by a disturbed placentation, whereas an overactive inflammatory maternal response reflects the second stage [6]. In normal early human pregnancy, roughly by week 5, specific placental cells, the cytotrophoblasts, invade the maternal endometrium. Cytotrophoblasts enter uterine spiral arteries and permanently dilate the vessels' walls in order to guarantee sufficient materno-placental blood flow. Insufficient trophoblast invasion and, as a consequence, impaired spiral artery remodeling have been suggested to play a central part in the pathogenesis of PE [7]. These pathophysiological incidences result in placental ischemia-reperfusion and hypoxia followed by an increased formation of reactive oxygen species and inflammatory factors [8]. In consequence, placental particles are extruded and released into the maternal circulation [9, 10], and, depending on maternal susceptibility, this leads to a systemic inflammatory response and endothelial activation [11]. Hypertension in PE is primarily due to marked vasoconstriction. Both, vasoconstriction and the development of glomerular lesions in the kidney, cause a decrement of renal plasma flow and glomerular filtration rate, leading to the second essential symptom of PE: proteinuria [12].

However, it is likely that PE is a heterogeneous disorder. The terms *placental* and *maternal* PE have been introduced to describe the two pathophysiological stages that seem to be most affected [13]. Placental PE comprises about 20% of all PE cases worldwide and usually occurs before the thirty-fourth week of gestation (early onset). It is usually a more severe form and pregnancy has to be terminated preterm in order to assure maternal and/or fetal survival. Most patients, however, suffer from the so-called ''late-onset'' form that typically affects patients after the thirty-fourth week of gestation. This form is often present in patients with predisposing factors, such as a history of renal or cardiac diseases, diabetes, and/or obesity. Moreover, it has been suggested to differentiate PE that has been further complicated by IUGR or by the HELLP syndrome from those that are not additionally affected [7, 14, 15]. Thus, PE can be subclassified according to clinical and molecular biological and/or laboratory chemical findings. It is likely that the development of PE involves several different pathophysiological mechanisms, as evidenced by the diversity of proteins that have been studied to date.

Several biomarkers have been considered for early detection of PE. Among them, serum concentrations of pro- and antiangiogenic factors, such as placental growth factor (PlGF), soluble vascular endothelial growth factor receptor-1 (sVEGFR-1 or sFlt-1), and soluble endoglin were found to be altered in maternal blood, even weeks before the onset of symptoms [16–18]. Moreover, extracorporal removal of sFlt-1 seems to be a promising approach to treat severe PE in order to prolong pregnancy and therefore improve outcome [19]. Other molecules that have been studied include activin A, inhibin A, pentraxin 3 (PTX3), pregnancy-associated plasma protein-A (PAPP-A), and placental protein 13 (PP13) [20–25]. However, neither a prediction model nor a prevention strategy exists by now that is sufficiently reliable for the prediciton of all forms of preeclampsia.

12.1.2
HELLP Syndrome

In 1954, Pritchard *et al.* [26] described three cases of PE/eclampsia, associated with intravascular hemolysis, thrombocytopenia, clotting defects, and evidence of hepatic dysfunction; two of their patients died. Several reports on case series followed until the acronym ''HELLP syndrome'' was introduced for the hematological changes seen in this disorder in 1982. HELLP stands for hemolysis, elevated liver enzymes, and low platelets [27]. The incidence of the HELLP syndrome is $<1\%$ of all pregnancies. Although a rare condition, it is a leading cause of maternal mortality in the western world. About 80% of women presenting with HELLP syndrome have pregnancy-related hypertension and/or proteinuria [28]. Hence, the HELLP syndrome was also regarded as a severe variant of PE. Whether the HELLP syndrome may represent a unique disease entity is still under debate. The pathophysiology is unknown. Hemolysis in HELLP syndrome presents as microangiopathic hemolytic anemia that is confirmed by schistocytes, burr cells, or by low serum haptoglobin concentration. Hepatic histopathology presents as focal parenchymal necrosis and periportal hemorrhage [29]. Inflammatory processes lead to swelling of the liver with distension of the Glisson's capsule. In consequence, epigastric or right upper abdominal pain can frequently be observed in the HELLP syndrome. A decrease in circulating platelets is secondary to an increased rate of platelet aggregation and consumption by the disturbed vascular endothelium. Common complications of the HELLP syndrome are placental abruption, disseminated intravascular coagulation (DIC), and acute renal failure. Less frequently, eclampsia, pulmonary edema, and subcapsular liver hematoma can be observed in association with HELLP [28]. The presenting symptoms and clinical and laboratory findings in women with HELLP syndrome overlap with a variety of other medical conditions. Hence, the HELLP syndrome might sometimes be misdiagnosed as ‘‘acute fatty liver,’’ ‘‘thrombotic thrombocytopenic purpura,’’ ‘‘hemolytic uremic syndrome,’’ or other hepatic diseases and vice versa [30]. Clinical management strategies between these conditions differ substantially, and hence, misdiagnosis leads to a delayed accurate treatment. As is the case for pure PE, delivery is the only definitive cure for HELLP to date. Even more, once a HELLP syndrome is diagnosed expedient delivery is often needed owing to its rapid progression. However, about 30% of HELLP syndromes occur in the post partum period, that is, after delivery. Hitherto, neither reliable preclinical recognition nor effective prevention strategies for the HELLP syndrome are available. As the course of HELLP is incalculable, rapidly determinable, reliable diagnostic markers, or marker profiles, are urgently needed.

12.1.3

Intrauterine Growth Restriction (IUGR)

IUGR affects about 3–8% of pregnancies. It is defined as a condition in that the fetus does not reach its genetically given growth potential, resulting in low birth weight. IUGR is an important cause of perinatal morbidity and mortality, thus contributing substantially to medically indicated preterm birth in order to prevent fetal death [15, 31].

Neonates with birth weight below the 10th (5th, 3rd) percentile are considered to be ‘‘small for gestational age’’ (SGA) [32]. Unfortunately, both terms, *SGA* and *IUGR*, are often used synonymously in the literature, which sometimes leads to confusion. It should be noted that the term *SGA* simply is a description for an underweight newborn baby. SGA, hence, neither refers to fetal growth nor does it take into account the underlying conditions that lead to the low birth weight. It needs to be stated firmly that a child that is born SGA has not necessarily suffered from IUGR [32]. Instead, considerable numbers of SGA infants are small at the time of birth simply because of factors determined by maternal ethnicity, parity, weight, or height. Therefore, some authors have used the term *constitutional small* to underline the physiologic condition in a subset of SGA children [33, 34].

By contrast, IUGR is diagnosed by a deceleration of fetal growth velocity in serial antenatal sonographic measurements of fetal biometry (crossing percentiles). Fetal growth is viewed as having three consecutive dynamic cell growth phases [35, 36]. Until week 16 of pregnancy, the early phase, fetal growth is primarily due to rapid cell division and an increase in cell numbers (hyperplasia). Between 16 and 32 weeks of gestation, concomitant increase of both, cell size and cell number, can be observed. The last phase, after 32 weeks, is mainly determined by cellular hypertrophy (increasing cell size) in which most fetal fat and glycogen deposits are built up. The clinical pattern of IUGR varies depending on the nature of the causative factors, stage of gestation, and duration of the intrauterine insult [37]. An IUGR-influencing factor that occurs within the first 16 weeks of gestation is more likely to lead to an overall diminished cell division, and the resulting growth-restricted fetus appears symmetric with proportional head to abdominal circumferences. Approximately 30% of growth-restricted infants exhibit a symmetric phenotype, and a variety of underlying causes have been described, including chromosomal anomalies, fetal infections, and multifactorial congenital malformations, or maternal diseases. On the contrary, asymmetric growth restriction occurs in 70% of IUGR cases and refers to a greater decrease in the size of the abdomen than that of the head, called *head-sparing phenomenon*. Asymmetric fetuses are therefore more likely to arise in the middle or last phase of fetal growth and it has been proposed that this phenomenon occurs secondary to placental insufficiency. In other words, the increasing fetal nutritional and oxygen demand with ongoing pregnancy exceeds placental nutritional capacity more and more. The diminished nutritional supply causes the fetus to redistribute its cardiac output in favor of vital organs. This phenomenon is reflected by changes in fetal blood flow resistance indices, which are measurable by fetal Doppler sonography. In clinical practice, IUGR is defined as low estimated fetal weight in addition to signs of compromised fetal well-being (pathological fetal cardiogram or resistance indices in Doppler sonographic measurements, asymmetry, and/or reduced amniotic fluid index in ultrasonographic examinations [31]).

The leading cause of placental insufficiency in the pathogenesis of asymmetric IUGR still remains unclear. Diminished cytotrophoblast invasion and uterine spiral artery remodeling has been hypothesized to play a crucial role. Hence, the pathomechanisms in IUGR are similar to those in PE, which might explain why both conditions occur simultaneously in 5–18% of the cases [6, 7].

Over the last decades it has become evident that abnormal intrauterine conditions also increase the infant's risk for cardiovascular and metabolic diseases later in life. The association of being born SGA and of developing atherosclerotic cardiovascular diseases later in life has been shown by several epidemiologic studies [38–40]. Such observations have led to the ''fetal origins of disease hypothesis'' or ''Barker's hypothesis'' in that abnormal conditions in the intrauterine environment may cause long-lasting structural and functional systemic alterations, predisposing an individual to the development of associated disorders. The mechanisms of ''fetal programming'' till now are unclear, but once noticeable disturbances in fetal blood composition toward an atherogenic phenotype in IUGR fetuses are found, biomarker and/or molecular-profile-guided research avenues are opened [41].

12.2
Mass Spectrometric Data Acquisition from Plasma Samples

Analyzing complex gestation-related pathophysiological conditions, such as PE, HELLP syndrome, and IUGR, requires methods that can cope with the complexity of the samples. One of the approaches to study such polygenic diseases that generated considerable interest due to its clinical potential is mass spectrometry (MS)-based proteomic pattern diagnostics. Protein MS with soft-ionizing properties, particularly matrix-assisted laser desorption/ionization-time of flight mass spectrometry (MALDI-TOF MS), proved in our studies to be the best choice for the required data sampling prerequisites. Owing to unsurpassed properties, such as low detection limits, multiplexing capability, rapidity, and facile sample preparation, and because of unbiased protein detection likelihood, which is independent from protein composition and structure, MALDI-MS combines many necessary features for blood profiling. MALDI-MS is an automated technique that can detect hundreds of peptide and/or protein ion signals from clinically obtained body fluids in one measurement with good reproducibility and robustness.

Simultaneously, in order to reduce the complexity of biological samples that typically contain numerous constituents, and particularly for detecting quantitative differences, mostly fractionation steps are applied before the above-mentioned MS-based screening analyses, in an attempt to facilitate detection of suitable markers but not to introduce unknown variables that may change the composition of the investigated samples in an unpredictable manner.

Here, we describe the steps of sample preparation, multiplexed data collection, and advanced multiparametric bioinformational data analysis, emphasizing on implementation and, equally important, the purpose for which a particular method is applied. The aim of our studies is to provide an easy to use reliable assay procedure that includes automated data analysis.

12.2.1

Mass Spectrometric Data Collection Without Sample Fractionation

MS-based screening approaches for describing peptide profiles in combination with fractionation of the proteins/peptides, such as peptidomics [42], surface-enhanced laser desorption/ionization (SELDI) [43], or the use of functionalized bead surfaces [44] have been reported. They have the advantage in common that no previous knowledge about the molecule of interest is needed for performing the assay. This stands in contrast to immunoassay-based techniques, such as ELISA (enzyme-linked immunosorbent assay), where the antigen needs to be known prior to carrying out the analysis.

We have developed a protein profiling method without fractionation [45] that relies on the use of a cryodetector mass spectrometer with principally unlimited mass range and ultra high detection sensitivity throughout the entire mass range [46]. This approach was successfully applied to the analysis of plasma samples from HELLP patients and from controls. The mass spectrometric profiling analysis included high molecular mass proteins that also displayed characteristic differences in the protein abundance profiles in plasma samples from HELLP patients and from healthy women prior to and after delivery.

The mass spectra that were obtained from all plasma samples using the cryodetector mass spectrometer were found to show only minor differences in the overall appearance in our case up to a mass range of m/z 200 000 (Figure 12.1). Mass accuracy of the cryodetector mass spectrometer is 100 ppm at 12.6 kDa and 1000 ppm at 1.5 MDa. In addition to ion signals with high abundance, the spectra showed numerous ion signals of lesser intensity due to the complexity of the protein mixture in plasma.

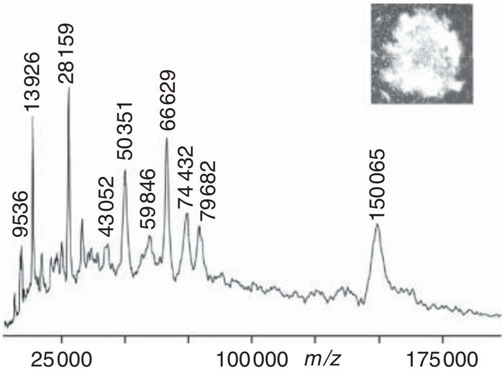

Figure 12.1 MALDI linear TOF cryodetector mass spectrum from plasma proteins of a HELLP patient after delivery; *m/z* range 5000–200 000. Ten selected ion signals are labeled. Ferulic acid was used as matrix. The inset shows a homogeneous sample/matrix distribution on the mass spectrometry target.

Reproducibility of experimental data was sufficient in the investigated cases. Differences in ion signal abundances between measurements of one and the same sample were by far smaller (typically by a factor of 10) than those resulting from the biological differences between samples. Some of the most intense ion signals were tentatively assigned to likely protein candidates, assuming that the corresponding protein ion signals represent the more abundant proteins in plasma [47, 48]. The 66.6 kDa ion signal, for example, is assigned to serum albumin.

The most striking difference in the spectra between most of the HELLP cases and those from the same persons after delivery (post-HELLP) was the presence or absence, respectively, of the so-called 11.8 kDa ion signal (absent in Figure 12.1). On the basis of results from previous studies with plasma samples [49, 50] and in accordance with UniProt data, this ion signal was assigned as serum amyloid A (SAA), although SAA is not an abundant plasma protein.

As indicated, monitoring of this one factor alone seemed not enough to come to a clinically relevant conclusion in all HELLP cases. Instead, statistical analysis of peak intensities of 10 selected ion signals clearly demonstrated that HELLP spectra were distinguishable from those of the post-HELLP samples. The mass spectrometric profiles were in fact different enough in their appearances to enable differentiation between the groups by statistical comparison of the peak intensities. Multifactorial analysis of these ion signal intensities proved reliable in all studied cases. At the same time, we noticed high homogeneity of the spectra within the groups and concluded that the observed intragroup differences were mirroring interindividual variations.

Our results showed that significant differences in ion intensities between post-HELLP (control) control samples and HELLP patients could be recorded without sample fractionation using the cryodetector MS equipment. The method described here is fast, very robust, and suitable to cope with large sample numbers. The assay is easily adaptable to current clinical sample collection procedures and shows high reliability when standard operating procedures are adopted, and, in principle, the method is easily adaptable to procedures that encompass pre-fractionation steps.

12.2.2
Mass Spectrometric Data Collection upon Sample Fractionation

In our next study we applied MALDI-TOF MS-based serum protein analysis as a means to detect PE patients by analyzing samples from pregnant women. We investigated the possibility of the method to reliably differentiate patient samples from those of control individuals, a prerequisite for potential clinical use. Again, from all individuals blood samples were taken and serum proteins were isolated with standardized procedures. However, in this study fractionation of serum proteins was conducted by applying a commercially available reversed-phase coated bead system (ClinProt® Profiling Kit MB-HIC 8).

This procedure proved to be well applicable for fractionation of serum proteins yielding samples suitable for MALDI-MS profiling without further work-up. An overview mass spectrum, using a commercially available time-of-flight (TOF) mass spectrometer equipped with a multichannel plate detector, showed abundant and well resolved protein ion signals between *m/z* 4500 and *m/z* 25 000 (Figure 12.2).

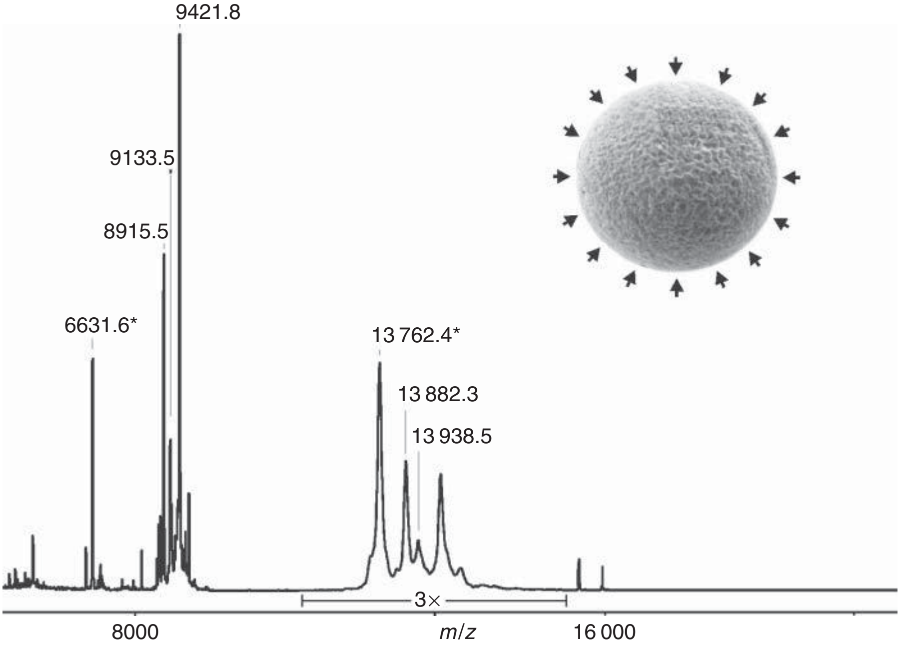

Figure 12.2 MALDI linear TOF mass spectrum of a serum sample after ClinProt® work-up from a preeclampsia patient; *m/z* range 4500–25 000. Selected ion signals are labeled. Signals marked with asterisks were used for calibration. Ferulic acid was used as matrix. The inset shows a magnified bead image to which plasma proteins bind selectively according to their physicochemical properties (indicated by arrows).

In order to better distinguish between the two groups under study and to more accurately assign a given spectrum to either the PE or the control group, a multiparametric analysis was performed in which the normalized ion signal areas within each spectrum were brought into context with each other [14].

In contrast to using the full mass spectrum as sample profile, we searched for a handful of distinctive signature signals by which a sample could be characterized. It turned out that the three most intense singly charged ion signals and the three best group-differentiating singly charged ion signals carried enough information to form rules that enabled accurate sorting of individual spectra, that is, of individual samples, when considering the relations of ion signal intensities in one spectrum (details are given in 12.3).

As a result, we obtained a group of protein ion signals that can be regarded as a "signature for PE" with the most prominent group of ion signals around m/z 13 715. Sodium dodecyl sulfate polyacrylamide gel electrophoresis (SDS PAGE) analysis and peptide mass fingerprinting suggested that these ion signals belonged to a protein called *transthyretin*. Consistent with this, nephelometric analyses showed lower transthyretin concentrations in samples from PE patients with respect to the control group. It should be noted that the transthyretin concentrations of all samples were below the reference value for serum, which is expected to be the case during pregnancy due to plasma volume expansion [51].

To the best of our knowledge, this is the first report of a decrease in transthyretin concentration in serum of the "subgroup of severe early-onset PE" before 34 gestational weeks with respect to transthyretin levels of individuals with uneventful pregnancies. In our experiments, it again turned out that just one marker protein ion signal was not sufficient to differentiate an individual PE sample from a control sample. By contrast, the so-called "multifactorial signatures" are believed to be more adequate for distinguishing two polygenic phenotypes [52–56].

12.3
Multiparametric Analysis of Mass Spectrometry Data

12.3.1
Recalibration and Standardization Strategies

Owing to their quite satisfactory performance, ClinProt® beads were applied to prefractionate serum samples also in other proteome profiling studies by us, as they enabled rapid work-up and yielded in high spectral quality (see preceding paragraph). Subsequent to mass spectrometric data collection, accurate ion signal assignments, that is, determination of correct m/z values for a given ion signal, had to be achieved in order to enable comparison of multiple spectra. The ClinProTools® 2.2 software (Bruker Daltonik, Bremen, Germany) was used to analyze the spectra from patients and controls. Settings had been specified and retained unchanged for all measurement analyses for (i) peak picking, which happened on the total average spectrum of the particular class, (ii) for signal to noise threshold (baseline), the value of which was set to 5.00, and (iii) the relative threshold base peak, the value of which was set to 0.00 (details on baseline effects are given in the next paragraph).

Particularly in order to enabling interassay comparisons with samples from different clinical centers, all mass spectra needed to be internally recalibrated using average masses of defined ion signals. As a calibration example, the ion signal for singly charged and unmodified transthyretin (UniProt accession number P02766) was set to m/z 13 762.4, and the ion signal for the singly charged and unmodified apolipoprotein C-I (UniProt accession number P02654) was set to m/z 6631.6. Transferring these settings to all spectra enabled to correct for calibration errors that needed to be eliminated prior to assigning matching ion signals in each spectrum (Figure 12.3). Precise assignment of ion signals was particularly

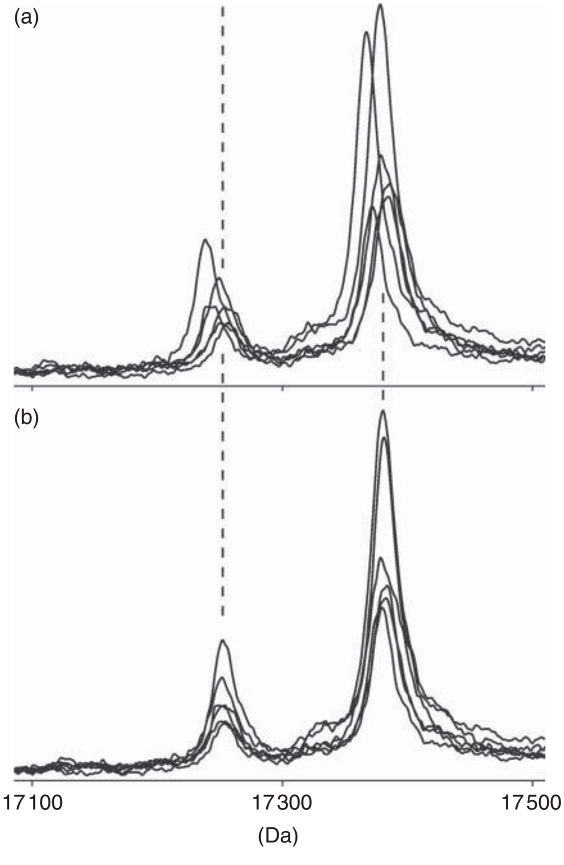

Figure 12.3 MALDI linear TOF mass spectrum of serum samples after ClinProt® work-up from cord blood samples; m/z range 17 100–17 500. (a) Ion signals are overlayed from six sample measurements prior to recalibration. (b) Overlay of the same ion signals after recalibration. The hatched vertical lines show the value of the determined m/z values 17 253.3 and 17 381.5, respectively.

important in regions with multiple ion signals in close proximity in order to exclude false assignments which otherwise would lead to poor overall assay results.

Spectra were recalibrated such that only those masses were taken into account which occurred in at least 30% of the spectra. The maximal mass tolerance between reference mass and peak mass was set to 1500 ppm. Hence, those spectra were excluded from analysis which either could not be recalibrated owing to larger mass differences or which contained too few ion signals for calibration. Smoothing of spectra was performed by applying the Savitsky–Golay algorithm, width 2.0 *m/z* for three cycles.

With successful assignment of correct *m/z* values to each ion signal in the spectrum, the decision of whether a given signal was regarded as belonging to the set of "signature ion signals" was enabled, fulfilling the first prerequisite of the clinically important assessment of whether a selected sample could be grouped into the patients cohort.

12.3.2
Statistical Procedures for Baseline Subtraction and Correction for Intercenter Offsets

Clearly, the next crucial issue to be addressed when analyzing ion signal intensities is the kind of baseline present around the ion signals, as the baseline shape is crucial for determining the area under the peak. As exemplified here, a linear baseline model (Figure 12.4) leads to different peak area values in comparison to a curved baseline approximation. The linear baseline approximation is generating correct peak area results when a flat baseline is present anywhere in the spectrum. By contrast, the curved baseline approximation regards the vicinity of the ion signals, and hence corrects for local baseline anomalies.

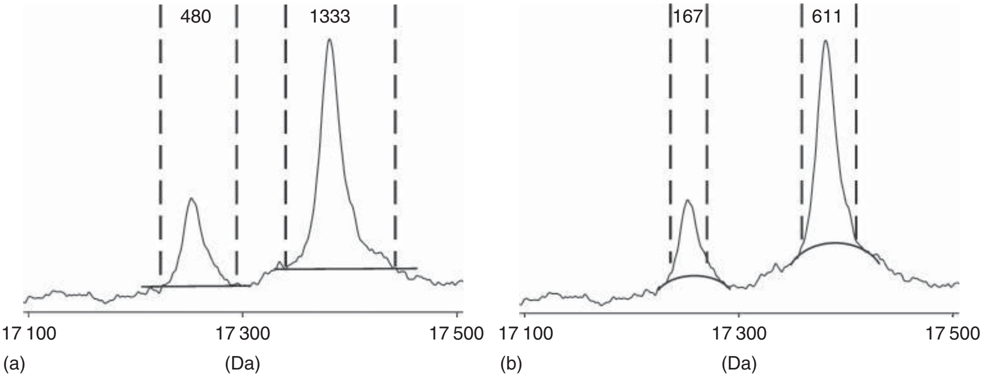

Figure 12.4 MALDI linear TOF mass spectrum of serum samples after ClinProt® work-up from cord blood samples; *m/z* range 17 100–17 500. (a) Areas under the curves of ion signals are determined assuming flat baselines. (b) Areas under the curves of ion signals determined with curved baseline approximation. Approximated baselines are shown as solid lines. The hatched vertical lines show the left and right margins of the ion signals that were set for integration. Calculated peak areas are given in arbitrary units.

In our experiments, baseline subtraction was performed in the ‘‘Top Hat Baseline mode’’ of the software. Further, all ion intensities in the spectra, measured as the integrated area of respective ion signals, were normalized to their own total ion count (TIC), which was determined as the sum of all intensities of all ion signals in the spectrum. Subsequently, single intensities of ion signals in this spectrum were divided by the summed-up TIC value obtained.

Even with precise matching of m/z values of ion signals and appropriate baseline subtraction in each spectrum, additional intercenter offsets in ion signal areas needed to be corrected when multicenter studies were performed. This was achieved using a standardization procedure for calculating the so-called z-scores for each peak area with Eq. (12.1), in which x describes an individual ion signal area, μ is the mean of the ion signal areas from all patients for the corresponding center, and σ is the standard deviation of μ.

$$z = \frac{x - \mu}{\sigma} \tag{12.1}$$

In our cases ‘‘+10’’ was added to all z-score values in order to avoid negative numbers for z [57]. This procedure cures unavoidable sample handling differences that come along when multicenter studies are performed. Multicenter studies are common in clinical research as they increase the available numbers of patient samples per cohort. Obviously, the analysis method of choice needs to be robust with respect to intercenter deviations that otherwise would add to the interindividual variability of sample values.

12.3.3
Determination of Cut-Off Values for Ion Signal Areas

As mentioned above, ion signals that were determined as being suitable for characterizing a spectrum, that is, sample, as either belonging to the group of patients or to the group of control individuals, were selected by statistical evaluation. Statistical significance was tested with a Wilcoxon rank-sum test [58] combined with a Kruskal–Wallis test [59], an Anderson–Darling test [60], and an ANOVA (analysis of variance) test combined with a Student’s t-test for two populations [61, 62]. All tests were performed on significance levels of 0.05. Using this approach, we generally obtained two kinds of ion signals when comparing spectra from both groups. The first category of ion signals encompassed those that displayed invariable areas regardless of their group origin. The second set of ion signals contained those that displayed on average quite distinct area values, and hence were considered suitable for differentiation of the groups. In our understanding, both kinds of ion signals carried valuable information about their sample. In order to make use of all available information, we calculated several quotients of the standardized and normalized areas of selected ion signals in pairs (Figure 12.5).

Graphical representations of the obtained values of the quotients were depicted as box-and-whisker plots [63], for example, using the Origin software (Version 6.1G, OriginLab Corporation, Northampton, MA, USA). With our MS data it turned out that the cutoff values for the scoring system were determined such that they had to

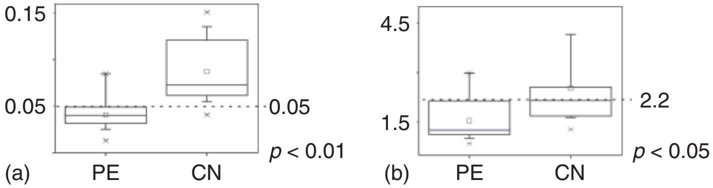

Figure 12.5 Distributions of peak area quotients from selected ion signal pairs derived from MS measurements of plasma samples after ClinProt® work-up (box and whiskers plots). Samples were from patients with preeclampsia (PE) and from healthy pregnant controls (CN). (a) Example with sufficient separation of the values, that is, little overlapping value ranges (P-value < 0.01). (b) Example with poor separation, that is, highly overlapping value ranges (P-value < 0.05). Boxes represent the upper (75% value) and lower quartile (25% value). The separation line in the box marks the 50% value (mean). Vertical bars indicate the standard deviation. Average values are depicted as little boxes. Upper and lower extreme values are indicated with a "minus sign." × symbols show the 99 and 1% range of the individual values, respectively. The horizontal hatched lines mark the cutoff values that were chosen for separation of the two groups.

be at least higher than the upper quartile (75% value) of the group that consistently showed lower values, and, ideally, lower than the lower quartile (25% value) of the group that consistently possessed higher values. There is no need to mention that the lesser the overlap between the values of the two groups, the better the separation by the cutoff line. In cases where the above-introduced criteria could not be reached, it was decided to still place the cutoff value higher than the upper quartile (75% value) of the group with consistently lower values. When the values of the quotients for the samples of patients were lower, as was the case in a few of our control assays [14], the number of true positives remained as high as desired; just the number of false positives increased. This effect turned out to be more tolerable in the overall assay outcome than the opposite.

Using the information of abundant but not differentiating ion signals of a given spectrum together with differentiating ones allowed the inclusion of internal check marks for each spectrum together with determining the individual sample profiles, which simultaneously corrected for mass spectrometric interassay variabilities, such as detector performance, ionization yields, and so on, and, most importantly, improved the overall data quality.

12.3.4
Biostatistical Assay Evaluation and Data Visualization

Testing whether in a given sample spectrum a defined area quotient reached the respective cutoff value provided a "yes" or "no" allocation for each test. When, for example, the value of one quotient was higher than the respective cutoff, a score of "1" was given to this respective sample. In the contrary case, the score for this sample was set to "0." This check was independently carried out n times for each of the defined ion signal ratios with each individual spectrum. Hence, each spectrum, that is, each sample, could ultimately reach a cumulative score between "0" and "n."

Subsequently, it was determined that a cumulative score above "$n - x$" was sorting the respective spectrum (sample) into the group of patients. Otherwise, it fell to the group of controls. Applying these dichotomic grouping rules enabled a clear-cut separation of PE samples into the PE group and control samples into the control group [57].

In the end, the results of this scoring system were compared to group assignments according to clinical criteria (the standard of truth). This enabled assessing biostatistical significance by calculating sensitivity, specificity, false positive rate, false negative rate, positive predictive value, and negative predictive value, and so on. In order to display clinically relevant quantities, for example, sensitivity, specificity, and likelihood ratios receiver operator characteristic (ROC) plots (Figure 12.6) have become increasingly popular.

Applying such ROC analyses is useful in general in evaluating a test system for its diagnostic performance or its accuracy [64, 65]. Areas under curves (AUC), for example, ROC, can be classified into groups that allow quality estimations. An AUC of 0.5 indicates "random" assignments, which is equal to an unacceptable test performance. An AUC of 1.0, on the other hand, is reached with a "perfect" assay that categorizes all samples into the correct groups–patients versus control individuals in our samples. Owing to cryptic sample inconsistencies that are lying outside of the control of the experimentator (a clinical cohort of patients is always an assembly of heterogeneous individuals), a "perfect" assay result is almost never observed in practice. An assay performance scaling in between "perfect" and "random" with decreasing AUC values uses the terms "excellent" ($\text{AUC} \geq 0.9$), "good" ($0.8 \leq \text{AUC} \geq 0.9$), "fair" ($0.7 \leq \text{AUC} \geq 0.8$), and "poor" ($\text{AUC} < 0.7$) [64, 66]. In our experience, an AUC category of at least "good" is required for clinically meaningful assays with the chosen group size [67]. Lesser AUC values may be of interest with very large sample sizes or in preclinical research for improving assays such that they gain in quality, ultimately reaching a level that makes them

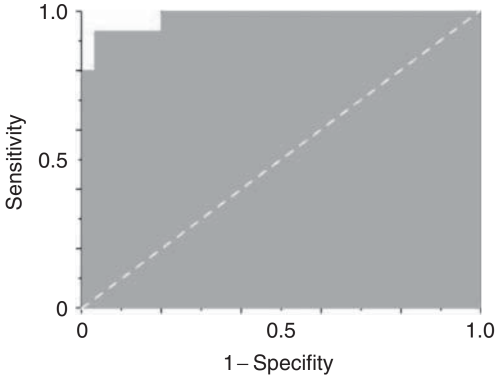

Figure 12.6 Receiver operator characteristic (ROC) curve for a cumulative score consisting of five additive criteria by which cord blood samples from IUGR infants were separated from those of controls. Calculated area under curve (AUC): 0.99. The hatched diagonal marks the 0.5 value.

interesting for clinical application. While testing, the biostatistical meaning of a given procedure is very helpful to describe the overall assay quality; in the end, the clinician is interested in getting access to a diagnostic (or even prognostic) procedure that is capable of identifying whether an individual sample is from a patient that carries the disease.

In order to display a complex data space with multiple entries but at the same time with individual sample resolution, the so-called ''heat maps'' derived from hierarchical clustering aligned in dendrograms is regarded as the ideal choice. In our examples, normalized values of selected ion signal area quotients are graphically represented in independent lines for each of the rules (quotients of normalized ion signal areas) that were selected for the assay (Figure 12.7). Individual patients and control samples are listed in columns from left to right.

Hierarchical clustering was performed on the basis of the complete linkage method and Spearman's correlation coefficient as a measure of similarity. Signal intensities were centered and scaled row-wise for visualization purposes [68] and enabled clear separation of the patients from the control samples with five independent classifier rules. Note that all PE patient samples were clustered correctly into the patient group. Only two control individuals were erroneously sorted into the patient group. All other control individuals were clustering in the control group. With this information, the clinician is instantly able to check clinical data of the patient/person of interest that may help interpret the overall assay result.

Interestingly, while in our example all patients are forking from one major branch of the tree (branch 3 at the left), the control group seemed to consist of two subgroups (separated by branches 1 and 2 at the right). The fact that the control

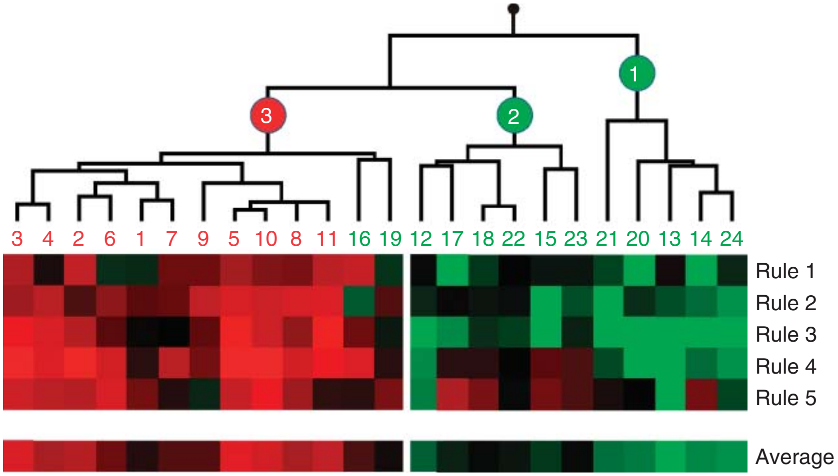

Figure 12.7 Hierarchical clustering of preeclampsia and control samples (PE; patient numbers in red) and control (CN; patient numbers in green). The vertical white line separates the main branches of the tree; branch 3 is on the left and branches 2 and 1 are on the right.

group displayed a broader heterogeneity than the patient group was observed quite frequently in clinical studies. Larger inhomogeneity of the control group seems system immanent because the clinical definition normally precisely describes the disease characteristics (Section 12.1), but gives no clear definition about the control group, except for defining the absence of the disease symptoms. Given these circumstances, such high accuracy of separation, as shown here, is considered satisfactory with respect to accurately identifying patient samples. In conclusion, the high reliability of the proteome signature that was defined with the above outlined approach was proven again.

12.4

Conclusion and Clinical Relevance

Proteomic pattern analysis of polygenic diseases generates considerable clinical interest owing to its diagnostic potential. With increasing power of computerized data analysis, it has become feasible to tackle the challenge to analyze data from complex clinical samples, such as blood serum. MALDI-TOF MS is an advanced technique that can detect hundreds of peptide and/or protein ion signals from clinically obtained body fluids in just one measurement with high fidelity and robustness. Hence, MALDI-TOF MS has enabled the multiparametric analysis of the reservoir of proteins derived from high-abundance endogenous circulating proteins. As a consequence, mass spectrometric measurements of the entire set of protein abundances in biological fluids allow the representation of proteome signatures for a particular pathology. An advantage of MS-based proteomics is that this approach does not require prior knowledge of the pathophysiological mechanisms underlying the condition of interest or even the existence of any single specific protein, as long as the signature of recorded signals remains differential. As a consequence, mass spectrometric measurements of the entire set of protein abundances in biological fluids (proteome signatures) allow the representation of a particular pathology, and the resulting signature is, in the best case, unique to the disease.

In all three gestation-related diseases mentioned, the placenta and/or the liver plays important roles. The placenta assumes dominating functions for life support of the fetus and contributes to the fetus' plasma/serum protein constitution. Owing to remarkable interconnections between the circulations of mothers and fetuses through the placenta, the likelihood of finding gestational disease-related alterations in the composition of the mothers' blood proteins is rather high, particularly, when the mothers' liver functions are also affected. Hence, comprehensive blood protein analysis during pregnancy provides sophisticated molecular diagnostics of such polygenic diseases, which is the key for forwarding our knowledge on gestational disease pathology. In our studies, we aimed at seeking disease-related plasma/serum protein constitution alterations that may become useful for diagnostics and perhaps even prognostics of gestational diseases. This endeavor has become feasible as with increasing power of computerized data analysis it has become possible to analyze complex data sets from clinical samples. Once the robustness of all involved steps is shown, clinics worldwide should be ready to adopt such analysis procedures on a routine basis. Hence, MALDI-TOF MS, either in combination with fractionation of the sample or without (as shown with the cryodetector system) enabled the multiparametric analysis of the reservoir of proteins derived from high-abundance endogenous circulating molecules from pregnant women, paving the way for fast decision-making for the best therapy and clinical care for each individual patient in the future.

References

1. Ciliberto, C.F. and Marx, G.F. (1998) Physiological changes associated with pregnancy. *Update Anaesth.*, **9**, 1–6.
2. Bellamy, L., Casas, J.-P., Hingorani, A.D., and Williams, D.J. (2007) Pre-eclampsia and risk of cardiovascular disease and cancer in later life: systematic review and meta-analysis. *Br. Med. J.*, **335** (7627), 974.
3. Sattar, N. and Greer, I.A. (2002) Pregnancy complications and maternal cardiovascular risk: opportunities for intervention and screening? *Br. Med. J.*, **325** (7356), 157–160.
4. Brown, M.A., Lindheimer, M.D., de Swiet, M., Assche, A.V., and Moutquin, J.-M. (2001) The classification and diagnosis of the hypertensive disorders of pregnancy: statement from the International society for the study of hypertension in pregnancy (ISSHP). *Hypertens. Pregnancy*, **20** (1), ix–xiv.
5. Roberts, J.M. and Redman, C.W.G. (1993) Pre-eclampsia: more than pregnancy-induced hypertension. *Lancet*, **341** (8858), 1447–1451.
6. Steegers, E.A.P., von Dadelszen, P., Duvekot, J.J., and Pijnenborg, R. (2010) Pre-eclampsia. *Lancet*, **376** (9741), 631–644.
7. Huppertz, B. (2008) Placental origins of preeclampsia. *Hypertension*, **51** (4), 970–975.
8. Burton, G.J., Yung, H.W., Cindrova-Davies, T., and Charnock-Jones, D.S. (2009) Placental endoplasmic reticulum stress and oxidative stress in the pathophysiology of unexplained intrauterine growth restriction and early onset preeclampsia. *Placenta*, **30** (Suppl. A), 43–48.
9. Knight, M., Redman, C.W.G., Linton, E.A., and Sargent, I.L. (1998) Shedding of syncytiotrophoblast microvilli into the maternal circulation in pre-eclamptic pregnancies. *Br. J. Obstet. Gynaecol.*, **105** (6), 632–640.
10. Lo, Y.M.D., Leung, T.N., Tein, M.S.C., Sargent, I.L., Zhang, J., Lau, T.K., Haines, C.J., and Redman, C.W.G. (1999) Quantitative abnormalities of fetal DNA in maternal serum in preeclampsia. *Clin. Chem.*, **45** (2), 184–188.
11. Redman, C.W., Sacks, G.P., and Sargent, I.L. (1999) Preeclampsia: an excessive maternal inflammatory response to pregnancy. *Am. J. Obstet. Gynecol.*, **180** (2, Pt. 1), 499–506.
12. Lindheimer, M.D., Taler, S.J., and Cunningham, F.G. (2010) Hypertension in pregnancy. *J. Am. Soc. Hypertens.*, **4** (2), 68–78.
13. Redman, C.W.G. and Sargent, I.L. (2010) Immunology of pre-eclampsia. *Am. J. Reprod. Immunol.*, **63** (6), 534–543.
14. Pecks, U., Caspers, R., Schiessl, B., Bauerschlag, D., Piroth, D., Maass, N., and Rath, W. (2011) The evaluation of the oxidative state of low-density lipoproteins in intrauterine growth restriction and preeclampsia. *Hypertens. Pregnancy*, **1–10**, 156–165.
15. Villar, J., Carroli, G., Wojdyla, D., Abalos, E., Giordano, D., Ba'aqeel, H., Farnot, U., Bergsjø, P., Bakketeig, L., Lumbiganon, P., Campodónico, L.,

Al-Mazrou, Y., Lindheimer, M., and Kramer, M. (2006) Preeclampsia, gestational hypertension and intrauterine growth restriction, related or independent conditions? *Am. J. Obstet. Gynecol.*, **194** (4), 921–931.

16. Levine, R.J., Lam, C., Qian, C., Yu, K.F., Maynard, S.E., Sachs, B.P., Sibai, B.M., Epstein, F.H., Romero, R., Thadhani, R., and Karumanchi, S.A. (2006) Soluble endoglin and other circulating antiangiogenic factors in preeclampsia. *N. Engl. J. Med.*, **355** (10), 992–1005.

17. Levine, R.J., Maynard, S.E., Qian, C., Lim, K.-H., England, L.J., Yu, K.F., Schisterman, E.F., Thadhani, R., Sachs, B.P., Epstein, F.H., Sibai, B.M., Sukhatme, V.P., and Karumanchi, S.A. (2004) Circulating angiogenic factors and the risk of preeclampsia. *N. Engl. J. Med.*, **350** (7), 672–683.

18. Verlohren, S., Galindo, A., Schlembach, D., Zeisler, H., Herraiz, I., Moertl, M.G., Pape, J., Dudenhausen, J.W., Denk, B., and Stepan, H. (2010) An automated method for the determination of the sFlt-1/PIGF ratio in the assessment of preeclampsia. *Am. J. Obstet. Gynecol.*, **202** (2), 161.e1–161.e11.

19. Thadhani, R., Kisner, T., Hagmann, H., Bossung, V., Noack, S., Schaarschmidt, W., Jank, A., Kribs, A., Cornely, O.A., Kreyssig, C., Hemphill, L., Rigby, A.C., Khedkar, S., Lindner, T.H., Mallmann, P., Stepan, H., Karumanchi, S.A., and Benzing, T. (2011) Pilot study of extracorporeal removal of soluble fms-like tyrosine kinase 1 in preeclampsia/clinical perspective. *Circulation*, **124** (8), 940–950.

20. Aquilina, J., Barnet, A., Thompson, O., and Harrington, K. (1999) Second-trimester maternal serum inhibin A concentration as an early marker for preeclampsia. *Am. J. Obstet. Gynecol.*, **181** (1), 131–136.

21. Bersinger, N.A., Smárason, A.K., Muttukrishna, S., and Groome, N.P. (2003) Women with preeclampsia have increased serum levels of pregnancy-associated plasma protein A (PAPP-A), inhibin A, activin A and soluble E-selectin. *Hypertens. Pregnancy*, **22** (1), 45–55.

22. Cetin, I., Cozzi, V., Pasqualini, F., Nebuloni, M., Garlanda, C., Vago, L., Pardi, G., and Mantovani, A. (2006) Elevated maternal levels of the long pentraxin 3 (PTX3) in preeclampsia and intrauterine growth restriction. *Am. J. Obstet. Gynecol.*, **194** (5), 1347–1353.

23. Huppertz, B., Sammar, M., Chefetz, I., Neumaier-Wagner, P., Bartz, C., and Meiri, H. (2008) Longitudinal determination of serum placental protein 13 during development of preeclampsia. *Fetal Diagn. Ther.*, **24** (3), 230–236.

24. Muttukrishna, S., Knight, P.G., Groome, N.P., Redman, C.W.G., and Ledger, W.L. (1997) Activin A and inhibin A as possible endocrine markers for pre-eclampsia. *Lancet*, **349** (9061), 1285–1288.

25. Nicolaides, K.H., Bindra, R., Turan, O.M., Chefetz, I., Sammar, M., Meiri, H., Tal, J., and Cuckle, H.S. (2006) A novel approach to first-trimester screening for early pre-eclampsia combining serum PP-13 and Doppler ultrasound. *Ultrasound Obstet. Gynecol.*, **27** (1), 13–17.

26. Pritchard, J.A., Weisman, R., Ratnoff, O.D., and Vosburgh, G.J. (1954) Intravascular hemolysis, thrombocytopenia and other hematologic abnormalities associated with severe toxemia of pregnancy. *N. Engl. J. Med.*, **250** (3), 89–98.

27. Weinstein, L. (2005) Syndrome of hemolysis, elevated liver enzymes, and low platelet count: a severe consequence of hypertension in pregnancy. *Am. J. Obstet. Gynecol.*, **193** (3), 859.

28. Rath, W., Faridi, A., and Dudenhausen, J.W. (2000) HELLP syndrome. *J. Perinat. Med.*, **28**, 249–260.

29. Barton, J.R., Riely, C.A., Adamec, T.A., Shanklin, D.R., Khoury, A.D., and Sibai, B.M. (1992) Hepatic histopathologic condition does not correlate with laboratory abnormalities in HELLP syndrome (hemolysis, elevated liver enzymes, and low platelet count). *Am. J. Obstet. Gynecol.*, **167** (6), 1538–1543.

30. Sibai, B.M. (2004) Diagnosis, controversies, and management of the syndrome of hemolysis, elevated liver enzymes, and low platelet count. *Obstet. Gynecol.*, **103** (5, Pt. 1), 981–991.

31. American College of Obstetricians and Gynecologists. Committee on Practice Bulletins (2001) Clinical management guidelines for obstetrician-gynecologists. Intrauterine growth restriction. *Int. J. Gynaecol. Obstet.*, **72** (1), 85–96.

32. Lee, P.A., Chernausek, S.D., Hokken-Koelega, A.C.S., Czernichow, P., and International SGA Advisory Board (2003) International small for gestational age advisory board consensus development conference statement: management of short children born small for gestational age, April 24-October 1, 2001. *Pediatrics*, **111** (6), 1253–1261.

33. Ananth, C.V. and Vintzileos, A.M. (2009) Distinguishing pathological from constitutional small for gestational age births in population-based studies. *Early Hum. Dev.*, **85** (10), 653–658.

34. Gardosi, J. (2006) New definition of small for gestational age based on fetal growth potential. *Horm. Res.*, **65** (Suppl. 3), 15–18.

35. Winick, M. (1971) Cellular changes during placental and fetal growth. *Am. J. Obstet. Gynecol.*, **109** (1), 166–176.

36. Rosso, P. and Winick, M. (1974) Intrauterine growth retardation: a new systematic approach based on the clinical and biochemical characteristics of this condition. *J. Perinat. Med.*, **2** (3), 147–160.

37. Lin, C.-C. and Santolaya-Forgas, J. (1998) Current concepts of fetal growth restriction: part I. Causes, classification, and pathophysiology. *Obstet. Gynecol.*, **92** (6), 1044–1055.

38. Barker, D.J.P., Osmond, C., Winter, P.D., Margetts, B., and Simmonds, S.J. (1989) Weight in infancy and death from ischaemic heart disease. *Lancet*, **334** (8663), 577–580.

39. Hales, C.N., Barker, D.J., Clark, P.M., Cox, L.J., Fall, C., Osmond, C., and Winter, P.D. (1991) Fetal and infant growth and impaired glucose tolerance at age 64. *Br. Med. J.*, **303** (6809), 1019–1022.

40. Phipps, K., Barker, D.J.P., Hales, C.N., Fall, C.H.D., Osmond, C., and Clark, P.M.S. (1993) Fetal growth and impaired glucose tolerance in men and women. *Diabetologia*, **36** (3), 225–228.

41. Pecks, U., Brieger, M., Schiessl, B., Fitzner, C., Bauerschlag, D.O., Maass, N., and Rath, W. (2011) Evaluating fetal cord blood lipids and oxidized LDL status in the intrauterine growth restriction and preeclampsia. *Pregnancy Hypertens.*, **1** (3–4), 261.

42. Schulz-Knappe, P., Zucht, H.D., Heine, G., Jurgens, M., Hess, R., and Schrader, M. (2001) Peptidomics: the comprehensive analysis of peptides in complex biological mixtures. *Comb. Chem. High Throughput Screen.*, **4** (2), 107–217.

43. Zhu, H. and Snyder, M. (2003) Protein chip technology. *Curr. Opin. Chem. Biol.*, **7** (1), 55–63.

44. Pusch, W., Flocco, M.T., Sau-Mei, L., Thiele, H., and Kostrzewa, M. (2003) Mass spectrometry-mased clinical proteomics. *Pharmacogenetics*, **4**, 463–476.

45. Koy, C., Heitner, J.C., Woisch, R., Kreutzer, M., Serrano-Fernandez, P., Gohlke, R., Reimer, T., and Glocker, M.O. (2005) Cryodetector mass spectrometry profiling of plasma samples for HELLP diagnosis: an exploratory study. *Proteomics*, **5** (12), 3079–3087.

46. Christ, P., Rutzinger, S., Seidel, W., Uchaikin, S., Proebst, F., Koy, C., and Glocker, M.O. (2004) High detection sensitivity achieved with cryogenic detectors in combination with matrix-assisted laser desorption/ionisation time-of-flight mass spectrometry. *Eur. J. Mass Spectrom.*, **10** (4), 469–476.

47. Manabe, T., Mizuma, H., and Watanabe, K. (1999) A nondenaturing protein map of human plasma proteins correlated with a denaturing polypeptide map combining techniques of micro two-dimensional gel electrophoresis. *Electrophoresis*, **20** (4–5), 830–835.

48. Anderson, N.L., Polanski, M., Pieper, R., Gatlin, T., Tirumalai, R.S., Conrads, T.P., Veenstra, T.D., Adkins, J.N., Pounds, J.G., Fagan, R., and Lobley, A. (2004) The human plasma proteome: a nonredundant list developed by combination of four separate sources. *Mol. Cell. Proteomics*, **3** (4), 311–326.

49. Sinz, A., Bantscheff, M., Mikkat, S., Ringel, B., Drynda, S., Kekow, J., Thiesen, H.-J., and Glocker, M.O. (2002) Mass spectrometric proteome analyses of synovial fluids and plasmas from patients suffering from rheumatoid arthritis and comparison to reactive arthritis or osteoarthritis. *Electrophoresis*, **23** (9), 3445–3456.

50. Heitner, J.C., Koy, C., Reimer, T., Kreutzer, M., Gerber, B., and Glocker, M.O. (2006) Differentiation of HELLP patients from healthy pregnant women by proteome analysis. *J. Chromatogr., B*, **840** (1), 10–19.

51. Sapin, V., Alexandre, M.C., Chaïb, S., Bournazeau, J.A., Sauvant, P., Borel, P., Jacquetin, B., Grolier, P., Lémery, D., Dastugue, B., and Azaïs-Braesco, V. (2000) Effect of vitamin A status at the end of term pregnancy on the saturation of retinol binding protein with retinol. *Am. J. Clin. Nutr.*, **71** (2), 537–543.

52. Alldridge, L., Metodieva, G., Greenwood, C., Al-Janabi, K., Thwaites, L., Sauven, P., and Metodiev, M. (2008) Proteome profiling of breast tumors by gel electrophoresis and nanoscale electrospray ionization mass spectrometry. *J. Proteome Res.*, **7** (4), 1458–1469.

53. Röwer, C., Vissers, J.P.C., Koy, C., Kipping, M., Hecker, M., Reimer, T., Gerber, B., Thiesen, H.-J., and Glocker, M.O. (2009) Towards a proteome signature for invasive ductal breast carcinoma derived from label-free nanoscale LC-MS protein expression profiling of tumorous and glandular tissue. *Anal. Bioanal. Chem.*, **395** (8), 2443–2456.

54. Seike, M., Kondo, T., Fujii, K., Yamada, T., Gemma, A., Kudoh, S., and Hirohashi, S. (2004) Proteomic signature of human cancer cells. *Proteomics*, **4** (9), 2776–2788.

55. Wang, M., You, J., Bemis, K.G., Tegeler, T.J., and Brown, D.P.G. (2008) Label-free mass spectrometry-based protein quantification technologies in proteomic analysis. *Brief. Funct. Genomic. Proteomic.*, **7** (5), 329–339.

56. Yamada, M., Fujii, K., Koyama, K., Hirohashi, S., and Kondo, T. (2009) The proteomic profile of pancreatic cancer cell lines corresponding to carcinogenesis and metastasis. *J. Proteomics Bioinform.*, **2** (1), 001–018.

57. Pecks, U., Schütt, A., Röwer, C., Reimer, T., Schmidt, M., Preschany, S., Stepan, H., Rath, W., and Glocker, M.O. (2012) A mass spectrometric multicenter study supports classification of preeclampsia as heterogenous disorder. *Hypertens. Pregnancy*, **31** (2), 278–291.

58. Wilcoxon, F. (1945) Individual comparisons by ranking methods. *Biomet. Bull.*, **1** (6), 80–83.

59. Kruskal, W.H. and Wallis, W.A. (1952) Use of ranks in one-criterion variance analysis. *J. Am. Stat. Assoc.*, **47** (260), 583–621.

60. Stephens, M.A. (1974) EDF statistics for goodness of fit and some comparisons. *J. Am. Stat. Assoc.*, **69** (347), 730–737.

61. Chambers, J.M. and Hastie, T.J. (1992) *Statistical Models in S*, Wadsworth & Brooks/Cole, Pacific Grove, CA.

62. Walpole, R.E. and Myers, R. (1993) *Probability and Statistics for Engineers and Scientists*, Macmillan, New York.

63. Tukey, J.W. (1977) *Exploratory Data Analysis*, Addison-Wesley, Reading, MA.

64. Metz, C.E. (1978) Basic principles of ROC analysis. *Semin. Nucl. Med.*, **8** (4), 283–298.

65. Zweig, M.H. and Campbell, G. (1993) Receiver-operating characteristic (ROC) plots: a fundamental evaluation tool in clinical medicine. *Clin. Chem.*, **39** (4), 561–577.

66. Van Cauwenberghe, E., Gubbels, J., De Bourdeaudhuij, I., and Cardon, G. (2011) Feasibility and validity of accelerometer measurements to assess physical activity in toddlers. *Int. J. Behav. Nutr. Phys. Acta*, **8** (1), 67.

67. Wölter, M., Koy, C., Röwer, C., Reimer, T., Rath, W., Pecks, U., and Glocker, M.O. (2012) An IUGR proteome signature derived from multifactorial analysis of mass spectrometry-based cord blood serum profiling. *Electrophoresis*, **33**, 1881–1893.

68. Eisen, M.B., Spellmann, P.T., Brown, P.O., and Botstein, D. (1998) Cluster analysis and display of genome-wide expression patterns. *Proc. Natl. Acad. Sci. U.S.A.*, **95** (25), 14863–14868.

13
Laser-Assisted Mass Spectrometry

David Touboul and Renato Zenobi

13.1
Introduction

Mass spectrometry (MS), defined as the analytical science related to the study of charged particles in the gas phase by measuring their mass-to-charge (m/z) ratio, has always profited from a large variety of different methods for vaporizing and ionizing the samples. The formation of gas-phase ions from solid, liquid, or gaseous neutrals is in fact the first key step of any mass spectrometric analysis. Classically, electron impact (EI) ionization, where the sample interacts with an electron beam, and chemical ionization (CI), a soft ionization method where an auxiliary ionized gas is utilized, have been used. Both EI and CI are, however, restricted to volatile or gaseous samples. Early on, energetic beams were used for direct ion production from nonvolatile solids. For example, in secondary ion mass spectrometry (SIMS), an energetic ion beam bombards a solid sample surface and liberates secondary ions that are indicative of the composition of the surface. In ^{252}Cf plasma desorption, the products of a nuclear fission event interact with a nonvolatile sample, again liberating ions that can be used to determine the sample composition. Incidentally, many of these desorption/ionization methods turned out to be quite soft, that is, little fragmentation occurred, even from complex organic molecules. It was only natural that laser beams were also employed for ion generation from nonvolatile solids. This method was called ‘‘laser desorption mass spectrometry’’ (LDMS).

In the 1970s, lasers become commercially available and more affordable, leading to their extensive use in physics. For example, experiments by Hillenkamp and coworkers in Germany [1] were conducted to locally deposit energy on surfaces by laser irradiation. Desorption/ionization of organic and inorganic nonvolatile compounds that showed optical absorption at the wavelength of the laser was demonstrated, opening a new field of investigation for MS. A decade later, the matrix-assisted laser desorption/ionization (MALDI) technique was discovered by Hillenkamp and Karas in Germany [2], and almost simultaneously by Tanaka in Japan [3]. Very large and fragile biological molecules can now be easily ionized by MALDI, a method which is widely used in bioanalysis, and especially proteomics.

Handbook of Spectroscopy, Second Edition. Edited by Günter Gauglitz and David S. Moore.

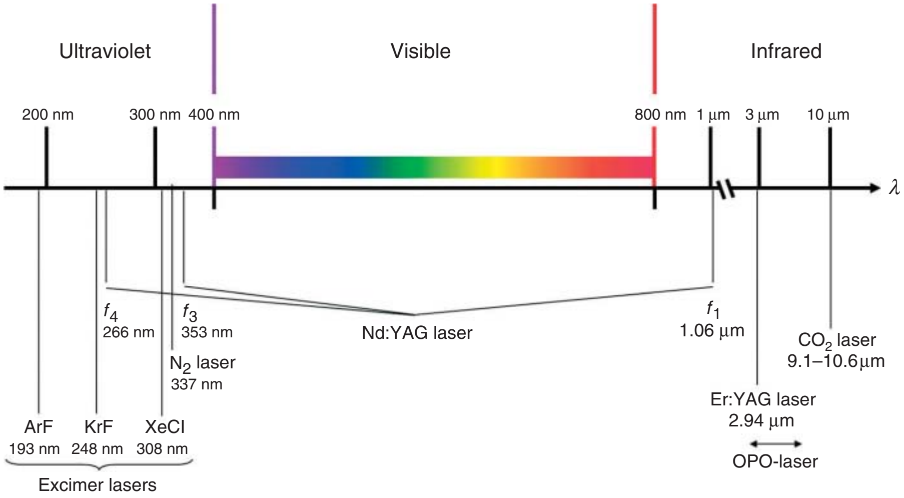

Figure 13.1 Wavelengths of lasers that are frequently used in mass spectrometry.

Lasers (Figure 13.1) also offer the possibility to deposit energy in gaseous ions at a variety of wavelengths, leading to the exploration of new fragmentation pathways that are often distinct from those usually observed by collision-induced dissociation (CID). This chapter thus covers not only ion generation by laser desorption/ionization (LDI) [4, 5] – arguably the most important use of lasers in MS – but also laser ablation and laser desorption for generating volatile species from solid samples that are then ionized by an alternative method, laser-induced dissociation, laser post-ionization, and laser spectroscopy of ions. We will explore the benefits of using lasers in MS by discussing some fundamentals aspects. At the end of the chapter, several typical applications of the use of lasers will be presented.

13.2
Laser Desorption/Ionization

13.2.1
Laser Microprobe Mass Spectrometry

In 1975, the group of Hillenkamp was the first to describe the use of lasers for the analysis of the chemical composition of surfaces [1]. A laser beam was focused on a spot a few micrometers in diameter on the target surface. With a pulse energy of some tenths of microjoules that is normally used, the resulting power density (irradiance) is $>10^8$ W cm^{-2}. An irradiance close to the threshold of ion formation favors the desorption/ionization of molecular ions from the sample surface, from an area with a diameter of 3–5 μm and a depth of some tenths of a micrometer. The great advantage of using lasers is the possibility to easily tune the irradiance in order to cover a wide range of ionization conditions. In fact, when the irradiance is 100–1000 times above threshold, evaporation of the total target volume occurs, along with extensive molecular rearrangement and fragmentation. This latter phenomenon is called *laser pyrolysis*. A commercial instrument, the so-called laser microprobe mass analyzer (LAMMA) became available for these analyses. The LAMMA was originally equipped with a frequency-doubled ruby laser ($\lambda = 347$ nm), and later with a frequency-quadrupled Nd:YAG (neodymium-doped yttrium aluminum garnet) laser ($\lambda = 266$ nm) (Figure 13.2).

The LAMMA instrument was capable of detecting light inorganic ions (Li^+, Na^+, K^+, Mg^{2+}, Ca^{2+}, and Co^{2+}) in the positive ion mode (Figure 13.3) and oxide ions $XO_n{}^-$ in the negative ion mode. The m/z values were measured with a time-of-flight (ToF) instrument [7]. For pulsed ion production by a laser, the ToF analyzer is the perfect choice and is in fact frequently used in all forms of LDMS. We will thus give some details here. A ToF analyzer works by accelerating the ions formed in the source region with a high voltage (2–20 kV) and by then measuring their

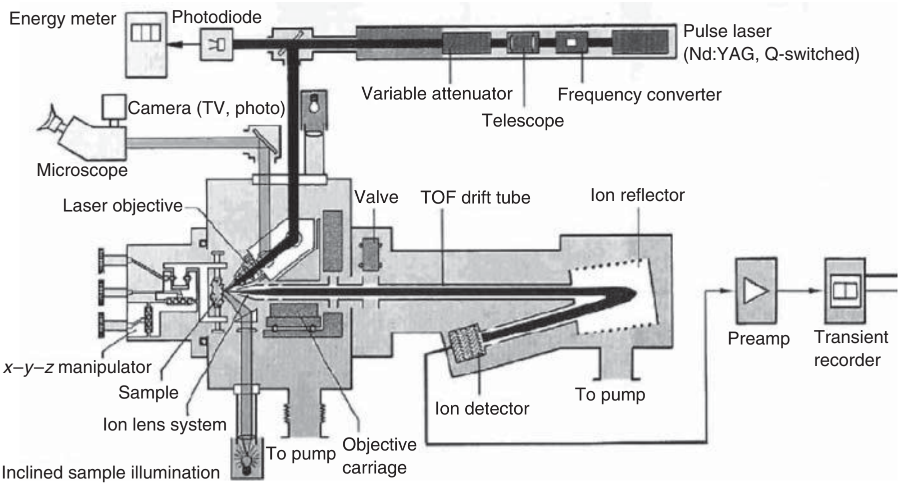

Figure 13.2 General scheme of a LAMMA or MALDI-TOF instrument [6]. (From [6]. Copyright Elsevier.)

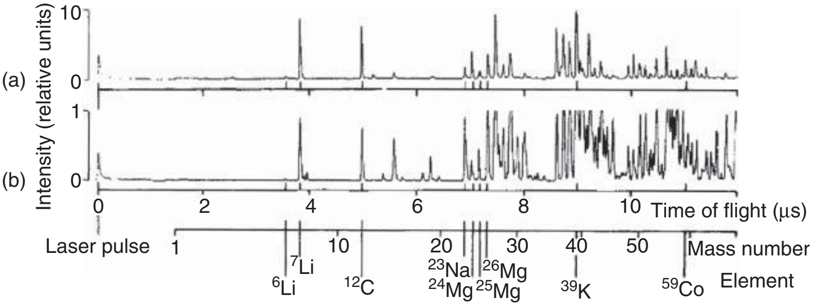

Figure 13.3 LAMMA-TOF mass spectra obtained from epoxy resin doped with lithium, manganese, and cobalt at (a) 40 and (b) 5 ppm [1]. (From [1]. Copyright Nature Publishing Group.)

ToF through a free-field drift region. The ToF is directly proportional to the square root of the mass-to-charge ratio (m/z) of the different ions. A small fraction of the laser beam is usually split onto a photodiode in order to provide a start pulse for the ion current measurement by a digital oscilloscope. The main advantages of the linear ToF analyzer are its simplicity, the possibility to simultaneously transmit a large number of ions to the detector without losses, few problems due to signal suppression, and reasonably good mass accuracy ($\sim$100 ppm). The mass resolution, however, is poor – only a few hundreds. However, mass resolution and accuracy can be improved to more than 10 000 and less than 10 ppm, respectively, when using an extraction delay between the ion generation pulse and the high voltage acceleration. Furthermore, an electrostatic mirror, also called *reflectron*, consisting of a series of ring electrodes creating a linear voltage gradient, is often introduced into the ion flight path. The reflectron counterbalances the difference in the velocity of ions with the same m/z and thus further improves resolution and mass accuracy. Both delayed extraction and the use of reflectron are nowadays standard in commercial ToF mass spectrometers.

It was later shown that singly charged molecular ions and cationized species could also be generated from aromatic compounds and nonvolatile species, respectively, by laser ablation [8]. Molecular ions mainly result from direct photoionization (PI) of the chemical compounds at the wavelength of the laser, whereas cationized species originate from the attachment of protons or inorganic cations, that is, mainly Na^+ or K^+, to neutral organic compounds. The LAMMA technique is usually considered as semi-quantitative because ionization yields differ for each species and each material. Relative detection limits in the parts per million range were claimed for inorganic species [1].

13.2.2
Matrix-Assisted Laser Desorption/Ionization (MALDI)

The main drawback of LAMMA experiments was the limited m/z range due to the difficulty in directly desorbing and ionizing large biomolecular species without fragmentation. A huge breakthrough was simultaneously achieved at the end of the 1980s by two groups – that of Hillenkamp and Karas in Germany [2] and that of Tanaka (Nobel Prize in Chemistry, 2002) in Japan [3]. Both groups were experimenting with additives and special sample preparation methods for large molecules in LDMS, and developed the MALDI. The key concept of MALDI is to mix fragile biomolecules with a chemical matrix, at a molar ratio between 10^{-2} (small molecules) and 10^{-4} (large molecules). One to five microliters of a solution containing a mixture of the sample and the matrix is then deposited on a metallic surface and allowed to dry. This standard sample preparation is called the *dried droplet technique*. Small crystals (Figure 13.4), with a size between one and several hundreds of micrometers, are formed and introduced into the vacuum of the ionization chamber. The chemical structure of the matrix is always chosen to exhibit a high absorption coefficient at the wavelength of the laser. The choice of the matrix (Table 13.1) is absolutely crucial and mainly depends on the type of

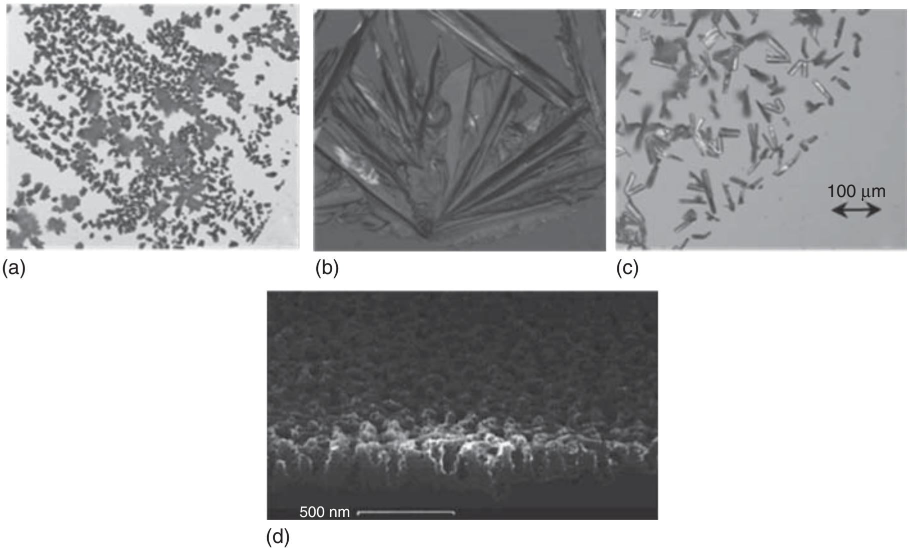

Figure 13.4 Microscopic views of (a) HCCA, (b) DHB, and (c) SA. (d) SEM (scanning electron microscopy) analysis of the ''double-etched'' porous silicon (DIOS) surface prepared from low-resistivity $n \pm$ Si material ($0.001 - 0.005\,\Omega$ cm) [9]. (From [9]. Copyright American Chemical Society.)

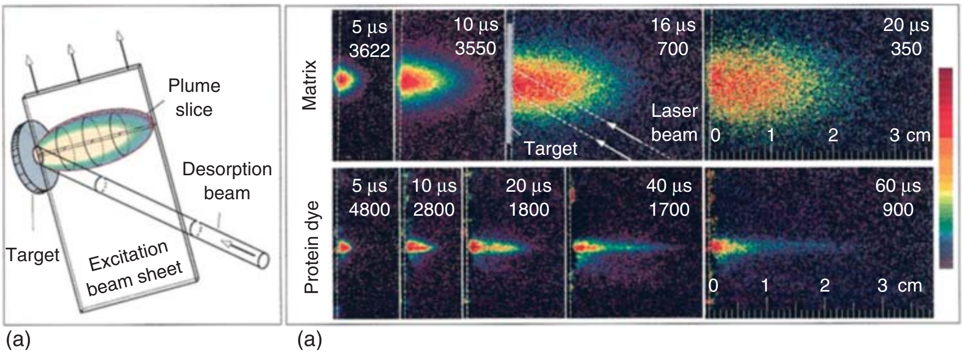

Figure 13.5 (a) Schematic of MALDI plume irradiation geometry. Desorption was induced with a KrF laser beam ($3.1 \times 3.6\,\text{mm}^2$ elliptical beam spot). LIF (laser-induced fluorescence) excitation utilizes a sheet beam from a second laser fired at variable time delay after the desorption laser pulse. (b) CCD (charge-coupled device) images (100 ns gate width, opened 50 ns prior to the LIF laser pulse) of LIF from matrix and dye-tagged protein molecules. Each image represents a different desorption event. Time delays after desorption and the maximum intensity (red, see palette) of each image are listed. Dashed lines show the target position. (Upper row) LIF images of 3-HPA matrix vapor plume (excitation: 308 nm XeCl, $1.6 \times 35.0\,\text{mm}^2$ rectangular beam spot); (lower row) LIF images of TMR-dye labeled DNase I protein (3.1×10^{-5} M) embedded within 3-HPA matrix and desorbed with a KrF laser (excitation: 532 nm, second harmonic of Nd:YAG laser, $0.3 \times 35\,\text{mm}^2$ beam spot). A 550 nm long-pass filter was used to cut off 532 nm scattered laser light [10]. (From [10]. Copyright American Physical Society.)

analytes and the polarity of the analysis. However, there is still no general rule to design an efficient matrix and to prepare the best matrix/analyte mixture, that is, MALDI sample preparation is still a kind of ‘‘art’’ (Figure 13.4).

For MALDI, a low irradiance (10^6 W cm^{-2}), which prevents nonvolatile, labile molecules from fragmentation, is used for the desorption/ionization process. (We note in passing that removal of a bulk volume is observed in MALDI when the laser hits the sample, that is, the term *desorption* is somehow misleading, and strictly speaking should be replaced by ‘‘ablation.’’) For infrared matrix-assisted laser desorption/ionization (IR-MALDI) with 100 ns-long erbium-doped yttrium aluminum garnet (ER:YAG)-laser pulses or for UV-MALDI (ultraviolet matrix-assisted laser desorption/ionization) [11], the ablation process is due to superheating of the sample to a temperature which is higher than the boiling temperature and to the ejection of material by heterogeneous nucleation in a plume (Figure 13.5). For 6 ns-long optical parametric oscillator (OPO)-laser pulses, the ablation mainly involves a strong thermoelastic wave, which is reflected at the sample vacuum surface, travels back through the sample, and leads to an explosion of the sample by homogeneous nucleation [11, 12]. In all cases, multiply charged clusters of the matrix and the analyte are extensively formed.

The exact mechanism leading to the formation of desolvated singly charged analyte ions is still unclear [11]. MALDI spectra in the positive ion mode are characterized by the presence of protonated/cationized molecules and radical cations of the matrix in the low m/z range, whereas deprotonated and radical anions of the matrix are detected in the negative mode. A characteristic of MALDI, as opposed to electrospray ionization (ESI), is that singly charged ions dominate in MALDI mass spectra. Sensitivity in the negative ion mode is usually lower compared to the positive ion mode. When an equimolar mixture of analytes is analyzed, different signal intensities are obtained for each compound (Figure 13.6), a phenomenon called *ion suppression effect*. During the crystallization step, exclusion of compounds from the crystal lattice is often observed, leading to different relative ion intensities at different locations of the MALDI sample crystals.

Several models for ion generation in MALDI have been thus proposed. The model developed by Knochenmuss and Zenobi [14] assumes that proton transfer occurs between neutral analyte molecules and primary ions formed from matrix molecules. However, with the typical UV-laser wavelength of 337 or 355 nm, the energy of more than two photons is needed for matrix PI, but the usual laser irradiance is too low for direct PI of the matrix in the gas phase. Energy pooling of excited matrix species in clusters has been suggested as a pathway for primary (matrix) ion formation. Another model for ion formation in MALDI, the ‘‘lucky survivor’’ model developed by Karas *et al.* [15], proposes that large biological analytes retain their solution charge state even when they are incorporated in the matrix crystals. After the desorption process, clusters are ejected, and desolvation, that is, loss of the neutral matrix molecules, occurs. Photoelectrons, presumably from PI of matrix molecules, are suggested to be captured by the free multiply charged analytes ions, leading to an extensive charge reduction. Most analytes should thus be reduced to charge state 0, but some analytes, called *lucky survivors*, can survive

Table 13.1 Commonly used MALDI matrices.

Matrix	Structure	Laser	Main applications
Nicotinic acid	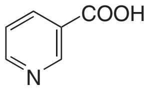	266 nm	Peptides, proteins
2,5-Dihydroxybenzoic acid (DHB)	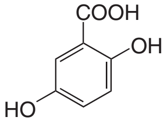	337, 353 nm	Peptides, proteins, carbohydrates, synthetic polymers
Sinapinic acid (SA)	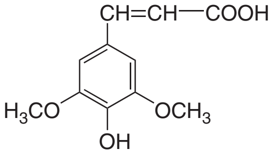	337, 353 nm	Peptides, proteins
α-cyano-4-hydroxycinnamic acid (HCCA)	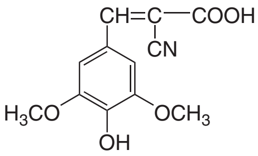	337, 353 nm	Peptides
2,4,6-Trihydroxyacetophenone (THAP)	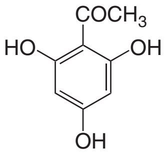	337, 353 nm	Nucleic acids
3-Hydroxy-picolinic acid (HPA)	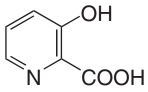	337, 353 nm	Nucleic acids
Dithranol (DIT)	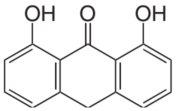	337, 353 nm	Carbohydrates, synthetic polymers
6-Aza-2 thiothymine (ATT)	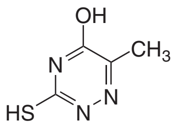	337, 353 nm	Peptides, proteins
Succinic acid	$HOOC{-}CH_2{-}CH_2{-}COOH$	2.79, 2.94 μm	Peptides, proteins
Glycerol	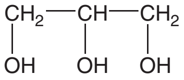 $CH_2(OH){-}CH(OH){-}CH_2(OH)$	2.79, 2.94 μm	Peptides, proteins

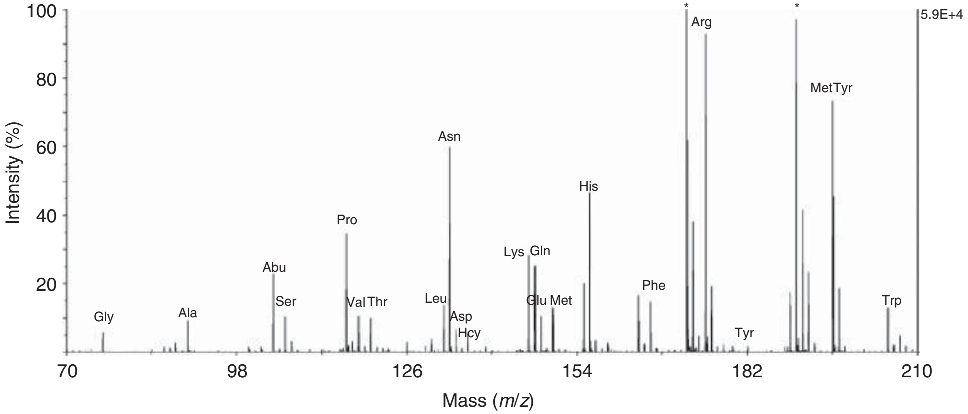

Figure 13.6 Positive ion MALDI-TOF MS spectrum of 21-amino acid standard mixture (equimolar mixture, 20 μM each) with HCCA as a matrix. Asterisks denote matrix ion peaks [13]. (From [13]. Copyright Elsevier.)

as singly charged ions. One issue that remains unclear is that photoelectrons cannot be formed in the gas phase. The probability that photoelectrons interact with desolvated multiply charged analytes in the gas phase is thus very low, and the neutralization process should not be so complete. Until now, no model can explain all the experimental observations. Most likely, several different ion pathways operate simultaneously, depending on the matrix and the sample. What is clear is that quantitative studies with MALDI-MS are difficult because of the number of parameters that must be controlled. Semiquantitative or mass fingerprinting studies, however, are very successfully done by MALDI. The sensitivity of MALDI analysis is normally in the low picomole range; some results were obtained that show a sensitivity down to the attomole range. The main applications are mass fingerprinting of peptides for proteomics, of lipids for lipidomics, carbohydrates, or drugs for industry and imaging MS. Some among them are described in Section 13.6.

Standard MALDI is a vacuum ionization technique. A general trend in modern MS, however, is to do ion production at atmospheric pressure outside the MS and guide the ions into the mass analyzer through a differentially pumped interface (''atmospheric pressure ionization,'' API). In 2000, the group of Burlingame introduced an atmospheric pressure-matrix-assisted laser desorption/ionization source (AP-MALDI) [16] using a specially designed interface. Even if the transfer leads to ion losses, the total ionization yield is probably at least as high as in vacuum MALDI because of the fast thermalization of ions at atmospheric pressure. AP-MALDI makes sample preparation easier, and allows direct analysis of very fragile analytes. Moreover, online coupling with high-performance liquid chromatography (HPLC) or capillary electrophoresis (CE) has been recently described [17]. Nevertheless, the m/z range is often limited to 2000, making the analysis of intact large biological analytes impossible.

13.2.3
Small-Molecule Desorption/Ionization

As described before, matrix ions give rise to intense peaks in the low m/z range in MALDI mass spectra, leading to unwanted effects such as detector saturation and analyte ion suppression effect. There have been a number of efforts to develop a matrix-free variant of MALDI. The earliest such attempt was in fact the particle matrices of Tanaka [3]. In 1999, a novel and very promising matrix-free desorption/ionization method was introduced by the group of Siuzdak [18]. The idea is to deposit the analyte onto a porous silicon surface and to desorb/ionize it by UV-laser. UV photons are absorbed by the silicon surface and the energy is transferred to the analyte molecules. This method, dubbed desorption/ionization on silicon (DIOS) is essentially background free (Figure 13.7) and quite soft, thus offering the possibility to analyze low molecular weight analytes ($m/z < 100$) with a very low yield of fragmentation. In addition, the sample preparation is very easy. DIOS-MS has been used to develop quantitative methods for the analysis of pharmaceutical compounds [19] and for complex matrices such as biological or environmental samples [20]. DIOS was further refined by using silicon nanowires grown on the surface of solid silicon as an LDI substrate [21]. The laser irradiance required is lower than for conventional DIOS-MS, leading to a very low background and an increase in sensitivity. Very recently, another DIOS variant called nanostructure-initiator mass spectrometry (NIMS) was introduced by the Siuzdak group [22]. NIMS works with a nanoporous Si surface, obtained by electrochemical etching of crystalline silicon using hydrofluoric acid, which serves to trap a liquid ''initiator.'' The ''initiator'' is transparent, whereas the nanostructured silicon surface has a high

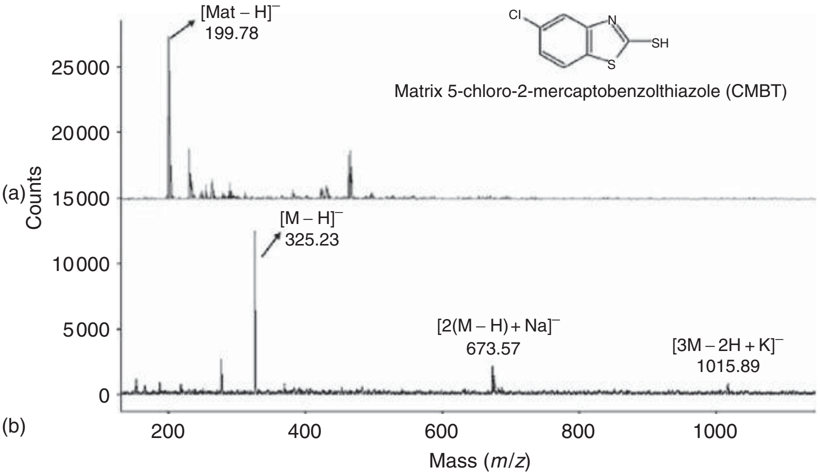

Figure 13.7 Negative ion mass spectra recorded for $C_{21}H_{42}O_2$ at 3 nmol µl^{-1} in (a) MALDI mode using the 5-chloro-2-mercaptobenzothiazole matrix (CMBT) and (b) in DIOS mode [23]. (From [23]. Copyright Wiley.)

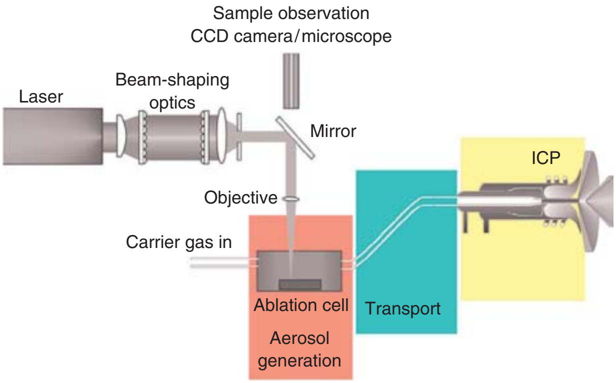

Figure 13.8 General scheme of a LA-ICP mass spectrometer [26]. (From [26]. Copyright American Chemical Society.)

absorption coefficient at the wavelength of the UV laser. A significant improvement in the signal-to-noise ratio was demonstrated for small organic compounds and peptide mixture compared to DIOS. Many other materials have been tried to enhance ion formation in LDI, including carbon nanotubes, functionalized carbon nanotubes, micro- and nanoparticles, sol–gels, ionic liquids, and so on. The main limitation of all these techniques is the low accessible m/z range, which is limited to a few thousands. Thus, studies of intact large biomolecules are usually conducted with MALDI-MS, whereas DIOS-MS and associated techniques are interesting alternatives for low mass compounds.

In parallel, bioaffinity MALDI formats were developed by several research teams, such as the groups of Nelson *et al.* [24] and of Chen [25]. These ‘‘assays’’ usually consist of a capture surface, for example, an antibody functionalized MALDI sample target or chemically modified particles, which is used for the concentration of specific analytes in a suspension of graphite particles in a mixture of glycerol, sucrose, and methanol. In the case of an antibody-functionalized MALDI target, a conventional matrix is applied to release the antigen. In the case of modified particles, they can be used as a ‘‘matrix’’ by themselves, thus serving not only for sample enrichment but for desorption/ionization as well.

13.3
Laser Ablation

In MALDI and DIOS, desorption and ionization steps are coupled and it is quite difficult to perfectly control both phenomena at the same time. Thus, several research laboratories have pursued the separation of the volatilization and ionization steps. Lasers, as spatially well-defined energy sources, can be easily focalized onto different surfaces in order to only ablate organic or inorganic materials. It is well known that the number of neutral species desorbed from an irradiated surface is much higher than the number of ions. Post-ionization of neutrals is therefore also attractive, especially for the detection of new analytes that cannot be analyzed by MALDI. Laser ablation has been successfully coupled to a large variety of ionization techniques [27]: electron ionization (EI), CI, Na^+-cationization, corona discharge atmospheric pressure chemical ionization (APCI), ^{63}Ni APCI, resonance-enhanced multiphoton ionization (REMPI), inductively coupled plasma (ICP), and vacuum-UV PI. At the present time, LA-ICP-MS (laser ablation inductively coupled plasma mass spectrometry; Figure 13.8) [28] is probably the most widely used among these techniques. In fact, it offers the unique possibility to combine the analysis of a very small volume of a sample with the simultaneous concentration determination of all chemical elements. Sensitivity is down to the parts per billion range for most elements, which makes it an efficient tool for ultratrace analysis of metals, semiconductors, or long-lived radionuclides.

Specific applications were developed for laser ablation followed by other post-ionization techniques, but most studies were restricted to the low mass range. To overcome this limitation, electrospray-assisted laser desorption/ionization (ELDI) was developed by Shiea *et al.* [27]. The idea was to couple an atmospheric MALDI source with an ESI source (Figure 13.9). In this case, the sample is directly deposited on a target plate and a laser is used for desorption of large biomolecules, which are then post-ionized by extensive proton exchanges with the charged solvent droplets formed by ESI. Typical ESI charge state distributions of proteins are observed, and found to be correlated with the initial conformation of proteins in solution, leading to the possibility of studying native proteins and noncovalent complexes by ELDI MS. The sensitivity of ELDI is comparable to that of ESI but still some orders of magnitudes worse than that of MALDI. ELDI was also applied to the analysis of drugs directly desorbed from tablets. A variant, called matrix-assisted laser desorption electrospray ionization, MALDESI, was developed by the group

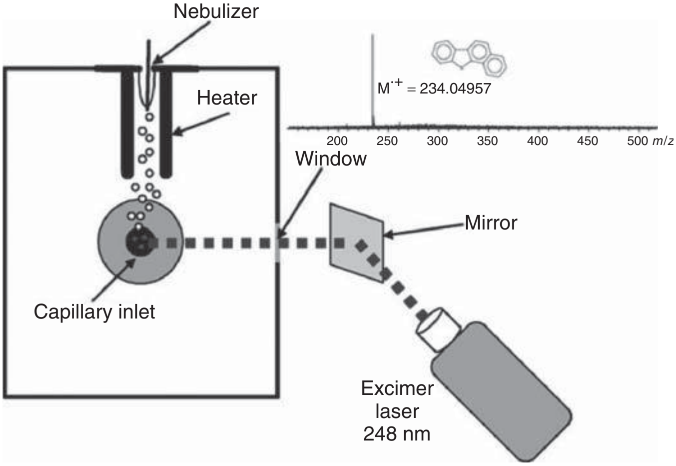

Figure 13.9 General scheme of a ELDI source coupled to a Fourier transform-ion cyclotron resonance (FT-ICR). Inset: typical mass spectrum obtained for benzonaphthothiophene [37]. (From [37]. Copyright 2008 The Royal Society of Chemistry.)

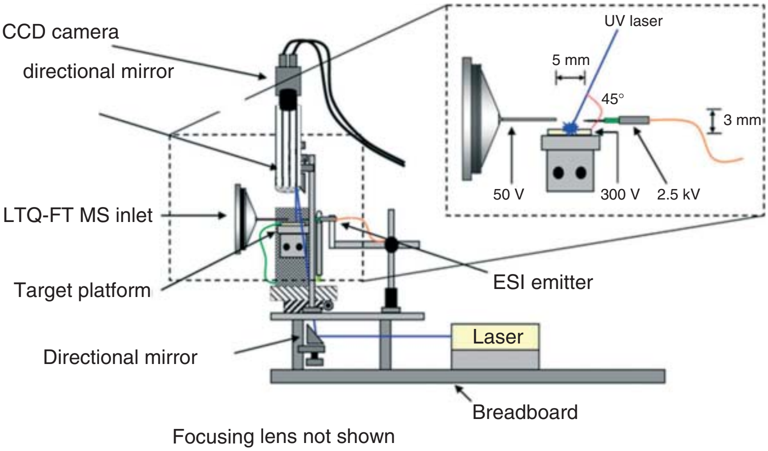

Figure 13.10 General scheme of a MALDESI source coupled to a hybrid linear triple quadrupole (LTQ) and Fourier transform-ion cyclotron resonance (FT-ICR) mass spectrometer [30]. (From [30]. Copyright 2008 American Society for Mass Spectrometry.)

of Muddiman (Figure 13.10) [29]. The setup is actually the same as in the case of ELDI, but in MALDESI the analytes are mixed with a matrix solution prior to deposition on the sample plate. A better sensitivity was achieved. Nevertheless, both ELDI and MALDESI are still in their infancy and need to prove their benefits compared to standard ESI or MALDI.

13.4
Laser Postionization

Lasers can be used for specific post-ionization of neutral gas-phase species in the nonresonant and resonant modes. Neutral species can be produced by laser ablation (two-step laser mass spectrometry, L2MS) [31], ion impact on a surface (laser secondary neutral mass spectrometry, SNMS) [32], evaporation (resonance ionization mass spectrometry, RIMS) [33], or thermospray/ESI (atmospheric pressure laser ionization mass spectrometry, APLI-MS) [34]. For L2MS, an IR-laser is first used for ablation of neutral molecules from the sample surface. Second, a pulse from a tunable UV laser is used for resonance-enhanced two-photon ionization (1+1 REMPI) of the desorbed species. The mass spectra are dominated by intact radical cations of those mixture components that strongly absorb the selected ionization laser wavelength. Little or no sample preparation is necessary, and direct analysis of complex matrices is possible with sensitivity in the picogram range. L2MS was extensively used for the quantitative analysis of polycyclic aromatic hydrocarbons in biological matrices or aerosols. SNMS and RIMS are based on laser post-ionization of neutrals desorbed by sputtering from a sample surface with 10–20 keV ion (Ga^+, In^+, Ar^+) beam, or by evaporation, respectively. A large variety of lasers have been employed, depending on the chemical structure of the analyte, to achieve high selectivity and efficiency in the ionization step. The main reported applications are quantitative elemental analysis of semi-conductors, ceramics, or biological samples, with sensitivities in the parts per billion to parts per trillion range. Instruments are generally home-made and SNMS and RIMS are only used in very few laboratories. Finally, APLI-MS was recently developed for the postionization of liquid samples, such as petroleum. Nonvolatile analytes that are not easily protonated are brought into the gas phase by an APCI probe, with no or little ionization taking place. A KrF ($\lambda = 248$ nm) laser then interacts with these neutrals, leading to specific 1+1 REMPI, for example, of aromatic compounds. Better sensitivity was achieved for this class of analytes compared to ESI or conventional atmospheric pressure photoionization (APPI); the latter is based on direct or indirect PI of the gaseous samples with a Xe ($\lambda = 147.6$ nm), Kr ($\lambda = 123.6$ nm), or Ar ($\lambda = 110.7$ nm) lamp.

13.5
Laser Ion Excitation

Photoexcitation of gaseous ions can be achieved using pulsed IR or UV–vis (ultraviolet–visible) lasers, or continuous IR laser irradiation. Absorption of UV–vis photons by ions leads to a population of excited electronic states and to photodissociation of the excited ion. With IR excitation, ions are slowly heated, that is, their internal energy increases by small steps. IR multiphoton absorption is required to reach the quasi-continuum of the vibrational states and to induce fragmentation of the gaseous ions. The so-called IRMPD (infrared multiphoton dissociation) is now widely used for efficient fragmentation of multiply charged ions from peptides, proteins, or oligonucleotides [35]. This technique is usually operated on Fourier transform ion cyclotron resonance mass spectrometers, or on RF ion trap instruments, and structural information can be obtained from the analysis of the fragments. The main drawback of IRMPD is that the required irradiation time is quite long – hundreds of milliseconds. Therefore, fragment ions that are produced early on can also absorb further IR photons leading to the formation of low mass secondary fragments, and generally to a loss of structural information. IRMPD with tunable lasers, such as free electron lasers, is also used as a spectroscopic tool. In this manner, a vibrational ‘‘action’’ spectrum of gaseous ions can be obtained by recording the photofragmentation rate as a function of irradiation wavelength. Comparisons between *ab initio* calculations and experimental results have yielded very interesting results on structural features of ions (e.g., Figure 13.11) [36].

13.6
Typical Applications of Laser Mass Spectrometry

Key application areas of laser MS that are focused on in this section are the application of MALDI-MS in proteomics, and the use of MS imaging with laser assistance, which is an emerging field in MS.

13.6.1
MALDI-MS in Proteomics

As described above, MALDI is suitable for the analysis of a wide range of compounds. Applications range from quantification of small compounds and analysis of digested or intact proteins, to sequencing of oligonucleotides, and to lipidomics. *Proteomics* is defined as the study of the entire complement of proteins, including their chemical modifications, that is posttranslational modifications, produced by a living object in a specific condition. Proteomes are of extremely high complexity. If all the modifications are counted, the number of different proteins contained in the human body is estimated to be around several millions. Furthermore, the protein content of a cell depends directly on cell activity, stimuli, or disease state. In fact, it is not possible to identify all these proteins and modifications in a single experiment. The classical approach consists in the specific extraction of a set of proteins. This can be done using acidic or basic extraction, immunochemical precipitation, centrifugation, microdissection, and so on. The second step is usually a chromatographic separation of the protein set using HPLC or two-dimensional gel electrophoresis. In the latter case, proteins are separated by migration in a polyacrylamide gel. The first separation dimension is related to the isoelectric point whereas the second dimension depends on the molecular weight. In order to find the proteins on the gel, chemical staining by coomassie blue or silver nitrate is done. All bands of interest are then cut out, the proteins are removed from the gel by various chemical procedures, and digested by enzymes such as pepsin and trypsin. Pepsin cleaves nonspecifically whereas trypsin cleaves peptide chains at the carboxyl side of the amino acids lysine and arginine, except when either of them is followed by proline. The peptides that are generated by this digestion are finally analyzed by MALDI-MS(/MS) or ESI-MS(/MS). In MALDI, a ‘‘peptide mass fingerprint’’ is obtained, that is, each peptide gives a single signal that corresponds to its protonated form in the positive ion mode. The high mass resolution and accuracy available on modern mass spectrometers allow the interrogation of online databases and often the unambiguous identification of proteins from their peptide mass fingerprint. MS/MS data are of interest in order to confirm the assigned peptides and to precisely localize posttranslational modifications on protein structures. Nowadays, high throughput analysis is possible owing to the high repetition rate of commercial N_2 or Nd:YAG lasers and the continuous improvement of electronics and informatics. Proteomics combined with MS has many potentially very interesting applications, such as the detection of protein markers of cancer [38, 39], predicting the effects of treatments [40], and helping to understand many biological processes [41].

13.6.2
Imaging Mass Spectrometry

Molecular imaging is of great interest in biology for understanding the spatial location of biomolecules at the tissue or cellular levels. Most widely used methods

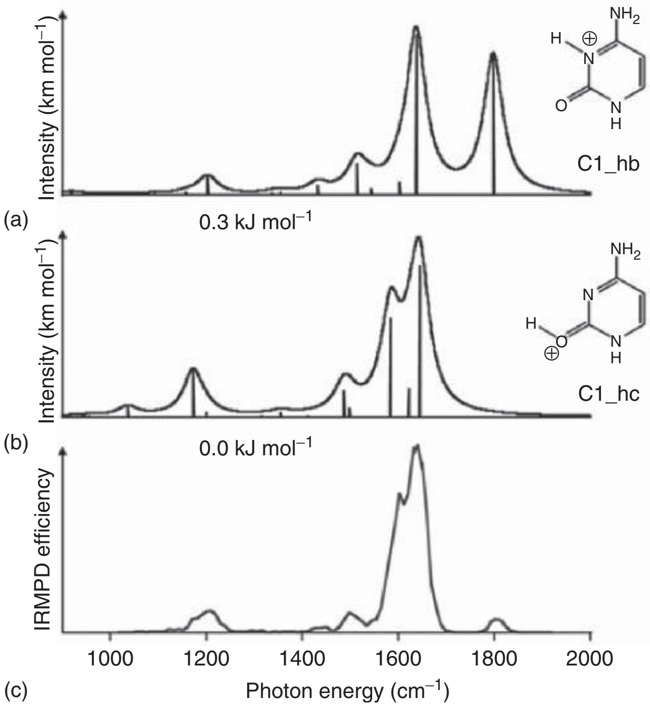

Figure 13.11 IR spectra of protonated cytosine. DFT calculated IR absorption spectra of the two lowest isomers C1_hb (a) and C1_hc (b) compared to the experimental IRMPD spectrum (c) recorded with two IR-FEL macropulses using our quadrupole ion trap device [42]. (From [42]. Copyright Wiley.)

are based on fluorescence, radiochemical tracers, positron emission tomography (PET), nuclear magnetic resonance (NMR), and so on. Nevertheless, all these techniques need chemical modifications of the interesting compounds and are related to very few chemical signals.

MS is more direct for chemical imaging, requiring no labels or tracers, and offering high spatial resolution by virtue of its sensitivity. One way to perform mass spectrometric imaging is by using laser ablation ICP-MS. LA-ICP-MS has in fact become of increasing interest in such different research areas as (i) physiology, pathophysiology, and anatomy, where trace elements play a role; (ii) development and *ex vivo* calibration of molecular imaging methods which use molecular probes carrying appropriate elements; (iii) development of metal-containing drugs; (iv) individual and environmental toxicology, and (v) gene–environment interactions concerning trace elements. Imaging LA-ICP-MS has been introduced and is being applied in several laboratories for the quantitative analysis of element distributions in biological tissue and in proteomics with a lateral resolution in the range of 10–200 μm, for example, for the mapping of Cu and Zn in sections of sheep liver or human brain tissue. An example of application area (ii) is given in Figure 13.12.

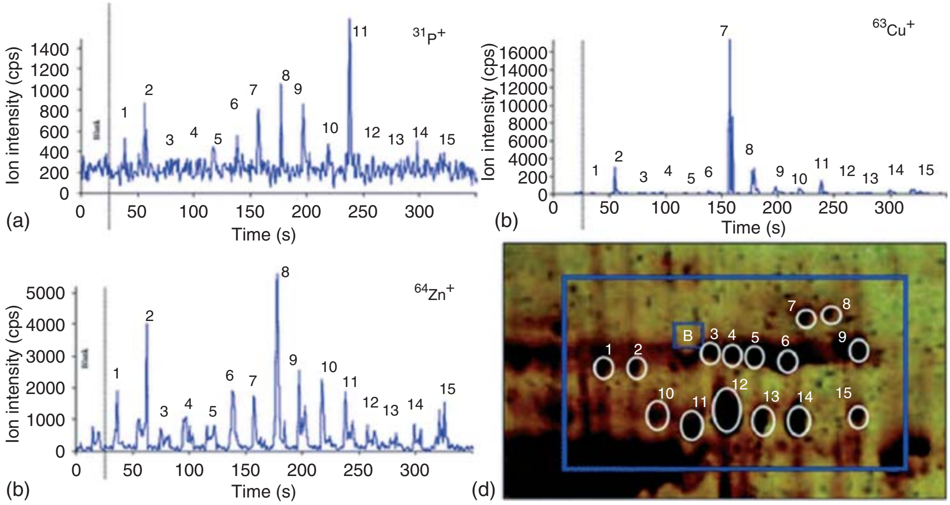

Figure 13.12 Example of LA-ICP-MS imaging [43]. Transient signals of (a) $^{31}\mathrm{P}^+$, (b) $^{63}\mathrm{Cu}^+$, and (c) $^{64}\mathrm{Zn}^+$, respectively, for protein spots 1–15 imaged directly in a 2D gel of human brain sample (d). The area marked with B in panel (d) is the blank. (From [43]. Copyright Royal Society of Chemistry.)

Imaging by molecular MS, for example, using MALDI-MS, offers the unique capability of analyzing several tens or hundreds of compounds at the same time on tissue surface. Modern MALDI mass spectrometers are equipped with lasers that have spot size of about 50 μm, allowing chemical imaging close to the cellular level.

MALDI-MS imaging was first described by Caprioli in 1997 [44]. The first step is to homogeneously deposit the matrix on the tissue section (Figure 13.13). This can be done manually with an air brush or automatically with a spotter or sprayer robot. It is absolutely crucial to control the matrix deposition in order to avoid delocalization of compounds. The sample is then introduced into vacuum. A first spectrum is recording at the top left of the sample. The sample plate is then moved in order to record a spectrum on the next position. The step between two locations will define the pixel size of the final images. At the end, a collection of spectra is recorded on the sample. Using these spectra it is then possible subsequently to plot the relative intensity of the individual m/z peaks in the mass spectrum across the tissue, and thus to visualize the distribution of the individual molecular ions. Depending on the matrix, spectra are focalized on the low mass range ($m/z < 2000$) or the high mass range ($m/z > 2000$). In the low mass range, the main information is related to lipid composition and localization [45]. This is why MALDI imaging in the low mass range is sometimes called a *lipid microscope*. Some studies are also linked to the distribution of drugs in different organs of a whole body mouse (Figure 13.14) [46] but high doses are usually needed because of a lack of sensitivity. MS/MS imaging can also be performed in order to improve the selectivity of the method. In the high mass range, peptides and light proteins can be localized. For example, markers of cancer have been identified on different tissues by the mean of

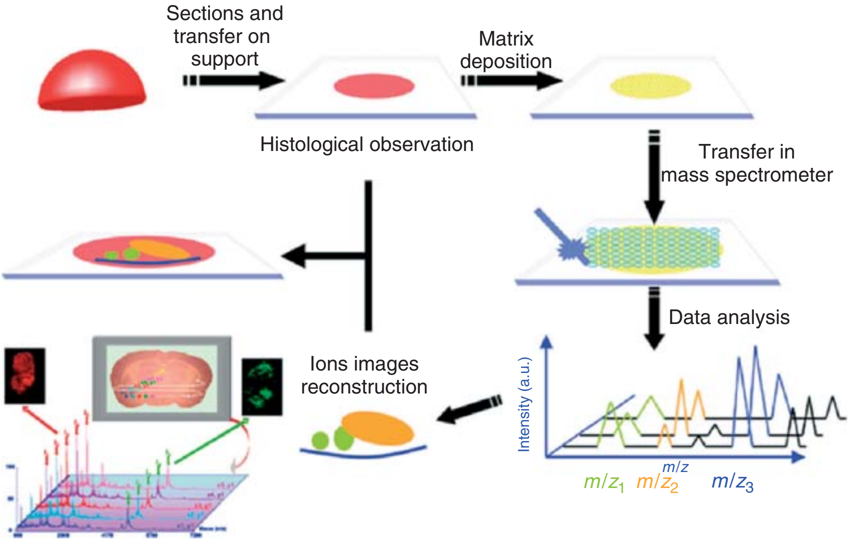

Figure 13.13 Representative scheme of MALDI imaging technology [49]. (From [49]. Copyright Bentham Science Publishers.)

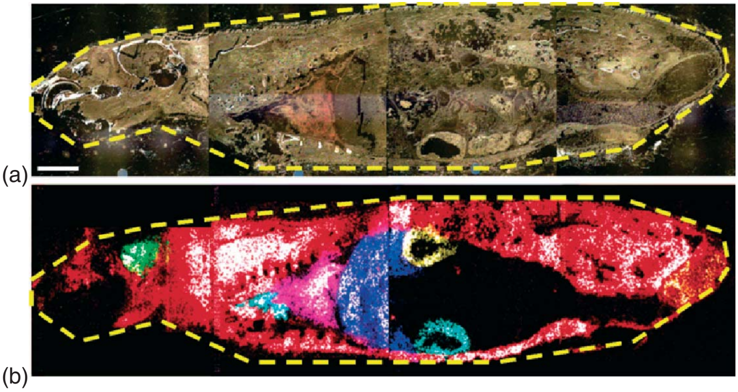

Figure 13.14 Whole-body protein analysis of rat sagittal tissue section by IMS (ion mass spectrometry). Optical image of rat sagittal tissue section across four gold MALDI target plates (a). Ion image overlay of unique organ signals: brain, green *m*/*z* 21 952; thymus, light blue *m*/*z* 6893; thoracic cavity, purple *m*/*z* 7921; liver, blue *m*/*z* 14 321; kidney cortex, yellow *m*/*z* 4643; cecum wall, cyan *m*/*z* 5155; testis, orange *m*/*z* 14 400; and muscle, red *m*/*z* 11 836 (b). Bar, 1 cm [46]. (From [46]. Copyright American Chemical Society.)

MALDI imaging [47]. Recently some attempts at local digestion by enzymes, such as trypsin, have been described [48]. Only fragments of highly abundant proteins were detected, limiting the interest in this approach. This technique is gaining attention in biology even if very careful sample preparation is needed in order to get reproducible data and to avoid false conclusions.

References

1. Hillenkamp, F., Unsöld, E., Kaufmann, R., and Nitsche, R. (1975) *Nature*, **256**, 119–120.
2. Karas, M., Bachmann, D., Bahr, U., and Hillenkamp, F. (1987) *Int. J. Mass Spectrom. Ion Processes*, **78**, 53–68.
3. Tanaka, K., Waki, H., Ido, Y., Akita, S., Yoshida, Y., and Yoshida, T. (1988) *Rapid Commun. Mass Spectrom.*, **2**, 151–153.
4. Lubman, D.M. (ed) (1990) *Lasers and Mass Spectrometry*, Oxford University Press, New York.
5. Vertes, A., Gijbels, R., and Adams, F. (eds) (1993) *Laser Ionization Mass Analysis*, John Wiley & Sons, Inc., New York.
6. Heinen, H.J., Meier, S., and Vogt, H. (1983) *Int. J. Mass Spectrom. Ion Phys.*, **47**, 19–22.
7. Cotter, J.C. (1997) *Time-of-Flight Mass Spectrometry: Instrumentation and Applications in Biological Research*, American Chemical Society Publication, Washington, DC.
8. Verbueken, A.H., Bruynseels, F.J., and Van Grieken, R.E. (1985) *Biomed. Mass Spectrom.*, **12**, 438–463.
9. Shen, Z., Thomas, J.J., Averbuj, C., Broo, K.M., Engelhard, M., Crowell, J.E., Finn, M.G., and Siuzdak, G. (2001) *Anal. Chem.*, **73**, 612–619.
10. Puretzky, A.A., Geohegan, D.B., Hurst, G.B., and Buchanan, M.V. (1999) *Phys. Rev. Lett.*, **83**, 444–447.
11. Hillenkamp, F. and Peter-Katalinić, J. (2007) *MALDI MS: A Practical Guide to Instrumentation, Methods and Applications*, Wiley-VCH Verlag GmbH, Weinheim.
12. Menzel, C., Dreisewerd, K., Berkenkamp, S., and Hillenkamp, F. (2002) *J. Am. Soc. Mass Spectrom.*, **13**, 975–984.
13. Alterman, M.A., Gogichayeva, N.V., and Kornilayev, B.A. (2004) *Anal. Biochem.*, **335**, 184–191.
14. Knochenmuss, R. and Zenobi, R. (2003) *Chem. Rev.*, **103**, 441–452.
15. Karas, M., Glückmann, M., and Schäfer, J. (2000) *J. Mass Spectrom.*, **35**, 1–12.
16. Laiko, V.V., Baldwin, M.A., and Burlingame, A.L. (2000) *Anal. Chem.*, **72**, 652–657.
17. Doroshenko, V.M., Laiko, V.V., Taranenko, N.I., Berkout, V.D., and Lee, H.S. (2002) *Int. J. Mass Spectrom.*, **221**, 39–58.
18. Wei, J., Buriak, J.M., and Siuzdak, G. (1999) *Nature*, **399**, 243–246.
19. Pihlainen, K., Grigoras, K., Franssila, S., Ketola, R., Kotiaho, T., and Kostiainen, R. (2005) *J. Mass Spectrom.*, **40**, 539–545.
20. Wall, D.B., Finch, J.W., and Cohen, S.A. (2004) *Rapid Commun. Mass Spectrom.*, **18**, 1403–1406.
21. Go, E.P., Apon, J.V., Luo, G., Saghatelian, A., Daniels, R.H., Sahi, V., Dubrow, R., Vertes, A., and Siuzdak, G. (2005) *Anal. Chem.*, **77**, 1641–1646.
22. Northen, T.R., Yanes, O., Northen, M.T., Marrinucci, D., Uritboonthai, W., Apon, J., Golledge, S.L., Nordström, A., and Siuzdak, G. (2007) *Nature*, **449**, 1033–1036.
23. Budimir, N., Blais, J.C., Fournier, F., and Tabet, J.C. (2006) *Rapid Commun. Mass Spectrom.*, **20**, 680–684.
24. Nelson, R.W., Krone, J.R., Bieber, A.L., and Williams, P. (1995) *Anal. Chem.*, **67**, 1153–1158.
25. Sunner, J., Dratz, E., and Chen, Y.C. (1995) *Anal. Chem.*, **67**, 4335–4342.
26. Hattendorf, B., Latkoczy, C., and Günther, D. (2003) *Anal. Chem.*, **75**, 341A–347A.
27. Shiea, J., Huang, M.Z., Hsu, H.J., Lee, C.Y., Yuan, C.H., Beech, I., and Sunner, J. (2005) *Rapid Commun. Mass Spectrom.*, **19**, 3701–3704.
28. Gy, A.L. (1985) *Analyst*, **110**, 551–556.
29. Sampson, J.S., Hawkridge, A.M., and Muddiman, D.C. (2006) *J. Am. Soc. Mass Spectrom.*, **17**, 1712–1716.
30. Sampson, J.S., Hawkridge, A.M., and Muddiman, D.C. (2008) *J. Am. Soc. Mass Spectrom.*, **19**, 1527–1534.
31. de Vries, M.S. (2000) *Rev. Anal. Chem.*, **19**, 269.
32. M.J. Pellin, W.F. Calaway, I.V. Veryovkin, in *ToF-SIMS: Surface Analysis by Mass Spectrometry*, (eds J. Vickerman,

D. Briggs), Surface Spectra Ltd, Manchester and IM Publications, Chichester, 2001, p. 375.

33. Letokhov, V.S. and Chebotayev, V.P. (1977) *Nonlinear Laser Spectroscopy*, Springer, Berlin, Heidelberg, New York.

34. Constapel, M., Schellentraeger, M., Schmitz, O.J., Gaeb, S., Brockmann, K.J., Giese, R., and Benter, T. (2005) *Rapid Commun. Mass Spectrom.*, **19**, 326–336.

35. Laskin, J. and Futrell, J.H. (2005) *Mass Spectrom. Rev.*, **24**, 135–167.

36. Lemaire, J., Boissel, P., Heninger, M., Mauclaire, G., Bellec, G., Metsdagh, H., Simon, A., Le Caer, S., Ortega, J.M., Glotin, F., and Maitre, P. (2002) *Phys. Rev. Lett.*, **89**, 273002.

37. Schrader, W., Panda, S.K., Brockmann, K.J., and Benter, T. (2008) *Analyst*, **133**, 867–869.

38. Steel, L.F., Shumpert, D., Trotter, M., Seeholzer, S.H., Evans, A.A., London, W.T., Dwek, R., and Block, T.M. (2003) *Proteomics*, **3**, 601–609.

39. Kulasingam, V. and Diamandis, E.P. (2008) *Int. J. Cancer*, **123**, 2007–2012.

40. Schriemer, D.C., Kemmer, D., and Roberge, M. (2008) *Comb. Chem. High Throughput Screen*, **11**, 610–616.

41. Kochanek, P.M., Berger, R.P., Bayir, H., Wagner, A.K., Jenkins, L.W., and Clark, R.S. (2008) *Curr. Opin. Crit. Care*, **14**, 135–141.

42. Salpin, J.Y., Guillaumont, S., Tortajada, J., MacAleese, L., Lemaire, J., and Maitre, P. (2007) *ChemPhysChem*, **8**, 2235–2244.

43. Becker, J.S., Zoriy, M., Becker, J.S., Dobrowolska, J., and Matusch, A. (2007) *J. Anal. At. Spectrom.*, **22**, 736–744.

44. Caprioli, R.M., Farmer, T.B., and Gile, J. (1997) *Anal. Chem.*, **69**, 4751–4760.

45. Trim, P.J., Atkinson, S.J., Princivalle, A.P., Marshall, P.S., West, A., and Clench, M.R. (2008) *Rapid Commun. Mass Spectrom.*, **22**, 1503–1509.

46. Khatib-Shashidi, S., Andersson, M., Herman, J.L., Gillepsie, T.A., and Caprioli, R.M. (2006) *Anal. Chem.*, **78**, 6448–6456.

47. Schwartz, S.A., Weil, R.J., Thompson, R.C., Shyr, Y., Moore, J.H., Toms, S.A., Johnson, M.D., and Caprioli, R.M. (2005) *Cancer Res.*, **65**, 7674–7681.

48. Groseclose, M.R., Andersson, M., Hardesty, W.M., and Caprioli, R.M. (2007) *J. Mass Spectrom.*, **42**, 254–256.

49. Wiztorski, M., Lemaire, R., Stauber, J., Menguelet, S.A., Croix, D., Jardin Mathé, O., Day, R., Salzet, M., and Fournier, I. (2007) *Curr. Pharm. Design*, **13**, 3317–3324.

Section V
Methods 4: Elemental Analysis

Handbook of Spectroscopy, Second Edition. Edited by Günter Gauglitz and David S. Moore.

14
X-ray Fluorescence Analysis

Koen Janssens

14.1
X-ray Fluorescence Analysis – Outline

XRF (X-ray fluorescence) analysis is a powerful analytical tool for the spectrochemical determination of almost all the elements present in a sample. XRF radiation is induced when photons of sufficiently high energy, emitted from an X-ray source, impinge on a material. These primary X-rays undergo interaction processes with the analyte atoms. High-energy photons induce ionization of inner-shell electrons by the photoelectric effect and thus electron vacancies in inner shells (K, L, M, . . .) are created. The prompt transition of outer shell electrons into these vacancies within some 100 fs can cause the emission of characteristic fluorescence radiation. Not all transitions from the outer shells or subshells are allowed, only those obeying the selection rules for electric dipole radiation. The creation of a vacancy in a particular shell results in a cascade of electron transitions, all correlated with the emission of photons with a well-defined energy corresponding to the difference in energy between the atomic shells involved. The family of characteristic X-rays from each element, including all transitions, allows the identification of the element. Next to this radiative form of relaxation, a competing process can take place: the emission of Auger electrons. Both processes have Z-dependent probabilities that are complementary: the Auger yield is high for light elements and the fluorescence yield is high for heavy elements.

The working principle of XRF analysis is the measurement of wavelength or energy and intensity of the characteristic photons emitted from the sample. This allows the identification of the elements present in the analyte and the determination of their mass or concentration. All the information for the analysis is stored in the measured spectrum, which is a line spectrum with all characteristic lines superimposed above a certain fluctuating background. Other interaction processes, mainly the elastic and inelastic scattering of the primary radiation on the sample and substrate, induce the background.

Measurement of the spectrum of the emitted characteristic fluorescence radiation is performed using wavelength-dispersive (WD) and energy-dispersive (ED) spectrometers. In wavelength-dispersive X-ray fluorescence analysis (WDXRF), the

Handbook of Spectroscopy, Second Edition. Edited by Günter Gauglitz and David S. Moore.

result is an intensity spectrum of the characteristic lines versus wavelength measured with a Bragg single crystal as dispersion medium while counting the photons with a Geiger–Müller, a proportional or scintillation counter. In energy-dispersive X-ray fluorescence analysis (EDXRF), a solid-state detector is used to count the photons, simultaneously sorting them according to energy and storing the result in a multichannel memory. The result is an X-ray energy versus intensity spectrum. The range of detectable elements ranges from Be ($Z = 4$) for the light elements and goes up to U ($Z = 92$) on the high atomic number Z side. The concentrations that can be determined with standard spectrometers of WD or ED type are situated in a wide dynamic range: from the percent to the microgram per gram level. In terms of mass, the nanogram range is reached with spectrometers having the standard excitation geometry.

By introducing special excitation geometries, optimized sources, and detectors, the picogram and even femtogram range of absolute analyte detection capacity can be reached; in terms of concentrations, the same improvement factor can be attained, that is, from the microgram per gram toward the pictogram per gram level under the best conditions.

In principle, XRF analysis is a multielement analytical technique and, in particular, the simultaneous determination of all the detectable elements present in the sample is inherently possible with EDXRF. In WDXRF, both the sequential and the simultaneous detection modes are possible.

The most striking feature of XRF analysis is that this technique allows the qualitative and quantitative analysis of almost all the elements (Be–U) in an unknown sample. The analysis is, in principle, nondestructive, has high precision and accuracy, has simultaneous multielement capacity, requires only a short irradiation time so that a high sample throughput is possible; online analysis is also possible and the running costs are low. The technique is extremely versatile for applications in many fields of science, research, and quality control; has low detection limits; and a large dynamic range of concentrations covering up to nine orders of magnitude. The physical size of an XRF spectrometer ranges from handheld, battery-operated field units to high-power laboratory units with compact tabletop units and larger ones requiring several cubic meters of space including a 10–20 kW electrical power supply and efficient cooling units with high-pressure water and a heat sink.

In contrast to all these attractive properties, there are some disadvantages. The absorption effects of the primary radiation and the fluorescence radiation created in the analyte result in a shallow layer a few tenths of a millimeter deep that provides information on its composition. This requires a perfectly homogeneous sample, which often occurs naturally but must sometimes be produced by acid dissolution into liquids or by grinding and the preparation of pressed pellets. In both examples, the feature of nondestructiveness is lost. Most ideally, thin films or small amounts of microcrystalline structure on any substrate are the ideal analytes, where the quantification process is also simple because there is linearity between fluorescence intensity and concentration. In thick samples, corrections for absorption and enhancement effects are necessary.

While the roots of the method go back to the early part of this century, where electron excitation systems were employed, it is only during the past 30 years or so that the technique has gained major significance as a routine means of elemental analysis.

14.2
Basic Principles

14.2.1
X-ray Wavelength and Energy Scales

The X-ray or Röntgen region of the electromagnetic spectrum starts at about 10 nm and extends toward the shorter wavelengths. The energies of X-ray photons are on the same order of magnitude as the binding levels of inner-shell electrons (K, L, M, . . . levels) and therefore can be used to excite and/or probe these atomic levels. The wavelength λ of an X-ray photon is inversely related to its energy *E* according to:

$$\lambda(\mathrm{nm}) = \frac{1.24}{E(\mathrm{keV})}$$

where 1 eV is the kinetic energy of an electron that has been accelerated over a voltage difference of 1 V ($1\,\mathrm{eV} = 1.602 \cdot 10^{-19}\,\mathrm{J}$). Accordingly, the X-ray energy range starts at 100 eV and continues toward higher energies. X-ray analysis methods most commonly employ radiation in the 1–50 keV (1–0.02 nm) range.

14.2.2
Interaction of X-rays with Matter

When an X-ray beam passes through matter, some photons will be absorbed inside the material or scattered away from the original path, as illustrated in Figure 14.1.

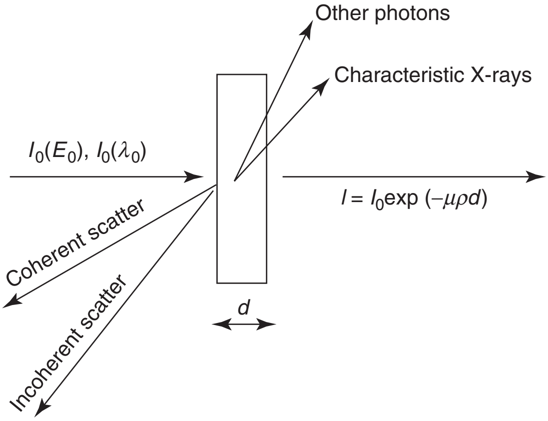

Figure 14.1 Interaction of X-ray photons with matter.

The intensity I_0 of an X-ray beam passing through a layer of thickness d and density ρ is reduced to an intensity I, according to the well-known law of Lambert–Beer:

$$I = I_0 e^{-\mu\rho d} \tag{14.1}$$

The number of photons (the intensity) is reduced but their energy is generally unchanged. The term μ is called the *mass attenuation coefficient* and has the dimension $\mathrm{cm}^2\,\mathrm{g}^{-1}$. The product $\mu_L = \mu\rho$ is called the *linear absorption coefficient* and is expressed in cm^{-1}. $\mu(E)$ is sometimes also called the *total cross section* for X-ray absorption at energy E.

Figure 14.2 shows a log–log plot of the energy dependence of the mass attenuation coefficient of several chemical elements in the X-ray energy range between 1 and 100 keV. The absorption edge discontinuities (due to photoelectric absorption – see subsequent text) are clearly visible. Low-Z materials attenuate X-rays of a given energy less than high-Z materials. A given material will attenuate high-energy (i.e., hard) X-rays less than low-energy (soft) X-rays.

The mass absorption coefficient $\mu(\mathbf{M})$ of a complex matrix $\mathbf{M}$ consisting of a mixture of several chemical elements (e.g., an alloy such as brass), can be calculated from the mass attenuation coefficient of the n constituting elements:

$$\mu(\mathbf{M}) = \sum_{i=1}^{n} w_i \mu_i \tag{14.2}$$

where μ_i is the mass attenuation coefficient of the ith pure element and w_i its mass fraction in the sample considered. This is called the *mixture rule*.

The mass absorption coefficient μ plays an important role in quantitative XRF analysis. Both the exciting primary radiation and the fluorescence radiation are attenuated in the sample. To relate the observed fluorescence intensity to the concentration, this attenuation must be taken into account.

As illustrated in Figure 14.1, the absorption of radiation in matter is the cumulative effect of several types of photon–matter interaction processes that take

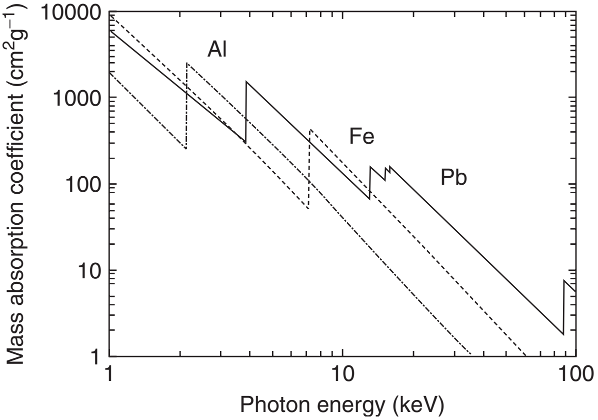

Figure 14.2 Energy dependence of the mass absorption coefficient μ of several elements.

place in parallel. Accordingly, in the X-ray range, the mass attenuation coefficient μ_i of element i can be expressed as

$$\mu_i = \tau_i + \sigma_i \tag{14.3}$$

where τ_i is the cross section for photoelectric ionization and σ_i the cross section for scattering interactions. All the above-mentioned cross sections are energy (or wavelength) dependent. Except at absorption edges (see subsequent text), μ is more or less proportional to $Z^4\lambda^3$.

14.2.3
Photoelectric Effect

In the photoelectric absorption process (Figure 14.3), a photon is completely absorbed by the atom and an (inner-shell) electron is ejected. Part of the photon is used to overcome the binding energy of the electron and the rest is transferred in the form of kinetic energy. After the interaction, the atom (actually an ion now) is left in a highly excited state as a vacancy has been created in one of the inner shells. The atom will almost immediately return to a more stable electron configuration by emitting an Auger electron or a characteristic X-ray photon. The latter process is called *X-ray fluorescence*. The ratio of the number of emitted characteristic X-rays to the total number of inner-shell vacancies in a particular atomic shell that gave rise to it is called the *fluorescence yield* of that shell (e.g., ω_K). For light elements ($Z < 20$), predominantly Auger electrons are produced during the relaxation upon K-shell ionization ($\omega_K < 0.2$), while the medium to heavy elements are preferentially relaxing in a radiative manner ($0.2 < \omega_K < 1.0$).

Photoelectric absorption can only occur if the energy of the photon E is equal to or higher than the binding energy ϕ of the electron. For example, an X-ray photon with an energy of 15 keV can eject a K-electron ($\phi_K = 7.112$ keV) or an L_3-electron ($\phi_{L_3} = 0.706$ keV) out of a Fe atom. However, a 5 keV electron can only eject L-shell electrons from such an atom.

Because photoelectric absorption can occur at each of the (excitable) energy levels of the atom, the total photoelectric cross section τ_i is the sum of (sub)shell-specific contributions:

$$\begin{aligned}\tau_i &= \tau_{i,\mathrm{K}} + \tau_{i,\mathrm{L}} + \tau_{i,\mathrm{M}} + \ldots \\ &= \tau_{i,\mathrm{K}} + (\tau_{i,\mathrm{L}_1} + \tau_{i,\mathrm{L}_2} + \tau_{i,\mathrm{L}_3}) + (\tau_{i,\mathrm{M}_1} + \ldots + \tau_{i,\mathrm{M}_5}) + \ldots\end{aligned} \tag{14.4}$$

In Figure 14.4, the variation of τ_{Mo} with energy is plotted. At high energy, for example, above 50 keV, the probability of ejecting a K-electron is rather low and that of ejecting an L_3-electron is even lower. As the energy of the X-ray photon decreases, the cross section increases, that is, more vacancies are created. At the binding energy $\phi_K = 19.99$ keV, there is an abrupt decrease in the cross section because X-rays with lower energy can no longer eject electrons from the K-shell. However, these photons continue to interact with the (more weakly bound) electrons in the L- and M-shells. The discontinuities in the photoelectric cross section are called *absorption edges*. The ratio of the cross section just above and just below the absorption edge

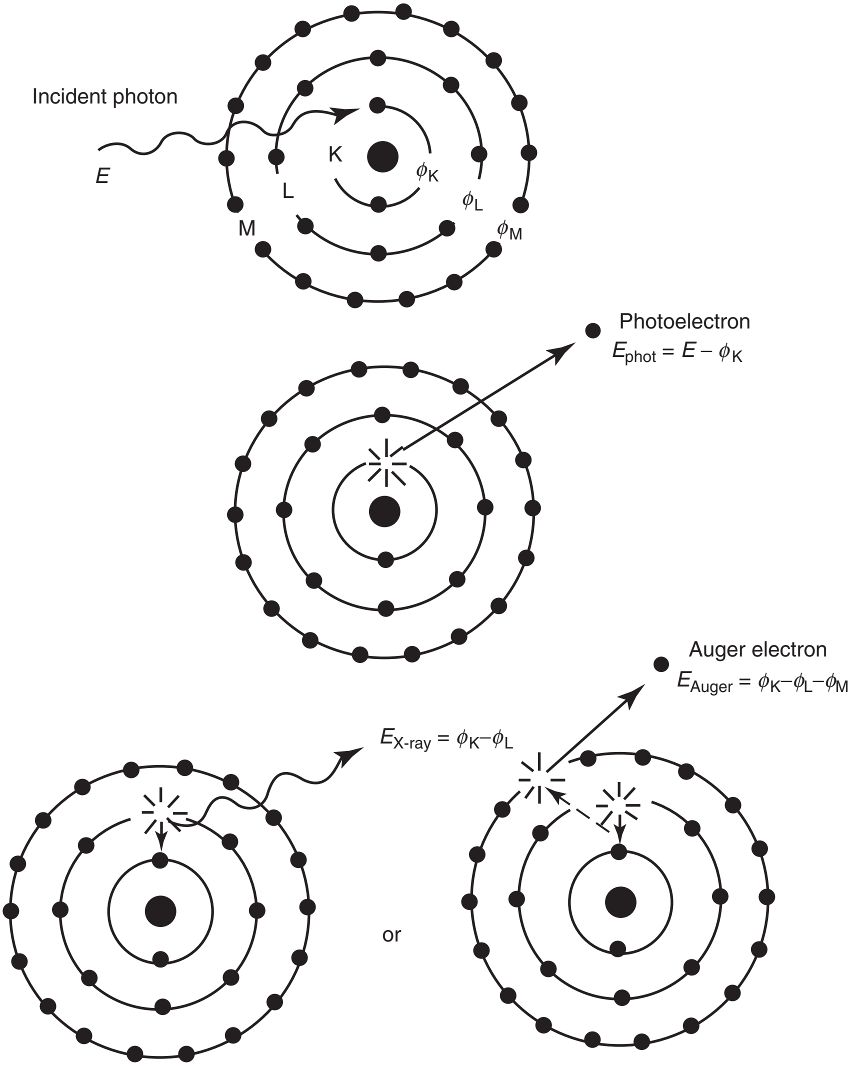

Figure 14.3 Photoelectric ionization can be followed by either radiative relaxation, causing the emission of characteristic fluorescent X-rays or nonradiative relaxation, involving the emission of Auger electrons.

is called the *jump ratio*, *r*. As XRF is the result of selective absorption of radiation, followed by spontaneous emission, an efficient absorption process is required. An element can therefore be determined with high sensitivity by means of XRF when the exciting radiation has its maximum intensity at an energy just above the K-edge of that element.

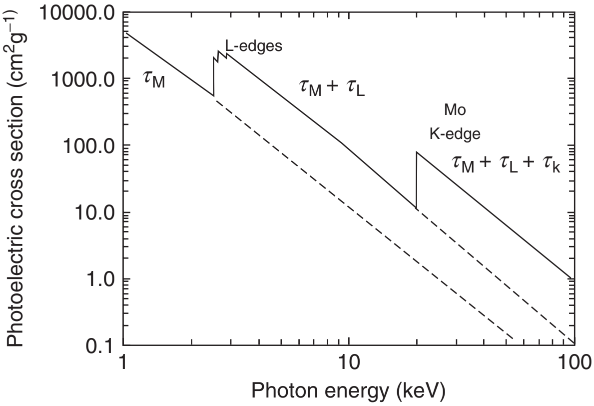

Figure 14.4 Variation of τ_{Mo} as a function of X-ray photon energy. The K, L_1, L_2, and L_3 absorption edges are clearly visible.

14.2.4
Scattering

Scattering is the interaction between radiation and matter that causes the photon to change direction. If the energy of the photon is the same before and after scattering, the process is called *elastic* or *Rayleigh scattering*. Elastic scattering takes place between photons and bound electrons and forms the basis of X-ray diffraction. If the photon loses some of its energy, the process is called *inelastic* or *Compton scattering*.

Accordingly, the total cross section for scattering σ_i can be written as the sum of two components:

$$\sigma_i = \sigma_{R,i} + \sigma_{C,i} \tag{14.5}$$

where $\sigma_{R,i}$ and $\sigma_{C,i}$, respectively, denote the cross sections for Rayleigh and Compton scattering of element i.

Compton scattering occurs when X-ray photons interact with weakly bound electrons. After inelastic scattering over an angle ϕ, a photon (Figure 14.5), with initial energy E, will have a lower energy E' given by the Compton equation:

$$E' = \frac{E}{1 + \frac{E}{m_0c^2}(1 - \cos\phi)} \tag{14.6}$$

where m_0 denotes the electron rest mass.

14.2.5
Bremsstrahlung

When an energetic electron beam impinges upon a (high-Z) material, X-rays in a broad wavelength band are emitted. This radiation is called *bremsstrahlung* because it is released during the sudden deceleration of the primary electrons, as a result

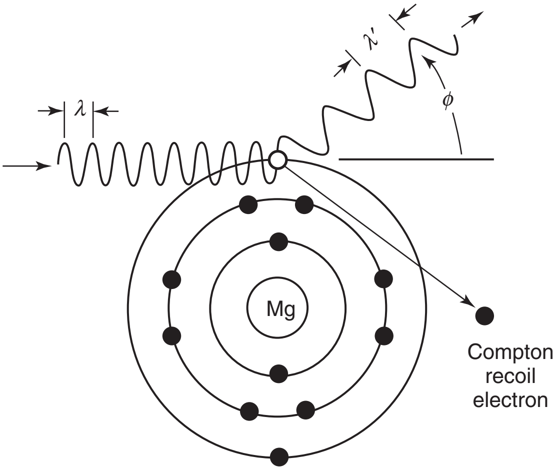

Figure 14.5 Geometry for Compton scattering of X-ray photons.

of their interaction with the electrons of the lattice atoms in the target. At each collision, the electrons are decelerated and part of the kinetic energy lost is emitted as X-ray photons. (In addition, characteristic X-ray lines (see subsequent text) of the target materials are produced.) As, during one collision, an electron of energy E can lose any amount between 0 and E, the resulting *bremsstrahlung* continuum features photons with energies in the same range. On a wavelength scale, the continuum is characterized by a minimal wavelength λ_{min} (nm) $= 1.24/E_{\mathrm{max}}$ (keV) $= 1.24/V$ (kV), where E_{max} is the maximum energy of the impinging electrons and V the potential used to accelerate them. The continuum distribution reaches a maximum at $1.5-2\lambda_{\mathrm{min}}$ so that an increase in the accelerating potential V causes a shift of the continuum toward shorter wavelengths. In Figure 14.6 *bremsstrahlung* spectra emitted by X-ray tubes operated at different accelerating potentials are shown.

14.2.6
Selection Rules, Characteristic Lines, and X-ray Spectra

Characteristic X-ray photons are produced following the ejection of an inner orbital electron from an excited atom, and the subsequent transition of atomic orbital electrons from states of high to low energy. Each element present in the specimen will produce a series of characteristic lines making up a polychromatic beam of characteristic and scattered radiation coming from the specimen. The systematic (IUPAC, International Union of Pure and Applied Chemistry) name of the X-ray line arising from a vacancy in the K-shell of an atom, which is filled by an electron originally belonging to the L_3-shell of that atom, is the $K-L_3$ transition. However, this transition is more commonly referred to as the $K_{\alpha 1}$-line (nonsystematic or Siegbahn nomenclature); similarly, fluorescent X-rays resulting from L_3-M_5 transitions are better known as $L_{\alpha 1}$*-photons*. Table 14.1 lists a number of observed X-ray lines and their corresponding IUPAC Siegbahn names.

Moseley first established the relationship between the wavelength λ of a characteristic X-ray photon and the atomic number Z of the excited element (Figure 14.7). Moseley's law is written as

$$\frac{1}{\lambda} = K(Z-s)^2 \tag{14.7}$$

where Z is atomic number and K and s are constants. s is the shielding constant and takes a value close to 1. K has a different value for each of the line series considered (e.g., the K_α-lines, the L_α-lines – see Table 14.1). Each unique atom has a number of available electrons that can take part in the transfer and, as millions of atoms are typically involved in the excitation of a given specimen, all possible de-excitation routes are taken. These de-excitation routes can be defined by a simple set of selection rules that account for the majority of the observed wavelengths.

Each electron in an atom can be defined by four quantum numbers. The first of these quantum numbers is the principal quantum number n, which can take all integral values. When n is equal to 1, the level is referred to as the *K level*; when n is 2, the L level, and so on. ℓ is the angular quantum number and this can take all values from $(n-1)$ to 0. m is the magnetic quantum number and can take values from $+\ell$ to $-\ell$. s is the spin quantum number with a value of $\pm\frac{1}{2}$. The total momentum J of an electron is given by the vector sum of $\ell + s$. As no two electrons within a given atom can have the same set of quantum numbers, a series of levels or shells can be constructed. Table 14.2 lists the atomic structures of the first three principal shells. The first shell, the K-shell, has a maximum of two electrons and these are both in the 1s level (orbital). As the value of J must

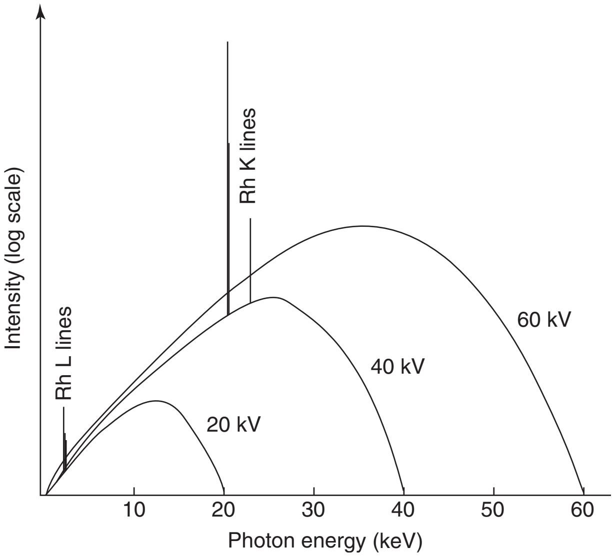

Figure 14.6 Polychromatic excitation spectra emitted by a Rh X-ray tube operated at various accelerating voltages. The excitation spectrum consists of a *bremsstrahlung* continuum upon which the characteristic lines of the anode material are superimposed.

Table 14.1 Principal X-ray lines (IUPAC and Siegbahn notations) and their approximate relative intensities relative to the major line in each subshell.

Series	IUPAC name	Siegbahn name	Relative intensity
K-lines	K-L_3	$K_{\alpha 1}$	100
	K-L_2	$K_{\alpha 2}$	~50
	K-M_3	$K_{\beta 1}$	~17
	K-M_2	$K_{\beta 3}$	~8
L_3-lines	L_3-M_5	$L_{\alpha 1}$	100
	L_3-M_4	$L_{\alpha 2}$	~10
	L_3-$N_{5,4}$	$L_{\beta 2,15}$	~25
	L_3-M_1	L_ℓ	~5
	M_3-N_1	$L_{\beta 6}$	~1
L_2-lines	L_2-M_4	$L_{\beta 1}$	100
	L_2-N_4	$L_{\gamma 1}$	~20
	L_2-M_1	L_η	~3
	L_2-O_1	$L_{\gamma 6}$	~3
L_1-lines	L_1-M_3	$L_{\beta 3}$	100
	L_1-M_2	$L_{\beta 4}$	~70
	L_1-N_3	$L_{\gamma 3}$	~30
	L_1-N_2	$L_{\gamma 2}$	~30
M-lines	M_5-N_7	$M_{\alpha 1}$	—
	M_5-N_6	$M_{\alpha 2}$	—
	M_5-N_6	M_β	—

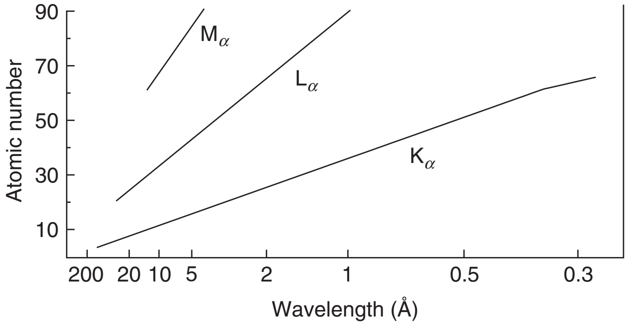

Figure 14.7 Moseley's law: relation between (inverse of the) wavelength of the K_α-, L_α-, and M_α-lines of the elements and their atomic number.

be positive in this instance, the only allowed value is $+\frac{1}{2}$. In the second shell, the L-shell, there are eight electrons: two in the 2s level and six in the 2p levels. In this instance, J has a value of $\frac{1}{2}$ for the 1s level and $\frac{3}{2}$ or $\frac{1}{2}$ for the 2p level, thus giving a total of three possible L transition levels. These levels are referred to as L_1, L_2, and

Table 14.2 Atomic structures of the first three principal shells.

Shell (number of electrons)	*n*	*ℓ*	*m*	*s*	Orbitals	*j*
K (2)	1	0	0	$\pm 1/2$	1s	$1/2$
L (8)	2	0	0	$\pm 1/2$	2s	$1/2$
	2	1	1	$\pm 1/2$	2p	$1/2$, $3/2$
	2	1	0	$\pm 1/2$	2p	$1/2$, $3/2$
	2	1	-1	$\pm 1/2$	2p	$1/2$, $3/2$
M (18)	3	0	0	$\pm 1/2$	3s	$1/2$
	3	1	1	$\pm 1/2$	3p	$1/2$, $3/2$
	3	1	0	$\pm 1/2$	3p	$1/2$, $3/2$
	3	1	-1	$\pm 1/2$	3p	$1/2$, $3/2$
	3	2	2	$\pm 1/2$	3d	$3/2$, $5/2$
	3	2	1	$\pm 1/2$	3d	$3/2$, $5/2$
	3	2	0	$\pm 1/2$	3d	$3/2$, $5/2$
	3	2	-1	$\pm 1/2$	3d	$3/2$, $5/2$
	3	2	-2	$\pm 1/2$	3d	$3/2$, $5/2$

L_3, respectively. In the M level, there are a maximum of 18 electrons: 2 in the 3s level, 6 in the 3p level, and 10 in the 3d level. Again, with the values of $\frac{3}{2}$ or $\frac{1}{2}$ for J in the 3p level and $\frac{5}{2}$ and $\frac{3}{2}$ in the 3d level, a total of five M transition levels are possible (M_1 to M_5). Similar rules can be used to build up additional levels: N, O, and so on.

The selection rules for the production of normal (diagram) lines require that the principal quantum number must change by at least 1 ($\Delta n \geq 1$), the angular quantum number must change by only one ($\Delta \ell = \pm 1$), and the J quantum number must change by 0 or 1 ($\Delta j = 0, \pm 1$). Application of the selection rules indicates that in, for example, the K series, only $L_2 \rightarrow K$ and $L_3 \rightarrow K$ transitions are allowed for a change in the principal quantum number of one. There are equivalent pairs of transitions for $n = 2$, $n = 3$, $n = 4$, and so on. Figure 14.8 shows the lines that are observed in the K series. Three groups of lines are indicated. The normal lines are shown on the left-hand side, consisting of three pairs of lines from the L_2/L_3, M_1/M_3, and N_2/N_3 subshells. While most of the observed fluorescent lines are normal, certain lines may also occur in X-ray spectra that, at first sight, do not abide by the basic selection rules. These lines are called *forbidden lines*; they arise from outer orbital levels where there is no sharp energy distinction between orbitals. As an example, in the transition elements, where the 3d level is only partially filled and is energetically similar to the 3p levels, a weak forbidden transition (the β_5) is observed. The satellite lines arising from dual ionizations form the third type. Following the ejection of the initial electron in the photoelectric process, a short, but finite, period of time elapses before the vacancy is filled. This time period is called the *lifetime* of the excited state. For the lower atomic number elements, this lifetime increases to such an extent that there is a significant probability that a second electron can be ejected from the atom before the first vacancy is filled. The

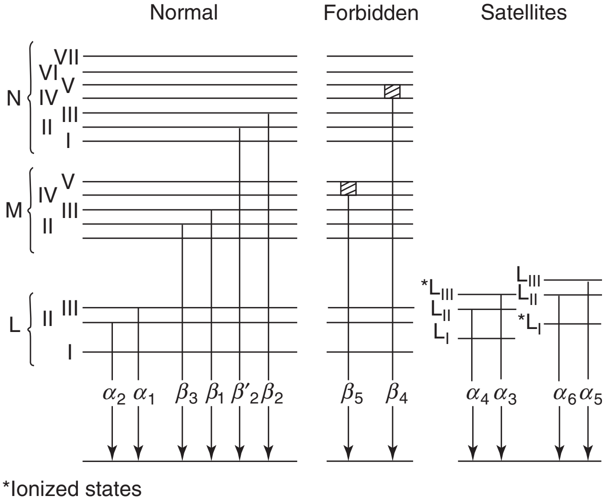

Figure 14.8 Observed lines in the K series.

loss of the second electron modifies the energies of the electrons in the surrounding subshells, and thus X-ray emission lines with other energies are produced. For example, instead of the Kα_1/Kα_2 line pair, a double ionized atom will give rise to the emission of satellite lines such as the Kα_3/Kα_4 and the Kα_5/Kα_6 pairs. As they are relatively weak, neither forbidden transitions nor satellite lines have great analytical significance; however, they may cause some confusion in the qualitative interpretation of spectra and may sometimes be misinterpreted as being analytical lines of trace elements.

14.2.7
Figures-of-Merit for XRF Spectrometers

14.2.7.1 Analytical Sensitivity

When XRF analysis of thin-film samples is performed (i.e., in samples where the product ρd of sample thickness d and sample density ρ is so small that absorption of the incoming exciting and of the outgoing fluorescent radiation in the material can be neglected – see Section 14.4), there is a linear relation between the collected net X-ray intensity N_{i} of a given characteristic line of element i and the irradiated mass m_i, which usually is also proportional to the concentration c_i of that element in the sample:

$$N_i = S_i^* \cdot m_i \cdot t = S_i \cdot c_i \cdot t \tag{14.8}$$

The proportionality constants S_i for the various elements are called the *sensitivity coefficients* of the XRF spectrometer for determination of these elements (expressed in counts per second per gram per cubic centimeter) and are important figures-of-merit of the instrument. In Figure 14.9, the variation with the atomic number of the sensitivity of a WDXRF spectrometer is plotted, for the case where either the

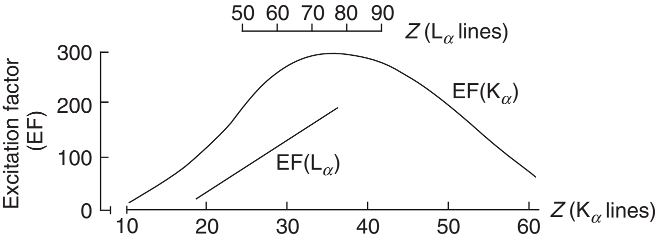

Figure 14.9 Variation in sensitivity coefficients with atomic number for a WDXRF spectrometer.

K_α ($10 < Z_i < 60$) or L_α ($40 < Z_i < 80$) peak intensities are used as analytical signals. By a selection of the excitation conditions (tube anode material, excitation voltage), the shape and location of the maximum in the sensitivity curve can be influenced to suit the needs of the application at hand.

Instead of using the X-ray intensity collected during a specific time t, it is often more convenient to use the net X-ray count rate R_i:

$$R_i = \frac{N_i}{t} = S_i \cdot c_i \tag{14.9}$$

14.2.7.2 **Detection and Determination Limits**

In reality, it is not possible to directly measure the net peak intensity N_i; rather, a total intensity $T_i = N_i + B_i$ is measured (see also Figure 14.27). The background intensity B_i can be written as the sum of various contributions:

$$B_i = B_i^{\text{scatter}} + B_i^{\text{detector}} + \sum_{j \neq i} B_{i,j}^{\text{overlap}} + B_i^{\text{blank}} \tag{14.10}$$

where B_i^{scatter} denotes the contribution to the spectral background below the analytical line of element i due to scattering of the primary radiation in the sample itself, in the sample environment gas (air or Helium, if any) and (in some cases) on the sample holder materials. These phenomena cause a continuous background upon which the characteristic peaks are superimposed. B_i^{detector} denotes the background contribution in the same energy/wavelength region due to detector artifacts, $B_{i,j}^{\text{overlap}}$ is the contribution to the peak intensity resulting from unresolved overlap between lines of an element $j \neq i$ and the analytical line of element i, and B_i^{blank} denotes the contributions to the peak intensity of element i not originating from the sample, that is, a blank value.

When the magnitude of B_i is experimentally determined and this measurement is repeated n times, the results will be distributed around a mean value $<B_i>$ with a standard deviation s_B. In modern instruments, most sources of systematic and random errors (e.g., due to mechanical or electrical instabilities) are small compared to the inherent uncertainty on the intensity measurements resulting from counting statistics. When B_i is obtained by means of a counting procedure (which usually is the case), Poisson (or counting) statistics govern the measurements so that $s^2{}_B = <B_i>$.

The IUPAC defines the limit of detection as "the lowest concentration level than can be determined to be statistically significant from an analytical blank." The lowest net X-ray intensity $N_{i,\mathrm{LD}}$ that still can be distinguished in a statistically significant manner from the average background level can be written as

$$N_{i,\mathrm{LD}} =< B_i > + k s_\mathrm{B} \tag{14.11}$$

where k is an integer constant depending on the significance level considered.

The limit of detection concentration $c_{i,\mathrm{LD}}$ corresponding to $N_{i,\mathrm{LD}}$ can be written as

$$c_{i,LD} = \frac{N_{i,LD} - \langle B_i \rangle}{S_i \cdot t} = \frac{k s_\mathrm{B}}{S_i \cdot t} = \frac{k\sqrt{R_\mathrm{B}}}{S_i \cdot \sqrt{t}} \tag{14.12}$$

where $R_\mathrm{B} = <B_i>/t$ is the background count rate. When the irradiation of a standard sample (with known concentration c_i) during a time t results in net and background intensities N_i^{std} and B_i^{std}, so that the sensitivity S_i can be approximated by the ratio $N_i^{\mathrm{std}}/c_i^{\mathrm{std}}/t$, it follows that the lowest detectable concentration (or relative detection limit) $c_{i,\mathrm{LD}}$ can be estimated from this measurement by using the relation:

$$c_{i,\mathrm{LD}} \cong c_i^{\mathrm{std}} \frac{k\sqrt{B_i^{\mathrm{std}}}}{N_i^{\mathrm{std}}} \tag{14.13}$$

When, during such an experiment, a known mass m_i^{std} was irradiated, the lowest detectable mass (or absolute detection limit) $m_{i,\mathrm{LD}}$ can be calculated by means of

$$m_{i,\mathrm{LD}} \cong m_i^{\mathrm{std}} \frac{k\sqrt{B_i^{\mathrm{std}}}}{N_i^{\mathrm{std}}} \tag{14.14}$$

Relative detection limits are useful figures-of-merit for bulk XRF equipment, where it usually is relevant to know the lowest concentration level at which the spectrometer can be used for qualitative or quantitative determinations. In instruments where very small sample masses are being irradiated (e.g., in the picogram range for microscopic X-ray fluorescence (μ-XRF) and total-reflection X-ray fluorescence (TXRF)), the absolute detection limit is another useful figure-of-merit as it provides information on the minimal sample mass than can be analyzed in a given setup.

In the literature, usually detection limit values for $k = 3$ (corresponding to a statistical confidence level of 99%) are reported. A related figure-of-merit is the *determination limit*, which is defined as the lowest concentration (or mass) at which a quantitative determination with a relative uncertainty of at least 10% is possible. This quantity can be calculated by setting $k = 10$ in the given expressions.

In Table 14.3, as an example, relative LD values for trace elements obtained by means of WDXRF in different matrices are listed. In Figure 14.10, a plot of typical absolute LD values for TXRF spectrometers is shown.

Table 14.3 WDXRF-obtained relative detection limits ($\mu g\,g^{-1}$) in various matrix and using different instruments.

Matrix	Element	c_{LD}
Terephthalic acid	Fe	0.15
	Co	0.18
Aluminum	Mg	10.5
	P	1.3
Al-Mg alloy	Mg	7
	Si	5
	Ti	3
	Mn	2
	Cu	1
Cement	Na_2O	36
	MgO	27
	Al_2O_3	22
	SiO_2	50
	SO_3	24
	P_2O_5	32
Low-alloy steel	C	80
	Al	4
	Si	2
	Cr	2
Copper alloys	Be	0.20%

14.3
Instrumentation

While most of the early work in X-ray spectrometry was carried out using electron excitation, the present-day use of electron-excited X-radiation is restricted mainly to X-ray spectrometric attachments to electron microscopes. Most modern stand-alone X-ray spectrometers use X-ray excitation sources rather than electron excitation. All conventional X-ray spectrometers comprise three parts: the primary source unit, the spectrometer itself, and the measuring electronics.

XRF spectrometry typically uses a polychromatic beam of short-wavelength/high-energy photons to induce the emission of longer wavelength/lower energy characteristic lines in the sample to be analyzed. Modern X-ray spectrometers may use either the diffracting power of a single crystal to isolate narrow *wavelength* bands (WDXRF) or an energy-selective detector may be employed to isolate narrow *energy* bands (EDXRF) from the polychromatic radiation (including characteristic radiation) that is produced in the sample.

Because the relationship between emission wavelength and atomic number is known, isolation of individual characteristic lines allows the unique identification of

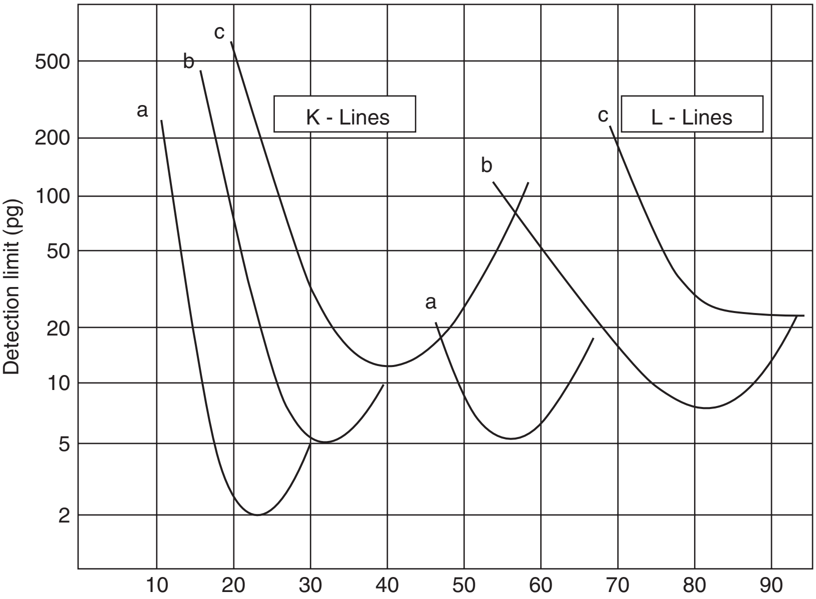

Figure 14.10 Typical absolute detection limit values for TXRF spectrometers. The labels a–c refer to different instrument settings.

an element to be made and elemental concentrations can be estimated from characteristic line intensities. Thus, this technique is a means of material characterization in terms of chemical composition.

WDXRF instrumentation is almost exclusively used for (highly reliable and routine) bulk analysis of materials, for example, in industrial quality control laboratories. In the field of EDXRF instrumentation, next to the equipment suitable for bulk analysis, several important variants have evolved in the past 20 years. Both TXRF and micro-XRF are based on the spatial confinement of the primary X-ray beam so that only a limited part of the sample (+support) is irradiated. This is realized in practice by the use of dedicated X-ray sources, X-ray optics, and irradiation geometries.

14.3.1
X-ray Sources

Four different types of X-ray sources are being employed in X-ray analysis: (i) sealed X-ray tubes and (ii) radioactive sources are the most commonly employed, while to a lesser extent primary X-rays produced in (iii) rotating anode tubes, and (iv) synchrotron radiation (SR) facilities are also utilized for analytical purposes.

Most commercially available X-ray spectrometers utilize a sealed X-ray tube as an excitation source, and these tubes typically employ a heated tungsten filament to induce the emission of thermionic electrons in a vacuum chamber. After acceleration by means of a high voltage V, the electrons are directed toward a layer of high purity metal (e.g., Cr, Rh, W, Mo, Rh, and Pd) that serves as the anode. In the metal layer, a *bremsstrahlung* continuum is produced, onto which the characteristic lines of the anode material are superimposed. The broad band radiation is well suited for the excitation of the characteristic lines of a wide range of atomic numbers. The higher the atomic number of the anode material, the more intense is the beam of radiation produced in the tube. Figure 14.11 shows a schematic cross section of a sealed X-ray tube.

In typical X-ray tubes employed in XRF spectrometers, accelerating voltages of 25–50 kV are used, while electron currents in the range 20–50 mA are employed. For WDXRF, frequently, 3 kW X-ray tubes are used; in EDXRF spectrometers, depending on the manner of sample excitation, tubes in the 50–1000 W range are employed. The efficiency of an X-ray tube is relatively low: only about 1% of the electric power is converted into X-rays, the rest is dissipated as heat. Accordingly, the tube anode of high-power tubes (>100 W) usually is water cooled to about meltdown of the metal block. A key factor in the design of an X-ray tube is the maximum powder loading (expressed in W mm^{-2}) it can stand. The high-voltage power supplies used together with X-ray tubes are highly stable so that a wide conical X-ray beam of nearly constant intensity (to within a small percentage relative) is emitted. For applications requiring higher power levels as 3 kW, rotating rather than fixed anode tubes are employed. In these devices, the anode is a fast-spinning water-cooled metal cylinder covered with the desired anode material. During each revolution of the anode, only a small area on the surface is bombarded by the electrons in a short fraction of the time, so that the rest of the period can be used for heat removal. Rotating anode tubes that can be operated up to a total power of 18 kW are commercially available.

The emission spectrum of an X-ray tube (Figure 14.6) consists of two components: a *bremsstrahlung* continuum upon which the characteristic lines of the anode material (that becomes ionized as a result of the electron bombardment) are

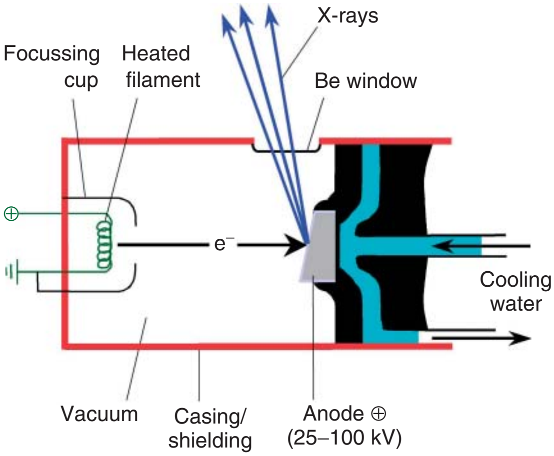

Figure 14.11 Cross section of a sealed X-ray tube.

superimposed. The shape of the emission spectrum can be modified by changing the electron acceleration voltage.

Radioactive α-, β-, and γ-sources may also be employed for (ED)XRF analysis. Generally, these sources are compact compared to X-ray tubes and can, for example, be used in portable analysis systems. α-sources are suited for the analysis of low atomic number elements. Frequently used sources are ^{244}Cm, with a half-life ($t_{\frac{1}{2}}$) of 17.8 years that emits 5.76 and 5.81 MeV α-particles, and ^{210}Po, having a half-life of 138 days and emitting 5.3 MeV α's.

β-sources can also be employed, either for direct EDXRF excitation of a sample or for producing *bremsstrahlung* radiation in a target to be used for subsequent sample excitation. ^{22}Na ($t_{\frac{1}{2}} = 2.6$ years), ^{85}Kr ($t_{\frac{1}{2}} = 10.7$ years), and ^{63}Ni ($t_{\frac{1}{2}} = 100$ years) are β-emitters that can be used for the former purpose, emitting, respectively, β^--particles of about 550, 670, and 66 keV. For *bremsstrahlung* production, ^{147}Pm ($t_{\frac{1}{2}} = 2.6$ years, 225 keV) in combination with a Zr target and ^{3}H ($t_{\frac{1}{2}} = 12.4$ years, 19 keV, Ti target) are useful.

In Table 14.4, some characteristics of radio sources emitting X-ray or γ-ray lines are listed. The X-ray emitting sources usually contain nuclides that decay by means of the electron-capture mechanism. During the decay, an inner-shell electron is captured by the neutron-deficient nucleus, transforming a proton in a neutron. This results in a daughter nuclide that has a vacancy in one of its inner shells, which results in the emission of corresponding characteristic radiation. For example, when a ^{55}Fe-nucleus (26 protons and 29 neutrons) captures a K-electron and becomes a ^{55}Mn nucleus, a Mn K-$L_{3,2}$ (Mn-K_α) or K-$M_{3,2}$ (Mn-K_β) photon will be emitted. Other sources (such as ^{241}Am or ^{57}Co) emit γ-rays of suitable energy as a result of different nuclear transformations.

In Figure 14.12, the range of elements that can be usefully analyzed by means of various radioactive and X-ray tubes sources is summarized.

In a number of specialized cases, XRF experiments also make use of synchrotron sources. SR is produced by high-energy (GeV) relativistic electrons or positrons circulating in a storage ring. This is a very large, quasi-circular vacuum chamber where strong magnets force the particles on closed trajectories. X-radiation is produced during the continuous acceleration (change in velocity vector in this case) of the particles. SR sources are several (six to twelve) orders of magnitude more

Table 14.4 Radioactive sources used for XRF analysis (flux in photons/s/sr).

Radio isotope	Half-life (years)	X-ray or γ-ray energy (keV)	Flux
^{55}Fe	2.7	5.9–6.5 (Mn-K X-rays)	7×10^6
^{244}Cm	88	14.6–22 (U L X-rays)	—
^{109}Cd	1.3	22–25 (Ag K X-rays)	8×10^6
^{125}I	0.16	27–32 (Te K X-rays)	—
^{241}Am	433	59.6 (γ-ray)	6×10^7
^{153}Gd	0.66	41.48 (Eu-K X-rays)	4×10^8
^{57}Co	0.74	122.136 (γ-ray)	4×10^6

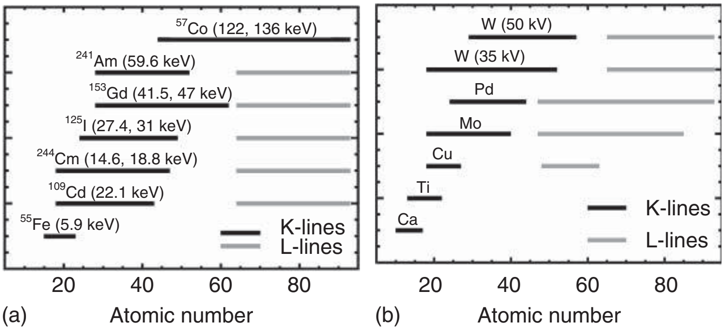

Figure 14.12 Range of elements that can be analyzed using (a) radioactive sources and (b) X-ray tubes with different anodes, showing excitation of K- and L-lines.

bright than X-ray tubes, have a natural collimation in the vertical plane, and are linearly polarized in the plane of the orbit. The spectral distribution is continuous or shows sharp maxima at a limited number of energies, called *harmonics*. By monochromatization of the continuum or by selection of one of the harmonics, it is possible to employ selective excitation of a series of elements in the sample, yielding optimal detection conditions (see subsequent text – TXRF). Because the SR originates from a source point of small dimensions and is released in a very narrow angular range, it is easily focusable into micro- and/or nanobeam (see subsequent text – micro-XRF). An additional advantage is the high degree of polarization of SR, causing spectral backgrounds due to scatter to be greatly reduced when the detector is placed at 90° to the primary beam and in the storage ring plane. The combination of a high primary beam intensity and a low spectral background causes DL values of SRXRF to go down to the parts per billion level (see, e.g., Figure 14.24).

14.3.2
X-ray Detectors

As any radiation detector, an X-ray detector is a transducer for converting X-ray photon energy into easily measurable and countable voltage pulses. All detector types work through a process of photoionization, in which interaction between the entering X-ray photon and the active detector material produces a number of electrons. By means of a capacitor and a resistor, the current produced by the electrons is converted to a voltage pulse, in such a way that one digital voltage pulse is produced for each X-ray photon that enters the detector.

Next to being sensitive to photons of the appropriate energy range, there are two other important properties that the ideal detector should possess: proportionality and linearity. A detector is said to be proportional when the height of the voltage pulse that is produced upon entry of a photon is proportional to the energy of the photon. Proportionality is needed when, through pulse-height selection, only pulses of a particular height, that is, corresponding to X-ray photons within a specific energy band, are to be measured.

When the rate with which voltage pulses are being recorded is the same as the rate with which X-ray photons enter the detector, the latter is said to have a linear response. This property is important when the recorded count rates of various X-ray lines are to be used as measures of the photon intensities of these lines produced in a sample.

The detector resolution is the precision/repeatability with which the energy of a specific type of X-ray photons (e.g., the Mn-K_α-line at 5.9 keV) can be determined and is therefore a measure of the capability of the detector to distinguish between X-rays of very similar energy but different origin (e.g., the As-$K_{\alpha 1}$-line at 10.543 keV and the Pb-Lα1-line at 10.549 keV).

In WD spectrometers, gas-flow proportional counters (for long wavelengths, $\lambda > 0.2$ nm) and scintillation counters (for wavelengths shorter than 0.2 nm) are used to count X-rays. Both types of detectors usually are combined in a tandem detector that covers the entire wavelength range used in WDXRF spectrometry. As neither of these detectors has sufficient resolution to separate multiple wavelengths/energies on its own, they are employed together with an analyzing crystal. In case of ED spectrometry, solid-state detectors of higher resolution are used.

A gas-flow proportional counter (Figure 14.13a) consists of a cylindrical tube about 2 cm in diameter, carrying a thin (25–50 mm) wire along its radial axis. The tube is filled with a mixture of inert gas and quench gas – typically 90% argon/10% methane (P-10). The cylindrical tube is grounded and a voltage of about 1400–1800 V is applied to the central wire. The wire is connected to a resistor shunted by a capacitor. An X-ray photon entering the detector produces a number of ion pairs (n), each comprising one electron and one Ar^+ ion. The first ionization potential for argon is about 16 eV, but competing processes during the conversion of photon energy to ionization cause the average energy required to produce an ion pair to be greater than this amount. The fraction relating the average energy to produce one ion pair, to the first ionization potential, is called the *Fano factor F*. For argon, F is between 0.5 and 0.3 and the average energy ε required to produce one primary ion pair is equal to 26.4 eV. The number of ion pairs produced by a photon of energy E will equal:

$$n = \frac{E}{\varepsilon} \tag{14.15}$$

Following ionization, the charges separate, with the electrons moving toward the (anode) wire and the argon ions to the grounded cylinder. As the electrons approach the high-field region close to the anode wire, they are accelerated sufficiently to produce further ionization of argon atoms. Thus, a much larger number N of electrons will actually reach the anode wire. This effect is called *gas gain* or *gas multiplication*, and its magnitude is given by $M = N/n$. For gas-flow proportional counters used in X-ray spectrometry, M typically has a value of around 10^5. Provided that the gas gain is constant, the size of the voltage pulse V produced is directly proportional to the energy E of the incident X-ray photon. In practice, not all photons arising from photon energy E will be exactly equal to V. There is a random process associated with the production of the voltage pulses and the resolution of a

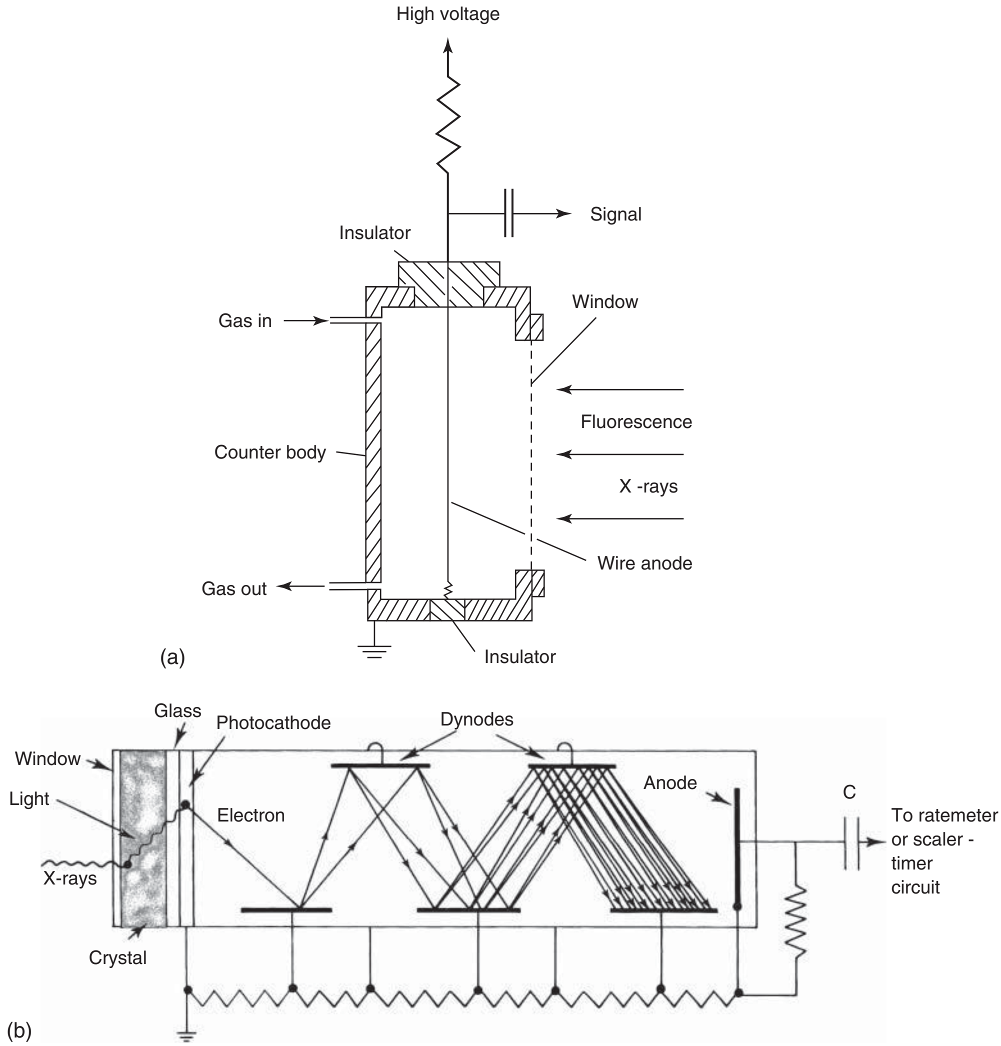

Figure 14.13 Schematic drawings of (a) a gas-filled proportional counter and (b) a scintillator detector.

counter is related to the variance in the average number of ion pairs produced per incident X-ray photon.

While the gas-flow proportional counter is ideal for measurement of longer wavelengths, it is rather insensitive to wavelengths shorter than about 0.15 nm. For this shorter wavelength region, it is common to use a scintillation counter (Figure 14.13b). The scintillation counter consists of two parts, the phosphor (scintillator) and the photomultiplier. The phosphor is typically a large single crystal of sodium iodide that has been doped with thallium, denoted as a NaI(Tl) crystal. When X-ray photons fall onto the phosphor, blue light photons are produced (with a wavelength of 410 nm), where the number of blue light photons is related to the energy of the incident X-ray photon. These visual light photons produce electrons by interaction with the surface of the photocathode in the photomultiplier, and the number of electrons is linearly increased by a series of secondary surfaces, called *dynodes*, inside the photomultiplier. The current produced by the photomultiplier is then converted to a voltage pulse, as in the case of the gas-flow proportional counter. As the number of electrons is proportional to the energy of the incident X-ray photon, the scintillation counter also has a proportional response. Because of inefficiencies in the X-ray/visual light/electron conversion processes, the average energy to produce a single event within a scintillation counter is more than a magnitude greater than the equivalent process in a flow counter. For this reason, the resolution of scintillation counters is much worse than that of flow counters.

The output pulses produced by both the above-mentioned detectors are further processed by a linear amplifier and a discriminator circuit. Usually the number of pulses is counted during a preset amount of time and the accumulated counts stored in computer memory for display and further processing. The processing of an X-ray event by the detector and its associated electronics takes a finite amount of time. After the arrival of one X-ray, the detection system is said to be ''dead'' during this length of time because X-rays arriving within this dead period will not be counted. The dead time is of the order of 200–300 ns after the arrival of each photon; this implies that count rates up to 10^6 photons per second can be handled.

The detectors used in the various forms of EDXRF are semiconductor detectors. Conventionally, two types, that is, lithium-drifted silicon (Si(Li)) and hyperpure germanium (HPGe) detectors are used. Their main advantages are their compact size, the nonmoving system components, and relatively good energy resolution, which optimally is of the order of 120 eV at 5.9 keV. Because of their operation principles, these detectors have an inherent simultaneous multielement capacity, which leads to a short measuring time for all elements as the detectors select the energy and collect counts at the same time. Disadvantages include the need for liquid nitrogen (LN_2) cooling during operation, the necessity of having a relatively thin (8–25 μm) Be window and the fact that the maximum processable number of counts is limited to about 40.000 cps. This figure can be increased to 100 000 cps, but with loss of optimal performance characteristics.

The detector crystal itself is a disk of very pure Si or Ge with dimensions of 4–10 mm diameter and 3–5 mm thickness. Even careful production of the Si ingots the disk are cut from will still leave some trace impurities in the Si lattice. To compensate for and bind all free electrons, lithium ions are drifted (allowed to diffuse at elevated temperature) into the silicon crystal to neutralize the Si crystal defects in a particular zone, the so-called intrinsic zone. Afterwards, Au contacts are evaporated onto the crystal and a reverse voltage applied. In the crystal, the energy difference ε (band gap) between the valence and conduction band is 3.8 eV. At room temperature, the conduction band is partially populated so that the crystal is a (semi)conductor. To keep the leakage current as low as possible, the crystal is cooled with LN_2 by placing it in a vacuum cryostat. At $-196\,^{\circ}$C, almost all electrons remain in the valence band. The radiation to be measured needs to enter the cryostat through a thin entrance window, usually made of Be. By applying a reverse voltage to the charge-carrier-free intrinsic zone, an absorbed X-ray photon is converted into charge by ionization. Electrons are promoted from the valence to the conduction band, leaving ''positive holes'' in the valence band; thus, the crystal temporarily becomes conducting. $n = E/\varepsilon$ of electron–hole pairs are created. The electrons and holes are quickly swept to the contact layers by the electric field created by the applied reverse bias on the crystal.

Figure 14.14 shows the operation principle schematically. The charge induces a signal at the gate of a cooled field-effect transistor (FET) that is the input stage of a charge-sensitive preamplifier. The output signal is fed to a pulse processor that shapes the pulse and amplifiers it further. This signal is in the range up to 10 V and is proportional to the energy of the absorbed photon. The pulse height is digitized by means of an analog-to-digital converter (ADC) and the resulting digital value stored in a multichannel analyzer (MCA). This is an array of memory cells called *channels*; by using the digital value associated with a single event as address offset into the memory array, the content of the appropriate channel is incremented with one count. Thus, all detector events having the same pulse height are stored in the same channel. For example, upon entry in the detector of a Cu-K$_{\alpha1}$ photon ($E = 8.05$ keV), 2117 electron–hole pairs will be generated, which may lead to the formation of a preamplifier voltage pulse of, for example, 42.0 mV. After further amplification and shaping, this is converted into a bell-shaped pulse of 4.20 V; the pulse height is then digitized by an ADC, resulting, for instance, in a digital number of 420. Ultimately, this causes the content of channel 420 to be incremented with one count. After readout, the MCA memory (typically 1024 or 2048 channels in size, each corresponding to a 10–20 eV wide energy range)

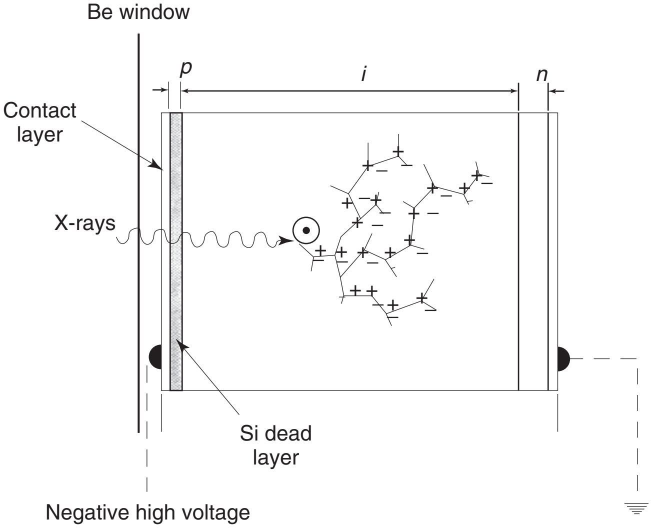

Figure 14.14 Scheme of the working principle of a Si(Li) detector.

yields a pulse-height distribution of the detected events or an ED X-ray spectrum, as shown in Figure 14.15.

In the spectra, a broadening of the X-ray lines can always be observed, that is, the counts associated with photons of a specific energy, which normally should end up in a single channel, are distributed in a quasi-Gaussian manner over several adjacent channels in the spectrum, thus giving rise to a bell-shaped X-ray peak in the spectrum. This line broadening is caused by statistical fluctuations in the number of electron–hole pairs created when an X-ray photon of a given energy enters the detector; electronic noise in the amplifiers causes the uncertainty on the pulse height to increase further. Even under conditions in which all noise contributions in the electronics are minimized, the line broadening remains a significant phenomenon, causing a frequent peak overlap to occur in X-ray spectra, for example, between lines of adjacent elements such as the Mn-K_β and Fe-K_α peaks. The resolution of ED detectors conventionally is expressed as the full width at half maximum (FWHM) of the Mn-K_α (Mn K-$L_{2,3}$) peak (at 5.98 keV) and typically is around 150 eV. In the most optimal case, this value can be also as low as 120 eV. The time to process an X-ray event (dead time) is of the order of 10–30 μs; conventional EDXRF spectrometers can therefore only operate at count rates up to 40 000 cps. In view of the presence of a Be window in the detector cryostat, X-ray photons below 2 keV are hard to detect in a conventional Si(Li) detector, although thin-window models are commercially available.

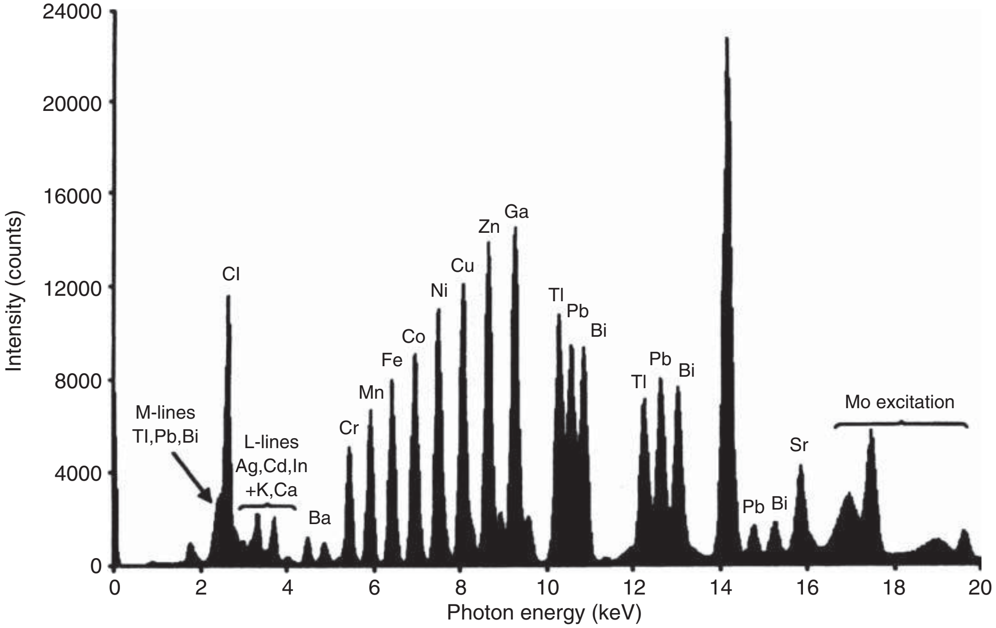

Figure 14.15 Energy-dispersive XRF spectrum of a multielement standard, obtained in a TXRF spectrometer.

Roughly since 1995, several types of compact and thermoelectrically cooled ED detectors have become available. The most significant advantage of these detectors is that they do not require LN_2 cooling, allowing the instrument they are incorporated in to be much smaller. These types of detectors are suitable for employment in portable equipment.

Thermoelectrically cooled Si-PIN, $Cd_{1-x}Zn_xTe$ (CZT), and HgI_2 detectors are fairly inexpensive devices. The currently available Si-PIN diode detectors mostly have a thickness of about 300 μm, which makes the detector useful up to X-ray energies of 20 keV and an energy resolution in the range of 180–200 eV at Mn-K_α, that is, slightly worse than that of Si(Li) or HPGe detectors. Some versions with 500 μm thickness or larger active areas (up to 25 mm^2 vs the standard 5–10 mm^2) are available as well. CZT detectors are targeted toward the higher energy range with a thickness of up to 2 mm and allow efficient detection of X-rays up to 150 keV with a resolution of about 250 eV at Mn-K_α (5.9 keV) and 1 keV at 60 keV. Similarly, HgI_2 detectors (with thicknesses of a few millimeters) can also be used in this range with a resolution of about 200 eV at Mn-K_α.

A high-quality type of solid-state detector is the solid-state drift (SSD) chamber detector, featuring excellent energy resolution at high count rates. An FWHM below 140 eV at 5.9 keV can be achieved by means of thermoelectrical cooling (Peltier effect). SSDs exist in a large variety of sizes up to 2 cm^2 diameter. They still show adequate spectroscopical behavior at count rates as high as several million counts per centimeter square per second. The compact design, the relatively low price, the absence of the need for LN_2 for cooling, the high count rate capability and the nonsensitivity to noise pickup make these systems attractive alternatives to conventional semiconductor detectors.

The resolution of a number of different X-ray detectors in the range 1–100 keV (about 1–0.01 nm) is compared in Figure 14.16. It is clear that scintillators and proportional counters are not even able to separate the K_α-lines of adjacent elements, whereas this is the case for most of the solid-state detectors.

14.3.3
Wavelength-Dispersive XRF

A typical WDXRF system consists of an X-ray tube, a specimen support holder, a primary collimator, an analyzing crystal, and a tandem detector. The typical WDXRF irradiation/detection geometry is shown in Figure 14.17. WD spectrometers employ diffraction by a single crystal to separate characteristic wavelengths emitted by the sample. A single crystal of known interplanar spacing d is used to disperse the collimated polychromatic beam of characteristics wavelengths coming from the sample, such that each wavelength λ will diffract at a specific angle θ, given by Braggs law:

$$n\lambda = 2d\sin\theta \tag{14.16}$$

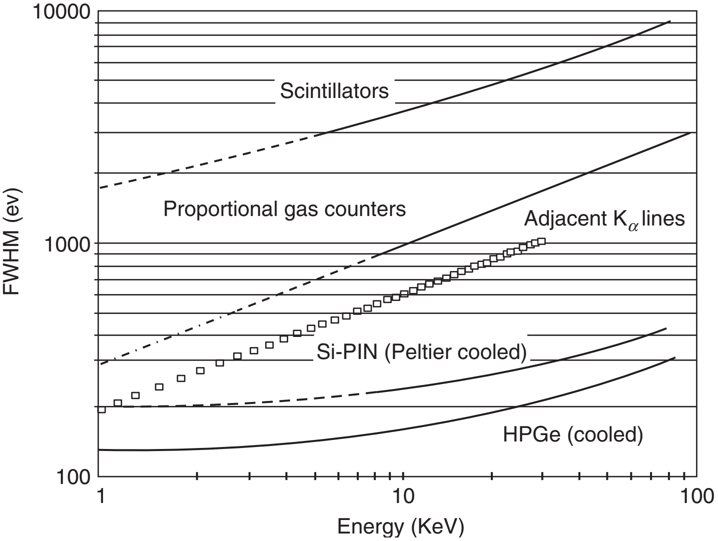

Figure 14.16 Energy resolution (expressed as FWHM of the K_α-line of a given energy), of different X-ray detectors in the 1–100 keV range. The difference in the K_α-line energy between adjacent elements is also shown (symbols).

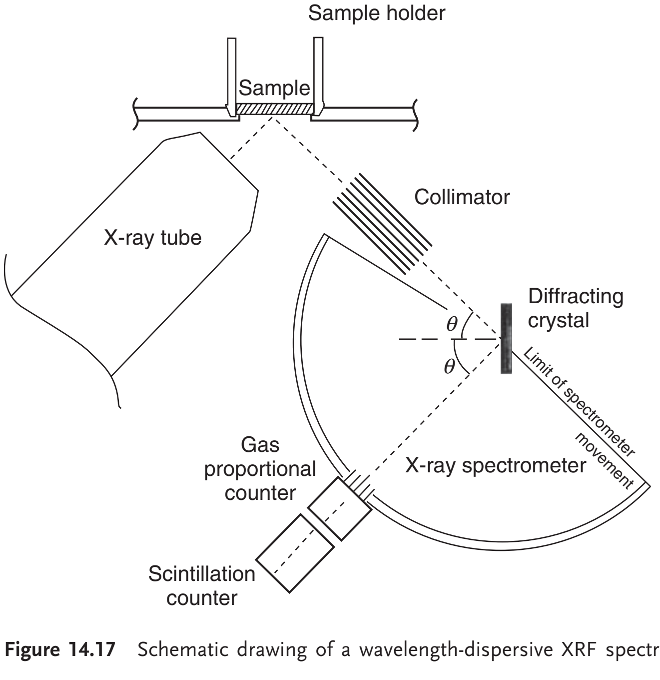

Figure 14.17 Schematic drawing of a wavelength-dispersive XRF spectrometer.

where n is an integer number denoting the order of the diffracted radiation. A goniometer is used to maintain the required $\theta/2\theta$ relationship between sample and crystal/detector.

Before impinging on the analyzer crystal, by means of a collimator or a slit, the spread in initial directions of the sample-to-crystal beam is limited. As the maximum achievable angle on a typical WDXRF spectrometer is around 73°, the maximum *wavelength* that can be diffracted by a crystal of spacing d is equal to about $1.9d$.

The angular dispersion $\mathrm{d}\theta/\mathrm{d}\lambda$ of a crystal with spacing $2d$ is given by

$$\frac{\mathrm{d}\theta}{\mathrm{d}\lambda} = \frac{n}{2d\cos\theta} \tag{14.17}$$

and is therefore inversely proportional to its d-spacing. Thus, high dispersion can only be obtained at the expense of reducing the wavelength range covered by a particular crystal. Several crystals therefore are likely to be employed for covering a number of analyte elements. Typically, four to six different analyzer crystals (with different d-spacings) and two different collimators are provided in this type of instrument, allowing for a wide choice in dispersion conditions. The smaller the d-spacing of the crystal, the better is the separation of the lines, but the smaller the wavelength range that can be covered. The separating power of the crystal spectrometer is dependent on the divergence allowed by the collimators (which mainly determine the width of the diffracted lines) in the 2θ spectrum, but the angular dispersion of the analyzing crystal itself and the intrinsic width of the diffraction lines also play a role.

In Table 14.5, some characteristics of a few commonly employed analyzer crystals are listed. Classically, large single crystals have been used as dispersive elements. For dispersion of long wavelengths (>0.8 nm), only a limited number of natural materials are available; the most commonly employed is thallium acid phthalate (TAP, $2d = 2.63$ nm), allowing measurement of the Mg-, Na-, F-, and O-K-lines. As an alternative, several other materials with large $2d$-spacings have been used and since the 1980s layered synthetic multilayers (LSMs) are in use. These consist of stacks of alternate electron-rich (e.g., W) and electron-poor (e.g., graphite) layers of atoms or molecules, deposited on a sufficiently smooth substrate. As the composition and interplanar distance of the LSM can, to a certain extent, be

Table 14.5 Analyzing crystals used in wavelength-dispersive X-ray spectrometry.

Crystal	Planes	2*d* (nm)	K-line range	L-line range
Lithium fluoride (LiF)	220	0.2848	>Ti	>La
Lithium fluoride (LiF)	200	0.4028	>K	>Cd
Pentaerythritol (PET)	002	0.8742	Al–K	—
Thallium acid phthalate (TAP)	001	2.64	F–Na	—
LSMs	—	5–12	Be–F	—

optimized for particular applications, a factor 4–6 improvement in peak intensities compared to TAP crystals can be achieved.

Among WD spectrometers, a distinction can be made between single-channel instruments and multichannel spectrometers. In the former type of instrument, a single dispersive crystal/detector combination is used to sequentially measure the X-ray intensity emitted by a sample at a series of wavelengths when this sample is irradiated with the beam from a high-power (2–4 kW) X-ray tube. In a multichannel spectrometer, many crystal/detector sets are used to measure many X-ray lines/elements simultaneously.

Single-channel instruments are also referred to as *scanning spectrometers*; this type is the most common. During an angular scan, the angle θ between sample and analyzer crystal is continuously varied; in order to maintain an identical angle between analyzer crystal and detector, the latter moves at the double angular speed as the crystal. In this manner, X-ray intensity versus 2θ diagrams are obtained. By means of tables, the recorded peaks can be assigned to the characteristic lines of one or more elements. In Figure 14.18, a typical 2θ spectrum obtained from a brass sample is shown.

Simultaneous WD spectrometers were introduced in the early 1950s, and sequential systems about a decade later. At this time, about 30 000 or so WD instruments have been supplied commercially. The two major categories of WD X-ray spectrometers differ mainly in the type of source used for excitation, the number of elements that they are able to measure at one time, the speed at which they collect data and their price range. For high-specimen throughput quantitative

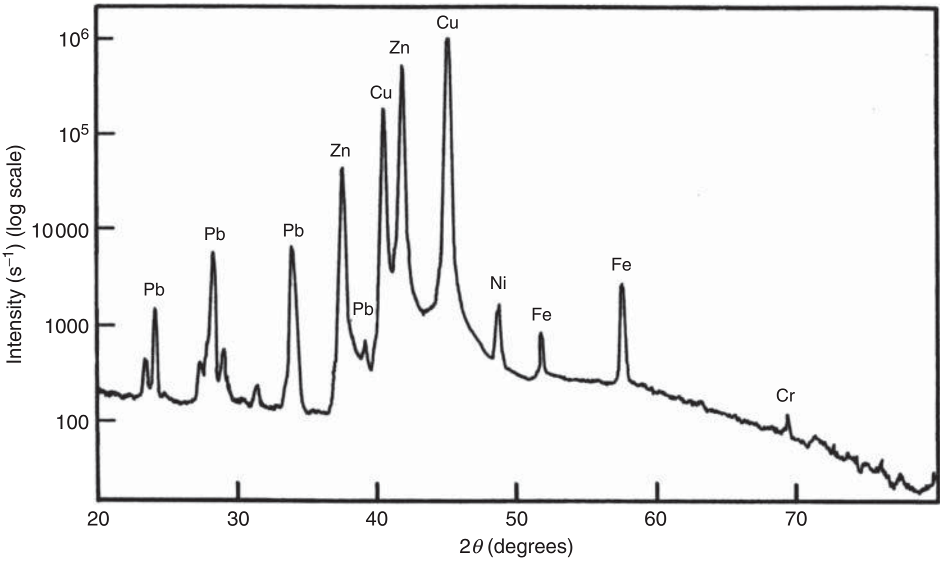

Figure 14.18 Wavelength-dispersive XRF of a brass sample recorded with a LiF analyzer crystal, showing the characteristic lines of the major elements Cu and Zn and the lines of Cr, Fe, Ni, and Pb superimposed on a continuous background.

analysis where speed is of the essence, and where a high initial cost can be justified, simultaneous WD spectrometers are optimal. For more flexibility, where speed is important but not critical and where a moderately high initial cost can be justified, sequential WD spectrometers are probably more suited. Both of the instruments are, in principle at least, capable of measuring all elements in the periodic classification from $Z = 9$ (F) and upwards, and most modern WD spectrometers can do some useful measurements down to $Z = 6$ (C). Both can be fitted with multiple sample-handling facilities and automated. Both are capable of precision of the order of a few tenths of 1% and both have sensitivities down to the parts per million level. Single-channel WD spectrometers are typically employed for both routine and nonroutine analysis of a wide range of products, including ferrous and nonferrous alloys, oils, slags and sinters, ores and minerals, and thin films. These systems are flexible but, relative to multichannel spectrometers, are somewhat slow. The multichannel WD instruments are used almost exclusively for routine, high-throughput analyses where there is need for fast accurate analysis, but where flexibility is of no importance.

14.3.4
Energy-Dispersive XRF

ED spectrometers became commercially available in the early 1970s, with the advent of high-resolution solid-state detectors; currently, there are of the order of 20 000 units in use. In principle, EDXRF instruments have a much simpler mechanical design than WDXRF instruments, as the detection system does not include any moving parts and the solid-state detector (most commonly a Si(Li) detector) itself acts as a dispersion agent. The high geometrical efficiency of the semiconductor detector permits a great variety in excitation conditions. The manner in which the radiation that originally exits from the X-ray tube is ‘‘pretreated’’ before it reaches the sample varies according to the type of EDXRF instrument. The final analytical capabilities and, in particular, the LD values that can be attained by the instrument strongly depend on the sophistication with which this is done.

In Figure 14.19a, the most simple of EDXRF instrumental configurations is shown. A low-power X-ray tube (e.g., 50 W) and a Si(Li) detector are both placed at an angle of 45° with respect to the sample. Collimators are used to confine the excited and detected beam to a sample area between 0.5 and 2 cm^2. In such a ‘‘direct-excitation’’ configuration, the distance between the components can be fairly small (typically a few centimeters) and as both the tube anode lines and the *bremsstrahlung* component of tube output spectrum are used to irradiate the sample, only a limited tube power is required. As the *bremsstrahlung* continuum not only ensures a uniform excitation of many elements but also causes a significant scatter background to be present in the recorded EDXRF spectra, most direct-excitation systems are equipped with a set of primary beam filters to alter the tube spectrum. By selection of an appropriate filter, the excitation conditions for a particular range of elements can be optimized. In order to facilitate the determination of low-Z

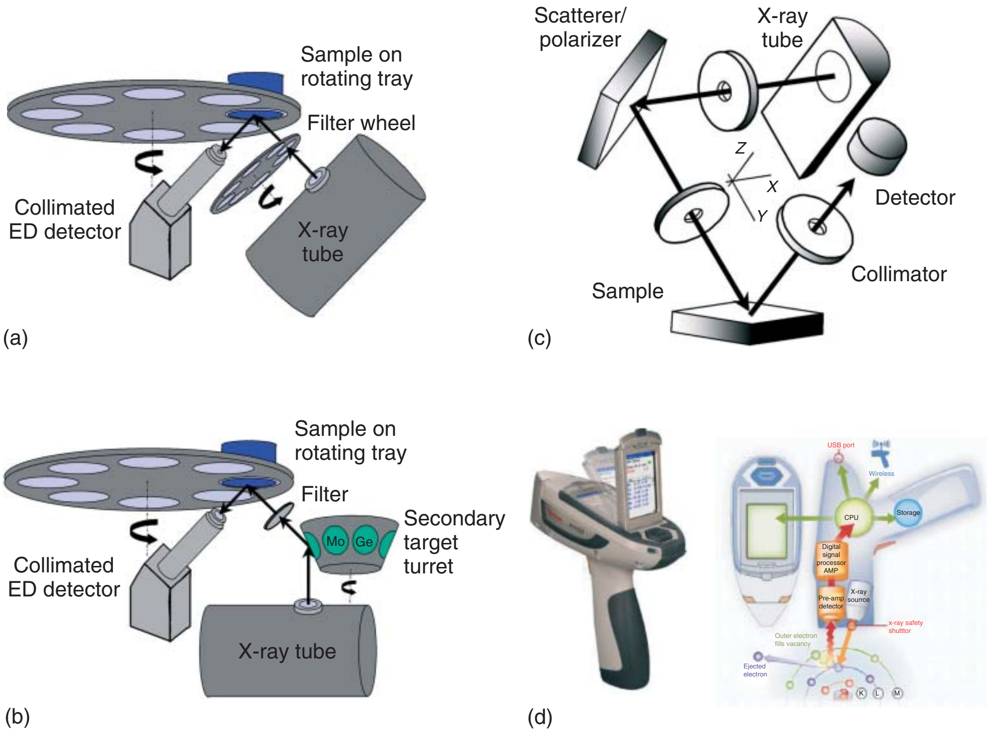

Figure 14.19 Schematic drawings of (a) a direct-excitation XRF instrument, (b) a secondary target XRF instrument, (c) a polarized XRF instrument employing a Cartesian (XYZ) irradiation geometry, and (d) a photograph a and schematic representation of a portable XRF device.

elements, commercial systems can be either evacuated or flushed with He, thus reducing the absorption of low-energy radiation and scatter.

The schematic of a ‘‘secondary target’’ EDXRF system is shown in Figure 14.19b. In such a configuration, a high-power (1 kW) X-ray tube irradiates a metal disk (the secondary target, e.g., made of Mo), causing it to emit its own characteristic radiation lines (Mo-K_α and Mo-K_β). This ‘‘bichromatic’’ fluorescent radiation is then used to excite the sample to be examined. The advantage of the secondary target scheme is that, as a result of the bichromatic excitation, the background in the resulting EDXRF spectra is significantly lower, as in the direct-excitation case. This leads to better detection limits. By using a filter that preferentially absorbs the K_β component of the secondary target radiation (e.g., a Zr foil in case of a Mo target), a quasi-monochromatic form of sample excitation can be realized. By interchanging the target (and matching filter), different element ranges can be excited optimally. For example, to obtain the best conditions for determination of trace concentrations of the elements Rb-Nb in geological samples, a Rh secondary target may be selected while for optimal detection of Cr in the same material, a Cu target would be more beneficial.

The ability to simultaneously measure a wide range of elements is one of the greatest advantages of EDXRF. This advantage is strongly reduced when the count rate limitation of the ED detection electronics is taken into consideration. This is due to simultaneous recording of the entire primary source radiation scattered on the specimen and is especially true for examinations on samples with light matrices.

The stationary arrangement of components used in EDXRF is ideally suited for geometrical configurations that exploit polarization phenomena to reduce background and thereby improve signal-to-noise ratios.

Figure 14.19c shows a configuration employed to achieve a reduction in the background level of EDXRF spectra obtained in direct-excitation conditions. In this case, one or more energy bands of the tube emission spectrum are scattered and/or diffracted under (nearly) 90° by means of a suitable scatterer material and/or diffraction crystal. Because scattering rather than fluorescence is used to ''reflect'' the primary tube spectrum onto the sample, the X-ray beam that impinges on the sample is linearly polarized in the plane perpendicular to the tube–scatterer–sample plane. When the Si(Li) detector is also positioned in the former plane at 90° relative to the scatterer–sample axis, the lowest background level will be recorded. The reason for this background reduction is that the polarized photons will preferentially be scattered out of the plane of polarization and therefore will not reach the detector. The optimal geometrical configuration is therefore that tube, scatterer, sample, and detector are arranged in an XYZ (also called ''*Cartesian*'') geometry, as shown in Figure 14.19c. For polarization of medium-to-hard radiation ($E > 10\,\mathrm{keV}$) by Barkla scattering, fairly thick slabs of low-Z materials such as Al_2O_3, B_4C, and B_3N are suitable materials. For polarization of softer radiation, the above-mentioned materials are not suitable given that for $E < 10\,\mathrm{keV}$, photoelectric absorption dominates over scattering. In the region 1–10 keV, radiation can be polarized through Bragg diffraction over $2\theta \approx 90^\circ$ by using a suitable crystal. For example, HOPG (highly oriented pyrolithic graphite) is an excellent Bragg polarizer for the (002) reflection of the Rh-L_α radiation ($\theta = 43.2^\circ$). Multiple-layer scatterers, for example, consisting of a thin layer of HOPG glued on top of an Al_2O_3 substrate, in combination with a Rh tube, are useful to determine a wide range of elements simultaneously with good detection limits and sensitivities.

In Figure 14.20, the spectra that result from direct-excitation, secondary excitation, and polarized direct excitation of a standard oil sample, containing 21 elements at the $30\,\mu\mathrm{g\,g}^{-1}$ level, are compared. The relative detection limits obtained from the three spectra are summarized in Table 14.6; they indicate that the DL values by means of polarized excitation are on average five times better than those determined by direct excitation. The secondary target results are factor 2.5 better than the polarized excitation values for elements efficiently excited by the Mo-Ka-line (e.g., Pb); however, elements such as Sn and Cd cannot be determined using the Mo secondary target, while they are well excited by the polarized *bremsstrahlung* radiation.

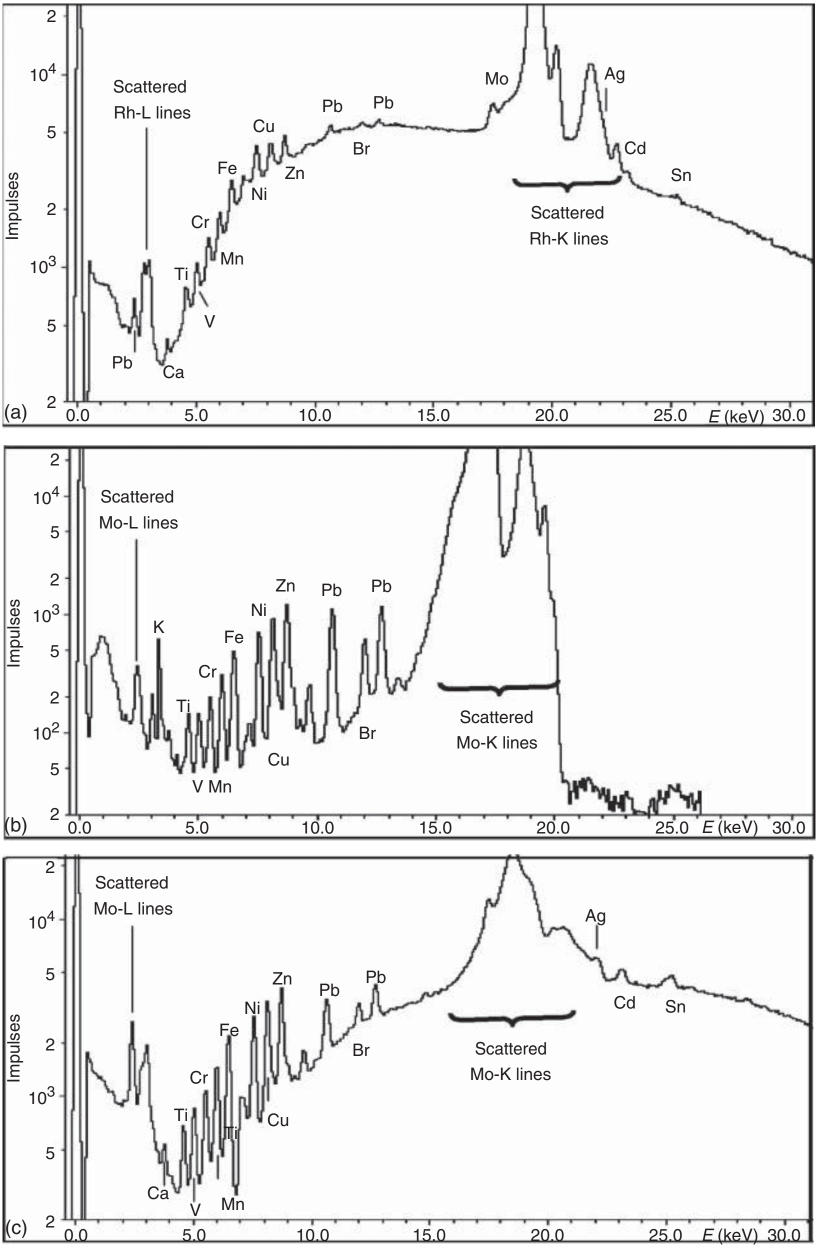

Figure 14.20 Comparison of EDXRF spectra of an oil standard containing 21 elements (e.g., Ca, Ti, V, Cr, Mn, Fe, Ni, Cu, Zn, Mo, Ag, Cd, Sn, Ba, and Pb) with concentrations of 30 μg g^{-1}. The spectra (log scale) are (a) nonpolarized, direct excitation by radiation from rhodium anode X-ray tube; (b) molybdenum secondary excitation; and (c) polarized excitation by scatter from a HOPG/Al_2O_3 target. The measuring time amounts 200 s for each spectrum. In all cases, a Rh end-window tube was used.

Table 14.6 Limits of detection (LD) (n.d. = not detectable), for some elements in base oil using direct excitation, monochromatic excitation using a Mo secondary target and direct excitation with linearly polarized X-rays (175 W for a measuring time of 200 s and a incident pulse density of about 60 000 cps).

Element	Limits of detection, ($\mu g\, g^{-1}$)		
	Direct excitation	Mo secondary target	Polarization
Ca	13	8.8	4.1
Ti	3.8	2.9	1.6
Cr	3.1	2	0.78
Mn	2.6	1.2	0.51
Cu	1.7	0.31	0.34
Zn	1.7	0.3	0.33
Mo	2.3	n.d.	0.95
Cd	18.0[a]	n.d.	1.6
Sn	12	n.d.	2
Pb	3.9	0.31	0.79

[a] Overlapping with Rh $K_{ß2}$.

From [1].

14.3.5
Portable and Radioisotope XRF

Next to EDXRF spectrometers that are intended for use in the laboratory, a number of portable EDXRF instruments are also available. These devices are used in various fields for on-site analysis of works of art, environmental samples, forensic medicine, industrial products and waste materials, and so on. In its simplest form, the instruments consist of one or more radioisotope sources combined with a scintillation or gas proportional counter. However, combinations of radio sources with thermoelectronically cooled solid-state detectors are also available in compact and lightweight packages (below 1 kg). In Figure 14.21, schematics of various types of radio-source-based EDXRF spectrometers are shown. In Figure 14.21a, the X-ray source is present in the form of a ring; radiation from the ring irradiates

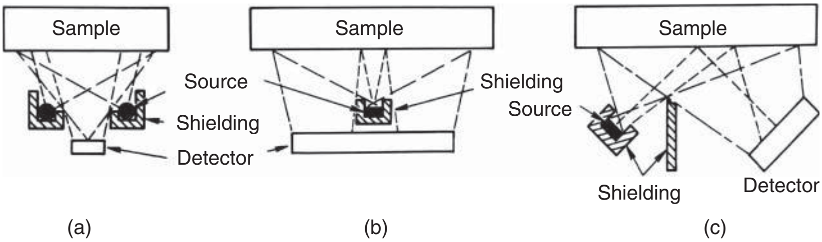

Figure 14.21 Radioisotope-excited X-ray fluorescence analysis by means of (a) an annular source, (b) a central source, and (c) a side-looking source.

the sample from below while the fluorescent radiation is efficiently detected by a solid-state detector positioned at the central axis. Shielding prevents radiation from the source entering the detector. In Figure 14.21b,c, the X-ray source has another shape, requiring a different type of shielding. Portable XRF analyzers (Figure 14.19d), however, have more or less completely replaced radioisotope-based XRF instruments. Figure 14.19d shows a photograph and the functional diagram of a portable or handheld XRF instrument. A miniaturized X-ray tube is combined with a compact Si-PIN or SDD detector into a lightweight enclosure. This type of XRF analyzers more or less have the dimensions and weight of a (lightweight) drilling machine and can run on batteries. They usually are controlled by means of a PDA (personal digital assistant)-style computer that is responsible for spectrum collection and storage, and on which spectrum evaluation software and quantification procedures can also be run.

14.3.6
Total Reflection XRF

When X-rays impinge (optically) upon a flat material under a very small angle (typically a few milliradians), that is, nearly grazing the surface, total external reflection occurs. This means that instead of penetrating the material, the X-ray photons will only interact with the top few nanometers of the material and then be reflected. Material that is present on top of the reflecting surface will be irradiated in the normal manner, and will interact with both the primary and the reflected X-rays. The major difference between conventional EDXRF and TXRF therefore is the excitation geometry. In the standard case of EDXRF, the angle between the primary incident radiation and the sample is 45°, while the detector is placed normal to the incident beam so that the angle between sample and detector is also 45°. The principle setup of TXRF is shown in Figure 14.22. A narrow, almost parallel beam impinges at angles below the critical angle on the surface of the

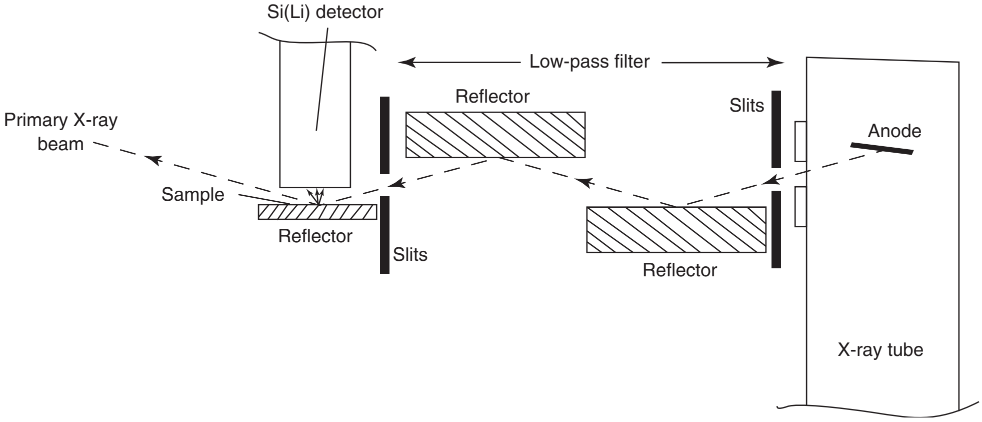

Figure 14.22 Schematic layout of a TXRF spectrometer.

reflector that carries the sample as randomly distributed microcrystals in the center part of its surface. As the X-rays scarcely penetrate the reflector, the contribution from scattered primary radiation from the substrate is minimized. As a result of the double excitation of the sample by both the primary and the reflected beam, the fluorescent signal is practically twice as intense as in the standard EDXRF excitation mode. The largest angle at which total external reflection still takes place is called the *critical angle* of total reflection ϕ_{crit}. The critical angles are in the range of a few milliradians for typical reflector materials such as quartz or Si and primary radiation of 9.4 keV (from a W-L tube) or 17.5 keV (from a Mo-anode X-ray tube). With higher energies in the exciting spectrum, adjustments must be made for the proper incident angle below the critical angle, which is given by

$$\phi_{\text{crit}}(\text{mrad}) = 20.7/E\ (\text{keV})\rho^{\frac{1}{2}}(\text{g}\,\text{cm}^{-3}) \tag{14.18}$$

The main advantages of TXRF are as follows:

1) The background caused by scattering of the primary radiation on the substrate is reduced.
2) The fluorescence intensity is doubled as the primary and reflected beams pass through the sample giving efficient excitation.
3) The distance between the sample on the reflector surface and the detector can be made small, and thus the solid angle for detection is large.
4) All these advantages lead to lower limits of detection (LD) compared to the standard EDXRF mode.

Depending on the X-ray source and the spectral modification devices, the LD are in the picogram range for 2–3-kW X-ray tubes and in the femtogram range with excitation by means of SR. Figure 14.15 shows a typical TXRF spectrum; the absolute detection limit values of typical TXRF instruments are shown in Figure 14.10. Thus, TXRF permits to simultaneously determine trace elements in samples of small volume. Additional advantages are insensitivity to matrix effects, easy calibration, fast analysis times, and low costs. In practice, the method is, in particular, applied to multielement determinations in water samples of various natures and for the routine analysis of Si-wafer surfaces employed in the microelectronics industry.

14.3.7
Microscopic XRF

The basic measuring strategy of μ-XRF analysis is illustrated in Figure 14.23. This microanalytical variant of bulk EDXRF is based on the localized excitation and analysis of a microscopically small area on the surface of a larger sample, providing information on the lateral distribution of major, minor, and trace elements in the material under study. Essentially, a beam of primary X-rays with (microscopically) small cross sections irradiates the sample and induces the emission of fluorescent X-rays from a microspot. A suitable detector system collects the fluorescent radiation that carries information on the local composition of the sample. When

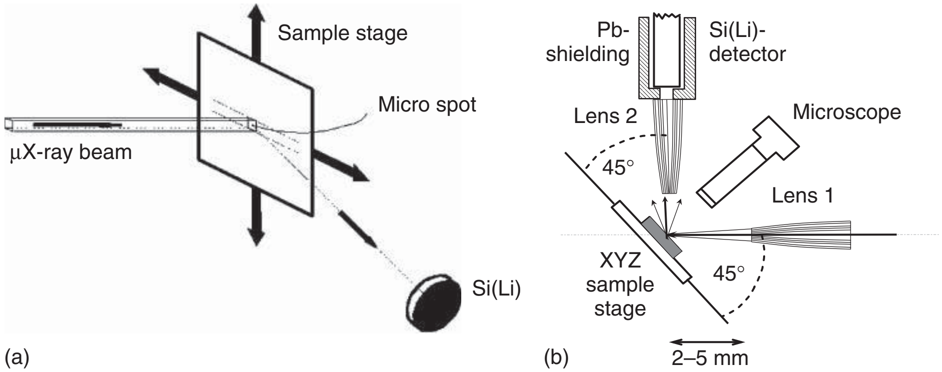

Figure 14.23 Principle of (a) conventional and (b) confocal μ-XRF.

the sample is moved either manually or under computer control in the X-ray beam path, spot analysis, line analysis, or image collection is possible.

The difficulties in the exploitation of this method reside in the production of sufficiently intense X-ray beams to allow sensitive microanalysis. Techniques to do this have only recently appeared; in the past, X-rays were considered to be notably difficult to focus to a small dimension beam. Any variants on the basic mode of operation either reside with the method employed for X-ray beam concentration/focusing or with the source type employed: conventional X-ray tubes or SR sources. Especially the increased performance of compact and relatively inexpensive X-ray focusing devices and in particular the development of (poly)capillary X-ray focusing optics, permitting X-ray beams to be focused to below 10 μm diameter spots, has made the development of μ-XRF possible. When used in combination with X-ray tubes, absolute detection limits in the picogram area are obtained for thin samples. In massive samples, relative LD values around 10 ppm have been reported. At synchrotron facilities, the capabilities of the μ-XRF method (both regarding spot sizes and detection limits) are significantly better: femtogram to lower attogram-level absolute detection limits are obtained with beams that are between 0.1 and 2 μm in diameter. Using monochromatic beams of polarized radiation, optimal peak-to-background ratios in the resulting EDXRF spectra can be obtained, resulting in relative LD levels in the 1–100 ppb range in biological materials. As an example, Figure 14.24 shows the LD values obtained within the 1000 section by using 14 and 21 keV synchrotron microbeams (of $2 \times 15\,\mu m^2$ diameter) to irradiate NIST SRM (standard reference material) 1577 bovine liver. At synchrotrons, the dimensions of the primary beams continuously shrink and currently (2010) beams with about 50 nm diameter and of sufficient intensity can be produced using various optical technologies. In recent years, the technique of confocal μ-XRF has been developed, where a secondary optic, placed between sample and detector prevents all XRF radiation, except that originating from a specific depth below the surface of the sample, to reach the detector. This allows to perform analysis of heterogeneous samples in three dimensions, with a resolution of about 10–50 μm.

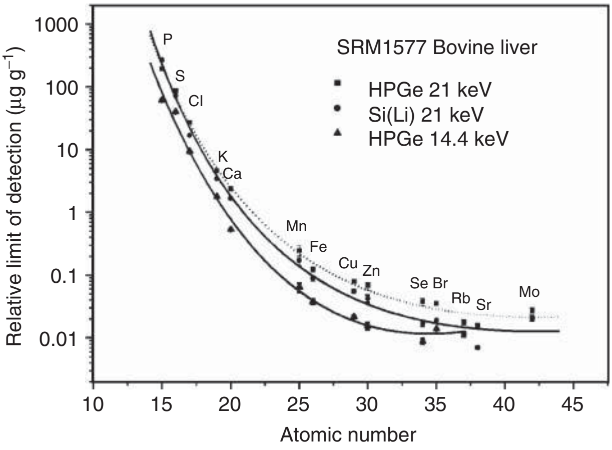

Figure 14.24 Relative LD values obtained by irradiation of NIST SRM 1577 bovine liver by means of 14.4 and 21 keV synchrotron microbeams and Si(Li) or HPGe detectors.

The application of μ-XRF to a great variety of problems and materials has been described, including geochemistry, archeology, industrial problems, and environmental studies. Especially the fact that quantitative data on (trace) constituents can be obtained at the microscopic level without sample damage is of use in many different circumstances. At synchrotron sources, (μ-)XRF investigations of heterogeneous materials is also frequently combined with other methods, providing speciation information on major, minor, and/or trace constituents.

14.4
Matrix Effects

14.4.1
Thin and Thick Samples

The simple linear relation between observed count rate R_i of analyte element i and its concentration c_i shown in Eq. (14.9) is only valid in a limited number of cases. In general, for monochromatic forms of excitation (with energy E_0) and in the absence of enhancement phenomena, the observed XRF count rate R_i of an element i (with energy E_i) is related to the sample thickness d and its concentration c_i is the following manner (see also Eqs. (14.34–14.36)):

$$R_i = S_i c_i \frac{1 - \mathrm{e}^{-\chi(E_0,E_i)\rho d}}{\chi(E_0, E_i)\rho d} = S_i c_i A_i \quad \text{with}$$
$$\chi(E_0, E_i) = \mu(E_0)\csc\alpha + \mu(E_i)\csc\beta \tag{14.19}$$

where α and β are the angles under which the X-rays impinge and takeoff relative to the sample surface (Figure 14.25) and ρ is the sample density. The absorption factor A_i is obtained by adding all contributions to R_i produced in a series of infinitesimal sample volumes at various depths z inside the sample and by considering an

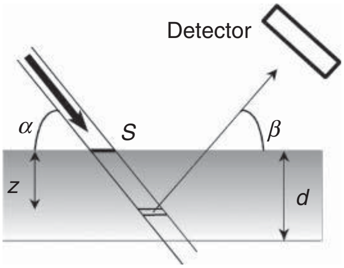

Figure 14.25 Basic XRF irradiation geometry.

attenuation factor $\exp[-\mu(E_0)\rho z \csc \alpha]$ for the primary radiation while penetrating into the sample until this depth and an attenuation factor $\exp[-\mu(E_i) z \csc \beta]$ for the fluorescent radiation when emerging from the sample toward the detector. When polychromatic forms of excitation are used, Eq. (14.19) is more complicated and involves an integral over the intensity distribution of the X-ray source (see subsequent text, Eq. (14.36)).

As a result of the attenuation of both primary and fluorescent radiation within the sample, these is a critical depth in the sample, d_{thick}, below the surface, beyond which any emitted photon is essentially absorbed and therefore will not make a significant contribution to the detected fluorescent intensity. This critical penetration depth varies as a function of matrix composition and is also strongly dependent on the energy of the (primary and) fluorescent radiation. Samples that have a thickness greater than the critical penetration depth for a specific kind of fluorescent radiation are sometimes referred to as ''*infinitely thick*'' or ''*massive*'' samples. In Table 14.7 values for d_{thick} in a geological (a silicate rock) and metallurgical (steel) matrix are listed for various fluorescent line energies. For low-energy photons (e.g., the K_α-photons of low-Z elements such as Al or Na), the critical penetration depth is very small (a fractional to a few micrometers), so that compositional information that exclusively pertains to the surface layers of the sample is obtained. When more penetrating fluorescent radiation is used (e.g., Rb-K_α at 13.39 keV), having d_{thick} values of several millimeters, compositional information from much deeper in the sample is obtained.

In many practical situations, it is important to ensure that the sample presented for analysis is sufficiently thick (i.e., thicker than the highest critical penetration depth among the various fluorescent signals being used), so that the observed analytical signals no longer depend on sample thickness but only on analyte concentration.

Next to the critical penetration depth, d_{thick}, it is also useful to define a critical thickness, d_{thin}, below which absorption and enhancement effects can be neglected. For analysis of such ''thin-film'' samples, the calibration relations of Eqs. (14.8) and (14.9) are valid and matrix effect corrections need not be applied. By convention, d_{thin} corresponds to the situation where the total attenuation in the sample is equal to 1%. Table 14.7 lists typical d_{thin} values for various fluorescent line energies in two matrices.

Table 14.7 Critical penetration depth and thin-film thickness of various fluorescent lines in two matrices.

Element	Energy/wavelength of K_α-line		Excitation spectrum tube anode	Critical penetration depth d_{thick} (μm)		Thin-film thickness d_{thin} (μm)	
	E (keV)	λ (nm)		Silicate	Steel	Silicate	Steel
C	0.28	4.4	Cr	—	0.1	—	0.002
Na	1.04	1.19	Cr	4.8	0.4	0.09	0.009
Si	1.74	0.713	Cr	13	1.6	0.2	0.03
Ca	3.69	0.336	Cr	36	9.6	0.7	0.2
Cr	5.41	0.229	Rh	90	30	1.7	0.7
Fe	6.4	0.194	Rh	180	43	3.4	0.9
Rb	13.39	0.0927	Rh	900	40	16	0.9
Nb	16.61	0.0748	Rh	1 400	62	25	1.3
Rh	20.21	0.0614	W	3 900	161	72	3.5
La	33.44	0.0373	W	10 600	580	190	13
Eu	41.53	0.0301	W	15 400	886	280	19

From [2].

14.4.2
Primary and Secondary Absorption, Direct and Third-Element Enhancement

In the context of XRF analysis, matrix effects are caused by attenuation and enhancement phenomena that influence the intensity of the fluorescent X-ray lines observed from a sample. As the magnitude of the matrix effects varies with elemental composition, the observed XRF intensity is no longer linearly proportional to the concentration of the analyte (Eq. (14.9)). Corrections must therefore be applied to the measured intensity data to account for the following:

1) *Primary absorption* (Figure 14.26a): this occurs because all atoms of the specimen matrix will absorb photons from the primary source. As there is competition for these primary photons by the atoms making up the specimen, the intensity/wavelength distribution of these photons available for the excitation of a given analyte element may be modified by other matrix elements. In this manner, the intensity and spectral distribution of the X-ray flux available to excite the sample atoms can change with penetration depth. This phenomenon is known as "*beam hardening*."
2) *Secondary absorption*: this refers to the effect of the absorption of characteristic analyte radiation by the specimen matrix. As characteristic radiation passes out from the specimen in which it was generated, it will be absorbed by all matrix elements, by amounts relative to the mass absorption coefficients of these elements.
3) *Direct (or second-element) enhancement* (Figure 14.26b): in situations where the energy of a fluorescent photon (e.g., Ni-K_α at 7.47 keV) is immediately above

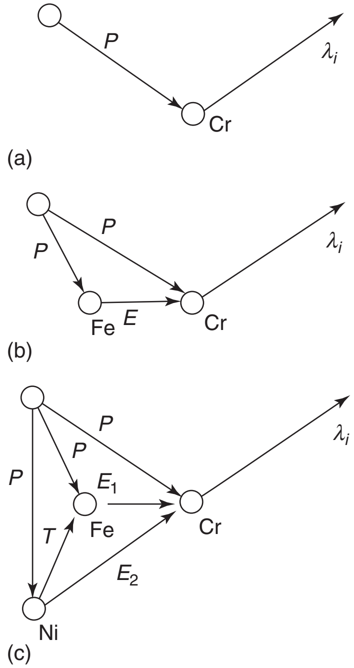

Figure 14.26 Primary excitation versus two-element and three-element enhancement. (a) Primary, (b) primary plus enhancement, and (c) primary, enhancement and third element.

the absorption edge of a second element (e.g., the K-edge of Fe at 7.11 keV), the fluorescence intensity of the second element (here, Fe-K_α and Fe-K_β radiation) will be enhanced as a result of the preferential excitation (here, by Ni-K_α radiation) within the sample. The magnitude of this effect is not always significant, but is readily observable in alloys of specific combinations of elements (e.g., Cr-Fe-Ni steels) and in multiplayer thin-film samples.

4) *Indirect (or third-element) enhancement* (Figure 14.26c): for example, in a stainless steel matrix, the observed intensity of the Cr-K characteristic radiation (Cr-K absorption edge at 5.99 keV) is enhanced by secondary excitation due to Fe-K (K_α at 6.40 keV) and Ni-K radiation. As the intensity of the Fe-K radiation is itself enhanced (see preceding text), part of the Cr enhancement due to Fe is a tertiary effect originating from Ni.

14.5
Data Treatment

The process of converting experimental XRF data into analytically useful information (usually in the form of concentration values of elemental constituents whose X-ray peaks are visible above the background in the spectrum) can be divided into two steps: first the evaluation of the spectral data, whereby the net height or the net intensity of the X-ray peaks is determined, taking care to correct for peak overlap (if any) between X-ray lines of different elements and, second, the conversion of the net X-ray intensities into concentration data, that is, the quantification. In this last step, especially, the appropriate correction of matrix effects is a critical issue.

14.5.1
Counting Statistics

The production of X-rays is a random process that can be described by a Gaussian distribution. As the number of photons counted is nearly always large, typically thousands of hundreds of thousands, rather than a few hundred, the properties of the Gaussian distribution can be used to predict the probable error for a given count measurement. There will be a random error, s_I, associated with a measured intensity value I, this being equal to $I^{\frac{1}{2}}$. As an example, if 10^6 counts are taken, the 1s standard deviation will be $[10^6]^{\frac{1}{2}} = 10^3$, or 0.1%. The measured parameter in WD X-ray spectrometry is generally the counting rate $R = I/t$ and, based on what has been already stated, the magnitude of the *relative* random counting error RSD(R) associated with a given measured rate R can be expressed as

$$\mathrm{RSD}(R)(\%) = 100\%\frac{s_R}{R} = 100\%\frac{s_I}{I} = 100\%\frac{\sqrt{I}}{I} = \frac{100\%}{\sqrt{Rt}} \tag{14.20}$$

Care must be exercised in relating the counting error (or indeed any intensity related error) with an estimate of the error in terms of concentration. Provided that the sensitivity of the spectrometer in counts per second per percent is linear, a count error can be directly related to a concentration error. However, where the sensitivity of the spectrometer changes over the range of measured response, a given fractional count error may be much greater when expressed in terms of concentration.

14.5.2
Spectrum Evaluation Techniques

Spectrum evaluation is a crucial step in X-ray analysis, as much as sample preparation and quantification. As with any analytical procedure, the final performance of X-ray analysis is determined by the weakest step in the process. Spectrum evaluation in EDXRF analysis is more critical than in WDXRF spectrometry because of the relatively low resolution of the solid-state detectors employed.

In general, it is possible to distinguish between amplitude and energy noise in (ED)X-ray spectra. Amplitude noise is the result of the statistical nature of the counting process in which random events (the arrival of X-ray photons in the detector) are observed during a finite time interval. Poisson statistics cause the typical channel-to-channel fluctuations observed in X-ray spectra. Energy noise, on the other hand, causes the characteristic X-ray lines in EDXRF spectra to appear much wider (on the order of 120–150 eV) than their natural line widths (typically

5–10 eV). It results partly from the photon-to-charge conversion process in the detector and partly from the electronic noise that is introduced in the amplification and processing steps that follow it. Accordingly, characteristic X-ray lines appear as nearly Gaussian peaks in EDXRF spectra.

In WDXRF spectra, where at least one of these noise contributions usually is absent (the noise in the energy/wavelength dimension is significantly lower as a result of the much higher resolution of the dispersion systems used), spectrum evaluation, in principle, is much more simple and sometimes can be discarded with altogether. Because the X-ray lines appear as narrow, well-defined peaks, their net X-ray intensities and that of the background in the same region can be determined with great accuracy. The few cases of peak overlap (e.g., between As-K_α and Pb-L_α, where the separation of 8 eV is less than the natural line width of As-K_α) can be dealt with on a case-by-case basis or avoided by the use of another, nonoverlapped, X-ray line of the elements involved as analytical signals (e.g., the As-K_β-line).

In both WDXRF and EDXRF, the net number of counts under a characteristic X-ray line (i.e., the integrated peak *intensity*) is proportional to the concentration of the analyte. At constant resolution, this proportionality also exists between concentration and net peak *height*. In EDXRF (where the detector resolution is low, and changes considerably with energy, and many peaks are low in intensity), the use of the net peak area as analytical signal is preferred, as this also results in a lower statistical uncertainty for the small peaks. In WDXRF (where the detector resolution is high and must be less dependent on the wavelength, while often sharp and intense peaks are encountered), the acquisition of the entire peak profile is often too time consuming so that the count rate is frequently measured only at the peak maximum.

14.5.2.1 **Data Extraction in WDXRF**

In WDXRF, most often the count rate, $R_{\max}$, at the angle of the peak maximum, corrected for background, is used as an analytical signal. In order to estimate the appropriate background below the line, the background count rate at slightly lower and higher 2θ values is measured and the average calculated. If T is the number of counts accumulated during a time interval t_T at the top of the peak and B is the corresponding background counts (during a time t_B), the net count rate R is given by the different of the total and background count rates R_T and R_B:

$$R = R_T - R_B = \frac{T}{t_T} - \frac{B}{t_B} \tag{14.21a}$$

and, considering that $s^2{}_T = T$ and $s^2{}_B = B$, the uncertainty s_R on the net count rate R is given by

$$s_R^2 = \frac{T}{t_T^2} + \frac{B}{t_B^2} = \frac{R_T}{t_T} + \frac{R_B}{t_B} \tag{14.21b}$$

Accordingly, in WDXRF, several counting strategies may be employed to keep this number as low as possible. In the "optimum fixed time" strategy, the minimum uncertainty is obtained within a time interval $t = t_T + t_B$ when t_T and t_B are chosen in such a way that

$$\frac{t_T^2}{t_B^2} = \frac{R_T}{R_B} \tag{14.22}$$

In this case, the uncertainty s_R can be written as

$$s_R = \frac{\sqrt{R_T} + \sqrt{R_B}}{\sqrt{t}} \tag{14.23}$$

14.5.2.2 Data Extraction in EDXRF – Simple Case: No Peak Overlap

The most straightforward method to obtain the net area of an isolated, nonoverlapped peak in an EDXRF spectrum is to interpolate the background under the peak and to sum the net channel contents in a window enclosing the peak. Thus, the net peak area N is given by

$$N = \sum_j [y_j - y_B(j)] = \sum_j y_j - \sum_j y_B(j) = T - B \tag{14.24}$$

where the summation runs over the spectral window (containing n_T channels) under consideration. Thus, the uncertainty s_N can be written as

$$s_N^2 = s_T^2 + s_B^2 = T + B \tag{14.25}$$

The background height $y_\mathrm{B}(j)$ in channel j of the peak window can be interpolated between the average background height to the left and right of the peak ($y_\mathrm{B,L} = B_\mathrm{L}/n_\mathrm{L}$ and $y_\mathrm{B,R} = B_\mathrm{R}/n_\mathrm{R}$, where B_L and B_R are the integrals of the left and right background windows and n_L, n_R their widths in channels) (Figure 14.27):

$$y_\mathrm{B}(j) = y_\mathrm{B,L} + \frac{y_\mathrm{B,R} - y_\mathrm{B,L}}{j_\mathrm{B,R} - j_\mathrm{B,L}} \cdot (j - j_\mathrm{B,L}) \tag{14.26}$$

where $j_\mathrm{B,L}$ and $j_\mathrm{R,L}$ represent the channels between which the background is linearly interpolated. When both background windows around the peak have equal

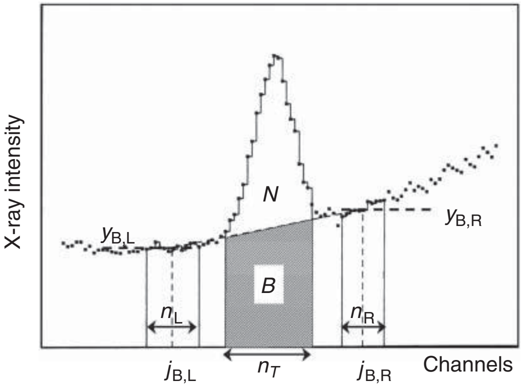

Figure 14.27 Background estimation below an isolated photo peak.

width (i.e., $n_\mathrm{L} = n_\mathrm{R} = n_\mathrm{B}/2$ channels) and are positioned symmetrically around the maximum, the uncertainty on N is given by

$$s_N^2 = T + \left(\frac{n_T^2}{n_\mathrm{B}^2}\right)\left(\frac{B_\mathrm{L}}{B_\mathrm{R}}\right) \tag{14.27}$$

14.5.2.3 **Data Extraction in EDXRF – Multiple Peak Overlap**

The above-described simple integration procedure is useful for explorative data analysis but implicitly assumes that within the energy window used, a single, nonoverlapped peak is present with a high peak-to-background ratio. In general, these assumptions are not valid: peak overlap frequently occurs in ED X-ray spectra when, especially for peaks corresponding to trace constituents, the background intensity below the peak may be on the same order or larger than the net peak intensity. In these cases, the use of too simple spectrum evaluation procedures may negate all the efforts that are made both during the data collection and during the further quantitative processing of the data to increase the reliability of the final (trace) element concentrations. An established way of proceeding is to use a nonlinear least squares strategy to minimize the weighted difference Π^2 between the experimental data y_i and a mathematical fitting function y_fit

$$\chi^2 = \frac{1}{n-m}\sum_i \left(\frac{\left[y_i - y_{\mathrm{fit},i}\,(i)\right]^2}{y_i}\right) \tag{14.28}$$

where y_i is the observed content of channel i in the spectrum being processed and $y_\mathrm{fit}(i)$ is the calculated fitting function in this channel. n is the total number of channels in the fitting window, while m represents the number of parameters in the fitting function. The latter consists of two parts, describing, respectively, the spectral background and the photo peaks:

$$y_\mathrm{fit}(i) = y_\mathrm{back}(i) + y_\mathrm{peak}(i) = y_\mathrm{back}(i) + \sum_j y_j(i) \tag{14.29}$$

where the index j runs over all characteristic line groups that appear in the spectrum. For each line group j (e.g., Fe-K, Pb-L$_3$), the contribution $y_j(i)$ to the ith channel is calculated as

$$y_j(i) = A_j \left(\sum_{k=1}^{N_j} r_{jk} G\left(E_{jk}, i\right) t(E_{jk})\right) \tag{14.30}$$

where A_j represents the total area of all photo peaks in line group j (comprised, e.g., of the Fe-K$_\mathrm{V}$- and -K$_\exists$-lines); these are optimizable parameters during the least squares fitting process. The index k runs over all lines in group j, each line having a relative abundance r_{jk} (with $\Gamma_k\, r_{jk} = 1$). G_{jk} represents a Gaussian function centered around E_{jk}; $t(E_{jk})$ denotes the total attenuation factor for X-rays with energy E_{jk} as defined by the absorption of radiation in the detector, in absorbers placed between sample and detector and in the sample itself. This model can also be expanded to account for spectral artifacts that are generated in the solid-state detector. In

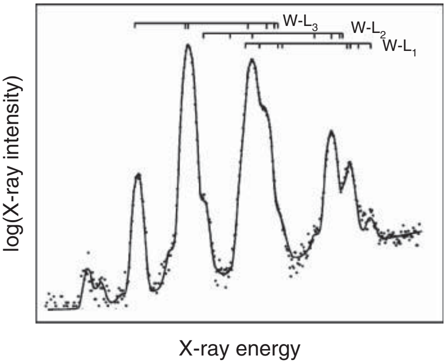

Figure 14.28 Spectral deconvolution in case of complex multiplets.

Figure 14.28, the result of nonlinear deconvolution of the complex multiplets constituted by the W-L$_1$-, L$_2$-, and L$_3$-lines is shown.

The background in the EDXRF spectra is the result of many processes and therefore can have a fairly complex shape. Although it is not impossible to calculate/predict this shape, during spectrum evaluation, usually a more empirical (and faster) approach is favored. Either the background shape is estimated a priori so that it can be subtracted from the experimental data before the actual fitting (‘‘background estimation’’) or it is described by a suitable mathematical function (usually a polynomial of some kind), of which the coefficients are optimized together with the other parameters of the fitting model (‘‘background modeling’’).

14.5.3
Quantitative Calibration Procedures

In the X-ray analytical laboratory, the quantitative method of analysis employed will be typically determined by a number of circumstances of which probably the four most common are the complexity of the analytical problem, the time allowable, the data processing and calibration software present, and the number of standards available. It is convenient to break quantitative analytical methods down into two major categories: single-element methods and multiple-element methods.

Single element methods	Internal standardization Standard addition
Multiple-element methods	Type standardization Use of influence coefficients Fundamental parameter techniques

The simplest quantitative analysis situation to handle is the determination of a single element in a known matrix. A slightly more difficult case might be the determination of a single element where the matrix is unknown. As shown in the table, three basic methods are commonly employed in this situation: use of internal standards, use of standard addition, or use of a scattered line from the X-ray source.

The most complex case is the analysis of all, or most, of the elements in a sample, about which little or nothing is known. In this case, a full qualitative analysis would be required before any attempt is made to quantify the matrix elements. Once the qualitative composition of the sample is known, again, one of three general techniques is typically applied: use of type standardization, use of an influence coefficient method, or use of a fundamental parameter technique. Both the influence coefficient and fundamental parameter technique require a computer for their application.

The correlation between the characteristic count rate, R_i, of an analyte element and the concentration c_i of that element is typically nonlinear over wide ranges of concentration because of interelement effects between the analyte element and other elements making up the specimen matrix. However, the situation can be greatly simplified in the case of homogeneous specimens, where severe enhancement effects are absent; here, the slope of a calibration curve S_i is inversely proportional to the total absorption factor A_i of the specimen for the analyte wavelength:

$$S_i = \frac{R_i}{c_i A_i^{-1}} \tag{14.31}$$

As an example, the data in Table 14.8 show how the net intensity of the Fe-K$_\alpha$-line (Fe K-L$_{3,2}$ transition) resulting from a concentration of 1% iron strongly depends on the matrix composition: the Fe-intensity obtained from a graphite sample, in which virtually no absorption takes place ($A \approx 1$) of the Fe-K$_\alpha$ radiation is about 600 times higher than that obtained from the same Fe concentration in a strongly absorbing lead sample. With the Ni sample, a higher intensity than in the Cr sample is observed, even though the absorption in the Ni matrix is higher. This is caused by the enhancement effect due to the Ni characteristic X-rays that additionally excite the Fe atoms. The combination of matrix absorption and enhancement effects causes the calibration curves in XRF to be nonlinear. Figure 14.29 shows calibration curves for Pb and Sn in binary Pb-Sn alloys. Different quantitative analysis schemes are used depending on the type of matrix, the concentration range, and the availability of the standards.

Table 14.8 Intensity (cps) of the Fe-K$_\alpha$-line obtained from a 1% concentration of Fe in various matrices.

Matrix	Intensity
C	1200
Al	108
Cr	22
Ni	79
Pb	20

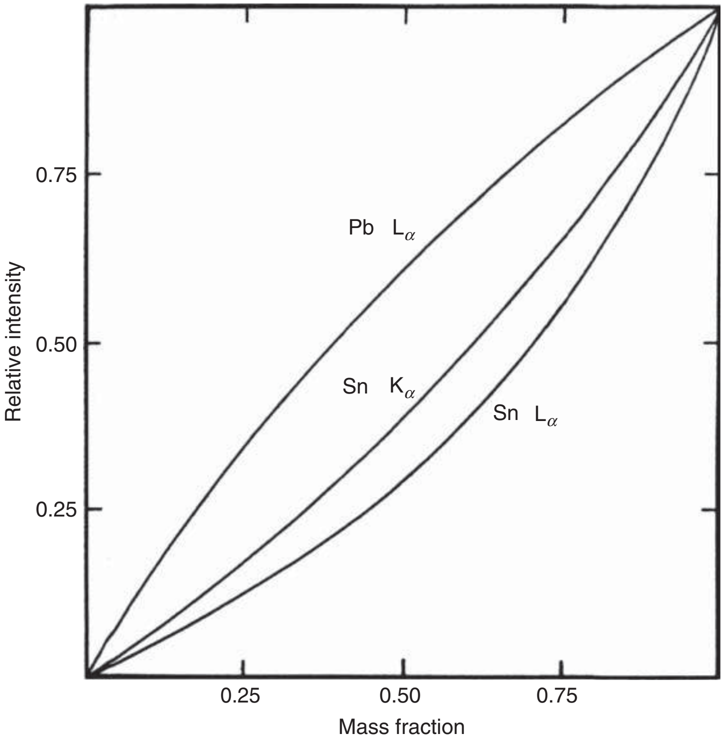

Figure 14.29 Calibration curves for Pb-L$_\alpha$, Sn-K$_\alpha$, and Sn-L$_\alpha$ in Pb-Sn binaries. The Pb-La intensity shows a slight enhancement effect (due to the Sn-K-lines); the Sn-K$_\alpha$ and Sn-L$_\alpha$ curves indicate different degrees of absorption in the sample. In case of Sn-L$_\alpha$, the absorption effect apparently dominates over the enhancement of the Sn-L$_\alpha$ intensity by both the Pb-L and Sn-K-lines.

14.5.3.1 **Single-Element Techniques**

Single-element techniques reduce the influence of the absorption term μ in Eq. (14.30), generally by referring the intensity of the analyte wavelength to a similar wavelength, arising either from an added standard or from a scattered line from the X-ray tube. In certain cases, limiting the concentration range of the analyte may allow the assumption to be made that the absorption value does not significantly change over the concentration range and the calibration curve is essentially linear.

Thin-film approach. Quantitative analysis of thin films, such as filters loaded with aerosol particles, can be done by simply comparing the count rate for a particular element in the sample with the count rate observed in a thin-film standard, because matrix effects are virtually absent. Special reference standards may be made up for particular purposes, and these may serve the dual purpose of instrument calibration as well as establishing working curves for analysis. As an example, two thin glass film SRMs specially designed for calibration of X-ray spectrometers are available from the National Institute of Standards and Technology in Washington as SRMs 1832 and 1833. They consist of a silica-based film deposited by focused ion-beam coating onto a polycarbonate substrate. SRM 1832 contains aluminum, silicon, calcium, vanadium, manganese, cobalt, and copper, and SRM 1833 contains silicon, potassium, titanium, iron, and zinc.

Internal standardization. One of the most useful techniques for the determination of a single-analyte element in a known or an unknown matrix is to use an internal standard. The technique is one of the oldest methods of quantitative analysis and is based on the addition of a known concentration of an element that features an X-ray line with a wavelength/energy close to that of the analyte wavelength. The assumption is made that the effect of the matrix on the internal standard is essentially the same as the effect of the matrix on the analyte element. Internal standards are best suited for the measurement of analyte concentrations below about 10%. The reason for this limit arises because it is generally advisable to add the internal standard element at about the same concentration level as that of the analyte. When more than 10% of the internal standard is added, it may significantly change the specimen matrix and introduce errors into the determination. Care must also be taken to ensure that the particle sizes of specimen and internal standard are about the same, and that the two components are adequately mixed. Where an appropriate internal standard cannot be found, it may be possible to use the analyte itself as an internal standard. This method is a special case of standard addition (spiking).

Type standardization. Provided that the total specimen absorption does not vary significantly over a range of analyte concentrations, and provided that enhancement effects are absent and that the specimen is homogeneous, a linear relationship will be obtained between analyte concentration and measured characteristic line intensity. Where these provisos are met, type standardization techniques can be employed.

In this way, linear calibration curves can be used to determine trace and minor element concentrations in alloys, mineral pellets, and liquids provided that the major element concentrations of standards and unknowns are very similar. In this case, the matrix effect remains the same.

It will also be clear from previous discussions that by limiting the range of analyte concentrations to be covered in a given calibration procedure, the range in absorption can also be reduced. Type standardization is probably the oldest of the quantitative analytical methods employed, and the method is usually evaluated by taking data from a well-characterized set of standards, and, by inspection, establishing whether a linear relationship is indeed observed. Where this is not the case, the analyte concentration range may be further restricted. The present-day analyst is fortunate in that many hundreds of good reference standards are commercially available. While the type standardization method is not without its pitfalls, it is nevertheless extremely useful and is especially useful for quality control type applications where a finished product is being compared with a desired product.

14.5.3.2 Multiple-Element Techniques

To determine major and minor elements in complex samples, more elaborate matrix correction algorithms need to be applied. They can be roughly divided into two categories: the influence coefficient and the fundamental parameter method.

14.5.3.2.1 Influence Coefficient Methods All these models have essentially the same form:

$$\frac{c_i}{R'_i} = K_i + \text{model-dependent term(s)} \tag{14.32}$$

describing the (empirical) relation between an analyte concentration c_i, its X-ray intensity ratio R'_i, an instrument-dependent term K_i that is equal to the inverse of the sensitivity of the spectrometer for the analyte in question ($K_i = 1/S_i$), and a term that corrects this sensitivity term for the effect of the matrix. R' is the ratio of the analyte intensity in the unknown sample to that obtained from a pure element standard, measured under identical circumstances. The different methods only vary in the form of the correction term. The relations used by some of the commonly employed influence methods are listed here:

$$\text{Linear model} \quad \frac{c_i}{R'_i} = K_i \tag{14.33a}$$

$$\text{Lachance–Traill} \quad \frac{c_i}{R'_i} = K_i + \sum_j \alpha_{ij} c_j \tag{14.33b}$$

$$\text{Claisse–Quintin} \quad \frac{c_i}{R'_i} = K_i + \sum_j \alpha_{ij} c_j + \sum_j \gamma_{ij} c_j^2 \tag{14.33c}$$

$$\text{Rasberry–Heinrich} \quad \frac{c_i}{R'_i} = K_i + \sum_j \alpha_{ij} c_j + \sum_{k \neq j} \beta_{ijk} \left[\frac{c_k}{(1 + c_i)} \right] \tag{14.33d}$$

$$\text{Lachance–Claisse} \quad \frac{c_i}{R'_i} = K_i + \sum_j \alpha_{ij} c_j + \sum_j \sum_{k>j} \alpha_{ijk} c_j c_k \tag{14.33e}$$

where all concentrations are expressed as mass fractions.

All the models are concentration correction models in which the product of the influence coefficient (α, β, or γ in the given equations) and the concentration of the interfering element are used to correct the slope of the analyte calibration curve. The Lachance–Traill model is the earliest model; after that, in the Rasberry–Heinrich model, the influence of the absorbing and enhancing elements is separated by the use of the α and β coefficients, respectively. When the physics of the X-ray excitation are thoroughly studied, it becomes clear that the above-mentioned models are too simple and that all binary coefficients (the α_{ij}'s and β_{ij}'s) systematically are dependent on the composition. Both the Claisse–Quintin and the Lachance–Claisse models use higher order cross-terms to correct for enhancement and third-element effects. Accordingly, these models are, in general, more suited for use in a very wide concentration range.

14.5.3.2.2 **Fundamental Parameter Method** The fundamental parameter method is based on the physical theory of X-ray production rather than on empirical relations between observed X-ray count rates and concentrations of standard samples. In general, the observed XRF count rate $R_{i,\mathrm{K}\alpha}$ of (the K_α-line of) an element i, obtained by polychromatic excitation of a sample with thickness d and density ρ, can be written as

$$\begin{aligned} R_{i,\mathrm{K}_\alpha} = &\int_{E=E_{i,\mathrm{abs}}}^{E_{\max}} \int_{z=0}^{d} I_0(E)\frac{G_1}{\sin\varphi}\sigma_{i,\mathrm{K}_\alpha}(E)c_i H_i(E)e^{-\chi(E,E_{i,\mathrm{K}_\alpha})\rho z} \\ &G_2 B(E, E_{i,\mathrm{K}_\alpha})\varepsilon(E_{i,\mathrm{K}_\alpha})\mathrm{d}z\mathrm{d}E \end{aligned} \tag{14.34}$$

where the quantity $\sigma_{i,\mathrm{K}_\alpha}$ is the effective cross section for production of K_α-radiation of element I:

$$\sigma_{i,K_\alpha}(E) = \tau_{i,K_\alpha}(E)\cdot\omega_{i,K}\cdot p_{i,K_\alpha} \tag{14.35}$$

(with p_{i,K_α} the probability of producing a K_α-fluorescent photon from a vacancy in the K-shell and $\omega_{i,\mathrm{K}}$ its fluorescence yield). $E_{i,\mathrm{abs}}$ is the absorption edge energy and E_{i,K_α} the K_α-line energy of element i, $I_0(E)\mathrm{d}E$ is the spectral distribution of the exciting radiation with $E_{\max}$ its maximum energy (see Figure 14.6), G_1 and G_2 are geometry constants, $\chi(E,E_{i,\mathrm{K}_\alpha})$ is defined in Eq. (14.19). $H_i(E,E_{i,\mathrm{K}_\alpha})$ is a factor describing secondary and higher order excitation (at low concentrations, $H_i = 1$), while the factor $B(E,E_{i,\mathrm{K}_\alpha})$ describes the absorption of the radiation in the medium between tube, sample, and detector (e.g., air, He). $\varepsilon(E_{i,\mathrm{K}_\alpha})$ is the efficiency of the detector. After integration over the sample depth, Eq. (14.34) becomes

$$\begin{aligned} R_{i,\mathrm{K}_\alpha} = &\int_{E=E_{i,\mathrm{abs}}}^{E_{\max}} I_0(E)\frac{G_1\rho d}{\sin\varphi}\sigma_{i,\mathrm{K}_\alpha}(E)c_i \times \frac{1-\mathrm{e}^{-\chi(E,E_{i,\mathrm{K}_\alpha})\rho d}}{\chi(E, E_{i,\mathrm{K}_\alpha})\rho d} \\ &\times G_2 B(E, E_{i,\mathrm{K}_\alpha})\varepsilon(E_{i,\mathrm{K}_\alpha})\mathrm{d}E \end{aligned} \tag{14.36}$$

This fundamental parameter equation relates the intensity of one element to the concentration of all elements present in the sample. A set of such equations can be written, one for each element to be determined. This set of equations can only be solved in an iterative way, making the method computationally complex. Moreover, an accurate knowledge of the shape of the excitation spectrum $I_0(E)\mathrm{d}E$, of the detector efficiency ε and of the fundamental parameters μ, τ, ω, and p is required. The fundamental parameter method is of interest because it allows for semiquantitative (5–10% deviation) analysis of completely unknown samples and is therefore of use in explorative phases of investigations. Several computer programs that allow to perform the necessary calculations at various levels of sophistication are available. As an example, in Table 14.9, the relative standard deviation between certified and calculated concentration of the constituents of series of tool steels are listed.

Table 14.9 Analysis of tool steels obtained by means of a fundamental parameter program and one calibration standard.

Element	Min (%)	Max (%)	Standard deviation (%)
Si	0.14	0.27	0.03
S	0.015	0.029	0.003
P	0.022	0.029	0.003
Mo	0.2	9.4	0.04
Mn	0.21	0.41	0.01
Cr	2.9	5	0.13
Co	0	10	0.2
C	0.65	1.02	0.16
W	1.8	20.4	0.52

Min., max.: minimum and maximum concentrations in the series of analyzed samples. Standard deviation on the basis of the difference between calculated and certified concentrations.
Adapted from [3].

14.5.4
Error Sources in X-ray Fluorescence Analysis

Table 14.10 lists the four main categories of random and systematic errors encountered in XRF analysis. The first category includes the selection and preparation of the sample to be analyzed. Two stages are generally involved before the actual prepared specimen is presented to the spectrometer, these being sampling and specimen preparation. The actual sampling is rarely under the control of the spectroscopist and it generally has to be assumed that the container containing the

Table 14.10 Sources of error in X-ray fluorescence analysis.

	Source	Random (%)	Systematic (%)
1	Sample preparation	0–1	0–5
	Sample inhomogeneity	—	0–50
2	Excitation source fluctuations	0.05–0.2	0.05–0.5
	Spectrometer instability	0.05–0.1	0.05–0.1
3	Counting statistics	Time dependent	—
	Dead time correction	—	0–25
4	Primary absorption	—	0–50
	Secondary absorption	—	0–25
	Enhancement	—	0–15
	Third-element effects	—	0–2

material for analysis does, in fact, contain a representative sample. It will be seen from the table that, in addition to a relatively large random error, inadequate sample preparation, and residual sample heterogeneity can lead to very large systematic errors. For accurate analysis, these errors must be reduced by the use of a suitable specimen preparation method. The second category includes errors arising from the X-ray source previously discussed. Source errors can be reduced to less than 0.1% by the use of the ratio counting technique, provided that high-frequency transients are absent. The third category involves the actual counting process and these errors can be both random and systematic. System errors due to detector dead time can be corrected either by use of electronic dead time correctors or by some mathematical approach. The fourth category includes all errors arising from interelement effects. Each of the effects listed can give large systematic errors that must be controlled by the calibration and correction scheme.

14.5.5
Specimen Preparation for X-ray Fluorescence

Because X-ray spectrometry is essentially a comparative method of analysis, it is vital that all standards and unknowns be presented to the spectrometer in a reproducible and identical manner. Any method of specimen preparation must give specimens that are reproducible and that, for a certain calibration range, have similar physical properties including mass attenuation coefficient, density, particle size, and particle homogeneity. In addition, the specimen preparation method must be rapid and cheap and must not introduce extra significant systematic errors, for example, the introduction of trace elements from contaminants in a diluent. Specimen preparation is an all-important factor in the ultimate accuracy of any X-ray determination, and many papers have been published describing a multitude of methods and recipes for sample handling. In general, samples fit into three main categories:

1) Samples that can be handled directly following some simple pretreatment such as pelletizing or surfacing. For example, homogeneous samples of powders, bulk metals, or liquids.
2) Samples that require significant pretreatment. For example, heterogeneous samples, samples requiring matrix dilution to overcome interelement effects, and samples exhibiting particle size effects.
3) Samples that require special handling treatment. For example, samples of limited size, samples requiring concentration or prior separation, and radioactive samples.

The ideal specimen for XRF analysis is one in which the analyzed volume of specimen is representative of the total specimen, which is, itself, representative of the sample submitted for analysis. There are many forms of specimen suitable for XRF analysis, and the form of the sample as received will generally determine the method of pretreatment. It is convenient to refer to the material received for analysis as the sample, and that which actually is analyzed in the spectrometer as the specimen. While the direct analysis of certain materials is certainly possible, more often than not some pretreatment is required to convert the sample to the specimen. This step is referred to as *specimen preparation*. In general, the analyst would prefer to analyze the sample directly, because if it is taken as received, any problems arising from sample contamination that might occur during pretreatment are avoided. In practice, however, there are three major constraints that may prevent this ideal circumstance from being achieved: sample size, sample size homogeneity, and sample composition heterogeneity. Problems of sample size are frequently severe in the case of bulk materials such as metals, large pieces of rock, and so on. Problems of sample composition heterogeneity will generally occur under these circumstances as well, and in the analysis of powdered materials heterogeneity must almost always be considered. The sample as received may be either homogeneous or heterogeneous; in the latter case, it may be necessary to render the sample homogeneous before an analysis can be made. Heterogeneous bulk solids are generally the most difficult kind of sample to handle, and it may be necessary to dissolve or chemically react the material in some way to give a homogeneous preparation. Heterogeneous powders are either ground to a fine particle size and then pelletized, or fused with a glass-forming material such as borax. Solid material in liquids or gases must be filtered out and the filter analyzed as a solid. Where analyte concentrations in liquids or solutions are too high or too low, dilution or preconcentration techniques may be employed to bring the analyte concentration within an acceptable range.

14.6
Advantages and Limitations

14.6.1
Qualitative Analysis

Qualitative analysis is, in principle, very simple with XRF and is based on the accurate measurement of the energy, or wavelength, of the fluorescent lines observed. As many WDXRF spectrometers operate sequentially, a 2θ scan needs to be performed. The identification of trace constituents in a sample can sometimes be complicated by the presence of higher order reflections or ‘‘satellite’’ lines from major elements. With EDXRF, the entire X-ray spectrum is acquired simultaneously. The identification of the peaks, however, is rendered difficult by the comparatively low resolution of the ED detector. In qualitative analysis programs, the process is simplified by overplotting the so-called KLM markers onto an (unknown) spectrum. These markers indicate the theoretical position of the K-, L-, and M-lines of a specific element; when these observed peaks coincide with the line markers, an element is positively identified.

14.6.2
Detection Limits

For a particular element, the detection limit depends on the sensitivity and on the count rate of the continuum below the peak and is inversely proportional to the measurement time. Detection limits can be improved by increasing the sensitivity (optimization of the excitation and detection efficiency), by reducing the background (as is done in TXRF) or by counting a longer period of time. The value of the attainable detection limits thus depends very much on the sample, the element considered and the experimental conditions. In WD instruments, values range from 0.1 to 10 ppm are obtained for medium-Z elements (such as Fe) upto 1–5% for the lightest elements (B, Be). Detection limits for unpolarized EDXRF are typically a factor 5–10 worse, except for TXRF that has absolute detection limits in the picogram range. Using synchrotron sources, the detection limits of XRF are generally several orders of magnitude better than in cases where conventional X-ray sources are employed.

14.6.3
Quantitative Reliability

The great flexibility, sensitivity, and range of the various types of XRF spectrometers make them ideal for quantitative analysis. In common with all analytical methods, quantitative XRF analysis is subject to a number of random and systematic errors that contribute to the final accuracy of the analytical result. As with all instrumental methods of analysis, the potential high precision of X-ray spectrometry can only be translated into high accuracy if the various systematic errors in the analysis process are taken care of. The precision of a WD system for the measurement of a single, well-separated line is typically on the order of 0.1%, and about 0.25% for the ED system. A good rule of thumb that can be used in XRF analysis to estimate the expected standard deviation σ at an analyte concentration level c is given by

$$\sigma = K(c + 0.1)^{\frac{1}{2}}$$

where K varies between 0.005 and 0.05. For example, at a concentration level $c \approx 25\%$, the expected value of σ would be between about 0.025 and 0.25%. A K value of 0.005 would be considered very high-quality analysis and a value of 0.05 rather poor quality. The value of K actually obtained under routine laboratory conditions depends on many factors but with reasonably careful measurements a K value of around 0.02–0.03 can be obtained.

14.7
Summary

When an element is bombarded by high-energy particles, orbital electrons may be ejected creating inner orbital atomic vacancies. These vacancies may be filled by transition of outer-level electrons giving rise to characteristic X-radiation.

XRF spectrometry provides the means of the identification of an element by measurement of its characteristic X-ray emission wavelength of energy.

The method allows the quantization of a given element by first measuring the emitted characteristic line intensity and then relating this intensity of element concentration.

While the roots of the method go back to the early part of this century, where electron excitation systems were employed, it is only during the past 30 years or so that the technique has gained major significance as a routine means of elemental analysis. WD spectrometers employ diffraction by a single crystal to separate characteristic wavelengths emitted by the sample. At present, nearly all commercially available X-ray spectrometers use the fluorescence excitation method and employ a sealed X-ray tube as the primary excitation source. The first commercial X-ray spectrometer became available in the early 1950s and although these earlier spectrometers operated only with an air path, they were able to provide qualitative and quantitative information on all elements above atomic number 22 (titanium). Later versions allowed use of helium or vacuum paths that extended the lower atomic number cutoff to around atomic number 9 (fluorine). X-ray detectors used include the flow counter, the scintillation counter, and the Si(Li) detector.

The X-ray method has good overall performance characteristics. In particular, the speed, accuracy, and versatility of XRF are the most important features among the many that have made it the method of choice in over 30 000 laboratories all over the world.

Most WD spectrometers fall into two broad categories – single channel and multichannel. Single-channel spectrometers are typically employed for both routine and nonroutine analysis of a wide range of products, including ferrous and nonferrous alloys, oils, slags, and sinters, ores and minerals, thin films, and so on. These systems are very flexible but relative to multichannel spectrometers are somewhat slow. The multichannel WD instruments are used almost exclusively for routine, high-throughout analysis where the great need is for fast accurate analysis, but where flexibility is of no importance. ED spectrometers exist in various forms, some designed for (on-site or laboratory) bulk analysis, others for surface-specific or microscopic analysis.

Interelement (matrix) effects often complicate quantitative analysis by XRF. However, a wide selection of methods is now available for minimizing these effects, allowing excellent accuracy to be obtained in many cases. Detection limits are achievable down to the low parts per million (ppm) range and it is possible to obtain reasonable responses from as little as a few milligrams of material.

References

1. Hechel, J. and Ryon, R.W. (2001) Polarized beam X-ray fluorescence analysis, in *Handbook of X-Ray Spectrometry*, 2nd edn (eds R.E. Van Grieken and A.A. Markowicz), Chapter 10, Marcel Dekker, New York.

2. Potts P. and West M. (eds.) (2008) *Portable X-ray Fluorescence Spectrometry: Capabilities for In Situ Analysis*, Royal Society of Chemistry, London.
3. Van Grieken, R.E. and Markowicz, A.A. (eds) (1993) *Handbook of X-Ray Spectrometry*, 1st edn, Chapter 5, Marcel Dekker, New York, p. 320, 453–489.

Further Reading

Bertin, E.P. (1975) *Principles and Practice of X-Ray Spectrometric Analysis*, 2nd edn, Plenum Press, New York.

Beckhoff, B., Kanngießer, B., Langhoff, N., Wedell, R., and Wolff, H. (eds) (2006) *Handbook of Practical X-Ray Fluorescence Analysis*, Springer.

Cesareo, R., Gigante, G.E., Castellano, A., and Iwanczyk, J.S. (2000) in *Encyclopedia of Analytical Chemistry* (ed. R.A. Meyers), John Wiley & Sons Ltd., Chichester, pp. 13327–13338.

Janssens, K.H., Adams, F.C., and Rindby, A. (2000) *Microscopic X-Ray Fluorescence Analysis*, John Wiley & Sons, Ltd, Chichester.

Janssens, K. and Adams, F. (1995) in *Encylopedia of Analytical Science*, Vol. 9 (ed. A. Townshend), Academic Press, London, pp. 5560–5574ISBN: 0 12 226709 5.

Jenkins, R. (1988) *X-Ray Fluorescence Spectrometry*, John Wiley & Sons, Inc., New York.

Jenkins, R., Gould, R.W., and Gedcke, D. (1981) *Quantitative X-Ray Spectrometry*, Marcel Dekker, New York and Basel.

Jenkins, R. (2000) in *Encyclopedia of Analytical Chemistry* (ed. R.A. Meyers), John Wiley & Sons Ltd, Chichester, pp. 13269–13288.

Jenkins, R. (2000) in *Encyclopedia of Analytical Chemistry* (ed. R.A. Meyers), John Wiley & Sons Ltd., Chichester, pp. 13422–13444.

Klockenkämper, R. (1997) *Total Reflection X-Ray Fluorescence Analysis*, John Wiley & Sons, Ltd, Chichester.

Potts, P. (1995) in *Encylopedia of Analytical Science*, Vol. 9 (ed. A. Townshend), Academic Press, London, pp. 5601–5611ISBN: 0 12 226709 5.

Potts, P. (1995) in *Encylopedia of Analytical Science*, Vol. 9 (ed. A. Townshend), Academic Press, London, pp. 5611–5622ISBN: 0 12 226709 5.

Potts, P. (1995) in *Encylopedia of Analytical Science*, Vol. 9 (ed. A. Townshend), Academic Press, London, pp. 5622–5633ISBN: 0 12 226709 5.

Selin-Lindgren, E. (2000) in *Encyclopedia of Analytical Chemistry* (ed. R.A. Meyers), John Wiley & Sons Ltd, Chichester, pp. 13315–13327.

Tsuji, K., Injuk, J., and Van Grieken, R.E. (2004) *X-Ray Spectrometry: Recent Technological Advances*, John Wiley & Sons Ltd., Chichester.

Wobrauschek, P. and Streli, C. (2000) in *Encyclopedia of Analytical Chemistry* (ed. R.A. Meyers), John Wiley & Sons Ltd., Chichester, pp. 13384–13414.

15

Atomic Absorption Spectrometry (AAS) and Atomic Emission Spectrometry (AES)

Erwin Rosenberg and Ulrich Panne

15.1

Introduction

Atomic absorption spectrometry (AAS) and atomic emission spectrometry (AES) were the first instrumental techniques to be established for elemental analysis. They are based on the pioneering work in the middle of the nineteenth century of Bunsen and Kirchhoff [1], who discovered that elements that are subjected to a hot flame emit light of a characteristic wavelength. On the other hand, this characteristic emission can be absorbed again by the vapor of the same element. These two discoveries formed the basis for atomic absorption and emission spectrometry and demonstrate the close interrelation and complementary nature of these two techniques. AAS and AES have many theoretical and practical considerations in common, and they can be described by the same formalism. The theory of AAS and AES will thus be treated together.

15.2

Theory of Atomic Spectroscopy

15.2.1

Basic Principles

The development of atomic spectroscopic techniques and their application to fundamental studies fostered the concurrent development of atomic theory and quantum mechanics. In turn, the better understanding of atomic theory led to the implementation of many beneficial techniques and instrumental features in atomic spectroscopy, particularly for the reduction or elimination of interferences and background.

A first step toward the interpretation of atomic spectra was made in 1885, when Balmer found a formula describing the different emission lines of hydrogen in the visible region:

$$\lambda = k \frac{n^2}{n^2 - 4} \tag{15.1}$$

Handbook of Spectroscopy, Second Edition. Edited by Günter Gauglitz and David S. Moore.

where λ is the wavelength (in nanometers), k a constant, and $n = 2, 3, 4$, and so on, represents the spectroscopic lines H_α, H_β, H_γ, and so on.

Equation (15.1) may be expressed in wavenumbers as

$$\nu' = \frac{1}{\lambda} = R\left(\frac{1}{2^2} - \frac{1}{n^2}\right) \tag{15.2}$$

where ν' is the frequency of the radiation in wavenumbers ($\mathrm{cm^{-1}}$) and R the Rydberg constant ($109\,677\ \mathrm{cm^{-1}}$). Equation (15.2) may be generalized to give the wavelength of the lines in all series of the hydrogen atom:

$$\nu' = R\left(\frac{1}{n_1^2} - \frac{1}{n_2^2}\right) \tag{15.3}$$

where $n_1 > n_2$. The numbers $n_1 = 1, 2, 3$ represent the Lyman, Balmer, and Paschen series, respectively. Formula (15.3) was further extended by Rydberg to yield

$$\nu' = RZ^2\left(\frac{1}{n_1^2} - \frac{1}{n_2^2}\right) \tag{15.4}$$

where Z stands for the atomic number (equivalent to the number of protons) of the particular element, which now gives the possibility of calculating the wavelength of lines of atoms other than the hydrogen atom. The two numbers n_1 and n_2 are the so-called spectral terms of the particular atom. These terms describe the defined energy levels of the electrons in their orbits around the nucleus. According to Bohr's theory of the atomic structure, no energy is taken up or emitted as long as the electron remains in its given orbit. Energy (E) is only taken up or emitted in the form of electromagnetic radiation when the transition of an electron between two energetic states occurs. The wavelength of this radiation is given by

$$E = h\nu = \frac{hc}{\lambda} \tag{15.5}$$

(with $h = 6.626 \times 10^{-34}\ \mathrm{J\,s}$, i.e., Planck's constant, ν is the frequency (in $\mathrm{s^{-1}}$), $c = 3 \times 10^8\ \mathrm{m\,s^{-1}}$ the speed of light in vacuum, and λ is the wavelength (m). The energy difference accompanying such a transition is thus

$$\nu' = \frac{1}{\lambda} = \frac{E}{hc} = \frac{E_1}{hc} - \frac{E_2}{hc} = T_1 - T_2 \tag{15.6}$$

where T_1 and T_2 are the Bohr energy levels. Considering systems with a single valence electron, the energy of this electron can be expressed as

$$E = \frac{2\pi Z^2 e^4 \mu}{n^2 h^2} \tag{15.7}$$

where μ is the reduced mass of the system; $\mu = m \times M/(m + M)$ with m representing the mass of the electron and M the mass of the nucleus, and n is the principal quantum number ($n = 1, 2, 3, \ldots$).

The orbital quantum number l, with $l = 0, 1, 2 \ldots (n-1)$, determines the orbital angular momentum $\boldsymbol{L}$.

$$||\boldsymbol{L}|| = \frac{h}{2\pi} = \sqrt{l(l+1)} \tag{15.8}$$

For an elliptical orbit, the possible orientations relative to an external electric or magnetic field are

$$\boldsymbol{L}_z = \frac{h}{2\pi} m_l \tag{15.9}$$

where $\boldsymbol{L}_z$ is the component of the orbital angular momentum $\boldsymbol{L}$ that is parallel to the external field with $m_l = \pm 1; \pm(n-1); \ \ldots \ 0$. m_l has $(2l+1)$ values. When an absorbing or emitting atom is brought into a strong magnetic field, the spectral lines display a hyperfine structure, called the *Zeeman effect*. The explanation of this effect requires the assumption that the electron rotates around its axis, thus exhibiting a spin angular momentum $\boldsymbol{S}$.

$$||\boldsymbol{S}|| = \frac{h}{2\pi} = \sqrt{S(S+1)} \tag{15.10}$$

The spin quantum number m describes the orientation of the axis of rotation of the electron and the external field.

$$\boldsymbol{s}_z = \frac{h}{2\pi} \ m_s \tag{15.11}$$

m_s may assume the values of $\pm 1/2$.

The total angular momentum $\boldsymbol{J}$ of an electron results from the vector sum of the orbital angular momentum and the spin angular momentum:

$$\vec{\mathrm{J}} = \vec{\mathrm{L}} + \vec{\mathrm{S}} \ \text{ with } \ ||\boldsymbol{J}|| = \frac{h}{2\pi} = \sqrt{j(j+1)} \tag{15.12}$$

$j = l \pm s$ is the total internal quantum number.

All electrons of an atom must differ in their energetic states. These are given by the quantum number in the following notation:

$$n^m l_j \tag{15.13}$$

where n stands for the principal quantum number; m for the multiplicity of the signal ($m = 2s+1$), and l ($l = 0, 1, 2, \ldots$) for the orbital quantum number. The corresponding terms are denoted by the symbols s (sharp), p (principal), d (diffuse), f (fundamental), and so on, which were initially used to describe the appearance of the different spectral lines. j is the total internal quantum number.

These term schemes are useful for expressing the energy levels of each element. They also allow defining which transitions between energy levels are allowed and which are forbidden. This is expressed by the so-called selection rules. These are

- $\Delta n = 0; \pm 1; \pm 2$ (the principal quantum number may change by any integer value);
- $\Delta l = \pm 1$ (the orbital quantum number must change by one integer);
- $\Delta j = 0$ or ± 1 (the total internal quantum number may either remain unchanged or change by one integer, but the transition $J = 0 \rightarrow J = 0$ is forbidden);
- $\Delta s = 0$ (the spin quantum number must not change, transitions between singulett and triplett spin systems are not allowed).

For larger systems (heavy atoms), however, the selection rules $\Delta l = \pm 1$ and $\Delta s = 0$ are sometimes violated.

The spectroscopic notation is easy to derive for elements with one valence electron, for example, the Na atom. Its electronic configuration in the ground state is $1s^2 2s^2 2p^6 3s^1$, or $3^2 S_{1/2}$ which results from $l = 0$ (*s*); $m = 2 \times (1/2) + 1 = 2$ (with $s = 1/2$), and $j = ||l \pm s|| = ||0 \pm 1/2|| = 1/2$. The spectroscopic notation corresponding to the excited states with the 3s electron being lifted to the 3p level is $3^2 P_{1/2}$ and $3^2 P_{3/2}$ (since $l = 1$(p); $m = 2 \times (1/2) + 1 = 2$ (with $s = 1/2$), and $j = ||1 \pm s|| = ||1 \pm 1/2|| = 1/2$ and $3/2$).

The term schemes of the elements have been compiled by Grotrian [2]. Two examples are given in Figure 15.1. The energy level diagram of the singly charged magnesium ion differs very little from that of the uncharged sodium atom (or of other alkaline metal atoms). A significant difference, however, consists in the energy difference between the 3p and 3s states, which is almost double for Mg^+ in comparison to Na_0 as a consequence of the larger charge of the nucleus of Mg.

For atoms with more than one valence electron, coupling of the spin and orbital angular momentum must be considered (Russel–Saunders or L–S coupling). The

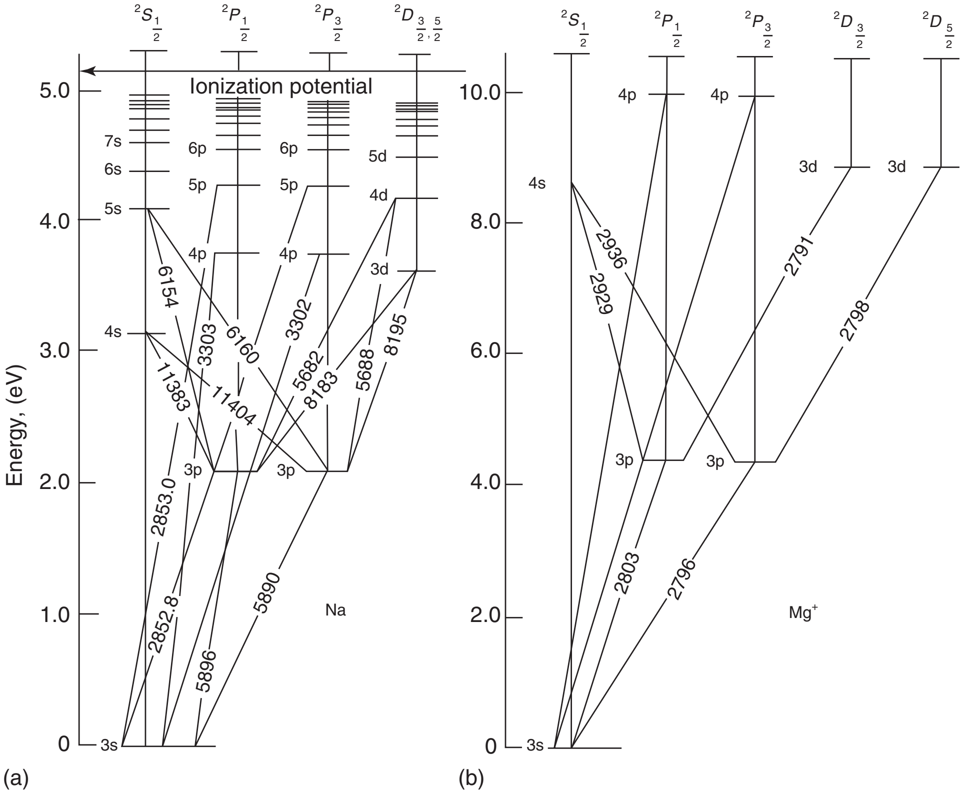

Figure 15.1 Energy level (Grotrian) diagrams for (a) atomic sodium and (b) magnesium (I) ion.

orbital momenta of all electrons have to be coupled to the total orbital momentum, and so are the spin momenta. The total quantum number L is obtained by replacing $L=\Sigma l$, $S=\Sigma s$, and $J=L-S, \ldots, L+S$. The term symbol thus becomes

$$^{\mathrm{M}}L_J \tag{15.14}$$

As an example, the ground state of Mg is denoted as 3^1S_0 (electron configuration: $1s^22s^22p^63s^2$, corresponding to $L=0$ as $l_1=0$ and $l_2=0$; $S=0$ as $s_1=1/2$ and $s_2=-1/2$; and $J=L+S=0$). The notation for the first excited state ($1s^22s^22p^63s^13p^1$) is, depending on the spin quantum number of the two valence electrons, 3^1P_1 (with $L=1$ as $l_1=0$ and $l_2=1$; $S=0$ as $s_1=1/2$ and $s_2=-1/2$; and $J=L+S=0$ and $J=|L\pm S|=1$) , as well as 3^3P_2, 3^3P_1, and 3^3P_0 (corresponding to parallel spins $s_1=1/2$ and $s_2=1/2 => S=1$ and consequently $J=0, 1, 2$). The energy level diagrams for ionic magnesium with one valence electron (Figure 15.1b) and atomic magnesium (Figure 15.2) differ significantly. For atoms with two outer electrons, two different term schemes exist upon excitation, the singlet and the triplet state with considerably different excitation energies. In the excited singlet state, the spins of the two electrons are of opposed orientation and they are paired. In the triplet state, the spins are parallel or unpaired. For this reason, the triplet excited state is of lower energy than the corresponding singlet state.

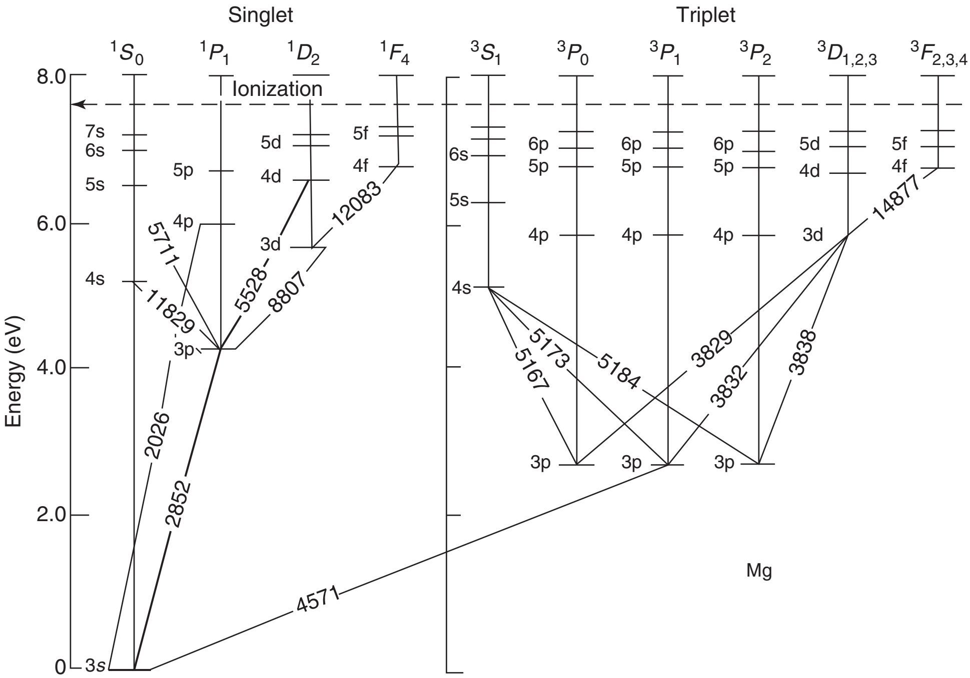

Figure 15.2 Energy level diagram for atomic magnesium. Strong lines indicate greater line intensities. The singlet/triplet transition has a significantly lower probability for occurrence than the singlet/singlet transition.

While the energy level diagrams and the corresponding spectroscopic transitions are relatively straightforward for light elements, they become very complex for heavier elements. The number of observed lines listed by Harvey [3] increases from the alkali metals with 30 (for lithium) to 645 (for cesium) to several thousand lines for the transition elements (chromium: 2277, iron: 4757, and cerium 5755).

15.2.2
Fundamentals of Absorption and Emission

Atomic absorption and emission require the prevalence of free atoms, which, in most instances, is achieved in a plasma or a plasma-like state. When a plasma is contained in a closed system and is in thermal equilibrium, the population of the excited levels may be described for one species by Boltzmann's law:

$$\frac{N_q}{N_0} = \frac{g_q}{g_0} \exp\left(\frac{-E_q}{kT}\right) \tag{15.15}$$

with N_q being the number of particles in the excited state, N_0 is the number of particles in the ground state, g_q and g_0 are the statistical weights of the corresponding energy levels, E_q is the excitation energy of the state q, k is the Boltzmann constant ($=1.38 \times 10^{-23}\ \mathrm{J\,K^{-1}}$), and T is the absolute temperature.

When the plasma is in the steady state, the number of particles that leave an energy level per unit time is equal to the number of particles that arrive at this level. A number of phenomena are responsible for the transition of species between energy levels in a plasma:

1) collisions of atoms, leading to the excitation of one species to a higher energy level (collisions of the first kind);
2) collisions of an excited species with another particle, leading to radiationless relaxation (collisions of the second kind);
3) excitation by collision with electrons;
4) de-excitation with the transfer of energy to an electron;
5) excitation of atoms or ions by the absorption of radiation;
6) de-excitation of atoms or ions by spontaneous or stimulated emission.

Assuming the presence of two species, with n being the concentration of one species and N that of the second species that is in large excess ($N \gg n$), we can set up the following equations:

$$\alpha N n_0 = \beta N n_q \tag{15.16}$$

$$\alpha_e n_e n_0 = \beta_e n_e n_q \tag{15.17}$$

$$B' \rho_\nu n_0 = (A + B\rho_\nu) n_q \tag{15.18}$$

A, B, and B' are the Einstein transition probabilities for spontaneous emission, stimulated emission, and absorption, respectively, and α_e, α, β_e, and β are the cross sections of the respective processes (which are also a function of the velocity distribution of the particles involved). n_e is the electron density and ρ_ν is the radiation density at a given frequency ν.

When the system is in thermodynamic equilibrium, the rate of formation and disappearance of charged particles and neutrals is equal, and at a given temperature T we can state

$$\frac{n_q}{n_0} = \frac{\alpha}{\beta} = \frac{\alpha_e}{\beta_e} = \frac{B'}{\frac{A}{\rho_\nu} + B} = \frac{g_q}{g_0} \exp\left(\frac{-E_q}{kT}\right) \tag{15.19}$$

The number of charged and uncharged species remains constant through excitation and de-excitation by collisions with neutrals, ions, and electrons. Absorption and emission, as they occur in a real radiation source, certainly also have to be considered, but they normally contribute only very little to the energy balance which is in the so-called local thermal equilibrium (LTE):

$$\alpha N n_0 + \alpha_e n_e n_0 + B' \rho_\nu n_0 = \beta N n_q + \beta_e n_e n_q + (A + B\rho_\nu) n_q \tag{15.20}$$

From Eq. (15.20), n_q/n_0 can be calculated. In the radiation source, the population of excited states is determined by the excitation process, as may be deduced from Eq. (15.20): Thus, for a DC arc source (which is said to be in LTE), $\alpha N \gg \alpha_e n_e + B' \rho_w$, and $\beta N \gg \beta_e n_e + (A + B\rho_\nu) n_q$.

As long as the radiation density is low (which is the case for the DC arc), the plasma can be assumed to operate under LTE. This is not the case for low-pressure discharges where both collisions with electrons and radiative de-excitation are very important. Also, for low-pressure plasmas, the assumption of a Maxwellian velocity distribution of the particles is no longer valid.

Species can decay from excited states through a number of processes, including collision with uncharged (molecules, atoms) or charged (ions, electrons) particles, or by the emission of electromagnetic radiation. In the case of radiative decay, the wavelength of emission is given by Planck's law. For the spontaneous decay from level q to level p, the number of events per unit time is

$$-\frac{\mathrm{d}N_q}{\mathrm{d}t} = A_{qp} N_q \tag{15.21}$$

A_{qp} is the Einstein coefficient for spontaneous emission (s^{-1}). Equation (15.21) must be adapted when several transitions starting from level q are to be considered.

$$-\frac{\mathrm{d}N_q}{\mathrm{d}t} = N_q \sum_p A_{qp} = N_q \nu_q \tag{15.22}$$

Here, ν_q is the lifetime of the excited state q. The typical lifetime of an excited state from which a species decays through an allowed radiative transition is of the order of 10^{-8} s. When radiative transitions are not allowed, the excited states are metastable (as is the case, e.g., for the Ar 11.5 and 11.7 eV states), and relaxation can only occur through collisions with other particles.

Absorption of electromagnetic radiation of frequency ν_{qp} and radiation density p increases the number density of excited particles N_q as

$$\frac{\mathrm{d}N_q}{\mathrm{d}t} = B'_{qp} N_q \rho_\nu \tag{15.23}$$

Stimulated emission takes place when atoms in the excited state q decay upon interaction with radiation of wavelength λ_{qp} and leads to a reduction in the number density of excited species according to

$$-\frac{\mathrm{d}N_q}{\mathrm{d}t} = B_{qp}N_q\rho_\nu \tag{15.24}$$

Under conditions of thermal equilibrium

$$g_q B_{qp} = g_p B_{pq} \tag{15.25}$$

where g_q and g_p are the statistical weights (degeneration factors) of levels p and q.

When species emit, the intensity of the emitted spectral line (denoted by the subscript a) is proportional to the number density of atoms in the excited state q:

$$I_{qp} = A_{qp}n_{aq}h\nu_{qp} \tag{15.26}$$

n_{aq} may be substituted using the Boltzmann equation

$$I_{qp} = A_{qp}h\nu_{qp}n_a\,\frac{g_q}{Z_a}\exp\left(\frac{-E_q}{kT}\right) \tag{15.27}$$

The sum $Z_a = \sum^{a} g_a \exp\left(\frac{-E_a}{kT}\right)$ is the partition function. It is a function of temperature, and the coefficients of this function are tabulated in the literature for a large number of atoms and ions. When the intensities of two emission lines a and b from the same ionization state of an element are used, the excitation temperature T may be calculated from

$$T = \frac{5040(V_a - V_b)}{\log[(g_aA_a)/(g_bA_b)] - \log(\lambda_a/\lambda_b) - \log(I_a/I_b)} \tag{15.28}$$

In this equation, energies are in electronvolts (eV), and V_a and V_b denote the excitation energies (eV) of lines a and b. The line pair Zn 307.206 nm/Zn 307.59 nm is very often used for calculating the excitation temperature. It is particularly suitable, as ionization of zinc is generally low (due to its high ionization energy), the difference between the two wavelengths is not too large, ensuring a uniform detector response, and the gA factors are precisely known.

15.2.2.1 **Absorption**

Between absorption and the number density of the absorbing atoms, the following relation holds:

$$\int K_\nu \mathrm{d}\nu = \frac{\pi e^2}{mc}Nf \tag{15.29}$$

where K_ν is the absorption coefficient at frequency ν, m is the electron mass and e its charge, c is the velocity of light, N is the number density of atoms, and f is the oscillator strength. As this relation is strictly valid only for monochromatic light, the use of a source that emits radiation with a very narrow spectral line width is required. Normally, atomic emission sources such as hollow cathode lamps (HCLs) or electrodeless discharge lamps (EDLs) fulfill this condition. The relation between the absorption A and the concentration c is given by the law of Lambert and Beer, which states that the intensity of incident radiation I_0 is diminished by the fraction dI by absorption in the incremental length dl (with l being the total optical path length):

$$-\mathrm{d}I = kI_0c\,\mathrm{d}l \tag{15.30}$$

Integration of Eq. (15.30) in the limits $I = I_0$ to I and $l = 0$ to l gives

$$-\int_{I=I_0}^{I} \frac{\mathrm{d}I}{I} = kc \int_{I=0}^{I} \mathrm{d}I \tag{15.31}$$

$$-\log\left(\frac{I}{I_0}\right) = kcl \tag{15.32}$$

As log I_0/I equals the absorbance A, Eq. (15.32) can finally be written as

$$A = kcl \tag{15.33}$$

The Lambert–Beer law is valid only within a restricted concentration range. Deviations from linearity are commonly observed – and most notably in atomic absorption – and may be due to a number of reasons.

15.2.2.2 **Line Broadening**

Because of the contribution from various broadening mechanisms, the line widths typically observed in atomic spectrometry are significantly larger than the natural width of a spectroscopic line that can be theoretically derived. The natural width of a spectral line is a consequence of the limited lifetime τ of an excited state. Using Heisenberg's uncertainty relation, the corresponding half-width expressed as frequency is

$$\Delta\nu_N = \frac{1}{2\pi\tau} \tag{15.34}$$

From this equation, a typical half-width of about 1–10 pm is obtained for most spectroscopic lines.

The first important line-broadening mechanism is *Doppler line broadening*. It results from the movement that emitting species make toward or away from the point of observation. The contribution to line broadening is

$$\Delta\nu_{\mathrm{D}} = \left[\frac{2\sqrt{(\ln 2)}}{c}\right]\nu_0\sqrt{\frac{2RT}{M}} \tag{15.35}$$

where c is the velocity of light, ν_0 is the frequency of the emission maximum, R is the gas constant, M is the atomic mass, and $\Delta\nu_{\mathrm{D}}$ is the observed Doppler line broadening, expressed as full width at half-maximum (FWHM). Equation (15.35) suggests that Doppler line broadening is strongly temperature dependent. It has therefore also often been termed *temperature broadening*. It may thus be used to determine the kinetic energy of the emitting atoms or ions. For example, Doppler broadening is about 0.8 pm for the Ca(I) emission at 422.6 nm at 300 K and reduced pressure, while it approaches 2 pm at 3000 K.

Pressure or *Lorentz broadening* is the second important factor for line broadening. It is a result of the interaction of the emitting species and other nonemitting particles. Its contribution to line broadening is

$$\Delta\nu_{\mathrm{L}} = \left(\frac{2}{\pi}\right)\sigma_{\mathrm{L}}^{2}N\sqrt{\left[2\pi RT\left(\frac{1}{M_1}+\frac{1}{M_2}\right)\right]} \tag{15.36}$$

where M_1 and M_2 are the atomic masses of the two interacting species. N is the concentration of the foreign atom species and σ_{L} is its cross-section. At low pressure, the contribution of pressure broadening is low: for example, for the Ca 422.6 nm line, only about 0.02 pm at 300 K and 0.9 kPa. However, with increasing pressure, this contribution becomes the dominant factor for line broadening.

Other factors contributing to line broadening are *isotopic effects* and *hyperfine structure* (due to the interaction between radiating and nonradiating atoms of the same species) and *Stark broadening* (which is due to the interaction with electric fields).

15.2.2.3 **Self-Absorption**

Self-absorption occurs when radiation emitted by the source is absorbed by atoms of the same species in the ground state. Since the probability of re-emission of an absorbed photon is always less than unity, self-absorption results in a reduction of the radiation produced. The intensity distribution of an emission line is $I_0P_{\mathrm{E}}(\nu)$, where I_0 stands for the intensity emitted at the line maximum, and $P_{\mathrm{E}}(\nu)$ the profile function. After passage through a layer of absorbing species with a number density n_{A} of absorbing species, the intensity distribution is

$$I(\nu) = I_0P_{\mathrm{E}}(\nu)\exp\left[\frac{-\rho P_{\mathrm{A}}(\nu)}{P_{\mathrm{A}}(\nu_0)}\right] \tag{15.37}$$

where ν_0 is the intensity in the line center, $P_{\mathrm{A}}(\nu)$ is the absorption profile function and $P_{\mathrm{A}}(\nu_0)$ its value at the line center, and ρ is an absorption parameter given by

$$\rho \sim BP_{\mathrm{A}}(\nu)n_{\mathrm{A}} \tag{15.38}$$

ρ increases with increasing Einstein coefficient for absorption and consequently is larger for transitions that are based on excitation from the ground state. It also becomes larger when the number density of species, n_{A}, increases in the source. Self-absorption is strongest in the center of the line where absorption reaches its maximum. Thus, flatter line profiles are observed in this case. When self-absorption is so pronounced that it leads to a minimum in the intensity profile and $\rho > 1$, this is called *self-reversal*. Self-reversal is seen only where the radiation source exhibits a strong temperature gradient and the number densities of the analyte are high in both the hotter and the cooler zones of the source.

15.2.2.4 **Ionization**

When the plasma is sufficiently energetic, atoms may be ionized. The degree of ionization depends on the temperature of the plasma and the ionization energy of the considered element. In particular, for easily ionizable species, ionic spectra also contribute to the emission spectra observed in a plasma to a great extent. The ionization of atoms a of a particular element into ions i with liberation of electrons e is an equilibrium reaction given by

$$n_a \rightleftarrows n_i + n_e \tag{15.39}$$

whose equilibrium constant $S_n(T)$ is the so-called Saha constant

$$S_n(T) = \frac{n_i n_e}{n_a} \tag{15.40}$$

As long as the degree of ionization α for the considered element is small, it can be expressed as follows:

$$\alpha = \frac{n_i}{n_{\text{total}}} = \frac{n_i}{n_i + n_a} \tag{15.41}$$

n_1 and n_2 are the concentrations of ions and atoms in the plasma, respectively, and can be expressed as fractions of the total element concentration.

$$n_a = (1-\alpha)n_{\text{total}} \quad \text{and} \quad n_i = \alpha n_{\text{total}} \tag{15.42}$$

This can be substituted into the Saha equation, giving

$$S_n(T) = \frac{\alpha}{1-\alpha} n_e \tag{15.43}$$

The Saha equation can also be expressed in partial pressures p as

$$S_p(T) = \frac{p_i p_e}{p_a} = \frac{\left[(2\pi m)^{\frac{3}{2}}(kT)^{\frac{5}{2}}\right]}{h^3\left(2\frac{Z_i}{Z_a}\right)\left[\exp\left(\frac{-E_i}{kT}\right)\right]} \tag{15.44}$$

The factor 2 is the statistical weight of the free electron (which has two possible orientations for its spin), k is the Boltzmann constant (1.38×10^{-23} J K^{-1}, m is the mass of an electron (9.11×10^{-28} g), and h is the Planck constant (6.63×10^{-34} J s). With the conversion to electron volts (1 eV $= 1.6 \times 10^{-19}$ J), the Saha equation reads

$$\log S_p = \frac{5}{2}\log\frac{T-5040}{T}V_i + \log\frac{Z_i}{Z_a} - 6.18 \tag{15.45}$$

where V_i is the ionization energy in electron volts.

The Saha equation is valid only when the plasma is in (at least local) thermal equilibrium. The temperature resulting from the Saha equation is then the ionization temperature of the observed species. Under these conditions, the degree of ionization can be calculated from the intensity of the atom and ion lines of the same element, I_{qp} and I_{qp}^{+}:

$$\log\left(\frac{\alpha}{1-\alpha}\right) = \log\left(\frac{I_{qp}^{+}}{I_{qp}}\right) - \log\left(\frac{g_q^{+}A_{qp}^{+}\nu_{qp}^{+}}{g_q A_{qp}\nu_{qp}}\right) + \frac{5040}{T}\,(V^{+} - V_q) + \log\left(\frac{Z_i}{Z_a}\right) \tag{15.46}$$

The temperature of the plasma must be precisely known and controlled for the calculation of the degree of ionization, as the partition functions Z_a and Z_i for the atom and ion species, respectively, are strongly temperature dependent. The accuracy of the values of gA determines the accuracy of the calculation of the degree of ionization. The line pairs Mg(II) 279.6 nm/Mg(I) 278.0 nm and Mg(II) 279.6 nm/Mg(I) 285.2 nm are very often used to calculate the degree of ionization of an element in a plasma. When the degree of ionization α is known, the electron pressure in the plasma can be determined. Starting from

$$\log\left(\frac{\alpha}{1-\alpha}\right) = \log\left(\frac{S_p(T)}{p_e}\right) \tag{15.47}$$

one can derive

$$\log p_e = -\log\left(\frac{\alpha}{1-\alpha}\right) + \log S_p(T) \tag{15.48}$$

This equation may be rephrased as

$$\log p_e = -\log\left(\frac{I_{qp}^{+}}{I_{qp}}\right) + \log\left(\frac{g_q^{+}A_{qp}^{+}\nu_{qp}^{+}}{g_q A_{qp} \nu_{qp}}\right) - \frac{5040}{T}(V_i + {V_q}^{+} - V_q) + \frac{5}{2}\log T - 6.18 \tag{15.49}$$

which indicates that the intensity ratio of the atom and ion lines of an element changes remarkably with the electron pressure. This is particularly true for elements with low ionization energy, such as the alkali metals. An important consequence of this is the occurrence of the so-called ionization interferences.

From the above, it can be concluded that there exists for each spectral line emitted by a radiation (plasma) source an optimum temperature at which its emission intensity reaches a maximum. This so-called standard temperature depends on the energy of ionization and excitation of this element, as well as on the electron pressure and temperature in the plasma. The standard temperature for many atom lines is around 4000 K, while the standard temperature of ionic lines is often around 10 000 K.

15.2.2.5 **Dissociation**

Although atomic spectroscopy requires the presence of free atoms, highly stable radicals or molecules are also present in a radiation source and contribute to the background emission. The atomic and ionic lines are then superimposed on the molecular bands. Common species encountered in plasmas are CN, NH, NO, OH, and N_2 or ${N_2}^+$, but refractory reaction products may also be observed (e.g., AlO^+, TiO^+, or YO^+). The dissociation of the molecular species within the plasma is an equilibrium reaction. It can be described by a formula similar to the Saha equation:

$$K_n = \left[\left(\frac{2\pi}{h^2}\right)\left(\frac{m_x m_y}{m_{xy}}\right)(kT)^{\frac{3}{2}}\right]\left(\frac{Z_x Z_y}{Z_{xy}}\right)\left[\exp\left(\frac{-E_d}{kT}\right)\right] \tag{15.50}$$

where K_n is the equilibrium constant and the indices x and y denote the species that are produced from the dissociation of xy.

$$K_n = \frac{n_x n_y}{n_{xy}}$$

If we take the example of a metal oxide in the plasma, the degree of dissociation can be calculated from the plasma temperature, the partial pressure of the reactant (oxygen, in this case), and the dissociation energy E_d.

15.2.2.6 Radiation Sources and Atom Reservoirs

In the discussion of the elementary steps of atomic spectroscopy, it is essential to distinguish between ''radiation sources'' and ''atom reservoirs.'' In the former, radiation is generated that is used for the spectroscopic measurement. The latter serve to produce free atoms (or ions) from the sample. The two devices may be separated, as is the case for atomic absorption (and also atomic fluorescence), or the atom reservoir may also be the radiation source, as for atomic emission.

The volatilization (vaporization) and dissociation of the sample usually require highly energetic conditions to be as complete as possible. This is essential to maximize sensitivity while minimizing matrix interferences at the same time. The effectiveness of volatilization, atomization, and excitation is dependent upon the supply of energy to the sample and is characterized by different spectroscopic temperatures. They represent an important diagnostic tool for the characterization of atomization conditions in the plasma:

Rotational temperature: This is important for all processes where molecules or radicals are involved. It can be determined from the intensity distribution from the rotational lines in rotational–vibrational spectra. In most cases, diatomic molecules or radicals such as OH and CN are used as thermometric probes.

Gas temperature: This depends on the kinetic energy of the atoms and ions in the plasma. It can be determined from the Doppler peak broadening. This is, however, not completely straightforward, as the contributions of Doppler and temperature line broadening have to be separated by mathematical deconvolution. Together with the rotational temperature, it is an indicator for the vaporization and atomization capability of a plasma.

Electron temperature: This is characteristic for the kinetic energy of the electrons. It is important for all excitation and ionization processes that are initiated by collisions with electrons. Electron temperatures are often determined from the intensity of the recombination continuum or from the energy distribution of the bremsstrahlung.

Excitation temperature: This characterizes the population of the excited levels of atoms or ions and is thus of fundamental importance for spectroscopic measurements. It can be determined from the intensity ratio of two lines of a given element in the same atomic or ionic state. Alternatively, it may be determined from a plot of the emission intensity at different lines over their excitation energies for the particular element at a defined state of ionization.

Ionization temperature: This describes the equilibrium between atoms, ions, and electrons in a plasma. When thermal equilibrium applies, the Saha equation can be used to calculate the ionization temperature from the intensity ratio of an ion and an atom line of the same element. Another possibility is to calculate the ionization temperature from the n_e value which

Table 15.1 Temperatures of different excitation sources and atom reservoirs used in atomic spectrometry.

Source	Temperature (K)				State
	Rotational, T_{rot}	Excitation, T_{ex}	Electron, T_e	Ion, T_i	
Arc (DC)	5 000	5 000	5 500	5 000	LTE
Spark	—	20 000	20 000	20 000	LTE
Inductively coupled plasma	4 800	5 000	6 000	6 000	~LTE
Microwave plasma	2 000	4 000	6 000	6 000	Non-LTE
Low-pressure discharge	600	20 000	30 000	30 000	Non-LTE

can be obtained from Stark broadening. In plasmas that are in thermal equilibrium, all the above temperatures are equal.

That means that

- the velocity distribution of all species in the plasma (molecules, atoms, ions, and electrons) can be described by the Maxwell equation;
- the population of the different energy levels follows the Boltzmann equation;
- the equilibrium between electrons, ions, and neutrals of the different species obeys the Saha equation.

Real plasmas provide, even in the best cases, just an approximation to LTE. However, their spatial inhomogeneity is very large, as far as the temperature and number density distributions of the different species are concerned. Consequently, the equilibria occur only within very small volume elements of the plasma. Table 15.1 gives an overview of the different temperatures observed in the most common excitation sources and reservoirs for atomic spectrometry.

15.3
Atomic Absorption Spectrometry (AAS)

15.3.1
Introduction

AAS is nowadays one of the most important instrumental techniques for quantitative analysis of metals (and some metalloids) in various types of samples and matrices. The history of AAS dates back to the discovery of dark lines in the continuous emission/spectrum of the Sun by Wollaston in 1802. The lines are caused by the absorption of the elements in the atmosphere of the sun. His work was taken up and further pursued by Fraunhofer in 1814. In 1860, Kirchhoff and Bunsen demonstrated that the yellow line emitted by sodium salts when introduced into a flame is identical with the so-called D-line in the emission spectrum of the

Sun [1]. However, it took nearly one century before this important discovery was transformed into a viable analytical technique. In 1955, Alan Walsh published the first paper on atomic absorption spectroscopy [4]. At the same time, and independently of Walsh, Alkemade and Wilatz published the results of their fundamental AAS experiments [5, 6]. But it was the vision of Walsh and his indefatigable efforts that eventually led to the general acceptance and commercialization of AAS instrumentation in the mid-1960s. Further instrumental achievements (such as the introduction of the graphite furnace and the hydride generation technique) in the second half of the 1960s further promoted the popularity and applicability of the technique [6b].

15.3.2
Instrumentation

The instrumental requirements of AAS will be discussed in the following section. In Figure 15.3, the essential components of an atomic absorption spectrometer are depicted schematically: a suitable radiation source, an atomizer, some optics and a monochromator, a detector, and suitable electronic signal processing [7, 8]. The individual components of an AAS instrument will be discussed in this order.

15.3.2.1 Radiation Sources

For absorption-based optical methods, one has to consider the line width of the excitation source in relation to that of the respective transition of the absorbing species.

The half-width of elemental lines is of the order of 0.002 nm when observed by emission spectroscopy with flame or electrothermal atomization. The broadening of the line can be due to a number of reasons, of which the most important and best understood are natural, pressure, resonance, and Doppler broadening. If a stable and sensitive detection is to be achieved, the line width of the excitation radiation must be narrower than the FWHM of the analyte line. Under these conditions, the entire radiant energy produced by the excitation source will be available for absorption by the analyte. The typical line sources used for atomic absorption are thus element-specific excitation sources such as the HCL or the EDL. More recent developments have demonstrated that even continuum sources can be used with appropriate instrumental designs.

15.3.2.1.1 **The Hollow-Cathode Lamp** Initially described in 1916 by Paschen, the HCL is probably the most versatile excitation source for AAS. A schematic of this excitation source is given in Figure 15.4. It consists of a Pyrex glass tube (“envelope”) in which the cathode and anode are located under an inert gas

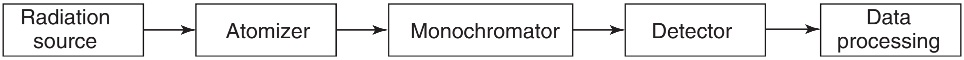

Figure 15.3 Essential components of an atomic absorption spectrometer.

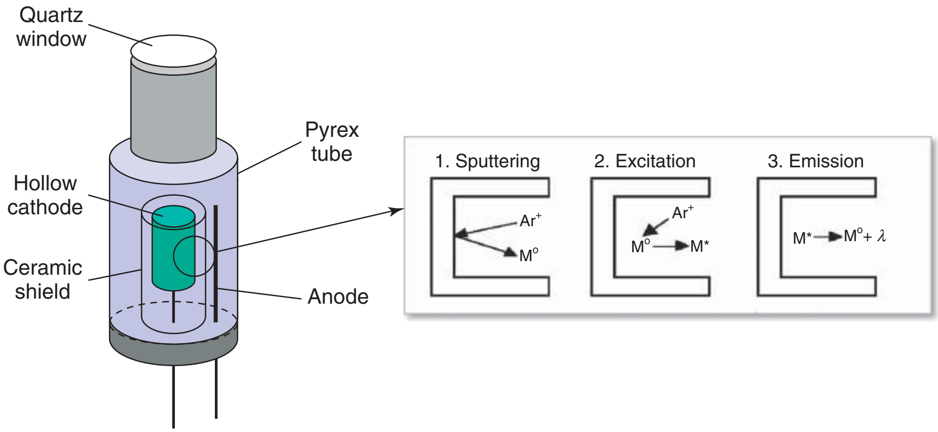

Figure 15.4 Schematic of a hollow cathode lamp (HCL). *Inset*: Signal formation mechanism in the HCL.

atmosphere (neon or argon; neon is typically preferred for its simpler spectral background, and preference is given to Ar only where spectral interferences by Ne emission lines are anticipated) at a pressure of typically 1–5 Torr. The hollow cathode is made from (or coated with) the respective pure element or the element alloyed with another suitable element. Alloying is used where the element is not available in an appropriate form, such as sodium, arsenic, and so on, to achieve a balanced output (Cd, Cr), or in the case of precious elements where significant cost savings can be made without compromising analytical performance. The anode is a strong nickel or tungsten wire. The anode often is coated with a getter material which assists in removing any impurities released from the cathode during the sputtering process from normal operation. The getter is also activated during lamp processing to collect any impurities remaining in the cathode material. This process deposits the impurities onto the glass bulb in such a form that they remain inert throughout the life of the lamp. It is this process that creates the dark colored ring on the wall of the envelope adjacent to the getter. The two electrodes are separated by a ceramic shield. At the front end of the HCL, a borosilicate glass (>400 nm), a special UV-transparent glass (240–400 nm), or a high-purity quartz glass window (>160 nm) is attached in order to achieve the optimum transmission of the key spectral lines of the cathode element.

The emission is generated by applying a voltage of typically 350–500 V across the electrodes, which leads to a current of 1–50 mA, resulting in an electrical discharge. Positive noble gas ions are accelerated toward the hollow cathode where their impact sputters atoms of the element to be determined from the hollow cathode. The sputtered metal ions are then excited through collisions with Ne or Ar ions in the gas phase. The metal ions return to the ground state by emitting radiation at characteristic wavelengths. The typical half-width of an atomic emission line produced by a HCL is approximately 0.2 pm, which fully complies with the requirements for an AAS line source discussed above.

The intensity of radiation produced by an HCL is proportional to the number of sputtered and excited atoms and will thus depend on the kinetic energy of the inert gas ions, which is controlled by the lamp current. Although the increase in lamp current produces a higher radiance and thus provides a higher sensitivity, there is, however, an upper limit for the HCL current for practical reasons (Figure 15.5): At high lamp currents, a large number of metal atoms are sputtered and brought into the gas phase. In this dense cloud of gas phase metal atoms, self-absorption reduces the intensity of the element-specific radiation, resulting in a reduction in sensitivity. Ideally, the sputtered metal atoms are redeposited on the hollow cathode upon radiative de-excitation. However, the metal atoms may also be transported and deposited on the glass walls of the HCL, thereby reducing the lifetime of the lamp. For this reason, the geometry of the cathode walls is optimized, and a protective shield is placed around the cathode.

In addition to single-element HCLs, multielement HCLs are also available and provide multielement excitation capabilities with one single HCL at a price that is comparable to a single-element HCL. More important than the cost advantage, however, is their ability to enable the simultaneous analysis of up to six elements without the need of changing the HCL for each element. Their principle of operation is the same as that of single-element lamps, with the cathode being made either from an alloy or from pressed powders of the respective elements (e.g., Al/Ca or Cr/Co/Cu/Fe/Mn/Mo). Although they represent a significant improvement for multielement AAS measurements (and make the exchange of HCLs obsolete when several elements are to be determined), they have some practical drawbacks. Their

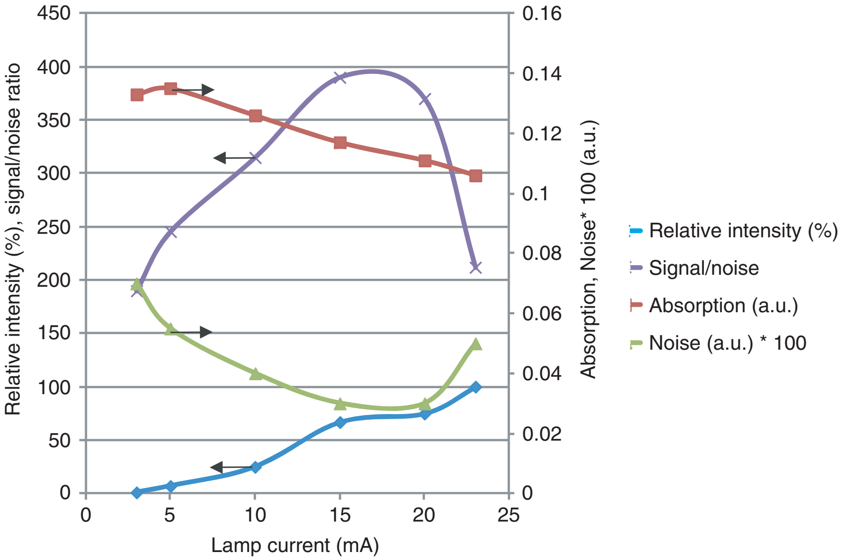

Figure 15.5 Relative intensity, noise, signal-to-noise ratio, and absorption for the determination of Cu (at 2 mg l^{-1}) by flame AAS as function of the lamp current.

lifetime is typically shorter than that of single-element HCLs, since the elements used for the production of the HCL have different volatilities. The element with the highest volatility will be preferentially sputtered and, with time, it will cover all other elements in the HCL, making them inaccessible to sputtering by accelerated gas ions. This will cause the sensitivity of the less volatile elements to diminish over time and will eventually shorten the effective lifetime of the HCL.

15.3.2.1.2 **The Boosted Hollow-Cathode Lamp** A very intense radiation source for AAS is the boosted HCL. It has been developed from the regular HCL and includes a second pair of electrodes between which a boost discharge is initiated, using the existing instrument lamp current supply. Via this discharge, the excitation of the sputtered atoms is increased significantly while self-absorption is minimized. As a result, the emission intensity is 5–15 times higher than for a standard HCL, which significantly improves the signal-to-noise ratio.

15.3.2.1.3 **The Electrodeless Discharge Lamp** The EDL is another atomic line source that allows one to produce a highly effective excitation source for elements that cannot be cast into hollow cathodes, such as mercury, arsenic, antimony, and some other elements.

The EDL is produced by filling a small quartz bulb with a few milligrams of the respective element under an inert gas atmosphere (usually argon) at reduced pressure and then sealing this tube. The quartz bulb is located at the center of a radio frequency (RF) coil (Figure 15.6). When an RF field, typically oscillating at 27.12 MHz, is applied to the coil, the argon atoms are ionized. The collision of free atoms of the particular element in the gas phase with the electrons produced by ionization of the argon leads to their excitation and subsequent radiative relaxation. While the EDL produces element-specific radiation of greater intensity than the HCL, its use is restricted to the more volatile elements. It also requires a separate power supply that provides the RF current.

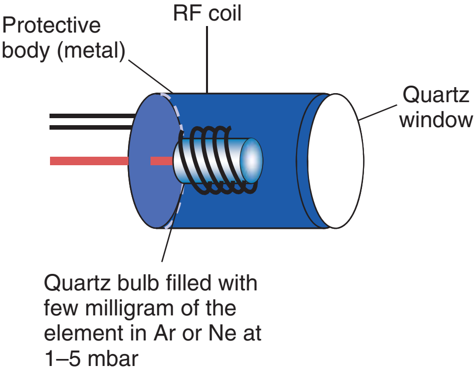

Figure 15.6 Scheme of an electrodeless discharge lamp.

15.3.2.1.4 **Continuum Sources** The disadvantage of having to change HCLs for each new element to be determined explains the interest in continuum light sources in AAS. However, as the line width of the absorbing species (0.0002 nm) is typically much smaller than the bandpass of common monochromators (0.1–0.2 nm), this approach is limited in practice [9]. This would mean that a large fraction of the light reaching the detector is not at the characteristic wavelength of the element. The small fraction of light that is actually absorbed by the atoms at their characteristic excitation wavelength would result in only a low analytical sensitivity. Echelle grating monochromators with their smaller spectral bandpass have, in part, overcome this shortcoming of AAS with continuum light sources, but still the sensitivity that can be reached is smaller than that with atomic line sources of narrow line widths.

Continuum sources that are currently used are the high-intensity xenon arc lamp and the deuterium lamp, the former being preferred owing to its higher brilliance. Although the presently realized continuum-source (CS) AA spectrometers are still operated sequentially for multielement detection, it may be anticipated that, with the use of suitable optics and multiarray detectors, this method will become a truly simultaneous multielement technique [10].

However, even as a single-element technique, CS-AAS provides a variety of advantages over conventional line source (LS) AAS. First, the atomic absorption can not only be measured at the center of the absorption line (with maximum sensitivity) but also at its wings (with reduced sensitivity). This leads to a greatly enhanced dynamic range of approximately 5–6 orders of magnitude in concentration or mass. This, together with very favorable detection limits as reported in recent literature, eliminates one of the classical disadvantages of AAS – its limited dynamic range.

Second, the setup shown in Figure 15.7 with a charge-coupled device (CCD) detector provides a lot of information about the spectral neighborhood around the analytical line, which eventually results in a much more reliable and accurate background correction, as essentially any pixel or set of pixels may be used for that purpose, depending on the nature of the background. In addition, as this wavelength-resolved absorbance is measured over time with each pixel, a three-dimensional absorbance pattern is obtained eventually for the background signal which is recorded simultaneously with the analytical signal – a unique property that not even Zeeman-effect background correction can provide which records the analyte and background absorbance sequential in time. In case of a structured background, background correction with a deuterium lamp is impossible, and presents a problem even for Zeeman-effect background correction. In the case of CS AAS, however, it is possible to eliminate the background almost completely by a least-squares background correction with the normalized spectra of the interfering species.

15.3.2.1.5 **Diode Laser Sources** Already in 1980, lasers had been suggested as excitation sources for AAS [11]. Tunable dye lasers can provide virtually any atomic line between 213 and 900 nm with a bandwidth corresponding to the natural line width of an atomic line and with a comparatively high intensity. However, they

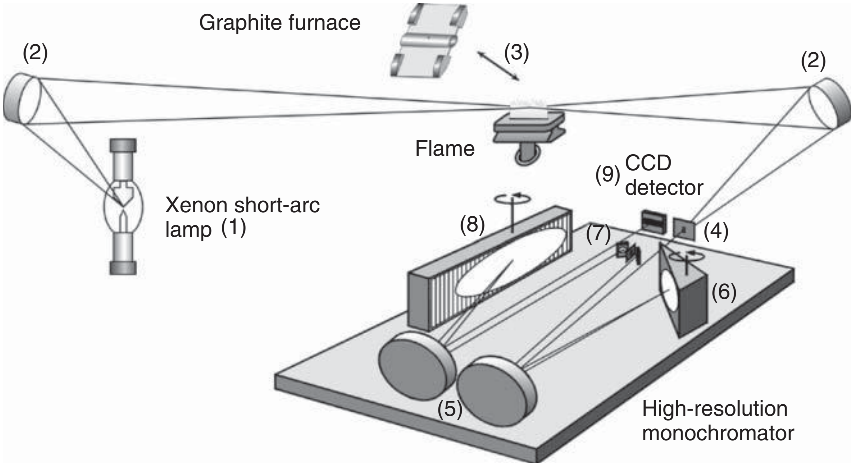

Figure 15.7 Experimental setup for CS AAS with double echelle monochromator. (1) Xenon short-arc lamp; (2) off-axis ellipsoid mirrors; (3) longitudinal Zeeman graphite furnace module (exchangeable with flame atomizer); (4) entrance slit; (5) off-axis parabolic mirrors; (6) Littrow prism; (7) deflection mirrors and intermediate slit; (8) echelle grating (75 grooves/mm, blaze 76°); and (9) linear CCD array detector. (Reprinted from Welz *et al*. [10b], with permission.)

have not found widespread acceptance for this application so far owing to their cost and complex operation compared to HCLs or EDLs. This situation seems to have changed with the advent of inexpensive, mass produced diode lasers (DLs) [12, 13].

DLs provide a radiant output that can be several orders of magnitude higher than that of common HCLs. Together with their excellent stability (both in terms of wavelength and intensity), this accounts for an improvement in signal-to-noise ratio, which brings about a 1–2 orders of magnitude improvement in the detection limit when compared with HCLs.

The typical line width of a commercial DL is approximately 2 orders of magnitude lower than that of atomic absorption lines in flames and furnaces. This allows one to expand the linear dynamic range of the method by tuning the DL to the wings of the absorption line where optically thin conditions prevail. Also, owing to the simplicity of DL emission (which basically consists of one single line), the requirements for the monochromator are much lower, allowing the construction of simpler instruments.

The possibility of modulating the emitted wavelength of DLs at gigahertz frequencies by the modulation of the diode current allows one to reduce the low-frequency (flicker) noise in the baseline, which again improves the detection limit. Emission wavelength modulation also provides a means of correcting for unspecific background absorption, thereby improving the selectivity of the technique.

DL AAS allows measurements that are almost shot-noise-limited with relatively high laser powers, leading to very low element detection limits (~1 ppt) if strong absorption lines are used. Although the wavelength range has been extended to the blue and near-UV spectral region with the introduction of new GaN-type laser diodes, the measurement of absorption lines down to 200 nm still needs frequency doubling of the laser radiation in optically nonlinear media which results in low radiation power and hence higher detection limits than theoretically possible. Further progress in the development of short wavelength laser diodes is needed, and is driven by the telecommunication and electronics industry.

The small line widths of DLs provide the opportunity of high-resolution spectroscopy, and thus the measurement of isotopes and isotope ratios. This allows the application of isotope dilution for improving the accuracy of elemental analysis, as known from mass spectrometry.

15.3.2.2 Atomizers

AAS requires that the species under investigation prevails in the gaseous and atomic state so that absorption of free atoms can be observed. The two most common methods for the production of atoms in the gas phase make use of thermal energy to vaporize and atomize the analyte. The sample transfer efficiency, that is, the amount of analyte that reaches the actual atomization zone, and the atomization efficiency that tells which fraction of the analyte is released in atomic form from its compounds, determine the overall efficiency. These two factors are important and directly related to the sensitivity that can be achieved with the particular method of atomization.

15.3.2.2.1 **Flame Atomization** In flame atomization, the sample solution is introduced into the flame with a specially designed nebulizer (Figure 15.8). The function of the nebulizer is to disrupt the continuous sample stream into a mist of fine droplets of typically 5–20 μm diameter which are swept into the mixing chamber. The aerosol is then mixed with the fuel gas and the oxidant gas before reaching the burner head. As a number of physical and chemical reactions, for example, vaporization, dissociation, reduction, or oxidation, may occur, it becomes evident that precise control of the operating conditions of flame atomization is required to obtain stable and sensitive signals. Optimization of flame atomic absorption measurements has thus the double role of maximizing the element's response and minimizing the undesired side reactions.

15.3.2.2.2 **Nebulizers** The most common type of nebulizer is the concentric tube nebulizer which consists of a capillary through which the liquid is introduced and an outer tube of larger diameter with a nozzle at its end. Through this outer tube, the nebulizer gas stream is directed at high pressure and achieves both transport of the liquid sample stream by aspiration and disruption of the continuous supply of sample. The advantages of this nebulizer type are its simple construction and the fact that it is self-aspirating. Other nebulizer types are in use, such as the cross-flow nebulizer where the high pressure gas flow is directed perpendicular to the capillary from which the liquid emerges. This type of nebulizer requires the liquid to be pumped through the capillary, which reduces the effect of viscosity on

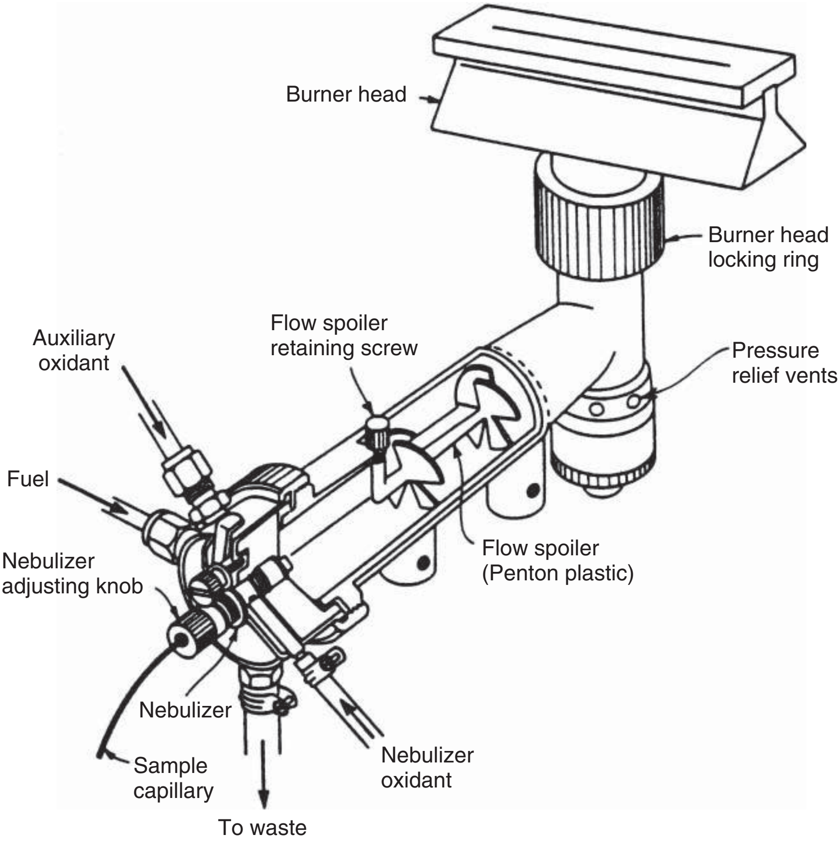

Figure 15.8 Design of a laminar flow burner. (Courtesy of the Perkin-Elmer Corporation, Norwalk, CT.)

sample introduction. The high-pressure gas is usually the oxidant, while the fuel gas is mixed subsequently with the sample aerosol.

15.3.2.2.3 **Burner Design** The aerosol is sprayed into the mixing chamber, which serves two functions. First, the fuel gas and additional oxidant gas are added (if required) and premixed to achieve optimum flame conditions. Second, droplets larger than about 20 μm in diameter are prevented from reaching the flame by arranging flow spoilers inside the mixing chamber. As a concentric tube nebulizer produces an aerosol of rather wide droplet size distribution, it is important to prevent droplets of larger diameter from being transported into the flame. Owing to the short residence time of the sample in the flame, large diameter droplets are not completely desolvated and atomized and thus increase the background noise of the flame. They are separated from the smaller diameter droplets by impacting on baffles and are drained to waste. Therefore, only less than 10% of the sample being converted to an aerosol actually reaches the burner head. High-efficiency nebulizers and flow-injection systems may introduce up to 30% of the aerosol into the flame, and high-pressure nebulizers even up to 50%.

The burner head is constructed in the form of a long, narrow slit (''laminar flow burner''). The long slit through which the flame expands (typically 10 or 5 cm) increases the absorption path length and thus also the sensitivity.

A point of critical importance in the AAS system is the optimization of fuel and oxidant gas flow ratios. Although fuel and oxidant gases are usually combined in approximately stoichiometric ratios, the determination of certain elements may require significantly different ratios.

Typical flame gas mixtures and resulting flame temperatures are given in Table 15.2. Early AAS work was carried out with natural gas/air and hydrogen/air flames and was focused mainly on those elements that, although easy to atomize, were difficult to excite because of the short excitation wavelengths, that is, Zn (213.8 nm), Cd (228.8 nm), Ni (232.0 nm), and Pb (283.3 nm). The use of hotter flames became necessary, however, as it was realized that a higher temperature is required for complete atomization (particularly for Al, Ti, or Si). While oxygen/natural gas or oxygen/acetylene mixtures can easily produce significantly higher flame temperatures, they require a particular burner head design that allows stable and safe operation even at the very high burning velocities of these gas mixtures.

The burning velocity is the velocity at which the flame expands in a premixed fuel/oxidant gas mixture. If the burning velocity is larger than the flow rate of the burner gas mixture, the flame propagates back into the burner, resulting in a flashback and potentially causing ignition of the explosive mixture in the mixing chamber. At higher flow rates, a point is reached where the flow velocity equals the burning gas velocity, so that a stable operation of the flame is achieved. If the flow velocity is further increased, the flame rises and eventually reaches a point where the flame is blown off the burner head. The extremely high burning velocities of oxygen/natural gas or oxygen/acetylene mixtures make their use in flame AAS very inconvenient and hazardous. A significant breakthrough was the introduction of the nitrous oxide/acetylene flame, which permits operation at reasonable burning velocities. However, the burner design has still to be modified

Table 15.2 Typical gas mixtures and flame properties for flame AAS.

Fuel	Oxidant	Flame temperature (°C)	Maximum burning velocity ($\mathrm{cm\,s^{-1}}$)	Burner slot (mm)
Natural gas	Air	1700–1900	39–43	100 × 1.5
Natural gas	Oxygen	2700–2800	370–390	—
Hydrogen	Air	2000–2100	300–440	—
Hydrogen	Oxygen	2550–2700	900–1400	100 × 1.5
Acetylene	Air	2100–2400	158–266	—
Acetylene	Oxygen	3050–3150	1100–2480	—
Acetylene	Nitrous oxide	2600–2800	285	50 × 0.5

for nitrous oxide/acetylene flames in contrast to air/acetylene or air/natural gas flames, that is, both the length and width of the burner head slit have to be of particular dimensions. This design provides a more efficient heat sink for the flame than with the larger dimension slit and thus reduces the risk of flashback.

Flames that operate in fuel-rich conditions are sometimes called *yellow flames*, while flames that are operated under fuel-lean conditions are often called *blue flames*. While the latter are oxidizing flames, the former provide reducing conditions which may be advantageous for the determination of certain elements. The atomization of an analyte is not homogenous throughout the flame, as the production of free atoms in the flame is governed by the variation in temperature in the different zones of the flame, as well as by the rate of diffusion of the flame gases that dilute the free atom population in the observation zone (Figure 15.9). For the highest sensitivity, the radiation from the light source must be directed through the zone of the flame that contains the highest fraction of free atoms. To meet this condition, the height and alignment of the burner head relative to the light path must be carefully optimized [13b].

15.3.2.2.4 **Electrothermal Atomization** In the late 1950s, L'vov made the first attempts to use a graphite furnace for the atomization of the sample in AAS [14]. It did, however, take until the early 1970s before the first graphite furnace (GF) or electrothermal (ET) atomizers were introduced to the market. Measurements by ET-AAS are discontinuous, and an analysis cycle comprises the following four steps: (i) the sample is introduced into the cold GF; (ii) the solvent is evaporated

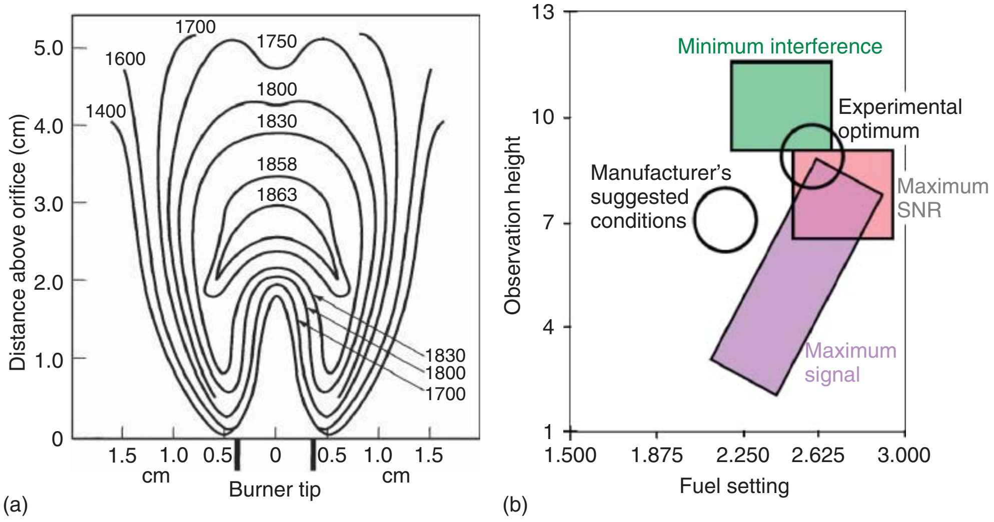

Figure 15.9 (a) Flame temperature as function of the observation height above the burner head for a natural gas/air flame. (Reprinted from Ebdon *et al.* [7], with permission.) (b) Regions of most suitable operation conditions for the flame AAS determination of Ca in the presence of Al. (Reprinted from Dockery *et al.* [13b], with permission.)

at temperatures of around 100 °C; (iii) the sample is ashed and any volatile sample constituents are removed by keeping the sample for about 1 min at 450–900 °C before; and (iv) the temperature is rapidly increased to 2000–3000 °C to vaporize and atomize the sample in a very short interval (milliseconds to a few seconds). The entire cycle can be accomplished in about 1 min because of the fast heating rates achieved by direct electrical (resistive) heating of the GF at currents of up to 400 A and a voltage on the order of 8 V (Figure 15.10).

The GF (Figure 15.11a) comprises the following features. The cylindrical graphite tube is open at both ends and has, typically, a length of 18–28 nm and an internal diameter of 6–10 mm. At its center, it has a small hole through which the sample (typically 5–20 μl) is introduced automatically. At its ends, the graphite tube is tightly fitted into a pair of water-cooled graphite ring electrodes through which the heating current is provided. The entire furnace is purged with argon to exclude air from the graphite tube and to prevent its incineration at high temperatures. An additional argon gas stream is directed from both ends of the tube toward the center to purge vapors from the sample matrix generated during the vaporization and ashing step. Argon has excellent optical transparency in the UV region, which is important for the detection of elements at short wavelengths. Despite the use of an inert gas atmosphere, the graphite tubes are severely affected during the heating cycles and must routinely be replaced after about 100 analyses.

Although this technique offers a much improved sensitivity in comparison with flame AAS owing to the fact that the entire sample is atomized and that the concentration of free atoms is very high in the restricted volume of the graphite tube (about 2 ml), some disadvantages arise from the use of graphite tubes with the above-mentioned design. As the graphite tube is rapidly heated, it will be considerably hotter than the gas phase in the center of the tube. Thus analyte

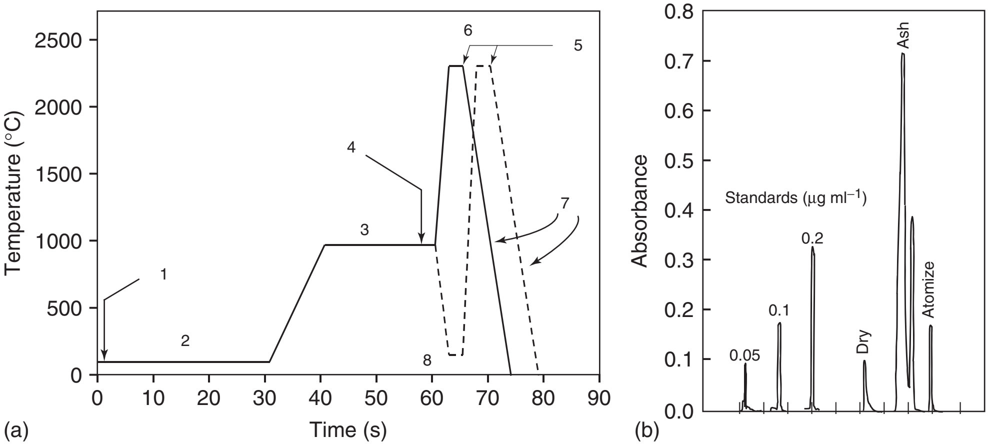

Figure 15.10 (a) Schematic temperature program of the graphite furnace: (1) Ar flow on; (2) drying; (3) ashing; (4) Ar flow off; (5) Ar flow on; (6) atomization step; (7) cooling period; and (8) cool-down procedure). (b) Typical signal output of a graphite furnace AAS measurement.

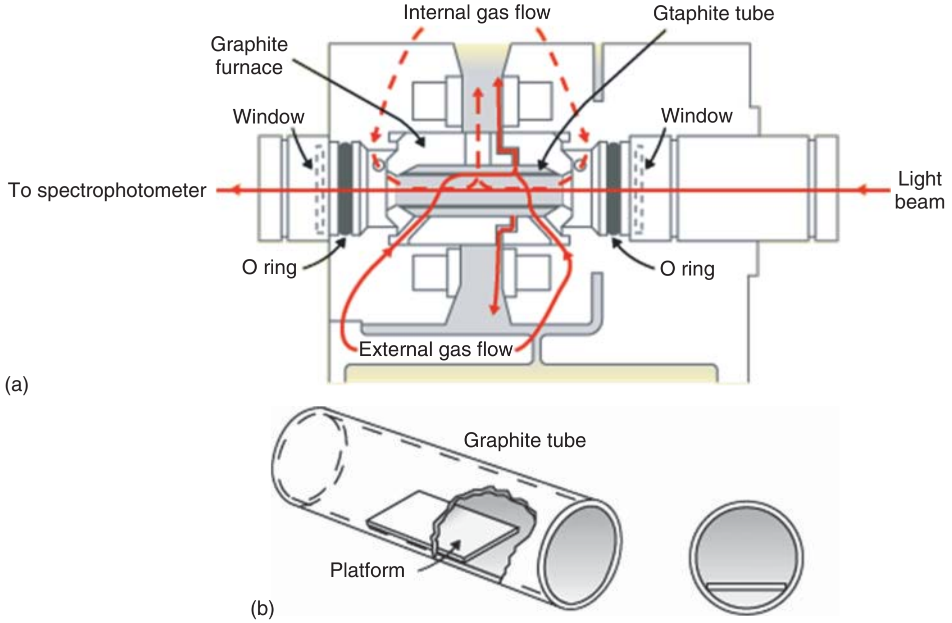

Figure 15.11 (a) Cross-sectional view of a graphite furnace and (b) graphite furnace with an L'vov platform inserted.

atoms are evaporated into a significantly cooler zone where they may recombine and further condense. This disadvantage has been alleviated by the introduction of the sample onto a small platform (L'vov platform) of graphite that is located in the center of the graphite tube (Figure 15.11b). The heating characteristics of the modified graphite tube remain essentially unaltered compared to those without a platform. However, since the platform has only a limited heat capacity, it will basically be heated by radiation from the tube walls. This will cause the temperature of the platform to lag somewhat behind the platform of the tube walls. The analyte will thus be volatilized with delay when compared to a graphite tube without platform, and it will also evaporate into an atmosphere that is significantly hotter than with wall atomization. In this way, the platform reduces interferences that arise from temporal non-isothermality. However, GFs of this design still have a remarkable spatial non-isothermality because of the water-cooled electrical contacts acting as effective heat sinks. The graphite tube has its highest temperature in the center and becomes cooler toward its ends. Elements of low volatility may therefore condense after initial volatilization or adsorb on cooler wall regions located away from the tube center. During a subsequent atomization sequence, revaporization of the analyte may occur and lead to memory effects since the ends of the tube initially also attain higher temperatures. For this reason, the transversely heated atomizer has been introduced which provides spatial isothermality through which condensation and memory effects are notably reduced (Figure 15.12). It has, furthermore, been observed that some of the sample matrix effects and the poor

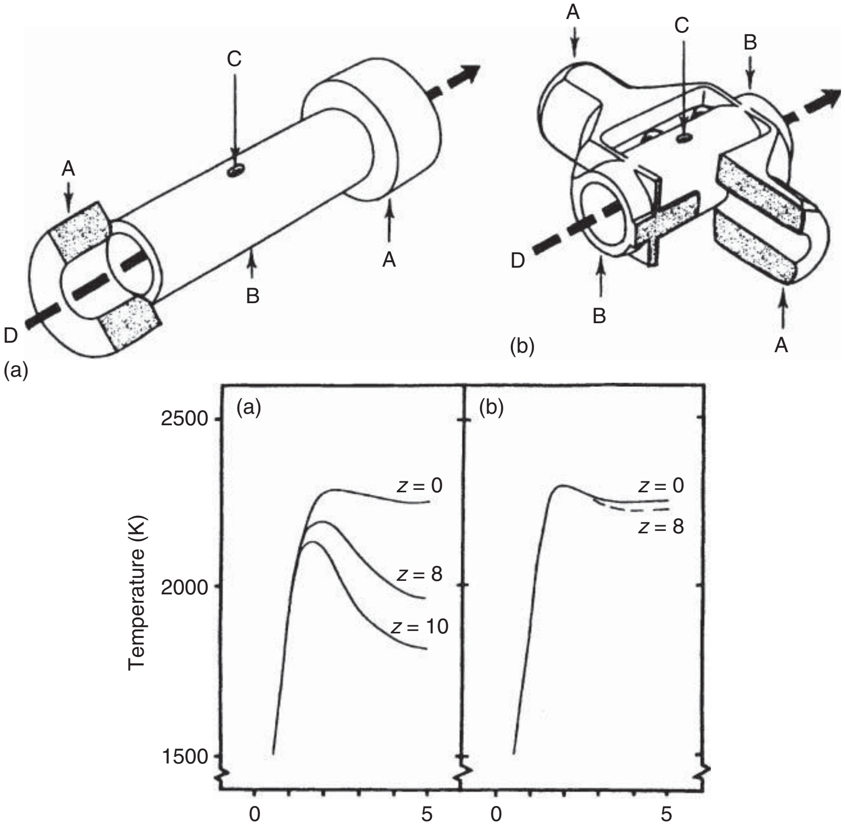

Figure 15.12 (a) End-heated and (b) side-heated electrothermal atomizer configuration and temperature profiles associated with these furnace designs. A, water-cooled electrical graphite contact cylinders; B, graphite tube; C, sample injection port; and D, light path of the spectrometer. The value of *z* denotes the distance from the center (in millimeters) at which the temperature profiles have been recorded for a graphite tube of 28 mm length.

reproducibility sometimes associated with GF atomization can be improved by reducing the natural porosity of the graphite tube. It appears that part of the analyte and matrix diffuse into the pores of the tube. This slows down the atomization process and causes smaller analyte signals or memory effects due to revaporization in a subsequent analysis cycle. To reduce the porosity, the graphite surfaces are covered with a thin layer of pyrolitic carbon through which the pores of the graphite tube are sealed.

15.3.2.2.5 **Vapor Generation Technique** The generation of gaseous analytes from the sample and their introduction into atomization cells for subsequent absorption spectrometric determination offer a number of advantages over the conventional sample introduction by pneumatic nebulization of the sample solution. These include the elimination of the nebulizer, the enhancement of the transport efficiency, which approaches 100%, and the presentation of a homogenous sample vapor to the atomizer. The most common and versatile techniques for the formation of volatile compounds are the hydride generation technique and the cold vapor technique.

Other techniques for the formation of volatile compounds, such as volatile chlorides or volatile organic complexes (e.g., β-diketonates or dithiocarbamates) have also been used, but rarely, and will thus not be discussed in the following.

The versatility and general acceptance of vapor formation techniques in AAS result from the various advantages that they offer:

- Separation of the analyte from the matrix is achieved, which improves the accuracy of the determination.
- Preconcentration of the analytes is easily implemented, which allows significant improvements in concentration detection limits.
- Different chemical species can be discriminated in some cases.
- The procedures are readily accessible to automation.

Only a few disadvantages are quoted for vapor generation techniques. These include the (chemical) interferences, notably in the presence of transition metals; a pronounced pH effect on the reaction, and its dependence on the oxidation state of the element, which, however, can also be advantageously used for speciation analysis; and finally gas-phase atomization interferences which may be caused by the presence of other volatile hydrides.

Vapor-generation techniques comprise the following three steps: (i) transformation of the analyte into a volatile form, (ii) its collection or preconcentration (if necessary) and transfer to the atomizer, and (iii) decomposition of the volatile compounds to liberate the free analyte atom (not necessary for mercury) with subsequent measurement of the atomic absorption signal.

15.3.2.2.6 **Hydride Generation Technique** A number of different reactions have been described for the formation of covalent volatile metal hydrides, which all have as a common denominator that they rely on the formation of atomic hydrogen as reducing agent [15]. For the generation of volatile hydrides of arsenic, antimony, and selenium (AsH_3, SbH_3, and H_2Se), the well-known reaction of Zn with concentrated hydrochloric acid may be employed [15b]:

$$\mathrm{Zn} + 2\mathrm{HCl} \rightarrow \mathrm{ZnCI}_2 + 2[\mathrm{H}]$$

$$\mathrm{E}^{m+} + k[\mathrm{H}] \rightarrow \mathrm{EH}_n + \mathrm{H}_2(\text{excess} \uparrow)$$

In the above equation, E represents the analyte element, and m may, but need not necessarily be, equal to n (e.g., when the analyte occurs in various oxidation states). Reduction by Zn/HCl requires that the analytes be present in their lower oxidation states prior to reaction. When this is not the case, the analytes must be reduced, for example, by $SnCl_2$ in an acidic medium. The formation of volatile hydrides (and of excess hydrogen) is then initiated by the addition of zinc metal.

This reaction is rather inconvenient, since it is slow, difficult to automate, and subject to high blank values due to the impurities of the zinc. Also its efficiency is limited as a consequence of incomplete reaction and the possibility of adsorption or entrapment in the zinc sludge of the volatile metal hydrides formed. Because of these disadvantages, the use of this procedure has nowadays been practically abandoned.

Instead, the far more effective sodium tetrahydroborate reagent is used, which reacts according to

$$NaBH_4 + 3H_2O + HCl \rightarrow H_3BO_3 + NaCl + 8[H]$$

$$E^{m+} + k[H] \rightarrow EH_n + H_2 \text{ (excess } \uparrow)$$

The higher reactivity of this reagent allows its use for the formation of volatile hydrides of antimony, arsenic, bismuth, germanium, lead, selenium, tellurium, and tin. This method is superior to the Zn/HCl method not only because of the wider range of elements that are accessible but also with respect to speed, efficiency of the reaction, and reduced contamination. The reaction is essentially completed within 10–30 s, and the reagent is typically added into the acidified samples as 0.1–10% (w/v) solution. These factors contribute to the ease of automation, which has been a key factor in the success of the hydride generation technique.

The preferred acid for this application is hydrochloric acid. HNO_3 and H_2SO_4 have also been used, although less frequently. The acid concentration is a parameter that has to be carefully optimized and may vary considerably, depending on the element and the matrix. It may range from as low as 0.1–0.2 $mol\,l^{-1}$ for tin and lead to up to 9 $mol\,l^{-1}$ for antimony, arsenic, and bismuth. Only two disadvantages have to be mentioned for the tetrahydroborate reduction. The reagent is not completely free from contaminants (particularly tin), which limits the achievable detection limits, and the generation of a large excess of hydrogen may be a significant hindrance, although this is usually not the case for atomic absorption unlike for other spectroscopic techniques.

Hydride generation-AAS may be carried out in batch systems (where the $NaBH_4$ may even be added as pellets) as well as in continuous generation systems where the sample and the reducing agent are pumped continuously into the reaction chamber, then further to a gas–liquid phase separator, and then into a flow injection (FI) system. In such a system, discrete amounts of the sample are injected into a flowing carrier stream which is merged with the reagent streams. Reaction takes place in a reaction coil, and the volatile hydrides are purged in a gas–liquid phase separator and carried to the atomization cell (Figure 15.13).

The most widely used atomizer for hydride generation is the heated quartz T-tube atomizer with a typical diameter of 10 mm and a length of 100–150 mm, making it compatible with the optical path of most AA spectrometers. The quartz tube is electrically heated to 700–1000 °C, which permits the optimization of the atomization temperature for each element. The quartz tube may either have open ends, or these ends may be sealed by removable quartz windows, and holes at the extreme ends of the quartz tube provide the gas flow outlets. This setup increases

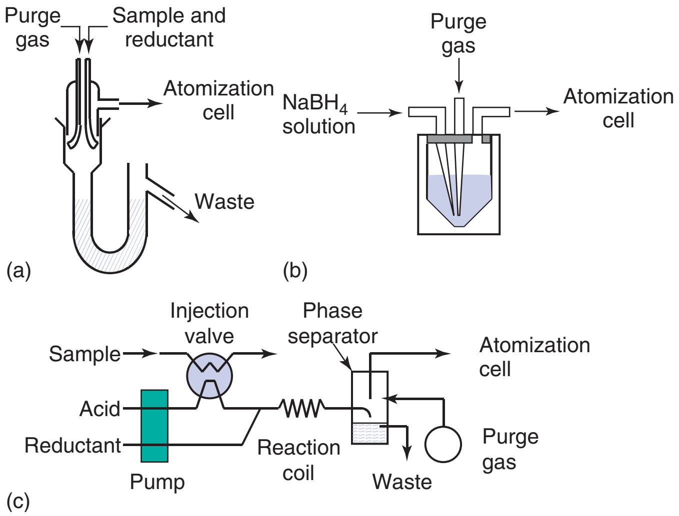

Figure 15.13 Hydride generation systems. (a) Batch generation. (b) Continuous generation. (c) Flow-injection generation.

the residence time of the atoms in the light path and thus improves sensitivity. With continued use, the performance of the quartz tube atomizer invariably deteriorates in terms of sensitivity and precision. This is attributed both to devitrification of the inner surface of the quartz tube to a less inert modification and to the contamination of the inner atomizer surface by deposition of small particles and droplets that were not efficiently removed by the gas–liquid phase separator.

The decomposition of hydrides to form free atoms is mainly due to the reaction with hydrogen radicals, but oxygen also plays an active role. The following reactions may take place within a quartz tube atomizer:

$$\mathrm{H}^{\bullet} + \mathrm{O}_2 \rightarrow \mathrm{OH}^{\bullet} + \mathrm{O}$$

$$\mathrm{O}^{\bullet} + \mathrm{H}_2 \rightarrow \mathrm{OH}^{\bullet} + \mathrm{H}^{\bullet}$$

$$\mathrm{OH}^{\bullet} + \mathrm{H}_2 \rightarrow \mathrm{H}_2\mathrm{O} + \mathrm{H}^{\bullet}$$

The concentration of the hydrogen radical in the atomizer tube is several orders of magnitude higher than that of the hydroxyl radical. Thus if a metal hydride is introduced into the quartz tube, it will undergo the following subsequent reactions, leaving finally the free atom in the gas phase:

$$\mathrm{EH}_x + \mathrm{H}^{\bullet} \rightarrow \mathrm{EH}^{\cdot}_{x-1} + \mathrm{H}_2$$

$$\mathrm{EH}^{\bullet} + \mathrm{H}^{\bullet} \rightarrow \mathrm{E} + \mathrm{H}_2$$

In addition to this process, thermal decomposition of the hydrides is also supposed to take place, but only if the oxygen supply to the atomizer is insufficient. Thermal decomposition is the dominant atomization process in the GF.

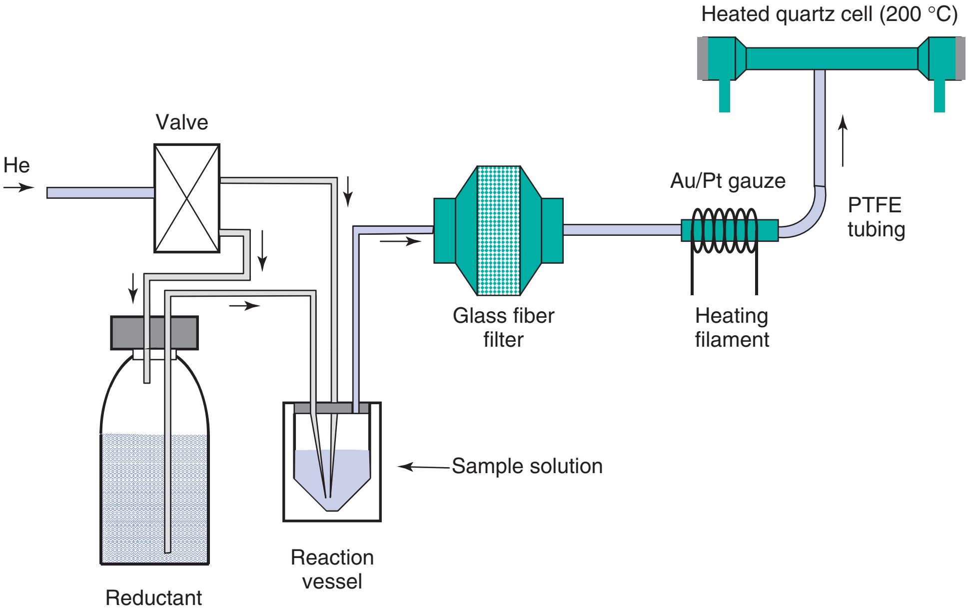

Figure 15.14 Scheme of a cold vapor generation system for mercury. (Redrawn from [16].)

15.3.2.2.7 **Cold Vapor Generation Technique** Mercury is the only metallic element that is liquid and sufficiently volatile at room temperature. These particular properties make this element uniquely suited for determination without an atomizer after reduction to the elemental state and transfer into the vapor phase and into the optical path of the absorption spectrometer [17]. As with hydride generation systems, the technique lends itself to both batch and flow-injection procedures which are becoming increasingly popular. A typical cold vapor generation system is depicted in Figure 15.14. For historical reasons, tin(II)chloride has been widely used as reducing reagent, but it is now being replaced by $NaBH_4$. Since the latter is a more powerful reducing reagent, particular precautions must be taken to avoid interferences that may have adverse effects on the preconcentration (amalgamation) trap which is normally used. Helium is preferred to purge elemental mercury from the sample solution. Either a chemical desiccant or a glass fiber filter is positioned between the reaction vessel and the amalgamation trap to prevent small water droplets from reaching the trap (which is more tolerant to water vapor). The material for the reaction vessels and all tubing must be selected with particular consideration to avoid permeation or adsorption of mercury. Quartz and fluorinated ethylene/propylene (FEP) are suitable materials showing only very little adsorption of mercury, while poly(tetrafluoroethylene) (PTFE) is said to be the most appropriate material for the transport of gaseous mercury.

Similar to hydride generation, the mercury vapor can be directly introduced into the absorption cell. However, because the vapor formation from the liquid phase is rather slow, requiring a period of typically 1–2 min, this would result in broad peaks of low intensity. Consequently, a trap is used to preconcentrate the generated Hg vapor and to improve the concentration detection limit for analysis in solution [16].

This is achieved by amalgamating mercury on a noble metal trap, from which it is subsequently thermally desorbed at 500–700 °C. In many instances, a gold–platinum gauze (90% Au, 10% Pt) is used for this purpose. It provides a high surface area, excellent thermal conductivity, ease of cleaning, and good physical stability. This results in excellent performance in terms of reproducibility and signal enhancement.

Since mercury is present already in the atomic state in the cold vapor technique, there is no need for an atomizer as such. The sample vapor is swept directly from the reduction cell or the amalgamation trap in the carrier gas stream to a 10-cm long T-shaped quartz tube that is moderately heated (to about 200 °C to prevent condensation of mercury). This quartz cell is located in the light path of a conventional AA spectrometer where the attenuation of a characteristic Hg line source is measured. Dedicated AA spectrometers (which, in this case, often have a continuum light source) may also be used with longer absorption cells (300 mm path length) to increase the sensitivity.

15.3.2.2.8 **Direct Introduction of Solid Samples** Both flame AAS and ET-AAS principally allow the direct introduction of solid samples. For flame AAS, cups may be used to introduce the solid sample, as suggested initially by Delves [18]. Alternatively, organic samples may be combusted and the vapors introduced directly into the flame. Although the direct introduction of solid powders into the GF had already been reported in the early 1980s [19], the analysis of sample slurries is preferable. Slurry sample introduction has been pioneered for flame AAS by Ebdon and Cave [20], who also demonstrated its applicability to GF-AAS. Solid sample introduction must, however, be carried out with particular attention. Since the amount of sample introduced is normally small – only a few milligrams is normally used – the sample homogeneity and the avoidance of potential sampling errors become important issues. For this reason, the use of larger furnaces, which may accept larger sample sizes, has been suggested. Calibration for solid sample analysis is generally difficult, since the nature and particle size of the solid affect analyte volatilization, transport, and, consequently, its response.

For the analysis of solid samples without prior digestion, the combination of cathodic sputtering with AAS has been proposed [21]. Jet-enhanced sputtering gives a high analyte number density, and the atom vapor cloud is introduced into the flame or ET atomizer. This approach is particularly feasible for the analysis of samples that are difficult to dissolve, such as refractory oxide-forming metals and alloys.

Laser ablation-AAS is also useful for insulating samples, where AA analysis is performed directly in the laser plume. Owing to the production of various particles in the measurement zone (solid particles, molecules, radicals) and the resulting background emission, appropriate techniques for the correction of spectral interferences must be used.

15.3.2.3 Optical Setup and Components of Atomic Absorption Instruments

Instruments for AAS can generally be divided into single- and double-beam designs. The sophistication and, consequently, the cost of the instruments span a very wide range.

The optical system of an AA spectrometer must provide a spectral resolution sufficient to separate the chosen analytical line from other lines that may interfere with it. Only in the case of some alkali metals, which have some few widely spaced resonance lines across the visible spectrum, may this be achieved by simple filter monochromators. For the determination of most elements, however, high-quality UV/vis monochromators are required that are capable of achieving a spectral bandwidth of the order of 0.1 nm. Such monochromators are nowadays incorporated in most commercial AA instruments. The optical components used (particularly, monochromators and detectors) are very similar to those used for emission spectroscopy and will be discussed in more detail later.

15.3.2.3.1 **Single-Beam Spectrophotometer** The typical design of a single-beam spectrophotometer is shown in Figure 15.15. It is constructed using an absolute minimum number of optical components with the evident advantage of high optical throughput and relatively low cost. The simplicity of this system is, however, at the price of limited signal stability, since any fluctuation in light source intensity will result in baseline variation.

15.3.2.3.2 **Double-Beam Spectrophotometer** The optical setup of a double-beam spectrophotometer is given in Figure 15.16. The beam from the light source is divided into two paths, one of which passes through the flame and the other is directed around the atomizer. These two light beams are subsequently recombined and modulated by a rotating (mirrored) chopper that alternately transmits the beams to the Czerny–Turner grating monochromator. The two signals are detected by a photomultiplier tube (PMT) and ratioed before further amplification and electronic signal processing. Double-beam spectrophotometers, being more complex and costly, offer the advantage of compensating any variations in light source intensity.

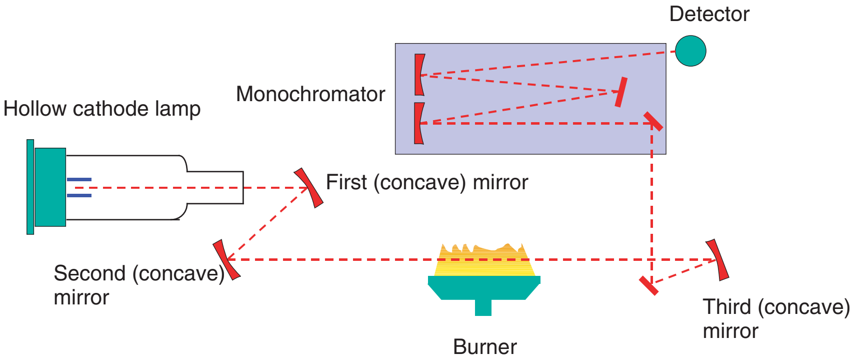

Figure 15.15 Optical system for a single-beam atomic absorption spectrophotometer.

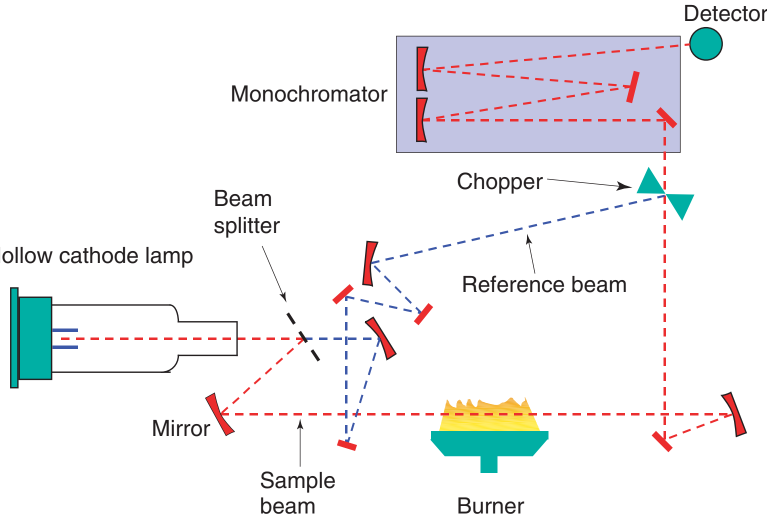

Figure 15.16 Optical system for a double-beam atomic absorption spectrophotometer.

However, radiant power loss through absorption and scattering effects in the flame is still not accounted for, since the reference beam bypasses the flame. Methods for the correction of these optical losses are discussed in the following section.

Detection is normally done with PMTs, or, for instruments that incorporate echelle-grating-based polychromators, with solid-state detectors consisting of a two-dimensional array of photodiodes.

15.3.3
Spectral Interferences

Two types of interference are encountered in atomic absorption spectroscopy: *Spectral interference* is the result of the absorption of an interfering species that either completely overlaps with the signal of interest or lies so close to this signal that it cannot be resolved by the monochromator. *Chemical interference* may be a consequence of the various chemical processes that occur during atomization and alter the absorption characteristics of the analyte.

Spectral interferences can, to a certain degree, be compensated or eliminated by suitable instrumental designs and analytical procedures.

15.3.3.1 Origin of Spectral Interference

As the emission lines of HCLs are very narrow, interference due to overlapping lines is rather unlikely. The separation between two spectral lines would have to be less than typically 0.01 nm for such an interference to occur. As an example, the vanadium absorption line at 308.211 nm interferes in the analysis of aluminum at

308.215 nm. A simple alternative is to carry out the measurement at a different (intense) aluminum absorption line, for example, at 309.270 nm.

Spectral interferences may also result from combustion products that exhibit broadband absorption or particulate matter, which causes scattering of the incident radiation. As both reduce the spectral radiance of the light source, they may erroneously lead to an overestimation of the absorbance and, consequently, the concentration. When the combustion or the particulate products arise from the fuel/oxidant mixture, they may be determined by measuring the absorbance while a blank is aspirated into the flame. The situation is more complicated if the absorption or scattering arises from a product associated with the sample or its matrix. For example, an elemental absorption line can be interfered by a molecular absorption line from reaction products of coexisting elements in the sample. In the case of Ba determination in the presence of Ca, the elemental absorption line at 553.6 nm can be overlapped by a broad $Ca(OH)^+$ absorption band in the range 548.0–558.0 nm. In many cases, such interference can be eliminated by replacing air by nitrous oxide as the oxidant. The resulting higher flame temperature leads to the decomposition of the $Ca(OH)^+$ and eliminates the absorption band.

In flame AA determination of elements such as Ti, Zr, and W, spectral interferences from the formation of refractory oxide particles with diameters greater than the wavelength of the light can increase the scattering. Interference due to scattering may also be observed when organic solvents are used. When these are combusted incompletely, carbonaceous particles may be generated and cause light scattering.

This interference is, however, not very frequently observed in flame AA, or they can easily be eliminated by the judicious choice and optimization of the analytical conditions. Alternatively, one may add the interfering substance (if this is known) in large excess to the sample. In that case, the interference due to the compound initially present in the sample will become insignificant in comparison to that of the compound added. Such a procedure is sometimes referred to as *spectral buffering*. While ET-AA was considered to be more susceptible than flame-AA to the interferences discussed above, this appears no longer true with the instrumental developments that have been realized over the past decades. Nowadays, GF-AA may be considered as being affected by interferences to a level not higher than observed with flame AA.

15.3.3.2 Methods for Correcting for Spectral Interferences

A number of methods have been developed for correcting spectral interference caused by matrix products. Perfect background correction can be achieved only when the background absorbance measurement corresponds exactly in space, time, and wavelength with the atomic absorbance measurement. Since this exact matching of all three parameters is impossible – at least with line source instruments – it is common to give priority to the equality in space and to make the difference in wavelength and/or time as small as possible. This is due to the fact that the background absorption can never be assumed to be completely constant over the considered (spectral or temporal) range.

In general, any type of background correction requires two measurements to be made, one of which is the measurement of the gross or total absorbance at the wavelength of the resonance line, A_{total}. Then, the background attenuation, $A_{\text{background}}$, is subtracted from the total absorbance to yield the absorbance of the analyte, A_{analyte}.

15.3.3.2.1 **Two-Line Background Correction**

The two-line correction method, which was proposed in the late 1970s [22], is based on measuring the absorption at a second, nonresonant line. This line should be close to the resonance line of the element that is measured but should not be absorbed by the analyte. If these conditions are met sufficiently well, it can be assumed that the attenuation at this second line is only due to the background absorption in the sample.

The reference line may, for example, be a neon or argon line from the gas in the HCL, or it may arise from an impurity in the hollow cathode material. Alternatively, another source of an element that is not present in the sample may be used for background measurement. The closer the reference line is to the analytical line, the better the background correction will be. In reality, this is not always easy to achieve. Particularly for short wavelengths of resonance absorption, the spectral distance of the two lines should not be more than 1 nm; otherwise, significant errors may arise from inadequate background correction since scattering is strongly dependent on the wavelength (and increases proportional to λ^{-4}).

15.3.3.2.2 **Continuum-Source Background Correction**

In a second, more widely used method for background correction, a deuterium lamp provides a source of continuous emission throughout the UV region. Deuterium lamps consist of an arc that is sustained in a deuterium atmosphere. They provide sufficient energy in the wavelength range between 190 and 330 nm, with an emission maximum near 250 nm. For longer wavelengths, a halogen lamp is used alternatively.

The radiations from the HCL and the deuterium lamp are directed alternately through a chopper to the (flame or GF) atomizer. The rotating chopper wheel allows the radiation of either source to pass alternately while the absorption is detected for one of the two beams (Figure 15.17). The absorbance of the deuterium lamp is then subtracted from that of the element-specific line source.

The continuous-source emission of the deuterium lamp is passed through a bandpass filter that has a transmission window of 0.2–1 nm. Since the half-width of an atomic absorption line is only about 2–5 pm, the attenuation of the comparatively wide spectral window of the continuous-emission source due to the specific absorption of the analyte will be negligible. It is thus possible to assume the attenuation of the continuous light source as being due only to the background absorption and scattering while the additional attenuation observed at the resonance wavelength is caused by element-specific absorption (Figure 15.18). In continuous-source background correction, it is assumed that the background is constant over the considered spectral range. If this is not the case, significant positive or negative correction errors may occur.

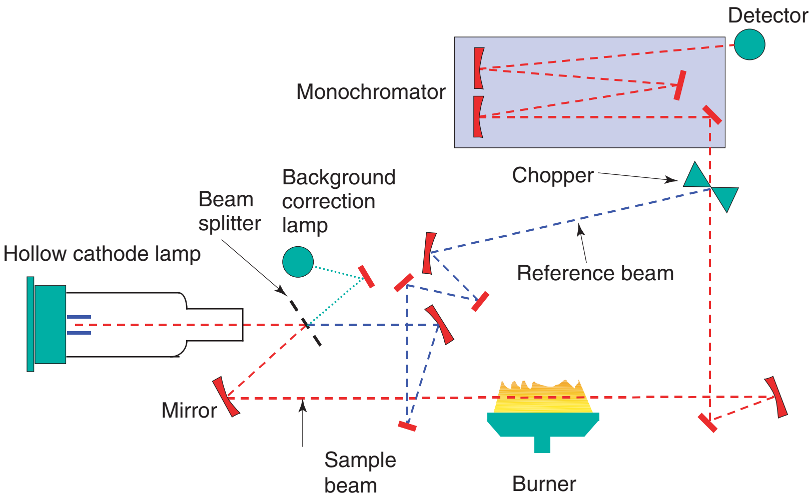

Figure 15.17 Schematic of a system used for continuous-source background correction. The chopper may be eliminated when each lamp is pulsed alternately.

Since the alteration between the two light sources is fast, continuum-source background correction can conveniently be used even with GF-AA instruments that produce fast transient signals. A few disadvantages have been reported for this type of background correction. These include the more complex (and thus more expensive) instrumental setup with two light sources, and the fact that, even if the two light sources are perfectly aligned, they will illuminate different sample volumes because of different light source geometries and also the differing intensity profiles across the beam.

However, continuum-source background correction is implemented in many commercial instruments and is particularly useful in combination with flame atomization or hydride generation.

15.3.3.2.3 **Zeeman Background Correction** In 1897, Zeeman observed a splitting of the electronic energy levels of a free atom that is introduced into a strong magnetic field (of 0.1–1 T). For each electronic transition, the Zeeman effect produces several absorption lines with a splitting in the order of 10 pm. The sum of the integrated absorbance of all lines equals the absorbance of the original line from which they derive. Different types of splitting exist, depending on the electronic state from which absorption occurs. In the simplest case (for singlet transitions), a single line is split into three components under the action of the magnetic field. The central (π) line is at the wavelength of the original line, while the other two (σ) lines are located symmetrically around this line. The absorbance of the π line is twice that of each σ line. With other transitions, the splitting pattern becomes more complex, which is often termed the *anomalous Zeeman effect* (in contrast to the "normal Zeeman effect" observed for the simpler systems). Zeeman patterns are observed in both absorption and emission.

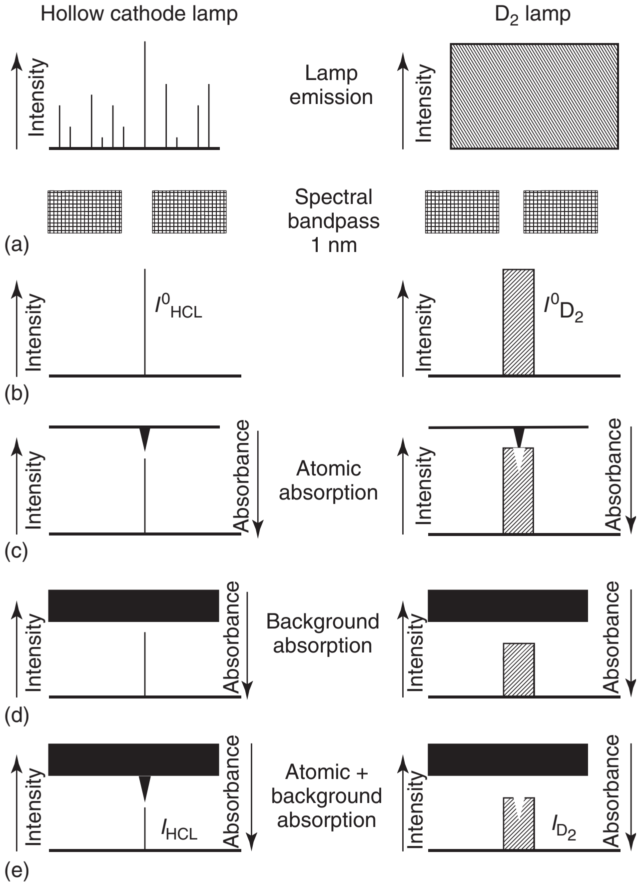

Figure 15.18 (a–e) Principle of background correction using a continuous source, for example, a deuterium lamp.

Use is made of the Zeeman effect for background correction, as the response of the two types of absorption peaks (π/σ) to polarized radiation is different: While the π peaks absorb only radiation that is polarized in a plane parallel to the external magnetic field, the σ peaks absorb only radiation that is polarized in a plane perpendicular to this field (Figure 15.19).

Generally the unshifted or only slightly shifted π components are used to measure the total absorbance of the analyte atoms and the background, while the shift of the σ components is used to measure the background absorbance. For background correction by the transverse Zeeman effect, a strong magnetic field is aligned perpendicular to the GF (Figure 15.19a). The element-specific absorption takes place only within the π component of the absorption line profile, while the σ components of the absorption line are shifted to different wavelengths λ_1 and λ_2. When a polarizer is inserted in the light path that rejects the π component, and the magnetic field is switched on and off at a sufficiently high frequency (e.g., at 50 Hz) by an alternating current, the gross absorbance and the background absorbance can be measured alternately. The net absorbance is obtained by subtracting the background absorbance from the gross absorbance. In this way, the background absorption is obtained at a single analyte wavelength λ_a, so that the background absorbance is measured correctly even for a structured background.

Alternatively, a permanent or DC magnet can be used in combination with a rotating polarizer. This allows alternate measurements with π- and σ-polarized radiation. The π-polarized radiation is absorbed by both the background and the element to be determined, providing the gross absorbance. In contrast, the σ-polarized radiation is absorbed by the background only, as these lines are shifted away from the resonance absorption wavelength λ_a. The net analyte absorbance again results from the difference of these two measurements (Figure 15.19b).

The longitudinal Zeeman effect for background correction employs a longitudinal magnetic field instead of transverse magnetic field. In this case (Figure 15.19c), the original atomic absorption line is split only into the two σ components which are circularly polarized. When the longitudinal magnetic field is modulated by application of an alternating current, then the gross absorbance is measured at zero field strength while the absorbance of the background is measured with the magnetic field. The advantage of the longitudinal Zeeman effect background

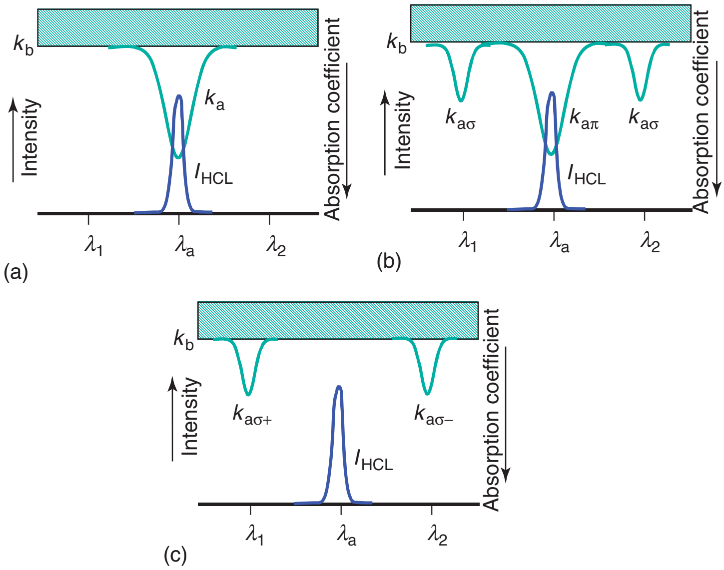

Figure 15.19 Principle of Zeeman background correction. The lower curve in each graph represents the emission of the hollow cathode lamp (I_{HCL}), while the upper line shows the absorption coefficient of the analyte (k_a) at wavelength in the presence of a background absorbance k_b. (a) Conventional AAS, no magnetic field applied; (b) in the presence of a transverse magnetic field; and (c) in the presence of a longitudinal magnetic field.

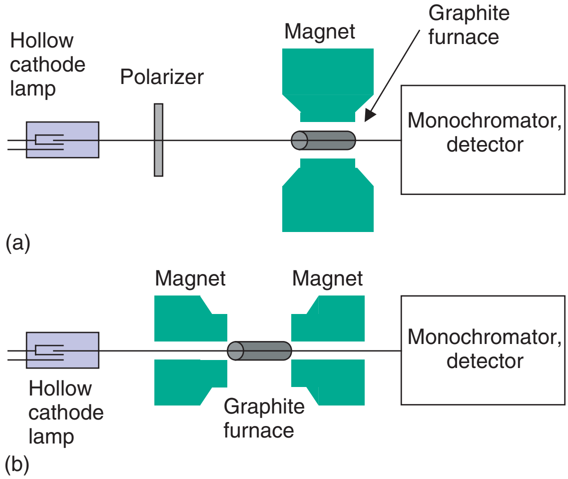

Figure 15.20 Schematic diagram of different Zeeman background correction systems for AAS: (a) Transverse magnetic field, that is, the magnetic field is perpendicular to the optical axis of the spectrometer. The rotating polarizer provides alternately p- and s-polarized radiation when the magnetic field is constant or transmits only p-polarized radiation if the magnetic field is modulated periodically by an AC current. (b) Instruments in which the longitudinal magnetic field is oriented parallel to the optical axis of the spectrometer do not require a polarizer.

correction is that no polarizer is required. For this reason, the full intensity of the HCL can be used in both measurement phases.

Principally, Zeeman background correction can be applied to either the source or the atomizer. When the magnetic field is located around the element-specific line source, its emission lines will be split into σ and π components. Depending on the polarizer orientation relative to the magnetic field, these will account for either only background absorption or the absorption of the analyte and background. For practical reasons, however, the arrangement is preferred where the GF is located in the magnetic field, since smaller magnets can be used. This is also the reason why Zeeman background correction is particularly popular with ET-AAS but hardly used with flame AAS, since the magnet would have to be large enough for the burner head to fit into its gap (Figure 15.20).

The use of the Zeeman effect for background correction in AAS was initially proposed in 1969 [23]. Six years later, the first commercial instruments became available [24]. Zeeman background correction is nowadays widely used in ET-AAS instruments. It is capable of reliably handling even highly nonspecific absorption. In particular, the more volatile elements Pb and Cd are preferably measured by ET-AAS with Zeeman background correction, since the relative volatility of the elements does not allow high temperatures to be used in the pyrolysis step to remove interferences.

Zeeman effect background correction is effective at any wavelength. There are, however, some disadvantages: A slight decrease in the sensitivity can be observed (about 20%), as well as a bending of the calibration curve (“rollover”).

15.3.3.2.4 **Pulsed-Lamp Background Correction**

A very simple method of background correction has been proposed by Smith and Hieftje [25] and is therefore known as the Smith–Hieftje method. It is based on the self-reversal behavior of the radiation emitted by HCLs when they are operated at high currents. This effect is seen when a large number of nonexcited atoms are brought into the vapor phase. These atoms absorb the characteristic radiation emitted by the excited species. At the same time, a significant broadening of the emission line is observed.

Altogether, this results in a broad emission line that has a minimum in intensity at its center, that is, exactly at the position of the atomic absorption line. Thus, at low lamp current, the sum of the specific and the nonspecific absorption is measured, while at high lamp currents effectively only the background emission is determined because of the intensity minimum at the wavelength of specific absorption and of the significantly broadened peak profile which is attenuated by the nonspecific absorption to the left and right of the characteristic absorption of the analyte. The difference between the two signals yields the background-corrected absorption of the analyte (Figure 15.21).

Background correction is thus achieved by modulating the lamp current to generate a longer pulse at low current (e.g., 9 ms at 5–10 mA), followed directly by a short pulse at high lamp current (e.g., 0.3 ms at 200–300 mA). As the atom cloud persists in the HCL for several milliseconds, a minimum pulse repetition time of typically 50 ms is required to allow the atom cloud to clear before the next measurement cycle is started.

Background correction by self-reversal is instrumentally very simple to implement and has consequently been used with flame and ET atomization and with hydride generation systems. It is particularly attractive since, like the Zeeman background correction, it does not require an additional radiation source. The efficiency of pulsed-lamp background correction depends on the degree of band broadening

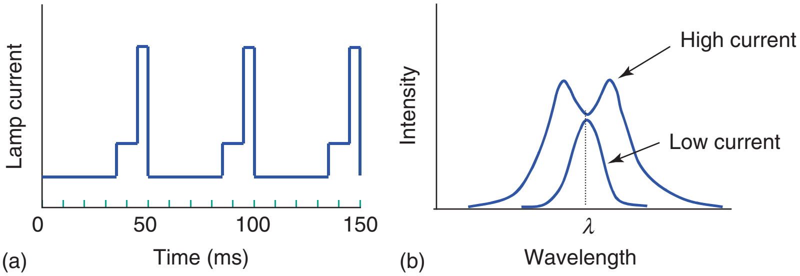

Figure 15.21 Background correction by source self-reversal. (a) Modulation of the lamp current that drives the hollow cathode lamp. (b) Resulting hollow cathode lamp emission line profiles generated at high and low current operation.

that can be achieved. This, however, differs from element to element and also varies strongly (increases) with the lamp current. At the same time, high lamp currents significantly reduce their lifetime. Thus, specially designed HCLs and lamp current modulation circuits must be used to achieve an acceptable compromise.

It is assumed that only the background absorption is measured at high lamp current (which is only a partially valid assumption); however, the broadening of the line profile is limited and self-reversal is not complete. Thus, radiation is still emitted at the center of the emission line and is absorbed by the analyte, and will subsequently be subtracted from the gross absorption of the analyte. This significantly reduces the sensitivity of the determination, with an average loss of sensitivity of about 45% being observed for the elements most commonly determined by AAS. Also, the efficiency of background correction becomes insufficient, particularly at high absorbance values ($A > 2$).

15.3.3.2.5 **Wavelength-Modulation Correction Methods** When a broadband, continuous emission source is used, background correction can easily be performed by measuring the background absorbance in the direct vicinity of the resonant absorption line. Where a constant spectral background absorption can be assumed, it is sufficient to measure the absorption at the position of the resonance line and at one point next to this wavelength. If the spectral background is sloping, two points on either side are required to interpolate the background at the position of the absorption line (cf. Figure 15.36 in Section 15.4.3.1). The analytical signal is then obtained as the difference of the gross absorption signal and the background absorption. It is evident that for a structured background this method would provide inadequate results, but as long as the wavelengths used as baseline points are close to the analytical line, the error is usually small. This method of background correction was first described by Snelleman in 1968 [26] and developed further by Zander *et al.* [27].

Its instrumental realization is achieved by a wavelength modulator, which is a vibrating mirror driven by an ac current and inserted in the light path between the atomizer and the monochromator. By the periodic movement of the wavelength modulator, a very narrow wavelength across the analytical resonance line is scanned, resulting in a modulated absorption signal as output. Phase-sensitive detection allows the discrimination of the background (DC) signal from the first harmonic AC component of the signal (due to specific absorption) and the calculation of the net absorption as the difference of the two signals.

Background correction by wavelength modulation is not widely used, but has already demonstrated to have considerable potential for simultaneous multielement AAS with continuum sources [10b]. Alternatively, high-resolution echelle gratings may be used that can detect both the elemental line and the background at the same time.

It becomes evident that there is no ideal method of background correction. Since each of the presented methods has its individual advantages and shortcomings, the choice of the most suitable technique depends on the instrumental design and particularly on the type of atomizer, as well as on the analyte and matrix.

15.3.4
Chemical Interferences

In addition to spectral interferences, chemical interferences are also significant in AA spectrometry. In many instances, however, they can be reduced by judicious optimization of the operating conditions. Chemical interferences are observed in AAS as a consequence of (i) the formation of compounds of low volatility, (ii) the influence on dissociation equilibria, and (iii) the ionization of the analytes.

15.3.4.1 Formation of Compounds of Low Volatility

This is perhaps the most common type of chemical interference. The presence of certain anions may cause refractory compounds to be formed with the analyte. As a consequence, its atomization is hindered and a decrease in response is observed. A well-known example is the suppression of the response of Ca with increasing concentrations of phosphate or sulfate. When the anion concentration in the flame is increased while keeping the calcium concentration constant, the absorbance decreases to about half its original value, which is attributed to the formation of hardly dissociated calcium phosphate or sulfate. At high anion concentrations, the analyte response again becomes independent of the anion concentration.

The co-occurrence of cations may also contribute to the formation of refractory compounds. The presence of aluminum has such an effect on the determination of magnesium. It is assumed that a refractory aluminum–magnesium oxide is formed, which reduces the sensitivity of the magnesium determination.

While an increase in atomizer temperatures (when possible) is an obvious way to reduce chemical interference, a second possibility is the use of matrix modifiers. An example of this is, for example, the addition of salts whose cations react preferentially with the interfering anion and thereby prevent their reaction with the analyte. The addition of Sr or La ions may, for instance, reduce the interference of phosphate in the analysis of calcium by forming a thermally stable compound with phosphate, with the effect that Ca will be released to form free atoms. An opposite approach is used when certain salts such as NH_4NO_3 are added to remove chloride salts by volatilization:

$$\mathrm{NaCl} + \mathrm{NH_4NO_3} \rightarrow \mathrm{NH_4Cl}\uparrow + \mathrm{NaNO_3}$$

In this case, NH_4Cl is removed during the ashing step and the residual $NaNO_3$ does not interfere during the atomization.

In a further approach, protective agents may be added to prevent the interfering substance from reacting with the analyte. Stable but volatile complexes or compounds are formed between the analyte and the protective agent. These protective agents are very often complexing agents, such as ethylenediaminetetraacetate (EDTA), ammonium pyrrolidone-dithiocarbamate (APDC), or 8-hydroxyquinoline.

15.3.4.2 Influence on Dissociation Equilibria

The influence of other elements present in the flame or GF on the dissociation equilibria of the analyte can be a significant cause of chemical interference. As the absorption requires that the analyte prevails in the atomic state, dissociation of its compounds must occur, following, for example, the equations

$$\mathrm{MO} \rightleftarrows \mathrm{M} + \mathrm{O}$$

$$\mathrm{M(OH)_2} \rightleftarrows \mathrm{M} + 2\mathrm{OH}$$

However, since the alkaline-earth metal oxides in particular are comparatively stable, molecular bands, arising from metal oxides or hydroxides, are frequently observed in the spectra of these elements. In contrast to this, the oxides of alkali metals are less stable, resulting in strong atomic lines.

A similar mechanism of interaction explains the increase in the response of vanadium in the presence of aluminum or titanium. This effect is observed more markedly in fuel-rich flames and depends critically on the concentration of oxygen-containing species (Ox), such as O and OH, in the flame. In the flame, the dissociation equilibria of the three metals

$$\mathrm{VOx} \rightleftarrows \mathrm{V} + \mathrm{Ox}$$

$$\mathrm{AlOx} \rightleftarrows \mathrm{Al} + \mathrm{Ox}$$

$$\mathrm{TiOx} \rightleftarrows \mathrm{Ti} + \mathrm{Ox}$$

coexist. The concentration of Ox is comparatively low in rich flames, so that the presence of Al or Ti in the flame shifts the dissociation equilibrium of the first equation to the right-hand side. The consequent increase in free metal concentration is accompanied by an increase in the absorption for vanadium. On the other hand, the concentration of Ox is high enough in lean combustion mixtures so that no significant shift is observed in the presence of Al or Ti. Thus, no particular shift of the dissociation equilibrium for vanadium is observed in flames with high oxidant concentration.

15.3.4.3 **Ionization in Flames**

Ionization in flames is a third mechanism that is largely responsible for chemical interference. In combustion mixtures that include air as oxidant, flame temperatures are usually not high enough to achieve a significant degree of ionization of the analyte. At the higher flame temperatures achievable with oxygen or nitrous oxide as oxidant, ionization is no longer negligible. Ionization can be treated as an equilibrium process according to the equation

$$\mathrm{A} \rightleftarrows \mathrm{A}^+ + \mathrm{e}^-$$

If we accept the treatment of ionization as an equilibrium process, it is evident that the degree of ionization will be affected by the presence of other ionizable species in the flame. As this interfering species B is also ionized to a certain degree in the flame, the degree of ionization of the analyte atom will be decreased, because of the law of mass action, by the electrons formed from B. The charge balance now requires consideration of the ionization of both species:

$$A \rightleftarrows A^+ + e^- \quad \text{with} \quad K_A = \frac{[A^+][e^-]}{[A]},$$

$$B \rightleftarrows B^+ + e^- \quad \text{with} \quad K_B = \frac{[B^+][e^-]}{[B]},$$

$$\text{and} \quad [e] = [A^+] + [B^+]$$

It can thus be concluded that, in the presence of an easily ionizable element B in the flame, the degree of ionization of the analyte A is reduced and thereby its absorption is increased. In all cases, it has to be borne in mind that at higher flame temperatures ionization is increased, which may counterbalance the increase in atomization. Thus, a hotter flame does not necessarily result in an improved sensitivity of AAS measurements.

The addition of an easily ionizable element at relatively high concentration as an *ionization buffer* allows the reduction of the effect of shifts in ionization equilibria. The ionization buffer (often an alkali metal salt such as potassium chloride) creates a high concentration of electrons in the flame, resulting in the suppression of the ionization of the analyte.

A generally useful and common approach to eliminate chemical interference in AAS is to use standard addition for quantitation. This will be described in more detail in the following section.

15.3.5
Data Treatment

15.3.5.1 Quantitative Analysis

Because of its principle and instrumental realization, AAS is a technique for quantitative analysis and is practically unsuitable for qualitative analysis. Quantitative response is governed by the law of Lambert and Beer, that is, the absorption A is proportional to the optical path length l, the absorption coefficient k at the observed wavelength, and the concentration c of the species (Equation 15.33).

In contrast to many other spectroscopic techniques, atomic absorption, however, often possesses only a very limited linear range. This deviation from linearity is the result of a combination of factors, including the finite width of the absorbing and the exciting lines, secondary lines within the pass band of the spectrometer, and stray light that reaches the detector. Also, spatial inhomogeneities of the excitation radiation and the atom cloud in the atomizer have been held responsible for these nonlinearities. The operating software of most spectrometers nowadays provides tools for curve-fitting nonlinear curves to optimize the useful dynamic range.

15.3.5.1.1 Quantitation by External Calibration The most common and straightforward method of calibration in AAS is the use of an external calibration with suitable standard solutions. It is based on the assumption that the standard solution matches the composition of the sample sufficiently well. This is an assumption that must always be examined with care, since, for example, samples of different viscosity may be aspirated at different rates in flame AAS, resulting in different sensitivities. Flame AAS normally produces step-function-like response curves as a result of the continuous introduction of sample or standard for a certain period (until a stable signal is reached). The height of this signal is evaluated. In ET-AAS, the transient signal is produced by subjecting the sample to a defined thermal cycle which produces a comparatively narrow signal of some few seconds (cf. Figure 15.12).

15.3.5.1.2 **Quantitation by the Standard Addition Technique** Matrix interferences result from the bulk physical properties of the sample, for example, viscosity, surface tension, and density. As these factors commonly affect nebulization efficiency, they will lead to a different response of standards and the sample, particularly with flame atomization. The most common way to overcome such matrix interferences is to employ the method of standard additions. This method, in fact, creates a calibration curve in the matrix by adding incremental sample amounts of a concentrated standard solution to the sample. As only small volumes of standard solutions are to be added, the additions do not alter the bulk properties of the sample significantly, and the matrix remains essentially the same. Since the technique is based on linear extrapolation, particular care has to be taken to ensure that one operates in the linear range of the calibration curve; otherwise significant errors may result. Also, proper background correction is essential. It should be emphasized that the standard addition method is only able to compensate for proportional systematic errors. Constant systematic errors can neither be uncovered nor corrected with this technique.

15.3.6
Hyphenated Techniques

The determination of the different forms (e.g., compounds or complexes) in which an element occurs (often referred to as the *speciation of an element* and *speciation analysis*, respectively) is in most cases performed by hyphenated techniques [28]. These are the combination of a high-performance separation technique such as gas or liquid chromatography (LC) or electrophoresis and an element- or compound-specific detector [29]. While the former provides the separation of the different elemental species present in the sample, the latter brings about selective and sensitive detection. In the case of AAS, only the hyphenation with gas or liquid chromatography has gained importance. The combination of AAS and electrophoresis has never proven successful, obviously due to the incompatibility of the extremely low flow rates of electrophoretic separations with the aspiration volumes of flame atomizers and the difficulties of interfacing the two techniques.

15.3.6.1 Gas Chromatography-Atomic Absorption Spectrometry

The combination of flame AAS and gas chromatography represents probably the first example of a hyphenated technique used for speciation analysis [30]. It is particularly favorable since the analytes arrive at the detector already in the gaseous state. Interfacing is straightforward, and in most cases a simple heated transfer line is used to direct the analytes to the atomizer. However, despite its apparent simplicity, the design of such a transfer line is critical since peak broadening due to dead volumes, cold spots, or lack of chemical inertness have to be avoided. In many cases, heated stainless steel capillaries or deactivated quartz capillaries inside a stainless steel tube of the shortest possible length are used, or the chromatographic column is directly interfaced to the premixing chamber of a flame atomizer. As the analytes are in the gaseous state, the transfer efficiency is in this case close to 100%. Capillary columns, as nowadays predominantly used in gas chromatography, are easier to interface than packed columns. They offer improved resolution, but the chromatographic peak width becomes much smaller, which poses higher demands on the speed of the data acquisition system. Also, capillary columns have a significantly smaller sample capacity than packed columns, which may result in less favorable relative detection limits.

The hyphenation of flame AAS and GC is easy to achieve, but it does not provide adequate sensitivity for most problems of environmental relevance. GF-AAS would provide trace-level sensitivity, but GF-AAS instruments are not designed for continuous operation. This prevents their use as online detectors for continuous chromatographic separation.

Hyphenated GC-AAS became successful by the introduction of quartz furnace-AAS(QF-AAS) with an electrothermally heated quartz T-tube furnace atomizer by Van Loon and Radziuk [31]. The system is designed for continuous operation, since the quartz tube can stand temperatures of up to about 1000 °C for an extended period, and combines the advantages of high sensitivity and low operation costs. QF-AAS appears to be an ideal detector for speciation analysis as long as the analytes are introduced in the vapor form. In most instances, the quartz furnace is operated at temperatures of 700–950 °C (Figure 15.22). For metal hydrides, atomization in the graphite furnace takes place according to the equations given already. Generally, the addition of O_2 and H_2 is required, which leads to the formation of $H^\bullet$ and $OH^\bullet$ radicals that initiate the atomization reaction.

For organometallic species, the decomposition of a molecule takes place via a series of electrophilic and nucleophilic reactions of the alkylated (or otherwise organically substituted) molecule with the hydroxyl and hydrogen radicals. For the example of an alkylated triorganotin compound, atomization can be described by the following reaction sequence:

$$R_3SnR' + HO^\bullet + H^\bullet \rightarrow R_3SnH + R'OH$$

$$R_3SnH + 2H^\bullet \rightarrow R_2SnH_2 + RH$$

$$R_2SnH_2 + 4H^\bullet \rightarrow Sn^0 + 2RH + 2H_2$$

The lifetime of the quartz tube atomizer is variable and can range up to several months. New tubes initially perform poorly and must be conditioned by several runs before achieving optimum sensitivity. Contamination of the quartz surface may result in significant signal suppression. As the electrothermal quartz furnace

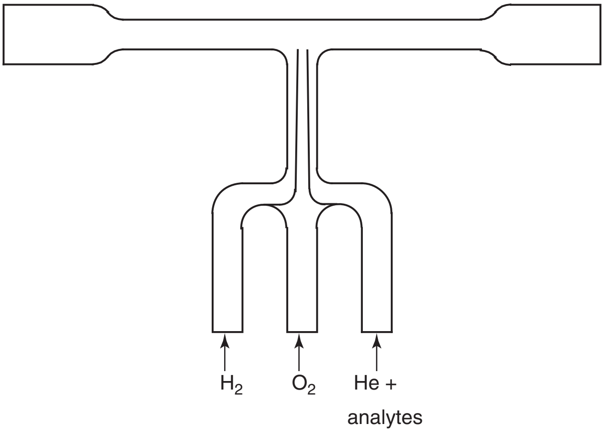

Figure 15.22 Design of a quartz T-tube atomizer (typical dimensions: length 20 cm, internal diameter 0.8 cm).

atomizer is comparatively robust and offers high overall efficiency and sensitivity at relatively low cost, it has found widespread application for the analysis of organometallic species of the elements Sn, Se, As, Sb, Pb, and Hg.

A simple, yet very efficient alternative to hyphenated GC-AAS is the use of a cryotrapping AAS system [32]. This technique combines an online aqueous derivatization of the ionic analytes, a preconcentration by cryofocussing, and chromatographic separation with detection by AAS. Details of the instrumental setup are presented in Figure 15.23. The analytes are derivatized *in situ* by $NaBH_4$ or $NaBEt_4$ and are purged to the cryotrap. Removal of the water vapor by a suitable dryer is required to avoid blocking of the trap at cryogenic temperatures. The cryotrap is a stainless steel U-tube (typically 300–450 mm long, 6 mm i.d.) that

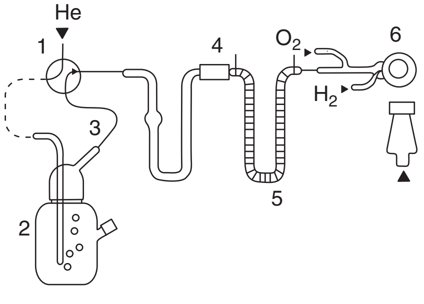

Figure 15.23 Schematic diagram of a hydride generation cryotrap-AAS HG/CT/AAS system for speciation analysis of organometallic compounds: (1) four-way valve; (2) hydride generator; (3) heated transfer lines; (4) moisture trap; (5) separation trap in liquid nitrogen; and (6) quartz furnace with inlets for hydrogen and oxygen gas. (Reproduced with permission from [33].)

is packed with a suitable adsorbent and immersed in liquid nitrogen and serves to trap the derivatized analytes. After removal of the liquid nitrogen, the trap eventually warms up or is actively heated by a Nichrome wire and the analytes are evaporated according to their volatility and transported with the carrier gas stream to the quartz furnace atomizer. Although the short packed column is only capable of achieving limited resolution (less than 1500 theoretical plates), this is often sufficient for speciation analysis of low molecular weight organametallic analytes such as organotin or organolead compounds. Because of the preconcentration effect that can be achieved by cryotrapping, detection limits in the low nanogram per liter range can be achieved for the analysis of samples of 100–500 ml volume.

15.3.6.2 **Liquid Chromatography-Atomic Absorption Spectrometry**

With its different modes of operation, high-performance liquid chromatography (HPLC) is the most suitable technique for the separation of less volatile, polar, or even ionic analytes. Depending on the column dimensions, HPLC separation provides a continuous eluent flow of typically few microliters up to 1 ml min^{-1} which can easily be introduced into the nebulizer of a flame AAS system. The interface design generally is a critical factor, since it may induce additional peak broadening which reduces both sensitivity and resolution [32b].

The column effluent is directly introduced into the mixing chamber of the flame atomizer. Since the transport efficiency of flame AAS is usually only 5–10%, this explains why the sensitivity of this type of coupling is limited, particularly in comparison with GC-AAS.

In part, this disadvantage can be overcome by using postcolumn derivatization for HPLC-flame AAS. The most versatile reaction is hydride generation, but aqueous phase ethylation has also been employed to form volatile derivatives *in situ* after liquid chromatographic separation. These are purged from the liquid phase in a nitrogen gas stream and carried into the flame atomizer. The advantage is that not only the analytes are converted to volatile forms and the transport efficiency is significantly increased thereby, but also a separation from the matrix is achieved. However, the application of this technique is obviously limited to hydride-forming elements or elements that can be alkylated by alkylborate reagents. Detection limits comparable to those of GF-AAS can be reached, for example, less than 1 ng absolute for Pb.

GF-AAS generally offers highly sensitive detection for small sample amounts; however, the sequential nature of the drying, ashing, and atomization steps makes it difficult to interface it to a continuous separation technique such as HPLC. As a simple solution, the autosampler of a commercial GF-AAS instrument may be modified in such a way that the effluent is passed through a PTFE flow-through cell from which the autosampler periodically injects a small aliquot (10–50 μl) into the furnace. Of course, this does not provide a continuous online signal, but the resulting discrete signals will allow one to reconstruct the chromatographic trace of the analytes.

Despite the better sensitivity of GF-AAS the coupling with HPLC has only found limited use, mainly due to the difficulties of coupling a continuous flow separation technique with the discrete nature of GF-AAS. Improvements may be expected by coupling HPLC and GF-AAS after online hydride generation as outlined for HPLC-flame AAS, but this technique has not been thoroughly investigated.

Although there may be niche applications where hyphenated techniques based on atomic absorption spectrometric detection are still used and provide valuable results, the use of these techniques is gradually declining. This is both due to the fact that the few existing instrumental platforms lack the continuing support of instrument manufacturers, and also that many of the applications where GC- or HPLC-AAS couplings were successful in the 1980s and 1990s have been taken over by GC and LC being coupled to either plasma emission spectroscopy or inductively coupled plasma mass spectrometry(ICP-MS), where ultratrace level sensitivity is required. These systems exist commercially, and allow integrated control of the separation and detection parameters, offering thus the convenience of use and excellent performance which as lacking in former AAS-based hyphenated systems.

15.3.6.3 **Conclusion and Future Directions**

Both flame AAS and GF-AAS can now be considered mature techniques. Flame AAS is very common, particularly in routine laboratories, as it is easy to use, inexpensive, and reliable. The technique is well understood, very little affected by interference, and provides satisfactory limits of detection. Where these are not sufficient, the use of GF-AAS is recommended. AAS is certainly the most widely employed method for elemental analysis in the routine laboratory.

Since AAS is classically a single-element technique, much effort has been spent in overcoming this disadvantage by the development of multielement spectrometers. While this is relatively easy to realize for the excitation sources by using multielement lamps which allow the analysis of up to six elements at least in a sequential mode, this is more difficult to achieve from the detection point of view, where a high-performance spectrometer must be used, consisting of an echelle spectrometer and a multichannel solid-state detector (Figure 15.24).

Such instruments have been available on the market, but have not been particularly successful. This is mainly due to the fact that these were GF instruments, which had to be operated under compromised conditions for the ashing and atomization steps for the simultaneously determined elements, but also due to the competition from emission spectrometers which by nature are more suitable for simultaneous multielement analysis.

Great interest has arisen in the direct introduction of solids in AAS. This technique has been introduced for GF-AAS [34] but has not yet been widely accepted because of the obvious difficulties in quantitative analysis. The introduction of solid suspensions (slurries) into the graphite furnace seems to be a further promising approach that has found better acceptance among users. After introduction of the sample slurry into the GF, it is subjected to a modified temperature program in the presence of modifiers as they are common for GF analysis of solutions. Thus, sample throughput is largely increased as there is no need for digestion of the sample material. It should be emphasized again that, since only very small sample amounts are analyzed, a problem arises for quantitative analysis from the

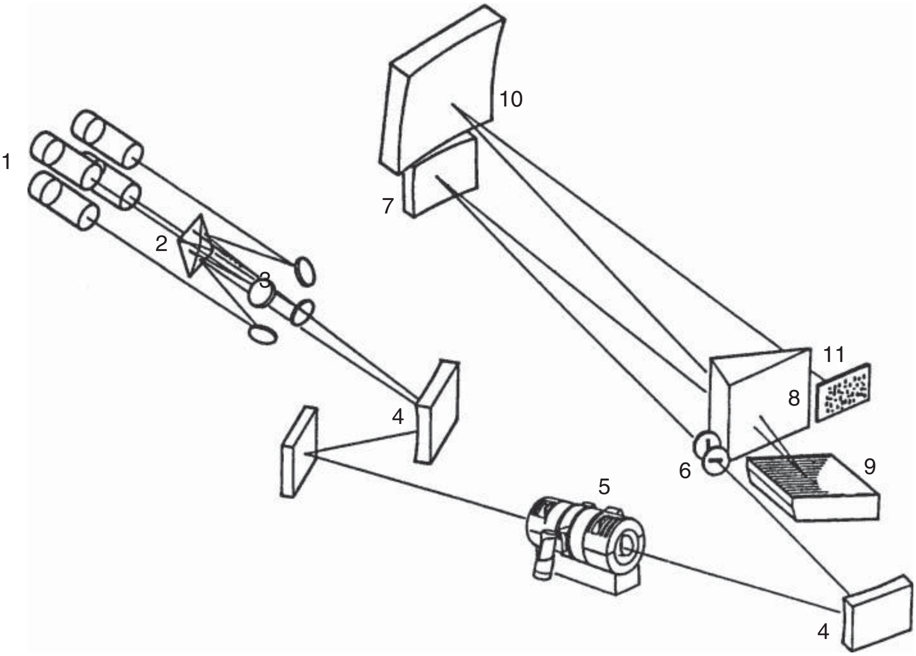

Figure 15.24 Scheme of a simultaneous graphite furnace AA spectrometer (SimAA 6100, Perkin Elmer Corp., Waltham, MA). (1) Manifold with four hollow cathode lamps; (2,3) beam unifier; (4) collimator mirror; (5) graphite furnace with Zeeman magnet; (6) entrance slit; (7) collimator mirror; (8) echelle prism; (9) echelle grating; (10) focusing detector mirror; and (11) CCD detector.

inhomogeneity of the original sample. However, as there is no need for sample digestion or dissolution, the advantage of this technique is still convincing and it has consequently been applied to a great variety of sample types such as biological materials, polymers, as well as industrial and environmental samples.

15.4
Atomic Emission Spectrometry (AES)

15.4.1
Introduction

AES has considerable potential for qualitative and quantitative analysis because all elements can, upon excitation, emit radiation at characteristic wavelengths. Unfortunately, the conditions for excitation are so variable that until now no single source exists to excite all elements [35–39]. Historically, AES dates back to the pioneering work of Bunsen and Kirchhoff in the mid-1800s. However, it was not before 1920 that flame emission spectrometry was established as a quantitative method. Arc and spark discharges were developed for solid samples by 1940 and continue to be valuable tools for today's metallurgical analysis. With the increasing interest in plasma sources in the 1960s, a new era began with the ICP commercially introduced in the mid-1970s. Because of its commercial success and widespread use in research and routine analysis, the discussion in many sections will be devoted mostly to ICP-AES.

15.4.2
Instrumentation

15.4.2.1 Atomization Devices

An atomic emission source serves a twofold purpose: the atomization of analytes with high efficiency, and the supply of energy to excite all analytes of interest. In addition, it would be desirable for an ''ideal source'' to control the excitation energy in order to optimize the analytical conditions (see Figure 15.25). Atomization and excitation should occur in an inert atmosphere to minimize formation of interfering species and reduce background emission. The source should tolerate the introduction of solid, liquid, or gaseous samples, while organic solvents can be accepted as well as aqueous samples with a high salt or particulate load. Further, the ideal source should provide reproducible atomization and excitation conditions to facilitate a high precision for multielement analysis at reasonable cost and maintenance. Naturally, none of the atomizers described below fulfills all the criteria.

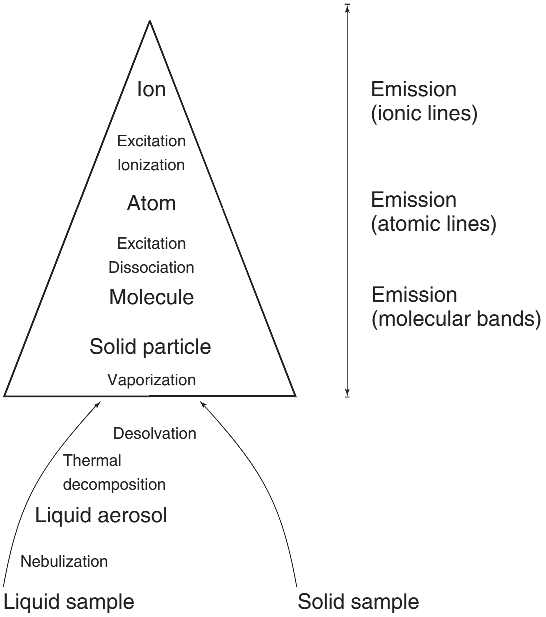

Figure 15.25 Main steps leading from a sample to atomic emission.

15.4.2.1.1 **Flame Atomizer** Historically, flames have been employed as the atomization source for various elements. Flames, as they are typically used for spectrochemical analysis, are characterized through a chemical reaction between a fuel, such as hydrogen, acetylene, or propane, and an oxidant, such as oxygen, air, or nitrous oxide. The burners are usually operated with premixed flames, in which fuel and oxidant are mixed before the combustion region. The sample is nebulized into the high-temperature region of the flame, where desolvation, volatilization, atomization, and excitation take place. The hotter flames, for example, acetylene–oxygen flames, generally produce a higher background emission, more ionization, and line-rich spectra of analytes and interferents. The background emission is typically reduced in cooler flames, for example, flames with hydrogen as fuel. However, problems can arise from nonvolatile matrix components. The fraction of excited atoms in a flame atomizer is rather low: less than 0.1% of all atoms are excited at temperatures around 2000 K and emit in the visible region between 500 and 700 nm; for elements emitting in the UV region, this fraction is even lower.

For multielement analysis, the significantly more energetic plasma sources are therefore by far superior to flames in most regards. Today, flames are used only for the determination of alkali metals, as these can be excited at low temperatures and give simple spectra free of interferences. The determination of these metals is especially important for the analysis of biological fluids, so that emission in acetylene–air flames is still routinely used in highly automated and simplified systems based on single or multiple interference filters and photomultiplier detection (see Figure 15.26). The systems often also include automatic addition of an internal standard and dilution [40].

15.4.2.1.2 **Inductively Coupled Plasma** Early types of plasmas that are the predecessors of the current ICP appeared in the early 1960s and were first reported independently by Fassel and Greenfield around 1964/1965 [41]. The ICP nowadays is probably the most common source in AES and has been widely used in routine elemental analysis since its commercial introduction in 1974. An ICP is formed

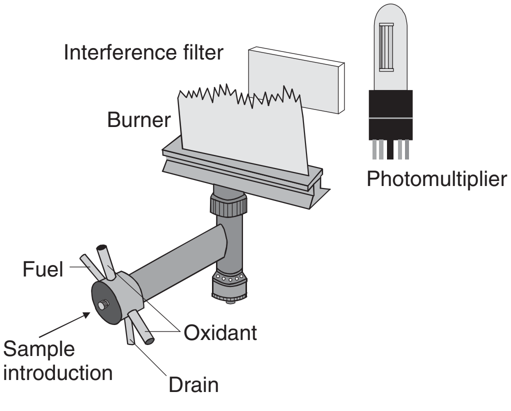

Figure 15.26 Schematic diagram of a simple flame photometer.

within the confines of three concentric quartz tubes, called a *torch*, through which a total flow of argon between 5 and 20 l min^{-1} is established. Figure 15.27 shows a schematic diagram of a torch with the outer tube, the intermediate tube, and the inner or carrier gas tube. A two- or three-turn water-cooled induction coil around the torch produces an intense oscillating magnetic field around the coil via an RF generator. These RF generators, producing 0.5–2 kW, are oscillators generating an alternating current at the desired frequency, typically at 27.12 or 40.68 MHz. In free-running oscillators, the frequency is fixed by the impedance of the components in the circuit itself. Alternatively, a piezoelectric crystal can stabilize the frequency through feedback. A higher frequency of oscillation leads to a lower excitation temperature and a lower electron density, which can result in a lower background emission and improved detection limit. With electrons and ions from a Tesla discharge, the ionization of the argon begins and a plasma is initiated in the toroidal region around the induction coil. The plasma is then sustained by inductive heating. The power delivered to the plasma will determine its temperature, with higher power resulting in higher excitation temperatures. Typical gas-kinetic temperatures in the ICP are about 5000–6000 K, while the excitation temperature is between 6500 and 7000 K and the electron temperature about 10 000 K. Because of the high temperatures inside the coil (about 5000 K), a vortex gas flow of about 10 l min^{-1} between the outer and the intermediate tube thermally isolates the outer tube and centers the plasma in a radial direction. The toroidal plasma core extends a few millimeters above the tube and emits a continuum which originates from ion–electron recombination and bremsstrahlung. On top of this continuum emission, atomic argon lines are superimposed. Between 10 and 30 mm above the core, the continuum background is reduced by several orders of magnitude so that the plasma is optically thin. The background in this second zone consists primarily of argon lines, OH bands, and some molecular bands. Because of the

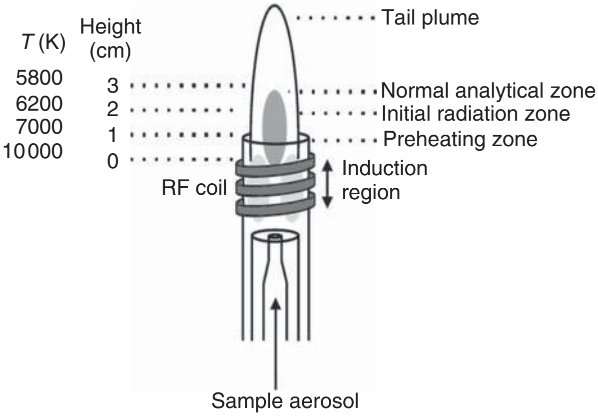

Figure 15.27 Schematic diagram of an inductively coupled plasma (ICP) assembly showing the three concentric tubes composing the torch, the RF coil, the different plasma regions, and the temperature as a function of height above the load coil. (Reprinted from Hou and Jones [42b], with permission.)

large temperature gradient, emission in this zone is observed from elements with a wide range of excitation energies. Above this zone, a flame tail is observed with temperatures similar to those of ordinary combustion flames, which can be used for easily excitable elements. Traditionally, the emission is viewed laterally through the plasma (side-on) and has the advantage of providing immediate venting of exhaust gases and heat to an overhead extraction system. Newer instruments also allow axial viewing, which permits a longer path length in the central channel and improved detection limits, by a factor of 4–10. For a long time, axial viewing had a poor reputation with regard to matrix effects, as the atomization zone within the coil and the recombination zone at the top of the plasma are also probed by the observation system. Recently, systems have appeared on the market that displace the cooler tail flame of the plasma away from the optical path either by a sampling cone or a directed gas flow. In this way, most of the original problems mentioned above can be solved.

The sample enters the plasma as an aerosol through the inner tube at a flow rate of about $1\,\mathrm{l\,min^{-1}}$ and has a residence time of about 2 ms in the plasma at temperatures between 4000 and 8000 K, after which it enters the observation zone above the core. The carrier flow shapes the plasma into the characteristic toroidal form. The intermediate gas flow is optional and can be employed, for example, for the analysis of samples in organic solvents to prevent soot deposition on the torch. The nebulizer or carrier gas flow affects not only the residence time in the plasma and the plasma conditions but also the size of the aerosols produced. With conventional nebulizers, the aerosol size increases at a low nebulizer gas flow, reducing the transport efficiency and decreasing the emission from all lines. However, lower flow rates also increase the residence time and the excitation temperature, enhancing the emission of ionic lines. For atomic lines, the excitation is improved by the increased residence time. On the other hand, the ionization rate is increased, resulting in a net decrease of atomic line emission.

The temperatures of an ICP are significantly higher than those in any combustion flame, and the atomization occurs in an inert gas atmosphere, which tends to enhance the lifetime of the free atoms by preventing oxide formation. As the temperature across the plasma is fairly uniform, self-absorption and self-reversal are not observed, thus permitting a considerable dynamic range (five orders of magnitude). Normally, the background intensities are rather low compared to other sources, which results in good detection limits in the parts-per-billion range.

15.4.2.1.3 **Direct Current Plasma** The direct current plasma (DCP) is an electrical discharge between two graphite anodes and a tungsten cathode, which are arranged in such a way that a tangentially flowing argon stream from the two anodes forms an inverted V-shaped plasma (see Figure 15.28). The cathode is located above the central apex into which the sample aerosol is directed. The plasma jet is built up by bringing the cathode and anodes into contact, resulting in ionization of the argon and development of a current (about 13–15 A). Although excitation temperatures of 6000 K can be reached, the sample volatilization is often not complete because of the relatively short residence times in the plasma. Spectra from a DCP generally have

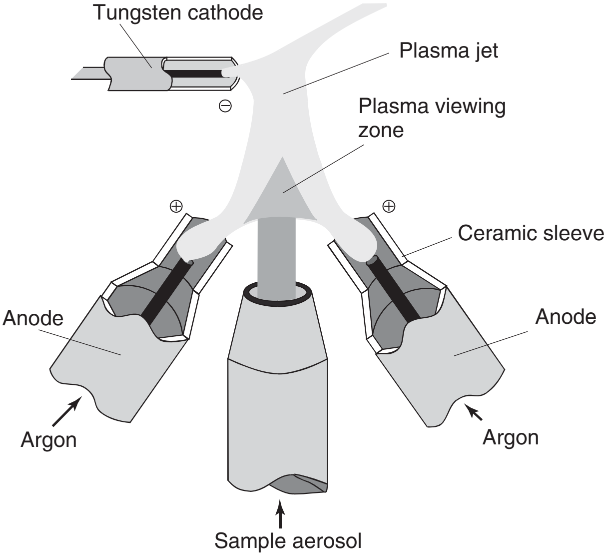

Figure 15.28 Schematic diagram of a direct current plasma (DCP).

fewer lines than those from an ICP and the lines are largely from atomic species. Problems arise from the small triangular region in which an optimal signal-to-background ratio can be achieved. The main advantage is the good stability and the ability to tolerate organic solvents as well as aqueous solutions and solutions with high solid contents. In addition, the power requirement is only 700 W and the argon consumption is, compared to the ICP, moderate, at around 7 l min^{-1}.

15.4.2.1.4 **Microwave Plasmas** Microwave plasmas can be differentiated into microwave-induced plasmas (MIPs) and capacitively coupled microwave plasmas (CMPs). In the case of MIPs, the plasma is usually generated in a flat, cylindrically shaped Beenakker-type cavity resonator (Figure 15.29) which is connected to a magnetron by coaxial or cavity waveguides. The power consumption is between 50 and 200 W at 2.45 GHz. A dielectric (quartz) capillary of 1–2 mm inner diameter is located at the center of the cavity in an axial direction. The plasma is formed within the capillary and ignited by a Tesla coil or an electrical spark. The sample is introduced into the capillary at a flow rate of 0.05–1 l min^{-1} with a carrier gas such as helium, nitrogen, or argon. The MIP is characterized by a high excitation temperature (4000–7000 K depending upon the carrier gas), which favors the atomic emission of nonmetals, but a low gas temperature (about 1000 K). Thus, there is little kinetic energy for dissociation of thermally stable compounds or high solvent loads, and the atomization efficiency is not much better than that of common flames. MIPs have been extensively used for detection of nonmetals in species separated by gas chromatography or supercritical fluid chromatography, as well as for the speciation analysis of organometallic compounds [43].

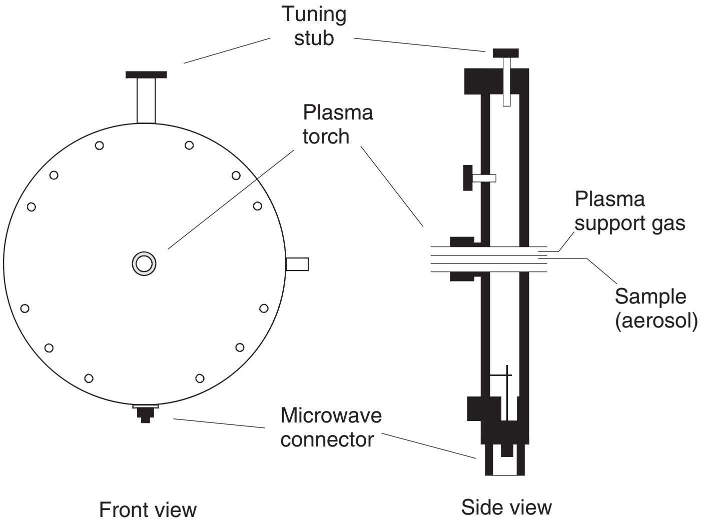

Figure 15.29 Schematic diagram of a Beenakker resonant cavity for microwave induced plasmas.

CMPs are operated at higher powers (0.5–3 kW) than MIPs, while the same frequency is used. A waveguide system transfers the energy into a plasma tube, where the plasma is ignited via a spark discharge. While excitation temperatures between 4900 and 8200 K, similar to MIPs, are achieved, gas temperatures between 4500 and 5700 K can be reached as a result of the higher power, so that CMPs are better suited for direct solution analysis.

15.4.2.1.5 **Arc and Spark Plasmas** Arc and spark discharges have been the workhorses for qualitative and quantitative emission spectrometry since the 1920s. Electrical discharges, classified into arcs and sparks, allow one to remove material from a sample surface and to excite it at the same time. Depending on the experimental conditions, the material is vaporized, eroded, or sputtered, usually in an argon atmosphere, for concurrent or subsequent excitation. The sample must be conductive, either naturally or through the addition of a conductive material such as powdered copper or graphite. Arcs are formed between a pair of metal or graphite electrodes a few millimeters apart. The DC arc, the most commonly used type, is ignited by a low-current spark and then sustained by thermal ionization. The kinetic temperature, typically between 4000 and 7000 K, depends upon the resistance between the electrodes and thus is a function of the atomization of material from the sample and the electrodes. Samples are generally introduced into the arc by evaporation from a cup-shaped electrode. Alternatively, liquid samples can be deposited on a graphite electrode and evaporated to dryness. The emission spectra contain mainly atomic lines and are interfered by those from the formation of CN radicals from the electrodes, even in an inert gas atmosphere. Because of the different rates of volatilization and excitation, the spectra of different species are time dependent, and long integration times are needed to record all species under study. On the other hand, selective volatilization can be used advantageously to enhance the signal-to-background ratio. The low-temperature outer regions of the arc contain high densities of ground-state species and are therefore prone to self-absorption and self-reversal. With the DC arc, about 70–80 elements can be excited; the analysis is mainly qualitative or semiquantitative because of the moderate precision of the arc.

Owing to their good precision (relative standard deviation (RSD) of the order of 1%), high-voltage spark source emission spectrometry is still popular for analysis of metallic samples down to concentrations of 1 ppm. For light elements, spark source AES easily outperforms X-ray fluorescence spectrometry. The high-voltage discharge is an intermittent discharge and lasts typically a few microseconds at a repetition rate of 100–1000 Hz. The sparking includes two phases. In the first phase, a low-energy discharge is produced by a primary circuit applying a potential difference of more than10 kV for a few microseconds across the electrodes to ionize the argon and create a conducting plasma. In the second phase, the main circuit of the spark generator discharges with an energy of 100–400 W at a moderate voltage of 300–500 V. In this phase, the sample is melted and evaporated at the impact point of the spark, while the different species are excited in the first phase in which excitation temperatures above 20 000 K can be reached for a short time. While in early spark systems the current waveform of the discharge was determined by the circuit resistance, inductance, and capacitance, today's systems allow excellent control of the waveform to improve detection limits and precision. Ionic spectra are more pronounced in a high-voltage spark source than in an arc. With a spark, electrode material is randomly sampled by many successive discharges on the surface, resulting in spatial averaging. To overcome changes in the surface, the integration is usually postponed for a prespark time of 1–2 min. Metallic samples for spark excitation are most often machined into the proper geometry to serve as electrodes.

15.4.2.1.6 **Laser Plasmas** Laser ablation (LA) AES is employed in two major fields of applications: bulk analysis with a spatial resolution between 100 and 1000 μm, and local microanalysis with a spatial resolution of 5–50 μm [42]. In the case of AES with the laser plasma, the technique is often denoted as laser-induced breakdown spectroscopy (LIBS) or laser-induced plasma spectroscopy (LIPS). For LIPS, an intense pulsed laser beam (typically a Nd:YAG or excimer laser) is focused on the sample of interest, resulting in evaporation, atomization, and partial ionization of the sample in an expanding plasma cloud. After a delay of some hundred nanoseconds to discriminate from the background, the elemental composition of the sample can be determined via the spectrally and temporally resolved detection of the characteristic atomic and ionic emissions. Because of the minimal sample preparation, the low cost for a single measurement, and the potential for extensive automation, LIPS is an attractive approach to environmental screening and monitoring and can be used to process solid, liquid, and gaseous samples. In addition, remote sensing is also possible either directly over a distance of some meters, or with fiber optics over a distance of 10–30 m. A microanalytical approach, either under atmospheric pressure or with Ar as buffer gas, has a considerable advantage compared to other beam techniques due to the higher sampling rate achievable with the laser. Quantitative determinations are often hampered by the lack of suitable matrix-matched standards or reference materials as well as by elemental fractionation.

15.4.2.1.7 **Reduced-Pressure Discharges** In addition to its widespread use as a light source for AAS, the hollow cathode discharge can also be used for AES. The sample is positioned in the hollow cathode and volatilized thermally and by cathode sputtering. The analyte vapor has a long residence time in the negative glow region of the plasma and is very efficiently excited, while the signal-to-background is very good because of the low electron densities. The time-consuming evacuation and gas-filling operation does not allow a fast throughput of samples, which makes the approach more suitable for solid samples, especially refractory materials.

Glow discharges with planar electrodes were introduced by Grimm in 1968 [44]. In this case, the glow discharge is confined to the sample, operating as cathode. The distance between the cathode and the anode block is below the mean free path of electrons so that the sample is volatilized by cathodic sputtering. Owing to the absence of thermal evaporation and separate atomization and excitation, matrix effects are low. Glow discharges are suitable for depth-profiling solid samples in the ppm range. Recently, glow-discharge emission spectrometry experienced a further impetus by the development of RF sources (see Figure 15.30), which allows direct analysis of nonconducting samples.

15.4.2.2 **Optical Setup and Detection**

In AES, the number of detectable elements is related to the wavelength coverage of the collimating and dispersive optical system. Alkali metal elements are usually observed above 500 nm, while elements such as Cl, Br, N, or As are detected in

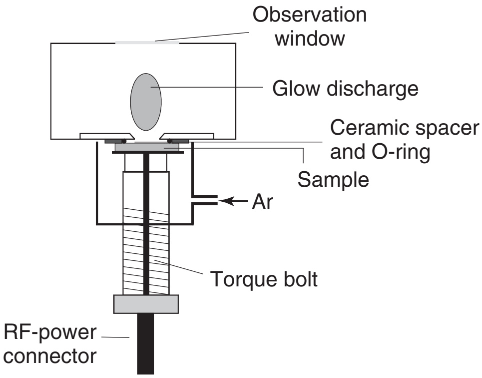

Figure 15.30 Schematic diagram of a discharge cell for RF glow-discharge atomic emission spectroscopy.

the vacuum ultraviolet (VUV) region between 130 and 190 nm. In addition, the selectivity is related to the spectral resolution of the system, which minimizes spectral interference from elements with line-rich spectra and the overall signal-to-background ratio. However, the high spectral resolution is accompanied by reduced light throughput, which can degrade the detection limits.

There are more than 50 000 documented spectral lines in ICP-AES, which makes a high-resolution spectrometer mandatory for analysis, especially when matrix effects have to be considered. The most versatile detection systems are characterized by large spectral coverage (120–770 nm) and high spectral resolution. The best spectral resolution achieved for the Ba(II) indicator line (see below) at 230.424 nm is currently below 5 pm. For high spectral resolution, all systems have to compensate for thermal and mechanical drifts by periodic spectral recalibration.

Design goals for an atomic emission spectrometer are (i) low spectral bandpass ($\lambda/\Delta\lambda > 40\,000$) and low stray light level, (ii) simultaneous measurement of the background and analyte line intensity, (iii) a detector with noise characteristics that are not the limiting noise sources, (iv) precise intensity reading <1% RSD at concentration levels 500 times the detection limit of the analyte under study, and (v) large dynamic range (6 orders of magnitude) of the detection system to record the emission intensity of major, minor, and trace constituents simultaneously.

15.4.2.2.1 **Sequential Instruments** Sequential systems are often based on a classical grating monochromator in a Czerny–Turner or comparable configuration with a holographic grating with 2400 to 3600 lines per millimeter. Scanning is performed by rotating the grating with a stepper motor, so that the different wavelengths are sequentially focused on the exit slit of the monochromator. PMTs are usually employed as detectors, though some instruments use dedicated photomultipliers for the UV and vis regions. In comparison with conventional linear-scanning monochromators, slew–scan monochromators provide significant savings in analysis time and sample consumption. Slew–scan systems can be programmed to scan slowly over or to stop momentarily at a wavelength region of interest, while the instrument moves rapidly between such regions.

To a certain extent, the linear dispersion and resolution can be improved by a finer ruled grating and a larger focal length. However, high resolution is more easily achieved with an echelle monochromator which utilizes diffraction orders greater than 80. The echelle grating provides high dispersion and a constant blaze at all wavelengths. The spectral coverage is much lower, so that a low-dispersion grating or a prism is needed as the order sorter or cross disperser (see Figure 15.31). Ambiguities in order overlap can be solved with a separate predispersion system, which also improves the overall optical throughput by removing the entrance slit height restrictions [45]. This results in a bandpass of the order of 0.007 nm at 200 nm with an accessible spectral range of 165–900 nm.

15.4.2.2.2 **Multichannel Instruments** In general, two types of multichannel instruments can be identified: polychromator instruments with several independent

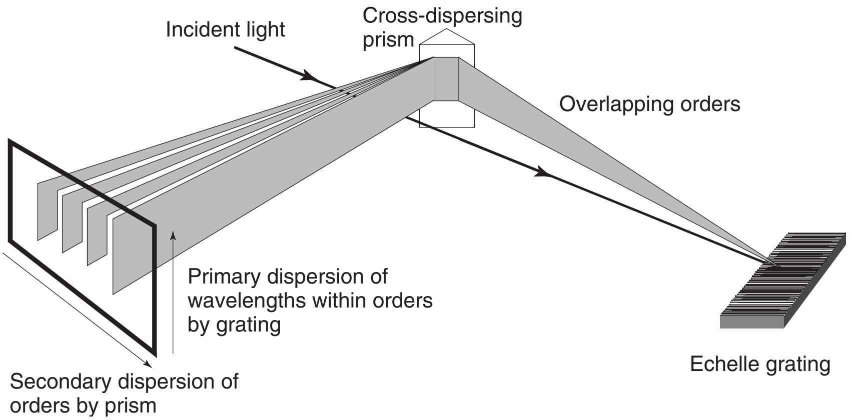

Figure 15.31 Principle of an echelle spectrograph.

detectors such as photomultipliers or small linear CCD arrays, and echelle spectrographs with solid-state array detectors such as CCDs or CIDs (charge-injection devices). Polychromators, such as the Rowland spectrometer in Figure 15.32, are based on a concave grating, which does both imaging and dispersion. This reduces the cost of optical components in the instrument, reduces alignment time, and also minimizes reflective and refractive losses. The spectral lines appear as astigmatically extended images of the entrance slit in a curved focal area. The entrance slit, the grating surface, and several exit slits with photomultipliers are arranged along the circumference of the Rowland circle. The circle diameter equals the radius of curvature of the grating. With holographic gratings with nonequidistant curved grooves, a nearly flat focal plane can be achieved for a defined spectral range. Then, an arrangement of small linear CCDs tangential to the circumference of the Rowland circle becomes possible, as employed in recent commercial systems. By moving the entrance slit tangentially to the Rowland circle, emission signals can be scanned and the background recorded. The dispersed light from the exit slits is directed with small mirrors to the corresponding photomultipliers (compare Figure 15.32), whose signals are processed by individual analog integrators. This allows very fast readout of the detectors, while the dynamic range and sensitivity for each line can be adjusted individually. Up to 60 elements can be determined simultaneously (with a 1-m Paschen–Runge spectrometer equipped with a 20-μm slit and a sampling time of 1 min), which makes polychromators the standard instrumentation for arc and spark analyzers.

In cases where no a priori information about the elemental composition is available, a more flexible approach is needed to cope with numerous emission lines and a potentially variable background. Echelle spectrographs (see Figure 15.31), based on an echelle grating and an order sorter, for example, a prism or second grating, disperse the spectrum in two dimensions in the focal plane [45]. With solid-state array detectors, a large spectral range can be addressed simultaneously with superior spectral resolution. Although CIDs have a poorer signal-to-noise

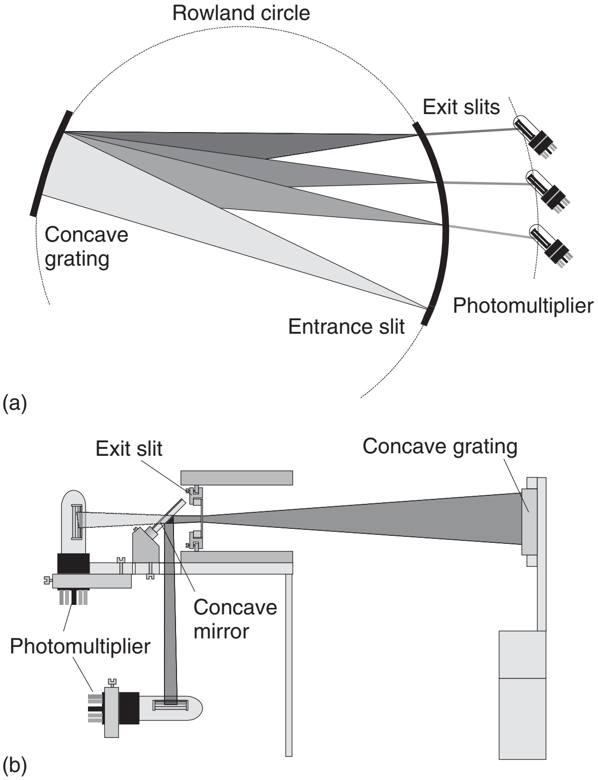

Figure 15.32 Schematic diagram of a polychromator based on a Paschen–Runge mount and photomultiplier detection. (a) General optical setup. (b) Side view and arrangement of the photomultipliers.

ratio compared to CCDs, their intermediate, that is, during an exposure, readout capability provides an improved dynamic range ($>10^5$).

Simultaneous detection permits in this way an increased sample throughput and a significant reduction in source flicker noise. Disadvantages of the two-dimensional dispersion are the reduced optical throughput and the fact that certain element combinations can be measured only in sequential groups because of different plasma conditions needed for their optimum determination. In addition, the dynamic range of the ICP-AES system itself (10^5–10^6) is larger than the dynamic range of today's CCDs (about 10^4), so that multiple exposures with different exposure times are needed for determination of trace, minor, and major components. This can also complicate the use of an internal standard if the elements under study are present in very different concentrations.

15.4.2.3 **Instrumentation for Solid Sample Introduction**

Although most samples are commonly presented as liquids for AES, direct solid sample analysis has the advantage that no major pretreatment or dissolution steps are required [46]. This minimizes dilution errors or contamination from reagents, and reduces the reagent and manpower cost per sample. In addition, improved detection limits may be obtained if microsamples or microanalyses are possible without any further dilution. However, the analyst has to ensure that the solid material sampled is representative of the bulk material. ICP-AES has generally a remarkable tolerance for total dissolved solids compared to ICP-MS or flame AAS so that, depending on the overall matrix, between 2 and 25% suspended solids can be coped with. Therefore, most of the solid sample introduction devices described below are dedicated for ICP-AES.

15.4.2.3.1 **Direct Insertion** The sample, ground into a powder, dried, and weighed, can be deposited on a probe made of graphite, tantalum, or tungsten and directly introduced into the plasma. An ICP torch can be modified, for example, by replacing the inner tube with a quartz tube which also guides the sample probe. The insertion process can be carried out in one or several defined steps by automatic positioning devices. Positioning the probe at successively closer positions to the plasma enables sample pretreatment and atomization steps, analogous to drying, ashing, and atomization in a graphite furnace. The signal is recorded as time-dependent intensity due to the differential volatilization of the sample. A typical precision of 7–15% is achieved because of the sample heterogeneity, irreproducible vaporization and sample insertion, or reactions of the sample with the probe material.

15.4.2.3.2 **Slurry Nebulization** Conventional pneumatic nebulizers are prone to serious losses and blockage if solids in the form of slurries are introduced. Usually, Babington-type nebulizers are employed, where the sample solution is pumped along a V-shaped groove and nebulized via a gas stream centered in this groove. Slurry nebulization is very suitable for small particles (particle diameter $<6\,\mu m$) and narrow size distributions. In this case, simple aqueous solutions can be used for calibration. The plasma conditions for slurries can differ considerably from solutions, and a separate optimization is needed. Apart from difficulties in the reproducible preparation of slurries, the inherent problem is the effect of particle size on evaporation and excitation. Slurry nebulization is especially interesting for fast monitoring studies, for example, geochemical and geological screening, or in the food industry [47].

15.4.2.3.3 **Electrothermal Vaporization** ET vaporization, analogous to the approach utilized in AAS, can be performed by resistive heating of sample devices such as boats, ribbons, rods, or tubes from graphite or a refractory element [48].

Usually, the vaporizer, exemplarily illustrated in Figure 15.33, can be sequenced through several heating stages, so that the solvent and matrix components can be temporally separated from each other and do not disturb the plasma conditions. The dry, highly dispersed aerosol produced under these conditions is swept into the plasma by an appropriate carrier gas stream. Because of the highly efficient sample vaporization and transport efficiency (30–80% compared to the typical 2% efficiency of a conventional cross-flow nebulizer), detection limits for aqueous

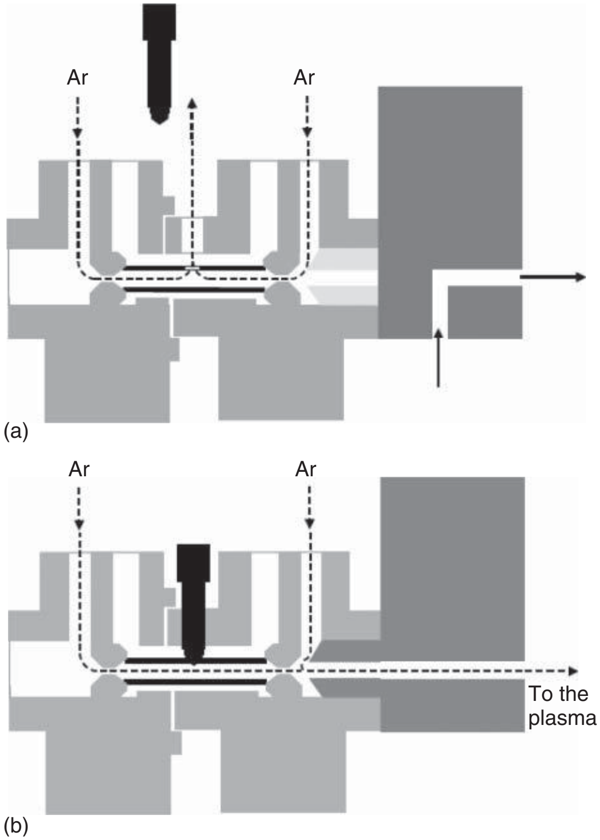

Figure 15.33 Layout of the modified graphite furnace for ETV operation during (a) the sample drying and ashing and (b) analyte vaporization. (Reprinted from Todolí and Mermet [48b] with permission.)

solutions are generally improved by a factor of 10–100. For solid samples, the maximum load is limited to 0.5 mg, with which absolute detection limits in the nanogram to picogram range can be achieved.

15.4.2.3.4 **Arc and Spark Ablation** Arc and spark ablation systems for sample introduction are similar to the respective atomization sources described above [49]. The DC arc equipped with metal or graphite electrodes is the most widely used form of the arc. Spark sources, as depicted in Figure 15.34, are frequently used for conducting samples because of their instantaneous high temperature whereas the arc temperature will increase during a measurement cycle, which can lead to fractionation effects.

15.4.2.3.5 **Laser Ablation** LA in combination with the ICP atomizer has become a powerful and flexible technique for solid sample introduction [49]. LA-AES

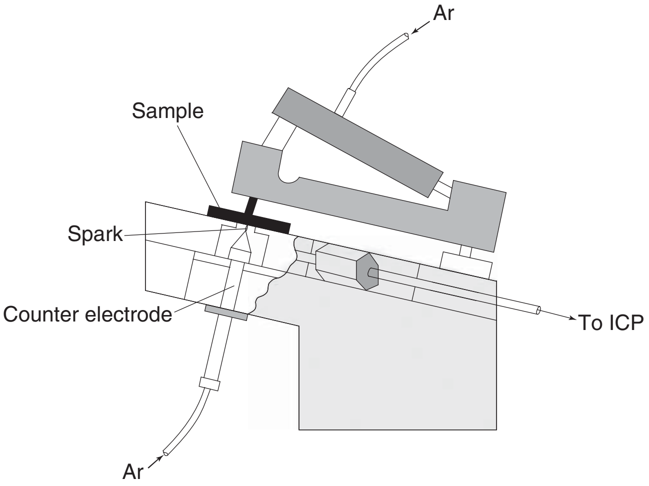

Figure 15.34 Spark chamber for solid sample introduction.

has found its niche primarily as a bulk sampling technique for the analysis of bulk solid materials with a large focal spot (500–1000 μm). It offers comparable detection capability to spark ablation/emission but is not dependent on the sample being conductive. The experimental setup, revealed in Figure 15.35, consists, in its simplest form, of a pulsed laser (excimer or Nd:YAG) with a defined pulse energy, some focusing optics, and a sample cell with a continuous Ar flow connected to the ICP torch with a simple plastic tube of 1–5 m length. For microanalysis, considerable efforts have been described in the literature to provide a homogeneous beam profile and suitable focusing optics for focal spots below 10 μm. Because of the superior sensitivity of ICP-MS, microanalysis with ICP-AES is usually limited to minor and main components. Calibration is typically based on solid reference standards, if possible with a suitable internal standard. Problems can arise from fractionation: that is, not all elements exhibit similar ablation and transport characteristics. The fractionation is related to the key parameters of a LA system, that is, laser wavelength, irradiance, and pulse width, and possibly transport phenomena or subsequent processes in the atomizer itself, and, of course, also depends on the sample itself. LA can be also used favorably in combination with other excitation sources such as microwave plasmas. The experimental setup is similar to that of LA-ICP-AES systems.

15.4.3
Matrix Effects and Interferences

In the early phase of ICP use, this technique was claimed to be free of matrix interference. Although the ICP was superior to earlier employed excitation sources and was less prone to interference than, for example, arc and sparks, matrix interference and spectral interference can still be observed.

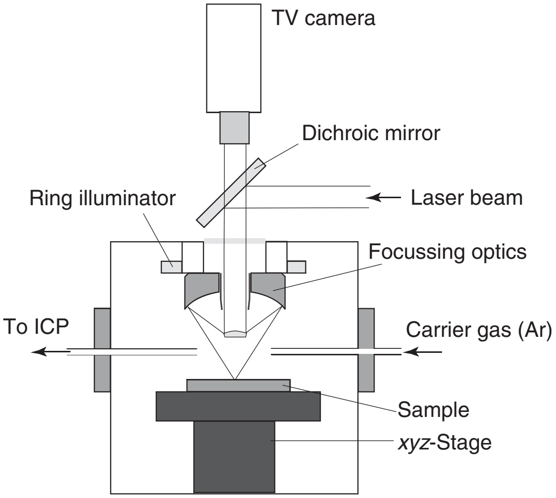

Figure 15.35 Laser ablation setup for solid sample introduction.

15.4.3.1 **Spectral Interferences**

Spectral interferences have been well studied and are probably best understood in AES. The usual remedy to alleviate a spectral interference is to either increase the spectral resolution of the spectrometer (which often is not possible with a given type of instrument) or to select an alternative emission line. Three types of spectral interference can be discriminated: (i) direct wavelength coincidence with another emission line, (ii) partial overlap of the line under study with an interfering line in close proximity, and (iii) a linear or nonlinear increase or decrease in background continuum (see Figure 15.36).

Interferences of types (i) and (ii) can occur not only from another element in the matrix but also from an argon line or molecular species such as OH or N_2. An example of a type (i) interference is the Zn(I) line at 213.856 nm overlapping with the Ni(I) line at 213.858 nm. As type (ii) can be eliminated only by improved spectral resolution, mathematical algorithms are used on a routine basis to solve this type. If the interference can be identified and quantified, then interelement correction factors can be inferred in a simple manner. First, a calibration for the analyte is constructed in the usual way, then different concentrations of the interfering element are studied, and the apparent analyte concentration is calculated at the emission line(s) of interest.

Type (iii) is easily solved by registering the background on either side of the line and modeling the background by an appropriate mathematical function. Provided that no fine structure is present, this approach should prove satisfactory. In general, the background emission decreases with wavelength, so most useful analytical lines are found in the UV region.

The selection of noninterfered lines is more critical for polychromator systems due to the limited number of channels. The major requirement is that the line is not spectrally interfered and provides sufficient sensitivity. However, for the

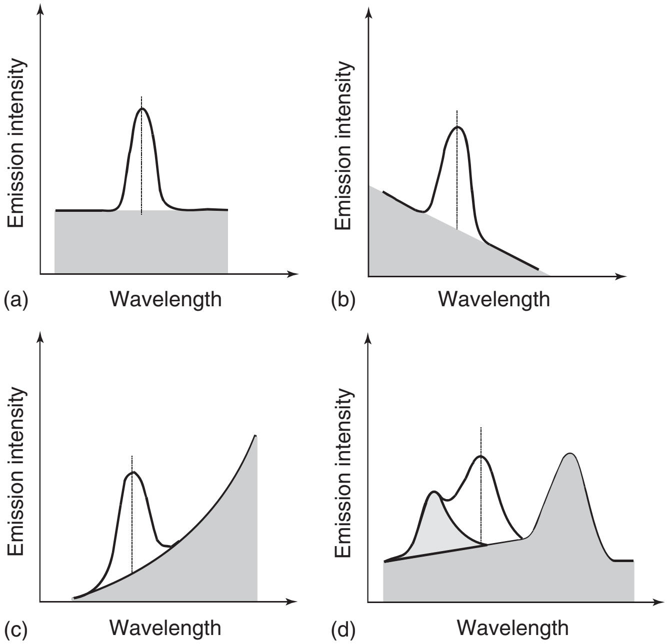

Figure 15.36 Typical spectral interferences and spectral background. (a) Flat background. (b) Sloped linear background. (c) Nonlinear background. (d) Structured background.

determination of minor and major components, less sensitive lines must also be included to allow for a better dynamic range.

15.4.3.2 Matrix Effects and Chemical Interferences

Matrix effects include nebulization interference, transfer and desolvation interference, chemical or ionization interference, and atomization and volatilization interference. Although the primary indication is a change in the emission intensity, it is often difficult to determine the origin of the interference.

As the spray chamber, through which samples are most commonly introduced into the ICP, can significantly affect the aerosol size distribution solely by its design, the trend is to use a direct-injection nebulizer (DIN). Matrix constituents, such as salts, organic compounds, or solvents altering the viscosity, surface tension, or solution density, can considerably change the quantity of the sample nebulized as a function of time. Interference by desolvation is due to the differences in volatility between the matrix and the analyte and is accompanied by a change in the analyte concentration in the aerosol during desolvation. Memory effects may be related to large tubing lengths or vessel surfaces used in the nebulization or desolvation system.

Mineral acids are widely used for sample preparation and solution storage and are therefore common matrices in AES. Depending on the nature and concentration of the acid, the atomic emission in ICP can be influenced. At low concentrations ($<1\%$ v/v), an increase in the analyte signal is observed, whereas higher acid concentrations lead to a decrease in net signal intensity. Possible explanations for this observation are a decrease in the sample uptake rate as a result of increased viscosity, a modified vapor pressure in the spray chamber, a change in the aerosol size distribution or transport efficiency, or a change in the ICP atomization and excitation conditions. Regarding the nature of the acid, it has been found that sulfuric and phosphoric acids result in an increased aerosol size due to the increased viscosity of the solution, while nitric, perchloric, and hydrochloric acids affect the excitation conditions in the plasma itself. Another well-known effect produced by acids is their influence on the duration of the nebulization period required to gain a steady-state signal.

Clogging of the injector tube by carbon or salt deposits is observed after prolonged spraying of organic samples, such as oils or organic solvents, or samples with a high salt content. Organic solvents, nebulized pneumatically, lead to a smaller aerosol size because of lower surface tension and viscosity. Hence, the solvent and analyte input in the plasma is increased and a signal enhancement may be observed. However, in some cases the solvent load may be too high, thus affecting the plasma stability and decreasing the excitation temperature and the electron density. Because of the high gas temperature of the ICP, long residence times, and inert gas atmosphere, chemical interference from the formation of thermally stable compounds or radicals is rarely observed for ICP sources, with low-power ICPs being the only exception. However, this interference is common in atomization sources with low gas temperatures, for example, the DCP, MIP, or flame.

Easily ionizable elements, such as alkali and alkaline-earth metal elements, can alter the emission intensity and may cause an enhancement or a depression. This problem is more serious with DCPs, MIPs, and CMPs, while less important with ICPs. Several mechanisms have been suggested to explain these changes, for example, lateral diffusion, changes in thermal conductivity, an altered volatilization rate, ambipolar diffusion or shifts in the ionization equilibrium, and the collisional processes.

15.4.4
Quantitative and Qualitative Analysis

Today, AES always makes use of relative quantitation, that is, unknown samples are quantitatively analyzed after calibration with samples of known composition. The most common approach to calibration is internal standardization. The underlying assumption, introduced by Gerlach in 1925, is that the ratio of the analyte mass to the mass of the internal standard, matching the analyte in its chemical properties, emission wavelength, energy of the line, and ionization potential, is constant, despite any fluctuations in the system. Internal standards thus compensate for instrumental fluctuations and improve the accuracy and precision of the determination.

Because many elements have several strong emission lines, AES can be regarded as a multivariate technique *per se*. Traditionally, for quantitative analysis in AES, a single strong spectral line is chosen, based upon the criteria of line sensitivity and freedom of spectral interferences. Many univariate attempts have been made to compensate spectral interferences by standard addition, matrix matching, or interelement correction factors. However, all univariate methods suffer from serious limitations in a complex and line-rich matrix.

On the other hand, atomic emission spectra are inherently well suited for multivariate analysis because of the fact that the intensity data can be easily recorded at multiple wavelengths. The only prerequisite is that the calibration set encompasses all likely constituents encountered in the real sample matrix. Calibration data are therefore acquired by a suitable experimental design. Not surprisingly, many of the present analytical schemes are based on multivariate calibration techniques such as multiple linear regression (MLR), principal components regression (PCR), and partial least-squares (PLS) regression, which have emerged as attractive alternatives.

Generally, AES systems are calibrated with multielement standard samples. In the case of sparks, arcs, glow discharges, and LA, solid samples are required, which are rarely available in large enough numbers to provide a satisfactory calibration. Hence, in solid sample analysis, secondary standards are usually prepared.

For conventional analysis by ICP or DCP, liquid standards are used, which are either easily prepared or commercially available. Interference problems are reduced to a minimum if the calibration solutions are matched to the samples with respect to their content of acids and easily ionizable elements (see above). Calibration curves obtained with sparks, arcs, and LA systems are usually curved, so that 8–15 calibration samples or more are needed to define a suitable calibration. In the case of liquid analysis by DCP and ICP, fewer calibration samples can be used because of the better linearity and dynamic range and absence of self-absorption effects. With the introduction of liquids, the spray chamber is the major source of flicker noise due to aerosol formation and transport. While shot noise can easily be compensated by longer integration times, the flicker noise is of multiplicative nature so that any element can be used as an internal standard provided that a true simultaneous measurement of the analyte and internal standard line intensity is possible.

To find optimal conditions for a given analysis, the principal parameters can be varied in a rational way. In the case of an ICP, to which the further discussion will be limited, this concerns the flow rate of aerosol carrier gas, the RF power input, the observation height above the induction coil, and the sample uptake rate. Numerous simple optimization schemes have been described in the literature, especially for ICP analysis. In addition, sophisticated and complex diagnostics have been suggested in the past to characterize the performance of ICP-AES systems, most of them requiring additional instrumentation. However, with commercial instruments, a simple approach based on several lines has been proposed by Mermet and others [50]. Table 15.3 gives an overview of the diagnostics that can be used to monitor the instrument performance. The spectral resolution is measured in the UV region where most analytical lines are found. Warm-up time and long-term stability are determined via the temporal behavior of three lines. Because of the all-solid-state RF generators, warm-up times are today usually about 15 min. The Mg(II)/Mg(I) ratio can be utilized to characterize the robustness of the plasma and the sensitivity of the method due to changes in the matrix. In the case

Table 15.3 Diagnostics to characterize ICP-AES performance.

Parameter	Diagnostics	Spectral line	Measurement
Selectivity	Resolution	Ba(II) 230.424	Line profile
Repeatability	RSD of signal	Mg(I) 285.213	RSD
Long-term stability	Warm-up time	Ar(I) 404.442 Ba(II) 455.403 Zn(II) 206.423	Intensity as function of time
	Stability	Ar(I) 404.442 Ba(II) 455.403 Zn(II) 206.423	RSD
Robustness	Mg(II)/Mg(I)	Mg(I) 285.213 Mg(II)280.270	Signal-to-background ratio
Limit of detection	Signal-to-background ratio RSD	Ni(II) 231.604 Background at 230 nm	Signal-to-background ratio RSD with optimized exposure time

Adapted from [50].

of a plasma, this corresponds to a constant excitation temperature and electron density as well as a similar spatial distribution of the species along the plasma axis. High RF power together with a low carrier gas flow, moderate solvent loading, and larger inner diameter of the injector usually results in robust conditions which are characterized by Mg(II)/Mg(I) ratios above 10, while, for example, a ratio of 4 indicates a high sensitivity to matrix effects. Lower power favors better signal-to-background ratio and improved detection limits.

For a long time, qualitative analysis was mainly carried out with DCP systems, while the sequential or direct reading ICP systems were too time and sample consuming for a general survey analysis. With the improved simultaneous observation of multiple emission lines via an echelle spectrometer, a general qualitative analysis of unknown samples becomes easily possible under robust plasma conditions.

15.4.5
Advantages and Limitations

15.4.5.1 Absolute and Relative Sensitivity

In the analysis of simple solutions with known composition, for ICP-AES, short-term precision between 0.2 and 3% RSD for analytes with concentrations 10 times the detection limits may be achieved, while over several hours a 5% RSD can be expected. This precision in combination with its robustness makes ICP-AES superior to ICP-MS for the determination of minor and major components. With ICP-AES, most elements (about 73) can be determined routinely at the $10\,\mu g\,l^{-1}$ level or better in solution with radial viewing. In favorable cases and for axial viewing, detection limits $<1\,\mu g\,l^{-1}$ can be achieved. For a single emission line, a linear range of 4 orders of magnitude may be easily attained and as many as 6 orders of magnitude can be observed in favorable cases. The linear range can be extended by multivariate calibration, as different emission lines with different sensitivities can be utilized for trace, minor, and major concentrations. While the speed of ICP-AES analysis will depend on whether simultaneous or sequential instruments are used for detection, generally this can vary between two and six samples per minute. Today, ICP-AES systems can be operated unattended overnight, because of the modern automated designs and safety inherent in the use of inert argon gas.

15.4.5.2 Hyphenated Techniques

Amongst the wide range of sample introduction methods available for AES, chromatographic methods are the most popular as they transform a complex mixture into a time-resolved separated analyte stream [43].

15.4.5.2.1 **Gas Chromatography and Atomic Emission Spectroscopy (GC-AES)** The combination of GS and plasma emission spectroscopy provides a specific and selective detection system for a large variety of analytes, for example, metallic elements, hydrogen, carbon, nitrogen, phosphorus, oxygen, sulfur, and the halogens. Compared to the Ar ICP, the hyphenation of a GC with normal-pressure helium MIP is extensively used, because of its superior performance in the determination of all elements that are particularly relevant in organic analysis (C, H, N, O, S, P, and halogens) and its significantly lower operation cost. In a first approximation, the emission intensity and mass response factor from an element in the plasma can be assumed to be independent of the structure of the parent compound. This is ideal for GC detection, since it significantly simplifies calibration. GC-MIP-AES is a universal, element-selective detector providing detection limits in the low picogram range. It is thus an ideal complement to GC-MS, particularly for screening purposes. The introduction of gaseous samples into a plasma offers several advantages over liquid introduction, as the transport efficiency approaches 100% in contrast to pneumatic nebulization where 95% of the sample is discarded. Sample introduction is achieved via a heated transfer line. In the case of hyphenated GC-ICP-AES, the carrier gas from the GC (normally He) is mixed with the Ar flow used to sustain the plasma and directly introduced into the plasma. The high sensitivity of ICP-AES detection, however, is partially offset by the large dilution of the GC effluent. Generally, the scope of analysis in GC-ICP-AES is limited, for example, to the determination of metal-organic species. These constitute a small group of compounds with similar chemical properties which are converted into volatile species, which, additionally, allows a substantial preconcentration and removal of interferents.

15.4.5.2.2 **Liquid Chromatography and Atomic Emission Spectroscopy (LC-AES)** LC is the most popular separation method for ionic, polar, nonpolar, and neutral compounds of intermediate to high molecular weight, low volatility, and low thermal stability. The LC effluent with a flow rate of up to 1 ml min^{-1} is connected directly to the nebulizer. The often-reported poor detection limits for LC-ICP-AES combinations are due to the ineffective conversion of the effluent into an aerosol.

This can be improved by utilizing an efficient nebulizer such as the DIN. While aqueous mobile phases are easily handled, organic phases are a greater challenge because of the increased spectral background and changes in the plasma characteristics. A simple solution is the use of a microbore LC with column diameters of ≤ 1 mm and, accordingly, lower mobile phase flow rates. Carbon deposition on the torch can be prevented with a cooled spray chamber or addition of 1–4% oxygen to the Ar plasma support gas. Microwave plasmas are difficult to use for LC detection. Because of the low plasma enthalpy, which is insufficient to desolvate and vaporize liquid aerosols effectively, they cannot tolerate the introduction of liquid phases at the usual LC flow rates. Again, the DIN or a thermospray interface can improve the coupling, but this adds significantly to the complexity of the system.

15.4.5.2.3 Capillary Electrophoresis and Atomic Emission Spectroscopy (CE-AES)

Capillary electrophoresis (CE) is a rapidly emerging tool for many routine clinical and pharmaceutical applications. Because of the high separation efficiency of the CE, this combination allows the speciation of elements even in rather complex matrices such as human serum. A challenge for this hyphenation is the interface compatible with the low flow rate of CE, which can be as little as a few nanoliters per minute, compared to a typical sample introduction rate of $1\,\mathrm{ml\,min^{-1}}$ into the ICP. Most interfaces reported in the literature contact the CE via a suitable Pt contact in a sheath buffer flow, which is mixed with the CE effluent, for example, in a polyether ether ketone (PEEK) tee. As the total flow is significantly increased by the make-up flow, a conventional nebulizer can be used for sample introduction.

15.4.5.2.4 Flow-Injection Analysis and Atomic Emission Spectroscopy (FIA-AES)

Flow-injection analysis (FIA) is a method in which small sample volumes, typically about 10–200 μl, are injected into a continuously flowing carrier stream. The corresponding transient signals can then be monitored each time a sample is introduced into the atomizer. The primary advantage of FIA as a means of sample introduction is that relatively high salt concentration in the sample can be tolerated, while viscosity effects and other interference are minimized. Further, FIA allows one to include several operations such as online dilution, standard addition, online preconcentration, and separation, which improve the sample throughput and ease of operation. For these reasons, many commercial ICP-AES systems can optionally be interfaced to highly automated FIA systems for unattended sample preparation and measurement.

15.5
Summary

Judging by a brief survey of the current literature, it can be concluded that the number of fundamental studies employing AAS is declining compared to those that use of ICP-AES and ICP-MS. At the same time, AAS continues to be one of

Table 15.4 Simplified comparison of ICP-AES, ICP-MS, flame AAS, and GF-AAS.

	ICP-AES	**ICP-MS**	**Flame AAS**	**GF-AAS**
Detection limits	Very good for most elements, ppb	Excellent for most elements, ppt	Very good for some elements, ppb	Excellent for some elements, ppt
Sample throughput	5–30 elements per min and sample	All elements per 2–6 min and sample	20 s per element and sample	5 min per element and sample
Linear dynamic range	10^5	10^5	10^3	10^2
Precision				
Short-term	0.2–3%	1–3%	0.1–1%	1–5%
Long-term	<5%	<5%	—	—
Acceptance of dissolved solids	2–25%	0.1–3%	0.5–3%	>20%
No. of elements detectable	>75	>73	>68	>50
Sample consumption	High	Low	Very high	Very low
Unattended operation	Yes	Yes	No	Yes
Operating cost	High	High	Low	Medium
Capital cost	High	Very high	Low	Medium/high

the workhorses of elemental analysis. This clearly indicates that AAS has become a mature analytical technique, both in instrumentation and analytical methodology, although some newer developments, such as continuous source-AAS, deserve particular mention and have the potential to even increase the analytical versatility of AAS. The differences in performance for different elements make AAS and ICP-AES not alternative but complementary analytical techniques. Table 15.4 illustrates this conclusion by a simplified comparison of the main analytical features of ICP-AES and ICP-MS, and flame AAS and GF-AAS, respectively. The operating cost for ICP-AES is still significantly higher than for AAS because of the considerable argon consumption during operation. Despite the generally very high performance of ICP-MS, which makes it a preferred analytical tool where available and where economically feasible, ICP-AES is a highly useful technique, as it offers excellent detection limits, particularly for those elements that are traditionally difficult to determine with ICP-MS due to interferences from elements such as Ca, Fe, and As.

In AES, flames, sparks, and MIPs will have their niche for dedicated applications, but ICP stays the most versatile plasma for multielement determination. The advances in instrumentation and the analytical methodology make quantitative analysis with ICP-AES rather straightforward once the matrix is understood and background correction and spectral overlap correction protocols are implemented. Modern spectrometer software automatically provides aids to overcome spectral and chemical interference as well as multivariate calibration methods. In this way, ICP-AES has matured in robustness and automation to the point where high-throughput analysis can be performed on a routine basis.

References

1. (a) Kirchhoff, G. and Bunsen, R. (1860) *Philos. Mag.*, **20**, 89–109. (b) Hieftje, G.M. (2000) *J. Chem. Educ.*, **77** (5), 577–583.
2. Grotrian, W. (1928) *Graphische Darstellung der Spektren von Atomen mit ein, zwei und drei Valenzelektronen*, Springer, Berlin.
3. Harvey, C.E. (1950) *Spectrochemical Procedures* Chapter 4, Applied Research Laboratories, Glendale, CA.
4. Walsh, A. (1955) *Spectrochim. Acta*, **7**, 108–117.
5. Alkemade, C.T.J. and Milatz, J.M.W. (1955) *Appl. Sci. Res.*, **B4**, 289–299.
6. (a) Alkemade, C.T.J. and Milatz, J.M.W. (1955) *J. Opt. Chem. Soc. Am.*, **45**, 583–584. (b) Welz, B. (1999) *Spectrochim. Acta, Part B*, **54** (14), 2081–2094.
7. Ebdon, L., Evans, E.H., Fisher, A., and Hill, S.J. (1998) *An Introduction to Analytical Atomic Spectrometry*, John Wiley & Sons Ltd, West Sussex.
8. Welz, B. and Sperling, M. (2008) *Atomic Absorption Spectrometry*, 3rd edn, Wiley-VCH Verlag GmbH, Weinheim.
9. Becker-Ross, H., Florek, S., Heilmann, U., and Weisse, R. (1996) *Fresenius J. Anal. Chem.*, **355**, 300–303.
10. (a) Harnly, J.M. (1999) *J. Anal. At. Spectrom.*, **14**, 137–146. (b) Welz, B., Borges, D.L.G., Lepri, F.G., Vale, M.G.R., and Heitmann, U. (2007) *Spectrochim. Acta, Part B*, **62**, 873–883.
11. Falk, H. (1980) *Prog. Anal. Spectrosc.*, **3**, 181–208.
12. Niemax, K., Zybin, A., Schnürer-Patschan, C., and Groll, H. (1996) *Anal. Chem.*, **68**, 351A–356A.
13. (a) Zybin, A., Koch, J., Wizemann, H.D., Franzke, J., and Niemax, K. (2005) *Spectrochim. Acta, Part B*, **60**, 1–11. (b) Dockery, C.R., Blew, M.J., and Goode, S.R. (2008) *J. Chem. Educ.*, **85** (6), 854–858.
14. L'vov, B. (1961) *Spectrochim. Acta*, **17**, 761–770.
15. (a) Long, Z., Luo, Y., Zheng, C., Deng, P., and Hou, X. (2012) *Appl. Spectrosc. Rev.*, **47** (5), 382–413. (b) Long, Z., Chen, C., Hou, X., and Zheng, C. (2012) *Appl. Spectrosc. Rev.*, **47** (7), 495–517. (c) Kumar, A.R. and Riyazuddin, P. (2007) *Int. J. Environ. Anal. Chem.*, **87** (7), 469–500.
16. Welz, B. and Melcher, M. (1984) *At. Spectrosc.*, **5**, 59–61.
17. Frech, W., Baxter, D.C., Dyvik, G., and Dybdahl, B. (1995) *J. Anal. At. Spectrom.*, **10** (10), 769–775.
18. Delves, H.T. (1970) *Analyst (London)*, **95**, 431–480.
19. Grobenski, Z., Lehmann, R., Tamm, R., and Welz, B. (1982) *Mikrochim. Acta*, **1**, 115–125.
20. Ebdon, L. and Cave, M.R. (1982) *Analyst (London)*, **107**, 172–187.
21. Gough, D.S. (1999) *Spectrochim. Acta, Part B*, **54**, 2067–2072.
22. Newstead, R.A., Price, W.J., and Whiteside, P.J. (1978) *Prog. Anal. At. Spectrosc.*, **1**, 267–298.
23. Prügger, M. and Torge, R. (1969) German Patent 1,964,469, filed Dec. 23, 1969.
24. Koizumi, H. and Yasuda, K. (1975) *Anal. Chem.*, **47**, 1679–1682.
25. Smith, S.B. and Hieftje, G.M. (1983) *Appl. Spectrosc.*, **37**, 419–424.
26. Snelleman, W. (1968) *Spectrochim. Acta, Part B*, **23**, 403–411.
27. Zander, A.T., O'Haver, T.C., and Keliher, P.N. (1978) *Anal. Chem.*, **48**, 1166–1175.
28. Lobinski, R. and Szpunar, J. (eds) (2003) *Hyphenated Techniques in Speciation Analysis*, RSC, Cambridge.
29. Rosenberg, E. (2004) in *Analytical Chemistry: A Modern Approach to Analytical Science* (eds R. Kellner, J.M. Mermet, M. Otto, M. Valcarcel, and H.M. Widmer), Wiley-VCH Verlag GmbH, Weinheim, pp. 865–896.
30. Kolb, B., Kemmner, G., Schleser, F.H., and Wiedeking, E. (1966) *Fresenius Z. Anal. Chem.*, **221**, 166–175.
31. Van Loon, J.C. and Radziuk, B. (1976) *Can. J. Spectrosc.*, **21**, 46–50.
32. (a) Donard, O.F.X. (1989) in *5th Colloquium Atomspektroskopische Spurenanalytik* (ed. B. Welz), Bodenseewerk Perkin- Elmer, Überlingen, p. 395.

(b) D'Haese, P.C., Van Landeghem, G.F., Lamberts, L.V., and De Broe, M.E. (1995) *Mikrochim. Acta*, **120** (1–4), 83–90.

33. Randall, L., Donard, O.F.X., and Weber, J.H. (1986) *Anal. Chim. Acta*, **184**, 197–203.
34. Bendicho, C. and de Loos-Vollebregt, M.T.C. (1991) *J. Anal. At. Spectrom.*, **6**, 353–374.
35. Broekaert, J.A.C. (2005) *Analytical Atomic Spectrometry with Flames and Plasmas*, 2nd edn, Wiley-VCH Verlag GmbH, Weinheim.
36. Montaser, A. and Golightly, D.W. (1992) *lnductively Coupled Plasmas in Analytical Atomic Spectrometry*, Wiley-VCH Verlag GmbH, New York.
37. Nölte, J. (2003) *ICP Emission Spectrometry: A Practical Guide*, Wiley-VCH Verlag GmbH, Weinheim.
38. Boumans, P.W.J.M. (1987) *lnductively Coupled Plasma Emission Spectroscopy, Part 1 and ll*, John Wiley & Sons, Inc., New York.
39. Tanner, S.D. and Holland, J.G. (eds) (2001) *Plasma Source Mass Spectrometry*, Royal Society of Chemistry, Cambridge.
40. Cresser, M.S. (1994) *Flame Spectrometry in Environmental Chemical Analysis*, Royal Society of Chemistry, Cambridge.
41. Montaser, A. (1998) *Appl. Spectrosc.*, **52**, 406A–426A.
42. (a) Radziemski, L.J. and Cremers, D.A. (eds) (1989) *Laser-lnduced Plasmas and Applications*, Marcel Dekker, New York. (b) Hou, X. and Jones, B.T. (2000) in *Encyclopedia of Analytical Chemistry* (ed. R.A. Meyers), John Wiley & Sons Ltd, Chichester, pp. 9468–9485.
43. Van Stee, L.L.P., Brinkman, U.A.T., and Bagheri, H. (2002) *Trends Anal. Chem.*, **21** (9–10), 618–626.
44. Payling, R., Nelis, T., Browner, R.F., and Chalmers, J.M. (2004) *Glow Discharge Optical Emission Spectroscopy*, Royal Society of Chemistry, Cambridge.
45. Becker-Ross, H. and Florek, S.V. (1997) *Spectrochim. Acta, Part B*, **52**, 1367–1375.
46. Sneddon, J. (1992) in *Advances in Atomic Spectroscopy*, vol. I (ed. J. Sneddon), JAI, Greenwich.
47. Sola-Larrañaga, C. and Navarro-Blasco, I. (2009) *Food Chem.*, **115** (3), 1048–1055.
48. (a) Hu, B., Li, S., Xiang, G., He, M., and Jiang, Z. (2007) *Appl. Spectrosc. Rev.*, **42** (2), 203–234. (b) Todolí, J.L. and Mermet, J.M. (2005) *Trends Anal. Chem.*, **24** (2), 107–116.
49. Wienold, J., Traub, H., Lange, B., Giray, T., Recknagel, S., Kipphardt, H., Matschat, R., and Panne, U. (2009) *J. Anal. At. Spectrom.*, **24** (11), 1570–1574.
50. Mermet, J.M. and Poussel, E. (1995) *Appl. Spectrosc.*, **49**, 12A–18A.

16
Inductively Coupled Plasma Spectrometry

José Alfons Clement Broekaert

16.1
The Inductively Coupled Plasma (ICP)

16.1.1
Historical Development

Atomic spectrometry is one of the oldest principles of instrumental analysis and goes back to the work of Kirchhoff and Bunsen, published in 1860 [1], who used flames both as radiation source for flame atomic emission spectrometry and as atom reservoir for atomic absorption spectrometry. Owing to the many developments in the sources, the spectrometers and the detectors, innovation in atomic spectrometry is still going on and analytical atomic spectrometry with flames and plasmas is one of the prominent methodologies in instrumental chemical analysis at present (for a treatment, see Ref. [2]). The flame remained of interest up to now but is only useful for the determination of easily ionized elements such as Na and the other alkali elements. Also, after the experiments with hot flames through the use of alternative burning gases, they could not be successfully used for the determination of further elements. Through experiments with electrical discharges in gases at the beginning of the twentieth century, their potential was also recognized for chemical analysis. DC arcs became famous for the direct analysis of solids, including both metals and alloys and electrically nonconducting materials in the powder form after mixing with an electrically conductive powder. DC arcs especially became popular for survey analysis in a wide field of applications such as geological samples analysis, soils analysis, plant residue elemental analyses and so on. In the same way, electrical sparks were recognized as a powerful tool for metal analysis and till date remained the main method for the production and product control in the metal industry. In view of their operation at low pressure, glow discharges were known as *narrow line sources* and became a main component of atomic absorption spectrometers as primary sources. However, since the 1960s it was found that sources of different geometry are also useful for the analysis of solids, which are then used as the cathode of the discharge and volatilized mainly by cathodic sputtering (for a discussion, see Ref. [3]). As this process progresses

Handbook of Spectroscopy, Second Edition. Edited by Günter Gauglitz and David S. Moore.

layer by layer, it can be used for in-depth analysis as it is currently used in the metals industry. By the use of RF sources, not only electrically conductive solids but also electrically insulator materials can be analyzed. Plasmas at atmospheric pressure, with the volume and the time and spatial stability of a chemical flame, were recognized as powerful sources for the atomic spectrometric analysis of liquid samples or solids after bringing them into solutions. Indeed, as a result of their higher temperatures and their inert gas atmosphere in contrast to flames, they enabled the determination of practically all elements with high sensitivity instead of the alkali elements only. Microwave discharges, as described by Margoshes and Scribner [4], and dc plasma jets, as the one described, for example, by Rieman [5], were discharges between electrodes; the latter suffered from erosion and regularly had to be replaced. Also, the spectral lines of the electrode material occurred in the spectrum. Therefore, the inductively coupled plasma (ICP), as it was described by Greenfield *et al.* [6] and Wendt and Fassel [7] in 1964, first was an electrodeless discharge in argon at atmospheric pressure. As a result of the so-called toroidal structure of the plasma, a wet aerosol could be introduced with high efficiency (Figure 16.1). As a rule, it is operated in argon at reasonably high gas flows of $10-20\,\mathrm{l\,min^{-1}}$ and a power of above 1 kW. This results in a plasma with a diameter of 15–20 mm and a length of some 6–7 cm. It is very stable and robust and its stability is only limited by the constancy of the gas flows and of the power line. Intensive research on the ICP started in many prominent groups and dealt with the optimization of the torch, together with the selection of the working frequencies in a range of 20–100 MHz. Further work on sample introduction devices started and continues up to these days. For liquid samples, pneumatic nebulization is the most common way. Different types of nebulizers were conceived, developed, and used for a wide diversity of applications. Ultrasonic nebulization was improved to a maturity for specific applications such as the analysis of drinking water. The generation of volatile species by suitable chemical reactions such as hydride generation enables it to obtain highest sample introduction efficiencies. This is also the case with electrothermal vaporization (ETV), where experience from atomic absorption work can be used very well. For direct solids analysis, spark and laser ablation were intensively investigated. Further work dealt with spectral interferences and figures of merit when the ICP was used as radiation source for atomic emission spectrometry. Currently, inductively coupled plasma optical emission spectrometry (ICP-OES) can be found together with atomic absorption spectrometry in almost every large analytical laboratory and is used in routine for element determinations in a wide variety of samples. In 1980, the use of an ICP as an ion source for elemental mass spectrometry was first described by Houk *et al.* [8] and was soon made commercially available. It is currently the most powerful tool for multielement determinations of trace and ultratrace elements in solutions. Here, the use of different types of mass spectrometers helps to cope with spectral interferences or transient signals, and in different ways they are useful for high-precision isotope determinations. Inductively coupled plasma mass spectrometry (ICP-MS) is also of use for elemental detection in combination with

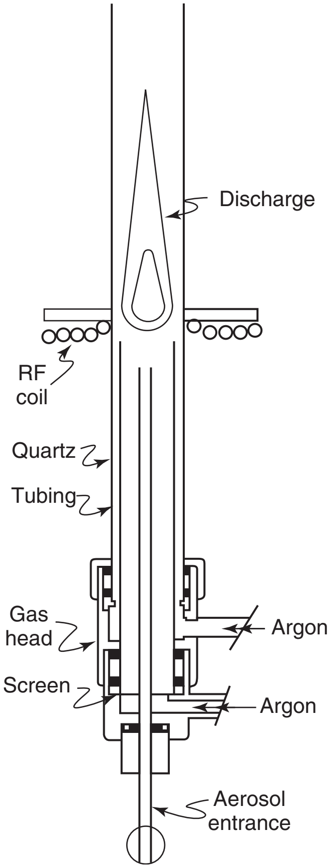

Figure 16.1 Plasma torch for ICP spectrometry. (Reproduced with permission from Ref. [7].)

chromatography and is very important for speciation in environmental and life sciences.

16.1.2
Excitation and Ionization Processes

The ICP in the form it first was described by Wendt and Fassel [7] is operated in a quartz torch consisting of three concentric tubes, of which the dimensions and form hardly have changed since the 1960s. Normally, the ICP is operated with argon in a torch with an external diameter of about 25 mm. There are three gas flows, namely, an external gas flow of 10–20 l min^{-1}, an intermediate gas flow, and the aerosol gas flow of about 1 l min^{-1}. The intermediate gas flow of 0.5–1 l min^{-1} must be used, namely, when analyzing organic solutions or when solutions with high salt contents are analyzed. However, in the original paper of Greenfield *et al.* [6] a larger torch was used and the outer gas flow could also be nitrogen, oxygen, or even air. Then, the power required is on the order of at least 2 instead of 1 kW. The plasma is powered by a high-frequency current delivered to the gas flow through a 1.5 turn coil, which is water cooled. Through a Tesla spark, some argon atoms are ionized and the charged species take up energy in the high-frequency field. A plasma is formed by ionization of additional gas atoms through the reactions:

$$\begin{aligned}\mathrm{Ar} + \mathrm{e} \rightarrow\ & \mathrm{Ar}^{+} + 2\mathrm{e}\ \text{(ionization energy : 15.7 eV) (electron impact)}\\ & \mathrm{Ar}^{*} + \mathrm{e}\\ & \mathrm{Ar}^{m} + \mathrm{e}\ \text{(metastable levels at 11.7 eV)}\end{aligned} \tag{16.1}$$

Indeed, the electrons can gain so much energy that they can ionize the omnipresent argon atoms and through this process the electron number density becomes so high that a high-temperature plasma is formed. In other cases, only excited argon atoms are formed, where electrons are promoted to higher energy levels. A special case is the population of the so-called metastable levels. As they are triplet states, they cannot decay directly by the emission of radiation and a transfer to lower energy states that are singlet states, because transitions between states with different multiplicities are forbidden. These metastable states can only decay by collisions and they have a considerable number density in analytical ICPs.

Because radiation is emitted by the decay of the excited states, a further important process is

$$\mathrm{Ar} + h\nu \rightarrow \mathrm{Ar}^{+} + \mathrm{e}\ \text{and}\ \mathrm{Ar}^{+} + h\nu \rightarrow \mathrm{Ar}^{2+} + \mathrm{e}\ \text{(radiation trapping)} \tag{16.2}$$

When analyte atoms (M) are brought into the ICP, they are excited through a number of processes, and during the decay of the excited species, element-specific radiation is emitted by the ICP. For the analyte excitation, the following processes may be important:

$$\mathrm{M} + \mathrm{e} \rightarrow \mathrm{M}^{*}, \mathrm{M}^{+*} + \mathrm{e}\ \text{(electron impact)} \tag{16.3}$$

$$\mathrm{M}^{+} + \mathrm{e} \rightarrow \mathrm{M} + h\nu \quad \text{(radiative recombination)} \tag{16.4}$$

$$\mathrm{Ar} + \mathrm{M} \rightarrow \mathrm{Ar} + \mathrm{M}^{*}\text{(collisions of the first kind)} \tag{16.5}$$

$$\mathrm{Ar}^{+} + \mathrm{M} \rightarrow \mathrm{Ar} + \mathrm{M}^{+*}\text{(charge transfer)} \tag{16.6}$$

$$\mathrm{Ar}^{m} + \mathrm{M} \rightarrow \mathrm{Ar} + \mathrm{M}^{+*} + \mathrm{e}\ \text{(Penning effect)} \tag{16.7}$$

The latter effect is especially interesting for ion lines, when the sum of the ionization energy of the element considered and the excitation energy of the respective line is near to the energy of the argon metastable levels (11.7 eV).

The high concentration of metastable argon species in the plasma even has been proposed in early studies on excitation mechanisms in the ICP to be responsible for the relatively high insensibility of the plasma to the injection of easily ionized elements. Indeed, changes in the ionization of analyte species as a consequence of introducing different concentrations of easily ionized elements such as Na, and so on, into the ICP are low, because of overionization as a result of the easy ionization of metastable argon [9]. Furthermore, the Penning effect may also explain the predominance of ion lines for a number of elements in ICP-OES. However, detailed spatially resolved measurements and probing of the excited species by laser-based techniques are still under investigation to draw up a more complete image of the relevant excitation and ionization processes in the different zones of the ICP at different working conditions (see, e.g., the recent work in the groups of Hieftje (see, e.g., Ref. [10]) and Farnsworth (see, e.g., Ref. [11])).

16.1.3
Diagnostics of the ICP

Plasmas contain not only molecules, radicals, and atoms but also ions and free electrons; all of these result from the coupling of energy with matter in the gaseous state. The species mentioned can be present in their ground states or in excited states; radiation can be emitted or absorbed when transitions from one to another state occur. The wavelength of the radiation can be obtained from Planck's law, whereas the intensities of the discrete lines depend on the number densities of the species and the states involved.

16.1.3.1 Excitation Temperatures

The transfer of energy for the different species in the ICP results from the nonradiative and radiative processes taking place. Nonradiative processes involve collisions and radiative processes involve emission, absorption, and fluorescence of radiation. The efficiency of collision processes is described by their cross section $\sigma(v)$, reflecting the loss in impulse that a particle with a mass m and velocity v undergoes when it collides with a particle with mass M. Apart from the cross section, however, the velocity distribution for a given species is important for describing the energy transfer in a plasma. In the absence of strong fields, as in the case of ICP, a Maxwell distribution can be assumed and the velocity distribution can be described by

$$\frac{\mathrm{d}n}{n} = \frac{2}{(\sqrt{\pi})} \cdot \sqrt{u'} \cdot \mathrm{e}^{u'} \cdot \mathrm{d}u' \tag{16.8}$$

with $u' = E / k{\cdot}T$, where E is the mean energy of the particles and T is the absolute temperature. For a plasma in a closed system and which is in so-called thermal equilibrium, that is, when each process is in equilibrium with its inverse process, the population of the excited levels for every type of particle is given by Boltzmann's law:

$$\frac{n_\mathrm{q}}{n_0} = \frac{g_\mathrm{q}}{g_0} \cdot \exp\left(\frac{-E_\mathrm{q}}{kT}\right) \tag{16.9}$$

where n_q is the number density of particles in the excited state, n_0 is the number density of particles in the ground state, g_q and g_0 are the statistical weights of the corresponding levels, E_q is the excitation energy of the state q, k is Boltzmann's constant (1.38×10^{-16} erg K), and T is the absolute temperature. In Eq. (16.9), a relationship is formulated between the temperature and the atom number density in a single excited state and in the ground state, respectively. The Boltzmann equation can be better formulated as a function of the total number of particles n

distributed over all states in the notations of Ref. [12] as

$$\frac{n_\mathrm{q}}{n} = \frac{\left[g_\mathrm{q} \cdot \exp\left(\frac{-E_\mathrm{q}}{kT}\right)\right]}{\left\{\Sigma_\mathrm{m} \cdot g_\mathrm{m} \cdot \exp\left[\frac{-E_\mathrm{m}}{(kT)}\right]\right\}} \tag{16.10}$$

where $n = \Sigma_\mathrm{m} n_\mathrm{m}$. The sum $Z_\mathrm{m} = \Sigma_\mathrm{m} \cdot g_\mathrm{m} \cdot \exp[-E_\mathrm{m} / (kT)]$ is the partition function. This is a function of the temperature and the coefficients of this function for a large number of neutral and ionized species are listed in the literature (see, e.g., Ref. [13]). When E_q is expressed in eV, Eq. (16.10) can be expressed as

$$\log n_\mathrm{q} = \log n + \log n_\mathrm{q} - \left[\frac{(5040)}{T}\right] \cdot V_\mathrm{q} - \log Z \tag{16.11}$$

Excited states are prone to decay, which may occur by collisions with surrounding particles or by emission of electromagnetic radiation. When this involves the levels q and p being involved, the number of spontaneous transitions per unit of time is given by

$$\frac{-\mathrm{d}n_\mathrm{q}}{\mathrm{d}t} = A_\mathrm{qp} \cdot n_\mathrm{q} \tag{16.12}$$

where A_qp is the Einstein coefficient for spontaneous emission (in s^{-1}). The intensity for the emitted spectral line (I_qp) is given by

$$I_\mathrm{qp} = A_\mathrm{qp} \cdot n_\mathrm{q} \cdot h \cdot \nu_\mathrm{qp} \tag{16.13}$$

After substitution of n_q for atomic species, according to Eq. (16.10):

$$I_\mathrm{qp} = A_\mathrm{qp} \cdot h \cdot \nu_\mathrm{qp} \cdot n \cdot \left(\frac{g_\mathrm{q}}{Z}\right) \cdot \exp\left[\frac{-E_\mathrm{q}}{(kT)}\right] \tag{16.14}$$

The excitation temperature T can be determined from the intensity ratio for two lines (a and b) of the same ionization stage of an element as

$$T = \frac{[5040(V_\mathrm{a} - V_\mathrm{b})]}{\left\{\log\left[\frac{(gA)_\mathrm{a}}{(gA)_\mathrm{b}}\right] - \log\left(\frac{\lambda_\mathrm{a}}{\lambda_\mathrm{b}}\right) - \log\left(\frac{I_\mathrm{a}}{I_\mathrm{b}}\right)\right\}} \tag{16.15}$$

For this purpose, often the line pair Zn 307.206/Zn 307.59 is used.

The excitation temperature can also be determined from the slope of the plot $\ln[I_\mathrm{qp} / (g_\mathrm{q} \cdot A_\mathrm{qp} \cdot \nu_\mathrm{qp})]$ or $\ln[I_\mathrm{qp} \cdot \lambda/(gA_\mathrm{qp})]$ versus E_q, which is equal to $-1/(k \cdot T)$ as

$$\ln\left[\frac{I_\mathrm{qp}}{\left(g_\mathrm{q} \cdot A_\mathrm{qp} \cdot \nu_\mathrm{qp}\right)}\right] = \ln\left(\frac{h \cdot n}{Z}\right) - \left[\frac{E_\mathrm{q}}{(k \cdot T)}\right] \tag{16.16}$$

For this purpose, often the iron lines Fe I 381.58, Fe I 383.04, Fe I 382.44, and Fe I 382.58 nm are used, of which the transition probabilities are well known.

After calculating the radial intensities from the laterally observed intensities at different distances away from the plasma center (through the application of Abel inversion – see Ref. [14]) – radially resolved temperature distributions can be calculated for the ICP. As shown by the results in Figure 16.2, for the ICP, temperatures close to 5000 K are obtained.

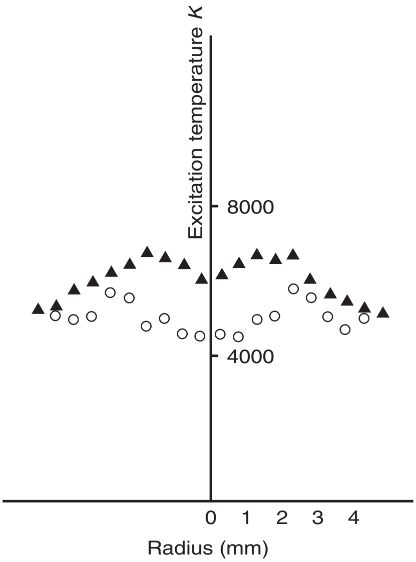

Figure 16.2 Radial distributions of excitation temperatures in ICP measured with Fe I lines. ○: with 4 mg $Na_2B_4O_7$ per ml and ▲: without $Na_2B_4O_7$; iron concentration: 100 µg ml^{-1}. (Reproduced with permission from Ref. [15].)

16.1.3.2 **Gas Temperatures**

Also, from the widths of the spectral lines, temperatures can be determined. The physical width of a spectral line results from several broadening mechanisms [16]:

The natural broadening of a spectral line is due to the finite lifetime τ of an excited state. The corresponding halfwidth in terms of the frequency is given by

$$\Delta\nu_N = \frac{1}{(2\pi\tau)} \tag{16.17}$$

For lines corresponding to transitions that are allowed according to the selection rules, lifetimes are on the order of 10^{-8} s and, accordingly, for most spectral lines this results in a natural broadening with a halfwidth on the order of 10^{-2} pm.

The Doppler linewidth results from the movement of the emitting atoms and their velocity component in the viewing direction. The respective halfwidth is given by

$$\Delta\nu_D = \left[\frac{2\cdot\sqrt{(\ln 2)}}{c}\right]\cdot\nu_0\cdot\sqrt{\left[\frac{(2\cdot R\cdot T)}{M}\right]} \tag{16.18}$$

where c is the velocity of light, ν_D is the frequency of the line maximum, R is the gas constant, and M is the atomic mass. The Doppler broadening thus strongly depends on the temperature and is often denoted as temperature broadening and reflects the kinetic energy of the radiating species (atoms, ions, or molecules). The relevant temperature is denoted as the gas temperature or Doppler temperature and the measurement of the Doppler width thus allows the determination of the gas temperature in a high-temperature plasma. In the case of the ICP, gas temperatures are on the order of 4000–5000 K.

Apart from natural and Doppler broadening, the pressure broadening and, for a number of lines, the Stark effect contribute to the line broadening.

16.1.3.3 **Ionization**

In the ICP, atoms are also ionized. The ionization of atoms (a) of an element j into ions (i) is an equilibrium:

$$n_{\mathrm{aj}} \rightleftarrows n_{\mathrm{ij}} + n_{\mathrm{e}} \tag{16.19}$$

The equilibrium constant $S_{\mathrm{nj}}(T)$ is known as the *Saha constant* and is given by

$$S_{\mathrm{nj}}(T) = \frac{(n_{\mathrm{ij}} \cdot n_{\mathrm{e}})}{n_{\mathrm{aj}}} \tag{16.20}$$

The degree of ionization α_{j} for an element is given by

$$\alpha_{\mathrm{j}} = \frac{n_{\mathrm{ij}}}{(n_{\mathrm{aj}} + n_{\mathrm{ij}})} \tag{16.21}$$

where n_{aj} and n_{ij} are the concentrations of the atoms (a) and the ions (i); these can be expressed as a function of the total number of atoms n_{j} by

$$n_{\mathrm{aj}} = (1 - \alpha_{\mathrm{j}}) \cdot n_{\mathrm{j}} \,\text{and}\, n_{\mathrm{ij}} = \alpha_{\mathrm{j}} \cdot n_{\mathrm{j}} \tag{16.22}$$

Accordingly, using the notations given in Ref. [9], the intensity of an atom line can be written as

$$I_{\mathrm{qp}} = \frac{A_{\mathrm{qp}} \cdot h \cdot \nu_{\mathrm{qp}} \cdot g_{\mathrm{q}}}{Z_{\mathrm{aj}}} \cdot (1 - \alpha_{\mathrm{j}}) \cdot n_{\mathrm{j}} \cdot \exp\left[\frac{-E_{\mathrm{q}}}{(kT)}\right] \tag{16.23}$$

while the intensity of an ion line is given by

$$I^{+}_{\mathrm{qp}} = \frac{A^{+}_{\mathrm{qp}} \cdot h \cdot \nu^{+}_{\mathrm{qp}} \cdot g^{+}_{\mathrm{qp}}}{Z_{\mathrm{ij}}} \cdot \alpha_{\mathrm{j}} \cdot n_{\mathrm{j}} \cdot \exp\left[\frac{-E^{+}_{\mathrm{q}}}{(kT)}\right] \tag{16.24}$$

These expressions for the intensities contain three factors that depend on the temperature, namely, the degree of ionization, the Boltzmann factors, and the partition functions. In particular, α_{j} can be written as a function of the electron number density and the Saha function as

$$\left[\frac{\alpha_{\mathrm{j}}}{\left(1 - \alpha_{\mathrm{j}}\right)}\right] \cdot n_{\mathrm{e}} = S_{\mathrm{nj}}(T) \tag{16.25}$$

However, the latter is also given by the well-known Saha equation. With the aid of wave mechanics and through differentiation of the Boltzmann equation, the Saha function in terms of the partial pressures can also be expressed as

$$S_{\mathrm{pj}}(T) = \frac{(p_{\mathrm{ij}} \cdot p_{\mathrm{e}})}{(p_{\mathrm{aj}})} = \frac{\left[(2\pi m)^{\frac{3}{2}} \cdot (kT)^{\frac{5}{2}}\right]}{h^3} \cdot \frac{2Z_{\mathrm{ij}}}{Z_{\mathrm{aj}}} \cdot \left\{\exp\left[\frac{-E_{\mathrm{ij}}}{(kT)}\right]\right\} \tag{16.26}$$

The factor of 2 is the statistical weight of the free electron (which can have two spin orientations).

This leads to the expression:

$$\frac{(p_{\mathrm{ij}} \cdot p_{\mathrm{e}})}{p_{\mathrm{aj}}} = S_{\mathrm{pj}}(T) = 6.58 \times 10^{-7} \times T^{\frac{3}{2}} \times \frac{Z_{\mathrm{ij}}}{Z_{\mathrm{aj}}} \times \left[\exp_{10}\left(-5040\frac{V_{\mathrm{ij}}}{T}\right)\right] \tag{16.27}$$

or in the logarithmic form:

$$\log S_{\mathrm{pj}} = \frac{5}{2}\log T - \frac{5040}{T} \cdot V_{\mathrm{ij}} + \log\frac{(Z_{\mathrm{ij}})}{(Z_{\mathrm{aj}})} - 6.18 \tag{16.28}$$

where V_{ij} is the ionization energy (eV).

The Saha equation is only valid for a plasma that is in local thermal equilibrium, that is, in which the balance of all energy processes is matched except for the radiative processes. Then the degree of ionization in a plasma can be determined from the intensity relationship between an atom and an ion line of the same element as

$$\log\left[\frac{\left(\alpha_{\mathrm{j}}\right)}{(1-\alpha_{\mathrm{j}})}\right] = \log\left(\frac{I^{+}_{\mathrm{qp}}}{I_{\mathrm{qp}}}\right) - \log\left[\frac{\left(g^{+}_{\mathrm{q}} \cdot A^{+}_{\mathrm{qp}} \cdot \nu^{+}_{\mathrm{qp}}\right)}{(g_{\mathrm{q}} \cdot A_{\mathrm{qp}} \cdot \nu_{\mathrm{qp}})}\right] + \left(\frac{5040}{T}\right)(V^{+} - V_{\mathrm{q}}) + \log\left(\frac{Z_{\mathrm{ij}}}{Z_{\mathrm{aj}}}\right) \tag{16.29}$$

In the case of the ICP, the line pair Mg II 279.6 nm/Mg I 278.0 nm has been used for the determination of the degree of ionization of elements and, depending on the ionization energies, values ranging from 10^{-5} to some percent have been found. Once α_{j} is known, the electron pressure can also be determined. Indeed, from

$$\log\left[\frac{\alpha_{\mathrm{j}}}{\left(1-\alpha_{\mathrm{j}}\right)}\right] = \log\left[\frac{S_{\mathrm{pj}}\,(T)}{p_{\mathrm{e}}}\right] \tag{16.30}$$

one can calculate that:

$$\log p_{\mathrm{e}} = -\log\left(\frac{I^{+}_{\mathrm{qp}}}{I_{\mathrm{qp}}}\right) + \log\left[\frac{\left(g^{+}_{\mathrm{q}} \cdot\ A^{+}_{\mathrm{qp}} \cdot \nu^{+}_{\mathrm{qp}}\right)}{(g_{\mathrm{q}} \cdot A_{\mathrm{qp}} \cdot \nu_{\mathrm{qp}})}\right] - \left(\frac{5040}{T}\right)(V_{\mathrm{ij}} + V^{+}_{\mathrm{q}} - V_{\mathrm{q}}) + \frac{5}{2}(\log T) - 6.18 \tag{16.31}$$

where:

$$\log n_{\mathrm{e}} = \log p_{\mathrm{e}} - \log T - \log k \tag{16.32}$$

In this manner, for the ICP, electron number densities of $n_{\mathrm{e}} = 10^{14}\,\mathrm{cm}^{-3}$ are found.

Independent of the fact that local thermal equilibrium is obtained, the electron number densities also can be determined from Stark broadening of the H_{β} line or of a suitable argon line. This contribution to broadening is a result of the electrical field of the quasi-static ions on one side and the mobile electrons on the other. As described in Ref. [17], it can be written as

$$d\lambda = 2[1 + 1.75\alpha(1 - 0.75\varsigma)]\omega \tag{16.33}$$

where ς is the ratio of the distance between the ions (ς_{m}) and the Debye path length (ς_{D}), ω is the broadening due to the interaction of the electrons ($\approx n_{\mathrm{e}}$), and α is the contribution of the interaction with the quasi-static ions ($\approx n_{\mathrm{e}}^{\frac{1}{4}}$).

$$\varsigma_{\mathrm{m}} = \left(4\pi \times \frac{n_{\mathrm{e}}}{3}\right)^{-\frac{1}{3}} \tag{16.34}$$

$$\varsigma_{\mathrm{D}} = \left[\frac{(k \times T)}{(4\pi \times \mathrm{e}^2 \times n_{\mathrm{e}})}\right]^{\frac{1}{2}} \tag{16.35}$$

$d\lambda$ can thus be calculated as a function of n_{e}. Accordingly, from the widths of the Ar I 549.59 or the Ar I 565.07 nm lines, which are mainly due to Stark broadening, n_{e} can be determined directly and this independent of the existence of LTE. For the ICP, values of 10^{16} cm^{-3} were obtained in this way. This shows that deviations of local thermal equilibrium exist.

16.1.3.4 Norm Temperatures

From Eqs. (16.23) and (16.24), which give the intensity from an atom and ion line, and from the Saha equation (16.28), it can be understood that for each spectral line emitted by a plasma source there is a temperature at which its intensity is maximum. This is the so-called norm temperature (T_{n}). In a first approximation [18], it can be written as

$$T_{\mathrm{n}} = \frac{(0.95V_{\mathrm{ij}} \times 10^3)}{\left[1 - 0.33\cdot\alpha + 0.37 \cdot \log\left(\frac{V_{\mathrm{ij}}}{10}\right) - 0.14 \log P_{\mathrm{e}}{}^*\right]} \tag{16.36}$$

where V_{ij} is the ionization energy, $\alpha = V_{\mathrm{a}}/V_{\mathrm{ij}}$ with V_{a} the excitation energy. $P_{\mathrm{e}}{}^*$ is the electron pressure (atm; 1 atm $\approx$ 101 kPa) and is a function of T and n_{e}:

$$P_{\mathrm{e}}{}^* = 1.263 \times 10^{-12} n_{\mathrm{e}} \times T \tag{16.37}$$

In cases where we have to consider the norm temperature for a line of an element that is only present as an impurity, as it is the case in an ICP formed in a noble gas, the dilution in the plasma (a) also has to be considered. For a system with more components, $P_{\mathrm{e}}{}^*$ is given by

$$P_{\mathrm{e}}{}^* = \left[\frac{(2i+1)}{(2i+3)}\right] \cdot \left(\frac{g_i}{g_{i+1}}\right) \cdot \left[\frac{4a}{(1+a)^2}\right] \cdot P \tag{16.38}$$

where g_i and g_{i+1} are the statistical weights of the ions with charge i and $i+1$, respectively. Accordingly, as a result of the dilution, the change in T_{n} after a dilution of the plasma by a factor of a will be given by

$$\frac{\Delta T_{\mathrm{n}}}{T_{\mathrm{n}}} = 0.14 \log\left[\frac{4a}{(1+a)^2}\right] < 1 \tag{16.39}$$

At a dilution of 0.1, the change in norm temperature will thus be −7.2%. In the ICP, the analyte dilution, however, is very high. It is on the order of 10^8, when 1 ml min^{-1} of a 1–10 μg ml^{-1} solution for an element with a mass of 40 is nebulized with an efficiency of 1% into an argon flow of 10 l min^{-1}. In the ICP, the norm temperatures for lanthanum atom lines such as La I 418.7 nm (with $V_{ij} = 6.61$ eV and $V_a = 2.96$ eV) will thus change from about 5000 K for a pure lanthanum plasma to 2830 K as a result of the large dilution. For atom lines of elements with relatively low ionization energies, the change in the norm temperatures as a result of the analyte dilution is high, but it is much less for ion lines. For the La II 412.3 nm line (second ionization energy: 11.43 eV and V_a: 3.82 eV), T_n is 9040 K. From the norm temperatures it becomes clear whether atom or ion lines will be optimally excited in a plasma of a given temperature, electron pressure, and gas composition. The norm temperatures further give important indications for line selection in a source of a given temperature. Atom lines often have their norm temperatures below 4000 K, especially at high analyte dilution, whereas those of ion lines often reach 10 000 K. The two types of lines are also often denoted as ''soft'' and ''hard'' lines, respectively. The fact that ion lines are predominant in the case of the ICP also is related to the overionization in the plasma, as these lines often have norm temperatures that are considerably higher than the temperatures in analytical ICPs.

16.1.3.5 **Dissociation**

The dissociation of molecular plasma gases (such as nitrogen and air in the case of the ICP) or analyte molecules that are brought into the plasma is an equilibrium reaction. Accordingly, thermally stable radicals, in particular, or molecules are often present in the ICP. They emit molecular bands that occur along with the atomic and ionic line spectra in the ICP emission spectrum. Radicals and molecules may also give rise to the formation of cluster ions, the signals of which will be present in the mass spectra in the case of ICP-MS. The main species stemming from the plasma gases are CN, NH, NO, OH, and N_2 (or ${N_2}^+$). From the analytes, predominantly thermally stable oxides remain (e.g., AlO^+, TiO^+, YO^+, etc.). A thorough treatment of molecular spectra is available in many classical textbooks (see, e.g., Refs. [19, 20]).

Molecules or radicals have different electronic energy levels ($^1\Sigma$, $^2\Sigma$, $^2\Pi$, ...), which have a vibrational fine structure ($\nu = 0, 1, 2, 3, \ldots$), and the latter again have a rotational hyperfine structure ($j = 0, 1, 2, 3, \ldots$). The total energy of a state is then given by

$$E_i = E_{el} + E_{vibr} + E_{rot} \tag{16.40}$$

E_{el} is on the order of 1–10 eV, the energy difference between two vibrational levels of the same electronic state is on the order of 0.25 eV, and for the case of two rotational levels of a vibrational band, the energy level is on the order of only 0.005 eV. A rotational line is emitted via a transition between two rotational levels. When the rotational levels considered belong to the same electronic level, the wavelength of the radiation emitted will be in the infrared region. When they belong to different electronic levels, the wavelength will be in the UV or in the visible region. Transitions are characterized by the three quantum numbers of the states involved, namely, n', ν', j' and n'', ν'', j''. All lines that originate from transitions between rotational levels belonging to different vibrational levels or two electronic states form a band: $n', \nu' \rightarrow n'', \nu''$. For these band spectra the selection rule is $\Delta j = j' - j'' = \pm 1, 0$. Transitions for which $j'' = j' + 1$ then give rise to the P-branch, $j'' = j' - 1$ to the R-branch and $j' = j''$ to the Q-branch of the band. The line corresponding to $j' = j'' = 0$ is the zero line of the band. When $\nu' = \nu'' = 0$, it is also the zero line of the system. The difference between the wave number of a rotational line (cm^{-1}) and the wave number of the zero line in the case of the P- and the R-branches is a function of the rotational quantum number j and the rotational constant B_ν, for which:

$$\frac{E_j}{(h \cdot c)} = B_\nu \cdot j(j+1) \tag{16.41}$$

The functional relationship is quadratic and is known as the *Fortrat parabola*.

For the CN radical and the N_2^+ molecular ion, the transitions give rise to band emission between 370 and 400 nm. For the violet system of the CN band, there is no Q-branch and the lowest j in the R-branch is $j = 1$.

Molecular and radical band spectra thus consist of electronic series, which in turn consist of many vibrational bands. They again consist of rotational lines, many of which are often only partially resolved. As in the case of atomic spectral lines, the intensity of a rotational line can be written as

$$I_{\mathrm{nm}} = N_{\mathrm{m}} \cdot A_{\mathrm{nm}} \cdot h \cdot \nu_{\mathrm{nm}} \cdot \frac{1}{(2\pi)} \tag{16.42}$$

where N_{nm} is the population of the excited level and ν_{nm} is the frequency of the emitted radiation. The transition probability for dipole radiation is

$$A_{\mathrm{nm}} = \frac{(64 \cdot \pi^4 \cdot \nu_{\mathrm{nm}}^3)}{(3k)} \times \frac{1}{g_{\mathrm{m}}} \times \Sigma |R_{\mathrm{nimk}}|^2 \tag{16.43}$$

The indices i and k refer to degenerated levels of the upper (m) and the lower state (n), R_{nimk} is a matrix element of the electrical dipole moment and g_{m} is the statistical weight of the upper state. N_{m} is given by the Boltzmann equation:

$$N_{\mathrm{m}} = N \cdot \frac{(g_{\mathrm{m}})}{Z(T)} \cdot \exp\left(\frac{-E_{\mathrm{r}}}{kT}\right) \tag{16.44}$$

where E_{r} is the rotational energy of the excited electronic and vibrational level and is given by

$$E_{\mathrm{r}} = h \cdot c \cdot B_{\nu'} \cdot J' \cdot (J' + 1) \tag{16.45}$$

$B_{\nu'}$ is the rotational constant and J' is the rotational quantum number of the upper state (m). For a ${}^2\Sigma_{\mathrm{g}} - {}^2\Sigma_{\mathrm{u}}$ transition, the term $\Sigma |R_{\mathrm{nimk}}|^2 = J' + J'' + 1$, where J' and J'' are the rotational quantum numbers of the upper and the lower states, respectively. Accordingly,

$$I_{\mathrm{nm}} = \frac{(16 \cdot \pi^3 \cdot c \cdot N \cdot \nu_{\mathrm{nm}}^4)}{[3Z(T)]} \cdot (J' + J'' + 1) \cdot \exp[-h \cdot c \cdot B_{\nu'} \cdot J'(J' + 1)] \tag{16.46}$$

or

$$\ln\left[\frac{I_{\mathrm{nm}}}{(J'+J''+1)}\right]=\ln\frac{[16\cdot\pi^3\cdot c\cdot N\cdot\nu_{\mathrm{nm}}^4]}{[3Z(T)]}-\left[\frac{h\ \cdot\ c\ \cdot\ B_{\nu'}\cdot\ J'\left(J'+1\right)}{(kT)}\right] \tag{16.47}$$

From a plot of $\ln[I_{\mathrm{nm}}/(J'+J''+1)]$ versus $J'(J'+1)$ for a series of rotational lines, a so-called rotational temperature can be determined. It characterizes the kinetic energy of the molecules and radicals responsible for emission of the band spectra. It is also a good approximation of the temperature, reflecting the kinetic energy of the neutrals and ions in a plasma. In the case of an ICP, rotational temperatures were measured with $N_2{}^+$, CN, and O_2 as thermometer species and radially resolved values published (see, e.g., Refs. [21, 22]). The values are at the 4000–5000 K level, being a bit lower than the excitation temperatures (5000–6000 K) commonly stated. This argues for the existence of deviations from local thermal equilibrium in an ICP.

The rotational temperatures are of the same level as the gas temperatures derived from the Doppler broadening of spectral lines.

As spectral lines of molecular bands may interfere with atomic spectral lines in ICP-OES or molecular fragments give rise to signals in mass spectrometry, which can also interfere with the signals from the ionized analyte atoms, it is important to consider the dissociation of molecular species in the ICP. The dissociation of gas-related species and molecule fragments is a function of the temperature and the plasma composition of the ICP. This dependence can be described by a dissociation equation, which is similar to the Saha equation:

$$K_{\mathrm{n}}=\left[\left(\frac{2\pi}{h^2}\right)\cdot\left(\frac{M_{\mathrm{X}}\cdot M_{\mathrm{Y}}}{M_{\mathrm{XY}}}\right)\cdot(k\cdot T)\right]^{\frac{3}{2}}\cdot\ (Z_{\mathrm{X}}\cdot\ Z_{\mathrm{Y}})\ \cdot\left[\exp\left(\frac{-E_{\mathrm{d}}}{(kT)}\right)\right] \tag{16.48}$$

where:

$$K_{\mathrm{n}}=\frac{(n_{\mathrm{X}}\cdot n_{\mathrm{Y}})}{n_{\mathrm{XY}}} \tag{16.49}$$

Z represents the partition functions for the different atomic and molecular species, M_{X}, M_{Y}, and M_{XY} are the respective masses, and E_{d} is the dissociation energy. This can be rewritten as

$$\begin{aligned}\log K_{\mathrm{n}}&=20.432+\frac{3}{2}\log\left(\frac{M_{\mathrm{X}}\cdot M_{\mathrm{Y}}}{M_{\mathrm{XY}}}\right)+\log\left(\frac{Z_{\mathrm{X}}\cdot Z_{\mathrm{Y}}}{Z_{\mathrm{XY}}}\right)-\log g+\frac{1}{2}\log T\\&\quad+\log B+\log\left(1-10^{-0.625\frac{\omega}{T}}\right)-\left(\frac{5040}{T}\right)\times V_{\mathrm{d}}\end{aligned} \tag{16.50}$$

For most diatomic molecules, the constants B and ω (cm^{-1}) have been listed in tables (see, e.g., [19]). V_{d} is then given in electron volts and for a diatomic molecule:

$$Z=\left[\frac{kT}{(h\cdot c\cdot B)}\right]\times\left[\frac{g\times\exp\left(-\frac{E_d}{(k\cdot T)}\right)}{\left\{1-\exp\left\{\frac{h\cdot c\cdot\omega}{(kT)}\right\}\right\}}\right] \tag{16.51}$$

Thus, for a metal oxide (XY), from $n_{\mathrm{XY}}/n_{\mathrm{X}} = n_{\mathrm{Y}}/K_{\mathrm{n}}$ the ratio of the number densities for the metal oxide and the metal atoms (n_{X}) as well as the degree of dissociation can be calculated when the plasma temperature, the partial pressure of oxygen in the plasma (p_{Y}), and the dissociation constant are known. This allows it to inform on the occurrence of band spectra and on the signal intensities for cluster ions in optical emission and mass spectra, respectively, in the case of the ICP.

16.2
Inductively Coupled Plasma Optical Emission Spectrometry

ICP-OES is a prominent method for multielement determinations of trace, minor, and major constituents in a wide variety of samples. Both its instrumentation, its optimization, and figures of merit as well as its application possibilities in different fields of chemical analysis are treated in this chapter.

16.2.1
Instrumentation

16.2.1.1 The Inductively Coupled Plasma

The energy of a high-frequency generator (in the frequency range of around 6–100 MHz) is transferred to a gas flow at atmospheric pressure (mostly argon) in a quartz tube system with the aid of a working coil. The electrons take up energy and collide with atoms, by which a plasma with a temperature of up to 6000 K is formed. At a suitable gas flow, geometry of the torch, and frequency, a ring-shaped toroidal plasma is formed, where the sample aerosol passes centrally through the hot plasma. The burner consists of three concentric quartz tubes. The aerosol is led with its carrier gas through the central tube. Between the outer and the intermediate tube a gas flow is introduced tangentially. It takes up the high-frequency energy and also prevents the torch from melting.

A torch of the type according to Fassel has a diameter of about 18 mm and it can be operated at 0.6–2 kW and with 10–20 l min^{-1} of argon. An intermediate argon flow (about 1 l min^{-1}) is useful when analyzing solutions of high salt content or organic solutions, so as to prevent salt or carbon deposition, respectively. In so-called low-consumption torches, the gas consumption could be brought down to about 6 l min^{-1} through the use of a special gas inlet or by reduction of the torch dimensions (see, e.g., Ref. [23]). It has been reported that ICPs in quasi-static operations can even be operated at powers of down to some 100 W and with an argon consumption as low as 1 l min^{-1} [24]. However, such plasmas are no longer robust sources that are capable of taking up wet aerosols of any aqueous sample solution with a sufficiently high sampling rate. Greenfield used a larger torch (outer diameter of up to 25 mm), in which an ICP can be operated at higher power and where argon, oxygen, or even air can be used for the outer gas flow (up to 40 l min^{-1}) [6].

ICP generators are R–L–C circuits producing a high-frequency current at high power. The stability of the power and the constancy of the gas flows are both essential in order to obtain the highest analytical precision. ICP generators with frequencies ranging from 27 to 100 MHz have been used and in general 27.12 and 40 MHz generators are now available. As a result of detailed investigations by Mermet and Michaud-Poussel, only slight differences in the performance in terms of detection limits and matrix interferences have been measured (see, e.g., Ref. [25]).

The ICP can be viewed side-on as well as end-on for atomic emission spectrometry. While in the beginning side-on observation only was used, end-on observation was later found to have a number of advantages: (i) the optical pathway is longer, which may remove detector noise limitations, especially when working at low UV and VUV wavelengths and (ii) it is easy to realize a system that is transparent at VUV wavelengths, enabling determinations to be made of elements such as the halogens, phosphorus, and sulfur, as well as of many metals with lines free of spectral interferences and with high line-to-background intensity ratios [26]. Therefore, limitations with respect to the linear dynamic range and higher easily ionized element interferences as a consequence of the larger influence of geometry changes of the plasma may occur [27].

16.2.1.2 **Sample Introduction**

In ICP spectrometry, the sample must be introduced into the source as a fine aerosol. The aerosol should enter the hot plasma zones with a low injection velocity so as to realize residence times in the millisecond range that are required for an efficient atomization and excitation. Therefore, the carrier-gas flow should not exceed $1–2\,\mathrm{l\,min^{-1}}$.

For solutions, sample introduction into the ICP in the rule makes use of *pneumatic nebulization*. The pneumatic nebulization of liquids is based on the viscous drag forces of a gas flow passing over a liquid surface and entraining parts of the liquid, by which small independent droplets are produced. This may occur when the liquid is forced through a capillary tube, and at the exit the gas then concentrically flows around the tube or perpendicularly with respect to the liquid stream. A fritted disk can also be used, which is continuously wetted and through which the gas flows.

Nebulizers are mounted in a nebulization chamber, which has the function of separating off the larger particles and leading them into the waste. Impact surfaces are often provided, so as to fractionate the aerosol droplets further, by which the efficiency of the aerosol production increases. In plasma spectrometry, a nebulization chamber according to Scott *et al*. [28] often is used. A cooling of the spray chamber may decrease the water vapor loading of the aerosol, which may increase the elemental signals and prevent cluster ion formation in ICP-MS (see later). The spray chamber needs some time to fill up with the aerosol produced and some tailing of the signals is seen, resulting from a removal of the sample aerosol by the new incoming gas and aerosol. These build-up and wash-out times limit the speed of analysis and lead to a flattening of transient signals, when a vapor

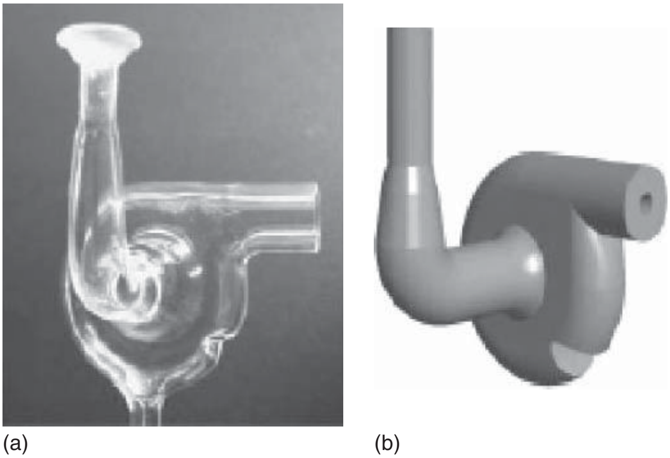

Figure 16.3 Photograph of a spray chamber according to Wu and Hieftje [29] (a) and a computer-generated 3D design (b). (Reproduced with permission from Ref. [30].)

cloud passes through the spray chamber, as is the case in flow injection analysis. In order to minimize these dead times, small spray chambers with short build-up and rinsing times have been constructed by decreasing their volume and optimizing their form with respect to ideal aerosol droplet fractionation and very efficient surface renewal. This resulted, for example, in the cyclone chamber described by Wu and Hieftje (Figure 16.3) [29]. They showed that with this spray chamber the wash-out times were very short without sacrificing analytical precision or power of detection.

In the pneumatic nebulizers used in ICP atomic spectrometry, the liquid flow is usually on the order of 1 to a few milliliters per minute and the full efficiency of the nebulizer (a small percentage) can actually be realized at gas flows below $2\,\mathrm{l\,min^{-1}}$. Even at lower gas flows, droplet diameters as low as about $10\,\mu\mathrm{m}$ and injection velocities below about $10\,\mathrm{m\,s^{-1}}$ can be obtained. Pneumatic nebulization in ICP spectrometry can be realized with concentric nebulizers, so-called cross-flow nebulizers, Babington nebulizers, and fritted-disc nebulizers (Figure 16.4). Concentric nebulizers consist of a narrow capillary through which the liquid is aspirated by the suction of gas flowing through a wider tube surrounding the capillary. At the tip of the capillary, small droplets are segmented from the liquid and with the gas form an aerosol. This type of nebulizer is known since the work of Gouy in the nineteenth century [31]. In ICP atomic spectrometry, the use of a concentric glass nebulizer (Meinhard Ass.) is typical. This nebulizer uses a gas flow of $1{-}2\,\mathrm{l\,min^{-1}}$ and is self-aspirating. The sample uptake rate is $1{-}2\,\mathrm{ml\,min^{-1}}$ and the aerosol efficiency is 2–5%. The gas pressure required is 2–7 bar and special types made of quartz also enable the analysis of dilute HF-containing solutions. Interesting developments are high-efficiency concentric nebulizers operated at very high pressures (tens of bars) [32] and microconcentric nebulizers [33], the latter allowing liquid flows in the sub-microliters per minute range as required

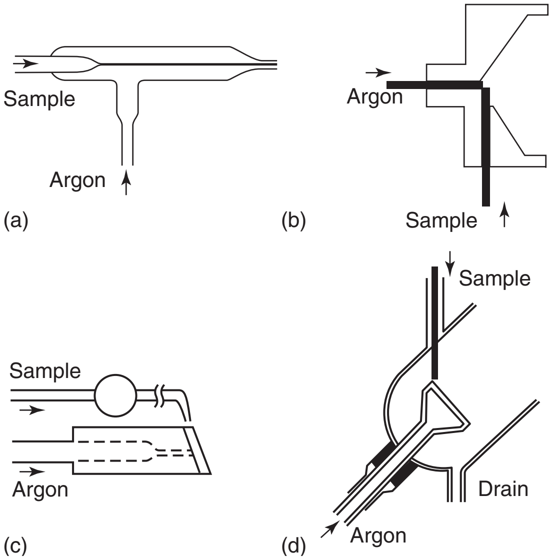

Figure 16.4 Types of pneumatic nebulizers: (a) concentric glass nebulizer, (b) cross-flow nebulizer, (c) Babington nebulizer, and (d) fritted-disc nebulizer. (Reproduced with permission from Ref. [36].)

in the coupling of liquid chromatography to ICP atomic spectrometry. Cross-flow nebulizers using glass or plastic nozzles are less sensitive to alkaline contents with respect to their stability but need to be fed with the aid of a peristaltic pump. Further, their characteristics are similar to those of concentric nebulizers. In the case of Babington nebulizers, the sample solution is pumped through a wide tube into a groove, where the film running off is nebulized by a gas flow entering perpendicular to the film of liquid. As the sample solution does not need to pass through a narrow capillary, solutions containing high salt concentrations and also slurries can be analyzed without the risk of clogging. This nebulizer, first described by Babington in 1973 [34], was later extensively used by Ebdon and Cave (see, e.g., Ref. [35]) especially for slurry nebulization.

Later on, direct injection nebulizers were designed, which allow it to work without a spray chamber. In this way, sample losses are low as are the dead times. This can only be achieved when the aerosol droplets are fine enough to avoid sample deposition or incomplete evaporation in the source. It ideally can be realized in the case of a high-efficiency nebulizer (DIHEN, direct injection high-efficiency nebulizer), as studied in Montaser's group [37] and is very useful when coupling liquid chromatography to ICP atomic spectrometry.

Further devices used for pneumatic nebulization make use of the expansion of liquid jets or impact nebulization.

In the optimization of pneumatic nebulizers, working conditions that give optimum droplet size and efficiency must be selected and where the droplets are brought with the highest possible residence time in the ICP. The so-called Sauter diameter d_0, that is, the diameter for which the volume-to-surface ratio equals that of the complete aerosol is approximated by the Nukuyama–Tanasawa equation (see Ref. [38]):

$$d_0 = \frac{C}{\nu_G} \cdot \left(\frac{\sigma}{\rho}\right)^{0.5} + C'\left\{\frac{\eta}{\left[(\sigma \cdot \rho)^{0.5}\right]}\right\}^{C''} \cdot \left[1000 \cdot \left(\frac{Q_L}{Q_G}\right)\right]^{C''} \tag{16.52}$$

where ν_G is the gas velocity, Q_G the gas flow, Q_L the liquid flow, η the viscosity, ρ the density, σ the surface density of the liquid, and C, C', C'', and C'' are constants. When the nebulizer gas flow increases, d_0 becomes smaller (through ν_G and Q_G) and the sample introduction efficiency will increase; as a result, the signals also increase. However, the higher gas flows through the ICP then cool the plasma and decrease the residence times of the droplets, and accordingly the atomization, excitation, and ionization also will decrease. These facts will counteract any increase in the signals as a result of the improved sampling. Accordingly, the highest signal intensity and thus the lowest detection limits will be achieved at a compromise gas flow. The physical properties of the liquid (σ, η, and ρ) also influence d_0, the efficiency and the analytical signals. Differences in the physical properties of the liquid samples to be analyzed thus lead to so-called nebulization effects and especially η has a large influence. It influences d_0 through the second term in Eq. (16.52). However, in the case of free sample aspiration, it also influences d_0 through Q_L, which is given by the Poiseuille law as

$$Q_L = \left[\frac{(\pi \cdot R_L^4)}{8 \cdot \eta \cdot l}\right] \cdot \Delta P \tag{16.53}$$

R_L is the radius and l the length of the capillary, ΔP is the pressure difference and is given by

$$\Delta P = \Delta P_U - g \cdot h \cdot \rho - f(\sigma) \tag{16.54}$$

where ΔP_U is the difference between the pressure inside and outside the nebulizer, h is the height, and $f(\sigma)$ a correction factor. In order to minimize the nebulization effects, one can utilize forced feeding with a peristaltic pump, the result of which is that Q_L is no longer a function of η. One also can operate the nebulizer at a high gas flow, by which Eq. (16.52) reduces to

$$d_0 = \frac{C}{\nu_G} \cdot \left(\frac{\sigma}{\rho}\right)^{0.5} \tag{16.55}$$

when Q_G/Q_L becomes >5000. However, the gas flow may then cool the source down through which incomplete atomization or signal depressions or enhancements may lead to even stronger interferences. Droplet sizes of most pneumatic nebulizers are at the 10 μm level and can be determined by measurements with cascade impactors or by stray light measurements. They are lower in the case of organic solutions than with aqueous solutions. As a lot of vapor can also accompany the aerosol droplets, desolvation of the sample aerosol may be required. This can be done by condensation of the vapor in a cooler or by diffusion through membranes such as

Nafion, which only can be permeated by the vapor and not by the droplets. Larger droplets, which represent a large fraction of the sample, may make the plasma unstable because of sudden evaporation effects. They have to be eliminated by the spray chamber and go into the waste as discussed earlier.

As an alternative to pneumatic nebulizers, *ultrasonic nebulizers* have been introduced in ICP atomic spectrometry for work with liquids. In these devices, the interaction of sufficiently energetic acoustic waves of a suitable frequency with the surface of a liquid leads to the formation of geysers by which an aerosol is produced. The diameter of the aerosol droplets produced depends on the frequency and on the physical properties of the liquid sample. In the case of water, for instance, aerosol droplets formed at a frequency of 1 MHz are about 4 μm in diameter. A system where the liquid flows over a transducer crystal was made commercially available. Because of the small droplet size, the aerosol production efficiency is high. As the accordingly high amount of liquid brought into the ICP cools the plasma more intensively, aerosol drying has to be applied. Then the power of detection is higher than with pneumatic nebulization. The approach, however, can only be used for samples with low salt loading such as drinking water, where the memory effects are high and the precision low.

Volatile species generation is a powerful approach for the determination of all elements that easily form volatile compounds as a result of chemical reactions. This has since long been applied for the determination of elements such as As, Se, Sb, Te, Bi, Sn, and so on, by atomic absorption spectrometry. Indeed, by *in situ* generation of the hydrides of these elements (AsH_3, etc.) from the sample solutions, the sampling efficiency can be increased from a small percentage in the case of pneumatic nebulization to virtually 100%.

Hydride generation can be performed efficiently by reduction with nascent hydrogen, as produced chemically by the reaction of acids with a solution of $NaBH_4$ in a flow cell. Also, electrolysis of acid solutions can be used for the production of nascent hydrogen. Here, the hydrogen is produced at the cathode and the oxygen at an anode separated from the cathode by a Nafion membrane, which prevents the mixing of both gases. Generally, the detection limits in ICP-OES for the elements mentioned in the case of flow-cell hydride generation can be improved by a factor of about 50 as compared to those of pneumatic nebulization (see, e.g., Ref. [39]). One can trap the hydrides and separate them from the excess of hydrogen produced by the use of a cooling trap with liquid nitrogen or by trapping the hydrides in a heated graphite furnace in which the hydrides are thermally decomposed (at about 700 K) and deposited as metals, which in turn can be volatilized at a temperature of >1500 K. In these cases, the power of detection of hydride generation, as a result of the preenrichment and the possibility of sweeping the collected analytes within a small time into the ICP, can be accordingly increased.

The accuracy in the case of hydride generation is limited by the fact that in different oxidation states the hydride generation species are formed with different efficiency, which in turn may be useful for speciation. Also, organometals in most cases first have to be mineralized to form the hydrides and heavy metals may influence the hydride generation efficiency as well. The latter interference can be prevented by complexing the interferents.

A similar volatilization reaction is possible in the case of Hg, where both under the use of a reducing agent such as $SnCl_2$ as well as through the use of $NaBH_4$ solutions, the volatile mercury metal can be formed with a high efficiency. Presently, research efforts are being made to expand the volatile species generation principle when using sodium tetraborate solutions to many more metals, and in the case of Cd, Au, and so on, this seems to be well possible [40].

Electrothermal evaporation of dry solution or suspension residues and transport of the released analyte with a carrier gas enable it to bring sample analytes with high efficiency into an ICP. As, here again, sample introduction efficiencies of theoretically up to 100% can be obtained, this is a technique with a high absolute power of detection, which is useful both for the analysis of small amounts of samples as well as for the determination of low concentrations. In the case of powders, the approach allows direct solids analysis after the preparation of slurries. Also, trace-matrix separations limiting the spectral interferences can be achieved by applying selective volatilization of the elements to be determined from the samples. For refractory powders, the approach seems to be very useful for the determination of volatile elements or of elements after converting them into volatile species by a suitable thermochemical reaction. Here, the principle of halogenation was found very useful as shown, for example, by a direct analyses of Al_2O_3 powders (see, e.g., Ref. [41]). The use of thermochemical reagents was found to be not only useful for volatile compound formation, but by radiotracer experiments it also could be shown that it may result in a considerable increase of the aerosol transport efficiency as a result of improved nucleation [42].

An extremely high absolute power of detection in ICP-OES can be obtained when *inserting the sample directly in the ICP*, as first shown by Salin and Horlick [43]. Here, detection limits of down to the sub-picogram level can be realized. The approach, however, was never made commercially available.

For direct solid analysis as in the case of compact solid samples, *ablation with both electrical discharges* and with *lasers* is important.

When applying a discharge between the electrically conductive sample and a counter electrode, material is ablated from the sample through local melting and evaporation of the material from the burning spot as well as by mechanical impact of atoms, ions, and clusters, for example, from ablated material or condensed droplets returning to the burning area. In the case of arc ablation, the heating of the sample and its local evaporation are predominant. In general, low burning voltages (below 100 V in argon) and high currents (up to several tens of ampere dc or ac) are used; for steel, copper base alloys, and so on, a material ablation of several milligrams per minute can be realized, which guarantees detection limits being in the same range as when the samples are dissolved and the solutions analyzed by ICP-OES using pneumatic nebulization. Owing to the evaporation process, selective volatilization of compounds with different thermal volatilities, such as Cu and Zn in the case of brass, may cause matrix effects. With spark ablation using medium-voltage sparks (burning voltages between 400 and 600 V) at medium frequencies (50 to several hundreds of Hertz), the cathodic sputtering may play a more pronounced role by which selective volatilization is lower. The ablation rates and detection limits are in the same range as with arcs. In both cases, burning spots of 6–8 mm are used, by which local analysis with lateral resolution is not possible.

Laser ablation enables to obtain much narrower burning spots at the sample surface (some micrometers) and accordingly is suitable for local analysis as well as for bulk analyses, where sample inhomogeneities, however, may become problematic. Laser ablation further has the advantage of being useful both for electrically conductive materials and isolators, such as glasses and ceramic samples. Several types of lasers have been used. While the first work was done with infrared solid-state lasers, now Nd-YAG-lasers are mostly used and instead of their basic wavelength of 105.4 nm one now uses frequency multiplexing to the UV range (also below 250 nm). In the case of laser ablation, craters produced at the sample surface with UV lasers and at atmospheric pressure have diameters of about 10 μm. They are determined by the diffraction of the laser radiation, heat conduction of the sample, the focal length of the focusing lens used, and the laser plasma effects. Because of the increase in the absorption of radiation toward shorter wavelengths but also because of the decrease in the diffraction limitations of the burning spots with smaller wavelengths, the use of UV lasers greatly increased the possibilities of laser ablation. While in the past lasers with pulses at best in the nanosecond range were exclusively used, one now gets access to lasers with pulses in the femtosecond range. It was found that not only the definition of the burning spot but also the level of selective volatilization in the latter case can be improved considerably (for an elaborate discussion, see Ref. [44]). Definitive answers here, however, have not yet been obtained. Also, modeling work now is done with the aim of further clearing the way of optimization and the finally achievable figures of merit, if possible, with these lasers. The concentration detection limits of laser ablation combined with ICP-OES are similar to those of arc and spark ablation, as are the matrix effects. A special procedure makes use of a rotation of the burning spot over the sample surface. Herewith an area of up to 8 mm in diameter can be covered, by which bulk information becomes less dependent on sample inhomogeneities. Applications of laser ablation combined with ICP-OES are in the field of studies on inclusions in geological samples, analyses of glasses and ceramics, forensic analysis of textiles, the analysis of aerosols, the investigation of welding, and so on.

16.2.1.3 **Spectrometers**

Spectrometers in optical atomic emission spectrometry are required to produce the spectrum. Dispersive spectrometers consist of an entrance collimator, a dispersive element, and an exit collimator, where a radiation detector is provided. With the entrance collimator, a quasi-parallel beam is produced from the radiation coming from the ICP through the entrance aperture. It essentially consists of a slit, with a slit width $s_{e,}$ and a collimating mirror with a focal length f_k and a width W. The exit collimator images the monochromated radiation, leaving the dispersive element on the exit focal plane. In the case of an exit window, in which one spectral area after another can be isolated by turning the dispersive element, we have a monochromator. In a polychromator, the dispersive element is fixed and different lines can be simultaneously measured at different locations in the focal plane. This is often done on a curved surface with a radius of curvature R (Rowland circle). Currently, a detector with two-dimensional resolution such as a charge-coupled device (CCD) is mostly used, with which a part of the spectrum over a certain wavelength range as well as the intensities of the signals, eventually at several locations in the ICP, can be recorded simultaneously. Virtually the only dispersive elements now used are diffraction gratings. Prisms are used only as predispersers. Distinction can be made between plane and concave gratings, of which the latter have imaging qualities. For a reflection grating, as a result of interference, a parallel beam of white radiation, inciding at an angle φ_1 with the grating normal, is dispersed and at an angle φ_2 radiation of wavelength λ is diffracted according to the Bragg equation:

$$\sin\varphi_1 + \sin\varphi_2 = m \cdot \frac{\lambda}{a} \tag{16.56}$$

where m is the order and a is the grating constant. It is the inverse of the number of grooves per millimeter. The theoretical resolving power R_0 equals the total number of grooves on the grating. The angular dispersion can be obtained by differentiation of Eq. (16.56) with respect to λ:

$$\frac{\mathrm{d}\varphi_2}{\mathrm{d}\lambda} = \frac{m}{(a\cos\varphi_2)} \tag{16.57}$$

The angular dispersion and the theoretical resolving power R_0 are related as $\mathrm{d}\varphi_2/\mathrm{d}\lambda = R_0/D_S{}'$, where $D_S{}'$ is the width of the monochromatic beam where it exits the dispersive element. The reciprocal linear dispersion is given by

$$\frac{\mathrm{d}x}{\mathrm{d}\lambda} = \left(\frac{\mathrm{d}x}{\mathrm{d}\varphi_2}\right)\left(\frac{\mathrm{d}\varphi_2}{\mathrm{d}\lambda}\right) = \left(\frac{f_k}{\cos\theta'}\right)\left[\frac{m}{(a\cdot\cos\varphi_2)}\right] \tag{16.58}$$

Here, θ' is the angle between the plane of the detector and the direction of the sorting beam.

With a plane grating, several mountings (Figure 16.5) can be used. In the Czerny–Turner mounting, two spherical mirrors with slightly different focal lengths are positioned at slightly different angles. In this way, spherical aberration can be adequately corrected for. This mounting is used for scanning ICP spectrometers with highly dispersive gratings (more than 1800 lines mm^{-1}). With the Ebert monochromator, there is only one mirror serving as the entrance and the exit collimator. Accordingly, aberrations such as coma occur.

Apart from gratings used at low orders, so-called Echelle gratings are also used in ICP spectrometers. Their groove density is low (up to 100/mm) but, therefore, order numbers of up to 70 can be used [45]. Here, the orders overlap and must be separated by using a second dispersive element (e.g., a prism) either with its axis parallel to that of the Echelle grating or in the so-called crossed-dispersion mode. In the latter case, the spectrum occurs as a number of dots with a height equaling

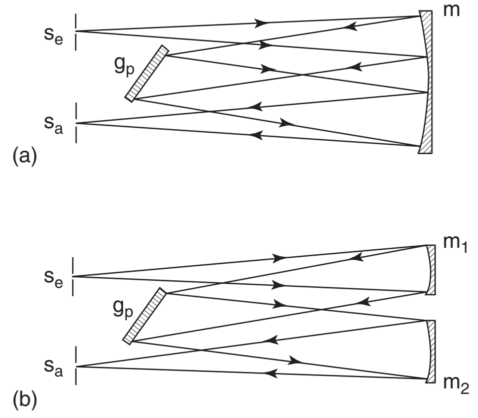

Figure 16.5 Ebert (a) and Czerny–Turner (b) mountings for monochromators. m: mirrors; s_e: entrance slit; s_a: exit slit, g_p: plane diffraction grating. (Reprinted with permission from Ref. [2].)

that of the entrance slit. The optical conductance is given by

$$\Phi = \frac{(B_\lambda \cdot t \cdot s \cdot h \cdot W \cdot H \cdot \cos \text{ß})}{f^2} \tag{16.59}$$

Here, B_λ is the spectral radiance, t the transmittance of the optics, W the width, and H is the height of the grating. Echelle spectrometers often use an Ebert mounting and allow a high spectral resolution to be obtained at low focal length (f). Therefore, they are thermally very stable. A two-dimensionally resolving array detector technology with high spatial resolution and sensitivity as well as high signal-to-noise ratios is now available. These detectors are much used in commercially available ICP-OES spectrometers. They allow large spectral regions to be collected on one detector of limited dimensions (e.g., 1 in. × 1 in.). The practical resolution then is finally limited by the pixel dimensions (e.g., 1000 pixels in one direction). In modern ICP spectrometers, a separate spectrometer is often built in to zoom into remote spectral areas, as required, for instance, for the alkali lines (Figure 16.6).

Mountings with a concave grating are also used. Here, the radius of the grating determines the so-called Rowland circle. In the direction of dispersion, the spectral lines are focused on the Rowland circle and are monochromatic images of the entrance slit. The Paschen–Runge mounting is most often used in simultaneous polychromators. Here, the grating, the entrance slit, and all detection elements are fixed on the Rowland circle. As the price of individual CCDs has come down, the whole relevant Rowland circle can be covered with CCDs. This allows more information as with classical polychromators, where, at the locations of the spectral lines, exit slits were provided and a photomultiplier was placed behind each individual exit slit. Indeed, by using CCDs information at any wavelength is accessible, whereas with photomultipliers one is limited to a number of lines (mostly below 30) and for background acquisition a scanning of the entrance slit has to be applied, which results in sequential measurements of line and background

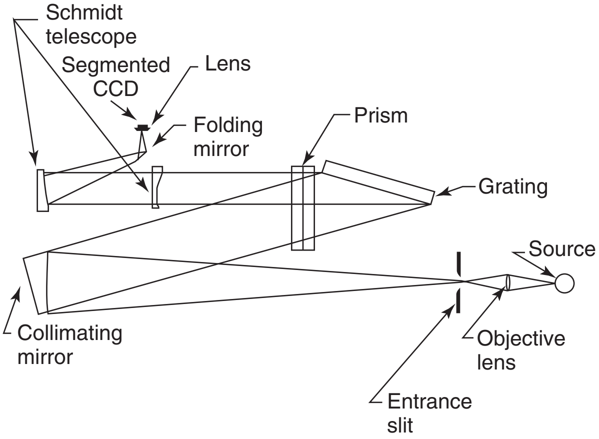

Figure 16.6 Echelle mounting in optical setup for CCD-ICP-OES (Optima) (Perkin Elmer Inc.).

intensities. The CCDs are positioned below and above the plane of the exiting radiation and mirrors placed at 45° are provided, by which a coverage of the whole spectrum, without missing any wavelength areas, becomes possible and a fully simultaneous spectrometer with data acquisition possibilities for analytical lines and background measurements at any wavelength can be realized (Figure 16.7). With such an instrument, the capacity of a photographically recording spectrograph for obtaining simultaneous information is now available for atomic spectrometry with the ease, precision, and time resolution of a photoelectrical system. However, some limitations in spectral resolution as a result of the minimum dimensions of

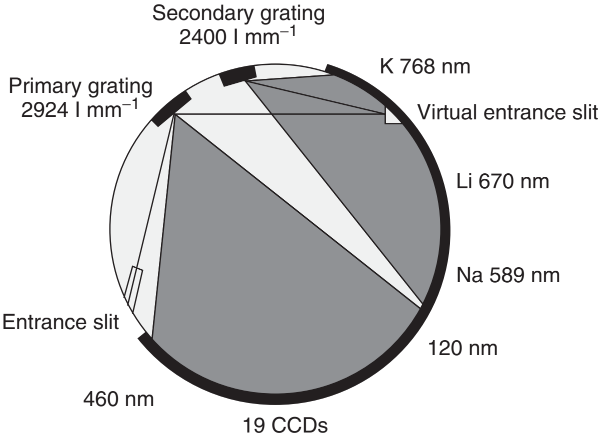

Figure 16.7 Optical setup for CCD-ICP-OES (CIROS) (Spectro Analytical Instruments GmbH).

the pixels and in signal-to-noise ratios as compared to classical photomultipliers especially at low UV wavelengths remain.

For the detection of radiation in the range of 150–500 nm, photomultipliers have been used for decades.

The photomultiplier has a photocathode and a series of so-called dynodes (for an in-depth treatment, see Ref. [46]). The radiation releases photoelectrons from the photocathode as a result of the Compton effect. After acceleration, these photoelectrons impact on the dynodes so that a large number of secondary electrons are produced, which, after successive action on a number of dynodes, leads to a measurable photocurrent at the anode (I_a). For a photon flux N_φ passing through an exit slit of a spectrometer and impacting on the photocathode, the flux of photoelectrons produced (N_e) is

$$N_e = N_\varphi \cdot \text{Q.E} \cdot (\lambda) \tag{16.60}$$

where Q.E. is the quantum efficiency (up to 20%). The cathode current (I_c) is given by

$$I_c = N_e \cdot e(e = 1.9 \times 10^{-19}\,\text{A} \cdot \text{s}) \quad \text{and } I_a = I_c \cdot \theta(V) \tag{16.61}$$

where $\theta(V)$ is the amplification factor (up to 10^6). The dark current I_d is the I_a measured when no radiation enters the photomultiplier (about 1 nA) and together with $\theta(V)$ and Q.E.(λ) is a characteristic for each photomultiplier. I_a is then fed to a preamplifier, amplifier, integrator, and digitizer. Photomultipliers for the spectral range between 160 and 500 nm usually have an S20 photocathode, but red-sensitive photomultipliers are also available. Below 160 nm, photomultipliers with a MgF_2 or LiF window are required. They have been the standard devices for high-precision measurements of radiation for decades.

Charge-transfer devices (CTDs) [47] are solid-state multichannel detectors and integrate signal information as radiation strikes them, just as a photographic film does. An individual detector in a CTD array consists of several conducting electrodes overlaying an insulating layer that forms a series of metal semiconductor (MOS) capacitors. The insulator separates the electrodes from a doped silica region used for photogenerated charge storage. In this n-doped silicon, the major current carrier is the electron, and the minor carrier is the hole. When the electrodes are negatively charged with respect to the silicon, a charge inversion region is created under the electrodes. This region is an energetically favorable location for mobile holes to reside in. The promotion of an electron into the semiconductor conducting band, such as by the absorption of a photon, creates a mobile hole that migrates to and is collected in the inversion region. The amount of charge generated in a CTD detector is measured either by moving the charge from the detector element, where it is collected to a charge-sensing amplifier, or by moving it within the detector element and measuring the voltage change induced by this movement. These two modes of charge sensing are employed by the CCD and the charge-injection device (CID), respectively. In the CCD, the charge from each detector element is shifted in sequence to an amplifier located at the end of a linear array or the corner of a two-dimensional array of detector elements. Charge

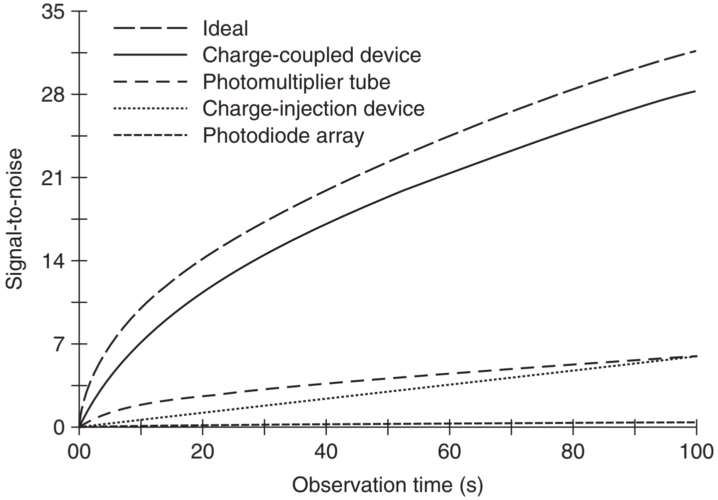

Figure 16.8 Calculated signal-to-noise ratios for different detectors at a photon flux of 10 photons s^{-1} for observation times ranging from 1 to 100 s at a wavelength of 600 nm. (Reprinted with permission from Ref. [47].)

is transferred to the on-chip amplifier by sequentially passing the charge packets through a row of detectors. Columns are read in parallel. With each reading, all of the charge in the imaging array is shifted toward the serial register by one row, whereas charge from the row adjacent to the serial register is transferred into the serial register. Once this is done, the charge packets are shifted sequentially to the on-chip amplifier. Modern CCDs are capable of thousands of transfers with almost immeasurable charge-transfer losses. By their ability to transfer the photogenerated signal from the photoactive element to an on-chip amplifier, high signal-to-noise ratios can be obtained, as compared with other detectors (Figure 16.8) [47]. With CIDs, the charge information can be read out nondestructively, further increasing the signal-to-noise ratios. With CCDs, binning can be applied, which is the process of summing the charge contained in multiple elements on the detector before sensing the total charge [48]. CTDs that can be used from the soft X-ray region to the IR are now commercially available and the signal-to-noise ratios achievable have become as high as with photomultipliers. The dynamic range has risen up to seven orders of magnitude in the case of a CID [49]. These two-dimensional detectors are ideally suited for coupling with Echelle spectrometers also for use as an alternative to photomultipliers in conventional spectrometers, where they allow simultaneous line measurements within a limited spectral range.

The ICP can be viewed axially and radially, of which the analytical possibilities are slightly different, as discussed further. In both cases, the radiation is focused through the entrance slit so that the entrance collimator is fully filled with radiation. This can be done with the aid of a lens, enabling a magnification of the relevant emission zone in the plasma (x) to the dimensions of the collimating mirror (W) by using the formulas:

$$\frac{1}{f} = \frac{1}{a} + \frac{1}{f_\mathrm{k}} \tag{16.62}$$

and

$$\frac{\mathrm{x}}{\mathrm{W}} = \frac{a}{f_\mathrm{k}} \tag{16.63}$$

Here, a is the distance between the source and the entrance slit, f is the focal length of the lens, and f_k is the focal length of the spectrometer.

Also, quartz fibers may be used to make the radiation transfer to the spectrometer more flexible. However, then the lower limit for the radiation transferred is at 220 nm. As an alternative, nowadays so-called light pipes, which make use of the total reflection of radiation, are also used.

16.2.2
Figures of Merit

16.2.2.1 Power of Detection

The detection limits (c_L), when determined according to the 3σ-concept [50], can be calculated from

$$c_\mathrm{L} = \left(\frac{I_\mathrm{X}}{I_\mathrm{U}}\right)^{-1} \cdot \left(\frac{1}{c}\right) \cdot 3\sqrt{2} \cdot 3\sigma_\mathrm{r}(I_\mathrm{U}) \tag{16.64}$$

where $I_\mathrm{X}/I_\mathrm{U}$ is the line (I_X) to background (I_U) intensity ratio measured for an analyte concentration c and $\sigma_\mathrm{r}(I_\mathrm{U})$ is the relative standard deviation of the background intensities. $I_\mathrm{X}/I_\mathrm{U}$ is a function of the nebulizer gas flow especially, the observation zone selected and the power, all of which have to be optimized so as to obtain the lowest possible detection limits for a given element or under compromise conditions. Generally, a power level of 1–1.5 kW is used and the observation window selected between 2 and 4 mm above the load coil.

The detection limits for most elements are at the 0.1 (Mg, Ca, ...) to 50 ng ml^{-1} level (As, Th, ...). In particular, for elements that have refractory oxides (such as Cr, Nb, Ta, Be, rare earths, ...), a fairly low ionization potential, and sensitive ion lines, the detection limits are lower than in AAS. On the contrary, the detection limits for elements with high excitation potentials, such as Cd, Zn, and Tl, are lower in AAS than in ICP-OES. For P, S, N, O, and F, the most sensitive lines are at VUV wavelengths and here with vacuum spectrometers and VUV transparent pathways and optics, values of 450 ng ml^{-1} (Br), 200 ng ml^{-1} (Cl), 3.9 ng ml^{-1} (P), and 3.5 ng ml^{-1} (S) can be obtained [51].

The detection limits obtained by radial and axial observation were found to be up to one order of magnitude lower in the axial as compared with the radial viewing, as reported by Ivaldi and Tyson [27]. These results were obtained with an Echelle spectrometer using CCD detection. The results were found to be partly due to better signal-to-noise ratios and also to lower RSD values. The latter may be understood from a better stabilization of the plasma.

In organic solutions, determinations can also be performed with ICP-OES using pneumatic nebulization. Indeed, solvents such as MIBK, xylene, or kerosene can also be nebulized (see, e.g., Ref. [52]). The addition of oxygen or the use of higher power is helpful so as to avoid carbon deposits. It also has been suggested that the use of burners with sharp edges and improved flow dynamics is helpful in preventing carbon deposits [53]. Oils can be analyzed after dilution 1 : 10 with xylene (c_L: 0.5–1 $\mu g\, g^{-1}$).

16.2.2.2 **Interferences**

Most interferences in ICP-OES are additive interferences and relate to coincidences of analyte lines with spectral background structures. These can be decreased by the use of high-resolution spectrometers and background correction procedures. Also, the line selection must be optimized in view of the sample matrix, for which atlases (see, e.g., Ref. [54] or tables where the resolution of the spectrometer also is considered, as worked out by Boumans [55], are useful.

Multiplicative interferences, however, also occur in ICP-OES. They may have several causes:

- *Nebulization effects*: as discussed earlier, differences in the physical properties of the different samples and calibration solutions lead to variations in the aerosol droplet size and thus also in the efficiency of the nebulizer and the sample introduction. This effect is strongest in the case of free sample aspiration and relatively low nebulizer gas flow and can be minimized.
- *Easily ionized elements have a complex influence*: first, they may shift the ionization equilibrium for partially ionized elements as they may influence the electron number densities through their easy ionization. They may also cause changes in the plasma volume as a result of ambipolar diffusion or eventually quench excited species such as metastables [15]. After correcting for the influence of easily ionized elements on the spectral background, signal enhancements or suppressions are negligible up to concentrations of 500 $\mu g\, ml^{-1}$ of Na, K, Ca, or Mg. At larger concentrations, matrix matching is required. It also was found that interferences caused by NaCl were nearly twice as large in the case of axial viewing than in radial viewing and that atom-to-ion line intensities were influenced more severely in the case of axial viewing [51]. Therefore, axial viewing allows it to exclude any air from entrainment into the ICP, by which many VUV lines can be used free of spectral interferences [56].

16.2.2.3 **Analytical Precision**

As the sample introduction is stable in ICP-OES using pneumatic nebulization, RSDs in ICP-OES can easily be brought down to below 1%. The dominant noise sources are nebulizer noise, fluctuations of the power and of the gas supply, especially. These sources can be at least partially eliminated, especially in the case of a CCD spectrometer where the signals can be freed from correlating spectral background fluctuations as the line and background intensities can be measured simultaneously. Accordingly, for PbBiSrCaCuOxide high-temperature supraconductor precursor materials, the main components could be determined with a precision of up to 0.25% [57] and this can still be improved by internal standardization, which, however, is critical with respect to internal standard element and line selection. The principles hereof have been discussed in detail by Fassel *et al.* [58]. For an intensity ratio of two atomic emission lines from two elements:

$$\frac{I_{\mathrm{qp(Xo)}}}{I_{\mathrm{sr(Ro)}}} = \left\{ \frac{\left[n_{\mathrm{(Xo)}} \cdot A_{\mathrm{qp}} \cdot \nu_{\mathrm{qp}} \cdot g_{\mathrm{q}} \cdot Q_{\mathrm{(Ro)}} \right]}{\left[n_{\mathrm{(Ro)}} \cdot A_{\mathrm{sr}} \cdot \nu_{\mathrm{sr}} \cdot g_{\mathrm{s}} \cdot Q_{\mathrm{(Xo)}} \right]} \right\} \cdot \left\{ \exp\left[\frac{\left(E_{\mathrm{s}} - E_{\mathrm{q}} \right)}{(k \cdot T)} \right] \right\} \tag{16.65}$$

Fluctuations in number densities of both elements X (analyte) and R (reference element) are canceled. In order to keep the influence of fluctuations in the temperature low, lines with similar excitation energies should be used and also the partition functions should be of the same order of magnitude. As ionization also has to be considered, the ionization energies should be similar, rendering the choice difficult. Finally, ICP-OES becomes as powerful as the most precise analytical methods, as, for example, shown for the determination of the mass fractions of Li and Al in $\mathrm{LiAlO_2}$ for which the Li/Al amount of substance ratio was 0.9793 ± 0.0017 (i.e., $\pm$ 0.17%) [59]. Internal standardization also could be used to minimize concomitant influences, as shown by Bauer and Broekaert [60], where matrix effects amounting up to 20% could be corrected for to below some percent, however, again with a very critical influence of the internal standard element and line selection.

16.2.2.4 **Multielement Capacity**

The multielement capacity of ICP-OES is high, as is the linear dynamic range (up to five orders of magnitude). It is restricted on the lower side by the limits of determination and at the higher concentrations by the beginning of self-reversal of the spectral lines. This only starts at concentrations of about $20\,000\,\mu\mathrm{g\,ml^{-1}}$, which is due to the fact that analyte atoms hardly occur in the cooler plasma zones. The linear range for axial viewing is lower than for radial viewing. The latter, in particular, is due to the somewhat longer optical pathway [27].

16.2.2.5 **Miniaturized ICPs**

While ICP-OES, as such, has reached maturity instrumentally, research now is being done with respect to the miniaturization of ICP-OES. This line of research is in the trend of the lab-on-a-chip approach. Of course, here one does not aim at robust plasma sources coping with a high variety of samples but to have sources with which well-defined tasks can be taken care of, online and in the field. Small ICPs with low power and gas consumption were developed along with other miniaturized sources, as reviewed by Karanassios [61] and is an ongoing line of research.

An ICP realized as μICP, for which the setup has planar load coils produced by photolithography and micromachining technology, was developed in the group of Hopwood (see Ref. [62]). Here, neither the load coil nor the matching network needed cooling and the device could be operated at low pressure (0.1–10 Torr) at a power of 4 W and with a frequency of 493 MHz. In the source (Figure 16.9),

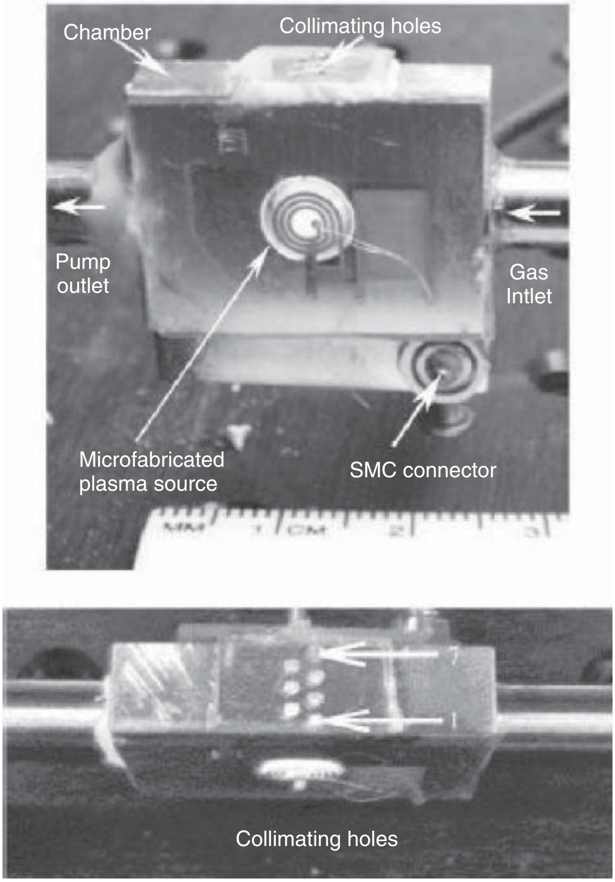

Figure 16.9 The microfabricated inductively coupled plasma-on-a-chip system is shown from the side and the top. The system includes a generator that is fabricated on a glass wafer and a miniature aluminum reaction chamber. (Reproduced with permission from Ref. [62].)

SO_2 could be detected in argon down to a concentration of 47 ppb using molecular bands (with the atomic S lines, the detection limits are four times higher). Thus, it was shown that the μICP could be of use for gas analysis. Even the ICP generator could be micromachined and its final dimensions reduced to 5 mm. Ichiki *et al.* [63] reported on an atmospheric pressure microplasma jet source exiting from a wafer. Here, the output power was 50 W at 144–146 MHz and the typical argon flow was $0.7\,\mathrm{l\,min^{-1}}$. Electron number densities on the order of $8 \times 10^{14}\,\mathrm{cm^{-3}}$ and excitation temperatures of 4000–5000 K were reported. With a miniaturized pneumatic nebulizer, in practice a capillary introduced directly into the discharge, a detection limit for sodium of $5\,\mathrm{\mu g\,ml^{-1}}$ was obtained, but no success could be achieved for other elements when introducing solutions. A number of other plasmas, especially microwave plasmas, were miniaturized and could be very well used in combination with gas-generating devices for spectrochemical analysis. Here, exemplarily, reference is to be made to the microwave strip plasma (MSP), designed by Engel *et al.* [64], which can also be used for the determination of volatile hydride-forming elements [65]. Further applications of the miniaturized sources certainly lie in their use for element-specific detection in gas chromatography.

16.2.3
Application Fields

ICP-OES is now a routine analytical method, which is of specific use when a large number of elements have to be determined in many samples. The latter can be solutions or dissolved solids. Therefore, in many cases, ICP-OES is complementary to AAS as the power of detection of furnace AAS cannot be rivaled for most elements. ICP-OES is of special interest in the analysis of geological samples, environmental analysis, clinical analysis, food analysis, metal analysis, chemical analysis, and for the certification of reference materials.

16.2.3.1 Geochemical Analysis

In the analysis of geological samples, sample dissolution with respect to not only nebulization but also to ionization interferences is important [15]. Indeed, in a number of cases, such as with carbonaceous minerals, a treatment with HCl will be sufficient; however, in a number of cases, it will be required to use strongly oxidizing acids. For samples with higher silicate contents, a treatment with HF even under the use of perchloric acid will be unavoidable. Here, fuming off will have to be performed carefully. Even fusion, for example, with sodiumtetraborate in a number of cases will be required, by which high amounts of alkali salts are entered into the sample solutions.

16.2.3.2 Environmental Analysis

The analysis of environmentally related samples is a major field of application of ICP-OES. On the basis of the early work of Garbarino and Taylor [66], a method has been proposed by the US EPA (Environmental Protection Agency) [67] and later on by DIN [68] for waste water analysis. The latter, standardized procedure describes the sample decomposition, the analytical range for 22 elements, and frequent interferences of ICP-OES in waste water analysis. For the analysis of natural waters, hydride generation [69], preconcentration based on liquid–liquid extraction of the dithiocarbamate complexes [70], adsorption of trace elements onto activated carbon [71], and also co-precipitation (e.g., with $In(OH)_2$)[72], and so on, have been reported; special emphasis has been given to online preconcentration as well [73]. For airborne aerosols, multielement determinations in large amounts of samples, collected with the aid of cascade impactors, allowing size-class differentiation can be performed by simultaneous ICP-OES subsequent to sample dissolution in HF/HNO_3 and complexation of the excess of HF with boric acid [74]. Here, many relevant elements, such as Ca, Mg, Fe, Ni, Pb, Cd, and so on, can be determined, which allows air pollution source appointment. The direct analysis of stack gases by

ICP-OES on the site has been investigated as well. However, the introduction of the air is difficult and therefore, other sources such as high-power microwave plasmas, which can be run on an air base, may be more suitable [75]. For the determination of heavy metals in soils, leaching under standardized conditions and analysis of the leachates by ICP-OES is a frequently applied procedure. In the case of fly ash, determinations of refractory elements are possible after decomposition of the samples by fusion or under the use of HF.

16.2.3.3 Analysis of Biological and Medical Samples

For the analysis of biological and medical samples, ICP-OES has some possibilities as well. In the clinical analysis, Ca, Fe, Cu, Mg, Na, and K can be determined directly even in microsized serum samples when calibrating with aqueous solutions of the elements to be determined, of which the viscosity has been adapted to one of the diluted serum samples (1 : 5) with Herrmann solution [76]. More elements can be determined in body fluids and tissues by the use of electrothermal evaporation of dry sample residues or by direct sample insertion; however, these techniques are not commercially available. For plant samples, sample drying and dissolution of the samples with oxidizing acids also allows the determination of a number of metals by ICP-OES. Furthermore, the power of detection of ICP-OES is too low for most of the analytical problems encountered in life sciences.

16.2.3.4 Analysis of Chemicals

This generally also applies to the analysis of high-purity chemicals. Therefore, however, online analysis of process fluids by ICP-OES is well possible and applied in the chemical industry.

16.2.3.5 Metals Analysis

Metals analysis, in particular, should be mentioned in the field of industrial products for which ICP-OES is of great use. It is used both in the ferrous industry and in the analysis of copper and aluminum samples. Also, for the analysis of by-products in the metal industry such as slags, the use of ICP-OES subsequent to fusion is useful. In the case of the metal bases, ICP-OES subsequent to acid dissolution of the samples is used for the characterization of laboratory samples, which are used for calibration of direct solids analysis methods such as XRF and spark OES. Apart from solution analysis, direct metals analysis by spark ablation is also useful [77]. This also applies for the use of a rotating laser sampling technique such as the LINA Spark coupled to ICP-OES, with which for a number of elements in different matrices low detection limits and linear calibration curves can be obtained [78].

In addition, the analysis of refractory powders by slurry nebulization for Al_2O_3 [79], SiC [80], and ZrO_2 [81] powder samples is to be mentioned. Here, a Babington nebulizer is used and calibration is done by adding aqueous solutions to slurries prepared from the powders. The results for sufficiently fine powders were found to be in good agreement with those of analyses subsequent to established sample decomposition methods, including the use of decomposition at high pressure with acids in autoclaves as well as under the use of microwave-assisted dissolution [79].

16.3
ICP Mass Spectrometry

Towards the end of the 1970s the ICP, which then was commercially available from a number of manufacturers in combination with different types of optical emission spectrometers, was first used as an ion source for quadrupole mass spectrometry by Houk in AMES Laboratory, and at the same time experiments were done by Gray *et al*. in the United Kingdom. The experimental realization of ICP-MS and its figures of merit were first described in a common paper in 1980 [8] and soon the approach became commercially available (for an in-depth treatment, see Ref. [82]).

16.3.1
Instrumentation

ICP-MS makes use of the ICP in the form it has been used for ICP-OES in a first approximation. The source, in all currently used instrumentation, is positioned horizontally and the ions are sampled from the plasma with the aid of a so-called sampler. This is a cone-shaped interface with an aperture of about 600 μm, which is water cooled. It separates the plasma, which is operated at atmospheric pressure, from the intermediate vacuum, which is realized with the aid of a powerful rotary oil pump. In the so-called interface region, a supersonic beam is formed and a number of collision processes take place as well as an adiabatic expansion. From this beam, ions are sampled into the vacuum of the mass spectrometer through a second aperture, named *skimmer*, which has a hole with a diameter similar to that of the sampler. The sampler and the skimmer are usually made of stainless steel and are both conically shaped with different cone angles. The sampler can also be made of copper, which has a better heat conductivity. In the case of HF-containing solutions, platinum cones can also be used. The distance between the sampler and the skimmer is critical with respect to maximum power of detection and minimal ionization interferences. This also applies to the power transmission to the RF coil, where considerable differences were found for coils powered centrally and coils powered at one of the ends [83]. The vacuum in the mass spectrometer itself is at the order of 10^{-5} mbar and is realized with the aid of turbomolecular pumps. The vacuum in the interface is monitored often with a capacitance pressure gauge, whereas in the mass spectrometer it is monitored with the aid of a Penning gauge.

16.3.1.1 Mass Spectrometers

Present day commercial instrumentation falls into three groups, namely, quadrupole-based instruments, high-resolution instruments, and time-of-flight instruments.

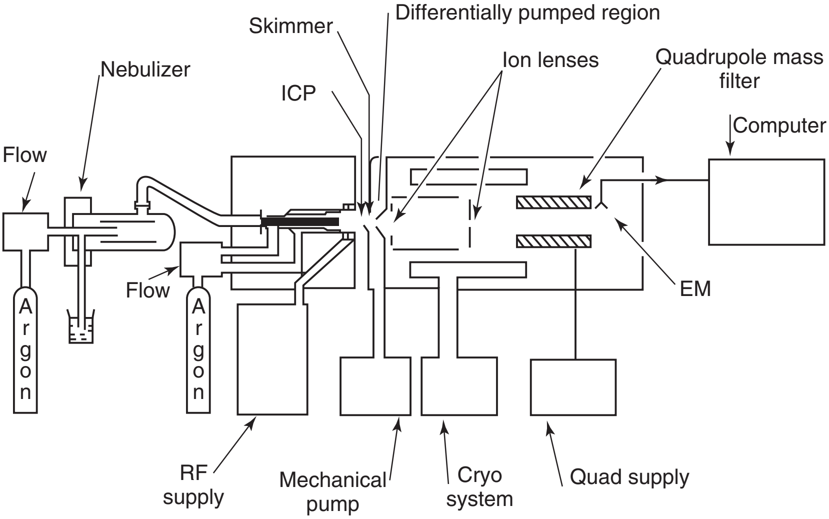

Figure 16.10 Instrumentation for quadrupole-based ICP-MS: (a) nebulizer, (b) sampler, (c) ion optics, (d) quadrupole, (e) electronics, (f) detector, (g) RF generator, (h) roughing pump, (i) turbomolecular pump, and (j) quadrupole RF generator. (Reprinted with permission from Ref. [2].)

In a *quadrupole-based* instrument, the spectrometer principally consists of four equidistant and parallel mounted rods (diameter: 10–12 mm) between which a DC voltage and in addition a high-frequency field (frequency up to 1 MHz) or $U + V.\cos(\omega t)$ is provided (Figure 16.10). By varying the alternating electrical field, ions with different m/z can leave the analyzer sequentially and scanning becomes possible. Ions within a narrow m/z range have a zone for stable oscillation at a well-defined DC voltage and a high-frequency field. Accordingly, ions of a certain mass can be filtered out by manual setting of the field or the spectrum can be scanned. The scanning velocity is normally limited to 30 000 Da s^{-1} as a result of the high frequency and the DC components used in a spectrometer. Thus, a mass interval of 0–300 Da can be scanned in about 30 ms. The mass resolution in the best case is about 1 Da. Spectral interferences occur as a result of line broadening, the isotopic abundances, and the occurrence of cluster ions. Quadrupole ICP-MS systems are rapid sequential measurement systems. Accordingly, the precision obtainable and the figures of merit of isotopic dilution techniques for calibration are limited by the noise occurring in the source. Therefore, the price of quadrupole instruments is reasonable and the transmission is high.

Magnetic mass analyzers make use of a curved flight tube located between the poles of an electromagnet, so that the field is perpendicular to the flight direction of the ions. The ions first pass through an electrical field and then enter a magnetic field where mass selection takes place. The electrical field is used to extract the ions, which then enter the magnetic field and start to follow a curved trajectory on which they are held by a centrifugal force. The radius of the curved trajectory depends on

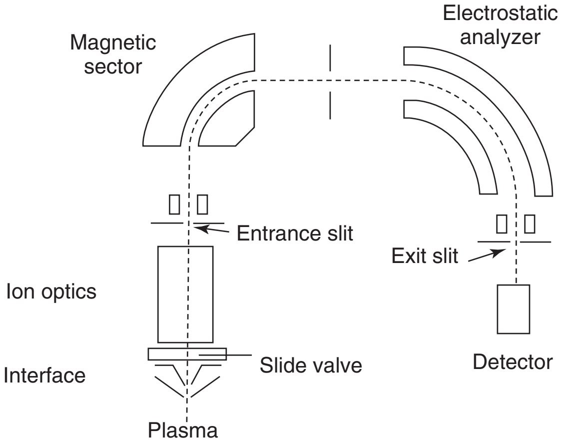

Figure 16.11 High-resolution ICP mass spectrometer. (Reprinted with permission from Ref. [85].)

m/z and the magnetic field. By sweeping the field, it is possible to scan the mass spectrum at an exit slit. As ions with different masses are deflected toward different locations in the focal plane, simultaneous detection of ions is thus possible with these spectrometers, provided that multichannel detection is applied. As the energy spread of the ion beam limits the resolving power of a deflecting magnetic sector mass analyzer, energy focusing must be applied. This can be done by providing an electrostatic analyzer in the ion optics. This electrostatic analyzer consists of two curved plates with a voltage on the order of 1.5 to 1 kV applied between them. When bringing the magnetic sector and the electrostatic sector together (Figure 16.11), a double-focusing instrument is obtained, where ions are selected by mass only and where the ion energy of the particles does not play a role. The use of a sector field mass spectrometer requires the source or the whole spectrometer to be brought at a high voltage, so as to realize a sufficient extraction yield. With sector field instruments, the resolution can easily be improved to below 0.1 Da (resolving power often up to 5000), enabling a number of spectral interferences in plasma mass spectrometry to be eliminated. The scanning speed cannot be increased in an unlimited manner, as hysteresis may hamper this. When the signals are transient and multielement detection is required, there are certainly limitations here. As the spectral background intensities are low, detection limits are lower than in quadrupole mass spectrometers, not only as a result of the absence of a number of spectral interferences but also because of better signal-to-background ratios [84].

The *time-of-flight mass spectrometer* is based on the detection of ions produced from a single well-defined event with high time resolution. The ions get an initial energy by passing an electrical field and then drift in a field-free region according to their mass. The principle is well known and has long been applied, for example, in secondary ion mass spectrometry (SIMS) [86]. As the velocity obtained by ions of a mass m in a field U is given by $1.4 \times 10^4 \sqrt{\left(\frac{U}{m}\right)}$ [87], the insertion of ions

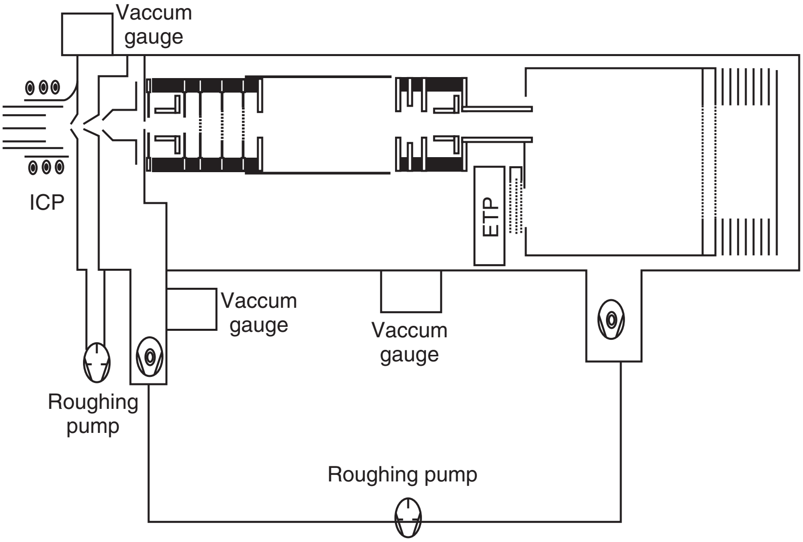

Figure 16.12 On-axis ICP time-of-flight mass spectrometer. (Courtesy of Leco Corporation, St. Joseph, MI (USA).)

of 50 Da in an electrostatic field of 5000 V results in a velocity of 1.4×10^5 m s^{-1}. Hence, for a flight tube with a length of 1.4 m one obtains, neglecting the time required to accelerate the ions, a flight time of 10^{-5} s. With modern electronics, one can differentiate very short times and thus obtain a mass resolving power of 2000. With this type of instrumentation, high transmission can be achieved and high mass resolution as well as high multiisotope capacity also for transient signals (see Ref. [88]). For time-of-flight ICP-MS, both orthogonal as well as linear end-on arrangements are used. The instruments commercially available use a reflectron to double the flight path (Figure 16.12) [89]. Now, *multicollector magnetic mass analyzers* are also used. They are particularly useful when a highly accurate recording of ratios of ion currents for different isotopes is required.A double-focusing instrument with a stigmatic focusing magnet and several individual detectors placed in the focal plane can be used to achieve such a system [90]. As in ICP-MS, isotope dilution is important for tracer work as well as for highly accurate calibration, these systems may gain considerable importance.

16.3.1.2 **Ion Detection**

As in ICP-MS ion currents between 10^{-20} and 10^{-9} A have to be measured, several detectors must be used. For a precise ion detection and relatively low signals ($<10^6$ ions s^{-1}), ion electron multipliers and pulse counting, as a rule, are used, whereas for higher ranges analog detection is used. In an ion counting device (Figure 16.13), the ions entering the analyzer are directed to a suitable surface held at high potential, so that the incident ions release several electrons. The surface may consist of a continuous dynode, the curvature of which guides the electrons, which

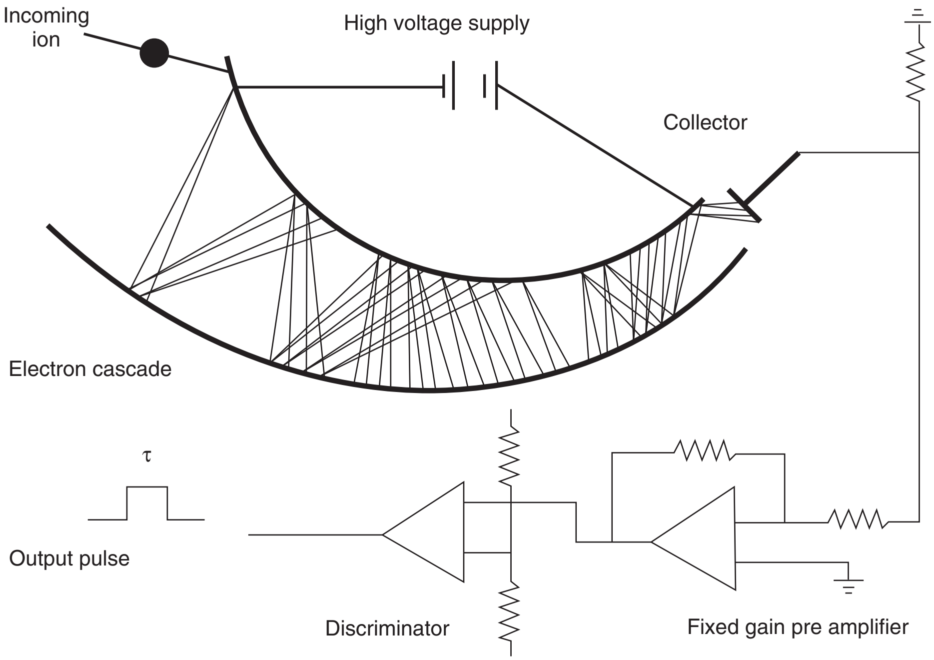

Figure 16.13 Continuous dynode electron multiplier. (Reprinted with permission from Ref. [94].)

increase in number at each interaction with the dynode surface. These detectors have a dead time, as the interaction of an ion takes a finite time (usually less than 10 ns), during which the detector is blind to the next ion. Accordingly, count rates beyond 1 MHz corrections are required, but damage to the detector may also occur. Further problems are related to the fact that the mass and ionization potential of the respective elements may influence the number of electrons released by the impact, which introduces bias, and, in addition, when high masses impact on a dynode, the lifetime of a diode may decrease considerably. Therefore, the ion current can be deflected onto a conversion dynode, which is more robust and is at a high negative potential for the ion impact, and the current carried by electrons then enters the dynode system. For the registration of larger signals, the voltage applied at the electron multiplier can be decreased and then a current is obtained, which in the case of ion currents above 10^6 ions s^{-1} is directly proportional to the input current. Another solution is the use of a so-called Faraday collector (Figure 16.14). With this system, currents of down to 10^{-15} A (10^4 ions s^{-1}) can be measured, corresponding to the upper range accessible with ion counting. The variable feedback resistor allows the measurement range to be adjusted and voltage-to-frequency conversion is applied for read-out. Faraday collectors have low mass bias and are robust but small. Through the use of novel microstructuring techniques, integrated multicollector array detectors for ions have also been realized. The most

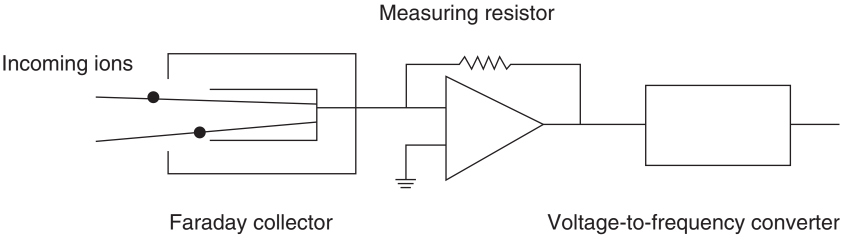

Figure 16.14 DC analog detector for mass spectrometry. (Reprinted with permission from Ref. [94].)

advantageous ion detectors are basically arrays of micro-Faraday cups. The charge-integrating detector, as described by Giffin *et al.* [91], responds to both positive and negative ions and also allows nondestructive read-outs. On top of each pixel of the charge-transfer detector, an island of electrically isolated conductive material is deposited. Each of the islands serves as a Faraday cup for the pixel below it. The conductive material responds to the incoming ion flux by supplying a neutralizing electron derived from the semiconductor band material beneath it. Each Faraday cup has its own low-capacitance integrator with a multiplexed read-out. In addition, each integrator can be read out nondestructively, which leads to an improved signal-to-noise ratio. The use of such a detector with a limited number of Faraday cups (128 strips of each 45 μm wide and set on 50 μm centers) [92] was described and with similar arrangements in the case of ICP-MS a relative precision for Ag isotope signals of 0.007% obtained [93].

16.3.1.3 **Ion Extraction and Optics**

For ion extraction in ICP-MS, Turner *et al.* [94] formulated the following requirements for the interface:

1) The pressure in the interface should be sufficiently low as to minimize chemical reactions.
2) The diameter of the sampling aperture should be as large as possible to maximize the analyte signal and to minimize orifice clogging, while keeping the pumps used for this section to a reasonable prize.
3) To sample the plasma in as undisturbed a state as possible, the diameter of the sampling orifice must be large compared with the Debye length in the plasma, which is a measure of the distance of the electrical field of an ion as ‘‘seen’’ by an electron, and is given by

$$\lambda_D = 6.9\sqrt{(T_e \cdot N_e)} \tag{16.66}$$

   Here, N_e is the electron number density and T_e is the electron temperature.
4) The gas flow through the sampler should not exceed the whole gas flow in the plasma, as only well-defined zones of the plasma (namely, those with the highest analyte concentrations) should be sampled.
5) Behind the sampler a concentric shock wave structure is formed, which surrounds a zone of silence and ends in a shock wave front called the *Mach*

disc. The interface should be such that the skimmer aperture still lies in the zone of silence for the optimal extraction.

In the case of the ICP a cooled sampler is used. Owing to the large pressure difference between the ICP and the first vacuum stage, the ions enter the interface with high energy. There is also a considerable adiabatic expansion of the plasma in the interface. This jet expansion is critical with respect to the analytical performance. Behind the skimmer the mutual repulsion of ions within the ion beam, known as *space charge effects*, also influence the ion trajectories. The magnitude of this effect depends on the total radial voltage drop (E_i), the current density (j), the total current (I), and the velocity (v) and is given by

$$\Delta\varphi = \int_0^a E_r \cdot \mathrm{d}r = \int_0^a \left[2 \cdot \pi j \cdot \left(\frac{r}{v}\right)\right] \mathrm{d}r = (9 \times 10^{11})\frac{I}{v} \tag{16.67}$$

Here, $v = 2.5 \times 10^5\,\mathrm{cm\,s^{-1}}$ and $\mathrm{I} = 10^{-6}\,\mathrm{A}$, $\Delta\varphi = 3.6\,\mathrm{V}$. With a field such as this, ions will move away from the beam axis and this movement is mass dependent and has to be corrected for with the aid of suitable ion optics. A cylindrically symmetric lens is used to transfer the ions sampled through the skimmer to an analyzer. To reduce the noise level, a metallic disk denoted as the ‘‘photon stop’’ is often placed in the center of the so-called Bessel box. Thus, radiation coming from the plasma sampled as it enters through the axially centered sampler and skimmer can be eliminated. Furthermore, the voltage at the lens is optimized so as to obtain as low a background (stemming from radiation and neutrals) as possible without decreasing the sensitivity. Alternatively, the mass spectrometer and/or the detector can be placed off-axis. A series of various lenses at different voltages is usually provided so as to direct the analyte ions as efficiently as possible into the analyzer. Often, three so-called Einzel lenses at negative potentials relative to the skimmer (varying from around −10 to −150 V) are used. The voltages applied determine the trajectories of the ions, which, however, also depend on their kinetic energies. The latter are element dependent and also relate to the zones in the ICP zones sampled. Computer programs, such as MacSimion (see Ref. [95]) and its more recent equivalents can be used to model the ion trajectories in ion optics after various assumptions. From these considerations, it becomes clear that in multielement determinations compromises must be made and that the analytical figures of merit at compromise conditions considerably can differ from those of single-element optimization.

16.3.2
Figures of Merit

The analytical features of ICP-MS are related to the production of ions in analytical ICPs as well as to the highly sensitive ion detection and the nature of the mass spectra themselves.

16.3.2.1 ICP Mass Spectra

In low-resolution ICP-MS, the resolution in the spectra at best is 1 Da and cluster ions are found, particularly in the low mass range, which in a number of cases cause spectral interferences with singly charged analyte ions, stemming from the analyte atoms for which the ionization degree is between 10^{-5}% (for Cl) and 9% (Ba). Cluster ions may be formed from different types of compounds, namely:

- solvents and acids: H^+, OH^+, H_2O^+, … , NO^+, NO^{2+}, … , Cl^+, … , SO^+, $SO_2{}^+$, SO_3H^+ (when residual H_2SO_4 is present in the measurement solution);
- radicals of gases in the surrounding atmosphere: $O_2{}^+$, CO^+, $CO_2{}^+$, $N_2{}^+$, NH^+, NO^+, …;
- reaction products of the above-mentioned species with argon: ArO^+, $ArOH^+$, … , $ArCl^+$, $Ar_2{}^+$, …

These cluster ions give strong signals in the mass range up to 80 Da and may hamper the determination of the light elements as a result of spectral interferences. At higher masses, the singly charged ions of the heavier elements are found, as are doubly charged ions of the light elements. They occur particularly for elements with low ionization energies.

In the mass spectra, signals for compounds of the analyte with various other species also occur, such as MO^+, MCl^+, MOH^+, $MOH_2{}^+$, …. These ions may be formed by the dissociation of nitrates, sulfates, or phosphates in the plasma or they may result from reactions between analyte ions and solvent residuals or oxygen in the plasma or eventually in the interface between the plasma and the mass spectrometer inlet.

In early work it was already recognized that the selection of the sampling zone in the plasma and the aerosol carrier-gas flow may strongly influence the occurrence of cluster ions and doubly charged analyte ions [85, 96]. This is clearly demonstrated by the results for lanthanum, where doubly and even triply charged ions may be expected in the argon plasma. This necessitates specific optimization of the power and especially of the carrier-gas flow, which influence both temperature and residence times of the sampled substance in the plasma. This is documented for the intensities of the signals for the ArO^+ and Cu^+ ions in Figure 16.15 [83]. Signals of all isotopes of the elements present in the sample are obtained. Their intensity ratios correspond to the isotopic abundances in the sample. Use can be made of this fact for calibration by isotopic dilution with stable isotopes and in tracer experiments. The isotopic abundances of the elements, however, are also useful for the recognition of spectral interferences. The spectra in ICP-MS are less line rich than in ICP-OES. With quadrupole mass spectrometers, however, the resolving power of the spectrometers is also lower than in ICP-OES. Accordingly, cluster ions will often cause spectral interferences, and appropriate correction procedures must be worked out. With high-resolution sector field instruments, which have a resolution of 5000 and more, a number of these interferences will not occur. This is shown by calculations of the minimum resolution that should be obtained so as to avoid the most frequent interferences occurring in ICP-MS (Table 16.1) [84]. In ICP-MS, the background intensities, mainly due to the dark current of the detector

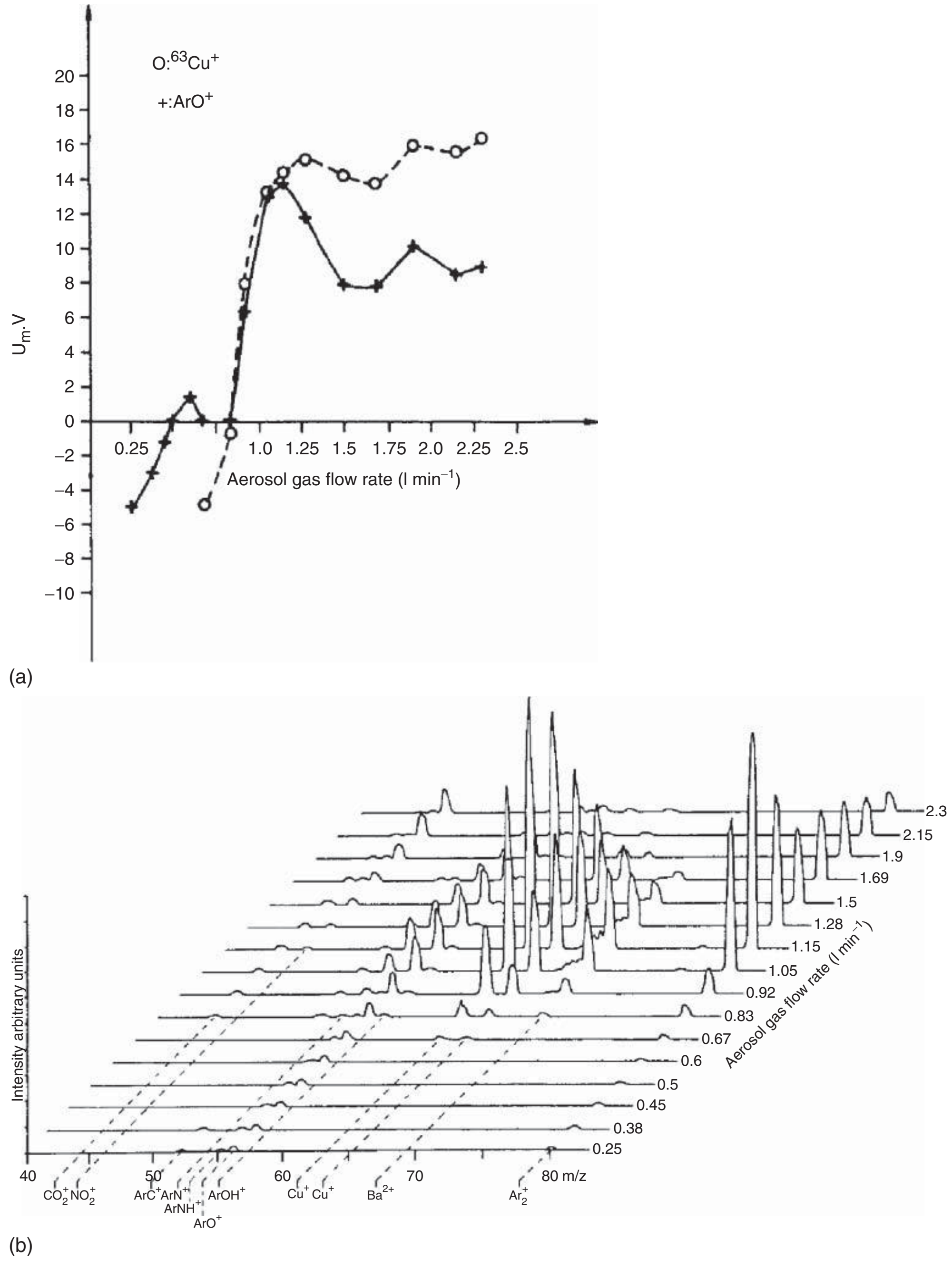

Figure 16.15 Maximum values of ion energies for two ion species (a) and mass spectra in the mass region 42–82 Da in ICP-MS (b) when sampling ions at different gas flow rates for a 1 μg ml^{-1} standard solution of Cu at radial distance 0 mm and 1.5 kW. (Reprinted with permission from Ref. [83].)

Table 16.1 Minimum required resolving power (*R*) in order to avoid spectral interferences in ICP-MS.

Isotope	Polyatomic ion	*R* required
^{27}Al	$^{12}C^{15}N$, $^{13}C^{14}N^+$, $^{12}C^{14}N^1H^+$	1454
^{51}V	$^{35}Cl^{16}O^+$	2572
^{52}Cr	$^{40}Ar^{12}C^+$	2375
	$^{35}Cl^{16}O^1H^+$	1671
^{53}Mn	$^{39}K^{16}O^+$	2670
	$^{37}Cl^{18}O^+$	2034
^{56}Fe	$^{40}Ar^{16}O^+$	2502
	$^{40}Ca^{16}O^+$	2479
^{60}Ni	$^{44}Ca^{16}O^+$	3057
	$^{23}Na^{37}Cl^+$	2409
^{63}Cu	$^{40}Ar^{23}Na^+$	2790
	$^{31}P^{16}O_2{}^+$	1851
^{64}Zn	$^{32}S^{16}O_2{}^+$	1951
^{75}As	$^{40}Ar^{35}Cl^+$	7775
^{77}Se	$^{40}Ar^{37}Cl^+$	9191

(Extracted from Ref. [84]).

and signals produced by ions scattered inside the mass spectrometer as a result of collisions with residual gas species or reflection, is generally low in contrast to ICP-OES.

16.3.2.2 **Optimization**

For the optimization of ICP-MS with respect to the highest power of detection, minimal spectral interferences and signal enhancements or depressions, as well as highest precision, the most important parameters are the power of the ICP, its gas flows (especially the nebulizer gas flow), the burner geometry, and the position of the samples, as well as the ion optics parameters. These parameters determine the ion yield and the transmission and accordingly also the intensities of the analyte and interference signals. At increasing nebulizer gas flow, the droplet size decreases; thus, the analyte introduction efficiency goes up, however, at the expense of the residence time in the plasma, the plasma temperature, and also of the ionization. The optimization of the carrier-gas flow, the ion sampling location, and the power also is more critical than in ICP-OES. This is due to the small sampling area. Furthermore, changes in the nebulizer gas flow also influence the formation and breakdown of cluster ions, requiring optimization with respect to minimum spectral interferences as well. The carrier gas flows also influence the ion energies and the geometry of the aerosol channel. Normally, it is between 0.5 and $1\,\mathrm{l\,min^{-1}}$. It must be optimized together with the power, which influences the plasma volume and thereby the kinetics of the processes taking place, and the position of the sampler. By changing the voltages at the different ion lenses, the transmission for a given ion can be optimized, enabling the optimization of the detection limits and the minimization of interferences. In multielement determinations, a compromise must always be made. For the easily ionized elements, working at so-called cool plasma conditions has been shown to be very successful. From the calculation of the degrees of ionization, it can be seen that mainly singly ionized species are formed instead of multiply ionized species (see detection limits listed in Ref. [84]). For Na, K, Ca, and Al, detection limits in the sub-parts per trillion range then become achievable.

16.3.2.3 Power of Detection

The lowest detection limits generally are obtained at a power between 0.6 and 2 kW and the sampler at about 10–15 mm above the tip of the injector. In general, it can be said that for the heavy elements the detection limits in ICP-MS are much lower than those in ICP-OES (Table 16.2) [2]. For most elements they are similar, except for the elements for which spectral interferences are a limiting factor. This

Table 16.2 Detection limits in ICP-OES and ICP-MS.

Element	**Detection limit**		
	ICP-OES (ng ml^{-1}) [97]	**ICP-MS (ng ml^{-1}) [98]**	**High-resolution ICP-MS (ng ml^{-1}) [84]**
Ag	7	0.03	0.4^a
Al	20	0.2	0.4^a
Au	20	0.06	0.8
B	5	0.04	5.4
Cd	3	0.06	0.5^a
Ce	50	0.05	—
Co	6	0.01	0.14^a
Cr	6	0.3	0.24^a
Fe	5	—	0.9
Ge	50	0.02	0.7
Hg	20	0.02	—
La	10	0.05	—
Li	80	0.1	0.012^a
Mg	0.1	0.7	0.2^a
Mn	1	0.1	0.14^a
Ni	10	—	0.3^a
Pb	40	0.05	0.12^a
Se	70	0.8	—
Te	40	0.09	—
Th	60	0.02	—
Ti	4	—	0.4
U	250	0.03	—
W	30	0.05	0.15
Zn	2	0.2	0.2^a

[a] cold plasma conditions.

applies to As ($^{75}As^+$ with $^{40}Ar^{35}Cl^+$), Se ($^{80}Se^+$ with $^{40}Ar^{40}Ar^+$), and Fe ($^{56}Fe^+$ with $^{40}Ar^{16}O^+$). The detection limits for elements with high ionization potential are usually very low because of the limited formation of positive ions.

The acids present in the measurement solution and the material of which the sampler is made (Ni, Cu, . . .) may influence the occurrence of spectral interferences considerably and accordingly the detection limits for a number of elements. This is particularly important when analyzing solids after dissolution by treatment with acids. Here, the measurement solution should not contain chlorine, phosphate, or sulfate ions. If it does, it is advantageous to remove these by precipitation or fuming off and taking up the analytes in dilute nitric acid. The detection limits for ICP-MS in the case of solids suffer from the necessary sample dilution, as the concentration of the sample in the measurement solution often is limited to $500\,\mu g\,ml^{-1}$ and is in contrast to ICP-OES where sample concentrations in the measurement solutions of 5 or even $50\,mg\,ml^{-1}$ often are possible. This is due to the risks in blocking the sampler. For elements such as B, Mg, Fe, and so on, the detection limits in solids in the case of ICP-OES thus may even become lower than in ICP-MS.

The detection limits obtained also depend on the type of mass spectrometer used. With quadrupole mass spectrometers, they are higher than in the case of high-resolution mass spectrometers. This applies particularly for strongly interfered elements such as Fe. With time-of-flight mass spectrometry, the detection limits in the case of the light elements were found to be one order of magnitude lower than in quadrupole-based ICP-MS. However, for the heavy elements, they are up to a factor of 5 worse [99].

16.3.2.4 Precision and Memory Effects

The constancy of the nebulizer gas flow is of prime importance for the precision achievable in ICP-MS. After stabilizing the nebulizer gas flows, relative standard deviations can be below 1%. They can be improved still further by internal standardization [100]. The tolerable salt contents (often below $500\,\mu g\,ml^{-1}$) are much lower than in ICP-OES, because of the risks of sampler clogging, and depend on the respective salts. The memory effects may become limiting, and in the case of a high matrix load rinsing times of 1–2 min are required.

A considerable portion of the noise originates from the nebulizer and the noise can generally be decreased by cooling the spray chamber. The latter is shown to decrease the white noise somewhat as well as some $1/f$ contributions and also the standard deviations for the blanks [101]. This directly leads to an improvement in the detection limits.

16.3.2.5 Interferences

Signal enhancements and depressions resulting from the matrix relate to the nebulization, influences on the ionization in the ICP, and to changes in the plasma geometry as well as in the ion energies. Changes in the nebulizer gas flow influence the nebulization effects (see Section 16.2.2.3); however, they also induce changes in the aerosol channel geometry and the plasma temperature and hence also the interferences of easily ionized elements [102]. Space charge effects have also been shown to play an important role in the suppression of signals as a result of alkali metals [103]. Up to a certain amount, these effects can be adequately corrected for by using an internal standard, the selection of which is only possible empirically. However, it is a guideline that elements with similar masses and ionization potentials should be chosen. Thus, it is often advisable to select more internal standards to cover elements in the whole analytical mass range, such as Sc for the low mass elements and Rh for the heavier elements. The use of internal standards was shown in early work to be successful for serum samples [100]. The matrix effects can be eliminated to such a degree that calibration with aqueous solutions in the case of diluted serum samples becomes possible.

In mass spectrometry, signals are obtained for each isotope present. With the low mass resolution of quadrupole mass spectrometers ($\approx$1 Da), this leads to a number of isobaric interferences, which can be corrected for with appropriate software. This type of interference depends only slightly on the working conditions, which is not the case for spectral interferences resulting from doubly charged ions, background species, or cluster ions. The background species at low masses [104] cause considerable spectral interferences, for example, for $^{28}Si^+$ (with $^{14}N^{14}N^+$), $^{31}P^+$ (with$^{16}N^{16}OH^+$), $^{80}Se^+$ (with $^{40}Ar^{40}Ar^+$), and so on. Species such as $^{40}Ar^{16}O^+$ not only interfere with $^{56}Fe^+$ but, due to all isotopic combinations and any hydrides present, also with other transition metal isotopes (^{52}Cr, ^{53}Cr, ^{54}Cr, ^{54}Fe, ^{55}Mn, ^{56}Fe, ^{57}Fe, ^{58}Ni, and ^{59}Co). In the case of HCl, additional interferences for further transitional metal isotopes will result from Cl^+, ClO^+, ClN^+, and $ArCl^+$ species. Under fixed working conditions, these interferences do not change very much with the matrix composition and can be corrected for by subtraction. However, they limit the power of detection. The interaction of signals from doubly charged ions and cluster ions change considerably with the power, the sampler position, and the nebulizer gas flow. These interferences are particularly important for elements that have relatively low ionization potentials or that form thermally stable oxides (e.g., Ba, Sr, Mg, Ti). This has been shown by measurements of the signals of singly charged (M^+) and doubly charged (M^{2+}) ions, as well as of metal oxides (MO^+) and hydroxides (MOH^+), for example, in the case of Ba [96, 105].

Considerable progress with respect to the elimination of spectral interferences in quadrupole mass spectrometry has been possible through the use of *collision- and reaction-induced dissociation of cluster species*. This approach goes back to the research of Douglas and French [106] and Barinaga *et al.* [107]. The theoretical aspects of collision- and direct-reaction cells, including the use of multipole devices have been treated in detail by Tanner *et al.* [108]. Ion-molecule reactions are of importance in decreasing the occurrence of polyatomic species in elemental mass spectrometry in two ways:

- *Collision-induced dissociation*: a transfer of energy from monoenergetic species such as He, Xe, and so on, during inelastic collisions results in an excitation of polyatomics, which may result in their subsequent dissociation. Here, purely mechanistic considerations are helpful to select appropriate gases for selected polyatomic species.

- *Reaction-induced dissociation*: through the chemical reaction of small molecules with the polyatomic species, unstable intermediates that subsequently dissociate may be formed. Here, thermodynamic considerations have been shown to be very helpful in predicting, or at least explaining, the effectiveness of gases with respect to the dissociation of polyatomic species.

Both types of process depend on the collision frequencies and hence on the pressure. The latter enhances the residence times of the polyatomic species in the collision or the reaction cell, respectively. The two principles have been realized in commercial ICP-MS instruments available from Agilent, Micromass, Perkin Elmer, Thermo, and Varian. It is possible to use several collision or reaction gases at different pressures and a lot of data are available on the effectiveness of the partial or complete removal of a number of potential interferents.

H_2 has been shown to be effective in the removal of polyatomics such as ArO^+ and ArH^+ for Fe and Ca, respectively, in work with dry aerosols as is the case in laser ablation ICP-MS [109]. This also is the case for Ne and CH_4 [110, 111]. He was also found to be of use for the dissociation of ArO^+ and $Ar_2{}^+$, interfering in the determination of Se and its species [112]. As shown for a hexapole cell, the ion energies are also relevant to the effectiveness of the according processes [113]. Much work has been done with NH_3 as the cell gas as well. Tanner *et al.* [114] proposed its use in a quadrupole reaction cell. Ben-Younes *et al.* [115] showed that it was useful for the removal of carbon-based interferents for the Si isotopes in ETV-ICP-MS, whereas Liu and Jiang [116] showed that NH_3 is effective in the reduction of interferences from $^{12}C^{16}O^+$ and $^{14}N_2{}^+$ for Si in steel. The use of O_2 was found to reduce the interferences of Hf, Ce, Ta, and Nb in noble metal determinations as a result of the formation of their oxides [117]. Pröfrock *et al.* [118, 119] showed that the use of Xe and an octopole cell may be effective in decreasing the interference signals for Cd, Cu, Zn, and S in the determination of metalloproteins by HPLC coupled to ICP-MS.

Further, the use of ion traps filled with He or Ne was mentioned to be effective in the removal of biatomic interferents such as GdO [120, 121].

16.3.2.6 **Isotope Dilution Analysis**

Dilution with stable isotopes not only offers the possibility of performing tracer experiments but also of circumventing systematic errors. The principle [122] can be applied to every element that has at least two stable or long-life isotopes. For its application, the analyte with a known isotopic composition but which differs from that of the sample is added to a known amount of sample, and mixed thoroughly. The isotopic abundance ratio then is given by

$$R = \frac{[N_S \cdot h_S(1) + N_A \cdot h_A(1)]}{N_S \cdot h_S(2) + N_A(2)} \tag{16.68}$$

N_S is the number of atoms of the element to be determined in the sample and N_A the number of atoms in the amount of standard added; h_S and h_A are the abundances of the isotopes (1) and (2) in the sample and the added standard. Thus,

N_S or the absolute mass G_S is given by

$$G_S = G_A \cdot \frac{[h_A(1) - R \cdot h_A(2)]}{[R \cdot h_S(2) - h_S(1)]} \tag{16.69}$$

R results from the signals for the isotopes; $h_S(1)$ and $h_S(2)$ as a rule are the natural abundances. G_A is the absolute amount of standard added, $h_A(1)$ and $h_A(2)$ are known from the isotopic composition. Isotope dilution in ICP-MS has been applied in studies on Pb (see, e.g., Ref. [123]). Tracer experiments for Fe in biological systems (see, e.g., Ref. [124]) have also been described. The precision achievable in the determination of isotope ratios for abundances that differ by a factor of less than 10 is in the lower percentage range.

For the determination of isotope ratios, the precision of TOF-ICP-MS has been studied and compared to the one obtained with other mass spectrometer systems. In a preliminary study already, typical isotope ratio precisions of 0.05% were obtained, thus overtaking sector field mass spectrometry with sequential detection, for which values of 0.1–0.3% for ^{63}Cu/^{65}Cu in Antarctic snow samples have been reported [125]. Similar results were obtained by Becker and Dietze [126] for Mg and Ca in biological samples (0.4–0.5 %). In principle, the features of TOF-ICP-MS may be superior to those of sequential sector field or quadrupole mass spectrometry; however, true parallel detection of the signals, as is possible with multicollector systems is more powerful, as shown by Hirata and Yamaguchi [90]. In fact, mass spectrometers with array detectors, as described by Schilling *et al.* [127] and investigated in detail in the Hieftje group, might be the perfect answer for isotope ratio measurements, as true parallel measurements of the signals within the relevant mass range, just as with CCDs for optical atomic emission spectrometry, are possible. Such systems allow it to obtain the full precision as the ratio signals are measured simultaneously and the impact of the noise of different signals, which is partially correlated here, can be canceled out. Indeed, in the case of the Ag isotopes, isotope ratio measurements with a precision of down to 0.015% have already been reported.

16.3.3
Alternative Methods for Sample Introduction

Apart from continuous pneumatic nebulization, all sample introduction techniques known from ICP-OES have been used and are of use for ICP-MS. In a number of cases, the advantages and limitations as compared to ICP-OES are quite different.

Similar to the situation with ICP-OES, the analysis of organic solutions is possible but somewhat more difficult [128]. The addition of oxygen was found to be helpful when nebulizing effluents from HPLC-containing organic eluents such as acetonitrile. This was useful when employing ICP-MS for online detection in speciation as well as in trace-matrix separations. Here, however, it is useful to use desolvation, even in the case of low-consumption, high-efficiency nebulizers, such as HEN or DIHEN. This can be done efficiently with membrane desolvation using Nafion membranes.

The use of ultrasonic nebulization just as in the case of ICP-OES allows the sampling efficiency to be increased. High water loading of the plasma has to be avoided, as is possible with desolvation, not only to limit the cooling of the ICP but also to keep the formation of cluster ions and the related spectral interferences low. These processes are complex, as, for example, a change in water loading also influences the pressure in the intermediate stage [129]. The use of high-pressure nebulization in ICP-MS has similar advantages and is suitable for coupling ICP-MS with HPLC. The setup that can be used is the same as the one that can be used for online trace-matrix separations [130].

With the formation of volatile hydrides, the detection limits for elements such as As, Se, and Sb can also be improved. As shown in Ref. [131], improvements for Pb were also obtained. They are due to improved analyte sampling efficiencies but also to the decrease in cluster ion formation, resulting from the introduction of a water-free analyte, which also applies to the cold vapor technique in the case of Hg.

ETV, in addition to its features for the analysis of microsamples, has the additional advantage in ICP-MS of introducing a dry analyte vapor into the plasma. Hence, it has been found to be useful for elements for which the detection limits are high as a result of spectral interferences with cluster ions. In the case of ^{56}Fe, which is subject to interference by ^{40}ArO^{+}, Park *et al.* [132] showed that the detection limit could be improved considerably by ETV. For similar reasons, the direct insertion of samples in ICP-MS leads to the highest absolute power of detection (detection limits in the picogram range and lower [133, 134]. Transient signals arise from ETV, where accordingly the number of elements that can be determined for one vaporization event is limited, unless drastic decreases in analytical precision and power of detection are accepted. In this respect, TOF-ICP-MS offers some advantages. Here, simultaneous measurements of different isotopes are possible during one evaporation event without losses in analytical performance. It is even possible to monitor the separation of the volatilization of interferents from the evaporation of the analytes in real time, which is helpful for removing both spectral and ionization interferences, as shown by Mahoney *et al.* [88].

Despite ICP-MS being mainly a method for the analysis of liquids and solids subsequent to dissolution, techniques for direct solids analysis have also been used. They are of use particularly when the samples are powders, which are difficult to bring into solution or, in addition, are electrically nonconducting and thus difficult to be analyzed with glow discharge or spark techniques. In the case of such powders, such as coal, slurry nebulization with a Babington nebulizer can be applied in ICP-MS as well [135]. ETV offers good possibilities not only for powders but also for granulates. With a novel furnace into which graphite boats can be introduced and where halogenated hydrocarbons can be used as volatilization aids, different volatile halide-forming elements can be successfully evaporated from Al_2O_3 [41]. When applying slurry sampling under continuous ultrasonic treatment of the slurry, accurate results for powered biological substances [136], and also for refractory powders such as Al_2O_3, down to the sub-micrograms per gram level [137] can be obtained. It could be shown that substances used as matrix modifiers in graphite AAS work, such as mixtures of Mg, Pd-nitrates, and soon, also may have a favorable influence here, as their use results in signal enhancements.

For the direct analysis of compact metals spark ablation can be used and the detection limits are in the nanograms per gram range as shown for steels [138]. The high ablation rates necessitate that measures be taken to limit a too high matrix load in the ICP. For the analysis of compact electrically nonconductive samples such as glasses, ceramics, rocks, and so on, laser ablation combined with ICP-MS is very powerful, commercially available, and widely used at present. The approach is treated in a separate chapter by Hattendorf and Günther.

Special attention is also to be given to the use of ICP-MS as an element-specific detection method in gas and liquid chromatography for speciation work. Here, special efforts had to be made in the coupling of the chromatographic and the spectrometric system and deals with

- suitable interfacing not to spoil chromatographic resolution;
- optimum sampling efficiency without analyte dilution to preserve the highest possible power of detection;
- optimization to allow a number of organic solvents entering the ICP without decreasing its stability of operation.

This field and its use in life sciences is especially addressed in a separate section by Rosenberg (see Chapter 15).

16.3.4
Time-of-Flight ICP-MS

Time-of-flight mass spectrometry has since long been known in instrumental analysis with SIMS, and so on, and been developed into a feasible detection system in ICP-MS [139]. Because of the mass range to be covered (1–238 amu), reasonable acceleration voltages (2 kV), and flight-tube lengths (1 m) permit the generation of 20 000–30 000 mass spectra per s. Both end-on and orthogonal geometry are possible and commercially available (LECO Renaissance and GBC Scientific Optimass 8000). In the end-on geometry, ions can be sampled from the ICP into the MS with an axial flight path, whereas with orthogonal geometry the incoming ions have a velocity component perpendicular to the extraction field, which can be compensated for by the use of steering plates. Therefore, in the axial geometry, the throughput is higher [140]. The figures of merit published with the two arrangements are rather similar. Indeed, as published for the axial geometry by Tian *et al.* [99], detection limits for 64 elements were at 0.5–20 pg ml^{-1}; with a long-term stability over 4 h between 1.0% for Li and 2.1% for ^{40}Ca under cool plasma conditions, and with RSDs between 0.07 and 0.7% for isotope ratios in SRM NIST 1643d. Sturgeon *et al.* [141] reported for the orthogonal geometry detection limits of 1 pg ml^{-1} and a resolution of 500 between ^{7}Li and ^{238}U.

Water-jacketed spray chambers have been shown to be helpful in reducing oxide signals [142], as well as the $1/f$ noise component on the signals [143]. Sanz-Medel and coworkers [144] found that the isotope ratio precisions and accuracies of TOF-ICP-MS surpassed those of quadrupole-based systems. This was impressively demonstrated for Pb by Carrion *et al.* [145], who reported RSDs of 0.08% for ^{85}Rb/^{87}Rb, 0.04% for ^{207}Pb/^{206}Pb, 0.49% for ^{204}Pb/^{206}Pb, and 0.07% for ^{208}Pb/^{206}Pb in the analog detection mode and respective values of 0.2, 0.3, 1.0, and 0.3% in the transient detection mode.

Besides isotope ratio measurements, a great strength of the ICP-TOF-MS lies in work with transient signals, where many isotope signals can be detected without spectral skew. By coupling flow injection to ICP-TOF-MS, Benkhedda *et al.* [146] were able to pre-enrich Pd, Pt, and Rh on diethylurea on the inner walls of a PTFE knotted reactor within 120 s and thereby could determine the elements in urine, blood serum, and road dust samples. For speciation, the online coupling of chromatography and ICP-TOF-MS has also been shown to be useful. Also, for a coupling with ETV where the signals are also transient, ICP-TOF-MS is very well suited. Mahoney *et al.* [88] already showed that in the case of Cd, Sn, and In, temperature programming could be used to avoid isobaric overlaps. Here, the interferences of Sn and Cd signals as a result of differences in their thermal volatilities could be removed, and absolute detection limits in the 10–80 fg range were obtained. Bings and Stefanka [147] showed that in the case of ETV from a tungsten filament, multielement determinations of Cr, Cu, Li, and Pb in 10 μl aliquots of blood serum could be directly performed when using a phosphate-based modifier. Here, all the elements present could be detected without any skew, as would have occurred with a sequentially measuring mass spectrometer. Moreover, laser ablation TOF-ICP-MS, can be efficiently used for the direct analysis of solids. Bings [148] optimized the method for the direct analysis of oils, such that a dilution with an organic solvent became unnecessary, and oils with particles suspended in them could be directly analyzed. Detection limits were at the 0.5 (Pb) to 28 $\mathrm{ng\,g^{-1}}$ level (Cr). Leach *et al.* [149] showed that a multitude of elements, in principle, can be determined from one laser pulse and, provided that all elemental signals are measured, absolute analyses of alloys become possible with a fairly good precision and accuracy. Indeed, one only has to add the signals for the various elements, to correct for their abundances, and to calculate the ratio of the signals for the respective elements. Finally, hydride and volatile species generation are also useful sampling techniques in ICP-TOF-MS. Bings *et al.* [150] used miniaturized electrochemical hydride generation, as described earlier, and obtained detection limits of 10–160 pg for As, Bi, Ge, Hg, and Sb and 1.1 ng for Se in simultaneous determinations of 12 isotopes in 200 μl samples; the method was shown to be useful for the analysis of natural waters.

16.3.5
Fields of Application

ICP-MS is a powerful method for multielemental trace determinations and therewith is especially promising for the areas where ICP-OES is applied, but where a higher power of detection is required. This is the case in trace analysis of geological samples, and especially of hydrogeological samples, as well as for trace determinations in metal samples, in the field of biology and medicine, as well as in environmental sciences.

16.3.5.1 Geological Samples

In the case of geological samples, ICP-MS especially is of interest where multi-element determinations are required and ICP-OES cannot be used because of the lack of power of detection or spectral interferences. This applies, for example, to the determination of low concentrations of the rare earth elements (see, e.g., Ref. [98, 151]). The optimization of the sample dissolution procedures with respect to ICP-MS has especially to be given attention to. When fusion is used to bring the samples into solution, the total salt contents of the solutions may necessitate a dilution of the measurement solutions in accordance with the consequences for the detection limits obtainable. Also, in the case of chemical dissolution involving oxidizing acids, problems may occur. Indeed, the presence of Cl in the measurement solutions may enhance the risks for cluster ion formation. Further, the use of HF may necessitate the use of HF-resistent nebulization systems (made of Ryton, e.g.) and ceramic injection tubes in the ICP burner. Clogging and corrosion of the sampler may be critical and requires rinsing and working with solutions having concentrations below 0.1%. Also, the use of a sampler made of Pt or a brass sampler covered with a ceramics layer may be required. Hydrogeological samples, as described by Garbarino and Taylor [152], can be analyzed very accurately for Ni, Cu, Sr, Cd, Ba, Tl, and Pb by isotope dilution ICP-MS. Isotope ratio work can be useful in dating or provenance studies and is well possible thanks to the high precision achievable with multicollector ICP-MS. For a series of trace elements, ETV was found to be useful so as to reduce spectral interferences. This applies particularly to volatile elements such as Tl [153], but in the case of a metal filament vaporizer also to Pt, Pd, Ru, and Ir [154]. For the investigation of inclusions in minerals, laser ablation ICP-MS is very powerful. It can even be used for the analysis of liquid inclusions in minerals, which can provide important information for geologists [155].

16.3.5.2 Metals and Ceramics

Trace determinations down to the sub-micrograms per gram level are possible in metals and ceramics, as the sample concentrations may be up to $5\,\mathrm{g\,l^{-1}}$. ICP-MS, therefore, is really an alternative for materials with line-rich matrix element optical emission spectra. This has been shown in the case of high-temperature alloys [156]. However, matrix interferences in ICP-MS may also limit the power of detection and the precision and the accuracy achievable, and matrix removal may be required so as to make further progress in these directions. All classical principles of trace-matrix separations are helpful in this respect. Innovative approaches where the classical trace-matrix separation principles are performed online with the determination step here are especially interesting. This has been shown by experiments with Al_2O_3 powders. After dissolution with strong acids, Al can be separated off by fixing the APDC complexes of the trace impurities on an Al_2O_3 column while the matrix passed through the column and nebulizing the liquid with which the complexes are eluted [157]. In the case where high-boiling inorganic acids are required so as to bring the samples into solution, as is the case with SiC, the acid residues have to be fumed off and the traces taken up in diluted HNO_3, by which the detection limits in ICP-MS can be decreased considerably [158]. Using high-resolution mass spectrometry can make it possible to prevent spectral interferences of the most abundant isotope signals with cluster ions, as is the case for $^{56}Fe^+$ and $^{40}Ar^{16}O^+$ or $^{52}Cr^+$ and $^{40}Ar^{12}C^+$ [85]. For a coupling of online matrix removal and ICP-MS, the use of suitable nebulization systems, such as high-pressure nebulization coupled with desolvation to HPLC or HENs in combination with capillary electrophoresis is very attractive. In the latter case, transient signals are obtained, which could be best measured in a multielemental mode with TOF-ICP-MS.

For material analysis also, direct solids analysis is possible in ICP-MS. For the direct analysis of steels by ICP-MS, Jiang and Houk [159] used arc ablation and reported detection limits down to the $0.1\,\mu g\,g^{-1}$-level. Further results were obtained by many groups by the use of laser ablation. Further, the direct coupling of slurry ETV to ICP-MS enabled trace determinations in ceramic powders very well, as shown in the case of Al_2O_3 by Wende *et al.* [41].

16.3.5.3 **Life Sciences**

For biological and medical samples, ICP-MS has considerably enlarged the series of elements that can be determined directly, and thus ICP-MS is of great importance for bioavailability studies. This is especially the case as the power of detection is sufficient to also determine different elemental compounds by coupling chromatography to ICP-MS, being the strongest approach for speciation studies. Speciation and the studies of the metal compounds in biotic materials under the name of metallomics [160] became a new field of research in the biosciences, where ICP-MS is one of the major tools. The determination of metalloproteins by a wide variation of methods and even sequencing of DNA became fields of research. At the ultratrace level, normal levels for many elements now can be determined in body fluids by ICP-MS, allowing biochemical studies [161]. In urine, for example, a good agreement of ICP-MS results with those of other techniques was obtained for Pb, Cd, Hg, and Tl. Deviations were found for As, Fe, and Se, which could be partly removed by a precipitation of the chlorides from the measurement solutions. With ICP-MS, Pb can be determined in blood [162] and the bioavailability of Zn has been studied [163]. For the analysis of small-volume samples, flow injection analysis found wide spread as well, as shown for blood analysis [164]. Also, in biotechnology, ICP-MS became a powerful tool for the determination of many metals and nonmetals within a wide concentration range.

16.3.5.4 **Environmental Sciences**

ICP-MS is a powerful method of analysis for chemical analysis in environmental work. Many elements can be determined directly in drinking water. In waste water analysis, sample digestion by a treatment with HNO_3/H_2O_2 is often required, and the most frequently occurring isobaric interferences have been described [165]. For seawater analysis, the salt content makes sample pretreatment necessary, and this can be done by chelate extraction. Beauchemin *et al.* [166] obtained a preconcentration of a factor of 50 by sorption of the trace elements onto a SiO_2 column treated with 8-hydroxyquinoline, and determined Ni, Cu, Zn, Mo, Cd, Pb, and U in seawater. In the case of river water, Na, Mg, K, Ca, Al, V, Cr, Mn, Cu, Zn, Sr, Mo, Sb, Ba, and U could be determined directly and Co, Ni, Cd, and Pb after the above-mentioned preconcentration procedure. For As, preconcentration by evaporation of the water from the sample was sufficient. Isotope dilution delivers the highest accuracy [167] and the procedure has been applied to the characterization of a standard reference sample [166]. ICP-MS, following sample decomposition with HNO_3/H_2O_2, has also been applied for trace determinations in marine sediments [168] and for the trace characterization of marine biological samples [169, 170]. Owing to the very high power of detection, ICP-MS can be used to determine very low background concentrations in unpolluted areas. With high-resolution ICP-MS and a microconcentric HEN, Rh, Pd, and Pt can be determined in ice samples with detection limits down to 0.02, 0.08, and 0.008 $pg\,g^{-1}$, respectively [171], as can be the actinides in environmental samples [172]. For speciation in the environment, ICP-MS coupled to chromatography also is very powerful.

16.4
Outlooks and Comparative Aspects

For elemental trace determinations, both ICP-OES and ICP-MS are now mature methods, and different types of instrumentation in the case of both methods are commercially available with a variety of sampling equipment. In the case of ICP-OES, the availability of different types of CCD optical emission spectrometers, especially, has widened the possibilities of the method in terms of interference recognition and correction for a broad range of real-life samples. Future developments may lie in the availability of more robust and still more stable RF power generators and burner technology. Fine work certainly will still be made on the side of sample introduction, where novel types of nebulizers can further improve the figures of merit. ICP-OES, however, is available in most laboratories just as AAS is. Especially for tasks such as waste water analysis, serum analysis, the characterization of metal standard samples, and so on, the method is a routine tool, which can also be handled by nonspecialists. The ease of calibration with synthetic elemental standard solutions is very attractive. Also, ICP-OES is valuable for in-line automated analyses.

ICP-MS now is the most accessible method for ultratrace element determinations. Both the quadrupole-based instrumentation, eventually with direct-reaction cell or collision cell, high-resolution sector field instruments, as well as time-of-flight and multicollector approaches have their respective strengths in terms of cost-effectiveness, the removal and prevention of spectral interferences, work with transient signals, or the achievement of high precision in isotope ratio measurements. ICP-MS will remain of prime importance for the analysis of samples with low matrix load, as they occur in water analysis, in the analysis of digested biological samples, in quality control for high-purity acids, and so on.

Much work is being done on lower cost alternatives to the ICP, especially when gases or vapor compounds are generated and the plasma used only serves for the excitation and or ionization of a gaseous compound. Here, low-power microwave plasmas and glow discharges, both at atmospheric and under reduced pressure, are good prospectives and will enable it to lower the supply and operation costs, without losing the required multielement detection capabilities or the required power of detection. These sources now play an important role in speciation work.

The field of solids analysis is only attractive for ICP atomic spectrometry when dissolution and calibration with synthetic solution samples can be used. This is the most common way for the characterization of new standard reference materials. For direct solids analysis, X-ray-based methods may be the more direct way, however, with the known limitations of the light elements and the restrictions on calibration, as a result of the absence of well-characterized standard reference samples in the case of most matrices. This also applies to glow discharge atomic spectrometry for bulk and microdistributional analysis of solids.

References

1. Kirchhoff, G.R. and Bunsen, R. (1860) Chemical analysis by spectrum-observation. *Philos. Mag.*, **20**, 89–98.
2. Broekaert, J.A.C. (2005) *Analytical Atomic Spectrometry with Flames and Plasmas*, 2nd Completely Revised and Extended edn, Wiley-VCH Verlag GmbH, Weinheim.
3. Marcus, R.K. and Broekaert, J.A.C. (eds) (2003) *Glow Discharge Plasmas in Analytical Spectroscopy*, John Wiley & Sons, Ltd, Chichester.
4. Margoshes, M. and Scribner, B. (1959) The plasma jet as a spectroscopic source. *Spectrochim. Acta*, **15**, 138–145.
5. Riemann, M.Z. (1966) Der Kaskadebogen als Anregungsquelle für die Spektralanalyse von Lösungen. *Z. Anal. Chem.*, **215**, 407–424.
6. Greenfield, S., Jones, I.L., and Berry, C.T. (1964) High-pressure plasmas as spectroscopic emission sources. *Analyst*, **89**, 713–720.
7. Wendt, R. and Fassel, V.E. (1965) Induction coupled plasma spectrometric excitation source. *Anal. Chem.*, **37**, 920–922.
8. Houk, R.S., Fassel, V.A., Flesh, G.D., Svec, H.J., Gray, A.L., and Taylor, C.E. (1980) Inductively coupled argon plasma as an ion source for mass spectrometric determination of trace elements. *Anal. Chem.*, **52**, 2283–2289.
9. Boumans, P.W.J.M. and de Boer, F.J. (1977) An experimental study of a 1-kW, 50-MHz RF ICP with pneumatic nebulizer and a discussion of experimental evidence for a non-thermal mechanism. *Spectrochim. Acta, Part B*, **32**, 365–395.
10. Huang, M., Hanselmann, D.S., Yang, P.Y., and Hieftje, G.M. (1992) Isocontour maps of electron temperature, electron number density and gas kinetic temperature in the Ar inductively coupled plasma obtained by laser-light Thomson and Rayleigh scattering. *Spectrochim. Acta, Part B*, **47**, 765–786.
11. Farnsworth, P.B., Woolley, A., Omenetto, N., and Matveev, O. (1999) Experimental studies of charge transfer reactions between argon and the third row metals Ca through Cu in the inductively coupled plasma. *Spectrochim. Acta, Part B*, **54**, 2143–2155.
12. Boumans, P.W.J.M. (1966) *Theory of Spectrochemical Excitation*, Hilger & Watts, London.

13. de Galan, L., Smith, R., and Winefordner, J.D. (1968) The electronic partition functions of atoms and ions between 1500 K and 7000 K. *Spectrochim. Acta, Part B*, **23**, 521–525.

14. Bockasten, K. (1961) Transformation of observed radiances into radial distribution of a plasma. *J. Opt. Soc. Am.*, **51**, 943–947.

15. Broekaert, J.A.C., Leis, F., and Laqua, K. (1979) Some aspects of matrix effects caused by sodium tetraborate in the analysis of rare earth minerals with the aid of inductively coupled plasma atomic emission spectrometry. *Spectrochim. Acta, Part B*, **34**, 167–175.

16. Junkes, J. and Salpeter, E.W. (1961) Linienbreiten in der photographischen Spektralphotometrie II. Das optische Linienprofil. *Ric. Spettrosc.*, **2**, 255–483.

17. Mermet, J.M. (1987) in *Inductively Coupled Plasma Emission Spectroscopy, Part II* (ed. P.W.J.M. Boumans), Wiley-Interscience, New York, pp. 353–386.

18. Diermeier, R. and Krempl, H. (1967) Thermische Anregungsfunktionen und Normtemperaturen von Atom-und Ionenlinien in Zweikomponentenplasmen. *Z. Phys.*, **200**, 239–248.

19. Herzberg, G. (1950) *Molecular Spectra and Molecular Structure*, 2nd edn, Van Nostrand Reinhold Ltd., New York.

20. Pearce, R.W.B. and Gaydon, A.G. (1953) *The Identification of Molecular Spectra*, Chapman and Hall Ltd., London.

21. Raeymaekers, B., Broekaert, J.A.C., and Leis, F. (1988) Radially resolved rotational temperatures in nitrogen-argon, air-argon and argon ICPs. *Spectrochim. Acta, Part B*, **43**, 941–949.

22. Ishii, I. and Montaser, A. (1991) Radially resolved rotational temperatures in nitrogen–argon, oxygen–argon, air–argon and argon ICPs, *Spectrochim Acta* A tutorial discussion on measurements of rotational temperature in ICP. *Spectrochim. Acta, Part B*, **46**, 1197–1206.

23. Rezaaiyaan, R., Hieftje, G.M., Anderson, H., Kaiser, H., and Meddings, B. (1982) Design and construction of a low-flow, low-power torch for ICP spectrometry. *Appl. Spectrosc.*, **36**, 626–631.

24. Van Der Plas, P.S.C. and De Galan, L. (1984) A radiatively cooled torch for ICP-AES using 1 L min1 of argon. *Spectrochim. Acta, Part B*, **39**, 1161–1169.

25. Michaud-Poussel, E. and Mermet, J.M. (1986) Influence of the generator frequency and the plasma gas inlet area on torch design in ICP-AES. *Spectrochim. Acta, Part B*, **41**, 125–132.

26. Brenner, J.B., Zander, A., Cole, M., and Wiseman, A. (1997) Comparison of axially and radially viewed inductively coupled plasmas for multielement analysis. Effect of sodium and calcium. *J. Anal. At. Spectrom.*, **12**, 897–906.

27. Ivaldi, J.C. and Tyson, J.F. (1995) Performance evaluation of an axially viewed horizontal inductively coupled plasma for optical emission spectrometry. *Spectrochim. Acta, Part B*, **50**, 1207–1226.

28. Scott, R.H., Fassel, V.A., and Kniseley, R.N. (1974) Inductively coupled plasmas for optical emission spectroscopy. *Anal. Chem.*, **46**, 75–80.

29. Wu, M. and Hieftje, G.M. (1992) A new spray chamber for ICP spectrometry. *Appl. Spectrosc.*, **46**, 1912–1918.

30. Schaldach, G., Berndt, H., and Sharp, B.L. (2003) An application of computational fluid dynamics (CFD) to the characterization and optimization of a cyclonic spray chamber for ICP-AES. *J. Anal. At. Spectrom.*, **18**, 742–750.

31. Gouy, G.L. (1879) Photometric research on colored flames. *Ann. Chim. Phys.*, **18**, 5–101.

32. Liu, H. and Montaser, A. (1994) Phase-Doppler diagnostic studies of primary and tertiary aerosols produced by a high-efficiency nebulizer. *Anal. Chem.*, **66**, 3233–3242.

33. Vanhaecke, F., Van Holderbeke, M., Moens, L., and Dams, R. (1996) Evaluation of a commercially available microconcentric nebulizer for inductively coupled plasma mass spectrometry. *J. Anal. At. Spectrom.*, **11**, 543–548.

34. Babington, R.S. (1969) Method of atomizing liquid in a mono-dispersed spray. US Patent 3,421,692.

35. Ebdon, L. and Cave, M.R. (1982) A study of pneumatic nebulisation systems for ICP emission spectrometry. *Analyst*, **107**, 172–178.

36. Broekaert, J.A.C. and Boumans, P.W.J.M. (1987) in *Inductively Coupled Plasma Emission Spectroscopy*, Vol. 1 (ed. P.W.J.M. Boumans), John Wiley & Sons, Inc., New York, pp. 296–357.

37. McLean, J.A., Zhang, H., and Montaser, A. (1998) A direct injection high-efficiency nebulizer for inductively coupled plasma mass spectrometry. *Anal. Chem.*, **70**, 1012–1020.

38. Nukuyama, S. and Tanasawa, Y. (1938, 1939) Experiments on the atomization of liquids in air stream. *Trans. Soc. Mech. Eng. (Jpn.)*, **4**, 86and **5**: 68.

39. Thompson, M., Pahlavanpour, B., Walton, S.J., and Kirkbright, G.F. (1978) Simultaneous determination of trace concentrations of arsenic, antimony, bismuth, selenium and tellurium in aqueous solution by introduction of the gaseous hydrides into an ICP source for emission spectrometry. *Analyst*, **103**, 568–579.

40. Feng, Y.L., Sturgeon, R.E., and Lam, J.W. (2003) Generation of atomic and molecular cadmium species from aqueous media. *Anal. Chem.*, **75**, 635–640.

41. Wende, M.C. and Broekaert, J.A.C. (2002) Analysis of Al_20_3 powders by direct solid sampling electrothermal vaporization powder and slurry sampling using inductively coupled plasma atomic emission spectrometry and mass spectrometry. *Spectrochim. Acta, Part B*, **57**, 1897–1904.

42. Peschel, B.U. and Broekaert, J.A.C. (2007) A radiotracer study on the volatilization and transport effects of thermochemical reagents used in the analysis of Al_2O_3 powders by slurry ETV-ICP-MS. *Spectrochim. Acta, Part B*, **62**, 109–115.

43. Salin, E.D. and Horlick, G. (1979) Direct sample insertion device for ICP emission spectrometry. *Anal. Chem.*, **51**, 2284–2286.

44. Hattendorf, B., Latkoczy, C., and Günther, D. (2003) Laser ablation ICP-MS. *Anal. Chem.*, **75**, 341A–347A.

45. Keliher, P.N. and Wohlers, C.C. (1976) Echelle grating spectrometers in analytical spectrometry. *Anal. Chem.*, **48**, 333A–340A.

46. Zworykin, V.K. and Ramberg, E.G. (1949) *Photoelectricity and Its Application*, John Wiley & Sons, Inc., New York.

47. Sweedler, J.V., Bilhorn, R.B., Epperson, P.M., Sims, G.R., and Denton, M.B. (1988) High-performance charge transfer device detectors. *Anal. Chem.*, **60**, 282A–291A.

48. Epperson, P.M. and Denton, M.B. (1989) Binning spectral images in a charge-coupled device. *Anal. Chem.*, **61**, 1513–1519.

49. Bilhorn, R.B. (1987) PhD Dissertation, University of Arizona.

50. Kaiser, H. and Specker, H. (1956) Bewertung und Vergleich von Analysenverfahren. *Z. Anal. Chem.*, **149**, 46–66.

51. Heitland, P. (2000) Verwendung von Spektrallinien in der ICP-OES im Wellenlängenbereich 125–190 nm. *GIT Labor Fachz.*, 847–850.

52. Broekaert, J.A.C., Leis, F., and Laqua, K. (1981) The application of an argon/nitrogen inductively-coupled plasma to the analysis of organic solutions. *Talanta*, **28**, 745–752.

53. Boumans, P.W.J.M. and Lux-Steiner, M.C. (1982) Modification and optimization of a 50 MHz inductively coupled argon plasma with special reference to analyses using organic solvents. *Spectrochim. Acta*, **37**, 97–126.

54. Harrison, G.R. (1991) *Wavelength Tables*, The MIT Press, Cambridge.

55. Boumans, P.W.J.M. (1984) *Line Coincidence Tables for ICP-OES*, Vol. 1 and 2, Pergamon Press, Oxford.

56. Schulz, O. and Heitland, P. (2001) Application of prominent spectral lines in the 125-180 nm range for inductively coupled plasma optical emission spectrometry. *Fresenius J. Anal. Chem.*, **371**, 1070–1075.

57. Geilenberg, D., Gerards, M., and Broekaert, J.A.C. (2000) Determination of the stoichiometric composition of high-temperature superconductors by ICP-OES for production control. *Mikrochim. Acta*, **133**, 319–323.

58. Barnett, W.B., Fassel, V.A., and Kniseley, R.N. (1968) Theoretical principles of internal standardization in analytical emission spectroscopy. *Spectrochim. Acta*, **23**, 643–664.

59. Salit, M.L., Vocke, R.D., and Kelly, W.R. (2000) An ICP-OES method with 0.2 expanded uncertainties for the characterization of $LiAlO_2$. *Anal. Chem.*, **72**, 3504–3511.

60. Bauer, M. and Broekaert, J.A.C. (2007) Investigations on the use of pneumatic nebulisers with dual solution loading for the correction of matrix effects for elemental determinations in inductively coupled plasma optical emission spectrometry. *Spectrochim. Acta, Part B*, **62**, 145–154.

61. Karannassios, V. (2004) Microplasmas for chemical analysis: analytical tools or research toys? *Spectrochim. Acta, Part B*, **59**, 909–928.

62. Minayava, O.B. and Hopwood, J.A. (2003) Microfabricated inductively coupled plasma-on-a-chip for molecular SO_2 detection: a comparison between global model and optical emission spectrometry. *J. Anal. At. Spectrom.*, **18**, 856–863.

63. Ichiki, T., Koidesawa, T., and Horiike, Y. (2003) *Plasma Sources Sci. Technol.*, **12**, S16–S20.

64. Engel, U., Bilgic, A.M., Haase, O., Voges, E., and Broekaert, J.A.C. (2000) A microwave-induced plasma based on microstrip technology and its use for the atomic emission spectrometric determination of mercury with the aid of the cold-vapor technique. *Anal. Chem.*, **72**, 193–197.

65. Pohl, P., Jiménez Zapata, I., Bings, N.H., Voges, E., and Broekaert, J.A.C. (2007) Optical emission spectrometric determination of arsenic and antimony by continuous flow chemical hydride generation and a miniaturized microwave microstrip argon plasma operated inside a capillary channel in a sapphire wafer. *Spectrochim. Acta, Part B*, **62**, 444–453.

66. Garbarino, J.R. and Taylor, M.E. (1979) An inductively-coupled plasma atomic-emission spectrometric method for routine water quality testing. *Appl. Spectrosc.*, **33**, 220–226.

67. U.S. Environmental Protection Agency 1979 Inductively Coupled Plasma-Atomic Emission Spectrometric Method for Trace Element Analysis of Water and Wastes, Washington, DC.

68. DIN (1987) 38 406 *Bestimmung der 24 Elemente Ag, Al, B, Ba, Ca, Cd, Co, Cr, Cu, Fe, K, Mg, Mn, Mo, Na, Ni, P, Pb, Sb, Sr, Ti, V, Zn und Zr durch Atomemissionsspektrometrie mit induktiv gekoppeltem Plasma (ICP-AES)(E22)*, Beuthe Verlag, Berlin.

69. Broekaert, J.A.C. and Leis, F. (1980) Application of two different ICP-hydride techniques to the determination of arsenic. *Fresenius' Z. Anal. Chem*, **300**, 22–27.

70. Miyazaki, A., Kimura, A., Bansho, K., and Umezaki, Y. (1982) Simultaneous determination of heavy metals in waters by ICP-AES after extraction into diisobutyl ketone. *Anal. Chim. Acta*, **144**, 213–221.

71. Berndt, H., Harms, U., and Sonneborn, M. (1985) Multielement-Spurenvoranreicherung aus Wässern an Aktivkohle zur Probenvorbereitung für die Atomspektroskopie (Flammen-AAS, ICP/OES). *Fresenius' Z. Anal. Chem*, **322**, 329–333.

72. Hiraide, M., Ito, T., Baba, M., Kawaguchi, H., and Mizuike, A. (1980) Multielement preconcentration of trace heavy metals in water by preconcentration and flotation with indium hydroxide for ICP-AES. *Anal. Chem.*, **52**, 804–807.

73. Hartenstein, S.D., Ruzicka, J., and Christian, G.D. (1985) Sensitivity enhancements for flow injection analysis ICP-AES using an on-line preconcentration ion-exchange column. *Anal. Chem.*, **57**, 21–25.

74. Broekaert, J.A.C., Wopenka, B., and Puxbaum, H. (1982) Inductively coupled plasma optical emission spectrometry for the analysis of aerosol samples collected by cascade impactors. *Anal. Chem.*, **54**, 2174–2179.

75. Seelig, M. and Broekaert, J.A.C. (2001) Investigations on the on-line determination of metals in air flows by capacitively coupled microwave plasma atomic emission spectrometry (CMP-OES). *Spectrochim. Acta, Part B*, **56**, 1747–1760.

76. Aziz, A., Broekaert, J.A.C., and Leis, F. (1982) The optimization of an ICP injection technique and the application to the direct analysis of small-volume serum samples. *Spectrochim. Acta, Part B*, **37**, 381–389.

77. Aziz, A., Broekaert, J.A.C., Laqua, K., and Leis, F. (1984) A study of direct analysis of solid samples using spark ablation combined with excitation in an inductively coupled plasma. *Spectrochim. Acta, Part B*, **39**, 1091–1103.

78. Kehden, A., Flock, J., Vogel, W., and Broekaert, J.A.C. (2001) Direct solids atomic spectrometric analysis of metal samples by laser induced argon spark ablation coupled to ICP-OES. *Appl. Spectrosc.*, **55**, 1291–1296.

79. Graule, T., von Bohlen, A., Broekaert, J.A.C., Grallath, E., Klockenkämper, R., Tschöpel, P., and Tölg, G. (1989) Atomic emission and atomic absorption spectrometric analysis of high-purity powders for the production of ceramics. *Fresenius' Z. Anal. Chem*, **335**, 637–642.

80. Docekal, B., Broekaert, J.A.C., Graule, T., Tschöpel, P., and Tölg, G. (1992) Determination of impurities in silicon carbide powders. *Fresenius J. Anal. Chem.*, **342**, 113–117.

81. Lobinski, R., Broekaert, J.A.C., Tschöpel, P., and Tölg, G. (1992) Inductively-coupled plasma atomic emission spectroscopic determination of trace impurities in ZrO2-powder. *Fresenius J. Anal. Chem.*, **342**, 569–580.

82. Montaser, A. (ed) (1998) *Inductively Coupled Plasma Mass Spectrometry*, Wiley-VCH Verlag GmbH, New York.

83. Jakubowski, N., Raeymaekers, B.J., Broekaert, J.A.C., and Stuewer, D. (1989) Study of plasma potential effects in a 40 MHz inductively coupled plasma mass spectrometry system. *Spectrochim. Acta, Part B*, **44**, 219–228.

84. Jakubowski, N., Moens, L., and Vanhaecke, F. (1998) Sector field mass spectrometers in ICP-MS. *Spectrochim. Acta, Part B*, **53**, 1739–1763.

85. Tittes, W., Jakubowski, N., Stuewer, D., Toelg, G., and Broekaert, J.A.C. (1994) Reduction of some selected spectral interferences in inductively coupled plasma mass spectrometry. *J. Anal. At. Spectrom.*, **9**, 1015–1020.

86. Benninghoven, A., Rüdenauer, F.G., and Werner, H.W. (1986) *Secondary Ion Mass Spectrometry*, John Wiley & Sons, Inc., New York.

87. Brunnee, C. (1987) The ideal mass analyzer: fact or fiction. *Int. J. Mass Spectrom. Ion Processes*, **76**, 125–237.

88. Mahoney, P.P., Ray, S.J., Li, G., and Hieftje, G.M. (1999) Preliminary investigation of electrothermal vaporization sample introduction for inductively coupled plasma time-of-flight mass spectrometry. *Anal. Chem.*, **71**, 1378–1383.

89. Mahoney, P.P., Ray, S.J., and Hieftje, G.M. (1997) Time-of-flight mass spectrometry for elemental analysis. *Appl. Spectrosc.*, **51**, 16A–28A.

90. Hirata, T. and Yamaguchi, T. (1999) Isotopic analysis of zirconium using enhanced sensitivity-laser ablation-multiple collector-inductively coupled plasma mass spectrometry. *J. Anal. At. Spectrom.*, **14**, 1455–1459.

91. Giffin, C.E., Boettger, H.G., and Norris, D.D. (1974) *Int. J. Mass Spectrom. Ion Phys.*, **15**, 437.

92. Schilling, G.D., Shelley, J.T., Broekaert, J.A.C., Sperline, R.P., Denton, M.B., Barinaga, C.J., Koppenaal, D.W., and Hieftje, G.M. (2009) Use of an ambient flowing atmospheric-pressure afterglow source for elemental analysis through hydride generation. *J. Anal. At. Spectrom.*, **24**, 34–40.

93. Barnes, J.H. IV,, Schilling, G.D., Sperline, R., Denton, M.B., Yound, E.T., Barinaga, C.J., Koppenaal, D., and Hieftje, G.M. (2004) Characterization of a focal plane camera fitted to a Mattauch-Herzog geometry mass spectrograph. 1. Use with an inductively coupled plasma. *Anal. Chem.*, **76**, 2531–2536.

94. Turner, P.J., Milis, D.J., Schröder, E., Lapitajs, G., Jung, G., Llacone, L.A., Haydar, D.A., and Montaser, A. (1998) in *Inductively Coupled Plasma Mass Spectrometry* (ed. A. Montaser), Wiley-VCH Verlag GmbH, New York, pp. 421–501.

95. Vaughan, M.A. and Horlick, G. (1990) Ion trajectories through the input optics of an inductively coupled plasma mass spectrometer. *Spectrochim. Acta, Part B*, **45**, 1301–1311.

96. Vaughan, M.A. and Horlick, G. (1986) Oxide, hydroxide and doubly charged analyte species in ICP mass spectrometry. *Appl. Spectrosc.*, **40**, 434–445.

97. Winge, R.K., Fassel, V., Peterson, V.J., and Floyd, M.A. (1985) *ICP-AES, an Atlas of Spectral Information*, Elsevier, Amsterdam.

98. Date, A.R. and Gray, A.L. (1985) Determination of trace elements in geological samples by inductively coupled plasma source mass spectrometry. *Spectrochim. Acta, Part B*, **40**, 115–122.

99. Tian, X., Emteborg, H., and Adams, F.C. (1999) Analytical performance of axial inductively coupled plasma time of flight mass spectrometry (ICP-TOFMS). *J. Anal. At. Spectrom.*, **14**, 1807–1814.

100. Vandecasteele, C., Nagels, M., Vanhoe, H., and Dams, R. (1988) Suppression of analyte signal in ICP-MS and the use of an internal standard. *Anal. Chim. Acta*, **211**, 91–98.

101. Pollmann, D., Pilger, C., Hergenröder, R., Leis, F., Tschöpel, P., and Broekaert, J.A.C. (1994) Noise power spectra of inductively coupled plasma mass spectrometry using a cooled spray chamber. *Spectrochim. Acta, Part B*, **49**, 683–690.

102. Crain, J.S., Houk, R.S., and Smith, F.G. (1988) Matrix interferences in ICP MS: some effects of skimmer orifice diameter and ion lense voltages. *Spectrochim. Acta, Part B*, **43**, 1355–1364.

103. Fraser, M.M. and Beauchemin, D. (2000) Effect of concomitant elements on the distribution of ions in inductively coupled plasma-mass spectroscopy. Part 1. Elemental ions. *Spectrochim. Acta, Part B*, **55**, 1705–1731.

104. Tan, S.H. and Horlick, G. (1986) Background spectral features in ICP mass spectrometry. *Appl. Spectrosc.*, **40**, 445–460.

105. Vaughan, M.A., Horlick, G., and Tan, S.H. (1987) Effect of the operating parameters on analyte signals in inductively coupled plasma mass spectrometry. *J. Anal. At. Spectrom.*, **2**, 765–772.

106. Douglas, D.J. and French, J.B. (1992) Collisional focusing effects in radio frequency quadrupoles. *J. Am. Soc. Mass Spectrom.*, **3**, 398–408.

107. Barinaga, C.J., Eiden, G.C., Alexander, M.L., and Koppenaal, D.W. (1996) Analytical atomic spectroscopy using ion trap devices. *Fresenius J. Anal. Chem.*, **355**, 487–493.

108. Tanner, S.D., Baranov, V.I., and Bandura, D.R. (2002) Reaction cells and collisions cells for ICP-MS: a tutorial review. *Spectrochim. Acta, Part B*, **57**, 1361–1452.

109. Günther, D., Hattendorf, B., and Audetat, A. (2001) Multi-element analysis of melt and fluid inclusions with improved detection capabilities for Ca and Fe using laser ablation with a dynamic reaction cell ICP-MS. *J. Anal. At. Spectrom.*, **16**, 1085–1090.

110. Hattendorf, B. and Günther, D. (2000) Characteristics and capabilities of an ICP-MS with a dynamic reaction cell for dry aerosols and laser ablation. *J. Anal. At. Spectrom.*, **15**, 1125–1131.

111. Hattendorf, B. and Günther, D. (2003) Strategies for method development for an inductively coupled plasma mass spectrometer with bandpass reaction cell. Approaches with different reaction gases for the determination of selenium. *Spectrochim. Acta, Part B*, **58**, 1–13.

112. Marchante-Gayon, J.M., Feldmann, I., Thomas, C., and Jakubowski, N. (2001) Speciation of selenium in human urine by HPLC-ICP-MS with a collision and reaction cell. *J. Anal. At. Spectrom.*, **16**, 457–463.

113. Dexter, M.A., Reid, H.J., and Sharp, B.L. (2002) The effect of ion energy on reactivity and species selectivity in hexapole collision/reaction cell ICP-MS. *J. Anal. At. Spectrom.*, **17**, 676–681.

114. Tanner, S.D., Baranov, V.I., and Vollkopf, U. (2000) A dynamic reaction cell for inductively coupled plasma mass spectrometry (ICP-DRC-MS). Part III. Optimization and analytical performance. *J. Anal. At. Spectrom.*, **15**, 1261–1269.

115. Ben-Younes, M., Gregoire, D.C., and Chakrabarti, C.L. (2003) Effectiveness of ammonia in reducing carbon-based polyatomic ion interferences in electrothermal vaporization collision cell inductively coupled mass spectrometry. *Spectrochim. Acta, Part B*, **58**, 361–372.

116. Liu, H.T. and Jiang, S.J. (2003) Dynamic reaction cell inductively coupled plasma mass spectrometry for determination of silicon in steel. *Spectrochim. Acta, Part B*, **58**, 153–157.

117. Simpson, L.A., Thomsen, M., Allooway, B.J., and Parker, A. (2001) A dynamic reaction cell (DRC) solution to oxide-based interferences in inductively coupled plasma mass spectrometry (ICP-MS) analysis of noble metals. *J. Anal. At. Spectrom.*, **16**, 1375–1380.

118. Pröfrock, D., Leonhard, P., and Prange, A. (2003) Determination of sulfur and selected trace elements in metallothionein-like proteins using capillary electrophoresis hyphenated to inductively coupled plasma mass spectrometry with an octopole reaction cell. *Anal. Bioanal. Chem.*, **377**, 132–139.

119. Pröfrock, D., Leonhard, P., and Prange, A. (2003) Determination of phosphorus in phosphorylated deoxyribonucleotides using capillary electrophoresis and high performance liquid chromatography hyphenated to inductively coupled plasma mass spectrometry with an octopole reaction cell. *J. Anal. At. Spectrom.*, **18**, 708–713.

120. Eiden, G.C., Barinaga, C.J., and Koppenaal, D.W. (1999) Analytical performance of the plasma source RF quadrupole ion trap in elemental and isotopic MS. *J. Anal. At. Spectrom.*, **14**, 1129–1132.

121. Jackson, G.P., King, F.L., and Duckworth, D.C. (2003) Electronic polyatomic interference reduction in plasma-source mass spectrometry via collision induced dissociation. *J. Anal. At. Spectrom.*, **18**, 1026–1032.

122. Heumann, K.G. (1982) Isotope dilution mass spectrometry for micro- and trace element determination. *Trends Anal. Chem.*, **1**, 357–361.

123. Dean, J.R., Ebdon, L., and Massey, R.J. (1987) Selection of mode for the measurement of lead isotope ratios by ICP mass spectrometry and its application to milk powder analysis. *J. Anal. At. Spectrom.*, **2**, 369–374.

124. Ting, B.T.G. and Janghorbani, M. (1987) Application of ICP-MS to accurate isotopic analysis for human metabolic studies. *Spectrochim. Acta, Part B*, **42**, 21–27.

125. Vanhaecke, F., Moens, L., and Dams, R. (1997) Applicability of high-resolution ICP-mass spectrometry for isotope ratio measurements. *Anal. Chem.*, **69**, 268–273.

126. Becker, J.S. and Dietze, H.J. (1998) Ultratrace and precise isotope analysis by double-focusing sector field inductively coupled plasma mass spectrometry. *J. Anal. At. Spectrom.*, **13**, 1057–1063.

127. Schilling, G.D., Andrade, F.J., Barnes, J.H. IV,, Sperline, R.P., Denton, M.B., Barinaga, C.J., Koppenaal, D.W., and Hieftje, G.M. (2007) Continuous simultaneous detection in mass spectrometry. *Anal. Chem.*, **79**, 7662–7668.

128. Hausler, D. (1987) Trace element analysis of organic solutions using ICP mass spectrometry. *Spectrochim. Acta, Part B*, **42**, 63–73.

129. Zhu, G. and Browner, R.F. (1988) Study of the influence of water vapor loading and interface pressure in ICP-MS. *J. Anal. At. Spectrom.*, **3**, 781–790.

130. Jakubowski, N., Feldmann, I., Stüwer, D., and Berndt, H. (1992) Hydraulic high pressure nebulization –application of a new nebulization system for inductively coupled plasma mass spectrometry. *Spectrochim. Acta, Part B*, **47**, 119–129.

131. Wang, X., Viczian, M., Lasztity, A., and Barnes, R.M. (1988) Lead hydride generation for isotope analysis by ICP-MS. *J. Anal. At. Spectrom.*, **3**, 821–828.

132. Park, C.J., Van Loon, J.C., Arrowsmith, P., and French, J.B. (1987) Sample analysis using plasma source mass spectrometry with electrothermal sample introduction. *Anal. Chem.*, **59**, 2191–2196.

133. Boomer, D.W., Powell, M., Sing, R.L.A., and Salin, E.D. (1986) Application of a wire loop direct sample-insertion device for ICP-MS. *Anal. Chem.*, **58**, 975–976.

134. Hall, G.E.M., Pelchat, J.C., Boomer, D.W., and Powell, M. (1988) Relative merits of two methods of sample introduction in ICP-MS: electrothermal vaporisation and direct sample insertion. *J. Anal. At. Spectrom.*, **3**, 791–797.

135. Williams, J.G., Gray, A.L., Norman, P., and Ebdon, L. (1987) Feasibility of solid sample introduction by slurry nebulisation for ICP-MS. *J. Anal. At. Spectrom.*, **2**, 469–472.

136. Fonseca, R.W., Miller-Ihli, N.J., Sparks, C., Holcombe, J.A., and Shaver, B. (1997) Effect of oxygen ashing on analyte transport efficiency using ETV-ICP-MS. *Appl. Spectrosc.*, **51**, 1800–1806.

137. Wende, M.C. and Broekaert, J.A.C. (2001) Investigations on the use of chemical modifiers for the direct determination of trace impurities in Al_2O_3 ceramic powders by slurry electrothermal evaporation coupled to inductively coupled plasma mass spectrometry (ETV-ICP-MS). *Fresenius J. Anal. Chem.*, **370**, 513–520.

138. Jakubowski, N., Feldmann, I., Sack, B., and Stüwer, D. (1992) Analysis of conducting solids by ICP-MS with spark ablation. *J. Anal. At. Spectrom.*, **7**, 121–125.

139. McClenathan, D.M., Ray, S.J., Wetzel, W.C., and Hieftje, G.M. (2004) Plasma source TOFMS. *Anal. Chem.*, **76**, 159A–166A.

140. Guilhaus, M. (2000) Essential elements of time-of-flight mass spectrometry in combination with the inductively coupled plasma ion source. *Spectrochim. Acta, Part B*, **55**, 1511–1525.

141. Sturgeon, R.E., Lam, J.W.H., and Saint, A. (2000) Analytical characteristics of a commercial ICP orthogonal acceleration time-of-flight mass spectrometer (ICP-TOFMS). *J. Anal. At. Spectrom.*, **15**, 607–616.

142. Longerich, H.P. and Diegor, R.W. (2001) Evaluation of a water-jacketed spray chamber using time-of-flight inductively coupled plasma mass spectrometry (TOF-ICP-MS). *J. Anal. At. Spectrom.*, **16**, 1196–1201.

143. Wetzel, W.C., Broekaert, J.A.C., McClenathan, D.M., and Hieftje, G.M. (2005) A contribution to the study of cooling a vertical-rotary spray chamber in inductively coupled plasma time-of-flight mass spectrometry. *J. Anal. At. Spectrom.*, **20**, 521–625.

144. Pelaez, M.V., Costa-Fernandez, J.M., and Sanz-Medel, A. (2002) Critical comparison between quadrupole and time-of-flight inductively coupled plasma mass spectrometers for isotope ratio measurements in elemental speciation. *J. Anal. At. Spectrom.*, **17**, 950–957.

145. Carrion, M.C., Andres, J.R., Rubi, J.A.M., and Emteborg, H. (2003) Performance optimization of isotope ratio measurements in transient signals by FI-ICP-TOFMS. *J. Anal. At. Spectrom.*, **18**, 437–443.

146. Benkhedda, K., Dimitrova, B., Infante, H.G., Ivanova, E., and Adams, F.C. (2003) Simultaneous on-line preconcentration and determination of Pt, Rh and Pd in urine, serum and road dust by flow injection combined with inductively coupled plasma time-of-flight mass spectrometry. *J. Anal. At. Spectrom.*, **18**, 1019–1025.

147. Bings, N.H. and Stefanka, Z. (2003) Development of a tungsten filament electrothermal vaporizer for inductively coupled plasma time-of-flight mass spectrometry and its possibilities for the analysis of human whole blood and serum. *J. Anal. At. Spectrom.*, **18**, 1088–1096.

148. Bings, N.H. (2002) Direct determination of metals in lubricating oils by laser ablation coupled to inductively coupled plasma time-of-flight mass spectrometry. *J. Anal. At. Spectrom.*, **17**, 759–767.

149. Leach, A. and Hieftje, G.M. (2001) Standardless semiquantitative analysis of metals using single-shot laser ablation inductively coupled plasma time-of-flight mass spectrometry. *Anal. Chem.*, **73**, 2959–2967.

150. Bings, N.H., Stefanka, Z., and Mallada, S.R. (2003) Flow injection electrochemical hydride generation inductively coupled plasma time-of-flight mass spectrometry for the simultaneous determination of hydride forming elements and its application to the analysis of fresh water samples. *Anal. Chim. Acta*, **479**, 203–214.

151. Date, A.R. and Hutchinson, D. (1987) Determination of rare earth elements in geological samples by ICP source mass spectrometry. *J. Anal. At. Spectrom.*, **2**, 269–281.

152. Garbarino, J.R. and Taylor, H.E. (1987) Stable isotope dilution analysis of hydrologic samples by ICP-MS. *Anal. Chem.*, **59**, 1568–1575.

153. Park, C.J. and Hall, G.E.M. (1988) Analysis of geological materials by ICP-MS with sample introduction by electrothermal vaporisation. *J. Anal. At. Spectrom.*, **3**, 355–361.

154. Gregoire, D.C. (1988) Determination of platinum, ruthenium and iridium in geological materials by ICP-MS with sample introduction by electrothermal vaporization. *J. Anal. At. Spectrom.*, **3**, 309–314.

155. Audetat, A., Guenther, D., and Heinrich, C.A. (1998) Formation of a magmatic-hydrothermal ore deposit: insight with LA-ICP-MS analysis of liquid inclusions. *Science*, **279**, 2091–2094.

156. McLeod, C.W., Date, A.R., and Cheung, Y.Y. (1986) Metal ions in ICP-mass spectrometric analysis of nickel-base alloys. *Spectrochim. Acta, Part B*, **41**, 169–174.

157. Pollmann, D., Leis, F., Tölg, G., Tschöpel, P., and Broekaert, J.A.C. (1994) Multielement trace determinations in Al_2O_3 ceramic powders by inductively coupled plasma mass spectrometry with special reference to on-line preconcentration. *Spectrochim. Acta, Part B*, **49**, 1251–1258.

158. Pilger, C., Leis, F., Tschöpel, P., Broekaert, J.A.C., and Toelg, G. (1995) Analysis of silicon carbide powders with ICP-MS subsequent to sample dissolution without and with matrix. *Fresenius J. Anal. Chem.*, **351**, 110–116.

159. Jiang, S.J. and Houk, R.S. (1986) Arc nebulisation for elemental analysis of conducting solids by ICP mass spectrometry. *Anal. Chem.*, **58**, 1739–1743.

160. Haraguchi, H. (2004) Metallomics as integrated biometal science. *J. Anal. At. Spectrom.*, **19**, 5–14.

161. Lyon, T.D.B., Fell, G.S., Hutton, R.C., and Eaton, A.N. (1988) Evaluation of ICAP MS for simultaneous multielement trace analysis in clinical chemistry. *J. Anal. At. Spectrom.*, **3**, 265–272.

162. Delves, H.T. and Campbell, M.J. (1988) Measurements of total lead concentrations and of lead isotope ratios in whole blood by use of ICP source MS. *J. Anal. At. Spectrom.*, **3**, 343–348.

163. Serfass, R.E., Thompson, J.J., and Houk, R.S. (1986) Isotope ratio determination by ICP MS for zinc bioavailability studies. *Anal. Chim. Acta*, **188**, 73–84.

164. Dean, J.R., Ebdon, L., Crews, H.M., and Massey, R.C. (1988) Characteristics of flow injection ICP MS for trace metal analysis. *J. Anal. At. Spectrom.*, **3**, 349–354.

165. Herzog, R. and Dietz, F. (1987) Anwendung der ICP MS in der Wasseranalytik. *Gewässerschutz, Wasser, Abwasser*, **92**, 109–141.

166. Beauchemin, D., McLaren, J.W., Mykytiuk, A.P., and Berman, S.S. (1988) Determination of trace metals in an open ocean water reference material by ICP-MS. *J. Anal. At. Spectrom.*, **3**, 305–308.

167. McLaren, J.W., Beauchemin, D., and Berman, S.S. (1987) Application of isotope dilution ICP mass spectrometry to the analysis of marine sediments. *Anal. Chem.*, **59**, 610–613.

168. McLaren, J.W., Beauchemin, D., and Berman, S.S. (1987) Determination of trace metals in marine sediments by ICP mass spectrometry. *J. Anal. At. Spectrom.*, **2**, 277–281.

169. Ridout, P.S., Jones, H.R., and Williams, J.G. (1988) Determination of trace elements in a marine reference material of lobster hepatopancreas (TORT-1) using ICP-MS. *Analyst*, **113**, 1383–1386.

170. Beauchemin, D., McLaren, J.W., Willie, S.N., and Berman, S.S. (1988) Determination of trace metals in marine biological reference materials by ICP MS. *Anal. Chem.*, **60**, 687–691.

171. Barbante, C., Cozzi, G., Capodaglio, G., Van de Velde, K., Ferrari, C., Veysseyse, A., Boutron, C.F., Scarponi, G., and Cescon, P. (1999) Determination of Rh, Pd, and Pt in polar and alpine snow and ice by double-focusing ICP-MS with microconcentric nebulization. *Anal. Chem.*, **71**, 4125–4133.

172. Becker, J.S., Dietze, H.J., McLean, J.A., and Montaser, A. (1999) Ultratrace and isotope analysis of long-lived radionuclides by inductively coupled plasma quadrupole mass spectrometry using a direct injection high-efficiency nebulizer. *Anal. Chem.*, **71**, 3077–3084.

17

Laser Ablation Inductively Coupled Plasma Mass Spectrometry (LA-ICPMS)

Bodo Hattendorf and Detlef Günther

17.1

Introduction

In laser ablation inductively coupled plasma mass spectrometry (LA-ICPMS) the aerosol analyzed by ICPMS is generated by evaporating (ablating) a solid sample by means of a high-energy pulsed laser beam, which is focused on the sample surface. The ability to concentrate laser energy into an area as small as 4 µm in diameter for current equipment enables spatially resolved elemental analysis of major, minor, and trace elements and isotope ratio measurements in almost any solid material [1–5]. The development of this technique started in 1985 when Alan Gray presented the very first attempt at quantitative analysis of geological materials using LA-ICPMS [6]. The general setup of LA-ICPMS has not undergone fundamental changes since this initial configuration, while technical improvements of laser sources, beam delivery optics, and ICPMS instrumentation led to better performance and an increasing range of applications until today. These applications range from geochemical studies over material sciences and technology into biochemical and even medical applications. Forensic studies of many kinds are routinely carried out, and quality control of production processes is an increasing field where this technique is employed. In general, LA-ICPMS is a valuable tool in elemental trace and ultra trace analysis whenever spatially resolved determinations are required or when sample consumption shall be minimized. Even for bulk analysis, LA-ICPMS may be considered as it eliminates the need for sample digestion and minimizes the occurrence of solvent-based spectral interferences, which can be a severe limitation in ICPMS when using conventional solution nebulization.

LA-ICPMS basically consists of the following components:

- *The laser source and beam delivery*. Different pulsed lasers are currently available for LA-ICPMS, which primarily differ in wavelength, pulse duration, and pulse energy as well as in beam geometry and energy distribution. The beam delivery in most cases consists of energy adjustment, steering and shaping elements, and an objective for focusing and observation. Beam shaping is carried out to

Handbook of Spectroscopy, Second Edition. Edited by Günter Gauglitz and David S. Moore.

minimize the variability of the energy density across the final beam in order to achieve a so-called flat-top energy distribution and to adjust the beam diameter at the sample surface, that is, the crater size at the ablation site.

- *The ablation cell and transport system*. The ablation cell forms an airtight enclosure around the sample area under investigation. It is usually mounted on a manually operated or computer-controlled x–y–z-stage for sample positioning under the laser beam. The cell interior, where the aerosol is generated by the laser pulse, is continuously flushed with argon or helium as carrier gas, transporting the material toward the ICPMS via flexible tubing. The transport system may contain devices for addition of a make-up gas or further aerosol manipulation such as removal of excessively large particles or pulse mixing to stabilize conditions inside the ICPMS.
- *The ICPMS instrument*. Many different types of ICPMS are available for elemental analysis of a laser-generated aerosol. The major difference with respect to the requirements of laser ablation (LA) may be seen in the type of mass spectrometer and detection system employed. Quadrupole systems represent the most widely used type here because of their simple operation and reliability. Sector field instruments can provide higher sensitivity and the capability of higher mass resolution. Comparably long magnet settling times however can lead to lower scan speed if the difference in m/z is large. The ability to detect ion signals for multiple isotopes simultaneously, when equipped with detector arrays, makes them ideally suited for isotope ratio measurements. Time of flight (TOF) systems probably resemble the smallest fraction of mass spectrometry (MS) used with LA, even though they would provide a quasi-simultaneous detection of the entire m/z range of interest. These instruments, however, appear to be limited in sensitivity and dynamic range.

Modern ICPMS instruments typically provide a linear dynamic range for detection of about 9–12 orders of magnitude, which is a valuable feature for LA sampling as it allows to register abundant isotope signals of major elements together with low abundant trace and ultra trace elements.

A typical set up of LA-ICPMS is shown in Figure 17.1. Commercial LA instruments typically utilize neodymium-doped yttrium aluminum garnet (Nd:YAG) lasers, operating at UV wavelengths (frequency quadrupled at 266 nm [7] or quintupled at 213 nm [8]) or gas lasers, almost exclusively employing an argon fluoride (ArF)-excimer laser (193 nm) [9–11]. Prototype instruments that were investigated included the F_2 excimer laser operating at 157 nm [12] or an all-solid-state Nd:YAG pumped OPO (optical parametric oscillator) system at 193 nm [13]. These laser are all nanosecond lasers with a pulse duration of approximately 5 ns (Nd:YAG) to 20 ns (excimers) and operate with pulse repetition rates of several tens of hertz. They exhibit a characteristic beam profile, with approximately Gaussian energy distribution in the radial direction (Nd:YAG) or perpendicular to the main axis (excimer). Since a constant energy density across the entire laser beam (the so-called flat top beam) leads to more uniform ablation craters [10], beam homogenization can be achieved by different approaches. In the so-called spatial filtering, the beam is expanded

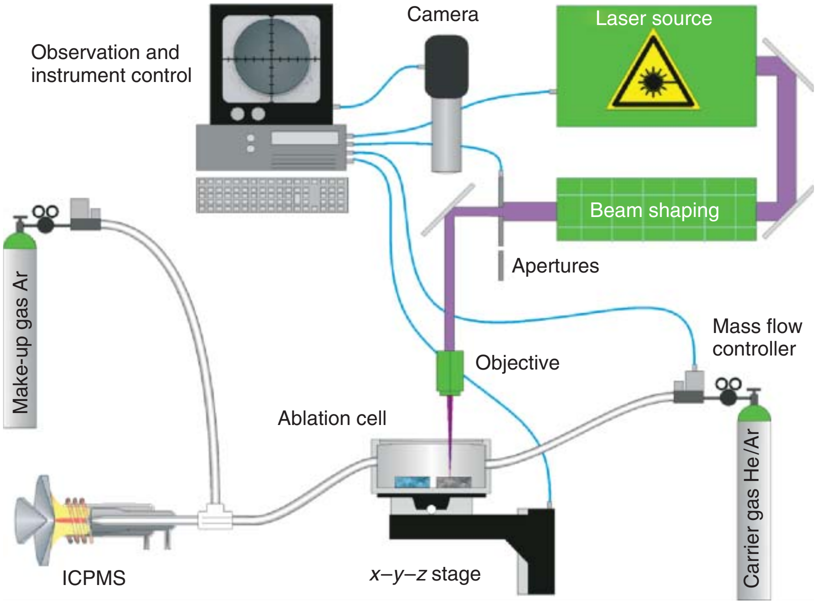

Figure 17.1 Schematic view of a typical LA-ICPMS configuration (MS not shown).

and only the central part of the beam, where variation of the energy is minimal, is transmitted and imaged onto the sample surface [11]. Lens array homogenization on the other hand achieves a homogenous field by splitting the raw beam into individual rays, which are subsequently superimposed at an image plane so that high-energy parts of the original beam coincide with their symmetrically opposite low-energy regions [10]. Both approaches can result in almost 90% loss of the initial beam energy and thus require laser sources of sufficiently high output energies. Recently, Nd:YAG lasers with approximately uniform energy distributions in the central part of the beam were developed, which thus avoid most of the losses associated with beam homogenization and allow the use of more compact laser sources and power supplies.

More recently, ''ultrafast'' laser sources with pulse duration in a range 150–300 fs (femtosecond lasers) have also been introduced [14, 15]. The most common type is the titanium-doped sapphire laser (Ti:sapphire), operating at a fundamental wavelength around 800 nm. Owing to the low energy available from the femtosecond laser, the pulse needs to be amplified using a so-called chirped pulse amplifier to generate laser pulses with sufficient energy density to allow ablation of a solid. UV wavelengths can be obtained after frequency tripling (≈266 nm) and quadrupling (≈200 nm) [16, 17], that is, similar to the wavelengths supplied by the Nd:YAG or the excimer lasers. The radial energy distribution is approximately Gaussian.

To adjust the size of the laser beam at the sample surface, it is usually directed onto a mask holding interchangeable apertures of various sizes and eventually different (circular or rectangular) geometries [9, 10]. An image of this aperture is then projected to the sample surface using an objective lens. Together with the aperture size, the demagnification provided through the objective determines the crater size, when the sample surface is placed at the respective image position. The energy density available for ablation is determined by the laser energy transmitted through the aperture and the crater size used. Additional loss of energy occurs by absorption by the optical elements in the beam path such as mirrors, the objective, and the cell window, as well as oxygen in the ambient air, especially for UV wavelengths. The optical elements within the beam path are usually coated specifically to ensure maximum transmission or reflectivity respectively at the wavelength used. Prolonged operation can lead to deposition of ablated material at the cell window, which not only affects the transmission of the incident light locally but may also lead to damage of the window's coating. It is thus critical to position the sample surface as far from the window as possible.

Sample observation is critical, especially when ablation shall be carried out at specific points of interest, which may be only several micrometers in size. Because of this, a LA unit is usually equipped with adjustable illumination and a digital observation system consisting of a charge-coupled device (CCD) camera and zoom optics, which may be supplemented by a microscope eyepiece for direct sample inspection.

Precise and reproducible positioning of the sample under the laser beam can be done using a motorized x–y–z-stage that is controlled by the instrument software. This stage can be used to either move to a specific position and keep that position during the entire ablation process (the so-called single-spot ablation) or to continuously traverse the sample along a predefined path, which may be a straight line or follow specific features at the sample surface (so-called scanning or raster mode ablation). Usually all three axes can be moved simultaneously, allowing the matching of the surface topography with the image point of the laser beam.

Aerosol transport from the ablation cell to the inductively coupled plasma (ICP) is achieved by the continuous flow of a carrier gas. Initially, argon was used for this purpose as it is commonly used in ICPMS instruments for sample introduction. In the late 1990s, however, helium was found to be better suited owing to higher analyte sensitivity and also reduced problems arising from elemental fractionation [9, 18], making it the preferred carrier gas today. The pressure inside the ablation cell may be considered atmospheric, as there should be little restriction of the flow after the ablation cell exit. The carrier gas is typically regulated by a mass flow controller, which may be available at the ICPMS or integrated in the LA unit and adjusted via the instrument software. The aerosol is then carried toward the ICP via flexible tubing. When helium is used as carrier gas, argon is admixed to the aerosol stream downstream the ablation cell to ensure stable operation of the ICP ion source.

The ICP shall transform the laser-generated aerosol into elemental ions, the currents of which can be registered using a mass spectrometer. Several competing processes inside the ICP, the vacuum interface, and ion optics, can greatly affect the sensitivity obtained in LA-ICPMS. In general, the processes are similar to those occurring in conventional ICPMS with solution nebulization but the absence of a solvent and the considerable amount of helium often used can change conditions inside the ICP substantially. The range of particle sizes generated during LA most likely imposes the greatest challenge on the optimization of the ICP ion source [19]. Ion extraction via the vacuum interface of the MS occurs at a fixed point in space and from a limited volume of the ICP. Thus, the ion density needs to be maximized at this position to attain the highest possible analyte sensitivity. The efficiency of particle vaporization depends mainly on gas temperature (T_{gas}) inside the central channel of the ICP and the residence time of the particles before reaching the sampler cone of the vacuum interface. Optimization of the ICP therefore has to balance T_{gas} and residence time between maximum vaporization of the laser-generated aerosol and potential analyte loss by diffusion out of the plasma volume sampled through the vacuum interface.

Extraction of the plasma via the vacuum interface should be governed by similar processes as in conventional ICPMS. The use of helium as a carrier gas, however, usually leads to higher interface pressure, and collisions during the transfer toward the high vacuum of the MS become more frequent. The absence of a solvent, on the other hand, reduces the abundance of molecular ions, formed in collisions during the extraction, significantly.

The transfer of the ions from the vacuum interface to the mass spectrometer is affected in a similar way. Since T_{gas} may be slightly higher when helium is used [20, 21], the ion kinetic energies may span over a greater range for different m/z after the supersonic expansion [22], and thus, focusing of the entire m/z range within the ion optics may become less efficient.

MS separation and detection should be least affected if LA is used in comparison to conventional nebulization. Owing to rapid changes in the ion densities created by the pulsed sample introduction, the scan duration of the MS should be as short as possible in order to maximize the correlation of the ion signals.

In the following chapters, more detailed descriptions of the respective components involved in LA-ICPMS and their effects on the analytical performance are given.

17.2
Fundamental Aspects of Laser Ablation

LA occurs when a material is irradiated by a laser pulse of sufficiently high energy density or fluence (expressed in joules per square centimeters). It results in a rapid heating of the sample material and ultimately evaporation of parts of the irradiated volume. In addition, within 50–200 nanoseconds after the laser pulse a plasma forms above the irradiated area [23]. The mass removal associated with these processes is utilized in many fields of technology (e.g., microfabrication, thin film production, and laser cutting) and also medicine (eye surgery). In spectrochemical analysis, LA is also used as a sampling and excitation tool for a variety of techniques. In laser-induced breakdown spectroscopy (LIBS, sometimes termed laser-induced plasma spectroscopy: LIPS), the material removed from the sample is excited either during ablation or within a localized plasma forming above the ablation crater [24–26]. By means of an optical spectrometer, it is thus possible to record the emission spectrum from the transient plasma. On the basis of this emission, elements present in the vaporized material can be identified and quantified using a calibration curve. A second – less common – application is laser ablation mass spectrometry (LAMS) [27, 28], where the ions formed during the ablation process are directly transferred into a mass spectrometer for analysis. Both former approaches are somewhat limited for quantitative analysis of samples, where matrix-matched calibration standards are not readily available [29–31]. Matrix-assisted laser desorption and ionization (MALDI) [32] may be considered an approach similar to LAMS. A major difference here is that a laser beam of comparably low energy density and large crater sizes are used, which results in the release of nondissociated molecules and molecular ions for analysis by MS. This technique has gained significant attention in the analysis of macromolecules, especially proteins and peptides, but analysis for the elemental composition of the sample is not easily achieved.

In elemental analysis using LA with ICP-based detection methods such as LA-ICPOES (laser ablation inductively coupled plasma optical emission spectroscopy) [33] and predominantly LA-ICPMS, the sampling process is completely separated from the excitation or ionization, which offers the opportunity to optimize both processes independently. This is most likely the key reason why especially LA-ICPMS has gained such significant attention in recent years.

The ultimate goal in LA for ICPMS detection is to create an aerosol that can be transformed into a mass spectrum representing the composition of the ablated material. This cannot be fulfilled in many practical applications because of the variability of the different processes that occur during the generation of the aerosol and the detection in the ICPMS. Elemental fractionation due to preferential vaporization during the ablation can change the composition in the aerosol formed during ablation and in the solid and also alter the thermodynamic properties of the sample material before the next laser shot occurs. On the other hand, vaporization and ionization of aerosols showing different particle size distributions inside the ICP ion source may further change the relative response of the elements when different materials are sampled.

17.2.1
Aerosol Generation and Transport

The aerosol analyzed finally with the ICPMS may be considered a result of various processes resulting from the different mechanisms of the laser–material interaction. These mechanisms change with respect to the sample material and the laser properties such as energy density, pulse duration, and wavelength. This chapter briefly introduces basic concepts of LA leading to aerosol formation from a solid with respect to experimental conditions.

17.2.1.1 Ablation Process

Initially, the laser beam will lead to excitation of electrons inside the solid. A fraction of these electrons may leave the surface by photoionization. The remaining excited electrons will subsequently transfer the energy to the lattice and heat the material. If the energy of the laser beam is above the ablation threshold, the near-surface temperature will rapidly rise above the respective point of vaporization and the vapor is ejected from the sample surface at a velocity in the range of $10^3 – 10^4$ m s^{-1} [34]. As ablation is carried out in an ambient gas at atmospheric pressure, a shock wave forms at the boundary between the expanding material and the background gas [35]. Moreover, ionization of the gas and the vapor released creates a plasma above the ablation crater. When the temperature in the vapor plume has fallen below the condensation temperature of its components, particles start to form [36]. The particles generated in these processes are typically in a range of several tens of nanometers and their overall composition should represent the ablated material unless the material contained species that can form volatile compounds at room temperature (e.g., CO_2 from carbonates). It is not well described yet whether the nucleation and condensation of these aerosol particles occur in a statistical manner or is driven by the thermodynamic properties of the vapor. Principally, an earlier onset of condensation of components with higher boiling temperatures has to be expected. This would ultimately result in a significant variability of the particle composition, size, and thermodynamic properties. In the presence of a considerable amount of melt within the ablation crater, particles can also be generated through splashing of droplets by the recoil pressure inside the expanding plume [37]. The size of these droplets depends to a large extent on the physical properties of the melt such as viscosity, thickness, and temperature and also on the aspect ratio of the ablation crater. Particles of several micrometers diameter were observed for shallow craters and thick molten layers, while their abundance decreases significantly for deeper craters [19]. The splashing of material is typically accompanied by the formation of a chimney-like structure at the top to the ablation crater.

The more rapidly the laser energy is converted into vaporization, the smaller is the degree of material melting, which is considered to represent an important source of elemental fractionation. The amount of energy density deposited within a specific sample volume depends on the fluence of the laser beam, the absorption of the respective wavelength, and the material-specific energy loss processes. A substantial fraction of the laser energy may be lost by reflection of the incident beam at the surface and the so-called ‘‘plasma shielding.’’ Both effects are difficult to estimate in their magnitude as optical reflectivity at the respective temperature is usually not known and because the extent of plasma formation above the laser crater depends to some extent on the ablation process (degree of photoionization, etc.). The latter, however, was estimated to cause as much as 50% loss of the incident beam, mainly due to inverse Bremsstrahlung [38]. Inside the material, the laser energy may further be lost as a result of the thermal conductivity of the material and by radiation [39]. The total energy available for vaporization is finally determined by the heat capacity of the material and its respective latent heat of melting. Especially, for natural samples with complex composition these are often difficult to determine making it difficult to estimate the relevance of the respective processes. Thus, prediction of the evaporation rates and vapor/melt ratios remain difficult for the majority of samples analyzed by LA-ICPMS. The optimization of the ablation process should thus ensure minimizing the extent of melting and maximizing the conversion of the laser energy into vaporization of the sample.

17.2.1.2 **Laser Pulse Energy**

The energy of the laser pulse ultimately determines how much of the solid material can be transferred into the vapor phase to subsequently form an aerosol. Ablation is only occurring if the energy density or fluence is sufficiently high. Depending on the type of material, the laser wavelength, and pulse duration, the ablation threshold lies in the order of some hundreds of millijoules per square centimeter up to several tens of joules per square centimeter. Such energy densities are obtained by focusing the original laser beam (output energy of several millijoules) to a size of typically 5–200 μm in diameter. A total beam energy of only 0.2 mJ output energy, concentrated in a crater size of 50 μm, is then sufficient to achieve an energy density of about 10 J cm^{-2}. Above the ablation threshold, the ablation rate usually increases over a wide range in proportion to the energy density [40] until at very high energy densities the ablation regime changes into a process termed *phase explosion* with significantly greater ablation rates [41].

When an aperture is illuminated by a homogenized beam and imaged onto the sample surface, the energy density remains constant for different crater sizes. Energy homogenization furthermore minimizes variations in the respective ablation processes that occur at different energy densities. In this case, the ablation crater is usually characterized by a regular and flat bottom. If, on the other hand, a focused Gaussian beam is used, the energy density and crater size depend on the focal position of the beam relative to the sample surface and its output energy. The respective energy density and ablation rate decrease along the radius of the beam.

17.2.1.3 **Laser Wavelength**

The absorption coefficient at the laser wavelength mainly influences the amount of energy that can be deposited within a given volume of the sample material. High absorption leads to smaller penetration depth and thus a higher temperature within the material. This is especially critical for transparent materials where the use of deep UV wavelengths (193 and 213 nm) was found to significantly improve the crater morphology and to reduce elemental fractionation during ICPMS detection [8, 13]. The higher the absorbance of the material at the laser wavelength, the more energy is concentrated in a volume at the surface. This leads to a higher vapor/melt ratio [36], which ultimately reduces the abundance of micrometer-sized particles in the aerosol. Deep UV wavelengths also benefit from smaller variability of the absorption for different materials.

17.2.1.4 **Crater Size**

Laser irradiation causes a part of the sample to undergo phase transitions including melting and evaporation. Apart from the area directly irradiated by the laser beam, a much larger volume is heated because of the thermal conductivity of the material (‘‘heat affected zone’’). The larger this volume, the greater is the corresponding amount of laser energy that cannot be converted into evaporation of the material, resulting in a smaller vapor/melt ratio. To avoid elemental fractionation, it is thus desirable to reduce the corresponding energy loss. For a constant fluence, however, the volume of the heat-affected zone relative to the ablation crater will decrease with increasing diameter of the laser beam. Furthermore, larger crater sizes reduce the aspect ratio of the ablation crater developing upon progressive ablation. Deep and narrow craters (high aspect ratio) have been found to enhance elemental fractionation in LA-ICPMS. Low-fluence irradiation at slightly tilted crater walls may cause preferential release of volatile components [42], which may further be enhanced by heating through the laser-induced plasma. Furthermore, transfer of larger particles into the carrier gas is probably less efficient for craters with a high aspect ratio. Finally, there is also the chance that vaporized material is deposited at the crater walls after the ablation event. Thus, especially when attempting to sample at high spatial resolution, the occurrence of elemental fractionation due to the formation of deep craters needs to be monitored. For glass samples and LA using 193 nm, for example, it was found that elemental fractionation is significant when an aspect ratio of six is exceeded, independent of the crater size used.

17.2.1.5 **Laser Pulse Duration**

The ablation of a solid is characterized by different processes occurring at different timescales [43]. In the subpicosecond (10^{-12} s) regime, photon–electron interactions dominate, leading to a rapid rise of the electron temperature inside the material with an instantaneous emission of electrons. The plasma is formed after several hundred femtoseconds (10^{-15} s) and at the same time the excited electrons transfer the energy into the lattice, thereby heating the material to the respective melting and boiling temperatures. Within a few nanoseconds (10^{-9} s) after the pulse, evaporation of the material starts. Currently, LA is most frequently carried out by nanosecond lasers, where the duration of the laser irradiation is sufficiently long to interact with all transformation stages of the material during the heating process and also with the laser-induced plasma above the ablation crater. Therefore, a significant fraction of the incident beam is shielded from the sample surface by heating the electrons in the plasma (inverse Bremsstrahlung) while heat conduction causes the energy deposited inside the ablation crater to be readily dissipated into the sample body. This ultimately limits the energy available for evaporation of the material and leads to a relatively large volume of molten material that may be splashed from the ablation crater [37]. When the pulse duration is reduced to the subpicosecond regime by using femtosecond lasers, energy loss by plasma shielding can be eliminated, and the laser energy is deposited inside the irradiated volume before relaxation of the electron energies into the lattice and thermal diffusion becomes significant. Owing to these major differences, femtosecond lasers are expected to improve the ablation characteristics for LA-ICPMS. First results indicate that especially ablation of metallic samples is significantly improved when femtosecond lasers are employed [17, 44–46]. Despite the typically lower fluencies available from femtosecond lasers, significantly higher ion signal intensities are observed in LA-ICPMS of metal samples, when compared to nanosecond lasers. For the ablation of dielectric materials such as glass, on the other hand, the use of femtosecond lasers may result in lower signal intensities [47]. This latter is attributed to the lower fluence supplied by current femtosecond-LA systems. Dielectric materials typically have significantly smaller thermal conductivity, which mitigates the energy loss by thermal diffusion, and the advantage of the shorter pulse duration diminishes to some extent. The higher fluence obtained from the nanosecond laser in this case results in greater ablation rates and correspondingly higher ion signal intensities.

17.2.1.6 Gas Environment

LA for sampling into the ICPMS has to be carried out in an inert gas, usually at atmospheric pressure. Argon is the common carrier gas for ICPMS operation and was thus initially also used in LA-ICPMS for aerosol transport [6]. Experiments using helium as the ambient gas during ablation, added to an argon flow for stable operation of the ICP, led to significant improvements with respect to analyte sensitivity, reduced the amount of material deposited near the ablation crater and showed smaller elemental fractionation effects [9, 18]. Both are ascribed to the change in the particle size distribution of the ablated material, which occurs when changing from argon to helium under otherwise similar ablation conditions [48]. Helium has an approximately 10-fold higher thermal conductivity and lower density than argon, resulting in a more rapid cooling of the evaporated material and greater dilution due to a wider expansion of the vapor plume. In addition, the shock applied to the molten surface of the sample during the expansion of the plasma is less pronounced in the less dense gas. These processes can explain the reduced abundance of micrometer-sized particles and solidified droplets in the sample aerosol when helium is used as carrier gas in LA-ICPMS.

17.2.1.7 Ablation Cell and Aerosol Transport System

The ablation cell provides a gas-tight enclosure of the ablation region connected via flexible tubing to the sample inlet of the ICPMS. It is continuously flushed by the carrier gas at flow rates between 0.3 and 1.1 $\mathrm{l\,min^{-1}}$. Ablation cells are often cylindrical in shape and equipped with a top window for observation, illumination, and delivery of the laser beam [6, 49]. The dependency of transport efficiency and signal dispersion on the volume and the shape of the ablation cell as well as differences in turbulent and laminar gas flow is still subject of intense research and also numerical modeling [46, 50]. It was observed, however, that the amount of mass transported from the ablation cell to the ICP is largely independent of the cell geometry or carrier gas flow rate if unrestricted flow to the ICP is attained [51]. Another important characteristic of the transport system is the aerosol dispersion. It may cause the aerosol generated from a single laser pulse to occur as a very sharp signal inside the ICPMS or stretched to a duration of several seconds. The dispersion of the aerosol is affected by the internal volume of the ablation cell and its geometry, and by the carrier gas flow rate and occurrence of laminar or turbulent flow regimes [52]. The effect of cell volume on signal dispersion is shown exemplarily in Figure 17.2. For a laser pulse repetition rate of 2 Hz, both ablation cells show distinct oscillations of the ion signals. The amplitude, however, is dramatically greater for the cell with only 0.25 $\mathrm{cm^3}$ internal volume compared to the 63 $\mathrm{cm^3}$ ablation cell. In addition, the smaller cell leads to a pronounced oscillation of the peak intensities at a frequency of approximately 0.3 Hz. This

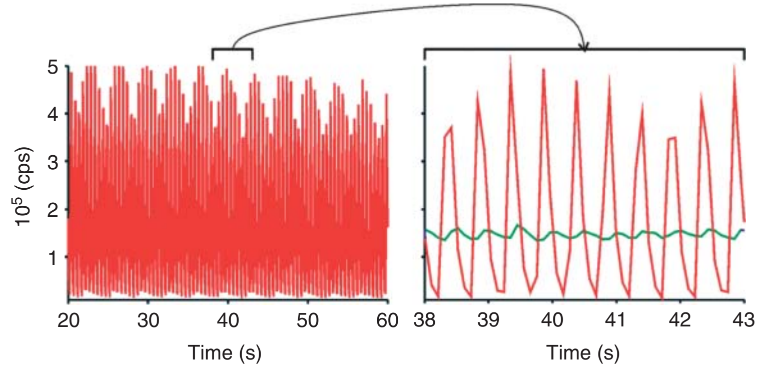

Figure 17.2 Influence of ablation cell volume on signal dispersion. Laser ablation carried out with 2 Hz pulse repetition rate. Red line: 0.25 cm^3 internal volume; green line: 63 cm^3 internal volume (not shown in the left panel). Average ion signals 158 kcps (0.25 cm^3) and 134 kcps (63 cm^3).

beat is originating in the rapid intensity change at 2 Hz and the data acquisition frequency of ≈9.71 Hz (103 ms scan duration of the MS). Averaged ion signal intensities obtained are fairly similar for both ablation cells. The smaller cell shows about 20% higher overall ion signal intensities, which is attributed to reduced deposition inside the cell due to flow dynamics.

High aerosol dispersion leads to tailing signals that can last for seconds and results in lower peak intensities from a single laser pulse. It is most pronounced for large cell volumes, low carrier gas flow rates, and especially when turbulent flow conditions prevail inside the ablation cell [46]. The volume of tube connections to the ICP was found not to have a major influence on the signal dispersion unless it becomes comparable to that of the ablation cell [52]. An advantage of higher dispersion, however, lies in smoother ion signal intensities that can be obtained. Therefore, additional pulse mixing devices have been employed in LA-ICPMS, which can be realized through volume holding baffle plates inserted between ablation cell and the ICP [9, 53]. Turbulences and abrupt changes in the flow direction, however, may lead to particle size dependent transport efficiency or changes in the respective transport times. Smaller particles tend to follow the gas flow more closely, while larger particles may be lost upon collisions with the tube walls. Vortexes in the transport system, on the other hand, may cause temporal trapping of smaller particles [50].

17.2.2
Requirements for Quantification

Elemental analysis using LA-ICPMS requires the transformation of the solid material into an aerosol that either resembles the composition of the analyzed volume or allows to asses and compensate for deviations in the aerosol composition by using a matrix matched material for calibration that shows identical effects.

In addition, the transient variation of the aerosol density in the carrier gas flow, caused by the use of pulsed lasers, in combination with aerosol dispersion affects the spatial resolution attainable owing to the mixing of aerosols generated by subsequent laser pulses. The pronounced variability of the dominating ablation mechanisms, which depends on the sample composition, can impose a challenge for the quantification of unknown samples. All processes involved can lead to varying ablation rates as well as sample- and time-dependent aerosol composition and particle size distributions. To minimize these effects with respect to quantitative analysis by LA-ICPMS, a few general remarks may be made.

- *When matrix-matched calibration standards are available*, the processes occurring during LA mainly affect the sensitivity of the method in general. As changes in the ablation rates, particle size distributions, and composition of the aerosol should be identical for the calibration standards and the unknown samples, the major limiting factors should cancel out in the calibration. It should be ensured, however, that the data acquisition for quantification is carried out for identical ablation conditions, that is, during the same ablation period when the ablation rates vary with time or crater depth.
- *When matrix matched calibration standards are not available*, it needs to be ensured that the stoichiometry of the aerosol is representative for the composition of the calibration standards and unknown samples respectively. In the case of dielectrics such as glasses, minerals, or ceramics, this appears to be mainly dependent on the wavelength used and the fluence applied. Deeper UV wavelengths and higher fluence were found to allow accurate quantification of these materials in a wide variety of applications. Elemental fractionation may, however, still be pronounced, especially when comparing volatile and refractory elements, but the extent is greatly reduced. For the analysis of metals, on the other hand, the duration of the laser pulse is more important. The use of femtosecond lasers was found to reduce elemental fractionation to a great extent in these materials. Currently, however, these systems still lack sufficient fluence in the deep UV to provide ablation rates in dielectric materials that are comparable to nanosecond lasers.

17.3
ICPMS Detection

Since the fundamental aspects and operating principles of ICPMS have been described in a previous section (Chapter 16), this chapter only discusses aspects that are considered important for LA sampling.

17.3.1
Instrumentation

In principle, the configuration of ICPMS for LA sampling is identical to solution-based sample introduction methods. Fundamental differences occur mainly in the composition of the carrier gas, which usually does not contain a solvent but a significant fraction of helium. The change in its composition, however, may affect the characteristics of the ICP with respect to sample vaporization and ionization to some extent. It will also alter the pressure in the vacuum interface and ion optics of the ICPMS as helium is less efficiently pumped by the vacuum system. Helium is typically supplied via mass flow controllers that may be incorporated in the ICPMS system or from an external unit fitted to the LA unit. The addition of argon to the carrier gas is typically performed using the nebulizer supply of the ICPMS.

17.3.1.1 **The ICP Source**

The laser-generated aerosol needs to be vaporized, atomized, and ionized before detection by the MS is possible. The abundance of the analyte ions in the ICP further needs to be maximized within the limited volume that is extracted via the sampler cone into the vacuum interface of the MS [54]. The residence time of the aerosol inside the ICP is limited to a few milliseconds only [55]. This will cause significant variations of particle evaporation when the laser-generated aerosol is characterized by a wide size distribution [21] and ultimately affect the efficiency of the sampling process. Figure 17.3 shows distribution of Rb^+, representing elements with higher volatility, and Y^+, representing more refractory elements inside the ICP when different LA configurations are employed.

The radial and axial distribution of analyte ions can be highly variable and dependent on the conditions used for LA sampling and inside the ICP. Generally, the distribution gets wider in the axial direction when argon is used as the carrier gas. At the same time, the volatility of the element has a significant influence on the distribution. Because of this, the more refractory Y^+ ions show a wider radial spread when the aerosol contains a significant amount of large particles (266 nm with argon as carrier gas) compared to Rb^+ ions. Changing to helium as carrier

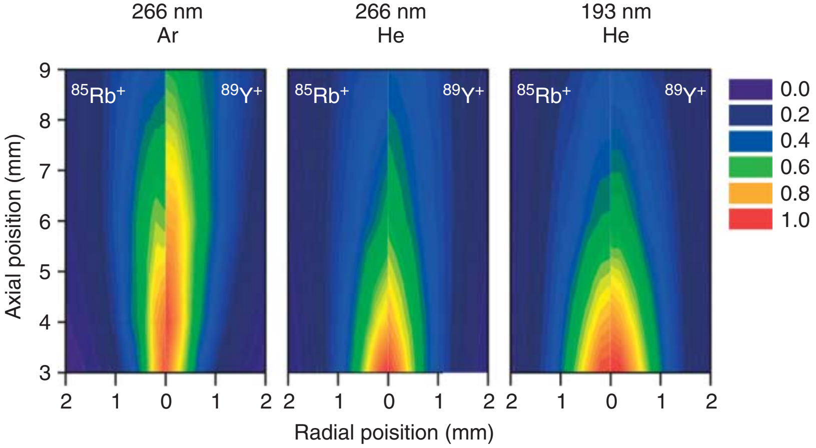

Figure 17.3 Radial and axial distribution of ion density in the ICP (normalized to the maximum signal) for aerosols from silicate glass, generated by different configurations of laser ablation (266 or 193 nm) and carrier gas (argon or helium). (Data according to [21].)

gas reduces the axial spread but leads to slightly wider radial distributions for both elements. When the laser-generated aerosol consists mainly of particles of around 100 nm (193 nm helium as carrier gas), the axial distributions of the elements are almost equal. The radial distribution then depends almost exclusively on the isotope mass and increases with decreasing isotope mass [21]. This would correspond to the higher diffusion rates for lighter isotopes and may therefore add to the mass dependency in the detection efficiency of the ICPMS (see also Figure 17.4).

An aerosol containing a significant fraction of large particles is thus disadvantageous, as the point where complete evaporation is achieved will vary substantially with particle size. Particles exceeding a certain limit may furthermore not be vaporized at a timescale of a few milliseconds, which is the typical transit time through the ICP [58]. The maximum particle size that can be vaporized in the ICP for MS detection will depend on its composition and is estimated to be in the order of 100 nm for silicate glass [59]. For comparison with solution nebulization, the mass of this particle would be equivalent to the dissolved fraction of only 20 mg l^{-1} in a droplet of 5 μm diameter.

Adjusting the ICP operating conditions to increase the residence time or the gas temperature within the plasma would allow for more efficient vaporization of larger particles. It will, however, also lead to more pronounced radial diffusion of the vaporized material and thus cause greater analyte losses due to incomplete ion sampling through the vacuum interface [56]. It is thus desirable that the aerosol predominantly consists of smaller particles to ensure complete vaporization of the entire aerosol in a narrow region to maximize sensitivity.

The extent to which the absence of the solvent in LA-ICPMS changes the plasma properties is not very well understood until today in detail. The gas temperature in the central channel of the ICP may increase because of the absence of the solvent

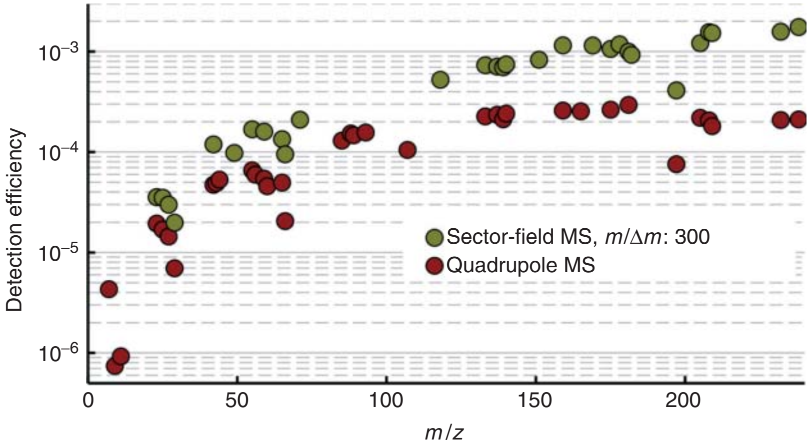

Figure 17.4 Typical detection efficiencies for LA-ICPMS when using quadrupole MS (Data from [56].) or sector field MS (Data from [57].) for isotope detection. (Data from [56].) and sector-field ICPMS (Data from [57].) for LA-ICPMS of silicate glass.

and thus the onset of particle vaporization may shift further upstream inside the ICP. In a similar manner, the presence of helium in the carrier gas can increase the gas temperature [20] because of its higher thermal conductivity. It may also lead to a higher evaporation rate due to faster diffusion of vapor away from the particle surface. Ionization, on the other hand, should not be affected to a remarkable degree by the presence of helium as its first ionization potential exceeds that of argon significantly. The relative degree of ionization thus should be similar to that observed in conventional ICPMS using solution nebulization.

17.3.1.2 **The Vacuum Interface and Ion Optics**

The use of helium as carrier gas can also affect the plasma expansion inside the vacuum interface and the ion optics. Helium is less efficiently evacuated by the vacuum pumps and thus the interface pressure is typically higher when it is present in the carrier gas. The plasma temperature on the other hand may be higher for the dry plasma, which can, to some extent, compensate for this effect. The influence on the respective transmission efficiencies is thus difficult to estimate. Only a few studies have tried to further optimize the vacuum interface for dry sampling by LA specifically [60, 61]. It was found that reducing the sampler cone aperture size or increasing the pump speed at the interface can, to some extent, improve transmission, especially for ions of high m/z. This is most likely a result of fewer collisions of the analyte ions with the background gas due to a lower interface and ion optics pressure. The fact that no improvement or even lower sensitivity was observed for low m/z ions indicates that a greater fraction of the lighter ions is lost owing to incomplete sampling of the ions from the ICP or because of greater diffusion in the vacuum interface at reduced pressure. Transmission through the ion optics may similarly become affected by increasing collision rates when helium is used as carrier gas. This may increase the magnitude of the mass bias observed to some extent. A greater influence on ion transmission, however, may result from variations in the total ion density due to varying sample mass introduced into the ICP. While the excess of solvent in conventional solution-based methods may act as a temperature buffer in the ICP, variations in the abundance of the dominating Ar^+ ions are reduced in most cases. In a dry plasma, on the other hand, varying amounts of the sample aerosol may induce larger variations of the abundance of Ar^+, which in turn would influence the magnitude of space charge effects to a greater degree.

The ion optics' mode of operation can further affect the abundance of background ions because of memory effects to some extent. Instruments utilizing extraction optics with highly negative potentials relative to the ion source such as sector field MS [62] typically provide higher analyte sensitivity when compared to instruments where only moderate extraction voltages or even positive potentials [63, 64] are applied. Highly negative potentials on the other hand are more prone to collect and transfer ions that can be sputtered from upstream surfaces and ionized. This can lead to increased background signals, especially for volatile species with low ionization energies such as the alkaline elements. Because the sputtered ions carry much smaller initial kinetic energies [65], ion optics with only moderate extraction or positive bias more efficiently discriminate against such background ions, which results in lower memory effects and improves the background equivalent concentrations.

17.3.1.3 Mass Spectrometers

The different mass spectrometers used for current ICPMS instruments have specific characteristics, which influence the performance for LA sampling in a similar way as with conventional solution nebulization. Because of the transient nature of the aerosol generation by the pulsed laser, however, the correlation of the individual ion signals depends on the scan frequency that can be achieved with the mass spectrometer.

Especially when the laser is operated at frequencies of <10 Hz or when the aerosol dispersion in the sample introduction system is small, the ion signals can exhibit a distinct oscillation at the laser pulse frequency (Figure 17.2). Depending on frequency and aerosol dispersion, the amplitude of this oscillation may span over more than an order of magnitude. Correlated ion signals are, however, important to allow correction for variations in the ablated mass with time and in between individual samples. Owing to the sequential nature of the signal acquisition in quadrupole and single-collector sector field mass spectrometers, the attainable correlation is limited by the duration for a mass scan covering all isotopes of interest. Therefore, the integration time (or dwell time) as well as the settling time need to be adjusted in order to maximize the correlation while still yielding sufficient reproducibility and accuracy of mass adjustment and ion signal acquisition. In most configurations, the dispersion of the aerosol is sufficient to minimize signal oscillations when pulse repetition rates >5 Hz are applied. In these cases, a scan duration of <1 s is usually appropriate to achieve sufficient signal correlation for quantitative analysis. Care should, however, be taken to adjust the scan duration not to be close or equal to a multiple integer of the time period between individual laser pulses, especially when the laser is fired at low repetition rates or the dispersion of the signal is low. Many applications with quadrupole instruments use a dwell time in the range of 10 ms, which, together with typical settling times between 1 and 3 ms, allows recording ion signals for more than 50 isotopes within 1 s. Sector field instruments may exhibit longer scan durations when wide m/z ranges are analyzed, where the magnet needs to be scanned. The dynamic range of the detection system for current instrumentation allows acquisition of ion signals over a range of 9 orders of magnitude by parallel read-out of pulse counting and analog signals at the secondary electron multiplier (SEM). This is sufficient to analyze for elements present at weight percentage concentrations to microgram/kilogram levels in a single mass scan. Recent developments also employ fast switching between an SEM and Faraday-cup for detection of even higher ion signal intensities [66]. If the analyte signals are acquired in different detector modes for different samples it needs to be ensured that the corresponding cross calibration is updated frequently in order to make pulse counting and analog signals comparable. Some instruments additionally allow attenuation of ion transmission for specific isotopes by dynamic adjustment of the mass resolution. This can further be used to include isotopes of the matrix elements into the acquisition, which would otherwise exceed the upper detector range in applications where large crater sizes and high laser fluence are used to increase sensitivity for trace and ultra-trace elements.

The mass resolution ($m/\Delta m$ at 10% peak height) achieved with sector field instruments is typically adjustable between $\approx$300 and $\approx$12 000 [62], allowing the separation of various spectral interferences from the analyte isotopes. In quadrupole instruments, on the other hand, the mass resolution is usually adjusted with m/z analyzed to obtain a peak width of 0.7–0.8 m/z at 10% of the peak height. Quadrupole ICPMS currently achieves detection efficiencies between 10^{-7} and 10^{-4} ions per atom present in the ablated volume. Sector field instruments can provide higher detection efficiency, most pronounced at high m/z (Figure 17.4). Limits of detection are additionally affected by the instrumental background and are thus much lower at high m/z where nanograms per gram detection limits can routinely be achieved at a lateral resolution of several tens of micrometers (Figure 17.13).

Time of flight mass spectrometer (TOFMS) acquires all isotope signals quasi-simultaneously at a rate of several 10^4 spectra per second [67]. This principally allows for a better ion signal correlation for rapidly changing ion signal intensities [68]. Even though this feature would make them ideally suited for LA sampling, the number of applications using these instruments has remained comparably small in comparison to quadrupole or sector field instruments. This may mostly be a result of their limited sensitivity due to a lower duty cycle and more pronounced space charge effects in the drift region. In addition, the dynamic range of current instruments is often limited to about 6 orders of magnitude because of the demands for high signal acquisition speed.

Sector field instruments with multiple detectors arranged at the focal plane of the MS (multi collector inductively coupled plasma mass spectrometry, MC-ICPMS) allow parallel detection of ion signals for more than 15 isotopes. An increasing number of applications use these instruments with LA for *in situ* isotope ratio measurements [16, 69–72]. Even though isotope ratio measurements with a precision in the sub permil range can be achieved, the accuracy is usually inferior to that with solution-based methods because of difficult-to-compensate-for variations in mass discrimination and spectral interferences from isobars and molecular ions. Elemental fractionation may further limit the applicability in application where decay products shall be analyzed simultaneously with the precursor elements, for example, in U/Pb dating. Because of the fact that the highest precision and accuracy is obtained by determination of the respective ion current using Faraday cups, the elements of interest have to be present at relatively high concentrations in the range of about 10–100 mg kg^{-1}. Low abundance isotopes can also be determined using ion counting detectors, whose precision though is limited because of greater drift of the detector gain (i.e., variation in the detector output for constant ion current) and poorer counting statistics.

The benefit of MC-ICPMS instruments by recording the ion signals simultaneously can be utilized for larger m/z ranges by using miniaturized, chip-based detectors in combination with a Mattauch–Herzog mass spectrometer [73]. The ongoing advances in chip technology and electronics design may lead to unique instrumentation that can avoid the limitations of the aforementioned instruments with respect to temporal correlation (sequential MS), duty cycle (TOFMS), or elemental coverage (MC). A potential limitation of this instrument type may arise from the unamplified analog ion current detection [74], which is typically affected by a greater detector noise, affecting the attainable limit of detection. The higher sensitivity of sector field instruments compared to a quadrupole or TOF-based system, however, may at least partially compensate for this [74].

17.3.2
Spectral Interferences

One of the advantages of LA sampling is the absence of a solvent in the sample aerosol, which dramatically reduces the abundance of the corresponding molecular ions in the mass spectrum. The abundance of polyatomic species containing oxygen, for example, is by at least an order of magnitude lower than in conventional solution-based methods. For optimized ICP operating conditions, the $\mathrm{ThO^+/Th^+}$ intensity ratio observed is typically <0.3%, $\mathrm{Th^+}$ being an elemental ion with a very high affinity to oxygen.

Owing to the limited resolution of quadrupole mass spectrometers, spectral interferences usually cannot be resolved. Sector field instruments can provide sufficient mass resolution for separating a range of potential analytes from these interferences albeit at the expense of sensitivity. Furthermore, a large number of polyatomic ions' m/z is still too close to the analyte ions to be resolved (Figure 17.5).

Identification of spectral interferences is usually possible by comparing the isotopic signature of an element with its natural distribution and relating the deviation to potential polyatomic ions on the basis of the composition of the sample. In the case of monoisotopic elements, however, this can only be achieved when

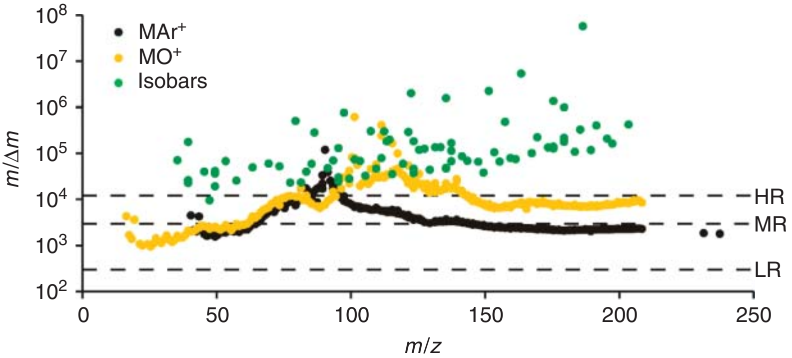

Figure 17.5 Representation of the mass resolution required to separate analyte and interference signals of equal height at the respective m/z for isobaric interferences and molecular ions containing oxygen or argon. Dashed lines indicate the resolution available from sector field instruments at typical instrumental settings of $m/\Delta m$: 300 (LR), 3000 (MR), and 12 000 (HR).

other elements in the same mass region show noticeable deviation from their natural pattern. It is thus generally advisable to know as much as possible about the approximate composition of the sample to allow estimating the occurrence of potential spectral interferences.

17.3.2.1 **Origin of Spectral Interferences**

All elements present in the ICP can principally form polyatomic ions, giving rise to spectral interferences. The magnitude of the interference depends on its respective abundance in the plasma and many possible species presumably occur at levels that do not contribute significantly to the measured ion signal intensities. The most abundant polyatomic ions are species consisting of argon, nitrogen, oxygen, and elements present at higher abundance in the sample aerosol. Furthermore, interferences from doubly charged ions occur at levels comparable to or slightly above those for solution-based methods owing to the potentially higher plasma temperature. Isobaric ions cannot be resolved by current instrumentation because of restricted mass resolution (one exception could be the overlap of $^{48}Ca^+$ and $^{48}Ti^+$, where the mass resolution of sector field instruments may just be sufficient). Nonetheless, all elements except for indium have at least one isotope free from isobaric overlap. Plasma background species are dominated by Ar, O, N, C, and several combinations of these elements, which are most abundant in the mass range between m/z 12 and 80 (Figure 17.6). Other components of the plasma gas as trace amounts of Kr and Xe are also present at detectable levels.

17.3.2.2 **Coping with Spectral Interferences**

Because it is difficult to modify the composition of the aerosol reaching the ICP with LA sampling, there are limited ways to remove an element causing spectral interference. One possibility, recently introduced, that may be useful for selected applications is thermal aerosol treatment, where ion signals of volatile elements could be selectively suppressed [75]. Passing the laser-generated aerosol through a graphite tube electrically heated to 2000 °C, for example, allowed attenuation of Rb by almost 2 orders of magnitude while not affecting the ion signal for Sr and thereby significantly reducing the spectral interference on ^{87}Sr. Apart from the rather complex setup, the approach is yet only applicable when the analyte and the interferent show sufficient difference in their respective volatility. The simplest approach to account for spectral interferences is thus to select an appropriate isotope for analysis, where spectral interferences do not occur at a significant level, instead of using the isotope yielding highest sensitivity. As an example, it would be more reasonable to determine copper using $^{65}Cu^+$ instead of the more abundant $^{63}Cu^+$ in samples with a high concentration of sodium to avoid interference from $^{23}Na^{40}Ar^+$. In many cases, however, an analyte isotope free from spectral interferences may not be available and other methods have to be employed.

Instrumental approaches to minimize spectral interferences include increasing the mass resolution with sector field instruments or the use of ion–neutral interactions in collision or reaction cell instruments. Both methods are yet limited in the general applicability.

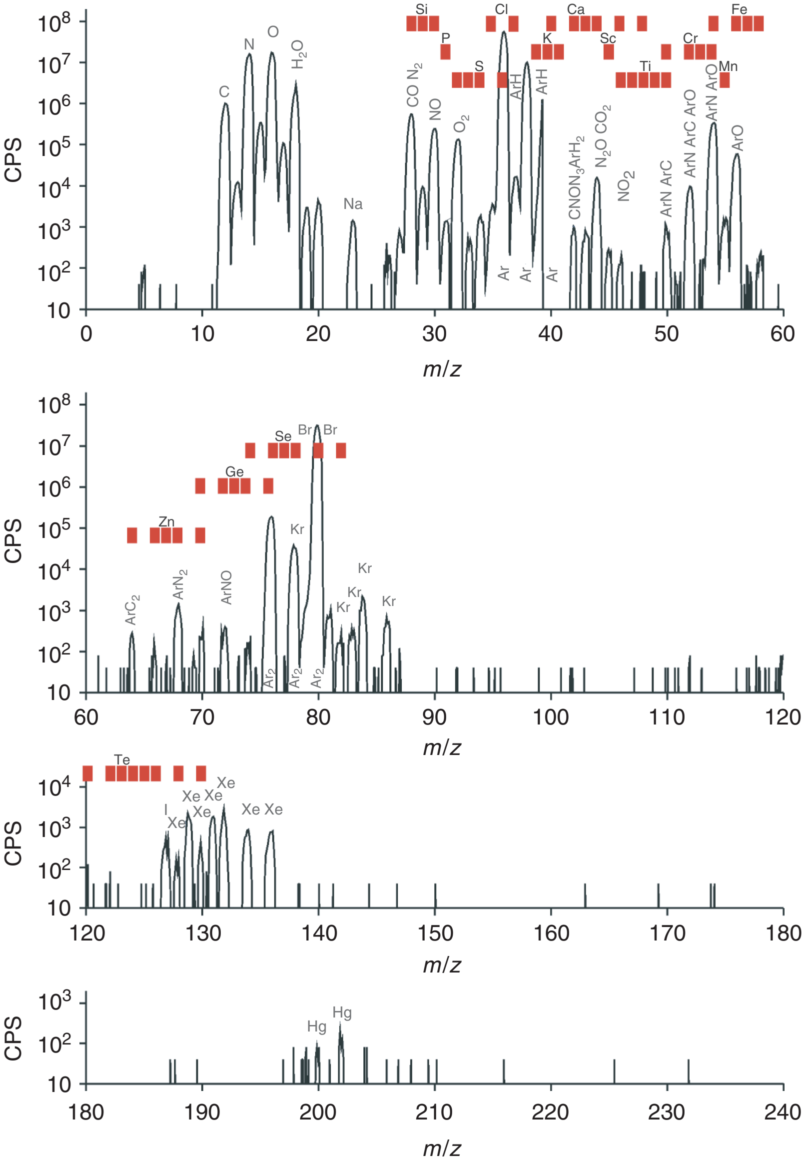

Figure 17.6 Example of a typical instrumental background or gas blank spectrum in LA-ICPMS (*m*/*z* 40 and 41 omitted). Tentative assignments for the background species are printed in blue. Red bars indicate the *m*/*z* of isotopes, where elements are affected by instrumental background signals. Several random signals of 40 cps result from single detector counts. Acquisition by quadrupole ICPMS using an integration time of 25 ms per point and 10 points per *m*/*z*.

Sector field instruments can resolve a wide variety of spectral interferences irrespective of their chemical composition. The mass resolution can typically be chosen depending on the requirements of the application and may reach values for $m/\Delta m$ of up to 12 000. Intermediate settings (usually around $m/\Delta m$ of 3000) are often sufficient to separate abundant spectral interferences from elemental ions (Figure 17.5). This reduces the loss in ion transmission and is less demanding with respect to a rapid and accurate adjustment of the magnetic field. Changing between mass resolution settings, however, requires adjustment of the entrance slit of the MS, which cannot be carried out on a timescale of milliseconds. In order to ensure a sufficiently high data acquisition speed, the instrument thus needs to operate at fixed mass resolution settings for all analytes of interest, which in turn reduces the sensitivity when measuring noninterfered isotopes. A variety of spectral interferences would also require much higher resolution values than 12 000 in order to avoid interference with analyte ions (Figure 17.5). Molecular ions with oxygen that occur in the range between m/z 100 and 140, SrO^+ or MoO^+ for example, cannot be resolved by current instrumentation.

Collision or reaction cell instruments utilize ion–neutral interactions (often termed *ion–molecule reactions*) to facilitate interference suppression in different ways [76]. The interaction of the gas with the ion beam from the ICP is facilitated by directing the ion beam through a chamber filled with the neutral gas at a pressure in the low millibar range [77]. A multipole ion guide is place inside the chamber to minimize transmission losses due to scattering processes with the background gas [78]. Reactive gases can be used, for example, to initiate charge transfer reactions, usually aiming at neutralization of the interfering species. Reactive gases can also be applied in atom transfer reactions, where the interference is resolved, for example, by transforming the analyte ion into a polyatomic ion of different m/z, where interference-free detection is possible [79, 80]. In a corresponding process, the interference may also be transformed into another species of a different m/z [81]. In LA applications, hydrogen may be useful for the removal of polyatomic ions containing argon because it is less reactive with other elemental ions and does not form adduct ions to a large extent [82]. Other highly reactive gases as ammonia or methane, however, are prone to induce undesired side reactions leading to the formation of unwanted molecular and cluster ions that may interfere with other isotopes of interest and reduce the sensitivity of the reaction partners [83]. In this view, it may be considered problematic to use these gases for multielement applications in complex matrices. Current instruments equipped with collision or reaction cells typically utilize either a dynamic bandpass filter [84] or kinetic energy discrimination (KED) [85] to minimize the abundance of cell-generated polyatomic ions in the mass spectrum. A bandpass filter is realized through a quadrupole ion guide, which transmits a range of m/z (bandpass). The bandpass can be adjusted dynamically with the m/z of the analyte isotopes. It is set to allow the analyte ions to pass through, while precursor ions of potential cell-generated ions are excluded. This approach is most efficient for large differences of the m/z of precursor and analyte ions because a very narrow bandpass also reduces transmission of the latter. KED on the other hand is making use of the higher collision frequency of the larger polyatomic ions with the background gas. Accordingly, they lose kinetic energy more rapidly than elemental ions. An electrostatic potential barrier before the MS can thus be adjusted to just allow the elemental ions with higher kinetic energy to pass through but to exclude the polyatomic ions from the MS. Both approaches can be fairly efficient, especially for interferences occurring at low to intermediate m/z. Nonetheless, they also reduce the sensitivity for elemental analyte ions, especially when a high degree of suppression is required and for ions at high m/z, where the relative energy or mass difference between the analyte and the interference is small [83].

When instrumental methods cannot be applied to resolve spectral interferences because of lack of mass resolution, or collision or reaction cell approaches are not feasible, mathematical correction of the measured ion signal intensities may be a last resort to account for spectral interferences. On the basis of known relative abundances of the isotopes of the interfering species it is, in many cases, possible to determine the respective contribution of the interference and the analyte to the measured ion signal intensities. The correction is then carried out by determining the contribution of the interference based on the measurement of another isotope that can be detected interference free and including the mass discrimination of the ICPMS:

$$I^{A}_{\text{isotope}} = I^{A}_{\text{raw}} - I^{B}_{\text{correction}} \cdot K\left(\frac{A}{B}\right)$$

where I represents ion signal intensities; isotope indicates the net signal for the isotope of interest (m/z: A); raw represents background-corrected ion signal (m/z: A); correction is the net ion signal intensity for the isotope used for correction (m/z: B); and $K(A/B)$ is the correction factor. $K(A/B)$ has to be determined from the intensity ratio of the interfering species, measured under identical conditions in a sample without the analyte isotope or calculated using mass bias approximations and the relative abundance of the isotopes of the interference (Section 17.5.3)

This process can principally be iterated a number of times to include potential interferences on ion signals used for correction or to include multiple interferences on one analyte isotope [86, 87]. The accuracy of this approach will, however, depend on the quality of the correction factors. The presence and variability of instrumental mass discrimination makes it impossible to simply use correction factors based on the isotopes' natural abundance. The correction factors thus need to be calibrated and eventually updated frequently and in dependence on the sample composition. This ultimately increases the uncertainty in the corrected signal intensities and the corresponding analytical results. Even greater uncertainties arise when corrections based on the abundance ratio of molecular ions relative to an elemental ion shall be employed. As an example, one may estimate the contribution from $^{181}\text{Ta}^{16}\text{O}^+$ on $^{197}\text{Au}^+$ (both almost monoisotopic) by assuming that the abundance ratio TaO^+/Ta^+ is constant and can be determined using any gold-free sample containing tantalum. Such abundance ratios, however, depend significantly on the operating conditions of the ICPMS and may show pronounced variability with time [88] and sample composition. Furthermore, the mass difference between the isotope used for correction and the analyte is comparably large and variations in mass discrimination can lead to significant bias.

17.3.3
Non-Spectral Interferences

Just as with solution nebulization methods, ICPMS with LA sampling is susceptible to non-spectral interferences or matrix effects [89]. They manifest in changes in the sensitivity ratios for different elements depending on the sample matrix or the ablation process in general. The origin of these interferences is manifold and related to a variety of processes that occur during the LA process and detection in the ICPMS.

- *Elemental fractionation occurring during LA*. This term was originally introduced to describe time-dependent sensitivity changes during a single spot ablation, caused by preferential vaporization of more volatile elements as the depth of the ablation crater increases [90]. A so-called ''fractionation index'' was derived by Fryer *et al*. [91] by splitting the measurement period in two halves and dividing intensity ratios obtained in the second half by those obtained in the first half. Any deviation from one would indicate elemental fractionation. When using calcium as reference element, several other elements showed fractionation indices greater than 1, indicating their relative enrichment in the aerosol as the ablation proceeded. Later, Mank and Mason [42] showed that, for the ablation of glass, this effect was largely independent of the crater size used but more closely related to the aspect ratio of the developing crater. Very recently, however, it was shown that the fractionation index is not showing the same trend in the entire ablation period but may actually reverse when calculated during the early ablation period [89] (see also Figure 17.7 and Figure 17.8).

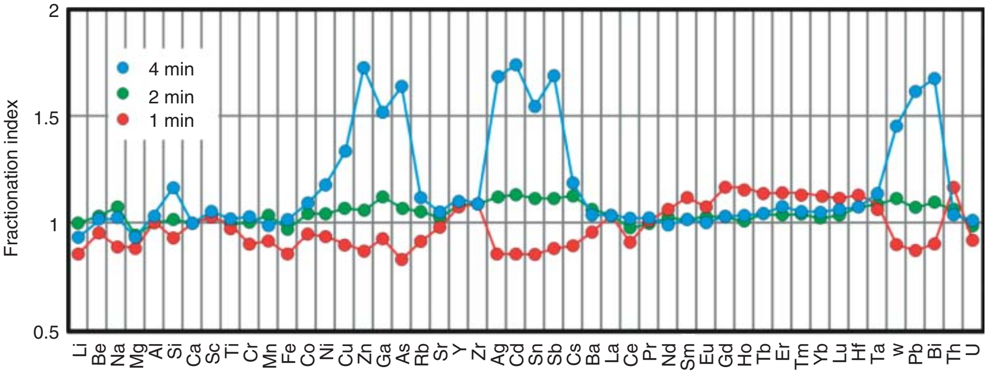

Figure 17.7 Fractionation indices of laser ablation of silicate glass (NIST SRM 610, 266 nm LA), calculated according to Fryer *et al*. [91] for different durations of the ablation. Short measurements show largely opposite trends compared with long ablation periods, while intermediate periods seem to exhibit no significant fractionation. (Reproduced from [89].)

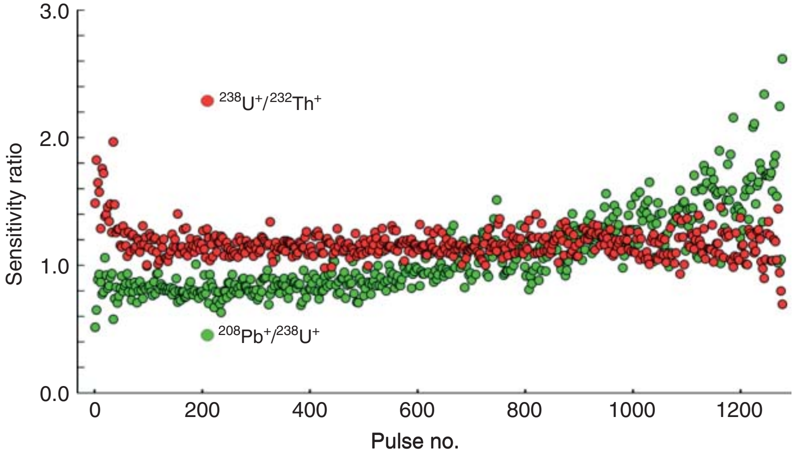

Figure 17.8 Representation of two distinctly different expressions of elemental fractionation occurring in single-spot LA-ICPMS measurements for silicate glasses. In the initial ablation pulses, the occurrence of large particles causes incomplete vaporization of Th, leading to high U^+/Th^+ sensitivity ratios. While the ablation proceeds, large particles are becoming less abundant and the sensitivity ratio remains stable. Pb^+/U^+ shows most pronounced deviation from their concentration ratio when the crater has deepened, which indicates that the more volatile elements are released preferentially.

- *Elemental fractionation occurring in the ICPMS*. The ICPMS may also cause elemental fractionation due to the dependence of vaporization, ionization, and ion transmission on the composition and size distribution of the particles in the laser-generated aerosol. Larger particles or particles that consist of a highly refractory matrix require longer residence time within the ICP or higher gas temperatures for complete vaporization [58, 92]. This can introduce a bias in the sensitivity ratios if the evaporation of the particles in the ICP is incongruent or if the composition of an aerosol particle varies with size [93]. Furthermore, the temperature inside the ICP will to some extent depend on the amount of aerosol present [94]. Thus, for highly variable mass loads in the ICP, the sensitivities of different elements may not change proportionally even when the particle size distributions are similar.

It will remain difficult to discriminate between elemental fractionation occurring during the ablation process and within the ICP as potential changes in the composition of the aerosol due to preferential vaporization during LA are usually accompanied by changes in the particle size distribution [59], which can cause fractionation within the ICP. Figure 17.8 demonstrates the different effects of elemental fractionation in LA-ICPMS that were frequently observed, for example, in Pb/U dating. In this measurement, the $^{238}U^+/^{208}Pb^+$ sensitivity ratio remains constant and close to 1 during the initial ablation period but continuously increases as the crater depth (or aspect ratio) exceeds a critical value (after ~500 laser pulses in this case). This would indicate that elemental fractionation is least significant at the beginning of the ablation, where only a slight but constant offset is observed, which is merely resulting from mass discrimination of the ICPMS. Pb appears to be preferentially released while the more refractory U remains as the ablation crater gets deeper. The sensitivities of $^{238}U^+$ and $^{232}Th^+$ on the other hand differ most significantly at the onset of ablation, where a significant fraction of micrometer-sized particles is present in the aerosol [19]. The relative depletion of Th^+ at this stage is thus considered to result predominantly from less efficient vaporization of Th relative to U within the ICP. The occurrence of preferential vaporization within the ICP is further supported by the fact that the change in the U/Th sensitivity ratio is significantly affected by the ICP operating conditions. Reducing gas temperature or residence time of the aerosol within the ICP usually leads to greater deviations of the corresponding sensitivities [95].

In general, elemental fractionation needs to be considered a phenomenon that is ultimately determined by the laser–sample interaction. The processes involved in the generation of the aerosol determine the composition and particle size distribution of the aerosol. The particle size distribution, however, can induce fractionation within the ICP even when the composition aerosol resembles the stoichiometry of the sample material. When elemental fractionation occurs, it may thus result in variations of measured sensitivity ratios for a sample upon prolonged ablation on the one hand and also in constant but biased sensitivity ratios for individual samples of different composition on the other.

17.3.4
Instrument Drift

Instrument drift can result from a variety of processes. It becomes notable by changing absolute intensities in the repetitive analysis of a homogeneous sample with time, using identical operating conditions. In many cases, drift is related to the thermal equilibration of the LA unit and/or the ICPMS. On the laser side, the output energy often depends on the actual temperature of the laser and optical components, for example, for generation of higher harmonics. In addition, there may be temporal changes in the absorption of UV radiation within the optical path owing to the formation of ozone when the laser is fired. Similarly, components of the ICPMS are sensitive to temperature (e.g., vacuum interface, electronics, and drift region), which can affect transmission efficiency. Apart from instrumental aspects, the composition of the carrier gas can drift over time after the ablation cell has been closed because of the washout of residual ambient air. The change in the concentration of molecular ions, however, was found to affect not only the abundance of molecular ions but also the sensitivities obtained with the ICPMS in an element-dependent manner [88]. Most processes described above equilibrate on timescales of several minutes, which is easily diagnosed by repetitive analyses of a reference sample. Ozone buildup and thermal equilibration of the laser head, however, may occur only within the duration of the measurement unless the laser is continuously fired against a shutter in between individual analyses.

17.4
Sampling Strategies

The ability to perform LA on practically any material at a lateral scale in the micrometer range and at ablation rates of 10 to several hundred nanometers per laser pulse allow for a wide range of sampling strategies. By using large crater sizes, extended ablation periods, and repetitive analyses, bulk concentrations can be assessed. Spatially resolved analysis can be carried out using finely focused laser beams or by analyzing individual layers in depth. The following chapters shall provide an overview about typical sampling strategies in the respective cases.

17.4.1
Bulk Analysis

The sample mass that is consumed during LA experiments is typically not more than some nanograms per laser pulse. Taking also into account that solid samples can a priori not be considered homogeneous on a scale of the laser beam diameter, determination of bulk concentration values by LA-ICPMS should be approached with some care. Typically, milligram amounts of a sample are analyzed for quantification of a sample when established techniques such as solution-based methods after sample digestion or X-ray fluorescence are used, for example. LA-ICPMS would thus require applying several million laser pulses to sample a comparable mass, which, at 10 Hz pulse repetition rate, would require several hours of measurement! In this sense, any ''bulk'' analysis carried out by LA under typical acquisition protocols should rather be considered an estimate for the true concentration – in many cases a good one however. Nonetheless, the degree to which the elemental concentrations vary needs to be verified by analyzing different regions of an unknown sample. Whether these regions are chosen randomly or using a pre-defined pattern (Figure 17.9) is not of importance. If a sample is suspected to contain concentration gradients, for example, due to the production process, it may be reasonable to follow such gradients if their orientation can be identified by other methods, for example, optical inspection in the simplest case.

The analysis can be carried out by multiple single spot ablations, line scans, or arbitrarily defined tracks of the laser beam across the sample surface (Figure 17.9), which generally does not affect the analytical results as long as representative amounts of the material are analyzed. Any type of scan, however, is much more affected by potential surface contamination and unfavorable particle size distributions in the laser-generated aerosol [19]. Single spot ablation, on the other hand, may suffer from laser-induced elemental fractionation when a large number of shots is applied because of the thermal effects in the vicinity of the ablation crater and the increasing degree of elemental fractionation when ablating from deeper cavities. Generally, approaching the ''true'' concentration value with uncertainties close to those obtained by solution nebulization methods requires comparably long measurement times, which may limit the cost-effectiveness of LA-ICPMS.

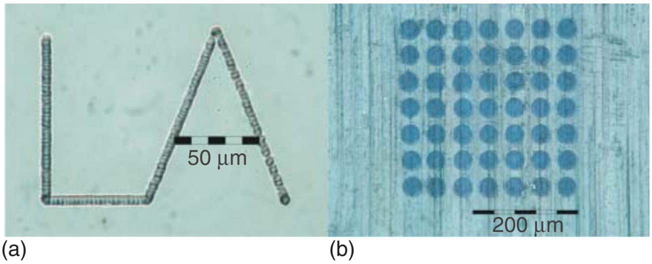

Figure 17.9 Laser ablation sampling. (a) Example for a line scan in a silicate glass with a beam diameter of 6 and a groove depth of 6 µm. The trench consists of four individually programmed segments ablated within a single scan. Thirty pulses were applied on each position. (b) Example for a single point raster on anodized aluminum using a beam diameter of 36 µm. One pulse applied at each position. A homogenized 193 nm laser ablation system with fluence of 15 J cm^{-2} was used in both experiments.

17.4.2
Depth Profiling

Depth profiling for layer thickness determination is typically performed by ablating the sample surface layer by layer and by comparing the number of pluses applied with the ablation rate of the material. Low-energy pulses increase the depth resolution but reduce the measurement sensitivity because less material is removed per laser pulse. The ion signals acquired by the ICPMS are then used to determine the penetration of the layer as indicated by the appearance of the substrate elements in the mass spectrum or from the decrease in the layer material [96–98]. The depth resolution of such an approach is ultimately dependent on the ablation rate per pulse and the energy distribution of the laser beam. The concave crater bottom obtained with near Gaussian energy distributions of the laser beam leads to ablation of material from all depths between the crater bottom and the sample surface, which limits the attainable resolution substantially. A homogenized beam, on the other hand, yields a constant ablation rate across the entire crater and a geometry that is close to cylindrical unless the aspect ratio of the crater is exceedingly large. Removal of material from the crater wall still occurs, but to a much lower extent, improving the resolution.

Compositional depth profiling, on the other hand, requires removing the surface layer by layer in a representative way while simultaneously registering ion signals for all isotopes of interest. To achieve a high definition of the depth profile in this case, mixing of the aerosols generated by successive laser pulses should be avoided as much as possible. Therefore, low laser pulse frequencies are most often employed. In addition, the aerosol transport system should be designed in order to minimize dispersion for increased peak signal intensities and to reduce the total measurement time. The depth profile can then be obtained by plotting ion signal intensities against the number of pulses or the crater depth if the ablation rate is known. When suitable calibration standards are available, the respective concentrations can be calculated as well. The theoretical depth resolution that can be obtained is again dependent on the ablation rate and can thus be adjusted over some range by the laser pulse energy. In practice, however, a certain degree of mixing of individual layers will always occur within the molten phase at the crater bottom and by removal of material from the crater wall. A further limitation for the characterization of very thick layers may occur through the laser-induced elemental fractionation, observed when the crater depth exceeds a critical value [42]. This will become most important when layers of a thickness of several hundred micrometers shall be analyzed. It may be more reasonable in this case to cut the sample and analyze the layers sideways.

At energy densities close to the ablation threshold for the respective laser used, ablation rates in the range of several tens of nanometers can be obtained. The depth resolution obtained in recent applications, however, ranges from about 100 nm to several micrometers [99], depending on the configuration and the sample material under investigation.

17.4.3
Lateral Profiling

Lateral profiling or elemental imaging refers to the analysis of element distributions in a surface layer of several micrometers or in thin sections of a solid sample. The sampling strategies for elemental profiling are generally similar to bulk analytical methods. The aim is, however, to identify and differentiate specific regions in the sample with respect to their elemental composition. Thus, in contrast to bulk analyses, variations of the respective ion signal intensities shall be explicitly determined in relation to the sampling position. The temporal correlation of the ion signal intensities should thus be as high as possible in order to be able to distinguish between real concentration changes and artifacts caused by the dispersion of the aerosol.

One or two dimensional profiles or images of the elemental distribution can be obtained in quasi-continuous approaches, when the sample is scanned by continuous line scans, and ion signal acquisition is carried out at high frequency. Alternatively, individual discrete positions can be analyzed using single-spot ablations distributed over the sample. Single-spot approaches ultimately provide the highest level of confidence in accurately assigning the measured ion signal intensities or element concentrations to a specific position at the sample surface. When the sample is continuously scanned under the laser beam, the dispersion of the transport system will lead to mixing of the aerosol generated from different positions. The temporal profile of the ion signal intensities in comparison with the actual concentration in the sample is therefore always blurred [100, 101]. In general, using a laser pulse repetition rate that ensures the occurrence of the aerosol in the ICP only after the previous cloud has diminished would reduce this effect but lead to exceedingly long analysis times when large samples need to be analyzed. Most applications therefore are carried out by using higher laser frequencies (typically between 5 and 10 Hz) and operate at low to moderate translation speed (between 5 and 50 $\mu m\, s^{-1}$) of the sample under the laser beam [102, 103]. This leads to greater overlap of the individual laser shots and deeper grooves. As more material is removed from each position, higher signal intensities are achieved as well but the aerosol always contains a mixture of material released from different depths. This may complicate an unambiguous assignment of the respective ion signal intensity or element concentration with a specific position in the sample, when the elemental composition varies substantially with depth [100]. In order to separate contributions from individual laser pulses or spatial positions of the sample in the sample aerosol, mathematical models may be employed.

An additional potential complication in spatially resolved analysis arises when sequential mass spectrometers are employed because of the discontinuous acquisition of the individual ion signal intensities. Every isotope will, in this case, be measured within a different time period relative to the arrival of the aerosol, generated by one specific laser pulse, in the ICP [104]. The smaller the dispersion of the aerosol transport system and the longer the duration of the mass scan, the larger is the deviation of the measured ion signal intensity ratios from those that would reflect the true concentration ratios within the entire aerosol cloud. The influence of this effect on the correlation between the measured intensity ratios and the respective concentrations in the sample can be minimized when many laser pulses are applied during each mass scan and when there is a substantial overlap of the individual ablation craters. In this case, the amplitude of the oscillation of the aerosol density is reduced and each laser pulse contains a significant fraction of material from the region ablated by the previous pulse. The depth of a groove generated by line scans will depend on the number of pulses applied on each position and the ablation rate of the material at the respective laser fluence. In order to estimate the influence of the individual operating parameters, the following expressions may be useful.

The number of pulses (N_{p}) applied on each position within the line is given by

$$N_{\mathrm{p}} = \frac{f}{v} \cdot D$$

where D is the diameter of a circular ablation crater or length of the side parallel to the translation direction for rectangular craters (µm), v is the translation speed of the sample under the laser beam ($\mu\mathrm{m\,s^{-1}}$), and f is the laser pulse repetition rate (Hz).

The number of pulses applied during one mass scan (N_{scan}) is given by

$$N_{\mathrm{scan}} = T \cdot f$$

where T is the mass scan duration (s); see Section 17.3.1.3.

In order to acquire ion signals for more than one laser pulse at each position of the sample, N_{p} has to be greater than N_{scan} or

$$\frac{D}{v} > T$$

The aspect ratio of the resulting scan line can be estimated if the ablation rate is known, using

$$\frac{d}{D} = \frac{N_\mathrm{p} \cdot R}{D} = \frac{f \cdot R}{v}$$

where d is the depth of the scan line (μm) and R is the ablation rate per laser pulse (μm pulse^{-1}).

It may be interesting to note that the aspect ratio resulting for a given combination of laser pulse repetition rate and translation speed is not dependent on the crater diameter when the ablation rate is constant.

The overlap of the areas for successive circular (O_c) or rectangular (O_r) ablation craters can be calculated according to

$$O_\mathrm{r} = \left[1 - \frac{1}{N_\mathrm{p}}\right] \times 100\%$$

$$O_\mathrm{c} = \frac{2}{\pi}\left[\arccos\left(\frac{1}{N_\mathrm{p}}\right) - \frac{\sqrt{N_\mathrm{p}{}^2 - 1}}{N_\mathrm{p}^2}\right] \times 100\%$$

Their dependencies on N_p are shown in Figure 17.10. There is little difference for the geometries for $N_\mathrm{p} > 10$ where the overlap is close or equal to 90% in both cases. More than 50% overlap is obtained in both cases for an N_p of 3.

It may further be interesting to compare the coverage of the trench obtained from circular crater geometries to that of a quadratic crater of identical D. When the sample is moved under the laser beam, a circular crater omits a fraction of the trench depending on N_p. If the length of the trench is much longer than the diameter of the ablation crater, the fraction omitted is always <2% if N_p is >2 and

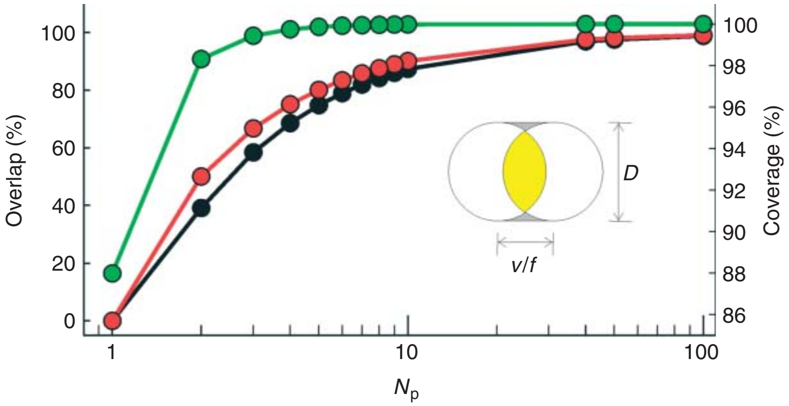

Figure 17.10 Overlap and coverage of successive laser craters for line scan ablation using circular or rectangular ablation craters. The overlap for a circular crater shape (black circles, yellow region in the inset) is only slightly smaller than for when a rectangular shape (red circles) is used. For a circular laser beam, the deviation of the coverage (green circles) from 100% is a result of omitting the gray area shown in the inset.

$<0.02\%$ for $N_p > 10$. One may thus consider the mass removed using a circular crater to closely represent that of a quadratic ablation crater.

If we consider a LA experiment with $D = 50\,\mu\text{m}$, $f = 10\,\text{Hz}$, $v = 10\,\mu\text{m}\,\text{s}^{-1}$, and $T = 0.52\,\text{s}$ (40 isotopes analyzed using 10 ms dwell time and 3 ms settling time) as an example, the resulting parameters will be

$N_p = 50$, $N_{\text{scan}} = 5.2$, $O_c = 97\%$, $O_r = 98\%$ and an aspect ratio equal to the value of R.

Increasing v to $50\,\mu\text{m}\,\text{s}^{-1}$ results in

$$N_p = 5,\ N_{\text{scan}} = 5.2,\ O_c = 75\%,\ O_r = 80\% \text{ and an aspect ratio equal to 0.1 R.}$$

The higher translation speed in the second set may be problematic because only one pulse will be applied at each position of the sample during acquisition of all isotopes within the duration of a mass scan. It will therefore be difficult to describe the respective element distributions, unless the dispersion of the aerosol transport system leads to a decay period of the ion signals from a single laser pulse that is much greater than the scan duration. This will lead to substantial mixing of the aerosol from successive laser shots and make an unambiguous assignment of the ion signals to a specific location at the sample difficult.

When line scans are used, repetitive parallel scans can be used to construct a two-dimensional image [102]. When the depth of the ablation crater or scan line is smaller or comparable to the crater sizes used, the images obtained by this approach represent the elemental distribution within the material reasonably well. The quality of such images with respect to spatial resolution is significantly affected by the instrumental conditions of the sampling process, aerosol dispersion, and detection by the ICPMS. Larger crater sizes will lead to coarser images but increase the measurement sensitivity of the ICPMS when trace element patterns are of interest.

17.4.4
Inclusion Analysis

Analysis of fluid or melt inclusions may be considered a specific case of lateral and depth profiling of solids. Melt inclusions of a size of several micrometers for solids, or fluid inclusions of some tens of micrometers may be characterized by ‘‘drilling’’ out the respective volume holding the inclusion in a single-spot ablation [105]. Homogeneous melt inclusions are often analyzed by polishing the sample material to bring the inclusion close to the sample surface. The laser beam diameter may then be chosen to limit ablation to the inclusion material without analyzing the grain boundary and avoid mixing with the host material. When the entire inclusion needs to be analyzed or, in the case of fluid inclusions where sampling the entire inclusion can only be accomplished by removal of surrounding material, discriminating between the contributions from the inclusion and the host material may become a challenge for the quantification [106]. Opening inclusions, present in a material that is prone to cracking, is commonly achieved by opening the inclusion with a small beam diameter and stepwise increasing the crater size until the entire inclusion is removed [107].

17.5
Data Treatment

Solid sampling by LA-ICPMS is inherently affected by potential variations of the aerosol composition due to concentration changes in the sample analyzed. It is thus recommended to acquire ion signal intensities in time-resolved mode and at high frequency [108]. This approach allows evaluation of the intensity profiles in retrospect and to identify peculiarities in the transient signal. Figure 17.11 shows an example of the transient signals obtained from ablation of a silicate glass reference material (NIST (National Institute of Standards and Technology) SRM (Standard Reference Material) 610). The laser is started about 40 s after the data acquisition to record the instrumental background. Afterwards, the laser is fired for 70 s and

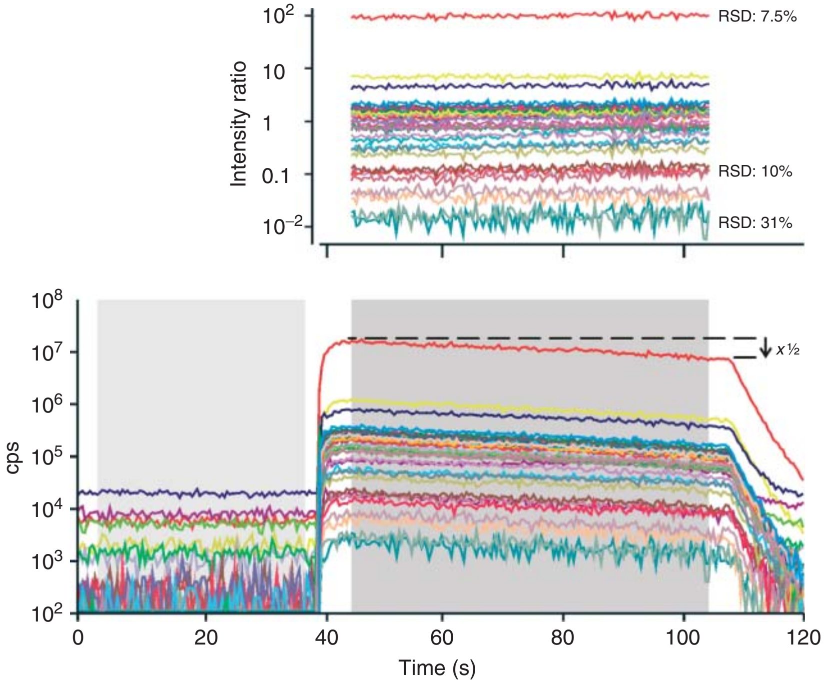

Figure 17.11 Time-resolved data acquired for single-spot ablation of a homogeneous sample (NIST 610 glass, 193 nm helium as carrier gas, quadrupole MS with 10 ms dwell time, 50 isotopes measured). Shaded areas indicate the integration period for instrumental background before ablation and the evaluated laser ablation signal. Top panel shows background-corrected ion signal intensities during the ablation period normalized to an internal standard (Ca).

the ion signal intensities (plus instrumental background) are registered. The raw ion signals exhibit a clear downward trend during the single-spot ablation, due to the increasing crater depth. While the ion signal intensities drop by 50%, the ratios of the background-corrected ion signal intensities, remain stable during the entire ablation period. The relative standard deviations (RSD) of the intensity ratios obtained depends mostly on the sensitivity of the isotope registered. For high-abundance isotopes, the intensity ratio is in the range of 7–10%, while isotopes of low abundance show a higher RSD of ≈30%.

Depending on the type of analysis, concentrations or intensity ratios may be calculated from the average ion signals measured, for example, for bulk analysis or single-spot ablation. Alternatively, when concentration profiles shall be obtained, a point-by-point evaluation is carried out, which can be transformed into the respective lateral or depth distribution. An example for ablation of an inhomogeneous synthetic sample is presented in Figure 17.12. In this case, element-specific profiles were obtained even for the chemically similar rare earth elements. Eu and Dy show high correlation to the internal standard cerium with relative standard deviations of 2%. Other rare earth elements show variations on the micrometer scale (Tm, Ho, Tb, and Pr) while especially Er exhibits a significantly different profile over the depth of the crater.

A remaining limitation before calculation of the ion signal intensities of a measurement is the lack of suitable blank samples that would allow determination of the true background signal intensities. Currently, most often only the instrumental background or gas blank is subtracted from the measured ion signal intensities. This approach is reasonably accurate as most isotopes of interest are not affected by

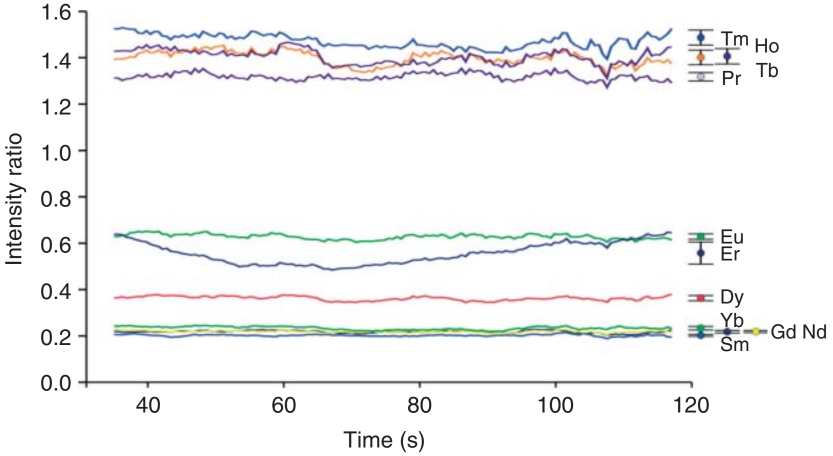

Figure 17.12 Intensity ratios of rare earth elements obtained from single-spot ablation, normalized to $^{140}Ce^+$. Average values of the intensity ratios are indicated by symbols with error bars representing one standard deviation of the measurement. Laser ablation was carried out using a crater diameter of 60 μm and reached a depth of ∼140 μm depth after 90 s.

spectral interferences from the instrument background or memory effects (Figure 17.6). Whenever such interferences occur, however, their abundance in the spectrum may differ from the gas blank when the laser-generated aerosol is introduced into the ICP [94]. This may especially impair the evaluation of Si, P, S, Cl, K, Ca, Cr, Mn, and Fe, where background intensities are significant on all major isotopes (Figure 17.6).

Data analysis in LA-ICPMS is most often carried out using off-line methods by importing raw analysis data into specific software or spreadsheet programs [109]. These allow setting specific integration periods covering the gas blank and the ablation signals. The average background signal intensity is then subtracted either from the raw ion signals of each data point or from the average signal intensity of the integrated ablation signal respectively. Average concentration values or concentration profiles can be directly obtained when the sensitivity ratios are available after a corresponding calibration.

To determine the limit of detection in LA-ICPMS one needs to take into account that the sample mass analyzed in each acquisition cycle of the ICPMS may change, for example, due to temporal variation of the ablation rate, leading to changes in element sensitivity during the analysis. In addition, when the transient signals shall be evaluated on a point-by-point analysis, the uncertainty of a single measurement is different from that represented by an average of a large number of measurements. To assess the low limit of ion signal intensities that can be determined above the instrumental background the following equation can be used [108]:

$$\mathrm{LOD} = 3 \times \mathrm{SD}_{\mathrm{BG}} \times \sqrt{\frac{1}{N_{\mathrm{BG}}} + \frac{1}{N_{\mathrm{Signal}}}}$$

where LOD is the limit of detection, expressed in ion signal intensities; $\mathrm{SD}_{\mathrm{BG}}$ is the standard deviation of the instrumental background measurements; N_{BG} is the number of data points acquired for the instrumental background, and N_{Signal} is the number of data points used for calculating the ion signal intensity.

As a consequence of this treatment, the average ion signal intensities that can be detected above the instrumental limit of detection depend on the mode of analysis. Point-by-point evaluation can lead to lower average signal intensity because a greater number of data points are excluded from the calculation of the average value when the ion signal intensities are close to the LOD of the individual measurement.

Because background signals often exhibit very low intensities, calculation of the standard deviation based on a normal distribution may not be adequate in all cases [110]. A normal distribution may be considered only if the background signal is >70 counts per acquisition on average. Until today, however LOD*s* are typically calculated by assuming a normal distribution for the background signals. It should be noted that this will typically underestimate the actual value, especially when the background signal intensities are close to zero.

17.5.1
Qualitative Analysis

Qualitative analysis in the context of *LA-ICPMS* refers to the evaluation of ion signal intensity ratios for different elements without calculation of absolute concentrations. This approach is most often applied when no suitable internal standard is available for quantification and when specific ‘‘fingerprints’’ of the intensity ratios are sufficient to discriminate individual samples by means of statistical analysis. Forensic [111–113] and authenticity testing [114, 115] are prominent fields of application where such fingerprinting is frequently used. The intensity ratios may be calculated from average ion signals, resembling the mean local concentration ratios or as a profile across a sample or in depth. Averaging an increasing number of data points will improve the uncertainty of the respective intensity ratios and thus the discriminating power of the approach. For lateral or depth profiles, the number of data points to be averaged needs to be balanced with respect to the desired spatial resolution.

17.5.2
Quantitative Analysis

When quantitative concentration values are to be calculated, the use of LA-ICPMS relies on the availability of one or more internal standard(s). This internal standard needs to compensate for matrix-dependent ablation rates, instrument drift, and potential variations in sensitivity, caused by the ICPMS. When the concentration of such an internal standard is known a priori or can be deduced from the chemical composition of the sample, the intensity ratios measured can be related to the sensitivity ratios, according to a calibration standard, to calculate the element concentration:

$$C_{\mathrm{E}}^{\mathrm{S}} = I_{\mathrm{E}}^{\mathrm{S}} \cdot \frac{C_{\mathrm{IS}}^{\mathrm{S}}}{I_{\mathrm{IS}}^{\mathrm{S}}} \cdot \frac{C_{\mathrm{E}}^{\mathrm{Cal}}}{I_{\mathrm{E}}^{\mathrm{Cal}}} \cdot \frac{I_{\mathrm{IS}}^{\mathrm{Cal}}}{C_{\mathrm{IS}}^{\mathrm{Cal}}}$$

where C *is the* concentration, I is the ion signal intensity (background corrected), S is the unknown sample, Cal is the calibration standard, E is the analyte element, and IS is the internal standard element.

This approach assumes that no non-spectral interferences are leading to changes of the relative sensitivities of the analyte element and the internal standard during the analysis or that the magnitude of these effects is identical for calibration standard and unknown sample. Furthermore, the ion signal intensities need to be acquired interference free or appropriate corrections have to be applied [108]. As mentioned earlier, true blank samples are usually not available for solid materials, which limit the effectiveness of the blank correction, by simply assuming that the abundance of background ions in the gas blank is not affected by the presence of the aerosol inside the ICP.

In an ideal case, matrix-matched calibration standards can be used to establish the sensitivity ratios necessary for quantification. The broad range of compositions of solids, however, renders this highly difficult for all materials under investigation. Unfortunately, the availability of calibration standards that contain a wide range of elements at concentration levels suitable for LA-ICPMS is still limited. Furthermore many of these materials are actually not certified for elemental concentrations at trace and ultratrace levels or even major and minor constituents. Nonetheless, LA-ICPMS has been employed for quantitative analysis in a wide range of applications. Many of these are related to geochemical investigations where reference materials of similar composition are available for a wide range of matrices. The NIST glass standard reference materials 612 and 610 are fairly frequently used because they contain most elements of the periodic table at concentration levels readily detectable by LA-ICPMS. In addition, a variety of vitrified natural geological samples are being used (e.g., BCR-2G), which have been characterized for a wide range of elements. Glasses are particularly attractive as calibration standards because they can be produced most homogeneously. Moreover, there is a wide range of metallic reference materials available, which have been characterized by a variety of methods and thus should be suitable as calibration standards for related applications. For many other materials, such as polymers or tissue, for example, calibration standards may be very difficult to obtain. In this case, quantification may be carried out after calibration with materials of similar matrix composition, which have been characterized by independent methods. The calibration standard's homogeneity with respect to the elements of interest, however, is often not explicitly known and needs to be tested before the material can be used.

Provided that the calibration material is long-term stable with respect to composition and that the element concentrations are well established, a single reference sample may be used to establish the sensitivity ratios for calibration. When this cannot be assumed, various reference materials have to be considered to estimate the respective uncertainty of the sensitivity ratios and this uncertainty ultimately needs to be included in the quantification.

A few reports have proposed the use of isotope dilution (ID) as an alternative to external calibration also for LA-ICPMS. ID, however, requires the chemical equilibration of an isotopically enriched spike with the sample matrix, which is more difficult to ensure when solid samples are under investigation. The only approach that may ensure the equilibration is fusion of the material with the spike into glasses that can be analyzed with LA [116]. Several other approaches have applied addition of dissolved spike solutions to a powdered sample and pressing the thoroughly mixed, dried powder into pellets before analysis [117–119]. The accuracy obtained in these analyses was satisfactory but not in all cases was better than when using external calibration methods. This may be partly because the ablation of pressed powders often results in ''noisy'' ion signal intensities, caused by the release of large particulates from the pressed pellets. In addition, it may be questioned whether chemical equilibration of the isotope spike is actually always ensured in this approach. Equilibration can only be ensured when no preferential evaporation of the spike from the surface of the powder particles occurs and when the entire aerosol reaching the ICP is formed by condensation of a well-mixed vapor phase after the ablation. Both conditions may not be assumed to be fulfilled in general, and any deviation will induce some bias in the analytical results. However, even though ID can only be applied for elements where at least two isotopes can be detected interference free by ICPMS, it may be a viable way for the characterization of materials, where calibration standards of similar matrix are not accessible at all.

In specific cases also, external calibration using nebulized solutions may be applied. Here, the aerosol generated by LA is mixed with an aerosol from solution nebulization before entering the ICP. Calibration curves can then be obtained from synthetic solutions that contain the analyte elements and the internal standard without firing the laser [120–122]. During analysis by LA a blank solution is nebulized to achieve comparable ICP operating conditions. Despite the flexibility of this approach, drawbacks may occur through increased abundance of polyatomic ions from the solvent, potentially higher blank signal intensities due to contamination, and, most importantly, differences in the sensitivity ratios of analyte and internal standard due to different vaporization efficiencies for droplets and laser-generated particles.

17.5.2.1 **Internal Standardization**

The internal standard for LA-ICPMS measurements mainly compensates for instrumental drift and changes in the ablation rate of the sample and between samples and calibration standards. In most cases, a matrix element is therefore used, whose concentration can be determined by an independent method such as X-ray fluorescence or electron probe microanalysis (EPMA). It needs to be present in calibration standards and samples and should be sufficiently abundant to ensure reproducible measurements and to mitigate influence from potential spectral interferences. When elemental fractionation occurs and no calibration standard of very similar composition is available, individual elements may be classified in accordance to their fractionation trend [90] and more than one internal standard needs to be employed for quantitative analysis.

As an alternative to single element internal standardization, matrix or 100% normalization has been applied [123, 124]. In this case, initially the sensitivity ratios of the elements to one reference element are determined by relating the sensitivity ratios to those of an external standard. After calculating the concentration ratios for all elements, each concentration ratio can be normalized to the sum of all ratios, resulting in the respective mass fractions present in the analyzed sample:

$$C_{\mathrm{E}}^{\mathrm{S}} = \frac{\frac{I_{\mathrm{E}}^{\mathrm{S}}}{I_{\mathrm{IS}}^{\mathrm{S}}} \cdot \frac{C_{\mathrm{E}}^{\mathrm{Cal}}}{I_{\mathrm{E}}^{\mathrm{Cal}}} \cdot \frac{I_{\mathrm{R}}^{\mathrm{Cal}}}{C_{\mathrm{R}}^{\mathrm{Cal}}}}{\sum \frac{I_{\mathrm{E}}^{\mathrm{S}}}{I_{\mathrm{IS}}^{\mathrm{S}}} \cdot \frac{C_{\mathrm{E}}^{\mathrm{Cal}}}{I_{\mathrm{E}}^{\mathrm{R}}} \cdot \frac{I_{\mathrm{R}}^{\mathrm{Cal}}}{C_{\mathrm{R}}^{\mathrm{Cal}}}} \times 100\%$$

where C is the concentration, I is the ion signal intensity (background corrected), S is the unknown sample, Cal is the calibration standard, E is the analyte element, R is the reference element, and IS is the internal standard element.

In order to make use of this approach, however, all elements contained in the sample would have to be detectable by the ICPMS. In the presence of elements that cannot be detected by ICPMS such as H, N, O, or F, this procedure can still be used when the stoichiometry of each element is known. For silicate glasses, for example, one may assume that the elements are present in the form of oxides whose stoichiometry is known. In this case, all concentration ratios can be transformed into the respective element–oxide concentration ratios, which can be normalized in the same way. When compounds are present where none of the elements can be determined by ICPMS such as crystal water, for example, the normalization factor (100%) may be adjusted to the fraction of the detectable elements if the difference can be estimated or determined by another method.

17.5.3
Isotope Ratio Determination

A steadily increasing number of applications utilize LA-ICPMS for *in situ* isotope ratio measurements. It is particularly attractive when sample specimens are very small; spatially resolved profiles of isotope ratios within a sample shall be acquired or if the samples are difficult to digest for analysis by conventional ICPMS methods [125, 126]. In most cases, MC-ICPMS are used for such applications because the parallel detection of the isotope signals substantially improves the isotope ratio precision compared to single collector instruments [69]. Furthermore, sector field MC-ICPMS provides very high sensitivities, allowing detection of isotopes with very low abundance. Typical applications include age determinations based on parent/daughter decay series such as U/Pb [126], U/Th [127], or Sr isotopes [128]. Other investigations study isotope fractionation by natural processes (e.g., S, Fe, and Os) [16, 129, 130] or for discriminating sample populations based on the isotope signature of characteristic elements (e.g., Sr in teeth and bones) [131, 132].

As in MC-ICPMS, with conventional nebulization, an important aspect in the accuracy of the measured isotope ratios is the correction for mass discrimination [133]. In addition, isobaric and polyatomic interferences become a greater problem because separation of the elements of interest from the sample is not possible with LA sampling [131]. Furthermore, it has been demonstrated that isotope fractionation may occur during the ablation process [134, 135]. The precision of the isotope ratios determined with LA sampling is thus by about an order of magnitude inferior to those achievable with conventional methods for comparable ion signal intensities.

As in conventional solution-based methods, the accuracy of the isotope ratio measurement depends to large extent on the quality of the correction for mass discrimination. Standard sample bracketing requires availability of a solid sample with well-known isotope abundance to establish the mass discrimination correction of the instrument before and after analysis of the unknown sample. This approach is most effective when the bracketing standard is of very similar composition as the unknown sample and when only a small drift occurs on the timescale of the measurements. Also, internal normalization is possible when the element has at last two isotopes whose abundance ratio is known a priori. In this case, the mass discrimination can be assessed from the measured ratio of the invariant isotope pair using mathematical approximations [136]. The most frequently used approximations of mass discrimination make use of the power law

$$r = R \cdot g^{(m_1 - m_2)}$$

or the exponential law

$$r = R \cdot \left(\frac{m_1}{m_2}\right)^{\beta}$$

where r is the measured isotope ratio, R is the true isotope ratio, m_1 is the mass of the heavier isotope, m_2 is the mass of the lighter isotope, and g, β are the mass discrimination coefficients.

Both methods are successfully used to improve the accuracy of isotope ratio determinations. One should keep in mind however that these correction formulae have been derived empirically and do not necessarily describe the relative ion transmission in the ICPMS accurately. In a similar manner, heteroelement normalization can be used, where the mass discrimination coefficient is determined from the measured isotope ratio of another element with known isotope abundance [137]. This element is either present in the sample at detectable levels or added to the laser-generated aerosol, for example, by continuous solution nebulization. Minute differences in the mass bias coefficients of different elements, however, will lead to greater inaccuracies and uncertainty of the result. Correction for spectral interferences is also usually carried out by using a single mass discrimination coefficient for analyte and interference isotopes. Thus, unless the contribution of the interference is comparably small, the deviation in the actual mass discrimination from the assumed value may introduce an additional bias.

17.6
Summary and Outlook

LA-ICPMS has grown into a mature technique for direct elemental analysis of solid samples in many applications. The technique has several advantages based on the conceptual simplicity of combining an atmospheric pressure ion source with a sampling system that allows spatially resolved analysis at the micrometer scale. Depending on the spatial and depth resolution, high elemental sensitivity can be obtained, providing limits of detection in the low milligram/kilogram or even microgram/kilogram range (Figure 17.13). LA-ICPMS furthermore offers the possibility to optimize the sampling and detection process individually, which helps reduce the matrix dependence of analyte sensitivities. Thus, non-matrix-matched calibration can be performed in many applications, significantly relaxing the requirements with respect to the composition of the calibration standards, compared to other direct solid analytical techniques.

Prevailing shortcomings predominantly lie in the still limited detection efficiency, especially for ions of low m/z and the occurrence of elemental fractionation effects in specific samples. Ongoing developments of ICPMS and LA instruments, especially the availability of femtosecond-lasers, are nonetheless expected to further improve the general applicability of the technique.

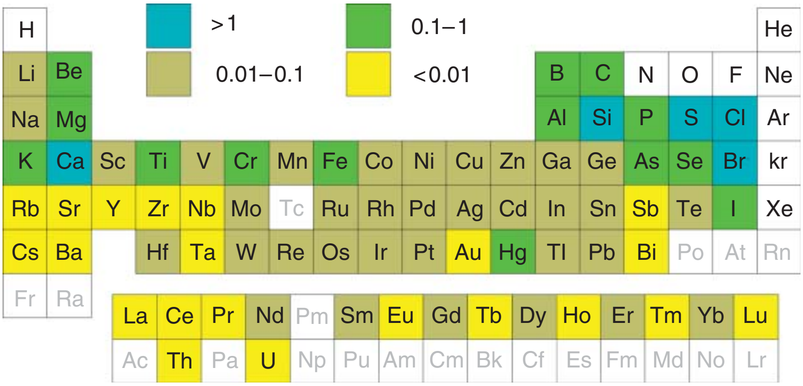

Figure 17.13 Approximate limits of detection in milligram/kilogram for elements in silicate glass using LA-ICPMS, determined using a 193 nm excimer laser, 40 µm crater diameter, 10 Hz pulse repetition rate, 20 J cm^{-2} fluence and helium as carrier gas coupled to a quadrupole ICPMS.

The roots of the technique are in geochemical research, where the distinct advantages of the technique were realized first, and LA-ICPMS is expected to remain an important analytical tool in this context. The distinct improvements in the past 20 years, however, have led to a significantly broader range of applications, which is expected to further increase in the near future.

In comparison with other techniques for spatially resolved solid sample analysis, LA-ICPMS may be positioned between EPMA and secondary ion mass spectrometry (SIMS), in terms of detection capabilities. Avoidance of high vacuum at the sampling site, on the other hand, increases the spectrum of applications significantly.

Future developments with respect to the ICPMS may include the development of more robust ion sources, to reduce fractionation effects caused by preferential vaporization. Furthermore, higher detection efficiencies may be realized to allow analysis from even smaller sample quantities and eventually approach the sub-micrometer range in spatial resolution. On the side of LA, more powerful femtosecond lasers may become available, which would achieve higher ablation rates for transparent materials and reduce elemental fractionation during the sampling process. Broader use as a routine technique will depend on the availability of integrated data acquisition schemes that allow unattended operation and automated data reduction for a large set of samples.

17.6.1
Characteristics, Figures of Merit, Applications

LA instrumentation used in commercially available systems and laboratory prototypes for LA-ICPMS are given below.

Laser type	**Wavelength (nm)**	**Pulse duration**	**Beam profile**	**Output energy (mJ)**	**Pulse repetition rate (Hz)**
Nd:YAG	266 (λ/4) 213 (λ/5)	5–10 ns	Flat top	≈5	≤20
ArF-Ecximer	193	5–20 ns	Homogenized	≈5	≤100
Ti:sapphire	≈800	≈150 fs	Gaussian	<5	≤10 000
	≈265 (λ/3)			<0.5	
	≈200 (λ/4)			<0.05	

Mass spectrometer configurations and their characteristics with respect to LA sampling are as follows:

Type	**Mass resolution ($m/\Delta m$)**	**Scan frequency**[a]	**Detection efficiency**[b]	**Detector range**
Quadrupole	<350	2–500 Hz	10^{-7} to 10^{-4}	10^9 SEM
Sector field	300	2–500 Hz	$10^{-6}$to 10^{-3}	10^9 (10^{12} with FC)
	3000		$10^{-7}$to 10^{-4}	
	12 000		10^{-8} to 10^{-5}	
Multicollector	300 (<10 000)[c]	N.a.	10^{-6} to 10^{-3}	10^3 (FC), 10^6 (SEM)
Time of flight	<3000	20–30 kHz	10^{-8} to 10^{-5}	10^6 SEM

FC, Faraday cup; SEM, secondary electron multiplier.

[a] Depends on number of isotopes, dwell time, and settling time of the MS.

[b] Typical values for analyses of silicate glass. Depends on particle size distribution and composition of the laser-generated aerosol.

[c] Mass resolving power in "pseudo high resolution" mode.

Figures of merit for LA-ICPMS instrumentation are as follows:

Beam diameter/lateral resolution	4–200 µm
Ablation rate	0.01–0.3 µm/pulse
Typical analysis time	120 s/sample (single-spot analysis)
Reproducibility	5–30% RSD ($C > 10 \times$ LOD)
Isotopes/analysis	2–50[a]
Elements detectable	68[b]

[a] Principally, more than 50 isotopes can be analyzed in LA-ICPMS but correlation of ion signal intensity degrades when acquired by sequential MS.

[b] Only considering naturally occurring elements. Radiogenic or synthetic isotopes are principally also detectable when not affected by spectral interferences.

Applications are as follows:

Geochemistry	Bulk element composition of mineral grains [138] Partition coefficients of elements among different phases [139, 140] Analysis of melt and fluid inclusion [105, 141–143] Isotope ratio measurements for age determination [144–146] Tracer studies
Materials science	Bulk element composition of difficult-to-digest materials [147] Elemental distribution Characterization of composition and thickness of layers [97, 148] Impurities and contamination from the production process Characterization of inclusions Trace element determination in plastics [149]
Forensic science	Elemental fingerprints of specimens from scenes of crime, investigation of authenticity, or origin [112]
Bioscience	Metal, sulfur, or phosphorus determination in macromolecules after separation using gel electrophoresis in one or two dimensions [150, 151]
Gemology	Authenticity of gemstones [152, 153] Identification of gemstones that were synthetically enhanced by trace element doping
Medicine	Trace element distribution in thin sections of tissue, bone, hair, and nails [154, 155]
Anthropology	Trace element and isotope ratio patterns in bones for identification of migration of a species [115, 132]
Archeology	Trace element and isotope ratio analysis for dating and identification of origin of artifacts [142, 156, 157]
Chemistry	Element composition of new materials [158], stoichiometric determination [159]

References

1. Günther, D. and Hattendorf, B. (2005) Solid sample analysis using laser ablation inductively coupled plasma mass spectrometry. *TRAC-Trends Anal. Chem.*, **24**, 255.
2. Sylvester, P.J. (2005) Laser ablation ICP-MS developments and trends for 2003. *Geostand. Geoanal. Res.*, **29**, 41.
3. Becker, J.S. (2002) Applications of inductively coupled plasma mass spectrometry and laser ablation inductively coupled plasma mass spectrometry in materials science. *Spectrochim. Acta, Part B*, **57**, 1805.
4. Russo, R.E., Mao, X.L., and Borisov, O.V. (1998) Laser ablation sampling. *TRAC-Trends Anal. Chem.*, **17**, 461.
5. Durrant, S.F. (1999) Laser ablation inductively coupled plasma mass spectrometry: achievements, problems, prospects. *J. Anal. At. Spectrom.*, **14**, 1385; 2000, **15**, 237.
6. Gray, A.L. (1985) Solid sample introduction by laser ablation for inductively coupled plasma source-mass spectrometry. *Analyst*, **110**, 551.
7. Jackson, S.E., Longerich, H.P., Dunning, G.R., and Freyer, B.J. (1992)

The application of laser-ablation microprobe; inductively coupled plasma-mass spectrometry (LAM-ICP-MS) to in situ trace-element determinations in minerals. *Can. Mineral.*, **30** (Part 4), 1049.

8. Jeffries, T.E., Jackson, S.E., and Longerich, H.P. (1998) Application of a frequency quintupled Nd:YAG source (lambda = 213 nm) for laser ablation inductively coupled plasma mass spectrometric analysis of minerals. *J. Anal. At. Spectrom.*, **13**, 935.
9. Eggins, S.M., Kinsley, L.P.J., and Shelley, J.M.G. (1998) Deposition and element fractionation processes during atmospheric pressure laser sampling for analysis by ICP-MS. *Appl. Surf. Sci.*, **129**, 278.
10. Günther, D., Frischknecht, R., Heinrich, C.A., and Kahlert, H.J. (1997) Capabilities of an argon fluoride 193 nm excimer laser for laser ablation inductively coupled plasma mass spectrometry microanalysis of geological materials. *J. Anal. At. Spectrom.*, **12**, 939.
11. Horn, I., Rudnick, R.L., and Mcdonough, W.F. (2000) Precise elemental and isotope ratio determination by simultaneous solution nebulization and laser ablation-ICP-MS: application to U-Pb geochronology. *Chem. Geol.*, **164**, 283; 2000, **167**, 403.
12. Telouk, P., Rose-Koga, E.F., and Albarede, F. (2003) Preliminary results from a new 157 nm laser ablation ICP-MS instrument: new opportunities in the analysis of solid samples. *Geostand. Newsl. J. Geostand. Geoanal.*, **27**, 5.
13. Horn, I., Günther, D., and Guillong, M. (2003) Evaluation and design of a solid-state 193 nm OPO-Nd: YAG laser ablation system. *Spectrochim. Acta, Part B*, **58**, 1837.
14. Russo, R.E., Mao, X.L., Gonzalez, J.J., and Mao, S.S. (2002) Femtosecond laser ablation ICP-MS. *J. Anal. At. Spectrom.*, **17**, 1072.
15. Poitrasson, F., Mao, X.L., Mao, S.S., Freydier, R., and Russo, R.E. (2003) Comparison of ultraviolet femtosecond and nanosecond laser ablation inductively coupled plasma mass spectrometry analysis in glass, monazite, and zircon. *Anal. Chem.*, **75**, 6184.
16. Horn, I., von Blanckenburg, F., Schoenberg, R., Steinhoefel, G., and Markl, G. (2006) In situ iron isotope ratio determination using UV-femtosecond laser ablation with application to hydrothermal ore formation processes. *Geochim. Cosmochim. Acta*, **70**, 3677.
17. Koch, J., Wälle, M., Pisonero, J., and Günther, D. (2006) Performance characteristics of ultra-violet femtosecond laser ablation inductively coupled plasma mass spectrometry at similar to 265 and similar to 200 nm. *J. Anal. At. Spectrom.*, **21**, 932.
18. Günther, D. and Heinrich, C.A. (1999) Enhanced sensitivity in laser ablation-ICP mass spectrometry using helium-argon mixtures as aerosol carrier–plenary lecture. *J. Anal. At. Spectrom.*, **14**, 1363.
19. Kuhn, H.R., Guillong, M., and Günther, D. (2004) Size-related vaporisation and ionisation of laser-induced glass particles in the inductively coupled plasma. *Anal. Bioanal. Chem.*, **378**, 1069.
20. Sesi, N.N., Mackenzie, A., Shanks, K.E., Yang, P.Y., and Hieftje, G.M. (1994) Fundamental studies of mixed-gas inductively coupled plasmas. *Spectrochim. Acta, Part B*, **49**, 1259–1282.
21. Wang, Z.K., Hattendorf, B., and Günther, D. (2006) Vaporization and ionization of laser ablation generated aerosols in an inductively coupled plasma mass spectrometer–implications from ion distribution maps. *J. Anal. At. Spectrom*, **21**, 1143.
22. Niu, H. and Houk, R.S. (1996) Fundamental aspects of ion extraction in inductively coupled plasma mass spectrometry. *Spectrochim. Acta, Part B*, **51**, 779.
23. Lowndes, D.H. (1997) in *Laser Ablation and Desorption, Experimental Methods in the Physical Sciences*, Vol. 30 (eds J.C. Miller and R.F. Haglund),

p. 475–571, Academic Press, New York.

24. Rusak, D.A., Castle, B.C., Smith, B.W., and Winefordner, J.D. (1997) Fundamentals and applications of laser-induced breakdown spectroscopy. *Crit. Rev. Anal. Chem.*, **27**, 257.

25. Song, K., Lee, Y.I., and Sneddon, J. (2002) Recent developments in instrumentation for laser induced breakdown spectroscopy. *Appl. Spectrosc. Rev.*, **37**, 89.

26. Tognoni, E., Palleschi, V., Corsi, M., and Cristoforetti, G. (2002) Quantitative micro-analysis by laser-induced breakdown spectroscopy: a review of the experimental approaches. *Spectrochim. Acta, Part B*, **57**, 1115.

27. Scott, R.H., Jackson, P.F.S., and Strashei, A. (1971) Application of laser source mass spectroscopy to analysis of geological material. *Nature*, **232**, 623.

28. Poels, K., Vanvaeck, L., and Gijbels, R. (1998) Microprobe speciation analysis of inorganic solids by Fourier transform laser mass spectrometry. *Anal. Chem.*, **70**, 504.

29. Tognoni, E., Cristoforetti, G., Legnaloli, S., Palleschi, V., Salvetti, A., Mueller, M., Panne, U., and Gomushkin, I. (2007) A numerical study of expected accuracy and precision in calibration-free laser-induced breakdown spectroscopy in the assumption of ideal analytical plasma. *Spectrochim. Acta, Part B*, **62**, 1287.

30. Fantoni, R., Caneve, L., Colao, F., Fornarini, L., Lazic, V., and Spizzichino, V. (2008) Methodologies for laboratory laser induced breakdown spectroscopy semi-quantitative and quantitative analysis-a review. *Spectrochim. Acta, Part B*, **63**, 1097.

31. Vanvaeck, L. and Gijbels, R. (1990) Laser microprobe mass-spectrometry–potential and limitations for inorganic and organic micro-analysis. 1. Technique and inorganic applications. *Fresenius' J. Anal. Chem.*, **337**, 743.

32. Hillenkamp, F., Karas, M., Beavis, R.C., and Chait, B.T. (1991) Matrix-assisted laser desorption ionization mass-spectrometry of biopolymers. *Anal. Chem.*, **63**, A1193.

33. Moenkeblankenburg, L. (1993) Laser-ICP-spectrometry. *Spectrochim. Acta Rev.*, **15**, 1.

34. Mikhailov, V.A., Putilin, F.N., and Trubnikov, D.N. (1997) Particle velocities at the complex solids laser ablation in vacuum and in gas ambients. *Appl. Surf. Sci.*, **110**, 591.

35. Russo, R.E., Mao, X.L., Liu, H.C., Yoo, J.H., and Mao, S.S. (1999) Time-resolved plasma diagnostics and mass removal during single-pulse laser ablation. *Appl. Phys. A*, **69**, S887.

36. Hergenroeder, R. (2006) A model for the generation of small particles in laser ablation ICP-MS. *J. Anal. At. Spectrom.*, **21**, 1016.

37. Hergenroeder, R. (2006) Hydrodynamic sputtering as a possible source for fractionation in LA-ICP-MS. *J. Anal. At. Spectrom.*, **21**, 517.

38. Bogaerts, A., Chen, Z.Y., Gijbels, R., and Vertes, A. (2003) Laser ablation for analytical sampling: what can we learn from modeling? *Spectrochim. Acta, Part B*, **58**, 1867.

39. Hergenroeder, R. (2006) A model of non-congruent laser ablation as a source of fractionation effects in LA-ICP-MS. *J. Anal. At. Spectrom.*, **21**, 505.

40. Horn, I., Guillong, M., and Günther, D. (2001) Wavelength dependant ablation rates for metals and silicate glasses using homogenized laser beam profiles–implications for LA-ICP-MS. *Appl. Surf. Sci.*, **182**, 91.

41. Liu, H.C., Mao, X.L., Yoo, J.H., and Russo, R.E. (1999) Nonlinear changes in plasma and crater properties during laser ablation of Si. *Appl. Phys. Lett.*, **75**, 1216.

42. Mank, A.J.G. and Mason, P.R.D. (1999) A critical assessment of laser ablation ICP-MS as an analytical tool for depth analysis in silica-based glass samples. *J. Anal. At. Spectrom.*, **14**, 1143.

43. Rethfeld, B., Sokolowski-Tinten, K., von der Linde, D., and Anisimov, S.I. (2004) Timescales in the response of materials to femtosecond laser excitation. *Appl. Phys. A*, **79**, 767.

44. Liu, C., Mao, X.L., Mao, S.S., Zeng, X., Greif, R., and Russo, R.E. (2004) Nanosecond and ferntosecond laser ablation of brass: particulate and ICPMS measurements. *Anal. Chem.*, **76**, 379.

45. Bian, Q.Z., Garcia, C.C., Koch, J., and Niemax, K. (2006) Non-matrix matched calibration of major and minor concentrations of Zn and Cu in brass, aluminium and silicate glass using NIR femtosecond laser ablation inductively coupled plasma mass spectrometry. *J. Anal. At. Spectrom.*, **21**, 187.

46. Koch, J., We, M., Dietiker, R., and Günther, D. (2008) Analysis of laser-produced aerosols by inductively coupled plasma mass spectrometry: transport phenomena and elemental fractionation. *Anal. Chem.*, **80**, 915.

47. Walle, M., Koch, J., and Gunther, D. (2008) Analysis of brass and silicate glass by femtosecond laser ablation inductively coupled plasma mass spectrometry using liquid standard calibration. *J. Anal. At. Spectrom.*, **23**, 1285.

48. Horn, I. and Günther, D. (2003) The influence of ablation carrier gasses Ar, He and Ne on the particle size distribution and transport efficiencies of laser ablation-induced aerosols: implications for LA-ICP-MS. *Appl. Surf. Sci.*, **207**, 144.

49. Arrowsmith, P. (1987) Laser ablation of solids for elemental analysis by inductively coupled plasma mass-spectrometry. *Anal. Chem.*, **59**, 1437.

50. Autrique, D., Bogaerts, A., Lindner, H., Garcia, C.C., and Niemax, K. (2008) Design analysis of a laser ablation cell for inductively coupled plasma mass spectrometry by numerical simulation. *Spectrochim. Acta, Part B*, **63**, 257.

51. Garcia, C.C., Lindner, H., and Niemax, K. (2007) Transport efficiency in femtosecond laser ablation inductively coupled plasma mass spectrometry applying ablation cells with short and long washout times. *Spectrochim. Acta, Part B*, **62**, 13.

52. Bleiner, D. and Günther, D. (2001) Theoretical description and experimental observation of aerosol transport processes in laser ablation inductively coupled plasma mass spectrometry. *J. Anal. At. Spectrom.*, **16**, 449.

53. Iizuka, T. and Hirata, T. (2005) Improvements of precision and accuracy in in situ Hf isotope microanalysis of zircon using the laser ablation-MC-ICPMS technique. *Chem. Geol.*, **220**, 121.

54. Stewart, I.I., Hensman, C.E., and Olesik, J.W. (2000) Influence of gas sampling on analyte transport within the ICP and ion sampling for ICP-MS studied using individual, isolated sample droplets. *Appl. Spectrosc.*, **54**, 164.

55. Tanner, M. and Günther, D. (2007) Signal acquisition in mu s time resolution for in-torch LA-ICP-MS. *J. Anal. At. Spectrom.*, **22**, 1189.

56. Wang, Z.K., Hattendorf, B., and Günther, D. (2006) Analyte response in laser ablation inductively coupled plasma mass spectrometry. *J. Am. Soc. Mass Spectrom.*, **17**, 641.

57. Latkoczy, C. and Günther, D. (2002) Enhanced sensitivity in inductively coupled plasma sector field mass spectrometry for direct solid analysis using laser ablation (LA-ICP-SFMS). *J. Anal. At. Spectrom.*, **17**, 1264.

58. Aeschliman, D.B., Bajic, S.J., Baldwin, D.P., and Houk, R.S. (2003) High-speed digital photographic study of an inductively coupled plasma during laser ablation: comparison of dried solution aerosols from a microconcentric nebulizer and solid particles from laser ablation. *J. Anal. At. Spectrom*, **18**, 1008.

59. Kuhn, H.R. and Günther, D. (2004) Laser ablation-ICP-MS: particle size dependent elemental composition studies on filter-collected and online measured aerosols from glass. *J. Anal. At. Spectrom.*, **19**, 1158.

60. Günther, D., Longerich, H.P., Jackson, S.E., and Forsythe, L. (1996) Effect of sampler orifice diameter on dry plasma inductively coupled plasma mass spectrometry (ICP MS) Backgrounds, sensitivities, and limits of detection using laser ablation sample introduction. *Fresenius' J. Anal. Chem.*, **355**, 771.

61. Günther, D., Longerich, H.P., and Jackson, S.E. (1995) A new enhanced sensitivity quadrupole inductively-coupled plasma-mass spectrometer (ICP-MS). *Can. J. Appl. Spectrosc.*, **40**, 111.

62. Feldmann, I., Tittes, W., Jakubowski, N., Stuewer, D., and Giessmann, U. (1994) Performance characteristics of inductively coupled plasma mass spectrometry with high mass resolution. *J. Anal. At. Spectrom.*, **9**, 1007.

63. Denoyer, E.R., Jacques, D., Debrah, E., and Tanner, S.D. (1995) Determination of trace elements in uranium–practical benefits of a new icp-ms lens system. *At. Spectrosc.*, **16**, 1.

64. Sakata, K., Yamada, N., and Sugiyama, N. (2001) Ion trajectory simulation of inductively coupled plasma mass spectrometry based on plasma-interface behavior. *Spectrochim. Acta, Part B*, **56**, 1249.

65. Carter, J., Ebdon, L., and Evans, E.H. (2003) Ion stopping experiment to determine the origin of background ions in ICP-MS. *J. Anal. At. Spectrom.*, **18**, 142.

66. Hamester, M., Rottmann, L., and Wills, J. (2005) Element XR: increased linear dynamic detection range sector field ICP-MS for geological applications. *Geochim. Cosmochim. Acta*, **69**, A797.

67. Myers, D.P., Li, G., Mahoney, P.P., and Hieftje, G.M. (1995) An inductively coupled plasma time-of-flight mass spectrometer for elemental analysis. 3. Analytical performance. *J. Am. Soc. Mass Spectrom.*, **6**, 411.

68. Tanner, M. and Günther, D. (2008) A new ICP-TOFMS. Measurement and readout of mass spectra with 30 mu s time resolution, applied to in-torch LA-ICP-MS. *Anal. Bioanal. Chem.*, **391**, 1211.

69. Halliday, A.N., Lee, D.C., Christensen, J.N., Walder, A.J., Freedman, P.A., Jones, C.E., Hall, C.M., Yi, W., and Teagle, D. (1995) Recent developments in inductively-coupled plasma magnetic-sector multiple collector mass-spectrometry. *Int. J. Mass Spectrom. Ion Processes*, **146**, 21.

70. Hirata, T. (2002) In-situ precise isotopic analysis of tungsten using laser ablation multi-collector inductively coupled plasma mass spectrometry (LA-MC-ICP-MS) with time resolved data acquisition. *J. Anal. At. Spectrom.*, **17**, 204.

71. Jochum, K.P., Pfander, J., Woodhead, J.D., Willbold, M., Stoll, B., Herwig, K., Amini, M., Abouchami, W., and Hofmann, A.W. (2005) MPI-DING glasses: new geological reference materials for in situ Pb isotope analysis. *Geochem. Geophys. Geosyst.*, **6**. Q10008, p. 1–15.

72. Kosler, J., Pedersen, R.B., Kruber, C., and Sylvester, P.J. (2005) Analysis of Fe isotopes in sulfides and iron meteorites by laser ablation high-mass resolution multi-collector ICP mass spectrometry. *J. Anal. At. Spectrom.*, **20**, 192.

73. Barnes, J.H., Schilling, G.D., Hieftje, G.M., Sperline, R.P., Denton, M.B., Barinaga, C.J., and Koppenaal, D.W. (2004) Use of a novel array detector for the direct analysis of solid samples by laser ablation inductively coupled plasma sector-field mass spectrometry. *J. Am. Soc. Mass Spectrom.*, **15**, 769.

74. Barnes, J.H. and Hieftje, G.M. (2004) Recent advances in detector-array technology for mass spectrometry. *Int. J. Mass Spectrom.*, **238**, 33.

75. Brogioli, R., Hattendorf, B., Koch, J., Wiltsche, H., Flamigni, L., and Gunther, D. (2011) Online electrothermal heating of laser-generated aerosols: effects on aerosol particle size and signal intensities in ICPMS. *Anal. Bioanal. Chem.*, **399**, 2201.

76. Tanner, S.D., Baranov, V.I., and Bandura, D.R. (2002) Reaction cells and collision cells for ICP-MS: a tutorial review. *Spectrochim. Acta, Part B*, **57**, 1361.

77. Bandura, D.R., Baranov, V.I., and Tanner, S.D. (2001) Reaction chemistry and collisional processes in multipole devices for resolving isobaric interferences in ICP-MS. *Fresenius' J. Anal. Chem.*, **370**, 454.

78. Gerlich, D. (2004) Applications of rf fields and collision dynamics in atomic mass spectrometry. *J. Anal. At. Spectrom.*, **19**, 581.

79. Bandura, D.R., Baranov, V.I., and Tanner, S.D. (2002) Detection of ultratrace phosphorus and sulfur by quadrupole ICPMS with dynamic reaction cell. *Anal. Chem.*, **74**, 1497.
80. Moens, L.J., Vanhaecke, F.F., Bandura, D.R., Baranov, V.I., and Tanner, S.D. (2001) Elimination of isobaric interferences in ICP-MS, using ion- molecule reaction chemistry: Rb/Sr age determination of magmatic rocks, a case study. *J. Anal. At. Spectrom.*, **16**, 991.
81. Simpson, L.A., Thomsen, M., Alloway, B.J., and Parker, A. (2001) A dynamic reaction cell (DRC) solution to oxide-based interferences in inductively coupled plasma mass spectrometry (ICP-MS) analysis of the noble metals. *J. Anal. At. Spectrom.*, **16**, 1375.
82. Hattendorf, B. and Günther, D. (2000) Characteristics and capabilities of an ICP-MS with a dynamic reaction cell for dry aerosols and laser ablation. *J. Anal. At. Spectrom.*, **15**, 1125.
83. Hattendorf, B. and Günther, D. (2004) Suppression of in-cell generated interferences in a reaction cell ICP-MS by bandpass tuning and kinetic energy discrimination. *J. Anal. At. Spectrom.*, **19**, 600.
84. Tanner, S.D. and Baranov, V.I. (1999) A dynamic reaction cell for inductively coupled plasma mass spectrometry (ICP-DRC-MS). II. Reduction of interferences produced within the cell. *J. Am. Soc. Mass Spectrom.*, **10**, 1083.
85. Yamada, N., Takahashi, J., and Sakata, K. (2002) The effects of cell-gas impurities and kinetic energy discrimination in an octopole collision cell ICP-MS under non-thermalized conditions. *J. Anal. At. Spectrom.*, **17**, 1213.
86. VAUGHAN, M.A. and Horlick, G. (1990) Correction procedures for rare-earth element analyses in inductively coupled plasma-mass spectrometry. *Appl. Spectrosc.*, **44**, 587.
87. Vanveen, E.H., Bosch, S., and Deloosvollebregt, M.T.C. (1994) Spectral interpretation and interference correction in inductively-coupled plasma-mass spectrometry. *Spectrochim. Acta, Part B*, **49**, 1347.
88. Kovacs, R. and Gunther, D. (2008) Influence of transport tube materials on signal response and drift in laser ablation-inductively coupled plasma-mass spectrometry. *J. Anal. At. Spectrom.*, **23**, 1247.
89. Kroslakova, I. and Günther, D. (2007) Elemental fractionation in laser ablation-inductively coupled plasma-mass spectrometry: evidence for mass load induced matrix effects in the ICP during ablation of a silicate glass. *J. Anal. At. Spectrom.* doi: 10.1039/b606522h
90. Longerich, H.P., Günther, D., and Jackson, S.E. (1996) Elemental fractionation in laser ablation inductively coupled plasma mass spectrometry. *Fresenius' J. Anal. Chem.*, **355**, 538.
91. Fryer, B.J., Jackson, S.E., and Longerich, H.P. (1995) Design, operation and role of the laser ablation microprobe coupled with an inductively coupled plasma mass spectrometer (LAM-ICP-MS) in the earth sciences. *Can. Mineral.*, **33**, 303.
92. Figg, D.J., Cross, J.B., and Brink, C. (1998) More investigations into elemental fractionation resulting from laser ablation inductively coupled plasma mass spectrometry on glass samples. *Appl. Surf. Sci.*, **129**, 287.
93. Koch, J., von Bohlen, A., Hergenroeder, R., and Niemax, K. (2004) Particle size distributions and compositions of aerosols produced by near-IR femto- and nanosecond laser ablation of brass. *J. Anal. At. Spectrom.*, **19**, 267.
94. Leach, A.M. and Hieftje, G.M. (2000) Methods for shot-to-shot normalization in laser ablation with an inductively coupled plasma time-of-flight mass spectrometer. *J. Anal. At. Spectrom.*, **15**, 1121.
95. Hattendorf, B. and Günther, D. (2003) Strategies for method development for an inductively coupled plasma mass spectrometer with bandpass reaction cell. Approaches with different reaction gases for the determination of selenium. *Spectrochim. Acta, Part B*, **58**, 1.

96. Bleiner, D., Plotnikov, A., Vogt, C., Wetzig, K., and Günther, D. (2000) Depth profile analysis of various titanium based coatings on steel and tungsten carbide using laser ablation inductively coupled plasma–"time of flight" mass spectrometry. *Fresenius' J. Anal. Chem.*, **368**, 221.

97. Pisonero, J., Koch, J., Wale, M., Hartung, W., Spencer, N.D., and Günther, D. (2007) Capabilities of femtosecond laser ablation inductively coupled plasma mass spectrometry for depth profiling of thin metal coatings. *Anal. Chem.*, **79**, 2325.

98. Plotnikov, A., Vogt, C., Hoffmann, V., Taschner, C., and Wetzig, K. (2001) Application of laser ablation inductively coupled plasma quadrupole mass spectrometry (LA-ICP-QMS) for depth profile analysis. *J. Anal. At. Spectrom.*, **16**, 1290.

99. Pisonero, J. and Gunther, D. (2008) Femtosecond laser ablation inductively coupled plasma mass spectrometry: fundamentals and capabilities for depth profiling analysis. *Mass Spectrom.*, **27**, 609.

100. Plotnikov, A., Vogt, C., Wetzig, K., and Kyriakopoulos, A. (2008) A theoretical approach to the interpretation of the transient data in scanning laser ablation inductively coupled plasma mass spectrometry: consideration of the geometry of the scanning area. *Spectrochim. Acta, Part B*, **63**, 474.

101. Bleiner, D., Belloni, F., Doria, D., Lorusso, A., and Nassisi, V. (2005) Overcoming pulse mixing and signal tailing in laser ablation inductively coupled plasma mass spectrometry depth profiling. *J. Anal. At. Spectrom.*, **20**, 1337.

102. Woodhead, J.D., Hellstrom, J., Hergt, J.M., Greig, A., and Maas, R. (2007) Isotopic and elemental imaging of geological materials by laser ablation inductively coupled plasma-mass spectrometry. *Geost. Geoanal. Res.*, **31**, 331.

103. Bi, M., Ruiz, A.M., Gornushkin, I., Smith, B.W., and Winefordner, J.D. (2000) Profiling of patterned metal layers by laser ablation inductively coupled plasma mass spectrometry (LA-ICP-MS). *Appl. Surf. Sci.*, **158**, 197.

104. Günther, D., Horn, I., and Hattendorf, B. (2000) Recent trends and developments in laser ablation-ICP-mass spectrometry. *Fresenius' J. Anal. Chem.*, **368**, 4.

105. Heinrich, C.A., Pettke, T., Halter, W.E., Aigner-Torres, M., Audetat, A., Günther, D., Hattendorf, B., Bleiner, D., Guillong, M., and Horn, I. (2003) Quantitative multi-element analysis of minerals, fluid and melt inclusions by laser-ablation inductively-coupled-plasma mass-spectrometry. *Geochim. Cosmochim. Acta*, **67**, 3473.

106. Halter, W.E., Pettke, T., Heinrich, C.A., and Rothen-Rutishauser, B. (2002) Major to trace element analysis of melt inclusions by laser-ablation ICP-MS: methods of quantification. *Chem. Geol.*, **183**, 63.

107. Günther, D., Audetat, A., Frischknecht, R., and Heinrich, C.A. (1998) Quantitative analysis of major, minor and trace elements in fluid inclusions using laser ablation inductively coupled plasma mass spectrometry. *J. Anal. At. Spectrom.*, **13**, 263.

108. Longerich, H.P., Jackson, S.E., and Günther, D. (1996) Laser ablation inductively coupled plasma mass spectrometric transient signal data acquisition and analyte concentration calculation. *J. Anal. At. Spectrom.*, **11**, 899.

109. Sylvester, P. (ed.) (2008) *Laser Ablation in the Earth Sciences: Current Practices and Outstanding Issues*, Short Course Series, Vol. 40 Appendix, Mineralogical Association of Canada, Quebec.

110. Tanner, M. and Gunther, D. (2009) Short transient signals, a challenge for inductively coupled plasma mass spectrometry, a review. *Anal. Chim. Acta*, **633**, 19.

111. Bajic, S.J., Aeschliman, D.B., Saetveit, N.J., Baldwin, D.P., and Houk, R.S. (2005) Analysis of glass fragments by laser ablation-inductively coupled plasma-mass spectrometry and principal component analysis. *J. Forensic Sci.*, **50**, 1123.

112. Latkoczy, C., Becker, S., Dücking, M., Günther, D., Hoogewerff, J.A., Almirall, J.R., Buscaglia, J., Dobney, A., Koons, R.D., Montero, S., van der Peijl, G.J.Q., Stoecklein, W.R.S., Trejos, T., Watling, J.R., and Zdanowicz, V.S. (2005) Development and evaluation of a standard method for the quantitative determination of elements in float glass samples by LA-ICP-MS. *J. Forensic Sci.*, **50**, 1327.

113. Watling, R.J., Lynch, B.F., and Herring, D. (1997) Use of laser ablation inductively coupled plasma mass spectrometry for fingerprinting scene of crime evidence. *J. Anal. At. Spectrom.*, **12**, 195.

114. Devos, W., Moor, C., and Lienemann, P. (1999) Determination of impurities in antique silver objects for authentication by laser ablation inductively coupled plasma mass spectrometry (LA-ICP-MS). *J. Anal. At. Spectrom.*, **14**, 621.

115. Stadlbauer, C., Reiter, C., Patzak, B., Stingeder, G., and Prohaska, T. (2007) History of individuals of the 18th/19th centuries stored in bones, teeth, and hair analyzed by LA-ICP-MS-a step in attempts to confirm the authenticity of Mozart's skull. *Anal. Bioanal. Chem.*, **388**, 593.

116. Reid, J.E., Horn, I., Longerich, H.P., Forsythe, L., and Jenner, G.A. (1999) Determination of Zr and Hf in a flux-free fusion of whole rock samples using laser ablation inductively coupled plasma-mass spectrometry (LA-ICP-MS) with isotope dilution calibration. *Geostand. Newsl.*, **23**, 149.

117. Tibi, M. and Heumann, K.G. (2003) Isotope dilution mass spectrometry as a calibration method for the analysis of trace elements in powder samples by LA-ICP-MS. *J. Anal. At. Spectrom.*, **18**, 1076.

118. Boulyga, S.F., Heilmann, J., and Heumann, K.G. (2005) Isotope dilution ICP-MS with laser-assisted sample introduction for direct determination of sulfur in petroleum products. *Anal. Bioanal. Chem.*, **382**, 1808.

119. Fernandez, B., Claverie, F., Pecheyran, C., and Donard, O.F.X. (2008) Solid-spiking isotope dilution laser ablation ICP-MS for the direct and simultaneous determination of trace elements in soils and sediments. *J. Anal. At. Spectrom.*, **23**, 367.

120. Günther, D., Cousin, H., Magyar, B., and Leopold, I. (1997) Calibration studies on dried aerosols for laser ablation inductively coupled plasma mass spectrometry. *J. Anal. At. Spectrom.*, **12**, 165.

121. Falk, H.F., Hattendorf, B., Krengelrothensee, K., Wieberneit, N., and Dannen, S.L. (1998) Calibration of laser-ablation ICP-MS. Can we use synthetic standards with pneumatic nebulization? *Fresenius' J. Anal. Chem.*, **362**, 468.

122. Bi, M., Ruiz, A.M., Smith, B.W., and Winefordner, J.D. (2000) Study of solution calibration of NIST soil and glass samples by laser ablation inductively coupled plasma mass spectrometry. *Appl. Spectrosc.*, **54**, 639.

123. Leach, A.M. and Hieftje, G.M. (2001) Standardless semiquantitative analysis of metals using single-shot laser ablation inductively coupled plasma time-of-flight mass spectrometry. *Anal. Chem.*, **73**, 2959.

124. Halicz, L. and Günther, D. (2004) Quantitative analysis of silicates using LA-ICP-MS with liquid calibration. *J. Anal. At. Spectrom.*, **19**, 1539.

125. Walder, A.J., Abell, I.D., Platzner, I., and Freedman, P.A. (1993) Lead isotope ratio measurement of NIST 610 glass by laser ablation inductively coupled plasma mass spectrometry. *Spectrochim. Acta, Part B*, **48**, 397.

126. Fryer, B.J., Jackson, S.E., and Longerich, H.P. (1993) The application of laser-ablation microprobe-inductively coupled plasma-mass spectrometry (Lam-ICP-MS) to in-situ (U)-Pb geochronology. *Chem. Geol.*, **109**, 1.

127. Potter, E.K., Stirling, C.H., Wiechert, U.H., Halliday, A.N., and Spotl, C. (2005) Uranium-series dating of corals in situ using laser-ablation MC-ICPMS. *Int. J. Mass Spectrom.*, **240**, 27.

128. Ramos, F.C., Wolff, J.A., and Tollstrup, D.L. (2004) Measuring Sr-87/Sr-86 variations in minerals and groundmass from basalts using LA-MC-ICPMS. *Chem. Geol.*, **211**, 135.

129. Clough, R., Evans, P., Catterick, T., and Evans, E.H. (2006) d(34)S measurements of sulfur by multicollector inductively coupled plasma mass spectrometry. *Anal. Chem.*, **78**, 6126.

130. Pearson, N.J., Alard, O., Griffin, W.L., Jackson, S.E., and O'Reilly, S.Y. (2002) In situ measurement of Re-Os isotopes in mantle sulfides by laser ablation multicollector-inductively coupled plasma mass spectrometry: analytical methods and preliminary results. *Geochim. Cosmochim. Acta*, **66**, 1037.

131. Horstwood, M.S.A., Evans, J.A., and Montgomery, J. (2008) Determination of Sr isotopes in calcium phosphates using laser ablation inductively coupled plasma mass spectrometry and their application to archaeological tooth enamel. *Geochim. Cosmochim. Acta*, **72**, 5659.

132. Prohaska, T., Latkoczy, C., Schultheis, G., Teschler-Nicola, M., and Stingeder, G. (2002) Investigation of Sr isotope ratios in prehistoric human bones and teeth using laser ablation ICP-MS and ICP-MS after Rb/Sr separation. *J. Anal. At. Spectrom.*, **17**, 887.

133. Foster, G.L. and Vance, D. (2006) In situ Nd isotopic analysis of geological materials by laser ablation MC-ICP-MS. *J. Anal. At. Spectrom.*, **21**, 288.

134. Jackson, S.E. and Günther, D. (2003) The nature and sources of laser induced isotopic fractionation in laser ablation-multicollector-inductively coupled plasma-mass spectrometry. *J. Anal. At. Spectrom.*, **18**, 205.

135. Kuhn, H.R., Pearson, N.J., and Jackson, S.E. (2007) The influence of the laser ablation process on isotopic fractionation of copper in LA-MC-ICP-MS. *J. Anal. At. Spectrom.*, **22**, 547.

136. Albarede, F., Telouk, P., Blichert-Toft, J., Boyet, M., Agranier, A., and Nelson, B. (2004) Precise and accurate isotopic measurements using multiple-collector ICPMS. *Geochim. Cosmochim. Acta*, **68**, 2725.

137. Marechal, C.N., Telouk, P., and Albarede, F. (1999) Precise analysis of copper and zinc isotopic compositions by plasma-source mass spectrometry. *Chem. Geol.*, **156**, 251.

138. Prince, C.I., Kosler, J., Vance, D., and Günther, D. (2000) Comparison of laser ablation ICP-MS and isotope dilution REE analyses–implications for Sm-Nd garnet geochronology. *Chem. Geol.*, **168**, 255.

139. Ertel, W., Walter, M.J., Drake, M.J., and Sylvester, P.J. (2006) Experimental study of platinum solubility in silicate melt to 14 GPa and 2273 K: implications for accretion and core formation in Earth. *Geochim. Cosmochim. Acta*, **70**, 2591.

140. Klemme, S. and Dalpe, C. (2003) Trace-element partitioning between apatite and carbonatite melt. *Am. Mineral.*, **88**, 639.

141. Pettke, T., Halter, W.E., Webster, J.D., Aigner-Torres, M., and Heinrich, C.A. (2004) Accurate quantification of melt inclusion chemistry by LA-ICPMS: a comparison with EMP and SIMS and advantages and possible limitations of these methods. *Lithos*, **78**, 333.

142. Resano, M., Perez-Arantegui, J., Garcia-Ruiz, E., and Vanhaecke, F. (2005) Laser ablation-inductively coupled plasma mass spectrometry for the fast and direct characterization of antique glazed ceramics. *J. Anal. At. Spectrom.*, **20**, 508.

143. Tomlinson, E., De Schrijver, I., De Corte, K., Jones, A.P., Moens, L., and Vanhaecke, F. (2005) Trace element compositions of submicroscopic inclusions in coated diamond: a tool for understanding diamond petrogenesis. *Geochim. Cosmochim. Acta*, **69**, 4719.

144. Yuan, H.L., Gao, S., Liu, X.M., Li, H.M., Günther, D., and Wu, F.Y. (2004) Accurate U-Pb age and trace element determinations of zircon by laser ablation-inductively coupled plasma-mass spectrometry. *Geostand. Geoanal. Res.*, **28**, 353.

145. Yuan, H.L., Gao, S., Dai, M.N., Zong, C.L., Günther, D., Fontaine, G.H., Liu, X.M., and Diwu, C. (2008) Simultaneous determinations of U-Pb age, Hf isotopes and trace element compositions of zircon by excimer laser-ablation quadrupole and multiple-collector ICP-MS. *Chem. Geol.*, **247**, 100.

146. Jackson, S.E., Pearson, N.J., Griffin, W.L., and Belousova, E.A. (2004) The application of laser ablation-inductively coupled plasma-mass spectrometry to in situ U-Pb zircon geochronology. *Chem. Geol*, **211**, 47.

147. Frei, C., Schenzel, J., Waibel, F., and Günther, D. (2008) Stoichiometry of various Ag(In)SbTe phase change materials (PCMs) determined using LA-ICP-MS. *J. Anal. At. Spectrom.*, **23**, 217.

148. Margetic, V., Bolshov, M., Stockhaus, A., Niemax, K., and Hergenroeder, R. (2001) Depth profiling of multilayer samples using femtosecond laser ablation. *J. Anal. At. Spectrom.*, **16**, 616.

149. Dobney, A.M., Mank, A.J.G., Grobecker, K.H., Conneely, P., and de Koster, C.G. (2000) Laser ablation inductively coupled plasma mass spectrometry as a tool for studying heterogeneity within polymers. *Anal. Chim. Acta*, **423**, 9.

150. Becker, J.S., Zoriy, M., Pickhardt, C., Przybylski, M., and Becker, J.S. (2005) Investigation of Cu-, Zn- and Fe-containing human brain proteins using isotopic-enriched tracers by LA-ICP-MS and MALDI-FT-ICR-MS. *Int. J. Mass Spectrom.*, **242**, 135.

151. Seuma, J., Bunch, J., Cox, A., McLeod, C., Bell, J., and Murray, C. (2008) Combination of immunohistochemistry and laser ablation ICP mass spectrometry for imaging of cancer biomarkers. *Proteomics*, **8**, 3775.

152. Rege, S., Jackson, S.E., Griffin, W.L., Davies, R.M., Pearson, N.J., and O'Reilly, S.Y. (2005) Quantitative trace-element analysis of diamond by laser ablation inductively coupled plasma mass spectrometry. *J. Anal. At. Spectrom.*, **20**, 601.

153. Guillong, M. and Günther, D. (2001) Quasi 'non-destructive' laser ablation-inductively coupled plasma-mass spectrometry fingerprinting of sapphires. *Spectrochim. Acta, Part B*, **56**, 1219.

154. Becker, J.S., Zoriy, M., Wu, B., Matusch, A., and Becker, J.S. (2008) Imaging of essential and toxic elements in biological tissues by LA-ICP-MS. *J. Anal. At. Spectrom.*, **23**, 1275.

155. Becker, J.S., Su, J., Zoriya, M.V., Dobrowolska, J., and Matusch, A. (2007) Imaging mass spectrometry in biological tissues by laser ablation inductively coupled plasma mass spectrometry. *Eur. J. Mass Spectrom.*, **13**, 1.

156. Resano, M., Garcia-Ruiz, E., Alloza, R., Marzo, M.P., Vandenabeele, P., and Vanhaecke, F. (2007) Laser ablation-inductively coupled plasma mass spectrometry for the characterization of pigments in prehistoric rock art. *Anal. Chem.*, **79**, 8947.

157. Wagner, B., Garbos, S., Bulska, E., and Hulanicki, A. (1999) Determination of iron and copper in old manuscripts by slurry sampling graphite furnace atomic absorption spectrometry and laser ablation inductively coupled plasma mass spectrometry. *Spectrochim. Acta, Part B*, **54**, 797.

158. Becker, J.S., Pickhardt, C., and Pompe, W. (2004) Determination of Ag, Tl, and Pb in few milligrams of platinum nanoclusters by on-line isotope dilution in laser ablation inductively coupled plasma mass spectrometry. *Int. J. Mass Spectrom.*, **237**, 13.

159. Ottinger, F., Kroslakova, I., Hametner, K., Reusser, E., Nesper, R., and Günther, D. (2005) Analytical evidence of amorphous microdomains within nitridosilicate and nitridoaluminosilicate single crystals. *Anal. Bioanal. Chem.*, **383**, 489.

Section VI
Methods 5: Surface Analysis

Handbook of Spectroscopy, Second Edition. Edited by Günter Gauglitz and David S. Moore.

Introduction

Surface analysis uses different means of the *probe* techniques of the surface leading to a *response*, an *analytical signal* serving as a source of *analytical information*. The probe/response combinations used in surface analysis are very bright, including electrons, ions, photons, neutrals, heat, and electric field. Practically all combinations may form the basis of techniques used in surface analysis and so their list is rather long and should by no means be considered to be complete. This is also due to fact that very subtle variations of a technique sometimes become known by their own name and acronym. Some of these acronyms along with the references to the text are listed in the Appendix.

There are several ways of classifying the surface analysis techniques [1, 2].

According to the used probe, we have:

1) *photon probe techniques*, divided further according to fundamental process to:
   a. scattering techniques (Raman spectroscopy),
   b. absorption techniques (infrared spectroscopy, extended X-ray absorption fine structure (EXAFS), surface extended X-ray absorption fine structure (SEXAFS), and near-edge X-ray absorption fine structure (NEXAFS)),
   c. emission techniques (ultraviolet photoelectron spectroscopy (UPS), X-ray photoelectron spectroscopy (XPS), laser micro mass spectrometry (LAMMS)).
2) *electron probe techniques*, based on:
   a. elastic scattering processes (transmission electron microscopy (TEM), reflection electron microscopy (REM), low-energy electron microscopy (LEEM), backscattered electron imaging (BSE), transmission high-energy electron diffraction (THEED), low-energy electron diffraction (LEED), reflection high-energy electron diffraction (RHEED)),
   b. inelastic processes (reflection electron energy loss spectroscopy (REELS), transmission electron energy loss spectroscopy (TEELS), electron probe X-ray microanalysis (EPXMA), Auger electron spectroscopy (AES), and scanning electron microscopy (SEM)).
3) *ion probe techniques*, based on
   a. elastic scattering processes (Rutherford backscattering spectrometry (RBS), medium energy ion scattering (MEIS), ion scattering spectroscopy (ISS), and elastic recoil detection (ERD)),

Handbook of Spectroscopy, Second Edition. Edited by Günter Gauglitz and David S. Moore.

   b. inelastic processes (nuclear reaction analysis (NRA), charged particle activation analysis (CPAA), secondary ion mass spectrometry (SIMS), and sputtered neutral mass spectrometry (SNMS)).
4) *field probe techniques* (scanning tunneling microscopy (STM)).

International Union of Pure and Applied Chemistry (IUPAC) Compendium of Analytical Nomenclature, Definitive Rules 1997 [2] recommends following schema:

1) *the electron, photoelectron, and related spectroscopies*
   a. The photoelectron emission spectroscopies (UPS/UPES, XPS/XEPS, DSPES (depth-selective photoelectron spectroscopy), synchrotron radiation photoelectron spectroscopy (SRPES), scanning electron spectroscopy for chemical analysis (SECSA), photoelectron diffraction (PED), angle-resolved photoelectron spectroscopy (ARPS/ARPES)),
   b. Electron impact spectroscopies (high-resolution electron energy loss spectroscopy/high electron energy loss spectroscopy (HREELS/HEELS), electron energy loss spectroscopy (EELS), electron energy loss fine structure/extended electron energy loss fine structure (EELFS/EXELFS), ionization spectroscopy (IS), and electron transmission spectroscopy (ETS)),
   c. Electron-induced photon emission spectroscopies (inverse photoemission spectroscopy (IPS), Bremsstrahlung isochromat spectroscopy (BIS), and Bremsstrahlung spectroscopy (BS)),
   d. Appearance potential spectroscopies (soft X-ray appearance potential spectroscopy (SXAPS), Auger electron appearance potential spectroscopy (AEAPS), disappearance potential spectroscopy (DAPS), total current spectroscopy (TCS), X-ray excited electron appearance potential spectroscopy (XEAPS), extended (electron) appearance potential fine structure analysis (EAPFS), and inelastic electron tunneling spectroscopy (IETS)),
   e. Auger electron spectroscopies (electron-excited Auger electron spectroscopy (EAES), scanning Auger microscopy (SAM), angle-resolved Auger electron spectroscopy (ARAES), spin-polarized Auger electron spectroscopy (SPAES), ion-excited Auger electron spectroscopy (IAES), and Auger electron (emission) spectroscopy (AEES)),
   f. The electron coincidence spectroscopies.
2) the photon spectroscopies resulting from the use of electromagnetic radiation (total reflection X-ray fluorescence (TXRF)),
3) neutron and ion scattering
   a. Ion scattering (ISS, RBS),
   b. Inelastic neutron scattering (INS),
   c. Ion neutralization spectroscopy (INS).
4) mass spectroscopy
   a. Secondary ion mass spectrometry (SIMS),
   b. Fast-atom bombardment mass spectroscopy (FAB MS),
   c. Field-ion mass spectroscopy (FIMS).
5) other spectroscopic techniques
   a. Metastable desorption spectroscopy (MDS),

    b. Inverse photoelectron spectroscopy (IPES/BIS).
6) desorption and related techniques
    a. Thermal desorption spectroscopy (TPD),
    b. Temperature-programmed reaction spectroscopy (TPRS).
7) spectroscopy/diffraction hybrids
    a. X-ray photoelectron diffraction (XPD),
    b. Extended X-ray absorption fine structure,
    c. Surface extended X-ray absorption fine structure (SEXAPS),
    d. Near-edge X-ray absorption fine structure/X-ray absorption near-edge structure (NEXAFS/XANES).

For practical purposes, a discrimination of the methods can be done according to information obtained on:

- surface elemental composition
- chemical bonding and molecular composition
- surface electronic structure.

In this section, an attempt is made to present the fundamentals of some of the spectroscopic methods used for characterization of surfaces. As shown, the spectroscopic methods represent a very important part of the arsenal used for characterization of surfaces, but in many cases it is difficult to separate the spectroscopic principals of a particular method from those of closely related techniques. Also, the usage of the term *spectroscopy* is sometimes confusing. A broader definition of spectroscopy will be accepted here, embracing not only an interaction of matter with electromagnetic radiation/photons but also the interactions with particles (electrons, ions, and molecules). Diffraction, desorption, microscopic, and imaging methods have been excluded from the discussion, but we are not quite rigorous in some cases where these methods are very closely connected with related spectroscopic methods.

Definition of the Surface

Surface is a poorly defined term. The IUPAC recommendation is to distinguish three terms: surface in general, physical surface, and experimental surface [2–4].

Surface (general) is the ‘‘outer portion’’ of a sample of undefined depth. This term is to be used in general discussions of the outside regions of the sample.

Physical surface is the outermost atomic layer of a sample (this is the layer that would be in direct contact with the vacuum if the sample were placed in a vacuum).

Experimental surface is that portion of the sample with which there is significant interaction with the particles or radiation used for excitation. It is the volume of sample required for analysis, or the volume corresponding to the escape of emitted radiation or particles, whichever is larger.

A typical problem of surface analysis is a study of a material deposited or adhered to a substrate. Coverage of a substrate by one atomic or molecular layer of a species is called *monolayer*. The term *multilayer* designates that more than one layer of a species covers the substrate. In contrast to the monolayer, in this case not all elementary units of the layer are in contact with the surface layer of the substrate. *Surface coverage* for both monolayer and multilayer coverage is defined as the ratio of the amount of substance covering the surface to the monolayer capacity. Coverage equals unity for one complete monolayer on the substrate. The *film* is a material which has been deposited or adhered to a substrate and has a uniform thickness within 20% of its average thickness, which is $<10\,\mu m$.

A major problem of all surface methods is their sensitivity. Among the surface techniques, only a limited number of atoms must be detected. Contained in a $1\,cm^3$ bulk sample is about 10^{22} molecules, in one $1\,cm^2$ of the surface only about 10^{15}, and when following a component present at the 1% level, a technique sensitive to about 10^{13} atoms is needed. A *surface-sensitive technique* is more sensitive to the atoms located near the surface than to the atoms in the bulk. A *surface-specific technique* gives signals due to atoms of the physical surface only. The mass fraction of the component in the experimental surface divided by its total amount in the volume of interest is often called *surface concentration*. It can be given in terms of atoms (particles) (ppm) or in terms of mass ($\mu g\,g^{-1}$).

Selection of Method

There are many criteria according to which the method can be selected [5]. A detailed discussion of the decision steps has been described in detail elsewhere. A survey of the method is given in the Reference data table along with some characteristics (Table 1). This table allows one to select the method according to information needed and its parameters. Some tentative figures are also given, allowing an estimate of the price and availability of a suitable laboratory to be made.

At present, the most popular techniques for chemical surface characterization are XPS, AES, SIMS, and also infrared (IR) techniques, which bring different and complementary information.

The critical point of surface analysis is to prevent any changes to the surface before or during the experiment; because of this, most methods do not allow one to carry out the technique *in situ*, as ultrahigh vacuum(UHV)isneeded.

UHV is required for most surface analysis techniques for several reasons:

- to have sufficient mean free path of the probe and detected particles (electron, ions, and atoms),
- to eliminate the signal from interaction of the probe particle with the molecules in the gas phase,
- to preserve a reproducibly clean surface during all measurement.

Even though the first two requirements allow work at pressures better than 10^{-2} Pa, contamination of the surfaces occurs in <1 s at this pressure. It means that for maintenance of a clean surface, pressures lower than 10^{-7} Pa are needed. These pressures are now routinely obtainable.

Another problem is connected with sputtering and heating of the surface.

Table 1 Reference data table.

Technique[a]	Sample[b]		Conditions[b]	Surface specificity		Resolution		Time needed for analysis		
	Form/type	Size[c]		Information depth	Detectability	Depth	Lateral	Preparation	Measurement	Evaluation
AES	s	1 cm^2	UHV	3 nm	0.1 at.%	3 nm	100 nm	1 h	3 h	10 min
APECS	s	5 mm	UHV	0.5 nm	0.5 ML	0.2	0.5 mm	1 h	5 h	2 h
APFIM	s	50 nm	UHV	0.1 µm	10 at.%	0.2 nm	1 nm	8 h	8 h	8 h
ARUPS	cr	>1 mm	UHV	1 nm	0.1 ML	0.5 nm	1 mm	1 h	1 h	1 h
ATR	s(flat), l	mm–cm	—	>10 µm	ML	—	—	5 min	5 min	1 h
CPAA	s	1 cm^3	HV	Bulk	1 ng g^{-1}	—	—	5 min	10–100 h	10 min
DAPS	s	5 mm	UHV	0.5 nm	0.05 ML	2 nm	1–100 µm	1 h	30 min	1 h
Ellipsometry	s(flat)/l	0.2–1		10 nm	<1 ML	1 µm	10–100 µm	Min	10 s to 10 min	1 h
EMS	s	5 mm	UHV	0.5 nm	0.1 ML	2 nm	1–100 µm	1 h	10 h	1 h
EPMA	s, powder	10 nm–1 cm	V	2 µm	0.1 at.%	1 µm	1 µm	15 min	5 min to 5 h	5 min to 1 h
ERD	s	0.5 cm^2	V	1 µm	0.1 at.%	20 nm	1 mm	1 min	10 min	30 min
ESD	s	5 mm	UHV	0.5 nm	0.01 ML	0.5 nm	1–100 µm	1 h	30 min	1 h
ESDIAD	s	5 mm	UHV	0.5 nm	0.01 ML	0.5 nm	1–100 µm	1 h	5 h	1 h
EWCRDS	s	cm	—	—	0.01 ML	—	—	—	—	—
GDOES	s (flat)	>12 mm	V	100 µm	10**14 at.cm^{-1}	2 nm	2 mm	2 min	15 min	5 min
GEXRF	th	>10 cm2	—	1–100 nm	10**11 at.cm^{-2}	0.1 nm	5 cm	30 min	10 min to 3 h	1 h
GIXRF	s	>0.5 cm2	—	3 nm to 1 µm	10**12 at.cm^{-3}	0.3–100 nm	1 cm	0	2 h	1 h to 1 day
HEELS	cr	1 mm	—	0.2 nm	<1 ML	—	—	Days	Days	Weeks
IETS	s/th	5 mm	—	0.5 nm	0.01 ML	0.5 nm	5 mm	1 h	30 min	1 h
IPES	s	>1 mm	UHV	0.5 mm	0.1 ML	0.5 nm	1 mm	1 h	5 h	1 h
ISS	s	1 cm^2	UHV	1–2 ml	0.001 ML	1 ml	150 µm	30 min	10 min	15 min
LEIS	s	1 cm^2	UHV	0.01 mm	0.01–0.1 at.%	0.1 nm	—	1 min	10 min	10 min

(*continued overleaf*)

Table 1 (*Continued*)

Technique	Sample		Conditions	Surface specificity		Resolution		Time needed for analysis		
	Form/type	Size		Information depth	Detectability	Depth	Lateral	Preparation	Measurement	Evaluation
LMMS	s	mm^2	V	10–50 nm	10**7 at	—	3 µm	10 min	10 min	4 h
MDS	s,l,cr	5 mm	UHV	—	0.1 ML	—	1 µm	1 h	30 min	1 h
NDP	s	0.5 cm2	HV	Bulk	10**15 at. cm^{-2}	10–20 nm	—	5 min	0.5–1 h	10 min
NEXAFS	s	5 mm	UHV	0.5 nm	0.01 ML	0.5 nm	1 mm	1 h	30 min	1 h
NRA	s	3 mm	V	0.1–1 µm	0.1–100 ppm	5–100 nm	1 mm	0	10 min	15 min
PAES	c	>1 mm	UHV	0.2 nm	0.1 at.%	0.1 nm	100 nm	1 h	2 h	2 h
PAS	s, l	0.2–1 cm	—	10 nm	1 ML	—	10 µm	10 min	10 min	10 min
PEEM	s	5 mm	UHV	5 nm	0.1 ML	0.5 nm	30 nm	30 min	>1 h	5 min to 1 h
PIES	s	>1 mm	UHV	0.2 nm	0.1 ML	0.2 nm	0.05 mm	2 h	2 h	2 h
PIGE	s, pellet	>mg	V	50 µm	>10 ppm	—	10 µm	0–2 h	>10 min	5 min
PIXE	s, powder	1 mm	V	50 µm	0.12 ppm	10 µm	1 µm	2 h	10 min	3 min
RBS	s	0.25 cm^2	V	2–10µm	0.1 at.%	25 nm	0.5 mm	1 min	10 min	5 min
REELS	c	5 mm	UHV	0.5 nm	0.01 ML	2 nm	1–100 µm	1 h	30 min	1 h
SEM	s, powder	1 nm to 1 cm	V	0.2 nm–10 µm	0.1 at.%	0.2 nm	0.2 nm	15 min	5 min to 5 h	5 min to 1 h
SEMPA	s, powder	10 nm to 1 cm	V	2 µm	0.1 at.%	1 µm	1 µm	15 min	15 min to 5 h	5 min to 1 h
SERS	th	µm–mm	—	—	1 ML	—	5 µm	10 min	10 min	1 h
SFG	Transparent s,l	0.1–1 mm^2	—	1 nm to 1 µm	0.1 ML	0.3 nm	11 µm	30 min	2 h	30 min
SHG	Transparent s,l	1 mm^2	—	10 nm to 1 µm	0.1 ML	0.3 nm	10 µm	30 min	2 h	30 min
SIMP	s	0.25 cm^2	V	—	—	—	0.1 mm	1 min	10 min	15 min
SIMS/dyn	s	0.01–2.5	V	10 nm to 100 µm	ppb–ppm	10 nm to 5 µm	0.1–5 µm	20 min	5 min to 20 h	2 h
SIMS/static	s, powder	>0.5 mm	UHV	1 nm	10**9 at cm^{-2}	—	0.5 µm	0	10 min	10 min
SNMS	s	0.25 cm^2	UHV	>100 µm	0.1 ng g^{-1}	0.5	—	20 min	5 min to 2 h	2 h
SPEELS	c	5 mm	UHV	0.5 nm	0.01 ML	2 nm	1–100 µm	1 h	5 h	1 h

SPIPES	c	>1 mm	UHV	0.5 mm	0.1 ML	0.5 nm	1 mm	1 h	5 h	1 h
SPUPS	c	5 mm	UHV	0.5 nm	0.5 ML	0.5 nm	1 mm	1 h	>1 h	1 h
SPXPS	c	5 mm	UHV	0.5 nm	0.5 ML	0.5 nm	1 mm	1 h	>1 h	1 h
STS	s	1 mm	UHV	0.5 nm	0.001 ML	0.5 nm	0.1 nm	1 h	5 min	1 h
TXRF	l, thin film, p		—	5 nm	10**10 at.cm^{-1}					10 min
UPS	c	5 mm	UHV	0.5 nm	0.01 ML	2 nm	1 mm	1 h	30 min	1 h
XAFS	s	5 mm	—	1–5 nm	0.01 ML	1–5 nm	1 mm	1 h	30 min	1 h
XPS	s	5 mm	UHV	10 nm	0.1 at.%	0.2 nm	0.01–1 mm	30 min	>1 h	5 min to 1 h
XPD	cr	5 mm	UHV	5 nm	0.1 at.%	0.2 nm	0.01–1 mm	1 h	>2 h	>1 h
XRF	s,l,th	8–500 μm	—	30 nm to 8 μm	ppm	2%	0.2 mm	5 min	3–60 s	5 min
XSW	cr	5 mm	—	1 nm to 8 μm	ppm	0.2 nm to 1 μm	0.1 mm	2 h	3 h	3 h

---

[a] Data for techniques in the normal fonts are taken from Ref. [5] and have been compiled from a questionnaire action; data given in italics are only an estimate of the authors of this chapter.

[b] s, solid; l, liquid; cr, crystal; c, (solid), conductor; V, vacuum; UHV, ultra high vacuum; ML, monolayer; th, thin film.

[c] Diameter or area.

Surfaces in UHV are initially covered in ‘‘crud’’ that is associated with prior exposure to atmosphere. This normally consists of several monolayers of oxide and adsorbed hydrocarbons that need to be cleaned away by argon ion bombardment to permit analysis of the sample by a surface-sensitive technique. This process of sputter cleaning can change the surface composition and/or structure, and is not always successful at removing all contamination.

Interaction of the highly energetic particles with the sample may also result in heating of the targeted parts (especially for thermally nonconductive samples) and additional cooling may be required to minimize this effect.

For some methods, erosion of the surface is inherent. This is typical for dynamic SIMS, where the sputtered particles are analyzed.

A survey of the individual techniques will be given in three chapters, divided up according to whether the excitation source used is electrons (Chapter 18), ions or neutrals (Chapter 19), or photons (Chapter 20). Owing to limited space, only selected techniques are discussed in detail and characterized by its underlying principle, instrumentation, sample requirements, characteristic spectral features, extractable analytical information, performance criteria, and main areas of application.

Acknowledgments

The authors thank Graham Beamson, RUSTI, Daresbury Laboratory, Warrington, UK, for the permission to use data from the Scienta X-ray Photoelectron Spectrometer and to Jiri Homola, Institute of Radioengineering and Electronics, Academy of Sciences of the Czech Republic and University of Washington, Department of Electrical Engineering, Seattle, USA, for cooperation on some parts of this chapter.

References

1. Kellner, R., Mermet, J.-M., Otto, M., and Widmer, H.M. (1998) *Analytical Chemistry*, Wiley-VCH Verlag GmbH, Weinheim.
2. IUPAC (1998) *Compendium of Analytical Nomenclature, Definitive Rules 1997*, Blackwell Science, Oxford.
3. Attard, G. and Barnes, C. (1998) *Surfaces*, Oxford Science Publications, Oxford.
4. Nix, R. An Introduction to Surface Chemistry, *http://www.chem.qmw.ac.uk/surfaces/scc/* (accessed 19 March 2013).
5. Brune, D., Hellborg, R., Whitlow, H.J., and Hunderi, O. (1997) *Surface Analysis*, Wiley-VCH Verlag GmbH, Weinheim.

18
Electron Probe Techniques

Christopher George Havelock Walker

Excitation of surfaces with electrons is accompanied by the release and detection of secondary electrons or photons and only a limited number of techniques use detection of neutrals or ions, for example, electron-stimulated desorption. To the first group, detecting secondary electrons, belongs Auger electron spectroscopy (AES) that is the workhorse technique for characterizing the elemental constituents of a surface. Another popular technique is electron energy loss spectroscopy (EELS) that can provide information regarding the electronic and optical dielectric properties of a surface. As for photon excitation, energy dispersive X-ray spectroscopy (EDXS) is in common use, although the volume to which it is sensitive is typically a micron or more below the surface and so not as surface sensitive as many techniques. More recently, developed techniques such as scanning tunneling spectroscopy can provide details of the electronic structure at very high spatial resolution. Certain techniques can use a spin-polarized source beam or detect spin-polarized emission. These techniques often find uses in the analysis of magnetic samples.

Individual techniques are presented in alphanumerical order.

18.1
Appearance Energy Spectroscopy

18.1.1
Introduction

Also known as Appearance Potential Spectroscopy. The energy of an incident ionizing radiation (usually electrons) is gradually increased such that the energy passes over the ionization threshold of a core level of an atom in the surface being studied [1]. This is the basis of the appearance potential spectroscopies. In the case of disappearance potential spectroscopy (DAPS), the onset of ionization is detected by a reduction in the intensity of the elastically scattered beam. For Auger electron appearance potential spectroscopy (AEAPS), the Auger electron current is measured as the incident beam energy is increased. For soft X-ray appearance potential spectroscopy (SXAPS), it is the appearance of X-ray emission

Handbook of Spectroscopy, Second Edition. Edited by Günter Gauglitz and David S. Moore.

that is detected. If the incident radiation is X-rays, then the methods are more generally known as extended X-ray absorption fine structure (EXAFS) and related techniques. It should be noted that the term *appearance potential* is deprecated. However, alternative names for the various appearance potential spectroscopies have not been decided upon.

18.1.2
Instrumentation

The measurement is carried out in an ultrahigh vacuum (UHV) chamber. Electrons from an electron gun in the energy range 50–2000 eV are directed onto the sample. The incident electron energy is gradually increased. In the case of DAPS, the elastically scattered primary electrons are detected using a retarding field analyzer (RFA). As the energy of the incident beam passes through an ionization edge, the number of elastically scattered electrons drops slightly.

In the case of AEAPS, it is not necessary to detect individual Auger peaks, as the total secondary electron yield can be measured instead. The electron cascade within the material can act as an electron multiplier increasing the AEAPS signal. Hence, an RFA could be used or an electron detector of a type used in a scanning electron microscope (SEM).

For SXAPS, the instrumentation is very simple. A filament is used as a source of electrons and is mounted close to the sample. The electrons from the filament are accelerated toward the sample. A screening mesh in front of the detector allows X-rays to pass into the detector, but not electrons. The X-rays cause photoelectrons to be emitted from the wall of the detector and these photoelectrons are collected on a thin wire. The detector has a superficial similarity to a Geiger–Muller tube. UHV is not needed for the instrumentation (this is especially true for SXAPS), but a clean surface is necessary for reliable data.

18.1.3
Sample

Conducting samples that survive well in UHV are normally studied. Insulating or biological samples will usually degrade in the beam.

18.1.4
Analytical Information

The elemental composition within the surface may be determined, but quantification is difficult. In addition, information regarding the empty density of states (DOSs) can be revealed. Therefore, it supplies complementary information to inverse photoelectron spectroscopy (IPES) and scanning tunneling spectroscopy (STS).

18.1.5
Performance Criteria

Typically, a content of ~5 at% in the surface region can be determined or alternatively ~20% of one monolayer covering the surface. These estimates are very much dependent on the material as there are large variations in sensitivity depending on the density of empty states within the sample.

The change in the elastically scattered yield when the primary beam energy passes through an ionization threshold is typically 0.1%. Hence, electronic differentiation is used to enhance the weak signal. AEAPS is ~10 times more sensitive than DAPS. SXAPS is ~10 000 times less sensitive than DAPS and hence is the least used despite its simple instrumentation.

18.1.6
Applications

Appearance potential spectroscopy (APS) is used to determine the empty DOSs and elemental composition of conducting materials. Currently, a little used technique.

18.1.7
Other Techniques

Total (or target) current spectroscopy (TCS) is similar to DAPS, but it is a very low-energy technique (0–15 eV) and all the secondary electrons originate from the valence band.

18.2
Auger Electron Spectroscopy

18.2.1
Introduction

An incident-exciting beam (normally electrons) is directed at a surface [2–8]. The atoms in the surface enter an excited state and can relax by the emission of an Auger electron, which has a characteristic energy. The energy spectrum of Auger electrons (20–2000 eV) emitted following the primary ionization of a core energy level can reveal the chemical composition of the surface layers.

18.2.2
Instrumentation

The measurement is carried out in an UHV chamber. Fixed energy electrons from an electron gun in the energy range 100 eV to 10 keV are directed on to the sample (beam diameter 3 nm to 1 mm). The electrons from this primary beam excite electrons from the surface (known as *secondary electrons*) and some of the primary electrons are scattered from the nuclei of the surface atoms to create backscattered primary electrons. The primary beam of electrons can also cause atoms in the surface to emit Auger electrons, which have energies characteristic of the element that emitted them. Some of the electrons emitted from the surface pass through an aperture and into an electron energy analyzer, which selects electrons over a narrow range of energies, and these electrons are then detected. A spectrum is obtained as the first or second derivative of the secondary electron current by changing the voltages on the electron energy analyzer such that the energy of electrons that passes through the analyzer is gradually changed. Spectra can also be acquired by pulse counting the electrons that passes through the analyzer with the aid of a channeltron or microchannel plate. The hyperbolic field analyzer can acquire spectra in few seconds. However, this device is not in common use.

18.2.3
Sample

Conducting samples that survive well in UHV are normally studied. Insulating or biological samples degrade in the beam.

18.2.4
Analytical Information

The first or second derivative of secondary electron current, with respect to the analyzer energy is measured (Figure 18.1). The secondary electron current can also be measured by electron counting techniques. The resultant electron spectrum reveals a series of peaks at different electron energies. The energy of the peaks is characteristic of the element that produced the electrons. The electrons rapidly lose energy within the solid and 1–10 nm they will no longer have the same energy with which they started. Therefore, the elements composing only the top few monolayers of the surface can be determined. Depth profiles can be obtained by sputtering the surface with Ar ions and simultaneously acquiring an Auger spectrum. Chemical bonding information can be determined from the line shape of the Auger spectra. In addition, whether the element is only on the top surface layer, or subsurface can be determined by examining the shape of the peaks and the near background. Estimates of the composition of the surface layers can be made by comparison with pure element standards. An accuracy of ∼3–10 at% is achievable.

18.2.5
Performance Criteria

Energy resolution is normally in the range of 0.5–2 eV.

Typically, a concentration of ∼0.5 at% in the surface region can be determined or alternatively ∼2% of one monolayer covering the surface. This depends on the intensity of Auger emission for the element concerned. Typically, Auger electron

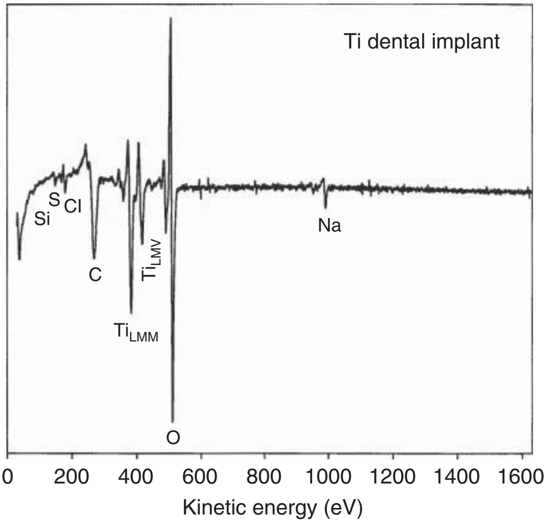

Figure 18.1 Auger electron survey spectrum from a titanium dental implant surface, showing that the surface consists of a titanium surface oxide, with a carbon contamination overlayer and some trace impurities (3 keV primary electrons, 250 nA primary beam current). (Reprinted with permission from Ref. [2].)

emission is high for low atomic number elements and gradually drops as the atomic number increases.

Auger electrons are not emitted by hydrogen and helium.

18.2.6
Applications

This method is a workhorse technique for surface science experiments in UHV. Typically, it is used to determine surface cleanliness prior to the main experiment. The usual contaminants are carbon and oxygen. It is also used in metallurgy, microelectronics, catalysis, and corrosion science.

18.2.7
Other Techniques

If the primary beam consists of ions, then the technique is known as *ion-excited Auger electron spectroscopy* or (IAES). This offers no major advantages in sensitivity of the technique, but simultaneous Auger emission and depth profiling can be carried out. By varying the take off angle of the detected electrons, some information regarding the depth profile of the elements under study can be obtained. This technique is known as *angle-resolved Auger electron spectroscopy* (ARAES). Owing to the longer path length, angle-resolved X-ray photoelectron spectroscopy (ARXPS) is a better method in this regard. Spin-polarized AES is possible by using a Mott detector as with other spin-polarized techniques. This can provide information regarding the spin-resolved DOSs for different elements. The low detection rate of the Mott detector makes data collection very slow for SPAES.

18.3
Cathodoluminescence Spectroscopy

18.3.1
Introduction

Cathodoluminescence (CL) occurs when a beam of high-energy electrons (typically 1–20 keV) strikes the surface of a luminescent material causing light emission [9]. It is used as the source of light in cathode-ray tube televisions. It can be used to study minerals, semiconductors, insulators, and so on (but not metals). Electrons within the valence band are excited into the conduction band. A hole remains within the valence band and when recombination of the excited electron and the hole occurs, light is emitted. Direct bandgap semiconductors such as GaAs and ZnS tend to emit more CL than indirect bandgap semiconductors such as Si as a phonon is required in the light emission for the latter. There is a sharp increase in the photoabsorption with light frequency, which corresponds to the bandgap. At low temperatures, the electrons and holes can form bound pairs known as *excitons*. This can lead to sharp emission lines below the edge emission frequency.

CL can also be used to study organic substances, where the excitation and subsequent emission occurs within a single molecule. Electrons from a ground state are excited to other singlet states, which then decay using a combination of radiationless and radiative transitions.

18.3.2
Instrumentation

This technique requires vacuum conditions. A tightly focused beam of high-energy electrons (2–100 keV or higher) strikes the surface of the sample. Cathodoluminescence studies are normally carried out in a SEM. The light emission can be detected using a photodetector. However, in order to carry out spectroscopy on the light emission, a spectrometer is required. The light can be collected by an elliptical mirror and passed down through an optical fiber. The light spectrum is then detected with the aid of a monochromator.

18.3.3
Sample

Vacuum compatible semiconducting or insulating solids.

18.3.4
Analytical Information

Variation in the bandgap can be determined in semiconductor compounds such as $Ga_xAl_{1-x}As$, which can then be used to determine the composition in hetereostructures or graded layers. The concentration of donors or acceptors may be revealed.

18.3.5
Performance Criteria

Exposure to intense electron beams may cause damage to the sample. This is especially the case for organic molecules.

18.3.6
Applications

SEM is one of the most widely used analytical techniques across all fields of science, technology, and industry. Cathodoluminescence can be used to image dislocations on Si and to identify defects on Si wafers. By strobing the beam source, estimates of the lifetime of the luminescence can be obtained. Dislocations can influence the lifetime and intensity of CL.

18.4
Electron Momentum Spectroscopy

18.4.1
Introduction

Electron momentum spectroscopy (EMS) measures the electronic structure of materials whereby an incoming electron with known energy and momentum scatters from an electron in a solid, transferring some of its energy; hence, this electron is also ejected from the solid [10]. If the energy and momentum of both the ejected and scattered electrons are measured in coincidence then it is possible to calculate, using the elemental laws of energy and momentum conservation, the energy and momentum of the ejected electron before the collision.

18.4.2
Instrumentation

In some experiments, the primary electrons have energies of ~50 keV. The two electrons after the collision have energies of 25 keV and are decelerated after emerging from the sample. They pass through electron energy analyzers to ensure that each electron has precisely the right energy. If there are simultaneous events on both detectors, the event is counted. Such high-energy electrons result in poor surface sensitivity. In other coincidence experiments, much lower (10–100 eV) electrons are used and this results in much higher surface sensitivity.

18.4.3
Sample

Metals, insulators, semiconductors, and gases.

18.4.4
Analytical Information

By using high-energy primary electrons, this technique provides information concerning the energy and momentum of electrons within the sample. By using low-energy electrons, the technique provides information on the spin–orbit coupling and exchange coupling in magnetic materials.

18.4.5
Performance Criteria

The technique is sensitive to the surface for low-energy primary electrons.

High voltages are needed. High vacuum or UHV is required if lower energy electrons are used.

18.4.6
Applications

EMS is used to determine electron momenta and energies within solids and (for the low-energy primary electrons) to shed light on the role of exchange coupling and spin–orbit coupling in the dynamic interaction of low-energy electrons in the valence band of solids.

18.5
Electron Probe Microanalysis

18.5.1
Introduction

Energy Dispersive X-ray Spectroscopy (EDS or EDX or XEDS) also goes under the name of Electron Probe Microanalysis (EPMA) [11–14]. An electron beam is made to strike a surface using an electron gun from a SEM. The X-rays generated by the electrons striking the surface contain elemental composition information from the sample surface down to a depth of $\sim 2\,\mu m$. This depth is sufficient to make it representative of the bulk rather than a surface sensitive technique. The X-ray energy range of operation lies from 1 to 20 keV.

18.5.2
Instrumentation

Electrons from a primary beam are made to strike a surface and the resulting X-ray emission from that surface is detected. The X-rays can be detected using a solid-state detector, which gives rise to the energy dispersive X-ray (EDS) technique. Alternatively, the X-rays can be dispersed by a crystal and then detected, which gives rise to the wavelength dispersive X-ray spectroscopy (WDS) technique. In EDS, the detector is normally a lithium-drifted silicon detector called *Si(Li) detector*, which needs to be kept at a low temperature using liquid nitrogen. However, a recent development is the silicon drift detector (SDD) that allows a much greater flux of X-rays to be detected. X-rays that strike the detector generate electron–hole pairs and the larger the energy of the X-ray, the more electron–hole pairs that are generated. The electron–hole pairs are prevented from recombining by application of a large electric field within the Si(Li) detector. The electrons and the holes travel to opposite ends of the detector where they generate an electric pulse. The larger the pulse, the higher the energy of the X-ray. Hence, an X-ray spectrum can be acquired with all X-ray energies in parallel, with each pulse being assigned to a different bin in a histogram. This can be performed with the aid of a multichannel analyzer. A higher energy resolution than the Si(Li) detector can be achieved using a microcalorimeter (also parallel acquisition). In this case, the detector has to be cooled to a much greater degree.

An alternative approach to obtaining higher energy resolution is to use WDS. The X-rays strike a crystal and the diffracted beams strike a detector. Different crystals may be used (e.g., quartz or lithium fluoride) that provide sensitivity to different X-ray energies. Several different crystals are normally available on a single SEM. By rotating the crystals, different energy X-rays can be made to strike the detector. The WDS spectrum acquisition is serial, whereas the EDS approach is parallel making EDS much faster than WDS. However, the much higher energy resolution of the WDS (and microcalorimeter) method provides a much greater sensitivity to lower concentration elements.

18.5.3
Sample

Conducting samples are usually studied. Some samples degrade under electron bombardment.

18.5.4
Analytical Information

For EDS, the Si(Li) detector is capable of detecting X-rays down to ∼200 eV, which implies that all elements from beryllium upwards can be detected. The sensitivity rises as the X-ray energy increases as a result of the fluorescence yield, which increases with atomic number. The elements composing the top ∼2 μm of the surface are determined from analyzing the X-ray spectrum. It is sensitive to ~0.5 at%, depending on the particular peak and possible peak overlaps, and so on.

With regard to WDS, it is sensitive to all elements mentioned earlier and including Boron. It can be sensitive to parts per million levels and if the elements concerned are solely on the surface and not in the bulk, then it can have high surface sensitivity.

In both approaches, the beam can be scanned across the surface to create images of each element in the scanned area (Section 18.13).

18.5.5
Performance Criteria

Spatial resolution is normally in the region of ~2 μm. For EDS, the energy resolution varies with X-ray energy, but typically varies from 50 eV at an X-ray energy of 1.5 keV to 200 eV at an X-ray energy of 6 keV. For WDS, the energy resolution depends on the crystal used in the diffracting geometry, but 5–10 eV can be achieved.

The electron beam spreads out as the primary electrons strike the surface. This means that the spatial resolution is limited based on the beam spreading within the material (~2 μm). The probability of X-ray emission reduces with atomic number; hence, elements with low atomic number are difficult to detect and helium and hydrogen have never been detected using EDS. The depth of penetration of the electron beam into the material is ~2 μm. This means that EDS is not a truly surface sensitive technique, but is more sensitive to the bulk.

18.5.6
Applications

EPMA is typically used in metallurgy, microelectronics, and corrosion science.

18.6
Electron-Stimulated Desorption

18.6.1
Introduction

Low-energy electrons are directed at the surface and can cause an atom or molecule on the surface to be desorbed [1, 15–17]. Electron-stimulated desorption usually occurs by electronic energy transfer and not by direct momentum transfer. Other processes include conversion of one binding energy state to another and desorption of atomic and molecular species, which may be charged (positive or negative) or neutral (ground state or excited). This technique also has a more specialized form called electron-stimulated desorption ion angular distributions (ESDIAD) (see later). Incident electron energy is typically <500 eV for electron-stimulated desorption (ESD).

18.6.2
Instrumentation

An electron beam strikes the surface of a single crystal at glancing incidence, and a small fraction of the ions ejected from the surface are collected using a mass spectrometer. The detection of positively charged ions is generally favored over negatively charged ions as a voltage can suppress interference from the primary electrons in the detection system. A quadrupole system cannot measure total desorption cross sections. For this purpose, a series of concentric grids can be used similar to a low-energy electron diffraction (LEED) system.

18.6.3
Sample

Samples that can be studied include metals, highly ionic oxides, alkali-halide solids, and semiconductors among others, usually with an adsorbed layer of gas or other atom/molecule.

18.6.4
Analytical Information

The incident electron energy is varied and the ejected ion current is measured. The experiments can be carried out at different temperatures. The resultant spectra provide information on intermolecular forces and bonding length of defect surface structure. By comparison with computer models, thermal dynamics of adsorbed species can be obtained. Desorption of an adsorbed molecular species can occur by the breaking of an intramolecular bond or the breaking of a molecule–surface bond.

18.6.5
Performance Criteria

The desorption cross section varies considerably depending on substrate and adsorbed species. As such the performance varies considerably on the system being studied. Different desorbing species can be selected using a mass spectrometer. This technique requires a good vacuum. Most of the desorption may originate from minority states and desorption cross sections vary enormously from species to species. The cross sections for metallic adsorbates (e.g., Cs on W or Th on W) are low. The information provided by ESD is semiquantitative.

18.6.6
Applications

Used for the study of adsorbates on metals or semiconductors.

18.7
Electron-Stimulated Desorption Ion Angular Distributions

18.7.1
Introduction

Low-energy electrons are directed at the surface and can cause an atom or molecule on the surface to be desorbed [1, 15–17]. By measuring the intensity of the desorbed species as a function of take off angle information regarding how the molecule is oriented on the surface can be determined (i.e., bond directionality). ESD usually occurs by electronic energy transfer and not by direct momentum transfer.

Range of operation is 0–3 eV.

18.7.2
Instrumentation

An electron beam strikes the surface of a single crystal at glancing incidence, and a small fraction of the ions ejected from the surface are collected by a channeltron mounted on a motor driven, computer-controlled goniometer. The detector can traverse a spherical surface and map out ESD ion intensity as a function of angle. Digital data is displayed in three-dimensional form, and digital background subtraction can be utilized to enhance the appearance of ESDIAD patterns.

An alternative approach is to arrange for the particles that are ejected to encounter a four-grid electrostatic lens array. All positive ion and neutral ESD species pass through the grid system, striking the first of two microchannel plates (MCPs), which produce ∼1 million electrons for each positive ion (or excited state neutral). This electron pulse is accelerated into a resistive anode, causing an expanding ring of charge, centered at the pulse arrival point, to propagate across the thin conductive film. The position analysis computer translates it into a three-dimensional image.

18.7.3
Sample

Samples that can be studied include metals, highly ionic oxides, alkali-halide solids, and semiconductors among others.

18.7.4
Analytical Information

A map of ion intensity versus the direction of take off is acquired. By comparison with model structures a number of characteristics can be determined, such as the bonding geometry of surface species from adsorbates on single crystal surfaces, intermolecular forces, bonding length, and orientations of defect surface structures. This leads to an understanding of the thermal dynamics of adsorbed species.

18.7.5
Performance Criteria

The performance criteria are similar to ESD. Different desorbing species can be selected using a mass spectrometer. This technique requires single crystals and a good vacuum. Most of the desorption may originate from minority states and desorption cross sections vary enormously from species to species. The information provided is semiquantitative.

18.7.6
Applications

It is used for the study of adsorption site symmetry of molecules on single crystal surfaces such as in the production and observation of synthetic catalytic intermediate species at high coverage. There are overlaps with techniques such as LEED and surface extended X-ray absorption fine structure (SEXAFS).

18.8
Extended Energy Loss Fine Structure

18.8.1
Introduction

Extended energy loss fine structure (EXELFS) is generally carried out in a conventional transmission electron microscope (TEM) [1, 18]. The electron beam loses energy through various mechanisms, but includes characteristic energy losses by the excitation of an electron from a core state. This results in a sudden rise in the number of loss events at certain energy below that of the primary beam energy corresponding to an absorption edge of an element contained within the sample. The excited core electron has a certain probability of being backscattered to the emitting atom. This can in turn affect the initial probability of ionization by the incident beam. This gives rise to oscillations in the ionization probability with electron energy loss (better known as *X-ray absorption fine structure*, oscillations).

Hence, information regarding the local structure around the atom whose absorption edge is acquired can be obtained. A much higher spatial resolution can be obtained with EXELFS than with EXAFS.

Range of operation: incident electron energy is typically hundreds of kiloelectron volt.

18.8.2
Instrumentation

A conventional TEM is required, as well as an electron energy analyzer, to measure the electron energy loss spectra. The EXELFS signal is very weak, and thus direct electron detection using a photodiode array for parallel detection is preferable.

18.8.3
Analytical Information

EXELFS spectra provide information regarding the local environment surrounding the atom whose absorption edge is studied. The specific local information includes the atom type of neighboring atomic shells, the distance of those shells from the central (absorbing) atom, and the static or dynamic disorder. The latter is given by the Debye–Waller value. The two-electron final state can make the interpretation of EXELFS spectra more complicated than EXAFS. Normally, EXELFS would be regarded as a bulk sensitive technique. However, by the use of grazing incidence electrons, it is possible to probe the near-surface region.

18.8.4
Performance Criteria

Primary electron energy is 100–500 keV.

The sample should be able to withstand the intense incident electron beam. As in EXAFS, it can be difficult to distinguish elements in the shells surrounding the central atom if they are close in atomic number and it can also be difficult to distinguish static from dynamic disorder.

18.8.5
Applications

EXELFS is used in many applications where local state information is required such as materials analysis (for example, structure of amorphous materials). It can be used where the amount of material is too small for conventional EXAFS experiments, or where a high spatial resolution of the local structure is required.

18.8.6
Other Techniques

Parallel electron energy loss spectroscopy (PEELS) is a method whereby electron energy loss spectra can be acquired in a TEM with great rapidity. This is accomplished by the use of a multielement solid-state detector. Typically, PEELS is used to determine the composition of the sample under study and does not have sufficient energy resolution to provide EXELFS data. Improvements in detector technology may change this.

18.9
High-Resolution Electron Energy Loss Spectroscopy

18.9.1
Introduction

A highly monochromated primary electron beam (energy 1–50 eV) impinges on a sample [1, 2, 19]. Many electrons are elastically scattered directly from the surface, whereas others undergo inelastic scattering by exciting a vibrational state of atoms in the surface layers. The scattered electrons reflected back from the surface are collected and their energies are analyzed.

18.9.2
Instrumentation

The electron beam from an electron gun is passed through a monochromator that results in a highly monochromatic electron beam with an energy spread <10 meV at a typical primary beam energy between 1 and 10 eV. The electrons are often made to strike the surface at grazing angles of incidence. The reflected electrons pass through an electron energy analyzer before being detected.

18.9.3
Sample

Samples should have flat surfaces and should preferably be conducting.

18.9.4
Analytical Information

The source of information is a dependence of electron current on electron energy loss.

There are three important scattering mechanisms in high-resolution electron energy loss spectroscopy (HREELS) – dipole scattering, impact scattering, and negative ion resonance scattering.

For dipole scattering, the electron is scattered to a long distance from the sample (~10 nm) and generates surface phonons. Only vibrational modes that are perpendicular to the surface are normally excited in dipole scattering and the low-energy losses result only in a small angle of deflection from the original direction.

For impact scattering, electrons scatter at much shorter range (~0.3 nm) and over a much wider angle than dipole scattering. Impact scattering has a much lower probability than dipole scattering and can be distinguished from dipole scattering by moving the analyzer away from the specular direction.

18.9.5
Performance Criteria

HREELS probes vibrational features from ~0 to >4000 cm^{-1} with resolution of <1 meV (8 cm^{-1}). It has a much more limited resolution in comparison with the infrared (IR)-based methods.

The method is sensitive to all elements, but only to the top few atomic layers for metals or to fractions of a monolayer (much <1%) for bands with large dipole moment changes. It can be possible to detect vibrational (<0.5 eV) and electronic losses (1–50 eV) in the same instrument.

It is possible to monitor vibrational modes below 1000 cm^{-1}, where reflection–absorption infrared spectroscopy (RAIRS) has problems with sufficient intensity of the infrared (IR) source.

HREELS has poor spatial resolution (1–5 mm) and it requires an UHV chamber with very good magnetic shielding. Stray charges may build up in the spectrometer, which then requires frequent baking. HREELS is difficult to quantify. It is best for small, nonmagnetic single crystals. HREELS is not very sensitive to insulating materials, as surface charging makes the analyzes difficult. It has poor sensitivity for rough surfaces and is difficult to use with depth profiling.

HREELS equipment is expensive (minimum $80 000) and there are a few number of commercial suppliers. HREELS instruments are very complex and bulky, and it is difficult to optimize the electron optics for the primary beam.

18.9.6
Applications

HREELS is used to investigate vibrational scattering mechanisms on surfaces. It helps to provide molecular orientation information for molecules on surfaces as well as bond strengths, adsorption geometry and surface acoustic, and optical phonon information.

18.9.7
Other Techniques

Reflection electron energy loss spectroscopy (REELS, energy loss spectroscopy (ELS)), and extended electron energy loss fine structure (EXELFS) work with a higher fixed energy of the primary electrons (50–200 eV and 10–80 keV, respectively) and higher energy losses of the scattered primary electrons ranging from 0.005 eV to several hundreds and from 200 to 4000 eV, respectively.

REELS provides information concerning higher energy loss mechanisms than HREELS, such as plasmons, interband transitions, and characteristic energy losses. EXELFS is a technique used in TEM. It provides information similar to EXAFS (i.e., data regarding the immediate neighborhood of atoms of certain elements in the sample). EXELFS is bulk sensitive.

Transmission electron energy loss spectroscopy (TEELS) is another technique that is used in a TEM. The electron energy loss is much higher than in EXELFS and characteristic energy losses can be observed. This provides information concerning the elemental composition of the sample. The spectra are detected using a multi-element solid-state semiconductor detector that results in spectra being acquired in parallel. Hence, it is known as parallel electron energy loss spectroscopy (PEELS).

18.10
Inelastic Electron Tunneling Spectroscopy

18.10.1
Introduction

Electrons (0–1 eV) are caused to tunnel between two conducting substrates through an insulating layer, which has a film of material deposited on it [20–22]. Electrons can tunnel through the insulating layer and attached film without losing any energy (i.e., an elastic process) or some energy may be lost (i.e., an inelastic process). Hence, the technique is sensitive to the empty states, vibrational molecular states, phonons, and magnons.

Range of operation is 0–3 V

18.10.2
Instrumentation

The current–voltage ($I-V$) characteristic of the metal-insulator-film-metal (M–I–x–M) junction is measured. AC modulation of the voltage can be used with lock-in amplifiers to obtain a plot of the $\mathrm{d}^2I/\mathrm{d}V^2$ against ΔV (i.e., against electron energy). Liquid helium temperatures are typically required for inelastic electron tunneling spectroscopy (IETS) experiments.

18.10.3
Sample

The sample is a film placed on a thin insulating substrate and then sandwiched between two metallic plates. Molecules adsorbed on an oxide or oxide-supported metal can be studied in such a way.

18.10.4
Analytical Information

Vibrational modes of the molecules in the film are displayed as sharp peaks on the plot of d^2I/dV^2 against ΔV. Even though both Raman and IR active modes are also active in IETS, only modes perpendicular to the surface are observed (as is also the case in reflection-spectroscopy-based techniques).

18.10.5
Performance Criteria

Resolution of the order $10\,\text{cm}^{-1}$ is reached. IETS has ultrahigh sensitivity; $<10^{13}$ molecules are needed for a spectrum. Overtone and combination bands are very weak. Optically forbidden transitions may be observed. The fact that the layer being studied is buried has made it difficult for other surface science techniques to be used in combination with IETS.

18.10.6
Applications

IETS is applied to the study of films such as self-organized monolayers. Adsorption experiments are limited by the low temperature required for the experiment.

18.10.7
Other Techniques

IETS provides information complementary to vibrational spectroscopies, such as Raman, IR, or HREELS. In addition, the technique has gained a new lease of life, in recent years, because of its use in association with scanning tunneling microscopy (STM). This has given rise to the technique known as *STM–IETS*.

18.11
Inverse Photoelectron Spectroscopy

18.11.1
Introduction

A beam of low-energy electrons with a fixed energy (5–50 eV) and momentum illuminates the sample where they couple with the unoccupied bands above the

Fermi energy [23, 24]. The electrons lose energy by emitting a photon and dropping down into another unoccupied band at a lower energy. The initial energy of the electron is known; hence, by measuring the energy of the photon that is emitted the remaining energy of the final state can be determined to produce a spectrum that is representative of the unoccupied DOSs above the Fermi level.

18.11.2
Instrumentation

This technique requires UHV conditions. An electron gun is used to direct a beam of low-energy electrons onto the sample. The electrons couple with unoccupied states above the Fermi level from which they decay into lower unoccupied states by emission of a photon. This photon hits a diffraction grating and is diffracted (at an angle that is dependent on its energy) onto a position (and hence energy) sensitive photon detector such as a charge-coupled device (CCD). As the initial energy of the electron is known, and the energy of the photon has been measured, the energy of the final unoccupied band can then be determined. Hence, a spectrum that is representative of the unoccupied DOSs above the Fermi level can be produced. Alternatively, photons of a fixed energy can be measured while the energy of the electron beam is scanned to produce the spectrum, a mode known as Bremsstrahlung isochromat spectroscopy (BIS).

By varying the angle of incidence of the electrons their momentum (*k*) can be varied to produce ‘‘band maps’’ of the unoccupied states as a function of momentum that are analogous to those of the occupied states produced in angle-resolved ultraviolet photoelectron spectroscopy (ARUPS). This is known as *k*-resolved inverse photoemission spectroscopy (KRIPES) or angle-resolved inverse photoemission spectroscopy (ARIPES).

If a spin-polarized electron gun is used then separate spectra of the unoccupied ‘‘spin-up’’ and ‘‘spin-down’’ DOSs can be produced that are analogous to the ‘‘spin-up’’ and ‘‘spin-down’’ spectra of the occupied states produced by spin-resolved ultraviolet photoemission spectroscopy (SRUPS). This is known as spin-resolved inverse photoelectron spectroscopy (SPIPES).

18.11.3
Sample

- UHV compatible conductors for IPES/BIS.
- Single crystal UHV compatible conductors for ARIPES/KRIPES.
- Magnetic UHV compatible conductors for SPIPES.
- Owing to the low count rates obtained in all variations of IPES the sample must be stable under intense electron beams in UHV for prolonged periods.

18.11.4
Analytical Information

This technique determines the density of unoccupied states above the Fermi level. Hence, IPES is complementary to ultraviolet photoelectron spectroscopy (UPS) that measures the density of occupied states below the Fermi level. As in UPS, angle- or spin-resolved variants on the technique can be used to perform band mapping of single crystals or to produce spin-resolved spectra of magnetic samples.

18.11.5
Performance Criteria

The inverse photoemission process is much less efficient than the photoemission process (by some five orders of magnitude). This can be offset somewhat because electron beams can generally be made more intense than X-ray beams. However, count rates are still much lower, and acquisition times much longer than in UPS.

The energy range of IPES is typically 5–50 eV, the energy resolution is generally ∼0.2 eV and the spatial resolution is generally ∼1 mm. Surface sensitivity is similar to UPS, that is, limited primarily to the top five atomic layers.

UHV is required for this technique. High surface sensitivity combined with long acquisition time means that IPES is limited to samples that will remain stable and clean in vacuum for many hours under the electron beam.

The low energies of the electrons involved means that the technique can be vulnerable to stray magnetic fields and magnetic shielding may be required. Spectra can be influenced by the particular crystal structure of the sample's top few atomic layers, which may not be completely representative of the bulk material. IPES is generally not suitable for insulating materials.

18.11.6
Applications

The empty states immediately above the Fermi level play a vital role in surface chemistry, optical properties, and the electrical conduction of semiconductors and so IPES and its variants can reveal vital information about these properties that is complementary to the information on the occupied DOSs obtained from UPS.

18.12
Reflection Electron Energy Loss Spectroscopy

18.12.1
Introduction

A primary electron beam (energy typically 100–2000 eV) impinges on a sample [15, 25]. The electrons are elastically and inelastically scattered back from the surface. Those electrons that undergo inelastic scattering typically do so by exciting a plasmon or interband/intraband transition in the surface layers. The energies of the reflected electrons are analyzed to produce an energy loss spectrum. This loss spectrum consists of a series of loss peaks at different energies and intensities. The technique is normally available on instrumentation designed primarily for AES (or X-ray photoelectron spectroscopy (XPS)) where an electron gun has been fitted) and thus provides useful extra information on the sample surface under study.

18.12.2
Instrumentation

The electron beam from a simple electron gun is directed at the sample surface. The beam normally has an energy spread of ~1–2 eV at typically primary beam energy between 100 and 2000 eV. The reflected electrons pass through an electron energy analyzer before being detected.

18.12.3
Sample

Samples should have reasonably flat surfaces and preferably be conducting.

18.12.4
Analytical Information

The source of information is dependent on electron current, primary beam energy and electron energy loss. The plasmon losses are typically of the order of ~10 eV and can provide information on the dielectric function of the material under study. EELS is, thus, complementary to optical reflectivity techniques. Interband transitions can be compared with theoretical models of the electronic structure of the material. Estimates of the inelastic mean free path (IMFP) can be determined from the dielectric function.

18.12.5
Performance Criteria

The method is sensitive to energy losses of greater than ~1 eV. Hence, it cannot detect vibrational losses as in HREELS. The detection volume is limited to the top few atomic layers for metals.

REELS requires an UHV chamber with magnetic shielding; stray charges may build up in the spectrometer, which then requires frequent baking. REELS is difficult to quantify. It is best for small, nonmagnetic single crystals, and has poor sensitivity for rough surfaces. It is not very sensitive for insulating materials as surface charging makes their analysis difficult. REELS equipment is relatively low cost in comparison to HREELS.

18.12.6
Applications

EELS spectra can be used to estimate the dielectric function of the material under investigation, which can in turn be used to derive the IMFP and the energy loss of electrons as they travel through materials. Such information can assist in the quantitative understanding of AES and XPS spectra.

18.12.7
Other Techniques

Scanning low-energy electron loss microscopy (SLEELM) can provide a map of electron energy loss peaks across a surface.

Extended electron energy loss fine structure (EELFS, EXELFS) works with higher fixed energy of primary electrons (10–80 keV) and higher energy losses of the scattered primary electrons ranging from 200 to 4000 eV. EXELFS is a technique used in TEMs. It provides information similar to Extended X-ray absorption fine structure (EXAFS), that is, data regarding the immediate neighborhood of atoms of certain elements in the sample. EXELFS is bulk sensitive. Transmission electron energy loss spectroscopy (TEELS) is another technique that is used in a TEM. The electron energy loss is much higher than in EXELFS and characteristic energy losses can be observed. This provides information concerning the elemental composition of the sample. The spectra are detected using a multielement solid-state semiconductor detector, which results in a spectrum being acquired in parallel. Hence, it is known as *PEELS*.

18.13
Scanning Electron Microscopy

18.13.1
Introduction

A tightly focused beam of high-energy electrons (typically 10 keV) is rastered back and forth across the surface of the sample [2, 9]. The impact of the high-energy electrons ejects low-energy secondary electrons from the sample, which are collected by a detector to produce a real-time magnified image of the sample.

18.13.2
Instrumentation

This technique requires vacuum conditions. A tightly focused beam of high-energy electrons (2–100 keV or higher) is rastered across the surface of the sample. This generates a number of effects including emission of low-energy secondary and Auger electrons from the surface, generation of X-rays from within the sample and the backscattering of the primary electrons. The analysis of these different forms of emission reveals complementary information about the sample. The output from an electron or X-ray detector within the instrument is sent to a display that is synchronized to the raster frequency of the beam to produce a real-time magnified image of the sample. The magnification is changed by keeping the size of the image constant while increasing or decreasing the size of the area of the sample being scanned by the electron beam. Hence, electron microscopy does not require the use of multiple sets of focusing optics for different magnifications as would be the case in optical microscopy.

The emission of secondary electrons is very sensitive to surface topography and so the collection of these electrons allows a topographic image of the sample to be obtained that has a much greater depth of field and a much higher ultimate magnification that would be possible with conventional optical microscopy techniques. Secondary electron microscopy also has a high surface sensitivity of a few tens of angstroms.

When secondary electrons are emitted from a magnetic material they become polarized and so by using a polarization sensitive detector such as a Mott detector to collect the secondary electrons an image can be obtained that has magnetic contrast, allowing magnetic domain structures to be studied. This technique is known as scanning electron microscopy with polarization analysis (SEMPA).

Images with elemental contrast can be obtained by detecting the high-energy backscattered electrons whose intensity is a function of the atomic number of the elements in the sample; these electrons also have a greater penetration depth than secondary electrons and so can be used for studying buried structures.

Quantitative information about the elemental distribution and concentration can be obtained by analyzing the energies of the X-rays emitted, which are characteristic of the elements involved. This is known as *energy dispersive X-ray analysis* or electron probe microanalysis (EPMA). It is essentially a bulk technique that reveals composition down to a depth of several microns.

Quantitative information regarding the surface (~1 nm depth) elemental distribution and concentration can be obtained by analyzing the energies of the Auger electrons emitted, which are also characteristic of the elements involved. This is known as scanning Auger microscopy (SAM). The instrumentation involved in detecting the Auger electrons is the same as in AES and the reader should refer to that technique to learn more. UHV is required for SAM.

18.13.3
Sample

Vacuum compatible conducting solids–nonconductors such as biological samples are generally coated with a thin layer of gold to render than conductive. Biological or insulating sample may also degrade under electron bombardment.

18.13.4
Analytical Information

Secondary electron mode – real-time magnified topographic contrast images.

Backscattering mode – real-time magnified elemental contrast images.

EDS mode – quantitative analysis of elemental composition and distribution at particular points of interest in the secondary or backscattered images. In addition, magnified elemental contrast images.

SEMPA – magnified magnetic contrast images of domain structures.

SAM – quantitative analysis of surface (~1 nm depth) elemental composition and distribution at particular points of interest in the secondary or backscattered images. In addition, magnified elemental contrast images.

18.13.5
Performance Criteria

Magnifications ranging from ×3 to ×500 000 are possible depending on the instrument. Spatial resolution may be as good as 20 Å.

One of the major strengths of SEM is that the depth of field is very large (generally 10–60% of the width of the field), ranging from 1 μm at high magnifications up to several millimeters at low magnifications. This is much larger (by some ×300) than the depth of field obtainable in conventional optical microscopy at equivalent magnifications. Hence, SEM allows realistic looking images of highly three-dimensional samples, such as biological structures, to be obtained.

Depth sensitivity depends on the analysis mode and energy range used. SEM with low-energy secondary electrons can result in a surface sensitivity of 20 Å, while EDS reveals information about the top few microns of the sample. Depth sensitivity for backscattered electrons is greatly dependent upon the electron beam energy and the elemental composition of the sample, but is generally hundreds of nanometers.

Elemental sensitivity in EDS mode is 0.1% depending on the elements in question with an accuracy of 1–3% achievable. The elemental sensitivity for the SAM mode is ~1% with an accuracy of ~5% achievable.

EDS is not sensitive to elements lighter than carbon in the periodic table and has only limited sensitivity for elements lighter than sodium. SAM is not sensitive to H or He, but has better sensitivity to lower atomic number elements.

EDS is not able to produce the sort of information on chemical states than can be obtained in XPS as the obtainable resolution is only some 3 eV. SAM can produce some information regarding chemical state.

Quantitative EDS and SAM are most effective on flat-polished samples.

Count rates in EDS are generally much lower than in backscattering or secondary electron mode and so it is often used for quantitative analysis of particular points of interest within a backscattered or secondary electron image, although EDS images can also be acquired if necessary. The same is true of SAM.

Mott scattering is a very inefficient means of electron detection and so magnetic contrast SEMPA images will require much longer acquisition times.

Exposure to intense electron beams may cause damage to the sample.

18.13.6
Applications

SEM is one of the most widely used analytical techniques across all fields of science, technology, and industry. Applications include imaging of highly three-dimensional biological structures, imaging and microanalysis of semiconductor structures, magnetic domain imaging for data storage applications, and imaging of fracture surfaces in component failure analysis.

18.14
Scanning Tunneling Spectroscopy

18.14.1
Introduction

Scanning tunneling spectroscopy is a technique that is carried out using a STM [6, 26, 27]. The STM is one of a family of scanned probe techniques that can provide atomic level (or near atomic level) resolution. A sharp conducting tip is brought within a tenth of nanometers from a surface such that an electric current can flow by quantum tunneling between the tip and sample. By rastering the tip across the surface a map of the surface defined by the tunneling current can be acquired. In the case of STS, the voltage (V) at each point can be varied and the corresponding variation in the current (I) can be measured. The resulting $I-V$ curve is characteristic of the electronic structure at the particular tip position. Hence, images of the electronic structure can be acquired at atomic resolution.

18.14.2
Instrumentation

A STM is the principal piece of equipment. The microscope should be placed in an UHV chamber in order to ensure clean surfaces. A lock-in-amplifier can be used to acquire $\mathrm{d}I/\mathrm{d}V$ or $\mathrm{d}I/\mathrm{d}z$ (where z is the height of the tip above the surface) curves. However, simple numerical differentiation of the $I-V$ curve usually suffices. The experiments are often carried out at cryogenic temperatures.

18.14.3
Sample

Samples should have reasonably flat surfaces and preferably be metallic or semiconducting. However, it has been shown that very thin films of insulators can also be analyzed.

18.14.4
Analytical Information

The electrons tunnel from filled states to empty states. The filled states can be in the tip or sample. Hence, by varying the sample tip voltage both filled and empty states in the sample can be probed. In such a way, STS provides information similar to UPS and IPES. STS is a much more local probe, but cannot achieve the angular resolution of UPS or IPES. The value of $\mathrm{d}I/\mathrm{d}V$ is proportional to the surface local DOSs, but contains an exponential dependence of the transmission probability on the tip-sample bias. The data is often displayed in the form $(\mathrm{d}I/\mathrm{d}V)/(I/V)$ that is known as the *normalized conductance*, which removes the voltage dependence and provides an improved approximation to the local DOSs of the sample. A good understanding of the electronic structure of the tip is also necessary to understand the data.

18.14.5
Performance Criteria

The technique is sensitive to surface contamination. The nature of the tip can affect both the spatial resolution and the I/V curves of the acquired STS data.

18.14.6
Applications

STS spectra are used to acquire information regarding the electronic structure at atomic resolution. For example, in the study of chemical reactions on a Si (111) surface it is possible to image reacted and unreacted sites or establishing the whether dimers on a Si surface are symmetric or asymmetric. Superconductors have been studied in order to determine the local energy gap in both conventional and high-temperature superconductors.

18.14.7
Other Techniques

Current imaging tunneling spectroscopy (CITS) is a technique whereby an STS spectrum is acquired at each point in an image. Multivariate techniques such as principal component analysis (PCA) can then be applied. Electrons injected from an STM tip can give rise to photon emission from the sample-probe area from both semiconductors and metals. The STS technique can be carried out at a solid–liquid interface (e.g., in an electrochemical cell). This leads to the technique of electrochemical tunneling spectroscopy (ETS) or voltage tunneling spectroscopy (VTS). This technique is used to analyze electrochemical interfaces at the nanometric scale. It is influenced by the presence of oxygen in the electrolyte, speed of the measurement, and unisolated areas of the tip and sample that are exposed to the electrolyte.

Another related technique is ballistic electron emission spectroscopy (BEES) that is the spectroscopic version of ballistic electron emission microscopy (BEEM). With BEES and BEEM, a semiconductor is coated with a metal film and an STM tip is brought close to the surface. A voltage is applied to the tip relative to the sample. Current flows from the tip to the metal film. However, only the current from the substrate semiconductor is measured to create the BEEM image or BEES spectrum. Only when the electrons from the tip have sufficient energy to overcome the Schottky barrier can the current be measured. Hence, only ballistic electrons contribute to the current measurements. By varying the voltage on the tip, the Schottky barrier height can be determined.

The technique of atomic force spectroscopy (AFS) uses an AFM to measure the mechanics of individual molecules on a surface. The tip adheres to a molecule and then is pulled from the surface. The resultant ''spectrum'' is a force distance curve and therefore AFS is not a spectroscopy in the strictest sense. AFS has been used to study polymers, proteins, and DNA/RNA molecules.

The scanning near-field optical microscopy (SNOFM) method can also provide standard far field optical spectroscopy techniques, but at resolutions down to a few nanometers.

18.15
Scanning Tunneling Microscopy – Inelastic Electron Tunneling Spectroscopy

18.15.1
Introduction

STM–IETS is one of a family of spectroscopies based on the STM (STM) (e.g., see STS) [28, 29]. In the case of STM–IETS, the voltage (V) is modulated with an amplitude of $\sim$1 meV and the modulation in the tunneling current is detected. STM–IETS can provide information regarding the vibrational properties of molecules on a surface and at a very high spatial resolution. Indeed, the vibration modes of single molecules can be studied with this technique. Electrons tunneling from the tip can excite a vibrational mode within a molecule lying on the surface.

18.15.2
Instrumentation

A STM is the principal piece of equipment. The microscope should be placed in an UHV chamber in order to ensure clean surfaces. A lock-in-amplifier can be used to acquire d^2I/dV^2 curves. The experiments are often carried out at cryogenic temperatures.

18.15.3
Sample

Samples should have reasonably flat surfaces (at an atomic scale). Typically, the surface will be coated with the molecule(s) of interest.

18.15.4
Analytical Information

STM–IETS experiments provide information regarding the vibrational modes of single molecules on a surface. Resonant states are excited in STM–IETS that is important to take into account when interpreting the spectra.

18.15.5
Performance Criteria

The technique is sensitive to surface contamination. The nature of the tip can affect both the spatial resolution and the $\mathrm{d}^2I/\mathrm{d}V^2$ curves of the acquired STM–IETS data.

18.15.6
Applications

An STM can be used to cleave molecules in a process known as *electron-induced dissociation*. This can be used to modify surfaces and create structures on an atomic scale. This could lead to applications involving lithography.

18.15.7
Other Techniques

STM–IETS is based on a combination of the techniques of STM and IETS. Although the instrumental setup is similar to STS, it provides different information regarding vibrational modes of surface molecules rather than the densities of states. Hence, the technique is similar to HREELS, Raman spectroscopy, and IR spectroscopies in the nature of the data that it provides.

18.16
Secondary Electron Emission Spectroscopy

18.16.1
Introduction

Although the term *secondary electron spectroscopy* could include both AES and REELS, the SEES technique generally refers to a beam of low-energy electrons (typically 20–100 eV) striking a sample [9, 30]. The impact of the primary beam of electrons ejects low-energy secondary electrons from the sample, which are energy analyzed and then collected by a detector. A spectrum is produced by ramping the analysis energy in a similar manner that occurs for AES and REELS except that the main interest is in the structure of the spectrum of secondary electrons at very low energy (0–50 eV). The spectrum shows a low-energy peak between and often has very little structure. However, fine details on the secondary electron background have been observed and it is these that are generally of interest.

An alternative technique that is also referred to as *secondary electron spectroscopy* ramps the primary electron energy while acquiring the entire (<50 eV) secondary electron emission. The ratio of the secondary electron emission to primary electron current is known as the *secondary electron coefficient*.

18.16.2
Instrumentation

This technique requires vacuum (preferably UHV) conditions. A beam of electrons (20–100 eV) is directed at the surface of the sample. This generates emission of low-energy secondary electrons from the surface. The emitted secondary electrons are energy analyzed using an electron energy analyzer such as a cylindrical mirror analyzer (CMA), concentric hemispherical analyzer (CHA) or a RFA. The electrons that pass through the analyzer are amplified using a channeltron or MCP, which are then detected using a charge sensitive preamplifier. It is difficult to amplify very low-energy electrons using a channeltron or MCP, so they may need a small acceleration prior to striking these devices. In the case of the RFA, the current to ground measured from a hemispherical grid is measured to detect the SEES signal. The energy dependence of low-energy electrons can be determined using through the lens detectors on modern SEMs.

18.16.3
Sample

Vacuum compatible conducting solids.

18.16.4
Analytical Information

The emission can be influenced by the DOS (both the filled and empty) below and above the Fermi level as the emitting electrons have such a low energy. These states are in turn influenced by the band structure of the solid. Angle-resolved measurements are thus of interest as the band structure will create a directionality in the emission. Hence, the analysis of the secondary electron emission can reveal information regarding the DOS of filled and empty states and the band structure. However, the data is more difficult to interpret than UPS, ARUPS, or IPES.

Information regarding local surface potential and fine structure caused by plasmon decay is also possible to acquire. The energy dependence of secondary electrons can be influenced by the dopant concentration in semiconductors. This can lead to dopant contrast in SEMs.

Although the IMFP for low-energy electrons is larger than that for most Auger electrons, secondary electron emission spectroscopy still has a high surface sensitivity of a few nanometers. An estimate of the IMFP of the secondary electrons can be made by studying the secondary electron coefficient as a function of primary beam energy.

18.16.5
Performance Criteria

Exposure to intense electron beams may cause damage to the sample.

18.16.6
Applications

SEES is used to study the empty DOSs near the Fermi level, the band structure, local surface potential, and plasmon decay.

18.16.7
Other Techniques

Some SEES experiments provide information regarding the empty DOSs and in this sense gives data complementary to IPES, IETS, and STS.

References

1. Woodruff, D.P. and Delchar, T.A. (1994) *Modern Techniques of Surface Science*, Cambridge University Press, Cambridge.
2. Brune, D., Hellborg, R., Whitlow, H.J., and Hunderi, O. (1997) *Surface Analysis*, Wiley-VCH Verlag GmbH, Weinheim.
3. Prutton, M. (1984) *Surface Physics*, Oxford University, Oxford.
4. Walls, J.M. (1990) *Methods of Surface Analysis, Techniques and Applications*, Cambridge University Press, Cambridge.
5. Briggs, D. and Seah, M.P. (eds) (1990) *Practical Surface Analysis*, Auger and X-Ray Photoelectron Spectroscopy, Vol. 1, John Wiley & Sons, Ltd., Chichester.
6. Clark, R.J.H. and Hester, R.E. (1998) *Spectroscopy for Surface Science*, John Wiley & Sons, Ltd., Chichester.
7. Briggs, D. and Grant, J.T. (2003) *Surface Analysis by Auger and X-Ray Photoelectron Spectroscopy*, IM Publicationsa and Surface Spectra, Chichester.
8. Prutton, M. and El Gomati, M.M. (2006) *Scanning Auger Electron Microscopy*, John Wiley & Sons, Ltd., Chichester.
9. Reimer, L. (1998) *Scanning Electron Microscopy, Physics of Image Formation and Microscopy*, Springer, Berlin.
10. Weigold, E. and McCarthy, I.E. (1999) *Electron Momentum Spectroscopy*, Kluwer Academic Publishers/Plenum Publisher, New York.
11. Kellner, R., Mermet, J.-M., Otto, M., and Widmer, H.M. (1998) *Analytical Chemistry*, Wiley-VCH Verlag GmbH, Weinheim.
12. Goldstein, J.I., Newbury, D.E., Joy, D.C., Lyman, C.E., Echlin, P., Lifshin, E., Sawyer, L.C., and Michael, J.R. (2003)

Michael Scanning Electron Microscopy and X-Ray Microanalysis, Springer Science+Business Media Inc., New York.

13. Alfassi, Z.B. (ed.) (2001) *Non-destructive Elemental Analysis*, Blackwell Publishing, Oxford.
14. Scott, V.D., Love, G., and Reed, S.J.B. (1995) *Quantitative Electron-Probe Microanalysis*, Ellis Horwood, New York.
15. Zangwill, A. (1990) *Physics at Surfaces*, Cambridge University Press, Cambridge.
16. Hudson, J.B. (1998) *Surface Science: An Introduction*, Wiley-IEEE, New York.
17. Czanderna, A.W., Madey, T.E., and Powell, C.J. (1998) *Beam Effects, Surface Topography, and Depth Profiling in Surface Analysis*, Springer, New York.
18. Channing, C.A. (2004) in *Transmission Electron Energy Loss Spectrometry in Materials Science* (ed. C.C. Ahn), Wiley-VCH Verlag GmbH, Weinheim, pp. 97–126.
19. Kesmodel, L. (2007) in *Encyclopedia of Surface and Colloid Science* (eds P. Somasundaran and A. Hubbard), Taylor & Francis, New York, pp. 2765–2772.
20. Lewis, D.M., Spencer, J.E.D., and Fiels, B.O. (1988) *Spectrochim. Acta*, **44A**, 247–261.
21. Pascual, J.I. and Lorente, N. (2006) in *Scanning Probe Microscopies Beyond Imaging: Manipulation of Molecules* (ed. P. Samori), Wiley-VCH Verlag GmbH, Weinheim, pp. 77–97.
22. Maekawa, S. and Shinjo, T. (2002) *Spin Dependent Transport in Magnetic Nanostructures*, CRC Press, London.
23. Smith, N.V. (1988) *Rep. Prog. Phys.*, **51**, 1227–1294.
24. Hüfner, S. (2003) *Photoelectron Spectroscopy: Principles and Applications*, Springer, Berlin.
25. Wang, Z.L. (1996) *Reflection Electron Microscopy and Spectroscopy for Surface Analysis*, Cambridge University Press, Cambridge.
26. Wiesendanger, R. (ed.) (1998) *Scanning Probe Microscopy: Analytical Methods (Nanoscience and Technology)*, Springer, Berlin, Heidelberg.
27. Morgenstern, M. (2005) in *Scanning Probe Microscopy: Characterization, Nanofabrication and Device Application of Functional Materials* (eds M. Vilarinho, Z. Rosenwaks, and A. Kingon), Springer, Dordrecht, pp. 251–274.
28. Komeda, T. (2005) *Prog. Surf. Sci.*, **78**, 4185.
29. Samori, P. (2006) *Scanning Probe Microscopies beyond Imaging: Manipulation of Molecules*, Wiley-VCH Verlag GmbH, Weinheim.
30. Kazemian, P., Mentink, S.A.M., Rodenburg, C., and Humphreys, C.J. (2007) *Ultramicroscopy*, **107**, 140–150.

19
Ion/Neutral Probe Techniques

Anna Macková and Andrew Pratt

Excitation of surfaces with ions or neutrals gives rise to elastic or inelastic scattering processes or to nuclear reactions. As a result of this processes, a variety of secondary particles, such as electrons, photons, positive or negative ions, or neutrals may be emitted. Numerous combinations of the excitation and emitted particles are used for analytical purposes. From these combinations, some of the most popular spectroscopies are ion Auger electron spectroscopy (IAES) (which is based on electron detection), secondary ion mass spectrometry or secondary neutral mass spectrometry (SIMS or SNMS), Rutherford back-scattering spectroscopy (RBS), low-energy ion scattering (LEIS), elastic recoil detection analysis (ERDA), or nuclear reaction analysis (NRA) (which are all based on ion detection), and glow discharge optical emission spectrometry (GD-OES) or ion beam spectrochemical analysis (IBSA) (which are both based on photon detection) for photon detection.

Individual techniques are presented in alphanumerical order.

19.1
Atom Probe Field Ion Microscopy

19.1.1
Introduction

Atom probe field ion microscopy (APFIM) is a combination of field ion microscopy (FIM) and TOF mass spectrometry [1–3]. Hence, although strictly speaking this technique is not a spectroscopy, it is judged sufficiently close to warrant inclusion in this handbook. In FIM, an atomically sharp metallic tip is kept in an atmosphere of gas and a high electric field is then applied in the region of the sharp tip. Gas atoms on the tip are emitted from it and impinge on a phosphor screen. The very small area of gas emission from the tip can be viewed on the screen giving images of the tip at atomic resolution. With APFIM, a mass spectrometer is added to the instrumental setup. This provides the ability to identify which atoms are being emitted from the surface. A sudden pulse is applied to the tip and this can cause a layer of atoms to be removed from it. The atoms emitted enter a drift

Handbook of Spectroscopy, Second Edition. Edited by Günter Gauglitz and David S. Moore.

tube and the time of arrival of the atoms at the detector enables their mass to be determined. This enables atomic resolution images in three dimensions of the material comprising the tip.

19.1.2
Instrumentation

A ultrahigh vacuum (UHV) chamber containing the sample in the form of a sharp tip is required. A time-of-flight (TOF) mass spectrometer to identify the type of atoms emitted from the surface is also needed.

19.1.3
Analytical Information

APFIM provides information concerning the three-dimensional arrangement of elements within the sample at atomic resolution.

19.1.4
Performance Criteria

The sample should be in the form of a sharp tip and be electrically conducting. The form of the sample is less convenient than for the scanning probe methods, but APFIM does provide extra elemental information.

19.1.5
Applications

APFIM is used where the elemental composition of the material at the very highest spatial resolution is needed.

19.2
Charged Particle Activation Analysis

19.2.1
Introduction

Charged particle activation analysis (CPAA) is an analytical method for determining the elemental concentration of trace elements in the near-surface region. The activated region in CPAA is prescribed by both the penetration range (it is defined as the thickness of appropriate material that stops the charged particle) and the charged particle beam diameter. Activation analysis is a highly sensitive, nondestructive technique for the detection of trace amounts of elements in a variety of matrices. The sample to be analyzed is activated by irradiation with an ion beam of a suitable type and energy. Artificial radioisotopes are created by nuclear reactions with nuclides present in the sample. The half-life of the produced radionuclides and the type and energy of the emitted radiation are used to identify the elements present.

19.2.2
Instrumentation

For CPAA, protons and deuterons have to be accelerated to energies between a few megaelectronvolts and 20–30 MeV and twice as high for helium-3 or -4 particles. An isochronous cyclotron, designed as a variable energy accelerator, covers this energy range. The energy of the beam should be well defined (an accuracy of 0.1 MeV) and reproducible. An important consideration is the beam uniformity for even irradiation of the beam spot area. If the beam energy is higher than that required for sample activation, the energy can be reduced by energy loss in a filter foil of a carefully chosen thickness [1, 4–6].

19.2.3
Sample

CPAA has no special limitations on the type of samples that can be studied. The sample should have a size in the order of centimeters in the usual case of solid samples. The simplest measurement is possible for solid samples with good thermal conductivity, not powdered and available as a foil or sheet with the thickness slightly larger than the range of the charged particles in the material (it means that charged particles should be stopped in the sample). However, CPAA offers a number of possibilities for the determination of trace elements in biological materials also.

19.2.4
Analytical Information

Qualitative analysis is based on the identification of the created radioisotopes, mainly using high-resolution gamma-ray spectroscopy. In CPAA, a related method is mostly used, whereby a sample and a standard are irradiated and the activity from the analyzed element is measured in both the sample and the standard. The concentration in the sample can then in principle be calculated from the concentration in the standard and the ratio of the activities measured in the sample and the standard.

19.2.5
Performance Criteria

For optimum analytical sensitivity, it is desirable to produce the maximum amount of activity in the sample to determine and measure that activity with the maximum efficiency. The measurement of activities with short half-lives should be carried out as soon as possible after the irradiation. It follows from the basic equation of activation analysis that 50% of the maximum activity is obtained after irradiation time equal to one half-life and more then 90% after four half-lives.

Detection limit down to 1 ng g^{-1} can be reached for certain isotopes. The choice of ion type and energy provide versatility for optimizing sensitivity and selectivity to suit particular problems. Proton energies from 5 to 20 MeV are needed to obtain a sufficiently high cross section for good sensitivity in CPAA. CPAA has excellent sensitivity especially for light elements, such as B, C, N, and O. CPAA is unique among activation techniques for determination of H and He with detection limits below 1 μg g^{-1}. CPAA can also be performed after radiochemical separations of products to improve detection limits.

The main disadvantages of CPAA are its complexity and cost, its lower suitability for liquid samples, and heating of the sample during irradiation. Special precautions have to be taken for samples that are not massive and are poor thermal conductors. Samples may need to be mounted on a cooled background to prevent overheating during irradiation. Even then, the temperature of the sample surface may rise by many hundreds of degrees of Celsius with beam currents of the order of 10 μA. A conducting surface layer or foil may be needed when irradiating insulating materials to prevent overheating and consequent sample damage. Cross sections are generally lower than those for neutron activation analysis (NAA). Counting times of 10–120 h are necessary to achieve high sensitivity and this reduces the number of samples that can be analyzed. Ionization energy loss prevents the irradiation of large volumes and so the ion range limits the produced activity.

19.2.6
Application

Activation analysis is primarily a technique used for detection of impurities in bulk materials. CPAA offers a number of interesting possibilities for the determination of trace elements in biological materials. It allows the determination of those elements that are difficult or impossible to determine by neutron activation, such as Al, Si, V, Cr, Ni, Cd, Sn, Tl, and Pb.

It makes CPAA a powerful technique when a sufficiently powerful accelerator is available.

19.2.7
Other Technique

NAA is similar to CPAA, but uses thermal neutrons (typically from a nuclear reactor), to activate the sample rather than charged particles. In general, the detection limits of NAA are in the range of 10^{-8} to 10^{-14} g. There is no intrinsic depth sensitivity in NAA because of activation of the whole sample. Neutron losses in the sample are negligible.

19.2.8
Related Techniques

Neutron depth profiling (NDP).

19.3
Elastic Recoil Detection Analysis

19.3.1
Introduction

ERDA is one of the most useful ion beam analysis techniques for depth profiling of light elements. A beam of energetic ions is directed toward the sample. When the incident ion's mass is bigger than the mass of the target atoms in the sample, a forward scattering geometry can be used to detect the recoiling light atoms, which emerge after colliding with the heavier incident ions. Atoms recoiled from the surface appear at different energies for the different elements (Figure 19.1b; [7]).

19.3.2
Instrumentation

The basic experimental equipment is similar as in RBS, but the glancing geometry with very small incident angles is usually used (Figure 19.1a). ERDA relies on the ability to discriminate between forward scattered incident ions and recoiling light atoms [1, 4–7]. The typical experimental arrangement is Mylar foil placed in front of the detector to block out the scattered incident ions but allow the lighter recoiled atoms, which suffer considerably less energy loss, to pass through toward the detector. Note that 10 μm Mylar foil completely stops 2.6 MeV He^+ ions, but megaelectronvolt recoiled protons go through with low-energy loss. Thus, He^+ ions are used for hydrogen profiling. Heavy ion-ERDA (HIERDA) is able to analyze light and medium elements, so typically heavier probe ions are used, for example, Cl^{n+}, I^{n+} with energy tens of megaelectronvolts [8]. In the case where the system parameters are calibrated, ERDA is standardless, and the analysis is independent of the matrix material. ERDA with heavy projectiles needs an appropriate detection technique to distinguish between a large number of different particles that are recoiled simultaneously. The technique is based either on the simultaneous measurement of the energy and velocity of the detected particles (TOF measurement) to separate a mass of recoils or a gas-filled ionization chamber is used for mass separation. The velocity in TOF measurement is determined by measuring the time elapsed between the detection of a particle in two sequential detectors that are placed at a fixed distance from each other. The full TOF measurement also requires a two-dimensional multichannel analyzer, which is not

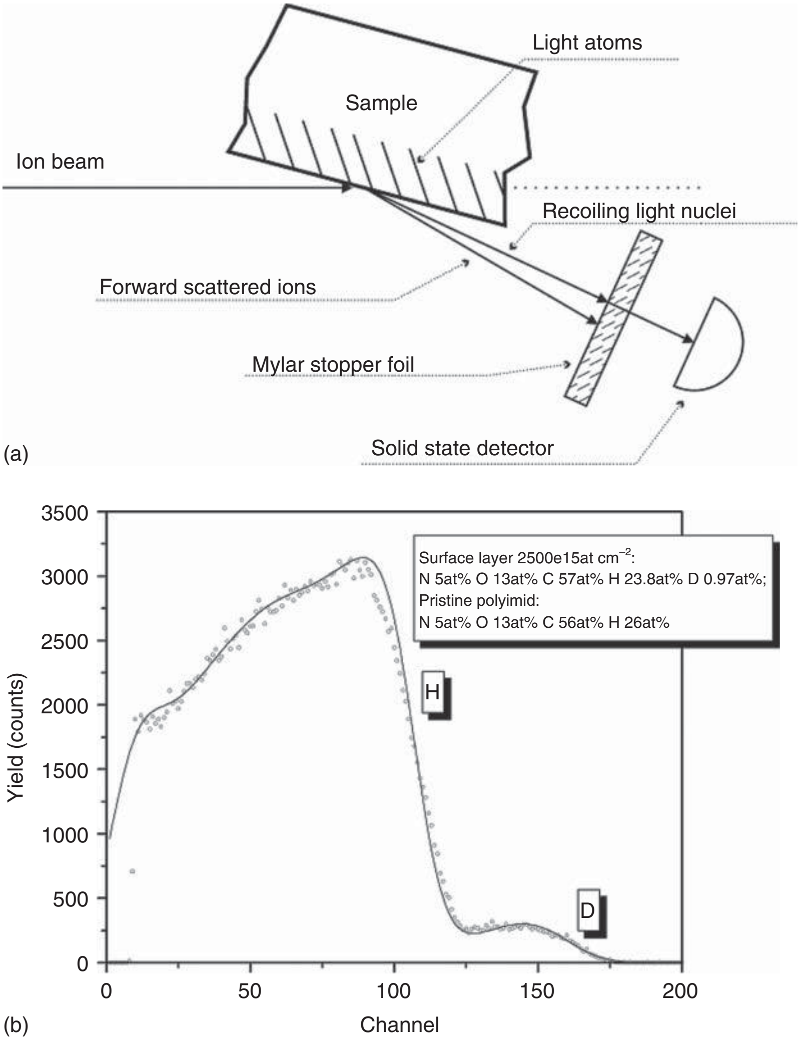

Figure 19.1 The forward recoil geometry (a) and the forward recoiled spectrum of ^{1}H and ^{2}H from 2.18 MeV ^{4}He^{+} ions incident on a thin deuterated polyimide film (b).

commonly found in every ion beam laboratory and enables us to measure the yield of recoiled particles depending on energy and TOF.

19.3.3
Sample

The sample could be multilayer system or bulk material. The lateral and interlayer homogeneity is important for a nondeformed spectrum for quantitative analysis to be obtained.

19.3.4
Analytical Information

The spectra of the forward recoiled sample atoms are detected (Figure 19.1b). In contrast to RBS, where light masses produce a signal at low energies with a low ion yield the detected energy and yield of the ERDA signals for the different masses depends strongly on the stopping power and thickness of the range foil. Each element in the spectrum has its own depth scale with a unique energy-to-depth transformation because of the difference in stopping powers for the different recoiled atoms. Using TOF spectrometer, the two-dimensional spectra are recorded, and the number of recoiled particles is separated according to energy (channels) and mass (time). Thus, the signal for each element can be worked out separately to get elemental depth profiles (Figure 19.2).

19.3.5
Performance Criteria

The sensitivity of ERDA depends on the experimental arrangement and the system-dependent background levels. Typically, 0.1 at% of ^{1}H is observable and from 0.1 to 1 at% of heavier atoms. Simple ERDAs are performed using charged particle detectors with a stopping foil and have a depth resolution of typically 20–60 nm. Accessible analytical depths depend on the projectile, its energy and sample composition: for example, 2.8 MeV He$^+$ ions have a range of around 2.75 μm in silicon. In a simple arrangement with megaelectronvolt He$^+$ ions, it is possible to profile only H to depth up to 1 μm in common materials (e.g., Si). With higher mass projectiles, heavier elements such as N, O, and F can also be analyzed by ERDA technique.

Absolute measurement of light atom contents by ERDA is best achieved by using standards. The stopping foil must be uniformly thick, free of pinholes, and its thickness must be greater than or equal to the projectile penetration range in the foil and less than the recoil range in the foil. The stopping foil method is not suitable for analyses of heavier elements using heavy projectiles than heavy ion elastic recoil detection analysis (HIERDA) or TOF-ERDA could be used.

19.3.6
Applications

As ERDA is complementary to RBS analysis, this method should be a part of every megaelectronvolt ion beam analysis system. When it is employed on small Van de Graaf accelerators, ERDA can be used for determining concentration depth profiles or areal densities of H and D [9].

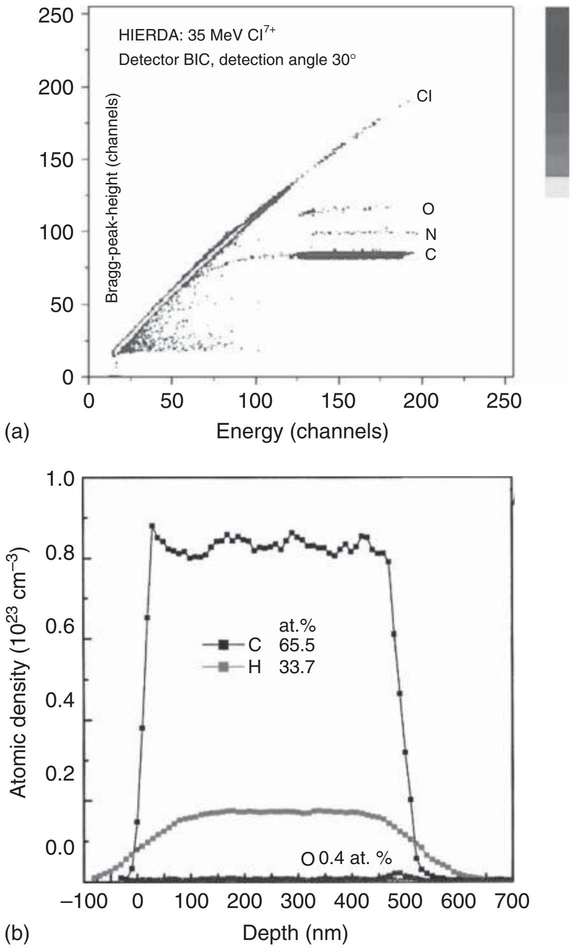

Figure 19.2 Spectrum of HIERDA measurement of layer prepared by magnetron sputtering containing O, C, N, and H elements using Cl^{7+} probing ions with energy 35 MeV (a) and the extracted elemental depth profiles are presented in (b). The worse depth resolution of hydrogen is caused by different detection technique. Although recoiled O, N, and C are detected by Bragg ionization chamber (BIC), hydrogen is detected simultaneously by semiconductor detector covered by Al foil.

19.3.7
Other Techniques

Another possible geometry for ERDA is the transmission mode. In this case, the sample must be thinner than the range of the recoiled atom to be profiled (its penetration depth in that material). The main advantage of transmission ERDA is an increased sensitivity (by up to two orders of magnitude) in comparison to conventional reflection geometry ERDA.

Elastic recoil coincidence spectrometry (ERCS) is a variation of transmission ERDA. Two detectors are used – one to detect the scattered incident particle and the other to detect the recoiled target atom. This technique is well suited to the study of polymers, which can be easily made as thin self-supporting films.

19.4
Glow Discharge Optical Emission Spectrometry

19.4.1
Introduction

This destructive method enables the rapid simultaneous determination of a variety of elements, including nonmetals and the in-depth profiling analysis of conductive samples. Atoms sputtered from the sample are excited in the glow discharge plasma by collisions with ions and electrons. The emitted characteristic radiation is in the visible and UV range.

19.4.2
Instrumentation

A GD-OES device consists of two main parts: a Grimm lamp and an optical spectrometer, which is usually a polychromator. First, the lamp is evacuated and then filled by the working gas (usually argon). The discharge is initiated by applying a voltage of typically 500–1000 V. Ar^+ ions are created as projectiles that bombard the surface of the sample. The sputtered sample atoms diffuse into the plasma. The sputter rate depends on the sample material and the discharge parameters. Some sample atoms are excited by collisions with electrons and the emitted light is analyzed with an optical spectrometer.

Heavy projectiles in the energy range of 30 eV to 100 keV are generally recommended for the excitation, but also high energy of 50 keV to 3 MeV Ar^+ ions have been applied. The usual sputter rates are in the range of 5–200 nm s^{-1}.

19.4.3
Sample

A flat solid sample is needed and the size should be of the order of centimeters.

19.4.4
Analytical Information

The intensities of emission lines of selected elements are recorded continuously by a computer during measurement. Using calibration curves obtained by means of calibration standards under identical discharge conditions, concentration depth profiles of the chosen elements in the analyzed sample are determined from the recorded intensity.

19.4.5
Performance Criteria

Owing to the well-known high sensitivity of optical emission spectrometry, detection limits reach from $\sim 10^{-5}$ g g^{-1} for metals such as C, S, P, and B to $\sim 10^{-3}$ g g^{-1} for elements such as H, O, and N, considering instantaneous analysis. For quantitative analysis using calibration standards, accuracy 0.2–1 at% has been reported for thin layer analysis. For the bulk analysis, we have to expect inferior accuracy in the range of 5–10% and also for the general case of instantaneous in-depth analysis.

The simplicity and speed of GD-OES have made it a powerful tool for rapid and accurate in-depth profiling, especially of iron and steel thin films, and selvage routine analysis. In routine analysis, a calibrated depth profile of 40–50 elements can be obtained in 1 min. Using an integration time of 0.1 s, this could result in a depth resolution of ~0.5 nm. The disadvantage of GD-OES is the need for calibration standards, which are not available for all elements and concentration ranges. The typical lateral resolution is ~2 mm.

The disadvantages of GD-OES could be the lateral resolution and the fact that calibration standards are not available for all elements and concentration ranges. GD-OES is a destructive method [10–12].

19.4.6
Application

The field of application for GD-OES is very broad and includes surface treatment studies of samples prepared by different techniques such as galvanization, nitriding, carbonitriding, carburization, diffusion, chemical and thermochemical treatments, thermal treatments, physical vapour deposition (CVD) and chemical vapour deposition (CVD), coating, electrodeposition, painting, and semiconductor multilayer growth.

19.4.7
Other Techniques

GDMS (glow discharge mass spectrometry) is a similar technique as GD-OES, but GDMS uses a mass spectrometer instead of an optical emission spectrometer.

The optical radiation, which is emitted from sputtered particles, is measured in a technique called SCANIIR (surface composition by analysis of neutral and ion impact radiation), IBSCA), or BLE (bombardment-induced light emission). Heavy particles in the energy range of 30 eV to 100 keV are recommended for the excitation in BLE. LAMMA (laser microprobe mass analysis), or LAMMS, or LMMS (Laser Microprobe Mass Analysis or Spectroscopy), is based on laser ablation. A high-frequency laser scans the area of the sample in a minimum step size, TOF mass spectra of each scan are evaluated with respect to several ion signals and transformed into two-dimensional distribution plots.

19.5
Ion Microprobe Analysis

19.5.1
Introduction

Ion probe microanalysis is a technique in which the sample is bombarded by a well-focused beam of primary ions (diameter ~1–10 μm, nanoprobes were constructed recently). The backscattered ions, emitted X- and γ-rays, or transmitted ions from the sample are detected using a detector according to a type of the produced signal, see RBS, particle-induced X-ray emission (PIXE), and particle-induced gamma-ray emission (PIGE). Lateral resolution, which is determined by ion beam diameter, gives opportunity to make an elemental mapping.

When a beam of charged particles passes through a thin specimen, the beam transmitted in the forward direction includes some particles that scattered elastically off atomic nuclei or lost energy as a result of interaction with electrons (inelastically scattered) as well as those particles that were left unscattered. An image formed with this forward transmitted beam is referred to as a *bright field image*.

19.5.2
Instrumentation

A fully equipped proton microprobe (PMP) chamber should include microscopes for transmission and reflective viewing of the specimen, a Si(Li) detector for detection of X-rays, surface barrier detectors for backward and forward scattering, and a detector for gamma-rays. It is important for microprobe work that the ion source produces a beam of the maximum possible brightness and that this brightness is maintained during transmission of the beam through the accelerator and associated beam optics. Charged particle beams are focused by means of magnetic or electrostatic lenses. The focal length of such lenses depends on the energy of the particles. The achievement of good spatial resolution requires a good ion optics design, high precision in fabrication, careful alignment, and careful elimination of sources of interference.

19.5.3
Sample

Ion probe microanalysis is suited to high-sensitivity multielement analysis of both thick and thin specimens. This method can be used for both surface analysis and element depth profiling. It is not possible to perform elemental analysis for an extended structure of irregular shape except by repeated measurements with a fixed beam at many selected points.

19.5.4
Analytical Information

In order to measure the distribution of elements along a line or map elemental distribution over an area, the focused beam spot must be scanned and the detector signal recorded as a function of the displacement of the beam from its normal position. When a beam of ions scans an area of a specimen, the emitted radiation carries information in 3 degrees of freedom – the two scanning dimensions and the energy.

Scanning ion microprobe (SIMP) and scanning proton microprobe are very useful techniques for *in situ* element or isotope distribution analysis. With protons or heavy ions, the mean free path between ionizing events is generally much shorter than the specimen thickness and hence multiple inelastic scattering occurs. The energy-loss spectrum is then a measure of specimen thickness rather then elemental content. If the specimen thickness exceeds the range of the slow heavy ions in an IMP (ion microprobe), then transmission signals are not available. However, in a PMP, where the typical energy is 3 MeV, the proton range may be some tens of micrometers and the mean free path between inelastic collisions will be <100 nm [13, 14].

19.5.5
Performance Criteria

With bright-field transmission imaging in which the unscattered transmitted beam is running directly into a detector, it may necessary restrict the beam current to $\sim 10^4$ particles s^{-1}. PMP gives 1 μm spatial resolution for microanalysis with 100 pA beams of protons or alpha particles. Each image is collected over 20 min.

Sample discoloration may occur and is usually because of ionization (whereas overheating causes physical deformation). It affects only sensitive specimens under intense bombardment. The sensitivity depends inversely on the beam diameter. Some effects must be taken into account, such as the charging of insulating components, and the sputter removal of some components, which prevents repeat investigations. Image contrast may also arise from chemical or topographic rather than isotopic differences.

19.5.6
Application

Metallurgy–metals provide an ideal specimen for microbeam analysis, their high thermal conductivity minimizes thermal damage and their high electrical conductivity removes any possibility of specimen charging giving rise to a beam deflection.

It is possible to extract a microbeam from the vacuum system to use external beam measurement for specimens that cannot be placed in the vacuum, but the beam will suffer considerable scattering from the air or gas as well as from any exit foil. Nevertheless, such an external microbeam can be very useful for low-resolution studies, for example, in archaeology or biological sciences. The technique has successfully been applied to the examination of nuclear membranes and the processes of etching of latent tracks in polymers.

19.5.7
Other Techniques

IPM can be used simultaneously with RBS, NRA, PIXE, or PIGE. More specialized examples include the FIM that gives better than atomic resolution in the study of high melting point materials.

19.6
Low-Energy Ion Scattering Spectrometry

19.6.1
Introduction

LEIS is a typical surface-specific method that detects particles scattered only from the uppermost surface layer of the solid. The scattering of low-energy ions of inert gases from the surface of a sample is measured. At low energies (<5 keV), the ions are neutralized, if they penetrate below the top two or three monolayers, so only a few monolayers of the solid participate in the ion scattering process. In this way, LEIS differs from RBS, in which the neutralization processes are negligible.

19.6.2
Instrumentation

LEIS uses a low-energy ion beam to interact with the sample surface. Ion source producing ions by electron impact ionization of noble gases (He, Ne, and Ar) or by heating of wafer containing alkali atoms is used (alkali ion scattering spectroscopy, AISS). The range of energies most often in LEIS is 500 eV to 20 keV. In LEIS, either electrostatic energy analyzers or drift tube in TOF setup are used to detect velocities and energy of scattered ions, electrostatic analyzers are suited to a low-energy analysis, they are simple to operate, and they provide good energy resolution. LEIS is a surface-sensitive technique and it should be performed under clean high vacuum conditions. In most research systems, 10^{-8} Pa in the target chamber is a minimum requirement. Any inert gas ions from the beam penetrating below the surface are neutralized [15–17].

19.6.3
Sample

The sample should be solid, with a size of around 1 cm. The requirements are the same as for RBS measurements and the sample must be cleaned because of atmospheric and other surface contaminants, to obtain a pure surface composition measurement.

19.6.4
Analytical Information

LEIS measurements result in an energy spectrum of the backscattered ions from the sample surface. The energy of scattered ions provides information on the mass of the surface atoms, which is directly related to their chemical identity. The cross section, solid angle, and transmission factors (the analyzer acts as an energy filter, with transmission characteristics that depend on the mode of operation) are used for these calculations. The most reliable method for quantitative analysis using LEIS involves a comparison with elemental standards to determine concentrations in alloys or chemical compounds. There is an inherent assumption that the scattered ion fraction does not change significantly between the elemental surface and the alloy surface [15–17].

19.6.5
Performance Criteria

In order to optimize the mass resolution of LEIS, it is advisable to use a projectile with a mass close to that of the target atom and to employ the largest possible scattering angle. Under these conditions, it is possible to detect low levels of contaminants on the surface. For high atomic mass impurities, the ultimate sensitivity is 5.10^{-4} monolayers using He^+ ions and 1.10^{-4} monolayers using Ar^+ ions, while the detection limit for O is between 10^{-2} and 10^{-1} monolayers. The ultimate accuracy of quantitative elemental composition analysis is 5–10% when applying a suitable calibration procedure.

The use of LEIS for the determination of ordered atomic positions at the surface atomic layer is based on its extreme surface selectivity. When other atoms, which result in, may shadow changing the scattering geometry by rotating the crystal, different atoms in the first atomic layer changed intensities of the respective LEIS signals. The limited mass resolution is the major problem in LEIS. This method is insensitive for the detection of low levels of C on surfaces. The detection sensitivity is also a function of the state of the surface. A highly contaminated (O or CO) or insulating surface produces an energy spectrum of scattered ions with a relatively high background. The charge-exchange phenomenon is simultaneously one of the greatest strengths of LEIS and one of its greatest weaknesses. The preferential neutralization of inert gas ions that penetrate below the surface atom layer is responsible for the extreme surface sensitivity of LEIS. The weakness is introduced by the uncertainty in ion yield that results from surface scattering.

19.6.6
Application

The main characteristic of LEIS is its high selectivity for the outermost layer of a solid owing to the large scattering cross section. For practical analysis, this results in the requirement of cleaning the solid surface in UHV before analysis to remove contamination and adsorbed layers. LEIS is frequently used for segregation, adsorption, and reaction studies on well-defined surfaces, which were carefully prepared within the UHV system rather than for the analysis of thin unknown layers. LEIS is a powerful tool in studies of chemistry, crystallography, and electronic structure in the monolayer range on a solid surface.

19.6.7
Other Techniques

In general, LEIS is based on the same principle as RBS, high-energy ion scattering (HEIS), and medium energy ion scattering (MEIS), but it uses a low-energy ion beam. HEIS and MEIS work with high- or medium-energy projectiles, respectively. The energy range of initial projectiles is chosen with respect to the measured sample characteristics (especially the elements present) and taking into account what information is needed about the sample.

Low-energy electron diffraction (LEED) is often used in combination with LEIS in order to have detailed structural information about a sample including surface superstructures and alignment of adsorbates.

19.7
Metastable Deexcitation Spectroscopy

19.7.1
Introduction

The sample is exposed to a beam of low-energy metastable rare gas atoms [18]. Interaction with the surface results in deexcitation of the atoms causing the emission of electrons. These are collected by an electron energy analyzer to reveal information regarding the surface electronic, chemical, and magnetic properties.

19.7.2
Instrumentation

This technique requires UHV conditions. A thermal energy ($\sim$0.1 eV) beam of metastable rare gas atoms is created (usually by electron collision in a DC discharge source) and directed onto the sample surface. Approximately 0.3–0.5 nm from the surface the atom deexcites through a mechanism that depends on the conducting properties of the sample. For conducting surfaces, the electron in the metastable state of the rare gas atom tunnels into a degenerate empty level of the solid, a process known as resonance ionization (RI). The rare gas ion formed is then neutralized by an electron from the surface with the excess energy causing the liberation of a second electron from the surface in a process known as Auger neutralization (AN). For semiconducting and insulating surfaces, or for low work function metals, an alternative deexcitation process called *Auger deexcitation* generally occurs (also referred to as *Penning ionization*). In this case, an electron from the surface fills the ground state of the atom causing the release of the electron in the excited metastable state through an Auger process. In both deexcitation mechanisms, the electron emitted as a result of the atom–surface interaction is detected with an electron energy analyzer such as a hemispherical energy analyzer to build up an ejected electron energy spectrum measuring the intensity of electrons as a function of kinetic energy.

Magnetic lenses or resonant laser light forces may be applied to intensify the metastable atom beam, which usually comprises helium atoms in the 2^3S metastable state because of its high internal energy (19.82 eV) and long lifetime ($\sim$8000 s).

To study magnetic samples, the metastable atom beam is electron spin polarized using optical pumping, and the technique is then referred to as spin-polarized MDS (SPMDS).

19.7.3
Sample

Any vacuum-compatible solids, whether metals, semiconductors, or insulators, and in some cases liquids. Magnetic samples may be studied with SPMDS.

19.7.4
Analytical Information

As the energies of the metastable states are in the range of 11–21 eV, MDS reveals complementary information to ultraviolet photoemission spectroscopy (UPS) regarding the surface valence band electronic density of states. However, as the cross section for deexcitation is so large, there is no penetration into the sample making MDS extremely surface sensitive, with no contribution from the bulk as may be the case for UPS (Figure 19.3). This allows a direct comparison between MDS spectra and the surface electronic density of states and may also enable the identification of the orientation of molecular adsorbates. Spin polarizing the metastable atom beam allows the study of spin-resolved adsorbate and electronic structure.

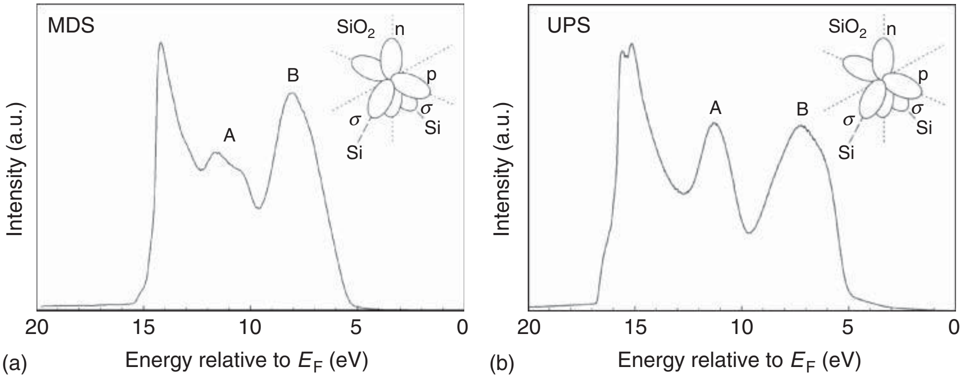

Figure 19.3 Comparison of (a) MDS and (b) UPS spectra from a Si(111)-SiO$_2$ surface demonstrating the surface sensitivity of MDS. Emission as a result of nonbonding orbitals normal (n) and parallel (p) to the surface (peak B) is enhanced in MDS when compared with emission from surface bonds (σ, peak A).

19.7.5
Performance Criteria

With modern energy analyzers, the energy resolution may be <1 meV with a spatial resolution in the micrometer range.

The excitation energy may be changed by using different metastable states of the rare gases.

The technique is extremely surface sensitive and may determine the composition and molecular orientation of the topmost atomic layer of a sample. However, this surface sensitivity makes MDS vulnerable to contamination, necessitating the use of UHV procedures. The low energy of the emitted electrons means the technique is also vulnerable to stray magnetic fields and so magnetic shielding is normally required.

Analysis of spectra is complicated by the presence of multiple deexcitation channels and the convolution of features although spectra may be deconvolved for interpretation.

19.7.6
Applications

The high surface sensitivity and nondestructive nature of the technique means MDS is suitable to the study of the surface properties of a wide range of materials, including semiconductors, magnetic thin films, and biomedical and organic surfaces.

19.7.7
Other Techniques

Ion neutralization spectroscopy is very similar to MDS, but makes use of ions (of energy no <5 eV) rather than metastable rare gas atoms.

19.8
Neutron Depth Profiling

19.8.1
Introduction

NDP is a prompt nuclear analysis technique, which employs a nuclear reaction that results in emission of charged particles with a specific kinetic energy. It is one of the most powerful nondestructive techniques for depth profiling of some light elements especially for ^{10}B and ^{6}Li, which have very high thermal neutron capture cross sections of 3837 and 940 barn, respectively.

19.8.2
Instrumentation

The samples are kept in a vacuum chamber and are irradiated with thermal neutrons produced by the nuclear reactor. Neutron flux $\sim 10^7\,\mathrm{cm}^{-2}\,\mathrm{s}^{-1}$ is used. NDP analysis leaves only trace amounts of residual radioactivity. Conventionally, a silicon charged particle detector or passivated implanted planar silicon (PIPS) detector is used for measurement of the residual energies of charged particles. In this configuration, the semiconductor detector is placed opposite to the surface of the sample being analyzed, and an energy spectrum of charged particles emitted by the neutron-induced reaction is acquired. TOF-NDP is a variation of the traditional NDP. It uses TOF techniques with superior resolution compared to conventional energy measurements conducted with semiconductor detectors.

19.8.3
Sample

Solid sample is required that can be placed into a vacuum chamber.

19.8.4
Analytical Information

If the thermal neutron capture takes place beneath the sample surface, the energy loss of charged particle stopping in the sample can be used to obtain information

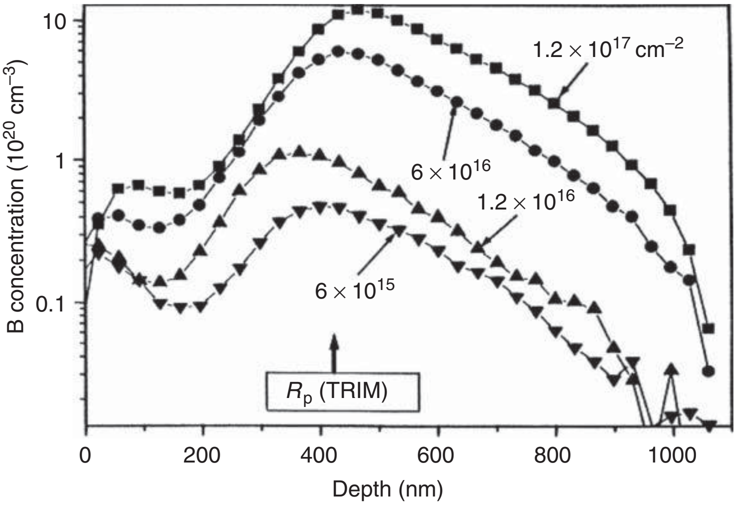

Figure 19.4 Concentration depth profiles of boron atoms implanted at 100 keV into polyimid to the fluences indicated. *R*p (TRIM) is typical range of 100 keV atoms simulated by TRIM code.

about the Li or B concentration profile (Figure 19.4). The amount of energy loss is related to the distance that the charged particle has traveled within the specimen isotopic sensitive, and exhibits the irreplaceable ability to probe the light NDP-active elements in materials up to tens of micrometers depth.

19.8.5
Performance Criteria

In each of the reactions ^{10}B (n,α) ^{7}Li and ^{6}Li (n,α) T, two charged particles are emitted. These particles carried out characteristic energy given by the reaction. The coincidence method, where both produced are detected can be used for very thin samples. It leads to improvement in the lithium or boron detection limit by several orders of magnitude. The element depth distribution can be reconstructed with a resolution of 10–20 nm. NDP is extensively used for the determination and depth profiling of the following elements (typical detection limit in 10^{15} at cm^{-2} is given in the parentheses): ^{3}He (10^{-3}), ^{6}Li (10^{-3}), ^{10}B (10^{-2}), ^{14}N (1), and ^{35}Cl (10). NDP technique is suitable for determination only of a few light elements [19, 20].

19.8.6
Application

The NDP method is an excellent tool for studying numerous problems in solid-state physics (diffusion and sputtering), materials science (corrosion), and life science and especially in microelectronics, where the tight control of boron distribution and transport is vital to semiconductor device fabrication.

19.9
Nuclear Reaction Analysis

19.9.1
Introduction

As a result of ion beam irradiation of a material, two distinct phases exist during which the emission of a particle (NRA) and gamma-rays (PIGE) or X rays (PIXE) takes place. Nuclear reactions are isotope specific (the nuclear reaction takes place on the specific isotope only) with no direct relationship between the mass of the target nucleus and the energy of the emitted particles. The detection of small amounts of isotopes is very easy, especially in the case of a sharp nuclear resonance cross section for the reaction, which is used in RNRA (resonant nuclear reaction analysis). NRA is induced by protons, deuterons, or alpha particles with an energy from 100 keV up to several megaelectronvolts. NRA in combination with RNRA has become very popular for depth profiling of light elements. RNRA uses the resonant cross section dependence on the initial ion beam energy, which can be many times higher than the nonresonant one. As RNRA is not only depth sensitive but also selects particular target isotopes, this technique opens the way to detailed isotope-sensitive studies.

19.9.2
Instrumentation

The equipment required for ion–ion analysis is typically a vacuum chamber, a solid-state detector, and an accelerator, which produces the ions (protons, He^+ ions, and deuterons) with energies 0.5–2 MeV. Energies above 3 MeV make the (d, p) reaction useful for the study of metals. The samples are irradiated by the ion beam and the products of the reaction can be monitored by measuring the emitted charged particles and/or subsequent gamma-radiation of the resulting nucleus. Magnetic analyzers should be used to separate reaction products from scattered ions and to achieve better energy resolution. In general, the probing ion beam hits the sample at normal incidence. If the ion energy used is equal to the resonant energy, the resonance reaction takes place on the nuclei located at the surface. If the beam energy is higher than the resonant energy, the resonance occurs at depth because of the energy losses of the initial ions. By measuring the yield for constant cumulated charge and varying the beam energy in small steps, the yield as a function of ion beam energy can be interpreted as the amount of the element at various depths, that is, it provides the concentration depth profile. Of course, the finite resonance width, the beam energy spread of the accelerator, and the energy straggling of the ion beam projectiles in the target have to be considered in the analysis. Incident ion energies from 0.5 to 2 MeV are most useful for minimizing interference from reactions on heavy isotopes [5, 21].

19.9.3
Sample

The sample should be a solid material; usually, the trace elements or impurities in the bulk material are investigated.

19.9.4
Analytical Information

The spectrum of charged products of the nuclear reaction is measured. The yield of nuclear reaction products is directly dependent on the cross section (which defines the probability of a specific type of interaction) and the density of target atoms in the sample.

High peak cross sections at resonances give high sensitivity of RNRA. Energy loss by the incident ion can be used to determine depth profiles by resonance scanning. Energy loss by both incident and product ions may be used for depth profiling of particular isotopes in the manner analogous to RBS. The advantage of RNRA is that there is no natural background from the high Z components of the target in comparison with methods using backscattering, where the ions backscattered from the heavy elements in the sample produce a background in the spectra and hence decreases the sensitivity for the light elements.

19.9.5
Performance Criteria

The nuclear reaction methods are suitable for the determination of several isotopes from ^{1}H to ^{32}S. The most frequently used reactions are (p,α), (d,p), and (d,α) providing useful alternative methods for the determination of isotopes, such as ^{2}D, ^{12}C, and ^{16}O compared with RBS or ERDA. Alpha-induced reactions have a limited use. Some ^{6}Li-induced reactions have been tested and the (^{11}B,α) reaction has been used for hydrogen determination and profiling. Cross sections of 10–100 mb sr^{-1} are observed for proton- and deuteron-induced reactions with light isotopes, such as D, Li, Be, and B. Detection limits of the order of 10 μg g^{-1} or even less are then possible with measuring times of the order of tens of minutes. Isotopes up to ^{32}S can be determined in heavier matrices at milligrams per gram levels depending on the maximum beam current that the sample can withstand.

The use of glancing incidence or emergence for heavy incident ions or produced ions, respectively, can give typical depth resolutions at the surface of 10–100 nm. The maximum analysis depth is usually limited to 1 μm. The composition of the target usually cannot be estimated from one measurement.

19.9.6
Application

This method is very useful especially for the determination of light elements (isotopes) in the sample due to the specific nuclear reactions. RNRA is complementary method to RBS, PIXE, and PIGE; therefore, final analysis gives more complex information about the sample.

19.9.7
Other Technique

NDP and CPAA. See following part.

19.10
Particle-Induced Gamma Emission

19.10.1
Introduction

PIGE or particle-induced gamma-ray emission (PIGME) is a versatile nondestructive depth profiling technique, which is complementary to other ion beam technique (especially PIXE). It is the most common application of nuclear analysis.

19.10.2
Instrumentation

The high-energy proton beam from an accelerator is used to irradiate the sample. PIGE is mostly based on the (p,γ), $(p,p'\gamma)$, and $(p,\alpha\ \gamma)$ nuclear reaction induced by megaelectronvolt protons where nuclear gamma rays are produced. In most cases, high purity germanium (HPGe) detector or scintillation detectors with multichannel acquisition systems are used for detection of gamma rays. A typical detector solid angle is 0.1–0.5 sr, the sample to detector distance is typically a few centimeters. The lower the incident ion energy, the fewer resonances are involved in ion–gamma reactions and nonuniform angular distributions are more likely to be observed. The choice of geometry affects the depth of ion penetration and hence the thickness of the layer that can be analyzed. For metals and other good thermal conductors, it is possible to use a beam current of the order of 1 μA without special cooling arrangements. The energy scale, including nonlinearity, can be calibrated using radioactive sources [19, 22, 23].

19.10.3
Sample

The same requirement as PIXE, but the gamma ray absorption in the sample is negligible.

19.10.4
Analytical Information

The PIGE method is typically less sensitive than the related methods utilizing X-ray detection (PIXE). The gamma-ray peaks are generally well isolated and the energy is high enough that no correction for absorption is necessary. The energy and intensity of the γ-ray lines produced indicate the elements that are present and their amounts, respectively. Sophisticated peak search and fitting routines are widely used for computer analysis of complex γ-ray spectra. The effect of multiple scattering causes the continuum to be higher at the low-energy side of a peak than on the high-energy one. The background elimination in the analysis should be taken into account.

19.10.5
Performance Criteria

For protons with energies from 1 to 3 MeV, the best sensitivities are found for Li, B, F, Na, and Al. These elements can be determined simultaneously in many cases. For example, a precision of better than 1% can be obtained for F and Na determination with a measuring time of a few minutes. At proton energies above 3 MeV, the gamma-ray emission from medium and heavy elements begins to compete with the light elements. The highest cross sections are for light isotopes (A-mass number <30), which can be determined with good sensitivity ($1\,\mu g\,g^{-1}$ or less). Many reactions have resonances, which are suitable for depth profiling with a resolution of 1–10 nm. In PIGE analysis, the γ-ray yield from many heavy elements is sufficiently high that these can be determined provided that light elements are not present in high concentrations.

19.10.6
Application

The most notable application of PIGE has been in the depth profiling of hydrogen using beam of ^{7}Li and ^{11}B. Analysis of heavier isotopes can be carried out with heavy ions by exploiting Coulomb excitation. The main improvement in the use of PIGE in the last decade has been introduction of external beams. The external beams offer several advantages, such as the ability to measure organic sample (even volatile ones) or large specimen (e.g., paintings) that cannot be placed within the normal analysis chamber.

19.11
Particle-Induced X-Ray Emission

19.11.1
Introduction

PIXE is a method using X-ray emission for elemental analysis. A high energetic proton beam excites emission of characteristic X-rays from the sample atoms because of inner-shell ionization. PIXE is not a true nuclear technique, as the ionization of the atoms by the ion beam and the subsequent emission of characteristic X-rays are purely atomic electromagnetic (rather than nuclear) processes. Methods and data for using K and L lines of X-rays, produced by ion beams (mostly proton beams) are well established and thick or thin samples can be analyzed with an absolute precision of 10% or better PIXE's main advantages are its good sensitivity, multielement capability, and speed of analysis.

19.11.2
Instrumentation

Ions, in particular protons from a particle accelerator, in the energy range 1–4 MeV, are used for excitation with beam spots 1 μm to 10 mm in diameter. Alpha-particles from radioactive sources (^{241}Am) can also be used for excitation of X-ray emission. The X-ray photons emitted from the sample are detected by means of wavelength dispersive (WD) Bragg spectrometer or an energy-dispersive (ED) semiconductor detector (Si(Li) or Ge(Li) detectors). Methods and data on K and L X-ray production by ion beam (mostly proton beam) are well established and thick or thin samples can be analyzed with precision of 10% or better.

19.11.3
Sample

PIXE is able to investigate solid samples with sizes of the order of a centimeter and thickness on the scale of micrometers. However, PIXE can also be used for unusual samples such as liquids and gasses. Owing to low absorption of X-rays in the sample it is better to investigate thin samples, the composition of which can be determined with better accuracy.

19.11.4
Spectrum

The typical PIXE spectrum of the sample from environmental research is shown in Figure 19.5.

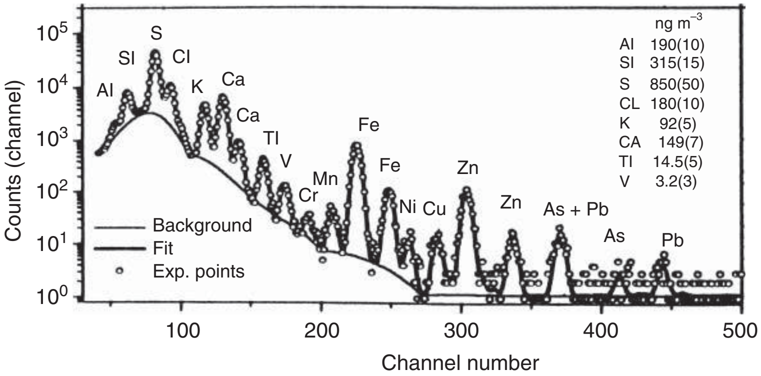

Figure 19.5 PIXE spectrum and composition of fine aerosol fraction collected on nucleopore filter at a suburban station.

19.11.5
Analytical Information

The energy dependence of the emitted X-rays is a monotonously increasing function of atomic number (Moseley law). Hence, the position of the peaks in the spectrum is characteristic of individual elements. Intensities of the characteristic X-ray lines can be converted into concentration data. X-ray yield depends on the number of atoms in the sample, the ionization cross section, the detector angle, intensity of the ion beam, and so on, and so the determination of an absolute concentration of an element in an unknown matrix represents a complicated problem. In practice, the evaluation of the sample composition involves the comparison of X-ray yields from the unknown sample with that from known standards. It is necessary in PIXE to take into account some correction factors for thickness evaluation as a result of X-ray absorption in the sample [21, 24–28].

19.11.6
Performance Criteria

PIXE should achieve sensitivities for all elements in the range of 0.1–1 $\mu g\,g^{-1}$, but this depends on the target and measurement arrangement. PIXE has a very low detection limit of 10^{-8} to 10^{-10} g in standard practice. This method is not used for elemental depth profiling, because of its low depth resolution. The depth accessibility for approximately megaelectronvolt protons is a few tens of micrometers. In PIXE, strong matrix effects are encountered. The major advantage of PIXE's use of ions is a reduction in the background in comparison to that obtained when electrons are used (electron microprobe-induced X-ray emission, EDX). The optimal depth range for useful results appears to be between 0.1 and 10 μm. PIXE enables the determination of composition for all elements with Z, atomic number, higher than 5. An examination of PIXE spectra shows that the characteristic X-ray peaks are superimposed on a background, which forms a limiting factor in sensitivity. It is possible to obtain limited depth profile information using ion-induced X-ray emission. The depth resolution is angle- and ion-energy dependent and is not as good as for other techniques.

19.11.7
Application

PIXE is the preferred method for such applications as the analysis of 15–20 elements in a thin sample, such as air filters (detection limit $1\,\mu g\,g^{-1}$) or for automated analysis of large numbers of geological or archaeological samples, as a result of its short measurement time. The low absolute detection limit and good sensitivity for elements, such as S, P, Cl, K, and Ca, Fe make PIXE of great importance in biological and medical applications.

Particle-induced X-rays can be generated with a microbeam (of order 1–10 μm) to perform high sensitivity-lateral mapping of trace elements distributions. Such a beam can also be brought into air for analysis of biological and vacuum-degradable samples.

19.11.8
Other Techniques

X-ray-induced fluorescence (XRF) is the main alternative to PIXE. However, electrons or gamma photons can stimulate X-ray fluorescence too. If large samples that cannot be placed in the usual vacuum chamber are involved (such as archeological samples or artifacts that might have dimensions of meters), then XRF may be the preferred, but for small samples or microprobe application PIXE is more advantageous.

TRXRFA (total reflection X-ray fluorescence analysis) offers very good element resolution and is especially useful for profiling medium Z (proton number) atoms in a low Z substrate. From experiment, it was concluded that this technique is best at glancing geometry (small incidence and exit angles with respect to the surface plane).

19.12
Positron Annihilation Auger Electron Spectroscopy

19.12.1
Introduction

A beam of low-energy positrons is directed onto the sample [29–32]. The positrons thermalize within a few 100 nm and move back to the surface and remain in a surface state until the positron is annihilated. Some of the positrons annihilate core electrons of the surface atoms, leaving them in an excited state, which decays by Auger emission of an electron. The energies of the Auger electrons are characteristic of the atoms involved and so measurement of the electron energies reveals information about the elemental composition of the sample surface.

Typical emitted electron energy range is 50–2000 eV.

19.12.2
Instrumentation

This technique requires UHV conditions. A low-energy positron source is required. Traditionally, ^{22}Na source beams are used, but the low-beam intensities result in spectra requiring days to acquire. More intense positron sources are becoming available, but these are expensive. Positron energies of ∼10–15 eV are used.

This technique is identical to Auger electron spectroscopy (AES) with the exception that positron annihilation is used to excite the core hole rather than a beam of high-energy electrons. The use of a positron beam has a number of distinct advantages. An electron beam that is energetic enough to excite core holes for AES will also produce a huge background signal of backscattered and secondary electrons, which is many times larger than the Auger signal of interest and must be removed during data analysis. This background is completely absent in positron annihilation Auger electron spectroscopy (PAES) resulting in true peak shapes that are free of distortions caused by background subtraction.

The electron beam used in AES delivers a large energy dose and a high electric charge density to the surface of the sample that can cause extensive damage to some materials. The energy dose in PAES is some five orders of magnitude lower than in AES and has charge densities 1000 times lower, eliminating any damage or charging.

Positron annihilation occurs almost exclusively in the topmost atomic layer, making the technique much more surface sensitive than AES.

19.12.3
Sample

UHV compatible materials. PAES may be used on insulators or delicate samples, such as weakly physisorbed molecules that cannot be studied easily with conventional AES.

19.12.4
Analytical Information

Elemental composition of the topmost atomic layer with peak shapes that are free of data manipulation artifacts.

19.12.5
Performance Criteria

This technique is extremely surface sensitive. Virtually, all positron annihilation occurs in the very topmost atomic layer.

Contents of 1% of the surface layer can be detected, depending on the intensity of Auger emission for the element concerned. Typically, Auger electron emission is high for low atomic number elements and gradually drops as the atomic number increases.

PAES is sensitive to all elements except hydrogen and helium.

Its extreme surface sensitivity makes this technique vulnerable to the presence of contamination.

Access to low-energy positron beams is extremely limited and so PEAS is only available at a few facilities.

Peak overlaps can make some element identification difficult.

19.12.6
Applications

PAES can be used to study weakly adsorbed molecules and insulators that cannot be studied easily by AES.

PAES is also used where the composition of the very topmost layer is important, such as in catalysis.

PAES is, particularly, useful in studies where determining the true shape and relative magnitude of the Auger peak free from background subtraction errors is important, such as for the compilation of Auger reference standards, instrument calibration, and verification of theoretical models of Auger emission.

19.12.7
Other Techniques

Auger photoelectron coincidence spectroscopy (APECS) is another technique that is used to produce background-free Auger spectra.

19.13
Rutherford Backscattering Spectrometry

19.13.1
Introduction

RBS is the most commonly used nondestructive nuclear method for elemental depth analysis of nanometer to micrometer thin films. It involves measurement of the number and energy distribution of energetic ions (usually protons or He^+) elastically backscattered within the near-surface region of solid targets. From such measurements, it is possible to determine, with some limitations, both the atomic mass and concentration of elemental target constituents as a function of depth below the surface.

19.13.2
Instrumentation

An ion beam with an energy of the order of several megaelectronvolts is provided by an accelerator and impinges on a sample located in a vacuum chamber (vacuum of the order 10^{-3} to 10^{-5} Pa). Samples are mounted, several per load, on the table of a goniometer, which allows 3 degrees of freedom, two for the sample position and one for the angle, so as to enable sample changing and manipulation without breaking vacuum. PIPS detector or surface barrier detectors are primarily used for ion detection.

19.13.3
Sample

The sample could be multilayer system or bulk material. The lateral and interlayer homogeneity is important for a nondeformed spectrum for quantitative analysis to be obtained. In case RBS is applied on study of nanoparticles, composites, or colloids, additional microscopic information is needed to interpret data obtained from RBS.

19.13.4
Analytical Information

Two main phenomena provided the analytical information: (i) the energy transfer and (ii) the kinematics in elastic collisions between atomic nuclei and ions. The Rutherford scattering cross section is a function of atomic number, target mass, and scattering angle and depends on the initial projectile energy. From the number of detected scattered particles, the content of a particular element in the target can be determined. Finally, the incident particle loses energy in penetrating the solid both along the incident path before scattering and the exit path. The measured energy loss can be transformed into a depth measurement using known stopping cross section (ion stopping in material). Thus, energy differences in the energy spectra can be used to identify scattering depths and hence provide a depth profile of target constituents [21, 33–37]. An example of an RBS spectrum is shown in Figure 19.6.

19.13.5
Spectrum

The RBS spectrum is yield of ions versus channels. The channel scale can be transformed into energy scale by means of energy losses determined by sample composition.

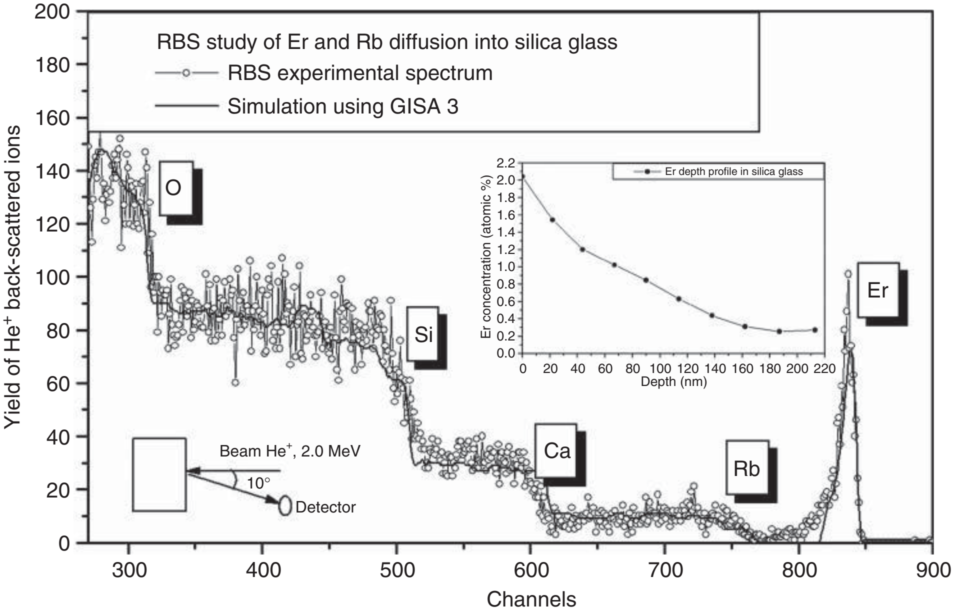

Figure 19.6 Measured and simulated RBS spectra of shallow Er depth profile in silica glass for optical applications measured by RBS, extracted depth profile in the inset.

19.13.6
Performance Criteria

The sensitivity of RBS for the detection of trace impurities in bulk samples depends strongly on the sample composition and the experimental conditions. For impurities heavier than the substrate, the signal of which lies in the background-free region, it is possible to measure infinitesimal amounts of impurities simply by increasing the integrated charge.

It would be possible to measure heavy impurity concentration ~0.01 at%. The lowest detectable amount by RBS is usually indicated $\sim 10^{14}$ atoms cm^{-2}. For near surface, the depth resolution can be improved by selecting glancing angle incident or exit geometry to the value lower than 10 nm, this improvement results from the increased path length through the surface region. The example of measurement of very shallow depth profile of indiffused Er into the glass substrate is shown in Figure 19.6.

Impurities that are lighter than the substrate are usually detected with poor sensitivity and several atomic percent are needed for their detection. The major strengths of RBS are absolute composition measurement of layered structures or trace impurity concentration through a precise knowledge of the cross section. RBS is not usually employed for the analysis of samples of totally unknown composition or for the depth profiling of sample containing a multitude of unknown elements. A problem arises if the material contains several elements with overlapping signals in the RBS spectra, or if the sample is inhomogeneous, resulting in deformed spectra.

19.13.7
Applications

Principal applications include bulk composition analysis and major element profiling, minor element identification, and study of multilayered systems including depth profiling. Thin film analysis is used for studies of solid-state reactions, interdiffusion, stoichiometry, film thickness, uniformity, and impurity content. Investigated systems are prepared by various techniques, for example, by conventional and reactive evaporation, RF and DC magnetron sputtering, laser ablation, ion-beam-assisted deposition, sol–gel techniques, ion implantation, or plasma surface treatment. The investigated materials are used for optics, microelectronics, hard and protective coatings, diffusion studies, magneto-optic recording media, and so on.

19.13.8
Other Techniques

Non-Rutherford backscattering spectrometry (non-RBS or n-RBS) measurement improves the detection sensitivity of light impurities, the light elements have a resonant cross section for light highly energetic projectiles (e.g., protons), which could be many times higher than for RBS. The measurement at resonant energy is sensitive to the light elements, for example, C (proton energy 1742 keV), N, and O.

RBS has also been combined with nuclear microscopy, in which a focused ion beam is scanned across a surface in a manner similar to a scanning electron microscope. The energetic analysis of backscattered signals in this kind of application provides compositional information about the surface; although the microprobe itself can be used to examine features such as periodic surface structures. Rutherford backscattering spectrometry-channeling (RBS-C) is a method for the investigation of adventitious atoms in the interstitial space of monocrystals (see next chapter).

19.14
RBS-Channeling Spectrometry

19.14.1
Introduction

RBS-C spectrometry is a method for investigation of adventitious atoms in the interstitial space of single crystals. Channeling is the steering of a beam of energetic ions into open spaces (channels) between close-packed rows or planes of atoms in a crystal.

19.14.2
Instrumentation

A channeling experiment requires the following basic components: a source of collimated high-energy ions from an accelerator, a detector of scattered particles (the same as for RBS), and an accurate crystal manipulator (called a *goniometer*). A goniometer is a crucial part of the channeling equipment. With this equipment, the crystal axes can be aligned with the collimated beam of particles.

19.14.3
Sample

A single crystal of a good quality is needed. Typically, bulk or thick single-crystalline layers are investigated using RBS/C analysis, which enables the channeling effective. Epitaxially grown layers could also be studied. Single-crystal quality is necessary to find the alignment of the crystal with the probing ion beam.

19.14.4
Analytical Information

The energy transfers or kinematics in elastic collisions between atomic nuclei and ion are used to get information about the composition and structure of the investigated sample. The number of scattered particles measured by a detector can be converted to the concentration of a particular element in the target. The incident particle energy losses are much lower in the channeling regime compared to random incidence. The energy spectrum of particles scattered back from an aligned crystal is dramatically different from that of nonaligned, randomly placed crystal (Figure 19.7). In the aligned spectrum, the scattering yield from the bulk of the solid is reduced of about two orders of magnitude and the surface peak occurs. The presence of defects can significantly enhance the dechanneling yield comparing to a perfect crystal. Distortions and dislocations in the crystal lattice also enhance dechanneling. The backscattering yield from nonsubstitutional atoms does not exhibit the same decrease as that of the host crystal and can be used either for evaluation of the impurity position in a host crystal lattice or for the study of the displacement of host atoms from their lattice sites [38–40].

19.14.5
Performance Criteria

The sensitivity of RBS/C for detecting trace impurities in bulk samples depends very much on the sample composition and the experimental conditions. For impurities heavier than the substrate, it would be possible to measure low amounts of impurities simply by increasing the integrated charge similar to RBS (see earlier). The major strength of RBS/C is an ability to determine the position of impurity atoms in a host crystal lattice. RBS/C is usually employed for the analysis

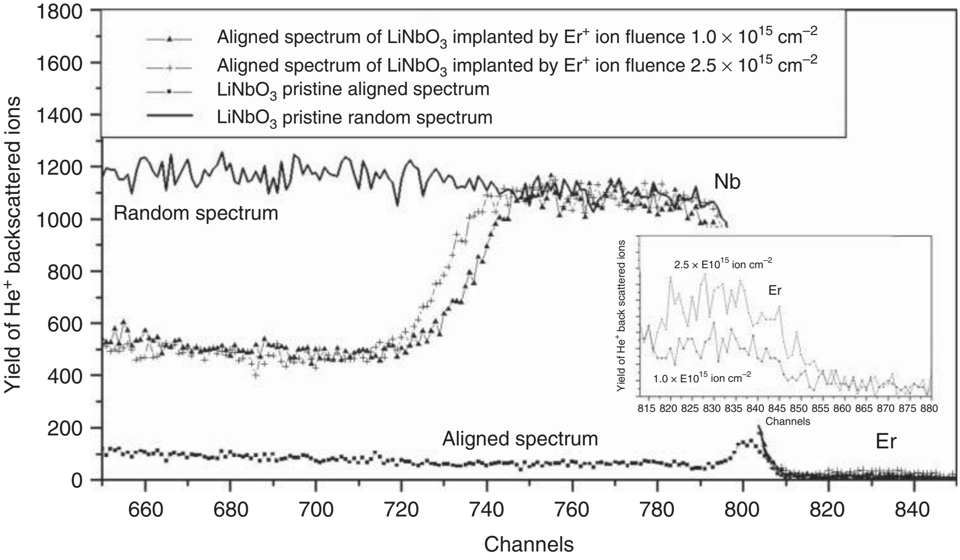

Figure 19.7 RBS/C spectra of $LiNbO_3$ along <11−20> axis of the modified layer in the host lattice caused by implantation of Er^+ ions, 330 keV. Yield of backscattered He^+ ions from the surface-modified layer in aligned spectra is comparable to the yield in random spectra. Thus, the fluences of Er^+ ions 1.10^{15} and 2.5×10^{15} ions cm^{-2} were so high that the implanted layer of crystal lattice was amorphized. Enlarged Er signal in the inset.

of samples of known composition with the focus on impurity atoms or number of defects. The study of impurity sites in the host lattice implies that the impurity is heavier than the host lattice atoms.

19.14.6
Application

The application of channeling to thin crystalline films, ion-implanted crystals, crystalline interfaces, and epitaxial structures is possible. Channeling is used to study many surface properties, such as surface reconstruction and relaxation of the outermost atom layer. Study of optical and semiconductor single crystals are provided using RBS/C to get information about the crystal quality, amount, and position of dopant atoms in a host lattice. Study of ion-implanted single crystals (semiconductor crystals, optical crystals, doped single crystal, etc.) are provided using RBS/C analysis BS/C spectra of lithium niobate implanted by Er^+ ions for photonics application are shown in Figure 19.7. When the signal is channeled to remove the bulk signal, manipulation of the incident and detection angles can be used to determine the relative positions of the first few layers of atoms using blocking effects. Surface reconstruction or relaxation can be detected if a higher-than-usual intensity or a wider surface peak appears to indicate that the first layers of atoms are failing to block the layers beneath.

19.14.7
Other Techniques

RBS/C analysis is combined very often with X-ray diffraction measurement or microscopy study (transmission electron microscopy – TEM). This complex multi-analytical study can give the full information about the studied structural changes in the crystal lattice.

19.15
Secondary Ion Mass Spectrometry

19.15.1
Introduction

In SIMS, a beam of ions (with an energy a few kiloelectronvolts) is used to sputter the surface of a solid sample. The resulting secondary positively or negatively charged ions are analyzed in a mass spectrometer. There are two modes of SIMS application differing primarily in the ion current and energy used. In the static mode, an extremely low primary ion current density of $1\,\mathrm{nA\,cm^{-2}}$ with a low primary ion energy of 0.5–2 keV is used resulting in a negligible sputtering rate of $0.1\,\mathrm{nmol\,h^{-1}}$. Dynamic mode uses a higher ion current density and the sputtering rate is typically $1\,\mu\mathrm{mol\,h^{-1}}$. Hence, in the static mode, the outermost surface layer may exist for hours before being completely removed in contrast to the dynamic mode where the surface layers are stepwise removed and depth profile analysis is possible.

19.15.2
Instrumentation

The primary ions, generated by plasma discharge ($O_2{}^+$, O^-, and Ar^+), by thermionic surface emission (Cs^+ and Li^+) or by liquid metal field emission (Ga^+ and In^+), are accelerated (2–50 kV) and focused onto the sample. The secondary ions are transferred by ion optics into a mass spectrometer.

Three types of instrumentation exist for dynamic SIMS: nonimaging ion probes, direct-imaging ion microanalyzers, and scanning ion microprobes–microscopes. Nonimaging ion probes are often an accessory of AES, electron spectroscopy for chemical application (ESCA), or electron microscopy systems and allow a point analysis. Imaging equipment allows a point-to-point analysis of the surface with a primary beam of the size 10–300 μm (microanalyzers) or below 10 μm (microprobes–microscopes). SIMS requires clean UHV conditions to avoid contamination and reaction with residual gas components and normally has a relatively large analyzed area.

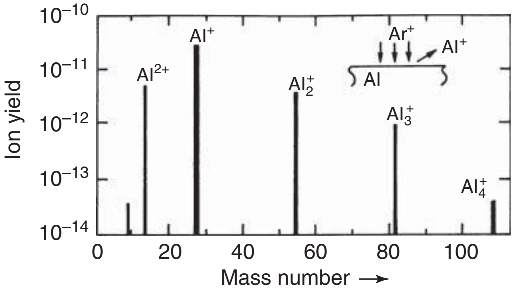

Figure 19.8 Secondary ion cluster spectrum from Ar bombardment of Al (note that the ordinate is a log scale).

19.15.3
Sample

The secondary ion yield is sensitive to surface roughness and contamination, which may change the relation between ion yield and element concentration.

19.15.4
Analytical Information

Analytical information is extracted from the mass spectrum, that is, from the dependence of intensity (total counts) on the mass-to-charge ratio. The spectra of both positive and negative secondary ions are complex exhibiting not only singly and multiply charged atomic ions but also all ionized clusters of target atoms (Figure 19.8). All elements including hydrogen can be detected. In static mode, the conditions are optimized to detect large molecular ions free from the ions formed in some recombination processes. Elemental micromapping combined with depth profiling provides a three-dimensional analysis of the elemental structure.

Quantitative analysis is not easy because of extremely large variations in secondary ion yield (as a result of the matrix effects – the target matrix affects the secondary ion yields markedly), up to five orders of magnitude, and the lack of simple quantitative algorithms. The best accuracy for quantitative SIMS analysis can be achieved by calibration using suitable standards [41–43].

19.15.5
Performance Criteria

High mass resolution is necessary for avoiding peak interference in SIMS. However, relative intensity is strongly reduced with the increasing mass resolution because of narrower entrance slits in the mass spectrometer. Lateral resolution of 0.3 μm or less is possible, but the sensitivity is reduced in proportion to the resolution. The excellent mass resolution, very low detection limits, and a wide dynamic range are available for many elements. SIMS is a method with a very low detection limit, typical $10^{-7}\,\mathrm{g\,g^{-1}}$ range. The main limitation in trace analysis arises from interference in the SIMS spectra as a result of detected clusters, hydrocarbons, oxides, and hydrides. SIMS is an excellent and powerful analytical destructive technique, but it is based on processes that are not yet sufficiently understood.

19.15.6
Application

SIMS applications cover a wide range of fields from pure research to industrial material control.

19.15.7
Other Techniques

SNMS makes use of the sputtered neutral particles by using post-sputter ionization. This is accomplished by laser (laser beam SNMS or SALI-surface analysis by laser ionization) or electron beams (e-beam SNMS), collisions of electrons generated by RF discharge (electron gas SNMS), excitation in various forms of plasma or discharge cell, or surface ionization. A major difference from a conventional SIMS lies in the insertion of an ionizing plasma chamber in front of the mass spectrometer. The grids placed before the plasma environment for postionization act as an electrical diaphragm between the sample and the chamber, which prevents ions entering or leaving the chamber. Thus, only neutral species enter the ionizing chamber, and species ionized within the chamber cannot reach the sample. Ionization of neutral species within the chamber is achieved by low-pressure high-frequency plasma.

Further Information

Information on some other techniques or acronyms, software for surface science studies, surface science databases, research centers and institutes, user groups and bulletin boards, academic research groups, teaching resources for surface science, conferences, commercials services and suppliers, sources of practical information, and also, a collection of links to lecture courses and tutorials covering a broad range of surface science can be found on Web sites, for example: *http://www.uksaf.org/tech/list.html* and *http://www.chem.qmw.ac.uk/surfaces/*.

References

This list of references represents only a selection of the literature having relevance to the given text and it is not complete by any means.

1. Brune, D., Hellborg, R., Whitlow, H.J., and Hunderi, O. (1997) *Surface Analysis*, Wiley-VCH Verlag GmbH, Weinheim.
2. Woodruff, D.P. and Delchar, T.A. (1994) *Modern Techniques of Surface Science*, Cambridge University Press, Cambridge.

3. Miller, M.K., Cerezo, A., Hetherington, M.G., and Smith, G.D.W. (1996) *Atom Probe Field Ion Microscopy*, Oxford University Press, Oxford.
4. Fink, D., Biersack, J.P., Stumpff, C., and Schlosser, S. (1986) *Nucl. Instrum. Methods Phys. Res. B*, **15**, 740–743.
5. Alfassi, Z.B. (ed.) (1994) *Chemical Analysis by Nuclear Methods*, John Wiley & Sons, Ltd., Chichester.
6. Yagi, M. and Masumuto, K. (1987) *J. Radioanal. Nucl. Chem.*, **109**, 237.
7. Tirira, J., Serruys, Y., and Trocellier, P. (1996) *Forward Recoil Spectrometry*, Plenum Press, New York.
8. Grigull, S., Kreissig, U., Huber, H., and Assmann, W. (1997) *Nucl. Instrum. Methods. Phys. Res. B*, **132**, 709–717.
9. Alfassi, Z.B. and Peisach, M. (1991) *Elemental Analysis by Particle Accelerators*, CRC Press, Boca Raton, FL.
10. Nelis, T. and Payling, R. (2004) *Glow Discharge Optical Emission Spectroscopy: A Practical Guide*, Royal Society of Chemistry, Cambridge.
11. Ohashi, Y., Yamamoto, Y., Tsuivoyama, K., and Kishidaka, H. (1979) *Surf. Interface Anal.*, **1**, 53–57.
12. Payling, R. (1994) *Mater. Forum*, **18**, 195.
13. Munnik, F., Sjöland, K.A., and Wätjen, U. (2000) *Nucl. Instrum. Methods Phys. Res. B*, **161–163**, 348–353.
14. Murr, L.E. (1991) *Electron and Ion Microscopy and Microanalysis: Principles and Applications*, Marcel Dekker, New York.
15. Werner, H.W. and Garten, R.P.H. (1984) *Rep. Prog. Phys.*, **47**, 221–344.
16. Rabalais, J.W. (2002) *Principles and Applications of Ion Scattering Spectrometry*, John Wiley & Sons, Inc., New York.
17. Englert, W., Taglauer, E., and Heiland, W. (1982) *Surf. Sci.*, **117**, 124–133.
18. Harada, Y., Masuda, S., and Ozaki, H. (1997) *Chem. Rev.*, **97**, 1897–1952.
19. Alfassi, Z.B. (ed.) (1990) *Activation Analysis*, CRC Press, Boca Raton, FL.
20. Downing, R.G., Lamaze, G.P., Langland, J.K., and Hwang, S.T. (1993) Neutron depth profiling: overview and description of NIST facilities. *NIST J. Res.*, **98**, 109.
21. Tesmer, J.R. and Nastasi, M. (1995) *Handbook of Modern Ion Beam Materials Analysis*, Material Research Society, Pitsburg, PA.
22. Bird, J.R. (1990) *Nucl. Instrum. Methods Phys. Res. B*, **45**, 516.
23. Borderie, B., Barrrandon, J.N., Delaunay, B., and Basutsu, M. (1979) *Nucl. Instrum. Methods Phys. Res. B*, **163**, 441.
24. Johansson, S.A.E., Campbell, J.L., and Malmqvist, K.G. (eds) (1995) *Particle Induced X-Ray Emission Spectrometry*, John Wiley & Sons, Inc., New York.
25. Bird, J.R. and Williams, J.S. (eds) (1989) *Ion Beams for Materials Analysis*, Academic Press, Sydney.
26. Bosch, F., ElGoresy, A., Herth, W., Martin, B., Nobiling, R., Povh, B., Reiss, H.D., and Traxel, K. (1980) *Nucl. Sci. Appl.*, **1**, 1.
27. Volfinger, M. and Robert, J.L. (1994) *J. Radioanal. Nucl. Chem.*, **185**, 273–291.
28. Kucera, J., Havranek, V., Smolik, J., Schwarz, J., Vesely, V., Kugler, J., Sykorova, I., and Santroch, J. (1999) *Biol. Trace Elem. Res.*, **71–2**, 233–245.
29. Lei, C., Mehl, D., Koymen, A.R., Gotwald, F., Jibaly, M., and Weiss, A. (1989) *Rev. Sci. Instrum.*, **60**, 3656–3660.
30. Jensen, K.O. and Weiss, A. (1990) *Phys. Rev. B*, **41**, 3928–3936.
31. Yang, S., Zhou, H.Q., Jung, E., Weiss, A.H., and Citrin, P.H. (1997) *Rev. Sci. Instrum.*, **68**, 3893–3897.
32. Dupasquier, A., Mills, A.P., and Mills, A.P. Jr., (1995) *Positron Spectroscopy of Solids*, IOS Press, Amsterdam.
33. Mackova, A., Havranek, V., Vacik, J., Salavcova, L., and Spirkova, J. (2006) *Nucl. Instrum. Methods Phys. Res. B*, **249**, 856–858.
34. Naramoto, H., Yamamoto, S., and Narumi, K. (2000) *Nucl. Instrum. Methods Phys. Res. B*, **161–163**, 534–538.
35. Svorcik, V., Kolarova, K., Slepicka, P., Mackova, A., Novotna, M., and Hnatowicz, V. (2006) *Polym. Degrad. Stab.*, **91**, 1219–1225.
36. Hobbs, C.P., McMillan, J.W., and Palmer, D.W. (1988) *Nucl. Instrum. Methods Phys. Res. B*, **30**, 342–348.
37. Spencer, N.D. and Moore, J.H. (1995) *Encyclopedia of Chemical Physics and Physical Chemistry*, Institute of Physics Publisher, Bristol.
38. Feldman, L.C., Mayer, J.W., and Picraux, S.T. (1982) *Materials Analysis by Ion Channeling*, Academic Press, New York.

39. Mackova, A., Groetzschel, R., Eichhorn, F., Nekvindova, P., and Spirkova, J. (2004) *Surf. Interface Anal.*, **36**, 949–951.

40. Nowicki, L., Ratajczak, R., Stonert, A., Turos, A., Baranowski, J.M., Banasik, R., and Pakula, K. (2000) *Nucl. Instrum. Methods Phys. Res. B*, **161–163**, 539–543.

41. Wilson, R.G., Stevie, F.A., and Magee, C.W. (1989) *Secondary Ion Mass Spectrometry*, John Wiley & Sons, Inc., New York.

42. Herbert, C.G. and Johnstone, R.A.W. (2003) *Mass Spectrometry Basics*, CRP Press, New York.

43. Kellner, R., Mermet, J.-M., Otto, M., and Widmer, H.M. (1998) *Analytical Chemistry*, Wiley-VCH Verlag GmbH, Weinheim.

20

Photon Probe Techniques

Simon Morton

The interaction of probing photons with surfaces is closely linked to various processes, including absorption, emission or scattering, changes in polarization, nonlinear effects, and so on. From the wide variety of techniques that are based on the detection of photons, the following will be discussed in detail: infrared reflection–absorption spectroscopy (IRRAS), ellipsometry (ELL), surface-enhanced Raman scattering (SERS) spectroscopy, sum frequency generation vibrational spectroscopy (SFG), laser-induced breakdown spectroscopy (LIBS), and total reflection X-ray fluorescence spectroscopy (TXRF). The discussion of techniques that are based on detection of released electrons will include X-ray photoelectron spectroscopy (XPS), electron spectroscopy for chemical analysis (ESCA), or ultraviolet photoelectron spectroscopy (UPS).

Individual techniques are presented in alphanumerical order.

20.1

Angle-Resolved Ultraviolet Photoelectron Spectroscopy

20.1.1

Introduction

Samples are exposed to monochromatic ultraviolet radiation (typically 10–100 eV) and the energies and emission angles of the ejected photoelectrons are measured to reveal information on the valence-band electronic structure [1–3].

20.1.2

Instrumentation

The measurement is carried out in an ultrahigh vacuum (UHV) chamber. Ultraviolet photons from a source such as a He lamp (21.2 or 40.8 eV) or synchrotron radiation (SR) illuminate the sample in order that photoelectrons are emitted from the surface. The emitted electrons are collected by an electron energy analyzer, such as a hemispherical mirror analyzer that has a narrow angular acceptance, to

Handbook of Spectroscopy, Second Edition. Edited by Günter Gauglitz and David S. Moore.

produce a spectrum of the number of electrons emitted with a given kinetic energy and at a given angle. Varying the emission angle by moving the sample or the analyzer enables spectra to be acquired across a range of emission angles. Such data sets allow the momentum vectors of the emitted electrons to be determined to produce ‘‘bandmaps’’ of the electronic structure of the valence bands. By using a synchrotron source instead of a He lamp, the momentum of the emitted electrons can be varied by changing the photon energy, enabling different regions of the band structure to be explored for a given range of emission angles.

20.1.3
Sample

Samples must be single-crystal metallic or semiconducting UHV compatible materials.

20.1.4
Analytical Information

‘‘Bandmaps’’ of the electronic structure of the top few atomic layers. Evidence of energy gaps such as in superconductors.

20.1.5
Performance Criteria

Spatial, angular, and energy resolutions are strongly dependent on the electron energy analyzer and photon source used. However, spatial resolution may be as good as 10 μm, energy resolution as good as 5 meV (or 1 meV using SR), and angular resolution as good as 10 mrad.

Typically, concentrations of a few atomic percentages at the surface can be detected, depending strongly on the cross section of the particular elements present. Sensitivity decreases rapidly with depth below the surface and is often negligible below a depth of approximately five atomic layers.

High surface sensitivity makes the technique vulnerable to contamination, necessitating the use of UHV procedures. The low energy of the emitted electrons makes the technique vulnerable to the presence of stray magnetic fields and hence magnetic shielding may be required.

The spectrum is influenced by the particular crystal structure of the sample’s top few atomic layers, which may not be completely representative of the bulk material. The technique is only applicable to single-crystal materials and is generally not suitable for insulating materials.

20.1.6
Applications

Angle-resolved ultraviolet photoemission spectroscopy (ARUPS) is used to probe the three-dimensional band structure of the electronic states near the Fermi level that are responsible for determining a material's electronic properties as well as to study the nature of the bonding between the atoms in the sample or between the sample and adsorbate molecules on its surface.

20.1.7
Other Techniques

UPS is similar to ARUPS, but spectra are collected at a fixed angle to determine the sample's overall valence band density of states (DOS). UPS is not restricted to single-crystal samples. Spin-polarized ultraviolet photoelectron spectroscopy (SPUPS) allows the DOS to be determined independently for the spin-up and spin-down electrons of a magnetic material by using a polarization sensitive detector.

20.2
Attenuated Total Reflection Spectroscopy

20.2.1
Introduction

The attenuation of a beam of radiation passing through an optical element from a high-refractive index material, under the condition of total internal reflection, is measured [4–6]. The sample must be in good optical contact with the surface of the optical element at which total internal reflection occurs.

Ranges of operation are from ultraviolet to infrared, but mid-infrared typical.

20.2.2
Instrumentation

Attenuated total reflection (ATR) spectroscopy is realized on standard spectrometers using an attachment introduced into the sampling area. Different geometric arrangements are used to direct the radiation through the optical element and onto the detector. The primary difference is in the shape of the optical element. Single (usually denoted as ATR) or multiple reflections (typically 8–20 for multiple internal reflection (MIR) or frustrated multiple internal reflection (FMIR)) can be achieved. Typical materials (crystalline and amorphous) for the optical element are As_2Se_3, AgCl, CdTe, diamond, Ge, KRS-5 (thallous bromide iodide), quartz, Si, ZnSe, and glass. The choice of material depends on the frequency range of operation.

20.2.3
Analytical Information

The ATR spectrum (i.e., the dependence of the reflectance on the wave number) for a sample resembles the transmission spectrum, but two features exclude a direct comparison:

- The depth of penetration is directly proportional to the wavelength; this means that the absorption bands at shorter wave number are intensified in the ATR spectra.
- The maximum shifts and intensity distortions can occur as a result of optical dispersion. These differences are more pronounced for smaller band separations and stronger bands.

A Kramers–Kronig analysis allows us to separate the absorption index and refractive index spectra. Different algorithms for this analysis are available.

20.2.4
Performance Criteria

The penetration depth is a complex function of the absorption and refractive indexes of the sample and ATR element.

The angular dependence of the penetration depth allows depth profiling, but because of superposition of the contributions from different depths an analysis can be difficult.

20.2.5
Applications

This method is not suitable for powders (particularly if they are hard). Study of the surfaces of compact samples is very sensitive to the quality of the optical contact reached between the sample and the ATR attachment. Good contact can be easily obtained when analyzing surfaces of elastomeric materials. The optical contact is usually poor for rough and rigid samples.

By using the MIR or FMIR techniques, a longer effective path length can be obtained through multiple reflections.

On the other hand, the ATR technique is very useful in cases when the ATR attachment can be used as an integral part of the surface experiment. If covered by an optically transparent thin-layer electrode (e.g., Pt), electrode phenomena can be studied. Langmuir–Blodgett monolayers can be transferred onto the attachment or *in situ* experiments can be carried out with the ATR attachment in optical contact with the hydrophobic part of the Langmuir–Blodgett layer.

20.3
Auger Photoelectron Coincidence Spectroscopy

20.3.1
Introduction

In coincidence spectroscopy, two or three particles originating from a single event are detected simultaneously [7–10]. In Auger photoelectron coincidence spectroscopy (APECS), an X-ray beam is directed at a sample to excite photoelectrons from core levels, leaving behind excited core-hole states. These decay virtually immediately by Auger emission of an electron. Simultaneous detection of the photoelectron/Auger electron pair allows all other electrons not directly involved in that event to be eliminated. This produces spectra that are completely free of background signal from scattered secondary electrons and eliminates overlapping peaks from closely related decay events.

20.3.2
Instrumentation

An electron energy analyzer such as a cylindrical mirror analyzer (CMA) is used to detect photoelectrons emitted at a kinetic energy precisely corresponding to the core level of interest. A second CMA is used to sweep continuously through the energy range of the corresponding Auger peak. Only those Auger electrons whose detection coincides exactly with the simultaneous detection of a photoelectron by the first CMA are counted. This eliminates all electrons not directly involved in the particular photoemission process of interest, including secondary electrons or Auger electrons that have been generated by photoemission from other core levels with very similar energies. This produces Auger spectra that are free of backgrounds and other, superimposed, peaks, allowing the true Auger peak shape to be determined. The process can also be reversed, scanning the first (photoelectron) CMA while keeping the second CMA at a fixed (Auger) energy to produce true, background-free photoelectron peaks instead.

20.3.3
Sample

UHV-compatible conductors that are stable over an extended period of UHV and X-ray exposure.

20.3.4
Analytical Information

True peak shapes for Auger electron spectroscopy (AES) or XPS that are free from the backgrounds, overlapping peaks, and satellite features that are present in conventional AES or XPS are obtained.

20.3.5
Performance Criteria

The requirement that only events where both emitted electrons are detected significantly reduces the count rate compared to standard XPS or AES as the probability of both electrons entering the correct analyzers is very low. Count rates are between 1 count min^{-1} and 1 count s^{-1}.

Energy resolution of 0.5–1 eV is significantly worse than in conventional AES or XPS as emphasis must be placed on maximizing the achievable count rate at the expense of overall resolution. Spatial resolution is around 0.5 mm. Typical energy range is 50–2000 eV. APECS is sensitive to all elements except H and He.

The requirement that both electrons must be ejected from the sample without undergoing scattering, combined with the geometrical effects resulting from the angle between the two detectors, means that APECS is significantly more surface sensitive than either XPS or AES alone, by about a factor of 2. Hence, sensitivity is negligible, below about five atomic layers.

UHV is required for this technique. High surface sensitivity combined with long acquisition time means that it is limited to samples that will remain stable and clean in vacuum for many hours under the X-ray beam.

20.3.6
Applications

APECS is used in studies where determining the true shape of the XPS or Auger peaks free of background subtraction errors or overlapping features is important, such as for compiling standard reference spectra, instrument calibration, and verification of theoretical models of photoelectron and Auger emission.

20.3.7
Other Techniques

Positron annihilation Auger electron spectroscopy (PAES) is another technique for producing true AES peak shapes that are free of the secondary electron background. PAES is identical to conventional AES except that the sample excitation is attained using a low-energy beam of positrons rather than a higher energy beam of electrons.

20.4
Diffuse Reflection Spectroscopy

20.4.1
Introduction

The diffusely scattered radiation from a sample is collected, refocused, and detected [5, 11]. Typical range of operation is from ultraviolet to infrared.

20.4.2
Instrumentation

Special reflectometers or emission photometers are constructed for measurement of diffuse reflectance, but, by using a suitable attachment, the measurement can be realized, in principle, using any spectrometer. The main requirement is an integrating sphere (Ulbricht sphere) or mirrors covering a large solid angle (particularly in the infrared region). Separation of the specular and diffuse reflection components is critical for the quality of diffuse reflection spectra that rely on spatial filtering (irradiation normal to the surface or out-of-plane configuration) or mechanical beam stops (blocker).

20.4.3
Analytical Information

It is not usually possible to measure the absolute reflectance of a sample and so, instead, the relative reflectance is measured as the ratio of the reflectance of the sample to the reflectance of a reference nonabsorbing material. Powdered samples are usually diluted with a nonabsorbing particulate matrix such as KBr. This helps meet the prerequisites of the Kubelka–Munk model. KBr is then also used as a reference medium.

If the scattering coefficient is independent of wavelength, the information obtained is similar to that obtained from transmission measurements. Under this condition, a linear dependence between the Kubelka–Munk function and the concentration should be found. For low absorption, the sensitivity of diffuse reflectance is greater than that of transmittance, while strong absorption bands are less pronounced in the diffuse reflection. The scattering coefficient increases with diminishing particle size, while the depth of penetration of the radiation diminishes. The mean layer thickness penetrated within the sample becomes smaller and hence the absorbed fraction is reduced. This fact is particularly useful for investigating adsorbed species on finely dispersed samples. Restrahlen bands can sometimes complicate the spectrum and their elimination is very difficult. The origin of these bands lies in the total reflection that occurs when the refractive index of air is higher than the refractive index of the sample.

20.4.4
Performance Criteria

The quality of the spectra depends critically on the sample material (its crystal form, refractive index, and absorbance), particle shape and size, packing density, and texture of the macroscopic surface as well as on the experimental arrangement (angles of incidence and observation, prevention of the specular fraction from reaching the detector). The presence of the specular component results in strong compression of the spectrum. This compression also occurs in the case of strong absorption in the sample, when the specular component can be the main contribution to the detected signal. The usual method of overcoming band suppression is a dilution of the sample as mentioned.

In general, the reproducibility of the measurements is often limited.

20.4.5
Applications

Diffuse reflection spectroscopy is particularly useful for measuring the spectra of adsorbed molecules, chemically modified surfaces, and catalysts. All spectral ranges from the UV to the infrared are used. Different information can be obtained in different spectral ranges. Adsorption under the influence of van der Waals forces generally only slightly changes the electronic spectrum of the substrate, but significant changes are observed in the case of chemisorption. Acid–base reactions, charge–transfer complexes, redox reactions, reversible cleavage reactions, and photochemical reactions of the adsorbed substance can all be studied.

20.5
Evanescent Wave Cavity Ring-Down Spectroscopy

20.5.1
Introduction

Evanescent wave cavity ring-down spectroscopy (EWCRDS) is based on the measurement of the rate of attenuation of a radiation pulse during intracavity total internal reflection [12, 13].

20.5.2
Instrumentation

A laser beam is focused on a cavity formed by two mirrors and a Pellin–Broca prism and the time behavior of the radiation intensity inside the cavity is monitored by the small fraction of radiation that is transmitted through the second mirror to a detector. Another arrangement uses a properly shaped monolithic, totally internally reflecting polygonal minicavity (from square to octagonal, with at least one convex facet to induce stability). Photon tunneling through the piezoelectrically driven prism introduces radiation into the cavity and extracts a small portion for monitoring. The time needed for attenuation of the pulse to $1/e$ of the original intensity is denoted as the *base ring-down time*.

20.5.3
Performance Criteria

This technique is critically dependent on the quality of the mirrors and cavity, respectively. Super polishing to <0.05 nm root-mean-square of surface roughness is essential. Under such conditions, the arrangement with the Pellin–Broca prism exhibits a base ring-down time of ~1 μs and yields a minimum detectable absorbance change of ~32 ppm. A ring-down time of ~800 ns is found for a 1 cm^2 minicavity.

20.5.4
Applications

Submonolayer detection of adsorption phenomena is possible (e.g., 0.04 monolayer of I_2 on fused silica).

20.6
Near-Edge X-Ray Absorption Fine Structure Spectroscopy

20.6.1
Introduction

A monochromatic X-ray beam is directed onto a sample, which typically has a molecular film on the surface [14–16]. The wavelength of this beam is ramped through an absorption edge of one of the elements that constitutes part of the film. As a monochromatic beam of X-rays at various wavelengths is needed, SR is used as the X-ray source for near-edge X-ray absorption fine structure (NEXAFS) spectroscopy. Data are acquired from a region near to the absorption edge (~50 eV wide).

20.6.2
Instrumentation

SR of high intensity and polarity (>90%) is required. The X-rays must pass through a monochromator before striking the sample. The sample is usually placed in a low-vacuum chamber for experiments in the soft X-ray energy range. The NEXAFS signal can be detected through a number of routes; often, the total electron yield (TEY) from the sample is measured and this signal is divided by the total photon flux striking the sample to normalize out any variations that might result simply from changes in the flux of SR.

20.6.3
Sample

The sample is usually not <2 mm across and must be able to withstand the intense X-ray beam from the synchrotron.

20.6.4
Analytical Information

NEXAFS spectra are frequently dominated by intramolecular resonances of π or σ symmetry. The energy, intensity, and polarization dependence of these resonances can be used to determine the orientation and intramolecular bond lengths of the molecule on the surface. NEXAFS probes the element-specific empty electronic states and has local electronic and bonding structure sensitivity. The orientation of the molecules can be determined using angular-resolved spectra and analysis of the π^* resonances.

20.6.5
Performance Criteria

The primary X-ray energy is typically 1000–4000 eV. NEXAFS is sensitive to ~1% of a single monolayer. Samples need to be able to survive intense doses of X-ray radiation.

20.6.6
Applications

NEXAFS is used to determine the orientation of and bonding structure of adsorbates on a surface. For instance, it is used for the analysis of self-organizing monolayers.

20.6.7
Other Techniques

Extended X-ray absorption fine structure (EXAFS) is similar to NEXAFS but makes use of a wider energy region around the adsorption peak to determine information about the type of atoms surrounding the atom of interest and their distances from it.

20.7
Photoacoustic Spectroscopy

20.7.1
Introduction

Photoacoustic spectroscopy (PAS) is a technique based on the so-called optoacoustic effect [17, 18]. When a short pulse of electromagnetic radiation interacts with condensed matter, the absorbed energy is converted into heat by fast nonradiative relaxation processes. Subsequently, the thermal expansion of the instantaneously heated medium causes an acoustic pulse, which is detected.

20.7.2
Instrumentation

A PAS spectrometer consists of a source of intensity-modulated electromagnetic radiation, a monochromator if necessary, a photoacoustic cell, and the electronics for detecting and storing the photoacoustic signal. The photoacoustic cell is the section containing the sample and the microphone, with its preamplifier, or a piezoelectric detector in intimate contact with the sample. In the infrared range, a Michelson scanning interferometer is used. The moving mirror is additionally sinusoidally driven to obtain a modulation of the output radiation.

20.7.3
Analytical Information

Analytical information is gained from the dependence of relative acoustic signal on wavelength, which represents the absorption spectra of the compound. By changing the modulation frequency, absorption information from different depths of the studied material can be obtained. For materials with low thermal diffusivity, this layer can be $\sim 0.1\,\mu\text{m}$ at a chopping frequency of 10–100 kHz, but 10–100 μm for a frequency of 5 Hz.

20.7.4
Performance Criteria

Temperature changes of 10^{-7} to 10^{-6} °C can be detected with a piezoelectric detector in intimate contact with the sample, detection with microphone is 10–100 times less sensitive. As only absorbed radiation contributes to the detected signal absorption spectra of highly scattering materials, such as powders, amorphous solids, gels, and colloids, can be obtained. A wide range of electromagnetic radiation can be used with the same detection system, the only limitation being sufficient energy of the source (minimum of $10\,\mu\text{W cm}^{-2}$) and sufficient transparency of the other optical components of the measuring system across the full energy range of interest. Hence, spectra from the UV to infrared range can be measured with the same equipment. PAS is not considered suitable for fast measurements and it is limited by the speed of sound, the slow microphone ($<20\,\mu\text{s}$), or the piezoelectric response time ($<0.1\,\mu\text{s}$).

20.7.5
Application

Spectra of adsorbed or chemisorbed species on nonabsorbing or highly reflecting substrates can be measured. PAS is a simple and highly sensitive method for identification of compounds separated on TLC plates and catalysts.

20.8
Photoemission Electron Microscopy

20.8.1
Introduction

X-rays are directed onto a sample to eject photoelectrons [19–21]. These are collected and focused onto a phosphor screen to produce a magnified, real-time, high-resolution image of the distribution of elements, and/or magnetic domains over the sample surface.

20.8.2
Instrumentation

This technique generally requires UHV. An X-ray beam from an anode or synchrotron source is used to excite photoelectrons from the sample. These pass through a series of electrostatic lens, which focus them to form a magnified real-time image of photoelectron distribution on a phosphor screen in a manner that is analogous to optical microscopes but which is element specific. This image can either be viewed directly by eye or with a CCD camera interfaced to image analysis software.

The tunable photon energies available at a synchrotron source can be used to significantly enhance the elemental contrast available in photoemission electron microscopy (PEEM) by choosing a photon energy that corresponds to an absorption edge of a particular element of interest, thus greatly increasing the number of photoelectrons emitted from those areas that specifically contain that element.

By using circularly polarized X-rays from a synchrotron source, the intensity of photoemission becomes dependent on the magnetization of the sample. This can be used to provide element-specific magnetic contrast for imaging magnetic domains, whose behavior can then be studied in real time.

Topographical features of the sample produce distortions in the image and this effect can be used to provide additional topographical contrast.

20.8.3
Sample

UHV-compatible, solid samples. Samples must be reasonably flat to avoid excessive topographic distortions.

20.8.4
Analytical Information

PEEM provides high-resolution real-time images of elemental or magnetic domain distribution with topographic sensitivity.

20.8.5
Performance Criteria

- Energy range is 50–2000 eV.
- Spatial resolution as good as 30 nm.
  Magnification up to ×10 000.
- Element-specific magnetic contrast capability for imaging magnetic domains.
- Real-time element-specific imaging.
- PEEM is sensitive to all elements except hydrogen and helium.
  Atomic sensitivities of a small percentage of a monolayer at the surface.

When used for element-specific magnetic imaging, PEEM is sensitive to all three components of the magnetization.

The technique can be used to study both ferromagnetic and antiferromagnetic domains, depending on the polarization of the X-rays.

Sensitivity decreases rapidly with depth and is generally negligible below ~10 atomic layers depending on energy.

Its surface sensitivity makes the technique vulnerable to surface contamination; hence, it is generally carried out under UHV conditions.

Magnetic imaging is limited to use at SR facilities because of the requirement for circularly polarized X-ray beams.

Electrostatic electron focusing is susceptible to the presence of stray magnetic fields and therefore magnetic shielding may be necessary.

20.8.6
Applications

PEEM is particularly useful for imaging semiconductor microstructures, doing microparticle analysis, studying real-time processes such as surface diffusion, or for magnetic domain imaging in data-storage applications as well as in other applications where real-time high-resolution imaging of elemental or magnetic domain distribution is required.

20.9
Raman Spectroscopy

20.9.1
Introduction

By irradiation of the sample with monochromatic radiation, a small proportion of the radiation is reemitted (scattered), with the wavelengths differing by frequencies corresponding to the vibrational modes of the sample [5, 14, 22–24]. Frequencies smaller (Stokes process) or higher (anti-Stokes process) than the excitation frequency are observed. The strength of the effect is determined by the derivative of the molecular polarizability of the sample with respect to the vibrational coordinates.

20.9.2
Instrumentation

Dispersive Raman spectrometers are used with excitation in the visible range (typically He–Ne or Ar^+ lasers are used), Fourier transform Raman spectrometers are used with excitation in the near-infrared range (Nd : YAG laser). For both ranges, microscopic techniques working with a laser beam diameter of micrometer size are commercially available.

20.9.3
Sample

Raman spectroscopy is not particularly surface sensitive but a surface-enhanced Raman scattering (SERS) effect is observed on some metals (copper, gold, silver, nickel, etc.). On an appropriately prepared (roughened) surface or on metal colloids, the surface coverage of molecules can be measured by Raman spectroscopy with high sensitivity. Tip-enhanced Raman scattering technique (TERS) reaches the same effect by scanning of a sample by a tip (metal nanoparticle or metallized tip of diameter of apex <30 nm) irradiated with laser light. It allows a nanoscale chemical analysis.

20.9.4
Analytical Information

The Raman spectrum, represented as the dependence of the relative intensity of the detected signal on the wave number, provides information on the sample's composition, structure, and vibrational modes that is complementary to the infrared spectrum (Figure 20.1).

20.9.5
Performance Criteria

The Raman effect is a very weak effect in comparison with inherently accompanying Rayleigh scattering (which can be eliminated by using good quality monochromatization or filtering) and with fluorescence of the sample or any accompanying impurities. The last effect can be eliminated using near-infrared radiation for excitation of the Raman spectra.

SERS effect allows an enhancement of the signal on the order of 10^3–10^6. It means that even subnanomolar amount of the component in the irradiated area can be detected.

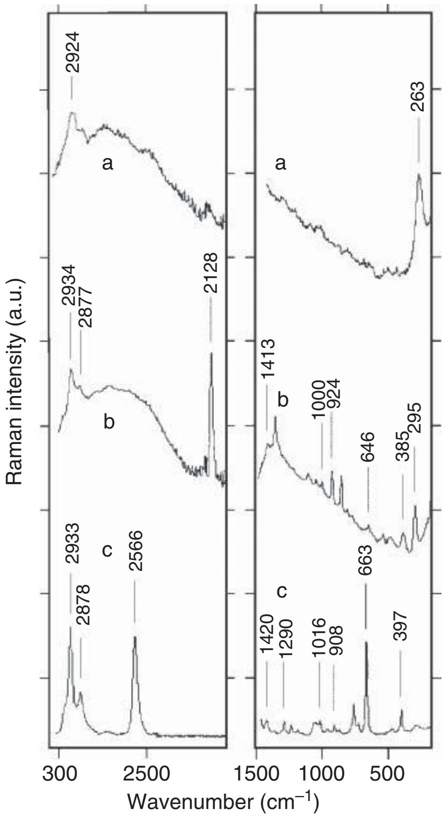

Figure 20.1 FT Raman spectra of a layer of 2-mercaptoethanol on polished (a) and (b) rough gold substrate compared with the spectrum of (c) pure 2-mercaptoethanol.

20.9.6
Application

Used in the study of catalysis and electrochemistry.

20.10
Reflection–Absorption Spectroscopy

20.10.1
Introduction

Measurement of sample layers of thickness ranging from many times the wavelength down to fractions of a monolayer placed on a mirror [5, 14, 25–27]. Absorption by the sample reduces the mirror's reflectance.

Range of operation is typically mid-infrared.

20.10.2
Instrumentation

In a typical setup (constructed as an accessory to be mounted in the sample compartment of a commercial FT spectrometer), infrared radiation is focused on the sample surface at a defined angle. The reflected beam is focused onto a detector. Irradiation with a polarized IR beam is often used.

Reflection–absorption spectra of fairly thick surface films (i.e., thickness between 0.2 and 20 μm) are easily achieved using standard accessories for specular reflectance spectrometry with incidence angles from 15° to 75°. Incidence angles $<15^\circ$ are difficult to attain with conventional optics as it becomes difficult to separate the incident and reflected rays. A so-called grazing angle accessory is needed to attain angles of incidence $>75^\circ$. Grazing incidence geometry leads to an increase in the path length in comparison with the transmission experiment, an increase in the irradiated area proportional to the secant of the angle of incidence, and an enhancement in the electric field vector of the IR photon perpendicular to the surface. Near grazing incidence, the contribution of the incoming wave interferes constructively with the 180° – phase-shifted reflected wave. In total, a sensitivity increase on the order of a factor of 20 in comparison with the transmission methods is to be expected on a highly reflective sample, such as a metal single-crystal surface.

In the extreme case of grazing incidence, the component of the electric field perpendicular to the plane of incidence is very small.

20.10.3
Sample

Mirror-like surfaces are required.

20.10.4
Analytical Information

Reflection–absorption infrared spectroscopy RAIRS results in a spectrum that is similar to that of a transmission measurement. For grazing incidence geometry, only molecular vibrations giving rise to a dynamic dipole perpendicular to the surface are infrared active; this is termed as the *surface selection rule* for surface vibrational spectroscopy.

20.10.5
Performance Criteria

Grazing incidence allows us to measure monomolecular or submonomolecular layers. For a thickness of ~1 nm, band absorbances on the order of 10^{-3}–10^{-4} are measured with an 85° angle of incidence. The overall size of the sampled area achieved with the given geometrical arrangement is critical for sensitivity.

An outstanding gain in sensitivity, allowing us to identify and quantify surface layers of some nanometer thickness, can be observed for strong oscillators owing to the Berreman effect.

20.10.6
Limitations

Strong dispersion associated with intense absorption bands can cause significant changes in the absorption peak position and shape, for example, 1–4 cm^{-1} for moderately absorbing species (benzene and acetone) and 22 cm^{-1} for strongly absorbing species (copper oxide on copper).

With layers of the thickness comparable to the measured wavelengths, the increase in the absorption with the thickness can be corrupted by a modulation connected with the regularly varying standing wave formed. With a thickness below one-quarter wavelength, the response decays not only with the thickness but also with the field amplitude approaching the node. Thus, zero sensitivity is to be expected at the very surface of the metal substrate.

For a number of practical reasons, low-frequency modes ($<600\,\mathrm{cm}^{-1}$) are not generally observable. This means that it is not usually possible to see the vibration of the metal–adsorbate bond and attention is instead concentrated on the intrinsic vibrations of the adsorbate species in the range of 600–3600 cm^{-1}.

20.10.7
Applications

RAIRS is used for characterization of adsorbates on metal surfaces, their transformations and kinetics (e.g., CO on metallic surfaces), catalytic reactions, characterization of semiconductor structures, high-temperature oxidation of metals (use of the so-called Berreman effect), electrode/electrolyte interface, Langmuir–Blodgett, and other ultrathin organic films.

20.10.8
Other Techniques

Modulation spectroscopy uses a periodic (sinusoidal) variation of a parameter influencing the reflectivity of the sample, such as wavelength, angle of incidence, electric field (electroreflectance), temperature (thermoreflectance), surface charge density (piezoreflectance), and magnetic field strength (magnetoreflectance). This technique allows the effect of an external perturbation on the sample to be studied and also enhances otherwise weak details on a large background.

If a photoelastic modulator is used to generate alternately parallel and perpendicular polarized radiation, the AC signal detected will be due to the difference in the absorption of radiation of each polarization. The effect of the background can be eliminated in this way. In the infrared region, this type of experiment is denoted as *polarization modulation*, PM FTIRRAS.

20.11
Spectroscopy of Surface Electromagnetic Waves

20.11.1
Introduction

A thin dielectric film deposited on a metal increases surface electromagnetic waves (SEWs) attenuation, which becomes stronger as eigenfrequencies of the film vibrations are approached [28].

20.11.2
Instrumentation

Modulated radiation from a tunable IR laser falls onto a prism at the condition of attenuated total reflection. Arising evanescent radiation can excite SEW on a metal surface at a suitable distance from the prism base. SEW propagates along the metal surface and can be attenuated by a thin dielectric film deposited on this metal. By means of a similar prism placed at a certain distance from the first one, the SEW is transformed into normal radiation and detected by a pyroelectric detector.

20.11.3
Performance Criteria

The SEW excitation efficiency is affected by both the angle of incidence in the prism and the gap height, the last being different for the coupler and decoupler prism. The size of the gap depends on the metal and the conditions of its evaporation. An absorption spectrum is obtained by a differential method in which the ratio of intensities is measured for an SEW on the metal surface with a film and without a film at various distances between the prisms.

20.11.4
Applications

Very thin films of organic and inorganic substances on metal surfaces can be measured down to monolayers.

20.12
Sum Frequency Generation Vibrational Spectroscopy

20.12.1
Introduction

SFG is a second-order nonlinear optical process in which two laser beams overlap in a medium and generate the sum frequency [14, 25, 29, 30]. As a second-order process, it is allowed on surfaces or interfaces, where the inversion symmetry is broken. In a typical experiment, one beam of infrared and the other of visible wavelength are mixed, allowing SFG vibrational spectroscopy.

20.12.2
Instrumentation

A typical experimental setup consists of a pulse Nd : YAG laser, which is used to pump an optical parametric/difference frequency generation system to produce tunable infrared radiation with a wavelength up to 9 μm. The infrared beam is then overlapped with a frequency-doubled output beam from the laser (532 nm) at the sample surface. A photomultiplier is used for detection. Sum-frequency vibrational spectra are generated by scanning the IR frequencies through the energy range of vibrational excitations.

20.12.3
Analytical Information

Information about molecular orientation and conformation at a surface, and sometimes even surface structure, is gained from the dependence of the SFG signal on wave number.

20.12.4
Performance Criteria

Typically, a spot of several hundred micrometers of the sample is irradiated by the infrared and visible pulse energies at 100 μJ and 1 mJ, respectively. A gain of ∼100 photons per pulse is observed, but the maximum signal we can get is limited only by the local maximum input intensity that the interface can tolerate without damage.

The strength of the resonant SFG response depends on several factors: the surface density of the molecule of interest, the line width of the transition, the IR transition moment, and the Raman transition strength. The last two factors restrict the technique to the study of vibrational modes, which are both infrared and Raman active.

Some of the disadvantages include low-detected signal levels and difficulties in determining a quantitative relationship between the peak intensities and the number of sampled molecules.

20.12.5
Applications

Although solid–solid interfaces can be studied, SFG represents the most powerful analytical tool for liquid interfaces. A wide range of systems has been studied including neat liquid–vapor, liquid mixture–vapor, neat liquid–solid, and neat liquid–liquid interfaces, and also surfactants at liquid–air, liquid–solid, and/or liquid–liquid interfaces, and electrochemistry at solid–liquid interfaces.

20.12.6
Other Methods

Second harmonic generation (SHG) spectroscopy is based on the same principles (two photons of frequency ν are converted to one photon of frequency 2ν). SFG has appeared to be the more successful and versatile technique to date.

20.13
Surface Plasmon Resonance Spectroscopy

20.13.1
Introduction

The surface resonance phenomenon in a thin metallic film is measured by attenuated total reflection as a function of either incident angle (using monochromatic light) or excitation wavelength (at a constant value of the incident angle) [31–33].

Ranges of operation are from visible to infrared, typically visible.

20.13.2
Instrumentation

A surface plasmon resonance (SPR) spectrometer has the following four principal components: a source of radiation, an optical coupling element, a thin metallic film, and a detector. Thin layers of SPR-active metals are most often produced by vacuum evaporation or sputtering.

Two arrangements of ATR optical prism couplers are used: the Kretschmann-type arrangement with a metallic film deposited directly onto the coupling prism and the Otto-type arrangement with a metallic film separated from the coupling prism, by air or other dielectric material of a thickness of about one wavelength of the radiation used in the experiments. The Kretschmann configuration is more convenient and is used in most applications.

SPR sensing platforms are combined with transducing layer(s) to enable the use of SPR for chemical sensing and biosensing.

20.13.3
Analytical Information

SPR is a general spectroscopic method for sensing refractive index changes near the surface of a metal film. The dependence of reflectance on the incident angle or excitation wavelength is defined as an *SPR spectrum*. The corresponding curve is characterized by position, width, and depth of the resonance dip in reflectance as a function of incident angle or wavelength. These features depend on the nature of the metal and thickness of its film. The position of the reflectivity minimum is the quantity that is most sensitive to the refractive index of the adjacent medium, and therefore it is usually used for the purpose of sensing. By fixing the wavelength or the angle of incidence at an appropriate constant value, the resonance can be positioned at any particular value of the incident angle or wavelength, respectively. The thickness, reflection, and absorption indexes and optical parameters of the thin layer under study may be determined from SPR reflectivity spectra.

20.13.4
Performance Criteria

Amplitude-based SPR sensing devices typically attain a refractive index resolution in the range of 10^{-6}–10^{-5}. Angular- and spectral-interrogation-based systems provide even better resolution, allowing the measurement of refractive index changes as small as 10^{-7}. This corresponds to a detection limit for an adsorbed protein layer of $<1\ \mathrm{pg\,mm^{-2}}$.

20.13.5
Applications

SPR is used in sensors and biosensors, but this method can also be used for the study of adsorption or chemical reactions in thin films as well as for the study of molecular interactions, conformational changes, and so on.

20.14
Time-Resolved Two-Photon Photoemission Spectroscopy

20.14.1
Introduction

A laser pulse strikes the sample and an electron is photoexcited to an unoccupied level [34–37]. A second laser pulse then causes the excited electron to be photoemitted. The kinetic energy of the electron can be used to estimate the energy of the unoccupied state. The time delay between pump and probe pulses can be used to determine the lifetime of the excited state. The non-time-resolved technique is known as *2PPE*.

20.14.2
Instrumentation

The experiment is carried out in UHV. The laser sources are capable of producing femtosecond pulses. Repetition rates between 10 and 250 kHz are typical. The photoelectrons are detected by an electron energy analyzer such as a concentric hemispherical analyzer.

20.14.3
Sample

The sample must be conducting and capable of withstanding UHV.

20.14.4
Analytical Information

For non-time-resolved data, this technique provides more precise information than inverse photoelectron spectroscopy (IPES) concerning the spectral line shapes and line widths of unoccupied states. In the time-resolved mode, we can obtain detailed information regarding the electron dynamics. The lifetimes of excited electrons can be compared with theoretical GW and GW + T calculations. Relaxation times can be determined from line-width measurements from high-energy resolution 2PPE experiments and cross correlations from TR-2PPE.

20.14.5
Performance Criteria

Better time-resolved experiments can be performed but only by reducing energy resolution. For extremely short-lived excited states (<1 fs), it can be difficult to make estimates of the relaxation times.

20.14.6
Applications

Image potential states, electron dynamics, coherence phenomena, interface states, and electrical currents.

20.14.7
Other Techniques

The information acquired by TR-2PPE is related to that obtained by IPES and STS (i.e., unoccupied states) and by UPS (i.e., filled states).

20.15
Total Reflection X-Ray Fluorescence Spectroscopy

20.15.1
Introduction

An X-ray beam hits a flat sample at a highly grazing angle so that total external reflection occurs [14, 38]. As a result, the X-rays only penetrate the top few atomic layers, where they cause X-ray fluorescence (XRF) emission. Thus, this technique combines high surface sensitivity with the high atomic sensitivity of the (otherwise normally bulk sensitive) fluorescence technique.

Typical energy range is 1–20 keV.

20.15.2
Instrumentation

A narrow beam of X-rays is directed at a flat sample at grazing incidence, typically <10 mrad, so that total external reflection of the X-rays occurs. As a result, the X-rays only penetrate the top few atomic layers, where they excite X-ray fluorescence. The emitted photons are then detected with a Si(Li) detector. Fluorescence detection is extremely sensitive to very low concentrations (1 part in 10^8 for transition metals and 1 part in 10^{10} for low atomic mass elements) but is normally a bulk-sensitive technique; TXRF allows it to be used in a surface-specific manner. TXRF is used particularly in semiconductor wafer processing for quantitative analysis of surface contamination present at very low concentrations. A map of contamination over the whole wafer can be obtained by rotating the sample in the beam.

UHV is not required and the technique can even be used to study liquids; however, the emphasis on detecting low levels of surface contamination means that either UHV or clean room conditions will normally be used. This technique may be used in conjunction with a high-intensity synchrotron source or with the X-ray standing wave (XSW) technique to boost sensitivity still further.

20.15.3
Sample

The sample need not be conducting but must be very flat because of the grazing incidence of the beam, and TXRF is often used on silicon wafers.

20.15.4
Analytical Information

Quantitative element-specific and surface-specific measurement of extremely low atomic concentrations on flat surfaces.

20.15.5
Performance Criteria

- Angle of incidence is generally 1–10 mrad.
- Energy range is 1–20 keV.
- Beam size is a few square millimeters.
- Beam spot size on sample – a few millimeters across the beam, but the full width of the sample along the beam axis as the grazing incidence angle that is required spreads out the beam spot considerably. Thus, by rotating the sample, the whole area of a wafer can be mapped in a few minutes.

This technique is not restricted to UHV, and it can be used in atmosphere or in clean room conditions.

Increased sensitivity can be obtained by using a powerful synchrotron source or by using TXRF in conjunction with the XSW technique. When X-rays are incident on a material that contains distinct boundaries between different layers, standing waves of X-rays will form. The standing waves are used to obtain a depth profile of the fluorescence signal for different angles of incidence or exit. The acronyms GIXRF (grazing incidence X-ray fluorescence) and GEXRF (grazing-exit X-ray fluorescence) are used for these methods.

- The spatial resolution of TXRF is generally only several millimeters.
- Analysis area is several square centimeters.
- Atomic contents of 1 part in 10^8 for transition metals or 1 part in 10^{10} for low-atomic mass elements are possible.
- Depth sensitivity is 50 Å.

TXRF can detect all elements with atomic masses from sulfur to uranium.

20.15.6
Applications

Nondestructive, non-UHV measurement of very low concentrations of impurities on the surfaces of flat samples, particularly, Si wafers.

20.16
Transmission Spectroscopy

20.16.1
Introduction

The ratio of the radiant power after and before the transmission of the electromagnetic radiation through the absorbing layer, that is, transmittance, is measured [14].

Range of operation is mid- and far-infrared.

20.16.2
Instrumentation

Conventional dispersive or Fourier transform spectrometers are used. Transmission spectroscopy of surfaces employs the same basic experimental geometry as that used for bulk samples.

20.16.3
Performance Criteria

The transparency of the substrate and the ability to compare the combined transmissivity of the substrate and its deposited surface layer with that of the substrate without this layer is crucial. A film thickness on the order of 1 μm is typical.

For characterization of surfaces or adsorbed molecules on fine powders, a mixture of the sample with KBr powder pressed into a disk is used. The so-called scattered transmission method is based on the measurement of the transmittance of a very thin layer of pulverized material. This method takes advantage of the fact that with increasing wavelength, the scattering media, which are composed of very small particles, become more transparent, and it is possible to record good absorption spectra with scattered transmission, especially in the mid-infrared region. Disks are usually prepared by pressing the powdered sample into a wafer between 0.1 and 0.25 mm thick. Good results can be obtained for solids with a high surface area.

20.16.4
Applications

Adsorption and heterogeneous catalysis have been studied by this method.

20.17
Ultraviolet Photoelectron Spectroscopy

20.17.1
Introduction

Samples are exposed to monochromatic ultraviolet radiation (typically in the range of 10–100 eV), and the energies of the emitted photoelectrons are measured to reveal information on the valence-band electronic structure of the sample [1–3, 14, 39].

20.17.2
Instrumentation

The measurement is carried out in a UHV chamber. Ultraviolet photons from a He lamp (21.2 or 40.8 eV) are directed at the sample to eject photoelectrons. The emitted electrons are collected by an electron energy analyzer, such a hemispherical mirror analyzer, to produce a spectrum showing the number of electrons emitted with a given kinetic energy. Such spectra are representative of, although not identical to, the sample's valence-band electronic DOS.

By using a synchrotron source instead of a He lamp to provide the ultraviolet photons, photon energy that preferentially favors emission from a particular element by exploiting variations in photoemission cross section can be selected. The partial DOS contribution from each individual element can then be determined.

20.17.3
Sample

Samples are normally metallic or semiconducting UHV-compatible materials.

20.17.4
Analytical Information

The valence-band electronic structure of the top few atomic layers can be determined from the variation in photoelectron intensity as a function of electron kinetic energy and incident photon energy.

20.17.5
Performance Criteria

Spatial and energy resolutions are strongly dependent on the particular type of electron energy analyzer and photon source used. However, the spatial resolution may be as good as 10 μm and the energy resolution may be as good as 5 meV.

Typically, concentrations of a few atomic percentages at the surface can be detected, depending strongly on the cross section of the particular elements present. Sensitivity decreases rapidly with depth below the surface and is often negligible below a depth of approximately five atomic layers.

High surface sensitivity makes the technique vulnerable to contamination, necessitating the use of UHV procedures. The low energy of the emitted electrons makes the technique vulnerable to the presence of stray magnetic fields and hence magnetic shielding is normally required. The spectrum can be influenced by the particular crystal structure of the sample's top few atomic layers, which may not be completely representative of the bulk material. This technique is generally not suitable for insulating materials.

20.17.6
Applications

UPS is used to probe the electronic states near the Fermi level that are responsible for determining a material's electronic properties and to study the nature of the bonding between the atoms in the sample or between the sample and adsorbate molecules on its surface.

20.17.7
Other Techniques

Measurement of the photoelectron intensity from single-crystal samples as a function of both their kinetic energy and emission angle allows the total momentum of the photoelectrons to be determined, enabling bandmaps of the electronic DOS of the material to be produced (see ARUPS).

Filled DOS information can also be obtained from metastable deexcitation spectroscopy (MDS).

By combining the electron energy analyzer with a polarization-sensitive Mott detector separate spin-up and spin-down valence-band DOS spectra can be produced for magnetic samples. This technique is known as *spin-polarized ultraviolet photoelectron spectroscopy*.

20.18
X-Ray Absorption Fine Structure

20.18.1
Introduction

A monochromatic X-ray beam is directed onto a sample [25, 39]. The wavelength of the beam is ramped through an absorption edge of an element, which is a constituent of the sample, while the extent of the X-ray absorption is measured to produce an absorption spectrum. As a monochromatic beam of X-rays at various wavelengths is needed, SR is used as the X-ray source for X-ray absorption fine structure (XAFS).

For XANES, the energy range ($<50\,\text{eV}$) near to absorption edge is studied. However, for EXAFS, the spectrum is acquired much further from the absorption edge. Information regarding the local structure around the atom whose absorption edge is acquired can be obtained.

Range of operation is incident photon energies in the range of 1–20 keV.

20.18.2
Instrumentation

An SR source is required. EXAFS and XANES are normally regarded as bulk-sensitive techniques. However, by measuring the total electron current emitted from the sample, both methods can be made relatively surface sensitive. The detection of the electron current is called *total electron yield*. The sample is normally placed inside a ''cell'' containing noble gas atoms (Ar and He). These gases prevent the electrons from combining with atoms in the air, which might otherwise affect the acquisition of the data. The intensity of the incident synchrotron light may vary and hence its flux is continuously measured by passing the light through another cell before striking the sample. The ratio of the TEY to the incident flux provides the spectral data. Improved detection of the EXAFS signal could be carried out using gas microstrip detectors. These detectors allow a more surface-sensitive signal to be acquired.

20.18.3
Analytical Information

EXAFS spectra provide information regarding the local environment surrounding the atom whose absorption edge is studied. The specific local information includes the atom type of neighboring atomic shells, the distance of those shells from the central (absorbing) atom, and the static or dynamic disorder. The latter is given by the Debye–Waller value. EXAFS spectra can be acquired in a gaseous environment. This allows data to be acquired in non-UHV environments and gas adsorption and *in situ* catalyst studies to be undertaken.

XANES spectra provide local structure information and the oxidation state. In the XANES region, electrons that are excited from the core level (usually the K level) jump into unfilled bound states, nearly bound states (resonances), or continuum states. Owing to multiple electron scattering, XANES spectra are harder to interpret than EXAFS spectra.

20.18.4
Performance Criteria

Primary X-ray energy is 1–20 keV.

The sample should be able to withstand the intense X-ray beam from the synchrotron. For the TEY technique, the sample should be conducting. XAFS study of low atomic number elements $Z < 11$ provides less information. It can be difficult to distinguish elements in the shells surrounding the central atom if they are close in atomic number. It can be difficult to distinguish static from dynamic disorder.

20.18.5
Applications

EXAFS is used in many applications where local state information is required, such as materials analysis, catalysis, protein crystallography, or the structure of liquids and amorphous materials. XANES can also be used to determine the oxidation state of an element in a sample.

20.18.6
Other Techniques

Surface-extended X-ray absorption fine structure (SEXAFS) uses Auger or photoelectrons to detect the EXAFS signal. This ensures that this technique has a much higher surface sensitivity than EXAFS acquired using the TEY method. SEXAFS requires UHV and the detection instrumentation normally associated with the AES or XPS techniques.

20.19
X-Ray Photoelectron Spectroscopy

20.19.1
Introduction

Samples are exposed to monochromatic X-ray radiation (typically with an energy range of 1–2 keV, but energies up to 10 keV may be used) and the characteristic energies of the emitted photoelectrons are measured to reveal information about the elemental composition, elemental distribution, and chemical bonding characteristics of the near-surface region [1, 3, 14, 39–41].

20.19.2
Instrumentation

The measurement is carried out in a UHV chamber. Monochromatic X-ray photons, typically from an AlK_α (1486.6 eV) or MgK_α (1253.6 eV) X-ray source, are directed at the sample to eject photoelectrons. These electrons have energies ranging from 0 eV up to almost the same energy as the incident photons, but most are emitted at a few discrete energies that are characteristic of the elements present in the sample. The photoelectrons are collected by an electron energy analyzer such as a hemispherical mirror analyzer (HMA) to produce a spectrum of the number of electrons versus their kinetic energy. Analysis of this spectrum provides quantitative information about the composition of the near-surface region of the sample.

Although XPS generally only reveals information about a particular point on the sample surface that is typically 100 μm to 1 mm across, a number of different approaches can be used to generate image maps of the elemental distribution over a wider area. By using a microfocused X-ray source, images with a resolution of some 10 μm may be obtained by scanning the sample under the beam or scanning the beam across the sample surface. Alternatively, images may be produced by scanning the area of analyzer sensitivity across the surface using electrostatic electron deflector plates. This method is more straightforward and cheaper to implement but has significantly poorer resolution (100 μm). Many modern electron energy analyzers have imaging optics and detectors that collect XPS spectra from many discrete points simultaneously to produce an image of elemental distribution. This method produces the highest resolution spatial images with a resolution of better than 10 μm.

Tilting the sample so that the analyzer collects electrons that are emitted at a more grazing angle increases the surface sensitivity of the technique. By acquiring spectra at several different angles, which have different surface sensitivities, quantitative information about the depth distribution of the elements in the top few nanometers of the sample can be extracted; this is known as angle-resolved X-ray photoelectron spectroscopy (ARXPS).

The energy resolution of XPS may be as good as 0.2 eV, which is sensitive enough to detect the small chemical shifts in the kinetic energy of the photoelectrons that result from variations in the chemical environment of a particular element. By analyzing the shape of an XPS peak, the relative contribution from different chemical states can be determined, revealing important information about the sample chemistry and atomic bonding.

By using a synchrotron source to provide the X-rays, a photon energy that preferentially enhances emission from a particular peak by exploiting variations in photoemission cross section as a function of photon energy to increase sensitivity to the given element can be selected.

20.19.3
Sample

Samples are generally metallic or semiconducting UHV-compatible materials. However, insulating samples such as polymers can also be studied if a low-energy ‘‘flood gun’’ electron source is used to supply electrons to the surface of the sample, replacing those ejected by photoemission and preventing net sample charging that would otherwise distort the position and shape of the XPS peaks.

20.19.4
Analytical Information

XPS reveals quantitative information about the elemental composition of the top 10 nm or sample (Figure 20.2). Using higher energy X-rays from a source such as a TiK_α (2040 eV) gun, or a high-energy synchrotron, can increase the kinetic energy of the photoelectrons and hence the analysis depth.

Images of the elemental distribution across a wider area of the sample surface can be obtained either by using an imaging electron energy analyzer or by scanning the position of the sample, the X-ray beam, or the analysis spot.

Quantitative elemental depth profiles can be obtained by collecting XPS spectra at different emission angles, which have differing depth sensitivities, and on analyzing the resulting changes in the peak intensities from the different elements in the sample (ARXPS).

Small chemical shifts in the XPS peaks can be used to discriminate between contributions coming from the different chemical states of a particular element. This reveals important quantitative information about the nature of the chemical and bonding environment for each element in the sample. This is particularly important in the study of polymers where the material’s properties are determined by small changes in the bonding of the carbon atoms.

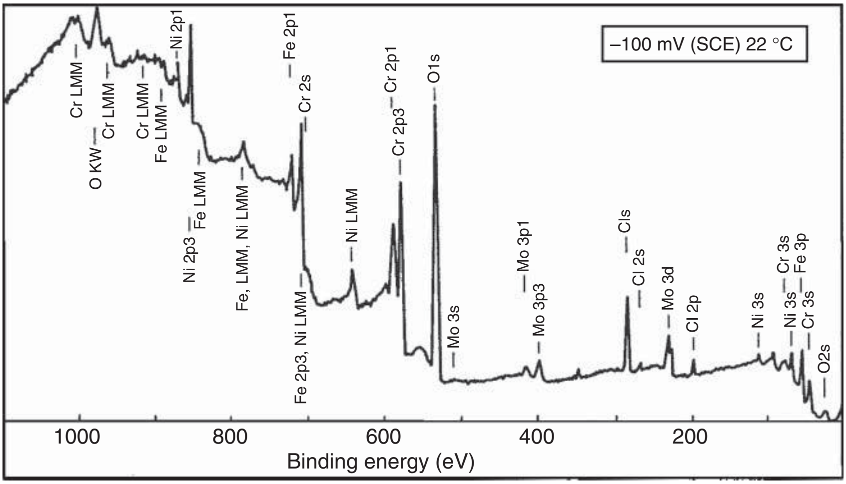

Figure 20.2 XPS survey spectrum recorded after polarization of the steel $20Cr_{18}Ni_{6}.1Mo\,0.2\,N$ to −100 mV (SCE) at 22 °C in 0.1 M HCl + 0.4 M NaCl. (Reproduced with permission from Ref. [14].)

20.19.5
Performance Criteria

Spatial and energy resolutions are strongly dependent on the particular type of electron energy analyzer and X-ray source used. However, spatial resolution may be as good as 10 μm, depth resolution may be as good as 0.2 nm, and the energy resolution may be as good as 0.2 eV.

Typically, concentrations of 1% or less at the surface can be detected, depending strongly on the photoemission cross section of the particular elements present. Using various corrections to the signal intensities, the accuracy of the surface concentration measurement can be as good as ±10%. Sensitivity decreases rapidly with depth below the surface and is often negligible below a depth of approximately 5–10 nm, depending on electron energy. All elements can be detected directly with the exception of hydrogen and helium.

High surface sensitivity makes the technique vulnerable to contamination, necessitating the use of UHV procedures. Spectra taken on crystalline samples can be influenced by diffraction effects, which can lead to variations in the peak intensity at different emission angles (see X-ray photoelectron diffraction, XPD). The composition of the surface as probed by XPS may not be completely representative of the bulk material because of surface segregation, degradation, or contamination.

Some samples such as polymers may be damaged by exposure to the intense X-ray beam.

An electron flood gun must be used to avoid charging distortions when studying insulators.

20.19.6
Applications

XPS is one of the most widely used surface and materials analysis techniques in both academia and industry. Applications include semiconductor wafer defect analysis, identification of surface contamination in industrial processes, adhesion chemistry analysis, catalysis, analysis of fracture or failure surfaces, and analysis of the strength and type of carbon bonding in polymers.

20.19.7
Other Techniques

AES requires equipment very similar to XPS and the two techniques are frequently integrated into the same analytical system to provide complementary information about a sample.

UPS is a technique very similar to XPS that makes use of much lower energy photons to emphasis variations in the low-energy valence-band electronic structure.

XPD is closely related to XPS but exploits the variations in XPS peak intensity that occur at different emission angles in crystalline samples to reveal element-specific crystallographic information.

20.20
X-Ray Standing Wave

20.20.1
Introduction

When single-crystal samples are exposed to a narrow beam of monochromatic X-rays, the regular arrangement of the atoms leads to diffraction of these X-rays at certain critical angles, a condition known as *Bragg reflection* [42–45]. The incoming and outgoing X-rays then interfere to form a standing wave that permeates the material and even extends beyond it. The resulting periodic spatial variations in the amplitude of the X-rays within the lattice mean that the X-ray absorption signal from a given element becomes very sensitive to its relative position in that lattice. Thus, XSW provides a sensitive, element-specific, probe of crystal structure, or of the bonding site of an absorbed molecule on a surface. Energy range is typically 2–80 keV.

20.20.2
Instrumentation

A narrow beam of monochromatic X-ray photons from a synchrotron is directed onto a single-crystal sample at an angle that satisfies the Bragg condition for that material in order to establish an XSW throughout the sample. The X-ray absorption signal from the element of interest is then monitored by a technique such as AES, XPS, or XRF as the relative position of the standing wave is gradually shifted through the lattice by changing the reflection angle or photon energy slightly. The relative position of the standing wave with respect to the crystal lattice can be calculated from theory for any given combination of angle and photon energy and hence by studying how the absorption signal of a particular element changes as the wave moves through the lattice the position of that element's atoms within that lattice can be established precisely. As the standing wave extends some distance beyond the surface of the sample, the technique is particularly useful for studying the bonding of absorbed molecules. Although UHV conditions are not a requirement for XSW, the emphasis on using XSW to study molecular absorption means that UHV is frequently used to avoid contamination problems. This technique normally requires a synchrotron X-ray source so that the standing wave conditions can be altered by changing the photon energy rather than the experimental geometry. Synchrotrons also have the additional advantages of producing a highly collimated X-ray beam that is extremely bright and therefore can be used for studying dilute systems.

20.20.3
Sample

Single-crystal materials, buried interfaces, and adsorbates on single-crystal surfaces.

20.20.4
Analytical Information

Element-specific and/or chemical-species-specific crystallographic and bonding information.

20.20.5
Performance Criteria

When XPS is used to detect the element of interest in the XSW experiment, the energy resolution may be as good as 0.2 eV and hence XSW can be used to probe the bonding of a particular chemical species within the lattice or on the sample surface by making use of small chemical shifts in the XPS peaks. XSW is very good at distinguishing between adsorption occurring at slightly different sites within the lattice that would otherwise appear very similar in complementary techniques such as SEXAFS.

An X-ray beam with energy 2–5 keV is required, and energies may be as high as 80 keV for some applications.

Minimum spot size for the X-ray beam is generally 0.5–1 mm.

The requirement for highly collimated intense X-ray beams with variable photon energy often restricts the technique to use at synchrotron sources, although for certain applications a laboratory X-ray source may be sufficient.

XSW has the advantage of not being inherently restricted to use in UHV conditions, and it can be used to study buried interfaces.

The depth sensitivity of XSW is dependent on the technique used to detect the X-ray absorption. If AES or XPS is used, then the technique is surface sensitive with negligible sensitivity below 5–10 atomic layers, whereas using fluorescence detection results in bulk sensitivity. Typically, concentrations of a few atomic percentage of a monolayer at the surface can be detected. The use of XPS for element detection can also make the XSW technique chemical species specific.

Very high angular resolution is required for this experiment as the width of the ‘‘rocking curve’’ of angles over which the standing wave condition is satisfied can be mere seconds of arc. However, it may be more than a degree in some configurations where the beam hits the sample at close to normal incidence (normal incidence X-ray standing wave) NIXSW.

XSW was initially restricted to very high-quality single crystals such as semiconductors owing to its extreme sensitivity to the degree of crystal perfection; however, the recent development of NIXSW techniques, which have wider angular rocking curves (and are hence less sensitive to crystal perfection), has now made it applicable to conventional single-crystal metallic samples.

XSW does not give a direct measurement of the position of a given atom; rather, it gives the atom’s position relative to the bulk unit cell of the lattice. XSW of adsorbates yields poor results in systems where extensive reconstruction of the surface has occurred, as it cannot determine where adsorbate atoms are relative to this reconstructed surface, only relative to the unreconstructed bulk lattice.

The quality of XSW data is very sensitive to the angular spread and photon energy resolution of the X-ray beam, which normally makes it necessary to use a synchrotron source.

20.20.6
Applications

Element-specific crystallography of single crystals. Study of the site-specific and/or chemical state-specific bonding of adsorbates to single-crystal surfaces. Structure of buried interfaces. Applications where UHV-specific techniques are not applicable.

References

This list of references represents only a selection of the literature having relevance to the given text and it is not complete by any means.

1. Prutton, M. (1984) *Surface Physics*, Oxford University Press, Oxford.
2. Zangwill, A. (1990) *Physics at Surfaces*, Cambridge University Press, Cambridge.
3. Hüfner, S. (2003) *Photoelectron Spectroscopy: Principles and Applications*, Springer, Berlin.
4. Urban, M.W. (1996) *Attenuated Total Reflectance Spectroscopy of Polymers*, American Chemical Society, Washington, DC.
5. Schrader, B. (1995) *Infrared and Raman Spectroscopy*, Wiley-VCH Verlag GmbH, Weinheim.
6. Räty, J.A., Peiponen K.E., Asakura, T. (2004) *UV-Visible Reflection Spectroscopy of Liquids*, Springer, Berlin.

7. Jensen, E., Bartynski, R.A., Hulbert, S.L., Johnson, E.D. (1992) *Rev. Sci. Instrum.*, **63**, 3013–3026.
8. Bartynski, R.A., Jensen, E., Hulbert, S.L., Kao, C.-C. (1996) *Prog. Surf. Sci.*, **53**, 155–162.
9. Arena, D.A., Bartynski, R.A., Hulbert, S.L. (2000) *Rev. Sci. Instrum.*, **71**, 1781–1787.
10. Berakdar, J., Kirschner, J. (2004) *Correlation Spectroscopy of Surfaces, Thin Films, and Nanostructures* Wiley-VCH Verlag GmbH, Weinheim.
11. Davydov, A., Sheppard, N. (2003) *Molecular Spectroscopy of Oxide Catalyst Surfaces*, John Wiley & Sons, Inc., New York.
12. Pipino, A., Jeffrey W., Hudgens, J.W., Huie, R.E. (1997) *Chem. Phys. Lett.*, **280**, 104.
13. Pipino, A., Jeffrey W., Hudgens, J.W., Huie, R.E. (1997) *Rev. Sci. Instrum.*, **68**, 2978.
14. Brune, D., Hellborg, R., Whitlow, H.J., Hunderi, O. (1997) *Surface Analysis*, Wiley-VCH Verlag GmbH, Weinheim.
15. Ade, H. (2002) in *Chemical Applications of Synchrotron Radiation* (T. K. Sham, ed.), World Scientific, Singapore.
16. Stöhr, J. (1992) *NEXAFS Spectroscopy*, Springer, New York.
17. Rosencwaig, A. (1980) *Photoacoustics and Photoacoustic Spectroscopy*, John Wiley & Sons, Inc., New York.
18. Demtröder W. (2003) *Laser Spectroscopy: Basic Concepts and Instrumentation*, Springer, Berlin.
19. Swiech, W., Fecher, G.H., Ziethen, C., Schmidt, O., Schonhense, G., Grzelakowski, K., Schneider, C.M., Fromter, R., Oepen, H.P., Kirschner, J. (1997) *J. Electron Spectrosc. Relat. Phenom.*, **84**, 171–188.
20. Anders, S., Padmore, H.A., Duarte, R.M., Renner, T., Stammler, T., Scholl, A., Scheinfein, M.R., Stohr, J., Seve, L., Sinkovic, B. (1999) *Rev. Sci. Instrum.*, **70**, 3973–3981.
21. Hopster H., Oepen H.P. (2004) *Magnetic Microscopy of Nanostructures*, Springer, Berlin.
22. Ferraro, J.R., Nakamoto K., Brown C.W. (2003) *Introductory Raman Spectroscopy*, Academic Press, San Diego, CA.
23. Smith, E., Dent G. (2005) *Modern Raman Spectroscopy: A Practical Approach*, John Wiley & Sons, Ltd, Chichester.
24. Yeo B.-S., Stadler J., Schmid T., Zenobi R., Zhang W. (2009) *Chem. Phys. Lett.*, **472**, 1–13, doi: 10.1016/j.cplett.2009.02.023
25. Clark R.J.H., Hester R.E. (1998) *Spectroscopy for Surface Science*, John Wiley & Sons, Ltd, Chichester.
26. Niemantsverdriet, J.W. (2000) *Spectroscopy in Catalysis: An Introduction*, Wiley-VCH Verlag GmbH, Weinheim.
27. Imae T. (2007) *Advanced Chemistry of Monolayers at Interfaces: Trends in Methodology and Technology*, Academic Press, Amsterdam.
28. Agranovich, V.M., Mills, D.L. (1982) *Surface Polaritons*, North Holland, Amsterdam.
29. Lambert A.G., Davies P.B., Neivandt D.J. (2005) *Appl. Spectrosc. Rev.*, **40**, 103–145.
30. McGilp J.F. (1996) *J. Phys. D: Appl. Phys.*, **29** 1812–1821.
31. Miranda, P.B., Shen, Y.R. (1999) *J. Phys. Chem. B*, **103**, 3292–3307.
32. Kambhampati, D.V., Knoll, W. (1999) *Curr. Opin. Colloid Interface Sci.*, **4**, 273–280.
33. Schasfoort R.B.M, Tudos A.J. (eds) (2008) *Handbook of Surface Plasmon Resonance*, Royal Society of Chemistry, Cambridge.
34. Chulkov, E.V., Borisov, A.G., Gauyacq, J. P., Sanchez-Portal, D., Silkin, V. M., Zhukov, V. P., Echenique, P. M. (2006) *Chem. Rev.*, **106**, 4160–4206.
35. FKP *http://www.fkp.uni-erlangen.de/methoden/2ppetutor/menu.html* (accessed 19 March 2013).
36. Zhu, X.-Y. (2002) *Annu. Rev. Phys. Chem.*, **53**, 22147.
37. Ueba H., Gumhalter, B. (2007) *Prog. Surf. Sci.*, **82**, 193–223.
38. Frutos, A. G., Corn, R. M. (1998) *Anal. Chem.*, **70**, 449A–455A.
39. Woodruff, D.P., Delchar, T.A. (1994) *Modern Techniques of Surface Science*, Cambridge University Press, Cambridge.
40. Walls, J.M. (1990) *Methods of Surface Analysis, Techniques and Applications*, Cambridge University Press, Cambridge.
41. Briggs, D., Seah M.P. (eds) (1990) *Practical Surface Analysis*, Vol. 1,

Auger and X-Ray Photoelectron Spectroscopy, John Wiley & Sons, Ltd, Chichester.

42. Stoev, K.N., Sakurai, K. (1999) *Spectrochim. Acta*, **B54**, 41–82.
43. Bedzyk, M. J., Materlik, G. (1985) *Phys. Rev. B*, **31**, 4110.
44. Woodruff, D.P., Seymour, D.L., McConville, C.F., Riley, C.E., Crapper, M.D., Prince, N.P., Jones, R.G. (1987) *Phys. Rev. Lett.*, **58**, 1460–1462.
45. Woodruff, D.P., Seymour, D.L., McConville, C.F., Riley, C.E., Crapper, M.D., Prince, N.P., Jones, R.G. (1988) *Surf. Sci.*, **195**, 237–254.
46. IUPAC (1998) *Compendium of Analytical Nomenclature, Definitive Rules 1997*, Blackwell Science, Oxford.

Appendix to Chapters 18–20: List of Acronyms Related to Surface Analysis

(e,2e)	(e,2e) spectroscopy
AEAPS	Auger electron appearance potential spectroscopy
AEES	nuclear Auger electron (emission) spectroscopy
AES	Auger electron spectroscopy
AFS	atomic force spectroscopy
AISS	alkali ion scattering spectroscopy
APECS	Auger photoelectron coincidence spectroscopy
APFIM	atom probe field ion microscopy
APS	appearance potential spectroscopy
ARAES	angle-resolved Auger electron spectroscopy
ARIPES	angle-resolved inverse photoemission spectroscopy
ARPES	angle-resolved photoelectron spectroscopy
ARPS *.viz*	ARPES
ARUPS	angle-resolved ultraviolet photoemission spectroscopy
ARXPS	angle-resolved X-ray photoelectron spectroscopy
ATR	attenuated total reflection
BEES	ballistic electron emission spectroscopy
BIS	Bremsstrahlung isochromat spectroscopy
BLE	bombardment-induced light emission
BS	momentum-resolved Bremsstrahlung spectroscopy
BSE	backscattered electron imaging
CITS	current imaging tunneling spectroscopy
CL	cathodoluminescence
CPAA	charged particle activation analysis
DAPS	disappearance potential spectroscopy
DRIFTS	diffuse reflectance (or reflection) infrared Fourier transform spectroscopy
DSPES	gamma-ray (or depth-selective) photoelectron spectroscopy
EAES	electron-excited Auger electron spectroscopy.*viz* AES
EAPFS	extended (electron) appearance potential fine structure
EDX	energy-dispersive X-ray analysis
EEAES	electron-excited Auger electron spectroscopy
EELFS	extended electron energy loss fine structure
ELS	energy loss spectroscopy.*viz* REELS
EMPA	electron microprobe analysis.*viz* EPMA
EMS	electron momentum spectroscopy
EPMA	electron probe microanalysis
EPXMA	electron probe X-ray microanalysis
ERCS	elastic recoil coincidence spectrometry
ERDA	elastic recoil detection (analysis)
ESCA	electron spectroscopy for chemical applications (originally analysis)

ESD	electron-stimulated desorption
ESDIAD	electron-stimulated desorption ion angular distributions
ESTS	electrochemical scanning tunneling spectroscopy
ETS	electron transmission spectroscopy
EWCRDS	evanescent wave cavity ring-down spectroscopy
EXAFS	extended X-ray absorption fine structure
EXELFS	extended electron energy loss fine structure.*viz* EELFS
FIM	field ion microscopy
FIMS	field ion mass spectroscopy.*viz* APFIM
FMIR	frustrated multiple internal reflections
FRS	forward recoil scattering
GDMS	glow discharge mass spectrometry
GDOES	glow discharge optical emission spectrometry
GIS	grazing incidence spectroscopy
HEIS	high-energy ion scattering spectrometry
HFS	hydrogen forward scattering
HIAA	high-energy ion activation analysis
HIERDA	heavy ion-ERDA
HREELS or HEELS	high-resolution electron energy loss spectroscopy
IBSCA	ion beam spectrochemical analysis
IEAES	ion-excited Auger electron spectroscopy
IETS	inelastic electron tunneling spectroscopy
INS	inelastic neutron scattering
Ion excited AES.*viz*	AES
IPES	inverse photoelectron spectroscopy
IPMA	ion probe microanalysis
IPS	inverse photoelectron spectroscopy.*viz* IPES
IRAS.*viz*	IRRAS
IRRAS	infrared reflection–absorption spectroscopy
IS	ionization spectroscopy
ISS	ion scattering spectrometry
ISS	ion scattering spectrometry
KRIPES	*k*-resolved inverse photoemission spectroscopy
LAMMA	laser microprobe mass analysis or spectroscopy
LAMMS.*viz*	LAMMA
LEED	low-energy electron diffraction
LEEM	low-energy electron microscopy
LEIS	low-energy ion scattering spectrometry
LMMS.*viz*	LAMMA
MDS	metastable desorption spectroscopy
MEIS	medium energy ion scattering spectrometry
MEIS	medium energy ion scattering
MIES	metastable impact electron spectroscopy
MIR	multiple internal reflection
MQS	metastable quenching spectroscopy

NAA	neutron activation analysis
NDP	neutron depth profiling
NEXAFS	near-edge X-ray absorption spectroscopy
NIXSW	normal incidence X-ray standing wave
NRA	nuclear reaction analysis
PAES	positron annihilation Auger electron spectroscopy
PAS	photoacoustic spectroscopy
PEELS	parallel electron energy loss spectroscopy
PEEM	photoemission electron microscopy
PESIS	photoelectron spectroscopy of inner shell
PIES	penning ionization electron spectroscopy
PIGE	particle-induced gamma ray emission
PIGME.*viz*	PIGE
PIXE	particle-induced X-ray emission
PM	FTIRRAS
PMP	proton microprobe
RAIRS	reflection–absorption infrared spectroscopy
RBS	Rutherford backscattering spectrometry
RBS/C	RBS-channeling spectrometry
REELS	reflection electron energy loss spectroscopy
REM	reflection electron microscopy
RHEED	reflection high-energy electron diffraction
RNRA	resonant nuclear reaction analysis
RS	recoil spectrometry
SALI	surface analysis by laser ionization
SAM	scanning Auger microscopy
SCANIIR	surface composition by analysis of neutral and ion impact radiation
SECSA	scanning electron spectroscopy for chemical analysis
SEM	scanning electron microscopy
SEMPA	scanning electron microscopy with polarization analysis
SEMPA	scanning electron microscopy with polarization analysis
SERS	surface-enhanced Raman scattering
SEW	surface electromagnetic waves spectroscopy
SEXAFS	surface-extended X-ray absorption fine structure
SEXAPS	soft X-ray appearance potential spectroscopy
SFG	sum-frequency generation
SHG	second harmonic generation spectroscopy
SIMP	scanning ion microprobe
SIMS	secondary ion mass spectrometry
SLEEM	scanning low-energy electron loss microscopy
SNMS	secondary neutral mass spectrometry
SPAES	spin-polarized Auger electron spectroscopy
SPUPES	spin-resolved ultraviolet photoemission spectroscopy
SPIPES	spin-resolved inverse photoelectron spectroscopy

SPMDS	spin-polarized metastable deexcitation spectroscopy
SPMP	scanning proton microprobe
SPR	surface plasmon resonance spectroscopy
SRPES	synchrotron radiation photoelectron spectroscopy
SRUPS	spin-resolved ultraviolet photoemission spectroscopy
STM	scanning tunneling microscopy
STS	scanning tunneling spectroscopy
SXAPS	soft X-ray appearance potential spectroscopy
SXPS	soft X-ray photoelectron spectroscopy
TCS	total (or target) current spectroscopy
TEELS	transmission electron energy loss spectroscopy
TEM	transmission electron microscopy
TERS	tip-enhanced Raman scattering
THEED	transmission high-energy electron diffraction
TOF-ERDA	time-of-flight elastic recoil detection analysis
TOF-NDP	time-of-flight neutron depth profiling
TPD	thermal desorption spectroscopy
TPRS	temperature-programmed reaction spectroscopy
TRXRFA	total reflection X-ray fluorescence analysis
UHV	ultrahigh vacuum
UPS	ultraviolet photoelectron spectroscopy
UVPES.*viz*	UPS
UVPS.*viz*	UPS
VTS	voltage tunneling spectroscopy
WDS	wavelength-dispersive X-ray spectroscopy
XAFS	X-ray absorption fine structure
XANES	X-ray absorption near-edge spectroscopy
XAPS	X-ray appearance potential spectroscopy
XEAES	X-ray excited Auger electron spectroscopy
XEAPS	X-ray excited electron appearance potential spectroscopy
XPES.*viz*	XPS
XPS	X-ray photoelectron spectroscopy
XRF	X-ray induced fluorescence
XSW	X-ray standing wave

Note: Usage of acronyms is very typical for surface analysis methods. Synonyms or different acronyms are used often for very subtle clones of the techniques; therefore, this list cannot be regarded as complete. A system for generation of acronyms for the names of the individual techniques is given by IUPAC recommendation [46].

Further Information

Information on some other techniques or acronyms, software for surface science studies, surface science databases, research centers and institutes, user groups and bulletin boards, academic research groups, teaching resources for surface science, conferences, commercials services and suppliers, sources of practical information, and also, a collection of links to lecture courses and tutorials covering a broad range of surface science can be found on web sites, for example: *http://www.uksaf.org/tech/list.html*.

Section VII
Methods 6: Spectroscopy in Nano Dimensions

Handbook of Spectroscopy, Second Edition. Edited by Günter Gauglitz and David S. Moore.

21
Single-Molecule Spectroscopy

Frank Schleifenbaum, Christian Blum, Marc Brecht, and Alfred J. Meixner

21.1
Motivation and Necessity of Single-Molecule Studies

All types of spectroscopy have in common that they are concerned with information about molecular structures, may it be the monitoring of individual chemical bonds, the observation of an electronic structure and its interaction with its environment, or the spatial composition of atoms in a crystal lattice. As powerful as these methods are, they typically refer to averaged data derived from a huge number of molecules and thus report on the typical, but not on individual features of these types of molecules. However, the ultimate goal of any science is to go to the innermost item of nature, which is considered to represent the properties observed in bulk studies. This innermost item can, for example, be regarded as an individual molecule as the basis of the current understanding of the composition of nature. Thus, an approach to single-molecule spectroscopy would open the field to investigate the most reduced functional fraction in nature. This becomes even more obvious regarding, for example, chemical symbolic language [1]. Here, the incorporated models depict chemical reactions of single molecules, such as $A + B \rightarrow C$, whereas the observation is ensemble. Thus, specific details typically remain concealed, but might be uncovered by the investigation of a single molecule. Moreover, a single molecule, given that it is not isolated in the gas phase, is always accompanied by neighboring molecules, the so-called local chemical environment, which might affect its individual (spectral) properties [2]. Thus, single-molecule spectroscopy does not only provide information about the basic functional composition element of nature but it might also be useful as a reporter for the local chemical environment.

In this chapter, we first discuss the intrinsic problems to be solved toward optical single-molecule detection. We present approaches to overcome these problems with both methodical and technological respect. After that we proceed to a chronological journey through the field of single-molecule spectroscopy, demonstrating the huge potential of these techniques. Starting from a very general concept, the different peculiarities that have developed are shown along with what modern single-molecule spectroscopy is capable of in order to provide a deeper understanding of

Handbook of Spectroscopy, Second Edition. Edited by Günter Gauglitz and David S. Moore.

molecular processes in nature. Finally, novel applications and developments are discussed in a compact outlook.

21.2
Intrinsic Problems and Difficulties in Optical Single-Molecule Techniques

It was not until the 1990s that the first optical single-molecule studies could be carried out [3–6]. The basic reason this technique developed so late simply lies in the intrinsic properties of a single molecule. This is small in size, is expected to give low signals, and typically is accompanied by neighboring species interfering unspecifically with the target molecule [7]. These were the main challenges that have to be fought on the course to single-molecule spectroscopy. The first concern of the low signal level is mainly a technical issue. Here, highly efficient detectors, in combination with decent computation power for instrument control and data analysis, were required. Regarding typical absorption cross sections in different regimes of the electromagnetic spectrum, it becomes obvious that the amount of radiation absorbed by an individual molecule is too weak to be separated from the excitation radiation [1]. This, in turn, limits the types of spectroscopies capable of single-molecule detection to those that are self-emitting rather than solely absorbing. We utilize the fact that generally it is more feasible to detect a weak signal in the dark than to identify a missing fraction in a bright signal. For illustration, imagine a big city at night. We probably would not notice one single light turned off. Contrarily, we would immediately identify a single bulb turned on in a lonely cottage in the mountains at night. The most prominent technique that fulfills this basic requirement is the optical fluorescence spectroscopy [3]. Here, the emitted light is shifted both spectrally and temporally with respect to the excitation radiation, which, accordingly, can be easily separated from the fluorescence signal.

So far, we have already learned that fluorescence-based techniques are one method of choice for single-molecule detection. This leads us to the next problem, which is about discrimination: if we do not work in the gas phase (which is experimentally very challenging and would not give any information about the interaction of an individual molecule with its local chemical environment), the ‘‘single’’ molecule to be investigated is always surrounded by neighboring molecules. Accordingly, in a sample volume, which is spatially more extended than a molecular structure (which is typically the case), a large number of molecules would be simultaneously addressed. To nevertheless perform single-molecule studies, one out of these many molecules in the sample volume has to be special, for example, one molecule in the investigated area must provide a recordable signal, whereas the moiety remains undetected. This important criterion can again be met by fluorescence-based approaches if a fluorescent molecule is embedded in a nonfluorescent surrounding matrix. In this way, merely the fluorescent label can be addressed optically to emit fluorescence photons, whereas the surrounding matrix remains invisible. However, although we claimed that the molecules of interest are embedded in a nonfluorescent matrix, the summation of a vast multitude of ''nonfluorescent'' species, will result in a noticeable signal due to, for example, nonperfect materials or impurities. Hence, the matrix typically will contribute to an unspecific background signal that overlaps with the desired molecular emission. If the amount of background signal gets too dominant, the signal-to-noise ratio (SNR) drops under the detection level and the emission of the individual target molecule cannot be resolved. To overcome this problem, the easiest way is to keep the amount of background signal as small as possible by reducing the detection volume, that is, the sample volume from which emitted light is detected, to a minimum. Accordingly, a preferably small sample volume, which confines the contribution of undesired neighboring molecules, is a prerequisite for single-molecule spectroscopy and imaging. A more detailed discussion is given in Section 21.3.

The need for luminescent species suited for single-molecule spectroscopic studies actually does not limit the number of molecular systems suited for single-molecule studies as much as we might expect at a first glance [8]. Currently, there is a huge variety of different fluorescent dyes, commercially available and absorbing and emitting over the entire visible spectral range [3, 9, 10]. Moreover, biotechnological progress offers a number of autofluorescent proteins (AFPs) with emission from the dark blue over green and yellow to the dark red spectral region [11–15]. These proteins are of high interest, as they can be expressed by a living organism and external staining can be avoided. Moreover, nanometer-sized quantum emitters based on inorganic semiconductors are available as highly photostable luminescent species [16–21]. Recently, even metallic nanoparticles have been reported as promising systems for single-molecule spectroscopy [22–25].

21.3
Technical Realization

These thoughts lead to the issue as to how these requirements can technically be met. Unlike in typical classical spectrometers, cuvette-based techniques cannot be used for single-molecule spectroscopy because of the large sample volumes. Here, a single dye molecule is surrounded by a huge number of solvent molecules, which induce background signals. These corrupt the SNR and thus hamper single-molecule detection as discussed earlier.

The most appropriate tool to achieve a minimal detection volume is given by microscopic techniques, especially by confocal microscopy, where the detection volume is confined by the diffraction limit of electromagnetic waves [26, 27]. For a typical wavelength of 500 nm, the diffraction-limited focal volume of a confocal microscope becomes as small as 0.2 fl (2×10^{-16} l). To further reduce the detection volume, the molecules can be embedded in a thin polymer film, strongly confining the sample volume in the axial direction [28]. In this case, regarding a surrounding matrix with a typical thickness of 50 nm and assuming a molecular size of 1 nm^3, in the focal volume there are roughly 1–5 million molecules. Accordingly, to detect one individual molecule out of 1 million, the product of absorbance cross section and the fluorescence quantum yield of this target molecule as a measure for molecular brightness have to exceed the sum of this product from all matrix molecules to obtain a reasonable SNR. This requirement is met for the combination of typical transparent polymers such as polystyrene (PS), polyvinylalcohol (PVA), or poylmethylmethacrylate (PMMA) with typical fluorescent dyes with high fluorescence quantum yields such as xanthene and perylene derivatives.

The technical requirements for a confocal microscope feasible of single-molecule spectroscopy are relatively moderate as depicted in Figure 21.1.

The collimated monochromatic excitation light, typically from a laser source, is focused onto the sample via a high NA microscope objective, resulting in a diffraction-limited excitation spot. The emitted light is collected by the same objective and led through a dichroic beamsplitter, which reflects the excitation light while the bathochromically shifted (i.e., shifted to higher wavelengths) emission signal is transmitted. To filter out backscattered excitation light, which even after passing the dichroic beamsplitter is still orders of magnitude more intense than the weak fluorescence signal, steep-edge longpass filters are inserted into the beam

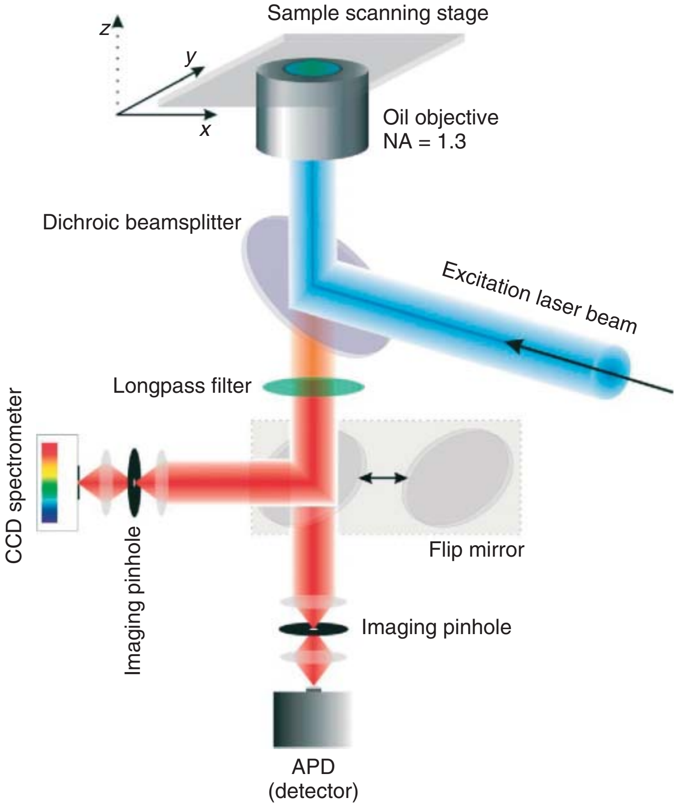

Figure 21.1 Confocal sample scanning setup.

path. The light is then focused through a pinhole onto the active area of a detector unit.

The kind of detector depends on the spectroscopic requirement. To record an intensity image of the sample or to record the intensity behavior of single molecules overtime, spectral integrating detectors such as avalanche photodiodes (APDs) with single photon sensitivity and a high time resolution, are used. To record frequency-resolved spectra of the individual emitters, the emitted light can be led to a spectrometer, typically consisting of a spectrograph coupled to a highly sensitive CCD camera. This configuration is crucial for single-molecule spectroscopy and deviates from standard ensemble spectrometers. However, in these spectrometers, fluorescence spectra are recorded by rotating a grating or a prism and directing the spectrally dispersed light onto a point detector. For single-molecule detection, it is not feasible to rotate the dispersive element due to the digital characteristics of single-molecule emission, which will be discussed in detail later on. Using a two-dimensional CCD chip, we can record the entire spectrum at a time, and thus the spectrum is not corrupted by, for example, temporal unstable emission.

The confocal principle comprises point-to-point imaging of a sample area [29]. Accordingly, to generate an image, the sample must be raster scanned relative to the detection volume. Currently, there are several methods to accomplish this raster scanning (e.g., beam scanning and spinning disk), but for single-molecule studies, the sample-scanning technique has prevailed in most cases because of high spatial precision together with superior beam quality. In the sample- or stage-scanning technique, the sample is scanned through the focus of a stationary objective via a feedback-controlled piezo-driven sample stage. Thus, a position accuracy of a few nanometers is obtained, while the optical beam path remains unaffected from the scanning routines. An alternative technique utilizes a movable excitation beam, which is raster scanned along the back aperture of the microscope objective. Although this technique allows for fast image acquisitions, the excitation profile is inhomogeneous over the sample and not every molecule experiences the identical excitation field.

21.4
How it Began: Low-Temperature Studies

The first single-molecule spectroscopy studies were carried out in the early 1990s by W.E. Moerner and M. Orrit at liquid helium temperatures [6, 30–32]. In those early days, the available equipment could not meet all requirements reported earlier. Especially, high-precision scanning stages were not available and the necessity of precisely scanning a sample had to be circumvented. Moreover, it was necessary to detect as many photons as possible from an individual molecule.

Still, it had to be ensured that the addressed molecule was different from its surrounding medium so that it could be observed individually. This was met by keeping the detection volume small and by utilizing some characteristics observable at cryogenic temperatures below 4 K. Here, special characteristics of molecular emission that are covered by thermal noise at room temperature come into play, which is discussed in brief in the following [33].

Typical fluorescence spectra at room temperature are very broad and unstructured because of various mechanisms increasing the linewidth. Most of these mechanisms can be suppressed by lowering the temperature. In the low-temperature limit, the linewidth of a fluorescence spectrum is solely defined by the excited-state lifetime, that is, the timespan a molecule remains in the excited S_1 state after the absorption of a photon [34]. The resulting natural, homogeneously broadened spectral linewidth is as small as 10–100 MHz for typical fluorescent molecules with nanosecond excited-state lifetimes as shown, for the example of terylene at different temperatures, in Figure 21.2.

The transition energy of a fluorophore basically represents its electronic properties. However, the local chemical environment wherein a fluorophore is embedded holds the ability to tune the transition energy remarkably. Depending on the matrix, the composition of the environment of every individual fluorophore can be different. Accordingly, each fluorophore in this host matrix experiences slight differences in its local chemical environment, leading to slight shifts in the frequency of the transition for both, the excitation ($S_0 \rightarrow S_1$) and the emission ($S_1 \rightarrow S_0$). At very low temperatures, these differences become visible in the excitation and emission

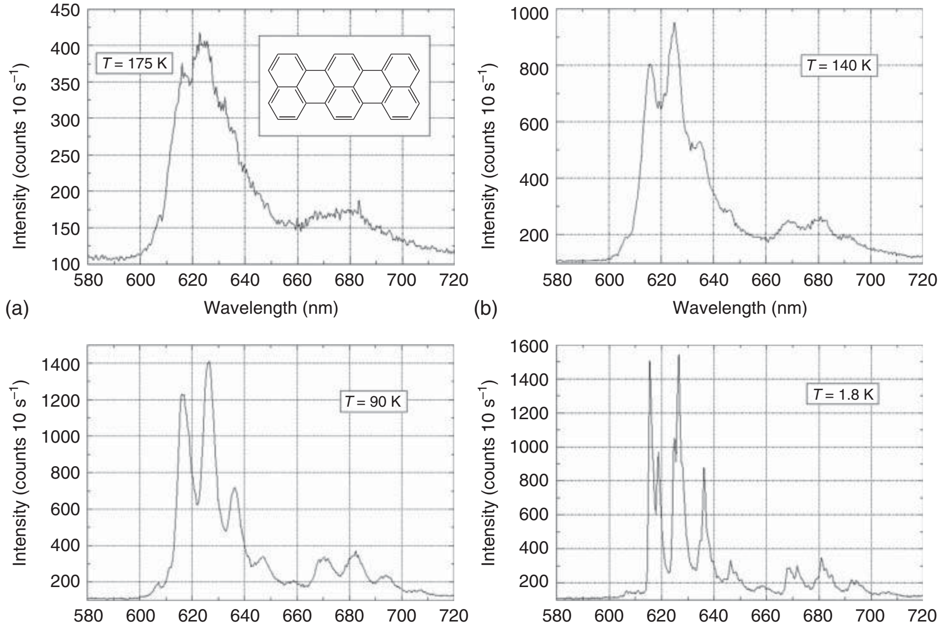

Figure 21.2 (a–d) Fluorescence spectra of an ensemble of terylene dyes in a Sphol'skii matrix at different temperatures.

spectrum of an individual molecule [35, 36]. This, in turn, can be used to selectively address individual emitters among others, as will be explained in the following.

For an ensemble of emitters, all molecules in the focal volume contribute to the measured signal, which results in an averaged spectrum that is broadened to a full width at half maximum (FWHM) of up to 30 GHz as shown in Figure 21.3.

While this broadening might definitely tell us something about the heterogeneity of the matrix system, still we are not investigating single molecules. Yet, the inhomogeneous line broadening opens the way to single-molecule detection. Two strategies are applicable: (i) using a single-mode laser source with a spectral linewidth comparable to the homogeneous broadened linewidth of a molecule, we can scan the excitation wavelength along the inhomogeneously broadened ensemble spectrum. At the very edges of the distribution (blue curve in Figure 21.3), finally we achieve an excitation wavelength, where exactly one molecule in the focal volume is in resonance with the excitation light. As a result, we can monitor the emission of an individual emitter at low temperatures by exactly tuning the excitation wavelength of a small bandwidth laser source. (ii) The other, maybe more straightforward, approach uses diluted dye solutions. Thus, for a given excitation wavelength, the number of molecules in the detection volume, which are in resonance with the excitation, can be reduced to an extent, where exactly one molecule is excited.

As discussed earlier, narrow line spectra were crucial for the first single-molecule investigations in solids at cryogenic temperatures. The line shape of these molecules depends thereby remarkably on the properties of the solid. The main differences

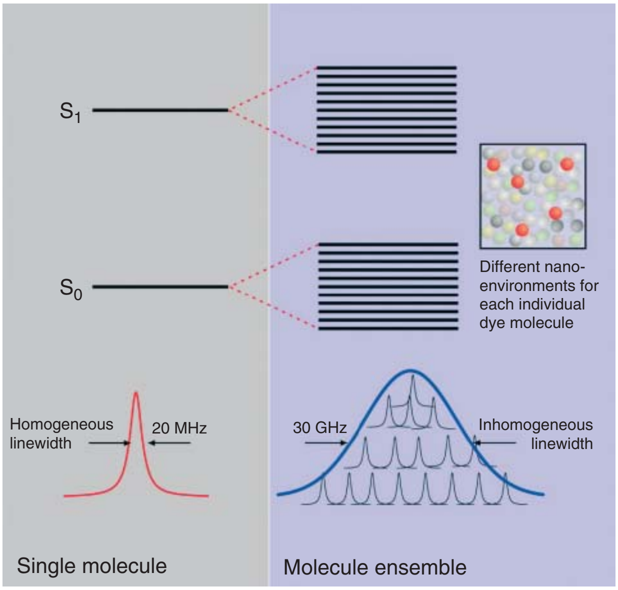

Figure 21.3 Homogeneous and inhomogeneous spectral line broadening at low temperatures.

between the optical bands of a molecule embedded in a solid and those in the gas phase are due to the interaction of the molecules with lattice vibrations (phonons). The shape of vibronic bands is determined by the electron–phonon coupling. At low temperature, the emission of every vibronic band consists of a narrow zero-phonon line (ZPL) and a relatively broad phonon wing (PW) at the long-wave side of the ZPL. The ZPL corresponds to a transition of the molecule without changing the number of phonons in the matrix, whereas the PWs are related to the transitions that create or annihilate phonons. The intensity Z of the optical band profile can be described in the form

$$I(\upsilon, T) = I_{\mathrm{ZPL}}(\upsilon, T) + I_{\mathrm{PW}}(\upsilon, T) \tag{21.1}$$

The ZPL has a Lorentzian shape with width γ. The ratio of ZPL and PW intensities can be characterized by the Huang–Rhys factor S [37] that is closely related to Debye–Waller factor $\alpha(T)$, which depends on temperature according to

$$\alpha(T) = I_{\mathrm{ZPL}}/(I_{\mathrm{ZPL}} + I_{\mathrm{PW}}) = \exp(-S(T)) \tag{21.2}$$

When temperature is increased, $S(T)$ increases, so that I_{ZPL} and $\alpha(T)$ decrease rapidly. Therefore, sharp ZPLs can only be observed at low temperatures and weak electron–phonon couplings.

The dependency of the I_{ZPL} and I_{PW} for the emission of a single fluorophore on the electron–phonon coupling is shown in Figure 21.4 by simulations. Values of $S \leq 0.7$ are considered as weak electron–phonon coupling. In those cases, needlelike ZPLs can be easily observed in fluorescence emission. For larger values of S, the intensity of the ZPL becomes much smaller. In this case, a much higher S/N ratio is necessary to observe ZPLs.

The requirements needed to observe the ZPLs in emission are perfectly matched for crystalline systems, and line narrowing was demonstrated for such samples. However, it is little convenient to dope solid-state crystals with organic (poly-) aromatic dye systems. Therefore, we have to find a host matrix with a quasi-crystalline structure, which simultaneously is capable of dissolving organic dye molecules. This requirement is met by low-molecular-weight linear alkanes, referred to as *Shpol'skii matrices* [40], and low-molecular-weight nonpolar fluorophores. Alkanes have strong absorption bands in the UV but are transparent in the visible regime, where fluorescent dyes are excited and emitted. Owing to their chemical nature, alkanes are good solvents for nonpolar aromatic compounds such as typical organic fluorophores. Moreover, at cryogenic temperatures, these compounds form crystal-like ordered structures, providing a uniform environment for the embedded chromophores. However, as the chromophores are not actually integrated into a crystal lattice, the chromophore–matrix coupling is minimized, leading to small Hunag–Rhys factors. Owing to this weak coupling, not only the fluorescence linewidths are narrowed but the PW of the fluorescence spectrum is also suppressed. This wing is caused by collective vibrations of the chromophore and the host matrix. A weak coupling reduces the probability for these vibrations to form. As a result, the spectral bandwidth of the molecular emission is reduced as

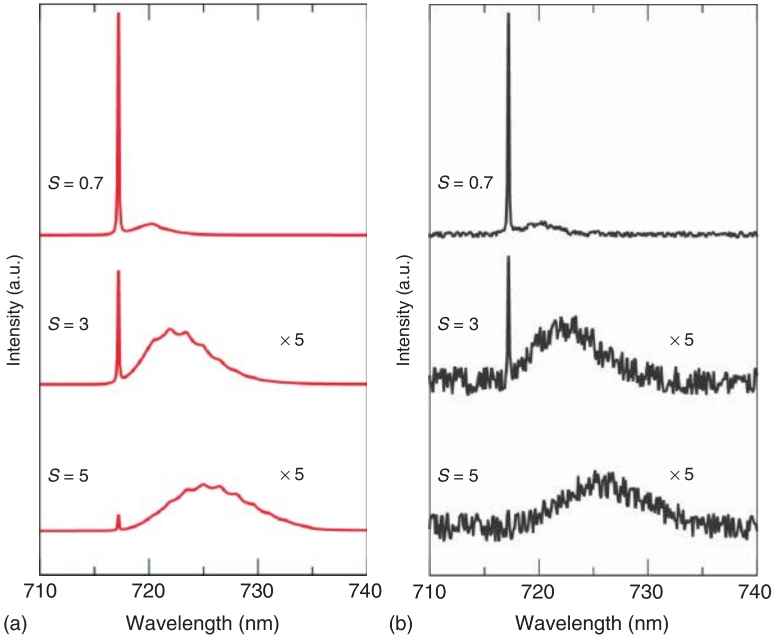

Figure 21.4 Simulations of the line shape of a single emitter as a function of the strength of the electron–phonon coupling. The Huang–Rhys factor S was changed as indicated in the plots (a). A noise level was added to these data, while the integrated intensity of the whole emission line (ZPL and phonon wing) was kept constant (b). The comparison illustrates clearly that observability of an ZPL depends on S. Simulation parameters are width of the ZPL, $\gamma ZPL = 2\,\mathrm{cm}^{-1}$; mean frequency of the phonon distribution $\omega = 30\,\mathrm{cm}^{-1}$; width of the phonon distribution, $\Delta\omega = 30\,\mathrm{cm}^{-1}$. For simulation, the expressions given in Ref. [39] were used.(The figure is adapted from [38].)

a prerequisite for the frequency selective single-molecule spectroscopy described earlier.

Figure 21.5 shows a typical fluorescence spectrum of a single terylene dye molecule at 1.8 K in a Shpol'skii matrix. Clearly, the inhomogeneous broadening dominating at higher temperatures (see Figure 21.2 for comparison) vanishes and the spectrum is composed of sharp, natural lifetime limited lines. Owing to the line narrowing, even the distinct vibronic levels of the molecule become accessible, enabling fluorescence spectroscopy for vibronic studies. Typically, in the ensemble, these lines cannot be resolved because of averaging over a large number of emitters (Figure 21.2d). However, if a single molecule is investigated, the individual vibronic levels appear and can be assigned to distinct vibration energies (Figure 21.5).

To unequivocally prove that in fact an individual emitter has been observed, the nonclassical properties of an individual molecule have to be considered. Molecular fluorescence is a successive one-photon process of excitation and emission. Accordingly, if only one single emitter is investigated, it is impossible to observe

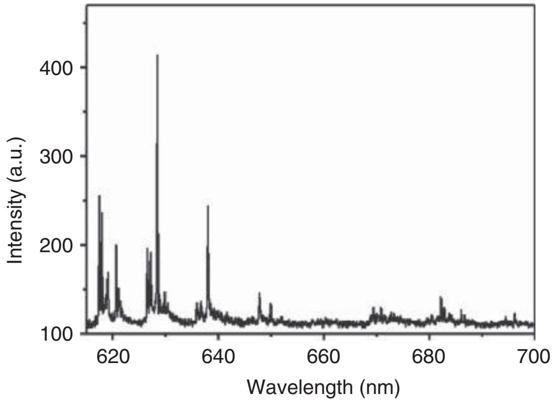

Figure 21.5 Emission spectrum of a single terylene molecule at 1.8 K in a Shpol'skii matrix.

two-fluorescence photons at a time. On the contrary, as soon as more than one emitter is observed, there is a certain probability of detecting two or more photons simultaneously at the same time [31].

One experimental demonstration based on photon correlation measurements can be achieved using a Hanbury–Brown and Twiss (HBT) setup [41, 42] (Figure 21.6a).

In an HBT configuration, photons emitted from a sample are split in two paths by a beam splitter. The photons are detected by two independent detectors A and B, and the time correlation between the arrival times is calculated numerically. Note that typically two detectors are used to compensate for detector dead times after a photon-counting event. For a detailed explanation of the experimental setup,

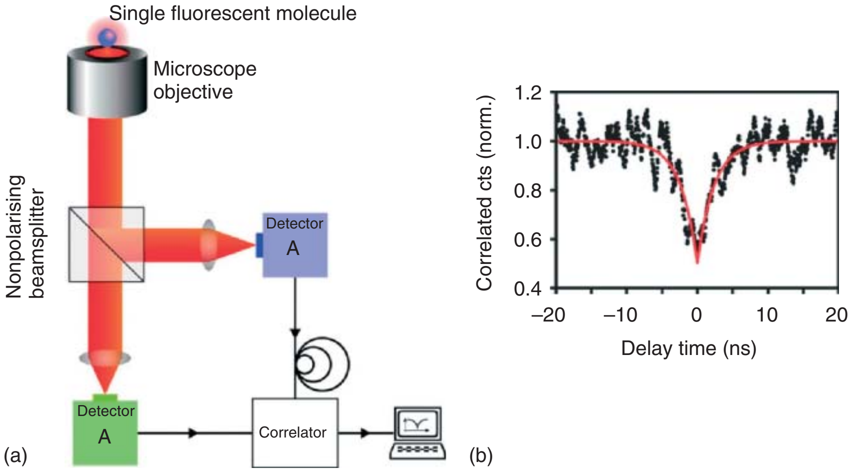

Figure 21.6 (a) A schematic representation of a Hanbury–Brown and Twiss configuration and (b) photon antibunching curve of a single molecule at cryogenic temperatures.

see [43]. The time correlation of photon arrival times provides the probability of detecting a photon on both detectors in a given time interval $t_0 + \Delta t$. For $\Delta t = 0$, this probability becomes zero for a single emitter because of the successive excitation–emission process discussed earlier. Accordingly, simultaneous photon detection on both detectors A and B is impossible. Therefore, correlating the photon arrival times on both detectors reveals a zero correlation at a certain time t_0, representing the zero probability of detecting two photons at this time.

This zero correlation is only expected for an isolated molecule and is represented by a dip in the correlation curve (Figure 21.6b), due to the isolated, ''antibunched'' photons emitted by a single quantum emitter. In Figure 21.6b, such a photon antibunching curve recorded from a single terylene dye molecule at 1.8 K is depicted. Strictly, we would expect the correlation function $g^2(\tau)$ to be zero at t_0. However, owing to a certain amount of dark counts generated randomly by the solid-state detectors and electronic noise, we have recorded some photon-counting events without a photon reaching the detector, causing the $g^2(\tau)$ curve not to drop to zero at t_0. Typically, $g^2(\tau)$ values ≤ 0.5 are accepted as a proof for single-molecule detection [44].

21.4.1
Recent Applications of Single-Molecule Spectroscopy at Low Temperatures

In the first period of single-molecule research, the interest was focused on the properties of single molecules that became observable for the first time. Soon after the initial stage, the newly developed techniques were also used to study much more complex systems such as light-harvesting systems of the photosynthetic apparatus [45].

The interaction of the chromophores within a protein is different from that in crystalline matrices. One reason for this difference is the ''material'' of which a protein is made. In its largest parts, this material consists of chains of amino acids that differ in their side chains (residues) attached to their alpha carbon. The size of the attached residues can vary remarkably in size from just one hydrogen atom in glycine to a large heterocyclic group (indol) in tryptophan. Among the amino acid residues, there are polar and unpolar as well as charged and neutral groups. The fold of the amino acid chain is one key component that determines the shape and function of the proteins in general. At the molecular level, the fold determines geometrical and chemical composition of the pocket wherein the chromophores are bound.

For one kind of protein, the composition of the amino acid chains is identical. Thus, the binding pockets are also similar. The transition energy of a chromophore is tuned by the electrostatic properties of the binding pocket. This type of tuning gives proteins the ability to modify the transition energy of the chromophores to maintain optimal protein function.

The forces holding a protein in its conformation are mostly much weaker than the forces of a covalent bond. As a consequence, there is not one well-defined conformational state of a protein, but a huge number of conformational states that differ only slightly in energy. It depends on the availability of energy and/or heights of the barrier between two conformations whether a protein remains in its present conformational state or it undergoes a conformational change.

The best description of this type of conformational dynamics is the picture of an energy landscape. On the basis of this description, the dynamic occurs on a complex, rugged energy landscape characterized by a large number of different conformational substates, as shown by the pioneering experiments of Frauenfelder and co-workers [46] on myoglobin, which is also called the *H-atom* of biophysics. The conformational substates correspond to local minima in the potential energy surface. Protein energy landscapes are characterized by the existence of many, nearly isoenergetic, local minima, which are organized in a hierarchical structure. At ambient temperatures, this results in fast fluctuations between many conformational states involving also large-scale motions as visualized in Figure 21.7c).

The motion of proteins also influences their bound chromophores. The largest effect on the site energy is due to the conformation of the chromophore itself and/or its close surrounding. The variation in the site energy over time is also called *spectral diffusion* (Figure 21.7c). A huge number of these spectral changes undergo much faster than the actual time needed to acquire an emission spectrum from a single protein ($\ll$1 ms). As a consequence, the acquired spectra are much broader than it is expected for a single emitter; and the determination of the electron–phonon coupling or the properties of the binding pocket is not possible. One option to reduce conformational motion is to lower the temperature. At low temperature, the activation energy for crossing the barriers between conformational states in the highest hierarchical levels of the energy landscape is no longer available. An additional advantage for investigations at low temperature is the increased photostability of chromophores [47]. Under these preconditions, spectroscopic investigations with high spectral resolution are possible. The advantage of this approach was well demonstrated in single-molecule experiments on light-harvesting complexes, where different absorption properties of individual chromophores were found as well as a dynamical hopping between conformational substates of single chromophores [48]. An example of the power of low-temperature spectroscopy on proteins is shown in Figure 21.8. The emission of two different chromophores bound to one photosystem I complex is visible in the sequence of emission spectra (Figure 21.8a). In both cases, the ZPL and the PW are resolved. The ZPLs undergo changes in the wavelength, which are visible as a shivering as well as line jumps in the range of several nanometers (Figure 21.8b). It is possible to determine the strength of the electron–phonon coupling for both emitters (Figure 21.8c) based on the intensity distributed between the ZPL and the PW [38].

The observed spectral hopping of lines in single-molecule experiments relies often on the higher barrier crossing probability between conformational substates in the excited state of the chromophore than in the ground state. These activated barrier crossings enable single chromophores to map the energy landscape even at low temperatures and thus provide a spectroscopic tool to obtain general insights into the characteristics of protein energy landscapes [49].

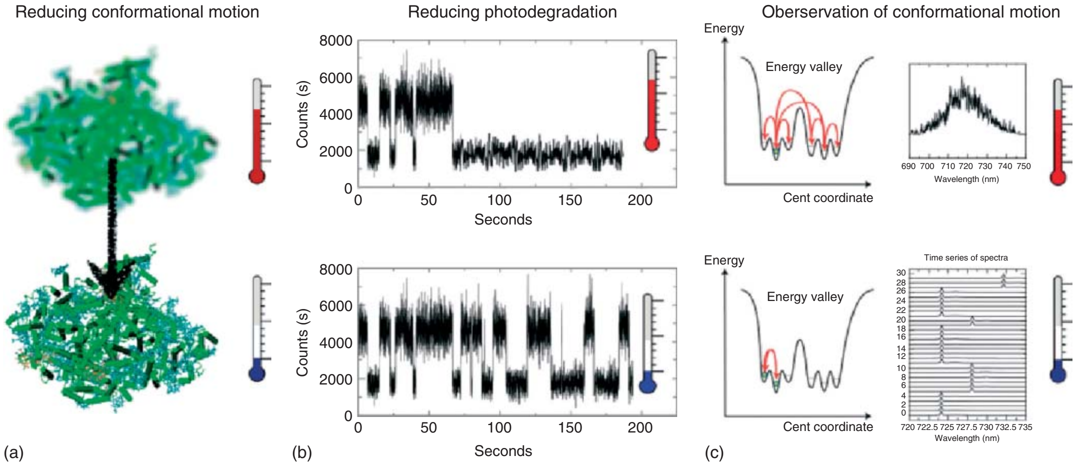

Figure 21.7 (a–c) Illustration of the advantages of single-molecule spectroscopy on proteins at low temperatures.

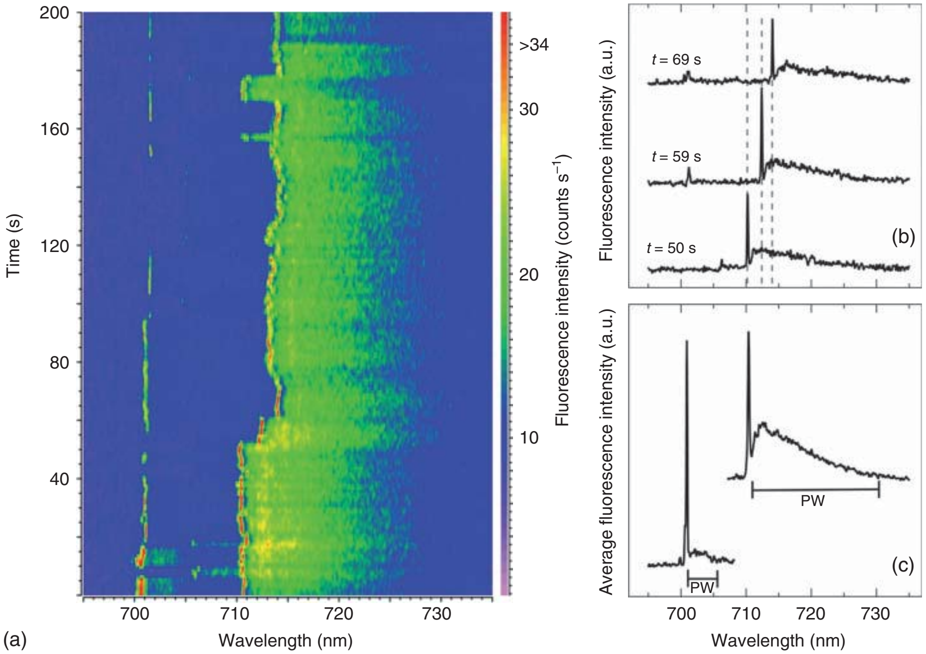

Figure 21.8 (a) Sequence of 200 fluorescence spectra taken continuously from a single photosystem I complex from Synechocystis PCC 6803. The acquisition time of the single spectra was 1 s. (b) Three single spectra out of the sequence given in (a). (c) For the emitter in the range of 710–715 nm, 16 spectra where the ZPL resides almost on the same position were summed up, and the assumed width of the PW (710.8–730 nm) is given by a bar. (a) On the basis of the width of the phonon wing, a value of the Huang–Rhys factors $S = 2.9 \pm 0.5$ was determined. For the ZPL in the range 700–706 nm the spectra between 15 and 17 s were summed up, the assumed width of the PW (from 701.3 to 705.5 nm) is indicated by a bar resulting in $S = 0.53 \pm 0.05$.(The figure is adapted from [38].)

21.5
Single-Molecule Spectroscopy at Room Temperature

Although the low-temperature studies already gave a fascinating new insight into the molecular world and demonstrated phenomena that could not be seen before in an ensemble, it was desirable to develop techniques that allow for single-molecule spectroscopy also at room temperature for several important reasons: obviously, investigations at temperatures as low as a few Kelvin are experimentally demanding and expensive. Hence, they are only available in a few laboratories to investigate scientific questions, which require cryogenic temperatures where, for instance, molecular diffusion or molecular folding are frozen or hardly observable. However, in many fields, such dynamic processes are essential, for example, in life sciences. Accordingly, it was desirable to detect single molecules to room temperature conditions. Similar to cryogenic studies, the basic requirements of (i) a small detection volume and (ii) sample systems where the target molecules are isolated and embedded in a nonfluorescing environment have to be met. A small detection volume is achieved by confocal microscopy techniques, allowing for the investigation of sample volumes as small as a few femtoliters [29]. For the second requirement, the isolation of an individual molecule, the major low-temperature strategy, which uses line narrowing of the fluorescence spectrum to address single molecules, cannot be applied. As both, absorbance and fluorescence spectra are inhomogeneously broadened at room temperature, resulting in unstructured fluorescence bands of several tens of nanometers at FWHM, spectral selection using narrow-band laser sources is not feasible. To circumvent this problem, a very straightforward approach was established: diluting a dye solution down to the picomolar range results in spatially isolated chromophores statistically dispersed in the overall volume. In this way, in a given detection volume, typically we will observe just one molecule at a time [1].

21.5.1
Single-Molecule Room-Temperature Studies in Solution

This approach was indeed used successfully in the early single-molecule detection experiments performed at room temperature in solution either in a hydrodynamic flow, in microdroplets, or freely diffusing through the diffraction-limited focus of a confocal microscope in the early 1990s [50] techniques, which were developed independently from cryogenic single-molecule spectroscopy. In a highly diluted solution of dye, molecules such as Rhodamine 6G in water and ethanol as a solvent were allowed to freely diffuse through the focus of a confocal fluorescence microscope as the detection volume. In such studies, the detection volume is irradiated with laser light for exciting the molecules and each time one chromophore passes by, the Stokes-shifted fluorescence light is recorded with an APD with millisecond time resolution. Histograming the integrated intensity versus the measurement time reveals a constant background level with single intense bursts (Figure 21.9).

These bursts are fluorescence signals from individual molecules, which diffuse into the confocal detection volume where they are excited and thus emit fluorescence photons. After a characteristic time, the molecule diffuses out of the focal volume

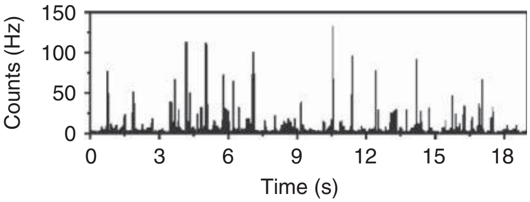

Figure 21.9 Intensity trajectory recorded from a highly diluted Rhodamine 6G dye solution in a confocal detection volume. Every time a molecule diffuses through the focus, a fluorescence burst is observed.

and the intensity abruptly drops back to the background level. Such liquid-phase intensity trajectories have been among the first examples demonstrating the feasibility to study single molecules at room temperature. Although the information content of these measurements seems to be rather low at first glance, direct information about, for example, the viscosity of the solvent and the free diffusion of molecules can be gained from these studies. As is discussed in the section about fluorescence correlation spectroscopy (FCS), even a quantitative determination of aggregation sizes of individual molecules can be achieved by an adoption of this measurement procedure. Nonetheless, the most important impact of these early room-temperature studies was the demonstration of the technical feasibility to detect the weak signal of a single molecule under relevant room-temperature conditions.

21.5.2
Single-Molecule Studies in Solid Hosts

Although it was a great progress that single-molecule studies could be performed at room temperature, it was desirable to keep the target molecules spatially fixed during the investigation. This would open the way for a careful spectroscopic characterization of molecular emission, which was expected to increase the insight into molecular matter. However, before the first studies of spatially fixed and isolated emitters were reported, some major requirements had to be met. First, for solid-host single-molecule spectroscopy, the technical issue of high-precision sample scanning had to be addressed. Contrary to liquid-phase studies, the molecules under investigation had to be actively shifted into the detection volume, that is, the confocal focal volume. For that, high-precision piezo-controlled scanning stages, which could precisely scan the sample through the focal spot, were mandatory. For further confining the excitation volume below the diffraction limit, single molecules were excited in the optical near-field of small apertures of ∼100 nm diameter at the end of pointed optical fiber probes. A specific advantage of this technique is that the sample topography can be obtained simultaneously to the optical measurement from the feedback control used to keep the aperture at nanometer distance from the sample surface [51].

Feedback-controlled piezo-based scanning stages, which allow for repeatedly addressing a defined sample position, are commercially available since mid-1990s and considerably helped to detect and localize single molecules in solid matrices or on surfaces [52].

An important requisite for such studies is the solid matrix, which is capable of solving the target dye molecules and is simultaneously nonfluorescent at the chosen excitation wavelength. While organic solvents, composed of small molecules, are often nonfluorescent at wavelengths in the visible regime, this is not necessarily true for solids. Here, owing to larger and stronger interacting molecules, side products can be formed or impurities embedded. Both can lead to the formation of impurities, which might interact with the excitation light. This, in turn, would cause a luminous matrix background, corrupting the SNR and thus hampering the detection of single-molecule fluorescence. However, it turned out that polymers such as PS [53], PMMA, or PVA [54] meet the requirements for a sufficiently low-fluorescence background and can serve as a host material for unpolar (PS and PMMA) or polar (PVA) dye systems for recording sequences of many spectra from one and the same single molecule and observing considerable spectral dynamics essentially until the molecule photobleaches.

For sample preparation, a diluted polymer solution (1–2% by weight) is doped with a highly diluted dye solution ($c_{\text{dye}} = 10^{-9}$ to 10^{-10} M). Afterwards, this sample solution is spincoated on a glass substrate, typically a microscope coverslip, to form a thin film of dye-doped polymer. The achieved film thickness, which can be adjusted by the rotation speed and the number of droplets from the polymer solution, is conveniently around 50 nm. Thus, the confocal detection volume is reduced by one order of magnitude down to 0.02 fl. As a consequence, the SNR is enhanced, which is then high enough for extended single-molecule spectroscopy in solid film at room temperature.

Before any spectroscopic investigation, the individual molecules have to be localized. This is typically accomplished by raster scanning a certain area of the sample through the confocal volume. Thus, an intensity image is obtained, where individual molecules appear as diffraction-limited bright spots. The spot size accounts for the fact that the physical dimension of a molecule can be neglected compared to the diffraction-limited focal size. Therefore, a single molecule can be regarded as a point emitter and thus reflects the point-spread function of the optical setup (Figure 21.10).

The most intuitive type of investigation possible with this polymer film sample systems is, in analogy to the liquid-phase studies, the measurement of the fluorescence intensity evolution with time. For an ensemble of emitters, we observe

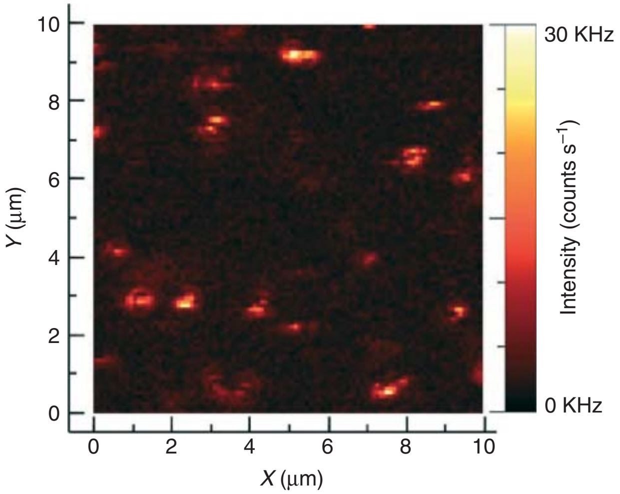

Figure 21.10 Raster scan image of single perylene dye molecules appearing as diffraction-limited fluorescence spots embedded in a thin PS polymer layer at room temperature.

a steady decrease in intensity as a function of time due to photobleaching of the chromophores. These trajectories obey a simple exponential decay and can be used to determine the photostability of a given dye system. This behavior is expected in the ensemble where a multitude of undistinguishable emitters contributes to the recorded signal. Photobleaching of a certain amount of these emitters hence results in the corresponding decrease of fluorescence intensity.

For an individual molecule, we have to consider its singular, binary nature, for example, a single molecule emits photons one by one on excitation until the molecule changes its structure permanently, for example, by the interaction with the environment such that it can no longer be excited or emit photons. At this moment, the molecule abruptly photobleaches and stays dark. Hence, recording the intensity trajectory, we expect to observe a binary behavior when photobleaching occurs.

Figure 21.11a depicts a typical example of an intensity trajectory of a single fluorescent molecule fixed in a polymer film. Clearly, we find two distinguishable intensity levels, as indicated by the histogram in the inset. The molecule is in a strongly radiating ''on-state'' at the beginning of the measurement, revealing photon counting rates of 16 KHz. After ∼19 ms, photobleaching occurs and the intensity abruptly drops to a low level with a photon counting rate of 5 KHz, representing background level. This switching behavior between ''on-'' and ''off-state'' is a clear demonstration of the binary nature of a single fluorescent molecule and thus is well accepted as a proof for single-molecule detection [55–57]. Note that the duration of the time interval for which a molecule emits fluorescence photons under constant illumination until it photobleaches abruptly (i.e., the photobleaching time) is an arbitrary process and hence the summation of photobleaching times of a large ensemble of individual emitters reveals a steadily decreasing function, which exactly samples the ensemble photobleaching behavior of these molecules in the same environment.

Although this binary behavior is often observed in single-molecule studies, more complex intensity trajectories are also frequently observed as shown, for

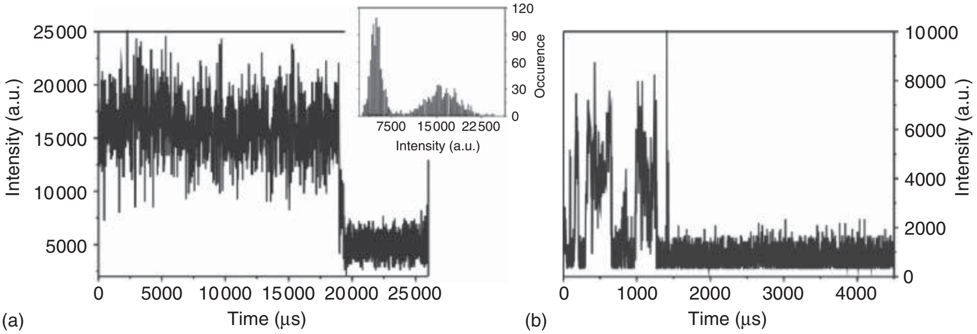

Figure 21.11 Single-molecule fluorescence trajectories. (a) Binary transition from an emitting on-state to a dark off-state and (b) instable fluorescence emission with short-lived off-states, causing intermittencies of the emission intensity [58].

example, in Figure 21.11b. Contrary to Figure 21.11a, here we do not observe stable emission, before photobleaching sets in after ∼14 ms, but the signal exhibits strong intensity fluctuations, flickering, or blinking. This observation is astonishing for a binary system, where stable emission (on-state) is expected before the molecule photobleaches and the intensity drops to background level. However, if blinking events are observed, at least a different nonradiative but reversible state of the molecule must be postulated. These fluctuations are often observed in addition to photobleaching in single-molecule studies [55]. Interestingly, Figure 21.11b reveals intensity values, which lie in between the defined on- and off-state intensities. Accordingly, these intermediate intensities can be interpreted as fast fluctuations between an on- and off-state below the temporal resolution of the experiment [59]. As a result, in the experimentally defined time interval, we observe the averaging between short-lived on- and off-states of the molecule.

The molecular origins of these fluctuations are widely discussed in the literature and range, depending on the dye systems and the dye/host arrangements, from fast cis/trans isomerizations or the formation of short-lived charge-transfer complexes to changes in the transition energy between S_0 and S_1, which tune the molecule to be off resonant with the excitation wavelength [60–62]. In addition to these short-lived off-states, single-molecule intensity trajectories often reveal long-lived dark states in the range between milliseconds and even seconds. These states are discussed to originate from reversible excitation energy migration from the dye to the host matrix (fluorescence quenching) or arise when a molecule undergoes intersystem crossing (ISC) to be trapped in a long-lived triplet state [7, 63, 64]. Especially, transitions to the triplet state are of great interest, if the characteristic triplet lifetime, that is, the average time a molecule remains in the triplet state before relaxation, is determined, for example, by transient methods. Then, single-molecule on–off statistics can be used to monitor triplet dynamics induced by external triggering such as specific and local host–matrix interactions [65]. Accordingly, these single-molecule triplet dynamics can be used to characterize a crystalline or amorphous host system for homogeneity. Clear enough, these dynamics are concealed in ensemble studies owing to averaging and local diversities in a matrix system remain unseen. Moreover, the described single-molecule triplet dynamics can be directly used in highly sensitive applications: oxygen, which, because of its electronic configuration, occupies a triplet level in its ground state, is known to be an effective triplet state quencher, transferring an excited molecule back into its singlet state. This effect can be used for oxygen-sensing applications [63, 66, 67], that is, as soon as oxygen diffuses through a porous material and permeates a dye-doped polymer matrix, the average triplet lifetime as derived from the offstate statistics is reduced. This technique is much more accurate than ensemble techniques that monitor overall intensity changes due to dye–oxygen interactions.

Intensity-based fluorescence studies are intrinsically problematic as the fluorescence intensity depends on many influences such as excitation power, detection efficiency, or photostability of the fluorescent dyes. In single-molecule-based sensor system, most of these limitations are circumvented, as the absolute intensity value is not used as quantification parameter, but data analysis can rely on the binary discrimination between two digital states. However, photostability still remains an issue, but might be circumvented, for example, by active dye-refreshing techniques that continuously provide new dye molecules to the system.

As discussed in the earlier sections, even the most straightforward approach, spectrally integrated intensity studies with moderate time resolution, provide significant insight into molecular processes, which are concealed in the ensemble. However, the significance of single-molecule studies can be extended if additional experimental parameters are accessible. In the following, two prominent approaches are presented.

21.5.2.1 Polarization-Resolved Measurements

A typical organic dye molecule is characterized by its transition dipole moment. Generally, the orientation of this dipole moment describes the direction of oscillations of delocalized electrons in resonance with an external (optical) field [7]. In other words, an absorbing (and emitting) dye molecule can be regarded as an antenna for both receiving (absorption) and sending (fluorescence). Accordingly, the emission is not isotropic, but highly directed and is described by a dipole emission pattern (Figure 21.12).

This intrinsic characteristic of molecular emission can be used to monitor molecular orientations and rotational motion of individual molecules in their host matrix, if polarization-sensitive techniques come into play [68].

After excitation with circularly polarized light, the fluorescence radiation is directed via a polarizing beam splitter to two detectors, each of which thus detects only horizontally and perpendicularly polarized light, respectively (Figure 21.13). As shown, the molecules are statistically oriented in the sample and the two detectors measure different intensities for the same molecule dependent on the orientation of its transition dipole moment. For data analysis, the ratio of the measured intensity can be used to determine the exact spatial orientation of the molecule under investigation. Plotting the intensity ratio of the two detectors in a false color

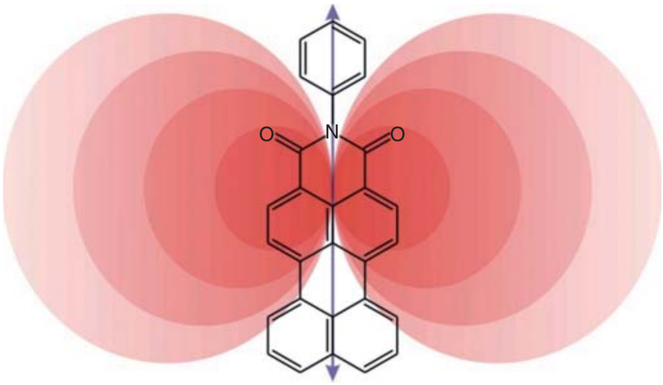

Figure 21.12 Dipole radiation characteristics of an organic dye molecule.

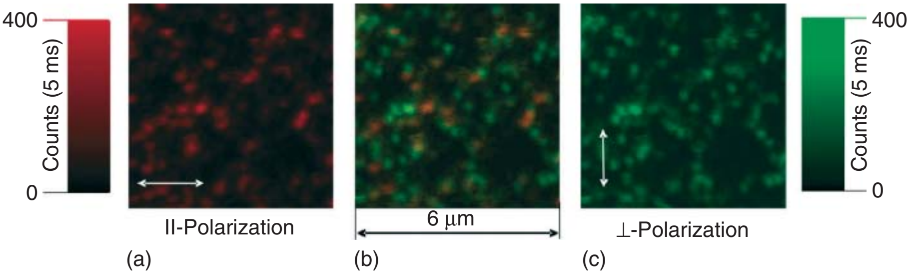

Figure 21.13 Polarization-resolved raster scan images of the fluorescence emitted by single Rhodamine 630 dye molecules. (a) Vertically polarized detection, (c) horizontally polarized detection, and (b) merged images for both polarizations.

scheme (Figure 21.13b) we can directly derive the molecule's orientation from the color map.

If a series of images is recorded with a sufficient time resolution, even molecular dynamics can be resolved. Here, a rotation of a molecule within its embedding matrix will result in a change of the polarization of the emitted light. This, in turn, can be detected by a changed intensity ratio of the two detectors, represented by a changing color in the merged image and molecular motion can be visualized.

21.5.2.2 **Single-Molecule FRET Detection**

One prominent way to investigate molecular interactions on the nanometer scale is fluorescence- or Förster resonance energy transfer (FRET) [69]. As an introduction to FRET, we consider two dye molecules that are only a few nanometers apart. If the fluorescence emission of one dye molecule, which will be called *donor* in the following, spectrally overlaps with the absorption spectrum of the second dye molecule, the latter being called *acceptor* in the following, energy can efficiently be transferred from the donor to the acceptor when the donor is excited via dipole–dipole coupling. This energy transfer leads to a quenching of the donor fluorescence and the appearance of redshifted acceptor fluorescence when the donor and the acceptor are approaching each other. As FRET is a near-field effect, the efficiency of the energy transfer is highly distance dependent and decays with $1/r^6$ of the distance r between the two chromophores [70]. Accordingly, even slight changes in the distance of donor and acceptor result in significant changes in the FRET efficiency.

Single-molecule spectroscopy can be used to analyze FRET on the single-molecule level and thus is a powerful method to monitor molecular interactions with a spatial resolution of a few nanometers [71–74]. Only recently, single-molecule FRET studies were used to quantify the internal friction in proteins by determining the reconfiguration times of unfolded proteins [75].

One approach to identify single-molecule fluorescence energy transfer uses two detectors, which operate in different spectral windows to match the donor and the acceptor emissions, respectively.

For data analysis, the anticorrelated fluorescence emission intensity of donor and acceptor in FRET pairs is used. If no FRET occurs, we observe a high-donor signal, whereas the acceptor channel remains at background level. In case of FRET, a fraction of the excitation energy is transferred to the acceptor, resulting in lower donor emission and increased acceptor intensities.

A good example of single-molecule FRET by the Chu group is shown in Figure 21.14. The upper panel shows the intensity trajectories of Cy3 as a donor (green) and Cy5 as an acceptor (orange). Chu and coworkers [76] investigated the activation of the enzyme GTPase, which is induced by binding of the ternary Cy5-labeled complex of EF-Tu, GDPNP, and aa-tRNA to Cy3 marked t-RNA p-site. At the start of the measurement, no interaction was observable, as expressed by high donor intensities. After 1 s, the acceptor-labeled complex is approached and a short interaction is observed by the anticorrelated donor-intensity drop with simultaneous acceptor intensity rise. A successful binding event leading to GTPase activation is identified after ~10 s and lasts until photobleaching occurred after 39 s indicated by zero intensity on both detection channels. In the lower panel, the FRET efficiency is plotted versus time according to

$$E_{\mathrm{ET}} = 1 - \frac{I_{\mathrm{DA}}}{I_{\mathrm{D}}} \tag{21.3}$$

where E_{ET} is the normalized transfer efficiency and I_{D} is the donor fluorescence intensity without an acceptor present. I_{DA} denotes the quenched donor fluorescence intensity in the presence of an acceptor.

In the example depicted in Figure 21.14, the GTPase activation is indicated by an abrupt rise in the FRET efficiency to a value of 0.5. Figure 21.14b demonstrates the reversibility of the GTPase activation, with a successful activation between $t = 2{-}3$ s and several subsequent unsuccessful binding attempts after ~5, 7, and 10 s. These data demonstrate the high potential of single-molecule FRET studies, which are

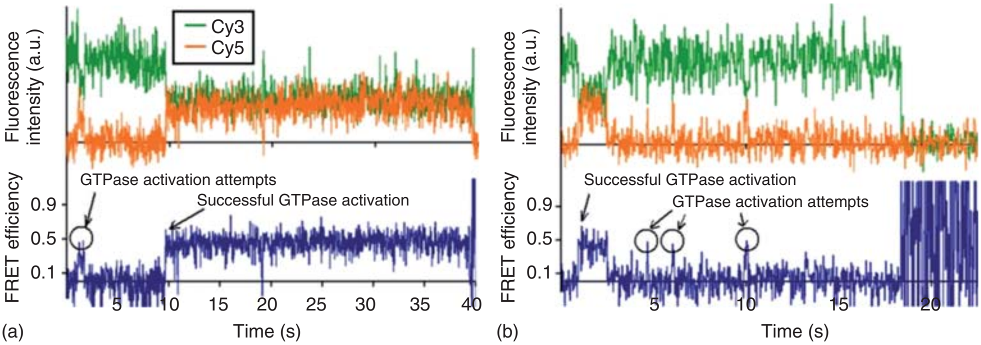

Figure 21.14 (a,b) Single-molecule FRET trajectories of a Cy3 (donor) and Cy5 (acceptor) FRET pair to monitor the activation of GTPase by binding of a Cy5-labeled complex (EF-Tu, GDPNP, and aa-tRNA) to Cy3-labeled r-RNA. The upper panels exhibit the anticorrelated donor and acceptor fluorescence intensities. The lower panels depict the calculated FRET efficiency overtime [76].

capable of monitoring essential biological interaction processes on a molecular scale.

21.5.2.3 Pulsed Interleaved Excitation FRET

Although the studies presented earlier are illustrative and demonstrate the high capability of single-molecule FRET studies, a robust and quantitative analysis of these data is often hampered by the limited stability of single fluorescent dyes against photobleaching. Moreover, a quantitative labeling of the target molecules with the marker dyes cannot be guaranteed. While this can be ignored for the donor (if no donor is present, then the entire system remains invisible in both detection channels), it becomes relevant for the acceptor; if the acceptor is trapped in a nonemitting and nonabsorbing dark state or is not present at all, single-molecule FRET analysis as described earlier will identify a noninteraction, even if the binding event was successful. To circumvent this major restriction, an alternative single-molecule measurement protocol, called pulsed interleaved excitation (PIE), has been developed [77]. Here, two pulsed laser sources are utilized, with one laser being in resonance with the donor absorption and the second with the acceptor. The repetition rates of the lasers are chosen to be well below the inverse fluorescence lifetime (typically 10–20 MHz for each laser). During a PIE-FRET measurement, the sample is alternately excited by the two lasers. Starting with the donor laser, acceptor fluorescence is detected because of FRET and, for example, on a second channel, residual donor emission owing to incomplete energy transfer (i.e., $E_{\text{ET}} < 1$) is recorded. The acceptor laser irradiates the sample after an electronic delay longer than the excited lifetime of the acceptor chromophore. This second pulse directly excites the acceptor and thus the presence of an acceptor can be registered. In this way, only intact FRET pairs contribute to subsequent data analysis and artifacts are excluded by ignoring fragmentary FRET pairs (Figure 21.15).

21.5.2.4 Single-Molecule-Based Superresolution Techniques

Single-molecule studies attracted the attention of a broader scientific community with the introduction of superresolution microscopy techniques such as stochastic optical reconstruction microscopy (STORM) or photoactivated-optical light microscopy (PALM). Both techniques rely on the photoswitching between an emitting and a nonemitting state or the irreversible photoconversion between two spectral

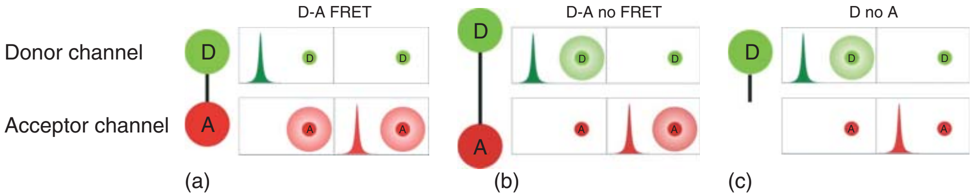

Figure 21.15 (a–c) Schematic illustration of PIE FRET. Both donor and acceptor emission is detected in distinct channels and by analyzing the (anti) correlation of the intensity signals, FRET activity is determined.

states of a single molecule. Tuning the equilibrium of these two states, we can adjust a sample system in a way that in average one or less molecules are radiating in the diffraction-limited volume in a given time interval. These molecules exhibit an isolated diffraction-limited spot in a microscopy image, which then can be fitted to a known point spread function. Having an analytical expression at hand, we can now calculate the position of the molecule with high precision, and spatial resolutions as high as 15 nm have been reported [78]. To generate a detailed image of a sample, the measurement and fitting routine are repeated several hundred times, taking advantage of the fact that the individual molecules are switched on and off in an arbitrarily manner. In this way, for each subimage, different molecules contribute and a summation of all recalculated subimages reveals a super-resolution image of the complete sample.

The prerequisite for these super-resolution techniques is the reversible switching between at least two spectroscopically different states. While it has been shown that this requirement can be met by conventional fluorescent dyes such as cyanine derivatives, which are known to be photoswitchable by a photoactivated cis/trans isomerization [79], photoactivatable fluorescent proteins (PAFPs) have great potential as they allow for the genetically encoded labeling of a protein *in vivo*. Habuchi *et al.* [80] contributed some pioneering work to this field by the first single-molecule investigation of the photoinduced switching processes in the GFP (green fluorescent protein) variant DRONPA. DRONPA was known to transit into a dark state on intense radiation with $\lambda_{\mathrm{exc}} = 488$ nm. This dark state can be recovered by illumination with 405 nm light. Using a confocal setup featuring two excitation wavelengths with $\lambda_{\mathrm{exc}} = 405$ nm and $\lambda_{\mathrm{exc}} = 488$ nm, the authors demonstrated the reversible photoswitching from an on- to an off-state of DRONPA on the single-molecule level. In contrast to other photoswitchable fluorescent proteins, DRONPA revealed a fast switching between the two states with high efficiency and repeatability as high as 170 switching events for a single protein (Figure 21.16a) [80]. On the basis of a statistical analysis of the on- and off times derived from the single-molecule studies correlated with photoswitching rate constants obtained from ensemble measurements, the authors were able to propose a kinetic scheme illustrating the photoswitching of DRONPA (Figure 21.16b). In this scheme, excitation into the 488 nm band B, which corresponds to the deprotonated form of the chromophore, a relaxation into the corresponding ground state or into the ground states of the photoswitched protonated form A_2 or a so far unknown dark state D, which is metastable and can convert into the ground state B. Interestingly, the authors found that although A_2 is a protonated form of the chromophore, a conversion into the original protonated form A_1 at a given pH is not possible. Excitation with 405 nm into either of the protonated forms A_1 or A_2, respectively, results in a very efficient nonradiative deactivation. In addition, A_2 can convert into the B ground state by an excited-state proton transfer (ESPT) process as the basis for the reversible photoswitching back to the bright form of the chromophore. However, as the ESPT from A_2 to B is very inefficient (ensemble studies revealed no emission from the deprotonated form of the chromophore for excitation with $\lambda_{\mathrm{exc}} = 388$ nm into the

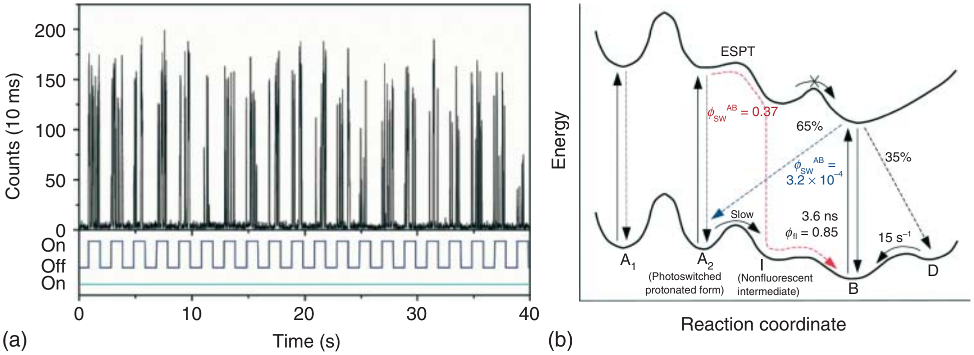

Figure 21.16 (a) Reversible photoswitching of DRONPA. The on–off scale refers to the intensity switch of the 405 nm irradiation to recover the fluorescent emission. (b) Proposed energy switching scheme in DRONPA as derived from ensemble and single-molecule spectroscopic data. (Figure adapted from [80]).

protonated form), another nonfluorescent intermediate state has to be proposed, which in turn can convert into the B ground state with high efficiency.

On the basis of this early work, the photoswitchable fluorescent proteins were further optimized and a new family of proteins was introduced, which combines irreversible spectral photoconversion from a green to a red form with reversible photoswitching known from DRONPA, opening the field of pulse-chase super-resolution imaging [81].

21.5.2.5 Spectrally Resolved Single-Molecule Fluorescence

In the earlier sections, the characteristics and potential of purely intensity-based single-molecule fluorescence studies was demonstrated. Despite the undisputable impact of these studies, access to further parameters such as a fluorescence spectrum are desirable for a deeper analysis and characterization of single-molecule fluorescence. For that, confocal microscopes can be equipped with a spectrometer consisting of a monochromator and a highly sensitive CCD camera as described earlier (see section on low-temperature studies). After a sample is raster scanned through the confocal focus, individual molecules can be identified in the intensity image. Subsequently, an identified molecule can be put into the detection volume and the detection path can be switched to enter the spectrometer and a series of fluorescence spectra of the molecule under investigation can be recorded. In this way, for example, spectral subpopulations concealed in the ensemble or distinct spectral dynamics can be investigated [82, 83]. In the following, two examples, demonstrating the ability of this technique, are introduced and briefly discussed.

Figure 21.17 depicts an example where distinct conformational states of an individual perylene molecule could be identified by single-molecule spectroscopy [84]. Here, an amino-substituted perylene imid-derivative (9-amino-*N*-(2,6,diisopropylphenyl)-perylene-3,4-dicarboximide, API) was investigated. The fluorescence spectrum of API strongly depends on the orientation of the terminal amino substituent relative to the delocalized π system of the chromophore backbone.

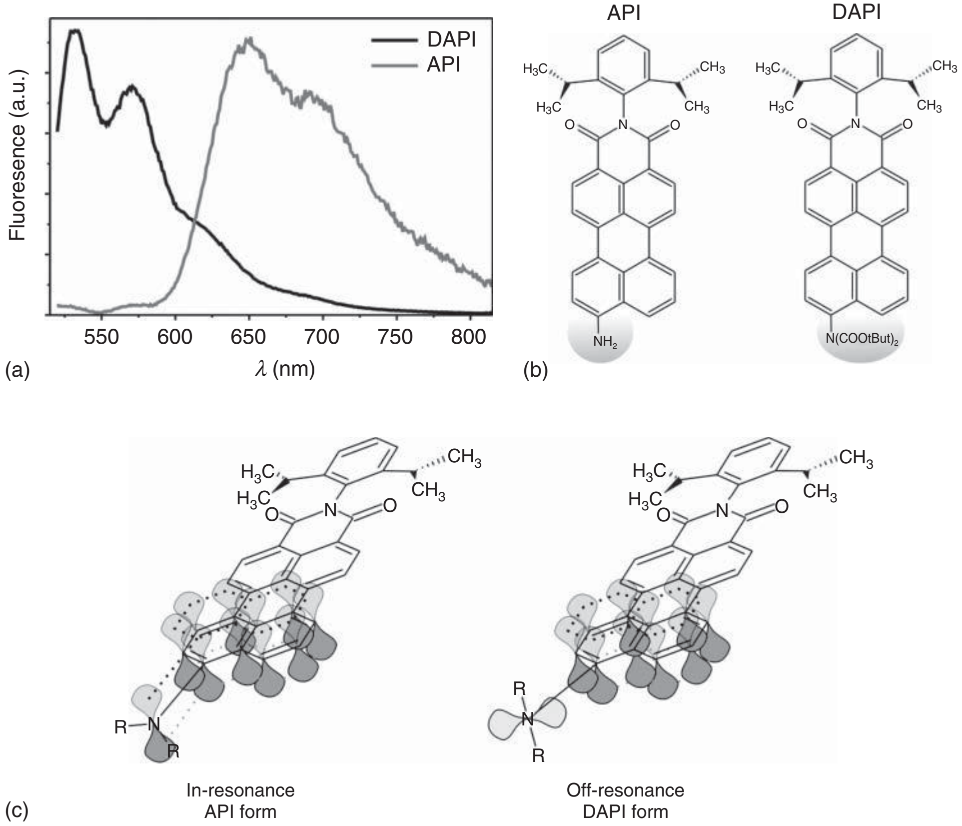

Figure 21.17 (a) Fluorescence spectra of the two perylene dyes API and DAPI. In the ensemble, DAPI exhibits a structured spectrum, while the API spectrum is less profiled and bathochromically shifted. (b) Chemical structure of API and DAPI. (c) Sketch of the two conformeric forms of API, showing the nitrogen lone pair in resonance with the chromophoric p-system (left) and off resonance with the p system (right) [58].

Investigation of derivatives of this molecule in solution revealed that in the presence of the amino substituent the fluorescence spectrum becomes less structured and shifts toward longer wavelengths as the electron lone pairs of the amino function can extend the delocalized π system. If sterically demanding, substituents such as COOtBut (*N*,*N*-di-(*tert*-butoxycarbonly)-9-amino-*N*-(2,6-diisopropyl-phenyl)-perylene-3,4-dicarboximide, DAPI) are introduced at the amino function, a free rotation around the C–N bond is inhibited, and the nitrogen lone pairs will orient perpendicular to the π system on account of sterical reasons (Figure 21.17).

For these *N*-substituted perylene derivatives, we observe a well-structured fluorescence spectrum hypsochromically shifted by ∼100 nm in the ensemble. For the amino-substituted API molecules, we find the discussed redshifted fluorescence spectrum in solution, whereas the picture entirely changes when API is embedded in a highly viscous polymer matrix and investigated on the single-molecule level. Here, for the majority of bright molecules, we observe the blueshifted emission with the nitrogen lone pairs off resonant with the chromophoric π system. The typical redshifted API spectrum as known from the ensemble could only be found from molecules, which only appeared as dim features in the raster scan image. This observation can be explained by a low-fluorescence quantum yield for the in-resonance form, that is, the lone pair in resonance with the chromophoric π system, compared to the off-resonance form. In contrast to ensemble studies in solution, a free rotation of the C–N bond is hindered because the rigid polymer matrix and transitions between the two conformeric forms are hindered. However, we found examples of single API molecules, which undergo a transition from the in-resonance to the off-resonance form and vice versa (Figure 21.18).

Switching between the two conformers as displayed for two individual API molecules as shown in Figure 21.18, which clearly demonstrates the different quantum efficiencies of the on- and off-resonant form. Although the off-resonance DAPI-like form exhibits a significantly higher fluorescence quantum yield, in the ensemble we only observe the dimmer in-resonance form. This form is energetically more favorable owing to the interaction between the nitrogen lone pair and the chromophoric π system. Hence, in solution, owing to rotation around the C–N bond, the molecules will be found in the in-resonance form, whereas in the rigid polymer matrix used in single-molecule studies the rotation is hindered and the different conformations are preserved. Thus, even with a moderate time resolution, we have access to a significant number of molecules in the energetically unfavored off-resonance form. These examples demonstrate that molecular processes such

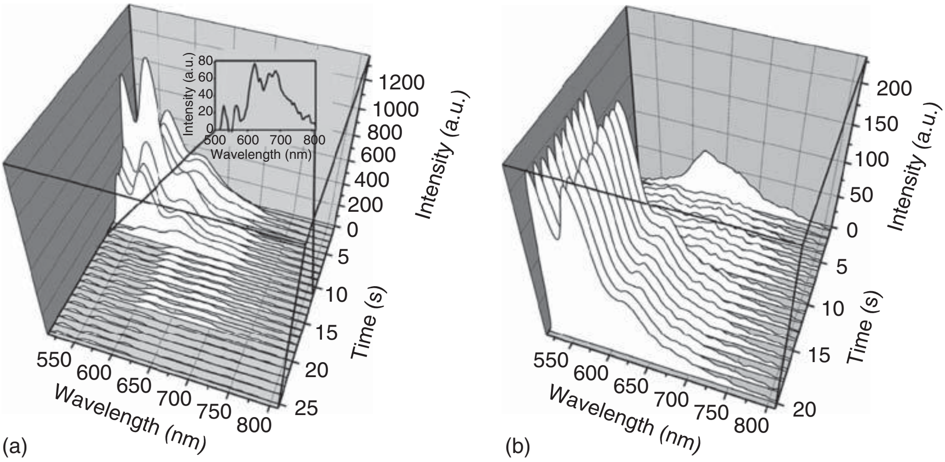

Figure 21.18 Spectral series from single API molecules demonstrating conformeric changes from the off-resonance to the in-resonance form (a) and vice versa (b) (sequence order from back to front). The inset in (a) displays spectrum number 11, where the off-resonance fluorescence has fully converted into an in-resonance spectrum [58].

as conformational changes can be visualized on a molecular level by spectrally resolved single-molecule studies.

Another prominent field of application for spectrally resolved single-molecule microscopy is the identification of spectral subpopulations hidden in the ensemble [83]. This is possible because, in contrast to the ensemble, in single-molecule studies dominant and minor spectral forms are addressed separately and, hence, mainly differ in their frequency of occurrence. In this way, the dominant forms are found more frequently, whereas a few molecules show the signature of the rare forms, which, in contrast to the ensemble, is not interfered by superposition of the dominant form. However, even at room temperatures, single-molecule spectra exhibit slight diversities such as spectral shifts, which are caused by slightly deformed energy hypersurfaces. Hence, to verify different subensembles in single-molecule studies, spectral features such as the emission maxima positions of a large number of investigated molecules must be histogrammed. In these histograms, subpopulations clearly become visible by a multimodal distribution of the maxima positions.

This can be used to, for example, examine the biologically relevant class of visible AFPs. These proteins are of great significance as they can be genetically fused to target proteins in a living organism. In this way, many biological processes such as protein expression, protein localization, or protein–protein interaction can be monitored *in vivo*. However, although the chromophore of these AFPs is shielded toward its external environment by a defined barrel structure composed of a well-known sequence of amino acids, a great variety of spectral forms has been observed. This photophysical versatility, which must be attributed to different chemical processes leading to different chromophores and to specific interactions between the chromophore and its adjacent protein scaffold, often hampers the quantitative and accurate interpretation of experimental data based on AFP studies.

In the example of the prominent yellow fluorescent protein (YFP), three interconvertible spectral forms, which have been identified by low-temperature studies, could be observed undisturbed by single-molecule spectroscopy at ambient conditions. On the basis of these room-temperature single-molecule spectra, the spectral forms could be assigned to distinct protonation states of the chromophoric system in combination with a conformational change in the chromophore environment [83]. Here, an intermediate state (I-form), formed during the transition from the deprotonated, anionic chromophore (B-form) to the neutral form (A-form) was found. The dominant redshifted B-form with an emission maximum at 527 nm is formed as a result of a $\pi-\pi$ interaction between the electronic system of the chromophore and a tyrosine residue at position 203 of the protein barrel. Interestingly, the I-form was found to be a spectral homolog to the chromophore of the GFP, where π stacking is impossible because of the amino acid composition. Accordingly, the occurrence of the I-form, as identified by single-molecule spectroscopy, points toward a conformational change in the chromophoric surrounding in YFP, most likely due to a turn or tilt of the phenolic group of the tyrosine residue, thus hampering $\pi-\pi$ interaction, which leads to the redshifted B-form.

If single-molecule studies are carried out with a sufficient temporal resolution and a series of single-molecule spectra are recorded, the said conformational change leading to the B-form and the I-form of YFP can be directly monitored. As can be derived from Figure 21.19, spectral dynamics of an individual YFP protein can be monitored, exhibiting the switching between the two spectral forms, which reveals that an interconversion is possible. Moreover, the two spectral forms and, hence, the two conformers must be isolated by an energy barrier that is small enough to be transcended at room temperature. However, this barrier is not negligible as the conversion between the two forms is slow enough that the spectra can be resolved isolated and no mixture of the B- and I-forms is detected.

Moreover, the single-molecule spectral series revealed that no direct transition from the B-form to the I-form and vice versa is possible but that the interconversion in all cases proceeds as a two-step mechanism via a dark intermediate state. As these data are not accessible in the ensemble, this example highlights the capability of spectrally resolved single-molecule studies to elucidate inter- and intramolecular dynamic processes.

21.5.2.6 Time-Resolved Single-Molecule Spectroscopy

In the earlier chapter, the possibilities of spectrally resolved single-molecule studies have been demonstrated. Another parameter accessible by fluorescence methods

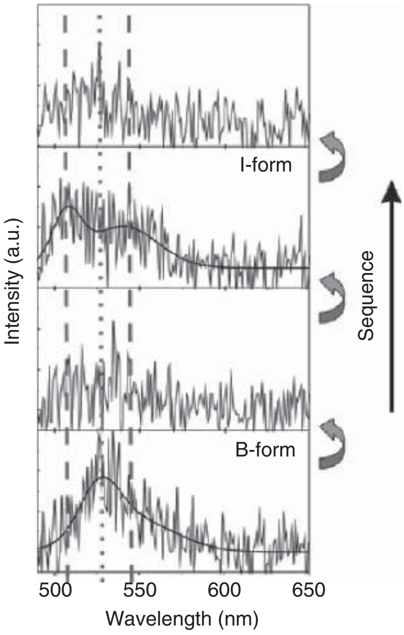

Figure 21.19 Spectral sequence of a single EYFP protein, revealing a transition from the B-form to the I-form. The transition does not occur directly, but proceeds via a nonemitting intermediate state (spectrum 2) [58].

is the fluorescence lifetime, which can be determined by time-correlated single-photon-counting (TCSPC) measurements [85–87]. In short, for a TCSPC study, a sample is excited with a short laser pulse with a pulse width of a few to a hundred picoseconds and the arrival time of the first photon is measured and its arrival time is stored. Here, the power density is adjusted in a way that maximum one photon is detected per pulse. Typically, we use excitation powers that reveal a photon count for 1% of the excitation pulses. This procedure is repeated many times and the distinct arrival times are histogrammed. This histogram represents the fluorescence intensity decay versus time and can be described by exponential decay functions (Eq. 21.4)

$$I = \sum_{i=1}^{n} A_n \times \exp\left(-\frac{t}{\tau_n}\right) \tag{21.4}$$

where the τ_n represent the excited-state lifetimes for the respective n emitting species. For a single emitting species, Eq. (21.4) becomes monoexponential with $n = 1$ and from τ the characteristic time a molecule remains in the excited state can be extracted [7]. Although this lifetime is characteristic for a molecular species, it strongly depends on the local chemical and physical environment. Parameters that can influence the fluorescence lifetime are, for example, the local pH value, physical stress, energy transfer to adjacent molecules, or the local refractive index of the surrounding matrix [88, 89]. Hence, single-molecule fluorescence lifetime data can be used as a highly sensitive local probe in complex samples.

Again, the class of AFPs deserves special attention. The chromophore of these compounds is well shielded against the protein environment by the outer protein shell. As a result, many external factors, which influence the fluorescence lifetime, can be neglected and only a limited number of parameters have to be considered as origins for variations in the fluorescence lifetime.

This finding can be used for quantitative FRET studies. In addition to intensity-based investigations discussed in Section 21.5.2.2, which are mainly applicable for qualitative FRET analysis, the energy-transfer efficiency can be monitored by the fluorescence lifetime of the donor chromophore [7, 69]. This technique utilizes the fact that because of the energy transfer an additional nonradiative relaxation channel is formed for the donor. This results in a reduced fluorescence lifetime τ_{DA} for an energy-donor chromophore that is energy transfer coupled to an acceptor molecule compared to the pure donor lifetime τ_{D} without an acceptor present. This relation can be quantified by the energy-transfer efficiency E_{ET} according to

$$E_{\mathrm{ET}} = 1 - \frac{\tau_{\mathrm{DA}}}{\tau_{\mathrm{D}}} \tag{21.5}$$

Note that in these time domain FRET measurements missing or nonabsorbing acceptor molecules can also distort data analysis. Therefore, single-molecule lifetime FRET measurements are often accompanied by PIE, as described in Section 21.5.2.3 [90–92].

Even at the single-molecule level, it is possible to combine both, spectrally and time-resolved studies on the same individual molecule. In this way, two independent spectral parameters can be determined experimentally for the same single emitter, and the correlation of these two parameters can extend the insight into molecular properties compared to the separated summation of the two spectral information. Thus, for example, coupled energy migration processes can be disentangled in a complex multichromophoric system [72, 87]. This will briefly be presented for the example of the red-fluorescent protein DsRed. DsRed natively forms tetramers, composed of green- and red-fluorescent subunits with a stoichiometry of 1 : 1 [93]. The subunits appear in a random composition and are coupled by FRET. In the ensemble, however, it is not possible to quantitatively investigate these transfer processes because fundamental photophysical parameters cannot be accessed as it is not possible to separate the native tetramers into functional monomeric subunits. However, as discussed earlier, single-molecule spectroscopy is capable of uncovering spectral subpopulations. Owing to the efficient energy transfer, we observe red acceptor emission for any tetrameric composition comprising a red-emitting chromophore. Accordingly, owing to the random composition of the tetramers, we find a major population exhibiting red emission. However, a considerable amount of tetramers is composed of solely green-emitting chromophores and hence appears as a purely green-emitting subspecies. In this way, single DsRed proteins can be sorted by spectrally resolved fluorescence spectroscopy and the green-emitting donor is accessible to further spectroscopic investigations without being interfered by any adjacent acceptor chromophore. Subsequent time-resolved measurements of the solely green-emitting tetramers provide fluorescence lifetime data of the unquenched donor chromophore of DsRed. This lifetime τ_D is indispensable for a quantitative description of the energy-transfer processes within the tetramer as the energy-transfer efficiency is dependent on this unquenched donor lifetime as demonstrated by Eq. (21.5). Furthermore, knowing τ_D gives direct quantitative access to the Förster distance R_0 of the FRET pair inherent in DsRed and thus the donor fluorescence quantum yield. Using these parameters, any energy migration pathway within the tetrameric structure can be quantitatively described and measuring the quenched donor lifetimes τ_{DA} of the red-emitting tetramers allows for a direct determination of the stoichiometric composition of the individual tetramer. This example is to show that a multiparametric approach on the single-molecule level can significantly increase the information content of a measurement, allowing for a molecular-specific analysis hampered in any ensemble-based studies.

21.5.2.7 **Dynamic Single-Molecule Studies in Solution**

One major drawback of single-molecule studies in highly viscous matrices is the hindrance of dynamical processes due to interaction of the molecule with its local host. Moreover, considering biological systems, a molecule in its native environment is not fixed at a certain position but is rather allowed to freely roam, for example, in the cytosol or diffuse along a membrane. However, to monitor the spectroscopic characteristics of an individual emitter, the molecule has to be fixed with respect to the probing volume and this fixation affects dynamic processes and emission properties and, hence, it remains equivocal to which extent the derived single-molecule data can be applied to a deeper understanding of native processes [94]. To circumvent these restrictions, Goldsmith and Moerner [95] introduced a technique that allows trapping an individual molecule in its native environment, thus making it accessible for spectroscopic investigations. A contact-free immobilization of a single emitter is achieved by using an anti-Brownian electrokinetic (ABEL) trap, which consists of four electrodes circularly mounted in an angle of 90° in a flow cell setup. If a potential difference is applied to two opposing electrodes, the solvent is displaced as a result of an electroosmotic flow with a velocity proportional to the potential gradient. If the position of a fluorescent molecule is constantly monitored, a feedback loop can trap the molecule to remain in a defined volume as small as a micrometer in square [96]. Using an intelligent triggering of all four electrodes, molecular motion in a two-dimensional space can be compensated for and the molecule under investigation is trapped in a confined space without any external mechanical distortion. By constantly rotating the excitation focus of the laser beam around the center of the trap, every detected photon can be assigned to a certain position of the focus and, hence, of the molecule at a given time. Moreover, the ABEL trap can verify that exactly one molecule is investigated. This is because the Brownian motion of different molecules is statistically uncorrelated. As the feedback-controlled voltage scheme only compensates for the motion of one specific molecule, any other fluorescent species will be pushed out of the trap by the electrokinetic forces after a short time. Goldsmith and Moerner [95] demonstrated the potential of the ABEL trap by investigating allophycocyanin (APC) proteins. These light-harvesting complexes from red algae and cyanobacteria are known to be highly sensitive to the conformation and dynamics of the protein subunits. This sensitivity is reflected by highly complex intensity trajectories in single APC studies. Moreover, results obtained from classical solid-host single-molecule studies were not consistent and significantly varied depending on the nature of the solid host. Using the ABEL trap, these inconsistencies could be compensated for and a plausible molecular model explaining the observed dynamics has been proposed. One remarkable outcome of these studies was the noncorrelation between radiative lifetime and fluorescence intensity. This suggests that the radiative lifetime depends on the local dielectric environment of the chromophore, which changes because of controlled shifts in the protein structure and conformational reordering processes. Accordingly, the protein tends to lose its native structure in a light-dependent manner. These findings would neither be possible in ensemble studies nor in a solid-host system where structural dynamics of a molecule are significantly constrained.

21.5.3
Single-Molecule Surfac-Enhanced Raman Scattering (SERS)

In the earlier sections, the capability of single-molecule studies has been demonstrated for different examples. However, as these investigations are all based on fluorescence measurements, the structural insight, which can be gained, is rather limited because of the broad and unstructured fluorescence spectra. Hence, an optical single-molecule spectroscopic technique, which provides access to structural information of, for example, distinct chemical bonds, is desirable. This requirement is met by Raman spectroscopic approaches, which utilize inelastically scattered light after monochromatic excitation of a molecule [97]. This radiation depends on the sampled material and reflects vibrations of distinct chemical groups of a molecule, which classifies Raman spectroscopy as an analytical spectroscopic technique.

However, Raman signals intrinsically suffer from a scattering cross section in the order of magnitude of $\sigma = 10^{-30}\,\text{cm}^2$, which is ∼12–13 orders of magnitude smaller than the absorbance cross section of typical fluorescence dye molecules ($\sigma_F = 10^{-16}\,\text{cm}^2$). As discussed in Section 21.2, this cross section is a limiting parameter for single-molecule detection as it defines the obtainable SNR and thus the ability of the target signal to extend over the background level. Hence, to apply Raman spectroscopy in single-molecule research, strategies to enhance the weak Raman signal have to be established.

The underlying principle of Raman scattering is the induction of a dipole moment within a molecule upon electromagnetic irradiation according to

$$\mu = \alpha \times E \tag{21.6}$$

where α is the molecular polarizability and E is the strength of the incident electromagnetic field.

Using $\alpha = \alpha_0 + \alpha_x \cos(2\pi(\nu \pm \upsilon_x) \times t)$, Eq. (21.6) reads

$$\mu = \alpha_0 E_0 \cos(2\pi \upsilon t) + {}^1\!/\!{}_2\alpha_x E_0[\cos(2\pi(\upsilon + \upsilon_x)t) + \cos(2\pi(\upsilon - \upsilon_x)t)] \tag{21.7}$$

where ν is the frequency of the excitation light and υ_x is the Stokes shifted frequency, respectively.

Equations (21.6) and (21.7) reveal that the induced dipole moment emerges to be dependent on only two parameters, the polarizability α of the molecule under investigation and the field strength of the external electromagnetic radiation $\vec{E}$. Accordingly, to enhance a Raman signal at least either of these parameters has to be increased.

One prominent approach to obtain Raman enhancement was introduced by Fleischmann *et al.* [98] in 1974 and is referred to as surface-enhanced resonance Raman scattering (SERRS). SERRS utilizes an enormous increase of up to 17 orders of magnitude of Raman intensity for molecules attached to rough noble metal surfaces. To explain the origin of this enhancement, we distinguish between an electromagnetic (EM) effect (Figure 21.20a), affecting the electrical field strength $\vec{E}$ and effects, which influence the polarizability α (Figure 21.20b,c) [99, 100].

The EM effect utilizes the field enhancement adjacent to defined nanostructures. To obtain a field enhancement, the versatile conduction band electrons of the metal particle must collectively follow the oscillation of incoming electromagnetic (light) waves, which is known as the *formation of surface plasmons*. These plasmons lead to noncompensated surface charges, which result in high local field strengths at the metal surface. For particles with a small radius compared to the light wavelength, $r \ll \lambda$, the occurrence of surface plasmons can be estimated from the polarizability

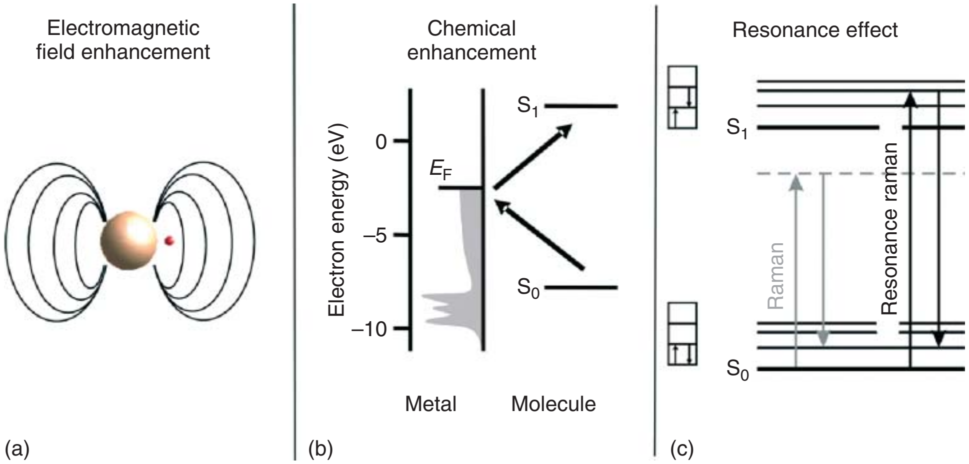

Figure 21.20 Raman enhancement effects. (a) Electromagnetic field enhancement in the vicinity of small metal particles. (b) Chemical enhancement due to the formation of charge-transfer complexes between metal and target molecule. (c) Resonance effect (black lines) with transition to a real electronic level versus conventional Raman (gray lines) to a so-called virtual level.

of the metal α_m given by Eq. (21.8)

$$\alpha_m = 4\pi r^3 \frac{\varepsilon(\upsilon) - \varepsilon_0}{\varepsilon(\upsilon) + 2\varepsilon_0} \tag{21.8}$$

where $\varepsilon(\upsilon)$ denotes the dielectric function of the metal for the respective field oscillation frequency υ and ε_0 describes the dielectric constant of the surrounding medium, which can be treated as a constant for transparent substances. For a maximal polarizability, the dielectric function of the metal must be $\varepsilon \to -2\varepsilon_0$. This condition for the appearance of surface plasmons is fulfilled in the regime of visible light for a couple of metals, the most prominent ones being the noble metals gold, silver, and copper.

Assuming a spherical metal particle, irradiation with light induces a dipole moment in the central point of the sphere, corresponding to the electrical field $E_{\text{ind}}(\upsilon_0)$ as described in Eq. (21.9)

$$E_{\text{ind}}(\upsilon_0) = r^3 \frac{\varepsilon(\upsilon_R) - \varepsilon_0}{\varepsilon(\upsilon_R) + 2\varepsilon_0} \times E_0(\upsilon_0) \times \frac{1}{(r+d)^3} \tag{21.9}$$

where d denotes the distance to the metal center. Hence, a molecule close to the metal particle experiences the superposition of the two fields E_{ind} and E_0.

The described effects are valid for the electromagnetic field emitted by the molecule $E_M(\upsilon_r)$ in an analog way. Hence, $E_M(\upsilon_r)$ induces a dipole moment in the metal particle, which leads to an increase in the detected Raman intensity. Accordingly, for big field strengths, the absolute electromagnetic enhancement factor Ω_{em} is given by the combination of the field enhancement factors for incoming and scattered light $\Phi(\upsilon)$ (Eq. 21.10)

$$\Omega_{\mathrm{em}} = |\Phi(\upsilon_0)|^2 \times |\Phi(\upsilon_\mathrm{S})|^2 = \frac{\varepsilon(\upsilon_0) - \varepsilon_0}{\varepsilon(\upsilon_0) + 2\varepsilon_0} \times \frac{\varepsilon(\upsilon_\mathrm{R}) - \varepsilon_0}{\varepsilon(\upsilon_\mathrm{R}) + 2\varepsilon_0} \times \left(\frac{r}{r+d}\right)^{12} \tag{21.10}$$

Equation (21.10) clarifies that the enhancement strongly depends on the distance between molecule and metal particle by an inverse 12th power law. However, for a monolayer of molecules with direct contact to the metal, this dependence drops to be d^{-10} (first-layer effect) [101]. Hence, molecules directly attached to the metal experience the highest electromagnetic enhancement. Signal enhancement due to the discussed EM effect can reach factors of up to 10^{10}. In addition, the fluorescence of luminescent molecules attached to a metal surface is effectively quenched as a result of excitation energy transfer to the metal electrons. Therefore, the strong fluorescence signal, which overlies the Raman signal in conventional resonant Raman measurements, is effectively reduced.

The second major approach to enhance the Raman effect by increasing the polarizability α can be met by what is referred to as the *chemical effect*. This enhancement factor is aroused by a direct interaction between the metal particle and the molecule under investigation. Although the chemical effect, which was introduced as a third dominant enhancement factor within SERRS, is widely accepted, its origin is still subject to ongoing controversial discussions. A prominent theoretical approach is given by Lombardi *et al.* [102] and Otto [103, 104], who postulate active sites at rough particle edges with localized state energies above the Ag-4d band, but well below the Fermi level. These states are understood as a starting point for a photoinduced electron transfer from the metal to the molecule. Within those charge-transfer complexes, the electron is shifted over a relatively big distance, resulting in an increased polarizability, because the electron is weakly bound to the molecule. With this chemical enhancement effect, enhancement factors of 10^2–10^3 can be obtained.

Resonance Raman scattering as a third approach to enhance the Raman effect is not directly connected to surface enhancement effects but is a commonly used effect for Raman enhancement at the single-molecule level [105]. Given that the irradiated light matches an electronic transition of the target molecule and does not excite the emitter into a virtual level (see Figure 21.20 for explanation), the molecule and its vibronic states experience a stronger interaction with the electromagnetic field, leading to a stronger charge displacement due to the electronic transition. As a result, the polarizability α is increased for resonance processes, allowing for an enhancement of the Raman signal by a factor of up to 10^2–10^4 or even, in exceptional cases, 10^6. However, merely exciting the molecule with a wavelength matching an electronic transition often involves fluorescence emission, which is still 8 orders of magnitude more intense and thus hides the Raman information. However, an excited molecule in close proximity to a metal can efficiently transfer its excitation energy to the metal and thus fluorescence emission is quenched.

A graphical illustration of the enhancement factors for Raman scattering is sketched in Figure 21.20a–c.

If the three reported enhancement factors discussed earlier, which are the resonance Raman effect, the electromagnetic, and the chemical effects, are combined, we obtain a resulting amplification factor of up to 10^{14} or even 10^{17}. Hence, the resulting scattering cross section σ can be calculated to reach values of up to 10^{-16} to 10^{-13} cm^2. Thus, it is possible to investigate the Raman signal of a single-emitting molecule with highly efficient detection techniques by SERRS.

Obviously, the metal substrate plays a decisive role in any single-molecule SERRS study. Therefore, many efforts were made to create suitable metal structures, providing highest Raman enhancement. These structures may be subdivided into three categories, pursuing different effect (Figure 21.21). The most common one is based on colloidal metallic nanoparticles, which can be produced chemically by redox reactions from aqueous solutions [106]. The various synthesis strategies reported in the literature have in common that the noble metal is utilized in its oxidized form and then carefully reduced to form nanoparticles. For that, micelle-building substances are added, which create a core–shell system on the metal surface. Thus, the particle growth can be controlled and the produced colloids are prevented from clustering.

Another approach to obtain SERRS-active substrates uses evaporation techniques. If a metal is evaporated onto a carrier substrate under high-vacuum conditions with a low deposition rate and the layer thickness is controlled to not extend a few nanometers, metal island films will form and homogeneously cover the substrate [107, 108]. By carefully controlling the evaporation conditions and layer thickness, these island films can be adjusted to consist of metal particles of a size, which matches the plasmonic resonance of the material.

The last approach uses lithographic techniques to produce highly ordered metal structures on a carrier substrate. Using this method, the size as well as the shape of the metallic nanoparticles can precisely be adjusted and the surface-enhanced Raman scattering (SERS) substrate can be designed to perfectly match the requirements of a specific measurement. For example, nanopillar structures

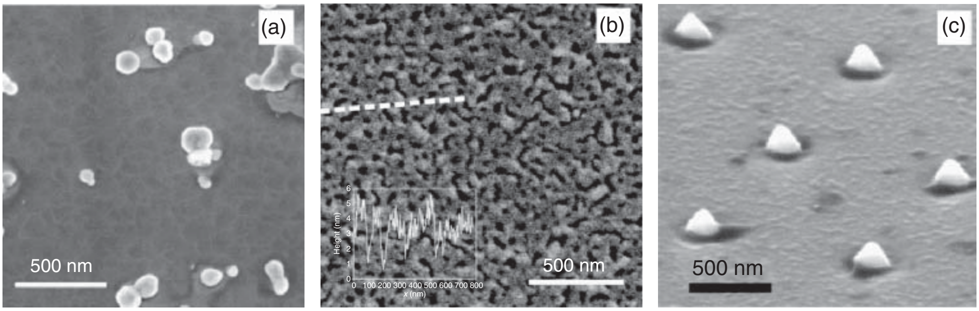

Figure 21.21 SERS substrates. (a) Silver colloids, (b) silver island film, and (c) lithographically produced silver cones.

can be built or even grating structures with highest SERS enhancement have been produced.

It is hard to judge which of the three approaches is most suited for SERS measurements; the colloidal approach does not depend on expensive equipment but can be carried out in any chemical laboratory. Moreover, working in an aqueous phase opens up the possibility to, for example, work in solution without the necessity of surface coatings and thus maintains physiological conditions for biological samples. On the contrary, the island films are easy and reliable to produce and provide a high reproducibility. Moreover, owing to the homogeneous covering of the substrate with structures well below the diffraction-limited focal spot of an optical microscope, SERS imaging is possible. Lithographically produced SERS substrates finally provide the most ordered structures and even high-performance particle arrangements such as bow-tie systems can be created. The latter ones use two particles in proximity to the molecule to enhance the Raman signal. In this way, outstanding SNRs can be obtained and thus the integration time per spectrum might be reduced, enabling the monitoring of fast molecular dynamics. However, these lithographically engineered substrates are challenging to produce and require specialized and expensive equipment. Moreover, SERS imaging is limited to the raster format of the produced substrates.

Similar to fluorescence studies, where the recorded spectra can be influenced either by the local molecular environment or by the internal properties of the individual emitter, for SERS spectra, we have to consider external and internal origins for spectral characteristics and dynamics [100]. Owing to the strong distance dependence of the SERS effect, scaling with an inverse 12th power law, even marginal variations in the distance between metal particle and the molecule or fluctuations of the morphology of the metal can cause dramatic changes in the overall Raman intensity. Moreover, as SERS spectra monitor the vibrational energy of distinct chemical bonds, any structural changes of the molecule must influence distinct Raman bands, whereas others remain unaffected. Accordingly, in SERS spectra, we can distinguish external influences, which appear as concerted fluctuations of the entire spectrum, from intrinsic structural changes within the molecule, which result in variations of the energies of distinct, isolated Raman bands. This is exemplarily shown in Figure 21.22. Figure 21.22a displays an SERRS spectra series of a single Rhodamine6G molecule, which exhibits intensity fluctuation of the entire spectrum, pointing toward a change in the enhancement efficiency caused by external factors. On the contrary, in Figure 21.22b, an SERRS spectra series of a Rhodamine6G molecule is shown, where distinct bands undergo fluctuations in their spectral position, while the overall Raman enhancement is maintained. This behavior is indicative of intrinsic dynamics of the molecule caused, for example, by the deformation of the molecule or slight conformational changes of distinct functional groups. As such spectral dynamics cannot be observed in the ensemble as a matter of principle, the observation of single SERRS band dynamics, whereas others remain fixed, is accepted as undoubted proof that SERRS provides single-molecule sensitivity [106, 109]. In Figure 21.22c, an interesting example of two SERRS spectra taken from a single Rhodamine6G molecule is

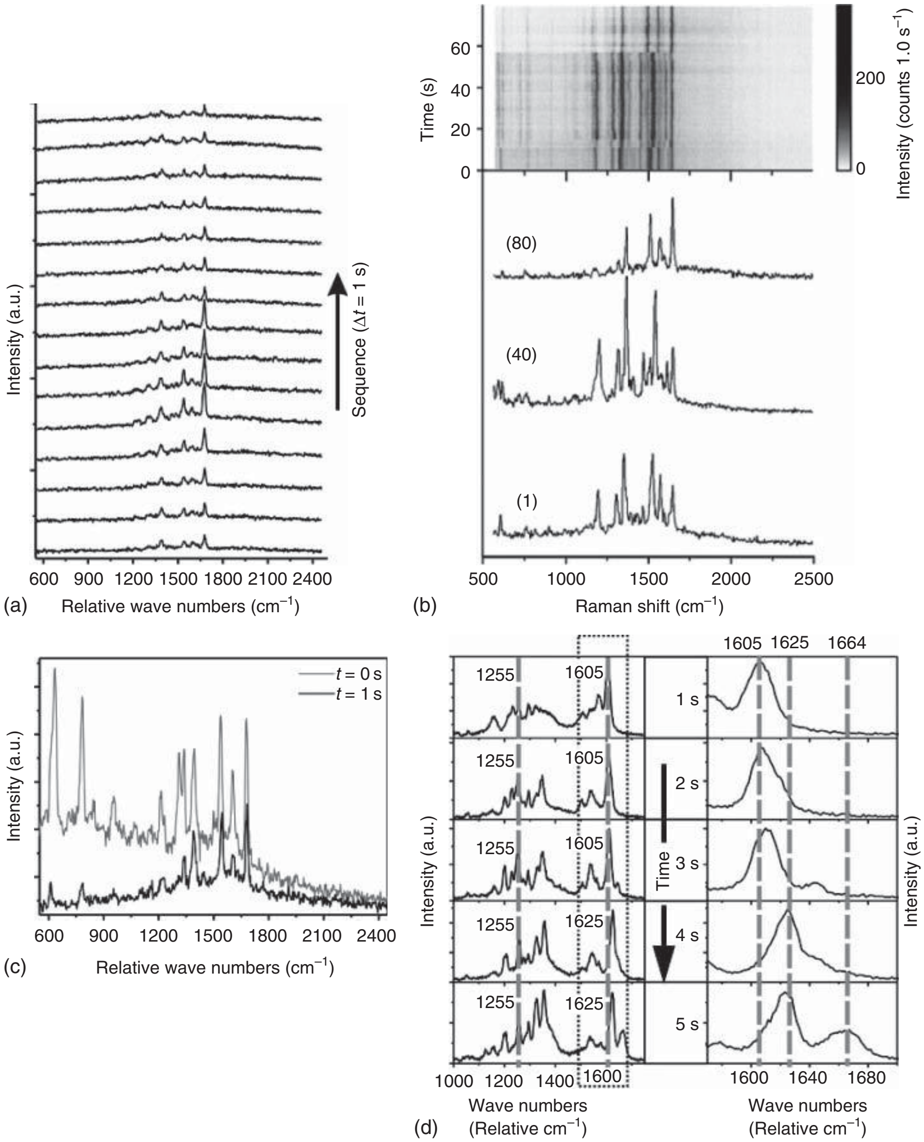

Figure 21.22 Spectral dynamics observed in SERRS spectra. (a) Intensity fluctuations of the entire Raman spectrum of a single R6G molecule point toward a change in the enhancement efficiency because of external factors rather than to a change in the target molecule. (b) Spectral changes and frequency jumps of distinct Raman bands of a single R6G molecule are definitive proof that single-molecule Raman spectroscopy is feasible. (c) Intensity changes of distinct Raman bands of a single R6G molecule reveal spatial fluctuations of molecular groups with respect to the enhancing metal particle [106]. (d) Spectral dynamics of distinct Raman lines of a single-fluorescent DsRed_N42H protein. The protein undergoes photodegradation and the Raman fingerprint switches from a red to a green signature [58].

presented. Here, a number of Raman lines exhibit intensity fluctuations, whereas others remain rather unaffected. Moreover, the spectral position of all bands is fixed. Obviously, no internal processes can cause this kind of dynamics as any changes in the molecular structure result in frequency changes of distinct Raman bands. Rather, these dynamics must be interpreted as a reorientation of distinct groups of the dye molecule with respect to the metal particle. Hence, some bonds of the molecule experience a weaker Raman enhancement and thus appear as less intense bands in the SERRS spectrum.

Figure 21.22d displays a spectrum series recorded from an AFP DsRed_N42H. As in DsRed, two different chromophoric species, with similar but slightly different chemical structures, can be present (Section 21.5.2.4), SERS spectra can show the Raman fingerprint of either of these species. It could be shown that the SERS spectra of the red- and the green-emitting chromophore can be distinguished by the anticorrelated presence of the Raman lines around 1565 and 1630 cm^{-1} [108]. The example shown in Figure 21.22d exhibits the 1565 cm^{-1} band, which is indicative of the observation of a red-emitting chromophore. During the course of the measurement, this band vanishes while a band at 1630 cm^{-1}, representative of the green-emitting chromophore, is detected. Accordingly, this protein underwent a conversion of the Raman fingerprint of the red to the green spectral form. This is of particular interest, as the red chromophore is known to be a dead-end product and no equilibrium between the two chromophores has been reported. This, in turn, yields that fluorescence studies cannot observe a transition from red to green species. However, the red chromophore can be degradated during intense irradiation, which leads to bond breaking and thus a reduction of the delocalized π system. In fluorescence measurements, these photodegradation products typically cannot be addressed as they are mostly nonfluorescent. However, SERS does not necessarily require an intact and emitting chromophore and hence even photodegradation products are accessible on the single-molecule level by this spectroscopic technique.

21.5.4
Recent Advances in Single-Molecule Spectroscopy

In the earlier sections, the underlying principle of single-molecule spectroscopic techniques has been demonstrated and distinct examples demonstrating the ability of these methods have been given. In the following, recent advances in single-molecule research shall shortly be presented.

21.5.4.1 Mode Density-Controlled Fluorescence

Although single-molecule fluorescence studies have become a valuable tool in life sciences, till date the inherent problem of low-signal intensities combined with a limited photostability is a problem. As a result, the duration of observation and the achievable brightness are critical as excitation powers are kept low enough to avoid excessive photodestruction. Accordingly, recent efforts explore strategies to enhance the fluorescence signal and the photostability of a given single molecule.

One prominent approach to this aim is metal-enhanced fluorescence, which, similar to SERS, utilizes plasmonic resonances of a metal particle in close proximity to a fluorescent molecule [110–112]. In principle, two competing effects have to be considered; on the one hand, a molecule experiences an increased local electromagnetic field next to a metal particle. On the other hand, fluorescence quenching is observed, where the excitation energy of the molecule can be transferred nonradiatively to the metal where it may dissipate. The interaction of the molecule and the metal is accompanied by a reduction of the excited-state lifetime of the molecule which in turn decreases the probability of photodestruction and hence enhances the photostability of the molecule. The underlying effects of metal-enhanced fluorescence are complex and only understood in parts. Moreover, a precise prediction whether the molecular fluorescence is quenched or enhanced is hard to make and the effects strongly depend on the nature and morphology of the metal particle [113].

However, while these effects incorporating plasmonic resonances are near-field effects, fluorescence properties, especially the fluorescence lifetime, of a molecule can also be effected by the far field of propagating electromagnetic waves [114]. In this regard, we may consider the metal particle acting as a mirror. Hence, we have to account for the electromagnetic field directly emitted by the molecule, which interferes with the field reflected by the mirror, that is, the mirror image of the molecule's emission. As a consequence, dependending on the distance between the molecule and metal particle we will find alternating constructive and destructive interferences. These interferences cause distance-dependent variations in the local photonic density of states, that is, the local mode density of the electromagnetic field. This mode density defines the probability for light of a given wavelength to propagate through space. In other words, an electromagnetic mode serves as a carrier for a photon [115].

All spectroscopic and most fluorescence studies have in common that they are investigative rather than manipulative. However, the fluorescence characteristic of a dye molecule depends on external parameters such as the (local) optical mode density. Hence, if we succeed in externally manipulating this mode density, for example, by the presence of a mirror, it is possible to control the light propagation properties and as a result the spectral characteristics of molecular emission. According to Fermi's golden rule, the probability for a transition between two states, for example, the S_1 and S_0 state ($P_{S_1 \rightarrow S_0}(t)$), depends on the mode density of the electromagnetic field [116]

$$P_{S1\rightarrow S0}(t) = \Gamma_{SpE} = \frac{1}{\tau_{SpE}} = \frac{2\pi}{\hbar^2}|\vec{\mu} \times \vec{\boldsymbol{E}}|^2 \times \rho(\omega) \tag{21.11}$$

where $\vec{\mu}$ is the transition dipole moment, $\vec{E}$ denotes the electromagnetic field vector, and $\rho(\omega)$ is the wavelength-dependent mode density of the electromagnetic field. Note that Eq. (21.9) only accounts for the electric part of the electromagnetic field, as the magnetic component can be neglected for optical transitions.

As discussed earlier, Eq. (21.11) reveals that a change of $\rho(\omega)$ directly affects the spontaneous emission rate Γ_{SpE}. As a consequence, we observe oscillations of Γ_{SpE}

and accordingly the fluorescence lifetime of a molecule for increasing distances to the metal interface [115].

While this approach already demonstrates the effect of a changed mode density by the interference of an incident and a reflected beam, the influence of the mode density on the fluorescence lifetime can even be enhanced when multiple interferences are considered.

One way to generate multiple interferences by controlling the mode density can be achieved by an optical Fabry–Perot interferometer setup with the dye molecules embedded between the plan-parallel resonator mirrors [117, 118].

As discussed earlier, Eq. (21.11) reveals that a change of $\rho(\omega)$ directly affects the spontaneous emission rate Γ_{SpE}. In the free space (i.e., no field confining components present), the mode density is represented by a continuum. On the contrary, for a Fabry–Perot microresonator $\rho(\omega)$ changes as a function of the mirror spacing L and has its maximum alteration amplitude in the first interference order m when exactly one-half of the light wavelength fits between the resonator mirrors according to the Fabry–Perot resonance condition

$$L\cos\theta = \left(m - \frac{\delta_{1,2}}{2\pi}\right) \times \frac{\lambda}{2n} \tag{21.12}$$

where $\delta_{1,2} = \sum_{i=1,2} \Delta\phi(d_i, \phi, \lambda)$ represents angle-dependent phase changes at the resonator mirrors and θ is the angle of incidence.

An experimental realization of such a microresonator is sketched in Figure 21.23 [118]. In short, a silver-coated microscope coverslip serves as a lower mirror. Here, spacer and protection layers are applied and a polymer layer with dye molecules embedded is spin coated on top. The upper mirror comprises a silver-coated plano-convex lens, which is connected to three piezo actuators. In this way, the mirror spacing L can be externally adjusted with high precision. To monitor the mirror spacing, it is suggested that white-light transmission measurements, which reveal concentric Newton rings in all colors of the rainbow, each of which represents a distinct resonance wavelength according to Eq. (21.12), be used.

In Figure 21.24, the microresonator effect on the emission spectrum of a single perylene imide (PI) molecule is depicted. Figure 21.24a–c shows spectra derived from one and the same dye molecule for different mirror spacings [119]. Clearly, the free space spectrum (gray-shaded area in Figure 21.24) is effectively redistributed to follow the mode characteristics of the microresonator.

The blue lines in Figure 21.24a–c denote theoretical simulations of the spectral shape based on a semiclassical approach and show a remarkable agreement with the experimental data (red dots). The simulations take into account that the coupling of the molecular emission to the electromagnetic modes inside the microresonator is strongly frequency dependent (Eq. 21.11). As the emission spectrum of a typical fluorescence dye is rather broad at room temperature, different spectral contributions experience different mode densities. Accordingly, distinct wavelengths have a high-coupling efficiency to the resonator modes. This results in an enhanced emission probability for these wavelengths, reflected by

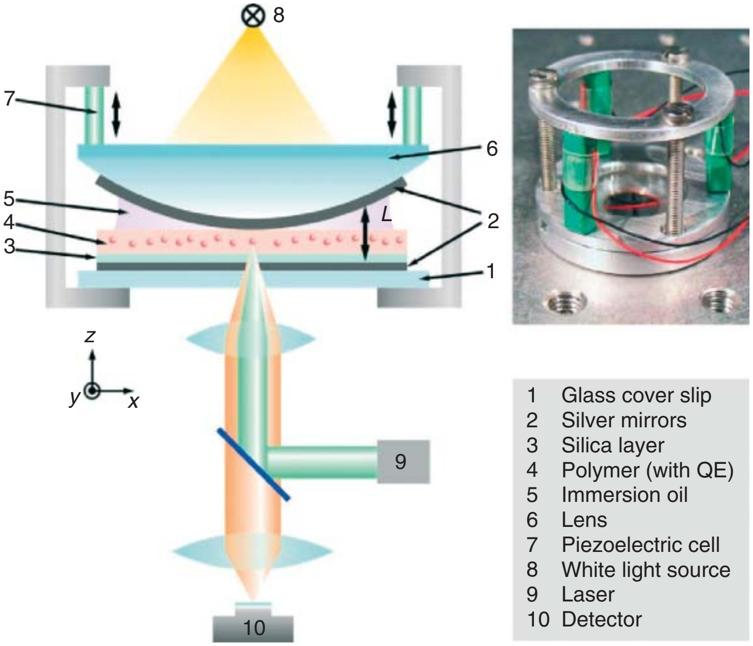

Figure 21.23 Schematic of an optical microresonator setup with tunable mirror spacing capable of single molecule detection.

an enhanced spontaneous emission rate (Eq. 21.11), while others are inhibited, an effect that is known as the *Purcell effect* [120]. The Purcell effect can also directly be visualized by measuring the fluorescence lifetime of a single molecule for different mirror spacings as shown in Figure 21.25. Clearly, the fluorescence lifetime changes according to the resonance condition of the microresonator (Figure 21.25a). However, Figure 21.25b reveals that the fluorescence lifetime variations, that is, the magnitude of the Purcell effect, are also dependent on the orientation of the molecular transition dipole moment. This is due to the fact that the resonator is composed of plan-parallel mirrors and thus the field confinement is anisotropic in space, resulting in a high confinement in the z-direction and a weaker confinement in the x,y plane. Thus, the effective resonator impact on the molecular emission is strongly dependent on the orientation of the transition dipole moment relative to the resonator mirrors.

As a result, the single-molecule emission experiences a significant and controllable spectral and temporal redistribution, making the microresonator a valuable tool to externally tailor molecular emission, for example, for new-generation single photon sources or quantum computing applications.

Besides these future applications, using the microresonator setup can also provide access to the fluorescence quantum yield of a single emitter [121]. The Purcell effect only influences radiative transitions. Accordingly, the amplitude of the microresonator length-dependent fluorescence emission rate variation is

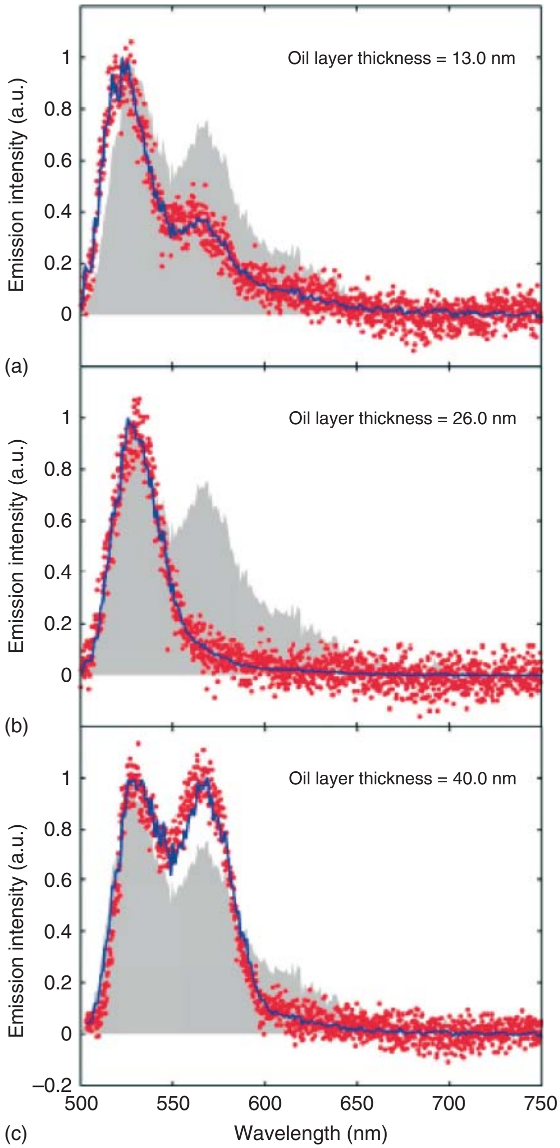

Figure 21.24 (a–c) Microresonator-controlled fluorescence spectra of one single PI molecule (red dots). The blue lines represent theoretical simulations of the spectral shape using a semiclassical approach. The gray-shaded area reflects the free space PI emission spectrum [119].

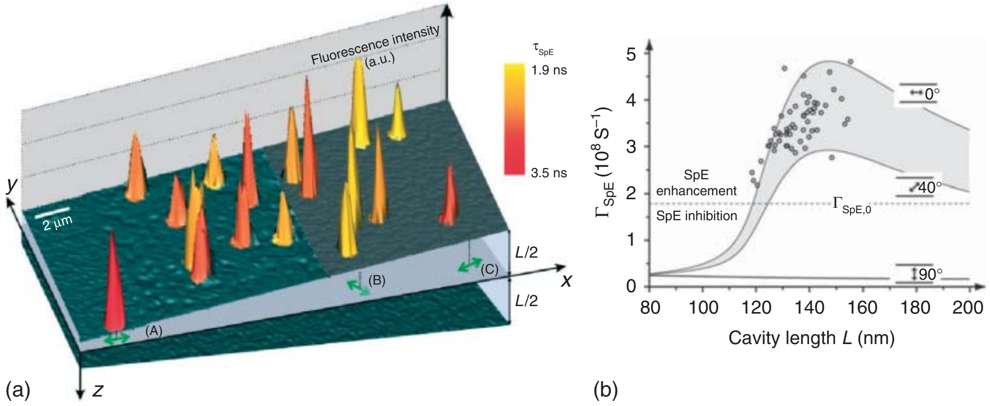

Figure 21.25 (a) FLIM (fluorescence lifetime imaging microscopy) Image of single perylene dyes embedded in a $\lambda/2$ microresonator and (b) fluorescence lifetimes of single perylene molecules for different mirror spacings [117].

maximal, if all relaxation processes are radiative, that is, the fluorescence quantum yield is 1, and decreases when nonradiative relaxation contributes. Hence, if it is possible to precisely determine the three-dimensional orientation of a single emitter embedded in the microresonator, the only free parameter to quantitatively describe the radiative rate is the fluorescence quantum yield. While the exact determination of the transition dipole orientation of a single emitter is critical using common excitation sources with a Gaussian intensity distribution, the use of doughnut-shaped higher order laser modes provides direct access to the 3D orientation of the emitter [122, 123]. A more detailed introduction in the generation, application, and data analysis of these laser modes is given in the respective section. The determination of single-molecule quantum yields revealed a broad scattering of the individual values, which reflect a strong nanoscopic inhomogeneity of the host environment of the single emitters [124].

21.5.4.2 **Single-Molecule Excitation Spectroscopy**

All the studies reported so far have in common that they rest on the analysis of the Stokes-shifted luminescence emission, either spectrally integrated or even with a spectral resolution. Indeed, it is desirable to get access to even more spectral parameters of a single molecule to further enhance the information content, which can be obtained from a single-molecule measurement,

For example, it is so far not possible to record a single-molecule absorbance spectrum for a couple of technical reasons. Thus, up to now, frequency-resolved monitoring of the electronic coupling of a quantum mechanical emitter (QME), such as a single molecule to an external electromagnetic field, is not possible. Fluorescence excitation spectroscopy, where the excitation wavelengths is swept over a broad spectral range while the fluorescence emission intensity is monitored in defined spectral window, is one approach, if certain presumptions (e.g., a constant fluorescence quantum yield over the excitation wavelength regime) are fulfilled.

While this is a standard technique in ensemble studies, it requires reasonable technical effort to adopt this spectroscopic method to single-molecule studies at ambient conditions and two major requirements have to be fulfilled. First, the excitation wavelength must be continuously tunable over a certain wavelength area. Second, the excitation source must be intense enough to ensure a sufficient number of excitation cycles of the single molecule to obtain a reasonable SNR. In very recent years, new-generation super-continuum laser sources providing white-light laser radiation over a broad wavelength regime, which meet these requirements, have become accessible. Combining these super-continuum lasers with a confocal microscope with single-molecule sensitivity then allows for excitation spectroscopy on individual emitters, if a dispersive element is introduced into the excitation path, which has a sufficient blocking efficiency combined with fast wavelength changing ability. For that, classical grating monochromators or, alternatively, new-generation acousto-optic tunable filters (AOTFs) can be utilized [125].

With a single-molecule fluorescence excitation spectroscopy setup as described earlier, a couple of open questions can be addressed. To name a few, a direct observation of FRET processes would be possible. Moreover, it is worth studying whether excitation spectra of individual emitters do slightly differ from each other because of different energy spacings per molecule. This, in turn, would help gain a deeper insight into the interaction between the chromophore and its local environment as, for example, the individual Stokes shift becomes accessible on a single-molecule level.

As an overview, results obtained from single-molecule excitation spectroscopy of individual semiconductor CdSe quantum dots (QDs) shall be briefly discussed. QD excitation spectra are known to exhibit a continuous slope toward short excitation wavelengths and are confined by a relatively sharp so-called excitonic peak close to the band edge of the material [21]. The spectral form can also be observed in single-molecule excitation spectra as depicted in Figure 21.26. Here, we also find features characteristic of single molecules such as instable emission due to blinking to various degrees. These blinking events are due to a transition of the QD to a nonemitting dark state and gets visible in the excitation spectrum as data acquisition is accomplished successively for each excitation wavelength. As a guide to the eye, the ensemble excitation spectrum is plotted as a dashed line. Along with

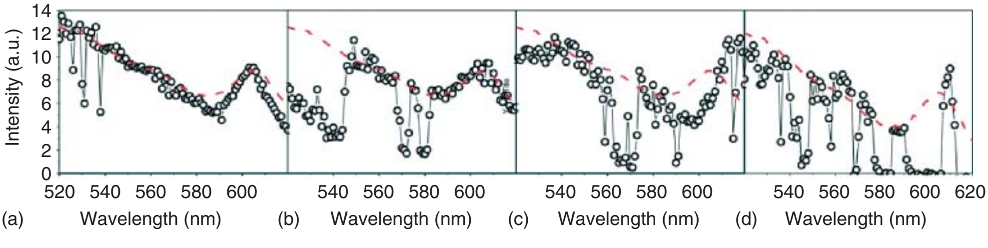

Figure 21.26 (a–d) Single QD fluorescence excitation spectra (open circles). Dashed lines are ensemble excitation spectrum [125].

the intensity fluctuations, photon antibunching curve measurements confirm the observation of single emitters (compare Section 21.4).

In addition to blinking, a number of QD dots revealed transitions to long-lasting dark states and did not recover until the end of the measurement. Interestingly, if the wavelengths where these transitions can be observed are histogrammed we find certain distinct wavelengths with a pronounced occurrence of these transitions. These wavelengths coincide with plateaus in a sum-spectrum derived from summing up all single QD excitation spectra. This finding is astonishing and has to be taken into consideration if high-performance setups with QDs as a (single-photon) light source are concerned. For such studies, the distinct excitation wavelengths derived from the single-molecule excitation spectra should be avoided as here the QD dot performance and stability is reduced.

21.5.4.3 **Single-Molecule Absorption Studies**

Even though it is not possible to record absorption spectra of individual molecules, there are some recent developments that enable spectrally integrated absorption studies at the single-molecule level. The most straightforward approach introduced by Celebrano *et al.* [126] directly detects the attenuation of irradiation light. Typically, the absorption cross sections of an individual molecule are as small as a few square angstroms and, hence, the attenuation of a focused laser beam is $\sim$0.0001%. Considering that inherent fluctuations in light sources are in the order of magnitude of 1%, the attenuation of the incident light by a single molecule is concealed. Celebrano *et al.* circumvented this restriction by using a dual-beam configuration, which essentially mimics the setup of a conventional absorption spectrometer. While one beam is tightly focused and probes the sample, the second one bypasses the sample volume before it is led to a detector. Thus, the second beam serves as a reference and by balanced detection even marginal intensity fluctuations, such as those provoked by a single-molecule absorption event, can be detected. If a polarization-sensitive detection scheme is introduced, the sensitivity can be further enhanced, thus allowing relatively short data acquisition times. However, as this approach monitors the attenuation of the incident light, discrimination between absorption and scattering processes is not intrinsically possible and a minimized surface roughness has to be ensured to scale the latter effect down.

A different approach to single-molecule absorption detection introduced by the Orrit group makes use of a two-color pump probe excitation schema in combination with a fast amplitude modulation to reduce measurement noise. Orrit *et al.* [127] detected the molecular absorption indirectly by monitoring the local heating, which is caused by the energy loss from the vibration of excited molecules. This photothermal effect can be probed with a second laser, which is not in resonance with an electronic transition of the sample (i.e., the sample appears transparent to this beam). Owing to the local heating, the refractive index experiences a slightly altered refractive index, which causes locally enhanced scattering. Using an amplitude modulation of the pump beam, these modulations also appear in the detection schema of the probe beam in case a molecule was excited by the pump beam. Providing a very good SNR, which outperforms the direct method, the main drawback of this photothermal technique is due to the inherent dependence on heat-induced changes in the refractive index and the level of heat conduction. These points especially become an issue for aqueous sample systems such as living cells, as here small changes in temperature only marginally affect the refractive index.

The third approach to single-molecule absorption has been established by the group of Sunny Xie, which probed an effect called *ground state depletion*. Using an experimental setup similar to the approach of Gaiduk *et al.* [127], the sample is excited with two laser beams of different wavelengths, both of which are in resonance with an electronic transition of the molecules under investigation. The first (pump) beam is used to prepare the molecules in their excited state. Accordingly, they are no longer resonant to the second (probe) beam and a fast on–off switching of the pump beam results in a modulated detection scheme of the probe beam [128]. While a high SNR is obtained and any restrictions concerning the temperature dependence of the local refractive index are circumvented by this approach, the technique requires high laser powers for the pump beam to drive the molecules into a saturated excited state, which highly strain the chromophores. Moreover, the excited-state lifetime is a crucial parameter as it defines the time evolution of the excited-state population after the pump pulse and the applicability to nonfluorescent molecules with short excited-state lifetimes remains to be demonstrated.

In conclusion, new techniques to approach single-molecule absorption measurements have been reported recently, driving single-molecule techniques to a new level. However, still a lot of effort has to be performed to make these approaches more sensitive, robust, and suitable for a broad range of sample systems. After these requirements have been fulfilled, even spectroscopic information might be gained from these absorption studies on individual molecules, further enhancing the information content of single-molecule studies.

References

1. Moerner, W. (2002) A dozen years of single-molecule spectroscopy in physics, chemistry, and biophysics. *J. Phys. Chem. B* **106** (5), 910–927.
2. Barkai, E., Jung, Y., Silbey, R. (2004) Theory of single-molecule spectroscopy: beyond the ensemble average. *Annu. Rev. Phys. Chem.*, **55**, 457–507.
3. Guttler, F., Irngartinger, T., Plakhotnik, T., Renn, A., Wild, U.P. (1994) Fluorescence microscopy of single molecules. *Chem. Phys. Lett.* **217** (4), 393–397.
4. Ambrose, W.P., Goodwin, P.M., Martin, J.C. (1994) Alterations of single-molecule fluorescence lifetimes in near-field optical microscopy. *Science* **265**, 364–367.
5. Ambrose, W.P., Goodwin, P.M., Martin, J.C. (1994) Single-molecule detection and photochemistry on a surface using near-field optical excitation. *Phys. Rev. Lett.* **72**, 160–163.
6. Moerner, W.E., Kador, L. (1989) Optical detection and spectroscopy of single molecules in a solid. *Phys. Rev. Lett.* **62**, 2535–2538.
7. Lakowicz, J.R. (2006) *Principles of Fluorescence Spectroscopy*, 3rd edn. Kluwer Academic Publishers, New York.
8. Lounis, B., Orrit, M. (2005) Single-photon sources. *Rep. Prog. Phys.* **68**, 1129–1179.
9. Vale, R.D. (2008) Microscopes for fluorimeters: the era of single molecule measurements. *Cell* **135**, 779–785.

10. Moerner, W.E. (2007) New directions in single-molecule imaging and analysis. *Proc. Natl. Acad. Sci. U.S.A.* **104** (31), 12596–12602.
11. Shaner, N., Campbell, R., Steinbach, P., Giepmans, B., Palmer, A., Tsien, R. (2004) Improved monomeric red, orange and yellow fluorescent proteins derived from Discosoma sp. red fluorescent protein. *Nat. Biotechnol.* **22** (12), 1567–1572.
12. Shu, X.K., Shaner, N.C., Yarbrough, C.A., Tsien, R.Y., Remington, S.J. (2006) Novel chromophores and buried charges control color in mFruits. *Biochemistry* **45** (32), 9639–9647.
13. Shaner, N.C., Campbell, R.E., Steinbach, P.A., Giepmans, B.N.G., Palmer, A.E., Tsien, R.Y. (2004) Improved monomeric red, orange and yellow fluorescent proteins derived from Discosoma sp. red fluorescent protein. *Nat. Biotechnol.* **22** (12), 1567–1572.
14. Zhang, J., Campbell, R.E., Ting, A., Tsien, R.Y. (2001) Creating new fluorescent probes for cell biology. *Nat. Rev. Mol. Biol.* **3**, 906–918.
15. Blum, C., Subramaniam, V. (2009) Single molecule spectroscopy of fluorescent proteins. *Anal. Bioanal. Chem.* **393** (2), 527–541.
16. Walling, M.A., Novak, J.A., Shepard, J.R.E. (2009) Quantum dots for live cell and in vivo imaging. *Int. J. Mol. Sci.* **10**, 441–491.
17. Freeman, R., Gill, R., Shweky, I., Kotler, M., Banin, U., Willner, I. (2008) Biosensing and probing of intracellular metabolic pathways by NADH-sensitive quantum dots. *Angew. Chem. Int. Ed.* **121** (2), 315–319.
18. Kahl, M., Thomay, T., Kohnle, V., Beha, K., Merlein, J., Hagner, M., Halm, A., Ziegler, J., Nann, T., Fedutik, Y., Woggon, U., Artemyev, M., Pe'rez-Willard, F., Leitenstorfer, A., Bratschitsch, R. (2007) Colloidal quantum dots in all-dielectric high-Q pillar microcavities. *Nano Lett.* **7** (9), 2897–2900.
19. Michalet, X., Pinaud, F., Bentolila, L., Tsay, J., Doose, S., Li, J., Sundaresan, G., Wu, A., Gambhir, S., Weiss, S. (2005) Quantum dots for live cells, in vivo imaging, and diagnostics. *Science* **307** (5709), 538.
20. Smith, A.M., Gao, X., Nie, S. (2004) Quantum dot nanocrystals for in vivo molecular and cellular imaging. *Photochem. Photobiol.* **80**, 377–385.
21. Empedocles, S., Norris, D., Bawendi, M. (1996) Photoluminescence spectroscopy of single CdSe nanocrystallite quantum dots. *Phys. Rev. Lett.* **77** (18), 3873–3876.
22. Wang, H., Huff, T., Zweifel, D., He, W., Low, P., Wei, A., Cheng, J. (2005) In vitro and in vivo two-photon luminescence imaging of single gold nanorods. *Proc. Natl. Acad. Sci. U.S.A.* **102** (44), 15752.
23. Farrer, R., Butterfield, F., Chen, V., Fourkas, J. (2005) Highly efficient multiphoton-absorption-induced luminescence from gold nanoparticles. *Nano Lett.* **5** (6), 1139–1142.
24. Jiang, Y., Horimoto, N., Imura, K., Okamoto, H., Matsui, K., Shigemoto, R. (2009) Bioimaging with two-photon-induced luminescence from triangular nanoplates and nanoparticle aggregates of gold. *Adv. Mater.* **21** (22), 2309–2313.
25. Kim, H., Xiang, C., Guell, A., Penner, R., Potma, E. (2008) Tunable two-photon excited luminescence in single gold nanowires fabricated by lithographically patterned nanowire electrodeposition. *J. Phys. Chem. C* **112** (33), 12721–12727.
26. Nie, S.M., Chiu, D.T., Zare, R.N. (1994) Probing individual molecules with confocal fluorescence microscopy. *Science* **266**, 1018–1021.
27. Nie, S., Chiu, D., Zare, R. (1994) Probing individual molecules with confocal fluorescence microscopy. *Science* **266** (5187), 1018.
28. Stracke, F., Blum, C., Becker, S., Müllen, K., Meixner, A.J. (2000) Intrinsic conformer jumps observed by single molecule spectroscopy in real time. *Chem. Phys. Lett.* **325**, 196–202.
29. Webb, R. (1996) Confocal optical microscopy. *Rep. Prog. Phys.* **59**, 427–471.
30. Orrit, M., Bernard, J. (1990) Single pentacene molecules detected

by fluorescence excitation in a p-terphenyl crystal. *Phys. Rev. Lett.* **65** (21), 2716–2719.

31. Basché, T., Moerner, W., Orrit, M., Talon, H. (1992) Photon antibunching in the fluorescence of a single dye molecule trapped in a solid. *Phys. Rev. Lett.* **69** (10), 1516–1519.
32. Ambrose, W., Moerner, W. (1991) Fluorescence spectroscopy and spectral diffusion of single impurity molecules in a crystal. *Nature* **349**, 225–227.
33. Bolton, D., Winefordnert, J.D. (1983) Laser-excited fluorescence line-narrowing: an analytical study. *Talanra* **30** (9), 713–716.
34. Yu, Z., Barbara, P. (2004) Low-temperature single-molecule spectroscopy of MEH-PPV conjugated polymer molecules. *J. Phys. Chem. B* **108** (31), 11321–11326.
35. Ambrose, W.P., Basché, T., Moerner, W.E. (1991) Detection and spectroscopy of single pentacene molecules in a p-terphenyl crystal by means of fluorescence excitation. *J. Chem. Phys.* **95**, 7150–7163.
36. Bopp, M.A., Meixner, A.J., Tarrach, G. (1996) Direct imaging single molecule diffusion in a solid polymer host. *Chem. Phys. Lett.* **263**, 721–726.
37. Huang, K., Rhys, A. (1950) Theory of light absorption and non-radiative transitions in F-centres. *Proc. R. Soc. London, Ser. A* **204** (1078), 406–423.
38. Brecht, M., Studier, H., Radics, V., Nieder, J.B., Bittl, R. (2008) Spectral diffusion induced by proton dynamics in pigment–protein complexes. *J. Am. Chem. Soc.* **130** (51), 17487–17493.
39. Pieper, J., Voigt, J., Renger, G., Small, G.J. (1999) Analysis of phonon structure in line-narrowed optical spectra. *Chem. Phys. Lett.* **310** (3–4), 296–302.
40. Shpol'skii, E., Il'ina, A., Klimova, L. Fluorescence spectrum of coronene in frozen solutions. *Dokl. Akad. Nauk SSSR*, 1952, **87** 935–938.
41. Hanbury-Brown, R., Twiss, R.Q. (1957) Interferometry of the intensity fluctuations in light. I. Basic theory: the correlation between photons in coherent beams of radiation. *Proc. R. Soc. Lond., A* **242**, 300–324.
42. Hanbury-Brown, R., Twiss, R.Q. (1958) Interferometry of the intensity fluctuations in light. II. An experimental test of the theory for partially coherent light. *Proc. R. Soc. Lond., A* **243**, 291–319.
43. Sýkora, J., Kaiser, K., Gregor, I., Bonigk, W., Schmalzing, G., Enderlein, J. (2007) Exploring fluorescence antibunching in solution to determine the stoichiometry of molecular complexes. *Anal. Chem.* **79**, 4040–4049.
44. Zwiller, V., Blom, H., Jonsson, P., Panev, N., Jeppesen, S., Tsegaye, T., Goobar, E., Pistol, M., Samuelson, L., Björk, G. (2001) Single quantum dots emit single photons at a time: antibunching experiments. *Appl. Phys. Lett.* **78**, 2476.
45. Berlin, Y., Burin, A., Friedrich, J., Köhler, J. (2007) Low temperature spectroscopy of proteins. Part II: experiments with single protein complexes. *Phys. Life Rev.* **4** (1), 64–89.
46. Frauenfelder, H., Wolynes, P.G., Austin, R.H. (1999) Biological physics. *Rev. Mod. Phys.* **71** (2), S419–S430.
47. Hofmann, C., Kulzer, F., Zondervan, R., Köhler, J., Orrit, M. (2008) *Single Biomolecules at Cryogenic Temperatures: From Structure to Dynamics Single Molecules and Nanotechnology*, Springer Series in Biophysics, Vol. 12, eds. Rigler, R., Vogel, H., Springer, Berlin, Heidelberg, pp. 25–51.
48. Hofmann, C., Aartsma, T.J., Michel, H., Köhler, J. (2003) Direct observation of tiers in the energy landscape of a chromoprotein: a single-molecule study. *Proc. Natl. Acad. Sci. U.S.A.* **100** (26), 15534–15538.
49. Hofmann, C., Aartsma, T., Michel, H., Köhler, J. (2003) Direct observation of tiers in the energy landscape of a chromoprotein: a single-molecule study. *Proc. Natl. Acad. Sci. U.S.A.* **100**, 15534–15538.
50. Nie, S.M., Chiu, D.T., Zare, R.N. (1994) Probing individual molecules with optical fluorescence microscopy. *Science* **266** (5187), 1018–1021.

51. Pohl, D.W., Fischer, U.C., Dürig, U.T. (1988) Scanning near-field optical microscopy (SNOM). *J. Microsc.* **152** (3), 853-861.

52. Lu, H.P., Xie, X.S. (1997) Single-molecule spectral fluctuations at room temperature. *Nature* **385**, 143–146.

53. Blum, C., Stracke, F., Becker, S., Müllen, K., Meixner, A.J. (2001) Discrimination and interpretation of spectral phenomena by room-temperature single-molecule spectroscopy. *J. Phys. Chem. A* **105**, 6983–6990.

54. Blum, C., Subramaniam, V., Schleifenbaum, F., Stracke, F., Angres, B., Terskikh, A., Meixner, A.J. (2002) Single molecule fluorescence spectroscopy of mutants of the Discosoma red fluorescent protein DsRed. *Chem. Phys. Lett.* **362**, 355–361.

55. Dickson, R.M., Cubitt, A.B., Tsien, R.Y., Moerner, W.E. (1997) On/off blinking and switching behavior of single green fluorescent protein molecules. *Nature* **388**, 355–358.

56. Garcia-Parajo, M.F., Koopman, M., van Dijk, EMHP., Subramaniam, V., van Hulst, N.F. (2001) The nature of fluorescence emission in the red fluorescent protein DsRed, revealed by single-molecule detection. *Proc. Natl. Acad. Sci. U.S.A.* **98** (25), 14392–14397.

57. Schleifenbaum, F., Blum, C., Subramaniam, V., Meixner, A.J. (2009) Single molecule spectral dynamics at room temperature. *Mol. Phys.* **107** (18), 1923–1942.

58. Schleifenbaum, F., Blum, C., Subramaniam, V., Meixner, A.J. (2009) Single molecule spectral dynamics at room temperature. *Mol. Phys.* **107** (18), 1923–1942.

59. Lippitz, M., Kulzer, F., Orrit, M. (2005) Statistical evaluation of single nano-object fluorescence. *ChemPhysChem* **6**, 770–789.

60. Cotlet, M., Goodwin, P.M., Waldo, G.S., Werner, J.H. (2006) A comparison of the fluorescence dynamics of single molecules of a green fluorescent protein: one- versus two-photon excitation. *ChemPhysChem* **7**, 250–260.

61. Huang, Z., Ji, D., Wang, S., Xia, A. (2006) Spectral identification of specific photophysics of Cy5 by means of ensemble and single molecule measurements. *J. Phys. Chem. A* **110** (1), 45–50.

62. Kao, W.Y., Davis, C.E., Kim, Y.I., Beach, J.M. (2001) Fluorescence emission spectral shift measurements of membrane potential in single cells. *Biophys. J.* **81** (2), 1163–1170.

63. Furuto, T., Lee, S-K., Asai, K., Okura, I. (1998) Novel oxygen sensor based on quenching of triplet-triplet absorption of zinc tetraphenylporphyrin. *Chem. Lett.* **27** (1), 61.

64. Valeur, B. (ed) (2002) *Molecular Fluorescence: Principles and Applications*. Weinheim, Wiley-VCH Verlag GmbH.

65. Veerman, J., Garcia-Parajo, M., Kuipers, L., Van Hulst, N. (1999) Time-varying triplet state lifetimes of single molecules. *Phys. Rev. Lett.* **83** (11), 2155–2158.

66. Opitz, N., Rothweil, P.J., Oeke, B., Schwille, P. (2003) Single molecule FCS-based oxygen sensor (O2-FVSensor): a new intrinsically calibrated oxygen sensor utilizing fluorescence correlation spectroscopy (FCS) with single fluorescent molecule detection sensitivity. *Sens. Actuators B* **96** (1–2), 460–467.

67. Rasnik, I., McKinney, S.A., Ha, T. (2006) Nonblinking and longlasting single-molecule fluorescence imaging. *Nat. Methods* **3** (11), 391–393.

68. Ha, T., Enderle, T., Chemla, D., Selvin, P., Weiss, S. (1996) Single molecule dynamics studied by polarization modulation. *Phys. Rev. Lett.* **77** (19), 3979–3982.

69. Jovin, T.M., Lidke, D.S., Jares-Erijman, E.A. (2005) *From Cells to Proteins: Imaging Nature across Dimensions*. Springer Dordrecht, pp. 209–216.

70. Förster, T. (1948) Intermolecular energy migration and fluorescence. *Ann. Phys.* **2**, 55–75.

71. Roy, R., Hohng, S., Ha, T. (2008) A practical guide to single-molecule FRET. *Nat. Methods* **5** (6), 507–516.

72. Schleifenbaum, F., Blum, C., Elgass, K., Peter, S., Subramaniam, V., Meixner, A.J. (2009) Multiparameter single molecule spectroscopy gives insight into the complex Photophysics of Fluorescence Energy Transfer (FRET) coupled biosystems. *SPIE Proc.* **7190**, 71900U.

73. Ha, T. (2001) Single-molecule FRET. *Single Mol.* **2** (4), 283–284.

74. Schuler, B., Eaton, W. (2008) Protein folding studied by single-molecule FRET. *Curr. Opin. Struct. Biol.* **18** (1), 16–26.

75. Soranno, A., Buchli, B., Nettels, D., Cheng, R.R., Müller-Späth, S., Pfeil, S.H., Hoffmann, A., Lipman, E.A., Makarov, D.E., Schuler, B. (2012) Quantifying internal friction in unfolded and intrinsically disordered proteins with single-molecule spectroscopy. *Proc. Natl. Acad. Sci. U.S.A.*, **109**, 17800–17806.

76. Lee, T., Blanchard, S., Kim, H., Puglisi, J., Chu, S. (2007) The role of fluctuations in tRNA selection by the ribosome. *Proc. Natl. Acad. Sci. U.S.A.* **104** (34), 13661.

77. Müller, B., Zaychikov, E., Bräuchle, C., Lamb, D. (2005) Pulsed interleaved excitation. *Biophys. J.* **89** (5), 3508–3522.

78. Matsuda, A., Shao, L., Boulanger, J., Kervrann, C., Carlton, P.M., Kner, P., Agard, D., Sedat, J.W. (2010) Condensed mitotic chromosome structure at nanometer resolution using PALM and EGFP-histones. *PLoS ONE* **5** (9), e12768.

79. Heilemann, M., van de Linde, S., Schüttpelz, M., Kasper, R., Seefeldt, B., Mukherjee, A., Tinnefeld, P., Sauer, M. (2008) Subdiffraction-resolution fluorescence imaging with conventional fluorescent probes. *Angew. Chem. Int. Ed.* **47** (33), 6172–6176.

80. Habuchi, S., Ando, R., Dedecker, P., Verheijen, W., Mizuno, H., Miyawaki, A., Hofkens, J. (2005) Reversible single-molecule photoswitching in the GFP-like fluorescent protein Dronpa. *Proc. Natl. Acad. Sci. U.S.A.* **102** (27), 9511–9516.

81. Adam, V., Moeyaert, B., David Charlotte, C., Mizuno, H., Lelimousin, M., Dedecker, P., Ando, R., Miyawaki, A., Michiels, J., Engelborghs, Y., Hofkens, J. (2011) Rational design of photoconvertible and biphotochromic fluorescent proteins for advanced microscopy applications. *Chem. Biol.* **18** (10), 1241–1251.

82. Blum, C., Meixner, A.J., Segers-Nolten, I., Subramaniam, V. (2005) Spectrally resolved single molecule spectroscopy reveals photophysical versatility of fluorescent proteins. *Biophys. J.* **88** (1), 184A–184A.

83. Blum, C., Meixner, A.J., Subramaniam, V. (2004) Room temperature spectrally resolved single-molecule spectroscopy reveals new spectral forms and photophysical versatility of Aequorea green fluorescent protein variants. *Biophys. J.* **87** (6), 4172–4179.

84. Stracke, F., Blum, C., Becler, S., Müllen, K., Meixner, A.J. (2000) Intrinsic conformer jumps observed by single molecule spectroscopy in real time. *Chem. Phys. Lett.* **323**, 196–200.

85. Weiss, S. (1999) Fluorescence spectroscopy of single biomolecules. *Science* **283** (5408), 1676.

86. Tinnefeld, P., Buschmann, V., Herten, D., Han, K., Sauer, M. (2000) Confocal Fluorescence Lifetime Imaging Microscopy (FLIM) at the single molecule level. *Single Mol.* **1** (3), 215–223.

87. Schleifenbaum, F., Blum, C., Elgass, K., Subramaniam, V., Meixner, A.J. (2008) New insights into the photophysics of DsRed by combined spectral and time domain spectroscopy on single proteins. *J. Phys. Chem. A* **112** (25), 7669–7674.

88. Elgass, K., Caesar, K., Schleifenbaum, F., Stierhof, Y.D., Meixner, A.J., Harter, K. (2009) Novel application of fluorescence lifetime and fluorescence microscopy enables quantitative access to subcellular dynamics in plant cells. *PLoS ONE* **4** (5), e5716.

89. Manen, H-Jv., Verkuijlen, P., Wittendorp, P., Subramaniam, V., Berg. TKvd, Roos, D., Otto, C. (2008) Refractive index sensing of green fluorescent proteins in living cells using fluorescence lifetime imaging microscopy. *Biophys. J.: Biophys.*

Lett., **94** L67–L69. doi: 10.1529/biophysj.107.127837.

90. Kapanidis, A., Laurence, T., Lee, N., Margeat, E., Kong, X., Weiss, S. (2005) Alternating-laser excitation of single molecules. *Acc. Chem. Res.* **38** (7), 523–533.

91. Eggeling, C., Widengren, J., Brand, L., Schaffer, J., Felekyan, S., Seidel, C. (2006) Analysis of photobleaching in single-molecule multicolor excitation and forster resonance energy transfer measurements. *J. Phys. Chem. A* **110** (9), 2979–2995.

92. Rüttinger, S., Macdonald, R., Krämer, B., Koberling, F., Roos, M., Hildt, E. (2006) Accurate single-pair Förster resonant energy transfer through combination of pulsed interleaved excitation, time correlated single-photon counting, and fluorescence correlation spectroscopy. *J. Biomed. Opt.* **11**, 024012.

93. Gross, L.A., Baird, G.S., Hoffman, R.C., Baldridge, K.K., Tsien, R.Y. (2000) The structure of the chromophore within DsRed, a red fluorescent protein from coral. *Proc. Natl. Acad. Sci. U.S.A.* **97** (22), 11990–11995.

94. Clifford, J.N., Bell, TDM., Tinnefeld, P., Heilemann, M., Melnikov, S.M., Hotta. J-I, Sliwa, M., Dedecker, P., Sauer, M., Hofkens, J., Yeow, EKL. (2007) Fluorescence of single molecules in polymer films: sensitivity of blinking to local environment. *J. Phys. Chem. B* **111** (25), 6987–6991. doi: 10.1021/jp072864d.

95. Goldsmith, R.H., Moerner, W.E. (2010) Watching conformational- and photodynamics of single fluorescent proteins in solution. *Nat. Chem.* **2** (3), 179–186.

96. Cohen, A.E. (2005) Control of nanoparticles with arbitrary two-dimensional force fields. *Phys. Rev. Lett.* **94** (11), 118102.

97. Long, D. (1977) *Raman Spectroscopy*. McGraw-Hill New York.

98. Fleischmann, M., Hendra, P.J., McQuillan, A.J. (1974) Raman spectra of pyridine adsorbed at a silver electrode. *Chem. Phys. Lett.* **26**, 163.

99. Kneipp, K., Wang, Y., Kneipp, H., Perelman, L.T., Itzkan, I., Dasari, R.R., Feld, M.S. (1997) Single molecule detection using Surface-Enhanced Raman Scattering (SERS). *Phys. Rev. Lett.* **78**, 1667–1670.

100. Otto, A. (2002) What is observed in single molecule SERS, and why? *J. Raman Spectrosc.* **33** (8), 593–598.

101. Otto, A. (2001) Theory of first layer and single molecule Surface Enhanced Raman Scattering (SERS). *Phys. Status Solidi A* **188** (4), 1455–1470.

102. Lombardi, J.R., Birke, R.L., Lu, T., Xu, J. (1986) Charge-transfer theory of surface enhanced Raman spectroscopy: Herzberg–Teller contributions. *J. Chem. Phys.* **84**, 4174–4181.

103. Otto, A., Mrozek, I., Grabhorn, H., Akemann, W. (1992) Surface enhanced Raman scattering. *J. Phys. Condens Matter* **4**, 1143–1212.

104. Otto, A. (1984) In: Cardona, M. (ed) *Light Scattering in Solids*, Vol. IV. Springer, Berlin, p. 289.

105. Strommen, D., Nakamoto, K. (1977) Resonance Raman spectroscopy. *J. Chem. Educ.* **54** (8), 474.

106. Vosgröne, T., Meixner, A.J. (2005) Surface- and resonance-enhanced micro-Raman spectroscopy of xanthene dyes: from the ensemble to single molecules. *ChemPhysChem* **6**, 154–163. doi: 10.1002/cphc.200400395.

107. Weitz, D.A., Garoff, S., Hanson, C.D., Gramila, T.J., Gersten, J.I. (1982) Fluorescent lifetimes of molecules on silver-island films. *Opt. Lett.* **7** (2), 89–91.

108. Schleifenbaum, F., Peter, S., Meixner, A.J. (2010) Detecting the same individual protein and its photoproducts via fluorescence and surface-enhanced Raman spectroscopic imaging. *J. Phys. Chem. A* **114** (1), 143–150.

109. Meixner, A.J., Vosgröne, T., Sackrow, M. (2001) Nanoscale surface-enhanced resonance Raman scattering spectroscopy of single molecules on isolated silver clusters. *J. Lumin.* **94**, 147–152.

110. Mackowski, S., Wörmke, S., Maier, A.J., Brotosudarmo, THP., Hartyunyan, H., Hartschuh, A., Govorov, A.O., Scheer, H., Bräuchle, C. (2007) Metal–enhanced fluorescence of chlorophylls in single light-harvesting complexes. *Nano Lett.*, **363**, 507–511.

111. Matveeva, E.G., Gryczynski, I., Barnett, A., Leonenko, Z., Lakowicz, J.R., Gryczynski, Z. (2007) Metal particle-enhanced fluorescent immunoassays on metal mirrors. *Anal. Biochem.* **363**, 239–245.

112. Zhang, J., Fu, Y., Chowdhury, M.H., Lakowicz, J.R. (2007) Metal-enhanced single-molecule fluorescence on silver particle monomer and dimer: coupling effect between metal particles. *Nano Lett.* **7** (7), 2101–2107.

113. Lakowicz, J.R. (2005) Radiative decay engineering 5: metal-enhanced fluorescence and plasmon emission. *Anal. Biochem.* **337**, 171–194.

114. Drexhage, K.H. (1970) Influence of a dielectric interface on fluorescence decay time. *J. Lumin.* **1** (2), 693–701.

115. Cesa, Y., Blum, C., Broek, JMvd., Mosk, A.P., Vos, W.L., Subramaniam, V. (2009) Manipulation of the local density of photonic states to elucidate fluorescent protein emission rates. *Phys. Chem. Chem. Phys.* **11**, 3636–2531.

116. Fermi, E. (1932) Quantum theory of radiation. *Rev. Mod. Phys.* **4**, 87–132.

117. Steiner, M., Schleifenbaum, F., Stupperich, C., Failla, A.V., Hartschuh, A., Meixner, A.J. (2005) Microcavity-controlled single-molecule fluorescence. *ChemPhysChem* **6**, 2190–2196.

118. Steiner, M., Schleifenbaum, F., Stupperich, C., Failla, A.V., Hartschuh, A., Meixner, A.J. (2006) A new microcavity design for single molecule detection. *J. Lumin.* **119** (120), 167–172.

119. Chizhik, A., Schleifenbaum, F., Gutbrod, R., Chizhik, A., Khoptyar, D., Meixner, A.J., Enderlein, J. (2009) Tuning the fluorescence emission spectra of a single molecule with a variable optical sub-wavelength metal microcavity. *Phys. Rev. Lett.* **102**, 073002–073006.

120. Purcell, E.M. (1946) Spontaneous emission probabilities at radio frequencies. *Phys. Rev.* **69**, 681.

121. Chizhik, A.I., Chizhik, A.M., Khoptyar, D., Baär, S., Meixner, A.J., Enderlein, J. (2011) Probing the radiative transition of single molecules with a tunable microresonator. *Nano Lett.* **11** (4), 1700–1703.

122. Züchner, T., Failla, A.V., Meixner, A.J. (2011) Light microscopy with doughnut modes: a concept to detect, characterize, and manipulate individual nanoobjects. *Angew. Chem. Int. Ed.* **50** (23), 5274–5293.

123. Gutbrod, R., Khoptyar, D., Steiner, M., Chizhik, A.M., Chizhik, A.I., Baär, S., Meixner, A.J. (2010) Three-dimensional orientation of single molecules in a tunable optical $\lambda/2$ microresonator. *Nano Lett.* **10** (2), 504–508.

124. Chizhik, A.I., Gregor, I., Schleifenbaum, F., Müller, C.B., Röling, C., Meixner, A.J., Enderlein, J. (2012) Electrodynamic coupling of electric dipole emitters to a fluctuating mode density within a nanocavity. *Phys. Rev. Lett.* **108** (16), 163002.

125. Blum, C., Schleifenbaum, F., Stopel, M., Peter, S., Sackrow, M., Subramaniam, V., Meixner, A.J. (2011) Room temperature excitation spectroscopy of single quantum dots. *Beilstein J. Nanotechnol.* **2**, 516–524.

126. Celebrano, M., Kukura, P., Renn, A., Sandoghdar, V. (2011) Single-molecule imaging by optical absorption. *Nat. Photonics* **5** (2), 95–98.

127. Gaiduk, A., Yorulmaz, M., Ruijgrok, P.V., Orrit, M. (2010) Room-temperature detection of a single molecule's absorption by photothermal contrast. *Science* **330** (6002), 353–356.

128. Chong, S., Min, W., Xie, X.S. (2010) Ground-state depletion microscopy: detection sensitivity of single-molecule optical absorption at room temperature. *J. Phys. Lett.*, **1**, 3316–3322.

22

Single-Molecule Interfacial Electron-Transfer Dynamics

Hong Peter Lu

22.1

Introduction

Interfacial electron transfer (ET) plays a critical role in catalysis, solar energy conversion, photosynthesis, environmental remediation technologies, and energy technologies. The fundamental information related to the energy flow between molecules and substrate surfaces as a function of surface site geometry and molecular structure are critical for understanding interfacial ET mechanism and dynamics. Specifically, interfacial ET processes involving dye molecules on titanium oxide (TiO_2) surfaces have been extensively investigated by ensemble-averaged studies [1–7]. As shown in Figure 22.1, in such studies, photoexcited dye molecules, such as organic dye molecules or porphyrin molecules, adsorbed on TiO_2 serve to inject electrons into the substrate conduction band (CB), where the excess electrons rapidly thermalize and relax to the CB minimum. The relaxed electrons may then diffuse into the bulk, becoming a part of the photochemical cycle, trap near the surface or in the bulk, or undergo back ET to an adsorbed molecule [4–20]. The forward electron transfer (FET) kinetics in various dye–TiO_2 ET systems are nonexponential or dispersive, with half-times disseminated in the femtoseconds to several hundred picoseconds range [6–20]. Following the FET, the thermalized-injected electron is localized to either subband states or surface states of the TiO_2 semiconductor [1–20]. Typically, a backward electron transfer (BET) from the semiconductor to the oxidized dye molecules will follow. In interfacial ET systems, a BET process is possible by thermal detrapping of the electrons from the total electron density of the reduced semiconductor and recombining the electrons with the oxidized dye molecules. When compared to ultrafast FET processes, BET processes take place at a longer timescale, ranging from subnanoseconds to several milliseconds, probably as a result of the existence of trap states and non-Brownian diffusion motions of the electrons in semiconductors. Furthermore, the dynamics of the BET processes are often nonexponential or dispersive [4–20]. Ensemble-averaged approaches, although valuable, cannot resolve important nanoscale aspects of interfacial ET. In particular, the geometry of the adsorption site, the orientation and the motion of the adsorbed molecule, and their relationship to the excited-state

Handbook of Spectroscopy, Second Edition. Edited by Günter Gauglitz and David S. Moore.

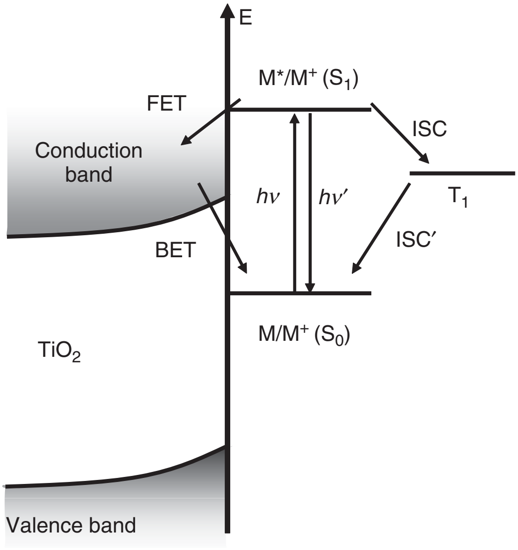

Figure 22.1 Schematic representation of a model of photoinduced processes in a dye-sensitized TiO_2 system. FET, forward electron transfer; BET, backward electron transfer; ISC, intersystem crossing; T, triplet state; M^*/M^+ (S_1), dye molecule excited state; and $M/M^+(S_0)$, dye molecule ground state.

dynamics are often averaged out as the ensemble-averaged measurements cannot dissect complex interfacial ET processes at a site-specific level. The difficulty comes from both intrinsic spatial and temporal inhomogeneities of the interfacial ET dynamics, which can be identified, measured, and analyzed by studying specific one molecule at a time and a location at an interface.

Single-molecule spectroscopy was first demonstrated in 1997 [21]. Since then, the single-molecule spectroscopy has been a powerful approach for studying complex systems and inhomogeneous dynamics [21–39] and has also been applied to intramolecular [40] and interfacial ET investigations [21–39]. In this chapter, we will discuss on the single-molecule interfacial ET work carried out at our laboratory, and we will only briefly discuss the work carried out at a number of laboratories worldwide in recent years [39, 41–45].

22.2
Single-Molecule Spectroscopy Applicable for Studying Electron-Transfer Dynamics

22.2.1
Single-Molecule Time-Stamping Spectroscopy

A confocal microscope with a focused laser was typically used to image the individual molecules and measure the single-molecule fluorescence intensity trajectories. The output of the Coherent MIRA900 femtosecond laser at an 850–1000 nm wavelength and 75.7 MHz repetition rate was frequency doubled and coupled through a single-mode optical fiber (Figure 22.2). The beam was collimated after the fiber and passed through a polarizer, and the excitation light was attenuated to 0.1–1 μW. The beam was sent into the microscope from its epiport, reflected up by a dichroic beamsplitter, and focused by a 100× oil immersion objective lens (Zeiss Fluar numerical aperture (NA) 1.3) onto the upper sample surface of a microscope coverslip (Fisher Scientific, 0.17 mm thick). The sample can be raster scanned or moved to a particular position with respect to the laser focus using an x–y

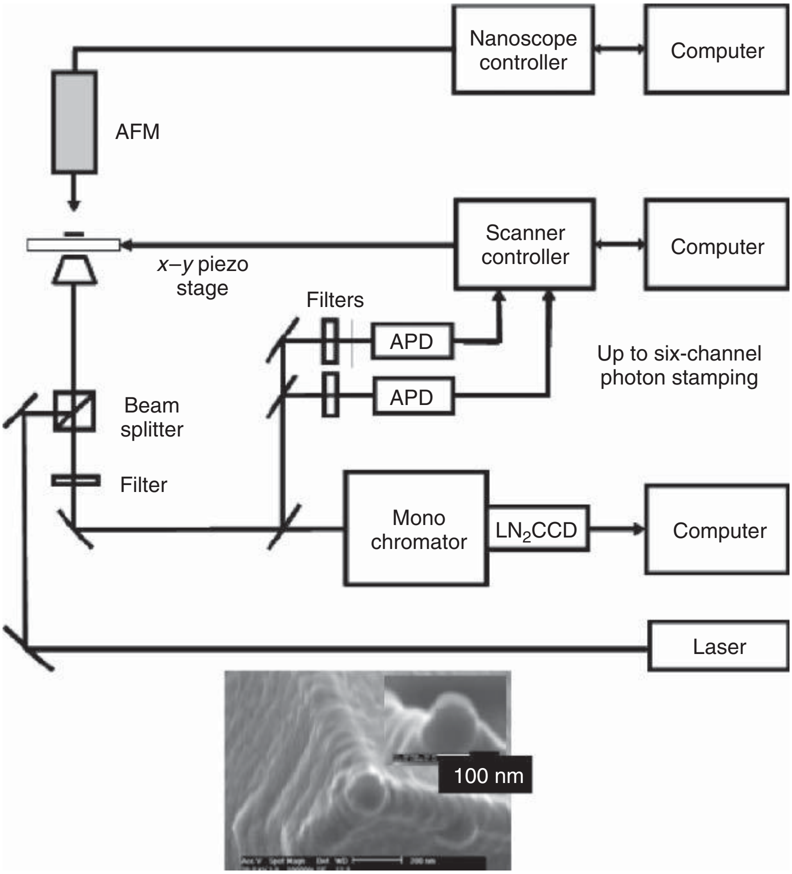

Figure 22.2 Schematic representation of the combined AFM tip-enhanced imaging and single-molecule fluorescence imaging experimental setup. Different continuous wave (CW) or pulse lasers and multicolor excitation are selected to improve the signal-to-noise ratio and the time resolution. A 2D piezoelectric closed-loop scanning stage is used to scan the sample in nanoscale precision for a 20 × 20 μm dynamic range and align the laser focal spot with the fluorescent molecule. APD, Avalanche photodiode; CCD (charged couple device camera). Inset: the AFM tip is typically coated with Au or Ag metal to facilitate tip-enhanced imaging and spectroscopy through surface plasmon enhancement and energy-transfer mechanisms.

piezoelectric closed-loop position scanning stage (Physik Instrumente, Germany). The fluorescence was collected by the same objective lens and was directed to the camera port of the microscope after going through the dichroic beamsplitter. The fluorescence signal was split by a polarizing beamsplitter or a color beamsplitter so that the two beams detected were the parallel and perpendicular components or the fluorescence resonant energy-transfer (FRET) donor and acceptor of the fluorescence, respectively. The two-channel (or four-channel) signals were imaged onto a (two pairs) pair of photon-counting detectors, either avalanche photodiodes (APDs; Perkin Elmer, SPCM-AQR-16 and SPCM-AQRH-14) or photomultiplier tube (PMT) (Hamamatsu H7522-40).

The detection electronics were derived from typical time-correlated single-photon counting. The two APD signals were directly sent to two time-to-amplitude converters (TACs) (Canberra, Model 2145) as a ‘‘start’’ signal. The photodiode signal from Mira 900 fs laser system was used as a ‘‘stop’’ signal for the TAC. The two TAC outputs were sent to a homemade two-channel digitizer instead of a multichannel analyzer. A recorded trajectory usually contains hundreds to thousands of photons

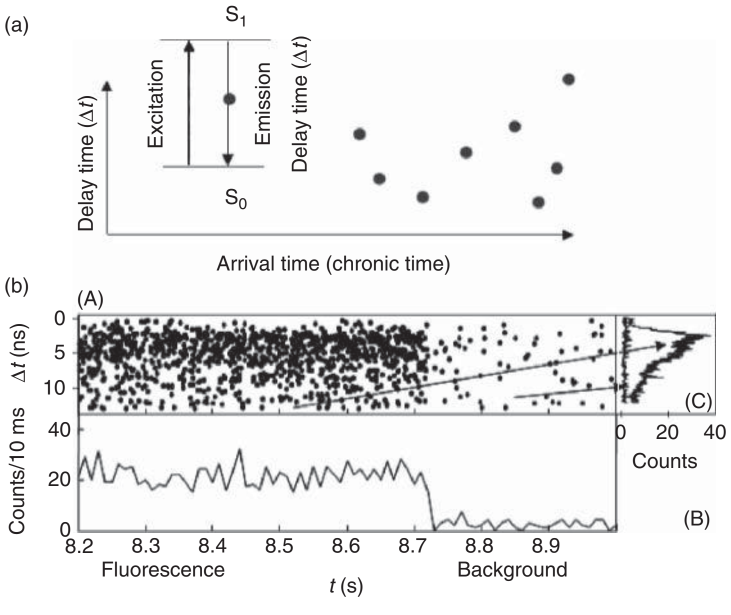

Figure 22.3 Schematic representation of a single-molecule confocal microscope with two-channel photon time-stamping spectroscopy. (a) It allows a study of the fluorescence intensity, lifetime, and anisotropy of a single molecule simultaneously by recording the arrival and delay time of each fluorescence photon. (b) An example of the raw data of the photon timestamping of a detector channel (A). Each dot corresponds to a photon-detected plot by its arrival time (t) and delay time (Δt). The fluorescence intensity trajectory (B) is calculated from the histogram of arrival time (t) with 0.01 s time bin resolution. The molecule was photobleached at 8.71 s. The nanosecond fluorescence decay curves (C) are the histograms of the delay time of the fluorescence photons ($t < 8.1$ s) and background photons ($t > 8.1$ s).

(Figure 22.3). For each photon, the detector identification, arrival time, and the delay time between laser excitation pulse and detected photon in nanoseconds or picoseconds were stored in the computer photon-by-photon for future data analysis. The recording of each photon is similar to receiving a mail with two stamps on the envelope showing when the mail was sent out and when the mail was received: this is where the name of the single-molecule photon-stamping spectroscopy originated from as an analogy to the mails [24, 27, 30, 39, 46, 47].

22.2.2
Tip-Enhanced Near-Field Fluorescence Lifetime Microscopy

A near-field optical imaging approach to correlate single-molecule optical spectroscopy with scanning tip topographic characterization [26, 28, 48–50] has been applied to studying interfacial ET, especially, to correlate the time-resolved spectroscopic temporal analysis and atomic force microscopy (AFM) topographic spatial analysis of the interfacial electron at a specific site (Figure 22.4). The method combines metallic tip scanning (either Au-coated AFM or STM metallic tips) with fluorescence lifetime imaging microscopy (FLIM) [48]. The AFM metallic tip was formed by sputter coating a Si tapping mode tip with Au, in a way that forms a globular tip apex (Figure 22.2, inset). The Au-coated tip generates high local electric field enhancement under laser illumination, which provides a strong electric field interaction between the AFM tip and the fluorescent molecule under

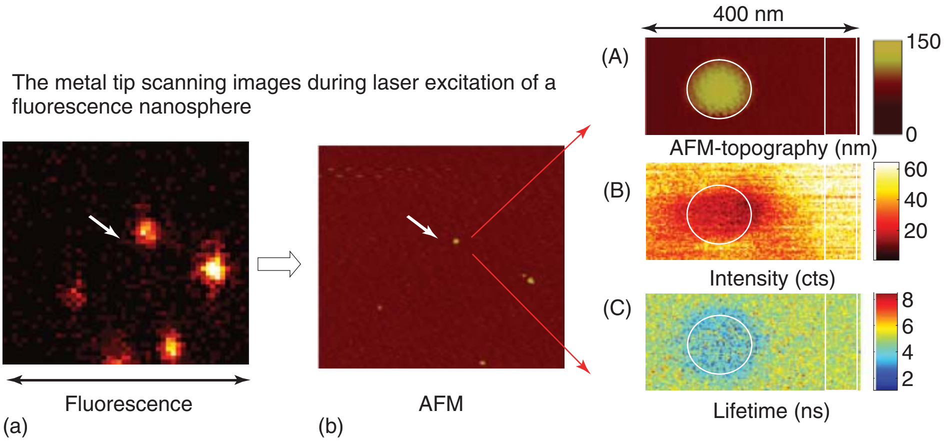

Figure 22.4 Proof-of-concept metallic tip-enhanced FLIM imaging. The fluorescence intensity image (a) and AFM image (b) of the same sample area containing 40 nm fluorescence nanospheres. The sample was first imaged by sample scanning confocal fluorescence microscopy and then by tip scanning AFM of the same area. The arrows on the images indicate the area zoomed-in for further high-resolution imaging shown in the three panels (A–C). The three nanosphere scanning probe images are obtained by (A) AFM; (B) the fluorescence intensity; and (C) the perturbation of the fluorescence lifetime [48].

the tip. The fluorescence lifetime is perturbed only when the tip is on top of the molecule within a nanometer range. The induced fluorescence lifetime changes provide the AFM–FLIM imaging contrast. Then imaging can be performed at an AFM spatial resolution typically defined by the tip diameter (Figure 22.4). Conceptually, an STM metallic tip can also facilitate correlated STM–FLIM imaging (Figure 22.5).

22.2.3
Tip-Enhanced Near-Field and Confocal Raman Spectroscopy Analysis of Vibronic Coupling of Interfacial Electron Transfer

AFM tip-enhanced site-specific resonance Raman microscopy studies on the interfacial ET of a dye-sensitization system has been applied to study interfacial ET energetics and dynamics [26]. A Raman excitation laser frequency resonant with the interfacial charge-transfer absorption band can be used in the Raman microscopic imaging measurements. For example, measuring the resonant-enhanced Raman signal associated with the chemical bonds that controls the interfacial ET dynamics [5, 47, 51, 52], we were able to observe the Raman peak intensity and peak-to-peak intensity ratio that are different from site to site at dye–TiO_2 nanoparticle (NP) layer. This approach allows quantitative analyses of vibrational relaxation energy barriers of the interfacial ET and surface chemical bonding and coupling between

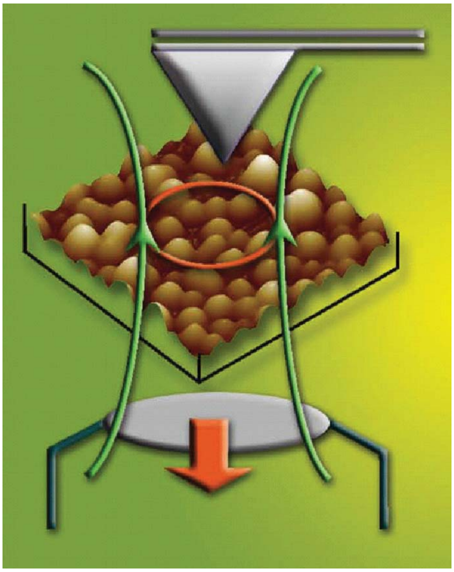

Figure 22.5 Schematic representation of AFM or STM metal tip-enhanced Raman spectroscopy of single TiO_2 nanoparticles. The optical detection and excitation are conducted using inverted confocal microscope coupled with monochromator-CCD or single-photon counting detectors (APD) [26, 28, 48, 49].

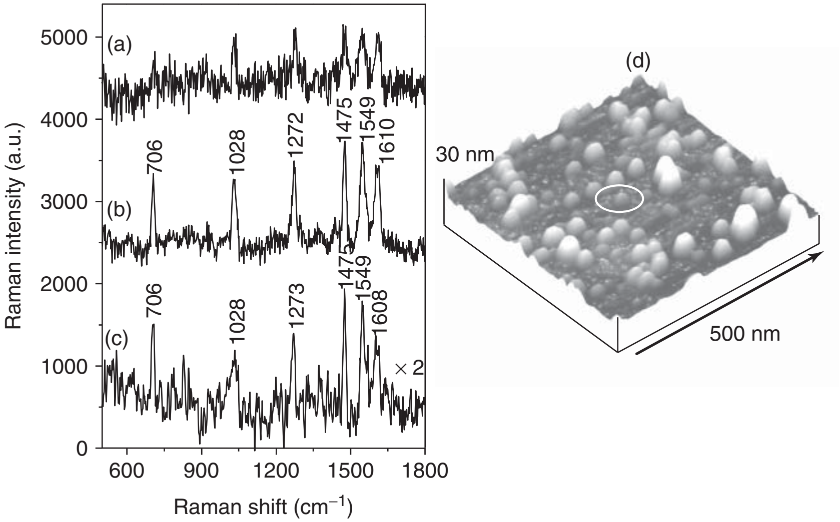

Figure 22.6 Tip-enhanced Raman spectroscopy and AFM characterization of N_3–TiO_2 interfacial electron transfer: (a) Raman spectrum without a tip, (b) Raman spectrum with a silver-coated AFM tip, (c) near-field Raman spectrum, and (d) an AFM image. The marked part in the AFM image corresponds to the nanoscale site where the near-field Raman spectrum was collected. In the near-field Raman spectrum, the most prominent bands, at 1475, 1549, and 1608 cm^{-1}, were assigned to the bipyridine ring stretching mode. The intense band at 1028 cm^{-1} was assigned to the ring breathing mode. The C–C interring stretch combined with the C–O stretching mode corresponds to the band at 1273 cm^{-1}. The 706 cm^{-1} band is attributed to an in-plan ring deformation mode [26].

the molecules and the substrates. A metallic-coated AFM tip can be used to enhance the Raman signals and help on achieving high spatial resolution beyond the optical diffraction-limited spatial resolution (Figure 22.6) [26, 53–55].

22.3
Intermittent Interfacial Electron Transfer in Organic Dye-Sensitized TiO_2 Nanoparticles

Here, we discuss a specific single-molecule spectroscopic study of photosensitized interfacial ET processes in Coumarin 343 (C343)–TiO_2 NP and Cresyl Violet (CV^+)–TiO_2 NP systems, using time-correlated single-photon stamping coupled with scanning confocal fluorescence microscopy. In this work, fluorescence intensity trajectories of individual dye molecules adsorbed on a semiconductor NP surface showed fluorescence fluctuations and blinking, with time constants distributed from milliseconds to seconds. The fluorescence fluctuation dynamics were found to be inhomogeneous from molecule to molecule and from time to time, showing significant static and dynamic disorders in the interfacial ET reaction dynamics. We attribute fluorescence fluctuations to the interfacial ET reaction rate fluctuations, associating redox reactivity intermittency with the fluctuations of molecule–TiO_2 electronic and Franck–Condon coupling. The intermittent interfacial reaction dynamics that likely occur among single molecules in other interfacial and surface chemical processes can typically be observed by single-molecule studies but not by conventional ensemble-averaged experiments.

With single-molecule spectroscopy, this study of interfacial ET dynamics of individual molecules avoided interference from (i) molecular aggregation, (ii) multiple electron injection to a single particle, and (iii) multiple electron–cation recombinations on the surface of a single particle.

C343–TiO_2 NP, CV^+–TiO_2 NP, and porphyin–TiO_2 systems were chosen for the studies of single-molecule interfacial ET (Figure 22.7). These systems exhibit a number of amenable properties for such research: (i) TiO_2 semiconductor being an essential substrate in many solar cells, interfacial ET processes in dye–TiO_2 NP systems have a potential industrial importance [1, 2]; (ii) the high fluorescence quantum efficiencies of C343 ($\Phi_f = \sim 0.7$) [56] and CV^+ ($\Phi = \sim 0.545$) [40] make it feasible to use single-molecule fluorescence spectroscopy to study interfacial ET processes; (iii) it has already been demonstrated that C343 [40, 56, 57] and CV^+ [58] adsorbed on semiconductor surfaces are efficient electron donors under photoexcitation; (iv) the systems can be used to validate single-molecule spectroscopy as a way to study interfacial ET processes involving chromophores that absorb in the near-UV (C343) and visible region (CV^+); (v) the oxidized dye molecules have different charge densities, +2 charges on CV and +1 charge on C343, making them an informative comparison; and (vi) STM and AFM can be applied to obtain single-molecule topographic images of single porphyin molecules on a single-crystal surface of TiO_2, rutile, or anatase.

Interfacial ET processes involving C343 have been explicitly proved by probing the ultrafast ET processes and ET products (cation radical of C343 and trapped electron in TiO_2 colloidal particles) in thorough ensemble-averaged studies of the C343–TiO_2 system [35, 40, 57]. Interfacial ET processes involving monomers or aggregates of CV^+ as electron donor have been reported in a previous single-molecule ET study [36] and in other ensemble-averaged ET studies [1–20, 40, 57, 58].

We examined the single-molecule interfacial ET processes by recording and analyzing the fluorescence intensity trajectories of individual C343 and CV^+ molecules adsorbed on the surface of TiO_2 NPs. In our experiments, a thin layer of TiO_2 NPs was spin coated on a glass coverslip (Figure 22.7) followed by spin coating a solution (0.1 nM) of C343 or CV^+. The dye molecules were covered using a thin film of poly(methyl methacrylate) (PMMA) by spin coating a toluene solution of PMMA (1 mg ml^{-1}). Fluorescence intensity trajectories of C343 and CV^+ single molecules adsorbed on bare glass surfaces and the surfaces of TiO_2 NPs were measured by single-photon time stamping (Figure 22.8) [24]. Uninterrupted fluorescence states, that is, no fluorescence blinking or fluctuation, were observed for both C343 and CV^+ molecules in the absence of TiO_2 NPs on insulating glass surfaces. Figure 22.8a shows a typical fluorescence intensity trajectory of a single C343 molecule

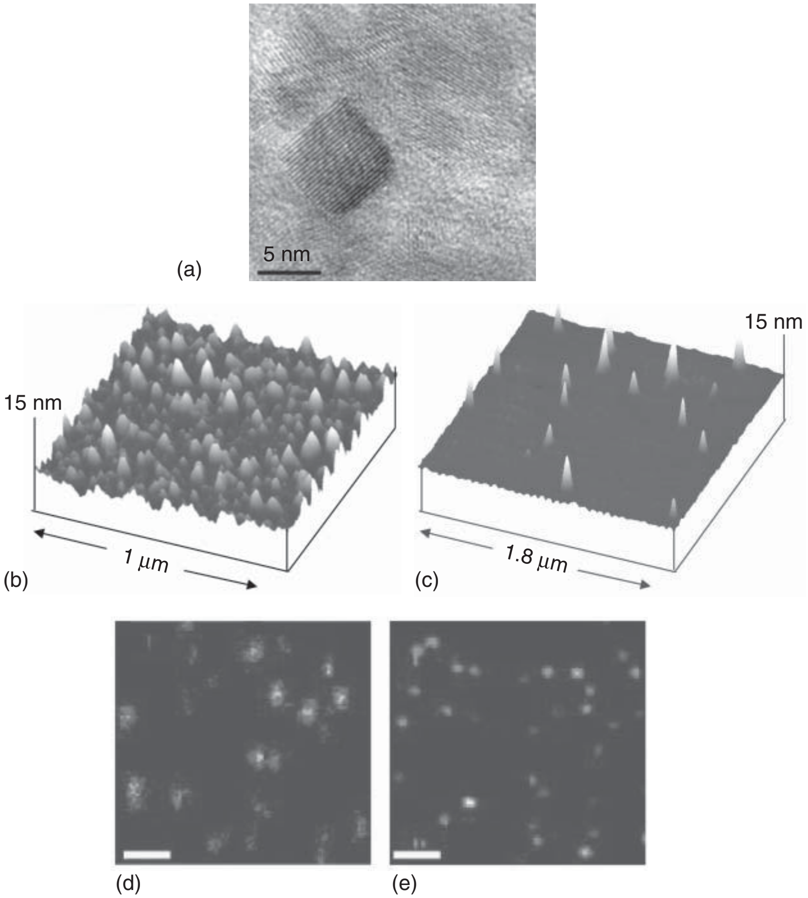

Figure 22.7 (a) A high-resolution TEM image of TiO_2 NPs obtained under 300 kV acceleration and 600 k magnification. (b) AFM images obtained for a 0.8 μM colloidal TiO_2 NP solution spin coated on a glass coverslip (samples prepared under this condition were overcoated with C343 or CV^+ dye molecules and used in single-molecule fluorescence studies) and (c) a 40 nM colloidal TiO_2 NP solution spin coated on a freshly cleaved mica surface. Fluorescence images of single molecules of (d) C343 and (e) CV^+ spin coated on TiO_2 NP-coated glass coverslips (topographies of these samples are identical to those in (b)). The scale bar in (a) is 5 nm and in (d) and (e) are 2 μm [24].

on a glass surface. Dye molecules at the singlet excited states exhibit different excited-state electronic deactivation processes: internal conversion, fluorescence emission, and intersystem crossing (ISC) to a dark triplet state (Figure 22.1). Under ambient conditions and millisecond temporal resolutions, it is rare to observe fluorescence blinking of these molecules as a result of ISC to the dark triplet-state and ground-state recovery. These processes usually occur in a much shorter timescale, for example, quenching of the triplet state by oxygen is in submillisecond timescale [24, 59]. In our experiments, we used submillisecond temporal resolution

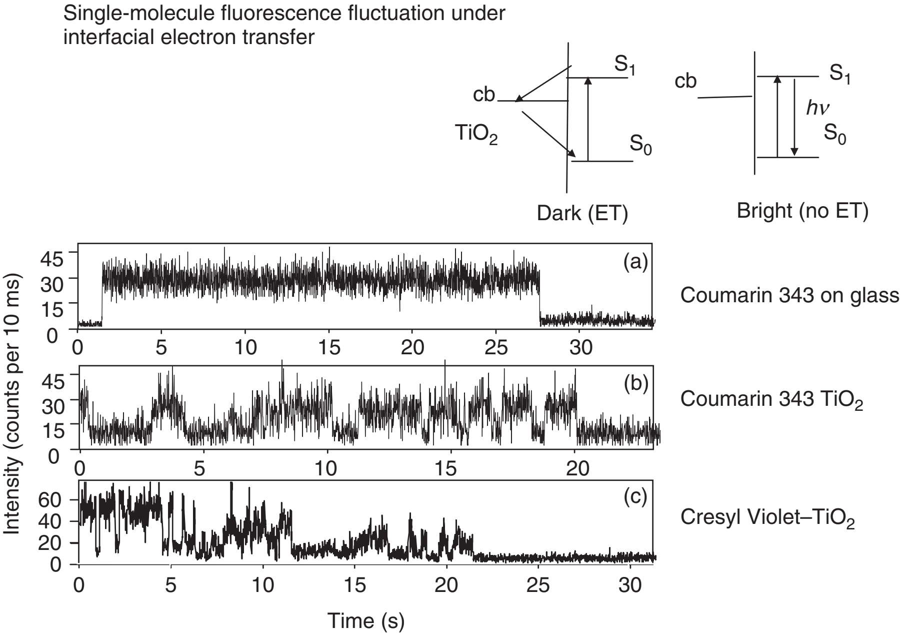

Figure 22.8 Fluorescence intensity trajectories collected in air for single molecules of C343 or CV^+, with samples prepared by spin coating aqueous dye solutions (0.1 nM) on glass coverslips or on TiO_2 NP-coated glass coverslips and overlaid with thin film of PMMA: (a) trajectory of C343 in the absence of TiO_2 NP; (b) trajectories of C343 in the presence of TiO_2 NPs; and (c) trajectory of CV^+ in the presence of TiO_2 NPs. The binning time for the trajectories was 10 ms. The fluorescence intermittency and blinking characteristics observed (b,c) are as a result of intermittent interfacial ET reactivity.

for single-photon counting and a 10 ms bin time for recording and analyzing single-photon arrival time. These timescales allowed any fast fluorescence intensity fluctuations or blinking of the dye molecules to be averaged out within our measurements.

A typical fluorescence intensity trajectory obtained for a single C343 molecule, adsorbed on the surface of TiO_2 NPs and recorded in air, is shown in Figure 22.8b. Figure 22.8c shows a typical fluorescence intensity trajectory of a single CV^+ molecule adsorbed on the surface of a TiO_2 NP and recorded in air. Under these conditions, fluorescence intensity trajectories of both C343 and CV^+ single molecules showed fluctuation behavior. The single-molecule fluorescence intensities stochastically dropped to either a lower or the background level. For both the C343 and CV^+ single molecules, the timescales of fluorescence intensity fluctuations ranged from several milliseconds to several seconds and also the fluctuation behavior was found differed among the single molecules.

On the basis of our experimental results and the literature, we are able to attribute the fluorescence intensity fluctuation behavior of single molecules adsorbed on TiO_2 NP surfaces to interfacial ET reactions for the following reasons: (i) the oxidized state of the dyes is essentially nonfluorescent, in contrast to their bright reduced forms; [24, 60] (ii) ensemble-averaged fluorescence and transient absorption studies have demonstrated that photoexcited C343 molecules inject electrons to the CB or energetically accessible surface states of the TiO_2 semiconductor, and both ensemble-averaged and single-molecule studies have identified interfacial ET reactions of CV^+ on semiconductor surfaces; (iii) fluorescence intensity trajectories of single molecules of C343 (Figure 22.8a) and CV^+ (not shown) in the absence of TiO_2 NPs in our control experiments showed essentially continuous fluorescence until the molecules were irreversibly photobleached; (iv) ET between the dye molecules and a PMMA film is unlikely, based on our control experiment (Figure 22.8a) in which the dye molecules were directly deposited on a glass surface and followed by covering with a PMMA layer; and (v) the fluorescence intensity fluctuations are not due to triplet states or the rotation of the transition dipoles of the dye molecules (see reference [24] for details).

We have investigated the possibility that transient changes in the transition dipole orientations of the single molecules, as a result of molecular rotational or translational motions, are responsible for the observed fluorescence fluctuations and blinking in subseconds to seconds (Figure 22.8b,d). Dye molecules adsorbed on TiO_2 NP surfaces may change their orientations as a result of the collective motions of the molecular environment or rotational and translational motions of the dye molecules. Under linearly polarized laser excitation, changes in the excitation cross section as a result of changes in molecular orientation result in fluorescence intensity changes. In our single-molecule control experiments, we recorded single-molecule fluorescence photon-stamping time trajectories using an orientation angle-modulated linear polarized laser excitation.

We determined the transition dipole orientation angles of single molecules by analyzing the fluorescence intensity trajectories. We identified that more than 80% of the single-molecule fluorescence intensity trajectories showed that the transition dipole orientations of single molecules do not change significantly. However, the intensity fluctuated along the trajectory. These observations substantiate the conclusion that molecular rotation or translation is not primarily responsible for the fluorescence fluctuation and blinking in the intensity trajectories (Figure 22.8b,c).

The nature of the lower fluorescence intensity levels has been further investigated. One possibility is that emission from the oxidized states of the dye molecules ($C343^+$ and CV^{2+}) may be responsible for lower fluorescence intensity levels. However, it is known in the literature that the oxidized states of the dye molecules ($C343^+$ and CV^{2+}) produce no fluorescence or extremely weak fluorescence that would not be significant compared to background. Another possibility is the fluorescence quenching by ET process. The timescale of the FET processes are known to be from femtoseconds to subnanoseconds [40, 57], whereas the fluorescence lifetimes of C343 and CV^+ are in nanoseconds. On the basis of the rates of FET and fluorescence, extremely low fluorescence quantum efficiency is expected.

It is an apparent paradox that single-molecule fluorescence is observed along with ET processes. We investigated this intriguing observation by analyzing the fluorescence lifetimes of single molecules. In this experiment, the arrival and the delay times of every detected photons were recorded using time-stamping technique [61]. The arrival time was used to construct an intensity trajectory and the delay time to analyze single-molecule fluorescence lifetimes. Figure 22.9a shows the intensity trajectory of a typical single CV^+ molecule constructed from the photon arrival time. The photon delay time of the same single molecule can be used to derive the fluorescence lifetime correlated to the intensity trajectory. For this, the trajectory was separated into higher and lower levels, based on a photon count threshold of 30 per 10 ms. Then, the nanosecond fluorescence decay curves were plotted, based on delay time of photons in each group (Figure 22.9). The curves were fitted to single exponential decays with time constants of 2.6 ns (for the profile "a" in Figure 22.9b) and 3.4 ns (for the profile "b" in Figure 22.9b). We found that the fluorescence lifetimes of the higher and the lower intensity states are very close

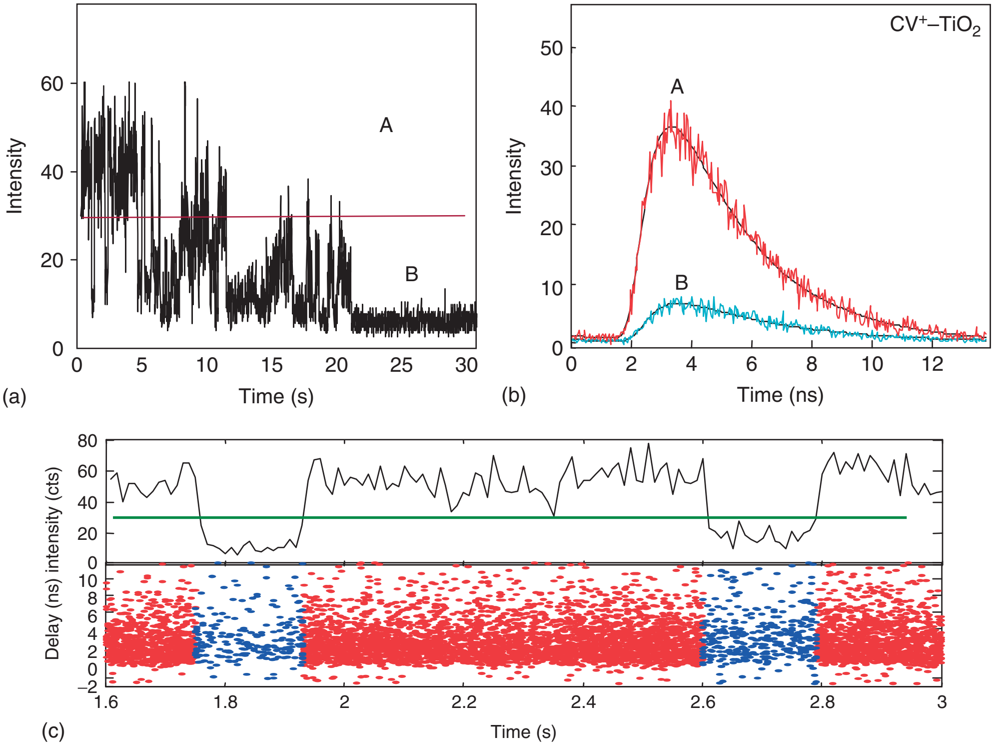

Figure 22.9 Fluorescence decay profiles of a single CV^+ molecule, whose intensity trajectory is provided in Figure 22.4d. The trajectory (Figure 22.4D) is separated into higher and lower levels based on a photocount threshold of 30 per 10 ms: (a) and (b) are the nanosecond fluorescence decay curves of the photons emitted within the higher and lower intensity periods, respectively. The curves are fitted to single exponential decays with time constants of 2.6 ns for (a) and 3.4 ns for (b). Both the curves are normalized based on their total accumulation time. The ratio of the preexponential amplitudes of the higher and the lower intensity curves is 6.

for the molecule, as shown in Figure 22.9. However, the preexponential amplitude of the higher intensity state was six times higher than that of the lower. Therefore, the intensity difference between the profiles (traces "a" and "b" in Figure 22.9) was attributed to the difference in the preexponential amplitudes. On the other hand, quenching of the singlet excited state as a result of interfacial ET reactions occurs at hundreds of picoseconds or below and is much faster than our instrument response time. The observed timescale of this fast quenching process of single molecules agrees with the reported fast FET rates in general. Similar behavior was observed in the analyzes of the intensity trajectories of other single molecules.

The fluorescence intensity level is determined by the fraction of time during which the intermittent ET process takes place. The fluctuations in the fluorescence intensity trajectories are as a result of high and low ET reactivities of the single dye molecules with TiO_2 NPs. It is unlikely that interfacial ET processes are completely turned "on" and "off" during the periods of the lower and higher fluorescence intensity states, respectively. On the other hand, each lower and higher intensity states likely include occurrences of multiple FET and BET events. Therefore, only the time-binning-averaged intensities were recorded in the single-molecule trajectories. The fluorescence intensity fluctuations reflect that interfacial ET reactivity changes from time to time stochastically, resulting different time span of the lower and higher intensity states. When the interfacial ET reactivity is high, the ultrafast redox reactions dictate the fate of the singlet excited state of the dye molecules, and the fluorescence quantum efficiency is low or close to zero. In contrast, when the redox reactivity is low or nonexistent, the fluorescence quantum efficiency is high and the fluorescence intensity is high. This concept is illustrated in Figure 22.10.

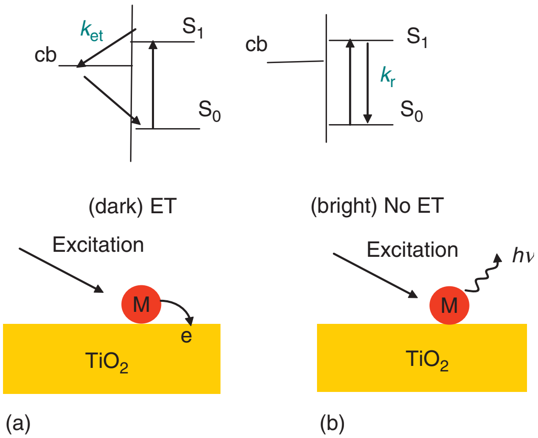

Figure 22.10 The ET activity is intermittent in nature and does not always dominate the excited-state process of the dye–TiO_2 NP system. (a) The dark state in the fluorescence trajectory is due to ET process with high activity quenching the fluorescence, (b) and the bright state is due to natural fluorescence emission cycles from $S_1 \rightarrow S_0$ and low activity in ET process.

Our control experiments support the conclusion that (i) the single-molecule interfacial ET is ultrafast and not directly time resolved by our single-molecule photon-stamping measurements; (ii) the single-molecule fluorescence intensity fluctuation reflects the single-molecule interfacial ET reactivity fluctuation; (iii) when the interfacial ET activity is low, the $S_1 \rightarrow S_0$ radiative emission dominates the signal, and the detected fluorescence intensity is high giving the bright states; (iv) whereas, when the interfacial ET activity is high, the ET quenches the $S_1 \rightarrow S_0$ radiative transition, and the detected fluorescence intensity is low giving the dark states; and (v) therefore the variations of the dark times represent the single-molecule ET reactivity fluctuation; statistically, a longer dark time represents a higher reactivity, and vice versa.

The molecular fluorescence intensity is typically characterized by the fluorescence quantum yield (Q) of the molecules. The value of Q is determined by the ratio of the number of emission photons to the number of excitation photons absorbed. As the intensity of the CW laser is stable and has almost no drift with time, the excitation photon flux is thereby held stable. Furthermore, the rotation motions of dye molecules are rare events within seconds as shown in Figure 22.2; the absorbed photon number is also held stable. Therefore, the single-molecule fluorescence intensity fluctuation, reflected by Q value fluctuation, is due to the emission photon number density fluctuation. Once an excitation photon is absorbed, a single-molecule dye is excited from S_0 ground state to the S_1 excited state (Figure 22.11). The probability of an emission transition from the S_1 excited state depends on both radiative decay rate constant k_{rad} and nonradiative decay rate constant, k_{nr}, and is given by the relation, $Q = k_{\mathrm{rad}}/(k_{\mathrm{rad}} + k_{\mathrm{nr}})$. If there is no nonradiative decay

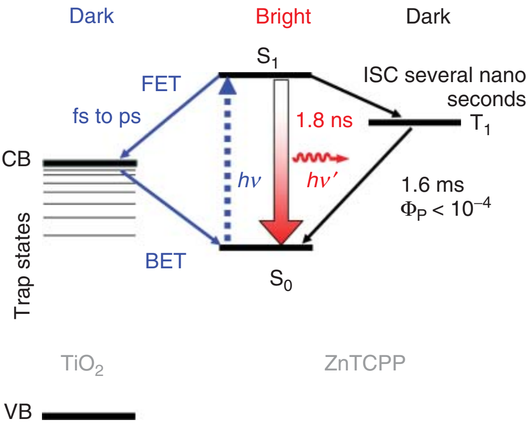

Figure 22.11 Schematic representation of energy levels and basic photoinduced process in dye–TiO_2 system. In this case, the dye molecule is a zinc porphyrin molecule (ZnTCPP); [39] nevertheless, the concept is generally applied to other interfacial electron dynamics discussed in this section. CB, conduction band; VB, valence band; FET, forward electron transfer; BET, backward electron transfer; and ISC, intersystem crossing. The dark state on the left is due to that the high ET reactivity quenches the photon emission and the dark state on the right is due to the triplet state of dye molecule.

process ($k_{nr} = 0$) or the nonradiative decay is much slower than the radiative decay ($k_{nr} \ll k_{rad}$), then the $Q = 1$ and the chromophore is bright. If the nonradiative decay is much faster, then the $Q \to 0$ and the chromophore are dark. As there is always a nonradiative decay process, and the decay time can be comparable to the radiative decay time, the Q has a finite value between 0 and 1. In a dye–TiO_2 NP system, the k_{rad} is the reciprocal fluorescence lifetime of nanosecond, and k_{nr} is dominated by FET time of femtoseconds to picoseconds as both the internal conversion from S_1 to S_0 (nanoseconds to microseconds) and the intersystem cross from S_1 to T_1 state (several nanoseconds) are much slower (Figure 22.4). The natural fluorescence lifetime is unlikely to fluctuate at milliseconds to seconds under the single-molecule experimental condition; therefore, it is the k_{nr} fluctuation that contributes to the Q fluctuation, which in turn contributes to the fluorescence intensity fluctuation (for example, Figure 22.4).

It is still not technically possible to measure the subpicoseconds and femtoseconds single-molecule ET dynamics directly, although measurements of the ultrafast single-molecule excited-state dynamics has been demonstrated [29]. In our single-molecule fluorescence spectroscopy experiments, what has been measured is the nanosecond emission photons from the $S_1 \to S_0$ radiative transition, which is related to the quantum efficiency of the excited state involving in FET as a dominated nonradiative transition, radiative transition, and intersystem cross transition from the singlet S_1 excited state to the triplet state (Figure 22.4). In other words, it is the $S_1 \to S_0$ nanosecond transition that serves as a clock to regulate the decay pathway of the excited state of dye molecule: the FET time apparently fluctuates in a wide timescale from femotoseconds to nanoseconds or even slower. This is because that if the FET as a nonradiative decay is constant in a femtosecond to picosecond timescale, the excited-state radiative emission efficiency at nanosecond timescale should be as low as 10^{-3} to 10^{-6}, and the single molecules should be essentially nonfluorescent or not observable by photon detection. However, we have observed that the single-molecule fluorescence intensity is blinking between the dark and bright states. When the nonradiative FET process is much faster than the nanosecond radiative decay, the single molecule is dark; when the nonradiative FET process is much slower than the nanosecond radiative decay, the single-molecule is bright; when the nonradiative FET time is comparable to the nanosecond radiative decay, the single-molecule fluorescence state is in between bright and dark states. The comparative nonradiative and radiative decay processes determined the fate of the excited states, and in turn determined the brightness of the single molecules. The fluctuation of the single-molecule emission intensity is a reflection of the rate fluctuation of the nonradiative FET process; and the fluctuation of the FET dynamics is practically probed by the nanosecond radiative decay process in determining the fluorescence quantum efficiency.

The single-molecule interfacial ET processes in C343–TiO_2 and CV^+–TiO_2 systems were found to be inhomogeneous, both dynamically and statically. The static inhomogeneity originates from different interfacial ET reactivity fluctuations from molecule to molecule, whereas dynamic inhomogeneity is associated with the ET reactivity fluctuations from time to time for the same individual molecules, resulting fluorescence fluctuations. On the basis of extensive literature on ensemble-averaged ET dynamics and mechanisms, we attributed the origins of these static and dynamic inhomogeneities in the single-molecule interfacial ET processes to fluctuation of the molecular properties, including donor–acceptor distance, redox potentials of the donor and the acceptor, Frank–Condon factors, donor–acceptor electronic coupling, and the solvent reorganization energy [5, 12, 24, 39, 62, 63]. Among these critical parameters, the changes in Frank–Condon coupling and associated nuclear motions are most likely to determine the ET rate fluctuation of a single molecule, assuming that other parameters do not change considerably for a single molecule overtime. However, limited by the sensitivity of the single-molecule fluorescence spectroscopy, we are not yet able to detect the changes of these parameters. There are two possible origins: (i) the changes in molecule–surface vibronic coupling as a result of nuclear motions, and (ii) the changes in Frank–Condon coupling as a result of fluctuations of the energy gap between the reactants and products are responsible for the dynamic inhomogeneity of the interfacial ET processes. We observed the dynamic inhomogeneity of the interfacial ET reactions by obtaining and analyzing autocorrelation functions (insets of Figure 22.12a,b) of single-molecule fluorescence intensity fluctuations and blinking. The autocorrelation decays are typically dispersive and fitted using

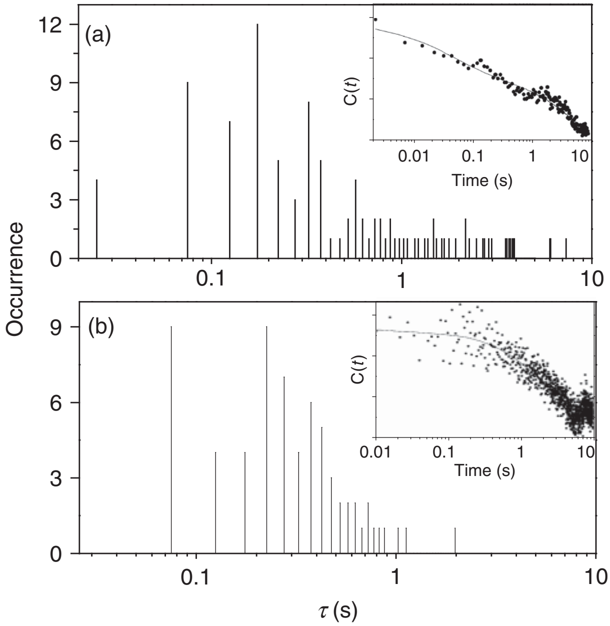

Figure 22.12 Histograms of fluorescence intermittency time constants, obtained from intensity trajectory autocorrelations, for >100 single molecules of C343 (a) and CV^+ (b) adsorbed on TiO_2 NP surfaces. The insets in (a) and (b) are typical fluorescence intensity trajectory autocorrelation traces for single C343 and CV^+ molecules, respectively.

biexponential decays, with the decay times ranging from 10 ms to 30 s. The dispersive and power-law behavior [64–68] of the autocorrelation function decays, which stretched across wide timescales, from submilliseconds to minutes, shows the dynamic inhomogeneity of the single-molecule interfacial ET reactivities. The cutoff at submilliseconds of the power-law decay is due to our measurement system response limitation, and it is highly likely that the dynamic inhomogeneity extends to shorter timescales.

Single-molecule interfacial ET dynamics has also been studied for zinc-tetra (4-carboxyphenyl) porphyrin (ZnTCPP)–TiO_2 NP system. The single-molecule fluorescence trajectories show strong fluctuation and blinking between bright and dark states. The intermittency and fluctuation of the single-molecule fluorescence are attributed to the variation of the reactivity of interfacial ET. The nonexponential autocorrelation function and the power-law distribution of the probability density of dark times imply the dynamic and static inhomogeneities of the interfacial ET dynamics. On the basis of the power-law analysis, the variation of single-molecule interfacial ET reactivity is analyzed as a fluctuation according to the Lévy statistics. We will focus on discussing the statistical analysis of the interfacial ET dynamics fluctuations in the following part of this section, and so far, the analysis approach has been applicable to the interfacial ET dynamics fluctuations in various dye–TiO_2 systems [24, 39].

To analyze the single-molecule interfacial ET dynamics that is associated with the fluctuation of the single-molecule fluorescence trajectories, a histogram of emission intensity is first constructed and then a threshold is determined. The

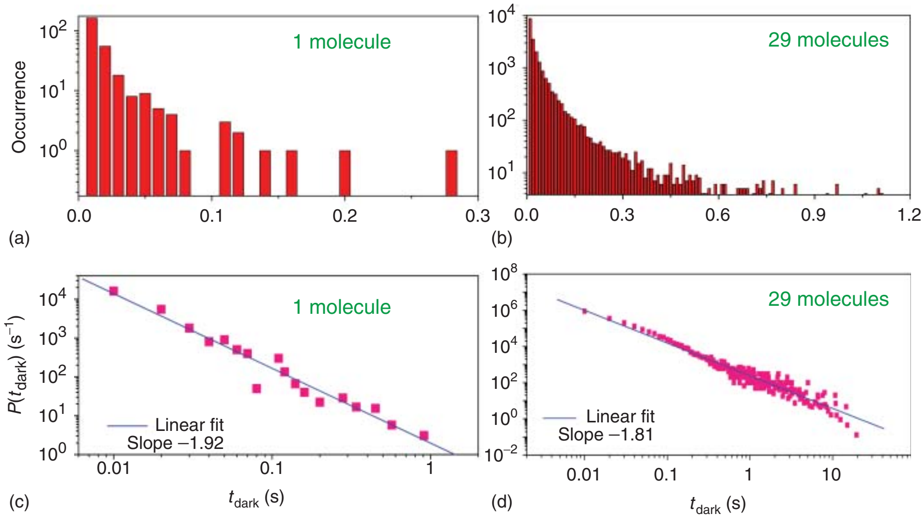

Figure 22.13 Distributions of occurrence (a,b) and probability density (c,d) of dark state for 1 molecule and 29 molecules. In (a) and (b), the occurrence and dark time are plotted in a semilog to linear scale. There are about 240 and 20 K dark states recorded for single molecule (a) and 29 molecules (b), respectively.

time durations of the dark or bright states are then obtained. Figure 22.13a,b shows the distributions of the time durations of the dark states for a single molecule and 29 molecules, respectively. The duration of the dark states spans a broad range from subseconds to seconds. It is interesting that, for the single molecules, non-Poisson behavior is observed evidenced by a nonexponential dark time distributions, as shown in Figure 22.13. This non-Poisson dark time distribution suggests that the intrinsic physical mechanism is not originated from a single Poisson event under an exponential rate dynamics, which reflects that the interfacial ET involves complex rate process that cannot be defined by a static rate constant and the rate changes from time to time. This fluctuation behavior has been characterized as dynamic disorder [24, 39, 69, 70], which is beyond the conventional scope of chemical kinetics.

To analyze the ET reactivity fluctuation dynamics associated with the non-Poisson dark time distributions, we have constructed the probability density [71] distributions of the dark states ($P\ (t_{\text{dark}}) = \text{Occurrence}\ (t)/\Delta t$). Each data point of the histogram is weighted by the average time between nearest neighbor events. The calculated log–log plots (Figure 22.13c,d) of the single-molecule dark time probability density distributions show typical power-law behavior, which can be mathematically described as $P(t_{\text{dark}}) \propto t_{\text{dark}}^{-m_{\text{dark}}}$. This power-law kinetics quantitatively demonstrates that the dark time probability density distributions are nonexponential and should correspond to non-Poisson dynamics associated with dynamically inhomogeneous ET activity, that is, the ET reaction activity fluctuates from time to time. Power-law behaviors have been extensively investigated in emission blinking dynamics of quantum dots and other single emitters [71, 72]. Distributed-traps model and diffusion-controlled models have been proposed to rationalize the power-law behavior of quantum dots [73, 74]. The former model proposed the quantum dots that enter dark state once it loses an electron into the surface traps and become bright again after a nonradiative Auger recombination. The latter model suggests that the blinking is controlled by the diffusion of the energy of electron or trap state, and the model agrees well with the experimental results. For the power-law behavior in single-molecule blinking, power-law-distributed dark states are found to be the main pathway of photobleach for single organic molecules, and it has been suggested that the power-law blinking of organic molecules seems to require dynamic disorder dynamics. Connected with experiment, the origin of power-law distribution in single-molecule conformation dynamics has been theoretically studied [72, 75]. In our experiment, the power-law statistical behavior is intrinsically determined by the interfacial ET dynamics. For ZnTCPP–TiO_2 system, the power-law behavior reflects the disorder of the ET reactivity, and the power exponent m_{dark} represents nonexponential distribution nature of the probability of the dark times.

We have calculated the power exponents, m_{dark}, for 28 molecules and obtained a distribution of m_{dark} (Figure 22.14a). The value ranges from 1.02 to 2.68, which reflects the inhomogeneity of the ET activity fluctuation from molecule to molecule. The mean value of the power exponents $<m_{\text{dark}}>$ is 1.79. To further understand the ET reactivity fluctuation and the dark state properties, we calculated the autocorrelation functions of the single-molecule fluorescence intensity trajectories.

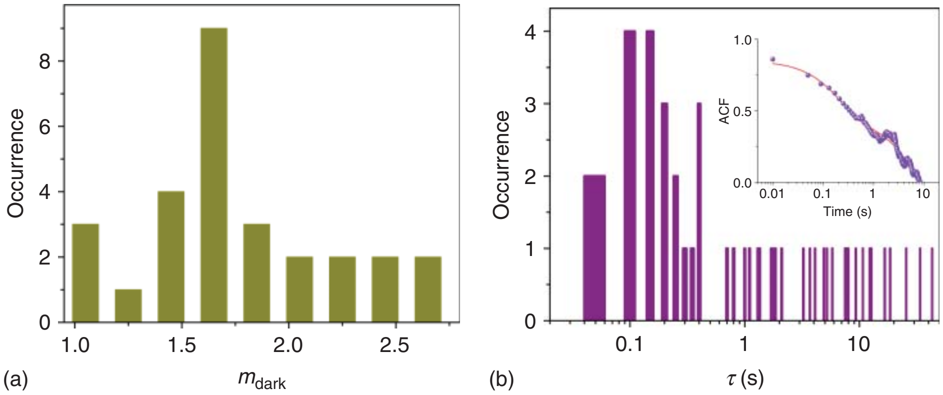

Figure 22.14 (a) Histogram of power-law exponents for 28 ZnTCPP molecules. (b) Histogram of fluctuation times derived from the autocorrelation function of the fluorescence intensity for 29 ZnTCPP molecules. Inset: a typical nonexponential autocorrelation function calculated from a single-molecule fluorescence intensity time trajectory. For autocorrelation function of emission intensity, $1/\tau$ represents the fluctuation rate, that is, interfacial ET reactivity fluctuation rate in the ZnTCPP–TiO_2 system.

Most of the autocorrelation functions show nonexponential decays, which is consistent with our previous findings on single-molecule Coumarin 343–TiO_2 and CV–TiO_2 interfacial ET dynamics [24]. The nonexponential autocorrelation function indicates the dynamic disorder of the interfacial ET reactivity, that is, the reactivity fluctuation rate changes from time to time during a single-molecule measurement.

Both the autocorrelation function decay time τ and the power-law exponent m_{dark} are critical factors characterizing the interfacial ET reactivity fluctuation dynamics. These two parameters correspond to the basic properties of single-molecule fluorescence fluctuations. The autocorrelation function fluctuation time τ represents the ET reactivity fluctuation time, and the power-law exponent m_{dark} represents nonexponential distribution nature of the probability of the dark times. The τ determines the fluctuation timescale for a single molecule to shift from a bright state to a dark state statistically. Although power-law exponent m_{dark} indicates the relative probability for the dark state duration: a larger m_{dark} suggests a relatively higher distribution probability for a shorter dart time states. As we have discussed earlier, the single-molecule fluorescence fluctuation as well as the dark states are as a result of the interfacial ET dynamics fluctuation, and the longer a dark state lasts, the longer the interfacial ET process dominates the ZnTCPP excited-state dynamics.

For a power-law distribution expressed as $P(t_{\text{dark}}) \propto t_{\text{dark}}^{-m_{\text{dark}}}$, the distribution is dominant by Lévy statistics at $1 < m_{\text{dark}} = 1 + \alpha < 2$ [76]

$$P(t_{\text{dark}}) \propto 1/t_{\text{dark}}^{1+\alpha}, \qquad 0 < \alpha < 1$$

Lévy statistics is usually observed in complex systems with nonlinear interactions, such as in physics and biology. Its typical characteristic is the diverging variance and a broad distribution expressed by power-law rule. In single-molecule spectroscopy, Lévy statistics has been extensively investigated in the blinking dynamics of quantum dots [61, 67]. Some abnormal properties due to Lévy statistics, such as statistical aging and ergodicity breaking, have been deduced by calculating the evolution time of on (off) state or time-averaged correlation function or power spectra [61, 68].

Figure 22.13a shows that there are 21 power-law exponents met with $1 < m_{\mathrm{dark}} < 2$, suggesting that the distribution of the dark states of 75% molecules examined obey Lévy statistics. We have calculated the evolution time of a ZnTCPP–TiO_2 system that spends in the dark states, that is, the total time spent in the dark state in the first N dark periods. For a single-molecule trajectory, the evolution time of the dark state is defined as [61]

$$\theta(N) = \sum_{i=1}^{N} t_{dark}^{i}$$

where $\theta(N)$ is the total evolution time, t_{dark} is the duration of a dark state, and N is the state index in a single-molecule fluorescence intensity trajectory. Figure 22.15 shows the evolution time trace for two single-molecule trajectories with m_{dark} of 1.39 and 2.68. Obviously, the Lévy type evolution performs a nonlinear increase with N, and the sum $\theta(N)$ is almost dominated by few long-time events of the order of $\theta(N)$ itself, which unambiguously shows the diverging variance in Lévy statistics. The Lévy statistics of dark states quantitatively reveal the fluctuation mode of the interfacial ET reactivity in ZnTCPP–TiO_2 system. We suggest that Lévy statistics of the interfacial ET can be ascribed to the complex interfacial site- and time-specific interactions between single ZnTCPP molecules and nanoscale local environments.

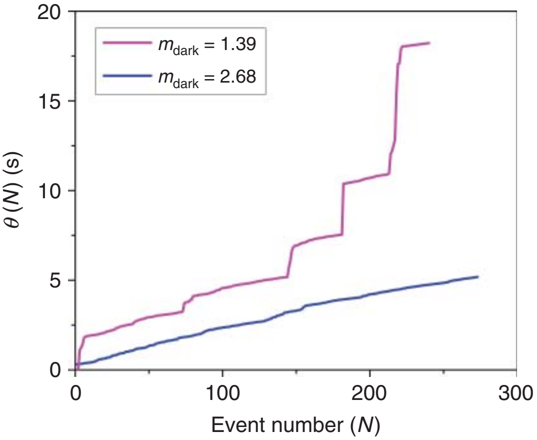

Figure 22.15 Evolution of total time spent in dark states $\theta(N)$ with the event index N. The curve with $m_{\mathrm{dark}} = 1.39$, which obeys Lévy statistics, shows rapid and nonlinear increase. The evolution is dominated by few events of the order of $\theta(N)$ itself.

Nevertheless, complex interfacial ET dynamics has been reported over the last 30 years from ensemble-averaged experiments, and it is often that different ET times (from femtoseconds to nanoseconds for FET time and nanoseconds to milliseconds for BET time) were reported for the same dye-sensitization system but from the different spectroscopy approach at different time resolutions. Our observation of the static and dynamic disordered interfacial ET dynamics fluctuating across a wide timescale is consistent with the ensemble-averaged results and reveals partially the origin of the complexity of the interfacial ET dynamics.

According to this work and our previously reported work [24, 39], the highly inhomogeneous ET dynamics is most likely common for the interfacial chemical reactions that are strongly regulated by the molecular interaction between adsorbed molecules and substrate surfaces. The spontaneous thermal fluctuations of the local environment and the molecular interactions occur at a wide timescale at room temperature, resulting in the interfacial ET reaction rate fluctuation and inhomogeneous dynamics. Our single-molecule spectroscopy analysis provides detailed information about the inhomogeneity of the interfacial ET, which is consistent but not obtainable from the conventional ensemble-averaged experiments.

22.4
Probing Inhomogeneous Vibrational Reorganization Energy Barriers of the Interfacial Electron Transfer

The complex fluctuations of the interfacial ET dynamics show characteristic dynamic and static disorders. We have attributed that the fluctuations are primarily originated from the rate fluctuation in a wide range across from ultrafast to nanoseconds and to even longer timescales. It is well known that the interfacial ET rate is highly sensitive to the molecular interactions between the adsorbed dye molecules and the TiO_2 substrate in a TiO_2-based dye sensitization system. The primary parameters of the molecular interaction are, for example, the ET driving force of free energy gap between the excited state of molecule and the CB of TiO_2 semiconductor, the vibrational relaxation energy of the adsorbed molecules and the surface vibrational modes of TiO_2, the electronic coupling between the molecules and the TiO_2, and so on. Among these parameters, the electronic coupling parameter is the most critical one on the interfacial ET rate from the excited state of dye molecules to the CB of TiO_2. The inhomogeneous surface state distribution and specific surface states that in contact with the single-molecule dye molecules play a critical role in the electronic coupling parameter. Specifically, the formation, stability, and rupture of surface bonding to TiO_2 may change and perturb electronic coupling significantly, and the electronic coupling can be energetically perturbed by local environment thermal fluctuation at room temperature. A powerful approach to analyze these energetic parameters is the electron transfer resonant Raman spectroscopy and microscopy [5, 25, 26, 47, 51, 52, 77]. We have applied an AFM-tip-enhanced Raman spectroscopic approach to analyze the surface vibrational modes and the vibrational relaxation energies of the relevant molecular vibrational modes and the TiO_2 surface vibrational modes. In this section, we will discuss our work on revealing that for alizarin–TiO_2 interfaces, the vibrational reorganization energy barriers of interfacial ET are inhomogeneous from TiO_2 NP to NP and from molecular site to site [25, 26].

Applying a microscopic AFM–Raman characterization and Heller theory (time-dependent wave packet scattering theory) analysis, we revealed that for alizarin–TiO_2 interfaces, the vibrational reorganization energy barriers of interfacial ET are inhomogeneous at a submesoscale (~250 nm). We found that (i) the total vibrational reorganization energy was inhomogeneous from site to site; (ii) the alizarin–TiO_2 bridging normal modes were the primary contributor to the total vibrational reorganization energy and its inhomogeneity; (iii) the mode-specific analyses indicated that the energy distributions were inhomogeneous for bridging normal modes and homogeneous for nonbridging normal modes, especially for modes far away from the alizarin–TiO_2 coupling hydroxyl modes; and (iv) the vibrational reorganization energy inhomogeneity was closely associated with the local environmental heterogeneity of the alizarin–TiO_2 interface (Figure 22.16). It is most likely that the vibrational reorganization energy inhomogeneities contributed to the inhomogeneous dynamics of the interfacial ET processes. Our results demonstrated that correlated AFM–confocal Raman microscopy is a promising approach for a quantitative understanding of inhomogeneous interfacial charge transfers.

Our spectral analysis was based on the Heller theory, that is, the resonance Raman and absorption cross sections were calculated using the following time-dependent wave packet propagation formalism: [5, 25, 26, 58, 78, 79]

$$\sigma_{Ri\to f}(\omega_L) = \frac{8\pi(\mathrm{eM})^4\,\omega_L\omega_S^3}{9\hbar^2c^4}\sum_i P_i\left|\int_0^\infty dt\langle f\right| i(t)\rangle\exp\left[i(\omega_\mathrm{L}+\omega_i-\omega_0)t-\gamma t/2\right]^2 \tag{22.1}$$

$$\sigma_A(\omega) = \frac{4\pi(\mathrm{eM})^2\omega}{3\hbar^2c}\sum_i P_i\ \mathrm{Re}\int_0^\infty dt\langle i|i(t)\rangle\exp[i(\omega+\omega_i-\omega_0)t-\gamma t/2] \tag{22.2}$$

where ω_L and ω_S are the incident (laser) and scattered photon frequencies, respectively; (eM) is the electronic transition dipole moment; $|i\rangle$ and $|f\rangle$ are the initial and final vibrational states on the ground-state potential energy surface, respectively; P_i is the Boltzmann population of initial vibrational state; ω_i is the vibrational frequency at the vibrational level of $|i\rangle$ or $|f\rangle$; ω_0 is the electronic zero–zero energy; γ is the inverse lifetime of the excited state; and $|i(t)\rangle$ is the vibrational wave packet function propagating in time t on the excited-state potential surface. In our treatment, the $\langle i|i(t)\rangle$ and $\langle f|i(t)\rangle$ overlaps are dependent on the displacement, Δ, in dimensionless normal coordinates between ground- and excited-state equilibrium geometries along each normal coordinate. The initial guesses for Δ were given from the relative resonance Raman intensities, assuming that the intensity ratios

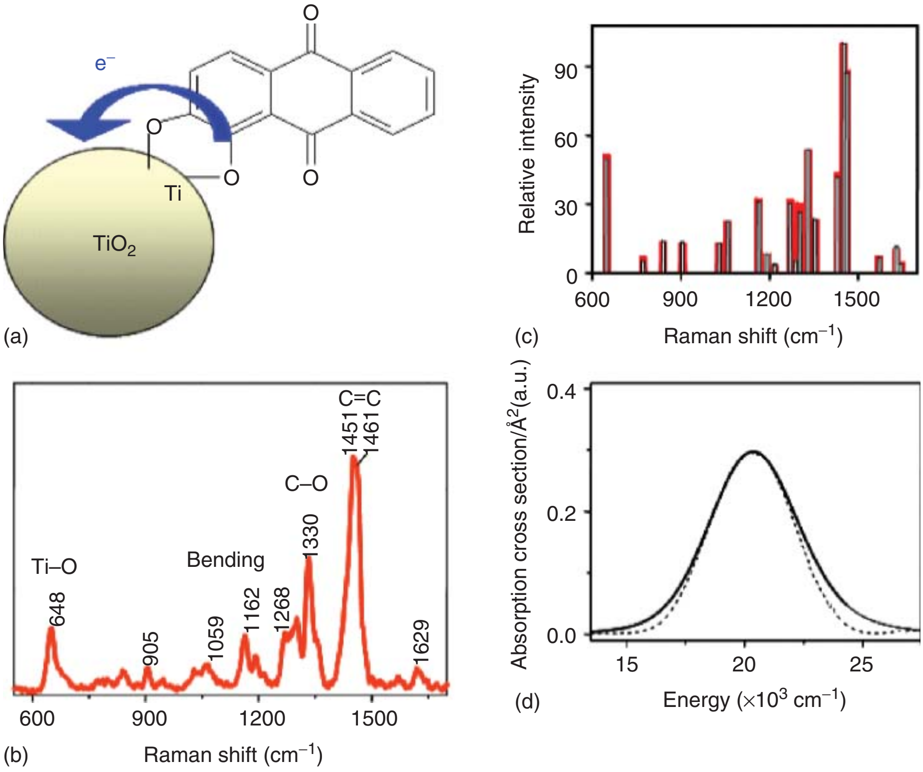

Figure 22.16 (a) Sketch of alizarin–TiO_2 nanoparticle surface adsorption of alizarin via the hydroxyl group bonding to the TiO_2 nanoparticles. (b) Resonance microscopic Raman spectrum of alizarin–TiO_2 nanoparticles. (c) Time-dependent wave packet analysis of Raman spectra. Comparison of experimental (white) and calculated (red) resonance Raman intensities of all observed modes for a specific microscopic site. (d) Time-dependent wave packet analysis of absorption spectra. The absorption cross section of experimental (solid) and calculated (dotted) charge-transfer-associated excitation band of the alizarin–TiO_2 complex in solution.

were proportional to $\Delta^2\nu^2$ ratios, where ν is the vibrational frequency. The homogeneous broadening (Γ) was calculated from the homogeneous line width function. The inhomogeneous broadening (Φ), a standard deviation of the normalized inhomogeneous Gaussian distribution function, was determined by the absorption band shape and resonance Raman intensity. The energy gap between potential surfaces, ω_0, was initially determined by the wavelength of the absorption spectrum maximum arising from the ET reaction. The parameters were optimized iteratively until the calculated and experimental absorption spectrum and resonance Raman intensities were in agreement. Finally, the mode-specific reorganization energy (λ_ν), assuming the vibrations to be harmonic, was calculated by

$$\lambda_\nu = \frac{1}{2}\nu\Delta^2 \tag{22.3}$$

The resonance Raman spectra in the alizarin–TiO_2 complex (Figure 22.16) exhibited 20 vibrational bands, consistent with the ensemble-averaged Raman measurement [25, 26]. The most prominent bands, at 1450 and 1461 cm^{-1}, were assigned to the ring C=C stretches. The C–O stretch combined with the ring C=C stretch mode corresponds to the intense bands at 1330 cm^{-1} and in the region of 1268–1300 cm^{-1} (Figure 22.16b). The 648 cm^{-1} band was attributable to a Ti–O stretching mode from a bridging Ti–O–C bond. On comparing with free molecules, the increased Raman intensity in the C–O stretching at 1330 cm^{-1} revealed that the hydroxyl groups provided the primary bridging bonds to the interfacial charge transfer.

To specify and characterize such an inhomogeneity, we used the time-dependent wave packet calculations to analyze correlatively the Raman and absorption spectra, obtaining the vibrational reorganization energy of individual normal modes of the alizarin–TiO_2 complex under interfacial charge-transfer reaction at each microscopic site. We analyzed the resonance Raman cross sections, the charge-transfer absorption spectrum (to determine the spectral broadening and Raman damping parameters), and the electronic transition energy. The analysis provided detailed information about changes in nuclear equilibrium geometry for both the electron donor–acceptor and the surrounding local environment in the interfacial charge-transfer processes. Figure 22.16c,d shows a typical fitting of the experimental Raman intensities for the observed Raman peaks from a specific spot. Figure 22.16d presents the corresponding experimental and fitting absorption spectral band at 496 nm, a strong charge-transfer interaction band [25, 26]. The model generates a good fit to both the relative intensities of the Raman peaks and the charge-transfer absorption spectrum with the parameters of electronic zero–zero energy ($\omega_0 = 20010\ cm^{-1}$), homogeneous broadening ($\Gamma = 550\ cm^{-1}$), inhomogeneous broadening ($\Phi = 1600\ cm^{-1}$), and frequencies and intensities of the 20 resonant Raman modes (Figure 22.16c). From the time-dependent wave packet analysis of the Raman and absorption spectra, we obtained unitless normal-coordinate displacements, Δ, for each electron-transfer-associated resonant Raman mode. The vibrational reorganization energies along each of the observed Raman modes were calculated from the unitless normal-coordinate displacement by Eq. (22.3). Our spectral analysis yielded a total vibrational reorganization energy of 0.045 eV for this specific spot, which is consistent with the result obtained from the ensemble-averaged Raman excitation profile [25, 26].

The most significant finding from our experiments is that the vibrational reorganization energy is inhomogeneous, that is, different from microscopic site to site of this alizarin–TiO_2 interfacial ET system. Correlating the topographic AFM imaging, we measured the resonance Raman spectra at different microscopic spots and found that relative Raman intensities of the Ti–O, C–O, and ring stretching modes were significantly different from site to site. These relative Raman intensity changes presumably resulted from properties intrinsic to interfacial charge transfer. The reorganization energy for the C–O bridge mode changes was measured from 63 to 97 cm^{-1}, the Ti–O bridge mode gave measurable vibration reorganization energy from 12 to 28 cm^{-1}, and the ring C=C stretching mode yielded a range from 30 to 65 cm^{-1}. Consequently, the total vibrational reorganization energy, λ_{total}, was obtained from values between 242 and 380 cm^{-1}. The λ_{total} was predominately contributed from the bridging modes at the alizarin–TiO_2 interface. We observed that not all of the vibrational modes associated with ET had inhomogeneous energies. The vibrational reorganization energy distributions of the specific normal modes in the alizarin–TiO_2 complex were homogeneous for those modes located away from direct bonding with the TiO_2. For example, the vibrational reorganization energy distributions of two C–H in-plane bending modes, revealing the distributions to be within the measurement error bars and significantly narrower than distributions of bridging modes.

It is desirable to obtain a correlated topographic and spectroscopic characterization with high chemical sensitivity, high spatial resolution, and spectroscopic selectivity for ET systems. The correlated metallic tip-enhanced near-field Raman spectroscopy and AFM technique was applied to measuring the tip-enhanced Raman spectrum for characterizing the vibrational relaxation energy barrier of dye-sensitized TiO_2 NPs. We have obtained the near-field Raman spectra that are associated with the photoinduced charge-transfer reaction in Ru(4,4′-dicarboxy-2,2′-bipyridine)$_2$(NCS)$_2$-sensitized TiO_2 single NPs. This method demonstrates that tip-enhanced near-field Raman spectroscopy is an effective approach for understanding inhomogeneous interfacial ETs with nanoscale spatial resolution. Near-field scanning optical scanning microscopy makes use of the strongly enhanced electric field around a sharp metal tip under laser illumination [26, 28, 48, 49, 53–55]. The spatial resolution achievable with this technique is determined primarily by the metallic tip size and shape, and the signal-to-noise is defined by the strength of the field-enhancement effect.

Correlated AFM images were obtained for the microscopic Raman spectral collection at optical diffraction-limited imaging sites. In contrast, as a result of the high fluorescence background and off-resonant excitation, no Raman bands were detected from an alizarin-alone sample under the same experimental conditions (Figure 22.16) because there were no contributions from the electron-transfer resonance Raman enhancement.

Figure 22.6 shows the correlated near-field Raman spectrum and the topographic AFM image of a larger area around the Raman measurement site at a single TiO_2 NP. In this measurement, a far-field Raman spectrum without a metallic tip for a specific microscopic site was first collected (Figure 22.6a), and then under the same microscopic site, the tip-enhanced Raman spectrum was detected when a silver-coated AFM tip was engaged over an N_3-sensitized TiO_2 NP (Figure 22.6b). The Raman signal with the near-field contribution caused by the tip was a factor of 2.1 higher than the signal measured without the tip. The near-field Raman spectrum (Figure 22.6c) was obtained after subtracting the far-field component from the tip-enhanced Raman spectrum. Figure 22.6d shows the topography of the dye-sensitized TiO_2 NPs on a nanoscale site (<50 nm) where the near-field Raman spectrum (Figure 22.6c) was collected. In the near-field Raman spectrum, the most prominent bands, at 1475, 1549, and 1608 cm^{-1}, were assigned to the bipyridine ring stretching mode. The intense band at 1028 cm^{-1} was assigned to the ring breathing mode. The C–C interring stretch combined with the C–O stretching mode corresponds to the band at 1273 cm^{-1}. The 706 cm^{-1} band is attributed to an in-plan ring deformation mode.

In this work, we achieved a Raman measurement from a single N_3 dye-loaded TiO_2 NP. Near-field Raman scattering enhancement is confined within the vicinity of the metallic tip axis, which provides a higher spatial resolution beyond the optical diffraction limit. Tip-enhanced Raman spectroscopy combined with simultaneous AFM measurement extends our ability to characterize the spatial inhomogeneity of interfacial ET dynamics at a spatial scale comparable to the AFM imaging scale.

We have moved forward to achieve higher spatial resolution and spectral sensitivity in order to obtain nanoscale site-specific characterization of the inhomogeneous vibrational reorganization energy barriers. The most needed technical and scientific advances include the following: (i) AFM-tip-enhanced near-field Raman spectroscopic measurements for dye-sensitized semiconductor NPs; (ii) higher measurement sensitivity to measure a small number of molecules or even single molecules at nanoscale sites; and (iii) a molecule-level understanding of the relationship between topographical nanoscale structures and surface chemical bonding structures.

22.5
Single-Molecule Triplet-State Photon Antibunching Analysis of Back Charge-Transfer Dynamics

Using photon antibunching measurements under CW laser excitation, nonclassical photon statistics, and excitation power-dependent measurements, we were able to selectively measure the single-molecule metal-to-ligand charge-transfer (MLCT) state lifetime that is a direct measurement of MLCT back charge-transfer time. This work demonstrated the single-molecule photon antibunching of triplet excited state and presented a step forward in studying single-molecule ET in proteins using MLCT complex as an ET donor or acceptor. Photon antibunching, a type of nonclassical photon statistical behavior, is the signature of phosphorescence from a single quantum system and can reveal information about transition rates between the photophysical states [80, 81]. Photon antibunching has been demonstrated for organic dye molecules [81, 82], polymer molecules [83], and quantum dots [84, 85].

Transition-metal complexes such as ruthenium complexes, having MLCT states, are being extensively investigated for their involvement in solar energy conversion [76], interfacial ET [86], and ET in biological systems [87–90]. The dynamics of this process can be highly complex and inhomogeneous, especially when molecules are involved in interactions and perturbations with heterogeneous local environments such as at interfaces or in covalent interactions with electron-transfer proteins. In this section, we discuss the use of photon antibunching to measure triplet-state lifetimes at room temperature at a microsecond timescale. We apply this approach to the studies of the MLCT state dynamics of a ruthenium complex, with the potential application of studying ET processes in biological systems at the single-molecule level.

In our experiments, $Ru(dpp)_3$ (Aldrich) was diluted to 3×10^{-10} M in methanol and was spin coated on polymethylmethacrylate-coated glass coverslips. The single-molecule sample was under constant nitrogen gas purge during the experiments, and all experiments were conducted at room temperature. A CW HeCd laser with 442 nm wavelength was used for photoexcitation. The intensity was modulated by a Pockel cell (Lasermetrics 3079) with a specific frequency and wave form controlled by a function generator. The laser was coupled through single-mode optical fiber and brought to the epiport of an inverted microscope (Zeiss Axiovert 200). The laser was reflected by a dichroic beamsplitter (Chroma 460DCLP) and focused by an objective (Fluar, 100×, NA1.3). The phosphorescence from a single-molecule $Ru(dpp)_3$ was collected by the same objective and passed through an emission filter (Chroma E470LP). The emission photons were detected by an APD (Perkin-Elmer SPCM-AQR-15). The detected photon time was recorded by a home-built time-stamping device based on the National Instrument data acquisition card (multiple-channel digital I/O Board (PCI-DIO)-32HS). The arrival time of every photon was digitized with the increment of 0.1 μs.

Single $Ru(dpp)_3$ molecules typically produce a kilohertz-level detected photon flux and several hundreds of thousand photons total before an irreversible photobleaching. The excitation laser intensity was modulated by a square wave function. Within every 0.1 s, there is a 0.03 s period of high power and a 0.07 s period of low power. The power ratio is 3.0 (high and low at 1.2 and 0.4 μW, respectively). The detected photons were separated into two groups according to the power level at their arrival time. Both the histogram of the interphoton time and the autocorrelation of the photon arrival time trajectory reveal the antibunching phenomena by showing the decreased probability of two photons arriving within the MLCT state lifetime. The autocorrelation was calculated for each group of photons under both high and low excitation powers (Figure 22.17b,c). Both autocorrelation curves show a dip near time zero, suggesting that there is less probability of two photons arriving at the same time or within the excited-state lifetime. This is a signature of photon antibunching, a characteristic property of emission photons from a single molecule.

The photophysical process of $Ru(dpp)_3$ can be considered as the hopping of a two-level system because the ISC in an excited state is much faster than the excitation and excited-state relaxation due to heavy metal effect on spin–orbit coupling in our experiments. The analytical relations between the transition rates of the photophysical states and the autocorrelation for a two-level system are presented in Eqs. (22.4) and (22.5). The autocorrelation $g(t)$ is an exponential rising curve [27]

$$g(t) = A[1 - \exp(-kt)] \tag{22.4}$$

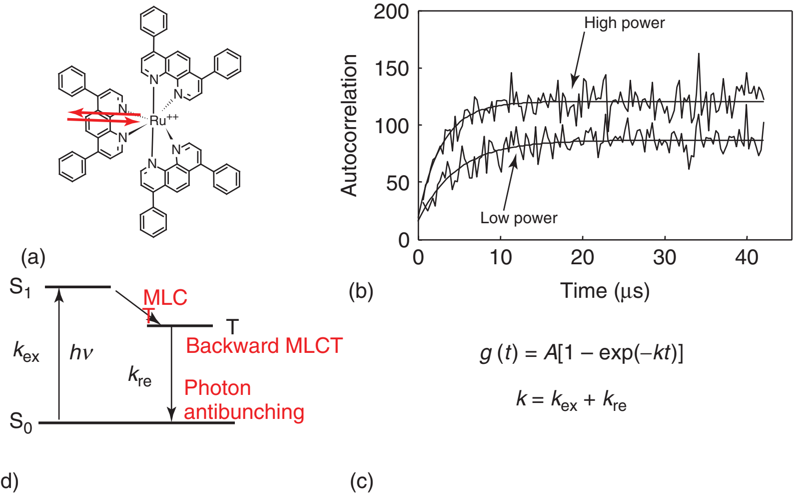

Figure 22.17 (a) The molecular structure of Ru(dpp)$_3$, tris(4,7-diphenyl-1,10-phenanthrolin)ruthenium(II) dichloride; forward and backward MLCT are depicted by the arrows. (b,c) The autocorrelation of the photon trajectory. The upper one is the molecule under high excitation power, and the lower is the same molecule under low excitation power. They are both fitted by single exponential curves. (d) The three-state energy diagram of the MLCT dynamics.

where the exponential decay rate constant k is the sum of the excitation rate k_{ex} and excited-state relaxation rate k_{re}

$$k = k_{\text{ex}} + k_{\text{re}} \tag{22.5}$$

To determine the individual rate of k_{ex} and k_{re}, we analyzed the results of excitation power modulation experiment, assuming that k_{re} is not affected by the excitation power and k_{ex} is proportional to the excitation power. The autocorrelation rates at high and low excitation power were measured, with k_{ex} and k_{re} then calculated [27]. Both autocorrelation curves of Ru(dpp)$_3$ in Figure 22.17b were fitted by a single exponential. The rate constants are $k_{\text{(high)}} = 3.0 \times 10^5\ \text{s}^{-1}$ and $k_{\text{(low)}} = 1.7 \times 10^5\ \text{s}^{-1}$ for high- and low-power excitations, respectively. By assuming an excitation rate ratio of 3.0, we obtained the excitation rate and excited-state relaxation rate by solving linear equations (Eq. (22.5)) at high- and low-power excitations. The results were $k_{\text{re}} = 1.1 \times 10^5\ \text{s}^{-1}$, $k_{\text{ex(low)}} = 6.2 \times 10^4\ \text{s}^{-1}$, and $k_{\text{ex(high)}} = 1.9 \times 10^4\ \text{s}^{-1}$. Thus, we derived the MLCT excited-state lifetime from photon statistics under CW laser excitation.

For further confirmation and characterization of the antibunching photons [27], we have calculated the photon statistics using Mandel's parameter [91] to verify the sub-Poisson or super-Poisson statistics of the detected photons at different timescales. The time-dependent Mandel parameter $Q(T)$ is defined as

$$Q(T) = \frac{\langle I^2 \rangle - \langle I \rangle^2}{\langle I \rangle} - 1$$

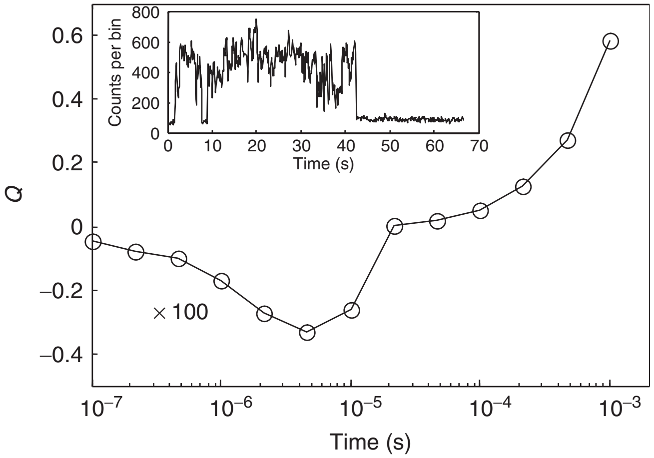

Figure 22.18 The Mandel parameter of a single molecule. The negative values are magnified by a factor of 100 to enhance the view. This single-molecule's phosphorescence intensity trajectory in the 0.1 s bin is shown in the inset.

where I is the intensity counts at the bin time T. A negative Q indicates sub-Poisson statistics (antibunching), while a positive Q indicates super-Poisson statistics (bunching). We have analyzed the Mandel parameter of a single $Ru(dpp)_3$ molecule's phosphorescence. The Mandel parameter result of a typical molecule is illustrated in Figure 22.18. The excitation power is at constant level without modulation. In the timescale of $<10\,\mu s$, the Mandel parameter is negative, which indicates photon antibunching dynamics. In contrast, at the longer timescale of milliseconds, the Mandel parameter is positive, indicating photon bunching due to the "blinking" of the single-molecule emission intensity.

Transition-metal complexes have been widely used as an electron donor or acceptor in studying conformational gated ET in redox electron-transfer proteins. Single-molecule photon antibunching studies will be particularly effective in resolving the ET dynamics in such complex systems. In this single-molecule photon antibunching study of MLCT state excitation and relaxation dynamics of $Ru(dpp)_3$ at room temperature, we provide a new method of probing single-molecule triplet-state dynamics. Using an excitation modulation measurement, we were able to obtain both single-molecule excitation and emission rate constants associated with MLCT dynamics.

22.6
Concluding Remarks and Perspective

Single-molecule spectroscopy has already changed the landscape of studying interfacial ET dynamics that often involve complex mechanism and spatial heterogeneity. The nonexponential ET rate processes can now be interrogated one molecule at one specific nanoscale site at a time. In an earlier study [21], the single-molecule ET dynamics shows single exponential for each individual molecules, but at different rate constants from molecule to molecule in a system of CV–indium tin oxide (ITO) interfacial ET; in recent years, a number of dye–TiO_2 interfacial ET systems have shown rate fluctuation in interfacial ET dynamics [24, 39, 45]. The intermittency of the single-molecule interfacial ET dynamics associated with single-molecule fluorescence blinking is one of the most significant discoveries made by single-molecule spectroscopy. In an ensemble-averaged measurement, these types of intermittency are not observable and are often averaged out as typical nonexponential or dispersive dynamics because the interfacial ET time constants involve fluctuations ranged from femtoseconds to microseconds. Since the intermittent single-molecule interfacial ET dynamics first reported in 2004 [24], similar intermittent interfacial ET dynamics has been observed for a few other interfacial systems and reported in 2008 [43–45]. Since 2004, significant efforts have been made to reveal the physical origins for the interfacial ET rate fluctuations, and AFM-correlated Raman spectroscopic analysis has revealed the inhomogeneous surface bonds, bonding energy, and vibrational relaxation energies at a single-TiO_2 NP level [25, 26], which suggests that thermal-induced conformational motions of adsorbed molecules may contribute to fluctuations of electronic and vibrational couplings between the dye molecules and the TiO_2 NPs, and these energetic fluctuations result the interfacial ET rate fluctuations. This new discovery suggests that the non-exponential and complex dynamics observed in ensemble-averaged experiments are most likely intrinsic for the interfacial ET dynamics, and the interfacial ET time constants contain in typical ensemble-averaged results may be widely ranged from femtoseconds to nanoseconds. The single-molecule analyses on both dynamics and energetics will be critical. The dynamics analysis will include application of femtosecond single-molecule spectroscopy, and the energetics analysis will involve analyzing of the fluctuations and inhomogeneity of the driving force, electronic and vibrational coupling, solvent and vibrational relaxation energy, and local electronic work function. It is anticipated that the single-molecule spectroscopy will provide more profound and fundamental understanding of the interfacial ET dynamics related to catalysis, surface redox reaction dynamics, environmental sciences, and solar energy sciences.

Acknowledgments

The author gratefully acknowledges Yuanmin Wang, Vasudevanpillai Biju, Donhai Pan, Dehong Hu, Micky Micic, Xiefei Wang, and Sujit Ghosh for their crucial contributions to the work discussed here. The work was supported by the Office of Basic Energy Sciences within the Office of Science of the US Department of Energy (DOE). A number of experiments were conducted in the Environmental Molecular Sciences Laboratory (EMSL) at Pacific Northwest National Laboratory (PNNL). The EMSL is a national scientific user facility and supported by the US DOE's Office of Biological and Environmental Research. PNNL is a multiprogram national laboratory operated for the US Department of Energy by Battelle Memorial Institute under contract number DE-AC06-76RLO 1830. After 2006, the work was conducted at the Center for Photochemical Sciences, Department of Chemistry of the Bowling Green State University in Bowling Green, OH. Part of the text appeared in our previous publications referenced.

References

1. Fujishima, A. and Honda, K. (1972) *Nature*, **238**, 37–38.
2. O'Regan, B. and Grätzel, M. (1991) *Nature*, **353**, 737–740.
3. Kamat, P.V. (2007) *J. Phys. Chem. C*, **111**, 2834–2860.
4. Lu, H., Prieskorn, J.N., and Hupp, J.T. (1993) Fast interfacial electron-transfer–evidence for inverted region kinetic-behavior. *J. Am. Chem. Soc.*, **115**, 4927.
5. (a) Hupp, J.T. and Williams, R.D. (2001) Using resonance Raman spectroscopy to examine vibrational barriers to electron transfer and electronic delocalization. *Acc. Chem. Res.*, **34**, 808. (b) O'Regan, B. and Grätzel, M. (1991) Colloidal TiO_2 films. *Nature*, **353**, 737.
6. Gray, K.A., Stafford, U., Dieckmann, M.S., and Kamat, P.V. (1993) Mechanistic studies in TiO_2 systems: photocatalytic degradation of chloro- and nitrophenols, in *Photocatalytic Purification and Treatment of Water and Air*, Elsevier Science, Amsterdam.
7. Fox, M.A. and Dulay, M.T. (1993) Heterogeneous photocatalysis. *Chem. Rev.*, **93**, 341.
8. Liu, D., Fessenden, R.W., Hug, G.L., and Kamat, P.V. (1997) Dye capped semiconductor nanoclusters. Role of back electron transfer in the photosensitization of SnO_2 nanocrystallites with cresyl violet aggregates. *J. Phys. Chem. B*, **101**, 2583.
9. (a) Liu, D., Kamat, P.V., Thomas, K.G., Thomas, K.J., Das, S., and George, M.V. (1997) Picosecond dynamics of an IR sensitive squaraine dye. Role of singlet and triplet excited stat es in the photosensitization of TiO_2 nanoclusters. *J. Chem. Phys.*, **106**, 6404. (b) Hao, E., Anderson, N.A., Asbury, J.B., and Lian, T. (2002) *J. Phys. Chem. B*, **106**, 10191–10198.
10. Oregan, B. and Gratzel, M. (1991) A low-cost, high-efficiency solar-cell based on dye-sensitized colloidal TiO_2 films. *Nature*, **353**, 737.
11. Hagfeldt, A., Bjorksten, U., and Gratzel, M. (1996) Photocapacitance of nanocrystalline oxide semiconductor films: band-edge movement in mesoporous TiO_2 electrodes during UV illumination. *J. Phys. Chem.*, **100**, 8045.
12. Adams, D.M., Brus, L., Chidsey, C.E.D., Creager, S., Creutz, C., Kagan, C.R., Kamat, P.V., Lieberman, M., Lindsay, S., Marcus, R.A., Metzger, R.M., Michel-Beyerle, M.E., Miller, J.R., Newton, M.D., Rolison, D.R., Sankey, O., Schanze, K.S., Yardley, J., and Zhu, X.Y. (2003) Charge transfer on the nanoscale: current status. *J. Phys. Chem. B*, **107**, 6668.
13. Durrant, J.R. (2002) Modulating interfacial electron transfer dynamics in dye sensitised nanocrystalline metal oxide films. *J. Photochem. Photobiol., A*, **148**, 5.
14. Linsebigler, A.L., Lu, G.Q., and Yates, J.T. (1995) Photocatalysis on TiO_2 surfaces–principles, mechanisms, and selected results. *Chem. Rev.*, **95**, 735.
15. Kamat, P.V. (2002) Photophysical, photochemical and photocatalytic aspects of metal nanoparticles. *J. Phys. Chem. B*, **106**, 7729.
16. (a) Marcus, R.A. (1964) Chemical and electrochemical electron-transfer theory. *Annu. Rev. Phys. Chem.*, **15**, 155; (b) Marcus, R.A. and Sutin, N. (1985) Electron transfers in chemistry and biology. *Biochim. Biophys. Acta*, **811**, 265.
17. Newton, M.D. (1991) Quantum chemical probes of electron-transfer kinetics–the nature of donor–acceptor interactions. *Chem. Rev.*, **91**, 767.

18. Miller, R.J.D., Miller, G.L., Nozik, A., Schmickler, W., and Willig, F. (1995) *Surface Electron-Transfer Processes*, Wiley-VCH Verlag GmbH, Weinheim.

19. Gratzel, M. (1987) *Heterogeneous Photochemical Electron Transfer*, CRC Press, Boca Raton, FL.

20. Ernstorfer, R., Felber, S., Storck, W., Galoppini, E., Wei, Q., and Willig, F. (2005) Distance dependence of heterogeneous electron transfer probed in ultra-high vacuum with femtosecond transient absorption. *Res. Chem. Intermed.*, **31**, 643.

21. Lu, H.P. and Xie, X.S. (1997) Single-molecule kinetics of interfacial electron transfer. *J.Phys. Chem. B*, **101**, 2753.

22. Bopp, M.A., Jia, Y., Haran, G., Morlino, E.A., and Hochstrasser, R.M. (1998) Single-molecule spectroscopy with 27 fs pulses: time-resolved experiments and direct imaging of orientational distributions. *Appl. Phys. Lett.*, **73**, 7.

23. VandenBout, D.A., Yip, W.T., Hu, D.H., Fu, D.K., Swager, T.M., and Barbara, P.F. (1997) Discrete intensity jumps and intramolecular electronic energy transfer in the spectroscopy of single conjugated polymer molecules. *Science*, **277**, 1074.

24. Biju, V., Micic, M., Hu, D.H., and Lu, H.P. (2004) Intermittent single-molecule interfacial electron transfer dynamics. *J. Am. Chem. Soc.*, **126**, 9374.

25. Pan, D.H., Hu, D.H., and Lu, H.P. (2005) Probing inhomogeneous vibrational reorganization energy barriers of interfacial electron transfer. *J. Phys. Chem. B*, **109**, 16390.

26. Pan, D., Klymyshyn, N., Hu, D.H., and Lu, H.P. (2006) Tip-enhanced near-field Raman spectroscopy probing single dye-sensitized TiO_2 nanoparticles. *Appl. Phys. Lett.*, **88**, 063121.

27. Hu, D.H. and Lu, H.P. (2005) Single-molecule triplet-state photon antibunching at room temperature. *J. Phys. Chem. B*, **109**, 9861.

28. Lu, H.P. (2005) Site-specific Raman spectroscopy and chemical dynamics of nanoscale interstitial systems. *J. Phys. Condens. Matter*, **17**, R333.

29. van Dijk, E., Hernando, J., Garcia-Lopez, J.J., Crego-Calama, M., Reinhoudt, D.N., Kuipers, L., Garcia-Parajo, M.F., and van Hulst, N.F. (2005) Single-molecule pump-probe detection resolves ultrafast pathways in individual and coupled quantum systems. *Phys. Rev. Lett.*, **94**, 078302.

30. Hu, D.H. and Lu, H.P. (2003) Single-molecule nanosecond anisotropy dynamics of tethered protein motions. *J. Phys. Chem. B*, **107**, 618.

31. Tan, X., Hu, D.H., Squier, T.C., and Lu, H.P. (2004) Probing nanosecond protein motions of calmodulin by single-molecule fluorescence anisotropy. *Appl. Phys. Lett.*, **85**, 2420.

32. Xie, X.S. and Dunn, R.C. (1994) *Science*, **265**, 361–364.

33. Lu, H.P. and Xie, X.S. (1997) *Nature*, **385**, 143–146.

34. VandenBout, D.A., Yip, W.T., Hu, D.H., Fu, D.K., Swager, T.M., and Barbara, P.F. (1997) *Science*, **277**, 1074–1077.

35. Moerner, W.E. and Orrit, M. (1999) *Science*, **283**, 1670–1676.

36. Lu, H.P. and Xie, X.S.J. (1997) *Phys. Chem. B*, **101**, 2753–2757.

37. Xie, X.S. and Trautman, J.K. (1998) *Annu. Rev. Phys. Chem.*, **49**, 441.

38. Peter Lu, H. (2005) Probing single-molecule protein conformational dynamics. *Acc. Chem. Res.*, **38**, 557–565 (invited review article).

39. Wang, Y., Wang, X., Ghosh, S.K., and Peter Lu, H. (2009) Probing single-molecule interfacial electron transfer dynamics of porphyrin on TiO_2 nanoparticles. *J. Am. Chem. Soc.*, **131**, 1479–1487.

40. Kamat, P.V. (1998) Electron transfer processes in nanostructured semiconductor thin films, in *Nanoparticles in Solids and Solutions* (ed. J. Fendler), John Wiley & Sons, Inc., New York.

41. (a) Palacios, R.E., Fan, F.R., Grey, J.K., Suk, J., Bard, A.J., and Barbara, P.F. (2007) *Nat. Mater.*, **6** (9), 680. (b) Palacios, R.E., Fan, F.-R.F., Bard, A., and Barbara, P.F. (2006) *J. Am. Chem. Soc.*, **128**, 9028.

42. Bolinger, J., Lee, K.-J., Palacios, R.E., and Barbara, P.F. (2008) *J. Phys. Chem. C*, **112**, 18608.

43. Issac, A., Jin, S.Y., and Lian, T.Q. (2008) *J. Am. Chem. Soc.*, **130**, 11280–11281.

44. Xu, W., Kong, J.S., Yeh, Y.-T.E., and Chen, P. (2008) Single-molecule nanocatalysis reveals heterogeneous reaction pathways and catalytic dynamics. *Nat. Mater.*, **7**, 992–996.

45. Cui, S.C., Tachikawa, T., Fujitsuka, M., and Majima, T. (2008) *J. Phys. Chem. C*, **112**, 19625–19634.

46. Fries, J.R., Brand, L., Eggeling, C., Kollner, M., and Seidel, C.A.M. (1998) Quantitative identification of different single molecules by selective time-resolved confocal fluorescence spectroscopy. *J. Phys. Chem.*, **102**, 6601–6613.

47. Pettinger, B. (2006) *Tip-Enhanced Raman Spectroscopy (TERS)*, Topics in Applied Physics, Vol. 103, Springer-Verlag, Berlin, pp. 217–240.

48. Hu, D.H., Micic, M., Klymyshyn, N., Suh, Y.D., and Lu, H.P. (2003) Correlated topographic and spectroscopic imaging beyond diffraction limit by atomic force microscopy metallic tip-enhanced near-field fluorescence lifetime microscopy. *Rev. Sci. Instrum.*, **74**, 3347.

49. Micic, M., Klymyshyn, N., Suh, Y.D., and Lu, H.P. (2003) Finite element method simulation of the field distribution for AFM tip-enhanced surface-enhanced Raman scanning microscopy. *J. Phys. Chem. B*, **107**, 1574.

50. Suh, Y.D., Schenter, G.K., Zhu, L.Y., and Lu, H.P. (2003) Probing nanoscale surface enhanced Raman-scattering fluctuation dynamics using correlated AFM and confocal ultramicroscopy. *Ultramicroscopy*, **97**, 89.

51. Myers, A.B. (1997) Resonance Raman intensity analysis of excited state dynamics. *Acc. Chem. Res.*, **30**, 519.

52. Meyers, A.B. and Mathies, R.A. (1988) in *Biological Applications of Raman Spectroscopy*, Vol. 2 (ed. T.G. Spiro), Wiley-Interscience, New York, p. 1.

53. Van Duyne, R.P. (2004) Molecular plasmonics. *Science*, **306**, 985–986.

54. Hayazawa, N., Yano, T., Watanabe, H., Inouye, Y., and Kawata, S. (2003) *Chem. Phys. Lett.*, **376** (1–2), 174–180.

55. (a) Hartschuh, A., Sanchez, E.J., Xie, X.S., and Novotny, L. (2003) *Phys. Rev. Lett.*, **90**, 95503. (b) Bouhelier, A., Beversluis, M.R., and Novotny, L. (2004) *Ultramicroscopy*, **100**, 413.

56. Stockle, R.M., Suh, Y.D., Deckert, V., and Zenobi, R. (2000) *Chem. Phys. Lett.*, **318**, 131.

57. Miller, R.J.D., McLendon, G.L., Nozik, A., Schmickler, W., and Willig, F. (1995) *Surface Electron Transfer Processes*, Wiley-VCH Verlag GmbH, Weinheim.

58. Liu, D. and Kamat, P.V. (1996) *J. Phys. Chem.*, **105**, 965–970.

59. Birks, J.B. (1973) *Organic Molecular Photophysics*, John Wiley & Sons, Inc., New York.

60. Huber, R., Moser, J.E., Grätzel, M., and Wachtveitl, J. (2002) *Chem. Phys.*, **285**, 39–45.

61. Brokmann, X., Hermier, J.P., Messin, G., Desbiolles, P., Bouchaud, J.P., and Dahan, M. (2003) *Phys. Rev. Lett.*, **90** (1–4), 120601.

62. Marcus, R.A. (1956) *J. Chem. Phys.*, **24**, 966–978.

63. Newton, M.D. (1991) *Chem. Rev.*, **91**, 767–792.

64. Wang, J. and Wolynes, P. (1995) *Phys. Rev. Lett.*, **74**, 4317–4320.

65. Jung, Y.J., Barkai, E., and Silbey, R.J. (2003) *Chem. Phys.*, **284**, 181–194.

66. Toniolo, C., Provenzale, A., and Spiegel, E.A. (2002) *Phys. Rev. E*, **66**, 066209-1 –066209-12.

67. Barkai, E., Jung, Y.J., and Silbey, R. (2004) *Annu. Rev. Phys. Chem.*, **55**, 457–507.

68. Margolin, G. and Barkai, E. (2006) *J. Stat. Phys.*, **122**, 137–167.

69. Zwanzig, R. (1990) *Acc. Chem. Res.*, **23**, 148.

70. (a) Peter Lu, H., Xun, L., and Sunney Xie, X. (1998) Single-molecule enzymatic dynamics. *Science*, **282**, 1877. (b) Sunney Xie, X. and Peter Lu, H. (1999) Single-molecule enzymology. *J. Bio. Chem.*, **274**, 15967. (c) Sunney Xie, X. and Peter Lu, H. (2003) in *Single Molecule Spectroscopy Nobel Conference Lectures* (eds R. Rigler, M. Orrit, and T. Basche), Springer, Berlin, pp. 227–240.

71. Kuno, M., Fromm, D.P., Hamann, H.F., Gallagher, A., and Nesbitt, D.J. (2001) *J. Chem. Phys.*, **115**, 1028–1040.

72. Wang, J., Xu, L., Xue, K., and Wang, E. (2008) *Chem. Phys. Lett.*, **463**, 405–409.

73. Bel, G., Zheng, Y., and Brown, F.L.H. (2006) *J. Phys. Chem. B*, **110**, 19066–19082.

74. Efros, A.L. and Rosen, M. (1997) *Phys. Rev. Lett.*, **78**, 1110–1113.

75. (a) Lee, C.L., Stell, G., and Wang, J. (2003) *J. Chem. Phys.*, **118**, 959–968. (b) Leite, V.B.P., Alonso, L.C.P., Newton, M., and Wang, J. (2005) *J. Phys. Rev. Lett.*, **95** (1–4), 118301.

76. Wang, P., Zakeeruddin, S.M., Moser, J.E., Nazeeruddin, M.K., Sekiguchi, T., and Gratzel, M. (2003) *Nat. Mater*, **2**, 402.

77. McHale, J.L. (2001) *Acc. Chem. Res.*, **34**, 265.

78. Heller, E.J. (1981) *Acc. Chem. Res.*, **14**, 368.

79. (a) Tutt, L. and Zink, J.I. (1986) *J. Am. Chem. Soc.*, **108**, 5830. (b) Kelley, A.M. (1999) *J. Phys. Chem. A*, **103**, 6891.

80. Verberk, R. and Orrit, M. (2003) *J. Chem. Phys.*, **119**, 2214.

81. Basche, T., Moerner, W.E., Orrit, M., and Talon, H. (1992) *Phys. Rev. Lett.*, **69**, 1516.

82. Fleury, L., Segura, J.-M., Zumofen, G., Hecht, B., and Wild, U.P. (2000) *Phys. Rev. Lett.*, **84**, 1148.

83. Kumar, P., Lee, T.H., Mehta, A., Sumpter, B.G., Dickson, R.M., and Barnes, M.D. (2004) *J. Am. Chem. Soc.*, **126**, 3376.

84. Lounis, B., Bechtel, H.A., Gerion, D., Alivisatos, P., and Moerner, W.E. (2000) *Chem. Phys. Lett.*, **329**, 399.

85. Michler, P., Imamoglu, A., Mason, M.D., Carson, P.J., Strouse, G.F., and Buratto, S.K. (2000) *Nature*, **406**, 968.

86. Hupp, J.T., Neyhart, G.A., Meyer, T.J., and Kober, E.M. (1992) *J. Phys. Chem.*, **96**, 10820.

87. Arkin, M.R., Stemp, E.D.A., Holmlin, R.E., Barton, J.K., Hörmann, A., Olson, E.J.C., and Barbara, P.F. (1996) *Science*, **273**, 475.

88. Millett, F. and Durham, B. (2002) *Biochemistry*, **41**, 11315.

89. Olson, E.J.C., Hu, D., Hormann, A., Jonkman, A.M., Arkin, M.R., Stemp, E.D.A., Barton, J.K., and Barbara, P.F. (1997) *J. Am. Chem. Soc.*, **119**, 11458.

90. Olson, E.J.C., Hu, D., Hörmann, A., and Barbara, P.F. (1997) *J. Phys. Chem. B*, **101**, 299.

91. Short, R. and Mandel, L. (1983) *Phys. Rev. Lett.*, **51**, 384–387.

23

Scanning Near-Field Gap-Mode Microscopy

Dai Zhang and Alfred J. Meixner

23.1

Introduction

The central part of scanning near-mode microscopy (SNGM) is a nanometer gap between the apex of a sharp metallic tip and the sample surface that is optically excited. A metallic tip focuses the electric field of the incident radiation into the sub-diffraction volume of the gap via the coherent light-induced oscillation of the conducting electrons in the metal tip. Dieter Pohl, a pioneer in near-field optical microscopy, pointed out the analogy of this configuration to the radio antenna. Such a configuration serves to collect energy from an electromagnetic wave and to deliver it to an oscillator circuit that has dimensions much smaller than the wavelength; or vice versa to emit an electromagnetic wave that has an additional signal imprinted onto it, that is, the information to be broadcasted. This gap-mode configuration is strikingly similar to the first antennas constructed by Heinrich Hertz, which he used to experimentally verify the generation of electromagnetic radiation. This comment is by no means to diminish the achievements in the developments of SNGM. We will see in the pace of this chapter that the electric field and emission enhancement in near-field optics has many similarities to radio antennas, however there is much more to it than simply downscaling the wavelength from centimeters to nanometers. The reader who is interested in a more in-depth treatment on nanoantennas is referred to an excellent recent review article and the references therein [1].

In the following sections, we will mainly focus on the aspects of electromagnetic enhancement important to high-resolution SNGM. In the visible frequency range, the phenomenon of electromagnetic enhancement has been introduced since 40 years ago to explain the tremendously enhanced Raman signals observed from organic molecules deposited on roughened noble metal surfaces or particles [2–4]. Today, surface-enhanced Raman spectroscopy, or surface-enhanced Raman scattering (SERS), has developed to a well-established surface-sensitive spectroscopic technique [5]. The enhancement factor can reach several orders of magnitude, which allows the technique to be sensitive enough to detect single molecules [6, 7].

Handbook of Spectroscopy, Second Edition. Edited by Günter Gauglitz and David S. Moore.

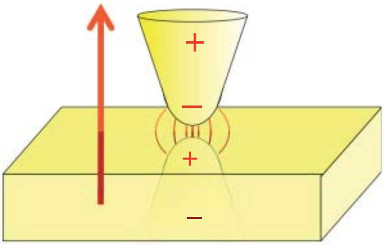

Figure 23.1 The gap width is on the order of some nanometers, that is, much smaller than the optical wavelength. The tip is polarized by the electric field of the incident beam, which is indicated by the red arrow. Electromagnetic radiation leading to a surface charge at the tip apex and its mirror on the sample surface. The surface charges establish a strongly enhanced electric field (indicated by the curved red lines) in the gap.

In Figure 23.1, we sketch the fundamental configuration of the optical antenna used in SNGM, consisting typically of a sharp gold or silver tip approaching the sample surface as close as a few nanometers and illuminated by incident laser radiation. Toward the end of the conical tip, its lateral diameter becomes smaller than the penetration depth of the incident optical field into the metal, and the electric field component of incident radiation induces a coherent oscillation of the conduction electrons – a so-called plasmon oscillation. The energy quanta of the charge oscillation are called *plasmon* in analogy to the photon as energy quanta of an oscillating electromagnetic field or wave. As the plasmon oscillation is always coupled with an optical field oscillation, it is termed as *plasmon polariton*. If the incident electric field is oriented along the tip axis, the freely moving charge in the metal is periodically driven up and down along the tip shaft bouncing periodically against the tip apex. It leads there to an oscillating surface charge with a maximum at the tip apex and, as a consequence, to a greatly enhanced local field. The response of the sample to the tip-enhanced field can be easily explained with the concept of mirror charges and leads to a local polarization that acts back on the tip. Hence, the tip and the sample form a system of coupled oscillators influencing each other via the electric field in the gap as sketched in Figure 23.2, and the magnetic field outside. The oscillating surface charges of the tip-sample system again emit radiation, with most of it at the incident laser frequency, that is, elastic or Rayleigh scattering. A small fraction resulting from inelastic processes [e.g., Raman scattering, photoluminescence (PL), or fluorescence] that is frequency-shifted. The emission pattern has radial symmetry about the antenna axis and the emitted power must constantly be refed to the antenna by the incident radiation; else the charge oscillation of the antenna would quickly fade away. From the optical reciprocity theorem, it remains clear that the antenna is most efficiently excited by an incident wave that is the time reversal of the emitted wave. Such excitation conditions can conveniently be realized by focusing a radially polarized laser beam by an objective lens with high numerical aperture (NA) or by a high NA parabolic mirror, an important issue to which we come back in Section 23.2.

In a simple way, we can view the electromagnetic field emitted by this system as the superposition of the fields created by two aligned and coupled dipoles that are separated by a short distance, one being from the oscillating charges at the end of the tip and the other being from the induced mirror dipole at the sample beneath the tip. The strength and the phase of these dipoles depend on the illumination conditions, polarizability of the tip, and local polarizability or the responsiveness of the sample to the locally enhanced field at the tip apex. Hence, it is easy to understand that the local variations of the dielectric properties of the sample can be probed by recording the optical signal point by point with a resolution and signal intensity limited by the tip radius, the tip-sample distance, and the polarizability of tip and the sample.

Furthermore, if we consider now a molecule in the gap, it can contribute to the optical signal via different processes, such as (i) tip-enhanced Rayleigh- and Raman scattering, (ii) tip-enhanced fluorescence or luminescence excitation under resonant condition, or (iii) tip-induced molecular fluorescence quenching by transferring energy to the tip as a result of absorptive losses of the metal. All three processes have been observed and the balance of the branching ratio between the signal enhancement and quenching depends on the spectral overlap between the molecule's emission and the tip absorption, the orientation of its emission dipole moment with respect to the local field in the gap and the distance with respect to the tip, the quantum yield of the molecule, and so on.

In summary, the laser-irradiated tip close to the sample surface leads to locally enhanced scattering and excitation as a result of the enhanced field in the gap. In addition, it leads to enhanced emission as a result of the enhanced optical mode density close to the gap offering a molecule more degrees of freedom to emit photons via the near-field to the far-field as compared to the situation without a tip. Finally, absorptive losses from an excited molecule to the tip could lead to luminescence quenching at very short distances between the molecule and the tip.

23.1.1
Enhancement Factor

An important measure for the local signal enhancement in the gap is the phenomenological enhancement factor. As there is no standard way for its definition in the literature that allows comparing data measured under different experimental conditions, we dedicate the following section to the definition of such a term that will allow us to compare different measurements.

First of all, we note that all photons are recorded in the far-field, that is, a macroscopic distance away from the gap. Second, a confocal optical configuration is used both for illuminating the tip-sample gap and for collecting the scattered photons from there. Hence, we can distinguish between the signals recorded from the far-field detection volume when the tip is at close distance to the sample such that a nanometer gap is formed and near-field phenomena play a role, from the optical signal when the tip-sample separation is so large that near-field effects can be neglected. Such measurements can easily be performed by recording spectra

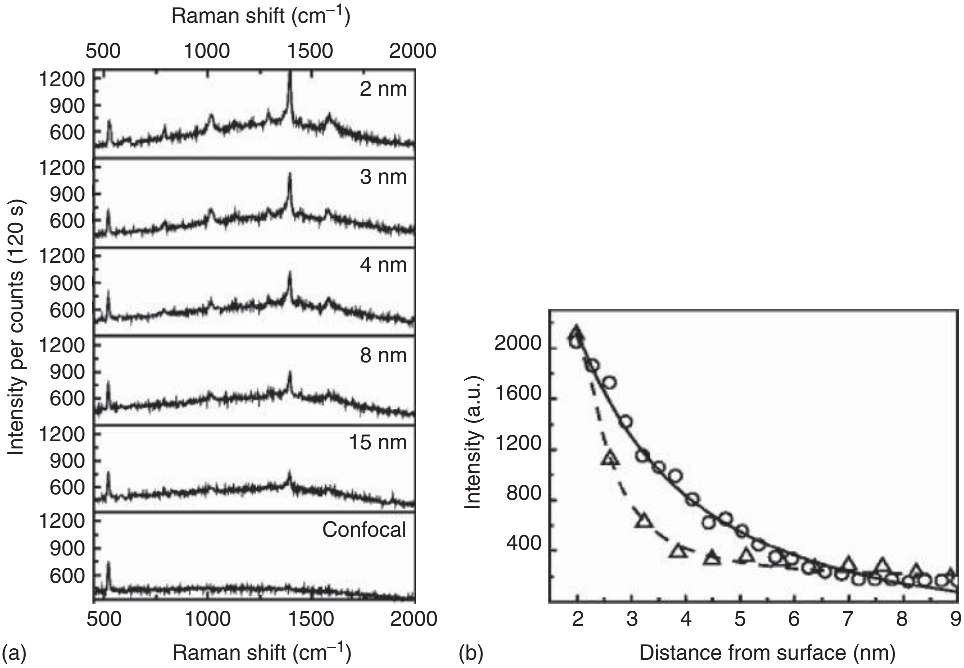

Figure 23.2 (a,b) Tip-enhanced Raman spectra of BTA on a smooth gold layer for decreasing tip–surface distances. Every spectrum was taken with an integration time of 120 s. The line at 520 cm^{-1} originates from the Si substrate under the gold layer and serves as an internal standard. (Copyright (2008) by Wiley-VCH Verlag GmbH & Co. KGaA, Weinheim. Reprinted from [8].)

for decreasing gap widths. An example is demonstrated in Figure 23.2, where a series of tip-enhanced spectra is shown that were taken from a monolayer of benzotriazole (BTA) molecules adsorbed on a smooth gold film when a sharp gold tip approaches to the sample surface [8]. The spectra show the appearance of a smooth luminescence background that originates both from the sample surface and from the gold tip, and in addition, the appearance of distinct Raman lines of BTA with decreasing tip-sample distances. The Raman line at 520 cm^{-1} is present in all spectra independent of tip–sample distance. It originates from the Si substrate below the Au film and is too far away from the tip to experience the near-field enhancement. This signal can, hence, conveniently serve as a reference to prove that the z-position (parallel to the optical axis of the microscope) of the sample in the focus stayed constant while the sequence of spectra was recorded.

Obviously, the increase in signal arises from the increasing optical near-field in the gap between the tip apex and the sample as they approach each other. Hence, the optical signal recorded at the detector is the sum of photons emitted from the confocal detection volume consisting of those arises from the near-field effect at close tip–sample distance, and the rest from the far-field focus illuminated area that can be considered as the confocal far-field background.

At a close tip–sample distance, the enhanced signal, $\int S_{\mathrm{enh}}(\omega)\mathrm{d}\omega$, can formally be divided into three fractions: the signal that originates only from the gap, $\int S_{\mathrm{gap}}(\omega)\mathrm{d}\omega$, and a confocal far-field background signal that originates from the sample, $\int S_{\mathrm{sample}}(\omega)\mathrm{d}\omega$, and the tip, $\int S_{\mathrm{tip}}(\omega)\mathrm{d}\omega$

$$\int S_{\mathrm{gap}}(\omega)\mathrm{d}\omega = \int S_{\mathrm{enh}}(\omega)\mathrm{d}\omega - \int S_{\mathrm{sample}}(\omega)\mathrm{d}\omega - \int S_{\mathrm{tip}}(\omega)\mathrm{d}\omega \tag{23.1}$$

The fraction of the background that originates from far-field illumination of the sample can be determined straightforwardly by retracting the tip and performing independent confocal measurements of the sample. Similarly, the contribution of the tip-emitted photons to the background signal can be evaluated by recording a confocal spectrum from the tip alone.

Since the near-field-enhanced signal originates from the sample surface and the tip apex within the tip–sample gap, it hence makes sense to define a near-field spot area A_{gap}, for example, given by the waist diameter of the enhanced field in the gap. The phenomenological spectral integrated enhancement factor (G) can thus be defined as the ratio between the spectral-integrated enhanced signal from the gap divided by A_{gap} and the confocal background divided by the diffraction-limited confocal far-field-illuminated area A_{conf}:

$$G = \frac{\dfrac{\int S_{\mathrm{gap}}(\omega)\mathrm{d}\omega}{A_{\mathrm{gap}}}}{\dfrac{\int S_{\mathrm{sample}}(\omega)\mathrm{d}(\omega) + \int S_{\mathrm{tip}}(\omega)\mathrm{d}\omega}{A_{\mathrm{conf}}}} \tag{23.2}$$

We would like to note that the enhancement factor accounts for the total spectral-integrated enhanced signal that is the sum of the enhanced luminescence background arising both from the sample surface and from the metallic tip as well as the tip-enhanced Raman signal from the adsorbed molecules at the metallic surface.

23.1.1.1 Physical Interpretation of the Enhancement Factor

23.1.1.1.1 Tip-Enhanced Photoluminescence (TEPL) Tip-enhanced photoluminescence (TEPL) results from the radiative decay of molecules or excitons electronically excited in the optical near-field between the tip apex and the sample. To explain the origin of the PL enhancement, we must take into account the enhancement of the excitation rate as well as the PL quantum yield. While the excitation rate is determined by the local optical field and, thus, follows directly the enhancement of the energy density in the optical near-field, the emission rate depends on the balance between the radiative decay rate Γ_{r} and the nonradiative decay rate Γ_{nr} leading to

$$I_{\mathrm{PL}} \propto \Gamma_{\mathrm{exc}} \times \left[1 - \frac{\Gamma_{\mathrm{nr}}}{\Gamma_{\mathrm{r}} + \Gamma_{\mathrm{nr}}}\right] \tag{23.3}$$

where the term in brackets represents the quantum yield in terms of the radiative and nonradiative rates. The excitation rate of a molecule or the rate for generating an exciton is proportional to the square of the transition dipole moment $\vec{D}$ between the electronic ground state and the excited state as well as the spectral energy density $\rho(\omega_{\mathrm{exc}}) = \frac{1}{2}\varepsilon_0 \vec{E}_0^2$ of the incident radiation at the location of the dipole as

$$\Gamma_{\mathrm{exc}} = \frac{\pi}{\varepsilon_0 h^2} |\vec{D}\vec{n}|^2 \rho(\omega_{\mathrm{exc}}) \tag{23.4}$$

where $\vec{n}$ is a unit vector along the direction of the electric field component with the amplitude $\vec{E}_0$. If we assume that the transition dipole is not affected by the presence of the tip, the excitation enhancement of the excitation process G_{exc} is given by

$$G_{\mathrm{exc}} = \frac{\rho(\omega)_{\mathrm{gap}}}{\rho(\omega)_{\mathrm{conf}}} \tag{23.5}$$

where $\rho(\omega)_{\mathrm{gap}}$ is the spectral energy density at the position of the transition dipole moment in the gap and $\rho(\omega)_{\mathrm{conf}}$ is the spectral energy density in the focus at the same position when the tip is infinitely far way. Hence, it is easy to understand that the enhanced optical near-field in the gap leads to an enhanced excitation rate. With respect to the confocal far-field situation, the enhancement of the optical near-field in the gap depends on the details of the tip and the sample, such as the materials they consist of and their geometries. Field enhancement factors of more than two orders of magnitude have been reproducibly achieved, giving excitation enhancement factors of up to five orders of magnitude.

The reasons for the enhancement of the emission process are less obvious to spectroscopists used to work with classical systems. According to Fermi's golden rule, the spontaneous radiative decay rate per frequency interval is

$$\frac{\partial \Gamma_{\mathrm{r}}(\omega_{\mathrm{em}})}{\partial \omega} = \frac{2\omega_{\mathrm{em}}}{3\hbar\varepsilon} |\vec{D}_{\mathrm{em}} \times \vec{n}|^2 \rho(\omega_{\mathrm{em}}) \tag{23.6}$$

where $\vec{D}_{\mathrm{em}}$ is the transition dipole for emission, the same definition as that of formular (23.4)? which is excited by the emission dipole, and $\rho(\omega_{\mathrm{em}})$ is the photonic mode density surrounding the emission dipole. In classical spectroscopy, usually samples with an ensemble of molecules homogeneously dispersed at high dilution in a transparent, dielectric solvent, or matrix are investigated, with an observation volume much larger than the optical wavelength. Under these conditions, the optical mode density is given by $\rho(\omega) = \frac{n^3\omega^2}{\pi^2 c^3}$ with n as the refractive index of the medium and has no spatial variation [9].

The situation is different for molecules in a resonator or for those very close to metallic nanoparticles. There $\rho(\omega)$ can vary dramatically within half a wavelength.

In order to determine the emission enhancement for a molecule in a gap, we have to compare the signal of an emitting dipole placed on or close to a surface adjacent to open space with the same situation, however with an additional tip pointing from the free space toward the surface such that the emitting dipole is enclosed in the small cavity between the surface and the tip apex. Both situations are rather complex when compared to a dipole emitting in free space and a quantitative analysis requires substantial numerical simulations.

The tip increases locally the photonic mode density in the gap between the apex and the sample surface when compared to a surface adjacent to open space and thus increases the radiative recombination rate Γ_r. Also absorptive losses from the emitting dipole to a metal surface increase the nonradiative decay rate at nanometer distances [10] and lead to complete fluorescence quenching for a molecule at an infinitely extended metal surface. However, as the radius of the tip apex gets smaller (e.g., some nanometers), the increase in the radiative rate may outweigh absorptive losses at short tip–sample distances as a result of the giant near-field enhancement. On the basis of this analysis, the PL enhancement G_{PL} can be expressed as the product of the excitation enhancement $G_{\mathrm{PL,exc}}$, and the emission enhancement $G_{\mathrm{PL,em}}$:

$$G_{\mathrm{PL}} = G_{\mathrm{PL,exc}} \times G_{\mathrm{PL,em}} = \left(\frac{\rho_{\mathrm{gap}}}{\rho_{\mathrm{conf}}}\right) \times \left(\frac{1 - \frac{\Gamma_{\mathrm{nr,gap}}}{\Gamma_{\mathrm{r,gap}} + \Gamma_{\mathrm{nr,gap}}}}{1 - \frac{\Gamma_{\mathrm{nr,conf}}}{\Gamma_{\mathrm{r,conf}} + \Gamma_{\mathrm{nr,conf}}}}\right) \tag{23.7}$$

As we will see in $G_{\mathrm{PL,exc}}$ and $G_{\mathrm{PL,em}}$, sensitivity depends on the tip and the sample properties such as their wavelength-dependent susceptibilities; the geometrical parameters such as the tip–sample distances and the tip geometries, in particular, apex radius, the illumination conditions; and on the optical properties of the molecules under consideration.

23.1.1.1.2 **Tip-Enhanced Raman Scattering (TERS)** The electromagnetic enhancement in TERS can in principle be analyzed in the same manner as for the PL enhancement. Estimating the local enhancement of Raman scattering would require solving the problem of a radiating dipole that is coherently driven by the gap field and comparing this with the solution for the same radiating dipole on the sample substrate under far-field excitation conditions, for example, in a diffraction-limited spot. This is a challenging task, being a matter of current research [11, 12]. In the following section, we discuss the intuitive arguments borrowed from the theory developed to explain electromagnetic enhancement in SERS [13, 14]. If we consider a single molecule located in the gap, the Raman enhancement factor, G_{R}, can be expressed as

$$G_{\mathrm{R}} = G_{\mathrm{R,exc}}(\omega_{\mathrm{L}}) \times G_{\mathrm{R,rad}}(\omega_{\mathrm{R}}) \tag{23.8}$$

where the excitation enhancement $G_{\mathrm{R,exc}}(\omega_{\mathrm{L}})$ is proportional to the enhancement of the local energy density of the excitation field at the position of the molecule versus the energy density at the same molecule under confocal far-field excitation. Other experimental conditions are kept constant

$$G_{\mathrm{R,exc}}(\omega_{\mathrm{L}}) = \frac{\rho_{\mathrm{gap}}}{\rho_{\mathrm{conf}}} = \frac{|\vec{E}_{\omega_{\mathrm{L}},\mathrm{gap}}|^2}{|\vec{E}_{\omega_{\mathrm{L}},\mathrm{conf}}|^2} \tag{23.9}$$

where $|\vec{E}_{\omega_{\mathrm{L}},\mathrm{gap}}|^2$ and $|\vec{E}_{\omega_{\mathrm{L}},\mathrm{conf}}|^2$ are the squared electric field amplitudes in the gap and confocally, respectively. A very simple approximation for the enhancement factor often used in SERS is motivated by the optical reciprocity theorem and assumes that the frequency difference between the Raman-scattered photons and the incident laser radiation has a minor effect and can be neglected. Also, neglecting polarization effects and absorptive losses by the metal and the radiative enhancement factor can be approximated as

$$G_{\mathrm{R,rad}}(\omega_{\mathrm{R}}) \approx \frac{\rho_{\mathrm{gap}}(\omega_{\mathrm{R}})}{\rho_{\mathrm{conf}}(\omega_{\mathrm{R}})} \approx \frac{\rho_{\mathrm{gap}}(\omega_{\mathrm{L}})}{\rho_{\mathrm{conf}}(\omega_{\mathrm{L}})} = \frac{|E_{0,\mathrm{gap}}|^2}{|E_{0,\mathrm{conf}}|^2} \tag{23.10}$$

Assuming similar enhancement levels for the incident and the scattered light, the total enhancement factor can be approximated by

$$G_{\mathrm{TERS}} \approx \frac{|E_{0,\mathrm{gap}}|^4}{|E_{0,\mathrm{conf}}|^4} \tag{23.11}$$

This result states that the tip-enhanced Raman signal increases with the fourth power of the local field enhancement. This expression is very popular in the SERS literature, where it is referred to as the $|E|^4$-*approximation* for the SERS enhancement. It must be kept in mind, however, that it is an approximation hiding an important part of the physics of TERS, namely, the enhancement in the scattering process is also strongly influenced by the magnitude of the local field enhancement.

23.2
Instrumentation

23.2.1
Tip Antenna

23.2.1.1 Tip Material

As has been explained in the introduction section, tip material is one of the crucial factors for an excellent SNGM performance. Metals with negative real permittivity can support collective oscillations of free charges (surface plasmon propagation) in the materials at an applied electromagnetic field. However, metals are plagued by large losses, especially in the visible and UV spectral ranges, arising partly from interband electronic transitions [15]. Even the metals with the highest conductivities suffer from large losses at optical frequencies [16–18]. Therefore, in practical applications, there are not many metallic materials that can be good candidates for tip fabrication. For example, Pettinger *et al*. [19] had reported that the Raman intensity of malachite green isothiocyanate (MGITC) adsorbed on Au (111) was increased by a factor of 2 when a He–Ne laser-illuminated Ir tip was approached at a distance of 1 nm away from the molecules. Under the comparable experimental condition, when the Ir tip was replaced by an Au tip, the average increase in the Raman intensity was ~8000. The explanation of the poor enhancements from an Ir tip was that a significant damping of the confined electric field occurred despite the excitation of localized surface plasmon in the Ir/Au (111) crystal cavity.

Among the metallic elements, Ag has the smallest total damping rate and the lowest loss in the visible and near-infrared spectrometer (NIR) ranges. Au, which has a larger damping rate than Ag, is often the metal of choice at lower NIR frequencies. However, Au has high interband losses in the visible spectrum for wavelengths below ~500 nm. Cu has an excellent conductivity (only less than Ag) among metals; hence, it is expected to exhibit promising plasmonic properties. Indeed, the imaginary part of the permittivity of Cu is comparable to that of Au from 600 to 750 nm. However, Cu has large interband losses over most of the visible spectrum. Al has not been an attractive plasmonic material because of the low-energy threshold (around 800 nm, 1.5 eV) of its interband transition, resulting in a large imaginary part in the visible wavelength range. However, in deep UV, the real part of its permittivity is negative while the imaginary part is still relatively low. Therefore, Al is a better plasmonic material than either Au or Ag in the blue and UV range [20].

An important issue concerning tip antenna is its chemical stability. Ag, Cu, and Al all form oxides at atmospheric conditions, leading to a complete loss or deteriorated antenna effect [21]. Concerning this practical problem, Au has a stable chemical stability and, therefore, is of an excellent candidate for tip antenna fabrication. Freshly prepared Ag tips are also used because of its attractive plasmonic properties [22]. To minimize the oxidation, the prepared sharp Ag tips can be stored and used either in a vacuum condition or under inert atmosphere protection.

23.2.1.2 **Tip Fabrication**

Different fabrication techniques exist for producing suitable tips for SNGM. In this section, we will shortly review some of the most employed methods for tip preparations.

23.2.1.2.1 **Metal Evaporation on Atomic Force Microscopy (AFM) Tip** SNGM combines scanning probe microscopy and optical microscopy. The manipulation of the tip antenna, such as approaching it to the vicinity of the sample surface, based on atomic force, is one of the most popular methods. As the AFM cantilever tips are typically made from Si, the tip apex needs to be coated by Au or Ag to create surface plasmon in the visible or near-UV regime. A simple manufacturing method is to evaporate a 20–50 nm thick metal layer over the cantilever, which results in a final tip radius in the range 20–50 nm [23]. A thinner film is promising for giving sharper tip apex, but is mechanically less stable. The advantage of this method is that we can easily employ the commercially available AFM sharp tip as a base, coating with various metals, for tip fabrication. Notably, the main disadvantage of such a method is the ill reproducibility of the tip apex geometry, which often leads to a large fluctuation in the near-field enhancement among different tips.

23.2.1.2.2 **Nanostructure at Different Tip Bases** Other techniques include attaching individual gold particles to the end of an optical fiber tip and using ion beam milling to fabricate tailored plasmonic structures.

For example, the antennas were fabricated at the apex of the pyramidal Si_3N_4 AFM cantilever tips (Figure 23.3a). The electric field, in this case, is confined by the

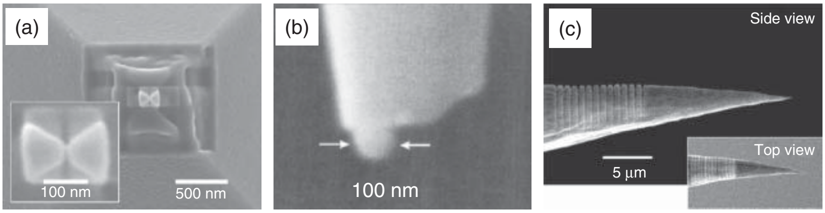

Figure 23.3 (a) Optical antenna at the apex of an AFM tip. (Copyright (2005) by the American Physical Society. Reprinted from [24].) (b) SEM images of an Au nanoparticle was fixed to a fiber tip. (Copyright (2001) by the Royal Microscopical Society. Reprinted from Ref. [25].) (c) Grating-coupling of surface plasmons on a tip. (Copyright (2010) by the American Chemical Society. Reprinted from [27].)

excitation of the antenna gap. After evaporating a homogeneous 40 nm thickness aluminum film to the AFM tip, a bowtie-shaped metallic structure was sculptured from the film by means of focused ion beam (FIB) milling. This includes, in a final step, cutting of a narrow gap between the two arms of the antenna right at the apex. The flare angle, radius of curvature of the antenna arms at the feed gap, and the feed gap width are 40°, 30 nm, and approximately 50 nm, respectively. The overall antenna length is 170 nm, which is in between the length of the half-wave dipole, estimated to be near 120 nm under consideration of the average dielectric properties of the environment, with the first minimum of the antenna responsively at about twice that length [24]. Figure 23.3b illustrates another approach that an Au nanoparticle can be attached to the end of a glass fiber tip as a local electric field confiner [25]. The advantage of such method lies in the fact that the size and geometry of the nanoparticle are well confined. However, the reproducibility and the flexibility of handling are under debate. Recently, a new type of tip of fabricating grating structure at the tip shaft is introduced [26, 27], as shown in Figure 23.3c. This local light source is based on spatially focusing surface plasmon polariton (SPPs) on nanofabricated, three-dimensionally tapered conical tips with apex radii of a few tens of nanometers. One-dimensional grating was written onto the tip shaft by FIB sputtering, which is more than 10 µm away from the apex. Illumination of the grating with a broadband femtosecond laser leads to resonant excitation of SPPs, which travel to the tip apex and radiates. This sort of tip is potentially very plausible for significant reduction of background illumination in SNGM.

23.2.1.2.3 **Electrochemical Etching of Au or Ag Wires** Electrochemical etching of Au or Ag wires to generate sharp tip apex is often used in fundamental research laboratories [28]. The setup for etching the Au tip is based on a commonly used configuration, as shown in Figure 23.4, placing a gold ring of ~8 mm diameter made from 1 mm gold wire on the surface of the solution (about 3/4 height of the ring is immersed in the solution).

A gold wire of 0.25 mm diameter after a quick flame annealing was immersed in the center of the ring. The immersed length is normally 2–3 mm. The etching solution was prepared using analytical grade fuming hydrochloric acid and ethanol

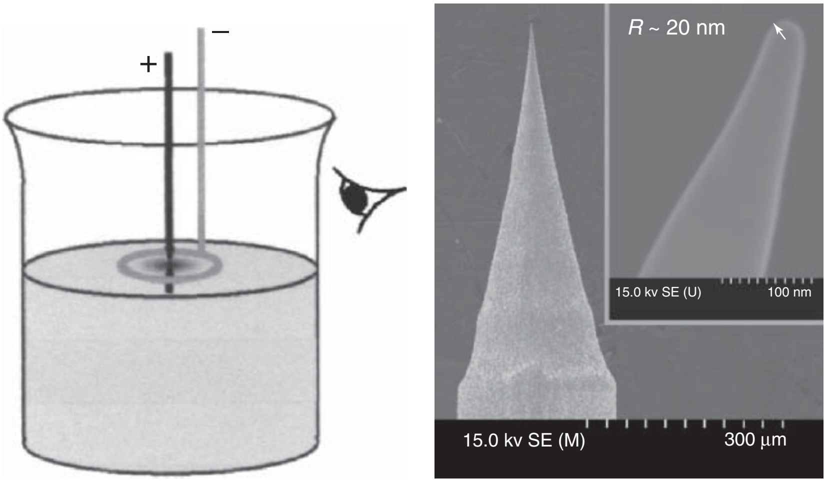

(a) (b)

Figure 23.4 (a) The schematic diagram of the setup for preparing the gold tip. (b) The smooth, pencil-shaped Au STM tip produced by electrochemical etching. (Copyright (2006) by the American Institute of Physics. Reprinted from [28].)

from Merck. The chemical reactions occurred during the tip etching procedure are

$$\mathrm{Au} + 4\mathrm{Cl}^- \rightarrow \mathrm{AuCl}_4^- + 3\mathrm{e}^-, E_0 = 1.002\ \mathrm{V}$$

$$\mathrm{Au} + 2\mathrm{Cl}^- \rightarrow \mathrm{AuCl}_4^- + \mathrm{e}^-, E_0 = 1.154\ \mathrm{V}$$

$$\mathrm{AuCl}_2^- + 2\mathrm{Cl}^- \rightarrow \mathrm{AuCl}_4^- + 2\mathrm{e}^-, E_0 = 0.926\ \mathrm{V}$$

According to authors' observation, a stable current oscillation only occurs at DC voltage more positive than 1.4 V with respect to a saturated calomel electrode. Notably, when the etching voltage is too high, side reactions such as the bubble evolution of Cl_2 and O_2 may occur, leading to severely roughened surface. The addition of ethanol is suggested in their method to reduce the bubbling and hence to produce a smooth surface during the etching process. After systematic comparisons of the different mixture ratios between ethanol and HCl, as well as the etching voltages, the authors suggested a series of optimized-electrochemical etching parameters: ethanol and fuming HCl are mixed with equal amount and the etching voltage is selected as 2.4 V. Although they did not rule out that other combinations of etching voltage and solution composition can produce better tips, they can achieve, with the earlier-mentioned parameters, well-defined tip shape and very smooth surface structure (a typical tip picture, as shown in Figure 23.4).

23.2.2
Microscope Configurations

The commonly used experimental configurations for SNGM, based on the arrangements of the optical paths for laser illumination and signal collection, can be divided into three main streams: transmission, side illumination, and top illumination.

23.2.2.1 Transmission Configuration

Laser illumination and signal collection in a transmission configuration is mostly employed to perform near-field optical microscopy. In such a configuration (Figure 23.5), the laser beam is delivered from below the sample and is focused by a lens at the apex of an AFM tip coated with metal. The scattered signal will be collected by the lens and be delivered to the detector. There are several advantages of working with such a configuration. (i) It can be a relatively convenient setup by integrating commercial available confocal optical microscope and scanning probe microscope, such as AFM. So far, most SNGM instruments on the market are based on this configuration. (ii) High NA oil immersion lens can be used in this configuration, which allows a tight laser focusing for minimizing the background signal and an efficient signal collection for achieving higher sensitivity.

Concurrently, there is a prerequirement that the sample substrates have been restricted to be transparent in order to let the laser illuminate the sample and the signal being collected through the substrate [29, 30, 23]. Transparent substrates such as mica and glass or ultrathin metal films have to be used, which limits the applicability of this technique. As shown later, for nontransparent samples, side illumination and top illumination were employed [31–34].

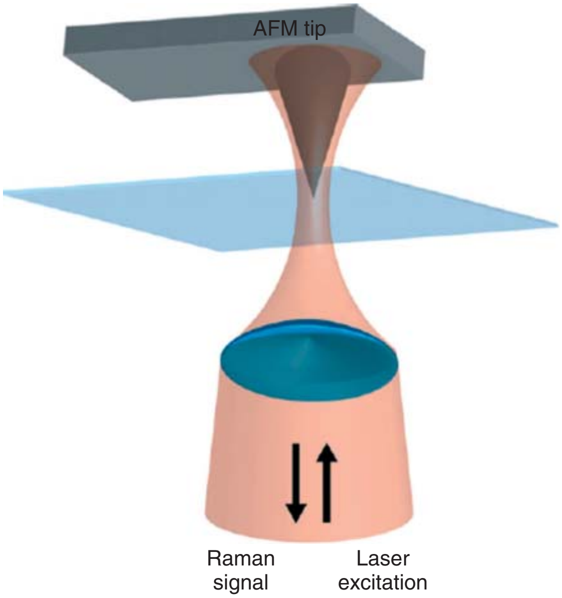

Figure 23.5 A schematic diagram of a tip-enhanced Raman scattering setup working in back reflection mode. (Copyright (2008) by the Royal Society of Chemistry. Reprinted from [29].)

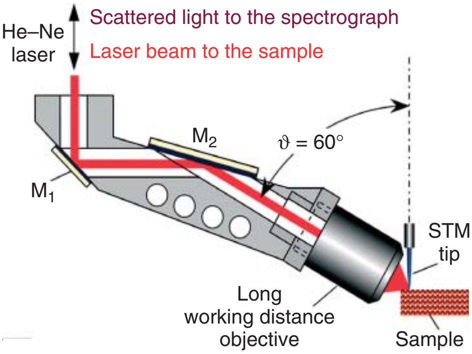

Figure 23.6 A schematic representation of a side-illumination configuration. (Copyright (2009) by the Elsevier B.V. Reprinted from [35].)

23.2.2.2 Side-Illumination Configuration

In this configuration, the laser illumination and signal collection are carried out at the side of the tip antenna with a certain angle (Figure 23.6).

In order to maximize the electric enhancement at the tip apex, the electric field of the incident light should be aligned along the tip axis, which is similar to the case of optimizing the electric enhancement in an elliptical metal particle. Such sort of requirement is difficult for the bottom-illumination method, especially when nontransparent sample is used; side-illumination configuration where a *p*-polarized laser beam [36] is directed to the tip antenna from a tilted angle versus the sample surface is proved to be an effective solution regarding this problem. The tilted angle has been suggested theoretically as between 45° and 60°. Practically, 60° [33] or 65° tilting angle is commonly used. The tip can be approached to the sample surface at a desired distance via tunneling current [35] and force [32].

Such an SNGM configuration allows a broad choice of samples, and no limitation regarding the sample transparency need to be taken account of. On the other hand, the limited NA of the air objective inevitably leads to some signal lose. In addition, the signal produced from the sample is collected only at ~60° from one side of the tip shaft, which may lead to artificial picture when using side-illumination configuration to do microscopic imaging.

23.2.2.3 Top-Illumination Configuration

In this reflection-type configuration (Figure 23.7), a high NA ($\mathrm{NA} = 0.998$) parabolic mirror is placed above the sample for laser focusing and signal collection [37]. Instead of commonly used lineally polarized beam, higher order laser beam such as radially polarized beam has been intensively employed. Compared to the focus of a linearly polarized beam, the radial symmetry of the field vectors in a radially polarized beam leads to a perfectly symmetric focus with a strong longitudinal component centered on the optical axis [38, 39]. When focused by the high NA

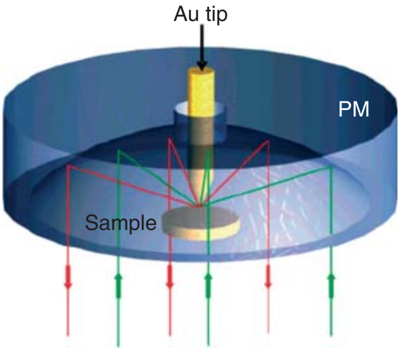

Figure 23.7 Sketch of a parabolic mirror situated above a sample and the tip antenna approached through an axial hole into the focus of a radially polarized laser beam. Green arrows indicate the incoming laser beam and the red arrows indicate the outgoing laser beam and optical signals. (Copyright (2010) by John Wiley & Sons, Ltd. Reprinted from [42].)

parabolic mirror, the electric field distribution along the longitudinal direction is ∼14.6 times stronger than that of the transverse direction and has a decay constant on the order to λ [40]. The tip is brought into the center of the focus through an axial hole at the center top of the parabolic mirror and is kept at a defined distance from the sample surface by shear force control [41, 42] or tunneling current [43, 44].

Similarly to the side-illumination configuration, top-illumination also has no limitation regarding the sample transparency. Besides this, on comparing with common air objective, a NA of nearly 1 can be achieved by a parabolic mirror, allowing an efficient and symmetric signal collection over a solid angle of π above the sample surface. Only a minor fraction of the signal is lost as a result of the small axial hole opened at the top of the parabolic mirror and the blockage of the tip shaft. In addition, a tighter focus that is slightly smaller than $\lambda/2$ can be achieved by a parabolic mirror, which helps to minimize the background signals from the far-field focus illuminated sample area [45]. A further advantage is that parabolic mirror focusing is based on reflection and is free from chromatic aberration, and thus, adaptable to different laser wavelengths. Notably, different from objective lens that has wide field of view and high degree of correction function; parabolic mirror has limited off-axis imaging property. Slight deviation of the incident beam from the optical axis or parallelism leads to large aberrations [40]. Therefore, the quality and the precise alignment of parabolic mirror are critical in such sort of configuration.

23.3
Applications

23.3.1
Materials Science

23.3.1.1 Carbon Nanotube and Graphene

Semiconducting single-walled carbon nanotubes (SWNTs) are photoluminescent quasi-one-dimensional quantum wires with great promise for application in photonics as well as opto and nanoelectronics. The unique optical and electronic properties observed in SWNTs are largely because of the one-dimensional confinement of electronic and phonon states, resulting in the so-called van Hove singularities in the nanotube [46]. Raman spectroscopy has been popularly employed to characterize SWNTs [47, 48]. The diameter and chirality of an SWNT can be determined by the shift of the radial breathing mode (RBM) at 100–400 cm^{-1} [49]. The detect defects in the nanotube structure can be detected by the disorder-induced D band at $\sim$1350 cm^{-1} [50], whereas the types of the SWNTs, be it semiconductor or metallic, can be distinguished from the shape of the tangential stretching G band ($\sim$1590 cm^{-1}) [51].

Near-field Raman and PL imaging of SWNTs have been performed by several groups [52–54]. Hartschuh *et al.* [55, 56] reported the TERS investigation of SWNTs with a spatial resolution of better than 15 nm. Highly localized excitation is used to visualize the spatial extent of the contributing excited states. Figure 23.8 shows the simultaneously near-field PL, Raman, and topographic imaging of micelle-encapsulated SWNTs on mica. The PL image and the Raman image were formed by detecting the light intensity that is transmitted by the band-pass filters centered at 950 nm (PL from the (8,3)-nanotubes) and 700 nm (G-band Raman scattering), respectively [57].

Recently, Maciel *et al.* [58] have shown the use of TERS and TEPL to detect spatially local charged defects along individual doped SWNTs. They observed a high degree of spatial localization of the PL along the SWNT, which is related to trapped excitons. They also reported a new peak in the G′ peak in the Raman spectra from the defect sites. This new peak can be shifted to lower or higher frequencies relative to that of the pristine tubes. They suggested that this additional G′ peak originates from the charged defects (dopants), having its frequency up/downshifted for p/n dopants.

As the basic structural element of carbon nanotube, graphene is one-atom-thick planar sheet of sp^2-bonded carbon atoms that are densely packed in a honeycomb crystal lattice [59]. The carbon–carbon bond length in graphene is $\sim$0.142 nm. Graphene sheets stack to form graphite with an interplanar spacing

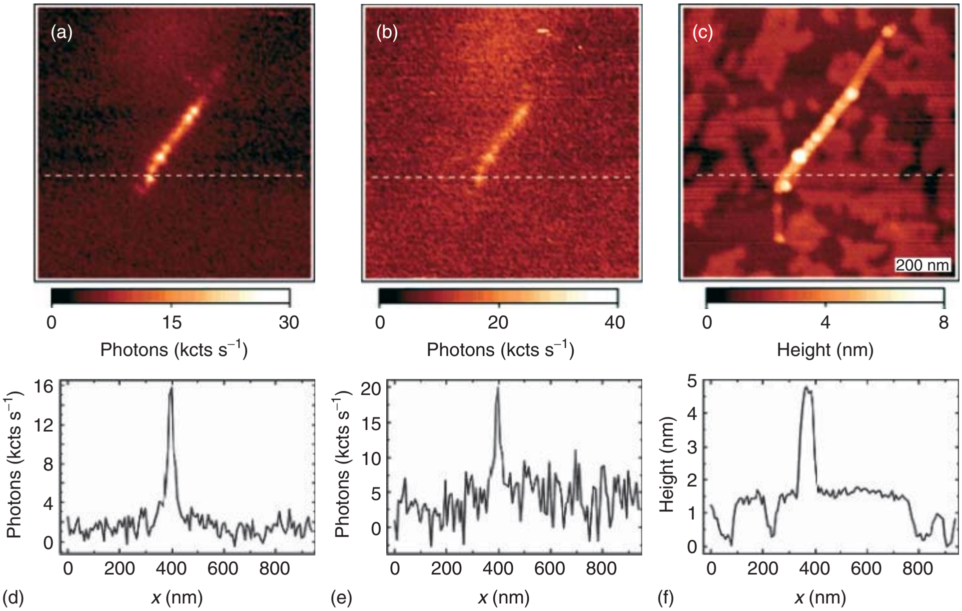

Figure 23.8 (a) Near-field PL, (b) Raman, and (c) topography image detected simultaneously for micelle-encapsulated SWNTs. (d–f) Optical and topographic cross sections taken along the dashed lines in (a–c), respectively. (Copyright (2005) by American Chemical Society. Reprinted from [55].)

of 0.335 nm. The extraordinary electronic and optical properties of graphene have attracted tremendous interests these days. In 2010, the Nobel prize in Physics was awarded to Andre Geim and Konstantin Novoselov "for groundbreaking experiments regarding the two-dimensional material graphene." Spectroscopic methods have been proved to be effective to identify the number of graphene layers, as well as to study the intermolecular interactions, molecular orientations, and symmetry distortions of graphene [60]. Saito *et al.* [61] has reported TERS analysis of n-graphene layers. Continuous change of intensity and peak shift of the G-band and the second-order overtone of the defect mode 2D band across the layer boundaries has been observed. They have suggested a near-field optical method to estimate the number of graphene layers and the thickness distribution in ultrathin graphite flakes. Snitka *et al.* [57] presented the TERS imaging of single-layer and multilayer graphene flakes with tips fabricated by flattering Au microwires. They reported an enhancement up to 10^6 of the D- and G-band of graphene, and by careful control of the tip, sample pressure, the shift in G-band wavelength was produced. In addition, the peak fluctuation in the 2D band also suggests the local stress distribution produced as a result of graphene–tip interaction. The number of layers and stress analysis in 2D imaging allows nondestructive identification of graphene layers critical for the evaluation of this material in future device applications.

23.3.1.2 **Inorganic Semiconductor**

Technology based on strained silicon has been widely used in semiconductor devices fabrications because it boosts the speed and reduces the power consumption of electronic devices [62–64]. For example, the strain introduced in active regions of complementary metal-oxide-semiconductors (CMOSs) devices can modify the electronic band structure and improve the mobility of charge carriers, hence enhancing the speed of high-performance microprocessors [65]. The device performance depends strongly on the level and the spatial distribution of the stress that is artificially imposed on the silicon lattice. Therefore, nondestructive characterization techniques of local stress with a lateral resolution below 100 nm are required for the quality control of high-performance electronic devices using silicon substrate [66]. Raman spectroscopy is one of the popular characterization tools to monitor the Si strain because of the linear dependence of the Si–Si phonon mode Raman shift on the strain level [67, 68]. The deviation from this peak position shows the amount of strain. Depending on the property of the strain, whether it is compressive or tensile, the Raman frequency of the Si–Si phonon mode shifts to either blue or red with respect to that of the nonstrained Si. A frequency change of at least 0.02 cm^{-1} can currently be detected [69]. Although Raman spectroscopy is in principle a powerful tool to characterize Si strain, this technique is less satisfactory regarding the sensitivity and the diffraction-limited optical resolution, that is, at a scale of several hundreds of nanometer.

TERS investigations of the Si strain have been performed by some research groups to cope with the earlier-mentioned problems. As shown in Figure 23.9, Ogawa *et al.* [70] have reported the nanometer-scale mapping of Ge/Si ODs that were grown on a Si substrate using TERS with a spatial resolution of less than 100 nm comparable with the dot sizes. In order to create a concentrated near-field, they deposited a gold particle at the apex of a fiber tip. On the basis of their TERS imaging, they discussed the strain in the Si substrate and the intermixing of single quantum dots (QDs). It was found that Ge–Ge and Si–Ge modes in the Raman spectra are significantly enhanced only when the AFM tip with a gold nanoparticle is positioned on the dots. It is also found that the Si substrate peak at 520 cm^{-1} is shifted considerably in the neighborhood of the dots. This implies that a large stress acts on the Si substrate around the dots. The Ge content reduces at the center of the dots. This result suggests that the dots consist of a Si-rich core and a Ge-rich shell. The Ge content decreases and the strain in the Si substrate increases with an increase in the dot height. Their work shows that the TERS technique is fully applicable to evaluation of the lattice structure and electronic properties of nanomaterials. Hanafusa *et al.* [71] studied the strain distribution of sputter-formed strained Si by TERS. A transparent cantilever tip with a gold nanoparticle deposited on top was used as the TERS probe. They carried out simultaneous measurements of the strain and surface undulation distribution for strained Si layers at a quadruple-$\mathrm{Si}_{1-x}\mathrm{Ge}_x$-layer. Their results show a strong relationship between the surface flatness and the strain distribution uniformity. The TERS analyses suggest that the compositional fluctuation of the underlying

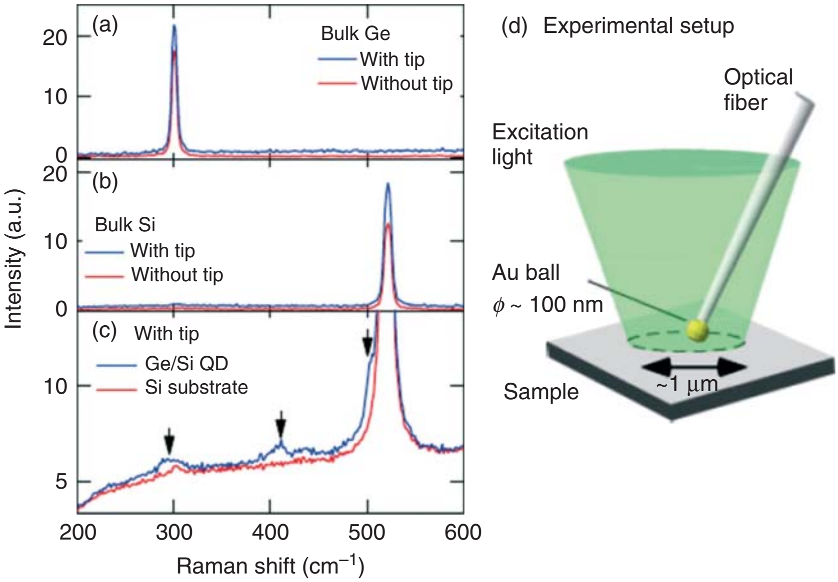

Figure 23.9 Raman spectra of bulk (a) Ge and (b) Si with tip [blue (black) line] and without tip [red (gray) line]. (c) Tip-enhanced Raman scattering (TERS) spectra of Ge/Si quantum dots (QDs) [blue (black) line] and Si substrate [red (gray) line]. The 2TA mode of the Si substrate is observed at 300 cm^{-1}. The three peaks of Ge/Si QDs observed at 294, 410, and 500 cm^{-1} belong to the Ge–Ge, Si–Ge, and Si–Si modes, respectively. (d) Experimental setup for TERS measurement. The TERS probe was made up of glass fibers and single gold nanoparticle with a size of ~100 nm attached to it; this particle was positioned on the samples in the focal spot during the measurements and was controlled by using a tapping-mode atomic force microscope. (Copyright (2011) by the American Physical Society. Reprinted from [70].)

$Si_{1-x}Ge_x$ is largely related to the weak Si strain fluctuation, which may also be related to the multidirectional lattice plane slips, which cause the surface flattening.

In addition to the Raman signal from the nanometer-sized area excited by the tip-induced near-field, an even overwhelming optical signal from the sample volume illuminated by the diffraction-limited focus (as discussed in Section 23.1.1) contributes as well to the collected TERS spectrum. This leads to the well-known problem of far-field signal interference when using TERS to characterize thin-strained Si layer. To minimize such a far-field interference without sacrificing the Raman signal from the strain Si, two major alternatives have been suggested. (i) UV illumination can be employed as the excitation source because of its thin penetration depth into the unstrained bulk Si substrate [72]. Owing to the frequency-dependent dielectric constant, Al has been recommended for the TERS measurement using UV light. Poborchii *et al.* [73] have optimized the tip materials and its shape for near-UV TERS of Si structures. They show both theoretically and experimentally that Al is a good Raman enhancer at the excitation of 363.8 nm. Employing an inclined Al-coated Si AFM tip, they succeeded in detecting weak

TERS signal of strained Si. (ii) The second alternative is based on the manipulation of the well-defined polarization properties of the Si crystalline sample relative to the polarization and propagation of the incident light. Such a method has been implemented by the reflective type side-illumination TERS configuration [74, 75]. They also proposed far-field suppression by depolarization configuration [76]. In this configuration, the tip depolarizes the incident beam from *p*-polarized light to *s*-polarized light or vice versa. The resulting depolarized light will incur a depolarized Raman signal that can be detected through an analyzer while blocking the Raman signal from the originally polarized light to minimize the far-field Raman signals. Ossikovski *et al.* [77, 78] proposed a simple model that describes polarized TERS to characterize the tip enhancement process. The model is based on a tip amplification tensor describing the interaction of the tip with both the incident and scattered optical field. The interference signal from the underlying bulk Si substrate can be reduced by appropriately setting the polarizer and analyzer relative to the material crystalline axis.

23.3.1.3 **Semiconductor Organic Thin Film**

Semiconducting organic materials have been studied intensively because of their interesting optoelectronic properties, giving rise to a broad range of applications such as organic field-effect transistors [79], organic light emitting diodes, or organic solar cells. The electronic properties of thin film semiconductors are usually different from the monomer or bulk crystal properties; moreover, they depend strongly on the microscopic film morphology, such as grain boundaries.

Zhang *et al.* [80] had reported the near-field imaging of a diindenoperylene (DIP) thin film based on the plasmon–polariton coupling between the excited gold tip and the semiconductor film. A near-field optical image of the DIP film and the simultaneously recorded topographic image are shown in Figure 23.10a,b. A sharp optical resolution of $\sim$17 nm at one molecular boundary is demonstrated. The DIP molecular domain boundaries being one to four molecular layers (1.5–6 nm) high are resolved topographically by a shear force scanning tip and optically by the 6×10^5 times enhanced PL (Figure 23.10c). The excitation is four magnitudes enhanced and the intrinsically weak PL yield of the DIP film is 15-fold enhanced by the tip. The enhanced PL contrast results from the local film morphology via stronger coupling between the tip plasmon and the exciton–polariton in the DIP film. The increasing and redshifted PL intensity with the tip approaching closer to the DIP sample indicate a stronger plasmon–polariton coupling (Figure 23.10d). The boundary of the DIP thin film appears to be brighter because of a stronger tip–sample coupling when compared to that of inside the thin film (Figure 23.10e).

On the basis of conjugated semiconductor polymers, organic solar cell is a promising candidate for new generation of low-cost and flexible photovoltaic devices. With blends of poly(3-hexylthiophene) and [21]-phenyl-C_{61} butyric acid methyl ester (P3HT:PCBM) that have been intensely used as electron donor and acceptor in organic solar cells devices. One of the main factors affecting the power conversion efficiency of P3HT:PCBM solar cells is the nanoscale morphology issue [81, 82].

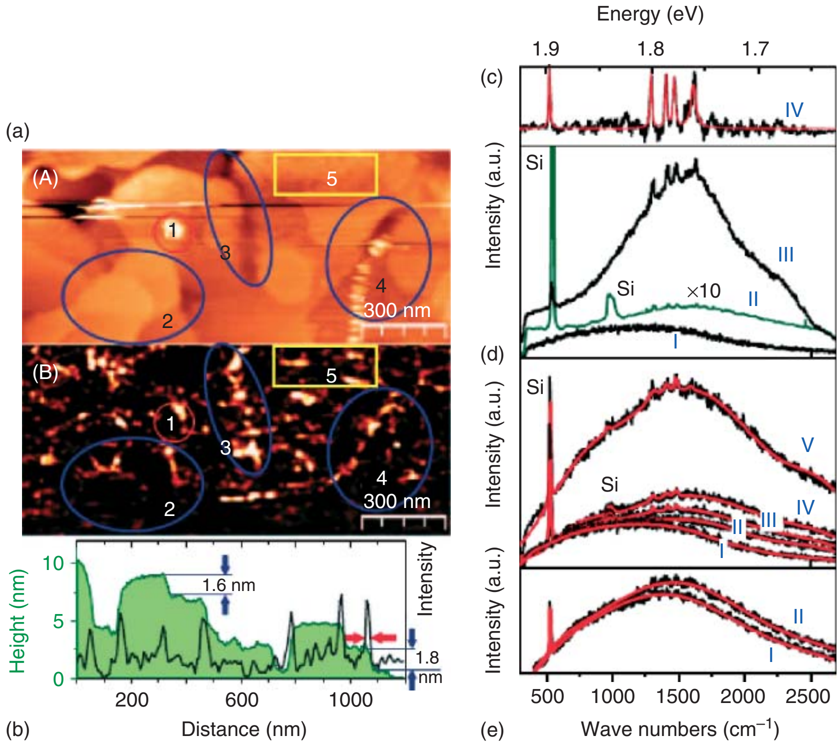

Figure 23.10 (a) Simultaneously recorded topographic (A) and near-field optical images (B). Scan area of 1.5 × 0.7 µm^2, laser power at the focus is 170 µW, tip–sample distance is 3 nm. (b) Line profile through the topographic image with its correlated optical intensity. (c) Confocal far-field PL spectrum (I) of a tip alone integrated for 10 s, (II) DIP film integrated for 900 s, and (III) tip-enhanced spectrum integrated for 10 s at a tip–DIP distance of 3 nm. Excitation power is 170 µW. (IV) tip-enhanced Raman spectrum obtained from (III) after subtraction of PL background with fitted spectrum (red curve). (d) Spectra collected at different tip–sample distance. (II) 3 nm, (III) 2.5 nm, (IV) 2 nm, (V) 1.5 nm, and (I), spectrum of tip alone. Integration time is 10 s. (e) PL spectra, (I) from inside a domain and (II) from a domain edge. Tip–sample distance is 3 nm. Excitation power is 170 µW. Acquisition time is 30 s. (Copyright (2010) by the American Physical Society. Reprinted from [80].)

Wang *et al.* [83] had reported the correlated topographical and near-field spectroscopic mapping images obtained from the blend film, which has been thermally annealed for 30 min (Figure 23.11). The PL intensity variation reflects the efficiency of charge generation at the P3HT:PCBM interface. Raman spectroscopy that is very sensitive to the degree of π-electron delocalization along the chain axis of conjugated polymers, studies nanoscale changes in morphology by monitoring the vibrational modes of P3HT polymer chains that are involved in electronic transitions.

Figure 23.11a shows the AFM image of a sample area. The corresponding near-field mapping image (Figure 23.11b), obtained by summing the total spectral

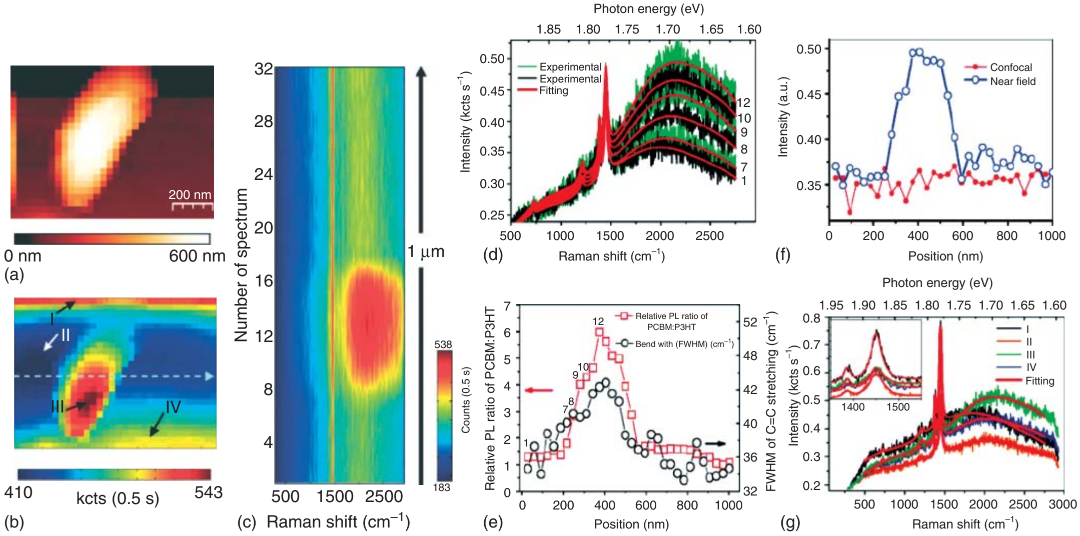

Figure 23.11 (a) Topographical image. (b) Near-field spectroscopic mapping images obtained by summing the total spectral pixel intensity from 283 to 2926 cm^{-1}. (c) Thirty-two spectra extracted from a line scan (1 μm) the position of which is indicated in (b) with an arrow. (d) Comparisons of several spectra extracted from the Raman line mapping sequence are shown in (c). The green and black spectra are the experimental data while the red curves are the fitted spectra. (e) The relative PL ratios between PCBM and P3HT (curves labeled with red open rectangles) and the FWHM changes of the P3HT C=C stretching Raman peaks (curves labeled with black open circles) along the line indicated in (b). (f) Comparison of the near-field and confocal spectroscopic mapping along the same line indicated in (b). The optical signals plotted here are derived from the PCBM PL intensities. (g) Near-field spectra collected at positions I, II, III, and IV as indicated in (b). The red curves are the fitting spectra. The inset figure shows the enlarged spectra from 1350 to 1550 cm^{-1}. Sample is thermally annealed at 140 °C for 30 min. Scan area is 1 × 0.75 μm. Laser power is 250 μW. Acquisition time is 0.5 s per spectrum. (Copyright (2010) by Wiley-VCH Verlag GmbH & Co. KGaA, Weinheim. Reprinted from [83].)

intensity from 283 to 2926 cm^{-1}, shows intense optical signals at the places where the island is located. Gradually decreasing optical intensity from the maximum height of the island to the flat area is clearly resolved. Figure 23.11c stacks 32 Raman spectra taken from a one-line near-field spectroscopic map (1 μm) along the arrow indicated in Figure 23.11b. Although the P3HT Raman peak at 1450 cm^{-1}, represented by the red line across Figure 23.11c, indicates the presence of P3HT molecules throughout this region, a clear optical signal evolution in the range from 1600 to 2600 cm^{-1}, corresponding to PCBM PL, is observed following the one-line scan. Figure 23.11c shows that from spectra No.7–12, PCBM tends to aggregate more and more severely as supported by the PCBM PL increase and the topographically obvious clustering. The full-width-at-half-maximum (FWHM) of the C=C stretching Raman peaks is broadened where the PL ratio of PCBM against P3HT is larger (Figure 23.11e). From spectra No.1–12, the PL ratio of PCBM against P3HT increases six times. Correspondingly, the FWHM of the P3HT C=C stretching Raman vibration peak increases by ~10 cm^{-1}, indicating that the increasing clustering of PCBM induces reduced crystallinity of the P3HT domain. The fine optical information given earlier cannot be revealed by the conventional far-field microscopy because of its resolution limitation (Figure 23.11f).

23.3.1.4 **Life Science**

To apply TERS to studying biological structures is of greatly interesting as a result of its high sensitivity, nanometer spatial resolution, and no need for complicated labeling [84]. Many biological molecules, such as DNA or RNA, have large cross sections and allow extremely sensitive detection, even down to single-molecule level. Domke *et al.* [85] have reported the distinctively different TER spectra of DNA bases (adenine, thymine, guanine, and cytosine) adsorbed on Au (111) crystal surface (Figure 23.12a). The pronounced near-field enhancement induced by the tip–Au crystal coupling realized the detection of even picomolar amount of adenine, which is ~400 molecules. Zhang *et al.* [86] have investigated the hydrogen bonding between adenine and thymine molecules using TERS. Hennemann *et al.* [87] has immobilized calf thymus DNA strands on a Au crystal surface. Using the top-illuminated parabolic mirror setup, the authors have reported the TERS spectra from a fraction of the DNA strands. A Raman enhancement factor of at least 1400 has been achieved when compared to the measurement without tip enhancement (Figure 23.12b).

Despite of its promising potential, the practical implementation of TERS in the biology field encounters several distinctive problems that may not appear in the solid-state physics. For example, a biological structure bearing its characteristic biological functions and compositions requires most often in its presence in a native biological environment. Therefore, to provide convincing analysis often needs to perform TERS measurements *in vivo*. Such sort of requirement is a great hindrance limiting the wide exploration of TERS in the biological field. (i) From the scanning probe microscopy point of view, the precise approaching of the TERS tip requires a stable feedback from the sample surface. Feedback via tunneling current is very much unlikely in the biological samples investigating with TERS as

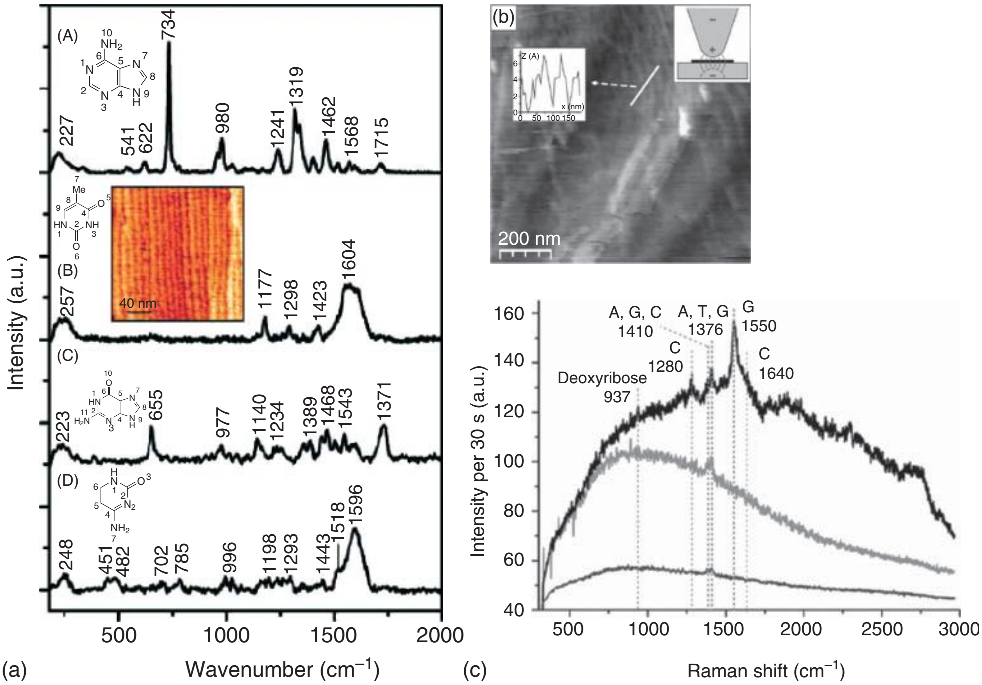

Figure 23.12 (a) TER spectra (background corrected) of DNA bases adsorbed at Au (111): (A) adenine, (B) thymine, (C) guanine, and (D) cytosine; normalized to 1 s integration time at 2 mW incident power. The inset shows an example STM image of a thymine self-assembled monolayer on Au (111) recorded after 12 h adsorption with a Au probe; tunneling current is 1 nA, bias is 150 mV, scan area as indicated. (b) TERS measurements of a (sub)monolayer of calf thymus DNA on a gold (111) crystal. (b) Shear force topographical image of the sample, including a line cut (inset graph). Sketched inset: illustration of producing a "hot spot" in the gap between a fine gold tip and the substrate. The + and − signs symbolize the dipole arising inside the tip induced via excitation with a radially polarized donut beam. The curved vertical streaks represent the electrical field lines connecting the tip and its mirror charge inside the gold crystal. (c) Three Raman spectra taken consecutively at one specific spot on the sample. From bottom to top: confocal far-field spectrum, acquisition time is 2 min but normalized to 30 s; spectrum with the tip close to the surface, acquisition time is 30 s; spectrum with the tip approached further to the surface, acquisition time is 30 s. A tentative assignment of some of the Raman bands was undertaken (A, adenosine; T, thymine; G, guanine; and C, cytosine). (632.8 nm He–Ne laser, laser power is 250 μW. (a) Copyright (2007) by the American Chemical Society. Reprinted from Ref. [85]. (b,c) Copyright (2010) by IOS press. Reprinted from [87].)

a result of the conductivity of the biological sample and the complicated influence of the applied bias voltage on the native function of the biological sample. To use force as the feedback has been proved to be rather successful as seeing from the popular application of AFM in biology. However, due to the fact that relative rigid sample surface is required to give a stable force feedback, only a limited number of nonmotile biological systems can be investigated. In addition, tremendous problems occur if we targets at molecules that are encapsulated in a closed compartment, such as a cell wall. The probing of such targets seems only possible if a sliced sample is used. (ii) From the spectroscopic point of view, the complex constitutions of the real biological samples produce large fluorescence background and complicated Raman fingerprints making the precise determination of one certain species extremely demanding. In addition, within the nanometer-sized TERS probing volume, the diffusion of biological compartment or molecules cannot be neglected, which could be one of the main reasons for producing great spectral fluctuation. The far-field interference in this case can also be overwhelming. (iii) From the biological point of view, biological systems are characterized by their complex structures and their vast amount of kinetic processes necessary for proper biological function. The TERS technique based on continuous wave excitation lacks time resolution; hence, could not provide a real picture of the kinetic biological processes. (iv) When using tip-enhanced fluorescence to investigate the biological samples, the possible photobleaching from the laser irradiation and the strongly confined near-field at the tip apex should be carefully taken into account. An effective alternative is tip-enhanced two-photon excitation fluorescence, which suffers much less from photobleaching, and does not require the removal of the far-field background signal. Si tips have been used recently for this purpose, despite having a lower enhancement, they cause less quenching and allow more excitation power.

Despite the earlier-mentioned difficulties, some research groups have successfully carried out TERS investigations of biological samples *in vitro*, such as DNA deposited on gold [87], tobacco mosaic virus on glass [88], lipid domain in supported lipid layer [89], histidine on silver substrate [90], and so on. These samples have the advantage of being nonmotile and being easy to deposit on a substrate.

Bailo *et al.* [29] have demonstrated experiments on a single-strand RNA homopolymer of cytosine (poly(C)) immobilized on mica and demonstrate the potential of single-base identification, for example, sequencing, when the tip is scanned along the strand. For their TERS measurement, RNA strands were attached to a mica surface via phosphate groups, by adding Mg^{2+} cations to the sample. Figure 23.13 shows the TERS measurements from seven locations along the RNA strand. The TER spectra were assigned to the fingerprint of cytosine with significant fluctuations in band intensities and slight shift of the band positions. The spectral intensity changes were likely related to the minuscule variation of the tip–sample distance. The shift of the band positions was suggested to be due to the molecular orientation differences in a fixed RNA strand with respect to the scanning tip. In addition, the polarization condition and the electromagnetic field distribution could also induce the spectral fluctuations. The authors proposed that this principle can be applied to the sequencing of peptides and proteins in a general manner [33, 91]. To further improve the TERS sensitivity when using a transmission setup, thin gold plates that are transparent for the visible light was recommended as the substrate for biomolecule immobilization [92].

One of the first successful TERS measurements of whole cells was conducted on the Gram-positive bacterium *Staphylococcus epidermidis* (*S. epidermidis*) [93].

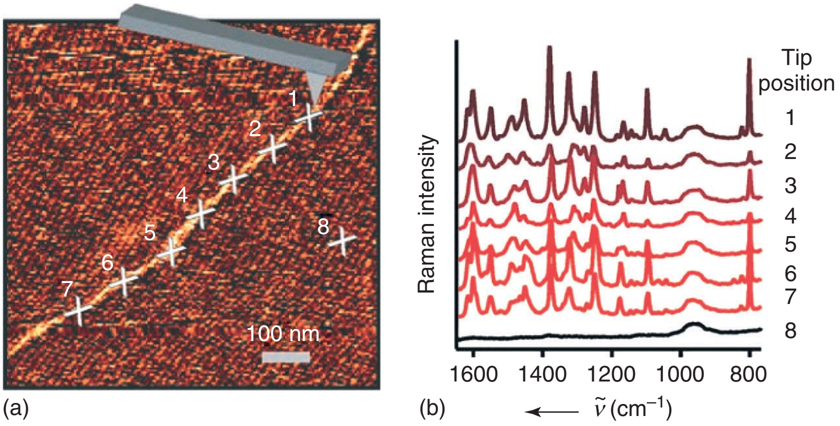

Figure 23.13 TERS experiment along an RNA strand. (a) Topography image showing seven adjacent spots corresponding to the positions of the TERS experiments and one additional spot for the reference measurement (position 8). (b) The Raman spectra of the positions in (a). (Copyright (2008) by the Royal Society of Chemistry. Reprinted from [29].)

This type of cell represents a wise choice for proof-of-concept, as it is nonmotile, reasonably stiff, phototolerant, and does not require an aqueous environment. Neugebauer *et al.* showed TER spectra for five individual cells, within each spectrum being averaged from 15 1 s acquisitions as a result of the significant tip enhancement achieved from an ultrasharp silver-coated AFM tip. The enhancement factor was calculated to be around 10^4–10^5. The majority of TERS peaks on the bacteria surface could be tentatively assigned to peptides, lipids, and carbohydrates abundant on the cell surface of bacteria.

The latest application of TERS in the samples besides cell surfaces [94], viruses, and isolated molecules were presented by Wood *et al.* [95] They have detected hemozoin crystals at <20 nm spatial resolution in the digestive vacuole of a sectioned malaria parasite-infected cell. The TER spectra show characteristic bands of hemozoin that can be correlated to a precise position on the crystal by comparison with the corresponding AFM image. They foresee that the combination of AFM/TERS paving a new way to independent drug screening modality for detection of drugs binding to the hemozoin surface within the digestive vacuole of the malaria trophozoite.

23.4
Conclusions

In the earlier sections, we have systematically explained the principle, the concept of design, the instrumentation, and the applications of SNGM. Benefiting from the near-field confinement in the gap of the tip antenna and the sample surface, SNGM achieves tight confinement of the optical field and high spectroscopic sensitivity from a nanometer-sized illuminated area. In addition, the sharp tip and the sample/substrate form an integrated unit in near-field optical microscopy. Therefore, the tip material, the tip–sample distance, and the substrate material are all key factors that need to be seriously taken into account in order to achieve an optimal performance. From the instrumentation point of view, designs such as side illumination and top illumination help to break the limitation concerning the transparency of the sample/substrate, which enables the application of high-resolution near-field optical microscopy in a variety of fields ranging from fundamental research to industrially oriented topics. Furthermore, the combination of optical microscopy and scanning probe microscopy in SNGM provides both optical and topography information correlated at the nanometer scale, which defines its extraordinary position compared with conventional optical microscopy. In summary, high-resolution SNGM is finding its way to a broad acceptance and application in the development of nanophotonics and nanotechnology.

References

1. Biagioni, P., Huang, J.S., and Hecht, B. (2012). Nanoantennas for visible and infrared radiation. *Rep. Prog. Phys.* **75**, 024402.
2. Albrecht, M.G., and Creighton, J.A. (1977). Anomalously intense Raman spectra of pyridine at a silver electrode. *J. Am. Chem. Soc.* **99**, 5215–5217.
3. Fleischmann, M., Hendra, P.J., and McQuillan, A.J. (1974). Raman spectra of pyridine adsorbed at a silver electrode. *Chem. Phys. Lett.* **26**, 163–166.
4. Jeanmaire, D.L., and Van Duyne, R.P. (1977). Surface raman spectroelectrochemistry: part I. Heterocyclic, aromatic, and aliphatic amines adsorbed on the anodized silver electrode. *J. Electroanal. Chem. Interfacial Electrochem.* **84**, 1–20.
5. Kneipp K., M. Moskovits, Kneipp H. (2006). *Surface-Enhanced Raman Scattering, Physics and Applications*, Heidelberg: Springer.
6. Kneipp, K., Wang, Y., Kneipp, H., Perelman, L.T., Itzkan, I., Dasari, R.R., and Feld, M.S. (1997). Single molecule detection using Surface-Enhanced Raman Scattering (SERS). *Phys. Rev. Lett.* **78**, 1667–1670.
7. Nie, S., and Emory, S.R. (1997). Probing single molecules and single nanoparticles by surface-enhanced Raman scattering. *Science* **275**, 1102–1106.
8. Sackrow, M., Stanciu, C., Lieb, M.A., and Meixner, A.J. (2008). Imaging nanometre-sized hot spots on smooth Au films with high-resolution tip-enhanced luminescence and Raman near-field optical microscopy. *ChemPhysChem* **9**, 316–320.
9. Demtröder, W. (1982). *Laser Spectroscopy* Heidelberg: Springer.
10. Drexhage, K.H. (1974).Interaction of light with monomolecular dye layers *Prog. Opt.* **12**, 163–232.
11. Blackie, E. (2010). *Quantification of the Enhancement Factor in Surface-Enhanced Raman Scattering* Victoria University of Wellington, Wellington.
12. Le Ru, E.C., Blackie, E., Meyer, M., and Etchegoin, P.G. (2007). Surface enhanced Raman scattering enhancement factors: a comprehensive study. *J. Phys. Chem. C* **111**, 13794–13803.
13. Le Ru, E.C., and Etchegoin, P.G. (2006). Rigorous justification of the E 4 enhancement factor in surface enhanced Raman spectroscopy. *Chem. Phys. Lett.* **423**, 63–66.
14. Moskovits, M. (1985). Surface-enhanced spectroscopy. *Rev. Mod. Phys.* **57**, 783–826.
15. Drachev, V.P., Chettiar, U.K., Kildishev, A.V., Yuan, H.-K., Cai, W., and Shalaev, V.M. (2008). The Ag dielectric function

in plasmonic metamaterials. *Opt. Express* **16**, 1186–1195.

16. Johnson, P.B., and Christy, R.W. (1972). Optical constants of the noble metals. *Phys. Rev. B* **6**, 4370–4379.

17. Marton, J.P., and Jordan, B.D. (1977). Optical properties of aggregated metal systems: interband transitions. *Phys. Rev. B* **15**, 1719–1727.

18. West, P.R., Ishii, S., Naik, G.V., Emani, N.K., Shalaev, V.M., and Boltasseva, A. (2010). Searching for better plasmonic materials. *Laser Photonics Rev.* **4**, 795–808.

19. Pettinger, B., Ren, B., Picardi, G., Schuster, R., and Ertl, G. (2004). Nanoscale probing of adsorbed species by tip-enhanced Raman spectroscopy. *Phys. Rev. Lett.* **92**, 096101.

20. Taguchi, A., Hayazawa, N., Furusawa, K., Ishitobi, H., and Kawata, S. (2009). Deep-UV tip-enhanced Raman scattering. *J. Raman Spectrosc.* **40**, 1324–1330.

21. Chan, G.H., Zhao, J., Hicks, E.M., Schatz, G.C., and Van Duyne, R.P. (2007). Plasmonic properties of copper nanoparticles fabricated by nanosphere lithography. *Nano Lett.* **7**, 1947–1952.

22. Downes, A., Salter, D., and Elfick, A. (2006). Finite element simulations of tip-enhanced Raman and fluorescence spectroscopy. *J. Phys. Chem. B* **110**, 6692–6698.

23. Hayazawa, N., Inouye, Y., Sekkat, Z., and Kawata, S. (2001). Near-field Raman scattering enhanced by a metallized tip. *Chem. Phys. Lett.* **335**, 369–374.

24. Farahani, J.N., Pohl, D.W., Eisler, H.J., and Hecht, B. (2005). Single quantum dot coupled to a scanning optical antenna: a tunable superemitter. *Phys. Rev. Lett.* **95**, 017402.

25. Kalkbrenner, T., Ramstein, M., Mlynek, J., and Sandoghdar, V. (2001). A single gold particle as a probe for apertureless scanning near-field optical microscopy. *J. Microsc.* **202**, 72–76.

26. Neacsu, C.C., Berweger, S., Olmon, R.L., Saraf, L.V., Ropers, C., and Raschke, M.B. (2010). Near-field localization in plasmonic superfocusing: a nanoemitter on a tip. *Nano Lett.* **10**, 592–596.

27. Ropers, C., Neacsu, C.C., Elsaesser, T., Albrecht, M., Raschke, M.B., and Lienau, C. (2007). Grating-coupling of surface plasmons onto metallic tips: a nanoconfined light source. *Nano Lett.* **7**, 2784–2788.

28. Ren, B., Picardi, G., and Pettinger, B. (2004). Preparation of gold tips suitable for tip-enhanced Raman spectroscopy and light emission by electrochemical etching. *Rev. Sci. Instrum.* **75**, 837–841.

29. Bailo, E., and Deckert, V. (2008). Tip-enhanced Raman spectroscopy of single RNA strands: towards a novel direct-sequencing method. *Angew. Chem. Int. Ed.* **47**, 1658–1661.

30. Hartschuh, A., Anderson, N., and Novotny, L. (2003). Near-field Raman spectroscopy using a sharp metal tip. *J. Microsc.* **210**, 234–240.

31. Hayazawa, N., Tarun, A., Inouye, Y., and Kawata, S. (2002). Near-field enhanced Raman spectroscopy using side illumination optics. *J. Appl. Phys.* **92**, 6983–6986.

32. Mehtani, D., Lee, N., Hartschuh, R.D., Kisliuk, A., Foster, M.D., Sokolov, A.P., and Maguire, J.F. (2005). Nano-Raman spectroscopy with side-illumination optics. *J. Raman Spectrosc.* **36**, 1068–1075.

33. Pettinger, B., Ren, B., Picardi, G., Schuster, R., and Ertl, G. (2005). Tip-enhanced Raman spectroscopy (TERS) of malachite green isothiocyanate at Au(111): bleaching behavior under the influence of high electromagnetic fields. *J. Raman Spectrosc.* **36**, 541–550.

34. Zhang, W., Yeo, B.S., Schmid, T., and Zenobi, R. (2007). Single molecule tip-enhanced Raman spectroscopy with silver tips. *J. Phys. Chem. C* **111**, 1733–1738.

35. Pettinger, B., Domke, K.F., Zhang, D., Picardi, G., and Schuster, R. (2009). Tip-enhanced Raman scattering: influence of the tip-surface geometry on optical resonance and enhancement. *Surf. Sci.* **603**, 1335–1341.

36. Hayazawa, N., Inouye, Y., Sekkat, Z., and Kawata, S. (2002). Near-field Raman imaging of organic molecules by an apertureless metallic probe scanning optical microscope. *J. Chem. Phys.* **117**, 1296–1301.

37. Stanciu, C., Sackrow, M., and Meixner, A.J. (2008). High NA particle- and tip-enhanced nanoscale Raman spectroscopy with a parabolic-mirror microscope. *J. Microsc.* **229**, 247–253.

38. Dorn, R., Quabis, S., and Leuchs, G. (2003). Sharper focus for a radially polarized light beam. *Phys. Rev. Lett.* **91**, 233901.
39. Quabis, S., Dorn, R., Eberler, M., Glöckl, O., and Leuchs, G. (2000). Focusing light to a tighter spot. *Opt. Commun.* **179**, 1–7.
40. Lieb, M., and Meixner, A. (2001). A high numerical aperture parabolic mirror as imaging device for confocal microscopy. *Opt. Express* **8**, 458–474.
41. Karrai, K., and Grober, R.D. (1995). Piezoelectric tip-sample distance control for near-field optical microscopes. *Appl. Phys. Lett.* **66**, 1842–1844.
42. Zhang, D., Wang, X., Braun, K., Egelhaaf, H.-J., Fleischer, M., Hennemann, L., Hintz, H., Stanciu, C., Brabec, C.J., Kern, D.P., *et al.*(2009). Parabolic mirror-assisted tip-enhanced spectroscopic imaging for non-transparent materials. *J. Raman Spectrosc.* **40**, 1371–1376.
43. Steidtner, J., and Pettinger, B. (2007). High-resolution microscope for tip-enhanced optical processes in ultrahigh vacuum. *Rev. Sci. Instrum.* **78**, 103104.
44. Steidtner, J., and Pettinger, B. (2008). Tip-enhanced Raman spectroscopy and microscopy on single dye molecules with 15 nm resolution. *Phys. Rev. Lett.* **100**, 236101.
45. Stadler, J., Stanciu, C., Stupperich, C., and Meixner, A.J. (2008). Tighter focusing with a parabolic mirror. *Opt. Lett.* **33**, 681–683.
46. Saito, R.D., G. Dresselhaus, M. S. Dresselhaus (1998). *Physical Properties of Carbon Nanotubes* London: Imperial College Press.
47. Dresselhaus, M.S., Dresselhaus, G., Saito, R., and Jorio, A. (2005). Raman spectroscopy of carbon nanotubes. *Phys. Rep.* **409**, 47–99.
48. Hartschuh, A., Pedrosa, H.N., Novotny, L., and Krauss, T.D. (2003). Simultaneous fluorescence and Raman scattering from single carbon nanotubes. *Science* **301**, 1354–1356.
49. Jorio, A., Saito, R., Hafner, J.H., Lieber, C.M., Hunter, M., McClure, T., Dresselhaus, G., and Dresselhaus, M.S. (2001). Structural (n, m) determination of isolated single-wall carbon nanotubes by resonant Raman scattering. *Phys. Rev. Lett.* **86**, 1118–1121.
50. Maultzsch, J., Reich, S., and Thomsen, C. (2001). Chirality-selective Raman scattering of the D mode in carbon nanotubes. *Phys. Rev. B* **64**, 121407.
51. Piscanec, S., Lazzeri, M., Robertson, J., Ferrari, A.C., and Mauri, F. (2007). Optical phonons in carbon nanotubes: Kohn anomalies, Peierls distortions, and dynamic effects. *Phys. Rev. B* **75**, 035427.
52. Peica, N., Thomsen, C., and Maultzsch, J. (2011). Studying the local character of Raman features of single-walled carbon nanotubes along a bundle using TERS. *Nanoscale Res. Lett.* **6**, 174.
53. Picardi, G., Chaigneau, M., and Ossikovski, R. (2009). High resolution probing of multi wall carbon nanotubes by tip enhanced Raman spectroscopy in gap-mode. *Chem. Phys. Lett.* **469**, 161–165.
54. Vannier, C., Yeo, B.S., Melanson, J., and Zenobi, R. (2006). Multifunctional microscope for far-field and tip-enhanced Raman spectroscopy. *Rev. Sci. Instrum.* **77**, 023104.
55. Hartschuh, A., Qian, H., Meixner, A.J., Anderson, N., and Novotny, L. (2005). Nanoscale optical imaging of excitons in single-walled carbon nanotubes. *Nano Lett.* **5**, 2310–2313.
56. Hartschuh, A., Sánchez, E.J., Xie, X.S., and Novotny, L. (2003). High-resolution near-field Raman microscopy of single-walled carbon nanotubes. *Phys. Rev. Lett.* **90**, 095503.
57. Snitka, V., Rodriguez, R.D., Lendraitis, V. (2011). Novel gold cantilever for nano-Raman spectroscopy of graphene *Microelectron. Eng.*. **88**, 2459.
58. Maciel, I.O., Anderson, N., Pimenta, M.A., Hartschuh, A., Qian, H., Terrones, M., Terrones, H., Campos-Delgado, J., Rao, A.M., Novotny, L., *et al.* (2008). Electron and phonon renormalization near charged defects in carbon nanotubes. *Nat. Mater.* **7**, 878–883.

59. Geim, A.K., and Novoselov, K.S. (2007). The rise of graphene. *Nat. Mater.* **6**, 183–191.

60. Dresselhaus, M.S., Jorio, A., Hofmann, M., Dresselhaus, G., and Saito, R. (2010). Perspectives on carbon nanotubes and graphene Raman spectroscopy. *Nano Lett.* **10**, 751–758.

61. Saito, Y., Verma, P., Masui, K., Inouye, Y., and Kawata, S. (2009). Nanoscale analysis of graphene layers by tip-enhanced near-field Raman spectroscopy. *J. Raman Spectrosc.* **40**, 1434–1440.

62. Le Thanh, V. (2001). New insight into the kinetics of Stranski–Krastanow growth of Ge on Si(001). *Surf. Sci.* **492**, 255–269.

63. Tarun, A., Hayazawa, N., and Kawata, S. (2009). Tip-enhanced Raman spectroscopy for nanoscale strain characterization. *Anal. Bioanal. Chem.* **394**, 1775–1785.

64. Welser, J., Hoyt, J.L., and Gibbons, J.F. (1994). Electron mobility enhancement in strained-Si n-type metal-oxide-semiconductor field-effect transistors. *IEEE Electron Device Lett.* **15**, 100–102.

65. Sun, Y., Thompson, S.E., and Nishida, T. (2007). Physics of strain effects in semiconductors and metal-oxide-semiconductor field-effect transistors. *J. Appl. Phys.* **101**, 104503.

66. Kolanek, K., Hermann, P., Dudek, P.T., Gotszalk, T., Chumakov, D., Weisheit, M., Hecker, M., and Zschech, E. (2010). Local anodic oxidation by atomic force microscopy for nano-Raman strain measurements on silicon–germanium thin films. *Thin Solid Films* **518**, 3267–3272.

67. Anastassakis, E.M. (1980). *Dynamical Properties of Solids*, Disordered Solids, Optical Properties, Vol. 4, North Holland, Amsterdam, pp. 157–375.

68. Nakashima, S., Mitani, T., Ninomiya, M., and Matsumoto, K. (2006). Raman investigation of strain in Si/SiGe heterostructures: precise determination of the strain-shift coefficient of Si bands. *J. Appl. Phys.* **99**, 053512–053517.

69. De Wolf, I. (1996). Micro-Raman spectroscopy to study local mechanical stress in silicon integrated circuits. *Semicond. Sci. Technol.* **11**, 139.

70. Ogawa, Y., Toizumi, T., Minami, F., and Baranov, A.V. (2011). Nanometer-scale mapping of the strain and Ge content of Ge/Si quantum dots using enhanced Raman scattering by the tip of an atomic force microscope. *Phys. Rev. B* **83**, 081302.

71. Hanafusa H., Hirose. N., Kasamatsu A., Mimura T., Matsui T., Chong H. M. H., Mizuta H. and Suda Y. (2011). Strain distribution analysis of sputter-formed strained Si by tip-enhanced Raman spectroscopy. *Appl. Phys. Exp.* **4**, 025701.

72. Holtz, M., Duncan, W.M., Zollner, S., and Liu, R. (2000). Visible and ultraviolet Raman scattering studies of Si1-xGex alloys. *J. Appl. Phys.* **88**, 2523–2528.

73. Poborchii, V., Tada, T., Kanayama, T., and Geshev, P. (2009). Optimization of tip material and shape for near-UV TERS in Si structures. *J. Raman Spectrosc.* **40**, 1377–1385.

74. Lee, N., Hartschuh, R.D., Mehtani, D., Kisliuk, A., Maguire, J.F., Green, M., Foster, M.D., and Sokolov, A.P. (2007). High contrast scanning nano-Raman spectroscopy of silicon. *J. Raman Spectrosc.* **38**, 789–796.

75. Motohashi, M., Hayazawa, N., Tarun, A., and Kawata, S. (2008). Depolarization effect in reflection-mode tip-enhanced Raman scattering for Raman active crystals. *J. Appl. Phys.* **103**, 034309.

76. Poborchii V., T. Tada, and Kanayama.T. (2005). Subwavelength-resolution Raman microscopy of Si structures using metal-particle-topped AFM probe. *Jpn. J. Appl. Phys.* **44**, L202–204.

77. Ossikovski, R., Nguyen, Q., and Picardi, G. (2007). Simple model for the polarization effects in tip-enhanced Raman spectroscopy. *Phys. Rev. B* **75**, 045412.

78. Picardi, G., Nguyen, Q., Ossikovski, R., and Schreiber, J. (2007). Polarization properties of oblique incidence scanning tunneling microscopy tip-enhanced Raman spectroscopy. *Appl. Spectrosc.* **61**, 1301–1305.

79. Schreiber, F. (2004). Organic molecular beam deposition: growth studies beyond the first monolayer. *Phys. Status Solidi A* **201**, 1037–1054.

80. Zhang, D., Heinemeyer, U., Stanciu, C., Sackrow, M., Braun, K., Hennemann, L.E., Wang, X., Scholz, R., Schreiber, F., and Meixner, A.J. (2010). Nanoscale spectroscopic imaging of organic semiconductor films by plasmon-polariton coupling. *Phys. Rev. Lett.* **104**, 056601.

81. Hoppe, H., Niggemann, M., Winder, C., Kraut, J., Hiesgen, R., Hinsch, A., Meissner, D., and Sariciftci, N.S. (2004). Nanoscale morphology of conjugated polymer/fullerene-based bulk- heterojunction solar cells. *Adv. Funct. Mater.* **14**, 1005–1011.

82. Thompson, B.C., and Fréchet, J.M.J. (2008). Polymer–fullerene composite solar cells. *Angew. Chem. Int. Ed.* **47**, 58–77.

83. Wang, X., Zhang, D., Braun, K., Egelhaaf, H.J., Brabec, C.J., and Meixner, A.J. (2010). High-resolution spectroscopic mapping of the chemical contrast from nanometer domains in P3HT:PCBM organic blend films for solar-cell applications. *Adv. Funct. Mater.* **20**, 492–499.

84. Elfick, A., Downes, A., and Mouras, R. (2010). Development of tip-enhanced optical spectroscopy for biological applications: a review. *Anal. Bioanal. Chem.* **396**, 45–52.

85. Domke, K.F., Zhang, D., and Pettinger, B. (2007). Tip-enhanced Raman spectra of picomole quantities of DNA nucleobases at Au(111). *J. Am. Chem. Soc.* **129**, 6708–6709.

86. Zhang, D., Domke, K.F., and Pettinger, B. (2010). Tip-enhanced Raman spectroscopic studies of the hydrogen bonding between adenine and thymine adsorbed on Au (111). *ChemPhysChem* **11**, 1662–1665.

87. Hennemann, L.E., Meixner, A.J., and Zhang, D. (2010). Surface- and tip-enhanced Raman spectroscopy of DNA. *Int. J. Spectrosc.* **24**, 119–124.

88. Cialla, D., Deckert-Gaudig, T., Budich, C., Laue, M., Möller, R., Naumann, D., Deckert, V., and Popp, J. (2009). Raman to the limit: tip-enhanced Raman spectroscopic investigations of a single tobacco mosaic virus. *J. Raman Spectrosc.* **40**, 240–243.

89. Opilik, L., Bauer, T., Schmid, T., Stadler, J., and Zenobi, R. (2011). Nanoscale chemical imaging of segregated lipid domains using tip-enhanced Raman spectroscopy. *Phys. Chem. Chem. Phys.* **13**, 9978–9981.

90. Deckert-Gaudig, T., and Deckert, V. (2009). Tip-enhanced Raman scattering studies of histidine on novel silver substrates. *J. Raman Spectrosc.* **40**, 1446–1451.

91. Rasmussen, A., and Deckert, V. (2006). Surface- and tip-enhanced Raman scattering of DNA components. *J. Raman Spectrosc.* **37**, 311–317.

92. Deckert-Gaudig, T., and Deckert, V. (2009). Ultraflat transparent gold nanoplates—ideal substrates for tip-enhanced Raman scattering experiments. *Small* **5**, 432–436.

93. Neugebauer, U., Schmid, U., Baumann, K., Ziebuhr, W., Kozitskaya, S., Deckert, V., Schmitt, M., and Popp, J. (2007). Towards a detailed understanding of bacterial metabolism—spectroscopic characterization of staphylococcus epidermidis. *ChemPhysChem* **8**, 124–137.

94. Richter, M., Hedegaard, M., Deckert-Gaudig, T., Lampen, P., and Deckert, V. (2011). Laterally resolved and direct spectroscopic evidence of nanometer-sized lipid and protein domains on a single cell. *Small* **7**, 209–214.

95. Wood, B.R., Bailo, E., Khiavi, M.A., Tilley, L., Deed, S., Deckert-Gaudig, T., McNaughton, D., and Deckert, V. (2011). Tip-Enhanced Raman Scattering (TERS) from hemozoin crystals within a sectioned erythrocyte. *Nano Lett.* **11**, 1868–1873.

Section VIII
Applications 1: Bioanalysis

Handbook of Spectroscopy, Second Edition. Edited by Günter Gauglitz and David S. Moore.

24
Trends in Bioanalytical Spectroscopy

Willem M. Albers

24.1
Introduction

In the new millennium, many new breakthrough technologies in the field of bioanalysis have emerged, spurred, among others, by the efforts in microsystems and biosensor development in the United States, Japan, and Europe from the 1990s onward. For instance, two microarray platforms for bioanalysis with optical detection have recently been commercialized [1, 2], and various lab-on-a-chip systems for bioanalysis have also appeared on the market, although they still have to show their ultimate potential [3]. The general trend is to combine bioanalytical devices increasingly with nanotechnology, because of the nanomolecular scale of the analytes themselves [4]. In the near future, miniature bioanalytical systems for self-monitoring will likely become portable and, for instance, easy to linkup with mobile phones or other mobile devices. At the other end, in the area of laboratory medicine, highly automated facilities have been developed that reduce hand labor. A recent example of this kind is the DNA analysis facility for forensic analysis that was installed in Pretoria by Tecan AG, as an initiative of the European Union, to reduce the crime rates in South Africa [5]. The major bioanalysis application fields are forensic analysis, food analysis, environmental analysis, and clinical diagnostics, while the field of *biodefence* has also received increased attention. Although the main focus of this chapter is on clinical diagnostics, some of the trends and prospects of the others will also be indicated.

In the realm of biosensor technology, there has been a steady pace of development and commercialization since 1990. In the European Union especially, there have been many European Commission-funded programs that modify and integrate biosensors, and various novel prototype devices have been constructed. The results of most of these programs can be found in the journals *Biosensors and Bioelectronics* [6] and *Sensors and Actuators B* [7]. Besides new approaches, the more conventional techniques of evanescent wave-based methods, particularly surface plasmon resonance (SPR), have steadily matured. The theory and applications of SPR have been covered in a handbook and various reviews [8–12], and more than 20 commercial vendors have emerged during the last 10 years.

Handbook of Spectroscopy, Second Edition. Edited by Günter Gauglitz and David S. Moore.

Particularly in the context of *omic* methods of bioanalysis, optical methods, and biosensor array systems hold new, exciting possibilities, although in many cases the new concepts still need to ripen, and the techniques further polished, such that they can become useful for the common user, or in the application laboratories. Although in the majority of cases, novel bioanalytical methods are still based on conventional sample handling, separation, and detection techniques, certain basic skills and know-how will always be required. The increase of technological possibilities, however, has given rise to a new bottleneck in this respect: novel technologies call for novel skills, and the training of skilled personnel does not always proceed in pace with the rates of development of new equipment [13]. For instance, the ‘‘Flexchip’’ SPR protein array system for functional proteomics research, originally developed by HTS Biosystems, and later marketed by Biacore, may have the power of simultaneous real-time measurement of up to 400 molecular interactions, but the attachment of a large collection of receptors on the surface is still a far from trivial matter. At present, the Flexchip system is no longer available, because of lack of demand. Thus, in many cases, it may prove useful to downscale the instrumentation such that it is more compatible with the size of the problem. Another persistent problem, particularly with designing assays for protein analytes, is that many novel detection methodologies reported in the technical literature have not been assessed in realistic matrices, such as serum or urine [14]. Therefore, this chapter will also briefly discuss some of the demands that are required of diagnostic tests.

24.2
Recent Progress in Holistic Methods of Bioanalysis

The mapping and functional analysis of all substances present in the human body, ranging from inorganic compounds and small organic compounds to large biopolymers (carbohydrates, proteins, and nucleic acids) has always been of primary concern in medicine, both for diagnosis and therapy, but at present is a driving force behind *theranostics* and *personalized medicine*. The main idea of comprehensive *omic* technologies – such as *genomics* and *proteomics* – is to come closer to a holistic understanding of biological processes, starting from the gene sequence, and through this improve our concept of medicine in practice, in which we identify more and more the underlying *causes* of disease instead of merely fighting *symptoms*. This paragraph pertains to give only a brief outline of the methodologies that have lately appeared. The *-ome* suffix likely has its origin in the word *Biome*, coined in 1916 to refer to an ecological community of organisms in a confined environment. *Biomes* were defined as: *the world's major communities, classified according to the predominant vegetation and characterized by adaptations of organisms to that particular environment* [15]. Biomes have changed and moved continuously during the history of life on our planet, and it is evident that human activities have drastically altered it in the last century.

In many cases, the prefix *functional* can be added to the basic *omic* term to imply the mapping of function of the components, such as *functional genomics* to map the function of genes [16, 17], and *functional proteomics*, to map the functions of proteins [18, 19]. With respect to the knowledge of the functions of genes, the situation has long been in an infant stage, as the functions of the majority of the human genes are not yet fully understood after sequencing of the human genome. Initially, the scientific community has irreverently referred to >95% of the genome as *Junk* DNA, but this picture is now changing [20]. Especially, the ENCODE consortium, founded in 2003, has set the goals to identify all functional elements in the human genome sequence, and the first pilot results, covering 1% of the human genome, were recently published in *Nature* in 2007 [21]. The most relevant *omic* technologies are summarized in Table 24.1, with references to the important internet sites for compiled databases or important projects. The annotated proteomic databases have been setup in 1990s, and they have been continuously expanded, while new ones have been added. All these databases will likely have a large impact on diagnostic and therapeutic product development and biomarker and drug discovery in the near future.

Drug discovery is mainly concerned with screening of small organic compounds against a range of receptors relevant in disease control, but screening of peptides, either produced by organisms or by combinatorial chemistry methods, has also become an important area of focus. Completely new approaches for screening very large numbers of biochemicals have been devised [22]. In *Pharmacogenomics*, the main purpose is to map the influence of genetic variation on drug response in patients by correlating gene expression or single-nucleotide polymorphisms with a drug's efficacy or toxicity. This would pave the way for a rational means to optimize drug therapy and arrive at some form of *personalized medicine*, in which drugs and drug combinations are optimized for each individual's unique genetic constitution [23].

The field of *genomics* is at present the most extensive. Valuable results have sprouted from the human genome project and these have spurred the development of novel, advanced tools for replication, sequencing, and analysis of nucleic acids. As a logical consequence of the advances in genomics, the *proteomics* field appeared in tow [24–27]. Both genomics and proteomics rely heavily on gel electrophoresis (GE), capillary electrophoresis (CE), and capillary array electrophoresis (CAE) [28, 29].

From a spectroscopic point of view, the most interesting methods for detection of nucleic acids still lie in fluorescence detection in the visible and near-infrared (vis–NIR) region (400–1100 nm) [30]. The most important techniques are laser-induced fluorescence (LIF) and fluorescence *in situ* hybridization (FISH), while upconverting phosphor particles (UPTs) have also been used as highly effective labels for laser detection with very low background [31]. FISH comprises many variants for probing DNA sequences for diagnostic purposes [32] and is particularly suited for lab-on-a-chip devices [33], while LIF is still much used in sequencing technologies. The UPTs, however, have been used in very sensitive nucleic acid assays in a lab-on-chip format, technology that has been recently commercialized and clearly points in the direction of future POC devices (point-of-care) for bioanalysis.

Table 24.1 Established omic methodologies and their main databases on the internet.

Name	Scope	On-line databases	Other sites (projects)
Genome	The sum total of an organism's genes at the DNA level (genotype)	NCBI/Entrez (OMIM and others) *http://www.ncbi.nlm.nih.gov/sites/gquery* Ensembl: *http://www.ensembl.org/*	Functional genomics initiative ENCODE: *www.genome.gov/10005107* and *http://genome.ucsc.edu/ENCODE/*
Proteome	Characterization of all proteins of an organism	UniProt: *http://www.uniprot.org/* (PDB) *http://www.pdb.org/*	*http://www.eupa.org/*
Transcriptome	The mRNA complement of an entire organism, tissue type, or cell	Genevestigator: *https://www.genevestigator.ethz.ch*	—
Metabolome	The collection of all metabolites in a biological organism, which are the end products of its gene expression	*http://www.hmdb.ca/* *http://www.husermet.org/70.php* *http://www.bmrb.wisc.edu/metabolomics/* *http://mmcd.nmrfam.wisc.edu/*	*http://www.metabolomics.ca/* *http://www.husermet.org/*
Lipidome	Large-scale study of non-water-soluble metabolites	*http://www.lipidmaps.org/* *http://lipidbank.jp/*	*http://www.lipidomics.net/*
Glycome	Entire collection of carbohydrates of an organism	Not yet established (2008)	Various small projects
Epigenome	A whole-genome approach to map environmental or developmental epigenetic effects on gene function	*www.epigenome.org*	*http://epigenome.eu/en/4,11,0* *http://www.epitron.eu* *http://www.gen-au.at*

The mapping of functions of genes relies heavily on *expression mapping* by DNA microarray technology [34]. This technology is based on fluorescent labels and utilizes a large number of DNA probes immobilized on glass slides by a photolithographic, combinatorial technique. For instance, the field of *transcriptomics* – which attempts to map the total messenger RNA expressed in a cell or tissue at a given point of time – makes extensive use of the gene chip technology.

Apart from fluorescence detection, mass spectroscopic methods have gained momentum in various genomics and proteomics methodologies [35–37], particularly, in *lipidomics* [38, 39]. The mass spectroscopic methods invariably make use of novel time-of-flight (TOF) or quadruple time-of-flight (Q-TOF) systems coupled to high-performance liquid chromatography/mass spectrometry (LC/MS), usually through electrospray ionization techniques (ESI) or via spotting on plates and subsequent matrix assisted laser desorption ionization time-of-flight (MALDI-TOF) analysis. In addition, chromatography coupled to tandem mass spectroscopy is more and more applied to the determination of whole panels of small metabolites, for example, in the field of lipidomics [40] and in endocrinology [41]. In addition to mass spectroscopy, NMR spectroscopy has become important, for example, in the field of *metabolomics* [42, 43].

Much effort has been put recently in *functional proteomics*, which attempts to map specific functions of proteins. This field is evolving fast, and various novel tools have been introduced for the study of protein–protein interactions, quantification, and comparisons of protein expression [44]. Array biosensor systems, particularly, are considered attractive in this field, although their use is still not common owing to the problem of routinely constructing large protein arrays [45].

Maybe the most significant activity in the last five years has been the search for new biomarkers by hyphenated methods, in which mass spectroscopy is coupled to other separation/detection techniques, such as microfluidic devices, solid-phase extraction, chromatography, or electrophoresis [46]. In this area, surface-enhanced laser desorption ionization (SELDI)-TOF has emerged as a popular, high-throughput tool, in which the proteins are fractionated by adsorption onto surfaces with different functionalities [47–49]. The method, however, suffers from the disadvantages that certain proteins can be missed [50], and that, for routine clinical practice, the reproducibility still needs to be improved [51]. Although analytical methods, particularly when coupled to database search capabilities, have the potential of speeding up the process of biomarker discovery, it should be realized that this is only the first step in a longer chain that includes prioritization, sample preparation, validation, marker development, and final product development. Sample preparation seems to be already a critical stumbling block in this process [52].

In the realm of bioanalytical sciences, antibody technology has kept its firm position as a tool for molecular recognition. Moreover, the *hybridoma* technique has still kept its prominent place. It is based on a sequence of (i) immunization and expression of antibodies in mice, (ii) selection of cell lines from the spleen that produce the appropriate antibody, and (iii) their fusion to cancerous myeloma cells to give a good yield of highly specific, high-affinity antibodies in cell culture. With this technique, antibodies can be produced with sufficiently high affinity and selectivity to tackle the most difficult problems of protein analysis. The recently introduced *immunoproteomics* field, which is concerned with the characterization of all proteins with ligand recognition capabilities, may yield interesting new possibilities in this area [53]. However, standard immunization approaches sometimes fail to give monoclonal antibodies with the desired specificity. Recently, *subtractive immunization* has been used for the production of monoclonal antibodies, which are otherwise unobtainable, by targeting specific epitopes within the proteome. This has given rise to the field of *epitomics* [54]. The adaptive immune system has acquired a large store of recognition DNA sequences, which are generated from peptides of microbial pathogens. This process takes place via the major histocompatibility complex (MHC). The MHC is a large collection of proteins that keep up a cycle of antigen recognition, processing, and representation to effector cells of the adaptive immune system (B and T cells). Changes in the profile of the signaling peptides give rise to an alert to the effector cells. The changes may be related to infection, but also to malignant transformations or anomalous cellular processes. This gives a cascade of microbiological reactions that ultimately results in the elimination of the affected cells, and generates an immunological memory.

For comprehensive characterization of bioactive peptides, the field of *peptidomics* has been recently introduced [55, 56]. Peptidomics aims to construct databases of all peptides that exist in a tissue or body and the changes in their expression. Already highly sensitive techniques for the separation and sequence determination of peptides with very low abundance have been devised, enabling the screening of peptides that could earlier not be easily identified [57]. For instance, a peptidomic approach has recently been applied to the identification of specific peptides with a role in cardiac failure [58].

The field of *metabolomics* is directed to characterization of all low-molecular-weight metabolites in an organism. Recently, a Canadian consortium of scientists compiled a preliminary draft of the human metabolome, in which some 2500 metabolites, 1200 drugs, and 3500 food components were listed that could be identified in the human body [59]. *Lipidomics*, a related field, is also rapidly expanding, and is concerned with multiple techniques to characterize hundreds of chemically distinct lipids in cells and determine the molecular mechanisms through which they facilitate cellular function. Recent developments in ESI-MS have enabled the precise identification and quantification of alterations in a cell's lipidome after cellular perturbations [60]. Within the collection of low-molecular-weight compounds with biological function, ions also play a key role, and the term *ionome* was recently introduced to include all the mineral nutrient and trace elements found in an organism [61]. A subset of the ionome, the *metallome*, has also been proposed to designate all the metal ions in an organism [62, 63].

Phosphorylation – by protein kinases – takes place in all fundamental cellular processes, and is a major signaling mechanism in eukaryotic cells. Nearly every property of a protein is regulated by phosphorylation. Thus, characterization of all protein kinases is an important task, and for this purpose the *kinome* has been introduced, which is the *kinase complement of the human genome* [64]. At present, the methodology only provides a starting point. For understanding the scale of the problem, it should be realized that the kinome consists of ''only'' 518 kinases, but each kinase phosphorylates a distinct collection of substrates in a regulated manner. Approximately one-third of all intracellular proteins are phosphorylated and this may give rise to as many as 20 000 states of phosphorylation.

The field of *epigenomics* had already been proposed in 1999 [65] and, at present, *epigenetics* is a particularly hot topic [66, 67], having its origin in the gene regulation theories of Waddington, who proposed the terms *epigenotype* and *epigenomic* *landscape* in 1939 to describe developmental processes of gene expression that were above, or in addition to, the classical genotype [68]. The primary subfield of epigenomics now is *methylomics*, a term coined in 2001 by Feinberg, concerned with the characterization of methylation patterns on the CpG sites of the genome [69]. The bioanalytical methods used to detect genome-wide methylations are very similar to those for normal DNA analysis, and make extensive use of bisulfite modification of methylated DNA [70].

To conclude the conspicuous list of *omes*, the *bibliome* should not be missed out: the bibliome pertains to data mining of the scientific literature, and novel ways of classifying and sorting scientific results. Indeed, new computing tools are needed to effectively scan the growing amount of scientific literature for useful information [71]. In fact, with the growth of the genomic/proteomic databases, such as (Online Mendelian Inheritance in Man), and various new developments in bioinformatics, this is already slowly materializing for the life science sector, and may serve as a good example for other, more technical sciences. At least the *Chemical Abstracts Service* has already come closer to the ideal of the bibliome by providing a new, intelligent search facility: *SciFinder* [72].

24.3
The Road to Personalized Medicine

Clinical research is at present strongly focused on the use of new devices and analysis platforms for future personalized medicine and theranostic approaches to medical treatment. Key roles in this development have initially been those of biosensor research and new nanotechnological innovations, such as microfluidics. These were combined into new lab-on-chip devices, which started to flourish strongly in 1990s [73]. At present, there are many successful commercial lab-on-chip type analyzers on the market. The first ones were the *Affymetrix GeneChip®* systems [74], based on photolithographically produced high-density DNA arrays. At present, Invitrogen has commercialized various high-density protein arrays (*ProtoArray®*) [75]. Furthermore, microfluidic electrophoresis-based devices have been introduced by Agilent, the *Agilent 2100 Bioanalyzer*, which is used for DNA, RNA, protein, and cell analysis on a single platform [76].

The first key enabling technology toward personalized medicine comprised that of biosensors. According to the definition, biosensors are devices that utilize a biomolecule for the determination of an analyte by intimate coupling of the biomolecule to a suitable detection device. Although biosensors can be based on electrochemical, piezoelectric or calorimetric principles, many biosensor types are based on optical phenomena and can therefore be placed in a spectroscopic context [77–81], such as fiber-optic biosensors based on novel molecular probes [82, 83]. Unfortunately, conventional *molecular probes* or *indicators* are repeatedly designated as sensors, even when they are applied *in vivo* as biosensors. In addition, the more recent term *colorimetric sensor arrays* has been used for indicator arrays, which are also not real sensors, but merely indicator strips, albeit more versatile ones. This misuse of terminology has given rise to a small dilemma when classifying the literature properly for reviewing. According to the IUPAC definition, a biosensor is a device that uses specific biochemical reactions mediated by isolated enzymes, immunosystems, tissues, organelles, or whole cells to detect chemical compounds usually by electrical, thermal, or optical signals [84]. A more recent definition states that ''*a chemical sensor is a device that transforms chemical information, ranging from the concentration of a specific sample component to total composition analysis, into an analytically useful signal. Chemical sensors usually contain two basic components connected in series: a chemical (molecular) recognition system (receptor) and a physicochemical transducer. Biosensors are chemical sensors in which the recognition system utilizes a biochemical mechanism*'' [85]. Some additional requirements, however, were also introduced in the latter IUPAC definition: (i) a biosensor should use a compound of biological origin as the sensing element, (ii) biosensors should be ''*self-contained, all parts being packaged together in the same unit, usually small, the biological recognition element being in direct spatial contact with the transducing element*,'' and (iii) biosensors should be clearly distinguished from an analytical system, which uses additional separation steps and sample processing, such as reagent addition. Thus, ideally a biosensor should work, for instance, as a pH meter, providing a real-time readout of the concentration of an analyte in its natural environment and follow the changes in concentrations reversibly without the need for flow cells or other devices for liquid handling. This ideal has been realized to date only for very few catalytic sensors (e.g., based on enzymatic action). For affinity biosensors, however, the term *single-use biosensor* or *dosimeter* would be more appropriate. Some have allowed a slightly broader definition of a biosensor as a device that provides a quick readout of the concentration of an analyte without the need for adding reagents [86]. This would mean, however, that affinity-based assays in which a regeneration step is included to enable multiple use of the sensor, as is the case with some immunoassay systems, may not be called *biosensors*. However, it is difficult to find equipment in the clinical laboratory that does not do any sample handling, because of the great amount of samples that need to be processed. Furthermore, the samples all need to be ''sensed'' under standardized conditions, meaning that at least a measurement medium (matrix) will need to be added, as is the case for all clinical samples, which are collected in standardized vacuum tubes with appropriate collection media. In the light of a vast number of new publications in the area of biosensors, more appropriate definitions might still be formulated.

Biosensors can be generally divided into catalytic and affinity biosensors, the former making use of enzymes and the latter of antibodies and various types of receptors. Immunoassay fits particularly well in the realm of spectroscopy, because the majority of immunoassay techniques are based on colorimetric enzyme-linked immunosorbent assay (ELISA), fluorescent [fluoroimmunoassay (FIA), fluorescence resonance energy transfer (FRET)], or electrochemiluminescent labeling techniques, sometimes enhanced by evanescent wave phenomena at surfaces. However, novel, sensitive, nonoptical detection methodologies are also gaining ground, such as methods based on as magnetic labels, and these are already forming a strong competition [87].

The first (real) biosensor system was commercialized in the early 1970s by Yellow Springs Instrument Co. (YSI) and was used for the determination of glucose in blood, urine, and bioprocesses. In 1980s, relatively little commercial activity was observed, but new sensor types were developed at a rapid pace in many research laboratories. There were many successful demonstrations of biosensors based on electrochemical, optical, microcalorimetric, and piezoelectric transducers, and an amperometric biosensor based on ferrocene mediators for glucose determination was soon commercialized [88].

In the 1990s, a number of new sensor technologies moved successfully from the research laboratory into the market place, and the amount of commercial biosensor systems for bioanalytical applications has been constantly growing thereafter. At present, biosensor technology is a mature research field that is yielding many new commercial applications in the form of rapid test devices and larger laboratory instruments. Today, biosensing instruments have application potential in diagnostics, functional proteomics, environmental monitoring, drug discovery, process industry, and food analysis [89].

Advances in optical biosensors have contributed significantly to the speed of bioanalysis by supplying real-time monitoring of biological binding reactions, without the need for labeling of biomolecules (real-time bio-interaction analysis or BIA). Optical sensor platforms have traditionally been used in a number of proteomics subfields, such as antibody screening and epitope mapping, or in drug discovery [90, 91]. For instance, the new Octet® sensor, which has been recently introduced on the market, is able to follow protein reactions through the use of eight parallel disposable sensors applicable directly in microtiter plates [92]. SPR, however, has still kept its leading position. With SPR, very small refractive index changes close to a metal surface can be detected, and this technique has flourished over the last 20 years [93–96]. The use of the SPR technology in clinical diagnostics, however, is not yet firmly established, mainly because of the fact that direct detection of low-molecular-weight compounds or detection below nanomolar concentrations has serious limitations [97]. However, the use of amplified SPR techniques have recently shown great potential, in which the SPR signal has been enhanced with nanoparticles (latex or gold labels) [98, 99].

Although optical biosensor research efforts have contributed much to the development of the large analysis platforms for DNA and protein analysis that will find their place in the realization of theranostics and personalized medicine in the near future, still there are serious technological, educational, economical, and legislative hurdles to be overcome before personalized medicine can be adopted in the wide sense as it has come to be understood in the last 10 years [100–103]. However advanced the technology may become, the more conventional clinical diagnostic practices should not be or lost out of sight and some pertinent issues related to this subject are further summarized in the following.

24.4
Clinical Diagnostics

24.4.1
Introduction

Clinical diagnostics is generally concerned with the determination of biochemical substances for a variety of purposes. This can be

1) *screening*–the early detection of disease in a segment of the population;
2) *clinical diagnosis*–confirmation or rejection of a disease;
3) *monitoring*–in which the history of a disease or response to treatment is followed in time; and
4) *prognosis*–which assesses the outcome of a disease or treatment.

Clearly, all these types of diagnostic measures place their own specific demands on the test. Screening tests generally need to be cheap and fast. For instance, the screening test for phenylketonurea (PKU) in newborn babies is – in most test kits – still based on a *fluorometric* test designed in 1962, utilizing the formation of a fluorescent product of phenylalanine by reaction with copper and Ninhydrin [104]. The modern version of this test is a mere adaptation to microtiter plate format [105]. Screening tests generally need to have a large sensitivity, such that positives are not missed. Follow-up testing is generally used to verify the positive cases, and diagnose the illness further. In case of PKU, the follow-up testing generally means a genetic test to determine the severity of the disease [106]. For clinical diagnosis, however, the testing needs to be more precise. The occurrence of false positive or false negative results has to be minimized as much as possible (Section 24.4.2). Monitoring of a disease state requires the possibility to do either continuous measurements (biosensors are ideally suited for this) or to easily provide for repeated measurements (such as with blood glucose monitoring for diabetics).

In diagnostics, yet another division can be made into three types, depending on the *closeness* of the test to the patient:

1) Over-the-counter (OTC) tests, which are sold to the common user, such as pregnancy and glucose test devices, and which need to be economically priced. The result should also be simple (generally a *yes* or *no*), and produce no ambiguity to the end user.
2) POC devices, which are used near the patient in health centers, doctor's offices, and also in hospitals, for instance near the emergency unit. These instruments should present a more reliable quantitative result and can be more expensive.
3) *Centralized* (*hospital*) *testing* by dedicated instruments that are routinely used to test a large amount of substances with great reliability. The price of these instruments is generally very high, but the price per sample can be low, owing to high throughput. The main issue is reliable measurement and validation at various levels.

For the larger part, diagnostic tests are based on immunological reactions, in which antibodies are used for the selective binding of the analyte (immunoassay).

The two most common formats of immunoassay are briefly explained in Figure 24.1. In the field of research and development of POC devices by small, pioneering firms, the goal is generally to design instruments that are capable of reliable quantitative testing, but are at the same time affordable to the smaller health centers or at home. For devices based on immunological reactions, this forces the multistep procedure to be simplified, for example, by fluid handling in a microfluidic device. The main driving force behind POC diagnostics is the increasing interest of the public for self-monitoring and the demand for quantitative results. The term *worried well* has often been coined, to describe an increasing segment of the population that is *well off*, but *worried* about their health condition, and this is seen as a new opportunity for small instrument producers. Even then, interpretation and validation of the test result by physicians is needed in most cases, and this may be an inhibiting factor for many types of home testing devices. The major challenge, at present, is to extend the applicability of POC devices to molecular diagnostics, that is, DNA detection or DNA sensing.

To conclude, with regard to methods for collecting samples, it is fortunate that nowadays samples are taken in a standardized manner, which is particularly the case for blood sampling (venipuncture or *phlebotomy*), where the use of vacuum tubes has greatly reduced the risk of infection and increased reproducibility of the determinations. When the test includes a part that will be come in contact with the patient sample, however, that part always needs to be disposable. Sometimes, it is important that tests are adapted to a specific format (e.g., microtiter plate) to facilitate better logistics and throughput.

24.4.2
Evaluation of Diagnostic Tests

The acceptance of a clinical test or method is, just like drug acceptance, a multistage process in which various sources of variance and error are rigorously evaluated, because a wrong test result may give an incorrect diagnosis, and thus a wrong decision, which may endanger human life. Although evaluation of new bioassays is generally performed in laboratories of the pharmaceutical and diagnostic industry, many new developments are offered by universities and contract research organizations, and these institutions should be aware of some of the common pitfalls in bioassay development.

Clinical diagnosis comprises various forms of testing, and each type imposes its own set of requirements to the analytical methodology. The usual chain in the diagnosis of disease starts on the technical level, with evaluation of the measured quantity and the analytical result, in which error checking, quality control, analytical evaluation, and evaluation of interferences are the main activities [107]. On the technical level, there are many possible sources of error and deviation, which are inherent to the test itself, but which also have an origin in the disease statistics. One important factor, frequently overlooked in the research phase, is the occurrence of interfering species that may invalidate the test [108]. Therefore, methods that use more specific detection schemes will always be preferred. For instance, in

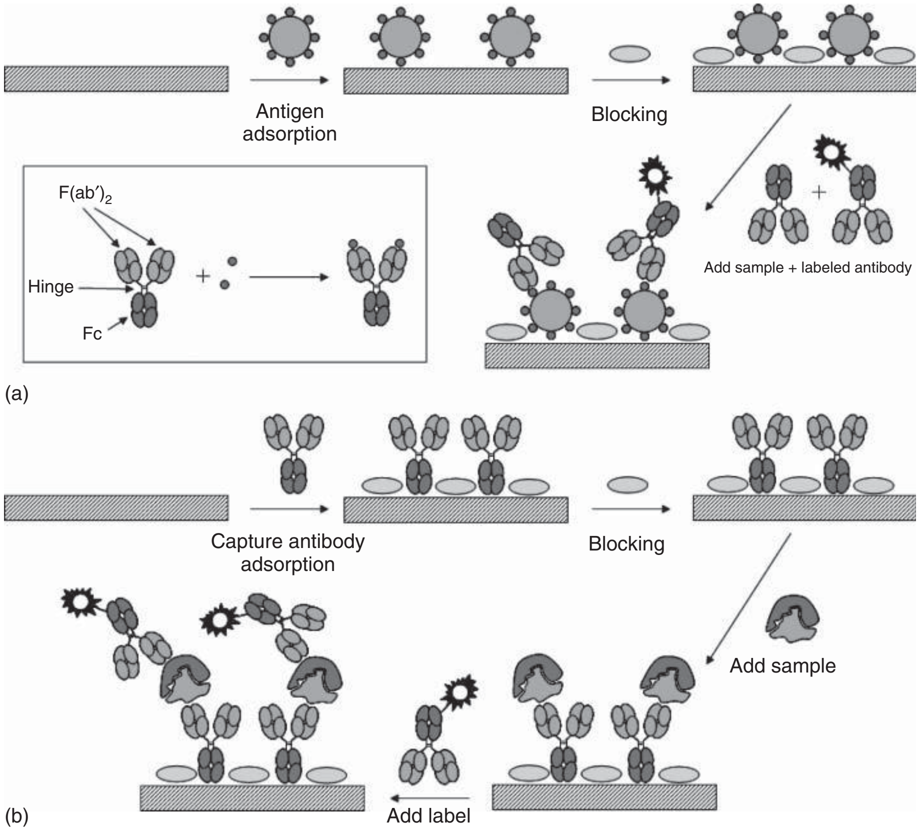

Figure 24.1 Two common formats used in clinical immunoassays. The inset shows the structure of an IgG molecule, consisting of one Fc domain and two Fab domains, linked together by a hinge. The Fab domains are ‘‘antibody binding’’ and one IgG is able to bind two antigen molecules. (a) Competitive assays are based on the competition of a labeled species with another species in solution for a limited amount of binding sites on the surface. Competitive assays can be designed in a variety of ways. In this example, a competitive assay is depicted for determining the antibody concentration in a sample, using a surface-immobilized antigen conjugate. First, an antigen conjugate is immobilized onto a suitable surface. After washing the surface, remaining space on the surface is filled up with suitable ‘‘blocking’’ protein that effectively blocks the surface from further nonspecific adsorption reactions. After washing, a sample is added that contains an unknown amount of unlabeled antibody against the antigen and a known amount of labeled antibody. The bound amount of labeled antibody will thus have a reciprocal dependence on the antibody concentration; if there is more antibody in solution, a lower proportion of labeled antibody will bind. (b) Noncompetitive (sandwich) assay making use of two antibodies that recognize different sites of the antigen (‘‘epitopes’’). One antibody is immobilized on the surface and the other one is labeled. After the sample is added, the antigen molecules will be bound to the surface; the labeled antibody is added after a washing step. The amount of label is measured after washing the excess of label from the surface. Labels can be enzymes, fluorophores, gold particles, or latex particles.

immunological tests, a sandwich assay is (in principle) more specific than a direct binding or competitive assay, because the analyte is detected by two antibodies instead of one. However, interfering species may also exist in sandwich assays and give rise to a false positive result [109].

Diagnosis of a disease is not solely dependent on the type and characteristics of the analytical method but it also depends on the *disease statistics* and the *purpose* of the test. Obviously, the analytical method should have selectivity, sensitivity, lower limit of detection, dynamic range, and accuracy sufficient for quantitation of the analyte or biomarker to establish a reliable diagnosis. Sometimes, these demands are not particularly stringent, sometimes they are. The validity of a test is defined as the *agreement of the test result with what the test was intended to determine*, such as presence of a bacterium, virus, or an abnormal value of a metabolite, protein, or drug. In addition, a valid diagnosis needs a correct assessment on the *biological level* (for the patient) and needs to be interpreted correctly in the frame of the known disease statistics (*nosological level*). Already in the former, the diagnosis of disease is far from straightforward, because the gender, age, disease history, and background of the patient will all have a bearing on the final diagnosis. A valid clinical result may even indicate more than one possible disease. Generally, a longitudinal evaluation (related to the history of the individual patient) and a transversal evaluation (related to the general disease statistics of healthy subjects compared to subjects with a disease) is performed for any new prospective diagnostic test. The largest uncertainties in laboratory findings arise from the classification of disease at the nosological level, where, in the end, new insights in disease patterns may give cause to search for new, more reliable analytes and markers [110].

When a diagnosis is based on the determination of abnormal values of a biochemical compound (analyte or marker), there will usually be some overlap of the distribution of concentrations in healthy subjects and the distribution of concentrations found in subjects with the disease (Figure 24.2a). There is nearly always a *gray area* where both distributions overlap, and it is in this area that false positive and false negative results are found. Although it may seem that this statistical factor is independent of the analytical characteristics of a test, the fact remains that some tests produce higher amounts of false negatives or false positives in comparison with other tests. Generally, hospitals will set the diagnostic cutoff concentration (Figure 24.2a) to a value, where the specificity and the sensitivity[1] of the test are both maximized to acceptable levels, but this will never completely remove the chance of encountering a false positive or false negative result. Instead, the location of the cutoff value of the test will depend on the prognostic purpose of the test: when the sensitivity of the test is more important than the selectivity (e.g., in screening where positives may not be missed), the diagnostic cutoff will be put at a lower value in the overlap area, but it will reduce the selectivity of the test.

---

[1] Note: Here the terms *ensitivity* and *specificity* have a different meaning compared to the normal analytical context: specificity indicates the incidence of negative results in persons that are free of the disease, and sensitivity indicates the incidence of a positive result in patients that have the disease.

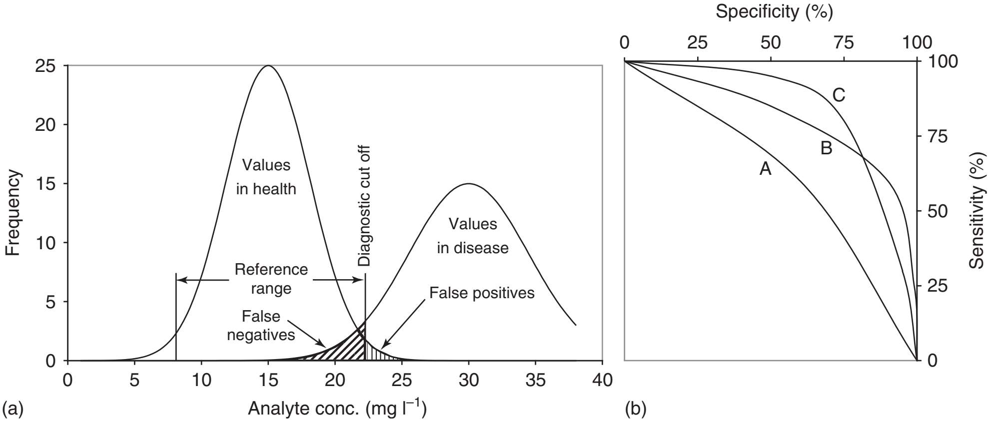

Figure 24.2 (a) Schematic representation of the overlap of concentration distributions of healthy subjects and subjects with disease. The efficiency of the test, corresponding to the overlap of the curves, is (TP + TN)/(TP + TN + FN + FP), where TP is the amount of true positives, TN is the amount of true negatives, FN the amount of false negatives, and FP the number of false positives. The specificity of the test is defined as TN/(TN + FP) and the sensitivity of the test as TP/(TP + FN). The diagnostic cutoff of the test was chosen slightly to the right, such that the specificity of the test is relatively high, but the sensitivity is relatively low. The predictive value for a positive result (PV+) is TP/(TP + FP) and the predictive value for a negative result (PV−) is TN/(TN + FN). (b) ROC curves for three hypothetical tests A, B, and C. In case of test A, the performance is relatively poor: both specificity and sensitivity are low. In test B, it has predominantly better performance, and a particularly good specificity, while test C has the highest sensitivity. Test C could be preferred as a screening tool over A and B.

Diagnostic tests are generally compared by the use of ROC curves (*receiver operating characteristic curves*), in which the specificity is plotted against sensitivity by varying the diagnostic cutoff, as illustrated in Figure 24.2b. Any new test should have at least a similar ROC curve as the preferred test, before it can be accepted.

Although nosological evaluations are usually not available to the researcher, knowledge of them is always needed. The best designers of clinical tests are the ones that actually work with patients on the hospital ward, because they know the demands in great detail and have experience in accessing how patient variables and factors of disease classification and statistics are to be taken into account. Therefore, it is favorable to include a major hospital laboratory or a clinical chemist in the research projects, if not to participate actively, at least to sit in the project meetings. Despite the fact that some of the higher aspects of clinical evaluation are out of reach of research organizations, it is favorable to include the following assessments in the development work:

1) work with real clinical samples at an early stage;
2) test for some common, known interferences;
3) make a correlation test with an established assay.

Once these three principles are followed, we may actually get to the point that clinicians start to have some interest in a new detection method.

24.4.3
Analytes of Clinical Interest

24.4.3.1 Inorganic Ions and Blood Gasses

To give a short overview of the substances of analytical interest that can be found in the human body, we begin with the first class of substances, which comprise inorganic ions and dissolved gasses. The majority of inorganic ions of biological importance are routinely determined with ion-selective electrodes, the operation of which is based on the permselective exchange of ions into a hydrophobic membrane phase [111, 112]. To achieve optical transduction, the ion–receptor complex formation will be intrinsically coupled to a physicochemical process of a light-absorbing or fluorescent dye compound. Such sensing matrices are used frequently in conjunction with fiber optics for the construction of miniature optical sensors, or *opt*(*r*)*odes* [113]. Another way to interrogate the binding of ions to ionophores at the boundary of two phases is to use second harmonics generation (SHG) [114].

A first means to achieve optical transduction is to include a lipophilic acidochromic dye (chromoionophore) into the membrane phase together with the receptor. The complexation of the metal ion by the ligand will expel a proton, which changes the absorbance spectrum. When a change in fluorescence properties is accomplished, we generally refer to *fluoroionophores*. The advantage of the approach is that no synthetic modification of the receptor or dye is needed, but the disadvantage is that these sensors have pH dependence, and buffering at an appropriate pH is necessary. Originally, lipophilic Nile blue (phenoxazine) derivatives were much used, but acridine, fluoresceine, and various other synthesized chromoionophores have also been described with signal-transducing properties [115–118]. Many of these ion receptors are commercially available from Fluka AG [119]. These sensors also have *practical* significance in clinical assays, as illustrated by Hisamoto *et al.* [117] and Wang *et al.* [116], who have described the measurement of common ions directly in serum.

In an alternative approach, the complexation of the metal ion may influence the partition of the lipophilic dye in the membrane phase, which can affect the fluorescence yield of the dye. This principle has been demonstrated with potentially sensitive dyes by Wolfbeis and Mohr [120, 121]. This approach is also applicable to the sensing of neutral species, such as 2-phenethylamine [122]. Although the majority of chromo- and fluoroionophores are cast in hydrophobic, (polyvinyl chloride type) membranes, sol–gel matrices have also become very popular [123]. Another interesting technique for making sensing layers is the electrostatic layer-by-layer technique (LBL), which has been recently used in fiber-optic pH sensors [124]. A well-established approach that enables intracellular sensing of various analytes with fluoroionophoresis is the technique called *PEBBLE*, which was acronymized from either *photonic explorer for bioanalysis with biologically localized embedding* or *probes encapsulated by biologically localized embedding*. This technique was initially used for pH and calcium sensing [125] and for potassium sensing [126], but now it is also used for the imaging of Mg^{2+} [127], Cu^{2+} [128], Zn^{2+} [129], glucose [130], and dissolved oxygen [131].

In a third approach, the dye is made an integral part of the receptor, such that absorbance and/or fluorescence parameters are directly modified by the complexation reaction. This is a more developed form of indicator chemistry – *semiochemistry* [132]. Receptor molecules modified with photosensitive groups may display very large changes in their photophysical properties on the binding of analytes, and can enable very sensitive detection. For instance, Chapoteau *et al.* [133] have already reported in 1992 a colorimetric method for the determination of lithium in blood serum, not requiring any sample pretreatment or solvent extraction steps. The chromogenic ionophore exhibited exceptionally high selectivity for lithium over sodium (>4000 : 1). In the same year, Shinkai *et al.* 134 and Diamond *et al.* [135] reported on different azophenol-modified calixarenes for quantitation of lithium. Akkaya *et al.* have reported dyes modified with phenylboronic acid groups for the detection of zinc ions [136] and calcium ions [137]. Zinc detection and imaging in neurons has also been recently reported using a new receptor [138]. Finally, the modulation of luminescent lifetime of luminescent particles in a polymeric material has been used for the simultaneous detection of carbon dioxide and oxygen in plant tissues [139]. With phosphate ion detection, optrodes are still rare, but recently some interesting ionophores for phosphate detection with ion-selective electrodes have been reported [140, 141], and therefore optical transduction may also be feasible. Besides sensors for the clinically relevant analytes, as listed in Table 24.2, sensor materials have been devised for many other ions to be applied in environmental or food analysis, such as nitrate [142, 143], bisulfite [144], mercury, and silver [145].

24.4.3.2 **Low-Molecular-Weight Analytes**

The most relevant low-molecular-weight metabolites and hormones are listed in Tables 24.3 and 24.4. Many metabolites can be determined with enzymatic biosensors, as all metabolites are in principle substrates for enzymes. Thus, electrochemical and optical biosensors have been widely reported [78, 197]. For some smaller-sized analytes, synthetic receptors have been devised, such as receptors for choline and carnitine [198], and creatinine [199]. In the latter, extensive hydrogen-bonding interactions were designed between the analyte and receptor. Signal-transducing synthetic receptors based on azophenol [133, 200], spirobenzopyran [201], antracene [202], or coumarine [203] dyes have also been synthesized. Calixarenes, with covalently linked chromogenic or fluorogenic groups, are especially the most intensively investigated [204]. Modified calixarenes have been produced for sensing of anions [205] and small organic molecules, such as dopamine [206] and 2-phenethylamine [122], and they have been used even for chiral recognition [207]. Moreover, calixarenes have been produced in which fluorescence can be switched on upon binding of the analyte, a principle that can afford far more sensitive sensors than the ones that are based on fluorescence quenching [208]. Recently, a variety of novel squarilium dyes with signal-transducing properties, for example, for carbohydrate detection, have been reported in the literature [209].

Table 24.2 Inorganic and gaseous analytes.

Substance	**Normal values**[a]	**Relevance**	**References**
Hydrogen ion, pH, H^+, and H_3O^+	35–46 nM pH = 7.36–7.44	Hyperventilation, lactic or respiratory acidosis, metabolic or respiratory alkalosis, and hyperkalemia	[124, 125, 146–153]
Sodium, Na^+	135–145 mM	Hypo- and hypernatremia	[115–117, 154–159]
Potassium, K^+	3.6–5.0 mM	Hypo- and hyperkalemia	[115–118, 126, 159–161]
Ammonia, $NH_4{}^+$, and NH_3	10–47 µM	Renal disorders, acidosis, and alkalosis	[116, 162–165]
Chloride, Cl^-	—	—	[117, 166–169]
CO_2 (bi)carbonate (total)	$p(CO_2) = 4.5–6.0$ kPa (arterial blood) 22–3.0 mM	Acidosis and alkalosis	[170–175]
Phosphate	0.8–1.4 mM	Hyper- and hypophosphatemia, acidosis, alkalosis (related to renal function), and hypercalcemia (via PTH calcium regulation)	[176–178]
Oxygen	$p(O_2) = 11–15$ kPa	Hypoxemia	[131, 179–183]
Calcium, Ca^{2+}	2.2–2.6 mM	Hypo- and hypercalcemia	[115, 117, 125, 137, 184]
Copper, Cu^{2+}	3.3–6.7 mM	Renal disorders, anemia, and Wilson's disease	[128, 185–187]
Iron, Fe^{2+}, Fe^{3+}	free: < bound:	Anemia and hemochromatosis	[188–191]
Magnesium, Mg^{2+}	0.7–1.0 mM	Hyper- and hypomagnesemia	[127, 192, 193]
Selenium, Se^{2+}	Traces	Myopathy and thyroid function	[194]
Zinc, Zn^{2+}	12–20 µM	Dermatitis and wound healing	[129, 136, 195, 196]

[a] In adults, serum, or plasma.

Home glucose monitoring and *in vivo* monitoring of glucose for diabetic care keeps receiving much attention in research and commercial R&D, owing to the large incidence of diabetes and its strong increase worldwide. Glucose detection still comprises the largest single-analyte market in diagnostics. Although most home glucometers are electrochemical sensors, some tests for detection of glucose in urine still use an older colorimetric method. The most important references for optical glucose detection have been included in Table 24.3. The very first optrode for glucose was reported by Schultz in 1982, and was based on the concanavalin A receptor [271]. This sensor has recently been further improved, and a glucose working range between 0.2 and 30 mM was attained [228]. More recently, the sensor dyes were switched so that the sensor operates in the near-infrared, making it less prone to background fluorescence from serum samples [272]. These sensors are capable of sensitive, long-term glucose monitoring, but have a strong interference from fructose. A much more sensitive and selective receptor for glucose from *Escherichia coli* has also been used [273].

Table 24.3 Some common metabolites.

Substance	Normal values	Relevance	References
Urea	3.3–6.7 mM	Renal function	[133, 153, 210–213]
Uric acid	0.1–0.4 mM	Renal function	[214–216]
Creatinine	60–120 µM	Liver function	[199, 217–221]
Glucose	2.8–5.0 mM	Diabetes and obesity	Reviews: [222] Synthetic receptors: [223–228] Biosensors: [229–234] Noninvasive: [235, 236] Intracellular: [130, 182]
Ethanol	—	Forensics and liver function (antidiuretic hormone, ADH)	[237–241]
Bilirubin	3–20 µM	Liver function	[242–244]
Cholesterol	Total: <5.2 mM* HDL: >1.2 mM* LDL: <3.5 mM*	Obesity	[245–247]
(acetyl) Choline	—	Brain function	[248–251]
Lactic acid	—	Acid lactosis and sports medicine	[251–255]
Triglycerides (lipids)	0.4–1.8 mM	Energy storage and various metabolic diseases	[256]
Adenosine triphosphate (ATP)	—	Energy storage	[257, 258]

For noninvasive monitoring, some direct photoacoustic spectroscopic approaches in the near- and mid-infrared are still under evaluation [259–262]. The new field of terahertz spectroscopy also offers new prospects to probe glucose directly in living tissues (see Chapter 27) [263]. Various intracellular approaches to the ''sensing'' of a range of metabolites, including the PEBBLE technique, have been reviewed by Yotter *et al.* [264], and these methods are compatible with lab-on-a-chip devices.

For the human hormones thyroxine, triiodothyronine, and the steroids (Table 24.4), immunological recognition is commonly used. In fact, the very first radioimmunoassays were applied to T3 and T4 determinations, and they are still in force [268]. Direct optical sensors for the human hormones of low molecular weight are relatively rare, mainly due to the extremely high sensitivity needed. Only one study has described a direct assay for thyroxine by fluorescence quenching of thyroxine-binding globulin [274]. The measurement, however, needed 2 h to reach the maximum signal, and the lower detection limit was still a 100-fold compared to the clinically relevant concentration of free thyroxine in serum. Schrader *et al.* [275] have recently described the fluorescence activation of receptors for catecholamines embedded in cross-linked vesicles consisting of phospholipids and diacetylenes. Measurements could be performed directly in urine at micromolar concentrations.

Table 24.4 Some relevant low-molecular-weight hormones.

Substances	Normal values	Relevance	References
Catechol and catecholamines (dopamine, epinephrine, norepinephrine, e.o.)	—	Parkinson's disease and stress	[259–265, 313]
Phenethylamines (2-phenethylamine, phenylephrine, amphetamine e.o.)	—	Neurotransmitters and drugs	[122, 312]
Thyroxine (T4)	Total: 60–150 nM Free: 9–26 pM	Thyroid function	[266–268]
Triiodothyronine (T3)	Total: 1.2–2.9 nM Free: 3.0–8.8 pM	Thyroid function	[267, 268]
Cortisol	Daytime: 140–690 nM Night: <100 nM	Sleep, day/night rhythm	[269]
Testosterone	Adult males: 9–30 nM Adult females: 0.5–2.5 nM	Key role in health, well-being, and sexual functioning (both in men and women)	[270]

Molecularly imprinted polymers (MIPs) have yielded interesting possibilities for recognition and detection of low-molecular-weight analytes, such as the steroids, phenethylamines, and catecholamines, and a variety of drug compounds [276–278]. The principle of molecular imprinting is basically simple: a well-optimized mixture of monomers with various functional groups is polymerized in the presence of the analyte, the latter functioning as a *template*. Hereafter, the analyte/template is eluted from the polymer matrix, which leaves cavities in the polymer to which the analyte/template or an analog can be rebound [279–281]. This polymer can then be used in an analytical system or sensor. Artificial enzymes can also be produced by molecular imprinting, in which a transition state analog of a chemical reaction is used as the template molecule [282]. Some reports have already appeared on the combination of fluorescence with imprinted polymers [283]. If the functional monomers are fluorescent and are designed to have specific chemical interactions with the analyte, it is possible to monitor the binding via changes in fluorescence of the polymer directly [284, 285]. For reasons of background and sensitivity, the activation of fluorescence by the binding of analyte to an imprinted polymer would be the most preferred situation, as previously mentioned for the catecholamine sensor [275]. Turkewitsch *et al.* [284] described a first prototype of this novel sensing scheme for template-selective recognition sites in imprinted polymers with cyclic AMP (cAMP). The polymer included a fluorescent dye, a dimethylaminostyryl-pyridinium derivative, as an integral part of the recognition cavity, thus serving as both the receptor and transducing element for the fluorescence detection of cAMP in aqueous media. The imprinted polymer displayed a quenching of fluorescence in the presence of cAMP in aqueous solution, whereas almost no effect was observed in the presence of cGMP. The affinity constant of the polymer for cAMP was about $10^5\ M^{-1}$.

Recently, the possibility to make imprinted molecular thin films has also been investigated with amperometric, capacitive, and SPR-based detection schemes [286–288]. Self-assembled monolayers (SAMs) of organic thiols and disulfides can be formed on gold surfaces in a highly defined way, and when a template molecule is included that does not interact so strongly with gold, it may become coadsorbed with the organic thiol onto the surface. The template molecule can be eluted with a suitable washing solution, and *footprints* may be formed that have the size and shape of the template molecule, allowing rebinding of the template (or an analog), as illustrated in Figure 24.3. The approach may be designated by the *imprinted self-assembled monolayer* (*i-SAM*) technique. The footprint can be formed with hydrophobic, hydrophilic, or bifunctional SAM-forming compounds. After screening several bifunctional lipoate derivatives, the highly effective imprinting of the model drug *morphine* to *i-SAM* layers of a tris(hydroxymethyl)aminomethane-derivative of lipoic acid was observed in an SPR study [288]. When the (re)binding was compared to the binding to an antibody against morphine, very similar binding characteristics were observed (Figure 24.4) [289]. This illustrates that synthetic receptors may have the same application potential as natural receptors in analytical methods.

24.4.3.3 **Protein Analytes**

Proteins are most abundant in the human body, and – although far from complete– Table 24.5 lists some of the most relevant protein analytes from the point of clinical diagnosis. Since many of these proteins are analyzed with immunoassays, no further references are included to specific optical/spectroscopic methods for their

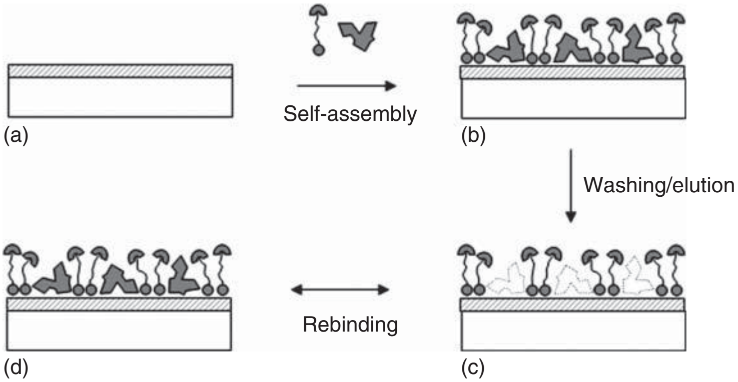

Figure 24.3 Principle of i-SAM formation. To a cleaned gold surface (a) a mixture of bifunctional ligands is added mixed with template (dark grey). The template forms weak complexes with the ligands and settle via one moiety of the ligands onto the gold surface (b). After washing, the self-assembled ligands are left in an arrangement favorable for rebinding the template (binding site shown in dotted lines) or similar compounds (c,d).

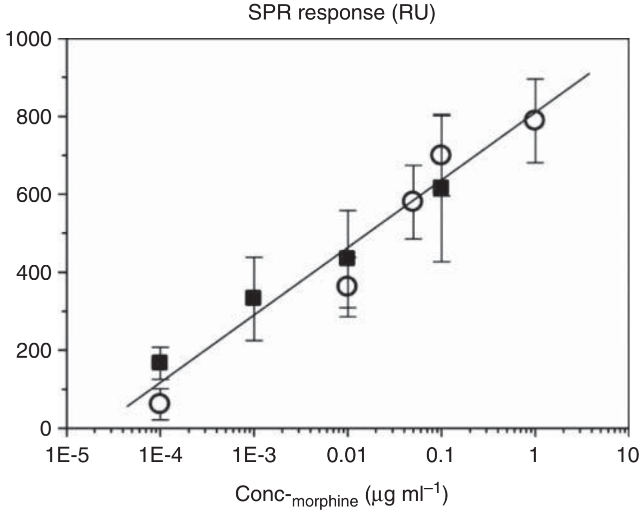

Figure 24.4 Binding of morphine to an imprinted self-assembled monolayer in comparison with the binding to an antibody. (■ response of i-SAM, ○ response of antibody to morphine) (From Ref. [289].)

detection, but some references are included to functional and structural data of these proteins in the OMIM and PDB databases. Proteins are less suited for the conventional imprinted polymer approaches, because of the susceptibility of tertiary and quaternary structure elements to denaturation in nonaqueous environment and because of the high concentration of monomers, but some recent progress has also been made toward imprinting of proteins [290, 291].

A number of plasma proteins are very abundant and amenable to direct detection. Albumin and immunoglobulins have been determined with various optical sensor systems, of which only a few are mentioned [292–294]. As part of the biological markers, tumor markers are at present in the center of interest, and also the object of large efforts in diagnostics R&D [295]. The most important of these are the ones that are routinely tested in central hospital laboratories and are listed in Table 24.5.

A typical example of a cancer marker is prostate-specific antigen (PSA) an indicator of prostate cancer in men. PSA is a glycoprotein with a molecular weight between 30 and 34 kDa, and is secreted by the prostate gland. PSA is found at high concentrations in semen, and thus it is an important analyte in forensic analysis too. It is an enzyme belonging to the kallikrein family of serine endopeptidases (serine protease EC 3.4.21.77), and sometimes referred to as *kallikrein-related peptidase 3* (KLK3). In clinical assays, PSA concentrations need to be assessed in the concentration range of 0.05–20 ng ml^{-1}, and thus an affinity constant of around 10^{10} M^{-1} or higher would be required of the antibody or receptor in a specific test [296]. PSA detection with biosensors has recently been the subject of intense investigation, predominantly with mass-sensitive sensors and SPR. The direct detection of PSA has been studied by the group of David Myszka, making

Table 24.5 Some human protein analytes.

Protein (MW (kDa))	Normal values in adults	Function/relevance	OMIM and PDB entries
Plasma proteins			
Albumin	35–50 $\mathrm{g\,l^{-1}}$	Oncotic pressure and drug/metabolite transport	103 600/1e78, 1bm0, 1uor, 1ao6
Immunoglobulins (IgM, IgG, IgA, OgD, and IgE)	Total approximately 20 $\mathrm{g\,l^{-1}}$	Immune response and allergy	(IgG) 147 100[a]/1hzh, 1mco (IgM) 147 020[a]/2rcj
Fibrinogen (340)	1.5–4.0 $\mathrm{g\,l^{-1}}$	Blood clotting	134820[a]/1fzc
Hemoglobin (68)	Males: 130–180 $\mathrm{g\,l^{-1}}$ Females: 120–160 $\mathrm{g\,l^{-1}}$	Oxygen transport	141 800 (α1), 141 850 (α2), 141900 (β)/1gzx
Transferrin (76.5)	2.04–3.60 $\mathrm{g\,l^{-1}}$	Iron carrier	190 000/1a8e, 1a8f, 1b3e, 1bp5, 1btj[a]
Ferritin (450 without iron)	Males: 30–300 $\mathrm{\mu g\,l^{-1}}$ Females: 15–200 $\mathrm{\mu g\,l^{-1}}$	Iron carrier	134 790/1lb3
C-reactive protein, CRP (250)	$<$5 $\mathrm{mg\,l^{-1}}$	General inflammation marker and chronic cardiac diseases	123 260/1b09, 1gnh, 1lj7
Protein hormones			
Follicle stimulating hormone, FSH (30)	Adult males: 2–10 $\mathrm{U\,l^{-1}}$ females: follicular phase: 2–8 $\mathrm{U\,l^{-1}}$ post-menopausal: $>$ 15 $\mathrm{U\,l^{-1}}$	Regulates the development, growth, pubertal maturation, and reproductive processes	136 530/1fl7, 1xwd
Growth hormone, GH (22.1)	Following glucose load: $<$2 $\mathrm{mU\,l^{-1}}$ Following stress: $>$20 $\mathrm{mU\,l^{-1}}$	Stimulates growth and cell reproduction	139 240, 139 250/1a22, 1huw, 1hgu[a]
Insulin (5.8)	Fasting: 3–15 $\mathrm{mU\,l^{-1}}$ Hypoglycemia: $<$3 $\mathrm{mU\,l^{-1}}$	Metabolic regulator (e.g., for glucose uptake)	176 730/
Parathyroid hormone, PTH (±10)	10–65 $\mathrm{ng\,l^{-1}}$	Calcium regulation	168 450/1bwx, 1et1, 1fvy, 1hph, 1hpy
Prolactin (±24)	50–400 $\mathrm{mU\,l^{-1}}$	Milk production in the breast	176 760/1n9d
Thyroid stimulating hormone, TSH (±30)	0.3–4.0 $\mathrm{mU\,l^{-1}}$	Stimulates the thyroid gland to secrete thyroxine (T4) and triiodothyronine (T3)	118 850 (α), 118 840 (β)/

Table 24.5 (*Continued*).

Protein (MW (kDa))	**Normal values in adults**	**Function/relevance**	**OMIM and PDB entries**
Human chorionic gonadotropin, hCG (±46)	Highly variable ($0–100\,000\ \mathrm{IU\,l^{-1}}$)	Indicator of pregnancy, also tumor marker	118 860/1hcn, 1hrp, 1qfw
Luteinizing hormone, LH (±26)	Adult males: $2–10\ \mathrm{U\,l^{-1}}$ Females: follicular phase: $2–10\ \mathrm{U\,l^{-1}}$ post-menopausal: $> 20\ \mathrm{U\,l^{-1}}$	In females, a rise of LH triggers and indicates ovulation. In male, LH stimulates Leydig cell production of testosterone	152 780/
Cardiac markers			
Myoglobin (16.7)	$< \pm 100\ \mathrm{\mu g\,l^{-1}}$	Oxygen carrier in muscle	160 000/1m6c, 1m6m, 1mdn, 1mnh, and 1mni^{+}
Creatine kinase, CK-MB	25 and $200\ \mathrm{U\,L^{-1}}$	Energy supply in muscle	123 310/1i0e
Cardiac Tropinin I, cTnI	$< \pm 0.1\ \mathrm{\mu g\,l^{-1}}$	Binds to actin in thin heart myofilaments	191 044/1mxl, 1a2x, 1vdi
Cardiac Tropinin T, cTnT	$< \pm 0.1\ \mathrm{\mu g\,l^{-1}}$	Binds to tropomyosin, in heart myofilaments	191 045/
Tumor markers			
α-Fetoprotein (AFP)	$<10\ \mathrm{\mu g\,l^{-1}}$	Hepatocellular carcinoma and endodermal sinus tumors	104 150/
Calcitonin (3.5)	$<10\ \mathrm{ng\,l^{-1}}$	Calcium regulator, and indicator of medullary thyroid carcinoma	114 130/2glh
Carcinoembryonic antigen, CEA		Colorectal, gastric, pancreatic, lung and breast carcinoma, and medullary thyroid carcinoma	12 different types of proteins in humans, for example: CEACAM1: 109 770/2gk2
Prostate specific antigen, PSA (±33)	$<4\ \mathrm{\mu g\,l^{-1}}$	Prostate cancer in men, possibly various forms of cancer in women	176 820/1z8l, 2zch, and 2zcl

[a] Indicates multiple entries.

use of a large group of participants, to investigate the differences that may arise in the determination of the affinity constant using a selected monoclonal antibody to PSA [297]. The native antibody used in this study had a reported affinity constant of about 0.75 nM^{-1}. The anti-PSA was immobilized onto a carboxydextran surface ("CM5," from Biacore) via the amino groups of the antibody, and the binding of PSA was studied by kinetic binding experiments in a buffer supplemented with 0.2 $\mathrm{mg\,ml}^{-1}$ bovine serum albumin. Three different antibody loadings in three different flow channels were employed (500, 1000, and 2000 RU), while one channel was left blank. This channel functioned as a reference to compensate for long-term drift. The variability in antibody loading yielded the possibility to relate the maximum PSA response to the antibody loading. In this way, an immobilization efficiency of 44% was inferred for the antibody/CM5 combination. At the highest antibody loading, the maximum response was from 160 to 350 RU ($\approx$pg mm^{-2}), and a distribution constant (K_D) was found of 1.1 nM (i.e., $K_A = 0.91\,\mathrm{nM}^{-1}$) with a coefficient of variation of 18%. These results prove that the SPR method is able to give a direct assay of PSA, although it should be noted that for reliable diagnostic tests, on real samples, the method has not yet been employed. Moreover, in the survey, the reported affinity is a decade lower and the variation in affinity is much higher than required in a diagnostic assay.

PSA has also been the object of various other studies pertaining to direct detection. For instance, single-chain dromedary antibodies against PSA have been immobilized in a highly ordered way through the use of fusion proteins of the antibody with an S-layer protein, and regular immobilization yielded up to 78% immobilization efficiency [298]. The amount of antibody bound to gold was 5770 RU, and under saturating conditions 1074 RU of PSA was bound. Binding isotherms and detection limits for PSA, however, were not reported, although the affinity constant of the antibody was separately assayed as 11 nM^{-1}.

In a recent study by Besselink *et al.* [98], various detection techniques for PSA were compared, all based on SPR detection, and the results have also been underpinned with theoretical calculations. Employing a new type of hydrogel-modified gold surface (commercially available from Ssense, Hengelo, the Netherlands) a very high antibody loading could be attained (20 500 RU) and it showed a saturation response of 3280 RU for PSA (at 34 $\mu\mathrm{g\,ml}^{-1}$). At the lower concentration of 300 $\mathrm{ng\,ml}^{-1}$ PSA, however, the response was only 98 RU, which still lies far above the clinically interesting concentration range. Highest sensitivity could be obtained, however, for particle amplification on planar surfaces, enabling detection down to 0.6 and 2.4 $\mathrm{ng\,ml}^{-1}$ respectively for gold and latex particles. Finally, Choi *et al.*, [299] using recombinant protein G to orient the (monoclonal) capture antibody and a polyclonal antibody gold label, claimed to have achieved a detection limit of 0.3 pM for PSA (0.01 $\mathrm{ng\,ml}^{-1}$). Indeed, in most cases in the literature, the detection of PSA without further amplification was conducted at concentrations far above the clinically interesting range, and only amplification with secondary antibody, gold, or latex particles gave the possibility to detect PSA at the required low concentrations.

Besides SPR phenomena on flat gold surfaces, localized surface plasmon resonance (LSPR) phenomena in dilute solutions of gold colloids have been successfully used for direct and highly sensitive detection of various clinical analytes such as theophiline, digoxine, troponin I, and hCG [300, 301]. The binding of an antigen to gold colloids coated with monoclonal antibodies gives a measurable shift of the absorbance spectrum. The effect is largest for gold colloids of 50 nm, because they still have a pronounced absorbance peak, with optimal sensitivity to local perturbation of the LSPR. With this size of nanoparticles, ratiometric absorbance measurements at 530 and 620 nm afford real-time analysis of association and dissociation constants. The issues discussed earlier thus, clearly, illustrate the possibilities (but also limitations) for plasmonic techniques in bioanalysis.

24.5
Conclusion

An important issue remaining, which is also of some bearing to optical sensing, is the immobilization of receptors and biological compounds on the surface of sensor devices. Immobilization techniques have been developed for proteins, DNA, aptamers, and cells for a variety of purposes. As outlined in the review by Borisov and Wolfbeis [80], immobilization materials are emerging increasingly as active ingredients of optical sensing devices. The general issues related interfacial aspects of biomolecule immobilization have been recently reviewed [302, 303], and many practical protocols have been published [304]. In SPR biosensors, the general issues of surface chemistry have been reviewed by Gedig [305].

Site-directed immobilization, that is, the attachment of biomolecules to a surface in an oriented manner to maximize the amount of available binding sites or activity, is particularly important with antibodies, owing to the fact that the antigens with which they need to interact are generally rather bulky. Proteins A, G, and L, have been used to orient whole antibodies on gold surfaces via the Fc part, with which they specifically interact (see Figure 24.1 for a schematic structure of an antibody) [299]. Unfortunately, these scaffold proteins do not always interact strongly enough with the antibody for stable attachment during the measurement, and therefore, immobilization of biotinylated antibodies onto surfaces via various avidins [306] or covalent attachment [307] may be preferred . One of the first site-directed methods for antibody immobilization was by activation of the carbohydrate moiety in the Fc part of antibodies and their attachment to amino surfaces [308]. IgG molecules can also be split into $F(ab')_2$-fragments with pepsin digestion, and bound directly to hydrophilic gold [309] or to SAMs via the terminal thiol groups [310]. Various polymeric matrices have also been used for immobilization. The efficacy of carboxy dextran matrices, as introduced by Pharmacia Biosensor in 1990, has been one of the factors that contributed to the success of the Biacore® SPR biosensing system. At present, there have emerged a few alternative providers of chips coated with similar matrices: Xantec Bioanalytics GmbH, in Germany, and Ssense, in the Netherlands. In the design of new polymers with low protein binding, various biocompatible functional groups can be considered, such as the ones screened by Ostuni *et al.* [311].

Clearly, there are very many important developments in bioanalytical methods, and it was only possible to give a small cross section of the literature in this introductory chapter. As everything nowadays converges to miniaturization, some preference has been given to biosensor and solid-state devices in this chapter, and to a few issues related to bionalysis that are not discussed in the chapters that follow in this section.

As a concluding outlook it can be stated that (i) synthetic receptors are clearly gaining territory next to the receptors given by nature, (ii) detection schemes become more and more integrated with immobilization, as evidenced by new discoveries in imprinted polymers and self-assembled molecular layers, and (iii) the operation of many new prototype devices in the field of clinical chemistry still needs to be evaluated in more realistic sample matrices.

References

1. Rich, R.L., Cannon, M.J., Jenkins, J., Pandian, P., Sundaram, S., Magyar, R., Brockman, J., Lambert, J., and Myszka, D.G. (2008) *Anal. Biochem.*, **373**, 112.
2. Beusink, J.B., Lokate, A.M.C., Besselink, G.A.J., Pruijnand, G.J.M., and Schasfoort, R.B.M. (2008) *Biosens. Bioelectron.*, **23**, 839.
3. RSC Publishing (xxxx) *Lab Chip*, *http://www.rsc.org/publishing/journals/LC/Index.asp* (accessed 21 March 2013).
4. Bogue, R. (2008) *Sens. Rev.*, **28**, 12.
5. Nederlands Forensisch Insituut 2006 *Tecan J.*, **3/2006**, *http://www.dnasporen.nl/docs/nieuws/Tecan_Journal_03_06_page14-17.pdf* (accessed 21 March 2013).
6. 2013 *Biosens. Bioelectron.*, **47**, *http://www.sciencedirect.com/science/journal/09565663* (accessed 21 March 2013).
7. 2013 *Sens. Actuators B: Chem.*, **182**, *http://www.sciencedirect.com/science/journal/09254005* (accessed 21 March 2013).
8. Schasfoort, R.B.M. and Tudos, A.J. (eds) (2008) *Handbook of Surface Plasmon Resonance*, RSC Publishing, Cambridge.
9. Hoa, X.D., Kirk, A.G., and Tabrizian, M. (2007) *Biosens. Bioelectron.*, **23**, 151.
10. Sharma, A.K., Jha, R., and Gupta, B.D. (2007) *IEEE Sens. J.*, **7**, 1118.
11. Boozer, C., Kim, G., Cong, S., Guan, H., and Londergan, T. (2006) *Curr. Opin. Biotechnol.*, **17**, 400.
12. Rich, R.L. and Myszka, D.G. (2006) *J. Mol. Recognit.*, **19**, 478.
13. Myszka, D.G. (2008) in *Handbook of Surface Plasmon Resonance* (eds R.B.M. Schasfoort and A.J. Tudos), RSC Publishing, Cambridge.
14. Peters, F.T. and Maurer, H.H. (2002) *Accred. Qual. Assur.*, **7**, 441.
15. Campbell, N.A. (1996) *Biology*, The Benjamin/Cummings Publishing Company, Inc., Menlo Park, CA.
16. Town, C. (ed.) (2002) *Functional Genomics*, Kluwer Academic Publishers, Dordrecht.
17. Hunt, S. and Livesey, F. (eds) (2000) *Functional Genomics: A Practical Approach*, Oxford University Press, Oxford.
18. Wilkins, M.R., Williams, K.L., Appel, R.D., and Hochstrasser, D.F. (eds) (1997) *Proteome Research: New Frontiers in Functional Genomics*, Springer-Verlag, Berlin.
19. Kamp, R.M., Kyriakidis, D., and Choli-Papadopoulou, T. (eds) (1999) *Proteome and Protein Analysis*, Springer-Verlag, Berlin.
20. Lynch, M. and Conery, J.S. (2003) *Science*, **302**, 1401.
21. ENCODE Project Consortium (2007) *Nature*, **447**, 799.
22. Hensly, P. and Myszka, D.G. (2000) *Curr. Opin. Biotechnol.*, **11**, 9.

23. Licinio, J. and Wong, M.-L. (eds) (2002) *Pharmacogenomics: The Search for Individualized Therapies*, Wiley-VCH Verlag GmbH, Weinheim.
24. Thongboonkerd, V. (ed) (2007) *Proteomics of Human Bodyfluids: Principles Methods, and Applications*, Humana Press, Totowa, NJ.
25. Dutt, M.J. and Lee, K.H. (2000) *Curr. Opin. Biotechnol.*, **11**, 176.
26. Wilkins, M.R., Williams, K.L., Appel, R.D., and Hochstrasser, D.F. (eds) (1997) *Proteome Research: New Frontiers in Functional Genomics (Principles and Practice)*, Springer-Verlag, Berlin.
27. Wasinger, V., Cordwell, S., Cerpa-Poljak, A., Yan, J., Gooley, A., Wilkins, M., Duncan, M., Harris, R., Williams, K., and Humphrey-Smith, I. (1995) *Electrophoresis*, **16**, 1090.
28. Koutny, L., Schmalzing, D., Salas-Solano, O., El-Difrawy, S., Adourian, A., Buonocore, S., Abbey, K., McEwan, P., Matsudaira, P., and Ehrlich, D. (2000) *Anal. Chem.*, **72**, 3388.
29. Kheterpal, I. and Mathies, R.A. (1999) *Anal. Chem.*, **71**, 31A.
30. Lakowicz, J.R. (ed.) (1994) *Topics in Fluorescence Spectroscopy: Probe Design and Chemical Sensing*, Vol. 4, Plenum Press, New York.
31. Wang, J., Chen, Z., Corstjens, P.L.A.M., Mauk, M.G., and Bau, H.H. (2006) *Lab Chip*, **6**, 46.
32. Volpi, E.V. and Bridger, J.M. (2008) *Biotechniques*, **45**, 385.
33. Wagner, M., Horny, M., and Daimsz, H. (2003) *Curr. Opin. Microbiol.*, **6**, 302.
34. Russell, S., Meadows, L.A., and Russell, R.R. (2008) *Microarray Technology in Practice*, Academic Press, San Diego, CA.
35. Takahashi, N., Isobe, T., Desiderio, D.M., and Nibbering, N.M. (2008) *Proteomic Biology Using LC/MS*, John Wiley & Sons, Inc., Hoboken, NJ.
36. Andersen, J.S. and Mann, M. (2000) *FEBS Lett.*, **480**, 25.
37. James, P. (ed.) (2001) *Proteome Research: Mass Spectrometry (Principles and Practice): Mass Spectrometry (Principles and Practice)*, Springer-Verlag, Berlin.
38. Wenk, M.R. (2005) *Nat. Rev. Drug Discov.*, **4**, 594.
39. van Meer, G. (2005) *EMBO J.*, **24**, 3159.
40. Zehethofer, N. and Pinto, D.M. (2008) *Anal. Chim. Acta*, **627**, 62.
41. Vogeser, M. and Parhofer, K.G. (2007) *Exp. Clin. Endocrinol. Diabetes*, **115**, 559.
42. Grivet, J.P., Delort, A.M., and Portais, J.C. (2003) *Biochimie*, **85**, 823.
43. Serkova, N.J., Spratlin, J.L., and Eckhardt, S.G. (2007) *Curr. Opin. Mol. Ther.*, **9**, 572.
44. Banks, R.E., Dunn, M.J., Hochstrasser, D.F., Sanchez, J.-C., Blackstock, W., Pappin, D.J., and Selby, P.J. (2000) *Lancet*, **356**, 1749.
45. Usui-Aoki, K., Shimada, K., Nagano, M., Kawai, M., and Koga, H. (2005) *Proteomics*, 2396.
46. Hamdan, M.H. (2007) *Cancer Biomarkers: Analytical Techniques for Discovery*, John Wiley & Sons, Inc., Hoboken, NJ.
47. Tang, N., Tornatore, P., and Weinberger, S.R. (2004) *Mass Spectrom. Rev.*, **23**, 34.
48. Hutchens, T.W. and Yip, T.T. (1993) *Rapid Commun. Mass Spectrom.*, **7**, 576.
49. Wright, G.L. Jr.,, Cazares, L.H., Leung, S.-M., Nasim, S., Adam, B.-L., Yip, T.-T., Schellhammer, P.F., Gong, L., and Vlahou, A. (1999) *Prostate Cancer Prostatic Dis.*, **2**, 264.
50. Sadiq, S.T. and Agranoff, D. (2008) *Proteome Sci.*, **6**, 16.
51. Whistler, T., Rollin, D., and Vernon, S.D. (2007) *Proteome Sci.*, **5**, 14.
52. Luque-Garcia, J.L. and Neubert, T.A. (2007) *J. Chromatogr., A*, **1153**, 259.
53. Purcell, A.W. and Gorman, J.J. (2004) *Mol. Cell. Proteomics*, **3**, 193.
54. Zijlstra, A., Testa, J.E., and Quigley, J.P. (2003) *Biochem. Biophys. Res. Commun.*, **303**, 733.
55. Schrader, M. and Schults-Knappe, P. (2001) *Trends Biotechnol.*, **19**, –S55.
56. Soloviev, M. and Finch, P. (2005) *J. Chromatogr., B*, **815**, 11–24.
57. Minamino, N. (2001) *Tanpakushitsu Kakusan Koso*, **46** (Suppl. 11), 1510.
58. Minamino, N. and Sasaki, K. (2007) *J. Card. Fail.*, **13**, S10.

59. Wishartet, D.S. *et al.* (2007) *Nucleic Acids Res.*, **35**, D521.
60. Han, X. and Gross, R.W. (2003) *J. Lipid Res.*, **44**, 1071.
61. Lahner, B. *et al.* (2003) *Nat. Biotechnol.*, **21** (10), 1215–1221.
62. Williams, R.J.P. (2001) *Coord. Chem. Rev.*, **583**, 216.
63. Szpunar, J. (2005) *Analyst*, **130**, 442.
64. Johnson, S.A. and Hunter, T. (2005) *Nat. Methods*, **2**, 17.
65. Beck, S., Olek, A., and Walter, J. (1999) *Nat. Biotechnol.*, **17**, 1144.
66. Goldberg, A.D., Allis, C.D., and Bernstein, E. (2007) *Cell*, **128**, 635.
67. Esteller, M. (ed.) (2008) *Epigenetics in Biology and Medicine*, CRC Press.
68. Waddington, C.H. (1957) *The Strategy of the Genes: A Discussion of Some Aspects of Theoretical Biology*, Allen & Unwin, London.
69. Feinberg, A.P. (2001) *Nat. Genet.*, **27**, 9.
70. Beck, S. and Rakyan, V.K. (2008) *Trends Genet.*, **24**, 231.
71. Searls, D.B. (2001) *Pharm. J.*, **1**, 88.
72. CAS *http://www.cas.org/* (accessed 21 March 2013).
73. Herold, K.E. and Rasooly, A. (eds) (2009) *Lab-on-a-Chip Technology: Biomolecular Separation and Analysis*, Caister Academic Press.
74. Affymetrix *http://www.affymetrix.com* (accessed 21 March 2013).
75. Life Technologies *http://www.invitrogen.com* (accessed 21 March 2013).
76. Agilent Technologies *http://www.genomics.agilent.com* (accessed 21 March 2013).
77. Turner, A.P.F., Karube, I., and Wilson, G. (eds) (1987) *Biosensors: Fundamentals and Applications*, Oxford University Press, Oxford.
78. Kress-Rogers, E. (ed.) (1996) *Handbook of Biosensors and Electronic Noses*, CRC Press.
79. Ligler, F.S. and Taitt, C.R. (eds) (2002) *Optical Biosensors: Present and Future*, Elsevier, Amsterdam, London, New York, Oxford, Paris, Shannon, Tokyo.
80. Borisov, S.M. and Wolfbeis, O.S. (2008) *Chem. Rev.*, **108**, 423.
81. Nirschl, M., Reuter, F., and Vörös, J. (2011) *Biosensors*, **1**, 70.
82. Wolfbeis, O.S. (ed.) (1991) *Fiber Optic Chemical Sensors and Biosensors*, Vol. 1 and 2, CRC Press, Boca Raton, FL.
83. Wolfbeis, O.S. (2006) *Anal. Chem.*, **78**, 3859. (2008) *Anal. Chem.*, **80**, 4269.
84. Nagel, B., Dellweg, H., and Gierasch, L.M. (1992) *Pure Appl. Chem.*, **64**, 143.
85. Thévenot, D.R., Toth, K., Durst, R.A., and Wilson, G.S. (1999) *Pure Appl. Chem.*, **71**, 2333.
86. Scheller, F.W., Wollenberger, U., Warsinke, A., and Lisdat, F. (2001) *Curr. Opin. Biotechnol.*, **12**, 35.
87. Dittmer, W.U., de Kievit, P., Prins, M.W., Vissers, J.L., Mersch, M.E., and Martens, M.F. (2008) *J. Immunol. Methods*, **338**, 40.
88. Cass, A.E.G., Davis, G., Francis, G.D., Hill, H.A.O., Aston, W.J., Higgins, I.J., Plotkin, E.V., Scott, L.D.L., and Turner, A.P.F. (1984) *Anal. Chem.*, **56**, 667–671.
89. Spichiger-Keller, U.E. (2007) *Chemical Sensors and Biosensors for Medical and Biological Applications*, Wiley-VCH Verlag GmbH, Weinheim.
90. Fan, X., White, I.M., Shopova, S.I., Zhu, H., Suter, J.D., and Sun, Y. (2008) *Anal. Chim. Acta*, **620**, 8.
91. Cooper, M.A. (2003) *Nat. Rev. Drug Discovery*, **1**, 515.
92. Abdiche, Y., Malashock, D., Pinkerton, A., and Pons, J. (2008) *Anal. Biochem.*, **377**, 209.
93. Daiss, J.L. and Scalice, E.R. (1994) *Methods Companion Methods Enzymol.*, **6**, 143.
94. Johne, B. (1998) *Mol. Biotechnol.*, **9**, 65.
95. Myszka, D.G. and Rich, R.L. (2000) *Pharm. Sci. Technol. Today*, **3**, 310.
96. Homola, J. (2008) *Chem. Rev.*, **108**, 462.
97. D'Orazio, P. (2003) *Clin. Chim. Acta*, **334**, 41.
98. Besselink, G.A.J., Kooyman, R.P.H., van Os, P.J.H.J., Engbers, G.H.M., and Schasfoort, R.B.M. (2004) *Anal. Biochem.*, **333**, 165.
99. Liu, X., Sun, Y., Song, D., Zhang, Q., Tian, Y., and Zhang, H. (2006) *Talanta*, **68** (3), 1026.
100. Bates, S. (2010) *Drug Discov. Today*, **15**, 115–120.

101. Gurwitz, D., Weizman, A., and Rehavi, M. (2003) *Trends Pharmacol. Sci.*, **24**, 122–125.

102. Aspinall, M.G. and Hamermesh, R.G. (2007) *Harv. Bus. Rev.*, 10.

103. Vogenberg, R.F., Barash, C.I., and Purcel, M. (2010) *Pharm. Ther.*, **35** (10Pt. 1), 560–576. (11, Pt. 2), 624–642; (12, Pt. 3), 670–675.

104. McCaman, M.W. and Robins, E. (1962) *J. Lab. Clin. Med.*, **59**, 885.

105. Perkin-Elmer Inc.(2013) The Neonatal Phenylalanine Kits. Life Sciences.

106. Guldberg, P. *et al.* (1998) *Am. J. Hum. Genet.*, **63**, 71.

107. Haeckel, R. (ed.) (1993) *Evaluation Methods in Laboratory Medicine*, Wiley-VCH Verlag GmbH, Weinheim.

108. Büttner, J. (1991) *Mitt. Dtsch. Ges. Klin. Chem.*, **22**, 3.

109. Kricka, L.J. (1999) *Clin. Chem.*, **45**, 942.

110. Babuin, L. and Jaffe, A.S. (2005) *Can. Med. Assoc. J.*, **173**, 1191.

111. Mohr, G.J. *et al.* (2002) *Anal. Sci.*, **18**, 109.

112. Bobacka, J., Ivaska, A., and Lewenstam, A. (2008) *Chem. Rev.*, **108**, 329.

113. Baldini, F., Chester, A.N., Homola, J., and Martellucci, S. (eds) (2006) *Optical Chemical Sensors*, Springer, Dordrecht.

114. Tohda, K., Yoshiyagawa, S., and Umezawa, Y. (1997) *J. Mol. Struct.*, **408–409**, 155.

115. O'Neill, S., Conway, S., Twellmeyer, J., Egan, O., and Diamond, D. (1999) *Anal. Chim. Acta*, **398**, 1.

116. Wang, E., Zhu, L., Ma, L., and Patel, H. (1997) *Anal. Chim. Acta*, **357**, 85.

117. Hisamoto, H., Miyashita, N., Watanabe, K., Nakagawa, E., Yamamoto, N., and Suzuki, K. (1995) *Sens. Actuators, B*, **29**, 378.

118. Suzuki, K., Ohzora, H., Tohda, K., Miyazaki, K., Watanabe, K., Inoue, H., and Shirai, T. (1990) *Anal. Chim. Acta*, **237**, 155.

119. Fluka AG (1998) Selectophore Product Range.

120. Wolfbeis, O.S. (1995) *Sens. Actuators, B*, **29**, 140.

121. Mohr, G.J., Murkovic, I., Lehmann, F., Haider, C., and Wolfbeis, O.S. (1997) *Sens. Actuators, B*, **39**, 239.

122. Kawabata, Y., Yamashiro, T., Kitazaki, Y., and Imasaka, T. (1995) *Sens. Actuators, B*, **29**, 135.

123. Podbielska, H., Ulatowska-Jarża, A., Müller, G., and Eichler, H.J. (2006) Sol-gels for optical sensors, in *Optical Chemical Sensors* (eds F. Baldini, A.N. Chester, J. Homola, and S. Martellucci) Chapter 17, Springer, Dordrecht.

124. Goicoechea, J., Zamarreño, C.R., Matias, I.R., and Arregui, F.J. (2008) *Sens. Actuators, B*, **132**, 305.

125. Clark, H.A., Kopelman R., Tjalkens R., and Philbert M.A. (1999) *Anal. Chem.*, **71**, 4837.

126. Brasuel, M., Kopelman, R., Miller, T.J., Tjalkens, R., and Philbert, M.A. (2001) *Anal. Chem.*, **73**, 2221.

127. Park, E.J., Brasuel, M., Behrend, C., Philbert, M.A., and Kopelman, R. (2003) *Anal. Chem.*, **75**, 3784.

128. Sumner, J.P., Westerberg, N.M., Stoddard, A.K., Fierke, C.A., and Kopelman, R. (2006) *Sens. Actuators, B*, **113**, 760.

129. Sumner, J.P., Aylott, J.W., Monson, E., and Kopelman, R. (2002) *Analyst*, **127**, 11.

130. Xu, H., Aylott, J.W., and Kopelman, R. (2002) *Analyst*, **127**, 1471.

131. Cao, Y., Lee Koo, Y.-E., and Kopelman, R. (2004) *Analyst*, **129**, 745.

132. Czarnik, A.W. (ed.) (1993) *Fluorescent Chemosensors for Ion and Molecule Recognition*, ACS Symposium Series, Vol. 538, American Chemical Society, Washington, DC.

133. Chapoteau, E., Czech, B.P., Zazulak, W., and Kumar, A. (1992) *Clin. Chem.*, **38**, 1654.

134. Iwamoto, K., Araki, K., Fujishima, H., and Shinkai, S. (1992) *J. Chem. Soc., Perkin Trans. 1*, **92**, 1885.

135. Harris, S.J., Barrett, G., McKervey, M.A., and Diamond, D.J. (1992) *J. Chem. Soc., Chem. Commun.*, **92**, 1287.

136. Dilek, G. and Akkaya, E.U. (2000) *Tetrahedron Lett.*, **41**, 3721.

137. Akkaya, E.U. and Turkyilmaz, S. (1997) *Tetrahedron Lett.*, **38**, 4513.

138. Nolan, E.M. and Lippard, S.J. (2008) *Acc. Chem. Res.*, **42**, 193.

139. Borisov, S.M., Krause, C., Arain, S., and Wolfbeis, O.S. (2006) *Adv. Mater.*, **18**, 1511.
140. Hartley, A.M., House, W.A., Callow, M.E., and Leadbeater, B.S.C. (2000) *Int. J. Environ. Anal. Chem.*, **76**, 199.
141. Kivlehan, K., Mace, W.J., Moynihan, H.A., and Arrigan, D.W.M. (2007) *Anal. Chim. Acta*, **585**, 154.
142. Mohr, G.J. and Wolfbeis, O.S. (1995) *Anal. Chim. Acta*, **316**, 239.
143. Hauser, P.C. *et al.* (1990) *Anal. Chem.*, **62**, 1919.
144. Mohr, G.J. (2002) *J. Chem. Soc., Chem. Commun.*, 2646.
145. Shamsipur, M. *et al.* (2006) *Sens. Actuators, B*, **113**, 892.
146. Korostynska, O., Arshak, K., Gill, E., and Arshak, A. (2007) *Sensors*, **7**, 3027.
147. Mohr, G.J. and Wolfbeis, O.S. (1994) *Anal. Chim. Acta*, **292**, 41.
148. Zhang, X. *et al.* (2001) *Anal. Chim. Acta*, **445**, 57.
149. Dong, S., Luo, M., Peng, G., and Cheng, W. (2008) *Sens. Actuators, B*, **129**, 94.
150. Seki, A., Katakura, H., Kai, T., Iga, M., and Watanabe, K. (2007) *Anal. Chim. Acta*, **582**, 154.
151. McCulloch, S. and Uttamchandani, D. (1997) *IEE Proc. Optoelectron.*, **144**, 162.
152. Talley, C.E., Jusinski, L., Hollars, C.W., Lane, S.M., and Huser, T. (2004) *Anal. Chem.*, **76**, 7064.
153. Tsai, H.-C. and Doong, R.-A. (2005) *Biosens. Bioelectron.*, **20**, 1796.
154. Ozawa, S. (1991) *Anal. Chem.*, **63**, 640.
155. Seiler, K. and Fresenius, J. (1990) *Anal. Chem.*, **337**, 109.
156. Brasuel, M., Miller, T.J., Kopelman, R., Philbert, M.A., and Kasman, I. (2002) *Proc. IEEE Sensors.*, **1**, 288.
157. Buchholz, F., Buschmann, N., and Cammann, K. (1992) *Sens. Actuators, B*, **9**, 41.
158. Ngeontae, W., Xu, C., Yea, N., and Wygladacz, K. (2007) *Anal. Chim. Acta*, **599**, 124.
159. Szmacinski, H. and Lakowicz, J.R. (1999) *Sens. Actuators, B*, **60**, 8.
160. Wang, K. (1990) *Anal. Sci.*, **6**, 7.
161. Krause, C., Werner, T., Huber, C., Wolfbeis, O.S., and Leiner, M.J.P. (1999) *Anal. Chem.*, **71**, 1544.
162. West, S.J. *et al.* (1992) *Anal. Chem.*, **64**, 533.
163. Chen, H., Cheng, H., Oh, M.-C., Kim, J.-H., Choi, H.-J., Kim, H.-S., Lee, J., and Koh, K. (2007) *Anal. Lett.*, **40**, 3373.
164. Wolfbeis, O.S. and Li, H. (1991) *Proc. SPIE.*, **1587**, 48.
165. Reichert, J., Sellien, W., and Ache, H.J.W. (1991) *Sens. Actuators, A*, **26**, 481.
166. Tan, S.S. *et al.* (1991) *Anal. Chim. Acta*, **255**, 35.
167. Huber, C., Krause, C., Werner, T., and Wolfbeis, O.S. (2003) *Microchim. Acta*, **142**, 245.
168. Bey, A.K. *et al.* (2008) *Sens. Actuators, A*, **141**, 390.
169. Schazmann, B., Alhashimy, N., and Diamond, D. (2006) *J. Am. Chem. Soc.*, **128**, 8607.
170. Weigl, B.H. and Wolfbeis, O.S. (1995) *Sens. Actuators, B*, **28**, 151.
171. Müller, B. and Hauser, P.C. (1996) *Analyst*, **121**, 339.
172. Burke, C.S., Markey, A., Nooney, R.I., Byrne, P., and McDonagh, C. (2006) *Sens. Actuators, B*, **119**, 288.
173. Moelders, N., McNeal, M.P., Pralle, M.U., Last, L., Ho, W., Greenwald, A.C., Daly, J.T., Johnson, E.A., George, T., and Choi, D.S. (2001) *Proc. SPIE Int. Soc. Opt. Eng.*, **4561**, 305.
174. Cajlakovic, M., Bizzarri, A., and Ribitsch, V. (2006) *Anal. Chim. Acta*, **573–574**, 57.
175. Segawa, H., Ohnishi, E., Arai, Y., and Yoshida, K. (2003) *Sens. Actuators, B*, **94**, 276.
176. Shimizu, Y., Furuta, Y., and Yamashita, T. (1999) *Trans. Inst. Electric. Eng. Jpn., Part E*, **119**, 285.
177. Sasaki, S.-I., Citterio, D., Ozawa, S., and Suzuki, K. (2001) *J. Chem. Soc., Perkin Trans. 2*, 2309.
178. Morais, I.P.A., Miro, M., Manera, M., Estela, J.M., Cerda, V., Souto, M., Renata, M.S., and Rangel, A.O.S. (2004) *Anal. Chim. Acta*, **506**, 17.
179. Roche, P., Al-Jowder, R., Narayanaswamy, R., Young, J., and Scully, P. (2006) *Anal. Bioanal. Chem.*, **386**, 1245.

180. McCulloch, S. and Uttamchandani, D. (1999) *Proc. IEE Sci. Meas. Technol.*, **146**, 123.

181. Voraberger, H.S., Kreimaier, H., Biebernik, K., and Kern, W. (2001) *Sens. Actuators, B*, **74**, 179.

182. Schaffar, B.P.H. and Wolfbeis, O.S. (1990) *Biosens. Bioelectron.*, **5**, 137.

183. Porterfield, D.M., Rickus, J.L., and Kopelman, R. (2006) *Proc. SPIE Int. Soc. Opt. Eng.*, **6380**, 63800S.

184. Morf, W.E. (1990) *Anal. Chem.*, **62**, 738.

185. Yari, A. and Afshari, N. (2006) *Sens. Actuators, B*, **119**, 531.

186. Gholivand, M.B., Niroomandi, P., Yari, A., and Joshagani, M. (2005) *Anal. Chim. Acta*, **538**, 225.

187. Aksuner, N., Henden, E., Yilmaz, I., and Cukurovali, A. (2008) *Sens. Actuators, B*, **134**, 510.

188. Lopes da Conceicao, A.C., Tena, M.T., Correia dos Santos, M.M., and SimoesGoncalves, M.L. (1997) *Anal. Chim. Acta*, **343**, 191.

189. Pons, C., Forteza, R., and Cerda, V. (2005) *Anal. Chim. Acta*, **528**, 197.

190. Oter, O., Ertekin, K., Kirilmis, C., Koca, M., and Ahmedzade, M. (2007) *Sens. Actuators, B*, **122**, 450.

191. Lee, S.T., Kumar, P., Suresh, U.K.P., Nampoori, V.P.N., Vallabhan, C.P.G., Sugunan, S., and Radhakrishnan, P. (2003) *Meas. Sci. Technol.*, **14**, 858.

192. Saris, N.-E.L., Mervaala, E., Karppanen, H., Khawaja, J.A., and Lewenstam, A. (2000) *Clin. Chim. Acta*, **294**, 1.

193. Capitan-Vallvey, L.F., Fernandez-Ramos, M.D., Lapresta-Fernandez, A., Brunet, E., Rodriguez-Ubis, J.C., and Juanes, O. (2006) *Talanta*, **68**, 1663.

194. Coo, L.D. and Martinez, I.S. (2004) *Talanta*, **64**, 1317.

195. Rastegarzadeh, S. and Rezaei, V. (2008) *Sens. Actuators, B*, **129**, 327.

196. Jeronimo, P.C.A., Araujo, A.N., Montenegro, M., and Conceicao, B.S.M. (2004) *Sens. Actuators, B*, **103**, 169.

197. Choi, M.M.F. (2004) *Microchim. Acta*, **148**, 107.

198. Ballester, P., Shivanyuk, A., Far, A.R., and Rebek, J. Jr., (2002) *J. Am. Chem. Soc.*, **124**, 14014.

199. Beckles, D.L., Maioriello, J., Santora, V.J., Bell, T.W., Chapoteau, E., Czech, B.P., and Kumar, A. (1995) *Tetrahedron*, **51**, 363.

200. Sandanayake, K.R.A.L. and Sutherland, I.O. (1993) *Tetrahedron Lett.*, **34**, 3165.

201. Kimura, K., Yamashita, T., and Yokoyama, M. (1992) *J. Chem. Soc., Perkin Trans.*, **92**, 613.

202. Fages, F., Desvergne, J.-P., Kampke, K., Bouas-Laurent, H., Lehn, J.-M., Meyer, M., and Albrecht-Gary, A.-M. (1993) *J. Am. Chem. Soc.*, **115**, 3658.

203. Bourson, J., Pouget, J., and Valeur, B. (1993) *J. Phys. Chem.*, **87**, 4552.

204. Diamond, D. and Nolan, K. (2001) *Anal. Chem.*, **73**, 22A.

205. Gale, P.A., Chen, Z., Drew, M.G.B., Heath, J.A., and Beer, P.D. (1998) *Polyhedron*, **17**, 405.

206. Odashima, K., Yagi, K., Tohda, K., and Umezawa, Y. (1999) *Bioorg. Med. Chem. Lett.*, **9**, 2375.

207. Grady, T., Harris, S.J., Smyth, M.R., and Diamond, D. (1996) *Anal. Chem.*, **68**, 3775.

208. Aoki, I., Sakaki, T., Tsutsui, S., and Shinkai, S. (1992) *Tetrahedron Lett.*, **33**, 89.

209. Kukrer, B. and Akkaya, E.U. (1999) *Tetrahedron Lett.*, **40**, 9125.

210. Sansubrino, A. and Mascini, M. (1994) *Biosens. Bioelectron.*, **9**, 207.

211. Wolfbeis, O.S. and Li, H. (1993) *Biosens. Bioelectron.*, **8**, 161.

212. Kovacs, B., Nagy, G., Dombi, R., and Toth, K. (2003) *Biosens. Bioelectron.*, **18**, 111.

213. Bell, T.W. and Hou, Z. (1997) *Angew. Chem., Int. Ed. Engl.*, **36**, 1536.

214. Schrenkhammer, P. and Wolfbeis, O.S. (2008) *Biosens. Bioelectron.*, **24**, 1000.

215. Wu, F., Huang, Y., and Li, Q. (2005) *Anal. Chim. Acta*, **536**, 107.

216. Gong, Z. and Zhang, Z. (1996) *Anal. Lett.*, **29**, 695.

217. Subrahmanyam, S., Piletsky, S.A., Piletska, E.V., Chen, B., Karim, K., and Turner, A.P.F. (2001) *Biosens. Bioelectron.*, **16**, 631.

218. Tsai, H.-A. and Syu, M.-J. (2005) *Anal. Chim. Acta*, **539**, 107.

219. Hsieh, R.-Y., Tsai, H.-A., and Syu, M.-J. (2006) *Biomaterials*, **27**, 2083.

220. Bell, T.W., Hou, Z., Luo, Y., Drew, M.G.B., Chapoteau, E., Czech, B.P., and Kumar, A. (1995) *Science*, **269**, 671.

221. Subat, M., Borovik, A.S., and Konig, B. (2004) *J. Am. Chem. Soc.*, **126**, 3185.

222. Duerkop, A., Schaeferling, M., and Wolfbeis, O.S. (2006) in *Topics in Fluorescence Spectroscopy*, Vol. 11 (eds C.D. Geddes and J.R. Lakowicz), Springer-Verlag, New York, p. 351.

223. Van de Bovenkamp, H.J., Antonisse, M.M.G., Engbersen, J.F.J., Reinhoudt, D.N., Hesselink, G.L.J., Lambeck, P.V., and Popma, T.J.A. (1995) *Sens. Actuators, B*, **29**, 312.

224. Striegler, S. (2003) *Curr. Org. Chem.*, **7**, 81.

225. Horgan, A.M., Marshall, A.J., Kew, S.J., Dean, K.E.S., Creasey, C.D., and Kabilan, S. (2006) *Biosens. Bioelectron.*, **21**, 1838.

226. Peng, B. and Qin, Y. (2008) *Anal. Chem.*, **80**, 6137.

227. Friggeri, A., Kobayashi, H., Shinkai, S., and Reinhoudt, D.N. (2001) *Angew. Chem. Int. Ed.*, **40**, 4729.

228. Ballerstadt, R. and Schultz, J.S. (2000) *Anal. Chem.*, **72**, 4185.

229. Stuart, D.A., Yuen, J.M., Shah, N., Lyandres, O., Yonzon, C., Glucksberg, M.R., Walsh, J.T., and Van Duyne, R.P. (2006) *Anal. Chem.*, **78**, 7211.

230. Pasic, A., Koehler, H., Schaupp, L., Pieber, T.R., and Klimant, I. (2006) *Anal. Bioanal. Chem.*, **386**, 1293.

231. Cavaliere-Jaricot, S., Darbandi, M., Kucur, E., and Nann, T. (2008) *Microchim. Acta*, **160**, 375.

232. Wu, M., Lin, Z., Duerkop, A., and Wolfbeis, O.S. (2004) *Anal. Bioanal. Chem.*, **380**, 619.

233. Schaeferling, M., Wu, M., and Wolfbeis, O.S. (2004) *J. Fluoresc.*, **14**, 561.

234. Wu, M., Lin, Z., Schaeferling, M., Duerkop, A., and Wolfbeis, O.S. (2005) *Anal. Biochem.*, **340**, 66.

235. Kim, D.-H., Ilev, I.K., Kang, J.U., (2007) proceedings IEEE Lasers and Electro-Optics Society Annual Meeting, LEOS 2007, p. 226.

236. Lambrecht, A., Beyer, T., Hebestreit, K., Mischler, R., and Petrich, W. (2006) *Appl. Spectrosc.*, **60**, 729.

237. Mohr, G. and Spichiger, U. (1997) *Anal. Chim. Acta*, **344**, 215.

238. Bezunartea, M., Estella, J., Echeverria, J.C., Elosua, C., Bariain, C., Laguna, M., Luquin, A., and Garrido, J.J. (2008) *Sens. Actuators, B*, **134**, 966.

239. De Marcos, S., Galban, J., Albajez, R., and Castillo, J.R. (1997) *Anal. Chim. Acta*, **343**, 117.

240. Xie, X., Suleiman, A.A., Guilbaut, G.G., Yang, Z., and Sun, Z. (1992) *Anal. Chim. Acta*, **266**, 325.

241. Penza, M., Cassano, G., Aversa, P., Antolini, F., Cusano, A., Cutolo, A., Giordano, M., and Nicolais, L. (2004) *Appl. Phys. Lett.*, **85**, 2379.

242. Vidal, M.M., Delgadillo, I., Gil, M.H., and Alonso-Chamarro, J. (1996) *Biosens. Bioelectron.*, **11**, 347.

243. Baldini, F. (2003) *Anal. Bioanal. Chem.*, **375**, 732.

244. Li, X. and Rosenzweig, Z. (1997) *Anal. Chim. Acta*, **353**, 263.

245. Marazuela, M.D., Cuesta, B., Moreno-Bondi, M.C., and Quejido, A. (1997) *Biosens. Bioelectron.*, **12**, 233.

246. Trettnak, W. and Wolfbeis, O.S. (1990) *Anal. Biochem.*, **184**, 124.

247. Wu, X.J. and Choi, M.M.F. (2003) *Anal. Chem.*, **75**, 4019.

248. Gerlach, J., Pohn, B., Karl, W., Scheideler, M., Uray, M., Bischof, H., Schwab, H., and Klimant, I. (2006) *Sens. Actuators, B*, **114**, 984.

249. Marquette, C.A., Leca, B.D., and Blum, L.J. (2001) *Luminescence*, **16**, 159.

250. Tsafack, V.C., Marquette, C.A., Leca, B.D., and Blum, L.J. (2000) *Analyst*, **125**, 151.

251. Wu, M.-H., Wang, J., Taha, T., Cui, Z., Urban, J.P.G., and Cui, Z. (2007) *Biomed. Microdevices*, **9**, 167.

252. Ignatov, S.G., Ferguson, J.A., and Walt, D.R. (2001) *Biosens. Bioelectron.*, **16**, 109.

253. Trettnak, W. and Wolfbeis, O.S. (1989) *Fresenius' J. Anal. Chem.*, **334**, 427.

254. Blum, L.J., Gautier, S.M., Berger, A., Michel, P.E., and Coulet, P.R. (1995) *Sens. Actuators, B*, **29**, 1.

255. Scheper, T. and Buckmann, A.F. (1990) *Biosens. Bioelectron.*, **5**, 125.

256. Kotsira, V.P. and Clonis, Y.D. (1998) *J. Agric. Food Chem.*, **46**, 3389.

257. Gautier, S.M., Blum, L.J., and Coulet, P.R. (1990) *Anal. Chim. Acta*, **235**, 243.

258. Michael, P.E., Gautier-Sauvigne, S.M., and Blum, L.J. (1998) *Talanta*, **47**, 169.

259. Christison, G.B. and MacKenzie, H.A. (1993) *Med. Biol. Eng. Comput.*, **31**, 284.

260. Bednov, A., Karabutov, A., Savateeva, E., March, W., and Oraevsky, A. (2000) *Proc. SPIE Int. Soc. Opt. Eng.*, **3916**, 9.

261. von Lilienfeld-Toal, H., Weidenmuller, M., Xhelaj, A., and Mantele, W. (2005) *Vib. Spectrosc.*, **38**, 209.

262. Kinnunen, M. and Myllyla, R. (2005) *J. Phys. D: Appl. Phys.*, **38**, 2654.

263. Upadhya1, P.C., Shen, Y.C., Davies, A.G., and Linfield, E.H. (2003) *J. Biol. Phys.*, **29**, 117.

264. Yotter, R.A., Lee, L.A., and Wilson, D.M. (2004) *IEEE Sens.*, **4**, 395.

265. Herm, M., Molt, O., and Schrader, T. (2002) *Chem. Eur. J.*, **8**, 1485.

266. Wang, X., Chen, H., Lin, J.-M., and Ying, X. (2007) *Int. J. Biol. Sci.*, **3**, 274.

267. Stefan, R.-I., van Staden, J.F., and Aboul-Enein, H.Y. (2004) *Talanta*, **64**, 151.

268. Mitsuma, T., Colucci, J., Shenkman, L., and Hollander, C.S. (1972) *Biochem. Biophys. Res. Commun.*, **24**, 2107.

269. Zhou, J.C., Chuang, M.H., Lan, E.H., Dunn, B.S., Gillman, P.L., and Smith, S.M. (2003) *Proc. SPIE Int. Soc. Opt. Eng.*, **4878**, 27.

270. Tschmelak, J., Kumpf, M., Käppel, N., Proll, G., and Gauglitz, G. (2006) *Talanta*, **69**, 343.

271. Schultz, J.S., Mansouri, S., and Goldstein, I.J. (1982) *Diabetes Care*, **5**, 245.

272. Ballerstadt, R., Polak, A., Beuhler, A., and Frye, J. (2004) *Biosens. Bioelectron.*, **19**, 905.

273. Marvin, J.S. and Hellinga, H.W. (1998) *J. Am. Chem. Soc.*, **120**, 7.

274. Reck, B., Himmelspach, K., Opitz, N., and Luebbers, D.W. (1988) *Analyst*, **113**, 1423.

275. Kolusheva, S., Molt, O., Herm, M., Schrader, T., and Jelinek, R. (2005) *J. Am. Chem. Soc.*, **127**, 10000.

276. Piletsky, S. and Turner, A.P.F. (eds) (2006) *Molecular Imprinting of Polymers*, Landes Bioscience, Georgetown, TX.

277. Hishiya, T., Shibata, M., Kakazu, M., Asanuma, H., and Komiyama, M. (1999) *Macromolecules*, **32**, 2265.

278. Dong, H., Tong, A.-J., and Li, L. (2003) *Spectrochim. Acta, Part A*, **59A**, 279.

279. Piletsky, S.A. and Turner, A.P.F. (2002) in *Optical Biosensors: Present and Future* (eds F.S. Ligler and C.R. Taitt), Elsevier, Amsterdam, London, New York, Oxford, Paris, Shannon, Tokyo, p. 397.

280. Kriz, D., Ramström, O., Svensson, K., and Mosbach, K. (1995) *Anal. Chem.*, **67**, 2142.

281. Ye, L. and Mosbach, K. (2008) *Chem. Mater.*, **20**, 859.

282. Kim, J.-M., Ahn, K.-D., and Wulff, G. (2001) *Macromol. Chem. Phys.*, 1105–1108.

283. Wolfbeis, O.S., Terpetschnig, E., Piletsky, S., and Pringsheim, E. (1999) in *Appied Fluorescence in Chemistry, Biology and Medicine* (ed. W. Rettig), Springer-Verlag, Heidelberg, p. 277.

284. Turkewitsch, P., Wandelt, B., Darling, G.D., and Powell, W.S. (1998) *Anal. Chem.*, **70**, 2025–2030.

285. Rathbone, D.L., Su, D., Wang, Y., and Billington, D.C. (2000) *Tetrahedron Lett.*, **41**, 123–126.

286. Piletsky, S.A., Piletskaya, E.V., Sergeyeva, T.A., Panasyuk, T.L., and El'skaya, A.V. (1999) *Sens. Actuators, B*, **60**, 216.

287. Mirsky, V.M., Hirsch, T., Piletsky, S.A., and Wolfbeis, O.S. (1999) *Angew. Chem. Int. Ed.*, **38**, 1108.

288. Tappura, K., Albers, W.M., and Vikholm-Lundin (2007) *Biosens. Bioelectron.*, **22**, 912.

289. Vikholm-Lundin, I., Pulli, T., Albers, W.M., and Tappura, K. (2008) *Biosens. Bioelectron.*, **24**, 1036.

290. Baggiani, C. and Giovannoli, C. (2006) Bioimprinting, in *Molecular Imprinting of Polymers* (eds S. Piletsky and A.P.F. Turner), Landes Bioscience, Georgetown, TX.

291. Takeuchi, T. and Hishiya, T. (2008) *Org. Biomol. Chem.*, **6**, 2459.

292. Bright, F.V., Betts, T.A., and Litwiler, K.S. (1990) *Anal. Chem.*, **62**, 1065.

293. Zhou, Y., Magill, J.V., De La Rue, R.M., and Laybourn, P.J.R. (1993) *Sens. Actuators, B*, **11**, 245.

294. McCormack, T., O'Keeffe, G., MacCraith, B.D., and O'Kennedy, R. (1997) *Sens. Actuators, B*, **41**, 89.

295. Rasooly, A. and Jacobson, J. (2006) *Biosens. Bioelectron.*, **21**, 1851.

296. Black, M.H., Grass, C.L., Leinonen, J., Stenman, U.-H., and Diamandis, E.P. (1999) *Clin. Chem.*, **45**, 347.

297. Katsamba, P.S., Navratilova, I., and Myszka, D.G. (2006) *Anal. Biochem.*, **352**, 208.

298. Pleschberger, M., Saerens, D., Weigert, S., Sleytr, U.B., Muyldermans, S., Sára, M., and Egelseer, E.M. (2004) *Bioconjugate Chem.*, **15**, 664.

299. Choi, J.W., Kang, D.Y., Jang, Y.H., Kim, H.H., Min, J., and Oh, B.K. (2008) *Colloids Surf., A*, **313**, 655.

300. Englebeinne, P., van Hoonacker, A., and Verhas, M. (2003) *Spectroscopy*, **17**, 255.

301. Englebeinne, P. (1998) *Analyst*, **123**, 1599.

302. Déjardin, P. (ed.) (2006) *Proteins at Solid–Liquid Interfaces (Principles and Practice)*, Springer-Verlag, Berlin.

303. Albers, W.M., Vikholm, I., Viitala, T., and Peltonen, J. (2001) Interfacial and materials aspects of the immobilisation of biomolecules onto solid surfaces, in *Handbook of Surfaces and Interfaces of Materials*, Vol. 5 Chapter I (ed. H.S. Nalwa), Academic Press, San Diego, CA.

304. Cass, T. and Ligler, F.S. (1998) *Immobilized Biomolecules in Analysis*, Oxford University Press, Oxford.

305. Gedig, E.T. (2008) Surface chemistry in SPR technology, in *Handbook of Surface Plasmon Resonance* (eds R.B.M. Schasfoort and A.J. Tudos) Chapter 6, RSC Publishing, Cambridge.

306. Cui, X., Pei, R., Wang, Z., Yang, F., Ma, Y., Dong, S., and Yang, X. (2003) *Biosens. Bioelectron.*, **18**, 59.

307. Shriver-Lake, L.C., Donner, B., Edelstein, R., Breslin, K., Bhatia, S.K., and Ligler, F.S. (1997) *Biosens. Bioelectron.*, **12**, 1101.

308. Hoffman, W.L. and O'Shannessy, D.J. (1988) *J. Immunol. Methods*, **112**, 113.

309. Vikholm-Lundin, I. and Albers, W.M. (2006) *Biosens. Bioelectron.*, **21**, 1141.

310. Bonroy, K., Frederix, F., Reekmans, G., Dewolf, E., De Palma, R., Borghs, G., Declerck, P., and Goddeeris, B. (2006) *J. Immunol. Methods*, **312**, 167.

311. Ostuni, E., Chapman, R.G., Holmlin, R.E., Takayama, S., and Whitesides, G.M. (2001) *Langmuir*, **17**, 5605.

312. Molt, O., Rubeling, D., and Schrader, T. (2003) *J. Am. Chem. Soc.*, **125**, 12086.

313. Abdullah, J., Ahmad, M., Heng, L.Y., Karuppiah, N., and Sidek, H. (2007) *Sensors*, **7**, 2238.

25

Quality Assessment of Spectroscopic Methods in Clinical Laboratories

Heike Schneider, Georg Kurz, and Peter B. Luppa

25.1

Introduction

Clinical chemistry is concerned with the clinical diagnosis and prognosis of disease and with patient therapy monitoring through the analyses of body fluids for specific (patho)physiological constituents. Diagnostic inputs by clinical chemistry analyses are important for more than 60% of all diseases treated in hospitals and in outpatient clinics. Specimens of blood, serum, plasma, urine, cerebrospinal fluids, other body fluids, and feces provide the samples for the various measurements in order to diagnose illness or to monitor the disease progress.

The modern clinical laboratory is characterized by the mostly automated utilization of a wide variety of techniques and equipment. These analyzers require constant maintenance and performance surveillance, as well as internal quality control and external ring trials. In Figure 25.1, some examples of commonly used analyzers with photometric units are shown.

25.2

Spectroscopic Methods in Clinical Chemistry

25.2.1

Overview

More than 90% of the analyses in clinical laboratories are based on photometric methods. Analyses done by spectroscopic methods vary from high concentrated analytes such as electrolytes, substrates, metabolites, or enzymes to the low concentrated micronutrients. In addition, spectroscopic methods are used for drug monitoring in different concentration ranges. The methods include an assortment of detection methods such as UV–Vis (ultraviolet and visible), fluorescence spectroscopy, and infrared spectroscopy in the field of molecular assays as well as flame atom emission spectrometry (F-AES) and atom absorption spectrometry (AAS) in the field of atom quantitation. Each method requires a superior specificity

Handbook of Spectroscopy, Second Edition. Edited by Günter Gauglitz and David S. Moore.

Abbott diagnostics:
Architect c8000 series

Roche diagnostics:
Cobas 6000 series

Beckman coulter:
UniCel® DxC 800 Synchron® system

Siemens healthcare diagnostics:
Dimension Vista® 3000 T system

Figure 25.1 Examples of automated clinical chemistry analyzers.

for the analyte and should be coupled with efficient sample preparation and/or separation technologies.

When choosing an appropriate analytical method in the clinical laboratory – as in other fields – a compromise must be found for the pivotal issues requirements, feasibility, practicability, and affordability. Adjacent to analytical aspects, the fundamentals of the already established quality assessment schemes in clinical chemistry have to be applied during method development.

25.2.2
Basic Requirements for Quality Assessment in Clinical Chemistry

Four main fields contributing to quality assessment in clinical chemistry in general have to be focused on:

- method validation;
- standardization;
- instrument performance surveillance;
- statistical quality control (internal, external).

The latter two, that is, the application of statistical quality control and the instrument surveillance performance are the central topics of this chapter. The first two aspects are typically part of the assay certification and covered by assay manufacturers. These issues are not the main subject of this chapter, but as there is a close relation to the instrument performance and statistical quality control, some important facets are discussed here.

Basic requirements for the utilized methods are adequate sensitivity and specificity for the analyte as well as the required precision and the linearity of the calibration. For the application in clinical chemistry analysis, particular attention should be paid to possible interference and the robustness of the method. In addition, calibrator and control material have to be internationally standardized.

Sensitivity and linearity are well characterized by the lower limit of quantification (LLOQ), the upper limit of quantification (ULOQ) as well as the r^2 value. These characteristics are determined during method validation, but might change during application. Thus, instrument performance surveillance as well as statistical quality assessment are strongly advised (Figure 25.2).

25.3
Quality Assessment by Basic Technical Prerequisites

25.3.1
Instrument Performance Surveillance and Preclusion of Sample-Dependent Variations in Different Spectroscopic Methods

A series of instrument factors and requirements dictate the sensitivity, stability, selectivity, robustness, and accuracy of the measurement. But the principle of

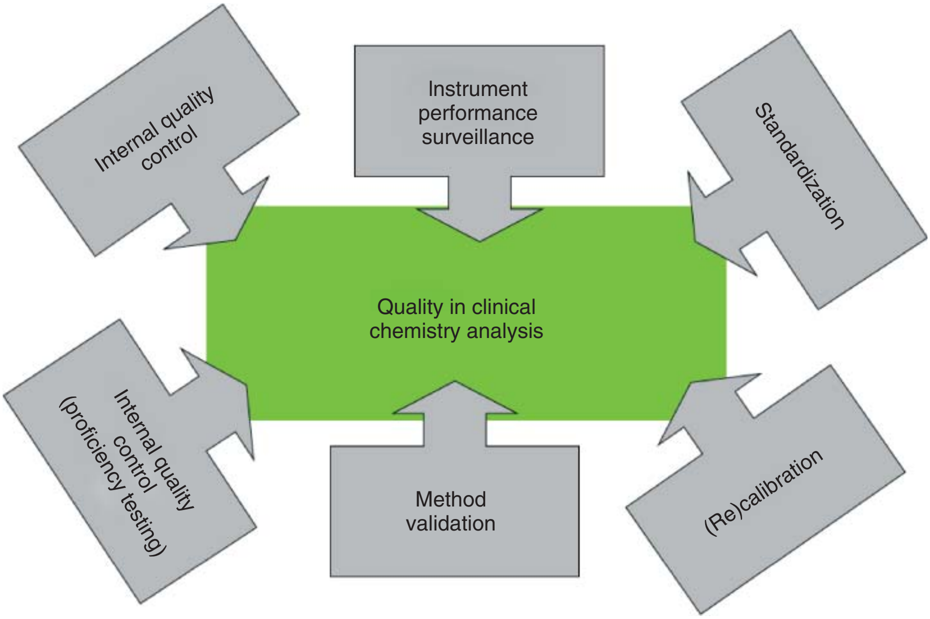

Figure 25.2 Capital fields contribute to quality assessment in clinical chemistry in general: instrument performance surveillance, method validation, standardization and statistical quality control, (re)calibration, and proficiency testing.

operation and the nature of the detected optical signal also contribute to the analytical performance.

Most of the above-mentioned basic requirements have to be considered before or checked during method validation. There are a series of factors that shift during the use of the instrument. For example, changes in the intensities of the light source affect the sensitivity of *AAS*, *flame atom emission spectroscopy* (*F-AES*), *Fourier transform infrared* (*FTIR*) spectroscopy, *fluorescence* or *UV–Vis measurements* and therefore the LLOQ. As most methods are performed using external standard calibration curves, the linearity and the ULOQ might also be affected by instrument changes. Some factors are monitored by modern instruments before the start of routine measurements as so-called *instrument self-check*. Otherwise, the instrument has to be checked by the user. Instrument self-checks and/or user-induced checks (to be defined for each instrument and each test configuration) should be passed according to a defined timetable and invariably after every service intervention.

An automated processing mode should warrant the requirements for analyzing the samples. The requirements to analyze samples refer to sample-dependent variations, given by the *matrix effects* of biological materials used in clinical chemistry. Some of the matrix effects are well known, such as hemolysis-caused effects. Some others, however, are patient specific and hard to define. Certain effects can be compensated for, for example, by using internal standards (ISs), but others lead to determination errors. These samples have to be excluded from the analysis.

Subsequently, it is stated which instrument and sample specific provisions are made for the different spectroscopic methods in clinical chemistry.

25.3.2
FTIR

Urinary tract concrements are investigated by the use of middle infrared (MIR) or classical infrared (MIR; wave number: 4000 to 400 cm^{-1}; wave length: 2.5–25 μm). The qualitative analysis of urinary stones (mostly urates, calcium oxalates, and phosphates) and, infrequently, gallstones is, at present, the only routine application of FTIR in the clinical laboratory [1].

There are two methods to prepare solid materials as urinary stones for FTIR. First, it is possible to dilute the well-pestled stone in dry potassium bromide (KBr) to prepare a KBr pellet. Second, attenuated total reflectance (ATR) can be used to analyze the pestled urinary stone directly. Sample preparation for ATR is quite simple, as the material is directly placed onto the diamond face of the measuring chamber. The preparation of KBr pellets is time consuming and needs well-trained technicians, as nonuniformly prepared KBr pellets lead to poorly reproducible analytical results. However, to date, KBr pellets are still used more frequently than ATR to analyze urinary stones. This refers to the interpretation of the data.

Both, ATR and KBr pellet spectra are analyzed by the comparison to databases entries in a qualitative mode. Almost all commercially available databases are established for KBr pellets. A switch between the ATR and KBr technique may lead to shifts in band intensities and result in worse spectra comparability. Presently, databases using ATR for measuring are in preparation. On completion of this databases, ATR can be used for routine analysis of urinary stones, to make sample preparation much simpler.

FTIR is used for qualification of urinary stones without calibration in terms of concentration, as there is no clinical need to quantify the composition better than ±10%. Nevertheless, there are some quality issues that should be considered using the FTIR system. The exact and reproducible position and band intensities should be guaranteed. Interferences should be avoided or at least identified.

During initialization, modern FTIR systems automatically check source, laser, scan, and calibration. A user-initialized system validation should be performed at least once a month. For this purpose a polystyrene sample is integrated into the system. In the automatically performed validation process, the position of the bands, band intensities, as well as the noise of the system are tested. A background correction is carried out per working day by the user.

Water leads to interferences in the FTIR spectrum; for this reason, urinary concrements are to be dried well and exhaustively dried KBr should be applied. In addition, each measurement is assessed automatically regarding interferences and weak or overloaded bands, resulting from disproportional sample amounts.

The qualification of urinary stones by FTIR is coupled to a database match of the spectra. To ease the match to the databases, modern FTIR systems offer correction facilities: baseline correction and absorbance expansion (ABEX) are often used. The baseline correction mathematically eliminates disruptive effects caused by scattering without distortion of the bands. ABEX processes the data to correct changes in sample concentration or thickness. By simply autoscaling the transmission, band shapes would be expressed incorrectly, leading to poor database matches.

In addition, it is possible to retrofit the databases by own entries. For this purpose, urinary stones with exactly known composition are measured. The use of own entries into the database, however, should be done carefully, as the database match provides the base of the evaluation process by the analyst. The database matches deliver a list of matches sorted by the quality of fit. The 10 best matches are given as a list and the best fitted spectrum is overlaid by the measured spectrum of the patient's urinary stone. The final classification of the urinary stone, however, depends on the professional judgment of the database match by the analyst [2].

25.3.3
AAS and F-AES

Although there are more sensitive methods than AAS, this method is still the gold standard for the determination of monovalent and divalent cations at low concentrations in human serum and urine. AAS is used for the quantification of micronutritions such as Cu^{2+} and Zn^{2+} in serum as well as Cu^{2+}, Mg^{2+}, and Fe^{3+} secretion in urine. Higher concentrated analytes such as Na^{+}, K^{+}, Ca^{2+}, or Li^{+} are determined by F-AES. AAS and F-AES are relative measurements using an external standard to get absolute molar concentrations [3].

In AAS, spectral interferences are revised or lowered at least by background correction. For this purpose, beside a hollow cathode lamp (radiant source for AAS) an additional deuterium lamp (D_2-lamp) is placed into the optical path. Alternatively, the Zeeman effect can be used to compensate for elevated background signals in AAS: if a special spectral band of an atom is viewed without exposure to a magnetic field, only a single wavelength is recorded. If a magnetic field is turned on, most elements display additionally three or even more bands. The light component polarized in the direction of the magnetic flux is absorbed by the atom, but the light component polarized perpendicular to the magnetic flux is only scarcely absorbed. On the contrary, molecules, particles, or the background do not show this effect.

Besides these actively performed corrections, it should be stated that interferences are minimized by using a powerful detector, which is able to completely separate all relevant spectral lines. For this reason, the incident light intensity (I_o according to the Lambert–Beer law) has to be controlled by the instrument after each start of the lamp.

F-AES systems compensate for matrix effects by using the reference line method [4]. For the reference line method, an F-AES-sensitive element is added in exactly the same concentration to each sample. In most cases Li^+ is added, as the human body contains only minute amounts of Li^+ without essential biological function. Only samples from patients under antidepressant therapy with Li^- salts (resulting in concentrations between 0.5 and 1.5 $mmol\,l^{-1}$ Li^+, higher concentrations being toxic) have to be measured without the correction by the reference line method. In contrast, Li-heparinate plasma samples can be used to measure Na^+, K^+, and Ca^{2+} applying the reference line correction. A prerequisite for this approach is, however, the knowledge of the exact Li^+ content of the Li-heparinate tube batch and test series with the Li^+ program of the flame photometer. The Li^+ concentration contributed by the Li-heparinate (mostly $<0.5\,mmol\,l^{-1}$) has to be integrated into the correction factor (see subsequent text).

In practice, all samples are diluted with a 5 $mmol\,l^{-1}$ Li^+ solution. With any variation in nebulization, the air and gas pressure has nearly the same effect on the measured electrolytes (e.g., Na^+, K^+, and Ca^{2+}) as referenced to lithium. During the calibration with the external standard, the Li^+ concentration is determined and set to 1. Each change in Li^+ in patient or control samples is converted into a correction factor being used to correct the concentration of the measured electrolyte.

25.3.4
HPLC-Coupled Methods

High-performance liquid chromatography (HPLC)-coupled methods are used in clinical chemistry in cases where for a certain analyte no satisfying selectivity can be achieved by simpler methods. There are HPLC methods available with fluorescence, UV–Vis, and partly diode array detection mode [5]. The alternative electrochemical and mass spectrometric detection systems are not related to spectroscopic methods. As expected, those quality control principles, which are applied for enzyme-coupled UV–Vis spectroscopic methods, are equally used with HPLC-coupled methods. There is, however, one important advantage of HPLC-coupled methods: the principle of using an IS can be implemented easily. As specified before, the best opportunity to exclude effects caused by individual sample characteristics or by the preparation of the sample is the use of ISs. Preferred ISs are as similar to the analyte as possible without changing the analyte-specific signal. For HPLC with UV–Vis fluorescence or electrochemical detection mode, ISs with a structure similar to the analyte are used. However, for this detection method, a separation by the retention time is essential. The best choice by far is the use of deuterated ISs, as they have the highest level of analogy with the analyte. A chromatographic separation of deuterated substances from nondeuterated, however, is not possible. Thus, the use of deuterated standards is only feasible for a mass spectrometric detector. Besides, the general quality assessment HPLC-coupled methods using an IS have to be additionally checked for the signal of the IS. The signal intensity should not vary for more than 20% if the same sample matrix is used, for example, serum or urine. Larger differences from sample preparation should be avoided, even if manual sample preparation, for example, by solid-phase extraction (SPE) is used. If larger differences are observed, they might be the result of an interference factor. In this case, the sample should be analyzed again. If the rerun gives no better result, another patient sample should be requested [6].

Besides the important advantage of using an IS, HPLC methods hold the special risk of sample mix-up; as always, a sample preparation in a secondary sample tube is necessary. And the sample preparation is carried out ‘‘offline’’ in most HPLC applications. That is why the user has to take special care, even if microplates are used for autosampling. There is one straightforward control that can be performed, in particular for drug monitoring applications: solely changing the sequence position of the control material. As controls have to have special composition, on the brink controls might assist the position control in offline measurements.

25.3.5
Automated Systems with UV–Vis Detection

25.3.5.1 Serum Index Measurement

Clinical laboratory tests can be affected by endogenous constituents in the sample matrix. Some of these potentially interfering factors can be recognized in the preanalytical phase by a colored appearance of the sample. Interferences due to lipemia (turbidity), hemolysis, and hyperbilirubinemia are difficult to predict because of their strong method-dependent interference.

A quantification of these interfering substances is possible by applying the serum index (SI) measurement, which can be performed on automated clinical chemistry analyzers. They are capable of semiquantitative measurement and reporting of the lipemia index (L), hemolysis index (H), and icteric index (I) [7].

Lipemia is observed as a visible turbidity in serum and plasma samples. The turbidity leads to an increased scattering of the irradiated light. The most frequent cause of lipemia is elevated triglyceride and/or chylomicron (remnants) concentration plasma and serum. This may be caused by diet, a disturbance of lipoprotein metabolism, or intravenous infusion of lipids.

Hemolysis is defined as the release of intracellular components of erythrocytes and other blood cells into the blood plasma. It can appear *in vivo* (e.g., due to a transfusion reaction or during malaria parasite infection) as well as *in vitro* during the preanalytical phase (sampling, sample transport, or storage). After the separation of blood cells, hemolysis is observed in serum or plasma samples by the red color of hemoglobin.

Hyperbilirubinemia (icterus) is defined as an elevated level of different conjugated and unconjugated bilirubin species in serum and plasma. Increased levels can be caused by diseases or conditions that, through hemolytic processes, produce bilirubin. Rapid bilirubin liberation overstrains the clearance capability of the liver. Liver immaturity and several other diseases in which the bilirubin conjugation mechanism is impaired cause similar elevations of circulating unconjugated bilirubin. Bile duct obstructions or damages to hepatocellular structures also increase the levels of both conjugated and unconjugated bilirubin in plasma.

The SI measurement is based on calculations of absorbance measurements of diluted samples at different bichromatic wavelength pairs to provide a semiquantitative representation of levels of lipemia, hemolysis, and hyperbilirubinemia present in serum and plasma samples [8].

The primary wavelength is at or near the peak absorbance of the chromogenic product and the second wavelength at which only a negligible absorbance of the desired chromogenic substance occurs.

Any absorbance (A_2) that occurs, due to interference from other substances in the sample, is measured at the secondary wavelength. This amount is then subtracted from the total absorbance (A_1) occurring at the primary wavelength to yield the net absorbance (A^C) (Figure 25.3).

The analyzer pipettes an aliquot of the diluted patient specimen to measure the absorbances for lipemia at 660/700 nm (primary/secondary wavelength), for hemolysis at 570/600 nm, and for hyperbilirubinemia at 480/505 nm (Figure 25.4). From these absorbance values the instrument calculates SI values using appropriate correcting factors that correct overlapping interference spectra. A measured SI result (L, H, or I) exceeding the specified value indicates that the corresponding test is affected by endogenous interferences beyond an acceptable deviation (Figure 25.4).

25.3.5.2 **Liquid Level and Clot Detection**

The sample and reagent probes are equipped with a *liquid-level detection system* checking the availability of sufficient sample and reagent volumes in the respective containers. In addition, the liquid-level detection serves to control the correct immersion depth of the probes in the samples and reagents for proper pipetting. If the sample or reagent level falls below a predetermined height, an alarm

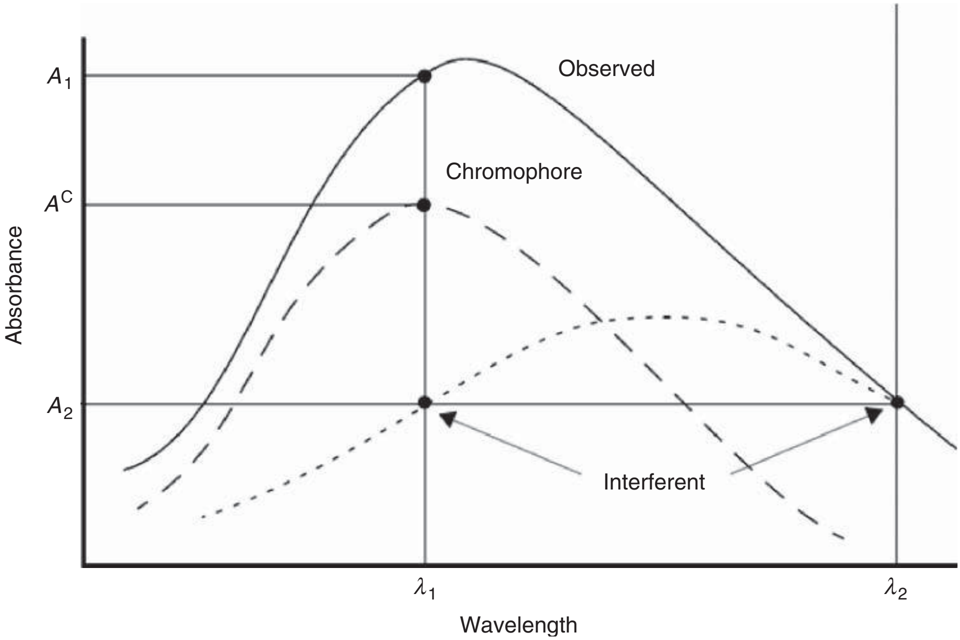

Figure 25.3 Photometric test using two wavelength readings to calculate results (bichromatic measurement).

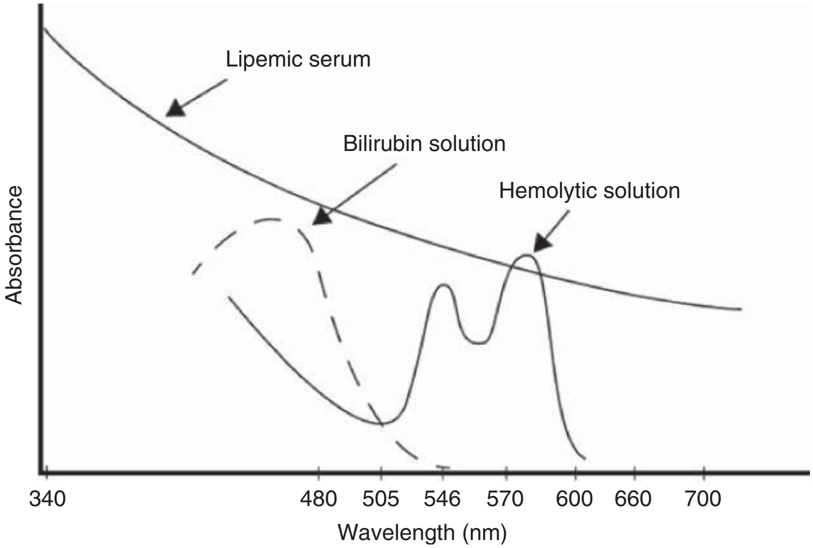

Figure 25.4 Absorbance against wavelength of the different interferences factors: lipids, hemoglobin, and bilirubin.

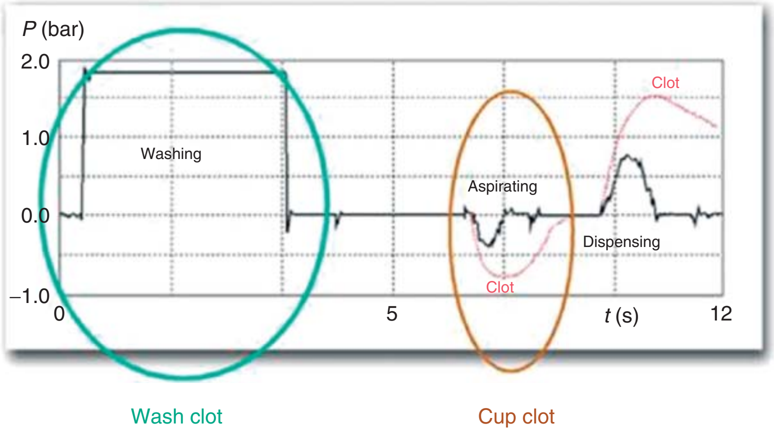

Figure 25.5 Clot detection: the sample probe is equipped with a pressure sensor that detects pressure changes during aspiration.

message is displayed. The liquid-level detection is accomplished by a highly sensitive capacitance measurement. The probe carries a high-frequency, low-voltage electrical charge. Changes in frequency and electrical amplitude characteristics are evaluated to detect the contact of the probe with the liquid. The liquid-level detection is a component of the pipetting integrity check of a clinical chemistry analyzer and increases the result security.

The *clot detection* is a further component of the pipetting integrity check. The sample probe is equipped with a pressure sensor that detects clots during the sample aspiration. Evaluating the clogging of the probe avoids false sample volume pipetting. The aspiration of a clot causes the measured pressure profile to exceed predefined threshold values, subsequently triggering an alarm message (Figure 25.5).

25.3.5.3 **Instrument Checks**

Multiple instrument checks are used to detect abnormalities during the measurement and result calculation and thereby significantly increase the result integrity. Results of calibrations or measurement results of patient or control samples are flagged accordingly. Some of the most important instrument checks are listed here.

- *Absorbance limit check*. The absorbance limit check induces a flag, if the absorbance value used for the calculation exceeds the photometer linearity limit. A potential cause might be that the sample concentration is too high or the sample is lipemic. The measurement has to be repeated after adequate dilution.
- *Antigen excess check*. Another possibility of ruling out high sample concentrations in assays that use antigen–antibody reactions is the antigen excess check. If the sample contains excess antigen concentrations, a valid result cannot be calculated. This is caused by an effect shown in the “Heidelberger curve” for turbidimetry. If the antigen exceeds the antibody concentration by a certain ratio, the signal decreases (Figure 25.6, [9]).

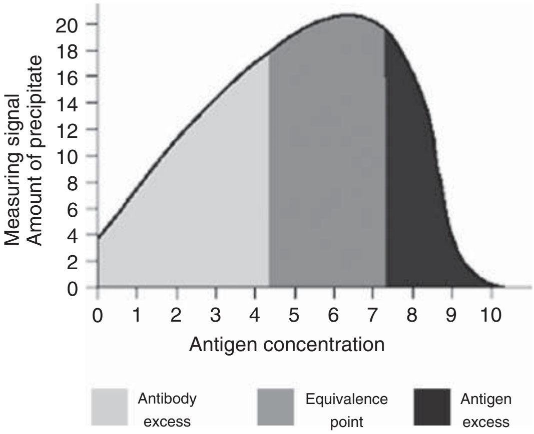

Figure 25.6 Heidelberger curve.

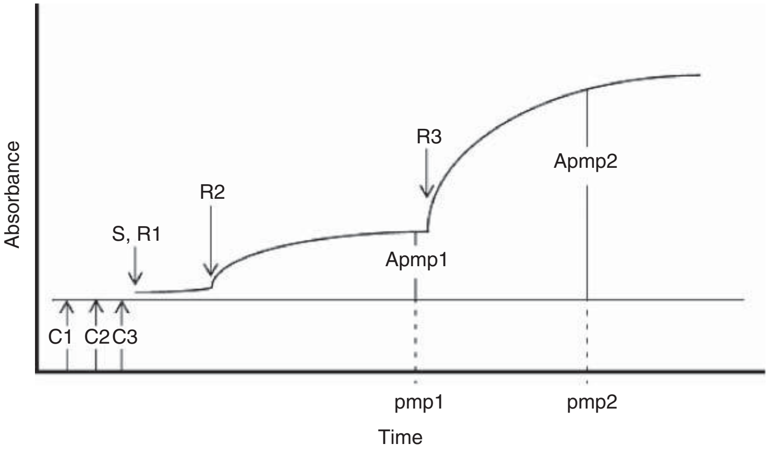

C1, C1, C3	Reaction cell s water blank values
S	Pipetting of sample
R1, R2	Pipetting of R1 and R2
R3	Pipetting of antigen excess reagent
pmp1, pmp2	Prozone measuring points 1 and 2
Apmp1, Apmp2	Absorbance at pmp1 and pmp2

Figure 25.7 Antigen excess check.

Antigen excess checks applying the antigen readdition method compare the absorbance before and after the addition of an antigen excess reagent, as indicated in Figure 25.7. If the signal height at Apmp2 underruns a limit value, the measurement should be repeated after adequate dilution.

- *Linearity check*. If the first and the second half of the reaction curve have different slopes exceeding a specified limit value, a flag appears (Figure 25.8).

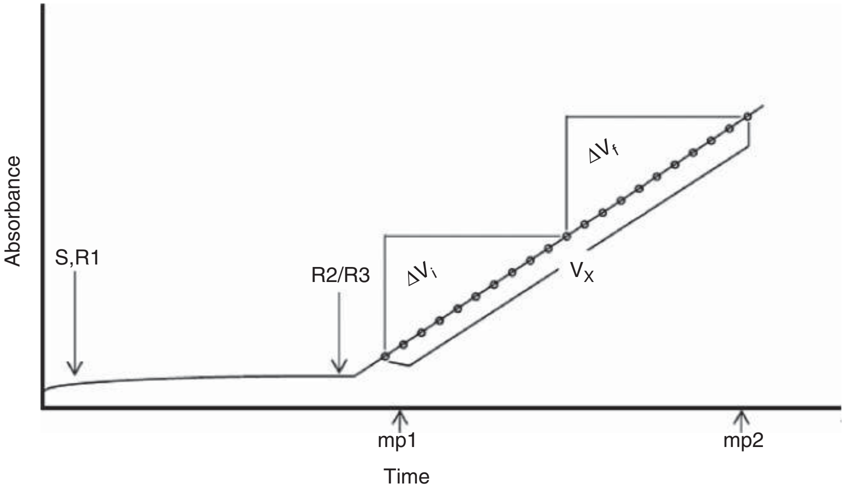

S	Pipetting of sample
R1, R2, R3	Pipetting of R1, R2, or R3
mp1	First photometric measuring point
mp2	Last photometric measuring point
Vx	Rate of change in absorbance calculated for all measuring points between mp1 and mp2 by least square analysis
Vi	Rate of change in absorbance calculated for the first half of the reaction curve
Vf	Rate of change in absorbance calculated for the half of the reaction curve

Figure 25.8 Linearity check.

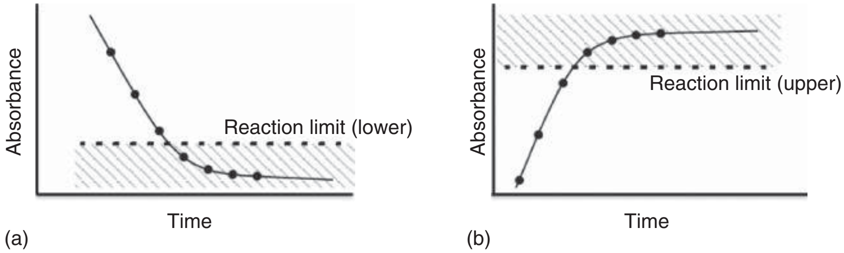

Figure 25.9 Reaction limits for (a) ascending and (b) descending rate assays.

The nonlinearity flag may have different causes (e.g., sample is lipemic). It is recommended that the measurement be repeated after adequate dilution.

- *Substrate deletion check*. If the substrate is depleted, the enzymatic reaction runs out of the linear area. The rate of change in the main wavelength absorbance exceeds the predefined limit value (reaction limit). This flag is caused, for example, by an extremely high sample concentration (Figure 25.9). The measurement should be repeated after adequate dilution.

In general, it must be stated that fully automated analyzers can be programmed in such a way that the above-mentioned ''flags'' trigger automatic reruns using predefined sample dilutions.

25.3.6
Sample Measurements and Calibrations with Photometric Analyzers

25.3.6.1 Routine Photometric Measurements

Photometric measurements on a clinical chemistry analyzer should be performed at the respective optimum wavelengths. Specific measure points – part of the so-called application parameters – for each individual test have to be selected.

There are two fundamental types of photometric tests: *endpoint* and *rate tests*.

If measurements are performed after the reactions are completed, the intensity of the colored product or the turbidity serves as indicators of the sample component's concentration. These are called *endpoint tests*.

If measurements are taken as the reaction proceeds, the rate of the reaction is directly proportional to the sample component's concentration or activity being analyzed. These are called *rate reactions*. Modifications of these two techniques are also possible, as well as a combination of the two.

The reaction time of samples on most clinical chemistry analyzers is approximately 10 min or less.

Absorbance readings are performed each time the reaction cell rotates past the photometer. When the reaction cell passes through the light path, absorbance at 12 wavelengths for each individual test is measured. When the light beam enters the photometer, it strikes a diffraction grating that separates the light into its constituent wavelengths and reflects them onto a fixed array of 12 photodiodes (340–800 nm). Each photodiode is permanently positioned to detect light at a certain wavelength (Figure 25.10).

There are some rare methods in clinical chemistry that are still manually performed and either measured by (spectro)photometers or by microtiter plate readers. Most of the quality checks for these types of instruments are done as described, with the following additional aspects:

Some ring trial organizations (see subsequent text) offer control material for quality control measurements of stand-alone spectrophotometers. These samples consist of aqueous solutions of dyes. The dyes have specific extinctions at the following wavelengths: 260, 280, 334, 340, 365/366, 405, 546, and 560 nm.

The quality control samples are used as ring trials and serve as sensitive photometer checks. They help to localize (mostly monochromator) defects of the photometer earlier than they would cause erroneous analytical results.

Microtiter plate readers are often used with multichannel detection depending on the plate format that is used. In this case, a control should check each channel even if not for every measurement, but in a fixed time frame.

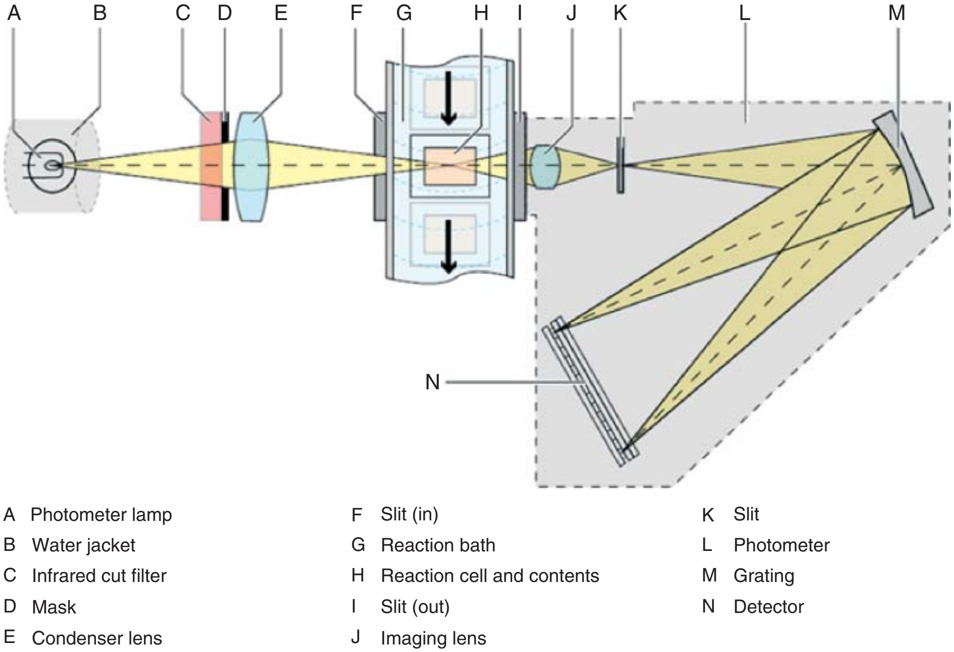

Figure 25.10 Assembly schema of a modern photometer (photometric absorbance reading). (With copyright permission of Roche Diagnostics.)

25.3.6.2 External Standard Calibration

Almost all clinical chemistry methods use external standards for quantification. Right from the method validation stage, it has to be worked out which standards have to be used and which calibration frequency is needed. As a routine, aqueous external standards are used. If quenching effects, however, occur, the use of matrix-loaded standards is required. Within this context, the assay supplier always specifies which calibrator has to be applied and which material (serum, plasma, urine, or special material) is valid for analysis. The calibration frequency also depends on the manufacturer's guidelines.

In general, in immunoassay methods a calibration is carried out for each test, whatever the detection method used. Enzyme immunoassays might be detected by different UV–Vis active or other dyes, but the signal height always depends on the immunoreactions carried out before the detection step. Exceptions to this calibration mode are made in fully automated systems: in these systems, the reaction sequence and all used reaction solutions are mostly standardized. For this reason, it is possible to reduce the calibration frequency significantly even for multistep enzyme-coupled reactions. If the calibration stability is high, the manufacturer might reduce calibration duty for the user. Thus, a one- or two-point recalibration is needed only when using a new lot of reagent, as the fully calibrated curve is provided within the product code. No further calibration of fully automated systems is required as long the criteria of all internal quality control measurements are fulfilled and the same reagent lot is used.

In HPLC-coupled methods and for AAS, a calibration is made within each batch to balance measurement deviations. In F-AES, the calibration is carried out even more often. Some systems, in particular F-AES systems for emergency laboratories, recalibrate at least every 15 min with a zero calibrator and one medium concentrated calibrator.

25.4
Quality Assessment – Regulatory Issues

The contemporary concepts of quality assessment of clinical chemical analyses (e.g., the Westgard rules [10–13]; see also *www.westgard.com*) have led to improvements in reliability of the analytical results, and also to marked improvements in equipment, methodology, reagents, calibration materials, and control specimens. But the statistical bases have also been improved in the past two decades [14]. Moreover, clinical chemistry measurements should be comparable and independent of the analytical system. Thus, establishing metrological traceability of results improves patient care and disease monitoring [15–17].

The goal of producing reliable analytical results for the benefit of the patient has enabled various assessment schemes in a series of different countries in the United States [12, 13], in Europe [11], and other parts of the world, but the underlying principle of the dual internal and external quality control is found in all of these concepts. These assessment schemes are dedicated to a variety of parameters. The various analytical chemistry techniques do not influence these rules. Also, intense efforts toward harmonization of quality systems and accreditation issues were spent [18–20]. Norms of the International Organization for Standardization (ISO) regarding the requirements for quality and competence in medical laboratories were devised [21].

Thus, this chapter aims to give an example of these quality assurance schemes, which are due for all of the applied spectroscopic methods.

German law mandates a set of quality regulations, known as the ''RiliBÄK'' (Richtlinie der Bundesärztekammer) [22], which govern medical devices in laboratory medicine. These regulations are further tied to the European IVD (*in vitro* diagnostic) directive and the ISO standards, for example, 15189 [21]. They are updated periodically to reflect changes in clinical need of regulated analytes, as well as improvements in technological capability of the clinical chemistry devices. The most recent update was proposed in 2008 with full implementation by April 2010.

RiliBÄK is the term for ''Guideline of the German Federal Medical Association (Bundesärztekammer, BÄK) for quantitative analytical measurements in the medical laboratory.'' The system described in this guideline is aimed at safeguarding the quality of analysis carried out in medical laboratories [23]. In other words, the quality assurance of medical laboratory examinations as part of the medical care should improve patient safety.

The guideline aims to ensure, in particular

- minimization of influence factors and *in vitro* effects during the preanalytical phase;
- proper performance of medical laboratory examinations including identify cation and minimization of factors interfering with the tests;
- correct assignment and documentation of results, including the generation of a report.

The RiliBÄK also defines the structure of medical laboratories: organizations in which medical laboratory analyses are performed must be legally identifiable. The responsibility, duties, and competence of the staff performing medical laboratory analysis must be clearly defined and documented. Medical laboratories must be headed by professionally qualified persons. The responsibility of the management encompasses all technical, organizational, administrative, educational, and advisory functions. Medical laboratory tests must only be performed by professionally qualified persons who fulfill the legal requirements. The number of personnel must be sufficient with regard to the amount of work. Regular participation in continued training and education programs must be ensured for all staff members. Participation in training and continued education programs must be documented. It must be stipulated and documented who is responsible for the training of new employees or training for new devices and new test methods and how such training is to be performed. The performance of mandatory training and educational sessions must be documented.

There are also strictly defined rules concerning:

- accommodation and environmental conditions;
- equipment;
- medical laboratory examinations concerning the pre- and postanalytical period; and
- medical laboratory test procedures for all analytical methods applied.

Very similar to the CLIA (Clinical Laboratory Improvement Amendments) in the United States [24], the RiliBÄK rule is meant to provide minimum requirements for the quality of quantitative clinical chemistry test results. The described quality requirements are in close relationship with the well-known ISO 15189:2007 standards. The RiliBÄK mandates quality requirements/allowable analytical errors/uncertainty recommendations for 67 analytes in serum and whole blood, as well as 10 analytes in urine, and seven in cerebrospinal fluid. The guideline also gives a decided statistical method for determining specifications for any unlisted (‘‘non list B1’’) analytes, as well as the permission for laboratories to apply the specifications of listed analytes to similar unlisted analytes.

The RiliBÄK guideline covers both *internal* quality assessment as well as *external* quality assessment. The internal assessment guideline is designed to assess a laboratory's quality using only a target value (TV) supplied by the manufacturer and the laboratory's routine QC data. These assessments are done on a daily basis as well as retrospective over a period of time (the so-called control cycle, CC). A laboratory must perform external quality tests, or peer comparison testing for any analytes that they test. For those analytes not listed in the RiliBÄK, laboratories are strongly encouraged to do also external quality testing. If the laboratory fails two successive external quality assessment events for the same analyte being listed in Table B1, a report must be filed with the government. Germany's equivalent (Bundesinstituts für Arzneimittel und Medizinprodukte, BfArM) (*www.bfarm.de*) of the Food and Drug Administration (FDA) in the matter of medical products is to receive the notice and investigate the deficiencies. Further failures of the laboratory are prosecuted by exclusion from the reimbursement system.

25.4.1
Internal Quality Assessment

All quantitative tests performed by medical laboratories are subject to internal quality assurance procedures. If several instruments are used to analyze a measurand, internal quality assurance procedures need to be performed on each of these instruments. The RiliBÄK from 2008 introduced a new quality metric for internal assessments, *root-mean-square deviation*, abbreviated as $\%RMSD$ and expressed as a percentage relative to a TV [25]. Previous versions used disconnected quality goals for bias and imprecision. These were replaced by the %RMSD as indicator of a total analytical error type of metric, being in accordance with the ISO concept of uncertainty. The %RMSD is computed from data acquired during a CC, which is a time period containing at least 15 observations, generally about 1 month of data, but not more than 3 months.

$$\%\mathrm{RMSD} = \frac{\sqrt{k^2(\mathrm{SD}_{\mathrm{CC}}^2) + \mathrm{Bias}^2}}{\mathrm{TV}}$$

where

$\mathrm{SD}_{\mathrm{CC}}$ = standard deviation,

Bias = difference of observed mean from TV,

k = statistical coverage factor to account for uncertainty (1 for metric, 3 to calculate specification), and

TV = target value for the control sample (from manufacturer).

The RiliBÄK provides a set of explicit goals for the uncertainty limits of the listed analytes. The tables also provide a concentration range for the tests – if your test value is within the specified range, then you can use the specification given in column 3 of Table B1, of the RiliBÄK (see *www.bundesaerztekammmer.de*; Richtlinien). Note that multiple ranges are provided in several cases (e.g., total bilirubin, digoxin, ethanol) where performance goals at low-analyte concentrations are different than that for the rest of the range. The statistical evaluation using a

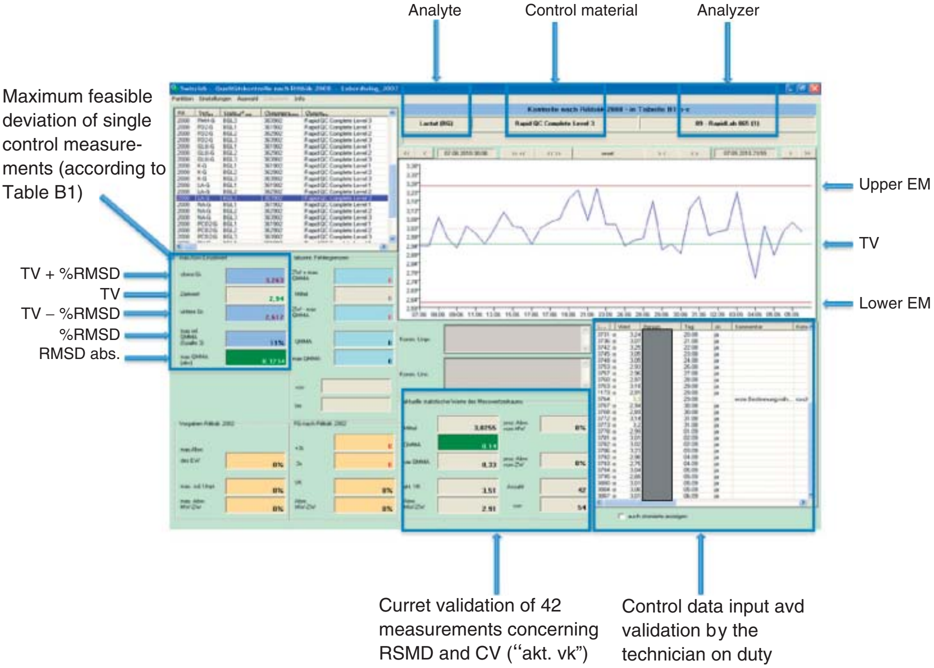

Figure 25.11 Internal quality control LIS screen for lactate in serum, according to the RiliBAK rules. (With copyright permission of Roche Diagnostics.)

commercial laboratory information system (LIS) is depicted in Figure 25.11 for one of the list B1 analytes.

For parameters not found on the B1 list, or for concentration ranges not found on the list, the establishment of internal laboratory limits of permissible error for the individual control sample measurement has to be installed as follows: a control sample result per day is chosen for each used control sample covering a period of at least 15 days and at most one CC. The selection is based on the same pattern, that is, each time the first, the xth, or the last value is used. Selecting values based on the statistic principles of random is also admissible. Subsequently, the limits of permissible error are calculated on the basis of TV $\pm\,\Delta_{\max}$. The calculation of $\Delta_{\max}$ is based on the following formula:

$$\Delta_{\max} = \sqrt{(k^2 \mathrm{SD}_{\mathrm{ep}}^2) + \mathrm{Bias}_{\mathrm{ep}}^2}$$

where

k = 3, coverage factor to calculate the internal laboratory limits of permissible error,

$\mathrm{SD}_{\mathrm{ep}}$ = experimental standard deviation of the control sample measurements used for the calculation during the specified period (ep), and

Bias_{ep} = difference of observed mean from TV used for the calculation during the specified period (ep).

To make it more simple, the correction of the variance SD_{ep}^2 with $(n-1)/n$ is dispensed with. In order to calculate the relative internal laboratory limits of permissible errors, Δ_{max} must be divided by the TV. This calculated %RMSD result becomes the *laboratory observed specification* and is done separately for each level of control used in the laboratory.

Once the %RMSD goal is reached by applying the RiliBÄK tables or the calculated laboratory observed specification, one can start the internal assessment. There are two periods of time when this internal assessment should be performed. First, there should be a daily assessment of control results versus the *error margin* (TV ± %RMSD). The laboratory's daily control values should not exceed the respective error margin. Second, there should be a retrospective check for CC. For each level of control, calculate the mean, SD, bias, and %RMSD from the daily control results over the entire CC. The calculated values should not exceed the respective %RMSD goals.

If an individual daily control result exceeds its error margin, the method is out of control and results are not released until an analytical or procedural cause is identified and corrected. Often, it is advisable to run additional QC or validation for resuming the method. If the monthly retrospective result fails the goal, it is also called *out-of-control* method. One must perform the same corrective actions as with the individual control result failure, but one must do more to revalidate the method. The consequences of failing consecutive retrospective assessments are more severe, requiring significantly more effort and documentation to revalidate the method, as well as potentially needing to notify the BfArM. The laboratory has to inform this federal authority as soon as it fails two times (2 months) in a row.

There are some additional rules in the context of internal QC: as to the period used to establish the internal laboratory limits of permissible errors, the ranges given by the manufacturer of the control samples apply. The internal laboratory limits of permissible error need to be within these ranges. Internal laboratory limits of permissible error do not need to be established for control samples with a lifetime of a lot below 12 weeks. Concerning these, the ranges indicated by the manufacturer of the control samples apply.

25.4.2
External Quality Assessment

The external assessment goals in the RiliBÄK are intended so that the analytes and specifications in the tables will be regularly reviewed and updated. Medical laboratories must take part in ring trials, at least every 6 months for the mandated analytes, as a certificate of passing from the RiliBÄK is only good for 6 months. Depending on the analyte, however, testing may be offered more frequently, up to eight times a year. Ring trial organizations in Germany are the Referenzinstitut für Bioanalytik (RfB) of the Deutsche Vereinte Gesellschaft für Klinische Chemie und Laboratoriumsmedizin (DGKL) (*www.dgkl-rfb.de*) and the Gesellschaft zur

Förderung der Qualitätssicherung in medizinischen Laboratorien e.V. (INSTAND) (*www.instandev.de*).

A special feature of the RiliBÄK is that the goals also indicate the grading system. Nearly half the mandated analytes are supposed to be graded against a reference method [designated in the table as ''Referenzmethodenwert'' reference method value (RMV)], the others only against the peer group median (designated in the table as ''Zielwert'' TV). Part of this reflects the sustained effort of the German DGKL to establish reference methods for the external quality assessment.

25.4.3
Quality Management Manual

The RiliBÄK demands for a quality management manual (QMM). This is depicted in part A of the guideline and is valid for all following parts B1, B2, and so on. The QMM has to describe the quality management system and the documentation used in the medical laboratory. The quality manual must include or make reference to all procedures. Laboratory personnel must be instructed on the use and practical application of the quality manual and all referenced documents. The quality manual must be kept up to date at all times.

The QMM also implies chapters for document control, resolution of complaints, examinations by referral laboratories, and procedures for nonconformities.

References

1. Daudon, M., Bader, C.A., and Jungers, P. (1993) Urinary calculi: review of classification methods and correlations with etiology. *Scanning Microsc.*, **7**, 1081–1106.
2. Hesse, A. and Straub, M. (2006) Rational evaluation of urinary stone disease. *Urol. Res.*, **34**, 126–130.
3. Welz, B. and Sperling, M. (1997) *Atomabsorptionsspektrometrie*, 4th edn, Wiley-VCH Verlag GmbH, Weinheim.
4. Johansson, A. and Nilsson, L.E. (1976) A multiple grating flame photometer for the simultaneous determination of five elements. *Spectrochim. Acta, Part B*, **31**, 419–428.
5. Snyder, L.R., Kirkland, J.J., and Dolan, J.W. (eds) (2010) *Introduction to Modern Liquid Chromatography*, 3rd edn, John Wiley & Sons, Inc., Hoboken.
6. Haefelfinger, P. (1981) Limits of the internal standard technique in chromatography. *J. Chromatogr. A*, **218**, 73–81.
7. Simundic, A.M., Nikolac, N., Ivankovic, V., Ferenec-Ruzic, D., Magdic, B., Kvaternik, M., and Topic, E. (2009) Comparison of visual vs. automated detection of lipemic, icteric and hemolyzed specimens: can we rely on a human eye? *Clin. Chem. Lab. Med.*, **47**, 1361–1365.
8. Pearson, J.R., Wells, R., and Wells, A. (1991) Serum index identifies lipemic samples causing interference with bilirubin assay on Hitachi 717. *Clin. Chem.*, **37**, 2014–2015.
9. Stokinger, H.E. and Heidelberger, M. (1937) A quantitative theory of the precipitin reaction: VI. The reaction between mammalian thyroglobulins and antibodies to homologous and heterologous preparations. *J. Exp. Med.*, **66**, 251–272.
10. Whitehead, T.P. and Woodford, F.P. (1981) External quality assessment of clinical laboratories in the United Kingdom. *J. Clin. Pathol.*, **34**, 947–957.

11. Stamm, D. (1986) Experience with quality control in clinical chemistry. *Z. Lebensm. Unters. Forsch.*, **182**, 372–384.
12. Westgard, J.O. (1999) The need for a system of quality standards for modern quality management. *Scand. J. Clin. Lab. Invest.*, **59**, 483–486.
13. Westgard, J.O. (2003) Internal quality control: planning and implementation strategies. *Ann. Clin. Biochem.*, **40**, 593–611.
14. Parvin, C.A. (2007) Statistical topics in the laboratory sciences. *Methods Mol. Biol.*, **404**, 353–375.
15. Stamm, D. (1991) Reference materials. *Eur. J. Clin. Chem. Clin. Biochem.*, **29**, 247–252.
16. Thienpont, L.M., Van Uytfanghe, K., Marriot, J., Stokes, P., Siekmann, L., Kessler, A., Bunk, D., and Tai, S. (2005) Metrologic traceability of total thyroxine measurements in human serum: efforts to establish a network of reference measurement laboratories. *Clin. Chem.*, **51**, 161–168.
17. Vesper, H.W. and Thienpont, L.M. (2009) Traceability in laboratory medicine. *Clin. Chem.*, **55**, 1067–1075.
18. Jansen, R.T., Blaton, V., Burnett, D., Huisman, W., Queralto, J.M., Zerah, S., and Allman, B. (1997) Essential criteria for quality systems in medical laboratories. *Eur. J. Clin. Chem. Clin. Biochem.*, **35**, 121–122.
19. Jansen, R.T., Blaton, V., Burnett, D., Huisman, W., Queralto, J.M., Zerah, S., and Allman, B. (1998) Additional essential criteria for quality systems of medical laboratories. European community confederation of clinical chemistry (EC4) working group on harmonisation of quality systems and accreditation. *Clin. Chem. Lab. Med.*, **36**, 249–252.
20. Spitzenberger, F. and Edelhäuser, R. (2006) Accreditation of medical laboratories in Europe: statutory framework, current situation and perspectives. *Transfus. Med. Hemother.*, **33**, 384–392.
21. DIN EN ISO (2007) 15189:2007. *Medical Laboratories – Particular Requirements for Quality and Competence*, International Organization for Standardization, Geneva.
22. Bundesärztekammer (2008) Richtlinie der Bundesärztekammer zur Qualitätssicherung laboratoriumsmedizinischer Untersuchungen RILIBÄK. *Dtsch. Ärtzebl*, **105**, A341–A355.
23. Wood, W.G. (2005) Some practical thoughts on restructuring the current guideline of the Federal Medical Council (Richtlinie der Bundesärztekammer [RiliBAK]) in Germany for quality control of clinical laboratory analyses based on results from external quality assessment surveys. *Clin. Lab.*, **51**, 547–573.
24. Rivers, P.A., Dobalian, A., and Germinario, F.A. (2005) A review and analysis of the clinical laboratory improvement amendment of 1988: compliance plans and enforcement policy. *Health Care Manage. Rev.*, **30**, 93–102.
25. Macdonald, R. (2006) Quality assessment of quantitative analytical results in laboratory medicine by root mean square of measurement deviation. *J. Lab. Med.*, **30**, 111–117.

26
UV–Vis and NIR Fluorescence Spectroscopy

Gabor Patonay, Garfield Beckford, and Pekka Hänninen

26.1
Introduction

The development of fluorescent dyes for optical spectroscopy has attracted considerable new interests in quantitative and qualitative bioanalytical science. Although common separation techniques such as gel electrophoresis (GE), capillary electrophoresis (CE), and high-performance liquid chromatography (HPLC), as well as gene probe and immunoassays, relied on detection in the visible region of the spectrum, scientists are now taking full advantage of mid-red and infrared regions because of the comparative optical advantages. The application of these fluorescent molecules continues to demonstrate a plethora of photophysical properties, making them unique for bioanalyses [2–6]. Table 26.1 provides an overview of the use of fluorescent probes in bioanalytical applications.

Traditional fluorescent probes, for example, rhodamines and fluoresceins, absorb and emit in the ultraviolet or visible (300–700 nm) region of the spectrum. With the development of new excitation sources, and in particular light-emitting diodes (LEDs) and diode lasers, optical spectroscopy in the short range near-infrared (NIR) (700–900 nm) and NIR (900–2000 nm) regions have proven more advantageous and profitable. Optical light sources and detectors in this spectral window become continuously cheaper through large-scale use in the telecommunication industry and opto-digital recording. Among the benefits of using the NIR region is the inherent reduced Rayleigh and Raman light scattering, which is the reciprocal of the wavelength to the fourth power dependence and diminished autofluorescence of biological tissues, thereby making biomedical applications in particular very attractive [46]. In addition, the NIR region is favorable in fiber-optic sensing because of the reduced light intensity loss associated with quartz fibers at higher wavelengths. A comparative list of these benefits is illustrated in Table 26.2.

Handbook of Spectroscopy, Second Edition. Edited by Günter Gauglitz and David S. Moore.

Table 26.1 Overview of fluorescent probes [1, 2].

Application area	Subfield or teaching technology	Typical dyes or assay system used	Description	References
Ion indicator dyes	pH	Near-neutral pH: ruthenium-1,2-dicarbonylhydrazide, fluorescein diacetate, carboxyfluorescein, and its ester, 5-sulfofluorescein diacetate, BCEFC	Physiological detection of pH is presently performed with various new fluorescent dyes. BCEFC and its membrane-permanent ester have become the most widely used fluorescent indicators for estimating intracellular pH. Studies are related to the role of intracellular pH in diverse physiological and pathological processes, cell proliferation, apoptosis, muscle contraction, malignancy, multidrug resistance, ion transport, and homeostasis, endocytosis, and Alzheimer's disease	[7]
	Na^+ and K^+	Crown ethers conjugated to the benzofuranyl fluorophore (SBFI and PBFI), sodium green, CoroNa Red, and squaraines	Detection of physiological concentrations of Na^+ and K^+ in the presence of other monovalent cations. Applications are estimation of Na^+ gradients in isolated mitochondria measurement of intracellular Na^+ levels or Na^+ efflux in cells from a variety of tissues. Blood (platelets, monocytes, and lymphocytes), brain (astrocytes, neurons, and presynaptic terminals), muscle (prefused heart, cardiomyocytes, and smooth muscle), secretory epithelium cells correlation of changes in intracellular Na^+ with Ca^{2+} concentration, intracellular pH, and membrane potential has been used in combination with other fluorescent techniques	[8]
	Ca^{2+}, Mg^{2+}, and Al^{3+}	Calcein, fura-2, BTC, various derivatives of calcium green, fluo-3 AM and fluo-4 AM, and some of their dextran conjugates	Measurement of intracellular and extracellular, Ca^{2+} concentrations (fluorescence microscopy, flow cytometry, and fluorescence spectroscopy). Conjugates with dextrans are used to confine the indicator to the cytosol. Major applications to the study of calcium regulations and transport	[9]
		EGTA, APTRA, and BAPTA aequorin (bioluminescence indicator for Ca^{2+})	—	
		Calcein, mag-fura-2, Magnesium Green™, and others	Mg^{2+} detection is important for studies of enzymatic reactions, DNA synthesis, hormonal secretion, and muscular contraction. For example, mag-fura-2 was first used to detect Mg^{2+} fluctuation in embryonic chicken heart cells	

Zinc and other metal ions	Newport Green™ DCF and PDX, FuraZin, FluoZin, and TSQ indicators (Zn^{2+})	Zn^{2+} is an important divalent cation in biological systems, influencing DNA synthesis, microtubule polymerization, gene expression, apoptosis, immune system function, and the activity of enzymes such as carbonic anhydrase and matrix metalloproteinases (MMPs)	[10]
	Calcein, Phen Green™ FL, and SK (Fe^{2+}, Cu^{2+}, Cu^{+}, Hg^{2+}, Pb^{2+}, Cd^{2+}, and Ni^{2+})	Zn^{2+} is functionally active in synaptic transmission and is a contributory factor in neurological disorders including epilepsy and Alzheimer's disease	
	2,3-Diaminonaphthalene (selenium)		
F^{-}, Cl^{-}, Br^{-}, I^{-}	Calcein, 6-methoxyquinolium derivatives (SPQ), MQAE, MEQ, cell-permanent DiH-MEQ, and lucigenin	Measurement of intracellular Cl^{-} has renewed relevance to research on cystic fibrosis, and can be performed with a variety of probes. Conventional applications of Cl^{-} detection are membrane chloride transport (e.g., sodium-dependent transport, renal brush border, $GABA_A$ receptor) intracellular chlorine activity in the quenching of Al^{3+}-calcein complex, fluorescence has been used as the basis of the method for fluoride determination with a detection limit of $0.2\,mg\,ml^{-1}$ detection of Cl^{-}, Br^{-}, and I^{-} are also much performed via chemiluminescence	[11]
CN^{-}	*O*-Phthaldialdehyde and naphthalene-2,3-dicarboxaldehyde	Determination of cyanide in blood, urine, and other samples via reaction of fluorophore in presence of primary amine	[12]
Sulfide	5,5′-Dithiobis-(2-nitrobenzoic acid) (DTNB OE Ellman's reagent) and monobromobimane	Sulfide has been determined for histochemical studies, probing of dynamic changes of red cell membrane thiol groups, subcellular location of cathepsin D, and studies related to glucose-6-phosphate dehydrogenase, glutathione, and glutathione transferase, 6-mercaptopurine	[13]
Phosphate and pyrophosphate	DCIP, NBT, and Amplex red/resorufin	Detection of free phosphate in solution through the formation of the fluorescent products (e.g., resorufin via maltose phosphorylase, glucose oxidase, and HRP resorufin)	[14]

(*continued overleaf*)

Table 26.1 (*continued*)

Application area	Subfield or teaching technology	Typical dyes or assay system used	Description	References
	Nitric oxides	4-Amino-5-methylamino-2′,7′-difluorofluorescein (DAF), 2,3-diamino-naphthalene, and *N*-methyl-4-hydra-zino-7-nitrobenzofurazan	Role of nitric oxide in signal transduction has been recently realized, yielding new fluorimetric assays for NO^{2-} and NO	[15]
Gases	Oxygen, peroxide, and so on	Fluorophores that generate or detect reactive oxygen species, such as singlet oxygen, superperioxide, hydroxyl radical, peroxides. These include merocyanine 540, rose bengal diacetate, and xanthene dyes for the detection of peroxide via HRP	Various applications in bioscience: oxidation/peroxidation of lipids, fatty acids, and cholesterols, NADH, NADPH, dopamines, ascorbic acid, histidine, tryptophan, tyrosine, cysteine, glutathione, proteins, and nucleic acids. Relevance to research of Alzheimer's disease	[16]
General biomolecule detection	Functional group labeling and detection with single-dye molecules	Nearly, all known fluorescent dye conjugates of drugs, haptens, proteins, immunoglobulins, and nucleic acid: coumarins, fluorescein cyanines, rhodamines, specialized dyes: BODIPY and Alexa Fluor® and various extended cyanine dyes	Main application in diagnostic, laboratory assays, immunoassay, histochemistry, immunohistochemistry, flow cytometry, and cellular diagnostics	[1–6]
	Labeling and detection with fluorescent proteins and other fluorescent biomolecules	Phycobiliproteins, green fluorescent proteins	Diagnostic assay use, histochemical staining, imaging of live organisms and their functions	[17]

	Functional group labeling and detection with fluorescent latex particles	Fluorescent dye-loaded micro- and nanoparticles	Diagnostic assay use (particularly in immunochromatography tests) and flow cytometry	[18]
	Enzyme-labeled fluorescence (ELF)	Various phosphate-labeled fluorescent dye, ELF 97	Uses phosphatase-based signal amplification. Applicable to immunohistochemical and cytological staining, mRNA *in situ* hybridization, detection of endogenous phosphatase activity, and blot analyses	[19]
	Tyramide signal amplification (TSA) Technology	Various tyramide-labeled dyes	Utilizes the catalytic activities of horse-radish peroxidase (HRP) to generate high-density labeling of target (also *in situ*). Involves coupling of tyramide-fluorescent dye conjugate to protein tyrosine side chains via peroxidase-mediated formation of an *O*,*O*′-dityrosine adduct. Applied to immunohistochemical staining and *in situ* hybridization	[20]
Protein and nucleic acid detection	Protein quantification in solution in gels, in CE and 2DE, and on blots	SYTO, SYBR, fluorescamine and ophthaldialdehyde, novel dyes: BODIPY, NanoOrange$^{®}$, CBQCA, and SYPRO$^{®}$ protein gel stains	In addition to the conventional dyes for protein staining (Coomassie blue, colloidal gold), many novel fluorescent stains have been developed that allow highly sensitive protein quantification in solution and in gels, particularly the SYPRO protein gel stains	[21]
	Peptide analysis, sequencing, and synthesis	All fluorescent dye labels with reactive groups for amine, dansyl chloride, and dabsyl chloride	N-terminal amino acid analysis, peptide sequencing, peptide synthesis, labeling peptides in solution, and solid-phase synthesis of labeled peptides	[22]
		Fluorescent isothiocyanates		
	Detection of cytoskeletal proteins (actin, tubulin)	Fluorescent, Alexa Fluor, BODIPY, and other conjugates of actin, tubulin, and phallotoxins	Study of *in vivo* cytoskeleton dynamics. Labels of phalloidin and phallacidin are used for selective labeling of F-actin. Tubulin conjugates are used for observation of cell cycle-dependent microtubule dynamics, mitotic spindle morphogenesis, and visualization of tubulin transport in neurons	[23]
	—	SYBR$^{®}$ dyes for sensitive detection in cells and blots	The three classes of ‘‘classic’’ nucleic acid stains are	[24]

(*continued overleaf*)

Table 26.1 (*continued*)

Application area	Subfield or teaching technology	Typical dyes or assay system used	Description	References
		Chemically reactive SYBR dyes for bioconjugates	Intercalating dyes (ethidium bromide and propidium iodide)	
			Minor-groove binders, (DAPI and the Hoechst dyes)	
			Miscellaneous nucleic acid stains with special properties (acridine orange, 7-AAD, and hydroxystilbamidine)	
	Hybridization detection including FISH (fluorescence *in situ* hybridization)	Chromatide nucleotides	Fluorophore- and hapten-labeled nucleotides for enzymatic incorporation into DNA of RNA probes for FISH (fluorescence *in situ* hybridization), for DNA arrays and microarrays and for other hybridization techniques	[25]
	—	SYBR Green	Real-time quantitative nucleic acid gel stain used in PCR	[26]
	—	Universal Linkage System™ (ULS)	Platinum-based chemistry for producing bright, fluorophore-labeled hybridization probes	[27]
	—	Enzyme-labeled fluorescence (ELF)	Phosphatase-based signal amplification assay also applicable to nucleic acid labeling	[28]
	—	Tyramide signal amplification (TSA™) technology	HRP-based assay with tyramide-fluorescent dye conjugate also applicable to nucleic acid labeling	[29]
Membrane and lipid research	General lipid and cell membrane labeling	Fluorescence-labeled lipids and fatty acids are generally used to investigate lipid traffic, for example, fluorescence recovery after photobleaching (FRAP) and other techniques examine lipid–lipid and lipid–protein interactions via FRET measurements	—	[30]

		characterize lipid domains by fluorescence correlation spectroscopy (FCS) characterize lipid domains by near-field scanning optical microscopy detect phospholipase activity investigate the cellular uptake of lipids investigate lipid metabolism and signaling study membrane fusion (pyrene eximer formation) and structural dynamics		
	Membrane potential-sensitive probes	Various styryl dyes (ANEP, RH) and Indo-, thia and oxa-carbocyanines, merocyanines, bisoxonols, and rhodamines	Dynamic optical detection and imaging or membrane potential changes	[31]
Detection of enzymatic actions	Glycosidases, glucuronidases, and so on	A large variety of β-galactosidase, β-glucuronidase, amylase, neuraminidase, sialidase, chitinase, and cellulose substrate	Endogenous glycosidase activity is frequently used to characterize strains of microorganisms and to selectively label organelles of mammalian cells. Defects in glucosidase activity are characteristic of several diseases. β-ᴅ-glucuronide activity is used primarily for contamination detection of *Escherichia coli*. β-amylase level in various fluids of the human body are of clinical importance. Plant and microbial β-amylase are important industrial enzymes. Cellulase enzymes are relevant in food, fuel, animal feed, and clothing applications	[32]
	Proteases and peptidases	7-Aminocouramins, rhodamine 110, fluorescein casein	Peptidase and proteases play essential roles in protein activation, cell regulation, and signaling, in the generation of amino acids for protein synthesis or utilization in other metabolic pathways	[33]

(continued overleaf)

Table 26.1 (*continued*)

Application area	Subfield or teaching technology	Typical dyes or assay system used	Description	References
	Metabolism of phosphates and polyphosphates, ATP phosphatases	Phosphatase substrates (classic chromogenic substrates: BCIP and NBT. Novel fluorescent substrates: fluorescein diphosphate, methylumbelliferyl phosphates, ELF 97e.o.) of bioluminescent determination of ATP	Detection of phospholipases phosphordiesterases, alkaline phosphates, ATPases, GTPases, DNA, and RNA polymerases	[34]
	Oxidoreductases	Fluorogenic reagent for H_2O_2 in conjunction with peroxidases (HRP) and catalase. (Amplex Red/resorufin, and so on). Electrochemical and chemiluminescence approaches are also much used	Systems are used in a wide variety of bioassays by linking various oxidases to HRP via hydrogen peroxide	[35]
			Determination of glucose, cholesterol, choline glutamate, xantine, and uric acid	
	Miscellaneous enzymes	Various probes for microsomal dealkylase, lipase, acetylcholinesterase, acetyltransferase, and carbonic anhydrase	—	[35e, 36]
Carbohydrate analysis	Lectins	Fluorescent concanavalin A, wheat germ agglutinin (WGA) fluorescein conjugates, lectins from *Griffonia simplicifolia, Phaseolus vulgaris, Arachis hypogaea, Helix pomatia, Glycine max*, cholera toxin subunits A and B	Lectins and other carbohydrate-binding proteins that bind to specific configurations of sugar molecules can serve to identify cell types or cellular components, making them versatile primary detection reagents in histochemical applications and flow cytometry	[37]

			Fluorescent derivatives of carbohydrate-binding proteins have been used to detect cell surface and intracellular glycoconjugates by microscopy and flow cytometry, to localize glycoproteins in gels and on protein blots, to precipitate glycoproteins in solution, and to cause agglutination of specific cell types	
Cellular biochemistry	Probes for mitochondria	Rhodamines and rosamines, carbocyanines, styryl dyes, lipophilic acridine orange, lucigenin, Mito-Tracker®, and MitoFluor™ Probes	Mitochondrion-selective reagents for assessment of mitochondrial activity, localization, and abundance, monitoring effects of pharmacological agents, such as anesthetics that alter mitochondrial function. Important role in apoptosis	[38]
	Probes for the endoplasmic reticulum (ER) and Golgi apparatus	The flattened membranous sacs of the ER and the Golgi apparatus can be stained with a variety of lipophilic probes and then distinguished on the basis of their morphology	The ER, and Golgi apparatus are responsible for the proper sorting of lipids and proteins in cells. Cell-permanent probes for these organelles are lipids or chemicals that affect protein movement. Enzymes in the ER are involved in synthesis of cholesterol and the membranes in the detoxification of hydrophobic drugs through the cytochrome P-450 system. Several enzymes in the Golgi glycosylate lipids and proteins, resulting in some fluorescent lectins being useful markers for this organelle	[39]
		Probes for the Golgi apparatus are fluorescently labeled ceramides and sphingolipids, which tend to associate preferentially with the trans-Golgi		

(continued overleaf)

Table 26.1 (*continued*)

Application area	Subfield or teaching technology	Typical dyes or assay system used	Description	References
	Calcium regulation	Cyclic adenosine 5′-diphosphate ribose (aADP-ribose), 3-deaza-cADP-ribose, Ryanodine derivatives, BODIPY FL thapsigargin, and so on Fluorescent-labeled calmodulin	Studies of calcium release. Calmodulin mediates many of the regulatory functions of calcium ions. Fluorescently labeled calmodulin is used to study the *in vitro* behavior of the protein (e.g., in the mammalian mitotic spindle). *In vitro*, fluorescently labeled calmodulin has been used for following the binding of protein kinase substrates by calmodulin studying the interaction of myogenic basic helix-loop-helix transcription factors with calmodulin investigating the molecular mechanisms for calmodulin trapping by calcium/calmodulin-dependent protein kinase I characterizing inhibitors of calmodulin activation of MLCKA-catalyzed phosphorylation of the smooth-muscle regulatory chain	[40]
	Blood coagulation	Fluorescent heparin conjugation	Study of heparin binding to thrombin, low-density lipoproteins, lipoproteins, lipase, circulatory serine proteases, proteinase inhibitors, heparin-binding growth factors, blood vessel-associated proteins (fibronectin and laminin), and binding to cells and tissues. Study of anticoagulant activity and the modulation of the structure, function, and metabolism of many proteins and enzymes	[41]
	Protein kinases, protein phosphatases, and nucleotide-binding proteins	Bisindolylmaleimides, fluorescent polymyxin B analogs, hypericin, hypocrellins, blue-fluorescent *N*-methylanthraniloyl (MANT) analog of cGMP, and fluorescent forskolin	Studies on protein kinase inhibitors and activators, cyclic nucleotides, adenylate cyclase, and so on	[42]

Receptor binding	Various acetylcholine receptors (probes to α-bungarotoxin probes, fluorescent derivatives of pirenzepine), andrenergic receptors (derivatives of prazosi and CGP 12177), GABA_A receptor (muscimol conjugates), neurokinin receptors (conjugates of substance P), neuromedin C receptor, angiotensin II receptor, and opioid receptors (naloxone and naltrexone probes), and so on Ca^{2+} channels α-conotoxin probes, fluorescent dihydropyridines, and verapamil ryanodine, and so on Probes for the Na^+ channel and the Na^+/H^+ antiporter. Amiloride analogs Na^+/K^+-ATPase: ouabain probes Probes for K^+ channels and carriers: glibenclamide conjugates for ATP-dependent K^+ channel, apamin probes for small-conductance Ca^{2+}-activated K^+ channels Probes for Cl^- channels and carriers: ivermectin probes for glutamate-gated Cl^- channels, stilbene disulfonates: (anion-transport inhibitors)	Fluorescent receptor ligands can provide a sensitive means of identifying and localizing some of the most pivotal molecules in cell biology. Many types of fluorescently labeled and unlabeled ligands exist for various cellular receptors, ion channels, and ion carriers. Many of these site-selective fluorescent probes may be used on live or fixed cells, as well as in cell-free extracts. Many new dyes provide extremely sensitive detection, which enables the measurement of low-abundance receptors. Various methods for further amplifying detection of these receptors have been reported. A variety of probes for Ca^{2+}, Na^+, K^+, and Cl^- ions channels and carriers have been described. Ion flux that affects the cell membrane potential, can be indicated with potential-sensitive probes	[43]

(continued overleaf)

Table 26.1 (*continued*)

Application area	Subfield or teaching technology	Typical dyes or assay system used	Description	References
	Phagocytosis	Dichlorodihydrofluorescein diacetate and OxyBURST® technology	Monitoring of the oxidative "burst" produced by activation of an NADPH oxidase in a chain of events starting with the binding of surface-bound immunoglobulin G (IgG) immune complexes interaction with Fc receptors	[44]
	Apoptosis	Various fluorescence-based kits, for example, those using annexin V conjugates Caspase protease activity	Apoptosis is a genetically controlled cell death. Various approaches are used in studying apoptosis, in distinguishing live cells from early and late apoptotic cells, and in forming necrotic cells. Apoptosis assay may be based on nucleic acid and stains annexin V conjugates protease activity mitochondrial stains free radicals ion indicators esterase activity ATP–ADP ratio	[45]

Table 26.2 Comparison of noise levels in the NIR and visible regions [2].

Source of noise	Visible region	NIR region
Detector	High	Low
Scatter (Rayleigh/Raman)	Greater at lower wavelengths (scattering is 1/4 dependent on λ)	Reduced
Autofluorescence	Most biomolecules exhibit fluorescence	Reduced

26.2
Chemistry of Vis–NIR Dyes

The application of new NIR sensors in the detection of key biomarkers continues to advance primarily because of an increasing scope of clinical application and the need for better microenvironmental monitoring. Interestingly, most commercially available fluorescent dyes self-aggregate in aqueous solutions resulting from π-stacking of the planar π-electron conjugation systems giving rise to both H-(hypsochromic) and J-(bathochromic) aggregation. Self-aggregation depends primarily on solvent polarity, but may also be affected by temperature, pH, dye concentration, and ionic strength [46]. Besides the aggregation properties of conventional fluorescent, they also suffer from low photostability, poor quantum efficiency, low Stoke shifts, and severe quenching of the fluorescence of cyanine dyes in biopolymer conjugates, for example, quenching of Cy5 and Cy7 dye variants on conjugation [47, 48]. Visible and NIR fluorescent dyes, which are relatively stable in the solid state, are, however, susceptible to photochemical degradation, which may result in photobleaching. Given the propensity to self-aggregate and photooxidize, the application of fluorescent dyes in solution is rather limited, thus, many new analogs are being developed with enhanced solubility and reduced photosensitivity.

26.3
UV–Vis Fluorescent Dyes

26.3.1
Rhodamines

Rhodamines are fluorescent molecules belonging to a family of 3,6-di(substituted-amino)-9-benzoate derivatives of xanthenes, and are commonly used as fluorescent probes in trace metal analysis [48], labeling of biological compounds, for example, antibodies or DNA [49], and as fluorescent tracers in histochemical studies [38]. These molecules can be derivatized with either an isothiocyanato group, for example, tetramethylrhodamine isothiocyanate or an *N*-hydroxysuccinimidyl

(NHS) ester functionality, for example, 5-carboxytetramethyl-rhodamine succinimidyl ester for covalent labeling at the amino group of proteins or amino-functionalized nucleotides. As hydrophobic compounds, rhodamines and their derivatives usually display poor water solubility, a prerequisite of effective conjugation reactions involving biologically relevant macromolecules (proteins, nucleic acids, and carbohydrates). In addition, the suitability of rhodamines as fluorescent probes may be further limited by poor solubility in aqueous solutions, which enhances aggregation and dimerization reactions [50, 51] (Figure 26.1).

To overcome the disadvantages of aggregation and unspecific absorption, a simple and efficient method is used to increase the water solubility of rhodamine and its derivatives. Recent studies have reported the successful synthesis of water-soluble sulfonated rhodamine 6G with rigidized xanthenes fragments. Besides reducing aggregate formation, sulfonation of the probes proved quite useful in inhibiting fluorescence quenching associated with conjugation, enhancing the photostability and pH sensitivity [49]. In addition, with the advantageous spectral characteristics displayed on sulfonation of the rhodamine molecules, further spectral tunability can be achieved with variation at the c-*meso* substituent [52, 53]. There are only a few discussed synthetic routes that yield novel rhodamine derivatives with ideal spectral properties suitable for biomolecular labeling. Wu and Burgess [53] demonstrated the preparation of new rhodamine analogs by modification of the 2-carboxylate group to yield fluorescein, rosamine, Tokyo green, and Pennsylvania green (Figure 26.2 and Table 26.3).

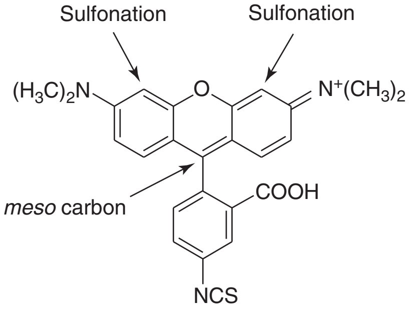

Figure 26.1 Structure of isothiocyanato-functionalized fluorescein.

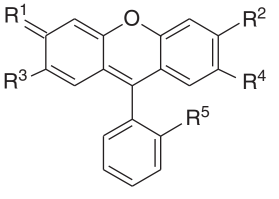

Figure 26.2 General structure of rhodamine derivatives.

Table 26.3 Substituted rhodamine derivatives [52, 53].

R^1	R^2	R^3	R^4	R^5	Compound
$N^+(CH_3)_2$	$N(CH_3)_2$	H	H	CO_2H	Rhodamine
$N^+(CH_3)_2$	$N(CH_3)_2$	H	H	H	Rosamine
O	OH	H	H	CO_2H	Fluorescein
O	OH	F	F	CH_3	Pennsylvania Green
O	OH	H	H	CO_2H	Tokyo Green

26.3.2
Coumarins

Coumarin is a group of low-molecular-weight fluorescent dyes with maximum absorbance in the 320–530 nm region of the spectrum. Similar to most fluorescent compounds previously discussed, coumarins exhibit strong fluorescent intensity in the UV–Vis range; thus, making them applicable in laser-active media, optical brighteners, and LEDs [54]. Coumarins are synthesized as heterocyclic aromatic molecules derived from cinnamic acid via the ortho-hydroxylation synthetic pathway. Derivatization of the molecular structure results in unique photophysical behavior and may further induce photosensitizer properties [55]. Unlike most fluorescent dyes, coumarins and its derivatives are produced naturally in plants as essential oils; thus, further enabling their pharmaceutical suitability. Bryantseva *et al.* [55] studied the fluorescent characteristics of coumarin photosensitizers using furocoumarins; a class of derivatized coumarins (**CD1**, **CD2**, **CD3**, **CD4**, and **CD5**) that absorb in the 320–400 nm spectral range. Intersystem crossing in the order of $\sim 10^{10}$ to $10^{11}\ s^{-1}$ was reported, which confirms the applicability of the substituted dyes as prime photosensitizers (Figure 26.3).

In addition, new sequential biosynthetic oxidation and alkylation reactions of coumarins (to form furanocoumarins) that have been reported enable the molecules to act as bifunctional photoreagents, capable of conjugating double-stranded DNA by cross-linking both strands (Scheme 26.1) [54, 56–59].

26.4
Near-Infrared Fluorescent Dyes

26.4.1
Carbocyanine Dyes

Among the large variety of commercially available fluorescent probes, carbocyanine dyes are highly recognized because of their intense absorption in the NIR region. These probes typically comprise two heterocyclic rings that are bound together

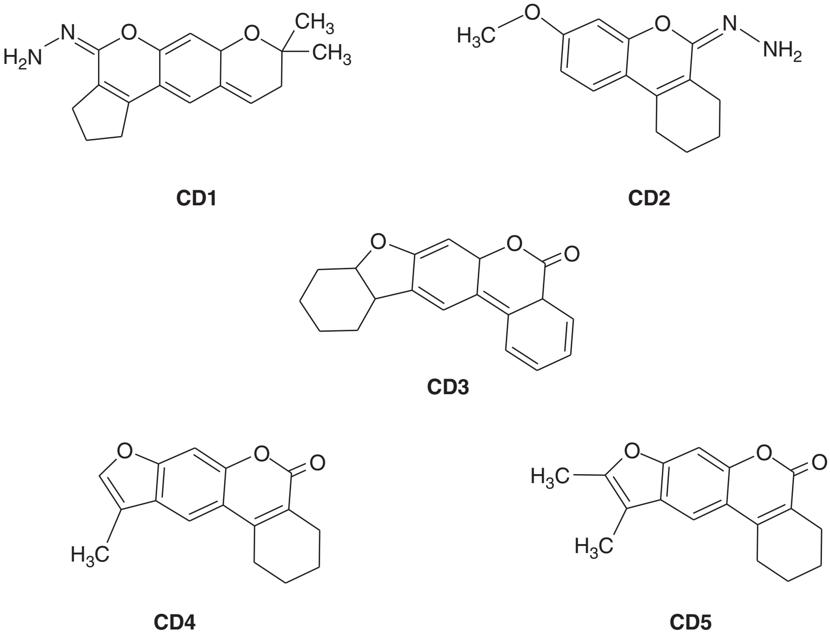
CD1 CD2 CD3 CD4 CD5

Figure 26.3 Substituted coumarin dyes characterized by Bryantseva *et al.* [55].

by a polymethine linker; each heterocyclic ring system incorporates one or more nitrogen atoms as shown in the general structure of Figure 26.4.

Variation in the length of the polymethine linker affects the absorption and emission properties on these NIR dyes and their common names denote the number of methine groups in the polyene chain [60]. In fact, it is reported that incorporation of an additional methine group can result in redshifts of up to 100 nm in the absorbance maxima [48]. Kim *et al.* [46, 61] have proposed a new synthetic pathway for the preparation of novel dimeric bis(heptamethine) carbocyanine dyes (BHmC)-***n***; ***n*** = **4**, **6**, **8**, and **10** that are relevant to the DNA labeling and *in vitro* studies of human serum albumin (HSA) with absorbance maxima in the order of 780 nm (Scheme 26.2).

Interestingly, there is a unique polymethine chain length-dependence spectral behavior observed with bis(heptamethine) dyes. Although the monomeric molecules exhibit strong fluorescence intensity in the 780 nm region, there is a common reduced photoactivity in the H-band of this class of compounds. In addition to low fluorescence that is observed, there is reduced quantum efficiency with the intermolecular H-aggregates of the monomeric analogs **4**. This highlights the unique spectral properties associated with aggregate formation in NIR fluorophores.

Carbocyanine dyes are popular in the development of digital data processing, optical communication, molecular labeling, light harvesting, and drug delivery agents. In a more recent study, Ma *et al.* [62] investigated the application of NIR cyanine dyes in the development of an organic light-emitting diode (OLED) for

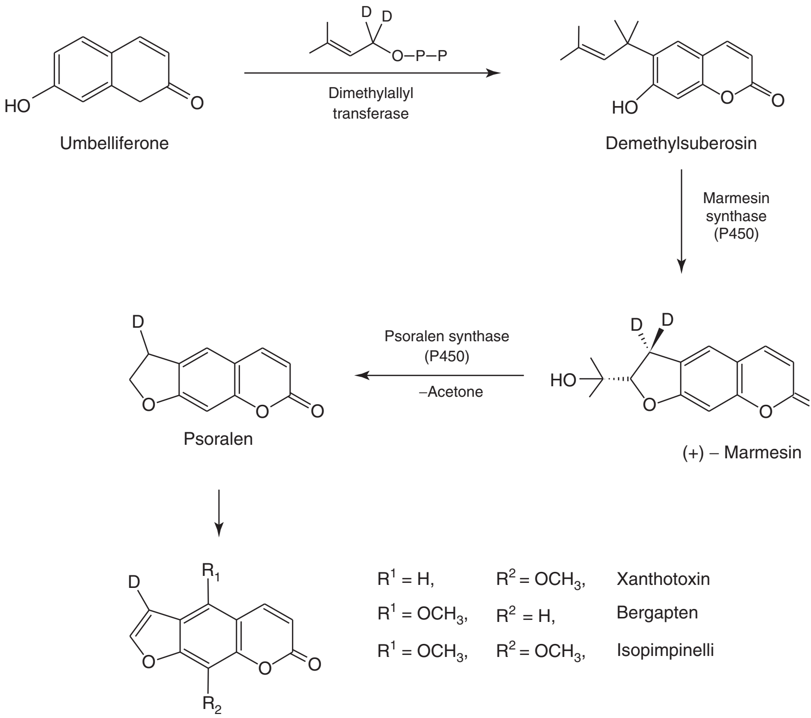

Scheme 26.1 Biosynthetic pathway reported by Stanjek *et al.* [57] toward the formation of furanocoumarins: xanthotoxin, bergapten, and isopimpinellin from umbelliferone (a coumarin compound).

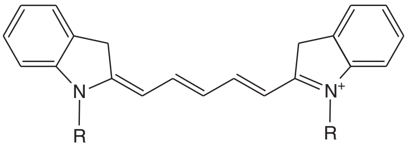

Figure 26.4 General structure of a carbocyanine dye.

use in optical communication and information processing. The optical properties of a fluorescence conjugate of poly(*N*-vinylcarbazole) (PVK) doped with the commercial NIR cyanine dye, 2-[2-[2-Chloro-3-[2-(1,3-dihydro-1,1,3-trimethyl-2H benzo[e]-indol2ylidene)ethylidene]-1-cyclohexen-1-yl]-ethenyl]-1,1,3-trimethyl-1H-benzo[e]-indolium-4-methylbenzenesulfonate (ADS830AT) was studied by spin-casting techniques [63]. In this work, the investigator developed an OLED of improved electroluminescence (EL) efficiency and reduced overlap from ultraviolet emission.

Most of the light-emitting materials reported in literature are ionic cyanine dyes with limited practical applications because of low EL efficiency. During the studies,

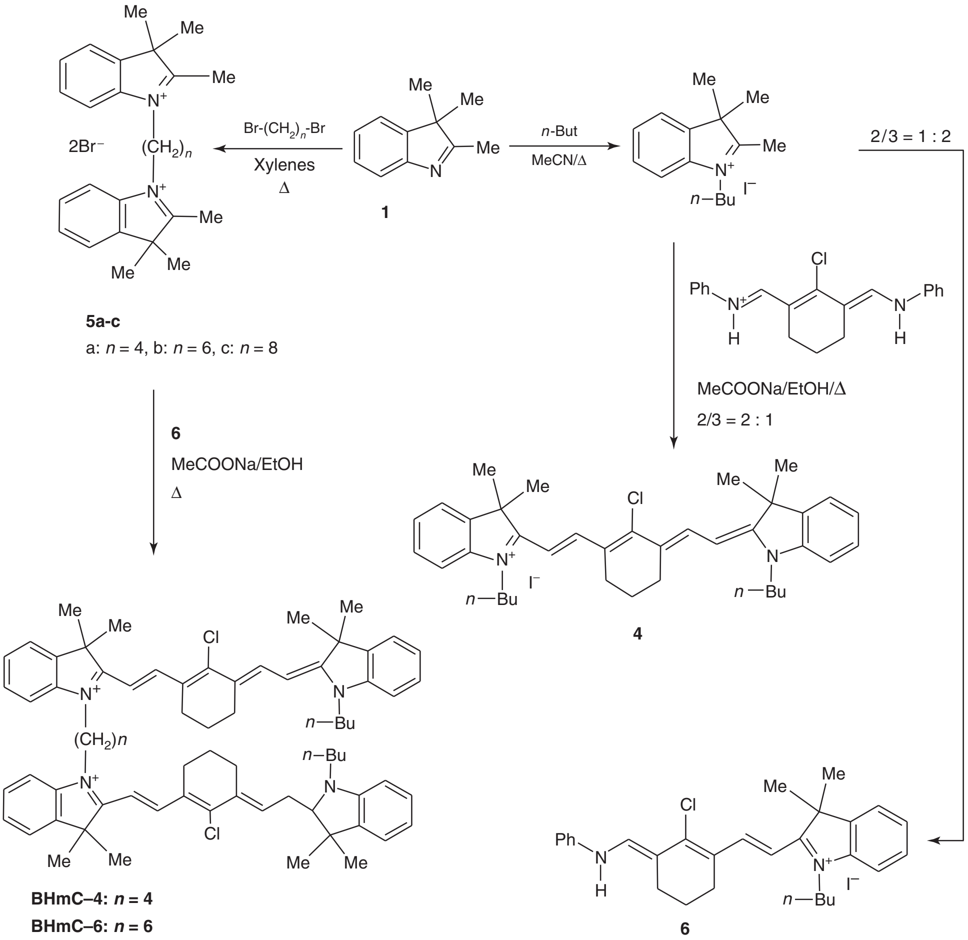

Scheme 26.2 Synthetic route to symmetrical indoleum bis(heptamethine) dyes by Kim *et al.* [46, 61].

Ma [63] discovered that in addition to improved EL efficiency, a single-emission layer PVK OLED device doped with NIR dye emits pure monochromatic NIR radiation at 890 nm and displayed stable spectral properties with forward bias voltages. Further advancements around the NIR region of the spectrum led to the fabrication of other optoelectronic cyanine analogs. New acidochromic molecules were synthesized and studied. Alonso *et al.* [64] developed novel heptamethincyanine dyes that have proven useful in the fabrication of inexpensive communication components. The rapid technological growth in the telecommunication field propelled an increased demand for new and less-expensive optochemical sensors. This resulted in the proliferation of chromoionophoric-embedded plasticide polyvinyl chloride (PVC) optodes capable of detecting the optical transduction signal generated by chemical reactions. Although classic acid–base indicators with absorption maxima in the visible region of the spectrum are suitable as potential chromoionophores, their applicability as plasticide PVC optodes is limited by spectral interferences. Only few classes of molecules fluoresce in the NIR region thus, enabling reduced spectral interferences and enhanced sensitivity. Puyol *et al*. further characterized three types of chromoionophores (Figure 26.5): nortricarbocyanine dyes (**3**), norindosquarocyanine dyes (**5**), and norindocrococyanine dyes (**7**) based on acid–base equilibrium with an aim to optimize the spectral characteristics by lowering the pK_a values.

This work highlights the effects of acid–base equilibrium on the optochemical properties of newly synthesized cyanine dyes. New trends in PVC optodes are geared toward widening the scope of chromoionophore applications by miniaturization of chemical analytical platforms, with a subsequent reduction in the size and complexity of optical systems. Laser diodes emitting at 670 and 780 nm are most suited for this purpose because of the high molar absorptivities of the dyes used with them, the high intensity of the laser diodes and low overall cost [64, 65]. It was demonstrated that the improved spectral characteristic and subsequent chromoionophore suitability in optochemical sensing of cyanine dyes, depend primarily on the conjugated chromophoric system and the nature of the polymethine side chain. Nortricarbocyanine dyes commonly consist of longer polymethine chains than its norindosquarocyanine and norindocyanine counterparts, thereby displaying favorable absorption characteristics for longer wavelength in the NIR region of the spectrum. Besides, the ability to induce ring formation of the side chain further

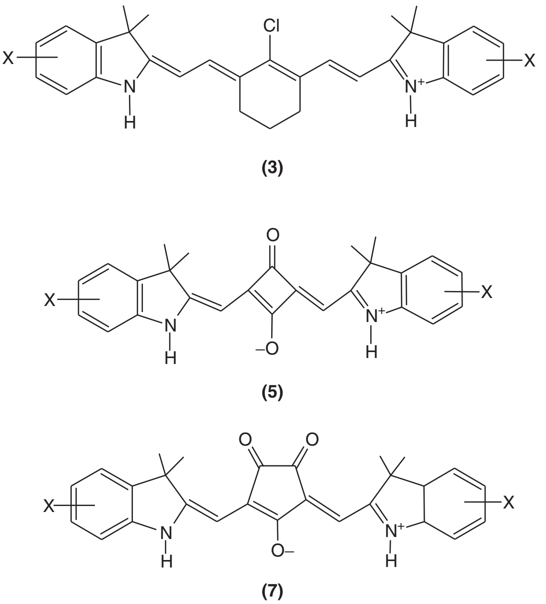

Figure 26.5 Norcyanine dyes prepared by Puyol *et al*. [64–66] for use as pH chromoionophores.

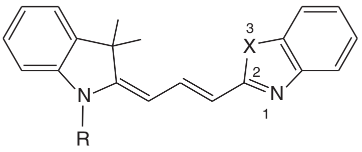

Ia: $R = (CH_2)_5COOH$, $X = C(CH_3)_2$
Ib: $R = (CH_2)_5COOH$, $X = CH_2$
IIa: $R = (CH_2)_4SO^-_3$, $X = C(CH_3)_2$
IIb: $R = (CH_2)_4SO^-_3$, $X = CH_2$

Figure 26.6 Structure of asymmetrical cyanine dyes prepared by Xu *et al*. [67] to study pH sensitivity.

enhances spectral stability and thus greater potential for optochemical fabrication and chemical-sensing capabilities [66]. Similar to the approach used by Puyol, Qian *et al*. characterized the spectral behavior of two groups (one symmetrical and the other asymmetrical) of novel NIR cyanine dyes (Figure 26.6) as fluorescent pH sensors by monitoring the pK_a value of the molecules. The studies indicated strong fluorescence enhancement, as well as distinct bathochromic shifts, of the absorption peaks from 525 to 570 nm as a result of the protonation of two of the symmetrical NIR fluorescence analogs. In addition, R-group substitution at the C-3 position of the indole ring resulted in distinct spectral changes to the emission maxima and the quantum efficiency of these cyanine dyes (Table 26.4).

Table 26.4 Spectral characteristics of novel cyanine dyes bearing different R groups at the C-3 position indoleum ring, developed by Xu *et al*. [67].

	Cyanine dyes			
	Ia	**IIa**	**Ib**	**IIb**
Methanol				
λ_{max}	550.3	549.5	493.9	495.4
$\lambda_{EM\ max}$	553.0	554.5	496.3	500.3
$\lambda_{EM\ max}$	569.4	571.4	528.0	525.1
Δ_S	16.4	15.9	34.1	24.8
Φ	0.129	0.164	0.005	0.003
Water				
λ_{max}	540.3	540.3	490.4	489.5
$\lambda_{EM\ max}$	546.7	547.5	494.1	494.1
$\lambda_{EM\ max}$	566.6	567.2	516.1	521.6
Δ_S	19.9	19.7	22.0	27.5
Φ	0.060	0.060	0.007	0.004

However, such favorable spectral changes could not be explained through mere proton deprotonation or resonance effect within the molecule. It was reported that pH sensitivity is attributed to changes from photoinduced electron transfer (PET) to intramolecular charge transfer (ICT) mechanisms, thus the compound can be fabricated into a pH sensor of high pK_a [66, 67]. Zhang *et al.* [67] also prepared a modified analog to a novel fluorescent molecule for improved spectral properties as a fluorescent pH indicator.

As reported by Zhang and Achilefu *et al.* [67], norcarbocyanines dyes such as indocyanine green (ICG) and cypate conjugates are easily prepared as target-specific pH indicators, through substitution on the indole ring for conjugation of the free carbonyl groups in biomolecules [63, 68] (Scheme 26.3).

26.4.2
NIR Dyes for *In Vivo* Molecular Imaging

In recent years, the development of new sensors for the detection of key biomarkers continued to advance primarily because of an increasing scope of clinical application and the need for better microenvironmental monitoring. For example, redox-active dinuclear ruthenium conjugates are functionalized with cyanine dyes for clinical monitoring of important biochemical substances such as glucose or hydrogen peroxide under physiological conditions. Xun *et al.* [68] have successfully synthesized various redox-active conjugates of ruthenium-1,2-dicarbonylhydrazide, and these complexes display intense absorbance in the NIR region of the spectrum when present in the mixed valence state as Ru^{2+} and Ru^{3+} because of the oxidative potential of hydrogen peroxide or any strong available biological oxidant. Glucose

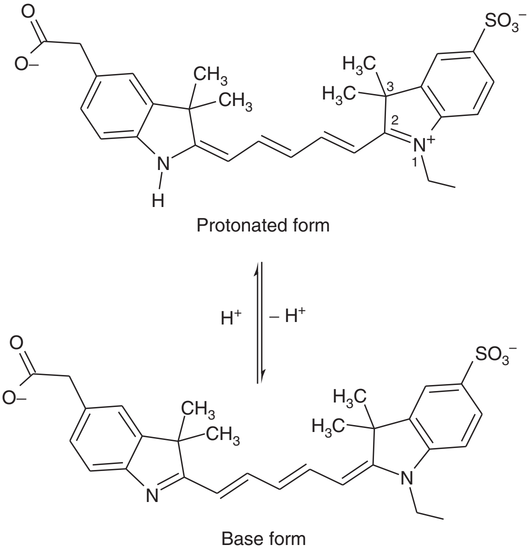

Scheme 26.3 The NIR cyanine base-form pH-sensitive fluorescence probe [64, 66, 67].

oxidation to hydrogen peroxide provided a suitable oxidative pathway for the formation of the ruthenium-mixed valence complexes and as such creates the ideal platform for the fabrication of the glucose NIR optical sensors [69]. The combination of simplicity in design and low electrical interferences further propelled the development of redox-based NIR optical sensors.

Research has shown that synthesized monosubstituted Vis–NIR cyanine dyes are suitable for use as transducers in distributed fiber-optic ammonia sensors [70, 71]. While most commercially available Vis–NIR fluorescent molecules display diminished optical properties and are less suitable for sensing chemically and biologically important substances such as ammonia. Simon *et al.* [72] reported a cyanine dye displaying ammonia-induced absorption peak at 620–680 nm. These newly developed fluorescence probes are been designed for the near to mid-infrared (MIR) regions with diminished light-scattering interference and background autofluorescence. The application of these dyes has even been extended to incorporate the fabrication of optical fiber sensors utilized in evaluating the decomposition of heavy hydrocarbons in transformer oil. The application of NIR dyes to detect slight changes in refractive indices incorporates the partial discharge of gaseous hydrocarbons, such as methane, ethane, propane, and butane, resulting from chemical disturbances in liquid hydrocarbons, for example, transformer fluids. This technique involves evanescent field absorption (EFA) measurements with an NIR optical sensors-coupled spectrometer, for enhanced performance. Although the intensity of the C–H, N–H, or O–H bond vibration is reduced by as much as a factor of 100 in the NIR as opposed to the corresponding ground modes at higher wavelength, such as, the MIR region, the former is preferred for its advantage of enhanced spectral purity and improved signal-to-noise ratio [46]. Furthermore, hydrocarbon sensing by EFA-MIR techniques requires the use of silver halide fibers, which, because they are sensitive to chemical attacks, suffer from UV degradation and high-transmission loss, making them less attractive for optical fiber development. As a result, the NIR-fabricated devices are more applicable for both their mechanical and optical properties, hence are more suitable for practical sensing applications [73–75].

The field of NIR spectroscopy has undergone an unprecedented surge in the application of NIR fluorophores specifically in the areas of optoelectronics and optochromic technology. More researchers are taking advantage of improved sensitivity resulting from lower background autofluorescence and reduced light scattering for deep tissue *in vivo* imaging. Typical examples of NIR cyanine dyes reported in literature include ICG and the IRDye78 [76]. Chen *et al.* [77] discussed noninvasive imaging and quantification of $\alpha_v\beta_3$-positive integrin level in the blood. $\alpha_v\beta_3$ integrin is believed to be responsible for the regulation of tumor growth and metastasis as well as angiogenesis. Increased blood level of this target molecule is a key factor in the evaluation of the aggressiveness of the disease. In this work, the researchers outlined the integrin receptor specificity of the newly synthesized peptide-dye conjugate arginine-glycine-aspartic acid (RGD)-Cy5.5 as a contrast agent *in vitro*, *in vivo*, and *ex vivo* imaging. An intravenous injection of a 3 nM dose of the fluorescent probes resulted in an instantaneous whole-body imagery of an athymic nude mice specimen. However, after 4 h postinjection, the U87MG tumor could be distinctly differentiated from the background tissue. Although the uptake and decomposition of the fluorescent probe was rapid in healthy tissue, it was rather slow in affected tissue. *Ex vivo* evaluations were also performed and results revealed improved sensitivity, achieving enhanced emission intensity and tissue contrast. This fluorescence probe is ideal for intraoperative NIR imaging because of its superb tissue contrasting capabilities and overall low toxicity. ICG-polyamine (polyethylamine, PEI) (IR820-PEI) is also a prime NIR dye conjugate developed specifically for *in vivo* NIR fluorescence imaging with improved photostability and reduced aggregation formation. With a large Stoke's shift of 115 nm in aqueous solution, this NIR fluorophore displayed strong binding affinity for DNA. Coupled to the low molecular weight and relatively high-quantum efficiency of ICG, this newly synthesized conjugated NIR fluorescent dye facilitates improved deep tissue imagery for the evaluation of liver function and noninvasive angiography in ophthalmology [78]. Similar results are achieved with *in vitro* optical NIR-imaging studies using novel carbocyanine–glucosamine conjugates. In addition to improved quantum efficiency and decreased aggregation tendencies in polar environments, NIR dye–glucosamine conjugates exhibit low toxicity and moderate-to-low pH response at physiological pH range. Owing to improved solubility in aqueous solutions and increased quantum yields, conjugation results in enhanced cellular uptake and a concomitant intracellular NIR fluorescence enhancement in breast epithelial cell lines [79]. NIR fluorescence monitoring of glucosamine levels has also enabled *in vivo* assessment of lysosomal proteins and provided a viable option for the evaluation of cancer and metastasis in their early stages [80]. Similar approaches have being attempted in order to study lysosomal target cells using NIR dyes. This is achieved primarily by binding a self-quenching targeting moiety, which is subsequently internalized into the lysosomal target cells. The application of this self-quenched avidin-rhodamine X conjugate (Av-ROX) facilitates the *in vivo* targeting as well as NIR-imaging differentiation of the aberrant tumor cells and the healthy background tissue. While intracellular degradation within the lysosomes leads to dequenching and subsequent fluorescence reactivation within the target cells, virtually no effect is observed within the surrounding tissue [81]. Besides achieving high-fluorescence signal-to-noise ratios for the targeted tumor cells, this technique allows improved molecular imaging.

NIR dyes have found application for *in vivo* molecular imaging of cellular events in early aortic valve disease. NIR dyes are used to visualize endothelial cells, macrophages, proteolysis, and osteogenesis in the aortic valve of hypercholesterolemic apolipoprotein E-deficient mice. Early detection of aortic valve diseases, such as macrophage activation, osteogenesis, and protein intramolecular degradation, can be achieved by utilizing NIR molecular imaging [82] also, and it is reported that NIR molecular imaging visualization of valvular cell functions *in vivo* may identify therapeutic targets in early atherosclerosis diagnosis.

A free-radical precipitation polymerization method was used to prepare thermally responsive poly(*N*-isopropylacrylamide-co-acrylamide) (P(NIPA-co-AAm)) nanohydrogels, which can later be evaluated by *in vivo* NIR fluorescence imaging on healthy and S180 tumor-infected denuded mice specimens. Fluorescent imaging studies may be performed by evaluating the overall fluorescence intensity of an entrapped novel NIR dye NIRD-12 into P(NIPA-co-AAm) nanohydrogels on both sets of specimens, which may or may not be exposed to controlled hyperthermic treatment. The researchers have reported passive and nonspecific thermally targeted behavior. In reality, the thermal-responsive, fluorescence-tagged nanohydrogels are only accumulated at higher temperatures in both healthy- and tumor-affected tissues. Although in other research experiments, the affected cells are differentiated by the NIR fluorescence, in the current experiments these results were not fully observed. Nonetheless, the thermal response of P(NIPA-co-AAm) nanohydrogels, regardless of health status, provided a viable option as a thermal carrier of drugs, especially for tumor diagnosis. In addition to the key thermal response of the P(NIPA-co-AAm) nanohydrogels, NIR dye conjugate is indicated by a distinct bathochromic shift at the absorption maxima. This is further characterized by enhanced photostability resulting from the entrapment of the fluorescent probe within the nanohydrogel polymer [83]. The technique improves molecular imaging and enables extending the overall time available for *in vivo* monitoring of the dynamic process of dye-loaded nanohydrogel polymers.

26.4.3
Squaraines and Rotaxane Dyes

Squaraines are a class of dyes that are well known for their intense fluorescence in the NIR region of the spectrum. These NIR molecules exhibit significant triplet quantum yields and are characterized by their unique aromatic four-membered ring system derived from squaric acid [84–88]. A number of squarylium derivatives are now being developed for application as such as chemosensors [89], *in vivo* imaging [90] photovoltaics, and low cost, large-area solar cells [91]. Unlike most of the other commonly encountered fluorophores, the applicability of squaraines is limited by the high electron-deficient four-membered ring, which inherently undergoes nucleophilic attacks [86]. As a result, Xue *et al*. [88] have proposed a new synthetic pathway for the preparation of a pair of triptycene-based tetralactan macrocycles, which can protect the squaraine molecules from polar solvents by formation of a dye–macrocycle complex. Furthermore, there is currently a vast number of commercially available squaraine-derived rotaxanes that have been developed for improved protection from nucleophilic attacks and enhanced spectral characteristics such as reduced aggregate formation [92]. Most often, the rotaxanes analogs exhibited the same excellent photophysical properties as the precursor squaraines, as well as improved spectral properties as a result of the encapsulating macrocyclization [88].

A common spectral improvement to the rotaxanes is the retardation of photobleaching tendencies of the molecules. In fact, Arunkumar *et al*. [92] reported the preservation of the color of the rotaxane molecule in aqueous solution after several weeks as oppose to the squarylium precursor, which undergoes photobleacing within 48 h at similar experimental conditions. In addition, incorporation of the encapsulating macrocycle results in diminished adsorption band broadening by inhibiting interchromophoric interactions both in solution and in the solid state. The spectral versatility of squaraine dyes make them quite unique as fluorescent probes and NIR labels for biomedical applications [93]. Terpetschnig *et al.* described a novel *N*-succinimidyl ester-derivatized indolium squaraine dye, which displayed strong conjugation affinity for HSA. Conjugation of the water-soluble NIR fluorophore yielded fivefold improved quantum efficiency and enhanced fluorescence lifetime [98]. In addition to the common ''methylene base'' synthetic pathway involving squaric acid or its derivatives, a novel synthetic route for monosubstituted squaraines by reacting with malononitrile, cyano-, and nitroacetic esters, barbituric acid, and 1,3-indanedione was proposed [94]. Interestingly, these monosubstituted squaraine dyes are in a similar spectral range of the more popularly known Cy5 and Cy5.5 NIR fluorescent dyes and are even considered more stable in aqueous solutions with molar coefficients in excess of 265 000 M^{-1} cm^{-1} [95] (Scheme 26.4).

26.4.4
Phthalocyanines and Naphthalocyanins

Similar to the squaraines, phthalocyanine (Pc) and naphthalocyanin (Npc) dyes are versatile planar fluorophores exhibiting strong fluorescent intensity in the NIR of the spectrum. Pcs and Npcs have been recently attracting enormous popularity for their use in the fabrication of molecular devices, such as electrochromic displays [100], LEDs [101], gas sensors [101–103], and photodynamic therapy agents [104]. While Pcs exhibit the natural tendency to self-aggregate owing to the large aromatic π-system [105, 106] as a result of coplanar Pc ring association, the general spectral characteristics are easily ''fine-tuned'' by a central metal and peripheral substitution at the rings [102, 107]. Thus, these NIR fluorophores are usually prepared as metal-free or metal-complexed conjugates. Generally, the peripheral substituents are used to modulate the hydrophobic character of these compounds making them more or less soluble in polar solvents. Consequently, the octasubstituted Pcs usually exhibit reduced solubility in comparison to the tetrasubstituted counterparts. In addition to modifying the solubility and hydrophobic behavior, peripheral substitution to these compounds yields a diverse range of functionalities enabling greater applicability. For example, the electrochemical and spectroelectrochemical behaviors of copper–Pc complexes have been investigated in relation to the position of tetrasubstituted phenylthio groups in the alpha and beta positions [108].

Similar to the squarylium dyes, rotaxanes belong to a unique class of fluorescent compounds. Rotaxanes are supramolecular compounds comprising macrocyclic and dumbbell-shaped components [87, 109, 110]. These molecules also consist of a ring and a threadlike component incorporating two recognition sites (stations). Within the last decade, there has been tremendous progress in the development of new synthetic pathways of these interlocked molecules. In recent work, Michaels *et al.* [111] have proposed the synthesis of novel conjugated polyrotaxane compounds by an aqueous Suzuki polymerization pathway, using hydrophobic binding to promote threading of cyclodextrin units. In this study, new cyclodextrin-encapsulated

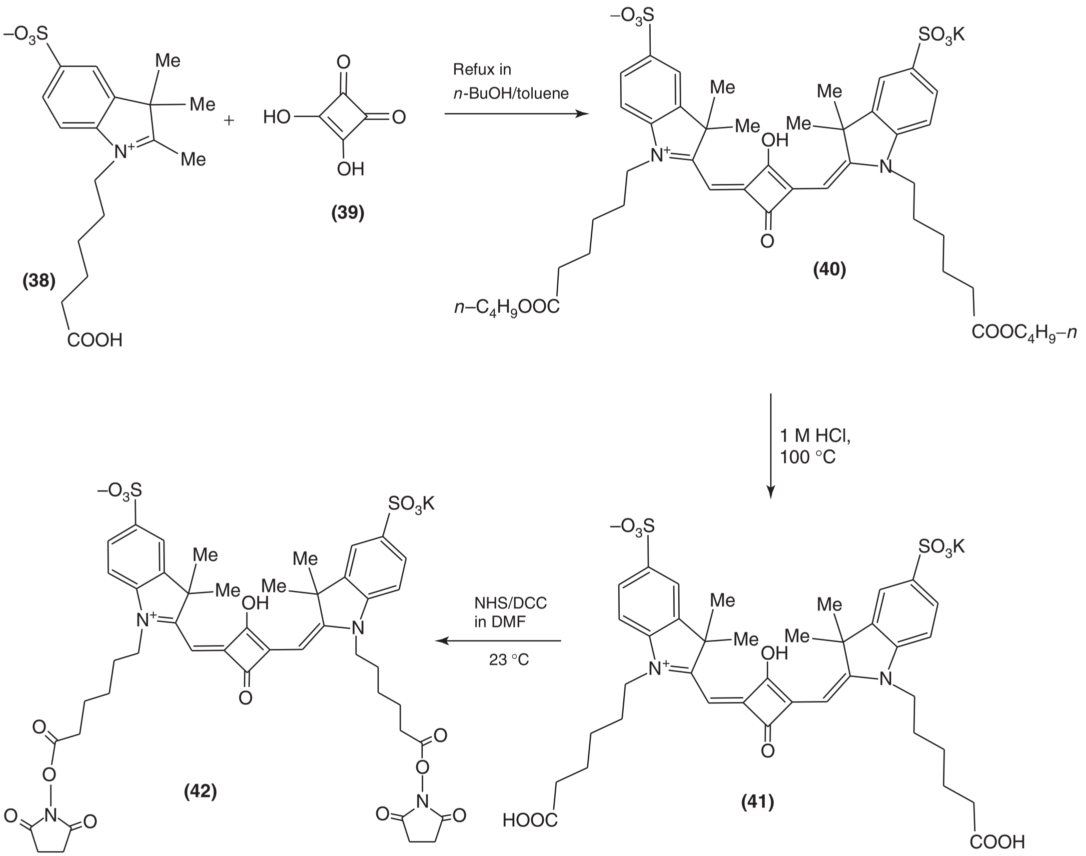

Scheme 26.4 Synthetic route to Sq635 squaraine dye **42** containing *N*-succinimidyl ester moieties. Sq635 is utilized in fluorescence resonance energy transfer (FRET) immunoassay by Terpetschnig *et al*. [2, 96–99].

fluorescent compounds were fabricated with conjugated polymer cores based on poly(*para*-phenylene), polyfluorene, and poly(diphenylene-vinylene), threaded through 0.9–1.6 cyclodextrins per repeat units. Besides improved overall quantum efficiency, these conjugated fluorescent rotaxanes molecules exhibit enhanced chemical stability, attracting widespread interest for optoelectronic applications [111]. Recently, there have been increased interests in insulated π-conjugated systems with high stability, high solubility, and improved quantum efficiency as a result of the isolation of the π–π-conjugated systems from the external environment and reduced π–π interactions among the conjugates [110].

Among the most notable characteristics of the rotaxanes is their photoswitching capability [112–115]. The photophysical properties of the bistable rotaxane molecules are attributed to molecular movements stimulated by external stimuli and are controlled by the two recognition sites as a shuttling process, which may alter the ring position [97, 113, 114, 116–132]. Most of the rotaxane-based molecular switches reported in literature involve mechanical movement of a ''ring'' component between the two ''thread'' components induced by pH [122], electrical potential [128, 132], chemical interactions [116, 123–125], and photochemical stimuli [126] (Figure 26.7).

However, new research is focused on developing alternative switching principles such as photoinduced charge–transfer interactions of a tetracationic ring with a photoactive electron donor. This subsequently reduces conformational changes to the rotaxane supramolecules and maintains overall molecular structure [117]. This principle of switching involves a rapid PET cascade that last only a few seconds, with the rotaxanes being in their tropylium state. It is believed that

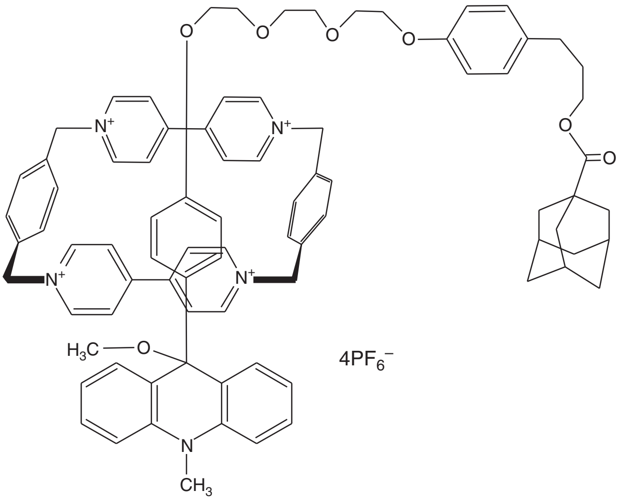

Figure 26.7 Switching mechanism reported by Abraham [97, 117]. Charge–transfer interaction between the tetracationic ring (cyclobis (paraquat-4,4′-bisphenylene) with photoelectron donors (arylcycloheptatriene) into an aryltropylium electron acceptor.

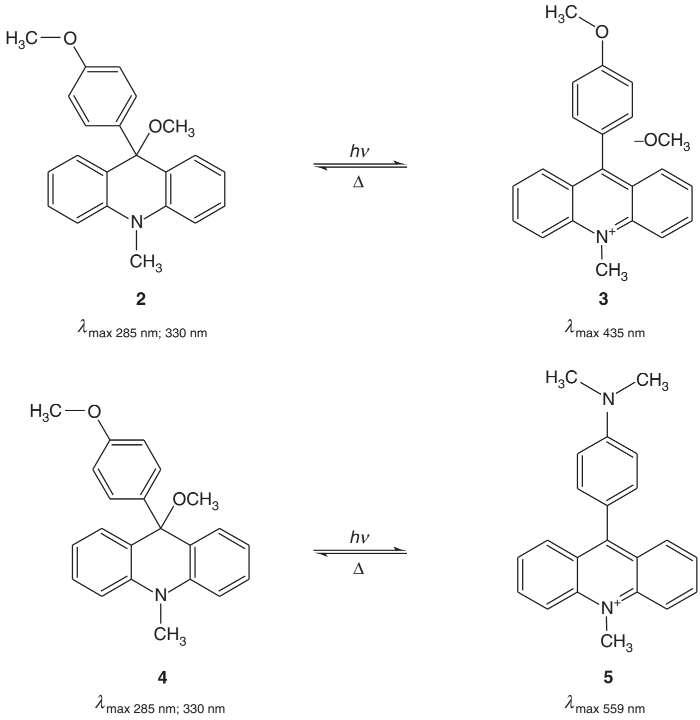

Scheme 26.5 Two types of photoswitches in rotaxanes were developed by Abraham *et al.* [97, 117].

the irradiation of the arylcycloheptatrienes molecules **2** ($\lambda_{\text{max}} = 285$ nm) and **4** ($\lambda_{\text{max}} = 285$ nm) shown in Scheme 26.5, results in a single-step photoreaction to form the respective acridinium salts; **3** ($\lambda_{\text{max}} = 435$ nm) and **5** ($\lambda_{\text{max}} = 559$ nm). Although the conventional chemical or pH-triggered shuttling processes often lead to undesired side reactions, photoswitching eliminates the formation of waste products, enabling these bistable rotaxanes to serve as archetype molecules for nanoscale photoelectronic systems [121, 133]. Nonetheless, although the use of fluorescence detection in sensors is widely explored, there are still only a few fluorescence-triggered rotaxane photoswitches [126, 133] reported in the literature.

References

1. Haugland, R.P. (1999) *Handbook of Fluorescent Probes and Research Chemicals*, 7th edn, Molecular Probes Inc., Eugene, OR.
2. Gauglitz, G. and Vo-Dinh, T. (2003) *Handbook of Spectroscopy*, Wiley-VCH Verlag GmbH, Weinheim.
3. Lakowicz, J.R. (ed.) (1994) *Topics in Fluorescence Spectroscopy: Probe Design and Chemicas Sensing*, Vol. 4, Plenum Press, New York.
4. Rettig, W., Strehmel, B., Schrader, S. *et al.* (eds) (1998) *Applied Fluorescence*

in Chemistry, Biology and Medicine, Springer-Verlag, Berlin.

5. Mason, W.T. (ed) (1999) *Fluorescence and Luminescence Probes for Biological Activity*, Academic Press, New York.
6. (a) Martin, M.M. and Lindqvist, L. (1975) *J. Lumin.*, **10**, 381. (b) Khodorov, B., Valkina, O., and Turovetsky, V. (1994) *FEBS Lett.*, **341**, 125. (c) Thomas, J.A., Buchsbaum, R.N., Zimniak, A., and Racker, E. (1979) *Biochemistry*, **18**, 2210–2218. (d) Paradiso, A.M., Tsien, R.Y., and Machen, T.E. (1984) *Proc. Natl. Acad. Sci. U.S.A.*, **81**, 7436. Sun, W.-C. *et al.* (1997) *J. Org. Chem.*, **62**, 6469. (e) Nedergaard, M., Desai, S., and Pulsinelli, W. (1990) *Anal. Biochem.*, **187**, 109. (f) Huang, C.S., Kopacz, S.J., and Lee, C.P. (1983) *Biochim. Biophys. Acta*, **722**, 107–115. (g) Overly, C.C., Lee, K.D., Berthiaume, E., and Hollenbeck, P.J. (1995) *Proc. Natl. Acad. Sci. U.S.A.*, **92**, 3156.
7. (a) Minta, A. and Tsien, R.Y. (1989) *J. Biol. Chem.*, **264**, 19449–19457. (b) Meuwis, K., Boens, N., De Schryver, F.C., Gallay, J., and Vincent, M. (1995) *Biophys. J.*, **68**, 2469–2473. Szmacinski, H., Lakowicz, J.R., and Johnson, M.L. (1994) *Methods Enzymol.*, **240**, 723–748. Jayaraman, S., Song, Y., Vetrivel, L., Shankar, L., and Verkman, A.S. (2001) *J. Clin. Invest.*, **107**, 317–324.
8. (a) Lambert, D. (ed) (1999) *Calcium Signaling Protocols*, Methods in Molecular Biology, Vol. 114, Humana Press. (b) Nuccitelli, R. (ed) (1994) *A Practical Guide to the Study of Calcium in Living Cells*, Methods in Cell Biology, Vol. 40, Academic Press, p. 342. (c) Williams, D.A., Fogarty, K.E., Tsien, R.Y., and Fay, F.S. (1985) *Nature*, **318**, 558–561. (d) Iatridou, H., Foukaraki, E., Kuhn, M.A., Marcus, E.M., Haugland, R.P., and Katerinopoulos, H.E. (1994) *Cell Calcium*, **15**, 190–198. (e) Girard, S., Luckhoff, A., Lechleiter, J., Sneyd, J., and Clapham, D. (1992) *Biophys. J.*, **61**, 509–517. (f) Takahashi, A., Camacho, P., Lechleiter, J.D., and Herman, B. (1999) *Physiol. Rev.*, **79**, 1089–1125. (g) Tsien, R.Y. (1980) *Biochemistry*, **19**, 2396–2404. (h) Ohmiya, Y. and Hirano, T. (1996) *Chem. Biol.*, **3**, 337–347. (i) Murphy, E., Freudenrich, C.C., Levy, L.A., London, R.E., and Lieberman, M. (1989) *Proc. Natl. Acad. Sci. U.S.A.*, **86**, 2981–2984. (j) van der Wolk, J.P., Klose, M., de Wit, J.G., den Blaauwen, T., Freudl, R., and Driessen, A.J. (1995) *J. Biol. Chem.*, **270**, 18975–18982.
9. (a) Canzoniero, L.M., Turetsky, D.M., and Choi, D.W. (1999) *J. Neurosci.*, **19**, RC31. (b) Frederickson, C.J., Kasarskis, E.J., Ringo, D., and Frederickson, R.E. (1987) *J. Neurosci. Methods*, **20**, 91–103. (c) Kuhn, M.A. *et al.* (1995) *Proc. SPIE-Intl. Soc. Opt. Eng.*, **2388**, 238.
10. (a) Wolfbeis, O.S. and Urbano, E. (1982) *J. Heterocycl. Chem.*, **19**, 841. (b) Verkman, A.S., Sellers, M.C., Chao, A.C., Leung, T., and Ketcham, R. (1989) *Anal. Biochem.*, **178**, 355–361. (c) Biwersi, J. and Verkman, A.S. (1991) *Biochemistry*, **30**, 7879–7883. (d) Biwersi, J., Tulk, B., and Verkman, A.S. (1994) *Anal. Biochem.*, **219**, 139–143. (e) Li, H.B. and Chen, F. (2000) *Fresenius' J. Anal. Chem.*, **368**, 501–504.
11. Sano, A., Takezawa, M., and Takitani, S. (1986) *Anal. Sci.*, **2**, 491.
12. (a) Deakin, H., Ord, M.G., and Stocken, L.A. (1963) *Biochem. J.*, **89**, 296. (b) Kosower, N.S., Kosower, E.M., Newton, G.L., and Ranney, H.M. (1979) *Proc. Natl. Acad. Sci. U.S.A.*, **76**, 3382–3386.
13. Upson, R.H., Haugland, R.P., Malekzadeh, M.N., and Haugland, R.P. (1996) *Anal. Biochem.*, **243**, 41–45.
14. (a) Komija, H. (1999) *Angew. Chem. Int. Ed.*, **21**, 3209. (b) Misko, T.P., Schilling, R.J., Salvemini, D., Moore, W.M., and Currie, M.G. (1993) *Anal. Biochem.*, **214**, 11–16. (c) Buldt, A. and Karst, U. (1999) *Anal. Chem.*, **71**, 3003–3007.
15. (a) Krieg, M. (1992) *Biochim. Biophys. Acta*, **1105**, 333–335. (b) Bottiroli, G., Croce, A.C., Balzarini, P., Locatelli, D., Baglioni, P., Lo Nostro, P., Monici, M., and Pratesi, R. (1997) *Photochem. Photobiol.*, **66**, 374–383. (c) Neckers, D.C. and Valdes-Aguilera, O.M. (1993) *Adv. Photochem.*, **18**, 315. (d) Miranda, S., Opazo, C., Larrondo, L.F., Munoz, F.J., Ruiz, F., Leighton, F., and

Inestrosa, N.C. (2000) *Prog. Neurobiol.*, **62**, 633–648.

16. (a) Tsien, R.Y. (1999) *Nat. Biotechnol.*, **17**, 956. (b) Baird, G.S., Zacharias, D.A., and Tsien, R.Y. (2000) *Proc. Natl. Acad. Sci. U.S.A.*, **97**, 11984.

17. (a) Armbruster, A., Schwarzhoff, R.H., Hubster, E., Edward, C., and Monica, K. (1993) *Clin. Chem.*, **39** (10), 2137–2146. (b) Szollosi, J., Damjanovich, S., and Matyus, L. (1998) *Cytometry*, **34** (4), 159–179. (c) Zhang, Y.Z., Kemper, C., Bakke, A., and Haugland, R.P. (1998) *Cytometry*, **33**, 244–248. (d) Luchtel, D.L., Boykin, J.C., Bernard, S.L., and Glenny, R.W. (1998) *Biotech. Histochem.*, **73**, 291–309. (e) Brinkley, J.M., Haugland, R.P., and Singer, V. (1994) US Patent 5, 326,692.

18. (a) Diwu, Z., Klaubert, D.H., and Haugland, R.P. (1999) *Proc. SPIE-Intl. Soc. Opt. Eng.*, **3602**, 265. (b) Larison, K.D., BreMiller, R., Wells, K.S., Clements, I., and Haugland, R.P. (1995) *J. Histochem. Cytochem.*, **43**, 77–83.

19. (a) Breininger, J.F. and Baskin, D.G. (2000) *J. Histochem. Cytochem.*, **48**, 1593–1599. (b) Bobrow, M.N., Harris, T.D., Shaughnessy, K.J., and Litt, G.J. (1989) *J. Immunol. Methods*, **125**, 279–285. (c) van Gijlswijk, R.P., Zijlmans, H.J., Wiegant, J., Bobrow, M.N., Erickson, T.J., Adler, K.E., Tanke, H.J., and Raap, A.K. (1997) *J. Histochem. Cytochem.*, **45**, 375–382.

20. (a) Lowry, O.H. *et al.* (1951) *J. Biol. Chem.*, **193**, 265. (b) Fazekas de St Groth, S., Webster, R., and Datyner, A. (1963) *Biochim. Biophys. Acta*, **71**, 377. (c) Bradford, M.M. (1976) *Anal. Biochem.*, **72**, 248–254. (d) Udenfriend, S., Stein, S., Bohlen, P., Dairman, W., Leimgruber, W., and Weigele, M. (1972) *Science*, **178**, 871–872. (e) Goodno, C.C., Swaisgood, H.E., and Catignani, G.L. (1981) *Anal. Biochem.*, **115**, 203–211. (f) Smith, P.K., Krohn, R.I., Hermanson, G.T., Mallia, A.K., Gartner, F.H., Provenzano, M.D., Fujimoto, E.K., Goeke, N.M., Olson, B.J., and Klenk, D.C. (1985) *Anal. Biochem.*, **150**, 76–85. (g) Jones, L.J. *et al.* (1996) *FASEB J.*, **10**, A1512Abstract #2954. (h) Liu, Y., Foote, R.S., Jacobson, S.C., Ramsey, R.S., and Ramsey, J.M. (2000) *Anal. Chem.*, **72**, 4608–4613. (i) Patton, W.F. (2000) *Electrophoresis*, **21**, 1123–1144. (j) Patton, W.F. (2000) *Biotechniques*, **28**, 944–994. (k) Yan, J.X., Harry, R.A., Spibey, C., and Dunn, M.J. (2000) *Electrophoresis*, **21**, 3657–3665.

21. (a) Rinderknecht, H. (1960) *Experientia*, **16**, 430. (b) Felton, L.C. and McMillion, C.R. (1961) *Anal. Biochem.*, **2**, 178. (c) Weber, G. (1952) *Biochem. J.*, **51**, 155. (d) Seiler, N. (1970) *Methods Biochem. Anal.*, **18**, 259–337. (e) Lin, J.K. and Chang, J.Y. (1975) *Anal. Chem.*, **47**, 1634–1638. (f) Muramoto, K., Kamiya, H., and Kawauchi, H. (1984) *Anal. Biochem.*, **141**, 446–450. (g) Jin, S.W., Chen, G.X., Palacz, Z., and Wittmann-Liebold, B. (1986) *FEBS Lett.*, **198**, 150–154. (h) Maggiora, L.L., Smith, C.W., and Zhang, Z.Y. (1992) *J. Med. Chem.*, **35**, 3727–3730. (i) Maeda, H. and Kawauchi, H. (1968) *Biochem. Biophys. Res. Commun.*, **31**, 188–192.

22. (a) Taylor, D.L. and Wang, Y.L. (1978) *Proc. Natl. Acad. Sci. U.S.A.*, **75**, 857–861. (b) Barber, K., Mala, R.R., Lambert, M.P., Qiu, R., MacDonald, R.C., and Klein, W.L. (1996) *Neurosci. Lett.*, **207**, 17–20. (c) Szczesna, D. and Lehrer, S.S. (1993) *J. Muscle Res. Cell Motil.*, **14**, 594–597.

23. (a) Le Pecq, J.B., Le Bret, M., Barbet, J., and Roques, B. (1975) *Proc. Natl. Acad. Sci. U.S.A.*, **72**, 2915–2919. (b) Morgan, A.R., Lee, J.S., Pulleyblank, D.E., Murray, N.L., and Evans, D.H. (1979) *Nucleic Acids Res.*, **7**, 547–569. (c) McMaster, G.K. and Carmichael, G.G. (1977) *Proc. Natl. Acad. Sci. U.S.A.*, **74**, 4835–4838. (d) Schnedl, W., Mikelsaar, A.V., Breitenbach, M., and Dann, O. (1977) *Hum. Genet.*, **36**, 167–172. (e) Weisblum, B. and Haenssler, E. (1974) *Chromosoma*, **46**, 255–260. (f) Crissman, H.A., Darzynkiewicz, Z., Steinkamp, J.A., and Tobey, R.A. (1990) *Methods Cell Biol.*, **33**, 305–314. (g) Saiki, I., Bucana, C.D., Tsao, J.Y., and Fidler, I.J. (1986) *J. Natl. Cancer Inst.*, **77**, 1235–1240. (h) Muller, W. and Crothers, D.M. (1968) *J. Mol. Biol.*, **35**, 251–290. (i) Festy, B. and Daune, M. (1973) *Biochemistry*, **12**, 4827–4834. (j) Netzel, T.L. *et al.* (1995) *J. Phys. Chem.*, **99**, 17936. (k) Poot, M., Gibson, L.L., and Singer, V.L. (1997) *Cytometry*, **27**, 358–364. (l) Popa, L.M., Winter, S., and Lober, G. (1994) *Biochem. Mol. Biol. Int.*, **34**, 1189–1196. (m) Beisker, W., Weller-Mewe, E.M., and Nusse, M. (1999) *Cytometry*, **37**, 221–229. (n) Mansfield, E.S., Worley, J.M., McKenzie, S.E., Surrey, S., Rappaport, E., and Fortina, P. (1995) *Mol. Cell. Probes*, **9**, 145–156. (o) Ahn, S.J., Costa, J., and Emanuel, J.R. (1996) *Nucleic Acids Res.*, **24**, 2623–2625. (p) Reyderman, L. and Stavchansky, S. (1996) *J. Chromatogr., A*, **755**, 271–280. (q) Jones, L.J., Yue, S.T., Cheung, C.Y., and Singer, V.L. (1998) *Anal. Biochem.*, **265**, 368–374. (r) Fujita, M., Tomita, S., Ueda, Y., and Fujimori, T. (1998) *Mol. Pathol.*, **51**, 342. (s) Karlsen, F., Steen, H.B., and Nesland, J.M. (1995) *J. Virol. Methods*, **55**, 153–156. (t) Schmidt, D.M. and Ernst, J.D. (1995) *Anal. Biochem.*, **232**, 144–146. (u) Hamaguchi, Y. *et al.* (1997) *Environ. Health*, **60**, 14.

24. (a) Schrock, E., du Manoir, S., Veldman, T., Schoell, B., Wienberg, J., Ferguson-Smith, M.A., Ning, Y., Ledbetter, D.H., Bar-Am, I., Soenksen, D., Garini, Y., and Ried, T. (1996) *Science*, **273**, 494–497. (b) Forghani, B., Yu, G.J., and Hurst, J.W. (1991) *J. Clin. Microbiol.*, **29**, 583–591.

25. (a) Schneeberger, C., Speiser, P., Kury, F., and Zeillinger, R. (1995) *PCR Methods Appl.*, **4**, 234–238. (b) Huang, J., DeGraves, F.J., Gao, D., Feng, P., Schlapp, T., and Kaltenboeck, B. (2001) *Biotechniques*, **30**, 150–157.

26. (a) Wiegant, J.C., van Gijlswijk, R.P., Heetebrij, R.J., Bezrookove, V., Raap, A.K., and Tanke, H.J. (1999) *Cytogenet. Cell Genet.*, **87**, 47–52. (b) Tanke, H.J., Wiegant, J., van Gijlswijk, R.P., Bezrookove, V., Pattenier, H., Heetebrij, R.J., Talman, E.G., Raap, A.K., and Vrolijk, J. (1999) *Eur. J. Hum. Genet.*, **7**, 2–11. (c) Alers, J.C., Rochat, J., Krijtenburg, P.J., van Dekken, H., Raap, A.K., and Rosenberg, C. (1999) *Genes Chromosomes Cancer*, **25**, 301–305.

27. Paragas, V.B., Zhang, Y.Z., Haugland, R.P., and Singer, V.L. (1997) *J. Histochem. Cytochem.*, **45**, 345–357.

28. Speel, E.J., Hopman, A.H., and Komminoth, P. (1999) *J. Histochem. Cytochem.*, **47**, 281–288.

29. (a) Kaiser, R.D. and London, E. (1998) *Biochim. Biophys. Acta*, **1375**, 13–22. (b) Monti, J.A., Christian, S.T., Shaw, W.A., and Finley, W.H. (1977) *Life Sci.*, **21**, 345–355. (c) Chattopadhyay, A. and London, E. (1988) *Biochim. Biophys. Acta*, **938**, 24–34. (d) Galla, H.J. and Sackmann, E. (1975) *J. Am. Chem. Soc.*, **97**, 4114–4120. (e) Barenholz, Y., Cohen, T., Haas, E., and Ottolenghi, M. (1996) *J. Biol. Chem.*, **271**, 3085–3090. (f) Waggoner, A.S. and Stryer, L. (1970) *Proc. Natl. Acad. Sci. U.S.A.*, **67**, 579–589. (g) Luan, P. and Glaser, M. (1994) *Biochemistry*, **33**, 4483–4489. (h) Sklar, L.A., Hudson, B.S., and Simoni, R.D. (1975) *Proc. Natl. Acad. Sci. U.S.A.*, **72**, 1649–1653.

30. (a) Sims, P.J., Waggoner, A.S., Wang, C.H., and Hoffman, J.F. (1974) *Biochemistry*, **13**, 3315–3330. (b) London, J.A., Zecevic, D., and Cohen, L.B. (1987) *J. Neurosci.*, **7**, 649–661. (c) Fluhler, E., Burnham, V.G., and Loew, L.M. (1985) *Biochemistry*, **24**, 5749–5755. (d) Smiley, S.T., Reers, M., Mottola-Hartshorn, C., Lin, M., Chen, A., Smith, T.W., Steele, G.D. Jr., and Chen, L.B. (1991) *Proc. Natl. Acad. Sci. U.S.A.*, **88**, 3671–3675. (e) Loew, L.M. (1993) *Methods Cell Biol.*, **38**, 195–209. (f) Schaffer, P., Ahammer, H., Muller, W., Koidl, B., and Windisch, H. (1994) *Pflugers Arch.*, **426**, 548–551. (g) Tsau, Y., Wenner, P., O'Donovan, M.J., Cohen, L.B., Loew, L.M., and Wuskell, J.P. (1996) *J. Neurosci. Methods*, **70**, 121–129. (h) Grinvald, A., Frostig, R.D., Lieke, E., and Hildesheim, R. (1988) *Physiol. Rev.*, **68**, 1285–1366. (i) Zochowski, M., Wachowiak, M., Falk, C.X., Cohen, L.B., Lam, Y.W., Antic, S., and Zecevic, D. (2000) *Biol. Bull.*, **198**, 1–21.

31. (a) Rakhmanova, V.A. and MacDonald, R.C. (1998) *Anal. Biochem.*, **257**, 234–237. (b) Jones, D.E. Jr., Cui, D.M., and Miller, D.M. (1995) *Oncogene*, **10**, 2323–2330. (c) Rao, A.G. and Flynn, P. (1990) *Biotechniques*, **8**, 37. (d) Young, D.C., Kingsley, S.D., Ryan, K.A., and Dutko, F.J. (1993) *Anal. Biochem.*, **215**, 24–30. (e) Zhou, M., Zhang, C., Upson, R.H., and Haugland, R.P. (1998) *Anal. Biochem.*, **260**, 257–259. (f) Tronsmo, A. and Harman, G.E. (1993) *Anal. Biochem.*, **208**, 74–79.

32. (a) Lottenberg, R., Christensen, U., Jackson, C.M., and Coleman, P.L. (1981) *Methods Enzymol.*, **80** (Pt. C), 341–361. (b) Rosser, B.G., Powers, S.P., and Gores, G.J. (1993) *J. Biol. Chem.*, **268**, 23593–23600. (c) Leytus, S.P., Melhado, L.L., and Mangel, W.F. (1983) *Biochem. J.*, **209**, 299–307. (d) Twining, S.S. (1984) *Anal. Biochem.*, **143**, 30–34.

33. (a) Rotman, B., Zderic, J.A., and Edelstein, M. (1963) *Proc. Natl. Acad. Sci. U.S.A.*, **50**, 1. (b) Leiraa, F., Vieitesa, J.M., Vieytesb, M.R., and Botanac, L.M. (2000) *Toxicon*, **38**, 1833–1844. (c) Avrameas, S. (1992) *J. Immunol. Methods*, **150**, 23–32. (d) Gee, K.R., Sun, W.C., Bhalgat, M.K., Upson, R.H., Klaubert, D.H., Latham, K.A., and Haugland, R.P. (1999) *Anal. Biochem.*, **273**, 41–48. (e) Petty, R.D., Sutherland, L.A., Hunter, E.M., and Cree, I.A. (1995) *J. Biolumin. Chemilumin.*, **10**, 29–34.

34. (a) Zhou, M., Diwu, Z., Panchuk-Voloshina, N., and Haugland, R.P. (1997) *Anal. Biochem.*, **253**, 162–168. (b) Amundson, D.M. and Zhou, M. (1999) *J. Biochem. Biophys. Methods*, **38**, 43–52. (c) Zhou, M. and Panchuk-Voloshina, N. (1997) *Anal. Biochem.*, **253**, 169–174. (d) McElroy, K.E., Bouchard, P.J., Harpel, M.R., Horiuchi, K.Y., Rogers, K.C., Murphy, D.J., Chung, T.D., and Copeland, R.A. (2000) *Anal. Biochem.*, **284**, 382–387. (e) Zhou, M., Zhang, C., and Haugland, R.P. (2000) *Proc. SPIE-Intl. Soc. Opt. Eng.*, **3926**, 166.

35. (a) Rosenberg, D.W., Roque, H., and Kappas, A. (1990) *Anal. Biochem.*, **191**, 354–358. (b) Solito, E., Raguenes-Nicol, C., de Coupade, C., Bisagni-Faure, A., and Russo-Marie, F. (1998) *Br. J. Pharmacol.*, **124**, 1675–1683. (c) Hendrickson, H.S., Hendrickson, E.K., Johnson, I.D., and Farber, S.A. (1999) *Anal. Biochem.*, **276**, 27–35. (d) Hendrickson, H.S. and Rauk, P.N. (1999) *Anal. Biochem.*, **116**, 553–558. (e) She, H.S., Garsetti, D.E., Steiner, M.R., Egan, R.W., and Clark, M.A. (1994) *Biochem. J.*, **298**, 23–29. (f) Hendrickson, H.S., Kotz, K.J., and Hendrickson, E.K. (1990) *Anal. Biochem.*, **185**, 80–83. (g) Trievel, R.C., Li, F.Y., and Marmorstein, R. (2000) *Anal. Biochem.*, **287**, 319–328. (h) Hruby, D.E. and Wilson, E.M. (1992) *Methods Enzymol.*, **216**, 369–376. (i) Lefevre, C.K., Singer, V.L., Kang, H.C., and Haugland, R.P. (1995) *Biotechniques*, **19**, 488–493. (j) Brubaker, K.D., Mao, F., and Gay, C.V. (1999) *J. Histochem. Cytochem.*, **47**, 545–550.

36. (a) Guasch, R.M., Guerri, C., and O'Connor, J.E. (1993) *Exp. Cell Res.*, **207**, 136–141. (b) Renthal, R., Steinemann, A., and Stryer, L. (1973) *Exp. Eye Res.*, **17**, 511–515. (c) Miller, M.W. and Hanover, J.A. (1994) *J. Biol. Chem.*, **269**, 9289–9297. (d) Ito, N., Imai, S., Haga, S., Nagaike, C., Morimura, Y., and Hatake, K. (1996) *Histochem. Cell Biol.*, **106**, 331–339. (e) Virtanen, I. (1990) *Histochemistry*, **94**, 397–401. (f) Kenworthy, A.K., Petranova, N., and Edidin, M. (2000) *Mol. Biol. Cell*, **11**, 1645–1655. (g) Sahagun, G., Moore, S.A., Fabry, Z., Schelper, R.L., and Hart, M.N. (1989) *Am. J. Pathol.*, **134**, 1227–1232.

37. (a) Chen, L.B. (1989) *Methods Cell Biol.*, **29**, 103–123. (b) Habicht, J. and Brune, K. (1980) *Exp. Cell Res.*, **125**, 514–518. (c) Bereiter-Hahn, J. (1990) *J. Int. Rev. Cytol.*, **122**, 1–63. (d) Septinus, M., Seiffert, W., and Zimmermann, H.W. (1983) *Histochemistry*, **79**, 443–456. (e) Septinus, M., Berthold, T., Naujok, A., and Zimmermann, H.W. (1986) *Histochemistry*, **82**, 51–66. (f) Rembish, S.J. and Trush, M.A. (1994) *Free Radic. Biol. Med.*, **17**, 117–126. (g) Poot, M., Zhang, Y.Z., Kramer, J.A., Wells, K.S., Jones, L.J., Hanzel, D.K., Lugade, A.G., Singer, V.L., and Haugland, R.P.

(1996) *J. Histochem. Cytochem.*, **44**, 1363–1372. (h) Pereira, A.J., Dalby, B., Stewart, R.J., Doxsey, S.J., and Goldstein, L.S. (1997) *J. Cell Biol.*, **136**, 1081–1090. (i) Sakanoue, J., Ichikawa, K., Nomura, Y., and Tamura, M. (1997) *J. Biochem. (Tokyo)* , **121**, 29–37.

38. (a) Pagano, R.E. and Martin, O.C. (1998) in *Cell Biology: A Laboratory Handbook*, 2nd edn, Vol. 2 (ed. J.E. Celis), Academic Press, New York, pp. 507–512. (b) Terasaki, M., Song, J., Wong, J.R., Weiss, M.J., and Chen, L.B. (1984) *Cell*, **38**, 101–108. (c) Cole, L., Davies, D., Hyde, G.J., and Ashford, A.E. (2000) *J. Microsc.*, **197**, 239–249. (d) Terasaki, M. and Jaffe, L.A. (1991) *J. Cell Biol.*, **114**, 929–940. (e) Cole, L., Davies, D., Hyde, G.J., and Ashford, A.E. (2000) *Fungal Genet. Biol.*, **29**, 95–106.

39. (a) Guse, A.H., da Silva, C.P., Berg, I., Skapenko, A.L., Weber, K., Heyer, P., Hohenegger, M., Ashamu, G.A., Schulze-Koops, H., Potter, B.V., and Mayr, G.W. (1999) *Nature*, **398**, 70–73. (b) Cui, Y., Galione, A., and Terrar, D.A. (1999) *Biochem. J.*, **342**, 269–273. (c) Wong, L., Aarhus, R., Lee, H.C., and Walseth, T.F. (1999) *Biochim. Biophys. Acta*, **1472**, 555–564. (d) Zhang, X., Wen, J., Bidasee, K.R., Besch, H.R. Jr., Wojcikiewicz, R.J., Lee, B., and Rubin, R.P. (1999) *Biochem. J.*, **340**, 519–527. (e) Abrenica, B. and Gilchrist, J.S. (2000) *Cell Calcium*, **28**, 127–136. (f) Malencik, D.A., Huang, T.S., and Anderson, S.R. (1982) *Biochem. Biophys. Res. Commun.*, **108**, 266–272. (g) Baudier, J., Bergeret, E., Bertacchi, N., Weintraub, H., Gagnon, J., and Garin, J. (1995) *Biochemistry*, **34**, 7834–7846. (h) Putkey, J.A. and Waxham, M.N. (1996) *J. Biol. Chem.*, **271**, 29619–29623. (i) Torok, K., Cowley, D.J., Brandmeier, B.D., Howell, S., Aitken, A., and Trentham, D.R. (1998) *Biochemistry*, **37**, 6188–6198.

40. (a) Ogamo, A., Matsuzaki, K., Uchiyama, H., and Nagasawa, K. (1982) *Carbohydr. Res.*, **105**, 69–85. (b) Sobel, M., Soler, D.F., Kermode, J.C., and Harris, R.B. (1992) *J. Biol. Chem.*, **267**, 8857–8862. (c) Berry, L., Stafford, A., Fredenburgh, J., O'Brodovich, H., Weitz, L., Mitchell, J., Andrew, M., and Chan, A.K. (1998) *J. Biol. Chem.*, **273**, 34730–34736. (d) Bentley, K.L., Klebe, R.J., Hurst, R.E., and Horowitz, P.M. (1985) *J. Biol. Chem.*, **260**, 7250–7256.

41. (a) Chen, C.S. and Poenie, M. (1993) *J. Biol. Chem.*, **268**, 15812–15822. (b) Newton, B.A. (1955) *J. Gen. Microbiol.*, **12**, 226. (c) Takahashi, I., Nakanishi, S., Kobayashi, E., Nakano, H., Suzuki, K., and Tamaoki, T. (1982) *Biochem. Biophys. Res. Commun.*, **165**, 1207–1212. (d) Hiratsuka, T. (1982) *J. Biol. Chem.*, **257**, 13354–13358.

42. (a) Anderson, M.J. and Cohen, M.W. (1974) *J. Physiol.*, **237**, 385–400. (b) Salzman, N.H. and Maxfield, F.R. (1993) in *Subcellular Biochem: Endocytic Components: Identification and Characterization*, Vol. 19 (eds J.J.M. Bergeron and J. Robin Harris), Kluwer Academic/Plenum Publishers, pp. 95–123. (c) Wang, Y., Gu, Q., Mao, F., Haugland, R.P., and Cynader, M.S. (1994) *J. Neurosci.*, **14**, 4147–4158. (d) Reid, J.L. and Vincent, J. (1986) *Cardiology*, **73**, 164–174. (e) Heithier, H., Hallmann, D., Boege, F., Reilander, H., Dees, C., Jaeggi, K.A., Arndt-Jovin, D., Jovin, T.M., and Helmreich, E.J. (1994) *Biochemistry*, **33**, 9126–9134. (f) Wang, H., Standifer, K.M., and Sherry, D.M. (2000) *Vis. Neurosci.*, **17**, 11–21. (g) Tota, M.R., Daniel, S., Sirotina, A., Mazina, K.E., Fong, T.M., Longmore, J., and Strader, C.D. (1994) *Biochemistry*, **33**, 13079–13086. (h) Walker, B., Gray, J., Burns, D.M., Wang, Q., Adrian, T.E., Nichols, D.H., Murphy, R.F., and Nelson, J. (1995) *Peptides*, **16**, 255–261. (i) Haller, H., Lindschau, C., Erdmann, B., Quass, P., and Luft, F.C. (1996) *Circ. Res.*, **79**, 765–772. (j) Kolb, V.M., Koman, A., and Terenius, L. (1983) *Life Sci.*, **33** (Suppl. 1), 423–426. (k) Jones, O.T., Kunze, D.L., and Angelides, K.J. (1989) *Science*, **244**, 1189–1193. (l) Schild, D., Geiling, H., Bischofberger, J., and Neurosci, J. (1995) *Methods*, **59**, 183–190. (m) Kleyman, T.R. and Cragoe, E.J. Jr., (1988) *J. Membr. Biol.*, **105**, 1–21. (n)

Fortes, P.A. (1977) *Biochemistry*, **16**, 531–540. (o) Lohrke, B., Derno, M., Kruger, B., Viergutz, T., Matthes, H., and Jentsch, W. (1997) *Pflugers Arch.*, **434**, 712–720. (p) Fricker, G., Gutmann, H., Droulle, A., Drewe, J., and Miller, D.S. (1999) *Pharm. Res.*, **16**, 1570–1575.

43. (a) Bass, D.A., Parce, J.W., Dechatelet, L.R., Szejda, P., Seeds, M.C., and Thomas, M. (1983) *J. Immunol.*, **130**, 1910–1917. (b) Ryan, T.C., Weil, G.J., Newburger, P.E., Haugland, R., and Simons, E.R. (1990) *J. Immunol. Methods*, **130**, 223–233.

44. Aubry, J.P., Blaecke, A., Lecoanet-Henchoz, S., Jeannin, P., Herbault, N., Caron, G., Moine, V., and Bonnefoy, J.Y. (1999) *Cytometry*, **37**, 197–204. Thornberry, N.A. and Lazebnik, Y. (1998) *Science*, **281**, 1312–1316.

45. Kim, J.S., Kodagahally, R., Strekowski, L., and Patonay, G. (2005) *Talanta*, **67**, 947–954.

46. Zhang, Y.Z., Xiang, J.F., Tang, Y.L., Xu, G.Z., and Yan, W.P. (2008) *Dyes Pigm.*, **76**, 88–93.

47. Jin, J.K., Sun, J.Z., Dong, Y.Q., Xu, H.P., Yuan, W.Z., and Tang, B.Z. (2009) *J. Lumin.*, **129**, 19–23.

48. Shandura, M.P., Poronik, Y.M., and Kovtun, Y.P. (2007) *Dyes Pigm.*, **73**, 25–30.

49. Eggeling, C., Widengren, J., Rigler, R., and Seidel, C.A.M. (1998) *Anal. Chem.*, **70**, 2651–2659.

50. Romieu, A., Brossard, D., Hamon, M., Outaabout, H., Portal, C., and Renard, P.Y. (2008) *Bioconjugate Chem.*, **19**, 279–289.

51. Folling, J., Belov, V., Kunetsky, R., Medda, R., Schonle, A., Egner, A., Eggeling, C., Bossi, M., and Hell, S.W. (2007) *Angew. Chem. Int. Ed.*, **46**, 6266–6270.

52. Wu, L.X. and Burgess, K. (2008) *J. Org. Chem.*, **73**, 8711–8718.

53. Antropova, I.G., Fenin, A.A., and Revina, A.A. (2007) *High Energy Chem.*, **41**, 61–64.

54. Bryantseva, N., Sokolova, I., Tsyrenzhapova, A., Selivanov, N., Khilya, V., and Garazd, Y. (2008) *J. Appl. Spectrosc.*, **75**, 700–705.

55. Dobrikov, M.I. (1999) *Usp. Khim.*, **68**, 1062–1079.

56. Stanjek, V., Piel, J., and Boland, W. (1999) *Phytochemistry*, **50**, 1141–1145.

57. Bissonnette, L., Arnason, J.T., and Smith, M.L. (2008) *Phytochem. Anal.*, **19**, 342–347.

58. Smith, M.L., Gregory, P., Bafi-Yeboa, N.F.A., and Arnason, J.T. (2004) *Photochem. Photobiol.*, **79**, 506–509.

59. Strekowski, L. (2008) *Heterocyclic Polymethine Dyes: Synthesis, Properties and Applications*, Springer, Berlin.

60. Patonay, G., Kim, J.S., Kodagahally, R., and Strekowski, L. (2005) *Appl. Spectrosc.*, **59**, 682–690.

61. Ma, N., Sargent, E.H., and Kelley, S.O. (2009) *Nat. Nanotechnol.*, **4**, 121–125.

62. Xuan, Y., Qian, G., Wang, Z.Y., and Ma, D.G. (2008) *Thin Solid Films*, **516**, 7891–7893.

63. Encinas, C., Miltsov, S., Otazo, E., Rivera, L., Puyol, M., and Alonso, J. (2006) *Dyes Pigm.*, **71**, 28–36.

64. Puyol, M., Encinas, C., Rivera, L., Mijtsov, S., and Alonso, J. (2007) *Dyes Pigm.*, **73**, 383–389.

65. Puyol, M., Encinas, C., Rivera, L., Miltsov, S., and Alonso, J. (2007) *Sens. Actuators, B*, **122**, 53–59.

66. Xu, Y.F., Liu, Y., and Qian, X.H. (2007) *J. Photochem. Photobiol. Chem.*, **190**, 1–8.

67. Zhang, Z.R. and Achilefu, S. (2005) *Chem. Commun.*, **47**, 5887–5889.

68. Xun, S.D., LeClair, G., Zhang, J.D., Chen, X., Gao, J.P., and Wang, Z.Y. (2006) *Org. Lett.*, **8**, 1697–1700.

69. Malins, C., Landl, M., Simon, P., and MacCraith, B.D. (1998) *Sens. Actuators, B*, **51**, 359–367.

70. Scorsone, E., Christie, S., Persaud, K.C., Simon, P., and Kvasnik, F. (2003) *Sens. Actuators, B*, **90**, 37–45.

71. Simon, P., Landl, M., Breza, M., and Kvasnik, F. (2003) *Sens. Actuators*, **90**, 9–14.

72. Jorge, P.A.S., Caldas, P., Da Silva, J., Rosa, C.C., Oliva, A.G., Santos, J.L., and Farahi, F. (2005) *Fiber Integr. Opt.*, **24**, 201–225.

73. Benounis, M., Aka-Ngnui, T., Jaffrezic, N., and Dutasta, J.P. (2008) *Sens. Actuators, A*, **141**, 76–83.

74. Benounis, M., Jaffrezic-Renault, N., Dutasta, J.P., Cherif, K., and Abdelghani, A. (2005) *Sens. Actuators*, **107**, 32–39.

75. Klohs, J., Wunder, A., and Licha, K. (2008) *Basic Res. Cardiol.*, **103**, 144–151.

76. Chen, X.Y., Conti, P.S., and Moats, R.A. (2004) *Cancer Res.*, **64**, 8009–8014.

77. Perlitz, C., Licha, K., Scholle, F.D., Ebert, B., Bahner, M., Hauff, P., Moesta, K.T., and Schirner, M. (2005) *J. Fluoresc.*, **15**, 443–454.

78. Li, C., Greenwood, T.R., Bhujwalla, Z.M., and Glunde, K. (2006) *Org. Lett.*, **8**, 3623–3626.

79. Glunde, K., Foss, C.A., Takagi, T., Wildes, F., and Bhujwalla, Z.M. (2005) *Bioconjugate Chem.*, **16**, 843–851.

80. Hama, Y., Urano, Y., Koyama, Y., Kamiya, M., Bernardo, M., Paik, R.S., Shin, I.S., Paik, C.H., Choyke, P.L., and Kobayashi, H. (2007) *Cancer Res.*, **67**, 2791–2799.

81. Aikawa, E., Nahrendorf, M., Sosnovik, D., Lok, V.M., Jaffer, F.A., Aikawa, M., and Weissleder, R. (2007) *Circulation*, **115**, 377–386.

82. Zhang, J., Chen, H.Y., Xu, L., and Gu, Y.Q. (2008) *J. Controlled Release*, **131**, 34–40.

83. Matveeva, E.G., Terpetschnig, E.A., Stevens, M., Patsenker, L., Kolosova, O.S., Gryczynski, Z., and Gryczynski, I. (2009) *Dyes Pigm.*, **80**, 41–46.

84. Wang, M.Z., Xie, H., Zhu, J.Q., Xie, M.G., Li, T.K., and Li, Y. (2007) *J. Mater. Sci.*, **42**, 7678–7683.

85. Ros-Lis, J.V., Garcia, B., Jimenez, D., Martinez-Manez, R., Sancenon, F., Soto, J., Gonzalvo, F., and Valldecabres, M.C. (2004) *J. Am. Chem. Soc.*, **126**, 4064–4065.

86. Gassensmith, J.J., Barr, L., Baumes, J.M., Paek, A., Nguyen, A., and Smith, B.D. (2008) *Org. Lett.*, **10**, 3343–3346.

87. Xue, M. and Chen, C.F. (2008) *Chem. Commun.*, 6128–6130.

88. Sreejith, S., Divya, K.P., and Ajayaghosh, A. (2008) *Angew. Chem. Int. Ed.*, **47**, 7883–7887.

89. Devi, D.G., Cibin, T.R., Ramaiah, D., and Abraham, A. (2008) *J. Photochem. Photobiol., B*, **92**, 153–159.

90. Ravirajan, P., Haque, S.A., Durrant, J.R., Bradley, D.D.C., and Nelson, J. (2005) *Adv. Funct. Mater.*, **15**, 609–618.

91. Arunkumar, E., Forbes, C.C., and Smith, B.D. (2005) *Eur. J. Org. Chem.*, 4051–4059.

92. Volkova, K.D., Kovalska, V.B., Losytskyy, M.Y., Bento, A., Reis, L.V., Santos, P.F., Almeida, P., and Yarmoluk, S.M. (2008) *J. Fluoresc.*, **18**, 877–882.

93. Tatarets, A.L., Fedyunyaeva, I.A., Terpetschnig, E., and Patsenker, L.D. (2005) *Dyes Pigm.*, **64**, 125–134.

94. Tatarets, A.L., Fedyunyayeva, I.A., Dyubko, T.S., Povrozin, Y.A., Doroshenko, A.O., Terpetschnig, E.A., and Patsenker, L.D. (2006) *Anal. Chim. Acta*, **570**, 214–223.

95. Patsenker, L., Tatarets, A., Kolosovaa, O., Obukhova, O., Povrozin, Y., Fedyunyayeva, I., Yermolenko, I., and Terpetschnig, E. (2008) Fluoresc methods and appl: spectroscopy, imaging and probes. *Anna. N. Y. Acad. Sci.*, **1130**, 179–187.

96. Abraham, W., Buck, K., Orda-Zgadzaj, M., Schmidt-Schaffer, S., and Grummt, U.W. (2007) *Chem. Commun.*, 3094–3096.

97. Terpetschnig, E., Szmacinski, H., Ozinskas, A., and Lakowicz, J.R. (1994) *Anal. Biochem.*, **217**, 197–204.

98. Oswald, B., Lehmann, F., Simon, L., Terpetschnig, E., and Wolfbeis, O.S. (2000) *Anal. Biochem.*, **280**, 272–277.

99. Juricek, M., Kouwer, P.H.J., Rehak, J., Sly, J., and Rowan, A.E. (2009) *J. Org. Chem.*, **74**, 21–25.

100. Wang, R., Liu, W., Chen, Y., Zuo, J.L., and You, X.Z. (2009) *Dyes Pigm.*, **81**, 40–44.

101. Basova, T.V., Jushina, I.V., Gurek, A.G., Atilla, D., and Ahsen, V. (2009) *Dyes Pigm.*, **80**, 67–72.

102. Hacivelioglu, F., Durmus, M., Yesilot, S., Gurek, A.G., Kilic, A., and Ahsen, V. (2008) *Dyes Pigm.*, **79**, 14–23.

103. Hu, Y.Y., Lai, G.Q., Shen, Y.J., and Li, Y.F. (2005) *Dyes Pigm.*, **66**, 49–53.

104. Bayar, S., Dincer, H.A., and Gonca, E. (2009) *Dyes Pigm.*, **80**, 156–162.

105. Martynov, A.G., Zubareva, O.V., Gorbunova, Y.G., Sakharov, S.G., and Tsivadze, A.Y. (2009) *Inorg. Chim. Acta*, **362**, 11–18.

106. Zimcik, P., Miletin, M., Novakova, V., Kopecky, K., and Dvorakova, Z. (2009) *Dyes Pigm.*, **81**, 35–39.

107. Villano, M., Amendola, V., Sandona, G., Donzello, M.P., Ercolani, C., and Meneghetti, M. (2006) *J. Phys. Chem. B*, **110**, 24354–24360.

108. Farcas, A., Jarroux, N., Guegan, P., Fifere, A., Pinteala, M., and Harabagiu, V. (2008) *J. Appl. Polym. Sci.*, **110**, 2384–2392.

109. Tsuda, S., Terao, J., and Kambe, N. (2009) *Chem. Lett.*, **38**, 76–77.

110. Michels, J.J., O'Connell, M.J., Taylor, P.N., Wilson, J.S., Cacialli, F., and Anderson, H.L. (2003) *Chem. – Eur. J.*, **9**, 6167–6176.

111. Francesco, Z., Fanti, M., Leigh, D.A., Zhang, S.W., and Asakawa, M. (1999) *Abstr. Pap. Am. Chem. Soc.*, **218**, 337-PHYS.

112. Asakawa, M., Brancato, G., Fanti, M., Leigh, D.A., Shimizu, T., Slawin, A.M.Z., Wong, J.K.Y., Zerbetto, F., and Zhang, S.W. (2002) *J. Am. Chem. Soc.*, **124**, 2939–2950.

113. Bermudez, V., Chollet, P.A., Kajzar, F., Lorin, A., Bottari, G., Gatti, F.G., and Leigh, D.A. (2002) *Mol. Cryst. Liq. Cryst.*, **374**, 343–356.

114. Choi, J.W., Flood, A.H., Steuerman, D.W., Nygaard, S., Braunschweig, A.B., Moonen, N.N.P., Laursen, B.W., Luo, Y., DeIonno, E., Peters, A.J., Jeppesen, J.O., Xu, K., Stoddart, J.F., and Heath, J.R. (2006) *Chem. – Eur. J.*, **12**, 261–279.

115. Nikitin, K., Lestini, E., Stolarczyk, J.K., Muller-Bunz, H., and Fitzmaurice, D. (2008) *Chem. – Eur. J.*, **14**, 1117–1128.

116. Abraham, W., Wlosnewski, A., Buck, K., and Jacob, S. (2009) *Org. Biomol. Chem.*, **7**, 142–154.

117. Hirva, P., Haukka, M., and Pakkanen, T.A. (2008) *J. Mol. Model.*, **14**, 879–886.

118. DeIonno, E., Tseng, H.R., Harvey, D.D., Stoddart, J.F., and Heath, J.R. (2006) *J. Phys. Chem. B*, **110**, 7609–7612.

119. Jagesar, D.C., Hartl, F., Buma, W.J., and Brouwer, A.M. (2008) *Chem. – Eur. J.*, **14**, 1935–1946.

120. Schmidt-Schaffer, S., Grubert, L., Grummt, U.W., Buck, K., and Abraham, W. (2006) *Eur. J. Org. Chem.*, 378–398.

121. Tuncel, D. and Katterle, M. (2008) *Chem. – Eur. J.*, **14**, 4110–4116.

122. Altobello, S., Nikitin, K., Stolarczyk, J.K., Lestini, E., and Fitzmaurice, D. (2008) *Chem. – Eur. J.*, **14**, 1107–1116.

123. Trabolsi, A., Hmadeh, M., Khashab, N.M., Friedman, D.C., Belowich, M.E., Humbert, N., Elhabiri, M., Khatib, H.A., Albrecht-Gary, A.M., and Stoddart, J.F. (2009) *New J. Chem.*, **33**, 254–263.

124. Zhao, Y.L., Dichtel, W.R., Trabolsi, A., Saha, S., Aprahamian, I., and Stoddart, J.F. (2008) *J. Am. Chem. Soc.*, **130**, 11294–11296.

125. Jun, S.I., Lee, J.W., Sakamoto, S., Yamaguchi, K., and Kim, K. (2000) *Tetrahedron Lett.*, **41**, 471–475.

126. Braunschweig, A.B., Northrop, B.H., and Stoddart, J.F. (2006) *J. Mater. Chem.*, **16**, 32–44.

127. Bermudez, V., Capron, N., Gase, T., Gatti, F.G., Kajzar, F., Leigh, D.A., Zerbetto, F., and Zhang, S.W. (2000) *Nature*, **406**, 608–611.

128. Brouwer, A.M., Fazio, S.M., Frochot, C., Gatti, F.G., Leigh, D.A., Wong, J.K.Y., and Wurpel, G.W.H. (2003) *Pure Appl. Chem.*, **75**, 1055–1060.

129. Brouwer, A.M., Frochot, C., Gatti, F.G., Leigh, D.A., Mottier, L., Paolucci, F., Roffia, S., and Wurpel, G.W.H. (2001) *Science*, **291**, 2124–2128.

130. Gatti, F.G., Lent, S., Wong, J.K.Y., Bottari, G., Altieri, A., Morales, M.A.F., Teat, S.J., Frochot, C., Leigh, D.A., Brouwer, A.M., and Zerbetto, F. (2003) *Proc. Natl. Acad. Sci. U.S.A.*, **100**, 10–14.

131. Bermudez, V., Gase, T., Kajzar, F., Capron, N., Zerbetto, F., Gatti, F.G., Leigh, D.A., and Zhang, S. (2003) *Opt. Mater.*, **21**, 39–44.

132. Collier, C.P., Mattersteig, G., Wong, E.W., Luo, Y., Beverly, K., Sampaio, J., Raymo, F.M., Stoddart, J.F., and Heath, J.R. (2000) *Science*, **289**, 1172–1175.

133. Zhou, W.D., Li, J.B., He, X.R., Li, C.H., Lv, J., Li, Y.L., Wang, S., Liu, H.B., and Zhu, D.B. (2008) *Chem. – Eur. J.*, **14**, 754–763.

27

Principles of Vibrational Spectroscopic Methods and their Application to Bioanalysis

David S. Moore, Peter Uhd Jepsen, and Karel Volka

27.1
Fourier Transform Infrared Absorption Spectroscopy

27.1.1
Introduction

The ability of infrared spectra to elucidate even minute changes in the chemical structure or composition of a sample has stimulated many studies of biological objects or their components. The opportunity to obtain relationships between the parameters derived from the spectra and the symptoms of disease, pathology, injury due to environmental pollution, and so on, has driven the research for medical, clinical, biological, environmental, and many other applications.

A great potential of infrared spectroscopy, especially when combined with Raman spectroscopy, lies in the fact that information about the structure or content/concentration of individual components can be gained with some of the following advantages:

- no treatment or separation of the sample;
- reagent-free analysis;
- all state forms (solid, liquid, and gas) measurable;
- rapid analysis;
- macro as well as micrometer size objects measurable;
- measurements possible *in situ, in vivo*, or at the point of care;
- noninvasive, that is, without direct contact between the transducer and the probed biological object.

Naturally, these applications are inherently faced with the following problems of complexity of the objects and the properties of infrared radiation:

- Low penetrability of the infrared radiation, which is of the order of tens of micrometers in the mid-infrared region. The low penetrability is determined by the strong absorption of infrared radiation by water and other components of the tissues. Water absorption also limits the applicability in the near-infrared

Handbook of Spectroscopy, Second Edition. Edited by Günter Gauglitz and David S. Moore.

region, but there are several transmission windows for which the thickness of the measured layer can be as large as 10 mm.

- Heterogeneity of the measured medium, responsible for strong scattering of radiation. Even infrared spectra of single biological cells are strongly distorted because the size of the nuclei and other organelles are of the same dimensions as the wavelength of mid-infrared radiation (1–10 μm). Only a small fraction of the photons passes through the measured medium without change in the optical path, but for the majority of photons, the length of the optical path is poorly defined.
- Spatial (inhomogeneous arrangement of cellular elements) and temporal variability (aging) of the biomaterial.
- Complexity of the measured spectra. Absorption bands of the individual components, usually of macromolecular nature, strongly overlap. This fact in most cases excludes quantitative or even qualitative conclusions without extensive computational processing of the spectral data.

27.1.2
Instrumentation

Bioanalytical applications of infrared spectroscopy greatly profit from the advantages of the Fourier-transform (interferometric) technique over the dispersive technique. Nowadays, research has shown that infrared spectrometers nearly exclusively use the interferometric technique of measurement, but for routine applications and in single-purpose/dedicated equipments, especially in the near-infrared region, they also work with the dispersive elements or optical filters (e.g., temperature-controlled acousto-optical tunable filters).

The Jacquinot advantage of Fourier-transform infrared (FTIR) spectrometers has made routine a number of techniques, for example, ATR (attenuated total reflection), IRRAS (infrared reflection-absorption spectroscopy or transflection spectroscopy), GIR (grazing incidence reflection), and DRIFTS (diffuse reflection infrared Fourier transform spectroscopy), which were unthinkable in the era of dispersive spectrometers because of inadequate signal-to-noise ratios. It also provides an opportunity to use optical fibers for remote measurements or as an ATR element, which has special attraction for medical *in vivo* measurements in real time. Unfortunately, infrared spectroscopy is handicapped in this respect compared to Raman spectroscopy, as only a limited number of suitable (and expensive) materials exist with sufficient spectral transmission in the mid-infrared range (e.g., silver halide, chalcogenide, or fluoride fibers). In addition to the required transparency and low-optical attenuation in the required range, these materials must be nontoxic, flexible, nonhygroscopic, and stable long term. Nevertheless, promising applications of silver halide fibers in ATR and reflection modes already have been demonstrated for *in vivo* applications [1].

Infrared microscopy enjoys a prominent position in bioanalytics without regard to the diffraction limit. Infrared microspectroscopy allows the study of individual regions within a sample in different modes (transmission, reflection, transflection, or ATR) by mapping (sequential, point-by-point measurement of the spectra of neighboring regions of a sample), imaging (acquiring an image of the sample on an array detector), or hyperspectral imaging (an image recorded at multiple wavelength bands by a 2D-array detector) [2]. Recent progress in this field has been demonstrated using the new generation of focal plane array detectors with mercury cadmium telluride elements of dimensions $40 \times 40\,\mu\text{m}$ that can operate with frame rates of 3000 Hz [3]. Usage of synchrotron infrared radiation allows a number of studies requiring extremely high source brilliance [4].

The commercial availability of vibrational circular dichroism (VCD) accessories to FTIR spectrometers has significantly improved the study of chiral compounds. VCD spectroscopy measures IR absorption difference spectra using left and right circularly polarized radiation. In contrast to the widespread electronic circular dichroism spectrometers, the spectral bands in VCD spectra are more easily assigned to individual groups and hence allow a more straightforward interpretation of the spectra [5].

The main progress in the understanding of the conformational dynamics lies in the exploitation of two-dimensional infrared spectroscopy. Theoretical and experimental aspects of this nonlinear technique have been reviewed by Woutersen and Hamm [6].

An inseparable part of the instrumentation of FTIR spectroscopy for bioanalytics is the software, allowing processing of the spectral data and application of chemometric methods. There are only limited cases where a simple library search for an identification or single-band absorbance for determination can be used. Multivariate classification (pattern recognition) and multivariate regression techniques need to be applied in bioanalytics [7]. The algorithms applied in infrared (and Raman spectroscopy) include [3] Mahalanobis distance, principal component analysis (PCA) and soft independent modeling of class analogies (SIMCAs), cluster analysis, linear discriminant analysis (LDA), partial least-squares regression (PLSs), artificial neural networks (ANNs), Bayes rule, support vector machines, and ensemble methods.

27.1.3
Applications

It is very difficult to briefly map all the fields of application that stem from the origin sometime in 1950s, as noted by Henry Mantsch [8] in his historical survey. This situation is documented in a great number of recently available books or chapters related to these topics [9–22].

Bioanalytics is a typical border discipline for which the spectroscopist has full insight into the relation of spectrum and structure only in the simplest cases. To this type of analysis belong structural studies, where support from model calculations allows the assignment of the spectral bands in the way typical for analysis of small organic molecules. The increasing complexity of the mixtures typical of biomaterials excludes such detailed analysis and a comparison of the spectra with known patterns or their clusters is only possible. To proceed from this type of information to the information relevant for clinical diagnostics, medicine, biology, and so on, an expertise in many fields is needed, including chemometrics, microscopy, clinical biochemistry, pathology, and cytology.

The following text is an attempt to give some examples from this broad field and is not intended to be exhaustive.

27.1.3.1 Structural Studies

The analysis of the infrared spectra of peptides and proteins, with the aim to determine the secondary structure, conformational changes, or unfolding processes, belongs to ''classical'' tasks of infrared spectroscopy. The manifold problems of use and misuse of FTIR in the determination of protein structure has been analyzed by Jackson and Mantsch [23].

Recent progress in this field is tightly wedded to the progress in the computational modeling of vibrational spectra [24]. Studies using *ab initio* Hartree–Fock, density functional theory (DFT) as well as excitonic coupling models are used to support interpretation of normal infrared spectra, as well as VCD spectra [24]. This approach allows not only the elucidation of the effect of secondary structure on the most relevant amide modes (amides I, II, and III) but also to make conclusions on the participation of the tertiary structure in the overall band shape formation. VCD spectra of chiral moieties are more sensitive to conformational changes than conventional infrared spectra.

Biomolecules undergo complex conformational dynamics, ranging from seconds to the pico and sub-picosecond timescales. To study the very fast timescales, two-dimensional infrared spectroscopy (2D IR) is the method of choice [6]. The present state of the analysis of the amide I band has been reviewed [25]. Theoretical and experimental considerations for interpretation of amide I bands in tissue have also been published [26].

27.1.3.2 Identification of a Component in the Biological Material

A typical bioanalytical task is the identification of kidney stones or its components. There are now available commercial spectral databases of real kidney stones (212 stones found in human kidneys), spectra of the primary components found in typical kidney stones, or synthetic spectra of kidney stone samples. In this case, the identification of the main kidney stone components can be carried out by suitable library search software [27] and, in some cases (for synthetic spectra), quantitative information can also be obtained.

Similarly extensive studies exist for gallstones [28–31].

27.1.3.3 Determination of a Selected Component

The determination of components in *food or agricultural products* using near-infrared spectroscopy is now widely accepted as simple, accurate, rapid, and inexpensive and it is routinely used [9, 15, 16].

On the other hand, the determination of *clinically important analytes* in human blood, urine, saliva, and other body fluids is still seeking acceptance as an official alternative to the standard biochemical methods in spite of the great research effort.

Of considerable interest is the *in vitro* determination of *glucose in blood*, which represents a very important piece of information. There are numerous studies by NIR and mid-IR spectroscopy on model mixtures, whole bovine blood, whole human blood, human blood plasma, or human blood serum (Table 27.1) using different sampling techniques, including microdialysis for quasi-continuous monitoring. The studies often included determination of other accompanying analytes, as indicated in the table.

The advantage of reagentless analysis, the possibility of the simultaneous determination of several analytes, or the possibility to use only a minimal sample volume (1 µl and even smaller) makes these techniques very attractive. Results are very encouraging, but unfortunately they still do not fully meet the requirements for clinical adoption. The low analyte concentration and mutual interference of the components makes the calibration process very difficult, which should cover the full physiological range of all individual components. A solution seems to be to waive the advantage of using the native fluid (as liquid or dry film) and preprocess the sample before spectroscopic measurement [83].

The noninvasive *in vivo* determination of glucose is another challenge for infrared spectroscopy, which could substitute the painful and inconvenient test-strip technique used by patients with diabetes mellitus. Unfortunately, only near-infrared radiation has a chance to penetrate deep enough into the human body. There are numerous attempts to do it noninvasively by near-infrared spectroscopy [84–93] using the drift technique on human skin [94–97] (also on rat skin [98]), lips [99, 100], or finger [101]. Fiber probes have also been applied [102, 103]. It remains clear that all the problems of *in vitro* determination of glucose are multiplied for *in vivo* analysis.

To date, no commercial product exists for noninvasive measurement of blood glucose [104]. One of the obstacles to the success of NIR spectroscopy is the problem of chance correlation induced by instrument drift or interference [104]. There are several critical parameters that should be respected to obtain valid data [105]: optical path length, wavelength range, instrumental performance, model dimensionality, and the chemical basis of model selectivity. Calibration models based purely on statistical data, not incorporating chemically specific information, can be misused [104].

27.1.3.4 **Identification of Biological Objects**

In many cases, there is no need to characterize and identify individual components, but rather to characterize and identify entire objects, for example, bacteria, yeasts, tissues, or cells.

The characterization and identification of *microorganisms* by infrared spectroscopy is considered to be one of its best-developed and most frequent applications

Table 27.1 Some details on the *in vitro* determination of glucose in blood by infrared spectroscopy.[a]

Techniques						Accompanying analyte										Sample						References
NIR	MID IR	ATR	Dry film	Fibers	Transmission	Urea	Triglycerides	Cholesterol	Creatinine	Protein	Lactate	Uric acid	Albumin	Bilirubin	Globulin	Whole blood bovine	Whole blood human	Human blood plasma	Human blood serum	Model solutions	Quasi-continuous monitoring	
■																■						[32, 33]
■																■				■		[32, 33]
■																	■					[34, 35]
■						■	■	■		■								■				[36–38]
■					■	■	■	■	■	■		■	■	■	■			■				[39]
■					■													■				[40]
■																			■	■	■	[41]
■																			■			[42]
■				■	■	■	■	■		■	■		■		■				■			[43]
■													■		■				■	■		[44]
■																				■		[45]
	■																■					[46–55]
	■		■					■									■		■			[56]
	■	■															■					[57]
	■	■				■	■	■		■			■				■	■				[58]
	■																■					[59]
	■		■			■											■					[60]
	■																■					[61]
	■				■												■					[62–64]
	■	■																■		■	■	[65]
	■	■				■	■	■		■								■				[66]
	■	■																■		■	■	[67, 68]
	■		■															■				[69]
	■										■							■				[70]
	■	■	■																■		■	[71]
	■	■																	■		■	[72]
	■	■				■		■		■									■		■	[73]
	■	■				■	■	■	■	■		■							■			[74]
	■					■		■		■		■			■				■			[75]
	■					■	■	■		■		■							■			[76]
	■	■				■		■												■		[77]
	■	■																		■		[78]
	■					■					■										■	[79]
	■																				■	[80]
	■																				■	[81, 82]

[a] This table contains information available from published abstracts only and a simplified notation is used for some components.

and it is now routinely used in microbiological laboratories [106–108]. The full advantages of infrared spectroscopy predominate if used as microspectrometry, which allows identification of microcolonies of a few hundred cells. This approach allows significant speedups in the process of identification [109]. FTIR spectroscopy can also be used to monitor the response of yeast cells to stresses induced by chemical, physical, or biological agents [110].

Valuable results for chemotaxonomy of horticultural and agricultural corps can be obtained from the combination of mid-infrared spectroscopy and multivariate analysis: primary constituents (proteins, lipids, and carbohydrates) as well as secondary plant metabolites (phenolic substances, terpenoids, and alkaloids) can be identified or determined [111].

To the same type of tasks belong the characterization and identification of tissues. To distinguish healthy, precancerous, and cancerous tissues, a deep understanding of the cellular and tissue architecture is needed, as well as of the spectral changes related to tissue or cell composition, which vary because of differentiation, maturation, and different stages of the cell life cycle [112]. Understanding of the processes and distribution of individual components in the tissue provides an opportunity for the early detection of diseases and their treatment and hence there are numerous applications to the characterization of bone, brain, breast, lung, skin, or tooth tissues [3, 113]. The spectral data detect molecular changes, which precede any morphological changes, thus enabling earlier diagnosis [114]. An effort to use FTIR spectroscopy as a diagnostic tool can be illustrated by discrimination between normal and tumor brain tissue, carried out on thin cryosections during tumor resection surgery [3].

Progress in this field is strongly related to the developments in FTIR microimaging and also to the availability of the synchrotrons around the world. Synchrotron IR microspectroscopy has significantly enhanced worldwide capabilities in protein structure analysis [115] and in single biological cells, as well as cell nuclei [116]. Unfortunately, the relative sizes of the cells to the employed wavelengths give rise to a strong scattering (dominated by Mie scattering), which strongly distort the spectra [117].

27.1.3.5 Concluding Remark

There are many other fields of applications not mentioned here, for example, a noninvasive method for measuring blood flow through an organ [118] or blood oxygenation by NIR spectroscopy [118], the study of structural changes of proteins in fingernails [119] or the permeation of drugs through the outer layer of human skin [120] by mid-IR spectroscopy, and so on. The application of infrared spectroscopy in bioanalytics has a great chance for further development. Experience of the past shows two key points that should be respected to achieve precise and accurate results: (i) the cooperation of all experts in the field and (ii) the development of standardized procedures and protocols for every stage of the study.

27.2
Raman Spectroscopy in Bioanalysis

27.2.1
Introduction

Raman spectroscopy has enjoyed a tremendous increase in usage in the past decade as a result of great advances in Raman instrumentation, including lasers, spectral filtering, spectrometers, detectors, and fiber optic probes. These advances have paved the way for wider application of Raman to bioanalysis, not only because of the large amount of information contained in a Raman spectrum but also because of ease of use and its noninvasive character. For example, disease can be linked to changes in the molecular makeup of tissues. Raman spectra contain detailed information on the molecular composition and structure without the need for labels or dyes and in a nondestructive manner, enabling its use *in vivo* for early disease diagnosis or to guide clinical intervention or treatment. There have been a large number of publications and reviews on the application of Raman to bioanalysis, including reviews by Pappas *et al*. [121] and Baena and Lendl [122], to which the reader is referred for additional information. Recent books with large portions devoted to the subject have been written by Salzer and Siesler [2], and McCreery [123]. Therefore, the material presented here is constructed as a tutorial rather than an exhaustive review.

27.2.2
Raman Systems

27.2.2.1 Laser Sources

A common laser source in the latest Raman systems is the frequency-stabilized diode laser, because of its small size, reasonable power, and low-cost considerations. Wavelength stabilization is usually accomplished using distributed Bragg reflector (DBR) lasers, where the laser resonator is made with at least one DBR outside the gain medium. A DBR is a wavelength-selective mirror based on Bragg reflection with a periodic structure [124]. Some other laser sources used for Raman bioanalysis include diode-pumped solid-state lasers, such as Nd:YAG (and its harmonics), and gas lasers, such as argon ion and helium neon.

27.2.2.2 Spectral Filtering

Compact Raman systems have been made possible by the introduction of optical filters with very high extinction (>OD 6) at the excitation wavelength and very sharp spectral cutoff edges to drastically reduce the intensity of the Rayleigh scattering before entering the spectrometer. These Rayleigh filters were accomplished first using a double spectrometer (additive or subtractive) as a prefilter or using resonance atomic absorption (e.g., mercury resonance radiation for excitation and a mercury vapor cell as notch filter). Other early notch filters were interference band, edge or line filters [125], or a chevron arrangement of bandpass filters [125].

In the early 1990s, holographic notch filters using volume hologram methods became available [126]. More recently, multiple-cell, thin-film filter designs have achieved the same level of rejection as holographic notch filters at a reduced cost [127]. The stringent requirements of optical filters used in dense wavelength division multiplexing in the optical fiber telecom industry has resulted in dramatic improvements applicable to fiber Raman probes. For example, the notch filter can be replaced by a fiber Bragg grating filter [128]. While these are only presently applicable to single-mode fibers, the methodology bodes well for future advances, especially for use *in vivo* or *in vitro* where diameter and flexibility are important.

27.2.2.3 Spectrometers

At first, Fourier transform Raman instruments were utilized for bioanalysis, because the Raman excitation laser was in the near-infrared (usually 1064 nm from an Nd:YAG laser) avoiding most of the fluorescence problems in biological materials and reducing the photochemical damage [129]. FT Raman also has a Jacquinot (optical conductance) advantage and a multiplex advantage versus grating-based spectrometers [125, 129].

Nevertheless, with the advent of high-efficiency charge-coupled device (CCD) multichannel detectors, the advantage shifted back to grating-based spectrometers, because the entire Raman spectrum could be obtained simultaneously, effectively negating the multiplex advantage of FT Raman systems. In addition, further advances in CCD technology (e.g., back thinning and antireflection coating) drastically improved their NIR response allowing NIR excitation, which dramatically reduces fluorescence interference, and photochemical damage, but at the cost of Raman signal strength (the ν^4 dependence) [125, 129]. The grating-based spectrometers utilized at present include high-resolution, long focal length spectrometers down to small monolithic aberration-corrected single-optical-element spectrometers with lower (typically $\sim 4\,\text{cm}^{-1}$) resolution. These latter devices are perfectly adequate for most liquids and solids, especially for analytical (detection and identification) purposes or for dedicated Raman instruments for *in vivo* or clinical use.

27.2.3
Fiber Optic Probes

In order to best obtain Raman spectra *in vivo*, fiber optic coupling between the larger portions of the Raman system (laser, spectrometer, detector, and computer) and the probe is usually used. Transmission of the excitation laser through silica (usually) optical fibers produces confounding Raman signals that must be suppressed. This suppression has been accomplished by use of optical filters in the probe, usually a short wavelength pass or bandpass filter on the excitation fiber and a long wavelength pass filter in front of the Raman signal fibers, as shown schematically in Figure 5 of Chapter 56, as well as in Figure 27.1 and Figure 27.2. A number of probes are available [130–132], as well as a novel, small-diameter, internally filtered probe (IFP) design (Enviva, Visionex Inc.) that moves the optimal Raman signal collection volume close to the probe end [133]. The IFP allowed large improvements

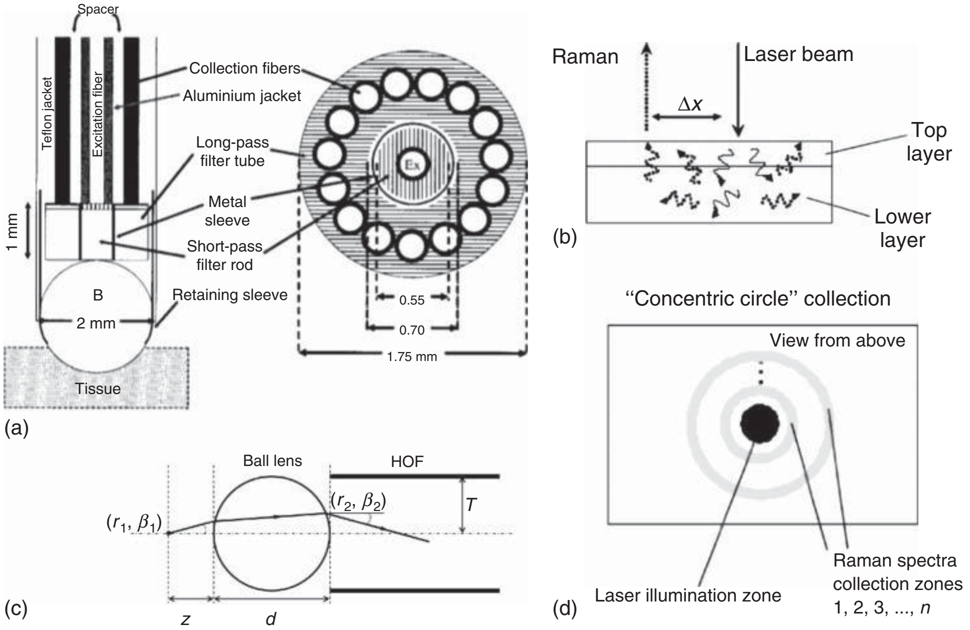

Figure 27.1 Optical fiber Raman probes for bioanalysis. Fifteen around one arrangement with in-line short-pass (excitation) and long-pass (collection) filters and a sapphire ball lens [134] (a). Hollow-core fiber/sapphire ball lens design [138] (b). SORS probe with offset collection fibers, concept (c) and concentric ring design (d) [139]. (Reprinted with permission from a) Optical Society of America, b) SPIE, c) and d) Society for Applied Spectroscopy.)

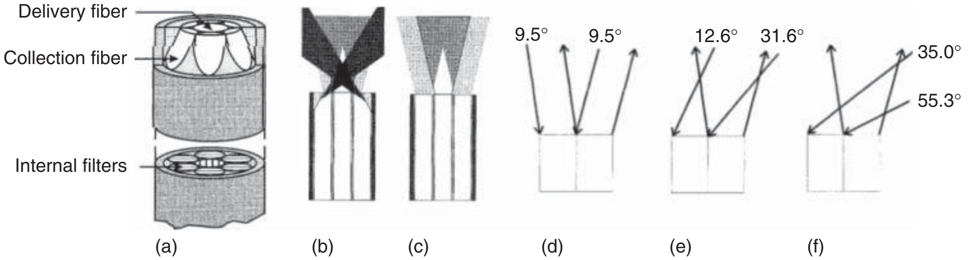

Figure 27.2 Enviva probe design. (a) Enviva probe with in-line filtering and beveled tips to increase overlap with the excitation close to the probe end (comparison of standard probe (c) to beveled probe (b), and illustrated for three different bevel angles in the (d–f) [133]. (Reprinted with permission from Society for Applied Spectroscopy.)

in Raman signal quality, as well as Raman-to-baseline signal ratios, by controlling the sampling depth in a variety of tissue types, and can be manufactured in very small diameters (<1 mm) for possible endoscopic use. Another design in clinical use involves an excitation fiber filtered using a short-pass filter rod and a circular array of collection fibers filtered using a long-pass filter tube, as well as a simple sapphire sphere as focusing element [134]. Their probe was used for *in vivo* Raman spectral pathology of human atherosclerosis [135]. Similarly, Komachi *et al.* [136, 137] have used custom filters to reduce their probe diameter to <1 mm and demonstrated its use *in vitro*. They also developed a confocal Raman endoscopy probe using a silvered, hollow-core fiber to carry both the excitation laser to the probe tip and the Raman signal back to the spectrometer. The internally silvered, hollow-core fiber does not generate spurious fiber Raman signals that must be removed at the distal end of the probe, greatly simplifying the probe design [138]. A sapphire ball lens version of their probe is small enough and sealed to allow sterilization for use in endoscopy.

Fiber optic probes are being used in other ways to obtain depth-resolved information, using a method called spatially offset Raman spectroscopy (SORS) [139–141]. The offset distance between excitation and Raman collection at the sample interface determines the average depth interrogated. The offset could be point to point, but more Raman signal is collected using concentric circle collection. The latter can be efficiently accomplished using a circular array of optical fibers surrounding the excitation fiber at some radial offset, followed by a circular to linear arrangement transition for optimal coupling into the spectrometer slit, as shown in Ref. [141]. Another embodiment of this concept uses a dielectric filter at the end of the optical fiber in direct contact with the sample [142]. The filter has high transmission for normal incidence excitation wavelength, but high reflection for non-normal incidence photons. It passes the collimated incident laser into the sample, but reflects most of the random-direction, sample-scattered excitation light back into the sample, enhancing the Raman signal level. A small hole in the center of the filter allows the Raman signal to pass back into the signal collection fiber.

27.2.4
Raman Imaging

There are several instrumental variations for performing Raman imaging of biological samples. Adar [143] has discussed these recently at the tutorial level. The global imaging scheme bathes the imaged area of the sample in laser excitation light and records the microscope image through a narrowband filter that selects the Raman spectroscopic feature of interest. The method has little depth resolution because it is nonconfocal and does not work well for complex biological samples, which usually do not have well-separated Raman features that can be isolated. Alternatively, the sample can be point illuminated and the full Raman spectrum obtained at each point, scanning the sample in x-, y-, and z-directions to obtain the full Raman image hypercube. In between, line-focus or line-scanning methods acquire full spectra along a line of points by imaging the illuminated line onto the slit of the Raman spectrograph, with y- and z-scanning to obtain the full Raman image hypercube. Because the Raman spectra of biological samples are complex, multivariate methods must usually be used to extract Raman images from the spectral hypercubes (Section 27.2.5).

The power of Raman imaging in bioanalysis has been illustrated in many publications. For example, van Manen and collaborators [144] showed that lipid bodies (LBs) rich in arachidonate as revealed by their Raman spectra associate with latex bead-containing phagosomes in neutrophilic granulocytes. The images show that different LB accumulation in phagosomal membranes is mediated by a flavohemoprotein, which is a catalytic subunit of the NADPH oxidase enzyme that plays a critical role in innate immunity. Puppels and collaborators [145] have demonstrated a large number of applications of Raman imaging to bioanalysis. For example, they have provided an overview of Raman imaging applied to mapping of tissue sections [146]. They have also demonstrated the effect of skin care products on molecular concentration-depth profiles using *in vivo* confocal Raman microspectroscopy [147].

27.2.5
Spectral Data Analysis

The key to use Raman spectroscopy in bioanalysis is not just obtaining a spectrum, but rather in much larger part how that spectrum is treated and interpreted within the enormous and exponentially increasing body of available bioanalytical Raman data. In another chapter 56 in this Handbook, the methods used to establish and search Raman spectral libraries are discussed, including both multivariate and spectral analysis tools. Some available commercial spectral libraries contain upward of 15 000 spectra of pure chemicals. To identify a pure material, the spectral search algorithms return usually unambiguous results. Mixtures present another set of difficulties. For the most part, biological materials are complex mixtures, necessitating the use of chemometric or multivariate classification tools to categorize and understand their complex nature. The huge number of investigators and clinicians using Raman tools to measure biological specimens and making their spectra available is producing a constantly growing data volume, which needs to be processed and analyzed in order to highlight the useful information, as well as to cope with noise, collinearities, and missing data.

A simple approach that has achieved much success is multivariate projection [148], wherein the table of observational data (spectra) is represented as a swarm of points, K (K is the number of variables), which is projected down to a low-dimensional plane or hyperplane. Methods used are PCA, soft independent modeling of class analogy (SIMCA), and partial least-squares discriminant analysis (PLS-DA) for classification, and principal component regression (PCR) and PLS for latent variable regression. To simplify interpretation of experiments with many variables, hierarchical PLS and PCA are recent modifications, which help divide the variables into conceptually meaningful blocks. A recent open source toolbox for MATLAB – called *Biodata* – to help accomplish this task for Raman spectral data has been developed and made available [149]. Other approaches include the sequential application of PCA and discriminant functional analysis (DFA), as well as hierarchical cluster analysis (HCA). PCA is usually used to identify those parameters that give the greatest differentiation between dimensions of multivariate data. DFA then discriminates between groups based on these retained principal components (PCs) and any a priori knowledge of which spectra were replicates. DFA is performed to maximize between-group variance and minimize within-group variance. To validate discrimination performed by DFA, projection analysis is also employed to project test data to PCA space and DFA space generated by the training set [148].

27.2.6
Pathology and Cytopathology

The number of pathology studies using Raman spectroscopy increased dramatically in the late 1990s and more recently, apparently coinciding with the availability of compact simple-to-use instrumentation (Figure 27.3) and acceptance of the efficacy of Raman data to differentiate tissue types.

The capabilities of micro-Raman imaging and spectroscopy have been used extensively to detect and differentiate cell types. Singular-value decomposition to remove noise has been among the various types of data analysis used [150]. HCA can be performed on Raman imaging data matrices to visualize regions in cells with high-Raman spectral similarities. In the cluster analysis routine, PCA scores are taken as input variables, squared Euclidean distances used as distance measure, and Ward's algorithm used to partition Raman spectra into clusters. HCA has also been used for rapid epidemiological analysis of bacterial strains [151].

Recently, spatially offset Raman spectroscopy (SORS) has been applied to measurement of bone tissue composition for studies of bone development, biomechanics, and bone health. The study compared five different fiber optic probe

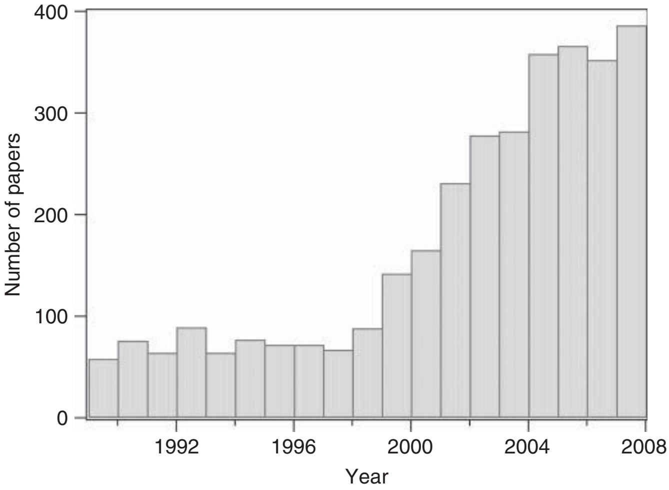

Figure 27.3 The dramatic increase in Raman pathology studies in recent years. (Data from Scisearch using "Raman <and> (pathology <or> cytopathology).")

configurations for *in vivo* bone signal intensity, variance, and power distribution, validated by measurements of exposed bone [152].

27.2.7
Single-Cell Analysis

Most recently, laser tweezer Raman spectroscopy (LTRS) has been used to obtain baseline spectra from single-tumor and healthy tissue cells [153]. PCA and PCR were used to reveal the cell structural changes or biochemical variations associated with the normal-to-cancer transition. Sabelnikov and Kempf [154] analyze the ramifications of whether a single cell picked for interrogation is representative of the whole, using a probability approach in LTRS. Spiers and coworkers [155] report on the capabilities of discriminate functional analysis of single-cell Raman spectroscopy to report on the whole-cell chemical composition of bacteria providing phenotypic classification with minimal physiological interference [153]. Zheng *et al.* [156] have shown the power of LTRS coupled with binary feedforward neural network spectral analysis for diagnosis of colorectal cancer.

27.2.8
Surface-Enhanced Raman Spectroscopy (SERS)

In the 35 years since its discovery [157], the new method of surface-enhanced Raman spectroscopy (SERS) has seen nearly exponential growth, particularly in bioanalytical applications [158]. The field has grown in spite of controversy about the detailed understanding of the enhancement mechanism, especially the variability in enhancement factors – particularly, the presence of hot spots at which the enhancement factor can be 10^9 or larger and at which single molecules have been detected [Ref 158] – which affect the use of SERS in bioanalysis. A recent article in *Science* by Dlott *et al.* [159] provides a method to measure the distribution of site enhancement factors on a given SERS substrate, establishing a methodology to achieve a greater level of understanding of whence SERS signals emanate.

The recent explosion in the use of SERS for bioanalysis was the subject of a special issue in *Chemical Society Reviews*, edited by Graham and Goodacre [160], which is an excellent resource for practitioners and newcomers. Among the articles in this special issue, Tian [161] introduces early work on SERS and then the development of electrochemical SERS to date. The importance of electronic resonance enhancement coupled with surface enhancement is discussed by Smith [162]. Mirkin [163] reviews the rational design of SERS nanostructures, and the tailoring or plasmonic substrates is detailed by Halas [164]. Another recent review of plasmonic nanostructures for SERS bioanalysis has been published by Vo-Dinh and his collaborators [165].

In addition to the traditional approach of using Raman spectroscopy, alternative measurement techniques for enhanced Raman measurements are being developed. Deckert provides an in-depth overview of tip-enhanced Raman scattering (TERS) as an alternative to the traditional approach to surface-enhanced Raman spectra, with its additional advantage of very high (beyond the diffraction limit) spatial resolution for imaging and mapping [166]. Blanch discusses combining surface-enhanced Raman spectroscopy with Raman optical activity (SEROA) to gain chiral-specific information from biochemical species [167].

Recent progress in the fundamental mechanisms and application of SERS at the single-molecule level is reviewed in articles by Aroca [168] and Kneipp [169]. The latter article also presents surface-enhanced hyper Raman scattering (SEHRS) as a tool for two-photon-excited vibrational spectroscopy, with its potential for greatly reduced phototoxicity and stress to the sample due to the longer wavelength excitation. Qian and Nie [170] discuss the considerable recent progress in understanding the mechanism of enormous enhancements of certain classes of SERS substrates and then present their use as SERS nanoparticle tags for *in vivo* imaging.

The abilities of SERS and Surface enhanced resonance raman spectroscopy (SERRS) for quantitative analysis are provided as a tutorial review by Bell and Sirimuthu [171], including the factors that need to be controlled to generate stable and reproducible SERRS calibrations. Graham and Faulds [172] discuss the use of SERRS for the analysis of specific DNA sequences by using spermine as the aggregation agent because of its abilities to produce highly enhancing aggregates of excellent reproducibility. SERS as a detection method for bioanalytes is reviewed by Porter who discusses the fundamentals, design, and applications of SERS as a viable bioassay platform [173].

Finally, Jarvis and Goodacre [174] illustrate how SERS can be used for the identification of low numbers of bacteria. Hildebrandt [175] furthers the understanding of the interfacial redox processes of proteins and Sockalingum [176] gives an interesting overview of intracellular SERS and the potential effect it has for single-cell imaging.

27.3
Terahertz Spectroscopy in Bioanalysis

27.3.1
Introduction

The terahertz (THz) region of the electromagnetic spectrum can loosely be defined as frequencies between 0.3 and 30 THz. Electromagnetic radiation with a frequency of 1 THz has a free-space wavelength of 300 μm and photon energy of 4.1 meV. At the same time, this frequency can be associated with a temperature of 47 K. Hence, a range of important low-energy interactions in physical, chemical, and biological processes involving interaction between the electromagnetic field and matter can be studied with a suitable spectroscopic technique covering the relevant spectral range. Particularly, THz spectroscopy has been widely used for the analysis of vibrational modes in molecular crystals [177–185].

As an example of a spectroscopic study of vibrational modes in the solid state, Figure 27.4a shows the absorption spectrum of the sucrose crystal together with

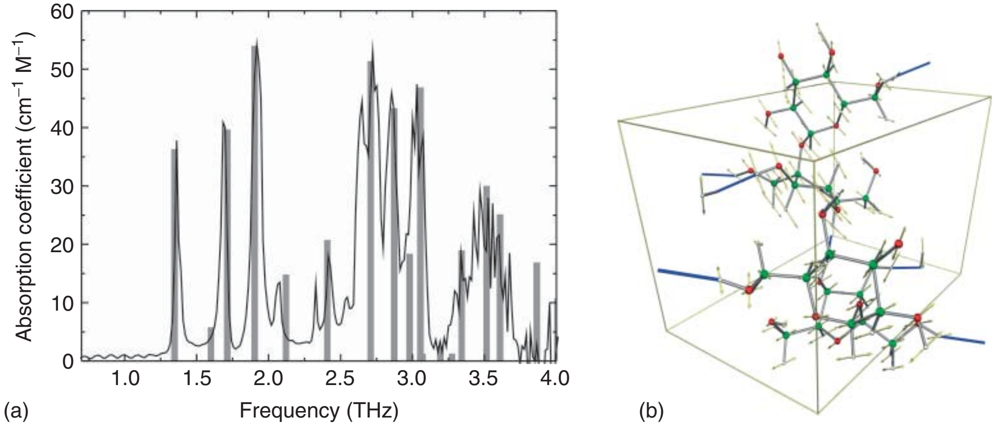

Figure 27.4 (a) Absorption spectrum of microcrystalline sucrose (solid curve) with simulated resonance frequencies (gray bars). (b) Normal-mode motion of the 1.9 THz resonance.

results of a simulation of the vibrational modes of the lattice, based on density functional perturbation theory (DFPT) [185]. The vibrational modes that contribute to the low-frequency absorption spectrum of the crystal are in general modes, which involve motion of all atoms in the unit cell, and in the general case, there is no clear distinction between molecular modes and intermolecular modes in the THz range. This is in contrast to vibrational modes in the mid-IR, which are typically localized at specific positions and functional subunits of the molecules with a relatively weak coupling to intermolecular modes.

In the THz range, the coupling between molecular modes and intermolecular modes is strongest when the intermolecular forces are relatively strong, for instance, in hydrogen-bonded crystals such as saccharides. In Figure 27.4b, the normal mode corresponding to the 1.9 THz absorption peak in sucrose is illustrated.

In crystals with weaker intermolecular forces, such as van der Waals-bonded systems, there is a correspondingly weaker coupling between the internal molecular modes and the external intermolecular modes [186, 187].

THz spectroscopy of gases reveals the rotational structure of the gas molecules. In Figure 27.5, we show the absorption spectrum of water vapor, which has been used extensively as a reference spectrum for calibration of THz spectrometers owing to the presence of water vapor in normal laboratory air, and thus in the beam path of an unpurged spectrometer. THz spectroscopy has been used extensively for the analysis of the rotational spectra of gases, including interstellar gases. THz time-domain spectroscopy, which will be described in the following, has unique capabilities that have been utilized for the detailed analysis of periodic rephasing of manifolds of rotational transition [188], collisional line broadening in gases at high pressures [189], and the study of hot molecular species in flames [190].

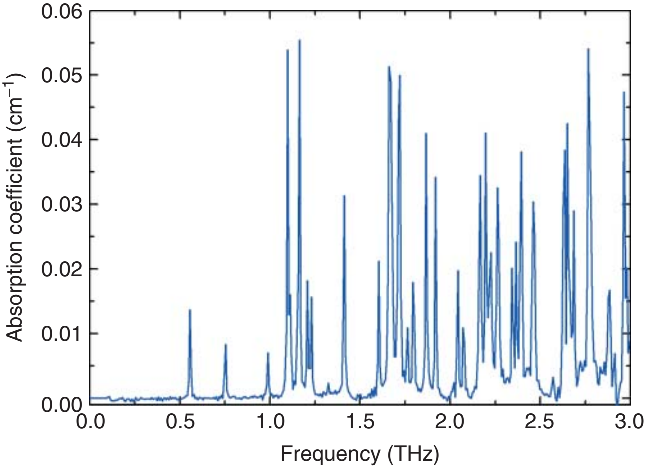

Figure 27.5 Absorption spectrum of water vapor in the THz range. Each absorption line corresponds to a rotational transition of the asymmetric top molecule H_2O.

Here, we will present an overview of a new technique known as terahertz time-domain spectroscopy (THz-TDS), which in the recent years has enabled a wealth of new studies of low-energy interactions between light and matter. In particular, the technique has recently offered unique insight into structural dynamics of biological systems, charge-transfer processes in molecules in solution, and transient behavior of photosensitive systems.

The development of the femtosecond laser in the 1980s enabled an alternative method for spectroscopy in the THz range with completely new functionalities. This method, first introduced in 1989 by Grischkowsky *et al.* [191], relies on the optical excitation of photoconductive dipole antennas and is now known as *terahertz time-domain spectroscopy*. The development of THz-TDS has been closely linked to the more general development of ultrafast laser technology, for instance, the Ti:sapphire femtosecond laser [192]. At the same time, the principles behind THz-TDS are heavily related to microwave technology as well as methods developed for FTIR. The different aspects of THz technology, components, spectroscopic methods, and imaging modalities are discussed in recent textbooks dedicated to THz science and technology [193–197].

27.3.2
Amplitude- and Phase-Resolved Detection of THz Fields

In a classical spectroscopic measurement, the intensity of electromagnetic radiation from a suitable light source is recorded in a manner that allows analysis of the spectral content of the light transmitted through or reflected from a sample. In FTIR spectroscopy, this analysis is performed interferometrically, and in a grating- or prism spectrometer, diffractive, or refractive optics is used to separate the wavelengths of the light. In all cases, the detection efficiency is determined by the dynamic range of the spectrometer and the capability of suppressing undesired background light from the beam path into the detector.

In the most basic implementation, FTIR as well as diffractive and refractive spectrometers detect only the intensity of the spectral distribution of the light. Hence, the recorded information is insufficient for the full reconstruction of the complex dielectric function of the sample material. With a sufficiently high bandwidth of the spectroscopic measurement, the Kramers–Kronig relations can, in principle, be applied for the determination of the full dielectric function. However, this procedure relies on certain assumptions about the behavior of the dielectric function outside the frequency range, and the accuracy of the analysis then naturally relies on the correctness of these assumptions.

Several spectroscopic methods exist for the direct measurement of the full dielectric function of a sample. The traditional method is dispersive FTIR [198], where the sample is placed as an integral part of one of the arms of the Michelson interferometer of the spectrometer.

27.3.3
Instrumentation for THz Spectroscopy

27.3.3.1 Coherent Generation and Detection of Broadband THz Light

Broadband, coherent THz radiation can be generated in a photoconductive switch on a semiconductor substrate excited by a femtosecond laser pulse or in a suitably phase-matched nonlinear crystal by difference frequency mixing of the frequency components of a femtosecond laser pulse. Generally speaking, the bandwidth of several THz of a femtosecond laser pulse can be used for the generation of broadband THz radiation with comparable bandwidth.

When driven by a train of femtosecond laser pulses synchronized to the laser pulses used for THz generation, photoconductive switches and electro-optic crystals can also be used for a field-resolved detection of the THz field.

In the following, we discuss the method of photoconductive generation and sampling of broadband THz radiation. We refer the reader to excellent reviews on the generation and detection of THz pulses by electro-optic methods [199–204].

The electric field from an electric dipole oscillating at a frequency of $\nu = \omega/2\pi$ can be expressed as [205]

$$E = \frac{1}{4\pi\varepsilon_0}\left[k^2\left(\hat{\boldsymbol{n}} \times \overrightarrow{\boldsymbol{p}}\right) \times \hat{\boldsymbol{n}}\frac{\mathrm{e}^{\mathrm{i}kr}}{r} + \left[3\hat{\boldsymbol{n}}\left(\hat{\boldsymbol{n}} \times \overrightarrow{\boldsymbol{p}}\right) - \overrightarrow{\boldsymbol{p}}\right]\left(\frac{1}{r^3} - \frac{\mathrm{i}k}{r^2}\right)\mathrm{e}^{\mathrm{i}kr}\right] \tag{27.1}$$

where $\overrightarrow{p}$ is the electric dipole moment, $\hat{n}$ is the unit vector in the direction of observation, r is the distance between the dipole and the observation point, and $k = \omega/c$ is the propagation constant of the electric field in free space.

If we assume that the temporal evolution of the electric dipole moment can be found by a Fourier analysis of its frequency components, then the electric field component perpendicular to the direction of observation from an electric dipole can be expressed in the time domain in the following form by a Fourier transformation of Eq. (27.1):

$$E_\theta(r,\theta,t) = \frac{1}{4\pi\varepsilon_0}\left[\frac{1}{r^3}\vec{\boldsymbol{p}}\left(t_\mathrm{r}\right) + \frac{1}{cr^2}\frac{\mathrm{d}\vec{\boldsymbol{p}}\,(t_\mathrm{r})}{\mathrm{d}t} + \frac{1}{c^2 r}\frac{d^2\vec{\boldsymbol{p}}\,(t_\mathrm{r})}{\mathrm{d}t^2}\right]\sin\theta \tag{27.2}$$

where θ is the angle between the electric dipole moment vector and the direction of observation and $t_\mathrm{r} = t - r/c$ is the retarded time. In the far field ($r \gg \lambda \gg d$, where d is the spatial extent of the electric dipole) only the last term in Eq. (27.2) survives, and hence the radiated electric field is proportional to the second temporal derivative of the dipole moment, or, the first temporal derivative of the current density $j(t)$.

This fundamental principle can be exploited for the generation of ultrabroadband electromagnetic transients with frequencies in the THz range. The frequency content of the electromagnetic field is closely linked to the dynamics of the transient current that generated the field. Consequently, a current transient that evolves on the timescale of a few hundred femtoseconds to a few picoseconds will generate a characteristic radiation signature with frequencies in the terahertz range. Such ultrafast current impulses can be generated by impinging an ultrafast laser pulse onto a biased semiconductor surface. The photons excite electrons across the electronic bandgap of the semiconductor, and the bias field subsequently accelerates the free charges, which subsequently recombine with the characteristic recombination time of the material. Using femtosecond laser pulses, current impulses with bandwidths well into the THz range can be generated in this manner. A photoconductive switch for generation of such ultrashort THz pulses is illustrated in Figure 27.6.

The metallic electrodes supply the bias field to the photoconductive gap between the electrodes. This gap is excited by femtosecond laser pulses, and the resulting

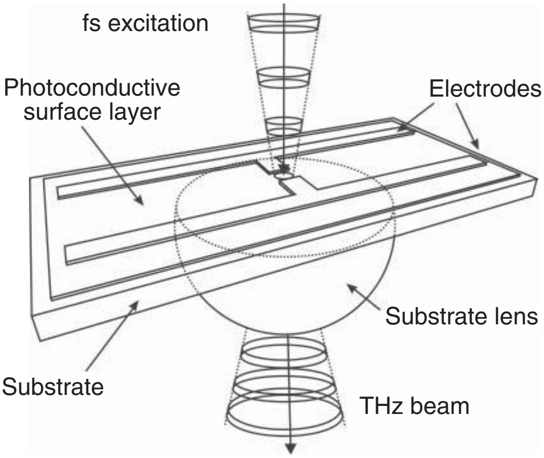

Figure 27.6 Photoconductive switches for generation and detection of ultrabroadband THz transients.

current transients generate the THz pulses that are emitted into the substrate by a THz dipole antenna structure, which in the simplest case is formed by the metalized bridge between the two electrodes. The THz radiation is collected into a collimated beam by a substrate lens attached to the structure.

27.3.3.2 **Detection of Broadband THz Transients**

Detection of the THz pulses generated in a broadband THz antenna can be detected by photoconductive sampling in an antenna structure identical to the THz emitter structure. A portion of the femtosecond laser pulse train, synchronized to the femtosecond pulse train used for the THz generation, is split off and used to excite, or gate, the detector structure. In contrast to the THz emitter antenna, the detector antenna is not biased by an external circuit. The electric field required to drive a photocurrent in the antenna is supplied by the THz pulses, which arrive in synchronism with the gate pulses. The photocurrent in the antenna circuit is then a convolution of the electric field picked up by the antenna and the transient photoconductivity induced by the gate pulse

$$j(\tau) \propto \int_{-\infty}^{\infty} E_{\mathrm{THz}}(t)g(t-\tau)\mathrm{d}t \tag{27.3}$$

The transient photoconductivity of the detector can be described by the same kinetics as discussed earlier for the generation of THz radiation. In the limit of a transient photoconductivity response $g(t)$ much faster than the duration of the THz field, the detected current is directly proportional to the THz field strength, corresponding to a frequency response of $j(\omega) \propto E_{\mathrm{THz}}(\omega)$. In the other limit, with long-lived photoconductivity, the measured current is proportional to the temporal integral of the THz field, corresponding to a frequency response of $j(\omega) \propto E_{\mathrm{THz}}(\omega)/\omega$. In the intermediate case, which is the normal case, the detected photocurrent will have a frequency response that can be described as [206]

$$j(\omega) \propto I(\omega)R(\omega)E_{\mathrm{THz}}(\omega) \tag{27.4}$$

where $I(\omega)$ is the spectrum of the excitation laser pulse and $R(\omega)$ is the frequency response of the photoexcited carriers in the semiconductor switch. Hence, the bandwidth of the detector is limited by the trapping and recombination times of the photoexcited carriers, and the transient photoconductivity can be seen as a low-pass filter function that is applied to the frequency spectrum of the THz pulse incident on the detector.

Ultrafast carrier lifetime is advantageous for a high bandwidth of the detected THz signal. Materials such as low-temperature-grown (LTG) GaAs, which have carrier lifetimes as low as a few hundred femtoseconds, are often used as active materials in photoconductive detectors. While the detection bandwidth in most systems described in the literature are in the low THz range, it was recently demonstrated that by removing all absorbing elements in the THz beam path and using the shortest possible laser pulses, photoconductive detection of frequencies approaching 100 THz is possible [206].

27.3.3.3 Ultrabroadband THz Optics

The photoconductive THz emitters described in the previous section are remarkably stable and reproducible with respect to the generated signal shape. Therefore, such emitters are well suited for spectroscopic measurements when combined with a similar THz detector. As illustrated in Figure 27.7, the THz emitter and THz detector must be excited with fractions of the same synchronized train of femtosecond pulses.

The beam of THz pulses can be transported from the emitter to the detector with either reflective or transmissive optics. The most commonly used reflective optics are off-axis paraboloidal mirrors with metallic reflectors, but elliptical mirrors can also be used, depending on the required focusing and imaging of the THz beam through the optical system. Reflective optics offer very low loss and minimal dispersion due to the high conductivity of most metals in the THz range, but may be difficult to align properly. On the other hand, transmissive optics can be aligned more easily than reflective optics, but usually suffer from frequency-dependent absorption that often leads to attenuation of the high-frequency components of the THz radiation and thus hinders high-frequency operation of the spectroscopy system.

Transmissive optics typically takes the form of lenses with spherical or aspherical surfaces. Such lenses are usually manufactured from transparent polymer materials such as polyethylene (PE) or teflon, and recently more transparent and low-dispersion materials based on cyclic olefin copolymers have been characterized [207, 208] and used. In addition, high-resistivity silicon is widely used as lens material for THz applications because of its exceptionally low loss and low dispersion [209].

High-resistivity silicon hyperhemispherical lenses are often used to couple the THz radiation from the emitter antenna into free space, and to couple the THz radiation from free space and onto the detector antenna. Hyperhemispherical lenses were first introduced by Fattinger and Grischkowsky [210, 211]. The THz radiation patterns from hyperhemispherical silicon lenses have been

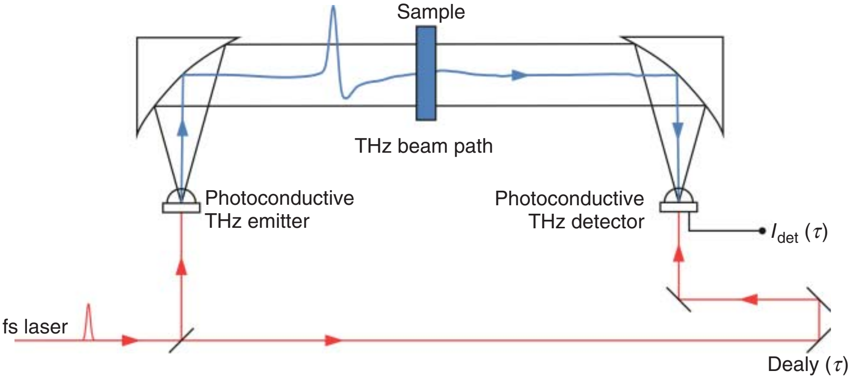

Figure 27.7 Schematic configuration of a full THz-TDS system for transmission spectroscopy, using broadband THz antennas driven by femtosecond laser pulses.

characterized [212, 213] and found to be described, at least approximately, by a fundamental Gaussian beam with beam waist at the surface of the hyperhemispherical lens. Different lens shapes (collimating, hemispherical, and hyperhemispherical shapes) have been thoroughly characterized by Rudd and Mittleman [214]. Reiten *et al.* [215, 216] performed careful measurements and simulations of the propagation of THz beams through hyperhemispherical lenses and the subsequent optical system of a THz-TDS setup. They showed that the THz beam profile emerging from a lens-coupled photoconductive emitter is accurately described by a superposition of Laguerre–Gauss modes, and also discussed the influence of spherical aberration and surface waves on the propagation. Recently, Lo and Leonhardt [217] devised aspheric lens designs with optimized focusing properties for high-resolution THz imaging applications.

27.3.4

Terahertz Time-Domain Spectroscopy (THz-TDS)

In this section, we review the most common configurations of THz-TDS and present an overview of the most widely used spectroscopic configurations, namely, transmission spectroscopy, reflection spectroscopy, and ATR spectroscopy. Each configuration has its own strengths, and we give examples of measurements with each experimental configuration. Transmission measurements are most suitable in situations with low- or medium-absorption strength of the sample. Examples include oils, solid-state materials such as molecular crystals, and powders of organic molecules. Transmission measurement requires the recording of a reference signal and a sample signal, either in the form of two different sample thicknesses (variable sample path length) or in the form of a measurement on an empty sample cell followed by a full sample cell.

Measurements in reflection are useful when the sample is a strong absorber. Reflection spectroscopy allows self-referenced measurements, where the reference signal and the sample signal can be obtained in a single scan, for instance, as reflections from the front side of a window in contact with the sample (the reference signal) and the reflection from the backside of the window in contact with the sample material (the sample signal). In such geometry, the sample and reference signals are separated in time, and by appropriate time gating of the signal, quantitative spectroscopy is possible with a single data recording.

In particular, the use of the ATR configuration can be shown to be the most sensitive method for the characterization of strongly absorbing materials with relatively low index of refraction. Examples include polar liquids, such as water, aqueous solutions, and electrolyte solutions. However, similar to transmission measurements, the ATR technique requires the recording of a reference signal followed by a sample signal.

Here, we describe the basic methods used in transmission and reflection spectroscopy, and discuss the influence of the dynamic range and the signal-to-noise ratio in a typical THz-TDS measurement. The first application of transmission THz-TDS was on water vapor in the ambient atmosphere [191] and subsequently

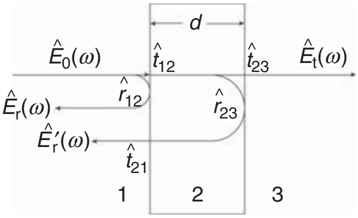

Figure 27.8 Schematic representations of the geometries for transmission and reflection spectroscopy.$E_0(\omega)$ is the incident field, $E_t(\omega)$ is the transmitted field, and $E_r(\omega)$ and $E_t{'}(\omega)$ are the fields reflected from the first and second interface of the sample, respectively.

the absorption coefficient and index of refraction of a range of dielectrics and semiconductors were reported [218].

In Figure 27.8, the general geometries for transmission and reflection measurements are illustrated.

The incident THz pulse is characterized by its spectral amplitude and phase $E_0(\omega)$, obtained by Fourier transformation of the raw experimental data and the time-domain representation of the pulse, as illustrated in Figure 27.9.

The transmitted and reflected signals are in this geometry given by

$$\begin{aligned}
\hat{E}_t(\omega) &= \hat{E}_0(\omega)\hat{t}_{12}\hat{t}_{23}\exp(-\alpha d/2)\exp(\mathrm{i}n\omega d/c),\\
\hat{E}_r(\omega) &= \hat{E}_0(\omega)\hat{r}_{12},\\
\hat{E}_r{'}(\omega) &= \hat{E}_0(\omega)\hat{t}_{12}\hat{r}_{23}\hat{t}_{21}\exp(-\alpha d)\exp(2\mathrm{i}n\omega d/c)
\end{aligned} \qquad (27.5)$$

where $\hat{t}_{12}$, $\hat{t}_{23}$, $\hat{t}_{21}$, $\hat{r}_{12}$, and $\hat{r}_{23}$ are the various complex Fresnel field transmission and reflection coefficients, as defined in Figure 27.8.

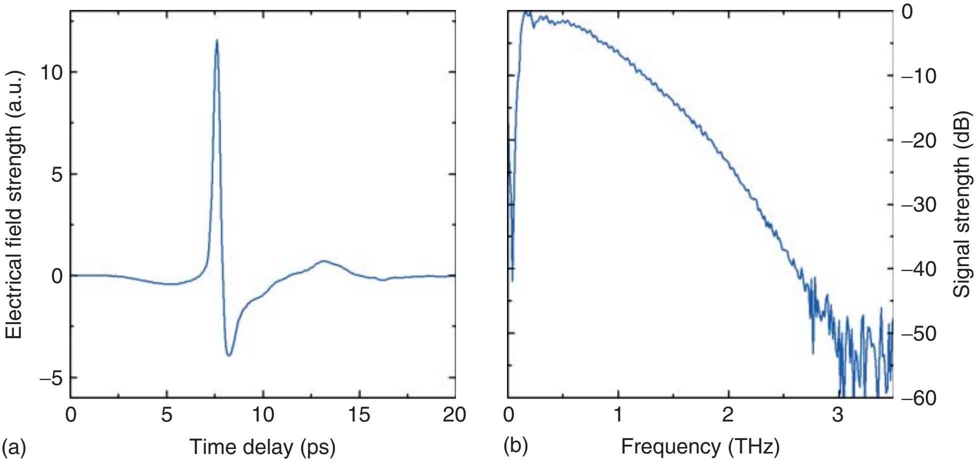

Figure 27.9 (a) THz-bandwidth transient recorded in the time domain and (b) its corresponding frequency spectrum.

Measurements carried out either in transmission and reflection can be used for the extraction of the complex index of refraction of the sample $\hat{n}(\omega) = n(\omega) + \mathrm{i}\kappa(\omega)$. Here, $\kappa(\omega)$ is the extinction coefficient, related to the absorption coefficient $\alpha(\omega)$ through $\kappa(\omega) = \alpha(\omega)c/2\omega$.

27.3.4.1 **Transmission THz-TDS**

In the simplest transmission experiment, two THz pulses–propagating through air and the sample, respectively–are recorded and their spectral amplitudes and phases are compared as

$$\frac{E_{\mathrm{sam}}(\omega)}{E_{\mathrm{ref}}(\omega)} = T(\omega)\exp(\mathrm{i}\phi(\omega)) = \hat{t}_{12}\hat{t}_{23}\exp(-\alpha d/2)\exp(\mathrm{i}(n-1)\omega d/c) \tag{27.6}$$

For simplicity, if we limit the analysis to sample materials with low absorption coefficient then the Fresnel transmission coefficients are real valued, and at normal incidence, we find

$$\begin{aligned} n(\omega) &= 1 + \frac{\phi(\omega)c}{\omega d}. \\ \alpha(\omega) &= -\frac{2}{d}\ln\left(\frac{(n+1)^2}{4n}T(\omega)\right) \end{aligned} \tag{27.7}$$

In Figure 27.10, we have shown an example of a transmission THz-TDS measurement. The sample was a mixture of the pure DNA base cytosine and PE filler material [219].

Figure 27.10a shows the time traces of the reference and sample signals, recorded after transmission through dry air and the sample pellet, respectively. Figure 27.10b shows the frequency spectra of the two signals, and Figure 27.10c shows the extracted absorbance (the product of absorption coefficient α and sample thickness d), together with a curve showing the highest detectable absorbance in the given experiment. Figure 27.10d shows the extracted index of refraction of the cytosine sample.

Figure 27.10b shows that the THz signal reaches the noise floor of the experiment at high frequencies, here at 4 THz. Naturally, at frequencies above this cutoff point, no meaningful measurements are possible, but also at frequencies below the cutoff the results might be impeded by the limited frequency-dependent dynamic range of the experiment, defined as the strength of the reference signal with respect to the noise floor of the experiment. The highest absorbance that can be measured with a given dynamic range DR corresponds to the situation where the sample signal is at the same level as the noise floor [220]. This can be expressed as

$$(\alpha d)_{\max} = 2\ln\left(\mathrm{DR}\frac{4n}{(n+1)^2}\right) \tag{27.8}$$

The curve showing the largest detectable absorbance in the given experiment is shown together with the extracted absorption coefficient in Figure 27.10c. The strongest absorption lines in the measured spectrum are clearly saturated, and the rolloff of the absorption at high frequencies is a direct consequence of the limited dynamic range of the experiment.

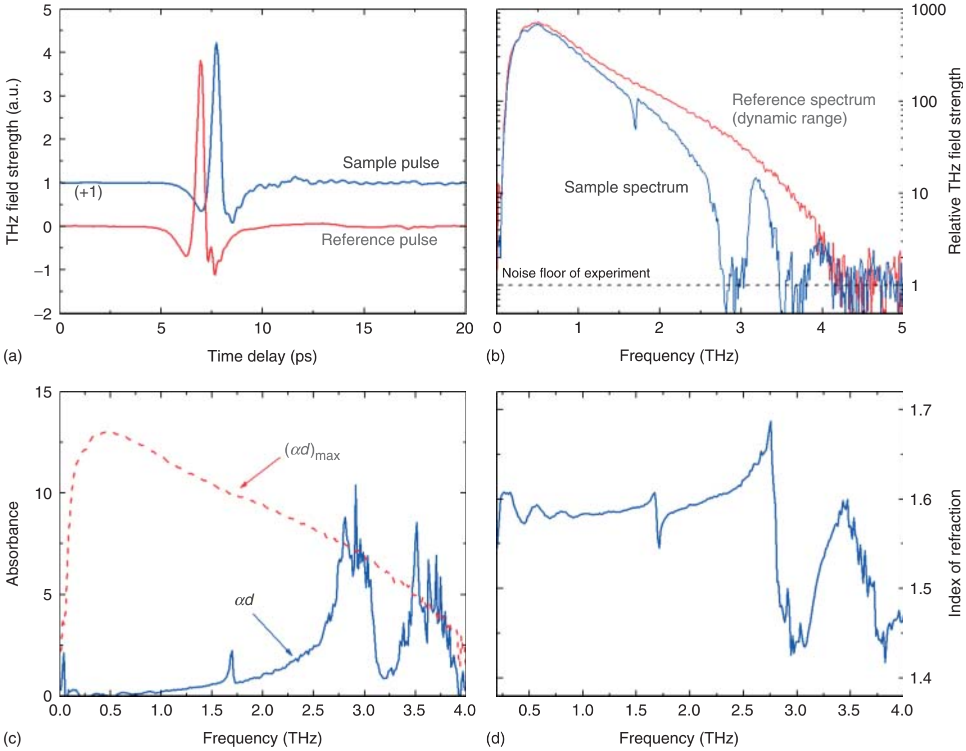

Figure 27.10 Time traces of the reference and sample pulses in a transmission THz-TDS experiment, (b) frequency spectra of the reference and sample pulses with respect to the noise floor of the experiment, (c) the extracted absorbance αd and the highest detectable absorbance αd_{max}, and (d) index of refraction of the sample material. The sample consisted of a mixture of cytosine and PE filler.

The analysis outlined gives analytical, closed-form solutions to the inversion of the equations linking the measured transmission amplitude and phase to the optical properties of the sample. However, Eq. (27.7) is only strictly valid for samples with vanishing absorption and infinite thickness. Finite absorption leads to additional phase shifts due to the complex-valued Fresnel transmission coefficients. For thin samples with high absorption (e.g., liquid water or highly doped semiconductors) the phase change due to the Fresnel coefficients becomes comparable to the accumulated phase change due to propagation through the sample. Hence, the separate calculation of the real part of the refractive index from the phase of the sample signal relative to the reference signal is no longer possible. In Figure 27.11, the effect of the additional phase shift at the sample interfaces is demonstrated. The dielectric function of liquid water was measured using a transmission cell with a water layer thickness $d = 76$ μm. The dashed lines show the result of an analysis using Eq. (27.7) to calculate the dielectric function $\hat{\varepsilon}(\omega) = \varepsilon\prime(\omega) + \mathrm{i}\varepsilon\prime\prime(\omega) = (n + \mathrm{i}\kappa)^2$, and the solid lines show the results of

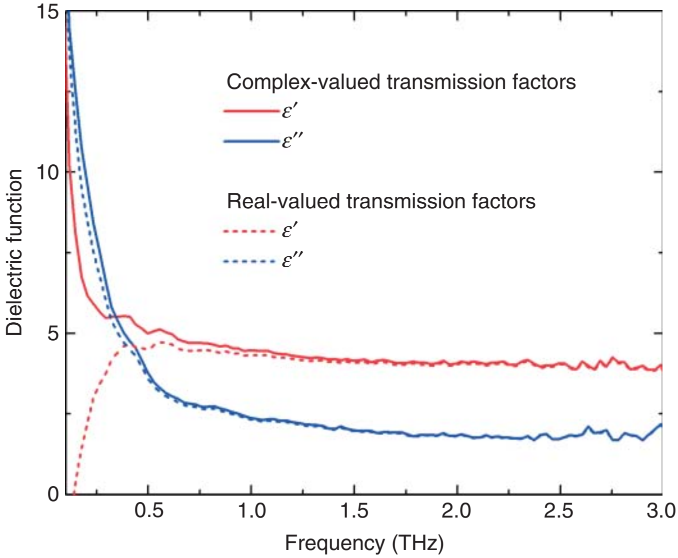

Figure 27.11 Real and imaginary parts of the dielectric function $\hat{\varepsilon} = \varepsilon\prime + \varepsilon\prime\prime$ of pure water at room temperature, extracted from transmission THz-TDS data measured with a 76 µm thick water layer using complex- (solid lines) and real-valued (dashed lines) Fresnel transmission coefficients.

a full analysis, including the phase shift due to the imaginary part of the index of refraction in the Fresnel transmission coefficients.

The correct extraction of the real part of the dielectric function is especially strongly dependent on the inclusion of the interfacial phase shifts. Although the full analysis correctly reproduces the known dielectric function of water [221–226], the simpler analysis completely fails to reproduce the sharp increase of $\varepsilon\prime$ toward its static value $\varepsilon_{\mathrm{DC}}$ at low frequencies.

The THz frequency range addresses low-energy processes (1 THz corresponds to a photon energy of 4.1 meV). In biological systems, there is a wide range of important questions that can be addressed by THz spectroscopy. Large macromolecules such as proteins and DNA have a large density of vibrational states in the THz region, because of the large masses and low-binding energies involved. For this reason, transmission THz spectroscopy has been applied to address the mechanisms, which control flexibility and conformational state of biological macromolecules [227]. As prominent examples of work on proteins, Markelz and coworkers [228, 229] have studied the influence of the conformational state of proteins on the density of states in the far-infrared, protein–ligand binding in solution [230], oxidation of proteins [231], and the dynamical transition near 200 K in proteins [232, 233]. Havenith *et al.* [234] have demonstrated a time-resolved THz-TDS technique, which is capable of studying the solvation kinetics in protein solution. THz spectroscopic studies on DNA material have focused on the difference in dielectric properties in the THz range on the binding state of DNA, as studied by Brucherseifer *et al.* [235] who later applied THz sensing in resonant waveguide structures for label-free sensing of hybridization of DNA with femtomolar sensitivity [236]. The broadband absorption differences between two types of artificial RNA could be used as contrast mechanism for free-space imaging of arrays of RNA spots [237]. Finally, the dielectric properties of water confined in nanometer-sized micelles has been studied by the Mittleman *et al.* [238, 239], who demonstrated that water in such confined environments displays strong resonances originating from vibrational modes of the nanometer-sized water pool.

27.3.4.2 **Reflection THz Spectroscopy**

Spectroscopy of liquids is typically carried out in either transmission geometry or reflection geometry, depending on the absorption strength of the liquid. The highest absorption that can be measured in a transmission experiment is limited by the dynamic range, defined as the frequency-dependent reference signal amplitude with respect to the noise floor of the experiment, of the spectrometer because the signal must be transmitted through the sample [220]. In contrast, it is the signal-to-noise ratio of the spectrometer, that is, frequency-dependent fluctuations of the signal strength, which determines the largest measurable absorption coefficient in a reflection experiment as the absorption of the sample is detected as a small additional phase of the reflected signal [220].

Owing to the rather strong absorption of polar liquids, and in particular of water, spectroscopy in the THz region of such liquids are typically carried out in a reflection geometry on bulk quantities of the liquid or by transmission through a very thin liquid layer. While THz transmission measurements of liquid water are certainly possible for thin water layers, the subsequent analysis becomes plagued with multiple reflections of the THz beam in the water cell, especially at low frequencies. In the region above 1 THz transmission, experiments are difficult owing to strong absorption, and in recent work targeting the frequency range of 1–6 THz, reflection-type spectroscopy seems the method of choice. Here, we briefly review different techniques applied for reflection THz spectroscopy.

Historically, the technique of dispersive Fourier transform spectroscopy (DFTS) [198] was the first method for accurate determination of the full dielectric function of materials in the far infrared. Afsar and Hasted [240] used DFTS to characterize the full dielectric function of liquid water in the 0.2–13.5 THz range of 6–450 cm^{-1}. In their spectroscopic setup, water was kept behind a single-crystal, high-resistivity silicon window, highly transparent to the far-infrared radiation, but with sufficiently high and constant index of refraction [218] to also serve as a useful beam splitter for the THz radiation. The liquid cell was placed in one of the arms of the modified Michelson interferometer in the spectrometer, as illustrated schematically in Figure 27.12a. Hence, phase-sensitive measurements were possible by measuring the interferogram $I(\tau)$ of the incoherent, broadband light source. This allowed a direct evaluation of both the real and the imaginary parts of the frequency-dependent permittivity $\varepsilon(\nu) = \varepsilon'(\nu) + i\varepsilon''(\nu)$ from the experimental data.

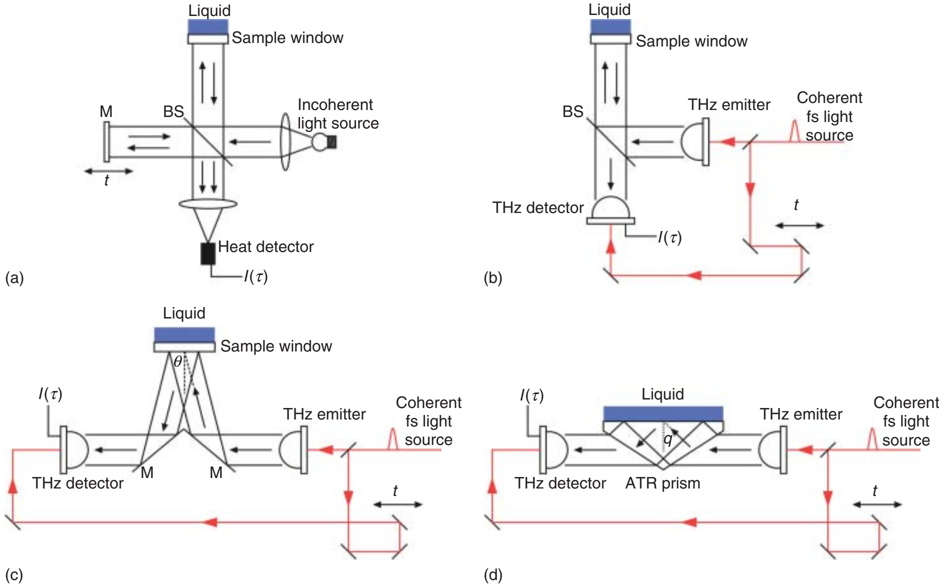

Figure 27.12 Experimental configurations for (a) dispersive Fourier transform spectroscopy (DFTS), (b) normal-incidence reflection THz time-domain spectroscopy (THz-TDS), (c) generalized reflection THz-TDS with an incidence angle theta, and (d) attenuated total reflection (ATR) THz-TDS with an internal angle theta larger than the total internal reflection angle.

In DFTS, temporally separated interferograms of the incoherent light reflected from the different dielectric interfaces in the sample arm of the spectrometer are recorded by scanning the position $\tau = 2x/c$ of the mirror in the variable arm of the interferometer. The part of the interferogram $I_{\mathrm{aw}}(\tau)$ associated with the window–air interface of the empty cell is used as a reference for the sample interferogram $I_{\mathrm{wl}}(\tau)$ from the window–liquid interface of the filled liquid cell. The ratio of the Fourier transformations of these interferograms can then, in combination with the standard expressions for the Fresnel reflection coefficients at the interfaces, be used for the calculation of the optical properties of the liquid

$$R\exp(\mathrm{i}\phi) = \frac{I_{\mathrm{wl}}(\nu)}{I_{\mathrm{aw}}(\nu)} = \frac{\hat{\boldsymbol{r}}_{\mathrm{wl}}(\nu)}{\hat{\boldsymbol{r}}_{\mathrm{aw}}(\nu)} = \frac{(\hat{\boldsymbol{n}}_{\mathrm{l}}(\nu) - n_{\mathrm{w}}(\nu))(1 + n_{\mathrm{w}}(\nu))}{(\hat{\boldsymbol{n}}_{\mathrm{l}}(\nu) + n_{\mathrm{w}}(\nu))(1 + n_{\mathrm{w}}(\nu))} \tag{27.9}$$

where R and ϕ are the measured amplitude and phase of the ratio of the Fourier transformations of the two interferograms. When inverted, Eq. (27.9) gives the complex index of refraction of the liquid, $\hat{\boldsymbol{n}}_{\mathrm{l}}(\nu) = n_{\mathrm{l}}(\nu) + \mathrm{i}\kappa(\nu) = n_{\mathrm{l}}(\nu) + \mathrm{i}\alpha(\nu)c/4\pi\nu$, assuming that the index of refraction n_{w} of the window material is known

$$\begin{aligned} n_{\mathrm{l}} &= \frac{1 - R^2(1 - n_{\mathrm{w}})^2/(1 + n_{\mathrm{w}})^2}{1 + R^2(1 - n_{\mathrm{w}})^2/(1 + n_{\mathrm{w}})^2 - 2R\cos\phi(1 - n_{\mathrm{w}})/(1 + n_{\mathrm{w}})}, \\ \alpha_l &= \frac{4\pi\nu}{c}\,\frac{2R\sin\phi(1 - n_{\mathrm{w}})/(1 + n_{\mathrm{w}})}{1 + R^2(1 - n_{\mathrm{w}})^2/(1 + n_{\mathrm{w}})^2 - 2R\cos\phi(1 - n_{\mathrm{w}})/(1 + n_{\mathrm{w}})} \end{aligned} \tag{27.10}$$

Thrane *et al.* [222] established a reflection-type THz-TDS technique with an experimental arrangement of the liquid cell similar to reflection-type DFTS [240], adapted for the technique of reflection THz-TDS, with normal incidence of the THz field onto the liquid surface. This experimental geometry is illustrated in Figure 27.12b. In the geometry shown here, the full set of spectroscopic data is obtained within the same temporal scan, by using the reflection from the interface between air and window material as the reference signal $E_r(\tau)$ and the reflection from the interface between the window and the liquid as the sample signal $E_s(\tau)$. The sample signal is separated in time from the reference signal as a result of the propagation delay of the sample signal through the window material. With normal incidence of the THz beam on the window, the ratio of the spectra of the sample and reference pulses is

$$\begin{aligned}
&\frac{\hat{\boldsymbol{E}}_s(\nu)}{\hat{\boldsymbol{E}}_r(\nu)} = \frac{t_{aw}t_{wa}}{r_{aw}} \exp\left(\mathrm{i}\frac{4\pi n_w d_w \nu}{c}\right) \frac{\hat{\boldsymbol{n}}_l - n_w}{\hat{\boldsymbol{n}}_l + n_w} \quad \Leftrightarrow \\
&R\exp(\mathrm{i}\phi) \equiv \frac{\hat{\boldsymbol{E}}_s(\nu)}{\hat{\boldsymbol{E}}_r(\nu)} \frac{r_{aw}}{t_{aw}t_{wa}} \exp\left(-\mathrm{i}\frac{4\pi n_w d_w \nu}{c}\right) = \frac{\hat{\boldsymbol{n}}_l - n_w}{\hat{\boldsymbol{n}}_l + n_w}
\end{aligned} \tag{27.11}$$

where R and ϕ are the measured spectral amplitude and phase of the ratio of the sample and reference signals, corrected for the transmission and reflection coefficients of the air–window interface and the acquired phase as a result of propagation through the window material.

Inverting Eq. (27.11) yields the index of refraction and absorption coefficient of the liquid

$$\begin{aligned}
n_l &= \frac{n_w(1-R^2)}{1+R^2+2R\cos\phi}, \\
\alpha_l &= \frac{4\pi n_w \nu}{c} \frac{-2R\sin\phi}{1+R^2+2R\cos\phi}
\end{aligned} \tag{27.12}$$

The methodology described here for the calculation of the dielectric properties of the liquid can be extended to an analysis at non-normal incidence at an angle θ of the THz beam on the sample window. This experimental geometry is shown schematically in Figure 27.12c. Compared to normal-incidence reflection spectroscopy, the configuration with non-normal incidence of the THz beam has significantly higher signal strength as the THz beam splitter is no longer required. In this situation, the generalized reflection and transmission coefficients must be used; in addition, the polarization state of the THz beam becomes important [225].

27.3.4.3 **Attenuated Total Reflection THz-TDS**

The most sensitive method for determination of the full dielectric function of a strongly absorbing liquid is offered by ATR THz-TDS [241, 242].

ATR THz-TDS has proved to be instrumental for detailed studies of the dielectric function of water and aqueous solutions as well as studies of solvation of organic molecules in water. The Tanaka group has demonstrated that spectroscopy in the THz range makes it possible to measure the size of the solvation shell of water molecules around molecules and aggregates of molecules in aqueous solution [243, 244]. Furthermore, the increased sensitivity of ATR THz-TDS compared to reflection THz-TDS has enabled the same group to study fast relaxation at several THz in water isotopes [245, 246].

In the ATR configuration, the THz beam is transmitted through a Dove prism where it undergoes total internal reflection at a facet of the prism in contact with the liquid. The geometry of an ATR THz-TDS system is schematically shown in Figure 27.12d. The angle θ refers to the internal incidence angle of the THz beam onto the interface in contact with the liquid. The highest sensitivity to small changes in the dielectric properties of the sample is obtained when that incidence angle is larger than, but close to, the critical angle for total internal reflection. The measurement is carried out by recording a reference pulse $E_\mathrm{r}(\tau)$ transmitted through the prism with air above the interface and, subsequently, a sample pulse $E_\mathrm{s}(\tau)$ is recorded with liquid in contact with the prism. The ratio of the spectra of these two signals is, as in the previous cases discussed here, analyzed in order to extract the complex index of refraction of the liquid. If we assume *p*-polarization of the THz light incident on the ATR interface, we have [242]

$$R\exp(\mathrm{i}\phi) = \frac{\hat{\boldsymbol{E}}_\mathrm{s}(\nu)}{\hat{\boldsymbol{E}}_\mathrm{r}(\nu)} = \frac{\hat{\boldsymbol{r}}^\mathrm{p}_\mathrm{wl}}{\hat{\boldsymbol{r}}^\mathrm{p}_\mathrm{wa}} \tag{27.13}$$

where R and θ again represent the amplitude and phase of the ratio of the spectra of the sample and reference pulses. Using the Fresnel reflection coefficients for total internal reflection of *p*-polarized light, Eq. (27.13) can be inverted to find an expression for the complex permittivity $\hat{\varepsilon}_1 = \varepsilon_1{\prime} + \mathrm{i}\varepsilon_1{\prime\prime} \equiv (n_1 + \mathrm{i}\kappa_1)^2$ [242]

$$\hat{\varepsilon}_1 = \frac{B \pm \sqrt{B^2 - AB\sin^2 2\,\theta}}{2A\cos^2\theta} \tag{27.14}$$

where $A = (\hat{\boldsymbol{r}}^\mathrm{p}_\mathrm{wl} - 1)^2$ and $B = (\hat{\boldsymbol{r}}^\mathrm{p}_\mathrm{wl} + 1)^2$. All typical material systems without gain show a positive $\varepsilon{\prime\prime}$ and hence the solution with $\varepsilon{\prime\prime} \geq 0$ should be chosen.

References

1. Bindig, U. and Muller, G. (2005) Fibre-optic laser-assisted infrared tumour diagnostics (FLAIR). *J. Phys. D: Appl. Phys.*, **38**, 2716–2731.
2. Salzer, R. and Siesler, H.W. (eds) (2009) *Infrared and Raman Spectroscopic Imaging*, Wiley-VCH Verlag GmbH, Weinheim ISBN: 978-3-527-31993-0.
3. Steiner, G. and Koch, E. (2009) Trends in Fourier transform infrared spectroscopic imaging. *Anal. Bioanal. Chem.*, **394**, 671–678.
4. Evans, J. (2006) Brilliant opportunities across the spectrum. *Phys. Chem. Chem. Phys.*, **8**, 3045–3058.
5. Dukor, R.K. and Nafie, L.A. (2000) in *Encyclopedia of Analytical Chemistry* (ed. R.A. Meyers), John Wiley & Sons, Ltd, Chichester, pp. 662–676 ISBN: 978-0-4719-7670-7.
6. Woutersen, S. and Hamm, P., Nonlinear two-dimensional vibrational spectroscopy of peptides, *J. Phys.: Condens. Matter* **14**, R1035–R1062 (2002).
7. Wang, L.Q. and Mizaikoff, B. (2008) Application of multivariate data-analysis techniques to biomedical diagnostics based on mid-infrared spectroscopy. *Anal. Bioanal. Chem.*, **391**, 1641–1654.

8. Mantsch, H.H. (1998) Vibrational spectroscopy of lipids: a historical perspective. *Chem. Phys. Lipids*, **96**, 3–7.
9. Burns, D.A. and Ciurczak, E.W. (eds) (2001) *Handbook of Near-Infrared Analysis*, CRC Press, Boca Raton, FL ISBN: 978-0-8493-7393-0.
10. Clark, R.J.H. and Hester, R.E. (eds) (1996) *Biomedical Applications of Spectroscopy*, John Wiley & Sons, Ltd, London ISBN: 0-471-95918-9.
11. Gregoriou, V.G. and Braiman, M.S. (2006) *Vibrational Spectroscopy of Biological and Polymeric Materials*, Taylor and Francis Group, London ISBN: 1-57444-539-1.
12. Gremlich, H.-U. and Yan, B. (2001) *Infrared and Raman Spectroscopy of Biological Materials (Practical Spectroscopy)*, Marcel Dekker, New York ISBN: 0-8247-0409-6.
13. Lasch, P. and Kneipp, J. (2009) *Biomedical Vibrational Spectroscopy*, John Wiley & Sons, Inc., Hoboken, NJ ISBN: 987-0-470-22945-3.
14. Mantsch, H.H. and Chapman, D. (eds) (1996) *Infrared Spectroscopy of Biomolecules*, Wiley-Liss, New York ISBN: 0-471-02184-9.
15. Ozaki, Y., McClure, W.F., and Christy, A.A. (eds) (2006) *Near-Infrared Spectroscopy in Food Science and Technology*, Wiley-Interscience ISBN: 978-0-471-67201-2.
16. Roberts, C.A., Workman, J. Jr., and Reeves, J.B. III, (2004) *Near-Infrared Spectroscopy in Agriculture*, American Society of Agronomy, Madison, WI ISBN: 0-89118-155-5.
17. Sasic, S. and Ozaki, Y. (eds) (2010) *Raman, Infrared, and Near-Infrared Chemical Imaging*, John Wiley & Sons, Inc., Hoboken, NJ ISBN: 978-0-470-38204-2.
18. Siebert, F. and Hildebrandt, P. (2008) *Vibrational Spectroscopy in Life Science (Tutorials in Biophysics)*, Wiley-VCH Verlag GmbH, Weinheim ISBN: 978-3-527-40506-0.
19. Siesler, H.W., Ozaki, Y., Kawata, S., and Heise, H.M. (eds) (2002) *Near-Infrared Spectroscopy: Principles, Instruments, Applications*, Wiley-VCH Verlag GmbH, Weinheim ISBN: 978-3-527-30149-2.
20. Srinivasan, G. (2010) *Vibrational Spectroscopic Imaging for Biomedical Applications*, McGraw-Hill ISBN: 978-0-071-59699-2.
21. Stuart, B.H. and Ando, D.J. (1997) *Biological Applications of Infrared Spectroscopy*, John Wiley & Sons, Inc., New York ISBN: 0 471 97413 7.
22. Uversky, V.N. and Permyakov, A.E. (eds) (2007) *Methods in Protein Structure and Stability Analysis: Vibrational Spectroscopy*, Molecular Anatomy and Physiology of Proteins(Series ed. V.N. Uversky), Nova Science PublishersISBN: 978-1-60021-703-6.
23. Jackson, M. and Mantsch, H.H. (1995) The use and misuse of FTIR spectroscopy in the determination of protein structure. *Crit. Rev. Biochem. Mol. Biol.*, **30**, 95–120.
24. Schweitzer-Stenner, R. (2006) Advances in vibrational spectroscopy as a sensitive probe of peptide and protein structure: a critical review. *Vib. Spectrosc.*, **42**, 98–117(A Collection of papers presented at the 3rd International Conference on Advanced Vibrational Spectroscopy (ICAVS-3), Delavan, Wisconsin, August 14–19, 2005 – Part 1).
25. Ganim, Z., Chung, H.S., Smith, A.W., Deflores, L.P., Jones, K.C., and Tokmakoff, A. (2008) Amide I two-dimensional infrared spectroscopy of proteins. *Acc. Chem. Res.*, **41**, 432–441.
26. Gough, K.M., Tzadu, L., Kastyak, M.Z., Kuzyk, A.C., and Julian, R.L. (2010) Theoretical and experimental considerations for interpretation of amide I bands in tissue. *Vibr. Spectrosc.*, **53**, 71–76(Advanced Vibrational Spectroscopy (ICAVS 2009), A Selection of papers presented at the 5th International Conference on Advanced Vibrational Spectroscopy).
27. NICODOM Kidney Stone Analysis Kit (2006) *http://www.ftir.cz/KID.html* (accessed 18 March 2013).
28. Yoo, E.H., Oh, H.J., and Lee, S.Y. (2008) Gallstone analysis using Fourier transform infrared spectroscopy

(FT-IR). *Clin. Chem. Lab. Med.*, **46**, 376–381.

29. Channa, N.A., Khand, F.D., Khand, T.U., Leghari, M.H., and Memon, A.N. (2007) Analysis of human gallstones by Fourier transform infrared (FTIR). *Pak. J. Med. Sci.*, **23**, 546–550.
30. Sayers, C., Wyatt, J., Soloway, R.D., Taylor, D.R., and Stringer, M.D. (2007) Gallbladder mucin production and calcium carbonate gallstones in children. *Ped. Surg. Int.*, **23**, 219–223.
31. Schafmayer, C., Hartleb, J., Tepel, J., Albers, S., Freitag, S., Voelzke, H., Buch, S., Seeger, M., Timm, B., Kremer, B., Foelsch, U.R., Faendrich, F., Krawczak, M., Schreiber, S., and Hampe, J. (2006) Predictors of gallstone composition in 1025 symptomatic gallstones from northern Germany. *BMC Gastroenterology*, **6**, 36.
32. Amerov, A.K., Chen, J., Small, G.W., and Arnold, M.A. (2005) Scattering and absorption effects in the determination of glucose in whole blood by near-infrared spectroscopy. *Anal. Chem.*, **77**, 4587–4594.
33. Amerov, A.K., Chen, J., Small, G.W., and Arnold, M.A. (2004) The influence of glucose upon the transport of light through whole blood. *Prog. Biomed. Opt. Imaging*, **5**, 101–111.
34. Ding, Q., Small, G.W., and Arnold, M.A. (1999) Evaluation of data pretreatment and model building methods for the determination of glucose from near-infrared single-beam spectra. *Appl. Spectrosc.*, **53**, 402–414.
35. Mattu, M.J., Small, G.W., and Arnold, M.A. (1997) Determination of glucose in a biological matrix by multivariate analysis of multiple band-pass-filtered Fourier transform near-infrared interferograms. *Anal. Chem.*, **69**, 4695–4702.
36. Haaland, D.M., Robinson, M.R., Koepp, G.W., Thomas, E.V., and Eaton, R.P. (1992) Reagentless near-infrared determination of glucose in whole-blood using multivariate calibration. *Appl. Spectrosc.*, **46**, 1575–1578.
37. Kim, Y.J. and Yoon, G. (2002) Multicomponent assay for human serum using Mid-infrared transmission spectroscopy based on component-optimized spectral region selected by a first loading vector analysis in partial least-squares regression. *Appl. Spectrosc.*, **56**, 625–632.
38. Marbach, R. and Heise, H.M. (1989) Comparison of multivariate calibration with PCR and PLS for glucose using infrared-spectra of human whole-blood. *Proc. Soc. Photo-Opt. Instrum. Eng. (SPIE)*, **1145**, 437–438.
39. Heise, H.M., Bittner, A., and Koschinsky, T. (1998) Clinical chemistry and near infrared spectroscopy: multicomponent assay for human plasma and its evaluation for the determination of blood substrates. *J. Near Infrared Spectrosc.*, **6**, 361–374.
40. Zhao, X.L., Zhang, L., Wang, Y., Xu, K.X., Wang, Y., Zhang, K., and Wang, X.Q. (2002) Preliminary investigation of simultaneous measurement of multi-components in human plasma by near-infrared spectroscopy. *Proc. Soc. Photo-Opt. Instrum. Eng. (SPIE)*, **4916**, 490–497.
41. Heise, H.M. and Bittner, A. (1998) Multivariate calibration for near-infrared spectroscopic assays of blood substrates in human plasma based on variable selection using PLS-regression vector choices. *Fresenius' J. Anal. Chem.*, **362**, 141–147.
42. Damm, U., Kondepati, V.R., and Heise, H.M. (2007) Continuous reagent-free bed-side monitoring of glucose in biofluids using infrared spectrometry and micro-dialysis. *Vibr. Spectrosc.*, **43**, 184–192.
43. Ham, F.M., Cohen, G.M., Kostanic, I., and Gooch, B.R. (1996) Multivariate determination of glucose concentrations from optimally filtered frequency-warped NIR spectra of human blood serum. *Physiol. Meas.*, **17**, 1–20.
44. Hazen, K.H., Arnold, M.A., and Small, G.W. (1998) Measurement of glucose and other analytes in undiluted human serum with near-infrared transmission spectroscopy. *Anal. Chim. Acta*, **371**, 255–267.
45. Li, B.Y., Kasemsumran, S., Hu, Y., Liang, Y.Z., and Ozaki, Y. (2007) Comparison of performance of partial least

squares regression, secured principal component regression, and modified secured principal component regression for determination of human serum albumin, gamma-globulin and glucose in buffer solutions and in vivo blood glucose quantification by near-infrared spectroscopy. *Anal. Bioanal. Chem.*, **387**, 603–611.

46. Arimoto, H., Tarumi, M., and Yamada, Y. (2003) Temperature-insensitive measurement of glucose concentration based on near infrared spectroscopy and partial least squares analysis. *Opt. Rev.*, **10**, 74–76.

47. Arimoto, H. and Yamada, Y. (2003) Spectroscopic blood component measurement by using reduced ranges of absorption spectra. *Proc. Soc. Photo-Opt. Instrum. Eng. (SPIE)*, **5138**, 323–330.

48. Heise, H.M. and Bittner, A. (1998) Essential absorption data for in-vitro and in-vivo near infrared spectrometric biotic fluid assays. *AIP Conf. Proc.*, **430**, 274–277.

49. Kramer, K.E. and Small, G.W. (2009) Digital filtering and model updating methods for improving the robustness of near-infrared multivariate calibrations. *Appl. Spectrosc.*, **63**, 246–255.

50. Kramer, K.E. and Small, G.W. (2007) Blank augmentation protocol for improving the robustness of multivariate calibrations. *Appl. Spectrosc.*, **61**, 497–506.

51. Mcshane, M.J., Cote, G.L., and Spiegelman, C.H. (1998) Assessment of partial least-squares calibration and wavelength selection for complex near-infrared spectra. *Appl. Spectrosc.*, **52**, 878–884.

52. Saptari, V. and Youcef-Toumi, K. (2004) Design of a mechanical-tunable filter spectrometer for noninvasive glucose measurement. *Appl. Opt.*, **43**, 2680–2688.

53. Saptari, V.A. and Youcef-Toumi, K. (2000) Sensitivity analysis of near infrared glucose absorption signals: toward noninvasive blood glucose sensing. *Proc. Soc. Photo-Opt. Instrum. Eng. (SPIE)*, **1**, 45–54.

54. Saptari, V.A., Youcef-Toumi, K., and Zhang, J. (2004) NIR measurements of glucose in synthetic biological solutions using high-throughput angle-tuned filter spectrometer. *Proc. Soc. Photo-Opt. Instrum. Eng. (SPIE)*, **5325**, 1–10.

55. Sulub, Y. and Small, G.W. (2009) Spectral simulation protocol for extending the lifetime of near-infrared multivariate calibrations. *Anal. Chem.*, **81**, 1208–1216.

56. Bhandare, P., Mendelson, Y., Peura, R.A., Janatsch, G., Krusejarres, J.D., Marbach, R., and Heise, H.M. (1993) Multivariate determination of glucose in whole-blood using partial least-squares and artificial neural networks based on midinfrared spectroscopy. *Appl. Spectrosc.*, **47**, 1214–1221.

57. Budinova, G., Salva, J., and Volka, K. (1997) Application of molecular spectroscopy in the mid-infrared region to the determination of glucose and cholesterol in whole blood and in blood serum. *Appl. Spectrosc.*, **51**, 631–635.

58. Heise, H.M., Marbach, R., Janatsch, G., and Krusejarres, J.D. (1989) Multivariate determination of glucose in whole-blood by attenuated total-reflection infrared-spectroscopy. *Anal. Chem.*, **61**, 2009. 1995) , **67**, 775.

59. Hosafci, G., Klein, O., Oremek, G., and Mantele, W. (2007) Clinical chemistry without reagents? An infrared spectroscopic technique for determination of clinically relevant constituents of body fluids. *Anal. Bioanal. Chem.*, **387**, 1815–1822.

60. Kim, Y.J., Hahn, S., and Yoon, G. (2003) Determination of glucose in whole blood samples by mid-infrared spectroscopy. *Appl. Opt.*, **42**, 745–749.

61. Low-Ying, S., Shaw, R.A., Leroux, M., and Mantsch, H.H. (2002) Quantitation of glucose and urea in whole blood by mid-infrared spectroscopy of dry films. *Vibr. Spectrosc.*, **28**, 111–116.

62. Shen, Y.C., Davies, A.G., Linfield, E.H., Elsey, T.S., Taday, P.F., and Arnone, D.D. (2003) The Use of Fourier-transform infrared spectroscopy for the quantitative determination of glucose concentration in whole blood. *Phys. Med. Biol.*, **48**, 2023–2032.

63. Shen, Y.C., Davies, A.G., Linfield, E.H., Taday, P.F., Arnone, D.D., and

Elsey, T.S. (2003) Determination of glucose concentration in whole blood using Fourier-transform infrared spectroscopy. *J. Biol. Phys.*, **29**, 129–133.

64. Ward, K.J., Haaland, D.M., Robinson, M.R., and Eaton, R.P. (1992) Postprandial blood-glucose determination by quantitative midinfrared spectroscopy. *Appl. Spectrosc.*, **46**, 959–965.

65. Vonach, R., Buschmann, J., Falkowski, R., Schindler, R., Lendl, B., and Kellner, R. (1998) Application of mid-infrared transmission spectrometry to the direct determination of glucose in whole blood. *Appl. Spectrosc.*, **52**, 820–822.

66. Bittner, A., Heise, H.M., Koschinsky, T., and Gries, F.A. (1997) Evaluation of microdialysis and FT-IR ATR-spectroscopy for in-vivo blood glucose monitoring. *Mikrochim. Acta*, 827–828.

67. Heise, H.M. and Bittner, A. (1997) Rapid and reliable spectral variable selection for statistical calibrations based on PLS-regression vector choices. *Fresenius' J. Anal. Chem.*, **359**, 93–99.

68. Heise, H.M. and Bittner, A. (1995) Investigation of experimental errors in the quantitative-analysis of glucose in human blood-plasma by Atr-Ir spectroscopy. *J. Mol. Struct.*, **348**, 21–24.

69. Heise, H.M., Bittner, A., Koschinsky, T., and Gries, F.A. (1997) Ex-vivo determination of blood glucose by microdialysis in combination with infrared attenuated total reflection spectroscopy. *Fresenius' J. Anal. Chem.*, **359**, 83–87.

70. Zhou, Y.P., Xu, L., Tang, L.J., Jiang, J.H., Shen, G.L., Yu, R.Q., and Ozaki, Y. (2007) Determination of glucose in plasma by dry film-based Fourier transformed-infrared spectroscopy coupled with boosting support vector regression. *Anal. Sci.*, **23**, 793–798.

71. Petibois, C., Gionnet, K., Goncalves, M., Perromat, A., Moenner, M., and Deleris, G. (2006) Analytical performances of Ft-Ir spectrometry and imaging for concentration measurements within biological fluids, cells, and tissues. *Analyst*, **131**, 640–647.

72. Diessel, E., Kamphaus, P., Grothe, K., Kurte, R., Damm, U., and Heise, H.M. (2005) Nanoliter serum sample analysis by mid-infrared spectroscopy for minimally invasive blood-glucose monitoring. *Appl. Spectrosc.*, **59**, 442–451.

73. Bhandare, P., Mendelson, Y., Stohr, E., and Peura, R.A. (1994) Glucose determination in simulated blood-serum solutions by Fourier-transform infrared-spectroscopy–investigation of spectral interferences. *Vibr. Spectrosc.*, **6**, 363–378.

74. Bhandare, P., Mendelson, Y., Stohr, E., and Peura, R.A. (1994) Comparison of multivariate calibration techniques for Mid-IR absorption spectrometric determination of blood-serum constituents. *Appl. Spectrosc.*, **48**, 271–273.

75. Fujii, T., Miyahara, Y., and Watanabe, Y. (1995) Reduction of glucose interference in biochemical analyses based on infrared-spectroscopy. *Bunseki Kagaku*, **44**, 465–469.

76. Kim, Y.J. and Yoon, G. (2006) Prediction of glucose in whole blood by near-infrared spectroscopy: influence of wavelength region, preprocessing, and hemoglobin concentration. *J. Biomed. Opt.*, **11**, 041128.

77. Rohleder, D., Kocherscheidt, G., Gerber, K., Kiefer, W., Kohler, W., Mocks, J., and Petrich, W. (2005) Comparison of mid-infrared and Raman spectroscopy in the quantitative analysis of serum. *J. Biomed. Opt.*, **10**, 031108.

78. Fujii, T., Miyahara, Y., and Watanabe, Y. (1997) Highly sensitive biochemical analysis using low-temperature infrared spectroscopy measurements. *Appl. Spectrosc.*, **51**, 1682–1686.

79. Nakamura, A., Hasegawa, T., Nishijo, J., Kanazawa, M., Aizawa, K., and Sota, T. (2002) Spectroscopic evaluation of glucose concentration in phosphate-buffered saline solution using principal component analysis. *Jpn. J. Appl. Phys. Part 2 Lett.*, **41**, L440–L442.

80. Heise, H.M., Damm, U., Bodenlenz, M., Kondepati, V.R., Kohler, G., and Ellmerer, M. (2007) Bedside monitoring of subcutaneous interstitial glucose in healthy individuals using microdialysis and infrared spectrometry. *J. Biomed. Opt.*, **12**, 024004.

81. Heise, H.M., Damm, U., and Kondepati, V.R. (2006) Reliable long-term continuous blood glucose monitoring for patients in critical care usling micro-dialysis and infrared spectrometry. *Proc. Soc. Photo-Opt. Instrum. Eng. (SPIE)*, **6093**, 9303.

82. Heise, H.M., Damm, U., Kondepati, V.R., Mader, J.K., and Ellmerer, M. (2007) Bed-side monitoring of subcutaneous interstitial glucose in type 1 diabetic subjects using micro-dialysis and infrared spectrometry with optimal correlation to blood glucose concentrations. *Proc. Soc. Photo-Opt. Instrum. Eng. (SPIE)*, **6445**, 44502.

83. Shaw, R.A., Rigatto, C., Reslerova, M., Ying, S.L., Man, A., Schattka, B., Battrell, C.F., Matthewson, J., and Mansfield, C. (2009) Toward point-of-care diagnostic metabolic fingerprinting: quantification of plasma creatinine by infrared spectroscopy of microfluidic-preprocessed samples. *Analyst*, **134**, 1224–1231.

84. Araujo-Andrade, C., Ruiz, F., Martinez-Mendoza, J.R., and Terrones, H. (2004) Non-invasive in-vivo blood glucose levels prediction using near infrared spectroscopy. *AIP Conf. Proc.*, **724**, 234–239.

85. Arnold, M.A., Burmeister, J.J., and Small, G.W. (1998) Phantom glucose calibration models from simulated non-invasive human near-infrared spectra. *Anal. Chem.*, **70**, 1773–1781.

86. Li, L.N., Li, Q.B., and Zhang, G.J. (2009) A weak signal extraction method for human blood glucose noninvasive measurement using near infrared spectroscopy. *J. Infrared Millimeter Terahertz Waves*, **30**, 1191–1204.

87. Li, L.N., Zhang, G.J., and Li, Q.B. (2009) Pretreatment method research of near-infrared spectra in blood component non-invasive measurement. *Mod. Phys. Lett. B*, **23**, 925–937.

88. Liu, R., Gu, X.Y., and Xu, K.X. (2008) Research on the background correction in the non-invasive sensing of glucose by near-infrared spectroscopy. *Spectrosc. Spect. Anal.*, **28**, 1772–1775.

89. Marquardt, L.A., Arnold, M.A., and Small, G.W. (1993) Near-infrared spectroscopic measurement of glucose in a protein matrix. *Anal. Chem.*, **65**, 3271–3278.

90. Samann, A., Fischbacher, C., Jagemann, K.U., Danzer, K., Schuler, J., Papenkordt, L., and Muller, U.A. (2000) Non-invasive blood glucose monitoring by means of near infrared spectroscopy: investigation of long-term accuracy and stability. *Exp. Clin. Endocrinol. Diabetes*, **108**, 406–413.

91. Wang, H., Li, Q.B., Liu, Z.Y., and Xu, K.X. (2002) Application of genetic algorithms in fundamental study of non-invasive measurement of human blood glucose concentration with near infrared spectroscopy. *Chin. J. Anal. Chem.*, **30**, 779–783.

92. Zhang, G.J., Li, L.N., Li, Q.B., and Xu, Y.P. (2009) Application of de-noising and background elimination based on wavelet transform to blood glucose noninvasive measurement of near infrared spectroscopy. *J. Infrared Millimeter Waves*, **28**, 107–110.

93. Liu, R., Chen, W.L., Gu, X.Y., Luo, Y.H., and Xu, K.X. (2005) Extraction of glucose information in blood glucose measurement by non-invasive near-infrared spectra. *Proc. Soc. Photo-Opt. Instrum. Eng. (SPIE)*, **5702**, 30–38.

94. Heise, H.M., Bittner, A., and Marbach, R. (1998) Clinical chemistry and near infrared spectroscopy: technology for non-invasive glucose monitoring. *J. Near Infrared Spectrosc.*, **6**, 349–359.

95. Heise, H.M., Haiber, S., Licht, M., Ihrig, D.F., Moll, C., and Stucker, M. (2006) Recent progress in non-invasive diabetes screening by diffuse reflectance near-infrared skin spectroscopy. *Proc. Soc. Photo-Opt. Instrum. Eng. (SPIE)*, **6093**, 9310.

96. Maruo, K., Oota, T., Tsurugi, M., Nakagawa, T., Arimoto, H., Tamura, M., Ozaki, Y., and Yamada, Y. (2006) New methodology to obtain a calibration model for noninvasive near-infrared blood glucose monitoring. *Appl. Spectrosc.*, **60**, 441–449.

97. Maruo, K., Tsurugi, M., Chin, J., Ota, T., Arimoto, H., Yamada, Y., Tamura, M., Ishii, M., and Ozaki, Y. (2003) Noninvasive blood glucose assay using a newly developed near-infrared system. *IEEE J. Sel. Top. Quantum Electron.*, **9**, 322–330.

98. Olesberg, J.T., Liu, L.Z., Van Zee, V., and Arnold, M.A. (2006) In vivo near-infrared spectroscopy of rat skin tissue with varying blood glucose levels. *Anal. Chem.*, **78**, 215–223.

99. Heise, H.M., Bittner, A., and Marbach, R. (2000) Near-infrared reflectance spectroscopy for noninvasive monitoring of metabolites. *Clin. Chem. Lab. Med.*, **38**, 137–145.

100. Marbach, R., Koschinsky, T., Gries, F.A., and Heise, H.M. (1993) Non-invasive blood-glucose assay by near-infrared diffuse-reflectance spectroscopy of the human inner lip. *Appl. Spectrosc.*, **47**, 875–881.

101. Robinson, M.R., Eaton, R.P., Haaland, D.M., Koepp, G.W., Thomas, E.V., Stallard, B.R., and Robinson, P.L. (1992) Noninvasive glucose monitoring in diabetic-patients–a preliminary evaluation. *Clin. Chem.*, **38**, 1618–1622.

102. Jagemann, K.U., Fischbacher, C., Muller, U.A., and Mertes, B. (1995) Application of near-infrared spectroscopy for noninvasive determination of blood-tissue glucose using neural networks. *Z. Phys. Chem.-Int. J. Res. Phys. Chem. Chem. Phys.*, **191**, 179–190.

103. Muller, U.A., Mertes, B., Fischbacher, C., Jageman, K.U., and Danzer, K. (1997) Non-invasive blood glucose monitoring by means of near infrared spectroscopy: methods for improving the reliability of the calibration models. *Int. J. Artif. Organs*, **20**, 285–290.

104. Bai, C., Graham, T.L., and Arnold, M.A. (2008) Assessing and advancing technology for the noninvasive measurement of clinical glucose. *Anal. Lett.*, **41**, 2773–2793.

105. Arnold, M.A. and Small, G.W. (2005) Noninvasive glucose sensing. *Anal. Chem.*, **77**, 5429–5439.

106. Naumann, D. (2008) FT-IR spectroscopy of microorganisms at the Robert Koch-institute: experiences gained during a successful. *Proc. Soc. Photo-Opt. Instrum. Eng. (SPIE)*, **6853**, G8530.

107. Burgula, Y., Khali, D., Kim, S., Krishnan, S.S., Cousin, M.A., Gore, J.P., Reuhs, B.L., and Mauer, L.J. (2007) Review of mid-infrared Fourier transform-infrared spectroscopy applications for bacterial detection. *J. Rapid Methods Autom. Microbiol.*, **15**, 146–175.

108. Harz, P., Rosch, P., and Popp, J. (2009) Vibrational spectroscopy-a powerful tool for the rapid identification of microbial cells at the single-cell level. *Cytometry Part A*, **75A**, 104–113.

109. Ngo-Thi, N.A., Kirschner, C., and Naumann, D. (2003) Characterization and identification of microorganisms by FIF-IR microspectrometry. *J. Mol. Struct.*, **661**, 371–380.

110. Corte, L., Rellini, P., Roscini, L., Fatichenti, F., and Cardinali, G. (2010) Development of a novel, FTIR (Fourier transform infrared spectroscopy) based, yeast bioassay for toxicity testing and stress response study. *Anal. Chim. Acta*, **659**, 258–265.

111. Schulz, H. and Baranska, M. (2007) Identification and quantification of valuable plant substances by Ir and Raman spectroscopy. *Vibr. Spectrosc.*, **43**, 13–25.

112. Diem, M., Boydston-White, S., and Chiriboga, L. (1999) Infrared spectroscopy of cells and tissues: shining light onto a novel subject. *Appl. Spectrosc.*, **53**, 148A–161A.

113. Krafft, C., Steiner, G., Beleites, C., and Salzer, R. (2009) Disease recognition by infrared and Raman spectroscopy. *J. Biophoton.*, **2**, 13–28.

114. Kendall, C., Isabelle, M., Bazant-Hegemark, F., Hutchings, J., Orr, L., Babrah, J., Baker, R., and Stone, N. (2009) Vibrational spectroscopy: a clinical tool for cancer diagnostics. *Analyst*, **134**, 1029–1045.

115. Yu, P.Q. (2006) Synchrotron Ir microspectroscopy for protein structure analysis: potential and questions. *Spectrosc. Int. J.*, **20**, 229–251.

116. Pijanka, J.K., Kohler, A., Yang, Y., Dumas, P., Chio-Srichan, S., Manfait, M., Sockalingum, G.D., and Sule-Suso, J. (2009) Spectroscopic signatures of single, isolated cancer cell nuclei using synchrotron infrared microscopy. *Analyst*, **134**, 1176–1181.

117. Bassan, P., Kohler, A., Martens, H., Lee, J., Byrne, H.J., Dumas, P., Gazi, E., Brown, M., Clarke, N., and Gardner, P. (2010) Resonant Mie scattering (RMieS) correction of infrared spectra from highly scattering biological samples. *Analyst*, **135**, 268–277.

118. Edwards, A.D., Richardson, C., Vanderzee, P., Elwell, C., Wyatt, J.S., Cope, M., Delpy, D.T., and Reynolds, E.O.R. (1993) Measurement of hemoglobin flow and blood-flow by near-infrared spectroscopy. *J. Appl. Physiol.*, **75**, 1884–1889.

119. Sakudo, A., Kuratsune, H., Kato, Y.H., and Ikuta, K. (2009) Secondary structural changes of proteins in fingernails of chronic fatigue syndrome patients from Fourier-transform infrared spectra. *Clin. Chim. Acta*, **402**, 75–78.

120. Andanson, J.M., Hadgraft, J., and Kazarian, S.G. (2009) In situ permeation study of drug through the stratum corneum using attenuated total reflection Fourier transform infrared spectroscopic imaging. *J. Biomed. Opt.*, **14**.

121. Pappas, D., Smith, B.W., and Winefordner, J.D. (2000) *Talanta*, **51**, 131–144.

122. Baena, J.R. and Lendl, B. (2004) *Cur. Opin. Chem. Biol.*, **8**, 534–539.

123. McCreery, R.L. (2000) *Raman Spectroscopy for Chemical Analysis*, John Wiley & Sons, Inc., New York.

124. Paschotta, R. 2008 *Encyclopedia of Laser Physics and Technology*, **2** Vols. 844 p., Wiley-VCH Verlag GmbH, Weinheim, *http://www.rp-photonics.com/distributed_bragg_reflector_lasers.html* (accessed 18 March 2013).

125. Schrader, B. (1994) *Infrared and Raman Spectroscopy*, Wiley-VCH Verlag GmbH, Weinheim.

126. Kaiser Optical Systems, Inc. Holographic Notch and SuperNotch® Filters, *http://www.kosi.com/Holographic_Filters/notchfilters.php* (accessed 18 March 2013).

127. For example: Semrock (http://www.semrock.com/edge-filters-vs-notch-filters-for-raman-instrumentation.aspx accessed 24 June 2013); Omega Optical (http://www.omegafilters.com/Capabilities/Applications/Raman_Spectroscopy/Raman_General accessed 24 June 2013); Ondax Incorporated (http://www.ondax.com/products/sureblock%E2%84%A2-narrow-band-notch-filters accessed 24 June 2013); and many others.

128. Othonos, A. (1997) Fiber Bragg gratings. *Rev. Sci. Instrum.*, **68**, 4309–4341.

129. Hirschfeld, T. and Chase, B. (1986) *Appl. Spectrosc.*, **40**, 133–137.

130. Raman Systems, *http://www.ramansystems.com/* accessed 24 June 2013.

131. Kaiser Optical Systems, Inc. Raman Probe Heads and Optics, *http://www.kosi.com/Raman_Spectroscopy/ramanprobeheads-optics.php* (accessed 18 March 2013).

132. InPhotonics Inc. The RamanProbeTM, *http://www.inphotonics.com/probes.htm* (accessed 18 March 2013).

133. Shim, M.G., Wilson, B.C., Marple, E., and Wach, M. (1999) *Appl. Spectrosc.*, **53**, 619–625.

134. Motz, J.T., Hunter, M., Galindo, L.H., Gardecki, J.A., Kramer, J.R., Dasari, R.R., and Feld, M.S. (2004) *Appl. Opt.*, **43**, 542–554.

135. Motz, J.T., Fitzmaurice, M., Miller, A., Gandhi, S.J., Haka, A.S., Galindo, L.H., Dasari, R.R., Kramer, J.R., and Feld, M.S. (2006) *J. Biomed. Opt.*, **11**, 021003.

136. Komachi, Y., Sato, H., Aisawa, K., and Tashiro, H. (2005) *Appl. Opt.*, **44**, 4722–4732.

137. Komachi, Y., Sato, H., Matsuura, Y., Miyagi, M., and Tashiro, H. (2005) *Opt. Lett.*, **30**, 2942–2944.

138. Katagiri, T., Komachi, Y., Hattori, Y., Matsuura, Y., Miyagi, M., Tashiro, H., and Sato, H. (2006) *Proc. SPIE*, **6083**, 60830E-1.

139. Matousek, P., Clark, I.P., Draper, E.R.C., Morris, M.D., Goodship, A.E., Everall, N., Towrie, M., Finney, W.F., and Parker, A.W. (2005) *Appl. Spectrosc.*, **59**, 393–400.

140. Matousek, P., Morris, M.D., Everall, N., Clark, I.P., Towrie, M., Draper, E., Goodship, A., and Parker, A.W. (2005) *Appl. Spectrosc.*, **59**, 1485–1491.

141. Matousek, P., Draper, E.R.C., Goodship, A.E., Clark, I.P., Ronayne, K.L., and Parker, A.W. (2006) *Appl. Spectrosc.*, **60**, 758–763.

142. Eliasson, C. and Matousek, P. (2008) *J. Raman Spectrosc.*, **39**, 633–637.

143. Adar, F., 2007, *Spectroscopy* **22** *http://spectroscopyonline.findanalytichem.com/spectroscopy/article/articleDetail.jsp?id=476139* (accessed 18 March 2013).

144. van Manen, H.J., Kraan, Y.M., Roos, D., and Otto, C. (2004) Intracellular chemical imaging of heme-containing enzymes involved in innate immunity using resonance Raman microscopy. *J. Phys. Chem. B*, **108**, 18762–18771.

145. Wolthuis, R., Bakker Schut, T.C., Caspers, P.J., Buschman, H.P.J., Romer, T.J., Bruining, H.A., and Puppels, G.J. (1999) in *Fluorescent and Luminescent Probes for Biological Activity, Biological Techniques* (ed W.T. Mason), Academic Press, London, pp. 431–455.

146. Bakker Schut, T., Koljenovic, S., van der Pol, S., de Jong, B., Wolthuis, R., and Puppels, G.J. (2004) Fotonica Magazine (Dec. 2004), pp. 23–24.

147. Zhang, S.L., Caspers, P.J., and Puppels, G.J. (2005) *Microsc. Microanal.*, **11**, 790.

148. Eriksson, L., Antti, H., Gottfries, J., Holmes, E., Johansson, E. *et al.* (2004) *Anal. Bioanal. Chem.*, **380**, 419–429.

149. Optics InfoBase The Biodata Toolbox for MATLAB, *http://www.analchem.ugent.be/Raman/Html/Biodata.php* (accessed 18 March 2013).

150. van Manen, H.J., Kraan, Y.M., Roos, D., and Otto, C. (2005) *Proc. Natl. Acad. Sci. U.S.A.*, **102**, 10159–10164.

151. Maquelin, K., Dijkshoorn, L., van der Reijden, T.J.K., Puppels, G.J., and Microbiol, J. (2006) *Methods*, **64**, 126–131.

152. Schulmerich, M.V., Cole, J.H., Kreider, J.M., Esmonde-White, F., Dooley, K.A., Goldstein, S.A., and Morris, M.D. (2009) *Appl. Spectrosc.*, **63**, 286–295.

153. Huang, W.E., Griffiths, R.I., Thompson, I.P., Bailey, M.J., and Whiteley, A.S. (2004) *Anal. Chem.*, **76**, 4452–4458.

154. Sabelnikov, A. and Kempf, C.R. (2008) *Anal. Biochem.*, **383**, 346–348.

155. Wang, W.E., Bailey, M.J., Thompson, I.P., Whiteley, A.S., and Spiers, A.J. (2007) *Microb. Ecol.*, **53**, 414–425.

156. Zheng, F., Qin, Y.-J., and Chen, K. (2007) *J. Biomed. Opt.*, **12**, 034002.

157. Fleischmann, M., Hendra, P.J., and McQuillan, A.J. (1974) *Chem. Phys. Lett.*, **26**, 163.

158. Baker, G.A. and Moore, D.S. (2005) *Anal. Bioanal. Chem.*, **382**, 1715–1770.

159. Fang, Y., Seong, N.-H., and Dlott, D.D. (2008) *Science*, **321**, 388–392.

160. Graham, D. and Goodacre, R. (2008) *Chem. Soc. Rev.*, **37**, 883.

161. Wu, D.-Y., Li, J.-F., Ren, B., and Tian, Z.-Q. (2008) *Chem. Soc. Rev.*, **37**, 1025.

162. Smith, W.E. (2008) Practical understanding and use of surface enhanced Raman scattering/surface enhanced resonance Raman scattering in chemical and biological analysis. *Chem. Soc. Rev.*, **37**, 955–964.

163. Banholzer, M.J., Millstone, J.E., Qin, L.-D., and Mirkin, C.A. (2008) Rationally designed nanostructures for surface-enhanced Raman spectroscopy. *Chem. Soc. Rev.*, **37**, 885–897.

164. Lal, S., Grady, N.K., Kundu, J., Levin, C.S., Lassiter, J.B., and Halas, N.J. (2008) Tailoring plasmonic substrates for surface enhanced spectroscopies. *Chem. Soc. Rev.*, **37**, 898–911.

165. Vo-Dinh, T., Yan, F., and Stokes, D.L. (2005) Plasmonics-based nanostructures for surface-enhanced Raman scattering bioanalysis, in *Protein Nanotechnology, Protocols, Instrumentation, and Applications*, Methods in Molecular Biology, Vol. **300** (ed T. Vo-Dinh), Humana Press Inc., Totowa, NJ.

166. Bailo, E. and Deckert, V. (2008) Tip-enhanced Raman scattering. *Chem. Soc. Rev.*, **37**, 921–930.

167. Abdali, S. and Blanch, E.W. (2008) Surface enhanced Raman optical activity (SEROA). *Chem. Soc. Rev.*, **37**, 980–992.

168. Pieczonka, N.P.W. and Aroca, R.F. (2008) Single molecule analysis by surface-enhanced Raman scattering. *Chem. Soc. Rev.*, **37**, 946–954.

169. Kneipp, J., Kneipp, H., and Kneipp, K. (2008) SERS – a single molecule and nanoscale tool for bioanalytics. *Chem. Soc. Rev.*, **37**, 1052–1060.

170. Qian, X.-M. and Nie, S.M. (2008) Single-molecule and single-nanoparticle SERS: from fundamental mechanisms to biomedical applications. *Chem. Soc. Rev.*, **37**, 912–920.

171. Bell, S.E.J. and Sirimuthu, N.M.S. (2008) Quantitative surface-enhanced Raman spectroscopy. *Chem. Soc. Rev.*, **37**, 1012–1024.

172. Graham, D. and Faulds, K. (2008) Quantitative SERRS for DNA sequence analysis. *Chem. Soc. Rev.*, **37**, 1042–1051.

173. Porter, M.D., Lipert, R.J., Siperko, L.M., Wang, G.-F., and Narayanan, R. (2008) SERS as a bioassay platform: fundamentals, design, and applications. *Chem. Soc. Rev.*, **37**, 1001–1011.

174. Jarvis, R.M. and Goodacre, R. (2008) Characterisation and identification of bacteria using SERS. *Chem. Soc. Rev.*, **37**, 931–936.

175. Murgida, D.H. and Hildebrandt, P. (2008) Disentangling interfacial redox processes of proteins by SERR spectroscopy. *Chem. Soc. Rev.*, **37**, 937–945.

176. Chourpa, I., Lei, F.H., Dubois, P., Manfait, M., and Sockalingum, G.D. (2008) Intracellular applications of analytical SERS spectroscopy and multispectral imaging. *Chem. Soc. Rev.*, **37**, 993–1000.

177. Korter, T.M., Balu, R., Campbell, M.B., Beard, M.C., Gregurick, S.K., and Heilweil, E.J. (2005) Terahertz spectroscopy of solid serine and cysteine. *Chem. Phys. Lett.*, **418**, 65.

178. Allis, D.G., Prokhorova, D.A., and Korter, T.M. (2006) Solid-state modeling of the terahertz spectrum of the high explosive HMX. *J. Phys. Chem. A*, **110**, 1951.

179. Allis, D.G. and Korter, T.M. (2006) Theoretical analysis of the terahertz spectrum of the high explosive PETN. *ChemPhysChem.*, **7**, 2398.

180. Siegrist, K., Bucher, C.R., Mandelbaum, I., Hight Walker, A.R., Balu, R., Gregurick, S.K., and Plusquellic, D.F. (2006) High resolution THz spectroscopy of crystalline trianiline: extreme sensitivity to beta-sheet structure and co-crystallized water. *J. Am. Chem. Soc.*, **128**, 5764.

181. Saito, S., Inerbaev, T.M., Mizuseki, H., Igarashi, N., and Kawazoe, Y. (2006) Terahertz vibrational modes of crystalline salicylic acid by numerical model using periodic density functional theory. *Jpn. J. Appl. Phys.*, **45**, 4170.

182. Saito, S., Inerbaev, T.M., Mizuseki, H., Igarashi, N., Note, R., and Kawazoe, Y. (2006) First principles calculation of terahertz vibrational modes of a disaccharide monohydrate crystal of lactose. *Jpn. J. Appl. Phys.*, **45**, L1156.

183. Allis, D.G., Fedor, A.M., Korter, T.M., Bjarnason, J.E., and Brown, E.R. (2007) Assignment of the lowest-lying THz absorption signatures in biotin and lactose monohydrate by solid-state density functional theory. *Chem. Phys. Lett.*, **440**, 203.

184. Allis, D.G., Zeitler, J.A., Taday, P.F., and Korter, T.M. (2008) Theoretical analysis of the solid-state terahertz spectrum of the high explosive RDX. *Chem. Phys. Lett.*, **463**, 84.

185. Uhd Jepsen, P. and Clark, S.J. (2007) Precise ab-initio prediction of terahertz vibrational modes in crystalline systems. *Chem. Phys. Lett.*, **442**, 275.

186. Gervasio, F.L., Cardini, G., Salvi, P.R., and Schettino, V. (1998) Low-frequency vibrations of all-trans-retinal: far-infrared and Raman spectra and density functional calculations. *J. Phys. Chem. A*, **102**, 2131.

187. Walther, M., Fischer, B., Schall, M., Helm, H., and Uhd Jepsen, P. (2000) Far-infrared vibrational spectra of all-trans, 9-cis and 13-cis retinal measured by THz time-domain spectroscopy. *Chem. Phys. Lett.*, **332**, 389.

188. Harde, H., Keiding, S., and Grischkowsky, D. (1991) THz commensurate echoes: periodic reshaping of molecular transitions in free-induction decay. *Phys. Rev. Lett.*, **66**, 1834.

189. Harde, H., Katzenellenbogen, N., and Grischkowsky, D. (1995) Line-shape transition of collision broadened lines. *Phys. Rev. Lett.*, **74**, 1307.

190. Cheville, R.A. and Grischkowsky, D. (1995) Far-infrared terahertz time-domain spectroscopy of flames. *Opt. Lett.*, **20**, 1646.

191. Van Exter, M., Fattinger, C., and Grischkowsky, D. (1989) Terahertz time-domain spectroscopy of water vapor. *Opt. Lett.*, **14**, 1128.

192. Kafka, J.D., Watts, M.L., and Pieterse, J.-W.J. (1992) Picosecond and femtosecond pulse generation in a regeneratively mode-locked Ti :sapphire laser. *IEEE J. Quantum Electron.*, **28**, 2151.

193. Mittleman, D. (ed) (2002) *Sensing with Terahertz Radiation*, Springer Series in Optical Sciences, Springer-Verlag ISBN: 978–3540431107.

194. Dexheimer, S.L. (ed) (2007) *Terahertz Spectroscopy: Principles and Applications*, CRC Press ISBN: 978–0849375255.

195. Sakai, K. (ed) (2005) *Terahertz Optoelectronics*, Springer-Verlag, New York ISBN: 978–3540200130.

196. Lee, Y.-S. (2008) *Principles of Terahertz Science and Technology*, SpringerISBN: 978–0387095394.

197. Zhang, X.-C. and Xu, J. (2010) *Introduction to THz Wave Photonics*, Springer, New York ISBN: 978–1441909770.

198. Parker, T.J. (1990) Dispersive Fourier transform spectroscopy. *Contemp. Phys.*, **31**, 335.

199. Wu, Q. and Zhang, X.-C. (1996) Design and characterization of traveling-wave electrooptic terahertz sensors. *IEEE J. Select. Top. Quantum Electron.*, **2**, 693.

200. Leitenstorfer, A., Hunsche, S., Shah, J., Nuss, M.C., and Knox, W.H. (1999) Detectors and sources for ultrabroadband electro-optic sampling: Experiment and theory. *Appl. Phys. Lett.*, **74**, 1516.

201. Kaindl, R.A., Eickemeyer, F., Woerner, M., and Elsaesser, T. (1999) Broadband phase-matched difference frequency mixing of femtosecond pulses in GaSe: experiment and theory. *Appl. Phys. Lett.*, **75**, 1060.

202. Gallot, G. and Grischkowsky, D. (1999) Electro-optic detection of terahertz radiation. *J. Opt. Soc. Am. B*, **16**, 1204.

203. Planken, P.M.C., Nienhuys, H.-K., Bakker, H.J., and Wenckebach, T. (2001) Measurement and calculation of the orientation dependence of terahertz pulse detection in ZnTe. *J. Opt. Soc. Am. B*, **18**, 313.

204. van der Valk, N.C.J., Wenckebach, T., and Planken, P.C.M. (2004) Full mathematical description of electro-optic detection in optically isotropic crystals. *J. Opt. Soc. Am. B*, **21**, 622.

205. Jackson, J.D. (2001) *Classical Electrodynamics*, 3rd edn, John Wiley & Sons, Inc.

206. Ashida, M. (2008) Ultra-broadband terahertz wave detection using photoconductive antenna. *Jpn. J. Appl. Phys.*, **47**, 8221.

207. Sengupta, A., Bandyopadhyay, A., Bowden, B.F., Harrington, J.A., and Federici, J.F. (2006) Characterization of olefin copolymers using terahertz spectroscopy. *Electron. Lett.*, **42**, 1477.

208. Nielsen, K., Rasmussen, H.K., Adam, A.J.L., Planken, P.C.M., Bang, O., and Uhd Jepsen, P. (2009) Bendable, low-loss Topas fibers for the terahertz frequency range. *Opt. Express*, **17**, 8592.

209. Dai, J., Zhang, J., Zhang, W., and Grischkowsky, D. (2004) Terahertz time-domain spectroscopy characterization of the far-infrared absorption and index of refraction of high-resistivity, float-zone silicon. *J. Opt. Soc. Am. B*, **21**, 1379.

210. Fattinger, C. and Grischkowsky, D. (1988) Point source terahertz optics. *Appl. Phys. Lett.*, **53**, 1480.

211. Fattinger, C. and Grischkowsky, D. (1989) Terahertz beams. *Appl. Phys. Lett.*, **54**, 490.

212. Uhd Jepsen, P. and Keiding, S.R. (1995) Radiation patterns from lens-coupled terahertz antennas. *Opt. Lett.*, **20**, 807.

213. Uhd Jepsen, P., Jacobsen, R.H., and Keiding, S.R. (1996) Generation and detection of terahertz pulses from biased semiconductor antennas. *J. Opt. Soc. Am. B*, **13**, 2424.

214. Van Rudd, J. and Mittleman, D.M. (2002) Influence of substrate-lens design in terahertz time-domain spectroscopy. *J. Opt. Soc. Am. B*, **19**, 319.

215. Reiten, M.T., Harmon, S.A., and Cheville, R.A. (2003) Terahertz beam propagation measured through three-dimensional amplitude profile determination. *J. Opt. Soc. Am. B*, **20**, 2215.

216. Reiten, M.T. and Cheville, R.A. (2005) Effect of spherical aberration and surface waves on propagation of lens-couples terahertz pulses. *Opt. Lett.*, **30**, 673.

217. Lo, Y.H. and Leonhardt, R. (2008) Aspheric lenses for terahertz imaging. *Opt. Express*, **16**, 15991.

218. Grischkowsky, D., Keiding, S., van Exter, M., and Fattinger, C. (1990) Far-infrared time-domain spectroscopy with terahertz beams of dielectrics and semiconductors. *J. Opt. Soc. Am. B*, **7**, 2006.

219. Fischer, B.M., Walther, M., and Uhd Jepsen, P. (2002) Far-infrared vibrational modes of DNA components studied by terahertz time-domain spectroscopy. *Phys. Med. Biol.*, **47**, 3807.

220. Uhd Jepsen, P. and Fischer, B.M. (2005) Dynamic range in terahertz time-domain transmission and reflection spectroscopy. *Opt. Lett.*, **30**, 29.

221. Rønne, C., Thrane, L., Åstrand, P.-O., Wallqvist, A., Mikkelsen, K.V., and Keiding, S.R. (1997) Investigation of the temperature dependence of dielectric relaxation in liquid water by THz reflection spectroscopy and molecular dynamics simulation. *J. Chem. Phys.*, **107**, 5319.

222. Thrane, L., Jacobsen, R.H., Uhd Jepsen, P., and Keiding, S.R. (1995) THz reflection spectroscopy of liquid water. *Chem. Phys. Lett.*, **240**, 330.

223. Kindt, J.T. and Schmuttenmaer, C.A. (1996) Far-infrared dielectric properties of polar liquids probed by femtosecond terahertz pulse spectroscopy. *J. Phys. Chem.*, **100**, 10373.

224. Kitahara, H., Yagi, T., Mano, K., Takeda, M.W., Kojima, S., and Nishizawa, S. (2005) Dielectric characteristics of water solutions of ethanol in the terahertz region. *J. Korean Phys. Soc.*, **46**, 82.

225. Uhd Jepsen, P., Møller, U., and Merbold, H. (2007) Investigation of aqueous alcohol and sugar solutions with reflection terahertz time-domain spectroscopy. *Opt. Express*, **15**, 717.

226. Møller, U., Cooke, D.G., Tanaka, K., and Uhd Jepsen, P. (2009) Terahertz reflection spectroscopy of Debye relaxation in polar liquids. *J. Opt. Soc. Am. B*, **26**, A113.

227. Markelz, A.G. (2008) Terahertz dielectric sensitivity to biomolecular structure and function. *IEEE J. Select. Top. Quantum Electron.*, **14**, 180.

228. Markelz, A., Whitmire, S., Hillebrecht, J., and Birge, R. (2002) THz time domain spectroscopy of biomolecular conformational modes. *Phys. Med. Biol.*, **47**, 3797.

229. Whitmore, S.E., Wolpert, D., Markelz, A.G., Hillebrecht, J.R., Galan, J., and Birge, R.R. (2003) Protein flexibility and conformational state: a comparison of collective vibrational modes of wild-type and D96N bacteriorhodopsin. *Biophys. J.*, **85**, 1269.

230. Chen, J.-Y., Knab, J.R., Ye, S., He, Y., and Markelz, A.G. (2007) Terahertz dielectric assay of solution phase protein binding. *Appl. Phys. Lett.*, **90**, 243901.

231. Chen, J.-Y., Knab, J.R., Cerne, J., and Markelz, A.G. (2005) Large oxidation dependence observed in terahertz dielectric response for cytochrome c. *Phys. Rev. E*, **72**, 040901.

232. Markelz, A.G., Knab, J.R., Chen, J.Y., and He, Y. (2007) Protein dynamical transition in terahertz dielectric response. *Chem. Phys. Lett.*, **442**, 413.

233. He, Y., Ku, P.I., Knab, J.R., Chen, J.Y., and Markelz, A.G. (2008) Protein dynamical transition does not require protein structure. *Phys. Rev. Lett.*, **101**, 178103.

234. Kim, S.J., Born, B., Havenith, M., and Gruebele, M. (2008) Real-time detection of protein-water dynamics upon protein folding by terahertz absorption spectroscopy. *Angew. Chem. Int. Ed.*, **47**, 6486.

235. Brucherseifer, M., Nagel, M., Haring-Bolivar, P., Kurz, H., Bosserhoff, A., and Büttner, R. (2000) Label-free probing of the binding state of DNA by time-domain terahertz sensing. *Appl. Phys. Lett.*, **77**, 4049.

236. Nagel, M., Haring Bolivar, P., Brucherseifer, M., Kurz, H., Bosserhoff, A., and Büttner, R. (2002) Integrated planar terahertz resonators for femtomolar sensitivity label-free detection of DNA hybridization. *Appl. Opt.*, **41**, 2074.

237. Fischer, B.M., Hoffmann, M., Helm, H., Wilk, R., Rutz, F., Kleine-Ostmann, T., Koch, M., and Uhd Jepsen, P. (2005) Terahertz time-domain spectroscopy and imaging of artificial RNA. *Opt. Express*, **13**, 5205.

238. Boyd, J.E., Briskman, A., Colvin, V.L., and Mittleman, D.M. (2001) Direct observation of terahertz surface modes in nanometer-sized liquid water pools. *Phys. Rev. Lett.*, **87**, 147401.

239. Boyd, J.E., Briskman, A., Sayes, C.M., Mittleman, D., and Colvin, V. (2002) Terahertz vibrational modes of inverse micelles. *J. Phys. Chem. B*, **106**, 6346.

240. Afsar, M.N. and Hasted, J.B. (1977) Measurements of the optical constants of liquid H_2O and D_2O between 6 and 450 cm^{-1}. *J. Opt. Soc. Am.*, **67**, 902.

241. Hirori, H., Nagai, M., and Tanaka, K. (2005) Destructive interference effect on surface plasmon resonance in terahertz attenuated total reflection. *Opt. Express*, **13**, 10801.

242. Nagai, M., Yada, H., Arikawa, T., and Tanaka, K. (2006) Terahertz time-domain attenuated total reflection spectroscopy in water and biological solution. *Int. J. Infrared Millimeter Waves*, **27**, 505.

243. Arikawa, T., Nagai, M., and Tanaka, K. (2008) Characterizing hydration state in solution using terahertz time-domain attenuated total reflection spectroscopy. *Chem. Phys. Lett.*, **457**, 12.

244. Arikawa, T., Nagai, M., and Tanaka, K. (2009) Hydration structures of 2-butoxyethanol monomer and micelle in solution. *Chem. Phys. Lett.*, **477**, 95.

245. Yada, H., Nagai, M., and Tanaka, K. (2008) Origin of the fast relaxation component of water and heavy water revealed by terahertz time-domain attenuated total reflection spectroscopy. *Chem. Phys. Lett.*, **464**, 166.

246. Yada, H., Nagai, M., and Tanaka, K. (2009) The intermolecular stretching vibration mode in water isotopes investigated with broadband terahertz time-domain spectroscopy. *Chem. Phys. Lett.*, **473**, 279.

28
Bioanalytical NMR Spectroscopy

Perttu Permi

28.1
Introduction

Nuclear magnetic resonance (NMR) spectroscopy is likely the most versatile method for the study of biomolecules. The power of NMR originates from the fact that practically every atom with a magnetic nucleus gives rise to an individual signal in the NMR spectrum that carries spatial and temporal information of the local chemical environment of that atom. Solution conditions in high-resolution NMR experiments mimic the natural biological environment and results relate to functional assays.

Proteins, owing to their many biological functions, display versatile phenomena to investigate. In addition, there are spectroscopic reasons in favor of proteins. Proteins, as a class of molecules, give particularly well-dispersed NMR spectra because of rich local diversity in their physical–chemical structures. Proteins can also be obtained using methods of molecular biology, in large quantities enriched uniformly or selectively with ^{13}C and ^{15}N as well as deuterated or specifically reprotonated to make use of a large repertoire of heteronuclear NMR experiments. These are the main reasons why NMR spectroscopy of proteins is highly developed.

Today, NMR spectroscopy is one of the most important experimental techniques for protein structure determination – 15% of new structures published in the protein data bank (PDB) have been solved using NMR. NMR has been found to be especially useful for the studies of small- and medium-sized proteins. The structure determination process can be accomplished within 1–3 months for proteins with $<$180 amino acid residues, provided that a good quality ^{1}H, ^{15}N correlation spectrum can be obtained, which shows a properly folded protein and no sign of aggregation. Recent technological advances such as cryogenically cooled probe heads as well as breakthroughs in NMR methodology, computational methods, data analysis, and sample production have resulted in astonishingly versatile and powerful methods well documented in the original papers, recent reviews [1–7], and textbooks on NMR spectroscopy [8, 9]. Recent progress has demolished many obstacles earlier hindering the studies of larger proteins. To date, the largest systems studied on the amino acid residue scale has been the

Handbook of Spectroscopy, Second Edition. Edited by Günter Gauglitz and David S. Moore.

110 kDa homooctameric *Staphylococcus aureus* 7,8-dihydroneopterin aldolase [10] and the 81.4 kDa *Escherichia coli* malate synthase G (MSG) containing 723 residues [11]. In addition, the number of membrane protein structures solved by solution-state NMR in detergent micelles has been steadily increasing during the past 5 years. It is very likely that molecular complexes with a molecular size approaching 1000 kDa are feasible under certain conditions.

The most important recent innovations in the field of NMR include the introduction of weakly aligned systems [12] and transverse relaxation-optimized spectroscopy (TROSY) [13]. These discoveries have significantly expanded the realm of high-resolution NMR spectroscopy by including new directional and range-independent information and by significantly enlarging the set of molecules amenable to NMR. Many of the NMR methods that were originally developed for proteins have been amended suitably for studies of other classes of molecules, in particular, nucleic acids and carbohydrates.

28.2
Protein Sample

28.2.1
Solubility and Stability

Successful NMR spectroscopy begins from successful sample preparation [14]. Usually, it is very difficult to compensate for a poorly ‘‘behaving’’ molecule by spectroscopic means. Indeed, the preparation of a highly soluble labeled protein sample is often the limiting factor, not the spectroscopy, in the studies of proteins and their complexes by NMR. Problems with samples manifest themselves typically as low signal-to-noise ratio (SNR) or fast transverse relaxation, that is, broad lines or multiple signals. These can be signs of poor solubility, oligomerization, aggregation, conformational isomerism, or perhaps paramagnetic ion impurities, all deleterious to carrying out detailed NMR studies. However, low-quality spectra may also be indicative of interesting phenomenon perhaps itself worthy of an investigation.

There has been a manifold increase in the SNR of NMR over the decades as a result of the progress in instrumentation and methodology. Nevertheless, NMR remains a comparatively insensitive method, owing to minute nuclear magnetic moments, compared with many forms of optical spectroscopy. Therefore, fairly large amounts of material are required for experiments. Even though compounds in a nanogram scale can be detected using special NMR probes, detailed structural studies, for example, determination of three-dimensional structures, need at least a few hundred micromolar protein solutions in few hundred microliter volumes. Proteins, that are obtained by overexpression in bacterial or eukaryote hosts and subsequently purified by affinity, ion exchange or gel filtration, and so on, come in large quantities and are usually sufficiently pure for NMR spectroscopy. Small molecule impurities are easy to detect and often indifferent to heteronuclear NMR spectroscopy, unless occurring in much higher concentrations than the solute of interest or unless they happen to possess a particular activity on the system of interest.

The high solubility of a biomolecule required for NMR cannot be taken for granted. The spectral characteristics might be compromised even without an apparent aggregation seen as weak signals or broad lines. Often it is not obvious if or how unspecific binding or aggregation or oligomerization that leads to increase in rotational correlation times can be avoided. Temperature, pH, and ionic strength are among the easiest parameters to vary in search of appropriate solvent conditions. Knowledge of the protein's properties, such as isoelectric point (pI), acquired during the production and purification may provide valuable clues about the conditions and additives, that is, cosolvents that may improve the spectral appearance. Some of the commonly used cosolvents include surfactants, such as CHAPS, octylglucoside, and SDS; alcohols such as trifluoroethanol; zwitterionic compounds such as glycine and also denaturants such urea and DMSO are sometimes applied. Ligands or inhibitors of enzymes or cofactors of proteins may improve the spectral appearance. Chimeric constructs have also been used to improve the behavior [15]. Nevertheless, it is difficult to take into account all aspects that have an influence on the spectral appearance and suitable conditions are often found after trial and error.

The presence of more than one conformation may give rise to multiple signals or broadened lines due to exchange and may significantly reduce SNR, complicating assignment and interpretation of the spectra. The solvent conditioning may alter the equilibrium toward a single conformation, provided that there is some evidence or even hypothesis of conformational heterogeneity, for example, proline cis–trans isomerism or flexibility in the catalytic site due to the lack of ligand or hinge motions in a multidomain structure may help to understand and eventually to solve the problem of conformational isomerism by protein engineering [16]. Of course, it should be kept in mind not to change the solvent conditions or to engineer the protein to render the original biological question meaningless. Functional assays help to judge the appropriateness of the solvent conditioning or protein engineering. NMR itself, for example, when used to follow reaction kinetics, can be used to assess functional properties.

A stable sample is a necessity for extensive studies, such as the determination of three-dimensional structure, which require several weeks of measurement time.

Bacterial growth, owing to nonsterile conditions, in the sample tube can be largely eliminated by using sodium azide (NaN_3) in 0.02% (w/v). Proteins are also subject to degradation by proteolytic enzymes that may be present in the sample in minute amounts after the purification. Application of a ''cocktail'' of inhibitors against the common proteases eliminates largely the enzymatic breakdown. Exposed cysteine residues not paired in disulfide bonds may with time form intermolecular disulfide bonds generating dimers or higher oligomers depending on the number of exposed cysteins. Dithiothreitol (DTT) in a stoichiometric excess to cysteines can be used to keep *all* cysteins in the reduced state. Alternatively, the unpaired cysteines could be mutated often to serines to avoid the problem of unnatural pairing. Deamidation of asparagine (Asp) over time is a potential problem in certain sequences, but can be avoided by engineering the corresponding sequence.

In practice, it is difficult to take into account or rationalize all aspects that influence the sample solubility and stability. Fortunately, the protein stability and solvent conditions are easy to monitor, in particular, by heteronuclear correlation spectroscopy. Amide resonances are sensitive reporters of changes in the protein structure or in the solvent conditions. Mass spectroscopy that requires very little material is a very practical method to monitor the protein sample. Once optimal conditions are found, experiments should be conducted promptly.

28.2.2
Isotope Labeling

The purpose of isotope labeling is to produce the molecule of interest enriched with isotopes of preferred nuclear magnetic properties in order to extract more information or to facilitate the interpretation of the information and more frequently to make the study feasible in the first place. In many applications, it is advantageous to increase the proportions of ^{13}C and ^{15}N that are both spin-$\frac{1}{2}$ nuclei, from their natural abundance of 1.1% and 0.4% respectively, as high as possible to nearly 100% for the detection. The labels facilitate assignment by multidimensional heteronuclear correlation spectroscopy. In other applications, selective labeling provides means to simplify the interpretation, for example, to distinguish intermolecular correlations from intramolecular signals or segmental labeling [17, 18], for example, to reduce the number of signals.

In large systems, perdeuteration is the efficient way to slow the transverse relaxation [19–22] and specific reprotonation serves to maintain crucial information [23]. The labels allow measurements of dihedral angles via scalar couplings [24] and projection angles via cross-correlation rates [25] as well as internuclear directions via residual dipolar couplings (RDCs) [26]. Furthermore, site-specific spin labels, that is, paramagnetic electrons, can be used to extract long-range distance information [27]. Today, isotope labeling is an integral part of biomolecular NMR spectroscopy [3].

28.2.2.1 ^{13}C and ^{15}N Labeling

Uniform ^{13}C and ^{15}N labeling provides improved signal dispersion and editing by multidimensional experiments or filtering by isotope or spin state as well as various routes for coherence transfer and ways to measure scalar and dipolar couplings. Solvent suppression in heteronuclear correlation experiments is also much easier than in homonuclear correlation experiments. Uniformly labeled proteins are customarily obtained via overexpression in bacteria grown in a culture medium having enriched metabolites as sole sources of carbon and nitrogen. For bacterial expression, ^{13}C-glucose (or ^{13}C-acetate) and ^{15}N-ammonium chloride or sulfate are commercially available and commonly used. The use of the minimal medium easily leads to reduction in growth and to a reduced yield compared to the use of rich medium. The choice of a host strain and vector and at times also the codon usage have to be optimized to reach a yield that is sufficient, given the current price of ^{13}C-glucose. The ^{15}N-compounds are inexpensive and thus can be used for testing much of the performance of the protein. More recently, rich growth media with isotope labels have become commercially available to facilitate the uniform enrichment. To make proteins with posttranslational modifications expression in eukaryote hosts primarily in yeast is reaching sufficient expression levels [28].

For studies of protein complexes, intermolecular correlations can be distinguished from intramolecular correlations by filtered heteronuclear experiments provided that one of the components is labeled selectively and differently from the other. This approach is also useful for large protein complexes to acquire simplified spectra to alleviate the assignment. For the same end, segments of polypeptide chain can selectively be labeled by ^{13}C and ^{15}N using inteins, splicing enzymes [18]. The inteins also provide the way to obtain cyclic peptides with labels that are significantly less expensive than labeled amino acids from the solid-state peptide synthesis.

Nowadays, *E. coli* is the primary organism for production of recombinant, isotopically enriched proteins. *E. coli* cells are easy to handle and by far serve the most economic way of producing uniformly ^{15}N, ^{13}C (^{2}H)-labeled proteins. Conventional labeling strategy, based on NH_4Cl and glucose precursors, yields homogeneously labeled proteins and is a very powerful method leading to high protein yield. Unfortunately, the protein expression in *E coli* has several limitations, for example, the proteolytic degradation of the target protein, the solubility problems, and improper protein folding, as a result of distinct folding machinery and posttranslational modifications between eukaryotics and prokaryotics. Additionally, only proteins that do not interfere with host cell physiology can be produced.

During the past few years, cell-free *in vitro* protein synthesis has become an important protocol in production of isotopically labeled proteins. The commercially available cell-free protein expression systems are based on *E. coli* or wheat germ cell extracts, where the necessary components for protein translational machinery are purified from the aforementioned organisms. Cell-free methods overcome many problems encountered in the protein production in *E. coli* cells. Proper folding of the mammalian protein can be achieved by using the eukaryotic protein translation/folding machinery extracted from wheat germs. Advantages of the cell-free protein production method rise from its open system nature, where components assisting the biosynthesis, folding, and stability of the protein, can be utilized during the protein synthesis. Although uniformly labeled proteins can be expressed in *E. coli* by simple protocols, selective labeling of the proteins is not achieved accurately. Severe scrambling of the isotopes is observed during the expression, due to the metabolism of the living organism. On the contrary, the metabolism of the amino acids the cell-free system is restricted, which enables highly selective labeling of the proteins. In addition, the usage of precursors, such as amino acids with selective isotope labeling, is also very flexible.

In addition, DNA and RNA molecules are, nowadays, obtained with labels from the cell-free synthesis using uniformly labeled ribonucleotide triphosphates (NTPs) [29–32].

28.2.2.2 **Deuteration**

Perdeuteration has become an indispensable means for circumventing problems of transverse relaxation (T_2) inherent to large biomolecules and their complexes [22]. Protons because of their large nuclear magnetic moment are the main cause of dipolar relaxation of protons themselves as well as the directly bound heteronucleus. The relaxation problem can largely be reduced by uniform deuteration. Perdeuterated proteins are obtained by growing host microorganisms in deuterium oxide (D_2O) often concurrently with ^{15}N and/or ^{13}C labeling. The expression levels in D_2O are usually comparable to that in H_2O, but the growth is compromised. When the labeled protein is dissolved in H_2O, the amide deuterons are exchanged for protons, which serve as the main source of magnetization for coherence transfer in heteronuclear correlation experiments, and also for the direct detection of the signal during the acquisition. The high degree of labeling is advantageous to reduce the transverse relaxation of the aliphatic carbons and amide protons in TROSY at high magnetic fields [13, 33]. Obviously, perdeuteration reduces significantly the distance information available via interproton nuclear Overhauser enhancements (NOEs). A compromise between the favorable relaxation properties and the extent of NOE data may be found by adjusting the degree of deuteration with the D_2O content in the culture medium. Suitable degree of random fractional deuteration is often $>50\%$.

Alternatively, an important portion of the conformational restrictive NOEs can be recovered by relabeling for protonated methyl rotors of aliphatic residues [23]. This is accomplished using either selectively labeled amino acids that are more readily incorporated during the expression than *de novo* synthesized amino acids or more affordably by using selectively protonated nonglucose carbon sources. It depends on the metabolism of a particular metabolite how the protons become incorporated in specific positions in the amino acids. The methyl group of pyruvate is a precursor for the methyls of alanine, valine, leucine, and γ rotor of isoleucine. More recently, protonated methyl rotors of valine, leucine, and isoleucine have been derived using α-ketoglutarate. It has been demonstrated that these labeling strategies are sufficient to obtain short-range distance data for determination of three-dimensional structures when the reduced distance information from highly perdeuterated proteins is compensated partly by using the directional restraints and hydrogen bond restrains. More sophisticated labeling strategies are designed to reprotonate $C\alpha$ to be used as the sole source of magnetization for experiments in D_2O.

The TROSY effect is not limited to IS spinning systems only. Substantial improvement in sensitivity and resolution can also be obtained for I_3S spin moieties of methyl groups, provided that one of the methyl groups of Ile$\delta1[^{13}CH_3]$, Leu$[^{13}CH_3/^{12}CD_3]$, and Val$[^{13}CH_3/^{12}CD_3]$ are selectively protonated in an otherwise highly perdeuterated protein [34].

The Stereo-array isotope-labeling (SAIL) scheme is an optimal isotopic labeling method in which cell-free translation system is used for assembling proteins from synthetic stereo-isotope-labeled amino acids [35]. The leading principle is to maximize sensitivity and resolution of protein spectra without losing vital NOE distance information from side chains. This is accomplished by stereospecific labeling of methylene $^{13}CH_2$ and methyl $^{13}CH_3$ moieties with ^{13}CHD and $^{13}CHD_2$ units. One of the prochiral methyl groups in Leu and Val residues is quenched by replacing the $^{13}CH_3$ moiety with $^{12}CD_3$. In addition, six-membered aromatic rings are labeled with alternating $^1H-^{13}C$ and $^2H-^{12}C$ moieties. Advantages of the SAIL labeling are significant. The resolution in NMR spectra is improved because more than 50% of carbon-bound protons are replaced by deuterons. These protons are mainly originating from methylene groups, which, without stereospecific assignment of geminal protons, contribute solely to spectral overlap in uniformly ^{13}C-labeled samples. Additional improvement in both resolution and sensitivity can be obtained through diminished ^1H and ^{13}C transverse relaxation rates and reduced long-range $^1H-^1H$ scalar coupling interactions. Moreover, coherence transfer efficiency can be optimized and improved owing to the absence of heterogeneous spin moieties.

28.2.3
Dilute Liquid Crystals

Perhaps surprisingly, biomolecules as large as proteins tumble in water so stochastically that it is difficult to observe any degree of a molecular alignment [36]. It is only proteins with prosthetic groups of high-magnetic anisotropy susceptibility, such as globins with hemegroups, which acquire a noticeable degree of alignment in isotropic milieu [37]. In general, it is first when molecules are dissolved in a dilute liquid crystal that they assume a minute, but measurable degree of molecular alignment [12]. The molecular alignment arises from the interaction between the molecule of interest and the liquid crystal particles. The steric hindrance, that is, the shape of the molecule, determines the size and direction of alignment [38]. In addition, the surface charges on the biomolecule, the charge texture on the liquid crystalline particle, and the ions or cosolvents in the solution may give a contribution to the size and direction of alignment.

The molecular alignment manifests itself as RDCs and chemical shift anisotropy (CSA) that carry information about directions and molecular shape. The preferred degree of molecular alignment is small on the order of 10^{-3} to retain essentially all characteristics of high-resolution NMR spectra. Otherwise, a full span of dipolar couplings and CSAs would render the spectrum of complex molecule hopelessly uninterpretable. RDCs reveal the directions of internuclear vectors and frequency shifts the directions of the components of CSA tensors [39]. The information content is highly complementary to the torsion angles available from three-bond scalar couplings and to the interproton distances available from NOEs when determining the three-dimensional structure. Furthermore, the anisotropy data implicitly contain information about the molecular shape via simulations [38]. The directional dependence of dipolar couplings and chemical shifts is easy to interpret and to compare with values computed from known three-dimensional structures. In this way, structures and conformational changes and formation of quaternary structures are easy to examine and to analyze without extensive structure determination.

A number of aqueous liquid crystalline media suitable for inducing a weak alignment of biomolecules are known [6]. It should be understood that the choice for a particular liquid crystalline system depends on the properties of the biomolecule, liquid crystalline particles and temperature, ionic strength, and eventual cosolvents. Some of the critical factors affecting the formation of the liquid crystal and the size and direction of the solute alignment may be difficult to anticipate beforehand and preliminary experiments are often required to find a suitable system. Furthermore, the set of aqueous liquid crystals for aligning biomolecules is likely to continue to expand as the search for novel media is currently in progress.

28.2.3.1 **Liquid Crystal Composed of Organic Compounds**

Certain amphiphatic molecules arrange themselves in discoidal-bilayered structures known as *bicelles*. The bicelles have highly anisotropic magnetic susceptibility and thus the property to align themselves in the magnetic field with the plane normal perpendicular to the field [40]. This results in a uniaxial medium suitable for aligning solute molecules. Bicelles can be prepared, for example, from a mixture of (1 : 3) dry dihexanoylphosphatidylcholine and dimyristoylphosphatidylcholine and dissolved in water to a concentration >3% (w/v) [41]. The long-chain lipid is thought to make the bilayer and the short-chain lipid confines and protects the perimeter of the disk. The solubilization is best carried out at low temperature near 0 °C, where the viscosity is low and components mix properly. The liquid crystalline phase is stable in the temperature range of ∼30–50 °C, depending slightly on the exact composition of the medium. The correctly prepared phase should be uniform and transparent. The presence of the liquid crystalline phase is easy to confirm by measuring the deuterium quadrupolar splitting of D_2O or from the shifted phosphor signals of the phosphatidylcholine head groups (Figure 28.1).

The size of the alignment can be tuned by varying the concentration of the liquid crystal, however, above the critical concentration required for the liquid crystalline phase to form [41]. The tuning is a convenient way to adjust the range of RDCs and CSA optimal for the measurements. Provided that the alignment is induced not only exclusively by the molecular shape but also by the electric interactions between the surfaces of the solute and liquid crystal particle, the ionic strength of the solution will influence both the size and the direction of the alignment. This phenomenon can be exploited by ‘‘doping’’ the bicelles with a small amount of charges. In this way, it is possible to create several nonredundant alignments and to collect nonredundant data for the structure determination.

Liquid crystal phases can be prepared, also, by dissolving various polyethylene glycols, referred to as *CmEn compounds* such as C12E5, to water >3% (w/v) [42]. A small amount of short-chain alcohol such as hexanol helps to form the phase by stabilizing the exposed edges of the lamellae. The liquid crystalline phase is found in the temperature range from 30 to 40 °C. However, the actual composition of polyethylene glycol or their mixtures or any of their derivatives may noticeably alter the phase diagram and transition temperatures. The phase transitions to and from

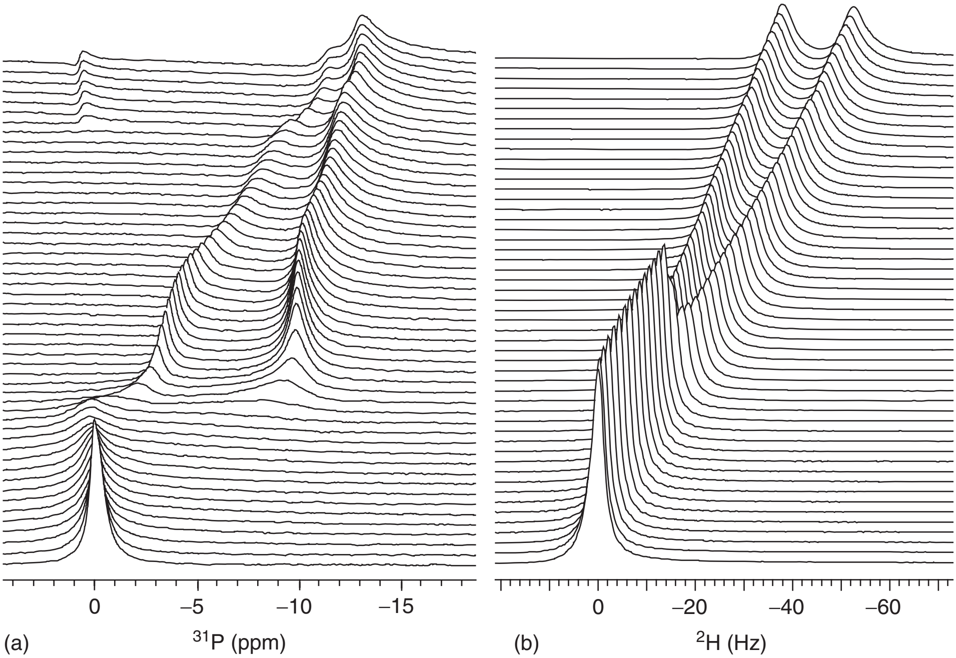

Figure 28.1 Deuterium (a) and phosphorus (b) spectra as a function of temperature of a liquid crystal.

the liquid crystalline phase, again depending on the composition, show hysteresis as a function of temperature. Another lamellar phase can be prepared from cetylpyridinium bromide/hexanol/sodium bromide [43]. The liquid crystalline phase is stable and robust, tolerating different buffer conditions, temperature ranges, and concentrations.

28.2.3.2 Liquid Crystals Prepared from Biological Material

Many particles of biological origin are also suitable for making lyotropic liquid crystals. For example, filamentous phages most notably Pf1, fd, and tobacco mosaic virus (TMV) readily align their long axis along the magnetic field [44–46]. The full degree of alignment of Pf1 is obtained already at modest field strengths, for example, at the field of a 300 MHz NMR spectrometer. The liquid crystalline phase is stable over a wide range of temperatures >5 °C, and it does not depend on the concentration as the phage particles align individually unlike bicelles and lamellae, where a critical concentration has to be exceeded. It is in the nature of the phages to carry high charge on their surfaces. Consequently, electric interactions often play a role in the alignment, in addition, to the molecular shape. The presence of electric contributions can be often deduced by varying the salt concentration. The Pf1 particles are negatively charged and therefore suitable for work with DNA, which is also negatively charged. On the other hand, an attractive Coulombic interaction may lead to an exchange-dominated alignment [47]. Likewise, when using particles of biological origin more specific interactions may come into the play and express themselves readily at very dilute concentrations of liquid crystalline particles as very large dipolar couplings.

The low pI ~4 of Pf1 implies that particle aggregation becomes a problem in acidic conditions. The bacterial phages can be produced in an infected bacterial culture and harvested after cell lysis and purified by precipitation and finally in a salt gradient by an ultracentrifuge.

Fragments of purple membranes (PMs) of *Halobacterium salinarum* align in the magnetic field [48]. The amount of the alignment can be tuned by varying the concentration of PMs and the solute alignment is also affected by salt that screens electric interactions between the negatively charged membranes and solutes. At tens of millimolar concentrations of monovalent ions, however, the PM membranes undergo transition to a gel, where the membrane patches can no longer be oriented with the magnetic field. An order of magnitude lowers the concentration of the divalent salt, which is required for a similar phase transition to gel.

28.2.3.3 **Oriented Matrices**

A cross-linked polyacrylamide gel customarily used in electrophoresis can be compressed or strained to bring about an oriented medium suitable for weakly aligning biomolecules [49]. The oriented matrix is robust, that is, insensitive to the solvent conditions, such pH, temperature, and cosolvents, which makes it suitable medium to study, for example, denatured proteins. Furthermore, the matrix is expected to be insensitive to the surface charge of the biomolecule. The direction of the medium is determined by the direction of the strain, not by the magnetic field, which opens possibilities to acquire data of a sample in different orientations with respect to the magnetic field. The main disadvantage of the polymeric systems is that the solute molecule has to be included in the solution before the polymerization or driven to the matrix by electrophoresis or diffusion.

Oriented matrices can also be prepared from the liquid crystal composed of membranes and bacterial phages by the polymerization to the acrylamide gel. The resulting "frozen" medium is no longer a liquid crystal, but an oriented matrix whose director is independent of the magnetic field.

28.3
Proton NMR Experiments

The large magnetic moment of proton, a spin-½ particle, and its high natural abundance are the reasons for the historical predominance of ^{1}H NMR spectroscopy. There are numerous homonuclear ^{1}H experiments, however, and some of them have proved to be most applicable to biomolecular NMR spectroscopy and are mentioned here. The emphasis is on the principles of the experiments, their processing, and information content. The reader is encouraged to consult textbooks (8 and 9) for the proper description of the experiments using the appropriate nomenclature that is not possible to introduce in this context. Furthermore, directions for operating an NMR spectrometer and procedures for setting up experiments including calibrations are usually found in textbooks or spectrometer manuals and are not discussed in this context.

In general, all present day pulse sequences employ pulsed field gradients (PFGs) for selection of desired coherences and/or for removal of artifacts. Furthermore, phase-sensitive experiments are preferred over their magnitude mode counterparts as a result of the superior resolution and possibilities to analyze the multiplet patterns for coupling constants. For the quadrature detection, the States-TPPI protocol [50] is often the most advantageous to displace artifacts to the edges of spectra. For small proteins and peptides and for many other biomolecules, the basic proton correlation experiments are the most practical and require no isotope labeling. Many of the elements of the basic proton correlation experiments are also embedded in many heteronuclear experiments.

28.3.1
One-Dimensional NMR Experiment

Customarily, studies of a biomolecule by NMR spectroscopy will begin by recording a one-dimensional (1D) proton spectrum. The 1D spectrum allows consideration of the SNR for further studies. Signals must be easily visible above the noise from a spectrum acquired by averaging 32 scans or preferably less for two-dimensional correlation experiments to be feasible (Figure 28.2). For equimolar concentrations, larger proteins have lower apparent SNR because of their larger linewidths compared to those of smaller proteins and peptides.

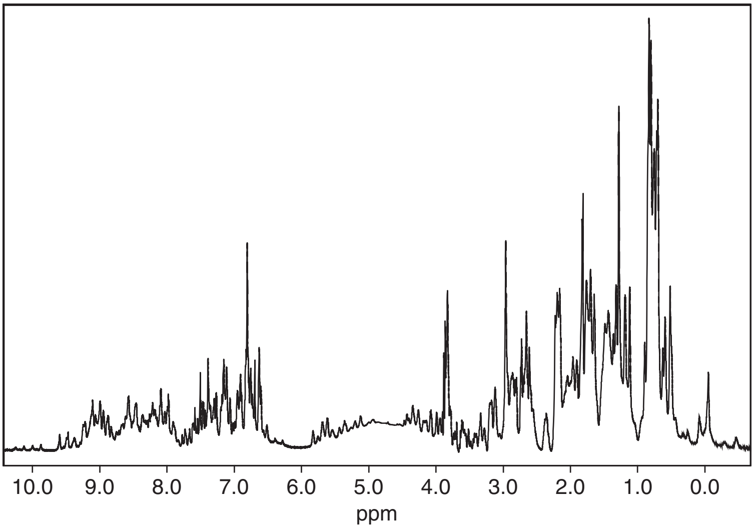

Figure 28.2 One-dimensional spectrum of a 3 mM human SH3 domain of TEC protein dissolved in H_2O/D_2O.

One-dimensional spectra of peptides and small proteins usually permit to judge from the linewidths, if aggregation or exchange processes are likely to compromise the performance. For larger proteins, in particular, it may be difficult to find sufficiently isolated signals in the 1D spectrum to measure linewidths. Furthermore, the proton linewidths of a large protein may not be adequate to evaluate feasibility of further experiments. Feasibility of larger proteins for NMR studies is better judged on the basis of heteronuclear experiments and at least an ^{15}N-labeled sample is required.

The overall dispersion of the signals seen in 1D is an important attribute of the structural characteristics of a protein. Well-structured proteins display signals over large spectral regions, in particular, the chemical shift dispersion in amide, alpha, and methyl proton resonance regions is indicative of the structure. On the contrary, resonances of unstructured or unfolded proteins lump together and have values similar to those found in short (random-coil) peptides. For example, amide proton dispersion in an unfolded protein is about four to five times smaller than in a well-folded protein of a similar size. One dimension can be used to monitor various effects, such as pH, temperature, ionic strength, or cosolvents on SNR and dispersion of signals, or on stability of a protein. It is also possible to estimate structural integrity of protein mutants with respect to wild-type proteins. So-called water-suppressed longitudinal encode decode (water-sLED) sequence [51] with its various variants is a powerful tool for studying translational diffusion and hydrodynamic radii of macromolecules and hence, aggregation state as well as folding/unfolding of proteins in solution [52]. Furthermore, one-dimensional, relaxation- and diffusion-edited proton NMR can also be used for screening of small molecule ligands that bind to a target [53]. The rate of diffusion of a small molecule is much higher than that of a macromolecule, for example, protein. A molecule that binds to a target protein can be readily identified from a cocktail of small molecules by recording 1D diffusion-edited spectra from a cocktail with and without a target protein. Subtracting these two spectra from each other reveals only signals whose rate of diffusion have changed on binding to a slowly diffusing target protein.

However, when using nondeuterated cosolvents the solvent signal suppression may become problematic. Owing to the high concentration of water, it is necessary to record the 1D proton spectrum using solvent suppression. The same applies to other nondeuterated solvents. There are various ways to reduce the solvent lines to a level comparable to the signals of the solute to utilize the full dynamic range of the detection of the NMR spectrometer. Saturation of the water line by selective radiation during the recycle delay is a simple, effective, and robust method. Therefore, the presaturation method is commonly in use. The main disadvantage of the method is that the solute signals near the solvent signals are also easily saturated to complicate the assignment. Even a partial saturation will compromise the quantitative spectroscopy. In addition, the exchangeable protons such as amide protons are subject to the saturation transfer that diminishes their signal intensity.

More selective schemes for solvent suppression employ selective pulses, spin-lock purge pulses, and field gradient pulses. Some of these methods aim to saturate the water signal in milliseconds rather than during the recycle delay, while others are designed to maintain the water magnetization in equilibrium. To destroy the water magnetization, selective pulses are used to generate orthogonal components for the solvent and solute magnetizations and subsequently to destroy the solvent signal by rf inhomogeneity or to dephase the solvent coherence by PFGs. To place the water magnetization along z-axis during the acquisition, selective pulses or binomial sequences are employed for selective excitation and PFGs are used to destroy any residual transverse magnetization caused by pulse imperfections [54]. In this way, radiation damping is largely avoided and also noticeable gains in the signal intensity of exchangeable protons are obtained. Although sensitivity loss by saturation transfer from water protons to labile amide protons is drastically diminished when PFGs are used for dephasing of water magnetization, significant sensitivity gain can be obtained by minimizing saturation of water magnetization. To this end, the so-called water flip-back procedure is employed, that is, water magnetization is turned back to positive z-axis before acquisition. This approach has now routinely been applied in protein NMR also in case of more complicated pulse sequences. A very recent innovation dubbed *selective optimized flip-angle short-transient heteronuclear multiple-quantum coherence* (*SOFAST-HMQC*) prevents excitation of water magnetization, which dramatically shortens longitudinal T_1 relaxation time of amide protons enabling the use of much faster repetition rates in NMR experiments (Section 28.5.4).

Post-acquisition methods are used to improve the *appearance* of the spectrum. The filtering of the low-frequency components by convolution is one of the most widely used methods to suppress the residual solvent signal [55]. The filtered dataset is constructed by subtracting the data ‘‘smeared’’ by the filter function from the original FID (Figure 28.2). If the solvent signal is away from the carrier frequency, that is, high-frequency components are to be removed, then the original data are initially digitally frequency shifted to zero by multiplication with an exponential function and subsequently filtered and finally restored to the original position by multiplication by the complex conjugate of the exponential function. A flat baseline is obviously an important merit of a spectrum of any dimensionality. There are various reasons for a poor baseline. The baseline will have an offset and curvature, if the signal phase at the beginning of the acquisition period or the indirect dimension is not a multiple of 90°, and if the sampling delay is not adjusted to zero, that is, $t_0 = 1$, or to the inverse of twice of the spectral width, that is, $t_0 = 1/(2 \times \mathrm{sw})$. The Hahn echo can be used to adjust the initial sampling delay for the acquisition dimension.

For the indirect dimensions in two- or higher-dimensional spectra, the phase evolution during, for example, off-resonance pulses and mixing periods must be taken into account to set the initial sampling delay correctly. The baseline distortions may also result from corrupted data points at the beginning of the acquisition period. These can be corrected by reconstruction of the initial points by a backward linear prediction. A receiver gain that is too high compared with the dynamic range of the analog-digital converter (ADC) will result in signals with ‘‘wiggles.’’ In addition, a finite rise time of audio filters may cause a baseline roll.

In modern spectrometers, this is circumvented by oversampling, that is, by using a sampling signal with the maximal frequency of the ADC and reconstructing the signal mathematically afterwards for processing.

28.3.2
Correlation Experiments

The principle purpose of correlation experiments is to establish a one-to-one mapping from the signal to its source, that is, to the particular atomic nucleus in the molecule. This assignment task involves identification of the members in the coupling network, referred to as the *spin system*. In addition, correlation experiments as such or with modifications are suitable for measurements of scalar and dipolar couplings.

Correlation in the two dimensions is the most natural dimensionality because the spin–spin interactions are pairwise. Three-dimensional or experiments of higher dimensionality are constructed from concatenated two-dimensional (2D) experiments. Homonuclear three-dimensional experiments, such as TOCSY-NOESY (total correlation spectroscopy-nuclear Overhauser enhancement spectroscopy), are not considered here because in many cases the multidimensional heteronuclear experiments are superior.

For all homonuclear experiments, there are certain common guidelines to follow. When preparing a correlation experiment, it is the expected lineshapes and widths that determine the lengths of acquisition and indirect dimension and the processing. Narrow in-phase lines allow considerable degree of freedom for the setup of experiments, whereas broad antiphase lines are the most difficult. The repetition rate of the acquisition for signal averaging should be adjusted properly to reach optimal SNR or to obtain quantitative spectra.

28.3.2.1 **COSY-Type Experiments**

Correlated spectroscopy (COSY) is the first 2D NMR experiment realized [56, 57] and it is still among the most useful NMR experiments. COSY generates cross peaks in the 2D spectrum at the intersection of resonances of coupled spins (Figure 28.3). In proteins, cross peaks are observed for geminal protons, that is, over two bonds, and vicinal protons, that is, over three bonds, and in small peptides, couplings over four bonds may also be detected. Thus, the COSY spectrum allows the identification of spin systems for the assignment.

However, apart from peptides, the overlap and degeneracy in chemical shifts is likely to prevent obtaining entire spin systems exclusively from the COSY spectrum, for which additional experiments are required.

The COSY spectrum also provides information about the coupling constants in the fine structures of cross peaks. The value of the three-bond scalar coupling is related to the torsion angle via the Karplus equation [58] and knowledge of the couplings together with NOEs provides stereospecific assignment. The coupling can be determined from the frequency separation of the antiphase absorptive doublet. For two-coupled spins, that is, without a passive coupling partner such

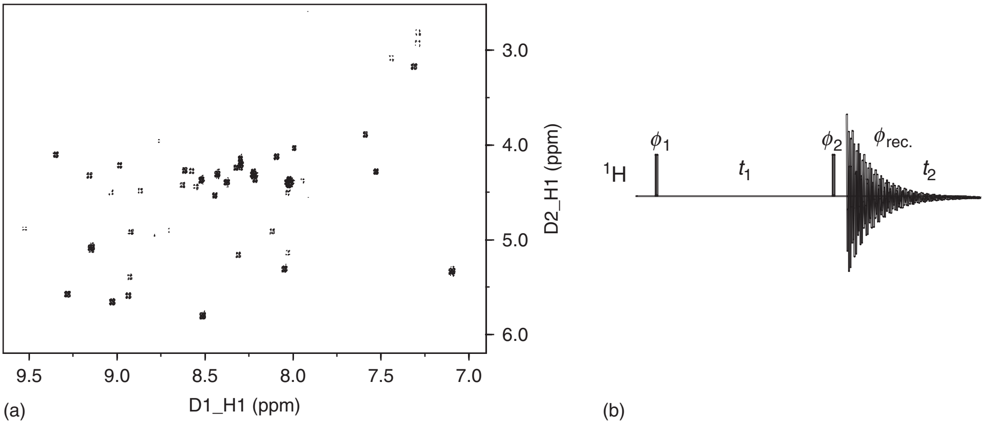

Figure 28.3 (a,b) COSY spectrum of a 1 mM SH3 sample in H_2O/D_2O (90/10 v/v).

as the ^3JHNHα of residues other than glycines (that have two Hα) the lobes of the cross peak are separated along the directly observed direction by the coupling constant. However, if the linewidth increase is comparable to the coupling constant or even larger, the positive and negative lobes of the antiphase line began to cancel each other more and more, thereby increasing the apparent separation of the multiplet components. This aberration from the true coupling value has to be taken into account when measuring coupling constants. Analyses of the antiphase lines for extracting the true separation of the multiplet components require that the spectrum to be processed to maintain Lorentzian lineshapes. In practice, when the linewidth is twice as large as the coupling constant or more, it is difficult to obtain accurate values. Therefore, scalar coupling constants are preferably measured by heteronuclear experiments. Owing to the self-cancellation of the broad antiphase lines, the sensitivity of the experiment also decreases with increasing molecular weight. COSY is, otherwise, among the most sensitive experiments for peptides and small proteins.

The COSY pulse sequence is very simple, consisting of the recycle delay, the first 90° pulse succeeded by the incremental delay t_1, and the other 90° pulse followed by the acquisition period t_2 (Figure 28.3). The phases of the pulses and the receiver are cycled according to CYCLOPS and axial peaks are suppressed by inverting the phases of the first pulse and receiver. The residual axial peaks are moved to the edges of the spectrum by the States-TPPI protocol. A product operator analysis shows that the cross peak has an antiphase lineshape and that the diagonal peak differs by 90° and thus cannot be phased simultaneously for absorption. The nature of the antiphase lines requires that the data in the indirect dimension t_1 are collected for a sufficiently long time, at least longer than $1/(4J)$, otherwise the signal intensity is reduced because of self-cancellation of the antiphase lines. For the measurement of couplings, the acquisition dimension t_2 can well be longer than $1/(2J)$ as the recycle delay can be shortened correspondingly. The COSY spectra are customarily processed for resolution using sine bell weight functions.

The analysis of coupling constants requires that the F_2 slices have been adequately zero filled, for example, to about 0.5 Hz per point.

There are a number of variant COSY experiments and extensions to COSY. One of the main goals of the descendants has been to remove the dispersive tails of the diagonal peaks that may obscure the near-diagonal cross peaks. The double-quantum filtered (2QF) COSY experiment [59] also yields a spectrum with absorptive antiphase lines for the diagonal peaks of the coupled spins and the attenuated diagonal resonance of the uncoupled spins. The drawback of 2QF-COSY over COSY is the twofold decrease in sensitivity. In addition, the total acquisition time for a concentrated sample may become long because of the longer phase cycle. The PCOSY experiment is designed for the same purpose as 2QF-COSY, but offers greater sensitivity.

E-COSY is an abbreviation for methods to generate coupling patterns exclusively with the active components. The fine structure of the E-COSY cross peak is a superposition of two-quantum (2Q) and three-quantum (3Q) COSY peaks so that the two components that stem from the passive couplings cancel each other to leave a simplified coupling pattern. The active coupling can be measured directly from the antiphase separation on either of the multiplets as usual and the passive couplings can be measured from the displacements of the two antiphase multiplets. Importantly, the method will not be subject to the errors as a result of finite linewidths. Furthermore, the E-COSY experiment serves to determine the relative sign of the passive couplings. The same principle is used in heteronuclear experiments. The pre-TOCSY COSY experiment aims to recover resonances attenuated by the solvent presaturation. The mixing sequence before the first 90° pulse serves to transfer the magnetization to Hα that are near the irradiated water line.

Relayed COSY [60] is a straightforward extension to COSY. An additional coherence transfer delay is inserted in the pulse sequence before the acquisition period with the purpose of relaying coherence from the second spin further to a third spin. This will result in a spectrum with a cross peak between the first and the third spin even if they are not directly coupled, but only via the second spin. The chemical shifts are monitored before, that is, t_1, and after, that is, t_2, the coherence transfer steps. The mixing time for the second coherence transfer depends, of course, on the couplings; for proteins, the delay from 20 to 40 ms usually makes a good compromise between transfer efficiency and relaxation losses. There is no new information compared to COSY, however, in the case of degenerate shifts; R-COSY provides means to assess if the spins belong to the same spin system. The acquisition and processing of R-COSY is similar to that of COSY.

28.3.2.2 **Multiple-Quantum Spectroscopy**

Multiple-quantum (MQ) spectroscopies offer complementary information to COSY to elucidate scalar coupling networks [61]. The multiple-quantum transitions are observed indirectly during t_1. A 2Q experiment is commonly used to circumvent problems in COSY due to diagonal peaks, self-cancellation of signals, and solvent suppression.

The idea is to generate the 2Q coherence that evolves with the frequency sum of the chemical shifts $\Omega_1 + \Omega_2$ of two coupled spins I_1 and I_2. The active coupling J_{12} will not evolve during t_1. During the acquisition, cross peaks appear along F_2 at frequencies of Ω_1 and Ω_2 with the absorptive antiphase splittings corresponding to J_{12} and along F_1 at a frequency of $\Omega_1 + \Omega_2$ with absorptive in-phase lineshape along with a dispersive antiphase component that add constructively. These cross peaks are referred to as *direct peaks*. In addition, three-spin coherences that originate from the J_{12} and J_{13} couplings and from the J_{13} and J_{23} couplings become observable and result in cross peaks along F_2 at frequencies of Ω_3 and along F_1 at frequencies of $\Omega_1 + \Omega_2$. These cross peaks with double antiphase dispersive nature along F_2 and with dispersive antiphase and absorptive in-phase components along F_1 are referred to as *remote peaks*. In general, the direct and remote peaks can be distinguished from each other by the opposite lineshape along F_2. Considering the lineshapes, the acquisition and processing parameters along t_2 are similar to those used in COSY, whereas along the indirect dimension t_1 it is not necessary to collect data extensively and cosine apodization is appropriate.

28.3.2.3 **Total Correlation Spectroscopy**

TOCSY, also known as the homonuclear Hartmann–Hahn (HOHAHA) experiment, provides all relayed connectivities within a spin system [62, 63]. The primary intention in TOCSY as in other relayed experiments is to establish connectivities in less-crowded spectral regions to facilitate the assignment of spin systems.

The key idea in TOCSY is to transfer in-phase magnetization from spin to spin throughout the spin system by an isotropic mixing sequence rather than to rely on transferring antiphase coherence during free precession periods. During the mixing sequence, the system is governed by the strong coupling Hamiltonian. The intensity of a cross peak will depend on the topology of the spin system, that is, the ways spins are coupled, the various coupling constants, and properties of the mixing sequence. There are several mixing sequences. The DIPSI-2 sequence [64] is better than WALTZ-16 or MLEV-17 when relaxation is neglected. The actual performance of a mixing sequence over the others depends on the implementation and accuracy of calibrations.

Dipolar couplings during the mixing period may give rise to the rotating-frame Overhauser effect (ROE). Attenuation of the in-phase TOCSY peaks due to the ROE peaks of opposite sign can be particularly important for larger proteins, but can be largely eliminated by interrupting the mixing train so that laboratory-frame NOEs with opposite sign to ROEs can develop to cancel each other. These sequences are referred to as *clean TOCSY*. Furthermore, adiabatic mixing sequences (WURST-8) [65] have low sensitivity to RF field inhomogeneity and miscalibration of the field strength. The sensitivity-enhanced TOCSY pulse sequence retains two orthogonal components of magnetization for postacquisition reconstruction of the spectrum to achieve a gain of $\sqrt{2}$ in SNR (Figure 28.4).

The evolution during the indirect dimension and acquisition are not constrained by the scalar couplings because the peaks in TOCSY are mostly in-phase and only resolution should be considered both when setting the acquisition and indirect

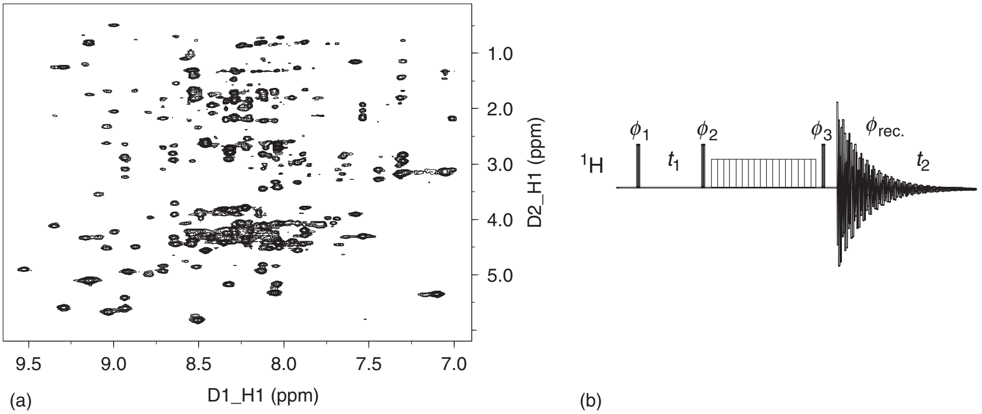

Figure 28.4 (a,b) TOCSY spectrum of a 1 mM SH3 sample in H_2O/D_2O (90/10 v/v).

dimensions and weight functions in processing. It is seldom worthwhile to collect t_1 longer than $1.5 \times T_2$, where T_2 is the transverse relaxation time. The length of the isotropic mixing sequence is subject to two opposing conditions. On one hand, a long mixing sequence is preferred to obtain a correlation between the spins at the opposite ends of the network and, on the other hand, all correlations are preferably observed. These constraints are difficult to meet simultaneously and therefore usually two or more TOCSY spectra with mixing times from 30 to 120 ms depending on the relaxation are collected. The interpretation of TOCSY is subject primarily to two concerns. As the experiment provides correlations along the network of spins, it may remain uncertain which nucleus in the spin system gives rise to which signal, in particular, when chemical shifts are not unambiguous. The other concern is that cross peaks may not always be observed because of the intensity variation of the signal as a function of the mixing time.

Furthermore, if TOCSY is used to estimate coupling constants it must be kept in mind that the signal intensity depends on *all* couplings in the spin system. Short mixing times transfer mostly via a single scalar coupling and are more reliable for coupling constant measurements.

28.3.3
Cross-Relaxation Experiments

The elucidation of the scalar coupling network by the correlation experiments is, apart from small molecules, not enough for the unambiguous, sequential, and stereospecific assignment. The complementary information of spatially adjacent protons is obtained via cross-relaxation experiments, the laboratory-frame NOESY, and the rotating-frame nuclear Overhauser effect spectroscopy (ROESY). These experiments also provide the distance restraints for the structure determination and help to recognize exchange processes.

28.3.3.1 Nuclear Overhauser Enhancement Spectroscopy

The NOESY experiment is composed of the frequency-labeling part, that is, t_1 flanked by two 90° pulses, ensued by the magnetization transfer via dipolar couplings during the mixing period τ_m before the read pulse for the acquisition t_2 (Figure 28.5). During the mixing period, relaxation processes govern the longitudinal magnetization. The autorelaxation results in the diagonal peak and the cross-relaxation results in the cross peaks in the NOESY spectrum. Both peaks are absorptive in-phase in both dimensions. The phase cycling will remove coherences higher than zero.

Consequently, in addition to the longitudinal magnetization, the cross peak may have an undesirable zero-quantum contribution. The zero-quantum peak is antiphase in both dimensions just as a COSY peak, but dispersive with respect to the NOE peaks. The intensity of the zero-quantum peak depends on the chemical shift difference of the spins in question and the mixing time. Furthermore, the transverse zero-quantum term relaxes during the mixing period faster than the desirable longitudinal magnetization.

Therefore, the zero-quantum artifacts are usually observed when the mixing time is short, but can further be suppressed by varying the length of the mixing time, a procedure known as *z-filtration*. However, for short mixing times it may be difficult to vary the mixing time enough without introducing problems in the interpretation due to the averaging.

When setting the NOESY experiment, it is worthwhile to make sure that the baseline is flat and the total measuring time will yield adequate SNR. The recycle delay should be $3 \times T_1$, where T_1 is the longitudinal relaxation time, otherwise the intensity of the cross peaks can be affected by the steady-state conditions. The length of the mixing time is subject to contradictory demands. A long mixing time, on the order of T_1, will give high intensities for the cross peaks and have small zero-quantum artifacts. On the other hand, multiple magnetization transfers, referred to as *spin diffusion*, will affect the intensity and obscure the interpretation.

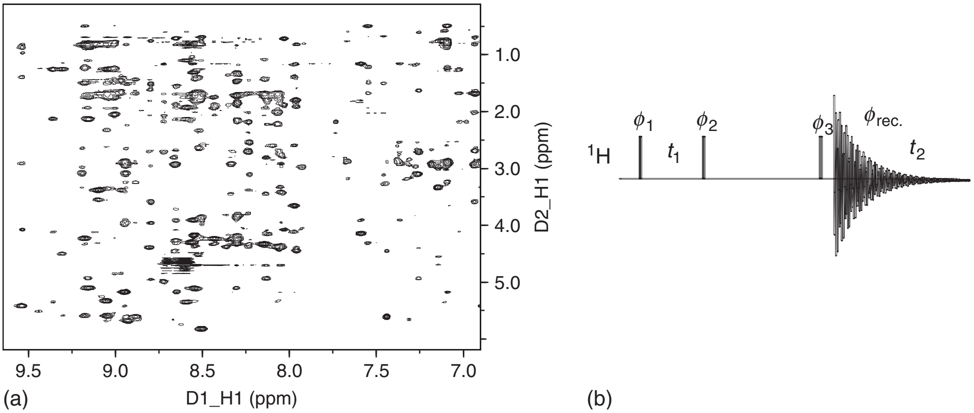

Figure 28.5 (a,b) NOESY spectrum of a 1 mM SH3 sample in H_2O/D_2O (90/10 v/v).

Therefore, a compromise depending on the size of the protein has to be made or a series of NOE spectra is to be collected for more precise calibration of intensities to distances. For large proteins, the dipolar relaxation is effective and short mixing times are appropriate, whereas for small proteins or peptides longer mixing times are required. Furthermore, the cross-relaxation rate constant depends on the rotational correlation time and changes its sign at short correlation times, thereby making the observation of NOEs for small molecules difficult unless there is a freedom to change temperature so as to affect the rotational correlation time. For proper integration of the cross peaks during processing, window functions for the resolution enhancement are to be applied with a caution because signals differing in their linewidths will then not retain relative intensities.

Otherwise, the in-phase absorptive peaks allow considerable freedom for choosing lengths of acquisition and indirect dimensions and their apodization. Chemical exchange, not too slow compared with the mixing time, can result in cross peaks in the NOESY spectrum. The chemical exchange peaks are hard to distinguish from the NOE peaks, but they have a different sign from the ROE peaks. Furthermore, coupled exchange and spin diffusion can result in complicated spectra.

28.3.3.2 **Rotating-Frame Nuclear Overhauser Effect Spectroscopy**

The ROESY experiment [66, 67] follows the cross relaxation in the rotating frame that is established by locking the spins with a train of rf pulses. During the spin lock any components of magnetization orthogonal to the rf field are dephased by the inhomogeneity of the rf field. The longitudinal magnetization is governed by rotating-frame relaxation rates. The rotating-frame cross-relaxation rate constant is positive for all correlation times, which makes ROESY particularly, suitable for studies of small peptides. The ROESY cross peaks depend, in addition, on the resonance offset from the carrier. The offset dependence appears as phase error along F_1 and F_2, which can be removed during processing. However, the intensity of cross peaks for the off-resonance spins will have an opposing NOE contribution in addition to that by ROE. The offset dependence has to be taken into account in quantitative analysis of the cross-peak intensities. The ROE mixing time is usually kept shorter than the corresponding NOE mixing time because the ROE buildup is twice as fast as the NOE buildup. The in-phase absorptive cross peaks and diagonal peaks, but of opposing sign to each other, allow considerable freedom in setting the parameters for the acquisition and indirectly detected dimensions and their processing.

The ROE experiment is potentially subject to artifacts rising from isotropic mixing. The TOCSY transfer will reduce the intensity of the ROE cross peak and obscure the quantification. In particular, consequent TOCSY and ROE transfers have the same sign as the authentic ROE peaks and may easily be misinterpreted. Therefore, as long as the long spinlock is not sufficiently strong to match the Hartmann–Hahn condition, there is need to watch only for artifacts for those spins that have closely similar chemical shifts or shifts that are placed on opposite sides with respect to the carrier. Eventual artifact-related problems can be noticed by taking spectra with different carrier positions and varying the strength of the spinlock.

Contrary to the NOE experiment, the cross peaks of the ROE experiment are of opposite sign with respect to the chemical exchange peaks. This is a particularly valuable property in studies of complex formation where peaks rise both from cross relaxation and chemical exchange. Furthermore, the assignment of stereospecific restraints to the methylene protons that are often subject to spin diffusion can be facilitated by the ROESY measurement. The ROE cross peaks that stem from the relayed transfer have opposite sign with respect to the direct transfer and thus the methylene ROE signals do not tend to have equal values.

28.3.4
Heteronuclear NMR Experiments

Heteronuclear NMR experiments have many virtues over the homonuclear ^{1}H experiments when labeled samples are available for the measurements. It is for the high-molecular-weight proteins and protein complexes that the heteronuclear experiments are imperative. Compared with homonuclear experiments, heteronuclear methods provide improved resolution via increased dimensionality, editing and filtering possibilities, and various ways for coherence transfer and measurement of scalar and dipolar couplings to increase the information content. It is in the nature of amino acids in folded proteins to contain distinguishable nuclei that are coupled to each other with various strengths of couplings that lays the foundation for the rich repertoire of heteronuclear experiments. Furthermore, relaxation measurements of ^{15}N and also ^{13}C are much more amenable to interpretation than those of protons. Today, heteronuclear experiments are indispensable for biomolecular NMR spectroscopy.

28.3.4.1 Basic Heteronuclear Correlation Experiments

Many heteronuclear multidimensional correlation experiments appear superficially complicated, but actually comprise simple building blocks for coherence transfer and for recording chemical shift and/or coupling evolution. These basic elements are simple and robust. The usual protocol begins by transferring proton magnetization to the heteronucleus, that is, ^{15}N or ^{13}C, which is subject to further actions, and finally the coherence is returned to the proton for detection. This indirect detection scheme is superior in sensitivity over direct methods because of the proton's large gyromagnetic ratio and favorable relaxation properties. The most frequently used experiments are the heteronuclear multiple-quantum coherence (HMQC) [68, 69] and heteronuclear single-quantum coherence (HSQC) experiments [70] More recently, it was discovered that significant gains in SNR for large proteins at high magnetic fields is obtained by selecting particular multiple components for the detection to result in TROSY [13]. Polarization transfer in high-molecular-weight systems has been further improved by designing novel pulse-sequence elements such as CRIPT and CRINEPT, which utilize elevated cross-correlation rates for magnetization transfer [71].

28.3.4.1.1 **Heteronuclear Multiple-Quantum Coherence** The HMQC experiment begins with a coherence transfer from a proton to the heteronucleus during a delay matched to $2\tau = 1/(2J)$, $J\mathrm{HN} = 94$ Hz, and $J\mathrm{HC}\alpha = 140$ Hz, to result in a MQ coherence that evolves during t_1. The heteronuclear coupling is not active under MQ coherence during t_1, but the ^{1}H chemical shift evolution must be refocused by a 180° proton pulse. The MQ coherence is transferred to the proton for detection. Before the acquisition, antiphase dispersive components can be purged by a 90° proton pulse. During the acquisition t_2, heteronuclear decoupling is employed. Homonuclear scalar couplings during the coherence transfer periods will cause a phase error along F_1. The size of the error is fairly small, but it depends on the size of the coupling and cannot be simply compensated. The HMQC experiment is very simple with only few pulses and it is therefore a favored building block in more complicated experiments.

28.3.4.1.2 **Heteronuclear Single-Quantum Coherence** The HSQC experiment (Figure 28.6) is based on the INEPT (insensitive nuclei enhanced by polarization transfer) sequence [72], which converts proton magnetization to the antiphase single-quantum (SQ) coherence that evolves during t_1. The scalar coupling evolution is refocused by a 180° proton pulse or decoupled. Homonuclear scalar couplings do not contribute to the lineshape along F_1. The reverse transfer from the heteronucleus to the proton is analogous. Homonuclear scalar couplings during the coherence transfer periods will affect the amplitude of the peak and cause an antiphase dispersive contribution along F_1, which can be purged by a 90° proton pulse just before the acquisition. During the acquisition t_2, the heteronucleus is decoupled.

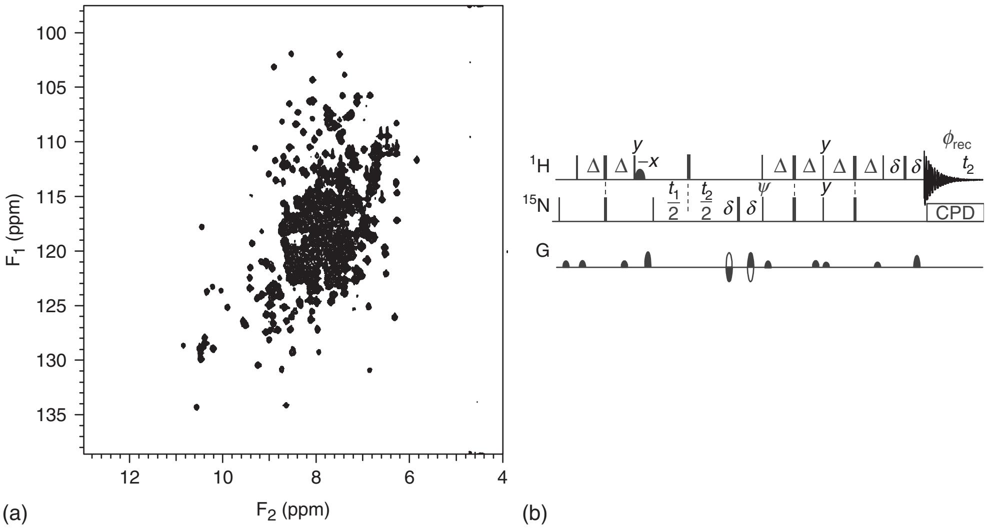

Figure 28.6 (a,b) ^{1}H–^{15}N HSQC spectrum of a 1 mM maltose-binding protein in complex with beta-cyclodextrin in H_2O/D_2O (93/7 v/v).

The decoupled HSQC experiment employs the refocused INEPT sequence to generate an in-phase SQ coherence that is desirable, for example, for measurements of heteronuclear relaxation rates. The transfer function of the refocused INEPT depends on the proton multiplicity, that is, the number of protons bound to the heteronucleus. This can be used to edit the spectrum or when an overall maximal transfer efficiency is required, $2\tau = 1/(3J)$ makes a good compromise. The constant time (CT) HSQC has an evolution period $t_1 = \mathrm{CT}$ fixed in length. This brings in two advantages. The homonuclear couplings do not modulate the signal during t_1 and consequently there is no homonuclear multiplet structure along F_1. This is particularly useful for fully ^{13}C-enriched samples to remove the ^{13}C–^{13}C couplings of aliphatic carbons that cannot be selectively decoupled. The other advantage is the narrow lines. The linewidth along the indirect dimension does not depend on the transverse relaxation rate, but is mainly determined by the window function used for processing. The transverse relaxation rate appears as only a constant factor that scales the intensity. The optimum trade-off between intensity and resolution depends on each particular case. Another favorable feature of the experiment is that when the CT delay is set to $1/(J_{\mathrm{CC}})$, the sign of the emerging signal depends on the number of adjacent carbons owing to the $\cos^n(\pi J_{\mathrm{CC}}\mathrm{CT})$ modulation ($n =$ number of carbons). Therefore, carbons that have an odd number of directly bound aliphatic carbons are in opposite phase with respect to the carbons having an even number of adjacent carbons. The CT scheme can also be implemented into a number of sophisticated triple-resonance experiments to facilitate the protein side-chain assignment procedure.

28.3.4.1.3 **Transverse Relaxation-Optimized Spectroscopy** At high-magnetic field strengths the CSA interaction of ^{15}N is a comparable source of relaxation as the dipole–dipole (DD) interaction. The same is true for the amide proton CSA and DD. Therefore, the four multiplet components of the amide spin pair have different relaxation rates depending on whether the DD and CSA mechanism interfere constructively or destructively. When other sources of relaxation such as those due to remote protons are negligible, the differential relaxation effect on the multiplet components is large and also in practice attainable at high magnetic fields for large perdeuterated proteins. It is the most slowly relaxing multiplet component that is of a particular interest and it is possible to filter away the other multiplet components for spectral simplification. This is the essence of the TROSY [13]. The resulting spectrum is superior to an HSQC experiment under the aforementioned conditions. The pulse sequence resembles superficially that of the sensitivity-enhanced HSQC. Obviously, neither proton during t_1 nor ^{15}N during the acquisition t_2 should be decoupled to maintain the multiplet components. It is the latter part of the pulse sequence used for the reverse transfer from ^{15}N to ^{1}H including the gradient selection that chooses the most slowly relaxing multiplet component for detection (Figure 28.7).

The intensity of TROSY component can be further boosted by sensitivity enhancement and more importantly by taking advantage of the ^{15}N steady-state

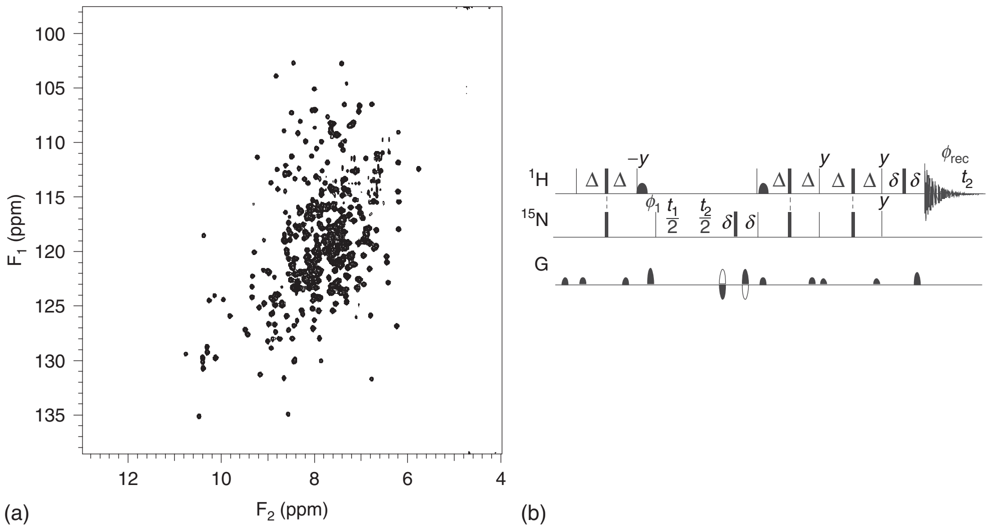

Figure 28.7 (a,b) ^{1}H–^{15}N TROSY spectrum of a 1 mM maltose-binding protein in complex with beta-cyclodextrin in H_2O/D_2O (93/7 v/v).

magnetization [73]. The TROSY principle has been implemented in many heteronuclear correlation experiments such as those used for the main-chain assignment and measurement of scalar and dipolar couplings that exploit coherence transfer between the amide nuclei before the acquisition. The TROSY principle works also for the CH pairs in aromatic rings and side-chain NH_2 groups [74]. TROSY has significantly increased the molecular size limit of proteins and their complexes feasible to NMR studies [75, 76].

Transverse Relaxation Optimized Polarization Transfer Polarization transfer in HSQC and TROSY experiments is based on the aforementioned INEPT sequence. INEPT utilizes scalar spin–spin couplings in order to create antiphase coherence between proton and nitrogen. Although the transfer based on INEPT is highly sensitive in small proteins, it rapidly becomes inefficient with increasing molecular weight. Another polarization transfer scheme, CRIPT [71] utilizes transverse relaxation optimization during the polarization transfer step by omitting the 180° pulse on nitrogen in the middle of the transfer delay. Thus, fast and slow relaxing spin states are not interchanged during the transfer period resulting in suppression of the fast relaxing doublet component, while the slowly relaxing component sustains. There are few characteristic features in CRIPT that differ from the INEPT-based transfer. Polarization transfer is obtained solely through cross-correlated relaxation DD and CSA interactions. In addition, only 50% of the available ^{1}H polarization can be transferred to heteronucleus, albeit the transfer efficiency does not depend on rotational correlation time of the molecule (τ_c). The optimal transfer time, however, depends on molecule's τ_c owing to the decay of the fast relaxing doublet component. Sensitivity of the CRIPT transfer has been improved (20–30%) by a sophisticated TROPIC sequence developed using the optimal control theory [77].

Another transverse relaxation-optimized polarization transfer scheme is CRINEPT [71]. It takes a full benefit from cross-correlated relaxation based transfer, but also maintains scalar-coupling-mediated transfer. This results in a significant improvement in polarization transfer efficiency. However, as no refocusing ^{1}H pulse is applied during the CRINEPT step, there is an inherent loss of sensitivity owing to ^{1}H chemical shift modulation during the CRINEPT transfer.

Interestingly, the TROSY or polarization transfer is not limited to the ^{1}H–^{15}N spin pair. The TROSY principle can be utilized in ^{1}H–^{13}C methyl correlation experiments as well [78]. Half of the originating proton magnetization relaxes slowly in both ^{13}C and ^{1}H domains during the methyl-TROSY experiment, which is essentially a methyl-HMQC pulse scheme. The pulse sequence selects a central line of the MQ methyl triplet during t_1 and transfers it to the slowly relaxing proton coherence for acquisition. In this way, dramatic sensitivity improvement of methyl correlations in very large proteins and complexes has been obtained. The isotopic-labeling scheme, where methyl groups of structurally and biologically important residues, that is, Leu, Val, and Ile (δ_1 only) are selectively protonated in otherwise perdeuterated proteins, plays a crucial role in the success of the methyl-TROSY experiment. It ensures that dipolar relaxation pathways from external protons are minimized, enabling cancellation of intramethyl ^{1}H–^{1}H and ^{1}H–^{13}C dipolar interactions. Methyl TROSY has been especially valuable in studies of high-molecular-weight systems including the 670 kDa 20S proteasome [79].

Application of Heteronuclear NMR Experiments for Studying Protein Dynamics One of the most fascinating attributes of solution-state NMR spectroscopy is its unique sensitivity toward molecular dynamics. In comparison to many other spectroscopic methods, NMR provides simultaneously a very broad range of timescales ranging from picoseconds to seconds (up to hours in H/D exchange experiments) and nearly atomic resolution, enabling site-specific characterization of macromolecular dynamics. Motions of proteins take place in various timescales, most of which can be studied by NMR spectroscopy through use of various relaxation probes or parameters. Fast internal motions, that is, interaction of surface atoms with water, side-chain rotations, or Brownian tumbling of small proteins, take place in the picosecond–to-nanosecond timescale, which can be readily probed by T_1, T_2, and heteronuclear ^{15}N NOE experiments [80]. These are in the essence ^{15}N-HSQC or ^{15}N-TROSY experiments, which include an implemented period for probing, for example, T_2 relaxation within the ^{15}N-HSQC experiment.

Local unfolding and catalysis-related motions in enzymatic reactions or conformational exchange, in general, take place in the microsecond-to-millisecond timescale, which can be characterized through analysis of $T_{1\rho}$ and T_2 relaxation times. These can be readily probed by Carr–Purcell–Meiboom–Gill (CPMG) relaxation dispersion methodology [81]. Relaxation dispersion NMR spectroscopy enables full characterization of both kinetics and thermodynamics of the exchange process [82]. It is even possible to determine the structures of very low populated excited states, which are invisible in traditional NMR spectra but can be accessed by using relaxation dispersion spectroscopy [83]. Kinetic molecular processes taking place in slow or very slow (millisecond-to-subsecond) timescales, for example, protein folding and proton–deuterium exchange, can be studied with exchange spectroscopy or real-time NMR spectroscopy. Real-time NMR spectroscopy has been plagued by inherently slow data collection in indirectly detected dimensions, which makes application of 2D NMR techniques for studying protein kinetics in the second timescale impossible. Fortunately, a novel SOFAST-HMQC technique opens the avenue for kinetic studies in the second timescale [84]. There is a gap between the sub-nanosecond and microsecond timescales, which is not accessible by T_1, $T_{2,}$ and heteronuclear NOEs or CPMG methodology. RDCs are sensitive to motions taking place in the picosecond-to-millisecond timescales, which ideally bridges the gap between the supra-nanosecond and microsecond timescales, facilitating studies of secondary structure fluctuations and domain movements occurring in the microsecond-to-millisecond timescale. This renders RDCs very suitable for their characterization.

28.3.4.2 Edited and Filtered Experiments

The basic heteronuclear experiments are easy to combine with the two-dimensional homonuclear experiments to produce three- or four-dimensional edited spectra. In this terminology, editing means selection of the protons that are attached to the heteronucleus. The main purpose of these experiments is to reduce the signal overlap of the homonuclear two-dimensional experiments.

Combinations of NOESY with HSQC (or HMQC) and TOCSY with HSQC are among the most useful edited three-dimensional experiments [85, 86]. For example, the NOESY-HSQC (Figure 28.8) begins by the NOESY sequence and is followed directly by the HSQC sequence. It is important to acquire enough data points (typically 128 and 2048) along the proton dimensions (t_1) and (t_3), whereas

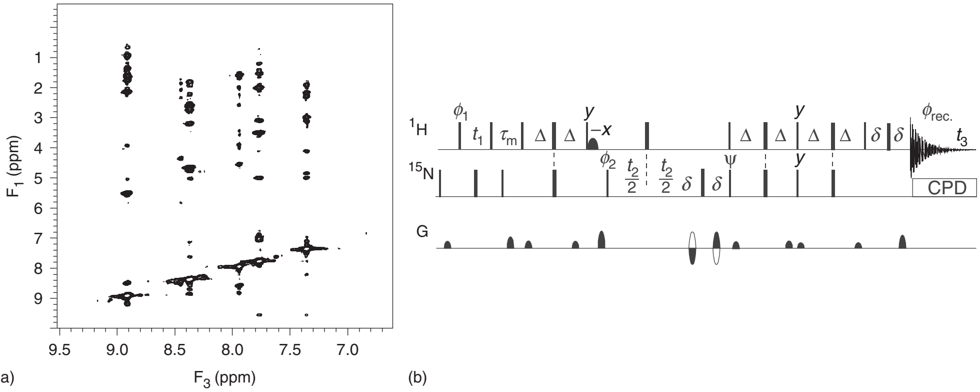

Figure 28.8 (a,b) Plane ^1H–^1H of ^1H–^{15}N-NOESY-HSQC spectrum of a 1 mM SH3 sample in H_2O/D_2O (90/10 v/v).

fewer increments (typically 32) along the ^{15}N editing dimension (t_2) will suffice. The F_1-F_3 plane at each F_2 displays the homonuclear correlations just as in the two-dimensional spectrum, but edited with respect to the heteronucleus. It will take about one day to acquire a spectrum with good SNR.

Clearly, the homonuclear and the heteronuclear experiments could be combined in the reverse order, that is, HSQC-NOESY and HSQC-TOCSY. The main advantage in these schemes relates to ^{15}N-edited experiments in which the narrower amide proton spectral width is sampled during t_1 and the full proton spectral width is collected during t_3. On the other hand, water suppression is more effective when HSQC follows NOESY. In addition, the sensitivity enhancement can be incorporated to the NOESY-HSQC experiment. For the TOCSY-HSQC or HSQC-TOCSY, this does not matter because both the TOCSY and HSQC sequences can be implemented with sensitivity enhancement. It should be mentioned that the TOCSY type of transfers is more effective between ^{13}C nuclei than between protons and therefore HCCH-TOCSY experiment is preferred when a doubly labeled sample is available.

Even if the heteronuclear editing provides a big advantage over the 2D homonuclear experiments, this is not enough when two protons with a mutual correlation have degenerate chemical shifts. This can be of importance, in particular, in NOESY that contains a large number of cross peaks. The 4D HMQC-NOESY-HMQC experiment provides editing in two dimensions to alleviate the overlap problem. The NOESY part is flanked by two HMQC sequences. Obviously, the two HMQC parts can be chosen to edit with respect to the same or different heteronucleus, that is, ^{15}N or ^{13}C. The total acquisition times tend to be long, taking several days to achieve sufficient resolution along the indirect dimensions. This can be alleviated by employing nonlinear sampling to indirectly detected dimensions (Section 28.3.5.3).

For studies of intermolecular interactions, filtered experiments are valuable. The essence of filtered experiments is to distinguish protons on the basis of the heteronucleus to which it is bound. In the terminology, filtering means rejection of the protons that are bound to the heteronucleus. Therefore, provided that the heteronuclei in the subunits that make the quaternary complex are labeled differently, that is, either the target protein or the ligand is labeled, it is possible to employ filtering experiments to distinguish, for example, intermolecular proton NOEs from intramolecular NOEs. While for the heteronuclear-edited experiments, it is sufficient to have only modest degree of labeling, it is mandatory for the filtered experiments to have very high degree of labeling, that is, >98%. The most robust filters are of the double spin echo type.

However, it should be kept in mind that none of the filter sequence will work properly, if the labeling degree is not close to 100%. Leakage of signal may lead to misinterpretation.

28.3.4.3 **Triple-Resonance Experiments**

The assignment of signals is, of course, a prerequisite for any detailed interpretation of NMR spectra. The advent of triple-resonance experiments [87] for double-labeled and, more recently, for perdeuterated proteins, has been very important to work out the assignment problem. The fundamental principle of all triple-resonance experiments is a directional relay of the magnetization from nucleus to nucleus via the scalar coupling network concurrent with a multidimensional detection of the resonance frequencies. In this way, it is possible to correlate several nuclei with enough dispersion to avoid degeneracy even for large proteins. Today, many of the triple-resonance experiments are well established (e.g., Refs. [1, 5, 88, 89]). The principles of how to use them are described later, whereas a more thorough discussion can be found in the reviews. In addition, the triple-resonance experiments are the skeletons for experiments designed to measure scalar and dipolar couplings.

The assignment of resonances to the chemical structure commences from the main-chain atoms HN, N, CA, CO, and CB. The experiments, that is, the pulse sequences for this purpose appear superficially complex, but are in fact built from concatenated parts of heteronuclear polarization transfers. The magnetization is often derived from the amide proton and also from the amide nitrogen when using TROSY. Subsequently, the polarization is relayed to amide nitrogen and further to carbons. Three-dimensional spectra are produced by acquiring frequencies of the amide proton directly and recording indirectly the frequencies of amide nitrogen and either aliphatic carbon or carbonyl carbon (or both, in four-dimensional experiments).

It is the coupling network that dictates the possibilities to select correlations to be observed. The key idea is to produce a mutually complementary pair of spectra, for example, HNCA and HN(CO)CA. The former displays both intra- and interresidue correlations and the latter exclusively the intercorrelations. Alternatively, an exclusive intraresidue HNCA can be recorded [90, 91] The pair of spectra, displaying both intra- and intercarbon resonances for each amide nuclei resonance, allow one to trace the polypeptide backbone from one residue to another. The sequential walk is interrupted at prolines and, at times, potentially due to exchange broadening.

The other commonly used pair of experiments also involves resonances of CB, that is, HNCACB and HN(CO)CACB. Of course, these experiments are less sensitive as the total intensity is divided among CA and CB, but extension of magnetization transfer to CBs facilitates the sequential assignment significantly. Besides that, signal dispersion of beta carbons is superior to that of CAs. The CB resonances carry vital information on residue type, which can be utilized for establishing certain anchor points during the assignment. Particularly, alanine, serine, and threonine residues have very distinctive CB chemical shifts. These residues and their respective linear combinations in the sequence, together with glycine that does not have a CB, form robust templates for the sequential assignment.

The third pair of experiments is the HNCO and HN(CA)CO. The principle is the same as that mentioned earlier, but now the carbonyl carbon frequencies are used instead of CAs or CBs. The former experiment, which correlates amide proton and nitrogen with carbonyl carbon of the preceding residue, is the most sensitive triple-resonance experiment, whereas the latter is among the least sensitive, making this pair unbalanced. Certain modifications to the latter experiment improve the performance, however, at the cost of nonuniform performance for the various amino acid residues.

Today, there are many variants of the basic sequences. The most important modifications are the transverse relaxation-optimized experiments suitable for perdeuterated proteins, the sensitivity-enhanced versions, and the CT implementations for improved resolution. Furthermore, there are many experiments based on the basic sequences designed to measure scalar dipolar couplings and RDCs, often also implemented with spin-state selection as exemplified in Figure 28.9.

The assignment of side-chain resonances is a more laborious undertaking. The proton-detected versions of the aforementioned experiments such as HN(CACB)HAHB and HBHA(CO)NH reveal the protons at the stem of the side chain.

Assignment of the protein's aliphatic side chains can readily be obtained using H(CC)(CO)NH and (H)CC(CO)NH experiments [92]. These experiments correlate either aliphatic ^{1}H or ^{13}C frequencies in the first indirectly detected dimension, after which the magnetization is relayed through aliphatic carbons and carbonyl carbon to the amide nitrogen of the sequential residue. After ^{15}N frequency

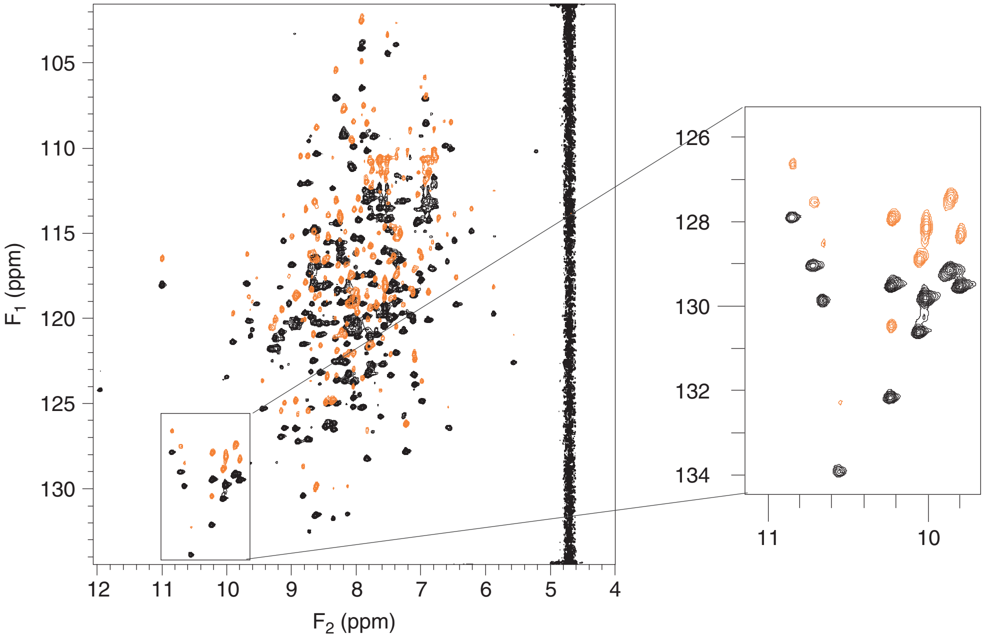

Figure 28.9 Spin-state edited ^{15}N–^{1}H correlation spectra of a 1 mM cellulase sample in H_2O/D_2O (90/10 v/v) recorded at 40 °C in a dilute liquid crystal composed of filamentous phages with an 600 MHz NMR spectrometer using the gradient selected TROSY sequence, modified to select TROSY (black contour) and semi-TROSY (red contour) spin states. The displacement of the multiplets contains in addition to the 94 Hz scalar-coupling-residual dipolar contributions. The inset shows linebroadening of the semi-TROSY component in ^{15}N dimension.

labeling, the coherence will be transferred to the directly bound amide proton for detection. In this way, provided that assignment of the protein main chain has been accomplished earlier, side-chain resonances can be assigned in a trouble-free manner for small- and medium-sized proteins. Inherent sensitivity of these C,C-TOCSY-NH experiments is low owing to relatively long transfer periods from side-chain protons/carbons to main-chain amide protons. HCCH-TOCSY and HCCH-COSY experiments, which correlate protons and carbons with their neighbors in aliphatic side chains, provide superior sensitivity in comparison to NH-detected counterparts. These spectra are, however, more tedious to assign.

Assignment of aromatic side chains is more troublesome owing to significant frequency difference between aromatic and aliphatic carbon resonances, which renders TOCSY transfer inefficient between aromatic and aliphatic carbons. Further difficulties are due to modest cross-peak dispersion among aromatic ring protons and carbons in combination with broad linewidth. For small- and medium-sized proteins, aromatic rings can be connected to the protein backbone by (HB)CB(CGCD)HD and (HB)CB(CGCDCE)HE experiments, which establish connectivities between CBs and aromatic ring protons [93]. There are also sophisticated experiments for the assignment of tryptophans and histidines [94] as well as polar side chains of Arg, Gln, Glu, Asn, and Asp [95–97]. Special techniques have been developed for the assignment of proline-rich sequences, which are abundant in many intrinsically unfolded proteins [98].

28.3.5
Methodology for Fast Data Collection

Traditionally, biological NMR spectroscopy has been limited by sensitivity, that is, experimental time of a key triple-resonance experiment such as HNCACB has been several days in order to accumulate spectrum adequately to meet a useful SNR. In total, this results in several weeks of expensive spectrometer time during which the stability of the sample can be of serious concern. Recent advances in NMR instrumentation, especially development of cryogenically cooled probe heads and higher polarizing magnetic fields, have improved the attainable SNR tremendously. The cryogenically cooled probe head decreases the thermal noise and resistance that originates in detector coils and preamplifiers by cooling them to 10–30 K. This results in an increase of SNR in NMR spectrum by a theoretical factor of 4. In biomolecular NMR applications, where the protein of interest is usually dissolved in aqueous solution comprising ionic buffer and some salt, this theoretical factor of 4 is not reached. Instead, sensitivity improvement by a factor of 3 is typically obtained. Nevertheless, owing to the $\mathrm{SNR} \sim \sqrt{t}$ relation, where t is the effective experimental time or more accurately the number of transients used for accumulating the NMR spectrum, the overall experimental time can, in principle, be reduced by an order of magnitude in cryogenically cooled probe heads, which has marshaled NMR spectroscopy of small- and medium-sized proteins to a new era – the sampling-limited regime. Thus, the overall duration of the NMR experiment is no more limited by the time required to obtain a feasible SNR, but instead to collect adequate number of time points to attain appropriate resolution in multidimensional experiments. Data collection or sampling in this way is a very slow process as each indirectly detected dimension has to be browsed in a point-by-point manner resulting in unnecessarily long experimental times, where expensive spectrometer time is wasted for obtaining adequate resolution. In recent years, several approaches have been introduced, which try to overcome the issue of sampling-limited regime. These methods, although referred here generally to as *fast acquisition NMR methodology* reach the same goal often in conceptually different ways. At least two main categories exist: approaches that (i) employ sparse sampling of NMR data and (ii) increase pulsing rate, that is, shorten the repetition delay between experiments. New methodologies belonging to the first category are reduced dimensionality (RD) and projection reconstruction techniques as well as experiments utilizing nonlinear or nonuniform sampling. Methods belonging to the second category are mainly SOFAST-HMQC experiments and their applications.

28.3.5.1 **Reduced Dimensionality Techniques**

The G-matrix Fourier transform (GFT) projection NMR spectroscopy speeds up data collection by obtaining high-resolution spectral data from low-dimensional projections. The technique is based on RD NMR methodology, which had already been introduced in the early 1990s [99], where two nuclei are jointly sampled in indirectly detected dimension. Therefore, conventional N-dimensional data can be ‘‘reduced’’ to be presented in an $(N-1)$-dimensional subspace. One of the two jointly sampled dimensions is detected as a simple cosine modulation, which creates a chemical shift doublet to this domain. Another dimension is detected in a conventional phase-sensitive manner. This then enables a phase-sensitive detection of a pair of peaks, which can be found as the sum and the difference of jointly sampled chemical shifts. The GFT projection NMR spectroscopy is a generalization of the RD NMR methodology [100]. Therefore, along with one phase-sensitively detected dimension, there is 2^n-fold repeated joint sampling of n indirectly detected chemical shift evolution periods. In addition, by taking linear combinations of these 2^n subspectra, we can generate separate, phase-sensitively detected spectra comprising peaks with a given linear combination of shifts. By using the GFT approach, even five- or six-dimensional data sets can be recorded using relatively short experimental times. For small proteins, overall time saving by a factor of 10–100 can be obtained. However, the experiment suffers from an inherent sensitivity loss by a factor of $(1/\sqrt{2})^n$ in comparison to the parent N-dimensional experiment. This can be partly compensated by symmetrization of subspectra.

28.3.5.2 **Projection Reconstruction Technique**

The projection reconstruction technique in NMR is related to a three-dimensionalX-ray imaging in anatomy, that is, a three-dimensional image is reconstructed from a set of plane projections taken from various angles of the object. By considering the NMR frequency space as a three-dimensional object, which is made of well-resolved discrete signals, a similar reconstruction of the three-dimensional spectrum can be obtained by collecting small number of 2D projections of the three-dimensional spectrum at different angles [101]. The full three-dimensional spectrum can then be reconstructed from the 2D projections. The peak lattice can be obtained using two orthogonal projections, but at least one or more tilted projections needs to be collected in order to select true cross peaks out of multiple possibilities. These tilted projections can be readily obtained by joint evolution of chemical shifts using fixed ratios, which defines the tilt angle. Although the projection reconstruction technique utilizes joint incrementation of two evolution parameters, similar to the RD approach, the data processing is different. It provides spectra with a familiar outlook, resembling the traditional three-dimensional spectrum. More importantly, sensitivity per unit time of the projection reconstruction method is identical to the conventional three-dimensional spectrum. Time savings on a spectrometer are significant, at least an order of magnitude in comparison to a conventional three-dimensional experiment.

28.3.5.3 Nonlinear Sampling

The principal idea behind nonlinear sampling, referred also to as *nonuniform* or *sparse sampling*, is to record multidimensional experiments through sparse and yet random sampling. In the sampling scheme, only a small subset of optimally selected data points are collected and the complete spectrum is then reconstructed by using nontraditional spectral-processing schemes such as nonuniform Fourier transform, maximum entropy, or multidimensional decomposition (MDD) [102–104]. For three-dimensional triple-resonance spectra, time savings by a factor of 5 can be readily obtained, enabling collection of data for protein backbone assignment within one day. By combining a nonlinear sampling scheme with the real-time targeted acquisition approach, additional time savings can be realized [105]. Fully automated data collection and on-line spectral processing during acquisition enables optimization of experimental time by following result-oriented criteria, that is, by stopping the experiment when the predefined spectral quality, completeness, or sensitivity, is adequate. This approach can be extended even further, that is, utilizing real-time data acquisition, hyperdimensional spectroscopy [106], and automated assignment, which results in blistering speed in backbone assignment of small proteins – the total time required for data collection and backbone assignment of 8.6 kDa human ubiquitin is ∼1 h [107].

28.3.5.3.1 **Selective Optimized Flip-Angle Short-Transient Heteronuclear Multiple-Quantum Coherence** RD and projection reconstruction techniques address the issue of sampling-limited data collection by joint sampling of several time domains and/or by collecting a limited set of 2D projections of a three-dimensional spectrum from various angles. The band-SOFAST-HMQC experiment is a conceptually very different approach [108, 109]. It hinges on standard sampling in indirectly detected dimensions but utilizes shortened longitudinal relaxation times of sample protons, which enables the use of very short interscan delay. Therefore, the repetition rate of the experiment can substantially be increased, resulting in significant time saving in overall experimental time. The key idea of the SOFAST-HMQC experiment is to avoid perturbation of protons, which are not directly detected. These protons serve as a reservoir for dipolar interactions (NOE effect) with the protons of interest, which reduces spin–lattice (T_1) relaxation time of detected protons substantially. Thus, the equilibrium spin polarization will be restored at a higher rate, enabling the use of a higher repetition rate in the pulse sequences. In comparison to the conventional HMQC, homonuclear J-modulation is not active during t_1 evolution period of SOFAST-HMQC as the 180° (^{1}H) pulse is band selective.

The general idea of fast pulsing in a manner of SOFAST-HMQC experiments can be used for acquiring three- or four-dimensional spectra with increased pace. With a suite of fast band-selective excitation short-transient (BEST) triple-resonance experiments [110]. High-quality 3D spectrum can be obtained within 10 min, provided that a sufficiently concentrated protein sample and a cryogenically cooled probe head are available.

References

1. Clore, G.M. and Gronenborn, A.M. (1998) *Curr. Opin. Chem. Biol.*, **2** (5), 564.
2. Ferentz, A.E. and Wagner, G.O. (2000) *Rev. Biophys.*, **33** (1), 29.
3. Gardner, K.H. and Kay, L.E. (1998) *Q. Rev. Biophys.*, **27**, 357.
4. Kay, L.E. (1998) *Biochem. Cell Biol.*, **76** (2–3), 145.
5. Pervushin, K. (2000) *Q. Rev. Biophys.*, **33** (2), 161.
6. Prestegard, J.H., Al-Hashimi, H.M., and Tolman, J.R. (2000) *Q. Rev. Biophys.*, **33** (4), 371.
7. Wider, G. (2000) *Biotechniques*, **29**, 1278–1292.
8. Cavanagh, J., Fairbrother, W., Palmer, A.G., and Skelton, N.J. (1996) *Protein NMR Spectroscopy Principles and Practice*, Academic Press, San Diego, CA.
9. van de Ven, F.J.M. (1995) *Multidimensional NMR in Liquids Basic Principles and Experimental Methods*, Wiley-VCH Verlag GmbH, Weinheim.
10. Salzmann, M., Pervushin, K., Wider, G., Senn, H., and Wüthrich, K. (2000) *J. Am. Chem. Soc.*, **122**, 7543.
11. Grishaev, A., Tugarinov, V., Kay, L.E., Trewhella, J., and Bax, A. (2008) *J. Am. Chem. Soc.*, **40**, 95.
12. Tjandra, N. and Bax, A. (1997) *Science*, **278**, 1111.
13. Pervushin, K., Riek, R., Wider, G., and Wüthrich, K. (1997) *Proc. Natl. Acad. Sci. U.S.A.*, **94**, 12366.
14. Bagby, S., Tong, K.I., and Ikura, M. (2001) *Methods Enzymol.*, **339**, 20.
15. Zhou, P., Lugovskoy, A.A., and Wagner, G. (2001) *J. Biomol. NMR*, **20**, 11.
16. Bagby, S., Tong, K.I., Liu, D., Alattia, J.R., and Ikura, M. (1997) *J. Biomol. NMR*, **10**, 279.
17. Yamazaki, T., Otomo, T., Oda, N., Kyogoku, Y., Uegaki, K., Ito, N., Ishino, Y., and Nakamura, H. (1998) *J. Am. Chem. Soc.*, **120**, 5591.
18. Otomo, T., Ito, N., Kyogoku, Y., and Yamazaki, T. (1999) *Biochemistry*, **38**, 16040.
19. LeMaster, D.M. and Richards, F.M. (1988) *Biochemistry*, **27**, 142.
20. Torchia, D.A., Sparks, S.W., and Bax, A. (1988) *J. Am. Chem. Soc.*, **110**, 2320.
21. Sattler, M. and Fesik, S.W. (1996) *Structure*, **4**, 1245.
22. Kay, L.E. and Gardner, K.H. (1997) *Curr. Opin. Struct. Biol.*, **7**, 722.
23. Goto, N.K., Gardner, K.H., Mueller, G.A., Willis, R.C., and Kay, L.E. (1999) *J. Biomol. NMR*, **13**, 369.
24. Bax, A., Vuister, G., Grzesiek, S., Delaglio, F., Wang, A.C., Tschudin, R.,

and Zhu, G. (1994) *Methods Enzymol.*, **239**, 79.

25. Schwalbe, H., Carlomagno, T., Hennig, M., Junker, J., Reif, B., Richter, C., and Griesinger, C. (2001) *Methods Enzymol.*, **338**, 35.

26. Bax, A., Kontaxis, G., and Tjandra, N. (2001) *Methods Enzymol.*, **339**, 127.

27. Battiste, J.L. and Wagner, G. (2000) *Biochemistry*, **39**, 5355.

28. Denton, H., Smith, M., Husi, H., Uhrin, D., Barlow, P.N., Batt, C.A., and Sawyer, L. (1998) *Protein Exp. Purif.*, **14**, 97.

29. Zimmer, D.P. and Crothers, D.M. (1995) *Proc. Natl. Acad. Sci. U.S.A.*, **92**, 3091.

30. Batey, R.T., Cloutier, N., Mao, H., and Williamson, J.R. (1996) *Nucleic Acids Res.*, **24**, 4836.

31. Nikonowicz, E.P. (2001) *Methods Enzymol.*, **338**, 320.

32. Werner, M.H., Gupta, V., Lambert, L.J., and Nagata, T. (2001) *Methods Enzymol.*, **338**, 283.

33. Salzmann, M., Pervushin, K., Wider, G., Senn, H., and Wüthrich, K. (1998) *Proc. Natl. Acad. Sci. U.S.A.*, **95**, 13585.

34. Tugarinov, V. and Kay, L.E. (2004) *J. Biomol. NMR*, **28**, 165.

35. Kainosho, M., Torizawa, T., Iwashita, Y., Terauchi, T., Ono, A.M., and Güntert, P. (2006) *Nature*, **440**, 52.

36. Tjandra, N., Grzesiek, S., and Bax, A. (1996) *J. Am. Chem. Soc.*, **118**, 6264.

37. Tolman, J.R., Flanagan, J.M., Kennedy, M.A., and Prestegard, J.H. (1995) *Proc. Natl. Acad. Sci. U.S.A.*, **92**, 9279.

38. Zweckstetter, M. and Bax, A. (2000) *J. Am. Chem. Soc.*, **122**, 3791.

39. Losonczi, J.A., Andrec, M., Fischer, M.W., and Prestegard, J.H. (1999) *J. Magn. Reson.*, **138**, 334.

40. Sanders, C.R. and Prestegard, J.H. (1990) *Biophys. J.*, **58**, 447.

41. Bax, A. and Tjandra, N. (1997) *J. Biomol. NMR*, **10**, 289.

42. Rückert, M. and Otting, G. (2000) *J. Am. Chem. Soc.*, **122**, 7793.

43. Barrientos, L.G., Dolan, C., and Gronenborn, A.M. (2000) *J. Biomol. NMR*, **16**, 329.

44. Hansen, M.R., Mueller, L., and Pardi, A. (1998) *Nat. Struct. Biol.*, **5**, 1065.

45. Hansen, M.R., Hanson, P., and Pardi, A. (2000) *Methods Enzymol.*, **317**, 220.

46. Clore, G.M., Starich, M.R., and Gronenborn, A.M. (1998) *J. Am. Chem. Soc.*, **120**, 10571.

47. Ojennus, D.D., Mitton-Fry, R.M., and Wuttke, D.S. (1999) *J. Biomol. NMR*, **14**, 175.

48. Sass, J., Cordier, F., Hoffmann, A., Rogowski, M., Cousin, A., Omichinski, J.G., Löwen, H., and Grzesiek, S. (1999) *J. Am. Chem. Soc.*, **121**, 2047.

49. Tycko, R., Blanco, F.J., and Ishii, Y. (2000) *J. Am. Chem. Soc.*, **122**, 9340.

50. Marion, D., Ikura, M., Tschudin, R. *et al.* (1989) *J. Magn. Reson.*, **85**, 393.

51. Altieri, A.S., Hinton, D.P., and Byrd, R.A. (1995) *J. Am. Chem. Soc.*, **117**, 7566.

52. Jones, J.A., Wilkins, D.K., Smith, L.J., and Dobson, C.M. (1997) *J. Biomol. NMR*, **10**, 199.

53. Hajduk, P.J., Olejniczak, E.T., and Fesik, S.W. (1997) *J. Am. Chem. Soc.*, **119**, 12257.

54. Piotto, M., Saudek, V., and Sklenar, V. (1992) *J. Biomol. NMR*, **2**, 661.

55. Marion, D., Ikura, M., and Bax, A. (1989) *J. Magn. Reson.*, **84**, 425.

56. Jeener, J. (1971) Lecture, Ampère Summer School, Basko Polje, Yugoslavia.

57. Aue, W.P., Bartholdi, E., and Ernst, R.R. (1976) *J. Chem. Phys.*, **64**, 2229.

58. Karplus, M. (1959) *J. Phys. Chem.*, **30**, 11.

59. Piantini, U., Sorensen, O.W., and Ernst, R.R. (1982) *J. Am. Chem. Soc.*, **104**, 6800.

60. Eich, G., Bodenhausen, G., and Ernst, R.R. (1982) *J. Am. Chem. Soc.*, **104**, 3731.

61. Dalvit, C., Rance, M., and Wright, P.E. (1986) *J. Magn. Reson.*, **69**, 356.

62. Braunschweiler, L. and Ernst, R.R. (1983) *J. Magn. Reson.*, **53**, 521.

63. Bax, A. and Davis, D.G. (1985) *J. Magn. Reson.*, **65**, 355.

64. Rance, M. (1987) *J. Magn. Reson.*, **74**, 557.

65. Kupce, E., Schmidt, P., Rance, M., and Wagner, G. (1998) *J. Magn. Reson.*, **135**, 361.

66. Bothner-By, A.A., Stephens, R.L., Lee, J.-M., Warren, C.D., and Jeanloz, R.W. (1984) *J. Am. Chem. Soc.*, **106**, 811.

67. Bax, A. and Davis, D.G. (1985) *J. Magn. Reson.*, **63**, 207.

68. Müller, L. (1979) *J. Am. Chem. Soc.*, **101**, 4481.

69. Bax, A., Griffey, R.H., and Hawkins, B.L. (1983) *J. Magn. Reson.*, **55**, 301.

70. Bodenhausen, G. and Ruben, D.J. (1980) *Chem. Phys. Lett.*, **69**, 185.

71. Riek, R., Wider, G., Pervushin, K., and Wüthrich, K. (1999) *Proc. Natl. Acad. Sci. U.S.A.*, **96**, 4918.

72. Morris, G.A. and Freeman, R. (1979) *J. Am. Chem. Soc.*, **101**, 760.

73. Salzmann, M., Wider, G., Pervushin, K., and Wüthrich, K. (1999) *J. Biomol. NMR*, **15**, 181.

74. Pervushin, K., Braun, D., Fernandez, C., and Wüthrich, K. (2000) *J. Biomol. NMR*, **17**, 195.

75. Tzakos, A.G., Grace, C.R.R., Lukavsky, P.J., and Riek, R. (2006) *Annu. Rev. Biophys. Biomol. Struct.*, **35**, 319.

76. Riek, R., Pervushin, K., and Wüthrich, K. (2000) *Trends Biochem. Sci.*, **25**, 462.

77. Frueh, D.P., Ito, T., Li, J.S., Wagner, G., Glaser, S.J., and Khaneja, N. (2005) *J. Biomol. NMR*, **32**, 23.

78. Tugarinov, V., Hwang, P.M., Ollerenshaw, J.E., and Kay, L.E. (2003) *J. Am. Chem. Soc.*, **125**, 10420.

79. Sprangers, R. and Kay, L.E. (2007) *Nature*, **445**, 618.

80. Peng, J.W. and Wagner, G. (1994) *Methods Enzymol.*, **239**, 563.

81. Palmer, A.G., Kroenke, C.D., and Loria, J.P. (2001) *Methods Enzymol.*, **339**, 204.

82. Korzhnev, D. and Kay, L.E. (2008) *Acc. Chem. Res.*, **41**, 442.

83. Vallupuralli, P., Hansen, D.E., and Kay, L.E. (2008) *Proc. Natl. Acad. Sci. U.S.A.*, **105**, 11766.

84. Schanda, P., Forge, V., and Brutscher, B. (2007) *Proc. Natl. Acad. Sci. U.S.A.*, **104**, 11257.

85. Marion, D., Driscoll, P.C., Kay, L.E., Wingfield, P.T., Bax, A., Gronenborn, A.M., and Clore, G.M. (1989) *Biochemistry*, **28**, 6150.

86. Zuiderweg, E.R.P. and Fesik, S.W. (1989) *Biochemistry*, **28**, 2387.

87. Ikura, M., Kay, L.E., and Bax, A. (1990) *Biochemistry*, **29** (19), 4659.

88. Clore, G.M. and Gronenborn, A.M. (1994) *Methods Enzymol.*, **239**, 349.

89. Clore, G.M. and Gronenborn, A.M. (1998) *Trends Biotechnol.*, **16** (1), 22.

90. Permi, P. (2002) *J. Biomol. NMR*, **23**, 201.

91. Tossavainen, H. and Permi, P. (2004) *J. Magn. Reson.*, **170**, 244.

92. Sattler, M., Schleucher, J., and Griesinger, C. (1999) *Prog. Nucl. Magn. Res. Spectrosc.*, **34**, 93.

93. Yamazaki, T., Forman-Kay, J.D., and Kay, L.E. (1993) *J. Am. Chem. Soc.*, **115**, 11054.

94. Löhr, F., Rogov, V.V., Shi, M.C., Bernhard, F., and Dötsch, V. (2005) *J. Biomol. NMR*, **32**, 309.

95. Iwahara, J.J. and Clore, G.M. (2006) *J. Biomol. NMR*, **36**, 251.

96. McIntosh, L.P., Brun, E., and Kay, L.E. (1997) *J. Biomol. NMR*, **9**, 306.

97. Pellechia, M., Wider, G., Iwai, H., and Wüthrich, K. (1997) *J. Biomol. NMR*, **10**, 193.

98. Kanelis, V., Donaldson, L., Muhandiram, D.R., Rotin, D., Forman-Kay, J.D., and Kay, L.E. (2000) *J. Biomol. NMR*, **16**, 253.

99. Szyperski, T., Wider, G., Bushweller, J.H., and Wüthrich, K. (1993) *J. Am. Chem. Soc.*, **115**, 9307.

100. Kim, S. and Szyperski, T. (2003) *J. Am. Chem. Soc.*, **125**, 1385.

101. Kupce, E. and Freeman, R. (2004) *J. Am. Chem. Soc.*, **126**, 6429.

102. Hoch, J.C. and Stern, A.S. (2001) *Nucl. Magn. Reson. Biol. Macromol.*, **338**, 159.

103. Marion, D. (2005) *J. Biomol. NMR*, **32**, 141.

104. Orekhov, V.Y., Ibraghimov, I., and Billeter, M. (2003) *J. Biomol. NMR*, **27**, 165.

105. Jaravine, V.A. and Orekhov, V.Y. (2006) *J. Am. Chem. Soc.*, **128**, 13421.

106. Kupce, E. and Freeman, R. (2006) *J. Am. Chem. Soc.*, **128**, 6020.

107. Jaravine, V.A., Zhuravleva, A.V., Permi, P., Ibraghimov, I., and Orekhov, V.Y. (2008) *J. Am. Chem. Soc.*, **130**, 3927.

108. Schanda, P. and Brutscher, B. (2005) *J. Am. Chem. Soc.*, **127**, 8014.

109. Schanda, P., Kupce, E., and Brutscher, B. (2005) *J. Biomol. NMR*, **33**, 199.

110. Schanda, P., van Melckebeke, H., and Brutscher, B. (2006) *J. Am. Chem. Soc.*, **128**, 9042.

29
Direct Optical Detection in Bioanalytics

Günter Gauglitz and Nicholas J. Goddard

29.1
Introduction

Apart from fluorescence techniques and the use of labeled compounds, direct optical detection of the biomolecular interaction process has increasingly gained interest in recent years. Especially, the monitoring of protein–protein interaction is in the focus of recent research. It takes advantage of direct optical detection since it reduces the problems with loss of bioactivity and requires no labeling. Accordingly, quite a few reviews dealing with optical biosensors for nonlabeled targets [1–5] have been published as well as an overall review of strategies for label-free optical detection. The latter is not just an overall review on optical biosensors covering only immunosensors but also refers to biosensors dealing with nucleic acids and whole-cell systems [6]. All these upcoming applications are discussed in a feature article in *Science* [7], ''Who needs labels,'' covering proteomics in life science technologies. These publications state the feasibility of direct optical detection as well as the advantages and disadvantages compared to microarrays based on labeled systems [8], and as optical techniques have to compete with optical microarray techniques using labeled systems that are commercially available [9]. Stimuli-responsive application is certainly done preferably by using direct optical techniques [10], and will help gain more information in the signaling chain or even to discriminate between agonists and antagonists [11].

In the meanwhile, quite a few commercially available systems for nonlabeled screening are available [12]. Further references to other commercialized products using different principles for direct optical detection are given in the related subchapters later. In addition, some specific realizations are discussed later.

Non-optical screening platforms relying on label-free screening such as impedance assays, acoustic systems, or micro-electromechanical sensors are also discussed in literature [13], but are not part of this chapter.

In principle, most of these direct optical detection techniques perform spectroscopy on biomolecules at the surface. In addition, they can monitor the interaction between a thin biomolecular layer containing recognition sites and a ligand or an analyte in solution. Typically, the behavior of radiation in

Handbook of Spectroscopy, Second Edition. Edited by Günter Gauglitz and David S. Moore.

reflectance is used. Thereby, in general, changes in the so-called optical thickness are monitored. This optical thickness is a product of the refractive index n and physical thickness d of this interaction layer. According to the Fresnel equation, white light interference or effects caused by changes in the evanescent field form the principle of these optical techniques [14].

The principles of both these approaches to use reflected radiation (inner or outer reflectance) is explained, demonstrating the advantages and disadvantages, and various applications are outlined.

29.2
Optical Fundamentals

29.2.1
Optical Absorption

The attenuation factor α links the imaginary part K of the complex refractive index n to the loss per unit length:

$$I_x = I_0 \mathrm{e}^{-\alpha x} \quad \text{or} \quad \ln \frac{I_x}{I_0} = -\alpha x \tag{29.1}$$

where I_0 is the initial intensity and I_x is the intensity after the light has propagated a distance x through the absorbing medium at wavelength λ, and

$$\alpha = \frac{4\pi K}{\lambda} \tag{29.2}$$

However, the Lambert–Beer law states that

$$\log \frac{I_0}{I_x} = \varepsilon c x \tag{29.3}$$

where ε is the molar extinction coefficient ($\mathrm{m}^2\ \mathrm{mol}^{-1}$) and c is the concentration ($\mathrm{mol\,m}^{-3}$). Combining Eqs. (29.1–29.3) yields

$$K = \frac{\varepsilon c \lambda \ln 10}{4\pi} \tag{29.4}$$

Thus, we can calculate the imaginary part of the complex refractive index of a dielectric medium if we know the extinction coefficient and the concentration of the absorbing species. If the lower index medium in a total internal reflection (TIR) configuration has a complex refractive index, that is, it is lossy, then the reflection coefficient is reduced from unity, even for angles of incidence above the critical angle.

29.2.2
Theory of Total Internal Reflection

29.2.2.1 Reflection and Refraction

At a dielectric interface, we can have both reflection and transmission, as shown in Figure 29.1 [14]. The following conditions must be satisfied:

$$\theta_3 = \theta_1$$

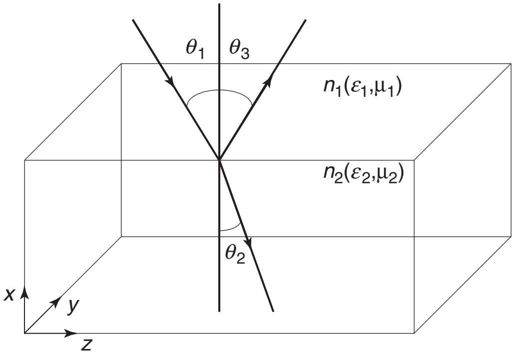

Figure 29.1 Reflection and refraction of light at the interface between two dielectric media having different refractive indices.

$$\frac{\sin\theta_2}{\sin\theta_1} = \frac{n_1}{n_2} = \left(\frac{\varepsilon_1}{\varepsilon_2}\right)^{1/2} \tag{29.5}$$

where n is the refractive index, ε is the permittivity, and μ is the permeability of the dielectric media. The incident, reflected, and refracted rays are coplanar (located in the x-z plane, the plane of incidence, in Figure 29.1). Transverse electric (TE), perpendicular (⊥) or s-polarized light has its electric vector perpendicular to the plane of incidence (x-z plane) in Figure 29.1, while transverse magnetic (TM), parallel (||) or p-polarized light has its magnetic vector perpendicular to the plane of incidence.

29.2.2.1.1 **The Fresnel Equations** The Fresnel equations describe the reflection and transmission coefficients at the interface of two optical media. The polarization of the incident light affects the magnitude of these coefficients. It is possible to derive expressions for the intensities of the reflected and refracted rays. These differ for the TE and TM polarizations as follows:

$$R_{\mathrm{TE}} = \frac{\sin^2(\theta_2 - \theta_1)}{\sin^2(\theta_2 + \theta_1)} = \frac{\left(n_1\cos\theta_1 - \sqrt{n_2^2 - n_1^2\sin^2\theta_1}\right)^2}{\left(n_1\cos\theta_1 + \sqrt{n_2^2 - n_1^2\sin^2\theta_1}\right)^2} \tag{29.6}$$

$$T_{\mathrm{TE}} = \frac{\sin 2\theta_1 \sin 2\theta_2}{\sin^2(\theta_2 + \theta_1)} = \frac{4n_1\cos\theta_1\sqrt{n_2^2 - n_1^2\sin^2\theta_1}}{\left(n_1\cos\theta_1 + \sqrt{n_2^2 - n_1^2\sin^2\theta_1}\right)^2} \tag{29.7}$$

$$R_{\mathrm{TM}} = \frac{\tan^2(\theta_1 - \theta_2)}{\tan^2(\theta_1 + \theta_2)} = \frac{\left(n_2^2\cos\theta_1 - n_1\sqrt{n_2^2 - n_1^2\sin^2\theta_1}\right)^2}{\left(n_2^2\cos\theta_1 + n_1\sqrt{n_2^2 - n_1^2\sin^2\theta_1}\right)^2} \tag{29.8}$$

$$T_{\mathrm{TM}} = \frac{\sin 2\theta_1 \sin 2\theta_2}{\sin^2(\theta_1+\theta_2)\, cos^2(\theta_1-\theta_2)} = \frac{4n_1 n_2^2 \cos\theta_1 \sqrt{n_2^2 - n_1^2 \sin^2\theta_1}}{\left(n_2^2 \cos\theta_1 + n_1\sqrt{n_2^2 - n_1^2 \sin^2\theta_1}\right)^2} \tag{29.9}$$

These expressions are only valid for non-normal incidence ($\theta_1 > 0$). For the special case of normal incidence, these expressions become

$$R = \left(\frac{n_1 - n_2}{n_1 + n_2}\right)^2 \tag{29.10}$$

$$T = \frac{4n_1 n_2}{(n_1 + n_2)^2} \tag{29.11}$$

Note that the polarization has no effect at normal incidence, as it is not possible to distinguish a particular plane of incidence.

29.2.2.1.2 **Total Internal Reflection (TIR)** If we have the condition $\theta_2 = \pi/2$, then the transmission coefficients for both TE and TM polarized light go to zero, because the term sin $2\theta_2$ becomes zero. Thus, the transmission coefficient is zero when $\theta_2 = \pi/2$. In this case,

$$\sin\theta_{\mathrm{c}} = \frac{n_2}{n_1} \tag{29.12}$$

and the angle of incidence at which this condition is true is called the *critical angle*. Since the sine function can only produce values from -1 to $+1$ for real angles, we can see that for this condition to be satisfied $n_2 < n_1$. In other words, TIR can only occur when light travels from a high index to a lower index medium. For angles of incidence greater than or equal to the critical angle, TIR occurs regardless of the polarization.

29.2.2.1.3 **Evanescent Waves** When the angle of incidence at a high–low refractive index boundary is greater than the critical angle, light is totally internally reflected. It can be shown that, although there is no energy transmitted across the interface, an electromagnetic wave, the evanescent wave, is present on the other side of the boundary. This wave propagates parallel to the interface and decays away exponentially with the distance from the boundary. The penetration depth of the evanescent wave is given by

$$d = \frac{\lambda}{2\pi\sqrt{n_1^2 \sin^2\theta_1 - n_2^2}} \tag{29.13}$$

where λ is the vacuum wavelength of the light. The penetration depth is the distance over which the intensity of the evanescent field decays to $1/e$ of its original intensity. This means that, except near the critical angle, the penetration of the evanescent wave into the optically rarer medium is no more than a wavelength. For example, if we take an SF10 prism ($n = 1.732$) in contact with water ($n = 1.333$) at a wavelength of 633 nm (HeNe laser), then the critical angle is 50.32°. If our angle of incidence is 60°, the penetration depth is approximately 146 nm.

While the evanescent field does not propagate into the rarer medium, it does propagate parallel to the interface and can interact with the lower index medium. Thus, if the lower index medium is absorbing, fluorescent, or scattering, some of the radiation will be absorbed, and the reflectivity will be reduced from unity. In the case of fluorescent or scattering media, fluorescence emission or scattered light from the evanescent field will be observed.

29.2.2.2 **Attenuated Total Internal Reflection (ATR)**

The small decrease in reflectivity observed when light is reflected by TIR at the interface between nonabsorbing and absorbing media is termed "attenuated total internal reflection" (ATR). If the light is scanned over a range of wavelengths, an absorption spectrum can be generated. Figure 29.2 illustrates the effect of the imaginary part of the refractive index on the reflectivity in a simple TIR configuration. When the imaginary part of the complex refractive index is quite small (0.001), the reflectivity curves deviate significantly from the curves for the no-loss situation only around the critical angle. At higher loss values, the curves deviate strongly from the no-loss values.

Figure 29.3 shows log(reflectivity) for internal reflection at the interface between dielectric media having a refractive index of 1.5 and $1.0 + iK$ for two angles of incidence, 60°, and the critical angle (41.8°). It can be seen that the TM polarization gives slightly higher sensitivity and that operating at the critical angle for $K \approx 0.1$ also gives higher sensitivity. Above these values of K, the reflectivity is a nonlinear function of K.

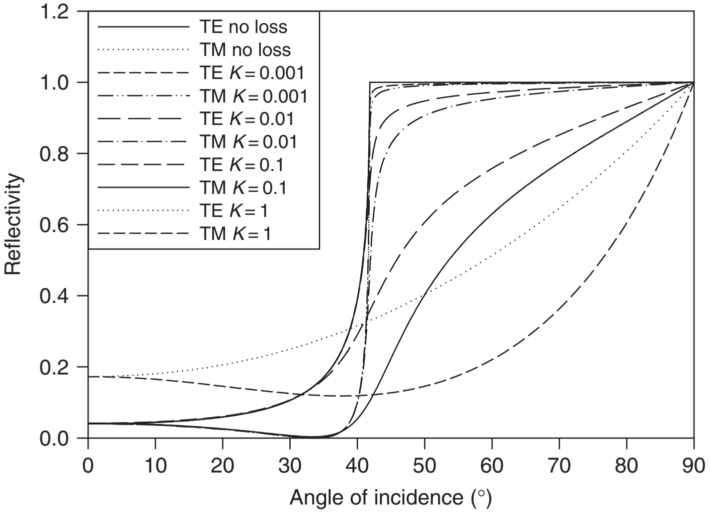

Figure 29.2 Reflectivities calculated for angles of incidence between 0 and 90° for internal reflection at the interface between dielectric media having refractive index 1.5 and $1.0 + iK$.

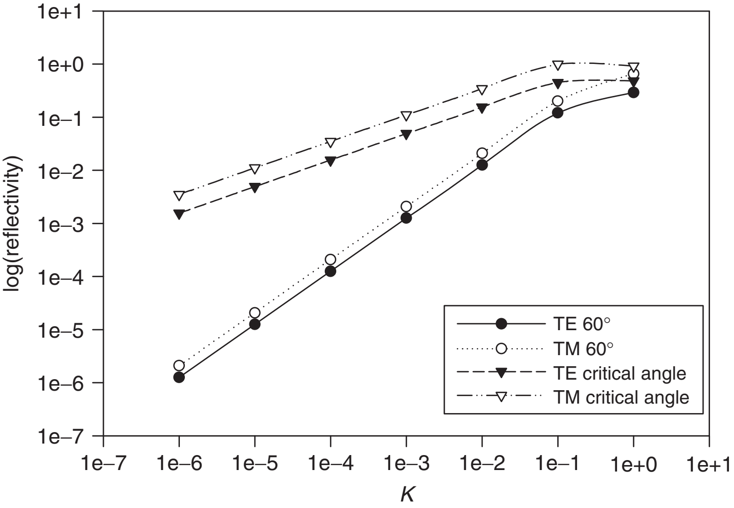

Figure 29.3 log(reflectivity) for internal reflection at the interface between dielectric media having refractive index 1.5 and $1.0 + iK$ for two angles of incidence, 60° and the critical angle (41.8°).

29.2.2.3 Effective Path Length and Sensitivity

We can use the preceding calculations to determine an effective path length for a material having a given value of K. This is calculated as a fraction of the path length of the material in a conventional spectrophotometer. Equation (29.4) can be rewritten as

$$\varepsilon c = \frac{4\pi K}{\lambda \ln 10} \tag{29.14}$$

In addition, we can use the reflectivity of the ATR configuration to calculate an effective absorbance or optical density:

$$A = \log \frac{I_0}{I} = -\log R \tag{29.15}$$

The ratio of the sensitivities for the ATR and conventional systems allows us to calculate an effective path length:

$$r_s = \frac{-\log R}{\varepsilon c l} = \frac{-\lambda \ln 10 \log R}{4\pi K l} = \frac{-\lambda \ln R}{4\pi K l} \tag{29.16}$$

For example, if we use ATR at the interface between dielectric media having a refractive index of 1.5 and $1.0 + 0.00001i$, we can calculate that $\varepsilon c = 86.24\,\text{m}^{-1}$ or $0.8624\,\text{cm}^{-1}$. Operating at the critical angle for such a system, using TM polarization, we obtain a value for R of 0.97487, which gives a value of 0.011055 for $-\log(R)$. This shows that the sensitivity of the ATR configuration is approximately 1/78 (0.011055/0.8624) of that of a conventional spectrophotometer, or the effective path length is 1/78 cm compared to a conventional 1-cm cell.

Although the effective path length is considerably shorter for a simple ATR configuration, the volume of material sensed is very small, since the penetration depth into the sensed material is generally very small. If we assume a circular input beam of radius r for both the conventional and ATR configurations, then the input beam will form an elliptical spot at the interface between the two media whose area is given by

$$A = \frac{\pi r^2}{\cos \theta_1} \tag{29.17}$$

The volume of material sensed is given by the product of the area of the spot and the penetration depth d:

$$V = \frac{\pi r^2 \lambda}{2\pi \ \cos \ \theta_1 \sqrt{n_1^2 \sin^2 \theta_1 - n_2^2}} \tag{29.18}$$

And, for the conventional cell the volume sensed is given by

$$V = \pi r^2 l \tag{29.19}$$

where l is the path length of the cell. The ratio of these two volumes is

$$r_{\mathrm{V}} = \frac{\lambda}{2\pi \mathrm{l} \ \cos \ \theta_1 \sqrt{n_1^2 \sin^2 \theta_1 - n_2^2}} \tag{29.20}$$

One obvious way to increase the sensitivity of ATR systems is to increase the number of reflections. This can be achieved by using a thin transparent slab and coupling the light in and out through the end faces of the slab. Many different configurations have been devised utilizing this method, including schemes where the light enters and exits by the same face and single- and double-sided slabs. If the reflectivity for a single TIR is R, then for n reflections the total reflectivity is R^n. ATR slab waveguides in IR-transparent materials such as silicon, germanium, zinc selenide, and KRS-5 are commercially available for fourier transform infrared (FTIR) instruments.

29.2.2.4 **Waveguides**

We can utilize the phenomenon of TIR to construct a waveguide. If we have a slab of transparent dielectric of a higher refractive index than its surroundings, light can be waveguided in the slab. Even a simple microscope slide can act as a slab waveguide if light can be coupled into it in such a way as to exceed the critical angle on reflection at the boundaries of the slab. Figure 29.4 shows a simple ray model of the propagation of light along the waveguide at a characteristic angle of incidence by successive reflections. To minimize losses, TIR is used as the reflection mechanism.

It might appear that θ can adopt any angle, but this is not the case. Consider an observer moving along the z-axis who sees only the transverse (x-direction) motion. For a self-consistent picture, this observer must see the ray having the same phase every time the ray reaches him or her. If this were not the case, over a large number of reflections the phase shifts would cancel out, giving an intensity of zero. For this not to occur, the total phase shift over a complete cycle from $x = 0$ to $2a$ and back to

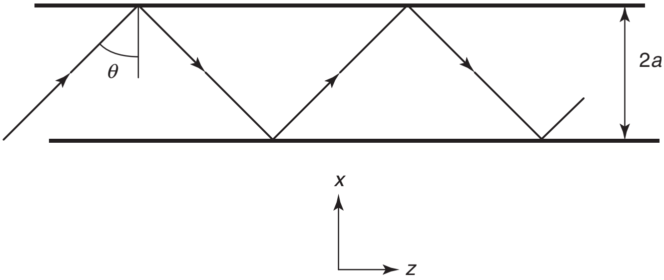

Figure 29.4 A simple model of a slab waveguide showing the propagation of light in a zig-zag path.

0 must again be an integral multiple of 2π. This is termed the *transverse resonance condition*.

If 2a is large compared to the wavelength of the light, then there will be a large number of angles θ that satisfy the transverse resonance condition. As the thickness of the waveguide is reduced, the number of possible solutions decreases until, in the limit, there is only one angle at which the light can propagate. Each discrete angle of propagation is termed a *mode,* and below a critical thickness (the cut-off thickness) no waveguide modes can be supported. Waveguides are termed *monomodal* if they can only support one mode, or multimodal if they can support more than one mode. Since a thin, monomodal waveguide will support the largest number of internal reflections, we find the sensitivity of monomodal waveguides to be higher than that of multimodal waveguides. Since the thickness of a monomodal waveguide is typically less than a wavelength, these waveguides are too fragile to be used without a thick substrate for support. This reduces the sensitivity, as only one side of the waveguide is exposed to the sample to be analyzed.

A guided mode in a waveguide also produces an evanescent field in the lower index layers outside the waveguide. In essence, some of the light is traveling outside the high-index waveguiding layer. The effective refractive index (N) of the waveguide depends on the bulk refractive indices of the waveguide and the cladding, and the relative proportions of the light in the waveguide and the cladding layers. This means that the effective index is always between the waveguide and the cladding indices.

The other implication of this is that if the refractive index of the cladding layer changes, the effective index of the waveguide changes also, which can be detected by a change in phase. Thus, waveguides are sensitive to changes in refractive index as well as to absorption outside the waveguide layer. To maximize this sensitivity, we need to increase the amount of light in the evanescent field. To do this, we require a large difference between the waveguide and the cladding refractive indices, and the waveguide should be thin enough to support only a single mode. Because of the nature of the equations that determine the supported modes of a waveguide, exact analytical solutions are not possible and numerical solutions are required. Figure 29.5 shows the sensitivity of a planar waveguide to changes in the external bulk refractive index as a function of waveguide thickness, Figure 29.6 shows the

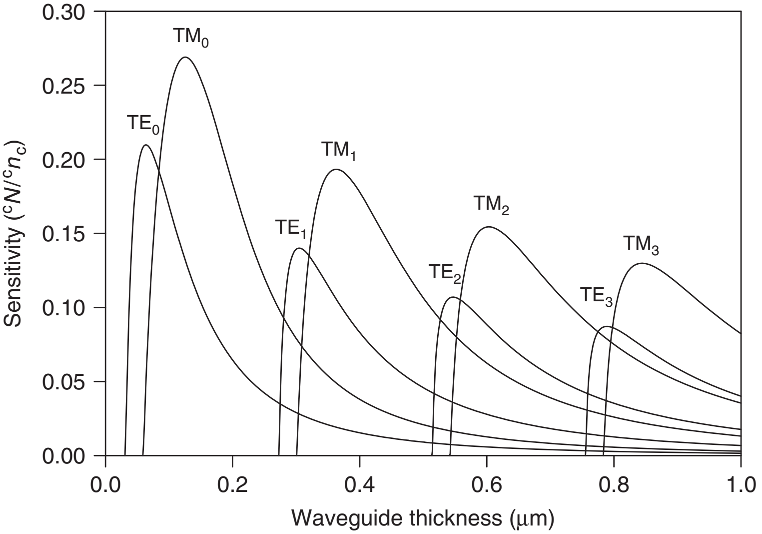

Figure 29.5 Graph of the sensitivity (ratio of the change of waveguide effective index to change in refractive index of cover layer) as a function of waveguide thickness for the first four TE and TM modes. Substrate index 1.46, waveguide index 2.00, and cover layer index 1.333, calculated for illumination at 660 nm.

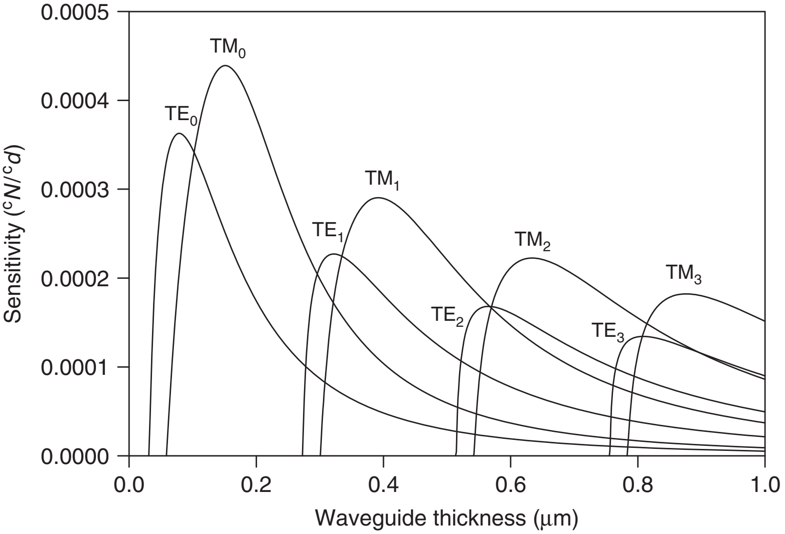

Figure 29.6 Graph of the sensitivity (ratio of the change of waveguide effective index to change in thickness of a thin adlayer) of the waveguide as a function of waveguide thickness for the first four TE and TM modes. Substrate index 1.46, waveguide index 2.00, adlayer index 1.45, and cover layer index 1.333, calculated for illumination at 660 nm.

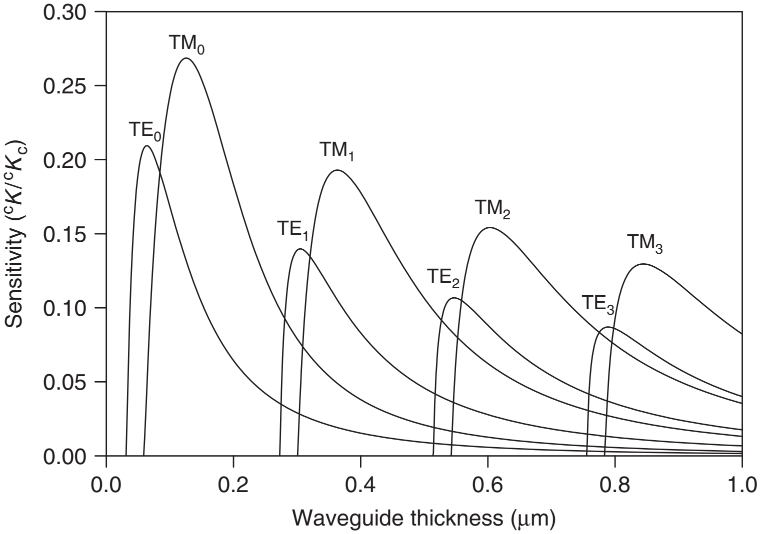

Figure 29.7 Graph of the sensitivity (ratio of the change of the imaginary part of waveguide effective index to change in the imaginary index of the cover layer) as a function of waveguide thickness for the first four TE and TM modes. Substrate index 1.46, waveguide index 2.00, and cover layer index 1.333 calculated for illumination at 660 nm.

sensitivity of the waveguide to changes in thickness of an adsorbed layer on the surface as a function of waveguide thickness, and Figure 29.7 shows the sensitivity of the waveguide to losses in the cover layer.

These graphs clearly show that there is an optimum waveguide thickness that maximizes sensitivity to refractive index changes for a particular mode, that these optimum thicknesses are different for TE and TM modes, that TM modes are generally more sensitive than TE modes, and that the zero-order modes are the most sensitive. The general form of all three graphs is the same, as they effectively measure the fraction of the light present in the evanescent field that is interacting with the material being sensed.

The calculations in the preceding paragraphs have been performed for a simple planar slab waveguide of infinite extent but finite thickness sandwiched between a semi-infinite substrate and cover layers. Other waveguide configurations are possible, most notably the cylindrically symmetrical case of a high refractive index rod surrounded by a lower index cladding. This is the fiber-optic configuration used widely in telecommunications.

The number of different optical methods depending on the optical thickness $n \times d$ (refractive index times physical thickness) is large. The following sections demonstrate that it is difficult to decide whether a device can be classified as a fiber or a waveguide, having read-outs influenced by evanescent fields, gratings, the waveguide structure, interferometric effects, or even a combination of these. Therefore, perhaps the best classification can be achieved by discriminating whether changes in refractive index or changes in the physical thickness of the layer are predominantly responsible for the measured effect. Thus, micro-refractometry or micro-reflectometry characterize the detection principle.

29.3
Measurement Configurations of Refractivity

29.3.1
General

There are various possible configurations that utilize evanescent waves for biomolecular sensing and spectroscopy [15–17]. Waveguides (either planar or in an optical fiber) can be used as prism couplers, grating couplers, mode couplers (interferometers), and in surface plasmon resonance (SPR), and FTR experiments. Grating couplers use a grating fabricated in either the substrate or waveguide to couple light in and out of the waveguide. As the surface refractive index changes, the in-coupling angle also changes, resulting in a change of the angular position of the out-coupled light on an appropriate detector. In this mode, grating couplers work very much like SPR and resonant mirror (RM) sensors. They can also be used purely as a means of coupling light in and out of the waveguide to permit detection of absorption or fluorescence changes. Interferometers (such as Mach–Zehnder, Michelson, or Young devices) use a separate reference channel that does not undergo the chemical binding stage to act as a phase reference. A periodic change in intensity at the output is observed, caused by interference between the sensing and reference channels as the refractive index on the sensing channel changes. A problem with interferometers is that the output can be ambiguous, as a large change in refractive index can take the output through more than one cycle. These devices are generally very sensitive.

Dual polarization sensors make use of the phase changes between the TM and TE modes propagating in a waveguide. If equal intensities of TE and TM are excited at the input, the polarization state of the output will depend on the relative phase shift between TE and TM at the output. Since the sensitivity of the waveguide is different for TE and TM modes, a change in refractive index on the waveguide surface will result in a change in polarization at the output. Similar to interferometric sensors using the evanescent field, the output is cyclic and can result in ambiguous outputs. The sensitivity is very high.

In FTR experiments, a leaky high index waveguide is used, which permits in- and out-coupling at well-defined coupling angles. The coupling angle depends strongly on the cover layer refractive index. They can also be used to monitor absorption, as the reflectivity is a strong function of the loss in the cover layer.

All these sensors are based on changes in the effective refractive index of the waveguide and use various forms of in-coupling and read-out techniques. A short review and comparison of these principles has been published [18a]. Design and fabrication of a complete optical interconnection scheme including the optoelectronic package, laser incoupling, and read-out has recently been published [18b].

29.3.2
Fiber Optics

Optical fibers are cylindrical waveguides consisting of a high-index core surrounded by a low-index cladding layer. Because of their low losses, fiber optics is widely used in the telecommunications industry, although the properties of telecommunications fiber optics make them poor sensors. Specially designed fiber optics can be used as biosensors, using a thin or no cladding layer on a monomode fiber core to permit interaction of the evanescent field with the material to be sensed [19–21]. Conventional fiber optics has also been widely used for sensing applications, but in the majority of cases, it has been used as a convenient means of delivering and collecting light for conventional spectroscopies.

29.3.3
End-Fire Coupling

End-fire coupling, as its name implies, is carried out by focusing a laser beam into a diffraction-limited spot centered on the waveguiding layer. Although end-fire coupling is conceptually very simple, it is not easy to perform in practice. One example where end-fire coupling has been successfully used in biological sensing applications is the difference interferometer [22–25].

If we consider Figure 29.6, we can see that there are waveguide thicknesses at which the difference in sensitivity between the TE and TM modes is at a maximum. If linearly polarized light is launched at 45° to the plane of the waveguide, equal intensities of the appropriate TE and TM modes will be launched. Since end-fire coupling will generally excite more than one mode, the waveguide thickness is chosen such that only monomode operation will be possible at the excitation wavelength and the difference in sensitivity between the TE and TM mode is maximized. As the surface refractive index changes, the retardation of the TE and TM modes will change by different amounts, changing the relative phase of the TE and TM modes, and hence the polarization state of the out-coupled light. When the TE and TM components are in phase, the out-coupled light will be polarized in the same direction as the in-coupled light. As the phase difference between TE and TM increases, the out-coupled light will become elliptically polarized, reaching circular polarization when the phase difference reaches $\pi/2$. At a phase difference of π, the light will be linearly polarized again, but at 90° to the polarization of the in-coupled light. As the phase difference increases further, the light will again become circularly polarized at $3\pi/2$, but with the opposite handedness, while at 2π the cycle will be complete and the out-coupled light will be polarized identically as the in-coupled light. This cycle can be followed using an appropriate arrangement of beam splitters, polarizers, and detectors, returning the TE–TM phase difference after processing the detector outputs. Since the phase difference is a cyclical function of the surface refractive index, this device does not give an unambiguous measurement of the surface refractive index. It can track slow changes in refractive index, but can only track the index successfully if the index change causes a phase change smaller than ±π between successive samples of the output. Because the path lengths employed in this type of sensor can be quite large (~10 mm), the sensitivity is quite high. Effenhauser *et al.* [26] were able to detect 10^{-11} M concentrations of human immunoglobulin G (IgG) using anti-human IgG antibodies with a difference interferometer configuration and a thin titanium dioxide waveguide. In studies with a bidiffractive grating coupler system, Kubitchko *et al.* [27] have used nanoparticles to enhance the sensitivity for the detection of analytes such as the thyroid-stimulating hormone (TSH). Without amplification, the detection limit was 430 pM, and with amplification by a latex-conjugated sandwich antibody, the detection limit dropped to 0.11 pM, which is the range of clinical interest (0.3–667 pM TSH).

29.3.4
Grating Couplers

A grating structure at the substrate–waveguide or waveguide–cover layer interface can be used to couple light into the waveguide [28]. A major advantage of this method is that the waveguide can be fabricated on a simple planar substrate and coupling can take place through the bottom of the substrate. Careful design of the waveguide and grating can permit the use of TM-polarized light at the Brewster angle, which eliminates reflection at the bottom surface of the substrate.

Dubendorfer and Kunz [29] employed a chirped grating coupler design, where the grating period varies continuously along the width of the coupling area. This means that light will only couple into the waveguide at the location where the grating equation is satisfied. Thus, the position in space of the out-coupled beam is a simple function of the surface refractive index. They were able to detect refractive index changes of 5×10^{-6}, corresponding to changes in surface loading of 5 pg mm^{-2}. An interesting read-out based on a rotating sample was compared to polyelectrolyte layers and biotin/streptavidin interactions in comparison to other waveguide devices [30].

Using grating couplers, the first instrumentation was developed by Tiefenthaler and Lukosz [31] based on optical principles realized by Lukosz and Tiefenthaler [32] in the small and medium sized enterprise (SME) *artificial sensing instruments* (*ASI*) in Zurich and found application in research. Tiefenthaler's goniometer has been modified by a precision-sensitive CCD (charge-coupled device) array, which avoids mechanical angle-scanning the optimum coupling angle [33]. Another possibility is a bi-diffractive coupler, which represents a ''mixed grating'' [34]. A second angle of out-coupling is achieved, which differs from that of normal reflection. By these means, the signal-to-noise ratio increases drastically, and the set-up is simpler than the *ASI* instrumentation. To reduce grating costs, embossed polycarbonate gratings as disposable chips can be considered. Varying either the grating constants across the chip or the waveguide height in which the grating is embedded, the resonance to the refractive index varies across the waveguide [35, 36]. Nowadays, the OWLS 210 from *MicroVacuum Ltd.* [37], an optomechanical grating coupler, is commercially available and provides biomolecular interaction applications [38a,b]. Details of the technology can be found in [39].

Best known is the *Corning Epic*, a broadband source grating coupler with a high-throughput platform that is used for biochemical and cell-based screening [40]. This system has been used to examine regulations of cell functions [41] or label-free cell-based screening of GPCR (G protein-coupled receptor) agonists and antagonists [42a]. Review on the screening of cellular targets using this system in comparison to other label-free platforms is given in [42b]. Since a few years, based on the Corning Epig System, Perkin Elmer offers a Multimode Plate Reader called EnSpire™ as the only bench-top plate reader available with optical label-free technology. Other modes of detection that are available in this configurable system include Alpha technologies, ultra-sensitive luminescence, fluorescence intensity, and absorbance in microplates up to 384 wells [42c].

Different optical principles of grating couplers have been reviewed in detail [33, 43].

29.3.5
Photonic Crystals

Photonic crystals have a periodic dielectric structure with a periodicity lower than the wavelength of radiation [44]. A one-dimensional ‘‘photonic crystal’’ just represents a simple grating. Therefore such devices can be considered as special types of grating couplers. A broadband source coupler system available from *SRU Biosystems*, described as a cost-effective platform for low to ‘‘ultrahigh’’ throughput, provides biochemical and cell-based applications [45]. On the basis of a former grating approach [46] below each well of a kind of microtiter plate a grating array and a scanning fiber read-out head are placed. The authors call this system the *BIND-system* [47]. *SRU* uses photonic crystals, given by periodical laterally resolved changes in refractive index on a polyester sheet (up to 1536 wells) [48]. Newer instrumentation even allows a combination of label-free and enhanced fluorescence detection [49a]. Publications use this system for interaction studies at membranes for regulations in neurosciences [49b]. Epic and BIND are compared for cellular-based screening [50].

These devices have been recently compared to other evanescent field techniques. Various arrangements and applications are given [1]. Recently, parameters for label-free biosensors have been theoretically calculated [51] and applications to ultrasensitive DNA detection are published [52].

29.3.6
Bragg Gratings

By embedding gratings in fibers by interchanging areas of different refractive indices (Figure 29.8), the grating conditions select a frequency to be reflected inside the core of the fiber [53]. Thus, a dip in intensity is formed in the bandwidth of the transmitted radiation, whereas the back propagating radiation exhibits a

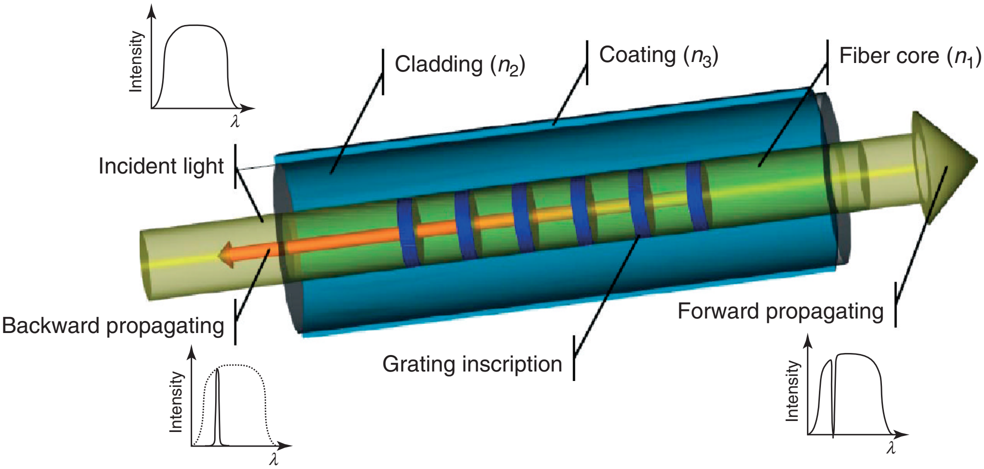

Figure 29.8 Fibers with Bragg grating, according to Meixner [56].

single line. Although Bragg gratings were first used in telecommunication and in temperature measurements, biosensing applications were published in the meantime. Maguis *et al.* [54] demonstrated the possibility of label-free immune sensing with BSA/anti-BSA interactions. These modified fibers are also used for locally resolved remote control. Changes of the refractive index in the coating or cladding can be read-out sensitively. Kashyap [55a] also proposed a Bragg grating assisted plasmon-polariton fiber for biomedical applications. A variety of applications of Bragg gratings and technical modifications have been published in the last years: for the determination of composition of fuel and biofuel [55b], label-free DNA detection [55c], or measuring of human osteoblastic cells [55d]. New possibilities to fabricate Bragg gratings are given in [55e].

29.3.7
Backscattering

A coherent single wavelength laser focuses onto a waveguide (or capillary) and a small sensing area, and results in another interference device. The reflected interference pattern is analyzed with respect to the wavelength using a detector, and monitors shifts dependent on changes in the refractive index. A newer review is given in [57], whereas various optical set-ups and applications are provided in [1]. One of the first applications of this approach is in packed-capillary high-performance liquid chromatography [58]. Label-free molecular interaction determination with nanoscale interferometry can be achieved on channels molded in PDMS (poly-dimethyl-siloxane) as perspective in proteomics [59a]. The use of nanoparticles in combination with back-scattering interferometry has been patented recently [59b] as well as using aptamer–protein interaction for biosensing [59c].

A variation of this principle is an arrangement on an optical disk comparable to a ''CD-player'' [60], which was commercialized by Quadraspec. This company changed its name in 2010 to Perfinity Biosciences Inc. and focused on protein sample preparation [61]. Recent achievements have been reviewed [62] and the detection of prostate-specific antigen in patient sera by a fluorescence-free BioCD protein array is given [63].

29.3.8
Resonant Mirror (RM)

The RM device consists of a high-index substrate (lead glass with a thickness of ~1 mm, $n_d = 1.72825$), a thin low-index spacer (about 1000 nm of magnesium fluoride or silica), and a very thin monomode waveguiding layer (about 100 nm of titanium oxide, zirconium oxide, hafnium oxide, or silicon nitride). It can be used to monitor the refractive index and the absorbing or fluorescent species within the evanescent field above the waveguide [64].

Light incident above the critical angle on the substrate/spacer interface is coupled into the waveguiding layer via the evanescent field in the spacer layer when the propagation constants in the substrate and waveguide match. For monochromatic light, this occurs over a very narrow range of angles, typically spanning <10 arcmin. The device has been termed the *resonant mirror* because it contains a resonant cavity (the waveguide), and it acts as a nearly perfect reflector for light incident above the critical angle. Since the waveguiding layer acts as a resonant cavity, the light reflected from the RM device undergoes a full 2π phase change as we scan across the resonance. To detect the resonance position, a phase reference must be provided, which is substantially constant in phase. This could be provided by splitting off part of the input beam and recombining it with the light from the sensor, but this is difficult with regard to instrumentation, and means that the object and reference beams travel by widely separated paths. Ideally, the two beams should travel by identical paths so that phase-shifting effects (such as temperature changes) are common to both beams. This can be accomplished in the RM sensor by using the TE mode as reference for the TM resonance and vice versa. This is only feasible because the resonance positions for TE and TM are widely separated.

The resonance positions may be determined in two ways:

1) in angle, using monochromatic input light covering a range of input angles (angular scan mode) [64];
2) in wavelength, using broadband input light at a fixed input angle (wavelength scan mode) [65].

To determine the resonance angles or wavelengths at which light couples into the waveguiding layer, linearly polarized light at 45° to the plane of the waveguiding layer is applied to the device, exciting equal intensities in the TE and TM modes. The output light from the device is passed to a crossed analyzer, which only passes light that has undergone a π phase change in the sensor device. In the angular measurement mode, the input light is a converging monochromatic wedge beam, covering a sufficiently wide range of input angles to permit the resonance angle (for the fixed wavelength) to be determined for the required range of surface refractive indices. In the wavelength measurement mode, the input light is a well-collimated beam of white light, covering a sufficiently wide range of wavelengths to permit the resonance wavelength (at the fixed input angle) to be determined.

Buckle *et al.* [66] used the RM to monitor antigen/antibody and enzyme/substrate/inhibitor interactions using several methods for immobilization of the biomolecules at the sensor surface. Sensitivities in the nanomolecular range were reported. Watts *et al.* [67] used the RM sensor to monitor the binding of microbial cells to antibodies immobilized on the surface of the sensor. They detected the binding of *Staphylococcus aureus* (Cowan-1 strain) to human immunoglobulin G (hIgG), covalently immobilized on the sensor surface via aminopropylsilane, at concentrations between 8×10^6 and 8×10^7 cells cm^{-3}. By employing a sandwich assay using a hIgG–gold particle conjugate, detection limits were reduced by a factor of 1000. It appeared feasible to detect between 4×10^3 and 1.6×10^6 cells cm^{-3} in spiked milk samples. Newer approaches use porous silicon for the measurement of very low DNA concentrations [68].

Some instruments based on the RM were commercially available (the *IASys* system of Thermo Labsystems/Affinity Sensors) [69], which used the angular scan mode to determine the resonance angles. According to the Internet, however, the product field of this company has changed.

29.3.9

Surface Plasmon Resonance (SPR)

Surface plasmon waves are excited in thin metal films when appropriate coupling conditions are met. The surface plasmon wave is an oscillation of the free electrons in the metal under the influence of the electric field of the light [17]. For sensor applications, the Kretschmann configuration [70–72] is most often used, where a thin metal layer (usually 50 nm gold) is deposited on a glass prism and light is coupled into the metal film at the coupling angle. This configuration is shown in Figure 29.9. Only TM polarized light shows this behavior where the mode is localized at the metal–cover layer interface. TE polarized light does not show this behavior. Since the metal film is very lossy (it has a large imaginary component of the complex refractive index), the reflected light is very strongly attenuated at the coupling angle. The coupling angle is a very strong function of the cover layer refractive index. Thus, as material binds to the metal layer there is a change in the angle at which the drop in reflectivity occurs. This is the basic sensing mechanism for SPR biosensors, as shown in Figure 29.10.

Instrumentation for SPR sensors generally comprises a monochromatic light source (a filtered incandescent lamp, LED, or laser) followed by a cylindrical lens to provide illumination over a wide range of angles. A CCD detector is then used to monitor the position of the dip in intensity (angle measurement mode), which indicates the coupling angle. Alternatively, a collimated beam of white light may be used at a fixed angle of incidence, and the wavelength position of the dip determined

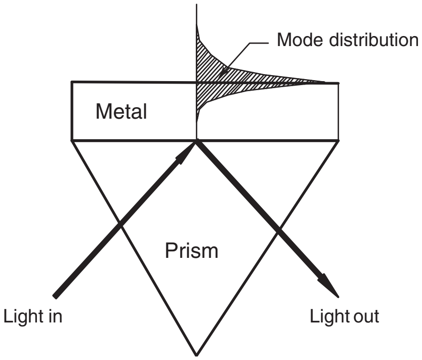

Figure 29.9 The Kretschman configuration for excitation of SPR in a thin metal layer.

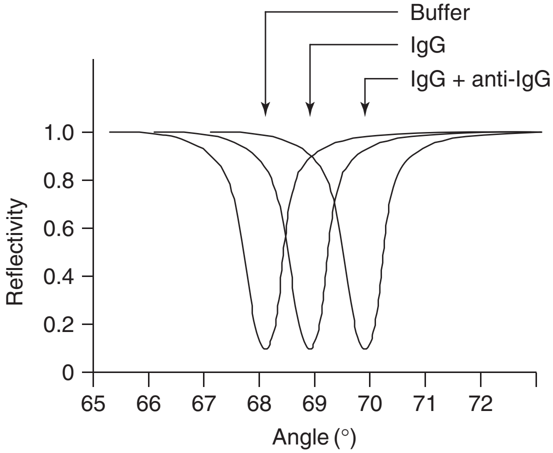

Figure 29.10 Illustration of the shift in resonance angle at various stages in the adsorption of biomolecules to the metal surface.

(wavelength measurement mode). Systems of this kind have no moving parts, and thus can follow very rapid changes in the angular position of the reflectivity dip. The metals most often used are gold or silver, but copper can also be used. These metals all have the high conductivity needed to give a relatively narrow dip in reflectivity, making the task of following small changes in the position of the dip easier.

Former reviews demonstrate the development in instrumentation, parallelization and application [73–78]. Instrumentation is reviewed in [79], and many new systems are considered for the future [80a]. Recent instrumentation and application are reviewed from a nanotechnology standpoint of view [80b]. Combination of SPR with Bragg gratings is gaining increasing interest [80c,d].

Since its commercialization, SPR has been used for the detection of a large variety of biomolecules. Reviews on the applicability of SPR detection have appeared rather regularly, discussing biomolecular interactions of proteins, nucleic acids, lipids, and carbohydrates, and demonstrating the fast growing interest in biomolecular interaction analysis (BIA) [81–86].

SPR has also shown some usefulness in the study of conformation changes of adsorbed proteins. For instance, Boussaad *et al.* [87] have used multiwavelength SPR to study conformational and electronic changes induced by the electron transfer reaction in cytochrome c, and Sota and Hasegawa [88] studied the acid-induced denaturation of an immobilized protein. DNA hybridization has also been studied by SPR [89]. Through many studies, much new knowledge has been acquired on the kinetics of antigen–antibody reactions at surfaces [90].

Besides, some other interesting applications have been published, dealing with global conformational transitions in human phenylalanine hydroxylase [91], examining peptides from the GH loop of the foot-and-mouth disease virus [92], measuring gentamicin residues [93], and determining penicillin residues in milk [94].

More recent applications deal with the detection of pathogenic microorganisms [95], review high-throughput label-free interaction analysis [96], even combining SPR microscopy and imaging to analyze kinetics quantitatively [97]. Refractometry can also be achieved using micro-optical fluidic systems [98]. Fragment-based screening is also possible using SPR [99], and the possibility of quantitative analysis of small molecule interactions with nucleic acids is demonstrated [100]. Recently, the benefits of SPR in food analysis have been reported [101a]. Development of portable and miniaturized SPR, even paper-based, opens new fields of simple applications [101b].

29.3.9.1 **Commercial SPR Biosensors**

Commercial systems using SPR sensing methods have become available from a number of suppliers. These systems range from large multichannel laboratory bench instruments to simple single-channel integrated devices in an integrated-circuit style package.

As the first direct optical detection technique, Pharmacia Biosensor AB (founded in 1984) commercialized SPR for studying biomolecular interactions; *Biacore®* was launched in the fall of 1990. Acquired by GE Healthcare in 2006, Biacore now offers a family of instruments for monitoring interaction processes in single channel fluidics and arrays. The Biacore system is based on the Kretschmann configuration, and is a multichannel instrument that has been extensively used for biological assay work and for monitoring both thermodynamic (dissociation constants) and kinetic (on and off rates) parameters of a wide range of biomolecular interactions. The present product range [102] of Biacore includes dual-channel instruments with varying specifications and the *Biacore Flexchip*, described as an array-based parallel kinetic profiling instrument with 400 spots on the sensor surface [103]. In a huge database, the newest publications can be found [104], dealing with a large number of interesting applications. The marketing concept of label-free protein interaction has been explained recently [105].

A competitive alternative to the Biacore, the *IBIS* series of biosensors, has been developed in the Netherlands at the Twente Technical University [106], which is based on the conversion of angle data into a time interval by the use of a vibrating mirror system [107]. An imaging application is given in [108].

The *Spreeta*™ device, formerly manufactured by Texas Instruments (now by Sensata Technologies in Attleboro, MA), is a low-cost miniaturized SPR sensor platform that allows real-time quantitative concentration, affinity, and kinetic analysis of biomolecular interactions [109]. Elkind *et al.* [110] describe the use of the Spreeta device as a refractive index sensor for a direct assay for human creatine kinase MB (CK-MB, a marker for heart attacks) using adsorbed anti-CK-MB antibodies, obtaining a change in index of $\sim 4 \times 10^{-4}$ for the binding of 100 ng ml^{-1} of CK-MB. They were also able to assay trinitrotoluene (TNT) using a competitive assay format by immobilizing a trinitrobenzene–bovine serum albumin adduct to the sensor surface, detecting 7 ng ml^{-1} of TNT. Sesay and Cullen [111] have used the Spreeta sensor to monitor endocrine disrupting chemicals (EDCs) in aqueous samples. The sensor surface can be regenerated by using a strong domestic detergent (Persil biological liquid) to remove all the biological material. The detection range was 10–150 ng ml^{-1}. The most recent published evaluation of the device is from 2003 [112].

Other companies have entered the market in recent years, such as *Reichert Life science* [113] and *BI Biosensing Instruments* [114]; the latter provides a large number of customer applications such as those described in [115], dealing with wild-type and mutant p53 proteins in cancer cell lysates and performed with a dual-channel SPR instrument. *Analytical* μ*-Systems*, a Department of Mivitec GmbH, offers to measure interaction of biomolecules (antigen–antibody and others) and binding constants with the *BIOSUPLAR 6 system* [116, 117].

Surface plasmon resonance imaging (SPRi) systems developed by *GenOptics* [118], a technology innovator in SPR, are now distributed worldwide by *HORIBA Jobin Yvon* [119]. With *ESPRIT, SPRINGLE*, and *TWINGLE*, *Ecochemie* in the Netherlands [120], a daughter of *Metrohm Autolab*, has brought a product family to the market dedicated to label-free measurement of biomolecular interaction processes, even in combination with electrochemical analysis. This business was outsourced to *Kinetic Evaluation Instruments BV* in the Netherlands [121]. This method is called *ESPR* (electrochemical surface plasmon resonance).

XanTec in Düsseldorf specializes in biosensor and bio-chip development [122], selling with their SPR Biosensor *SR7000DC* various chips and applications. *GWC Instruments* in Madison [123] offers Fourier transform and imaging SPR with applications to life science and material research, *Sierra Sensors* sells not only quartz micro balance sensors but also SPR equipment [124], and *DKK-TOA Corporation* [125] in Japan has entered the market with model *SPR-20. Biolin Scientific* [126] in Sweden in principle concentrates on quartz micro balance instrumentation. However, SPR is also part of their business, since this company acquired former *KSV Instruments* (Helsinki), which had long years of expertise in SPR development. These SPR *Navi*™ products are further developed by *BioNavis* [127] with applications in life sciences and material sciences. Recently, *Accurion* (former named *Nanofilm*) in Goettingen has developed an ellipsometric platform in combination with a SPR kit [128a]. It is called *nanofilm_SPR_microlab* and uses a cell design tailored for imaging ellipsometry and imaging SPR in the ellipsometric mode [128b].

29.3.9.2 Fiber and Waveguide SPR

Fiber-optic devices are attractive in many applications because they can be very small physically and provide remote operation and electrical isolation from the associated instrumentation. For these reasons, many designs for fiber-optic SPR sensors have been developed. They all rely on phase matching between the optical mode in the fiber and the surface plasmon wave. Since the control over the coupling angle is lost in a fiber, wavelength scanning is often employed. Slavik *et al.* [129] have shown that a wavelength-scanned fiber-optic SPR sensor can detect very low concentrations of proteins. They used a single-mode optical fiber with a cut-off wavelength of 724 nm, which was polished down to remove all but 500 nm of the cladding. The resulting device was coated with 65 nm of gold to support surface plasmons, and then with 19 nm of tantalum pentoxide to adjust the sensor's operating range to refractive indices between 1.329 and 1.353. This device was capable of detecting 40 ng ml^{-1} of human IgG using anti-human IgG antibodies immobilized on the sensor surface by cross-linking with glutaraldehyde.

A similar behavior is observed when a thin metal layer is coated on a planar waveguide. Harris and Wilkinson [130] have developed the theory of waveguide-coupled SPR sensors. Brecht and Gauglitz [131] have compared the performance of a waveguide-coupled SPR sensor against a grating-coupled waveguide, a channel waveguide interferometer, and a thin-film reflectance sensor for the detection of pesticides using a competitive assay format with anti-triazine antibodies. Instead of using a full spectrum scan, the intensity at a fixed wavelength was monitored. The limit of detection for triazine was found to be 0.15 ng cm^{-3}. Newer developments of fiber/SPR combination have been mentioned in Section 29.3.9.

29.3.9.3 Sensitivity and Applications of SPR-Based Biosensor Instruments

In a recent review by Homola *et al.* [73, 132], the analytical characteristics of various SPR instrumentation configurations have been compared with respect to the type of coupling (prism or grating) and the mode of measurement (angular, wavelength, and intensity read-out). In principle, the prism-coupler (Kretschman) configuration was assessed as being capable of yielding the highest sensitivity (in terms of refractive index change) in comparison to a grating-coupler-based set-up, particularly when the method of interrogation was based on intensity measurements. Lekkala and Sadowski [133] have used the Kretschmann configuration in conjunction with lock-in amplifiers for the highly sensitive detection of intensity changes at near-resonance conditions. The system was used for the optimization of antibody orientation on various lipid-modified surfaces [134].

Although the intrinsic sensitivity of SPR measurements (without any amplification schemes) had been initially assessed to be of the order of 1 nM or 150 μg l^{-1} for IgG [135], lower detection limits for small analytes have been reported [27, 136]. In most studies, equilibrium dissociation constants ranged from nanomolar to micromolar, with a few studies in the picomolar range [137, 138]. The resolution of

SPR measurements has, to some extent, been improved by using well-designed reference surfaces and sophisticated data-processing techniques [139]. SPR has been combined with other techniques, such as mass spectrometry [140] and atomic force microscopy (AFM) + electrochemistry [141]. Particularly, the combination of multichannel SPR with MALDI-TOF (matrix-assisted laser desorption/ionisation-time of flight) can be regarded as a powerful tool for proteomics research (Chapter 24).

In general, SPR-based biosensors have detection limits around 50 pM or 100 pg cm^{-2}. This is not always sufficient for the detection of low molecular weight analytes where concentrations fall below picomolar levels [142]. In such cases, amplification of the signal by sandwich assay formats or binding inhibition assays is presently the only solution. Already in 1988, Mandenius and Mosbach [143] had used quartz particles to amplify ellipsometric measurements of biospecific interactions. Similar labels, which have a large effect on the refractive index near the surface, will be suitable for use with SPR. For instance, Lyon et al. [144a] have described the use of colloidal Au nanoparticles to enhance the SPR response, through strong optical coupling between the film and the particle, achieving detection limits for human IgG down to 6.7 pM using a sandwich immunoassay format. Besides a large shift in incident angle, the colloidal gold gives a broadening of the plasmon resonance peak and an increase in minimum reflectance.

Combination of SPR with TIR increases sensitivity [145]. It was demonstrated that combining SPR and TIR devices to form a collinear, heterodyne interferometric system provided an enhanced sensitivity of real-time phase detection. Spatial variations of orientation of the reflected beam were also overcome. A refractive index sensitivity of $\approx 2 \times 10^{-7}$ was achieved. Small-angle applications in heterodyne interferometry use the two polarization states [144b]. Combination of surface plasmon resonance and total internal reflection ellipsometry (SPR-TIRE) is used for *in situ* monitoring of the growth of poly(*N*-isopropylacrylamide) brushes [144c].

29.3.10
Mach–Zehnder Interferometer

This optical detection principle combines interferometry with evanescent field effects. In substrate, waveguides are embossed, forming a bifurcation as shown in Figure 29.11a. In-coupled radiation, preferably from a laser, is split into two arms, one of which is covered with the biosensitive layer whereas the other serves as reference. The result is a phase shift ($\Delta\Phi$) dependent on the length L of the sensitive layer, its refractive index n, and the wavelength (given by the wave vector k). Details are given in [43]. Development, limits of measurable refractive index changes, modified arrangements, and comparison to other integrated optics devices have been reviewed recently [146a]. The resulting interferogram is shown in Figure 29.11b. *Lionix* in Twente supplies Mach–Zehnder interferometers commercially and gives some applications [146b].

The first applications to biosensing have been demonstrated [147, 148], and measurements of pesticides in water using immune reactions have been published [149]. Using surface structuring masks, parallelized waveguiding arms can be produced,

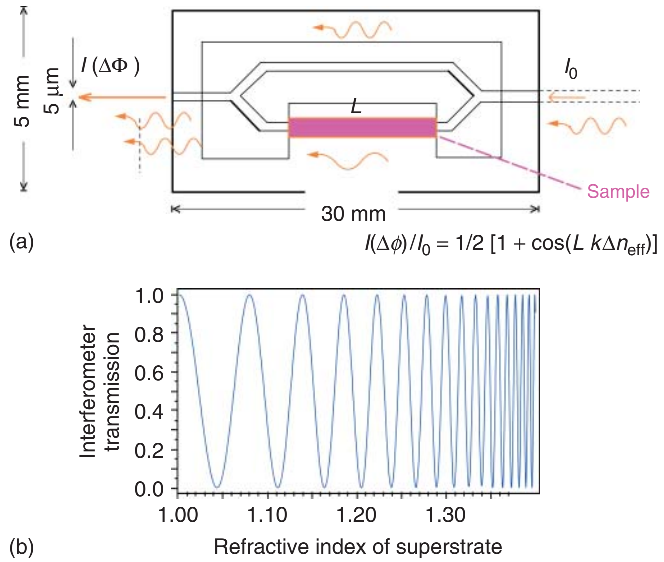

Figure 29.11 Mach–Zehnder direct optical biosensor with two waveguide arms, one covered with a biosensitive layer (a). The phase shift between this arm and the reference one causes an intensity signal at the outlet (left) dependent on refractive index, length L, and amount of interacting sample. This shift is schematically given below in dependence on the superstrate (b). (According to Ref. [15].)

which show good limits of detection combining grating in- and out-coupling with the Mach–Zehnder structure [150]. In principle, these devices are rather difficult to handle. Nevertheless, their high sensitivity makes them interesting for affinity sensing [151, 152]. Integration of microfluidics and using standard complementary metal-oxide semiconductor (CMOS)-compatible processed lab-on-chip systems have been realized to measure DNA [153a]. Modern applications are in the area of health care and point of care testing [153b].

To reduce the limit of detection, magneto-optic modifications have been patented [154] and parallelized. Applying external potential to the sensitive interferometer arm provides a zero phase-shift method, correlating the value of the external field to the analyte concentration. Since zero compensation is more sensitive in principle, better results are achieved [155, 156a]. An all-optic phase modulation system integrated in the Mach–Zehnder interferometer in general improves sensitivity [156b]. However, experimental expenditure increases [157].

29.3.11
Young Interferometer

If the two waveguide arms of the Mach–Zehnder interferometer are not combined, but form a free space arrangement, this device is called a *Young interferometer* [15, 158, 159]. The optical pathways are given in Figure 29.12a. The resulting

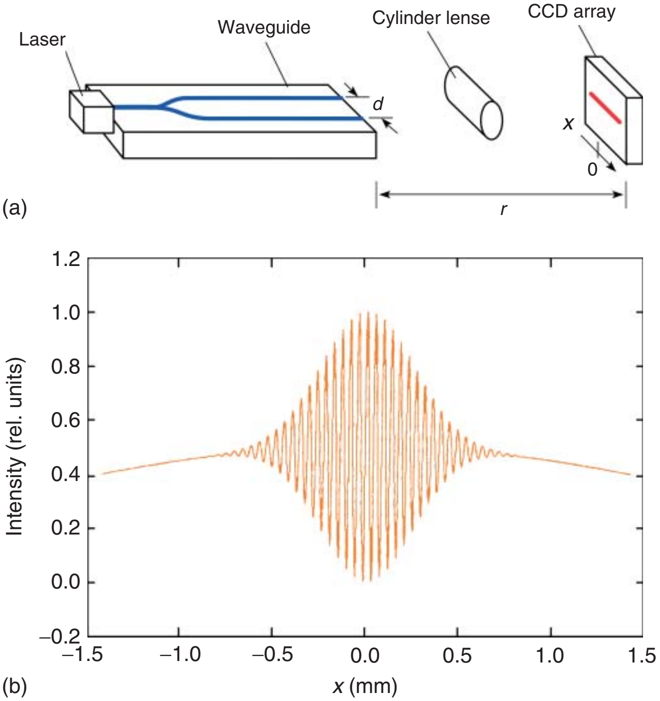

Figure 29.12 Young interferometer with free space optics (a). The resulting interference fringes are given below; this pattern shifts in the *x*-axis with changes in concentration of the interacting material (b). (According to Ref. [15].)

interference fringes of the superimposed partial beams leaving the two arms are given in Figure 29.12b. Such instrumentation was used to monitor an anti-human serum albumin/human serum albumin (α-HSA/HSA) immunoreaction in a microfluidic sensing system [160a]. Viruses can be detected [160b]. The biosensor was compared with others [161]. A dual polarization interferometer working as a Young interferometer has been realized [162].

A rather interesting modification uses two parallel waveguides in a chip in which radiation is coupled in by a grating and coupled out by another grating. This can be considered a free-space Young interferometer [163]. This principle can be seen in instrumentation commercialized by *Farfield* in Crewe (UK) [164] as a dual polarization interferometer (DPI). Polarized light from a laser is coupled-in down stacked waveguides. The evanescent field emanating from the top waveguide interrogates the immobilized molecules. Changes in the resulting optical interference pattern are caused by changes in the structure and/or mass of the immobilized molecules [165]. The *AnaLight®* instrument series provides a variety of instruments for biophysics and surface analysis in many applications [166]. It is used to interrogate DNA immobilization and DNA–small-molecule interactions in real-time [167].

29.3.12
Ring Resonators

It is known from attenuated total reflection spectroscopy used for absorbance sensors that the longer the interaction area, the better the signal-to-noise ratio. For this reason, the evanescent field absorbance sensor (EFAS) was a circular waveguide embedded in a glass substrate [168]. Accordingly, optical micro-ring resonators have gained much research interest in the last decade. Chip-based, stand-alone microsphere-based, and capillary-based opto-fluidic ring sensors are reviewed with a large number of technical modifications and biochemical applications [1].

The first applications to biosensing have been published in [169], modifying an integrated optics ring sensor for protein detection (avidin) at low concentrations (calculated detection limit: 0.1 nM (6.8 $\mu g\,l^{-1}$)). Liquid core optical ring resonators (LCORRs) use a glass capillary as both the fluidics and the ring resonator and show a measurable whispering gallery mode spectral shift of 30 pm/refractive-index-unit (RIU). This calculates a detection limit of approximately 10^{-6} RIU [170], allows quantitative real-time label-free detection of DNA sequences [171], and normally integrates optical ring resonator sensors into the microfluidic delivery system by using glass capillaries with a thin wall [172].

Other authors name similar sensing platforms that integrate the microfluidics and photonic sensing to an opto-fluidic ring resonator (OFRR) sensor. They demonstrate sensitive label-free virus detection [173] and use phage as a receptor for analyte detection [174]. Affinity selection from large libraries of random peptides displayed on phage provides a generic method of discovering receptors for detecting a wide range of analytes with high specificity and sensitivity. For such optical micro-ring resonators, numerical simulations of the distribution of the electromagnetic fields inside the waveguides, the micro-ring, and near the micro-ring surface have been done. Furthermore, all the functionalization reactions and the bio/non-bio interfaces have been studied and modeled by means of spectroscopic ellipsometry [175]. Finally, the design, fabrication, and characterization of an array of optical slot-waveguide ring resonator sensors, integrated with microfluidic sample handling in a compact cartridge, for multiplexed real-time label-free biosensing have been published [176].

29.4
Reflectometric Interference Spectroscopy (RIfS)

29.4.1
Principle

Reflectometric measurements are technically easy to perform and can yield useful information about thin films and their interfaces. The partial reflection of incident light from two interfaces of a thin film with a thickness of about 300–700 nm can function as a Fabry–Perot white light interferometer with low reflectance.

In the scenario depicted in Figure 29.13, the reflected light will show an interference pattern as a function of wavelength, according to

$$R = R_1 + R_2 + 2\sqrt{R_1 R_2}\cos\left(\frac{4\pi nd}{\lambda}\right) \tag{29.21}$$

where R is the reflectance, λ is the wavelength, n is the effective refractive index, and d is the effective physical thickness of the optical layer.

At the beginning, a white light source and a diode array were used to measure the spectral interference pattern according to Figure 29.13 (middle) and binding curves calculated from the spectrum shift on interaction as given in Figure 29.13 (right) [178, 179]. Among various algorithms for the evaluation of the interferograms, a polynomial fit proved to be the best [180]. After approximation of the cosine function in the wave number domain, the shift in extrema is correlated to the change in the product of refractive index and physical thickness according to

$$\Delta = \frac{4\pi}{\lambda} \times n \times d \tag{29.22}$$

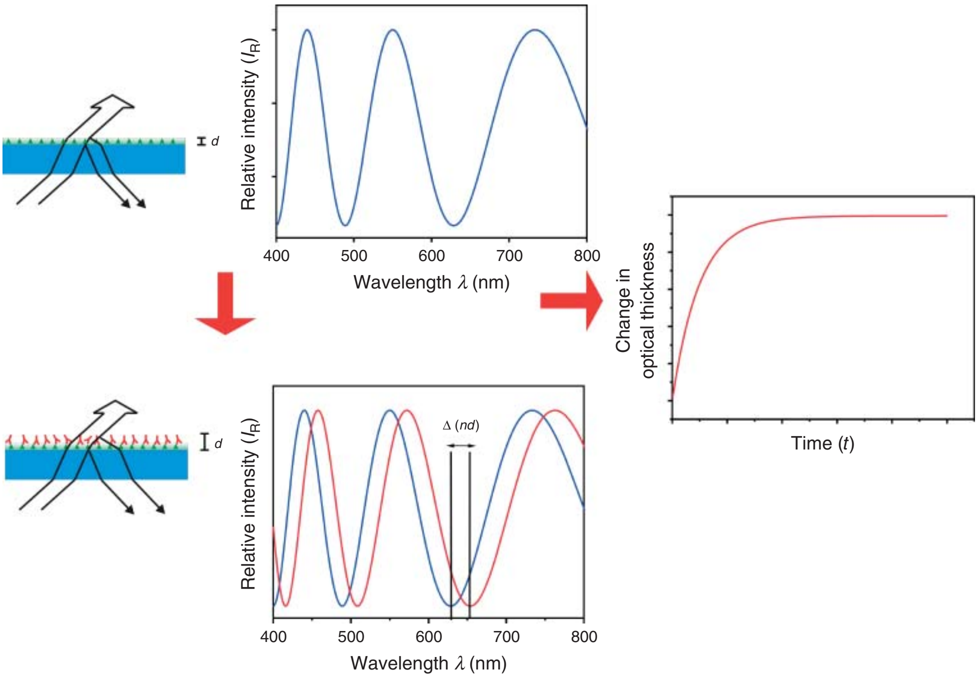

Figure 29.13 The principle of interference reflectometry at a thin film of increasing optical thickness: (left) The thin optical layer with several reflections from increasing optical thicknesses nd, changing physical thickness d by adding biomolecules gives (middle) the shift of the interference spectrum dependent on Δnd (top to bottom); from this shift the binding curve can be calculated (right). (Modified form from Ref. [177].)

This is the principle behind reflectometric interference spectroscopy, or RIfS. Evaluation can be more complex in multilayer systems, but can also be performed by means of Fresnel equations using matrix approaches for multiple reflections at interfaces of thin layer systems [181]. Fortunately, variation in temperature does not affect the signal, since increasing temperature increases the volume (physical thickness) and decreases the refractive index. Both effects nearly compensate each other; therefore, RIfS is only marginally dependent on temperature in contrast to other direct optical techniques based on read-out effects on evanescent fields. Owing to the high sensitivity of the detection, parts per million levels of phase shifts can be measured [182]. Thus, RIfS is a robust, simple, and potential low-cost direct optical detection technique. The principle was compared with other optical techniques and demonstrated limit of detections in the same order of magnitude as others [183, 184]. Also, affinity reactions of low molecular weight molecules such as biotin were detected [185].

29.4.2
Various Realizations

It could be demonstrated that spectral information can be substituted by just a few wavelengths to achieve simple and low-cost realizations. The spectrum was reduced to four selected wavelengths that supplied interpolation points for the parabola fit [186–188], and even a single carefully selected wavelength gives sufficient information [189]. Simulation allows finding the optimum wavelength depending on recognition layer and transducer properties [190]. This approach was transferred to a parallelized set-up improving the former solution, in which a microtiter format had been chosen [191] with a filter wheel sequentially selecting seven wavelengths. Avoiding the large and optically inconvenient microtiter plate format and using an object lens, a quantitative imaging system is achieved with approximately 700 spots cm^{-2} and noise representing less than 10 pm thickness incertainty which is equivalent to 2–5 pg mm^{-2} of biomaterial [192].

Latest developments focus on wavelength-selective detection using a multilayer semiconductor system, where the chip may be disposable in the future and which allows measurements at four wavelengths [193]. Such systems are planned to be used in point of care testing [194a]. A new technological approach together with application has been published using multilayer ‘‘photodiodes’’ to get wavelength-dependent detectivity [194b].

29.4.3
Applications

Starting with antigen/antibody interaction [195], in a next step immuno reactions were quantified [196] and RIfS was applied to directly measure triazine pollution of water [197, 198], opening new aspects in environmental analytics [199]. DNA–ligand interactions also can be quantified [200]. The ligand-induced assembling of the type I interferon receptor on supported lipid bilayers has been examined [201] and the adsorption of proteins on biomaterial surfaces has been quantitatively evaluated [202]. Some kind of RIfS has been used to rapidly detect mecA from methicillin-resistant *S. aureus* [203] and nucleic acid targets on optically coated silicon [204] as well as label-free oligonucleotides [205]. Biochips called *Fabry–Perot interferometer* have been examined [206]. Some additional applications have been reviewed in [207] recently. SPR and RIfS have been compared, giving practical tips for data evaluation and obtaining kinetic constants [208].

Another interesting approach is a Fourier transform version used as LC detector [209] for characterizing antibodies with respect to their affinity constants in affinity chromatography [210]. To qualify the surface modification, affinity constants of LNA (locked nucleic acid) and DNA duplex formation were determined [211] and endocrine receptors were examined [212];cell morphology also can be examined by RIfS [213]. Binding of ubiquitin to short peptide segments of hydrolase was studied in comparison to fluorescence correlation spectroscopy, isothermal calorimetry, and NMR [214].

Hyphenated techniques are frequently used in analytics. The spectroscopic detector can be substituted by RIfS, too. As in SPR, reflectometric interference can be combined with MALDI-TOF measurements by coating the glass type surface with ITO (indium tin oxide) to achieve a matrix for laser desorption; mixtures of the emergency antibiotics vancomycin have been examined [215]. Other applications are combining reflectometry and electrochemistry or applying electric field gradients along the optical chip. Electrophoretic flow conditions can be monitored [216] directly, since no metallic film is involved which would cause a breakdown of any applied electrical potential. Combining electrokinetics and reflectometric interference allows insights into hydrophobic and electrostatic interactions of fibronectins on biofilms and electrostatics of biopolymers [217, 218]. The combination of interferometry with AFM has been reported recently [219, 220]. A combination of infrared spectroscopy with RIfS, which apart from interaction kinetics also provides sample identification, is interesting [221a].

Reflectometry has been recently used to understand the interaction between cadmium and the estrogen receptor α [221b]. Label-free detection in high content screening [222] and the trends in fragment-based screening [223a] have been reported recently. In a very recent publication, reflectometric interference spectroscopy not only could be used to monitor and quantify bio-interaction processes but also to discriminate agonists and antagonists [11]. Further applications deal with label-free detection of C-reactive protein [223b] and the detection of whole cells [223c] and tumor cells [223d]. Auto antibodies directed against the β2-glycoprotein-I (β2GP-I) are known as the best markers for diagnosis of antiphospholipid syndrome (APS) ; however, detection of such antibodies is still a challenge and reflectometry can quantify the interaction process [223e].The use of molecular imprinted polymers allows monitoring in biotechnology [223f]. First applications of a parallelized set-up allowing the determination of kinetic data with up to 700 data points have been published [223g].

Commercialization of reflectometry has started a few years ago, later than SPR and with fewer companies. Reflectometric interference is a stripped-down ellipsometry method [224] that uses polarized radiation and is especially useful in characterizinge biolayers for biosensing [225, 226]. However, the technique is rather complex and not suitable for simple biosensing. Based on this principle, *Maven Biotechnologies* in Pasadena has developed the *LFIRE* [227] (Label-Free Internal Reflection Ellipsometry™), which allows precise real-time measurements of specific interactions between molecular entities in a microarray or well-plate format and combines the principles of ellipsometry and evanescent wave detection. However, the instrumentation thereby loses the advantage of simple RIfS of negligible temperature dependence. A typical application is given in [228] for reverse-phase protein arrays measuring antigen–antibody interaction or glycobiology. *ForteBio* [229] in Menlo Park avoids evanescent problems and utilizes proprietary biolayer interferometry (BLI). Coated fibers dip into the wells of a microtiter plate in this *OCTET* system and the read-out shifts in interference spectra for 16 wells are simultaneously measured to calculate binding curves. For applications, see [230]. Biametrics [231a] intends to bring a family of reflectometric interference instrumentation to the market, covering single-wavelength simple robust devices and quantitative imaging systems. At present, the single-wavelength system is on the market [231c] with its first applications [231b].

A rather special device is the *picoscope,* which in principle is based on correlation of two different interferometer positions [232a]. It can be combined with Fabry–Perot, Mach–Zehnder, or Michelson set-ups, and has also been used as a biosensor.

29.4.4
Ellipsometry

It had been mentioned that ellipsometry uses both polarization states of electromagnetic radiation to get more information on behavior of interaction processes at the recognition layer. Accordingly, some biosensor applications such as characterization and computational 3D reconstruction of flagellar filament protein layer structure [232b] or even gold nanoparticles enhanced ellipsometry have been published [232c].

Imaging ellipsometry has also been applied to monitor biomolecular interaction. A highly sensitive, label-free, real-time detection of the biomarker CA19-9 using microarray biosensors based on total internal reflection imaging ellipsometry (TIRIE) is published, in which anti-CA19-9 is immobilized onto the PEGylated phospholipid membrane [232d]. A special ellipsometry-based optical scanner for high throughput, label-free screening of small molecule compound libraries for protein-ligands in microarrays is discussed [232e].

29.5
Survey on Refractometry and Reflectometry

In recent years, direct optical detection techniques have gained increasing interest. Besides reviews on special methods, some manuscripts have been published that compare the different detection principles [233a]. Another review covers Mach–Zehnder interferometer, Young interferometer, diffraction optics, dual polarization, waveguide microresonators, SPR interferometry, and other reflective interferometry platforms including backscattering interferometry, also giving applications [233b]. A similar review is given focusing on point-of-care diagnostic applications [233c]. Refractometry as well as reflectometry measures the product of refractive index and optical thickness and its changes, respectively. Nevertheless, all the evanescent field techniques preferably determine the changes in refractive index and are dependent on good thermostating, accordingly. The advantage of reflectometry is the good independence on temperature, since changes in refractive index with temperature are widely compensated by changes in volume. Furthermore, reflectometry does not depend on penetration depth of the evanescent field into the observed medium, thus reducing problems of measuring layers thicker than 100 nm and, in addition, independent of layer thickness (evanescent field decays). For this reason, reflectometric techniques have gained interest for some bioapplications – also allowing easier parallelization.

29.6
Circular Dichroism

Circular dichroism (CD) is a form of light absorption spectroscopy that measures the difference in absorbance of right- and left-circularly polarized light (rather than the absorbance of isotropic light) by a sample in solution. CD is related to optical rotary dispersion (ORD), which is a variation of optical rotation as a function of wavelength. CD spectra recorded between 180 and 260 nm enable fast routine determination of secondary structural types in proteins, that is, the α-helix, parallel and antiparallel β-sheet, and β-turn content. Owing to the expanding markets for chiral compounds [233d], the use of CD spectroscopy in bioanalysis is expected to increase. Contemporary CD instrumentation allows levels of accuracy of 97% for the determination of α-helices, 75% for β-sheet, 50% for β-turns, and 89% for the other structure types. The most common application of CD is the study of conformation changes (secondary and tertiary structure). As such, the technique lends itself well to the study of folding and unfolding induced by temperature, pH, and chaotropic ions [234, 235]. Model synthetic peptides have been examined by CD to explore the physical basis of the formation of α-helix and β-sheets [236, 237]. CD is increasingly used to examine tertiary structural features of proteins through aromatic amino acid mutant proteins [238, 239]. The use of CD in membrane and surface adsorption studies has been, unfortunately, limited by differential light scattering and absorption flattening [240].

Vibrational circular dichroism (VCD) was developed as a supplementary technique in the 1970s, and is the IR counterpart of CD [241]. VCD measures the differential absorption of left and right circularly polarized IR light by chiral molecules. Since there are more spectral lines in the IR region than in the UV and each can have a chiral response, a more elaborate stereochemical and structural analysis is possible than on the basis of CD. Researchers have started to use VCD for conformational studies of all classes of chiral molecules, especially carbohydrates [242].

29.7
Other Optical Read-Outs

Even though cantilevers are no optical detectors, they should be briefly mentioned because they frequently use an optical read-out of force-dependent deflection of a cantilever, reflecting a laser source to a different angle [243–245]. Just a few applications are cited [246–249].

For measurements at membranes, nanotubes, or nanowires, mostly electrochemical methods are used [250, 251]. However, optical techniques can yield additional interesting behaviour effects in nanopores [252] or utilizing plasmon resonance scattering of nanocubes that are chemically coupled to a membrane [253].

Interesting approaches are combinations of electrochemical and optical read-outs [254, 255]. In the case of cell-based assays important to drug discovery processes, impedance and SPR measurements are considered in comparison [256].

References

1. Fan, X.-D., White, I.M., Shopova, S.I., Zhu, H.-Y., Suter, J.D., and Sun, Y.-Z. (2009) Sensitive optical biosensors for unlabeled targets: a review. *Anal. Chim. Acta*, **620**, 8–26.
2. Cooper, M.A. (2003) Label-free screening of bio-molecular interactions. *Anal. Bioanal. Chem.*, **377**, 834–842.
3. Rich, R.L. and Myszka, D.G. (2007) Higher-throughput, label-free, real-time molecular interaction analysis. *Anal. Biochem.*, **361**, 1–6.
4. Yu, X.-B., Xu, D.-K., and Cheng, Q. (2006) Label-free detection methods for protein microarrays. *Proteomics*, **6**, 5493–5503.
5. Borisov, S.M. and Wolfbeis, O.S. (2008) Optical biosensors. *Chem. Rev.*, **108**, 423–461.
6. Gauglitz, G. and Proll, G. (2008) in *Biosensing for the 21st Century*, Advances in Biochemical Engineering/Biotechnology (ed. T. Scheper), Springer-Verlag, Berlin, Heidelberg, pp. 395–432.
7. Perkel, J.M. (2009) Who needs labels? Macromolecular interaction sans labels. *Science*, **19**, 1561.
8. Seidel, M. and Niessner, R. (2008) Automated analytical microarrays: a critical review. *Anal. Bioanal. Chem.*, **391**, 1521–1544.
9. Bally, M., Halter, M., Vörös, J., and Grandin, H.M. (2006) Optical microarray biosensing techniques. *Surf. Interface Anal.*, **38**, 1442–1458.
10. Mendes, P.M. (2008) Stimuli-responsive surfaces for bio-applications. *Chem. Soc. Rev.*, **37**, 2512–2529.
11. Fechner, P., Proell, F., Carlquist, M., and Proll, G. (2009) An advanced biosensor for the prediction of estrogenic effects of endocrine-disrupting chemicals on the estrogen receptor alpha. *Anal. Bioanal. Chem.*, **393** (6–7), 1579–1585.
12. Cooper, M.A. (2006) Optical biosensors: where next and how soon? *Drug Discov. Today*, **11** (23/24), 1061–1067.
13. Cooper, M.A. (2006) Non-optical screening platforms: the next wave

in label-free screening? *Drug Discov. Today*, **11** (23/24), 1068–1074.

14. Hecht, E. (1997) *Optics*, 3rd edn, Addison-Wesley, London.
15. Gauglitz, G. (1996) in *Sensors Update*, Vol. I (eds H. Baltes, W. Göpel, and J. Hesse), VCH Verlagsgesellschaft, Weinheim, p. 1.
16. Cooper, M.A. (2002) Optical biosensors in drug discovery. *Nature*, **1**, 515–527.
17. Vo-Dinh, T. and Allain, L. (2003) in *Biomedical Photonics* (ed. T. Va-Dinh), CRC Press, Boca Raton, FL, pp. 20-1–20-40.
18. (a) Schmitt, K., Oehse, K., Sulz, G., and Hoffmann, C. (2008) Evanescent field sensors based on tantalum pentoxide waveguides – a review. *Sensors*, **8**, 711–738. (b) Van Hoe, B., Bosman, E., Missinne, J., Kalathimekkad, S., Van Steenberge, G., and Van Daele, P. (2012) Novel coupling and packaging approaches for optical interconnects. *Proc. SPIE*(Optoelectronic Interconnects XII), **8267**, 82670T–82670T-11.
19. Canzoniero, L.M., Turetsky, D.M., and Choi, D.W. (1999) Fluorescent ion indicators for detecting heavy metals. *J. Neurosci.*, **19**, RC31.
20. Frederickson, C.J., Kasarskis, E.J., Ringo, D. *et al.* (1987) A quinoline fluorescence method for visualizing and assaying the histochemically reactive zinc (bouton zinc) in the brain. *J. Neurosci. Methods*, **20**, 91–103.
21. Kuhn, M.A. *et al.* (1995) Fluorescent ion indicators for detecting heavy metals. *Proc. SPIE-Int. Soc. Opt. Eng.*, **2388**, 238.
22. Fattinger, C., Koller, H., Schlatter, D. *et al.* (1993) The difference interferometer: a highly sensitive optical probe for quantification of molecular surface concentration. *Biosens. Bioelectron.*, **8**, 99–107.
23. Huber, W., Barner, R., Fattinger, C. *et al.* (1992) Direct optical immunosensing (sensitivity and selectivity). *Sens. Actuator, B*, **6**, 122–126.
24. Stamm, C. and Lukosz, W. (1993) Integrated optical difference interferometer as refractometer and chemical sensor. *Sens. Actuator, B*, **11**, 177–181.
25. Stamm, C. and Lukosz, W. (1994) Integrated optical difference interferometer as biochemical sensor. *Sens. Actuator, B*, **18**, 183–187.
26. Schlatter, D., Barner, R., Fattinger, C. *et al.* (1993) The difference interferometer: application as a direct affinity sensor. *Biosens. Bioelectron.*, **8**, 109–116.
27. Kubitchko, J., Spinke, J., Bruckner, T. *et al.* (1997) Sensitivity enhancement of optical immunosensors with nanoparticles. *Anal. Biochem.*, **253**, 112–122.
28. Clerc, D. and Lukosz, W. (1994) Integrated optical output grating coupler as biochemical sensor. *Sens. Actuator, B*, **19**, 581–586.
29. Dubendorfer, J. and Kunz, R.E. (1998) Compact integrated optical immunosensor using replicated chirped grating coupler sensor chips. *Appl. Opt.*, **37**, 1890–1894.
30. Grego, S., McDaniel, J.R., and Stoner, B.R. (2008) Wavelength interrogation of grating-based optical biosensors in the input coupler configuration. *Sens. Actuator, B*, **131**, 347–355.
31. Tiefenthaler, K., Lukosz, W. (1986) Optical sensor for selectively detecting substances and for detection of the variation of refractive index in substances. PCT Int. Appl. WO8607149 A1 19861204, pp. 52.
32. Lukosz, W. and Tiefenthaler, K. (1983) Embossing technique for fabricating integrated optical components in hard inorganic waveguiding materials. *Opt. Lett.*, **8** (10), 537–539.
33. Brandenburg, A. and Gombert, A. (1993) Grating couplers as chemical sensors: a new optical configuration. *Sens. Actuator, B*, **17**, 35–40.
34. Fattinger, C., Mangold, C., Gale, M.T., and Schuetz, H. (1995) Bidiffractive grating coupler: universal transducer for optical interface analysis. *Opt. Eng. (Bellingham)*, **34**, 2744–2753.
35. Kunz, R.E. (1991) *Proc. SPIE-Int. Soc. Opt. Eng.*, **1587**, 98.
36. Kunz, R.E., Edlinger, J., Curtis, B.J., Gale, M.T., Kempen, L.U., Rudigier, H., and Schuetz, H. (1994) *Proc. SPIE-Int. Soc. Opt. Eng.*, **2068**, 313–325.

37. MicroVacuum Ltd OWLS 210 Label-free Biosensor, *http://www.owls-sensors.com/OWLS-System.aspx* (accessed 20 March 2013).

38. (a) Vörös, J., Ramsden, J.J., Csucs, G., Szendrõ, I., De Paul, S.M., Textor, M., and Spencer, N.D. (2002) Optical grating coupler biosensors. *Biomaterials*, **23**, 3699–3710. (b) Kaufmann, S., Kumar, K., and Reimhult, E. (2011) Preparation and dynamic patterning of supported lipid membranes mimicking cell membranes. *Bioconjugat. Protoc. Methods Mol. Biol.*, **751** (4), 453–463.

39. MicroVacuum Ltd *http://www.owls-sensors.com/technology-overview.aspx* (accessed 20 March 2013).

40. CORNING *http://www.corning.com/lifesciences/us_canada/en/whats_new/epic_system.aspx* (accessed 20 March 2013).

41. Schröder, R., Merten, N., Mosolff Mathiesen, J., Martini, L., Kruljac-Letunic, A., Krop, F., Blaukat, A., Fang, Y., Tran, E., Ulven, T., Drewke, C., Whistler, J., Pardo, L., Gomeza, J., and Kostenis, E. (2009) The C-terminal tail of CRTH2 is a key molecular determinant that constrains Gai and downstream signaling cascade activation. *J. Biol. Chem.*, **284** (2), 1324–1336.

42. (a) Fang, Y., Frutos, A.G., and Verklereen, R. (2008) Label-free cell-based assays for GPCR screening. *Comb. Chem. High Throughput Screen.*, **11**, 357–369. (b) Stuhmeier, F., Bradley, J., Fairman, E., Gbekor, E., Hayter, P., and Ramsey, S. (2011) in *Label-Free Technologies for Drug Discovery* (eds M. Cooper and L. Mayr), John Wiley & Sons, pp. 189–203. (c) PerkinElmer EnSpire Multimode Plate Reader Label-free System, *http://www.perkinelmer.com/Catalog/Product/ID/2300-001L* (accessed 20 March 2013).

43. Brandenburg, A., Hinkov, V., and Konz, W. (1992) in *Sensors*, Vol. 6 (eds W. Göpel, J. Hesse, and J.N. Zemel), Wiley-VCH Verlag GmbH, Weinheim, pp. 399–420.

44. Joannopoulos, J.D., Johnson, S.G., and Winn, J.N. (2008) *Photonic Crystals: Molding the Flow of Light*, Princeton University Press, Princeton, NJ.

45. SRU Biosystems, Inc. *http://www.srubiosystems.com* (accessed 20 March 2013).

46. Cunningham, B.T., Lin, B., Qiu, J., Li, P., Pepper, J., and Hugh, B. (2002) A plastic colorimetric optical biosensor for multiparallel detection of label-free biochemical interactions. *Sens. Actuators, B*, **85**, 219–226.

47. Cunningham, B.T., Li, P., Schulz, S., Lin, B., Baird, C., Gerstenmaier, J., Genick, C., Wang, F., Fine, E., and Laing, L. (2004) Label-free assays on the BIND system. *J. Biomol. Screen.*, **9**, 481–490.

48. SRU Biosystems, Inc. *http://www.srubiosystems.com/Products/plateBasedBiosensors.html* (accessed 20 March 2013).

49. (a) Cunningham, B.T., Chan, L., Mathias, P.C., Ganesh, N., George, S., Lidstone, E., Heeres, J., and Hergenrother, P.J. (2009) Photonic crystals: a platform for label-free and enhanced fluorescence biomolecular and cellular assays. *Mater. Res. Soc. Symp. Proc.*, 1133, 43–52 (b) Loers, G., Makhina, T., Bork, U., Dörner, A., Schachner, M., and Kleene, R. (2012) *J. Neurosci.*, **32** (11), 3917–3930.

50. Jerman, J., Brown, J., and Rocheville, M. (2011) in *Label-Free Technologies for Drug Discovery* (eds M. Cooper and L. Mayr), John Wiley & Sons, Inc, Hoboken, NJ, pp. 205J–222J.

51. Rindorf, L. and Bang, O. (2008) Sensitivity of photonic crystal fiber grating sensors: biosensing, refractive index, strain, and temperature sensing. *J. Opt. Soc. Am. B*, **25** (3), 310–324.

52. Li, M.-Z., He, F., Liao, Q., Liu, J., Xu, L., Jiang, L., Song, Y.-L., Wang, S., and Zhu, D.-B. (2008) Ultrasensitive DNA detection using photonic crystals. *Angew. Chem. Int. Ed.*, **120**, 7368–7372.

53. Kashyap, R. (1999) *Fiber Bragg Gratings*, Academic Press, San Diego, CA.

54. Maguis, S., Laffont, G., Ferdinand, P., Carbonnier, B., Kham, K., Mekhalif, T., and Millot, M.-C. (2008) Biofunctionalized tilted fiber Bragg gratings for label-free immunosensing. *Opt. Express*, **16** (23), 19049–19062.

55. (a) Nemova, G. and Kashyap, R. (2007) Novel fiber Bragg grating assisted plasmon-polariton for bio-medical refractive-index sensors. *J. Mater. Sci.: Mater Electron.*, **18**, 327–330. (b) Sadykov, I.R., Morozov, O.G., and Sadeev, T.S. (2012) The biosensor based on fiber Bragg grating to determine the composition of the fuel and biofuel. *Proc. SPIE*(Optical Technologies for Telecommunications), **8410**, 4100F–84100F-6. (c) Candiani, A., Sozzi, M., Coscelli, E., Poli, F., Cucinotta, A., Selleri, S., Veneziano, R., Corradini, R., Marchelli, R., Childs, P. *et al.* (2011) Double tilted fiber Bragg grating for label-free DNA detection. International Workshop on Biophotonics, Parma, Italy, June 8–10, 2011, pp. 16–18; (d) Carvalho, L., Alberto, N.J., Gomes, P.S., Nogueira, R.N., Pinto, J.L., and Fernandes, M.H. (2011) In the trail of a new bio-sensor for measuring strain in bone: osteoblastic biocompatibility. *Biosens. Bioelectron.*, **26** (10), 4046–4052. (e) Gagne, M. and Kashyap, R. (2012) New nanosecond Q-switched 213 and 224 nm lasers for fiber Bragg grating inscription in hydrogen-free fibers. *Proc. SPIE*(Laser Applications in Microelectronic and Optoelectronic Manufacturing XVII), **8243**, 824314/1–824314/6.
56. Zeh, T., Meixner, A., Koch, A.W., and Neumann, C. (2002) Faseroptische Bragg-Sensoren zur Dehnungs- und Temperaturmessung. Proceedings XVI. Messtechnisches Symposium des Arbeitskreises der Hochschullehrer für Messtechnik e.V. (AHMT), Kassel, November 30–October 2, 2002.
57. Bornhop, D.J., Latham, J.C., Kussrow, A., Markov, D.A., Jones, R.D., and Sørensen, H.S. (2007) Free-solution, label-free molecular interactions studied by back-scattering interferometry. *Science*, **317**, 1732–1736.
58. Kenmore, C.K., Erskine, S.R., and Bornhop, D.J. (1997) Refractive-index detection by interferometric backscatter in packed-capillar high-performance liquid chromatography. *J. Chromatogr., A*, **762**, 219–225.
59. (a) Markov, D.A., Swinney, K., and Bornhop, D.J. (2004) Label-free molecular interaction determinations with nanoscale interferometry. *J. Am. Chem. Soc.*, **126** (50), 16659–16664. (b) Weinberger, S., Rich, W., Dotson, S., and Bornhop, D.J. (2012) Interferometric detection using nanoparticles. PCT Int. Appl. WO2012060882 A2 20120510; (c) Olmsted, I.R., Xiao, Y., Cho, M., Csordas, A., Sheehan, J., Meiler, J., Soh, H., and Bornhop, D.J. (2011) Measurement of aptamer-protein interactions with back-scattering interferometry. *Anal. Chem.*, **83** (23), 8867–8870.
60. Varma, M.M., Nolte, D.D., Inerowicz, H.D., and Regnier, F.E. (2004) The BioCD: a high-sensitivity spinning-disk interferometer for antigen detection. *Trends Opt. Photonics*(Conference on Lasers and Electro-Optics), **96/B**, CThI6/1–CThI6/3.
61. Perfinity Biosciences, Inc. *http://www.perfinity.com/* (accessed 20 March 2013).
62. Nolte, D.D. (2009) Invited review article: review of centrifugal microfluidic and bio-optical disks. *Rev. Sci. Instrum.*, **80** (10), 101101/1–101101/22.
63. Wang, X., Zhao, M., Nolte, D.D., and Ratliff, T.L. (2011) Prostate specific antigen detection in patient sera by fluorescence-free BioCD protein array. *Biosens. Bioelectron.*, **26** (5), 1871–1875.
64. Cush, R., Cronin, J.M., Stewart, W.J. *et al.* (1993) The resonant mirror: a novel optical biosensor for direct sensing of biomolecular interactions part I: principle of operation and associated instrumentation. *Biosens. Bioelectron.*, **8**, 347–353.
65. Goddard, N.J., Pollard-Knight, D., and Maule, C.H. (1994) Real-time biomolecular interaction analysis using the resonant mirror sensor. *Analyst*, **119**, 583–588.
66. Buckle, P.E., Davies, R.J., Kinning, T. *et al.* (1993) The resonant mirror: a novel optical sensor for direct sensing of biomolecular interactions. *Biosens. Bioelectron.*, **8**, 355–363.

67. Watts, H.J., Lowe, C.R., and Pollard-Knight, D.V. (1994) Optical biosensor for monitoring microbial cells. *Anal. Chem.*, **66**, 2465–2470.

68. de Tommasi, E., De Stefano, L., Rea, I., Di Sarno, V., Rotiroti, L., Arcari, P., Lamberti, A., Sanges, C., and Rendina, I. (2008) Porous silicon based resonant mirrors for biochemical sensing. *Sensors*, **8**, 6549–6556.

69. IAsys *http://www.thermo.com/eThermo/CMA/PDFs/Product/productPDF_15190.pdf* (accessed 20 March 2013).

70. Kretschmann, E. and Raether, H. (1968) Radiative decay of nonradiative surface plasmons excited by light. *Z. Naturforsch. A*, **23**, 2135–2136.

71. Otto, A. (1968) Excitation of non-radiative surface plasma waves in silver by the method of frustrated total reflection. *Z. Phys.*, **216**, 398–410.

72. Liedberg, B., Nylander, C., and Lundström, I. (1993) Surface plasmon resonance for gas detection and biosensing. *Sens. Actuators*, **4**, 299–304.

73. Homola, J., Yee, S.S., and Gauglitz, G. (1999) Surface plasmon resonance sensors: review. *Sens. Actuators, B*, **B54** (1–2), 3–15.

74. Homola, J. (2003) Present and future of surface plasmon resonance biosensors. *Anal. Bioanal. Chem.*, **377** (3), 528–539.

75. Homola, J., Yee, S.S., and Myszka, D. (2008) in *Optical Biosensors*, 2nd edn (eds F.S. Ligler and C.R. Taitt), Elsevier B.V., Amsterdam, pp. 185–242.

76. Homola, J. (2008) Surface plasmon resonance sensors for detection of chemical and biological species. *Chem. Rev.*, **108** (2), 462–493.

77. Dudak, F.C. and Boyaci, I.H. (2009) Rapid and label-free bacteria detection by surface plasmon resonance (SPR) biosensors. *Biotechnol. J.*, **4** (7), 1003–1011.

78. Piliarik, M., Vaisocherova, H., and Homola, J. (2009) *Biosensors and Biodetection*, Methods in Molecular Biology, Vol. 503 Vol. 1, Humana Press, pp. 65–88.

79. Schasfoort, R.B.M. and McWhirter, A. (2008) in *Handbook of Surface Plasmon Resonance* (eds R.B.M. Schasfoort and A.J. Tudos), Royal Society of Chemistry, Cambridge, pp. 35–80.

80. (a) Schasfoort, R.B.M. and Schuck, P. (2008) in *Handbook of Surface Plasmon Resonance* (eds R.B.M. Schasfoort and A.J. Tudos), Royal Society of Chemistry, Cambridge, pp. 354–394. (b) Guo, X. (2012) Surface plasmon resonance based biosensor technique: a review. *J. Biophoton.*, **5** (7), 483–501. (c) Toma, M., Toma, K., Adam, P., Homola, J., Knoll, W., and Dostalek, J. (2012) Surface plasmon-coupled emission on plasmonic Bragg gratings. *Opt. Express*, **20** (13), 14042–14053. (d) Shevchenko, Y., Francis, T.J., Blair, D., Walsh, R., DeRosa, M., and Albert, J. (2011) In situ biosensing with a surface plasmon resonance fiber grating aptasensor. *Anal. Chem.*, **83** (18), 7027–7034.

81. Szabo, A., Stolz, L., and Granzow, R. (1995) Surface plasmon resonance and its use in bio-molecular interaction analysis (BIA). *Curr. Opin. Struct. Biol.*, **5**, 699–705.

82. Raghavan, M. and Björkman, P.J. (1995) BIAcore: a microchip-based system for analyzing the formation of macromolecular complexes. *Structure*, **3**, 331–333.

83. van der Merwe, P.A. and Barclay, A.N. (1996) Analysis of cell-adhesion molecule interactions using surface plasmon resonance. *Curr. Opin. Immunol.*, **8**, 257–261.

84. Myszka, D.G. (1997) Kinetic analysis of macromolecular interactions using surface plasmon resonance biosensors. *Curr Opin. Biotechnol.*, **8**, 50–57.

85. Schuck, P. (1997) Use of surface plasmon resonance to probe the equilibrium and dynamic aspects of interactions between biological macromolecules. *Annu. Rev. Biophys. Biomol. Struct.*, **26**, 541–566.

86. Fivash, M., Towler, E.M., and Fisher, R.J. (1998) BIAcore for macromolecular interaction. *Curr. Opin. Biotechnol.*, **9**, 97–101.

87. Boussaad, S., Pean, J., and Tao, N.J. (2000) High-resolution multiwavelength surface plasmon resonance spectroscopy for probing conformational and electronics changes in redox proteins. *J. Anal. Chem.*, **72**, 222–226.

88. Sota, H. and Hasegawa, Y. (1998) Detection of conformational changes in an immobolized protein using surface plasmon resonance. *Anal. Chem.*, **70**, 2019–2024.

89. Kai, E., Sawata, S., Ikebukuro, K. *et al.* (1999) Detection of PCR products in solution using surface plasmon resonance. *Anal. Chem.*, **71**, 796–800.

90. Myszka, D.G., He, X., Dembo, M. *et al.* (1998) Extending the range of rate constants available from biacore: interpreting mass transport-influenced binding data. *Biophys. J.*, **75**, 583–594.

91. Flatmark, T., Stokka, A.J., and Berge, S.V. (2001) Use of surface plasmon resonance for real-time measurements of the global conformational transition in human phenylalanine hydroxylase in response to substrate binding and catalytic activation. *Anal. Biochem.*, **294**, 95–101.

92. Gomes, P., Giralt, E., and Andreu, D. (2000) Molecular analysis of peptides from the GH loop of foot-and-mouth disease virus C-S30 using surface plasmon resonance: a role for kinetic rate constants. *Mol. Immunol.*, **37**, 975–985.

93. Haasnoot, R. and Verheijen, R. (2001) A direct (non-competitive) immunoassay for gentamicin residues with an optical biosensor. *Food Agric. Immunol.*, **13**, 131–134.

94. Gaudin, V., Fontaine, J., and Maris, P. (2001) Screening of penicillin residues in milk by a surface plasmon resonance-based biosensor assay: comparison of chemical and enzymatic sample pretreatment. *Anal. Chim. Acta*, **436**, 191–198.

95. Bergwerff, A.A. and Van Knapen, F. (2006) Surface plasmon resonance biosensors for detection of patogenic microorganisms: strategies to secure food and environmental safety. *J. AOAC Int.*, **98** (3), 826–831.

96. Boozer, C., Kim, G., Cong, S.-X., Guan, H.-W., and Londergan, T. (2006) Looking towards label-free biomolecular interaction analysis in a high-throughput format: a review of new surface plasmon resonance technologies. *Curr. Opin. Chem. Biol.*, **17**, 400–405.

97. Campbell, C.T. and Kim, G. (2007) SPR microscopy and its application to high-throughput analyses of biomolecular binding events and their kinetics. *Biomaterials*, **28**, 2380–2392.

98. Liu, A.Q., Huang, H.J., Chin, L.K., Yu, Y.F., and Li, X.C. (2008) Label-free detection with micro optical fluidic systems (MOFS): a review. *Anal. Bioanal. Chem.*, **391**, 2443–2452.

99. Neumann, T., Junker, H.-D., Schmidt, K., and Sekul, R. (2007) SPR-based fragment screening: advantages and applications. *Curr. Top. Med. Chem.*, **7**, 1630–1642.

100. Nguyen, B., Tanious, F.A., and Wilson, W.D. (2007) Biosensor-surface plasmon resonance: quantitative analysis of small molecule-nucleic acid interactions. *Methods*, **42**, 150–161.

101. (a) McWhirter, A. and Wahlström, L. (2008) in *Handbook of Surface Plasmon Resonance* (eds R.B.M. Schasfoort and A.J. Tudos), The Royal Society of Chemistry, pp. 333–353. (b) Breault-Turcot, J. and Masson, J.-F. (2012) Nanostructured substrates for portable and miniature SPR biosensors. *Anal. Bioanal. Chem.*, **403** (6), 1477–1484.

102. BiaCore *http://www.biacore.com/lifesciences/products/systems_overview/index.html* (accessed 20 March 2013).

103. BiaCore (2011) Biacore System Selection Guide, homepage: 29-0070-53 AA, October 2011.pdf.

104. BiaCore *http://www.biacore.com/lifesciences/Application_Support/publications/ refdb/index.html* (accessed 20 March 2013).

105. Löfås, S. (2007) in *Handbook of Biosensors and Biochips* (eds R.S. Marks, D.C. Cullen, I. Karube, C.R. Lowe, and H.H. Weetall), John Wiley & Sons, Ltd, pp. 1261–1271.

106. IBIS Technologies *http://www.ibis-spr.nl/* (accessed 20 March 2013).

107. Kooyman, R.P.H., Lenferink, A.T.M. *et al.* (1991) Vibrating mirror surface plasmon resonance immunosensor. *Anal. Chem.*, **63**, 83–85.

108. Lokate, A.M.C., Beusink, J.B., Besselink, G.A.J., Pruijn, G.J.M., and Schasfoort, R.B.M. (2007) Biomolecular interaction monitoring of autoantibodies by scanning surface plasmon resonance microarray imaging. *J. Am. Chem. Soc.*, **129** (45), 14013–14018.

109. Sensata Technologies *http://www.sensata.com/sensors/spreeta-analytical-sensor-highlights.htm* (accessed 20 March 2013).

110. Elkind, J.L., Stimpson, D.I., Strong, A.A. *et al.* (1999) Integrated analytical sensors: the use of the TISPR-1 as a biosensor. *Sens. Actuators, B*, **54**, 182–190.

111. Sesay, M. and Cullen, D.C. (2001) Detection of hormone mimics in water using a miniturised SPR sensor. *Environ. Monit. Assess.*, **70**, 83–92.

112. Chinowsky, T.M., Quinn, J.G., Bartholomew, D.U., Kaiser, R., and Elkind, J.L. (2003) Performance of the Spreeta 2000 integrated surface plasmon resonance affinity sensor. *Sens. Actuators, B*, **6954**, 1–9.

113. Reichert Technologies *http://reichertspr.com/* (accessed 20 March 2013).

114. Biosensing Instrument Inc. *http://www.biosensingusa.com/* (accessed 20 March 2013).

115. Wang, Y., Zhu, X., Wu, M., Xia, N., Wang, J., and Zhou, F. (2009) Simultaneous and label-free determination of wild-type and mutant p53 at a single SPR chip preimmobilized with consensus DNA and monocolonal antibody. *Anal. Chem.*, **81**, 8441–8446.

116. Mivitec GmbH *http://www.micro-systems.de/index.htm* (accessed 20 March 2013).

117. Mivitec GmbH *http://www.biosuplar.com/* (accessed 20 March 2013).

118. Genoptics Bio Interactions *http://www.genoptics-spr.com* (accessed 20 March 2013).

119. Horiba Scientific *http://www.horiba.com/de/scientific/products/surface-plasmon-resonance-imaging-spri/* (accessed 20 March 2013).

120. Metrohm *http://www.ecochemie.nl/?pag=8* (accessed 20 March 2013).

121. Kinetic Evaluation Instruments *http://www.ke-instruments.com/* (accessed 20 March 2013).

122. Xantec *http://www.xantec.com/new/index.php* (accessed 20 March 2013).

123. GWC *http://www.gwcinstruments.com/* (accessed 20 March 2013).

124. Sierrasensors *http://www.sierrasensors.com/* (accessed 20 March 2013).

125. DKK-TOA Corporation *http://www.dkktoa.net/productslpi4.html* (accessed 20 March 2013).

126. BiolinScientific *http://www.biolinscientific.com/* (accessed 20 March 2013).

127. BioNavis *http://www.bionavis.com/* (accessed 20 March 2013).

128. (a) Accurion Solutions for Science *http://www.nanofilm.de* (accessed 20 March 2013); (b) Accurion Solutions for Science *http://www.accurion.de/download/productflyer_ep__spr∼1.pdf* (accessed 20 March 2013).

129. Slavik, R., Homola, J., Ctyroky, J. *et al.* (2001) Novel spectral fiber optic sensor based on surface plasmon resonance. *Sens. Actuators, B*, **74** (1–3), 106–111.

130. Harris, R.D. and Wilkinson, J.S. (1995) *Sens. Actuators, B*, **29** (1–3), 261.

131. Brecht, A. and Gauglitz, G. (1997) *Anal. Chim. Acta*, **347** (1–2), 219.

132. Homola, J., Koudela, I., and Yee, S.S. (1999) *Sens. Actuators, B*, **54**, 16.

133. Lekkala, J.O. and Sadowski, J.W. (1994) in *Chemical Sensor Technology*, Vol. 5 (ed. M. Aizawa), Kodansha Ltd, Tokyo, p. 199.

134. Vikholm, I., Viitala, T., Albers, W.M. *et al.* (1999) *Biochim. Biophys. Acta*, **1421**, 39.

135. Eddowes, M.J. (1987/1988) *Biosensors*, **3**, 1.

136. Morton, T.A. and Myszka, D.G. (1998) *Methods Enzymol.*, **295**, 268.

137. Myszka, D.G. (2000) *J. Mol. Recognit.*, **12**, 390.

138. Pearson, J.E., Kane, J.W., Petraki-Kalloti, I. *et al.* (1998) *J. Immunol. Methods*, **221**, 87.

139. Myszka, D.G. (1999) *J. Mol Recognit.*, **12**, 279.

140. Williams, C. and Addona, T.A. (2000) *TIBTECH*, **18**, 45.

141. Badia, A., Arnold, S., Scheumann, V. *et al.* (1999) *Sens. Actuators, B*, **54**, 145.

142. Albers, W.M., Vikholm, I., Viitala, T. *et al.* (2001) in *Handbook of Surfaces and Interfaces of Materials*, Vol. 5 Chapter 1, 1–31 (ed. H.S. Nalwa), Academic Press, New York.

143. Mandenius, C.F. and Mosbach, K. (1988) *Anal. Biochem.*, **170**, 68.

144. (a) Lyon, L.A., Musick, M.D., and Natan, M.J. (1998) *Anal. Chem.*, **70**, 5177. (b) Wang, S., Chiu, J., Lee, L., Lee, C., and Hong, R. (2009) New type small-angle sensor based on the TIR and SPR theories in heterodyne interferomery. *Sens. Transducers J.*, **105** (6), 18–25. (c) Erber, M., Stadermann, J., and Eichhorn, K. (2011) *Macromol. Symp. Polym. Spectrosc.*, **305**, 101–107.

145. Wu, C.-M., Jian, Z.-C., Joe, S.-F., and Chang, L.-B. (2003) High-sensitivity sensor based on surface plasmon resonance and heterodyne interferometry. *Sens. Actuators, B*, **92**, 133–136.

146. (a) Lambeck, P.V. (2006) Integrated optical sensors for the chemical domain. *Meas. Sci. Technol.*, **17**, 93–116. (b) LioniX *http://www.lionixbv.nl/applications.html* (accessed 21 March 2013).

147. Ingenhoff, J., Drapp, B., and Gauglitz, G. (1993) Biosensors using integrated optical devices. *Fresenius' J. Anal. Chem.*, **346**, 580–583.

148. Ingenhoff, J. and Gauglitz, G. (1994) New integrated optical substrates for immunoanalytical applications. *Fresenius' J. Anal. Chem.*, **349**, 355–359.

149. Drapp, B., Piehler, J., Brecht, A., Gauglitz, G., Luff, B.J., Wilkinson, J.S., and Ingenhoff, J. (1997) Integrated optical Mach-Zehnder interferometers as simazine immunoprobes. *Sens. Actuators*, **B39**, 277–282.

150. Kempen, L.U. and Kunz, R.E. (1997) Replicated Mach-Zehnder interferometers with focusing grating couplers for sensing applications. *Sens. Actuators, B*, **38–39**, 295–299.

151. Brosinger, F., Freimuth, H., Lacher, M., Ehrfeld, W., Gedig, E., Katerkamp, A., Spener, F., and Cammann, K. (1997) A label-free affinity sensor with compensation of unspecific protein interaction by a highly sensitive integrated optical Mach-Zehnder interferometer on silicon. *Sens. Actuators, B*, **44**, 350–355.

152. Hong, J.-G., Choi, J.-S., Han, G.Y., Kang, J.-K., Kim, C.-M., Kim, T.-S., and Yoon, D.-S. (2006) A Mach-Zehnder interferometer based on silicon oxides for biosensor applications. *Anal. Chim. Acta*, **573–574**, 97–103.

153. (a) Sepúlveda, B., Sánchez del Río, J., Moreno, M., Blanco, F.J., Mayora, K., Domínguez, C., and Lechuga, L.M. (2006) Optical biosensor microsystems based on the integration of highly sensitive Mach-Zehnder interferometer devices. *J. Opt. A: Pure Appl. Opt.*, **8**, 561–566. (b) Duval, D., Gonzalez-Guerrero, A.B., Dante, S., Dominguez, C., and Lechuga, L.M. (2012) Interferometric waveguide biosensors based on Si-technology for point-of-care diagnostic. *Proc. SPIE*, **8431**, 84310P–84310P-11.

154. Heideman, R.G. and Lambeck, P.V. (2005) Integrated optical lightguide device. US Patent 6,956,982.

155. Lambeck, P.V., van Lith, J., and Hoekstra, H.J.W.M. (2006) Three novel integrated optical sensing structures for the chemical domain. *Sens. Actuators, B*, **113** (2), 718–729.

156. (a) Sepúlveda, B., Armelles, G., and Lechuga, L.M. (2007) Magneto-optical phase modulation in integrated Mach-Zehnder interferometric sensors. *Sens. Actuators, A*, **134**, 339–347. (b) Dante, S., Duval, D., Sepulveda, B., Gonzalez-Guerrero, A., Sendra, J., and Lechuga, L.M. (2012) All-optical phase modulation for integrated interferometric biosensors. *Opt. Express*, **20** (7), 7195–7205.

157. Laib, T. (2008) Anwendung moderner Auswerteverfahren in der Chemometrie und Geostatistik, Definition von Kenngrößvon Bioanalytsystemen und Charakterisierung eines Mach-Zehnder-Interferometers für die Bioanalytik, Dissertaion. Universität Tuebingen, *http://tobias-lib.uni-tuebingen.de/volltexte/2008/3471/* (accessed 12 June 2013).

158. Brandenburg, A. and Henninger, R. (1994) *Appl. Opt.*, **33**, 5941–5947.

159. Ymeti, A., Kanger, J.S., Greve, J., Lambeck, P.V., Wijn, R., and Heideman, R.G. (2003) Realization of a multichannel integrated young interferometer chemical sensor. *Appl. Opt.*, **42** (28), 5649–5660.

160. (a) Ymeti, A., Kanger, J.S., Greve, J., Besselink, G.A.J., Lambeck, P.V., Wijn, R., and Heideman, R.G. (2005) Integration of microfluidics with a four-channel integrated optical young interferometer immunosensor. *Biosens. Bioelectron.*, **20**, 1417–1421. (b) Ymeti, A., Greve, J., Lambeck, P.V., Wink, T., van Hoevell, S., Beumer, T., Wijn, R., Heideman, R., Subramaniam, V., and Kanger, J. (2007) Fast, ultrasensitive virus detection using a young interferometer sensor. *Nano Lett.*, **7** (2), 394–397.

161. Passaro, V.M.N., Dell'Olio, F., Casamassima, B., and De Leonardis, F.F. (2007) Guided-wave optical sensors. *Sensors*, **7**, 508–536.

162. Ronan, G. (2004) Doubling up. SPIEs oemagazine (Sep. 2004), pp. 17–20.

163. Schmitt, K., Schirmer, B., Hoffmann, C., Brandenburg, A., and Meyrueis, P. (2007) Interferometric biosensor based on planar optical waveguide sensor chip for label-free detection of surface bound bioreactions. *Biosens. Bioelectron.*, **22**, 2591–2597.

164. Farfield Group Ltd *http://www.farfield-group.com/index.asp* (accessed 21 March 2013).

165. Farfield Group Ltd *http://www.farfield-group.com/technology_dpi.asp* (accessed 21 March 2013).

166. Farfield Group Ltd *http://www.farfield-group.com/applications.asp* (accessed 21 March 2013).

167. Wang, J., Xu, X., Zhang, Z., Yang, F., and Yang, X. (2009) Real-time study of genomic DNA structural changes upon interaction with small molecules using dual polarization interferometry. *Anal. Chem.*, **81**, 4914–4921.

168. Bürk, J., Zimmermann, B., Mayer, J., and Ache, H.-J. (1996) Integrated optical NIR-evanescent wave absorbance sensor for chemical analysis. *Fresenius' J. Anal. Chem.*, **354** (3), 284–290.

169. Ksendzov, A. and Lin, Y. (2005) Integrated optics ring – resonator sensors for protein detection. *Opt. Lett.*, **30** (24), 3344–3346.

170. White, I.M., Ian, M., Zhu, H., Suter, J.D., Oveys, H., and Fan, X. (2006) Liquid core optical ring resonator label-free biosensor array for lab-on-a-chip development. *Proc. SPIE Int. Soc. Opt. Eng.*, **6380**, 63800F/1–63800F/7.

171. Suter, J.D., White, I.M., Ian, M., Zhu, H., Shi, H., Caldwell, C.W., and Fan, X. (2008) Label-free quantitative DNA detection using the liquid core optical ring resonator. *Biosens. Bioelectron.*, **23** (7), 1003–1009.

172. White, I.M., Zhu, H., Suter, J.D., Fan, X., and Zourob, M. (2009) Label-free detection with the liquid core optical ring resonator sensing platform. *Methods Mol. Biol. Biosen. Biodetect.*, **503**, 139–165.

173. Zhu, H., White, I.M., Suter, J.D., Zourob, M., and Fan, X. (2008) Opto-fluidic micro-ring resonator for sensitive label-free viral detection. *Analyst*, **133** (3), 356–360.

174. Zhu, H., White, I.M., Suter, J.D., Zourob, M., and Fan, X. (2008) Phage-based label-free biomolecule detection in an opto-fluidic ring resonator. *Biosens. Bioelectron.*, **24** (3), 461–466.

175. Iodice, M., De Stefano, L., Coppola, M., Mocella, V., Rea, I., De Tommasi, E., Orabona, E., and Rendina, I. (2009) Label-free biosensing by means of optical micro-ring resonator. *Proc. SPIE*(Optical Sensors), **7356**, 735603/1–735603/11.

176. Carlborg, C.F., Gylfason, K.B., Kazmierczak, A., Dortu, F., Banuls Polo, M.J., Maquieira Catala, A., Kresbach, G.M., Sohlstroem, H., Moh, T., Vivien, L., Popplewell, J., Ronan, G., Barrios, C.A., Stemme, G., and van der Wijngaart, W. (2010) A packaged optical slot-waveguide ring resonator sensor array for multiplex label-free assays in labs-on-chips. *Lab Chip*, **10** (3), 281–290.

177. Ewald, M. Entwicklung und Charakterisierung eines Sensors zum Nachweis von Salmonelleninfektionen mittels Reflektometrischer Interferenzspektroskopie (2009) Diploma thesis. University Tuebingen.

178. Gauglitz, G. and Nahm, W. (1991) *Fresenius' J. Anal. Chem.*, **341**, 279.

179. Brecht, A., Gauglitz, G., and Nahm, W. (1992) Interferometric measurements used in chemical and biochemical sensors. *Analusis*, **20**, 135–140.

180. Kraus, G. and Gauglitz, G. (1992) Application and comparison of algorithms for evaluation of typical interferograms. *Fresenius' J. Anal. Chem.*, **344**, 153–157.

181. Fowles, G.R. (1989) *Introduction to Modern Optics*, Dower Publications, New York.

182. Brecht, A. and Gauglitz, G. (1994) *Fresenius' J. Anal. Chem.*, **349**, 360.

183. Brecht, A. and Gauglitz, G. (1995) Optical probes and transducers. *Biosens. Bioelectron.*, **10**, 923–936.

184. Hänel, C. and Gauglitz, G. (2002) Comparison of reflectometric interference spectroscopy with other instruments for label-free optical detection. *Anal. Bioanal. Chem.*, **372**, 91–100.

185. Piehler, J., Brecht, A., and Gauglitz, G. (1996) Affinity detection of low molecular weight analytes. *Anal. Chem.*, **68**, 139–143.

186. Reichl, D., Krage, R., Krummel, C., and Gauglitz, G. (2000) Sensing of volatile organic compounds using a simplified reflectometric interference spectroscopy setup. *Appl. Spectrosc.*, **54**, 583–586.

187. Gauglitz, G., Seemann, J., Reichl, D., and Brecht, A. Mikroreflektometrie iP – verfahren und vorrichtung zum nachweis physikalischer oder chemischer wechselwirkungen. German Patent 197 29 259.3, 198 30 727.6.

188. Reichl, D. (2000) Aufbau, Charakterisierung und optimierung eines optischen sensorsystems zur reflektometrischen interferenzspektroskopie mit mehrfarbigen leuchtdioden. Dissertation. Uni Tübingen, Electronic thesis database at university library, *http://www.bsz-bw.de/cgi-bin/xvms.cgi?SWB8582767* (accessed 21 March 2013).

189. Frank, R., Möhrle, B., Fröhlich, D., and Gauglitz, G. (2005) A transducer-independent optical sensor system for the detection of biochemical binding reactions. *Proc. SPIE Int. Soc. Opt. Eng.*, **5993**, 49–59.

190. Markovic, G.. (2008) Einsatz von nanopartikeln und optimierten schichtsystemen für die signalverstärkung in reflektometrischen biosensoren. Dissertation. Uni Tübingen, Electronic thesis database at university library, *http://tobias-lib.ub.uni-tuebingen.de/volltexte/2008/3345/* (accessed 21 March 2013).

191. Rothmund, M., Brecht, A., Berthel, G., Gräfe, D., Schütz, A., and Gauglitz, G. (1997) Label free binding assay with spectroscopic detection for pharmaceutical screening. *Fresenius' J. Anal. Chem.*, **359**, 15–22.

192. Pröll, F., Markovic, G., Schweizer, N., and Gauglitz, G. (2008) Imaging Reflectometric Interference Spectroscopy (iRIfS): a versatile tool for high throughput biomolecular interaction analysis. Proceedings of the 10th World Congress on Biosensors, Shanghai, China.

193. Saemann, M., Steinle, L., and Schubert, M.B. (2008) Amorphous silicon based p-i-i-n photodetector detects 12 nm thin protein layers. *J. Non-Cryst. Solids*, **354** (19–25), 2575–2579.

194. (a) Furin, D. (2010) Book of Abstracts, Europt(r)ode X, Prag; (b) Saemann, M., Furin, D., Thielmann, J., Pfaefflin, A., Proll, G., Harendt, C., Gauglitz, G., Schleicher, E., and Schubert, M. (2010) Amorphous silicon based p-i-i-n photodetectors for point-of-care testing. *Phys. Status Solidi C*, **7** (3–4), 1160–1163.

195. Brecht, A., Ingenhoff, J., and Gauglitz, G. (1992) Direct monitoring of antigen-antibody-interactions by spectral interferometry. *Sensor. Actuators*, **6B**, 96–100.

196. Brecht, A., Gauglitz, G., and Polster, J. (1993) Interferometric immunoassay in a FIA-system – a sensitive and rapid approach in label-free immunosensing. *Biosens. Bioelectron.*, **8**, 387–392.

197. Lang, G., Brecht, A., and Gauglitz, G. (1994) Low molecular analytes in water by spectral interferometry using a competitive immunoassay. *Fresenius' J. Anal. Chem.*, **348**, 602–605.

198. Brecht, A., Piehler, J., Lang, G., and Gauglitz, G. (1995) A direct optical immunosensor for atrazine detection. *Anal. Chim. Acta*, **311**, 289–299.

199. Mouvet, C., Amalric, L., Broussard, S., Lang, G., Brecht, A., and Gauglitz, G. (1996) Reflectometric interference spectroscopy for the determination of atrazine in natural waters. *Environ. Sci. Technol.*, **30**, 1846–1851.

200. Piehler, J., Brecht, A., Gauglitz, G., Maul, C., Zerlin, M., Thiericke, R., and Grabley, S. (1997) Label-free monitoring of DNA-ligand interactions. *Anal. Biochem.*, **249**, 94–102.

201. Lamken, P., Lata, S., Gavutis, M., and Piehler, J. (2004) Ligand-induced assembling of the type I interferon receptor on supported lipid bilayers. *J. Mol. Biol.*, **341** (1), 303–318.

202. Lue, X.Y., Huang, Y., Qian, W.P., Tang, Z.M., and Lu, Z.H. (2003) An effective method for quantitative evaluation of proteins adsorbed on biomaterial surfaces. *J. Biomed. Mater. Res., Part A*, **66A** (3), 722–727.

203. Jenison, R., Haeberli, A., Yang, S., Polisky, B., and Ostroff, R. (2000) Thin film biosensor for rapid detection of mecA from methicillin-resistant Staphylococcus aureus. *Clin. Chem. (Washington)*, **46** (9), 1501–1504.

204. Jenison, R., Yang, S., Haeberli, A., and Polisky, B. (2001) Interference-based detection of nucleic acid targets on optically coated silicon. *Nat. Biotechnol.*, **19** (1), 62–65.

205. Lu, J.-H., Strohsahl, C.M., Miller, B.L., and Rothberg, L.J. (2004) Reflectric interferometric detection of label-free oligonucleotides. *Anal. Chem.*, **76** (15), 4416–4420.

206. Lee, J.-C., An, J.-Y., and Kim, B.-W. (2007) Application of anodized aluminium oxide as a biochip substrate for a Fabry-Perot interferometer. *J. Chem. Technol. Biotechnol.*, **82**, 1045–1052.

207. Gauglitz, G. and Proll, G. (2008) *Biosensing for the 21st Century*, Advances in Biochemical Engineering/Biotechnology, Vol. 109, Springer, pp. 395–432.

208. Gesellchen, F., Zimmermann, B., and Herberg, F.W. (2005) in *Protein-Ligand Interactions: Methods and Applications*, Methods in Molecular Biology, Vol. 305 (ed. G.U. Nienhaus), Humana Press, Totowa, pp. 17–44.

209. Shang, Y., Zhao, W., Xu, E., Erchao, T., Tong, C., and Wu, J. (2010) FTRIFS biosensor based on double layer porous silicon as a LC detector for target molecule screening from complex samples. *Biosens. Bioelectron.*, **25** (5), 1056–1063.

210. Proll, G., Kumpf, M., Mehlmann, M., Tschmelak, J., Griffith, H., Abuknesha, R., and Gauglitz, G. (2004) Monitoring an antibody affinity chromatography with a label-free optical biosensor technique. *J. Immunol. Methods*, **292**, 35–42.

211. Moehrle, B., Kumpf, M., and Gauglitz, G. (2005) Determination of affinity constants of locked nucleic acid (LNA) and DNA duplex formation using label free sensor technology. *Analyst*, **130** (12), 1634–1638.

212. Penttinen, P., Jaehrling, J., Damdimopoulos, A.E., Inzunza, J., Lemmen, J.G., van der Saag, P., Pettersson, K., Gauglitz, G., Mäkelä, S., and Pongratz, I. (2007) Diet-derived polyphenol metabolite enterolactone is a tissue-specific estrogen receptor activator. *Endocrinology*, **148** (10), 4875–4886.

213. Möhrle, B.P., Köhler, K., Jaehrling, J., Brock, R., and Gauglitz, G. (2006) Label-free characterisation of cell adhesion using reflectometric interference spectroscopy (RIfS). *Anal. Bioanal. Chem.*, **384** (2), 407–413.

214. Roth, G., Freund, S., Moehrle, B., Woellner, K., Bruenjes, J., Gauglitz, G., Wiesmueller, K.-H., and Jung, G. (2007) Ubiquitin binds to a short peptide segment of hydrolase UCH-L3: a study by FCS, RlfS, ITC and NMR. *ChemBioChem*, **8** (3), 323–331.

215. Mehlmann, M., Garvin, A.M., Steinwand, M., and Gauglitz, G. (2005) Reflectometric interference spectroscopy combined with MALDI-TOF mass spectrometry to determine quantitative and qualitative binding of mixtures of vancomycin derivatives. *Anal. Bioanal. Chem.*, **382** (8), 1942–1948.

216. Kumpf, M. and Gauglitz, G. (2006) Biomolecular interaction analysis under electrophoretic flow conditions. *Anal. Bioanal. Chem.*, **384** (5), 1129–1133.

217. Zimmermann, R., Osaki, T., Kratzmueller, T., Gauglitz, G., Dukhin, S.S., and Werner, C. (2006) Electrostatic switching of biopolymer layers. insights from combined electrokinetics and reflectometric interference. *Anal. Chem.*, **78** (16), 5851–5857.

218. Osaki, T., Renner, L., Herklotz, M., and Werner, C. (2006) Hydrophobic and electrostatic interactions in the adsorption of fibronectin at maleic acid copolymer films. *J. Phys. Chem. B*, **110** (24), 12119–12124.

219. Liu, C., Zhang, D., and Zhang, H. (2008) Study of in-situ measurement system for porous alumina film based on AFM and reflectometric interference spectroscopy. *Guang Pu Xue Yu Guang Pu Fen Xi*, **28** (7), 1679–1683.

220. Yang, Y., Wang, Y., Xiong, K., Liu, B., Tan, Y., Tan, H., and Chen, D. (2005) Study of the key technology of optical fiber biosensor. *Guangzi Xuebao*, **34** (1), 121–125.

221. (a) Leopold, N., Busche, S., Gauglitz, G. *et al.* (2009) IR absorption and reflectometric interference spectroscopy (RIfS) combined to a new sensing approach for gas analytes absorbed into thin polymer films. *Spectrochim. Acta, Part A*, **72** (5), 994–999. (b) Fechner, P., Damdimopoulou, P., and Gauglitz, G. (2011) Biosensors paving the way to understanding the interaction between cadmium and the estrogen receptor alpha. *PLoS ONE*, **6** (8), e23048.

222. Proll, G., Steinle, L., Pröll, F., Kumpf, M., Möhrle, B., Mehlmann, M., and Gauglitz, G. (2007) The potential of label-free detection in high-content-screening applications. *J. Chromatogr., A*, **1161**, 2–8.

223. (a) Pröll, F., Fechner, P., and Proll, G. (2009) Direct optical detection in fragment-based screening. *Anal. Bioanal. Chem.*, **393** (6–7), 1557–1562. (b) Choi, H., Sakata, Y., Kurihara, Y., Ooya, T., and Takeuchi, T. (2012) Label-free detection of C-reactive protein using reflectometric interference spectroscopy-based sensing system. *Anal. Chim. Acta*, **728**, 64–68. (c) Merkl, S., Vornicescu, D., Dassinger, N., Kehrel, M., Harpel, S., and Keusgen, M. (2012) Approaches to the detection of whole cells using reflectometric interference spectroscopy. *Phys. Status Solidi A*, **209** (5), 864–870. (d) Kumeria, T., Kurkuri, M., Mahaveer, D., Diener, K., Parkinson, L., and Losic, D. (2012) Label-free reflectometric interference microchip biosensor based on nanoporous alumina for detection of circulating tumour cells. *Biosens. Bioelectron.*, **35** (1), 167–173. (e) Hilbig, U., Bleher, O., LeBlanc, A., and Gauglitz, G. (2012) A biomimetic sensor surface to detect anti-β2-glycoprotein-I antibodies as a marker for antiphospholipid syndrome. *Anal. Bioanal. Chem.*, **403** (3), 713–717. (f) Kolarov, F., Niedergall, K., Bach, M., Tovar, G., and Gauglitz, G. (2012) Optical sensors with molecularly imprinted nanospheres: a promising approach for robust and label-free detection of small molecules. *Anal. Bioanal. Chem.*, **402** (10), 3245–3252. (g) Schwarz, B., Fechner, P., Pröll, F., Proll, G., and Gauglitz, G. (2011) Imaging Reflectometric Interference Spectroscopy (iRIfS) für die markierungsfreie biomolekulare Interaktionsanalyse von Peptid- und Proteinarrays. Deutsches BioSensor Symposium, Heilbad Heiligenstadt, Germany, 03-06 April 2011, p. S. 47. ISBN: 978-3-00-034073-4.

224. Azzam, R.M.A. and Bashara, N.M. (1989) *Ellipsometry and Polarised Light*, North Holland, Amsterdam.

225. Brecht, A., Gauglitz, G., and Striebel, C. (1994) Characterization of biomembranes by spectral ellipsometry. *Biosens. Bioelectron.*, **9**, 139–146.

226. Jin, G., Tengvall, P., Lundstrom, I., and Arwin, H. (1995) A biosensor concept based on imaging ellipsometry for visualization of biomolecular interactions. *Anal. Biochem.*, **232** (1), 69–72.

227. Maven Biotechnologies *http://www.mavenbiotech.com/about.asp* (accessed 21 March 2013).

228. Maven Biotechnologies *http://www.mavenbiotech.com/reversephase.pdf* (accessed 21 March 2013).

229. ForteBio *http://www.fortebio.com/* (accessed 21 March 2013).

230. ForteBio *http://www.fortebio.com/references.html* (accessed 21 March 2013).

231. (a) Biametrics *http://biametrics.com/en/about/* (accessed 21 March 2013); (b) Faulstich, K., Haberstroh, K., Gruler, R., Eberhard, M., Wiest, T., and Lentzsch, D. (2008) Handheld and portable test systems for immunodiagnostics, nucleic acid detection and more. *Proc. SPIE*(Optics and Photonics in Global Homeland Security IV), **6945**, 69450H/1–69450H/10. (c) Biametrics *http://biametrics.com/en/applications/* (accessed 21 March 2013).

232. (a) Nikitin, P.I. (2007) in *Handbook of Biosensors and Biochips* (eds R.S. Marks, D.C. Cullen, I. Karube, C.R. Lowe, and H.H. Weetall), John Wiley & Sons, Ltd, pp. 471–483. (b) Kozma, P., Kozma, D., Nemeth, A., Jankovics, H., Kurunczi, S., Horvath, R., Vonderviszt, F., Fried, M., and Petrik, P. (2011) In-depth characterization and computational 3D reconstruction of flagellar filament protein layer structure based on in situ spectroscopic ellipsometry measurements. *Appl. Surf. Sci.*, **257** (16), 7160–7166. (c) Moirangthem, R., Chang, Y., and Wei, P. (2011) Investigation of surface plasmon biosensing using gold nanoparticles enhanced ellipsometry. *Opt. Lett.*, **36** (5), 775–777. (d) Zhang, Y., Chen, Y., and Jin, G. (2011) Serum tumor marker detection on PEGylated lipid membrane using biosensor based on total internal reflection imaging ellipsometry. *Sens. Actuators, B*, **159** (1), 121–125. (e) Landry, J., Fei, Y., and Zhu, X.Y. (2012) High throughput, label-free screening small molecule compound libraries for protein-ligands using combination of small molecule microarrays and a special ellipsometry-based optical scanner. *Int. Drug Discov.*, **6** (6), 8–13.

233. (a) Gauglitz, G. (2010) Direct optical detection in bioanalysis: an update. *Aanal. Bioanal. Chem.*, **398** (6), 2363–2372. (b) Kussrow, A., Enders, C., and Bornhop, D.J. (2012) Interferometric methods for label-free molecular interaction studies. *Anal. Chem.*, **84** (2), 779–792. (c) Duval, D., Gonzalez-Guerrero, A., Dante, S., Dominguez, C., and Lechuga, L.M. (2012) Interferometric waveguide biosensors based on Si-technology for point-of-care diagnostic. *Proc. SPIE*(Silicon Photonics and Photonic Integrated Circuits III), **8431**, 84310P–84310P-11. (d) Zubritsky, E. (1999) *Anal. Chem.*, **71**, 545A.

234. Yang, Y.-W. and Teng, C.-C. (1998) *Int. J. Biol. Macromol.*, **22**, 81.

235. Georgieva, D.N., Stoeva, S., Ali, S.A. *et al.* (1998) *Spectrochim. Acta, Part A*, **54**, 765.

236. Padmanabhan, S., Jiménez, M.A., Laurents, D.V. *et al.* (1998) *Biochemistry*, **37**, 17318.

237. Blondelle, S.E., Forood, B., Houghten, R.A. *et al.* (1997) *Biochemistry*, **36**, 8393.

238. Juban, M.M., Javadpour, M.M., and Barkley, M.D. (1997) Circular dichroism studies of secondary structure of peptides. *Methods Mol. Biol.*, **78**, 73–78.

239. Kelly, S.M. and Price, N.C. (1997) *Biochim. Biophys. Acta*, **1338**, 161.

240. Hermel, H. (1997) in *Particle Surface Characterization Methods* (eds R.H. Mueller, W. Mehnert, and G.E. Hildebrand), Medpharm Scientific Publishers, Stuttgart, p. 159.

241. Nafie, L.A., Keiderling, T.A., and Stephens, P.J. (1976) *J. Am. Chem. Soc.*, **98** (10), 2715.

242. Bose, P.K. and Polavarapu, P.L. (1999) *J. Am. Chem. Soc.*, **121**, 6094.

243. Fritz, J. (2008) Cantilever biosensors. *Analyst*, **133**, 855–863.

244. Yue, M., Majumdar, A., and Thundat, T. (2007) in *Biomolecular Sensing, Processing and Analysis* (eds R. Bashir and S. Wereley), Springer-Verlag, pp. 21–33.

245. Lee, C.-K., Thillaigovindan, J., Chen, C.-C., Chen, X.-T., Chao, Y.-T., Tao, S.-H., Xiang, W.-F., Yu, A.-B., Feng, H.-H., and Lo, G.Q. (2008) Si nanophotonics based cantilever sensor. *Appl. Phys. Lett.*, **93**, 113113/1–113113/3.

246. Zheng, K.-C., Khalid, W., Wang, Z., Li, Y.-F., Katragadda, R.B., Zhao, Y.-J., Lin, Q., and Xu, Y. (2008) Optical lever based parylene cantilevers for biochemical sensing. *Open Opt. J.*, **2**, 86–93.

247. Campbell, G.A. and Mutharasan, R. (2008) Near real-time detection of cryptosporidium parum oocyst by IgM-functionalized piezoelectric-excited millimetre-sized cantilever biosensor. *Biosens. Bioelectron.*, **23**, 1039–1045.

248. Campbell, G.A., de Lesdernier, D., and Mutharasan, R. (2007) Detection of airborne Bacillus anthracis spores by an integrated system of an air sampler and a cantilever immunosensor. *Sens. Actuators, B*, **127**, 376–382.

249. Johansson, A., Blagoi, G., and Boisen, A. (2006) Polymeric cantilever-based biosensors with integrated readout. *Appl. Phys. Lett.*, **89**, 173505/1–173505/3.

250. Patolsky, F., Zheng, G., and Lieber, C.M. (2006) Nanowire-based biosensor. *Anal. Chem.*, **78** (13), 4260–4269.

251. Gyurcsanyi, R.E. (2008) Chemically modified nanopores for sensing. *Trend Anal. Chem.*, **27** (7), 627–639.

252. Deamer, D., Schmidt, H., and Hawkins, A.R. (2007) A nanopore - ARROW biosensor for life detection. *Proc. SPIE Int. Soc. Opt. Eng.*, **6694**, 669411/1–669411/7.

253. Galush, W.J., Shelby, S.A., Mulvihill, M.J., Tao, A., Yang, P., and Groves, J.T. (2009) A nanocube plasmonic sensor for molecular binding on membrane surfaces. *Nano Lett.*, **9** (5), 2077–2082.

254. Kerman, K., Endo, T., and Tamiya, E. (2007) in *Handbook of Biosensors and Biochips* (eds R.S. Marks, D.C. Cullen, C.R. Lowe, and H.H. Weetall), John Wiley & Sons, Ltd, pp. 925–937.

255. Ramanaviciene, A. and Ramanavicius, A. (2004) in *UV Solid-State Light Emitters and Detectors* (eds M.S. Shur and A. Žukauskas), Kluwer Academic Publishers, Dordrecht, pp. 287–296.

256. Xi, B., Yu, N.-C., Wang, X.-B., Xu, X., and Abassi, Y.A. (2008) The application of cell-based label-free technology in drug discovery. *Biotechnol. J.*, **3**, 484–495.

Section IX
Applications 2: Polymer Analysis

Handbook of Spectroscopy, Second Edition. Edited by Günter Gauglitz and David S. Moore.

30
Surface Plasmon Spectroscopy Methods and Electrochemical Analysis

Akira Baba and Rigoberto Advincula

30.1
Introduction

The surface plasmon resonance (SPR) optical technique is a powerful tool for the characterization and study of ultrathin films, interfaces, and kinetic processes on surfaces, and has been investigated in the applications of SPR sensors and plasmonic devices [1–5]. Many of these applications involve the increase in optical field by surface plasmon excitation at metal–dielectric interfaces. For example, in biosensor applications, this technique is used to investigate the adsorption–desorption of biomolecules onto surfaces and *in situ* time-dependent surface coverage [6].

The combination of SPR with electrochemical (EC) measurements has been demonstrated as a powerful analytical technique for the simultaneous characterization and manipulation of electrode–electrolyte interfaces [7–13]. In EC-SPR measurements, the gold substrate that carries the optical surface mode is simultaneously used as the working electrode in a standard three-electrode EC experiment. One of the advantages in using the EC-SPR technique is that the EC and optical properties are simultaneously obtained on surfaces and ultrathin films at the nanometer scale [14]. This involves the *in situ* monitoring of the film thickness and electrochromic properties during the anion doping–dedoping process of deposited conducting polymers. More recently, we have demonstrated the *in situ* electrochemical-surface plasmon resonance spectroscopy-atomic force microscopy (EC-SPR-AFM) technique for ‘‘real-time’’ dynamic and simultaneous acquisition of the dielectric (optical), surface morphological, and EC data of a depositing conducting polymer thin film at the electrode–electrolyte interface [15]. This enabled the differentiation of cyclic voltammetry (CV) and potentiostatically (chronoamperometrically) deposited films between their dielectric, EC, and morphological properties in real time.

The EC and optical quantitative analyses of π-conjugated polymer ultrathin films on oxidation–reduction and doping–dedoping are of great interest to a number of applications. This includes electrochromic displays [16], battery electrodes [17], sensors, and so forth. Many of these applications make use of the fact that the conductivity or color of the film can be controlled by its redox state [18]. On oxidation

Handbook of Spectroscopy, Second Edition. Edited by Günter Gauglitz and David S. Moore.

(doping), thin polymer films become positively charged, with their conductive state. Several chromic states have been observed at various degrees of doping, but these have never been fully understood. Thus, due to their complex properties, it is very intriguing to obtain more information in a single experiment. As polymer films change their optical, electrical, and morphological properties on various redox states, we need to combine complementary techniques *in situ*. Furthermore, because of their high conductivity and specific redox properties, which are essential for biological communication [19], conducting polymers are sensitive materials for monitoring and manipulating biological interactions. The redox properties of the conducting polymers change during biological interactions, and this change can be detected either as an EC signal or as an optical signal. Electroactive conducting polymers also provide the media for electron transfer to the electrode, enabling the detection of EC signals. Hence, EC-SPR techniques are very powerful tool to monitor these properties [20–23].

In this chapter, recent developments and applications on SPR methods and electroanalysis are overviewed.

30.2
Combined Surface Plasmon Resonance Methods and Electrochemical Measurements

Figure 30.1 shows the attenuated total reflection (ATR) setup used for the excitation of surface plasmons in the Kretschmann configuration combined with an EC cell. When a *p*-polarized laser beam is reflected at the incident angle θ from the base of a prism above the critical angle θ_c, a strong nonradiative electromagnetic

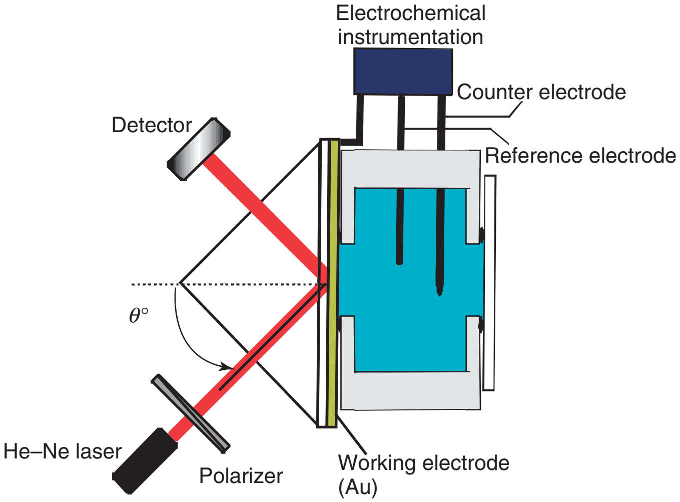

Figure 30.1 A schematic representation of the combined electrochemical-surface plasmon resonance spectroscopy setup.

wave is excited at the resonant angle. This surface plasmon propagates at the metal–electrolyte interface, with the coupling angle being given by the energy- and momentum-matching conditions between photons and surface plasmons. As the energy of the incident light is transferred toward excitation of the surface plasmon, a decrease of the reflectivity in the angular scan is observed. The resonance character of this excitation gives rise to an enhancement of the electric field at the interface by more than an order of magnitude, which is the origin of the remarkable sensitivity enhancements, for example, in scattered light [24], fluorescence [25, 26], or Raman spectroscopies [27, 28] when working with surface plasmon light. If the formation of a thin dielectric coating is observed *in situ*, for example, during the electropolymerization process of conducting polymers at the metal electrode–electrolyte interface, kinetic information can be obtained. This includes film deposition and diffusional transport of mass adjacent to the interface by cycling potentials. The experiment often involves monitoring the reflected intensity at a fixed angle of observation θ_{obs}. The Au–glass substrates used for the excitation of surface plasmons also serve as a working electrode in the EC measurements, with a counter and a reference electrode. For these experiments, the gold film thickness is chosen for optimum excitation of the surface plasmons with both wavelengths (42–45 nm).

30.3
Investigation of Electropolymerization Process of Conducting Polymer Thin Films by EC-SPR

First, the EC-SPR study during the electropolymerization of conducting polymer is shown. Figure 30.2 shows the cyclic voltammograms and SPR reflectivity curve with the first electropolymerization cycle. These were obtained at a concentration of 0.1 M aniline in 0.5 M H_2SO_4 with repeated potential cycling between −0.2 and 1.0 V at a scan rate of $20\,\text{mV}\,\text{s}^{-1}$. An increase in reflectivity with the SPR corresponds to the start of aniline oxidation as seen with the cyclic voltammogram. This was observed prominently in the anodic scan of the first cycle at about 0.8 V and is indicative of the oxidation of the aniline monomer to form polyaniline (PANI). From the SPR curve in the anodic scan of the first cycle, the slope can be divided into two regions, that is, 0.8–0.9 and 0.9–1.0 V. This corresponds to two separate phenomena, namely (i) the oxidation of aniline monomer started at the vicinity of the Au surface at 0.8 V; the SPR curve increased because the growing PANI film has a higher dielectric constant than aniline monomer and (ii) the growing PANI deposits and becomes insoluble to the H_2SO_4 solution at 0.9 V, that is, essentially precipitates out because of increasing chain length (PANI is insoluble to H_2SO_4 solution). In this way, the PANI was deposited onto the Au substrate, at the region where the SPR curve was steeper, that is, between 0.8 and 0.9 V. These phenomena are consistent with previous results using *in situ* electrochemical-quartz crystal microbalance (E-QCM) as reported by Park *et al.* [29]. They observed a time delay in PANI deposition with the oxidation peak of the cyclic

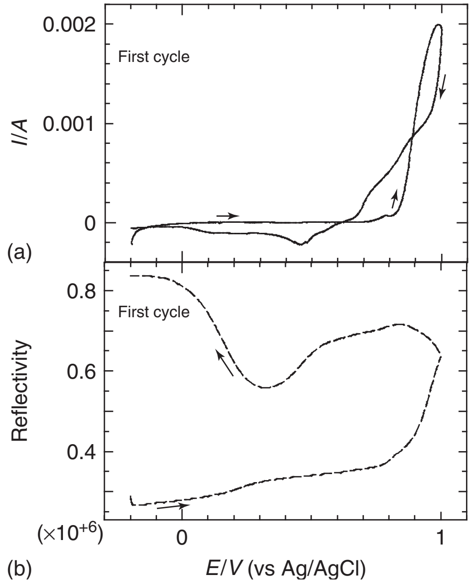

Figure 30.2 (a,b) Simultaneous observation of SPR kinetic curves and cyclic voltammograms during the electropolymerization of 0.1 M aniline in 0.5 M H_2SO_4 solution using repeated potential cycling between −0.2 and 1.0 V at a scan rate of 20 mV s^{-1}; first cycle. (From Ref. [6] with permission.)

voltammogram. For the cathodic scan of the first cycle, the SPR curve continued to increase until 0.88 V, then decrease until 0.52 V, and then subsequently increase again until 0 V. From the cyclic voltammogram, the first region corresponds to the reduction of deposited PANI. The reduction of deposited PANI causes the decrease of the SPR curve due to a change either in the dielectric constant or in film thickness [30]. The reflectivity in the SPR is high after anion dedoping. If the change of the SPR curve in this region is mainly due to the film thickness, the SPR curve should continuously decrease because of film contraction by anion dedoping and/or expulsion of water molecule into the solution. In this case, we believe that the behavior of the SPR curve is mainly due to the increase of the imaginary part of dielectric constant (refractive index). We have observed similar phenomena on our investigations with the layer-by-layer (LbL) PANI–sulfonate polyaniline film by using another surface plasmon technique [12]. This reduction region of the SPR curve consistently decreased during second and fifth redox processes in cathodic scans.

EC-SPR has been applied for *in situ* optical/EC investigations in order to determine the complex dielectric constants of conjugated polymer thin films. In order to be quantitative to all parameters of the films, that is, its thickness and real and imaginary parts of dielectric constant, we used EC-SPR data taken under potentiostatic measurement conditions. In Figure 30.3, the potentiostatic SPR scans are shown for both $\lambda = 632.8$ nm and $\lambda = 1152$ nm. Some very interesting information was obtained from the analysis of these curves. Firstly, it is noticeable

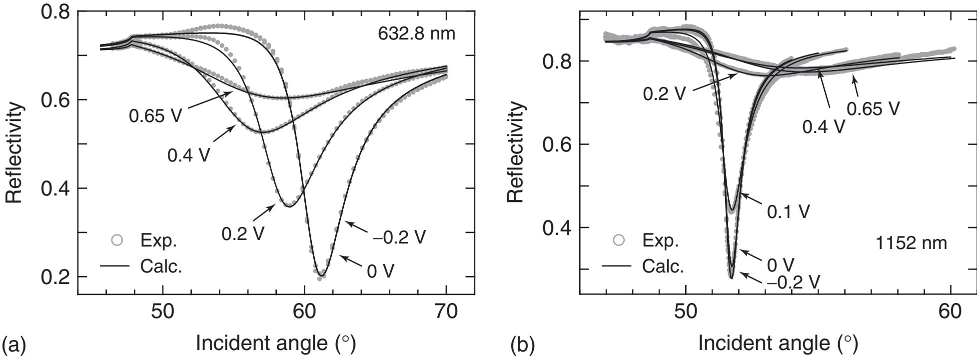

Figure 30.3 (a,b) Experimental angular SPR reflectivity curve (dotted) and calculated curve (solid) under applied potential at 632.8 and 1152 nm, respectively. (From Ref. [8] with permission.)

that the change in the reflectivity curves at around 0.2 V occurs when the PANI "base" film changes, on doping, into the corresponding conducting PANI salt. This process is reversible and many cycles can be performed without any noticeable variation (except for any degradation processes). If the film, in the absence of monomers, is kept at 0.9 V, the behavior of SPR is again likened to that of the insulating state, and subsequent SPR scans at 0.65, 0.4, −0.2, 0.4, and 0.65 V showed no difference. This indicates that in the absence of the aniline monomer, oxidation at potentials higher than 0.65 V leads to an irreversible degradation of the EC response of the PANI film.

As it is difficult to obtain independent information on the thickness and the real and imaginary parts of the dielectric constant from mere SPR measurement, we also used the quartz crystal microbalance (QCM) in a potentiostatic mode of the measurement. As explained earlier, the Sauerbrey equation [31] could be applied to relate frequency shifts to mass changes. The corresponding thickness is roughly estimated on the assumption of a mass density of 1.3 g cm^{-3} [32] for comparison with the EC-SPR results. In contrast to that of the SPR reflectivity curves, which show a large change at 0.2 V, the thickness from the QCM measurement was found to be roughly constant between −0.2 and 0.2 V. The loss of film thickness at 0.9 V was found to be 38% after 3 min. Fitting the experimental SPR reflectivity results with the thickness values obtained from QCM measurement (except the value of 0.9 V) gives the theoretical reflectivity curves that are also shown in Figure 30.3. The calculation was carried out by using Fresnel's equations for a Prism/Cr/Au/PANI/electrolyte solution architecture. Details for the fitting procedure can be found elsewhere [1]. Although the surface plasmons (SP) resonance at $\lambda = 1152$ nm is very broad at high potential, excellent fitting curves were obtained in most cases. The obtained fitting parameters are shown in Figure 30.4. Dramatic changes in both the real and the imaginary parts of the dielectric constants were determined at both wavelengths. The error bars in Figure 30.4 are based on the density fluctuation of the polymer on doping–dedoping, that is, 1.25–1.35. On

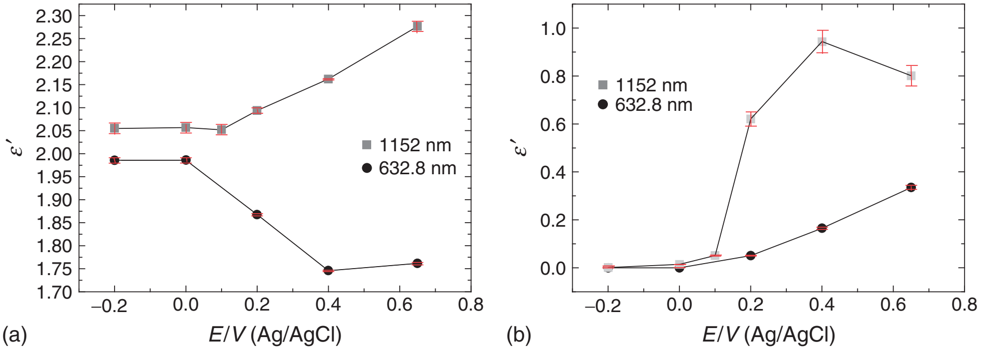

Figure 30.4 (a) Real part (ε') and (b) imaginary part (ε'') of dielectric constants at several potential. (From Ref. [8] with permission.)

the basis of these calculations, the accuracy for the determination of the complex dielectric constant is estimated to be better than ±0.02 for the real part and ±0.10 for the imaginary part of the dielectric constant in this density range, that is, EC-SPR measurements are able to determine the complex dielectric constants of the conducting polymer films in the doped–dedoped state rather independently of the uncertainty in the film density. Thus, the electrochromic phenomena of PANI films can be characterized by this EC-SPR technique with high sensitivity, which may lead to new designs for SPR-based sensors/biosensors based on the electrochromism of thin conducting polymer films.

30.4
Electrochemical SPR-surface plasmon light scattering (SPLS)

The incident light enhanced by surface plasmons and scattered off the substrate–electrode interface also enabled us to investigate the changes in the roughness of the conducting polymer films on the potential cycling. Light scattering due to the roughness of the electrode and/or deposited PANI/surfonate polyaniline (SPANI) LbL film enhanced by surface plasmons was detected by the photomultiplier detector, which was set on the backside of the prism.

Figure 30.5 shows the cyclic voltammogram, SPR, and surface plasmon field enhanced light scattering (SPFELS) data of four bilayers PANI/SPANI in 0.5 M H_2SO_4 solution during potential cycling from −0.2 to 0.9 V at a scan rate of $100\,\mathrm{mV\,s^{-1}}$. The solid line shows the cyclic voltammogram, the dashed line shows the SPR, and the dotted line shows the SPFELS curves. As reported by Orata and Buttry [33], the first redox process (at 0.22 V in the anodic scan and 0.13 V in the cathodic scan) corresponds to anion transport, that is, anion doping and dedoping, from the electrolyte solution to the PANI/SPANI film. The second redox process (~0.8 and 0.75 V, respectively) simply corresponds to the imine nitrogen deprotonation and protonation, that is, protons in the PANI/SPANI film are expelled into the electrolyte solution and inserted into the PANI film, respectively. The anion is also

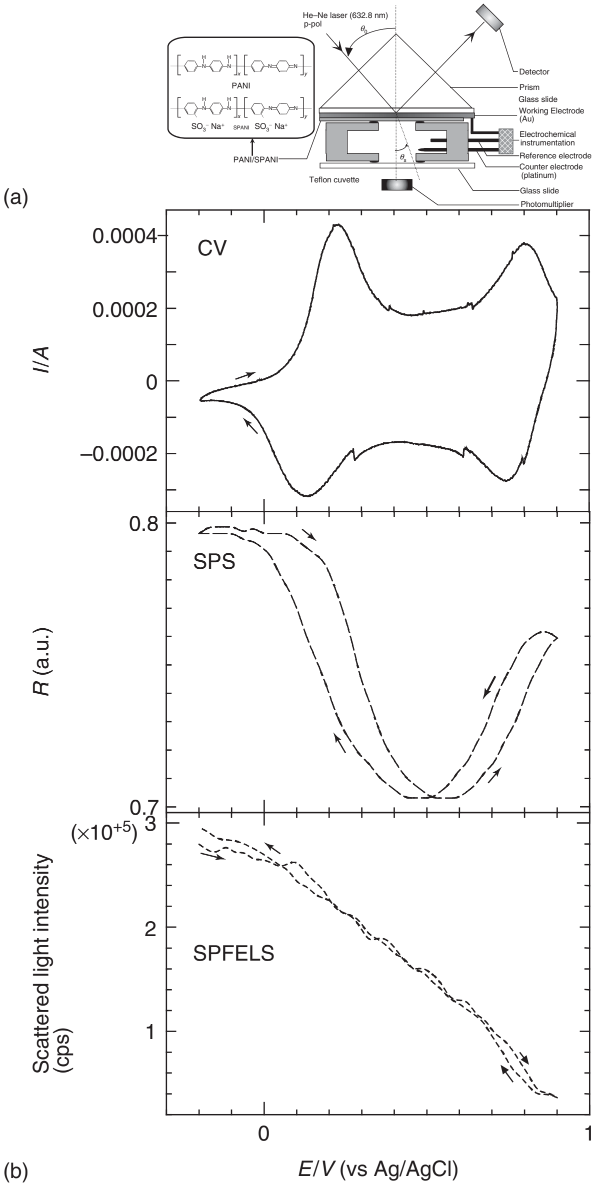

Figure 30.5 (a,b) Simultaneous observation of cyclic voltammogram, SPR curve, and SPFELS curve of four double layers of PANI/SPANI film during the potential cycling in 0.5 M H_2SO_4 solution at a scan rate of 100 mV s^{-1}. (From Ref. [27] with permission.)

inserted during the protonation of PANI/SPANI film and expelled from the film during the deprotonation as a counterion to the iminium cation formation (doping).

The SPR reflectivity decreases during doping by the anion and increases during dedoping of anion for the deposited PANI/SPANI, respectively. Moreover, an increase in the SPR during the deprotonation and a decrease during the protonation can be observed in the anodic and the cathodic scans, respectively. In this experiment, using E-QCM, Orata and Buttry [34] observed an increase in the film mass by the doping and a decrease in the film mass by the dedoping of the ion. This can be associated with changes in the density of the film or in its thickness. However, in our SPR measurements, the SPR reflectivity was observed to decrease by the doping with the ion. Normally, if measured at the low-angle slope of the reflectivity curve, an increase in SPR reflectivity is related to an increasing thickness assuming a constant refractive index. In this case, we believe that the dielectric constant plays a major role in the behavior of observed SPR reflectivity. From the above-mentioned observations, three possible explanations for the change of the SPR curve by anion doping–dedoping process can be considered. This includes the *thickness change*, Δd, of the PANI/SPANI film by anion doping–dedoping and the other two, the dependence of the reflectivity curves for *different dielectric constants*, ε_r and ε_i. If the change in thickness of a PANI/SPANI film is the main component of the SPR curve change, the reflectivity should increase during doping (if measured at angles lower than the resonance) because the insertion of the anion and, simultaneously, of water molecules into the PANI/SPANI film will result in film swelling. This was not observed in our data. Therefore, we believe that the change of the SPR curve in Figure 30.5 is dependent primarily on the change of the dielectric constants, ε_r, and ε_i of the PANI/SPANI film and not of its thickness. This finding then indicates that the dielectric constant of the PANI/SPANI film *decreases* on ion doping and increases on ion dedoping. These observations are consistent with a trade-off between the Δn and the Δd components of the SPR data. We consider this to be consistent with the E-QCM data by Orata and Buttry [34] where ion doping results in an increase in film mass and density (insertion of ions and protonation), thereby decreasing the dielectric constants but not necessarily increasing the optical thickness of the film as monitored by SPR.

30.5
Electrochemical SPR-SPPL

The combination of SPR and surface plasmon-enhanced photoluminescence spectroscopy (SPPL) with electrochemistry was demonstrated for the detection of weak photoluminescence materials such as poly(3,4-ethylenedioxythiophene) (PEDOT) films [35]. In this case, surface plasmons were excited at the metal–dielectric interface, on total internal reflection of polarized light from an He–Ne laser at a wavelength of 594 nm. SPPL from the deposited film was detected by a photomultiplier after passing through a low wavelength cutoff filter ($\lambda = 610$ nm) as schematically shown in the inset of Figure 30.6.

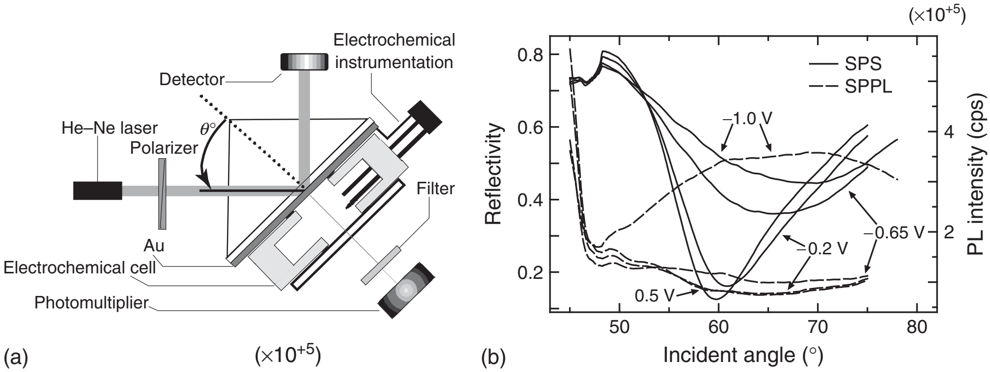

Figure 30.6 (a,b) Angular SPR and SPLS curves of a PEDOT film (solid curve: SPR; dotted curve: SPLS). (From Ref. [36] with permission.)

A most important question in this investigation is whether the photoluminescence can be detected from an ultrathin PEDOT film in the dedoped state. The He–Ne laser of 2.1 eV ($\lambda = 594$ nm), which correspond to the average transition energy from the valence band to the conduction band obtained from UV–vis–near infrared (NIR) spectra, was chosen for the excitation of surface plasmons. The angular measurements were performed under equilibrium conditions with several potentials being held constant. The SPR and SPPL curves of a thin PEDOT film at four different potentials are shown in Figure 30.6. For these measurements, an ultrathin film was prepared intentionally in order to excite the photoluminescence with the evanescent field associated with the surface plasmon mode. The thickness of the film was about 25 nm as deduced from Fresnel fitting curves. From the spectra in Figure 30.6, we can see that the minimum angle of the reflectivity curve increased with increasing negative potential. The minimum angle of the SPR resonance curve for the ultrathin film increases on decreasing the potential from 0.5 to −1 V, which indicates an increase of the real part, ε', of the dielectric constant ($\varepsilon' + i\varepsilon''$) of the PEDOT film. Furthermore, the SPR reflectivity curves significantly broadened at negative potentials. In SPR measurements, curve broadening is either due to an increase of the imaginary part of the dielectric constant, ε'', or to surface roughness. If this broadened curve would be due to surface roughness, the scattered light intensity enhanced by SPR should also increase. As, in our light scattering measurements, an increase of the scattered light intensity was not observed at negative potentials, this result indicates that the electrodeposited thin PEDOT film has a smooth surface, in which the surface roughness does not change with potential. Therefore, the broadening of the SP reflectivity curve is mostly due to an increase in the imaginary part, ε'', of the dielectric constant. This agrees with the observation that the absorption at 2.1 eV increased with negative potentials, that is, on dedoping.

To observe photoluminescence from the conducting polymer film, we needed to use a laser with a higher photon energy than the electronic bandgap energy, that is, in the region that has a strong imaginary part of the dielectric constant. At the same time, the excitation of a surface plasmon is required in order to enhance the electromagnetic field at the Au/PEDOT/electrolyte interface. However, a strong imaginary part of the dielectric constant dampens the excitation of a surface plasmon. An important point in this system is that the surface plasmon is still excited at the dedoped state (−1.0 V), which is only possible because we are dealing with an ultrathin film. Therefore, we can generate an evanescent optical field at the Au/PEDOT/electrolyte interface. The EC-SPPL measurements clearly show the different photoluminescence (PL) intensity properties at different potentials. Indeed, photoluminescence from PEDOT was observed in the dedoped state (−1.0 V) as shown in Figure 30.6. On the other hand, no significant PL intensity was observed at 0.5, −0.2, and −0.65 V. As can be seen, the SPR curve is sharper in the more doped state, which means that the enhanced optical field for the Au/PEDOT/electrolyte system is stronger in the more doped state. However, the enhanced optical field at 2.1 eV is not expected to generate an appreciable $\pi-\pi^*$ transition at 0.5, −0.2, and −0.65 V, and the presence of increased charge carriers might quench the generated exciton. Consequently, no enhancement of luminescence was observed. One possible explanation for the finding that can detect the weak photoluminescence by the EC-SPR/SPPL technique is that the strongly enhanced optical field by the excitation of surface plasmons overcomes the dissipation of the photoluminescence (very low quantum efficiency) in the ultrathin PEDOT film. Another advantage for the use of EC-SPR/SPPL is that we can obtain a strong variation of the photoluminescence by changing the incident angle.

To study the relation between the reflectivity and the photoluminescence, the chronoamperometric measurements using EC-SPR/SPPL were performed. The response of an ultrathin PEDOT film to a sequence of potential steps applied is shown in Figure 30.7. The potential was switched sequentially between the doped and the dedoped states, that is, applied in the following sequence: $0.5 \rightarrow -0.2 \rightarrow 0.5 \rightarrow -0.5 \rightarrow 0.5 \rightarrow -1.0 \rightarrow 0.5$ V. Each potential was applied for 20 s. Characteristic changes were observed in the SPR reflectivity and in the SPPL intensity. The reflectivity increased and decreased when the PEDOT film was dedoped and doped, respectively, whereas the increase of the SPPL signal was observed only when the potential was held at −1.0 V. This observation is quite interesting because it gives direct evidence of the differences between the SPR reflectivity and the SPPL emission. The phenomenon would be very useful in designing optical switching devices because we can obtain three independent signals by this technique. This switching property is in accordance with the result obtained from angular-reflectivity measurements. The reflectivity changed almost immediately if the potential step was applied, and reached a plateau characteristic for each potential applied. On the other hand, the SPPL intensity continued to increase gradually during the applied potential at −1.0 V. The change of the dielectric constant due to the dedoping should be a very fast process: the dielectric constant changed quickly and remained constant. One possible reason for the continued increase of the SPPL intensity is that during the applied potential at −1.0 V, the anion, which quenches the PL intensity in the PEDOT film, moved to the electrolyte solution, so that the PL intensity continued to increase at −1.0 V. Another possible

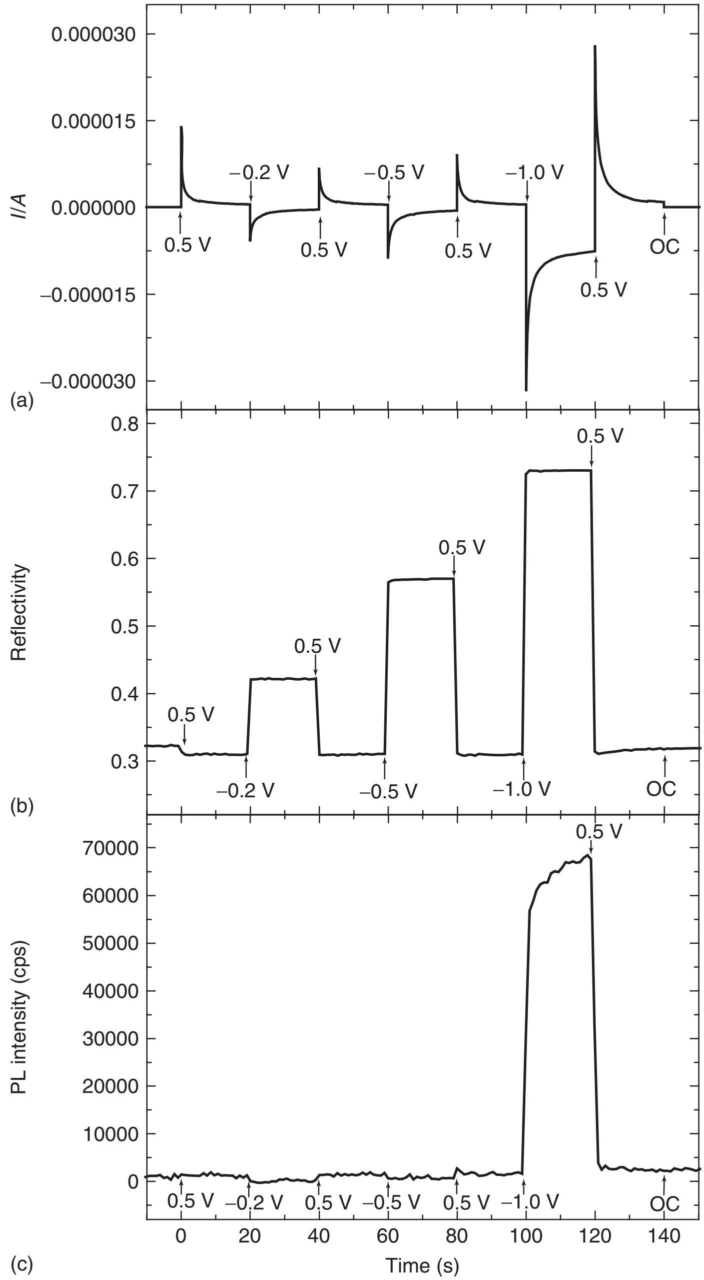

Figure 30.7 (a–c) Chronoamperometric measurements of a PEDOT film switched sequentially between the doped and the dedoped states (0.5 → −0.2 → 0.5 → −0.5 → 0.5 → −1.0 → 0.5 V), respectively. (From Ref. [36] with permission.)

explanation is that the injected charge carriers (leading to recombination and photoemission) might contribute to the enhancement of the light emission process. In fact, a negative current was observed even after 20 s. Even in the dedoped state, an electronic current is expected to exist together with the ionic current [37]. Note that the irradiated area for the excitation of surface plasmons is about 0.010 cm^2, whereas the electrode area is 0.785 cm^2. Therefore, the observed current cannot be mainly assigned to the photocurrent.

30.6
Applications to Biosensors

30.6.1
Glucose Sensing

Electrically conducting and π-conjugated polymers have been shown to be highly sensitive materials for monitoring and mediating enzymatic interactions. This is attributed to the high conductivity and specific EC redox properties of conducting polymers, which can be paired with redox events present in enzymatic reactions [38–40]. For example, the redox property of conducting polymers changes on reduction of the enzyme glucose oxidase (GOx). This change can then be detected either as an EC signal or as an optical signal. On introduction of glucose, GOx is reduced and glucose is converted to gluconic acid (gluconolactone). In the conventional glucose sensors without conducting polymer mediators, the reduced GOx drives the conversion of O_2 to H_2O_2, in the presence of O_2. The H_2O_2 can then undergo oxidation to give H_2O. On the other hand, in the case of with conducting polymer mediators, the oxidation of a reduced chemical species/polymer material can be directly measured by an electrode surface. Thus, electroactive conducting polymers can be considered as ‘‘wiring’’ materials for the EC activation of redox enzymes [41]. Redox enzymes usually have poor direct electrical conductivity contact and communication with metallic electrodes. An electroactive conducting polymer provides the matrix for electron transfer from the enzyme to the electrode, correlated with changes in the EC (I–V) signal. We have endeavored to apply a combined EC-SPR and waveguide approach to enable better differentiation of these factors. Firstly, a water-soluble, positively charged *N*-alkylaminated polypyrrole was synthesized for pairing with the negatively charged GOx. The composite enzyme electrode was fabricated by the assembly of the polypyrrole and the GOx via the LbL electrostatic self-assembly technique [42–44]. As compared to as-deposited LbL film, it was observed that an enhancement in sensitivity for an SPR/amperometric sensor can be achieved by taking advantage of the doping–dedoping effect of these films in a neutral buffer solution condition. As the LbL film can be homogeneously assembled, dips from both SPR and waveguide were obtained when the thick film was fabricated. We have harnessed the EC-SPR technique for demonstrating a glucose biosensor with possible applications for other enzymatic biological optoelectronic differentiation [45].

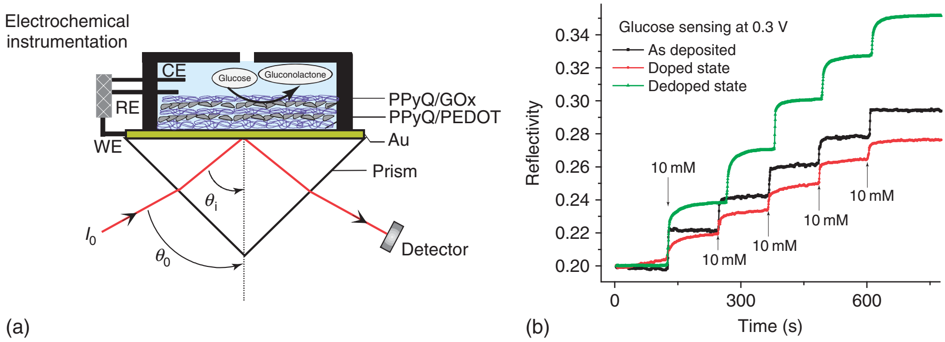

Figure 30.8 (a,b) SPR glucose sensing as a function of concentration (time) at different doping states. (From Ref. [42] with permission.)

As the electrochromic property was obtained in neutral solution, it should be possible to carry out glucose sensing after doping, dedoping, and at the as-deposited states as shown in Figure 30.8. The sensing was carried out in neutral buffer on the addition of 10 mM of glucose every 5 min. As shown in this figure, the change of the optical signal was different by changing the doped–dedoped state before the sensing. This indicates that the doped–dedoped state did not move back even the potential was set at 0.3 V during the sensing experiment. This is probably because the ions are more difficult to move out the LbL films in phosphate buffer solution (PBS) solution. Furthermore, this result indicates that the dedoped state has the highest reflectivity change. This is not counterintuitive as the polypyrrole film is oxidized in the glucose sensing (reduction) event and thus the dedoped state shows the highest change, that is, from a dedoped state to a more doped state. The results obtained also highlights the fact that the change of reflectivity can also be controlled by the doping state of the conducting polymer films. It should be noted that the magnitude of this shift is also a function of the electrochromic behavior of the films and the wavelength of the light source for the ATR experiment.

30.6.2
Detection of Catecholamine

The development of real time and selective detection of catecholamines faces many challenges, despite a high demand for such a technique in the diagnostic field. Catecholamines, such as adrenaline, noradrenaline, and dopamine, are adrenal cortical hormones and neurotransmitters involved in central and peripheral neuroendocrine responses to different types of stress [46, 47]. They are also related to the sympathetic medullar system, which is particularly sensitive to mental and physical stresses [48, 49]. Until now, high-performance liquid chromatography (HPLC) with EC [50–52] or optical [53] detections has been frequently used to detect catecholamines. Although catecholamines can be selectively detected from ascorbic acid and uric acid by the HPLC technique, this method requires a pretreatment process, and the detection measurements take time. Recent research has explored

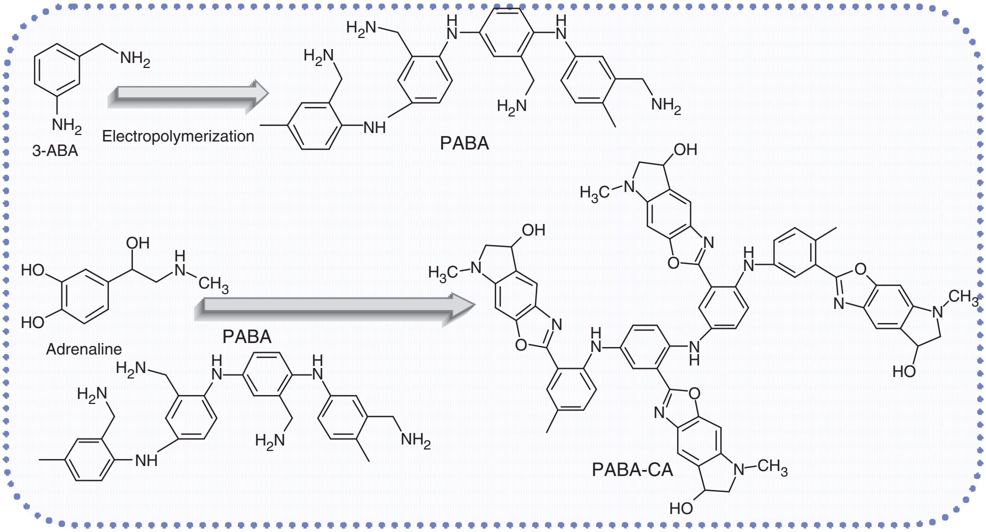

Figure 30.9 Strategy of immobilization of PABA film on electrode and the specific reaction of adrenaline to PABA.

the use of materials such as gold nanoparticles [54, 55], carbon nanotubes [56, 57], and CdSe nanocrystals [58] for the optical detections of catecholamines to obtain lower limit of detection or selectivity [59]. These methods involve distinct adsorption, optical emission, and optical quenching properties. We have reported a real-time detection of optical and EC signals from the specific reaction of adrenaline, which is used as one of the catecholamines, on para-amino benzoic acid (PABA) by EC-SPR. Benzylamines present in the structure of the PANI derivative, PABA, act as specific reaction sites for adrenaline, enabling detection of both optical and EC signals by the surface-sensitive EC-SPR technique, as shown in Figure 30.9 [60]. PABA was electropolymerized from electroactive 3-aminobenzylamine (ABA) monomers. The deposition process was investigated by EC-SPR. Electroactivity of PABA was confirmed from CV in PBS solution, indicating that the signals can be enhanced in the event of specific reactions with adrenaline. The reaction of adrenaline with PABA was studied by UV–vis spectroscopy and X-ray photoelectron spectroscopy (XPS) measurements, and adrenaline was detected within the PABA film by the EC-SPR technique. Signal enhancements were obtained in the case of PABA mediator, while PANI thin film, which was also electropolymerized, showed small enhancement, when the adrenaline was injected into each system. Furthermore, EC-SPR properties exhibited a distinct response for the adrenaline as compared to that for uric acid and ascorbic acid.

The SPR reflectivity and current responses on the detection of adrenaline were obtained at a constant potential of 0.65 V. Figure 30.10a,b shows simultaneous observation of current and SPR reflectivity changes on injection of 100 μM, 1 mM, and 10 mM adrenaline. The current responses exhibited a rapid increase followed by a gradual decrease, corresponding to the transient characteristics of electric double

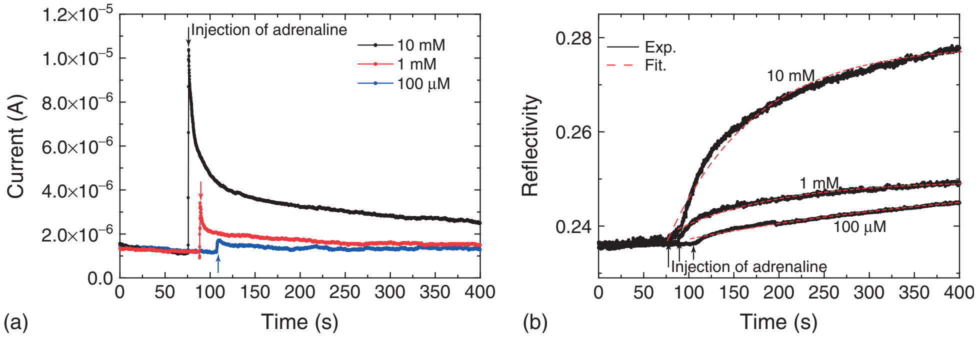

Figure 30.10 Simultaneous observation of (a) current and (b) SPR reflectivity changes on injection of 100 μM, 1 mM, and 10 mM adrenaline. (From Ref. [57] with permission.)

layer reformation at PABA–solution interface and the diffusion of adrenaline. An increase in anodic current was observed as the concentration of adrenaline increased. A gradual increase in the SPR reflectivity, which measures the binding reaction of adrenaline to the PABA film, was observed on injection of adrenaline. As the binding mechanism is based on the chemical reaction between benzylamine and adrenaline, each adsorption SPR reflectivity curve was analyzed using a kinetic model within the Langmuir approach [61, 62]

$$R(t) = (R_{\max} - R_0)\ \left\{1 - \exp\ \left(-k\ c_0\ t\right)\right\} \tag{30.1}$$

where $R_{\max}$ is the reflectivity measured at maximum coverage of the probes at the adrenaline concentration c_0, R_0 is the initial background reflectivity, k is the association rate constant, and $R(t)$ is the time-dependent reflectivity during the adsorption process, which is assumed to be proportional to the number of probe sites occupied by adrenaline at time t. As indicated by the solid lines (Figure 30.10b), the theoretical curves fit well with the experimental kinetic curves for all concentrations. In all cases, the R_2 was higher than 0.97. The k values are 1.0, 8.7, and 27 $\mathrm{M}^{-1}\,\mathrm{s}^{-1}$ for 10 mM, 1 mM, and 100 μM, respectively. The k values derived from the kinetic trace at different concentrations show a decrease with increasing concentration. This might be due to the increasing charge density on the specific reaction of adrenaline with the benzylamine in PABA. This corresponds with XPS and UV–vis results, indicating that the doping state of the PABA film changed after the reaction.

Figure 30.11a,b shows calibrated double-logarithmic plots of the change of the current and reflectivity as a function of concentration. The plot for the current demonstrates that the change in the signal is a linear function of the adrenaline concentration. This result indicates that the current response for the adrenaline detection in this system can be followed within the standard catalytic reaction equation [63, 64]. In the plot of SPR reflectivity change, the relation was also linear to the concentration of adrenaline, while the fitting for SPR kinetic curves shown in Figure 30.5 was carried out within Langmuir adsorption

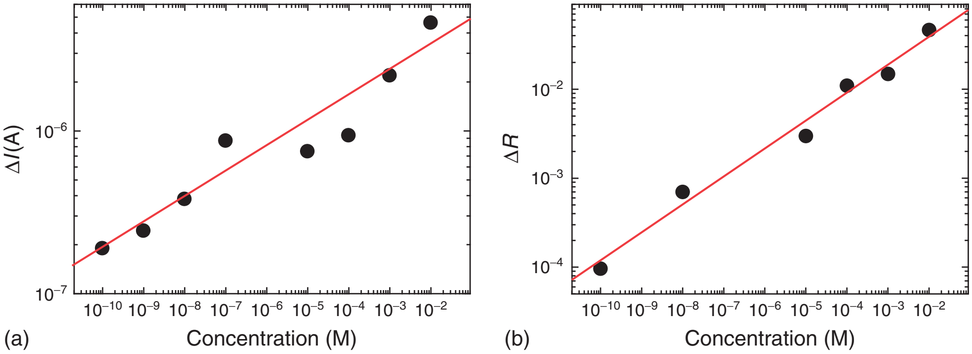

Figure 30.11 Calibrated double-logarithmic plots of the change of (a) the current and (b) reflectivity as a function of concentration. (From Ref. [57] with permission.)

model. This result of log–log plot indicates that the relation corresponds well with extended Langmuir model, that is, Langmuir–Freundlich model further than simple Langmuir model [65–67]. This might be because the PABA film has specific reaction site, benzylamine, not only on the surface but also inside the PABA film. The detection limit in the experiment was determined to be 100 pM from the response with the signal-to-noise ratio of 3 for current response and 10 for SPR reflectivity response.

30.7
Conclusions

In this review, we introduced the combination of SPR methods and EC analysis, which was further combined with a variety of surface-sensitive techniques such as light scattering and photoluminescence for the study of conducting polymer thin films. Their applications to biosensors were also introduced. Besides the combined techniques with EC-SPR shown in this review, other novel combinations such as with scanning EC microscopy [68, 69], microfluidic devices [70], and electrochemically tunable SP-enhanced diffraction gratings [71] have been reported for the study of polymer thin films or sensor applications. In these studies, two surface plasmon excitation methods, that is, prism-coupling method based on Kretschmann configuration and grating-coupling method, were demonstrated.

The introduced method should provide new opportunities both for basic studies and for sensor applications using conducting polymers.

Acknowledgments

We would like to thank all collaborators in this work at Max Planck Institute for Polymer Research, National University of Singapore, University of Houston and Niigata University.

References

1. Knoll, W. (1998) *Ann. Rev. Phys. Chem.*, **49**, 569.
2. Homola, J., Yee, S.S., and Gauglitz, G. (1999) *Sens. Actuators, B*, **54**, 3.
3. Baba, A., Tada, K., Janmanee, R., Sriwichai, S., Shinbo, K., Kato, K., Kaneko, F., and Phanichphant, S. (2012) *Adv. Funct. Mater.* doi: 10.1002/adfm.201200373
4. Baba, A., Wakatsuki, K., Shinbo, K., Kato, K., and Kaneko, F. (2011) *J. Mater. Chem.*, **21**, 16436.
5. Baba, A., Aoki, N., Shinbo, K., Kato, K., and Kaneko, F. (2011) *ACS Appl. Mater. Interfaces*, **3**, 2080.
6. Tamada, K., Nakamura, F., Ito, M., Xinheng, L., and Baba, A. (2007) *Plasmonics*, **2**, 185.
7. Tadjeddine, A., Kolb, D.M., and Kötz, R. (1980) *Surf. Sci.*, **101**, 277.
8. Iwasaki, Y., Horiuchi, T., Morita, M., and Niwa, O. (1997) *Electroanalysis*, **9**, 1239.
9. Baba, A., Advincula, R.C., and Knoll, W. (2002) *J. Phys. Chem. B*, **106**, 1581.
10. Raitman, O., Katz, E., Willner, I., Chegel, V., and Popova, G. (2001) *Angew. Chem. Int. Ed.*, **40**, 3649.
11. Baba, A., Tian, S., Stefani, F.D., Xia, C., Wang, Z., Advincula, R.C., Johannsmann, D., and Knoll, W. (2004) *J. Electroanal. Chem.*, **562**, 95.
12. Baba, A., Lübben, J., Tamada, K., and Knoll, W. (2003) *Langmuir*, **19**, 9058.
13. Chegel, V., Raitman, O., Katz, E., Gabai, R., and Willner, I. (2001) *Chem. Commun.*, **10**, 883.
14. Kang, X., Jin, Y., Chen, G., and Dong, S. (2002) *Langmuir*, **18**, 1713.
15. Baba, A., Knoll, W., and Advincula, R. (2006) *Rev. Sci. Instrum.*, **77**, 064101.
16. Kobayashi, T., Yoneyama, H., and Tamura, H. (1984) *J. Electroanal. Chem.*, **161**, 419.
17. MacDiarmid, A.G., Mu, S.L., Somarisi, N.L.D., and Mu, W. (1985) *Mol. Cryst. Liq. Cryst.*, **121**, 187.
18. Daifuku, H., Kawagoe, T., Yamamoto, N., Ohsaka, T., and Oyama, N. (1989) *J. Electroanal. Chem.*, **274**, 313.
19. Peter, K., Nilsson, R., and Inganäs, O. (2003) *Nat. Mater.*, **2**, 419.
20. Tian, S., Baba, A., Liu, J., Wang, Z., Knoll, W., Park, M.-K., and Advincula, R. (2003) *Adv. Funct. Mater.*, **13**, 473.
21. Baba, A., Sano, Y., Ohdaira, Y., Shinbo, K., Kato, K., and Kaneko, F. (2008) *IEICE Trans.*, **E91-C**, 1881.
22. Sriwichai, S., Baba, A., Phanichphant, S., Shinbo, K., Kato, K., and Kaneko, F. (2010) *Sens. Actuators, B*, **147**, 322.
23. Janmanee, R., Baba, A., Phanichphant, S., Sriwichai, S., Shinbo, K., Kato, K., and Kaneko, F. (2011) *Jpn. J. Appl. Phys.*, **50**, 01BK02.
24. Kretschmann, E. (1972) *Opt. Commun.*, **5**, 331.
25. Atteidge, J.W., Daniels, P.B., Deacon, J.K., Robinson, G.A., and Davidson, G.P. (1991) *Biosens. Bioelectron.*, **6**, 201.
26. Liebermann, T. and Knoll, W. (2000) *Colloids Surf., A*, **171**, 115.
27. Ushioda, S. and Sasaki, Y. (1983) *Phys. Rev. B*, **27**, 1401.
28. Knobloch, H., Duschl, C., and Knoll, W. (1989) *Chem. Phys.*, **91**, 3810.
29. Cui, S.-Y. and Park, S.-M. (1999) *Synth. Met.*, **105**, 91.
30. Baba, A., Park, M.-K., Advincula, R., and Knoll, W. (2002) *Langmuir*, **18**, 4648.
31. Sauerbrey, G. (1959) *Z. Phys.*, **155**, 206.
32. Stejskal, J. and Gilbert, R.G. (2002) *Pure Appl. Chem.*, **74**, 857.
33. Orata, D. and Buttry, D.A. (1987) *J. Am. Chem. Soc.*, **109**, 3574.
34. Orata, D. and Buttry, D.A. (1987) *J. Am. Chem. Soc.*, **109**, 3574.
35. Baba, A. and Knoll, W. (2003) *J. Phys. Chem. B*, **107**, 7733.
36. Huang, W.S., Humphrey, B.D., and MacDiarmid, A.G. (1986) *J. Chem. Soc., Faraday Trans.1*, **82**, 2385.
37. Johansson, T., Pettersson, L.A.A., and Inganäs, O. (2002) *Synth. Met.*, **129**, 269.
38. Wang, D., Gong, X., Heeger, P.S., Rininsland, F., Bazan, G.C., and Heeger, A.J. (2002) *Proc. Natl. Acad. Sci. U.S.A.*, **99**, 49.
39. Peter, K., Nilsson, R., and Inganäs, O. (2003) *Nat. Mater.*, **2**, 419.
40. Wallace, G.G. and Kane-Maguire, L.A.P. (2002) *Adv. Mater.*, **14**, 953.

41. Kros, A., Hövell, S., Sommerdijk, N., and Nolte, R. (2002) *Adv. Mater.*, **13**, 1555.

42. Hodak, J., Etchenique, R., Calvo, E.J., Singhal, K., and Bartlett, P.N. (1997) *Langmuir*, **13**, 2708.

43. Constantine, C.A., Gattás-Asfura, K.M., Mello, S.V., Crespo, G., Rastogi, V., Cheng, T.C., DeFrank, J.J., and Leblanc, R.M. (2003) *Langmuir*, **19**, 9863.

44. Ferreira, M., Fiorito, P.A., Oliveira, O.N., and Torresi, S.I.C. (2004) *Biosens. Bioelectron.*, **19**, 1611.

45. Baba, A., Ponnapati, R., Taranekar, P., Knoll, W., and Advincula, R. (2010) *ACS Appl. Mater. Interfaces*, **2**, 2347.

46. Codispoti, M., Gerra, G., Montebarocci, O., Zaimovic, A., Raggi, M.A., and Baldaro, B. (2003) *Psychophysiology*, **40**, 863.

47. Gerra, G., Zaimovic, A., Mascetti, G.G., Gardini, S., Zambelli, U., Timpano, M., Raggi, M.A., and Brambilla, F. (2001) *Psychoneuroendocrinology*, **26**, 91.

48. Lundberg, U. (1995) *Technol. Health Care*, **3**, 3.

49. Nikolajsen, R.P.H. and Hansen, A.M. (2001) *Anal. Chim. Acta*, **449**, 1.

50. Takahashi, M., Morita, M., Niwa, O., and Tabei, H. (1992) *J. Electroanal. Chem.*, **335**, 253.

51. Musso, N.R., Vergassola, C., Pende, A., and Lotti, G. (1990) *J. Liq. Chromatogr.*, **13**, 2217.

52. Chernyshov, D.V., Shvedene, N.V., Antipova, E.R., and Pletnev, I.V. (2008) *Anal. Chim. Acta*, **621**, 178.

53. Ragab, G.H., Nohta, H., and Zaitsu, K. (2000) *Anal. Chim. Acta*, **403**, 155.

54. Raj, C.R., Okajima, T., and Ohsaka, T. (2003) *J. Electroanal. Chem.*, **543**, 127.

55. Baron, R., Zayats, M., and Willner, I. (2005) *Anal. Chem.*, **77**, 1566.

56. Ali, S.R., Ma, Y., Parajuli, R.R., Balogun, Y., Lai, W.Y.C., and He, H. (2007) *Anal. Chem.*, **79**, 2583.

57. Yogeswaran, U. and Chen, S.M. (2008) *Sens. Actuators, B*, **130**, 739.

58. Ma, Y., Yang, C., Li, N., and Yang, X. (2005) *Talanta*, **67**, 979.

59. Hayashi, K., Iwasaki, Y., Kurita, R., Sunagawa, K., and Niwa, O. (2003) *Electrochem. Commun.*, **5**, 1037.

60. Baba, A., Mannen, T., Ohdaira, Y., Shinbo, K., Kato, K., Kaneko, F., Fukuda, N., and Ushijima, H. (2010) *Langmuir*, **26**, 18476.

61. Yao, D.F., Kim, J.Y., Yu, F., Nielsen, P.E., Sinner, E.K., and Knoll, W. (2005) *Biophys. J.*, **88**, 2745.

62. Knoll, W., Park, H., Sinner, E.K., Yao, D., and Yu, F. (2004) *Surf. Sci.*, **570**, 30.

63. Wang, X., Yang, N., Wan, Q., and Wang, X. (2007) *Sens. Actuators, B*, **128**, 83.

64. Aoki, K., Chen, J., Ke, Q., Armes, S.P., and Randall, D.P. (2003) *Langmuir*, **19**, 5511.

65. Norde, W. and Lyklema, J. (1991) *J. Biomater. Sci., Polym. Ed.*, **2**, 183.

66. Umpley, R.J. II,, Baxer, S.C., Ranpey, A.M., Rushton, G.T., Chen, Y., and Shimizu, K. (2004) *J. Chromatogr. B*, **804**, 141.

67. Yao, C. (2000) *Sep. Purif. Technol.*, **19**, 237.

68. Szunerits, S., Knorr, N., Calemczuk, R., and Livache, T. (2004) *Langmuir*, **21**, 9236.

69. Fortin, E., Defontaine, Y., Mailley, P., Livache, T., and Szunerits, S. (2005) *Electroanalysis*, **17**, 495.

70. Choi, S. and Chae, J. (2009) *Biosens. Bioelectron.*, **25**, 527.

71. Tian, S., Armstrong, N.R., and Knoll, W. (2005) *Langmuir*, **21**, 4656.

31

Applications of Fourier Transform Infrared (FTIR) Imaging

Al de Leon, Brylee Tiu, Joey Mangadlao, Katrina Pangilinan, Pengfei Cao, and Rigoberto Advincula

31.1

Introduction

Fourier transform infrared (FTIR) spectroscopy is a common method used to ascertain the molecular identity and composition of a sample. The technique relies on the absorption in the 2–15 μm^{-1} regions of the electromagnetic spectrum resulting to excitation of vibrational, rotational, and bending modes of constituent chemical moieties. The general selection rule for IR spectroscopy is the change in dipole moment during vibration. Although FTIR by itself offers a number of utilities in chemical characterization, coupling it with a microscope allows the elucidation of a chemical structure in a specific spatial region. This technique is called *FTIR microspectroscopy* or simply *FTIR microscopy*. In principle, the combination of spatial specificity and information on chemical makeup allows the construction of an FTIR map or FTIR image (a chemical map) providing information on the distribution of chemical species, morphological assemblies, diffusion profiles, and concentration gradients.

It is important to delineate the difference between FTIR mapping and FTIR imaging. FTIR mapping, also called *point mapping*, is a point-by-point measurement across the sample to obtain spatially resolved information [1]. In detail, an IR spectrum is collected at a particular point, and then the sample is moved to collect the spectrum of another location. The process is repeated within the area of interest. The spectra are then correlated by a computer to a specific and reproducibly obtainable sample position [2]. While a very good signal-to-noise ratio for very small single-point sample areas can be obtained, the method suffers from a number of limitations: firstly, low-spatial resolution at sample areas is restricted to squares $>15 \times 15\,\mu m^2$ [1, 2]. Secondly, diffraction effects and stray light compromise accuracy of the data.

Finally, as the technique is essentially a sequential mapping process, carrying out the analysis takes a long time and requiring very precise X–Y positioning and image reconstruction. In effect, studying dynamic processes with FTIR mapping is extremely challenging.

Handbook of Spectroscopy, Second Edition. Edited by Günter Gauglitz and David S. Moore.

FTIR imaging, on the other hand, was primarily developed to overcome the limitations of FTIR mapping. The use of focal plane array (FPA) detectors in FTIR imaging affords simultaneous collection of spectra at a single experiment thus, a “chemical snapshot” is obtained [1]. FPA detectors consist of a large number of small detectors laid out in a grid pattern. The spectrum, simultaneously acquired by each detector, is represented as a single pixel in the resulting FTIR image. As a given field of view is imaged in a single collection, the sample does not need to be moved and the use of aperture is not required to limit the sample area, and hence, the occurrence of stray light, which compromise spatial distribution, is eliminated [3]. In addition, in FTIR imaging, the collection time is decreased by a factor of n^2, where n is the number of spatial resolution elements in one direction of a square sample area imaged [3]. Koenig *et al.* [3] illustrated that a $500 \times 500\,\mu m$ sample area will take 10 h if it were analyzed by FTIR mapping, while it will only take less than a minute for FTIR imaging with the same image quality and spectral resolution. In addition, the use of mosaicking or assembly of several FTIR images enables sampling over a wider area. Thus, spatially and temporally resolved chemical information can be obtained. In combination with chemometrics or time-resolved studies, it makes a very powerful analytical technique.

Figure 31.1 shows the optical setup for a typical FTIR imaging spectrometer. The heart and soul of the configuration is the FPA detector and the step-scan interferometer. The beam from the interferometer is diverted through the microscope optics and then to the FPA detector. A step-scan interferometer maintains constant

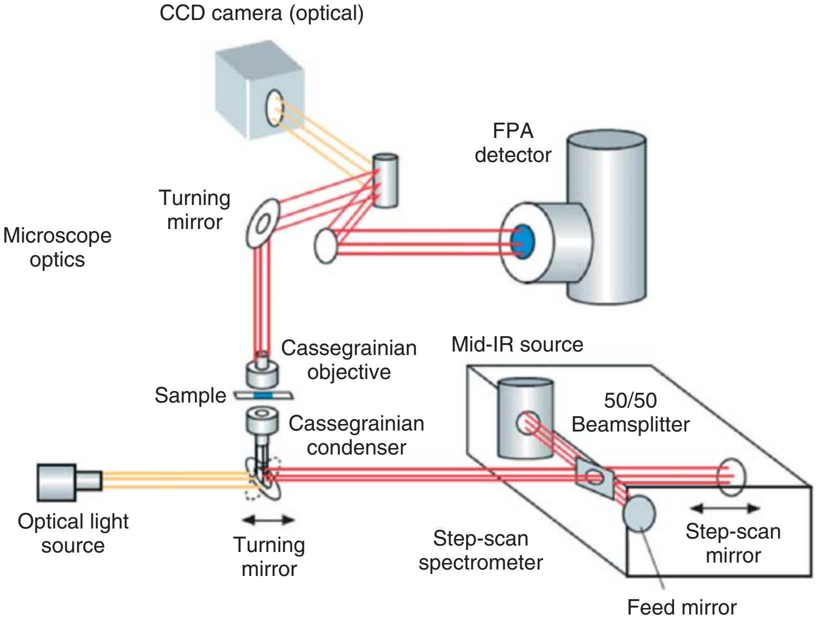

Figure 31.1 Optical setup for a typical FTIR imaging spectrometer. (Copyright from Ref. [1].)

optical retardation for an arbitrarily large time while the FPA coadds collected frames at each optical retardation point in order to improve signal-to-noise ratio. A Cassegraninan condenser and objective are also added to focus the radiation to the plane of the sample [1, 3]. This configuration allows for the imaging of a wide field of view in a single collection.

The speed of image acquisition and improved signal-to-noise ratio in FTIR imaging offer the advantage of real-time monitoring of dynamic phenomena and chemical processes in both biological and nonbiological systems. For example, FTIR imaging is essential in studying both static and dynamic phenomena in polymeric systems. It has been used to investigate single and mixed solvent diffusions in polymer films, polymer blends, polymer–liquid crystal systems, and composites [4–6]. The characterization of structure and morphology, as well as the determination of homogeneity in polymer systems, can also be analyzed by the technique [7, 8]. While much potential has to be exploited in the area of material, FTIR imaging has been widely used in biological arena where it has become useful in the characterization of biological samples, diagnosis, reaction dynamics of pharmaceuticals, and drug delivery [9, 10]. With FTIR imaging, chemical processes can be investigated, and specific molecules inside the cell can be mapped out in real time, because staining and labeling are not required for visualization. More recently, FTIR imaging has also been found useful in forensic science, microfluidics, and biofuels [11–13].

31.2
FTIR Imaging Applied to Polymeric Systems

The chemical nature of single polymer particles and polymer films has been effectively studied using FTIR imaging. While not exhaustive, the applications of the technique of various polymer materials will be described in the following sections.

31.2.1
Polymer Ultrathin Film Characterization

Our group has used FTIR imaging to confirm the successful polymerization of block copolymers from polyelectrolyte atom transfer radical polymerization (ATRP) macroinitiators. The macroinitiators were assembled via layer-by-layer (LbL) deposition onto an aminopropyltrimethoxysilane (APS)-functionalized silicon wafer [14]. Successful polymerization of poly(styrene-*b*-2,2,2-trifluoroethyl methacrylate) (p(St-*b*-TFEMA) was confirmed by comparing the chemical maps before and after polymerization of trifluoromethyl methacrylate (TFEMA) from the polystyrene (pSt) brush, which was polymerized via surface-initiated ATRP. Specifically, FTIR imaging for pSt homopolymer shows no absorbance at 1730 cm^{-1}, which corresponds to carbonyl region. After the polymerization of TFEMA, the carbonyl peak becomes apparent on some regions. The chemical heterogeneity is brought about by the fact that each layer in the LbL film acted as an initiating site. This resulted in varying heights of grafted pSt brush and unequal grafting of the pTFEMA block brushes.

We also utilized FTIR imaging to verify the successful grafting and the spatial distribution of binary mixed brush. Mixed brushes of poly(*N*-isopropylacrylamide) (pNIPAM) and pST were grown from LbL assembly of polyelectrolyte ATRP macroinitiators and 4-4′-azobis(4-cyanovaleric acid) free radical polymerization initiator [7]. IR images focused at 1650 cm^{-1} (–C=O), 2900 cm^{-1} (–CH), and 3300 cm^{-1} –NH) of (pNIPAM) and pNIPAM-pSt mixed brush were compared. The significant decrease in the maximum absorbance in the three regions for the pNIPAM-pST mixed brush relative to that for pNIPAM homopolymer brush confirms the successful grafting of both pSt and pNIPAM. In addition, by looking at the functional distribution, it was concluded that the surface was saturated with pNIPAM. This was also confirmed by ellipsometry studies, which revealed that the brush thickness of pNIPAM and pSt is 159 and 2 nm, respectively, for 20 layers of macroinitiators. This result was expected because with more layers of macroinitiators deposited on the surface, the initiator density increases accordingly, and thicker pNIPAM brush is polymerized. Thick pNIPAM brush limits the availability of the underlying free radical initiator for polymerization of styrene. In addition, the statistical distribution of the pNIPAM-pSt mixed brushes meant that the surface functionalities were randomly configured on the surface.

In another study performed by our group, we used FTIR imaging to estimate the degree of coverage of pNIPAM brush on ATRP-initiator-modified LbL assembly of chitosan and alginate [8]. Image focused at 1650 cm^{-1} (amide I carbonyl backbone stretch) shows that majority of the area is covered by pNIPAM. Comparison with the image focused at 1600 cm^{-1} (carboxylated region), led the author to conclude that about 85% surface was covered by pNIPAM and that its growth was favored on the amine regions derived from chitosan.

31.2.2
Polymer Nanostructures and Surface Patterning

Chemical composition of the patterned surface can also be mapped using FTIR imaging as exemplified by our group [15]. We presented a simple yet versatile route for patterning polymer brushes. This was made possible by using a molecule bearing an electroactive (carbazole) group and a photoactive (benzophenone) group. Two patterning routes available are (i) electrodeposition on patterned indium tin oxide (ITO) surface and then photografting of the spin-coated polystyrene (PS) film (Figure 31.2a,b) and (ii) electrodeposition on ITO and patterned photografting of spin-coated film using a photomask (Figure 31.2c,d).

FTIR imaging was conducted to gain information about the chemical composition of the patterns produced. All images are focused at 3034 cm^{-1}, which corresponds to aromatic –CH stretch of polystyrene. Green areas represent high concentration of pSt, while the blue areas represent either the glass substrate or the electrodeposited benzophenone. These patterns were only visible at this wave number, that is, images focused at different wave numbers (e.g., 1680–1800 cm^{-1}) do

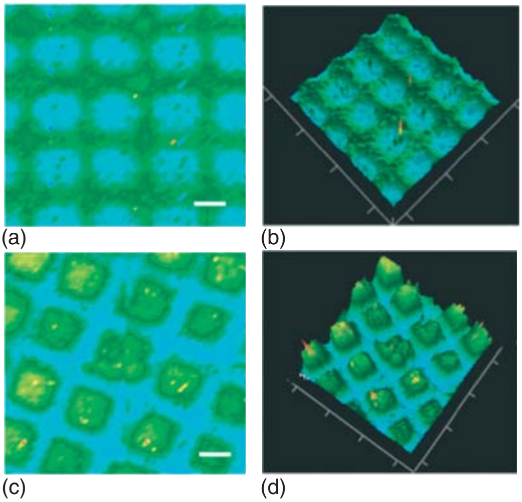

Figure 31.2 2D and 3D IR images for (a,b) electropatterned and (c,d) photopatterned pSt brushes. Scale bar = 30 μm. (Copyright from Ref. [15].)

not show any pattern. On a separate study, we utilized FTIR imaging to chemically characterize binary patterned brush systems initiated by electroactive monomer with chain transfer agent (CTA) moiety and by ATRP-initiator-functionalized silane [16]. CTA-functionalized carbazole was first electrodeposited on a glass substrate coated with patterned ITO, and then pSt brush was grown via surface-initiated reversible addition–fragmentation chain transfer (RAFT) polymerization. pNIPAM was then polymerized on the exposed glass prefunctionalized with ATRP initiator-functionalized silane. By focusing on peaks distinct to the polymer brushes, we obtained a clear image of the patterned surface. Image focused at 3020 cm^{-1}, corresponding to aromatic –CH stretch, reveals that pSt was successfully polymerized on the patterned ITO. On the other hand, image focused at 1650–1700 cm^{-1} (–C=O stretch), 1550–1600 cm^{-1} (amide II peak, –NH bending), or 3100–3400 cm^{-1} (–NH stretch) shows that pNIPAM was polymerized on the region where ITO was etched away.

Characterization of polymer nanostructures is another application of FTIR imaging, more effectively if combined with other characterization techniques. King *et al.* [17] reported the characterization of various polymer nanostructures and heterogeneous patterns of polymer nanostructures by the combination of atomic force microscope (AFM) and FTIR imaging spectroscopy. Hilt *et al.* [18] also demonstrated that FTIR imaging can be used to characterize the real-time photopolymerization of a patterned methacrylate-based hydrogel. The patterns were created by microcontact printing of 1-octadecanethiol on gold, application of monomer solution containing the cross-linker and photoinitiator on the unpatterned areas, and photopolymerization by UV light ($\lambda = 320$–500 nm) irradiation.

31.2.3
Diffusion and Dissolution of Polymer Films

Koenig *et al*. [4] are among the first to employ FTIR imaging to study the physical processes in polymeric systems, such as diffusion and dissolution processes. Their main objective is to spatially resolve the chemical functionalities to monitor the diffusion process involved in polymer–dispersed liquid crystal system. They monitored the diffusion of a low-molecular-weight liquid crystal into a solid polymer film in real time [19], and mapped the multiphase domains. They also studied the diffusion process for both cured and uncured blends of polybutadiene and diallyl phthalate by monitoring the domain compositions, sizes, shapes, and interfaces. In another study, they used FTIR imaging to characterize and calculate the dissolution rate of poly(α-methylstyrene) and poly(styrene-*b*-methyl methacrylate) as a function of solvent and temperature [20, 21].

31.2.4
Phase Separation

Siesler *et al*. [5, 22] demonstrated the applicability of FTIR imaging in phase separation of polymer blends. In their report, they imaged the chemical map of blends with varying compositions of poly(3-hydroxylbutyrate) (PHB) with poly(L-lactic acid) (PLA) [5].

Figure 31.3a shows that the islands of PHB, with a size of 30–40 μm, are embedded in a PLA matrix as confirmed by PLA- and PHB-specific FTIR images. On the other hand, no phase separation can be observed in the visible and FTIR images of 30 : 70 (w/w) blends as shown in Figure 31.3b. Integrated intensities from 1720 to 1700 cm^{-1} and 1770 to 1800 cm^{-1} were used to represent PHB and PLA in the FTIR images, respectively. In another study performed by the same group, they used FTIR imaging coupled with polarized irradiation to understand the orientation mechanism of incompatible and miscible polymer blends on uniaxial elongation [22].

Kazarian *et al*. [23] utilized FTIR imaging to study the CO_2-induced phase separation of pSt/poly(vinyl methyl ether) (PVME) blend, and poly(ethylene oxide) (PEO)/poly(methyl methacrylate) (PMMA) system. Moreover, several groups started to map the chemical composition of polymer spherulite [24, 25]. Recently, Morikawa *et al* [26]. successfully analyzed quantitatively the molecular chain orientation of the PEO spherulite by using the four-polarization method of FTIR imaging.

31.2.5
Polymer Degradation

We were the first to report the study of the photodegradation of PS polymer thin film by using FTIR imaging [27]. In this study, pSt was mixed with [1,12-dodecanediylbis(oxy-4,1-phenylene)][bis[phenylmethanone], a photoinitiator with

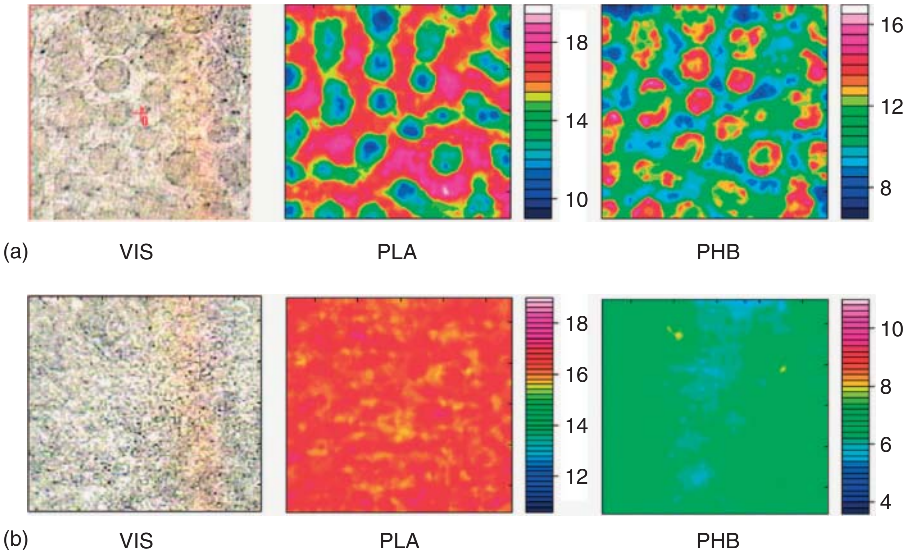

Figure 31.3 Visual image (left), PLA-specific FTIR image (center), and PHB-specific FTIR image (right) of a PHB/PLA (50 : 50% (w/w)) blend (a) and a PHB/PLA (30 : 70 (w/w)) blend (b). (Copyright from Ref. [5].)

two benzophenone moieties, and then spin-casted on silicon wafer. Both photodegradation and cross-linking were studied by irradiating the polymer film in the presence of air. IR images focused at three pertinent wave numbers, specifically 1640 cm^{-1} (–C=O stretch for benzophenone), 1735 cm^{-1} (–C=O stretch for degradation carbonyl), and 3350 cm^{-1} (–OH for hydroperoxide formation), which are shown in Figure 31.4.

It can be seen clearly that as the film was irradiated, the intensity for 1640 cm^{-1} decreases, while the intensities for 1735 and 3350 cm^{-1} increase. In addition, the changes in IR image of the pSt degradation products are more apparent than those for the benzophenone carbonyl. This was explained by considering that degradation of carbonyls and hydroperoxides begin from zero intensity. Furthermore, even after 150 min of irradiation, cross-linking does not proceed to completion. This was expected because not all benzophenone moieties in a film are within reasonable proximity to hydrogen donors.

31.3
Biomedical Applications of FTIR Imaging

31.3.1
Cell Imaging and Diagnosis

FTIR imaging has been applied in the investigation of molecular and metabolic processes due to its ability to probe samples on a molecular level. This imaging

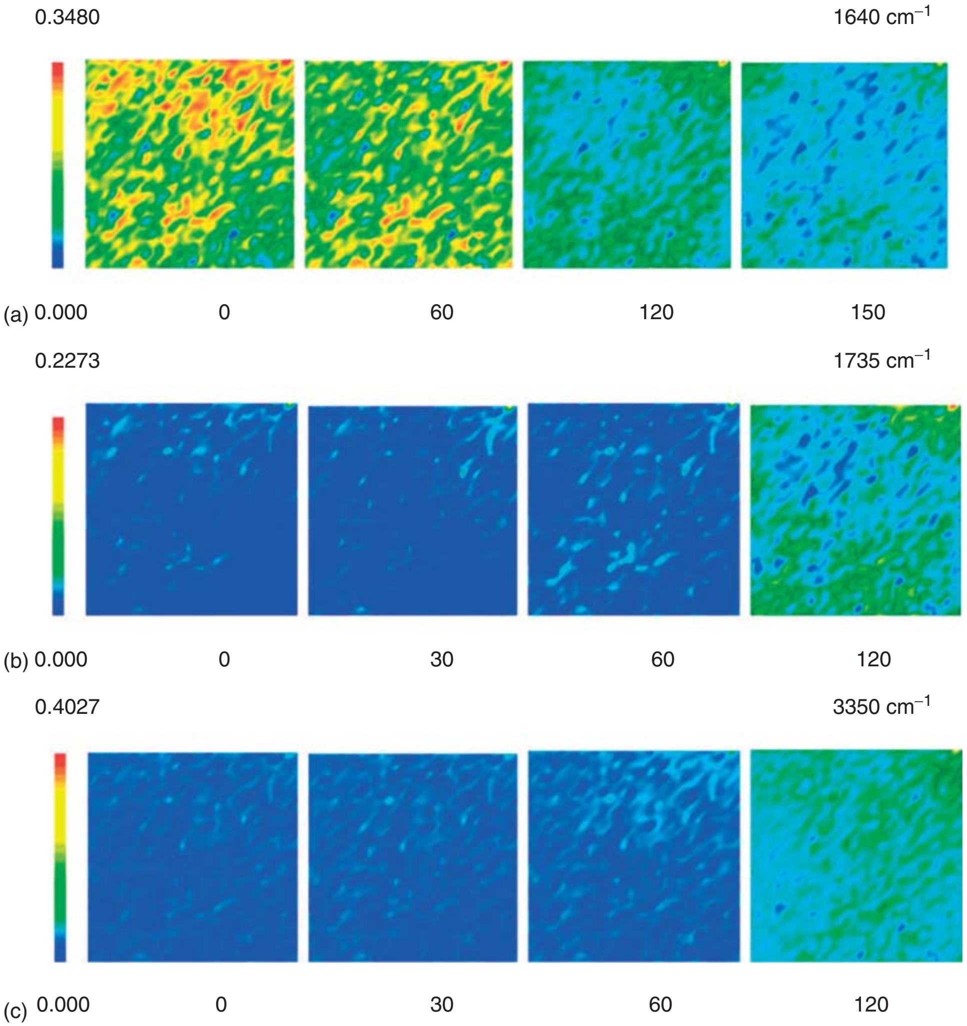

Figure 31.4 (a–c) 2D FTIR images focused at 1640, 1735, and 3350 $\mathrm{cm^{-1}}$ as a function of irradiation time in 30 min increment. Area = 176 × 176 μm^2. (Copyright from Ref. [27].)

technique offers a rapid, high-resolution, and nondestructive molecular analysis that requires neither staining nor labeling, an advantage. Subtle changes in the characteristic infrared signatures of biomolecules such as proteins, lipids, and nucleic acids have been used to characterize tissue specimens for diagnoses (e.g., early development of cancer cells) [28–32].

Cancer is probably one of the most important diseases that are needed to be diagnosed early. Traditionally, cancer is detected after it has already caused significant morphological changes in tissues. Breast cancer is the most common cancer among women, affecting one in eight women in the United States [33].

Mammography is used as a screening tool for the early detection of breast cancer. It works by using small doses of ionization radiation to create images where masses and microcalcifications can be seen. However, mammography by itself is not a very accurate tool and can easily overlook cancer. FTIR imaging, on the other hand, is very sensitive to changes in the structure of biomolecules, and therefore can serve as an effective replacement or complement technique to mammography. As cancer mutations in biomolecules appear before cellular manifestations, early detection with FTIR imaging is possible. This will eventually lead to an increase in patient survival. A recent report has shown that FTIR imaging can differentiate cancerous, benign lesions, calcifications in proliferative lesions, and normal breast tissues [9]. The FTIR imaging of the cancer cell sample was color-coded to show the extent of the disease. Comparison of the spectra for normal and cancer cells showed differences in the position of the peaks and their corresponding intensities. The normal collagen peak at 1203 cm^{-1} shifted to 1207 cm^{-1} for the cancer sample, which is broader and has lower intensity. This suggests changes in the collagen matrix. Another collagen peak for amide III of the cancer sample at 1236 cm^{-1} has lower intensity than for the normal cells. Both spectra have peaks around 1160 cm^{-1}, but only the cancer sample has a small shoulder at 1170 cm^{-1}. The amide I peak at 1600–1730 cm^{-1} for cancer stroma has stronger intensity and is slightly shifted to a lower wave number than for the normal stroma. The shift corresponds to a decrease in the number of random coils and turns in the secondary structure of proteins. Another protein band, the amide II peak at 1544 cm^{-1}, is shifted to a lower wave number. These differences indicate a change in protein conformation in the cancer tissues.

FTIR imaging has also been utilized in the study of other diseases such as leukemia [31, 34], lung cancer [35], ovarian carcinoma [36], and glioma [37]. Glioma is the most common type of brain tumor affecting 66 000 people per year. In a study by Manfait *et al.* [37], relative absorbance percentage fractions of normal and glioma brain tissue components from IR spectra were used to diagnose brain cancer. FTIR maps of healthy and cancer cells were taken based on a cluster analysis. Comparison of the spectra showed that a malignant brain tumor has a lower 1466 cm^{-1}/1396 cm^{-1} ratio corresponding to the amino acid side chain from peptides and proteins than for normal brain tissue. Moreover, the intensity of C=O stretching of the lipids of a malignant brain tumor is lower, consistent with what has been observed before the tumor growth is characterized by a decrease in phospholipid content. These studies show that FTIR imaging can aid in the early detection and quantification of biochemical changes related to cancer. However, it is important to separate the contributions of lipids, proteins, and nucleic acids in the spectra during analysis for proper diagnosis. Another limiting factor in FTIR imaging application in medicine is the brightness available from the blackbody light source, which dictates the resolution and signal-to-noise ratio; therefore, getting an image with a useful signal-to-noise ratio requires long acquisition times and imaging of dynamic living cells proves to be a challenge. To overcome this, Phillips and his colleagues [38] built a pulsed tunable optical parametric generator source that can produce an image at the subcellular level with 100 ps temporal resolution. With this modification, they were able to view cancer cells undergoing mitosis by mapping the characteristic vibrations of amide II band at 1540 cm^{-1} of proteins (Figure 31.5). This makes it possible to acquire *in vitro* IR spectral images of living cells for use in clinical studies.

31.3.2
Pharmaceutical Application

FTIR imaging has been used in evaluating the concentration and distribution of the different components of pharmaceutical formulations for manufacturing [39–41]. It also provides a fast screening tool for evaluating a large number of samples produced by pharmaceutical companies. Samples with controlled diameter are dispensed on attenuated total reflectance (ATR) crystal to form an array (Figure 31.6), and are characterized simultaneously at identical conditions [42].

FTIR imaging can be utilized in differentiating genuine and fake tablets because it is a very sensitive method for detecting trace materials [43–45]. A poor quality drug

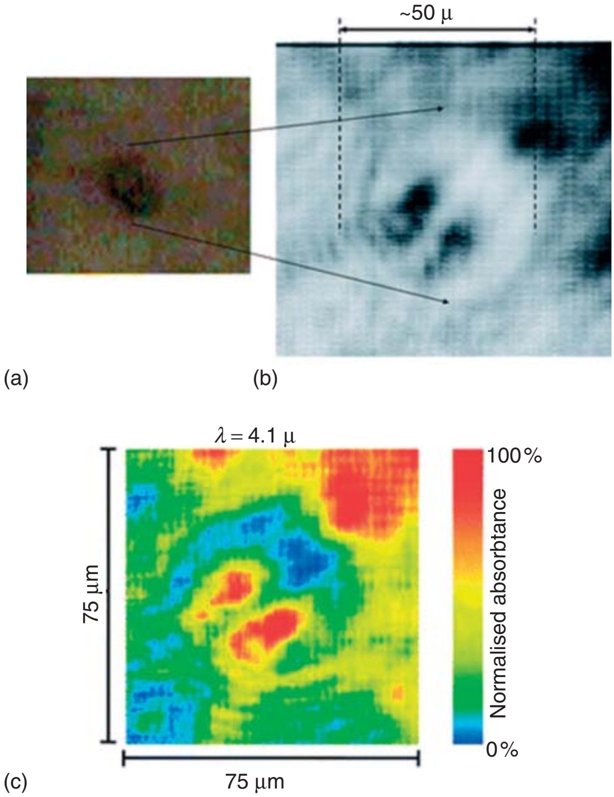

Figure 31.5 (a–c) IR image of a live SK-OV-3 human ovarian cancer cell undergoing mitosis in H_2O-based phosphate buffer solution. (Copyright from Ref. [38].)

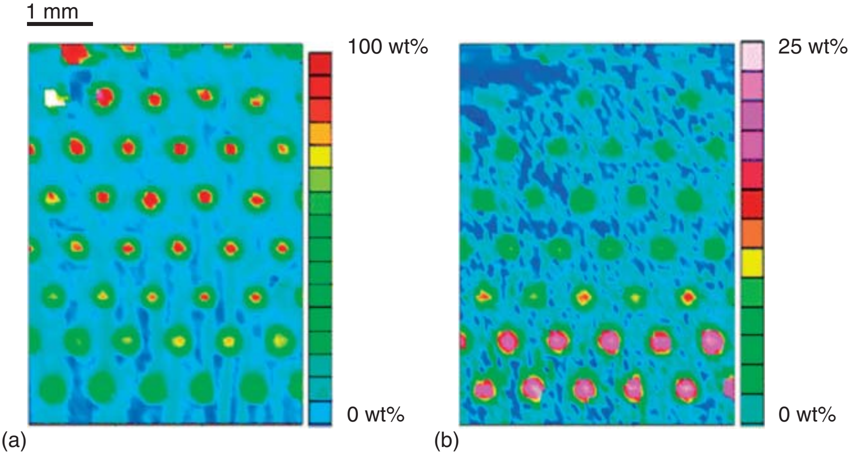

Figure 31.6 Distribution of (a) PEG and (b) ibuprofen in the same sample array. (Copyright from Ref. [42].)

contains inactive ingredients, contaminants, degraded drug, or incorrect dosage, all of which may be harmful to the consumer. Macro-ATR-FTIR imaging of fake tablets can be evaluated against the spectral and image features expected from a pure tablet. Traditional methods such as high-performance liquid chromatography (HPLC), gel permeation chromatography (GPC), and mass spectrometry (MS) are time-consuming, while macro-ATR-FTIR imaging is fast and nondestructive. Thus, this technique can be integrated with standard protocols for forensic investigation of pharmaceutical tablets.

FTIR imaging has also been used to study drug dissolution and drug release by measuring drug concentration as a function of time. The mechanism of drug release (e.g., diffusion of water into the polymer matrix, polymer swelling, polymer dissolution or degradation, or diffusion of drug out of the matrix), along with the chemical structure and morphology of the drug, can be effectively determined by using FTIR imaging. Drug release studies are often performed by imaging the tablet during dissolution. Kazarian *et al.* [10] used a combination of FTIR imaging in its macromode and the ATR–IR approach to study the polymer/drug formulations in contact with water (Figure 31.7).

Ibuprofen, which is slightly soluble in water, was dispersed in poly(ethylene glycol) (PEG), a water-soluble polymer. Figure 31.8 shows FTIR images of ibuprofen/PEG in contact with water. The images at the top row are based on the PEG band integration at 1020–1170 cm^{-1}, and images at the bottom are based on the integration of the C=O absorption band of ibuprofen at 1665–1760 cm^{-1}. Images of PEG show uniform dissolution within 40 min. On the other hand, the images of ibuprofen dissolution show drug accumulation on the surface as evidenced by the increase in intensity of the ibuprofen band (shown in red). The inset in Figure 31.8 shows that the peak of ibuprofen dispersed in and around the polymer. The shift

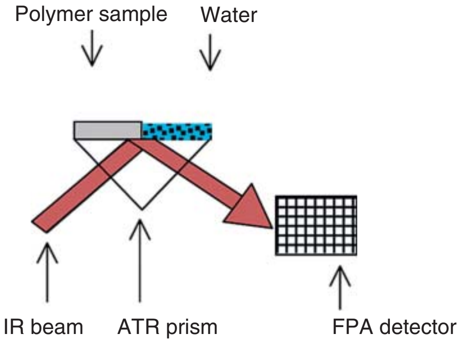

Figure 31.7 Schematic presentation for studying the polymer–water interface using the macro-ATR-imaging approach. (Copyright from Ref. [42].)

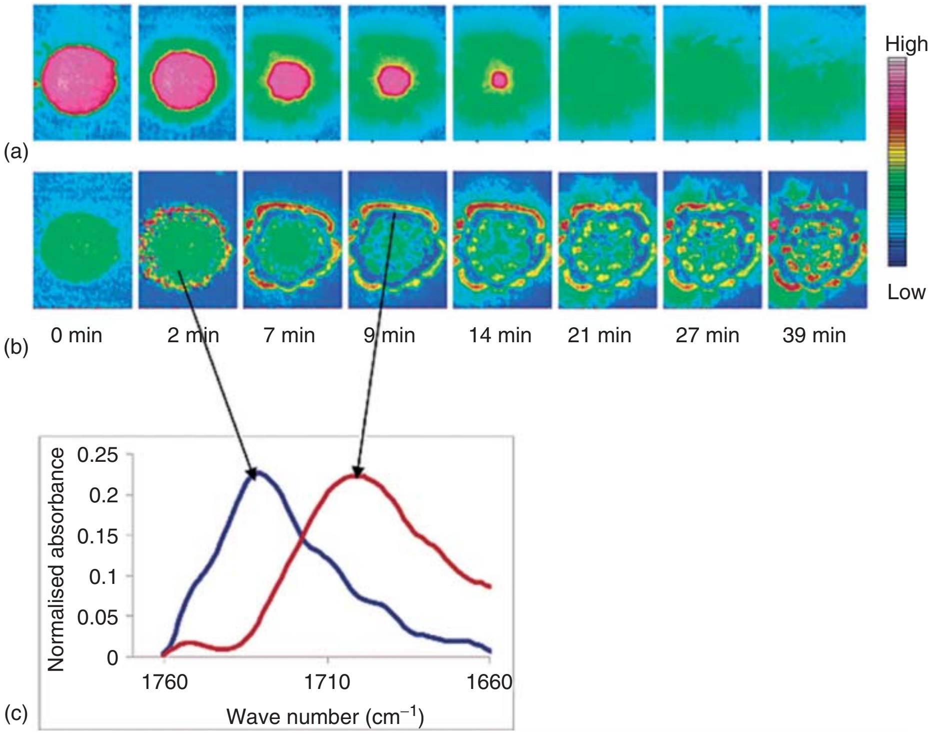

Figure 31.8 (a–c) Macro-ATR-IR images of PEG/ibuprofen formulation show distribution of PEG and ibuprofen as a function of time during contact with water. The inset shows representative IR spectra of ibuprofen to demonstrate the difference between molecularly dispersed (blue) and crystalline drug (red). (Copyright from Ref. [42].)

(blue to red) can be interpreted as crystallization of the drug as it is released in water. When the polymer matrix is dissolved, the initial layer becomes saturated with water-insoluble drug, which leads to its precipitation. In addition, the polymer chains at the interface decreased the rate of dissolution of the drug. As ibuprofen has a carboxylic group, the addition of pH modifiers can affect the dissolution and the rate of release of the drug [46]. The same group studied the drug release of other compounds such as niferidipine [47] and buflomedyl pyridoxal phosphate [48]. Koenig *et al.* [49] investigated the release of testosterone in PEO. From the IR image, the drug release mechanism was identified. It was determined that the homogeneity of the polymer/drug matrix, the drug particle size, the drug concentration, and the molecular weight, morphology, and dissolution of the polymer dictates the rate and uniformity of drug release. The information provided by dissolution studies are the basis for the design and optimization of the formulation for controlled drug delivery.

31.4
Other Applications of FTIR Imaging

31.4.1
Forensic Science

Owing to label-free and noninvasive sample collection and increased chemical information, spectroscopic methods have gained attention in the forensic community for fingermark and trace investigations [11, 46]. As compared to other spectroscopic techniques, the ability of FTIR imaging to analyze a wide sampling area and to identify small amounts of randomly distributed trace materials makes it one of the most promising tools in forensic science. Usually, significant information gained by detecting small particles of prohibited drugs, gunpowder, explosives, and other potential evidences present at localized regions throughout the sample is difficult to record using ‘‘mapping-type’’ spectroscopy methods, but an imaging approach enables fast access to this data in a single measurement [46].

Kazarian *et al.* [47] have demonstrated fingermark analysis via FTIR imaging on samples using two approaches: (i) directly imprinting on the ATR accessory used and (ii) lifting the fingerprint using gelatin adhesive tapes or polydimethylsiloxane (PDMS) films. The instrumentation for both approaches involves an FTIR spectrometer with an FPA detector coupled with a ZnSe crystal accessory in ATR approach. The combined imaging approach was able to provide more information on the composition and the distribution of a wide range of functionalities across the sample. For the first strategy, latent fingerprints were directly laid on the ZnSe ATR accessory under controlled temperatures and relative humidities. Resulting chemical images focused at certain spectral regions clearly show the heterogeneous distribution of lipids and amino acids present in the fingerprint residues. Absorption bands between 3000 and 2800 cm^{-1}, corresponding to antisymmetric and symmetric stretching vibrations for CH_2 groups, respectively, were used to confirm the presence of several types of lipids. Peaks at 1745 cm^{-1} and shoulder at 1712 cm^{-1} reveal the presence of triglycerides and/or phospholipids and fatty acids, respectively. Traces of amino acids and protein substances are identified using the absorption bands at 1654 cm^{-1} (–C=O), 1551 cm^{-1} (–NH in-plane bend), and around 3080–3100 cm^{-1} (weak –NH stretching vibrations corresponding to amide B).

Another approach is to lift and transfer the fingerprints to adhesive tapes or polymer films and subsequently analyzed in the laboratory. This is actually more practical for actual forensic investigations. The same group demonstrated this technique using different types of lifting media such as the BVDA gelatin lifter and the Dycem gel print lifter [48]. The fingers were damped on forehead or nose sebum (to enhance the signals of the samples) before touching a door handle, a mug handle, a curved glass surface, and a computer screen. The lifting material was placed on the fingermarks and was carefully peeled off. Similar to the previous approach, the presence and spatial distribution of lipids and amino acids were analyzed through the absorption bands between 2800 and 3000 cm^{-1} for both the gelatin tip and the Dycem gel lifter. The resulting FTIR images with corresponding IR spectra are shown in Figure 31.9.

Apart from lipid and amino acid analysis, forensic applications of FTIR imaging on fingerprints are expanding to identification of exogenous components such as drug particles [46]. In 2006, a model system of ibuprofen and paracetamol (diameter = 5–30 μm) was carefully lifted by a PDMS film or directly analyzed on a finger surface via FTIR imaging [46]. PDMS works perfectly with the matrix because, unlike the normal adhesive tapes, it does not have absorption bands between 1650 and 1750 cm^{-1} to which the absorption of C=O of ibuprofen is prominent. For paracetamol, the absorbance of the amide II band between 1580 and 1525 cm^{-1} can be used as the chemical marker. Analysis was performed using a (i) ZnSe ATR accessory (macro-ATR) and (ii) IR microscope and a Ge ATR objective (micro-ATR). The first method provided information on the distribution of the drug particles across the sample. However, small drug particles with sizes between 5 and 30 μm were not detected. Imaging resolution was significantly enhanced by incorporating the second method, and thus enabling the analysis of smaller particles. Owing to its success in the characterization and differentiation of the drug particles, the technique was also applied in analyzing small amounts of a street drug diacetylmorphine hydrochloride (heroin) concealed on a binary drug matrix with paracetamol adhered on a PDMS film and/or on the finger. Furthermore, other groups have also worked on the detection of explosive materials, such as hexahydro-1,3,5-trinitro-1,3,5-triazine and the RDX explosive solution (whose IR spectra can be characterized by strong NO_2 deformations and weak –CH stretching modes) [49, 50]. As shown in Figure 31.10a–c, FTIR images of the fingerprints before and after washing of RDX were generated, and results showed that even after washing localized residues can still be detected. This analysis may be used as an evidence for crime investigations to verify previous handling of explosives or other prohibited materials.

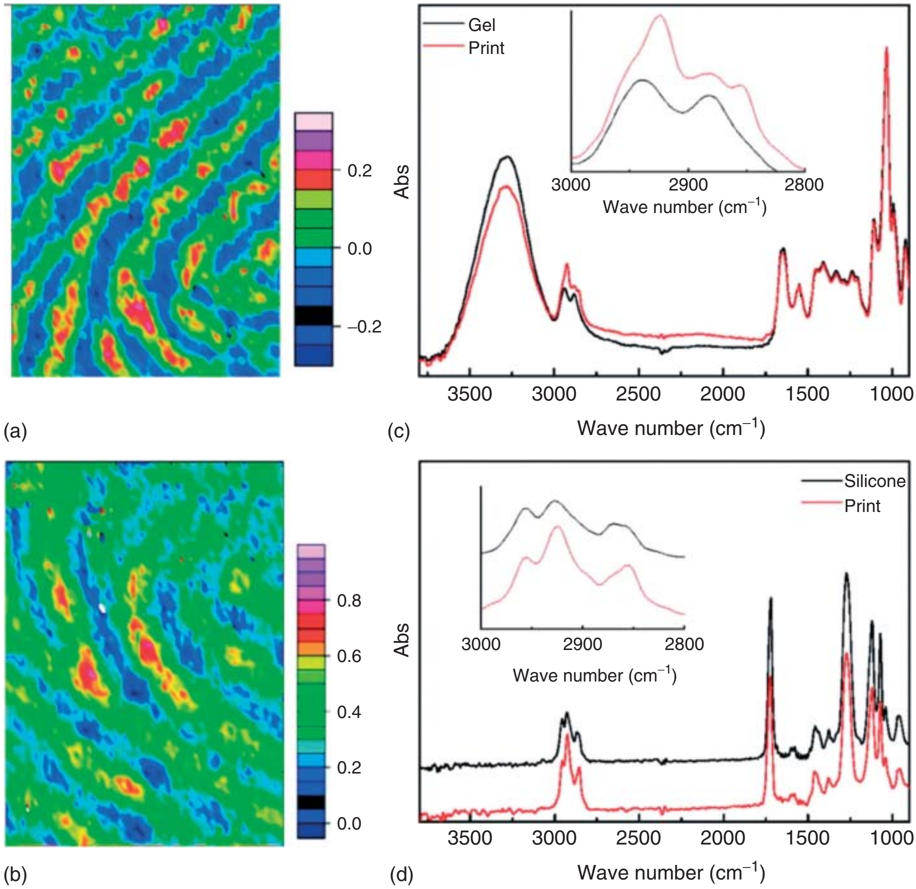

Figure 31.9 Latent fingerprint analysis via ATR-FTIR imaging using a BVDA gelatin tape (a,c) and a Dycem gel lifter (b,d). Measurements were made based on a sample area of $2.5 \times 3.6\,\text{mm}^2$. The integration range selected is between 2830 and 2870 cm^{-1} to highlight the ridges present on the fingerprints. (Copyright from Ref. [48].)

31.4.2
Microfluidics

In order to optimize traditional process systems, chemical reactions are recently being investigated in microfluidic or microfabricated devices. In these smaller scale systems, concentration gradients of the chemical components are being monitored *in situ* at various points in time and space. Before the development of more advanced techniques, reaction conditions are numerically simulated to determine the concentration gradients throughout the system. However, there is a growing need to develop real-time characterization methods to verify these simulations. Currently, fluorescence imaging is the most widely used technique for microfluidics owing to its sensitivity. However, the use of dyes and other fluorescent additives

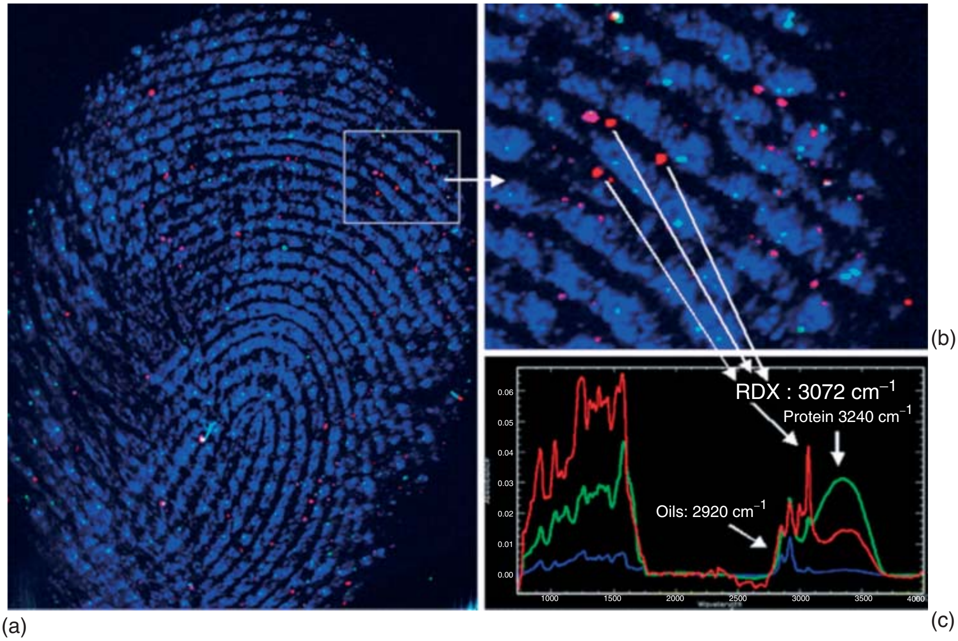

Figure 31.10 FTIR imaging for explosive material detection. These reconstructed images present distributions of oil secretions, proteins, and the RDX solution present across the sample. (a) Fingerprint, (b) Zoomed in region, (c) IR spectra differentiation. (Copyright from Ref. [50])

may cause disturbance and introduce contaminants to the systems. Furthermore, it does not necessarily give exact compositional and functional group information. As a result of which label-free spectroscopic techniques such as FTIR imaging have been gaining attention in these studies. Each pixel in an FTIR image contains spatially resolved infrared spectrum of the chemical components of the system; hence, absorption bands of various functional groups can accurately monitor the movement, emergence, or disappearance of any chemical component in a process system.

In 2009, the mixing behavior of deionized water and PEG in a y-junction PDMS microfluidic device, as depicted in Figure 31.11, was studied by using FTIR imaging [12, 51]. Both liquids were injected at steady state and the system was equilibrated before imaging. The IR images focused at $2800-3000\,\mathrm{cm}^{-1}$ and at $3100-3700\,\mathrm{cm}^{-1}$, for the −CH absorption band of PEG and for the −OH absorption band of water, respectively, were captured. In reference to Figure 31.11, the red colors represent high concentration of the component, while the darker regions correspond to zero concentration. On the basis of the images, it can be concluded that PEG occupies most areas and water slowly diffuses from the left side.

In the same report, FTIR imaging was also used in *in situ* monitoring of the H/D isotope exchange between H_2O and D_2O to produce HDO [12]. As signified by the emergence of two additional peaks at around 1451 and $2500\,\mathrm{cm}^{-1}$, the

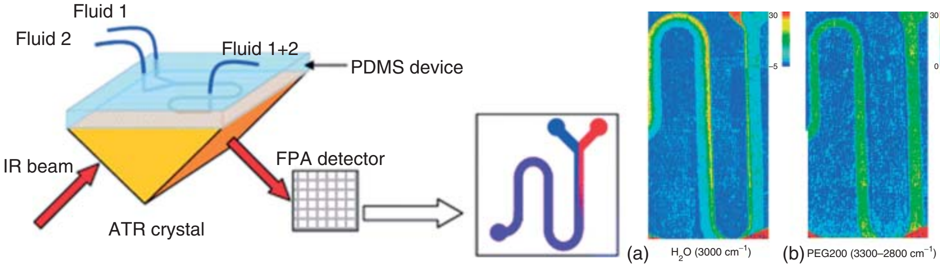

Figure 31.11 (a) A schematic representation of the y-junction PDMS-based microfluidic device integrated in the ATR-FTIR imaging system. (b) The flow patterns as water and PEG 200 is being injected at 75 and 25 μl h^{-1}. (Copyright from Ref. [12].)

formation of HDO occurs at the interface between the H_2O and D_2O streams. IR images not only provide the spatial distribution of the chemical components of the reaction but also present the actual quantitative concentrations of the components at certain points in the flow as correlated by the Beer–Lambert law. Analyzing the intersection of the normalized absorption spectra of the H_2O and D_2O streams at the dotted lines in Figure 31.11 shows that both the reaction kinetics and the equilibration are fast. Although this technique was successful in *in situ* monitoring of a chemical reaction, conventional FTIR imaging is still too slow for producing continuous chemical images of picoliter-sized droplets of various liquid streams. The same group was able to overcome this limitation using a model system of introducing small amounts of water and oil (FC40) that converges in a T-junction microfluidic device and measuring the spectra using a single wavelength measurement and a quantum cascade laser [52]. The resulting FTIR images were produced after a scanning time of 50 ms with a temporal resolution of 120 ms. This can potentially be used for making videos of chemical reactions. Another recent report on the application of FTIR imaging on microfluidics monitored *in situ* the chemical reaction in both laminar and segmented flows in two-phase systems [51].

31.4.3
Single-Particle Characterization

Ro *et al.* [53] studied the artificially generated aerosol particles of micrometer size, such as ascorbic acid and $NaNO_3$ aerosols, by using X-ray microanalysis (electron probe microanalyzer (EPMA)) techniques and FTIR imaging spectroscopy. These techniques provided information on the functional groups, molecular species, and crystal structure of the particles. Employing the same techniques, detailed characterization of mineral particles was also performed on a single-particle level for 24 mineral samples [54], which was later extended to the characterization of an atmospheric aerosol sample collected in Incheon, Korea [55], and aerosols samples collected at King George Island in the Antarctic [56].

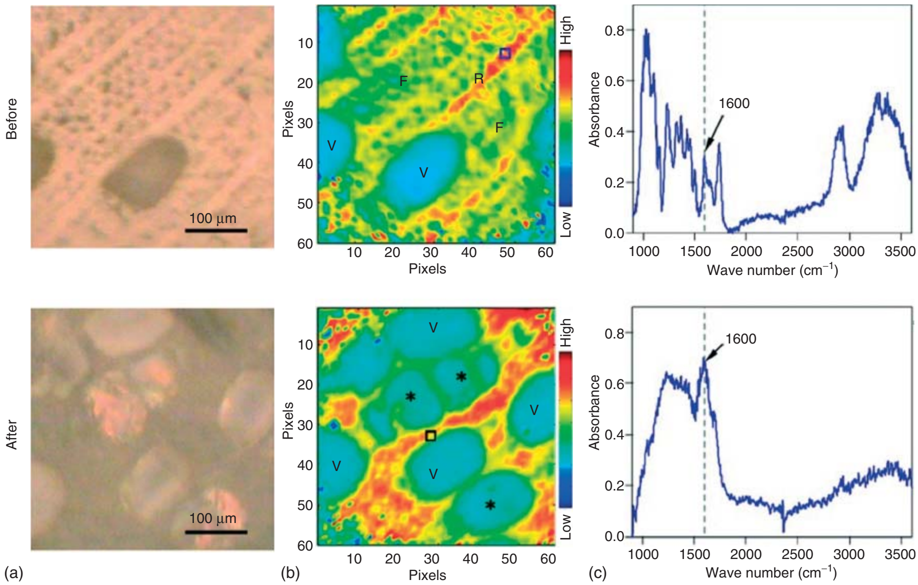

Figure 31.12 Cross section of poplar wood before and after pyrolysis. (a) Visible light images, (b) FTIR images, and (c) IR spectra highlighting the aromatic C=C at the region indicated by the blue box. For the FTIR images, F = fiber, R = ray cells, V = vessels, and * = empty spaces. (Copyright from Ref. [13].)

31.4.4
Biofuels

In the search for more cost-efficient and environment-friendly energy sources, thermochemical conversion of organic material or biomass through pyrolysis or gasification is continuously being developed as promising substitutes for crude oil. Pyrolysis, which is generally driven by phenomenological changes in chemical and physical properties, is the thermochemical decomposition of organic materials in the absence of oxygen. One of its main uses is to produce a lighter synthetic fuel from crops, agricultural residues, or other biological wastes. Recently, Nimlos *et al.* [13] investigated the changes in the structural and chemical compositions of poplar wood (biomass) after thermal decomposition using FTIR imaging coupled with various multivariate techniques. The FTIR images were analyzed at $1600\,\text{cm}^{-1}$ to monitor the presence of C=C functional groups. Before pyrolysis, the C=C absorption band represents the distribution of lignin; however, the emergence of polyaromatic compounds produced after the pyrolysis causes a broadening of the absorption band centered at $1600\,\text{cm}^{-1}$ ranging from $\sim$1550 to $1650\,\text{cm}^{-1}$. The resulting FTIR images are presented in Figure 31.12, which highlight the increase in empty spaces in the wood and the changes in aromatic C=C absorption band. Apart from lignin, other components of wood such as cellulose and hemicellulose were also analyzed by adding multivariate techniques.

31.5
Conclusion

In summary, FTIR imaging is a very powerful technique for the chemical mapping of surfaces, and for obtaining spatially and temporally resolved chemical information. It also enables the identification of chemical functionalities distributed from a corresponding diffraction-limited optical image, and it distinguishes the presence of overlapping species within the same location. The technique has found utility in studying polymer systems, in biomedical applications, forensic science, and biofuels. More powerful applications can be further developed if we harness the advantages and sampling methods that cannot be carried out by any other microspectroscopic method in a similar resolution or timescale. Furthermore, multivariate methods, chemometrics, and time-resolved spectroscopy enhance its utility in analytical chemistry.

References

1. Bhargava, R., Wang, S.Q., and Koenig, J. (2001) *Anal. Chem.*, **73**, 361A.
2. Bhargava, R., Wall, B., and Koenig, J. (2000) *Appl. Spectrosc.*, **54**, 470.
3. Bhargava, R., Wang, S.Q., and Koenig, J. (2003) *Adv. Polym. Sci.*, **163**, 137.
4. Challa, S.R., Wang, S.Q., and Koenig, J. (1997) *Appl. Spectrosc.*, **51**, 10.
5. Vogel, C., Wessel, E., and Siesler, H.W. (2008) *Biomacromolecules*, **9**, 523.
6. Gupper, A., Chan, K.L.A., and Kazarian, S.G. (2004) *Macromolecules*, **37**, 6498.

7. Estillore, N. and Advincula, R. (2011) *Langmuir*, **27**, 5997.
8. Fujie, T., Park, J., Murata, A., Estillore, N., Tria, M., Takeoka, S., and Advincula, R. (2009) *ACS Appl. Mater. Interfaces*, **1**, 1404.
9. Ooi, G.J., Fox, J., Siu, K., Lewis, R., Bambery, K.R., McNaughton, D., and Wood, B.R. (2008) *Med. Phys.*, **35**, 2151.
10. Chan, K.L.A. and Kazarian, S.G. (2003) *Macromolecules*, **36**, 9866.
11. Hazarika, P. and Russell, D.A. (2012) *Angew. Chem. Int. Ed.*, **51**, 3524.
12. Chan, K.L.A., Gulati, S., Edel, J.B., de Mello, A.J., and Kazarian, S.G. (2009) *Lab Chip*, **9**, 2909.
13. Bahng, M.K., Donohoe, B.S., and Nimlos, M.R. (2010) *Energy Fuels*, **25**, 370.
14. Estillore, N. and Advincula, R. (2011) *Macromol. Chem. Phys.*, **15**, 1552.
15. Tria, M., Park, J., and Advincula, R. (2011) *Chem. Commun.*, **47**, 2393.
16. Tria, M. and Advincula, R. (2011) *Macromol. Rapid Commun.*, **32**, 966.
17. Felts, J.R., Kjoller, K., Lo, M., Prater, C.B., and King, W.P. (2012) *ACS Nano*, **6**, 8015.
18. Biswal, D. and Hilt, J.Z. (2009) *Macromolecules*, **42**, 973.
19. Snively, C.M. and Koenig, J.L. (1998) *Macromolecules*, **31**, 3753.
20. Koenig, J. (2002) *Adv. Mater.*, **14**, 457.
21. Miller-Chou, B.A. and Koenig, J.L. (2003) *Macromolecules*, **36**, 4851.
22. Vogel, C., Wessel, E., and Siesler, H.W. (2008) *Macromolecules*, **41**, 2975.
23. Kazarian, S.G. and Chan, K.L.A. (2004) *Macromolecules*, **37**, 579.
24. Merten, C., Kowalik, T., Aßhoff, S.J., and Hartwig, A. (2010) *Macromol. Chem. Phys.*, **211**, 1627.
25. Cong, Y., Hong, Z., Qi, Z., Zhou, W., Li, H., Liu, H., Chen, W., Wang, X., and Li, L. (2010) *Macromolecules*, **43**, 9859.
26. Hikima, Y., Morikawa, J., and Hashimoto, T. (2012) *Macromolecules*, **45**, 8356.
27. Millan, M., Locklin, J., Fulghum, T., Baba, A., and Advincula, R. (2005) *Polymer*, **46**, 5556.
28. Ellis, D.I. and Goodacre, R. (2006) *Analyst*, **131**, 875.
29. Vahlsing, T., Damm, U., Kondepati, V.R., Leonhardt, S., Brendel, M.D., Wood, B.R., and Michael Heise, H. (2010) *J. Biophotonics*, **3**, 567.
30. Kim, D.H., Jarvis, R.M., Xu, Y., Oliver, A.W., Allwood, J.W., Hampson, L., Hampson, I.N., and Goodacre, R. (2010) *Analyst*, **135**, 1235.
31. Babrah, J., McCarthy, K., Lush, R.J., Rye, A.D., Bessant, C., and Stone, N. (2009) *Analyst*, **134**, 763.
32. Lamberti, A., Sanges, C., and Arcari, P. (2010) *Spectroscopy*, **24**, 535.
33. American Cancer Society (2012) October 31-November 26 2012, *http://www.cancer.org* (accessed 25 March 2013).
34. Babrah, J., McCarthy, K.P., Lush, R., Rye, A.D., Bessant, C., and Stone, N. (2007) Diagnostic optical spectroscopy in biomedicine IV. *Proc. SPIE*, **6628**, 66280R.
35. Krafft, C., Codrich, D., Pelizzo, G., and Sergo, V. (2008) *Vib. Spectro.*, **46**, 141.
36. Kuimova, M.K., Chan, K.L., and Kazarian, S.G. (2009) *Appl. Spectrosc.*, **63**, 164.
37. Beljebbar, A., Amharref, N., Lévèques, A., Dukic, S., Venteo, L., Schneider, L., Pluot, M., and Manfait, M. (2008) *Anal. Chem.*, **80**, 8406.
38. Amrania, H., McCrow, A.P., Matthews, M.R., Kazarian, S.G., Kuimovac, M.K., and Phillips, C.C. (2011) *Chem. Sci.*, **2**, 107.
39. Chan, K.L.A., Hammond, S.V., and Kazarian, S.G. (2003) *Anal. Chem.*, **75**, 2140.
40. Kolomiets, O., Hoffmann, U., Geladi, P., and Siesler, H.W. (2008) *Appl. Spectrosc.*, **62**, 1200.
41. Awotwe-Otoo, D., Zidan, A.S., Rahman, Z., and Habib, M.J. (2012) *AAPS PharmSciTech*, **13**, 611.
42. Chan, K.L.A. and Kazarian, S.G. (2005) *J. Comb. Chem.*, **7**, 185.
43. Ricci, C., Nyadong, L., Fernandez, F.M., Newton, P.N., and Kazarian, S.G. (2007) *Anal. Bioanal. Chem.*, **387**, 551.
44. Ricci, C., Eliasson, C., Macleod, N.A., Newton, P.N., Matousek, P., and Kazarian, S.G. (2007) *Anal. Bioanal. Chem.*, **389**, 1525.

45. Lanzarotta, A., Lakes, K., Marcott, C.A., Witkowski, M.R., and Sommer, A.J. (2011) *Anal. Chem.*, **83**, 5972.
46. Ricci, C., Chan, K.L.A., and Kazarian, S.G. (2006) *Appl. Spectrosc.*, **60**, 1013.
47. Ricci, C., Phiriyavityopas, P., Curum, N., Chan, K.L.A., Jickells, S., and Kazarian, S.G. (2007) *Appl. Spectrosc.*, **61**, 514.
48. Ricci, C., Bleay, S., and Kazarian, S.G. (2007) *Anal. Chem.*, **79**, 5771.
49. Chen, T., Schultz, Z.D., and Levin, I.W. (2009) *Analyst*, **134**, 1902.
50. Bhargava, R., Schwartz Perlman, R., Fernandez, D., Levin, I., and Bartick, E. (2009) *Anal. Bioanal. Chem.*, **394**, 2069.
51. Chan, K.L.A. and Kazarian, S.G. (2012) *Anal. Chem.*, **84**, 4052.
52. Chan, K.L.A., Niu, X., deMello, A.J., and Kazarian, S.G. (2011) *Anal. Chem.*, **83**, 3606.
53. Ryu, J.Y. and Ro, C.U. (2009) *Anal. Chem.*, **81**, 6695.
54. Jung, H.J., Malek, M.A., Ryu, J.Y., Kim, B.W., Song, Y.C., Kim, H.K., and Ro, C.U. (2010) *Anal. Chem.*, **82**, 6193.
55. Song, Y.C., Ryu, J.Y., Malek, M.A., Jung, H.J., and Ro, C.U. (2010) *Anal. Chem.*, **82**, 7987.
56. Maskey, S., Geng, H., Song, Y.C., Hwang, H.J., Yoon, Y.J., Ahn, K.H., and Ro, C.U. (2011) *Environ. Sci. Technol.*, **45**, 6275.

32
Photon Correlation Spectroscopy Coupled with Field-Flow Fractionation for Polymer Analysis

J. Ray Runyon and S. Kim Ratanathanawongs Williams

32.1
Introduction

Photon correlation spectroscopy (PCS), also known as *dynamic light scattering* or *quasielastic light scattering*, is a nondestructive analytical technique that provides an absolute determination of the normal diffusion coefficient (D) of submicrometer-sized analytes in solution. PCS has been used to characterize a wide array of analytes including biomacromolecules, synthetic and natural polymers, and nanoparticles. Information pertaining to the hydrodynamic diameter (d_h) of the sample, macromolecular chain conformation, and analyte interactions can be extracted from the measured D values [1–6]. d_h is calculated from the Stokes–Einstein equation $D = kT/3\pi\eta d_\mathrm{h}$, where k is Boltzmann's constant, T is the temperature in K, and η is the solvent viscosity.

PCS measurements are traditionally performed in batch mode where the sample volume, sample concentration, and timescale of the measurement are well controlled. Batch mode PCS yields average D values of the entire sample and is best suited for the characterization of monodisperse samples. Multimodal samples need to differ in size by two to three times for PCS to register the presence of distinct populations [1, 5, 7–9]. For a polydisperse sample with a continuous distribution of sizes, light scattered by a small number of large-sized analytes will mask the signal from small-sized components because the scattering intensity is proportional to the sixth power of the analyte radius. This sensitivity of PCS to large-sized analytes biases measured D to smaller values. Examination of low-concentration subpopulations within a polydisperse sample by batch mode PCS is difficult, if not impossible, without prior separation [1, 5, 7, 8, 10–13].

Size-based separation techniques including field-flow fractionation (FFF), size-exclusion chromatography (SEC), and hydrodynamic chromatography (HDC) have been coupled with online PCS detection to characterize D and d_h of eluting nanoparticles and macromolecules [5, 6, 12–31]. The separation stage parses the polydisperse sample into the more uniform size fractions required for accurate PCS measurements and makes it possible to obtain a more accurate representation of the analyte sizes.

Handbook of Spectroscopy, Second Edition. Edited by Günter Gauglitz and David S. Moore.

Analytical capabilities beyond diffusion or size measurements are possible when a separation technique such as thermal field-flow fractionation (ThFFF) is coupled with online PCS. ThFFF uses a temperature gradient to fractionate polymers by molecular weight (MW) and composition. The ThFFF separation mechanism relies on the analyte Soret coefficient (S_T), where S_T is a balance between the polymer thermal diffusion (D_T) and D. D_T is a characteristic property of the analyte–solvent pair [32] and has been shown to be independent of homopolymer MW and branching [32, 33] and to be linearly dependent on the mole fraction of one homopolymer component of a copolymer [34–38]. ThFFF separation of mixtures of compositionally different homopolymers has been demonstrated for polystyrene (PS) and poly(methyl methacrylate) and PS and polyisoprene mixtures in tetrahydrofuran (THF), and a PS and poly(*n*-butyl acrylate) (PBA) mixture in methyl ethyl ketone (MEK) [35, 36, 38, 39]. Polymer D_T values can be experimentally measured from ThFFF analyte retention times (Section 32.3) provided D values are accurately known from an external source such as SEC or batch mode PCS. The integration of online PCS with ThFFF would allow D to be measured as a function of retention time. This would enable the subsequent calculation of D_T and the simultaneous characterization of both the size and composition distributions of heterogeneous polymers and/or polymer mixtures.

The majority of reported studies involving online PCS have focused on hydrophilic analytes [5, 6, 12, 13, 17–25, 28–31, 40]. Very few have addressed synthetic polymers [14–16, 26, 27], and none has investigated ThFFF coupled with online PCS. The characterization of synthetic polymers with online PCS detection is demanding because of the weak scattering intensity of these analytes in common organic mobile phases. This problem is exacerbated for dilute samples, polymer–solvent combinations with low specific refractive indices (d_n/d_c), and low-MW polymers. The separation process can dilute sample by 15–100 times. Band broadening during the separation leads to further dilution. High concentrations of analyte can be injected to increase the eluting sample concentration, but at the expense of decreased resolution of the separation, column overloading, or complete column plugging (in the cases of SEC and HDC). The sensitivity of PCS to large-sized analytes has lead to the previous conclusion that online PCS is best used with relatively high-MW samples (>300 kDa) with higher d_n/d_c values [15, 16, 26].

PCS detectors often have preset scattering angles usually between 90° and 110°. Low-MW polymers (isotropic scatters where $d_h < 1/10$th the wavelength of incident light) are best measured at small angles to increase the timescale of data collection [3, 4, 16, 27, 41]. The D values for PS with MWs as low as 12 kDa and poly(hexylisocyanate) with MWs below 100 kDa were measured at scattering angles $<32^\circ$ [16, 27]. However, there was a large standard deviation in the measured data as a result of low-analyte concentration and small d_n/d_c values. For high-MW polymers (anisotropic scatters), small scattering angles yield the true translational diffusion while large scattering angles provide information about the intermolecular motion of the polymer [3, 6, 16, 25]. No systematic trends of angular dependence on D have been reported for online PCS of 200 nm PS latex particles but were observed in batch mode measurements of 13 million Da PS [17, 40].

Additionally, when using online PCS as a detector, the time interval for data collection is dictated by the flow rate used to achieve the separation. The separation flow rate has been shown to have an insignificant effect on measured D values for aqueous analytes [5, 21, 29], but this has yet to be confirmed for organosoluble polymers in common organic solvents. Liu *et al.* [26] measured batch mode D values for polydimethylsiloxane (PDMS) in 1,2,4-trichlorobenzene over different data collection times ranging from 10 to 600 s and concluded that accurate D values can be obtained in as little as 10 s (with an associated increase in the standard deviation).

This chapter focuses on the usage of online PCS as a detection method for liquid-phase separations. The specific objectives are to (i) establish guidelines for coupling online PCS with a flow-based separation technique utilized for polymer characterization and (ii) apply these guidelines in the characterization of synthetic organosoluble polymers fractionated by ThFFF and proteins and protein aggregates fractionated by flow field-flow fractionation (FlFFF). The coupling of online PCS with FFF provides a powerful new approach to polymer characterization rich with potential applications.

32.2
Photon Correlation Spectroscopy

PCS measures the timescale of fluctuations in the detected intensity of scattered light from analytes undergoing Brownian motion in a liquid. It differs from static light scattering in that the latter measures a time-averaged scattering intensity. In PCS, a plot of intensity (I) versus time (t) shows I fluctuating about an average value due to the phase changes of scattered light reaching the detector. The D values can be extracted from this fluctuation through the use of an autocorrelation function [1, 3, 4, 16, 41].

The intensity normalized autocorrelation function ($g_2(\tau)$) is defined in Eq. (32.1) [1, 41]

$$\frac{\langle I(t)I(t+\tau)\rangle}{\langle I\rangle^2} = 1 + bg_2(\tau) \tag{32.1}$$

where $I(t)$ is the intensity at time t, $I(t+\tau)$ is the intensity shifted by a delay time of τ, and b is an optical coherence factor that ranges from 0 to 1. Initially, at $\tau \to 0$, $I(t)$ equals $I(t+\tau)$ and $<I(t)I(t+\tau)>$ equals $<I^2>$ (where $<I^2>$ is the average of the squared scattering intensity). At long delay times ($\tau \to \infty$), the solutes greatly change their position in solution relative to one another and $I(t)$ and $I(t+\tau)$ become less correlated and $<I(t)I(t+\tau)>$ equals $<I>^2$ (where $<I>^2$ is the square of the average scattering intensity). The rate of decay of the autocorrelation function from $<I^2>$ to $<I>^2$ holds the information on the diffusion of the analyte. It is assumed that the long time average of the scattered intensity is equal to the ensemble average or the average over all possible positions and shapes of the analyte in solution.

Averaging over the total duration of the experiment yields Eq. (32.2) [1, 41]

$$g_2(\tau) = \frac{\lim}{t \to \infty} \frac{1}{\Omega} \int_0^{\infty} I(t) I(t+\tau) \mathrm{d}\tau \tag{32.2}$$

where Ω is the experiment duration. $g_2(\tau)$ is converted to the electric field normalized autocorrelation function ($g_1(\tau)$) by Eq. (32.3) [1, 41].

$$g_2(\tau) = \langle I \rangle^2 \lfloor 1 + b |g_1(\tau)|^2 \rfloor \tag{32.3}$$

When $g_1(\tau)$ is plotted against the log of the delay time (τ), the decay of the autocorrelation function can be represented as a function of the analyte diffusion coefficient by Eq. (32.4) [1, 41]

$$|g_1(\tau)| = \mathrm{e}^{(-\Gamma\tau)} \tag{32.4}$$

where Γ is the decay rate. Γ is related to the analyte diffusion through Eq. (32.5) [1, 41]

$$\Gamma = Dq^2 \tag{32.5}$$

where q is the scattering vector shown in Eq. (32.6) [1, 41].

$$q = \frac{4\pi n_0}{\lambda_0} \sin \frac{\Theta}{2} \tag{32.6}$$

where n_0 is the refractive index of the solvent, λ_0 is the wavelength of the incident light, and θ is the scattering angle normal to the path of the incident light. This derivation holds true for D values at infinite dilution (D_0), where analytes can be considered point masses that move independently of one another. The earlier discussion assumes a monodisperse sample and precisely controlled analyte concentrations and data collection times (conditions met by batch mode PCS).

In online PCS, data collection times are determined by the flow rate used to achieve the separation. In addition, the sample concentration at the detector is continuously changing due to band broadening and dilution of the analyte during the separation stage. Thus, investigation of the contribution of variables such as analyte concentration, flow rate, and scattering angle to the accuracy of measured online D values, along with understanding of the magnitude of the error associated with each variable, is important in establishing guidelines for accurate online PCS detection.

32.3
Field-Flow Fractionation

FFF is a family of techniques designed to separate and measure the physicochemical properties of complex macromolecular, colloidal, and particulate materials [35, 42, 43]. In an FFF experiment, a sample in solution is injected into a high-aspect ratio, thin ribbonlike channel devoid of packing material. Under laminar flow conditions, the carrier liquid has a characteristic parabolic flow velocity profile with the highest flow velocity at the center of the channel and decreasing flow velocities toward the channel walls. The analyte is subjected to an external field applied perpendicular to the sample flow as shown in Figure 32.1a. Different fields can be applied, that is, a cross flow of fluid, a temperature gradient, centrifugal force, an electrical potential, and so on, to probe different physicochemical properties of the analyte such as hydrodynamic size, composition, density, surface chemistry, and semiconductive properties [35]. The separation mechanism and open parallel plate channel impart important characteristics on FFF such as low shear rates (ideal for investigating fragile samples), low sample loss, tunable selectivity, and speed. FFF is applicable to diverse samples spanning a broad MW/size range (10^3–10^9 Da; ~2 nm–100 μm). Descriptions of FFF theory, the separation mechanism, channel designs, applied fields, and targeted sample physicochemical properties can be

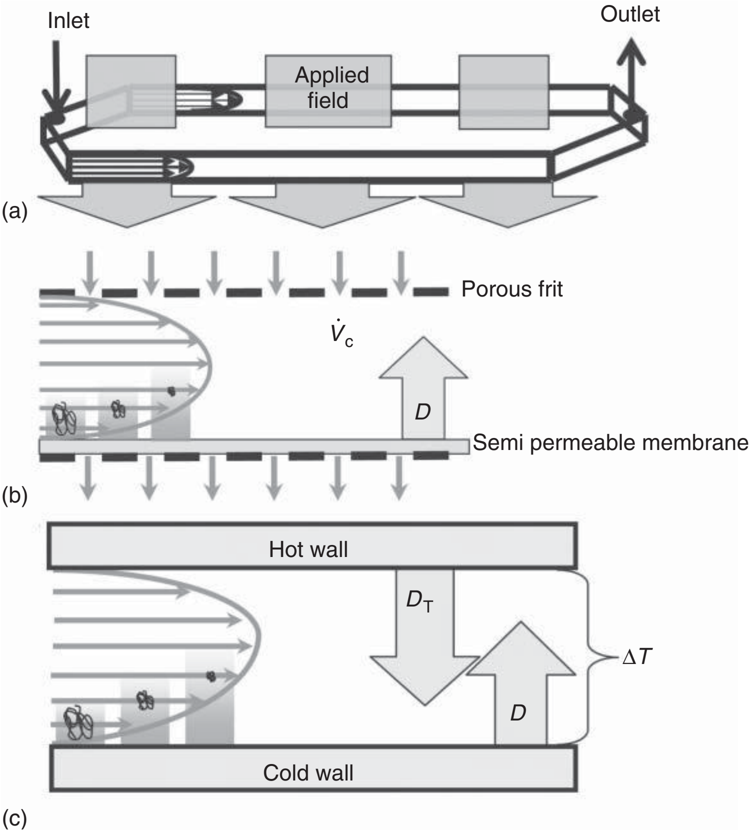

Figure 32.1 (a) FFF channel showing parabolic flow profile of carrier liquid and direction of applied field. (b) Longitudinal cross section of a symmetric FlFFF channel showing semipermeable wall and the two opposing transport processes denoted as the cross flow rate ($\dot{V}_c$) and the analyte D. (c) Longitudinal cross section of a ThFFF channel showing D_T and D. The gray-shaded rectangles on the left-hand side of (b) and (c) represent the exponential concentration profiles for three polymers.

found in previous publications and the reader is directed to Refs. [34, 35, 42–44] for more detailed discussions.

ThFFF utilizes a temperature gradient on the order of 10^4 K cm^{-1} as the applied field and is predominately utilized to fractionate organosoluble samples. FlFFF utilizes a cross flow of fluid as the applied field and has been mainly used to characterize water-based samples. Under the influence of the applied field, the injected analyte plug is compressed into slower velocity carrier liquid flow streams near one channel wall termed the *accumulation wall*. The accumulation wall is a semipermeable membrane in FlFFF and the cold wall in ThFFF as shown in Figure 32.1b,c. An exponential analyte concentration profile develops across the channel thickness with the highest concentration at the accumulation wall. This concentration gradient results in diffusion of the analyte away from the accumulation wall. Under steady-state conditions, the field- and the concentration-induced mass transport processes are balanced and the net flux of the analyte is zero. Retention is a result of the analyte residing in slower than average flow velocities within the channel. Separation occurs because of the differential distribution of analyte species across the parabolic flow velocity profile of the carrier liquid. In the normal mode of separation, small-sized analytes with larger D values will diffuse into fast-moving carrier liquid flow streams and be retained less. Hence, the expected order of elution is from small to large sizes, that is, low to high MW (Figure 32.1b,c) [34, 35, 44]. This statement holds true for ThFFF if the polymers are the same composition.

Equation (32.7) is the general retention equation for FFF [44]

$$R = \frac{t^0}{t_\mathrm{r}} = \frac{V^0}{V_\mathrm{r}} = 6\lambda\left[\coth\left(\frac{1}{2\lambda} - 2\lambda\right)\right] \tag{32.7}$$

where R is the retention ratio, t^0 and t_r are the retention times of nonretained and retained analytes, V^0 and V_r are the void and retention volumes, and λ is the retention parameter. The λ is a dimensionless parameter that represents the degree of zone compactness of the analytes relative to the channel thickness. It is also a measure of the extent of the interaction between the applied field and the sample components [34, 44]. Equation (32.7) is valid for FlFFF but must be adjusted for ThFFF to account for nonidealities in the carrier liquid parabolic flow profile that arise from changes in carrier liquid viscosity and thermal conductivity due to the applied temperature gradient. (The velocity profile is skewed toward the hot wall with the maximum velocity located above the midplane of the channel.) This adjustment is shown in Eq. (32.8), where ν is a velocity distortion factor and is equal to 0 when the parabolic profile is regained [44, 45]. Values for ν for several commonly used organic carrier liquids can be found in Ref. [45]

$$R = \frac{t^0}{t_\mathrm{r}} = \frac{V^0}{V_\mathrm{r}} = 6\lambda\left[\nu + (1 - 6\lambda\nu)\left[\coth\left(\frac{1}{2\lambda} - 2\lambda\right)\right]\right] \tag{32.8}$$

Let us assume λ as a different form for each FFF technique because of the different applied field. Equation (32.9) describes λ for FlFFF, where $\dot{V}_\mathrm{c}$ is the volumetric cross flow rate and w is the channel thickness [44]

$$\lambda_{\text{FlFFF}} = \frac{DV^0}{\dot{V}_c w^2} \tag{32.9}$$

Equation (32.9) shows that FlFFF is a size-based separation technique because the analyte physicochemical parameter that governs analyte retention is D. Changes in the hydrodynamic size of the analyte will result in a corresponding change in retention time.

Equation (32.10) describes λ for ThFFF, where D_T is the analyte thermal diffusion coefficient and ΔT is the temperature drop across the channel thickness [44]

$$\lambda_{\text{ThFFF}} = \frac{D}{D_T \Delta T} \tag{32.10}$$

Equation (32.10) shows that the Soret coefficient (D_T/D) is the physicochemical parameter that governs analyte retention in ThFFF. A change in the polymer size or composition will result in changes in D or D_T and be reflected in the analyte retention time.

This study coupling FFF with online PCS for polymer analysis was conducted in two parts. In the first part, the contribution of analyte concentration, MW, carrier liquid flow rate, and the scattering angle to the accuracy and precision of measured online D values was investigated. This was accomplished by introducing a large volume of sample directly into the PCS instrument (no FFF separation). These experiments enabled measurements of D at controlled and steady analyte concentrations in the presence of flow. These results were then used to establish guidelines for the second part of this study, which incorporated FFF with online PCS. This second set of experiments was complex because the concentration varied across each sample peak as it eluted from the FFF channel. The objective is to examine the accuracy and precision of D measurements and hence determine a best approach to processing the collected data. Online D values measured in the second part of the study are referred to as either *ThFFF/PCS* or *FlFFF/PCS D* values.

32.4
Materials and Methods

Table 32.1 lists the polymer and protein standards used in both parts of this work.

32.4.1
Direct Sample Introduction into the PCS Instrument

The polymer standards listed in Table 32.1 were prepared in uninhibited THF (Mallinckrodt Chemicals, Phillipsburg, NJ, USA). Five milliliters of each solution was filtered through a 0.2 μm polytetrafluoroethylene (PTFE) 13 mm syringe filter (Millipore, Billrica, MA, USA) before batch mode PCS measurements. Bovine serum albumin (BSA), bovine thyroglobulin (BTG), fibrinogen, and myoglobin protein solutions were prepared in 50 mM phosphate buffer saline (PBS) adjusted

Table 32.1 Polymer and protein standards.

Standard	MW (kDa)[a]	PDI[b]	Suppliers[c]
Polystyrene (PS20)	20.4	1.06	PCC
Polystyrene (PS52)	52	1.02	Waters
Polystyrene (PS90)	90	1.04	PCC
Polystyrene (PS254)	254	1.17	PE
Polystyrene (PS411)	411	1.1	Mann
Polystyrene (PS575)	575	1.06	PCC
Polystyrene (PS1800)	1800	<1.20	PCC
Polystyrene (PS250BR)	250	2.5	APSC
Poly(*n*-butyl acrylate) (PBA263)	263	1.13	PSI
Poly(methyl acrylate) (PMA171)	171	1.07	NSC
Poly(2-ethylhexyl acrylate) (P2EHA242)	242	1.16	PSI
Myoglobin	17 000	—	SA
Bovine serum albumin (BSA)	66 000	—	SA
Fibrinogen	340 000	—	SA
Bovine thyroglobulin (BTG)	670 000	—	SA

[a] Weight average MW.

[b] Polydispersity index (M_n/M_w).

[c] PCC, Pressure Chemical Company; PE, Perkin Elmer; Mann, Mann Research Laboratories; APSC, American Polymer Standards Corporation; PSI, Polymer Sources, Inc.; SA, Sigma–Aldrich; and NSC, National Starch and Chemical Company.

to pH 7.0. NaN_3 was added (0.02% w/w) to prevent bacterial growth. Five milliliters of each protein solution was filtered through a 0.1 μm Durapore (Millipore) inorganic membrane before batch mode PCS measurements.

Experiments were conducted by injecting each filtered sample directly into the PCS detector using a Valco injector (VICI Valco Instruments Co. Inc., Houston, TX, USA) equipped with a 500 μl sample loop. The large volume sample loop resulted in the formation of a plateau with a steady analyte concentration. Online *D* values were measured within this plateau region for PS and proteins in THF and 50 mM PBS solutions, respectively.

32.4.2
FFF Coupled with Online PCS for Polymer Analysis

ThFFF/PCS *D* values were measured for four different polymer samples and mixtures all prepared in MEK (Mallinckrodt Chemicals). The samples investigated were (i) a mixture 23.8, 411, and 1800 kDa PS standards with a polydispersity index (PDI) <1.2; (ii) a mixture of 390 kDa PS and 263 kDa PBA standards; (iii) a mixture of 242 kDa poly(2-ethylhexyl acrylate) (P2EHA242), 171 kDa poly(methyl acrylate) (PMA171), and PBA263 standards; and (iv) a 250 kDa broad MW PS standard with a PDI of 2.5. FlFFF/PCS *D* values were measured for BSA and BTG. Triplicate measurements were made for each sample.

32.4.3
Instrumentation

PCS measurements were made with a Wyatt quasielastic light scattering (QELS) that consisted of a fiberoptic cable connected to a DAWN-EOS multiangle light scattering (MALS) detector (Wyatt Technologies, Santa Barbara, California). The MALS is equipped with a 30 mW laser with a wavelength of 690 nm. The MALS detector can be used in either batch mode or online configurations. In batch mode, a 20 ml scintillation vial containing at least 5 ml of filtered sample solution is placed in the MALS detector. In the online configuration, a flow cell constructed from optical glass is placed in the MALS detector and sample eluting the FFF channel is pumped through this flow cell. The QELS fiberoptic cable can be moved to 1 of 18 different positions in the MALS detector allowing scattering data to be collected at different angles in both batch and online modes. The default manufacturer configuration connected the fiberoptic cable to position 13 on the MALS instrument (108° normal to the incident light). PCS angle-dependent studies were performed by placing the fiberoptic cable at positions 4, 8, 11, 13, and 16 (38°, 64°, 90°, 108°, and 134°) of MALS detector. All scattering data was collected using ASTRA V software (v. 5.1.8). A Waters 510 high-performance liquid chromatography (HPLC) pump (Milford, MA, USA) was used to maintain the desired carrier liquid flow rate.

A ThFFF system (Model TF2000; Postnova Analytics, Salt Lake City, Utah) was utilized for synthetic polymer separations. MEK was utilized as the carrier liquid because it yielded good sample retention. A symmetrical FlFFF system (Model F-1000; Postnova Analytics) equipped with a 5 kDa MW cutoff regenerated cellulose membrane was utilized for protein separations. Fifty millimolar of PBS at pH 7.0 (with 0.02% NaN_3 added to prevent bacterial growth) was used as the carrier liquid. Each FFF system was coupled with the Wyatt MALS and PCS detectors plus a Wyatt Optilab DSP differential refractive index (dRI) detector. Waters 510 and 590 HPLC pumps were used to set and maintain the desired carrier liquid flow rates.

32.5
Results and Discussion

32.5.1
Contribution of Individual Variables to the Accuracy of *D* Values Measured in Flowing Streams

The effect of sample concentration, carrier liquid flow rate, scattering angle, and analyte MW on the accuracy and precision of online *D* values measured from the introduction of the sample directly into the PCS instrument (without FFF) are discussed individually later. Measured online *D* values were compared against experimental and literature batch mode *D* values.

32.5.1.1 **Effect of Sample Concentration**

Solution concentrations were maintained below the overlap concentration, c^*, to ensure insignificant polymer chain overlap and entanglement as this could lead to errors in measured D values because of the presence of large aggregated species in solution [3, 16]. c^* was calculated using the equation $c^* = \mathrm{MW}/N_A \rho R_g{}^3$, where R_g is the radius of gyration, ρ is the polymer density, and N_A is Avogadro's number. For PS1800, the c^* value was calculated to be 6.7 mg ml^{-1}.

Figure 32.2a shows the effect of analyte concentration and flow rates on the measured D values for PS in THF. For the purpose of comparison, the D value for each flow rate was extrapolated to infinite dilution (D_0); therefore, the polymer chains can be considered point masses that move independently of one another. The measured online and batch mode D_0 values are within 5% of previously reported batch mode D_0 values, which were measured across a large concentration range from 1.0 to 20.0 mg ml^{-1} [46]. The lower end of the concentration range in Figure 32.2a is representative of analyte concentrations eluting from an FFF channel or SEC column and the upper end is typical of injected concentrations.

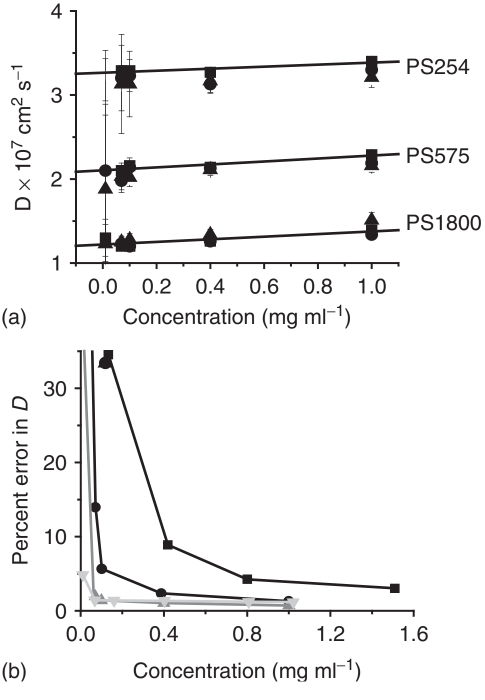

Figure 32.2 (a) Effect of analyte concentration on measured D values (at different flow rates) for PS standards prepared in THF (■, batch mode; ●, 0.1 ml min^{-1}; and ▲, 1.0 ml min^{-1}). The solid black lines are linear regression lines for batch mode values. (b) Measurement error for batch mode measurements (■, black line – PS20; ●, dark gray line – PS52; ▲, gray line – PS254; and ▼, light gray line – PS1800). Scattering angle: 108° for (a) and (b). The samples were introduced directly into the PCS detector.

The observed increase in D with increasing concentration agrees with previously reported trends [3, 8, 46, 47]. The observed slopes ranged from 0.2 to 0.4, which is in agreement with literature values of 0.007–0.3 ml mg^{-1} [46]. No systematic increase in the slope is observed with increasing MW. This is attributed to the low-concentration range at which the measurements were made.

The percentage error in D as a function of solution concentration is plotted in Figure 32.2b. For concentrations below 0.1 mg ml^{-1} (typical analyte concentrations eluting from an SEC column or FFF channel), the error in the measurement increases significantly even for high MWs. An error of <10% in D is observed for PS MWs as low as 52 kDa when concentrations >0.1 mg ml^{-1} were used.

Figure 32.3a,b shows analogous data for BSA, BTG, fibrinogen, and myoglobin protein standards. A similar pattern of increasing D values with increasing analyte concentrations and a concentration threshold of 0.1 mg ml^{-1} were observed.

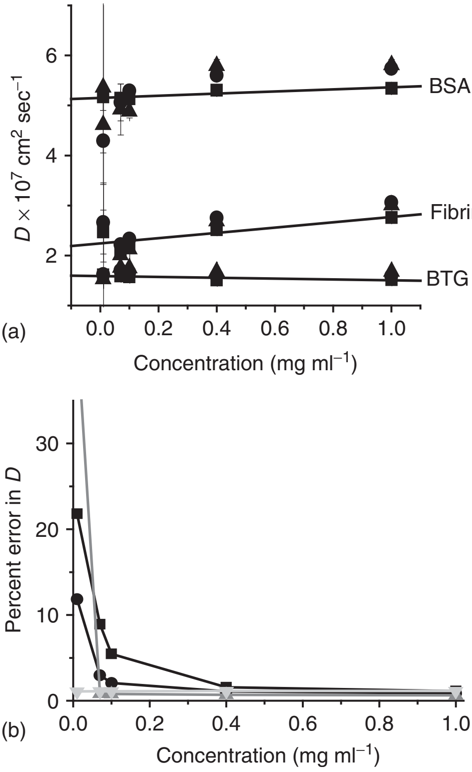

Figure 32.3 (a) Effect of analyte concentration on measured D values (at different flow rates) for protein standards prepared in 50 mM PBS (■, batch mode; ●, 0.1 ml min^{-1}; and ▲, 1.0 ml min^{-1}). The solid black lines are linear regression lines for batch mode values. (b) D measurement error for batch mode measurements (■, black line – myoglobin; ●, dark gray line – BSA; ▲, gray line – fibrinogen; and ▼, light gray line – BTG). Scattering angle: 108° for (a) and (b). The samples were introduced directly into the PCS detector.

The precision of online D measurements is better for low-MW proteins compared to analogous PS standards. For example, myoglobin had an error of 1.6% at a concentration of 0.4 mg ml^{-1} compared to PS20, which had an error of 8.9% at the same concentration. This is a result of the compact globular configuration of the proteins in PBS and the lower background scattering intensity of water compared to THF.

The PS and protein results demonstrate the importance of concentration on the accuracy of measured D values. An analyte concentration of at least 0.1 mg ml^{-1} is desirable to measure online D values within 2–4% of D_0. This is within experimental measurement error.

32.5.1.2 **Effect of Separation Flow Rate**

Figure 32.2 and Figure 32.3 show that flow rates <1.0 ml min^{-1} had a 2–6% impact on D_0 compared to batch mode measurements. Figure 32.4a,b shows the results of a more detailed systematic study of the effect of carrier liquid flow rate on the measured D values for PS and protein standards prepared at concentrations of

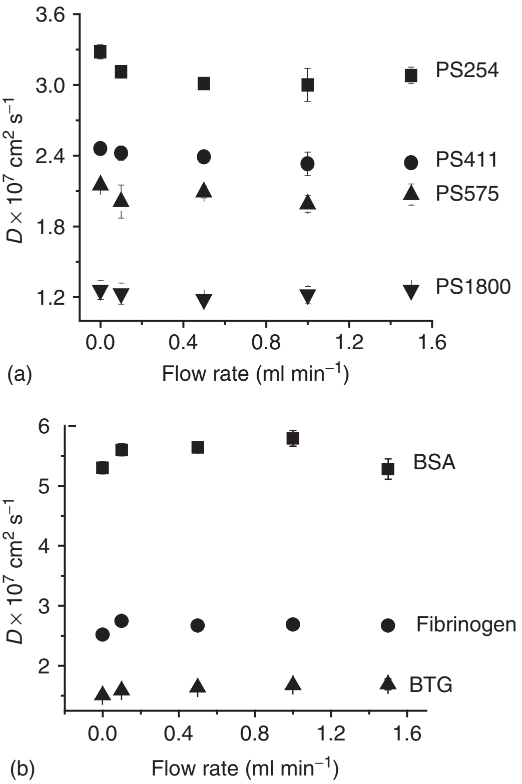

Figure 32.4 Effect of flow rate on measured D values for (a) PS standards in THF (0.1 mg ml^{-1}) and (b) protein standards in 50 mM PBS (0.1 mg ml^{-1}). The samples were introduced directly into the PCS detector.

$0.1\,\mathrm{mg\,ml^{-1}}$ in THF and 50 mM PBS, respectively. It is observed that flow rates in the typical ranges used for SEC and FFF separations do not have a significant effect on the measured D values. This conclusion is in agreement with data previously reported for BSA at concentrations of $5.0\,\mathrm{mg\,ml^{-1}}$ measured at flow rates ranging from 1 to $10\,\mathrm{ml\,min^{-1}}$ and for gold nanoparticles and PS sulfonate polyelectrolytes fractionated using FlFFF and flow rates up to $2\,\mathrm{ml\,min^{-1}}$ [5, 21, 29]. The scatter in the data in Figure 32.4a,b is observed to increase with decreasing MW of the analyte. This is likely a result of analyte concentration rather than changes in flow rate as discussed earlier.

Table 32.2 compares D_0 values for PS in THF and proteins in 50 mM PBS under different flow conditions and with literature values. Good agreement is observed between PS and fibrinogen online and literature D values [2, 44, 46]. The measured D values for unfractionated BSA and BTG are lower than reported literature values for protein monomers because of contributions from dimers or higher order aggregates [48–51]. It is concluded that the flow rates typically used for separation ($<2.0\,\mathrm{ml\,min^{-1}}$) have a small effect on the accuracy of D values obtained by online PCS.

32.5.1.3 **Effect of Scattering Angle**

Figure 32.5 shows the relationship between the scattering angle at which data is acquired and the measured D value for PS575 and PS1800 in batch mode and at $0.1\,\mathrm{ml\,min^{-1}}$. The data is plotted as D/D_{38} versus the scattering angle of the measurement to enhance the observed angular dependence of the measured D values. D is the value obtained at the scattering angle indicated on the x-axis and D_{38} is the value measured at 38°. Batch mode and online PCS data are in agreement and no significant angular dependence (deviation <5%) was observed for PS575. However, a systematic angular dependence is observed for PS1800 with measured

Table 32.2 Online PCS: comparison of D_0 values for polymers in THF and proteins in PBS under different flow rates.

		$D_0 \times 10^7\ \mathrm{cm^2\,s^{-1}}$				
Analyte	**Batch**	**0.1**[a]	**% Δ**[b]	**1.0**[a]	**% Δ**[a]	**Literature**
PS90	5.68 ± 0.06	5.58 ± 0.06	−1.8	5.53 ± 0.06	−2.6	5.54 [46]
PS254	3.24 ± 0.03	3.11 ± 0.11	−4	3.14 ± 0.22	−3.1	3.09 [46]
PS411	2.43 ± 0.01	2.44 ± 0.11	0.4	2.48 ± 0.12	1.6	2.35 [46]
PS575	2.07 ± 0.04	2.11 ± 0.09	1.9	2.04 ± 0.01	−1.4	1.95 [46]
PS1800	1.19 ± 0.01	1.19 ± 0.03	0	1.24 ± 0.01	4.2	1.01 [46]
BSA	5.15 ± 0.08	5.31 ± 0.13	3.1	5.05 ± 0.47	−1.9	6.0, 5.35 [2, 48–51]
Fibrinogen	2.12 ± 0.08	2.25 ± 0.09	6.1	2.06 ± 0.14	−2.8	1.98 [2, 44]
BTG	1.59 ± 0.02	1.66 ± 0.02	4.4	1.68 ± 0.06	5.7	2.32–2.57 [49, 51]

[a] 0.1 and $1.0\,\mathrm{ml\,min^{-1}}$, scattering angle: 38°.

[b] Percentage change from batch mode measurements.

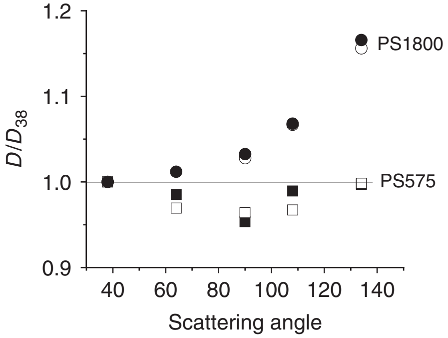

Figure 32.5 Effect of scattering angle on measured D values for PS575 (squares) and PS1800 (circles) prepared in THF ($0.1\ \mathrm{mg\,ml^{-1}}$) and measured in batch mode (solid symbols) and at $0.1\ \mathrm{ml\,min^{-1}}$ (open symbols). The horizontal line indicates no angular dependence. D measurement taken at the scattering angle indicated on the x-axis. D_{38} is the D value at a scattering angel of 38°.The samples were introduced directly into the PCS detector.

D values increasing up to 20% as the measurement angle increased from 38° to 134°. The observed increase in D values for higher MWs can be attributed to internal motions of the macromolecule [3, 6, 16, 25, 40].

This data shows that the measurement angle must be considered. Additional considerations arise from Eq. (32.5), which shows that the decay rate is linearly dependent on the square of the scattering vector q and the timescale of the decay can be increased by collecting data at smaller angles. For example, the time for the diffusion process viewed at 15° is 29 times longer than for the same process measured at 90°. Moreover, the amount of light scattered into the detector is proportional to the scattering volume and ~3.9 times as much light is collected at 15° compared to 90° [4]. Data collection at small angles is advantageous for low-MW polymers with extremely fast decay rates because data collection time and scattering intensity are effectively increased (compared to the standard 90° settings). For high-MW samples that exceed isotropic scattering dimensions ($d_h > 1/10$ the wavelength of the incident light) low-angle data collection yields the true center-of-mass diffusion. This is because contributions of internal motions of the polymer chain to D are eliminated in the limit of $q \rightarrow 0$ [3, 4, 6, 16, 25, 40, 41]. Therefore, small scattering angles should be used for online PCS to be applicable to the widest possible range of polymer MWs.

32.5.1.4 Effect of Sample Molecular Weight

Diffusion coefficient and MW are related through the well-known equation $D = A(\mathrm{MW})^{-b}$, where A and b are the intercept and slope of a plot of log D versus log MW. Log–log plots can be used to determine polymer MW from measured D values, assess the polymer configuration in solution (i.e., globular, random coil, or rodlike), and evaluate the thermodynamic goodness of a solvent for a polymer [3]. Deviation from the expected linearity of a log–log plot for linear polymers could indicate angular dependence of the scattering intensity or changes in the

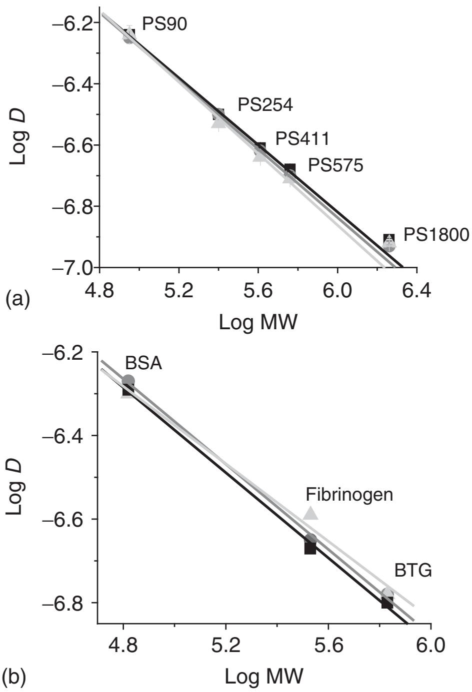

Figure 32.6 Effect of analyte MW on measured *D* values for (a) PS in THF and (b) protein standards in 50 mM PBS. The lines are linear regression lines for data collected under different flow conditions. (For both (a) and (b): ■, black line – batch mode; ●, gray line – 0.1 ml min^{-1}; and ▲, light gray line – 1.0 ml min^{-1}.) The samples were introduced directly into the PCS detector.

configuration of the polymer. Figure 32.6a shows the log–log plot for PS standards in THF. Literature reports of *b* values for PS in THF obtained from batch mode experiments range from 0.55 to 0.58 [32, 46, 47]. The experimental *b* values obtained in batch mode and for flow rates up to 1.0 ml min^{-1} also fell in a similar range. Experimental *A* values that ranged from 2.9 to 4.5×10^{-4} (for batch mode to 1.0 ml min^{-1}) were also in good agreement with literature [44, 46, 47]. The PS1800 standard was consistently observed to lie above the linear regression for each flow condition. This systematic overestimation of *D* for PS1800 is due to a combination of the angular dependence of the scattering intensity and inaccuracy in the nominal MW. The MW of PS1800 was measured to be $((1.42 \pm 0.23) \times 10^6$ Da).

Figure 32.6b shows that the diffusion behavior of proteins as a function of MW also follows the $D = A(\mathrm{MW})^{-b}$ relationship. The linear regression for batch and online *D* values yielded *b* values of ~0.50. The slope of this regression line is expected to be 0.33 for globular proteins such as BSA and BTG. Table 32.2 shows that the measured *D* value for BTG of $1.59 \times 10^{-7}\ \mathrm{cm^2\,s^{-1}}$ is significantly lower than the literature value of $\sim 2.6 \times 10^{-7}\ \mathrm{cm^2\,s^{-1}}$ for a BTG monomer due to the presence of aggregates. In addition, the *D* values for BSA are in better agreement with the values for dimer proteins. The measured *D* for fibrinogen agreed with literature values [2, 44].

It is concluded that the relationship between analyte *D* values and MW is similar for batch and online mode PCS measurements of unfractionated samples. However, the contribution of high-MW species, dimers, and/or higher order aggregates to measured *D* values resulted in unexpected *b* values because of the high sensitivity of PCS to large-sized analytes.

32.5.1.5 **Summary**

Accurate and precise online *D* values can be measured with PCS by utilizing low-scattering angles to increase the measurement timescale and analyte scattering intensity, and by maintaining an analyte concentration $>0.1\ \mathrm{mg\,ml^{-1}}$. Typical flow rates used to achieve FFF or SEC polymer separation have an insignificant effect on measured online *D* values.

32.5.2
Factors Affecting the Accuracy of *D* Values Measured by FFF-PCS

The previous sections demonstrated the contribution of individual variables such as analyte concentration and MW, carrier liquid flow rate, and scattering angle on the accuracy and precision of online *D* values. The two most critical variables were the analyte concentration (should be $\geq 0.1\ \mathrm{mg\,ml^{-1}}$) and the scattering angle (low angles will minimize the angular dependence of the scattering). These conditions will maximize analyte signal and provide more accurate and precise online *D* values by increasing the data collection time and sample scattering intensity. The results to this point have been obtained by direct injection of the sample solutions into the PCS detector.

Part 2 of this study demonstrates the application of ThFFF/PCS to lipophilic macromolecules (PS and polyacrylate standards) in organic solvent and FlFFF/PCS to proteins (BSA and BTG) in aqueous solution. These applications are preceded by a discussion about the criteria used to select retention time intervals for the online determination of *D* and further refinement of FFF/PCS instrument configuration. The four samples characterized by ThFFF/PCS were selected to demonstrate different capabilities of this combined technique. Sample 1, which is a mixture of PS homopolymers, demonstrates the capability of ThFFF/PCS to fractionate a polymer mixture based on size differences of the analytes and accurately measure *D* for each eluting component. Samples 2 and 3 demonstrate the ability of ThFFF/PCS to fractionate polymer mixtures based on differences in component chemistry. Sample 3 represents a challenging mixture of three different polyacrylates. Sample 4 demonstrates the capability to characterize high-PDI polymers.

32.5.2.1 **Selection of Retention Time Intervals**

The studies in the previous sections demonstrate the relative importance of analyte concentration, scattering angle, flow rate, and analyte MW on the accuracy of online *D* measurements. While it is important to examine the effect of each parameter individually and identify the major contributor(s) to potential inaccuracies in *D* measurements, it is also important to note that their effects are interdependent. For example, high-MW PS exhibits higher scattering intensities and thus the threshold concentration for accurate *D* measurement is lower than that for a lower MW PS. This becomes significant when coupling a separation stage with online PCS as the eluting sample peak varies in concentration and possibly composition. The scattering intensity of the eluting sample is a culmination of analyte properties and experimental conditions and hence can be related to percentage errors in *D*. A signal-to-noise (S/N) ratio >2.5 is used to guide the selection of the retention time interval over which *D* values are averaged for each component separated by FFF. This ratio corresponds with errors <10% in measured FFF/PCS *D* values as shown in Figure 32.7, which plots the percentage error in ThFFF/PCS *D* measurement versus S/N for PS in THF. This curve should be independent of the chosen solvent.

32.5.2.2 **Carrier Liquid Temperature**

ThFFF utilizes large temperature gradients to achieve polymer separations, which can cause elevated carrier liquid temperatures. Furthermore, the temperature gradient is often programmed to decrease from high to low ΔT values to reduce analysis times. This may result in a constantly changing carrier liquid temperature as it passes through the PCS detector. The temperature sensitivity of *D* and d_h necessitates that the carrier liquid temperature remains constant in the PCS instrument so that accurate values are measured. The temperature of the carrier liquid passing through the MALS detector was found to remain constant between 25 and 26 °C when either constant ΔT or programmed decay ΔT conditions were used. ThFFF/PCS *D* values for PS254 in THF using different constant ΔTs of 30, 50, 70, and 90 °C were measured to be 3.34 ± 0.12, 3.45 ± 0.14, 3.50 ± 0.14, and $3.42 \pm 0.14\,\text{cm}^2\,\text{s}^{-1}$, respectively. These results show that the carrier liquid temperature does not systematically contribute to measure online *D* values for the ThFFF/PCS setup used in this study. However, this potential effect should be evaluated for each individual ThFFF channel. If needed, the carrier liquid temperature

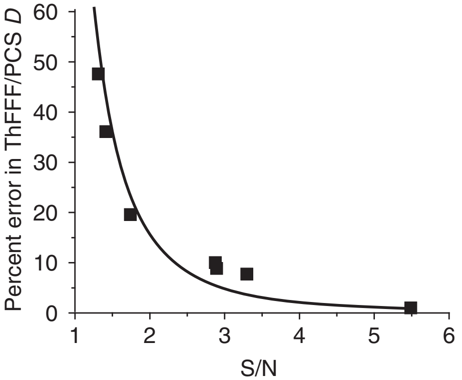

Figure 32.7 Percentage error in ThFFF/PCS *D* versus S/N for PS in THF.

can be accurately maintained at a desired constant temperature by using a column heater/exchanger in between the ThFFF outlet and the detector inlet [52].

32.5.2.3 Optimum Instrument Configuration

The results shown in Figures 32.2 and 32.3 were obtained by injecting a sufficiently large sample plug directly into the PCS detector so that a constant concentration is maintained throughout the D measurement. This situation is quite different when the PCS detector is connected to a separation instrument such as FFF. First, each separated sample component elutes as a peak that varies in concentration over time. Second, achieving an analyte concentration of 0.1 mg ml^{-1} at the detector is challenging because of significant dilution (15–100×) during the separation stage. Injecting higher concentration samples may cause channel overloading, which in turn leads to peak broadening, fronting/tailing, shifted retention times, and loss of resolution. Another alternative to optimizing the concentration of the eluting sample components is to minimize band broadening, particularly, those associated with the instrumental setup [44]. One facile instrumentation modification is to use a smaller volume sample loop. The contribution of sample injection volume to band broadening is represented by Eq. (32.11), where $\sigma_{\text{inj}}{}^2$ is the sample injection variance and Δt_{inj} is the time needed for the sample to flush out of the sample loop

$$\sigma_{\text{inj}}^2 = \frac{\Delta t_{\text{inj}}^2}{12} \tag{32.11}$$

Reducing the injected sample volume by 50-fold from 20 to 0.4 µl theoretically results in a 50-fold decrease in the sample injection volume contribution to the band broadening. To maintain the sample-injected amount, the sample concentration would need to increase 50×. However, in practice, the upper limit of sample concentration that can be injected using a 0.4 µl sample loop is determined by the viscosity of the polymer sample solution. Figure 32.8 compares fractograms obtained for PS411 in MEK using 0.4 and 20 µl sample loops. A higher signal intensity is measured when using the smaller volume sample loop with a higher concentration sample. The D value obtained using the 20 µl sample

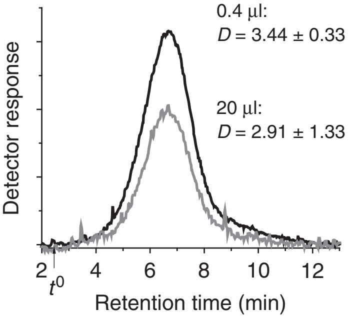

Figure 32.8 Comparison of ThFFF fractograms for PS411 in MEK obtained using a 0.4 µl (black trace) sample loop and a 20 µl (gray trace) sample loop. The D values are indicated for each peak ($\times 10^7$ cm^2 s^{-1}).

loop was $(2.91 \pm 1.33) \times 10^{-7}\,\mathrm{cm}^2\,\mathrm{s}^{-1}$. The D value measured using the 0.4 µl sample loop was $3.44 \pm 0.11 \times 10^{-7}\,\mathrm{cm}^2\,\mathrm{s}^{-1}$, which is in agreement with the value of $3.43 \times 10^{-7}\,\mathrm{cm}^2\,\mathrm{s}^{-1}$ obtained from batch mode measurements. These results demonstrate the advantage of injecting small volumes of high concentration analyte solutions.

Low angles for PCS data collection and the injection of concentrated low-volume samples were used in the ThFFF/PCS analysis of a mixture of three low PDI PS standards in MEK (shown in Figure 32.9). Three components can be easily identified and the elution order is as expected from low to high MWs. The shaded regions indicate the retention time ranges over which the S/N was >2.5 and ThFFF/PCS D values were averaged. The separation seen in Figure 32.9 was performed under both the manufacturer's instrument configuration (20 µl sample loop and 108° scattering angle) and the optimized instrument configuration (0.4 µl sample loop and 38° scattering angle). Triplicate measurements of ThFFF/PCS D values for each PS component in the separated mixture are compared in Table 32.3. Using the optimized configuration, the error in the measurement is reduced by almost 50% and an accurate value for D is obtained for the high MW sample, which was not obtained using the manufacturer's instrument configuration (recall 1800 in Figure 32.6a).

Figure 32.10 compares the ThFFF/PCS average D values listed in Table 32.3 to nominal batch mode values in a log–log plot. The linear regressions between the optimized instrument configuration and batch mode data are in excellent agreement and the slopes of these lines are also shown in Figure 32.10. The linear regression for the manufacturer's instrument configuration and the batch mode data deviates particularly for the high MW standard. It is not possible to discern whether this increase in D is due to contributions from internal motions of the

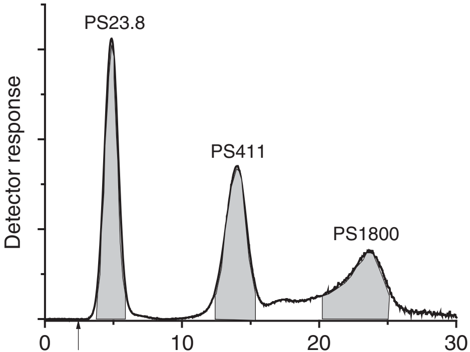

Figure 32.9 ThFFF separation of a three component mixture of low-PDI PS standards in MEK. Shaded regions mark the time interval over which the S/N was >2.5. ThFFF conditions: carrier liquid, MEK; ΔT, programmed exponential temperature decay (exponent of 2); initial ΔT, 80 °C for 5 min; flow rate, 0.4 ml min^{-1}; injection volume, 0.4 µl; scattering angle, 38°; and sample concentrations: PS23.8, 80 mg ml^{-1}; PS411, 4.0 mg ml^{-1}; and PS1800, 1.4 mg ml^{-1}.

Table 32.3 Comparison of ThFFF/PCS *D* values measured from the peaks of separated standards in MEK using different instrument configurations.

	$D \times 10^7$ cm^2 s^{-1}	
Sample	**Manufacturer configuration**[a]	**Optimized configuration**[b]
PS23.8	17.30 ± 1.35	16.93 ± 0.76
PS411	3.61 ± 0.34	3.48 ± 0.20
PS1800	2.53 ± N/A[c]	1.55 ± 0.11

[a] 20 μl Sample loop, 108° scattering angle, MEK, PS23.8, 411 and 1800–1810, and 0.5 and 0.17 mg ml^{-1}, respectively.

[b] 0.4 μl Sample loop, 38° scattering angle, MEK, PS23.8, 411 and 1800–1880, and 4.0 and 1.4 mg ml^{-1}, respectively.

[c] Only one of three injections yielded data.

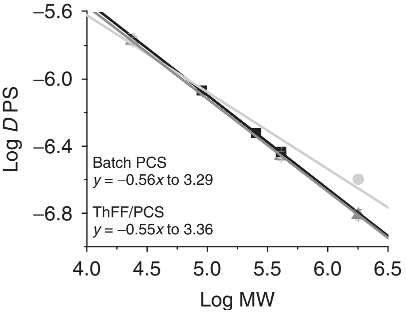

Figure 32.10 Comparison of ThFFF/PCS *D* values measured in MEK using the optimized instrument configuration (▲, gray line) and the manufacturer's instrument configuration (●, light gray line) with nominal batch mode values (■, black line).

polymer or because of poor precision, because *D* for only one of the three replicate injections was successfully measured.

Figure 32.11 demonstrates that ThFFF/PCS *D* values can be measured for weakly scattering polymers such as PBA and PMA when using the 0.4 μl sample loop and a scattering angle of 38°. Excellent agreement is observed between batch mode and online *D* values.

32.5.3
ThFFF/PCS Characterization of Synthetic Polymers

The optimum experimental conditions identified earlier were employed for ThFFF/PCS characterization of synthetic homopolymer mixtures and polydisperse samples. *D* and D_T values are simultaneously obtained at each slice of a fractionated sample eluting from the ThFFF channel, in addition, to average *D* and D_T values for the entire sample. This allows both the size and the composition distributions

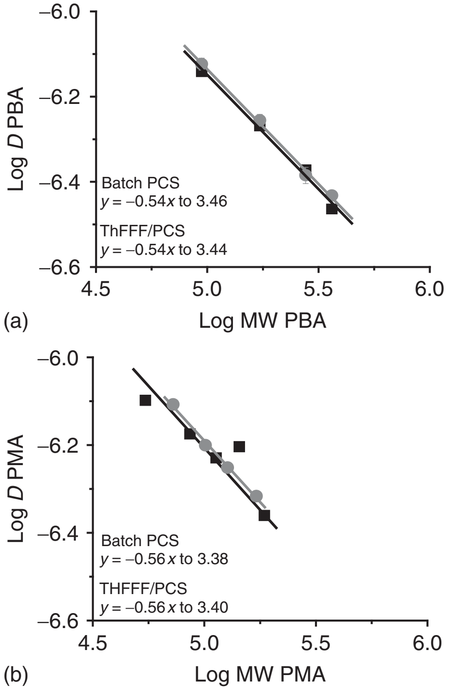

Figure 32.11 Comparison between batch mode (gray line) and ThFFF/PCS *D* (black line) values measured in MEK using the optimized instrument configuration for (a) PBA and (b) PMA homopolymers.

of homopolymers with broad MWs, heterogeneous polymers or polymer mixtures to be characterized.

Figure 32.12 shows a near baseline separation of a mixture of PBA and PS linear homopolymer standards. The average ThFFF/PCS D and D_T values for each component of the mixture were calculated from the time intervals ($S/N > 2.5$) indicated by the shaded regions. The similar D values for both homopolymers indicate that they have similar hydrodynamic diameters and that the separation is based on different homopolymer chemistries, which is reflected by their different D_T values. As expected, a longer retention time is observed for the analyte with the larger D_T value. The average D_T values for PBA263 and PS390 in MEK were calculated to be $(1.00 \pm 0.04) \times 10^{-7}$ cm^2 K^{-1} s^{-1} and $(1.69 \pm 0.03) \times 10^{-7}$ cm^2 K^{-1} s^{-1}, respectively. This is the first reported D_T value for PBA in MEK while the D_T value for PS in MEK agrees well with the range of $(1.39–1.9) \times 10^{-7}$ cm^2 K^{-1} s^{-1} reported in literature [32, 53].

ThFFF/PCS fractionation of a broad MW PS standard with a weight average MW of 250 kDa and a PDI of 2.5 (250BR) is shown in Figure 32.13a. Sample elution was also monitored by MALS-dRI detectors. The sample is well retained and the peak is broader than those seen in Figure 32.9 for low PDI PS standards. In this case, the additional complication is that the MALS and dRI traces in

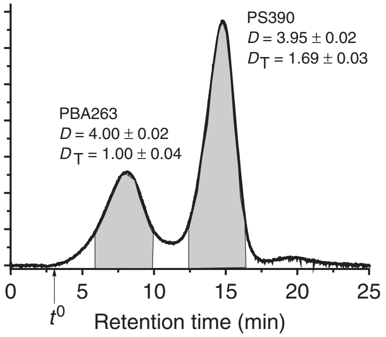

Figure 32.12 Composition-based ThFFF separation of a mixture of PS and PBA homopolymer standards with similar *D* values but different D_T values. Shaded regions mark the time interval over which the S/N was >2.5. ThFFF conditions: carrier liquid, MEK; flow rate, 0.4 ml min^{-1}; ΔT, 70 °C constant; injection volume, 0.4 µl; scattering angle, 38°; and sample concentrations: PS390, 4.0 mg ml^{-1} and PBA263, 20 mg ml^{-1}.

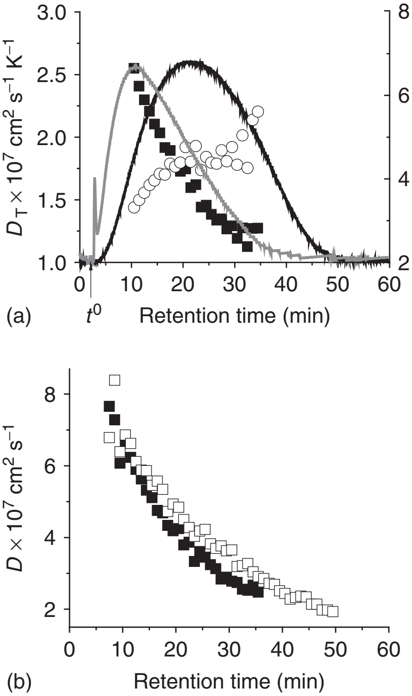

Figure 32.13 (a) ThFFF separation of a broad MW PS standard (MW: 250 kDa, PDI: 2.5) prepared at 50 mg ml^{-1}. MALS (black trace) and dRI (gray trace) fractograms are overlaid with *D* (■) and D_T (○) values taken at 1 min intervals across the peak. (b) Comparison of online *D* values taken at 1 min time intervals across the ThFFF fractogram of PS250BR injected at concentrations of 50 (■) and 100 mg ml^{-1} (□). ThFFF conditions: carrier liquid, MEK; flow rate, 0.4 ml min^{-1}; ΔT, 100 °C; injection volume, 0.4 µl; and scattering angle, 38°.

Figure 32.13a have different peak maximum retention times. Consequently, two average D_T values for PS250BR can be calculated using each peak maximum t_r. The question that arises is which average D_T value is most accurate. Average D_T values of $(0.98 \pm 0.02) \times 10^{-7}$ cm^2 K^{-1} s^{-1} (dRI) and $(1.83 \pm 0.07) \times 10^{-7}$ cm^2 K^{-1} s^{-1} (MALS) were calculated to be 40% lower and 10% higher, respectively, compared to the expected D_T value of $(1.67 \pm 0.14) \times 10^{-7}$ cm^2 K^{-1} s^{-1} for PS in MEK. The peak maximum of the MALS trace yields the more accurate average D_T value for polydisperse samples. The lower than expected D_T calculated from the dRI trace can be attributed to the shift of the peak maximum to shorter retention times because of a large amount of low-MW species. The higher than expected D_T calculated from the MALS trace may be a result of either a detector bias toward high-MW species due to their increased scattering intensity or to sample overloading.

Figure 32.13a shows D and D_T taken at 1 min time interval across the fractogram. D is observed to decrease across the peak width as expected with increasing retention times. D_T initially increases, then plateaus at 20 min, and increases again at 30 min. D_T should be constant across the elution peak because homopolymer D_T has been shown to be independent of MW and branching for polymers with MWs >10 kDa [32, 33, 54]. The deviation of D_T at short and long retention times can be attributed to inaccuracies in ThFFF/PCS D measurements because of low-sample concentrations (≤ 0.02 mg ml^{-1}) eluting the ThFFF channel. This concentration is 5× below the desired threshold of 0.1 mg ml^{-1} and results in larger errors in D measurements. D_T values within the plateau region between 20 and 30 min (which corresponds with MALS peak maximum) are observed to be $\sim 1.75 \times 10^{-7}$ cm^2 K^{-1} s^{-1}. This is in good agreement with literature values for PS in MEK and demonstrates that retention times near the MALS peak maximum can be used to calculate D_T values. Figure 32.13 b shows the effect of doubling the injected sample amount on measured ThFFF/PCS D values. Before 15 min, the measured D values for each concentration agree. Beyond 15 min, the D values increased by up to 30% for the more concentrated sample. This translates into an increase of D_T by the same amount. This current limitation of ThFFF/PCS to measure a constant D_T value across a sample elution peak warrants further investigation.

Analysis of mixtures composed of chemically similar polymers is difficult from both the separation and the characterization perspectives. Pressure-sensitive adhesives represent this class of sample as they are often formulated from mixtures of polyacrylate homopolymers. ThFFF/PCS can be used to accomplish separation and characterization in a single step because of ThFFF's composition- and size-based separation mechanisms. A partial separation of a mixture of P2EHA242, PBA263, and PMA171 is shown in Figure 32.14. D slightly decreases while D_T significantly increases across the fractogram. This indicates that the three components have similar hydrodynamic sizes and that the separation was driven by differences in their chemistry. Qualitative identification of each component was achieved by comparing the D_T value measured at peak maximum retention time with that measured from individual homopolymer injections. D_T from individual injections were measured to be 0.83 ± 0.13, 1.01 ± 0.06, and $1.88 \pm 0.26 \times 10^{-7}$ cm^2 K^{-1} s^{-1} for P2EHA, PBA, and PMA homopolymers, respectively. The observed elution order

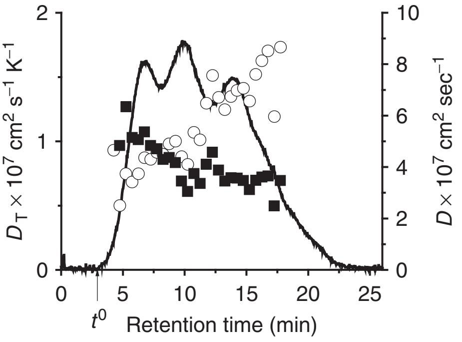

Figure 32.14 ThFFF/PCS characterization of a mixture of P2EHA242, PBA263, and PMA171 homopolymers. D (■) and D_T (○) taken at 30 s time slices overlay the MALS fractogram. ThFFF conditions: carrier liquid, MEK; flow rate, 0.4 ml min^{-1}; ΔT, 80 °C constant; injection volume, 0.4 μl; scattering angle, 38°; and sample concentrations: 22–40 mg ml^{-1}.

of P2EHA242, PBA263, and PMA171 follows the order of increasing D_T values as expected. Figure 32.12 and Figure 32.14 demonstrate ThFFF/PCS's potential for characterizing multiple component polymer mixtures.

32.5.4
FlFFF/PCS of Proteins

The established operational guidelines for online PCS are equally applicable to hydrophobic analytes such as proteins and protein aggregates. The fractograms for BSA and BTG are shown in Figure 32.15, which demonstrate FlFFF's ability to separate monomers from aggregates. The shaded regions signify the time interval where the S/N was >2.5 and measured D values have errors below 10%. Excellent agreement is observed between FlFFF/PCS D and literature values for both protein monomers (Table 32.3). The D for the aggregate peak in the BTG fractogram

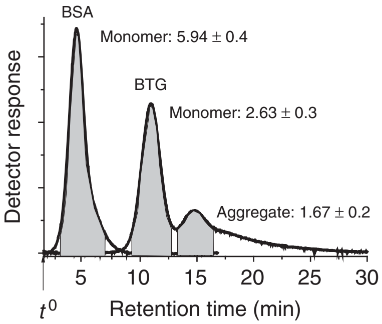

Figure 32.15 Overlay of BSA (gray trace) and BTG (black trace) FlFFF fractograms. FlFFF/PCS D values ($\times 10^7$ cm^2 s^{-1}). Shaded regions mark the time interval over which the S/N was >2.5. FlFFF/PCS conditions: $\dot{V}_c$, 2.85 ml min^{-1}; $\dot{V}$, 1.25 ml min^{-1}; and sample concentrations: BSA, 11.0 mg ml^{-1} and BTG, 2.0 mg ml^{-1}.

was measured to be $1.67 \times 10^{-7}\,\mathrm{cm^2\,s^{-1}}$ which, as expected, is lower than that for monomer. The plot of log D versus log MW of the protein monomers yielded a slope of 0.34 between the BSA and BTG monomers, which agrees with the literature value of 0.33 for globular proteins [51]. This is in contrast to the 0.54 slope observed in Figure 32.6b, which was obtained without any sample separation. The batch mode D values for the rod-shaped fibrinogen fall well below the linear regression for globular proteins as expected [51]. These results demonstrate that a separation stage is important to obtain accurate D values of broadly distributed or multimodal samples.

32.6
Conclusions

The effects of analyte concentration, flow rate, scattering angle, and MW on the accuracy of D measurements from online PCS were evaluated by comparison with values obtained in batch mode. Analyte concentrations $>0.1\,\mathrm{mg\,ml^{-1}}$ at the detector and measurement at small scattering angles are desired for accurate online D determinations. While the absolute numbers reported in this study are instrument specific, the general observations are expected to be applicable across different instruments.

An S/N ratio of >2.5 was established as the threshold for maintaining errors in D below 10%. This criterion was applied when obtaining average D results for ThFFF/PCS of polymers in organic solvent and FlFFF/PCS of proteins in aqueous solution. Excellent agreement was obtained between FFF/PCS and batch mode D values. The use of an optimized instrument configuration was crucial to successful ThFFF/PCS determinations of D and D_T. The combination of a separation stage with online PCS has enabled the successful characterization of subpopulations present in mixtures or high-polydispersity samples, which would otherwise remain hidden in traditional batch mode measurements. The guidelines presented for online PCS are shown to be valid for both lipophilic and hydrophilic analytes, and are expected to be applicable to other separation techniques.

Acknowledgments

The authors thank the National Science Foundation CHE-1013029 for supporting this work.

References

1. Filella, M., Zhang, J., Newman, M.E., and Buffle, J. (1997) Analytical applications of photon correlation spectroscopy for size distribution measurements of natural colloidal suspensions: capabilities and limitations. *Colloids Surf., A*, **120** (1–3), 27–46.
2. Gun'ko, V.M., Klyueva, A.V., Levchuk, Y.N., and Leboda, R. (2003) Photon correlation spectroscopy investigations of

proteins. *Adv. Colloid Interface Sci.*, **105** (1–3), 201–328.

3. Burchard, W. (1999) in *Branched Polymers II: Advances in Polymer Science*, Vol. 143 (ed. J. Roovers), Springer-Verlag, Berlin, pp. 113–194.
4. Xu, R. (2000) in *Particle Characterization: Light Scattering Methods* (ed. B. Scarlett), Kluwer Academic Publishers, Dordrecht, pp. 223–288.
5. Cho, T.J. and Hackley, V.A. (2010) Fractionation and characterization of gold nanoparticles in aqueous solution: asymmetric-flow field flow fractionation with MALS, DLS, and UV–Vis detection. *Anal. Bioanal. Chem.*, **398** (5), 2003–2018.
6. Rolland-Sabate, A., Mendez-Montealvo, M.G., Colonna, P., and Planchot, V. (2008) Online determination of structural properties and observation of deviations from power law behavior. *Biomacromolecules*, **9** (7), 1719–1730.
7. Filipe, V., Hawe, A., and Jiskoot, W. (2010) Critical evaluation of Nanoparticle Tracking Analysis (NTA) by nanosight for the measurement of nanoparticles and protein aggregates. *Pharm. Res.*, **27** (5), 796–810.
8. Faraone, A., Magazu, S., Maisano, G., Villari, V., and Maschio, G. (1999) Possibilities and limits of photon correlation spectroscopy in determining polymer molecular weight distributions. *Macromol. Chem. Phys.*, **200** (5), 1134–1142.
9. Brown, R.G.W., Burnett, J.G., Mansbridge, J., and Moir, C.I. (1990) Miniature laser light scattering instrumentation for particle size analysis. *Appl. Opt.*, **29** (28), 4159–4169.
10. Williams, S.K.R., Lee, H., and Turner, M.M. (1999) Size characterization of magnetic cell sorting microbeads using flow field-flow fractionation and photon correlation spectroscopy. *J. Magn. Magn. Mater.*, **194** (1–3), 248–253.
11. Clogston, J.D., Zheng, J., Ramalinga, U., Patri, A., and McNeil, S.E. (2008) Nanoparticle metrology: reporting the hydrodynamic size by DLS. 236th ACS National Meeting, Philadelphia, Pennsylvania, August 17–21, 2008.
12. Ma, P.L., Buschmann, M.D., and Winnik, F.M. (2010) One-step analysis of DNA/chitosan complexes by field-flow fractionation reveals particle size and free chitosan content. *Biomacromolecules*, **11** (3), 549–554.
13. Silveira, J.R., Raymond, G.J., Hughson, A.G., Race, R.E., Sim, V.L., Hayes, S.F., and Caughey, B. (2005) The most infectious prion protein particles. *Nature*, **437** (7056), 257–261.
14. Striegel, A.M. (2005) Multiple detection in size-exclusion chromatography of macromolecules. *Anal. Chem.*, **77** (5), 104A–113A.
15. Farmer, B.S., Terao, K., and Mays, J.W. (2006) Characterization of model branched polymers by multi-detector SEC in good and theta solvents. *Int. J. Polym. Anal. Charact.*, **11** (1), 3–19.
16. Cotts, P.M. (2003) in *Multiple Detection in Size Exclusion Chromatography* (ed. A.M. Striegel), American Chemical Society, Washington, DC, pp. 52–75.
17. Brewer, A.K. and Striegel, A.M. (2009) Particle size characterization by quadruple-detector hydrodynamic chromatography. *Anal. Bioanal. Chem.*, **393**, 295–302.
18. Brewer, A. and Striegel, A. (2011) Characterizing a spheroidal nanocage drug delivery vesicle using multi-detector hydrodynamic chromatography. *Anal. Bioanal. Chem.*, **399** (4), 1507–1514.
19. Lohrke, J., Briel, A., and Mader, K. (2008) Characterization of superparamagnetic iron oxide nanoparticles by asymmetrical flow field-flow fractionation. *Nanomedicine*, **3** (4), 437–452.
20. Chow, K.M., Stansfield, A.G., Carr, R.J.G., Rarity, J.G., and Brown, R.G.W. (1988) On-line photon correlation spectroscopy using fibre-optic probes. *J. Phys. E*, **21**, 1186–1190.
21. Carr, R.J.G., Rarity, J.G., Stansfield, A.G., Brown, R.G.W., Clarke, D.J., and Atkinson, T. (1988) Determination of protein size in chromatography column eluants by on-line photon correlation spectroscopy. *Anal. Biochem.*, **175** (2), 492–499.
22. Claes, P., Kenney, A., and Vardy, P. (1991) Instrumentation for molecular

size detection for analytical biotechnology. *Anal. Chim. Acta*, **249** (1), 227–230.

23. Choi, S.M. and Ma, C.Y. (2005) Study of thermal aggregation of globulin from common buckwheat (*Fagopyrum esculentum* Moench) by size-exclusion chromatography and laser light scattering. *J. Agric. Food Chem.*, **54** (2), 554–561.
24. Zhao, Y., Mine, Y., and Ma, C.Y. (2004) Study of thermal aggregation of oat globulin by laser light scattering. *J. Agric. Food Chem.*, **52** (10), 3089–3096.
25. Rolland-Sabate, A., Guilois, S., Jaillais, B., and Colonna, P. (2011) Molecular size and mass distributions of native starches using complementary separation methods: Asymmetrical Flow Field Flow Fractionation (A4F) and Hydrodynamic and Size Exclusion Chromatography (HDC-SEC). *Anal. Bioanal. Chem.*, **399** (4), 1493–1505.
26. Liu, Y., Bo, S., Zhu, Y., and Zhang, W. (2003) Determination of molecular weight and molecular sizes of polymers by high temperature gel permeation chromatography with a static and dynamic laser light scattering detector. *Polymer*, **44** (23), 7209–7220.
27. Ford, N., Havard, T., and Wallace, P. (1988) in *Particle Size Distribution III: Assessment and Characterization* (ed. T. Provder), American Chemical Society, Washington, DC, pp. 39–51.
28. Knappe, P., Bienert, R., Weidner, S., and Thunemann, A.F. (2010) Characterization of poly(N-vinyl-2-pyrrolidone)s with broad size distributions. *Polymer*, **51** (8), 1723–1727.
29. Thunemann, A.F., Knappe, P., Bienert, R., and Weidner, S. (2009) Online coupling of field-flow fractionation with SAXS and DLS for polymer analysis. *Anal. Methods*, **1** (3), 177–182.
30. Isaacson, C.W. and Bouchard, D. (2010) Asymmetric flow field flow fractionation of aqueous C60 nanoparticles with size determination by dynamic light scattering and quantification by liquid chromatography atmospheric pressure photo-ionization mass spectrometry. *J. Chromatogr. A*, **1217** (9), 1506–1512.
31. Le Cerf, D., Simon, S., Argillier, J.F., and Picton, L. (2007) Contribution of flow field flow fractionation with on line static and dynamic light scattering to the study of hydrosoluble polyelectrolyte complexes. *Anal. Chim. Acta*, **604** (1), 2–8.
32. Schimpf, M.E. and Giddings, J.C. (1989) Characterization of thermal diffusion in polymer solutions by thermal field flow fractionation. *J. Polym. Sci.: Polym. Phys. Edn.*, **27**, 1317–1332.
33. Schimpf, M.E. and Giddings, J.C. (1987) Characterization of thermal diffusion in polymer solutions by thermal field-flow fractionation: effects of molecular weight and branching. *Macromolecules*, **20** (7), 1561–1563.
34. Messaud, F.A., Sanderson, R.D., Runyon, J.R., Otte, T., Pasch, H., and Williams, S.K.R. (2009) An overview on field-flow fractionation techniques and their applications in the separation and characterization of polymers. *Prog. Polym. Sci.*, **34** (4), 351–368.
35. Williams, S.K.R., Runyon, J.R., and Ashames, A.A. (2010) Field-flow fractionation: addressing the nano challenge. *Anal. Chem.*, **83** (3), 634–642.
36. Schimpf, M.E., Wheeler, L.M., and Romeo, P.F. (1993) in *Chromatography of Polymers* (ed. T. Provder), American Chemical Society, Washington, DC, pp. 63–76.
37. Van Batten, C., Hoyos, M., and Martin, M. (1997) Thermal field-flow fractionation of colloidal materials: methylmethacrylate-styrene linear diblock copolymers. *Chromatographia*, **45**, 121–126.
38. Schimpf, M.E. and Giddings, J.C. (1990) Characterization of thermal diffusion of copolymers in solution by thermal field-flow fractionation. *J. Polym. Sci., Part B: Polym. Phys.*, **28** (13), 2673–2680.
39. Gunderson, J.J. and Giddings, J.C. (1986) Chemical composition and molecular-size factors in polymer analysis by thermal field-flow fractionation and size exclusion chromatography. *Macromolecules*, **19** (10), 2618–2621.
40. Co, C.C., Cotts, P., Burauer, S., de Vries, R., and Kaler, E.W. (2001) Microemulsion polymerization. 3. molecular weight and particle size distributions. *Macromolecules*, **34** (10), 3245–3254.

41. Teraoka, I. (2002) *Polymer Solutions: An Introduction to Physical Properties*, John Wiley & Sons, Ltd, Chichester.

42. Giddings, J.C. (1993) Field-flow fractionation: analysis of macromolecular, colloidal, and particulate materials. *Science*, **260** (5113), 1456–1465.

43. Giddings, J.C. (1995) Measuring colloidal and macromolecular properties by FFF. *Anal. Chem.*, **67** (19), 592A–598A.

44. Schimpf, M.E., Caldwell, K.D., and Giddings, J.C. (2000) *Field-Flow Fractionation Handbook*, John Wiley & Sons, Inc., New York.

45. Belgaied, J.E., Hoyos, M., and Martin, M. (1994) Velocity profiles in thermal field-flow fractionation. *J. Chromatogr. A*, **678** (1), 85–96.

46. Mandema, W. and Zeldenrust, H. (1977) Diffusion of polystyrene in tetrahydrofuran. *Polymer*, **18** (8), 835–839.

47. Mes, E.P.C., Kok, W.T., Poppe, H., and Tijssen, R. (1999) Comparison of methods for the determination of diffusion coefficients of polymers in dilute solutions: the influence of polydispersity. *J. Polym. Sci., Part B: Polym. Phys.*, **37**, 593–603.

48. Raj, T. and Flygare, W.H. (1974) Diffusion studies of bovine serum albumin by quasielastic light scattering. *Biochemistry*, **13** (16), 3336–3340.

49. Liu, M.K., Li, P., and Giddings, J.C. (1993) Rapid protein separation and diffusion coefficient measurement by frit inlet flow field-flow fractionation. *Protein Sci.*, **2**, 1520–1531.

50. Meechai, N., Jamieson, A.M., and Blackwell, J. (1999) Translational diffusion coefficients of bovine serum albumin in aqueous solution at high ionic strength. *J. Colloid Interface Sci.*, **218** (1), 167–175.

51. Tanford, C. (1961) *Transport Processes. Viscosity, in Physical Chemistry of Macromolecules*, John Wiley & Sons, Inc., New York.

52. Lee, D. and Williams, S.K.R. (2010) Thermal field-flow fractionation and multiangle light scattering of polyvinyl acetate with broad polydispersity and ultrahigh molecular weight microgel components. *J. Chromatogr. A*, **1217** (10), 1667–1673.

53. Giddings, J.C., Caldwell, K.D., and Myers, M.N. (1976) Thermal diffusion of polystyrene in eight solvents by an improved thermal field-flow fractionation methodology. *Macromolecules*, **9** (1), 106–112.

54. Rauch, J. and Kohler, W. (2005) On the molar mass dependence of the thermal diffusion coefficient of polymer solutions. *Macromolecules*, **38** (9), 3571–3573.

33
Surface Plasmon Resonance Spectroscopy and Molecularly Imprinted Polymer (MIP) Sensors

Allan Cyago and Rigoberto Advincula

33.1
Introduction

In the advent of new concerns over environmental pollution, diminishing sustainable clean water supplies, and contamination of food products, the need for novel analytical methods has prompted research on sensors with low-cost preparation and highly efficient capabilities. Chemical sensors and biosensors have gained a major role in the development of innovative techniques for the measurement and detection of biologically (pharmaceuticals and biomolecules) and environmentally (contaminants and pollutants) important substances. The focus of sensor preparation and research usually emphasizes on two fundamental parts, which are essential in the improvement of overall sensor device performance; first, the signal generation process or how the ''sensor response'' is made based on specific molecular interactions between the target molecule and the ''recognition site'' and second, on the signal transduction method employed, which directly affects the analytical figures of merit of the complete sensor.

Chemical sensors employ detection based on signal obtained from covalent or noncovalent types of interaction, such as metal–ligand complexation, van der Waals force, and electrochemical redox transport of electrons. On the other hand, biosensors use specific covalent and noncovalent types of interaction, but facilitated by biomolecules serving as recognition sites embedded on the sensor platform. Most biomolecules used in biosensors act via enzyme–substrate interaction, antigen–antibody bonding (immunosensors), or membrane-based proteins as ion-transport sensors. These natural receptors offer exceptional sensitivity and selectivity when coupled with a suitable detection method, but they require special handling conditions and are less stable chemically and mechanically, often more expensive. The success of the analytical method also depends strongly on the signal transduction process, especially techniques with high resolution and signal-to-noise ratio, which allows the detection of target molecules at trace concentrations. Common examples include various electrochemical methods [1], mass-sensitive techniques such as quartz crystal microbalance (QCM) [2], and also surface-based techniques such as atomic force microscopy (AFM) [3]. An important

Handbook of Spectroscopy, Second Edition. Edited by Günter Gauglitz and David S. Moore.

consideration in sensor design is the ability to incorporate the sensing platform directly to the transducer surface, which allows for more sensitivity as the signal generated is directly transported to the digital output device used. This effectively lowers the signal-to-noise ratio generated for the device and leads to higher calibration sensitivity and lower limits of detection (LODs).

An important class of signal transduction techniques that is capable of direct integration with the recognition element is the surface plasmon resonance (SPR) technique. This technique involves measurement of changes in property of reflected light from the surface of a thin film noble metal, such as gold or silver, as a result of the evanescent excitation of surface plasmon waves propagating on the metal–dielectric surface. Initially, SPR has been extensively studied for biosensors applications owing to high sensitivity and specificity, and as proof many instruments have since been commercialized successfully [4]. However, the drawbacks inherent to the use of biomolecules in sensor applications, such as short lifetime and loss of sensitivity due to deactivation have led to the research and discovery of novel and stable chemical-sensing platforms.

Molecular imprinting as a method of preparing recognition sites has now become a leading research field in the study of sensors. The technique has the ability to mimic the action of biomolecules, while having exceptional mechanical and chemical stabilities in otherwise harsh conditions. Molecular imprinting has become a widely preferred technique due to its effectiveness, low-cost preparation, and directness of approach. Molecular imprinting technique has been widely studied over the last decade [5] (Figure 33.1), with the number of publications increasing dramatically over the last few years. This has lead to a wide variety of applications, some of which have already been commercialized. In general, the technique is based on entrapment of molecules and other particles of interest in a predetermined scaffold,

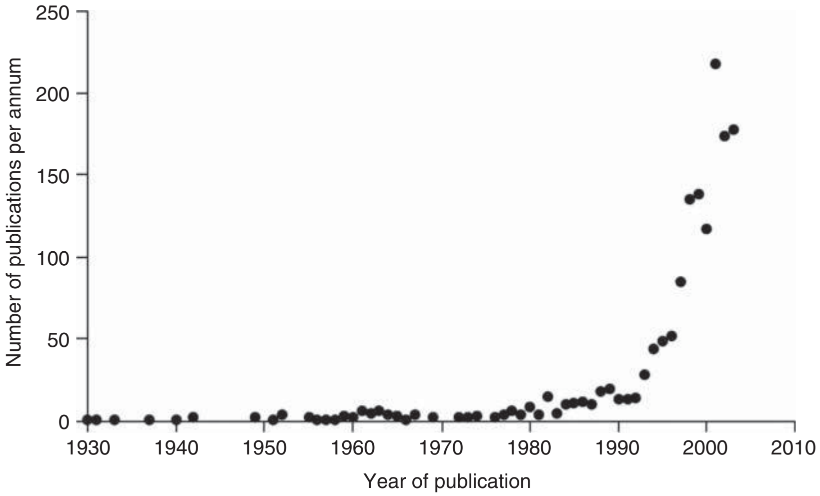

Figure 33.1 The number of publications within the field of molecular imprinting science and technology per annum for the period 1931–2003. (Taken from Ref. [5].)

after which a suitable washing step is performed to remove most of the originally entrapped material. The washing process leaves behind a cavity – the recognition site – that is sensitive toward the original or other similarly structured molecules. Another term for this model is the ''lock-and-key'' model, which is also used to refer to enzymes. For most of the molecular imprinting techniques currently applied in sensors, organic-based scaffolds, particularly polymers, are commonly used, and the number of original papers on ''molecularly imprinted polymers'' or MIPs have dramatically increased over the past decades [5, 6]. As the different methods of polymerization have now been well reported, this knowledge has been extensively applied in the preparation of MIPs, resulting in the formation of tunable recognition elements that have specific properties, for example, enhanced selectivity, enzymelike catalysis, and enantioselectivity. With a suitable signal transduction method, MIP-based sensors can achieve higher sensitivity, accuracy, and selectivity compared to similarly designed biosensors, making them more commercially viable and able to meet the demands of low-cost sensing. Flow injection process, microfluidics, and other miniaturization techniques should enable the MIP sensor setup to be portable and thus allow onsite monitoring of environmental pollutants and contaminants that may be considerably difficult for humans to handle. As a signal transduction technique, SPR allows the detection of molecules of interest down to picomolar levels. With MIPs as recognition element, it can achieve even more sensitive detection at ultratrace levels. One major advantage of combining MIP with SPR is the ability to prepare the imprinted polymers directly on the SPR substrate, thus lessening the time needed for sensor preparation and allowing enhanced sensitivity as the recognition event happens within the range of the evanescent field for plasmon absorption to occur. Research on MIP-SPR (Figure 33.2) sensors have increased steadily over the last few years, with efforts focused on more simple

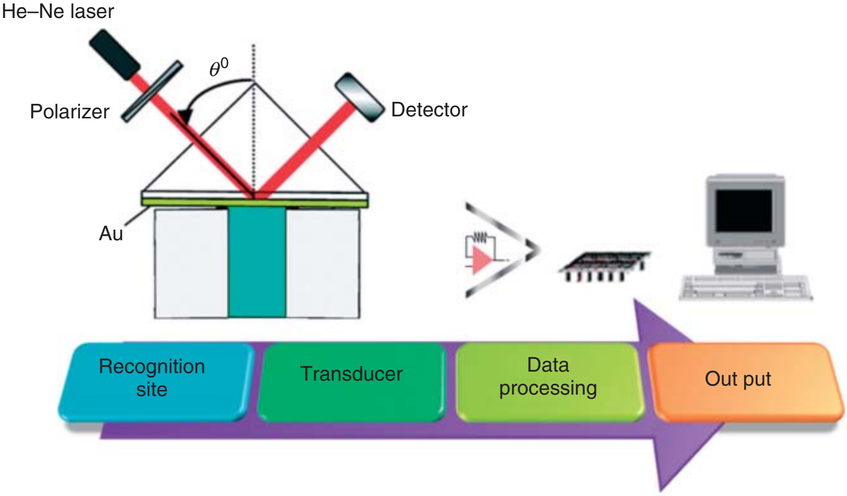

Figure 33.2 MIP-SPR setup.

methods of preparing the MIP-gold sensor chip and use of simple and more sensitive SPR setups. This review describes the research made on MIP sensors with SPR as a detection process, based on previous works and the current models that utilized novel preparation techniques and improvements on instrumentation setup.

33.2
Molecularly Imprinted Polymers

33.2.1
MIP Technique

Molecular imprinting on polymer scaffolds is a facile and versatile way of preparing artificial receptors. As different polymerization techniques had been discovered, it has become a widely used method in making the selective recognition element for sensors. MIP synthesis (Figure 33.3) starts with the introduction of monomers in solution together with the template – the molecule to be imprinted – based on a "prepolymer" condition. This allows the templates to interact more with the monomers and be dispersed evenly in solution. During polymerization, the template is entrapped along with the growing polymer chains, a process that essentially determines the number of active recognition sites. A subsequent washing step is performed to remove the bound template, leaving behind cavities with shape and size complementary to the original template. When the washed polymer is placed in a solution of same template or similarly structured molecules, selective adsorption takes place as the particles bind to the cavities, and with an appropriate transducer the accompanying change in properties of the polymer can be converted into a quantifiable signal. Such changes may be observed in terms of polymer porosity, dielectric/refractive index property, surface energy, mass variations, or conductivity (electrochemically conducting polymers (ECPs)). Vinyl-based free-radical polymerization is a very common route in preparing MIPs [5, 6], but other techniques have also been adopted, most notably electropolymerization with electroactive monomers, and polycondensations. Several

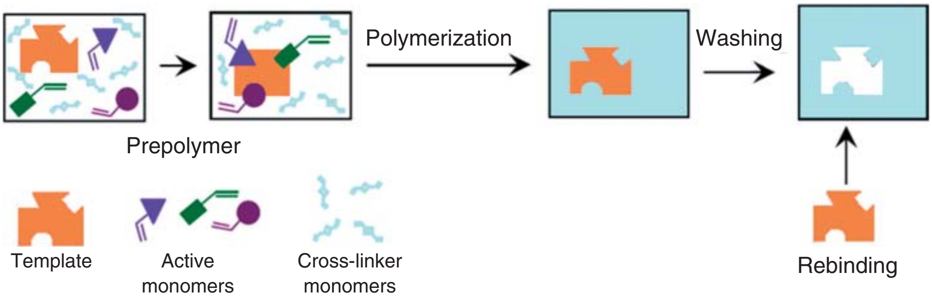

Figure 33.3 Diagram of MIP preparation.

methods have also been performed to introduce functionality in the MIP recognition sites. The noncovalent approach uses monomers with specific functional groups that enhance the ligand–template complex during the prepolymer step. This is, particularly, useful in preparing MIPs with special properties, such as enantioselectivity [7], catalysis [8], and transport capability [9]. In the covalent approach, the target molecule is attached covalently to one of the monomer components in the MIP. In a reported covalent MIP approach, a sialic acid template was covalently attached to the active monomer *p*-vinylbenzeneboronic acid ester. After preparation of the MIP, the system was shown to have greater binding affinity toward GM1 ganglioside, which contains a sialic acid moiety in its structure [10].

33.2.2
Methods of Preparing MIPs: from Bulk Imprinting to Surface Imprinting Techniques

The earliest reports on MIP synthesis were based on solution polymerization systems involving functionalized vinyl-based monomers, cross-linkers, and initiator mixed initially in a prepolymer solution condition. To prepare an MIP-sensing film, this prepolymer solution can be casted on the surface of a substrate followed by thermal or photocured, resulting in a ''grafted to'' polymer film. Another way is by initially grinding the resulting polymerized solid MIP (monolith) to make fine particles before dispersing with a suitable solvent, which is then casted on the transducer surface. These methods of preparation are proved to be simple and straightforward, and readily available for various modifications with additives. However, MIPs films prepared from this method suffer from a host of problems observed due to binding site heterogeneity and incompatibilities among the polymer, template, and porogen (solvent) [5, 11]. The application of molecular imprinting on large templates also poses difficulty in terms of regenerating the binding sites – as the polymer network encloses on the templates, they become more hindered and thus become more impeded from being washed off from the binding site cavities. The reverse also applies during the rebinding step, where target molecules are impeded from accessing the sites due to slow mass transfer [11]. These effects could be addressed by using an optimum monomer:cross-linker:template ratio to ensure homogeneous binding sites formation with good final polymer porosity. To enhance access of binding sites during washing and rebinding, polymerization methods such as suspension and emulsion polymerizations can be employed to make polymer spheres with defined particle size. With smaller polymer particle size, the surface area:volume ratio increases, thus allows enhanced washing/rebinding of templates. However, binding site heterogeneity is still an issue as the monomer–template complex envisioned in the prepolymer condition does not always result in an actual active binding site. This may be a result of several processes, including dissociation of monomer–template aggregates, leaching of template during polymerization process, random coiling processes giving clustered templates bound in the polymer, as well as binding site collapse after the washing step [12]. Attempts to minimize binding site heterogeneity in artificial sensor films prepared on transducer surfaces have led to the discovery of a class of imprinting processes that can be aptly called *surface molecular imprinting* technology. For MIP-SPR sensors, other than the ''grafting-to'' approach described earlier, two other methods are reported, namely surface-initiated polymerization (SIP) or ''grafting-from'' approach and electrochemical polymerization (electropolymerization). SIP as a surface molecular imprinting technique requires the initiator to be initially immobilized on a surface before polymerization takes place [13]. In electropolymerization, the conducting substrate serves as initiator-formation site by providing the current or potential necessary to cause radical-ion formation among the monomers [14]. In general, for any surface imprinting method, the resulting imprint cavities formed after polymerization are within the vicinity of the substrate surface, that is, thin to ultrathin film configuration, which allows ease of template removal and access during rebinding. Moreover, the polymerization mechanism of the growing thin film could ensure greater homogeneity among the imprint cavities, which should enhance the rebinding capability of the final imprinted polymer [14, 15]. These properties make surface molecular imprinting a more reliable route for preparing imprints of a variety of small and large templates [14–16]. Surface molecular imprinting finds great use in preparing recognition elements as thin films directly on the surface of transducers, showing improved qualities over conventional biosensor techniques [17]. *In situ* monitoring is particularly beneficial during the growth process of surface-grafted imprinted polymers, as it allows control over the final polymer properties, such as thickness and viscoelasticity [18]–which should help regulate the final MIP-sensor performance. With a suitable sensitive signal transduction technique, sensors with various configurations can now be prepared via surface molecular imprinting approach, which have found great use in many commercialized applications.

33.3
Surface Plasmon Resonance Spectroscopy as Signal Transduction Method

SPR spectroscopy is a special type of surface-sensitive optical signal transduction technique that has become a popular method for sensing due to its inherent high sensitivity and simple setup. Originally developed as a characterization method for thin films and processes occurring at metal–dielectric interfaces, SPR has been extended ever since for applications that involve chemical and physical changes occurring directly on the surface of the metal substrates, that is, interactions of immobilized biomolecules. The number of original research articles on SPR-based biosensors has increased dramatically over the last decade, with emphasis on sensing of important biomolecules such as DNA, RNA, proteins, pharmaceuticals, and other drugs [4, 19]. As antibody–antigen interactions are highly specific, affinity biosensors with SPR as signal transduction mode allow real-time investigation of biomolecular interactions without the use of labeled molecules, that is, label-free methods [20]. Since then, SPR has been extended to other sensor formats, shown to exhibit high robustness and have capability of being resolved to sensitivities of up to picomolar levels, depending on the setup configuration used as well as the recognition elements employed. The demand for onsite testing has also increased, and SPR-based sensors can serve this purpose and be developed for the detection of even trace levels of environmental pollutants and contaminants found in harsh conditions. As a substitute for natural receptors, MIPs have been prepared on the surface of SPR substrates, and with increasing innovative methods for surface imprinting, MIP-SPR sensors have been demonstrated to achieve the level of sensitivity observed in SPR biosensors. As SPR spectroscopy has now become an important signal transduction method, it is important to be familiar on SPR phenomenon and theory, which is vital for understanding important considerations for optimum sensitivity during analytical chemistry measurement. Several review journals [19, 21] have been specifically dedicated to this purpose, and so, only a brief discussion is included in this work, focusing mainly on concepts related to sensors development and control of conditions.

33.3.1
Basic SPR Theory

At a metal–dielectric interface, the resulting Coulombic and attractive forces among the surface-bound ‘‘sea of electrons’’ result in charge density oscillations known as *surface plasma oscillations*. The energy conditions (hence eigenvalues) for these oscillating electrons can be mathematically determined using quantum mechanical solutions, with a quantum of these oscillations being collectively referred to as a *surface plasmon*. The surface plasmon is considered an evanescent electromagnetic wave propagating along the metal–dielectric interface, as the longitudinal or plane-polarized electric field decays exponentially both in metal and toward the dielectric (Figure 33.4). Solving the Maxwell’s equation for metal–dielectric kind of refractive index distribution gives the propagation constant of surface plasmons, which shows dependence on the dielectric constants of the metal layer and dielectric medium. Metals such as gold and silver satisfy the conditions of the equation at optical wavelengths and are most commonly used in SPR applications. For an incoming light wave to couple with a surface plasmon, the wave vector of light parallel to the metal–dielectric interface should have energy and momentum, which matches the propagation constant of the surface plasmon. As a result, surface plasmons cannot be excited directly by light incident onto a smooth metal surface, but can be achieved with the use of a coupler. Most SPR sensors employ couplers in the form of a prism, waveguide, or grating device, which operate under the conditions of attenuated total reflection or diffraction. The most common configuration used for prism coupling is the Kretschmann configuration (Figure 33.5), wherein the prism is held in contact with a thin metal film (~50 nm) that faces the lower dielectric medium (air or sensing media). Incident photons approaching from the side of the prism are totally reflected at the prism–metal interface. At a particular incident angle θ, these photons can then excite a surface plasmon wave located at the outer boundary of the metal, via evanescent tunneling through the thin metal layer. By plotting the reflected light as a function of incident angle

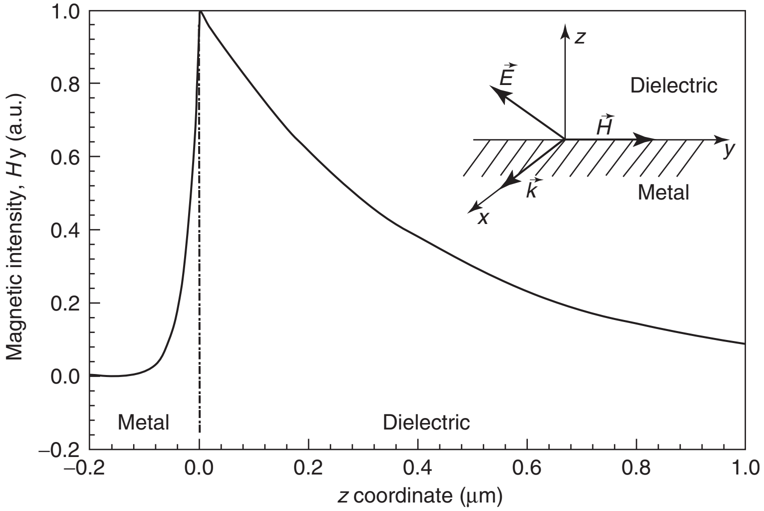

Figure 33.4 Spatial distribution of the magnetic intensity for a surface plasmon at the interface between gold and a dielectric ($n_d = 1.328$) in the direction perpendicular to the interface, $\lambda = 850$ nm. (Adapted from Ref. [21].)

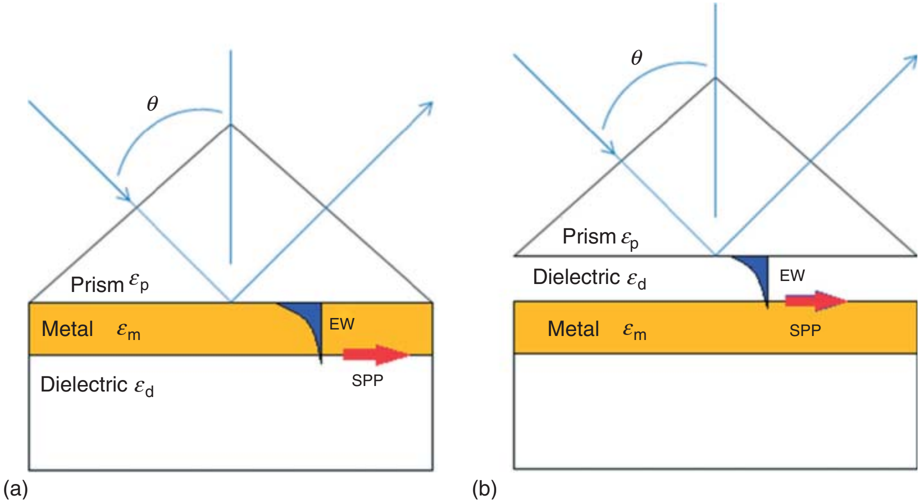

Figure 33.5 Kretschmann (a) and Otto (b) configurations of prism-based couplers showing evanescent wave (EW) and corresponding surface plasmon polariton (SPP) propagation.

(angular scanning or interrogation technique), a dip in the curve is observed, that is, minimum in reflectance owing to loss of reflected light, which corresponds to optical light energy being transferred to the surface plasmon wave (resulting in a surface plasmon polariton). SPR is exhibited at this point, which is then monitored to probe events occurring in the metal–dielectric surface. In particular, processes that result in changes of the optical properties of the dielectric adjacent to the metal layer can cause a shift in the incident angle θ required for optimum surface plasmon polariton formation. Other than the shift in incident angle for resonance to occur, parameters such as reflectance intensity, wavelength of incident light [22], polarization, and phase [23] may be measured and quantified to correlate with the changes occurring at the metal–dielectric interface. Another configuration that allows measurement of SPR based on prism couplers is the Otto configuration (Figure 33.5); however, the Kretschmann configuration has been widely used even in commercialized instruments and is discussed in detail later in the chapter.

33.3.2

Performance Characterization of SPR-Based Sensors

A typical SPR sensogram shows a plot of reflectivity change or shift in incident angle (at plasmon coupling condition) versus time as changes in refractive index takes place at a thin film (hence recognition element) found between the metal layer and the dielectric medium. Fresnel equations can be used to correlate the incident angle at which reflectivity is at minimum to the changes in refractive index based on three-layered system consisting of the prism, metal layer, and dielectric medium. This also allows calculation of the real and imaginary components of the dielectric constants for the film found on the surface of the metal, which may give further information on its properties. The refractive index of the thin film may change depending on particular interactions that occur, such as adsorption of particles on the metal surface, transport of material over the film, or changes in thickness. Sensitivity of an SPR sensor is therefore dependent on its ability to determine changes in the monitored SPR parameter with respect to the corresponding change in refractive index of the recognition element located at the metal–dielectric medium interface. In general, for SPR sensors based on angular interrogation, a positive shift in resonance angle indicates an increase in refractive index, and sensitivity is high if the corresponding resonance angle shift is large per change of refractive index (reported as degrees per refractive index units or deg RIU^{-1}). For wavelength-reflectance intensity domain type of SPR measurements, silver metal is a good choice for substrate, and sensitivity is increased when higher wavelength is used [24]. The sensitivity of SPR sensors using reflectivity prism couplers is shown to be higher than most SPR devices that use grating couplers [21, 24]. The thickness of surface-imprinted polymer films prepared as recognition elements on the surface of SPR substrates has been shown to affect the sensitivity of an SPR sensor device that uses the Kretschmann configuration; however, this can still be studied using waveguided modes during sensing [25]. In general, for MIP-SPR sensors based on the Kretschmann setup, thinner films result in better sensitivity during sensing [26]. SPR resolution is also another important property addressed in SPR-based sensors, which can be defined as the minimum change in measured parameter that can be detected by the sensing device. This depends strongly on the accuracy of measuring the sensor response elicited by changes in property of the corresponding recognition site. The resolution achieved by SPR devices is essentially limited by its own instrument noise level, which can come from sources similar to those observed in spectrophotometric devices, such as influences of temperature, light source, and photodetector used [27]. For angular scanning mode SPR method, the accuracy is directly affected by the width of the resonance curve, which is related to the thickness of the metal film substrate used. Narrower SPR curves often result in more accurate resonant angle response corresponding to refractive index changes at the sensor recognition site. Noise can also be generated from the signal response of the recognition element toward a blank medium (sensing solvent), which is quantitatively determined as part of the LOD measured for a particular SPR-sensing experiment. *LOD* is quantitatively defined as the concentration of analyte that produces sensor signal relative to three standard deviations of signal measured for a blank sample. The use of MIPs as recognition sites for SPR-based sensing has been demonstrated to enhance signal resolution using polymers that can generate localized dielectric changes during the specific recognition processes. This localized dielectric change is essentially translated into refractive index changes in the film, which affect the evanescent surface plasmon waves. Enhanced sensing of refractive index changes in the polymer can also be done by coupling the surface plasmon wave with localized surface plasmon resonance (LSPR) of metallic nanoparticles (NPs) embedded in the polymer film. These MIP-NP composites have been shown to amplify the signal generated by the local dielectric changes (refractive index changes) caused by molecules interacting with the recognition sites, leading to exceptionally high-sensor performance parameters [28]. Finally, resolution and sensitivity for a particular SPR sensor device are best determined on collective effects of the instrument configuration and the degree of optimization implemented, which collectively dictates the analytical figures of merit for a measurement process.

33.3.3
Configurations of SPR Instruments

A typical SPR instrument consists of a light source, coupler-sample stage, and optical detector (Figure 33.6). Prism-based SPR devices allow more flexibility in terms of measuring variations in refractive index as analyte interacts with metal substrate. High-quality optics employed in the SPR system can limit optical noise, which can lead to enhanced resolution measurements. Most MIP-SPR sensors that have been reported employ prism-based coupling on Kretschmann configuration for enhanced sensing. The prism is made from high-refractive index material, such as BK7 ($n = 1.52$) and LaSFN9 ($n = 1.85$), which allows total internal reflection of the incoming light to occur. A thin Au or Ag metal layer ($\sim$50 nm) is deposited onto a separate glass substrate that matches the material of the prism used. To ensure

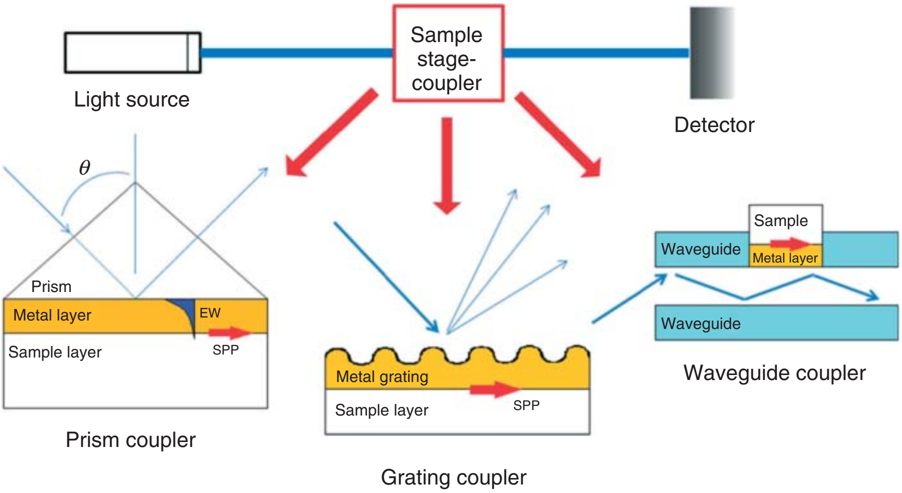

Figure 33.6 General SPR instrumentation diagram showing prism, grating, and waveguide types of couplers.

strong adhesion, an under layer coating of another material is initially deposited, usually Cr metal (~5 nm) or aluminum oxide. The prism and glass with metal film layer are clamped together (a liquid, usually an oil with refractive index matching the glass substrate is placed in between to form a continuous phase) to form a three-layered system consisting of the glass, metal surface, and dielectric (air, transparent medium such as water, or sensing material). Simultaneous angular scanning and reflectivity measurement are achieved by placing the prism-sample holder setup in a two-stage goniometer, with a laser as monochromatic light source and a CCD or PMT as detector. This instrument arrangement allows for dual domain analysis, as both angle and reflectance intensity are simultaneously measured, with resolution of up to 1×10^{-3} deg RUI^{-1} [29]. Excitation of the surface plasmon wave, hence SPR, is observed at the point of minimum reflectivity for a particular angle of incidence. Wavelength domain analysis or measurement via wavelength of incident light wave in resonance with the surface plasmon wave has also been demonstrated, with reported resolution of $6.9–8.0 \times 10^4$ nm RUI^{-1} for Jena-SPR device [22], and 1×10^5 nm RUI^{-1} using a parallel channel optics architecture [27]. Prism-based SPR sensors with a CCD array type of detector for angular scanning have been extensively commercialized by several companies, such as BIAcore and Autolab ESPRIT, which can attain a minimum resolution values in the range of 1.0×10^{-7} to 2.0×10^{-5} deg RIU^{-1} [30]. However, these instruments can only be used for measuring SPR within a short range of angle, and therefore have limited use for high-refractive index MIP films. The Kretschmann-ATR configuration is also attractive for the development of multichannel-sensing devices by adding several flow injection components, as well as microfluidic techniques on the prism-sample holder compartment. Miniaturization is also possible by integrating the light source, detector, and optical system for excitation and analysis of surface plasmon wave into a single component. A miniaturized device previously developed by Texas Instruments [31] relies on the detection of SPR angular position using a divergent light beam that passes through a polarizer and linear diode array detector. The sensor allows a resolution of 5×10^{-6} RIU, which shows that the Kretschmann-ATR SPR configuration can be adapted into a suitable format for the development of mobile, compact, and cost-effective sensing devices with potential for field applications.

Excitation of surface plasmon waves can also be achieved with the use of grating couplers. Periodic distortions on metal–dielectric interface will cause an incident optical wave to be diffracted and form reflected beams from the surface at different angles. If the component momentum and energy of the diffracted light is equal to the propagation constant for the surface plasmon, coupling occurs, which results in SPR. Most grating couplers used in SPR devices have specially designed patterns that result in optimum diffraction conditions for surface plasmon wave coupling to occur. An advantage on the use of grating couplers is the low-cost fabrication with the use of plastic and other materials useful for disposable sensors [32]. However, the mathematics involved in grating-based SPR is known to be more complex than planar prism-based systems [21], which make modeling and analysis of sensor data difficult. Grating-based MIP-SPR sensors have been demonstrated, using intensity, wavelength, and angular domain analysis for the detection of important substances [33].

Optical waveguiding is another method to excite surface plasmons in SPR sensors. The coupling process is essentially similar to the Kretschmann-ATR prism couplers, in that total internal reflection provides the energy and momentum necessary to excite the surface plasmon. As a light wave passes along the waveguide (fiber optic or slab slide), it enters a region with a thin metal overlayer that evanescently penetrates through the metal layer. If the surface plasmon wave and the waveguided light are phase-matched, SPR occurs at the outer interface of the metal. The sensitivity of most waveguide-based SPR devices is approximately similar to that of corresponding Kretschmann-ATR configurations. However, most SPR-waveguide sensor designs require more constraints compared to bulk prism-based SPR-sensing devices, which limit their use in MIP-SPR sensors [34].

33.4
MIP-SPR Sensors

Although SPR-based biosensor applications have been studied in the early 1980s, it is only in the late 1990s that MIPs were first successfully employed as a recognition element in combination with SPR. Sensitivity is a major issue encountered with the use of MIP-SPR sensor, particularly as the refractive index changes induced by target molecule–recognition site interaction may not be sensitive enough to be detected by the evanescent field, especially with small molecules. Consequently, detection can only be achieved at relatively high concentration levels. However, with advances in polymerization techniques, surface imprinting has now been applied to prepare polymer films capable of generating sensitive refractive index changes that can be detected by surface plasmon waves. Currently, MIP-SPR sensors have the advantage of being label-free sensing techniques and the majority requires only low-cost materials (commonly available monomers and initiators) in preparing the recognition films. A number of recently reported MIP-SPR sensors also show robustness in terms of longer response lifetime and even miniaturization (sources herein). This section discusses about MIP-SPR sensors published so far in research journals, and describes briefly specific categories, namely MIP recognition element and its properties, SPR instrumentation involved, and final sensor performance parameters obtained.

33.4.1
Sensor Film Preparation Methods for MIP-SPR Sensors

33.4.1.1 MIP Films Prepared via Solvent Casting

The successful integration of MIP as recognition site into an SPR setup was first reported by Lai and co-workers [35] in 1998. The bulk MIP was prepared from the polymerization of methacrylic acid (MAA) monomer, ethylene glycol dimethacrylate (EGDMA) cross-linker, and 2,2′-azobis(2-methylpropionitrile) (AIBN) as initiator, with theophylline, xanthine, and caffeine as imprint/analyte molecules. After polymerization, the solid MIP was ground into fine particles and dispersed in acetonitrile-acetic acid solvent. The sensing film was prepared by the drop cast method of dissolved MIP over a silver substrate. Using two different detectors in the prism-based SPR setup – photothermal deflection spectroscopy (for sensitivity enhancement) and photodiode array detection (for faster characterization), no cross-sensitivity was observed for theophylline-imprinted films toward structural analogs. An LOD of $0.4\,\mathrm{mg\,ml^{-1}}$ theophylline was reported, which is relatively high compared to other MIP-SPR methods prepared for theophylline. Morphological characteristics of the MIP film could have an effect on the sensor performance, although this was not discussed in the chapter. Kugimiya and Takeuchi [10] prepared an MIP thin film by placing a prepolymer solution composed of methacrylate monomers and sialic acid-modified *p*-vinylbenzeneboronic acid ester as active monomer in between a thiol-modified Au substrate and cover glass. This was then illumined by UV light to photoinitiate the polymerization process. The resulting MIP was shown to have imprints capable of detecting GM1 ganglioside, with minimum detected concentration of $0.1\,\mathrm{mg\,ml^{-1}}$. However, the reported MIP did not show response toward sialic and galacturonic acids, which are small molecules, indicating that the refractive index changes in the polymer induced by these molecules could not be detected by the surface plasmon wave (prism-based). Li and coworkers [36] prepared an enantioselective MIP-SPR toward imprinted L-phenylalanine ethyl ester (L-PHET), with a methacrylate-based MIP film prepared via spin coating on a gold substrate. Significant selective response to L-PHET over enantiomer D-PHET was observed at $1.0\,\mathrm{g\,l^{-1}}$ sensing solution concentration. Substantial improvement of MIP-SPR sensor properties prepared with spin-casted films was shown by Taniwaki *et al*. [37] by using an oligopeptide additive into the polysulfone-based MIP film. The oligopeptide serves as a highly specific recognition element for the template molecule 9-ethyladenine due to strong H-bonding. This significantly increased the MIP-SPR sensitivity toward adenosine molecule using prism-based optics, with increased apparent affinity constant (1.30×10^4 to $1.60 \times 10^4\ \text{mol}^{-1}\ \text{l}$) relative to decreasing imprinting ratio (1.0–0.25, respectively). Similarly, Roche and coworkers [38] prepared an MIP for dextromethorphan based on with poly(toluene diisocyanate-*co*-β-cyclodextrin) system. β-Cyclodextrins are known to form inclusion complexes with target organic molecules having complementary size with lypophilic inner cavity. With a waveguide-type of SPR setup (wavelength-intensity domain), a linear calibration range was obtained from 0.035 μM to 6.00 mM and an LOD of 0.35 μM was achieved for sensing dextromethorphan in aqueous buffer. Another specialized MIP-SPR sensor application was demonstrated by Raitman *et al*. [39] for studying noninvasive enzymatic reactions. The MIP film was prepared by casting a solution of NADH-imprinted acrylamide–acrylamidophenylboronic acid copolymer on the surface of gold substrate employed for prism-based Kretschmann-ATR SPR. The MIP-SPR displayed highly sensitive response toward the original template NADH at the concentration range of 1×10^{-6} to 1×10^{-3} M and showed significant selectivity in the presence of other similar cofactors. In addition, the NADH-imprinted films could be used to track the biocatalyzed oxidation of lactate to pyruvate, in the presence of NAD^+ and lactate dehydrogenase. This MIP-SPR setup represents a less destructive way in the detection of NADH compared to electrochemical detection, which often results in irreversible oxidation of the NADH molecule. The size of the polymer particles dispersed in the precasting solvent can affect the performance of the overall sensor. As described earlier, smaller polymer particle size results in higher surface area:volume ratio, which can effectively enhance washing–rebinding of templates. Lavine and coworkers [40] reported an MIP-SPR sensor for theophylline based on poly*N*-(*N*-propyl)acrylamide (polyNNPA) nanobeads synthesized via suspension polymerization. The sensing surface was prepared by spin coating an Au SPR substrate (Kretschmann configuration) with methanol-dispersed imprinted polyNNPA nanobeads. With angular and reflectivity domain analysis, they showed that the polyNNPA beads respond specifically toward theophylline, with decrease in angular incidence due to decreasing refractive index as theophylline swells the beads. Even at low level of cross-linking (20% as reported), the MIP-SPR sensor achieved an LOD of 200 ppb for theophylline, which is significantly better compared to the initial MIP-SPR sensor setup by Lai. MIP-SPR sensors with sensing films prepared from casted prepolymer solutions have also been shown to detect target molecules in nonaqueous media. Wei and Wei [41] prepared an MIP for testosterone using methacrylate monomers and benzophenone initiator. The sensing film was prepared via polymerization directly on the surface of the Au substrate. This was achieved by sandwiching the prepolymer mixture in between an alkane-thiol-modified Au-LaSFN9 substrate and a specialized microflow cell. After photoinitiation and curing, the resulting MIP film was about 50 nm in thickness. Subsequent washing and rebinding tests gave calibration sensitivity in the range of 10^{-12} to 10^{-8} M measured in acetonitrile. The authors suggest that the method is more simple and straightforward in preparing grafted MIP films compared to methods that use surface-attached polymer systems. A similar procedure was followed by Hao *et al.* [42] (same corresponding author) in preparing an MIP film for sensing morphine. With the use of an SPR device with Kretschmann-ATR configuration, the resulting linear calibration range was determined at 10^{-9} to 10^{-6} M in acetonitrile. The sensor was also tested for repeated injections of morphine and subsequent washing, which showed that it has good reproducibility at three cycles. In a proof-of-concept report, Matsui and coworkers [43] were able to prepare an MIP-NP composite film composed of poly(MAA-*co*-EDGMA)-thiolcarboxylic acid-modified Au nanoparticles (AuNPs) for nonaqueous sensing of atrazine herbicide. The use of Au NPs (4.28 ± 0.98 nm) was expected to enhance the electromagnetic field via coupling effects between gold NPs (LSPR) and a gold substrate (SPR) on the MIP-SPR sensor chip when the NPs are immobilized in close proximity to the substrate surface [28, 43]. Polymer-NP composite films were prepared by casting the prepolymer solution in between an SPR chip (mercaptan-modified) and glass substrate (thiol-modified), and subsequent thermal polymerization and curing. A thickness of about 251 ± 14 nm was obtained for the MIP film, which is considerably thicker than most films employed in MIP-SPR sensors. Their results show high sensitivity toward atrazine template, with an LOD value of about 1 pM in acetonitrile solvent, and also high selectivity against other similarly structured agrochemicals (prism-based Kretschmann-ATR configuration). Overall, the MIP polymer-AuNP composite-SPR sensor system is expected to be useful for other environmentally important molecules, and as low detection limits are obtainable, it can be applied for direct sample testing with limited use of solvent-consuming preconcentration steps.

The method of preparing MIP films by thermal or photocuring of solvent casted prepolymer solutions can be aptly called as a *grafting-to* approach as the resulting polymer films are physically attached on the surface of the sensor substrate. ‘‘Grafting-onto’’ techniques are also reported for film preparation of MIP-SPR sensors, wherein the monomers used are covalently linked on the surface. Nishimura *et al.* [44] prepared an MIP film by immobilizing MAA monomers on aminothiol-modified Au surface via ethyl(dimethylaminopropyl) carbodiimide/N-Hydroxysuccinimide (EDC/NHS) coupling, and then subsequent polymerization in the presence of template. The MIP-SPR sensor system showed good selectivity toward tetracaine original template. Another reported grafting-into approach using disulfide-linked monomers is that of Matsunaga and coworkers [45]. Self-assembled monolayer bearing vinyl groups on the Au-SPR sensor chips was prepared using *N*,*N*′-bis(acryloyl)cystamine. The prepolymerization mixture composed lysozyme (template), acrylic acid, 2-methacryloylethyl phosphorylcholine, and *N*,*N*′-methylenebisacrylamide were dissolved in aqueous buffer with varying amounts of NaCl. Their results indicated that presence of salt in the prepolymerization mixtures gives higher selectivity and decrease of nonspecific binding, which essentially demonstrates a way to enhance the selectivity on protein imprinting.

33.4.1.2 Grafted Initiators on Substrate: Surface-Initiated Polymerization Approach

SIP or ''grafting-from'' approach is a class of techniques employed in surface imprinting technology that is based on immobilization of initiator on the surface of sensor substrate. SIP differs from photo- or thermal-grafted polymerization described in the previous chapter as it allows more control on the properties of the resulting polymer (brush density, degree of functionalization, surface uniformity, etc.). The SIP approach as an MIP film preparation technique has been reported only a few times in several journals for MIP-SPR sensor applications (as compared to electropolymerization and grafting-to approaches), possibly due to the additional initiator immobilization step, which adds time and cost during preparation. Nevertheless, SIP techniques give more reliable MIP films compared to most solvent casted methods, in terms of morphological control and possible binding site homogeneity. Initiator immobilization is commonly done by self-assembly monolayers (SAMs) of thiol- or mercaptan-based molecules, followed by appropriate coupling reaction. With the use of a specific form of initiator, we can also perform living-radical polymerizations via atom-transfer radical approach (ATRP) [46] or reversible addition-fragmentation chain transfer approach (RAFT) [47] in preparing an MIP film. Although these methods have already been performed on substrates for MIP with other forms of signal transduction [47, 48], several authors have reported ATRP-based MIP film method on the surface of Au-SPR substrates.

Lotierzo and coworkers [49] first reported a surface-imprinted film prepared via free-radical SIP approach for the detection of domoic acid (DA). Cyanovaleric acid photoinitiator was first immobilized on a mercaptoethylamine SAM-modified Au substrate by carbodiimide coupling, followed by free-radical polymerization of pre-MIP mixture composed of 2-(diethylamino)ethyl methacrylate, *N*,*N*-methylenebisacrylamide, and template DA. Surface morphological analysis by AFM and contact angle measurement revealed a thickness of 40 nm for the grafted MIP layer and root-mean-square roughness (RMS) of 13 nm. The MIP performance characteristics were compared with a DA-antibody immunosensing scheme for the same SPR device (BIAcore 3000), and results showed that MIP had approximately three times higher detection limit compared to that of monoclonal antibody (5.0 vs $1.8\,g\,l^{-1}$ of DA, respectively). Although the calibration sensitivity of the MIP film was lower in value (half of observed) as compared to the monoclonal antibody, the detection range of the MIP sensor was considerably higher ($5-100\,g\,l^{-1}$), proving that there is significantly higher distribution of MIP binding sites present. The MIP film also appeared to be robust enough to withstand harsh treatment and multiple regeneration cycles. A similar method of preparing MIP films through SAM-immobilized free-radical SIP route was recently reported by Wei *et al.* [50] for MIP-SPR sensing of aqueous acephate (Figure 33.7). The ultrathin acephate-imprinted film was prepared on the surface of Au SPR sensor chip from dilute prepolymer solution of acephate, MAA, and trimethylolpropane trimethacrylate (TRIM) and finally photopolymerized via surface 4-aminobenzoic acid hydrazide (ABAH)-initiated radical polymerization. Their polymerization process was done at 4 °C, which the authors claim would ensure efficient noncovalent interaction between MAA and acephate in order to increase the imprinting efficiency. By using

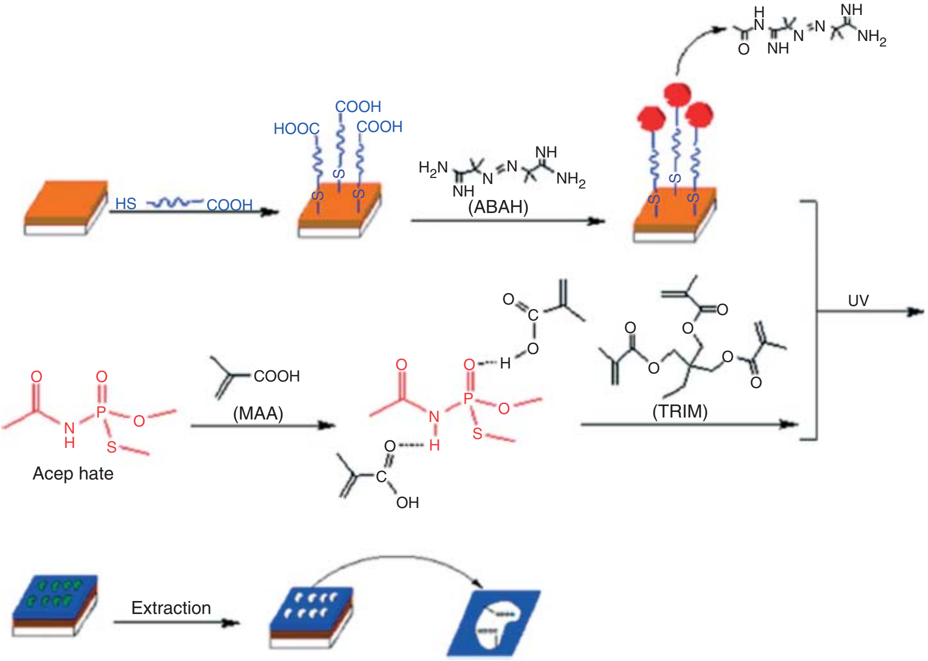

Figure 33.7 Schematic illustration of the formation of MIP ultrathin film by a surface-bound photoradical initiator. (Adapted from Ref. [50].)

a Fourier transform surface plasmon resonance (FT-SPR) (wavelength-reflectivity domain analysis), the group reported an affinity constant of $7.7 \times 10^{12}\ \mathrm{M}^{-1}$ for the acephate-MIP film system and linear response of $0.5–8.0 \times 10^{-12}$ M for acephate detection. The group also performed recovery analysis using their MIP film for sensing acephate in spiked real samples (apple and cole) and obtained percentage recovery values of up to 98%, proving the system can be used as an alternative sensitive technique for acephate measurement.

ATRP as an SIP-based film preparation method is known to produce high-polymer segment densities that shield the underlying substrate, and can form highly uniform polymer surfaces with controllable layer thicknesses at the nanoscale level. These properties therefore make ATRP suitable and advantageous in MIP film preparation in tandem with SPR detection method. An ATRP-based MIP film with SPR detection was reported by Li and Husson [51] for sensing dansylated cysteine (DDC) and dansylated lysine amino acids (DDK). SPR Au surfaces (BIAcore AB) with SAMs of mercaptoundecanoic acid-(4-chloromethyl)benzoyl chloride served as initiator-modified surface. ATRP was performed using Cu(I)-tris-(2-(dimethylamino)ethyl)amine as catalyst with *p*-vinylpyridine functional monomer and EDGMA cross-linker. Surface morphological characterization revealed MIP film thickness of about 7 nm and RMS of ~1.6 nm, indicating smoother and more uniform film distribution on the Au substrate. The kinetics of DDC rebinding toward DDC-MIP films was analyzed using SPR kinetic data, and their results show that dual-site Langmuir binding model more accurately describes the template molecule rebinding process, which can be attributed to heterogeneity of binding sites formed in the polymer film. Equilibrium binding studies also showed that the Langmuir–Freundlich (LF) model was found fit to model the adsorption behavior over the entire concentration region up to saturation, which supports the claim of having binding site heterogeneity. Cross-reactivity was observed between similar template compounds, but MIPs still showed selective binding, and selectivity was also shown to vary with pH values. The application of ATRP-prepared MIP-SPR sensor is expected to be extended over analysis of other nonfluorinated templates. A recent ATRP-based MIP film preparation scheme was described by Zhao *et al.* [52] for the FT-SPR sensing of ametryn herbicide. First, the initiator 2-bromo-2-methylpropionyl bromide was covalently coupled to an aminothiol SAM prepared on the Au SPR chip. Then, a prepolymer mixture containing MAA, EDGMA, and ametryn (13 : 15 : 1 mmol ratio) together with Cu(I)-tetra-azacyclotetradecane catalyst was placed on top of the modified Au chip to allow MIP film formation. The FT-SPR system allows SPR detection via reflectivity and wave number domain analysis. With an estimated film thickness of 75 nm, the MIP-SPR sensor was shown to have linear response toward ametryn in the range of 1.0×10^{-7} to 1.0×10^{-5} M, and an association constant of $1.09 \times 10^{4}\ \mathrm{M}^{-1}$ employing Langmuir isotherm. This system shows promising application of ATRP-based MIP-SPR sensor for the detection of herbicides and other environmental contaminants. A novel and way of activating the sensor surface with initiators for surface-initiated MIP preparation was described recently by Dong *et al.* [53]. Initiator AIBN was mixed with polyvinylchloride to form PVC-AIBN paste, which was spread on the Au SPR disk (Autolab ESPRIT). MAA and cross-linker EDGMA, together with malachite green (MG) as template, were polymerized on the surface of the paste-modified Au SPR disk, which gave approximately 40 nm MIP film sensitive to MG. The performance of the sensing film was compared to a similar film prepared from an SAM-initiator-modified Au SPR disk. Their results indicate that MIP film prepared from paste-initiator approach has more sensitivity toward MG at high-sensing concentration, while both MIP-paste and MIP-SAM systems showed almost similar response at low-sensing concentrations.

33.4.1.3 **Electropolymerization of Monomers for MIP Film Preparation**

Electropolymerization of monomers is now one of the most preferred approaches in preparing MIPs attached to transducer surfaces, owing to its high versatility and controllability in making thin films. Electrochemically synthesized polymers were only recently employed in sensing applications, but have been thoroughly investigated for their electronic properties, that is, conductivities and capacitances that can be modulated for use in electronic device applications. Electropolymerized molecularly imprinted polymers (E-MIPs) were studied for sensor applications early in the 1990s, primarily using electrochemical-based signal transduction methods, but it has only been recently employed as a sensing platform in tandem with SPR detection schemes [14, 15]. E-MIP in tandem with SPR offers several advantages over other signal transduction methods: (i) simultaneous electrochemical and

SPR *in situ* monitoring of E-MIP growth is achieved, allowing more control over film properties; (ii) dual-sensing capability is possible as the SPR signal can also be monitored along with changes in electronic properties of the E-MIP film; and (iii) simple instrumentation design as the Au substrate is compatible to both electrochemical signaling and surface plasmon wave generation at optimum thickness. Although E-MIP can also be tandem with other techniques, for example, electrochemical QCM as mass-sensitive technique [18], the inherent sensitivity of surface plasmon wave coupling with refractive index changes of the polymer matrix makes E-MIP-SPR still more advantageous for many sensing applications.

Yu and Lai [54] first reported the use of electropolymerized molecularly imprinted polymer polypyrrole films (MIPPy) for ochratoxin A (OTA) target molecule prepared on a Spreeta^{TM} Au-covered sensor surface. Growth of MIPPy film done by potentiostatic electropolymerization at +0.85 V with 1 : 20 OTA : pyrrole mole ratio in 1 : 9 ethanol:H_2O solvent. This was monitored *in situ* by SPR angle shifts as polypyrrole deposits on the surface of the Au substrate. Subsequent washing was successfully performed via pulsed elusion technique, which resulted in MIPPy films sensitive to OTA. The SPR angle increased when binding of OTA molecules occurred, and the linear calibration range was determined from 0.05 to 0.5 ppm and an LOD value of 0.01 ppm ($\sim 2.5 \times 10^{-8}$ M) OTA. The results demonstrated a novel combination of SPR device with E-MIP technique, with advantages in terms of short preparation time, low consumption of print molecules, and real-time sensing (flow injection setup added). However, the E-MIP-SPR sensor showed significant response when real samples (wine and wheat) were tested, which indicates that nonspecific interactions occur between other components coming from the real sample and MIPPy film. Choi *et al.* [55, 56] also prepared an E-MIP based on polypyrrole for imprinting mycotoxins zearalenone and deoxynivalenol with SPR detection setup (prism-based Kretschmann configuration). Electropolymerization of MIPPy together with the target templates were performed via potentiostatic process at 0.9 V and a current density of $5\,\mathrm{mC\,cm^{-2}}$ in acetonitrile solvent. The resulting E-MIP systems showed large calibration range of $0.3-3000\,\mathrm{ng\,ml^{-1}}$ for MIPPy-zearalenone and $0.1-100\,\mathrm{ng\,ml^{-1}}$ for MIPPy-deoxynivalenol. These results indicate that pyrrole is a good monomer for preparing low-cost E-MIP films with SPR detection, and can achieve high sensitivity and selectivity for sensing specific food contaminants.

The electropolymerization of carbazole-modified dendrimer molecules as recognition sites for E-MIP application was first reported by Taranekar *et al.* [57] for nanomolar detection and specific recognition of toxic nerve agent marker pinacolyl methyl phosphonate (PMP). In this system, fourth-generation polyamidoamine (CBZ-PAMAM) dendrimers with end-tethered carbazoles were used as active components for making PMP imprints. This CBZ-PAMAM component actually serves two purposes: first, imprinting of PMP happens through interaction with amine functional groups within the PAMAM structure; second, the carbazole units at the outer periphery of the dendrimer act as cross-linking (potentiodynamic, cyclic voltammetry method) component to make cavities and link the dendrimers to form a uniform film. Of the various films synthesized, the E-MIP film composed of

Cu(II)-modified CBZ-PAMAM with a thiol-carbazole SAM ad-layer gave the best performing sensor film. Dual sensing of PMP was achieved by doing simultaneous SPR monitoring and potentiostatic measurement in a Kretschmann-type configuration equipped with electrochemical flow cell (Figure 33.8). As low as 10^{-9} M PMP can be detected by the E-MIP-SPR system, which gives a promising procedure for aqueous-based sensing of nerve agent derivatives.

Functionalized terthiophenes and carbazoles were also used as monomers in preparing tailored E-MIP films for sensing theophylline [58], paracetamol, and naproxen [26] with SPR angle-reflectance scanning detection (Figure 33.9). Terthiophenes are beneficial in E-MIP preparation as electropolymerization can be set at lower-oxidation potentials, and hence lessening over oxidation of films. Advincula's group used mono- and bifunctional terthiophenes having orthogonal moieties (particularly –COOH, –OH, and $-NH_2$), which were expected to complex with selected template molecules by noncovalent interaction, specifically H-bonding. To ensure most favorable formation of binding site cavities, theoretical modeling was initially performed to determine optimum monomer:template ratios (generally 2 : 1), after which solutions of monomer:template were prepared and allowed to stand for 24–48 h before use. This ''prepolymerization step'' condition allows further contact and complexation between monomer and template in the synthesis medium before electrochemical polymerization. The use of the Autolab ESPRIT instrument, which enables simultaneous electrochemical SPR monitoring, allowed for further characterization of MIP film deposition from angular domain-based sensogram. Cyclic voltammetry was employed for the electrochemical polymerization of terthiophene monomers (0–1.1 V) and carbazole monomers (0–1.3 V). It was noted that the electropolymerization of the terthiophene monomers resemble cross-linking polymerization, suggesting that the regular α,α-coupling (2,5 position) could result in an ordered conjugated polymer network (CPN) film. On the basis of their results, it was also observed that –COOH and –OH functionalized monomers resulted in higher MIP rebinding ability compared with $-NH_2$ functional groups, which they claim as being attributed to weak H-bonding capability of amines. The SPR detection signal of bifunctional monomers bearing the –COOH and –OH functional groups was shown to be higher than that of monofunctional monomers, which was attributed to a higher number template–monomer complexes formed per unit volume of the MIP film. Another innovation shown in these works is the successful application of potential-induced template washing/removal at 0.4 V in acetonitrile (original porogen), which effectively reduces the washing time. It is possible that this process leads to an increase in swelling ability of polymer films, which then leads to easier release of imprinted molecules. For the theophylline-imprinted polyterthiophene sensor film, the linear concentration range was observed at $1.0–5.0 \times 10^{-5}$ M and has an LOD of 3.36 μM. Finally, good selectivity properties were demonstrated in all the systems, indicating the feasibility of this approach.

Most of the monomers used to prepare E-MIPs described earlier require anodic conditions, or application of oxidizing potential, to form the radical ion and therefore initiate polymerization. The first E-MIP prepared via cathodic electropolymerization

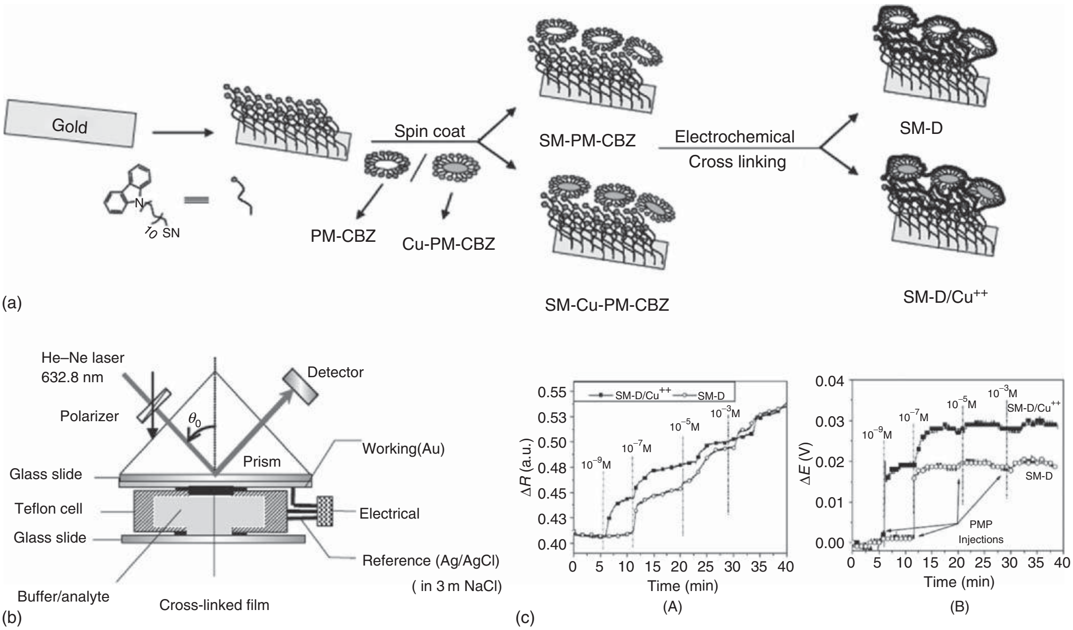

Figure 33.8 (a) Preparation of E-MIP for PMP using carbazole-tethered G4 PAMAM dendrimers. (b) Diagram of SPR-ATR configuration attached with electrochemistry cell for SPR-potentiometric dual sensing. (c) Nanomolar detection of PMP via reflectance (a) and potential (b) measurement. (Adapted from Ref. [57].)

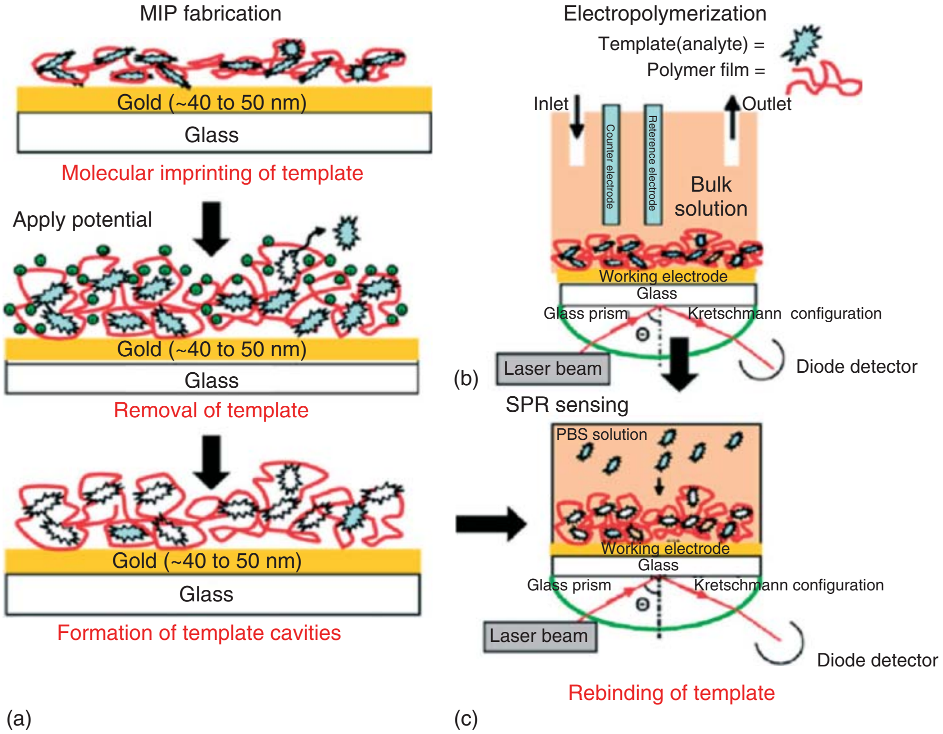

Figure 33.9 (a) Sensor film fabrication by molecular imprinting and template removal by constant potential wash at 0.4 V (vs Ag/AgCl). (b) ESPR *in situ* setup for electropolymerization. (c) SPR sensing of the imprinted guest molecule using. (Adapted from Ref. [58].)

condition is reported by Dutta and coworkers [59] for sensing dopamine using SPR-based detection. *p*-Aminostyrene was chosen as electroactive monomer because of its ability to interact with dopamine molecule through H-bonding interactions. The prepolymer solution consisted of *p*-PAS, *N*,*N*′-methylene bisacrylamide (cross-linker), and dopamine in dimethylformamide solvent, with $LiClO_4$ acting as supporting electrolyte. Electropolymerization was performed by cyclic voltammetry in the cathodic potential window of 0–1.0 V at 50 mV s^{-1} scan rate of (30 cycles) on the surface of Au substrate. The resulting polymer film was then washed with aqueous HCl to remove most of the imprinted dopamine molecules. Subsequent rebinding test using SPR detector (Multiskop, Kretschmann-ATR) showed that the film indeed has binding capability toward dopamine (aqueous). The group further optimized the sensing conditions by varying the amount of active monomer *p*-PAS, and their results revealed that more sensitive binding toward dopamine is observed when MIP is prepared from prepolymer solution containing 0.3 M *p*-PAS. Further tests showed that the E-MIP-SPR sensor can detect dopamine at a low concentration of 1×10^{-12} M, as well as having higher selectivity toward the original template compared with structural analogs (epinephrine, catechol, tyramine, and 2-(3,4-dihydroxyphenyl)acetic acid). Overall, the research demonstrates the feasibility of cathodic electropolymerization method in preparing E-MIP, which could be applied to other vinyl-based monomers, as a substitute for initiator-based free-radical polymerization.

Recently, Willner's group reported several E-MIP-SPR sensor platforms derived from the electropolymerization of *p*-aminothiophenol (*p*-ATP) or *p*-thioaniline together with *p*-ATP-capped AuNPs. The use of poly(*p*-ATP-AuNP) nanocomposite films gave exceptional levels of sensitivity, which may be attributed to the coupling effects of LSPR coming from the AuNPs and SPR of the Au substrate. This enhanced coupling process allows sensing of even minute changes in refractive index of the film during rebinding of target molecule, resulting in amplified signals at low sensing levels. In their first report [60], they prepared poly(*p*-ATP-AuNP) on a *p*-ATP SAM-modified Au substrate (Figure 33.10). Picric acid was initially used as "pseudotemplate," for the subsequent sensing of trinitrotoluene (TNT) analyte. Electropolymerization was done by applying 10 voltammetric cycles between −0.35 and +0.85 V versus Ag quasireference electrode, followed by an application of a fixed potential of 0.85 V for 30 min. This was probed *in situ* by the SPR shifts of

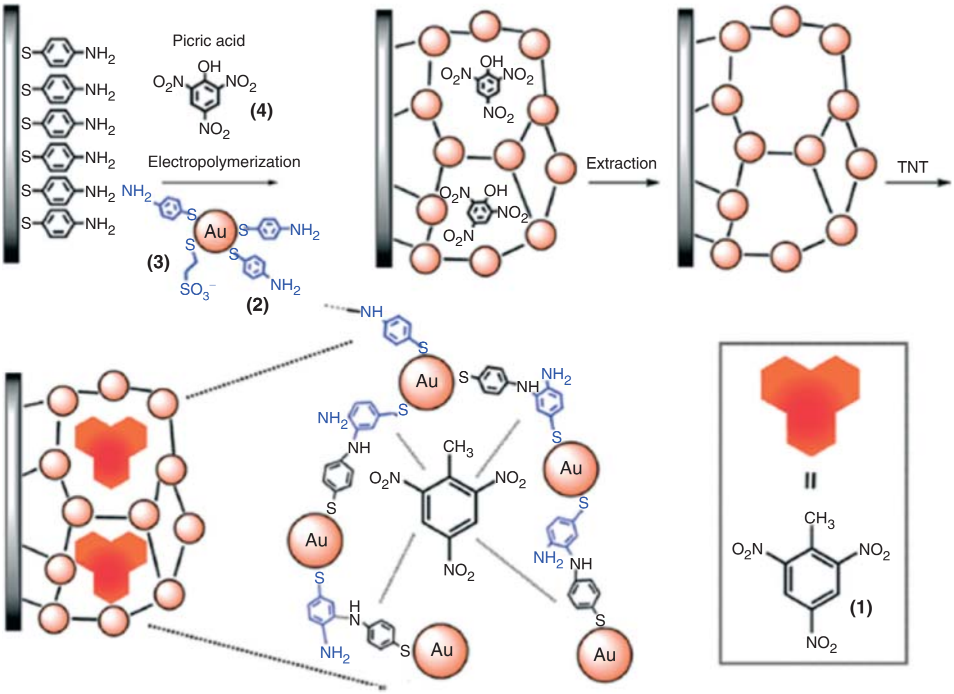

Figure 33.10 Imprinting of TNT molecular recognition sites using picric acid into the bis-aniline-cross-linked AuNPs composite associated with an Au substrate. (Adapted from Ref. [60].)

the SPR instrument (reflectance intensity domain, Kretschmann-type spectrometer NanoSPR 321). Aside from the effects of LSPR-SPR coupling, enhanced sensitivity is observed due to highly specific noncovalent interactions between template and monomer. With picric acid as template, strong $\pi-\pi$ donor–acceptor interactions are observed between the electron-rich ring of *p*-ATP and electron-deficient rings of picric acid. The imprinted poly(*p*-ATP-AuNP) composite revealed a two-step response that included an ultrasensitive analysis region in which TNT was detected at a limit of 10 fM, and was attributed to the analysis of TNT by the high-affinity imprinted association sites ($K_{\mathrm{ass.}}{}^{\mathrm{I}}$) $6.4 \times 10^{12}\ \mathrm{M}^{-1}$. A second detection region was observed in the 10^{-10} M TNT range and was attributed to the association of TNT by the nonimprinted bis-aniline π-donor sites ($K_{\mathrm{ass.}}{}^{\mathrm{NI}}$) $3.9 \times 10^{9}\ \mathrm{M}^{-1}$. By adding the molecule (*p*-mercaptophenyl)boronic acid to the same poly(*p*-ATP-AuNP) nanocomposite, the resulting film could now be used to imprint molecules with vicinal diol functionalities. In a separate research work, antibiotic template molecules neomycin (NE), kanamycin (KA), and streptomycin (ST) were successfully imprinted in the poly(*p*-ATP-AuNP-mercaptophenyl boronic acid) composite film [61]. After subsequent washing, the rebinding studies revealed exceptionally high sensitivities toward original antibiotic templates using identical SPR instrument (Kretschmann configuration). The reported calculated detection limits for analyzing NE, KA, and ST correspond to 2.00 ± 0.21 pM, 1.00 ± 0.10 pM, and 200 ± 30 fM, respectively. The MIP composite films were also successfully applied to analyze the presence of antibiotics in real milk samples. Selectivity analysis of specific antibiotic-imprinted MIP composite films suggests that the system could be used as an array-type of sensor for a possible lab-on-a-chip-based parallel SPR analysis of antibiotic samples. Using this same poly(*p*-ATP-AuNP-mercaptophenyl boronic acid) composite, imprinted films for enantioselective sensing of mono- and disaccharides were prepared, which were also shown to be sensitive down to pico- and femtomolar levels [62]. An extended application of the original poly(*p*-ATP-AuNP) MIP film was made for the imprinting of oligocarboxylic acid molecules [63]. These oligocarboxylic acid molecules served as ‘‘pseudotemplates’’ in preparing MIPs, which were subsequently used for sensing target nitrosubstituted molecules. The carboxylic acid residues present in the template molecules should exhibit similar dimensions and structural features to the nitro groups found in the target explosives. Possible ionic and/or H-bonding interactions between the carboxylic acid and the anilinium residues should generate imprinted sites with proper shape, size, and orientation of functional groups to structurally analogous nitrocompounds. This was proved to be the case as results showed higher affinity and sensitivity toward pentaerythritol tetranitrate and nitroglycerine using citric acid-imprinted film; and ethylene glycol dinitrate using fumaric acid-imprinted film. Overall, these series of works prove that with proper tuning of conditions, MIP films prepared from poly(*p*-ATP-AuNP) nanocomposite are very useful and applicable for sensing various important analytes, with remarkable sensitivity and selectivity resulting from amplification of detection signal by LSPR–SPR coupling.

33.4.2
MIP-SPR Configurations and Possible Commercial Applications

As emphasized earlier, the overall success of a sensing method – quantitatively determined in terms of figures of merit for sensitivity and selectivity – is dependent on the collective effects of the signal generating (recognition element) and signal transducing components used in the sensor device. Similarly, with other sensor formats, research is mainly focused on modifications in the signal-generating component for direct enhancement of analytical parameters. The improvements made on SPR instruments are based on the demands for more sensitive and robust biochemical sensing. Most of the SPR instruments described in Chapter 32 have already been applied for biosensor research; therefore, the improvements in these SPR instruments would also be beneficial for MIP-based sensing. Development of increasingly efficient SPR biosensors in terms of speed, throughput, and accuracy was pioneered by BIAcore, which launched the first commercial SPR biosensor on the market in 1990. Since then, other SPR instrument designs have been invented, which were geared toward specialized applications. On-site sensing can be achieved with the use of compact Spreeta^{TM} sensor system from Texas Instruments. Autolab developed the ESPRIT (dual channel) and Springle (single channel) SPR devices that have programmable-automated sampling capability, which makes it suitable for multiple batch analysis. The Autolab ESPRIT and Springle systems are also capable of carrying out simultaneous electrochemical analysis when connected with the PGSTAT electrochemical station that is convenient for most E-MIP film preparation. In general, these SPR instruments utilize the angular scanning of surface plasmon waves excited using prism couplers and are monitored by array-based detectors. The range of angles that can be scanned by the instrument is limited with the use of nonmobile detector or sample holder, which means that it cannot be used with high-refractive index MIP films. For wide-angle sampling ($>30^\circ$), SPR configurations with the sample stage connected to a dual-motor goniometer is more advantageous. This type of design enables complete scanning of angle versus intensity (or wave number vs intensity) that can be modeled with Fresnel formalisms. Wide-angle scanning SPR setups (manufactured by RES–TEC, Multiskop, or can be home-built) are therefore useful in analysis of MIPs with high-refractive index, as well as relatively thick films that approach waveguide modes [25]. Waveguided surface plasmon excitation for the use on MIP-SPR design has also been reported previously [38].

The SPR instruments just described are usually equipped with flow injection apparatus to enable real-time monitoring of target molecule interaction at the binding site cavities. Microfluidics fabrication technology can also be applied to facilitate the development of miniaturized instrumentation for SPR. Micromachined systems have several advantages over the common bulky flow injection counterparts, such as lower overall cost, disposability, low reagent and sample consumption, portability, and lower energy consumption. Microfluidics technology also enables preparation of multichannel SPR sensors vital for high-throughput analysis. Lee and coworkers [64, 65] developed a novel microfluidic system that incorporates a

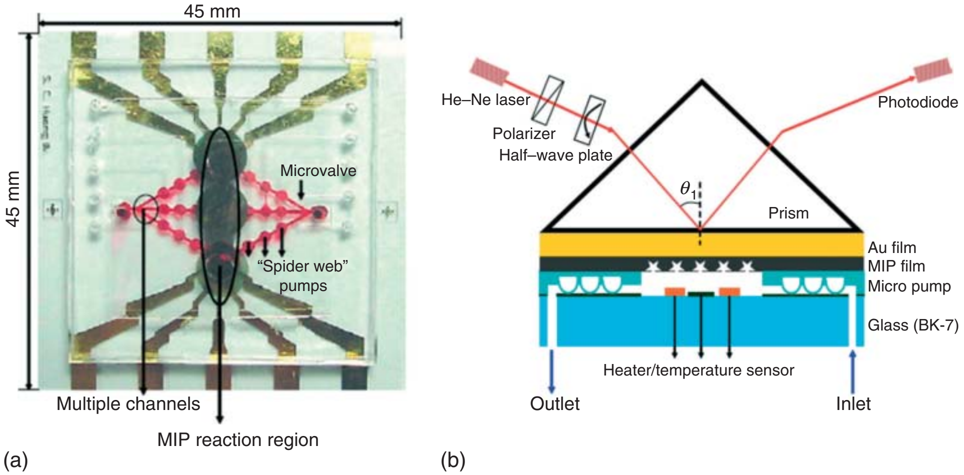

Figure 33.11 (a) Photograph of the assembled microfluidic SPR/MIP biochip with dimensions of 4.5 cm × 4.5 cm. (b) Schematic illustration of the microfluidic SPR/MIP biochip system designed for the detection of multiple nanoscale biomolecules. (Adapted from Ref. [65].)

"spider web" design (Figure 33.11) of micropumps and microvalves aimed to automate the transportation of samples on an SPR Au chip. The MIP films for sensing progesterone, testosterone, and cholesterol were synthesized by a "localized MIP deposition" technique in which different MIP films are spin-coated inside separate reaction chambers of the microfluidic system. The integrated micropumps and microvalves facilitate automation of the sample introduction process, which enables precise control on the amount of sample injected to the MIP-SPR-sensing chambers. The resulting apparent association rate for testosterone binding was reported to be 8.0×10^3 deg s^{-1} at optimum flow rate of 24 μl min^{-1}. The proposed microfluidic sensor chip has been shown to have significant potential for a variety of automatic nanoscale biosensing applications. A more recent study by Taguchi *et al.* [66] reported a slab-type optical waveguide (s_OWG) design that contains consecutive parallel Au and Ag deposition bands, which enabled double SPR signal analysis for sensing bis-phenol A (BPA). Two SPR peaks around 600 nm (Au band) and 550 nm (Ag band) were detected at an optimized angle of 12° between the propagation direction of light and horizontal direction. This procedure permitted the study of binding behaviors on both deposition bands independently and simultaneously. Their molecular recognition element is based on MIP NPs prepared from styrene, divinylbenzene, and template monomer *N*,*N*′-bis(3-vinylbenzylidene)-4,4′-diaminodiphenylmethane via seeded emulsion polymerization (same composition of seed NPs). To enhance SPW signal generation, BPA-modified AuNPs were synthesized and were made to interact on the surface of MIP-NP beads. On injection of BPA solutions, the SPR signals shifted owing to competitive binding of the free BPA molecules with the BPA-Au NPs. The final MIP-SPR design was tested for BPA sensing, and showed detectable response at low (0.1–1.0 mM) and high (1.0–2.0 M) concentration levels in toluene:methanol solvent medium. The proposed s_OWG-based coupling MIP-SPR device allows for label-free sensing in conjunction with the use of MIP-NP and BPA-AuNP, and can be further extended in other applications that could use other kinds of SPR-active metal pairs for multiple differential plasmon characterization.

33.5
Conclusions and Future Perspectives

Over the last two decades, a substantial amount of work has been given to MIP-based SPR sensing, and majority of the developments reported for this technique appeared only on the last decade. In order to illustrate the benefits of this new family of sensing method, namely MIP-SPR, the description of the MIPs used and corresponding SPR instrumentation have been reviewed. This therefore highlights the important views that – (i) MIP-SPR sensors can adequately be used for highly sensitive and selective measurements of substances in priority fields and (ii) MIP-SPR devices can provide solutions for the various problems encountered in detection and analysis of substances. MIP films prepared on the surface of sensor substrates present great potential as substitute to biomolecules acting as recognition element in sensors, mainly due to their comparable sensitivity and selectivity, while using low-cost materials and generally simple preparation steps. However, MIPs still possess inherent problems that arise from various conditions that can be traced starting from preparation to washing and finally rebinding tests, which essentially put certain limitations to their use. SPR spectroscopy as signal transduction method offers further enhancement of sensing properties as it possesses high flexibility and versatility in terms of its ability to modify instrument components depending on particular applications of the device. Nevertheless, other signal transduction strategies are now capable of high-throughput multianalyte sensing (e.g., electrochemical techniques and solution-based spectrophotometry), of which SPR (with MIP recognition) is still on its initial stages of development. With these in mind, it is therefore envisioned that further research and development of MIP-SPR-sensing strategies should focus on the following possible modifications:

1) *Better MIP preparation strategy*: imprinted polymers that allow multiple analyte recognition can be achieved by combining the MIP polymerizations described. An example would be SIP-electropolymerization approach, which could be developed to allow for two or more molecules to be imprinted in the final film. SIP based on living polymerization methods such as ATRP and RAFT could also be studied in the preparation of block copolymers, which may also have multiple-molecule imprinting capability. Other surface-based techniques that could be used are the layer-by-layer approach of polyelectrolytes for sensing charged templates, and self-assembly of oligomers following a molecularly imprinted monolayers (MIMs) format. Use of these surface imprinting strategies should enable the formation of recognition sites with high-homogeneous

binding site distribution and stable morphological characteristics while maintaining thin film thicknesses. In addition, the role of LSPR–SPR coupling should also be fundamentally considered in amplifying the recognition event signal, which can be done by adding appropriately modified AuNPs on the MIP system.

2) *Improvements on SPR instrumentation*: optical waveguide coupling using fiber optics is a key strategy in making lightweight, compact, and portable MIP-SPR sensors. Existing fiber optic-based SPR setups should be tailored to match the various MIP film preparation strategies, or find unique MIP systems that could be tailored with the SPR-fiber optic. Multichannel capability has already been demonstrated as an actual microfluidic sample platform for MIP-SPR setup, and this should also be considered in connection with SPR-fiber optic for possible advancements in miniaturization in the future.

References

1. Bakker, E. (2004) *Anal. Chem.*, **76**, 3285.
2. Cheng, C.I., Chang, Y., and Chu, Y. (2012) *Chem. Soc. Rev.*, **41**, 1947.
3. Giessibl, F.J. and Pielmeier, F. (2011) *Phys. Rev. B*, **84**, 125409.
4. Liedberg, B., Nylander, C., and Lundström, I. (1995) *Biosens. Bioelectron.*, **10**, i–ix.
5. Alexander, C., Andersson, H.S., Andersson, L.I., Ansell, R.J., Kirsch, N., Nicholls, I.A., O'Mahony, J., and Whitcombe, M.J. (2006) *J. Mol. Recognit.*, **19**, 107.
6. Haupt, K. and Mosbach, K. (2000) *Chem. Rev.*, **100** (7), 2496.
7. Maier, N.M. and Lindner, W. (2007) *Anal. Bioanal. Chem.*, **389**, 377–397.
8. Wulff, G. (2002) *Chem. Rev.*, **102** (1), 1–25.
9. Piletsky, S.A., Panasyuk, T.L., Piletskaya, E.V., Nicholls, I.A., and Ulbricht, M. (1999) *J. Memb. Sci.*, **157**, 263–278.
10. Kugimiya, A. and Takeuchi, T. (2001) *Biosens. Bioelectron.*, **16**, 1059–1062.
11. Nicholls, I.A. and Rosengren, J.P. (2002) *Bioseparation*, **10**, 301–305.
12. García-Calzón, J.A. and Díaz-García, M.E. (2007) *Sens. Actuators, B*, **123**, 1180–1194.
13. Dong, J., Gao, N., Peng, Y., Guo, C., Lv, Z., Wang, Y., Zhou, C., Ning, B., Liu, M., and Gao, Z. (2012) *Food Control*, **25**, 543–549.
14. Sharma, P.S., Pietrzyk-Le, A., D'Souza, F., and Kutner, W. (2012) *Anal. Bioanal. Chem.*, **402**, 3177–3204.
15. Malitesta, C., Mazzotta, E., Picca, R.A., Poma, A., Chianella, I., and Piletsky, S.A. (2012) *Anal. Bioanal. Chem.*, **402**, 1827–1846.
16. Bossi, A., Piletsky, S.A., Piletska, E.V., Righetti, P.G., and Turner, A.P.F. (2001) *Anal. Chem.*, **73**, 5281–5286.
17. (a) Hillberg, A.L., Brain, K.R., and Allender, C.J. (2005) *Adv. Drug Delivery Rev.*, **57**, 1875–1889. (b) Ye, L. and Haupt, K. (2004) *Anal. Bioanal. Chem.*, **378**, 1887–1897.
18. (a) Apodaca, D.C., Pernites, R.B., Ponnapati, R.R., Del Mundo, F.R., and Advincula, R.C. (2011) *ACS Appl. Mater. Interfaces*, **3** (2), 191–203. (b) Taranekar, P., Fulghum, T., Baba, A., Patton, D., and Advincula, R.C. (2007) *Langmuir*, **23**, 908–917.
19. (a) Homola, J., Yee, S.S., and Gauglitz, G. (1999) *Sens. Actuators, B*, **54**, 3–15. (b) Homola, J. (2003) *Anal. Bioanal. Chem.*, **377**, 528–539.
20. (a) Cooper, M.A. (2003) *Anal. Bioanal. Chem.*, **377**, 834–842. (b) Dudak, F.C. and Boyacı, I.H. (2009) *Biotechnol. J.*, **4**, 1003–1011.
21. (a) Knoll, W. (1998) *Annu. Rev. Phys. Chem.*, **49**, 569–638. (b) Homola, J. (2008) *Chem. Rev.*, **108**, 462–493.

22. Pfeifer, P., Aldinger, U., Schwotzer, G., Diekmann, S., and Steinrücke, P. (1999) *Sens. Actuators, B*, **54**, 166–175.

23. Kuo, W. and Chang, C. (2010) *Opt. Express*, **18** (19), 19656–19664.

24. (a) Homola, J. (1997) *Sens. Actuators, B*, **41**, 207–211. (b) Homola, J., Koudela, I., and Yee, S.S. (1999) *Sens. Actuators, B*, **54**, 16–24.

25. Baba, A., Taranekar, P., Ponnapati, R.R., Knoll, W., and Advincula, R.C. (2010) *ACS Appl. Mater. Interfaces*, **2** (8), 347–2354.

26. Pernites, R., Ponnapati, R., Felipe, M.J., and Advincula, R.C. (2011) *Biosens. Bioelectron.*, **26**, 2766–2771.

27. (a) Johansen, K., Stålberg, R., Lundström, I., and Liedberg, B. (2000) *Meas. Sci. Technol.*, **11**, 1630–1638. (b) Nenninger, G.G., Piliarik, M., and Homola, J. (2002) *Meas. Sci Technol.*, **13**, 2038–2046.

28. Bolduc, O.R. and Masson, J. (2011) *Anal. Chem.*, **83**, 8057–8062.

29. RES-TEC *http://www.res-tec.de/products.html* (accessed 20 March 2011).

30. (a) Metrohm *http://www.metrohm.co.th/Products/Autolab/SPRinstrumentation/AutolabEsprit.html* (accessed 20 March 2011); (b) GE Healthcare *http://www.biacore.com/lifesciences/products/systems_overview/Biacore_4000/System_Details* (accessed 20 March 2011).

31. Texas Instruments *http://www.ti.com/product/tspr1a150100 (product preview)* (accessed 20 March 2011).

32. Zhang, N., Liu, H., and Knoll, W. (2009) *Biosens. Bioelectron.*, **24**, 61783–61787.

33. Baggio, R., Carven, G.J., Chiulli, A., Palmer, M., Stern, L.J., and Arenas, J.E. (2005) *J. Biol. Chem.*, **280**, 4188.

34. (a) Kashyap, R. and Nemova, G. (2009) *J. Sens.*, **2009**, 645162. (b) Sharma, A.K., Jha, R., and Gupta, B.D. (2007) *IEEE Sens. J.*, **7** (8), 118–1128.

35. Lai, E.P.C., Fafara, A., VanderNoot, V.A., Kono, M., and Polsky, B. (1998) *Can. J. Chem.*, **76**, 265–273.

36. Li, P., Huang, Y., Hu, J., Yuan, C., and Lin, B. (2002) *Sensors*, **2**, 35–40.

37. Taniwaki, K., Hyakutake, A., Aoki, T., Yoshikawa, M., Guiver, M.D., and Robertson, G.P. (2003) *Anal. Chim. Acta*, **489**, 191–198.

38. Roche, P.J.R., Ng, S.M., Narayanaswamy, R., Goddard, N., and Page, K.M. (2009) *Sens. Actuators, B*, **139**, 22–29.

39. Raitman, O.A., Arslanov, V.V., Pogorelova, S.P., and Kharitonov, A.B. (2003) *Dokl. Phys. Chem.*, **392** (4–6), 256–258.

40. Lavine, B.K., Westover, D.J., Kaval, N., Mirjankar, N., Oxenford, L., and Mwangi, G.K. (2007) *Talanta*, **72**, 1042–1048.

41. Wei, Q.Q. and Wei, T.X. (2011) *Chin. Chem. Lett.*, **22**, 721–724.

42. Hao, H.X., Zhou, H., Chang, J., Zhu, J., and Wei, T.X. (2011) *Chin. Chem. Lett.*, **22**, 477–480.

43. Matsui, J., Takayose, M., Akamatsu, K., Nawafune, H., Tamaki, K., and Sugimoto, N. (2009) *Analyst*, **134**, 80–86.

44. Nishimura, S., Yoshidome, T., and Higo, M. (2001) *Bunseki Kagaku*, **50** (11), 733–738.

45. Matsunaga, T., Hishiya, T., and Takeuchi, T. (2007) *Anal. Chim. Acta*, **591**, 63–67.

46. Wei, X., Li, X., and Husson, S.M. (2005) *Biomacromolecules*, **6**, 1113–1121.

47. Mao, Y., Bao, Y., Gan, S., Li, F., and Niu, L. (2011) *Biosens. Bioelectron.*, **28**, 291–297.

48. Lu, C., Zhou, W., Han, B., Yang, H., Chen, X., and Wang, X. (2007) *Anal. Chem.*, **79** (14), 5457–5461.

49. Lotierzo, M., Henry, O.Y.F., Piletsky, S., Tothill, I., Cullen, D., Kania, M., Hock, B., and Turner, A.P.F. (2004) *Biosens. Bioelectron.*, **20**, 145–152.

50. Wei, C., Zhou, H., and Zhou, J. (2011) *Talanta*, **83**, 1422–1427.

51. Li, X. and Husson, S.M. (2006) *Biosens. Bioelectron.*, **22**, 336–348.

52. Zhao, N., Chen, C., and Zhou, J. (2012) *Sens. Actuators, B*, **166** (167), 473–479.

53. (a) Dong, J., Peng, Y., Gao, N., Bai, J., Ning, B., Liu, M., and Gao, Z. (2012) *Analyst*, **137**, 4571. (b) Dong, J., Gao, N., Peng, Y., Guo, C., Lv, Z., Wang, Y., Zhou, C., Ning, B., Liu, M., and Gao, Z. (2012) *Food Control*, **25**, 543–549.

54. Yu, J.C.C. and Lai, E.P.C. (2005) *React. Funct. Polym.*, **63**, 171–176.

55. Choi, S., Chang, H., Lee, N., Kim, J., and Chun, H.S. (2009) *J. Agric. Food Chem.*, **57**, 1113–1118.

56. Choi, S., Chang, H., Lee, N., and Chun, H.S. (2011) *Sensors*, **11**, 8654–8664.

57. Taranekar, P., Baba, A., Park, J.Y., Fulghum, T.M., and Advincula, R.C. (2006) *Adv. Funct. Mater.*, **16**, 2000–2007.

58. Pernites, R.B., Ponnapati, R.R., and Advincula, R.C. (2010) *Macromolecules*, **43**, 9724–9735.

59. Dutta, P., Pernites, R.B., Danda, C., and Advincula, R.C. (2011) *Macromol. Chem. Phys.*, **212**, 2439–2451.

60. Riskin, M., Tel-Vered, R., Lioubashevski, O., and Willner, I. (2009) *J. Am. Chem. Soc.*, **131**, 7368–7378.

61. Frasconi, M., Tel-Vered, R., Riskin, M., and Willner, I. (2010) *Anal. Chem.*, **82**, 2512–2519.

62. Ben-Amram, Y., Riskin, M., and Willner, I. (2010) *Analyst*, **135**, 2952–2959.

63. Riskin, M., Ben-Amram, Y., Tel-Vered, R., Chegel, V., Almog, J., and Willner, I. (2011) *Anal. Chem.*, **83**, 3082–3088.

64. Lee, K., Su, Y., Chen, S., and Lee, G. (2006) 19th IEEE International Conference on Micro Electro Mechanical Systems, MEMS 2006, Istanbul, Turkey, pp. 430–433.

65. Huang, S., Lee, G., Chien, F., Chen, S., Chen, W., and Yang, M. (2006) *J. Micromech. Microeng.*, **16**, 1251–1257.

66. Taguchi, Y., Takano, E., and Takeuchi, T. (2012) *Langmuir*, **28**, 7083–7088.

Section X
Applications 3: Environmental Analysis

Handbook of Spectroscopy, Second Edition. Edited by Günter Gauglitz and David S. Moore.

34

LC-MS in Environmental Analysis

Sophie Bourcier and Michel Sablier

34.1

Introduction

Liquid chromatography-mass spectrometry (LC-MS), or alternatively high-performance liquid chromatography-mass spectrometry (HPLC-MS), is an analytical technique that combines the physical separation capabilities of LC (or HPLC) with the mass analysis capabilities of MS. LC-MS is a powerful technique that has very high sensitivity and specificity and, therefore, is currently used for many analytical applications. MS, which gives information on both molecular weight and structure of chemical compounds, is more specifically oriented toward the specific detection and identification of target compounds in the presence of other chemicals in complex mixtures. Development of the concept of linking analytical instrumentation is motivated by the need for chemists to detect unequivocally, characterize, and quantify compounds in unknown mixtures: GC-MS represents the first example of chromatography hyphenated successfully to MS. The development of LC-MS arose initially from the need to extend the range of compounds studied to polar and thermally labile molecules not amenable to GC-MS or necessitating prior derivation steps for the analysis.

Experimentally, the major problem in the development of LC interfaces has been the incompatibility between a high mobile-phase flow rate in LC and MS pumping requirements for normal conditions of use. Two solutions have been proposed during the first years of development based on two different strategies to eliminate the solvent: (i) evaporation of solvent before the ionization and (ii) evaporation and ionization at the same time. Finally, the second strategy was chosen, and the development of atmospheric pressure ionization (API) has greatly facilitated the combination of LC with MS, as exemplified by the numerous applications found in the literature. The large possibility offered by API methods allows analyzing both polar and non-polar compounds. Electrospray ionization (ESI) is suitable for analyzing polar compounds, whereas atmospheric pressure chemical ionization (APCI) and atmospheric pressure photoionization (APPI) allow more specifically ionization of nonpolar compounds. All of these ionization techniques can be used in both positive and negative ion modes. Each method can be associated with either

Handbook of Spectroscopy, Second Edition. Edited by Günter Gauglitz and David S. Moore.

triple quadrupole (QqQ), quadrupole ion trap (QIT), quadrupole linear ion trap (QLIT), quadrupole time-of-flight (Q-TOF), ion trap time-of-flight (IT-TOF): this large panel of mass spectrometers allow solving different problems of identification, quantification, and detection of pollutants and their metabolites. Moreover, LC-MS is used in combination of sample preparation and/or sample preconcentration to improve selectivity. All these elements have largely contributed to the development of environmental LC-MS.

Many aspects of LC-MS are reported in the literature. In addition, Handbook (Method 3) covers the general principles and the applications of MS. Rather, this chapter describes briefly the principles of operation and the developments that have permitted routine analysis by LC-MS coupling. This chapter focuses also on some of the most striking examples of applications of LC-MS in the environmental field, and highlights recent developments in this area.

34.2
Developments in Interfacing for LC-MS

34.2.1
General Principle of Operation

The operational principle of most API interfaces is as follows: the column effluent from the LC is nebulized into an atmospheric pressure ion source region, ionized and sampled by a skimmer into a second pumping stage containing an ion-focusing and ion-transfer device to optimally transport and focus the ions to the mass analyzer region. In most systems, the ion-transfer device consists of a radio-frequency (RF)-only quadrupole, hexapole, or octapole, which should transfer onto the mass analyzer the maximum of ions.

Concerning vacuum pumping requirements, it is no longer important whether a high flow rate or a low flow rate of liquid is nebulized because the technical solution ultimately chosen for sampling orifice in the recent design of API source employs a fixed restriction between the atmospheric pressure region and the first pumping stage of the mass spectrometer. The trade-off between a high-throughput of liquid sample and ionic current detection has been solved by the use of off-axis geometries and optic transmission improvement (see subsequent text). The historical development of API interfaces for LC-MS has been well reviewed in detail elsewhere [1, 2] and the interested readers are invited to refer to these reviews.

A general schematic diagram of an API source is depicted in Figure 34.1. An API interface source consists in five parts: (i) the liquid introduction device or spray probe (not shown); (ii) the atmospheric pressure ion source region, where the ions are generated by means of an electric field (ESI), by a corona discharge (APCI), or by photoirradiation (APPI); (iii) an ion-sampling aperture; (iv) an atmospheric-pressure-to-vacuum interface; and (v) an ion optical system, where ions are subsequently transferred into the mass analyzer. Ion losses cannot be avoided in the transfer region, but must be kept to a minimum.

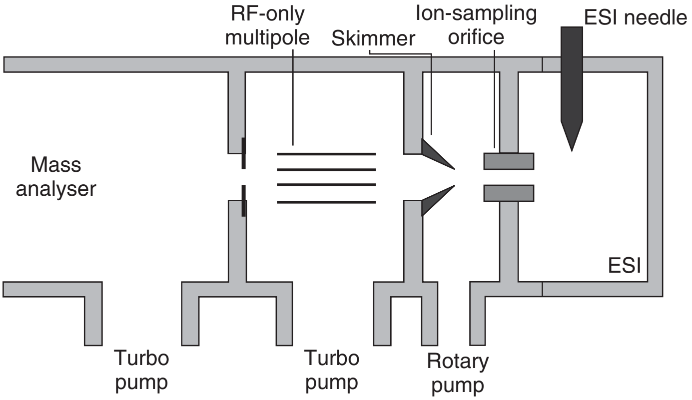

Figure 34.1 General schematic diagram of an ion source for atmospheric pressure ionization with, from the right to the left: (i) the atmospheric pressure ion source region, (ii) the ion-sampling aperture, (iii) the first pumping stage, and (iv) the ion optical system. (Reproduced from Ref. [3], with permission from Elsevier, copyright 2003.)

A large variety of API interfaces is now commercially available from a number of manufacturers. Initially, the spray probe was positioned on-axis. The major disadvantage of this setup is that all material in the spray may start clogging the ion-sample orifice. Several instrumental developments have been proposed to avoid such contamination problems : (i) a nitrogen curtain gas that flows between the orifice plate and curtain plates in the first pumping stage, (ii) a countercurrent of heated gas flow that promotes the desolvation of the droplets in the atmospheric pressure ion source region, and (iii) the orthogonal positioning of the spray probe by off-axis sampling that constitutes the most successful source modification to reduce contamination. This latter solution is applied in most commercial systems available for LC-MS currently. In LC-MS applications, one aims at introducing the highest possible flow rate into the ion source interface, manufacturers have optimized ESI interfaces in this purpose to permit increased introduction flow rates up to 1 ml min^{-1} of effluent. Moreover, to assist in the evaporation of the high flow of LC effluent, the source can be heated to increase desolvation processes. These modifications allowed the implementation of high-throughput methods, applied in particular for the newly developed ultrahigh pressure liquid chromatography (UPLC). This technique uses small diameter particles and short columns to reduce time analysis with the highest efficiency for the chromatographic separation.

34.2.2
Interfacing and Operations

34.2.2.1 Electrospray Ionization (ESI)

Several reviews [4–8] have documented the mechanisms of the electrospray process. Schematically, this process of ionization includes both the nebulization of a liquid into an aerosol of highly charged droplets and the ionization of solvated molecules

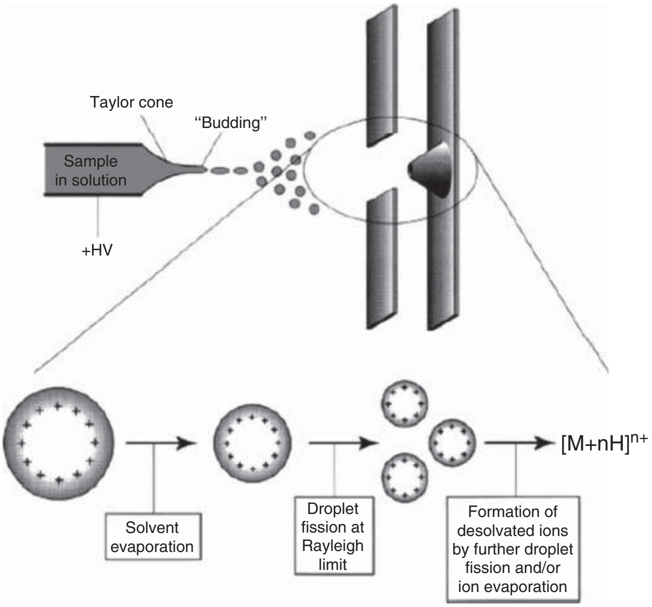

Figure 34.2 Droplet production in the electrospray interface. (Reproduced from Ref. [7], with permission from John Wiley & Sons Ltd., copyright 1997.)

after desolvation of the charged droplets (Figure 34.2). The electrospray process is initiated by applying a potential of several kilovolts to a liquid introduced through a capillary or a needle in the atmospheric pressure ion source region. By increasing the potential difference between the needle or capillary and the counter electrode, a series of processes takes place involving three main steps: (i) droplet formation, (ii) droplet explosion, and (iii) finally gaseous ion formation. Stability of spray depends on several parameters including solvent properties, liquid flow rates, and applied voltages. ESI is the result of the decrease of the size of the droplet by the evaporation of neutral solvent molecules. This size reduction is accompanied by an increase in the electrical field strength at the droplet surface favoring droplet explosion. ESI was originally a low flow rate ionization technique (allowing a few microliters per minute flow input). Compatibility of ESI with typical LC flow rates (0.2–0.5 ml min^{-1}) have been achieved by pneumatically assisted electrospray (also called *ionspray*), by the use of a heated gas (called *turboionspray*), and/or the adjunction of a heated sampling capillary.

34.2.2.2 **Atmospheric Pressure Chemical Ionization (APCI)**

In a heated-nebulizer APCI interface (Figure 34.3), the column effluent is nebulized into a heated vaporizer probe (350–500 °C) to evaporate the solvent [9]. The resulting vapor enters the atmospheric pressure ion source, where sample ionization is initiated by a corona discharge. The mobile phase vapor acts like a reagent gas. The ionization conditions in APCI are considered to be "harder" than those observed in

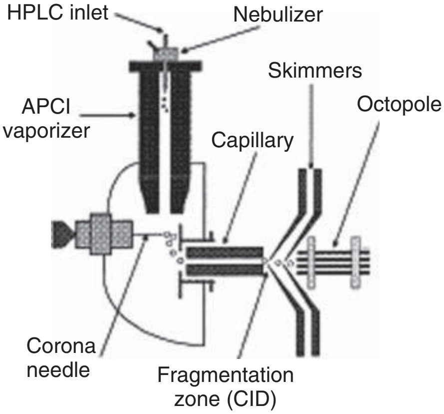

Figure 34.3 Schematic diagram of an atmospheric pressure chemical ionization source. (Adapted from Ref. [9], with permission from Elsevier, copyright 1998.)

ESI [10], and acid–base reactions are still the most frequently observed ionization mechanisms. This technique is currently reported as more suitable for less polar compounds. It is noteworthy that the effective higher flow input capacities of APCI constitute a potential drawback because the use of these high flows increases the propensity of source contamination, affecting both the sensitivity and the reproducibility of APCI experiments [3].

34.2.2.3 **Atmospheric Pressure Photoionization (APPI)**

APPI is the most recently developed methods among the soft ionization methods available currently in MS. Several authors have described the ionization methods in the recent years [11–14].

APPI complements the other two API techniques previously described and was principally developed to extend the range of compounds amenable to LC/MS analysis to nonpolar compounds, ordinarily inefficiently ionized by ESI and APCI. The technical setup for an APPI source is closely related to that of APCI sources, with a heated nebulizer for both eluent spraying and desolvation, but including a vacuum ultraviolet (VUV) lamp for the ionization process instead of the corona discharge used in APCI [14, 15]. A large number of reactions could be involved in the photoionization (PI) process. APPI is characterized as an alternative ionization process that is showing evidence of being relatively nondiscriminant for nonpolar compounds. The different steps taking place for the APPI process can be schematically described as follows: (i) photoexcitation of samples and/or solvent molecules, (ii) photodissociation, and (iii) ionization (by proton transfer and charge exchange for the positive mode of ionization and proton transfer; electron capture, and halide attachment for the negative mode of ionization). The nature of ions formed depends on the mixture of constituents and their associated physicochemical properties, (proton affinity (PA), and ionization energy (IE), [16]). For example, proton transfer from a reagent ion to a neutral molecule having higher PA can act as a common ionization reaction in APPI (Figure 34.4).

Bruins *et al.* [17] have introduced the use of ''dopants'' to increase ionization efficiency, taking advantage of the ion–molecule reactions observed during APPI: schematically, dopants are chosen for their propensity to be efficiently photoionized and form quantitatively dopant ionized species able to ionize molecules through proton transfer or charge transfer. Consequently, the molecule used as a dopant must be selected with an IE lower than the photon energy of the emitted light. The dopant is mixed with the sample stream in the liquid phase, often with a tee situated upstream from the source. The dopant-assisted APPI method is now the standard method in APPI source designs. Under conventional reversed-phase conditions, proton transfer reagent ions are generated via PI of toluene or acetone commonly used as a dopant. Toluene is known to generate photoions that react rapidly with either methanol or acetonitrile. To orientate the formation of ions between solvents or analytes, and to simplify the interpretation of mass spectra, the ultraviolet (UV) source energy can be modulated in such a manner that the operating photon energy is bracketed between sample IEs and solvent IEs (or molecules present in air). Table 34.1 gives PAs and IEs of some common solvents used together with the energies of some lamps commonly used in PI.

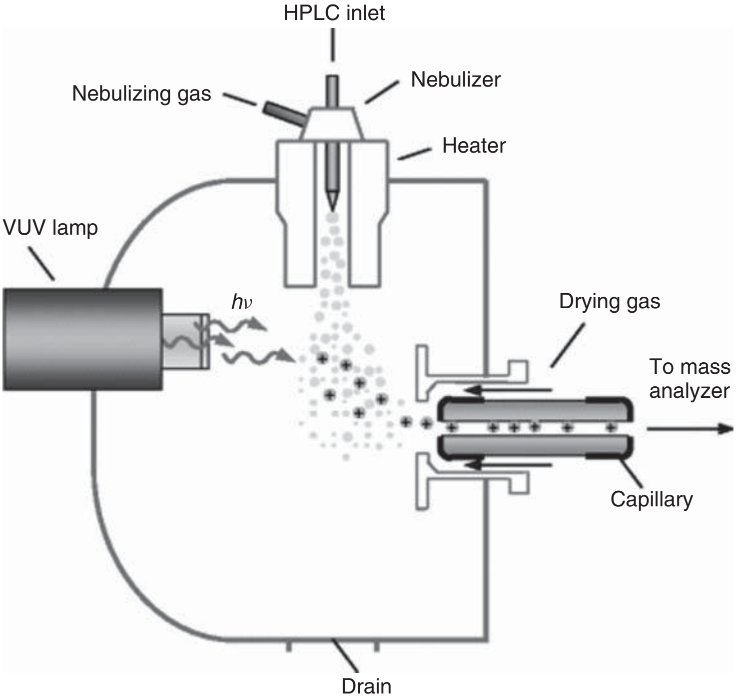

Figure 34.4 Schematic drawing of the orthogonal-source-type APPI interface. (Reproduced from Ref. [14], with permission from Springer-Verlag Ltd., copyright 2006.)

Table 34.1 Gas phase IE and PA values of commonly used solvents and gas in APPI.

Lamp	Gas and solvent	PA[a] (kJ mol^{-1})	IE[a] (eV)
—	Nitrogen	493.8	15.58
Ar 11.2 eV	Water	691	12.62
—	Acetonitrile	779.2	12.2
—	Oxygen	421	12.07
—	Methanol	754.3	10.84
Kr 10.0 eV	Isopropanol	793	10.17
—	Acetone	812	9.7
Xe 8.4 eV	Toluène	784	8.83
—	Triethylamine	981.8	7.53

[a] Reference [16].

Depending on the characteristics of the sample, the solvent and the dopant (if any), the APPI method has shown applications exceeding the field of nonpolar compounds and has proved to be effective for detecting a broad range of compounds, placing APPI as a complementary tool for LC-MS besides the ESI and APCI methods.

34.2.2.4 **Comparison between Ionization Methods**

API ionization techniques are soft ionization techniques, and cover different ranges of applications in terms of polarity and molecular mass of samples analyzed. ESI is particularly well adapted to polar compounds, while APCI and APPI ionizations are most suitable for nonpolar compounds. For a given sample, in order to choose between the various API methods, one must keep in mind that ESI more properly transfers ions in solution, whereas APCI and APPI ionize compounds in the gas phase [18]. Moreover, only the ESI ionization technique can be efficiently used for the analysis of high-molecular mass compounds because it is the only ionization technique leading to the formation of multicharged ions. One disadvantage of ESI is its reported likelihood of matrix effects [19–21]. A matrix effect consists in some suppression or an enhancement of sample response due to the co-eluted matrix components and/or conjugated counterions. It can be easily evaluated by comparing the response obtained from a standard solution and that from a spiked solution with internal standards (mostly labeled compounds) or chemical analogs. A matrix effect is essentially a liquid-phase process found to be related to the amount of nonvolatiles in the sample. Indeed, nonvolatiles appear to reduce the ion evaporation of preformed sample ions from solution. For this reason when combining LC with MS, it is necessary to optimize the LC separation carefully. In particular, LC additives must be suitable to LC-MS: for example, phosphate and borate buffers must be replaced by volatile mobile phase additives. The sensitivity of API-MS can then be optimized in improving the formation of ions and supporting the nebulization enhancing the desolvation process. Depending on the API method processed, the choice of solvent, dopant, pH, or flow rates consists of several parameters that must be taken into account to improve sensitivity and to obtain the best results. Post-column techniques can be used to set the optimal conditions of pH or solvent after the separation. Figure 34.5 reports the experimental design for the use of a post-column system [22], and Figure 34.6 illustrates the results obtained for the analysis of a mixture of β-lactam antibiotics [23]. In this application, the ion-pair reagent heptafluorobutyric acid (HFBA) for the reversed-phase LC separation was added to improve the chromatographic separation of compounds, but HFBA forms stronger ion pairs with the sample, reducing in return ESI sensitivity. The post-column addition of weaker acid such as propionic acid can displace adduct formation toward the more volatile counter-acid adduct formation depending on volatility or boiling point of this counter-acid (b.p.): for example, b.p. propionic acid >b.p. HFBA. The formation of weaker ion pairs between sample and propionic acid results in an improvement on the API sensitivity.

We can notice that the use of the post-column infusion system is limited to target compound analysis. In general, the matrix effects can be decreased by improving sample pretreatment or/and optimizing chromatographic separation parameters, as well as changing the ionization mode [15, 24–26]. It has been estimated that APCI and APPI sources can reduce matrix effects by a factor of 3–10. Moreover, this latter benefit observed with APPI over ESI is not restricted to nonpolar compounds [13].

Matrix effect can also be evaluated using post-column techniques. As such, Hanold *et al.* [15] proposed a test of ion suppression by introducing a continuous flow of a standard solution of fluphenazine after the LC column and noting the change in ion signal level due to LC elution of components from an injection of rat plasma. The results are reported in Figure 34.7, and give a comparison between ion suppression susceptibility during APPI, APCI, and ESI.

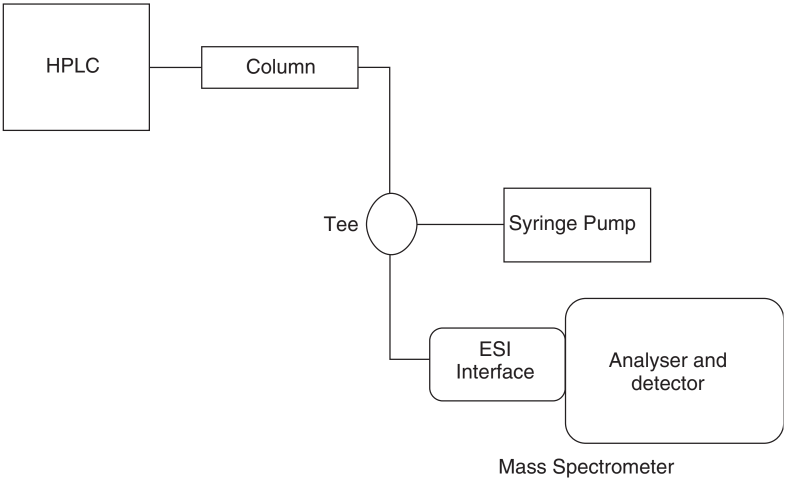

Figure 34.5 Schematic diagram of a post-column infusion system. (Reproduced from Ref. [22], with permission from John Wiley & Sons Ltd., copyright 2000.)

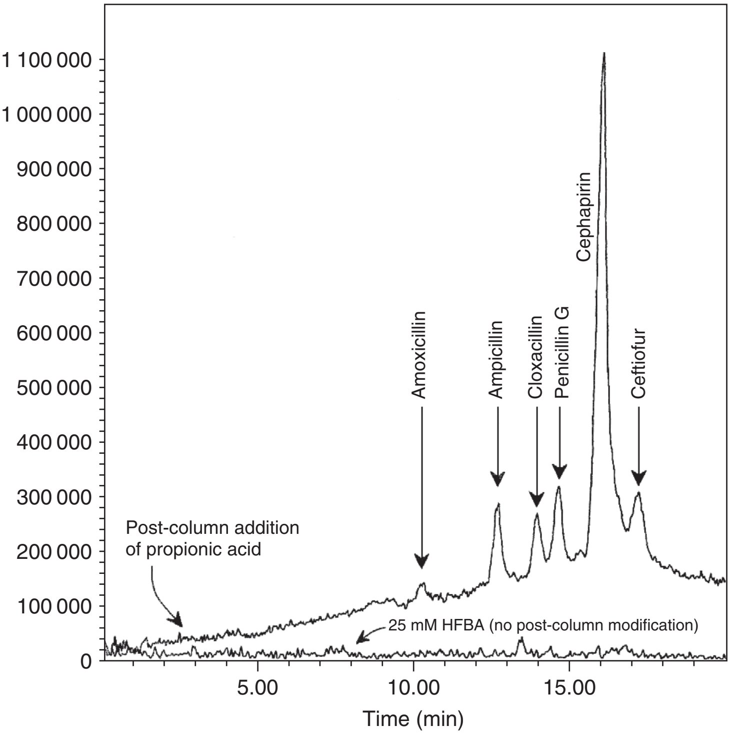

Figure 34.6 The LC-ESI-MS total-ion current chromatographic separations of a mixture of β-lactam antibiotics with and without the post-column addition of propionic acid. (Reproduced from Ref. [23], with permission from John Wiley & Sons Ltd., copyright 1997.)

The linear dynamic range of APPI has been reported at several times to be higher than those of ESI [15, 27]. Disadvantages of both APPI and APCI relative to ESI include a (mild) propensity to induce fragmentation or other changes in labile samples during the vaporization and/or chemical ionization steps. However, qualitative analysis using APPI may also be complicated by the presence of multiple peaks in the spectrum of a single compound, due to different ionization pathways. Additional practical disadvantages of APPI relate to the need to supply a dopant, which increases method complexity, so that some understanding of the mechanisms involved in the ionization process is generally required to achieve optimum results.

34.3
Developments in Mass Analyzers for LC-MS

The identification of compounds in complex matrices at very low levels with high selectivity and specificity implies the use of tandem MS. In this part, we present the tandem mass spectrometers currently used for environmental analysis and

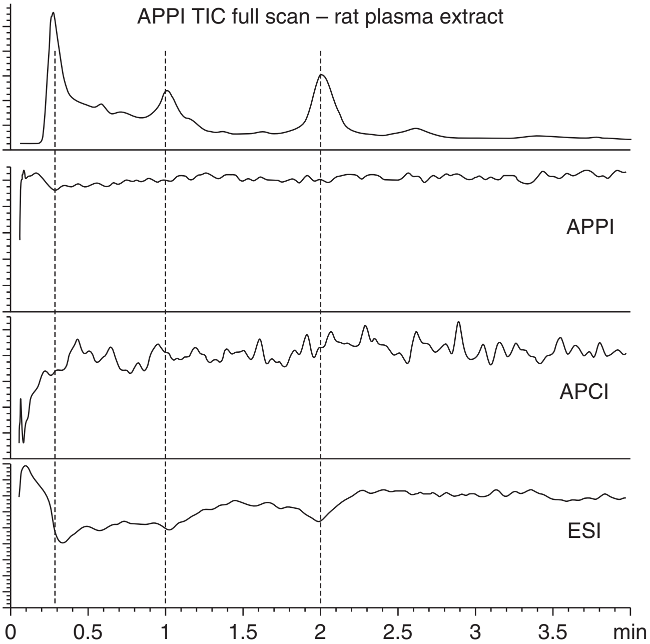

Figure 34.7 Comparison of ion suppression susceptibility for APPI, APCI, and ESI by post-column addition of fluphenazine to an LC separation of a rat plasma sample. (Reproduced from Ref. [15], with permission from ACS Ltd., copyright 2004.)

remind about their specificities. MS/MS allows a variety of experiments, which, in general, tends to improve the selectivity, specificity, and/or sensitivity of detection over single-stage-instrument experiments. Two mass analyzers in series, or two stages of mass analysis in a single instrument, are currently used in that purpose.

34.3.1
Triple Quadrupoles

The QqQ is the most frequently used mass analyzer to quantify target compounds on biological matrices with respect to the dynamic range, repeatability, and sensitivity. In a QqQ mass spectrometer, there are three sets of quadrupole filters, although only the first and third function as mass analyzers. The first quadrupole (Q1), acting as a mass filter, transmits and accelerates a selected ion toward the second quadrupole q, which acts as a collision cell. Although in some designs, q is similar to the other two quadrupoles, RF is imposed on it only for transmission, not mass selection. The pressure in q is higher, and the ions collide with a neutral gas in this collision cell. These collisions result in fragmentations by collision-induced dissociation (CID). The fragments are then accelerated into the third quadrupole Q3, another scanning mass filter, which sorts them before they enter a detector. Several acquisition modes are available on a QqQ: (i) multiple-reaction monitoring

(MRM) and selected reaction monitoring (SRM) modes, (ii) neutral loss (NL) scan, and (iii) precursor ion scan. The latter two acquisition modes allow identifying molecules belonging to the same chemical family.

The MRM mode is the most widely used for sensitive and selective quantification of target compounds. MRM operation is performed at fixed m/z values of the quadrupole Q1 and Q3. This acquisition mode allows obtaining of very low limits of detection (LODs) of target compounds present in complex matrices. We can notice that tandem MS coupled with ESI ionization provides an effective MS/MS/MS device because ESI ionization permits "in-source CID" to obtain additional structural information. Despite the high specificity of LC-QqQ, target compounds can still be mistakenly identified because of interferences from matrix components and metabolites. To further improve data quality and avoid false-positive results, the European Commission Decision 2002/657/ECD [28] requires two and more transitions to be used for the identification of any molecule in MRM mode. In addition, response ratios that arise from different transitions must be calculated and compared with those of a standard. Comparison of retention times for similar chromatographic conditions can be used to confirm identifications [29].

NL and precursor ion scans give the opportunity to detect other metabolites. In the NL scan, both Q1 and Q3 are scanned with a constant offset for Q3. In the precursor ion scan, Q1 is scanned while Q3 set at a fixed m/z value. To illustrate applications in the field of environmental analysis, NL scans have been used for identification of acidic naphthalene derivatives using the CO_2 NL corresponding to an m/z 44 ratio in the negative mode of detection [30, 31], while precursor ion scans have been well employed by Pozo *et al.* [32] to identify unknown anabolic steroids. One must concede that the efficient use of both NL and precursor ion scans imply the knowledge of fragmentation pathways.

34.3.2
Quadrupole Ion Trap

Three-dimensional (3D) QITs have found large application specifically in structure elucidation studies [33]. A QIT mass spectrometer has three electrodes; that is, one ring electrode between two hyperbolic end-cap electrodes to form a 3D ion trap. The main advance of QIT technology was the development of the mass-selective instability mode of mass analysis, which revolutionized the use of the ion trap as a mass analyzer. In this mode of operation, an RF voltage is applied to the central ring electrode of the ion trap, while the two end-cap electrodes are held at ground potential. By definition, each ion confined within the ion trap is associated with a value of the functioning q_z parameter correlated with a particular mass-to-charge m/z ratio. To record a mass spectrum, the RF voltage is increased with time so that ions of successively greater m/z ratio are ejected and detected as they develop unstable trajectories. The scanning sequence of the ion trap consists of three periods performed repeatedly: (i) ionization and storage of ions above a chosen m/z ratio, (ii) ejection of background ions below the m/z range of interest, and

(iii) ejection and detection of ions. The oscillating potential difference established between the ring and end-cap electrodes creates finally a store or pass ions in and out of the traps. Such a system combines ejection sequences for mass determination and multiples stages of MS/MS with high collision efficiency. All stages of ion manipulation occur within the same volume but at different times. This in-time operation procedure increases the scanning sensitivity of QIT relative to QqQ mass spectrometers.

34.3.3
Triple Quadrupole Linear Ion Trap

A triple quadrupole linear ion trap(QqQLIT) consists of a QqQ mass spectrometer with Q3 operated as a linear ion trap spectrometer with axial ion ejection. These instruments enable the accumulation of a higher number of ions with no loss due to charge effects compared to QIT. These instruments combine the advantages of QqQs for the quantification of target molecules and possess ion accumulation and fragmentation capacity for structural elucidation while softwares allow obtaining both quantitative and qualitative information. To analyze complex mixtures, the use of information-dependent acquisition (IDA) [34], where the m/z ions of highest intensities in the full-scan mode are automatically selected to conduct fragmentations, are currently processed.

34.3.4
Time-of-Flight Mass Analyzers

Time-of-flight (TOF) analyzers are conceptually the simplest mass analyzers: the ions are accelerated with the same kinetic energy from the exit of the ion source, the ions of different m/z values are separated in the field-free flight tube and are detected sequentially depending on their arrival time on the detector. TOF instruments are configured either alone or in tandem with a quadrupole analyzer Q-TOF. Both instruments offer a high resolution, accurate mass measurement, and good sensitivity on full scan. A Q-TOF instrument gives the opportunity of obtaining product ion spectra with high mass accuracy. This advantage allows the confirmation of compounds suspected to be present. A significant feature of a TOF instrument is the necessity for pulsed ion introduction, which is readily achieved by the use of a pulsed voltage to a repeller plate positioned at the opposite to the accelerating grid. However, this results in a reduced effective duty cycle: while ions are generated continuously, only part of these ions is sampled for mass analysis. To achieve higher duty cycles, in-line ion storage devices are used. With the programmable ‘‘dynamic range enhancement’’ function, the quantification with a Q-TOF instrument is feasible, but some applications demonstrate that the LODs are lower than those obtained with tandem quadrupole (TQ) instruments.

34.3.5
Other Instruments

Cyclotron instruments trap ions electrostatically in a cell using a constant magnetic field. Pulses of RF voltage create orbital ion motion, and the orbiting ions generate a small signal at the detection plates of the cell (the ion's orbital frequency). The frequency is inversely related to the ion's m/z ratio, and the signal intensity is proportional to the number of ions of the same m/z ratio in the cell. At very low cell pressures, a cyclotron instrument can maintain the ion's orbit for extended periods, providing very high resolution measurements. Fourier transform-ion cyclotron resonance (FT-ICR) mass spectrometers represent the extreme capability of measuring mass with the ability to resolve closely related masses. A 14.5-T magnet can then achieve a resolution of more than 3.5 million and thus display the difference between molecular entities whose masses vary by less than the mass of a single electron.

On-line electrospray FT-ICR-MS resulted in a more extensive analytical use of FT-ICR-MS instruments. As a consequence, electrospray interfaces for FT-ICR-MS instruments are commercially available. The instrumental problems related to ESI coupling to an FT-ICR-MS system relate to the working pressure in the FT-ICR ion cell, the kinetic energy that ions gain in the nozzle-skimmer region, which can limit ion trapping efficiency in the cell. Furthermore, drawbacks of FT-ICR in the environmental analysis relates to the lack of sensitivity. Recent instrumental improvements for ESI-FT-ICR-MS are the use of a capacitively coupled open cell to improve the signal-to-noise ratio and the use of an electrostatic ion guide in the post-source region to further enhance the sensitivity.

Magnetic instruments are almost abandoned in LC-MS applications for environmental analysis. The major difficulties in coupling an LC-API source to a sector instrument reside in the high acceleration voltage required in the ion source and the large pressure difference between ion source and analyzer. This pressure drop necessitates extensive pumping to avoid discharges and electrical breakdown, as well as extensive collision activation of the ions incompatible with high-resolution applications. All these factors have drastically limited the implementation of magnetic LC-MS instruments in environmental laboratories.

The newly developed hybrid linear ion trap (LIT) FT-Orbitrap mass spectrometer [35] could revolutionize the domain of environmental high-resolution analysis, but this apparatus is still in its infancy in LC-MS for environmental analysis.

34.4
Sample Preparation

As compounds of interest or degradation compounds are found at very low concentration in environmental samples, sample preparation is a determining step before the LC-MS analysis and depends on the nature of sample and on the analytical problem to be solved. Typically, liquid sample extraction can be done without presteps, whereas with homogenized solid samples it is often necessary. Several authors have reviewed recent advances in sample preparation [36–43]. Several operations are included in this preparation: (i) sample dissolution step, (ii) sample clean-up, and (iii) sample fractionation and preconcentration. According to the nature of the sample, several methods can be used: solvent extraction under reflux, liquid–liquid extraction (LLE), solid-phase extraction (SPE), and solid-phase microextraction (SPME). The two latter extraction procedures are the procedures more described in the literature. SPE allows a multitude of chemical specific phases to prepare the sample before LC-MS analysis. The SPE is very well adapted to extraction of target compounds. In the case of multiresidue methods, compounds are extracted in two or more SPE according to the chemical properties of compounds [40]. Most SPE procedures are used off-line but development and use of automated on-line sample preparations have been recently reported [44, 45]. Higher sensitivity is achieved under on-line configurations owing to the higher transfer efficiency and the resulting analysis of the totality of the sample. Moreover, this solution is attractive when large numbers of samples have to be analyzed. SPME [46, 47] can be easily coupled on-line with LC/MS. Moreover, new SPME–HPLC systems known as *in-tube SPME* are now available using an open tubular-fused silica capillary column as the SPME device instead of the SPME fiber. In-tube SPME is suitable for automation, provides better accuracy and precision relative to manual techniques, and such SPME methods have been reported for the determination of drugs and environmental contaminants by coupling with LC/MS/MS [48]. Another possibility to improve the selectivity in SPE can be obtained with molecular imprinted polymers (MIPs) [49, 50]. In addition to these methods, other sample pretreatment methods are described: on-line column switching with a restricted access media (RAM) column, liquid phase membrane extraction, and microdialysis [51, 52].

In association with the important step of sample preparation, one must not forget the crucial role of the chromatographic separation mode depending on analyte properties. The most used separation technique for environmental compounds is reversed-phase HPLC chromatography. Environmental contaminants are often polar compounds and their transformation products even more. Besides, monolithic LC columns have been introduced by column manufacturers to facilitate the analysis of very polar molecules and to conduct fast LC/MS analysis [40, 51].

34.5
Examples of Application

34.5.1
General

In the field of LC-MS, recent years have shown a tremendous increase in the use of time-of-flight-mass spectrometry (TOF-MS) and quadrupole time-of-flight mass spectrometry (Q-TOF-MS) for structural elucidation and compound confirmation.

TOF-MS and Q-TOF-MS provide increased resolution capability, which allows precise empirical formula assignments for unknowns and provides confidence for positive identification in quantitative work [53]. LC coupling to ESI and APCI continues to dominate the new methods developed for emerging contaminants, and the use of MRM with MS/MS has become commonplace for quantitative environmental analysis. As a consequence, the use of LC/MS/MS allows in most cases identification of highly polar organic pollutants down to nanogram per liter levels, avoiding derivatization [53, 54]. Also, the use of MRM provides increased selectivity and sensitivity, greatly reducing the presence of chemical background in LC/MS analysis. Of note, APPI is also increasingly being used with LC/MS because of its ionization efficiency for nonpolar compounds.

Besides instrumental developments in MS, trends in sampling and extraction include use of traditional SPME and SPE cartridges. One of the fastest growing trends in chromatography is the use of UPLC, a recently developed LC technique that uses small diameter particles in the stationary phase and short columns, to allow higher pressures and, ultimately, narrower LC peaks. In addition to better chromatographic separation, UPLC dramatically shortens total analysis times.

New analytical methods continue to push detection limits lower, while regulation law drastically decreases authorized LODs and limits of quantification (LOQs). Currently, it is common to see LODs that lay in the low-nanogram per liter range. A drop in these detection limits will continue to allow the detection of analytes at concentrations not attainable before, as well as their degradation products. Indeed, pollutants are generally present at nanogram per liter to low-microgram per liter levels in wastewater influents, and detection limits at the low-nanogram or sub-nanogram per liter level are necessary to determine their percentage removal.

The past years have seen some major successes in terms of global measurement and regulation of persistent, bioaccumulative, toxic chemicals, and persistent organic pollutants. There has been a major expansion of measurements and risk assessments of new chemical contaminants in the global environment. However, the list of chemicals measured represents only a small fraction of the thousands of chemicals widely used in commerce. One must concede that the vast majority of existing and new chemical substances in commerce are not monitored in environmental media [55].

LC-MS analysis in the field of environmental analysis commonly refers to the terms *persistent organic pollutants* or *emerging contaminants*. The definition of ‘‘emerging contaminants’’ has been addressed in the Editor’s introduction of a recent issue of Environmental Science and Technology [56], emphasizing the elusiveness of the term *emerging contaminant* itself due to the matter of perspective and timing inscribed in its acceptation. Indeed, better analytical methods have allowed for the low level detection of emerging organic contaminants, such as pharmaceuticals, antibiotics, endocrine-disrupting compounds, and so on. Analytical advances now permit the routine analysis of organic chemicals that cannot be observed previously, and led to the early discovery of many persistent organic pollutants. Once a substance is quoted as an emerging contaminant, assessing the effects of these contaminants in the environment remains a major time-consuming and a resource-intensive challenge. Therefore, it is not surprising that advances in the understanding of the potential adverse effects of the many thousands of chemicals being spread in the market are often rather slow. This fact introduces the concept of ''perspective'' and ''timing'' in the ''emerging'' character of these contaminants. As a consequence, a contaminant may be considered for several years to be ''emerging.'' *Emerging contaminants* can then be defined more properly as ''unregulated contaminants, which may be candidates for future regulation depending on research on their potential health effects and monitoring data regarding their occurrence'' [54].

Moreover, the issue of emerging contaminants is closely related to analytical capabilities. The increased sensitivity in MS, as a result of more efficient ionization techniques and better detectors, has enabled detection of virtually any new and potentially harmful contaminant at a very low level. Consequently, previously ignored or unrecognized contaminants as well as new contaminants have come under scrutiny. Analysis of emerging pollutants encompasses the monitoring of known environmental contaminants that have the potential to adversely affect human health: for example, chlorinated dioxins, pesticides, and metals [57]. As analytical instruments evolve, detection limits improve, and new analytical methods are developed, new compounds of potential concern emerge. Several groups of compounds [58] have emerged as particularly relevant: algal and cyanobacterial toxins, brominated flame retardants, disinfection by-products, gasoline additives, hormones and other endocrine-disrupting compounds, organometallics, organophosphate flame retardants and plasticizers, perfluorinated compounds, pharmaceuticals and personal care products, polar pesticides and their degradation products, and surfactants and their metabolites. All of these compounds will not be addressed here; only analysis of a few of them will be detailed later in the textto illustrate LC-MS capabilities in environmental analysis.

34.5.2
Pharmaceuticals, Veterinary Pharmaceuticals

Pharmaceuticals have become important emerging contaminants owing to their presence in environmental waters, threat to drinking water sources, and concern about adverse effects, both to wildlife and humans [59]. It is estimated that few thousands of different substances are used as pharmaceutical ingredients, whereas only a very small subset of these compounds has been investigated in environmental studies (less than a few hundred). Moreover, pharmaceuticals are an important group of potential endocrine-disrupting compounds that have recently attracted much attention to their likely detection in environmental samples. Pharmaceuticals are introduced not only by humans but also through veterinary use. Veterinary pharmaceuticals have been gaining interest, and, recently, a global perspective on the use, sales, exposure pathways, occurrence, fate, and effects of veterinary antibiotics in several countries was reported [60]. Veterinary antibiotics are widely used worldwide for treating diseases and protecting the health of animals. They are also incorporated into animal feed to improve growth rate and feed efficiency, as veterinary antibiotics became integrated into the growing animal food industry. Veterinary pharmaceuticals fall into several pharmaceutical categories, for example, anesthetic, steroidal, and nonsteroidal anti-inflammatory, antibacterial, antiseptic, tranquilizer, and are mainly delivered to the animals through feed or water. As antibiotics are poorly absorbed in the organism of the animals, they can be excreted unchanged in feces and urine, and, consequently, there is a potential for antibiotic resistance. This represents the main question remaining on the likely adverse effects of pharmaceuticals on humans or wildlife at low environmental levels (generally nanograms per liter), and a major concern for pharmaceuticals includes the development of bacterial resistance from the release of antibiotics in the environment. In order to guarantee safety of pharmaceuticals for human and environmental health in the future, the European Agency for the Evaluation of Medical Products has recently released a draft guideline based on EU (European Union) directives aimed at providing evaluation criteria for environmental risk assessment [61].

The ecotoxicology of human pharmaceuticals was recently reviewed [62], and the benefits of chemical analysis methods able to determine more polar compounds such as LC–tandem MS was emphasized. Examples of applications with the development of multiresidue analytical methods in groundwater and surface-water samples are reported in the subsequent text.

For identification of pharmaceuticals, LC-QqQ MS in the MRM mode has proved its suitability for target analysis [59]. The availability of Q-TOF MS has recently enlarged the scope of LC-MS-MS as a powerful identification tool. The accurate masses obtained by Q-TOF MS for both parent ion and transition ions, and the possibility of obtaining a full-scan product ion spectrum of the analytes present a great interest for final confirmation of compound identities in complex matrices. In this purpose, Stolker *et al.* [63] described a screening method based on LC-Q-TOF MS for the confirmation of the identity of residues of 13 pharmaceuticals in surface, drinking, and groundwater. Most of the pharmaceuticals investigated were medium-polar and polar compounds; therefore, placing reversed-phase LC as the separation method of choice. The use of MS-MS for detection enabled combination of screening and confirmation in one procedure. The set of pharmaceuticals investigated included analgesics (acetylsalicylic acid, diclofenac, ibuprofen, and paracetamol), antibiotics (sulfamethoxazole, erythromycin, and chloramphenicol), blood-lipid regulators and β-blockers (fenofibrate, bezafibrate, clofibric acid, bisoprolol, and metoprolol), and one antiepileptic drug carbamazepine. Reported LOQs ranged from 5 to 25 $\mathrm{ng\,l^{-1}}$. The analysis of a large number of samples (66) showed that 80% of the samples of groundwater contained up to three pharmaceuticals, while almost all surface waters showed the presence of two to eight pharmaceuticals. The concentrations of the individual target analytes were typically 10–100 $\mathrm{ng\,l^{-1}}$.

The development, optimization, and validation of an analytical method for the simultaneous detection and identification of 73 pharmaceutical residues, covering various therapeutic groups, in both surface and wastewaters has been recently described by Petrovic *et al.* [64]. The originality of the method resides in combining the simultaneous extraction of target compounds by SPE, using a hydrophilic–lipophilic balanced polymer with LC–tandem MS, and QqLIT. LODs ranging from 0.1 to 55 ng l^{-1} (depending on the matrix) were reported with SRM procedures of operation for the QqLIT mass spectrometer. This multiresidue analytical method based on off-line SPE-LC-MS/MS allowed the simultaneous extraction of 73 multiple-class pharmaceuticals in a single extraction step, simplifying noticeably the sample preparation. This work well demonstrated the potential of QqLIT, for an unambiguous and accurate identification of target compounds in effluent wastewaters. While Q-TOF is suitable for confirmation purposes, as well as identification of unknown compounds or metabolites because of their ability to provide exact mass measurements, QqLIT was shown to be appropriate for both quantitative and confirmational purposes owing to its unique scanning properties.

Hernández *et al.* [65] investigated the different approaches provided by the use of LC-MS with both QqQ and Q-TOF analyzers for the detection of antibiotics in environmental waters. A basis set of more than 100 groundwater and surface-water samples was used to further discuss the main achievements and pitfalls of LC-MS in the confirmation of positive findings. Confirmation of the identity of pollutants in environmental samples based on the acquisition of only one MS/MS transition in QqQ instruments proved insufficient for a safe confirmation. The acquisition of two specific SRM in QqQ instruments associated with the measurement of the retention time and the ion-intensity ratio is the minimum required for a safe confirmation. Meanwhile, the use of two transitions drastically reduced the risk for false positives. The use of Q-TOF instruments proved to eliminate definitely this risk of false positives, but at higher concentration levels. Nevertheless, one must keep in mind that the most reliable way of reducing the limitation observed in tandem MS is to improve chromatographic resolution, which undoubtedly helps confirmation by resolving interferent and analyte peaks, if any. The lower sensitivity of Q-TOF in comparison to QqQ can be one drawback of this approach, which can hamper the confirmation at very low analyte concentration levels.

An analytical methodology combining the use of two LC-MS techniques, LC-hybrid QqQ/LIT and LC-TOF instruments, has been investigated by Aguera *et al.* [66] to achieve both accurate and reliable target compound monitoring and identification of nontarget compounds. The strategy for the analysis was applied to a selected group of 56 organic pollutants in wastewater, comprising 38 pharmaceuticals and 10 of the most frequent metabolites. Quantification was performed by LC-QIT-MS operating under SRM mode in both positive and negative ESI. Unequivocal identification was provided by the acquisition of three SRM transitions per compound in most of the cases and by LC-TOF-MS analysis, which allows obtaining accurate mass measurements of the identified compounds with errors lower than 2 ppm. In addition, the use of TOF-MS allowed postanalysis from the full spectrum recorded at all times during the data acquisition. Methodology was applied to wastewater effluents of six sewage treatment plants in Spain. Mean concentration values ranged from 9 ng l^{-1} in the case of atrazine to 15 μg l^{-1} for paraxanthine, while LODs lie between 0.04 and 50 ng l^{-1}. The stimulants caffeine and nicotine, the antiseptics biphenylol and chlorophene, and the pharmaceuticals hydrochlorothiazide and furosemide (diuretics), atenolol (β-blocker), codeine, ketorolac, naproxen, and ibuprofen (analgesics/anti-inflammatory), gemfibrozil (lipid regulator), and ofloxacin (antibiotic) were the compounds present at the higher concentration level ($>1\,\mu g\,l^{-1}$).

Obviously, analytical methods for the pharmaceutical active compound analysis have evolved considerably and optimization of analytical instruments and specific methods – especially those based on use of LC-MS-MS systems – have reduced detection limits in such a manner that pharmaceuticals are being reported with increasing frequency worldwide. Nevertheless, further reduction of detection limits may be required to enable proper assessment of the true extent of the effect of pharmaceutical active compounds on human and ecosystem health. State-of-the-art of LC-MS-MS in the field of pharmaceutical active compounds has been reported in several reviews, and further information can be obtained there [29, 67].

A recent target analysis search for pharmaceuticals in the area of chemical water analysis provided the first example of application for the newly developed hybrid linear ion trap (LTQ) FT-Orbitrap mass spectrometer [68]. The use of the LTQ FT-Orbitrap MS–MS combines the tandem MS capability of the linear ion trap with the high-resolution and mass-accuracy capability of the FT-Orbitrap, allowing high-quality accurate mass MS^n spectra to be acquired. High-accuracy mass measurements in the LTQ FT-Orbitrap MS–MS are currently reported within the 2 ppm range using internal standard and within the 5 ppm range with external calibration [35]. Surface, ground, and drinking water samples searching for accurate masses corresponding to target compounds and their product ions known from priority lists of emerging pollutants and full-scan screening of water samples in search of ''unknown'' or unexpected masses followed by MS^n experiments were presented and discussed. In this work, results are reported for target analysis search for pharmaceuticals, benzotriazoles, illicit drugs, and for the identification of unknown compounds in a groundwater sample and in a polar extract of a landfill soil sample.

34.5.3
Endocrine-Disrupting Compounds: Estrogenes

There is growing alarm about the potential effects of endocrine- disrupting pollutants on wildlife and humans. Indeed, certain synthetic and natural chemicals have the ability to mimic hormones and, consequently, are able to interfere or disrupt normal hormonal functions of living creatures. In wildlife, endocrine-disrupting compounds are suspected in the decline of certain species favoring sterility, or change of sex in fish and shellfish [53]. Natural estrogens can easily reach the aquatic environment and particularly fishes through wastewater discharges, while humans can become exposed through the intake of this water into drinking water treatment plants. Compounds associated with these effects include natural compounds, such as estrogens and phytoestrogens, synthetic estrogens, and a wide variety of organic pollutants, including pharmaceuticals, pesticides, surfactants, plasticizers, and so on. Among them, estrogens are of particular interest owing to their high estrogenic potency, and their wide distribution in the aquatic environment [69]. According to recent reports [53, 70] physiologically active concentrations of these estrogens in the environment are ranging from picogram per liter to nanogram per liter. Furthermore, the reformation of estrogens from conjugates might be an explanation for the concentrations measured in many sewage treatment plant effluents: the less active conjugated forms, glucuronides and sulfates, excreted by the organism, can be deconjugated during wastewater treatment to regenerate the more potent parent compound. The key topics associated with the assessment of endocrine-disrupting activity in complex environmental mixtures reside mainly (i) in the improvement in chemical analysis to reduce LODs of target and (ii) in the development of integrated procedures combining chemical analysis and specific bioassays to identify the causes of the observed endocrine-disrupting effects [71]. The last key topic relates to the fact that chemical identification of all compounds responsible for the observed endocrine-disrupting effect represents an impossible task if one considers the number of new chemicals released per year in the environment. Consequently, the current state of new monitoring strategies implies the application of integrated chemical-biological procedures for the determination of endocrine-disrupting compounds [70]. These strategies are based on the effect-based analysis of environmental samples enabling determination of the causative agents. The results obtained by applying bioassays in the first step are used to direct attention to detailed chemical analysis of fractions until the correlation is achieved.

Many efforts have been undertaken for the accurate analysis of estrogens in aqueous and solid samples down to nanograms per liter and even subnanogram per liter concentrations. The first methods at the end of the 1990s used primarily GC/MS or GC/QIT-MS/MS detection [72]. Currently, an increasing number of methods use LC/MS and LC/MS/MS with the main benefits of lowering statistical errors and the absence of derivatization steps during analysis.

Moreover, the high polarity of many endocrine-disrupting compounds necessitates the use of LC/MS (or LC/MS/MS) for their analysis to typically measure compounds in environmental samples at low nanogram per liter levels. ESI and APCI are the most commonly used LC interfaces, even if APPI is sometimes used. Increasingly, tandem MS and MRM are being employed to provide added selectivity and sensitivity to these analyses. Coupling of API technology and TOF-MS combines high accuracy and excellent sensitivity due to the high-frequency sampling of all ions simultaneously recorded across a full mass range [70]. The advent of orthogonal-acceleration TOF-MS coupled to LC demonstrated its advantage for identification of endocrine-disrupting compounds in complex mixtures with accuracy of 5–10 ppm: an impressive improvement if one compares with the conventional nominal-mass information gained using a quadrupole instrument. Moreover, the tandem hybrid combination of a quadrupole analyzer to an orthogonal-acceleration Q-TOF increases the accuracy of mass measurement in diminishing accuracies down to 5 ppm: this gain in precision allows ruling out ambiguities in data interpretation, and makes easier the interpretation of decomposition tandem mass spectra.

The great concern at detection of trace quantities of endocrine-disrupting substances and their reported impact in the environment has led to the development of new methods for their characterization. As stated, endocrine-disrupting substances include a broad spectrum of compounds with large differences in polarities, structures (acidic or basic functional groups), and molecular weights, making the development of analytical techniques quite challenging. Efforts have been oriented to extraction steps in the recent work of Trenholm *et al.* [73] with the development of a comprehensive method for the analysis of several target potential endocrine-disrupting substances in various water matrices using sample volumes of 100 ml to 1 l and a single SPE step.

Description of the application of ultra-performance LC to Q-TOF-MS to the analysis of estrogens and phytoestrogens in water, associated to a semi-quantitative analysis of estradiol by ELISA (enzyme-linked immunosorbent assay) test combined with confirmatory analysis of estrogens was reported by Farré *et al.* [74]. This work has been developed for the need of cost-effective and rapid methods of screening, allowing the preselection of positive samples for further analysis, if necessary. Classical HPLC-MS/MS based on the use of QqQ or QIT analyzers operated in the SRM mode allows most often the determination of endocrine-disrupting compounds in the aquatic environment with enough sensitivity. Nevertheless, a trade-off remains between the gain of qualitative information needed to support the structural elucidation of analytes and the operation of mass analyzers in the full-scan mode associated with an inherent lack of sensitivity. Under such conditions, UPLC-Q-TOF-MS and UPLC-Q-TOF-MS/MS permitted quantitation and confirmation of target estrogens found in samples, and the screening of other structurally related compounds, phytoestrogens.

Zenobi *et al.* [75] demonstrated the potential of nanoelectrospray ionization mass spectrometry (nanoESI-MS) for the screening of suspected endocrine-disrupting compounds using chip-based nanoESI-MS. This method allows to detect specific noncovalent ligand binding to the human estrogen receptor α-ligand-binding domain (hERα LBD). As a wide variety of molecules, known as *endocrine disruptors*, can bind to the estrogen receptor and induce adverse health effects in wildlife and humans, this system represents an important environmental interest through the characterization of the binding affinity of sampled compounds toward the estrogen receptor by nanoESI-MS. NanoESI-MS allows ranking their relative affinity in consistence with binding affinities in solution. Speed of analysis (1 min/ligand), low sample consumption (90 pmol protein/ligand), and sensitivity for ligands (30 ng ml^{-1}) demonstrate how this technique must be promising as a screening method for suspected endocrine-disrupting compounds and to qualitatively evaluate their binding affinity in relation to expected adverse health effects.

34.5.4
Pesticides, Herbicides

Numerous extensive reviews on pesticide residue determination in environmental and food applications have been published in the past years [76–79]. In particular, these reviews stated how pesticide analysis initially carried out by means of GC-MS multiresidue methods evolved toward LC-MS analysis as new active ingredients appear in the industry of pesticide formulations with physicochemical properties (thermal instability and polarity) not anymore compatible with GC separation. Moreover, this trend is obviously favored by the recent improvements in LC-MS/MS instrumentation (sensitivity, selectivity, and robustness of the methods), enabling the increase in the number and diversity of pesticides that can be included in a single analysis [77]. This ability to measure more pesticides in a single run by LC/MS/MS compared to GC/MS stems from the broader peak width of LC versus GC. As stated by Richardson [53], the resulting longer cycle time in LC/MS compared to GC/MS allows more characteristic ions to be analyzed during a single analysis through MRM transitions monitoring.

Besides these potentialities of LC-MS/MS, the use of this technique allows, in most cases, reduction of the sample pretreatment, even facilitating the direct injection of the extracts due to the specificity of API. One of the major problems encountered in the quantitative analysis of pesticide residues using LC-MS is that compound and matrix-dependent response suppression or enhancement may occur, leading to the above-mentioned matrix effects. Related matrix effects of combined LC-MS using ESI or APCI have been well reviewed by Niessen *et al.* [21]. The use of LC coupled to LC-Q-TOF-MS to determine the presence of target and nontarget pesticides in water and food is detailed in the paper of Lacorte and Fernandez-Alba [80]. López de Alda *et al.* [81] reviewed the various works published from 1997 to 2005 for the determination of pesticides and their transformation products in water by means of LC coupled to tandem MS, with applications more specifically related to tandem quadrupole MS. The SRM transitions selected for the analysis of pesticides in water by QqQ tandem MS were reported in this chapter for about 70 compounds relevant to pesticide analysis in water.

In the field of pesticide residue determination, the majority of methods applied until now are mainly focused on the determination of parent compounds. However, the occurrence of pesticide transformation products can be often higher than unchanged pesticides [82]. Their inclusion in multiresidue methods represents an analytical challenge for several reasons: (i) they are still not well known, (ii) the number of potential analytes in water increases drastically, and (iii) they are usually more polar than the parent compounds and their extraction/preconcentration is consequently more difficult. Moreover, in adding more compounds in QqQ-based methods, analysis leads to a noticeable increase in the number of transitions to monitor, resulting in a likely decrease in sensitivity. The use of LC-MS/MS for residue determination can be employed to increase the selectivity of the method but the complexity of the sample can exceed the selectivity of MS detection. To circumvent these drawbacks, Hernández *et al.* [82] developed two on-line SPE-LC-ESI-MS/MS methods with the aim of rapid determination and confirmation of parent compounds and transformation products in surface and groundwater samples. This methodology allowed the simultaneous quantification and confirmation of 27 pesticides and transformation products after injection of only 2.2 ml of water sample. Quantitative recoveries in both types of samples were at the 0.025 and

$0.1\,\mu g\,l^{-1}$ levels, and LODs lower than $10\,ng\,l^{-1}$ by using the most intense MS/MS transition for quantification.

Obviously, future investigations on pesticide determination in environmental samples will focus on transformation products. Physical properties of these products can be noticeably modified compared to the parent molecule, rendering their detection more difficult. Kolpin *et al.* [83] proposed an illustration of this fact in their recent study on the widely used herbicide active compound glyphosate and its degradate aminomethyl phosphonic acid. The purpose of this study was to provide a better understanding of the potential contribution of glyphosate and its degradate aminomethyl phosphonic acid to streams derived from the urban use of this herbicide. The analytical results of 29 stream samples and 11 treated effluent samples collected around the United States during 2002 were described. LC-MS results documented the apparent contribution of waste water treatment plant effluent to stream concentrations of glyphosate and aminomethyl phosphonic acid with reporting limit of $0.1\,\mu g\,l^{-1}$ for both compounds. This confirmed that the urban use of glyphosate has contributed noticeably to glyphosate and aminomethyl phosphonic acid concentrations in the stream samples investigated. Finally, the overall results suggested that glyphosate and aminomethyl phosphonic acid are more mobile and persistent in aquatic environments than earlier researches have indicated.

One can expect that the success and future application of LC-MS instruments for trace determination of pesticides in complex matrices will be dependant on the development of accurate and precise quantification procedures using appropriate internal standards and on the availability of compound databases and mass spectral libraries. With no contest, the possibility of exact mass determination of unknown compounds in combination with the fragmentation pattern is a very valuable tool for screening polar nontarget pesticides or pesticide degradation products. In this aim, LC-TOF-MS might become one of the most applicable techniques to achieve LOD at the low parts per billion level, avoiding at the same time many difficulties related to matrix effects [80].

34.6
Conclusion

No one now disputes that LC-MS is really needed in a routine environmental laboratory to carry out monitoring of emerging contaminants (i.e., pesticides, herbicides, endocrine disruptors, pharmaceuticals, etc.). Clearly, the coupling of LC to MS has been a driving force for the development of commercial instruments, showing a mature setup that has greatly contributed to the customization of operating procedures for analytical purposes. As a matter of fact, LC-MS and LC-MS/MS has become increasingly important for both qualitative and quantitative analysis of a wide range of organic pollutants, the so-called emerging pollutants, and a large number of applications are now being found as reported in the numerous review articles quoted here.

There is still a question over which instrument should reflect better the most striking advances observed in the domain of LC-MS during the past few years. The answer seems a bit complex; nevertheless, exact mass seems more and more required in environmental analysis to identify unknown compounds. Thus, TOF and Q-TOF instruments provide sufficiently accurate mass to carry out unequivocal confirmation of target compounds, and to investigate complex environmental matrix. In this respect, it is rather easy with a TOF mass spectrometer to look for a comprehensive list of metabolites of a known target pesticide in a complex sample, even if it is still much more difficult to investigate real unknown samples. A point remains about the improvement on sensitivity in Q-TOF technology compared to QqQ mass spectrometers. The use of other types of high-resolution, that is, accurate mass instruments (e.g., Orbitrap) is well established for the environmental analysis.

However, we are sure that efforts are being made by mass spectrometer manufacturers, and, most probably within a few years, instruments will achieve improved sensitivity, linear range, and resolution in accordance with the most demanding field represented by environmental analysis.

References

1. Niessen, W.M.A. (1998) *J. Chromatogr. A*, **794**, 407–435.
2. Niessen, W.M.A. and Tinke, A.P. (1995) *J. Chromatogr. A*, **703**, 37–57.
3. Niessen, W.M.A. (2003) *J. Chromatogr. A*, **1000**, 413–436.
4. Fenn, J.B. (1993) *J. Am. Soc. Mass Spectrom.*, **4**, 524–535.
5. Fenn, J.B., Mann, M., Meng, C.K., Wong, S.F., and Whitehouse, C.M. (1990) *Mass Spectrom. Rev.*, **9**, 37–70.
6. Hager, D.B., Dovichi, N.J., Klassen, J., and Kebarle, P. (1994) *Anal. Chem.*, **66**, 3944–3949.
7. Gaskell, S.J. (1997) *J. Mass Spectrom.*, **32**, 677–688.
8. Kebarle, P. and Ho, Y. (1997) in *Electrospray Ionization Mass Spectrometry Fundamentals Instrumentation and Applications* (ed R.B. Cole), John Wiley & Sons, Inc., New York, pp. 3–63.
9. Rosenberg, E., Krska, R., Wissiack, R., Kmetov, V., Josephs, R., Razzazi, E., and Grasserbauer, M. (1998) *J. Chromatogr. A*, **819**, 277–288.
10. Niessen, W.M.A. (1999) *J. Chromatogr. A*, **856**, 179–197.
11. Raffaelli, A. and Saba, A. (2003) *Mass Spectrom. Rev.*, **22**, 318–331.
12. Robb, D.B. and Blades, M.W. (2008) *Anal. Chim. Acta*, **627**, 34–49.
13. Marchi, I., Rudaz, S., and Veuthey, J.L. (2009) *Talanta*, **78**, 1–18.
14. Bos, S.J., van Leeuwen, S.M., and Karst, U. (2006) *Anal. Bioanal. Chem.*, **384**, 85–99.
15. Hanold, K.A., Fischer, S.M., Cormia, P.H., Miller, C.E., and Syage, J.A. (2004) *Anal. Chem.*, **76**, 2842–2851.
16. NIST NIST Chemistry Web Book *http://webbook.nist.gov/chemistry/* (accessed 20 March 2013).
17. Robb, D.B., Covey, T.R., and Bruins, A.P. (2000) *Anal. Chem.*, **72**, 3653–3659.
18. Reemtsma, T. (2003) *J. Chromatogr. A*, **1000**, 477–501.
19. Matuszewski, B.K., Constanzer, M.L., and Chavez-Eng, C.M. (2003) *Anal. Chem.*, **75**, 3019–3030.
20. Lindsey, M., Meyer, M., and Thurman, E.M. (2001) *Anal. Chem.*, **73**, 4640–4646.
21. Niessen, W.M.A., Manini, P., and Andreoli, R. (2006) *Mass Spectrom. Rev.*, **25**, 881–899.
22. King, R., Bonfiglio, R., Fernandez-Metzler, C., Miller-Stein, C., and Olah, T. (2000) *J. Am. Soc. Mass Spectrom.*, **11**, 942–950.

23. Voyksner, R.D. (1997) in *Electrospray Ionization Mass Spectrometry Fundamentals Instrumentation and Applications* (ed R.B. Cole), John Wiley & Sons, Inc., New York, pp. 323–341.

24. Dams, R., Huestis, M.A., Lambert, W.E., and Murphy, C.M. (2003) *J. Am. Soc. Mass Spectrom.*, **14**, 1290–1294.

25. Souverain, S., Rudaz, S., and Veuthey, J.L. (2004) *J. Chromatogr. A*, **1058**, 61–66.

26. Rosenberg, E. (2003) *J. Chromatogr. A*, **1000**, 841–889.

27. Hakala, K.S., Laitinen, L., Kaukonen, A.M., Hirvonen, J., Kostiainen, R., and Kotiaho, T. (2003) *Anal. Chem.*, **75**, 5969–5977.

28. European Commission (2002) 2002/657/EC: Commission Decision of 12 August 2002 Implementing Council Directive 96/23/EC Concerning the Performance of Analytical Methods and the Interpretation of Results.

29. Hao, C., Clement, R., and Yang, P. (2007) *Anal. Bioanal. Chem.*, **387**, 1247–1257.

30. Ohlenbusch, G., Zwiener, C., Meckenstock, R.U., and Frimmel, F.H. (2002) *J. Chromatogr. A*, **967**, 201–207.

31. Steen, R.J.C.A., Bobeldijk, I., and Brinkman, U.A.T. (2001) *J. Chromatogr. A*, **915**, 129–137.

32. Pozo, J.O., Deventer, K., Van Eenoo, P., and Delbeke, F.T. (2008) *Anal. Chem.*, **80**, 1709–1720.

33. Wang, J. (2009) *Mass Spectrom. Rev.*, **28**, 50–92.

34. Decaestecker, T.N., Casteele, S.R.V., Wallemacq, P.E., Van Peteghem, C.H., Defore, D.L., and Van Bocxlaer, J.F. (2004) *Anal. Chem.*, **76**, 6365–6373.

35. Makarov, A., Denisov, E., Kholomeev, A., Balschun, W., Lange, O., Strupat, K., and Horning, S. (2006) *Anal. Chem.*, **78**, 2113–2120.

36. Moldoveanu, S.C. (2004) *J. Chromatogr. Sci.*, **42**, 1–14.

37. Huie, C.W. (2002) *Anal Bioanal. Chem.*, **373**, 23–30.

38. Kataoka, H. (2003) *Trends Anal. Chem.*, **22**, 232–244.

39. Hyötyläinen, T. (2009) *Anal. Bioanal. Chem.*, **394**, 743–758.

40. Gros, M., Petrovic, M., and Barcelo, D. (2006) *Anal. Bioanal.*, **386**, 941–952.

41. Koester, C.J., Simonich, S.L., and Esser, B.K. (2003) *Anal. Chem.*, **75**, 2813–2829.

42. Lopez de Alda, M.J., Diaz-Cruz, S., Petrovic, M., and Barcelo, D. (2003) *J. Chromatogr. A*, **1000**, 503–526.

43. Thurman, E.M. and Mills, M.S. (1998) *Solid Phase Extraction: Principles and Practice*, John Wiley & Sons, Inc., New York.

44. Ratola, N., Lacorte, S., Barcelo, D., and Alves, A. (2009) *Talanta*, **77**, 1120–1128.

45. Rodriguez-Mozaz, S., de Alda, M.J.L., and Barcelo, D. (2007) *J. Chromatogr. A*, **1152**, 97–115.

46. Kataoka, H., Heather, L., Lord, H.L., and Pawliszyn, J. (2000) *J. Chromatogr. A*, **880**, 35–62.

47. Mitani, K., Fujioka, M., Uchida, A., and Kataoka, H. (2007) *J. Chromatogr. A*, **1146**, 61–66.

48. Mitani, K. and Kataoka, H. (2006) *Anal. Chim. Acta*, **562**, 16–22.

49. Smith, R.M. (2003) *J. Chromatogr. A*, **1000**, 3–27.

50. Lasáková, M. and Jandera, P. (2009) *J. Sep. Sci.*, **32**, 779–812.

51. Kostiainen, R., Kotiaho, T., Kuuranne, T., and Auriola, S. (2003) *J. Mass Spectrom.*, **38**, 357–372.

52. Xu, R.N.X., Fan, L.M., Rieser, M.J., and El-Shourbagy, T.A. (2007) *J. Pharm. Biomed. Anal.*, **44**, 342–355.

53. Richardson, S.D. (2008) *Anal. Chem.*, **80**, 4373–4402.

54. Petrovic, M. and Barcelo, D. (2004) *Anal. Bioanal. Chem.*, **378**, 549–562.

55. Derek, C., Muir, G., and Howard, P.H. (2006) *Environ. Sci. Technol.*, **40**, 7157–7166.

56. Field, J.A., Johnson, C.A., and Rose, J.B. (2006) *Environ. Sci. Technol.*, **40**, 7105.

57. Koester, C.J. and Moulik, A. (2005) *Anal. Chem.*, **77**, 3737–3754.

58. Petrovic, M. and Barcelo, D. (2006) *Anal. Bioanal. Chem.*, **385**, 422–424.

59. Richardson, S.D. (2007) *Anal. Chem.*, **79**, 4295–4324.

60. Sarmah, A.K., Meyer, M.T., and Boxall, A.B.A. (2006) *Chemosphere*, **65**, 725–759.

61. EMEA (2003) Note for Guidance On Environmental Risk Assessment of Medicinal Products for Human Use.

Draft of the European Agency for the Evaluation of Medicinal Products (EMEA), 24 July 2003.

62. Fent, K., Weston, A.A., and Caminada, D. (2006) *Aquat. Toxicol.*, **76**, 122–159.

63. Stolker, A.M., Niesing, W., Hogendoorn, E.A., Versteegh, J.F.M., Fuchs, R., and Brinkman, U.A.T. (2004) *Anal. Bioanal. Chem.*, **378**, 955–963.

64. Gros, M., Petrovic, M., and Barcelo, D. (2009) *Anal. Chem.*, **81**, 898–912.

65. Pozo, O.J., Sancho, J.V., Ibáñez, M., Hernández, F., and Niessen, W.M.A. (2006) *Trends Anal. Chem.*, **25**, 1030–1042.

66. Martínez Bueno, M.J., Aguera, A., Gómez, M.J., Hernando, M.D., García-Reyes, J.F., and Fernández-Alba, A.R. (2007) *Anal. Chem.*, **79**, 9372–9384.

67. Nikolaou, A., Meric, S., and Fatta, D. (2007) *Anal. Bioanal. Chem.*, **387**, 1225–1234.

68. Hogenboom, A.C., van Leerdam, J.A., and de Voogt, P. (2009) *J. Chromatogr. A*, **1216**, 510–519.

69. Mueller, S.O. (2004) *Anal. Bioanal. Chem.*, **378**, 582–587.

70. Petrovic, M., Eljarrat, E., Lopez de Alda, M.J., and Barceló, D. (2004) *Anal. Bioanal. Chem.*, **378**, 549–562.

71. Barceló, D. and Kettrup, A. (2004) *Anal. Bioanal. Chem.*, **378**, 547–548.

72. Richardson, S.D. (2005) *Anal. Chem.*, **77**, 3807–3838.

73. Trenholm, R.A., Vanderford, B.J., Holady, J.C., Rexing, D.J., and Snyder, S.A. (2006) *Chemosphere*, **65**, 1990–1998.

74. Farré, M., Kuster, M., Brix, R., Rubio, F., Lopez de Alda, M.-J., and Barceló, D. (2007) *J. Chromatogr. A*, **1160**, 166–175.

75. Bovet, C., Wortmann, A., Eiler, S., Granger, F., Ruff, M., Gerrits, B., Moras, D., and Zenobi, R. (2007) *Protein Sci.*, **16**, 938–946.

76. Picó, Y., Blasco, C., and Font, G. (2004) *Mass Spectrom. Rev.*, **23**, 45–85.

77. Soler, C., Mañes, J., and Picó, Y. (2008) *Crit. Rev. Anal. Chem.*, **38**, 93–117.

78. Picó, Y., Font, G., Ruiz, M.J., and Fernández, M. (2006) *Mass Spectrom. Rev.*, **25**, 917–960.

79. Alder, L., Greulich, K., Kempe, G., and Vieth, B. (2006) *Mass Spectrom. Rev.*, **25**, 938–965.

80. Lacorte, S. and Fernandez-Alba, A.R. (2006) *Mass Spectrom. Rev.*, **25**, 866–880.

81. Kuster, M., López de Alda, M., and Barceló, D. (2006) *Mass Spectrom. Rev.*, **25**, 900–916.

82. Marín, J.M., Sancho, J.V., Pozo, O.J., López, F.J., and Hernández, F. (2006) *J. Chromatogr. A*, **1133**, 204–214.

83. Kolpin, D.W., Thurman, E.M., Lee, E.A., Meyer, M.T., Furlong, E.T., and Glassmeyer, S.T. (2006) *Sci. Total Environ.*, **354**, 191–197.

35

Ion Attachment Mass Spectrometry for Environmental Analysis

Yuki Kitahara, Seiji Takahashi, Masamichi Tsukagosi, Juhász Márta, and Toshihiro Fujii

35.1

Introduction

Mass spectrometry (MS) has proved to be one of the most powerful, sensitive, and versatile research techniques and has been applied analytically in a great variety of qualitative and quantitative studies. As a consequence, mass spectrometers have undergone endless cycles of optimization for a great variety of applications; however, so far, no completely satisfactory method has been developed for measurements on free radical intermediates and molecular and atomic species in ordinary gas-phase chemical reactions at the low, steady-state concentrations at which they usually occur. The combination of low concentration and short lifetime of intermediate radicals has provided a real challenge to scientists in identifying and quantifying particular compounds/mixtures in the chemical environment. Many radicals have been detected and characterized using low-energy electrons [1] and photons [2]; in practice, however, encountering a large number of interfering factors is unavoidable.

In 1971, a new method known as *alkali metal ion attachment chemical ionization mass spectrometry* (ACIMS) was proposed by Beauchamp [3] and others [4, 5]. In this method, alkali metal ions such as Li^+, Na^+, and K^+ form adduct ions (also referred to as *cationized molecules*) with molecular species through association reactions. In general, these cationized molecules are more stable than radical molecular ions or protonated molecules in the gas phase. Rollgen and Schulten [6] explored this approach for achieving cationization using the field desorption technique.

Introducing some additional features to this method, Beauchamp and coworkers [7] described a technique for obtaining mass spectra solely of quasi-molecular ions formed by the addition of Li^+ ions to the sample molecules. Several research groups have actively attempted to detect many organic complexes by attaching alkali metal ions to the sample molecules [8, 9]; however, all these experiments have generally been employed to investigate the chemical ionization reactions rather than to provide a complementary tool to identify the chemical species.

Handbook of Spectroscopy, Second Edition. Edited by Günter Gauglitz and David S. Moore.

Twenty years ago, Fujii and his group [10] developed the novel method for detection of radical species in the gas phase using Li^+ ion attachment (IA) to chemical species. As the potential of lithium ion attachment in mass spectrometry (Li^+IAMS) had not yet been realized, they attempted to reveal and explore some of the unique properties of Li^+IAMS [11–18]. It provides mass spectra of quasi-molecular ions formed by Li^+ IA to the radical species under high pressure [19–21]. Results are obtained in the form of trace of Li^+ adduct ions ($R+Li^+$) (also referred to as *cationized molecules*).

In this chapter, the development of a Li^+IAMS that is used to study the occurrence of free radical intermediates and molecular and atomic species (which are not found under ordinary conditions) on a real-time basis in the gas phase is briefly described. The newly developed device, IAMS, exhibits several advantages over conventional mass spectrometers. The performance of this equipment and unique features are also presented. Finally, the interesting applications for environmental analysis and possible future perspectives of this approach are reviewed.

35.2
Principle

Thermal IA (association) reactions are described [22, 23] by the termolecular process in this equation:

$$A^+ + R + N \rightarrow [A - R]^+ + N \tag{35.1}$$

where A denotes a positively charged alkali metal ion, R is a radical species, and N acts as a third body. The binding energy of the radical R to the alkali cation A^+ is defined by the enthalpy change for the preceding reaction. Deriving primarily from electrostatic forces, the binding energy of the reagent alkali metal ion A^+ to the radical must be high enough to permit a significant number of adducts to be formed at the partial pressure used in the experiments. As indicated, most association reactions are reversible, although not necessarily appreciably so for all experimental conditions. The bonding between ion and neutral species is generally found to be weak relative to normal chemical bond strengths; for (A–M) is typically $200\,\mathrm{kJ\,mol^{-1}}$ or less, often much less. It seems likely that the A–M bond derives primarily from electrostatic forces such as ion–dipole attraction.

Sensitivity is influenced by a large number of factors. Only a limited number of factors, however, can potentially contribute to a significant gain in sensitivity: (i) kinetic energy of the Li^+ ion and (ii) Li^+ affinity of the sample molecule. For stabilization of the adduct ionic complex, the cationization process should be carried out in a high-pressure environment because the added gas molecules serve as third bodies in the analyte addition reaction with the alkali metal ions. The voltage applied to the repeller provides sufficient kinetic energy to the reactant ion. The relationship between the Li^+ ion intensity and the repeller voltage should be considered at various ion source pressures: at higher ion source pressure, more adduct ions are produced at a higher repeller voltage. Low repeller voltage (E)

and high ion source pressure (P) favor adduct formation; as E/P is raised, the probability of this process decreases. This ion energy dependence is consistent with the reported mechanism of the IA reaction: the initial combination step of an ion–molecule association reaction is brought about by ion–dipole attraction between the reactants without any activation energy.

35.3
Instrumentation

35.3.1
Basics of Instrumental Design

An overview of the Li$^+$IAMS is sketched in Figure 35.1 [24–27]. It is composed of four major functional blocks: the sample inlet system, the reaction chamber (RC), the ion focusing system, and the mass analyzer. Three different vacuum pumps are employed to evacuate various sections of the system: the RC is maintained at 1–760 Torr by a rotary pump, and the ion focusing system and mass analyzer are held at $<2 \times 10^{-4}$ Torr and around 5×10^{-7} Torr, respectively, by two turbomolecular pumps (diffusion pumps). These functional blocks are discussed in more detail in the following sections.

35.3.1.1 Sample Inlet System

Samples may be introduced into the present MS system by several different methods, such as leaks, insertion probes, and online combinations with chromatography. Owing to the high-vacuum conditions, a controlled leak is a simple method to introduce samples but is restricted to samples with high vapor pressure. Solid and liquid samples can be introduced with a heatable insertion probe via

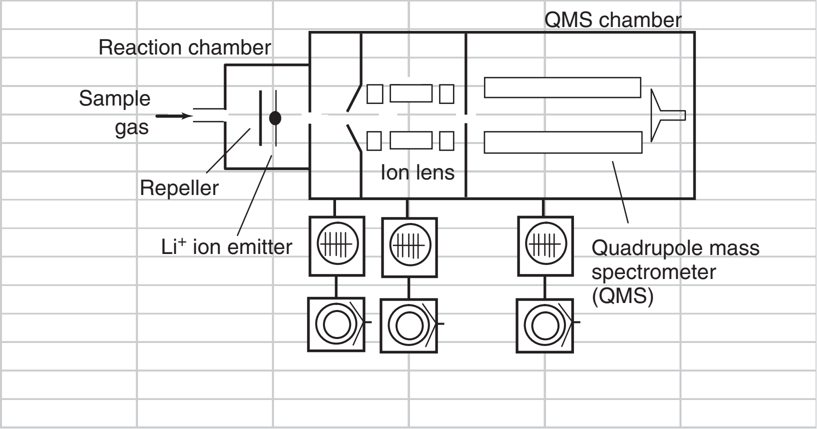

Figure 35.1 Basic scheme of ion attachment mass spectrometry.

a vacuum lock into the high vacuum. Either gas chromatography (GC) or liquid column chromatography can be easily applied as sample inlet systems. In principle, any gaseous sample whose components are to be identified can be introduced into the RC.

35.3.1.2 Reaction Chamber

The RC is a cylindrical tube (i.e., 5 cm) with a lithium ion source centered along one side. The chamber can be evacuated through a cone aperture with a rotary pump and can be maintained at high pressure by altering the pumping speed or the carrier gas flow rate.

The lithium ion source consists of a lithium ion emitter and a repeller. The Li^+ emitter is a small mineral bead (about 0.2 cm in diameter) fused to a 0.25-cm-diameter Ir wire; the bead is prepared [28] by thoroughly grinding a mixture of $Li_2O : Al_2O_3 : SiO_2$ (1 : 1 : 1 mole ratio), and primary Li^+ ions are produced by heating the bead. The emission of contaminants along with the Li^+ ions is unavoidable as emission begins, but in due course decreases to <0.1% of the total emission. The repeller electrode, consisting of a 1.5 cm diameter stainless steel disk, was placed 1 cm behind the emitter bead; its voltage was maintained at the same potential as the emitter.

35.3.1.3 Ion Focusing System

Adduct ions from the RC pass through an aperture and are directed into the differentially pumped lens region through a 1 mm diameter orifice drilled into the tip of a skimmer. No potential was applied to the skimmer. The ion focusing system is an electrostatic lens system (ELS).

35.3.1.4 Mass Analyzer and Detector

The mass analyzing chamber was equipped with a quadrupole mass spectrometer with rods biased below ground by connecting the DC-rod-driven circuit to separate DC supplies. Two possible modes of ion detection, analog and pulse counting, can be employed using a channeltron electron multiplier detector. In the pulsed mode, the channeled output from the multiplier is fed to the preamplifier–discriminator–counter system operated in the multichannel scaling mode.

35.3.2
IA-Lab

This type of mass spectrometer has recently become available commercially in a complete form [29]. It allows an easy linkup with GC, and hence the acquisition of the mass spectrum of pseudomolecular ions.

35.3.2.1 System

The optimal utilization of “direct measurements” is facilitated by the constitution of the IA-Lab (ion attachment Lab), which includes state-of-the-art features such as

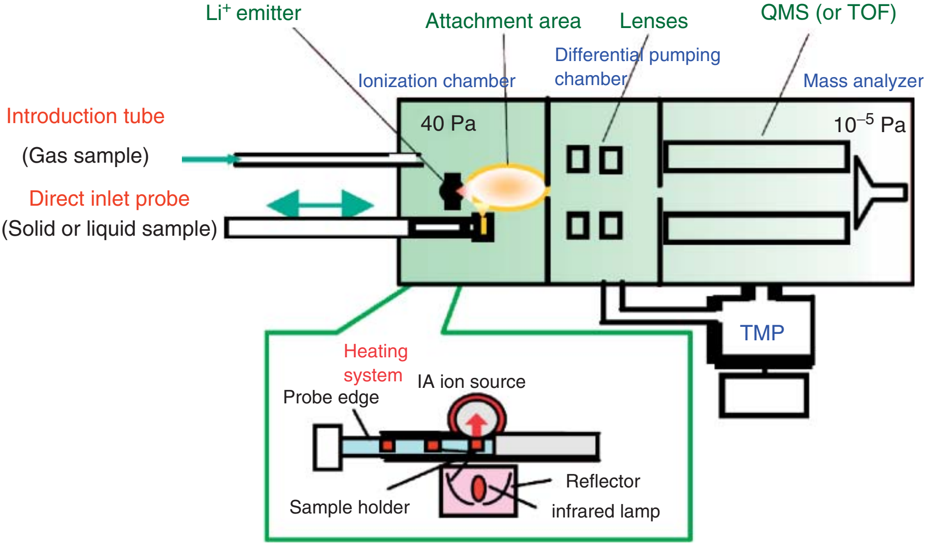

Figure 35.2 Schematics of IA-Lab. Li^+ is supplied by an Li^+ emitter. There are two types of interface for sample introduction: an introduction tube for gases and a direct inlet probe for solids and liquids. Using the direct inlet probe, the sample is heated by an infrared lamp and the temperature is controlled by the program. The range is room temperature to 500 °C. Li^+ attaches to the evolved gas in the attachment area. The ion $[M+Li]^+$ is then introduced to the mass analyzer after passing through focusing devices (lenses) in the differential pumping chamber.

a five-series direct probe, a mass spectrometer operating to 1000 m/z, and an easily maintained ion source. The sample is heated and vaporized with the infrared (IR) lamp, and ionized in the ion source, and its constituents are measured in the mass spectrometer (Figure 35.2). For vaporization in vacuum immediately under the ion source, there is little influence of pyrolysis or adsorption. In addition, use of the electron ionization (EI) source can furnish complementary fragment information. The IA-Lab can analyze not only liquid/solid samples but also adsorptive gases via a heating entry port (GC interface). A GC connection is possible, too.

35.3.2.2 **Sample Entry**

In "direct measurements," a small sample is introduced. The sample is weighed with a precision balance in the case of quantitative analysis.

35.3.2.3 **Operation**

After sample introduction, all operations are performed on a PC. In a measurement screen of standard heating, the selected ion monitoring (SIM) and a spectrum are displayed at the same time. The mass spectrometer is fully equipped with the software necessary for quantitative analysis calculations.

35.3.2.4 Application (Thermoresolution Process)

In thermogravimetric analysis-mass spectrometry (TG-MS) (outbreak gas analysis), a change in every constituent is not possible. Moreover, a continuous time change in pyrolysis gas chromatography mass spectrometry (py-GC/MS) is likewise not possible. However, thanks to the ‘‘direct measurement’’ feature of IA-Lab, a continuous change in each product generated by pyrolysis could be measured.

35.3.3
IA-TOF

Recently, the Japanese group made a unique development in this area. The alkali metal IA reaction has been applied to time-of-flight (TOF) MS [30]. Preliminary results have revealed the high efficiency of the lithium cation (Li^+) attachment reaction in the TOF mass spectrometer. The TOF MS/IA RC setup appears interesting, especially for the analysis of nonvolatile and thermally labile compounds. Studies are ongoing in a number of laboratories to develop this combination.

35.3.3.1 Main System

The tabletop IA-TOF system consists mainly of an IA ion source, a differential pumping system, and a TOF mass spectrometer. The main body of the IA-TOF system measures 50 cm × 80 cm. The adduct ions are transported by a guiding electrostatic field between the aperture at a DC potential and the skimmer at ground potential (Figure 35.3). The adduct ions that pass through the skimmer

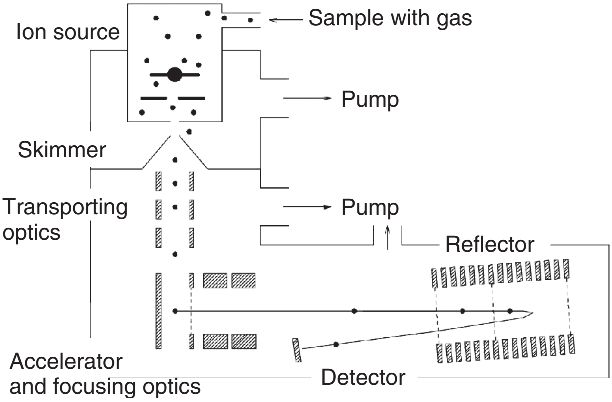

Figure 35.3 Schematic view of the IA-TOF system. Gas-phase sample molecules are ionized by alkali metal ion attachment and become adduct ions in the IA ion source. The adduct ions are extracted through the aperture into the differential pumping region, pass through the skimmer, and are introduced into the TOF mass spectrometer. Because 100 Pa of N_2 gas is introduced into the IA ion source, a differential pumping system is used to evacuate the gas as the TOF mass spectrometer must be kept in a high vacuum condition. The orthogonal acceleration reflector TOF mass spectrometer realizes mass spectrometry with a high mass resolution over a wide mass range.

are focused on the starting point in the acceleration region of the TOF mass spectrometer by an Einzel lens. Scattering of the adduct ions by collision with gaseous N_2 at the aperture and in the differential pumping region introduces spreading of the initial position and initial velocity (energy) in the acceleration region that reduces the mass resolution.

35.3.3.2 **Orthogonal Acceleration Reflector**

A TOF mass spectrometer consists mainly of a single-stage accelerator, ion focusing optics, a two-stage reflector, and an ion detector. Ions are accelerated by a pulsed electric field in the accelerator, then pass through a field-free TOF drift region, are next reflected by the reflector, and finally reach the detector. If all the ions have the same flight path and the same kinetic energy, their TOF (t_{TOF}), from the acceleration point to the detection point, is proportional to the square root of the mass m.

The mass resolution R of a TOF mass spectrometer is defined by the ratio of m to the detectable mass difference Δm:

$$R = \frac{m}{\Delta m} = \frac{t_{TOF}}{2\Delta t} \tag{35.2}$$

where Δt is the temporal broadening width of the TOF profile.

For the ion detection system, a fast-response microchannel-plate detector is used with a detection diameter of 14.5 mm (Hamamatsu F4655). The data-recording system involves a digital oscilloscope with a bandwidth of 2 GHz or a digital multistop time digitizer with 0.25 ns resolution (FAST ComTec P7887). Although the current-detection mode, where the ion signal is measured by accumulating the waveforms of the individual ion currents on the oscilloscope, is useful for qualitative measurement of the relative abundance of ions, the pulse-counting method with the multistop time digitizer permitted attainment of a wide dynamic range and sufficient ion count accuracy for quantitative measurement of the TOF spectrum. In the pulse-counting method, the intensity of the ion signal (the ion flux) should be reduced to a sufficiently low level so that multiple ions of identical mass do not hit the detector simultaneously. Mass measurements in this work were obtained by the pulse-counting method.

35.3.3.3 **IA-TOF Mass Spectrum**

Figure 35.4 depicts the mass spectrum of Ultramark 1621. Ions over a wide mass range up to m/z 3400 are clearly observed. Ions of $m/z < 350$ are due to traces of residual styrene monomers, dimers, and trimers from the pyrolysis of polystyrene samples. Two reference time peaks were adopted to obtain the conversion parameters: the time peak at m/z 111.079, corresponding to the styrene monomer $[^{12}C_8H_8 + {}^7Li]$, and the peak at m/z 1628, corresponding to Ultramark 1621 [31].

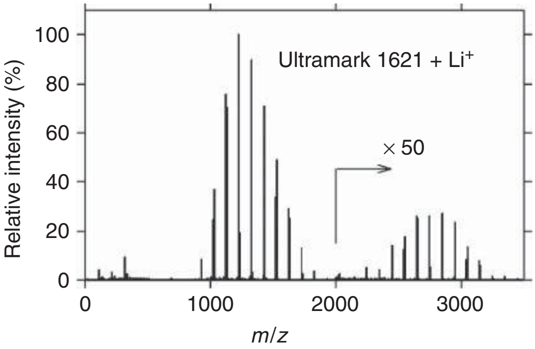

Figure 35.4 Typical mass spectrum of the mass marker Ultramark 1621. Compounds over a wide mass range up to *m*/*z* 3400 are clearly mass analyzed with high mass accuracy.

35.4
Performance and Response Characteristics and Features

35.4.1
Sensitivity

When an acetone sample was introduced at a rate of $2.6 \times 10^{-10}\,\mathrm{g\,s^{-1}}$ from the permeation tube at 25 °C, measurement of the adduct ion current was 2.9×10^{-10} A (with an ion multiplier gain of 2×10^3); hence, the sensitivity was calculated as $1.12\,\mathrm{A\,(g\,s^{-1})^{-1}}$.

The minimum detectable amount (MDA) can be estimated using the actual noise level of the system as the ultimate limitation on the minimum detectable sample size. A signal-to-noise ratio of 10 is a practical and conservative lower limit for quantitative detection; then, in pulse mode, a signal of $100\,\mathrm{counts\,s^{-1}}$ is required. For acetone, the MDA was estimated around $14.2 \times 10^{-18}\,\mathrm{g\,s^{-1}}$. On the other hand, in the analog detection mode, the MDA was calculated as $8.93 \times 10^{-15}\,\mathrm{g\,s^{-1}}$ (with a signal-to-noise ratio of 3), on the assumption that the capability of the ion detection system was around 1×10^{-14} A.

35.4.2
Linear Response Range

The signal response was linear over the chosen range of 7×10^{-11} to $8.2 \times 10^{-10}\,\mathrm{g\,s^{-1}}$. A plot of four introduction rates of acetone versus the corresponding peak heights produced an essentially straight line up to $8.2 \times 10^{-10}\,\mathrm{g\,s^{-1}}$ (data not shown); at this point, >5% of the total $\mathrm{Li^+}$ reactant ions have been used for attachment. As the cationized samples are depleted of alkali metal ion density, the response follows Beer's law, similar to that of the electron capture detector; hence, it could be concluded that for a linear response, the sample size must ensure a large excess of reactant ions in the cationizing chamber.

35.4.3
Li^+ Affinity

From Li^+ affinity data, the relative sensitivity of any organic of interest can be estimated. The production rate of the Li^+ adduct depends on the strength of the Li^+ affinity of the molecule or radical species under consideration, which ranges up to about 50 kcal mol^{-1}; this value, in turn, is heavily dependent on the polarity or polarizability of the target species. In other words, the chemical species captures the Li^+ ions and yields the $(M+Li)^+$ adduct if the Li^+ affinities are sufficiently high. Under conventional Li^+MS experimental conditions, compounds with Li^+ affinities weaker than 10 kcal mol^{-1} were barely detectable, even if they were present in abundance. Li^+ affinities of molecular species may be helpful in predicting whether the species can be detected using a minimum sample concentration.

35.4.4
Features

Some of the essential advantages and applications of the present IAMS system are as follows:

1) No dissociative ionization takes place. There is no possibility of fragmentation of the adduct ions; Li^+MS provides only molecular ions and hence can be exploited for the determination of molecular weight and the analysis of mixtures where no fragmentation is desired.
2) Mass spectra from a Li^+IAMS tend to be simple and hence it is easy to determine which form of which radical species is reacting.
3) Its sensitivity is high, especially for polar molecules, because of ion–molecule reactions.
4) Direct continuous measurements on a real-time basis of many radical species and stable molecules in a dynamic system are feasible.
5) It makes possible the analysis of any plasma via identification of both the ionic and neutral radical species and the correlation between them.
6) The detection of interstellar species and the identification of unfamiliar species, which would be immensely useful in astrophysical and astrochemical studies, are possible with this method.

These features can help widen the applications of MS.

35.5
Applications

Li^+IAMS has been done already for the interesting environmental analysis; (i) RoHS (restriction of hazardous substances) rapid analysis of brominated flame retardant (BFR); (ii) organic pollutants in atmospheric environment, exhaust gases from the automobiles, formaldehydes in doors, offensive odor species; (iii) pyrolysis of Teflon; (iv) BPA (bisphenol A) from polycarbonate (PoC) (EGA probe) (EGA, evolved gas analysis); (v) PFC (perfluoro compound); (vi) NO_x; and (vii) others such as pesticide residue in rice a volatile organic compound (VOC) in soil. Some of the studies are presented here.

35.5.1
RoHS Rapid Analysis of Brominated Flame Retardants

35.5.1.1 RoHS (Restriction of Hazardous Substances) Directive

No electronic electric apparatus can be marketed in an EU member state after July 2006 if it contains materials (e.g., polybrominated biphenyls (PBB), polybrominated diphenyl ethers (PBDEs), or heavy metals) in excess of a designated value of RoHS [32]. A fast analytical method is therefore required to quantify certain BFRs in plastic materials with a combination of instrumental techniques such as X-ray fluorescence spectrometry, thermal desorption GC, and MS. In practice, the differentiation of the various possible compounds (second screening) after bromine (Br) has been detected by X-ray fluorescence is important because many kinds of BFRs are used besides PBB and PBDEs, which are restricted by the RoHS directive in plastics products. After the second screening, an accurate measurement by GC/MS is usually carried out as for PBDEs, which are restricted by the RoHS directive. However, this may require a total of 20 h or more including the pretreatment (extraction and concentration) and calculations of the GC/MS.

IAMS is a method that can measure burned snippets or powders of RoHS samples directly, using a direct inlet probe; the peaks of the molecules of each component can be detected without separation and in real time. The total analysis time required with this method is generally 40 min, that is, very short. The IAMS method is faster than the GC/MS method and results in exact differentiation of Br compounds because there is no fragmentation. IAMS is a new method that is able to satisfy this demand. Examples of the measurement of Br compounds by IAMS are presented in Figure 35.5. Although the product of octabromodiphenyl ether is a mixture of homologs containing different numbers of Br atoms, the mass spectrum correctly shows the composition ratio.

35.5.2
Organic Pollutants in the Atmospheric Environment

Many kinds of pollutants can coexist in the atmospheric environment. Real-time measurements of pollutants are essential for the conformation of hazards and for safeguarding against chemical disasters. In this section, IAMS has been used to measure numerous kinds of volatile organic pollutants in the atmospheric environment.

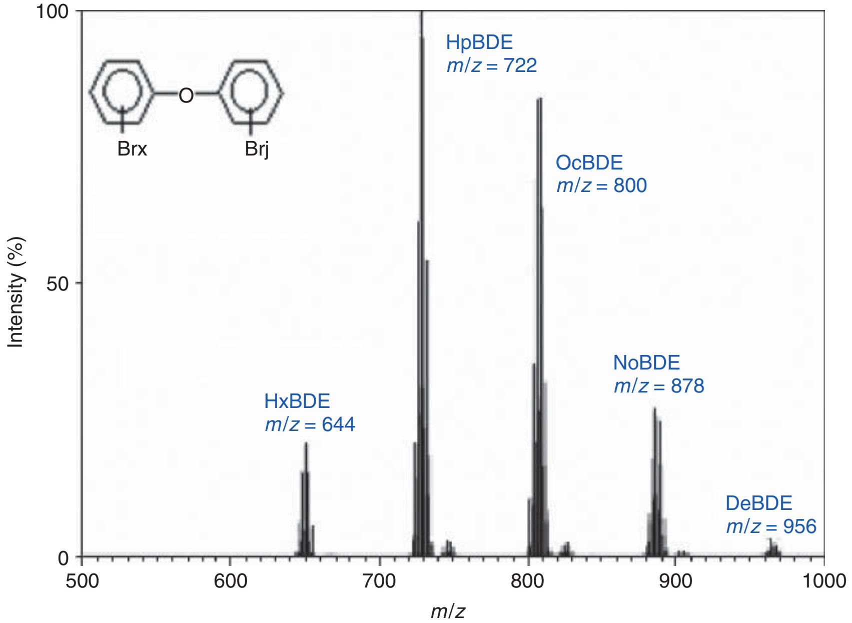

Figure 35.5 Mass spectrum of polybrominated diphenyl ethers (PBDEs).

35.5.2.1 Exhaust Gases from Automobiles

The hydrocarbon content of automobile exhaust gases varies with the engine speed; it approaches a steady state at high speed [33]. The harmful effects depend on the compounds in the exhaust gases, which can vary in nature and in concentration hour by hour. A real-time measurement of each element is demanded.

The Canon ANELVA people used the IAMS method to measure the fumes emitted by gasoline- and diesel-powered cars. The benzene content was followed in real time (Figure 35.6). The exhaust gases were measured by IAMS, with a detection limit of 0.03 ppm and a measurement interval of 10 s in selected ion monitoring. IAMS detected 1 ppm benzene 1 min after the start of the new gasoline engine instead of no detection after 3 min. It seemed that the elimination by the catalyst was not adequate after 1 min. Many kinds of organic compounds, such as aromatics, alkanes, alkenes, and dienes, were detected. The total amount of organic compounds from the new engine 3 min after the engine start was 0.05 ppm, that is, three orders less than from the old engine.

35.5.2.2 Formaldehydes Indoors

Formaldehyde (HCHO) emitted from the furniture and walls in rooms injures the eyes, the nose, and the respiratory organs and causes allergies; this is the sick house syndrome. Formaldehyde was a suspected carcinogen and in group 2A in the International Agency for Research on Cancer (IARC) classification system until 2004, when the working group of IARC reclassified it as a human carcinogen (1G) [34].

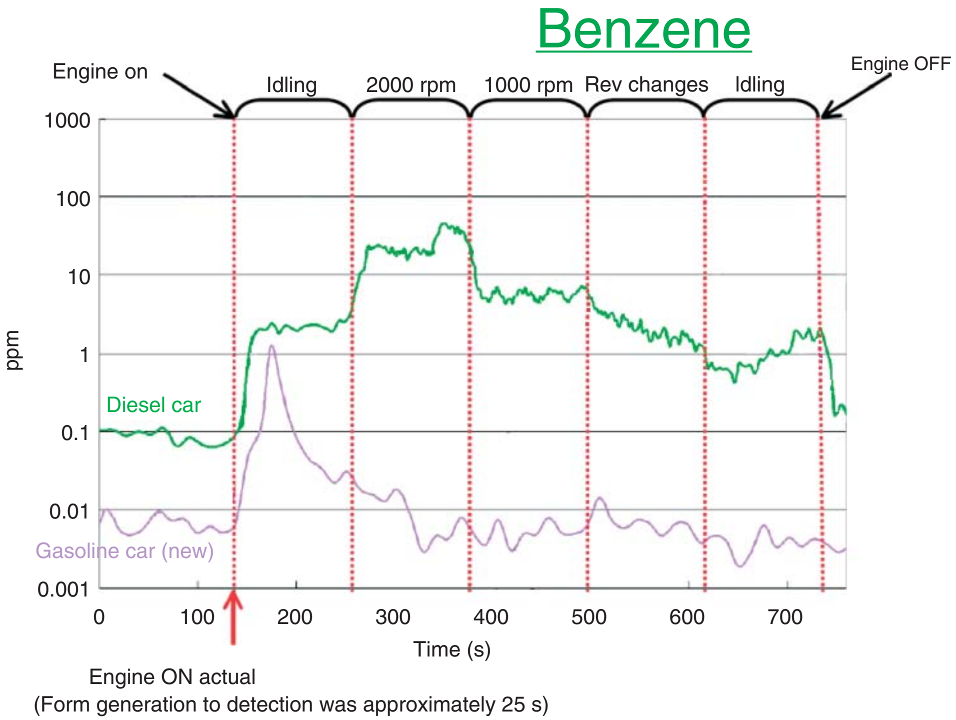

Figure 35.6 Emission behavior of benzene by revolution change of gasoline engine.

Direct measurements of formaldehyde have been attempted. As formaldehyde is a very unstable compound, pretreatment for derivatization is essential for GC, but not for IAMS. IAMS detects for formaldehyde itself in the mass spectrum and demonstrates changes in its concentration in real time in the selected ion monitor mode. The reported detection limit was 9.2 ppb and the correlation coefficient (R^2) was 0.999. The results indicate that IAMS can simultaneously monitor other atmospheric odorous substances (Figure 35.7).

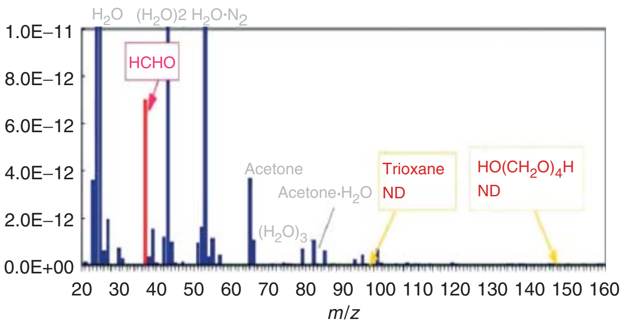

Figure 35.7 Detection of formaldehydes in doors.

35.5.2.3 Offensive Odorous Substances

Sulfide-containing compounds are among the most intense-smelling substances. The aromatic substances most generally found in food are H_2S, mercaptans, and thioalcohols present in coffee and onions, sulfides and thioethers in garlic, disulfides in garlic and leeks, trisulfides in garlic, and isothiocyanate, mustard oil, and others in Brassica nigra [35]. H_2S is responsible for most of the odor problems associated with brewing and food processing wastewater treatment. Heavier than air, colorless, corrosive, and extremely toxic, it raises serious workplace health and safety concerns [36].

H_2S was measured directly by IAMS, which yielded a calibration curve with 0.996 (R^2) and a detection limit of 0.05 ppm. On the other hand, the limit of detection by conventional MS with EI was 100 ppm, due to interference by the O_2 isotope. The IAMS mass spectrum of gases from putrefied onion indicated many kinds of sulfur compounds (Figure 35.8). These results demonstrate the possibility not only of measuring odors but also of monitoring the quality control of foods, industrial facilities, and so on.

35.5.3
Pyrolysis of Teflon

A well-established IA mass spectrometer has been combined with an IR image furnace specifically for thermal analysis studies [37]. With this system, it is

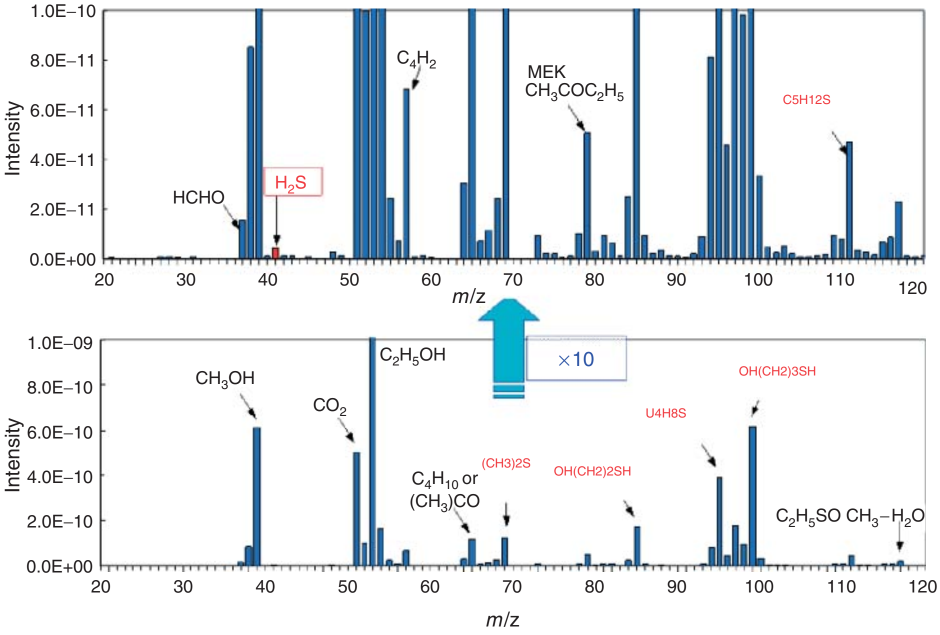

Figure 35.8 H_2S substances from decayed onion.

possible to detect any chemical species at atmospheric pressure, including radical intermediates, on a real-time basis, especially for the analysis of temperature-programmed pyrolysis products. The performance and applicability of the system is illustrated by polytetrafluoroethylene (PTFE) samples. The potential of the system for the analysis of oxidative pyrolysis has also been considered. The temperature-programmed decomposition of PTFE gave constant-slope plots of temperature versus signal intensity in a defined region and provided an apparent activation energy of 28.8 kcal mol^{-1} for the PFTE decomposition product $(CF_2)_3$.

35.5.3.1 Infrared Image Furnace (IIF)-IAMS System

The atmospheric pressure IIF interface system, and part of the Li^+IAMS developed by Canon Anelva Corporation (Kawasaki, Japan) is shown schematically in Figure 35.9. A Sinku-Riko IIF (Model RHL-E45P, Sinku-Riko, Tokyo, Japan) was used as heat source. We have developed a skimmer interface system between the IIF sample at atmospheric pressure and the high vacuum inside an MS. With this system coupled with Li^+IAMS, it is possible to detect any chemical species at atmospheric pressure, including radical intermediates, on an EGA basis.

35.5.3.2 Pyrogram

When an analyte at atmospheric pressure is introduced through the 70 μm orifice in the sample skimmer inlet, the pressure in the RC reaches 100 Pa. No deterioration or marked changes in the leak rate have been noticed over a long period of use.

The EGA of a PTFE polymer was carried out at atmospheric pressure with programmed temperature increases. The temperature was increased at a rate of

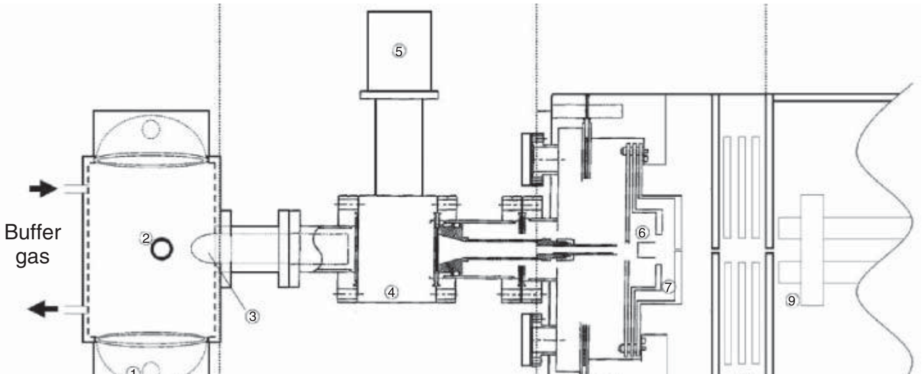

Figure 35.9 General scheme of the IIF attached to the Li^+ IAMS used in this study: (a) the IIF, showing the IR lamp unit (1) and position of the sample holder (2); (b) the interface, which has a concentric quartz tube with a 70 μm orifice at its center (3) and exit stainless steel tube (4), both of which are fixed to the flange of the gate valve (5); (c) the reaction (ionization) chamber, with the Li ion emitter bead fused onto the Ir wire (6), RC (7), and ELS (8); (d) the envelope for quadrupole MS (9).

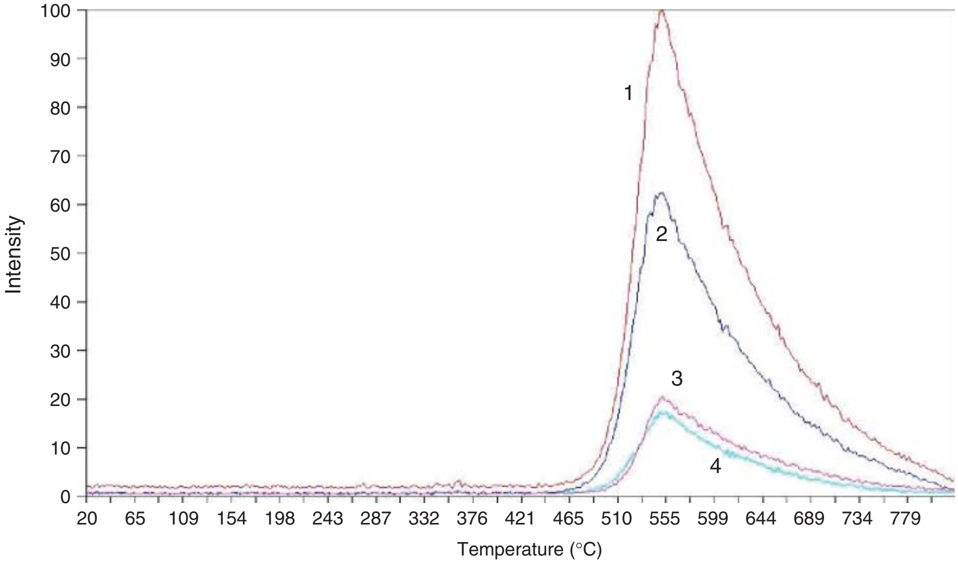

Figure 35.10 Evolution profiles of the thermal products from the pyrolysis of PTFE polymer as shown by total ion and selected ion chromatograms. (1) Total ion, (2) $(CF_2)_3$, (3) $(CF_2)_4$, and (4) $(CF_2)_2$.

$20\,^\circ\mathrm{C\,min^{-1}}$ until it reached 800 °C, after which the temperature was kept constant. In EGA, peaks caused by the decomposition products started to appear after the IIF temperature reached around 480 °C. The total ion yield of all the products increased continuously (Figure 35.10) to a maximum at 550 °C.

35.5.3.3 **Apparent Activation Energies for the Decomposition Products of PFTE**

The ionic signal (i) acquired from the real-time multiple ion detection of chemicals (Figure 35.10) released from thermally decomposed PTFE polymer is used to obtain the functional form of the kinetic rate expression. From ln[i] versus $1/T$ plots, the Arrhenius parameters (apparent activation energy) can be determined [38, 39]. We investigated the intensities of the $(CF_2)_3$ signals at m/z 157 over the temperature range 485–510 °C in order to obtain the rate expressions for PFTE degradation, on the assumption that (i) equilibrium is established between the chemical species via thermal degradation and the products are detected by $\mathrm{Li^+}$IAMS; (ii) a simple correlation exists between the adduct ion signal, the product concentrations and PFTE degradation; and (iii) the overall rate of decomposition of a heated polymer sample is constant within the limited ranges for which the degree of conversion (fraction of material decomposed, C) of the sample is in a defined range. According to the isoconversional method of Flynn and Wall, the apparent activation energy (E_a) values are invariant for conversions >5%. Therefore, we take the defined range to be from a C of 5% up to the percentage at which the slope of the ln[i] versus $1/T$ plots is no longer constant (better than $R^2 = 0.99$). The

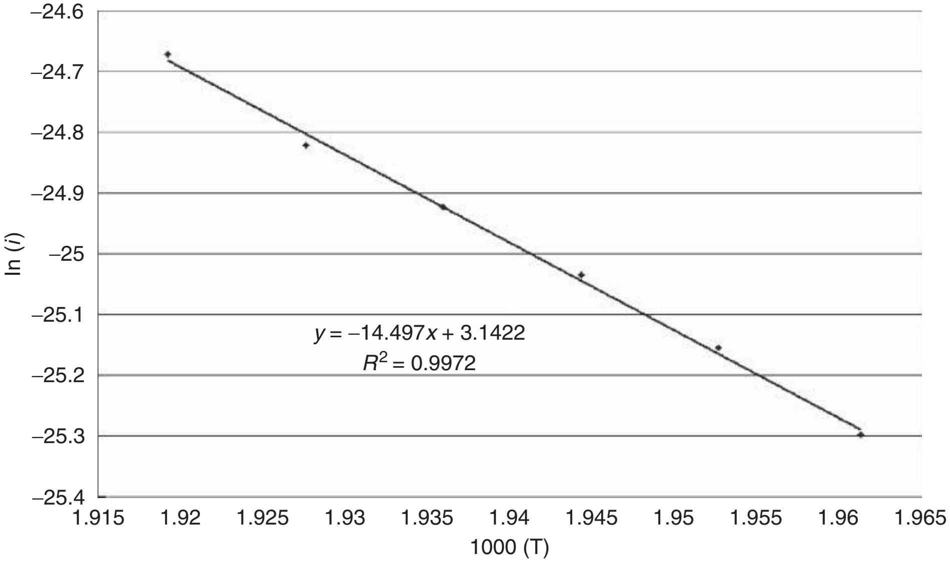

Figure 35.11 Plots of temperature versus signal intensity of $(CF_2)_3$ in the temperature range 485–510 °C.

slopes of the plots of temperature versus signal intensity in this limited region are constant (Figure 35.11). An E_a of 28.8 kcal mol^{-1} was calculated from the plots of $(CF_2)_3$. This value may be associated in some way with the nature of the bonding.

35.5.4
BPA from PoC (EGA-Probe)

The group of Fujii recently developed [40]a simple EGA system to act as an interface between solid samples at atmospheric pressure and the high vacuum inside a mass spectrometer. The newly designed stainless steel EGA system is simple, small and rugged, and fulfills all the basic requirements for EGA. With this system coupled with a Li^+IAMS, it is possible to study the temperature-programmed decomposition of a number of polymer materials by detecting any chemical species on a real-time basis. For illustrative purposes, pyrolysis experiments of some polymers were conducted.

35.5.4.1 EGA Probe

A schematic drawing of the cutaway side view of the EGA probe inlet system fabricated in this study, and part of the Li^+IAMS developed by Canon Anelva Technix Corporation (Fuchu, Japan) is shown in Figure 35.12. The newly designed inlet system for the mass spectrometer consists of a gas inlet set up as follows to ensure a consistent and streamlined entry of analytes into the mass spectrometer. There is a gas inlet in the inner tube through which a buffer gas is introduced to

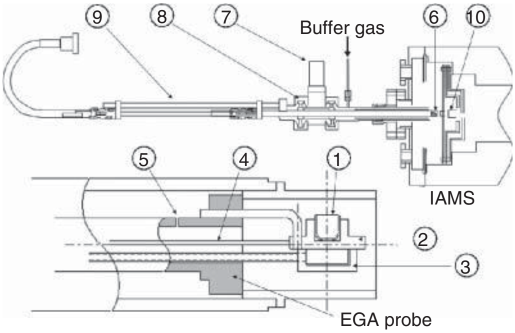

Figure 35.12 General overview of the EGA probe attached to the lithium ion attachment mass spectrometer used in this study; Extended view of EGA probe showing (1) sampler, (2) sampler holder, (3) heater, (4) thermocouple, (5) gas inlet, and the whole system of EGA probe and IAMS, showing (6) sampler, (7) isolation valve, (8) detachable flange, (9) slide guide, and (10) Li^+ emitter.

carry the product gas. This arrangement ensures that the analyte flows in a constant stream from the sampler into the mass spectrometer. The EGA probe consists of two concentric stainless steel tubes (200 mm long, 15.8 mm in outer diameter and 280 mm long, 6.4 mm in outer diameter); a holder with a sampler on it at its center is fastened to the end of this probe. The EGA probe is placed in front of the reaction (ionization) chamber of the mass spectrometer with a Conflat flange in such a way that the sampler is located 10 mm from the Li^+ emitter. The distance from the Li^+ emitter is adjustable, but 10 mm was found to be optimum.

The sample is introduced through a vacuum isolation valve into the MS. The purpose of the isolation valve is to permit the sampler, which is at atmospheric pressure, to be injected into the vacuum system while still keeping a good vacuum for the MS operation.

The sampler (Figure 35.12) is made of heat-resistant tantalum alloy. The heating element (a microceramic heater, 15 V, 15 W) is contacted on a holder body that holds the sampler on the upper end and a thermocouple at the bottom. An EGA probe controller (UP, UP150-VN) controls the programmable heating, in which the goal temperature, the rate of heating, and the length of constant-temperature periods in each step can be set up. The maximum operating temperature is 600 °C.

While the analytes are introduced directly into the mass spectrometer, the pressure of the RC is maintained between 60 and 133 Pa, which is the optimum pressure for the formation of Li^+ adducts through a termolecular association reaction.

35.5.4.2 **Pyrolysis of Polycarbonate: EGA/IAMS**

The accumulation of plastics in the environment is a matter of great concern [41–43]. One of the available solutions is waste reconversion; on the other hand, incineration can be used to transfer the waste plastics into energy. However, the combustion of plastics can produce many gaseous products, the nature of which depends mainly on the external conditions, that is, temperature and oxygen availability. Accordingly a series of experiments were conducted either in nitrogen or in an air atmosphere, to mimic the reductive environment and the conditions in incinerators.

Pyrolysis experiments were conducted with the EGA/IAMS systems (Figure 35.13). Li^+ IAMS has considerable advantages for product monitoring in the gas phase in comparison with traditional EI MS. Unlike traditional MS, employing ionization by high-energy electrons, IAMS much better preserves the profiles of the product molecules, allowing their detection as adduct ions without any fragmentation. The fundamental mass spectra are considered for the decomposition of polycarbonate. The present work also focuses on BPA, generated on increases of the pyrolysis temperature in the presence of metal chlorides. The source of BPA in nature is through contamination from incineration and it can be leached from the waste in landfills. From there, it passes into the soil and aquatic environment and potentially into water sources. BPA is an endocrine disruptor; although its acute toxicity is low, there is concern that long-term exposure to low doses of BPA may induce chronic toxicity in humans. Therefore, it is important to lower BPA emissions if possible.

Figure 35.13 illustrates the results of single ion experiments conducted with polycarbonate in nitrogen and air atmospheres respectively (Figure 35.13a,b). The mass peak at $m/z = 235$ indicates the amount of BPA emitted. It may be seen that in air (Figure 35.13b), another BPA emission peak is observed at lower temperature than in the case of the nitrogen atmosphere (Figure 35.13a). This clearly shows that there are two different mechanisms of BPA production, but at the moment this cannot be discussed in detail. Figure 35.13 c presents the results of experiments where a mixture of polycarbonate and $CuCl_2$ in a ratio of 1 : 3 was pyrolyzed [44]. The amount of BPA evolved is almost 100 times less than when no $CuCl_2$ is present. Thus, BPA emission can be successfully reduced by the addition of metal salts.

35.5.5
Perfluoro compounds

PFCs, widely used as fluorine sources in semiconductor manufacturing processes such as CVD (chemical vapor deposition) chamber cleaning and dry wafer etching, can be emitted as gaseous by-products, along with hazardous air pollutants (HAPs) and various other gases. There is a need for reliable methods [45] that are capable of measuring PFCs in the exhaust gas, in real time.

The Li^+IAMS method provides mass spectra of quasi-molecular ions formed by lithium IA to the chemical species under high-pressure conditions [13, 25, 26]. Results are obtained in the form of mass spectrum of Li^+ adducts. As an example, the method was successfully applied to the study of neutral species that emerge from CH_4/O_2 microwave (MW) discharge plasmas [46, 47], demonstrating that Li^+MS combines sensitivity with the capability of quantifying amounts of reactive products in detecting even free radical species [48].

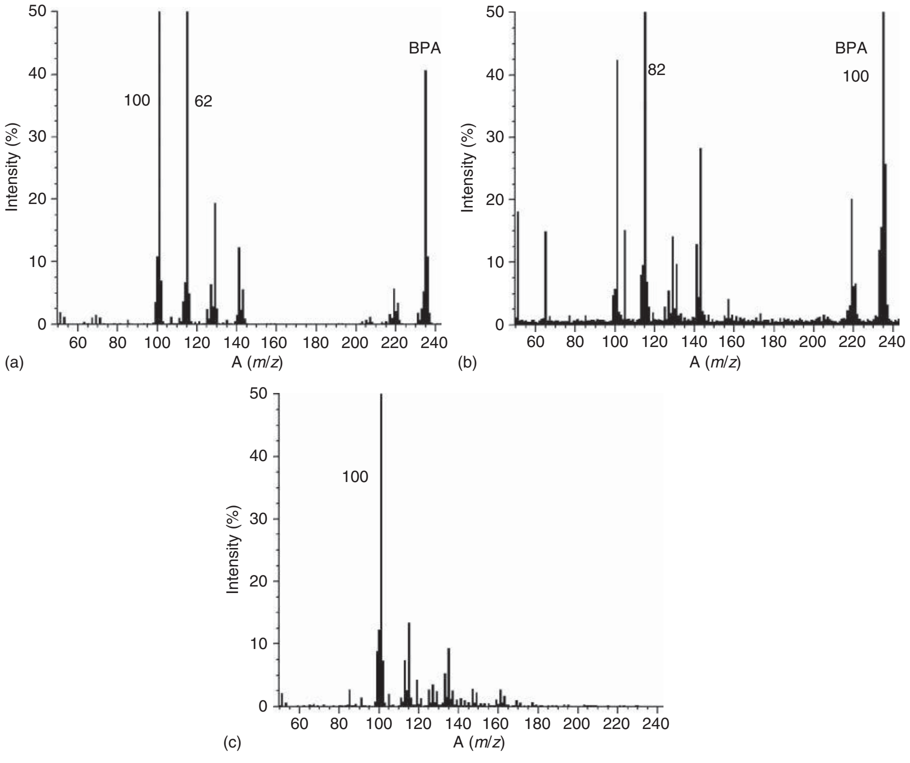

Figure 35.13 Spectra measured at 450 °C in N_2 atmosphere, air atmosphere, and with addition of $CuCl_2$ (ratio 1 : 3 in favor of $CuCl_2$) in N_2 atmosphere.

In order to support the emission reduction objectives of the semiconductor industry, the development of standardized analytical methodologies is necessary. To meet this requirement, we applied the Li^+IAMS technique to the development of a direct, real-time monitoring method for PFCs emitted from integrated circuit (IC) manufacturing facilities that we expect will significantly improve these areas of PFC measurement technology. The compounds studied were sulfur hexafluoride (SF_6), tetrafluoromethane (CF_4), trifluoromethane (CHF_3), perfluoroethane (C_2F_6), and perfluorocyclobutane (c-C_4F_8).

The c-C_4F_8 example was selected to show the performance and response characteristics possible with this analytical instrument in the optimal case. Figure 35.14a shows a typical mass spectrum in the mass range up to m/z 210 and Figure 35.14b a background spectrum, with no sample in the N_2 carrier gas. Only peaks due to Li^+ adduct molecular ion, with no fragmentation, are observed for the test compound, c-C_4F_8 (Figure 35.14a); this spectrum is completely different from the 70-eV EI mass spectrum (not shown), which shows many fragment ions, such as $C_2F_4{}^+$, $C_3F_5{}^+$, and CF^+ ions, but no molecular ions.

The c-C_4F_8 sample, diluted by 12 ml min^{-1} of N_2, was introduced at a rate of 1.8×10^{-6} g s^{-1} (0.012 ml min^{-1} of c-C_4F_8) from the needle valve at a temperature

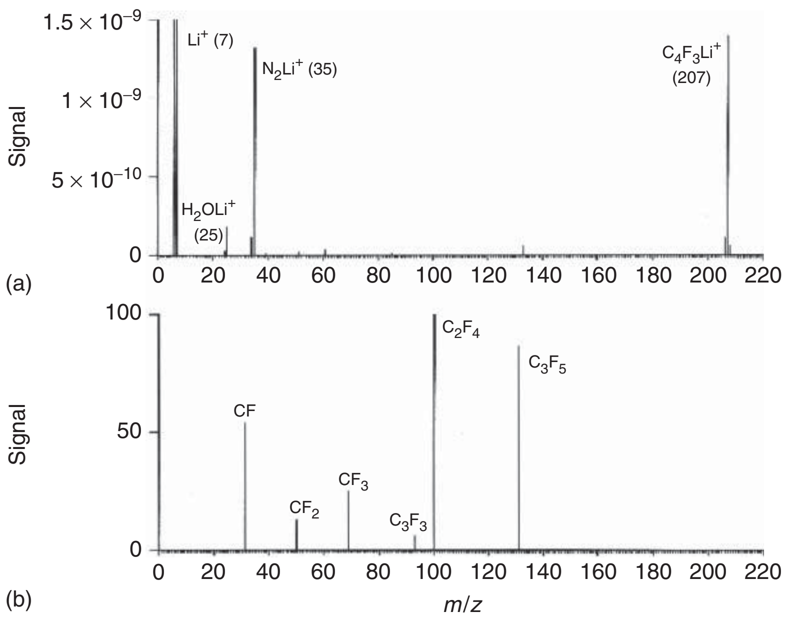

Figure 35.14 Ion attachment mass spectrum (a) obtained from 1000 ppm c-C_4F_8 in the N_2 gas, showing c-$C_4F_8Li^+$ (m/z 207). For comparison, the 70 eV electron ionization (EI) mass spectrum (b) was measured; the abundant ions observed and their relative intensities are C_2F_4 (100), C_3F_5 (87), CF (54), CF_3 (25), CF_2 (13), and C_3F_3 (6). The background mass spectrum of EI was measured with no c-C_4F_8 in the N_2 carrier gas.

of 25 °C. The measurement of the adduct ion current yielded a value of 4.4×10^{-9} A, which is the output of the ion multiplier with a gain of 7.8×10^2. Thus, the sensitivity coefficient is 2.4×10^{-3} A $(\mathrm{g\,s^{-1}})^{-1}$.

The study demonstrates [49, 50] the feasibility of measuring PFC concentrations in air by generating ions by Li^+ IA and mass analysis. The analytical method exhibited the following features: (i) high sensitivity, with the ability to detect 7 ppb c-C_4F_8 molecules in air; (ii) the ability to accept high-capacity sample introduction from atmospheric pressure and to allow easy coupling of various sample introduction sources to the MS analysis; (iii) the opportunity for real-time detection of any PFC species, including radical intermediates; (iv) the ability to identify compounds by the generation of ions that do not fragment, which is especially useful for determination of molecular weight; and (v) analysis of mixtures where no fragmentation is desired.

35.5.6
NO_x

Interest in NO_x species is fueled by the desire to understand their complex spectroscopic characteristics on a fundamental level, as well as by their importance in the Earth's atmosphere, especially with regard to key processes relating to ozone (O_3), hydroxyl radicals, and acid formation [51]. Model calculations indicate that background concentrations of NO_x in the troposphere may have risen by as much as 100%, causing a 20% increase in O_3 levels during much of the year. Beck and Ehhalt [52, 53] reported significant evidence that 30–50% of the NO_x in the upper troposphere is due to aircraft emissions.

Although nearly all (>90%) of the NO_x in the atmosphere is emitted as NO, NO is quickly converted to a variety of other species such as NO_2, HNO_3, N_2O_5, and HNO_2 [54]. There are indications that all these species may be involved in a complex way in the behavior of NO_x. A full understanding of atmospheric NO_x has not been achieved, and the existence of ionic ${NO_x}^+$ has not yet been reported. Atmospheric NO_x has been studied with the help of simulation experiments using plasma systems.

The use of an electric discharge to partially decompose a chemical compound so that the various free radicals, ions, excited molecules, and so on generated by the discharge react almost immediately with the undecomposed parent compound to generate daughter compounds is a technique that should have general applicability [55].

The Li^+IAMS technique provides mass spectra of quasi-molecular ions formed by lithium IA to chemical species under high pressure [13]. Results are obtained in the form of MS traces of Li^+ adducts. As an example, the method has been successfully applied to the study of neutral species that emerge from N_2/O_2 MW discharge plasmas [56]. This study demonstrated that Li^+MS produces only molecular ions, thus permitting the direct determination of unfamiliar and reactive species.

Because MW discharges through N_2/O_2 in the presence of water are used for simulations [57] of atmospheric chemistry, we believed that it would be desirable to examine the effects of water in detail. Therefore, we used Li^+MS with a flow system to qualitatively detect the product species, paying special attention to the effects of water.

Fujii reported on a series of experiments in which we measured the products of an MW discharge in airlike gas mixtures (80% N_2, 20% O_2, and water). The products of the discharge are molecules that are thought to exist in the atmosphere and are relevant to the study of atmospheric chemistry. The products are compared with species observed in the field. We believe that the nature of the $N_2/O_2/H_2O$ discharge plasma can be best understood after all the products have been fully identified.

The product species detected in this study were compared with the species detected in field observations [58]. Table 35.1 reveals that the neutral species observed in our laboratory resemble the constituents observed in the Earth's atmosphere. On the basis of this resemblance, we concluded that the MW-discharge-induced chemistry observed in the $N_2/O_2/H_2O$ plasma may be helpful for understanding atmospheric chemistry. We demonstrated that laboratory simulation experiments can yield results directly applicable to the Earth's atmosphere. It should be noted, however, that there are significant differences in the relative amounts of the products, especially for NO and HNO_2. They compared the ionic products we detected with those detected by Eisele *et al.* [59, 60] in a remote desert area of southeastern Arizona and on top of Mount Washington in New Hampshire. We found no agreement in terms of the products, except for one species

Table 35.1 Analysis of neutral products formed the MW discharge of the mixture of N_2 (80 Pa) : O_2 (20 Pa) : H_2O (2 Pa) and comparison with literatures.

m/z[a]	**Present study (relative intensity)**[b]	**From literature**[c] **(relative intensity)**[d]
37	NO (trace)	NO (56)
51	N_2O (310)	N_2O (trace)
53	NO_2 (100)	NO_2 (320)
54	HNO_2 (550)	HNO_2 (trace)
69	NO_3 (27)	NO_3 (trace)
70	HNO_3 (18)	HNO_3 (750)
86	—	HO_2NO_2 (3.2)
115	—	N_2O_5 (trace)

[a] The observed m/z due to Li^+-adduct.

[b] The percent intensity relative to the peak m/z 53 from the $N_2/O_2/H_2O$ system is given for all the products of MW plasmas.

[c] From Refs. [57, 58]. Distribution of reactive nitrogen species over Colorado (continental) during August and September 1984.

[d] Volume mixing ratio (ppt).

at m/z 60. We detected various kinds of ionic clusters of NO^+ and H_2O^+, but we did not detect the NH_4^+ products observed by Eisele. This difference remains unexplained at this time. The as-yet-unidentified ionic species at m/z 60 in both studies is probably $NO^+(NO)$, which is present with considerable intensity in our plasma at a H_2O partial pressure of <1 Pa. We predict that some of the ionic products found in our study that have not been reported by field investigators may eventually be detected in more sensitive *in situ* observations, especially in polluted areas.

In conclusion [61], MW discharge in an 80% N_2/20% O_2 gas mixture in the presence of water was used to simulate the Earth's atmosphere. In addition to the familiar NO and N_2O species, significant amounts of gas-phase neutral NO_2, NO_3, HNO_2, and HNO_3 were produced and detected in the form of their Li^+ adducts. A number of ionic clusters with NO^+ and H_2O^+ produced by gas-phase ion–molecule reactions were also detected.

35.5.7
Miscellaneous

35.5.7.1 Pesticide Residue in Rice

The fate and residues of pesticides in a rice paddy ecosystem were monitored because this is thought to contribute more to pesticide pollution of the environment than any agro-ecosystem in the tropics. The usual practice of harvesting rice 30–40 days after the last application of pesticide may be considered safe from the standpoint of consumption. In chlorpyrifos-treated rice fields, residues in soil were detected up to 15 days after application from high-pesticide users' farms while remaining only up to 5 days in the low-pesticide users' fields [62]. GC/MS and LC/MS are used for the analysis of the pesticide residue in fruits, vegetable, and grain. And the measurement conditions are extremely different; depending on agricultural chemicals, the demand for a rapid measurement has risen. The pesticide residue in the rice can be measured without any pretreatment other than lyophilization in IAMS at all (Figure 35.15).

35.6
Prospective

Applications to GC/MS mode are promising analytically in view of the simple mass spectra obtained where pseudo-molecular ions dominate. The compatibility of TG with Li^+MS may provide excellent temporal correspondence [63, 64] between TG and mass spectral data and the ability to identify and resolve complex coevolving products; this method appears to hold great promise for the analysis of nonvolatile d-metal complex [65] and thermally labile medicinal compounds [66–68].

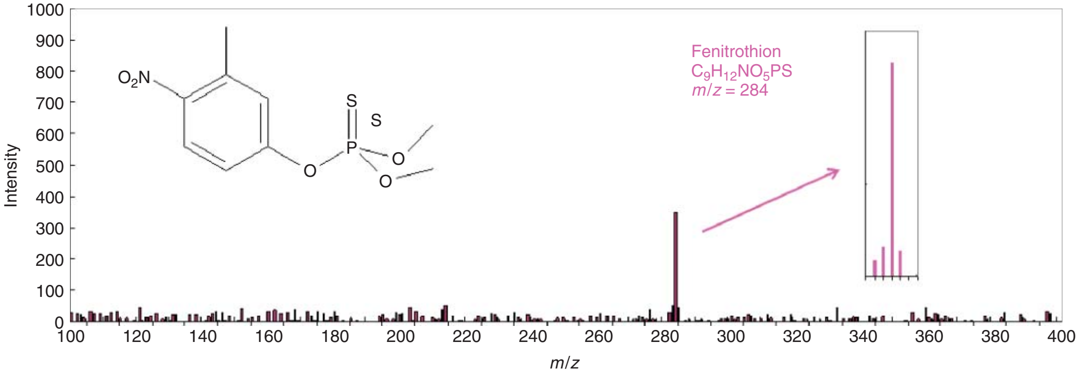

Figure 35.15 Mass spectrum of pesticide residue in rice by direct measurement.

Acknowledgments

The authors are very grateful to Canon ANELVA Technix people, especially to Dr. Y. Shiokawa, Dr. M. Nakamura, and Ms. H. Maruyama, for providing original results and for their assistance in collecting mass spectral data. This work was supported in part by a grant from the France–Japan Sasakawa Foundation (Code: 08-PT/6 & 12-PT/2).

References

1. Eltenton, G.C. (1947) *J. Chem. Phys.*, **15**, 455–465.
2. Jones, I.T.N. and Bayes, K.D. (1972) *J. Am. Chem. Soc.*, **94**, 6869–6871.
3. Beauchamp, J.L. (1971) *Annu. Rev. Phys. Chem.*, **22**, 527–561.
4. Kebarle, P. (1977) *Annu. Rev. Phys. Chem.*, **28**, 445–476.
5. Mark, T.D. and Castleman, A.W. Jr., (1984) *Adv. At. Mol. Phys.*, **20**, 65.
6. Rollgen, F.W. and Schulten, H.R. (1975) *Org. Mass Spectrom.*, **10**, 660–668.
7. Staley, R.H. and Beauchamp, J.L. (1975) *J. Am. Chem. Soc.*, **97**, 5920–5921.
8. Bombick, D., Pinkston, J.D., and Allison, J. (1984) *Anal. Chem.*, **56**, 396–402.
9. Bombick, D. and Allison, J. (1987) *Anal. Chem.*, **59**, 458–466.
10. Fujii, T. (l992) *Chem. Phys. Lett.*, **l9l**, 162–168.
11. Fujii, T. (2007) *Encyclopedia of Mass Spectrometry*, Ionization Methods, Vol. 6, America Society for Mass Spectrometry (Elsevier), pp. 327–334.
12. Sablier, M. and Fujii, T. (2002) *Chem. Rev.*, **102** (9), 2855–2924.
13. Fujii, T. (2000) *Mass Spectrom. Rev.*, **19**, 111–138.
14. Sablier, M. and Fujii, T. (2005) *Annu. Rep. Prog. Chem. Sect. C: Phys. Chem.*, **101**, 53–99.
15. Fujii, T. and Kareev, M. (2001) *J. Appl. Phys.*, **89**, 2543–2546.
16. Faye, T., Brunot, A., Sablier, M., Tabet, J.C., and Fujii, T. (2000) *Rapid Commun. Mass Spectrom.*, **14**, 1066–1073.
17. Fujii, T. (1998) *Phys. Rev. E.*, **58**, 6495–6502.
18. Fujii, T., Yashiro, M., and Tokiwa, H. (1997) *J. Am. Chem. Soc.*, **119**, 12280–12284.
19. Fujii, T. and Syouji, K. (l992) *Phys. Rev. A*, **46**, 3555–3557.
20. Fujii, T. and Syouji, K. (1993) *J. Appl. Phys.*, **74**, 3009–3012.
21. Fujii, T. (1997) *J. Appl. Phys.*, **82**, 2056–2059.
22. Good, A. (1975) *Chem. Rev.*, **75**, 561–583.
23. Castleman, A.W. and Keesee, R.G. (1986) *Acc. Chem. Res.*, **19**, 413–419.
24. Selvin, P.C. and Fujii, T. (2001) *Rev. Sci. Instrum.*, **72**, 2248–2252.
25. Fujii, T. (1992) *Anal. Chem.*, **64**, 775–778.
26. Fujii, T., Ogura, M., and Jimba, H. (1989) *Anal. Chem.*, **61**, 1026–1029.
27. Takahashi, S., Nakamura, M., and Fujii, T. (2012) *J. Am. Soc. Mass Spectrom.*, **23**, 547–552.
28. Fujii, T. and Ohta, M. (1995) *J. Phys. D: Appl. Phys.*, **28**, 1268–1272.
29. Canon Anelva Technix Corp *http://www.canon-anelva.co.jp/english/index.html.*
30. Saito, N., Nanjyo, J., Taneda, Y., Shiokawa, Y., and Tanimoto, M. (2007) *Rapid Commun. Mass Spectrom.*, **21**, 2654–2662.
31. Sugimura, Y. and Tsuge, S. (1978) *Anal. Chem.*, **50**, 1968–1972.
32. Samsonek, J., Puype, F., and Vit, D. (2007) *Comp. Opt. Disk.*, **69**, 1016/1–1016/4.
33. Walker, J.K. and O'Hara, C.L. (1955) *Anal. Chem.*, **27**, 825–828.
34. Suzuki, Y., Nakano, N., and Suzuki, K. (2003) *J. Am. Chem. Soc.*, **37** (24), 5695–5700.

35. Neukom, H. (1967) *Aroma-Geschmacksstoffe Lebensm*, Forster-Verlag A.-G., Ziirich, pp. 103–117.

36. Robbins, T.L. and Boillat, B. (2002) *Master Brew. Assoc. Am.*, **39** (1), 29–31.

37. Tsugoshi, T., Nagaoka, T., Nakamura, M., Shiokawa, Y., and Watari, K. (2006) *Anal. Chem.*, **78**, 2366–2369.

38. Kitahara, Y., Takahashi, S., Kuramoto, N., Sala, M., Tsugoshi, T., Sablier, M., and Fujii, T. (2009) *Anal. Chem.*, **81** (8), 3155–3158.

39. Coleman, W.E., Scheel, L.D., Kupel, R.E., and Larkin, R.L. (1968) *Am. Ind. Hyg. Assoc. J.*, **29**, 33–40.

40. Takahashi, S., Tsukagoshi, M., Kitahara, Y., Juhasz, M., and Fujii, T. (2010) *Rapid Commun. Mass Spectrom.*, **24**, 2625–2630.

41. Grubbs, G.R., Kleppick, M.E., and Magill, J.H. (1982) *J. Appl. Polym. Sci.*, **27**, 601–620.

42. Kitahara, Y., Takahashi, S., Tsukagoshi, M., and Fujii, T. (2010) *Chemosphere*, **80**, 1281–1284.

43. Arulmozhiraja, S., Coote, M.L., Kitahara, Y., Juhász, M., and Fujii, T. (2011) *J. Phys. Chem. A*, **115**, 4874–4881.

44. Sala, M., Kitahara, Y., Takahashi, S., and Fujii, T. (2010) *Chemosphere*, **78**, 42–45.

45. Green, D.S. (1996) PFC technical update. SEMICON WEST'96.

46. Fujii, T. and Syouji, K. (1993) *J. Phys. Chem.*, **97**, 11380–11384.

47. Fujii, T. and Syouji, K. (1994) *Phys. Rev. E*, **49**, 657–662.

48. Kitahara, Y., Takahashi, S., Tsukagoshi, M., and Fujii, T. (2011) *Chem. Phys. Lett.*, **507**, 226–228.

49. Fujii, T., Arulmozhiraja, S., Nakamura, M., and Shiokawa, Y. (2001) *Anal. Chem.*, **73**, 2937–2940.

50. Fujii, T. and Nakamura, M. (2001) *J. Appl. Phys.*, **90**, 2180–2184.

51. Crutzen, P.J. (1979) *Annu. Rev. Earth Planet. Sci.*, **7**, 443–472.

52. Beck, J.C., de Leeuw, R.F., and Penkett, S. (1992) *Atmos. Environ.*, **26A**, 17–29.

53. Ehhalt, D.H., Rohrer, F., and Wahner, A. (1992) *J. Geophys. Res.*, **97**, 3725–3738.

54. Johnson, C., Henshaw, J., and McInnes, G. (1992) *Nature*, **355**, 69–71.

55. Singh, H.B. (1987) *Environ. Sci. Technol.*, **21**, 320–327.

56. Niu, C., Lu, Y.Z., and Lieber, C.M. (1993) *Science*, **261**, 334–337.

57. Fujii, T. and Arai, N. (1999) *Astrophys. J.*, **519**, 858–863.

58. Folkins, I.A., Weinheimer, A.J., Ridley, B.A., Walega, J.G., Anderson, B., Collins, J.E., Sachse, G., Pueschel, R.F., and Blake, D.R. (1995) *J. Geophys. Res.*, **100**, 20913–20926.

59. Eisele, F.L. (1983) *Int. J. Mass Spectrom. Ion Processes*, **54**, 119–126.

60. Eisele, F.L. and McDaniel, E.W. (1986) *J. Geophys. Res.*, **91**, 5183–5188.

61. Fujii, T., Iwase, K., and Selvin, P.C. (2003) *J. Geophys. Res. Atmos.*, **108** (D4), 4148–4151.

62. Tejada, A.W., Varca, L.M., Ocampo, P., Bajet, C.M., and Magallona, E.D. (1994) *Environmental Toxicology in South East Asia*, VU University Press, Philippines, PA, pp. 145–156.

63. Kitahara, Y., Takahashi, S., and Fujii, T. (2012) Thermal analysis of polyethylene glycol: evolved gas analysis with ion attachment mass spectrometry. *Chemosphere*, **88**, 663–669 *http://dx.doi.org/10.1016/j.chemosphere.2012.03.054* (accessed 21 March 2013).

64. Kitahara, Y., Okuyama, K., Ozawa, K., Suga, T., Takahashi, S., and Fujii, T. (2012) *J. Therm. Anal. Calorim.*, **110**, 423–429.

65. Kitahara, Y. and Fujii, T. (2012) *Res. Chem. Intermed.*, **38**, 233–239.

66. Takahashi, S., Kitahara, Y., Nakamura, M., Shiokawa, Y., and Fujii, T. (2010) *Phys. Chem. Chem. Phys.*, **12**, 3910–3913.

67. Juhász, M., Kitahara, Y., and Fujii, T. (2011) *Food Chem.*, **129**, 546–550.

68. Takahashi, S., Suga, T., Kitahara, Y., and Fujii, T. (2012) *J. Phys. Chem. A*, **116**, 865–869.

36
Immunoassays

Günther Proll and Markus Ehni

36.1
Introduction

Immunoassays are biochemical tests based on the antibody/antigen interaction and can look back on a successful history of almost 50 years [1]. With this technology it is possible to measure the concentration of a compound in various matrices. Their commercial impact nowadays as a quantitative analytical technology is enormous. Thereby the area of application of immunoassays ranges from medical diagnostics to trace analytics in environmental and food samples. In the beginning, mainly radioimmunoassays (RIAs) and enzyme-linked immunosorbent assays (ELISAs) have been used in many variations [2]. These predominant test formats are commonly combined with the microplate format.

With the development of automated biosensors including flow injection analysis (FIA) [3–5] the drawback of complicated automation could be overcome. On the basis of this, new technologies have been developed for the automated handling of aqueous samples [6] and together with new test formats new fields of application were opened up. Within the past two decades, bioanalytics has become a well-established field of science. Since the introduction of biomolecules for quantitative analysis [7], the combination of FIA and biomolecular interactions could be established. For the combination of FIA with immunoassays, the term ‘‘flow injection immunoanalysis’’ (FIIA) was introduced by Fintschenko and Wilson [4]. Together with an ELISA-based test format, this technology was established for the automated, selective, and sensitive detection of small organic molecules in aqueous samples [8], especially in combination with fluorescence-based detection [9]. The main advantage of immunoassays compared to conventional analytical methods is the reduced complexity of sample pretreatment, especially the omission of the preconcentration step before the analysis. This leads to a significant saving of time and manpower. Furthermore, immunoassays allow simultaneous detection of chemical compounds of different chemical classes within a single measurement. This multianalyte approach is well established for environmental applications [10]. Current developments in microfluidics and microarray technology are the basis for multiplexed quantitative measurements in the area of environmental and food

Handbook of Spectroscopy, Second Edition. Edited by Günter Gauglitz and David S. Moore.

analysis as well as in clinical diagnostics [11–14]. Apart from the mentioned advantages, immunoassays are also very specific and cost effective.

This chapter focuses on automated immunoassays performed with biosensors at the heterogeneous phase. Therefore, after an introduction to antibodies and their properties, aspects related to thermodynamics and the particularities of biomolecular interactions at the sensor surface are discussed. The validation section is based on recommendations given by relevant institutions and covers the topics calibration and determination of validation parameters such as limit of detection (LOD) and limit of quantification (LOQ). Research in the area of automated immunoassays for biosensors is a very active field. Besides, the improvement and creation of new transduction technologies, especially the new recognition elements introduced in the last section, are a very important driving force in the development of new increasingly powerful biosensors.

36.2
Theory

Antibodies are the analytical tools in immunoassays. Their unique properties to bind an antigen with high specificity and high affinity have been designed by nature to protect vertebrates against microorganisms or other pathogens [15]. To set up an immunoassay, it is of great importance to have a good knowledge of the biochemical behavior and the structure of these glycoproteins. The best-known class of immunoglobulins used in immunoassays are the IgG antibodies with a molecular weight of approximately 150 000 Da. An IgG molecule (Figure 36.1) consists of two identical light chains (L-chains) with approximately 220 amino acid residues and two identical heavy polypeptide chains (H-chains) with approximately 450–600 amino acid residues.

These four chains are linked by covalent disulfide bonds and noncovalent forces [17]. Each H-chain is covalently linked to a carbohydrate chain, which varies from

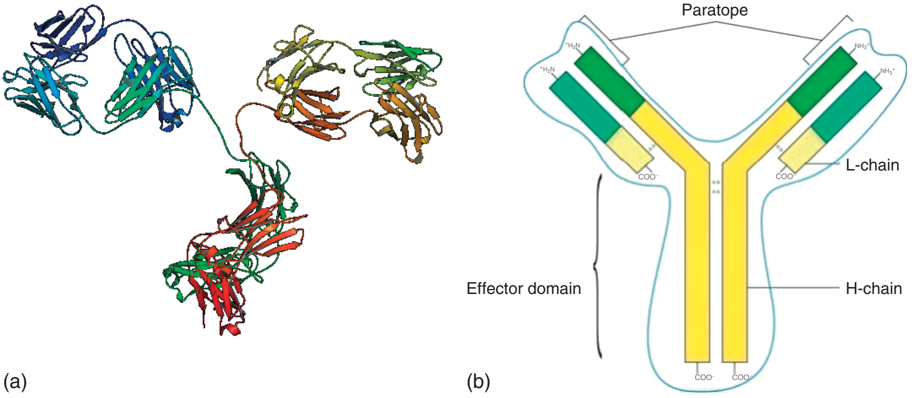

Figure 36.1 (a) Three-dimensional structure of an IgG antibody molecule based on X-ray data [16] and (b) schematic drawing of an IgG antibody molecule.

specie to specie. The typical Y-form of the molecule is the result of a bend in the middle of each H-chain. The site of an antibody molecule that binds to the antigen is called *paratope* and is complementary to the epitope of the antigen [18]. An IgG molecule has two paratopes and is therefore called *bivalent*, whereas an antigen can be monovalent or multivalent, offering multiple identical or different epitopes. Paratopes are formed by variable domains (V-region) at the N-terminal end of L- and H-chains. This variable region, composed of 110–130 amino acids, gives the antibody its specificity for binding an antigen.

Treating the antibody with a protease can cleave the V-region, producing the so-called Fab fragment, including the antigen-binding variable ends of an antibody. The use of Fab fragments can be interesting, especially in terms of a reduced molecular weight compared to a complete antibody. As will be discussed later in this chapter, a critical step during immunoassays is the diffusion-limited binding between antibodies and antigens, which can be accelerated by molecules offering a lower diffusion coefficient.

Antibodies are divided into five major classes, IgM, IgG, IgA, IgD, and IgE, based on their constant region (Fc domain) structure and immune function (Table 36.1). An overview of the different antibody classes and subclasses can be found in [16]. For most applications, for example, in molecular diagnostics or environmental analysis, antibodies from different IgG subclasses are used. For special applications such as the agglutination test during blood group typing, IgM antibodies offer interesting properties.

In nature and during the classical antibody production process [19, 20], the immune system of a vertebrate will produce many different IgG antibodies specifically for the same or for different epitopes of the antigen. These polyclonal antibodies are mixtures of antibodies with different paratopes. Using the so-called hybridoma technology [21], it is possible to produce identical antibody molecules, so-called monoclonal antibodies, all offering the same properties. Currently, there are hundreds and thousands of polyclonal and monoclonal antibodies commercially available. In addition, specialized companies offer custom antibody production. For example, in the case of monoclonal antibodies, many of these monoclonal antibodies are derived from mice cell lines and belong to the subclass IgG1. The information of the type and host is very important if an adaptor protein such as protein A or protein G will be used to bind antibodies oriented via their Fc region

Table 36.1 Antibody classes.

	IgM	**IgD**	**IgG**	**IgE**	**IgA**
H-chain	μ	δ	γ	ε	α
L-chain	κ or λ	κ or λ	κ or λ	κ or λ	κ or λ
Number of four-chain units	5	1	1	1	1
Serum concentration (mg l^{-1})	1	0.03	12	0.0003	2
Molecular weight (kDa)	950	180	150	160	190

to a surface. Furthermore, the chemical stability of an antibody is related to the host specie. Especially for applications working under nonphysiological conditions, this has to be taken into account during antibody selection. Interestingly, extreme thermodynamic stability has been reported, for example, for camelid antibody fragments [22].

The specific noncovalent binding of an antibody to an antigen is based on different distance-dependent binding forces, namely, hydrogen bonds, electrostatic, dipole–dipole, and dispersion interactions. For a stable and specific binding according to the induced fit model, the dissociation energy has to be higher than the association energy. The type of predominant binding forces responsible for an individual interaction changes with the chemical nature of an antigen, for example, whether it is more hydrophobic or hydrophilic. Nevertheless, antibodies do not bind a specific epitope at a perfect specificity. In fact, antibodies can bind other epitopes at a higher or lower specificity if there is a structural similarity. This phenomenon is called *cross-reactivity* and will be discussed in detail later.

36.2.1
Thermodynamics

After mixing an antibody with an antigen in solution, the biomolecular interaction process starts and after a short time – depending on concentrations and diffusion properties – the equilibrium between free antigen, free antibody, and antigen–antibody complex is reached:

$$\mathrm{Ag} + \mathrm{Ab} \underset{k_\mathrm{d}}{\overset{k_\mathrm{a}}{\rightleftharpoons}} \mathrm{AgAb} \tag{36.1}$$

where k_a and k_d are the association and the dissociation rate constants, respectively. According to the law of mass action, the equilibrium constant, here identical with the term *affinity constant* (K), is defined by

$$K = \frac{k_\mathrm{a}}{k_\mathrm{d}} = \frac{c_\mathrm{AgAb}}{c_\mathrm{Ag} \cdot c_\mathrm{Ab}} = \frac{c_\mathrm{AgAb}}{(c_{0,\mathrm{Ag}} - c_\mathrm{AgAb}) \cdot (c_{0,\mathrm{Ab}} - c_\mathrm{AgAb})} \tag{36.2}$$

with

K	affinity constant
Ag	antigen
Ab	antibody
AgAb	antigen–antibody complex
c_AgAb	equilibrium concentration of the antigen–antibody complex
c_Ab	equilibrium concentration of the antibody
c_Ag	equilibrium concentration of the antigen
$c_{0,\mathrm{Ab}}$	initial concentration of the antibody
$c_{0,\mathrm{Ag}}$	initial concentration of the antigen

For most antibodies, K is between 10^5 and 10^{11} M^{-1} [16]. However, it has to be pointed out that the term *affinity* describes the interaction between one paratope and one epitope. If the interaction takes place between multivalent antibody molecules and multivalent antigen molecules, multiple different bindings occur and the equilibrium constant is called *avidity* [23] or *functional affinity* [24]. The same applies to polyclonal antibodies, where the average functional affinity is the sum of the affinities provided by each clone taking into account the individual concentrations.

If the interaction between an antibody and a small antigen takes place in solution, the paratopes can bind to the epitopes independently without any structural influence on each other. In the case of surface-bound antigens at a high loading, both paratopes of an antibody can bind to an epitope at the heterogeneous phase. For this interaction, the equilibrium constant is equivalent to the avidity as a sum of the individual affinities. This is because of a reduced dissociation rate constant k_d caused by the fact that for dissociation both paratopes have to release their bound epitope at the same time [23]. The kinetics and impact of the heterogeneous phase is discussed in detail in Section 36.2.3.

In case of multianalyte immunoassays or immunoassays based on cross-reactive antibodies, the situation becomes more complicated. Here, many antigens and/or antibodies are present at the same time. Therefore, the interactions between the antigens and antibodies can be described as competing reactions according to the law of mass action reaching equilibrium after some time. To develop a mathematical model for this situation, the following assumptions are made: (i) each single reaction is reversible and in equilibrium; (ii) single binding sites B compete independently from each other against univalent analytes A; and (iii) there are no other reactions taking place:

$$A_i + B_j \rightleftharpoons A_iB_j \tag{36.3}$$

$$i = 1, 2, \ \ldots, \ n \qquad j = 1, 2, \ \ldots, \ m$$

where n is the number of different analytes and m is the number of different binding sites. The composition at equilibrium is given by

$$K_{A_iB_j} = \frac{c_{A_iB_j}}{c_{\mathrm{fA}_i} \cdot c_{\mathrm{fB}_j}} \tag{36.4}$$

$$i = 1, 2, \ \ldots, \ n \qquad j = 1, 2, \ \ldots, \ m$$

$$c_{\mathrm{tA}_i} = c_{\mathrm{fA}_i} + \sum_{i=1}^{n} c_{A_iB_j} \tag{36.5}$$

$$c_{\mathrm{tB}_j} = c_{\mathrm{fB}_j} + \sum_{j=1}^{m} c_{A_iB_j} \tag{36.6}$$

with

$K_{A_iB_j}$	affinity constant for each single reaction
c_{fA_i}	free equilibrium concentration of analyte i
c_{fB_j}	free equilibrium concentration binding site j
c_{tA_i}	total concentration of analyte i
c_{tB_j}	total concentration of binding site j
$c_{A_iB_j}$	equilibrium concentration of the complex formed by analyte I and binding site j

Combining Eqs. (36.4–36.6) yields a system consisting of n equations:

$$c_{\mathrm{tA}_i} = c_{\mathrm{fA}_i} + \sum_{j=1}^{m} \frac{K_{A_iB_j} c_{\mathrm{tB}_j} c_{\mathrm{fA}_i}}{1 + \sum_{k=1}^{n} K_{A_k,B_j} c_{\mathrm{fA}_k}} \tag{36.7}$$

If this system of n nonlinear equations is numerically solved for the concentration of the free binding sites ($c_{f\mathrm{B}_j}$) at known c_{tA_i}, c_{tB_j}, and $K_{A_iB_j}$, then c_{fB_j} can be calculated as

$$c_{\mathrm{fB}_j} = \frac{c_{\mathrm{tB}_j}}{1 + \sum_{i=1}^{n} K_{A_iB_j} c_{\mathrm{fA}_i}} \tag{36.8}$$

36.2.2
Cross-Reactivity

The existence of cross-reactivity is the normal case; however, a highly specific antibody shows a very low cross-reactivity, whereas especially for polyclonal antibodies or for antibodies directed against an antigen with potentially many different chemically similar derivatives cross-reactivity can be very high. Thus, cross-reactivity describes the ability of a specific paratope of an antibody to bind to another, structurally similar epitope. The extent to which that similar antigen is bound by that antibody is called *relative cross-reactivity* and its value is given in percentage (%CR). %CR is usually is determined by a titration experiment of the antibody with its specific analyte and with the potentially cross-reactive analytes. The measured values are normalized and plotted against the logarithm of the antigen concentration, and the test midpoint of an approximated logistic function is calculated (Section 36.4). %CR can now be calculated according to [25, 26]:

$$\%\mathrm{CR} = \frac{c_{\mathrm{saTMP}}}{c_{\mathrm{paTMP}}} \times 100 \tag{36.9}$$

with

c_{saTMP}	concentration of specific antigen at test midpoint
c_{paTMP}	concentration of the potentially cross-reactive antigen at test midpoint

On the one hand, cross-reactivity for many applications has to be carefully checked and minimized to avoid wrong results such as incorrect concentrations. On the other hand, there is a chance to use cross-reactivity as a tool, for example, to establish quantitative assays for the detection of similar compounds resulting in a sum concentration [27–30]. Another possibility can be the combination of cross-reactivity-based assay designs and data evaluation procedures derived from chemometrics to quantitatively distinguish unknown mixtures of similar analytes [31].

36.2.3
Biomolecular Interaction

Automated immunoassays in many cases include a heterogeneous phase, which at the same time can also be the transduction element, for example, of a biosensor setup. Having a look at the possible biomolecular interactions taking place in parallel, the situation compared to homogeneous assay formats becomes more complex. Figure 36.2 shows the interaction processes of an antibody with an antigen in solution and an antigen bound at the heterogeneous phase. In solution, according to the law of mass action, equilibrium is reached between free antigen, free antibody, and free antigen–antibody complex. Close to the surface, a diffusion layer is formed where no flow takes place independently from the situation of the bulk solution even in a flow cell. If the flow speed increases or the dimension of the flow cell is downsized, the thickness of this diffusion layer is reduced [32].

On the basis of this model, the interaction of an antibody with a surface-bound antigen can be divided into two steps because the antibodies have to come to the surface by diffusion before the binding event. Thereby, diffusion within a laminar

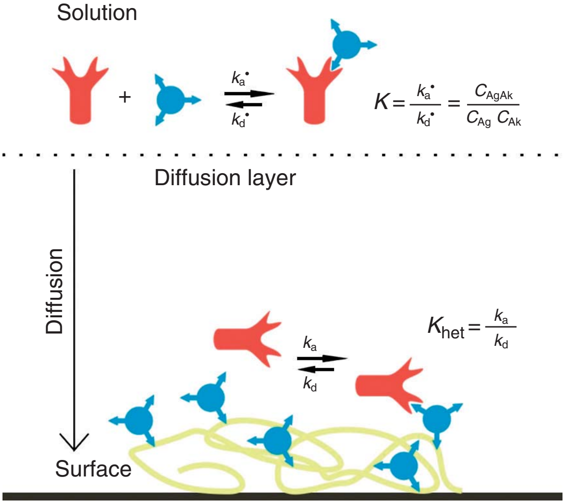

Figure 36.2 Biomolecular interactions at the heterogeneous phase.

flow can be described according to Fick's first law, which relates the diffusion flux to the concentration field:

$$J = -D \cdot \frac{dc}{dx} \tag{36.10}$$

with

J	diffusion flux
D	diffusion coefficient
c	concentration
x	length

If there is a steady state for the concentration gradient, as is the case for the flow through assay designs including a FIA, the diffusion speed depends only on the diffusion coefficient. Because D depends on the molecular weight [33], the diffusion speed increases with smaller molecules. For a typical IgG, the diffusion coefficient is approximately 4.1×10^{-7} cm^2s^{-1}. In case the diffusion of the antibody molecules to the surface is the rate-determining step, the reaction is called *mass transport controlled* or *diffusion controlled*. If the interaction between antibody and antigen at the surface determines the rate, the reaction is kinetically controlled [34].

With respect to the chosen test format (Section 36.3), it is important to consider the complex relationship between the interaction at the heterogeneous phase, diffusion and flow conditions with the performance of an immunoassay especially in terms of achievable LOD and needed incubation time.

36.3
Test Formats and Assay Design

During the past four decades, many different types of immunoassays have been developed. Each assay type or test format together with the applied detection principle provides individual properties suitable for various analytical applications. In this chapter, the focus is on six basic immunoassay principles developed for automated biosensor applications at the heterogeneous phase carried out under flow through conditions: direct test format, competitive test format, sandwich assay, replacement assay, displacement assay, and binding inhibition assay. The discussion of these different test formats covers aspects from fluorescence-based and label-free transduction principles as well as the necessity to adapt the chosen test format according to the analytical problem and the affinity of the antibody.

Classification of immunoassays at the heterogeneous phase starts with the immobilized component(s) on a surface (Figure 36.3). The first category is based on immobilized antibodies. Incubation of this sensor surface with antigen followed by label-free detection via surface plasmon resonance (SPR) [35] or reflectometric interference spectroscopy (RIfS) [36] leads to the direct test format which is noncompetitive (Figure 36.3, I.I). Because of its simplicity and easy automation it can be very powerful, for example, in diagnostics. However, there are many

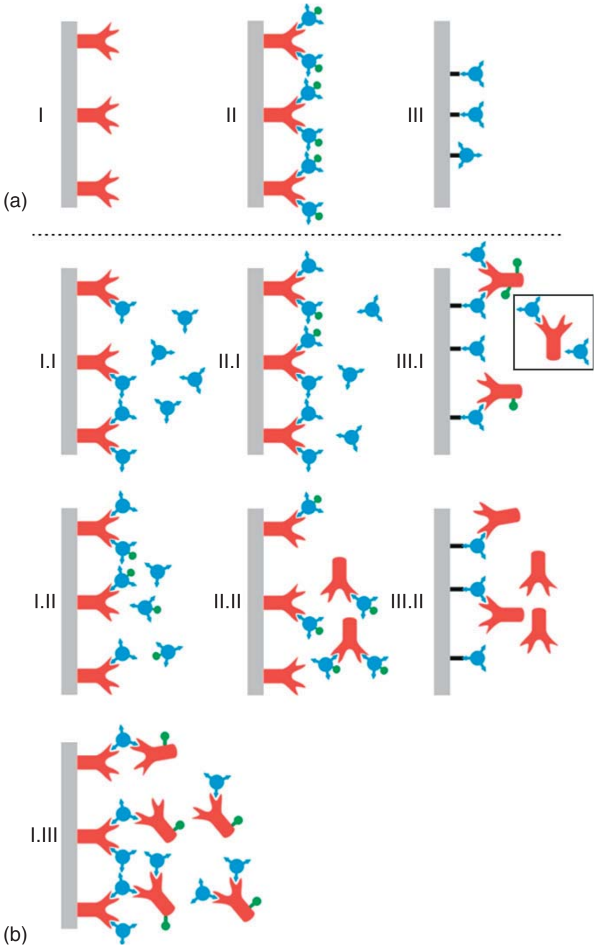

Figure 36.3 (a) Heterogeneous phase modified with antibody molecules (I), antibody molecules loaded with labeled antigen derivatives (II), or antigen derivatives (III). (b) Test formats derived from the different modified surfaces; direct test format (I.I), competitive test format (I.II), sandwich assay (I.III), replacement assay (II.I), displacement assay (II.II), binding inhibition test (III.I), and direct test format (III.II).

critical aspects to be considered: The antibody should provide a high affinity to the analyte (antigen), and during the immobilization process it is necessary to bind many antibodies (high surface loading) in a way that the paratopes are intact and accessible to the antigen. For an oriented immobilization procedure, it can be helpful to use adaptor proteins such as protein A or protein G [37] or a special chemistry protocol as published in [38]. A limitation for all label-free transduction technologies is the rather high LOD due to the mass sensitivity, which correlates with the molecular weight of the analyte [39]. Furthermore, nonspecific binding of matrix compounds to the sensor surface may affect the measurement and is the main source for artifacts. However, the direct test format plays an important role in current research, for example, on new assays for molecular diagnostics.

If a labeled analyte analog is added to the sample before the incubation step with an antibody-modified surface, the test format is called *competitive* (Figure 36.3, I.II) and usually combined with a fluorescence-based transduction method. During assay development for this type of immunoassay, it is necessary to select an antibody that offers good affinity for both analyte and labeled analyte analog, but still allows for competition. Therefore, the dissociation rate constant of the antibody should not be too high. For the sandwich assay (Figure 36.3, I.III), either fluorescence-based transduction, for example, scanning or total internal reflection fluorescence (TIRF) [40] or label-free transduction is possible. Here, either the sample is incubated with the sensor surface in a first step followed by a secondary antibody that can be modified with a fluorescence dye or the secondary antibody is mixed with the sample for preincubation. In case the antigen offers more identical epitopes, this secondary antibody can be the same as the surface-bound antibody, assuming that for this scenario the incubation of the surface with the analyte and the secondary antibody has to be carried out in two steps. In general, it is advantageous to select antibodies with very high affinities because it is a noncompetitive test format. The combination with fluorescence-based detection allows for a very low LOD. Especially for the sandwich assay, there is the additional advantage of very high selectivity because of the involved secondary antibody. Furthermore, this test format in the labeled mode is preferable when resistance against matrix compounds is important. Therefore, many of the currently used immunoassays for molecular diagnostics are based on the sandwich assay principles. The only relevant limitation of this test format exists for small molecules, which do not provide two epitopes to be bound by two antibody molecules simultaneously, for example, because of sterical hindrance.

Starting from a sensor surface modified with antibodies carrying labeled analyte analogs, two basic test formats can be created. The first one is called *replacement assay*, where the analyte in the sample replaces the bound labeled analogs during the incubation step (Figure 36.3, II.I). Replacement assays can handle large and small analytes and should be carried out with an antibody, providing a reasonable dissociation rate constant for the analyte analog. During the incubation step of a displacement assay, the labeled analyte is displaced by an antibody in the sample. This second type of immunoassays, starting from the modified surface shown in Figure 36.3, II.II, is also combined with fluorescence-based transduction methods.

A very powerful test format, especially for small analytes, for example, in environmental applications, is the binding inhibition test (Figure 36.3, III.I). During a preincubation step of the antibody with the sample, according to the law of mass action, the paratope can bind to their epitopes. Antibody molecules with at least one free binding site can bind to an immobilized antigen derivative at the sensor surface. Because the incubation step with the modified surface is mass transport controlled – this requires a very high surface loading with an antigen derivative to prevent a kinetically controlled biomolecular interaction – the binding inhibition test is noncompetitive. If high affinity antibodies are used together with a TIRF setup for the readout, extremely low limits of detection can be achieved [41].

The use of Fab fragments instead of complete antibody molecules is advantageous because of the reduced diffusion constant resulting in a higher mass transport to the surface. This test format can be easily used for multi-analyte immunoassays, when the surface modification is based on a spatially resolved chemistry protocol [42]. In addition, for surfaces modified with antigens coming from chemical classes such as steroid hormones, pesticides, or other small and robust organic molecules, there are regeneration protocols available to regenerate the sensor surface several hundred times [43].

The last test format discussed here is the second way to perform a direct immunoassay based on an antigen-modified surface (Figure 36.3, III.II). Compared to the direct test format discussed according to Figure 36.3, I.I, the only difference is that the analyte is now a specific antibody for the immobilized antigen. Because of the label-free detection mode of this test format, the same critical conditions have to be addressed but with the addition that antibodies offer a high molecular weight and therefore the weakness in terms of LOD is usually not a limitation. Furthermore, the regeneration of a sensor surface with immobilized antigens in many cases is much more robust because of the usually higher chemical stability of these molecules compared to antibodies.

Table 36.2 summarizes some important advantages and disadvantages of the most frequently used immunoassay test formats discussed. Together with the background given in Section 36.2, the choice of a proper test format for a given analytical problem must also take into account requirements coming from authorities, for example, the need for single test disposables or parallelization and miniaturization aspects related to the complete biosensor system.

Finally, the key to the functionality of all the discussed test formats is the introduction of a surface modification on the sensor surface. In addition, the requirements of this functionalization with regard to the different fluorescence-based or label-free transduction methods are different. Therefore, very special

Table 36.2 Comparison of advantages and disadvantages of important test formats.

	LOD	Mixing step	Complexity of automation	Complexity of disposables	Ability for regeneration
Sandwich assay according to Figure 36.3, I.III	+++	y	High	High	Low
Binding inhibition test according to Figure 36.3, III.I	+++	y	High	High	High
Direct test format according to Figure 36.3, I.I	−	n	Low	Low	Low
Direct test format according to Figure 36.3, III.II	+	n	Low	Low	High

+++, extremely low LOD achievable; ++, very low LOD achievable; +, low LOD achievable; −, not suitable for low LOD.

and smart surface properties are required in terms of selectivity, sensitivity, and stability, which must be provided by the introduced surface chemistry. An overview on biomaterials and processes already in use as well as an outlook for this important field is given in [44]. A review on immunosensor principles is given in [45].

36.4
Evaluation of Immunoassays

The characteristics of immunoassays are different from those of traditional analytical technologies, for example, chromatography. In this way, immunoassays show an indirect response together with a direct or inverse concentration–response relationship. Furthermore, the precision of immunoassays is usually lower owing to the higher interassay imprecision. The most important characteristic discussed here is the nonlinear behavior of the calibration curve owing to the nature of the underlying antibody/antigen interaction with respect to the statistical methods for determining validation parameters.

36.4.1
Calibration Curve

A special challenge is the fact that the classical calibration strategies and determinations of characteristic quantities for the validation described in the ISO (International Organization for Standardization) standards are not fully applicable facing the nonlinear behavior of the calibration curves [46]. If the logical principle of the best approximation of a mathematical function to the measurement results is used for the calibration, the linear model will have to be rejected for all immunoassays as a consequence. A typical calibration curve for an immunoassay – in this case, the test format was a binding inhibition test with typical inverse concentration–response relationship – is shown in Figure 36.4. With the logarithmic scaled abscissa, the data points form a sigmoid curve. Currently, in many publications dealing with calibration of immunoassays the four-parameter logistic function (Eq. (36.11) [47, 26]) is approximated to replica measurements of different concentration steps.

$$y = \frac{A_1 - A_2}{1 + \left(\frac{x}{x_0}\right)^p} + A_2 \tag{36.11}$$

with

A_1	upper asymptote
A_2	lower asymptote
X	analyte concentration
x_0	test midpoint (analyte concentration at inflection point)
p	slope at test midpoint after logarithmic transformation

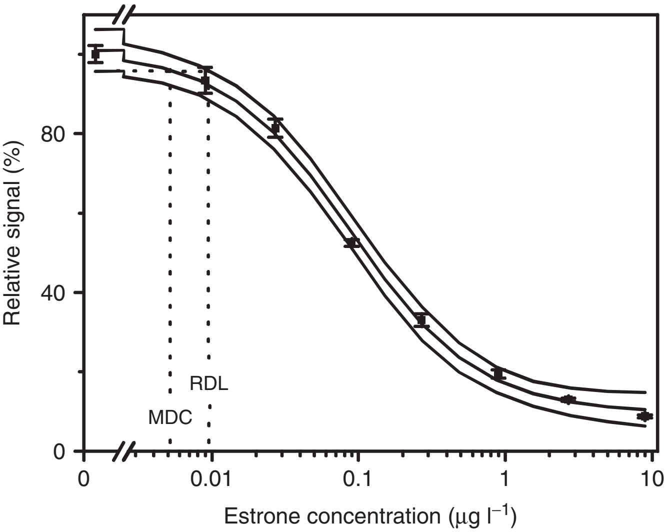

Figure 36.4 A typical calibration curve of an immunoassay performed with the binding inhibition assay as the test format. In this particular case, the sensor surface was covalently modified with an estrone derivative. A labeled polyclonal was used together with TIRF as transduction principle. The calibration curve was obtained by approximating the four-parameter logistic function to replica measurements at eight concentration steps including blanks. On the basis of a 95% confidence belt, the corresponding minimum detectable concentration (MDC) and reliable detection limit (RDL) are marked.

For the calibration shown in Figure 36.4, the parameter A_1 corresponds with the ''zero'' concentration response, and A_2 with the ''infinite'' concentration response. The approximated four-parameter logistic model assumes central symmetry of the curve. If this is not the case, a model taking into account variances of the ideal model, for example, effects caused by a changed binding statistic for bivalent antibodies, or effects of the fluidics, can improve approximation of the concentration–response relationship. Such a model shows also sigmoidal behavior but without central symmetry and therefore a more variable approximation is expressed by the five-parameter-based logistic model [48]:

$$y = \frac{A_1 - A_2}{\left[1 + \left(\frac{x}{x_0}\right)^p\right]^a} + A_2 \tag{36.12}$$

with a the asymmetry factor.

In the case of no asymmetry (asymmetry factor equals 1), the five-parameter-based logistic model changes into the four-parameter-based logistic model. A major disadvantage of the five-parameter-based logistic model is the dependence of the test midpoint from other parameters. Therefore, the test midpoint as an important quantity in assay development and especially the variation of the test midpoint cannot be calculated easily. A reparametrization can remedy this deficiency [49].

$$y = \frac{A_1 - A_2}{\left[1 + \left(2^{\frac{1}{a}} - 1\right)\left(\frac{x}{x_0}\right)^p\right]^a} + A_2 \tag{36.13}$$

Both calibration functions are recommended by the Federal Drug Administration (FDA) within the guidelines for industrial use [50]. If one wishes to benefit from the well-described regulations for linear calibration functions, a mathematical transformation of the sigmoidal curve into a linear response is possible, with limitations in the working range, by using a logit [51].

36.4.2
Validation

The recommendations given by the ISO standards for the determination of the characteristic quantities and the International Union of Pure and Applied Chemistry (IUPAC) for determining the LOD and the LOQ are dedicated to linear calibration responses. However, these rules are usually also applied to the nonlinear case of immunoassays and are partially recommended by the FDA [47]. In compliance with ''The Orange Book'' [52] as well as the ISO 32645, the LOD can be calculated as three times respectively 3.29 times the standard deviation (SD) of the blanks ($\mathrm{SD_b}$) and the LOQ is calculated as 10 times the $\mathrm{SD_b}$. However, one should consider that this is only a preliminary estimate for linear calibration curves, but also applicable to nonlinear curves. These estimations can be improved by taking into account heteroscedasticity, changing the probability of the type I and type II error, or using correct Student's *t*-test depending on the number of measurements [52]. In [53], a possibility of adapting the IUPAC definitions to sigmoidal response curves is given. As an alternative, the use of a 95% confidence belt and the associated minimum detectable concentration (MDC) and reliable detection limit (RDL), which can easily be calculated for the sigmoidal calibration curves [54], is possible. An example is given in Figure 36.4.

Usually, calibrations carried out with polyclonal antibodies providing a moderate avidity show a larger dynamic range (working range) and a smaller slope at the test midpoint compared to high affinity monoclonal antibodies. If needed, the dynamic range and the sensitivity of an immunoassay based on high-affinity antibodies can be tuned toward broader dynamic range and lower sensitivity by lowering the amount of used antibody, but this has to be carefully balanced with the expected analyte concentration range.

For immunoassays, it is important to perform the calibration with the matrix of the later application. A test to verify the accuracy of the obtained calibration curve is to perform measurements using real samples of known analyte concentrations and to determine the recovery rates according to:

$$\mathrm{RR} = \frac{\overline{x}}{x_t} \times 100 \tag{36.14}$$

with

RR	recovery rate
$\overline{x}$	mean value of measured analyte concentration
x_t	true analyte concentration

In addition, further principal analytic quantities, such as selectivity, accuracy, precision, and stability, are useful for the characterization and validation of a developed immunoassay method. In the guideline for industrial use [50], suggestions are made for immunoassays concerning the determination of these quantities. Furthermore, some annotations are given for when and which parameters should be determined.

36.4.3
Multi-Analyte Immunoassay for Water Analysis

For the development of a fully automated biosensor for water analysis, several important requirements have to be addressed. First of all, the concentrations of the small organic compounds that have to be quantified in a multianalyte approach are very low. For example, the EU directive for drinking water sets the limit for a single pesticide to 0.1 $\mu g\, l^{-1}$. Therefore, the LOD and LOQ of the immunoassays have to be below this threshold. Furthermore, a real-world application scenario of this biosensor would be the monitoring of surface water bodies implemented as a quasicontinuous measurement system. This can only be realized by a regenerative sensor element as part of an FIA-based analytical system.

The test format of choice is the binding inhibition test combined with fluorescence-based detection. In the following example, TIRF was used as the underlying transduction principle. In a first step, the biosensor system automated water analyser computer supported system (AWACSS) [43] was calibrated in a multianalyte approach for the analytes estrone, isoproturone, and atrazine. To improve the approximation of the logistic function the parameter A_1 was fixed to 100% as recommended by the FDA guidelines. The obtained validation parameters are summarized in Table 36.3.

Table 36.3 Validation parameters for the multianalyte calibration of the TIRF biosensor.

Validation parameter	Estrone	Isoproturone	Atrazine	Unit
A_1	100	100	100	%
A_2	20.55 ± 2.49	22.08 ± 5.65	20.76 ± 2.04	%
x_0	0.10 ± 0.025	0.70 ± 0.28	0.68 ± 0.09	$\mu g\, l^{-1}$
p	1.15 ± 0.29	0.74 ± 0.21	0.66 ± 0.04	—
LOD	0.003	0.007	0.003	$\mu g\, l^{-1}$
LOQ	0.007	0.040	0.018	$\mu g\, l^{-1}$

During a field test, the calibrated system was used to determine the concentrations of these compounds frequently fully automated and unattended [10]. Reference measurements performed with high-performance liquid chromatography with diode-array detection (HPLC-DAD) have been used to calculate the recovery rates. For the analyte isoproturone, the recovery rate was 80% and for atrazine 97%. Estrone was for both systems below the LOQ; therefore, quantification was not possible. These results demonstrate the reliability of this fully automated biosensor system capable of monitoring surface water quality under realistic operation conditions.

36.4.4
Immunoassay for Medical Diagnostics

The requirements for the development of a fully automated biosensor for medical diagnostics are nearly the same as for water analyses. The concentration ranges to be measured are also very low. The situation is even complicated by the fact that medical samples, such as blood plasma, have a complex composition. That places a lot of demands on the requirements of the developed assay, which can be proved by a detailed validation.

In [55], the inflammation marker CRP (C-reactive protein) was quantified. The test format was the sandwich assay measured in a TIRF-based biosensor system. For the calibration, the four-parameter as well as the five-parameter logistic functions were approximated (Figure 36.5).

It is obvious that the curve characteristics are nearly the same for both calibration curves. Performing a residual analysis leads to the conclusion that the five-parameter logistic function is the better fit in the specified concentration region of

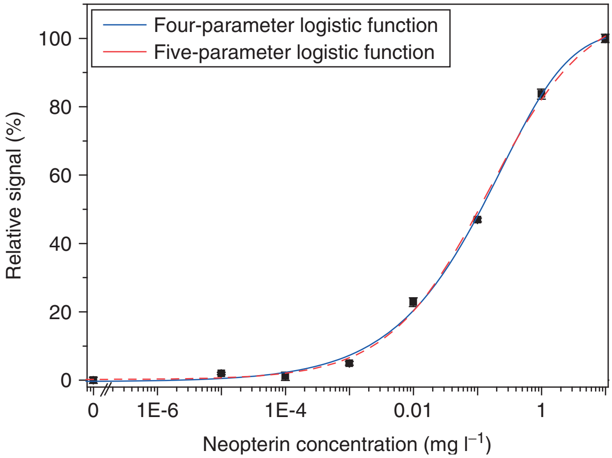

Figure 36.5 Approximation of the four-parameter and five-parameter logistic function. Analyte was C-reactive protein. The capture biomolecular recognition element was a special modified protein and the detection biomolecular recognition element was a fluorescence-labeled antibody.

interest. The calculations of the LOD and LOQ as well as the MDC and RDL are summarized in Table 36.4.

Assuming that the meaningfulness of the LOD and the MDC is quite similar, a discrepancy of several hundred percent can be observed. This leads to the conclusion that only characteristic quantities, calculated exactly the same way, can be compared with each other.

For the validation, parameters such as accuracy, precision, and the recovery rate were determined. Following the FDA validation procedure, multiple measurements in different concentration ranges were performed. At which the deviation should not exceed 15% respectively 20% in the lower concentration range (Table 36.5).

36.5
Trends

New production technologies for antibodies have drastically improved the properties of these molecules regarding affinity and stability. Especially, chimeric antibodies produced by the phage display technology can offer tailored antibodies, for immunoassays [56]. As an alternative to traditional monoclonal or polyclonal antibodies, new biological recognition elements (BREs) offer interesting properties. These BREs are commonly based on proteinaceous affibodies, aptamers, or

Table 36.4 Summary of the characteristic quantities of the CRP measurement.

Validation parameter	Neopterin	Unit
LOD	0.091	$\mu g\, l^{-1}$
LOQ	1.30	$\mu g\, l^{-1}$
MDC	0.417	$\mu g\, l^{-1}$
RDL	2.04	$\mu g\, l^{-1}$

Table 36.5 Analytical quantities for the CRP measurements.

Validation parameter	Real concentration ($\mu g\, l^{-1}$)	Deviation from real value (%)
Accuracy	0.2	12.00
	20	14.80
	2000	10.31
Precision	0.2	15.67
	20	6.76
	2000	3.56
Recovery rate	0.5	8.29
	50	9.18
	5000	8.86

All deviations are within the limits; consequently, the assay is validated within the limits set.

molecular imprinted polymers (MIPs). Besides the improvement of availability, the driving force behind these interesting research activities is the improvement of properties such as chemical stability and affinity.

Affibodies are affinity proteins and have been described for the first time in 1995 as a combinatorial protein engineering approach based on structures derived from protein A [57]. The described engineering approach is used to create a defined new specificity combined with high affinities. Affibodies have since been used for various applications such as diagnostics or biotechnology [58, 59]. Affibodies can be selected from libraries and offer, besides their robustness, usually a smaller molecular weight than that of antibodies, which is advantageous for test formats depending on the diffusion constant of the recognition structure. The smallest class of BREs discussed here are aptamers. These types of BREs include DNA and RNA oligonucleotides with high affinities for their target molecule [60]. The production of aptamers follows a systematic evolution of ligands by an exponential enrichment (SELEX) procedure [61, 62]. The temperature stability of aptamers and their robustness against chemicals and conditions used during regeneration procedures applied with affinity sensors makes these BREs ideal candidates in the area of diagnostics [63] and biosensors [64, 65].

MIPs follow a supramolecular approach, making synthetic recognition sites capable of specifically detecting small molecules in complex environments [66] or even whole cells [67]. The most significant advantages of MIPs are mechanical and chemical stability combined with high storage endurance. Usually, these polymers are used as surface coatings [68] for bioanalytical applications [69].

Besides these new developments of artificial recognition elements for specific targets, there is a trend to use receptors for a new type of analytical assays that are no longer classical quantification assays but effect-based assays. For example, the estrogen receptor in the human body recognizes a large variety of ligands that have estrogen, such as activity. For the estrogen receptor, it could be shown that not only natural estrogens can be detected but also environmental pollutants such as bisphenol A. On the basis of this example, effect-based detection of potential endocrines has been reported [70]. The main advantage of this effect-based analytic is the assessment of known and unknown active compounds. The challenge will be the stabilization of natural receptors and the statistical evaluation of these new assays.

References

1. Yalow, R.S. and Berson, S.A. (1959) Assay of plasma insulin in human subjects by immunological methods. *Nature*, **184**, 1648–1649.
2. Price, P. and Newman, D.J. (1997) *Principles and Practice of Immunoassay*, Stockton Press, New York.
3. Růžička, J. and Hansen, E.H. (1975) Flow injection analysis. Part I. A new concept of fast continuous flow analysis. *Anal. Chim. Acta*, **78** (1), 145–152.
4. Fintschenko, Y. and Wilson, G.S. (1998) Flow injection immunoassay: a review. *Mikrochim. Acta*, **129**, 7–8.
5. Hansen, E.H. (1996) Principles and applications of flow injection analysis in biosensors. *J. Mol. Recognit.*, **9**, 316–325.

6. Cerdà, V., Estela, J.M., Forteza, R., Cladera, A., Becerra, E., Altimira, P., and Sitjar, P. (1999) Flow techniques in water analysis. *Talanta*, **50**, 695–705.

7. Scheller, F. and Schubert, F. (1989) *Biosensoren*, 1st edn, Birkhäuser, Basel.

8. Krämer, P. and Schmid, R. (1991) Flow Injection Immunoanalysis (FIIA) – a new immunoassay format for the determination of pesticides in water. *Biosens. Bioelectron.*, **6** (3), 239–243.

9. Krull, I.S., Cho, B.Y., Strong, R., and Vanderlaan, M. (1997) Principles and practice of immunodetection in fluorescent immunoassay and HPLC analysis. *LC GC*, **15** (7), 620–629.

10. Tschmelak, J., Proll, G., Riedt, J., Kaiser, J., Kraemmer, P., Bárzaga, L., Wilkinson, J.S., Hua, P., Hole, J.P., Nudd, R., Jackson, M., Abuknesha, R., Barceló, D., Rodriguez-Mozaz, S., de Alda, L., Sacher, F., Stien, J., Slobodník, J., Oswald, P., Kozmenko, H., Korenková, E., Tóthová, L., Krascsenits, Z., and Gauglitz, G. (2005) Automated water analyser computer supported system (AWACSS) – Part I: project objectives, basic technology, immunoassay development, software design and networking. *Biosens. Bioelectron.*, **20** (8), 1499–1508.

11. Seidel, M. and Niessner, R. (2008) Automated analytical microarrays: a critical review. *Anal. Bioanal. Chem.*, **391**, 1521–1544.

12. Henares, T.G., Mizutani, F., and Hisamoto, H. (2008) Current development in microfluidic immunosensing chip. *Anal. Chim. Acta*, **611**, 17–30.

13. Suri, C.R., Boro, R., Nangia, Y. *et al.* (2009) Immunoanalytical techniques for analyzing pesticides in the environment. *TRAC, Trends Anal. Chem.*, **28** (1), 29–39.

14. Borrebaeck, C.A.K. (2000) Antibodies in diagnostics – from immunoassays to protein chips. *Immunol. Today*, **21** (8), 379–382.

15. Delves, P.J., Roitt, I.M., and Seamus, J. (2006) *MartinRoitt's Essential Immunology*, Blackwell Publishers.

16. Harris, L.J., Larson, S.B., Hasel, K.W., and McPherson, A. (1997) Refined structure of an intact IgG2a monoclonal antibody. *Biochemistry*, **36** (7), 1581–1597.

17. Lodisch, H., Baltimore, D., Berk, A., Zipursky, S.L., Matsudaira, P., and Darnell, J. (1996) *Molekulare Zellbiologie*, 2nd edn, Walter de Gryter, Berlin.

18. Janeway, C. and Travers, P. (1994) *Immunologie*, Spektrum Akad Verlag, Heidelberg.

19. Cohn, E. *et al.* (1949) *J. Am. Chem. Soc.*, **68**, 459.

20. Abuknesha, R.A., Gallacher, G., and Perry, L.A. (1987) The production and characterisation of antisera to 17-hydroxyprogesterone. *J. Steroid Biochem.*, **26** (3), 375–82.

21. Liddell, E. and Weeks, I. (1996) *Antikörpertechniken*, 1st edn, Spektrum Akademischer Verlag, Heidelberg.

22. Dumoulin, M., Conrath, K., Van Meirhaeghe, A., Meersman, F., Heremans, K., Frenken, L.G.J., Muyldermans, S., Wyns, L., and Andre, M. (2002) Single-domain antibody fragments with high conformational stability. *Protein Sci.*, **11** (3), 500–515.

23. Harlow, E. (1998) *Antibodies Lab Manual (P): A Laboratory Manual*, Cold Spring Harbor Laboratory, New York.

24. Mattes, M.J. (1999) Binding parameters of antibodies – a reappraisal. *Tumor Target.*, **4**, 63–69.

25. Abraham, G.E. (1969) Solid-phase radioimmunoassay of estradiol-17 beta. *J. Clin. Endocrinol. Metab.*, **29**, 866.

26. Oubina, A., Gascon, J., and Barcelo, D. (1997) Multianalyte effect in the determination of cross-reactivities of pesticide immunoassays in water matrices. *Anal. Chim. Acta*, **341**, 121.

27. Hock, B. and Niessner, R. (1995) *Immunochemical Assay of Environmental Pollutants Using Pesticides as an Example. Immunochemical Detection of Pesticides and their Metabolites in the Water Cycle*, Wiley-VCH Verlag GmbH, Weinheim, pp. 3–24.

28. Winklmair, M., Weller, M.G., Mangler, J., Schlosshauer, B., and Niessner, R.F. (1997) Development of a high sensitive enzyme-immunoassay for the determination of triazine herbicides. *J. Anal. Chem.*, **358**, 614–622.

29. Bjarnason, B., Bousios, N., Eremin, S., and Johansson, G. (1997) Flow injection enzyme immunoassay of atrazine herbicides in water. *Anal. Chim. Acta*, **347**, 111–120.

30. van Emon, J.M. and Lopez-Avila, V. (1992) Immunochemical methods for environmental analysis. *Anal. Chim. Acta*, **64**, 285–292.

31. Reder, S., Dieterle, F., Jansen, H., Alcock, S., and Gauglitz, G. (2003) Multi-analyte assay for triazines using cross-reactive antibodies and neural networks. *Biosens. Bioelectron.*, **19** (5), 447–55.

32. Guyon, E., Hulin, J.-P., and Petit, L. (1997) *Hydrodynamik*, 1st edn, Vieweg Verlag, Braunschweig, Wiesbaden.

33. Murphy, R.M., Yarmush, M.L., and Colton, C.K. (1991) Determining molecular weight distributions of antigen-antibody complexes by quasi-elastic light scattering. *Biopolymers*, **31** (11), 1289–1295.

34. Glaser, R.W. (1993) Antigen-antibody binding and mass transport by convection and diffusion to a surface: a two-dimensional computer model of binding and dissociation kinetics. *Anal. Biochem.*, **213** (1), 152–161.

35. Homola, J., Yee, S.S., and Gauglitz, G. (1999) Surface plasmon resonance sensors: review. *Sens. Actuators, B*, **54**, 3–15.

36. Brecht, A., Gauglitz, G., Kraus, G., and Nahm, W. (1993) Chemical and biochemical sensors based on interferometry at thin layers. *Sens. Actuators, B*, **11B**, 21–27.

37. Walker, J.M. (2002) *The Protein Protocols Handbook*, 2nd edn, Humana Press, Totowa, NJ.

38. Shmanai, V.V., Nikolayeva, T.A., Vinokurova, L.G., and Litoshka, A.A. (2001) Oriented antibody immobilization to polystyrene macrocarriers for immunoassay modified with hydrazide derivatives of poly(meth)acrylic acid. *BMC Biotechnol.*, **1**, 4.

39. Hänel, C. and Gauglitz, G. (2002) Comparison of reflectometric interference spectroscopy with other instruments for label-free optical detection. *Anal. Bioanal. Chem.*, **372**, 91–100.

40. Albrecht, C., Käppel, N., and Gauglitz, G. (2008) Two immunoassay formats for fully automated CRP detection in human serum. *Anal. Bioanal. Chem.*, **391** (5), 1845–1852.

41. Tschmelak, J., Prol, G., and Gauglitz, G. (2004) Immunosensor for estrone with equal limit of detection as common analytical methods. *Anal. Bioanal. Chem.*, **378**, 744–745.

42. Gauglitz, G. and Proll, G. (2008) Total internal reflection fluorescence sensing – quality assurance and application to water analysis, in *Standardization and Quality Assurance in Fluorescence Measurements I*, Springer Series on Fluorescence (ed. O.S. Wolfbeiß) (ed. U. Resch-Genger), Springer, Heidelberg.

43. Tschmelak, J., Proll, G., Riedt, J., Kaiser, J., Kraemmer, P., Bárzaga, L., Wilkinson, J.S., Hua, P., Hole, J.P., Nudd, R., Jackson, M., Abuknesha, R., Barceló, D., Rodriguez-Mozaz, S., de Alda, L., Sacher, F., Stien, J., Slobodník, J., Oswald, P., Kozmenko, H., Korenková, E., Tóthová, L., Krascsenits, Z., and Gauglitz, G. (2005) Automated water analyser computer supported system (AWACSS) – Part II: intelligent, remote-controlled, cost-effective, on-line, water-monitoring measurement system. *Biosens. Bioelectron.*, **20** (8), 1509–1519.

44. Ratner, B.D. and Bryant, S.J. (2004) Biomaterials: where we have been and where we are going. *Annu. Rev. Biomed. Eng.*, **6**, 41–75.

45. Knopp, D. and Niessner, R. (2004) *Waste Manag. Ser.*, **4**, 505.

46. Findlay, J.W.A. and Dillard, R.F. (2007) Appropriate calibration curve fitting in ligand binding assays. *Am. Assoc. Pharm. Sci. J.*, **9** (2), E260–E267.

47. Dudley, R.A., Edwards, P., Ekins, R.P., Finney, D.J., McKenzie, I.G.M., Raab, G.M., Rodbard, D., and Rodgers, R.P.C. (1985) Guidelines for imunnoassay data processing. *Clin. Chem.*, **31** (8), 1264–1271.

48. Gottschalk, P.G. and Dunn, J.R. (2005) The five-parameter logistic: a characterization and comparison with the four-parameter logistic. *Anal. Biochem.*, **343** (1), 54–65.

49. Liao, J.J.Z. and Liu, R. (2009) Re-parameterization of five-parameter logistic function. *J. Chemom.*, **23** (5), 248–253.
50. Food and Drug Administration (2001) Guidance for Industry Bioanalytical Method Validation, U.S. Department of Health and Human Services, Center for Drug Evaluation and Research (CDER), Center for Veterinary Medicine (CVM).
51. Govindarajulu, Z. (2001) *Statistical Techniques in Bioassay*, 2nd revised and enlarged edn, Karger Publishers, Basel.
52. Inczedy, J., Lengyel, T., and Ure, A.M. (1998) Compendium of analytical nomenclature. definitive rules 1997, in *The Orange Book*, 3rd edn, Blackwell Science, Oxford.
53. Hayashi, Y., Matsuda, R., Ito, K., Nishimura, W., Imai, K., and Maeda, M. (2005) Detection limit estimated from slope of calibration curve: an application to competitive ELISA. *Anal. Sci.*, **21**, 167–169.
54. O'Connel, M.A., Belanger, B.A., and Haaland, P.D. (1993) *Chemom. Intell. Lab. Syst.*, **20**, 97–114.
55. Ehni, M. (2012) Validierung und assayimplementierung im rahmen der entwicklung eines neuen optischen biosensorsystems für die medizinische diagnostik. Dissertation. Universität Tübingen.
56. Kretzschmar, T. and Rüden, T. (2002) Antibody discovery: phage display. *Curr. Opin. Biotechnol.*, **13** (6), 598–602.
57. Nord, N., Nilsson, U., and Nygren, A. (1995) Combinatorial library of an alpha-helical bacterial receptor domain. *Protein Eng.*, **8**, 601–608.
58. Nord, K. *et al.* (1997) Binding proteins selected from combinatorial libraries of an alpha-helical bacterial receptor domain. *Nat. Biotechnol.*, **15**, 772–777.
59. Nygren, P.-Å. (2008) Alternative binding proteins: affibody binding proteins developed from a small three-helix bundle scaffold. *FEBS J.*, **275**, 2668–2676.
60. David, H., Bunka, J., and Stockley, P.G. (2006) Aptamers come of age – at last. *Nat. Rev. Microbiol.*, **4**, 588–596.
61. Ellington, A.D. *et al.* (1990) In vitro selection of RNA molecules that bind specific ligands. *Nature*, **346**, 818–822.
62. Tuerk, C. *et al.* (1990) Systematic evolution of ligands by exponential enrichment: RNA ligands to bacteriophage T4 DNA polymerase. *Science*, **249**, 505–510.
63. Mascini, M. and Tombelli, S. (2008) Biosensors for biomarkers in medical diagnostics. *Biomarkers*, **13** (7), 637–657.
64. Tombelli, S., Minunni, M., and Mascini, M. (2005) Analytical applications of aptamers. *Biosens. Bioelectron.*, **20** (12), 2424–2434.
65. Song, S.P., Wang, L.H., Li, J. *et al.* (2008) Aptamer-based biosensors. *TRAC, Trends Anal. Chem.*, **27** (2), 108–117.
66. Haupt, K. and Mosbach, K. (2000) *Chem. Rev.*, **100**, 2495–2504.
67. Hayden, O., Mann, K.J., Krassnig, S., and Dickert, F.L. (2006) Biomimetic ABO blood-group typing. *Angew. Chem. Int. Ed.*, **45** (16), 2626–2629.
68. Uludag, Y., Piletsky, S.A., Turner, A.P.F. *et al.* (2007) Piezoelectric sensors based on molecular imprinted polymers for detection of low molecular mass analytes. *FEBS J.*, **274**, 5471–5480.
69. Lieberzeit, P.A. and Dickert, F.L. (2008) Rapid bioanalysis with chemical sensors: novel strategies for devices and artificial recognition membranes. *Anal. Bioanal. Chem.*, **391** (5), 1629–1639.
70. Scippo, M.L., Argiris, C., Van de Weerdt, C. *et al.* (2004) Recombinant human estrogen, androgen and progesterone receptors for detection of potential endocrine disruptors. *Anal. Bioanal. Chem.*, **378** (3), 664–669.

Section XI
Applications 4: Process Control

Handbook of Spectroscopy, Second Edition. Edited by Günter Gauglitz and David S. Moore.

Introduction

Process control is the application of analytical chemistry to a chemical, biological or physical process combined with the control of the process on the basis of knowledge and process understanding. Process control uses process analytical measurement technologies in combination with control technologies. There is a long tradition in the control of many types of physical and chemical transformations and still today fairly simple physical parameters such as temperature and pressure in combination with a clear understanding of the process are used for typical control tasks in many industries.

The definition and understanding of the terms *process control*, *process analytics*, and *process analytical technology* varies from industry to industry and is changing with development of technologies and software. Therefore, the detailed definitions are given in the context of the chapters related to industries in subsequent text. The general drivers for process control are always quality and costs, with variations in the major focus. Besides direct savings, the benefits of process control are typically a more consistent production and savings in raw material use, in less waste, and less energy consumption. High contributions typically arise from reduced cycle times. Examples from industry are unfortunately not often published but sometimes presented in oral presentations. In a few examples presented or published, it was shown that process analytical equipment has increased the product output of available equipment up to a factor of 2 and that the typical pay-off time of a process analytical instrument implementation is below 1 year [1, 2].

In the current sophisticated production systems from basic chemistry, fine chemicals, food production to pharmaceuticals, or many specialty products such as, for example, liquid crystals, even highly sophisticated analytical measurement tools are used in the control cycle. The type of process control strongly depends on the individual production process. In many basic chemical manufacturing systems as in the crude oil distillation physical parameter measurements such as temperature and pressure may be used as process control tools. In the case of these continuous/semicontinuous processes, the production equipment stays unmodified and only the variations in the raw materials and changes in the environment (such as ambient temperature and humidity) or changes in process components (as in the aging of a catalyst) lead to variations in the process. In these continuous processes also, the changes are typically continuous (drifts). In many other production processes, as, for example, in food manufacturing (beer

Handbook of Spectroscopy, Second Edition. Edited by Günter Gauglitz and David S. Moore.

brewing as a well-known example) a ‘‘pseudocontinuous’’ batch production process is applied. This means that a batch is produced in the production equipment and after finalizing the batch and cleaning the equipment the same equipment is used for the manufacturing of the next batch of the same product. In this case, in principle, the situation is the same as found in real continuous processes. The production process parameters are mainly influenced by the raw materials and environmental parameters. The difference is that the influences typically change discontinuously from batch to batch; for example, the changes in raw material from batch to batch. This also is often true for aging of equipment that typically fails suddenly, whereas in real continuous processes parameters drift slightly. In both cases, the implementation of process analytical equipment and control loops are part of the engineering of the equipment. This implementation is therefore discussed in engineering textbooks, taught in courses for engineers, and the basic work in this field is a well-understood part of engineering.

Moving forward to fine chemicals, pharmaceuticals, and specialty products, batch production processes typically dominate the scene. The difference here is that the basic installation is designed by engineers. This installation includes process analytical measurements, for example, temperature, pressure, flow meters, weight measurements, and so on; but for nearly each product, the equipment configuration is modified. For example, in the pharmaceutical industry, for the intermediate manufacturing of a drug substance, two stirred tank reactors are combined in a parallel configuration, whereas for the next chemical conversion step three stirred tanks may be combined in a top-down configuration. Additional equipment such as those for heating and cooling is attached and detached from process step to process step. This means that some parts of the equipment are changed from batch to batch and the combination may be new each time. The number of variations in the process increases and even the process analytics equipment used for one product is changed, moving on to the next production step; therefore, it is often only installed for one or a few batch(es) and is then replaced for the next step of the chemical conversion. Besides the variations from raw materials and the environmental parameters, as mentioned, here additional variations of the equipment may therefore influence the production process.

Besides this, typical calibration procedures are also different for continuous or batch processes. Typically, process control measurements are quantitative measurements. Often, in continuous processes, complex calibrations using, for example, chemometric models are applied to give a quantitative relationship between process information and the desired control unit of the process. Establishing these calibrations is expensive, but in such a process a calibration model can be used for a long time/a high number of batches (in pseudocontinuous processes). In real batch processes, for example, five batches of a drug substance intermediate may be produced using a chemical conversion and after this may be for 1 year or even longer this intermediate is not produced. After such a long time, a number of changes of typical wearing of parts has happened. For example, a seal in the stirrer has been replaced and therefore the stirrer speed is slightly different. Because a chemometric model includes all variables in a process, such slight changes would lead to the need for a recalibration. Therefore, in such processes, establishing chemometric models often would not pay off. This leads to the need for simple calibration models (e.g., linear models) that can be recalibrated with low to medium costs. These limitations sometimes restrict the number of analytical methods to be applied to such analytical tasks.

The more complex the production process the more sophisticated process analytics and control is needed. The control is applied to hold or to bring the product quality into a predefined specification or range, where the control loops may be both feed forward or feedback control. Typically, the spectroscopic tools in process control belong to the sophisticated tools and are therefore applied to the sophisticated process analytical challenges.

The typical control loops may be off-line in an analytical laboratory or at-line, which means that the sample is analyzed off-line but close to the process, for example, in the plant by plant personnel. Typically, these analyses include manual operations, and off-line/at-line analysis is performed if the frequency for adjusting the process needs only few measurements with time intervals of hours or even days. The process often is then adjusted manually. In control situations, where the analysis is needed in minute-to-hour frequency, on-line or in-line sampling technique is applied. On-line sampling means that a sample is taken from the process by an automated system and is analyzed without manual operation, whereas in-line means that the analysis is performed directly in the process without interfering with the process. In both cases, a direct coupling to the process control system is possible. The faster the conversion performed, the faster the process analytical technology is needed. Acquiring classical measurement data such as temperature and pressure is very fast. In the cases where detailed/sophisticated information on molecular basis is needed, chromatographic and spectroscopic information can fulfill this need. Typically, spectroscopic process analytical methods are much faster. This is an important reason why a high degree of spectroscopic technologies are applied in process analytics and control. Especially, if the information is needed within seconds, only an in-line solution using a spectroscopic technique is possible (Figure 1).

In addition, the choice of the applied approach in process control is strongly dependent on the sample to be analyzed. The samples ''in process'' may be solid (e.g., wood, steel, polymers, salts, and pharmaceutical formulations), they may be liquids (e.g., oil, water, and solutions in organic solvents for chemical reactions), or gases (e.g., in combustion plants, in chemical gas phase reactions). The temperature and pressure conditions vary from ambient to, for example, liquid aluminum and the pressure may vary from high vacuum (in semiconductor industry) to high-pressure chemical reactions. For the choice between on-line, in-line, and off-line/at-line process control, access to samples without counterfeiting the sample may be an important issue. Sometimes the concentration of the components of interest limits the use to some special techniques or coupling options. The examples given in the following chapters show an overview of typical sampling and analysis methods.

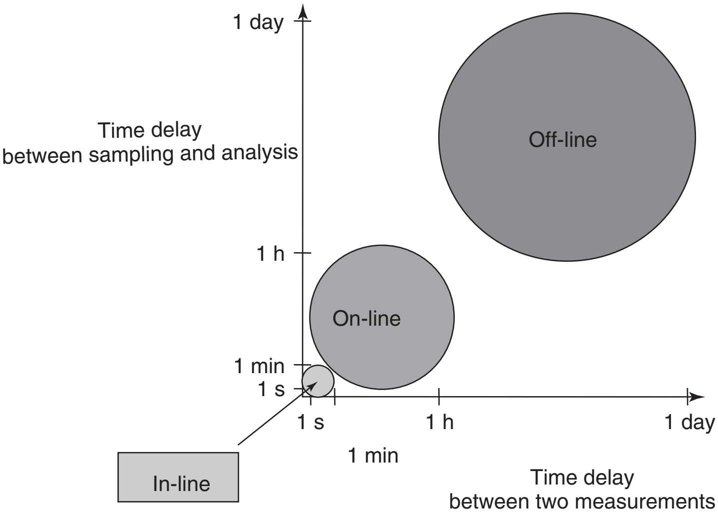

Figure 1 The correlation between off-line (including at-line), on-line, and in-line on the basis of timescales for sampling and analysis versus time delay between two measurements.

Process control is always a tool to support some kind of production process. Therefore, some general requirements for process control can be summarized. The current requirements for process control are as follows:

- Installation of process control equipment should be easy (plug and play).
- Equipment should be service-free (best case).
- Maintenance costs should be low.
- The whole system including the measurement results should be robust.
- Up-to-date equipment should
  - have wired or wireless control capability;
  - contain self-diagnosis of operation;
  - be capable of diagnosis, maintenance, and calibration by wire.
- Costs of ex-capability should be low.

From the very beginning, spectroscopic techniques have been applied to process control. Infrared spectroscopy, for example, was one of the techniques applied in this field for more than 100 years and is still one of the most important ones. In addition, a wide range of spectroscopic techniques are applied in process control currently. Besides spectroscopy, all other analytical techniques are also used in process control. Most of them are mentioned in the examples within the chapter. Although there are also other techniques, spectroscopy dominates the field. As a chromatographic-technique-only process, gas chromatography (GC) plays an important role in process control. A number of sensors such as pH and some selective electrodes are also widely used here. Flow injection analysis is used to couple various analytical techniques to the process; also spectroscopic, these kinds of couplings are only applied if a direct solution to the control problem is not available.

Although market researchers give various figures for market shares of different technologies for process analytical instrumentation in process control, the general figures show that more than 40% of the market are spectroscopic instrumentation, about 30% is dedicated to electrochemistry, and only about 10% of the market is located with chromatographic technologies [3]. The major advantage of spectroscopy for process control is the short analysis time and that most of the techniques can be applied on-line or in-line, which, in addition, allows reduction of the time between measuring a sample and the possibility of adjusting the process.

This section covers an overview of current applications and future trends including the general trends caused by the US Food and Drug Administration's (FDA's) process analytical technology (PAT)-initiative and changes caused by the ongoing globalization in industry. The first contribution of the section takes a look at the chemical industry. Here, process control is typically applied to control a process at minimum costs with a constant quality of the product. A general summary of the benefits of process analytical tools for this field of applications is given in Figure 2. Here, very often the benefits already reach a breakeven point at a few measurements per day, sometimes already at one measurement per day. A detailed discussion about the cost/benefit aspects of process control is included in this chapter.

In the second part of the section, the use of process analytical instruments in the pharmaceutical industry is described. In this industry, the quality of the product, documentation of the quality, and regulatory aspects are the key issues.

As already mentioned, optical spectroscopy techniques are used in many applications of process analytics in the control of chemical or physical techniques.

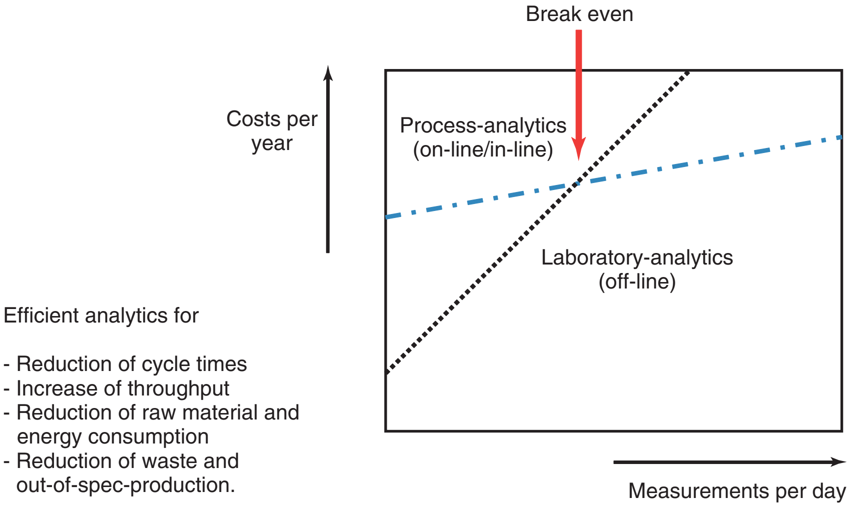

Figure 2 Summary of the benefits of process analytical measurements in production processes.

Therefore, the third contribution takes a look at some special aspects of optical spectroscopy in process environments independent of industry.

A quite young but fast developing field in process control is chemical imaging. Therefore, a contribution is dedicated to the field of chemical imaging in quality and process control.

Finally, one contribution takes a look at a wide number of different developing and special techniques and applications in process control and gives an overview of future trends.

One major issue for process control that is different from many other fields of spectroscopy (such as structure elucidation) is that the signal needs to be proportional to the information needed, but not necessarily is the chemical or physical correlation between the information and the signal known. A second and extremely important issue of process control compared to all other applications given in this book is the implementation of the process analytical instrumentation in a plant environment or any other process environment, together with an integration of data flows inside the control loop. While this contribution tries to look at process analytics from an application and industrial point of view, other contributions take a more technological view toward process analytics. A series of current reviews, which takes a more technological perspective, can be found in [4]. This review series gives an introduction to the technological developments for a short period in time with a strong focus on developments in the United States and from the American point of view. Another current review was given by Chew and Sharratt, who tried to focus on trends in process analytical technology starting from FDA's PAT-initiative [5].

One part of process control is also the data transfer, to control systems, data integration, data safety, the generation of signals for feedback and the feedback by changing a flow rate, a feed rate, the addition of feed, solvents, the maintenance of equipment and data infrastructure in a plant, and so on. This is a technological field covered by engineers and because these topics are part of the education of engineers these aspects are not covered in this section.

References

1. Hajduk, M. (2008) Presentation, Europact 2008, Frankfurt am Main, Germany, April 23–25, 2008, *www.euro-pact.org* (accessed 21 March 2013).
2. Clegg, I.M., Everall, N.J., King, B., Melvin, H., and Norton, C. (2001) *Appl. Spectrosc.*, **55**, 1138–1150.
3. SDI Inc. Market Forecast (2005) *PAT Instrumentation: The Pharmaceutical and Biotechnology Market for Process Analytical Technology*, Strategic Directions International, Inc., *www.strategic-directions.com/pdf/PAT-ProcessAnalyticalTechnology.pdf* (accessed 21 March 2013).
4. Workmann, J., Jr, M.K., Lavine, B., and Chrisman, R. (2009) *Anal. Chem.*, **81**, 4623–4643 and previous reviews of these authors.
5. Chew, W. and Sharratt, P. (2010) Trends in process analytical technology. *Anal. Methods*, **2**, 1412–1438.

37

Process Control in Chemical Manufacturing

Dieter Fischer, Stefan Stieler, and Stephan Küppers

37.1

Introduction to Chemical Manufacturing Processes

Typical process industries such as the petrochemical industry, monomer production, and polymerization reaction and polymer processing often work with dedicated equipment and continuous or semicontinuous production processes. This means a process with a feed of raw materials that goes into the process and an outcome of product(s) from the process that needs to be controlled. On one hand, the measurement of mass flow is a key to control these processes but because the raw materials are not pure or have an inherent variability, some kind of method for the determination of the concentration of the valuable components is needed to correct the masses going into the process/coming out of the process. For example, in many cases, natural materials contain varying amount of water or, to give another example, natural oils have a varying composition in aliphatic components, aromatics, and impurities such as sulfur-containing components. The process may consist of one conversion step or even a number of steps that are combined. Examples for one-step conversions are waste incineration or the generation of biogas, whereas most processes in manufacturing consist of a number of steps. In many cases, not all of the steps of a conversion process are controlled by process controls. The typical reasons for deciding on an analytical control step are not only cost and quality but also time, where speeding up a process typically also means that costs of the overall process are decreased.

In these industrial processes, first a large number of sensors are installed for measuring, for example:

- feed of raw materials, flow rates of components, weight (balance);
- pressure, temperature, and power consumption.

While the first set of sensors measures the pure quantities, the second type, in many cases, already gives information on the process status that allows the control of parts of the process. In some cases, such information is also combined with the so-called soft-sensors. In addition, specific sensors are installed depending on the industry, from pH-measurement, via density, viscosity to conductivity. Mostly,

Handbook of Spectroscopy, Second Edition. Edited by Günter Gauglitz and David S. Moore.

there is a linear correlation between the sensor signal and a step/part of the process. Therefore, the direct control to a specific need can be related.

Finally, in some cases, molecular information or element concentration is needed for tasks such as:

- the determination of the amount of additives that have to be used (e.g., the concentration of the desired metal in the ore);
- the end point of a chemical reaction;
- the conversion of an individual substance, that is, a monomer, and so on.

In these cases, sophisticated analytical techniques, which are often spectroscopic techniques, are implemented. The following examples will give a general overview of some of these implementations. The discussion will follow the supply chain of chemical industry from typical examples for starting or raw materials to the end-point/conversion control in later production steps and will move on to environmental control and close with some discussions on costs. Typically, in many industries in chemical manufacturing there is both an analytical chemical laboratory and a process control responsibility. While the laboratory is typically involved in the control of the starting material before use, for example, for release of the purchased material and the quality control of the final products, the process control is allocated in all of the intermediate steps. Depending on the size of the company and the industry, sometimes both responsibilities are found in one common organizational unit, but at least for large organizations there are two independent departments or groups. Figure 37.1 summarizes this discussion.

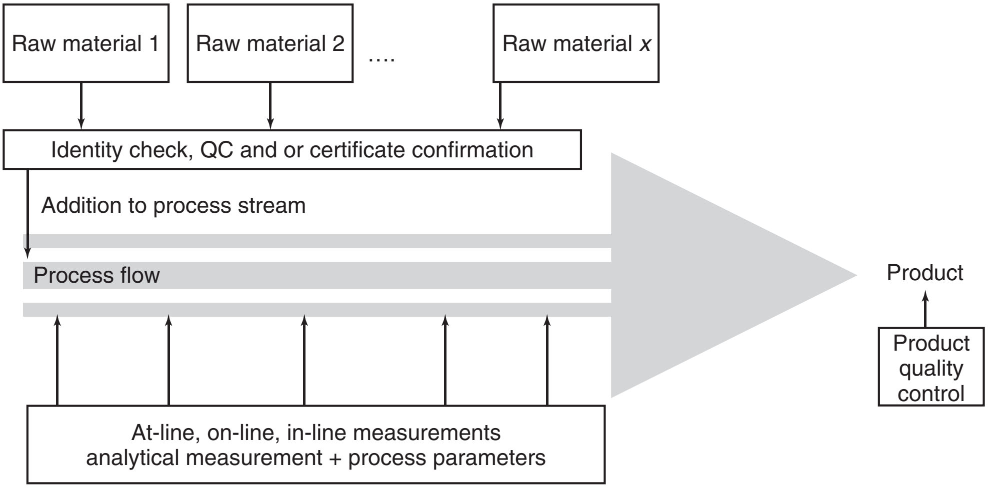

Figure 37.1 Typical workflow in process industries. QC, quality control.

37.2
Chemical Reaction Process Monitoring and Optimization

37.2.1
Monitoring of Pseudocontinuous Batch Processing

In classical industrial production processes such as steel or cement production, or similar processes, a number of process analytical techniques are currently applied. Among these techniques are a large number of spectroscopic techniques [1]. For organic production processes such as many dye productions, the optical spectroscopic techniques, as described later in this chapter, are typically applied, whereas in many inorganic production processes the amount, concentration, or weight of elements has to be determined. In many of these cases X-ray fluorescence (XRF) is a typical process spectroscopic method. Typically, in addition to a number of inorganic components such as nitrate, sulfate, or carbonate are determined by flow injection analysis (FIA), ion chromatography, or capillary electrophoresis, off-line or at-line in a laboratory. In many processes, gases such as carbon dioxide and carbon monoxide, for example, in iron and steel production, are also an important parameter. These gases are typically determined by commercially available gas sensors with a different working principle, some of them based on the infrared (IR) absorption principle.

For example, in cement production, XRF is used to control the raw material flow into the production process. The raw materials are transported via a continuous belt. Here, a weighing step is also included. After weighing, the components are mixed and directly behind the mixing point the implementation of a commercially available XRF spectrometer determines the element composition of the mixture. Here, the elements Ca, Si, Al, and Fe, which are critical for the process, are direct input variables for the process control system that controls the speed of the raw material feed belts. XRF has for a long time been used as an in-line sensor, using the same general instrumental setup as is known in laboratory instrumentation [2].

In a similar way, many floating processes are controlled by XRF. Typically, process flows or the addition of a feed to a process stream can be controlled with cycle times in the range of a few 10 s, and process flows or belt speed can be kept to optimum conditions. The important difference when compared to laboratory application of XRF is that reproducibility and or even precision of the results depends on the grain size distribution and the mineralogical composition of the raw material. The calibration of the measurements therefore needs to be performed on samples that are similar to the samples of interest with respect to type, degree of grinding, and so on. Still, techniques such as XRF are easy to implement in these cases because commercially available portable XRF instruments can be used. The in-line measuring is easy to implement directly in a production plant because the feed belts are typically at ambient conditions and the concentration range of interest is typically in the 0.1–50% range, which is easily stable calibrated by XRF. In cases where a different concentration range and/or a measurement at nonambient conditions is needed, other (typical laboratory) techniques are also implemented in the process.

Products such as steel are typically used as a starting material for the following production step, for example, for the manufacturing of vehicles. In such cases, the structure of the material may have an enormous importance in the stability/usability in the next step, as in the example of steel the corrosion stability, the mechanical plastic deformation stability, and so on. Therefore, X-ray diffraction (XRD) is a typical process control spectroscopy for grid structure of the produced steel. XRD, in this case, can also be applied as a continuous process in a similar way as XRF. Here again, the controls are typically applied on-line under ambient conditions for the measurement instrument.

Also, in other industries such as semiconductor or solar panel manufacturing, XRF and XRD are applied as control technologies on-line or at-line to determine the crystal structure or the content of a component. For example, in semiconductor manufacturing, the thickness of a wafer-coating process is typically determined by XRF. In this case, the analytics with XRF is used to determine the total amount of material coated onto the wafer. If the process is stable and the density of the material is determined once, this procedure allows the calculation of the thickness of the layer even in the nanometer range. In solar technology, in some cases the crystallinity of the material has to be determined. This can be applied on-line by Raman spectroscopy. All different types of Si crystallinity from noncrystalline (amorphous) – via polycrystalline – to monocrystalline – Si are used in production processes. Therefore, Raman or XRD can be used for the control of in-line, on-line, or at-line, depending on the question and or the industry. In the semiconductor industry, these techniques are typically installed as in-line process control instruments because only the in-line implementation inside a clean room and/or even directly connected to a high vacuum process do these tools allow the control of the process without contamination of the samples. Depending on the question, Raman spectroscopy can be applied in a transmission or a reflection configuration using standard commercial laboratory equipment with fiber optic coupling. For details, see subsequent text in this chapter.

In the semiconductor industry, in many cases extremely pure starting materials are needed. Therefore, a number of element and trace element techniques from total reflection XRF, atomic absorption spectrometry (AAS), inductively coupled plasma optical emission spectroscopy (ICP-OES), and inductively coupled plasma mass spectrometry (ICP-MS) are applied as laboratory control or at-line. In some cases, a direct transfer of the sample from the process to the laboratory has also been implemented; for example, in steel manufacturing, sampling processes that lead to a sample that is directly transferred to the laboratory have been implemented because any other sampling process would lead to contaminations of the liquid steel by the environment. In principle, in all the cases mentioned up to now, standard laboratory equipment for process analysis is still used, but a dedicated sampling and sample transfer system has to be established. Details of many of the analytical process controls including the detailed description of the processes themselves can be found in [1].

37.2.2
Monitoring of Continuous Processes

The heart of the chemical industry is chemical conversion. Important chemical conversions that are, in many cases, performed in continuous processes and therefore are measured and controlled by process analytics and control are reactions for monomer production and polymerization reactions.

A number of these chemical reactions are performed at high temperature in the gas phase. Typical examples are found in the petrochemical industry where both distillation and chemical conversions are performed at high temperature; chemical reactions in synthesis for various intermediates of chemical reactions; and the generation of basic chemicals, metathesis reactions, or other high-temperature gas-phase processes, for example, waste combustion or distillation processes for purification of chemicals and solvents. For these processes, gas chromatography (GC) [3] and mass spectrometry (MS) [4] are typical monitoring and control technologies; sometimes, the combination of GC with MS is also applied, but in many cases both technologies are direct competitors with each other and the application depends on which method is implemented. Mostly, the details of such implementations are not published because the manufacturing technology in many cases is one of the competitive advantages of the organizations. Although only a few examples are published, some information can be found in literature [5]. One example is the reaction of acidic acid to ketene. The reaction mechanism of the ketene process is given in Figure 37.2. The important point is that all components of the reaction are in equilibrium. Therefore, for process control a large number of components have always to be monitored.

The reaction is endothermic ($\Delta H = 140\,\mathrm{kJ/mol}$) at a temperature of 700 °C and a pressure of 500 mbar. The product contains acidic acid, acidic acid anhydride, carbon dioxide, methane, propadiene, hydrogen, diketene, carbon monoxide, and ethylene as well as some minor by-products. After the reaction, the mixture is cooled down to split the product from the acid that is transferred back into the reactor. The analytical challenge, as reported in the literature, can be monitored by process MS [5].

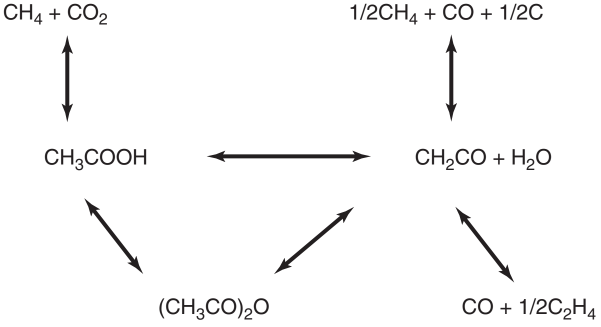

Figure 37.2 Schematic of the ketene reaction.

For better understanding of the system, the whole process from the reaction including distillation and hydrolysis was described by a model. The data for this model was received from on-line analysis. Measurements were performed in the reactor entrance and the reactor outlet. The reason for using process MS was the high reaction speed of the product, ketene. To receive data that is representative of the process, a high-speed process analysis was needed. The results of the on-line MS analysis and the optimization using the process model allowed the improvement of the process output of 13%. One of the key issues in the process analysis in this case was the sampling at high temperature with the need for fast analysis times.

The major advantages of process MS in this case are

- fast analysis times, up to 1 s per analysis;
- sensitivity to many components, parts per million to parts per billion, lower for special applications;
- a wide dynamic range, which allows to determine minor and major components in one analysis;
- because of the high speed, multiplexing is possible to analyze different processes and/or the same process at different stages/times in the process;
- because mostly full mass spectra are recorded, MS has the capability to detect unknowns in the process.

However, there are also disadvantages:

- Because process MS always works under high vacuum and at ambient temperature, the sample needs to be transferred to these conditions.
- The instrumentation is expensive compared to some other analytical techniques.
- The installment needs to be relatively close to the process.

The hardware used in process analytical applications is mostly based on laboratory equipment. Often, in process MS, quadrupole, sector field, or time-of-flight (ToF) instrumentation is used [6]. In contrast, in special cases, as in the above-mentioned example, special process mass spectrometers are developed for on-line applications. Other examples for the use of dedicated process mass spectrometers, for instance, can be found in steel manufacturing and in petrochemistry. The choice of the analyzer depends on the application. The mainly used analyzer is the quadrupole mass spectrometer because of price and speed, as also in the above-mentioned case. Sector field analyzers have the advantage of highest stability, which is sometimes needed for process applications, whereas the advantages of the ToF analyzers are the high mass resolution combined with a small analyzer size, which might be relevant for portable applications.

Typically, electron ionization is used. The sample inlet has to be adapted to the process. In case of MS, on-line configurations are always applied and the modifications of the inlet are less complex compared to optical spectrometry. In an ideal case, a direct capillary inlet can be used. Depending on the sample, this transfer line needs to be heated. In case of the sampling of liquids or components that are dissolved, membrane interfaces are applied [7] and in more special cases a GC is used as the interface to the process. The calibration of the mass spectrometer needs to be automated for process control. This can be achieved by sampling loops, sometimes also by direct adaption of a calibration gas bottle into the MS system.

Another typical example for mass-produced chemicals is polymers. The polymerization reactions are often continuous processes that are controlled by in-line and/or on-line methods. Temperature and pressure for polymerization reactions cover a wide range from low temperature to melting polymerizations and also sometimes accelerated pressure. Oxygen typically has to be kept out of the process, which means that coupling to the process and sampling is typically a challenge for the implementation of the analytical technique. Various techniques are used to control polymerization reactions. Besides the ‘‘classical techniques’’ from temperature, pressure, pH, density, viscosity, turbidity, and others, sometimes optical spectroscopy techniques are applied to receive molecular information on the process. For polymerization reaction monitoring techniques such as IR, NIR, and Raman spectroscopy are highly suitable. The advantage of spectroscopic techniques here is that they can be used on-line or in-line and time constants are short. The typical chemical conversion in polymeric reactions is the change in C=C double bonds, COH, NH, C=O bonds. In cases of, for example, NH and OH, hydrogen bonds can lead to shifts in the spectra, so especially for NIR with strongly overlapping bands and shifts caused by temperature, pH and, for example, the already-mentioned hydrogen bonds must be evaluated carefully [8]. Anyhow, multivariate methods are necessary for quantitative information in monitoring processes such as, for example, copolymerizations. Using Raman spectroscopy, the C=C double bond can be very sensitively monitored. This gives access to monitoring most of the typical vinyl- and acryl-based polymerization reactions on-line [9]. The laser excitation wavelength always is a compromise between prevention of fluorescence caused by impurities and by-products and efficiency. As reported in [8] for polymerization reactions monitoring the C=C double bond, a wavelength of 800 nm has been proved to be a good compromise. For safety reasons, the power of the laser radiation brought into the system has to be kept low, for example, below 30 mW [8].

The instrumentation used in the coupling of optical spectrometry to the process is typically laboratory equipment. The principle setup of the instrumentation, the detection systems, and so on are described elsewhere in this handbook. For the coupling of these instruments to the process, a number of strategies, depending on the process, are described in the same section.

Besides the polymerization reaction, the processing of polymers is also monitored by process control using spectroscopic tools. A typical example is the monitoring of extrusions. Extrusion is one of the most applied technologies for mixing and modifying of polymers in polymer processing. The example presented here is taken from the extrusion to create innovative multifunctional polymer materials such as polymer blends and nanocomposites, as presented elsewhere [10].

Off-line analytics does not display the current state of the material during the extrusion process. For an adequate characterization of the material, it is necessary to make real-time measurements at the extruder. Spectroscopic methods are outstanding for in-line monitoring [11–13]. In the example given, the opportunities of NIR and ultraviolet–visible (UV–vis) measurements as methods for in-line monitoring to characterize polymeric nanocomposites in the extrusion process are shown. Furthermore, the combination of in-line methods with off-line spectroscopic measurements, transmission electron microscopy (TEM), and atomic force microscopy (AFM) are demonstrated.

Measurements for the example described were performed on a twin screw extruder as shown. The sensors for ultrasonic, NIR, Raman, and light scattering (particle monitoring) are directly coupled to the extruder, as visible in the image (Figure 37.5), where the sensors can be seen lined up, along the outer wallet of the extruder.

The polymers used were polyamide 6 (PA6) and polypropylene (PP) modified with 5% maleic anhydride (PB 3200). Both polymers were mixed with different nanofillers (montmorillonite, sepiolite, and boehemite) in the concentration range from 1 to 12%.

Figures 37.3 and 37.4 show as an example the NIR spectra and the results of a chemometric analysis by partial least squares (PLS) for the nanocomposite PA6/montmorillonite. The NIR spectra of the PA6 series, with different montmorillonite concentrations in the wavelength range from 1 to 1.7 µm, are shown in Figure 37.3. The calculated concentrations by PLS analysis are in shown in Figure 37.4. The results of the in-line measurements show a good correlation between the predicted nanofiller concentrations in the polymer matrix and the NIR spectra.

The TEM and AFM investigations of the extruded samples show the state of intercalation and exfoliation and also the dispersion of the nanofillers in the polymer matrix.

A similar approach to characterize current polymer blends under research can be performed with ultrasonic measurements as technique for in-process monitoring of polymer nanocomposites in the melt [14–16]. An in-line process application was built up with a measuring adapter for the ultrasonic probes at the end of the

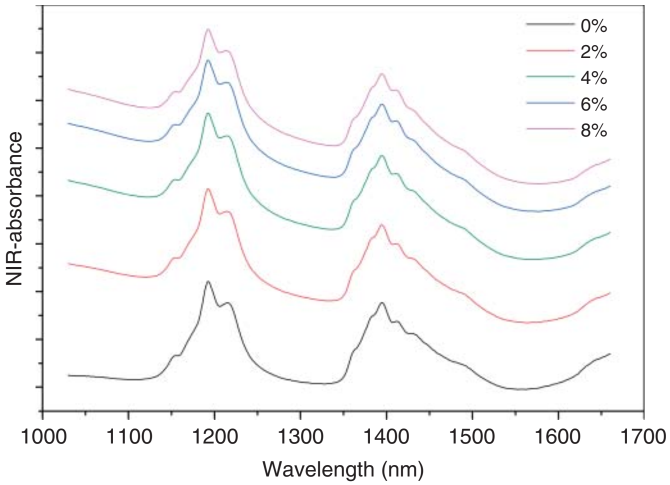

Figure 37.3 In-line NIR spectra of the nanocomposite PA6/montmorillonite.

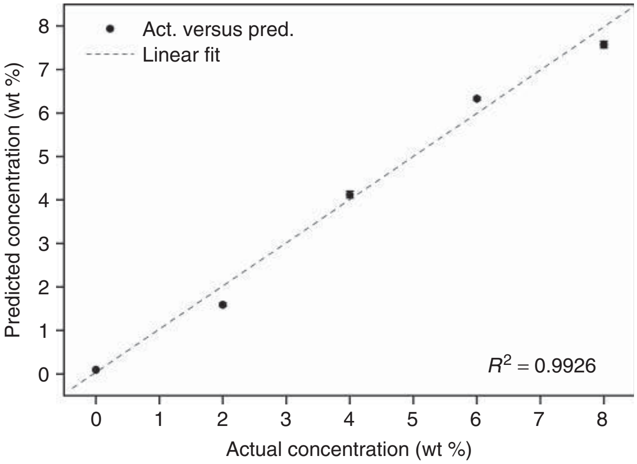

Figure 37.4 PLS results of the concentrations of the filler montmorillonite in the nanocomposite PA6/montmorillonite (2 PC) using NIR spectra.

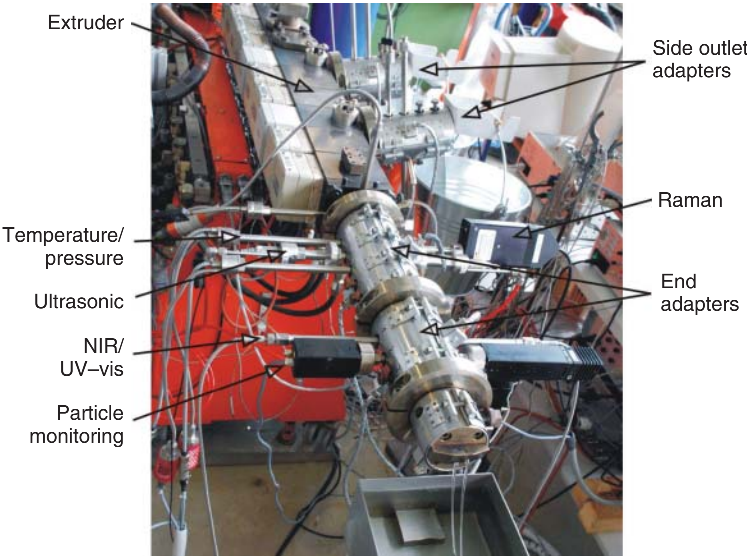

Figure 37.5 Laboratory setup of a twin screw extruder with an ultrasonic probe, a Raman probe, and an NIR probe.

same extruder shown in Figure 37.5. Different polymer/nanofiller mixtures were investigated during extrusion by ultrasonic velocity measurements and ultrasonic attenuation spectroscopy.

The data obtained show a decreasing sound velocity with an increasing content of the nanofiller and changes in the ultrasonic attenuation spectra. A frequency-dependent ultrasonic attenuation in the range from 3 to 12 MHz was measured, as shown in Figure 37.6. To find a correlation between the measured ultrasonic

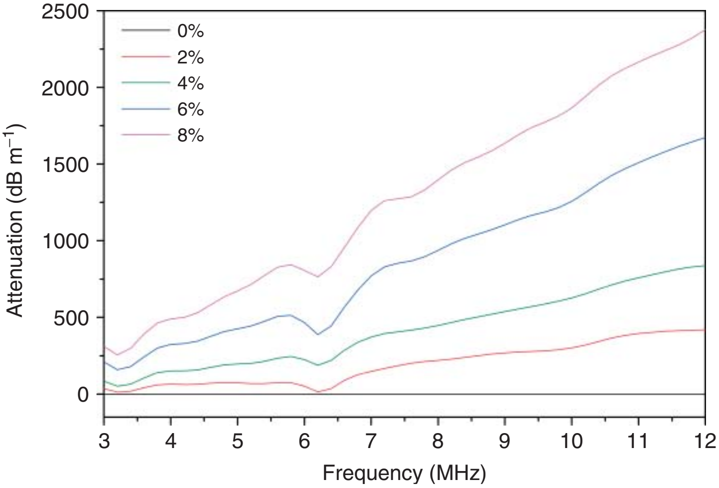

Figure 37.6 Ultrasonic attenuation spectra of the nanocomposite PA6/montmorillonite (2–8% content of montmorillonite).

spectra and the contents of nanofillers, a chemometric analysis was performed using the PLS method. The predicted concentrations, calculated from the ultrasonic attenuation spectra, show a very good correlation to the actual concentrations for all nanocomposites, as seen in Figure 37.7.

The difference between these examples and those given in the beginning is that, in this case, no commercial solutions were available and therefore the process analytical solution had to be developed especially for process control reasons. Other

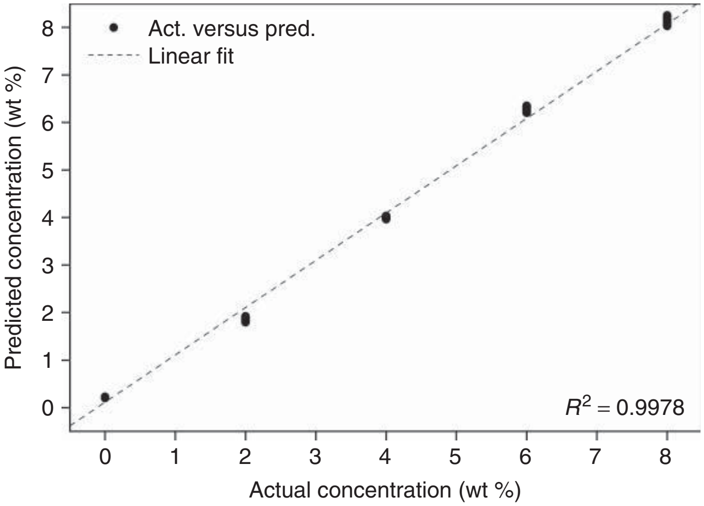

Figure 37.7 PLS results of the concentrations of the filler montmorillonite in the nanocomposite PA6/montmorillonite (2 PC) using US attenuation spectra.

techniques are currently evaluated for similar approaches as, for example, terahertz (THz)-spectroscopy for in-line monitoring of polymeric compounding processes [17]. A current overview of the techniques where the development is ongoing is given later in this section.

In many industrial manufacturing processes, the downstream processing is relevant for either quality of the product or even costs and therefore often is controlled by process control tools. The highest requirements for quality process control in downstream processing are found in biotechnology and pharmaceutical products. Many of the technologies already implemented in the chemical and food industry are under investigation in the pharmaceutical industry [18]. Examples for process control in downstream processing are therefore given in the subsequent text.

37.2.3

Monitoring of the Process Environment

Another key issue for many chemical production environments is the extreme corrosivity of the mechanical components of a plant. Typical chemical conversions that lead to high corrosion are reactions with acids at high temperature or, for example, reactions using halogen from fluorine to iodine, which are used in many chemical processes from polymers to pharmaceutical products. An example of a production process monitoring of a chlorine production plant was presented by Welmink [19]. Here, water was monitored in the plant, to ensure a safe, uninterrupted, and smooth operation because the water together with chlorine gives the extremely corrosive mixture. To keep the plant producing continuously, it is vital to prevent corrosion of piping and other production equipment and therefore keep the water content low. Besides routine checks of leakage of the pipelines in a plant, the monitoring of corrosive media is an opportunity to ensure a smooth, continuous operation of a plant. The continuous monitoring of the water vapor concentration in chlorine gas in several stages of chlorine production is an example of the use of process control with spectroscopic tools that can help predict corrosive situations at an early stage.

The moisture measurement in chlorine gas in-line or on-line is therefore an example of process analytics in chemical production, but in this case the infrastructure is secured by process analytical tools. Because tunable diode laser absorption spectroscopy (TDLAS) is not a widely known technology, this example is also an opportunity to describe a technique that is typically used only in process control or some special applications but not in the laboratory environment.

TDLAS relies on well-known spectroscopic principles and sensitive detection techniques, coupled with advanced diode lasers and optical fibers developed by the telecommunications industry. The principles are straightforward: gas molecules absorb energy at specific wavelengths in the electromagnetic spectrum. At wavelengths slightly different from these absorption lines, there is essentially no absorption. By transmitting a beam of light through a gas mixture sample containing a (usually trace) quantity of the target gas, and tuning the beam's wavelength to one of the absorption lines of the target gas, and accurately measuring the absorption of that beam, one can deduce the concentration of the target gas molecules integrated over the beam's path length. This measurement is usually in the parts per million concentration range.

In most TDLAS instruments, the laser's fast tuning capability is exploited to rapidly and repeatedly scan the wavelength across the selected gas absorption line [20–23]. While this scanning occurs, the fraction of emitted laser power that is transmitted through the gas mixture is monitored with a photodetector. When the wavelength is tuned to be off of the absorption line, the transmitted power is higher than when it is on the line. Measurement of the relative amplitudes of off-line to on-line transmission yields a precise and highly sensitive measure of the target gas concentration along the path transited by the laser beam. Furthermore, techniques known as *frequency* or *wavelength modulation spectroscopy* (WMS) and balanced ratiometric detection (BRD) are frequently employed in TDLAS instruments to make them exquisitely sensitive to even very weak absorption of the laser power. Thus, TDLAS instruments offer a combination of high sensitivity to trace concentrations of many gases, freedom from cross-species and external interference, and fast response. Examples of gases that can be sensed with TDLAS, and typical minimum detectable path-integrated concentrations, are listed in Table 37.1.

In many current implementations of TDLAS, the diode laser beam is coupled to optical fibers. This enables separating the laser, associated electronics, and microprocessor from the measurement head. This capability has led to the evolution of the TDLAS system architecture, utilized by many of today's practitioners for monitoring and controlling various chemical, combustion, or manufacturing processes, that has made the technology attractive for use in harsh, hazardous, or difficult-to-access industrial environments. The instrument is separated into two distinct, yet interconnected, components called the *system console* and the *measurement path*, illustrated in Figure 37.8. The laser beam originates within the

Table 37.1 Some gases measured by TDLAS (according to *http://www.tdlas.com/*).

Gas	Detection limit (ppm)
HF	0.2
H_2S	20
NH_3	5.0
H_2O	1.0
CH_4	1.0
HCl	0.15
HCN	1.0
CO	40
CO_2	40
NO	30.0
NO_2	0.2
O_2	50

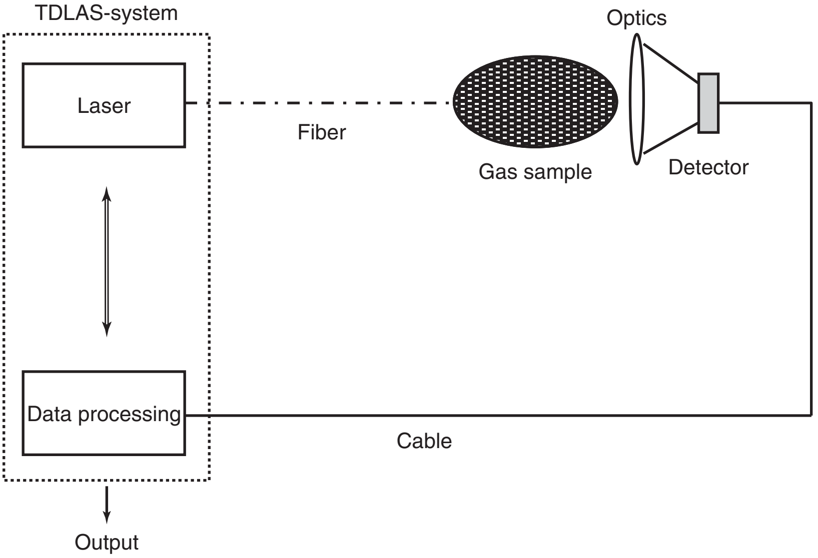

Figure 37.8 TDLAS gas detector system, according to *http://www.tdlas.com/theory.shtml*.

system console, which is usually installed in a general-purpose environment. An optical fiber conducts the beam to the measurement path, which is built to withstand the harsh installation environment. At the beginning of the measurement path, the laser beam exits the fiber and is transmitted into the gas sample. At the opposite end of the measurement path, the laser beam impinges on the photodetector, which converts the beam, and the information it carries, into an electrical signal that is returned to the system console via an electrical cable. At the console, the signal is processed and the path-integrated target gas concentration is reported. Noise reduction in sensitive BRD and WMS detection techniques is accomplished by use of an optical or electronic reference signal that connects directly from the laser transmitter module to the signal processor module.

Since a few years, such TDLAS systems are marketed as in-line process analytical equipment to measure various components in gases in various process environments [24]. TDLAS equipment is already in use for the measurement of oxygen and experiences are good until now. The TDLAS measuring principle can also be used in the measurement of moisture in chlorine gas at parts per million levels. If the TDLAS equipment can be used for moisture measurement, less maintenance effort can be expected. However, measuring moisture at parts per million levels is a totally different challenge from measuring oxygen at percentage levels. When the sample matrix contains corrosive gases such as chlorine or hydrochloric acid, additional issues are to be dealt with. Till now in most chlorine plants, the moisture content of chlorine is measured with instruments based on the coulometric phosphorus pentoxide (P_2O_5) principle (also named "Keidel"cell).

If the moisture content of the chlorine gas rises above certain limits, the protective ferric chloride ($FeCl3 \times aq$) coating on the inside of the plant piping will liquefy, resulting in severe corrosion. Therefore, a comparison between TDLAS equipment and the P_2O_5 cell in laboratory and field tests and by cost of ownership by TDLAS was performed and it was demonstrated that the TDLAS could be successfully applied. Because corrosion prediction is a typical challenge for process analytics in chemical manufacturing, it can be expected that such implementations will be routinely seen in coming years [19]. Besides corrosive gases, other extreme reactive materials, such as, for example, the halogen iodine, are used in chemical manufacturing, and other techniques are therefore used in the monitoring corrosive substances in production.

37.2.4
Environmental Monitoring in Industrial Processes by Process Analytics

A large number of process controls in industrial manufacturing are also related to control of emissions into the environment caused by manufacturing itself, recycling processes but also by waste incineration. This area of process controls is regulated by law, for example, by European and national law.

For example, in Germany the seventeenth BImSchV (''Bundes-Immissionsschutz-Verordnung'') sets limits for emissions into the environment. Therefore, for example, the continuous monitoring of waste incinerations is a typical field for process analytics and control and, depending on the waste, sometimes a challenging application (Table 37.2). The following table shows an overview of important components to be measured as well as typical devices applied for that, representing the current status of German law at the time of writing this contribution.

In some of these cases, for multicomponent analyzers, Fourier transform infrared (FTIR) spectrometers are applied. In case of only one component of interest, often nondispersive IR systems are used. Details of the implementation of such instruments are discussed in subsequent text. An overview of UV–vis applications in environmental applications is given elsewhere [25].

For a number of gases, the European guideline gives limits and requirements that have to be measured on a routine basis if emissions occur (European Directive 2000/76/EC and 2003/87/EC). The list contains a similar list of gases, as given,

Table 37.2 Emission and typical control according to German national law.

	Components to be measured	**Typical analytical system**
Gas	HCl, CO, NO, SO_2, O_2, TOC, Hg, if applicable: HF, dioxin/furan	Multicomponent analyzer (e.g., FTIR)Mercury measuring device Multicomponent analyzer (FTIR)
Dust	Dust concentration	*In situ* dust measuring device, extractive dust measuring device
Others	Temperature, flow, pressure humidity	Combined measuring devices multicomponent analyzer (e.g., FTIR)

from German national law but also a number of metals—Cd/Tl, Sb, As, Pb,Cr, Co, Cu, Mn, Ni, V, and Sn. The regulated limits are on a daily average or half hour average values. Especially, if more than one element has to be determined, spectroscopic analytical techniques are a powerful tool.

There are two major points with respect to the recent revisions of regulations and guidelines. On the one hand, a new demand is set on the availability of the plant and, on the other, quality requirements on the measuring equipment and its continuous operation are sharpened.

The measurement of gas emissions in a clean gas is normally performed by extraction and classical laboratory analysis. A representative measuring gas sample is continuously extracted by means of a heated gas sampling probe and led to the analyzer via a heated measuring gas line. Gas conditioning with a multicomponent analyzer may be installed directly in the analysis cabinet. The dust measurement can be performed either *in situ* or extractively using commercial solutions provided by various suppliers. The continuous measurement of the gas, for example, by the IR technique, needs a combination with a gas flow measurement to determine the overall emission. The elemental analysis of, for example, dust is normally performed in a classical laboratory environment by various spectroscopy techniques, often ICP-OES or XRF because of their multielement capability. The implementation of a solution strongly depends on company size and the products to be produced. Very large companies sometimes establish homemade solutions based on separation techniques or hyphenated approaches [26]. The reason, therefore, is the complexity of the samples that cannot be handled even byhighly sophisticated spectroscopic methods. One major advantage in these cases is also the longer time scale, because in case of ''normal'' emission the concentrations are so low that samples for each half hour or up to once per day are requested by authorities. For the optimization of waste incineration plants also, a number highly sophisticated techniques such as on-line, real-time MS combined with FTIR have been applied [27].

37.2.5
Investment, Return on Investment, Cost of Ownership

For the chemical industry in a global competitive situation, the most important motivation for implementing process analytical tools is the possibility of cost reduction. Therefore, the calculation of investment in process analytical instrumentation, the determination of the return for this investment, and the cost of ownership are important issues. Here, the industrial point of view is described for better understanding. In this context, a more general starting point has also to be applied because spectroscopy in many cases competes with other techniques; besides, the comparison between laboratory and process implementation often means comparinga spectroscopic with a nonspectroscopic method, if only costs and quality matter.

Starting with a general view of analytical chemistry in production, up to 4% of production costs are spent on analytical work. A major part of this work is done in the classical way – off-line by laboratory analysis. This is the case although most analyzers used in the laboratory are available as on-line working process analyzer versions. The decision to move from laboratory analysis to process analytical equipment in the chemical industry has three major reasons:

- Increase the safety of a production facility
- Improve the quality or yield of a product
- Reduce the costs of a product.

Typically, in production an overall cost balance has to be made. The costs of a product are determined by the cost of the raw materials, energy, workforce, the quality of the product, and the cost of equipment.

The costs of analytics in many cases are part of the costs of workforce and equipment. So, the benefits of an improvement of analytics by on-line or in-line in process control can be found in the workforce costs, equipment costs and also in the quality of the product and sometimes in raw materials costs. The balance of these factors, as listed here, has to give a positive benefit.

- Costs
  - Instrumentation
  - Implementation
  - Training of personnel
  - Calibration, maintenance, repair, and supplies.
- Benefits
  - Reduced cycle time
  - Higher quality of the product
  - Less usage of raw material
  - Documentation of testing
  - Higher process control stability, planning becomes easier
  - Transferability of processes to various plants.

Typically, the investment in instrumentation and implementation of process analytical equipment is low compared to the costs of the production equipment ($\ll$10%), but typically two to five times higher compared to similar laboratory equipment. This difference including the company's internal capital costs has to be justified by a turnover within typically 6 months to about 2 years.

The question is therefore which investment in process analyzers is profitable regarding a certain production process and the requirements for quality of measuring values. Such data would be valuable for the planning of new and optimization of existing production plants.

In the following, some guidelines for different measuring principles on the basis of long-term experience in process analyzer technology are given.

The examples of some standard analytical measurements in chemical and pharmaceutical processes are given in Table 37.3; see column 1.

Methods commonly used for process control are shown in column 2 process analytical technology (PAT), whereas the competing laboratory method is given in column 3.

Table 37.3 Measuring tasks and methods used for evaluation of process analytics versus laboratory analytics.

Measuring tasks regarded

Measuring task	**PAT method**	**Laboratory method**
pH-measurement	Potentiometric	Potentiometric
Nitrate in chemical wastewater	Titrator/automatic analyzer with a specific reagent	Titrator/automatic analyzer with a specific reagent or *photometer*
DOC + VOC in chemical wastewater	Thermic TOC with VOC-channel and dilution + filtering	Thermic or UV decomposition TOC with VOC channel
Gas analysis of five components	Filter photometer or *GC*	GC
Liquid analysis of five components	NIR spectrometer	GC
Gas analysis of one component	NDIR photometer	GC
DOC of ultrapure water (ppb-range)	Ultrapure water DOC (UV-decomposition + conductometry)	Ultrapure water DOC (UV-decomposition + conductometry)

NDIR (non-dispersive infrared) photometer.

Cost of ownership was determined on the basis of manifold experience with such measurements. Because investment and running costs vary within a wide range depending on the application, average values were taken. Assuming a lifetime of 15 years, the following costs have been taken into consideration:

1) Interests and depreciation of
   a. engineering, application, installation of measurement;
   b. fraction of analyzer room (it has been assumed, that an analyzer room contains 8–10 process analyzers).
2) Operating costs for
   a. maintenance (including functional tests and calibrations);
   b. repairs;
   c. expendable items (gases, buffers, and so on) and repair materials.

For the laboratory analysis methods, the following expenses were taken into account:

- Sampling
- Sample transport from the sampling point to the laboratory
- Laboratory hours/analyzing costs
- Enter results into plant data system (data sampling)
- Disposal of samples.

To give a more general estimate for this cost balance in a survey, a number of chemical and pharmaceutical companies were asked for quotations of such laboratory analysis services. In addition, prices from commercial analytical laboratories were collected. Finally, the results were averaged.

For two of the seven measuring tasks, two alternative solutions (indicated underlined) were investigated. An important finding was that – for the investigated applications – 45–75% of process analyzer ownership costs were caused by maintenance, inspection, and repair (Figure 37.9). The contribution of investment costs is relatively small. Therefore, in planning or applying a process analyzer, the focus should be more on maintenance and not too much on investment costs because cost optimization is achieved mainly in maintenance, which means that the decision between different analyzers with similar specifications is performed simply on maintenance effort or costs. For example, self-diagnosis and maintenance request status signals require higher investment but may help to reduce maintenance costs by switching from periodic to condition-oriented maintenance.

As a second result, it turned out that on-line analysis is often less costly than laboratory analysis (Figure 37.10). The breakeven point is about 1–2 analysis per day (nitrate in wastewater, multicomponent gas, and liquid analysis, dissolved organic carbon (DOC) plus volatile organic compound (VOC) of wastewater) and even less than 0.5 analysis per day for some measurements (pH, one-component gas analysis, DOC in ultrapure water).

The application of PAT can save a lot of money in chemical and pharmaceutical production processes. Examples with amortization times of 1–2 years are as follows:

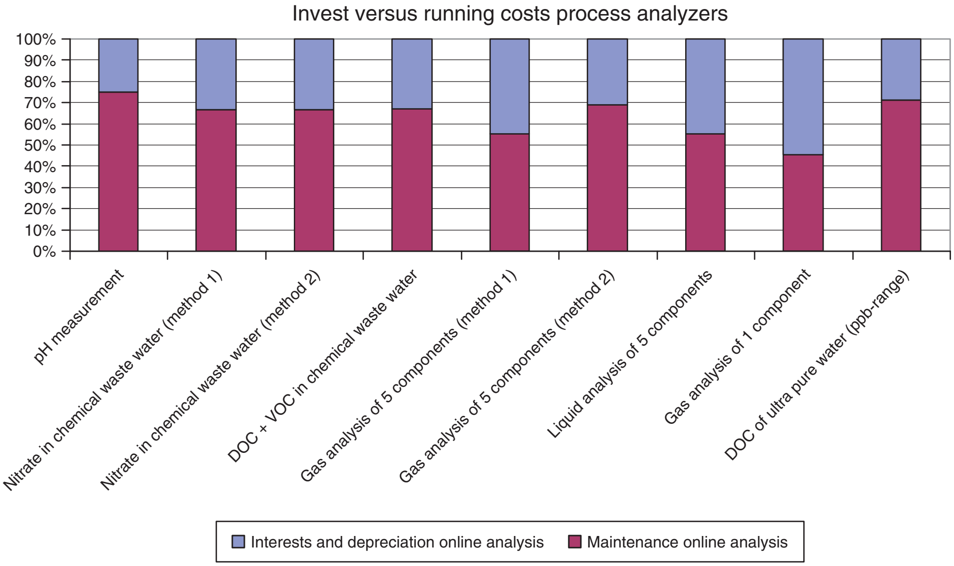

Figure 37.9 Ratio of investment and operation costs for the various process analyzer systems evaluated.

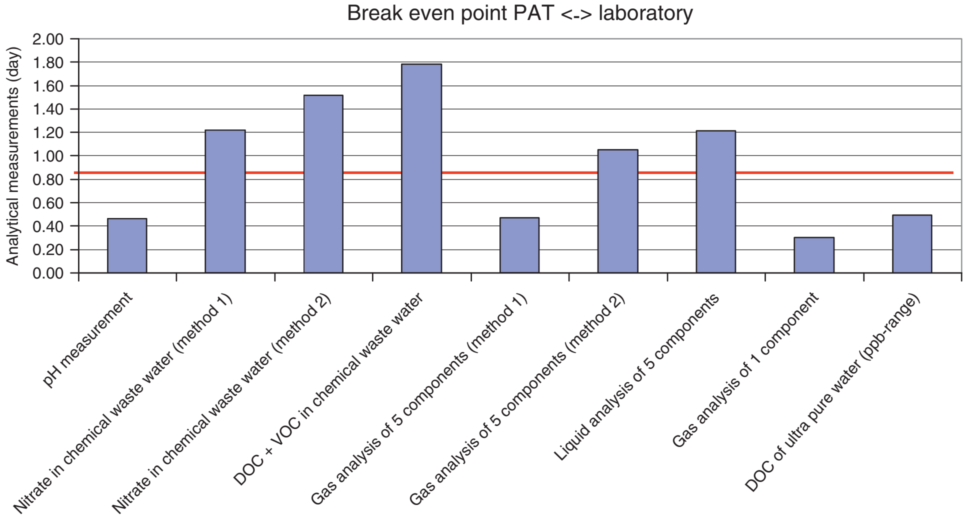

Figure 37.10 Results of the evaluation with mean value of measurements per day and the individual results for each technique.

- Supervision of distillation columns with an NIR-spectrometer
- Analysis of fractions after a preparative chromatography with on-line high performance liquid chromatography (HPLC)
- Supervision of boiler feed water.

As a rule of a thumb, it can be summarized that approximately for one analysis per day the costs of process analyzers are comparable with the costs of laboratory analysis. The main task for on-line analyzer specialists will be to optimize consulting, planning, and maintenance to reduce the breakeven point to laboratory analysis and to increase the benefits of the plant managers. Smart engineering, the introduction of diagnosis tools, and new analytical methods will help achieve this.

References

1. Koch, K.H. (1999) *Process Analytical Chemistry – Control, Optimization, Quality, Economy*, Springer, Berlin.
2. Steiner, G. (2005) in *Handbook of Spectroscopy*, (eds G. Gauglitz, T. Vo-Dinh), 2nd edn, Section V. Wiley, Weinheim.
3. Mahler, H. (2008) P&A Select Oil&Gas, 2008/2, pp. 22–24.
4. Nordsieck, H.O., Liu, Y., Kettrup, A., and Zimmermann, R. (2006) *Environ. Sci. Technol.*, **40** (1), 342–349.
5. List, T., Dempf, D., and Brudel, M. (2004) *Chem. Anlagen Verfahren*, **2**, 64–65.
6. Cook, K.D., Bennett, K.H., and Haddix, M.L. (1999) *Ind. Eng. Chem. Res.*, **38** (4), 1192–1204.
7. Cisper, M.E. and Hemberger, P.H. (1997) *Rapid Commun. Mass Spectrom.*, **11**, 1449–1453.
8. Hergeth, W.-D. and Krell, M. (2006) *Anal. Bioanal. Chem.*, **384**, 1054–1058.
9. Brink, M. van den, Pepers, M.L.H., Herk, A.M. van, and German, A.L. (2001) Thesis. Technical University of Eindhoven. Polymer Reaction Engineering, **9** (2), 101–133.

10. Müller, J., Kummer, S., Sahre, K., and Fischer, D. (2009) Proceedings of 3. Doktorandenseminar, Attendorn, Germany, 2009, pp. 9–12, ISBN: 978-3-032604-23-2.
11. Fischer, D., Sahre, K., Abdelrhim, M., Voit, B., Sadhu, V.B., Pionteck, J., Komber, H., and Hutschenreuter, J. (2006) *C. R. Chim.*, **9**, 1419–1424.
12. Fischer, D., Müller, J., Kummer, S., and Kretzschmar, B. (2011) *Macromol. Symp.*, **305**, 20–27.
13. Müller, J., Große, S., Kummer, S., Masarati, E., Consalvi, M., and Fischer, D. (2012) *J. Nanostruct. Polym. Nanocompos.*, **8**, 21–26.
14. Fischer, D., Alig, I., Steinhoff, B., Lellinger, D., and Hutschenreuter, J. (2006) *GIT Labor Fachz.*, (11), 1017–1020.
15. Alig, I., Fischer, D., Lellinger, D., and Steinhoff, B. (2005) *Macromol. Symp.*, **230**, 51–58.
16. Müller, J., Kummer, S., and Fischer, D. (2009) *Meas. Sci. Technol.*, **20**, 097002.
17. Kumbholz, N., Hochrein, T., Vieweg, N., Hasek, T., Kretschmer, K., Bastian, M., Mikulics, M., and Koch, M. (2009) *Polym. Test.*, **28** (1), 30–35.
18. De Beer, T., Burggraeve, A., Fonteyne, M., Saerens, L., Remon, J.P., and Vervaet, C. (2011) *Int. J. Pharm.*, **417** (1–2), 32–47.
19. Welmink, J.G. (2006) Presentation, 2. Kolloquium, AK Prozessanalytik, Dresden, Germany, November 7, 2006.
20. Cooper, D.E. and Martinelli, R.U. (1992) *Laser Focus World*, **28**, 133–146.
21. Bomse, D.S. (1995) *Photonics Spectra*, **29** (6), 88–93.
22. Bjorklund, G.C. (1980) *Opt. Lett.*, **5**, 15–17.
23. Bomse, D.S., Stanton, A.C., and Silver, J.A. (1992) *Appl. Opt.*, **31**, 718–731.
24. Schiff, H.I., Bechara, J., Pisano, T.J., and Mackay, G.I. (1994) *J. Air Waste Manage. Assoc.*, **SP-89**, 921.
25. Bosch Ojeda, C. and Sánchez Rojas, F. (2009) *Appl. Spectrosc. Rev.*, **44**, 245–265.
26. Wortberg, M., Ziemer, W., Kugel, M., Müller, H., and Neu, H.J. (2006) *Anal. Bioanal. Chem.*, **384** (5), 1113–1122.
27. Streibel, T., Hafner, K., Mühlberger, F., Adam, T., Warnecke, R., and Zimmermann, R. (2006) *Anal. Bioanal. Chem.*, **384** (5), 1096–1106.

38

Process Control Using Spectroscopic Tools in Pharmaceutical Industry and Biotechnology

Michael Brudel, Uwe Schmidt, Holger Mueller, and Stephan Küppers

38.1

Introduction to Pharmaceutical Industry

The company structure in the pharmaceutical industry typically is divided into a drug substance (active pharmaceutical ingredient (API)) production and a drug product production. The drug substance is either produced in a chemical or sometimes in a biotechnological process, as already mentioned. Typically, at least the drug substance – but in most cases also the drug product – is produced in multipurpose equipment using a batch production process. A chemical production plant produces between a few and up to 20 different products, which means also that quite often each chemical synthesis is only produced once a year. Very often, the drug substance is produced within a low number of batches, <3 to 10 batches per year. Afterwards the equipment is cleaned and used for the next product. The typical equipment of the chemical or biotechnological production process is the stirred tank reactor. A typical API synthesis has between 5 and 15 chemical or biotechnological steps. The typical processing time of a chemical conversion is hours and the process from preparation of equipment to the isolation of the product has a time scale from 1 day to a few days. This is different from the biotechnological processes, which typically need at least a few days/1 week to a few weeks.

Because of the strong batch and multipurpose orientation of chemical manufacturing in the pharmaceutical industry, special technologies, such as process analytical instrumentation, is used only if it can be applied to a large number of chemical synthesis steps.

In addition, a typical chemical manufacturing plant in the pharmaceutical industry has a large infrastructure of special process and/or downstream processing instrumentation, starting from distillation, wastewater plant to process chromatography, and so on. In this infrastructure part of the plant, typically different products are processed, but the various support processes are always the same. For example, in distillation different solvents are distilled but the distillation process stays the same and, therefore, in the infrastructure part of a chemical manufacturing plant much more process control instrumentation is applied, than in the chemical part of the pharmaceutical core facility. In solvent recovery (a distillation plant), in many

Handbook of Spectroscopy, Second Edition. Edited by Günter Gauglitz and David S. Moore.

cases, a process control instrumentation such as process GC (gas chromatography), process MS (mass spectrometry), or near infrared (NIR) is applied to receive the specified quality at lowest costs. Here, a point of view similar to chemical manufacturing is taken, and implementations are comparable to the examples described.

The pharmaceutical production process, starting from the API to produce the drug product, is also typically a batch-type process. Here, the equipment and processes slightly differ for solid, semisolid (ointments, crèmes), and liquid products. In addition, there are some special products such as suspensions, band-aid/plasters, and others. The key quality issues depend on the product. For example, for solid products, homogeneity of mixing of the API with the additives is the key issue; for semisolid products, this is only sometimes an issue; but, typically, the homogeneity is no issue at all for liquid products. This also means the process control and, therefore, the process control instrumentation is strongly dependent on the type of product.

Biotechnological manufacturing, in principle, is just another way of manufacturing the API. Sometimes, even some of the steps of the conversion from starting material to API are produced using biotechnological conversions. But there are some important differences compared to chemistry with respect to the importance of process controls. The most important differences are as follows:

- the biotechnological processes are much more complex on the molecular level;
- a biotechnological conversion takes much longer and therefore the control of the process is also possible with slower analytical tools;
- sampling is often much easier than in chemical conversions because the samples are water based and the processes are typically at ambient pressure and moderate temperatures.

Especially because of the second reason, process analytics has a much longer tradition in biotechnology. Because of this tradition, the modern (and often fast) spectroscopic analytical tools often have first been implemented in biotechnology and implementation in chemistry has been following slowly. In this chapter, therefore, much more examples from biotechnology are shown compared to the current importance of biotechnology in the pharmaceutical industry.

The overall workflow for pharmaceutical industry is given in Figure 38.1.

38.2
Regulatory Aspects

In the pharmaceutical industry, quality is still the key issue for a product. In development, a product is therefore tested by a toxicological study with healthy humans and then with patients. At the date of submission, the pharmaceutical company submits a ‘‘contract,’’ with a promise to produce the same quality with the same impurity profile to the regulatory agencies. This general procedure leads in combination with the fact that the pharmaceutical industry is interested in the shortest possible

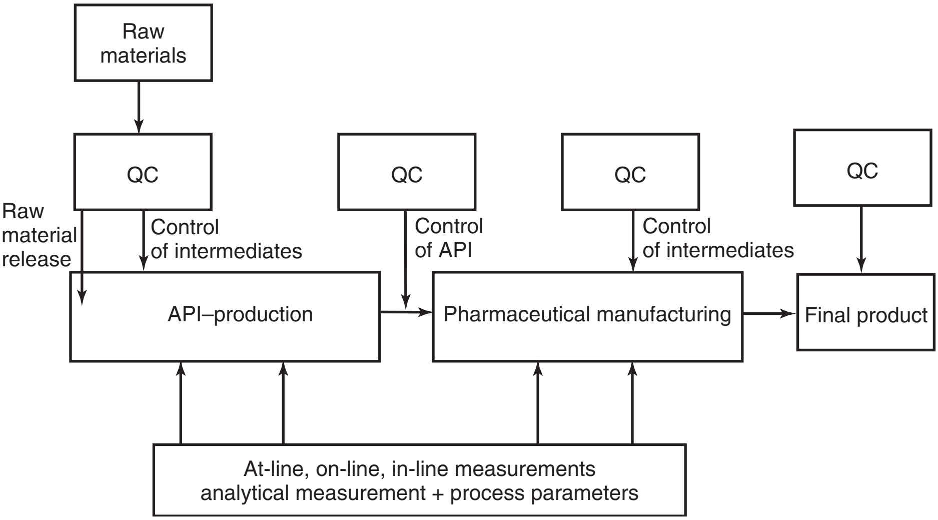

Figure 38.1 Typical workflow for the pharmaceutical industry.

time to market to a situation that the production processes are typically fixed before they are fully optimized. Every change (also an optimization) in the production process has to be accepted by the regulatory agencies. If the impurity profile is changed, a new study showing the comparability of the new product in clinics has to be applied and a new stability test is needed. Both tests typically take years and the costs are extremely high. Therefore, typically, in chemical and pharmaceutical manufacturing, only a few sophisticated process controls are implemented because they are not available at the time of the submission of a new product.

The situation slightly changes because of the FDA's (Food and Drug Administration) so-called Process Analytical Technology (PAT)-initiative. The PAT-initiative was initiated at the beginning of the century and is intended to present a new risk-based approach of the FDA for the twenty-first century. It is an interdisciplinary and process-oriented approach to the quality in production in the pharmaceutical industry. Because of the complexity of the approach, a number of scientific and business organizations are involved in the PAT-initiative.

The definition of PAT is

> A system for designing, analyzing, and controlling manufacturing through timely measurements (i.e., during processing) of critical quality and performance attributes of raw and in-process materials and processes with the goal of ensuring final product quality.

In a later part of the definition, the innovation orientation of the approach is clarified:

> Using this approach of building quality into products, this guidance highlights the necessity for process understanding and opportunities for

> improving manufacturing efficiencies through innovation and enhanced scientific communication between manufacturers and the Agency [1].

This approach is already changing the way the pharmaceutical industry thinks about process control. Process control is becoming more integrated into process development, as first examples show [2], and critical parameters in the production process are controlled to ensure product quality. An interesting part of the FDA definition is also:

> It is important to note that the term analytical in PAT is viewed broadly to include chemical, physical, microbiological, mathematical, and risk analysis conducted in an integrated manner.

Here, the widening of the scope of process control to include mathematical tools such as chemometrics will be important for further developments. A general introduction on the process initiated by the FDA's PAT-initiative can be found elsewhere [3, 4].

The new approach is oriented toward other industries such as the semiconductor industry, where also a very strict quality orientation is performed but the quality is produced by the following:

- a strict quality control (QC) system including statistical process control in each process step, between process steps;
- on-line and in-line controls are essential and an integral part of every process technology [5].

The PAT-initiative is currently changing the production in the pharmaceutical industry, which leads to a continuous increase in process analytical tools in manufacturing, especially in pharmaceutical production. Spectroscopic techniques are mainly used here. Therefore, the number of publications dealing with applications as well as reviews [4, 6–9] and on special aspects of the production process in this special field is growing strongly. In general, the interaction between regulatory agencies and industry leads to a strong integration of new technologies and evaluation processes. In this respect, a strong growth of integration of chemometric tools in industrial applications has been observed recently. One current aspect in the transformation process in the pharmaceutical industry is the definition of design spaces that describe a parameter space for the production of a product. Within this parameter space, the product reaches the necessary quality. The control of the parameters of the design space might be performed either by analytical measurement, as shown for the vaccine example later, or by settings of the optimized process parameters, as shown in the fluid bed granulation example [9]. The following discussion will therefore never be up to date. We more or less try to describe the process and give a few examples for a more general understanding.

38.3
Applications in Pharmaceutical Industry

As regulatory aspects play an extremely important role in the pharmaceutical industry, this aspect and its influences are explained in the following discussion. As shown in the workflow for the pharmaceutical industry, there are two major parts of manufacturing. As many chemical reactions in API production are similar to production processes in the chemical industry, only one example for the monitoring of a chemical reaction is given. In addition to chemical manufacturing, biotechnology as a manufacturing process is of increasing importance in the pharmaceutical industry for API production and also in food production, as discussed earlier. The monitoring of these types of products is therefore discussed in this chapter. As also visible from the workflow, the pharmaceutical part of manufacturing is an important part of the production process; this part is also discussed. The downstream processing is monitored in the chemical as well as in the pharmaceutical industry. Because of the strong regulatory influences, the specs for downstream processes are much tighter in the pharmaceutical part compared to the chemical and therefore the monitoring of downstream processes is performed much more rigidly in this industry. Here, a few examples are discussed.

38.3.1
Raw Material Control

In the pharmaceutical industry, each raw material that is purchased is tested with respect to identity, assay, and purity before use. Depending on the type of raw material, the supplier and the stage in the synthesis where the material is used, the tests are more or less complex. For many raw materials, the current test procedures are still laboratory tests, which contain wet chemical and physical parameters and often also a chromatographic purity test. NIR spectroscopy has changed the field because it can be used for identity and purity tests. In the purity test, not only are the individual impurities identified but the impurity profile is also identified to be ‘‘in-spec.’’ One of the advantages of the pharmaceutical industry is the high degree of standardization in production and the high regulatory standards. This means that the chemometric calibration models only need to include a relatively limited number of raw materials and a relatively low number of different qualities for the raw materials. The interface for the application of NIR in this field is typically an attenuated total reflectance (ATR) probe as described in the subsequent text, and both the NIR technique and the chemometric model are described in detail elsewhere [10].

38.3.2
API Production

Chemical reactions often lead to more than one product. In case of chemical products, often the by-products are recycled or used in a separate product. In API production, typically, a synthesis from 5 to 15 chemical, biological, microbiological, or their combinations lead to a single product that must have a purity of higher than 95%, often higher than 98%. This means on each step of such a synthesis, the control of the purity and the assay are essential to receive a high yield of the final product with the necessary quality. Therefore, the individual synthesis steps can be purified (which sometimes has to be performed in addition to process control) and or the chemical reactions can be controlled to lead to the optimum quality. In addition to the control of the chemical process, the endpoint detection of chemical reactions is useful to keep the desired product instead of forming degradation products. Endpoint detection also may save other resources such as energy, equipment time, solvents, and other resources. For a growing number of chemical synthesis steps, process controls, the so-called PAT-solutions, are under establishment. Historically, process control implementations only have been established if necessary because of the relatively high costs in a batch process environment with low annual batch numbers.

A chemical reaction that is widely investigated with respect to start and endpoint determination is the Grignard reaction. One of the major reasons is the safety control of this reaction in a production plant environment [11, 12]. The principle of the reaction is the reaction of an organic halide with solid magnesium in tetrahydrofuran (THF) to Grignard reagents R-Mg-X, which then is *in situ* used by the reaction. This first reaction is a spontaneous and extremely exothermic reaction. Therefore, it is vital to control the start of the reaction und extremely useful to monitor the whole reaction till the end. Although various approaches have been tested, Fourier transform infrared spectroscopy (FTIR) monitoring has been proved to be the most useful method [11–13]. In some cases, NIR has been used [14].

The implementation of a mid-IR (infrared) spectrometer in a plant environment is more complex compared to NIR because, typically, the coupling has to be direct to the process, whereas NIR can be coupled with a fiber optic to the process. The mid-IR spectrometer is coupled to the process using an ATR-type interface. The spectrometer itself has to be installed in an Ex-proven box directly connected to the reaction flask where the monitoring is performed. In case of defined chemical conversions, the advantage of mid-IR is that in some cases a single wavelength is characteristic for the conversion. Therefore, the evaluation is much easier compared to the complex mathematical evaluation typically performed in NIR monitoring, as shown in Figure 38.2. Here, the reaction monitoring for the Grignard reaction at three different wavelengths versus time is shown K. Lovis, unpublished, 2000.

Another field where process control applications are being implemented for a number of years is the final step of the chemical process that leads to the API itself, in case this step is a crystallization step under salt formation. The reason for using process control here is that different polymorphs could be generated and typically only one of the different polymorphs leads to the correct pharmaceutical formulation. Very few examples of pharmaceutical process monitoring for this final synthesis step have been published. A published process monitoring example is the formation of an HCl salt from a free base. In this reaction, the free base, the

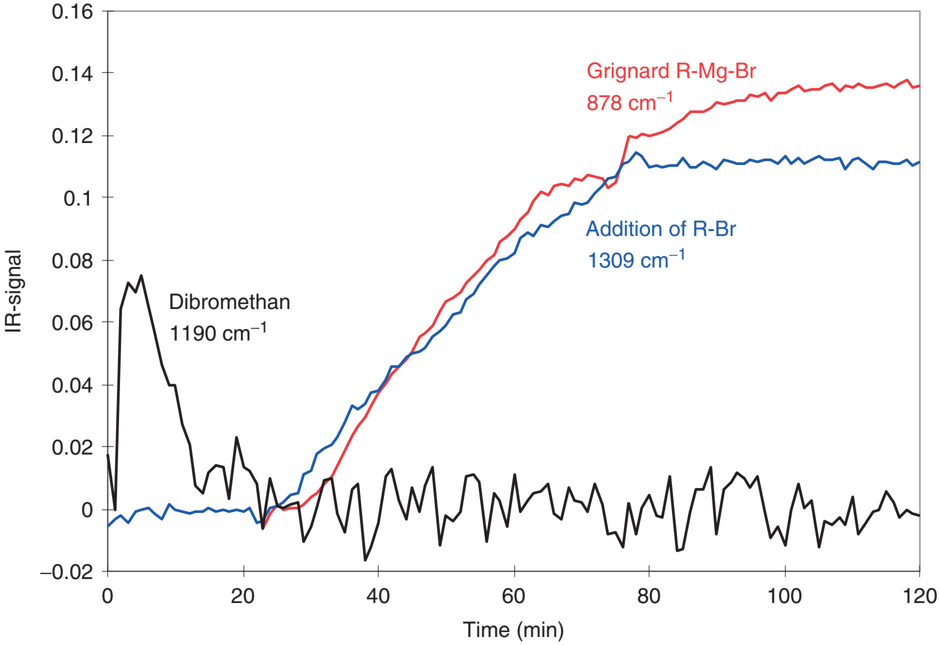

Figure 38.2 Mid-IR monitoring of a Grignard reaction.

mono- and the bis-HCl salt are found, where the free base and the bis-HCl salt can be monitored by IR. The mono-HCl salt is the desired product, whereas the bis-HCl salt is an impurity. The optimum of the reaction, where the salt formation/addition of HCl is stopped, is found at the flat point of the concentration profile of the free base. At this time, the concentration profile of the bis-salt starts increasing. The paper shows that the endpoint determination of a salt-formation process using mid-IR is possible; for details, see [15]. Another example of a combined process control for crystallization, where also the particle size control is discussed, is given later in this chapter.

38.3.3
Biotechnology

Biotechnology has been used for about 8000 years [16] for beer manufacturing and still has an extremely broad use in food manufacturing from wine, acetic acid, leaven, to various milk products. In general, the so-called classical biotechnology is understood as the use of microorganisms in technological processes besides food; fermentations including composting and waste water plants are also covered by this definition.

Currently, biotechnology has a much wider range and is structured in four fields of application:

- green biotechnology is the use of any kinds of plants including genetically modified plants;
- red biotechnology is the area of any kind of biotechnology for the manufacturing of drug substances;
- blue biotechnology has its focus in the marine area;
- white biotechnology is the industrial manufacturing and use of biotechnology for any kind of products from chemicals via textiles to food products.

The field of biotechnological products ranges from enzymes, vitamins, amino acids, antibiotics, aroma substances, vaccines, fine chemicals, monomers, and many others products. New areas such as energy conversion play an increasing role in the application area of biotechnological processes. The importance of biotechnological processes for the pharmaceutical industry is both changing in the area of chemical entities and growing for the area of biopharmaceuticals.

An overview of the products of the white biotechnology, where process control is typically applied, is given in subsequent text [17] (Table 38.1).

38.3.4
Technological Aspects of Biotechnology

For the discussion of process control in biotechnology, a few explanations on the technology itself have to be given as introduction. In biotechnology, reactions are preformed at room temperature and normal pressure. The control process has to take into account two major points. On one hand, the microorganisms themselves have to grow and produce biomass and, on the other hand, the concentration

Table 38.1 Important products of white biotechnology.

Product	World annual production in tons
Riboflavin (vitamin B2)	30 000
Vitamin C	80 000
L-Glutamic acid	1 500 000
L-Lysine	700 000
L-Threonine	30 000
Citric acid	1 000 000
Acryl amide	100 000
Polylactide	140 000
Bio-ethanol	>18 500 000
Beer/wine	165 766 000
Antibiotics	<80 000
Glucose	20 000 000
Iso-glucose (HFCS)	8 000 000

high fructose corn syrup (HFCS)

of the desired product should increase to the optimum. First, process control has to care about biomass. Typically, cells replicate within hours or days; that is, *Escherichia coli* (*E. coli*) under optimum conditions replicate every 20 min. For monitoring the biomass generation, a measurement cycle of one point per hour is typically sufficient and typically the input into a reactor is well known in the form of air (oxygen), additional sugar, additives, and so on. For monitoring the biomass growth, therefore, the output can be measured, which means measuring the gases CO_2, H_2, CH_4, pH, and acetate. In many cases, the monitoring of the gaseous compounds is routinely performed by gas sensors on the basis of IR sensors, commercially available for many years. In the past decade, in addition the monitoring of the target compounds has become state of the art. In the beginning, these analyses have been performed within the day-shifts off-line, whereas currently on-line- or in-line-analytical-systems are being implemented or are already state of the art. A detailed example is given in subsequent text.

Central to the concept of bioprocess monitoring are the sensors with which measurements are made. Nature has developed very efficient, highly precise methods of controlling biological processes. The challenge is to transfer these principles into technically applicable and precise analytical systems that can be used for many applications. Although this goal has not yet been met, it is nonetheless true that an impressive range of sensing devices has been developed over the years for measurement of chemical, biological, and physical parameters of both up and downstream bioprocesses. These devices are conveniently categorized as biosensors, chemosensors, or optical sensors, depending on their detection principle.

In addition to the measurement of traditional bioprocess parameters such as substrate, product and biomass concentrations, there will be an increasing need for new measurements. For example, as our design of therapeutic proteins becomes more sophisticated, it will be important to have measurements of particular glycosylation patterns. A drug with multiple chiral centers is another case of a complex analyte. Other motivations for sensors will come from systems biology: although sensors for some compounds of the metabolome have been described or even commercialized, these usually cover only some of the extracellular metabolome and only a small fraction of the range of intracellular compounds. On-line sensors of the transcriptome and proteome may also be needed in the future. Regardless of the sensor type, the target analyte, or application, sensors are expected to be sensitive, selective, and specific. Continuous signals and rapid responses to analyte changes are desirable, especially for process control purposes. An additional requirement, less recognized but perhaps more important, is for robustness and the ability to function in real bioprocess environments for extended periods. This includes the need for aseptic measurements, either by sterilization of the sensor or by incorporation of a sterile sampling device. Although perceived as less glamorous than the invention of a new sensing technique, creative ideas are also needed to solve practical problems so that new sensors can be commercialized and implemented [18].

38.3.5
Overview of Analytical Technologies Used in Biotechnology

38.3.5.1 Off-line/At-line

In biotechnological processes, a wide range of classical analytical techniques are applied; especially if the analysis is not time critical, the analysis is still often performed in a laboratory [19]. The techniques typically applied in the laboratory are high-performance liquid chromatography (HPLC), GC, nuclear magnetic resonance (NMR), and others depending on the process. For determination of the biomass concentration, often ultraviolet–visible (UV–vis) (optical light absorption) or gravimetric dry biomass is determined at-line. In addition, a number of analytical measurements such as density, titrations of acid concentration in the medium, and a large number of enzyme tests are performed off-line or at-line. As an example, for a spectrometric test typically performed close to the process in biotechnology, the glucose determination by the generation of glucose-6-phosphate may be mentioned. In this determination, the glucose-6-phosphate reacts with its dehydrogenase to the corresponding lactone. In this reaction, NADP+ is converted to NADPH (nicotinamide adenine dinucleotide phosphate), which is detected at 334 nm in a UV–vis spectrometer. Alternative tests are also commercially available on the basis of amperiometric detection [19].

38.3.5.2 On-Line

As already mentioned, a number of gas sensors based on IR detection are used in on-line biotechnology process control to monitor the gas flows of CO_2, O_2, N_2, and Ar through the fermentation [20]. The fermentation brow itself depending on the question is monitored on-line by many optical spectroscopic techniques from refractive index measurements, to UV–vis to IR and NIR spectroscopy [21]. The reason these techniques are applied on-line instead of in-line often is that the biomass in this case does not interfere with the optical path. In process development also, combined techniques consisting of HPLC and MS [22] are used to generate process understanding by structure elucidation of metabolites. MS has an additional advantage compared to other spectroscopic techniques such as NIR in case of unknown contaminations. While an NIR model typically can give only the information that there is something wrong, the MS is capable of structure elucidation of unknown components. In a process MS, the mass of the unknown component would become available and could give a first hint to the impurity or contamination.

38.3.5.3 In-Line

If the transparency of the fermentation brow allows use of optical techniques also in-line, in many cases UV–vis spectrometry and NIR are used directly in the process to determine mass growth, the concentrations of feed, the compounds of interest and also by-products such as acetate. The typical challenge for using in-line process control in biotechnology is that the sensor has to be sterilized. For NIR, in addition, the calibration is much more complex than in many other cases because of the very complex mixtures.

38.4
Examples of Applications of Process Control in Biotechnological Processes

As mentioned, the gas analysis of the reactor outlet is an important indicator for the growth of the cells in the fermentation process. The gases of interest are, for example, O_2, CO_2, or also ethanol. Because ethanol is difficult to measure, in the fermentation brow, the in-line measurement in the gas phase above the fermentation by IR sensors can be used alternatively. This measurement can either be performed by MS [23] or by IR sensors [24]. In the outlet pipe of the fermentation reactor, the on-line application of MS is also possible. The advantages of MS are the high analysis speed (within seconds) and the sensitivity down to the parts per million range. The disadvantage is the higher investment cost of a process mass spectrometer. This is partially compensated for by the quite low costs of maintenance [25].

The IR example described in detail in [24] shows an example of yeast fermentation. In this fermentation, first the increase in biomass is desired. Although the feed contains enough carbon source (e.g., sugar) the production of ethanol starts. Because the ethanol decreases the biomass production speed, this so-called Crabtree effect usually is unlikely. Therefore, for the control of all gases, CO_2 for the overall turnover in the process and ethanol for the type of turnover are used to control the fed-addition, that is, for example, the glucose, and by this way to minimize the effect of the Crabtree effect (Figure 38.3 and Figure 38.4).

The three sensors in the waste gas line are directly coupled to the control system of the fermentation. The sensors can in many cases be used to estimate

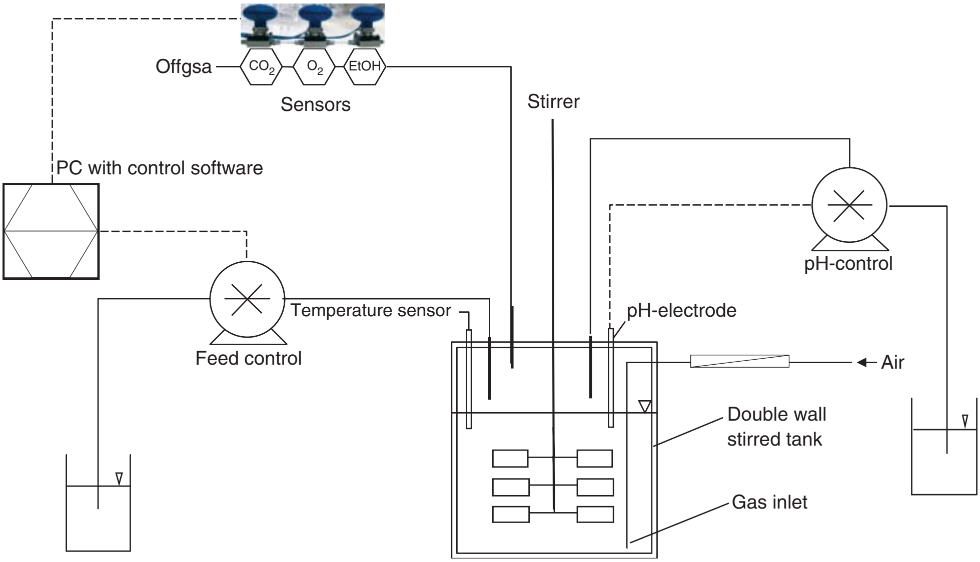

Figure 38.3 The experimental setup with the three gas sensors in the waste gas line.

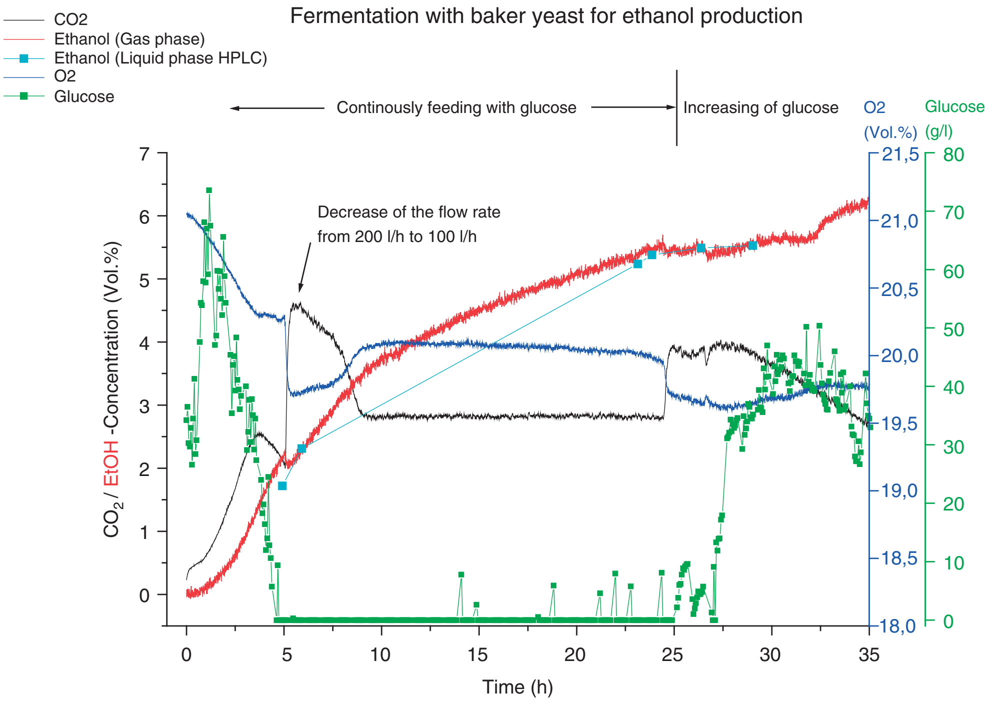

Figure 38.4 Typical results of a fermentation with the received sensor signals for CO_2, ethanol, and O_2. In addition, the added glucose and the determined ethanol concentration in the liquid phase (determined by HPLC) is shown.

the biomass generation by the carbon dioxide sensor, whereas the oxygen sensor shows the limitations of the process. In Figure 38.4, a typical curve of fermentation without process control is shown. This leads to a continuous increase in the ethanol concentration, which leads to the limitation of the fermentation. In Figure 38.5,a controlled fermentation is shown. Here, the ethanol concentration controlled by the sensors is nearly kept constant. For details, see [23].

Optical sensors have become more and more important for bioprocess monitoring. The term *optical sensors* is used here to encompass all analytical methods that are based on interactions of light with matter. Optical sensors offer the advantages of noninvasive, nondestructive, continuous, and simultaneous multianalyte monitoring. A major advantage is that no contamination is introduced into the process if on-line or in-line monitoring can be performed. Optical systems do not interfere with metabolism and thus *in vivo* measurements are possible. This can yield intracellular information that is difficult to obtain with other methods. As modern bioprocesses are extremely complex and differ greatly from process to process (e.g., fungal antibiotic production vs mammalian cell cultivation), appropriate analytical systems must be set up for each biotechnological process, designed to meet the special demands of the particular process.

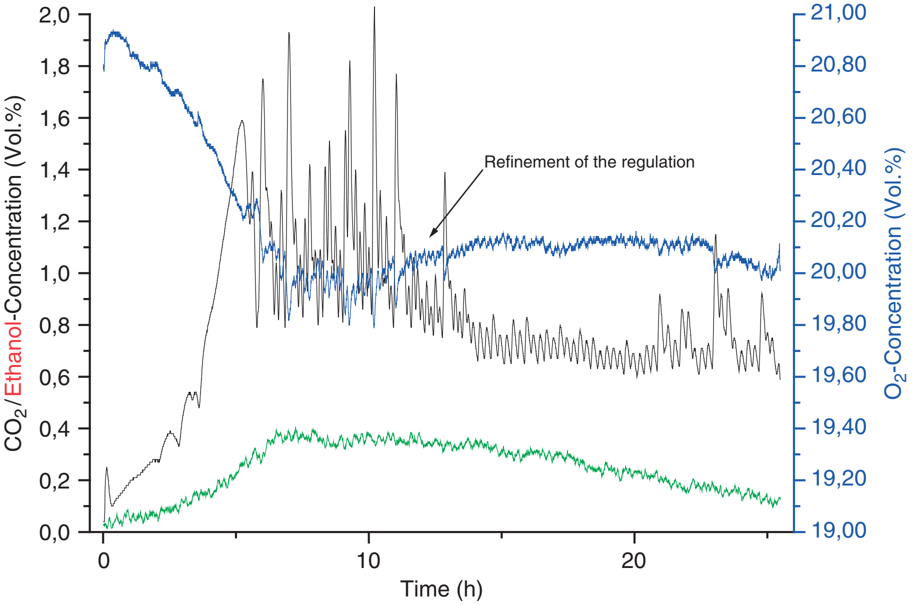

Figure 38.5 The resulting curves of a process-controlled fermentation. Here, the production of ethanol is limited to the desired range.

In most cases, the sensors are based on a few analytical principles, namely, ultraviolet (UV) spectroscopy, IR spectroscopy (NIR and FTIR), Raman spectroscopy, fluorescence spectroscopy, and pulsed terahertz spectroscopy (PTS).

Some current applications of these sensor types in biotechnology are described in subsequent text.

38.4.1
Application of UV Spectroscopy

UV spectrophotometers with high resolution are suitable for use in on-line monitoring of fermentation and downstream processes. New UV spectrometers have been developed in the past years [26] capitalizing on recent advances in electronics and especially in the development of new light detectors. One main advantage of these new devices is the use of charge-coupled devices (CCDs) or photodiode arrays to replace photomultipliers in conventional spectrometers. Because of lower costs combined with robustness, optical spectroscopy detectors are increasingly applied in industrial processes. The development of a high-resolution UV spectrometer that is suitable for the on-line monitoring of different kinds of bioprocesses is described by Noui *et al.* [26]. In this application, a deuterium light source was used to produce a light beam with an effective spectral radiation range of 185–400 nm. With this instrument, one is able to measure a continuous spectrum and this technique allows the simultaneous detection of several analytes. Another approach to sensing focuses not on detection of specific target analytes but rather on integrated parameters. This is especially useful in complex media, including classical culture media, as well as in domestic and/or industrial wastewater treated by biological processes.

Pons *et al*. [27] described more global methods based on UV spectroscopy that can be used to rapidly detect ‘‘accidents’’ such as the appearance of an undesirable by-product in a fermentation broth or of a toxic substance in wastewater. These methods combine a ‘‘hard’’ part, for sensing, and a ‘‘soft’’ part, for data treatment. In addition to the direct measurement of compounds of interest, increasingly chemometric tools are used [26, 28, 29].

38.4.2
Application of NIR and FTIR Spectroscopy

NIR spectroscopy enables detailed monitoring of substrates and products in many important types of industrial and food bioprocesses in order to document progress, ensure comparable end-product quality, and process control. Examples include the report by Jorgenson *et al*. [30], who described a newly developed modification of multivariate statistical process control charts based on on-line NIR. This enabled simple, efficient identification of abnormal fermentation runs, even at an early stage of the fermentation, which is critical for industrial production monitoring. Sorensen [31] has developed prediction models for determination of lactic acid, acetic acid, pH, NH_3, and ethanol in grass and corn silages by *in situ* NIR spectroscopy. The application of on-line NIR spectroscopy to measure simultaneously the concentration of substrates and products of acetic fermentation (ethanol, acetic acid, and biomass concentrations) was reported by Garrido-Vidal *et al*. [32].

Other examples of the application of in-line NIR monitoring in food biotechnology include fermentation of *Lactobacillus casei* [33], wine [34], and yogurt [35] fermentation. The application of NIR in-line to monitor and control an industrial fermentation process was investigated by Tosi *et al*. [36]. The determination of biomass, glucose, and lactic and acetic acids during fermentations of *Staphylococcus xylosus* was performed by an interactance fiber-optic probe immersed in the culture broth and connected to an NIR instrument. Thus, NIR seems to be one of the most promising spectroscopic techniques for the future of bioprocess control and modeling [37]. In addition to NIR-based technologies, FTIR has also been applied to bioprocess monitoring. For an example, a novel attenuated total-reflection-FTIR sensor was used for continuous on-line monitoring of chlorinated aliphatic hydrocarbons in a fixed-bed bioreactor. The sensor was based on an ATR internal reflection element coated with an extracting hydrophobic polymer, which prevented water molecules from interacting with the IR radiation [38].

FTIR spectroscopy, coupled to sequential injection analysis (SIA) was employed by Kansiz *et al*. [39] for the on-line monitoring of an acetone–butanol fermentation by simultaneously determining acetone, acetate, butanol, butyrate, and glucose from the mid-IR spectra of the samples.

38.4.3
Application of Raman Spectroscopy

Raman spectroscopy is based on the phenomenon of shifted wavelength scattering of molecules excited with monochromatic light due to inelastic collisions of photons with the molecule. The application of Raman spectroscopy to bioprocess analysis was made possible by the development of adjustable lasers. In principle, it is suitable for multianalyte monitoring of complex industrial bioprocesses on-line [40, 41] as well as for performing differentiated measurements of certain parameters, as demonstrated by Shaw *et al.* [42] and Lee [43]. The simultaneous estimation of glucose, acetate, formate, lactate, and phenylalanine concentrations in *E. coli* cultivations using *in situ* Raman spectroscopy was recently reported [44].

Challenges to the application of Raman spectroscopy to bioprocess monitoring lie in the strong fluorescence activity of many biological molecules that often overlies the Raman signal. One solution to this is ‘‘shifted subtracted Raman spectroscopy’’; using this approach, the resulting spectra have much lower apparent noise and fluorescence owing to the cancellation of irregularities in the detector response [44].

38.4.4
Application of Fluorescence Spectroscopy

Because many important biomolecules fluoresce, it is not surprising that fluorescence spectroscopy has been applied to bioprocess monitoring for several decades. A promising new version of the classic technique is two-dimensional (2D) fluorescence spectroscopy, in which a range of excitation and emission wavelengths are scanned. In comparison to traditional NAD(P)H fluorescence techniques, this method provides much more analytical information with a single measurement. With 2D fluorescence, all fluorophores present in a sample can be monitored simultaneously. Recently, a noninvasive 2D fluorescence sensor was developed for the measurement of the whole cell biotransformation of L-serine and indole to tryptophan [45] and for industrial downstream processing of sugar beet molasses [46].

Fermentation processes can be monitored using various spectroscopic techniques for growth and metabolic activity monitoring, as mentioned in detail earlier. The group of Scheper and Hitzmann [47, 48] demonstrated the use of 2D fluorescence spectroscopy for monitoring fermentations used for protein production. In this case, the excitation and emission wavelength in fluorescence spectroscopy are used in the range of 250–550 nm for excitation and 260–600 nm for emission. The evaluation is performed using the 2D plots of excitation versus emission. Some known fluorophores are used as markers for the quantitative evaluation of the protein production.

38.4.5
Pulsed Terahertz Spectroscopy

The ongoing developments in PTS may lead to new analytical applications for bioprocess monitoring. The potential for applications in chemical and biological identification [49] has already been shown and first examples of PTS to examine low-frequency collective vibrational modes of biomolecules have already been reported [50, 51]. Those results demonstrate that PTS is a viable technique for time-resolved measurements of protein folding.

One of the most important fermentation processes in health care is vaccine production. Here, safety and quality of the product are of extreme concern and this why a number of technological developments have been performed in this area. An example of vaccine production is therefore used to show the current status of PAT in the pharmaceutical industry.

38.5
Example Vaccine Production for the Control of a Biotechnological Process

The upstream part of a vaccine manufacturing line is a typical biotechnological fermentation process. Typically, measurements such as temperature, pH, dissolved oxygen, and flow rates are measured in this process, but the product is also monitored. This is either possible by on-line coupling of HPLC or high-performance liquid chromatography–mass spectrometry (HPLC-MS) [52, 53], but direct measurements using NIR have also been demonstrated [54, 55].

For a few years, PAT-approaches have been implemented in this field. A promising example has been developed by Streefland and colleagues from the Dutch National Vaccine Institute (NCI). For vaccines, the process can stay constant but the vaccine that is produced changes typically each year. Therefore, the process was described by a design space that was evaluated by systematic process variations and process controls. The result of the systematic approach is a controlled process. The major process control tool is NIR, and as a result of process control the product testing effort can be reduced, which in the case of vaccine production is an important issue because it saves time for the product to come to the market, an especially important issue for vaccines [56, 57]. The key parameter for QC of the vaccines consists of on-line monitoring of the nutrient concentration by NIR spectroscopy.

38.5.1
Downstream Processing

As already shown in the previous example, the production of a drug substance consists of the chemical and/or biotechnological step but this step is always followed by some kind of downstream processing to isolate, purify, or modify the product to bring it into an appropriate form for the next process step. In the case of vaccines, the downstream processing is closely related to the fermentation and both processes are nearly integrated currently, which can also be seen in the above-cited literature. In addition, in this case, downstream processing only consists of heat inactivation and concentration to yield the bulk product. This process step has only very low impact on quality. In chemical API manufacturing, the different chemical steps typically show a much larger change from one step to the next. Therefore, downstream processing may have an enormous impact on quality by the purity of the received intermediate. This importance of the purity of the material is therefore much higher and it gets an increasing importance the closer the chemical step comes to the final product. An important downstream processing technology is crystallization, which is often controlled by process analytics, now increasingly using a PAT-approach. After the purified product has been received, often a drying follows as the next process step. Here, the temperature could lead to the destruction of the product and therefore drying is the second important downstream processing in pharmaceutical industry, which is often controlled by process analytics, again with an increasing trend toward PAT-approaches. Examples for crystallization, drying, and mixing are discussed subsequently, as typical process control steps. During downstream processing, other changes might also appear, as, for example, polymorphic transformation. Many of these processes are currently observed offline, but might be also controlled on-line as the same technologies are used as shown elsewhere [58].

38.5.1.1 **Crystallization**

Crystallizations are a typical purification in the synthesis of organic products in API or fine chemical manufacturing. In many cases, besides elimination of by-products, the crystallization is also used to receive a desired polymorph of a product (in case of the final step of the synthesis). For further processing, the particle size (distribution) is adjusted to the desired range, to make washing, filtration, and drying as easy and robust as possible. In pharmaceutical manufacturing, the particle size/particle size distribution of the API may be also essential for the formulation. The monitoring of crystallizations therefore has received high attention since the FDA has started the PAT-initiative [1]. In this initiative, a regulatory agency for the first time has requested that the quality should be demonstrated within the process.

As already mentioned, the key issues in process design and scale-up of crystallization processes are

- robustness
- particle size/distribution
- polymorphic form.

To receive these goals, process control for critical crystallizations is necessary to control the thermodynamics of the process in a reproducible manner. Up till now very often in process development, the crystallization is investigated and in production a procedure based on the process knowledge is used to receive the needed quality. With respect to the PAT-view, this procedure does not demonstrate the quality of the process; here, a continuous process monitoring would allow the demonstration of the quality, and the product could be directly forwarded to micronizing, for example, without offline testing.

Therefore, the following paragraphs will describe the crystallization process and the techniques focused beam reflectance measurement (FBRM) and ATR–FTIR as tools to understand and control the crystallization in pharmaceutical production from process development via scale-up to process monitoring in manufacturing. For details, see also [59–62].

For any optimization in crystallization, first the solubility of the compound of interest in various solvents needs to be known. The solubility is a thermodynamic parameter and therefore is valid also for scale-up and other variations of other parts of the process. Unfortunately, the solubility may strongly depend on variations in impurities. The solubility data typically is achieved in laboratory experiments by either gravimetric or chromatographic (HPLC) methods. For some time, the use of ATR–FTIR measurements have been growing in importance [53]. Besides the solubility area (below the solubility curve (Figure 38.6)), there is a metastable area above the solubility curve where the system can exist as an oversaturated solution without spontaneous crystallization. The automatic determination of the solubility curve and the metastable area can be performed be in-line measurements with IR sensors (ATR–FTIR) and the solid product, in this case, is characterized, for example, by FBRM with respect to particle size and distribution. The crystallization its self is than optimized by changing the environmental parameters (temperature (cooling)), addition of seed or a so-called antisolvent, stirrer speed, and so on.

38.5.1.1.1 **Crystallization – Monitoring** FBRM [63] is one of the techniques that have been widely used for in-line crystallization monitoring for a few years. The probe is directly introduced into the reactor. The technique works even with a

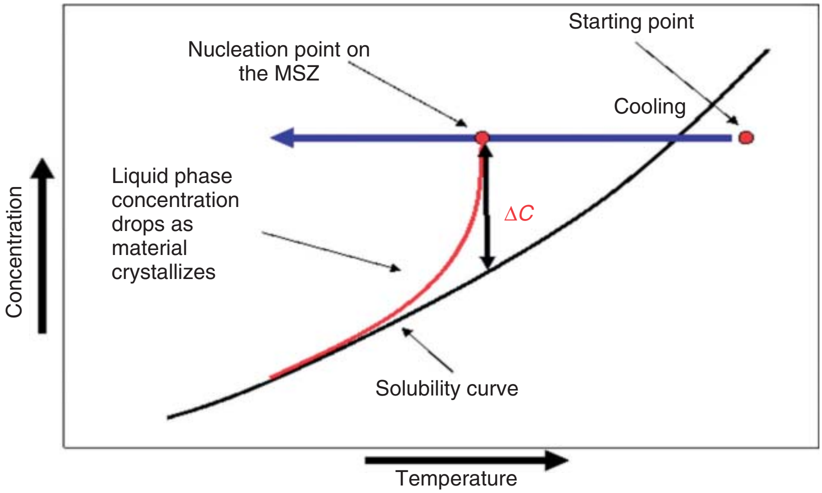

Figure 38.6 Schematic diagram of the cooling crystallization process (MSZ = metastable zone).

relatively high concentration of solid material in solution. In principle, FBRM is based on a focused, rotating laser beam. This laser beam is reflected by particles in solution. This reflected part of the light beam is analyzed and a so-called chord length distribution – CLD versus particle diagram is received in real time. This distribution is directly correlated to number, size, and form of the analyzed particles (Figure 38.6). The conclusion from the CLD/particle diagram provides information on the status of the crystallization, that is, if the process leads to growth of crystals or if the number of new crystals increases. The optimization by variation of parameters such as temperature (i.e., cooling) can be monitored in real time (Figure 38.7).

Figure 38.8 shows the typical change in the concentration of the compound of interest in solution during a cooling crystallization, as, for example, measured by IR. The concentration first increases because of the decreasing temperature. The concentration crosses the solubility curve into the metastable area and finally the crystallization starts, which leads to a decrease in concentration. This curve can be used both for process optimization and later on in manufacturing as a characteristic for process reproducibility. Figure 38.8, therefore, might be one parameter in a PAT-concept for a parametric release of the product.

Monitoring of a complex, real-world crystallization is shown in Figure 38.9. The crystallization is initiated by seeing and is then controlled by cooling. The figure shows the CLD plot of three different particle sizes (front) and in the background the temperature profile. In the beginning of the crystallization (A), the temperature is kept constant with a clear solution without particles. At B, the seed is added, which is seen in the FBRM signal. After the number of particles has become constant, the cooling starts. At this time (C), the particle size increases. This becomes visible because the number of larger particles increases dominantly. This also means that in C the generation of new particles is a process of low importance.

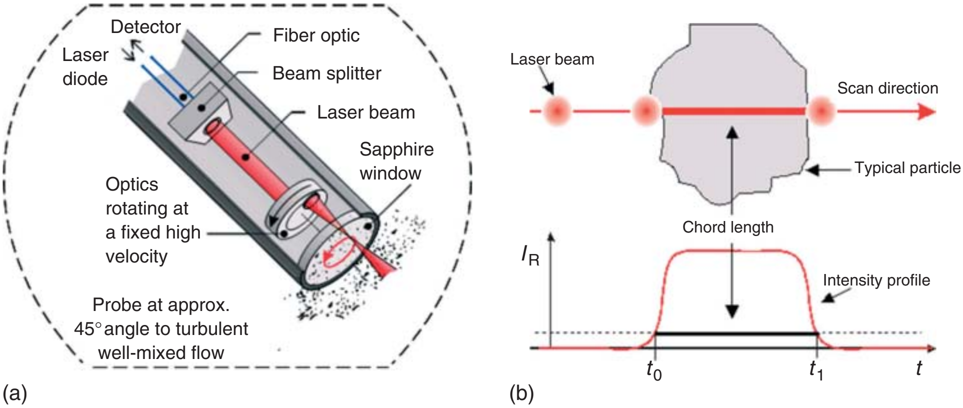

Figure 38.7 FBRM probe head (a) and the general measurement principle (b).

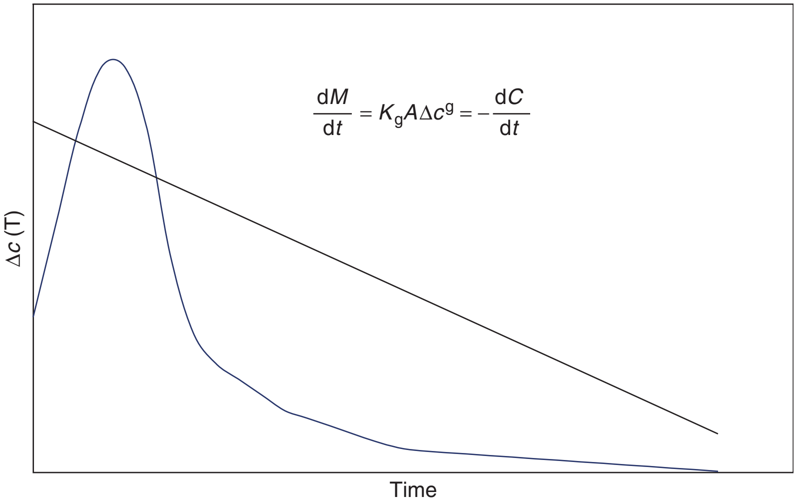

Figure 38.8 Schematic representation of the concentration profile of the component of interest during crystallization.

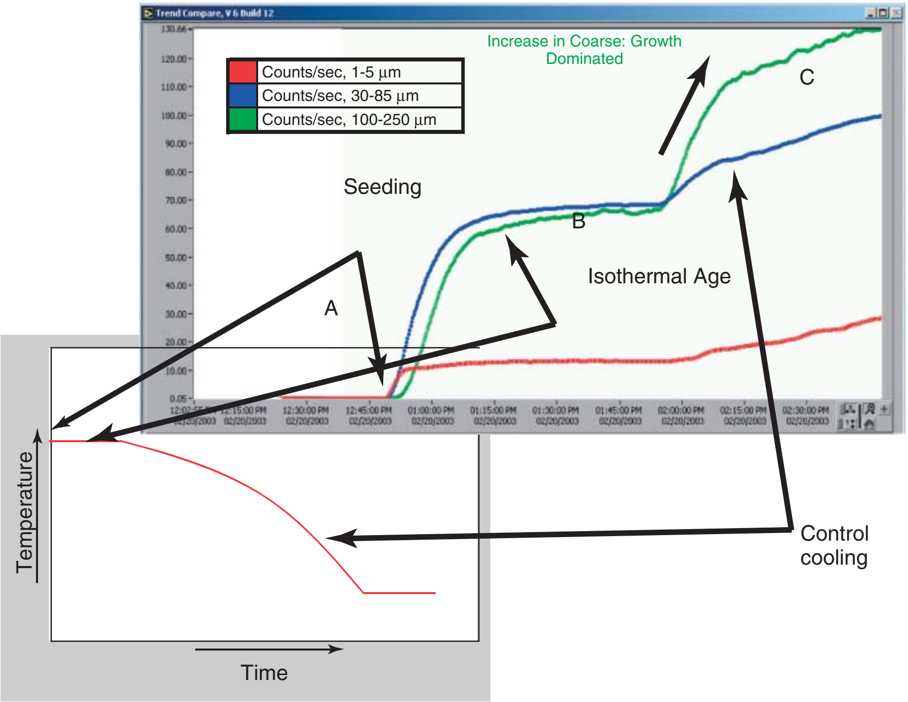

Figure 38.9 Evaluation of the FBRM measurement during cooling crystallization (for details, see text).

The knowledge of particle generation and growth kinetics allow the generation of a protocol for a robust process. The process stability is in addition supported by the independent optical techniques [62, 64].

Process control as described here as a tool improvement of quality is typical in the pharmaceutical industry. Up to now, most of these technologies were mainly used in process development, but since the PAT-initiative the number of implementations that allow real-time quality monitoring is increasing.

The product received so far either is transferred directly to the next process step or is isolated in a dry form, which typically is much more stable and can be stored for further processing, can be analyzed, may be released as a drug substance, and may then be also transferred to another site. But, typically, this drying process is also a process step with a high impact for the quality of the product and is therefore monitored by process analytical tools.

The current interest in many large scale batch processes is not only to control the process on the macroscopic scale but also to understand the process in different scales to molecular dimension during scale-up. This is of course of extremely high importance if phase changes are part of the process as in crystallization. Some attempts have been made in process tomography [65] and the combinations of spectroscopic tools with other techniques. A promising example is given by Simon *et al*. [66].

38.5.1.2 **Drying**

The partial or complete removal of solvents is an important process step in manufacturing pharmaceutical intermediate and final products. These drying processes extract water and other solvents from the substrate up to a precisely defined residual value. The extraction of solvents from a given batch is often accomplished considering substance- and plant-specific regimes of heating and evacuation cycles. In addition, many of these drying cycles use make-up or inert gas to support the drying process and protect product quality.

Batch production processes are dominant in the pharmaceutical industry and various drying apparatus types are used. The drying endpoint is reached at different times depending on the substance and solvent in the batch. The drying endpoint is the point where the residual content of solvent decreases to the required level. The current method to determine the solvent content of the batch is usually accomplished via manual sampling from the drying apparatus and offline analysis in the company laboratory. The repeated iterations on drying determinations are labor and time intensive using discrete sampling especially in the case of the vacuum drying processes, which often results in interruptions of the process vacuum and thus the drying processes.

On-line measuring methods offer a better alternative. The primary purpose is to draw conclusions about the progress of the drying process, to document the drying process as completely as possible and to reduce the number of manual samplings considerably or completely. The on-line measurements may be used advantageously for developing and optimizing a specific temperature and pressure behavior inside the drying apparatus with regard to reduced drying times.

The increased introduction of continuous process analytical technologies in the production schemes resulting from the PAT-initiative of the FDA may thus be supported effectively. Two spectroscopic techniques that are typically used are NIR for drying of water based drying, which are very often applied in the API step, or MS as a more general technique that can nearly detect every solvent. Applications for both types of drying procedures are presented. Besides these two spectroscopic techniques, the drying process often is monitored by IR-heating-based drying balances. These balances are used as a screening tool at-line in the plant. They are quite fast, do not need a calibration but because the heater is an IR lamp the balance does not work with all kinds of materials and all kinds of solvents. In some cases, these type of balances lack seriously in accuracy. The Karl Fischer (KF) titration is used in QC laboratories because of the high precision but currently it is no longer used in a plant environment. The drying of organic solvents in control laboratories is also monitored by GC, typically coupled to a headspace sampler. The analysis times are typically too long and data evaluation typically too complex for at-line analysis.

38.5.1.2.1 **Drying Monitoring by NIR** As known, NIR is very sensitive to water and therefore in the pharmaceutical industry, drying monitoring is very often monitored with this technique. NIR nearly has replaced the classical monitoring techniques such as KF-water-titration, which also has been used widely also in plants as an at-line process control by experienced technicians. One of the major problems of this technique is that the humidity in production plants is typically kept very high for explosion prevention. Therefore, for very hygroscopic products taking a sample and transferring it to the plant laboratory may be a major reason for wrong results.

In contrast, NIR can be coupled directly to various drying processes, also for the often used vacuum drying process. Especially again for later steps in a chemical/biotechnological synthesis, where the product value is high, and sometimes the product is temperature labile, vacuum drying is applied. In this case, there is a slow drying gas flow pumped through the system. The outlet line of the vacuum dryer can by directly coupled in-line to an NIR instrument.

But the NIR sensor can also be directly coupled to the various dryers where the NIR sensor directly measures the water content on the surface, which is proportional to the water content of the water in the bulk sample. There are various types of dryers. Very often, in the pharmaceutical industry static dryers are used, were the product is typically placed on a plate of about $50 \times 50\,\text{cm}^2$ and then the product is dried. In these dryers, the problem is that the sample drying kinetics is also part of the NIR calibration model because NIR only can analyze the first few nanometers of the material, whereas the material is lying in a layer of a few centimeter thickness on the plate. In these dryers also, for each product a separate calibration model is needed. Depending of the crystallization, there still might be deviations from the calibration model because the particles have slightly different sizes and this changes the drying kinetics. Later, an example of a high-shear fluid bed mixer and dryer for the granulation in pharmaceutical manufacturing is presented. In this case and in other examples where continuous mixing of the drying material is applied, the calibration of NIR [67] is much more stable and it has even been shown that the calibration may be widely independent of the drying material [68]. Also, NIR drying monitoring in a paddle dryer works extremely well [69]. A very special type of drying, freeze drying, was also monitored by the PAT-tools Raman and NIR. The authors compare and evaluate the strengths of the techniques during the process [70].

38.5.1.2.2 **Drying Monitoring by On-Line Process Mass Spectrometry** Similar to many biotechnological approaches, in drying also the analysis of the gas stream leaving the drying chamber can be used for the control of drying processes. In this case, for the complete drying process, the gas atmosphere inside the drying apparatus may be monitored and documented continuously with a process gas mass spectrometer. The interesting point for MS is that a wide range of solvents can be analyzed with one instrumental set up and one calibration strategy. Therefore, this approach is typically advantageous in multipurpose chemical production processes.

The continuous sampling of gas samples can be taken at the drying apparatus outlet, in the outlet gas stream, or in the vacuum suction line. When the drying is to be monitored both in the vacuum area and when working with carrier gas, the mass spectrometer will be equipped with a two-stage, pressure-controlled gas inlet to adjust constant pressure conditions for the mass spectrometer. The pressure control at the gas inlet is done independent of the gas type and for an inlet pressure range of 1–1200 mbar (absolute). The sampling lines and the gas inlet can be heated to measure solvents with low vapor pressures. Multiple drying apparatuses (up to 16) may be connected via a multiport valve unit and measured consecutively with one mass spectrometer.

Typically, quadrupole mass spectrometers are used for various reasons:

- Mass spectrometers allow for continuous measuring of the solvent concentration in the gas phase without interruption of the drying process. Measurement may be done inside the drying apparatus at various pressure ranges.
- Mass spectrometers have a high sensitivity (detection limit <0.1 ppm) and a wide dynamic measuring range (0.1 ppm to 100%), allowing for continuous monitoring of the drying process up to very low ‘‘loss-on-drying’’ (LOD) values.
- The measuring principle of MS has a high selectivity for the individual solvents. Partial pressure curves for all solvents may be determined and evaluated individually.
- In addition to the solvent concentrations in the gas phase, it is possible to measure further components such as, for example, nitrogen, oxygen, or argon and thus detect possible malfunctions or leakages of the drying apparatus at an early point of time.
- Solvent analysis can be accomplished fully automatically with measuring parameters [mass numbers (MNs)], selected for given solvents (Table 38.2).

38.5.1.2.3 **Vacuum Drying in a Blade Dryer as an Application Example**

Because many chemical intermediates of final products are temperature labile, on one hand, different types of dryers are used; sometimes, only the sophistication of the dryer alone will not guarantee the quality of the product. Therefore, in some cases process control is also implemented. In the example presented here, a quadrupole mass spectrometer was connected via a pressure-controlled gas inlet to the vacuum suction line of a blade dryer. During the drying process, the air constituents and the two solvents, water and isopropanol, were measured in the residual gas from the suction line of the drying apparatus.

Figure 38.10 shows the concentration curve for water, isopropanol, and nitrogen during the final phase of the drying process. For comparison, the results of five manual samplings with subsequent determination of the LOD are also stated in the figure. In the example, the target nominal value for the LOD is 6%.

The blade dryer was bathed with nitrogen. The sample lock chamber is flushed with nitrogen, resulting in considerable N_2 concentration increases during sampling.

Table 38.2 A selection of various solvents with mass numbers (MN 1–4) of the most important mass spectrometric fragment ions.

Solvent	MN 1	MN 2	MN 3	MN 4
Commonly used solvents				
Water	18	—	—	—
Methyl alcohol	31	32	29	—
Ethyl alcohol	31	45	29	46
Acetone	43	58	—	—
Isopropyl alcohol	45	—	—	—
Cyclohexane	56	84	41	—
N,*N*-Dimethylacetamide (DMA)	44	87	72	—
Methyl-*tert*-butylether (MTBE)	73	57	41	—
Toluene	91	92	—	—
Butylacetate	43	56	61	—
Some other solvents				
Acetonitrile	41	40	39	—
Butanone (MEK)	43	72	57	—
Tetrahydrofuran (THF)	42	71	72	—
N,*N*-Dimethylformamide (DMF, DMFA)	73	44	42	—
Isobutyl alcohol	43	41	42	74
Dimethyl sulfoxide (DMSO)	63	78	45	—
1,4-Dioxan	28	88	58	—
N-Methylpyrrolidinon (NMP)	99	98	44	—
Methyl isobutyl ketone (MIBK)	43	58	85	100
Isopropyl acetate	43	61	87	—
2,2,4-Trimethyl pentane (isooctane)	57	56	41	—

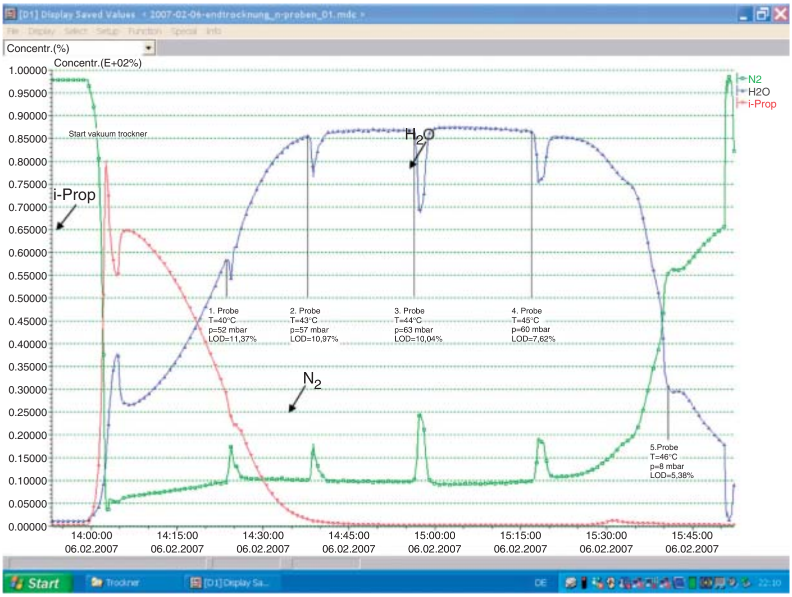

T: temperature in the drying apparatus

p: total pressure in the drying apparatus

LOD:Loss-on-drying

Figure 38.10 Example of a concentration curve of water (H_2O), isopropanol (i-Prop), and nitrogen (N_2) in the suction line of a blade dryer. (By courtesy of Boehringer-Ingelheim Pharma GmbH & Co. KG, Ingelheim.)

As shown in Figure 38.10, at the start of the drying apparatus evacuation, isopropanol is volatized first from the substance. After 50 min, the drying rate for isopropanol drops to <1% of the stationary value.

In this example, the necessary drying time is mainly determined by slower water vaporization. In the drying phase from 2:35 p.m. to 3:25 p.m., the concentration value for water remains nearly constant. The transition of water from the surface of the substance particles into the gas phase is the limiting effect on drying in this example. From about 3:25 p.m., the measured water concentration in the suction line starts to drop and may be related to the degree of dryness. If this correlation is once determined, it is no longer necessary to take samples for repeated determination of the LOD and the drying process can be controlled via parameters that are measured on-line.

The concentrations or partial pressures of the solvents measured with the mass spectrometer may be used directly or after calculation with further process quantities such as temperature or absolute pressure in the dryer. Calculation of the process variables may be done directly with the control software of the mass spectrometer.

The mass spectrometric determination of solvent concentrations or solvent partial pressures in the gas atmosphere of a drying apparatus results in data sets that are suitable for optimization of drying processes.

The drying curve may be tracked and documented on-line with the mass spectrometer. As soon as the correlation to the LOD values has been determined once, the end of the drying process can be inferred from the mass spectrometric data without delay. The time saving that results from this allows for an improved plant utilization and reduces energy costs. The avoidance of unnecessary offline analyses also contributes to cost reduction.

The mass spectrometric data gives important information for optimization of the temperature, pressure, and carrier gas parameters in process development, particularly with regard to influencing the sequence of individual drying steps if there are several solvents. It is also easy to detect critical dryer conditions (leakages, starting disintegration of the product, etc.).

38.6
Pharmaceutical Manufacturing

The API is the end-product of the chemical (biotechnological, and so on) process and also the starting point of the pharmaceutical process. In many cases, the API manufacturer and the pharmaceutical manufacturer are two different companies. The process therefore typically starts with the identification of the starting materials for this new process. Besides the API depending on the dosage form, different materials have to be identified, for example, microcrystalline cellulose, cellulose ethers, starch, additives, urea, fats, and so on. Currently, this is often performed by NIR identification. The NIR is used as a qualitative tool and sometimes also as a quantitative tool [71] in these cases. With a number of test substances, a chemometric model that allows discrimination of the product in the specified quality from other products and other qualities is established. Applications in detail can be found elsewhere; for example, see [9]. Some quality parameters may not be checked by process control tools; therefore, depending on material and specification, classical laboratory analysis is also performed at this stage of the process. An overview on the application of process control in pharmaceutical manufacturing is given elsewhere [72–74].

After all starting materials are released, the pharmaceutical manufacturing process consists of a formulation where typically the API and the other excipients have to be mixed to a homogeneous mixture. Often, this mixing and blending process is also monitored by process control currently, in many cases with optical spectroscopy such as NIR or IR. For the manufacturing of tablets, this mixture often undergoes a granulation process. This is a physical process of agglomeration of smaller particles to larger conglomerates. This step is necessary for the tablet compression process. In the granulation process, water is added to the mixture followed by drying. Here again, the homogeneity of the mixture, with respect to the distribution of the API, the water content, and the particle size distribution, have to be controlled. In addition, the drying process is critical for many pharmaceutical products because of possible degradation. Therefore, the water content is monitored – which is a typical NIR application. Current trends show that the blending, mixing, granulation, and drying are under way for integration. An example of such an application is discussed in detail in subsequent text.

38.7
Granulation

In-line NIR spectroscopy is already a common tool for the measurement of moisture in granulation and drying processes in fluid bed equipment [6, 75, 76]. Reliable and robust in-line measurements are a key factor for applying the PAT-philosophy in a production process. Many authors have proved the successful use of NIR spectroscopy for in-line moisture detection. The drawback of the NIR spectra is a high amount of influencing factors, which are all physical or chemical properties of products. These lead to a high amount of samples that are necessary to reach a high prediction accuracy of the methods. These circumstance hamper the application of the NIR in-line measurement in the daily production. An example o such a process is described in subsequent text. Alternatives to NIR are also reported in the literature, using microwave resonance technology [77], which is at least currently only a niche technique with only very few applications.

Relying on the high influence of the water content on the NIR spectra at selected wave length, the current scope is to establish moisture detection using several products and two different processes by employing the same calibration curve. This would allow considerable reduction of the calibration samples needed for each product and thus lead to higher acceptance of in-line IR spectroscopy in production.

The example shown uses an NIR spectrometer model Xone made by NIR-Online GmbH, Waldorf, Germany, including a software implementation based on a PLS (partial least squares) algorithm. Two different types of processes were evaluated in the fluid bed. In the first, the fluid bed was used as a dryer in a full closed in-line process subsequently after the high-shear granulator. In the second type of process, the fluid bed was used as a spray granulator where the whole granulation process was carried out in the fluid bed. The fluid bed system consists of different types of fluid bed mixers of Hüttlin GmbH (now a subsidiary of Bosch). Two different fluid beds (HKC 200 and one high-shear mixer HMG 600) were used to evaluate the influence of the equipment. Table 38.3 depicts the process equipment used to manufacture the different products.

The reference method for the moisture analysis was a thermogravimetric moisture meter type MA 100 (Sartorius AG, Göttingen Germany). The drying temperature was 130 °C and the endpoint was reached, when the changes were <1 mg during 5 min. The wide difference between the NIR spectra of the 16 products is shown in Figure 38.11.

In Figure 38.12 and Figure 38.13, the calibration curves of products 1 and 10 are presented. The standard error of prediction for the cross validation for these products was 0.22 and 0.24% relative humidity, respectively.

Figure 38.14 contains calibration curves of the 16 different products. The standard error of the prediction for the cross validation sums up to 0.33% relative humidity. Thus, it is only slightly higher when compared to the single product curves.

The application of only one calibration curve for the product moisture detection of 16 different products was successful. The standard error of prediction was only 0.22% relative humidity, which is acceptable in many production processes. Even

Table 38.3 Process equipment used for production.

Product	Batch size (kg)	Process equipment	Composition
Product 1	131	HKC 200[a]	94% Lactose; 6% PVP K25
Product 2	131	HKC 200[a]	76% Lactose; 19% starch; 5% PVP K25
Product 3	136	HKC 200[a]	88% Lactose; 9% HPC; 2% starch
Product 4	100	HKC 200[a]	85% Magnesium-carbonate; 9% HPC; 9% lactose
Product 5	100	HMG 600 + HKC 200[a]	46% MCC; 38% calcium-carbonate; 10% lactose, 5% croscarmellose (additive)
Product 6	125	HKC 200[a]	Blend of API and additives
Product 7	125	HKC 200[a]	95% Lactose; 5% PVP K25
Product 8	125	HMG 600 + HKC 200[a]	87% Lactose, 10% starch, 3% PVP K 25
Product 9	125	HMG 600 + HKC 200[a]	67% Lactose, 10% starch; 20% MCC, 3% PVP K 25
Product 10	100	HMG 600 + HKC 200[b]	Blend of API and additives
Product 11	200	HMG 600 + HKC 200[b]	46% Lactose; 30% MCC, 16% HPMC; 5% crosspovidone; 3% cellulose
Product 12	200	HMG 600 + HKC 200[b]	Blend of a mixture of different APIs with additives
Product 13	125	HMG 600 + HKC 200[b]	Blend of a mixture of different APIs with additives
Product 14	200	HKC 200[b]	Blend of a mixture of different APIs with additives
Product 15	200	HKC 200[b]	Blend of a mixture of different APIs with additives

HKC 200: fluid bed spray granulation process; HMG 600 + HKC 200: product processed in closed in-line equipment.

[a,b] Indicate the different HKC 200.

many *ex situ* measurement systems in the daily production have a lower accuracy. A further decrease in the standard error of correlation and prediction should also be achievable by applying a reference method with a higher accuracy such as KF titration instead of a drying balance [68, 78]. Also, the measurement of particle size is under establishment, which will introduce another spectroscopic method as an in-line process control into this process.

Typically, in the pharmaceutical industry, the mixing and granulation is performed in batches. For batch mixers, it is important to know how long the components have to be mixed. The reason is not only saving time and therefore money but also the risk of overmixing, as some bulk materials have the tendency to segregate after the mixing quality has passed through an optimum. The determination of the

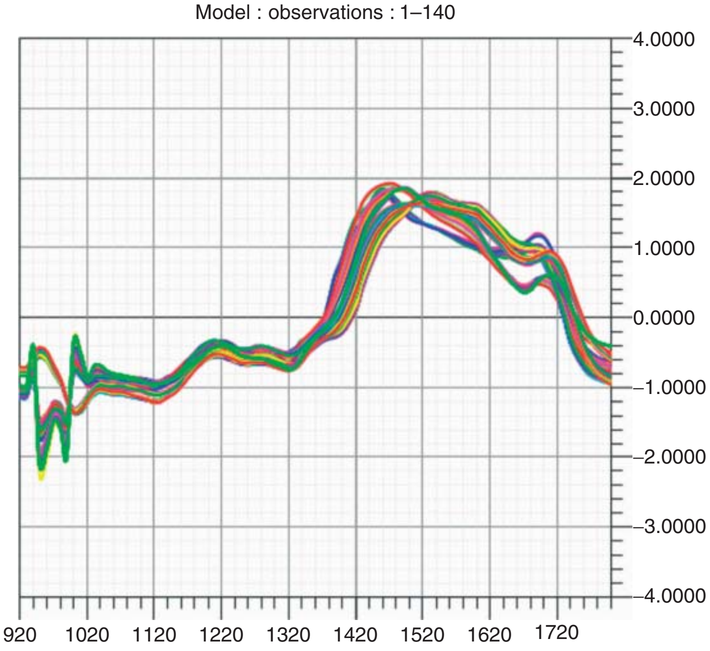

Figure 38.11 Near infrared spectra of 16 products.

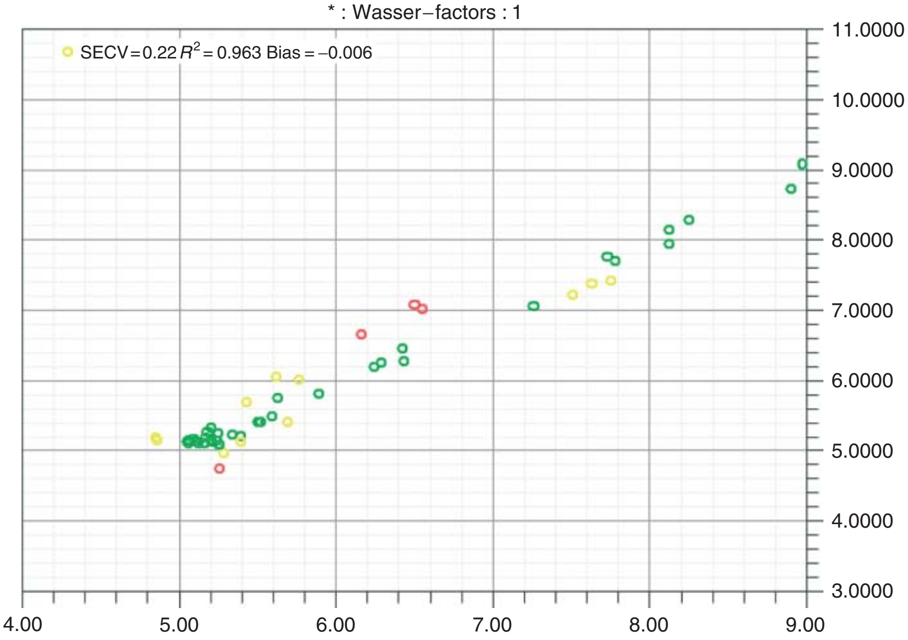

Figure 38.12 Calibration curve of product 1.

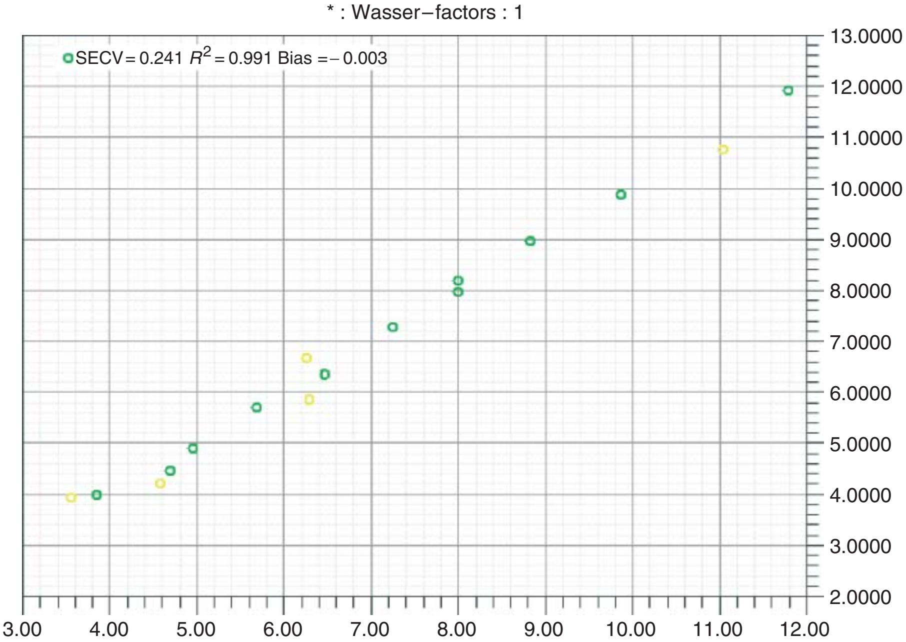

Figure 38.13 Calibration curve of product 10.

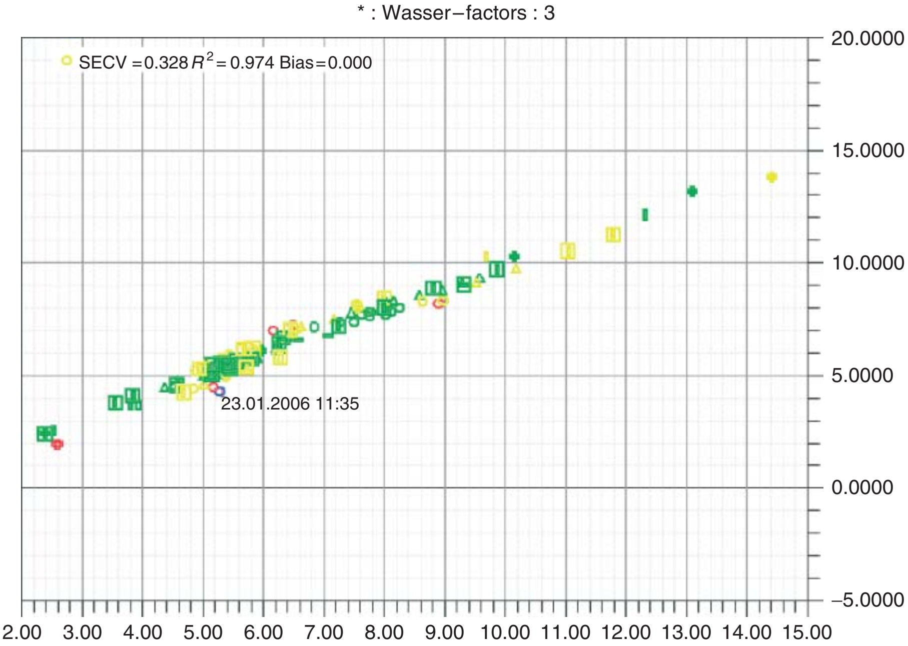

Figure 38.14 Calibration curve containing all 16 different products.

optimum mixing time is performed using the above-mentioned approach. In very few cases only in the pharmaceutical production of extremely large products is the currently continuous mixing used, whereas the process of continuous mixing and drying is also, for example, used in food processing. Here, it is a very import unit operation. In continuous mixing, there is a different reason for applying process control. Although the dimension of continuous mixers is relatively small, their throughput can be very high. In order to reduce or even avoid wastage, it is important to react as fast as possible to deviations of the product composition from the specification. An example for the control of a batch mixer has already been shown. Similar approaches can be found for instrumentation from various manufacturers, with different implementations of the sampling system [79]. The monitoring of a continuous mixing process in polymer manufacturing has also been shown in Chapter 2 of this section. Other authors [80] have developed an approach for applying NIR spectroscopy to receive a fast feedback process control of continuous mixing of powders for various industrial applications.

38.8
Final Product Control

After mixing and homogenizing of the product in the pharmaceutical industry, the product is filled into tubes, pressed to tablets, or filled into vials (liquid products). Further on, there is also some process control using NIR, typically for identification reasons. In many cases NIR is applied, but in some cases other techniques have also been described. An interesting application is the identification of tablets by Raman spectroscopy [81]. The interesting point here is that the peak-rich Raman spectra combined with chemometrics even allow the determination of the source of a tablet, for example, if a tablet is an original product or a generic product [82]. In recent years, counterfeited products are becoming a serious problem in the pharmaceutical industry. This has led to a number of investigations where spectroscopic techniques from NIR via IR to Raman have been used to identify the manufacturers' own products via profile intermediates, impurities, or, for example, by polymorphism [83]. A wide range of techniques has been applied to the characterization of the final product, mainly in research projects. Another interesting example with the potential to routine control is the nondestructive determination of film thickness of tablet coatings by optical spectroscopy [84] or terahertz spectroscopy [85]. Other examples describe the use of Raman spectroscopy to investigate multiple layers [86], which might also be relevant for the process control of tablet manufacturing.

38.9
Packaging

A very young application of spectroscopic tools in the pharmaceutical field is the filling control of vials, capsules, and injection solutions. In some drug cases, this is relevant because the amount of drug per dose is controlled by the filling level. A number of different techniques have been used for different cases from optical spectroscopy, via X-ray and time-domain nuclear magnetic resonance (TD-NMR) [87]. Some of these applications such as the fill level inspection via X-ray are already used in routine manufacturing, whereas others such as the TD-NMR techniques are still under evaluation.

References

1. FDA *http://www.fda.gov/cder/OPS/PAT.htm* (accessed 22 July 2013).
2. Hinz, D. (2006) *Anal. Bioanal. Chem.*, **384**, 1036–1042.
3. Wölbeling, C. (2008) *Pharm. Eng.*, **28** (3), 1–9.
4. Chew, W. and Sharratt, P. (2010) Trends in process analytical technology. *Anal. Methods*, **2**, 1412–1438.
5. Wu, H., Khan, M.A., and Hussain, A.S. (2007) *Chem. Eng. Commun.*, **194**, 760–779.
6. Johansson, J., Claybourn, M., and Folestad, S. (2010) in *Emerging Raman Applications and Techniques in Biomedical and Pharmaceutical Fields* (eds P. Matousek and M.D. Morris), Springer, Heidelberg, Berlin, New York, pp. 241–262.
7. Read, E.K., Park, J.T., Shah, R.B., Riley, B.S., Brorson, K.A., and Rathore, A.S. (2010) *Biotechnol. Bioeng.*, **105**, 285–295.
8. Rathore, A.S., Bhambure, B., and Ghare, V. (2010) *Bioanal. Chem.*, **398**, 137–154.
9. Hartung, A., Johansson, E., Knoell, M., Valthorsson, H., and Langguth, P. (2012) *Pharm. Ind.*, **74** (4), 644–650.
10. Bakeev, K.A. (ed) (2010) *Process Analytical Technology – Spectroscopic Tools and Implementation Strategies in the Chemical and Pharmaceutical Industries*, 2nd edn, John Wiley & Sons, Ltd, Chichester.
11. Kryk, H., Hessel, G., Schmidt, W., and Tefera, N. (2007) *Chem. Eng. Sci.*, **62**, 5198–5200.
12. Kryk, H., Hessel, G., and Schmidt, W. (2007) *Org. Process Res. Dev.*, **11**, 1135–1140.
13. Lovis, K., Dantan, N., Tilstam, U., Frenzel, W., and Küppers, S. (2000) Presentation Analytica Conference, Munich, Germany, April 11–14, 2000.
14. Thayer, A.-M. (2005) *Chem. Eng. News*, **83**, 63–67.
15. Lin, Z., Song, S., Ellison, D., Wang, T., Zhou, L., Mahajan, A., and Ge, Z. (2006) *J. Pharm. Biomed. Anal.*, **41** (1), 99–104.
16. Liese, A. (2000) in *History of Industrial Biotransformations – Dreams and Realities* (ed D. Vasic-Racki), Wiley-VCH Verlag GmbH, Weinheim, pp. 3–29.
17. DECHEMA (2004) Positionspapier des Ad-hoc Arbeitskreis der DECHEMA e.V.: Weiße Biotechnologie – Chancen für Deutschland.
18. Küppers, S., Oldiges, M., and Trauthwein, H. (2006) in *Prozessanalytik* (ed R.W. Kessler), Wiley-VCH Verlag GmbH, Weinheim, pp. 513–538.
19. Becker, T., Hitzmann, B., Muffler, K., Pörtner, R., Reardon, K.F., Stahl, F., and Ulber, R. (2007) *Adv. Biochem. Eng. Biotechnol.*, **105**, 249–293.
20. Fuchs, F. (2002) *Biochemie*, **84**, 1173–1179.
21. Workmann, J. (1999) *Appl. Spectrosc. Rev.*, **34**, 1–89.
22. Adams, V.M. (1986) *Am. Lab.*, **12**, 72–77.
23. Hayward, M.J., Lister, A.K., Kotiaho, T., Cooks, R.G., Austin, G.D., Narayan, R., and Tsao, G.T. (2005) *Biotechnol. Tech.*, **3**, 361–364.
24. Müller, H. and Eiden, F. (2008) *Bioforum*, (4), 2–4.
25. P & A - FORUM MARKTTREND P&A Select Biotech 2008/1, p. 53.
26. Noui, L., Hill, J., Keay, P.J., Wang, R.Y., Smith, T., Yeung, K., Habib, G., and Hoare, M. (2002) *Chem. Eng. Proc.*, **41** (2), 107–114.
27. Pons, M.N., Le Bonte, S., and Potier, O. (2004) *J. Biotechnol.*, **113** (1–3), 211–230.

28. Nomikos, P. and Mac Gregor, J.F. (1994) *AIChE J.*, **40** (8), 1361–1375.

29. Nomikos, P. and Mac Gregor, J.F. (1995) *Technometrics*, **37** (1), 41–59.

30. Jorgensen, P., Pedersen, J.G., Jensen, E.P., and Esbensen, K.H. (2004) *J. Chemom.*, **18** (2), 81–91.

31. Sorensen, L.K. (2004) *J. Dairy Sci.*, **87** (11), 3826–3835.

32. Garrido-Vidal, D., Esteban-Diez, I., Perez-del-Notario, N., Gonzalez-Saiz, J.M., and Pizarro, C. (2004) *J. Near Infrared Spectrosc.*, **12**, 15–27.

33. Sivakesava, S., Irudayaraj, J., and Ali, D. (2001) *Process Biochem.*, **37** (4), 371–378.

34. Cozzolino, D., Kwiatkowski, M.J., Parker, M., Cynkar, W.U., Dambergs, R.G., Gishen, M., and Herderich, M.J. (2004) *Anal. Chim. Acta*, **513** (1), 73–80.

35. Navratil, M., Cimander, C., and Mandenius, C.F. (2004) *J. Agric. Food Chem.*, **52** (3), 415–420.

36. Tosi, S., Rossi, M., Tamburini, E., Vaccari, G., Amaretti, A., and Matteuzzi, D. (2003) *Biotechnol. Prog.*, **19** (6), 1816–1821.

37. Suehara, K.I. and Yano, T. (2004) in *Recent Progress of Biochemical and Biomedical Engineering in Japan I*, Advances in Biochemical Engineering/Biotechnology, Vol. 90 (ed T. Kobayashi), Springer, Berlin, Heidelberg, New York, pp. 173–198.

38. Acha, V., Meurens, M., Naveau, H., and Agathos, S.N. (2000) *Biotechnol. Bioeng.*, **68** (5), 473–487.

39. Kansiz, M., Gapes, J.R., McNaughton, D., Lendl, B., and Schuster, K.C. (2001) *Anal. Chim. Acta*, **438** (1–2), 175–186.

40. McGovern, A.C., Broadhurst, D., Taylor, J., Kaderbhai, N., Winson, M.K., Small, D.A., Rowland, J.J., Kell, D.B., and Goodacre, R. (2002) *Biotechnol. Bioeng.*, **78** (5), 527–538.

41. Vankeirsbilck, T., Vercauteren, A., Baeyens, W., Van der Weken, G., Verpoort, F., Vergote, G., and Remon, J.P. (2002) *Trac, Trends Anal. Chem.*, **21** (12), 869–877.

42. Shaw, A.D., Kaderbhai, N., Jones, A., Woodward, A.M., Goodacre, R., Rowland, J.J., and Kell, D.B. (1999) *Appl. Spectrosc.*, **53** (11), 1419–1428.

43. Lee, H.L.T., Boccazzi, P., Gorret, N., Ram, R.J., and Sinskey, A.J. (2004) *Vib. Spectrosc.*, **35** (1–2), 131–137.

44. Bell, S.E.J., Bourguignon, E.S.O., Grady, A.O., Villaumie, J., and Dennis, A.C. (2002) *Spectrosc. Eur.*, **14** (6), 17–20.

45. Ulber, R., Protsch, C., Sölle, D., Hitzmann, B., Willke, B., Faurie, R., and Scheper, T. (2001) *Eng. Life Sci.*, **1** (1), 15–17.

46. Ulber, R., Faurie, R., Sosnitza, P., Fischer, L., Stärk, E., Harbeck, C., and Scheper, T. (2000) *J. Chromatogr. A*, **882** (1–2), 329–334.

47. Ganzlin, M., Marose, S., Lu, X., Hitzmann, B., Scheper, T., and Rinas, U. (2007) *J. Biotechnol.*, **132**, 461–468.

48. Boehl, D., Solle, D., Toussaint, H.J., Menge, M., Renemann, G., Lindemann, C., Hitzmann, B., and Scheper, T. (2001) *Proc. SPIE*, **4021**, 50–57.

49. Zhang, X.C. (2002) *Phys. Med. Biol.*, **47** (21), 3667–3677.

50. Chen, J.Y. and Markelz, A.G. (2003) *Biophys. J.*, **84** (2), 156A–156A.

51. Knab, J., Chen, J.Y., and Markelz, A. (2004) *Biophys. J.*, **86** (1), 84A–84A.

52. Rehorek, A. and Plum, A. (2007) *Anal. Bioanal. Chem.*, **388**, 1653–1662.

53. Liotta, V. and Sabesan, V. (2004) *Org. Process Res. Dev.*, **8** (3), 488–494.

54. van Sprang, E.N.M., Ramaker, H.-J., Streefland, M., van der Pol, L.A., Coen Beuvery, E., and Smilde, A.K. (2007) *Qual. Eng.*, **19** (4), 373–384.

55. Streefland, M., van der Pol, L.A., Martens, D.E., Coen Beuvery, E., van de Waterbeemd, B., and Happé, H. (2007) *J. Tramper*, **25** (16), 2994–3000.

56. Streefland, M., van de Waterbeemd, B., Kint, J., van der Pol, L.A., Beuvery, E.C., Tramper, J., and Martens, D.E. (2009) *Biotechnol. Bioeng.*, **102**, 161–167.

57. van de Waterbeemd, B., Streefland, M., Pennings, J., van der Pol, L., Beuvery, C., Tramper, J., and Martens, D. (2009) *Biotechnol. Bioeng.*, **103**, 900–908.

58. Heinz, A., Strachan, C.J., Gordon, K.C., and Rades, T. (2009) *J. Pharm. Pharmacol.*, **6**, 971–988.

59. Schöll, J., Lindenberg, C., Vicum, L., Mazzotti, M., and Brozio, J. (2007) *Cryst. Growth Des.*, **7** (9), 1653–1661.

60. Schöll, J., Vicum, L., Müller, M., and Mazzotti, M. (2006) *Chem. Eng. Technol.*, **29** (2), 257–264.

61. Schöll, J., Bonalumi, D., Vicum, L., Mazzotti, M., and Müller, M. (2006) *Cryst. Growth Des.*, **6** (4), 881–891.

62. Schöll, J., Lindenberg, C., Vicum, L., Brozio, J., and Mazzotti, M. (2007) *Faraday Discuss.*, **136**, 247–265.

63. Worlitschek, J. and Mazzotti, M. (2003) *Part. Part. Syst. Char.*, **20**, 12–17.

64. Schöll, J., Vicum, L., Müller, M., and Mazzotti, M. (2006) *Chem. Eng. Technol.*, **29** (2), 257–264.

65. Ding, Y. (2007) *Chem. Eng. J.*, **130** (2-3), 65–186.

66. Simon, L.L., Nagy, Z.K., and Hungerbuhler, K. (2009) *Org. Process Res. Dev.*, **13**, 1254–1261.

67. Cuirczak, E.W. (1987) *Appl. Spectrosc. Rev.*, **23** (1-2), 147–163.

68. Knoell, M., Sill, R., Schmidt, U., Langguth, P., and Küppers, S. (2008) *Process PharmaTEC*, **15**, 18–19.

69. Burgbacher, J. and Wiss, J. (2008) *Org. Process Res. Dev.*, **12**, 235–242.

70. De Beer, T.R.M., Vercruysse, P., Burggraeve, A., Quinten, T., Ouyang, J., Zhang, X., Vervaet, C., Remon, J.P., and Baeyens, W.R.G. (2009) *J. Pharm. Sci.*, **98** (9), 3430–3446.

71. Posch, A., Horl, G., Voura, C., Radl, S., Urbanetz, N., Fraser, S.D., Tritthart, W., Reiter, F., Schlingmann, M., and Khinast, J.G. (2011) *Powder Technol.*, **205** (1-3), 87–96.

72. Roggo, Y., Chalus, P., Maurer, L., Lema-Martinez, C., Edmond, A., and Jent, N. (2007) *J. Pharm. Biomed. Anal.*, **44**, 683–700.

73. Maurer, L. and Leuenberger, H. (2009) *Pharm. Ind.*, **71** (4), 672–678.

74. Patel, P., Kamani, R., Prajapati, B.G., Atara, S., and Suthar, A.M. (2009) Pharmaceutical Manufacturing, *www.pharmamanufacturing.com* (accessed 22 July 2013).

75. Hartung, A., Knoell, M., Schmidt, U., and Langguth, P. (2010) *Drug Dev. Ind. Pharm.*, **37** (3), 274–280.

76. Alcalà, M., Blanco, M., Bautista, M., and González, J.M. (2012) *J. Pharm. Sci.*, **99**, 336–345.

77. Buschmüller, C., Wiedey, W., Döscher, C., Plitzko, M., and Breitkreutz, J. (2009) *Pharm. Ind.*, **71** (8), 1403–1408.

78. Küppers, S. and Hartung, A. (2010) *Excellente Pharma Supply Chain – von der Vision zur Praxis*, 2nd edn, ECV, Aulendorf, pp. 117–124.

79. Märk, J., Karner, M., Andre, M., Rueland, J., and Huck, C.W. (2010) *Anal. Chem.*, **82**, 4209–4215.

80. Kehlenbeck, V. (2006) Continuous dynamic mixing of cohesive powders. PhD Thesis. Technical University of Munich.

81. Gendrin, C., Roggo, Y., and Collet, C. (2008) *J. Pharm. Biomed. Anal.*, **48** (3), 533–553.

82. Dégardin, K., Roggo, Y., and Fischer, A. (2009) 3. Doktorandenseminar Attendorn, Germany, February 15–17, 2009, p. 36, ISBN: 987-3-932604-23-2.

83. Ayala, A.P., Siesler, H.W., and Cuffini, S.L. (2008) *J. Raman Spectrosc.*, **39**, 1150–1157.

84. Koller, D.M., Hannesschläger, G., Leitner, M., and Khinast, J.G. (2011) *Eur. J. Pharm. Sci.*, **44** (1-2), 142–148.

85. Maurer, L. and Leuenberger, H. (2009) *Int. J. Pharm.*, **370**, 8–16.

86. Buckley, K. and Matousek, P. (2011) *J. Pharm. Biomed. Anal.*, **55** (4), 645–652.

87. Witt, K. and Posset, T. (2012) *Pharm. Ind.*, **74** (5), 826–832.

39
Applications of Optical Spectroscopy to Process Environments

Stephan Küppers

39.1
Optical Techniques Applied in Process Control

Optical spectroscopy covers the interactions of matter with the electromagnetic waves in the range between UV to far IR [1]. Details of the optical spectrum can be found above [2]. Nearly the whole wavelength range is used for spectroscopic applications. The way of interactions with matter may vary from adsorption via reflection of light to more complex processes such as scattering, fluorescence, or chemiluminescence. There are a number of different physical processes underlying these spectroscopic processes that are discussed in various textbooks of spectroscopy and also above [2]. All of these spectroscopic techniques with the underlying physical processes are used in process control, some of them in very few and even very special applications. Some applications are also mentioned in other chapters of this section.

In the mid-IR-region two fields of applications for process control are found. On one hand, the interaction with the IR range is used for the selective detection of individual components by a single characteristic wavelength that has no (or nearly no) interference with other component spectra in nondispersive infrared (NDIR) and the use of more than one characteristic wavelength, typically in complex reaction monitoring using Fourier transform infrared (FT-IR) spectrometry.

The NDIR instruments are used in many gas-analytical applications, for example, in safety monitoring. The general principle of NDIR is the use of one light source that is split into two separate beams and both beams are filtered through a fixed wavelength filter. The filter wavelength is chosen for the sample of interest and only the wavelength that leads to an adsorption of the sample goes through the filter. Typically, the reference beam goes directly to the detector, whereas the sample beam interacts with the sample in a flow cell. The difference between the two signals at the detector should be proportional to the sample concentration of the component of interest. NDIR instrumentation has been used for decades in the same way. Commercially available instruments currently show a number of different instrumental designs following the same principle with one or two beams, with one or multiple wavelengths. Typical applications are the gas

Handbook of Spectroscopy, Second Edition. Edited by Günter Gauglitz and David S. Moore.

monitoring devices, for example, for carbon dioxide, carbon monoxide, ethylene, nitrogen oxides, sulfur oxides, and so on. For details, see elsewhere [3].

For about a decade the use of near-infrared spectroscopy increases dramatically [4]. The reason is the use of chemometrics for the evaluation of NIR spectra. The difference between mid-IR and NIR mainly is that in the NIR area, overtones and combinations of various vibrations are summarized in one spectrum. In addition to the number of bands and the mixture of overtones and combined vibrations, the NIR bands are broad. All this made NIR spectra difficult to interpret for many years. This has changed with chemometric models that allow the fast evaluation of NIR data. Another important advantage of NIR versus mid-IR is the possibility of using fiber optics for the transmission of the light to the sample and NIR signals back to the spectrometer. Therefore, a standard NIR spectrometer can be installed outside the so-called Ex-area, whereas the fibers (up to 100 m) can transport the signal from the Ex-areas of a plant directly to the spectrometer. In cases of permanent installations, multiplexing capabilities of NIR can also be used to monitor a process stream at various places (i.e., stages of the process) or even different processes can be monitored. NIR is very sensitive to water and changes of water in various forms. Typical examples for applications of NIR therefore show a high correlation with the change in the water content, for example, drying process monitoring, granulation, and so on. Also, many food manufacturing processes are correlated with the change in the content of water or the bonding of water to other components of the product. Therefore, NIR has a large number of applications in food processing.

UV–vis spectrometry, instead, is a classical process control technique. Traditionally, UV–vis spectroscopy is/was used at-line. In some configurations, on-line or in-line implementations are used. The reasons for using UV–vis spectra is, on one hand, that color is an important specification in many products and, on the other hand, that the conversion of aromatic ring structures in many chemical processes can be used to monitor the rate of conversion or determine the endpoint of a chemical reaction. UV–vis spectroscopy in process control is comparable to the use in the laboratory; the instrumentation is also comparable. Typically, the low price of instrumentation for UV–vis instruments and the importance of color, besides the ease of use, are the reasons for using UV–vis spectroscopy. Often, process control still uses filter instruments, which means that a filter is used to select the wavelength at which quantitative information is gathered. These are used because they are cheap and robust. The instruments are built in the same general way as described for dispersive IR. Details on instrumentation in optical spectroscopy are also given above [2].

Raman spectroscopy has been a niche technique for a very long time owing to limited availability of laser sources and because for many years the so-called ‘‘notch filters’’ have not been available for nonmilitary use. The interest in Raman spectroscopy has for some time been growing strongly in laboratory and process control use. The Raman effect is a scattering effect, which means that a small number of molecules scatter light elastically. This scattering leads to a slight wavelength shift. The shift contains information on the molecule that has interfered with the light. Raman spectra show sharp bands and are information rich; this means that for process control selective information on the state or conversion of the molecules of interest can be extracted. In addition, this information is complementary to IR, which means that in some cases where IR does not give the desired selectivity Raman may be an interesting alternative. Water is a very weak Raman scattering molecule. This means that in contrast to NIR, Raman spectroscopy is especially of interest when the water content in a process is high but concentration changes of water do not correlate with the ongoing process.

Because the Raman effect is very small, most of the light collected from the sample has the same wavelength. This light has to be eliminated with the notch filter before the information can be extracted in a spectrometer. All this makes Raman spectrometry complex and expensive, but there are also some advantages for Raman spectroscopy for process control. Because nearly no mechanical parts are involved in a Raman spectrometer, the technique is robust and the excitation as well as the emission light can be transferred by fiber optics, which gives the same advantages for process control using Raman spectroscopy as for NIR spectroscopy with respect to explosion zones.

Laser diode techniques have been developed especially for process control. An application for the monitoring of gases using a tunable diode laser absorption (TDLAS) in chemical manufacturing has been described in detail before. The laser diode techniques are suitable and applied in various gas analytical tasks; see also further applications in this field in the literature [5]. One advantage of laser diode techniques is their usability at high temperatures. So, monitoring of gas components in harsh environmental conditions is possible. Although some of the examples are very interesting, laser diode techniques are currently expected to be niche solutions for the time being.

Another interesting niche technique in optical spectroscopy is fluorescence spectroscopy. The principle and the best-known application of fluorescence is the same as in the laboratory, the detection and determination of polycyclic aromatic hydrocarbons (PAHs). With fluorescence, this can be done in combination with high performance liquid chromatography (HPLC) in the laboratory but also in or on water in the environment. Similar applications are the determination of the film thickness of oil on water, which is described in detail elsewhere [6]. The advantages are the low sensitivity and the robustness of the systems.

39.2
Instrument Design for Process Control

In many cases, as described earlier, in process control, the same or similar basic instrumentation is used as in the laboratory environment. The software and the interfaces to the various process systems, depending on industry and product type, are always different from the laboratory instrumentation. In special cases, as in laser diodes or fluorescence, the whole setup is designed for the process application.

In many cases, the interface to the process is specially designed and adapted to the process. This is always necessary for in-line or on-line applications of optical spectroscopy. Besides the instrument manufacturers, there are some companies that have specialized in the field of interfacing the optical spectrometers to the process.

39.3
Coupling of Optical Techniques to the Process

Optical spectroscopy in measuring process control situations is applied in four different configurations:

- the transmission,
- reflexion,
- "transflection," and
- the ATR (attenuated total reflection)-mode.

Accordingly the geometries of the probes have to be different.

39.3.1
Transmission

Figure 39.1 displays the classical geometry of transmission measuring cells, suitable for most applications involving clear liquids. Measuring cells are available for measuring the concentration of transparent liquids directly in the pipe (production or bypass line). The transmission path length can often be set as variable or fixed. The so-called fixed settings are easy to change, with different distance bolts or base discs. The functionality is similar to that of a traditional cuvette setup. The light arrives from the transmitting fiber through an optic, passes the medium present in the pipe, and then is coupled to a second optic in the receiving fiber.

Depending on the application and installation points, transmission measuring cells (Figure 39.2) and transmission immersion probes are available.

The importance of crystallization has already been discussed. Besides the abovementioned approach other approaches are also used. One option is the monitoring

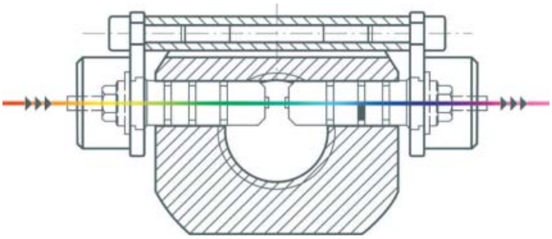

Figure 39.1 Transmission measuring cell schematic (courtesy of Solvias AG Basel).

Figure 39.2 Transmission measuring cell (courtesy of Solvias AG Basel).

using NIR. A typical way is that a pharmaceutically active ingredient (API) is crystallized from a solvent mixture containing two main components and one side component. The composition of the precrystallization solution is not accurately known. Efficient seeding is thus impossible and the product suffers from significant fluctuations in particle size and yield. The out-of-specification batches are either lost or need reprocessing, which is expensive and does not conform to cGMP. With NIR process spectroscopy, concentrations of all components (100% analysis) can be determined simultaneously. Such an application requires a process control, for example, by NIR spectrometer (in an Ex-free area) and an NIR transmission probe mounted in a bypass of the crystallizer and connected by fibers to the spectrometer. Application of NIR process spectroscopy has been shown to have a number of benefits: constant and increased yield; full control of polymorphs; reduced cycle time; uniform particle size distribution throughout all batches; elimination of expensive reprocessing steps; and savings in laboratory costs by fully automated determination of concentration.

Besides the examples discussed in previous chapters, further standard procedures for transmission measurements are

- color number determination according to American Public Health Association (APHA), Hazen, Lovibond, and Saybolt;
- reaction monitoring in chemical synthesis from UV to NIR range;
- control of process chromatography;
- solvent blending.

For gas measurements it is important to have a measuring cell with a long optical path length (OPL): ranging from 50 mm to over a meter; this is due to the low density of the molecules in the gas phase. For such special applications, there are fiber-optic transmission flow cells on the market, which allow measurement with such a long OPL. Examples are the measurement of UV–vis-absorbing gases (e.g., F_2, CL_2, Br_2, NO_x, SO_2, and ozone) and the measurement of UV–vis-absorbing substances in the gas phase (e.g., benzene, chlorobenzene, and phosgene). These measuring cells can also be used to monitor liquids used in cleaning validation programs for API production.

39.3.2
Transflection

In transflection mode – a combination of transmission and reflection – the sample is measured as in the transmission mode, only that the beam is reflected on a mirror; the OPL is thus doubled. Measurement in reflection mode is also possible with this type of probe (Figure 39.3).

Transflection probes have a multitude of applications – in multipurpose plants, in fermentation, or in organic-chemical process development – and thereby provide the user with a high degree of flexibility. For reaction monitoring in transmission mode, the OPL is in most cases easily and quickly adjustable to rapidly respond to changing concentration conditions. Typical are the examples for endpoint determination, where a pharmaceutical product is manufactured in a multistep chemical synthesis. One example where a successful implementation is possible is a condensation reaction, where an optimum product purity and yield is obtained only if the reaction is stopped as soon as the concentration of a certain reagent drops below 0.3%. This point is reached within roughly 4 h after the start of the reaction. Traditional laboratory analysis is slow and can therefore not be used for an accurate endpoint determination. For the real-time determination of concentrations of both the reagent and the product, an NIR spectrometer and an NIR transflection probe can be used. The probe is mounted in a reactor bypass and connected by fiber-optic cables to the spectrometer (in an Ex-free area). The bypass system allows easy cleaning of the transflection probe. The benefits are shorter cycle times, higher yield, avoidance of purification steps as the reaction is stopped before side products start to develop, and an optimized process due to ideal dosing profiles established on the basis of real-time reaction monitoring.

Besides the examples discussed in previous chapters, further standard procedures for transmission measurements are

- color number determination according APHA, Hazen, Lovibond, and Saybolt;
- reaction monitoring in chemical synthesis from UV to NIR range;
- control of process chromatography;
- concentration development monitoring in biotechnological fermentation processes.

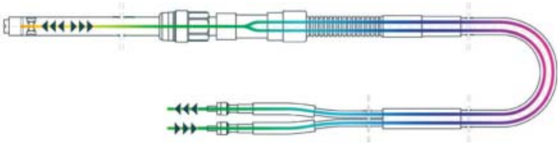

Figure 39.3 Transflection probe schematic (courtesy of Solvias AG Basel).

39.3.3
Diffuse Reflection

Diffuse reflection probes are particularly useful for heterogeneous reaction masses such as slurries, emulsions, or solids. Many processes involve transformation between or separations of liquid/liquid or liquid/solid phases. Optimal control of reaction steps can often be achieved with simple turbidity measurements. However, substantially greater quantities of information may be gained via the acquisition of diffuse reflection spectra throughout the course of the process. In diffuse reflection probes, light enters the medium through a window or fiber so that no light reflection is generated – which would otherwise lead to an unwanted offset. The measurement signal is produced through backscattering in the medium and is essentially proportional to the concentration (Figure 39.4).

Typical applications include the identity control, for example, of raw materials or the API used in a pharmaceutical formulation. Often, various APIs are delivered to a central storage facility. Before final processing, identities of all the ingredients must be checked. Conventionally, samples would be taken to the off-line QC lab for analysis, where the identification procedure takes up to a few days – a period far too long for efficient control of the process. On-site NIR analysis allows direct identification at the storage site within seconds and can easily be carried out by the stock-keeper through the polyethylene bags containing the APIs.

The identity control system consists of an NIR spectrometer and an NIR diffuse reflection probe connected via a fiber-optic bundle to the spectrometer. The benefits are redundancy of expensive laboratory analysis; time-saving, and more efficient storage due to on-site identification; improved work-place hygiene by avoiding sampling and analyzing through the PE bags; and elimination of potential error sources by simplifying the identity control procedure.

Besides the examples discussed in previous chapters, further standard procedures for transmission measurements are

- reaction monitoring in heterogeneous systems in NIR range;
- analysis of solids compositions directly in mixers;
- determination of residual solvents concentrations on solids directly in driers;
- noninvasive determination of residual solvents or water concentrations on lyophilisates directly in vials.

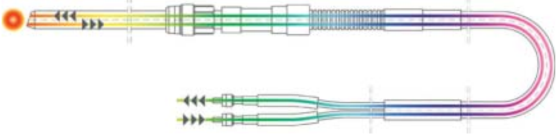

Figure 39.4 Diffuse reflection probe schematic (courtesy of Solvias AG Basel).

39.3.3.1 Raman and Fluorescence Probes

Raman scattering can also be utilized in rapid and efficient material characterization. In pharmaceutical manufacturing, *in situ* Raman spectroscopy has proved effective in monitoring crystallization processes in real time. Another widespread use of Raman spectroscopy can be found in the manufacturing of paint, where Raman immersion probes are used to monitor color during the mixing process. Similarly, *in situ* fluorescence spectroscopy is employed in the analysis of turbid and biologically active masses. Raman and fluorescence probes are very similar to turbidity probes, although Raman probes contain another in/out light coupling ratio as laser light is used to stimulate the sample, and well-selected filters are used to reject unwanted light.

39.3.4
Attenuated Total Reflection (ATR)

With ATR it is possible to take advantage of the total reflection of light transmitted from an optically dense medium to a less dense medium. The light at the boundary layer (e.g., sapphire/liquid) penetrates approximately a quarter of the wavelength into the less optically dense medium, where it can be absorbed. This method is applied mainly in the whole UV region and also in the analysis of dyestuffs in the visible region. Solid particles (e.g., catalysts) or bubbles do not interfere with the measurement. However, the path length is too small to acquire acceptable NIR spectra (Figure 39.5).

A typical example implemented was the hydrogenation of hydrazone, which is an important process in a fungicide production [7]. The reaction endpoint is critical because overhydrogenation produces unwanted by-products. Sample extraction under hydrogenation conditions is technically complex and does not yield representative process data. Immediate reaction monitoring with ATR spectroscopy offers two clear advantages: it allows for a direct and undiluted measurement of samples despite high absorbance in the UV range; and heterogeneous constituents such as catalysts have no influence on the spectrum, unlike in transmission measurements.

ATR probes are also used in heterogeneous catalysis (e.g., hydrogenations [8]) and where highly concentrated dyestuff is processed. Besides the examples discussed in previous chapters, further standard procedures for transmission measurements are

- reaction monitoring in heterogeneous catalyzed processes;
- on-line determination of concentrations in active ingredient- or color concentrates; and
- control of process chromatography.

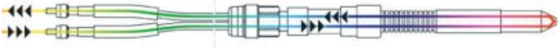

Figure 39.5 ATR probe schematic (courtesy of Solvias AG Basel).

39.3.5
Fiber Optics

For the transmission of light from the probe to the photometer, different types of optical fibers are available. Generally, there are two transmission regions: the UV–vis region (200–900 nm) and the vis/NIR region (400–2200 nm); measurement with the same glass fiber in both UV and NIR regions are not possible from a physically technical viewpoint. For every region there is a high quality glass fiber, with small absorption in the whole spectral region. There are many attractively priced glass fibers for the visible region, as for other spectral regions. These can be used as extension fibers in specialized applications where the whole spectrum is not needed. Transmission lengths up to 50 m are possible without problems for wavelengths above 270 nm; in the vis/NIR region, distances of over 100 m have been successfully realized.

The application and potential of fiber-optic probes for the NIR and ultraviolet–visible (UV–vis) spectral region is described here. Application examples are illustrated for the different spectroscopic techniques: transmission, reflection, transflection, and ATR. These are only a few examples of many successful applications in chemical and pharmaceutical plants.

In addition, in order to enable the in-line use of spectroscopy in various processes where samples could clog the window or the tip of the spectrometer, for example, with powder mixers [9] or chemical reactions [10] installations have been developed to clean the probe tip of the spectrometer with air or solvents.

39.4
Additional Application of Optical Spectroscopy

A few interesting new applications are very reviewed in short to demonstrate the enormous range of optical spectroscopy in process analytics and control applications.

For future applications of process control, small productions and privately used productions sites, such as the decentralized generation of electricity, are becoming higher in importance because in many small and medium-sized production units there is still high potential for optimizations. An interesting new application is the process monitoring and control in biogas plants, shown by Baumgarten and Busche [11], recently. The production of renewable energy by biogas plants is the focus of interest owing to amendments in German law. The efficiency of biogas plants is highly dependant on maximized exploitation of the substrates for fermentation. Nowadays, modern biogas plants are not running on the maximum of efficiency. A reduced yield of biogas, among others, caused by a lack in measurement technology, is directly resulting in a waste of biomass and a loss of money for the plant owner. A quantitatively and qualitatively constant production of biogas is needed for an economic operation of the plant. Therefore, the requirements on reliable and precise process monitoring and control become more and more important [12, 13].

The optimization of the biogas production by continuous analysis of the fermentation process and the monitoring of the status of the plant is one of the interesting technological approaches to improve the production of ''clean'' energy. The advantages that can be achieved are

- balancing of the parameters of the mass fluxes;
- control and optimization of the feeding of the plant with dry matter and nutrients with respect to the gas yield;
- control of the stability of the process within the fermentation reactor;
- modeling and trend analysis for the regulation of the biogas production.

NIR spectroscopy can be applied to obtain relevant parameters of the fermentation process. The plant is monitored by a fiber-coupled NIR spectrometer equipped with a multiplexer. Parameters, such as dry matter, acidity, and pH value, are monitored on representative locations within the plant and quantitative results are available in the control room and for remote maintenance.

A scheme of a biogas plant with integrated measuring and control technology with the different measurement points using only one spectrometer is shown in Figure 39.6. The contribution of NIR spectroscopy is found in the increase in efficiency of energy production [11, 12]. One of the interesting points is that all parameters needed for the control of the plant can be achieved by one NIR spectrometer using a combination of chemometric data models, fibers for coupling to the processes and a multiplexing device. Such approaches open the door for a wide range of applications in various fields on optimization of ''microplants.'' This is of special interest for commercial reasons as also for environmental reasons, because in large-scale production processes often are already optimized, whereas in many small production facilities there is still an enormous potential for optimization.

The control of bioprocesses, as already described in the previous example, is discussed in the next short summary of an application. Because of its wide

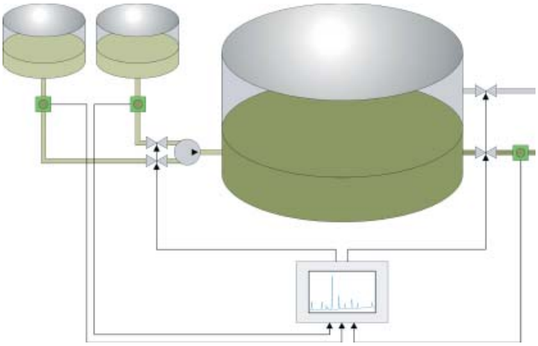

Figure 39.6 Scheme of a biogas plant with measurement and control system. The measurement points are the input lines of the substrate and the cosubstrate as also the gas phase and the liquid phase of the biogas reactor. The controlled units are the mass flow regulators of the substrate flows and the outlet of the reactor.

applicability, the monitoring of a bioprocess is described, in this case in order to ensure optimal biomass and product formation [13].

Till date, for product control in biotechnology off-line techniques such as HPLC or mostly HPLC-MS are often applied for nonvolatile components because the complexity of the sample mixtures typically does not allow to determine nutrients and products by NIR, even using chemometric modeling. The disadvantage of the off-line methods in general is that these measurements are performed with a time delay. To allow the determination of a number of different components of interest in a complex mixture, the information-rich mid-IR spectroscopy (FT-IR) was combined with data evaluation using PLS (partial least square) in an example presented by Hopf *et al.* [14].

Typically, FT-IR-spectroscopic methods are used for chemical process monitoring if the sample is not to complex and a direct correlation between one wavelength and the process is possible, whereas FT-IR-methods are not commonly applied for monitoring of biotechnological processes. For such a process, the ATR technique has been evolved as a suitable method for quantitative determination of components in bioprocesses in combination with FT-IR spectroscopy.

The advantages of IR spectroscopy in this case are

- the measurements are rapid,
- nondestructive,
- require minor sample preparation,
- provide the possibility of simultaneous constituent determination.

In their work, the authors presented an FT-IR spectroscopic method for monitoring the so-called dark fermentation, an anaerobic process for H_2 production. Special microorganisms are applied, converting different sugars to hydrogen and organic acids, such as acetic and lactic acid. Real substrates are conventionally hydrolyzed before their conversion. Considering the obtained sugar patterns, lignocellulosic material is mainly degraded to glucose and xylose, whereas fruit residues are composed of glucose and fructose. Therefore, it was aimed at generating a method to determine three monosaccharides and two organic acids simultaneously. A set of calibration (88) and test samples (47) was prepared according to a statistical plan. The measurements were performed using a standard FT-IR instrument with horizontal ATR with ZnSe-crystal with six reflections. Commercial Bruker OPUS Quant 2 Software was used for the PLS regression.

The results of calibration and validation are summarized in Table 39.1. The calibration yielded excellent data and regression coefficients close to one for several components. Similarly, the error of cross validation was very small, indicating promising applicability of this method. The validation with real samples and reference analysis by HPLC is in progress.

These few examples are intended to demonstrate the range of applications currently under development. In this field, a continuous process to more and more applications is under way, so that optical spectroscopy will go on dominating the field of process control.

Table 39.1 Calibration and validation results of the IR method for determination of glucose, fructose, xylose, acetate, and lactate in the range of 0–30 $g\,l^{-1}$.

Component	R^2	RMSECV	Used PCs
Glucose	0.9998	0.106	10
Fructose	0.9997	0.139	10
Xylose	0.9999	0.0838	8
Acetate	0.9999	0.0644	9
Lactate	0.9999	0.0862	10

References

1. Thiele S., and Salzer R. in *Handbook of Spectroscopy*, Part XI, 2nd edn. (ed. G. Gauglitz and T. Vo-Dinh) Wiley; Weinheim, 2005.
2. M. Hof, in *Handbook of Spectroscopy*, Part II, 2nd edn. (ed. G. Gauglitz and T. Vo-Dinh) Wiley; Weinheim, 2005.
3. W. Jessel, *Gase – Dämpfe – Gasmesstechnik*, Dräger Safety AG & Co. KGaA; Lübeck, 2001, ISBN: 3-9808076-0-6.
4. Bakeev, K.A. (ed.) (2010) *Process Analytical Technology – Spectroscopic Tools and Implementation Strategies in the Chemical and Pharmaceutical Industries*, 2nd edn, John Wiley & Sons, Ltd, Chichester.
5. Bomse, D.S. (1995) *Photonics Spectra*, **29** (6), 88–93.
6. Bublitz, J., Christophersen, A., and Schade, W. (1996) *Anal. Bioanal. Chem.*, **355**, 684–686.
7. Danigel, H., Graber, N., Länzlinger, M., Studer, M., Thies, H., and Zilian, A. (1997) Chemical Processing Technology International, Special Achema Issue 99.
8. Danigel, H. (1995) *Opt. Eng.*, **34**, 2665–2669.
9. Kehlenbeck, V. (2006) Continuous dynamic mixing of cohesive powders. PhD Thesis. Technical University of Munich.
10. Mannhardt, J. (2007) *Process PharmaTEC*, (1), **14**, 26–27.
11. Baumgarten, R. and Busche, S. (2008) Proceedings Europact 2008, p. 115.
12. Polytec, *http://www.analyticjournal.de/downloads_ak_pat_3kolloq2008/polytec_busche_biogas_s.pdf* (accessed 23 March 2013).
13. Holm-Nielsen, J.B., Andree, H., Lindorfer, H., and Esbensen, K.H. (2006) *J. Near Infrared Spectrosc.*, **15** (2), 123–135.
14. Hopf, R., Gruber, M., Ahrer, W., and Schnitzhofer, W. (2008) Proceedings Europact 2008, p. 94.

40
Spectral Imaging in Quality and Process Control

Rudolf W. Kessler and Waltraud Kessler

40.1
Introduction

Applications in chemical imaging have only a short history compared to the widespread and well-known field of machine vision [1]. Especially, the use of chemical imaging in quality and process control is still a young subject but with no doubt of growing importance [2–4].

Spectral imaging is the combination of three possibilities, to characterize a sample, that are integrated into one single system: the chemical characterization; the physical, morphological, or texture characterization; and the lateral visualization of the above-mentioned, which then gives the image of the sample. The term *hyperspectral imaging* is used when images of more than 10 wavelength regions are recorded simultaneously. Which spectral wavelength range is chosen to build the image is decided on the basis of the application. It is the objective of this short introduction to outline the present technological alternatives, the setup of a sound instrumentation and calibration, and also the handling of the huge amounts of data that are obtained with each image. The data reduction is commonly done by multivariate image analysis (MIA).

Applications of ''chemical imaging'' in process control are interested in visualizing the distribution of different chemical components within a sample. This can be the protein content in fish or the distribution of an active pharmaceutical ingredient (API) in a tablet [5] or the distribution of binder and strands in oriented strand boards (OSBs) [6], only to name a few. These examples demonstrate that distribution of a compound or the particle sizes and their distribution and sometimes also the layer thicknesses of the coating or other structural details might be of interest.

40.2
Instrumentation for Chemical Imaging

The techniques in chemical imaging are generally classified into mapping and imaging techniques and depend on the used wavelength range [7]. The common

Handbook of Spectroscopy, Second Edition. Edited by Günter Gauglitz and David S. Moore.

meaning of mapping is to measure a full spectrum of i wavelengths (λ_i) at one local point of spatial x_k- and y_l-coordinate of the sample. The complete image is obtained by adding the local information point by point to form a spatial image. The term imaging is used when the spatial image for several x_k- and y_l-coordinates is obtained simultaneously by measuring with a camera at different wavelengths (λ_i) sequentially. In addition, line scans are possible, which measure a full spectrum along a spatial line x in one go. In remote sensing, the different applied imaging technologies are labeled as [1]

- whiskbroom (''spot light'') imaging
- staring (''staredown'') imaging
- pushbroom imaging.

Figure 40.1 visualizes the different techniques. As mentioned, all techniques can be used in the wavelength ranges from UV to IR as well as with Raman and fluorescence spectroscopy.

A pushbroom imager is a line scanning system and acquires the full spectral information for all lateral x_l-coordinates in a single line, mostly called *x-pixels*, simultaneously. The system is a direct light imaging spectrograph that can be quickly combined with a broad range of matrix detectors to form a spectral imaging device. For process control, which is often applied to moving samples and therefore should be as fast as possible, the pushbroom acquisition mode is the best suited one. The sample is moved, for example, on a conveyor belt, in the y-direction and the imaging spectrograph measures a full spectrum (λ_i) for all x_l-pixels along the x-direction. A detailed description of the staring and whiskbroom imaging is given by Griffiths in [7].

Owing to cost efficiency and availability of technology, the focus for process control is emphasized to imaging in the spectral range of UV–vis, NIR, and also to IR and Raman spectroscopy [8] and to a certain extent even to fluorescence spectroscopy. They are reasonably inexpensive, readily available, and ideally suited and proved for in-line and on-line control. Using molecular or optical spectroscopy, several chemical components can be determined simultaneously.

When measuring opaque or scattering samples, special care has to be taken to the instrumental setup and the calibration procedures as well as the measurement procedures. This is described in detail by Boldrini *et al.* [9].

40.3
Chemometrics and Data Analysis in Chemical Imaging

The evaluation of hyperspectral image data for quality and process control is very much related to normal quality and process control in the way that the final decision parameters, which determine the quality of the product, can be qualitative as in ''pass'' or ''fail'' or quantitative such as the concentration of an analyte. The most obvious difference between hyperspectral image data and classical spectroscopic data is the sheer amount of data collected with each collected image. Another

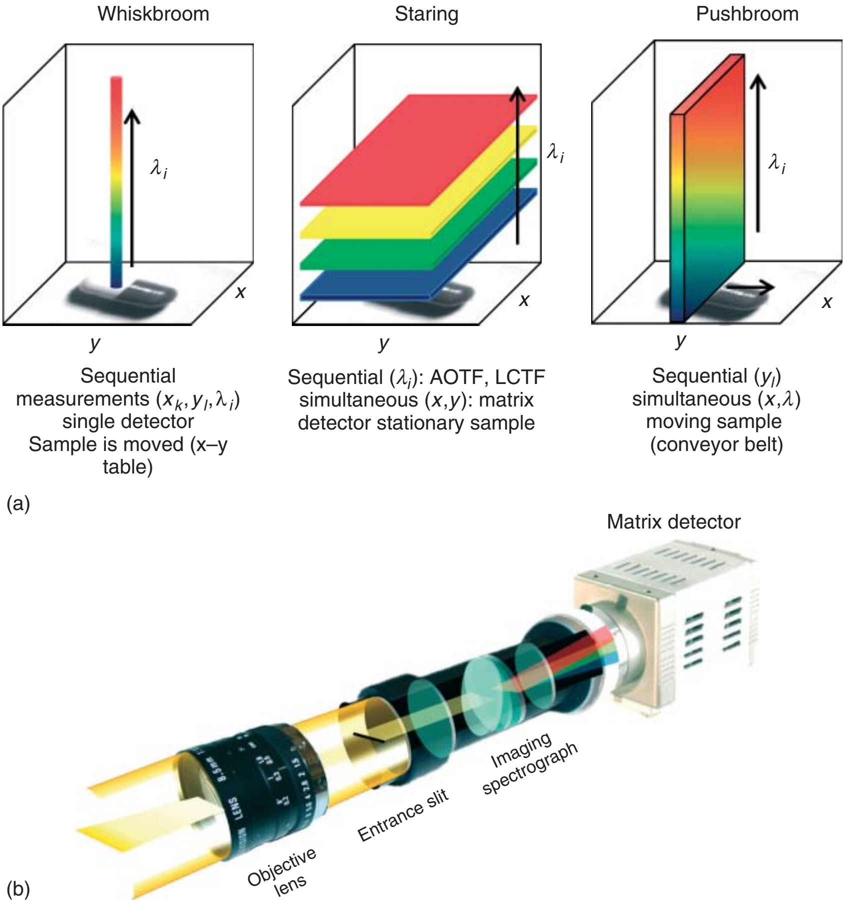

Figure 40.1 (a) Visualization of the different imaging technologies: whiskbroom imaging, staring imaging, pushbroom imaging and (b) a pushbroom imaging spectrograph. (Courtesy of Specim, *http://www.specim.fi*.)

important difference is the combination of spatial and chemical information in the hyperspectral image. By reducing the huge amount of data to the relevant information, chemometrics offers the possibility of using the full spectral information instead of extracting single-wavelength channels only. When chemometrics is applied, the relevant information is reduced to one or a few quality-defining so-called latent variables. Each spectrum is then represented by its score values, which are calculated from the latent variables. These scores are used to build either multivariate classification or regression models with the hyperspectral data. For images it is called *multivariate image analysis* and for qualitative analysis it is very often linked to principal component analysis (PCA). If a quantitative quality or process parameter is required, it is called *multivariate image regression* and is mostly related to partial least squares (PLSs) algorithms [10–12].

There has been constant development in chemometrics on the image analysis field and a number of good reviews and useful tutorials have been published [13, 14]. Multivariate curve resolution(MCR) methods belong to those chemometric tools that have been incorporated into the field of image analysis only recently and they have already revealed many successful applications [15–18].

Before a multivariate image analysis or regression is calculated, the data should be checked for obvious abnormal spectra due to instrumental artifacts such as bad pixels. A detailed description is given in [9, 19].

A very easy way to compress the original image is to bind two or more pixels together to form only one measurement. This can be done in the spatial and spectral dimension, but it is not advisable if a high resolution of the spectra is desired. In this case, data reduction by PCA is preferable in the spectral dimension. Often, three to five principal components (PCs) capture most of the relevant information of several hundreds of spectral pixels. The image is composed of the scores and can be looked at separately for the different scores or combining three scores to an RGB (red-green-blue) image. Figure 40.2 gives an example of the information contained in the different PCs (PC1 to PC3) of a hyperspectral image. The letters RRI (Reutlingen Research Institute) were written with a UF (urea formaldehyde) resin binder, which is commonly used in the production of OSBs. The image was recorded in the NIR wavelength range (900–1700 nm) with a pushbroom technique by moving the sample below the line scanning spectrograph. A PCA is calculated for the gathered spectra. Figure 40.2a shows the distribution maps of the scores for PC1. This score captures most of the binder information (dark blue letters), PC2 (Figure 40.2b) gives information on the morphology of the wood chip, and PC3 contains surface effects due to inhomogeneous illumination (Figure 40.2c).

The aim of PCA is more explorative but it is also possible to build regression models with the PCA scores, which are then regressed on target values as, for example, binder concentration as shown in the above-mentioned example. This is called *principal component regression* (PCR). But, as in traditional spectroscopy, the most commonly used algorithm for multivariate regression is PLSs regression (PLS regression, sometimes also called *projection to latent structures*) [11–13, 20].

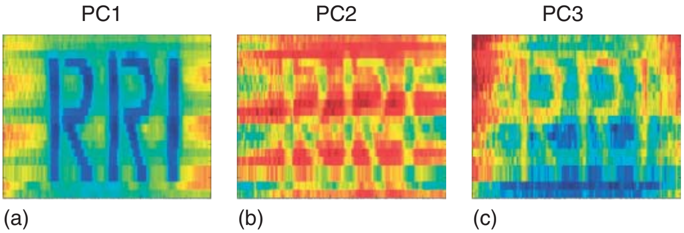

Figure 40.2 Example of data reduction by PCA: Three letters written with urea formaldehyde resin binder on a wood chip. Shown are the PCA scores of the measured spectra (a) PC1, which is the binder information; (b) PC2, which is the information of the morphology of the wood chip; and (c) PC3, which are surface effects due to inhomogeneous illumination.

When building calibration models for hyperspectral image data, the same problems of under- or overfitting arise and the same caution has to be taken when selecting the number of latent variables. The agreed procedure for building multivariate calibration models is first to divide the data set into a calibration and an internal validation data set, which is often referred to as a *cross validation data set*. The model size (number of latent variables) is determined by the internal validation data set by a cross validation and should be checked for correctness with an external data set [21]. The main difference between calibration models in classical spectroscopy and in image spectroscopy is that in classical spectroscopy for each spectrum a reference y value is available, whereas for images a reference value accounts for hundreds or thousands of pixel spectra. Most often, a bulk property is given as reference value, but the spectra can be very different from pixel to pixel. One possibility is to use a mean or median spectrum of all pixels of that sample and relate this mean or median spectrum to the bulk concentration. Another possibility is to find a region of interest on the sample that can be attributed to the reference value [22].

The combination of spectral image acquisition and multivariate data analysis has led to many successful applications. The objective of the following chapter is to give an overview on recent publication in the field of process industry.

40.4
Selected Applications

The majority of papers on spectral imaging are published in the field of food, feed, and pharmaceutical industries. And most of them use spectroscopy in the NIR range, which is still the workhorse in spectral imaging.

40.4.1
Food and Feed

Food and feed safety control as well as quality control are often carried out by human vision, especially for sorting out bad looking products. But by human vision it is often not possible to see chemical changes in the product. Combining NIR hyperspectral imaging spectroscopic techniques with chemometrics can greatly improve food and feed safety and improve quality control. An overview of several applications is given in [23, 24]. Chemical imaging is used for sorting apples [25–27] and tomatoes [28]. Furthermore, there are applications that determine the composition of food and feed [29, 30]. Even for safety reasons, to determine undesirable substances such as bacteria in food and feed chemical imaging has proved to be applicable [31, 32].

Daugaard *et al*. [33] showed that hyperspectral imaging has the potential for quality control in a continuous frying process. They used canonical discriminant analysis of the multispectral images of samples of fried minced meat and diced turkey to visualize the effect of different heat treatments. It was even possible to detect slight increases in the agglutination of the fried minced meat during the process, which is difficult to measure otherwise. Chemical imaging was also used to measure the tenderness of fresh beef [34] and the water holding capacity of beef muscles [35], thus facilitating the identification and classification of beef meat in a simple and fast way. Similar applications for quality control are found in the fish industry [36] and in bread [37] or pasta [38] making.

40.4.2
Pharma

The growing interest of the pharmaceutical industry in NIR chemical imaging is a result of its high usefulness for quality control analyses of drugs throughout the entire production process [39]. Focus is given mainly to these different uses: blend uniformity of powders and tablets [40], content uniformity [41], composition and morphological features of coated tablets [42] and granules, and spatial changes during hydration and degradation [43].

Counterfeit pharmaceutical products are a real threat to the health of patients. NIR chemical imaging provides a rapid method for detecting and comparing suspected counterfeit products without sample preparation. The advantage of imaging is that the discrimination of the tablets is not only caused by changes in the chemical composition but also from its spatial distribution. This reflects the use of different raw materials as well as different processing conditions, which change the distribution of the components in the tablet. The advantage of NIR chemical imaging over classical NIR spectroscopy is the potential to determine not only the amount but also the spatial distribution of ingredients within a single tablet. Furthermore, the combined chemical and morphological information provides an individual measure for the characterization of tablets [44, 45].

40.4.3
Recycling and Sorting

NIR and Raman spectroscopy is widely used in laboratory and industrial applications for material classification. While standard spectrometers only allow measurements at one sampling point at a time, chemical imaging techniques can identify, in real-time, both the size and shape of an object as well as the material it is made from. Sorting of materials requires the determination of the correct material, size, and shape of the entire object for reliable separation.

There are applications of industrial in-line material sorting system for cellulose-based materials such as pulp, paper, and cardboard [46]. Recent papers report the development of a hyperspectral imaging system in the NIR range (1000–1700 nm) to classify polyolefin particles from complex waste streams in order to improve their recovery, producing high-purity polypropylene (PP) and polyethylene (PE) granulates, according to market requirements [47]. Gosselin and coworkers [48] report an NIR hyperspectral imaging sensor for predicting spatiotemporal variations of extruded wood/plastic composite materials. Pushbroom imaging technology is

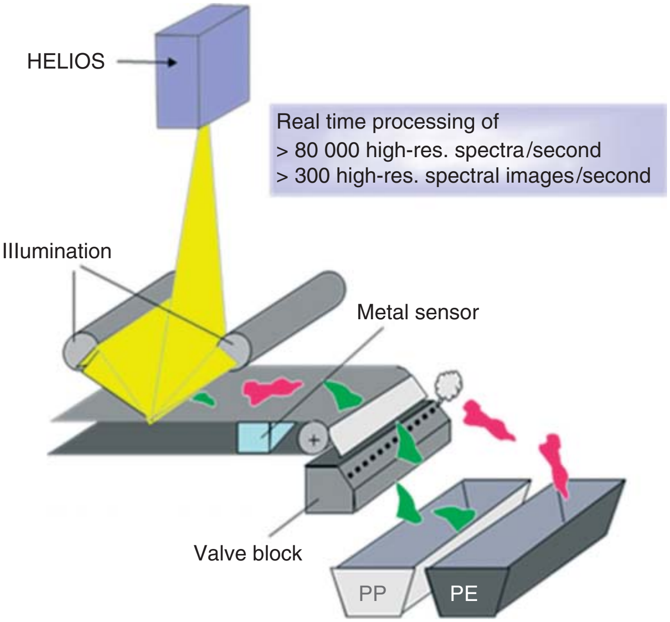

Figure 40.3 Real-time characterization of polymers in plastic waste separation. (Courtesy of EVK company, *http://www.evk.co.at*.)

also used to identify plastics in waste management systems [49, 50]. Figure 40.3 shows an example of a commercial application in separating the different polymers automatically on a conveyor belt.

References

1. G. Joseph *Fundamentals of Remote Sensing*, 2nd edn, 2005, Universities Press, India, ISBN: 8173715351, 9788173715358.
2. Bakeev, K.A. (ed.) (2010) *Process Analytical Technology – Spectroscopic Tools and Implementation Strategies for the Chemical and Pharmaceutical Industries*, 2nd edn, John Wiley & Sons, Ltd, Chichester.
3. Rebner, K., Kessler, W., and Kessler, R.W. (2009) in *Proceedings of the 14th International Conference on Near Infrared Spectroscopy, Bangkok, Thailand, 2009* (eds S. Saranwong, S. Kasemsumran, W. Thanapase, and P. Williams), IM Publications, Chichester, pp. 919–927.
4. Lewis, E.N., Schoppelrei, J.W., Lee, E., and Kidder, L.H. (2005) in *Process Analytical Technology* (ed K.A. Bakeev), Blackwell Publishing, Oxford, pp. 187–223.
5. Cruza, J., Bautista, M., Amigob, J.M., and Blanco, M. (2009) Nir-chemical imaging study of acetylsalicylic acid in commercial tablets. *Talanta*, **80**, 473–478.
6. Nishimura, T., Amin, J., and Ansell, M.P. (2004) Image analysis and bending properties of model OSB panels as a function of strand distribution, shape and size. *Wood Sci. Technol.*, **38**, 297–309.
7. Griffiths, P.R. (2009) in *Infrared and Raman Spectroscopic Imaging* (eds R. Salzer and H.W. Siesler), Wiley-VCH Verlag GmbH, Weinheim, pp. 3–64. doi: 10.1002/9783527628230.ch1

8. R. Salzer, H.W. Siesler (eds) *Infrared and Raman Spectroscopic Imaging* Wiley-VCH Verlag GmbH, Weinheim, 2009, ISBN 978-3-527-31993-0.

9. Boldrini, B., Kessler, W., Rebner, K., and Kessler, R.W. (2012) Hyperspectral imaging: a review of best practice, performance and pitfalls for in-line and on-line applications. *J. Near Infrared Spectrosc.*, **20**, 438–508.

10. Geladi, P. and Grahn, H. (1996) *Multivariate Image Analysis*, John Wiley & Sons, Ltd, Chichester.

11. Grahn, H.F. and Geladi, P. (eds) (2007) *Techniques and Applications of Hyperspectral Image Analysis*, John Wiley & Sons, Ltd, Chichester.

12. Amigoa, J.M., Ravn, C., Gallagherd, N.B., and Bro, R. (2009) A comparison of a common approach to partial least squares-discriminant analysis and classical least squares in hyperspectral imaging. *Int. J. of Pharm.*, **373**, 179–182.

13. Brown, S.D., Tauler, R., and Walczak, B. (2009) *Comprehensive Chemometrics*, Vol. 4, Elsevier, Amsterdam.

14. de Juan, A., Tauler, R., Dyson, R., Marcolli, C., Rault, M., and Maeder, M. (2004) Spectroscopic imaging and chemometrics: a powerful combination for global and local sample analysis. *Trends Anal. Chem.*, **23**, 70–79.

15. de Juan, A. and Tauler, R. (2003) Chemometrics applied to unravel multicomponent processes and mixtures: revisiting latest trends in multivariate resolution. *Anal. Chim. Acta*, **500**, 195–210.

16. Jaumot, J., Gargallo, R., de Juan, A., and Tauler, R. (2005) A graphical user-friendly interface for MCR-ALS: a new tool for multivariate curve resolution in MATLAB. *Chemom. Intell. Lab. Syst.*, **76**, 101–110.

17. de Juan, A., Maeder, M., Hancewicz, T., and Tauler, R. (2005) Local rank analysis for exploratory spectroscopic image analysis. fixed size image window-evolving factor analysis. *Chemom. Intell. Lab. Syst.*, **77**, 64–74.

18. Kandelbauer, A., Rahe, M., and Kessler, R.W. (2012) in *Handbook of Biophotonics*, Photonics in Pharmaceutics, Bioanalysis and Enviromental Research, Vol. 3 (eds J. Popp, V.V. Tuchin, A. Chiou, and S.H. Heinemann), Wiley-VCH Verlag GmbH, Weinheim, pp. 3–69.

19. Burger, J. (2009) Bad pixel detection in hyperspectral staring camera systems. *NIR News*, **20**, 9–12.

20. Amigo, J.M., Ravn, C., Gallagher, N.B., and Bro, R. (2009) A comparison of a common approach to partial least squares discriminant analysis and classical least squares in hyperspectral imaging. *Int. J. Pharm.*, **373**, 179–182.

21. Ravn, C., Skibsted, E., and Bro, R. (2008) Near-infrared chemical imaging (NIR-CI) on pharmaceutical solid dosage forms—Comparing common calibration approaches. *J. Pharm. Biomed. Anal.*, **48**, 554–561.

22. Pierna, J.A.F., Baeten, V., Dardenne, P., Dubois, J., Lewis, E.N., and Burger, J. (2009) in *Comprehensive Chemometrics* (eds S.D. Brown, R. Tauler, and B. Walczak), Elsevier, Amsterdam, pp. 173–197.

23. Baeten, V. and Dardenne, P. (2005) Applications of near-infrared imaging for monitoring agricultural food and feed products, in *Spectrochemical Analysis Using Infrared Multichannel Detectors* (eds R. Bhargava and I.W. Levin), Blackwell Publishing Ltd, Oxford.

24. V. Bellon-Maurel, J. Dubois in (eds R. Salzer and H.W. Siesler) *Infrared and Raman Spectroscopic Imaging* Wiley-VCH Verlag GmbH 2009, Weinheim, ISBN: 978-3-527-31993-0, pp. 259–294.

25. Mehl, P.M., Chao, K., Kim, M., and Chen, Y.R. (2002) Detection of defects on selected apple cultivars using hyperspectral and multispectral image analysis. *Appl. Eng. Agric.*, **18**, 219–226.

26. Ariana, D., Guyer, D.E., and Shrestha, B. (2006) Integrating multispectral reflectance and fluorescence imaging for defect detection on apples. *Comput. Electron. Agric.*, **50** (2), 148–161.

27. Peirs, A., Scheerlinck, N., de Baerdemaeker, J., and Nicolai, B.M. (2003) Starch index determination of apple fruit by means of a hyperspectral near infrared hyperspectral imaging system. *J. Near Infrared Spectrosc.*, **11**, 379–389.

28. Polder, G., van der Heyden, G.W.A.M., and Young, I.T. (2003) Tomato sorting using independent component analysis on spectral images. *Real Time Imaging*, **9**, 253–259.

29. Weinstock, B.A., Janni, J., Hagen, L., and Wright, S. (2006) Prediction of oil and oleic acid concentrations in individual corn kernels using near-infrared reflectance hyperspectral imaging and multivariate analysis. *Appl. Spectrosc.*, **60**, 9–16.

30. Fernandez Pierna, J.A., Baeten, V., and Dardenne, P. (2006) Screening of compound feeds using NIR hyperspectral data. *Chemom. Intell. Lab. Syst.*, **84**, 114–118.

31. Dubois, J., Lewis, E.N., Fry, F.S., and Calvey, E.M. (2007) Near infrared chemical imaging for high throughput screening of food bacteria. *NIR News*, **18**, 4–6.

32. Fernández Pierna, J.A., Vermeulen, P., Tossens, A., Dardenne, P., Baeten, V., and Amand, O. (2012) NIR hyperspectral imaging spectroscopy and chemometrics for the detection of undesirable substances in food and feed. *Chemom. Intell. Lab. Syst.*, **117**, 233–239.

33. Daugaard, S.B., Adler-Nissen, J., and Carstensen, J.M. (2010) New vision technology for multidimensional quality monitoring of continuous frying of meat. *Food Control*, **21**, 626–632.

34. ElMasry, G., Sun, D.-W., and Allen, P. (2012) Near-infrared hyperspectral imaging for predicting colour, pH and tenderness of fresh Beef. *J. Food Eng.*, **110**, 127–140.

35. ElMasry, G., Sun, D.-W., and Allen, P. (2011) Non-destructive determination of water-holding capacity in fresh beef by using NIR hyperspectral imaging. *Food Res. Int.*, **44**, 2624–2633.

36. Sivertsen, A.H., Kimiya, T., and Heia, K. (2011) Automatic freshness assessment of cod (Gadus morhua) fillets by Vis/Nir spectroscopy. *J. Food Eng.*, **103**, 317–323.

37. Soleimani Pour-Damanab, A.R., Jafary, A., and Rafiee, S. (2011) Monitoring the dynamic density of dough during fermentation using digital imaging Method. *J. Food Eng.*, **107**, 8–13.

38. Mokhtar, A., Hussein, M.A., and Becker, T. (2011) Monitoring pasta production line using automated imaging technique. *Procedia Food Sci.*, **1**, 1173–1180.

39. Lewis, E.N., Schoppelrei, J., and Lee, E. (2004) Near-infrared chemical imaging and the PAT initiative. *Spectroscopy*, **19**, 22–31.

40. Lyon, R.C., Lester, D.S., Lewis, E.N., Lee, E., Yu, L.X., Jefferson, E.H., and Hussain, A.S. (2002) Near-infrared spectral imaging for quality assurance of pharmaceutical products: analysis of tablets to assess powder blend homogeneity. *AAPS PharmSciTech*, **3**, 1–15, Article 17.

41. Lee, E., Huang, W.X., Chen, P., Lewis, E.N., and Vivilecchia, R.V. (2005) High-throughput analysis of pharmaceutical tablet content uniformity by near-infrared chemical imaging. *Spectroscopy*, **21**, 25–32.

42. Palou, A., Cruz, J., Blanco, M., Tomàs, J., de los Ríos, J., and Alcalà, M. (2012) Determination of drug, excipients and coating distribution in pharmaceutical tablets using NIR-CI. *J. Pharm. Anal.*, **2**, 90–97.

43. Möltgen, C.-V., Puchert, T., Menezes, J.C., Lochmann, D., and Reich, G. (2012) A novel in-line NIR spectroscopy application for the monitoring of tablet film coating in an industrial scale process. *Talanta*, **92**, 26–37.

44. Puchert, T., Lochmann, D., Menezes, J.C., and Reich, G. (2010) Near-infrared chemical imaging (NIR-CI) for counterfeit drug identification – a four-stage concept with a novel approach of data processing (Linear Image Signature). *J. Pharm. Biomed. Anal.*, **51**, 138–145.

45. Amigo, J.M. and Ravn, C. (2009) Direct quantification and distribution assessment of major and minor components in pharmaceutical tablets by NIR-chemical imaging. *Eur. J. Pharm. Sci.*, **37**, 76–82.

46. Tatzer, P., Wolf, M., and Panner, T. (2005) Industrial application for inline material sorting using hyperspectral imaging in the NIR Range. *Real-Time Imaging*, **11**, 99–107.

47. Serranti, S., Gargiulo, A., and Bonifazi, G. (2012) Classification of polyolefins from building and construction waste using NIR hyperspectral imaging system. *Resour. Conserv. Recycl.*, **61**, 52–58.

48. Gosselin, R., Rodrigue, D., and Duchesne, C. (2011) A hyperspectral imaging sensor for on-line quality control of extruded polymer composite products. *Comput. Chem. Eng.*, **35**, 296–306.
49. Leitner, R., Mairer, H., and Kercek, A. (2003) Real-time classification of polymers with NIR spectral imaging and blob analysis. *Real Time Imaging*, **9**, 245–251(Special Issue on Spectral Imaging).
50. Kulcke, A., Gurschler, C., Spöck, G., Leitner, R., and Kraft, M. (2003) Online classification of synthetic polymers using near infrared spectral imaging. *Near Infrared Spectrosc.*, **11**, 71–81.

41

Trends in Spectroscopic Techniques for Process Control

Michael Maiwald, Igor Gornushkin, and Markus Ostermann

41.1

Trends

As previously described, the science-based regulatory guidances such as the process analytical technology (PAT) guidance [1] and ICH Q8 [2] have recognized spectroscopic techniques as potentially useful tools on building quality into the product and manufacturing processes, as well as continuous process improvements [3]. The goal of PAT is to enhance understanding and thereby control the manufacturing process: quality cannot be tested into products; it should be built in or should be by design.

There is a considerable trend to recognize process analytical techniques as potentially useful tools for classical chemical production and manufacture in general [4–6]. A need to study complex multicomponent mixtures and gain insight into their behavior in the real process can be recognized. On-line spectroscopic methods can meet these demands when either flow probes are directly coupled to process equipment such as reactors for process monitoring – from laboratory size up to industrial scale. Likewise, commercial off-the-shelf offers for optrodes, light and radiation-guiding material (e.g., infrared (IR) transparent light fibers), as well as suited interfaces (e.g., flanges with spectroscopic windows) were significantly expanded on the market.

Besides the technical demands – and chances – of microanalytical sensors to become smaller and smaller (e.g., for analysis in microreactors or small amounts of samples), there is also need for precise local quantification in bulk materials or large-scale apparatuses (e.g., tomography, detection of hot spots).

41.2

Nuclear Magnetic Resonance Spectroscopy (NMR)

41.2.1

Process Analytical Applications of High-Resolution NMR Spectroscopy

Quantitative high-resolution on-line nuclear magnetic resonance (NMR) spectroscopy is the method of choice for the investigation of complex fluid mixtures

Handbook of Spectroscopy, Second Edition. Edited by Günter Gauglitz and David S. Moore.

with analytically similar compounds, where other analytical methods (e.g., optical spectroscopy such as UV–vis, (near) infrared (IR, NIR), Raman, or fluorescence spectroscopy) suffer from insufficient differentiation of components. In addition, the high value of NMR in determining chemical structure and accurate quantitative measurements, more subtle features such as speciation (e.g., protonation) are clearly indicated. The development of on-line (flow) techniques has tremendously increased the value of NMR spectroscopy for process development applications and became very attractive as noninvasive methods.

One of the most attractive features of quantitative NMR spectroscopy [7, 8] is that the coefficients relating the peak area to the number of nuclei are essentially identical for all nuclei of the same species in a mixture. Provided that spin saturation is attained, NMR peak areas can be directly used for quantification without further calibration. A major advantage of NMR spectroscopy is that the method features a high linearity between absolute signal area and sample concentration, which makes it an absolute analytical method independent of the matrix (Figure 41.1).

The NMR effect subject to atomic nuclei possessing a nuclear spin (spin quantum number $I \neq 0$). Among the most important isotopes are the NMR active proton (^{1}H, $I = 1/2$) and deuterium (^{2}H, $I = 1$). Only the isotope carbon ^{13}C shows nuclear magnetic effects ($I = 1/2$). Its relatively low natural abundance of 1.108% and other effects result in a relatively low sensitivity and hence to longer acquisition times for NMR experiments. From all elements of the periodic table in most cases, there are some that have a nuclear spin with very individual sensitivities.

A magnetic spin momentum μ arises from the nucleus' spin momentum L owing to its moving charge. The magnetogyric ratio $\gamma = \mu/L$ describes the ratio between the magnetic property μ of the nucleus with respect to its mechanical spin momentum L. It is responsible for the sensitivity of detection and is listed in tables [9]. A strong, homogeneous, and timely constant magnetic field B_0 provided by

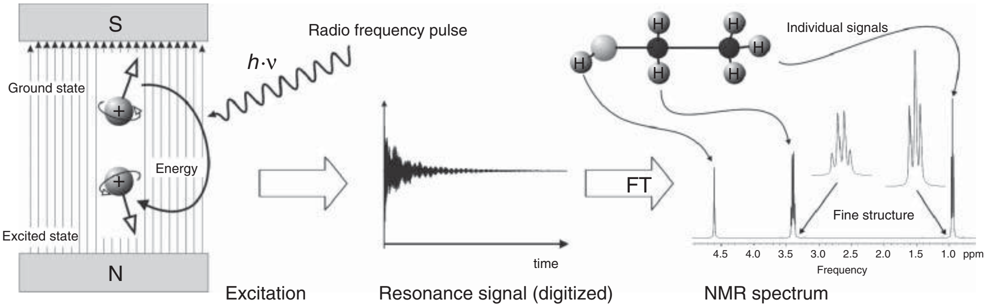

Figure 41.1 Schematic representation of an NMR experiment. A short radio frequency pulse leads to a temporal population difference between nuclei in its ground state and excited state, which affects the total magnetization of the system. This can be detected by the radio frequency receiver coil and is digitized. The NMR spectrum is derived by Fourier transform (FT). As individual atomic nuclei are magnetically shielded by individual electron currents, this leads to separate signals in the spectrum. A characteristic fine structure that allows for structural determination of the observed molecule (e.g., ethanol) is observed.

superconducting magnets leads to alignment of the magnetic spin moments into the direction of and contrary to B_0. Spins into the direction of B_0 are energetically preferred. Both states are indicated by an energy difference of

$$\Delta E = h\nu = 2\,\mu_z B_0 = \gamma\hbar\, B_0$$

This allows for spectroscopic excitation with radio frequency (RF) radiation (e.g., $B_0 = 9.4\,\mathrm{T}$ resulting in 400 MHz resonance frequency). As thermal energy counteracts with magnetic polarization, population differences are typically only several parts per million – in contrast to optical spectroscopy, for instance.

Excitation is typically achieved by using a high-energy short-time pulse of resonance frequency, which excites a broad frequency range of the resonant nuclei. The pulse changes the magnetization of the observed nuclei, which induce an alternating current into an RF detection coil. While the magnetization of the system relaxes back to its ground state, an impulse response is detected for several seconds [time domain (TD)] and digitized. A Fourier transform (FT) yields the NMR spectrum in the frequency domain [10]. Relaxation effects arise from various inter- and intramolecular effects and reflect molecular properties. Therefore, relaxation times grant access to molecular movements and segment movements.

On-line coupling of NMR spectrometers was first developed with high performance liquid chromatography (HPLC) and supercritical fluid chromatography SFC, using NMR as an analytical detector with high spectral dispersion [11–13]. Flow NMR probes were developed, and these have also been used for high-throughput NMR spectroscopy.

A major advantage of flow NMR probes is that they are less sensitive to changing magnetic properties of the sample because of the fixed fluid volume and the cell design. When used for on-line reaction monitoring, the pressure-handling capacity of the flow probe is an important design consideration. The shimming of deuterium-free samples can give excellent results when automated shim procedures based on pulsed magnetic field gradient experiments are used. These processes work reliably and without operator supervision, even for concentrated samples or solvent mixtures for which solvent peaks have the same order of magnitude as analyte peaks – and even under flow conditions. Shimming or tuning of the probe during an experiment is typically not necessary. The choice of a suitable solvent suppression pulse sequences of deuterium-free samples is possible but nontrivial.

Despite the high spectral resolution that follows from the use of a high-field magnet (about 500 MHz or better for ^{1}H), NMR signals may overlap because the interesting chemical species are structurally related. Solvent signals can, in most cases, only be reduced but not completely eliminated, so that the remaining signal may falsify quantitative results for close solute signals. In the worst case, the signal intensities can only be determined by peak deconvolution.

Various applications of chemical as well as pharmaceutical reaction and process monitoring of reactions and processes are described in the recent literature [14–16].

41.2.2
Time Domain NMR Spectroscopy

Since the mid-1990s medium resolution (MR) and TD NMR devices are commercially offered for laboratory quality control as well as process analytics, which typically work at field strengths under 1.41 T (60 MHz proton frequency). There are both desktop devices and process-suited devices available. Magnetic fields with small scattering fields are typically produced by a permanent magnet. Relaxation times, which are directly accessible from the measurements without accomplishment of a FT (decay of the free induction decay (FID) signal), represent the main valuable process variables.

In some cases, MR NMR spectra can be derived if a sufficient shim is provided [17]. Owing to the relatively low-field strengths of the magnets used in such instruments, the resulting spectral dispersions are clearly restricted. Usually for the interpretation of the spectrum or the pure TD information, chemometric methods are applied to allow for a multicomponent and/or a multiparameter correlation to the sample characteristics.

Desktop devices possess a modular design and can be supplemented for various options such as gradient units with bipolar rectangles and formed gradient pulses, excitation by shaped waveforms, 3D gradient experiments, and so forth. Various sample probes are offered, which are predominantly intended for the observation of ^{1}H, ^{19}F, and ^{31}P nuclei with acceptable sensitivity covering a wide temperature and pressure range. Likewise, custom-built sample probes can be integrated [18].

MR NMR process instruments are accordingly constructed for employment in direct proximity of production plants. They fulfill high safety standards and have internal control functions such as switching off functions or leakage control. Besides, a set of sample probes and components for observation of the above-mentioned nuclei are available, for example, for switching between different sample lines as well as for cleaning and rinsing. Likewise, standards can be brought into the spectrometer.

The uses of MR NMR spectrometers cover measurements of components and component conditions in technical process liquids with the need for direct transmission through the equipment using a bypass. Besides, measurements of physical and chemical parameters such as relaxation times, diffusion procedures, droplet size distributions, and so forth are possible. The devices are at present predominantly used for the investigation of process liquids from the refinery and chemical industry, for pharmaceutical products [19] and for food and dairy products [20, 21].

41.2.3
Process NMR Spectroscopy Outlook

Novel polarization transfer methods [22], spin–lattice relaxation time reduction techniques [23], and cryogenic NMR probes [24] have been utilized toward the improvement of NMR measurements. Because cryogenic magnets are not compatible with the industrial environment, the development of process capability of such instruments is highly appreciated, for example, by further developing MR NMR and microcoil capillary NMR techniques [25, 26]. The latter reduce the RF coil diameter [27] and allow application of suited tubing material.

Small, low-field NMR systems equipped with permanent magnet technology have already been developed and applied at-line and on-line [28–30].

41.3
Ion Mobility Spectroscopy (IMS)

Ion mobility spectroscopy (IMS) is an analytical technique with growing application in semiconductor, pharmaceutical, and medical device manufacturing, industrial monitoring, petrochemical and chemical plant security as well as for chemical agent detection, for example, in airports or military applications [31, 32]. Ion mobility has recently also been proved in the analysis of biological materials (proteomics and metabolomics [33, 34]) and for pharmaceutical applications, for example, cleaning validations.

In IMS, drift times under the influence of an electrostatic field of ionized species through a drift chamber are measured. The method is comparable to mass spectroscopy but works under ambient pressure, mostly with air as drift gas. The (diluted) sample enters the drift cell from a sampling system over a semipermeable membrane, which provides a degree of sample selectivity. Dopant materials can be added to enhance the ionization process and increase specificity. Purified air sweeps the membrane on the inside of the cell and delivers the sample to the ionizer. The molecules of the sample have to be ionized, usually by corona discharge, electrospray ionization (ESI), atmospheric pressure photoionization (APPI), or a radioactive source, for example, ^{63}Ni. An electrically biased shutter grid (gate) allows periodic introduction of the ions into a drift tube where they separate based on charge, mass, and shape while flowing counter to a drift gas flow, which is introduced at the end of the drift tube. The ions drift with constant velocity v_d in a homogeneous electric field E ranging from a few up to several hundreds of volts per centimeter.

$$v_\mathrm{d} = KE$$

Typical mobility coefficients K for swarms of ionized particles with atomic mass constants of 10–500 amu are on the order of 0.5–2.5 $\mathrm{cm^2\,V^{-1}\,s^{-1}}$ for an electric field of 150–300 $\mathrm{V\,cm^{-1}}$ and drift velocities of 1–10 $\mathrm{m\,s^{-1}}$. Typically, mobility coefficients K are normalized to standard pressure and standard temperature according to

$$K_0 = K\frac{p}{p^\ominus}\frac{T^\ominus}{T}$$

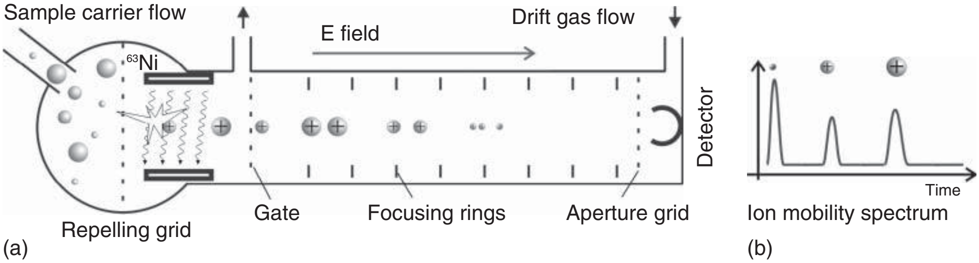

Figure 41.2 (a) Ion mobility spectrometer. The sample is delivered to the ionizer (here: radioactive ^{63}Ni) and periodically introduced into the drift tube with a homogeneous electric field while flowing counter to a drift gas flow. (b) Time-of-flight ion mobility spectrum with detector signals of the sample ions separated on the basis of charge, mass, and shape.

A Faraday plate located at the end of the tube serves as collector and detects the arrival of the ions, producing a current. This current is amplified to produce a time-of-flight spectrum (Figure 41.2).

IMS is a technique of growing interest for an expanding number of applications because of its versatility by properly selecting temperature, flow rates, membrane type, drift-tube polarity, and other parameters to specifically monitor selected compounds. Limits of detection are in the lower parts per billion level for many compounds. Real-time monitoring, sensitivity, selectivity, and speed of response (millisecond range) make this technique preferable to other monitoring methods.

IMS is applied in semiconductor manufacturing to detect bases such as ammonia, NMP (*n*-methylpyrrolidone), and other amines during photolithography processes. It is also employed to monitor acids in metal deposition, etch, and copper CMP processes. For accurate monitoring of HCl and HF at the parts per billion and parts per million levels, IMS is advantageous compared to other analytical techniques. In petrochemical production environments, IMS is used to analyze trace ammonia in ethylene and light hydrocarbon process streams, which causes catalyst poisoning in most production processes. Airport security and chemical agent detection are widely applied fields for IMS ownig to its sensitivity, selectivity, and speed of response.

41.4
Process Analytical Applications of Laser Spectroscopy

Extraordinary progress has been made in advancing the performance and manufacturability of quantum-cascade laser (QCL) materials. Proposals concerning the development of intraband lasers on quantum wells were formulated already in the 1970s, but such lasers only appeared several decades later. In a structure with quantum wells, or in a super lattice, emission of electromagnetic radiation can be influenced by a bias voltage, the spatial position of the conductance band, the energy levels in the wells, and populations of these levels. Transition between the wells can be induced by tunneling or phonons and by electromagnetic radiation [35]. The combination of quantum-cascade media with external-cavity lasers produces mid-IR radiation with narrowband output, broadband single-mode tuning abilities [36, 37]. The high optical power output, tuning range, and room temperature operation make QCLs useful for spectroscopic applications such as remote sensing of gases [38].

41.4.1
Cavity Ring-Down Spectroscopy (CRDS)

Cavity ring-down spectroscopy (CRDS) is a direct absorption technique that is normally used in a wide spectral region from the UV (200 nm) to the IR (10 μm). The technique is also known as cavity ring-down laser absorption spectroscopy (CRLAS). Pulsed or continuous light sources can be used. A broad variety of atoms and molecules have been studied with significantly higher sensitivity to trace amounts of substance or very weak absorbing species than obtainable in conventional absorption spectroscopy, including radicals, ions, clusters, and solids [39].

The experiment is based on detection of the rate of absorption rather than the magnitude of absorption of a light pulse, which is restricted to an optical cavity with a high Q factor. A short laser pulse is coupled to the optical cavity and reflected between the mirrors. With every reflection, a small fraction leaks out of the cavity. Instead of measuring the total intensity of the light exiting the cavity, one determines the decay time by measuring the time dependence of the light leaking out of the cavity. As the sample absorption increases the decay, the rate of absorption reflects the sample contribution. The resulting intrinsic insensitivity to light source intensity fluctuations and extremely long optical pathways in stable optical cavities (some 1000 m) are advantegous over normal absorption spectroscopy. Multimode excitations of the ring-down cavity were typically reported in the range of 10^{-6} to $10^{-10}\,\text{cm}^{-1}$, single-mode excitations between 10^{-9} and $10^{-12}\,\text{cm}^{-1}$. The difficult calibration is a disadvantage of this method, when used as an absolute detection method (Figure 41.3).

41.4.2
Tunable Diode Laser Absorption Spectroscopy (TDLAS)

Tunable diode laser absorption spectroscopy (TDLAS) is a technique for quantitative detection of certain species, for example, methane or water in a gaseous mixture using tunable diode lasers in combination with laser absorption spectroscopy. TDLAS achieves very low detection limits in the order of parts per billion. In addition, determination of temperature, pressure, velocity, or mass flux is possible. The method is the most common quantitative laser-based absorption technique for gases [40].

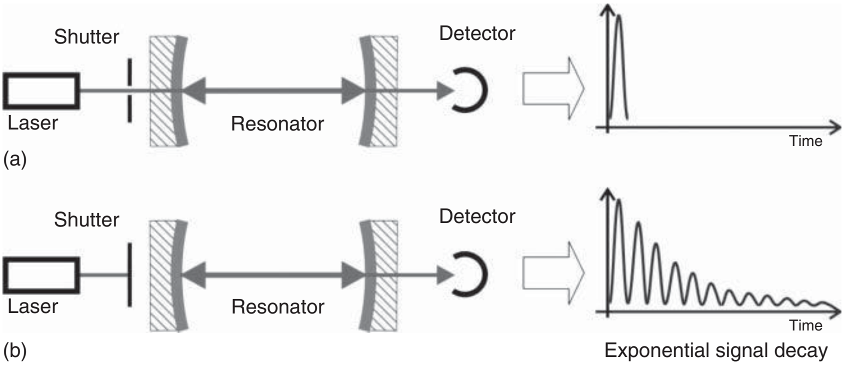

Figure 41.3 Schematic representation of a cavity ring-down experiment. (a) A laser pulse leads to a resonating signal between highly reflecting mirrors. (b) An exponentially decaying signal is detected after the laser is shut off. Spectrum-dependent absorptions of trace amounts of sample lead to an increasingly decaying signal in the spectrum.

41.4.3
Photothermal Techniques

Photothermal techniques are based on the production and proof of thermal waves. Frequency-dependent amplitudes and phase shifts of the thermal waves yield information on the thermal characteristics and their depth profile of a sample. Thermal waves are produced by a local periodic heating up of the sample, for example, with the help of an intensity-modulated laser beam. For the detection of oscillating temperature fields, various techniques are common [41], such as photo acoustics, photo-thermally modulated reflection, and photo-thermally modulated IR radiometry, where radiant heat is detected because of the periodic heating up. All techniques are particularly suitable for remote investigations within the industrial range.

Photoacoustical spectroscopy (PAS) has been increasingly used for selective identification of materials using their optical absorption characteristics. The technique is widely applied to samples in the vapor phase, where the vapor is kept in a chamber with optical windows. In novel approaches a quartz crystal tuning fork (QCTF) is used [42]. The reflected light absorbed by the QCTF generates pressure waves at the air–surface interface and thereby causes quartz to resonate and produce a piezoelectric voltage. These devices are highly sensitive and do not require microphones to detect the sound produced by the photoacoustic effect.

41.5
Laser-Induced Breakdown Spectroscopy (LIBS)

Laser-induced breakdown spectroscopy (LIBS) is a relatively simple plasma spectrochemical technique that uses short-pulsed lasers [43–47]. A laser is focused on a sample to create a microplasma. The microplasma is a transient event with high temperature (10 000–20 000 K) sufficient to break chemical bonds and to produce electronically excited atoms and ions. These excited species give off radiation at specific wavelengths depending on the element. By detecting the light from the microplasma within UV–vis spectral range elements are identified and chemical abundances are measured. LIBS is a real-time standoff measuring technique with typical working distances of 10–20 cm and record-long working distances of about 100 m. The technique requires no sample preparation and can be used for analysis of solids, liquids, and gases. It has the potential to be developed into a compact, rugged, and relatively low-cost instrument.

Currently, LIBS is used for compositional analysis, remote process monitoring, thin-film deposition, and nanofabrication [48–51]. In compositional analysis, concentrations are found by using certified standards. The use of matrix-matched standards is imperative; otherwise, results are biased by the matrix effect that is notorious for LIBS. There, an alternative calibration-free approach exists where the concentrations are calculated from the plasma spectrum using theoretical modeling [52–54]. The basic assumption is that the plasma composition represents exactly that of the solid.

In analytical practice, dual- or multiple-pulse laser systems are popular as they provide better figures of merits compared to that of single-pulse lasers [55]. A significant increase in detection sensitivity occurs because of the enhanced plasma excitation combined with the increased mass removal.

The vast majority of analyses are performed on solid samples [56]. Typical limits of detection are in the low part-per-million range with typical uncertainties of 5–10%. For hybrid techniques, such as laser ablation inductively coupled plasma mass spectrometry (LA-ICP-MS), even lower sensitivities at a part-per-trillion level can be achieved [57]. LIBS is often the technique of choice in heavy industry thanks to its remote capability and lack of sample preparation. It is used for microcharacterization of solid samples [58], *in situ* analysis of mineral and metal melts [59, 60], and industrial monitoring [61]. Applied to pharmaceutical products, LIBS allows for rapid multicomponent analysis, depth profiling, and the assessment of product homogeneity [62]. It has been demonstrated that LIBS is also capable of fast and reliable on-line *in situ* detection of hazardous chemical and biological agents [63], sorting industrial and recycled materials [64, 65], and classification of particulate systems [66]. The fingerprinting capability of LIBS improves when it is combined with Raman spectroscopy [67]. The remote capability of LIBS makes this technique ideal for planetary exploration [68].

The detection of trace elements in gases emitted by industrial and incinerator facilities is another important LIBS application [69]. It combines continuous monitoring with the possibility to remotely access a desirable testing site. LIBS proved to be also suitable for the detection of particles and aerosols, allowing the determination of both species composition and total particle mass and size [70, 71].

Thus, LIBS-based techniques become increasingly popular in many applied fields. Operational simplicity, versatility, and relatively low cost are the features that make LIBS the technique of choice for many industrial laboratories.

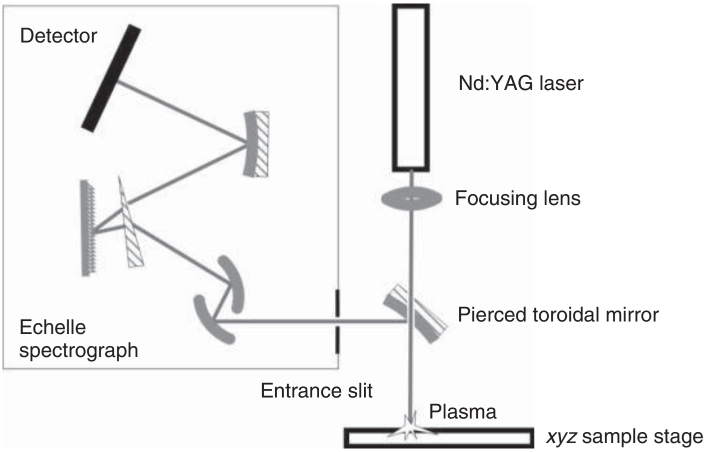

Figure 41.4 Schematic representation of an LIBS spectrometer using an Echelle spectrometer with CCD detector. The sample is excited with a pulsed Nd:YAG laser.

Several commercial LIBS instruments are available on the market and the number of companies offering the instruments steadily grows (Figure 41.4).

41.6
X-Ray Fluorescence Spectroscopy

X-ray fluorescence (XRF) analysis permits qualitative and quantitative evaluation of the elementary composition of a sample. In XRF, X-rays produced by a source irradiate the sample. The source is in most cases an X-ray tube, but it can also be a radioactive material. The elements present in the sample emit fluorescent X-rays with discrete energies that are characteristic for each individual element. By measuring the energies of the radiation emitted by the sample, it is possible to determine which elements are present for qualitative analysis. By measuring the intensities of the emitted energies, quantitative analysis is also straightforward [72].

There are two main types of XRF instruments available on the market: wavelength-dispersive X-ray fluorescence (WDXRF), which is achieved by diffraction using analyzer crystals, and energy-dispersive X-ray fluorescence (EDXRF), which does not use crystals. WDXRF systems provide application versatility, optimal measurement conditions, excellent light element performance, very high sensitivity, and low detection limits. While WDXRF systems are mostly used in laboratories, EDXRF systems offer a lower cost alternative for more routine applications as it is needed for process analytical purposes. Recent developments of new detectors bring significant analytical improvements to these systems [73–75].

Moreover, elemental analysis using EDXRF for *in situ* material flow in production processes is gathering importance nowadays. The use of X-ray radiation for the investigation of material streams is highly competitive and has been investigated extensively. The employment of on-line XRF analysis pays off both in financial as well in time aspects, as it can be used for the economic application of raw materials or, for example, for recycling [76, 77]. Thanks to these technical developments, XRF analysis can be used as information source in the elemental analysis of material in the industrial process without tedious sample preparation steps. It plays no role whether the sample is liquid or solid, a compact body or a bulk material. A smooth surface eases and improves the measurements; less ideal surfaces are also measurable as long as they are homogeneous [78, 79]. XRF analysis is a nondestructive measurement method. In principle, XRF is capable of measuring elements from beryllium (Be) to uranium (U) and beyond at trace levels and up to 100%.

The versatility of the method and the relatively easy sample preparation have paved the way for XRF in many application areas [80]. The technique has become widespread in chemical, food, pharmaceutical, cosmetic industries, as well as for cement, mining, and petrochemical applications, where it provides a valuable tool for manufacturing and quality assurance, monitoring environmental impact, and resource utilization [81]. In some industrial branches, as, for example, in the cement industry, XRF is used currently still off-line, that means that raw materials, intermediate products, process components, and end products are examined in the company's laboratory. This approach delivers temporal-shifted measuring values. For raw materials this approach is not very critical, as long as sufficient storage capacities are available. But because in process control measuring values must be available immediately in order to guarantee a constant and optimal process output and products of the highest quality, an implementation of the XRF instrumentation into the production line should be realized. This XRF on-line analytics for process control slowly becomes accepted. The comprehensive basis of understanding of the method, the easy sample preparation, and the moderate costs of the components produced inlarge scale are strong arguments for its use. Some good application examples in process control are the determination of the zinc content in converter dust for steel production [82], the monitoring of the coal supply to a blast furnace [83], or the application for the removal of impurities in glass recycling.

41.7
Terahertz Spectroscopy

Terahertz (THz) spectroscopy is a focus of research in applied optics [84–87]. At present, its applications include observation of vibrational modes in macromolecules [88], quality control of pharmaceutical products. The method also provides molecular fingerprints and has been demonstrated for explosives, polymorphic forms of active pharmaceutical ingredients (APIs), or illegal narcotic substances [89].

Conventional THz spectroscopy uses the Fourier transform infrared (FTIR) technique in the distant IR around 100 GHz to 10 THz (3–300 cm^{-1}) and it represents a complementary vibrational spectroscopic method to IR and Raman spectroscopy, providing information on lattice oscillations such as low energy molecular, intermolecular, and crystal vibrational processes. Absorption spectra of THz radiation are directly related to the three-dimensional arrangement and low-frequency motions of all atoms in a molecule. It is also sensitive to intermolecular interactions. Many materials are transparent to THz radiation and the radiation harmlessly penetrates several millimeters beneath the surface. THz radiation is nonionizing and therefore safe for biological tissues. As most materials are transparent to THz radiation, samples can be observed through normally opaque intervening layers such as clothing or packaging materials.

Terahertz time-domain spectroscopy (THz-TDS) measures the electric field of the reflected or transmitted radiation of a short pulse of THz radiation, for example, using a picosecond-pulsed laser, which contains frequency components covering the whole THz range.

The method shares similarities with pulsed ultrasonic waves. It provides the phase and amplitude changes of radiation from which the refractive index and the absorptions coefficient can be obtained, and therefore the technique provides more information than conventional FT spectroscopy, which is only sensitive to the amplitude. THz-TDS is typically used from 0.05 to 4 THz, for example, to investigate thickness, density, or defect location in multilayer specimens or composites on a quantitative background. THz-TDS imaging systems are also available. Images can have spatial resolutions down to 1 mm.

THz-pulsed spectrometers are particularly suited to study solids [90]. The terahertz-pulsed imaging (TPI) technology offers unique possibilities in the area of imaging and for investigation of APIs in pharmaceutical manufacturing [91, 92]. Of particular interest is the identification and characterization of drug polymorphs [93]. Femtosecond-pulsed THz radiation has also been utilized for nondestructive 3D internal imaging of pharmaceutical products, surface coating measurements, and for scanning living tissue [94, 95], where the absorption of THz radiation can be used to quantitatively and nondestructively measure the API contents.

41.8
Acoustic Spectroscopy (Ultrasound)

Acoustic and electroacoustic spectroscopy give a unique opportunity to study concentrated dispersions, emulsions, and microemulsions without dilution and hence without changes in equilibrium conditions of surface and rheological properties. The technique is also known as *ultrasound attenuation spectroscopy*. Applications include characterization of ceramics, mixed dispersed systems, emulsions, food emulsions, and microemulsions [96–99].

In acoustic spectroscopy, sound pulses are generated and passed through the sample. Typical operation frequencies are 1–100 MHz. Sound energy losses (attenuation) and sound speed are measured by a receiver, which is sensitive to changes in intensity and phase of the signal. Such changes are due to interaction of sound waves with particles and liquids in the sample system. Acoustics provides reliable *in situ* particle size information as an alternative to light scattering methods. The method works in concentrated dispersions and yields accurate particle sizes in undiluted technical systems eliminating the need for dilution or other sample preparation. The method covers volume fractions up to 0.5 as well as low dispersed systems with volume fractions down to 0.001. Advanced systems allow particle size ranges of, for example, 0.005–100 μm to be measured in a single run. Beyond this, acoustical stresses yield information about the microstructure of the dispersed system, for example, extensional and volume viscosity, and can therefore be treated as acoustic microrheometers.

The technique allows a wide range of technical sample types for investigation such as mixed systems of dissimilar materials, for example, zirconia/alumina or ceramic slip. Particles sizes can, for instance, be determined in polymer solutions with extremely high macroscopic viscosity. Measurements do not require charged particles and can take place with conducting as well as nonconducting material. Samples can be measured in a static sample chamber or circulated in a bypass using a pump.

Data analysis of attenuation data involves fitting of experimental results to theoretical models that are based on different acoustic loss mechanisms. There are several mechanisms of ultrasound interaction with a dispersed system: viscous, thermal, scattering, and intrinsic. Minor interactions are caused by structural and electrokinetic effects. Viscous losses are the dominant losses for small rigid particles below 3 μm and occur because of shear waves of the oscillating particles in the acoustic pressure field due to differences in densities of the particles compared to the surrounding medium. Shear waves are nonstationary, sliding movements of the liquid layers in the vicinity to the particle. For soft particles, the dominant effect is a thermal loss due to the thermodynamic coupling between pressure and temperature. Scattering mechanisms can be compared to light scattering, where acoustic energy is scattered and reflected from the particles. This mechanism becomes more important for high frequencies over 10 MHz as well as larger particles over 3 μm. Effects of direct molecular interactions of sound waves with either particles or the solvent, which result in dissipation of energy, are called *intrinsic effects*. Minor losses are also caused by oscillations of molecule or particle networks, which are bound by specific and nonspecific interactions and also result in attenuation of sound energy. Charged particles may also cause minor energy dissipations due to transformation of sound energy into electrical energy.

Electroacoustic techniques are different depending on the driving field applied [100]: electrokinetic sonic amplitude (ESA) involves generation of mechanical energy by the driving force of an electric field. Colloid vibration current (CVI) techniques detect resultant electric fields or currents by the vibration of colloid electric double layers, which are evoked by sound energy while disturbing the double layer surrounding the particles and shifting the neighboring cloud of counterions. This displacement evokes a dipole moment and can be measured as a resulting electric field by a two-electrode sensor.

Electroacoustic spectroscopy is used to determine the ζ-potential, an electro kinetic potential in colloidal systems describing the potential difference between the medium and the stationary layer of fluid attached to the dispersed particle. Its value can be related to the stability of colloidal dispersions, indicating the degree of repulsion between adjacent, similarly charged particles.

41.9
Dielectric and Microwave Spectroscopy

Dielectric (or impedance) spectroscopy measures the dielectric properties (permittivity) of a medium as a function of frequency and thus provides information on relaxational dynamics of soft matter in a wide frequency range [101–103]. The fluctuations of the sample dipoles are connected to the dynamics on a molecular scale.

Dielectric spectroscopy supplies information on temperature-dependent relaxational dynamics, for example, of polymeric materials and glass-forming liquids, or dynamic (AC) conductivities of polymeric ion conductors. It yields complementary information compared to neutron scattering, which has a limited frequency range but supplies spatial information, which is not obtainable by dielectric spectroscopy. The characteristic relaxation times vary over many orders of magnitude. Two major properties are typically detected for different application: the spatial distribution of the interrogation field and the interrogation frequency range. The former is used in dielectric spectroscopy and enables measurements of bulk or low-penetration surface information. Frequencies are optimized for a particular sample and typically vary from 10^6 to 10^{11} Hz. Normally, a parallel plate capacitor configuration is used to detect attenuation and phase shift of an electric field passing through a sample. One electrode delivers an excitation signal and another electrode measures the resulting signal after passing in an approximately linear manner through the sample. In an alternative setup, the so-called fringing-field sensing, one electrode delivers the excitation signal and a second electrode is placed in a coplanar manner on the same surface such that the original signal passes nonlinearly through the sample.

Dielectric spectroscopy is a continuously evolving PAT. It was applied to study physical properties of pharmaceutical solutions, colloids, microcapsules, gels, and emulsions. Various types of instrumentation, algorithms, and sensing systems present a wide range of applications and capabilities of this method. Principles and design features of dielectric sensors of pharmaceutical applications have recently been discussed [104, 105]. The static dielectric number of solutions can be used to study the solubility of cosolvent systems, reaction rates of pharmaceutical solutions, and drug stability [79]. Colloidal particles with its surrounding electrical layer influence the dielectric response when aggregation or dissociation of colloidal particles occurs. It thus provides information about particle size in the colloidal solutions. Studies of microcapsules as improved drug delivery systems show relations of the relative dielectric permittivity to the thickness of the capsule wall [106]. Impedance spectroscopy also provides volume fractions of microspheres in solution, which influence dissolution rates of microcapsules [79]. Dielectric spectroscopy was used to give insight into structural and interfacial properties of gels, which are complex systems with multiple dielectric relaxation processes, each reflecting different physical characteristics. The method, for example, was applied to differentiate relaxation of water, ions in cetostearyl alcohol bilayers, as well as migration of ions in channels between these bilayers [107]. It has been used to classify the types of emulsions and microemulsions, which act as effective drug delivery systems for drugs that are insoluble in water. Dielectric properties can be used to detect differences between water-in-oil and oil-in-water emulsions [79].

Dielectric spectroscopy, also applied for on-line property measurement, is a key technique for monitoring cure, where the liquid resin first gels and finally becomes a glassy solid. Owing to the dependence of dielectric properties to viscosity, glass transition temperature, cross-linking of the material, the method is used to monitor gelation and increase of viscosity [107]. Such studies can prevent failure of reaction of resins, use of incorrect proportions of resin components, poor mixing, insufficient curing, or incorrect processing conditions.

Microwave (MW) spectroscopy is a further process analytical method for monitoring and control of industrial processes for solids, liquids, gases as well as suspensions. MW spectroscopy is rotational spectroscopy of molecules in the MW range of 0.25–3.20 GHz of the electro magnetic spectrum. MWs normally penetrate all samples with low dielectric numbers such as glass, plastics, ceramics, and composite materials of several centimeter thicknesses but are reflected by metal surfaces. MW spectroscopy reflects the dielectric behavior of the sample such as the dielectric number. Usually, chemometrics is applied on spectral data. As a noninvasive method, it can be used to analyze large sample volumes to yield integral sample properties from the entire sample [108, 109].

Applications have been reported in areas of batch reaction monitoring, for example, on esterification reaction, the determination of acetonitrile or ethanol concentration in water [110] as well as monitoring drying processes, where MW spectroscopy had advances over NIR spectroscopy owing to a significantly reduced calibration data set [111].

References

1. U. S. Department of Health and Human Services, Food and Drug Administration (FDA), Center for Drug Evaluation and Research (CDER), Center for Veterinary Mediane (CVM), Office of Regulatory Affairs (ORA) (2004) Guidance for Industry, PAT – A Framework for Innovative Pharmaceutical Development, Manufacturing, and Quality Assurance, September 2004, *http://www.fda.gov/downloads/Drugs/GuidanceComplianceRegulatoryinformation/Guidances/UCM070305.pdf.* (accessed 14 June 2013).
2. International Conference on Harmonisation of Technical Requirements for Registration of Pharmaceuticals for Human Use (ICH) (2009) Harmonised Tripartite Guideline Q8(R2), Pharmaceutical Development, August 2009, *http://www.ich.org/fileadmin/Public_Web_Site/ICH_Products/Guidelines/Quality/Q8_R1/Step4/Q8_R2_Guideline.pdf* (accessed 14 June 2013).
3. Bakeev, K.A. (2005) in *Process Analytical Technology: Spectroscopic Tools and Implementation Strategies for the Chemical and Pharmaceutical Industries* (ed K.A. Bakeev), Blackwell, Oxford.
4. Workman, J. Jr., Koch, M., and Veltkamp, D. (2007) Process analytical chemistry. *Anal. Chem.*, **29**, 4345–4364.
5. Workman, J. Jr., Koch, M., Lavine, B., and Chrisman, R. (2009) Process analytical chemistry. *Anal. Chem.*, **81**, 4623–4643.
6. Chew, W. and Sharratt, P. (2010) Trends in process analytical technology. *Anal. Methods*, **2**, 1412–1438.

7. Shoolery, J.N. (1996) in *Encyclopedia of Nuclear Magnetic Resonance* (eds D.M. Grant and R.K. Harris), John Wiley & Sons, Ltd, Chichester, pp. 3907–3916.
8. Evilia, R.F. (2001) Quantitative NMR spectroscopy. *Anal. Lett.*, **34**, 2227–2236.
9. Harris, R.K., Becker, E.D., Cabral de Menezes, S.M., Goodfellow, R., and Granger, P. (2001) NMR nomenclature. nuclear spin properties and conventions for chemical shifts. *Pure Appl. Chem.*, **73**, 1795–1818.
10. Claridge, T.D.W. (2009) High-resolution NMR techniques in organic chemistry, in *Tetrahedron Organic Chemistry*, Elsevier, Oxford.
11. Bayer, E., Albert, K., Nieder, M., Grom, E., and Keller, T. (1979) On-line coupling of high-performance liquid chromatography and nuclear magnetic resonance. *J. Chromatogr.*, **186**, 497–507.
12. Dorn, H.C. (1996) High-performance liquid chromatography nuclear magnetic resonance, in *Encyclopedia of Nuclear Magnetic Resonance*, John Wiley & Sons, Ltd, Chichester, pp. 12070–12085.
13. Albert, K. (ed) (2002) *On-Line LC-NMR and Related Techniques*, John Wiley & Sons, Ltd, Chichester.
14. Maiwald, M., Fischer, H.H., Kim, Y.-K., Albert, K., and Hasse, H. (2004) *J. Magn. Reson.*, **166**, 135–146.
15. Bernstein, M.A., Stefinovic, M., and Sleigh, C.J. (2007) Optimising reaction performance in the pharmaceutical industry by monitoring with NMR. *Magn. Reson. Chem.*, **45**, 564–571.
16. Maiwald, M., Steinhof, O., Bernstein, M., Sleigh, C., Hasse, H. (2008) in: *NMR Spectroscopy in Drug Analysis*, Chapter 8 (ed. Holzgrabe, U.), Amsterdam: Elsevier, pp. 471–492 ISBN: 0444531734.
17. Dalitz, F., Cudaj, M., Maiwald, M., and Guthausen, G. (2012) Process and reaction monitoring by low-field NMR spectroscopy. *Prog. Nucl. Magn. Reson. Spectrosc.*, **60**, 52–70.
18. Dalitz, F., Guthausen, G., and Maiwald, M. (2012) Considerations on the design of flow cells in by-pass systems for process analytical applications and its influence on the flow profile using NMR and CFD. *Chem. Eng. Sci.*, **75**, 318–326.
19. Witt, K. and Posset, T. (2012) Non-destructive filling weight determination of solid drug powder in crimped and non-crimped vials. *Pharm. lnd.*, **74** (5), 826–832.
20. Corver, J., Guthausen, G., and Kamlowski, A. (2005) In-line non-contact check weighing (NCCW) with nuclear magnetic resonance (NMR) presents new opportunities and challenges in process control. *Pharma. Eng.*, **25**, 18–30.
21. Guthausen, A., Guthausen, G., Kamlowski, A., Todt, H., Burk, W., and Schmalbein, D. (2004) Measurement of fat content of food with single-sided NMR. *J. Am. Oil Chem. Soc.*, **81**, 727–731.
22. Dorn, H.C., Glass, T.E., Gitti, R., and Tsai, K.H. (1991) *Appl. Magn. Reson.*, **2**, 9–27.
23. Fischer, H.H., Seiler, M., Ertl, T.S., Eberhardinger, U., Bertagnolli, H., Schmitt-Willich, H., and Albert, K. (2003) *J. Phys. Chem. B*, **10**, 4879–4886.
24. Spraul, M., Freund, A.S., Nast, R.E., Withers, R.S., Mass, W.E., and Corcoran, O. (2003) *Anal. Chem.*, **75**, 1546–1551.
25. Krucker, M., Lienau, A., Putzbach, K., Grynbaum, M.D., Schuler, P., and Albert, K. (2004) Hyphenation of capillary HPLC to microcoil 1H NMR spectroscopy for the determination of tocopherol homologues. *Anal. Chem.*, **76**, 2623–2628.
26. Wensink, H., Benito-Lopez, F., Hermes, D.C., Verboom, W., Gardeniers, H.J., Reinhoudtb, D.N., and van den Berg, A. (2005) Measuring reaction kinetics in a lab-on-a-chip by microcoil NMR. *Lab Chip*, **5**, 280–284.
27. Olson, D.L., Lacey, M.E., and Sweedler, J.V. (1998) *Anal. Chem.*, **70**, 257A–264A.
28. McGill, C.A., Nordon, A., and Littlejohn, D. (2002) Comparison of in-line NIR, Raman and UV-visible spectrometries, and at-line NMR spectrometry for the monitoring of an

esterification reaction. *Analyst*, **127**, 287–292.

29. Nordon, A., Meunier, C., Carr, R.H., Gemperline, P.J., and Littlejohn, D. (2002) Determination of the ethylene oxide content of polyether polyols by low-field H-1 nuclear magnetic resonance spectrometry. *Anal. Chim. Acta*, **472**, 133–140.
30. Nordon, A., McGill, C.A., and Littlejohn, D. (2002) Evaluation of low-field nuclear magnetic resonance spectrometry for at-line process analysis. *Appl. Spectrosc.*, **56**, 75–82.
31. Eiceman, G.A. and Karpas, Z. (2004) *Ion Mobility Spectrometry*, 2nd edn, Taylor & Francis, Boca Raton, FL.
32. Baumbach, J.I. and Eiceman, G.A. (1999) Ion mobility spectrometry: arriving on-site and moving beyond a low profile. *Appl. Spectrosc.*, **53**, 338A–355A.
33. Baumbach, J.I. (2008) Ion mobility spectrometry in scientific literature and in the international journal for ion mobility spectrometry (1998–2007). *Int. J. Ion Mobility Spectrom.*, **11**, 3–11.
34. Baumbach, J.I. (2009) Ion mobility spectrometry coupled with multi-capillary columns for metabolic profiling of human breath. *J. Breath Res.*, **3**, 034001–0340017.
35. Andronov, A.A., Gordin, A.I., Zinchenko, D.I., Levichev, M.Y., Marugin, A.V., Nozdrin, Y.N., and Ustinov, A.V. (2003) Quantum cascade lasers and applications: state-of the-art and prospects. *Radiophys. Quantum Electron.*, **46**, 666–674.
36. Taubman, M.S., Myers, T.L., Cannon, B.D., and Williams, R.M. (2004) Stabilization, injection and control of quantum cascade lasers, and their application to chemical sensing in the infrared. *Spectrochim. Acta, Part A*, **60**, 3457–3468.
37. Gmachl, C., Capasso, F., Sivco, D.L., and Cho, A.Y. (2001) Recent progress in quantum cascade lasers and applications. *Rep. Prog. Phys.*, **64**, 1533–1601.
38. Normand, E., Howieson, I., and McCulloch, M.T. (2007) Quantum-cascade lasers enable gas-sensing technology. *Laser Focus World*, **43**, 90–92.
39. Berden, G., Peeters, R., and Meijer, G. (2000) Cavity ring-down spectroscopy: experimental schemes and applications. *Int. Rev. Phys. Chem.*, **19**, 565–607.
40. Werle, P., Slemr, F., Maurer, K., Kormann, R., Mucke, R., and Janker, B. (2002) Near- and mid-infrared laser-optical sensors for gas analysis. *Opt. Lasers Eng.*, **37**, 101–114.
41. Bein, B.K. and Pelzl, J. (1988) in *Plasma Diagnostics – Surface Analysis and Interactions*, Vol. 2 (eds O. Auciello and D.L. Flamm), Academic Press, New York, pp. 211–326.
42. Van Neste, C.W., Senesac, L.R., and Thundat, T. (2008) Standoff photoacoustic spectroscopy. *Appl. Phys. Lett.*, **92**, 234102.
43. Radziemski, L.J. and Cremers, D.A. (eds) (1989) *Laser-Induced Plasmas and Applications*, Marcel Dekker, New York and Basel.
44. Miziolek, A.W., Paleschi, V., and Schechter, I. (eds) (2006) *Laser Induced Breakdown Spectroscopy*, Cambridge University Press, Cambridge.
45. Cremers, D.A. and Radziemski, L.J. (2006) *Handbook of Laser-Induced Breakdown Spectroscopy*, John Wiley & Sons, Ltd, Chichester.
46. Singh, J.P. and Thakur, S.N. (2007) *Laser-Induced Breakdown Spectroscopy*, Elsevier, Amsterdam.
47. Noll, R. (2012) *Laser-Induced Breakdown Spectroscopy. Fundamentals and Applications*, Springer-Verlag, Berlin, Heidelberg.
48. Winefordner, J.D., Gornushkin, I.B., Correll, T., Gibb, E., Smith, B.W., and Omenetto, N. (2004) Comparing several atomic spectrometric methods to the super stars: special emphasis on laser induced breakdown spectrometry, LIBS, a future super star. *J. Anal. At. Spectrom.*, **19**, 1061–1083.
49. Ashfold, M.N., Claeyssens, F., Fuge, G.M., and Henley, S.J. (2004) Pulsed laser ablation and deposition of thin films. *Chem. Soc. Rev.*, **33**, 23–31.
50. Compagnini, G., Scalisi, A.A., and Puglisi, O. (2003) Production of gold nanoparticles by laser ablation in liquid alkanes. *J. Appl. Phys.*, **94**, 7874–7877.

51. Li, Y. and Qu, S. (2011) Femtosecond laser-induced breakdown in distilled water for fabricating the helical microchannels array. *Opt. Lett.*, **36**, 4236–4238.

52. Tognoni, E., Cristoforetti, G., Legnaioli, S., and Palleschi, V. (2010) Calibration-free laser-induced breakdown spectroscopy: state of the art. *Spectrochim. Acta, Part B*, **65**, 1–14.

53. Gornushkin, I.B., Kazakov, A.Y., Omenetto, N., Smith, B.W., and Winefordner, J.D. (2005) Experimental verification of a radiative model of laser-induced plasma expanding into vacuum. *Spectrochim. Acta, Part B*, **60**, 215–230.

54. Yaroshchyk, P., Body, D., Morrison, R.J.S., and Chadwick, B.L. (2006) A semi-quantitative standard-less analysis method for laser-induced breakdown spectroscopy. *Spectrochim. Acta, Part B*, **61**, 200–209.

55. Babushok, V.I., De Lucia, F.C. Jr., Gottfried, J.L., Munson, C.A., and Miziolek, A.W. (2006) Double pulse laser ablation and plasma: laser induced breakdown spectroscopy signal enhancement. *Spectrochim. Acta, Part B*, **61**, 999–1014.

56. Pasquini, C., Cortez, J., Silva, L.M.C., and Gonzaga, F.B. (2005) Laser induced breakdown spectroscopy. *J. Braz. Chem. Soc.*, **18**, 463.

57. Shuttleworth, S. and Kremser, D.T. (1998) Assessment of laser ablation and sector field inductively coupled plasma mass spectrometry for elemental analysis of solid samples. *J. Anal. At. Spectrom.*, **13**, 697–700.

58. Loebe, K., Uhl, A., and Lucht, H. (2003) Microanalysis of tool steel and glass with laser-induced breakdown spectroscopy. *Appl. Opt.*, **42**, 6166–6173.

59. Panne, U., Neuhauser, R.E., Haisch, C., Fink, H., and Niessner, R. (2002) Remote analysis of a mineral melt by laser-induced plasma spectroscopy. *Appl. Spectrosc.*, **56**, 375–380.

60. Gruber, J., Heitz, J., Strasser, H., Bäuerle, D., and Ramaseder, N. (2001) Rapid in-situ analysis of liquid steel by laser-induced breakdown spectroscopy. *Spectrochim. Acta, Part B*, **56**, 685–693.

61. Noll, R., Bette, H., Brysch, A., Kraushaar, M., Mönch, I., Peter, L., and Sturm, V. (2001) Laser-induced breakdown spectrometry – applications for production control and quality assurance in steel industry. *Spectrochim. Acta, Part B*, **56**, 637–649.

62. Mowery, M.D., Sing, R., Kirsch, J., Razaghi, A., Béchard, S., and Reed, R.A. (2002) Rapid at-line analysis of coating thickness and uniformity on tablets using laser induced breakdown spectroscopy. *J. Pharm. Biomed. Anal.*, **28**, 935–943.

63. Gotfried, J.L., De Lucia, F.C. Jr., Munson, C.A., and Miziolek, A.W. (2008) Standoff detection of chemical and biological threats using laser-induced breakdown spectroscopy. *Appl. Spectrosc.*, **62**, 353–363.

64. Werheit, P., Fricke-Begemann, C., Gesing, M., and Noll, R. (2011) Fast single piece identification with a 3D scanning LIBS for aluminium cast and wrought alloys recycling. *J. Anal. At. Spectrom.*, **26**, 2166–2174.

65. Gurell, J., Bengtson, A., Falkenstrom, M., and Hansson, B.A.M. (2012) Laser induced breakdown spectroscopy for fast elemental analysis and sorting of metallic scrap pieces using certified reference materials. *Spectrochim. Acta, Part B*, **74–75**, 46–50.

66. Gornushkin, I.B., Ruiz-Medina, A., Anzano, J.M., Smith, B.W., and Winefordner, J.D. (2000) Identification of particulate materials by correlation analysis using a microscopic laser induced breakdown spectrometer. *J. Anal. At. Spectrom.*, **15**, 581–586.

67. Hoehse, M., Mory, D., Florek, S., Weritz, F., Gornushkin, I., and Panne, U. (2009) A combined laser-induced breakdown and Raman spectroscopy Echelle system for elemental and molecular microanalysis. *Spectrochim Acta, Part B*, **64**, 1219–1227.

68. Lanza, N.L., Wiens, R.C., Clegg, S.M., Ollila, A.M., Humphries, S.D., Newsom, H.E., and Barefield, J.E. (2010) Calibrating the ChemCam laser-induced breakdown spectroscopy instrument for carbonate minerals on Mars. *Appl. Opt.*, **49**, C211–C217.

69. Zhang, H., Yueh, F.-Y., and Singh, J.P. (1999) Laser induced breakdown spectrometry as a multimetal continuous-emission monitor. *Appl. Opt.*, **38**, 1459–1466.

70. Hahn, D.W. and Omenetto, N. (2010) Laser-induced breakdown spectroscopy (LIBS), part I: review of basic diagnostics and plasma-particle interactions: still-challenging issues within the analytical plasma community. *Appl. Spectrosc.*, **64**, 335A–365A.

71. Hahn, D.W. and Omenetto, N. (2012) Laser-induced breakdown spectroscopy (LIBS), part II: review of instrumental and methodological approaches to material analysis and applications to different fields. *Appl. Spectrosc.*, **66**, 347–419.

72. Potts, P.J. and Webb, P.C. (1992) X-ray fluorescence spectrometry. *J. Geochem. Explor.*, **44** (1–3), 251–296.

73. Longoni, A., Fiorini, C., Guazzoni, C., Buzetti, S., Bellini, M., Strüder, L., Lechner, P., Bjeoumikhov, A., and Kemmer, L. (2005) A novel high resolution XRF spectrometer for elemental mapping based on a monolithic array of silicon drift detectors and on a polycapillary x-ray lens. *X-Ray Spectrom.*, **34**, 439–445.

74. Yonehara, T., Yamaguchi, M., and Tsuji, K. (2010) X-ray fluorescence imaging with polycapillary x-ray optics. *Spectrochim. Acta, Part B*, **65** (6), 441–444.

75. Revenko, A.G. (2007) Specific features of x-ray fluorescence analysis techniques using capillary lenses and synchrotron radiation. *Spectrochim. Acta, Part B*, **62** (6–7), 567–576.

76. Wacker, G., Hanning, S., Janßen, A. *et al.* (2009) Anwendung der RFA zur Bestimmung prozessrelevanter Elemente in Sekundärbrennstoffen. Proceedings of PRORA 2009, Fachtagung Prozessnahe Röntgenanalytik, Berlin, Germany.

77. Ostermann, M., Adamczyk, B., Brenneis, R. *et al.* (2008) In-situ Prozessanalytik im Lichtbogenofen zur Rückgewinnung von Wertstoffen. Proceedings of 4. Kolloquium GDCh/DECHEMA Arbeitskreis Prozessanalytik, Basel, Switzerland.

78. Al-Merey, R., Karajou, J., and Issa, H. (2005) X-ray fluorescence analysis of geological samples: exploring the effect of sample thickness on the accuracy of results. *Appl. Radiat. Isot.*, **62** (3), 501–508.

79. Denker, R., Oosten-Nienhuis, N., and Meier, R. (2008) Sample preparation for x-ray analytics. *Global Cem. Mag.*, **5**, 17–18.

80. Ostermann, M., Kühn, A., Bjeoumikhov, A. *et al.* (2011) Einsatz der röntgenfluoreszenzanalyse in der prozessanalytik. *Tech. Mess.*, **78** (12), 559–568.

81. Docenko, D., Sokolov, A., and Pechersky, A. (2009) On-line XRF measurements of ore composition and coating thickness. Proceedings of PRORA 2009, Fachtagung Prozessnahe Röntgenanalytik, Berlin, Germany.

82. Pilz, K., Heiss, J., Klein, A., Ritter, A., Langhoff, N., Bjeoumikhov, A., Günther, A., and Wedell, R. (2010) Prozessmessverfahren zur onlinebestimmung des zinkgehalts im konverterstaub. *Stahl Eisen*, **11** (130), 93–99.

83. Klein, A. (2008) Online X-ray Elemental Analysis of Coal and Bulky Minerals, IME Kolkata.

84. Mittelman, T. (2005) *Sensing with Terahertz Radiation*, Springer, Berlin.

85. Kimmitt, M.F. (2003) Restrahlen to T-rays – 100 years of terahertz radiation. *J. Biol. Phys.*, **29**, 77–85.

86. Krumbholz, N., Hochrein, T., Vieweg, N. *et al.* (2009) Monitoring polymeric compounding processes inline with THz time-domain spectroscopy. *Polym. Test.*, **28** (1), 30–35.

87. Wietzke, S., Jansen, C., Jordens, C., *et al.*, Industrial applications of THz systems, *Proc. SPIE*, **7385**, 738506. *http://proceedings.spiedigitallibrary.org/proceeding.aspx?articleid=1339973.* (accessed 13 July 2013)

88. Globus, T., Woolard, D., Crowe, T.W., Khromova, T., Gelmont, B., and Hesler, J. (2006) Terahertz Fourier transform characterization of biological materials in the liquid phase. *J. Phys. D: Appl. Phys.*, **39**, 3405–3413.

89. Taday, P.F. (2004) Applications of terahertz spectroscopy to pharmaceutical sciences. *Philos. Trans. R. Soc. London, Ser. A*, **362**, 351–363.

90. Globus, T., Khromova, T., Woolard, D., and Gelmont, B. (2004) Terahertz Fourier transform characterization of biological materials in solid and liquid phases. *Proc. SPIE Int. Soc. Opt. Eng.*, **5268**, 10–18.

91. Wu, H., Heilweil, E.J., Hussain, A.S., and Khan, M.A. (2008) Process analytical technology (PAT): quantification approaches in terahertz spectroscopy for pharmaceutical application. *J. Pharm. Sci.*, **97** (2), 970–984.

92. Wallace, V.P., Taday, P.F., Fitzgerald, A.J., Woodward, R.M., Cluff, J., Pye, R.J. *et al.* (2004) Terahertz pulsed imaging and spectroscopy for biomedical and pharmaceutical applications. *Faraday Discuss.*, **126**, 255–263.

93. Strachan, C.J., Taday, P.F., Newnham, D., Gordon, K., Zeitler, J.A., Pepper, M. *et al.* (2005) Using terahertz pulsed spectroscopy to quantify pharmaceutical polymorphism and crystallinity. *J. Pharm. Sci.*, **94**, 837–846.

94. Fitzgerald, A.J., Cole, B.E., and Taday, P.F. (2004) Nondestructive analysis of tablet coating thicknesses using terahertz pulsed imaging. *J. Pharm. Sci.*, **94**, 177–183.

95. Wallace, V.P., Fitzgerald, A.J., Shankar, S., Flanagan, N., Pye, R., Cluff, J. *et al.* (2004) Terahertz pulsed imaging of basal cell carcinoma ex vivo and in vivo. *Br. J. Dermatol.*, **151**, 424–432.

96. Dukhin, A.S. and Goetz, P.J. (2002) *Ultrasound for Characterizing Colloids*, Elsevier, Amsterdam.

97. Dukin, A.S., Goetz, P.J., Wines, T.H., and Somasudaran, P. (2000) Acoustic and electroacoustic spectroscopy. *Colloids Surf., A*, **173**, 127–158.

98. McClements, D.J. (1991) *Adv. Colloid Interface Sci.*, **37**, 33–72.

99. Hackley, V.A. and Texter, J. (eds) (1998) *Ultrasonic and dielectric Characterization Techniques for Suspended Particulates*, The American Chemical Society, Ohio.

100. Hunter, R.J. (1998) *Colloids Surf., A*, **141**, 37–65.

101. Hippel, A.R. (1954) *Dielectrics and Waves*, John Wiley & Sons, Inc., New York.

102. Kremer, F., Schonhals, A., and Luck, W. (2002) *Broadband Dielectric Spectroscopy*, Springer-Verlag, Berlin.

103. Volko, A.A. and Prokhorov, A.S. (2003) Broadband dielectric spectroscopy of solids. *Radiophys. Quantum Electron.*, **46**, 657–665.

104. Craig, D.Q.M. (1995) *Dielectric Analysis of Pharmaceutical Systems*, Taylor & Francis, London.

105. Mathur, A., Sundara-Rajan, K., Rowe, G., and Manishev, A.V. (2008) Dielectric spectroscopy: choosing the right approach. *Pharm. Technol.*, **9**, 82–93.

106. Sekine, K. and Hanai, T. (1991) Dielectric analysis of PMMA microcapsules containing an aqueous KCl solution to derive a distribution function of the release rate of KCl. *Colloid Polym. Sci.*, **269**, 880–888.

107. Dissado, L.A., Rowe, R.C., and Haidara, A. (1987) The characterization of heterogeneous gels by means of a dielectric technique. 1: theory and preliminary evaluation. *J. Colloid Interface Sci.*, **117**, 310–324.

108. Mulligan, D. (2003) *Cure Monitoring for Composites and Adhesives*, Rapra Technology, Shawbury.

109. Riebe, M.T. and Eustace, D.J. (1990) Process analytical chemistry. an industrial perspective. *Anal. Chem.*, **62**, 65A–71A.

110. Loades, V. and Walmsley, A.D. (2001) Determination of acetonitrile and ethanol in water by guided microwave spectroscopy with multivariate calibration. *Analyst*, **126**, 417–420.

111. Dane, A.D., Rea, G.J., Walmsley, A.D., and Haswell, S.J. (2001) The determination of moisture in tobacco by guided microwave spectroscopy and multivariate calibration. *Anal. Chim. Acta*, **429**, 185–194.

Section XII
Applications 6: Spectroscopy at Surfaces

Handbook of Spectroscopy, Second Edition. Edited by Günter Gauglitz and David S. Moore.

42
Optical Spectroscopy at Surfaces

Georgeta Salvan and Dietrich R. T. Zahn

42.1
Introduction

Optical spectroscopies are commonly not inherently surface sensitive owing to the large penetration depth of light that determines the information depth. Therefore, special experimental arrangements are necessary to achieve the required surface sensitivity. Among the optical characterization tools, Raman spectroscopy is a widely applied technique offering a wealth of information regarding, for example, chemistry at interfaces or electronic properties of interfaces. In order to make Raman spectroscopy surface sensitive, one prerequisite is the employment of resonance effects. Tuning the photon energy of the exciting laser light into an absorption feature of the species to be detected results in a strong signal enhancement and thus allows tiny amounts down to sub-monolayer (ML) coverage to be detected. The characterization of such amounts of material on surfaces usually requires a very clean environment, that is, the application of ultrahigh vacuum (UHV) conditions is needed and the coupling of a UHV chamber to a Raman setup is required. The UHV-Raman system also permits the formation of interfaces to be followed from clean surfaces to thicker films, that is, Raman spectra can be taken continuously during deposition of material. This *in situ* Raman monitoring technique is advantageous compared to *ex situ* Raman measurements as it unfolds the evolution of interface formation. Using the example of organic/inorganic interface formation, namely the UHV deposition of small molecules onto inorganic semiconductors, the capabilities of Raman spectroscopy will be illustrated. Moreover, the deposited organic layers serve as substrates for metal deposition for studying metal/organic semiconductor interfaces. This allows another extremely useful effect for surface/interface characterization to be demonstrated, namely, the surface-enhanced Raman scattering (SERS) effect. The clusters formed during metal deposition induce this effect and the enhanced Raman signal stems from those molecules in the intimate vicinity of the metal. Therefore, this effect is extremely sensitive to the interface formation. More widely used approaches to achieve SERS are based on molecules deposited on nanostructured substrates or on molecules in colloidal solutions, which are not in the focus of this review. Readers

Handbook of Spectroscopy, Second Edition. Edited by Günter Gauglitz and David S. Moore.

interested in the progress made in these fast developing branches of the SERS community are advised to consult recent reviews (e.g., [1–3]).

A widely used thin-film characterization technique, based on the change in polarization on reflection from the thin film surface is spectroscopic ellipsometry (SE). Under favorable conditions [4, 5] even sub-ML resolution can be attained for inorganic semiconductors [4] as well as for organic molecules [5] on semiconductor surfaces. A survey of methods to characterize thin absorbing films with SE appeared recently [6].

Reflection anisotropy spectroscopy (RAS), also known as *reflection difference spectroscopy* (*RDS*) was originally developed for the characterization of inorganic semiconductor surfaces and their reconstructions. RAS gains its surface sensitivity by measuring the difference in the reflection coefficients for two perpendicular directions within the sample surface plane. Considering the cubic symmetry of the most important semiconductors, the bulk contribution is eliminated and only surface contributions remain. Also, this technique can be coupled to a growth apparatus in order to monitor the evolution of the RAS spectra during growth. Especially, RAS was not only applied for UHV-deposition processes but also during gas phase processes such as metal-organic vapor phase deposition or even to study solid/liquid interfaces. This illustrates an important advantage, namely, the applicability of optical spectroscopies in environments other than UHV, compared to electron-based spectroscopy techniques that depend on UHV conditions. More recently, RAS has also been applied to the characterization of organic/inorganic interface formation for which an example will be given.

Impressive interface sensitivity was achieved using X-ray magnetic circular dichroism (XMCD). The absorption of circularly polarized X-rays in the soft-X-ray energy range is different for parallel and antiparallel orientation of the helicity of the incident light with respect to the magnetization direction of the sample [7]. This synchrotron-based technique was routinely applied to measure the magnetization of thin ferromagnetic layers on nonmagnetic substrates. Recently, it was applied to measure the exchange coupling of paramagnetic molecules to magnetic substrates (e.g., [8]).

Methods employing high electromagnetic field strengths that generate a nonlinear response are increasingly used to characterize surfaces and interfaces (see e.g., [9] for a recent review). Second harmonic generation (SHG), for example, is sensitive to surface and interface symmetry, and many experiments have exploited this. Extensive reviews of the application of SHG to semiconductor [10] and molecular interfaces were published [11]. The electric-field-induced optical second harmonic generation (EFISHG) was exploited to map the electric field profile along the channel region at the gate-insulator-active layer interface in pentacene-based organic field effect transistors (OFETs) (see, e.g., [12]). Time-resolved EFISHG measurements were furthermore employed to study the charge carrier dynamics in pentacene OFETs [13].

The development of reliable femtosecond laser systems has, on the other hand, driven the application of sum-frequency generation (SFG) to probe vibrational properties at surfaces and interfaces. The main advantages of SFG compared to conventional infrared (IR) spectroscopies is its surface sensitivity, arising from the detection at the sum-frequency wavelength. This allows the use of much more sensitive detectors operating in or near the visible region and the time resolution associated with short laser pulses. Comprehensive reviews of SFG can be found in [14, 15]. SFG vibrational spectra, in combination with theoretical simulations based on density functional theory (DFT), were successfully used to estimate the molecular orientation of self-assembled MLs [16]. Simultaneous SFG vibrational spectra and electrical measurements of pentacene-based OFETs showed a strong correlation between the dependence of the SFG nonresonant background on gate voltage on one hand and the electronic mobility on the other hand, suggesting that a common molecular structural packing element determines the magnitude of both the electronic mobility and higher order nonlinear optical susceptibilities in oligomeric thin films [17]. Further reports on the application of vibrational SFG to OFETs characterization are summarized in [18]. Elliott, Horvath, and Gordon [18] also present an up-to-date review of various vibrational spectroscopies used to probe various molecule-based devices.

The research interest in organic semiconductors is driven by manifold applications such as organic light-emitting devices (OLEDs), OFETs, and organic photovoltaic cells (OPVCs). Organic semiconductors could be devided in two groups containing either polymers or so-called small molecules. This chapter deals exclusively with the application of optical spectroscopies for the study of molecules within the latter class, demonstrated using two examples from the class of perylene derivatives, 3,4,9,10-perylene-tetracarboxylic-dianhydride (PTCDA) and *N*,*N*′-dimethyl 3,4,9,10-perylene-tetracarboxylic diimide (DiMe-PTCDI). The molecular structure of these two molecules is quite similar. Still, the ‘‘minor’’ change in the functional groups of these molecules has dramatic effects on both molecular orientation on inorganic substrates and interfacial chemistry when an interface with the organic semiconductor is formed by depositing a metal on top of the organic semiconductor. These dramatic effects motivate the choice of these two molecules. They are excellently suited to demonstrate how minor changes of molecular structures can be utilized to influence interfacial and layer properties. At the same time, they allow the sensitivity of the major experimental techniques used in this review, Raman spectroscopy and RAS, to be benchmarked.

PTCDA is an archetype organic molecule that has already been studied on a variety of inorganic substrates by a large number of experimental and theoretical methods [e.g. 19–22], with scanning probe techniques being the ones most widely used. The most commonly used substrate materials have been metals, highly oriented pyrolytic graphite and insulators (NaCl, SiO_2, Al_2O_3) [19], while investigations using the more reactive surfaces of common inorganic semiconductors such as silicon and gallium arsenide (GaAs) have been scarce. In this review, GaAs is the substrate of choice owing to the emphasis in our work on inorganic/organic semiconductor heterostructures.

This chapter is organized as follows. Section 42.2 introduces the molecules and their properties with particular emphasis on the solid phase as molecular crystals, the sample preparation, and the experimental methods, that is, Raman and RAS.

Section 42.3 deals with the initial adsorption of the molecules on GaAs surfaces studied by RAS and Raman spectroscopy, while Section 42.4 focuses on Raman spectroscopy investigations of metal deposition onto organic layers.

42.2
Experimental Methods and Theoretical Calculations

42.2.1
Properties of Perylene Derivatives

The two molecules that are the object of this work belong to the class of heteroaromatic systems, more specifically to the group of perylene derivatives (Figure 42.1): PTCDA and DiMe-PTCDI.

PTCDA is one of the most intensively studied organic molecular semiconductors, for example, for investigations of structural ordering during growth. This is because PTCDA is thermally stable, and very pure, well-ordered thin films can be fabricated by organic molecular beam deposition (OMBD) on various inorganic substrates. The structural formula of PTCDA is shown in Figure 42.1. PTCDA has a planar rectangular geometry consisting of a perylene core (20 carbon atoms, 8 hydrogen atoms) terminated by two electron-withdrawing anhydride (O=C–O–C=O) groups. Three C_2 axes of symmetry can transform the molecule into itself upon rotation by 180°, three planes show reflection symmetry ($\sigma(xy)$, $\sigma(xz)$, $\sigma(yz)$) and an inversion center I is present. The symmetry of all molecular orbitals can be described by the irreducible representations of the D_{2h} point group. All the symmetry classes that are even/odd with respect to the inversion center will be labeled with the indices *g*(*gerade*)/*u*(*ungerade*). Following Suzuki [23], the orbitals are usually denoted by lower case letters, and states by capital letters. As an example, the symmetry of HOMO (highest occupied molecular orbital) is $a_u(xyz)$, that of LUMO (lowest unoccupied molecular orbital) is $b_{1g}(yz)$, and the corresponding states are A_u and B_{1g}. All states are singlet and the usual notation found in literature for the

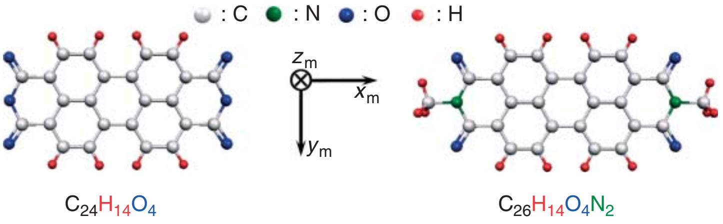

Figure 42.1 The chemical structure of PTCDA and DiMe-PTCDI. The molecular coordinate system is defined such that the x_m and y_m axes are parallel to the long and short axes of the molecules, respectively, and the z_m axis is perpendicular to the molecular planes. The molecular mass is 392 atomic mass units (amu) and 418 amu for PTCDA and DiMe-PTCDI, respectively. Adapted with permission from Ref. [24]. Copyright (2007) American Chemical Society.

corresponding vibronic (electronic plus vibrational) states is S_0 for HOMO, S_1 for LUMO, and S_2 for the next excited state accessible via a dipole-allowed transition. E_{0-0} designates the transition between the ground vibrational states of the electron ground state and first excited state.

DiMe-PTCDI is very similar to PTCDA, and it consists of 26 carbon atoms, 14 hydrogen atoms, 4 oxygen atoms, and 2 nitrogen atoms. The replacement of the bridging oxygen atom of the anhydride group with the three-dimensional methylimide group leads to a deviation from the planar geometry. The molecular structure is also shown in Figure 42.1. Two relative arrangements of the methyl groups are possible: in one of them the hydrogen atoms face each other (C_{2v} molecular symmetry), in the other they are rotated by 180° such that the molecule has an inversion center (C_{2h} symmetry). The electronic levels and vibrational frequencies are not influenced by the difference in the geometry; therefore, the C_{2h} group will only be considered further on for the ease of comparison with PTCDA.

The fact that perylene derivatives often grow in a well-ordered, sometimes even in a quasiepitaxial mode, when thermally evaporated under vacuum conditions was experimentally verified on a variety of substrates ranging from metals to ionic insulators. An exhaustive review was made by Forrest in 1997 [19]. In most cases, the monoclinic crystallographic system ($P2_1/c(C_{2h}{}^5)$) is preferred. For PTCDA two polymorphs are reported [19], whereas for DiMe-PTCDI only one crystal structure is known so far. PTCDA molecules were found to lie almost flat on the substrates [19].

Both molecular crystals have two molecules per unit cell arranged in a herringbone packing in the (102) lattice planes. The inclination of the molecular plane with respect to the (102) plane amounts to $\sim 5^\circ$ for PTCDA [25] and $\sim 8^\circ$ for DiMe-PTCDI (calculated from crystal data [26]). The distance between adjacent planes is ~ 3.2 Å, which is small compared to the other lattice constants. This causes fairly strong interactions of the π-electron systems within the stacks perpendicular to (102) plane.

Both HOMO and LUMO of perylene derivatives are mainly governed by the extended conjugated π-electron system composed of atomic $2p_z$ wave functions [27, 28] of the perylene core. The experimental ultraviolet–visible (*UV–vis*) absorption spectra of isolated molecules (monomer) obtained from diluted solutions of PTCDA in dimethyl-sulfoxide (DMSO) and of DiMe-PTCDI in chloroform are very similar in terms of line shape [29]. In both cases, the vibronic progression of the S_0–S_1 transition with the E_{0-0} peak at 2.38 eV (PTCDA) and 2.36 eV (DiMe-PTCDI) dominates the spectra. It must be noted, however, that the E_{0-0} values are affected by the dielectric constant of the solvent. The E_{0-0} values for PTCDA monomers in an inert environment was determined by means of laser-induced fluorescence of PTCDA in He droplets to be 2.6 eV [30]. A comprehensive analysis of the PTCDA monomer absorption was carried out by Scholz *et al.* [31] taking into account the participation of totally symmetric vibrations in the vibronic progression.

In thin films grown on quartz substrates, the E_{0-0} (S_0–S_1) transitions are red-shifted compared to monomers in solution and the first absorption peaks appear at 2.22 eV (PTCDA) and 2.16 eV (DiMe-PTCDI) (Figure 42.2). Moreover, the broadening is large so that the individual vibronic peaks are not resolved. The same holds for

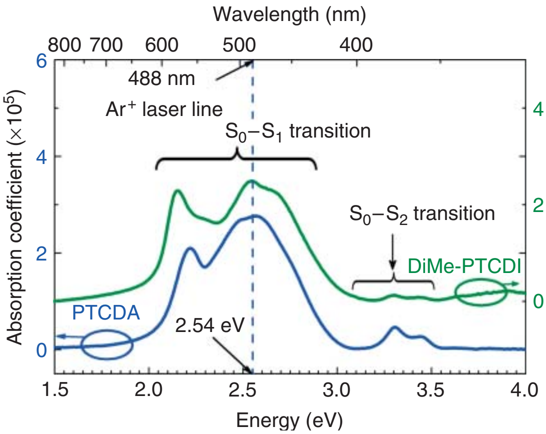

Figure 42.2 Absorption spectra of PTCDA (bottom) and DiMe-PTCDI (top) films (50 nm each) deposited on quartz substrates at RT. The energy position of the excitation line used in Raman experiments is indicated by the dashed vertical line. Adapted with permission from Ref. [24]. Copyright (2007) American Chemical Society.

the S_0-S_2 transition, the dipole of which is oriented along the short molecular axis y_m. The change in absorption line shape of films (crystal) compared to monomers in solution is known as *crystallochromy* and was observed for a large number of perylene derivatives [29]. For PTCDA, it was shown that this change can be related to the transfer of Frenkel excitons between neighboring molecules [31], considering a regular arrangement of the molecules in the crystalline domains having finite size.

42.2.2
Sample Preparation

42.2.2.1 Organic Molecular Beam Deposition (OMBD)

The experiments described in this chapter focus on thin films of PTCDA and DiMe-PTCDI grown on GaAs(100) by OMBD. The PTCDA material was purchased from Lancaster Synthesis, while the DiMe-PTCDI material was purchased from Sensient Imaging Technologies GmbH. Each material was further purified by double sublimation at 310 °C for PTCDA and 300 °C for DiMe-PTCDI under high vacuum ($\sim 10^{-6}$ mbar) and then filled into a quartz crucible mounted in a Knudsen cell. Before the evaporation of the organic material, the Knudsen cell was thoroughly degassed for a few hours at 200 °C. Organic thin films were prepared using OMBD from the Knudsen cells operated at approximately 280 °C for the two organic materials. During OMBD, the GaAs(100) substrates were kept at room temperature (RT). The organic films were deposited at a rate of $\sim 0.2\,\text{nm min}^{-1}$ as monitored by a quartz crystal microbalance located in the vicinity of the sample. A calibration of the microbalance was performed by correlating the frequency shift to the thickness determined by means of atomic force microscopy (AFM). The thickness of the organic coverage varies from submonolayer to 15 nm thick films. We define the thickness of one monolayer (ML) as the amount of PTCDA molecules ($7.6 \times 10^{13}\,\text{cm}^{-2}$) that covers the entire surface assuming flat-lying PTCDA molecules: 1 ML $\cong$ 0.32 nm.

The deposition was interrupted for the Raman and the RAS measurements at certain thicknesses.

42.2.2.2 **Metal Deposition**

The metals were evaporated from boron-nitride Knudsen cells kept at 380 °C for Mg, 830 °C for In, and 930 °C for Ag onto the organic films. Before use, all evaporation sources were thoroughly degassed. The metal was deposited at a rate of approximately 1.6 nm min^{-1} for Ag and 2 nm min^{-1} for In and Mg, in a stepwise manner. The amount of metal deposited onto the sample was monitored using a quartz crystal microbalance.

42.2.3
Reflection Anisotropy Spectroscopy

RAS, also called *reflectance difference spectroscopy*, is an optical technique developed originally by Aspnes [32] for real-time, *in situ* monitoring of semiconductor growth [33–35]. More recently, RAS was used to characterize the surface optical properties of metals [36–39] and even to monitor the growth of different organic molecular systems on metal surfaces [40–42] as well as on semiconductor surfaces [43, 44]. When applied to the investigations of the molecular film growth, RAS allows information on the bonding nature of the molecules on surfaces [45, 46] to be extracted as well as for the determination of the molecular orientation [40, 47, 48]. A complementary technique, differential reflectance spectroscopy (DRS) has also been used to investigate the growth of molecular films, especially on high-symmetry substrate surfaces (see, e.g., [49]), where the application of the RAS technique is limited because of the low signal level.

In the RAS technique, the difference in normal incidence in reflection for light linearly polarized (Figure 42.3) along two orthogonal directions in the sample surface as a function of photon energy is measured. In, for example, cubic materials where the bulk is optically isotropic, the RAS signal vanishes because of a cancellation of the bulk contribution by symmetry.

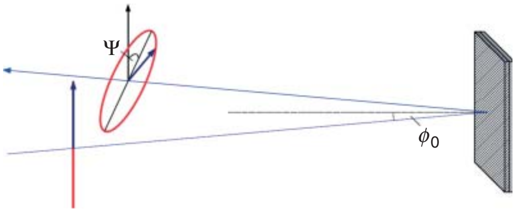

Figure 42.3 Schematic picture of the light propagation in a RAS experiment. The incidence angle ϕ_0 and the polarization states of the light beams before and after reflection on the surface are indicated.

The RAS signal, as defined by Eq. (42.1), measures the difference in reflectivity along two orthogonal axes.

$$\frac{\Delta r}{r} = \mathrm{Re}\left(\frac{\Delta r}{r}\right) + i\ \mathrm{Im}\left(\frac{\Delta r}{r}\right) = 2\frac{r_x - r_y}{r_x + r_y} \tag{42.1}$$

As the RAS measurement is performed at near-normal incidence, the ratio of Fresnel coefficients can be written as follows:

$$\rho = \frac{r_\mathrm{p}}{r_\mathrm{s}} = \frac{r_x}{r_y} \tag{42.2}$$

In the case of extremely small anisotropies, for $\Delta r \ll 1$, the RAS signal becomes

$$\begin{aligned} \mathrm{Re}\left(\frac{\Delta r}{r}\right) &\cong 1 - |\rho| = 1 - \tan\psi \\ \mathrm{Im}\left(\frac{\Delta r}{r}\right) &\cong 1 - \arg\rho \end{aligned} \tag{42.3}$$

For the *in situ* RAS measurements, a spectrometer similar in design to that described by Aspnes [32] (Figure 42.4) was employed. The spectrometer was operated at near-normal incidence in the photon energy range from 1.8 to 5.3 eV. The spectra were recorded by measuring the relative reflectance difference of the sample in two directions corresponding to the [−110] and [110] directions in the surface plane of GaAs(001).

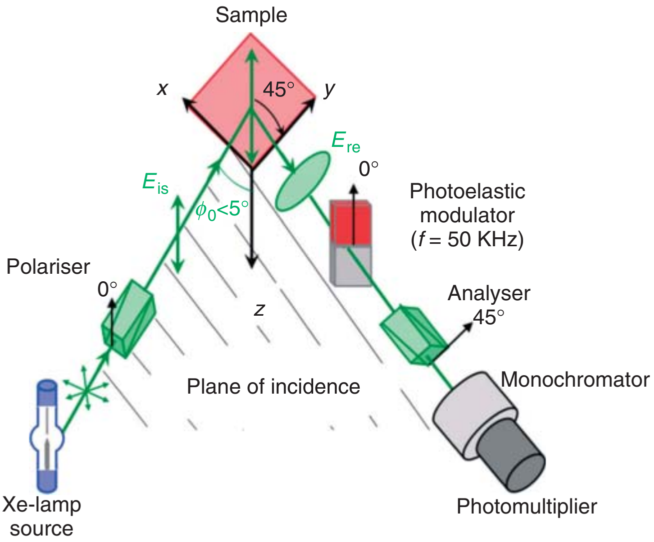

Figure 42.4 A general scheme of a RAS setup. The incident linearly *s*-polarized light (with the direction perpendicular to the plane of incidence) reflects from the sample elliptically polarized. The transmission axes of input polarizer and photoelastic modulator coincide. The transmission axis of analyzer is rotated by 45° with respect to the plane of incidence.

42.2.4
Raman Spectroscopy

In its classical description, Raman scattering is treated as the radiation of light produced by a time-dependent dipole $M(t)$, induced in a molecule by the incident electromagnetic light and modulated by the molecular vibrations. The highly monochromatic incident light required in Raman spectroscopy is provided by laser sources having a light frequency ν_L usually much larger than the vibrational frequency ν_j involving the motions of nuclei. Therefore, only electrons can respond to the external electromagnetic field. The dipole moment induced in the molecule can be written as

$$M(t) = \alpha(t) \cdot E(t) + {}^1\!/_2\beta(t) \cdot E^2(t) + \cdots \tag{42.4}$$

Here, $E(t) = E_L \cdot \cos(2\pi\nu_L t)$ is the electric field component of the incident light with the amplitude E_L, α is the electronic polarizability of the molecule (or susceptibility in inorganic crystals), and β is the hyperpolarizability, which is responsible for the hyper-Raman effect.

In general, the direction of the induced dipole M does not coincide with that of the electric field. Therefore, the polarizability in the relation $M = \alpha\ E$ must be a second-rank tensor:

$$\begin{pmatrix} M_x \\ M_y \\ M_z \end{pmatrix} = \begin{pmatrix} \alpha_{xx} & \alpha_{xy} & \alpha_{xz} \\ \alpha_{yx} & \alpha_{yy} & \alpha_{yz} \\ \alpha_{zx} & \alpha_{zy} & \alpha_{zz} \end{pmatrix} \begin{pmatrix} E_x \\ E_y \\ E_z \end{pmatrix} \tag{42.5}$$

The matrix constructed with the elements of the polarizability tensor derived with respect to the normal coordinate q_j of the vibration j is denoted as Raman or scattering tensor:

$$\delta\alpha^j = \begin{pmatrix} \alpha^j_{xx} & \alpha^j_{xy} & \alpha^j_{xz} \\ \alpha^j_{yx} & \alpha^j_{yy} & \alpha^j_{yz} \\ \alpha^j_{zx} & \alpha^j_{zy} & \alpha^j_{zz} \end{pmatrix} q_j \tag{42.6}$$

where

$$\delta\alpha^j_{\eta\sigma} = \alpha^j_{\eta\sigma} q_j = \left(\frac{\partial\alpha_{\eta\sigma}}{\partial q_j}\right)_0 q_j$$

Taking into consideration the wave-particle duality of the light, Raman scattering processes involve at least two quanta acting instantaneously (scattering time is on the order of 10^{-14} to 10^{-15} s) with the conservation of energy and momentum between the initial and final states of the light-matter system:

$$h\nu_L = h\nu_S \pm h\nu_j(k_j) - \text{energy conservation} \tag{42.7}$$

$$\mathbf{k}_L = \mathbf{k}_S \pm \mathbf{k}_j - \text{momentum conservation} \tag{42.8}$$

Here $h\nu_{L,S}$ and $\mathbf{k}_{L,S}$ are the energy and momentum of the incident (L) and scattered (S) light. $h\nu_j$ and $\mathbf{k}_j$ are the energy and momentum related to a transition between

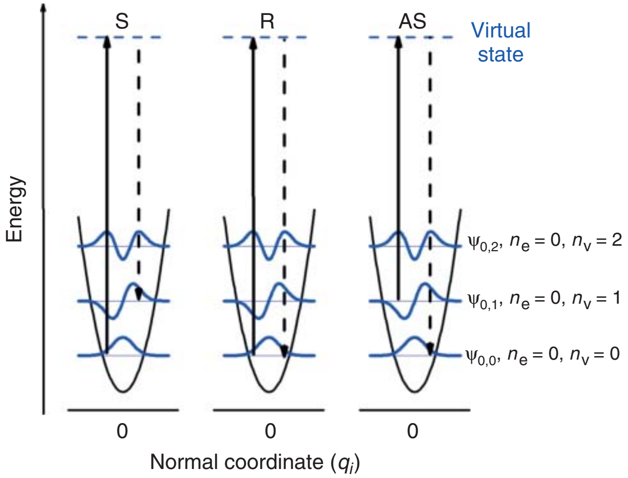

Figure 42.5 Comparison of energy diagrams for scattering processes: Raman Stokes (S), Rayleigh (R), and Raman anti-Stokes (AS). Each energy level of the harmonic oscillators is labeled with the electronic quantum number (n_e) and the vibrational quantum number (n_v).The energy of the exciting and emitted photon is indicated by a continuous and by a dash-dotted arrow, respectively. Adapted with permission from Ref. [24]. Copyright (2007) American Chemical Society.

the vibrational states of a normal vibration *j*. For a visualization of the energy diagram of the processes, see Figure 42.5.

In an elastic Rayleigh scattering process, a photon having the same energy as the incident one is emitted and the molecule/crystal remains in the initial vibrational state. In the case of an inelastic Raman process, the energy of the emitted photon is not the same as that of the impinging one and there is a net change in the vibrational state of the molecule. The Stokes process brings the molecule into a higher vibrational state, and the energy of the emergent photon is lower than ν_L (Figure 42.5). During the anti-Stokes (AS) process, the molecule suffers a transition to a lower energy vibrational state and the emitted photon has a higher energy compared to the incident one. Typically, the intensity of the Rayleigh line is about 10^{-3} of the incident light intensity, while the Raman bands are at least another factor 10^3 weaker. As the population of the ground vibrational state is higher by a Boltzmann factor compared to that of the first excited state, Stokes processes are more probable than AS ones [50]. Therefore, the more intense Stokes Raman spectrum on the low-energy side of the exciting line is usually recorded.

For PTCDA and DiMe-PTCDI, the excitation light (488 nm line of an Ar^+ laser) for the Raman spectroscopy experiments throughout this work falls in the S_0–S_1 absorption band (Figure 42.2). This provides favorable conditions for the resonant Raman effect. As the S_0–S_1 transition dipole moment lies along the x_m axis, mainly the vibrations with a large R_{xx} component of the Raman tensor will be enhanced during the process. For PTCDA, this condition is fulfilled by the 19 vibrations originating from the A_g modes of the isolated molecule. In the case of DiMe-PTCDI, only those A_g modes with low off-diagonal components in the Raman tensor will be resonantly enhanced by the 488 nm excitation line, that is, those modes preserving the rectangular symmetry of the perylene core. Therefore, a similar number of vibrations are expected to occur in the resonant Raman spectra of PTCDA and DiMe-PTCDI.

The total number of degrees of freedom associated with internal vibrations is $Z{\cdot}(3{\cdot}N\text{-}6)$, with Z being the number of molecules in the crystal unit cell. The remaining $6{\cdot}Z$ degrees of freedom determine the orientation of the Z molecules in space and can describe movements of entire molecules, that is, lattice vibrations. These vibrations will be termed as *external modes*, or simpler *phonons*. As in inorganic crystals, three of the phonons have an acoustic character. From the remaining $6{\cdot}Z-3$ of optical origin, three have a translational character and the rest involve rotations of the rigid molecules around their fixed axes. The symmetry of external vibrations is determined by irreducible representations of the crystal space group. As both PTCDA and DiMe-PTCDI belong to the same factor group with $Z = 2$, they have the same representation for the external modes:

$$\Gamma_{\text{ext}} = 3A_g + 3B_g + 3A_u + 3B_u \tag{42.9}$$

Six of the optical phonons are symmetric with respect to the inversion center of the unit cell and are Raman active and those with B_u symmetry are IR active. The acoustic phonons have A_u symmetry.

The broadening of the Rayleigh band is dominated by the spectrometer resolution and can thus serve for the determination of the experimental resolution. The line shape of a Stokes/AS band originates from the limited lifetime of the vibrations convoluted with the instrumental resolution. Generally, it can be described by a Lorentz function convoluted with a Gaussian function. When the width of the Gaussian function is small enough, the line shape of Raman bands can be approximated by a Lorentz function. Unless otherwise specified, the Raman spectra throughout this work were fitted with Lorentzian functions using a least square error algorithm.

The samples investigated by means of Raman spectroscopy were prepared in a UHV chamber (base pressure 2×10^{-10} mbar), which also serves as the analysis chamber. It is optically coupled to a Raman spectrometer allowing *in situ* measurements and *online* growth monitoring to be performed. The Raman spectra shown in this work were excited with the 488 nm (2.54 eV) emission line of an Ar^+ laser. The scattered light is collected by a Dilor XY 800 triple monochromator operated in the subtractive mode and equipped with a multichannel charge-coupled device detector. The spectral resolution ranged from 2 to $\sim$3.5 cm^{-1} as determined from the full width at half maximum (FWHM) of the Rayleigh line.

For the *in situ* measurements, the angle between the incident and scattered light is fixed by the position of the corresponding UHV windows. The sample surface was always oriented parallel to the collection window, that is, the scattered light was collected in the direction parallel to the sample normal. The incidence angle was 30°. The diameter of laser light focused on the sample was $\sim$300 μm and the collection angle was $\sim$18°.

The laser power was measured in front of the UHV window. Typical power values were in the range from 50 to 100 mW. The power densities lie below the damage threshold of the absorbing PTCDA and DiMe-PTCDI films and crystals in all configurations used.

Two polarization configurations were used in the present work. The polarization of the analyzer was always kept the same and only the polarization of incident light was rotated. For example, ''crossed polarization'' means that the electric field vector of the incident light was in the plane of incidence and the electric field vector of the analyzed scattered light was perpendicular to it; ''parallel polarization'' means that both electric field vectors are perpendicular to the plane of incidence and hence parallel to the sample surface. If the polarization configuration is not specified in the text, it means that the polarization of the scattered light was not analyzed.

As the incidence angle for the *in situ* measurements is rather small (30°), this quasi-backscattering geometry will be denoted in all cases according to the Porto notation, that is, $z(yx)\bar{z}$ and $z(xx)\bar{z}$ for the parallel and perpendicular polarization configurations, respectively. Here, z and $\bar{z}$ indicate that the direction of the incident and analyzed scattered light, respectively, are parallel to the sample surface normal, while x and y denote the direction of the electric field vector of incident and analyzed scattered light, respectively.

42.2.4.1 **Calculation of Vibrational Frequencies**

Vibrational frequencies are computed by determining the second derivatives of the energy with respect to the Cartesian nuclear coordinates and then transforming to mass-weighted coordinates. In general, DFT methods slightly overestimate vibrational frequencies [51]. Therefore, it is common practice to introduce scaling factors for the frequencies of 0.95–0.99 in order to get a lower root-mean-square error between calculated and experimental modes. However, in some cases, calculated modes can match experimental values or even underestimate them slightly. As the situation is rather complicated for oxygen-containing compounds such as PTCDA and DiMe-PTCDI, no general scaling for the calculated mode frequencies was performed. The relative order of the Raman-active and IR-active modes calculated using the 6-31G(d) basis set corresponds well to the ordering of the experimental frequencies. However, the smaller 3-21G basis set results in the best agreement with the experimental findings in terms of the root-mean-square deviations [51]. As it also requires less calculation time, in particular for larger systems such as PTCDA + Si, the 3-21G basis was used for all frequency calculations within this work.

42.2.4.2 **Vibrational Properties of *PTCDA***

The first vibrational spectra of PTCDA films were reported in 1987 by Akers *et al.* [52] who proposed an empirical assignment of internal modes. Several theoretical works were devoted in recent years to the study and identification of the vibrational modes. Scholz *et al.* [27] used a DFT code and compared the frequencies of the calculated A_g modes with those observed in thin PTCDA films. A similar DFT time-dependent method was used in the Gaussian 98 [53] package with several basis sets for the molecular wavefunctions. The correspondence between the resulting Raman-active modes and the experimental ones is discussed in detail in Ref. [28]. However, the calculations were all performed for nonresonant conditions, while the experimental spectra of films were obtained in resonance; therefore, a direct correspondence between the calculated cross sections and the experimental ones must be considered with care.

Polarization-dependent measurements performed on a single crystal using the 488 nm (2.54 eV) Ar^+ line enabled recently the first observation of the Davydov splitting in this system [54]. The Raman spectra from Ref. [54] are shown in Figure 42.6. For the determination of the Raman mode frequencies and intensities in the spectra shown in Figure 42.6, a least square fitting algorithm with Lorentzian peaks was employed. The Raman tensor for the A_g component of the Davydov doublet has three diagonal components of different magnitude and nondiagonal components, while the tensor of the B_g mode has only nondiagonal components [54]. For the experimental geometry employed by Tenne *et al.* [54], the B_g bands appear only in the crossed polarization geometry $z(yx)\bar{z}$, while the A_g modes are present in both configurations depending on the magnitude of their Raman tensor components.

Table 42.1 summarizes the assignment of the PTCDA modes observed under resonant conditions. The second and the third columns contain the frequencies of Davydov components observed in a crystal [54], while the fourth column gives the calculated frequencies in a free molecule [28]. The last two columns describe the symmetry of the corresponding vibrations in the isolated molecule and which part of the molecule is predominantly involved. As depicted in Figure 42.7, a PTCDA

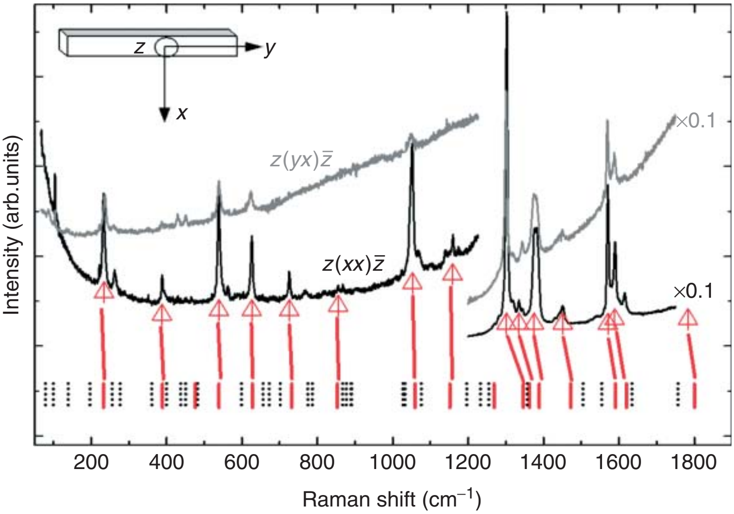

Figure 42.6 Raman spectra of a PTCDA single crystal recorded at RT in crossed (gray line) and parallel (black line) polarization configurations. The triangles represent experimental frequencies of A_g modes and the vertical lines represent calculated frequencies of A_g (thick lines) and B_g (dotted lines) modes.

Table 42.1 Vibrational modes for a PTCDA single crystal [54] and calculated vibrational properties for an isolated molecule using B3LYP:3-21G basis set of Gaussian 98.

PTCDA	Raman shift (cm^{-1})		B3LYP: 3-21G	Perylene* 0.8	Symmetry	Dominant character
	(*xx*)	(*yx*)	(cm^{-1})	(cm^{-1})		
External modes		37		32	B_g	Libronic
	41			42	A_g	
	60			67	B_g	
	75			75	A_g	
		88		81	B_g	
	106			96	A_g	
Internal modes	232.9	236.2	233		A_g	Breathing along x_m
	262.2	259.3	255		B_{3g} (xy)	$\nu_{C=O}$
	388.2	387.6	389		A_g	δ_{C-O-C}, $\delta_{C=O}$
	—	430	437		B_{3g} (xy)	$\delta_{C-C,}$ δ_{C-O-C} in-plane
	—	451	450		B_{2g} (yz)	$\delta_{C-O-C,}$ δ_{C-C} out of plane
	538.6	539.1	539		A_g	ν_{C-C} radial
	562	—	598		B_{3g} (xy)	δ_{C-C}, δ_{C-H}
	625.6	623.3	627		A_g	δ_{C-O-C}, $\delta_{C-C,}$ ν_{C-C} tangential
	725.7	—	732		A_g	δ_{C-C}, δ_{C-H}, δ_{O-C-C}
	855	—	853		A_g	δ_{C-C}, δ_{C-H}
	1052	1043.5	1059		A_g	δ_{C-O-C}, δ_{C-C}, δ_{C-H}
	1072	—	1075		B_{3g} (xy)	δ_{C-C}, δ_{C-H}
	1141	—	1196		B_{3g} (xy)	δ_{C-H}, δ_{C-C-C}
	—	1149	1151		A_g	δ_{C-H}, δ_{C-O-C}
	1159	—	1232		B_{3g} (xy)	δ_{C-H}
	1302.3	1300.6	1346		A_g	δ_{C-H}
	1321	—				
	—	1349	1356		B_{3g} (xy)	δ_{C-C}
	1335	—				
	1375.4	1373	1363		A_g	δ_{C-H}
	1383.6	1381.8	1389		A_g	δ_{C-H}, ν_{C-C}
	1451	—	1472		A_g	δ_{C-H}, ν_{C-C}
	1572	1585	1591		A_g	ν_{C-C}, δ_{C-H}
	1589.1	1588.3	1620		A_g	ν_{C-C}, δ_{C-H}
	1615	—	1634		B_{3g} (xy)	δ_{C-C} along short axis
	1783	—	1800		A_g	$\nu_{C=O}$

Adapted with permission from Ref. [24]. Copyright (2007) American Chemical Society.

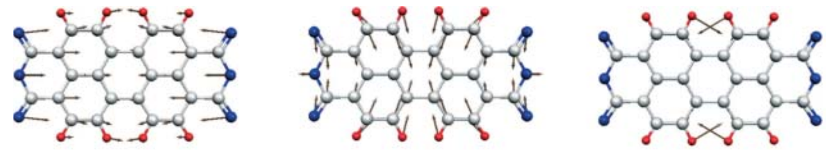

(a) Exp. 232.9 cm^{-1} Calc. 233 cm^{-1}

(b) Exp. 538.6 cm^{-1} Calc. 539 cm^{-1}

(c) Exp. 1302.3 cm^{-1} Calc. 1346 cm^{-1}

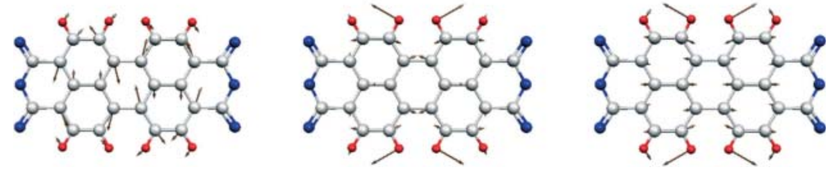

(d) Exp. 1321/1335 cm^{-1} Calc. 1356 cm^{-1}

(e) Exp. 1383.6 cm^{-1} Calc. 1389 cm^{-1}

(f) Exp. 1572 cm^{-1} Calc. 1591 cm^{-1}

Figure 42.7 (a–f) Elongation patterns of selected modes of a neutral PTCDA molecule obtained by DFT calculations with the B3LYP:3-21G basis set of the Gaussian 98 package along with their calculated frequencies and the frequencies measured for a crystal in the parallel polarization configuration. Adapted with permission from Ref. [24]. Copyright (2007) American Chemical Society.

molecular breathing along the x_m axis gives rise to the lowest frequency internal mode (233 cm^{-1}), while the mode at 1303 cm^{-1} – with the largest cross section – is related to C–H bending vibrations. The stretching of C–C bonds governs the modes around 1580 cm^{-1}. There are two groups of modes, namely, around $\sim$1150 cm^{-1} and between 1320 and 1360 cm^{-1} where the assignment is still ambiguous owing to their very similar cross section and polarization behavior.

The observation of external modes in PTCDA was reported in 2000 [54, 55, Figure 42.6, left]. The symmetry assignment was performed by analogy with the modes reported for β-perylene [56], which has the same monoclinic structure as PTCDA and therefore similar intermolecular forces can be assumed. Considering the difference in mass for the two molecules ($m_{\text{PTCDA}} = 392$ amu and $m_{\text{perylene}} = 252$ amu), the frequencies of PTCDA phonons were calculated using the proportionality relation of two harmonic oscillators with the same force constant:

$$\frac{\omega_{\text{perylene}}}{\omega_{\text{PTCDA}}} = \sqrt{\frac{m_{\text{PTCDA}}}{m_{\text{perylene}}}} = 0.8 \tag{42.10}$$

The properties of phonons observed in PTCDA are summarized in the first six rows in Table 42.1. The frequencies calculated as described are given in column five and their elongation patterns are displayed in Figure 42.8. The assignment of the mode at 60 cm^{-1} is not clear because, according to the comparison with the perylene phonons, it should be a B_g mode, but in PTCDA it is observed in parallel polarization as the A_g modes. The lowest energy phonons employ rotations around the x_m axis of the molecules, while for the higher energy ones the molecules rotate around their z_m axis [57]. A sketch of the vibrational pattern for selected modes can be seen in Figure 42.8. It must be noted that DFT methods (B3LYP:3-21G)

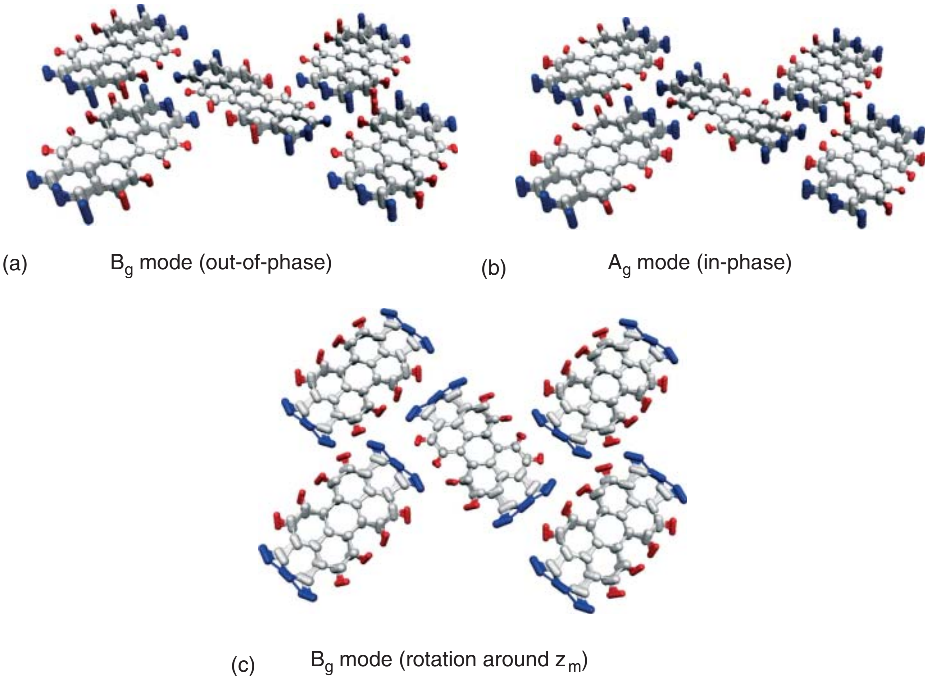

Figure 42.8 Elongation patterns of selected phonons of the α-PTCDA crystal: the lowest frequency phonons employ out-of-phase (a) and in-phase (b) rotations around the x_m axis of the molecules; in the highest frequency B_g phonon (c) the molecules rotate around their z_m axis. Adapted with permission from Ref. [24]. Copyright (2007) American Chemical Society.

predict the existence of three out-of-plane (OOP) internal modes below 150 cm^{-1}: one B_{2g} ($\delta_{C-C-C} + \delta_{C-O-C}$) mode at 78 cm^{-1}, and two B_{1g} (δ_{C-C-C}) modes at 99 and 138 cm^{-1}. In-plane (IP) and OOP modes stem for vibrational elongations involving movement of atoms within the molecular plane and perpendicular to it, respectively.

Muck *et al.* [57] reported the presence of more than six modes below 125 cm^{-1} in Raman spectra measured at 20 *K*, some of them showing strong polarization dependence. They proposed a model that explains the large number of modes based on the coupling between internal and external modes mediated by pure van der Waals interactions. Even though the number of the observed modes and their ordering were reproduced fairly well, the calculated frequencies were highly overestimated, in particular for the C–H and C=O related modes.

42.2.4.3 **Vibrational Properties of DiMe-PTCDI**

Gosh and Aroca [58] were again the first to report Raman spectra of films and proposed an empirical assignment. For the mode assignments used in this work, DFT was employed with the same basis set as for PTCDA (B3LYP:3-21G) (Figure 42.9).

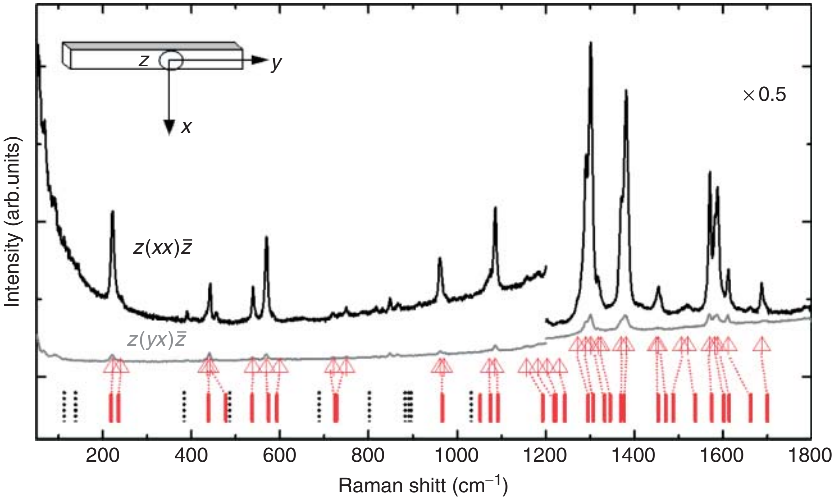

Figure 42.9 Raman spectra of a DiMe-PTCDI single crystal recorded at RT in parallel (black line) and crossed (gray line) polarization configuration. The triangles represent experimental frequencies of A_g modes and the vertical lines represent calculated frequencies of A_g (thick lines) and B_g (dotted lines) modes. Adapted with permission from Ref. [24]. Copyright (2007) American Chemical Society.

As in the case of PTCDA, polarization measurements on a single crystal were performed under resonant conditions using an excitation energy of 2.54 eV and a resolution of 2 cm^{-1}.

A concept widely used in the literature dedicated to quantitative analysis of the sample polarization response is the depolarization ratio [59]. This is defined as the ratio between the Raman signals obtained in crossed polarization configuration to that obtained in parallel configuration:

$$\mathrm{Dep} = \frac{I_{yx}}{I_{xx}} \tag{42.11}$$

The frequencies obtained for the parallel and crossed polarization spectra are tabulated in the second and third column of Table 42.2. In column five, the intensities in parallel polarization relative to the strongest mode at 1301.4 cm^{-1} are provided. The experimental depolarization ratios are listed in column six. The calculated frequencies, the mode symmetry, and their character are listed in column four, seven, and eight. Selected elongation patterns of several modes of a neutral DiMe-PTCDI molecule are displayed in Figure 42.10. No scaling factor was applied to the calculated frequencies for consistency with the model applied to PTCDA [51].

A large number of similarities can be found between the vibrational spectra of DiMe-PTCDI and PTCDA owing to their perylene core, which determines the rectangular symmetry of both molecules. For instance, the breathing mode at 220.5 cm^{-1} has the same character as the corresponding one in PTCDA and its frequency is by a factor 0.95 lower compared to the 233 cm^{-1} mode of PTCDA

Table 42.2 Vibrational modes of a DiMe-PTCDI single crystal and calculated vibrational properties for an isolated molecule using B3LYP:3-21G basis set of Gaussian 98.

DiMe-PTCDI	Raman shift (cm^{-1})		B3LYP: 3-21G	Intensity	Depolarization	Symmetry	Dominant character
	(*xx*)	(*yx*)	(cm^{-1})	(*xx*)			
External modes		30			—	B_g	Libronic
	37	37		0.05	0.18	A_g	
	50	50		0.05	1.22	B_g	
	57			0.11	0		
	69	68		0.06	0.18	A_g	
	89	88		0.03	0.20	B_g	
		96			—	A_g	
Internal modes	220.5	221.1	220	0.11	0.13	A_g	Breathing along x_m
	239.3	238.2	238	0.06	0.04	A_g	ν_{N-C}
	390.4	391	403	0.01	0.30	A_g	Core deformation $+\delta_{C-O-C}+\delta_{C=O}$
	434.8	—	442	0.01	0.41	A_g	$\delta_{C-C}+\delta_{C-O-C}$
	441.9	440.6	457	0.04	0.24	B_g	$\delta_{C-O-C}+\delta_{C-C}$, OOP
	538.9	539.1	542	0.03	0.30	A_g	Core stretch, radial+ $\delta_{C=O}$
	569.3	568.8	580	0.11	0.11	A_g	$\delta_{C-C}+\delta_{C-H}+\delta_{CH3}$
	720.4	718.9	733	0.01	0.64	A_g	$\delta_{C-C}+\delta_{C-N-C}+\delta_{C-H}$
	749.2	750.6	734	0.01	1.01	A_g	$\delta_{C-C}+\delta_{C-N-C}+\delta_{C-H}$
	848.7	847.5	882	0.01	0.47	B_g	δ_{C-H}
	961.4	962	975	0.07	0.12	A_g	CH_3 rocking
	1085.9	1086.1	1103	0.11	0.07	A_g	CH_3 rocking + δ_{C-H}
	1157	1155.7	1173	0.07	0.03	A_g	CH_3 rocking
	1181.7	1184.1	1205	0.04	0.11	A_g	δ_{C-H}
	1203.2	—	1232	0.04	—	A_g	δ_{C-H}
	1290	1289.6	1320	0.49	0.08	A_g	$\delta_{C-H}+\delta_{CH3}+\nu_{C-N}$
	1301.4	1301	1347	1.00	0.09	A_g	$\delta_{C-H}+\nu_{C-C}$
	1318.5	—	1358	0.04	—	A_g	Core deformation
	1370	1369	1383	0.35	0.14	A_g	$\delta_{CH}+\delta_{CH3}+\delta_{C-N-C}$
	1381.4	1380.2	1391	0.91	0.09	A_g	$\delta_{C-H}+\nu_{C-C}+\delta_{CH_3}$
	1454.6	1452	1469	0.11	0.27	A_g	$\delta_{CH_3}+\delta_{C-H}$
	1520	1517.4	1554	0.22	0.55	A_g	$\delta_{C-H}+\nu_{C-C}$
	1570.3	1568.9	1591	0.36	0.12	A_g	$\delta_{C-H}+\nu_{C-C}$
	1581.3	1581.1	1618	0.12	0.17	A_g	$\delta_{C-H}+\nu_{C-C}$
	1587.8	1587.2	1631	0.40	0.07	A_g	$\delta_{C-C}+\delta_{C-H}$
	1612.1	1610.8	1679	0.13	0.20	A_g	$\nu_{C=O}$
	1687.8	1689.0	1717	0.08	0.12	A_g	$\nu_{C=O}+\delta_{CH_3}$

Adapted with permission from Ref. [24]. Copyright (2007) American Chemical Society.

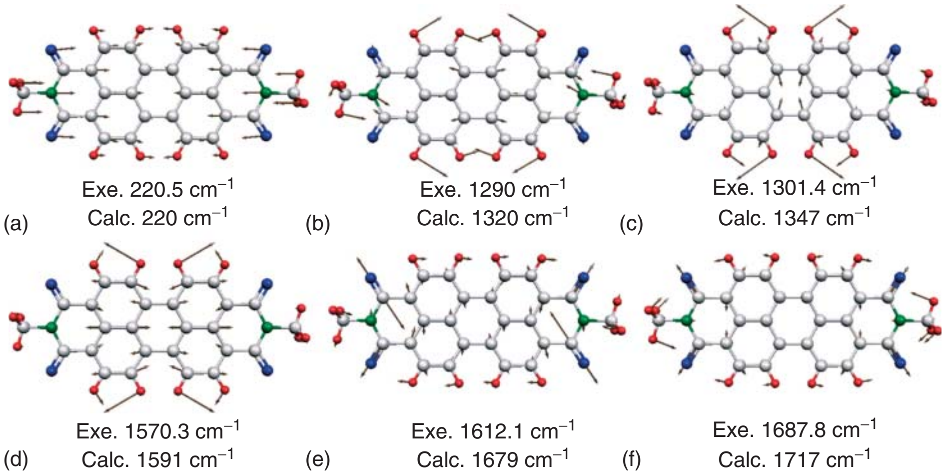

Figure 42.10 (a–f) Elongation patterns of several modes of a neutral DiMe-PTCDI molecule calculated using DFT methods with the B3LYP:3-21G basis set of the Gaussian 98 package along with their calculated and the corresponding experimental frequency. Adapted with permission from Ref. [24]. Copyright (2007) American Chemical Society.

(Figure 42.11). This factor is very close to the scaling factor obtained approximating both molecules ($m_{\text{PTCDA}} = 392\,\text{amu}$ and $m_{\text{DiMe-PTCDI}} = 418\,\text{amu}$) with linear oscillators having the same force constants (Figure 42.11):

$$\frac{\omega_{\text{DiMe-PTCDI}}}{\omega_{\text{PTCDA}}} = \sqrt{\frac{m_{\text{PTCDA}}}{m_{\text{DiMe-PTCDI}}}} = 0.97 \qquad (42.12)$$

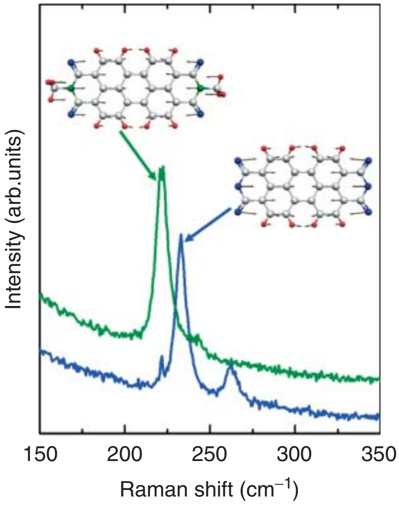

Figure 42.11 Raman spectra in the region of the breathing mode of PTCDA and DiMe-PTCDI together with the elongation pattern of the breathing mode. Adapted with permission from Ref. [24]. Copyright (2007) American Chemical Society.

As in the case of PTCDA, a mode with OOP character involving deformation of C–C and C=O bonds appears at 441 cm^{-1}. The C–H deformation modes with some contribution from CH_3 groups, C–N stretching or bending appearing around 1300 and 1380 cm^{-1}, dominate the spectra. The C–C stretching modes accompanied by C–H deformations govern the region around 1600 cm^{-1}. There are few modes originating exclusively from the methylimide groups ($-N-CH_3$) in the spectra: a shoulder at 239 cm^{-1} stems from the stretching of C–N bonds, and the modes at 961, 1086, and 1157 cm^{-1} are due to the rocking of CH_3 groups.

In crossed polarization configuration $z(yx)\bar{z}$, the internal modes almost vanish. This leads to low depolarization ratios (0.1–0.2) for most of the A_g modes involving vibrations of the perylene core. The few modes with depolarization above 0.5 have either *OOP* (B_g) or *IP* C–H or C–N–C deformation character. The amount of Davydov splitting is generally less than that observed in PTCDA owing to different relative orientation of the molecules in the unit cell.

The external vibrational modes of DiMe-PTCDI were observed for the first time in a Raman experiment in 2003 [60]. Their observation in a femtosecond pump-probe experiment was also reported by Hasche *et al.* [61].

Figure 42.12 shows the polarization dependence in the phonon region in both PTCDA and DiMe-PTCDI crystals for the experimental geometry shown in the insets. Even though the relative intensities are different for the two crystals, clear polarization dependence is observed in both cases. Modes that are strong in parallel polarization become very weak or even vanish in crossed polarization, enabling the symmetry assignment proposed for DiMe-PTCDI in Table 42.3. When rotating the DiMe-PTCDI crystal around the z axis, the polarization behavior changes and

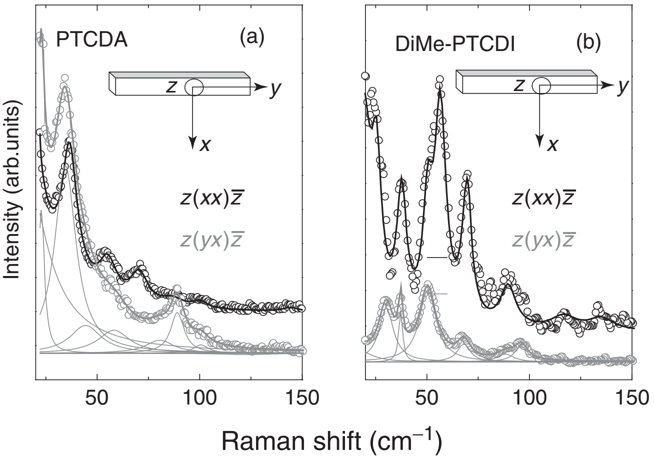

Figure 42.12 Raman spectra of (a) PTCDA and (b) DiMe-PTCDI crystals in the region of the external modes. The sketch of the measurement geometry is shown in the inset. Adapted with permission from Ref. [24]. Copyright (2007) American Chemical Society.

Table 42.3 Frequencies of modes observed below 125 cm^{-1} in a DiMe-PTCDI crystal compared with the experimental values from Ref. [61].

Crystal				**Reference [61]**	**Perylene*0.8**	**Symmetry**
$z(xx)\bar{z}$	$z(yx)\bar{z}$	$z(yy)\bar{z}$	$z(xy)\bar{z}$	(cm^{-1})	(cm^{-1})	
25				4.7 + 25	—	B_g
	30	31	33	33	32	B_g
37	37			43	42	A_g
50	50	50		57	67	B_g
57			54			
69	68	67	69	71	75	A_g
89	88	88	89	89	85	B_g
	96			105	96	A_g
		101	102			

The symmetry assignment is made following Ref. [61] by comparison to the molecular phonons of perylene. All values are in cm^{-1}.
Adapted with permission from Ref. [24]. Copyright (2007) American Chemical Society.

several modes appear at different frequencies. The frequencies are summarized for both situations in columns one to four of Table 42.3. In column five, the frequencies reported in Ref. [61] are provided. Columns six and seven contain the frequencies and the symmetry assignment proposed [61] by comparison with the phonons reported for perylene [56]. The correspondence in number of modes and frequency positions is good, except for the presence of two modes at 4.7 and 25 cm^{-1}. These were assigned to a Davydov splitted internal mode with B_g symmetry, which is predicted by DFT calculations to appear at 16 cm^{-1}. On the other hand, the B3LYP:3-21G methods predict the existence of four Raman-active internal modes with B_g(OOP) character below 125 cm^{-1}, but none of them has such a low frequency: 77, 86, 111, 112 cm^{-1} (A. Y. Kobitski, private communication). The mode at 25 cm^{-1} is also observed in the Raman spectra.

Moreover, it was found that three modes located at 50, 54, and 57 cm^{-1} correspond to the B_g mode at 57 cm^{-1} reported by Hasche *et al.* [61], whereby the mode observed at 50 cm^{-1} behaves rather like an A_g mode. Also, the Raman modes at 96 and 101 cm^{-1} correspond to the same A_g mode in the time-resolved experiment. The large number of modes could be understood in the frame of the model proposed by Muck *et al.* [57] as originating from the coupling between internal and external modes. Because a comprehensive theoretical model is still lacking, the modes below 125 cm^{-1} will be considered as external modes according to the assignments in Table 42.1 (for PTCDA) and Table 42.3 (for DiMe-PTCDI) throughout this work, even though a contribution from the internal modes cannot entirely be ruled out.

42.3
Initial Adsorption of Molecules on Inorganic Semiconductor Surface

Early studies of organic molecule adsorption on low-index faces of inorganic semiconductors such as GaAs (100) suggested that a passivated surface was necessary for ordered growth. It was found that, for example, PTCDA formed ordered layers on GaAs (100) if the surface had been passivated by a selenium (Se) ML, while the order was significantly poorer when the growth took place on clean GaAs surfaces [62]. It was proposed that the GaAs surface bonds are saturated by Se and the organic molecules attach through weak van der Waals bonding to the surface. As a result of this weak interaction, the molecules have sufficient mobility on the surface to arrange into an ordered, quasi-epitaxial overlayer. It is thus expected that the quality of the passivated surfaces will influence the organic film structure. On the other hand, the molecular functional groups, namely, the anhydride and the methylimide groups, may also play a role in determining the strength of interaction with the passivated surface and the surface defects. In this section, the nature of the interface bonding and its role in determining the structure of the organic film are investigated by combining Raman spectroscopy and RAS.

42.3.1
Reflection Anisotropy Spectroscopy Investigations

A typical reflectance anisotropy (RA) spectrum measured for a sulfur-terminated GaAs(001) surface is shown in Figure 42.13 and represents an RA fingerprint for

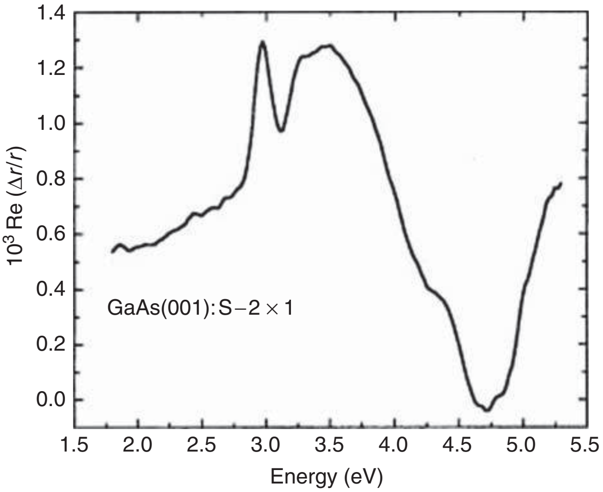

Figure 42.13 RAS spectrum of sulfur-passivated GaAs(001). Adapted with permission from Ref. [63]. Copyright (2001) American Vacuum Society.

the sulfur-induced (2 × 1) reconstruction of the GaAs surface. The sharp derivative-like feature around 3 eV is attributed to the E_1 and $E_1 + \Delta_1$ critical points of GaAs [64], while the broad dip at 4.7 eV is associated with the E'_0 and E_2 critical points of GaAs. The feature near 3.5 eV is related to the sulfur passivation. Its origin is, however, still under discussion. While Hughes *et al.* [65] attributed its occurrence to a transition involving sulfur dimers, other explanations such as transitions within Ga–S bonds are also possible [66].

The evolution of RA spectra with increasing PTCDA coverage is demonstrated in Figure 42.14 for layers with nominal thicknesses of 1, 3, 5, and 10 nm. Note that

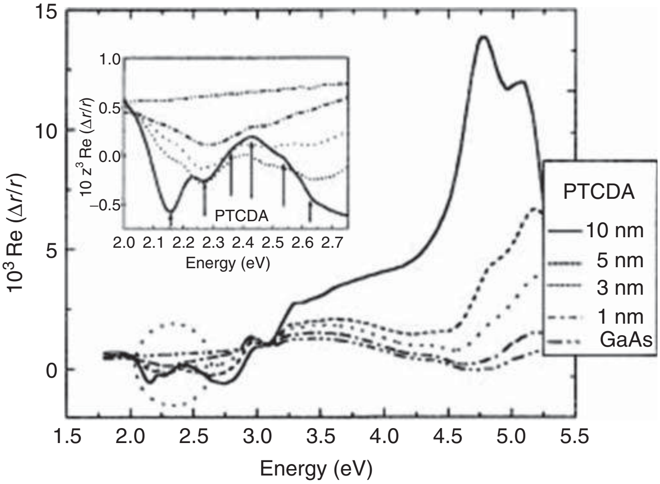

Figure 42.14 RAS spectra of chalcogen-passivated GaAs upon PTCDA deposition. Adapted with permission from Ref. [63]. Copyright (2001) American Vacuum Society.

Table 42.4 Spectral position of PTCDA features in the case of both reflectance anisotropy spectroscopy (RAS) and spectroscopic ellipsometry (SE).

Energy (eV)	
RAS	**SE**
2.15	2.21
2.29	
2.37	—
2.42	2.47
2.54	2.57
2.63	—
—	3.38
—	3.52

the features in the RA spectrum of clean GaAs appear as very weak in this figure, clearly illustrating the pronounced optical anisotropy induced by the presence of the PTCDA layer. Features indicated by arrows can clearly be assigned to PTCDA and their energy positions are listed in Table 42.4. It is important to note that these positions do not necessarily coincide with transition energies observed in optical absorption or ellipsometry ($\mathrm{Im}\langle\varepsilon\rangle$) spectra owing to the low symmetry of PTCDA. Still, a comparison of the region enlarged in the inset of Figure 42.14 with optical absorption spectra [67] reveals good correspondence strengthening the assignment of the indicated features to PTCDA. The observation of a finite RAS response in the energy range 2–2.7 eV, where no GaAs-related features are present and the anisotropy of the starting surface is small, rules out that crystallites are completely random in their azimuthal orientation.

The RA line shape of the GaAs-related feature at 3 eV hardly changes by deposition of PTCDA, thus suggesting that the underlying GaAs surface is quite likely to remain intact and chemical interaction between organic molecules and the sulfur passivated substrate is very weak.

42.3.2
Raman Investigations

To clarify the nature of the interaction between the PTCDA molecules and the GaAs substrate, Raman spectroscopy studies are employed. On one hand, the Raman modes of the GaAs substrate are monitored upon the PTCDA deposition to detect eventual changes in the band bending of the substrate. On the other hand, the spectral range containing the molecular modes with the strongest intensity, that is, the C–C and C–H modes, will be studied for very low molecular coverage of the substrate to prove that the chemical structure of the molecules adsorbed on the substrate remains intact.

42.3.2.1 Monitoring of the GaAs Substrate Modes During Organic Film Growth

One of the advantages when choosing a low frequency range for the monitoring of the film growth is the observation of the substrate phonons. An example of Raman monitoring of PTCDA film growth on S-GaAs(100):2×1 substrates kept at RT is presented in Figure 42.15. For each spectrum, an accumulation period of 1 min was taken at an incident power of 100 mW. The evaporation rate was about $\sim$0.3 nm min^{-1} and the final thickness of the film was 40 nm. From Figure 42.15 it can be deduced that the relative areas of longitudinal optical (LO) and Ω^- GaAs modes remain constant during the organic film deposition at RT. The band bending of the substrate can be determined from the ratio of the GaAs modes according to Refs. [68, 69]. The results are displayed in Figure 42.16.

The difference in the doping levels of the GaAs substrates used for the growth of the present PTCDA and DiMe-PTCDI films (1.8×10^{18} and 2.7×10^{18} cm^{-3}) and slight experimental variations in the S-passivation of the GaAs substrates are likely to be responsible for the difference in the band bending of the two substrates before the organic film growth. One source of errors in the evaluation

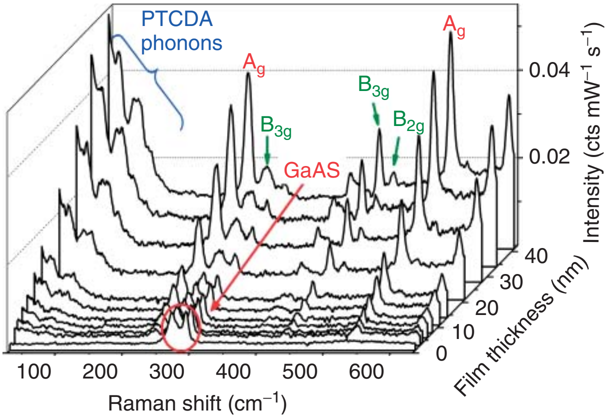

Figure 42.15 Raman spectra recorded *online* during the growth of PTCDA on S-GaAs(100):2 × 1 substrates at RT.

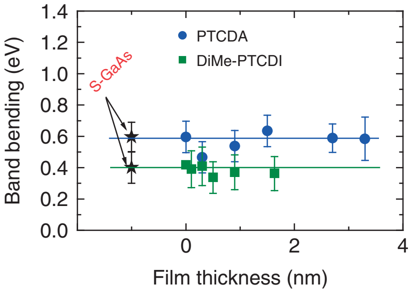

Figure 42.16 Evolution of the band bending of the GaAs substrates upon organic film deposition as determined from the Raman spectra. Adapted with permission from Ref. [24]. Copyright (2007) American Chemical Society.

of spectral intensities is the presence of a weak broad band stemming from an internal molecular vibration that overlaps with the Ω^- GaAs mode in films thicker than 4 nm: the B_{3g} mode at $\sim$262 cm^{-1} in PTCDA and the A_g mode at 239 cm^{-1} in DiMe-PTCDI.

From the RAS measurements it was concluded that no reacted layer is formed when PTCDA is deposited onto GaAs at RT. Therefore, it can be assumed that the relevant processes that might lead to a change in the substrate band bending should take place upon the deposition of the first MLs and the evolution of the GaAs phonons is followed up to an organic film thickness of 4 nm. Neither PTCDA nor DiMe-PTCDI changes the electronic band bending of the S-passivated substrate when deposited at RT. This is in very good agreement with photoemission results that demonstrated a preferential adsorption of molecules at defect sites, which leads to a reduction of the inhomogeneous Fermi level pinning leaving thereby the band bending unchanged [24].

42.3.2.2 Monitoring of the Molecular Modes During Organic Film Growth

In this section, the Raman spectra of sub-ML coverages of PTCDA on S-GaAs(100) surfaces are analyzed and compared with theoretical frequency calculations in order to explore the initial interface formation. Similar experiments were also performed for the PTCDA/Se-GaAs system. During the Raman monitoring of PTCDA deposition onto Se-passivated GaAs surfaces, the thickness-dependent spectra in the region of the most intense vibrational modes with C–H and C–C character resembled those of single crystals [55]. Hence, the interaction between the PTCDA molecules and the Se-passivated GaAs substrate was proposed to be weak and comparable with intermolecular interaction. It must be noted, however, that the lowest investigated thickness was 1.8 nm, which corresponds to roughly six ML.

The evolution of PTCDA modes with contributions from C–C and C–H vibrations as a function of film thickness was recorded in $z(y,x)\bar{z}$ polarization configuration (with $x = [001]$, $y = [010]$, $z = [100]$ defined by the main axis of the GaAs substrate) and is presented in Figure 42.17. All spectra are normalized to the height of the $\nu_{\text{C–C}} + \delta_{\text{C–H}}$ mode at 1572 cm^{-1}. Owing to the low signal-to-noise ratio, each spectrum required an accumulation time of up to 3 h, a period for which the growth was interrupted.

The Raman spectrum of a 40 nm thick PTCDA/S-GaAs(100) layer recorded *in situ* is considered as reference, as it resembles that of PTCDA single crystal in terms of line-shape and frequency positions.

Several differences can be noticed when comparing the spectra of the 0.18 nm with that of the 40 nm thick PTCDA film. A novel feature is observed with high intensity at 1290 cm^{-1}. The other modes are shifted toward lower frequencies, for example, by ~2.4 cm^{-1} for the totally symmetric (A_g) C–C stretching mode at 1572 cm^{-1}. The amount of shift is reduced for the modes at 1303 cm^{-1}(C–H

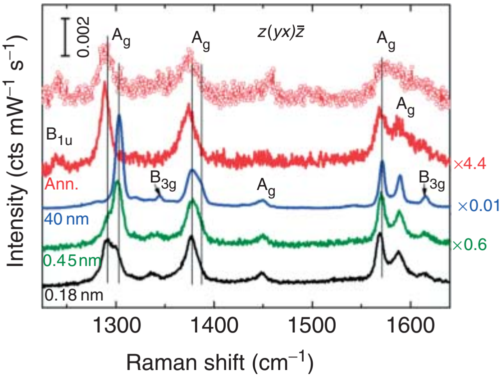

Figure 42.17 Raman spectra in the region of C–C and C–H modes for several thicknesses of PTCDA films (from bottom to top: 0.18, 0.45, and 40 nm) on S-GaAs(100) and after annealing a 14 nm thick film for 30 min at 350 °C (second from the top), taken in crossed polarization. The topmost spectrum was recorded after annealing a 20 nm thick film grown on H–Si(100) substrate at 410 °C for 15 min. Adapted with permission from Ref. [24]. Copyright (2007) American Chemical Society.

bending with A_g symmetry) and 1572 cm^{-1} upon increasing thickness to 0.45 nm. The intensities of these modes increase, while that of the 1290 cm^{-1} band remains almost constant. Obviously, there are molecules experiencing a different type of interaction in the initial phase of adsorption compared to the intermolecular interaction specific to thicker films and single crystal PTCDA. The spectral contribution, and hence the number of such molecules, remains almost constant upon increasing the coverage above 0.18 nm.

Further insight in the molecule–substrate interaction and the origin of the new band at 1290 cm^{-1} is obtained by annealing a 14 nm thick PTCDA film at 350 °C for 30 min. This temperature is higher than the desorption temperature for PTCDA multilayers, which is determined to be 325 °C for PTCDA on glass substrates [70]. Thus, only molecules experiencing a bonding to the substrate stronger than the intermolecular interaction should remain on the GaAs surface. The spectrum after annealing is shown in the upper part of Figure 42.17. By comparing the height of the C–C mode at 1572 cm^{-1} for the annealed and the as-deposited 0.18 nm film, a number of molecules corresponding to $\sim$0.04 nm nominal coverage are evaluated as remaining on the surface, that is, approximately 1/8 of an ML. However, it must be noted that a precise determination of the absolute number of molecules from the Raman peak intensities may be limited by a number of parameters, for example, the growth mode or the resonance conditions. The photoemission measurements have shown from the attenuation of the substrate core levels that at RT on Se- as well as on S-passivated GaAs(100) [71] surfaces, the first PTCDA ML should be completed before the second one starts to form. Hence, the signal from a 0.18 nm film most probably originates only from molecules in direct contact with the substrate. In the following, it will be shown that the interaction between the molecules and the surface after annealing does not involve the disruption of the molecule. It should thus not modify significantly the resonant conditions for Raman scattering and hence the relative intensities of the Raman modes. Therefore, the relative change in the intensity of the C–C mode when comparing the spectra of the as-deposited 0.18 nm and the annealed film is expected to give a fairly reasonable estimate on the number of the molecules remaining on the surface after annealing.

At the doping level used in this experiment ($N_d = 2.7 \times 10^{18}$ cm^{-3}), the number of Si dopant atoms on the GaAs (100) surface should be at least 10^{12} cm^{-2} among 6×10^{14} cm^{-2} surface atoms. Furthermore, previous investigations of ZnSe films grown on GaAs(100) have shown that already upon annealing at 280 °C for 40 min Si dopant impurities diffuse toward the GaAs surface, leading to the occurrence of silicon clusters [72]. Considering the PTCDA molecules lying flat on the substrate when grown at RT as well as after annealing, the nominal coverage of 1/8 ML ($\sim$0.04 nm) determined from the Raman spectra after annealing would correspond to $\sim 10^{13}$ cm^{-2}, that is, sufficient to cover all surface defect sites induced by Si dopant atoms. Further evidence of the interaction of molecules mainly with the Si dopant atoms is provided by the similarities between the spectra recorded after annealing the 14 nm PTCDA film grown on S-GaAs(100) and after annealing of a 20 nm PTCDA film grown on H-passivated Si(111) substrate (topmost spectrum in Figure 42.17). Additional defect sites such as missing S atoms, domain boundaries, and step edges [73] may also be present and can probably explain the large value of 10^{13} molecules cm^{-2}.

In the spectrum after annealing, the band at 1303 cm^{-1} is entirely replaced by the novel feature at 1290 cm^{-1}. This is a clear hint of the origin of the band at 1290 cm^{-1} as being a shifted variant of the 1303 cm^{-1} mode in agreement with the argument used for molecules adsorbed on Ag(111) substrates [74]. The band at 1290 cm^{-1} is thus proposed to be characteristic for molecules having direct contact with the surface defects, while the band at 1303 cm^{-1} is characteristic of molecules in a molecular crystalline-like environment.

The approximately 1/2 ML (~0.18 nm) coverage PTCDA corresponds to a number of molecules that are about four times larger than the number of molecules remaining on the surface after annealing. Thus, the corresponding Raman spectrum should contain three types of contributions: from molecules in contact with defects, from molecules in contact with the passivated surface, and from molecules also interacting with other molecules. The experimental spectrum, however, appears as a combination of the spectra of molecules interacting with defects and of the spectra of thick films. The intensity of the 1290 cm^{-1} mode is approximately equal to that of the 1303 cm^{-1} mode. The intensity ratio of these modes reflects that at least half of the molecules at the surface are not interacting exclusively with the surface defects. Consequently, the molecules interacting with the passivated surface must contribute to the spectrum in a similar way as the molecules involved in intermolecular agglomerations; hence, the strength of the interaction between the molecules and the passivated GaAs surface is likely to be comparable to that of the intermolecular interaction.

Considering the adsorption of the PTCDA molecules at surface Si dopant atoms (or other defects) at the GaAs surface, several mechanisms may be involved. The prediction of the Raman spectra corresponding to the PTCDA molecules interacting with Si defects requires the knowledge of the adsorption geometry as well as theoretical tools capable of handling systems with a large number of atoms comprising the PTCDA molecule and the topmost five layers of the S-GaAs substrate. To our knowledge, additional experimental evidence regarding the exact location of the Si defects with respect to the surface sites and the adsorption geometry of the PTCDA molecules on the defects is missing. The calculation of the Raman spectra within the Gaussian 98 package is possible only under coarse approximations of the interaction between single molecules and defects. Therefore, the calculated Raman spectra can be only qualitatively compared to the experimental ones.

Charge transfer between a molecule and one defect was first considered and approximated by charging an isolated PTCDA molecule with one positive or negative elementary charge. Frequency calculations with the B3LYP:3-21G functional predict dramatic shifts for the C–C stretching Raman modes [75] that are not detected in the spectra after annealing.

In a second approach, complexes consisting of a PTCDA molecule and one Si atom are considered and the corresponding Raman spectra are calculated with the same functional. The high affinity of Si atoms having dangling bonds to form σ-bonds with C atoms was experimentally proved by the chemisorption

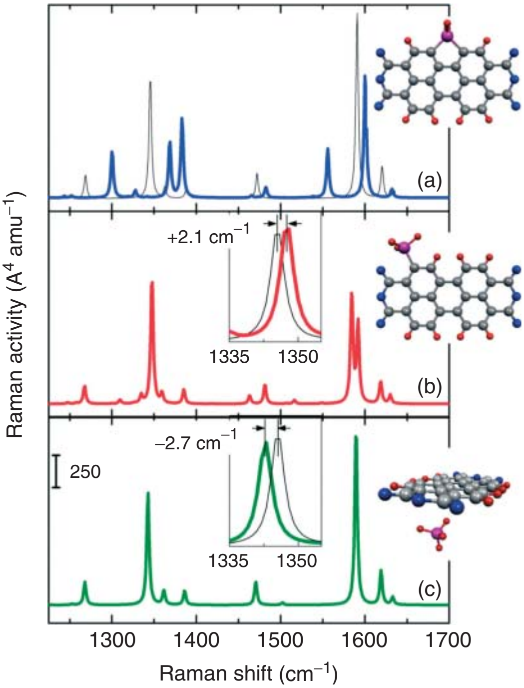

Figure 42.18 Calculated Raman spectra (thick lines) for a PTCDA molecule bonded to one Si atom via two σ-bonds (a), one σ-bond (b) and for a PTCDA molecule with a passivated Si atom below the molecular plane (c). The calculated spectrum of a neutral molecule is shown for comparison in the graph (a) and in the insets (b) and (c) by the thin continuous lines. The Raman bands were modeled with Lorentz oscillators having an FWHM of 3.5 cm^{-1}. Adapted with permission from Ref. [24]. Copyright (2007) American Chemical Society.

process of maleic anhydride onto clean nonpassivated Si(100):2 × 1 surfaces [76] accompanied by the rehybridization of the C atoms from sp^3 to sp^2. Therefore, complexes having σ-bonds between one Si atom and carbon atoms of the perylene core of PTCDA were considered.

As can be seen in the calculated Raman spectra in Figure 42.18 a,b, the formation of two σ-bonds between Si and PTCDA also leads to dramatic shifts of all modes, while the C–H Raman modes of the complex with a single σ-bond are slightly shifted toward higher frequencies. Thus, none of the two complexes can explain the spectral changes observed on annealing.

Finally, calculations for a single Si atom with all valence electrons saturated with H atoms situated below the molecular plane of PTCDA were performed. Most of the modes in the spectral region of interest shift to lower frequencies by at most 1.5 cm^{-1}, while the mode at 1346 cm^{-1} (calculated for isolated molecule, 1303 cm^{-1} in experiment) experiences the largest amount of shift (2.7 cm^{-1}) to lower frequencies (Figure 42.18c). This situation provides the best qualitative match to the experimentally observed shift, but the amount of shift is still lower than the experimentally observed one. The amount of accompanying static charge transfer from the PTCDA molecule is only 0.007 of an elementary charge. Besides strengthening the assignment of the mode at 1290 cm^{-1} as being a shifted variant of the 1303 cm^{-1}, these calculations also show that small changes in the molecular environment can lead to significant frequency shifts for modes with pure C–H deformation character.

An additional feature of the Raman spectra after annealing should be noted. A normally IR-active band ($B_{1u}(\gamma)$, $\delta_{\mathrm{C-H}}$) occurs at 1243 cm^{-1}. Its presence can either be explained by a symmetry lowering to C_v for the molecules adsorbed at defect sites (by analogy with the case of D_{6h} molecules [77]) or by a dynamical charge transfer [78]. Therefore, the molecules are proposed to interact with surface defects due to Si dopant atoms via a charge transfer modulated by molecular vibrations and/or accompanied by a molecular deformation. This conclusion is supported by the observation of the mode at 1243 cm^{-1} along with the one at 1290 cm^{-1} in the spectra of Ag/PTCDA or In/PTCDA interfaces (Section 42.4) or in the Raman spectra of PTCDA MLs on Ag(111) [79, 74].

In summary, the molecules with a different spectral signature compared to those in a molecular crystalline environment are proposed to be adsorbed at defects mainly due to Si dopant atoms at the GaAs surface. The interaction involved is sufficiently strong to retain these molecules at the surface upon annealing above the desorption temperature of PTCDA. A comparison of the experimentally observed characteristic features and the calculated spectra excludes static transfer of an elementary charge or the formation of σ-bonds between the Si atom and the molecule as being responsible for this interaction. However, the observed breakdown of selection rules points to an interaction mediated by dynamical charge transfer. From the similarity between the spectral response of molecules arriving at the surface after the defects are saturated and that of molecules in a crystalline environment, the interaction between PTCDA molecules and the S-passivated surface is estimated to be comparable to the intermolecular one.

The Raman spectra of DiMe-PTCDI on S-GaAs(100) starting from a sub-ML coverage are presented in Figure 42.19.

In order to verify if the DiMe-PTCDI molecules stick at the surface defect sites via interactions comparable to those between the PTCDA and the defects on S-GaAs(100), a ~15 nm thick DiMe-PTCDI was annealed at 325 °C for 10 min. This was sufficient to leave a coverage of only 0.08 nm DiMe-PTCDI on the substrate, which corresponds to a coverage fraction of 0.25 ML. This value was estimated by comparing the intensity of the C–C stretching band at 1570 cm^{-1} with that in the spectrum of a 0.36 nm thick film (taken under the same experimental conditions).

The spectrum of molecules remaining on the surface after annealing presents a B_u mode at 1248 cm^{-1} (Figure 42.19). The C–H modes at 1290 and 1300 cm^{-1} merge into one band, downshifted to 1287 cm^{-1}. The two modes at 1369 and at 1380 cm^{-1} also merge into one band at 1375 cm^{-1}. The shift of the C–C stretch band at 1570 cm^{-1} is very small (0.5 cm^{-1}) and toward larger frequencies, while the band at 1290 cm^{-1} shifts to lower frequencies.

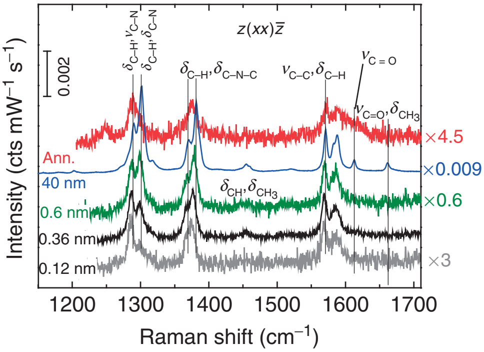

Figure 42.19 Raman spectra in the region of C–C and C–H modes for several thicknesses of DiMe-PTCDI films on S-GaAs(100) recorded in parallel polarization configuration. Spectra are normalized with respect to the height of the mode at 1570 cm^{-1}. Adapted with permission from Ref. [24]. Copyright (2007) American Chemical Society.

The number of bands, their broadening, and relative intensities are very similar to those observed in the parallel polarization configuration for the annealed PTCDA/S-GaAs sample. The frequency positions in the spectra of the annealed DiMe-PTCDI and PTCDA films on S-GaAs differ by at most 4.8 cm^{-1} (Table 42.5), which might be an indication of molecular fragmentation with a loss of CH_3 groups. Fragmentation of molecules adsorbed on Ag(110) substrates with the desorption of CH_3 groups was detected by mass spectroscopy when annealing the substrate at 455 °C [80], which is 100 °C higher compared to this experiment. We assume that the DiMe-PTCDI molecules remaining on the surface are involved in processes of fractional charge transfer with the defect sites similar to the case of PTCDA, that is, via the π orbitals. As a result, the $N-CH_3$ bonds are weakened, possibly enabling the molecular fragmentation already at 325 °C.

Let us consider now the spectrum of an as-deposited 0.12 nm thick film. Here the B_u mode is not observed. If the first deposited DiMe-PTCDI molecules

Table 42.5 Frequency positions (in cm^{-1}) of several modes in the spectra of annealed PTCDA and DiMe-PTCDI films recorded in parallel polarization.

PTCDA/S-GaAs	PTCDA/H–Si	DiMe-PTCDI/S-GaAs
1243	1240.7	1247.8
1290	1289.8	1287.2
1373.9	1375.5	1375
1570	1571.9	1570.4

Adapted with permission from Ref. [24]. Copyright (2007) American Chemical Society.

adsorb at superficial defects – following the interpretation proposed for PTCDA on S-GaAs(100) in the previous section – the defect sites must already be saturated at this coverage. Thus, the spectra of 0.12 nm and higher coverage should contain information about three types of molecules: molecules interacting with the surface defects, molecules interacting with the S-passivated GaAs(100):2 × 1 surface, and molecules having additional interactions with other molecules. All bands except for the one at 1300 cm^{-1} (see Figure 42.10c for its vibrational pattern) are shifted to lower frequencies compared to the reference spectrum. The largest shift is observed for the band at 1290 cm^{-1}, which originates from the vibrational deformation of C–H bonds as well as CH_3 groups (Figure 42.10b). The band appearing in thicker films at 1300 cm^{-1} is very broad and has a lower height compared to the band at 1290 cm^{-1}. The frequency position of the $\delta_{CH} + \nu_{CC}$ mode at 1570 cm^{-1} in thicker films is shifted downward by -1.5 cm^{-1}, less than the corresponding band in PTCDA. Moreover, the B_u mode is not observed. This might indicate that the interaction between the perylene core and the passivated GaAs substrate is weaker for DiMe-PTCDI than for PTCDA molecules. The umbrella deformation of CH_3 groups at 1454 cm^{-1} and the C=O deformations (Figure 42.10 e,f) are not observed.

For a DiMe-PTCDI coverage of 0.36 nm the mode at 1300 cm^{-1} becomes well resolved, probably due to the larger number of molecules interacting only with the passivated surface and with other molecules. The umbrella deformation of CH_3 groups at 1454 cm^{-1} is also resolved, although its intensity relative to the band at 1570 cm^{-1} is lower compared to thicker films. A broad band is observable at the position of the C=O antisymmetric stretching at 1610 cm^{-1}, while the symmetric C=O stretching at 1688 cm^{-1} is still not resolved.

In the next section, it is shown that in thicker films the DiMe-PTCDI molecules are oriented with their molecular plane making an angle of ~56° with the substrate plane. Assuming the same orientation also for the molecules at the interface, this would mean that the interaction between the molecule and the substrate takes place via the CH_3 group at one side of the molecule. This situation could be achieved through the formation of C–H–S bridges considering the high electron affinity of S. Such an adsorption geometry would explain the low activity of the CH_3 umbrella deformation and of the C=O vibrations in the Raman spectra of sub-ML coverages.

To summarize, the interface formation between the two perylene derivatives and differently treated GaAs(100) surfaces was assessed by means of Raman spectroscopy. It was proposed that initially molecules adsorb at the defects sites of the passivated surfaces additionally, leading to a reduction in inhomogeneous band bending as revealed by photoemission experiments [24].

Moreover, by means of Raman spectroscopy, the strength of the interaction between the molecules and the S-passivated surface is estimated to be comparable to the intermolecular one.

42.4 Metals on Organic Layers

Metal deposition onto 15 nm thick films of PTCDA and DiMe-PTCDI was monitored by means of Raman spectroscopy in two spectral regions: below 600 cm^{-1} where the interest is focused on the intermolecular phonon-like and intramolecular breathing modes, and between 1200 and 1700 cm^{-1} where the C–H deformation and C–C and C=O stretching modes are located. The latter is the only region where a sufficient signal was obtained from an ML organic coverage. Figure 42.20 shows the Raman spectrum of a bare 15 nm PTCDA film and its evolution upon the stepwise deposition of indium.

The overall signal intensity increases with the In thickness up to 15 nm and decreases for higher metal coverages, as shown by the normalization factors in Figure 42.20. The same behavior is observed when Ag is deposited onto PTCDA and for both metals deposited onto DiMe-PTCDI [81, 82]. This effect is known as *SERS* [83–85]. The SERS effect has been widely investigated for various molecules adsorbed on rough metallic surfaces or on metallic clusters in colloids. Reviews on this topic can be found, for example, in Refs. [85–87]. The enhancement of normally Raman-active modes is a consequence of the enhancement of the electric field of the incoming and scattered radiation in the vicinity of a rough metal film upon coupling with the dipolar plasmon resonances in the metal clusters. This enhancement affects molecules located up to even 10 nm away from the metal surface [84, 85]. The enhancement factors are essentially determined by the electronic properties of the metal and by the morphology of the metal film.

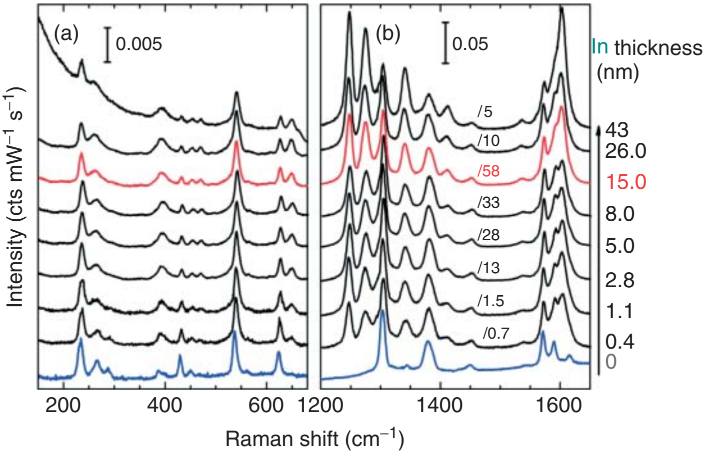

Figure 42.20 (a,b) Raman spectra of PTCDA acquired upon successive deposition of Indium onto a 15 nm PTCDA film. The spectra normalization is done with respect to the intensity of the C–C stretch modes (1572 cm^{-1}). Adapted with permission from Ref. [24]. Copyright (2007) American Chemical Society.

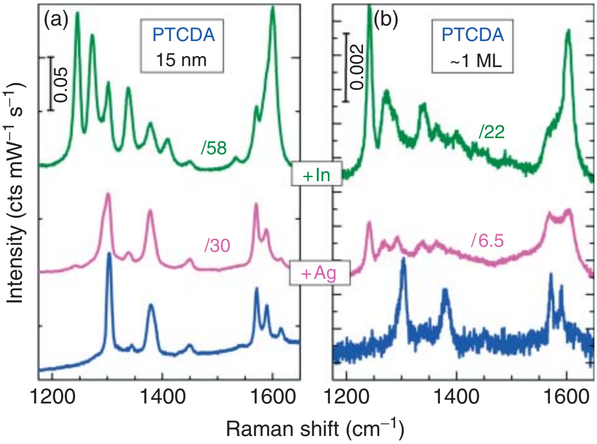

Figure 42.21 Raman spectra of a 15 nm (a) and of an ML (b) PTCDA film clean (bottom) and covered with nominally 15 nm of silver (middle) and indium (top) each. Adapted with permission from Ref. [24]. Copyright (2007) American Chemical Society.

In addition to the enhancement of the totally symmetric modes, the deposition of 0.4 nm In leads to the appearance of some modes in the higher frequency region. The same modes were also observed when depositing In or Ag onto an ML of PTCDA on S-GaAs, only with different relative intensities (Figure 42.21). They, therefore, must be a signature of the molecules in direct contact or in the very near vicinity of a metal surface. In general, such a breakdown of the selection

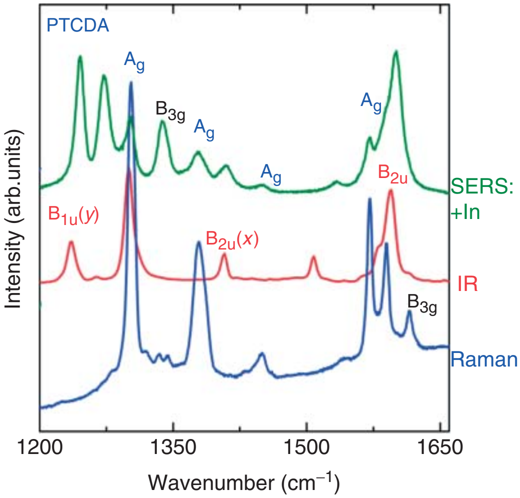

Figure 42.22 Example of the activation of infrared-active modes in the Raman spectrum for the case of indium deposition onto PTCDA. Adapted with permission from Ref. [24]. Copyright (2007) American Chemical Society.

rules accompanies the SERS effect and can be induced by several mechanisms: structural deformation of the molecule, charge transfer from the molecule into the metal or *vice versa*, or formation of new chemical bonds. Thus, the spectral changes induced by SERS can be used to extract information about chemical reactions at the interface, as well as about the morphology of the metal film.

The band at 1338 cm^{-1} was identified in Ref. [75] to be a B$_{3g}$ band based on its frequency and intensity in the crystal spectra, while a band 1292 cm^{-1} is likely to be a shifted variant of the C–H deformation A$_g$ mode at 1303 cm^{-1} in the single crystal [88]. The other bands correspond to modes that normally show IR activity (Figure 42.22).

Considering that all the modes occurring upon In and Ag deposition are normal modes of the PTCDA molecule, the observed breakdown of the Raman-IR selection rules was proposed to originate from a weak charge transfer between the molecules and the metal surface mediated by molecular vibrations [82]. This is in contradiction to previous findings of Hirose *et al.* [89] and Kera *et al.* [90], who proposed the formation of an In$_4$PTCDA complex.

In order to assess the effect of a metal-PTCDA complex formation on the vibrational frequencies theoretical calculations were preformed with the Gaussian 98 package on the In$_4$PTCDA complex using the B3LYP functional and the basis set LANL2DZ, which takes into account possible relativistic effects due to the presence of the heavy metal atoms [53]. Four In atoms were assumed to interact with the PTCDA molecule via the O atoms in the anhydride groups according to Ref. [90]. The optimized geometry, the electronic levels, and the charge distribution over the complexes are similar to those reported in Ref. [89]. Figure 42.23 shows the

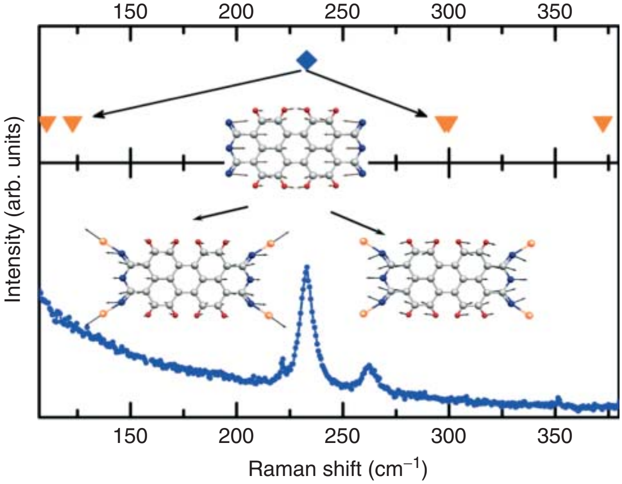

Figure 42.23 Raman spectrum of a PTCDA crystal along with calculated frequencies for a single molecule (rhombus) and for a In$_4$PTCDA complex (triangles). Adapted with permission from Ref. [24]. Copyright (2007) American Chemical Society.

spectrum of a PTCDA single crystal together with the calculated frequencies for a single PTCDA molecule (rhombus) and for an In_4PTCDA complex (triangles).

The most dramatic effect of the complex formation resides in the twofold splitting of the breathing mode at 233 cm^{-1} (see the elongation patterns in Figure 42.23). A first component originates from a breathing of the whole complex and the significant increment of mass compared to the single PTCDA molecule results in a dramatic shift toward lower frequencies (110 cm^{-1}). For the second component, the In atoms are fixed and constrain the breathing of the PTCDA molecule, increasing its frequency to 299 cm^{-1}. In the Raman experimental spectra (Figure 42.20) of the In/PTCDA interface formation, the molecular breathing mode is still observed at 233 cm^{-1}, ruling out the possibility of this chemical reaction. This conclusion is further supported by IR spectroscopic studies [82] and by high-resolution photoelectron spectroscopy (PES) results [24].

In Figure 42.24, the Raman spectra of 15 nm films of PTCDA are shown for metal coverages of 5 nm In, 4.5 nm Ag, and 5 nm Mg. The spectra in the low-frequency windows are normalized to the height of the molecular breathing mode at 233 cm^{-1}. The normalization in the high-frequency region is again performed with respect to the C=C stretch mode (1572 cm^{-1}).

The Raman spectra of the (5 nm) Mg/(15 nm) PTCDA system also exhibit the breakdown of selection rules, with the occurrence of the modes observed in the other two metal/organic heterostructures (Figure 42.24). In addition, several modes with significant intensity (marked with asterisks in Figure 42.24) appear at 307, 502, 598, 696, 1088 cm^{-1} as well as at 1225 and 1433 cm^{-1}. The assignment of

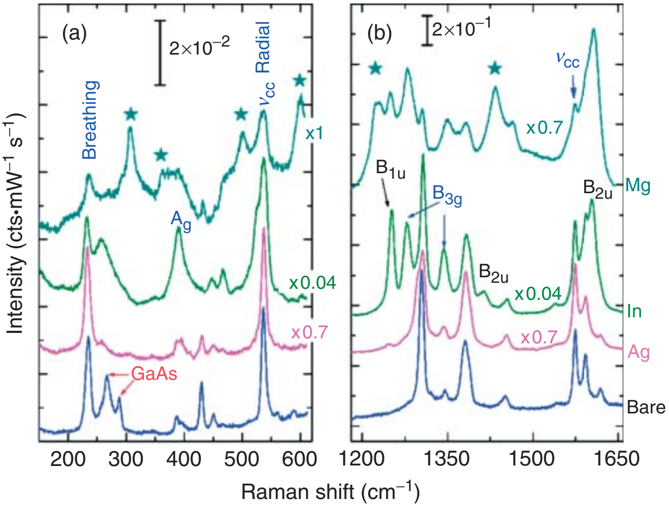

Figure 42.24 Raman spectra for In (5 nm), Ag (4.5 nm), and Mg (5 nm) coverages on 15 nm thick PTCDA films, compared with the spectrum of the bare PTCDA film in the spectral region of the internal breathing mode (a) and in the spectral region of C–H deformation and C=C stretching modes (b). Adapted with permission from Ref. [24]. Copyright (2007) American Chemical Society.

these modes cannot yet be done unambiguously. The frequency of the mode at 598 cm^{-1} is very close to the calculated value of 592 cm^{-1} for a B_{3g} mode of an isolated PTCDA molecule [51].

Frequency calculations performed with the same basis set and density functional methods in Gaussian 98 as in Ref. [51] but for a modified PTCDA molecule, in which the central O atom in the anhydride group is removed, deliver several frequencies that may be candidates for the assignment of the experimentally observed modes: 308, 500, 581, 702, and 1090 cm^{-1}. Raman-active modes in MgO (magnesium oxide) microcrystals [91] were observed at 595, 719, and 1096 cm^{-1}. Thus, the modes observed in the present work at 598, 696, and 1088 cm^{-1} may indicate the formation of MgO as a result of the interaction between Mg and PTCDA. No modes of PTCDA or the modified molecule are found in the vicinity of 1225 cm^{-1}.

Whatever the final assignment of the new modes, they are not activated in the molecules in contact with either Ag or with In. Therefore, it can be concluded that the model of weak charge transfer is not sufficient to describe the interaction at the Mg/PTCDA interface. Indeed a chemical reaction with the loss of the central O atom of the anhydride group and formation of MgO was confirmed by photoemission spectroscopy results [24].

In Figure 42.25, the spectra of 15 nm DiMe-PTCDI films for metal coverages of 5 nm In, 4.5 nm Ag, and 5 nm Mg are shown. The spectra in the low-frequency windows are normalized to the height of the breathing mode at 221 cm^{-1}. The normalization in the high-frequency region is performed with respect to the C–C stretching modes (1570 cm^{-1}).

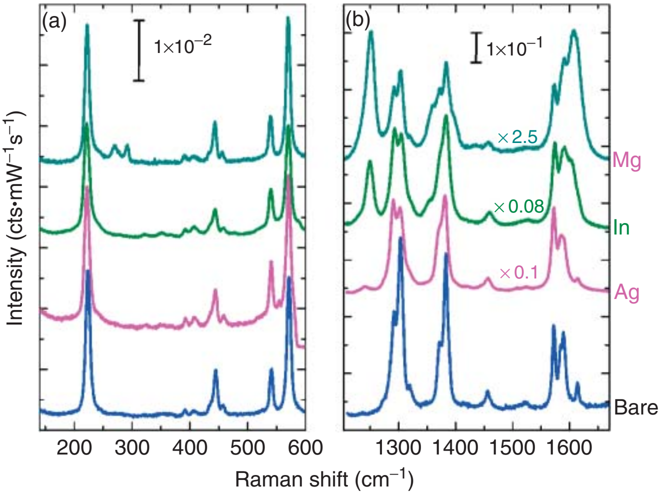

Figure 42.25 Raman spectra for In (5 nm), Ag (4.5 nm), and Mg (6 nm) coverages on 15 nm thick DiMe-PTCDI films, compared with the spectrum of the bare DiMe-PTCDI film. Adapted with permission from Ref. [24]. Copyright (2007) American Chemical Society.

In the case of DiMe-PTCDI, all the investigated metals, that is, Ag, In, and Mg, lead to the breakdown of selection rules with the occurrence of normally IR-active modes at 1246 and 1606 cm^{-1}. The breathing mode at 221 cm^{-1} survives with increasing metal coverage. Thus, a chemical reaction between these metals and the O atoms of DiMe-PTCDI molecules can be ruled out. Interestingly, the features potentially assigned to MgO phonons do not appear in the spectra even for higher coverages of Mg. It can thus be concluded that the methylimide group in the DiMe-PTCDI molecule is less reactive compared to the O atoms in the anhydride group of PTCDA.

Raman spectroscopy showed that Ag and In behave similarly in terms of chemical reactivity when deposited onto PTCDA and DiMe-PTCDI. Both metals induce a breakdown of selection rules, which was interpreted to be the result of a dynamical charge transfer process. The vibrational signature of Mg deposited onto PTCDA is very different compared with the other metals, indicating that a strong chemical interaction between the two partners takes place. High-resolution photoemission measurements, together with sophisticated core-level line-shape analysis, deliver a deeper insight into the physics and chemistry of the metal/organic interfaces and confirm the conclusions drawn from Raman experiments [24].

The external modes of PTCDA disappear almost completely after depositing 0.4 nm In, while they only get broader and decrease in intensity after Ag and Mg deposition (Figure 42.26).

In Figure 42.27, the spectra of the external modes are shown upon stepwise metal deposition onto 15 nm of PTCDA. For a quantitative evaluation, the spectra of Ag/PTCDA and Mg/PTCDA were fitted using Lorentzian functions.

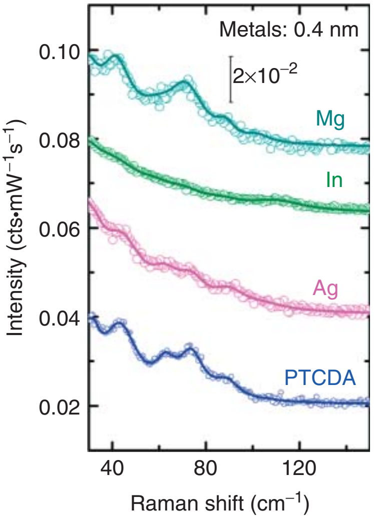

Figure 42.26 Raman spectra of 15 nm thick PTCDA films covered with Ag, In, and Mg in the region of the external modes. Adapted with permission from Ref. [24]. Copyright (2007) American Chemical Society.

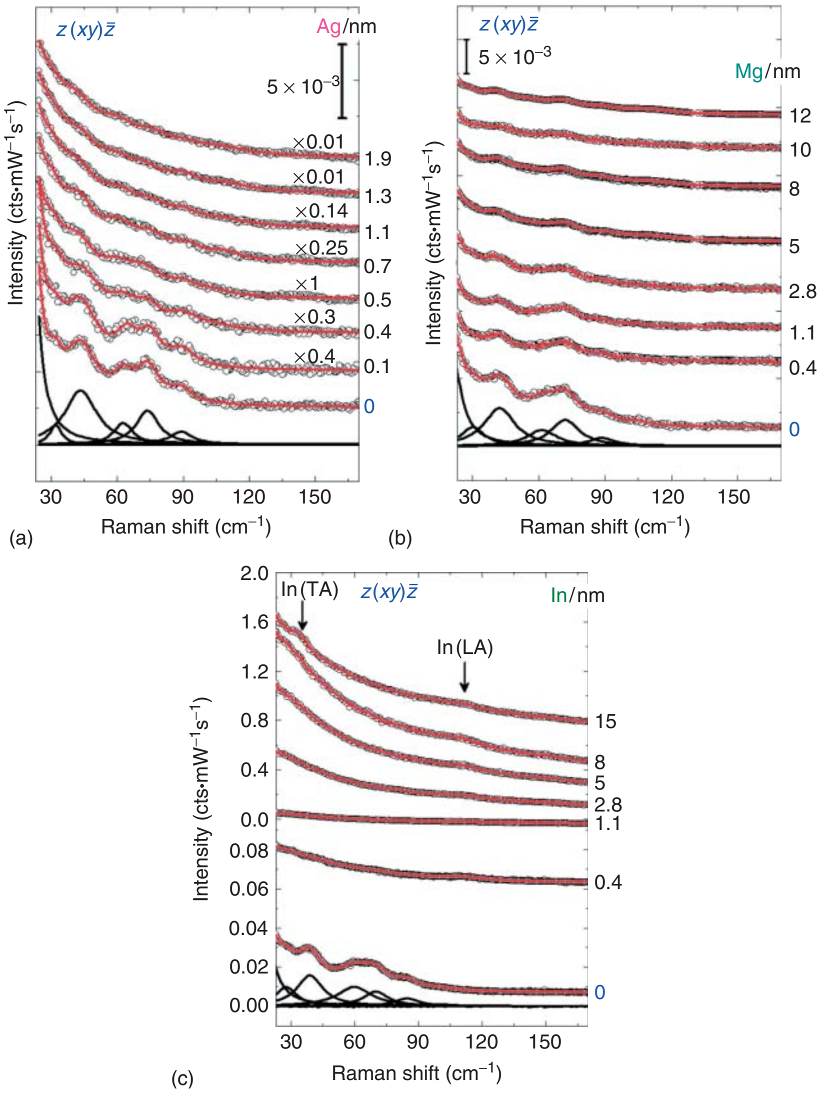

Figure 42.27 Raman monitoring in the external mode region upon metal deposition: Ag (a), Mg (b), and In (c). The experimental spectra are shown by open symbols and the fitted spectra by red lines. The Lorentzian functions used for curve fitting of the Raman spectrum of the pure PTCDA film are shown by lines in the lower part of the figures. The spectra are normalized for Ag/PTCDA for a better observation of the phonons. Adapted with permission from Ref. [24]. Copyright (2007) American Chemical Society.

The evolution of the FWHM as a function of Ag and Mg thickness is plotted in Figure 42.28 for the external mode at 41 cm^{-1}. This mode is fairly well separated from its neighbors and hence the fitting parameters of the corresponding Lorentzian function are less correlated. As the metal thickness increases, the FWHM of the external modes increases faster in Ag/PTCDA compared to Mg/PTCDA.

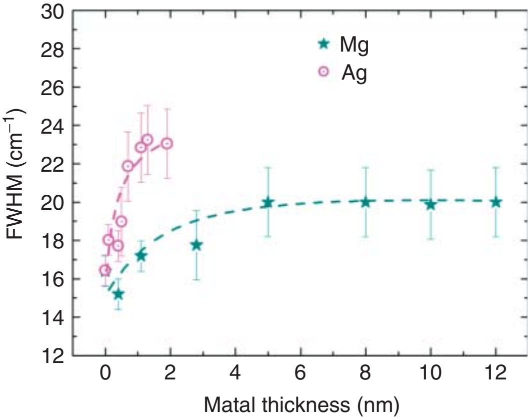

Figure 42.28 Evolution of the FWHM of the external mode at 41 cm^{-1} as a function of the metal coverage relative to the initial values before the metal deposition: for Ag (asterisk) and Mg (open circle). The dashed lines are guide for the eyes. Adapted with permission from Ref. [24]. Copyright (2007) American Chemical Society.

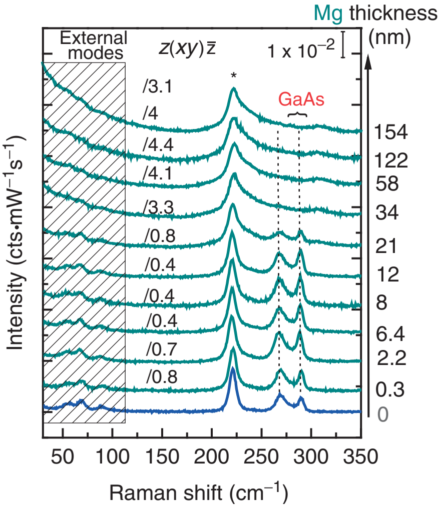

Figure 42.29 Raman spectra of DiMe-PTCDI upon Mg deposition in the region of external modes and GaAs phonons. The spectra are normalized with respect to the intensity of the breathing mode at 221 cm^{-1}. Adapted with permission from Ref. [24]. Copyright (2007) American Chemical Society.

For Mg the external modes are still visible at 12 nm coverage, whereas they are almost completely smeared out at 1.3 nm of Ag. This is a clear indication that the crystalline structure of the organic layers is less affected by the Mg deposition compared to Ag. However, it should be noted that curve fitting of the spectra in the case of Ag/PTCDA is complicated by the significant increase in the low-frequency background (which was already subtracted in Figure 42.26). The background evolution reflects an increasing degree of roughness, which is consistent with an increasing number of metallic clusters that diffusely scatter the light. A strong increase in the low-frequency background is also observed for the case of In deposition onto PTCDA, while it hardly affects the spectra of Mg/PTCDA, supporting the conclusion that the roughening due to Mg is lower compared to that of the Ag and In.

While the external molecular modes disappear in the first deposition stages for In/PTCDA, two new modes develop at 33 and 112 cm^{-1} above In coverage of 2.8 nm. They may correspond to the transverse acoustic and longitudinal acoustic phonons located at 34 and 114 cm^{-1}, respectively, in bulk indium [92, 93] activated because of the low dimension of the In clusters. This observation, corroborated by the concomitant increase in the low-frequency background, indicates the formation of metallic In clusters. Moreover, the enhancement of the internal modes also increases dramatically above 2.8 nm In, supporting the conclusion of metallic cluster formation.

In the case of Mg deposition onto DiMe-PTCDI, the external modes are attenuated only for an Mg nominal coverage above 21 nm, that is, similar to the case of Mg/PTCDA, indicating that the Mg atoms do not protrude into the crystalline molecular islands (Figure 42.29). On the other hand, the relative intensities of the GaAs-related features change already for low Mg coverages (Figure 42.29), reflecting a change in the GaAs band bending. This can only occur if the Mg atoms reach the GaAs surface in the large voids between the DiMe-PTCDI islands and react with it as also learned from the PES results [24].

References

1. Le Ru, E.C. and Etchegoin, P.G. (2009) *Principles of Surface-Enhanced Raman Spectroscopy*, Elsevier, Amsterdam.
2. Sharma, B., Frontiera, R.R., Henry, A.I., Ringe, E., and Van Duyne, R.P. (2012) *Mater. Today*, **15**, 16.
3. Cialla, D., März, A., Böhme, R., Theil, F., Weber, K., Schmitt, M., and Popp, J. (2012) *Anal. Bioanal. Chem.*, **403**, 27.
4. Bordo, V.G. and Rubahn, H.-G. (2005) *Optics and Spectroscopy at Surfaces and Interfaces*, Wiley-VCH Verlag GmbH, Weinheim.
5. Gordan, O.D., Himcinschi, C., Zahn, D.R.T., Cobet, C., Esser, N., and Braun, W. (2006) *Appl. Phys. Lett.*, **88**, 141913.
6. Hilfiker, J.N., Singh, N., Tiwald, T., Convey, D., Smith, S.M., Bakerand, J.H., and Tompkins, H.G. (2008) *Thin Solid Films*, **516**, 7979.
7. Chen, C.T., Sette, F., Ma, Y., and Modesti, S. (1990) *Phys. Rev. B*, **42**, 7262.
8. Wende, H., Bernien, M., Luo, J., Sorg, C., Ponpandian, N., Kurde, J., Miguel, J., Piantek, M., Xu, X., Eckhold, P., Kuch, W., Baberschke, K., Panchmatia, P.M., Sanyal, B., Oppeneer, P.M., and Eriksson, O. (2007) *Nat. Mater.*, **6**, 516.
9. McGilp, J.F. (2010) *J. Phys. Condens. Matter*, **22**, 084018.
10. Lüpke, G. (1999) *Surf. Sci. Rep.*, **35**, 75.

11. Zhang, W., Wang, H., and Zheng, D. (2006) *Phys. Chem. Chem. Phys.*, **8**, 4041.
12. Lim, E., Yamada, D., Weis, M., Manaka, T., and Iwamoto, M. (2009) *Chem. Phys. Lett.*, **477**, 221.
13. Manaka, T., Liu, F., Weis, M., and Iwamoto, M. (2010) *J. App. Phys.*, **107**, 043712.
14. Vidal, F. and Tadjeddine, A. (2005) *Rep. Prog. Phys.*, **68**, 1095.
15. Hopkins, A.J., McFearin, C.L., and Richmond, G.L. (2005) *Curr. Opin. Solid State Mater. Sci.*, **9**, 19.
16. Cecchet, F., Lis, D., Caudano, Y., Mani, A.A., Peremans, A., Champagne, B., and Guthmuller, J. (2012) *J. Phys. Condens. Matter*, **24**, 124110.
17. Ye, H., Huang, J., Park, J.-R., Katz, H.E., and Gracias, D.H. (2007) *J. Phys. Chem. C*, **111**, 13250.
18. Elliott, A.B., Horvath, R., and Gordon, K.C. (2012) *Chem. Soc. Rev.*, **41**, 1929.
19. Forrest, S.R. (1997) *Chem. Rev.*, **97**, 1793.
20. Glöcker, K., Seidel, C., Soukopp, A., Sokolowski, M., Umbach, E., Böhringer, M., Berndt, R., and Schneider, W.-D. (1998) *Surf. Sci.*, **405**, 1.
21. Seidel, C., Awater, C., Liu, X.D., Ellerbrake, R., and Fuchs, H. (1997) *Surf. Sci.*, **371**, 123.
22. Kendrick, C., Kahn, A., and Forrest, S.R. (1996) *Appl. Surf. Sci.*, **104–105**, 586.
23. Suzuki, H. (1967) *Electronic Absorption Spectra and Geometry of Organic Molecules*, Academic Press, New York.
24. Zahn, D.R.T., Gavrila, G., and Salvan, G. (2007) *Chem. Rev.*, **107**, 1161.
25. Möbus, M., Karl, N., and Kobayashi, T. (1992) *J. Cryst. Growth*, **116**, 495.
26. Hädicke, E. and Graser, F. (1986) *Acta Crystallogr. C.*, **42**, 189.
27. Scholz, R., Kobitski, A.Y., Kampen, T.U., Schreiber, M., Zahn, D.R.T., Jungnickel, G., Elstner, M., Sternberg, M., and Frauenheim, T. (2000) *Phys. Rev. B*, **61**, 13659.
28. Kobitski, A.Y. (2003) Time-resolved photo-luminescence and theoretical study of excitons in PTCDA. PhD thesis. TU Chemnitz, *http://archiv.tu-chemnitz.de/pub/2003/0055/index.html* (accessed 22 March 2007).
29. Hoffmann, M. (2000) Frenkel- and Charge-transfer excitons in quasi-one-dimensional molecular crystals with strong intermolecular orbital overlap. PhD thesis. TU Dresden, Dresden.
30. Wewer, M. and Stienkemeier, F. (2003) *Phys. Rev. B.*, **67**, 125201.
31. Scholz, R., Vragovic, I., Kobitski, Y.A., Salvan, G., Kampen, T.U., Schreiber, M., and Zahn, D.R.T. (2001) International School of Physics "'Enrico Fermi'', Proceedings of Enricon Fermi School, Varenna, Italy, *http://www.sif.it/attivita/scuola_fermi.*
32. Aspnes, D.E. (1985) *J. Vac. Sci. Technol., B*, **3**, 1498.
33. Aspnes, D.E. (1994) *Surf. Sci.*, **307–309**, 1017.
34. Richter, W. and Zettler, J.-T. (1996) *Appl. Surf. Sci.*, **100–101**, 465.
35. Weightman, P., Martin, D.S., Cole, R.J., and Farrell, T. (2005) *Rep. Prog. Phys.*, **68**, 1251.
36. Borensztein, Y., Mochan, W.L., Tarriba, J., Barrera, R.G., and Tadjeddine, A. (1993) *Phys. Rev. Lett.*, **71**, 2334.
37. Mochan, W.L. *et al.* (1994) *Physica A*, **207**, 334.
38. Hansen, J.K., Bremer, J., and Hunderi, O. (1998) *Phys. Status Solidi A*, **170**, 271.
39. Stahrenberg, K., Hermann, T., Esser, N., and Richter, W. (2000) *Phys. Rev. B*, **61**, 3043.
40. Cole, R.J., Frederick, B.G., Power, J.R., Perry, C.C., Chen, Q., Verdozzi, C., Richardson, N.V., and Weightman, P. (1998) *Phys. Status Solidi A*, **170**, 235.
41. Frederick, B.G., Power, J.R., Cole, R.J., Perry, C.C., Chen, Q., Haq, S., Bertrams, T., Richardson, N.V., and Weightman, P. (1998) *Phys. Rev. Lett.*, **80**, 4490.
42. Frederick, B.G., Cole, R.J., Power, J.R., Perry, C.C., Chen, Q., Richardson, N.V., Weightman, P., Verdozzi, C., Jenisson, D.R., Schultz, P.A., and Sears, M.P. (1998) *Phys. Rev. B*, **58**, 10883.
43. Kampen, T.U., Rossow, U., Schumann, M., Park, S., and Zahn, D.R.T. (2000) *J. Vac. Sci. Technol., B*, **18**, 2077.
44. Kampen, T.U., Paraian, A.M., Rossow, U., Park, S., Salvan, G., Wagner, T., Friedrich, M., and Zahn, D.R.T. (2001) *Phys. Status Solidi A*, **188**, 13707.

45. Passmann, R., Kropp, M., Bruhn, T., Fimland, B.O., Bloom, F.L., Gossard, A.C., Richter, W., Esser, N., and Vogt, P. (2007) *Appl. Phys. A*, **87**, 469.

46. Schmidt, W.G., Fuchs, F., Hermann, A., Seino, K.A., Bechstedt, F., Paßmann, R., Wahl, M., Gensch, M., Hinrichs, K., Esser, N., Wang, S., Lu, W., and Bernholc, J. (2004) *J. Phys. Condens. Matter*, **16**, S4323.

47. Hacker, C.A. and Hamers, R.J. (2003) *J. Phys. Chem. B*, **107**, 7689.

48. Hu, Y., Maschek, K., Sun, L.D., Hohage, M., and Zeppenfeld, P. (2006) *Surf. Sci.*, **600**, 762.

49. Proehl, H., Nitsche, R., Dienel, T., Leo, K., and Fritz, T. (2005) *Phys. Rev. B*, **71**, 165207.

50. Debe, M.K. (1987) *Prog. Surf. Sci.*, **24**, 1.

51. Yu Kobitski, A., Scholz, R., and Zahn, D.R.T. (2003) *J. Mol. Struct. THEOCHEM*, **625**, 39.

52. Akers, K., Aroca, R., Hor, A.M., and Loutfy, R.O. (1987) *J. Phys. Chem.*, **91**, 2954.

53. Frisch, M.J., Trucks, G.W., Schlegel, H.B., Scuseria, G.E., Robb, M.A., Cheeseman, J.R., Zakrzewski, V.G., Montgomery, J.A., Stratmann, R.E., Burant, J.C., Dapprich, S., Millam, J.M., Daniels, A.D., Kudin, K.N., Strain, M.C., Farkas, O., Tomasi,J., Barone, V., Cossi, M., Cammi, R., Mennucci, B., Pomelli, C., Adamo, C., Clifford, S., Ochterski, J., Petersson, G.A., Ayala, P.Y., Cui, Q., Morokuma, K., Malick, D.K., Rabuck, A.D., Raghavachari, K., Foresman, J. B., Cioslowski, J., Ortiz, J.V., Stefanov, B.B., Liu, G., Liashenko, A., Piskorz, P., Komaromi, I., Gomperts, R., Martin, R.L., Fox, D.J., Keith, T., Al-Laham, M.A., Peng, C. Y., Nanayakkara, A., Gonzalez, C., Challacombe, M., Gill, P.M.W., Johnson, B.G., Chen, W., Wong, M.W., Andres, J.L., Head-Gordon, M., Replogle, E.S., and Pople, J.A. (1998) Gaussian'98 Revision A.1, Gaussian, Inc., Pittsburgh, PA.

54. Tenne, D.A., Park, S., Das, A., Kampen, T.U., and Zahn, D.R.T. (2000) *Phys. Rev. B*, **61**, 15464.

55. Kampen, T.U., Salvan, G., Friedrich, M., Tenne, D.A., Park, S., and Zahn, D.R.T. (2000) *Appl. Surf. Sci.*, **166**, 387.

56. Kosic, T.J., Schosser, C.L., and Dlott, D.D. (1983) *Chem. Phys. Lett.*, **96**, 57.

57. Muck, T., Schneider, M., Umbach, E., Wagner, V., and Geurts, J. (2002) Spring Meeting of the German Physical Society Proceedings.

58. Guhatathakurta-Gosh, A. and Aroca, R. (1989) *J. Phys. Chem.*, **93**, 6125.

59. Ferraro, J.R. and Nakamoto, K. (1994) *Introductory Raman Spectroscopy*, Academic Press, San Diego, CA.

60. Kampen, T.U., Salvan, G., Paraian, A., Himcinschi, C., Kobitski, A.Y., Friedrich, M., and Zahn, D.R.T. (2003) *Appl. Surf. Sci.*, **212–213**, 501.

61. Hasche, T., Canzler, T.W., Scholz, R., Hoffmann, M., Schmidt, K., Frauenheim, T., and Leo, K. (2001) *Phys. Rev. Lett.*, **86** (18), 4060.

62. Hirose, Y., Forrest, S.R., and Kahn, A. (1995) *Phys. Rev. B*, **52**, 14040.

63. Paraian, A. M., Rossow, U., Park, S., Salvan, G., Friedrich, M., Kampen, T. U., and Zahn, D. R. T. (2001) *J. Vac. Sci. Technol. B*, **19**, 1658.

64. Aspnes, D.E. and Studna, A.A. (1983) *Phys. Rev. B*, **27**, 985.

65. Hughes, G., Springer, C., Resch, U., Esser, N., and Richter, W. (1995) *J. Appl. Phys.*, **78**, 1948.

66. Berkovits, V.L. and Paget, D. (1992) *Appl. Phys. Lett.*, **61**, 1835.

67. Kaiser, R., Friedrich, M., Schmitz-Hübsch, T., Sellam, F., Kampen, T.U., Leo, K., Zahn, D.R.T., and Fresenius, J. (1999) *Anal. Chem.*, **363**, 189.

68. Geurts, J. (1993) *Surf. Sci. Rep.*, **18**, 1.

69. Salvan, G.(2003) Metal/Organic/Inorganic semicoductor hetrostrctures characterized by vibrational spectroscopies. PhD thesis. TU Chemnitz.

70. Heutz, S., Salvan, G., Jones, T.S., and Zahn, D.R.T. (2003) *Adv. Mater.*, **15**, 131109.

71. Park, S., Querner, T., Kampen, T.U., Braun, W., and Zahn, D.R.T. (2000) *Appl. Surf. Sci.*, **166**, 376.

72. Schneider, A., Drews, D., Zahn, D.R.T., Wolfframm, D., and Evans, D.A. (1996) *J. Cryst. Growth*, **159**, 732.

73. Kendrick, C. and Kahn, A. (1998) *Appl. Surf. Sci.*, **123–124**, 405.

74. Wagner, V. (2001) *Phys. Status Solidi A*, **188**, 1297.

75. Kobitski, A.Y., Salvan, G., Scholz, R., Tenne, D., Kampen, T.U., Wagner, H.P., and Zahn, D.R.T. (2002) *Appl. Surf. Sci.*, **190**, 386.

76. Bitzer, T., Rada, T., and Richardson, N.V. (2001) *J. Phys. Chem. B*, **105**, 4535.

77. Moskovits, M. and DiLella, D.P. (1980) *J. Chem. Phys.*, **73**, 6068.

78. Lippitsch, M.E. (1984) *Phys. Rev. B*, **25**, 3101.

79. Wagner, V., Muck, T., Geurts, J., Schneider, M., and Umbach, E. (2003) *Appl. Surf. Sci.*, **212–213**, 502.

80. Seidel, C., Schäfer, A.H., and Fuchs, H. (2000) *Surf. Sci.*, **459**, 310.

81. Salvan, G., Tenne, D.A., Kampen, T.U., Scholz, R., Jungnickel, G., Frauenheim, T., and Zahn, D.R.T. (2001) *Appl. Surf. Sci.*, **179**, 113.

82. Zahn, D.R.T., Salvan, G., Paez, B.A., and Scholz, R. (2004) *J. Vac. Sci. Technol., A*, **22**, 1482.

83. Brouers, F., Blacher, S., Lagarkov, A.N., Sarychev, A.K., Gadenne, P., and Shalaev, V.M. (1997) *Phys. Rev. B*, **55**, 13234.

84. Creighton, J.A. (1988)Chapter 2: The selection rules for Surface-Enhanced Raman Spectroscopy: in *Spectroscopy of Surfaces* (eds R.J. Clark and R.E. Hester), John Wiley & Sons, Ltd, Chichester.

85. Otto, A., Mrozek, I., Graborn, H., and Akemann, W. (1992) *J. Phys. Condens. Matter*, **4**, 1134.

86. Kneipp, K., Kneipp, H., Itzkan, I., Dasari, R.R., and Feld, M.S. (1999) *Chem. Rev.*, **99**, 2957.

87. Otto, A. (2001) *Phys. Status Solidi A*, **188**, 1455.

88. Salvan, G. and Zahn, D.R.T. (2004) *Europhys. Lett.*, **67**, 827.

89. Hirose, Y., Kahn, A., Aristov, V., and Soukiassian, P. (1996) *Appl. Phys. Lett.*, **68**, 217.

90. Kera, S., Setoyama, H., Onoue, M., Okudaira, K., Harada, Y., and Ueno, N. (2001) *Phys. Rev. B*, **63**, 115204.

91. Böckelmann, H.K. and Schlecht, R.G. (1974) *Phys. Rev. B.*, **10**, 5225.

92. Fleischer, K., Chandola, S., Esser, N., Richter, W., and McGilp, J.F. (2003) *Phys. Rev. B*, **67**, 235318.

93. Bakulin, A.S., Overhauser, A.W., Kaiser, H., Werner, S.A., Fernandez-Baca, J.A., and Smith, H.G. (2001) *Phys. Rev. B*, **63**, 052301.

43
NEXAFS Studies at Surfaces

Maria Benedetta Casu and Thomas Chassé

43.1
Introduction

The interaction of electromagnetic radiation with matter is the basis of several spectroscopies.

Whenever electromagnetic radiation encounters matter, three events may occur: the radiation can be reflected, can propagate through matter, or can be absorbed. In particular, photon and matter interaction generates several phenomena, among others the photoelectric effect, the Compton scattering, and, in addition, two processes with very small energy transfer: Thomson (elastic) scattering on a ‘‘free’’ electron, that is, the redirection of low-energy photon without change in energy, and the Rayleigh (coherent) scattering that results from a combined (coherent) action of an atom as a whole. In the photoelectric effect, electrons are emitted from matter (metals and nonmetallic solids, liquids, or gases) as a consequence of their absorption of energy from electromagnetic radiation with a frequency greater than a critical threshold frequency. The emitted electrons that may be referred to as *photoelectrons* have kinetic energy E_{kin} determined by the Einstein relationship [1]

$$E_{\mathrm{kin}} = h\nu - E_{\mathrm{b}} \tag{43.1}$$

where $h\nu$ is the energy of the incident radiation and E_{b} is the binding energy of the emitted electrons. Equation (45.1) indicates that radiation will be absorbed for incident energies larger than the binding energy of the electrons in the system (Figure 43.1). X-rays have enough energy to ionize atoms by emission from both valence electrons and core electrons.

The concept of absorption spectroscopy refers to a bunch of techniques that measure the absorption of radiation. The sample absorbs energy from the radiating field. The intensity of the absorption varies as a function of frequency/energy, and this variation leads to an absorption spectrum. The X-ray absorption spectrum is typically divided into two regimes: near-edge X-ray absorption fine structure spectroscopy (NEXAFS) and extended X-ray absorption fine structure spectroscopy (EXAFS). Despite the fact that the two stem from the same physical origin, this distinction is convenient for the interpretation. NEXAFS is strongly sensitive to

Handbook of Spectroscopy, Second Edition. Edited by Günter Gauglitz and David S. Moore.

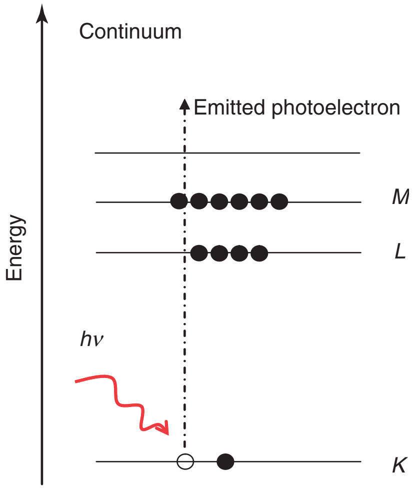

Figure 43.1 Schematic view of the photoelectron effect.

formal oxidation state and coordination chemistry (e.g., octahedral, tetrahedral coordination) of the absorbing atom, while EXAFS is used to determine the distances, coordination number, and species of the neighbors of the absorbing atom.

In this chapter, we report some basic concepts that represent the background of the photon absorption in the X-ray range by electrons distributed within specific orbitals in a population of molecules or atoms. In doing so, we refer to the classical work of Stöhr [2], Koningsberger and Prins [3], and Iwasawa [4]. Other specific references are also given in the following text.

43.2
Near-Edge X-Ray Absorption Fine Structure: Basic Principles

X-ray absorption is a process, for certain aspects, very similar to optical absorption. It obeys the Lambert–Beer law that relates the absorption of light to the properties of the material through which the light is traveling:

$$I = I_0 \exp(-\mu l) \tag{43.2}$$

where I is the transmitted light, I_0 the incident light, μ the absorption coefficient, and l the thickness of the absorbing medium (Figure 43.2). At most X-ray energies, the absorption coefficient μ is a smooth function of energy, with a value that depends on the sample density ρ, the atomic number Z, the atomic mass A, and the X-ray energy E roughly as

$$\mu \simeq \rho Z^4 / AE^3 \tag{43.3}$$

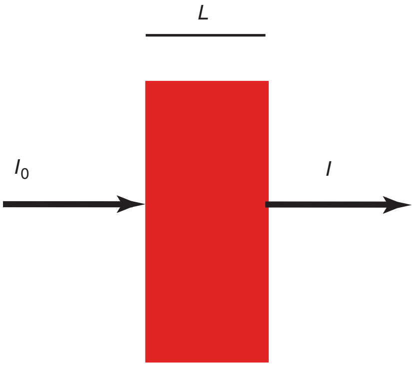

Figure 43.2 Schematic view of X-ray absorption. I_0 is the intensity of the incoming X-ray beam. After the X-ray has traveled a distance l into the material, the intensity has been reduced to $I = I_0 \exp(-\mu l)$, where μ is the definition of the absorption coefficient.

The strong dependence of μ on both Z and E is a fundamental property of X-rays.

Owing to the Z^4 dependence, the absorption coefficient, for example, for O, Ca, Fe, and Pb are very different, spanning several orders of magnitude, so that a good contrast between different materials can be achieved for nearly any sample thickness and concentration by adjusting the X-ray energy. This gives also the possibility of using X-ray absorption as a key technique in microscopy, as, for example, in scanning transmission X-ray microscopy or tomography.

As in optical absorption, the transition rate can be calculated by Fermi's golden rule that describes the transition rate (T) from one energy eigenstate ($\psi(i)$) of a quantum system into a continuum of energy eigenstates ($\psi(f)$), due to a perturbation H':

$$T_{\mathrm{if}} \ \alpha | < \psi(f) | H' | \psi(i) > |^2 \rho_f \tag{43.4}$$

where ρ_f is the density of final states, and the matrix element is $\mathrm{M}_{\mathrm{if}} = <\psi(f)\ |H'|\ \psi(i)>$.

In particular, NEXAFS is the absorption of X-ray radiation close to a given edge. In NEXAFS, the photon energy is scanned in a region of about 30 eV above the edge and the absorbed X-ray intensity is measured. NEXAFS is element specific because each element has its own binding energy, that is, absorption energy and, consequently, absorption edge. It is possible to gain information about the unoccupied states, the environment of specific chemical elements, bonding properties, and local charge distributions.

This means that NEXAFS is sensitive to the local order as well as to the middle- to long-range order and it can be used to investigate both amorphous and crystalline samples.

The NEXAFS spectra for a given K-edge are characterized by features at the pre-edge and at the edge, that stem from transitions from the 1s states to excited bound states; thus, they are also known as *resonances*. These transitions can be described within the framework of molecular orbitals or band structure for metals and semiconductors. In general, the NEXAFS features at slightly higher photon energy can be seen as transitions to an unbound final state or to the continuum, and they can be described by multiple scattering theories. Resonances related to shake up or multielectron excitation satellites are also visible. Shape, energy position, and intensities of NEXAFS features give information on chemical bonds, oxidation states, and coordination numbers for the element related to the investigated edge.

As mentioned, the transition rate in NEXAFS can be described by Fermi's golden rule (Eq. (45.4)) containing the perturbation operator H', which represents the electromagnetic radiation and can be approximated as

$$H' \propto -\frac{e}{2mc}(\widehat{p}\cdot\widehat{A}+\widehat{A}\cdot\widehat{p}) \tag{43.5}$$

where $\widehat{p}$ is the momentum operator and $\widehat{A}$ is the vector potential of the electromagnetic radiation. $\widehat{A}$ can be written as

$$\widehat{A}(\mathbf{r},\mathbf{t}) = \mathbf{e}\cdot A_0\cdot e^{i(\mathbf{kr}-\varpi t)}$$

where **e** describes the polarization direction of the light. In vacuum, the Coulomb calibration can be applied

$$\vec{\nabla}\cdot\widehat{A}=0\rightarrow\widehat{p}\cdot\widehat{A}=0$$

Thus, H' can be simplified as $2\cdot(\widehat{A}\cdot\widehat{p})$.

Now, if the wavelength of the type of electromagnetic radiation that induces or is emitted during transitions between different atomic energy levels is much larger than the typical size of an atom, the exponential term can be expressed as a series, and only its first term, 1, is taken into account (electric dipole approximation). It follows that

$$M_{if} \sim \langle\psi_f|\mathbf{e}\cdot\widehat{p}|\psi_i\rangle \tag{43.6}$$

is known as *dipole matrix element*.

At this point, we can understand why the interpretation of a NEXAFS spectrum is certainly a complicated issue. Looking at the dipole matrix element, we observe that the initial and the final state appear. There are several methods to determine the initial state that corresponds to the electronic ground state; for example, semiempirical methods, *ab initio* calculations, and density functional theory can describe this state. On the contrary, here the final state is a state with a core hole and an exited electron in a previously unoccupied state.

To solve this problem, there are essentially two approaches: the *ab initio* molecular orbital theory, and the multiple scattering theory.

The molecular orbital approach is based on Hartree, Hartree–Fock, and local density approximations applied to a system, just as a cluster surrounds the absorbing atom. In this approach, the final state is seen as a core-level photoemission state with an additional electron that occupies one of the previously unoccupied molecular orbitals. One of the most used methods of this kind is the *ab initio* method (GSCF3) that was developed by Kosugi [5–7]. These calculations have proved to give good values, for example, for the energy positions and intensities of the π*-resonances of large compounds, such as subunits of polymers [8–10].

The other approach consists in solving the one-electron Schrödinger equation. In this respect, good performances have been obtained, for example, with the effective scattering amplitude F_{eff} (FEFF) program [11]. FEFF is a self-consistent real-space multiple-scattering code for simultaneous calculations of X-ray absorption spectra and electronic structure. The approach builds in core-hole effects and can include local fields. It works for clusters and atoms, as well as for crystalline systems such as inorganic semiconductors [12].

The one-electron description of X-ray absorption works for all K edges; however, applying these codes to systems such as transition metal oxides one finds excellent agreement for the metal and oxygen K edges, whereas for the other edges, in particular metal $L_{2,3}$ edges, the agreement is poor. The reason for this discrepancy is that the density of states (DOS) is not observed in X-ray absorption processes, while it is calculated in the one-electron approach. The reason for the deviation from the DOS is the strong overlap of the core wave function with the valence wave functions. The overlap of core and valence wave functions is present also in the ground state, but because all core states are filled, it is not effective and it is possible to approximate the core electrons with their charge. In the final state of an X-ray absorption process, there is a partly filled core state. In case systems with a partly filled 3d-band are investigated, the final state will have an incompletely filled 3d-band. The 2p-hole and the 3d-hole have radial wave functions that overlap significantly. This wave function overlap is an atomic effect that can be very large. It creates final states that are found after the coupling of the 2p and 3d wave functions. This effect is well known in atomic physics and actually plays a crucial role in the calculation of atomic spectra. Experimentally, it has been shown that while the direct core-hole potential is largely screened, these so-called multiplet effects are hardly screened in the solid state. This implies that the atomic multiplet effects are of the same order of magnitude in atoms and in solids. Upon this approach, a bunch of codes have been developed. One of the most successful in calculating the X-ray absorption of metal oxides is the TT-multiplets (TT after Theo Thole, one of the authors) [13]. This is a set of computer programs designed to calculate core-level spectra of correlated systems. It is presently maintained by de Groot [14, 15]. He also developed his own version of the TT-multiplets' above-mentioned code, the CTM4XAS Charge Transfer Multiplet Program, packaged with a convenient graphical front end to allow for the simulation of the transition metal 2p and 3p X-ray absorption spectroscopy (XAS), X-ray photoemission spectroscopy (XPS), and X-ray magnetic circular dichroism (XMCD) spectra using atomic multiplets [16–18].

Coming back to the dipole matrix element (Eq. (45.6)), we can also observe that the intensity of the NEXAFS resonances depends on the mutual orientation of the molecular orbital involved in the given transition and the incident radiation. This aspect of the NEXAFS spectroscopy can be used to calculate the molecular orientation (angle between the molecular plane and the substrate) directly from the spectra when investigating adsorbates onto a substrate (Figure 43.3). This model

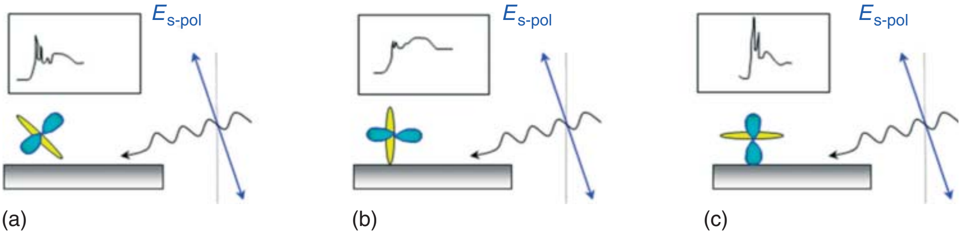

Figure 43.3 (a,b,c) Examples of changes in the π*-resonances intensities for different molecular orientation keeping a fixed geometry of the NEXAFS experiment.

was introduced for the first time by Stöhr [2, 19], and it is widely used for structural investigation of molecular thin films.

In this model, all molecules are classified into general groups depending on the fact that the final state molecular orbital points into a specific direction (vector case) or it is energy degenerate and it spans a plane (plane case). The general equations are derived for both cases, showing the angle dependence of the NEXAFS π* and σ* resonances on the polarization plane of the incident radiation.

In particular, it can be shown for a vector-type orbital and a threefold symmetry of the substrate that the resonance intensity along the direction of the dominant component of the incident electric field is given by [19] [20]

$$I \propto (\cos^2\theta \, \sin^2\alpha + 2\sin^2\theta \, \cos^2\alpha) \tag{43.7}$$

with α angle between the normal to the surface and the orbital, and θ angle between the incident radiation and the normal to the surface. Measuring the intensity for two different polarization directions with respect to the surface, in normal (θ_1) and in grazing incidence (θ_2), it is possible to determine α from the following equation:

$$\frac{1}{\tan^2\alpha} = \frac{1}{2P}\left(P - \frac{1-q}{\sin^2\theta_2 - q\sin^2\theta_1}\right) \tag{43.8}$$

where P is the polarization degree and q is the ratio between the intensities of the chosen resonances for the two different polarizations

$$q = \frac{I(\theta_2)}{I(\theta_1)} \tag{43.9}$$

43.3
NEXAFS Measurements and Data Analysis

We have seen previously that an X-ray absorption event creates a core hole. There are two main mechanisms for the decay of the excited state. The first is X-ray fluorescence, in which a higher energy core-level electron fills the deeper core hole, ejecting an X-ray of well-defined energy. The fluorescence energies emitted in this way are characteristic of the atom; thus, they can be used to identify the atoms in a system and to quantify their concentrations. The second process for the decay of the core hole is the Auger effect, in which an electron drops from a higher electron level and a second electron is emitted into the continuum. In the hard X-ray regime (>2 keV), X-ray fluorescence is more likely to occur than Auger emission, but for lower energy X-ray absorption, Auger processes dominate.

Now, to measure a spectrum, it is essential to realize a good measure of $\mu(E)$ (Eq. (45.3)). The main experimental challenge is getting a X-ray source that can be tuned in energy. Nowadays, the X-ray source typically used is a synchrotron, which provides a full range of X-ray wavelengths. In addition, this radiation has very peculiar properties necessary for NEXAFS such as high brightness and high intensity, many orders of magnitude more than with X-rays produced in conventional X-ray tubes, high level of polarization (linear or elliptical), high brilliance, exceeding other natural and artificial light sources by many orders of magnitude in third-generation sources [21].

Experimentally, different detection modes can be chosen. The traditional detection has been for a long time the transmission mode, as shown in Figure 43.2. However, this technique can be applied only to self-standing systems thin enough to allow the transmission of the X-ray radiation through the sample. As a consequence, the signal contains contributions that are due to the complete thickness of the investigated system. Unless the elements present at the surface are different from those in the bulk, as in the case of adsorbates, and the spectra can be chemically resolved, this technique is essentially bulk sensitive; thus, we do not further address its specifics in this chapter.

Further detection modes are total electron yield (TEY), partial electron yield (PEY), Auger electron yield (AEY), and fluorescence yield (FY), as shown in Figure 43.4.

In TEY, all emitted electrons (i.e., Auger plus secondary electrons) are detected. On the one hand, this detection method yields high signal intensity, on the other hand, there is a high background due to low-energy electrons. The electrons can be detected with a channeltron or microchannelplate. Alternatively, the sample current, that is, the current between sample and ground, can be measured

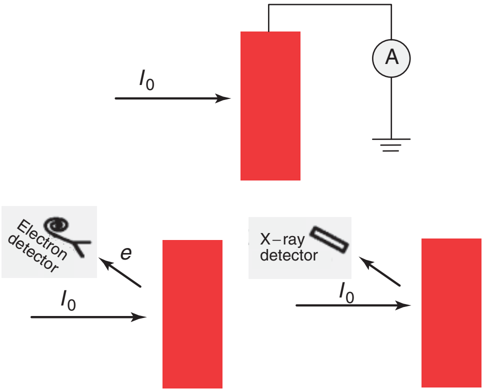

Figure 43.4 Different methods used for measuring NEXAFS are sketched.

with a multimeter down to the picoampere regime, which represents the least experimental effort for NEXAFS measurements.

To increase the signal-to-background ratio, a negative retarding field can be applied to a grid in front of the electron detector (channeltron/channelplate). This is done in PEY. Thus, the background signal from low-energy electrons can be drastically reduced.

A possible configuration of a PEY detector is shown in Figure 43.5. The photoemitted electrons travel trough a metal grid, kept at ground potential, while the low-energy electrons are repelled by a second grid kept at a negative retarding voltage. The retarding voltages depend on elements; typical values are −200 V for carbon, −320 V for nitrogen, and −450 V for oxygen K-shell [2]. The electron signal is amplified by two channel plates, whose voltages are supplied by metallic contact rings. The electron output is finally gathered by a collector, which is connected for current measurements to a floating battery box. The collector is kept at a voltage around 100 V higher than the ring contact of the second channel plate.

The best signal-to-background ratio can be obtained in AEY, if only the Auger electrons are detected with an electron energy analyzer. This detection mode also enhances the chemical sensitivity, as the analyzer energy is tuned to an element specific Auger line (e.g., C-KLL at 266 eV, O-KLL at 512 eV). In addition, NEXAFS has the highest surface sensitivity in the AEY mode because electrons from deeper layers, which lose energy on their way out of the sample, are not detected.

As mentioned, when X-rays are absorbed, the excited core hole can relax back also via emission of fluorescent X-rays. In FY, the fluorescence emission is detected. Fluorescence detection was principally used in experiments with hard X-rays because its use in the soft X-ray range was hampered by the extremely low values of the FY. With the availability of high-brilliance third-generation synchrotron radiation sources, new opportunities exist for the application of FY. However, this detection mode is also more bulk sensitive and therefore better suited when structural information from the bulk of the sample is needed.

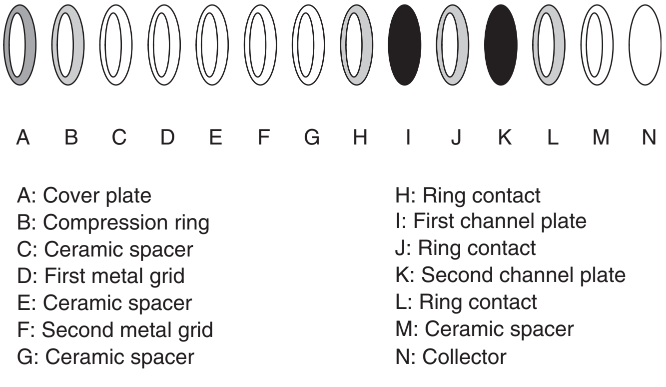

Figure 43.5 Schematic configuration of a double-channel plate partial electron yield detector.

Here, we mention for the first time the surface sensitivity of NEXAFS spectroscopy. Surface sensitivity in a technique is given by the relationship between kinetic energy of the photoemitted electrons and their inelastic mean free path. The inelastic mean free path is defined as the average distance traveled by an electron between inelastic collisions. It depends on the kinetic energy according to a general behavior that is similar for all materials, the so-called universal curve. The surface sensitivity is determined by the depth perpendicular to the surface from which the electrons escape, which is proportional to the inelastic mean free path via the cosines of the emission angle of the electrons relative to the surface normal. Thus, the surface sensitivity of an experiment can be varied accordingly: the inelastic mean free path has a minimum at around 50 eV, corresponding to a few Angstrom. For kinetic energies up to 2000 eV, its value is 70 Å large. Thus, in the X-ray regime, when the chosen detection mode collects emitted photoelectrons (e.g., PEY and AEY), their largest inelastic mean free path is on the order of magnitude of few nanometer [22].

Data analysis in NEXAFS represents a very crucial post-experiment phase. The recorded signal always contains also the absorption of the entire setup for a given edge. A traditional example is the absorption at the carbon edge of the mirrors used at beamlines. As in optical spectroscopy, the signal of the analyzed sample is multiplied by the signal due to the setup; thus, a normalization is necessary.

There are two methods to determine the normalizing signal: flux (I_0) current and clean substrate current [2].

The I_0 current method consists in measuring, when possible simultaneously, the TEY current of a clean metallic grid, usually of gold, put in front of the sample and the NEXAFS signal of the sample itself. The clean substrate method is useful when adsorbates are deposited onto a surface, that is, a substrate. The NEXAFS signal of the adsorbate is normalized in this case at each edge by using the NEXAFS signal of the substrate.

Upon normalization, which can be considered completely correct when the background line before the pre-edge region is simply a line parallel to the energy axis, that is, there is no absorption due to the investigated edge, we subtract a constant value corresponding to the smooth pre-edge function, to get rid of any instrumental background (this is the case, for example, with synchrotron radiation due to the slight small differences in the beam orbit after every injection), and absorption from other edges. At this point, it is usual to consider the signal in the region after the edge due to transitions to continuum, that is, the edge jump, equal to 1. This procedure gives the opportunity to compare NEXAFS spectra at a given edge taken at different synchrotrons, with different set ups, and so on.

The use of high-brilliance synchrotron radiation and ultrahigh-resolution monochromators has immensely broadened the potential of the NEXAFS method, given also the opportunity to resolve new fine structures. However, the high resolution requires even major care in handling of the data and it requires (i) accurate calibration of the energy scale and (ii) perfect intensity normalization in order to avoid errors such as spurious features. From this point of view, normalizing data taken at the carbon edge can be rather problematic and requires particular care and effort because of the unavoidability of carbon contaminations of the optical elements of a beamline.

Last but not least, the development of the modern synchrotrons (from third generation on) has had a real impact and importance in NEXAFS spectroscopy. Most of the recent not previously explored properties of gas, liquid, or solid state by using NEXAFS owe their discovery to the existence of such a powerful source in synergy with the high degree of knowledge reached in ultrahigh vacuum science and technology. We do not address it in detail and we suggest that the readers refer to the existent literature [21, 23].

43.4
Applications

In the following, we will report some NEXAFS experiments from the existing literature in order to show the potential of this technique, and how it can be used to answer questions ranging from basic research to solve problems also relevant in technology.

43.4.1
NEXAFS as a Fingerprint in Oxides

Single crystals of TiO_2 have been intensively studied. Titanium oxide is the most investigated single-crystalline system among all metal oxides [24]. The potential of applications is enormous, ranging from medicine to electronics [24, 25]. TiO_2 exists mainly in three different crystallographic phases: rutile, anatase, and brookite. Their electronic structure as well as their surface structure is well understood. NEXAFS spectra constitute a clear fingerprint of titanium oxides. Figure 43.6 shows the NEXAFS spectra at the Ti 2p edge of stoichiometrically well-ordered rutile $TiO_2(110)$ and anatase $TiO_2(101)$ surfaces. They show significant differences depending on the crystallographic phase as well as on the degree of Ti reduction [26–32]. In particular, TiO_2 single-crystal spectra show well-resolved peaks in the range between 455 and 470 eV corresponding to the various Ti 2p → 3d transitions [20, 21–24], as shown in Ref. [24]. The Ti 2p edge shows two groups of peaks arising from the spin-orbit splitting of the Ti 2p core level into $2p_{3/2}$ and $2p_{1/2}$ levels with $\sim$6 eV energy separation. These levels are further split because of crystal-field effects [26, 27]. This rich structure is absent in the case of TiO and Ti_2O_3 [26]. Their spectra present broader features, and the splitting due to crystal-field effects is quenched by the fact that the Ti 3d spectral weight is redistributed by the core-hole influence. An analogous behavior is seen in the spectra of metallic Ti [30].

Nowadays, there is the need to go beyond single-crystal characterization toward applications that require different types of surfaces. TiO_2, in polycrystalline form and as thin film, has already attracted a great deal of attention in biology and medicine because of the standard methods (e.g., machined or sandblasted Ti) used to build implant devices. In addition, titanium oxide thin films are also useful for

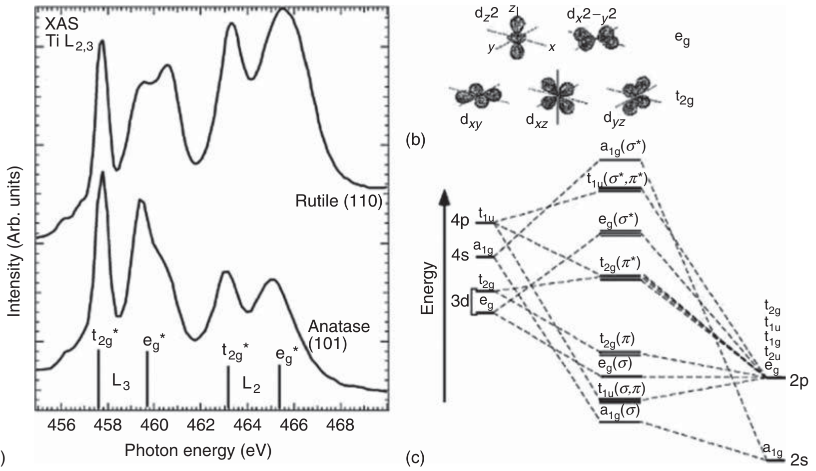

Figure 43.6 NEXAFS spectra at the Ti 2p edge of stoichiometric well-ordered rutile $TiO_2(110)$ and anatase $TiO_2(101)$ surfaces. The effect of the crystal field of the oxygen ligands is also sketched. (Reprinted from Ref. [24], Page 107, Copyright 2002, with permission from Elsevier.)

applications such as catalysis, optical coatings for selective filters, dye-sensitized photovoltaic cells, and electrochemical sensors [33–36]. A possible method of growing thin films of titanium oxide is given by magnetron sputtering [37–44]. Despite the large number of applications, only a few studies have been published investigating the electronic structure of titanium oxide films [45, 46], and not much has been done on magnetron-sputtered films [41].

For example, we have investigated two sets of magnetron-sputtered TiO_2 thin films by using NEXAFS [47]. The detailed analysis of the Ti 2p (Figure 43.7) and O 1s NEXAFS spectra allows determining the polymorphs and the degree of order of the investigated samples. We find that thin films grown by using reactive sputtering with a Ti target and lower deposition rates have a rutile-like character, while by using a TiO_2 target and higher deposition rates we obtain amorphous/mixed thin films. The NEXAFS results and the assignment to specific polymorphs are in good agreement with the corresponding X-ray diffraction (XRD) patterns. This work clearly shows the extension of possibilities given by the use of such a powerful tool as NEXAFS, not only to investigate single crystals but also TiO_2 thin films. The

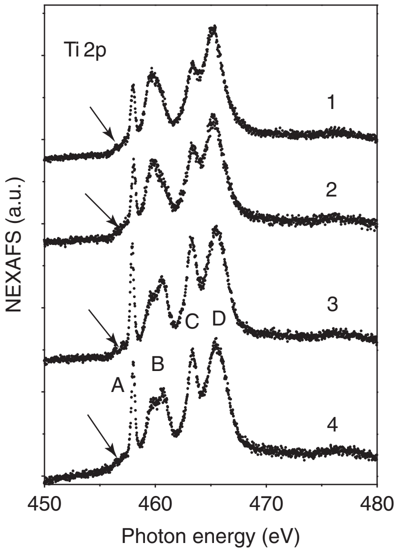

Sample	Target	Composition (sccm)	Time (min)	*P* (mbar)	Nominal thickness (nm)	Phase
1, 2	Ti	Ar : O = 80 : 30	120	7.7×10^{-3}	50	Rutile-like
3, 4	TiO_2	100 Ar	120	7.2×10^{-3}	100	Amorphous/mixed

Figure 43.7 Ti 2p NEXAFS spectra of sample set 1, subgroups 1 and 2, as indicated. A vertical offset is used for clarity. The arrows evidence pre-edge features. The table gives the preparation parameters of the investigated samples investigated and the phase of the films as obtained from the NEXAFS investigations.

strong correlation between the electronic structure and the structural phase allows assigning directly from the NEXAFS spectra the polymorphs, even in the case of very thin films for which diffraction techniques may not provide unambiguous information and for the surface region, which is important for the interface properties especially in case of implants.

43.4.2

Molecular Orientation, Interaction with the Substrate, and Intermolecular Interaction of an Organic Absorbate: Copper Phthalocyanine Thin Films on a Polycrystalline Gold Substrate

Organic small molecules have been extensively investigated in recent years because of the fascinating opportunities related to their use in electronics, ranging from flexible, stretchable displays to transparent ones, via new lighting concepts, where lamp structures or walls are the light-emitting objects themselves. To use the molecules in a device, it is necessary to grow a film. The orientation of the molecules is known to determine the electronic properties at the interfaces, and consequently the device performances. A method that can be used to determine this structural parameter is NEXAFS spectroscopy. As discussed previously, it is necessary to vary the polarization of the incident radiation and to measure NEXAFS spectra for at least two different polarization angles. At third-generation synchrotron radiation sources, given the high brilliance at undulator beamline, it is possible to investigate also very thin films, down to the submonolayer regime. It is worth mentioning that under these experimental conditions, the radiation damage issue has to be taken into account, and all possible precautions have to be taken to avoid data artifacts.

Among small molecules, the most investigated ones, because of their importance as a model system and as an active layer in devices, are certainly the acenes, the phthalocyanines (Pcs) and the perylene-based molecules [48, 49].

The family of Pcs is one of the most promising candidates for a variety of applications [50–52] owing to their electronic and optical properties and their variability in functional group substitution. Anisotropic electrical transport properties are often observed in these materials, caused by the preferred molecular orientation [53–55]. A very high degree of orientation in evaporated films was observed on several substrates [49, 56–60], even on relatively ill-defined technically relevant substrates [61].

A series of N1s edge NEXAFS spectra at different beam incidence angles were recorded from thin films with thicknesses up to 3 nm (Figure 43.8) [62]. For the spectra of the 0.5 nm thick film, a strong angle dependence is observed, with a maximum π^* absorption for grazing beam incidence and a minimum π^* absorption for normal beam incidence. This shows that the π^* molecular orbitals are perpendicular to the sample plane, indicating that the molecules are oriented parallel to the substrate surface. The data set for 1.0 nm film thickness shows reduced angle dependence with respect to the 0.5 nm film, whereas almost no angle dependence is observed for the 3.0 nm film. The observed initial growth mode of the first layers can be understood by means of the competing molecule–substrate and molecule–molecule interactions at the interface [61, 63, 64]. This has been

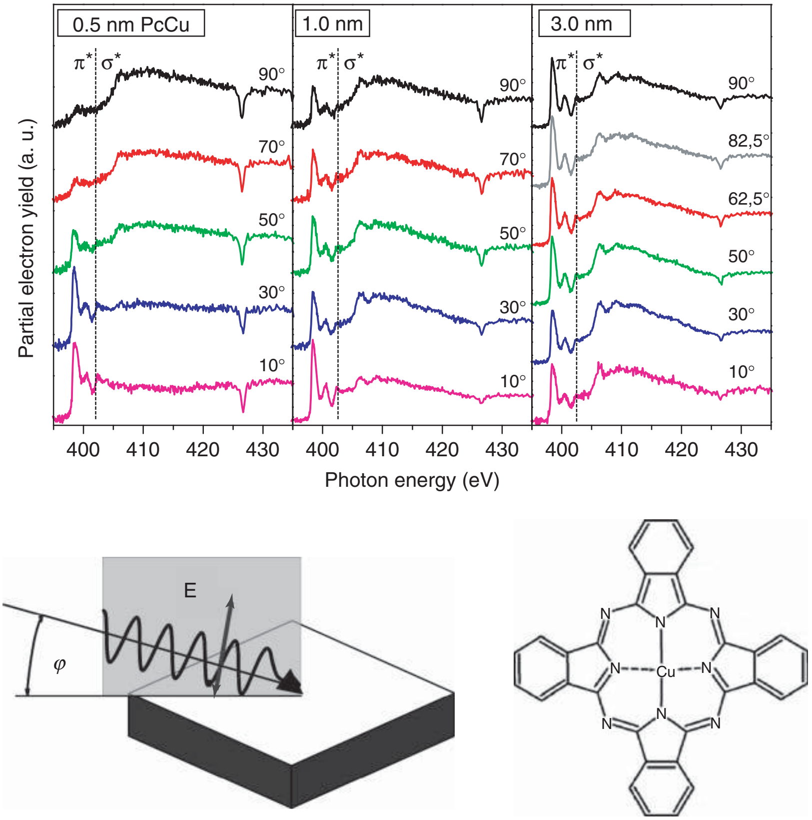

Figure 43.8 Series of N1s NEXAFS spectra of copper phthalocyanine thin films on gold foil substrates taken with different angles of beam incidence $\varphi = 90^\circ$ corresponds to normal, $\varphi = 10^\circ$ to grazing incidence, according to the geometry of the experiment that is also shown. The angular dependence of the π* features for the 0.5 nm film reveals the "lying orientation" of the molecules. The spectra for the 1.0 and 3.0 nm films show a weaker or almost no angle dependence, pointing to a change of molecular ordering with growing film thickness. The molecular structure of copper phthalocyanines is also shown.

observed for substituted and unsubstituted Pcs on single-crystalline metal substrates [65] and single-crystalline germanium [61], as well as for copper Pcs on molybdenum disulfide [66] and on native silicon [67]. For higher coverages, the molecule–substrate interaction becomes negligible, and the intermolecular interaction and surface energy of the molecular film are the structure-determining parameters [63, 64, 68]. The molecules may form stacks parallel to the sample surface consisting of standing molecules, as the interfacial layers act as a van der Waals substrate.

How the molecules oriented themselves in the film plays an important role also from a technological point of view. Photoelectron spectroscopy of conjugated organic compounds, an ω-dihexyl-sexithiophene and a-sexithiophene, on Ag(111), combined with first principles calculations have revealed the existence of a surface dipole built into molecular layers. Its magnitude depends on the orientation of molecules relative to the surface. In particular, the ionization potentials of the molecules change by up to 0.6 eV depending on whether they are flat lying or standing upright with respect to the substrate [69].

Thus, opportunely tuning the molecular orientation by appropriate preparation parameters, or substrate patterning, it is possible to optimize the barriers for charge injection in organic electronics.

43.4.3
Molecular Orientation and Growth Modes

Investigating the perylene deposited on $Al_2O_3/Ni_3Al(111)$ by NEXAFS spectroscopy [70], we found that it is possible to ''tune'' the molecular orientation by choosing an appropriate set of growth parameters during the deposition. The NEXAFS spectra show that there is no evidence of any reorientation of the molecules upon annealing.

This means that the possibility to tune the molecular geometry in the film is directly related to the adsorption mechanism. As a consequence, the monolayer can be deposited varying the molecules orientation from flat lying on the substrate toward a more upright standing position. Because of the relationship between the films thickness and the molecular orientation, we conclude that the molecules have their short axis parallel to the substrate plane, while the long axis is out of plane. In the multilayers, the minimum obtainable value for the molecular orientation is 53°. In this case, we cannot discern by using only NEXAFS data whether it is a real intermediate phase or it is a coexistence of several phases. In thicker films prepared by using higher deposition rate and keeping the substrate at room temperature (RT), we obtain an almost upright molecular orientation close to the single-crystal value. We have described the driven mechanisms in terms of the classical theory of nucleation.

Atomistic theories, based on a general thermodynamic approach, describe the role of individual atoms or small clusters during the earliest stage of the film formation [71, 72]. We apply this approach to molecules, seen now as the elemental building blocks. The reason for this choice is based on the fact that (i) this theory answers the questions why, how, and where different preparation conditions play a role in the film growth. (ii) It relates the preparation with a different dimensionality of the growth. (iii) It has been already applied to the growth of tetracene, pentacene, and perylene thin films, showing how the growth of organic thin films on inert substrates closely mimics the epitaxial growth of inorganic materials [73, 74].

The orientation of the molecules is the specific parameter that defines the difference between atomic and molecular growth. Thus, the most innovative aspect of this work is the relationship between the changes in the molecular orientation, investigated by NEXAFS, and the calculated supersaturation during growth (Figure 43.9).

This relationship, molecular orientation versus supersaturation, is a step forward in aiming at a general description of the organic thin-film growth.

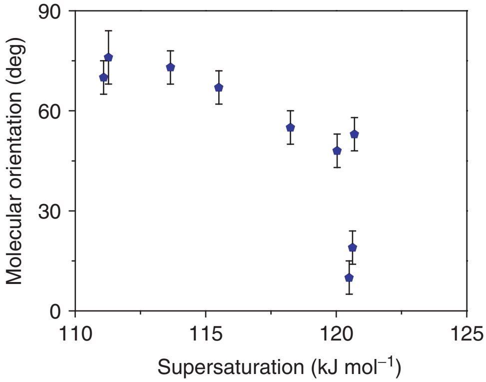

Figure 43.9 Molecular orientation as calculated from the NEXAFS spectra versus supersaturation.

43.4.4
Thickness Dependence of the Electronic Structure and Local Geometry in MnO: Differences between Bulk and Thin Film Properties

Binary transition-metal oxides have been attracting fundamental scientific interest for many years. Their strong electron–electron interaction combined with their compositional simplicity makes them important model compounds for understanding the effects of strong correlation in phenomena such as magnetism and electron transport. Novel properties are predicted for ultrathin films of these oxides on metallic substrates [75]. These properties are expected to differ from bulk properties because of both the reduced dimensionality and the influence of the interface. The metallic substrate may have a purely electronic contribution to the properties of ultrathin films by changing the electron density at the interface [76]. This may change either the ground state of the oxide film or the screening in response to an electronic excitation [77, 78]. In case of less inert metallic substrates, interface reactions, to various extent, can take place [79–83]. Furthermore, interface strain effects may be observed in epitaxial layer systems with a lattice mismatch [84]. It is of basic interest whether these different influences can be used to tune the properties of ultrathin films systematically. As discussed earlier, NEXAFS can probe the orientation of molecular orbitals. More generally, polarized X-ray absorption can sense the charge anisotropy of the valence states involved in the core excitation process. In most cases, the anisotropy of the charge in the atomic volume is caused by anisotropy in the bonding, that is, by the electrostatic potential.

Thus, NEXAFS is a very useful investigation method in this framework. Ultrathin films of MnO on Ag (001) have been investigated by using thickness-dependent XAS [85]. In the MnO bulk structure, manganese is octahedrally coordinated by oxygen. Therefore, no polarization dependence is expected in the XAS spectra of the MnO(001) crystal. The peak positions, the relative intensities, and the overall intensity after normalization with respect to the edge jump remain unchanged for the reference crystal when going from normal to grazing incidence. In contrast, clear changes in the peak positions and the relative intensities are visible in the polarization-dependent Mn $L_{2,3}$ edge spectra of the ultrathin films. These changes become evident in different angular-dependent sets of spectra recorded at the different film thicknesses, and shown in Figure 43.10a.

Subtracting the normalized spectra taken at an angle of 70° from the spectra at 0° (that is the definition of linear dichroism) and plotting them together (Figure 43.10b, also with the related simulations scaled by a factor of 10 to match

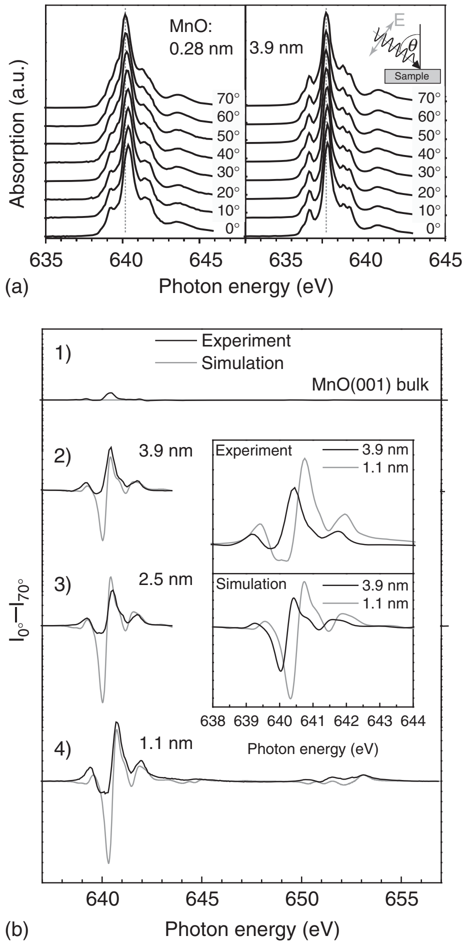

Figure 43.10 (a) Polarization-dependent Mn L_3 XA spectra of a 0.28 nm (left) and a 3.9 nm (right) MnO (001) film on Ag (001). (b) Linear dichroism of the Mn $L_{2,3}$ X-ray absorption spectra of (1) a MnO (001) single crystal, (2) a 3.9 nm, (3) a 2.5 nm, and (4) a 1.1 nm thick film of MnO (001) on Ag (001). The experimental spectra (black solid curves) are directly compared to the theoretical simulations (dashed gray curves). The inset shows the experimental and theoretical findings of the L_3 edge for two different film thicknesses.

the total intensity), it is clear that the linear dichroism plot of the bulk MnO shows only a small artifact at the position of the highest absorption intensity. On the contrary, in the linear dichroism plots of the films, the dichroism decreases and the features shift to lower energies with increasing film thickness. The synergy between experiment and simulation is a key point in understanding this behavior. The simulations were performed assuming that the epitaxially grown manganese oxide layers on a silver substrate are tetrahedrally distorted MnO_6 octahedrons. This describes the observed linear dichroism reasonably well. The influence of the substrate on the layer decreases with increasing film thickness. Consequently, the distortion of the MnO structure by the matching to the Ag substrate decreases with increasing film thickness, as also verified by the simulation.

43.4.5

Charge Transfer Between Metal 3d Electrons and Metal Surfaces in Transition-Metal Phthalocyanine/Metal Interfaces

X-ray absorption is also a technique that is proved to be useful to investigate the interface between transition-metal Pcs and metal surfaces. In addition to the well-known material properties of the Pcs family, transition-metal Pcs have magnetic properties because of the presence of the partially empty d levels of the central metal. This aspect makes them promising candidates for their use in spintronics.

Thickness-dependent angle-resolved NEXAFS measurements performed on well-ordered CoPc thin films deposited on Ag(111) show an evident dichroism at the Co L-edge that is different depending on thickness (Figure 43.11) [86]. The strong dependence of the Co L XAS on polarization reflects the different d-orbital character of the unoccupied metal atom states.

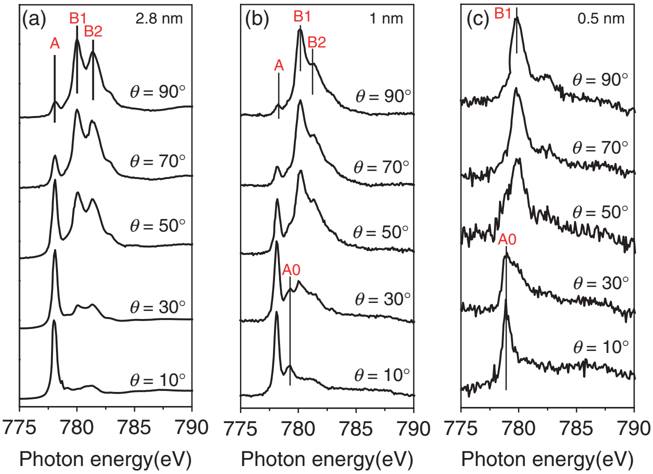

Figure 43.11 Co $L_{2,3}$ edge XAS spectra for the CoPc/Ag(111) system for different film thicknesses: (a) 2.8 nm, (b) 1 nm, and (c) 0.5 nm measured at different incident angles of the X-ray beam.

Petraki *et al*. demonstrate that this phenomenon is related to the occurrence of charge transfer between the metal 3d electrons of the Pcs and the metal surface underneath. A charge donation from the metal substrate to the central metal Co atom of the Pc molecules on top of the substrate itself leads to a redistribution of the 3d electron-inducing changes in the Co-related absorption spectra. A similar, although weaker, effect is also found at the interface in MnPc thin films deposited on Ag(111).

43.4.6
X-Ray Magnetic Circular Dichroism

XMCD is very commonly used currently to measure the difference in absorption of circular polarization with opposite helicity.

XMCD is the difference spectrum of two X-ray absorption spectra taken in the presence of a magnetic field, once with left circularly polarized light and once with right circularly polarized light. By closely analyzing the difference in the XMCD spectrum, information can be obtained on the magnetic properties of the atom, such as its spin and orbital magnetic moment. Because the allowed core-to-valence transition follows the dipole selection rule excitation at different absorption edges, XMCD provides selectivity to the angular momentum of the valence-electron states. For example, L-edge (2p) excitation in cobalt probes the cobalt 3d valence subshell, while K-edge (1s) excitation probes the cobalt 3p valence electrons [87, 88]. The large size of the circular dichroism effects (up to 30% in XMCD and tens of degrees in magnetooptical rotation) allow the study of very dilute and/or weak moments [89].

XMCD is a powerful technique that has been used to investigate various aspects. For example, XMCD at the Co L_3 and L_2 edges in Co/Pd multilayers gave evidence of a greatly enhanced orbital moment compared to that in bulk Co. The results also show that, in general, there is no simple relationship between the dichroism signal and either the spin moment or the total moment [90].

Magnetic impurities in solids cause manifold changes in their macroscopic properties, such as anomalous low-temperature resistance due to Kondo screening, reduction in the superconducting transition temperature due to local suppression of the order parameter. They create magnetic signatures in semiconductors and lead to inelastic spin excitations in tunnel junctions. With XMCD, it is possible to investigate the properties of such impurities and the huge difference with the bulk elemental spectra [91].

43.5
Conclusions and Future

The aim of this chapter has been to give an overview of a faceted technique as NEXAFS spectroscopy is. NEXAFS investigations not only give information on the unoccupied states but their use also shed light on several aspects as oxidation states, bonding of adsorbates with substrates, molecular orientation, and structural properties in thin films.

The detailed understanding of complex materials requires the use of state-of-the-art experimental techniques that provide information on electronic and magnetic properties of the materials. The advent of third-generation synchrotron sources has immensely increased the possibilities offered by NEXAFS because of the high energy resolution reached. However, the increasing miniaturization of components furthermore demands the use of techniques with spatial resolution down to the nanometer range. Thus, a good way to satisfy both requirements is to combine the distinctive properties of standard XAS with those of electron microscopy as in X-ray photoemission electron microscopy, which opens further ways to the use of XAS and to the investigations of not yet revealed phenomena.

References

1. Einstein, A. (1905) *Ann. Phys.*, **322**, 132.
2. Stöhr, J. (1998) *NEXAFS Spectroscopy*, Springer-Verlag, Berlin, Heidelberg, New York.
3. Koningsberger, D.C. and Prins, R. (eds) (1988) *X-Ray Absorption: Principles, Applications, Techniques of EXAFS, SEXAFS, and XANES*, John Wiley & Sons, Inc., New York.
4. Iwasawa, Y. (ed.) (1996) *X-Ray Absorption Fine Structure for Catalysts And Surfaces*, Series on Synchrotron Radiation Techniques and Applications, Vol. 2, World Scientific Publishing Co. Pte. Ltd., Singapore.
5. Kosugi, N. and Kuroda, H. (1980) *Chem. Phys. Lett.*, **74**, 490.
6. Kosugi, N. (1987) *Theor. Chim. Acta*, **72**, 149.
7. Kosugi, N. and Kuroda, H. (1983) *Chem. Phys. Lett.*, **94**, 377.
8. Urquhart, S.G., Hitchcock, A.P., Smith, A.P., Ade, H., and Rightor, E.G. (1997) *J. Phys. Chem. B*, **101**, 2267.
9. Urquhart, S.G. and Ade, H. (2002) *J. Phys. Chem. B*, **106**, 8531.
10. Oji, H., Mitsumoto, R., Ito, E., Ishii, H., Ouchi, Y., Seki, K., Yokoyama, T., Ohta, T., and Kosugi, N. (1998) *J. Chem. Phys.*, **109**, 10409.
11. Rehr, J.J. and Albers, R.C. (2000) *Rev. Mod. Phys.*, **72**, 621.
12. Chassé, T., Hallmeier, K.H., Hecht, J.-D., and Frost, F. (2002) *Surf. Rev. Lett.*, **9**, 381.
13. de Groot, F.M.F. and Kotani, A. (2008) *Core Level Spectroscopy of Solids*, Taylor & Francis, New York.
14. de Groot, F.M.F., Fuggle, J.C., Thole, B.T., and Sawatzky, G.A. (1990) *Phys. Rev. B*, **41**, 928.
15. de Groot, F.M.F., Fuggle, J.C., Thole, B.T., and Sawatzky, G.A. (1990) *Phys. Rev. B*, **42**, 5459.
16. de Groot, F.M.F. (1994) *J. Electron Spectrosc. Relat. Phenom.*, **67**, 529.
17. de Groot, F.M.F. (2001) *Chem. Rev.*, **101**, 1779.
18. de Groot, F.M.F. (2005) *Coord. Chem. Rev.*, **249**, 31.
19. Stöhr, J. and Outka, D. (1987) *Phys. Rev. B*, **36**, 7891.
20. Taborski, J. (1994) Doctoral Thesis, NEXAFS-Untersuchungen an organischen Adsorbaten auf verschiedenen (111)-Oberflächen. Universität Stuttgart.
21. Duke, P.J. (2000) *Synchrotron Radiation: Production and Properties*, Oxford Series on Synchrotron Radiation, Vol. 3, Oxford University Press, New York.
22. Powell, C.J., Jablonski, A., Tilinin, I.S., Tanuma, S., and Penn, D.R. (1999) *J. Electron Spectrosc. Relat. Phenom.*, **98**, 1.
23. Wiedemann, H. (2002) *Synchrotron Radiation*, Springer-Verlag, Berlin.
24. Diebold, U. (2003) *Surf. Sci. Rep.*, **48**, 53and references therein.
25. Jones, F.H. (2001) *Surf. Sci. Rep.*, **42**, 75 and references therein.
26. Lusvardi, V.S., Barteau, M.A., Chen, J.G., Eng, J. Jr.,, Frühberger, B., and Teplyakov, A. (1998) *Surf. Sci.*, **397**, 237.
27. Brydson, R., Williams, B.G., Engel, W., Sauer, H., Zeitler, E., and Thomas, J.M. (1987) *Solid State Commun.*, **64**, 609.

28. Brydson, R., Sauer, H., Engel, W., Thomas, J.M., Zeitler, E., Kosugi, N., and Kuroda, H. (1989) *J. Phys. Condens. Matter*, **1**, 797.

29. Yoshiya, M., Tanaka, I., Kaneko, K., and Adachi, H. (1999) *J. Phys. Condens. Matter*, **11**, 3217.

30. Soriano, L., Abbate, M., Vogel, J., Fuggle, J.C., Fernández, A., Gondález-Elipe, A.R., Sacchi, M., and Sanz, J.M. (1993) *Surf. Sci.*, **290**, 427.

31. Ruus, R., Kikas, A., Saar, A., Ausmees, A., Nõmmiste, E., Aarik, J., Aidla, A., Uustare, T., and Martinson, I. (1997) *Solid State Commun.*, **104**, 199.

32. De Groot, F.M.F., Grioni, M., Fuggle, J.F., Ghijsen, J., Swatzky, G.A., and Petersen, H. (1989) *Phys. Rev. B*, **40**, 5715.

33. Li, Y., Bu, W., Wu, L., and Sun, C. (2005) *Sens. Actuators B*, **107**, 921.

34. Ramírez-Salgado, J., Djurado, E., and Fabry, P. (2004) *J. Eur. Ceram. Soc.*, **24**, 2477.

35. O'Regan, B. and Grätzel, M. (1991) *Nature*, **353**, 737.

36. Xiang, J., Masuda, Y., and Koumoto, K. (2004) *Adv. Mater.*, **16**, 1461.

37. Dony, M.F., Ricard, A., Wautelet, M., Dauchot, J.P., and Hecq, M. (1997) *J. Vac. Sci. Technol., A*, **15**, 1890.

38. Tanemura, S., Miao, L., Wunderlich, W., Tanemura, M., Mori, Y., Toh, S., and Kaneko, K. (2005) *Sci. Technol. Adv. Mater.*, **6**, 11.

39. Vancoppenolle, V., Jouan, P.Y., Wautelet, M., Dauchot, J.P., and Hecq, M. (1999) *Surf. Coat. Technol.*, **116**, 933.

40. Vancoppenolle, V., Jouan, P.Y., Ricard, A., Wautelet, M., Dauchot, J.P., and Hecq, M. (2003) *Appl. Surf. Sci.*, **205**, 249.

41. Gouttebaron, R., Cornelissen, D., Snyders, R., Dauchot, J.P., Wautelet, M., and Hecq, M. (2000) *Surf. Interface Anal.*, **30**, 527.

42. Stamate, M.D. (2003) *Appl. Surf. Sci.*, **218**, 317.

43. Mwabora, J.M., Lindgren, T., Avendaño, E., Jaramillo, T.F., Lu, J., Lindquist, S.-E., and Granqvist, C.G. (2004) *J. Phys. Chem. B*, **108**, 20193.

44. Persson, C. and Da Silva, A.F. (2005) *Appl. Phys. Lett.*, **86**, 231912.

45. Sánchez-Agudo, M., Soriano, L., Quirós, C., Avila, J., and Sanz, J.M. (2001) *Surf. Sci.*, **482**, 470.

46. Sánchez-Agudo, M., Soriano, L., Quirós, C., Roca, L., Pérez-Dieste, V., and Sanz, J.M. (2002) *Surf. Sci.*, **507**, 672.

47. Casu, M.B., Braun, W., Bauchspieß, K.R., Kera, S., Megner, B., Thull, R., Heske, C., and Umbach, E. (2008) *Surf. Sci.*, **602**, 1599.

48. Witte, G. and Woll, C. (2004) *J. Mater. Res.*, **19**, 1889 and references therein.

49. Schreiber, F. (2004) *Phys. Status Solidi A*, **201**, 1037and references therein.

50. Horowitz, G. (1998) *Adv. Mater.*, **10**, 365.

51. Leznoff, C.C. and Lever, A.B.P. (eds) (1989) *Phthalocyanines–Properties and Applications*, Vol. 1, Wiley-VCH Verlag GmbH, Weinheim.

52. Forsythe, E.W., Abkowitz, M.A., Gao, Y., and Tang, C.W. (2000) *J. Vac. Sci. Technol., A*, **18**, 1869.

53. Ostrick, J.R., Dodabalapur, A., Torsi, L., Lovinger, A.J., Kwock, E.W., Miller, T.M., Galvin, M., Berggren, M., and Katz, H.E.J. (1997) *J. Appl. Phys.*, **81**, 6804.

54. Michaelis, W., Wöhrle, D., and Schlettwein, D. (2004) *J. Mater. Res.*, **19**, 2040.

55. Mathur, S.C. and Ramesh, N. (1975) *Chem. Phys. Lett.*, **37**, 276.

56. Ruocco, A., Evangelista, F., Attili, A., Donzello, M.P., Betti, M.G., Giovanelli, L., and Gotter, R. (2004) *J. Electron Spectrosc. Relat. Phenom.*, **137**, 165.

57. Barrena, E., Osso, J.O., Schreiber, F., Garriga, M., Alonso, M.I., and Dosch, H. (2004) *J. Mater. Res.*, **19**, 2061.

58. Alfredsson, Y., Aahlund, J., Nilson, K., Kjeldgaard, L., O'Shea, J.N., Theobald, J., Bao, Z., Mårtensson, N., Sandell, A., Puglia, C., and Siegbahn, H. (2005) *Thin Solid Films*, **493**, 13.

59. Sakurai, T., Kawai, S., Fukasawa, R., Shibata, J., and Akimoto, K. (2005) *Jpn. J. Appl. Phys., Part 1*, **44**, 1982.

60. Kera, S., Casu, M.B., Bauchspieß, K.R., Batchelor, D., Schmidt, T., and Umbach, E. (2006) *Surf. Sci.*, **600**, 1077.

61. Peisert, H., Schwieger, T., Auerhammer, J.M., Knupfer, M., Golden, M.S., Fink, J., Bressler, P.R., and Mast, M. (2001) *J. Appl. Phys.*, **90**, 466.

62. Biswas, I., Peisert, H., Nagel, M., Casu, M.B., Schuppler, S., Nagel, P., Pellegrin, E., and Chassé, T. (2007) *J. Chem. Phys.*, **126**, 174704.

63. Iwatsu, F. (1988) *J. Phys. Chem.*, **92**, 1678.

64. Ottaviano, L., Nardo, S.D., Lozzi, L., Passacantando, M., Picozzi, P., and Santucci, S. (1997) *Surf. Sci.*, **373**, 318.

65. Peisert, H., Biswas, I., Zhang, L., Knupfer, M., Hanack, M., Dini, D., Cook, M.J., Chambrier, I., Schmidt, T., Batchelor, D., and Chassé, T. (2005) *Chem. Phys. Lett.*, **403**, 1.

66. Okudaira, K.K., Hasegawa, S., Ishii, H., Seki, K., Harada, Y., and Ueno, N. (1999) *J. Appl. Phys.*, **85**, 6453.

67. de Oteyza, D.G., Barrena, E., Sellner, S., Osso, J.O., and Dosch, H. (2006) *J. Phys. Chem. B*, **110**, 16618.

68. Hamann, C. and Lehmann, G. (1973) *Phys. Status Solidi B*, **60**, 407.

69. Duhm, S., Heimel, G., Salzmann, I., Glowatzki, H., Johnson, R.L., Vollmer, A., Rabe, J., and Koch, N. (2008) *Nat. Mater.*, **7**, 326.

70. Casu, M.B., Schöll, A., Bauchspieß, K.R., Hübner, D., Schmidt, T., Heske, C., and Umbach, E. (2009) *J. Phys. Chem. C*, **113**, 10990.

71. Ohring, M. (2002) *Materials Science of Thin Films*, 2nd edn, Academic Press, London.

72. Zhang, Z. and Lagally, M.G. (1997) *Science*, **276**, 377.

73. Meyer zu Heringdorf, F.-J., Reuter, M.C., and Tromp, R.M. (2001) *Nature*, **412**, 517.

74. Verlaak, S., Steudel, S., Heremans, P., Janssen, D., and Deleuze, M.S. (2003) *Phys. Rev. B*, **68**, 195409.

75. Altieri, S., Tjeng, L.H., and Sawatzky, G.A. (2001) *Thin Solid Films*, **400**, 9.

76. Ferrari, A.M. (2005) *Surf. Sci.*, **584**, 269.

77. Altieri, S., Tjeng, L.H., Voogt, F.C., Hibma, T., and Sawatzky, G.A. (1999) *Phys. Rev. B*, **59**, R2517.

78. Altieri, S., Tjeng, L.H., Voogt, F.C., Hibma, T., Rogojanu, O., and Sawatzky, G.A. (2002) *Phys. Rev. B*, **66**, 155432.

79. de Masi, R., Reinicke, D., Müller, F., Steiner, P., and Hüfner, S. (2002) *Surf. Sci.*, **515**, 523.

80. Regan, T.J., Ohldag, H., Stamm, C., Nolting, F., Lüning, J., Stöhr, J., and White, R.L. (2001) *Phys. Rev. B*, **64**, 214422.

81. Benedetti, S., Luches, P., Liberati, M., and Valeri, S. (2004) *Surf. Sci.*, **572**, L348.

82. Nagel, M., Zhang, L., Peisert, H., and Chassé, T. (2006) *Microchim. Acta*, **156**, 27.

83. Krasnikov, S., Vinogradov, A., Hallmeier, K.-H., Höhne, R., Ziese, M., Esquinazi, P., Chassé, T., and Szargan, R. (2004) *Mater. Sci. Eng., B*, **109**, 207.

84. Haverkort, M.W., Csiszar, S.I., Hu, Z., Altieri, S., Tanaka, A., Hsieh, H.H., Lin, H.-J., Chen, C.T., Hibma, T., and Tjeng, L.H. (2004) *Phys. Rev. B*, **69**, 020408(R).

85. Nagel, M., Biswas, I., Nagel, P., Pellegrin, E., Schuppler, S., Peisert, H., and Chassé, T. (2007) *Phys. Rev. B*, **75**, 195426.

86. Petraki, F., Peisert, H., Latteyer, F., Aygül, U., Vollmer, A., and Chassé, T. (2011) *J. Phys. Chem. C*, **115**, 21334.

87. Samant, M.G., StoKhr, J., Parkin, S.S.P., Held, G.A., Hermsmeier, B.D., Herman, F., van Schilfgaarde, M., Duda, L.-C., Mancini, D.C., Wassdahl, N., and Nakajima, R. (1994) *Phys. Rev. Lett.*, **72**, 1112.

88. Pizzini, S., Fontaine, A., Giorgetti, C., Dartyge, E., Bobo, J.F., Piecuch, M., and Baudelet, F. (1995) *Phys. Rev. Lett.*, **74**, 1470.

89. Kortright, J.B., Awschalom, D.D., Stöhr, J., Bader, S.D., Idzerda, Y.U., Parkin, S.S.P., Schuller, I.K., and Siegmann, H.C. (1999) *J. Magn. Magn. Mater.*, **207**, 7.

90. Wu, Y., Stöhr, J., Hermsmeier, B.D., Samant, M.G., and Weller, D. (1992) *Phys. Rev. Lett.*, **69**, 2307.

91. Brune, H. and Gambardella, P. (2009) *Surf. Sci.*, **603**, 1812.

44
The X-Ray Standing Wave Technique

Alexander Gerlach and Frank Schreiber

44.1
Introduction

The X-ray standing wave (XSW) technique provides element-specific information on surface structures and adsorbate sites by combining a diffraction-based approach with spectroscopic measurements. After pioneering work by Batterman in the 1960s [1, 2] and various others thereafter, the increased availability of brilliant and tunable synchrotron light has stimulated the application of this technique to a wide range of problems in surface and interface science; see, for example, Refs. [3–5].

The conventional concept is based on the excitation of characteristic, element-specific signals, that is, photoelectrons, Auger electrons, or fluorescence light, in an XSW field, which is generated by the superposition of the incoming and the reflected wave. The interference character of this technique allows for high spatial resolution, typically a few percent of the wavelength used in the experiment. There are several variations of the XSW technique, which differ in the way the standing wave field is generated. While the most common approach is based on single-crystal Bragg reflections, the use of thin-film Bragg reflections, total external reflection, or reflection from layered synthetic multilayers are also well established in the study of interfaces at different length scales [4].

In this article, we first give a short overview of the theory used to describe X-ray wave field in crystals (Section 44.2), then we discuss briefly about some specific experimental requirements of the technique (Section 44.3). Finally, we look at some typical XSW applications in the field of organic adsorbates, where atomic length scales are probed (Section 44.4).

Handbook of Spectroscopy, Second Edition. Edited by Günter Gauglitz and David S. Moore.

44.2
Theory

44.2.1
Wave Fields in Crystals

The dynamical theory of X-ray diffraction derives the wave fields in crystals from the Maxwell equations [6] for a periodic electron density $\rho(\vec{r})$ at each point $\vec{r}$ inside the crystal. As shown in Figure 44.1, the wave vectors of the incident and diffracted waves, $\vec{K}_0$ and $\vec{K}_{\mathrm{H}}$, fulfill the Bragg condition

$$\vec{K}_{\mathrm{H}} = \vec{K}_0 + \vec{H} \tag{44.1}$$

with $|\vec{K}| = \lambda^{-1}$ and $\vec{H}$ being a reciprocal lattice vector. Because, in periodic media, Bloch functions are the solutions to linear differential equations, the fields are expanded as a sum of plane waves (with $\vec{\mathcal{A}}$ corresponding to the electric and magnetic vectors fields $\vec{\mathcal{E}}, \vec{\mathcal{D}}, \vec{\mathcal{H}}$, and $\vec{B}$)

$$\vec{\mathcal{A}} = \sum_H \vec{\mathcal{A}}_{\mathrm{H}} e^{-2\pi i \vec{K}_{\mathrm{H}}\cdot\vec{r}} = \left[\sum_H \vec{\mathcal{A}}_{\mathrm{H}} e^{-2\pi i \vec{H}\cdot\vec{r}}\right] e^{-2\pi i \vec{K}_0\cdot\vec{r}} e^{-2\pi i \nu t} \tag{44.2}$$

Using this representation, one finds that because the equations have to be valid for all points in space and time, the following conditions for each reciprocal lattice vector $\vec{H}$

$$\vec{K}_{\mathrm{H}} \times \vec{\mathcal{E}}_{\mathrm{H}} = \nu\mu_0\vec{\mathcal{H}}_{\mathrm{H}} \tag{44.3}$$

$$\vec{K}_{\mathrm{H}} \times \vec{\mathcal{H}}_{\mathrm{H}} = -\nu\vec{\mathcal{D}}_{\mathrm{H}} \tag{44.4}$$

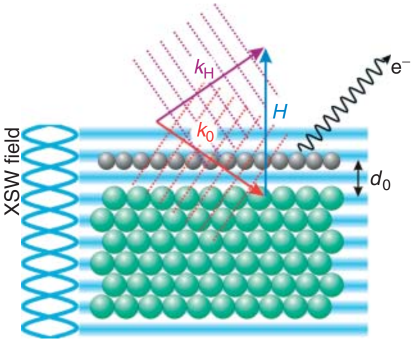

Figure 44.1 XSW principle. The standing wave field can be produced by Bragg reflection of monochromatic X-rays from a single-crystal substrate. The variation in the photo (or fluorescence) yield, when scanning the photon energy through the Bragg condition, depends on the adsorbate position d_0.

Here, the electron density $\rho(\vec{r})$ enters via the complex structure factor $\mathcal{F}_{\mathrm{H}} = \mathcal{F}_{\mathrm{H}} + i\mathcal{F}'_{\mathrm{H}}$ and the corresponding susceptibility χ given by

$$\mathcal{F}_{\mathrm{H}} = \int \rho(\vec{r}) e^{2\pi i \vec{H}\cdot\vec{r}} \mathrm{d}^3 r \tag{44.5}$$

$$\chi(\vec{r}) = 1 - \Gamma \sum_{H} \mathcal{F}_{\mathrm{H}} e^{-2\pi i \vec{H}\cdot\vec{r}} \tag{44.6}$$

with $\vec{\mathcal{D}} = \chi \epsilon_0 \vec{\mathcal{E}}$ (using $\Gamma = r_e \lambda^2/(\pi V)$ with the classical electron radius $r_e = 2.82 \times 10^{-5}$ Å and the unit cell volume V). From this it is found that

$$\vec{\mathcal{D}}_{\mathrm{H}} = \epsilon_0 \vec{\mathcal{E}}_{\mathrm{H}} - \epsilon_0 \Gamma \sum_{P} \mathcal{F}_{\mathrm{H}-P} \mathcal{E}_{\mathrm{P}} = \epsilon_0 (1 - \Gamma \mathcal{F}_0) \mathcal{E}_{\mathrm{H}} - \epsilon_0 \Gamma \sum_{P \neq H} \mathcal{F}_{\mathrm{H}-P} \mathcal{E}_{\mathrm{P}} \tag{44.7}$$

Inserting this into Eq. (44.3), one obtains a set of fundamental equations that describe the wave fields inside the crystal

$$\left[k^2(1 - \Gamma\mathcal{F}_0) - (\vec{K}_{\mathrm{H}} \cdot \vec{K}_{\mathrm{H}})\right] \vec{\mathcal{E}}_{\mathrm{H}} - k^2 \Gamma \sum_{P \neq H} \mathcal{F}_{\mathrm{H}-P} \vec{\mathcal{E}}_{\mathrm{P}} + (\vec{K}_{\mathrm{H}} \cdot \vec{\mathcal{E}}_{\mathrm{H}}) \vec{K}_{\mathrm{H}} = 0 \tag{44.8}$$

For the case that only one reciprocal lattice point contributes to the diffraction, that is, there is only the incidence wave $\vec{\mathcal{E}}_0$ and the reflected wave $\vec{\mathcal{E}}_{\mathrm{H}}$, this is reduced to two equations for σ-polarization

$$\left[k^2(1 - \Gamma\mathcal{F}_0) - \vec{K}_0 \cdot \vec{K}_0\right] \vec{\mathcal{E}}_0^{\sigma} - k^2 \Gamma \mathcal{F}_{\overline{\mathrm{H}}} \vec{\mathcal{E}}_{\mathrm{H}}^{\sigma} = 0 \tag{44.9}$$

$$-k^2 \Gamma \mathcal{F}_{\mathrm{H}} \vec{\mathcal{E}}_0^{\sigma} + \left[k^2(1 - \Gamma\mathcal{F}_0) - \vec{K}_{\mathrm{H}} \cdot \vec{K}_{\mathrm{H}}\right] \vec{\mathcal{E}}_{\mathrm{H}}^{\sigma} = 0 \tag{44.10}$$

This set of equations only has a nontrivial solution for $\mathcal{E}_0^{\sigma}/\mathcal{E}_{\mathrm{H}}^{\sigma}$ if the determinant is zero, that is, the wave vectors $\vec{K}_0$ and $\vec{K}_{\mathrm{H}}$ have to fulfill the equation

$$\begin{vmatrix} k^2(1 - \Gamma\mathcal{F}_0) - \vec{K}_0 \cdot \vec{K}_0 & -k^2 \Gamma \mathcal{F}_{\overline{\mathrm{H}}} \\ -k^2 \Gamma \mathcal{F}_{\mathrm{H}} & k^2(1 - \Gamma\mathcal{F}_0) - \vec{K}_{\mathrm{H}} \cdot \vec{K}_{\mathrm{H}} \end{vmatrix} = 0 \tag{44.11}$$

For Bragg diffraction from a centrosymmetric crystal ($\mathcal{F}_{\mathrm{H}} = \mathcal{F}_{\overline{\mathrm{H}}}$), this reduces to

$$\frac{\mathcal{E}_{\mathrm{H}}}{\mathcal{E}_0} = -[\eta \pm \sqrt{(\eta^2 - 1)}] \tag{44.12}$$

where η is the generalized angle

$$\eta = \frac{\Gamma\mathcal{F}_0 - \Delta\theta \sin(2\theta_{\mathrm{B}})}{\Gamma\sqrt{\mathcal{F}_{\mathrm{H}}\mathcal{F}_{\overline{\mathrm{H}}}}} \tag{44.13}$$

and $\Delta\theta = \theta - \theta_{\mathrm{B}}$ the deviation from the kinematical Bragg angle θ_{B}.

From Eqs. (44.12, 44.13) not only the intrinsic shape of the reflectivity curve can be calculated but also the phase ν between the incident and reflected wave. As shown in Figure 44.2, ν changes by π across the Bragg reflection. The corresponding shift of the nodes (and antinodes) of the standing wave field by half a lattice plane spacing is the key ingredient of the XSW technique.

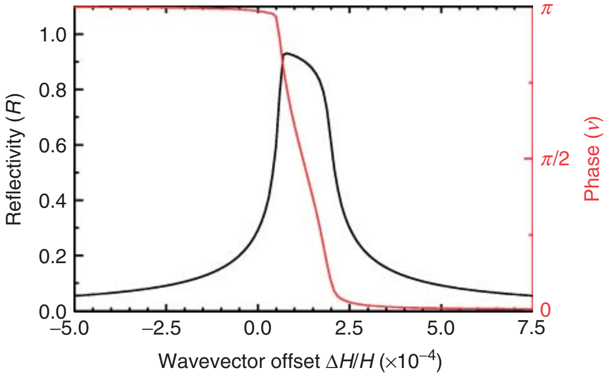

Figure 44.2 Theoretical angle/energy dependence of the reflectivity R and phase ν for Si(111) around the (111) Bragg reflection, that is, H along the [111] direction. Note that the x-axis denotes the wave vector offset relative to the Bragg condition in kinematical approximation.

44.2.2
Standing Waves

The two-beam approximation of dynamical theory assumes that only two wave vectors $\vec{K}_0$ and $\vec{K}_\mathrm{H}$ satisfying the Bragg condition contribute with a nonnegligible amplitude [6]. Therefore, the electrical field can be described by the superposition of the incident wave $\vec{\mathcal{E}}_0$ and the Bragg reflected wave $\vec{\mathcal{E}}_\mathrm{H}$, which are given by

$$\vec{\mathcal{E}}_0(r) = \sum_s \vec{e}_{0s}\mathcal{E}_0\, e^{-2\pi i \vec{K}_0\cdot\vec{r}} \tag{44.14}$$

$$\vec{\mathcal{E}}_H(r) = \sum_s \vec{e}_{\mathrm{H}s}\mathcal{E}_\mathrm{H}\, e^{-2\pi i \vec{K}_\mathrm{H}\cdot\vec{r}} \tag{44.15}$$

with the polarization vectors $\vec{e}_{is}$ of the two possible states $s = \sigma, \pi$ which for $\vec{e}_{0\sigma}$ and $\vec{e}_{\mathrm{H}\sigma}$ ($\vec{e}_{0\pi}$ and $\vec{e}_{\mathrm{H}\pi}$) are perpendicular (parallel) to the plane defined by the two wave vectors $\vec{K}_0$ and $\vec{K}_\mathrm{H}$ (Figure 44.3).

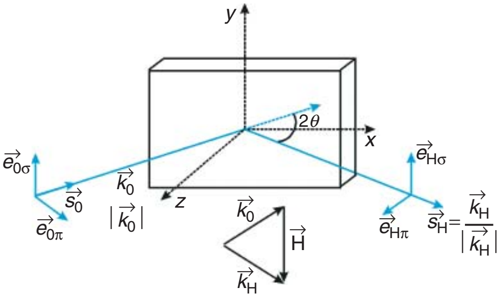

Figure 44.3 Scheme of the scattering geometry. The two plane waves $\mathcal{E}_0$ and $\mathcal{E}_\mathrm{H}$ with the wave vector $\vec{K}_0$ and $\vec{K}_\mathrm{H}$ and the polarization vectors $\vec{e}_0$ and $\vec{e}_\mathrm{H}$.

As the resulting electrical field is given by

$$\vec{\mathcal{E}}(\vec{r}) = \sum_s (\vec{e}_{0\mathrm{s}}\mathcal{E}_0\; e^{-2\pi i\vec{K}_0\cdot\vec{r}} + \vec{e}_{\mathrm{Hs}}\mathcal{E}_{\mathrm{H}}\; e^{-2\pi i\vec{K}_{\mathrm{H}}\cdot\vec{r}}) \tag{44.16}$$

an XSW field with the intensity $I(\vec{r}) = |\vec{\mathcal{E}}(\vec{r})|^2$ is generated. Inserting Eq. (44.13) and using the polarization factor

$$C = \vec{e}_{0\mathrm{s}} \cdot \vec{e}_{\mathrm{Hs}} = \begin{cases} 1, & \sigma\,\text{polarization} \\ \cos 2\theta, & \pi\,\text{polarization} \end{cases} \tag{44.17}$$

one finds

$$I(\vec{r}) = I_0(1 + R + 2C\sqrt{R}\cos(\nu - 2\pi\vec{H}\cdot\vec{r})) \tag{44.18}$$

where R is the reflectivity with $\mathcal{E}_{\mathrm{H}} = \sqrt{R}\mathcal{E}_0 e^{i\nu}$. The periodicity of the standing wave field is given by the lattice spacing $d_{\vec{H}} = |\vec{H}|^{-1}$.

44.2.3
The Photo Yield

Within the X-ray interference field, the atoms absorb some of the incoming photons (which is why one can see them as local probes for the standing wave field). As a result, photoelectrons or Auger electrons are excited from the core levels of specific atoms (Figure 44.4). As shown below the photoelectron yield, Y_{p} around the Bragg condition depends on the position of the emitting atom relative to the lattice planes.

According to Fermi's golden rule, the photoelectron yield Y_{p} for excitation from the initial state i to the final state f is proportional to the square of the transition

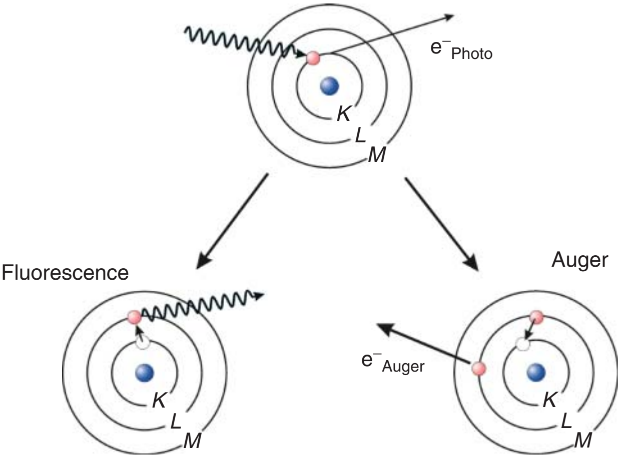

Figure 44.4 Photoelectrons excited from core levels because of the absorption of X-rays can be used as element-specific signals for XSW measurements. Also, secondary processes as fluorescence and Auger electron emission can be exploited.

matrix element M_{fi}, with

$$M_{fi} = \langle f | e^{2\pi i \vec{k}\cdot\vec{r}} \vec{e} \cdot \nabla | i \rangle \tag{44.19}$$

For two coherent wave fields, one therefore obtains [7]

$$Y_{\mathrm{p}}^{\mathrm{XSW}} \propto |M_{fi}^{\mathrm{XSW}}|^2 = |\mathcal{E}_0 \langle f | (e^{2\pi i \vec{K}_0\cdot\vec{r}} \vec{e}_0 \cdot \nabla) | i \rangle + \mathcal{E}_{\mathrm{H}} \langle f | (e^{2\pi i \vec{K}_{\mathrm{H}}\cdot\vec{r}} \vec{e}_{\mathrm{H}} \cdot \nabla) | i \rangle|^2 \tag{44.20}$$

In case $|\vec{K}_0 \cdot \vec{r}| \langle 1$ (long wavelength limit), the so-called dipole approximation can be used to evaluate this expression

$$\begin{aligned} Y_{\mathrm{p}}^{\mathrm{XSW}} \propto\ & |\mathcal{E}_0|^2 \ |\langle f | \vec{e}_0 \cdot \nabla | i \rangle|^2 + |\mathcal{E}_{\mathrm{H}}|^2 \ |\langle f | \vec{e}_{\mathrm{H}} \cdot \nabla | i \rangle|^2 \\ & + \left|\mathcal{E}_0 \mathcal{E}_{\mathrm{H}}\right| (e^{-i(\nu - 2\pi \vec{H}\cdot\vec{r}) \langle f|\vec{e}_0\cdot\nabla|i\rangle \times \langle f|\vec{e}_{\mathrm{H}}\cdot\nabla|i\rangle^*} + e^{i(\nu - 2\pi \vec{H}\cdot\vec{r}) \langle f|\vec{e}_0\cdot\nabla|i\rangle^* \times \langle f|\vec{e}_{\mathrm{H}}\cdot\nabla|i\rangle}) \end{aligned} \tag{44.21}$$

For σ polarized light, where $\vec{e}_0$ and $\vec{e}_H$ are parallel to each other, this can be simplified to

$$\begin{aligned} Y_{\mathrm{p}}^{\mathrm{XSW}} & \propto 1 + \left|\frac{\mathcal{E}_{\mathrm{H}}}{\mathcal{E}_0}\right|^2 + 2\left|\frac{\mathcal{E}_{\mathrm{H}}}{\mathcal{E}_0}\right| \cos(\nu - 2\pi \vec{H} \cdot \vec{r}) \\ & = 1 + R + 2\sqrt{R} \cos(\nu - 2\pi \vec{H} \cdot \vec{r}) \end{aligned} \tag{44.22}$$

This expression is similar to Eq. (44.18), and thus shows that under these conditions the photo yield $Y_{\mathrm{p}}^{\mathrm{XSW}}$ is proportional to the intensity $I(\vec{r})$ of the standing wave field at the center of the excited atom. Nondipolar effects in the photoemission process can be taken into account by modifying this equation. Related issues are discussed in detail in Refs. [8, 9] (theory) and Refs. [10–14] (experiment).

By scanning the angle θ or the photon energy E of the incident wave through the Bragg condition, the phase ν of the interference field changes by π and, as a consequence, the nodal planes of the standing wave field shift by half a lattice constant [3]. As the absorption of X-rays depends on the position $\vec{r}$ of the atoms within this wave field, the photoelectrons or Auger electrons [15, 16] can be used as element-specific signals, which reveal the position of the atoms. The measured photoelectron yield $Y_{\mathrm{p}}^{\mathrm{XSW}}$ exhibits a characteristic shape that is related to the position of a given atom. Figure 44.5 illustrates the effect that different atomic positions $\vec{r}$ have on the photo yield.

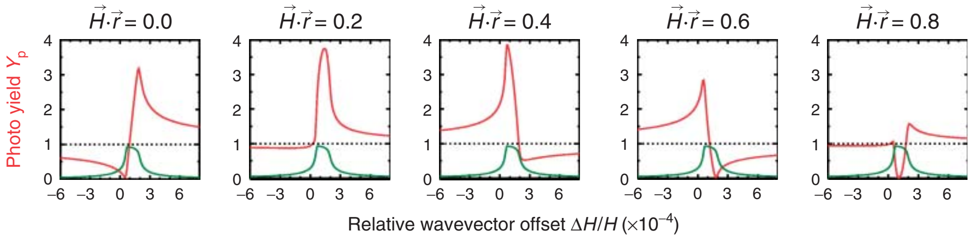

Figure 44.5 Theoretical normalized photo yields for different values of $\vec{H} \cdot \vec{r}$ in Eq. (44.22). The extraordinary sensitivity of Y_{p} to the position of the atom $\vec{r}$ is demonstrated.

For an (partly) incoherent system with atoms on nonequivalent atomic sites, a normalized distribution function $n(\vec{r})$ that describes the spread of atoms around their average lattice position has to be introduced [3–5]. Equation (44.22) is then generalized to

$$Y_{\mathrm{p}}^{\mathrm{XSW}} = \int Y_{\mathrm{p}}(\vec{r})n(\vec{r})\mathrm{d}^3r = 1 + R + 2C\sqrt{R}\int n(\vec{r})\cos(\nu - 2\pi\vec{H}\cdot\vec{r})\mathrm{d}^3r \tag{44.23}$$

with the polarization factor C given by Eq. (44.17).

A more convenient form of this averaging equation is obtained by introducing two new parameters: the *coherent position* $P_{\mathrm{H}} = \vec{H}\cdot\vec{r}$ and the *coherent fraction* f_{H}.

$$Y_{\mathrm{p}}^{\mathrm{XSW}} = 1 + R + 2C\sqrt{R}f_{\mathrm{H}}\cos(\nu - 2\pi P_{\mathrm{H}}) \tag{44.24}$$

This is the basic equation for most XSW experiments as P_{H} and f_{H} contain all structural information on the specific system. The coherent position $0 \le P_{\mathrm{H}} \le 1$ now gives the atomic position relative to the diffraction planes associated with the vector $\vec{H}$, whereas the coherent fraction $0 \le f_{\mathrm{H}} \le 1$ describes the degree of coherent order in the system.

This is best illustrated by considering two extreme cases: a random distribution of atoms on the surface, for example, a thick incoherent film of molecules, with $f_{\mathrm{H}} = 0$ results in $Y_{\mathrm{p}} = 1 + R$, that is, depending on the absorption $Y_{\mathrm{p}} \le 2$. A perfectly ordered adlayer with $f_{\mathrm{H}} = 1$, in contrast, amplifies the XSW yield to $Y_{\mathrm{p}} \le 4$.

The equivalence of Eqs. (44.23, 44.24) can be used to explore the physical meaning of the coherent fraction f_{H} [17]. By equating both expressions, we obtain a relation

$$f_{\mathrm{H}}\cos(\nu - 2\pi P_{\mathrm{H}}) = \int n(\vec{r})\cos(\nu - 2\pi\vec{H}\cdot\vec{r})\mathrm{d}\vec{r} \tag{44.25}$$

which has to hold for any value of ν. An expansion of the cosine sums on both sides now gives

$$\begin{aligned} \cos\nu\, f_{\mathrm{H}}\cos(2\pi P_{\mathrm{H}}) + \sin\nu\, f_{\mathrm{H}}\sin(2\pi P_{\mathrm{H}}) \;=\; & \cos\nu \int n(\vec{r})\cos(2\pi\vec{H}\cdot\vec{r})\mathrm{d}\vec{r} \\ & + \sin\nu \int n(\vec{r})\sin(2\pi\vec{H}\cdot\vec{r})\mathrm{d}\vec{r} \end{aligned} \tag{44.26}$$

As $\sin\nu$ and $\cos\nu$ are linear independent functions, this relation can only be satisfied if the individual coefficients are equal, that is,

$$f_{\mathrm{H}}\cos(2\pi P_{\mathrm{H}}) = \int n(\vec{r})\cos(2\pi\vec{H}\cdot\vec{r})\mathrm{d}\vec{r} \tag{44.27}$$

$$f_{\mathrm{H}}\sin(2\pi P_{\mathrm{H}}) = \int n(\vec{r})\sin(2\pi\vec{H}\cdot\vec{r})\mathrm{d}\vec{r} \tag{44.28}$$

Using complex numbers, this can finally be summarized by

$$f_{\mathrm{H}}\exp\;(2\pi iP_{\mathrm{H}}) = \int n(\vec{r})\exp\;(2\pi i\vec{H}\cdot\vec{r})\mathrm{d}\vec{r} \tag{44.29}$$

Therefore, the coherent fraction f_H is the first Fourier component of the distribution function $n(\vec{r})$ multiplied by a phase factor containing the coherent position P_H. This means that by measuring photo yields for sufficiently many reciprocal lattice vectors $\vec{H}$, it is, in principle, possible to determine the Fourier representation of the atomic density of a specific element [18].

44.3
Experiment

Different types of experimental setups have been used at various synchrotron light sources. The principal mode of detection (fluorescence light versus photoelectrons) and the accessible photon energies determine, to a large extent, the design of the instrument. Two typical examples are beamline 5ID-C at the APS (advanced photon source) (mostly fluorescence detection) and beamline ID32 at ESRF (European Synchrotron Radiation Facility) (mostly photoelectron detection).

Here, we briefly describe the setup used at the ESRF, which was used to measure the XSW data presented in the following section. The ultrahigh vacuum system shown schematically in Figure 44.6a is used for XSW studies and high-energy XPS (X-ray photoelectron spectroscopy) measurements. The chamber is equipped with a hemispherical electron analyzer (150 mm radius), a sample manipulator with five degrees of freedom (all motions stepper motor driven), a sample holder with possibilities of heating the sample up to 1000 K and cooling down to 30 K with a copper braid connected to a He-cryostat, a rear-view low-energy electron diffraction (LEED) system, a sputter gun for sample preparation, a load-lock chamber with a transfer rod to introduce samples into the main chamber under UHV (ultrahigh vacuum) conditions, a three-way gas line for different gases, a residual gas analyzer (RGA), several evaporation sources (Knudsen cells) for thin

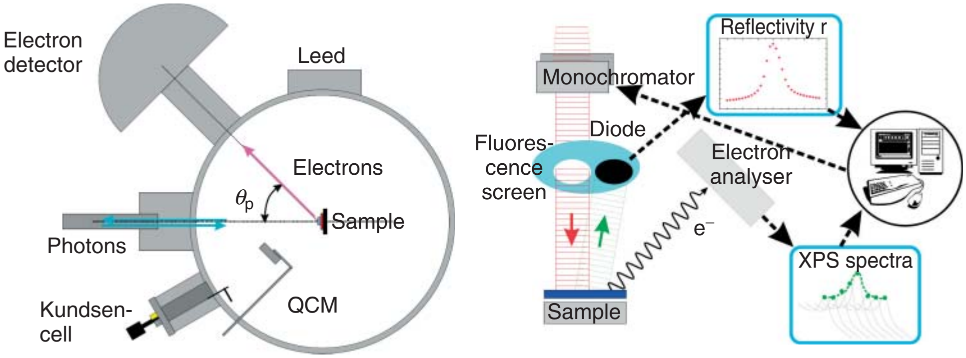

Figure 44.6 Experimental setup for XSW measurements at beamline ID32 at the ESRF. (a) Schematic of the UHV chamber. (b) Principle of XSW measurements.

film preparation, a quartz crystal microbalance (QCM) to control the deposition rate, a port for solid-state X-ray fluorescence detector and some spare ports for user-defined equipments.

44.4
Examples: Organic Adsorbates

The interaction strength between the adsorbed molecule and the substrate, possible distortions of the molecule on the substrate, and possibly the orientation of the molecules are fundamental properties of organic adsorbates. These structural details do not only influence the growth process beyond the first layer [19, 20] but are also important for the energy level alignment at the organic/metal interface and the corresponding efficiency of charge-carrier injection into the organic material [21]. Therefore, the precise and chemically resolved structural information, which can be obtained by normal incidence XSW experiments even for relatively large organic molecules [22], improve the general understanding of these systems.

Subsequently, we shall discuss a number of experimental results for the molecules shown in Figure 44.7, which illustrate that the strength of the substrate–adsorbate interaction—in particular for lying-down molecules on different substrates—varies considerably and that the complex interaction mechanisms result in a rich phenomenology of adsorption geometries.

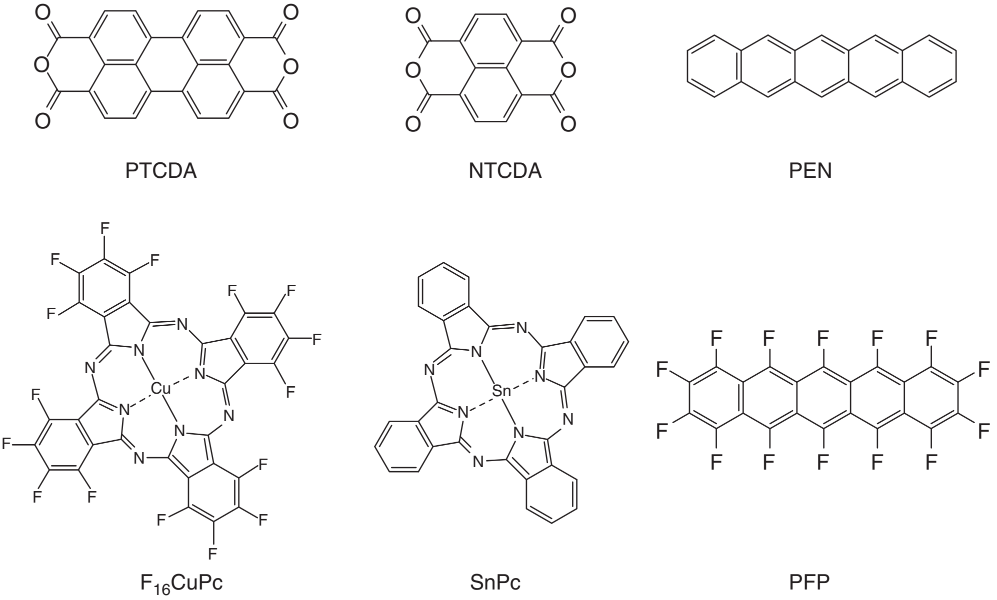
PTCDA
NTCDA
PEN
F_{16}CuPc
SnPc
PFP

Figure 44.7 Examples of organic semiconductor molecules described in Section 44.4.

Table 44.1 Bonding distances of organic molecules measured with XSW.

Molecule	Substrate	C (Å)	Other atoms (Å)	References
PTCDA (deposition at RT)	Ag(111)	2.86 ± 0.06	O: 2.97 ± 0.06 (anh.), 2.68 ± 0.06 (carb.)	[23]
PTCDA (deposition at LT)	—	2.80 ± 0.06	O: 2.83 ± 0.04 (anh.), 2.49 ± 0.04 (carb.)	[30]
NTCDA (relaxed) ML at LT	—	2.997	O: 3.004 (anh.), 2.747 (carb.)	[34, 35]
CuPc	—	3.05 ± 0.02	N: 3.00 ± 0.03	[44]
F_{16}CuPc (copper phthalocyanine)	—	3.25	F: 3.45	[36]
SnPc (incomm.)	—	3.17	N: 3.26, Sn(down): 2.41	[37]
SnPc (comm.)	—	2.93	N: 3.12, Sn(down): 2.59, Sn(up): 4.01	[37]
SnPc (incomm.) 1ML		3.09	N: 3.09, Sn(down): 2.25	[39]
SnPc (comm.) 0.8ML	—	2.92	N: 2.92, Sn(down): 2.23, Sn(up): 4.08	[39]
PFP	—	3.16	—	[45]
EC4T (end-capped quaterthiophene at RT)	—	—	Ave. S: 3.15 ± 0.05	[46]
Azobenzene	—	—	N: 3.07 ± 0.02	[47]
PTCDA	Cu(111)	2.66	O: 2.89 (anh.), 2.73 (carb.)	[24]
PEN	—	2.34	—	[40]
ZnPc (zinc phthalocyanine)	—	2.49	N: 2.55, Zn: 2.25	[48]
F_{16}CuPc	—	2.61	N: 2.70, F: 2.88	[36]
PFP	—	2.98	F: 3.08	[40]
F_4TCNQ	—	—	N: 2.7 ± 0.1, F: 3.3 ± 0.1	[41]
PTCDA	Au(111)	3.27 ± 0.02	—	[25]
F_{16}CuPc	—	3.05 ± 0.02	F: 3.26	[49]

RT, room temperature; LT, low temperature.

An overview of bonding distances determined with the XSW technique on different noble metal substrates is presented in Table 44.1 (summary as of 2010).

44.4.1
PTCDA/Ag(111), Cu(111), and Au(111)

PTCDA (3,4,9,10-perylene-tetracarboxylic acid dianhydride) has become the best-studied system in this field; see, for example, Refs. [23–32]. There are precise data on three different substrates, that is, Ag(111), Cu(111), and Au(111). A strong

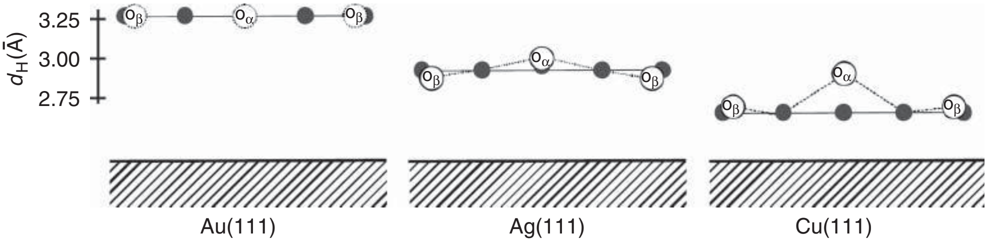

Figure 44.8 Different bonding distances and adsorption geometries of PTCDA on Au(111), Ag(111), and Cu(111) as measured by XSW. On copper, both oxygen species—distinguishable because of a chemical shift in the photoemission spectra—are located above the carbon plane. On silver, however, the carboxylic oxygen atoms are bent toward the surface. The position of the oxygen atoms on Au(111) was not measured with XSW. (From Ref. [27] with permission.)

interaction with the substrate ('chemisorption') is found for Ag(111) and Cu(111), with a bonding distance of 2.86 ± 0.01 Å and 2.61 ± 0.02 Å, respectively. Yet, a much weaker interaction is found for PTCDA on Au(111) with 3.27 ± 0.02 Å. The close correlation of these findings with the electronic properties of PTCDA on the different substrates is discussed in Ref. [27].

The XSW results of PTCDA/Ag(111) obtained in the monolayer regime agree with surface diffraction data [33] obtained from multilayer films of PTCDA. This indicates that the growth of further layers does not influence the first layer and the XSW measurements of d_0 discussed here are indeed relevant beyond the monolayer coverage. Moreover, a substrate-dependent distortion of the C=O bonds is found: for PTCDA on Ag(111) the carboxylic oxygen atoms are located below the molecular plane ($d_0 = 2.68$ Å), but for PTCDA on Cu(111) these atoms are above the plane ($d_0 = 2.73$ Å) (Figure 44.8). Theoretical efforts based mainly on density functional theory are being made to explain these findings, but are still hampered by the necessarily tedious computations.

44.4.2
NTCDA/Ag(111)

Recent XSW experiments demonstrate that the adsorption geometry of NTCDA (1,4,5,8-naphthalene tetracarboxylic dianhydride) on Ag(111) is similar to the one found for the larger PTCDA molecule [34, 35]. A slightly weaker substrate–adsorbate interaction results in a carbon distance of $d_0 = 2.997 \pm 0.016$ Å to the Ag(111) lattice. Therefore, the adsorption of NTCDA might be regarded as relatively strong (chemisorption). A nonplanar adsorption geometry is also reported for NTCDA. In essence, the distortion of the C=O bonds in NTCDA is similar to the case of PTCDA on Ag(111) in which the carboxylic oxygen atoms are located below the molecular plane. As no XSW data for Cu(111) or Au(111) are presently available, a substrate-dependent distortion of NTCDA—as found for PTCDA—has not yet been established.

44.4.3

F_{16}CuPc/Ag(111) and Cu(111)

The XSW results obtained on F_{16}CuPc (copper hexadecafluorophthalocyanine) show that perfluorinated copper-phthalocyanine molecules adsorb in a lying down, but significantly distorted configuration on Cu(111) and Ag(111) surfaces [36]. While on copper (silver) the central carbon rings reside 2.61 ± 0.05 Å (3.25 ± 0.05 Å) above the substrate, the outer fluorine atoms are located 0.27 Å (0.20 Å) further away from the surface. These results on F_{16}CuPc are in remarkable contrast to those on PTCDA on Cu(111) and Ag(111) mentioned earlier. First, a much larger difference between the adsorption distances d_0 on copper and silver is found. Second, the type of molecular distortion, that is, an upward bending of the C–F bonds in F_{16}CuPc, is the same on copper and silver despite the obviously weaker interaction of F_{16}CuPc with the Ag(111) surface. As for PTCDA, a thorough explanation for the nonplanar adsorption structure of the molecules is still missing. Yet, it is suggested that the results can be discussed in terms of the outer carbon atoms in F_{16}CuPc undergoing a partial rehybridization ($sp^2 \rightarrow sp^3$) with a concomitant change of the bonding angles. For details, see Ref. [36].

44.4.4

SnPc/Ag(111)

The adsorption geometry and orientation of the nonplanar phthalocyanine molecule SnPc (tin phthalocyanine) has been measured by XSW [37–39]. Depending on the preparation Conditions, SnPc monolayers exhibit different superstructures and molecular conformations on the Ag(111) surface. The existence of an incommensurate room-temperature (RT) phase with an average carbon bonding distance of 3.17 Å (Sn-down orientation) and a commensurate low-temperatures phase with a carbon bonding distance of 2.93 Å (mixed Sn-down and Sn-up orientation) was established [37]. Moreover, it is reported that for a monolayer of SnPc prepared via desorption of a multilayer film [37], the carbon atoms are bent toward the surface, whereas for deposition at 300 °C substrate temperature [38] the carbon atoms are bent away from the surface with $d = 3.61$ Å.

44.4.5

PEN/Cu(111) and PFP/Cu(111)

The adsorption geometry of pentacene (PEN) and perfluorinated pentacene (PFP) on Cu(111) has been studied using the XSW technique und other complementary techniques [40]. The element-specific structural information derived from the C(1s)and F(1s) photoelectron signals reveals the different bonding mechanism of both molecules (Figure 44.9).

While PEN interacts strongly with the copper substrate and adsorbs with an average bonding distance of only 2.34 ± 0.02 Å, the carbon core of the PFP molecule is located at 2.98 ± 0.07 Å. Despite the relatively weak interaction of PFP

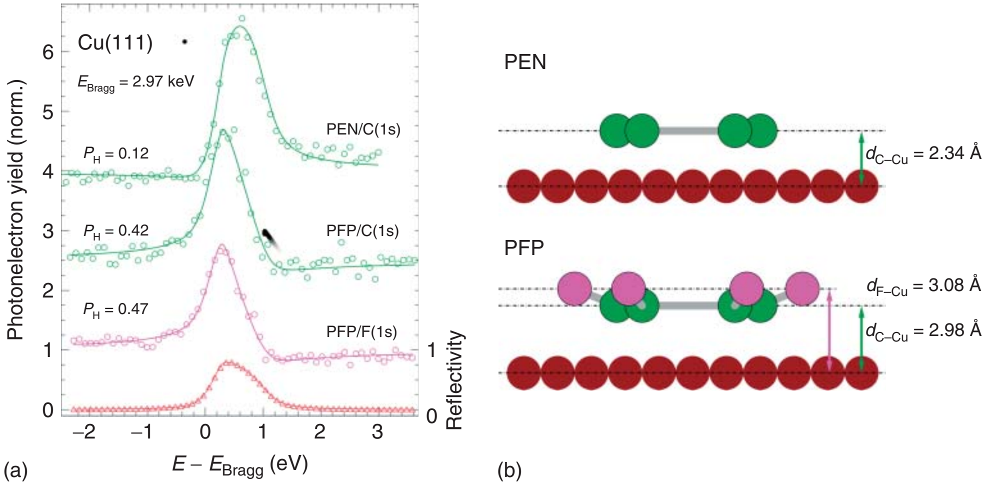

Figure 44.9 (a) X-ray standing wave scans obtained on submonolayers of PEN and PFP on Cu(111). The symbols represent the photoelectron yield (circles) and substrate reflectivity (triangles) data measured for both adsorbate systems. The solid lines show least-square fits based on the dynamical diffraction theory, which provide the coherent position P_H and coherent fraction f_H for each element. The coherent position thus reveals the adsorption distance d_0 of PEN and PFP, whereas the coherent fraction ($0 < f_H < 1$) with $f_H = 0.55$ for PEN/C1s and $f_H = 0.41$ for PFP/C1s and PFP/F1s, is related to disorder in the adsorbate system. (b) Schematic conformation of PEN (top) and PFP (bottom) on Cu(111) derived from XSW measurements, indicating the different average positions of the F and C atoms. (From Ref. [40] with permission.)

with the substrate, the molecules experience a mild distortion upon adsorption, with the fluorine atoms being slightly above the molecular plane at 3.08 ± 0.04 Å. On the basis of the XSW results, the influence of the intramolecular dipole on the charge transfer across the interface has been discussed in detail [40].

44.4.6
Other Systems

Besides these relatively large organic molecules with conjugated π-electron systems, there have been several XSW studies on smaller organic molecules on metal subtrates. For example, F_4TCNQ (tetrafluorotetracyanoquinodimethane) on Cu(111) [41], where a nitrogen bonding distance of 2.7 ± 0.1 Å is found, methanethiol on Pt(111) [42], where a Pt–S bonding distance of 1.67 Å is found, and tetrahydrofuran on Cu(111) [43], where a Cu–O bonding distance of 2.39 Å is found.

Acknowledgments

We thank J. Zegenhagen for giving numerous helpful comments and T. Hosokai for assembling Table 44.1.

References

1. Batterman, B.W. (1964) Effect of dynamical diffraction in x-ray fluorescence scattering. *Phys. Rev.*, **133**, A759.
2. Batterman, B.W. (1969) Detection of foreign atom sites by their x-ray fluorescence scattering. *Phys. Rev. Lett.*, **22**, 703.
3. Zegenhagen, J. (1993) Surface structure determination with x-ray standing waves. *Surf. Sci. Rep.*, **18**, 199.
4. Bedzyk, M.J. (2005) *Encyclodedia of Condensed Matter Physics*, Chapter Scattering: X-ray Standing Wave Techniques, Vol. 6, Elsevier, p. 330.
5. Woodruff, D.P. (2005) Surface structure determination using x-ray standing waves. *Rep. Prog. Phys.*, **68**, 743.
6. Authier, A. (2003) *Dynamical Theory of X-ray Diffraction*, Oxford University Press.
7. Berman, L.E. and Bedzyk, M.J. (1989) Angular distribution of the photoelectron yield excited by two coherently coupled photon beams. *Phys. Rev. Lett.*, **63**, 1172.
8. Vartanyants, I.A. and Zegenhagen, J. (1999) Quadrupole contribution to the angular resolved photoemission from an x-ray interference field. *phys. Stat. Sol. (b)*, **215**, 819.
9. Vartanyants, I.A. and Zegenhagen, J. (2000) Photoelectric scattering from an x-ray interference field. *Solid State Commun.*, **113**, 299.
10. Jackson, G.J., Cowie, B.C.C., Woodruff, D.P., Jones, R.G., Kariapper, M.S., Fisher, C., Chan, A.S.Y., and Butterfield, M. (2000) Atomic quadrupolar photoemission asymmetry parameters from a solid state measurement. *Phys. Rev. Lett.*, **84**, 2346.
11. Schreiber, F., Ritley, K.A., Vartanyants, I.A., Dosch, H., Zegenhagen, J., and Cowie, B.C.C. (2001) Non-dipolar contributions in XPS-detection of x-ray standing waves. *Surf. Sci. Lett.*, **486**, 519.
12. Lee, J.J., Fischer, C.J., Woodruff, D.P., Roper, M.G., Jones, R.G., and Cowie, B.C.C. (2001) Non-dipole effect in photoelectron-monitored x-ray standing wave experiments: characterization and calibration. *Surf. Sci.*, **494**, 166.
13. Nelson, E.J., Woicik, J.C., Pianetta, P., Vartanyants, I.A., and Cooper, J.W. (2002) Quadrupole effects in core and valence photoelectron emission from crystalline germanium measured via a spatially modulated x-ray interference field. *Phys. Rev. B* **65**, 165219.
14. Vartanyants, I., Lee, T.-L., Thiess, S., and Zegenhagen, J. (2005) Non-dipole effects in x-ray standing wave photoelectron spectroscopy experiments. *Nucl. Instrum. Methods Phys. Res.*, **547**, 196.
15. Shard, A.G. and Cowie, B.C.C. (1998) A demonstration of Auger electron emission stimulated by secondary radiation: implications for x-ray standing-wave analysis of surfaces. *J. Phys.: Condens. Matter.*, **10**, L69.
16. Pacile, D., Papagno, M., Cupolillo, A., Chiarello, G., and Papagno, L. (2004) A comparison between Auger and photoelectron emission detection in an x-ray standing-wave analysis of adsorbates. *J. Electron Spectrosc. Relat. Phenom.*, **135**, 201.
17. Hertel, N., Materlik, G., and Zegenhagen, J. (1985) X-ray standing wave analysis of bismuth implanted in Si(110). *Z. Phys. B: Condens. Matter*, **58**, 199.
18. Cheng, L., Fenter, P., Bedzyk, M.J., and Sturchio, N.C. (2003) Fourier-expansion solution of atom distributions in a crystal using x-ray standing waves. *Phys. Rev. Lett.*, **90**, 255503.
19. Witte, G. and Wöll, C. (2004) Growth of aromatic molecules on solid substrates for applications in organic electonics. *J. Mater. Res.*, **19**, 1889.
20. Gerlach, A., Sellner, S., Kowarik, S., and Schreiber, F. (2008) In-situ x-ray scattering studies of OFET interfaces. *Phys. Stat. Sol. A*, **205**, 461.
21. Koch, N. (2007) Organic electronic devices and their functional interfaces. *ChemPhysChem*, **8**, 1438.
22. Woodruff, D.P., Seymour, D.L., Riley, C.C.E., Crapper, M.D., and Prince, N.P. (1988) A simple x-ray standing wave technique for surface structure determination - Theory and an application. *Surf. Sci.*, **195**, 237.

23. Hauschild, A., Karki, K., Cowie, B.C.C., Rohlfing, M., Tautz, F.S., and Sokolowski, M. (2005) Molecular distortions and chemical bonding of a large π-conjugated molecule on a metal surface. *Phys. Rev. Lett.*, **94**, 036106.

24. Gerlach, A., Sellner, S., Schreiber, F., Koch, N., and Zegenhagen, J. (2007) Substrate dependent bonding distances of PTCDA - a comparative x-ray standing wave study on Cu(111) and Ag(111). *Phys. Rev. B*, **75**, 045401.

25. Henze, S.K.M., Bauer, O., Lee, T.-L., Sokolowski, M., and Tautz, F.S. (2007) Vertical bonding distances of PTCDA on Au(111) and Ag(111): relation to the bonding type. *Surf. Sci.*, **601**, 1566.

26. Zou, Y., Kilian, L., Schöll, A., Schmidt, T., Fink, R., and Umbach, E. (2006) Chemical bonding of PTCDA on Ag surfaces and the formation of interface states. *Surf. Sci.*, **600**, 1240.

27. Duhm, S., Gerlach, A., Salzmann, I., Bröcker, B., Johnson, R., Schreiber, F., and Koch, N. (2008) PTCDA on Au(111), Ag(111) and Cu(111): correlating bonding distance and interfacial charge transfer. *Org. Electron.*, **9**, 111.

28. Kilian, L., Umbach, E., and Sokolowski, M. (2004) Molecular beam epitaxy of organic films investigated by high resolution low energy electron diffraction (SPA-LEED): 3,4,9,10-perylenetetracarboxylicacid-dianhydride (PTCDA) on Ag(111). *Surf. Sci.*, **573**, 359.

29. Kilian, L., Umbach, E., and Sokolowski, M. (2006) A refined structural analysis of the PTCDA monolayer on the reconstructed Au(111) surface - ''Rigid or distorted carpet?''. *Surf. Sci.*, **600**, 2633.

30. Kilian, L., Hauschild, A., Temirov, R., Soubatch, S., Schöll, A., Bendounan, A., Reinert, F., Lee, T.-L., Tautz, F.S., Sokolowski, M., and Umbach, E. (2008) Role of intermolecular interactions on the electronic and geometric structure of a large π-conjugated molecule adsorbed on a metal surface. *Phys. Rev. Lett.*, **100**, 136103.

31. Tautz, F.S. (2007) Structure and bonding of large aromatic molecules on noble metal surfaces: the example of PTCDA. *Prog. Surf. Sci.*, **82**, 479.

32. Hauschild, A., Temirov, R., Soubatch, S., Bauer, O., Schöll, A., Cowie, B.C.C., Lee, T.-L., Tautz, F.S., and Sokolowski, M. (2010) Normal-incidence x-ray standing-wave determination of the adsorption geometry of PTCDA on Ag(111): comparison of the ordered room-temperature and disordered low-temperature phases. *Phys. Rev. B*, **81**, 125432.

33. Krause, B., Dürr, A.C., Schreiber, F., Dosch, H., and Seeck, O.H. (2003) Thermal stability and partial dewetting of crystalline organic thin films: PTCDA on Ag(111). *J. Chem. Phys.*, **119**, 3429.

34. Stanzel, J., Weigand, W., Kilian, L., Meyerheim, H.L., Kumpf, C., and Umbach, E. (2004) Chemisorption of NTCDA on Ag(111): A NIXSW study including non-dipolar and electron-stimulated effects. *Surf. Sci. Lett.*, **571**, 311.

35. Stadler, C., Hansen, S., Schöll, A., Lee, T.-L., Zegenhagen, J., Kumpf, C., and Umbach, E. (2007) Molecular distortion of NTCDA upon adsorption on Ag(111): a normal incidence x-ray standing wave study. *New J. Phys.*, **9**, 50.

36. Gerlach, A., Schreiber, F., Sellner, S., Dosch, H., Vartanyants, I.A., Cowie, B.C.C., Lee, T.-L., and Zegenhagen, J. (2005) Adsorption-induced distortion of F_{16}CuPc on Cu(111) and Ag(111): an x-ray standing wave study. *Phys. Rev. B*, **71**, 205425.

37. Stadler, C., Hansen, S., Pollinger, F., Kumpf, C., Umbach, E., Lee, T.-L., and Zegenhagen, J. (2006) Structural investigation of the adsorption of SnPc on Ag(111) using normal-incidence x-ray standing waves. *Phys. Rev. B*, **74**, 035404.

38. Woolley, R., Martin, C., Miller, G., Dhanak, V., and Moriarty, P. (2007) Adsorbed molecular shuttlecocks: an NIXSW study of Sn phthalocyanine on Ag(111) using Auger electron detection. *Surf. Sci.*, **601**, 1231.

39. Stadler, C., Hansen, S., Kröger, I., Kumpf, C., and Umbach, E. (2009) Tuning intermolecular interaction in long-range-ordered submonolayer organic films. *Nat. Phys.*, **5**, 153.

40. Koch, N., Gerlach, A., Duhm, S., Glowatzki, H., Heimel, G., Vollmer, A., Sakamoto, Y., Suzuki, T., Zegenhagen, J., Rabe, J.P., and Schreiber, F. (2008) Adsorption induced intramolecular dipole: correlating molecular conformation and interface electronic structure. *J. Am. Chem. Soc.*, **130**, 7300.
41. Romaner, L., Heimel, G., Bredas, J.L., Gerlach, A., Schreiber, F., Johnson, R.L., Zegenhagen, J., Duhm, S., Koch, N., and Zojer, E. (2007) Impact of bidirectional charge transfer and molecular distortions on the electronic structure of a metal-organic interface. *Phys. Rev. Lett.*, **99**, 256801.
42. Lee, J.J., Fisher, C.J., Bittencourt, C., Woodruff, D.P., Chan, A.S., and Jones, R.G. (2002) A structural study of the interaction of methanethiol with Pt(111) using x-ray standing waves. *Surf. Sci.*, **516** 1/2, 1.
43. Mulligan, A., Johnston, S.M., Miller, G., Dhanak, V., and Kadodwala, M. (2003) A TPD and NIXSW investigation of furan and tetrahydrofuran adsorption on Cu(111). *Surf. Sci.*, **541**, 3.
44. Kröger, I., Stadtmüller, B., Stadler, C., Ziroff, J., Kochler, M., Stahl, A., Pollinger, F., Lee, T.-L., Zegenhagen, J., Reinert, F., and Kumpf, C. (2010) Submonolayer growth of copper-phthalocyanine on Ag(111). *New J. Phys.*, **12**, 083038.
45. Duhm, S., Hosoumi, S., Salzmann, I., Gerlach, A., Oehzelt, M., Wedl, B., Lee, T.-L., Schreiber, F., Koch, N., Ueno, N., and Kera, S. (2010) Influence of intramolecular polar bonds on interface energetics in perfluoro-pentacene on Ag(111). *Phys. Rev. B*, **81**, 045418.
46. Kilian, L., Weigang, W., Umbach, E., Langner, A., Sokolowski, M., Meyerheim, H.L., Maltor, H., Cowie, B.C.C., Lee, T., and Bäuerle, P. (2002) Adsorption site determination of a large π-conjugated molecule by normal incidence x-ray standing waves: end-capped quaterthiophene on Ag(111). *Phys. Rev. B*, **66**, 075412.
47. Mercurio, G., McNellis, E.R., Martin, I., Hagen, S., Leyssner, F., Soubatch, S., Meyer, J., Wolf, M., Tegeder, P., Tautz, F.S., and Reuter, K. (2010) Structure and energetics of azobenzene on Ag(111): benchmarking semiempirical dispersion correction approaches. *Phys. Rev. Lett.*, **104**, 036102.
48. Yamane, H., Gerlach, A., Duhm, S., Tanaka, Y., Hosokai, T., Mi, Y.Y., Zegenhagen, J., Koch, N., Seki, K., and Schreiber, F. (2010) Site-specific geometric and electronic relaxations at organic-metal interfaces. *Phys. Rev. Lett.*, **105**, 046103.
49. de Oteyza, D.G., El-Sayed, A., Garcia-Lastra, J.M., Goiri, E., Krauss, T.N., Turak, A., Barrena, E., Dosch, H., Zegenhagen, J., Rubio, A., Wakayama, Y., and Ortega, J.E. (2010) Copper-phthalocyanine based metal–organic interfaces: the effect of fluorination, the substrate, and its symmetry. *J. Chem. Phys.*, **133**, 214703.

45

Photoelectron Spectroscopy Applications to Materials Science

Maria Benedetta Casu and Thomas Chassé

45.1

Introduction

The interaction of electromagnetic radiation with matter is the basis of several spectroscopies.

Whenever electromagnetic radiation encounters matter, three events may occur: the radiation can be reflected, can propagate through matter, or can be absorbed. In particular, photons and matter interaction generates several phenomena, among others, the photoelectric effect, the Compton scattering, and, in addition, two processes with very small energy transfer: Thomson (elastic) scattering on a “free” electron, that is, the redirection of low-energy photon without change in energy, and the Rayleigh (coherent) scattering that results from a combined (coherent) action of an atom as a whole. In the photoelectric effect, electrons are emitted from matter (metals and nonmetallic solids, liquids, or gases) as a consequence of their absorption of energy from electromagnetic radiation with a frequency greater than a critical threshold frequency. The emitted electrons that may be referred to as *photoelectrons* have kinetic energy E_{kin} determined by the Einstein relationship [1]

$$E_{\mathrm{kin}} = h\nu - E_{\mathrm{b}} \tag{45.1}$$

where $h\nu$ is the energy of the incident radiation and E_{b} the binding energy of the emitted electrons. Equation (45.1) indicates that radiation will be absorbed for incident energies larger than the binding energy of the electrons in the system (Figure 45.1).

Historically, Heinrich Hertz, in the 1880s during his studies on electromagnetic waves, noticed that metals in electrical systems when exposed to light reacted with a spark. In 1899, Joseph John Thomson found that light could be deflected by an electric field. He found that cathodes could emit rays or better “matter” and those emitted particles were lighter than the mass of the lightest atom, hydrogen. He concluded that the rays were composed of very light negatively charged particles, which he called *corpuscles*: he discovered the electrons. Finally, in 1905, Albert Einstein explained the real nature of the photoelectric effect, that is, a transfer of

Handbook of Spectroscopy, Second Edition. Edited by Günter Gauglitz and David S. Moore.

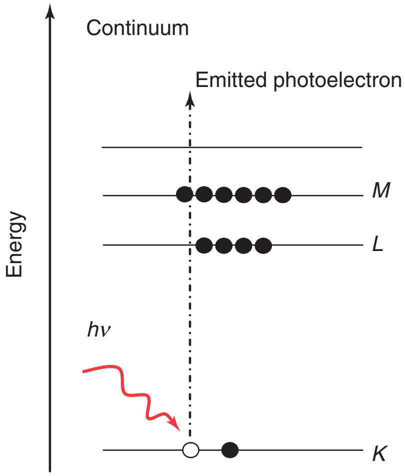

Figure 45.1 Schematic view of the photoelectron effect.

energy between a photon and an electron in an atom, resulting in the emission of the electron itself, with the concepts of quanta, proposed by Max Planck in 1900. Einstein was awarded the Nobel Prize in 1921 for his explanation.

In this chapter, we report some basic concepts that represent the background of the photon electron spectroscopy and its use in investigating surfaces and adsorbates. In doing so, we refer to the classical work of Hüfner [2], Briggs and Seah [3], and Cardona and Ley [4]. Other specific references are also given in the following paragraphs.

45.2
Photoelectron Spectroscopy: Basic Principles

Looking at Eq. (45.1), we can immediately derive some basic considerations on the photoelectric effect: there will be an emitted electron only when $h\nu > E_b$, that is, one has to expect that the effect has a threshold defined by the system, as each electron has a different binding energy due to its environment. Thus, for incident photon energy below E_b, no effect is possible. Keeping $h\nu$ as a fixed parameter, the kinetic energy of the emitted photoelectron is higher, the lower its binding energy, and vice versa. If we assume that the electron is emitted from an atom, the photoemission event is not influenced by different isotopes of the same element. This is due to the fact that although isotopes have different numbers of neutrons, they have the same nuclear charge and their difference does not influence the binding energy of the electrons.

How can we define the binding energy of the photoemitted electron?

In principle, E_b is defined as the difference between the energy $E_f(n-1)$ of the $(n-1)$ electron final state and the energy $E_i(n)$ of the n electron initial state:

$$E_b = E_f(n-1) - E_i(n) \tag{45.2}$$

If no rearrangement of the system took place, this difference would be identical to the negative binding energy of the electron in its orbital, ε_k. This approximation (with frozen orbitals) is the basis of the so-called Koopmans' theorem [5]. This energy can be calculated within a Harthree–Fock method. However, during emission of the photoelectron, a core hole is created and the system reacts to shield and minimizes the energy of its ionized state. The energy reduction caused by this rearrangement is called *relaxation energy*. In addition to the relaxation, electron correlation ($\delta\varepsilon_{\mathrm{corr}}$) and relativistic effects ($\delta\varepsilon_{\mathrm{rel}}$) are also neglected by the Koopmans' theorem. Consequently, in general, E_{b} is given by

$$E_{\mathrm{b}} = -\varepsilon_k - E_{\mathrm{r}}(k) - \delta\varepsilon_{\mathrm{corr}} - \delta\varepsilon_{\mathrm{rel}} \tag{45.3}$$

It is worth mentioning that the correlation and the relativistic corrections are very small and this is the reason why they can be neglected.

As mentioned in the introduction, the photoemission process has to be described with a quantum mechanical approach. On the other hand, a semiclassical model, the three-step model [6], gives the opportunity to interpret the photoemission events in a simpler but effective way.

In the three-step model, the photoemission process is broken up into three sequential steps: the optical excitation of the electron inside the bulk, the diffusion of the electron to the surface, and its transmission through the surface into the vacuum. Only those electrons that have enough kinetic energy along the direction normal to the surface are able to overcome the surface potential barrier and to escape. The remaining electrons are totally reflected, back to the bulk.

Depending on the photon energy, it is usual to distinguish between two measurement regimes: ultraviolet photoelectron spectroscopy (UPS) when $h\nu$ is lower than 100 eV and X-ray photoelectron spectroscopy (XPS) for values above 100 eV. X-rays have enough energy to ionize atoms by emission from both valence electrons and core electrons, while UPS gives detailed information on electrons coming from the valence band.

In the UPS regime, the photon momentum p is related to the photon frequency ν via the relationship $p = \hbar k$ with wave vector $\mathbf{k}$. In UPS, p is negligible and the photoexcited electrons have the same momentum in the initial and in the final state; it means that direct transitions occur. UPS spectra show energy and intensity variations depending on the incident energy, and this gives the opportunity to map out the energy band structure of well-ordered materials.

45.2.1
UPS Regime

As mentioned, the kinetic energy of the emitted electrons is given by Einstein's relationship (Eq. (45.1)). In a metal, the maximum kinetic energy, $E_{\mathrm{kin}}^{\mathrm{max}}$, that one electron escaping from the emitter can have is

$$E_{\mathrm{kin}}^{\mathrm{max}} = h\nu - \Phi_{\mathrm{m}} \tag{45.4}$$

where Φ_{m} is the work function of the metal (Figure 45.2).

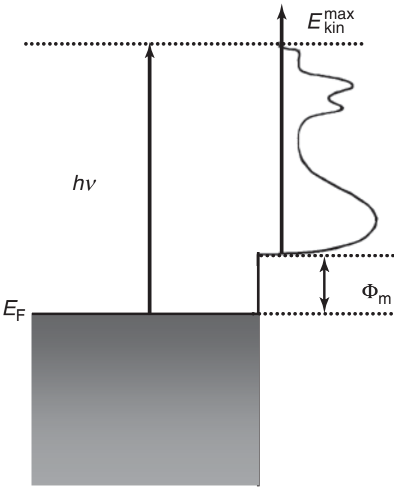

Figure 45.2 Photoemission from a metal.

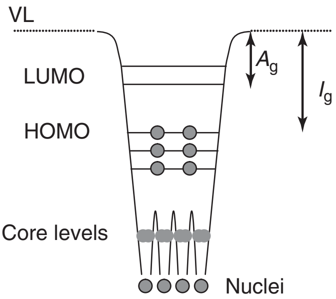

Figure 45.3 Potential well of a polyatomic molecule.

In a polyatomic molecule, the effective potential well seen by an electron is formed by the atomic nuclei and the other electrons. The deep atomic orbitals are still localized in the atomic potential well but the upper ones interact, forming delocalized molecular orbitals (MOs). The edge of the potential well is the vacuum level, VL, above which the electron can escape from the molecule or the chain. In a molecule, the separation from the highest occupied molecular orbital (HOMO) to the VL is the gas-phase ionization potential, I_g, and between the lowest unoccupied molecular orbital (LUMO) and the VL is the electron affinity, A_g (Figure 45.3). Thus, by using UPS, it is possible to determine the ionization potential of a molecule, analogously to the work function in the case of a metal.

UPS gives valuable information when investigating semiconductors also. For example, the ionization potential, I_P, and the electron affinity, E_A, of an organic semiconductor are still defined as in a molecule, but their values are different because (i) of the solid state effects, (ii) of the crystalline periodic potential, if the organic semiconductor is well ordered, and (iii) of the overlapping of the wave functions [7].

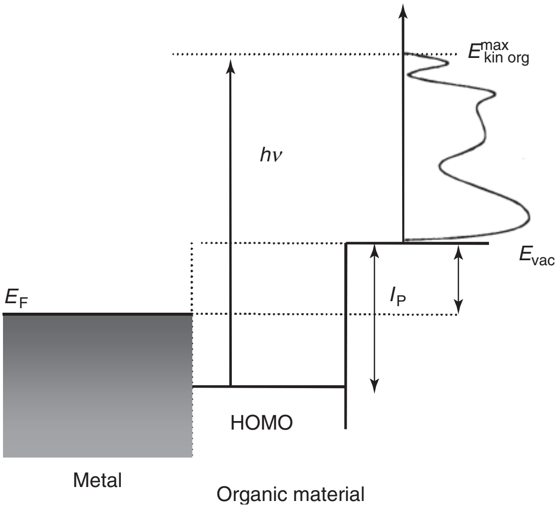

Figure 45.4 UPS at the interface organic/metal: $h\nu$, incident photon energy; E_F, Fermi level of the metal; I_P, ionization potential; HOMO, highest occupied molecular orbital; $E^{max}_{kin\ org}$, maximum kinetic energy of the photoelectron emitted from the organic material; and E_{vac}, VL of the organic layer.

Keeping this picture in mind, the photoelectrons of an organic adsorbate deposited on a metal surface come from the organic layer. The photoelectrons with highest kinetic energy, $E^{max}_{kin\ org}$, originate from the HOMO (Eq. (45.4)). Consequently, it is possible to obtain the ionization potential, I_P, of the organic layer as

$$I_P = h\nu - E^{max}_{kin\ org} \tag{45.5}$$

Several other physical parameters can be obtained from the UPS spectra such as the alignment of the HOMO of the organic layer with respect to the Fermi level, E_F, of the metal; the VL energy shift of the organic layer at the interface metal/organic with respect to the VL of the metal; and also the energy, ε^F_{vac}, of the VL of the organic layer relative to the E_F [8] (Figure 45.4 and Figure 45.5).

This means that UPS is a very powerful technique to study the interfacial electronic structure and the energy alignment at the organic/metal and organic/organic interfaces [9, 10].

A further interesting aspect of UPS that we like to mention in this chapter is the fact that UPS spectra are strongly dependent on energy dispersion of valence and conduction states and they give direct information about the resulting 2D band structure of surface states, the 2D band structure of adsorbates, as well as bulk band structure. In particular, when a well-ordered system is investigated with this technique, the spectra are very sensitive to the variation of the incident energy and to the variation of the angle of incidence, α, the takeoff angle, θ, and the azimuth angle, φ (Figure 45.6). Therefore, angle-resolved

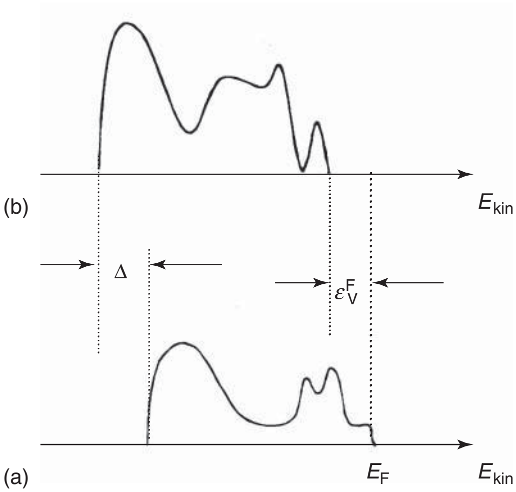

Figure 45.5 Comparison between the UPS spectra (a) from a metal and (b) from the deposited organic material. The abscissa is the kinetic energy of the emitted photoelectrons; the origin is fixed in an arbitrary point. E_F is the metal Fermi energy, Δ is the vacuum level shift at the interface, and ε_V^F is the energy alignment of the HOMO relative to E_F.

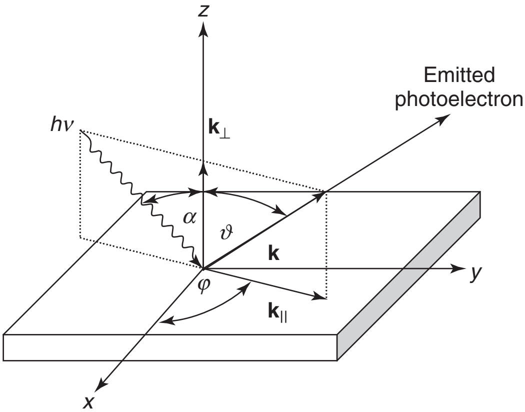

Figure 45.6 Geometry of an UPS experiment: α, angle of incidence; θ, takeoff angle; φ, azimuth angle; $h\nu$, incident photon energy; $\mathbf{k}$, wave vector of the emitted photoelectrons; and $\mathbf{k}_\perp$ and $\mathbf{k}_{||}$ are the components of $\mathbf{k}$, perpendicular and parallel, respectively, to the surface of the sample.

ultraviolet photoelectron spectroscopy (ARUPS) allows determining the energy band dispersion relation $E(\mathbf{k})$ between the energy E and the wave vector $\mathbf{k}$ of the photoelectrons [11].

To obtain the $\mathbf{k}$-resolved band structure, the peaks from the recorded spectra are related to $\mathbf{k}$-conserving transitions from occupied (E_{in}) to unoccupied bands (E_{fin})

of the material, satisfying the equation

$$E_{\text{fin}} = E_{\text{in}} \pm h\nu \tag{45.6}$$

in which direct transitions are assumed.

The measured quantity is the kinetic energy of the photoelectrons, E_{kin}, detected for a given energy and fixed angles α, θ, and ϕ, relatively to the substrate normal of the sample:

$$E_{\text{fin}} = E_{\text{kin}} + \Phi \tag{45.7}$$

where Φ is the work function of the system.

The kinetic energy and the momentum of the electron in the vacuum are related according to

$$E_{\text{kin}} = \frac{\hbar^2}{2m_{\text{e}}}(\mathbf{k}_{\perp}^2 + \mathbf{k}_{||}^2) \tag{45.8}$$

where $\mathbf{k}_{\perp}$ and $\mathbf{k}_{||}$ are the components of the momentum of the electron, perpendicular and parallel, respectively, to the surface.

In a photoemission process, only the component of the wave vector parallel to the surface is conserved because the translation symmetry is broken by the surface; therefore, this component will be given by the following equation:

$$\mathbf{k}_{||} = \left(\frac{2m_{\text{e}}}{\hbar^2}E_{\text{kin}}\right)^{1/2} \sin\theta \tag{45.9}$$

To determine $\mathbf{k}_{\perp}$ the free-electron model has been widely used [11–13]. In this model, the dispersion relation of the final state is assumed to be

$$E_{\text{fin}} = \frac{\hbar^2}{2m_{\text{e}}}(\mathbf{k} + \mathbf{G})^2 + E_0 \tag{45.10}$$

where $\mathbf{G}$ is a reciprocal lattice vector, $E_{\text{v}} - E_0$ is the inner potential, $V_0 = E_{\text{v}} - E_0 = |E_0| + \Phi$, that is, the potential well depth where the energies are measured with respect to the Fermi level.

In normal emission $\mathbf{k}_{||} = 0$, therefore, the momentum normal to the surface is given by

$$\mathbf{k}_{\perp}^2 = \frac{2m_{\text{e}}}{\hbar^2}(E_{\text{inc}} - E_{\text{b}} + V_0) \tag{45.11}$$

By means of Eqs. (45.9) and (45.11), it is possible to map out the complete band structure of materials.

Already in the 1990s, ARUPS was used to investigate the electronic structure and the energy dispersion of surface states [11], as well as bonding of adsorbed hydrocarbons, the orientation and symmetry of the adsorbate on the surface, the influence of lateral interactions, and the formation of two-dimensional adsorbate band structures. Several examples of energy band structure of simple hydrocarbon molecules such as benzene, ethylene, and acetylene deposited, for example, on Ni(110), Ni(111), Ru(001), and the reconstructed Pt(110)1 × 2 surface have been experimentally determined by Steinrück [14]. Ueno *et al.* [13] also investigated a variety of

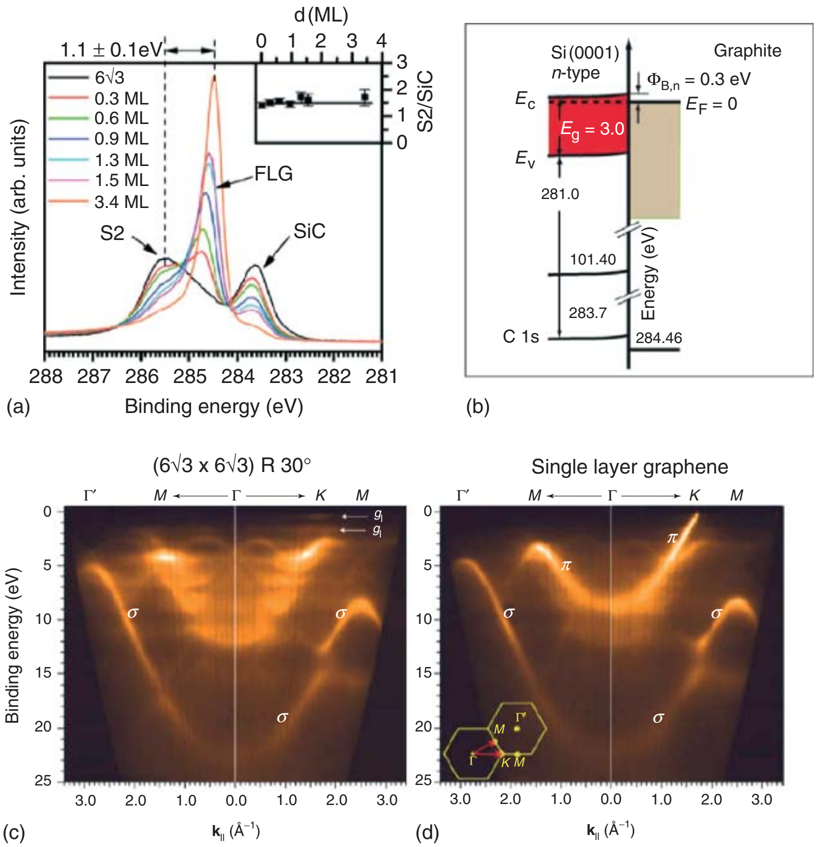

Figure 45.7 Photoelectron intensity map versus binding energy and parallel momentum of (a) C 1s core-level spectra of SiC(0001) – $(6\sqrt{3} \times 6\sqrt{3})$R30° as a function of graphene film thickness. (b) Band alignment at the SiC–graphene interface (FLG, few layer graphene). (c) Angle-resolved photoemission images of the SiC(0001) – $(6\sqrt{3} \times 6\sqrt{3})$R30° structure and (d) graphene on top of SiC(0001) – $(6\sqrt{3} \times 6\sqrt{3})$R30°, respectively. (Reprinted from [19], Copyright 2009, Ref. [19] with permission from Elsevier.)

adsorbates determining, among others, the valence-band energy dispersion of thin films of pentatriacontan-18-one [$CH_3(CH_2)_{16}CO(CH_2)CH_3$] on copper, comparing the results with theoretical calculations.

A recent application of the potential of ARUPS in band mapping is represented by graphene. Graphene is a strictly two-dimensional material that exhibits exceptionally high crystal and electronic quality, and has already revealed a world of new properties and potential applications [15]. It is a one-atom-thick planar sheet of sp^2-bonded carbon atoms that are packed in a honeycomb crystal lattice. Graphene can be recognized as the mother of all graphitic forms. From the theoretical point of view, most of its electronic properties were well known since 1947, when a calculation of the graphene band structure was performed on the basis of tight banding approximation [16]. This calculation already showed the dynamics of the electrons in such a single, one-atom-thick sheet of carbon atoms. However, there was no experimental evidence that 2D systems could ever exist as self-standing crystals, as it was believed that strictly 2D crystals were thermodynamically unstable: the nascent 2D crystallites would try to minimize their surface energy and morph into 3D structures. In graphene, the thermodynamic stability is reached by gentle crumpling in 3D. In 2004, Novoselov *et al.* [17] were able, by using a peeling technique, with adhesive tape to isolate a single layer of graphene. This was the fundamental step that allowed to prove all characteristics of this fascinating material, and that also led to Geim and Novoselov winning the Nobel Prize in Physics in 2010 [18]. This discovery literally propelled the curiosity of the scientists on graphene including the possibility of experimentally determining its band structure. This result was achieved in 2008 by Emtsev *et al.* [19] using ARUPS (Figure 45.7). Their experiment clearly shows the unusual band structure of a graphene single layer with its linear dispersion close to the Dirac points, without band gap, due to the fact that electrons in graphene behave as massless Dirac fermions [15–17, 19].

45.2.2
XPS Regime

As previously discussed, the binding energy of the emitted photoelectrons depends on the final and on the initial states. The effects of both natures are visible in the XPS spectra and they will be described in the following, starting with the initial state effects.

XPS spectra are characterized by high-intensity features that belong to core-level photoemission effects. Figure 45.8a shows the survey spectrum, that is, a wide scan, of a monolayer of hexadecanethiol (HDT). Alkanethiols are well known to form self-assembling monolayers (SAMs) on substrates such as gold, silver, and copper because of the strong affinity that the sulfur atoms show for these metals. They are molecules with an alkyl chain, $(\mathrm{C{-}C})_n$ chain, as the backbone, a tail group, and an S–H head group. They are extensively investigated because of their possible applications in optoelectronics and sensors [20]. In this case, HDT has been deposited on a semiconductor surface, that is, indium phosphide [21]. The spectrum has been excited by using Al Kα radiation ($h\nu = 1486.6\,\mathrm{eV}$). Several peaks may be attributed to either the In or P atoms of the substrate, and carbon and sulfur peaks of the film are also recognizable, in chemical agreement with the substrate + adsorbate system. It is clearly visible how the main lines have their binding energy position exactly where it has to be expected because of their element specificity. The peak assignment can be performed by using the tables of electron-binding energies for the elements in their natural form [22] or in a particular bond [23]. Thus, one can identify the main lines due to In 3s, In 3p, In 3d, In 4d, and P 2s and P 2p, which are contributions coming from the substrate, and the lines due to C 1s and S 2p due to the adsorbate. Looking at the survey spectrum at the energy positions of the main XPS lines, their binding energy represents the strength of the interaction between the electron and the atomic nucleus; consequently, they

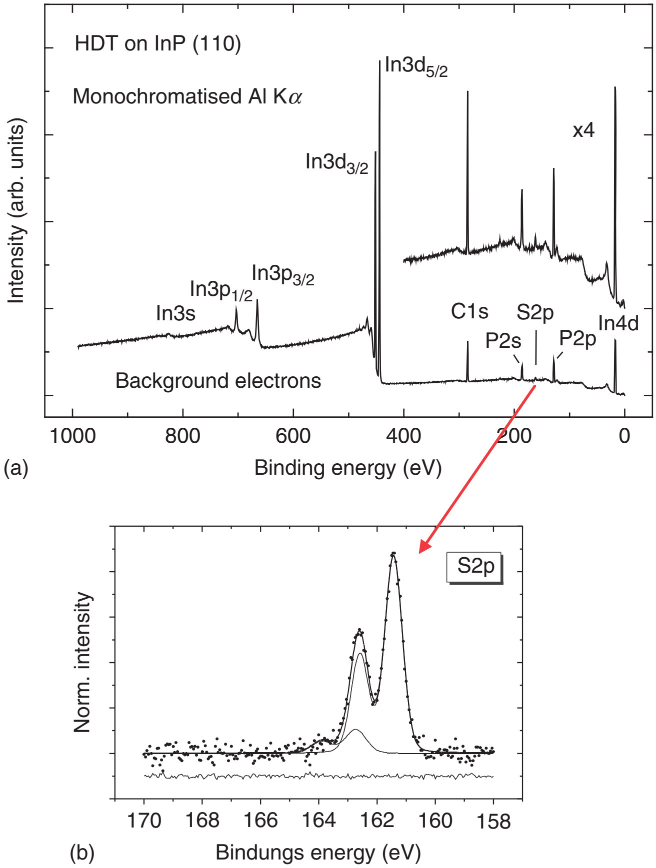

Figure 45.8 Hexadecanethiol (HDT) on InP (110). (a) Survey spectrum. (b) S 2p highly resolved core-level photoemission spectra.

follow the energy of the orbital and, for example, the binding energy of the 3s states is higher than the binding energy of the 3p states. In addition, the binding energy increases with the atomic number Z (i.e., the number of protons found in the nucleus of an atom and therefore identical to the charge number of the nucleus); thus, the main line assigned to 3s, 3p, 3d states of the In atoms have higher energy than the relative binding energies of the 2s and 2p core levels in P atoms.

Further examining the spectrum in Figure 45.8a, another relevant aspect of XPS spectra is visible: the background. The background has a typical step shape with higher intensity for higher binding energies (left of the main peak). This is due to the inelastic scattering processes that are caused by electrons that have lost a part of their energy because of inelastic collisions in the solid, but they have still enough energy to escape the surface. Continuous values of the energy are possible from zero kinetic energy to the photoemission peak for a given kinetic energy because the collision events have energies that are continuous themselves.

A survey spectrum is very useful to immediately characterize a system, to check whether extraneous atoms, due to unexpected chemical species, for example, are present. Figure 45.8a does not evidence any impurity, leading to the conclusion that the HDT monolayer is contamination-free.

However, additional information can be obtained from highly resolved spectra. Figure 45.8b shows the highly resolved S 2p core-level photoemission spectrum. The feature that seemed to be unique in the survey spectrum in Figure 45.8a in reality shows a more complex structure. This effect is again an initial state effect and it is due to the spin–orbit splitting, that is, the interaction of the electron spin with its momentum [24]. The 1s orbitals do not show any spin–orbit splitting and, in general, they appear as a singlet in XPS.

The electronic cloud around an atom is sensitively influenced by the electronegativity of the neighbor atoms. This is mirrored in the XPS spectra that show a difference, a shift toward higher energies, known as *chemical shift*, in the binding energy of the emitted photoelectrons involved in the bond between a more electronegative atom and a core electropositive atom, for example, in the case of functional groups and oxidation states. This effect is visible in XPS spectra of complex anions, alkali, alkaline earth compounds [25], and metal oxides. A case system is the Ti 2p core-level spectrum for metallic Ti and for TiO_2 [23]. The binding energy for Ti $2p_{1/2}$ and $2p_{3/2}$ are 460 and 454 eV, respectively. Owing to the presence of oxygen, which withdraws the electrons, titanium assumes an oxidation state 4+; consequently, the Ti 2p relaxes to higher binding energies, that is, 464.3 and 458.8 eV, respectively [23].

Till now, we have examined only initial state effects, but, as mentioned, XPS spectra show also features that are due to final state effects. Here, we briefly analyze these aspects. According to the Koopmans' theorem, we should expect the main lines having their binding energies exactly as if the electrons were in a system as the nonexcited one, but with one electron less (frozen orbital approximation). However, we cannot observe this state of the system because the system immediately reacts, screening the core hole. The binding energy is shifted toward the higher energy range. Analogously, we cannot observe the system in a fully relaxed state, that is, in the ground state of the ionized system because the photoemission event is faster than the full relaxation. Thus, we observe a series of complementary features at higher binding energies in the spectra, which depend on various excited states of the systems: (i) excitations of electron to bound state (shake-up satellite), (ii) excitations of electron to unbound (continuum) states (shake-off satellite), and (iii) excitations of hole states (shake-down satellite).

A particular final state effect is visible in spectra of metallic systems. It is well known how electrons in a metal behave as a Fermi gas, owing to the properties of the metallic bond and the strong delocalization of the electrons in metals [24]. The collective oscillations of the free-electron gas give rise to plasmons, that is, to quanta of a plasma oscillation. Plasmons, for example, are clearly visible not only in the XPS spectra of simple metals such as Na and Mg [2, 26, 27] and Al but also in semiconductors.

45.3
Photoemission Measurements and Data Analysis

Surface analysis of solid samples using electron spectroscopies are typically performed in ultrahigh vacuum (UHV) conditions at base pressures of about 10^{-10} mbar. Because of the very strong interaction cross sections of the electrons with matter, any interactions of the emitted electrons with molecules from the residual gas need to be avoided on their path from the samples toward the detecting unit, in order to record sufficiently intense electron spectra. In addition, both the photon sources (X-ray tubes or UV (ultraviolet) lamps) and electron detectors require better than high vacuum conditions to operate properly for long times. Further, an estimate using kinetic gas theory gives easily that even at 10^{-6} mbar within 1–3 s, about one monolayer is adsorbed from the residual gas due to the huge number of hits from the gas phase to the surface, provided any hit results in an adsorbate atom/molecule. But any recontamination of carefully prepared samples by hits from residual gas molecules needs to be carefully avoided during measurements, as will happen in time if the partial pressures are not sufficiently low enough. Therefore, dedicated stainless steel chamber systems equipped with two-or three-level pumping systems and, of course, adequate handling of the systems is strictly required.

As outlined in the previous chapters, during a photoemission experiment the photoelectrons coming from a sample, due to the excitation with an appropriate incident radiation, are collected. We can divide the required setup for a photoemission experiment into two blocks: source, and measuring chamber with analyzer and sample.

UPS measuring units are usually equipped with standard UV light sources such as He discharge lamps (He I = 21.2 eV and He II = 40.8 eV).

X-ray laboratory sources are obtained by focusing a beam of high-energy electrons (usually with energy above 10 keV) onto a target. In this way, core holes are created in the target (anode) that emits fluorescence X-rays. They represent the source of the radiation for the experiment. Several materials are used as an anode: Mg, Al, Si, Zr, Ag, Ti, and Cr. Their characteristic energies are given in Table 45.1. As a specific line is used because of the order of magnitude of its intensity (in principle, the background emission could also be used), each anode provides its

Table 45.1 Most common X-ray lines with their relative energy and line width.

Line	Energy (eV)	Line width (eV)
Na Kα	1041.0	0.70
Mg Kα	1253.6	0.70
Al Kα	1486.6	0.85
Zr Lα	2042.4	1.7
Ti Kα	4510.0	2.0
Cu Kα	8048.0	2.6

own fixed energy for the X-rays. The most used anode materials are Mg and Al, very often also in combination in the same setup. However, the obtained emission is not perfectly monochromatic; also, satellite background emission, high-energy electrons, Bremsstrahlung, and heat will reach the sample (the electron energy is mostly converted into heat; this is the reason a water cooling system is required for the X-ray source). Thus, an X-ray transparent window (usually Al for Mg and Al anodes) is placed in front of the X-ray source. A further optimization procedure is the use of a monochromator. This is very often found in combination with an Al anode and it is based on quartz crystals. The con of this system is the obvious reduction in the intensity that can be compensated for by using efficient detection methods.

We like to mention that in recent years a considerable improvement on the photoemission experiment came from the use of synchrotron radiation. Synchrotron light is intense, bright, and polarized. It covers a very broad spectral range if the emission is produced with a bending magnet; on the other hand, the emission from periodic arrays of magnets inserted in the linear parts of the electron storage rings occurs over a very narrow and tunable spectral band. Using an appropriate monochromator, the desired spectral range can be selected for the experiment. Because of all these important characteristics, a synchrotron source is, in principle, an ideal photon emitter [28]. The measuring line, or more commonly in a synchrotron, the so-called beamline, is of course structurally determined by the source. The main identifying part, which very often also gives the name to the beamline, is the monochromator, with gratings or crystals. It is used to select a narrow spectral bandwidth from the continuum of the radiation coming from the synchrotron ring, to modulate the flux, to scan the incident energy, and sometimes to focus the beam on the sample. More often, mirrors properly chosen and placed fulfill this task. In a synchrotron as well as in a beamline, the UHV is necessary to let the particles move at relativistic speed in the accelerator. The development of the modern electron storage rings (from third generation on) has had a real impact and importance in photoelectron spectroscopy. We do not further address this topic and we suggest that the readers refer to the existent literature [29, 30].

The analyzer usually has three sections: an electronic lens, a dispersive part, and a detector (usually a channeltron: channeltron is the trade name of one of the most commonly sold multipliers) (Figure 45.9). Its energy resolution depends on their geometry. The lens has to collect the emitted photoelectrons: this can be done by choosing the angular resolution, the spatial resolution, or maximizing the number of collected electrons; for example, it is possible to switch between detection from large or small areas as well as large or small acceptance angles. The dispersive part analyzes the electrons depending on their kinetic energy. It consists of two cylindrical or hemispherical deflection plates, kept at a certain voltage, that determine the energy of the electrons pulled into the electron multiplier. Electron spectra are preferably measured using constant analyzer pass energy of the electrons, which results in a constant energy resolution but an energy-dependent transmission. An electron multiplier is a vacuum-tube structure that

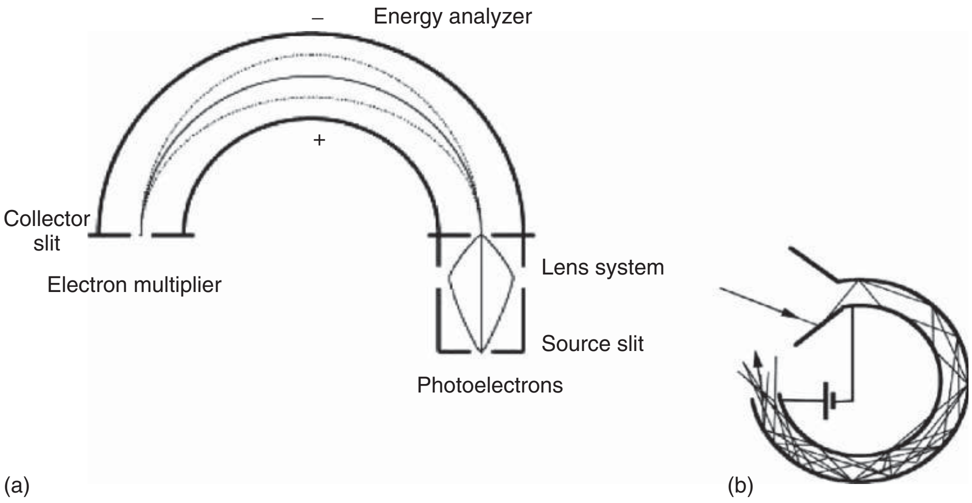

Figure 45.9 A schematic view of (a) an analyzer and (b) a multiplier.

multiplies incident charges, by using secondary emission. Electron bombarding a metal can induce the emission of a few electrons (1–3). Applying a potential between this metal and a second plate accelerates the emitted electrons to the next metal plate and induces secondary emission of further more electrons. This can be done as many times as necessary to amplify the signal, resulting in an avalanche of electrons collected by an anode. The electrons are detected by stacks of channeltron-type electron multipliers (typically 5–9) or position-sensitive channel plate detectors.

Here, we like to mention the surface sensitivity of photoelectron spectroscopy. Surface sensitivity in a technique is given by the relationship between kinetic energy of the photoemitted electrons and their inelastic mean free path (IMFP). The *IMFP* is defined as the average distance traveled by an electron between inelastic collisions. It depends on the kinetic energy according to a general behavior that is similar for all materials, the so-called universal curve [22]. The surface sensitivity is determined by the depth perpendicular to the surface from which the electrons escape, which is proportional to the IMFP via the cosines of the emission angle of the electrons relative to the surface normal. Thus, the surface sensitivity of an experiment can be accordingly varied: the IMFP has a minimum at around 50 eV, corresponding to a few Angstrom. For kinetic energies up to 2000 eV, its value is 70 Å large [22]. Thus, for example, in synchrotron, XPS experiments with different surface sensitivity can be carried on, taking advantage of the tuning of incident photon energy [31].

Another useful concept related with the surface sensitivity is the information depth. The information depth is the maximum depth, in the direction normal to the surface, from which the information is obtained. The number of emitted electrons trough matter with no energy loss decreases obeying the Lambert-Beer:

$$I = I_0 \exp(-d/\lambda \cos\theta) \tag{45.12}$$

where I and I_0 is the intensity of the emitted photoelectrons at d and $d = 0$ (i.e., the surface), λ the inelastic mean free path, and θ the angle between the normal to the surface, and the emitted photoelectrons. From simple numerical consideration, Equation (45.12) leads to the fact that 95% of the electrons comes from $d = 3\lambda$. This is the informatiom depth at which 95% of the electrons is emitted.

In a photoemission experiment, samples have also to fulfill important requirements: in particular, they must be conductive to avoid charging effects. The charging effects lead to artifacts in the spectra such as shift in the energy of the features, distorted peaks, and new peaks. However, insulators can also be investigated by photoelectron spectroscopy, provided that the positive charges are neutralized, for example, with an electron gun or with an electric field.

In addition, to measure the kinetic energy/binding energy of the photoemitted electrons, the sample is put in electrical contact with the spectrometer and grounded. This means that the Fermi edge of the two systems, sample, and spectrometer are aligned. To measure the binding energy, it is now necessary to overcome the work function of the spectrometer. It is possible to take Einstein relationship (Eq. (45.1)) into account, modified as follows:

$$E_B^F = h\nu - E_{kin} - \Phi_{sp} \tag{45.13}$$

where E_B^F indicates that the binding energy is referred to as the *Fermi level*, and Φ_{sp} is the work function of the spectrometer. This implies the necessity to determine this parameter. This can be done using a known sample with well-defined main lines, for example, gold or silver, and modulating the spectrometer settings in order to exactly match their binding energy. Once the spectrometer is calibrated, in principle, the calibration can be taken as fixed. However, changes in the UHV level, use of gases, and various preparations can change its work function; thus, a systematic calibration and check are a good laboratory practice.

Very often, in UPS, it is necessary to measure the work function of the sample, for example, to determine the energy-level alignment between a metal substrate and an organic adsorbate (Figure 45.5). This can be done by negatively biasing the samples with respect to the analyzer. This raises the energy levels and it overpasses the work function of the analyzer because the bias voltage adds to the photoelectron kinetic energy relatively to the analyzer itself, giving the opportunity to clearly measure the secondary electron cutoff. The work function is consequently determined by the excitation energy minus the width of the photoelectron spectrum.

Data analysis represents a very important issue, in XPS as well as in UPS. In both cases, information on occupied states (core levels and valence states, respectively) can be obtained by comparing experiments with calculations. This is a standard procedure that has been extensively applied, for example, to organic materials, when the first UPS investigations of this class of materials were performed. The first approach has been to use single-molecule calculations and compare the data of the simulated spectra with the experiments. Very little was known at that time about small molecules and polymer thin films; thus, this was certainly a successful method to gain as much information as possible on the new systems [32]. Nowadays, the necessity of model calculations that take into account intermolecular interactions, solid-state interactions, and a periodic potential have brought new challenges that have still to be completely addressed by theoreticians in this fields, in contrast to band structure calculation and optical absorption where brilliant results have been already obtained [33].

From a quantification point of view, XPS can provide information on the stoichiometry of the investigated films as well as on the atomic density of the elements on which the system is based. The area of the main lines, together with their relative satellites for a given element, is proportional to the percentage of the same element in the chemical formula of the investigated system. In highly resolved XPS spectra, the rich fine structure allows fitting the lines including contributions for different atomic sites of the same element that, owing to a different chemical environment, are expected to show differences in their binding energies [34, 35].

The fitting curves can be described with a Voigt profile, that is, a convolution of a Gaussian and a Lorenzian profile. This is due to the fact that different contributions influence the line shape of the XPS main features: intrinsic lifetime broadening leads to a Lorenzian profile, while experimental contributions and various inhomogenieties have a Gaussian profile. The lifetime of the core hole is determined basically by the Heisenberg uncertainty principle and consequently the intrinsic peak width. For example, the Lorenzian width for the C 1s orbital is around 80 meV, and for the O 1s orbital it is around 100 meV in organic materials [35]. The setup gives a contribution assumed to have a Gaussian lineshape due to the resolution of the analyzer, the not perfect monochromaticity of the X-ray, and inhomogeneities of different nature.

A background subtraction must be also taken into account before performing an appropriate fit procedure of the XPS curves. The most used method was developed by Shirley [36] in 1972. This method considers the background due to inelastically scattered electrons, it is assumed to arise only from the scattering of electrons of higher kinetic energy and it is proportional to the integrated photoelectron intensity of the higher kinetic energy. Later, Tougaard [37] described the transport of electrons after excitation with equations based on a convolution of the recorded data with an energy-loss probability distribution. Each material has its own characteristic loss function [38].

Regarding the atomic density, we can observe that the intensity of the signal for a given photon energy is proportional to the photon flux Φ_0, the photoionization cross section σ, the number of photoemitting atoms n, the transmission of the spectrometer T, and the detection efficiency A, according to the following formula

$$I(h\nu, E) = \Phi_0 \cdot \sigma(h\nu) \cdot n \cdot A \cdot \lambda(E) \cdot T(E) \tag{45.14}$$

where λ is the IMFP. The photoionization cross section, σ, represents the probability of the ionization of a subshell. It measures the ‘‘overlap’’ of the initial and the final state wavefunctions [22].

Adopting a ratio procedure, for example, for two elements 1 and 2, as following:

$$\frac{I_1}{I_2} = \frac{n_1 \cdot \sigma_1 \lambda_1 \cdot T_1}{n_2 \cdot \sigma_2 \lambda_2 \cdot T_2} \tag{45.15}$$

it is possible to determine the atom fraction for a certain element:

$$\frac{n_1}{n_2} = \frac{I_1/S_1}{I_2/S_2} \tag{45.16}$$

according to Eq. (45.16), and generalizing:

$$x_1 = \frac{n_1}{\sum_i n_i} \tag{45.17}$$

where S is the atomic density factor defined as $S_i = \sigma_i \lambda_i T_i$.

The differential ionization cross section, $\mathrm{d}\sigma/\mathrm{d}\Omega$, for isolated atoms using nonpolarized photons is given in the traditional dipole approximation as

$$\frac{\mathrm{d}\sigma}{\mathrm{d}\Omega} = \frac{\sigma}{4\pi}\left[1 - \frac{\beta}{4}\left(3\cos^2\theta - 1\right)\right] \tag{45.18}$$

where β is the asymmetry parameter, σ is the total photoionization cross section for a given subshell, θ is the angle between the photon and photoelectron propagation directions, and $\mathrm{d}\Omega$ is an element of the solid angle [39, 40]. More recent studies include quadrupole terms and these lead to a significantly different angular distribution [39].

The above-mentioned formalism is derived under the assumption that the photoelectron trajectories are linear from the depth of emission to the surface. In reality, photoelectrons may undergo elastic interactions with atoms of the solid and, as a result, the photoelectron trajectories are generally nonlinear and this formalism is not adequate anymore.

The effects of elastic scattering of the signal electrons in XPS can be accounted for by the introduction of two correction parameters, Q_x and β_{eff} [40], into the equation commonly used for quantitative analyses of homogeneous materials. Two formulae describe each parameter. One of these formulae is a function of the single-scattering albedo and the photoelectron emission angle, and is useful for emission angles between 0° and 80°. The other simpler formula is a function only of the single-scattering albedo and is useful for emission angles between 0°and 50° [40]. Hence, angle-resolved XPS reveals to be a nondestructive method for the determination of simple concentration depth profiles in perfectly flat surfaces [41].

Observing Eqs. (45.15–45.17), the necessity to know the value of λ for individual material in order to address a quantitative analysis of the XPS spectra is clear. The algorithm proposed by Tanuma, Powell, and Penn (TPP) have been applied to many solids, including organic and inorganic materials as well as elements. In particular, they also developed the so-called TPP-2M [42–47] equation to determine the IMFP according to the Bethe equation:

$$\lambda(\text{Å}) = \frac{E}{E_{\mathrm{p}}^2[\beta \ln(\gamma E) - CE^{-1} + DE^{-2}]}(\text{Å}) \tag{45.19}$$

$$E_p(\text{eV}) = 28.8\left(\frac{N_v\rho}{M}\right)^{1/2}(\text{eV}) \tag{45.20}$$

where E_p is the free-electron plasmon energy, N_v the number of valence electrons per atom/molecule, ρ the density, and M the atomic/molecular weight. The values of the parameters β, γ, C, and D have been determined for many materials [42–47]. By comparison with values of the IMFP experimentally obtained, it has been demonstrated that the TPP-2M equation constitutes a useful predictive equation for estimating λ in materials [48].

Seah [3] also contributed in a substantial way to address this aspect of quantification in XPS, developing, in addition, also the necessary equations to determine the thickness of adsorbates using the XPS signal.

45.4
Applications

In the following, we report some photoelectron experiments from the existing literature in order to show the potential of this technique, and how it can be used to answer questions ranging from basic research to solve problems also relevant in technology.

45.4.1
Ultraviolet Photoelectron Spectroscopy: Basic Research and Its Relevance in Technology

Already at the beginning of the 1940s, it was clear that the work function depends on the different crystallographic faces of the crystals of the same element [49]. The difference in values ranges from a few tenths of a volt to 1 V [49]. For example, for gold the calculated work function is 6.01, 6.16, and 5.40 eV, for the fcc (face-centered cubic) crystallographic directions (111), (100), and (110), respectively [50]. Analogously, it has recently been shown that thin films of well-organized molecules are also characterized by different ionization potentials depending on the different molecular orientation that the molecules themselves may assume in the film [51].

Figure 45.10 shows the experimental and the theoretical photoelectron spectra of α,ω-dihexyl-sexithiophene (DH6T). DH6T is a small organic molecule used in organic electronics; thus, it is important to know in a very accurate way its ionization potential in thin films because of device engineering. The figure indicates a shift of the binding energy of the molecular levels comparing a lying monolayer, and a second standing layer. Duhm *et al.* [51] have shown that the difference of 0.6 eV is due to a difference in the ionization potential in the two cases. By using photoelectron spectroscopy combined with density functional theory (DFT) calculations, they have demonstrated that the ionization potential changes are linked to the existence of a surface dipole built into the molecular layers, due to details of the molecular electronic structure. In particular, its magnitude depends on the orientation of molecules relative to the surface of an ordered assembly.

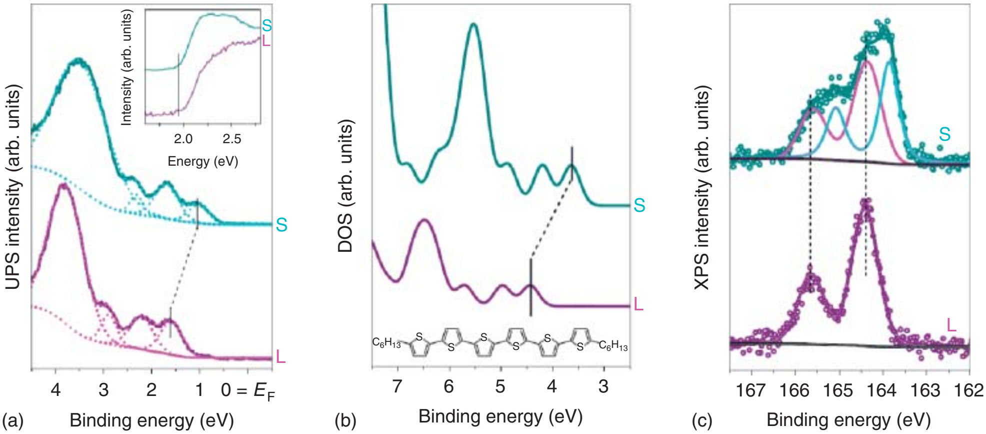

Figure 45.10 (a) Photoemission spectra of DH6T on Ag(111). Experimental UPS spectra of 4 Å of DH6T (purple), and 40 Å of DH6T (cyan). The dotted lines are a fit. The inset shows the secondary-electron cutoffs. (b) Density functional theory calculation of the density of states of a single layer of lying (purple) and standing (cyan) DH6T molecules. The inset shows the chemical structure of DH6T. (c) Experimental XPS S 2p spectra for 4 Å (purple), and 30 Å (cyan) of DH6T. L indicates a lying monolayer, and S a second standing layer. (Reprinted with permission from Macmillan Publishers Ltd [51] copyright 2008.)

As molecular orientation in organic thin films is influenced not only by the molecule–substrate interaction but also by several parameters such as preparation conditions [52, 53], topography [54], and morphology of the substrate [55, 56], including patterning [57], it is possible to design films with a certain molecular orientation to obtain the desired level of alignment to achieve the necessary optimization of working devices.

45.4.2
XPS as a Tool to Investigate Buried Interfaces

Organic small molecules have been extensively investigated in recent years because of the fascinating opportunities related to their use in electronics, ranging from flexible, stretchable displays to transparent ones, via new lighting concepts, where lamp structures or walls are the light-emitting objects themselves. As briefly mentioned earlier, to use the molecules in a device, it is necessary to deposit molecules onto a substrate. The orientation of the molecules must be known to determine the electronic properties at the interface, and consequently the device performances.

The family of phthalocyanines (Pcs) is one of the most promising candidates for a variety of applications [58–60] owing to their electronic and optical properties and their variability in functional group substitution. Anisotropic electrical transport properties are often observed in these materials, caused by the preferred molecular orientation [61–63]. A very high degree of orientation in evaporated films was observed on several substrates [64–68], even on relatively ill-defined technically relevant substrates [69].

Biswas *et al.* [70], by using near-edge X-ray absorption fine structure (NEXAFS), investigated copper phthalocyanines (CuPcs) deposited on gold foil. They found lying CuPc molecules in the first layer on top of the polycrystalline gold substrate. However, the NEXAFS dichroism was not evident for thicker films. This can be interpreted either as a rearrangement of the molecules during film growth or as a sum of signals from differently oriented, lying, and standing molecules. XPS investigations with different surface sensitivities have been performed to clarify this point. The C 1s photoemission spectrum of CuPc in Figure 45.11 shows two main features, one is derived from the benzene substructure (C1) and another from the atoms of the pyrrole substructure neighbored to nitrogen (C2). They can be used to distinguish standing and lying molecules within the uppermost layer. In the former case, the C2 atoms are located deeper inside the film compared to the C1, so the corresponding surface-sensitive photoemission signal of C2 atoms is weakened compared to the C1 signal from the outer parts of the molecule. In the latter case, C2 electrons from different parts of the lying molecule are not particularly attenuated, and the photoemission signal represents the stoichiometric ratio.

Figure 45.11 presents also the resulting C1–C2 ratios, calculated as (C1a + C1b + S1a + S1b)/(C2 + S2), as a function of the excitation energy for all

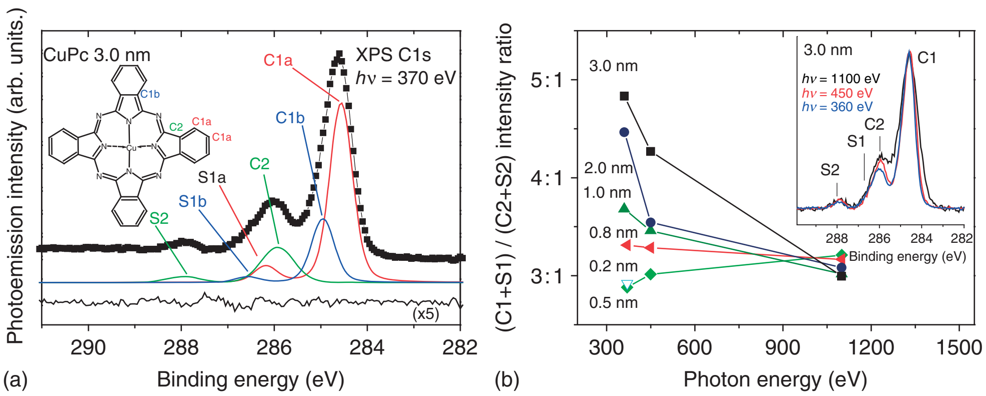

Figure 45.11 (a) Numeric peak fit of the C1s photoemission spectrum of the copper phthalocyanine films (3.0 nm thick film measured with an excitation energy of 370 eV). The spectrum is described by three components and the corresponding shake-up satellites, distinguishing the benzene components C1a and C1b and the pyrrole component C2. (b) The component ratios of the investigated copper phthalocyanine films show a distinct trend: for the film thicknesses of 1.0, 2.0, and 3.0 nm, they deviate from the 3 : 1 stoichiometric ratio, when the data are taken with lower excitation energies (enhanced surface sensitivity). This gives evidence for the overall standing orientation in the topmost molecules. In contrast, the signal ratio remains constant at each photon energy for film thicknesses below 1 nm, as expected for lying molecules. The lines are guides for the eye. As an example of a changing C1–C2 intensity ratio, the spectra for the 3.0 nm thick film are shown in the inset.

investigated films. The inset shows a direct comparison of the spectra for a 3.0 nm thick film for different photon energies. The spectra taken at 1100 eV are the least surface sensitive and the intensity ratios are in agreement with the stoichiometry for all investigated film thicknesses. As expected for lying molecules, the C1–C2 ratios for the film thicknesses below 1 nm also are about 3 : 1, reflecting the stoichiometric value. For the 1.0 nm thick film, the C1–C2 ratio only slightly depends on the excitation energy. A clear deviation from 3 : 1 can be seen for surface-sensitive spectra at 360 eV of the 2.0 and 3.0 nm thick films. The ratios of 4.5 : 1 and 4.8 : 1 for 2.0 and 3.0 nm, respectively, are close to the value of 4.9 : 1, that was found earlier for a 7.6 nm film of standing zinc Pc molecules under more surface-sensitive conditions [71]. Thus, it could be concluded that standing molecules form the topmost layer of the 2 and 3 nm thick films. From the disappearance of the anisotropy of the NEXAFS data, about half of the total film consists of lying molecules, that is, about three layers of lying molecules are covered by about one layer of standing molecules.

This example shows how XPS, coupled with the opportunity to use synchrotron radiation, that is, to tune the surface sensitivity of the experiment, delivers information on buried interfaces without destroying the investigated systems.

45.4.3
XPS as a Tool to Investigate Growth Modes

A model study of film growth typically involves deposition of a controlled amount of atoms/molecules onto a well-characterized crystalline substrate at a defined set of growth conditions. The precisely defined growth conditions, coverage, and deposition rates in such studies make it possible to decipher the rules governing the evolution of the growth front, and to explore ways of tailoring film morphology to obtain specific characteristics.

Essentially three basic growth modes can be observed: (i) island (or Volmer–Weber), (ii) layer-by-layer (or Frank–van der Merwe), and (iii) layer plus island (or Stranski–Krastanov) growth [72, 73].

Island growth occurs when the smallest stable cluster nucleates and grows in three dimensions to form an island. The molecules are more strongly bound to each other than to the substrate. The opposite characteristics are shown during the layer-by-layer growth: the smallest stable nucleus develops in two dimensions, resulting in the formation of planar layers. The molecules are more strongly bound to the substrate than to each other. The second layer grows on top of the first experienced, a slightly weaker bond with the substrate. The layer-by-layer mode will be sustained, provided the decrease in bonding energy is continuous toward the bulk-crystal value. The layer plus islands is an intermediate mechanism that can be seen as a combination of the previous two modes [72, 73].

Thickness-dependent XPS investigations offer the opportunity to identify the growth mode of an adsorbate on a given substrate. By monitoring the XPS signal attenuation of the substrate during growth, it is possible to identify which growth mode occurs.

For layer-by-layer growth, the substrate signal goes to zero as the overlayer buries the substrate. The intensity decrease is strictly linear up to the completion of the next full monolayer for ideal layer-by-layer growth. However, the envelope function for the overlayer peak intensities over an extended thickness range shows an exponential decay, with a characteristic decay length determined by the IMFP. In contrast, the intensity decay signal with increasing amount of material will be much slower with the nominal thickness of the film for a 3D growth mode. Its details will depend on the details of island shape and densities, which develop on the surface and are hard to generalize. An intermediate behavior is shown by the layer plus island growth [73, 74].

During the past decade, remarkable research efforts in the field of III nitrides have been achieved. GaN and related materials have attracted a lot of interest for applications in high-power electronics such as light-emitting diodes (LEDs) or high-mobility field-effect transistors [75–81]. In addition, the combination of wurtzite polytypes of AlN, GaN, and InN with band gaps of 6.2, 3.4, and ~0.8 eV allowed the development and commercialization of several devices, such as green and blue LEDs with exceptional efficiencies and brightness for a variety of applications [79]. Further potential applications of III-nitride-based alloys in spintronics and magneto-optics were recently suggested [82–84]. Different deposition techniques, such as metal-organic chemical vapor deposition (MOCVD), hydride vapor phase epitaxy, and plasma-assisted molecular beam epitaxy (PAMBE), have been applied to achieve a heteroepitaxial growth of III-nitride films [85]. However, the lack of matching substrates still limits the quality of the nitride films, especially with regard to GaN. Recently, Sidorenko *et al.* [86] have compared epitaxial growth of GaN films on 6H-SiC(0001)-($\sqrt{3} \times \sqrt{3})R30^\circ$ – Ga and on (0001)-sapphire. Predeposited Ga layers were nitrided by ion-beam-assisted molecular beam epitaxy. On SiC, the initially deposited Ga covers the substrate surface completely, while on sapphire only Ga droplets are present. The different distribution of the predeposited Ga affects the morphology of GaN significantly. The system was investigated with different techniques; in particular, XPS measurements revealed that metallic Ga resides also on top of the GaN films during the growth.

In Figure 45.12, a comparison of Ga 3d and Ga 2p3/2 core-level peak areas at successive stages of the GaN ion beam assisted molecular beam epitaxy (IBA-MBE) experiment are shown for GaN on SiC.

The data represent the surface coverage of the $\sqrt{3}$ structure by Ga, which corresponds to 1/3 ML of Ga. The experimental intensity ratio I(Ga 2p3/2)/I(Ga 3d) is about 5, which is close to the ratio of the corresponding IMFP values of 4.0, the largest value to be expected. The obtained value corresponds very well to the fact that all Ga is laterally distributed in the topmost layer of the sample. After Ga metal deposition, both the Ga 2p3/2 and Ga 3d peak intensities increase because of the additional Ga on the surface, but they remain significantly smaller than 1. The intensity ratio decreases from 5 to 2.5, but this latter value is still much larger than 1, expected for bulk GaN or islands thicker than the information depth. Thus, the Ga metal does not only reside in thick metallic droplets on the surface. Apparently, beside the droplets the metal distributes into a Ga layer, wetting the

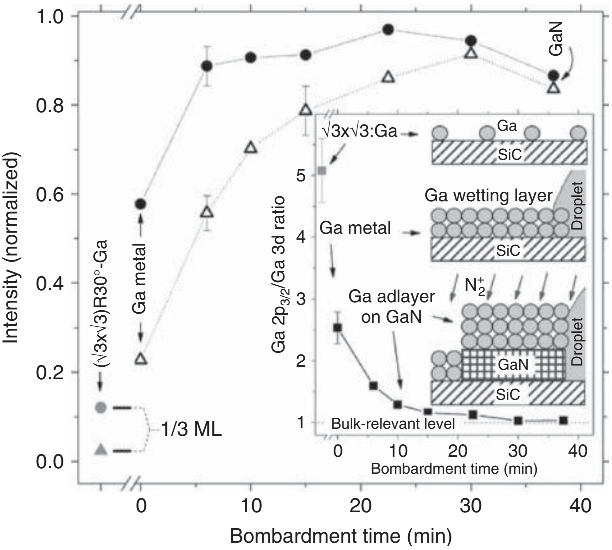

Figure 45.12 GaN on SiC: comparison of Ga 3d (triangles) and Ga 2p3/2 (circles) core-level peak areas at successive stages of the GaN IBA-MBE experiment. The areas are normalized related to the thick GaN film. Gray data points represent the surface. Black data points correspond to successive ion bombardment steps of the 30 nm Ga metal layer, bombardment times $t = 0$–37 min. All lines and arrows are guides for the eye. Inset: plot of the Ga 2p3/2/Ga 3d peak area ratio, related to the main panel. The dashed horizontal line indicates the area ratio expected for a bulklike homogeneous sample. From the detailed analysis of the peak intensities, a growth model is proposed, as illustrated in the inset. Top: as-prepared surface with 1/3 ML of Ga adatoms. Middle: deposited metal Ga film, which forms droplets and a wetting layer of about 2 ML. Bottom: during GaN growth (not completed ion bombardment) the film exhibits a mixture of GaN islands, covered by a Ga metal adlayer and Ga metal droplets. (Reprinted with permission from [86]. Copyright 2007, American Institute of Physics.)

SiC surface. The XPS data in Figure 45.12 allow estimating the thickness of this substrate wetting layer to be ~1.5–2.0 ML. During the initial steps of the GaN growth, a further increase in both Ga 2p3/2 and 3d intensities with the nitrogen bombardment time is observed, despite the fact that no further Ga was deposited. This can be explained by a redistribution of Ga from the droplets toward the growing GaN film, as mentioned earlier. The Ga 2p3/2 intensity approaches a saturation level 1 rather quickly. At this stage, the Ga/GaN film has reached a certain lateral extension on the substrate surface and its thickness exceeds the Ga 2p3/2 information depth, evidently. The increase in the corresponding Ga 3d intensity follows gradually, in this manner indicating the further increase in the GaN film thickness. This growth in thickness is also supported by the approach of the Ga peak intensity ratio toward 1. The slight intensity decrease after the final nitridation step has to be related to the consumption of the metallic Ga, which possesses higher Ga atom density compared to GaN. The final intensities are smaller than 1, which has to be explained by the incomplete surface coverage by the grown GaN film. The interpretation was also corroborated by atomic force and scanning transmission microscopy investigations.

In summary, the detailed analysis of the XPS intensities makes it possible to identify a laterally homogeneous film (Ga wetting layer on SiC) and additional droplets, which are apparently concentrated on a particular stacking termination, and a Ga adlayer resides on top of the GaN film during the growth process.

This experiment shows how by using XPS a reach characterization of growth modes is possible, with specific insights also in complicated growth regimes.

45.4.4

Laterally Resolved XPS as a Tool to Reveal New Aspects in Physics and Chemistry of Thin Film

In the previous paragraphs, we have shown how XPS is a very powerful technique to investigate a large range of effects related to the chemistry, the physics, and the growth modes of materials. However, standard XPS averages over the sample area illuminated by the incident light. If there is the opportunity to couple such information also with high lateral resolution, it is clear how such a technique may reveal aspects not yet investigated of materials.

A way to reach high lateral resolution in XPS is the use of a photoelectron emission microscopy (PEEM) [87]. The excitation is usually produced by UV light, synchrotron radiation, or X-ray sources. The illumination of the specimen with X-rays excites a broad electron spectrum consisting of the primary unscattered or elastically scattered photoelectrons, inelastically scattered electrons (secondary electrons), and Auger electrons. These instruments can reach lateral resolution of a few nanometers, and provide a unique combination of complementary imaging and diffraction methods with structural, chemical, and magnetic sensitivity. They allow a multitechnique investigation, in real time and *in situ*, of surfaces, interfaces, thin films, nanostructures, and the processes thereby occurring.

We have used PEEM to investigate thin films of diindenoperylene (DIP) deposited on Au(111) [88]. DIP is a perylene-based molecule that shows a high-hole mobility already in thin films, good film-forming properties, and thermal stability [89–94]. All these aspects suggest that it is a promising molecule for electronic applications.

The opportunity to use synchrotron radiation as a light source for a PEEM allows the simultaneous investigation of morphology, structure, and electronic characteristics. Figure 45.13 shows an *in situ* observation of DIP growth on Au(111) by using UV-PEEM (ultraviolet photoelectron emission microscopy) (Hg-lamp, $h\nu = 4.9\,\text{eV}$). The PEEM images show bright and dark regions. The work function of gold is higher than the photon energy of the Hg lamp; therefore, there is no contribution from the substrate (no PEEM intensity is shown by the substrate) [95]. However, the work function decreases to 4.35 eV within the first three layers [94], allowing the photoelectrons to escape and the consequent observation of a bright PEEM signal. With increasing film thickness, this contribution is attenuated by elastic and inelastic scattering of the photoelectrons that gives rise to dark regions [92, 95]. A layer-by-layer mechanism characterizes the initial growth (bright

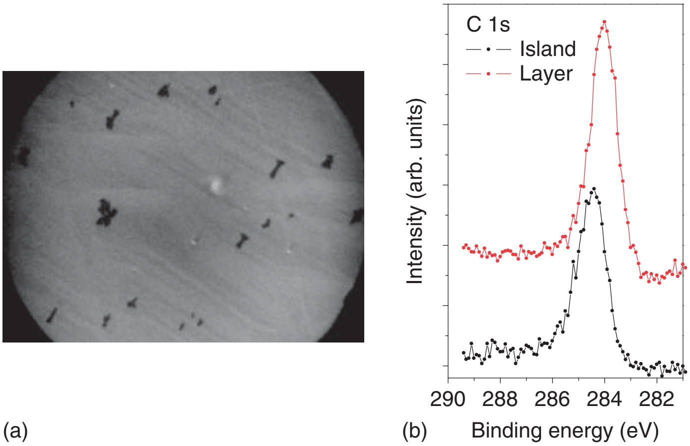

(a)

(b)

Figure 45.13 (a,b) UV-PEEM image of a nominal 53 Å thick DIP films showing islands on a Au(111) surface. The field of view is 25.0 × 18.7 μm. C 1s core-level spectra of the DIP film are shown in the image, obtained from an image stack integrated in the binding energy range between 281 and 289 eV, for an island and the monolayer on top of the gold substrate.

region) followed by island nucleation (dark regions), that is, the growth follows the Stranski–Krastanov mode (layer plus islands) [72, 73]. Investigating the C 1s core levels by PEEM, the spectra are obtained from an image stack taken in the binding energy range between 281 and 289 eV ($h\nu = 350$ eV) and analyzed for an island and for the monolayer on top of the gold substrate (Figure 45.13a). A strong peak at 284.4 eV dominates the spectrum of the island. Because of the molecular symmetry (the free DIP molecule belongs to the D_{2h} point group), the C 1s core-level features are expected to be composed of at least nine contributions, one for each different nonequivalent carbon site. Owing to their similar binding energy and the finite resolution of our experiment, their separation and energy determination by curve fitting would be quite speculative, and it will not be addressed in this context. Comparing the signal of the C 1s core levels of the island and the monolayer, a 0.4 eV shift toward the higher binding energy is clearly observable. This effect is analogous to the shift found comparing monolayer and multilayer with standard XPS [54]. It is due to the substrate-enhanced efficiency of the screening effect of the C 1s core hole in the monolayer. Because of the strength of spectromicroscopy, we are able to demonstrate that this screening effect actually depends on selectable different thickness in a given film, for which both preparation conditions and experimental setup are exactly identical.

We could observe several phenomena [88], such as different screening of the core hole, or different full width at half maximum of the XPS lines that have been previously shown comparing different samples consisting of monolayer and multilayer. On the contrary, we have shown their occurrence comparing islands versus monolayer in the same film. This could be done because of the high lateral resolution of the experiment (~30 nm) that allows speaking about nano-XPS.

45.4.5
X-Ray Photoelectron Diffraction (XPD) as a Tool to Investigate Structural Properties

Here, we briefly introduce an important application of the core-level spectroscopies, that is, photoelectron diffraction (PED). The appearance of PED was proposed by Liebsch [96] in 1974. PED is a phenomenon that occurs in angle-resolved core-level photoemission from ordered, crystalline samples. The directly emitted component of the photoelectron wave function from an emitting atom superimposes coherently with components of the same wave function, which are elastically scattered by the surrounding atoms. This interference leads to a modulation of the measured photoelectron intensity as a function of (i) emission angle or (ii) photoelectron energy. These modulations contain information on the relative positions of the emitter and the neighbored scatterers. Thus, the local geometrical structure of the investigated systems can be deduced from such experimental information (Figure 45.14). Diffraction patterns are specific to the local environments of the emitting atoms and in case of significant chemical shifts also for particular chemical species.

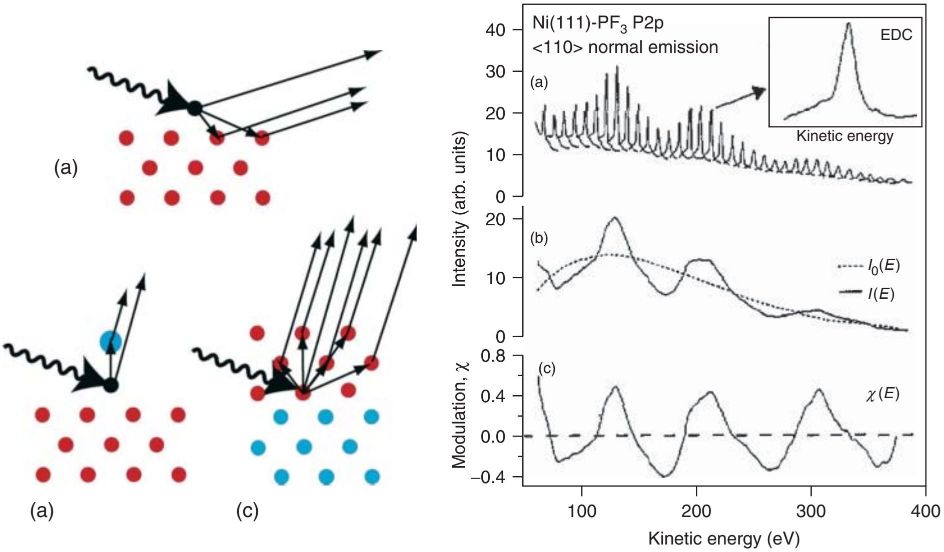

Figure 45.14 Left panel: Schematic diagrams showing some of the near-forward scattering paths in three different applications of XPD: (a) adsorbate site determination using grazing emission geometries; (b) intramolecular scattering in a simple diatomic adsorbate; (c) epitaxial growth characterization. (Reprinted with permission from [97]. Copyright 2010, Elsevier.) Right panel: The determination of the photoelectron diffraction modulation function. The P 2p level in the molecule PF$_3$ adsorbed on a Ni(111) surface is used as an example. Inset: a single P 2p electron energy distribution curve at $h\nu = 346$ eV. (a) Group plot of the raw energy distribution curves but showing only every third curve. (b) Integrated intensity of the P 2p energy distribution curves together with the sp line function used to normalize to the average value. (c) Resulting modulation function, $X(E)$. (Reprinted with permission from [98]. Copyright 1994, IOP Publishing Ltd.)

Extensive studies by Bradshaw and Woodruff [98–103] have demonstrated that energy-scanned PED may be applied to determine surface and adsorbate geometries. As shown in Figure 45.14, core-level intensities $I(E)$ are measured dependending on the electron kinetic energy E by varying the photon energy and referred to a *smoothly varying background* $I_0(E)$. The systematic comparison of the experimentally derived anisotropy $\chi(E) = (I(E) - I_0(E))/I_0(E)$ with a related quantity from multiple scattering cluster calculations (MSCCs) in the framework of R-factor analysis gives access to the structural parameters of atomic and small molecular adsorbate systems. Recently, this technique has also been extended to investigation of larger adsorbed molecules on surfaces, as nonplanar vanadyl phthalocyanine (VOPc) molecules on Au(111) single crystals [103]. The results showed that the molecular plane of VOPc is essentially parallel to Au(111) and the off-plane V=O vanadyl bond points away from the surface. The V=O bond length of 1.60 ± 0.04 Å determined by comparison to MSCC is close to the molecular value, but the V atom is found almost coplanar with the surrounding N atoms in the adsorbed molecule in clear contrast to the off-plane location of V in crystalline VOPc molecular solid. This indicates a significant interaction between the V atoms in adsorbed VOPc monolayers with the Au(111) surface, in this manner also supporting the notion that bonding of large near-planar molecules to metal surfaces can lead to modification of the internal conformation of the molecules.

In X-ray photoelectron diffraction (XPD) experiments, angular distribution curves (ADCs) of the intensity are measured in dependence on polar or azimuthal angles of photoemission. Owing to the higher energy of the laboratory X-ray sources, the information depth is typically larger in XPD rather than in a related PED experiment and therefore the method has been used to investigate structure of bulk samples and thin films in addition to LEED (low-energy electron diffraction) and STM (scanning tunneling microscopy). In particular, growth of metals on metals, for example, Cu on Ni(001) [98], or oxide film growth, for example, MnO on Ag(001) [104], have been investigated. In Figure 45.15, an angular distribution pattern (ADP) and an ADC curve taken from MnO(001) bulk (lattice constant $a = 445$ pm) are compared to an experimental ADC and simulations for a MnO film on lattice-mismatched Ag(001) ($a = 409$ pm). High-intensity features along low-index directions may be related forward scattering peaks, essentially, but satisfactory quantitative agreement between experiment and theory can only be achieved by taking multiple scattering into account. In this manner, geometric parameters and thus information on strained films and structural relaxations in dependence on film thickness may be obtained by XPD [104] (Figure 45.15).

45.4.6
Molecular Orbital Densities from Photoemission Spectra of Organic Molecules

A recent method that couples ARUPS with theoretical calculations in order to also gain information on MOs not directly accessible with conventional fitting techniques has been developed by *Puschnig et al*. They studied the interface of perylene-tetracarboxylicacid-dianhydride (PTCDA) deposited on Ag(110) by

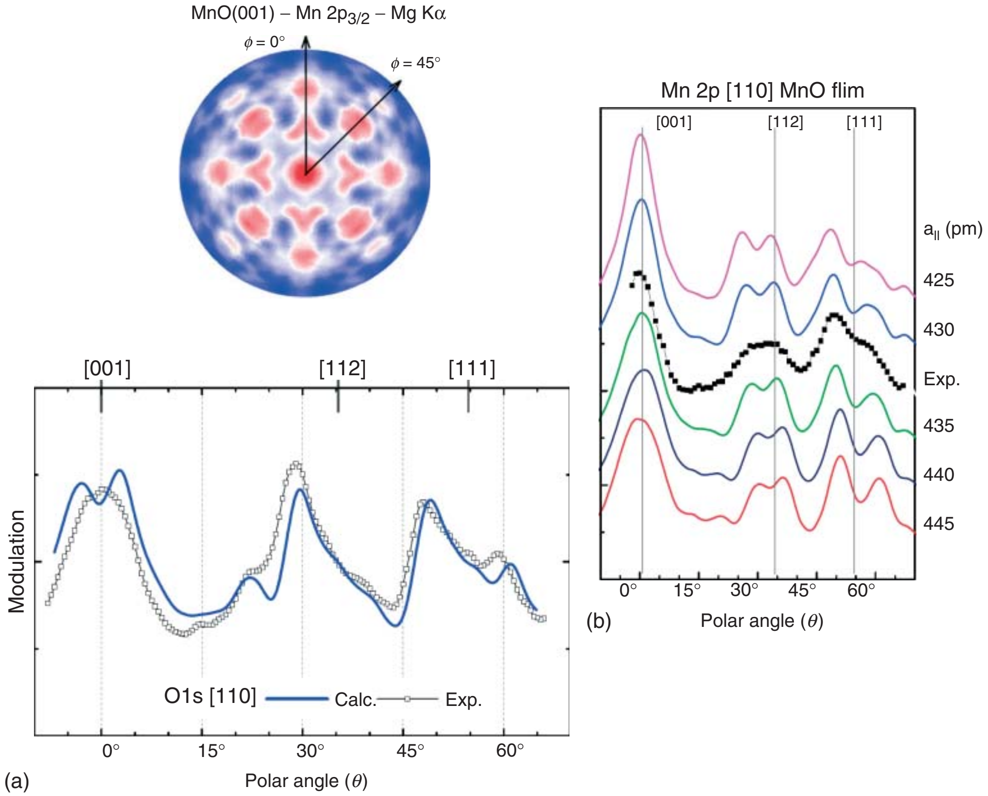

Figure 45.15 (a) Experimental 2π scans of Mn 2p of MnO(001) single crystal excited by Mg Kα-radiation together with the comparison of experimental and theoretical polar scan ADCs of O 1s photoelectrons of MnO(001) single crystal along the [110] direction. (b) Calculated polar scan ADCs of 6 ML MnO film in dependence on the degree of tetragonal distortion. The calculated spectra are compared to experimental results of a 6.5 ML thick film. (Reprinted with permission from Ref. [104]. Copyright 2011, Elsevier.)

ARUPS [105]. They measured the signal intensity from a constant initial-energy state in the full half-space above the sample surface, obtaining a set of data that contain a complete momentum- and energy-resolved density of state (DOS) of the sample in the measured binding energy range.

Analyzing the data in a plane-wave approximation for the final state in the photoemission process, they have assigned the emissions to specific molecular states. For the assignment, they have valuated the tomographic cross section through the momentum-resolved data set and searched for momentum space patterns that are characteristic of the corresponding MOs. In this approximation, the ARUPS intensity distribution from a molecular state corresponds to the respective Fourier transform of the MO. The combination of the simulated momentum maps and the tomographic data allows the deconvolution of the energy distribution

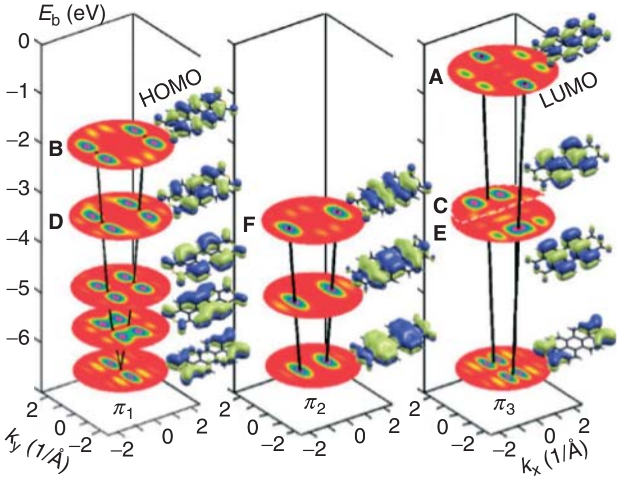

Figure 45.16 Molecular orbitals of free PTCDA together with the corresponding calculated (*kx*,*ky*) maps of 12 PTCDA π orbitals in a binding energy window between −7 and 0 eV. They are grouped into three bands: $\pi 1$ (left panel) dispersing along the *kx* direction and representing orbitals with an *xz* nodal plane, $\pi 2$ (middle panel) dispersing along *kx* with no node in the *xz* plane, and $\pi 3$ (right panel) dispersing along *ky* with an increasing number of nodal planes perpendicular to *y*. (Reprinted with permission from Ref. [105]. Published by the American Physical Society. Copyright under Creative Commons Attribution 3.0 License.)

curves (EDCs) into contributions from a single molecular state beyond the intrinsic limit of the line broadening and of the instrumental resolution. This is possible because the deconvolution is carried in the k-space using the full momentum space information of the MO.

The π-MOs of the free PTCDA molecule can be classified according to their symmetry and momentum distribution [106]. Figure 45.16 shows this classification based on the nodal structure of the MO. The first group is characterized by an *xz* nodal plane through the long molecular axis *x*. The second group has no nodes in the *xz* plane. The third group shows an increasing number of nodal planes in the *xz* plane. These moment patterns are the base for the search for the MO in the data set.

This model was proved to be appropriate for a number of different molecules [106–109] and may be considered useful to extract even more information from ARUPS experiments, providing an orbital-by-orbital characterization of large adsorbates, allowing also the estimation of the effects of bonding on individual orbitals.

45.5
Conclusions and Future

The aim of this chapter has been to demonstrate by a number of representative examples the power of photoemission spectroscopy. Photoemission experiments deliver a wealth of information on a large number of different aspects connected with the characterization of a system, ranging from core-level states to chemical environment, from interface effects and bonding to growth.

The detailed understanding of complex materials requires the use of state-of-the-art experimental techniques that provide information on electronics, structure, and morphology of the materials. The advent of third-generation synchrotron sources has immensely increased the possibilities offered by photoemission because of the high-energy resolution reached. The increasing miniaturization of components furthermore demands the use of techniques with spatial resolution down to the nanometer range. Thus, a good way of satisfying both requirements is to combine the distinctive properties of standard UPS/XPS with those of electron microscopy as in photoemission electron microscopy, which opens even further ways to the use of photoemission and to the investigations of not yet revealed phenomena.

Another aspect of XPS, less inherent to surfaces but that it is presently matter of a very rapid development, is high-energy XPS. It allows the extension of the probing depth typical of standard XPS giving the opportunity to apply XPS to various materials with nanolayered structures and nanoparticles. A straightforward way of extending the probing depth is to raise the photon energy for excitation. The recent progress of X-ray undulators at third- generation synchrotron light sources, as mentioned, delivers high photon flux as well as high flux density. These sources compensate for the decreases in cross section and analyzer transmission, problems to deal with in high energy, and make high-energy XPS accessible. The larger escape depth of photoelectrons with higher kinetic energy facilitates studies of electronic structures and/or chemical states of bulk materials, interfaces, and nanoscale buried layers, as the contribution to the detection of signal from the surface region is small [110].

There are fields where the use of XPS could deliver important information, but the related phenomena do not take place in UHV. Environmental and atmospheric chemistry, catalysis, and biomaterials require higher pressure. Thus, high-pressure XPS in the millibar range has become an important tool within the past years to explore particular phenomena as water deposition on several substrates [111, 112] or catalytically active phases [113]. Also, in this case, the application of this technique at a synchrotron radiation facility has an important role, and future applications will confirm the importance of using high-energy XPS also coupled with high-resolution XPS.

Last but not least, very recently the advent of lasers that emit pulses in the attosecond timescale allowed measuring the time delays between different photoemission processes generated by the same ultrashort light pulse. Photoemission from atoms is assumed to occur instantly in response to incident radiation: Schultze *et al.* [114, 115] found a delay of 21 as in the emission of electrons from the 2p orbitals of neon atoms with respect to those released from the 2s orbital by the same light pulse. Small differences in the timing of photoemission from different quantum states give the opportunity for modeling many-electron dynamics. This finding not only allows further studies of the timing of photoemission but also provides a new way to investigate electron interactions in atoms.

References

1. Einstein, A. (1905) *Ann. Phys.*, **322**, 132.
2. Hüfner, S. (2007) *Photoelectron Spectroscopy: Principles and Applications*, Springer-Verlag, Berlin.
3. Brigg, D. and Seah, M.P. (1990) *Practical Surface Analysis*, John Wiley & Sons Ltd., Chichester.
4. Cardona, M. and Ley, L. (1978) *Photoemission in Solids*, Springer-Verlag, New York.
5. Koopmans, T. (1934) *Physica*, **1**, 104.
6. Berglund, C.N. and Spicer, W.E. (1964) *Phys. Rev. A*, **136**, 1030.
7. Kronig, R.d.L. and Penney, W.G. (1930) *Proc. Roy. Soc. A*, **130**, 499.
8. Ishii, H., Sugiyama, K., Ito, E., and Seki, K. (1999) *Adv. Mater.*, **11**, 605.
9. Cahen, D., Kahn, A., and Umbach, E. (2005) *Mater. Today*, **8**, 32.
10. Koch, N. (2008) *J. Phys.: Condens. Matter*, **20**, 184008.
11. Courths, R. and Hüfner, S. (1984) *Phys. Rep.*, **112**, 53.
12. Dröge, H., Nagelstraßer, M., Nürnberger, J., Faschinger, W., Fleszar, A., and Steinrück, H.P. (2000) *Surf. Sci.*, **454–456**, 477.
13. Ueno, N., Seki, K., Sato, N., Fujimoto, H., Kuramochi, T., Sugita, K., and Inokuchi, H. (1990) *Phys. Rev. B*, **41**, 1176.
14. Steinrück, H.P. (1996) *J. Phys.: Condens. Matter*, **8**, 6465.
15. Geim, A.K. and Novoselov, K.S. (2007) *Nat. Mater.*, **6**, 183.
16. Wallace, P.R. (1947) *Phys. Rev.*, **71**, 622.
17. Novoselov, K.S., Geim, A.K., Morozov, S.V., Jiang, D., Zhang, Y., Dubonos, S.V., Grigorieva, I.V., and Firsov, A.A. (2004) *Science*, **306**, 666.
18. Nobelprize.org *http://nobelprize.org/nobel_prizes/physics/laureates/2010/* (accessed 21 March 2013).
19. (a) Emtsev, K.V., Speck, F., Seyller, T., Ley, L., and Riley, J.D. (2008) *Phys. Rev. B*, **77**, 155303. (b) A. Bostwick, J. McChesney, T. Ohta, E. Rotenberg, T. Seyller, K. Horn, *Progr. Surf. Sci.* **84** (2009) 380, 388 p.
20. Rubinstein, I., Sabatani, E., Maoz, R., and Sagiv, J. (1986) Organized monolayers on gold electrodes, in *Electrochemical Sensors for Biomedical Applications* (ed. C.K.N. Li), The Electrochemical Society, Pennington.
21. Zerulla, D. and Chassé, T. (1999) *Langmuir*, **15**, 5285.
22. Thompson, A.C. 2009 *X-Ray Data Booklet*, Lawrence Berkeley National Laboratory, Berkeley, CA, *http://xdb.lbl.gov/*
23. Moulder, J.F., Stickle, W.F., Sobol, P.E., and Bomben, K.D. (1992) *Handbook of X-Ray Photoelectron Spectroscopy, Physical Electronics Inc*, Perkin-Elmer Corporation, Eden Prairie.
24. (a) Gasiorowicz, S. (2003) *Quantum Physics*, John Wiley & Sons, USA. (b) Kittel, C. (1976) *Quantum Theory of Solids*, John Wiley & Sons, New York. (c) Dekker, A.J. (1962) *Solid State Physics*, Prentice-Hall, Englewood Cliffs.
25. Dupin, J.-P., Gonbeau, D., Vinatier, P., and Levasseur, A. (2000) *Phys. Chem. Chem. Phys.*, **2**, 1319.
26. Steiner, P., Reiter, F.J., Höchst, H., and Hüfner, S. (1978) *Phys. Status Solidi B*, **90**, 45.
27. Höchst, H., Steiner, P., and Hüfner, S. (1978) *Z. Phys. B*, **30**, 145.
28. Margaritondo, G. (1995) *Riv. Nuovo Cimento*, **18**, 1.
29. Duke, P.J. (2000) *Synchrotron Radiation: Production and Properties*, Oxford Series on Synchrotron Radiation, Vol. 3, Oxford University Press, New York.
30. Wiedemann, H. (2002) *Synchrotron Radiation*, Springer-Verlag, Berlin.
31. Casu, M.B., Zou, Y., Kera, S., Batchelor, D., Schmidt, T., and Umbach, E. (2007) *Phys. Rev. B*, **76**, 193311.
32. Salaneck, W.R., Stafström, S., and Brédas, J.L. (1996) *Conjugated Polymer Surfaces and Interfaces: Electronic and Chemical Structure of Interfaces for Polymer Light Emitting Devices*, Cambridge University Press, Cambridge.

33. Ambrosch-Draxl, C., Nabok, D., Puschnig, P., and Meisenbichler, C. (2009) *New J. Phys.*, **11**, 125010.
34. Schöll, A., Zou, Y., Schmidt, T., Fink, R., and Umbach, E. (2004) *J. Phys. Chem. B*, **108**, 14741.
35. Schöll, A., Zou, Y., Jung, M., Schmidt, T., Fink, R., and Umbach, E. (2004) *J. Chem. Phys.*, **121**, 10260.
36. Shirley, D.A. (1972) *Phys. Rev.*, **55**, 4709.
37. Tougaard, S. (1988) *Surf. Interface Anal.*, **11**, 453.
38. Tougaard, S. (1997) *Surf. Interface Anal.*, **25**, 137.
39. Seah, M.P. and Gilmore, I.S. (2006) *Phys. Rev. B*, **73**, 174113.
40. Jablonski, A. and Powell, C.J. (2010) *Surf. Sci.*, **604**, 327.
41. Paynter, R.W. (2009) *J. Electron. Spectrosc. Relat. Phenom.*, **169**, 1.
42. Tanuma, S., Powell, C.J., and Penn, D.R. (1987) *Surf. Sci.*, **192**, L849.
43. Tanuma, S., Powell, C.J., and Penn, D.R. (1988) *Surf. Interface Anal.*, **11**, 577.
44. Tanuma, S., Powell, C.J., and Penn, D.R. (1991) *Surf. Interface Anal.*, **17**, 911.
45. Tanuma, S., Powell, C.J., and Penn, D.R. (1991) *Surf. Interface Anal.*, **17**, 927.
46. Tanuma, S., Powell, C.J., and Penn, D.R. (1993) *Surf. Interface Anal.*, **20**, 77.
47. Tanuma, S., Powell, C.J., and Penn, D.R. (1993) *Surf. Interface Anal.*, **21**, 165.
48. Tanuma, S., Powell, C.J., and Penn, D.R. (2004) *Surf. Interface Anal.*, **36**, 1.
49. Smoluchowski, R. (1941) *Phys. Rev.*, **60**, 661.
50. Skriver, H.L. and Rosengaard, N.M. (1992) *Phys. Rev. B*, **46**, 7157.
51. Duhm, S., Heimel, G., Salzmann, I., Glowatzki, H., Johnson, R.L., Vollmer, A., Rabe, J., and Koch, N. (2008) *Nat. Mater.*, **7**, 326.
52. Casu, M.B., Yu, X., Schmitt, S., Heske, C., and Umbach, E. (2008) *J. Chem. Phys.*, **129**, 244708.
53. Casu, M.B., Schöll, A., Bauchspieß, K.R., Hübner, D., Schmidt, T., Heske, C., and Umbach, E. (2009) *J. Phys. Chem. C*, **113**, 10990.
54. Schuster, B.-E., Casu, M.B., Biswas, I., Hinderhofer, A., Gerlach, A., Schreiber, F., and Chassé, T. (2009) *Phys. Chem. Chem. Phys.*, **11**, 9000.
55. Marchetto, H., Groh, U., Schmidt, T., Fink, R., Freund, H.-J., and Umbach, E. (2006) *Chem. Phys.*, **325**, 178.
56. Casu, M.B., Biswas, I., Schuster, B.-E., Nagel, M., Nagel, P., Schuppler, S., and Chassé, T. (2008) *Appl. Phys. Lett.*, **93**, 24103.
57. Liu, S., Wang, W.M., Briseno, A.L., Mannsfeld, S.C.B., and Bao, Z. (2009) *Adv. Mater.*, **21**, 1217.
58. Horowitz, G. (1998) *Adv. Mater.*, **10**, 365.
59. C. C. Leznoff, A. B. P. Lever *Phthalocyanines–Properties and Applications*, Wiley-VCH Verlag GmbH, Weinheim, 1989.
60. Forsythe, E.W., Abkowitz, M.A., Gao, Y., and Tang, C.W. (2000) *J. Vac. Sci. Technol., A*, **18**, 1869.
61. Ostrick, J.R., Dodabalapur, A., Torsi, L., Lovinger, A.J., Kwock, E.W., Miller, T.M., Galvin, M., Berggren, M., and Katz, H.E.J. (1997) *J. Appl. Phys.*, **81**, 6804.
62. Michaelis, W., Wöhrle, D., and Schlettwein, D. (2004) *J. Mater. Res.*, **19**, 2040.
63. Mathur, S.C. and Ramesh, N. (1975) *Chem. Phys. Lett.*, **37**, 276.
64. Ruocco, A., Evangelista, F., Attili, A., Donzello, M.P., Betti, M.G., Giovanelli, L., and Gotter, R. (2004) *J. Electron. Spectrosc. Relat. Phenom.*, **137**, 165.
65. Barrena, E., Osso, J.O., Schreiber, F., Garriga, M., Alonso, M.I., and Dosch, H. (2004) *J. Mater. Res.*, **19**, 2061.
66. Alfredsson, Y., Aahlund, J., Nilson, K., Kjeldgaard, L., O'Shea, J.N., Theobald, J., Bao, Z., Mårtensson, N., Sandell, A., Puglia, C., and Siegbahn, H. (2005) *Thin Solid Films*, **493**, 13.
67. Sakurai, T., Kawai, S., Fukasawa, R., Shibata, J., and Akimoto, K. (2005) *Jpn. J. Appl. Phys. I*, **44**, 1982.
68. Kera, S., Casu, M.B., Bauchspieß, K.R., Batchelor, D., Schmidt, T., and Umbach, E. (2006) *Surf. Sci.*, **600**, 1077.
69. Peisert, H., Schwieger, T., Auerhammer, J.M., Knupfer, M., Golden, M.S., Fink, J., Bressler, P.R.,

and Mast, M. (2001) *J. Appl. Phys.*, **90**, 466.

70. Biswas, I., Peisert, H., Nagel, M., Casu, M.B., Schuppler, S., Nagel, P., Pellegrin, E., and Chassé, T. (2007) *J. Chem. Phys.*, **126**, 174704.
71. Zhang, L., Peisert, H., Biswas, I., Knupfer, M., Batchelor, D., and Chasse, T. (2005) *Surf. Sci.*, **596**, 98.
72. Bauer, E. (1958) *Z. Kristallogr.*, **110**, 395.
73. Venables, J.A. (2000) *Introduction to Surface and Thin Film Processes*, Cambridge University Press, Cambridge.
74. Lüth, H. (2001) *Solid Surfaces Interfaces and Thin Films*, 4th edn, Springer-Verlag, Berlin.
75. Ponce, F.A. and Bour, D.P. (1997) *Nature*, **386**, 351.
76. Nakamura, S. (1998) *Science*, **281**, 956.
77. Jain, S.C., Willander, M., Narayan, J., and Van Overstraeten, R. (2000) *J. Appl. Phys.*, **87**, 965.
78. Pearton, S.J., Ren, F., Zhang, A.P., and Lee, K.P. (2000) *Mater. Sci. Eng.*, **30**, 55.
79. Davis, R.F., Einfeldt, S., Preble, E.A., Roskowski, A.M., Reitmeier, Z.J., and Miraglia, P.Q. (2003) *Acta Mater.*, **51**, 5961.
80. David, A., Fujii, T., Sharma, R., McGroddy, K., Nakamura, S., Denbaars, S.P., Hu, E.L., Weisbuch, C., and Benisty, H. (2006) *Appl. Phys. Lett.*, **88**, 061124.
81. Palacios, T., Chakraborty, A., Heikman, S., Keller, S., DenBaars, S.P., and Mishra, U.K. (2006) *IEEE Electron Device Lett.*, **27**, 13.
82. Buyanova, I.A., Izadifard, M., Chen, W.M., Kim, J., Ren, F., Thaler, G., Abernathy, C.R., Pearton, S.J., Pan, C.-C., Chen, G.-T., Chyi, J.-I., and Zavada, J.M. (2004) *Appl. Phys. Lett.*, **84**, 2599.
83. Sakuma, M., Hyomi, K., Souma, I., Murayama, A., and Oka, Y. (2005) *J. Supercond.*, **18**, 325.
84. Pearton, S.J., Abernathy, C.R., Overberg, M.E., Thaler, G.T., Norton, D.P., Theodoropoulou, N., Hebard, A.F., Park, Y.D., Ren, F., Kim, J., and Boatner, L.A. (2003) *J. Appl. Phys.*, **93**, 1.
85. Liu, L. and Edgar, J.H. (2002) *Mater. Sci. Eng.*, **37**, 61.
86. Sidorenko, A., Peisert, H., Neumann, H., and Chassé, T. (2007) *J. Appl. Phys.*, **102**, 044907.
87. Bauer, E. (2001) *J. Electron. Spectrosc. Relat. Phenom.*, **114–116**, 975.
88. Casu, M.B., Schuster, B.-E., Biswas, I., Raisch, C., Marchetto, H., Schmidt, T., and Chassé, T. (2010) *Adv. Mater.*, **22**, 3740.
89. Karl, N. (2003) *Synth. Met.*, **133–134**, 649.
90. Dürr, A.C., Schreiber, F., Münch, M., Karl, N., Krause, B., Kruppa, V., and Dosch, H. (2002) *Appl. Phys. Lett.*, **81**, 2276.
91. de Oteyza, D.G., Krauss, T.N., Barrena, E., Sellner, S., Dosch, H., and Ossó, J.S. (2007) *Appl. Phys. Lett.*, **90**, 243104.
92. Casu, M.B., Biswas, I., Nagel, M., Nagel, P., Schuppler, S., and Chassé, T. (2008) *Phys. Rev. B*, **78**, 075310.
93. Casu, M.B., Schuster, B.-E., Biswas, I., Nagel, M., Nagel, P., Schuppler, S., and Chassé, T. (2009) *J. Phys. Condens. Matter*, **21**, 314017.
94. Dürr, A.C., Koch, N., Kelsch, M., Rühm, A., Ghijsen, J., Johnson, R.L., Pireaux, J.-J., Schwartz, J., Schreiber, F., Dosch, H., and Kahn, A. (2003) *Phys. Rev. B*, **68**, 115428.
95. Marchetto, H. (2006) High-resolution spectro-microscopic investigations of organic thin film growth. Doctoral thesis. Freie Universität Berlin.
96. Liebsch, A. (1974) *Phys. Rev. Lett.*, **32**, 1203.
97. Woodruff, D.P. (2010) *J. Electron. Spectrosc. Relat. Phenom.*, **178–179**, 186.
98. Woodruff, D.P. (1994) *Surf. Sci.*, **299–300**, 183.
99. Woodruff, D.P. and Bradshaw, A.M. (1994) *Rep. Prog. Phys.*, **57**, 1029.
100. Bradshaw, A.M. and Woodruff, D.P. (1995) Structure determination of molecular adsorbates using photoelectron diffraction, in *Applications of Synchrotron Radiation: High-Resolution Studies of Molecules and Molecular Adsorbates on Surfaces* (ed. W. Eberhardt), Springer-Verlag, Berlin.
101. Woodruff, D.P., Norman, D., Holland, B.W., Smith, N.V., Farrell, H.H., and Traum, M.M. (1978) *Phys. Rev. Lett.*, **41**, 1130.

102. Woodruff, D.P. (2007) *Surf. Sci. Rep.*, **62**, 1.

103. Duncan, D.A., Unterberger, W., Hogan, K.A., Lerotholi, T.J., Lamont, C.L.A., and Woodruff, D.P. (2010) *Surf. Sci.*, **604**, 47.

104. Chassé, A., Langheinrich, C., Nagel, M., and Chassé, T. (2011) *Surf. Sci.*, **605**, 272.

105. Puschnig, P., Reinisch, E.-M., Ules, T., Koller, G., Soubatch, S., Ostler, M., Romaner, L., Tautz, F.S., Ambrosch-Draxl, C., and Ramsey, M.G. (2011) *Phys. Rev. B*, **84**, 235427.

106. Koller, G., Berkebile, S., Oehzelt, M., Puschnig, P., Ambrosch-Draxl, C., Netzer, F.P., and Ramsey, M.G. (2007) *Science*, **317**, 351.

107. Berkebile, S., Puschnig, P., Koller, G., Oehzelt, M., Netzer, F.P., Ambrosch-Draxl, C., and Ramsey, M.G. (2008) *Phys. Rev. B*, **77**, 115312.

108. Puschnig, P., Berkebile, S., Fleming, A.J., Koller, G., Emtsev, K., Seyller, T., Riley, J.D., Ambrosch-Draxl, C., Netzer, F.P., and Ramsey, M.G. (2009) *Science*, **326**, 702.

109. Ziroff, J., Forster, F., Schöll, A., Puschnig, P., and Reinert, F. (2010) *Phys. Rev. Lett.*, **104**, 233004.

110. Kobayashi, K., Yabashi, M., Takata, Y., Tokushima, T., Shin, S., Tamasaku, K., Miwa, D., Ishikawa, T., Nohira, H., Hattori, T., Sugita, Y., Nakatsuka, O., Sakai, A., and Zaima, S. (2003) *Appl. Phys. Lett.*, **83**, 1005.

111. Ketteler, G., Yamamoto, S., Bluhm, H., Andersson, K., Starr, D.E., Ogletree, D.F., Ogasawara, H., Nilsson, A., and Salmeron, M. (2007) *J. Phys. Chem. C*, **111**, 8278.

112. Verdaguer, A., Weis, C., Oncins, G., Ketteler, G., Bluhm, H., and Salmeron, M. (2007) *Langmuir*, **23**, 9699.

113. Rupprechter, G. and Weilach, C. (2007) *Nano Today*, **2**, 20.

114. Schultze, M., Fieß, M., Karpowicz, N., Gagnon, J., Korbman, M., Hofstetter, M., Neppl, S., Cavalieri, A.L., Komninos, Y., Mercouris, T., Nicolaides, C.A., Pazourek, R., Nagele, S., Feist, J., Burgdörfer, J., Azzeer, A.M., Ernstorfer, R., Kienberger, R., Kleineberg, U., Goulielmakis, E., Krausz, F., and Yakovlev, V.S. (2010) *Science*, **328**, 1658.

115. van der Hart, H.W. (2010) *Science*, **328**, 1645.

Section XIII
Applications 7: Nano-Optics

Handbook of Spectroscopy, Second Edition. Edited by Günter Gauglitz and David S. Moore.

46
Miniaturized Optical Sensors for Medical Diagnostics

Seong-Soo Kim and Boris Mizaikoff

46.1
Introduction

The interactions between photons and molecules are among the most widely researched areas in physics, chemistry, and biology. Photons interact with molecular constituents in different ways depending on their energies. Photons with higher energies, that is, shorter wavelengths, excite predominantly electronic transitions within molecules, which is utilized in ultraviolet/visible/near-infrared (UV/Vis/NIR) absorption and fluorescence spectroscopy.

Photons with lower energies, that is, longer wavelength, do not provide sufficient energy for exciting transitions between electronic states, thus addressing energetically much closer spaced vibrational and rotational molecular states. In particular, electromagnetic (EM) radiation in the mid-infrared (MIR; 3–20 μm) spectral range provides photon energies compatible with the excitation of fundamental–vibrational and mixed rotational–vibrational modes spectroscopically addressable for molecules with a resulting net change of the permanent dipole moment. The interaction of MIR photons specifically with organic molecules gives rise to sharp transition in contrast to most interactions in the UV/Vis/NIR regime, thereby providing a particularly high discriminatory potential when analyzing complex mixtures. Within the MIR regime, the so-called fingerprint range, where each molecule is characterized by highly distinctive spectral patterns, provides a preferable spectroscopic window for detecting individual molecular species.

Although there is no strict definition for the analytically most useful spectral bands, EM radiation within a wavelength range of 20–100 μm is considered the far-infrared (FIR) regime, while the wavelength range of 100 μm (3 THz) to 1 mm (0.3 THz) is referred to as *terahertz (THz) radiation*. Compared to the aforementioned spectral ranges, the THz regime is to date the least researched area in terms of miniaturized optical diagnostic device technology, as relevant components such as, for example, appropriate light sources, radiation guiding media, and optical detectors have only recently emerged. Most recently, THz radiation has attracted increasing interest because of its potential for interaction with macromolecules via vibrational modes. Hence, it appears feasible to study macromolecules such

Handbook of Spectroscopy, Second Edition. Edited by Günter Gauglitz and David S. Moore.

as, for example, DNA or proteins, which have numerous vibrational modes, with low-energy radiation. As THz photons have typical photon energies of a few millielectronvolts, the analysis of, for example, protein folding, receptor binding, or the label-free detection of DNA hybridization appears within reach.

Raman spectroscopy provides another important optical platform amenable to medical diagnostics. While Raman spectroscopy typically relies on optical excitation of molecules in the UV/Vis/NIR spectral range, the relaxation from higher energy states results in molecular vibrations apparent at much longer wavelengths (in particular, within the spectral regime typical for MIR absorption spectroscopy) because of inelastic scattering. However, despite the inherent merit of significantly less interference by water and water vapor, the Raman process suffers from its optical inefficiency compared to, for example, MIR absorption spectroscopy. The analytical efficiency of Raman techniques may considerably be improved by taking advantage of signal enhancement effects arising at the surface of corrugated (noble) metal layers or particles, also referred to as *surface-enhanced Raman spectroscopy* (*SERS*).

While each fundamental optical process involving photon–molecule interactions has its own merits and weaknesses for detecting molecular constituents including inorganic compounds, small organic molecules, or macromolecules such as, for example, DNA or proteins, it is evident that this wide variety of optical sensing techniques provides complementary analytical information rather than competitive device platforms. Given their versatility, optical spectroscopic techniques are already applied in areas including industrial process monitoring, pharmaceutical development, biomedical research, and so on. However, for the development of diagnostic instrumentation in medical applications it is of primary importance to understand the relationship between the *in vivo* or *in vitro* analyzed chemical/biochemical reactions and molecular patterns, and the physiological or disease status characterized by such data. Any disease is characterized by a complex sequence of metabolic reactions, physiological reactions, and pathogenic reactions that involve a wide variety of *in situ* synthesized or transformed chemical/biochemical constituents. Hence, a ‘‘biomarker’’ may be considered a specific constituent (i.e., indicator) that is found only in a certain metabolic, pathogenic, or pharmacologically relevant reaction or environment and characterizes a certain biological status of the investigated organism. Given the complexity of most disease pathologies or the response of an organism to therapeutic treatment, usually several biomarkers or entire panels of biomarkers are required for a status determination. Therefore, the analysis of such biomarkers – ideally *in situ* and within their native environment – provides valuable information on the condition of a biological system. Consequently, diagnosing the status of physiological processes, metabolism, or disease/therapy progression is ideally enabled by monitoring corresponding biomarkers *in vivo* (e.g., the human body), or after appropriate sampling of representative matrices from the organism (e.g., blood, interstitial fluid, biopsy, etc.). Of particular interest is the analysis of biomarkers in excretions that may be noninvasively collected such as, for example, exhaled breath (EB) or breath condensate, urine, perspiration, saliva, or similar matrices.

From a practical point of view, miniaturization of optical devices and sensing system facilitates their clinical utility and daily operation, in particular, if *in vivo* applications are targeted. During the past few decades, engineering progress including, for example, novel light sources covering a wide spectral range, component and device fabrication processes taking advantage of microelectronic and microelectromechanical fabrication techniques, advances in integrated optical detectors, and so on has enabled the miniaturization of laboratory-style optical instrumentation toward biomedically more applicable optical device and sensor technology. Selected examples and recent developments will highlight the current state-of-the-art and future potential of miniaturized optical diagnostics in this field.

46.2
UV/Vis/NIR Plasmonic Sensors

While conventional absorption and fluorescence spectroscopy measurement schemes are well established in biosensing and imaging applications related to medical diagnostics, methods based on plasmonic sensing schemes utilizing metal nanostructures or thin metal films have recently attracted considerable interest because of the high sensitivity and selectivity achievable in the UV/Vis/NIR spectral range. A variety of plasmonic sensing schemes take advantage of nanostructures for detecting biomarkers; however, common to these techniques is the consequent utilization of plasmon resonance effects.

Surface plasmons result from efficient coupling between free electrons within the conduction band of metals, and incident EM radiation in a coherent manner. Generally, two types of surface plasmon resonances (SPRs) may be discriminated: (i) propagating surface plasmon polaritons (SPPs) and (ii) localized surface plasmon resonances (LSPRs). SPPs are excited at the surface of thin metal films

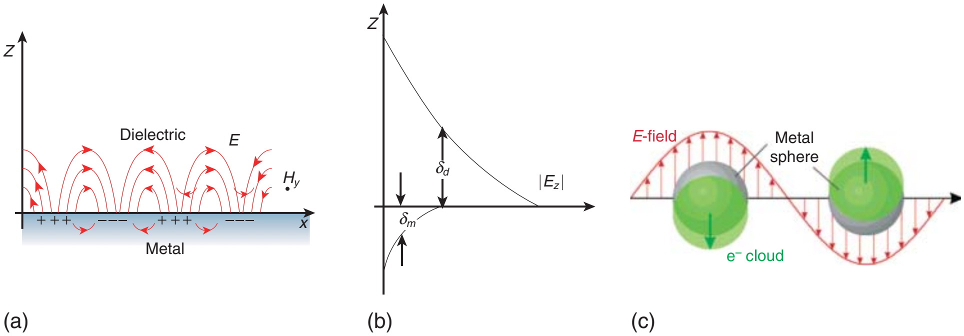

Figure 46.1 Two types of surface plasmon resonance (SPR): (a,b) surface plasmon polaritons (SPPs) and (c) localized surface plasmon resonances (LSPRs). SPR represents a coherent interaction between an electromagnetic field and charges at a metal–dielectric interface. The field lines in (a) represent the electromagnetic field (TM mode). (b) The electric field strength along the normal direction to the interface [1]. (c) LSPRs by the collective oscillation of the electron cloud at a metal sphere under the influence of an external electromagnetic field [2].

surrounded by dielectric media if the appropriate resonance conditions are satisfied, which are illustrated in Figure 46.1a,b. SPPs may propagate up to a few hundreds of micrometers along the metal/dielectric interface. In contrast, LSPR are nonpropagating plasmon excitations generated at metal nanostructures such as, for example, metallic nanoparticles (NPs), nanoshells, or nanoholes, which are surrounded by dielectric media, as shown in Figure 46.1c. In both cases, any change of the dielectric constant in the surrounding dielectrics results in a change of the plasmon resonance conditions, which may be detected by measurable experimental parameters such as, for example, change of intensity, wavelength, and coupling angle. Both types of plasmonic sensors are highly sensitive toward minute changes of the dielectric constant resulting from the presence of a target analyte near the metal/dielectric interface. However, the specificity of such plasmonic biosensors usually exclusively results from appropriate molecular recognition (bio)chemistry immobilized at the surface of or near the metal/dielectric interface for target molecule recognition such as, for example, antibody–antigen, ssDNA–ssDNA, or similar recognition events. Examples for appropriate antibody–antigen binding schemes are shown in Figure 46.2.

To date, SPP biosensor technologies have further evolved than LSPR biosensors, which are still at an early stage of research. Typically, SPP biosensors utilize prism couplers, grating couplers, or waveguide couplers based on optical fibers or channel waveguides [3]. Although SPP biosensors based on prism coupling are the most sensitive optical configuration, systems using optical fibers have advantages in terms of device miniaturization [3]. Optical fiber SPR biosensors usually exploit single-mode fibers with one side surface planar polished and coated with a thin metal film. The fundamental mode of the optical fiber is designed to couple to the SPP excitation mode with the biorecognition element immobilized at the metal surface.

Bench-top style SPR biosensors utilizing SPPs are commercially available, and are already frequently applied in biomedical and clinical analysis. For example, Besselink *et al.* [4] have reported the successful detection of prostate-specific antigen (PSA), a biomarker for prostate cancer, in PBS buffer using a commercial SPR sensor system based on SPPs.

Wittekindt *et al.* [5] have used SPP biosensors to detect antibodies against herpes simplex virus type I and type II from human sera. Wei *et al.* [6] have demonstrated the detection of troponin (cTn I), a biomarker for cardiac muscle injury, in serum. As an example of viable immobilization schemes, an avidin layer was prepared by amine coupling chemistry on alkanethiolate deposited as a self-assembled monolayer (SAM). Biotinylated antibodies against cTn I were then immobilized onto the avidin layer. The limits of detection (LOD) in this particular study were determined at 2.5 and 0.25 ng ml^{-1} for the direct and the sandwich format, respectively. The group of Books has used miniaturized optical fiber SPR sensors to detect cTn I with LODs equivalent to 3 ng ml^{-1} [7].

Nanostructured metals with surrounding dielectrics support a different type of plasmonic excitation, which is an active area of research for enhancing the sensitivity and selectivity of SPR-based biosensors [8]. LSPR at NPs significantly

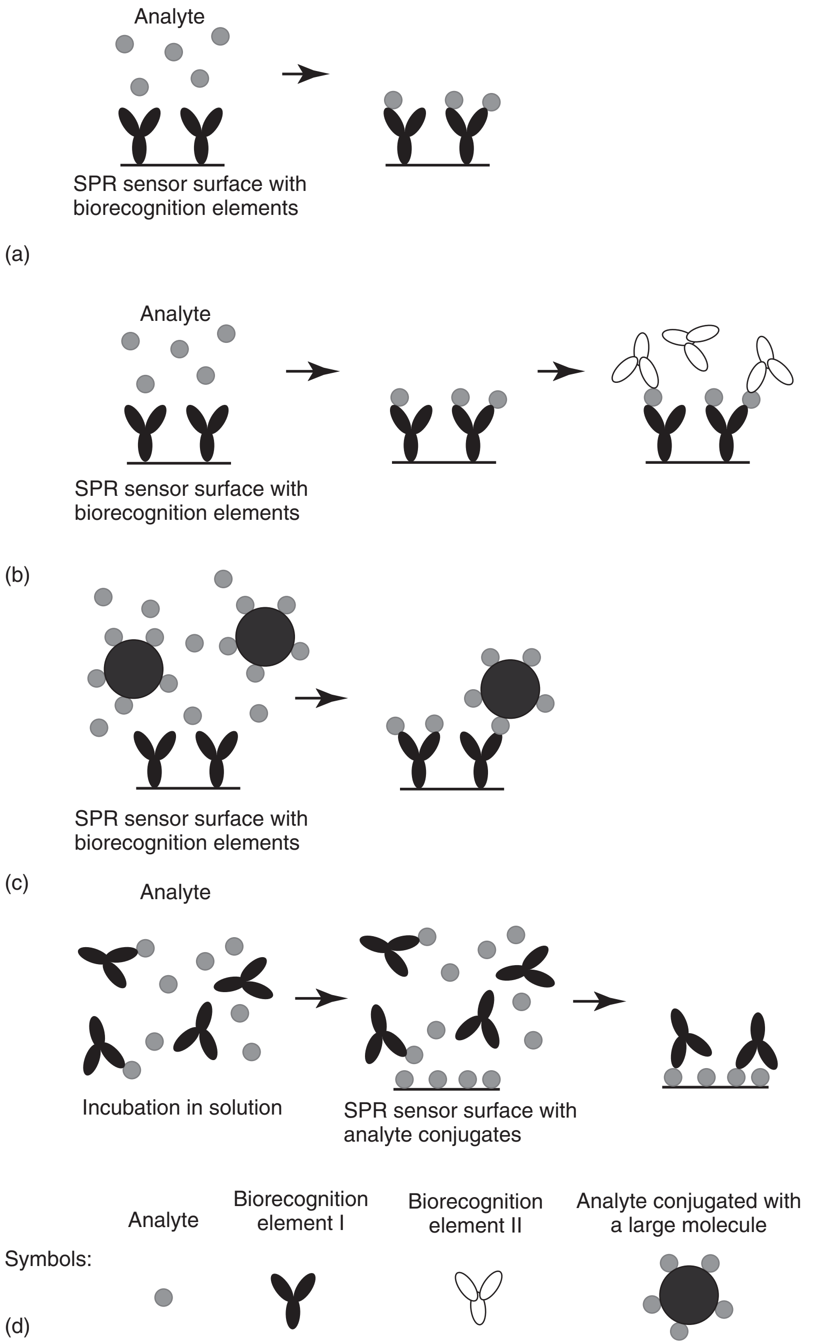

Figure 46.2 Selection of analyte detection schemes applicable in SPR [3]. (a) Direct detection, (b) sandwich detection, (c) competitive detection, and (d) inhibition detection.

enhance light scattering as well as light absorption [8, 9], with several interesting detection schemes based on NPs derived for biosensing applications.

Colorimetric detection schemes based on NP–NP coupling are probably among the most simple, yet effective methods taking advantage of LSPR. Mirkin and his research group [10] have successfully demonstrated a nucleic acid assay with oligonucleotide-functionalized Au NPs. Such oligonucleotide-functionalized Au NPs will aggregate in the presence of the nucleotide as the target analyte. As the distance between the Au NPs decrease as a result of NP aggregation and especially within the range of the LSPR-enhanced electric field, near-field coupling effects dominate, thereby resulting in a redshift of the absorption spectra.

Another highly interesting scheme is the hybridization of SPP biosensors with metal NPs to further enhance the sensitivity. Determining the rather minute changes of the dielectric constant after antigen–antibody binding events is frequently the limiting factor in sensitivity for SPR biosensors based on SPPs, as the change in dielectric constant due to the presence of a few – or small – (bio)molecules may be rather limited. In a hybrid approach, the metal surface of the SPR sensor is modified with an immobilized antibody followed by antigen exposure. To further improve the signal strength, the sensor is then exposed to an antibody-conjugated Au NP solution. The presence of Au NPs near the SPR sensor metal film significantly enhances the dielectric constant change, thereby resulting in higher sensitivity [11]. This method may be applicable for detection in immunoassays, DNA hybridization assays, protein conformation assays, or for analyzing nucleotide polymorphism with rather small sample amounts.

An alternative plasmonic measurement scheme is based on Rayleigh and Raman scattering at metal NPs for sensing and imaging purposes [9, 12–14]. Rayleigh scattering is a purely elastic process, that is, the wavelength of the incident radiation is not altered after scattering. In a Raman process, phonon absorption and generation is involved during scattering, thereby resulting in a wavelength shifting. El-Sayed and his group [9] have used Au NPs conjugated to ligands targeting cancer cell biomarkers for the detection and for imaging cancer cells by taking advantage of very strong Rayleigh scattering. The same methodology was later investigated for even treating cancers by photothermal therapy [9].

Raman spectroscopy is a molecularly highly specific detection technique, with SERS promising significant signal enhancements compensating the low optical efficiency of the Raman. Hence, the enhanced electric field provided by LSPRs at metal NPs significantly improves the Raman coupling efficiency [15–17]. By virtue of the inherent molecular specificity, metal NP-based Raman spectroscopy is complementary to LSPR assays, which has the advantage of high sensitivity and molecular selectivity on the same sensing platform.

A final LSPR biosensing scheme is based on spectral shifting of LSPRs resulting from the dielectric constant change due to the binding event between target biomarkers and appropriate immobilized receptors. While this scheme, similar to colorimetric sensors based on NP–NP coupling, takes advantage of the fact that the LSPR is shifted, one signal is caused by a dielectric constant change due to the biomarker binding event, while the other results from coupling of NPs themselves because of the presence of biomarkers. The group of Van Duyne [18] has developed nanostructured LSPR biosensors to detect amyloid-beta-derived diffusible ligands (ADDLs), a biomarker for Alzheimer's disease, from human brain extracts by LSPR shifting caused by a dielectric change because of the binding event.

46.3
Mid-Infrared Optical Sensors

MIR absorption spectroscopy in the 3–20 μm wavelength regime is characterized by high sensitivity and inherent molecular selectivity, due to sharp optical transitions via efficient direct phonon coupling, and the particular benefit of the ''fingerprint'' region enabling *ad hoc* molecular identification. The unique features of MIR absorption spectroscopy render sensing MIR schemes highly suitable for analyzing multiple analytes, that is, panels of biomarkers, at trace levels with minimal or in the absence of time-consuming sample preparation steps such as, for example, labeling. Mizaikoff and coworkers [19–21] have shown the detection of multiple analytes at trace levels by combining Fourier transform infrared spectroscopy (FT-IR) with hollow-core waveguide sensing modules for gas-phase analytes, or with solid-core fiberoptic or planar waveguides for liquid-phase analysis in many different application scenarios.

MIR absorption spectroscopy appears to be an ideal complementary platform for the detection of biomarkers in medical diagnostics, with the analysis of EB and exhaled breath condensate (EBC) among the most promising clinical fields of application [22]. EB is known to contain more than 1 000 different volatile organic compounds (VOCs) [23–29]. The blood matrix propagates many organic and inorganic compounds as a result of complex metabolic reactions, physiological and pathogenic processes, or pharmacologic responses. Many of these constituents may permeate across the alveolar membrane, thereby ending up in the EB matrix. While the correlation between the VOCs in EB and many distinct disease conditions or physiological reactions is not yet fully understood, some relations between EB composition and certain physiological conditions are already well established. Acetone is among the earliest and most studied VOCs in EB with respect to its potential for diagnostic detection and progression monitoring [30–32].

For example, patients suffering from diabetes show significantly altered acetone levels in their EB, as diabetes mellitus is a metabolic disorder causing higher glucose concentration, and thus, extensive lipolysis [33]. Diabetes increases the concentration of ketones in the blood including, in particular, acetoacetate, 3-β-hydroxybutyrate, and acetone, which result in elevated concentrations of acetone in EB.

As another example, the so-called breath methylated alkane contour (BMAC) appears to have potential as a biomarker for breast cancer [33]. A research team led by Phillips [34] reported breast cancer prediction with 88.2% sensitivity and 73.8% specificity by analyzing BMAC of C4–C20 alkanes and monomethylated alkanes with the aid of fuzzy logic algorithms. Breast cancer causes an increase in oxidative stress, and initiates the expression of polymorphic cytochrome P-450 mixed oxidase enzymes (CYP). Oxidative stress triggers lipid peroxidation of poly-unsaturated fatty acids, thereby resulting in alkanes and methylalkanes, while CYP contributes to the catabolism of these constituents. Therefore, the combined effect of oxidative stress and CYP significantly changes the alkane group profile, which may be of high diagnostic value. The same research group later improved the selectivity and specificity of these studies by additionally analyzing different VOCs with similar methods [35], and identified 2-propanol, 2,3-dihydro-1-phenyl-4(1H)-quinazolinone, 1-phenyl-ethanone, heptanal, and isopropyl myristate as biomarkers of breast cancer, even though their biological functionality is not yet fully understood.

For lung cancer, a diagnostic panel of 22 breath VOCs has been identified, which mainly consists of alkanes, alkane derivatives, and benzene derivatives with high sensitivity and specificity [36]. Furthermore, lung cancer has been diagnosed by detecting different combinations of VOCs, which comprise BMAC, C4–C20 alkanes, and monomethylated alkanes [37].

Furthermore, a variety of VOCs have been used to diagnose respiratory infection and inflammation.

Table 46.1 summarizes a selection of well-known biomarkers found in EB, and the corresponding disease conditions. As VOCs in EB are the ‘‘projection image’’ of constituents also present in the blood matrix, valuable information is provided to noninvasively diagnose the physiological status of the organism.

Recently, a number of efforts have focused on the application of MIR spectroscopy and sensing schemes to human EB analysis for the identification of diseases [26, 38, 39]. The group of Mizaikoff [21] has constructed MIR broadband gas sensing systems based on FT-IR spectrometers, a 1 m long hollow-core waveguide gas cell, and a mercury-cadmium-telluride (MCT) detector, thereby successfully demonstrating simultaneous multianalyte sensing with detection sensitivities of 15.8 ppb for CO_2 and 517 ppb for CH_4. This broadband MIR absorption sensing system requires only ∼1.5 ml of sample for analysis, which is ideally suited for small EB samples. The advantage of the MIR broadband sensing system is the wide spectral coverage, so that most VOCs in EB can be simultaneously addressed. However, the broad spectral band results in limited energy density per wavelength, and thus, limited sensitivity for target analysis.

In order to improve the sensitivity for selected constituents, compact semiconductor MIR lasers are used as light source. While trading in spectral bandwidth and, to a certain extent, multicomponent detection capability, increased sensitivity within a narrow spectral band is gained using narrow bandgap heterostructure semiconductor laser diodes or quantum cascade lasers (QCLs).

Narrow bandgap semiconductor laser diodes are usually made of lead salt materials or IV–VI compound semiconductors, which generate photons by radiative recombination of electrons from the conduction band, and holes from the valence band. The emitted photon wavelength is compatible with the energy gap between the conduction band and the valence band. The operational principle of QCLs is

Table 46.1 Diseases and associated biomarkers commonly found in exhaled breath and exhaled breath condensate.

Disease/health status	Biomarker in EB	Biomarker in EBC
Breast cancer	BMAC, pentane, formaldehyde	—
Lung cancer	BMAC, NO, acetaldehyde	H_2O_2, nitrite
Asthma	NO, CO	H_2O_2, leukotriene E4, isoprostanes, TBARs
COPD	NO, CO	H_2O_2, leukotrienes, prostanoids, isoprostanes
CF	NO, CO	H_2O_2, isoprostanes
ARDS	NO	H_2O_2
Diabetes	Acetone	—
Schizophrenia	CS_2, pentane	—
Renal function	NH_3, dimethylamine, trimethylamine	—
Liver function		
Liver transplant rejection	COS	—
Helicobacter pylori infection	^{13}C-urea breath test	—

Thiobarbituric acid-reactive products (TBARs), carbonyl sulfide (COS).
Adapted from [22].

quite different from such conventional laser diodes, and had already been suggested by Kazarinov and Suris in the 1960s; experimentally, the first QCL was demonstrated in 1994 by Capasso and his colleagues at the Bell Laboratory [40, 41]. In QCLs, the conduction band consists of several repeating intersubbands, which are engineered by designing appropriate quantum well heterostructures. Electrons in the upper intersubband are forced into the lower intersubband, thereby generating MIR photons whose energy is compatible with the energy difference between the upper and the lower intersubband. As QCLs are usually composed of several cascaded stages, each electron may generate several photons depending on the number of cascades present in the device. Simplified energy band diagrams for bandgap diode lasers and QCL are illustrated in Figure 46.3a,b.

Roller *et al.* [38] have constructed a tunable diode laser absorption spectroscopy (TDLAS) sensing system utilizing IV–VI narrow bandgap MIR diode lasers with an emission wavelength of 5.2 μm combined with a 107 m long multipass White cell to quantitatively detect NO and CO_2 in human breath for the diagnosis of asthmatic conditions in EB, as shown in Figure 46.4. Similar measurement techniques have later been applied in veterinary medicine by analyzing EB from animals. Although narrow bandgap semiconductor laser diodes have shown initial success in EB analysis, and have contributed to the first steps toward miniaturization of MIR sensor systems, they have several disadvantages. They usually require cryogenic temperatures (15–80 K) for operation, and their emitted optical power is usually

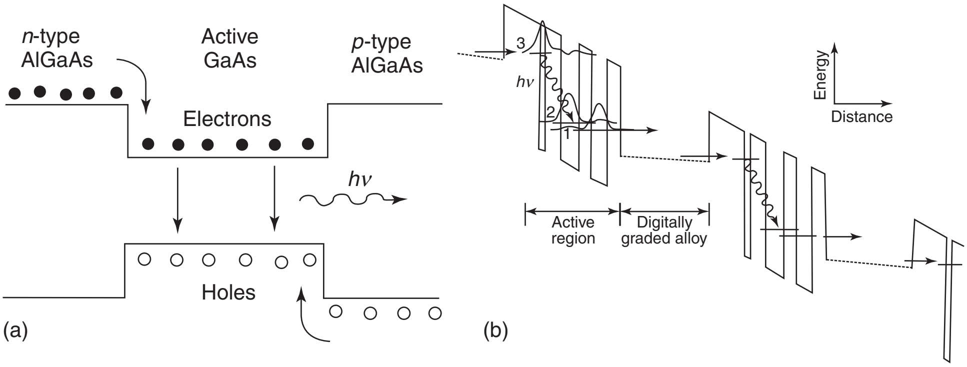

Figure 46.3 Photon generation schemes in conventional bandgap laser diodes (double heterostructure), and in quantum cascade lasers (QCL). (a) In a double heterostructure laser diode, a relatively narrower bandgap layer is sandwiched by a p-type and an n-type layer. The double heterostructure laser diode is under forward bias during operation; the p-type layer supplies holes to the valence band of the active region, while the n-type layer supplies electrons to the conduction band of the active region. Electrons and holes in the active region recombine, resulting in the emission of photons with an energy compatible to the bandgap of the active region. For MIR emission, IV–VI semiconductors are usually applied [42]. (b) In QCLs, the conduction band structure of active regions and injection regions (digitally graded alloy) is schematically shown. The digitally graded alloy region also consists of several quantum wells (superlattice) with the fine structure omitted for simplicity in this diagram. QCL may consist of >20 active regions separated by injection regions. The active region has three coupled quantum wells forming several delocalized electron eigenstates. Optical transitions from level 3 to level 2 release photons within the active region. The electrons in level 1 tunnel through the potential barrier of the injector region, and are transferred to level 3 of the next active region [41]. (Reproduced with permission from [41] copyright © 1994 AAAS.)

low, that is, in the range of several milliwatts. Furthermore, their beam quality is not consistent, and because of material limitations, which are governed by the bandgap of the materials and thus difficult to engineer, the entire MIR spectral range is not covered. While the need for cryogenic cooling adds to the technical complexity of the sensing system, the rather low optical output power limits the detection sensitivity of the system and requires either the detection of biomarkers present at acceptable concentration levels, or additional preconcentration schemes. Furthermore, limitations in emission wavelength due to the material restrictions prevent access to certain biomarkers with absorption peaks within these spectral ranges.

Some of the main disadvantages of conventional narrow bandgap semiconductor lasers have recently been overcome by QCLs. Meanwhile, a wide variety of studies have demonstrated superior sensitivity and selectivity in gas sensing applications using QCL light sources in combination with types of gas cells and at different laser tuning ranges. Mizaikoff and coworkers [43] have reported the detection of 30 ppb ethyl chloride from a 1.5 ml sample volume with an integrated MIR sensing system using a 1 m long photonic bandgap optical fiber serving as the waveguide and as the miniaturized sample cell and a QCL with a lasing wavelength of 10.3 μm, as described in Figure 46.5.

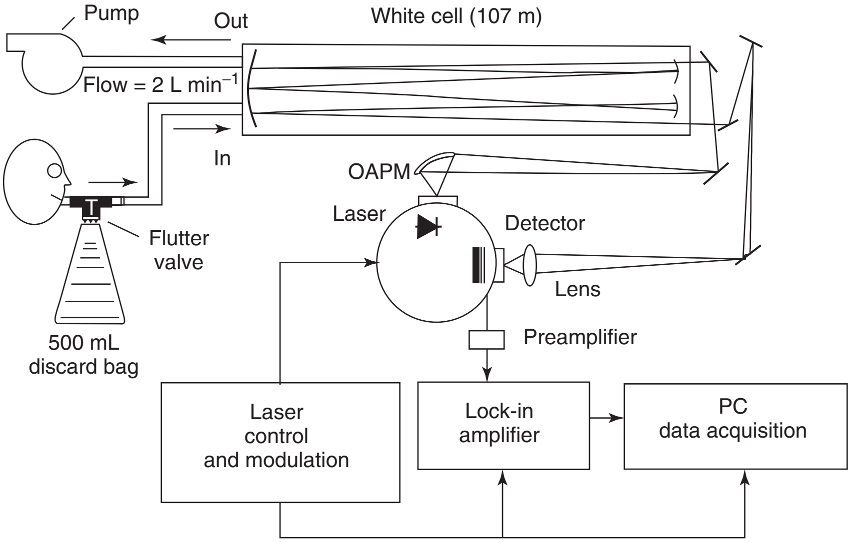

Figure 46.4 Diagram of an exhaled breath (EB) analysis system by Ekips Technologies, Inc. The system consists of a tunable MIR diode laser made from narrow bandgap semiconductor materials, a multipass gas cell in a White configuration, and a cooled detector [38].

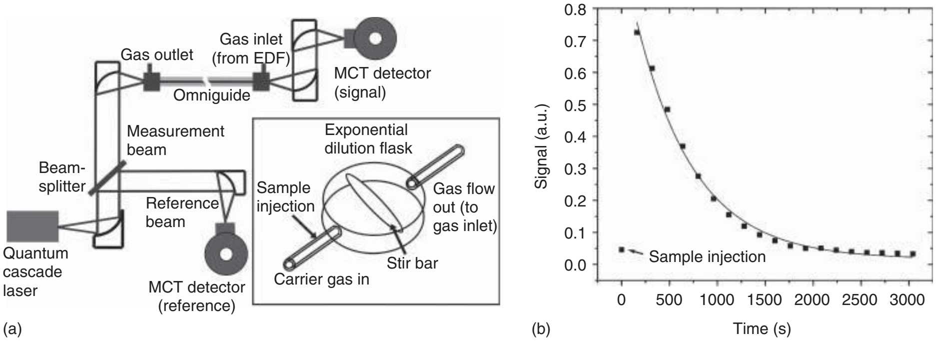

Figure 46.5 (a) Diagram of a gas sensing system comprising a room-temperature-operated QCL with a lasing wavelength of 10.3 μm, and a 1 m long photonic bandgap hollow waveguide with a transmission window matched to the QCL emission [43]. The inset shows an exponential dilution chamber. (Reproduced with permission from [43] copyright © 2005 AIP Publishing LLC.) (b) Experimental results determining the LOD for ethyl chloride at approximately 30 ppb via exponential dilution.

Tittel *et al.* [44] have shown the applicability of tunable laser absorption spectroscopy (TLAS) sensing system to detect approximately 30 ppb carbonyl sulfide (COS), which is a biomarker for failure of the liver function and acute lung transplant rejection. The TLAS sensing system comprises a thermoelectrically cooled QCL lasing at 4.86 μm, and an optical multipass gas cell providing 36 m absorption path length.

QCLs coupled with integrated cavity output spectroscopy (ICOS) sensing systems have detected approximately 3.6 ppb NO, and 15 exhaled human breath samples were tested with this device [45].

While the application of MIR lasers for detecting biomarkers has been proved successfully with regard to sensitivity, it remains critical to match the emission wavelength of the laser with the absorption peak of the target analyte for optimized sensitivity and selectivity. Consequently, the capability of tuning the emission wavelength of the laser deliberately within a certain spectral range is vital for improved selectivity and multicomponent analysis. Therefore, tunable MIR laser diode spectroscopy systems have the potential of serving as miniaturized spectrometers with high sensitivity and adequate discriminatory power for multiple constituents. While the lasing wavelength of semiconductor laser diodes including QCLs usually tunes with temperature or injected current, the tuning ranges thus achieved are limited to a few wavenumbers. An alternative strategy to tuning is to use a parallel array of fixed wavelength MIR semiconductor lasers with different lasing wavelengths, thereby establishing a quasi-broadband coherent MIR radiation source [46, 47]. However, the most effective way to achieve wide tunability is the construction of external-cavity quantum cascade lasers (EC-QCLs), where external-angle-tunable gratings provide wavelength-selective feedback to the coupled QCL [48, 49]. Figure 46.6 shows a diagram of an EC-QCL and its tunable lasing characteristics. In this configuration, continuous tuning over 250 cm^{-1} has been achieved [50]. Young *et al.* [51] have constructed a gas sensing module comprising an EC-QCL and a hollow-core waveguide, thereby achieving multianalyte sensing with excellent sensitivity. It was possible to achieve LODs as low as 4 ppb for ethyl chloride, 7 ppm for dichloromethane, and 11 ppb for trichloromethane by precisely tuning the lasing wavelength of EC-QCL to the Q-branch of each analyte absorption peak.

Another interesting MIR sensing technique is photoacoustic spectroscopy (PAS) coupled with QCLs [52, 53]. PAS takes advantage of a different signal transduction

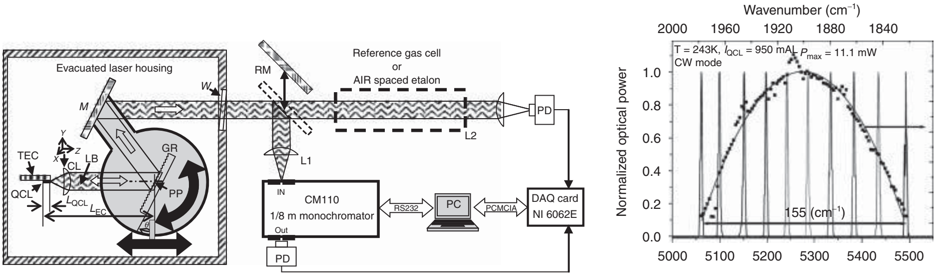

Figure 46.6 (a) Schematic of a typical tunable EC-QCL setup with thermoelectric cooler (TEC), diffraction grating (GR), and pivot point (PP) of the grating rotation [50]. (Reproduced with permission from [50] copyright © 2008 Springer Science & Business Media.) (b) Tuning characteristics of a tunable EC-QCL with a laser emission centered at 5.3 μm; the EC-QCL is operated in cw at 950 mW.

scheme compared to MIR absorption spectroscopic sensing. In PAS, modulated MIR radiation is absorbed by the target analyte similar to conventional absorption spectroscopy. However, instead of directly detecting the remaining intensity of the radiation after absorption, PAS takes advantage of the fact that modulated MIR radiation leads to the periodic excitation of vibrations of the absorbing molecules, thus giving rise to an oscillating pressure wave, if the sample is enclosed in a resonant or nonresonant cell. This modulated pressure change generates an acoustic wave, which may be detected by a microphone(s) or by a quartz tuning fork(s) without the need for an optical detector [42]. There have been several reports about achieving ultralow detection levels of analytes in air at the parts-per-billion (ppb) to parts-per-trillion (ppt) concentrations using this scheme [53–56].

For example, QCL-PAS sensing systems were able to detect ammonia, a biomarker for asthma, to levels of 66 ppb [54]. The introduction of a quartz-tuning-fork-enhanced PAS system has considerably increased the sensitivity, and the degree of miniaturization for such devices [57]. The typical dimensions of a quartz tuning fork are in the range of approximately 1 mm^3, such that the overall device footprint can be as small as approximately 5 mm^3. Therefore, quartz-enhanced photoacoustic sensors (QEPASs) only require small volumes of a gas sample, which is again ideal for EB analysis. A small device footprint is particularly important for handheld diagnostic applications such as, for example, posthospitalization therapeutical progress monitoring, and biohazard exposure monitoring in work places.

While gas cells and hollow-core waveguides serve as excellent transducers for gas phase analytes, solid-core optical fibers, planar waveguides, channel waveguides, or advanced photonic structures such as, for example, disk or ring resonators are the transducers of choice for liquid- or solid-phase analytes. Especially in medical diagnostics, several types of bodily secretions and constituents of the human body exist as forms of liquid and solid. However, the interaction mechanism of transducers is quite different from that of the gas-phase analyte. In the gas cell or hollow-core waveguide, the gas-phase sample and MIR radiation are simultaneously present inside the transducer, such that MIR radiation and target analyte molecules directly interact. Solid-core optical fibers or planar waveguides confine MIR radiation inside the waveguide by forming a guided mode due to total internal reflection (TIR), while the liquid or solid or liquid-phase analytes reside at the surface of the optical waveguide. However, radiation may interact with analytes at or close to the waveguide surface via evanescently guided modes emanating at the waveguide surface, if the internally reflected radiation is incident at the waveguide/adjacent medium interface below the so-called critical angle, and if the refractive index of the adjacent medium is smaller than the refractive index of the waveguide material. Therefore, analyte molecules need to be present within the penetration depth of the evanescent field, which, in the MIR, extends a couple of micrometers into the adjacent medium. Solid-core optical fibers or planar waveguides are composed of MIR transparent materials such as, for example, GaAs, chalcogenide glass, or silver halides [58]. Although such solid-core waveguides are efficient MIR transducers, the sensitivity may be considerably enhanced by coating the waveguide surface with appropriate enrichment membranes or molecular recognition structures. An enrichment membrane may increase the concentration of target analytes compared to the concentration in the native samples by several orders of magnitude, if the partition coefficient favorably facilitates diffusion of the analyte(s) into the enrichment matrix. Such signal enhancement strategies lead to significantly higher detection sensitivity, and may also reduce interferences of other matrix constituents. In particular, for the MIR regime, hydrophobic enrichment membranes reduce water interferences within the evanescent field, thereby further facilitating the detection of trace constituents such as, for example, small organic molecules in the aqueous matrix. Water is among the most prominent interferants in MIR absorption spectroscopy owing to its pronounced dipole moment giving rise to strong MIR absorptions.

Liquid- and solid-phase MIR sensing systems utilizing QCLs as a compact MIR light source and silver halide [20] or GaAs/AlGaAs [59] waveguides as the transducer have successfully detected precipitated solid-phase urea samples at 80.7 μg, and solution concentrations of 10.8 μg of acetic anhydride in 0.01 μl of acetonitrile, as shown in Figure 46.7. These fundamental studies are considered

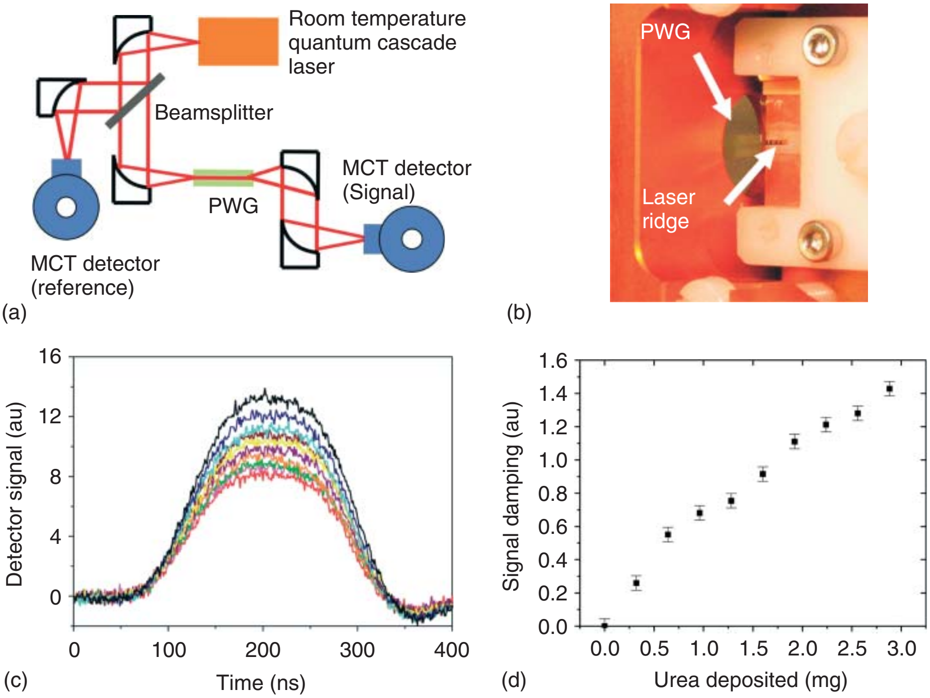

Figure 46.7 (a) Diagram of solid-core waveguide sensing system for liquid- and solid-phase analytes. PWG is a planar silver halide waveguide with MIR radiation coupled from a room-temperature-operated QCL via an off-axis parabolic mirror. (b) The PWG is shown directly coupled to the QCL. (c) QCL PWG sensor response evaluating the area of the laser signal as a function of the amount of urea precipitated at the waveguide surface (calibration function shown in (d)) [20]. (Reproduced with permission from [20] copyright © 2005 American Chemical Society.)

the first proof-of-concept for MIR absorption spectroscopy sensing systems with sufficient sensitivity applicable to bodily secretions including, for example, EBC, urine, interstitial fluid, or saliva. EB not only contains VOCs but also nonvolatile organic compounds, which provide relevant information on the physiological status of an organism. Such nonvolatile compounds are usually collected as EBC at a cooled surface for further analysis [60, 61]. Usually, patients suffering from asthma, chronic obstructive pulmonary disease (COPD), or cystic fibrosis (CF) show markedly elevated concentrations of H_2O_2, leukotrienes, lipid peroxidation products, and isoprostanes in EBC, which are considered biomarkers of oxidative stress [62, 63]. Nitric oxide metabolites in EBC have also been used as biomarkers for airway inflammation in asthma, CF, COPD, and adult respiratory distress syndrome (ARDS) [64–67]. EBC is less researched than VOCs in EB despite its potential for medical diagnostics, predominantly as analysis methods are comparatively cumbersome. Recently, increased research efforts adopting microfluidics, optofluidics, and advanced photonic structures such as, for example, photonic crystals or microdisk/ring resonators for further miniaturization and enhanced sensing performance may provide a viable solution for direct analysis of EBC constituents utilizing lab-on-chip or monolithically integrated devices [68–71].

For example, the research team of Capasso [69] has achieved a detection sensitivity equivalent to a 170 μm thin absorption cell for a liquid-phase sample with a volume of approximately 10 pl using a sensing platform a few hundreds of micrometers in size. An intracavity absorption spectroscopic device using a narrow ridge microfluidic QCL with a 9 μm laser emission was established, as shown in Figure 46.8a,b.

Loncar *et al*. [70] have developed photonic crystal QCLs combined with an optofluidic structure, which is suitable for miniaturized liquid-phase chemical sensing, as shown in Figure 46.8c,d. Consequently, advanced MIR photonic sensors provide a promising platform for molecularly selective analysis of clinically relevant samples, and are certainly among the most attractive optical sensing techniques once advanced photonic structures are readily available.

46.4
Terahertz Optical Sensors

In the past decade, the THz spectral range has attracted increasing interest for many applications including biological analysis and biomedical diagnostics [72–74]. However, as THz spectroscopy has been less explored compared to any other spectral regime of analytical interest, the relevant device technologies including light sources, waveguides, and detectors are less developed. This also reflects in the expression ‘‘THz gap’’ referring to the difficulty in accessing this spectral regime from a device optics and electronics point of view. However, recent progress in THz technology has significantly revitalized this field and promises the transition of THz spectroscopy from a niche technology to a bioanalytically relevant tool.

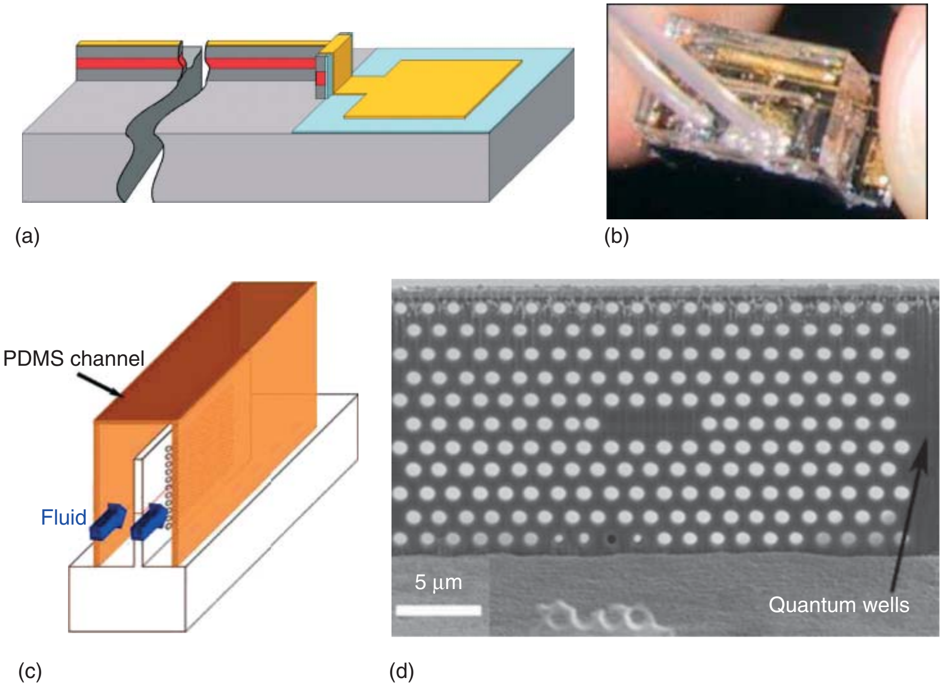

Figure 46.8 Advanced miniaturized photonic sensors. (a) Diagram of a narrow-ridge waveguide QCL for intracavity absorption spectroscopy [69]. (b) Optical image of a QCL intracavity absorption spectroscopic sensor with microfluidic liquid channels connected to tubing [69]. (c) Diagram of a photonic crystal QCL with microfluidic analyte guiding channel [70]. (d) SEM image of a photonic crystal waveguide microfabricated by focused ion beam milling [70].

While there is no strict definition of the THz spectral range, it is usually considered to cover the frequencies from 0.3 THz (1 mm or 10 cm^{-1}) to 3 THz (100 μm or 100 cm^{-1}); however, occasionally the FIR region from 20 to 100 μm is included into the THz regime. With respect to (bio)sensing applications, several research groups have recently applied THz spectroscopy for protein folding, label free detection of DNA hybridization, general disease diagnostics, monitoring of receptor binding events, dental diagnostics, and medical imaging [74–76]. Before discussing details of THz biomedical or medical diagnostic applications, it is essential to highlight the unique nature of THz radiation compared to more commonly applied UV/Vis/NIR or MIR radiation, and the consequences of these unique properties for biomedical applications.

The energy of THz radiation matches well with the phonon energy associated with macromolecules at different conformational states, which implies that useful resonances should be available for molecular studies. Owing to the long wavelength, less scattering and more penetration depth are anticipated with typical spatial resolution of approximately 170 μm at 1 THz. Finally, the photon energy of THz radiation is far below the ionization energy (4 meV at 1 THz), thus ensuring minimal effects on the probed molecules.

Consequently, THz radiation appears particularly suitable for studying biological samples or organisms given the opportunity of addressing a variety of biologically relevant macromolecules including proteins, RNA, and DNA, as THz radiation provides an efficient optical window to monitor conformational or structural changes, or binding events of such macromolecules. However, it should be noted that water vapor and liquid water are highly absorptive in the THz regime, that is, the absorption coefficient of liquid water varies from 100 to 1000 cm^{-1} [72]. Although some of the water absorption peaks are not yet firmly assigned, it is evident that THz radiation is efficiently absorbed via intramolecular vibrational and rotational modes, as well as intermolecular vibrational modes associated with hydrogen bonds [73]. The high absorptivity of THz radiation by water plays an important role in biomedical applications, and renders imaging or tomographical applications for visualizing, for example, the human body rather challenging. However, by taking advantage of the strong absorption of water, it is indeed feasible to image tissues utilizing their water content as contrast mechanism, which is difficult to obtain with other spectroscopic techniques.

For example, THz images utilizing the tissue water content provide a discrimination between, for example, muscle from adipose tissues, and tumors from normal tissues [77]. By virtue of the deep penetration ability, such images may carry information not only from the tissue surface but also from the bulk material. The low energy of THz radiation is ideal for noninvasive diagnostics with minimal risk of ionization.

From the instrumental perspective, there are different schemes for generating THz radiation. Initially, the photoconductive method developed by Auston in 1975 at the Bell Laboratory was predominantly used for THz radiation generation and detection [78, 79]. In this scheme, EM pulses in the THz range are generated during acceleration of electrons in the conduction band of a semiconductor material such as, for example, GaAs. During this process, ultrashort laser pulses with photon energies higher than the bandgap of the semiconductor material are propagated between two electrodes on the semiconductor material, while a DC bias voltage is applied to the electrodes. The applied DC bias voltage accelerates electrons that are photoexcited by the ultrashort laser pulses into the conduction band. A typical setup is shown in Figure 46.9 [74]. This type of THz source may generate broadband radiation up to 5 THz.

Another interesting paradigm is based on nonlinear optical frequency generation such as, for example, different frequency generation (DFG) or optical parametric oscillation (OPO). Both techniques do not directly generate THz radiation, but convert a fundamental pump laser beam in the Vis/NIR range to THz radiation via nonlinear optical processes. Optical crystals without structural inversion symmetry are able to generate EM radiation (ω_1, idler) from a pump beam (ω_3, pump) with or without another input beam (ω_2, signal) utilizing the second order nonlinear optical coefficient $\chi^{(2)}$, which is referred to as *DFG* (with ω_2 external input) or

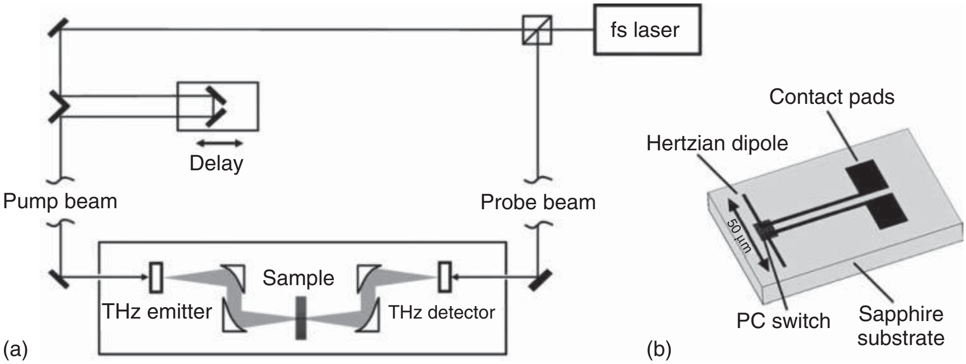

Figure 46.9 (a) Diagram for THz radiation measurement and (b) photoconductive Aston THz switch [74].

OPO (without ω_2 external input), respectively. Typical nonlinear optical crystals are GaAs, $LiNbO_3$, $LiTaO_3$, potassium titanyl phosphate (KTP), or organic nonlinear materials. The relationship among the three involved lightwaves follows energy conservation and momentum conservation:

$$\hbar\omega_1 = \hbar\omega_3 - \hbar\omega_2$$

$$\Delta k = k_1 + k_2 - k_3 = 0$$

$$P(\omega_1 = \omega_3 - \omega_2) = 2\chi^{(2)} E_3 E_2^*$$

The main benefit of frequency down-conversion is the fact that readily available laser light sources with appropriate output power, beam quality, and so on may be applied and converted to the THz regime, where only a few compact high-power coherent light sources are currently available [80, 81].

Another important scheme for direct generation of THz radiation are QCLs, which have been described in the section on MIR optical sensors. QCLs are already considered the most advanced light source for MIR radiation, and may be tailored toward THz emission by reducing the energy gap of the intersubbands. Recently, cw THz emission from QCLs was demonstrated at 66, 87, and 100 μm [82–85]. While QCLs are still predominantly applied in the MIR to FIR radiation regime, recent progress on THz QCLs promises coherent compact semiconductor light sources at these long wavelengths.

Nagel *et al.* [86] recently demonstrated DNA detection with THz biosensors. As THz radiation resonates well with different vibrational modes of the DNA molecular backbone, a potential sensing platform for label-free monitoring of DNA binding is provided. As an advancement, biosensors based on ring resonators with integrated THz waveguides coupled with two photoconductive switches, as shown in Figure 46.10, have demonstrated 5 orders of magnitude higher sensitivity compared to the free space version [74].

Probably the first application of THz radiation for medical diagnostics was the detection of early dental caries by THz imaging [87]. In dental caries, mineral is lost

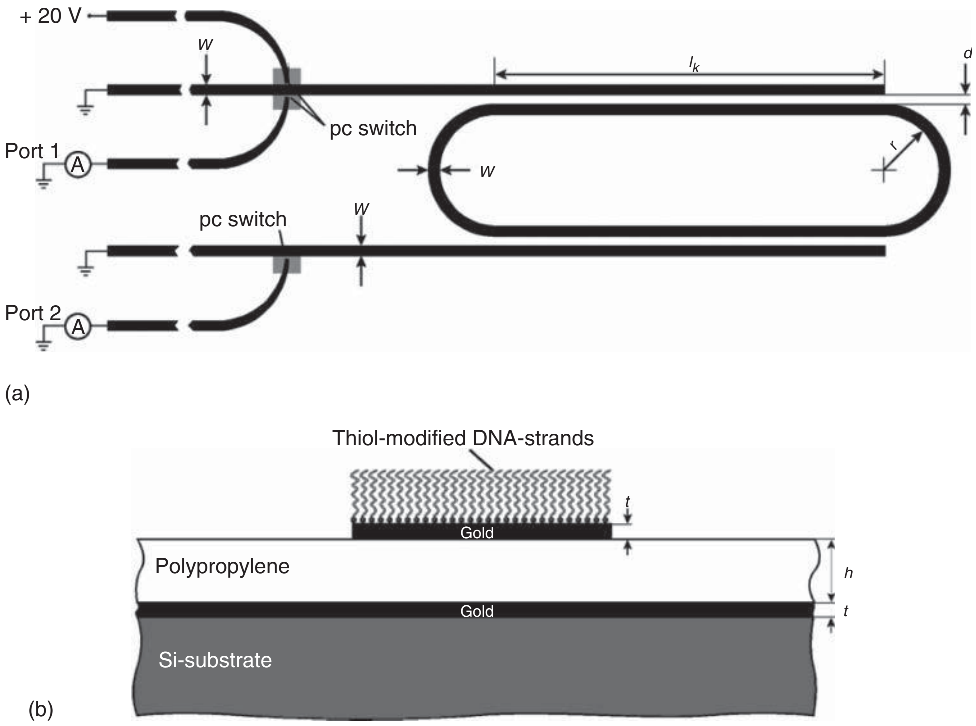

Figure 46.10 Diagram of integrated photonic THz biosensors [74]. (a) Top view of an integrated photonic THz biosensor with racetrack resonator. (b) Cross-sectional view of the device. Top and bottom gold films at the polypropylene layer form thin-film microstrip-style THz guiding structures. The racetrack resonator acts as a filter for THz radiation, which may couple to the detector side only if a resonating mode is formed mediated by the binding event of the target analytes.

from the enamel, which results in a change of the refractive index. THz radiation may noninvasively locate dental caries by imaging using refractive index changes of enamel as a contrast mechanism.

Similar strategies have been applied to investigate the human skin and the human breast for the detection of cancers [88]. Cancer cells and other malignant tissues have different refractive indices and attenuation coefficients compared to healthy tissues, thus providing contrast mechanisms for imaging in the THz regime. Table 46.2 summarizes related results for the THz spectral range. Figure 46.11 compares a visible image and a THz image of the same tissue area containing carcinoma. In this case, a photoconductive emitter was used as the THz light source operated in pulsed mode. Given recent progress in THz QCL technology, similar THz images obtained for a rat brain using a QCL emitting at 3.4 THz indicate the future potential of this technology based on advanced light sources, as shown in Figure 46.12 [89].

Table 46.2 Absorption coefficient (α) and refractive index (n) of healthy and abnormal tissues in the THz spectral regime [73].

	α (mm^{-1})		n	
	0.5 THz	1 THz	0.5 THz	1 THz
Normal skin	11.0	16.8	2.20	2.06
BCC	13.1	19.3	2.26	2.09
Normal breast	10.5	16.4	2.01	1.90
Breast carcinoma	12.5	18.6	2.23	2.08
Breast adipose	1.3	2.2	1.56	1.54
Water	16.3	23.0	2.28	2.09

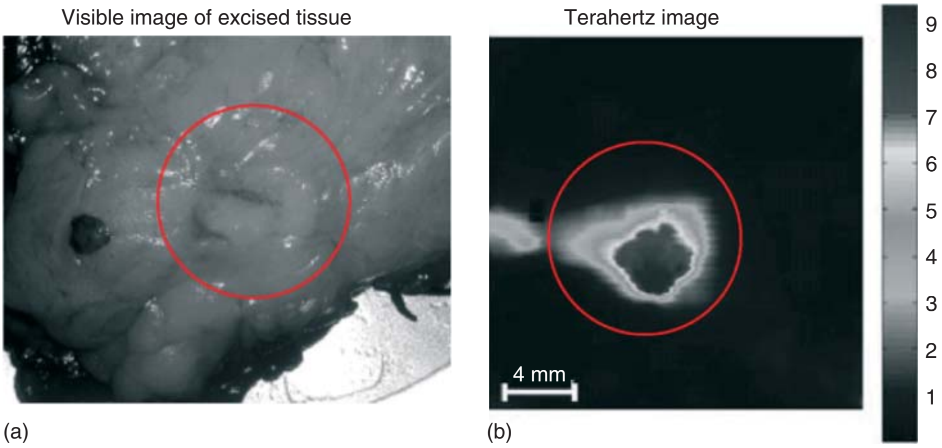

Figure 46.11 (a) Visible image versus (b) THz image of invasive lobular carcinoma (circled area) from a 52-year-old patient [73]. The THz radiation source was a photoconductive Aston switch.

46.5
Conclusions and Outlook

Medical diagnostics are among the fastest growing application areas for optical sensor technologies, especially if miniaturized devices provide access to a wide variety of measurement scenarios. Here, the current status of selected advanced optical sensor technologies has been summarized in reference to the EM spectrum from the UV/Vis/NIR to THz regime. Each spectral range provides individual merits, if appropriate optical sensor technology is applied to address (bio)medically relevant questions. Furthermore, it is evident that the optical sensor technologies presented are at significantly different levels of maturity, thus requiring continuous effort in research and development for transitioning promising laboratory or prototype concepts into the clinical reality.

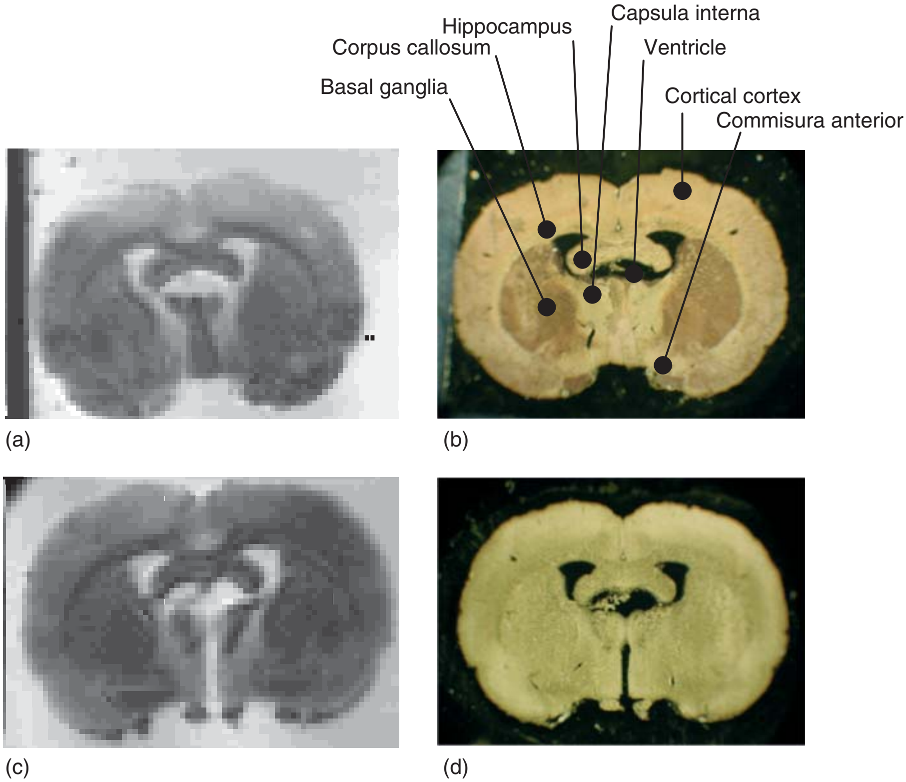

Figure 46.12 Images with (a,b) visible light source and (c,d) THz light source of the frontal section of a rat brain [89]. THz light source was a semiconductor QCL with an emission frequency of 3.4 THz.

While some of the optical (bio) sensor technologies discussed are still at a research stage, SPR-based biosensors using SPPs are already commercially available, and are routinely applied in clinical settings for disease diagnostics. In addition, LSPR biosensors utilizing metal nanostructures have already been proved a successful strategy for detection and imaging of diseases such as, for example, cancers, and Alzheimer's disease. Finally, MIR plasmonics appears to be an emerging novel technology facilitating the combination of inherent molecular selectivity with the benefits of SPR sensing technology [90, 91]. Taking advantage of further signal enhancement via Rayleigh scattering or Raman scattering, it is evident that plasmonic sensors operating in the UV/Vis/NIR spectral range will continue their evolution among the most sensitive optical detection schemes in bioanalytics.

MIR absorption and PAS are among the most promising optical sensing techniques in medical diagnostics because of the inherent molecular selectivity along with high sensitivity [92]. MIR photons directly interact with organic and inorganic molecules via well-structured vibrational and rotational modes, thereby providing the opportunity for close to real-time medical diagnostics without any labeling. In particular, breath analysis appears among the most suitable application areas for MIR optical sensor [93–98]. Recent technological advancements including QCL light sources and thin-film waveguide transducers further accelerate the development of miniaturized MIR sensing techniques toward biomedical applications [99–101].

While the THz spectral regime has only recently attracted interest in bioanalytics and medical diagnostics, rapid progress in light source, detector, and waveguide technology promises an interesting analytical platform for label-free biomolecular analysis. The low photon energy, with no risk of ionization and resonances particularly with biomacromolecules, renders THz radiation an interesting label-free detection scheme for analyzing, for example, conformational changes or binding events of macromolecules such as DNA or proteins. Furthermore, THz imaging applications utilizing water absorptivity within tissues or refractive index changes resulting from tissue compositions as contrast mechanisms maximize the utility of optical sensing and imaging techniques within a possibly broad spectral band.

References

1. Chen, Y.-B. (2009) Development of mid-infrared surface plasmon resonance-based sensors with highly-doped silicon for biomedical and chemical applications. *Opt. Express*, **17**, 3130–3140.
2. Esteban, O., González-Cano, A., Mizaikoff, B. *et al.* (2012) Generation of surface plasmons at waveguide surfaces in the mid-infrared region. *Plasmonics*, **7**, 647–652.
3. Homola, J. (2008) Surface plasmon resonance sensors for detection of chemical and biological species. *Chem. Rev.*, **108** (2), 462–493.
4. Besselink, G.A.J., Kooyman, R.P.H., van Os, P. *et al.* (2004) Signal amplification on planar and gel-type sensor surfaces in surface plasmon resonance-based detection of prostate-specific antigen. *Anal. Biochem.*, **333** (1), 165–173.
5. Wittekindt, C., Fleckenstein, B., Wiesmuller, K.H. *et al.* (2000) Detection of human serum antibodies against type-specifically reactive peptides from the N-terminus of glycoprotein B of herpes simplex virus type 1 and type 2 by surface plasmon resonance. *J. Virol. Methods*, **87** (1–2), 133–144.
6. Wei, J.Y., Mu, Y., Song, D.Q. *et al.* (2003) A novel sandwich immunosensing method for measuring cardiac troponin I in sera. *Anal. Biochem.*, **321** (2), 209–216.
7. Masson, J.F., Obando, L., Beaudoin, S. *et al.* (2004) Sensitive and real-time fiber-optic-based surface plasmon resonance sensors for myoglobin and cardiac troponin I. *Talanta*, **62** (5), 865–870.
8. Stewart, M.E., Anderton, C.R., Thompson, L.B. *et al.* (2008) Nanostructured plasmonic sensors. *Chem. Rev.*, **108** (2), 494–521.
9. Jain, P.K., El-Sayed, I.H., and El-Sayed, M.A. (2007) Au nanoparticles target cancer. *Nano Today*, **2** (1), 18–29.
10. Mirkin, C.A., Letsinger, R.L., Mucic, R.C. *et al.* (1996) A DNA-based method for rationally assembling nanoparticles into macroscopic materials. *Nature*, **382** (6592), 607–609.
11. Lyon, L.A., Musick, M.D., and Natan, M.J. (1998) Colloidal Au-enhanced surface plasmon resonance immunosensing. *Anal. Chem.*, **70** (24), 5177–5183.
12. Aslan, K., Lakowicz, J.R., and Geddes, C.D. (2005) Plasmon light scattering in biology and medicine: new sensing

approaches, visions and perspectives. *Curr. Opin. Chem. Biol.*, **9** (5), 538–544.
13. Anker, J.N., Hall, W.P., Lyandres, O. *et al.* (2008) Biosensing with plasmonic nanosensors. *Nat. Mater.*, **7** (6), 442–453.
14. Zhang, X.Y., Young, M.A., Lyandres, O. *et al.* (2005) Rapid detection of an anthrax biomarker by surface-enhanced Raman spectroscopy. *J. Am. Chem. Soc.*, **127** (12), 4484–4489.
15. Stockman, M.I. (2006) *Surface-Enhanced Raman Scattering: Physics and Applications*, Topics in Applied Physics, Springer-Verlag, Berlin, pp. 47–65.
16. Schatz, G.C., Young, M.A., and Van Duyne, R.P. (2006) *Surface-Enhanced Raman Scattering: Physics and Applications*, Topics in Applied Physics, Springer-Verlag, Berlin, pp. 19–45.
17. Nie, S.M. and Emery, S.R. (1997) Probing single molecules and single nanoparticles by surface-enhanced Raman scattering. *Science*, **275** (5303), 1102–1106.
18. Haes, A.J., Chang, L., Klein, W.L. *et al.* (2005) Detection of a biomarker for Alzheimer's disease from synthetic and clinical samples using a nanoscale optical biosensor. *J. Am. Chem. Soc.*, **127** (7), 2264–2271.
19. Mizaikoff, B. (2003) Mid-IR fiber-optic sensors. *Anal. Chem.*, **75** (11), 258A–267A.
20. Charlton, C., Katzir, A., and Mizaikoff, B. (2005) Infrared evanescent field sensing with quantum cascade lasers and planar silver halide waveguides. *Anal. Chem.*, **77** (14), 4398–4403.
21. Kim, S.S., Menegazzo, N., Young, C. *et al.* (2009) Mid-infrared trace Gas analysis with single-pass FT-IR hollow waveguide gas sensors. *Appl. Spectrosc.*, **63** (3), 331–337.
22. Kim, S.S., Young, C., Vidakovic, B. *et al.* (2010) Potential and challenges for mid-infrared sensors in breath diagnostics. *IEEE Sens.*, **10**, 145–158.
23. Pauling, L., Robinson, A.B., Teranish, R. *et al.* (1971) Quantitative analysis of urine vapor and breath by gas-liquid partition chromatography. *Proc. Natl. Acad. Sci. U.S.A.*, **68** (10), 2374–2376.
24. Phillips, M., Herrera, J., Krishnan, S. *et al.* (1999) Variation in volatile organic compounds in the breath of normal humans. *J. Chromatogr., B*, **729** (1–2), 75–88.
25. Wallace, L., Buckley, T., Pellizzari, E. *et al.* (1996) Breath measurements as volatile organic compound biomarkers. *Environ. Health Perspect.*, **104** (Suppl. 5), 861–869.
26. Mansfield, C.D., Mantsch, H.H., and Rutt, H.N. (2002) Application of infrared spectroscopy in the measurement of breath trace compounds: a review. *Can. J. Anal. Sci. Spectrosc.*, **47** (1), 14–28.
27. Manolis, A. (1983) The diagnostic potential of breath analysis. *Clin. Chem.*, **29** (1), 5–15.
28. Cao, W.Q. and Duan, Y.X. (2006) Breath analysis: potential for clinical diagnosis and exposure assessment. *Clin. Chem.*, **52** (5), 800–811.
29. Phillips, M. and Greenberg, J. (1992) Ion-trap detection of volatile organic-compounds in alveolar breath. *Clin. Chem.*, **38** (1), 60–65.
30. Henderson, M.J., Karger, B.A., and Wrenshall, G.A. (1952) Acetone in the breath – a study of acetone exhalation in diabetic and nondiabetic human subjects. *Diabetes*, **1** (3), 188–193.
31. Rooth, G. and Ostenson, S. (1966) Acetone in alveolar air and control of diabetes. *Lancet*, **2** (7473), 1102–1105.
32. Sulway, M.J. and Malins, J.M. (1970) Acetone in diabetic ketoacidosis. *Lancet*, **2** (7676), 736–740.
33. Kalapos, M.P. (1999) Possible physiological roles of acetone metabolism in humans. *Med. Hypotheses*, **53** (3), 236–242.
34. Phillips, M., Cataneo, R., Ditkoff, B. *et al.* (2003) Volatile markers of breast cancer in the breath. *Breast J.*, **9** (3), 184–191.
35. Phillips, M., Cataneo, R.N., Ditkoff, B.A. *et al.* (2006) Prediction of breast cancer using volatile biomarkers in the breath. *Breast Cancer Res. Treat.*, **99** (1), 19–21.
36. Phillips, M., Gleeson, K., Hughes, J.M.B. *et al.* (1999) Volatile organic compounds in breath as markers of

lung cancer a cross-sectional study. *Lancet*, **353** (9168), 1930–1933.

37. Phillips, M., Cataneo, R.N., Cummin, A.R.C. *et al.* (2003) Detection of lung cancer with volatile markers in the breath. *Chest*, **123** (6), 2115–2123.
38. Roller, C., Namjou, K., Jeffers, J. *et al.* (2002) Simultaneous NO and CO_2 measurement in human breath with a single IV-VI mid-infrared laser. *Opt. Lett.*, **27** (2), 107–109.
39. Namjou, K., Roller, C.B., and McCann, P.J. (2006) The breathmeter – a new laser device to analyze your health. *IEEE Circ. Dev. Mag.*, **22** (5), 22–28.
40. Kazarinov, R.F. and Suris, R.A. (1971) Possible amplification of electromagnetic waves in a semiconductor with a superlattice. *Fiz. Tekh. Poluprovodn. (Sankt-Peterburg)*, **5** (4), 797–800.
41. Faist, J., Capasso, F., Sivco, D.L. *et al.* (1994) Quantum cascade laser. *Science*, **264** (5158), 553–556.
42. Young, C., Kim, S.-S., and Mizaikoff, B. (2008) Quantum cascade laser based gas and liquid chemical sensors, in *Lasers in Chemistry* (ed. M. Lackner), Wiley-VCH Verlag GmbH, Weinhem.
43. Charlton, C., Temelkuran, B., Dellemann, G. *et al.* (2005) Midinfrared sensors meet nanotechnology: trace gas sensing with quantum cascade lasers inside photonic band-gap hollow waveguides. *Appl. Phys. Lett.*, **86** (19), 194102–194102-3.
44. Roller, C., Kosterev, A.A., Tittel, F.K. *et al.* (2003) Carbonyl sulfide detection with a thermoelectric ally cooled mid-infrared quantum cascade laser. *Opt. Lett.*, **28** (21), 2052–2054.
45. Bakhirkin, Y.A., Kosterev, A.A., Curl, R.F. *et al.* (2006) Sub-ppbv nitric oxide concentration measurements using cw thermoelectrically cooled quantum cascade laser-based integrated cavity output spectroscopy. *Appl. Phys. B*, **82** (1), 149–154.
46. Lee, B.G., Kansky, J., Goyal, A.K. *et al.* (2009) Beam combining of quantum cascade lasers. *Appl. Phys. B*, **92** (3), 16216–16224.
47. Young, C., Cendejas, R., Howard, S.S. *et al.* (2009) Wavelength selection for quantum cascade lasers by cavity length. *Appl. Phys. Lett.*, **94**, 0911091–0911092.
48. Luo, G.P., Peng, C., Le, H.Q. *et al.* (2002) Broadly wavelength-tunable external cavity mid-infrared quantum cascade lasers. *IEEE J. Quantum Electron.*, **38** (5), 486–494.
49. Maulini, R., Beck, M., Faist, J. *et al.* (2004) Broadband tuning of external cavity bound-to-continuum quantum-cascade lasers. *Appl. Phys. Lett.*, **84** (10), 1659–1661.
50. Wysocki, G., Lewicki, R., Curl, R.F. *et al.* (2008) Widely tunable mode-hop free external cavity quantum cascade lasers for high resolution spectroscopy and chemical sensing. *Appl. Phys. B*, **92** (3), 305–311.
51. Young, C., Kim, S.S., Luzinova, Y. *et al.* (2009) External cavity widely tunable quantum cascade laser based hollow waveguide gas sensors for multianalyte detection. *Sens. Actuators, B*, **140** (1), 24–28.
52. Bell, A.G. (1881) Upon the production of sound by radiant energy. *Philos. Mag.*, **11**, 510–528.
53. Elia, A., Lugara, P.M., and Giancaspro, C. (2005) Photoacoustic detection of nitric oxide by use of a quantum-cascade laser. *Opt. Lett.*, **30** (9), 988–990.
54. Filho, M.B., da Silva, M.G., Sthel, M.S. *et al.* (2006) Ammonia detection by using quantum-cascade laser photoacoustic spectroscopy. *Appl. Opt.*, **45** (20), 4966–4971.
55. Grossel, A., Zeninari, V., Parvitte, B. *et al.* (2007) Optimization of a compact photoacoustic quantum cascade laser spectrometer for atmospheric flux measurements: application to the detection of methane and nitrous oxide. *Appl. Phys. B*, **88** (3), 483–492.
56. Pushkarsky, M.B., Dunayevskiy, I.G., Prasanna, M. *et al* (2006) High-sensitivity detection of TNT. *Proc. Natl. Acad. Sci. U.S.A.*, **103** (52), 19630–19634.
57. Kosterev, A.A., Bakhirkin, Y.A., and Tittel, F.K. (2005) Ultrasensitive gas detection by quartz-enhanced photoacoustic spectroscopy in the fundamental molecular absorption bands region. *Appl. Phys. B*, **80** (1), 133–138.

58. Lendl, B. and Mizaikoff, B. (2002) in *Handbook of Vibrational Spectroscopy*, Vol. 2 (eds J.M. Chalmers and P.R. Griffiths), John Wiley & Sons, Ltd, pp. 1541–1550.

59. Charlton, C., Giovannini, M., Faist, J. *et al.* (2006) Fabrication and characterization of MBE grown thin film GaAs waveguides for mid-infrared evanescent field chemical sensing. *Anal. Chem.*, **78**, 4224–4227.

60. Phillips, M. (1997) Method for the collection and assay of volatile organic compounds in breath. *Anal. Biochem.*, **247** (2), 272–278.

61. Kharitonov, S.A. and Barnes, P.J. (2002) Biomarkers of some pulmonary diseases in exhaled breath. *Biomarkers*, **7** (1), 1–32.

62. Paredi, P., Kharitonov, S.A., and Barnes, P.J. (2002) Analysis of expired air for oxidation products. *Am. J. Respir. Crit. Care Med.*, **166** (12, Pt. 2), S31–S37.

63. Kharitonov, S.A. and Barnes, P.J. (2001) Exhaled markers of pulmonary disease. *Am. J. Respir. Crit. Care Med.*, **163** (7), 1693–1722.

64. Silkoff, P.E., Sylvester, J.T., Zamel, N. *et al.* (2000) Airway nitric oxide diffusion in asthma – role in pulmonary function and bronchial responsiveness. *Am. J. Respir. Crit. Care Med.*, **161** (4), 1218–1228.

65. Tate, S., MacGregor, G., Davis, M. *et al.* (2002) Airways in cystic fibrosis are acidified: detection by exhaled breath condensate. *Thorax*, **57** (11), 926–929.

66. Gessner, C., Hammerschmidt, S., Kuhn, H. *et al.* (2003) Exhaled breath condensate acidification in acute lung injury. *Respir. Med.*, **97** (11), 1188–1194.

67. Montuschi, P. (2005) Exhaled breath condensate analysis in patients with COPD. *Clin. Chim. Acta*, **356** (1–2), 22–34.

68. Armani, A.M., Kulkarni, R.P., Fraser, S.E. *et al.* (2007) Label-free, single-molecule detection with optical microcavities. *Science*, **317** (5839), 783–787.

69. Belkin, M.A., Loncar, M., Lee, B.G. *et al* (2007) Intra-cavity absorption spectroscopy with narrow-ridge microfluidic quantum cascade lasers. *Opt. Express*, **15** (18), 11262–11271.

70. Loncar, M., Lee, B.G., Diehl, L. *et al.* (2007) Design and fabrication of photonic crystal quantum cascade lasers for optofluidics. *Opt. Express*, **15** (8), 4499–4514.

71. Loncar, M., Hochberg, M., Scherer, A. *et al.* (2004) High quality factors and room-temperature lasing in a modified single-defect photonic crystal cavity. *Opt. Lett.*, **29** (7), 721–723.

72. Siegel, P.H. (2004) Terahertz technology in biology and medicine. *IEEE Trans. Microw. Theory Tech.*, **52** (10), 2438–2447.

73. Pickwell, E. and Wallace, V.P. (2006) Biomedical applications of terahertz technology. *J. Phys. D: Appl. Phys.*, **39** (17), R301–R310.

74. Nagel, M., Forst, M., and Kurz, H. (2006) THz biosensing devices: fundamentals and technology. *J. Phys.: Condens. Matter*, **18** (18), S601–S618.

75. Lawrence, A.F., McDaniel, J.C., Chang, D.B. *et al.* (1987) The nature of phonons and solitary waves in alpha-helical proteins. *Biophys. J.*, **51** (5), 785–793.

76. Vanzandt, L.L. and Saxena, V.K. (1989) Millimeter-microwave spectrum of DNA-6 predictions for spectroscopy. *Phys. Rev. A*, **39** (5), 2672–2674.

77. Fitzgerald, A.J., Berry, E., Zinov'ev, N.N. *et al.* (2003) Catalogue of human tissue optical properties at terahertz frequencies. *J. Biol. Phys.*, **29** (2–3), 123–128.

78. Auston, D.H. (1975) Picosecond optoelectronics switching and gating in silicon. *Appl. Phys. Lett.*, **26** (3), 101–103.

79. Smith, P.R., Auston, D.H., and Nuss, M.C. (1988) Subpicosecond photoconducting dipole antennas. *IEEE J. Quantum Electron.*, **24** (2), 255–260.

80. Kawase, K., Sato, M., Nakamura, K. *et al.* (1997) Unidirectional radiation of widely tunable THz wave using a prism coupler under noncollinear phase matching condition. *Appl. Phys. Lett.*, **71** (6), 753–755.

81. Kawase, K., Hatanaka, T., Takahashi, H. *et al.* (2000) Tunable terahertz-wave generation from DAST crystal by dual signal-wave parametric oscillation of periodically poled lithium niobate. *Opt. Lett.*, **25** (23), 1714–1716.
82. Rochat, M., Ajili, L., Willenberg, H. *et al.* (2002) Low-threshold terahertz quantum-cascade lasers. *Appl. Phys. Lett.*, **81** (8), 1381–1383.
83. Faist, J., Ajili, L., Scalari, G. *et al.* (2004) Terahertz quantum cascade lasers. *Philos. Trans. R. Soc. London, Ser. A*, **362** (1815), 215–229.
84. Scalari, G., Ajili, L., Faist, J. *et al.* (2003) Far-infrared (lambda similar or equal to 87 mu m) bound-to-continuum quantum-cascade lasers operating up to 90 K. *Appl. Phys. Lett.*, **82** (19), 3165–3167.
85. Williams, B.S., Ku, S., Callebaut, H. *et al.* (2003) Terahertz quantum-cascade laser at lambda approximate to 100 mu m using metal waveguide for mode confinement. *Appl. Phys. Lett.*, **83** (11), 2124–2126.
86. Nagel, M., Bolivar, P.H., Brucherseifer, M. *et al.* (2002) Integrated THz technology for label-free genetic diagnostics. *Appl. Phys. Lett.*, **80** (1), 154–156.
87. Crawley, D.A., Longbottom, C., Cole, B.E. *et al.* (2003) Terahertz pulse imaging: a pilot study of potential applications in dentistry. *Caries Res.*, **37** (5), 352–359.
88. Fitzgerald, A.J., Wallace, V.P., Jimenez-Linan, M. *et al.* (2006) Terahertz pulsed imaging of human breast tumors. *Radiology*, **239** (2), 533–540.
89. Darmo, J., Tamosiunas, V., Fasching, G. *et al.* (2004) Imaging with a Terahertz quantum cascade laser. *Opt. Express*, **12** (9), 1879–1884.
90. Barnes, W.L., Dereux, A., and Ebbesen, T.W. (2003) Surface plasmon subwavelength optics. *Nature*, **424** (6950), 824–830.
91. Kelly, K.L., Coronado, E., Zhao, L.L. *et al.* (2003) The optical properties of metal nanoparticles: the influence of size, shape, and dielectric environment. *J. Phys. Chem. B*, **107** (3), 668–677.
92. Mizaikoff, B. (2013) Waveguide-enhanced mid-Infrared Chem/Bio sensors. *Chem. Soc. Rev*. doi: 10.1039/c3cs60173k
93. Young, C., Menegazzo, N., Riley, A.E. *et al.* (2011) Infrared hollow waveguide sensors for simultaneous gas phase detection of benzene, toluene, and xylenes in field environments. *Anal. Chem.*, **83**, 6141.
94. Wilk, A., Seichter, F., Kim, S.-S. *et al.* (2012) Toward the quantification of the $^{13}CO_2/^{12}CO_2$ ratio in exhaled mouse breath with mid-infrared hollow waveguide gas sensors. *Anal. Bioanal. Chem.*, **402**, 397.
95. Seichter, F., Wilk, A., Woerle, K. *et al.* (2013) Multivariate determination of $^{13}CO_2/^{12}CO_2$ ratios in exhaled mouse breath with mid-infrared hollow waveguide gas sensors. *Anal. Bioanal. Chem.*, **405**, 4945.
96. Woerle, K., Seichter, F., Wilk, A. *et al.* (2013) Breath analysis with broadly tunable quantum cascade lasers. *Anal. Chem.*, **85**, 2697.
97. Perez-Guaita, D., Wilk, A., Kuligowski, J. *et al.* (2013) Improving the performance of hollow waveguide based infrared gas sensors via tailored chemometrics. *Anal. Bioanal. Chem.* doi: 10.1007/s00216-013-7230-5
98. Fortes, P.R., Wilk, A., Seichter, F. *et al.* (2013) Combined sensing platform for advanced diagnostics in exhaled mouse breath. *Proc. SPIE*, **8570**, 85700Q.
99. Wang, X., Kim, S.-S., Roßbach, R. *et al.* (2012) Ultra-sensitive mid-infrared evanescent field sensors combining thin-film strip waveguides with quantum cascade lasers. *Analyst*, **137**, 2322.
100. Wang, X., Sieger, M., and Mizaikoff, B. (2013) Toward on-chip mid-infrared chem/bio sensors using quantum cascade lasers and substrate-integrated semiconductor waveguides. *Proc. SPIE*, **8631**, 86312M.
101. Sieger, M., Balluff, F., Wang, X. *et al.* (2013) On-chip integrated mid-infrared GaAs/AlGaAs mach-zehnder interferometer. *Anal. Chem.*, **85**, 3050.

47
Tip-Enhanced Near-Field Optical Microscopy

Achim Hartschuh

47.1
Introduction

Fluorescence and Raman spectroscopy are powerful tools for the nondestructive analysis of sample materials providing detailed chemical, structural, and physical information (see Section II of this Handbook). Combined with microscopy, three-dimensional spatial maps with spectroscopic contrast can be constructed. On shrinking the sample dimensions down to the nanometer regime, both spatial resolution and signal detection sensitivity become crucial. However, as conventional microscopes rely on the detection of propagating waves, diffraction limits their spatial resolution to about half the wavelength. The main aim of nano-optics is to extend optical microscopy down to nanometer length scales below the limit imposed by diffraction. Nano-optical concepts are distinguished into far-field and near-field techniques. Far-field techniques rely on the detection of propagating waves at distances from the source larger than the wavelength of light while near-field techniques exploit short-ranged evanescent waves.

Near-field optical microscopy, initiated by the pioneering work of Pohl, Lewis, and others [1, 2] in the late 1980s and beginning of the 1990s, raised high expectations and gave access to nanoscale resolution for the first time. The history of near-field optics is reviewed in articles by Pohl and Novotny [3, 4]. In addition, numerous reviews and books exist describing fundamentals and applications (e.g., [5–10]). Here, we focus on recent developments of a particular type of near-field technique that is based on a laser-illuminated metal tip, termed tip-enhanced near-field optical microscopy (TENOM). TENOM is shown to be *the most powerful tool* for the optical characterization of surfaces not only providing superior spatial resolution down to 10 nm but also enormous signal enhancement.

This chapter is organized as follows: after this short introduction, the basic physical principles of evanescent and propagating waves are outlined. In the following sections the origin of electromagnetic field enhancement at a metal tip and schemes to utilize it for signal enhancement are described. Experimental realizations and recent examples for tip-enhanced Raman scattering (TERS) and tip-enhanced fluorescence (TEF), which highlight the capabilities of the techniques,

Handbook of Spectroscopy, Second Edition. Edited by Günter Gauglitz and David S. Moore.

are reviewed. The summary reviews the main aspects of TENOM and addresses future prospects and remaining challenges.

47.2
Principles of Near-Field Optics

Near-field optics aims at overcoming the diffraction limit of optical imaging [11, 12]. Diffraction results from the formation of the optical far field by propagating waves, described as photons in a particle picture, for which $k_z = \sqrt{4\pi^2/\lambda^2 - k_x^2 - k_y^2}$ is real. Their evanescent counterparts with complex k_z dominate the near field of a radiation source or smaller distances z decaying according to $\exp(-|k_z|z)$. According to Heisenberg's uncertainty principle relating the spread in transverse momentum Δk_x and position Δx of a particle according to $\Delta k_x \Delta x \geq 2\pi$, the spatial resolution corresponding to Δx needs to remain finite. The spread in momentum of a focused beam can be expressed through $\Delta k_x = 2k_{x,\max} = 2|k| n \sin\alpha = 4\pi/\lambda n \sin\alpha$ with n being the refractive index, $\lambda = 2\pi/|k|$ the wavelength of light and the focusing angle α illustrated in Figure 47.1a. The resulting resolution limit of $\Delta x \geq \lambda/2\pi\, NA$ illustrates its dependence on the wavelength and the numerical aperture $\mathrm{NA} = n \sin\alpha$ of the microscope objective. Following Rayleigh's criterion for the spatial resolution the well-known equation $\Delta x = 0.61\lambda/NA$, can be derived [4, 11].

To overcome this limitation, both far-field and near-field concepts have been developed. A comprehensive review of the principles, progress, and prospects of high-resolution, far-field techniques is given in [13]. Near-field optical microscopy achieves high spatial information through interactions between the sample and a pointed probe mediated by the electromagnetic near field. Raster scanning

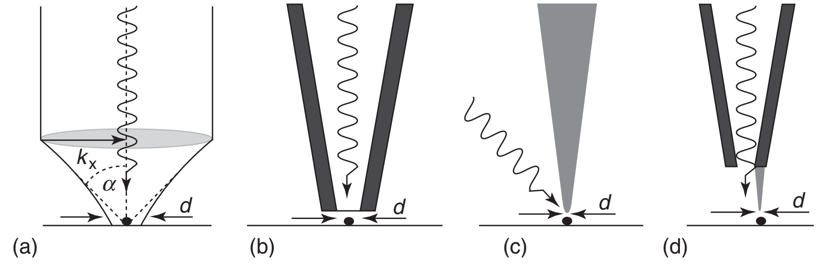

Figure 47.1 Focusing concepts: far-field focusing using a lens (a). The angular frequency range of propagating waves k_x and thus the focus diameter d is limited by the aperture angle α of the lens $k_{x,\max} = 2\pi n/\lambda \sin\alpha$, with n being the refractive index and λ the wavelength of light. (b–d) Near-field optical microscopy exploiting evanescent waves offers subdiffraction resolution limited only by the probe dimension d. In aperture-type scanning, near-field optical microscopy (aperture SNOM (b)), d is given by the aperture diameter. For tip-enhanced near-field optical microscopy (TENOM (c)) combining high spatial resolution and signal amplification, d corresponds to the tip diameter. Tip-on-aperture approach (TOA (d)) combining the advantages of (b,c) (Reprinted from Ref. [9]. Copyright 2008, with permission from Wiley VCH.)

the probe and simultaneous signal detection then allows for image formation. As higher spatial frequencies k_x, k_y are connected to faster exponential decay (see earlier definition of k_z), high-resolution imaging requires nanoscale probe-sample distances. As a consequence, near-field microscopy is limited to surface or subsurface studies or, in other words, the technique provides surface sensitivity. Four different focusing concepts are illustrated in Figure 47.1 including lens-based far-field focusing (Figure 47.1a), the widely used aperture-type approach (aperture scanning near-field optical microscopy(SNOM)) , Figure 47.1b], and tip-enhancement (Figure 47.1c,d) that is at the center of this chapter.

In TENOM, enhanced optical fields in the proximity of a sharp metallic probe are used to locally excite the sample and to extract the emitted light (Figure 47.1c). Shown in Figure 47.1d is the so-called tip-on-aperture (TOA) probe that combines the advantages of aperture-type and TENOM. The use of laser-illuminated metal tips for near-field imaging was suggested by Wessel in 1985 [14]. In general, three different approaches can be distinguished: (1) scattering-type microscopy [15–17] in which the sample response is detected in the far-field at the frequency of the incident light; (2) tip-enhanced nonlinear optical frequency generation and mixing such as second-harmonic generation (SHG) and four-wave mixing (4WM) [6, 18–21]; and (3) tip-enhanced microscopy that utilizes the locally enhanced fields to increase the inelastic spectroscopic response of the system [6, 7, 22–26]. Local signal enhancement not only serves to achieve high spatial resolution but also increases the detection sensitivity enormously. The technique is therefore applicable to weak emitters with low quantum yield and intrinsically weak signals such as Raman scattering. Moreover, the versatility of the technique allows the study of a variety of spectroscopic signals including local time-resolved fluorescence or Raman spectra. In this chapter, we focus on the third approach and refer the interested reader to the references listed for the other two approaches. The next section contains a brief theoretical description of field enhancement at a metal tip and how these fields modify the optical signals.

47.3
Field Enhancement at a Metal Tip

Field enhancement at metal structures is a phenomenon we encounter almost in daily life, forming the principle of a lightning rod, a radio antenna, and the coloring based on metallic nanoparticles. In fact, the three examples also illustrate the different contributions to field enhancement: the electrostatic lightning rod effect is caused by geometric singularities, leading to highly localized surface charge densities that also form the basis for field emission (Figure 47.2a). Surface plasmon resonances of metal particles reflect shape and dielectric properties, causing characteristic extinction spectra (Figure 47.2b). Antenna resonances become relevant if the length of the metal structure matches multiples of half the wavelength of radiation (Figure 47.2c) [26–28]. Antenna and plasmon resonances exhibit distinct wavelength dependencies, with pronounced maxima in

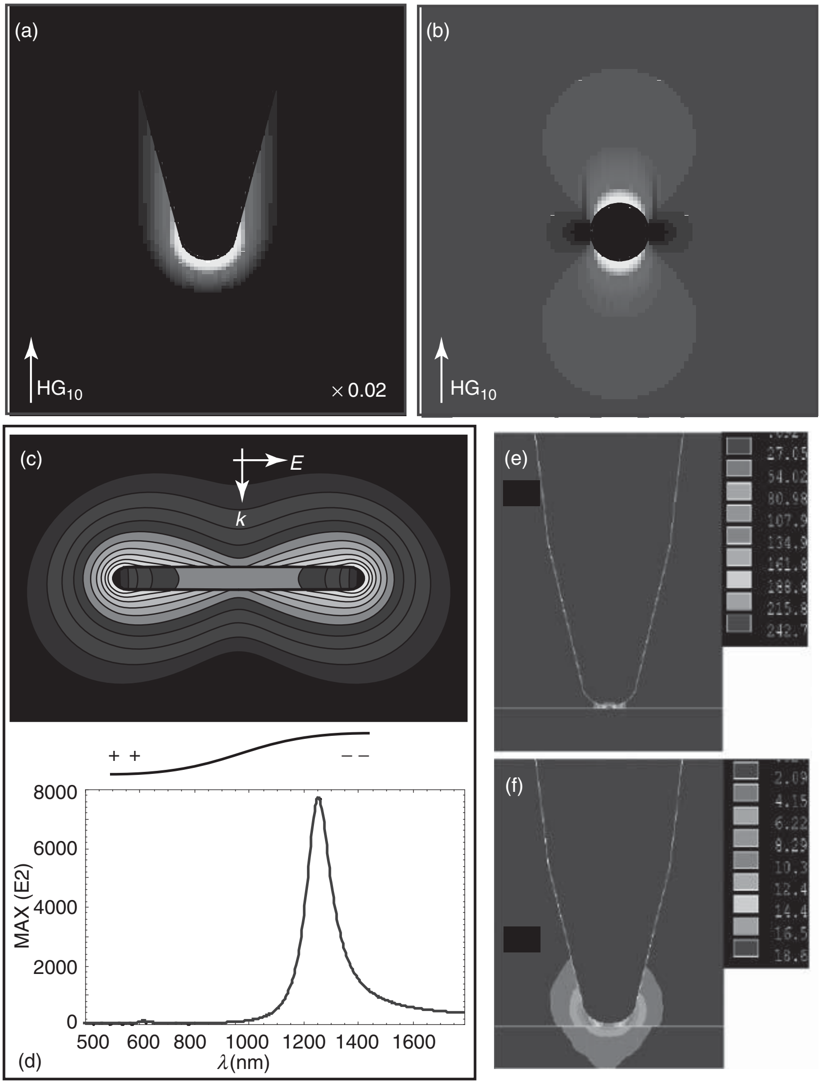

Figure 47.2 Field enhancement at nanostructures results from three different contributions. The quasistatic lightning-rod effect requires a geometric singularity and is observable for semi-infinite pointed probes (a). Surface plasmon resonances result from collective excitations of electrons reflecting both shape and dielectric properties of metal particles (b). In (a,b), calculated field distributions $|E_{local}(\mathbf{r},\omega)|^2$ near a gold tip (a) and sphere (b) located above a glass substrate and irradiated by an on-axis focused HG$_{10}$ laser mode are shown. (Reprinted from Ref. [30]. Copyright 2006, with permission from Annual Reviews. 3.) Antenna resonances occur when the tip length is related to an effective wavelength (c,d). (Reprinted from Ref. [31]. Copyright 2007, with permission from Elsevier.) Electric field enhancement and confinement at a metal tip is strongly increased for metallic (e) as compared to glass substrates (f). ((e,f) Reprinted from Ref. [32]. Copyright 2005, with permission from the American Chemical Society.)

the field intensity tunable through the visible spectral range, while the contribution from the electrostatic lightning rod effect depends on the conductivity of the material at light frequencies typically increasing toward the IR spectral range [27, 29].

Numerous theoretical studies have been presented in the literature, employing a variety of techniques to quantify the contributions from different field enhancement mechanisms and to find the optimum tip structure. The difficulty in describing metallic structures in the optical regime results from the fact that metals do not behave as perfect conductors at these frequencies. This leads to finite skin depth, that is, fields are not confined to surfaces, and ultimately results in deviations from the simple antenna theory. Another consequence is the formation of surface plasmon polaritons at the boundary between metals and dielectrics. The influence of tip shape and material on the field enhancement has been discussed in a series of publications with the aim of finding the optimum tip [31, 33, 34]. For simple tip structures, highest enhancement is predicted theoretically and verified experimentally to occur in the retarded regime, when antenna length is related to an effective wavelength [28, 35]. Results from different numerical techniques need to be compared quantitatively to assess technical difficulties and to maximize the impact of theoretical predictions [36].

From theory and experiments on surface-enhanced Raman scattering (SERS), it is evident that highest enhancement results for two or multiple particle configurations as realized by the combination of spheres, antennas, or in more complex colloidal aggregates [21, 35, 37–43]. Similarly, field enhancement is increased enormously for tips over metal surfaces [32, 44–46] combined with higher localization (Figure 47.2d,e). For samples covered by a thin dielectric layer, on the other hand, field enhancement is expected to drop rapidly [47]. The interaction between tip and sample substrate leads to surface- and distance-dependent spectral shifts of plasmon Resonances, complicating the quantification of field enhancement achieved in a particular configuration [48– 52].

Experiments using tips on metallic substrates revealed that fields are enhanced additionally by sub- or a few nanometer-sized surface features that are hardly observable in atomic force microscopy (AFM) images [51, 53] (see also Figure 47.8). In order to avoid roughness-related artifacts in TERS mapping, atomically smooth metal substrates are necessary for quantitative TERS imaging. For TENOM applications, maximized fields are not sufficient as they also have to be accessible in scanning probe configuration and therefore have to occur at the extremities of the particle or tip [28]. Moreover, the probe dimensions should be small as they directly determine the topographic resolution and the possibility of topographic artifacts resulting from tip–sample distance variations [54, 55].

Resulting field distribution and localized enhancement do not only depend on particle configuration and wavelength but also on the polarization state of the excitation light. To establish a strong field enhancement at tips formed by sharpened wires, the electric field of the exciting laser beam needs to be polarized along the tip axis [27]. Initially, field distributions are calculated for continuous-wave (cw)-excitation by plane waves. In the retarded regime, where light propagation becomes relevant such as in the case of extended antenna structures, tightly focused excitation or excitation with evanescent waves will lead to modified field distributions. Advanced approaches utilize surface plasmon propagation and retardation for field engineering. Chirp- and polarization-controlled laser pulses can be designed, and adaptive subwavelength control of nano-optical fields at metal structures has been recently developed into an efficient tool giving way to the field of ultrafast nano-optics [56–59].

47.4
Tip-Enhancement of Optical Signals

Although the enhanced electromagnetic fields are localized to the tip apex as discussed in the previous section and in Figure 47.2, the image contrast formed by raster scanning the sample does not simply reflect the tip shape. In other words, tip-enhanced optical imaging does not correspond to AFM with optical information. In particular, because Raman scattering and fluorescence are distinct optical processes involving different electronic states of the sample material with a different degree of coherence, the enhancement effects for either type of sample and thus the image contrast is expected to vary.

The enhanced fields at the tip lead to enhanced excitation rates corresponding to an increase in the excitation density provided by the light source. In general, the enhancement of the excitation rate k^{ex} will be identical for Raman scattering and fluorescence if electronic dephasing is not changed. By defining the field enhancement factor f as the ratio between the electric field at the tip $E_{\mathrm{tip}(x)}$ and without tip $E_0(x)$, the excitation rate enhancement is expressed as $k^{\mathrm{ex}}_{\mathrm{tip}}/k^{\mathrm{ex}}_0 = f^2$. In analogy with a radio, which can be used both as receiver and sender, the enhanced fields can also promote radiative decay expressed by the rate k^{rad}. Radiative rate enhancement can be discussed in terms of the Purcell effect and is expressed by Fermi's golden rule in the weak coupling regime [60, 61].

47.4.1
Enhancement of Raman Scattering

In the case of Raman scattering, the total signal depends on the product of the transition rates $k^{\mathrm{ex}}(\lambda^{\mathrm{ex}})k^{\mathrm{rad}}(\lambda^{\mathrm{rad}})$. As a consequence, the total signal enhancement scales with the fourth power of the field enhancement for small differences between the excitation and emission wavelength $\lambda^{ex,rad}$ and assuming that the field enhancement at the tip does not depend sensitively on the wavelength.

$$M_{\mathrm{Raman}} = k^{\mathrm{ex}}_{\mathrm{tip}}/k^{\mathrm{ex}}_0 \cdot k^{\mathrm{rad}}_{\mathrm{tip}}/k^{\mathrm{rad}}_0 \approx f^4 \tag{47.1}$$

For the general case of SERS, Raman enhancement factors are reported reaching up to 12 orders of magnitude for particular multiple particle configurations involving interstitial sites between particles or sharp protrusions on the outside surface [37, 62]. As the signal scales with the fourth power, the already moderate field enhancement, predicted for a single spherical particle to be in the range of $f = 2 - 5$, is sufficient for significant signal enhancement.

47.4.2
Enhancement of Fluorescence

The fluorescence intensity, on the other hand, depends on the excitation rate k^{ex} and the quantum yield η, denoting the fraction of transitions from excited state to ground state that give rise to an emitted photon. The quantum yield is expressed in terms of the radiative rate k^{rad} and the nonradiative rate k^{nonrad} through $\eta = k^{\text{rad}}/(k^{\text{rad}} + k^{\text{nonrad}})$. Accordingly, the fluorescence enhancement due to the presence of the metal tip can be written as

$$M_{\text{Flu}} = (E_{\text{tip}}/E_0)^2(\eta_{\text{tip}}/\eta_0) = f^2(\eta_{\text{tip}}/\eta_0) \tag{47.2}$$

Here, we assume that the system is excited far from saturation. From Eq. (47.2) it is clear that TENOM works most efficiently for samples with small fluorescence quantum yield η_0 and fast cycling rates such as, for example, semiconducting single-walled carbon nanotubes (SWNTs) [63, 64]. For highly fluorescent samples such as dye molecules, the quantum yield η_0 is already close to unity and cannot be enhanced further.

Because of the small separation between emitter and metal tip required for high spatial resolution (below 10 nm in typical experiments) nonradiative transfer of energy from the electronically excited molecule to the metal followed by nonradiative dissipation in the metal has to be taken into account. This process represents an additional nonradiative relaxation channel and reduces the number of detected fluorescence photons. While the theory of energy transfer between molecules and flat metal interfaces is well understood in the framework of phenomenological classical theory [65, 66], nanometer-sized objects are more difficult to quantify. Tip- and particle-induced radiative rate enhancement and quenching have been studied in literature theoretically [42, 61, 67– 70].

Experiments on model systems formed by single-dipole emitters such as molecules and semiconductor nanocrystals and spherical metal particles revealed a distance-dependent interplay between competing enhancement and quenching processes [71–75]. Besides amplifying emission signals, particle-induced radiative rate enhancement can also lead to a substantial spatial and spectral redistribution of the emission [52, 73, 76, 77]. Of major importance for the resulting radiative rate modification is the orientation of the emitter dipole with respect to the antenna structure [73]. While semiconducting tips will cause less efficient quenching [78, 79], they will also provided weaker enhancement because of lower conductivity at optical frequencies.

As signal enhancement and high spatial resolution are the result of near-field interactions between probe and sample as discussed earlier, TENOM spectra can differ substantially from their far-field counterpart. Large wave vectors k, for example, are expected to initiate optical transitions beyond standard dipole approximations assuming constant excitation fields [80–82]. Large field gradients could influence Raman spectra, leading to different selection rules [83]. An improved understanding of near-field optical interactions and phenomena would enable their controlled exploitation, leading to additional and new spectroscopic information.

47.5
Experimental Realization

47.5.1
Near-Field Microscopes

As field enhancement is localized to the tip apex, mechanisms for tip–sample distance control working on the length scale of a few nanometers are required. Experimental implementations are based on normal or shear-force detection used in AFM or current detection as in scanning tunneling microscopy (STM) [84, 85]. A variety of TENOM probes are employed, including sharp gold or silver tips fabricated by electrochemical etching of thin wires and metal-coated AFM probes that are commercially available (e.g., [6, 23, 25]). Alternatively, field-enhancing metal particles are attached to sharpened glass probes (e.g., [86–88]). More elaborate approaches combine etching and focused ion beam (FIB) milling, leading to tailored plasmonic structures such as bow-tie antennas [71, 89, 90].

Illumination schemes can be divided in two classes based on their applicability to nontransparent samples (Figure 47.3). Side illumination allows studying nontransparent samples for which the polarization requirement along the tip axis can be easily fulfilled (Figure 47.3c). In the case of transparent samples, on-axis illumination can benefit from high NA objectives with NA > 1 that decrease the size of the confocal volume contributing to the far-field background as discussed later and that maximize the collection efficiency of the emitted light (Figure 47.3a). The later point is paramount in the case of weakly fluorescence species for which photobleaching at high excitation densities becomes an issue. For on-axis illumination, however, light propagation is parallel to the polarization direction required to excite efficient field enhancement at the tip. This requirement can be fulfilled using higher order laser modes such as the radially polarized doughnut mode [91, 92]. Nontransparent samples can be investigated at high NA, employing parabolic mirror objectives instead of glass objectives (Figure 47.3c) [51, 93–95]. Moreover, parabolic mirrors do not exhibit chromatic aberrations and can be used at all temperatures and ultra-high vacuum (UHV) conditions, making them ideally suited for surface sciences. Their alignment is delicate because already minor deviations lead to substantially altered focal fields and reduced detection sensitivity [93].

To acquire an image, the tip is positioned in the focus of the objective and illuminated by laser light. The optical signal is typically collected through the same objective and detected either using sensitive avalanche photodiodes APDs or CCD-equipped spectrometers after rejecting the fundamental laser light. Raster

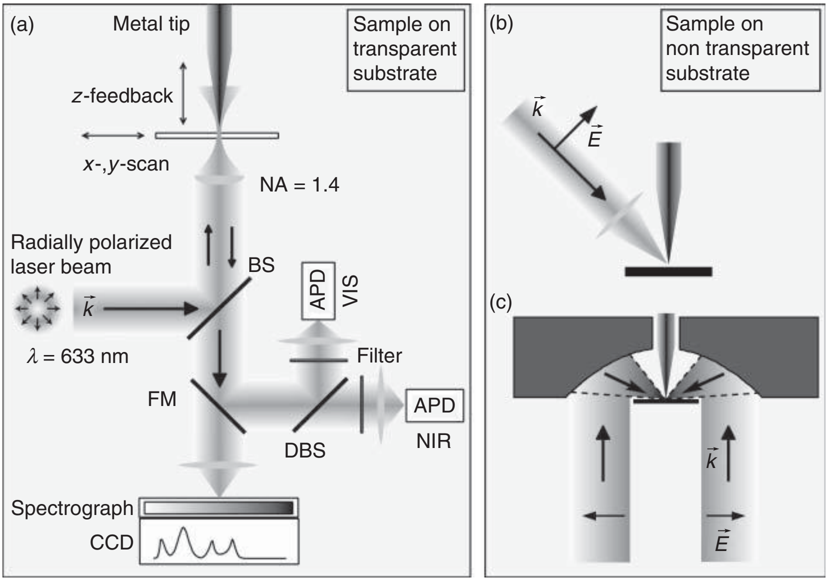

Figure 47.3 (a) Schematic of an experimental setup employing on-axis illumination of a transparent sample used to observe simultaneous Raman scattering and photoluminescence of carbon nanotubes [63]. A sharp metal tip is positioned in a tightly focused radially polarized laser beam. The optical signal is detected after passing the beam splitter (BS) either by two avalanche photodiodes (APDs) for the visual (Vis) and near infrared (NIR) spectral range or by a combination of a spectrograph and a charge-coupled device (CCD). DBS, dichroic beam splitter; FM, flip mirror (b) Side illumination of the tip on top of a nontransparent substrate. (c) Focusing of light using a parabolic mirror with high numerical aperture. To generate a strong field component parallel to the tip axis required for efficient field enhancement, schemes (a,c) utilizes a radially polarized laser mode [51, 91, 92]. (Reprinted from Ref. [9]. Copyright 2008, with permission from Wiley VCH.)

scanning the sample then allows for the simultaneous detection of near-field optical signals and the topography of the sample. Spectroscopic images formed by acquiring spectra at each pixel of the scan provide most detailed information, allowing for true spectroscopic contrast.

47.5.2
Far-Field Background

The configurations discussed so far utilize far-field illumination of the metal tip, and, as mentioned, besides the signal resulting from the near-field interaction between tip and sample, a far-field signal without the tip is detected. This is referred to as *far-field background*. The present configurations therefore rely on a substantial near-field enhancement of the signal as it needs to compete with the far-field background that results from the much larger diffraction-limited sample volume. For high-resolution imaging, the signal results approximately from a circular sample surface area of $\pi(5\text{ nm})^2$, whereas the confocal area is about $\pi(200\text{ nm})^2$ resulting in a surface area ratio of 40000/25. Considering bulk samples and taking into account the finite decay length of the near field of about 10 nm and the longitudinal focal depth of about 500 nm in far-field microscopy, this ratio increases further by a factor of 50. From this discussion it is apparent that TENOM works best for low-dimensional structures such as 1D quantum wires and nanotubes or isolated single emitters such as semiconductor quantum dots and single fluorescent molecules.

Several approaches to minimize or distinguish the background contribution have been developed. The first makes use of the rapid decay of the near-field signal on increasing tip–sample distance. In this approach, a tapping-mode AFM is used to probe the sample while the optical signal is demodulated at the fundamental or higher harmonics of the tapping-mode frequency. This approach also forms the basis of elastic scattering microscopy mentioned previously in Section 47.2. In the case of weakly emitting samples such as single fluorescent molecules, time tagging of the detected photons with respect to the tapping oscillation is used to differentiate between photons generated during small tip–sample distances related to dominating near-field interactions and those detected while the tip–sample distance is increased corresponding to far-field contributions [45, 96, 97]. At present, the corresponding demodulation of CCD-signals is challenging, precluding the acquisition of complete spectra at higher harmonic tapping-mode frequencies.

Different approaches utilize particular probes that avoid far-field excitation of the sample area. The so-called TOA (Figure 47.1d) combines the best of two worlds, namely, high spatial resolution and signal enhancement provided by sharp tips and illumination of the tip with an evanescent wave resulting from a subwavelength aperture [98, 99]. In addition, tip fabrication allows tuning the tip length to match antenna resonances, further maximizing field enhancement [100]. Other schemes make use of surface plasmon propagation [101]. The challenge of coupling propagating light to plasmons can be achieved through grating coupling, in which laser excitation of a grating written by FIB into a tapered gold tip is used to launch surface plasmons propagating to the tip apex [102]. Efficient excitation of propagating plasmons can also be achieved using higher order laser mode coupled into opaque metal-coated tapered glass fibers [69, 103, 104].

In a simplified view, a tip-enhanced near-field optical microscope is built by combining a confocal microscope with a setup for tip–sample distance control, for example, an AFM or a STM. While these microscopic techniques are fully developed, their combination certainly adds substantial complexity and will require careful design modifications to achieve a high degree of user friendliness. Although there is a huge variety of different probes for AFM, including chemically functionalized and magnetic probes, most of the commercially available tips to date cannot be efficiently used for TENOM, being based on semiconductor materials that provide only weak signal enhancement (Section 47.4). At present, the development of well-defined large-scale fabrication processes of metallic or metallized probes with maximized field enhancement factors at high reproducibility is a key issue.

47.6
Tip-Enhanced Fluorescence (TEF)

Confocal microscopes offer detection efficiencies sufficient for fluorescence imaging of single molecules with high fluorescence quantum yield. Here, the signal enhancement provided by the tip is aiming mainly at increasing spatial resolution. In the literature, many examples of TEF microscopy utilizing one- or two-photon excitation exist [22, 63, 72, 73, 96, 99, 100, 105–108]. In the following, selected examples are reviewed to highlight the capabilities of fluorescence-TENOM and to illustrate the discussions in the previous sections.

47.6.1
Single-Molecule Fluorescence Enhancement

Several experiments report on the competition of field enhancement and tip-induced quenching in clearly defined single-molecule experiments (see also Section 47.4). Metallic spheres have been used for which the field distribution can be calculated analytically [72–74, 99, 109]. Figure 47.4a shows the distance-dependent fluorescence signal for a single molecule oriented perpendicular to the substrate plane. Substantial signal enhancement is observed on decreasing the tip–sample distance, while at below about 10 nm fluorescence quenching is observed to dominate. Good agreement between theoretical and experimental curves, including different dipole orientations with respect to the tip-connecting line between dipole and tip, indicate that this effect is well understood and can be accounted for in experiments [110].

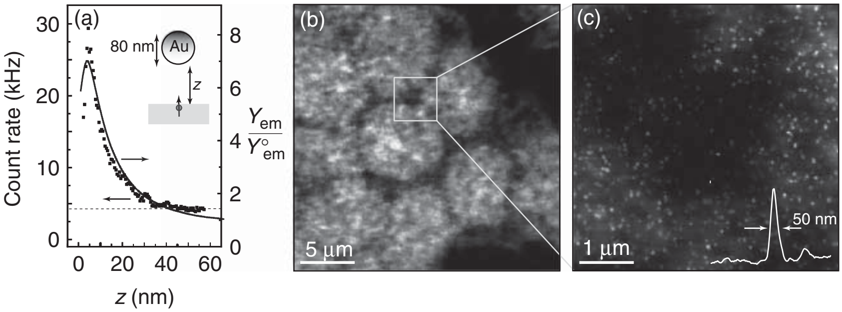

Figure 47.4 (a) Distance dependence of the fluorescence enhancement of a single dye molecule provided by an 80 nm gold nanoparticle antenna. The solid curve displays the theoretically expected enhancement. (Reprinted from Ref. [72]. Copyright 2006, with permission from the American Physical Society.) (b) Confocal fluorescence image of individual erythrocyte plasma membranes. (c) Near-field fluorescence image of the area marked in (b) resolving individual PMCA4 proteins. The image was acquired with a 60 nm gold nanoparticle antenna irradiated by a tightly focused, radially polarized laser beam. The inset shows a cross section through one of the fluorescence spots, indicating a resolution of 50 nm. ((b,c)Reprinted from Nano Letters, 2008, 8, 642. Copyright 2008, with permission from the American Chemical Society.)

As Figure 47.4a indicates an optimum tip sample distance for signal enhancement, several experiments used additional inert polymer spacer layers covering the investigate emitter [100, 111]. However, as shown in [47], this is connected to a substantial loss in field enhancement and resolution because of the drop in field strength caused by the dielectric [47]. The different distance dependencies for fluorescence enhancement and quenching indicate that there is an optimum tip–sample distance for fluorescence imaging (Section 47.6).

47.6.2
Imaging of Fluorescently Labelled Biosurfaces

The applicability of TENOM in fluorescence imaging of biological surfaces has been demonstrated in [112]. Figure 47.4c shows near-field fluorescence imaging of erythrocyte plasma membrane.

Figure 47.5 presents fluorescence imaging of single Cy3 dye molecules covalently bound to the termini of short DNA strands [96]. In the present example, efficient far-field background suppression has been achieved by time tagging each detected

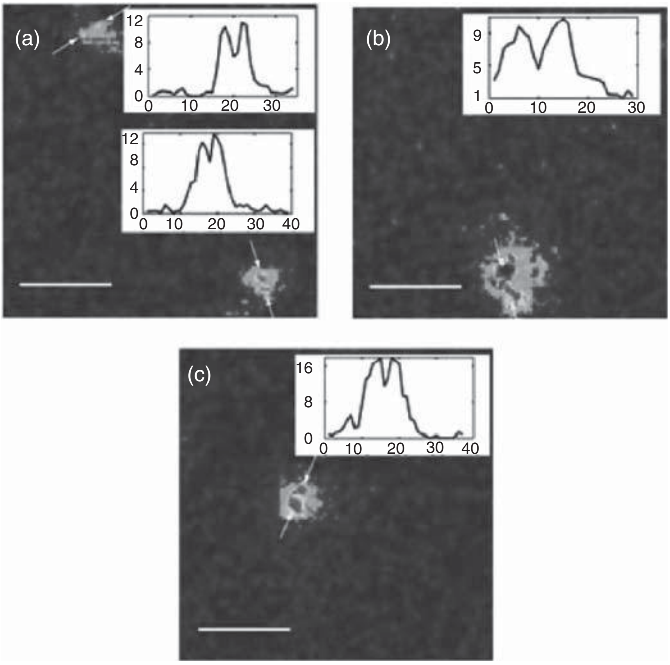

Figure 47.5 (a–c) Near-field images of Cy3 pairs on surface. The signal-to-noise ratio (SNR) is 12.4 and 15.9 for (a), 16.1 for (b), and 20.4 for (c). The insets show the profiles with line cut through the image centers (indicated by arrows), where the horizontal axis is in pixels (1 pixel = 1.95 nm) and the vertical axis is the pixel signal. Scale bars: 50 nm. (Reprinted from Ref. [96]. Copyright 2006, with permission from the American Physical Society.)

photon followed by optimized temporal filtering (Section 47.5). Dye molecules spaced by <10 nm are resolved with high signal-to-noise ratio (SNR). As spectra from highly sensitive CCD cameras cannot be demodulated at typical tapping-mode frequencies in the range of 100 kHz at present, time tagging of photons comes at the cost of reduced spectral information.

Images acquired with a TOA probe of dye-labeled DNA have been presented in [99]. Besides providing high spatial resolution, the radially symmetric field distribution at the tip allows for visualizing the 3D orientation of the transition dipole moment. As the sample is not excited in far field, this approach minimizes the far-field background and simultaneously reduces the irreversible photobleaching bleaching [99, 100].

Besides fluorescent molecules typically used for labeling of biological structures, TENOM is particularly well suited to investigate the photoluminescence (PL) of semiconducting SWNTs [63, 113, 114]. SWNTs are photoluminescent quasi-one-dimensional systems with great promise for applications in photonics, opto- and nanoelectronics [115]. While all SWNTs consist of a hexagonal lattice of carbon atoms rolled up to form a cylinder, their electronic properties vary dramatically depending on the roll-up vector that is expressed by the index tuple (n, m) specifying the nanotube chirality.

Figure 47.6a,b shows the simultaneously acquired topography and PL image of a single nanotube. The PL image is constructed from emission spectra recorded for each position while raster scanning the sample. The PL image shows the intensity within the spectral window ranging from 970 to 1030 nm corresponding to emission from (6, 5) nanotubes [115]. The two spectra detected for the positions marked in (c) are shown in (d,e), respectively. Figure 47.6c shows the spatial dependence of the emission energy, which is seen to vary within a few 10 nm [114]. Energy variations are ascribed to nonuniform wrapping by short DNA segments.

For carbon nanotubes and inorganic nanowires, simultaneous near-field Raman and PL imaging is possible and has been shown in several publications [63, 108, 116, 117]. The enhancement of PL and Raman signals detected simultaneously from the same nanotubes can be used to compare the different enhancement mechanisms [63, 117]. Typically, the observed signal enhancement is stronger in the case of PL. This is somewhat surprising because the Raman signal scales with the fourth power of the field enhancement factor, whereas the PL signal is expected to scale only quadratically. Equations (47.2) and (47.1) indicate that $M_{\text{Flu}} > M_{\text{Raman}}$ is only possible if $(\eta_{\text{tip}}/\eta_0) \geq 1$. Because the quantum yield cannot be larger than unity, $M_{\text{Flu}} > M_{\text{Raman}}$ requires an unperturbed (intrinsic, in the absence of the tip) quantum yield that is very small, that is, $\eta_0 \ll 1$ as in the case of nanotubes. As the nonradiative rate k^{nonrad} is not expected to be decreased by the tip, an increased quantum yield requires substantial enhancement of the radiative rate k^{rad} in the presence of the metal tip, as discussed in Section 47.4.

Predicted by the simple formula discussed in Section 47.4, TEF microscopy is best suited to study weak emitters [63, 64]. The present results demonstrate that TEF is particularly promising for fluorescence imaging of the biosurface in solution. TOA approaches are of major importance because, while reducing the

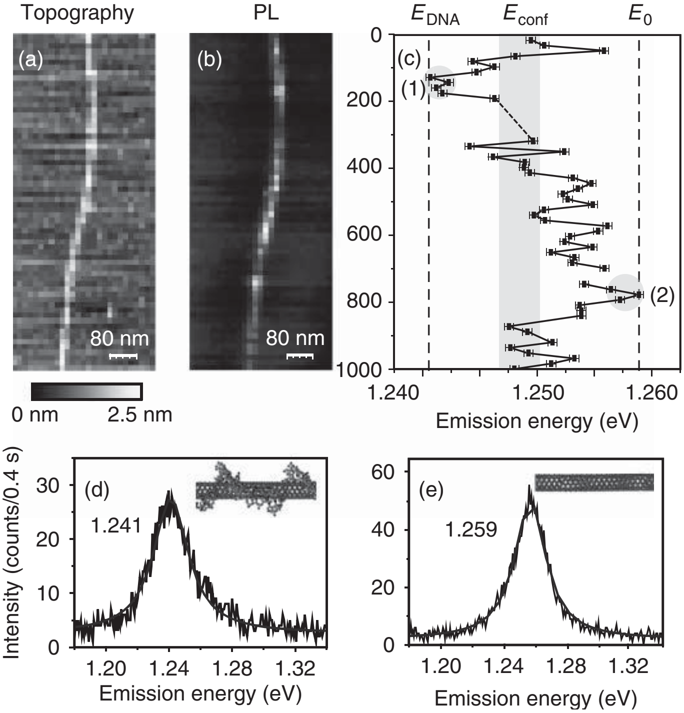

Figure 47.6 Simultaneously recorded topography (a) and near-field PL image (b) of a DNA-wrapped (6,5) nanotube on mica. The PL image was obtained by measuring spectra at each pixel and represents the integrated intensity between 970 nm and 1030 nm covering the emission range of (6,5) nanotubes [115]. For each pixel, the emission spectrum was fitted by a single Lorentzian line shape function to extract the central emission energy that is plotted in (c). Strong energy variations occur on a length scale of about 20 nm, which are assigned to nonhomogeneous wrapping by short DNA strands. PL spectra of wrapped and unwrapped DNA segments detected at positions (1) and (2) along the nanotube are shown in (d,e), respectively [114] Reprinted with permission from Nano Letters, 2008, 8, 2706. Copyright 2008 American Chemical Society.

far-field contribution, they also minimize photobleaching of the emitters caused by long light exposure during raster scanning the sample.

47.7
Tip-Enhanced Raman Scattering (TERS)

Raman scattering probes the unique vibrational spectrum of a sample and directly reflects its chemical composition and molecular structure. A main drawback of Raman scattering is the extremely low scattering cross section, which is typically 10–14 orders of magnitude smaller than the cross section of fluorescence in the case of organic molecules. Clearly, both the high spatial resolution and signal enhancement provided by TENOM are needed for the detection of nanoscale sample volumina. In the following, we review selected examples to illustrate the possibilities, limitations, and perspectives of TERS.

47.7.1
Signal Enhancement and Detection Sensitivity

A comprehensive list of reported enhancement factors achieved in TERS is given in [6], reaching up to 5×10^9 [44]. As discussed in the experimental Section 47.5, the measured relative signal enhancement, the ratio between enhanced near-field signal and background far-field signal, also reflects the different sample areas probed and the field enhancement factors cannot be quantified directly. In the derivation of these ratios, uniform sample properties, that is, uniform coverage for molecular films and uniform signal characteristics along one-dimensional structures, are assumed.

Figure 47.7 demonstrates the signal enhancement experimentally. Raman spectra detected from SWNTs in the presence of the tip and without the tip are shown in Figure 47.7a. In Figure 47.7b the near-field Raman image of SWNTs on glass is Shown, acquired by detecting the intensity of the G band around 1600 cm^{-1} after laser excitation at 785 nm using a radially polarized laser mode while raster scanning the sample. The spatial resolution can be determined from the width of the signal to be about 15 nm. The signal enhancement factor is derived from the present data using the amplitude ratio of enhanced to nonenhanced G-band signal of 3000/100 scaled by the length ratio of the probe nanotube sections of ≈400 nm/15 nm to be about 900 [118].

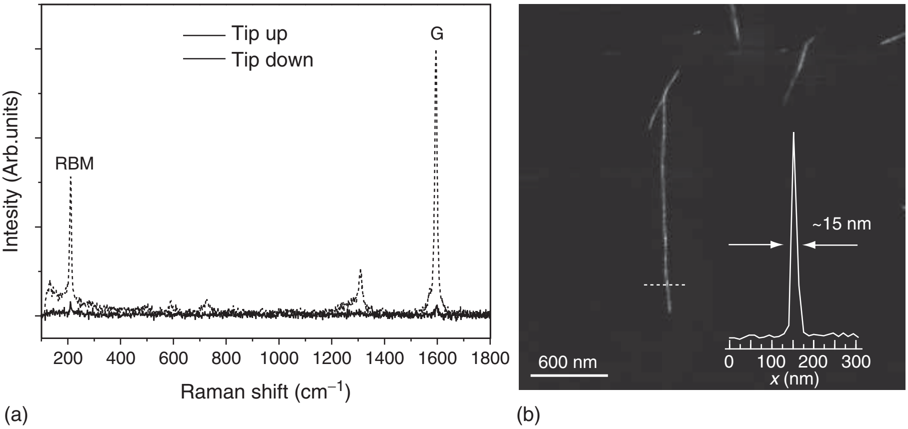

Figure 47.7 Illustration of the signal enhancement provided by a sharp gold tip. (a) Spectra taken at the position of the nanotube with tip (“tip down”, dashed line) and without tip (“Tip up”, solid line). RBM, radial breathing mode. (b) Near-field Raman image (raw data) of single-walled carbon nanotubes on glass, acquired by detecting the intensity of the Raman G band marked in (a) on laser excitation at 785 nm [115]. The cross section shown in the inset features a width of about 15 nm. (Data courtesy of G. Cancado, The Institute of Optics, University of Rochester.)

The sharpest images observed so far for glass substrates feature an optical resolution of about 10 nm, limited by the tip diameter [119]. In general, the measured optical width is smaller than the topographic width by about a factor of 1.3 [25, 119]. While the topographic image of nanometer-sized objects will reproduce the tip shape, the 4th-order dependence of the Raman signal on the field enhancement will render steeper traces (Eq. (47.1)), [117]). Nanoscale Raman spectroscopy probing the structural properties along single carbon nanotubes has been presented in several publications [120–122], clearly demonstrating the enormous capabilities of TENOM.

Corresponding to the time-tagging approach used for fluorescence imaging as described in Section 47.6, confocal background suppression can be achieved in TERS by correlating the detection event with the tapping-mode oscillation [45]. Additional amplification is achieved in tip-enhanced coherent anti-Stokes Raman scattering (TE-CARS) as demonstrated in [123] for DNA networks. High spatial image contrast can also be achieved using other local tip-induced effects not relying on enhanced optical fields. Pressure-induced spectral shifts of Raman bands have been utilized in [124]. In [125], chemical imaging of DNA bases is discussed on the basis of local bond formation with Ag atoms at the tip.

Several publications demonstrate that single-molecule sensitivity can be achieved in tip-enhanced Raman measurements in the case of single dye molecules on metal substrates, providing both additional field and electronic resonance enhancement [44, 126–131]. For extremely high field strength, photochemical modifications of the molecules need to be considered and distinguished in the spectral data [85, 132]. In general, signal fluctuations can also result from temporal fluctuation of the enhancement efficiency caused by physical/chemical changes of the adsorption sites and physical instabilities of the TERS tip during the experiment. Signal losses have also been attributed to tip-induced sample heating, leading to weaker field enhancement by reducing the surface roughness as well as surface diffusion of adsorbates [133].

47.7.2
Chemical Analysis of Surfaces

The chemical analysis of molecular species on surfaces is one of the main driving forces for the development of TERS, holding huge promise for applications in different areas such as catalysis. An example of near-field imaging with chemical contrast is shown in Figure 47.8. A thin layer of benzotriazole (BTA) molecules, a species that does not provide additional resonance enhancement at the laser excitation energy used in the experiment, is imaged on a smooth gold film by a gold tip in the focus of a parabolic mirror objective. Here, the optical signal results from a superposition of Raman scattering from BTA and PL from gold. As described in the section on the fundamentals of field enhancement (Section 47.3), additional signal amplification results from nanoscale protrusions within the metal film, leading to the very bright and highly localized features in the optical image (Figure 47.8a).

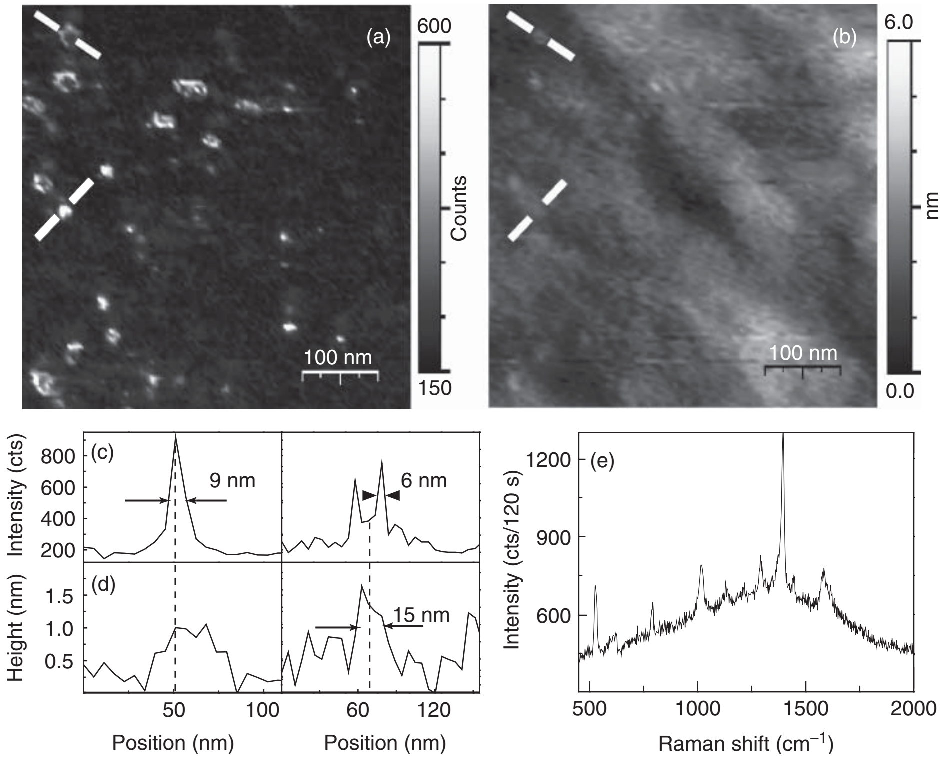

Figure 47.8 (a) Near-field optical image of a smooth Au film covered with a layer of benzotriazole molecules (BTA), which shows the Raman signal of BTA on top of the photoluminescence signal of Au. Simultaneously recorded (b) topography revealing only subnanometer height variation. Strongest near-field enhancement is observed for nanoscale protrusions. (c,d) Intensity height profiles over two small gold islands marked with dashed lines. (e) Raman spectrum detected at one of the bright features in (a). (Reprinted from Ref. [51]. Copyright 2008, with permission from Wiley-VCH Verlag.)

In analogy to TEF imaging (Section 47.6) the detected TERS signal will reflect the mutual orientation of the Raman scattering tensor and the enhanced fields. More specifically, the relative amplitudes of certain Raman lines can be utilized to extract orientational information and to monitor orientational mobility. In the case of chemical binding of the scatterer to the surface, additional Raman lines, line splitting, or shifts that can help to explore the details of the surface chemistry can occur.

47.7.3
Biopolymers and Biosurfaces

DNA bases feature characteristic Raman signatures, and direct optical sequencing of DNA on substrates using TERS is a long-standing dream stimulating the development of the technique. Recent experiments on single RNA strands and picomole quantities of DNA bases indicate that this goal could come within reach [127, 134]. In the past years, several studies using TERS on biological samples were Presented, including ommatidial lens surfaces [135], adenine nanocrystals [136], cytochrome c [137], bacteria [138], and hemoglobin crystals [139], demonstrating the broad applicability of the technique.

47.7.4
Stress Imaging in Semiconductors

As the length scales in semiconductor devices continuously shrink, nanoscale imaging of dedicated stress, for example, in transistor structures is of enormous technological relevance regarding further progress in stress engineering [6, 140, 141]. Stress in silicon causes a spectral shift of the Si–Si Raman peak of about 4 cm^{-1} for 1 GPa of biaxial stress. For realistic (3D) stress states in actual device structures, a shift of about 1 cm^{-1} can be expected. The main challenge for nanoscale Raman measurements results from the far-field to near-field sample volume ratio, making the resulting surface signal variations extremely difficult to extract from the strong confocal background. Moreover, sample heating upon laser excitation also leads to significant Raman shifts in the order of 50 $\mathrm{K/cm}^{-1}$, making the identification of purely stress-induced features difficult [142, 143]. Because of the large reflectivity of silicon, artifacts, in particular for periodic and layered structures, could result [140]. Different schemes based on polarization filtering have been developed for contrast enhancement and background suppression [6, 144, 145], and TERS is very likely to become a useful tool for the investigation of semiconductor surfaces.

47.7.5
Nanoscale Optoelectronic Probing

In the previous examples, tip-enhanced near fields have been used to locally increase the optical response of nano-objects such as Raman scattering and fluorescence. The scheme of tip enhancement or antenna enhancement is, in fact, more general as described in [26] and can, in principle, be used also for probing other sample properties such as local photovoltaic response and electroluminescence efficiency [146]. In [147], antenna-enhanced photocurrent microscopy has been used for the first time for the detection of optical and photocurrent signals with nanoscale spatial resolution and improved detection sensitivity. The enhanced photocurrent signal was shown to result from locally increased absorption by comparing it to the simultaneously obtained Raman signal. The technique was then used to study the direction and decay length of the band bending at the electrical contacts of metallic SWNT devices and to probe local variations in the electronic structure along a single SWNT that cannot be detected by confocal microscopy. These results further underline the wide applicability of the optical antenna concept in nanophotonics, merging the fields of plasmonics and photovoltaics.

47.8
Summary

The results presented in this chapter clearly demonstrate that TENOM has developed into a powerful and versatile tool. With this technique, the highest spatial resolution optical measurements of surfaces have been achieved up to date combined with enormous signal enhancement. In addition, TENOM provides detailed structural information based on the observation of Raman scattering with ultrahigh detection sensitivity. A brief checklist for the applicability of TENOM to the characterization of a particular sample comprises the following points:

1) the surface can be characterized by AFM or STM, providing the basis for tip–sample distance control and the required proximity;
2) the optically active elements (e.g., Raman scatterers, fluorescent molecules) are close to the surface;
3) the sample renders a stable confocal microscopy signal.

Because of the far-field background and the unfavourable near-field to far-field volume ratio, TENOM works particularly well for 0D and 1D structures such as point dipoles or wires. The observation of bulk materials with small spectral contrast, however, remains challenging. Active research currently addresses this issue, and significant improvements also regarding signal enhancement and spatial resolution, eventually reaching a single nanometer, can be expected within the next years.

Compared to far-field techniques, TENOM is likely to retain slightly higher spatial resolution being limited essentially by the tip-apex diameter. For fluorescence imaging of high-quantum yield emitters, far-field techniques however provide much faster acquisition times than scanning-probe-based TENOM at 20 nm resolution. In fact, stimulated emission depletion (STED) microscopy already permits video-rate fluorescence imaging [13].

Because the signal in TENOM results from electromagnetic near-field interactions between a metallic probe and the sample, the detected optical response can differ essentially from the far-field response. In order to exploit this fact for sample characterization and to quantify the near-field optical contrast, tip-induced signal modifications need to be modeled and understood in detail for molecular point dipoles and also for extended crystal-type structures.

To develop into a standard tool and for the broad applicability of TENOM, the controlled, reproducible, and ideally parallel fabrication of tips with a high field enhancement factor needs to be achieved. This will be particularly challenging in the case of background-minimizing probe schemes such as TOA. Compact designs integrating optical microscopy and AFM/STM exist and can be optimized further to yield even more user-friendly microscope systems. Besides providing a tool for unprecedented sample analysis, TENOM is certainly a fascinating research field both with respect to novel physical phenomena and our understanding of near-field optical interactions.

References

1. Pohl, D.W., Denk, W., and Lanz, M. (1984) Optical stethoscopy: image recording with resolution λ/20. *Appl. Phys. Lett.*, **44**, 651–653.
2. Lewis, A., Isaacson, M., Harootunian, A., and Muray, A. (1984) Development of a 500 Å resolution light microscope. *Ultramicroscopy*, **13**, 227–231.
3. Pohl, D.W. (2004) Optics at the nanometre scale. *Philos. Trans. R. Soc. London, Ser. A*, **362**, 701–717.
4. Novotny, L. (2007) The history of near-field optics in *Progress in Optics*, Vol. 50 (ed. E. Wolf), Elsevier, Amsterdam, The Netherlands, pp. 137–184.
5. Novotny, L., and Hecht, B. (2006) *Principles of Nano-optics*, Cambridge University Press, Cambridge.
6. Kawata, S. and Shalaev, V. M. (2007) *Tip Enhancement*, Advances in Nano-Optics and Nano-Photonics, Elsevier, Amsterdam.
7. Hartschuh, A., Beversluis, M.R., Bouhelier, A., and Novotny, L. (2004) Tip-enhanced optical spectroscopy. *Philos. Trans. R. Soc. London, Ser. A*, **362**, 807–819.
8. Bouhelier, A. (2006) Field-enhanced scanning near-field optical microscopy. *Microsc. Res. Tech.*, **69**, 563–579.
9. Hartschuh, A. (2008) Tip-enhanced near-field optical microscopy. *Angew. Chem. Int. Ed.*, **47**, 8178–8198.
10. Pettinger, B., Schambach, P., Villagómez, C.J., and Scott, N. (2012) Tip-enhanced Raman spectroscopy: near-fields acting on a few molecules. *Annu. Rev. Phys. Chem.*, **63**, 379–99.
11. Abbe, E. (1873) Beirträge zur Theorie des Mikroskops und der mikroskopischen Wahrnehmung. *Archiv. f. Mikroskop. Anat.*, **9**, 413.
12. Rayleigh, L. (1879) Investigations in optics, with special reference to the spectroscope. *Philos. Mag.*, **8**, 261–274.
13. Hell, S. (2007) Far-field optical nanoscopy. *Science*, **316**, 1153–1158.
14. Wessel, J. (1985) Surface-enhanced optical microscopy. *J. Opt. Soc. Am. B*, **2**, 1538–1541.
15. Knoll, B. and Keilmann, F. (1999) Near-field probing of vibrational absorption for chemical microscopy. *Nature*, **399**, 134–137.
16. Hillenbrand, R., Taubnerm, T., and Keilmann, F. (2002) Phonon-enhanced light matter interaction at the nanometre scale. *Nature*, **418**, 159–27.
17. Keilmann, F. and Hillenbrand, R. (2004) Near-field microscopy by elastic light scattering from a tip. *Philos. Trans. R. Soc. London, Ser. A*, **362**, 787–805.
18. Zayats, A. and Sandoghdar, V. (2000) Apertureless scanning near-field second-harmonic microscopy. *Opt. Commun.*, **178**, 245–249.
19. Zayats, A.V. and Smolyaninov, I.I. (2004) Near-field second-harmonic generation. *Philos. Trans. R. Soc. London, Ser. A*, **362**, 843–860.
20. Bouhelier, A., Beversluis, M., Hartschuh, A., and Novotny, L. (2003) Near-field second-harmonic generation induced by local field enhancement. *Phys. Rev. Lett.*, **90**, 013903.
21. Danckwerts, M. and Novotny, L. (2007) Optical frequency mixing at coupled gold nanoparticles. *Phys. Rev. Lett.*, **98**, 026104.
22. Sánchez, E.J., Novotny, L., and Xie, X.S. (1999) Near-field fluorescence microscopy based on two-photon excitation with metal tips. *Phys. Rev. Lett.*, **82**, 4014–4017.
23. Stöckle, S.M., Suh, Y.D., Deckert, V., and Zenobi, R. (2000) Nanoscale chemical analysis by tip-enhanced raman spectroscopy. *Chem. Phys. Lett.*, **318**, 131–136.
24. Hayazawa, N., Inouye, Y., Sekkat, Z., and Kawata, S. (2001) Near-field raman scattering enhanced by a metallized tip. *Chem. Phys. Lett.*, **335**, 369–374.

25. Hartschuh, A., Sánchez, E.J., Xie, X.S., and Novotny, L. (2003) High-resolution near-field raman microscopy of single-walled carbon nanotubes. *Phys. Rev. Lett.*, **90**, 095503.

26. Bharadwaj, P., Deutsch, B., and Novotny, L. (2009) Optical antennas. *Adv. Opt. Photon.*, **1**, 438–483.

27. Novotny, L., Bian, R.X., and Xie, X.S. (1997) Theory of nanometric optical tweezers. *Phys. Rev. Lett.*, **79**, 645–648.

28. Kappeler, R., Erni, D., Xudong, C., and Novotny, L. (2007) Field computations of optical antennas. *J. Comput. Theor. Nanosci.*, **4**, 686–691.

29. Neascu, C.C., Steudle, G.A., and Raschke, M.B. (2005) Plasmonic light scattering from nanoscopic metal tips. *Appl. Phys. B*, **80**, 295–300.

30. Novotny, L. and Stranick, S. (2006) Near-field optical microscopy and spectroscopy with pointed probes. *Annu. Rev. Phys. Chem.*, **57**, 303–31.

31. Novotny, L. (2007) Effective wavelength scaling for optical antennas. *Phys. Rev. Lett.*, **98**, 266802.

32. Notingher, I. and Elfick, A. (2005) Effect of sample and substrate electric properties on the electric field enhancement at the apex of SPM nanotips. *J. Phys. Chem. B*, **109**, 15699–15706.

33. Martin, Y.C., Hamann, H.F., and Wickramasinghe, H.K. (2001) Strength of the electric field in apertureless near-field optical microscopy. *J. Appl. Phys.*, **89**, 5774–5778.

34. Krug, J.T.I., Sánchez, E.J., and Xie, X.S. (2002) Design of near-field probes with optimal field enhancement by finite difference time domain electromagnetic simulation. *J. Chem. Phys.*, **116**, 10895–10901.

35. Mühlschlegel, P., Eisler, H.-J., Hecht, B., and Pohl, D.W. (2005) Resonant optical antennas. *Science*, **308**, 1607–1609.

36. Grosges, T., Vial, A., and Barchiesi, D. (2005) Models of near-field spectroscopic studies: comparison between Finite-Element and Finite-Difference methods. *Opt. Express*, **13**, 8483–8497.

37. Baker, G.A. and Moore, D.S. (2005) Progress in plasmonic engineering of surface-enhanced Raman-scattering substrates toward ultra-trace analysis. *Anal. Bioanal. Chem.*, **382**, 1751–1770.

38. Bakker, R.M., Yuan, H.-K., Liu, Z., Drachev, V.P., Kildishev, A.V., Shalaev, V.M., Pedersen, R.H., Gresillon, S., and Boltasseva, A. (2008) Enhanced localized fluorescence in plasmonic nanoantennae. *Appl. Phys. Lett.*, **92**, 043101–043103.

39. Olk, P., Renger, J., Härtling, T., Wenzel, M.T., and Eng, L.M. (2007) Two particle enhanced nano Raman microscopy and spectroscopy. *Nano Lett.*, **7**, 1736–1740.

40. Xu, H., Bjerneld, E.J., Käll, M., and Börjesson, L. (1999) Spectroscopy of single hemoglobin molecules by surface enhanced Raman scattering. *Phys. Rev. Lett.*, **83**, 4357–4360.

41. Muskens, O.L., Giannini, V., Sánchez-Gil, J.A., and Rivas, J.G. (2007) Strong enhancement of the radiative decay rate of emitters by single plasmonic nanoantennas. *Nano Lett.*, **7**, 2871–2875.

42. Rogobete, L., Kaminski, F., Agio, M., and Sandoghdar, V. (2007) Design of plasmonic nanoantennae for enhancing spontaneous emission. *Opt. Lett.*, **32**, 1623–1625.

43. Alú, A. and Engheta, N. (2008) Tuning the scattering response of optical nanoantennas with nanocircuit loads. *Nat. Photon.*, **2**, 307–310.

44. Neacsu, C.C., Dreyer, J., Behr, N., and Raschke, M.B. (2006) Scanning-probe Raman spectroscopy with single-molecule sensitivity. *Phys. Rev. B*, **73**, 193406.

45. Yano, T., Ichimura, T., Taguchi, A., Hayazawa, N., Verma, P., Inouye, Y., and Kawata, S. (2007) Confinement of enhanced field investigated by tip-sample gap regulation in tapping-mode tip-enhanced Raman microscopy. *Appl. Phys. Lett.*, **91**, 121101.

46. Hayazawa, N., Ishitobi, H., Taguchi, A., Tarun, A., Ikeda, K., and Kawata, S. (2007) Focused excitation of surface plasmon polaritons based on gap-mode in tip-enhanced spectroscopy. *Jpn. J. Appl. Phys.*, **46**, 7995–7999.

47. Anderson, N., Anger, P., Hartschuh, A., and Novotny, L. (2006) Subsurface Raman imaging with nanoscale resolution. *Nano Lett.*, **6**, 744–749.

48. Kalkbrenner, T., Hakanson, U., Schädle, A., Burger, S., Henkel, C., and Sandoghdar, V. (2005) Optical microscopy via spectral modifications of a nanoantenna. *Phys. Rev. Lett.*, **95**, 200801.

49. Pettinger, B., Domke, K.F., Zhang, D., Schuster, R., and Ertl, G. (2007) Direct monitoring of plasmon resonances in a tip-surface gap of varying width. *Phys. Rev. B*, **76**, 113409.

50. Yeo, B.S., Schmid, T., Zhang, W., and Zenobi, R. (2007) Towards rapid nanoscale chemical analysis using tip-enhanced Raman spectroscopy with Ag-coated dielectric tips. *Anal. Bioanal. Chem.*, **387**, 2655–2662.

51. Sackrow, M., Stanciu, C., Lieb, M.A., and Meixner, A.J. (2008) Imaging nanometre-sized hot spots on smooth Au films with high-resolution tip-enhanced luminescence and Raman near-field optical microscopy. *Chem. Phys. Chem.*, **9**, 316–320.

52. Bek, A., Jansen, R., Ringler, M., Mayilo, S., Klar, T.A., and Feldmann, J. (2008) Fluorescence enhancement in hot spots of AFM-designed gold nanoparticle sandwiches. *Nano Lett.*, **8**, 485–490.

53. Zhang, W., Cui, X., Yeo, B.S., Schmid, T., Hafner, C., and Zenobi, R. (2007) Nanoscale roughness on metal surfaces an increase tip-enhanced Raman scattering by an order of magnitude. *Nano Lett.*, **7**, 1401–1405.

54. Hecht, B., Bielefeldt, H., Inouye, Y., Pohl, D.W., and Novotny, L. (1997) Facts and artifacts in near-field optical microscopy. *J. Appl. Phys.*, **81**, 2492–2498.

55. Bozhevolnyi, S.I. (1997) Topographical artifacts and optical resolution in near-field optical microscopy. *J. Opt. Soc. Am. B*, **14**, 2254–2259.

56. Stockman, M.I., Faleev, S.V., and Bergman, D.J. (2002) Coherent control of femtosecond energy localization in nanosystems. *Phys. Rev. Lett.*, **88**, 067402.

57. Brixner, T., Garcia de Abajo, F.J., Schneider, J., and Pfeiffer, W. (2005) Nanoscopic Ultrafast Space-Time-Resolved Spectroscopy. *Phys. Rev. Lett.*, **95**, 03901–03904.

58. Stockman, M.I., Kling, M.F., Kleineberg, U., and Krausz, F. (2007) Attosecond nanoplasmonic-field microscope. *Nat. Photon.*, **1**, 539–544.

59. Aeschlimann, M., Bauer, M., Bayer, D., Brixner, T., Garcia de Abajo, F.J., Pfeiffer, W., Rohmer, M., Spindler, C., and Steeb, F. (2007) Adaptive subwavelength control of nano-optical fields. *Nature*, **466**, 301–304.

60. Purcell, E.M. (1946) Spontaneous emission probabilities at radio frequencies. *Phys. Rev.*, **69**, 681.

61. Thomas, M., Carminati, R., Arias-Gonzalez, J.R., and Greffet, J.-J. (2004) Single-molecule spontaneous emission close to absorbing nanostructures. *Appl. Phys. Lett.*, **85**, 3863–3865.

62. Xu, H., Aizpurua, J., Käll, M., and Apell, P. (2000) Electromagnetic contributions to single-molecule sensitivity in surface-enhanced raman scattering. *Phys. Rev. E*, **62**, 4318–4323.

63. Hartschuh, A., Qian, H., Meixner, A.J., Anderson, N., and Novotny, L. (2005) Nanoscale optical imaging of excitons in single-walled carbon nanotubes. *Nano Lett.*, **5**, 2310–2313.

64. Aslan, K., Gryczynski, I., Malicka, J., Matveea, E., Lakowicz, J.R., and Geddes, C.D. (2005) Metal-enhanced fluorescence: an emerging tool in biotechnology. *Anal. Biotechnol.*, **16**, 55–62.

65. Chance, R.R., Prock, A., and Silbey, R. (1974) Lifetime of an emitting molecule near a partially reflecting surface. *J. Chem. Phys.*, **60**, 2744–2748.

66. Barnes, W.L. (1998) Fluorescence near interfaces: the role of photonic mode density. *J. Mod. Opt.*, **45**, 661–699.

67. Bek, A., Jansen, R., Ringler, M., Mayilo, S., Klar, T.A., and Feldmann, J. (2005) Gold nanoparticles quench fluorescence by phase induced radiative rate suppression. *Nano Lett.*, **5**, 585–589.

68. Carminati, R., Greffet, J.J., Henkel, C., and Vigoureux, J.M. (2006) Radiative and non-radiative decay of a single molecule close to a metallic nanoparticle. *Opt. Commun.*, **261**, 368–375.

69. Issa, N.A., and Guckenberger, R. (2007) Fluorescence near metal tips: the roles of energy transfer and surface plasmon polaritons. *Opt. Express*, **15**, 12131–12144.

70. Baffou, G., Girard, C., Dujardin, E., Colas des Francs, G., and Martin, O.J.F. (2008) Molecular quenching and relaxation in a plasmonic tunable system. *Phys. Rev. B*, **77**, 121101-R–121101-4.

71. Farahani, J.N., Pohl, D.W., Eisler, H.-J., and Hecht, B. (2005) Single quantum dot coupled to a scanning optical antenna: a tunable superemitter. *Phys. Rev. Lett.*, **95**, 017402–017405.

72. Anger, P., Bharadwaj, P., and Novotny, L. (2006) Enhancement and quenching of single molecule fluorescence. *Phys. Rev. Lett.*, **96**, 113002–1130-4.

73. Kühn, S., Hakanson, U., Rogobete, L., and Sandoghdar, V. (2006) Enhancement of single molecule fluorescence using a gold nanoparticle as an optical nano-antenna. *Phys. Rev. Lett.*, **97**, 017402–017405.

74. Bharadwaj, P., Anger, P., and Novotny, L. (2007) Nanoplasmonic enhancement of single molecule fluorescence. *Nanotechnology*, **18**, 044017–044022.

75. Eckel, R., Walhorn, V., Pelargus, C., Martini, J., Enderlein, J., Nann, T., Anselmetti, D., and Ros, R. (2007) Fluorescence-emission control of single CdSe nanocrystals using gold-modified AFM tips. *Small*, **3**, 44–49.

76. Taminiau, T.H., Stefani, F.D., Segerink, F.B., and van Hulst, N.F. (2008) Optical antennas direct single-molecule emission. *Nat. Photon.*, **2**, 234–237.

77. Böhmler, M., Hartmann, N., Georgi, C., Hennrich, F., Hersam, M.C., and Hartschuh, A. (2010) Enhancing and Redirecting Carbon Nanotube Photoluminescence by an Optical Antenna. *Opt. Express*, **18**, 16443–16451.

78. Stavola, M., Dexter, D.L., and Knox, R.S. (1985) Electron-hole pair excitation in semiconductors via energy transfer from an external sensitizer. *Phys. Rev. B*, **31**, 2277–2289.

79. Azoulay, J., Débarre, A., Richard, A., and Tchénio, P. (2000) Quenching and enhancement of single-molecule fluorescence under metallic and dielectric tips. *Europhys. Lett.*, **51**, 374–380.

80. Zurita, J.R. and Novotny, L. (2002) Multipolar interband absorption in a semiconductor quantum dot. I. Electric quadrupole enhancement. *J. Opt. Sco. Am. B*, **19**, 1355–1362.

81. Hohenester, U., Goldoni, G., and Molinari, E. (2004) Optical near-field mapping of excitons and biexcitons in naturally occurring semiconductor quantum dots. *Appl. Phys. Lett.*, **84**, 3963–3965.

82. Hohenester, U., Goldoni, G., and Molinari, E. (2007) Dark-state luminescence of macroatoms at the near-field. *Phys. Rev. Lett.*, **95**, 216802.

83. Ayars, E.J., Hallen, H.D., and Jahncke, C.L. (2000) Electric field gradient effects in raman spectroscopy. *Phys. Rev. Lett.*, **85**, 4180–4183.

84. Karrai, K. and Grober, R.D. (1995) Piezoelectric tip-sample distance control for near field optical microscopes. *Appl. Phys. Lett.*, **66**, 1842–1844.

85. Pettinger, B., Ren, B., Picardi, G., Schuster, R., and Ertl, G. (2004) Nanoscale probing of adsorbed species by tip-enhanced Raman spectroscopy. *Phys. Rev. Lett.*, **92**, 096101.

86. Kalkbrenner, T., Ramstein, M., Mlynek, J., and Sandoghdar, V. (2001) A single gold particle as a probe for apertureless scanning near-field optical microscopy. *J. Microscopy*, **202**, 72–76.

87. Barsegova, I., Lewis, A., Khatchatouriants, A., Manevitch, A., Ignatov, A., Axelrod, N., and Sukenik, C. (2002) Controlled fabrication of silver or gold nanoparticle near-field optical atomic force probes: Enhancement of second-harmonic generation. *Appl. Phys. Lett.*, **81**, 3461–3463.

88. Vakarelski, I.U. and Higashitani, K. (2006) Single-nanoparticle-terminated tips for scanning probe microscopy. *Langmuir*, **22**, 2931–2934.

89. Schuck, P.J., Fromm, D.P., Sundaramurthy, A., Kino, G.S., and Moerner, W.E. (2005) Improving the mismatch between light and nanoscale objects with gold bowtie nanoantennas. *Phys. Rev. Lett.*, **94**, 017402.

90. Farahani, J.N., Eisler, H.-J., Pohl, D.W., Pavius, M., Flückiger, P., Gasser, B., and Hecht, P. (2007) Bow-tie optical antenna probes for single-emitter scanning near-field optical microscopy. *Nanotechnology*, **18**, 125506.

91. Novotny, L., Sánchez, E.J., and Xie, X.S. (1998) Near-field optical imaging using metal tips by higher-order hermite-gaussian beams. *Ultramicroscopy*, **71**, 21–29.

92. Quabis, S., Dorn, R., Glöckl, O., Eberler, M., and Leuchs, G. (2000) Focusing light to a tighter spot. *Opt. Commun.*, **179**, 1–7.

93. Lieb, A., and Meixner, A.J. (2001) A high numerical aperture parabolic mirror as imaging device for confocal microscopy. *Opt. Express*, **8**, 458–474.

94. Steidtner, J., and Pettinger, B. (2007) High-resolution microscope for tip-enhanced optical processes in ultrahigh vacuum. *Rev. Sci. Instrum.*, **78**, 103104.

95. Zhang, D., Wang, X., Braun, K., Egelhaaf, H.-J., Fleischer, M., Hennemann, L., Hintz, H., Stanciu, C., Brabec, C.J., Kern, D.P., and Meixner, A.J. (2009) Parabolic mirror-assisted tip-enhanced spectroscopic imaging for non-transparent materials. *J. Raman Spectrosc.*, **40** (10), 1371–1376.

96. Ma, Z., Gerton, J.M., Wade, L.A., and Quake, S.R. (2006) Fluorescence near-field microscopy of DNA at sub-10 nm resolution. *Phys. Rev. Lett.*, **97**, 260801.

97. Yoskovitz, E., Oron, D., Shweky, I., and Banin, U. (2008) Apertureless near-field distance-dependent lifetime imaging and spectroscopy of semiconductor nanocrystals. *J. Phys. Chem. C*, **112**, 16306–16311.

98. Frey, H.G., Keilmann, F., Kriele, A., and Guckenberger, R. (2002) Enhancing the resolution of scanning near-field optical microscopy by a metal tip grown on an aperture probe. *Appl. Phys. Lett.*, **81**, 530–532.

99. Frey, H.G., Witt, S., Felderer, K., and Guckenberger, R. (2004) High-resolution imaging of single fluorescent molecules with the optical near-field of a metal tip. *Phys. Rev. Lett.*, **93**, 200801–200804.

100. Taminiau, T.H., Moerland, R.J., Segerink, F.B., Kuipers, L., and van Hulst, N.F. (2007) $\lambda/4$ Resonance of an optical monopole antenna probed by single molecule fluorescence. *Nano Lett.*, **7**, 28–33.

101. De Angelis, F., Das, G., Candeloro, P., Patrini, M., Galli, M., Bek, A., Maksymov, I., Liberale, C., Andreani, L.C., and Di Fabrizio, E. (2010) 3D adiabatic compression of surface plasmon polaritons for nano-mapping at 10 nm spatial resolution. *Nat. Nanotechnol.*, **5**, 67–72.

102. Ropers, C., Neacsu, C.C., Elsaesser, T., Albrecht, M., Raschke, M.B., and Lienau, C. (2007) Grating-coupling of surface plasmons onto metallic tips: a nanoconfined light source. *Nano Lett.*, **7**, 2784–2788.

103. Eckert, J.M., an Freyland, R., Gersen, H., Heinzelmann, H., Schürmann, G., Noell, W., Staufer, U., and de Rooij, N.F. (2000) Near-field fluorescence imaging with 32 nm resolution based on microfabricated cantilevered probes. *Appl. Phys. Lett.*, **77**, 3695–3697.

104. Bouhelier, A., Renger, J., Beversluis, M.R., and Novotny, L. (2003) Plasmon-coupled tip-enhanced near-field optical microscopy. *J. Microsc.*, **210**, 220–224.

105. Huang, F.M., Festy, F., and Richards, D. (2005) Tip-enhanced fluorescence imaging of quantum dots. *Appl. Phys. Lett.*, **87**, 183101.

106. Frey, H., Bolwien, C., Brandenburg, A., Ros, R., and Anselmetti, D. (2006) Optimized apertureless optical near-field probes with 15 nm optical resolution. *Nanotechnology*, **17**, 3105–3110.

107. Zhang, D., Heinemeyer, U., Stanciu, C., Sackrow, M., Braun, K., Hennemann, L.E., Wang, X., Scholz, R., Schreiber, F., and Meixner, A.J. (2010) Nanoscale spectroscopic imaging of organic semiconductor films by plasmon-polariton coupling. *Phys. Rev. Lett.*, **104**, 056601–056604.

108. Böhmler, M., Wang, Z., Myalitsin, A., Mews, A., and Hartschuh, A. (2011) Optical Imaging of CdSe Nanowires with Nanoscale Resolutio. *Angew. Chem. Int. Ed.*, **50**, 11536.

109. Seelig, J., Leslie, K., Renn, S., Kühn, A., Jacobsen, V., van de Corput, M., Wyman, C., and Sandoghdar, V. (2007) Nanoparticle-induced fluorescence lifetime modification as nanoscopic ruler: demonstration at the single molecule level. *Nano Lett.*, **7**, 685–689.

110. Kühn, S. and Sandoghdar, V. (2006) Modification of single molecule fluorescence by a scanning probe. *Appl. Phys. B*, **84**, 211–217.

111. Kramer, A., Trabesinger, W., Hecht, B., and Wild, U.P. (2002) Optical near-field enhancement at a metal tip probed by a single fluorophore. *Appl. Phys. Lett.*, **80**, 1652–1654.

112. Höppener, C. and Novotny, L. (2008) Antenna-based optical imaging of single Ca^{2+} transmembrane proteins in liquids. *Nano Lett.*, **8**, 642–646.

113. Qian, H., Georgi, C., Anderson, N., Green, A.A., Hersam, M.C., Novotny, L., and Hartschuh, A. (2008) Exciton energy transfer in pairs of single-walled carbon nanotubes. *Nano Lett.*, **8**, 1363–1367.

114. Qian, H., Araujo, P.T., Georgi, C., Gokus, T., Hartmann, N., Green, A.A., Jorio, A., Hersam, M.C., Novotny, L., and Hartschuh, A. (2008) Visualizing the local optical response of semiconducting carbon nanotubes to DNA-wrapping. *Nano Lett.*, **8**, 2706–2711.

115. Jorio, A., Dresselhaus, M.S., and Dresselhaus, G. (eds) (2008) *Carbon Nanotubes*, Topics in Applied Physics, Vol. 111, Springer, Berlin / Heidelberg.

116. Qian, H., Gokus, T., Anderson, N., Novotny, A.J., Meixner, L., and Hartschuh, A. (2006) High-resolution optical imaging of single-walled carbon nanotubes. *phys. Stat. Sol. B*, **13**, 3146–3150.

117. Böhmler, M. and Hartschuh, A. (2012) Tip-enhanced near-field optical microscopy of single quasi-1D nanostructures. *Chem. Phys. Chem.*, **13**, 927.

118. Hartschuh, A., Anderson, N., and Novotny, L. (2003) Near-field raman spectroscopy using a sharp metal tip. *J. Microsc.*, **210**, 234–240.

119. Anderson, N., Hartschuh, A., and Novotny, L. (2005) Nanoscale vibrational analysis of single-walled carbon nanotubes. *J. Am. Chem. Soc.*, **127**, 2533–2537.

120. Anderson, N., Hartschuh, A., and Novotny, L. (2007) Chirality changes in carbon nanotubes studied with near-field Raman spectroscopy. *Nano Lett.*, **7**, 577–582.

121. Maciel, I.O., Anderson, N., Pimenta, M.A., Hartschuh, A., Qian, H., Terrones, M., Terrones, H., Campos-Delgado, J., Rao, A.M., Novotny, L., and Jorio, A. (2008) Electron and phonon renormalization near charged defects in carbon nanotubes. *Nat. Mater.*, **7**, 878–883.

122. Georgi, C. and Hartschuh, A. (2010) Tip-enhanced Raman spectroscopic imaging of localized defects in carbon nanotubes. *Appl. Phys. Lett.*, **97**, 143117.

123. Ichimura, T., Hayazawa, N., Hashimoto, M., Inouye, Y., and Kawata, S. (2004) Tip-enhanced coherent anti-Stokes Raman scattering for vibrational nanoimaging. *Phys. Rev. Lett.*, **92**, 220801–220804.

124. Yano, T., Inouye, Y., and Kawata, S. (2006) Nanoscale uniaxial pressure effect of a carbon nanotube bundle on tip-enhanced near-field Raman spectra. *Nano Lett.*, **6**, 1269–1273.

125. Hayazawa, N., Watanabe, H., Saito, Y., and Kawata, S. (2006) Towards atomic site-selective sensitivity in tip-enhanced Raman spectroscopy. *J. Chem. Phys.*, **125**, 244706.

126. Zhang, W., Yeo, B.S., Schmid, T., and Zenobi, R. (2007) Single molecule tip-enhanced Raman spectroscopy with silver tips. *J. Phys. Chem. C*, **111**, 1733–1738.

127. Domke, K.F., Zhang, D., and Pettinger, B. (2007) Tip-enhanced Raman spectra of picomole quantities of DNA nucleobases at Au(111). *J. Am. Chem. Soc.*, **129**, 6708–6709.

128. Domke, K.F., Zhang, D., and Pettinger, B. (2006) Toward raman fingerprints of single dye molecules at atomically smooth au (111). *J. Am. Chem. Soc.*, **128**, 14721–14727.

129. Neacsu, C.C., Dreyer, J., Behr, N., and Raschke, M.B. (2007) Reply to “Comment on ’Scanning-probe Raman spectroscopy with single-molecule sensitivity’”. *Phys. Rev. B*, **75**, 236402.

130. Ward, D.R., Halas, N.J., Ciszek, J.W., Tour, J.M., Wu, Y., Nordlander, P., and Natelson, D. (2008) Simultaneous measurements of electronic conduction and Raman response in molecular junctions. *Nano Lett.*, **8**, 919–924.

131. Steidtner, J. and Pettinger, B. (2008) Tip-enhanced raman spectroscopy and microscopy on single dye molecules with 15 nm resolution. *Phys. Rev. Lett.*, **100**, 236101.

132. Domke, K.F., Zhang, D., and Pettinger, B. (2007) Enhanced Raman spectroscopy: Single molecules or carbon?. *J. Phys. Chem. C*, **111**, 8611–8616.

133. Zhang, W., Schmid, T., Yeo, B.S., and Zenobi, R. (2008) Near-Field heating, annealing, and signal loss in tip-enhanced Raman spectroscopy. *J. Phys. Chem. C*, **112**, 2104–2108.

134. Bailo, E. and Deckert, V. (2008) Tip-enhanced Raman spectroscopy of single RNA strands: towards a novel direct-sequencing method. *Angew. Chem. Int. Ed.*, **47**, 1658–1661.

135. Anderson, M.S. and Gaimari, S.D. (2003) Raman-atomic force microscopy of the ommatidial surfaces of Dipteran compound eyes. *J. Struct. Biol.*, **142**, 364–368.

136. Watanabe, H., Ishida, Y., Hayazawa, N., Inouye, Y., and Kawata, S. (2004) Tip-enhanced near-field Raman analysis of tip-pressurized adenine molecule. *Phys. Rev. B*, **69**, 155418–155-11.

137. Yeo, B.S., Mädler, S., Schmid, T., Zhang, W., and Zenobi, R. (2008) Tip-Enhanced Raman spectroscopy can see more: the case of cytochrome c. *J. Phys. Chem. C*, **112**, 4867–4873.

138. Neugebauer, U., Rösch, P., Schmitt, M., Popp, J., Julien, C., Rasmussen, A., Budich, C., and Deckert, V. (2006) On the way to nanometer-sized information of the bacterial surface by tip-enhanced Raman spectroscopy. *Chem. Phys. Chem.*, **7**, 1428–1430.

139. Wood, B.R., Asghari-Khiavi, M., Bailo, E., McNaughton, D., and Deckert, V. (2012) Detection of nano-oxidation sites on the surface of hemoglobin crystals using tip-enhanced raman scattering. *Nano Lett.*, **12** (3), 1555–1560.

140. Georgi, C., Hecker, M., and Zschech, E. (2007) Raman intensity enhancement in silicon-on-insulator substrates by laser deflection at atomic force microscopy tips and particles. *Appl. Phys. Lett.*, **90**, 171102.

141. Tarun, A., Hayazawa, N., Motohashi, M., and Kawata, S. (2007) Highly efficient tip-enhanced Raman spectroscopy and microscopy of strained silicon. *Rev. Sci. Instrum.*, **79**, 913706.

142. Hart, T.R., Aggarwal, R.L., and Lax, B. (1970) Temperature dependence of Raman scattering in silicon. *Phys. Rev. B*, **1**, 638–642.

143. Georgi, C., Hecker, M., and Zschech, E. (2007) Effects of laser-induced heating on Raman stress measurements of silicon and silicon-germanium structures. *J. Appl. Phys.*, **101**, 123104.

144. Ossikovski, R., Nguyen, Q., and Picardi, G. (2007) Simple model for the polarization effects in tip-enhanced Raman spectroscopy. *Phys. Rev. B*, **75**, 045412.

145. Motohashi, M., Hayazawa, N., Tarun, A., and Kawata, S. (2008) Depolarization effect in reflection-mode tip-enhanced Raman scattering for Raman active crystals. *J. Appl. Phys.*, **103**, 034309.

146. Burghard, M. and Mews, A. (2012) High-resolution photocurrent mapping of carbon nanostructures. *ACS Nano*, **6** (7), 5752–5756.

147. Rauhut, N., Engel, M., Steiner, M., Krupke, R., Avouris, P., and Hartschuh, A. (2012) Antenna-enhanced photocurrent microscopy on single-walled carbon nanotubes at 30 nm resolution. *ACS Nano*, **6** (7), 6416–6421.

48
Optical Waveguide Spectroscopy

James S. Wilkinson

Total internal reflection (TIR) elements are well-established components for the optical interrogation of chemical processes at surfaces, with attenuated total reflection (ATR) spectroscopy and total internal reflection fluorescence (TIRF) having a long pedigree and surface plasmon resonance (SPR) finding widespread use in biomolecular research, for example. Key attributes of these devices are that the optical fields are confined to a submicrometer region above the solid surface of the transducer and that the light is delivered to the surface without passing through the bulk of the sample. Optical waveguides take this TIR approach to its most sensitive conclusion by engineering the dimensions and refractive index profile of the waveguide to maximize the interaction of the incident light with the surface integrated optical waveguides to exploit the technological approaches of microelectronics and guided-wave optics to realize optical waveguides performing TIR functions at the surface of an optical chip, allowing miniaturization of sample volumes, integration of multiple optical functions, and robust ‘‘solid-state’’ interconnection. Owing to precise control of local optical velocity and intensity distribution, these waveguides provide strong and well-controlled evanescent interaction of light with chemical species at a surface in a very small sample volume, yielding benefits in terms of sensitivity, speed, or spatial localization. Integrated optical waveguides are able to probe a wide range of optical phenomena, and are compatible with microfluidic systems for sample delivery and with optical fiber for connection to instrumentation. In this chapter, the application of integrated optical waveguides to spectroscopy is described, including a brief introduction to waveguide optimization for spectroscopy, describing the performance of devices implemented to date, and drawing conclusions for the application of these devices in practical applications.

48.1
Introduction

The use of TIR elements for optical spectroscopy at surfaces was proposed and developed by Harrick [1] and Fahrenfort [2] and has since found widespread application. Absorption spectra are obtained from this technique, which is often

Handbook of Spectroscopy, Second Edition. Edited by Günter Gauglitz and David S. Moore.

referred to as *ATR spectroscopy* or *internal reflection spectroscopy* (*IRS*), by reflecting broadband light from the interface between a transparent internal reflection element (IRE) and the sample, resulting in absorption in the evanescent field that extends typically a submicrometer distance into the sample. ATR spectroscopy thus provides spectra for a thin layer (typically 100–500 nm) on the IRE surface, allowing collection of strong spectra from extremely small volumes and from thin films such as monomolecular layers adsorbed at surfaces. Further advantages include reduction of interference from (often scattering) bulk media, determination of absorption spectra of powdered samples without scattering, and external analysis of materials in a closed chamber. Many applications are specifically directed at studying surface layers, so that the IRE surface is part of the system under study, while others simply use the IRE to enhance sensitivity, reduce the effect of scattering, or provide a convenient measurement geometry. It should be recognized that the spectrum of the material at a surface is not necessarily the same as that of the bulk medium and, whether this is a desired effect that is to be observed or a spurious effect to be minimized, it must be taken into account. TIR absorption spectra depend on the extent of the evanescent field in the sample medium, and hence on incident angle; and this also results in the distortion of the spectrum compared with the spectrum of the bulk medium as the extent of the evanescent field is wavelength dependent. However, this dependence is usually readily predicted so that the undistorted spectrum can be determined. The first ATR experiments employed a single reflection, but it was soon realized that using multiple reflections (Figure 48.1) offered a great advantage in terms of the strength of the absorption spectra, or spectral contrast, so that more than 500 reflections are routinely used, by repeated TIR from the sample side and the parallel underside of the IRE as shown in Figure 48.1.

For absorption spectroscopy of thin films, the principal sensitivity advantage of the ATR configuration over transmission spectroscopy comes from these multiple reflections. Multiple IREs are in fact optical waveguides, albeit usually highly multimoded ones. The bouncing rays in an IRE can be described in terms of the superposition of the modes of the IRE, interfering along the length of the structure to produce the resultant reflecting rays. Once the IRE thickness becomes comparable to the wavelength of light, the modal description becomes the more convenient, and Harrick [3] indicates this in his description of a frustrated total

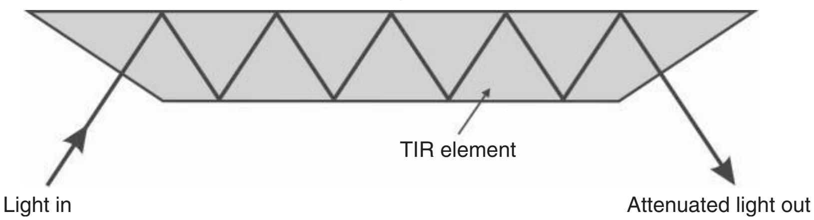

Figure 48.1 Multiple reflection TIR element.

reflection (FTR) optical cavity with enhanced sensitivity and presents a waveguide and prism coupler as an example of IRE geometry.

In 1971, Midwinter [4] presented a theoretical description of the use of optical waveguides for IRS. Noting the similarity between Harrick's FTR cavity and work at the Bell Laboratories on prism coupling into optical waveguides [5], Midwinter asked "if these waveguide techniques could be used with advantage in the examination of internal reflection spectra." Concentrating on designs for minimum distortion of the sample spectrum compared to conventional transmission spectroscopy, he proposed *in situ* use of miniature waveguide probes fabricated by microelectronic techniques, for chemical and biological processes. Polky and Harris [6] studied the theoretical optimization of waveguides for highest sensitivity and described absorption measurements on bulk dye, emphasizing the strong absorption obtained and the effect of adsorption of dye molecules at the surface, and pointing to future applications *in vivo*. The principal differences between these waveguide devices and multiple reflection IREs were that the waveguides would normally consist of a thin film on a solid substrate (Figure 48.2) and that the film would normally be much thinner than an IRE. In a conventional IRE, the number of reflections per unit length is inversely proportional to its thickness. While this ray model breaks down as the thickness becomes comparable to the wavelength, the trend continues so that thin-film waveguides can exhibit the ultimate sensitivity. Taken to its furthest extreme, very thin waveguides, which support only one mode (usually one in each polarization), can be designed to have the highest sensitivity, and also present advantages in stability owing to unique and well-defined surface intensity distribution. In 1974, Mitchell *et al.* [7] demonstrated the application of waveguide spectroscopy to bilirubin measurement in blood samples, emphasizing the minimization of the sample volume and the suppression of scattering and absorption from red blood cells that dominates in bulk transmission spectra, and the selective measurement of the blood plasma.

Optical waveguides for IRS are the natural extension of TIR elements, exhibiting all the same advantages plus ultimate sensitivity, extreme miniaturization, easy integration of multiple sensors and reference sensors, robust fabrication techniques, and the economies of mass-production techniques employed in microelectronics manufacturing. Against these advantages may be traded greater complexity in

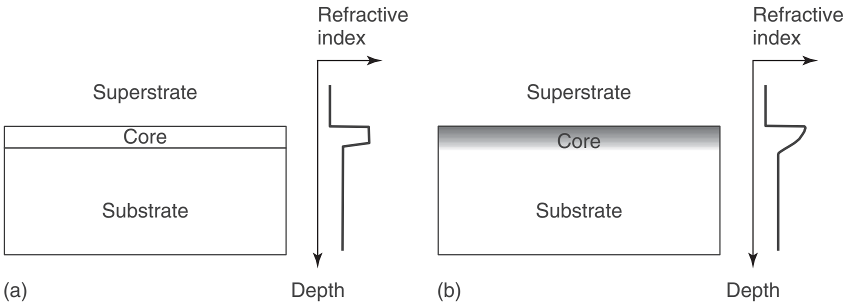

Figure 48.2 Planar waveguides: (a) slab waveguide and (b) graded-index waveguide.

use, particularly connection to instrumentation, and the expense of the fabrication equipment, but the all-pervasive nature of microelectronic devices demonstrates that the additional complexity of microminiaturized devices need be no barrier to successful commercialization.

This introduction has concentrated on the use of IREs for absorption spectroscopy and their natural evolution toward optical waveguide implementations. Since their invention, IREs have been used for a much wider range of broadly spectroscopic applications including TIRF, Raman spectroscopy and surface-enhanced Raman spectroscopy (SERS), SPR, and critical angle refractometry. In this chapter, optical waveguide implementations of these spectroscopic techniques will be discussed, concentrating on truly spectroscopic studies of the sample materials rather than on single-wavelength absorption, fluorescence, and refractive index measurements, despite their great importance in sensing applications, or on studies that interpret changes in waveguide mode velocity ''spectra'' to determine refractive index changes at a single wavelength.

48.2
Integrated Optical Waveguides

The principles of integrated optical waveguide design, fabrication, and operation are briefly reviewed to place the specific configurations and applications to be described in the remainder of this chapter in context and to define important parameters. Detailed descriptions of waveguide principles are given in many excellent textbooks, including those by Adams [8], Ghatak and Thyagarajan [9], Lee [10], and Okamoto [11]. The optimization of waveguides for absorption, index, and fluorescence sensing is well documented [12–15] and, while these studies are directed primarily at single-wavelength sensing, the principles and mathematical descriptions may be applied to broadband spectroscopy.

High-sensitivity waveguide spectroscopy usually requires structures that, for a given power in the waveguide, optimize either the intensity at the waveguide/analyte interface in the case of ultrathin-film spectroscopy or the power in the analyte medium in the case of bulk analyte spectroscopy, leading to significantly different designs. For thin-film spectroscopy, the discrimination between surface effects and bulk effects may need to be maximized, favoring waveguides with rapid evanescent decay into the sample medium [16]. A further important consideration is the efficiency with which power is coupled into the waveguide, which often results in a further trade-off in waveguide design. This may drive the choice of how light is coupled into the waveguide and full optimization requires analysis of the detected optical signal strength, the system noise sources, and the effect of stray light. These aspects, which are strongly dependent on the specific system configuration, are addressed in Section 48.8 on instrumentation. Here, it should simply be borne in mind that optimization of the waveguide element alone is not sufficient, and that the entire system, including drift and noise sources in the optical detection system, must be considered in order to arrive at the highest sensitivity, lowest limit of detection (LoD), or the most cost-effective solution.

The homogeneous planar or slab waveguide is the simplest integrated optical waveguide, consisting of a thin homogeneous film of dielectric material of refractive index n_{co} supported by a substrate of index n_s and overlaid with a superstrate or cladding of index n_{cl}, where $n_{co} > n_s$ and $n_{co} > n_{cl}$, as shown in Figure 48.2a. Most practical slab waveguides are asymmetric, so that $n_s \neq n_{cl}$, and are formed by a wide variety of film deposition techniques such as sputtering, evaporation, or chemical vapor deposition [10].

The graded-index planar waveguide, shown in Figure 48.2b, is similar to the slab waveguide except that one or both discrete dielectric boundaries are replaced by smooth variations in the refractive index profile. In terms of ray optics, TIR is no longer from a discrete boundary; rather, a ray propagating into the lower-index region is turned back into the high-index region by continuous refraction through the index gradient. Graded-index planar waveguides are usually formed by the diffusion of a dopant into a substrate material, for example, by deposition of a thin metallic or dielectric film onto the substrate followed by annealing, or by immersion in a molten source of dopant atoms. The dopant is chosen such that the refractive index of the substrate material increases with increasing dopant concentration.

The planar waveguides described confine light in one dimension and allow it to propagate freely in two dimensions, so that phenomena such as refraction, diffraction, and interference occur in the waveguide plane. In many cases, however, guidance of light in the plane is also required and this is achieved by confining light in two dimensions using channel waveguides. The simplest homogeneous channel waveguide consists of a core of index n_{co} surrounded in two dimensions by media of lower refractive index. It has a geometry similar to a step-index optical fiber except that the cross section of the core is often rectangular rather than circular and it is normally deposited on or buried in a flat substrate as shown in Figure 48.3a,d.

In a basic channel waveguide, propagation of guided modes is along the axis of the channel. However, the additional guidance in the plane of the substrate allows bends and tapers to be introduced into the waveguides and many optical circuit elements such as couplers and power splitters have been realized using the photolithographic techniques developed for the microelectronics industry [11]. Channel waveguides thus allow guidance of light to specific locations on the surface of an optical chip and integration of multiple branches, leading to, for example, the integrated equivalent of dual-beam spectrophotometry.

Homogeneous channel waveguides are usually formed by deposition of a homogeneous slab waveguide on a suitable low-index substrate (or buffer layer) followed by etching of the film to form channels using ion-beam milling, reactive-ion etching, chemical etching, or a combination of these. Outside the core region, the film may be etched fully down to the substrate, in which case a strip waveguide (Figure 48.3a) is formed; alternatively, the film may be only partially removed, in which case a rib waveguide (Figure 48.3b) is formed. Depending on the application, the strip or rib waveguide may then be overlaid with a suitable low-index cladding material as shown in Figure 48.3c. A cladding is used to isolate the waveguide

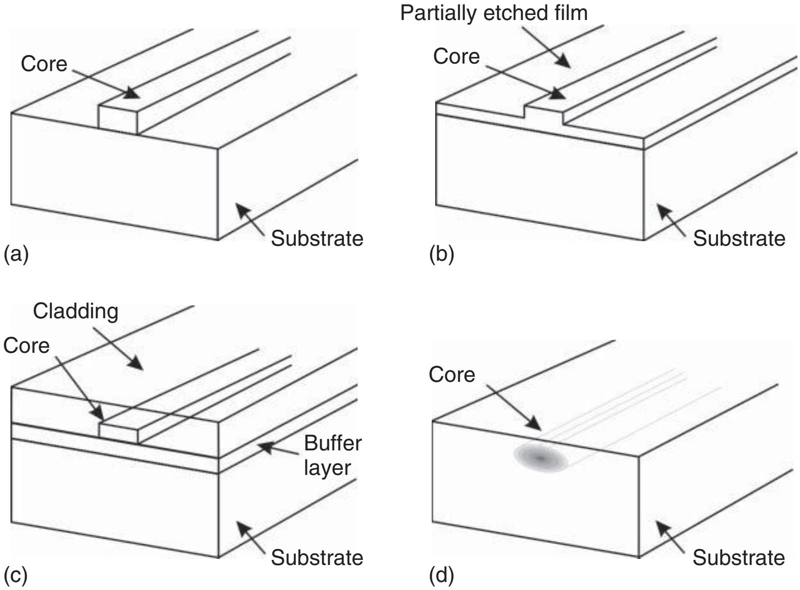

Figure 48.3 Channel waveguides: (a) unclad homogeneous strip waveguide, (b) unclad homogeneous rib waveguide, (c) clad homogeneous strip waveguide, and (d) buried graded-index waveguide.

mode from external influences and to make the mode more symmetrical for ease of coupling light in with an optical fiber. However, in evanescent spectroscopy, the cladding is omitted or reduced in thickness in the measurement region to allow strong evanescent interaction. Figure 48.3c also shows a buffer layer between the substrate and the core layer; this may be appropriate where the substrate does not have the refractive index or transparency required to optimize the waveguide for absorption or refractive index sensitivity. It also relaxes the constraints on the substrate itself, allowing independent optimization for reasons of cost, availability, mechanical properties, or the availability of other features in a convenient substrate material, such as in the case of microfluidic devices in silicon [17].

The graded-index channel waveguide is similar to the homogeneous channel waveguide except that some or all of the discrete dielectric boundaries are replaced by smooth variations in the refractive index profile. Graded-index channel waveguides are usually formed by diffusion from a strip of dielectric or metallic material deposited on a substrate, or by diffusion through a mask deposited on the substrate surface. Unless multistep diffusion processes are used, the discrete dielectric boundary at the substrate surface usually remains, while all other boundaries are graded. Multistep diffusion is usually used to produce a buried waveguide (Figure 48.3d) for the same reasons as homogeneous waveguides are clad. As this reduces the evanescent field at the surface, it is usually not used for applications in waveguide spectroscopy. However, either a cladding or a burial step may be convenient to isolate the waveguide from an analyte (or from a sample cell attached to the waveguide surface) outside the spectroscopic measurement region.

An intriguing special case is the ‘‘zero-mode’’ waveguide that exploits evanescent fields in nanoscale holes in metal films and has been applied to single-molecule studies at high concentrations [18, 19]. The hole is considered to be a metal-clad waveguide below cutoff in which light is confined laterally by the walls of the hole and along the length of the hole by the evanescent decay length (as no mode can propagate). Cutoff occurs for hole diameters $<0.586\ \lambda_m$, where λ_m is the wavelength in the medium filling the hole. In [18], holes of diameters including 43 and 66 nm were opened in an 89 nm thick aluminum film deposited on a fused silica substrate. Illumination through the substrate with light at a free-space wavelength of 488 nm results in an evanescent decay length of order 10–20 nm and thus a probed volume of 10^{-19} to 10^{-20} l, compared with order 10^{-13} l for conventional diffraction-limited optics. This allows measurements to be made on individual molecules at million-fold higher concentrations, allowing single-molecule studies at concentrations relevant to observing normal molecular behavior. These waveguide arrays have been applied to fluorescence correlation spectroscopy (FCS) of single-labeled molecules using a single excitation wavelength and counting fluorescent photons with time as the molecule diffuses into and out of the excitation volume. Applications including diffusion in lipid bilayers and live cells ‘‘exploring’’ zero-mode waveguide structures are described by Moran-Mirabal and Craighead [19]. The vast majority of truly spectroscopic studies using waveguides have applied conventional monomode or multimode dielectric waveguide structures, which will be addressed in the remainder of this chapter.

48.3

Optimization of Dielectric Optical Waveguides for Evanescent Spectroscopy

The key pieces of information required to design or analyze integrated optical waveguides for evanescent spectroscopy are the modal intensity profile at any cross section of the waveguide and the modal velocity v_m, which is most conveniently expressed through the modal effective index $N_m = c/v_m$, where c is the vacuum speed of light. Both the intensity distribution and the velocity are functions of wavelength, resulting in predictable distortion of spectra measured using waveguides. They are found by obtaining wave equations for electromagnetic radiation in the waveguide media and matching tangential components of electric and magnetic fields across the dielectric boundaries, yielding discrete modal solutions effectively corresponding to resonances across the core of the waveguide, as described in several textbooks [8–10]. Chapter 1 of [20] written by the pioneers of waveguide techniques for Raman spectroscopy, JF Rabolt and JD Swalen, provides a very good theoretical introduction to waveguide design and operation with a particular emphasis on surface studies.

Most practical waveguides require numerical techniques to determine their modal distributions and velocities, and there are several good commercial Computer

Aided Design (CAD) packages available to design such waveguides and devices and to convert the designs to photolithographic mask layouts. Here, we discuss only the basic considerations and interrelationships between quantities to aid understanding of waveguide optimization for evanescent spectroscopy. Often, the choice of waveguide *materials* is dominated by pragmatic considerations such as their chemical durability and wavelength transmission windows (polymers; glasses; and crystals, such as silicon, sapphire, and lithium niobate, among many others, may be used to create practical waveguides). The choice of waveguide *design* may sometimes be dominated by the need to couple light in easily, rather than for achieving the maximum possible sensitivity.

The homogeneous slab waveguide shown in Figure 48.2a is a conveniently simple structure with which to illustrate the basic behavior of optical waveguides. In the following discussion, it will be assumed that the refractive index of the substrate is higher than that of the superstrate, $n_s > n_{cl}$, which is usually the case, for example, when the superstrate is air ($n \approx 1.0$) or water ($n \approx 1.33$), and the substrate is, for example, glass ($n \approx 1.5$). The core index must be higher than the substrate index and the core thickness, a, must be great enough to guide at least one mode. For the slab waveguide, this requires that (with m set to zero to correspond to the fundamental mode):

$$a > \frac{\lambda}{2\pi\sqrt{n_{co}^2 - n_s^2}} \left[\tan^{-1}\left\{ \eta \sqrt{\frac{n_s^2 - n_{cl}^2}{n_{co}^2 - n_s^2}} \right\} + m\pi \right] \tag{48.1}$$

where $\eta = 1$ for the transverse electric (TE) polarization (electric field parallel to the dielectric interfaces) and $\eta = (n_{co}/n_{cl})^2$ for the transverse magnetic (TM) polarization (magnetic field parallel to the interfaces). Note that for a symmetrical slab waveguide, where $n_s = n_{cl}$, the cutoff thickness for the fundamental ($m = 0$) mode is zero. In practice, losses and mode size place a lower limit on the practical thickness of symmetrical slab waveguides. The waveguide becomes multimoded where the inequality in Eq. (48.1) is satisfied for $m = 1$; here, we will concentrate on monomode waveguides as these are most suitable for high-performance spectroscopic applications. For a homogeneous slab waveguide, the modes display sinusoidal or cosinusoidal field distributions across the core, with exponentially decaying fields into the superstrate and substrate, as shown for the TE_0 and TE_1 modes in Figure 48.4a. Matching these field solutions at the two boundaries results in discrete modes with well-defined field profiles and effective indices, N_m, which are wavelength dependent. The modal effective indices for a homogeneous slab waveguide with $n_s = 1.51$, $n_c = 1.52$, and $n_{cl} = 1.0$ are plotted against normalized core thickness in Figure 48.4b, where $t_{norm} = a/\lambda$ [21], for the first three TE and TM modes. This clearly shows cutoff, where the fundamental mode is no longer supported, below $t_{norm} \approx 1.25$. The effective index is equal to the substrate index at cutoff and increases toward the refractive index of the core as core thickness increases, as a greater proportion of the power travels in the core and the power in the evanescent fields diminishes for thicker waveguides. To emphasize the

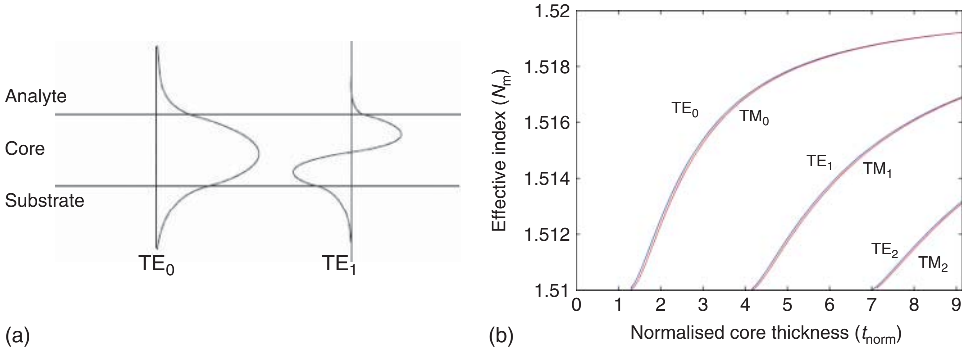

Figure 48.4 (a) Modal field distributions and (b) modal effective indices.

application of waveguides to spectroscopy, the superstrate will be referred to as the *analyte* in what follows.

Each mode travels with a phase velocity given by c/N_m where $n_{co} > N_m > n_s$, and the distance at which the field has decayed into the analyte by $1/e$ of its surface value or at which the intensity has fallen to $1/e^2$ of its surface value is given by

$$d_{cl} = \frac{\lambda}{2\pi\sqrt{N_m^2 - n_{cl}^2}} \tag{48.2}$$

Note that for the common situation of a glass waveguide in water, d_{cl} takes a value close to $\lambda/4$, so that the evanescent field probes a region about one-quarter of a wavelength beyond the dielectric interface. For a higher index waveguide, such as $LiNbO_3$ in water, d_{cl} is closer to $\lambda/10$, so that it is more surface specific. However, while the evanescent decay length in a given medium is dictated by the effective index of the mode, the proportion of modal power in the analyte and the surface intensity depend strongly on the refractive index contrast of the core/substrate interface. The decay distance in the substrate is given by the same expression as Eq. (48.2) with the subscripts "cl" replaced by "*s*." In most situations, this interface has a much weaker refractive index contrast so that the decay length is much longer than in the analyte. For example, a conventional glass or lithium niobate waveguide may have a decay length of several wavelengths in the substrate. This strong asymmetry leads to a rather small proportion of the modal power traveling in the analyte as shown in Figure 48.5, where the analyte fills the space corresponding to $x > 0$. Note from the inset how the surface intensity increases with decreasing core thickness, *over this range of thicknesses*.

Tiefenthaler and Lukosz [15] and Parriaux, Veldhuis *et al.* [12, 13] have reported comprehensively on waveguide optimization for evanescent sensing, which must be addressed distinctly for "bulk" analyte measurements where the analyte fills the evanescent field and "thin-film" measurements where the film to be measured is on the waveguide/analyte interface and is thin compared with the extent of the evanescent field. The *sensitivity* S is defined as the rate of change of the effective index of the mode with changes in the refractive index of the analyte which, for

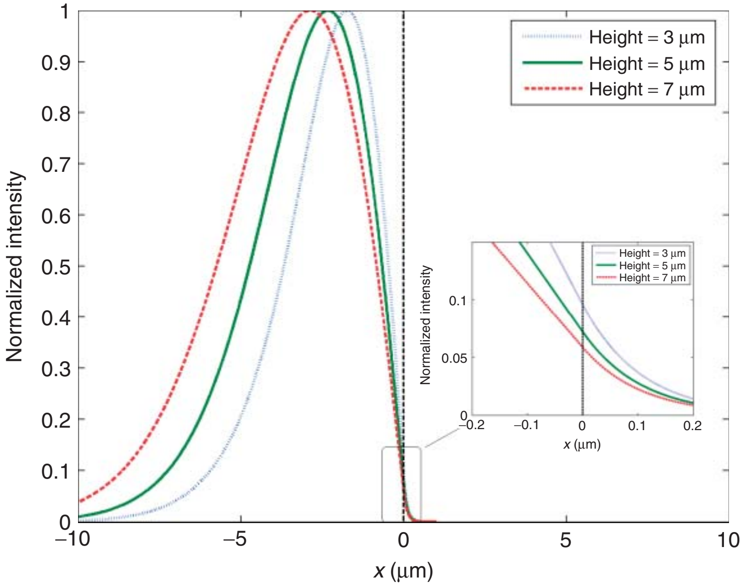

Figure 48.5 Intensity distribution across waveguide core for three core thicknesses. $\lambda = 750\,\text{nm}$, $n_{\text{cl}} = 1.0$, $n_{\text{co}} \approx 1.52$, $n_{\text{s}} = 1.51$.

a bulk analyte is $S = \delta N_{\text{m}}/\delta n_{\text{cl}}$. This applies to sensitivity to the refractive index including sensitivity to absorption, as absorption may be described in terms of the imaginary part of refractive index through the expression:

$$\alpha \cong \frac{2k_0}{2.3}\text{Im}\{n\}$$

where α is the absorption coefficient in the base 10 form of the Beer–Lambert law and k_0 is the free-space wavenumber $(2\pi/\lambda_0)$. It will be assumed that the imaginary part of the analyte index is small compared with the real part, as is usually the case.

48.3.1
Optimization for Bulk Analyte Spectroscopy

To the first order, optimizing the waveguide design for sensitivity to a bulk analyte comes down to maximizing the fraction of modal power carried in the analyte, so that, in general (i) the substrate index should be as low as possible to shift the waveguide mode into the analyte, leading ultimately to "reverse-symmetry" waveguides [22] where the analyte index is higher than the substrate index, and (ii) the waveguide core index should be as high as possible, assuming that its thickness can then be chosen to optimize the waveguide at the wavelength of operation. To clarify this last point, if the core thickness is kept constant, then the evanescent power will *reduce* with increasing core index. However, practical constraints such as available materials, fabrication tolerances, efficiency of coupling light into and out of the waveguides and waveguide losses usually limit the maximum practically useful core index.

An example showing the proportion of power traveling in the analyte against normalized core thickness, for the TE_0 mode in a homogeneous slab waveguide with $n_s = 1.51$, $n_c = 1.52$, and $n_{cl} = 1.33$ (corresponding to a typical glass waveguide in water) is given in Figure 48.6, where $t_{norm} = a/\lambda$ [21]. This clearly shows cutoff, where the fundamental mode is no longer supported, at $t_{norm} \approx 1.25$ and a maximum analyte power at $t_{norm} \approx 1.7$. In other words, *for this set of refractive indices*, the core thickness required for maximum sensitivity to the analyte is close to two free-space wavelengths. For core thicknesses below the optimum, for this asymmetrical waveguide, the modal power is increasingly carried in the substrate. In the case of sensing, which is usually carried out at a single wavelength, the optimization procedure is straightforward. However, in the case of spectroscopy over a wide range of wavelengths, it is clear that the fraction of evanescent power in the analyte can change dramatically with wavelength, distorting the spectra obtained. If this is an important design issue, then choosing a thicker waveguide, and one with a lower core index, will reduce this distortion, at the cost of absolute sensitivity, as pointed out by Midwinter [4] in his original paper. Furthermore, for broadband spectroscopy, the dispersion of all the materials including the analyte must be taken into account. For a more precise optimization for bulk analytes and applying to slab waveguides, the following expression should be used for the sensitivity [15]:

$$S = \frac{n_{cl}}{N_m}\frac{P_{cl}}{P_{tot}}\left\{2\left(\frac{N_m}{n_{cl}}\right)^2 - 1\right\}^q \tag{48.3}$$

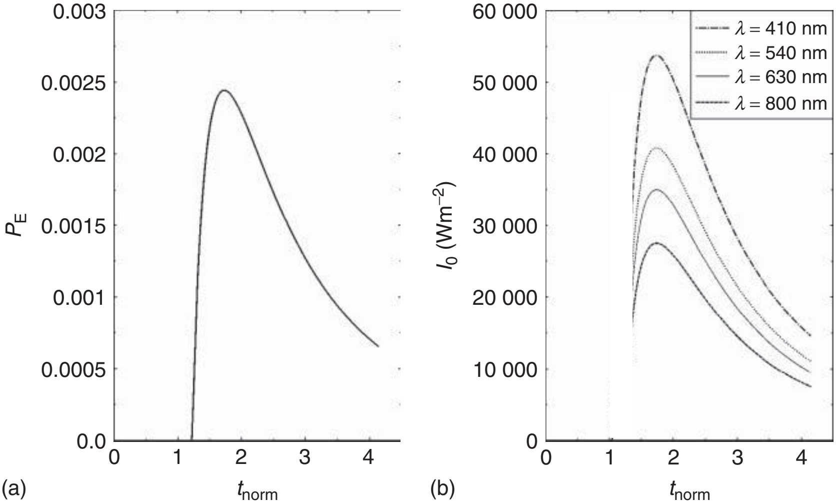

Figure 48.6 (a) Fraction of power in the analyte. (b) Surface intensity. $n_{cl} = 1.33$, $n_{co} = 1.52$, $n_s = 1.51$. (From [21] reprinted with permission.)

where $q=0$ for TE modes and $q=1$ for TM modes. In the case of the TM polarization, this is conveniently rearranged in [13] to yield the following expression:

$$S_{\mathrm{TM}} = \frac{N_{\mathrm{m}}}{n_{\mathrm{cl}}} \left\{ 1 + \frac{\left(N_{\mathrm{m}}^2 - n_{\mathrm{cl}}^2\right)}{N_{\mathrm{m}}^2} \right\} \frac{P_{\mathrm{cl}}}{P_{\mathrm{tot}}} \tag{48.4}$$

It can be seen that in addition to the fraction of modal power in the analyte there are two further factors that must be taken into account. The first is the velocity of the mode relative to the velocity of a wave in the bulk analyte (as described by the term $N_{\mathrm{m}}/n_{\mathrm{cl}}$) and the second is a term correcting for the additional component of electric field along the direction of propagation in the case of the TM polarization [13].

Because the effective index must always be higher than the superstrate index to allow a guided mode to be supported, the first two terms in Eq. (48.3) are always greater than unity, giving a sensitivity advantage to the TM polarization. However, the power fraction term is not the same for the two polarizations and will be optimized at different thicknesses for the two polarizations, so this must be calculated for the specific waveguide design before the relative sensitivities can be finally determined. For the usual case of a waveguide where the substrate has a higher index than the analyte, the optimized sensitivity is greater and the optimum core thickness is larger for the TM polarization, so this is likely to be preferred [12, 13]. While the same arguments apply to channel waveguides as to slab waveguides, precise optimization of the sensitivity usually requires numerical solution of the modal equations.

48.3.2
Optimization for Thin-Film Spectroscopy

Here, we consider the case where a film much thinner than the evanescent field depth, d_{cl}, is present at the waveguide/analyte interface. In this case, the sensitivity to the optical properties of the film is dominated by the optical intensity at the core/analyte interface. This surface intensity is shown in Figure 48.6b, for the waveguide modeled in Figure 48.6a, and where the mode is carrying a power of $1\,\mathrm{W\,m^{-1}}$ of (infinite slab) waveguide width. It can be seen that the surface intensity is maximized for close to the same thickness. As a rough approximation, $1\,\mathrm{W\,m^{-1}}$ (1 Watt per metre of slab waveguide width) in the slab waveguide is equivalent to 5 mW of total power carried in a typical $5\,\mu\mathrm{m}$ wide channel waveguide mode. The peak surface intensity is higher for the shorter wavelengths because the optimized waveguide is thinner and the light is therefore confined more tightly, yielding higher intensity for the same total modal power.

The broad considerations for waveguide design for evanescent spectroscopy have been discussed here. There are many variants depending on the specific spectroscopic application and these are discussed in the sections that follow according to classes of spectroscopic measurement. Many approaches have been taken to reaching a compromise between sensitivity and ease of use, and some of these are discussed in Section 48.8 on instrumentation.

48.4
Absorption Spectroscopy

The majority of measurements of absorption of bulk analytes and thin films have been carried out using lasers at single wavelengths or at a few discrete wavelengths, probably because of the perceived difficulty of coupling broadband light into waveguides. Plowman *et al.* [23] presented an excellent review of waveguide-based spectroscopies up to 1997. Here, a very brief review of the historical development is given followed by a more detailed description of developments since 2000, concentrating on broadband absorption spectroscopy. In 1972, Polky and Harris [6] at the University of Washington made single-wavelength absorption measurements of solutions of methylene blue (MB) using sputtered glass waveguides. They observed enhanced absorption due to adsorption of MB at the waveguide surface and reconciled the measurements with theoretical models. In 1974, extending this work, Mitchell *et al.* [7] conducted single-wavelength measurements of bilirubin in blood plasma samples, emphasizing the suppression of the effects of scattering by erythrocytes using evanescent techniques compared with conventional absorption spectroscopy, the lack of blood sample preparation needed, and the subnanoliter volumes required for waveguide spectroscopy. In 1979, Swalen [24] reviewed the use of waveguides for surface spectroscopy and pointed out that the causal relationship between the imaginary (absorptive) part and the real part of the refractive index of an analyte distorts an absorption spectrum and that simultaneous measurement of the real part of the analyte refractive index (in this case through measuring prism-coupling angles) improves quantification. Measurements were made of monolayers of cadmium arachidate on glass and polyvinyl alcohol (PVA) waveguides, determining the optical anisotropy of the films over the visible spectrum, demonstrating the determination of molecular orientation in monomolecular films, and emphasizing the complementary nature of measurements of refractive index and absorption. In 1990, DeGrandpre *et al.* [25] applied high-index (tantalum pentoxide) planar waveguides to single-wavelength absorption spectroscopy of bromothymol blue in phosphate buffer, achieving a micromolar detection limit. Waveguide spectroscopy with multimoded waveguides may be attractive because of the ease of incoupling more power, but usually results in fluctuations in measured absorption because each mode has a different effective absorption coefficient and the distribution of power between modes tends to fluctuate. However, in 1995, Gnewuch and Renner [26] reported that multimode waveguides with linear refractive index profiles display mode-independent evanescent absorption. In the same year, Kato *et al.* [27] at the National Institute of Materials and Chemical Research in Japan demonstrated broadband (380–650 nm) spectroscopy of a Cu–porphyrin complex in a Langmuir–Blodgett (LB) film on a monomode ion-exchanged glass waveguide. Polarized absorption spectra were obtained, yielding information on bandsplitting due to aggregate formation and on molecular orientation. In 1999, the same group [28] extended this technique further into the UV by using highly multimoded Suprasil (silica) slab waveguides supported on a low-index fluoropolymer, and a pulsed Xenon lamp. In both [27] and [28], broadband light was coupled in by focusing onto an incoupling prism. The UV-visible spectrum of adsorbed cytochrome *c* was measured between 230 and 600 nm. This approach was then exploited for a wide range of surface spectroscopic measurements including absorption spectroscopy of a hemoglobin submonolayer [29], kinetic studies of cytochrome *c* adsorption [30], simultaneous determination of mixed MB and new MB adsorption at a waveguide surface using an artificial neural network approach [31], coadsorption of myoglobin and MB [32], and metal nanoparticle self-assembly on protein-functionalized glass [33]. In 1996, Mendes *et al.* [34] at the University of Arizona measured the absorption spectrum of a hydrated cytochrome *c* monolayer at the surface of a sputtered glass monomode waveguide using broadband light from 500 to 600 nm. The absorption spectrum yields information on ligand binding, oxidation, and protein conformation. Conventional transmission spectroscopy is insufficiently sensitive to achieve absorption measurements on these ∼3 nm thick films, and waveguide spectroscopy achieved an enhancement in absorption of order 10^4, by evanescent absorption along a ∼1 cm long protein film. A broadband (achromatic) input coupler was used to couple light into the 400 nm thick waveguide and an output grating was used to disperse the transmitted light onto a charged-coupled device (CCD) camera, yielding transmission spectra without the need for an external monochromator. More recently, Araci *et al.* [35] have used a silver-diffused waveguide with high sensitivity and improved short-wavelength transmission (∼400 nm) to study the Soret band at 406 nm in a submonolayer film of cytochrome *c*, and employed channel waveguides due to their efficient coupling to lasers and detectors using optical fiber. In a dramatic demonstration of the suppression of scattering in the measurement of absorption spectra of powdered materials without pretreatment, using evanescent spectroscopy, Ogawa *et al.* [36] obtained UV-visible absorption spectra of naphthalene and salicylideneaniline powders placed directly on the waveguide surface. Infrared waveguide spectroscopy was demonstrated by Plunkett *et al.* [37], by using a multimoded germanium slab waveguide on a ZnS substrate with an Fourier transform infrared (FTIR) spectrometer. This extended conventional infrared IREs by reducing the slab thickness to improve sensitivity, necessitating support on a substrate. Absorption spectra of deuterated water were obtained at wavelengths in the range of approximately 2–10 μm, and spectroscopy using the wider range of IR waveguides which are now available [38], is likely to be a significant area for growth. Further extension of waveguide spectroscopy to the Terahertz region has been demonstrated by Zhang and Grischowsky [39], where a parallel-plate metallic waveguide was used to determine the refractive index and absorption of a 20 nm film of water on the internal waveguide walls at frequencies up to 2.5 THz. Terahertz spectroscopy has many potential applications in environmental monitoring, medicine, security, and biomolecular film characterization, and novel Terahertz waveguide materials and configurations for spectroscopy are under intense investigation. Laamiri *et al.* [40] have recently demonstrated evanescent spectroscopy of a film of photoresist using a grating-coupled silicon slab waveguide at frequencies up to 1 THz.

The examples of waveguide absorption spectroscopy described here illustrate the advantages of the technique, in particular for high-sensitivity spectroscopy of ultrathin films, spectroscopy of bulk analytes avoiding the effects of transmission through the medium, particularly scattering, and analysis of surface-specific interactions. Many of the approaches have used readily available low-cost highly multimoded slab waveguides, which differ only slightly from conventional IREs, but the examples cited here emphasize the sensitivity advantages that can be gained as the waveguides become thinner and, ultimately, monomode.

Waveguide technology has primarily been developed for the telecommunications industry so the materials systems have been optimized for operation at wavelengths between 800 and 1600 nm. However, interest in mid-IR waveguiding at wavelengths from 2 to 20 μm is increasing and it is expected that the study of new waveguide systems appropriate for evanescent spectroscopy over a much wider range of wavelengths will continue to expand. There are many glass compositions that support transmission into the IR and which are now being developed for application to mid-IR waveguide spectroscopy. The majority of optical waveguide approaches to mid-IR sensing demonstrated to date have concentrated on silver halide [41] and chalcogenide glasses [42, 43]. The $AgCl_{0.4}Br_{0.6}$ waveguides were excited with a 6 μm quantum cascade laser (QCL) to detect urea and a 10 μm QCL to detect acetic anhydride, and FTIR spectroscopy was also carried out to validate these results. While yielding excellent transmission into the IR, these waveguides were essentially free-standing bulk ATR elements reduced to the thickness of a silicon wafer by hot pressing. This is incompatible with the thin-film processing techniques required for high sensitivity and mass production, and the halides are not ideal in terms of chemical durability. The chalcogenide waveguides first used for mid-IR studies were formed from Germanium-Antimony-Selenide [43] and Germanium-Antimony-Sulfide [42] glasses. For the selenides, a thin-film cladding and waveguides were evaporated on silicon, and human IgG was successfully immobilized on the films, but only external (nonwaveguiding) mid-IR spectra were reported, confirming successful immobilization. The thin-film sulfide waveguides were thermally evaporated directly onto an oxidized silicon wafer; measurements were reported in the NIR for the N−H bond absorption near 1.5 μm from *N*-methylaniline. Microdisk resonators for cavity-enhanced IR absorption have now been integrated and used to measure enhanced absorption of *N*-methylaniline in carbon tetrachloride [38]. Recently, the group at the University of Rennes realized high-quality sulfide waveguides by RF sputtering directly on oxidized silicon and reactive-ion etching and immobilization of avidin [44] has been monitored through NIR spectroscopy. More advanced biochemical systems have recently been studied through mid-IR evanescent absorption spectroscopy, using surface-modified zinc selenide waveguides and an FTIR spectrometer, to detect DNA hybridization through direct observation of vibrational modes [45]. In a further development by the same group, extremely sensitive detection of acetic anhydride has been achieved using monomode GaAs/GaAlAs strip waveguides and a QCL [46], achieving 1000-fold improvement in detection limit when compared with the multimoded silver halide waveguides [41].

48.5
Waveguide Spectroelectrochemistry

The planar geometry, surface sensitivity, and microfabrication technology employed in integrated optical waveguides render them ideal for integration with thin-film electrodes for spectroelectrochemical measurements, as first identified by Itoh and Fujishima [47] in 1988. Electrochemical absorption spectroscopy on waveguides is usually achieved by depositing a thin (10–100 nm) film of indium tin oxide (ITO) on the waveguide surface by sputtering or electron-beam deposition and using the waveguide as mentioned, but in a conventional three-electrode cell with the ITO film as the working electrode. The high sensitivity of waveguides to optical absorption requires that the ITO film be kept as thin as possible to minimize the excess attenuation, as ITO is strongly absorbing compared with most optical materials. However, the requirement of low sheet resistance for electrochemical cycling favors the use of thick films, resulting in a trade-off that depends on the exact configuration and measurement being carried out. Furthermore, the high index ($1.75 < n < 2.1$) of the ITO films will also pull the optical fields in the waveguide up to the surface, increasing the sensitivity of these waveguides to absorption [48], but, unfortunately, this also increases the loss due to the ITO absorption. These ITO loading losses are often reduced to an acceptable level by placing a low-index transparent layer (such as SiO_2) between the waveguide and the ITO, but this reduces sensitivity, emphasizing that careful design and well-controlled fabrication are required to optimize the device for the particular application.

Itoh and Fujishima [47] first demonstrated an optical waveguide combined with a thin-film ITO electrode for the oxidation and reduction of MB. A ~100 nm thick film of ITO was deposited directly on a potassium ion-exchanged slab waveguide by spray pyrolysis. Gratings were used to couple light from a He–Ne laser into and out of the waveguide, which was covered with a 1 cm long cell containing 10^{-3} M aqueous solution of MB. Both the transmitted optical power and a cyclic voltammogram were recorded as the electrode potential was swept between −1.0 and +0.5 V, showing a clear correlation between the oxidation and reduction current and the optical absorption. Subsequent measurements with the MB solution replaced by 0.1 M KCl showed similar behavior, indicating that the observed redox reaction is mainly due to adsorbed MB molecules. Piraud *et al.* [49] studied oxidation and reduction of a 10 nm thick film of lutetium biphthalocyanine ($Lu(PC)_2$) of length 4.5 mm on a potassium ion-exchanged channel waveguide, as an electrochemically resettable chlorine sensor. The waveguide was coated with a 200 nm thick film of silica and a 10 nm thick film of ITO by vacuum evaporation followed by annealing, achieving low losses and acceptable sheet resistance. White light was coupled from a tungsten halogen lamp into the waveguide via a monomode optical fiber, and a monochromator and avalanche photodiode (APD) were used to obtain transmission spectra at wavelengths between 550 nm and 1 μm as the electrode potential was swept between −0.1 and +0.8 V, with the cyclic voltammogram being recorded simultaneously. Strong absorption spectra were obtained for both the oxidized and reduced forms of these very thin $Lu(PC)_2$ films. Dunphy *et al.* [50] used a moderately high-index-sputtered glass slab waveguide ($n = 1.56$ on a substrate of index 1.51) to achieve highly sensitive single-wavelength measurement of the oxidation and reduction of a submonolayer film (<0.4% of a full monolayer) of MB, achieving enhancement in signal by a factor of 40 000 compared with conventional transmission. The waveguide film was 400 nm thick and it was coated with a 200 nm silica film followed by a 50 nm ITO film. Gratings were used to couple light from a He–Ne laser into and out of the waveguide. It was observed that the ITO film increases the sensitivity of the measurement because of its high refractive index. Cycling the electrode potential between 50 and −450 mV caused clear changes in waveguide absorption, which correlated well with the voltammetry. The device was then used to study the formation of Prussian Blue during the reduction of ferricyanide, showing that the complementary optical information helped in identifying otherwise concealed electrochemical processes. The authors then used a prism-based broadband coupling approach combined with an ITO layer on a similar waveguide with a flow-cell, to obtain broadband (500–700 nm) spectra of submonolayers of cytochrome *c* [51], in both the oxidized state when held at +0.4 V and reduced state when held at −0.4 V (with respect to an Ag/AgCl electrode). Similar measurements were then made on the weakly absorbing chromophore 1,1′-ferrocenedicarboxilic acid ($Fc(COOH)_2$). Ross *et al.* built upon earlier work combining ITO-coated IREs with a selective film into which the analyte is selectively partitioned [52] by combining a potassium ion-exchanged waveguide with a 150 nm thick ITO electrode coated with an anionically charge-selective sol–gel derived poly(dimethyldiallylammonium chloride): SiO_2 composite film [53]. This allowed both electrical and optical measurements, as in the earlier examples, but added the advantage of preconcentration of the electroactive species in the selective film. The same authors went on to realize a channel waveguide design with gold electrodes placed on either side of the waveguide, partially avoiding the problems of spurious absorption and unwanted interference from modulation of the optical properties of the electrode encountered when directly loading the waveguide with the electrode [54]. Matsuda *et al.* [55] used an ITO-coated slab waveguide to observe absorption spectra during electrochemical reduction and oxidation of adsorbed heptylviologen cation radicals, extending their work on waveguide absorption spectroscopy [27]. The addition of a Nafion film on the ITO allowed separation of the contribution to the absorption spectrum due to the Br^- ion, which is unable to enter the Nafion film. This was followed by a detailed quantitative study of the potential dependence of the optical properties of MB adsorbed on a 30 nm thick ITO electrode on a 50 μm thick glass plate acting as a slab waveguide [56]. To relax the requirement for a transparent electrode, Fujita *et al.* [57] demonstrated "noncontact optical waveguide spectroscopy," in which the molecules to be studied were adsorbed on a carbon electrode spaced by ∼120 nm from the waveguide surface, still within the evanescent field, in a configuration reminiscent of the "Otto" SPR configuration. Latex beads were used to space the carbon electrode from the highly multimoded quartz slab waveguide and oxidation and reduction of adsorbed cytochrome *c* was studied, with absorption spectra being obtained from 350 to 600 nm.

In summary, waveguide devices offer similar advantages in spectroelectrochemistry as they do in simple absorption spectroscopy, with particular convenience due to the simplicity with which planar electrodes and electrode arrays can be integrated with waveguides and waveguide arrays, using microfabrication techniques.

48.6
Fluorescence Spectroscopy

The advantages of internal reflection fluorescence spectroscopy were first laid out by Hirschfeld [58] in 1965 for a conventional IRE, and the approach was developed by Harrick and Loeb [59] for multiple internal reflection to observe both enhanced absorption and enhanced collection of fluorescence spectra. They noted a small shift of the emission spectrum compared with solution fluorescence possibly due to the changed environment of the molecules. TIRF brings the advantages of *enhanced absorption* as in the case of absorption spectroscopy, *enhanced emission* due to strong evanescent tunneling into the higher index medium, and the potential for *enhanced collection* of fluorescence spectra within the IRE. As in the case of absorption spectroscopy, improvements in sensitivity are achieved using thinner IREs, driving developments in TIRF toward ultrathin optical waveguides, as pioneered by Reichert [60] in 1987. Optimization of waveguides to maximize fluorescence from an analyte on an optical waveguide follows trends similar to maximization of the strength of absorption spectra, and is discussed in detail in several papers [14, 61, 62]. Key points to consider are (i) that the emission from a fluorophore in an evanescent field is increased compared with that in the homogeneous medium in which it is bathed, due to tunneling into the higher index medium and/or into the (higher effective index) modes of a waveguide [63] and (ii) that the angular emission pattern is strongly distorted by the presence of the high-index medium [64], so that optimization of collection efficiency must consider emission into waveguide modes and the angular distribution of emission into the substrate. Collection of light by most (asymmetrical) waveguides is usually quite inefficient, so that most waveguide fluorescence measurements exploit absorption from the waveguide mode but collect the emitted fluorescence conventionally with a high numerical aperture (NA) lens above or below the waveguide. A further advantage of evanescent fluorescence spectroscopy in real samples is the strong suppression of background fluorescence from the bulk of the sample due to the short evanescent penetration depth into the analyte.

Although many fluorescence assays have been demonstrated using waveguides, where total fluorescence intensity has been measured (e.g., [65–69]), rather few measurements of the fluorescence spectra themselves have been made, and these will be the focus of this description of the use of waveguides for spectroscopy. Plowman *et al*. [70] employed a silicon oxynitride channel waveguide to carry out fluorescence immunoassays with femtomolar sensitivity, using a He–Ne laser at 633 nm with prism coupling into the waveguides and monochromator and CCD detector normal to the waveguides to collect the fluorescence spectra. They made the important observation that while waveguide optimization may increase the fluorescence signal, the detection limit will improve only if the waveguide itself shows low fluorescence and low loss, leading to their choice of silicon oxynitride waveguides and a pump wavelength of 633 nm rather than the shorter wavelengths usually used. Fluorescence spectra for Cy5-tagged bovine serum albumin (BSA) at a wide range of concentration were obtained over a wavelength window from 650 to 750 nm. Simpson *et al.* [71] studied the fluorescence spectra of self-assembled monolayers (SAMs) of phthalocyanines having mercaptoalkyl chains of different lengths, on gold-coated glass slides acting as highly multimoded waveguides. A laser diode at 670 nm was used for excitation and the fluorescence was collected using a monochromator and photomultiplier. A significant redshift in the fluorescence spectrum was observed compared with solution spectra, potentially due to the ordered nature of the film on the surface. The molecule with the longer mercaptoalkyl chain yielded much stronger spectra, and this is believed to be due to reduction in quenching by the gold film. Exposure to NO_2 gas was found to cause partially reversible quenching of the fluorescence. Kelly *et al.* [72] formed a phospholipid bilayer containing donor and acceptor dye-tagged glycolipid receptors on a sputtered Corning 7059 glass waveguide 400 nm thick to study the dependence of fluorescence emission spectra from 550 to 700 nm on binding of cholera toxin. Excitation was by light from a frequency-doubled yttrium aluminum garnet (YAG) laser emitting at 532 nm, coupled into the waveguide using a grating. The fluorescence spectrum, collected from underneath the waveguide through the substrate using a fiber-coupled spectrometer, showed combined emission from the Bodipy TMR (donor) and the Bodipy TR (acceptor) fluorophores. The multivalent cholera toxin binds multiple receptors, increasing the proximity of donors and acceptors, leading to energy transfer and increased long-wavelength emission. Binding of cholera toxin was shown to cause an increase in the acceptor emission at 625 nm and a reduction in emission from the donor at 575 nm, and the ratio of these was correlated with cholera toxin concentration, allowing picomolar detection. Recently, this team extended their approach, with silicon oxynitride waveguides, to quantification of tumor markers [73] using a sandwich immunoassay for carcinoembryonic antigen (CEA) with Alexafluor 647 dye. Fluorescence spectra were recorded between 650 and 800 nm, and a detection limit of <0.5 pM CEA, an order of magnitude below the normal physiological concentration, was achieved.

A strong fluorescence signal from low densities of fluorophores usually requires collection over a waveguide length of some millimeters, requiring nonideally long devices and large sample volumes. The use of a microresonator can reduce the sample size and waveguide length by storing energy, for example, in whispering gallery modes [74]. The pump power circulating in the resonator is then greater than the power in the supply waveguide, owing to energy storage, so that stronger fluorescent emission is obtained as long as photobleaching is not a limiting factor. Enhanced waveguide fluorescence spectroscopy was demonstrated using an integrated optical disk resonator by Krioukov *et al.* [75]. The fluorescence spectrum of indocyanine green dye on a 30 μm diameter silicon nitride disk coupled was obtained by tunnelling from an underlying silicon nitride channel waveguide, through a silica layer, and collecting the fluorescence from above with a high NA lens. The volume probed by the evanescent field may be as low as ~10 fl and acquisition of spectra from 20 molecules with 1 μW input power was projected, with the use of an even lower fluorescence ZnO waveguide system to potentially allow single-molecule detection being proposed.

48.7
Waveguide Raman Spectroscopy

Enhanced Raman spectroscopy of thin-film materials acting as waveguides was proposed and demonstrated by Levy *et al.* [76] in 1974 using thin (1 and 6 μm) methyl methacrylate films on glass substrates. Strong Raman spectra were obtained, due to the high pump intensity maintained over a long path-length but, for the thinner film, the greater fraction of modal power traveling in the substrate caused interference in the polymer spectrum by the Raman spectrum of the glass substrate. Rabolt *et al.* [77] at Intercontinental Ballistic Missiles (IBM) subsequently improved the discrimination between film and substrate for thin polymer films by using a low-index substrate, which caused the waveguide mode to be better confined in the film, and then went on to use a purpose-built waveguide, rather than the film under analysis, to guide the light, allowing Raman measurements to be made on nonguiding submicrometer films. Here, the strong surface intensity over a long path length in an appropriately designed waveguide was exploited. The effects of molecular orientation on polarized waveguide Raman measurements were then explored in polymethyl methacrylate (PMMA) and polystyrene waveguiding films by Schlotter and Rabolt [78]. Rabe *et al.* [79] conducted waveguide Raman studies of LB films of cadmium arachidate, using both the polarizations of the waveguide mode (TE and TM) to study anisotropy and order in these films. A 1 μm thick sputtered layer of Corning 7059 glass on silica or Pyrex was used as the waveguide. Raman emission from the multilayer LB films was collected normal to the waveguide from above, and analyzed using a double monochromator and cooled photomultiplier. Excitation was at 488 nm and waveguide fluorescence caused some interference in the 800–1600 cm^{-1} range but was insignificant for the C–H stretching region around 2900 cm^{-1}. Measurements at temperatures up to 150 °C showed Raman peak broadening, yielding information on chain tilting in the multilayer. Zimba *et al.* [80] studied films of cellulose acetate doped with 4% 2-nitro-5-(N-methyl-N octadecylamino) benzoic acid, for example, using longer wavelength excitation (1064nm) to reduce background fluorescence and avoid resonant excitation of the chromophore, and employed a Fourier transform infra-red (FTIR) spectrometer for detection. A substantial reduction in fluorescence was obtained when compared with excitation at 488 nm. Walker *et al.* [81] reported the first observation of Raman spectra from a protein film adsorbed to a *dielectric* surface, using a low-fluorescence silicon oxynitride waveguide, of core refractive index 1.523, to which was bound horse heart cytochrome *c*. This study combined waveguide ATR (absorption) measurements of linear dichroism with polarized resonance Raman spectroscopy of the protein film, using radiation at 514.5 nm to both measure the Cyt C absorption near 520 nm and to excite the resonance Raman spectra. The orientation of the heme group of the Cyt C was partially inferred from the measured dichroism and differences in the Raman spectra with polarization. Surface coverage of the Cyt C was estimated from the absorption measurements to be $\sim$50 ng cm^{-2}. Kanger *et al.* [82] used a very thin ($\sim$120 nm) much higher index low-fluorescence ZnO waveguide ($n_{co} \approx 2.0$) to achieve high-sensitivity *spontaneous* Raman spectroscopy of a monolayer of bovine albumin, using excitation at 514.5 nm.

SERS is a topic of growing importance that exploits metallic nanostructures to enhance Raman signals by factors of up to 10^8, on average, with electromagnetic hotspots exhibiting much higher local enhancements [83]. There have been several reports of Raman spectroscopy studies combining dielectric waveguides with metallic nanoparticles to achieve SERS in waveguide geometry. Ellahi *et al.* [84] obtained strong resonance Raman spectra from thick (73 μm) and thin (3.5 μm) PVA film waveguides doped with ruthenium(II) tris(bipyridine) ($Ru(bpy)_3{}^{2+}$) adsorbed to colloidal silver, excited at 457.9 and 514.5 nm; detection of about 40 pg of $Ru(bpy)_3{}^{2+}$ was achieved. Baldwin *et al.* [85] attached colloidal silver nanoparticles to the surface of a glass optical waveguide to achieve SERS at the surface of the waveguide. The SERS spectra of 2-mercaptopyridine (2-MPy) and 4-mercaptopyridine (4-MPy) were obtained and, to demonstrate metal ion detection, 4-MPy spectra were collected during exposure to aqueous $Cu(NO_3)_2$. Cu/pyridine complexation resulted in irreversible changes to the Raman spectrum, which was interpreted as binding of the pyridine nitrogen to the cations in solution. Acid/base titration of the surface-bound 4-MPy using HCl or NaOH showed strong and reversible changes in the Raman bands corresponding to protonated 4-MPy. Lal *et al.* [86] studied the interaction between the resonances of gold-coated silica spheres of approximate radius 30 nm and a waveguide structure on which they were randomly distributed. Strong dependence was observed on the nanoparticle-waveguide separation with a redshift in the spectra with decreasing separation, having important implications for the design of SERS structures on waveguides and the interpretation of the spectra obtained.

The waveguide geometry is particularly advantageous for coherent Raman spectroscopy as the Raman signals depend strongly on the pump and probe intensities, which can be very high in waveguides, and grow quadratically with the length of the waveguide. Coherent Raman scattering from monolayers on dielectric waveguides was proposed by Stegeman *et al.* [87] and the Raman spectrum of a polystyrene waveguide itself was then determined [88] using two dye lasers, one fixed at 564 nm and the other tuned between 596.6 and 598.8 nm, as the pump and probe beams, resulting in strong coherent Stokes Raman spectra. Cancellation of contributions to the Raman spectrum from the waveguiding medium itself may be minimized using modal interference in the waveguide [87], allowing signals from a surface adlayer to be detected. Coherent anti-Stokes Raman spectra were obtained from pyridine and phenol adsorbed on the surface of ZnO optical waveguides [89]. Wijekoon *et al.* [90] went on to apply this technique to obtain the Raman spectrum of benzene adsorbed on a ZnO planar waveguide, with the objective of determining the frequency of the symmetric ring-stretch mode of the benzene ring, and its dependence on the nature of the adsorption. Kanger *et al*. [91] applied stimulated Raman gain spectroscopy to 30 nm thick polystyrene films on silicon nitride waveguides, proposing the advantages of reduced complexity over waveguide coherent anti-Stokes Raman scattering (CARS) due to self-phase-matching and lack of nonresonant background from the waveguide material.

48.8
Instrumentation

In all configurations, the precise determination of spectroscopic information from thin films and bulk media is governed by the signal-to-noise ratio (S/N), where noise is considered in its broadest sense. This observation is not confined to waveguide spectroscopies, so a full treatment of these aspects of instrumentation is beyond the scope of this chapter, being treated very well in many texts, such as [92]. However, it is worth pointing out a few important factors to consider when using waveguides for spectroscopy, partly because optical waveguide researchers often devote huge effort to increasing the sensitivity of devices (and hence signal) while paying little attention to the equally important aspects of noise, drift, and signal processing, which often yield greater gains in detectability more simply and more cheaply, and partly because there are specific issues associated with using waveguides for spectroscopy that need to be borne in mind. The accuracy and precision with which spectra are obtained is also dependent on system calibration and the variability in sample preparation, dwell times, and interactions of chemicals with surfaces. Micropumps and microfluidic devices are making a significant contribution to reducing the variability of samples and their presentation to sensing devices [17], and will make a similar contribution in miniature spectroscopic systems. From the point of view of the developer of the waveguide device and the surrounding instrumentation and software, it is usually sufficient to provide a protocol for calibration and to reduce the optical and electronic noise sources and mechanical and thermal drifts to the point where it is the lack of repeatability in sample preparation that dominates uncertainties in the data acquired.

Spectroscopy using waveguides normally operates in the low-light-level regime where the dominant noise source is thermal noise in the receiver. The effect of this on S/N may be reduced by low-pass filtering or integrating for longer durations (reducing noise bandwidth) and using phase-sensitive detection. The power coupled into a monomode waveguide from a source such as a tungsten lamp for white-light absorption spectroscopy is fundamentally limited, but 30 dB of dynamic range is easy to achieve if a monomode optical fiber is used to spatially filter the light, and is butt coupled to a waveguide which has been well matched to the fiber (by matching mode field dimensions), and assuming that the spectrum is not fast varying. A well-mode-matched fiber ensures not only that the power entering the waveguide is maximized but that any light scattered into the substrate and superstrate, which may reach the detector, is minimized. For fast measurements of absorption spectra, higher brightness sources of white light such as supercontinuum sources [93] may provide benefits, as much more power may be launched into a mode, requiring less stringent noise reduction.

Unfortunately, most surface-sensitive waveguides are usually poorly mode matched to conventional optical fiber, in which case a mode transformer must be incorporated, or it may be better to use a grating or a prism to couple light into the waveguide, as described later. Itoh *et al.* [94] described a composite device comprising a fiber-compatible potassium ion-exchanged input/output waveguide with mode transformers to a thin high-index high-sensitivity waveguide overlayer, and subsequently replaced the high-index overlayer with a diffused high-index silver-ion-exchanged region [95, 96], both approaches effectively relaxing the trade-off between sensitivity and coupling efficiency. A compromise approach with the advantage of simplicity but the potential disadvantages of increased scattering loss or lower sensitivity is to simply deposit a short section of high-index film directly onto the fiber-compatible waveguide surface without mode transforming tapered velocity couplers [48, 97].

Coupling of light into waveguides with optical fiber is probably the best approach for spectroscopy if the waveguide is fiber compatible and if the fiber may be permanently fixed to the waveguide, as problems with alignment and mechanical drift are minimized and the light is spatially filtered by the fiber. However, issues of cost and disposability of waveguide devices often dictate that a permanent connection is not practical, in which case a grating- or prism-based approach is preferred. In this case, a ‘‘free-space’’ beam is directed at the grating (see, e.g., [67]) or prism (see, e.g., [27]) at an angle that allows phase matching of the incident beam to the waveguide mode. For monomode waveguides, the prism or grating approach may relax positional tolerances on input coupling and removes the need for tricky and expensive fiber ‘‘pigtailing’’ but places a severe constraint on the phase-matching angle. In the case of single-wavelength input, for example, for fluorescence or Raman spectroscopy, this constraint can be readily met. However, in the case of broadband input coupling for absorption spectroscopy, the coupling angle is usually different for each wavelength. Nonetheless, this can usually be overcome by appropriate focusing of the input light to provide a range of coupling angles or by using more sophisticated broadband input couplers [34]. In all cases, the power coupling efficiency and the effects of light not coupled into the waveguide must be considered carefully and weighed up against cost.

Once coupled power has been maximized and fundamental noise sources have been reduced to an acceptable level, other common limiting factors such as mechanical, thermal, and instrumental drift and sources of spurious radiation such as ambient light, background fluorescence, and any incident light not coupled into the waveguide but arriving at the photodetector must be reduced. These are mostly common to any spectroscopic system and may suggest the use of light-tight enclosures, phase-sensitive (lock-in) detection, background subtraction, and spectral correlation or principal component analysis, for example. Issues associated specifically with waveguides depend on the application, but for fluorescence and Raman spectroscopy may include choosing low-fluorescence substrates as described by Walker *et al.* [98], and filtering the output of the pump laser before coupling into the waveguide, to improve its spectral purity, especially in the case of semiconductor lasers. Mechanical stability is usually the next most important issue, and is effectively solved by permanently pigtailing input and output fiber to the waveguide where this is practical, or providing a very robust assembly for prism or grating coupling. Residual mechanical drift can be compensated for by including a reference branch in the waveguide device, as shown in the example in Figure 48.7, to allow a differential measurement to be made. A simple approach to reduce the effects of scattered light is to coat the unused surfaces of the waveguide substrate with an absorbing medium, bearing in mind that Fresnel reflection occurs even from poorly matched absorbing media, and to spatially filter the waveguide output to reduce the collection of light from the substrate on the receiver. Thermal effects at the waveguide are often minimized by monitoring and controlling the waveguide, sample, and mount temperatures. Whether any or all of these are required depends, of course, on the specification of the spectroscopic measurements to be made.

External commercial spectrometers are usually used to analyze the spectrum at the output of a waveguide device, and there are many suitable high-performance, compact, low-cost fiber-coupled spectrometers now available. Several groups have implemented waveguide spectrometers for chemical analysis, and these include arrayed waveguide grating (AWG) spectrometers where the optical detection and spectrometer were integrated on the same chip for absorption spectroscopy [99] and fluorescence spectroscopy [100], and AWG spectrometers for external Raman spectroscopy [101]. Fourier transform spectrometers have several well-known advantages over dispersive spectrometers and recent demonstrations have shown the potential for waveguide FTIR spectrometers [102–104], which may find application in integrated systems for waveguide spectroscopy of chemical species.

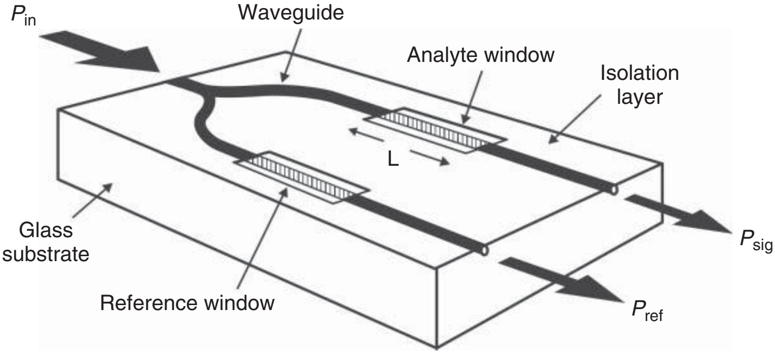

Figure 48.7 Illustration of a simple integrated optical chip.

48.9
Conclusions

Optical waveguides have been employed for spectroscopic measurements since 1971–1972 when it was realized that this approach would drive the technique of TIR spectroscopy to its ultimate sensitivity and bring the benefits of mass production and integration, in terms of cost, robustness, and stability. Integrated optical waveguides may be fabricated from a vast range of materials and these must be selected carefully with the particular spectroscopic application and analytes and the required optical performance in mind. Optical waveguides have primarily been developed for optical telecommunications systems and therefore tend to employ materials that are transparent between 500 and 1800 nm. However, recently, waveguides for short wavelengths (400 nm and below) and for mid-IR (and even Terahertz) wavelengths are becoming increasingly available for new spectroscopic applications. The principles of optimization of waveguides for surface spectroscopy are quite straightforward, to the first order, and guidelines for optimization have been given in this chapter. Waveguide techniques lend themselves particularly well to the spectroscopy of ultrathin films, for example, of submonolayer protein films, where a strong optical interaction can be built up by integration over a long length, and where interferences from the bulk of an analyte medium are minimized because of the rapid decay of the evanescent field into the analyte. The microfabrication techniques employed for optical waveguides, and their surface sensitivity, render them ideal for integration with electrodes for spectroelectrochemical measurements, bringing an extra dimension to the spectroscopic technique. While fluorescence sensing using optical waveguides is well established, there have been rather few demonstrations of fluorescence spectroscopy on optical waveguides, despite the advantages of enhanced absorption and enhanced emission. This may be due to the historic expense of low-light-level spectrometers, combined with the high background fluorescence of many waveguide materials, but with the advent of high-performance miniature CCD spectrometers at low cost, and lower fluorescence waveguides, this may be expected to change. Raman spectroscopy lends itself to waveguide techniques for the same reasons, and with the same caveats, as fluorescence spectroscopy. SERS requires a structured metallic surface so that integrated optical waveguides, which are realized using photolithographic techniques, lend themselves well to integration with a structured metallic surface for repeatable SERS. In general, improvements in the sensitivity of spectroscopic techniques are achieved as much by focusing on noise and drift reduction as they do on the enhancement of signal strength. Careful consideration of noise reduction, signal referencing, data processing, and mechanical and thermal stability allows the potential for ultrahigh sensitivity of optical waveguide spectroscopies to be fully exploited.

Acknowledgments

I thank Mr Chris Nash, Dr Hamish Hunt, Dr Li Na Ng, and Dr Yuwapat Panitchob for their contributions to this chapter, and Prof. Olivier Parriaux of Université Jean

Monnet St-Etienne and Dr Hugo Hoekstra of the University of Twente for very helpful discussions.

References

1. Harrick, N.J. (1960) Study of physics and chemistry of surfaces from frustrated total internal reflection. *Phys. Rev. Lett.*, **4**, 224.
2. Fahrenfort, J. (1961) Attenuated total reflection. A new principle for the production of useful infrared spectra of organic compounds. *Spectrochim. Acta*, **17**, 698.
3. Harrick, N.J. (1967) *Internal Reflection Spectroscopy*, Wiley-Interscience, New York, pp. 148–163.
4. Midwinter, J.E. (1971) On the use of optical waveguide techniques for internal reflection spectroscopy. *IEEE J. Quantum Electron.*, **7**, 339.
5. Tien, P.K., Ulrich, R., and Martin, R.J. (1969) Modes of propagating light waves in thin deposited semiconductor films. *Appl. Phys. Lett.*, **14**, 291.
6. Polky, J.N. and Harris, J.H. (1972) Absorption from thin-film waveguides. *J. Opt. Soc. Am.*, **62**, 1081.
7. (a) Mitchell, G.L., Harris, J.H., and Yee, S. (1974) Bilirubin Determination in Whole Blood Using Integrated Optics. Electrical Engineering Department Report 185, University of Washington; (b) Mitchell, G.L. (1977) Absorption spectroscopy in scattering samples using integrated optics. *IEEE J. Quantum Electron.*, **13**, 173.
8. Adams, M.J. (1981) *An Introduction to Optical Waveguides*, Wiley-Interscience, New York.
9. Ghatak, A. and Thyagarajan, K. (1998) *Introduction to Fiber Optics*, Cambridge University Press, New York.
10. Lee, D.L. (1986) *Electromagnetic Principles of Integrated Optics*, John Wiley & Sons, Inc., New York.
11. Okamoto, K. (2006) *Fundamentals of Optical Waveguides*, 2nd edn, Academic Press, New York.
12. Parriaux, O. and Veldhuis, G.J. (1998) Normalised analysis for the sensitivity optimisation of integrated optical evanescent wave sensors. *J. Lightwave Technol.*, **16**, 573.
13. Veldhuis, G.J., Parriaux, O., Hoekstra, H.J.W.M., and Lambeck, P.V. (2000) Sensitivity enhancement in evanescent optical waveguide sensors. *J. Lightwave Technol.*, **18**, 677.
14. Srivastava, R., Bao, C., and Gómez-Reino, C. (1996) Planar surface waveguide evanescent wave chemical sensors. *Sens. Actuators, A*, **51**, 165.
15. Tiefenthaler, K. and Lukosz, W. (1989) Sensitivity of grating couplers as integrated-optical chemical sensors. *J. Opt. Soc. Am. B*, **6**, 209.
16. Kunz, R.E. and Cottier, K. (2006) Optimising integrated optical chips for label-free (bio)-chemical sensing. *Anal. Bioanal. Chem.*, **384**, 180.
17. Hunt, H.C. and Wilkinson, J.S. (2008) Optofluidic integration for microanalysis. *Microfluid. Nanofluid.*, **4**, 53.
18. Levene, M.J., Korlach, J., Turner, S.W., Foquet, M., Craighead, H.G., and Webb, W.W. (2003) Zero-mode waveguides for single-molecule analysis at high concentrations. *Science*, **299**, 682.
19. Moran-Mirabal, J.M. and Craighead, H.G. (2008) Zero-mode waveguides: sub-wavelength nanostructures for single molecule studies at high concentrations. *Methods*, **46**, 11.
20. Clark, R.J.H. and Hester, R.E. (eds) (1988) *Spectroscopy of Surfaces*, Advances in Spectroscopy, Vol. 16, John Wiley & Sons, Ltd, Chichester.
21. Ng, L.N., Luff, B.J., Zervas, M.N., and Wilkinson, J.S. (2000) Forces on a Rayleigh particle in the cover region of a planar waveguide. *J. Lightwave Technol.*, **18**, 388.
22. Horváth, G., Lindvold, L.R., and Larson, N.B. (2002) Reverse-symmetry waveguides: theory and fabrication. *Appl. Phys. B*, **74**, 383.

23. Plowman, T.E., Saavedra, S.S., and Reichert, W.M. (1998) Planar integrated optical methods for examining thin films and their surface adlayers. *Biomaterials*, **19**, 341.
24. Swalen, J.D. (1979) Optical wave spectroscopy of molecules at surfaces. *J. Phys. Chem.*, **83**, 1438.
25. DeGrandpre, M.D., Burgess, L.W., White, P.L., and Goldman, D.S. (1990) Thin film planar waveguide sensor for liquid phase absorbance measurements. *Anal. Chem.*, **62**, 2012.
26. Gnewuch, H. and Renner, H. (1995) Mode-independent attenuation in evanescent field sensors. *Appl. Opt.*, **34**, 1473.
27. Kato, K., Takatsu, A., Matsuda, N., Azumi, R., and Matsumoto, M. (1995) A slab-optical waveguide absorption spectroscopy of Langmuir-Blodgett films with a white light excitation source. *Chem. Lett.*, **437**.
28. Kato, K., Takatsu, A., and Matsuda, N. (1999) UV-visible slab optical waveguide spectroscopy of cytochrome c adsorbed on a liquid–solid interface. *Chem. Lett.*, **31**.
29. Qi, Z., Matsuda, N., Yoshida, T., Asano, H., Takatsu, A., and Kato, K. (2002) Optical waveguide spectrometer based on thin-film glass plates. *Opt. Lett.*, **27**, 2001.
30. Qi, Z., Matsuda, N., Takatsu, A., and Kato, K. (2003) A kinetic study of cytochrome c adsorption to hydrophilic glass by broad-band time-resolved optical waveguide spectroscopy. *J. Phys. Chem. B*, **107**, 6873.
31. Sun, L.-X., Reddy, A.M., Matsuda, N., Takatsu, A., Kato, K., and Okada, T. (2003) Simultaneous determination of methylene blue and new methylene blue by slab optical waveguide spectroscopy and artificial neural networks. *Anal. Chim. Acta*, **487** (109).
32. Qi, Z., Matsuda, N., Takatsu, A., and Kato, K. (2004) In situ investigation of coadsorption of myoglobin and methylene blue to hydrophilic glass by broadband time-resolved optical waveguide spectroscopy. *Langmuir*, **20**, 778.
33. Qi, Z., Matsuda, N., Santos, J., Yoshida, T., Takatsu, A., and Kato, K. (2004) In situ monitoring of metal nanoparticle self-assembly on protein-functionalised glass by broadband optical waveguide spectroscopy. *J. Colloid Interface Sci.*, **271**, 249.
34. Mendes, S.B., Li, L., Burke, J.J., Lee, J.E., Dunphy, D.R., and Saavedra, S.S. (1996) Broad-band attenuated total reflection spectroscopy of a hydrated protein film on a single mode planar waveguide. *Langmuir*, **12**, 3374.
35. Araci, I.E., Mendes, S.B., Yurt, N., Honkanen, S., and Peyghambarian, N. (2007) Highly sensitive spectroscopic detection of heme-protein submonolayer films by channel integrated optical waveguides. *Opt. Express*, **15**, 5595.
36. Ogawa, K., Harada, J., Fujiwara, T., and Takahashi, H. (2004) UV–vis absorption spectra of powdered materials: direct measurements by optical waveguide spectroscopy. *Chem. Lett.*, **33**, 1446.
37. Plunkett, S.E., Propst, S., and Braiman, M.S. (1997) Supported planar germanium waveguides for infrared evanescent-wave sensing. *Appl. Opt.*, **36**, 4055.
38. Hu, J., Carlie, N., Petit, L., Agarwal, A., Richardson, K., and Kimerling, L.C. (2009) Cavity-enhanced IR absorption in planar chalcogenide glass microdisk resonators: experiment and analysis. *J. Lightwave Technol.*, **27**, 5240.
39. Zhang, J. and Grischowsky, D. (2004) Waveguide terahertz time-domain spectroscopy of nanometer water layers. *Opt. Lett.*, **29**, 1617.
40. Laamiri, Y., Garet, F., and Coutaz, J.-L. (2009) Thin-film characterisation by terahertz time-domain spectroscopy using grating-assisted excitation of guided modes. *Appl. Phys. Lett.*, **94**, 071106.
41. Charlton, C., Katzir, A., and Mizaikoff, B. (2005) Infrared evanescent field sensing with quantum cascade lasers and planar silver halide waveguides. *Anal. Chem.*, **77**, 4398.
42. Hu, J.J., Tarasov, V., Agarwal, A., Kimerling, L., Carlie, N., Petit, L., and Richardson, K. (2007) Fabrication and

testing of planar chalcogenide waveguide integrated microfluidic sensor. *Opt. Express*, **15**, 2307.

43. Yu, C.X., Ganjoo, A., Jain, H., Pantano, C.G., and Irudayaraj, J. (2006) Mid-IR biosensor: detection and fingerprinting of pathogens on gold island functionalized chalcogenide films. *Anal. Chem.*, **78**, 2500.
44. Anne, M.L., Keirsse, J., Nazabal, V., Hyodo, K., Inoue, S., Boussard-Pledel, C., Lhermite, H., Charrier, J., Yanakata, K., Loreal, O., Le Person, J., Colas, F., Compere, C., and Bureau, B. (2009) Chalcogenide glass optical waveguides for infrared biosensing. *Sensors*, **9**, 7398.
45. Riccardi, C.S., Hess, D.W., and Mizaikoff, B. (2011) Surface-modified ZnSe waveguides for label-free infrared attenuated total reflection detection of DNA hybridization. *Analyst*, **136**, 4906.
46. Wang, X., Kim, S.-S., Roßbach, R., Jetter, M., Michler, P., and Mizaikoff, B. (2012) Ultra-sensitive mid-infrared evanescent field sensors combining thin-film strip waveguides with quantum cascade lasers. *Analyst*, **137**, 2322.
47. Itoh, K. and Fujishima, A. (1988) An application of optical waveguides to electrochemistry: construction of optical waveguide electrodes. *J. Phys. Chem.*, **92**, 7043.
48. Stewart, G., Muhammad, F.A., and Culshaw, B. (1993) Sensitivity improvement for evanescent-wave gas sensors. *Sens. Actuators B*, **11**, 521.
49. Piraud, C., Mwarania, E., Wilkinson, J., O'Dwyer, K., and Schiffrin, D.J. (1992) Optoelectrochemical thin-film chlorine sensor employing evanescent fields on planar optical waveguides. *Anal. Chem.*, **64**, 651.
50. Dunphy, D.R., Mendes, S.B., Saavedra, S.S., and Armstrong, N.R. (1997) The electroactive integrated optical waveguide: ultrasensitive spectroelectrochemistry of submonolayer adsorbates. *Anal. Chem.*, **69**, 3086.
51. Bradshaw, J.T., Mendes, S.B., Armstrong, N.R., and Saavedra, S.S. (2003) Broadband coupling into single-mode electroactive integrated optical waveguide for spectroelectrochemical analysis of surface-confined redox couples. *Anal. Chem.*, **75**, 1080.
52. Shi, Y., Slaterbeck, A.F., Seliskar, C.J., and Heineman, W.R. (1997) Spectroelectrochemical sensing based on multimode selectivity simultaneously achievable in a single device. 1. Demonstration of concept with ferricyanide. *Anal. Chem.*, **69**, 3679.
53. Ross, S.E., Seliskar, C.J., and Heineman, W.R. (2000) Spectroelectrochemical sensing based on multimode selectivity simultaneously achievable in a single device. 9. Incorporation of planar waveguide technology. *Anal. Chem.*, **72**, 5549.
54. Ross, S.E., Shi, Y., Seliskar, C.J., and Heineman, W.R. (2003) Spectroelectrochemical sensing: planar waveguides. *Electrochim. Acta*, **48**, 3313.
55. Matsuda, N., Takatsu, A., Kato, K., and Shigesato, Y. (1998) In situ observation of adsorbed heptylviologen cation radicals by slab optical waveguide spectroscopy utilising indium-tin-oxide electrode. *Chem. Lett.*, **125**.
56. Matsuda, N., Santos, J.H., Takatsu, A., and Kato, K. (2003) In situ observation of adsorbed species of methylene blue on indium-tin-oxide electrode by slab optical waveguide spectroscopy. *Thin Solid Films*, **445**, 313.
57. Fujita, K., Suzuki, C., and Ohno, H. (2003) Non-contact spectral analysis of cytochrome c on carbon electrodes with optical waveguide spectroscopy. *Electrochem. Commun.*, **5**, 47.
58. Hirschfeld, T. (1965) Total reflection fluorescence. *Can. Spectrosc.*, **10**, 128.
59. Harrick, N.J. and Loeb, G.I. (1973) Multiple internal reflection fluorescence spectrometry. *Anal. Chem.*, **45**, 687.
60. Reichert, W.M., Ives, J.T., Suci, P.A., and Hlady, V. (1987) Excitation of fluorescent emission from solutions at the surface of polymer thin-film waveguides: an integrated optics approach for the sensing of fluorescence at the polymer/solution interface. *Appl. Spectrosc.*, **41**, 636.
61. Marcuse, D. (1988) Launching light into fiber cores from sources located in

the cladding. *J. Lightwave Technol.*, **6**, 1273.

62. Bernini, R., Cennamo, N., Minardo, A., and Zeni, L. (2006) Planar waveguides for fluorescence-based biosensing: optimisation and analysis. *IEEE Sensors J.*, **6**, 1218.
63. Lukosz, W. and Kunz, R.E. (1977) Light emission by magnetic and electric dipoles close to a plane interface. I. Total radiated power. *J. Opt. Soc. Am.*, **67**, 1607.
64. Lee, E.-H., Benner, R.E., Fen, J.B., and Chang, R.K. (1979) Angular dispersion of fluorescence from Liquids and monodispersed spheres by evanescent wave excitation. *Appl. Opt.*, **18**, 862.
65. Zhou, Y., Laybourn, P.J.R., Magill, J.V., and De La Rue, R.M. (1991) An evanescent fluorescence biosensor using ion-exchanged buried waveguides and the enhancement of peak fluorescence. *Biosens. Bioelectron.*, **6**, 595.
66. Plowman, T.E., Durstchi, J.D., Wang, H.K., Christensen, D.A., Herron, J.N., and Reichert, W.M. (1999) Multiple-analyte fluoroimmunoassay using an integrated optical waveguide sensor. *Anal. Chem.*, **71**, 4344.
67. Duveneck, G.L., Abel, A.P., Bopp, M.A., Kresbach, G.M., and Ehrat, M. (2002) Planar waveguides for ultra-high sensitivity of the analysis of nucleic acids. *Anal. Chim. Acta*, **469**, 49.
68. Ligler, F.S., Taitt, C.R., Shriver-Lake, L.C., Sapsford, K.E., Shubin, Y., and Golden, J.P. (2003) Array biosensor for detection of toxins. *Anal. Bioanal. Chem.*, **377** (469).
69. Hua, P., Hole, J.P., Wilkinson, J.S., Proll, G., Tschmelak, J., Gauglitz, G., Jackson, M.A., Nudd, R., Griffith, H.M.T., Abuknesha, R.A., Kaiser, J., and Kraemmer, P. (2005) Integrated optical fluorescence multisensor for water pollution. *Opt. Express*, **13**, 1124.
70. Plowman, T.E., Reichert, W.M., Peters, C.R., Wang, H.K., Christensen, D.A., and Herron, J.N. (1996) Femtomolar sensitivity using a channel-etched thin film waveguide fluoroimmunosensor. *Biosens. Bioelectron.*, **11**, 149.
71. Simpson, T.R.E., Revell, D.J., Cook, M.J., and Russell, D.A. (1997) Evanescent wave excited fluorescence from self-assembled phthalocyanine monolayers. *Langmuir*, **12**, 460.
72. Kelly, D., Grace, K.M., Song, X., Swanson, B.I., Frayer, D., Mendes, S.B., and Peyghambarian, N. (1999) Integrated optical biosensor for detection of multivalent proteins. *Opt. Lett.*, **24**, 1723.
73. Mukundan, H., Kubicek, J.Z., Holt, A., Shively, J.E., Martinez, J.S., Grace, K., Grace, W.K., and Swanson, B.I. (2009) Planar optical waveguide-based biosensor for the quantitative detection of tumor markers. *Sens. Actuators B*, **138**, 453.
74. Owen, J.F., Barber, P.W., Dorain, P.B., and Chang, R.K. (1981) Enhancement of fluorescence induced by microstructure resonances of a dielectric fiber. *Phys. Rev. Lett.*, **47**, 1075.
75. Krioukov, E., Klunder, D.J.W., Driessen, A., Greve, J., and Otto, C. (2002) Integrated optical microcavities for enhanced evanescent wave spectroscopy. *Opt. Lett.*, **27**, 1504.
76. Levy, Y., Imbert, C., Cipriani, J., Racine, S., and Dupeyrat, R. (1974) Raman-scattering of thin-films as a waveguide. *Opt. Commun.*, **11** (66).
77. Rabolt, J.F., Santo, R., and Swalen, J.D. (1980) Raman measurements on thin polymer films and organic monolayers. *Appl. Spectrosc.*, **34**, 517.
78. Schlotter, N.E. and Rabolt, J.F. (1984) Raman spectroscopy in polymeric thin film optical waveguides. 1. Polarised measurements and orientational effects in two-dimensional films. *J. Phys. Chem.*, **88**, 2062.
79. Rabe, J.P., Swalen, J.D., and Rabolt, J.F. (1987) Order–disorder transitions in Langmuir-Blodgett films. III. Polarised Raman studies of cadmium arachidate using integrated optical techniques. *J. Chem. Phys.*, **86**, 1601.
80. Zimba, C.G., Hallmark, V.M., Turrell, S., Swalen, J.D., and Rabolt, J.F. (1990) Applications of Fourier transform Raman spectroscopy to studies of thin polymer films. *J. Phys. Chem.*, **94**, 939.

81. Walker, D.S., Hellinga, H.W., Saavedra, S.S., and Reichert, W.M. (1993) Integrated optical waveguide attenuated total reflection spectrometry and resonance Raman spectroscopy of adsorbed cytochrome c. *J. Phys. Chem.*, **97**, 10217.

82. Kanger, J.S., Otto, C., Slotboom, M., and Greve, J. (1996) Waveguide Raman spectroscopy of thin polymer layers and monolayers of biomolecules using high refractive index waveguides. *J. Phys. Chem.*, **100**, 3288.

83. Kneipp, J., Kneipp, H., and Kneipp, K. (2008) SERS – a single-molecule and nanoscale tool for bioanalytics. *Chem. Soc. Rev.*, **37**, 1052.

84. Ellahi, S.B. and Hester, R.E. (1995) Waveguide surface-enhanced resonance Raman spectroscopy of Ru(bpy)3^{2+}. *Anal. Chem.*, **67**, 108.

85. Baldwin, J., Schühler, N., Butler, I.S., and Andrews, M.P. (1996) Integrated optics evanescent wave surface enhanced Raman scattering (IO-EWSERS) of mercaptopyridines on a planar optical chemical bench: binding of hydrogen and copper ion. *Langmuir*, **12**, 6839.

86. Lal, S., Wetscott, S.L., Taylor, R.N., Jackson, J.B., Norlander, P., and Halas, N.J. (2002) Light interaction between gold nanoshells plasmon resonance and planar optical waveguides. *J. Phys. Chem. B*, **106**, 5609.

87. Stegeman, G.I., Fortenberry, R., Karaguleff, C., Moshrefzadeh, R., Hetherington, W.M. III,, Van Wyck, N.E., and Sipe, J.E. (1983) Coherent anti-stokes Raman scattering in thin-film dielectric waveguides. *Opt. Lett.*, **8**, 295.

88. Hetherington, W.M. III,, Van Wyck, N.E., Koening, E.W., Stegeman, G.I., and Fortenberry, R.M. (1984) Observation of coherent Raman scattering in thin-film optical waveguides. *Opt. Lett.*, **9**, 88.

89. Hetherington, W.M. III,, Ho, Z.Z., Koening, E.W., Stegeman, G.I., and Fortenberry, R.M. (1986) Surface CARS spectroscopy of pyridine and phenol on ZnO optical waveguides. *Chem. Phys. Lett.*, **128**, 150.

90. Wijekoon, W.M.K.P., Koening, E.W., and Hetherington, W.M. III, (1993) Coherent anti-Stokes Raman scattering spectroscopy with guided waves applied to adsorption of benzene on planar (0001) surface of zinc oxide. *J. Phys. Chem.*, **97**, 1065.

91. Kanger, J.S., Otto, C., and Greve, J. (1996) Stimulated Raman gain spectroscopy of thin layers using dielectric waveguides. *J. Phys. Chem.*, **100**, 16293.

92. Johnson, M. (2003) *Photodetection and Measurement: Maximising Performance in Optical Systems*, McGraw-Hill, New York ISBN: 0-07-140944-0.

93. van der Sneppen, L., Hancock, G., Kaminski, C., Laurila, T., Mackenzie, S.R., Neil, S.R.T., Peverall, R., Ritchie, G.A.D., Schnippering, M., and Unwin, P.R. (2010) Following interfacial kinetics in real time using broadband evanescent wave cavity-enhanced absorption spectroscopy: a comparison of light-emitting diodes and supercontinuum sources. *Analyst*, **135**, 133.

94. Itoh, K. and Madou, M. (1991) Optical waveguides for surface spectroscopy: $FePO_4$ thin film/K^+ -doped glass composite optical waveguide systems having tapered velocity couplers. *J. Appl. Phys.*, **69**, 7425.

95. Itoh, K., Chen, X.-M., and Murabayashi, M. (1993) Ion-exchanged glass optical waveguide systems for surface spectroscopy. Composite structures for realisation of high sensitivity and low loss. *Chem. Lett.*, 1991.

96. Yimat, A., Rossberg, A.G., Amemiya, T., and Itoh, K. (2005) Thin film composite optical waveguides for sensor applications: a review. *Talanta*, **65**, 1102.

97. Quigley, G.R., Harris, R.D., and Wilkinson, J.S. (1999) Sensitivity enhancement of integrated optical sensors by use of thin high-index films. *Appl. Opt.*, **38**, 6036.

98. Walker, D.S., Reichert, W.M., and Berry, C.J. (1992) Corning 7059, silicon oxynitride and silicon dioxide thin-film integrated optical waveguides – in search of low-loss nonfluorescent, reusable glass waveguides. *Appl. Spectrosc.*, **46**, 1437.

99. Kodate, K. and Komai, Y. (2008) Compact spectroscopic sensor using an arrayed waveguide grating. *J. Opt. A: Pure Appl. Opt.*, **10**, 044011.
100. Hu, X., Glidle, A., Ironside, C.N., Sorel, M., Strain, M.J., Cooper, J., and Yin, H. (2012) Integrated microspectrometer for fluorescence based analysis in a microfluidic format. *Lab Chip*, **12**, 2850.
101. Ismail, N., Choo-Smith, L.-P., Wörhoff, K., Driessen, A., Baclig, A.C., Caspers, P.J., Puppels, G.J., de Ridder, R.M., and Pollnau, M. (2011) Raman spectroscopy with an integrated arrayed-waveguide grating. *Opt. Lett.*, **36**, 4629.
102. Bentini, G.G., Bianconi, M., Cerutti, A., Nubile, A., Cerabolini, P., Chiarini, M., Pennestri, G., Dinicolantonio, W., and Guzzi, R. (2006) A new miniaturised optical system for chemical species spectroscopic detection based on a scanning integrated Mach-Zehnder microinterferometer on $LiNbO_3$. *Origins Life Evol. Biosphere*, **36**, 597.
103. Florjanczyk, M., Cheben, P., Janz, S., Scott, A., Solheim, B., and Xu, D.X. (2007) Multiaperture planar waveguide spectrometer formed by arrayed Mach-Zehnder interferometers. *Opt. Express*, **15**, 18176.
104. Okamoto, K., Aoyagi, H., and Takada, K. (2010) Fabrication of Fourier-transform, integrated-optic spatial heterodyne spectrometer on silica-based planar waveguide. *Opt. Lett.*, **35**, 2103.

Section XIV
Hyphenated Techniques

Handbook of Spectroscopy, Second Edition. Edited by Günter Gauglitz and David S. Moore.

49

Mass Spectral Detection

John C. Fetzer

49.1
Introduction

49.1.1
Mass Spectrometers

There are several books that specifically cover the use of GC–MS and LC–MS in certain application areas, including pharmaceutical and illicit drug analysis [1], toxicology [2], essential oils [3], food analysis [4], wines and spirits [5], and environmental analyses [6], among many topical areas.

49.1.1.1 **GC**

GC–MS is now a routine analytical procedure with turnkey instrumentation. This is due to the development of interfaces that readily remove the large excesses of helium carrier gas and leave only a small amount of material to go into the high vacuum of the MS. These interfaces rely on the vastly different diffusion and momentum of flowing helium gas molecules compared to the analytes. MS technology has improved, so that new approaches such as MS-MS detection are now common. In MS–MS, the initial ions of an analyte molecule are each passed onto a second MS that monitors specific fragments. This MS–MS approach allows much greater specificity in detection. A typical commercial MS–MS detector is shown in Figure 49.1.

49.1.1.2 **LC**

Mobile-phase removal or limitations on mobile-phase composition have been an inherent requirement to do LC–MS. The flow rates used in LC are large enough that even when the mobile phase can be completely volatilized, there is still too much material to be compatible with the high vacuum of an MS (it must be remembered that a liquid volume of 1 ml becomes more than 20 ml of gas). This problem is compounded by the widespread use of aqueous mobile phases as water is a more difficult solvent for MS and for vacuum systems to remove [7, 8].

Handbook of Spectroscopy, Second Edition. Edited by Günter Gauglitz and David S. Moore.

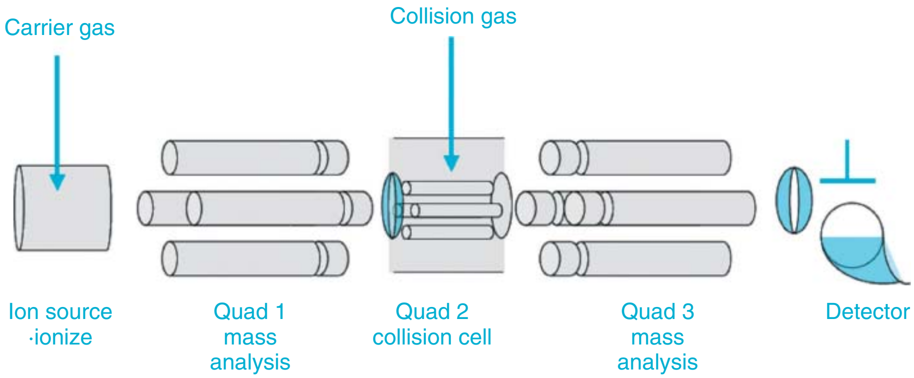

Figure 49.1 A typical quadrupole MS–MS as used for GC–MS–MS analyses.

49.1.2
Ionization Approaches for LC–ESI versus APCI

The mobile phase in LC determines, most often, which of the two main sample introduction approaches are used. A brief description will be given first.

Electrospray ionization (ESI) is based on nebulization of the LC effluent.

Atmospheric pressure chemical ionization (APCI) is an ambient-pressure method in which the mobile phase is heated and nebulized. Once evaporated, it is used as a chemical-ionization medium and reagent. This is accomplished by creating a plasma of the vaporized solvents.

ESI is a harder ionization source than APCI. Fragmentation of analytes and the creation of multiple charges on the ions can occur. Fragmentation reduces detection limits because not all of the analyte can be detected as the same ion. This fragmentation, however, can be used to determine structural details of an analyte. This is analogous to the fragmentation of molecules in normal electron-sector mass spectrometry. Multiple charges also reduce detection limits.

In chemical ionization, a chemical with certain affinities for compounds of interest is ionized. Through collisional deactivation, the charges are transferred to the analytes from the charged mobile-phase molecules. It is considered to be a ‘‘soft’’ ionization with little fragmentation of the analytes because the energy level is much lower than in traditional electron-impact ionization. Small amounts of chemicals can be added to the mobile phase, which do not affect the LC retention behavior but produce select detection. These dopant reagents undergo specific reactions with certain classes of compounds, yielding ions of a specific mass increase.

ESI is good for nonaqueous mobile phases but not for aqueous ones. Droplet formation and ionization kinetics can be problematic with aqueous mixtures.

Conversely, APCI is good with aqueous phases. APCI is also compatible with most organic and inorganic salts, so the buffered mobile phases used in pharmaceutical and clinical analyses are usable.

49.1.3
Application Examples for GC–MS and LC–MS

Applications of GC–MS and LC–MS are now commonplace and numerous. It would be impossible to cover most of the wide range of applications in a short chapter. That task would be the subject of a very long book. Instead, this section is an overview touching on several uses as examples of what LC–MS can do to give the reader a flavor of its scope and what kinds of information can be gained through using it.

This section gives a few recent examples of the variety of analyses published in tens of thousands of papers that utilized either GC–MS or LC–MS in the past few years. In most of these chapters, the authors function only as users of the instrumentation and techniques. They rely on the computer software and libraries to identify peaks and do little traditional mass spectrometry as it would be conceived of as a hyphenated technique. The chromatograph separates, the MS detector gathers data, and the data system gives results. These two techniques have become so commonplace and the instruments are so turnkey that any user can now produce high-level results.

Numerous example conditions for specific analyses have been developed by the instrument and column manufacturers. These are offered as a support service. One such chromatogram is shown in Figures 49.1–49.6. Figure 49.2 shows the separation of polybromodiphenyl ethers, formerly used as flame retardants until their health effects became known. The isomer groups severely overlap, so the specificity of MS detection is required.

Figure 49.3 shows the separation of the trimethylsilane derivatives cocaine and three of its major metabolites. Figure 49.4 is a total ion chromatogram, the sum of all ion responses to increase sensitivity, for the four tocopherol (vitamin E) iosomers. Figure 49.5 is a chromatogram of the many flavorants and additives found in a citrus-flavored soft drink. The complexity of gasoline is reflected in the chromatogram of Figure 49.6.

Ultrahigh-pressure liquid chromatography (UPLC) uses columns packed with particles of 1–2 μm in diameter. The LC systems for UPLC have extremely small dead volumes and operate at much higher pressures than conventional HPLC. The result is much greater resolution and shorter retention times. One example is shown in Figure 49.7. The detection was with fast-scanning MS over targeted mass ranges of analytes during ranges around their expected elution times (retention-time window monitoring) [9–11].

As in other areas of chromatography, GC–MS has benefited by the use of solid-phase extraction (SPE) and solid-phase microextraction (SPME) for sample cleanup or fractionation. Using reversed-phase SPME, very low levels of polycyclic

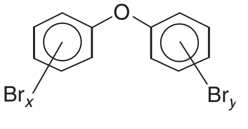

Figure 49.2 The structure of the polybromodiphenyl ethers and a SIM monitoring of the various degrees of bromination.

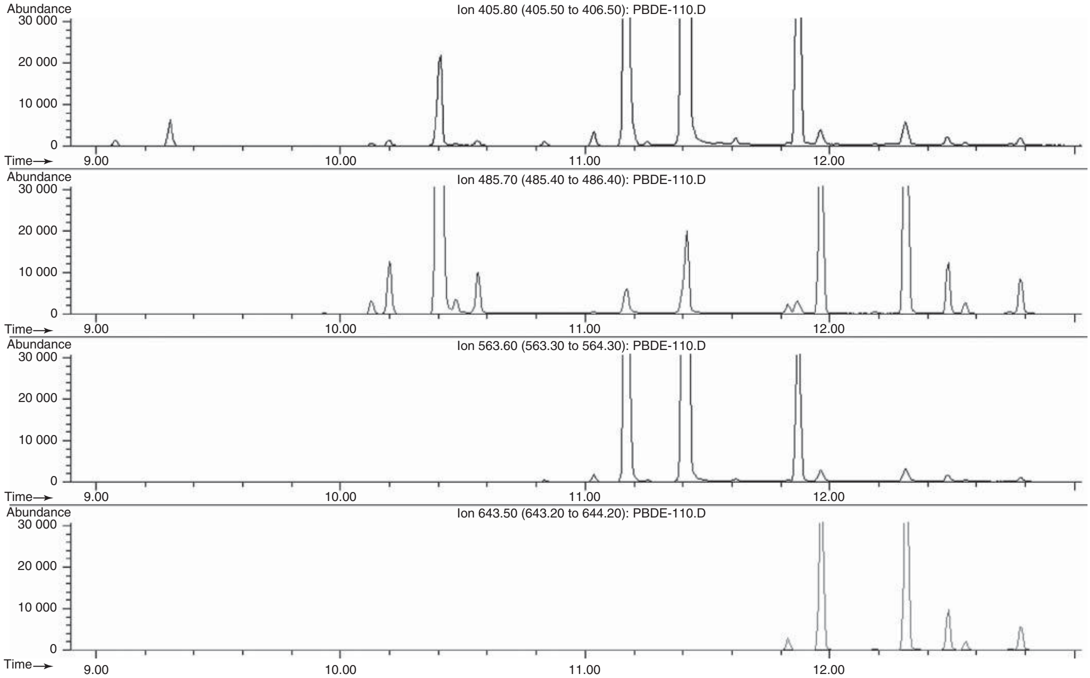

Figure 49.3 Commercial fire-retardant-containing polybrominate diphenyl ethers. Top to bottom are tribromo-, tetrabromo-, pentabromo-, and hexabromo derivatives monitored at ranges starting at 405, 485, 563, and 643 and covering the isotope pattern for each isomer.

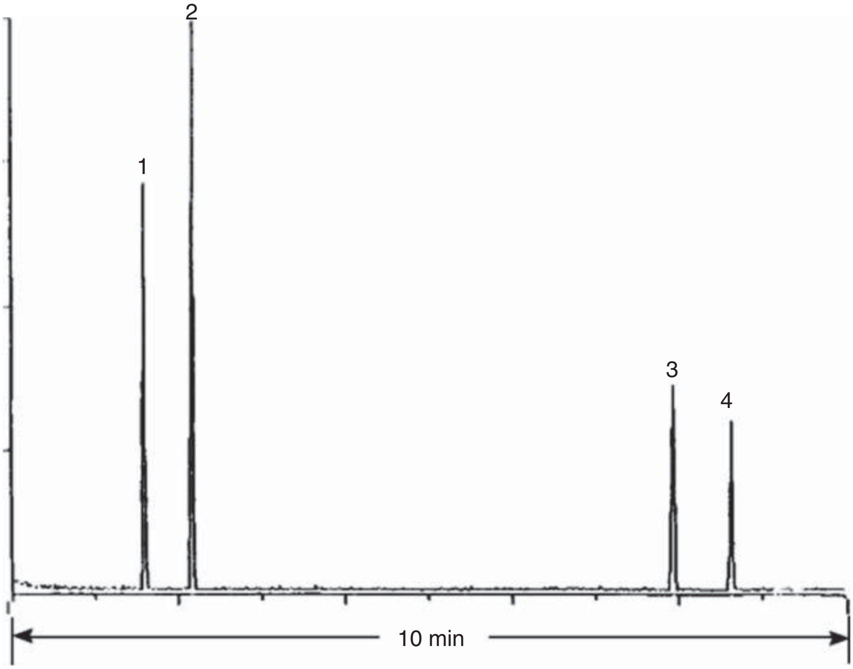

Figure 49.4 Cocaine and some of its metabolites as their trimethylsilane derivatives by GC–MS: 1. ecgonine methyl ester; 2. ecgonine; 3. cocaine; 4. benzoylecgonine.

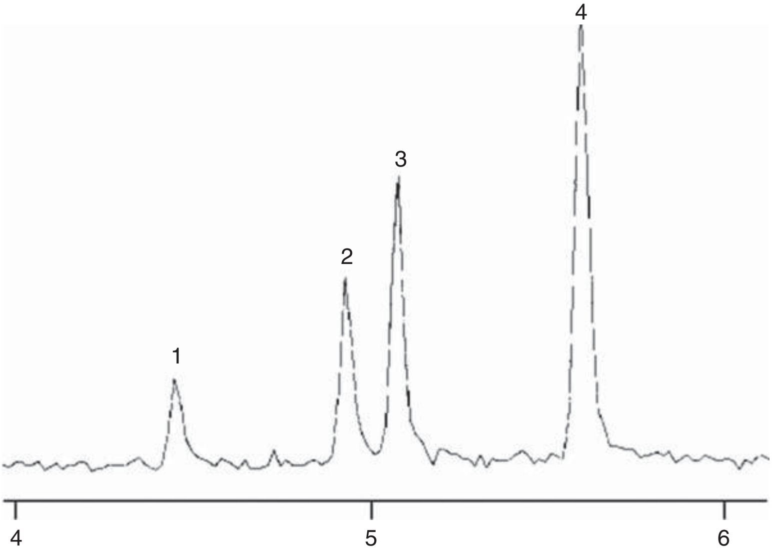

Figure 49.5 Total ion current chromatogram for the four tocopherol isomers: 1. *d*-δ-tocopherol; 2. *d*-β-tocopherol; 3. *d*-γ-tocopherol; 4. *d*-α-tocopherol.

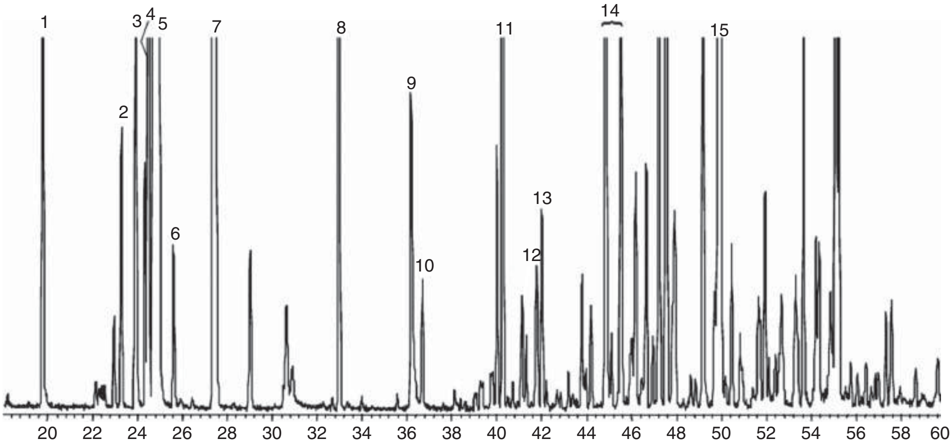

Figure 49.6 Volatile molecules in a citrus-flavored soft drink, total ion chromatogram: 1. (*S*)-(−)-limonene; 2. *p*-cymene; 3. (*R*)-(+)-limonene; 4. octanol; 5. γ-terpinene; 6. nonanol; 7. 2-ethyl-1-hexanol; 8. linalool; 9. decanol; 10. terpinen-4-ol; 11. phenethyl-alcohol; 12. α-terpineol; 13. BHT (butylated hydroxytoluene).

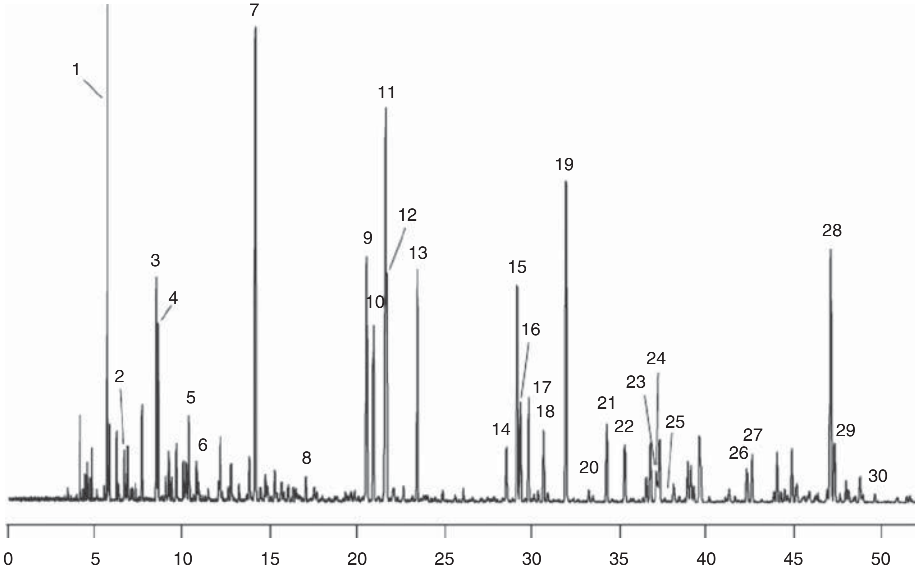

Figure 49.7 Hydrocarbons in a gasoline by GC–MS: 1. methyl-*tert*-butyl-ether (MTBE); 2. *n*-hexane; 3. benzene-d_6 (IS); 4. benzene; 5. isooctane; 6. *n*-heptane; 7. toluene; 8. *n*-octane; 9. ethylbenzene-d_{10} (IS); 10. ethylbenzene; 11. *m*-xylene; 12. *p*-xylene; 13. *o*-xylene; 14. *n*-propylbenzene; 15. 1-methyl-3-ethylbenzene; 16. 1-methyl-4-ethylbenzene; 17. 1,3,5-trimethylbenzene; 18. 1-methyl-2-ethylbenzene; 19. 1,2,4-trimethylbenzene; 20. *n*-decane; 21. 1,2,3-trimethylbenzene; 22. indan; 23. 1,4-diethylbenzene; 24. *n*-butylbenzene (valley); 25. 1,2-dimethylbenzene; 26. 1,2,4,5-tetramethylbenzene; 27. 1,2,3,5-tetramethylbenzene; 28. naphthalene-d_8 (IS); 29. naphthalene; 30. *n*-dodecane.

aromatic hydrocarbons in water samples were found [12, 13]. These techniques can be automated and even done within sample vials within the GC sample carousel, leading to high throughputs for routine analyses.

Many compounds of interest are biological or within an aqueous matrix. The polar functionalities of these molecules that lend them to aqueous solubility also create similar molecular interactions that decrease their volatilities. Increasing volatility by using higher temperature separations is often not possible because of potential degradation. Derivatization still remains the method of choice for GC–MS analyses of nonvolatile analytes. Ledauphin and coworkers used GC–MS of the 3-methylbenzothiazolin-2-one hydrazone derivatives of C5 to C11 *n*-aldehydes found in beverages [14]. Ten estrogen metabolites were analyzed by a GC–MS method [15]. Samples were cleaned through SPE on C18 cartridges and the analytes were derivatized with *O*-trimethylsilyl ether derivatization.

In contrast to GC, where derivatization is predominantly used to make compounds volatile, in LC derivatization is mainly used to make analytes detectable through increases in sensitivity or selectivity. An example in which this was done was the derivatization of amines by 1,2-benzo-3,4-dihydrocarbazole-9-isopropyl chloroformate [16]. In APCI mode, the $M+1$ ion of these derivatives is very intense, improving the sensitivity to around 1 ppm of the injected amount.

Selective ion monitoring (SIM) is a very important methodology in environmental analysis. In SIM, target ions are monitored in the retention-time window for the analytes' expected elution. The environmental pollutant dinitropyrene isomers have been separated by GC and monitored by MS [17]. Yeast metabolites were identified and quantified using GC–MS [18].

LC–MS has seen an even greater increase in application over the past decade than that of GC–MS. LC–MS once required a knowledge of both techniques to ensure their compatibility. Now, interface or the use of APCI means that the instrumentation no longer has these limitations. Therefore, users can essentially be operators only. Although much published work shows more sophistication than this, the need for knowledge of both LC and MS principles is much, much less. Figure 49.8 shows a chromatogram of 224 pesticides by LC-MS-MS.

Trace analytes are now routinely examined by LC–MS techniques. One was for 12 pesticide contaminants in various fruit samples of oranges, strawberries, cherries, peaches, apricots, and pears [19]. The pesticide amitraz and its degradation products were determined in pears using LC–MS after sample extraction and supercritical fluid extraction (SFE) cleanup [20].

Such sensitivity and the ability to identify molecules have led to LC–MS being used widely in clinical application. The identification of impurities within [21] and the metabolites [22–24] of pharmaceuticals and dietary supplements are common applications.

The metabolites of the important dietary flavonol quercetin were examined by LC–ESI–MS–MS [25]. A specific metabolite, tribendimidine, of the pharmaceutical tribendimidine was determined through the use of LC–MS techniques [26]. The evidence of traces levels of illicit steroids were found through the use of SPE sample preparation and reversed-phase LC–MS [27].

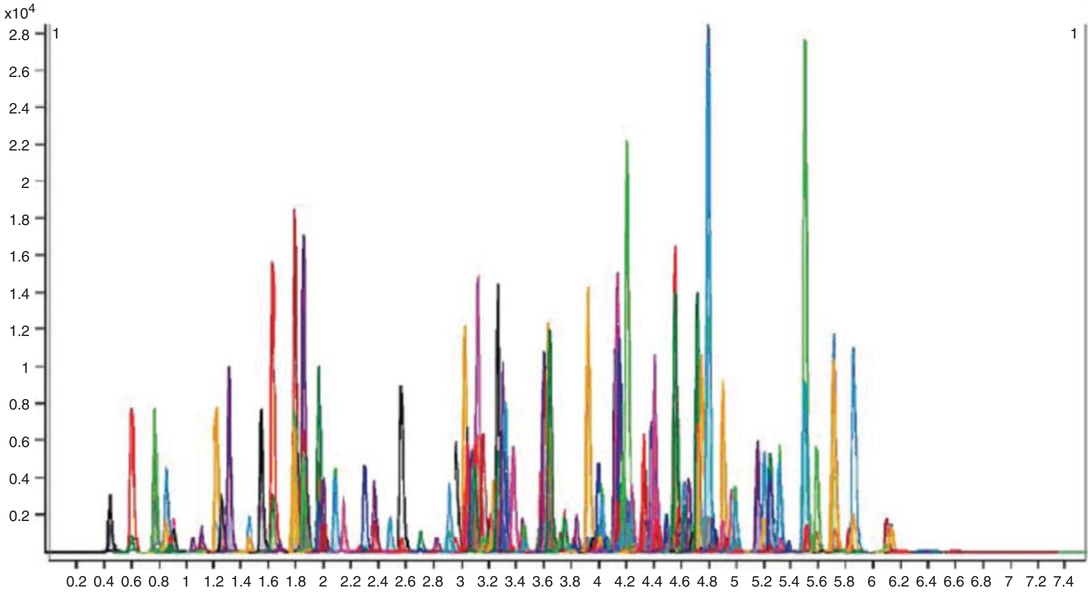

Figure 49.8 LC–MS separation utilizing ultrahigh-pressure LC and MS monitoring of retention windows for target masses in the analysis of 224 pesticides in a standard mixture.

The fungus *Fusarium verticillioides* infests many plants, including maize and other grains. *F. verticillioides* is a pathogen of many plants and produces fumonisins, which are both toxic to animals and humans and it affects the sprouting and growth of crops. An LC–MS method to determine the presence of the fumonisins was used to determine if this fungal contamination had occurred in maize samples [28]. An LC–MS method could determine 18 illegal drugs in samples of human saliva [29]. A method for the anticholesterol medication pravastatin and its metabolites in human plasma samples used LC–MS [30]. It provided both sensitivity and high throughput. An analogous type of method for the antipsychotic medication risperidone and its metabolites also utilized LC–MS–MS [31]. The method used positive ion detection and the separation was able to differentiate the various enantiomers of 9-hydroxyrisperidone.

The testing of animals for drugs and toxins is now routinely done by LC–MS to ensure food safety. One example is the analysis of antiinflammatory drugs in cattle used for milk and beef production [32]. Similarly, the antibiotic nitrofurazone was looked for in a variety of meat, poultry, dairy, and fish samples [33]. Yatsukawa and coworkers used LC–MS to analyze the antibiotics sedecamyin and terdecamycin (TDM) in meat and dairy products [34].

Acknowledgment

The help of Dr. Matthew S. Klee of Agilent Technologies is gratefully appreciated, as is the approval to use the figures.

References

1. Weber, A., Maurer, H.W., and Pfleger, K. (2007) *Mass Spectral and GC Data of Drugs, Poisons, Pesticides, Pollutants and Their Metabolites*, Wiley-VCH Verlag GmbH, Weinheim ISBN: 3-527-31538-1.
2. Bertholf, R. and Winecker, R. (eds) (2004) *Chromatographic Methods in Clinical Chemistry and Toxicology*, John Wiley & Sons, Ltd, Chichester ISBN: 0-470-02309-0.
3. Adams, R.P. (2007) *Identification of Essential Oil Components by Gas Chromatography/Mass Spectrometry*, Allured Publishing Co., ISBN: 1-932633-21-9.
4. Mossoba, M.M. (ed.) (1998) *Spectral Methods in Food Analysis: Instrumentation and Application*, Taylor & Francis, Carol Stream, IL ISBN: 08-247-0223-9.
5. Flamini, R. (ed.) (2008) *Hyphenated Techniques in Grape and Wine Chemistry*, Wiley-Interscience ISBN: 0470061871.
6. Loconto, P.R. (ed.) (2008) *Trace Environmental Quantitative Analysis, Principles, Techniques and Applications*, 2nd edn, Taylor & Francis, Boca Raton, FL ISBN: 0-8247-5853-6, CRC Press.
7. Ardrey, B. and Ardrey, R.E. (2003) *Liquid Chromatography Mass Spectrometry: An Introduction*, John Wiley & Sons, Ltd, Chichester ISBN: 0-471-49801-7.
8. Cappiello, A. (ed) (2007) *Advances in LC-MS Instrumentation*, Elsevier, Amsterdam ISBN: 0-444-52773-7.
9. Nováková, L., Solichová, D., and Solich, P. (2006) Advantages of ultra performance liquid chromatography over high-performance liquid chromatography: comparison of different analytical approaches during analysis of diclofenac gel. *J. Sep. Sci.*, **29**, 2433–2443.
10. Nováková, L., Matysová, L., and Solich, P. (2006) Advantages of application

of UPLC in pharmaceutical analysis. *Talanta*, **68**, 908–918.

11. Swartz, M.E. (2005) UPLC: an introduction and review. *J. Liq. Chromatogr.*, **8**, 1253–1263.
12. ElBeqqali, A., Kussak, A., and AbdelRehim, M. (2006) Fast and sensitive environmental analysis utilizing microextraction in packed syringe online with gas chromatography–mass spectrometry–determination of polycyclic aromatic hydrocarbons in water. *J. Chromatogr. A*, **1114**, 234–238.
13. Ravindra, K., Godoi, A.F., Bencs, L., and VanGrieken, R. (2006) Low-pressure gas chromatography-ion trap mass spectrometry for the fast determination of polycyclic aromatic hydrocarbons in air samples. *J. Chromatogr. A*, **1114**, 278–281.
14. Ledauphin, J., Barillier, D., and BeljeanLeymarie, M. (2006) Gas chromatographic quantification of aliphatic aldehydes in freshly distilled Calvados and Cognac using 3-methylbenzothiazolin-2-one hydrazone as derivative agent. *J. Chromatogr. A*, **1115**, 225–232.
15. Knust, U., Strowitzki, T., Spiegelhalder, B., Bartsch, H., and Owen, R.W. (2007) Optimization of an isotope dilution gas chromatography/mass spectrometry method for the detection of endogenous estrogen metabolites in urine samples. *Rapid Commun. Mass Spectrom.*, **21**, 2245–2254.
16. You, J.M., Chen, X.M., Zhao, X.N., Suo, Y.R., Wang, H.L., and Li, Y.L. (2006) Pre-column derivatization of amines with 1,2-benzo-3,4-dihydrocarbazole-9-isopropyl chloroformate followed by LC-fluorescence and LC-APCI-MS. *Chromatographia*, **63**, 337–343.
17. Nakao, T., Aozasa, O., Ohta, S., and Miyata, H. (2007) Analytical method for determination of dinitropyrenes using gas chromatography-high-resolution mass spectrometry. *J. Chromatogr. A*, **1157**, 352–357.
18. Mohler, R.E., Dombek, K.M., Hoggard, J.C., Pierce, K.M., Young, E.T., and Synovec, R.E. (2007) Comprehensive analysis of yeast metabolite GC x GC-TOFMS data: combining discovery-mode and deconvolution chemometric software. *Analyst*, **132**, 756–767.
19. Soler, C., James, K.J., and Pico, Y. (2007) Capabilities of different liquid chromatography tandem mass spectrometry systems in determining pesticide residues in food–application to estimate their daily intake's'. *J. Chromatogr. A*, **1157**, 73–84.
20. Pico, Y., la Farre, M., Tokman, N., and Barcelo, D. (2009) Rapid and sensitive ultra-high-pressure liquid chromatography-quadrupole time-of-flight mass spectrometry for the quantification of amitraz and identification of its degradation products in fruits. *J. Chromatogr. A*, **1203**, 36–46.
21. Vogeser, M. and Seger, C. (2008) A decade of HPLC-MS/MS in the routine clinical laboratory–goals for further developments. *Clin. Biochem.*, **4**, 649–662.
22. Yamada, K., Miyazaki, T., Shibata, T., Hara, N., and Tsuchiya, M. (2008) Simultaneous measurement of tryptophan and related compounds by liquid chromatography/electrospray ionization tandem mass spectrometry. *J. Chromatogr. B*, **867**, 57–61.
23. Li, J.L., Wang, X.D., Wang, C.X., Fu, Q., Liu, L.S., Huang, M., and Zhou, S.F. (2009) Rapid and simultaneous determination of tacrolimus (FK506) and diltiazem in human whole blood by liquid chromatography-tandem mass spectrometry: application to a clinical drug-drug interaction study. *J. Chromatogr. B*, **867**, 111–118.
24. Chen, Y., Song, W., Peng, Z.H., Ge, B.Y., and Han, F.M. (2008) Identification of metabolites of tectoridin in-vivo and in-vitro by liquid chromatography-tandem mass spectrometry. *J. Pharm. Pharmacol.*, **60**, 709–716.
25. Duenas, M., MingoChornet, H., PerezAlonso, J.J., DiPaolaNaranjo, R., GonzalezParamas, A.M., and SantosBuelga, C. (2008) Preparation of quercetin glucuronides and characterization by HPLC-DAD-ESI/MS. *Eur. Food Res. Technol.*, **227**, 1069–1076.
26. Yuan, G.Y., Wang, B.J., Wei, C.M., Zhang, R., and Guo, R.C. (2008) LC-MS determination of p-(1-dimethylamino ethylimino)aniline: a metabolite of

tribendimidine in human plasma. *Chromatographia*, **68**, 139–142.

27. Strahm, E., Kohler, I., Rudaz, S., Martel, S., Carrupt, P.A., Veuthey, J.L., Saugy, M., and Saudan, C. (2008) Isolation and quantification by high-performance liquid chromatography-ion-trap mass spectrometry of androgen sulfoconjugates in human urine. *J. Chromatogr. A*, **1196**, 153–160.
28. Zitomer, N.C., Glenn, A.E., Bacon, C.W., and Riley, R.T. (2008) A single extraction method for the analysis by liquid chromatography/tandem mass spectrometry of fumonisins and biomarkers of disrupted sphingolipid metabolism in tissues of maize seedlings. *Anal. Bioanal. Chem.*, **391**, 2257–2263.
29. Concheiro, M., de Castro, A., Quintela, O., Cruz, A., and LopezRivadulla, M. (2008) Determination of illicit and medicinal drugs and their metabolites in oral fluid and preserved oral fluid by liquid chromatography-tandem mass spectrometry. *Anal. Bioanal. Chem.*, **391**, 2329–2338.
30. Wang, X.D. and Wang, Y.C. (2008) On-line extraction coupled with liquid chromatography tandem mass spectrometry for quantitation of pravastatin and its metabolite in human serum. *Biomed. Chromatogr.*, **22**, 719–726.
31. De Meulder, M., Remmerie, B.M.M., de Vries, R., Sips, L.L.A., Boom, S., Hooijschuur, E.W.J., van de Merbel, N.C., and Timmerman, P.M.M.B.L. (2008) Validated LC-MS/MS methods for the determination of risperidone and the enantiomers of 9-hydroxyrisperidone in human plasma and urine. *J. Chromatogr. B*, **870**, 8–16.
32. Gentili, A. (2007) LC-MS methods for analyzing anti-inflammatory drugs in animal-food products. *TrAC, Trends Anal. Chem.*, **26**, 595–608.
33. Horie, B.M., Tabarai, Y., Ishii, R., Hashimo, K., and Yamagish, Y. (2008) Determination of nitrofurazone in livestock products and seafoods by liquid chromatography-tandem mass spectrometry. *J. Food Hyg. Soc. Jpn*, **49**, 204–210.
34. Yatsukawa, Y., Fujita, K., Nakamura, M., Watai, M., Murayama, M., and Maitani, T. (2008) Simultaneous determination of sedecamycin and terdecamycin in livestock products by LC/MS. *J. Food Hyg. Soc. Jpn*, **49**, 239–243.

50

Optical Detection

John C. Fetzer

50.1

UV Detection

The photodiode array detector is the most used UV absorbance detector. Different instrument vendors abbreviate this as PDA or DAD (diode-array detector). PDA will be used in this review. PDAs are commonly utilized even when only single-wavelength monitoring is used and are produced by a wide variety of instrument companies.

The PDA relies on simultaneous detection of the intensity of light at all wavelengths within a selected range. This is accomplished through the use of an optical design and optical devices that are very different from what was formerly used for UV detection in liquid chromatography (LC). One such commercial design is shown in Figure 50.1.

In the past, only a single wavelength was monitored. The light from the source was separated by a prism or diffraction grating, and a monochromator passed only the one selected wavelength through the chromatographic sample cell. No spectral information could be collected, except through stop-flow scanning techniques.

The photodiode array detector (abbreviated as DAD or PDA by various instrument manufacturers – and DAD will be used here) passes the total beam from the light sources through the flow cell. In contrast to the monochromator-based detector, both the tungsten and deuterium light sources are used simultaneously if both high and low wavelengths are needed (in the monochromator-based system, the scanning aspect precluded the need for this). As all wavelengths obey the Beer–Lambert law independently, a separated sample component will absorb the wavelengths according to its UV spectral responses. The diffraction grating is placed after this, spreading the light into a band. This is focused onto a row of photodiodes, semiconductor devices that respond to light intensity. Each photodiode, thus, covers a small range of the diffracted light. The current from each photodiode correlates with the intensity each receives. The responses of all of the series of photodiodes correspond with the analyte's absorbance spectrum.

As a spectroscopic approach, UV is, in general, inherently less informative than other molecular spectroscopy techniques. The presence of a chromophore within

Handbook of Spectroscopy, Second Edition. Edited by Günter Gauglitz and David S. Moore.

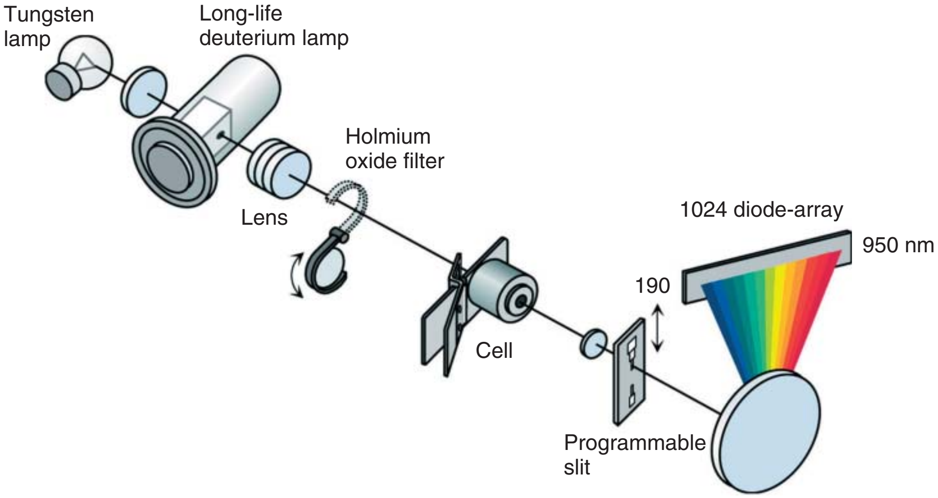

Figure 50.1 Schematic diagram of a typical diode-array UV detector. (By courtesy of Agilent Instruments.)

the viewing range of the mobile phase is one limitation. Some common LC solvents, such as tetrahydrofuran, acetone, and ethyl acetate, have high UV absorbances in the range where many molecules have their own absorbances.

UV activity usually involves electronic transitions of π or lone-pair electrons. These transitions are broad and featureless for most chemical structures, being 50–100 nm wide and having only a single, rounded peak. Minor differences in the location occur because of derivatization. A methyl group, for instance, shifts the spectrum upward by 1–2 nm, while deuteration shifts downward a similar amount. These are due to electron-withdrawing and electron-donating tendencies.

Solvent choices also have an effect on the use of UV spectral detection as the technique. The location of an absorbance band is usually solvent dependent. The range of shift may be as great as 15–20 nm from a nonpolar solvent, such as hexane, to a very polar mixture containing water and methanol. This limits the use of spectral atlases and library-matching programs to solvents of very similar interactions or necessitates corrections. Most software do not have such a feature, so this must be done manually.

Because UV bands are so broad and featureless, their use in identifying compounds is not often used unless a pure standard is available for comparison of the spectrum and chromatographic retention time. If that is the case, spectra of the standard and unknown peak can be directly compared without worries over solvent shifts and other artifacts.

The best-known exception to this generality for organic compounds is the class of polycyclic aromatic hydrocarbons. Their UV spectra are determined by the arrangement of the multiple fused aromatic rings in their structures. These various arrangements result in UV spectra with numerous bands, generally a dozen

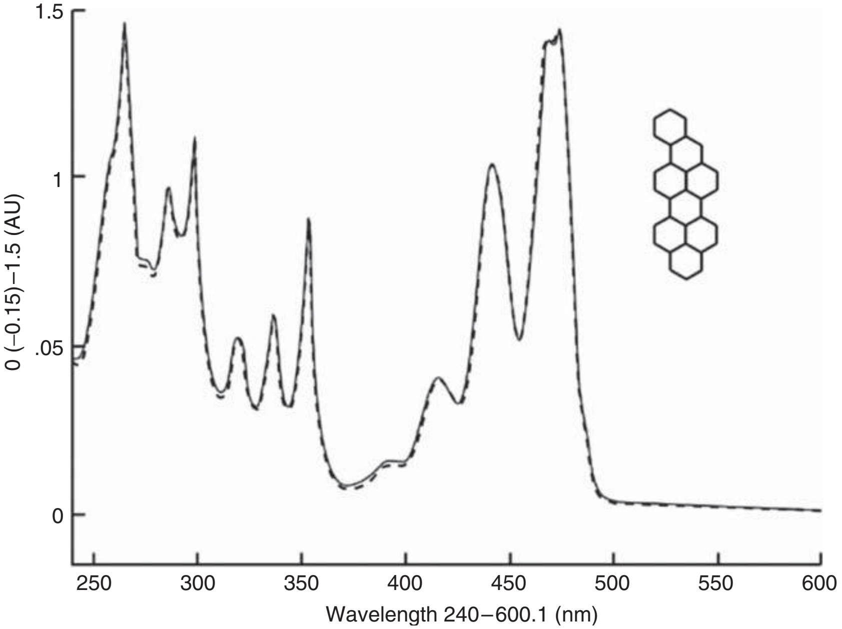

Figure 50.2 The UV spectrum of the nine-ring PAH.

or more, arranged in distinct patterns of different intensities and with narrow widths [1]. A typical UV spectrum obtained during a chromatographic run of a polycyclic aromatic hydrocarbon (PAH) is shown in Figure 50.2. These are often very intense, with molar absorptivities of five or six orders of magnitude. Figure 50.3 shows the separation of several eight-ring PAH isomers by reversed-phase high-performance liquid chromatography (HPLC).

Inorganic ions often have distinct UV spectra, so UV detection can be used both qualitatively and quantitatively. The ions of many transition metals have high-wavelength absorbance bands (thus, their characteristic colors that change with oxidation state). The best example of this is the lanthanide group of elements. In them, their buried f-shell electrons are what are seen in UV absorbance spectra. By not being involved in chelation or bonding, these electrons have many very narrow UV bands. These are distinct for each lanthanide.

A DAD detector is slightly less sensitive than a monochromator-based detector, typically 3–10 times less. The typical detection level is in the range of 0.1 milliabsorbance units (mAU) to 0.05 mAU. The lower limit for a typical intensity for a usable spectrum is 1–2 mAU, but analytes with very sharp and narrow bands may be identifiable below this level.

The resolution of a DAD is usually 1–2 nm. This is sufficient to even see the small upward shift in a spectrum when there is methyl or other alkyl substitution. The spectra of pyrene and three of its alkyl derivatives are shown in Figure 50.4, also showing that the basic pattern in the spectra does not change.

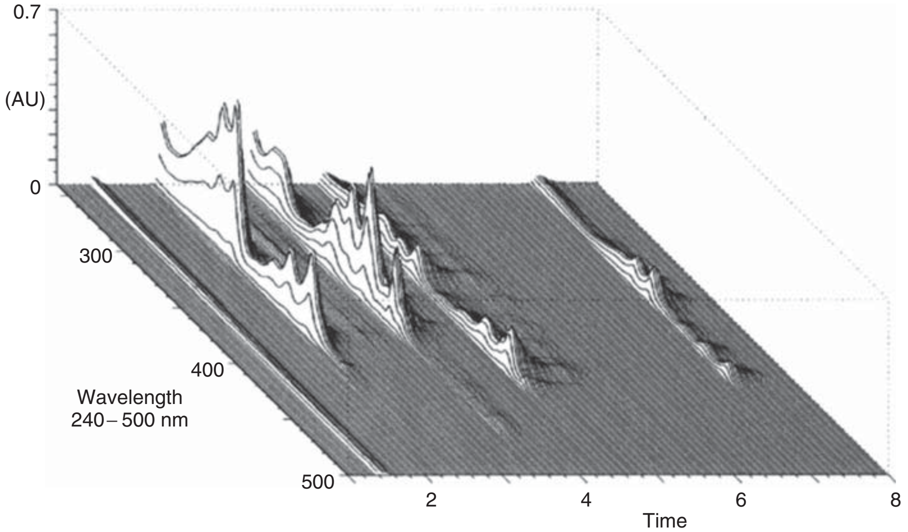

Figure 50.3 A three-dimensional chromatogram of PAHs separated by nonaqueous reversed-phase HPLC.

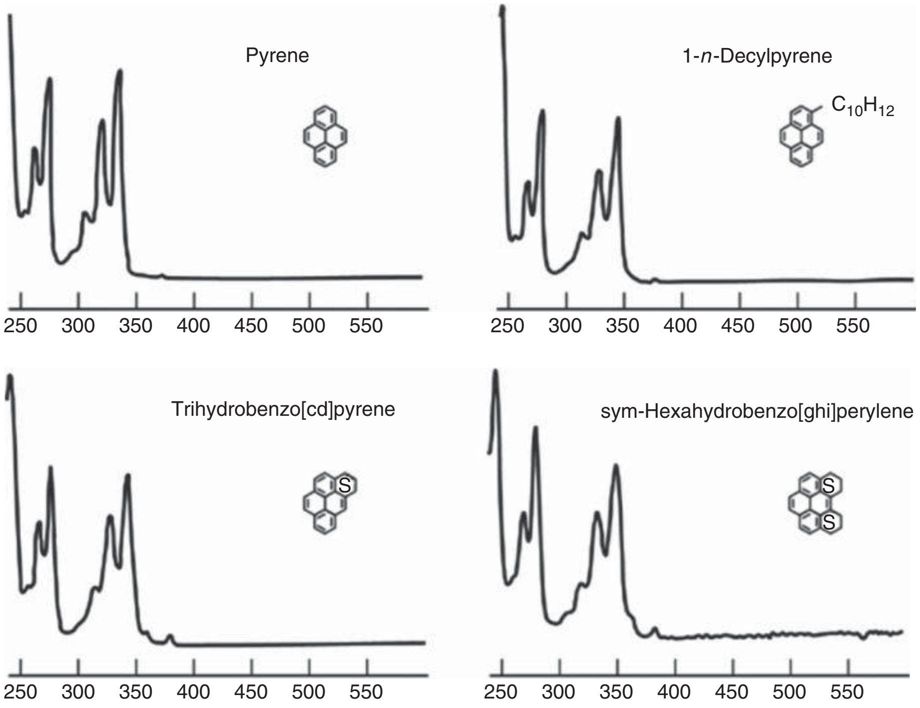

Figure 50.4 DAD spectra of pyrene and some of its alkyl derivatives showing the slight upward shifts.

50.2
Fluorescence Detection

Fluorescence excitation and UV absorbance involve the same electronic transition, that of an electron going from a ground state to an excited state. UV absorbance, however, involves all such transitions. Fluorescence excitation, as it is monitored by the resulting emission from the lowest excited state to the highest ground state, only involves the excitation of an electron upward through those two states. Therefore, a fluorescence excitation spectrum is usually only about 50–150 nm wide, in contrast to an absorbance spectrum that might be several hundred nanometer wide.

A typical spectral pair for a PAH is shown in Figure 50.5. The mirror-image quality between excitation and emission is common in PAHs.

How does this affect the use of a spectrofluorometer as a detector? With such a short range (the range for the emission spectra are similarly short), a fast-scanning spectrofluorometer might scan a peak in a short enough time where there is little change in concentration that might distort the spectrum. Stopping the flow to scan, however, is often the common practice when collecting fluorescence spectra.

There has been a commercially available diode-array-based detector. Unfortunately, its slit width settings were very wide, 15 nm, and not adjustable. This leads to much higher light throughput and better sensitivity for monitoring in the

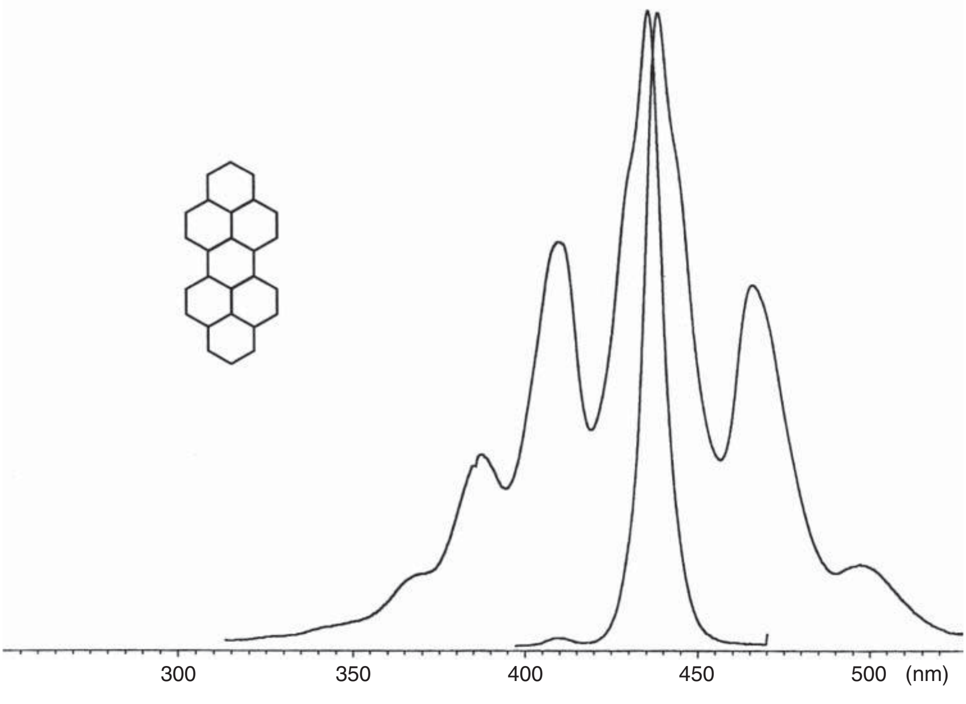

Figure 50.5 The fluorescence excitation and emission spectra of dibenzo[cd,lm]perylene.

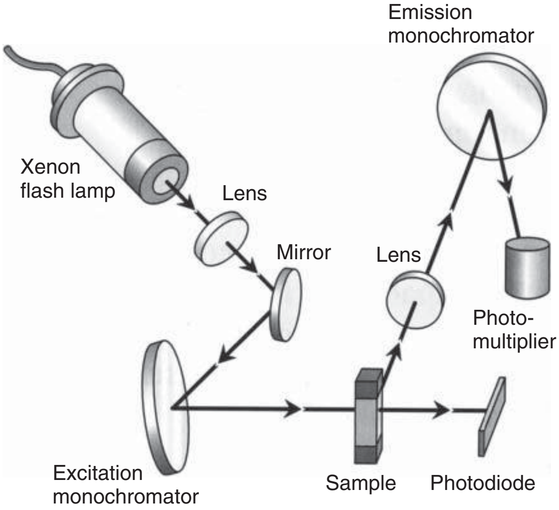

Figure 50.6 A schematic of a full-spectrum fluorescence detector. (By courtesy of Agilent Instruments.)

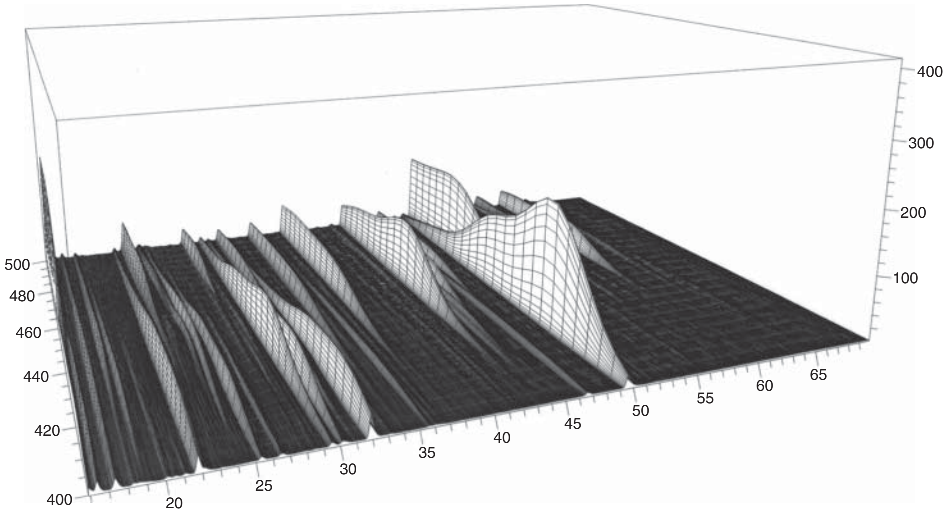

Figure 50.7 Chromatogram of a complex mixture of PAHs in a carbon-black extract. Each peak is in the nanogram-injected range.

chromatogram mode. The spectra, however, are broader. Any spectral features, such as the multiple bands seen in PAH spectra, are lost and peak identification is more difficult. The optical schematic of this detector is shown in Figure 50.6. A chromatogram of its output is shown in Figure 50.7, with the obvious broad and featureless spectra. If the resolution were better, these should be similar in pattern to the excitation spectrum in Figure 50.5.

50.3
Infrared Detection

The same separators developed for GC–MS are amenable for GC–FTIR. Griffiths describes the use of GC-FTIR to differentiate the four butylbenzene isomers. MS detection was unable to show the differences between two of the four.

Gas-phase infrared spectra can be quite different from solution ones. Two factors contribute to this, the much narrower transition lines for gas-phase molecular motions and the much higher experimental temperatures of the GC effluent than the room temperature. Reference spectra in the literature are almost always taken at room temperature and are solid-phase mixtures of neat liquids or solids mixed with potassium bromide.

This means that literature and library spectra cannot be matched to peaks found in the GC chromatogram. This necessitates building a library of gas-phase spectra by running standard compounds. Although this can be both tedious and limiting, it does add the chromatographic retention time as another confirming piece of data. The limitation is brought on by the requirement that a standard compound be available.

In LC, the mobile phase is present in hundred or even thousand times higher concentrations than the analytes. This results in large and significant spectral ranges being unavailable or limits the chromatography to several or more transparent solvents that may not perform the best separations.

50.4
Applications

UV detection is common in HPLC. Its application, therefore, is widespread. Multiwavelength and spectral detection are used to assess peak purity because a single component ought to obey the Beer–Lambert law throughout the peak, excepting in the very front and back portions where noise may be an issue. In addition, the absorbance spectra are used to identify the individual peaks.

One series of chapters uses HPLC-DAD to a high degree to identify PAHs produced in pyrolysis and combustion. The UV spectra are used both to identify unknown peaks through comparison to standard compounds and through interpretation of the locations of absorbance bands and the patterns within the spectra. In the latter methodology, several previously unknown large PAHs are identified [2–6].

An HPLC-DAD method was developed for quantification of aripiprazole and dehydro-aripiprazole, in human plasma. After a simple liquid–liquid extraction, chromatographic separation was carried out on a C18 reversed-phase column, using an ammonium buffer-acetonitrile mobile phase (40 : 60, v/v). The total run time was only 7 min at a flow rate of 1.0 ml min^{-1}. The precision values were less than 12% and the accuracy values were ranging from 98 to 113% and the lower limit of quantification was 2 ng ml^{-1} for both compounds. Calibration curves were linear over a range of 2–1000 ng ml^{-1}. The mean trough plasma concentrations in patients treated with aripiprazole were 157 and 29 ng ml^{-1} for aripiprazole and dehydro-aripiprazole, respectively [7].

The roles of isoflavones in the prevention of several hormone-dependent cancers and osteoporosis are of great interest. Despite many pharmacokinetics studies of the isoflavones, the actual types of conjugates circulating in the body and the position(s) of conjugation sites on the flavone skeleton are still uncertain because, in general, conjugated compounds in biological fluids have been evaluated by measuring the free aglycones obtained after selective enzymatic hydrolysis. Using a high-performance (HPLC)-UV-DAD method combined with solid-phase extraction, we have obtained HPLC profiles of isoflavone glycosides [daidzin (Din) and genistin (Gin)] and of intact isoflavone metabolites in human plasma: daidzein, genistein, daizein-7-glucuronide, daidzein-4′-glucuronide, genistein-7-glucuronide, genistein-4′-glucuronide, daidzein-7-sulfate, daidzein-4′-sulfate, genistein-7-sulfate, and genistein-4′-sulfate. We investigated the plasma profile of intact isoflavone metabolites in plasma obtained 1–7 h after oral administration of 50 g of kinako (baked soybean powder) to two healthy volunteers. The results of DAD analysis indicated that the main isoflavone metabolite peaks were identified on the HPLC chromatogram. Furthermore, the intact glycosides Din and Gin were detected in 1-h plasma samples by their positive electrospray ionization mass spectra, demonstrating that the glycosides Din and Gin can be absorbed from the gut [8, 9].

We report an offline multidimensional HPLC technique for the group separation and analysis of PAHs in a heavy gas oil fraction (boiling range 287–481 °C). Waxes present in the heavy gas oil fraction were precipitated using cold acetone at $-20\,^{\circ}$C. Recovery studies showed that the extract contained 93% (±1%; $n = 3$) of the PAHs that were originally present, while the wax residue contained only 6% (±0.5%; $n = 3$). PAHs present in the extract were fractionated, on the basis of the number of rings, into five fractions using a semipreparative silica column (normal-phase HPLC). These fractions were analyzed using reverse-phase high-performance liquid chromatography (RP-HPLC) coupled to a DAD. The method separated alkyl and unsubstituted PAHs on two reverse-phase columns in series using an acetonitrile/water mobile phase. UV spectra of the chromatographic peaks were used to differentiate among PAH groups. Further characterization of PAHs within a given group to determine the substituent alkyl carbon number used retention time matching with a suite of alkyl-PAH standards. Naphthalene, dibenzothiophene, phenanthrene and fluorene, and their C1–C4 alkyl isomers were quantified. The concentrations of these compounds obtained using the current method were compared with that of a GC–MS analysis obtained from an independent oil chemistry laboratory.

References

1. Fetzer, J.C. (2000) *The Chemistry and Analysis of the Large Polycyclic Aromatic Hydrocarbons* Chapter 3, Wiley-Interscience, New York, pp. 67–83.
2. Ona, J.O. and Wornat, M.J. (2007) Identification of the $C_{30}H_{16}$ polycyclic aromatic hydrocarbon benzo[cd] naphtho[1,2,3-lm] perylene as a product of the supercritical

pyrolysis of a synthetic jet fuel. *Polycyclic Aromat. Compd.*, **27**, 165–183.

3. Somers, M.L., McClaine, J.W., and Wornat, M.J. (2007) The formation of polycyclic aromatic hydrocarbons from the supercritical pyrolysis of 1-methylnaphthalene. *Proc. Combust. Inst.*, **31** (1), 501–509.
4. Somers, M.L. and Wornat, M.J. (2007) UV spectral identification of polycyclic aromatic hydrocarbon products of supercritical 1-methylnaphthalene pyrolysis. *Polycyclic Aromat. Compd.*, **27** (4), 261–280.
5. McClaine, J.W., Ončа, J.O., and Wornat, M.J. (2007) Identification of a new $C_{28}H_{14}$ polycyclic aromatic hydrocarbon as a product of supercritical fuel pyrolysis: Tribenzo[cd,ghi,lm]perylene. *J. Chromatogr. A*, **1138** (1–2), 175–183.
6. Marsh, N.D., Wornat, M.J., Scott, L.T., Necula, A., Lafleur, A.L., and Plummer, E.F. (2000) The identification of cyclopenta-fused and ethynyl-substituted polycyclic aromatic hydrocarbons in benzene droplet combustion products. *Polycyclic Aromat. Compd.*, **13** (4), 379–402.
7. Lancelin, F., Kayssa, D., Tabaouti, K., Linda, K., Sophie, B.A., Paubel, P., and Piketty, M.L. (2008) *J. Chromatogr. B: Anal. Technol. Biomed. Life Sci.*, **867**, 15–19.
8. Hosoda, K., Furuta, T., Yokokawa, A., Ogura, K., Hiratsuka, A., and Ishii, K. (2008) *Drug Metab. Dispos.*, **36** (8), 1485–1495.
9. Aravanabhavan, G.S., Helferty, A., Hodson, P.V., and Brown, R.S. (2007) A multi-dimensional high performance liquid chromatographic method for fingerprinting polycyclic aromatic hydrocarbons and their alkyl-homologs in the heavy gas oil fraction of Alaskan North Slope crude. *J. Chromatogr. A*, **1156** (1–2), 124–133.

51

Atomic Spectral Detection

John C. Fetzer

51.1

Introduction

Atomic spectroscopy has been used for chromatographic detection for many years. Its use has become more widespread as a result of two factors: the importance of the elemental-speciation information that it generates is now of greater interest and the major advances in instrumentation. Plasma-based instruments are used because they offer continuous input of sample (the chromatographic effluent), multielement observation and robust, reliable operation.

Bioinorganic studies have grown rapidly in the past two decades. Before that, it was possible only to know the presence of an inorganic element through bulk analysis using techniques such as atomic absorption or X-ray fluorescence. Over 30 years ago, plasmas were first used in atomic spectroscopy. In the 1970s and 1980s, a variety of plasma sources were developed to atomize samples and then do optical emission spectroscopy (OES). The three main types of plasmas were the microwave-induced plasma (MIP), the direct-current plasma (DCP), and the inductively coupled plasma (ICP). Their history and features are not the scope of this chapter, but can be found in review articles [1, 2] and in other chapters of this book. In this chapter, the focus will be on the strengths and weaknesses of each for chromatographic detection.

51.2

Atomization and Plasmas

As the aim is to monitor individual elements, molecules must be broken down into their constituent atoms. This is generally readily done through generation of a plasma. A plasma is a low-pressure mixture of individual atoms and their ions.

Certain elements do form stable multiatomic fragments. Calcium and barium, for example, can occur as their oxides in some plasmas.

Interferences are not as prevalent as in molecular spectroscopy detection, but do occur. For mass spectral detection, isotopes can be numerous and overlapping with

Handbook of Spectroscopy, Second Edition. Edited by Günter Gauglitz and David S. Moore.

other elements. This leads to the need for deconvolution algorithms based on the normal relative abundances for the isotopes of each element (a few elements have only one isotope). This process is generally straightforward because most elements contain a limited number of isotopes, the spread in masses between elements can limit the overlap, and chemically many of the overlapping elements are unlikely to occur together. The lanthanides, however, are chemically similar and possess numerous isomers, so quantitation can be more difficult because the deconvolution algorithms are not designed to deal with numerous interfering elements.

The type of atomization source determines operating conditions. These, in turn, define and limit the application. There must be compatibility between the type of chromatography and the type of atomization. The carrier gas in GC and the mobile phase in LC most often determine this, but flow rates are also an important factor.

An MIP is inherently incompatible with samples containing water. Microwave generators radiate at 2.45 GHz. This is a rotational resonance for water, so the energy is lost to that mode rather than to plasma formation. Thus, they cannot be used as part of a detector for LC because most separations are aqueous. In addition, the focal volume of an MIP is relatively small compared to that of the other sources. This limits its use in nonaqueous LC, as well, just as quenching and thermal effects can lower the atomization efficiency if normal LC flow rates are used.

The ICP does not work as well with helium as it does with argon, while the DCP and MIP do. This is an advantage in coupling to GC because the carrier gas is helium. For an ICP to be used, argon makeup gas must be introduced. This dilutes the analyte atoms and raises detection limits. In addition, the higher energy of the ICP requires that the gases dissipate some of the energy so that the surrounding instrumentation is not heated too highly. Argon has a higher heat capacity than helium. This would require a higher helium makeup gas flow, more than 50% greater than the $20\,\mathrm{l\,min^{-1}}$ usually used with argon. This adds to the potential cost of a GC-ICP instrument. Transfer lines may also melt or deform in extended use.

For LC, in contrast, ICP with either optical emission (OE) or MS detection has become the dominant plasma source for atomic detection. This has led to the development of numerous commercial instruments. Their pricing has greatly been reduced as these instruments are produced in greater numbers and market competition has grown. These instruments are now robust, turnkey, and reliable.

A secondary factor is the stability of the background, which translates into baseline stability in a chromatogram. This was one limit of the DCP, as the electrodes used to generate the plasma are consumed over time, creating an inherent background of the major elements (often, carbon from a graphite electrode, but also varying amounts of any trace-level contaminants). In some designs, a tungsten cathode is used with carbon anodes.

None of the plasmas are very robust with respect to changes in ionization energy and efficiency when a liquid stream is injected into it. The ICP is the most stable, but can tolerate only a few microliters per minute of flow. The development of narrow-bore HPLC columns and micro-LC, however, has given matching flow rates that have made LC-ICP possible.

The detection limits found when using the atomic emission spectroscopy (AES) version of an ICP instrument are approximately 1000 times greater than those of the MS version of the technique. This leads to a detection delay or hysteresis effect in which the incoming flows must expand and fill the detection volume of the spectrometer to levels above the detection limit. This leads to peak broadening and less apparent chromatographic resolution (it creates a large detection volume that merges resolved peaks back together). MS does not suffer from this because of the lower detection limits.

This difference in the optimum benefits of helium and argon in GC versus ICP use can be overcome by using helium as the GC carrier gas and argon as the makeup gas for a sensitive method such as ICP-MS.

The plasma in a DCP is very sensitive to longer term drift, which in chromatographic detection is seen as a gradual change in the baseline. The few applications of LC-DCP include the monitoring of the various oligomers in polyphosphate species from size-exclusion chromatography and the vanadium and nickel porphyrin species in heavy crude oils.

51.3
Spectrometric Detection

Once a sample has been atomized, there are two main ways of detecting the atoms, OES and MS. Both methods have multielement capabilities. The MS is less sensitive, but suffers from fewer interferences than atomic emission detector (AED).

51.4
MIP for GC Detection

Most gas chromatographs use either helium or hydrogen as the carrier gas because of the higher diffusion coefficients for molecules in them. The microwave plasma is more stable with helium as a medium than the other plasma sources. Helium has a very low thermal conductivity compared to many other permanent gases. This can lead to overheating in the plasma cavity. This in turn can cause melting and deformation of instrument parts. This can be a critical failure if it causes misalignment of the carrier-gas-containing analytes and the MIP focal volume.

Commercial MIPs for use in GC-AED are now robust and reliable. One commercial design of the plasma area is shown in Figure 51.1. The optical unit consists of a diffraction grating and a diode-array detector for multielement monitoring.

There have been many applications of GC-AED within the petroleum industry. The use of carbon, sulfur, and nitrogen monitoring in diesel fuel has been used to see the effects of various types of processing [3]. Not only can an AED monitor specific elements of interest, such as sulfur, oxygen, or metals, but it can be used as a universal detector because it can monitor carbon (Figure 51.2). This mode can be used with specific element monitoring to identify heteroatom-containing

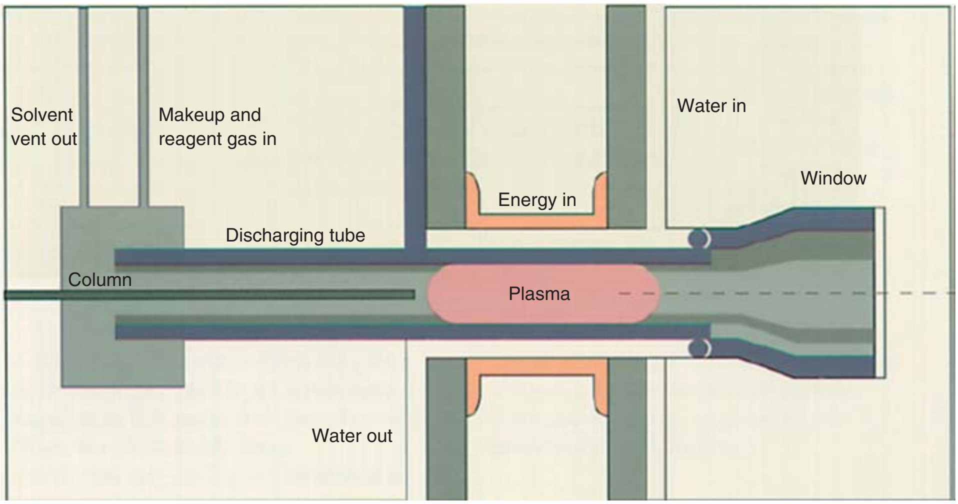

Figure 51.1 The arrangement of the plasma source within a commercial GC-AED.

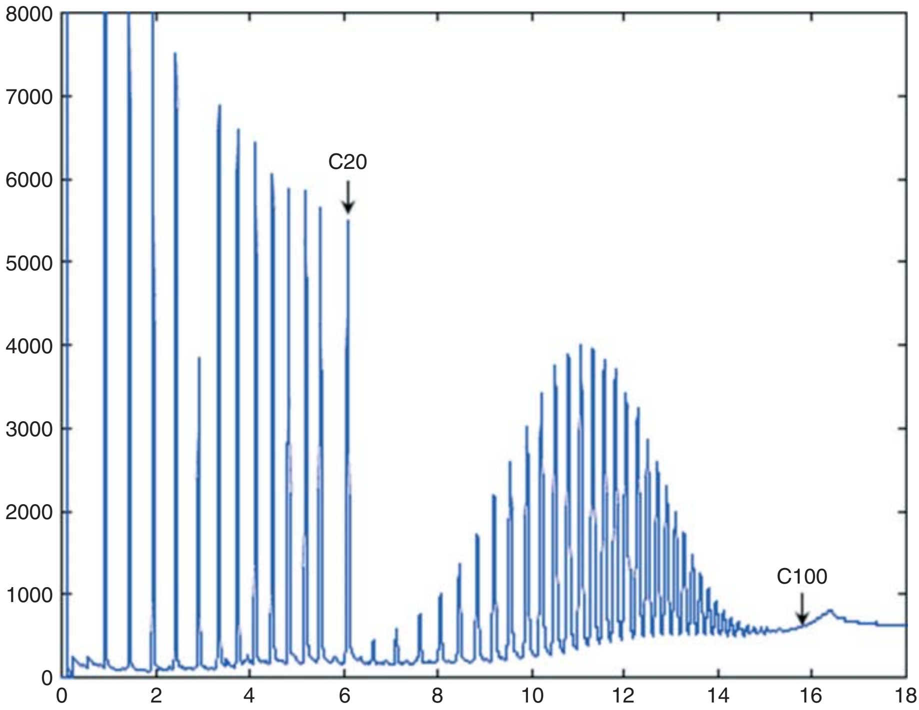

Figure 51.2 The use of carbon monitoring for universal detection in GC of a low-molecular-weight polystyrene.

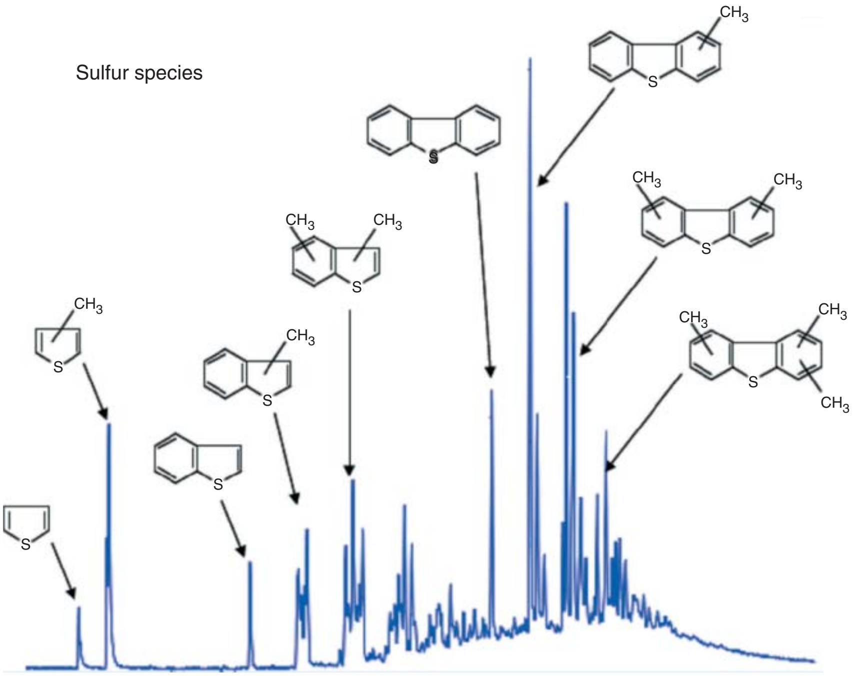

Figure 51.3 The determination of sulfur heterocyclics in a diesel fuel by GC-AED.

compounds. This is particularly important in the petroleum processing industry as certain molecule types have been shown to persist or to be formed during processing. In the case of sulfur- and oxygen-containing compounds, these are the source of sulfur and nitrogen oxides important in controlling air pollution. Other processing issues can be aided by GC-AED analyses. Vanadium and nickel naturally occur in petroleum as porphyrinic structures. These metals can poison certain processing catalysts and must be removed in steps before their use as feeds [4–7] (Figure 51.3, Figure 51.4, and Figure 51.5).

GC-AED was used to separate and identify several organotin compounds (Figure 51.6). These compounds are used as biocides, particularly for antifungal agents in paper products, wood pulp, and textiles; in the water systems of paper mills, breweries; and industrial cooling systems. Organotin compounds are also used in marine antifouling paint to lessen algal and barnacle growth on ship hulls (Figure 51.7).

51.5
ICP for LC Detection

The development of interfaces for LC–MS also spurred the use of other spectral detectors where mobile-phase removal was necessary. The mobile phase in LC puts several limits on the use of plasma detection and the type of plasma used.

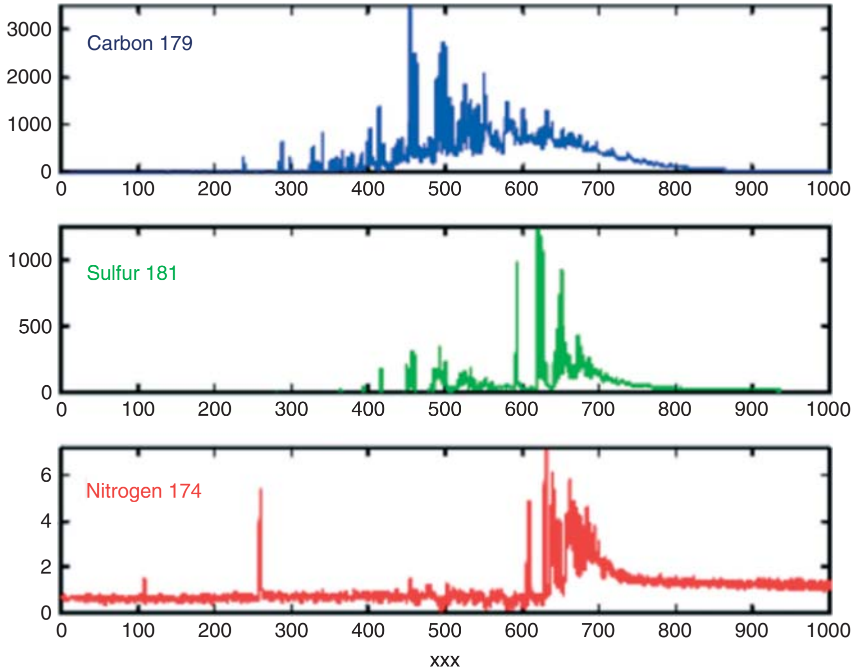

Figure 51.4 (a,b,c) A comparison set of chromatograms of the same type as in Figure 51.3, but with carbon monitoring to be used as a universal detection method and nitrogen detection to show the presence of carbazole-type nitrogen heterocyclics within the diesel fuel.

The amount of mobile phase nebulized into the plasma must be limited so as not to quench or alter the plasma ionization characteristics. Flow rates of 100 ml or less are often cited as the requirement as water has more effect than most organic solvents. The cooling due to thermal expansion of some solvents can alter the plasma. This effect also was the reason why MIP cannot be used for LC detection as it is even more sensitive to these effects. The microwave plasma that is very good in GC is not amenable at all to LC because of the widespread use of aqueous mobile phases. The microwave sources use 2.45 GHz. This is a rotation resonance line of water (and why microwave ovens work for cooking foods). This is incompatible with an aqueous mobile phase.

51.6
Application of LC-ICP MS

LC with atomic detection is now a commonly used technique when identification of peaks can be done by monitoring specific elements. This has become very useful in areas such as the study of metalloenzymes and of toxicity mechanisms for elements like arsenic and mercury.

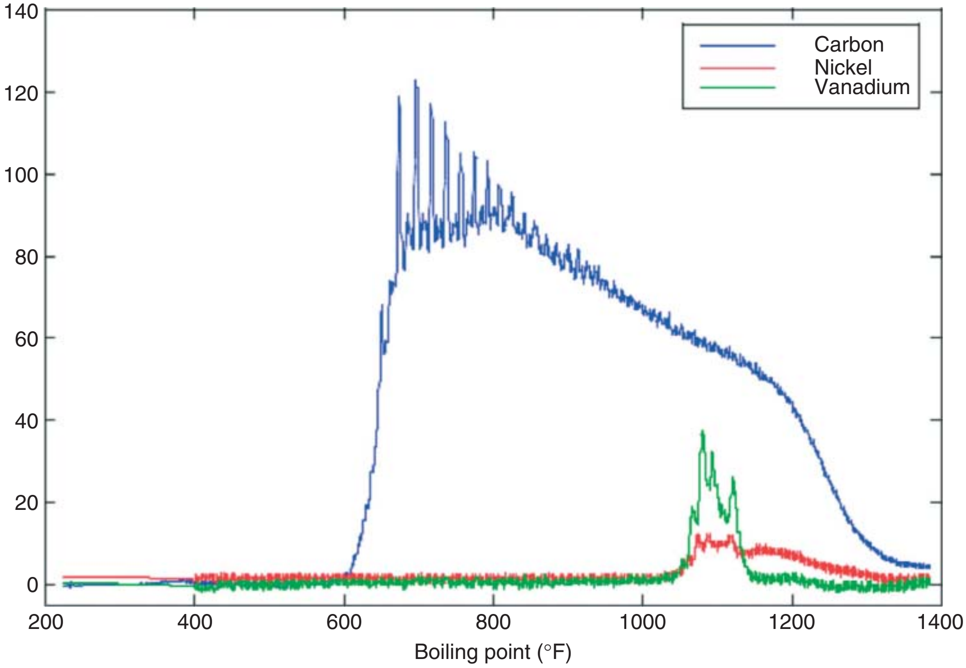

Figure 51.5 The monitoring of vanadium and nickel in a heavy oil residuum fraction. The vanadium is predominantly free porphyrin structures.

A GC has been coupled to an ICP-MS equipped with a novel detector array that permits simultaneous monitoring of up to 15 mass values. With this coupling, absolute limits of detection are in the sub-picogram range for organometallic species and in the picogram range for halogenated hydrocarbons [8, 9].

High-temperature aqueous LC with ICP-MS was used to detect Br in the disposition and metabolic fate of 2-, 3-, and 4-bromobenzoic acids [10]. A method was developed for the simultaneous determination of selenomethionine and selenocysteine in meat by HPLC-ICP-MS [11].

The mechanism of Cisplatin in chemotherapy by HPLC-ICP-MS of the Pt-bound proteins [12]. The nature of As species in algae from the Antarctic region. As speciation was obtained using anion- and cation-exchange chromatography with MS detection [13]. As species in groundwater samples was obtained by anion ion chromatography with ICP-AES [14].

A procedure for the simultaneous determination of 6 Se species and 6 Ar species in human urine by HPLC-ICP-MS was described [15]. The simultaneous detection by HPLC-ICP-MS of arsenic and sulfur as thioarsenicals in a fortified National Institute of Standards and Technology (NIST) freeze-dried urine sample. The molecular oxygen interference at m/z 32 was reduced through both sample introduction and collision-cell parameters optimizing. A 34-fold improvement in the detection limit was achieved using Xe instead of He as the collision gas [16].

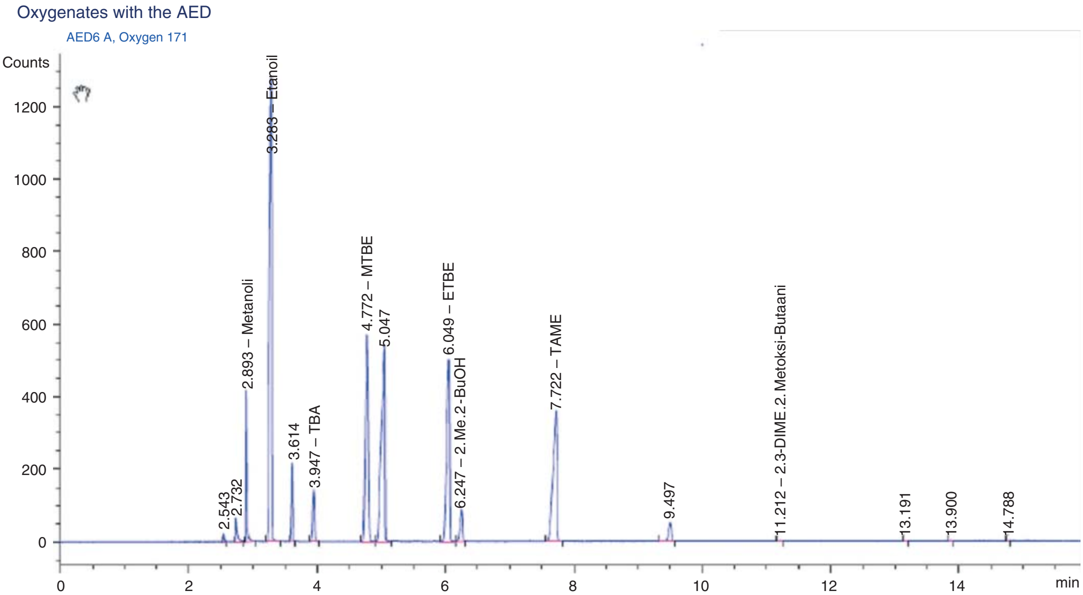

Figure 51.6 The monitoring of oxygen to identify fuel-additive molecules: *tert*-butyl alcohol (TBA); methyl *tert*-butyl ether (MTBE), ethyl *tert*-butyl ether (ETBE), *tert*-amyl-methyl-ether (TAME).

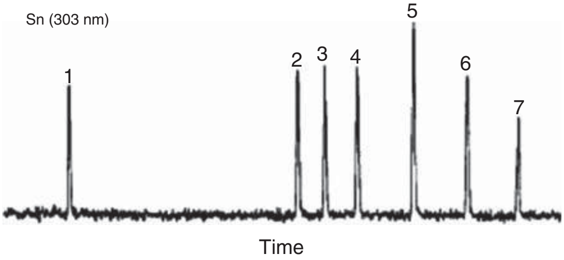

Figure 51.7 Separation of organotin biocides.

Organophosphorus fire retardants and plasticizers were determined at trace levels in wastewater by GC-ICP-MS for P [17].

Seven nerve agent degradation products were analyzed by GC-ICP-MS is described. The nonvolatile alkyl phosphonic acid degradation products included ethyl methylphosphonic acid, isopropyl methylphosphonic acid, ethyl hydrogen dimethylamidophosphate sodium salt, isobutyl hydrogen methylphosphonate (IBMPA, as well as pinacolyl methylphosphonic acid, methylphosphonic acid, and cyclohexyl methylphosphonic acid. The method separated and detected all seven, as well as phosphate, in <10 min. Detection limits for the developed method were <5 pg. This method was successfully applied to river water and soil matrices [18].

Speciation of selenium in dill, supplemented with sodium selenite during its growth, used ion-pairing reversed-phase and cation exchange chromatography. The chromatograms from different parts of the plant revealed differences in selenospecies as well as their concentrations. The major selenospecies found in different parts of the plant was Se-methyl-selenocysteine. Another major Se species identified was Se-methyl-selenomethionine, which had the highest relative concentration in the root, indicating possible Se volatilization from that plant part. Selenomethionine was present in minor quantities in all parts of the plant [19].

Acknowledgments

I thank Dr. Geoffrey N. Coleman for several helpful discussions on plasma behavior and uses, Dr. Matthew S, Klee for help in being able to use figures from Agilent Technologies, Dr. David A. Grudoski of We-measure-it, Inc., for information on GC-AED, and Dr. Axel Strebel and Dr. Joachim Gerstel for figures from Joint Analytical Systems (JAS), Moers, Germany.

References

1. Broekaert, J.A.C. (2008) Innovation in plasma atomic spectrometry from the direct current arc to plasmas on a chip. *Appl. Spectrosc.*, **62**, 227A–234A.
2. Montaser, A. (1992) in *Inductively Coupled Plasmas in Analytical Atomic Spectrometry* (eds A. Montaser and D.W. Golightly) Chapter 1, John Wiley & Sons, Inc., New York, pp. 1–1018.

3. Quimby, B.D., Grudoski, D.A., and Giarroco, V. (1996) Improved measurement of sulfur and nitrogen compounds in refinery liquids using gas chromatography–atomic emission detection. *J. Chromatogr. Sci.*, **26**, 436–443.
4. Reynolds, J.G., Biggs, W.R., Fetzer, J.C., Gallegos, E.J., Fish, R.H., Komlenic, J.J., and Wines, B.K. (1984) Molecular characterization of vanadyl and nickel non-porphyrin compounds in heavy crude petroleums and residua. *Collect. Colloq. Semin. (Inst. Fr. Pet.)*, **40**, 153–9.
5. Biggs, W.R., Fetzer, J.C., Brown, R.J., and Reynolds, J.G. (1985) Characterization of vanadium compounds in selected crudes: porphyrin and non-porphyrin separations. *Liq. Fuels Technol.*, **3**, 397–422.
6. Reynolds, J.G., Biggs, W.R., and Fetzer, J.C. (1985) Characterization of vanadium compounds in selected crudes: electron paramagnetic resonance studies in porphyrin and non-porphyrin fractions. *Liq. Fuels Technol.*, 423–447.
7. Sundararaman, P., Biggs, W.R., Reynolds, J.G., and Fetzer, J.C. (1988) Vanadylporphyrins, indicators of kerogen breakdown and generation of petroleum. *Geochim. Cosmochim. Acta*, **52**, 2337–2341.
8. Barnes, J.H. IV,, Schilling, G.D., Sperline, R.P., Denton, M.B., Young, E.T., Barinaga, C.J., Koppenaal, D.W., and Hieftje, G.M. (2004) *J. Anal. At. Spectrom.*, **19** (6), 751–756.
9. Barnes, J.H. IV,, Schilling, G.D., Stone, S.F., Sperline, R.P., Denton, M.B., Young, E.T., Barinaga, C.J., and Hieftje, G.M. (2004) *Anal. Bioanal. Chem.*, **380** (2), 227–234.
10. Smith, C.J., Shillingford, S., Edge, A.M., Bailey, C., and Wilson, I.D. (2008) Quantification of the in vitro and in vivo metabolic fates of 2-, 3- and 4-bromobenzoic acids using high temperature LC coupled to ICP-MS and linear ion trap MS. *Chromatographia*, **67**, 673–678.
11. Bierla, K., Dernovics, M., Vacchina, V., Szpunar, J., Bertin, G., and Lobinski, R. (2008) Determination of selenocysteine and selenomethionine in edible animal tissues by 2D size-exclusion reversed-phase HPLC-ICP MS following carbamidomethylation and proteolytic extraction. *Anal. Bioanal. Chem.*, **390**, 1789–1798.
12. Esteban-Fernaćndez, D., Montes-Bayoćn, M., Blanco Gonzaćlez, E., Goćmez Goćmez, M.M., Palacios, M.A., and Sanz-Medel, A. (2008) Atomic (HPLC-ICP-MS) and molecular mass spectrometry (ESI-Q-TOF) to study cisplatin interactions with serum proteins. *J. Anal. At. Spectrom.*, **23**, 378–384.
13. Wuilloud, R.G., Altamirano, J.C., Smichowski, P.N., and Heitkemper, D.T. (2006) Investigation of arsenic speciation in algae of the Antarctic region by HPLC-ICP-MS and HPLC-ESI-Ion Trap MS. *J. Anal. At. Spectrom.*, **21** (11), 1214–1223.
14. Gettar, R.T., Garavaglia, R.N., Gautier, E.A., and Batistoni, D.A. (2000) Determination of inorganic and organic anionic arsenic species in water by ion chromatography coupled to hydride generation-inductively coupled plasma atomic emission spectrometry. *J. Chromatogr. A*, **884** (1–2), 211–221.
15. Pan, F.M., Tyson, J.F., and Uden, P.C. (2007) Simultaneous speciation of arsenic and selenium in human urine by high-performance liquid chromatography inductively coupled plasma mass spectrometry. *J. Anal. At. Spectrom.*, **22**, 931–937.
16. Ellis, J.L., Conklin, S.D., Gallawa, C.M., Kubachka, K.M., Young, A.R., Creed, P.A., Caruso, J.A., and Creed, J.T. (2008) Complementary molecular and elemental detection of speciated thioarsenicals using ESI-MS in combination with a xenon-based collision-cell ICP-MS with application to fortified NIST freeze-dried urine. *Anal. Bioanal. Chem.*, **390** (7), 1731–1737.
17. Ellis, J., Shah, M., Kubachka, K.M., and Caruso, J.A. (2007) Determination of organophosphorus fire retardants and plasticizers in wastewater samples using MAE-SPME with GC-ICPMS and GC-TOFMS detection. *J. Environ. Monit.*, **9** (12), 1329–1336.

18. Richardson, D.D. and Caruso, J.A. (2007) Derivatization of organophosphorus nerve agent degradation products for gas chromatography with ICPMS and TOF-MS detection. *Anal. Bioanal. Chem.*, **388** (4), 809–823.

19. Cankur, O., Yathavakilla, S.K.V., and Caruso, J.A. (2006) Selenium speciation in dill (Anethum graveolens L.) by ion pairing reversed phase and cation exchange HPLC with ICP-MS detection. *Talanta*, **70** (4), 784–790.

52

NMR as a Chromatography Detector

Klaus Albert

52.1

Structural Assignment Techniques

The structural assignment of all peaks of a chromatographic separation is a demanding task. Hints on the structure of a separated compound can be derived from the retention behavior with respect to the employed stationary phase and the mobile phase composition. A wide range of mass selective detection techniques such as ultraviolet (UV), refractive index (RI), and electrochemical flame ionization detection can be used for selective detection but do not yield sufficient structural information. Diode-array detection at different wavelengths reveals more information if a UV-active chromophore is part of the molecule under investigation. A very sensitive and unique detection technique is mass spectrometry (MS). Therefore, hyphenated techniques such as GC–MS (gas chromatography–mass spectrometry) and HPLC–ESI–MS^n and HPLC–APCI–MS^n are versatile tools for deriving structural information. Especially in target analysis, where the mass of the investigated molecule is known, these techniques are a matter of choice. For instance, in water quality control, peak identification can be performed at the picogram sensitivity level with the help of hyphenated MS techniques.

In the case of nontarget analysis, with only the information of the retention time of the peak under investigation, the combination of hyphenated GC–MS, HPLC–MS with GC-NMR, and HPLC-NMR or HPLC-SPE-NMR (solid phase extraction) techniques has to be employed. MS^n techniques yield very important structural data, but only from NMR spectroscopic investigation can stereochemical information be derived. For instance, structural and stereoisomers can be assigned unambiguously only with the help of NMR techniques. Despite NMR spectroscopy not being as sensitive as MS, the methodical developments performed in the past years have rendered this technique a versatile tool in the online structure analysis of chromatographic separations [1–47].

Handbook of Spectroscopy, Second Edition. Edited by Günter Gauglitz and David S. Moore.

52.2
NMR in a Flowing Liquid

NMR spectra are usually recorded by exciting nuclei (^{1}H, ^{13}C, ^{31}P) with a radio frequency (RF) pulse from the ground state level to the excited state level. The energy difference between the ground state level and the excited state level as well the population difference of nuclei (Boltzmann distribution) is dependent on the strength of the applied magnetic field Bo. Thus, a stronger magnetic field results in a higher sensitivity. Owing to two relaxation processes, the spin–lattice relaxation and the spin–spin relaxation, the excited nuclei move back from the excited state to the ground state. The spin–lattice relaxation time is named T_1 and the spin–spin relaxation time is named T_2. The decay of magnetization is observed in the transmitter detection coil as ''free induction decay (FID)'' with the time constant T_2. Employing the Fourier transformation technique, the time-dependent FID is converted to a frequency domain with distinct NMR signals [40]. NMR signal intensity is dependent on T_1, whereas NMR signal half width is dependent on T_2.

In the flowing mode, nuclei only stay for a distinct residence time τ within the NMR transmitter/detection coil. This results in an increase in relaxation rates (inverse relaxation times T_1 and T_2):

$$1/T_{n\ \text{flow}} = 1T_{n\ \text{static}} + 1/\tau$$

The overall effect of continuous-flow NMR is an increase in sensitivity versus given acquisition time and an increase in signal half width increasing flow rates. For instance, a residence time of 5 s leads to a signal broadening of 0.2 Hz, a residence time of 0.5 s to a signal broadening of 2 Hz.

52.3
Design of Continuous-Flow NMR Probes

52.3.1
Continuous-Flow ^{1}H NMR Probe for LC-NMR

Continuous-flow NMR probes should exhibit good flow characteristics for the chromatographic separation, for example, no peak broadening. On the other hand, the highest possible sensitivity for the NMR detection should be obtained. Thus, it is clear that a compromise between chromatographic and NMR spectroscopic requirements has to be obtained. Figure 52.1 shows the picture of one of the first continuous-flow NMR probes used at a 400 MHz NMR superconducting spectrometer. The NMR RF folio is directly attached to the glass of the up-leading part of the U-type detection cell, defining a detection volume of about 44 μl. The whole assembly is inserted in a glass dewar, enabling temperature-dependent measurements (Figure 52.1) [2]. The whole arrangement is centered in the glass dewar of a conventional probe body. The internal diameter of the glass tube varies between 2 and 4 mm, resulting in detection volumes between 30 and 120 μl. The

Figure 52.1 Continuous-flow ^{1}H NMR probe for HPLC-NMR.

glass walls of the flow cell are parallel within the length of the proton detection coil (18 mm) and taper at both ends to fit to polytetrafluorethylene (PTFE) tubings (ID 0.25 mm). PTFE tubings and glass tubes are connected by shrink-fit tubings. ‘‘Inverse’’ continuous-flow probes contain an additional coaxial coil (matched to the ^{13}C resonance frequency) surrounding the ^{1}H NMR detection coil for heteronuclear ^{1}H/^{13}C shift correlated experiments.

Newer probes are fabricated with Helmholtz saddle-type coils or cryogenic coils cooled with liquid helium. These cryoprobes show three to four times high sensitivity levels, leading to limits of detection in the lower nanogram range.

52.3.2
Solenoidal NMR Microprobe for Capillary HPLC-NMR and GC-NMR

An alternative probe design is shown in Figure 52.2. Besides the Helmholtz saddle-type coil (in analogy to conventional NMR probes) the solenoidal-type probe design

Figure 52.2 Solenoidal NMR microprobe for capillary HPLC-NMR and GC-NMR.

[40, 48–54], which is constructed by directly wrapping the RF coil around a capillary column, has successfully been utilized for capillary HPLC-NMR and GC-NMR coupling. Here, a copper coil is directly wound around an 180 μm internal diameter fused-silica (360 μm OD) capillary, resulting in a detection volume between 1.5 and 5 μl within the NMR radiofrequency coil. The polyimide coating of the capillary is removed over the length of the NMR detection window. The microcoil is immersed in a container containing perfluorotributylamine to compensate for susceptibility distortions between copper and air [48, 49]. The solenoidal probe design shows a threefold better sensitivity than saddle-shaped coils and therefore is especially beneficial in the case of the hyphenation of capillary HPLC to NMR. Owing to the use of a susceptibility-matching fluid high-resolution ^{1}H NMR spectra are obtained, but there might be problems with interfering signals in ^{13}C NMR measurements.

The solenoidal NMR microprobe shown in Figure 52.2 can be used for capillary HPLC-NMR and GC-NMR detection [48–64].

52.3.3
On-Line HPLC-NMR

For on-line HPLC-NMR, GPC-NMR (gel permeation chromatography), and SFC (supercritical fluid chromatography)-NMR experiments, the chromatographic separation system, consisting of either an HPLC or SFC pump together with an injection valve, separation column (250 × 4.6 mm ID) and an UV or RI detector, is located at a distance of 1.5–2.5 m besides the unshielded cryomagnet (Figure 52.3). If a shielded cryomagnet without any magnetic stray field is used, the chromatographic equipment can be directly placed besides the cryomagnet.

The outlet of the UV (RI) detector is connected by stainless steel capillaries (0.25 mm ID) to a switching valve. It is used for trapping a desired peak in the NMR flow cell in stopped-flow experiments. For online experiments with continuous registration of NMR spectra in distinct time intervals (1–8 s), the switching valve is open for a continuous flow through the probe into the waste. Instead of the switching valve, a Bruker peak sample unit (BPSU) can be used or the eluted peaks can be trapped on SPE cartridges. These techniques are advisable when long NMR experiment times are expected. With the help of the peak-sample unit or SPE cartridges, desired peaks of a separation can be stored in small capillary loops. When a separation is finished, every single peak can be transferred into the probe and the desired stopped-flow experiment can be conducted.

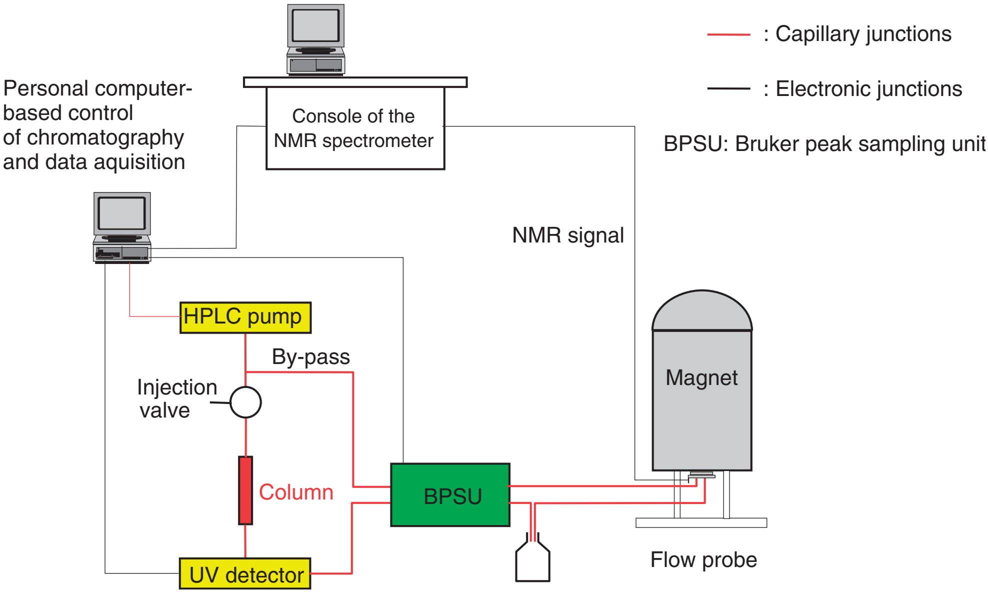

Figure 52.3 Experimental setup for HPLC-NMR.

52.4
Solvent Signal Suppression

Most HPLC separations are performed in the reversed-phase mode with surface-modified stationary phases and using binary solvent mixtures such as acetonitrile (ACN)/water or methanol/water as mobile phase. The intensity ratio of the protonated solvent versus sample signals is in the order 10 000 : 1 in a routine analytical HPLC-NMR run with about 10–25 μl of injected compound. For proper adjustment of the receiver gain of the NMR instrument, the intensity of the solvents should be reduced to the height of the sample signals either by the use of deuterated solvents (which can be easily and economically implemented in capillary separation techniques because of the low flow rates (1–10 μl min^{-1}) applied) or by the application of a solvent suppression technique. Efficient solvent suppression in the continuous-flow and in the stopped-flow mode can be performed by application of a nuclear Overhauser effect spectroscopy (NOESY)-type presaturation scheme. Figure 52.4 shows the effect of solvent signal suppression.

The gain in sensitivity by reducing the intensity of the methyl signal of ACN by a factor of 100 to the intensity of the ^{13}C satellites of ACN is clearly visible at the signal's retinoic acid between 5.6 and 8.0 ppm. With residence times in the order

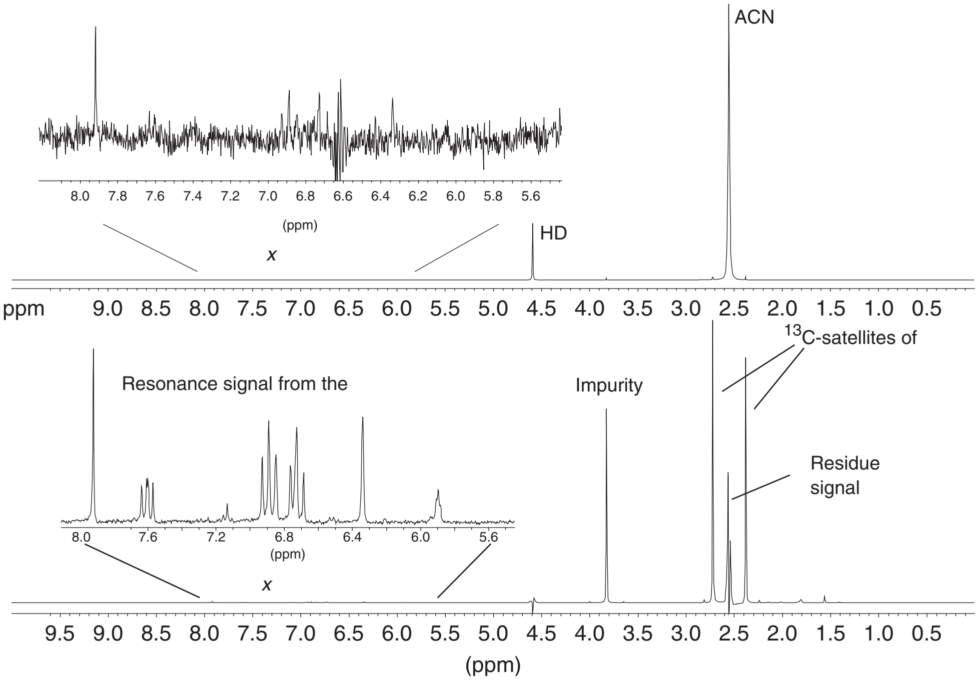

Figure 52.4 Effect of solvent signal suppression.

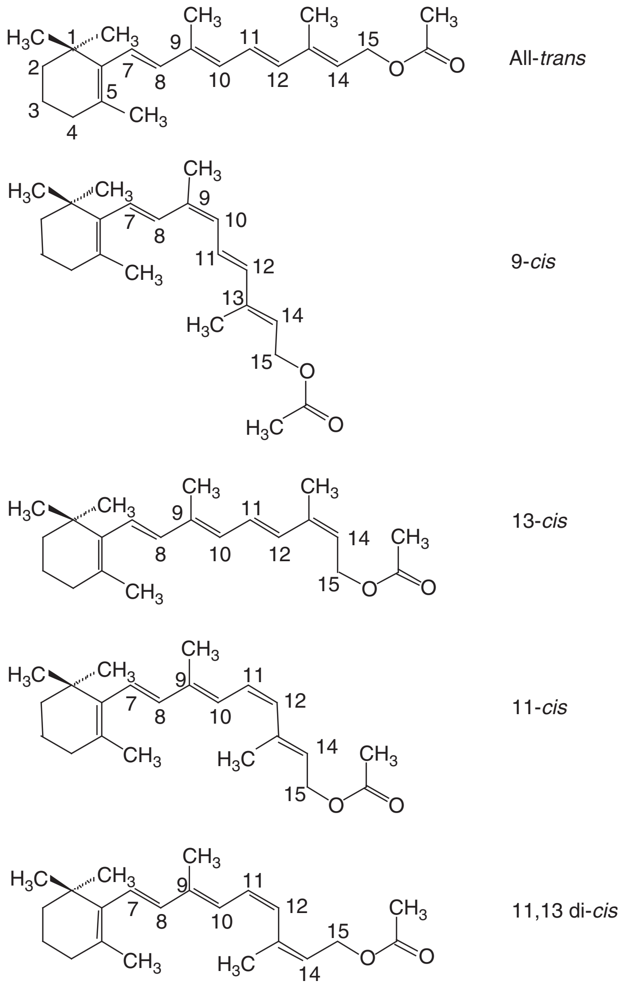

Figure 52.5 Structures of isomers of vitamin A acetate.

of 5 s and acquisition times for one transient of about 1 s, sufficient presaturation time is left even in the continuous-flow mode.

The acquisition of NMR spectra in the hyphenated HPLC-NMR techniques is possible in the continuous-flow and the stopped-flow mode. An example of the continuous-flow recording is the separation of different isomers of vitamin A acetate, whose structures are shown in Figure 52.5 [14].

The acquisition of online continuous-flow NMR spectra results in a two-dimensional contour plot of ^{1}H NMR signals of the separated compounds (x axis = ^{1}H chemical shift) against the retention times (y axis). Figure 52.6 shows the gained continuous-flow HPLC-NMR spectra of the continuous-flow ^{1}H NMR detection of the separation of vitamin A acetate isomers, the chemical shift is

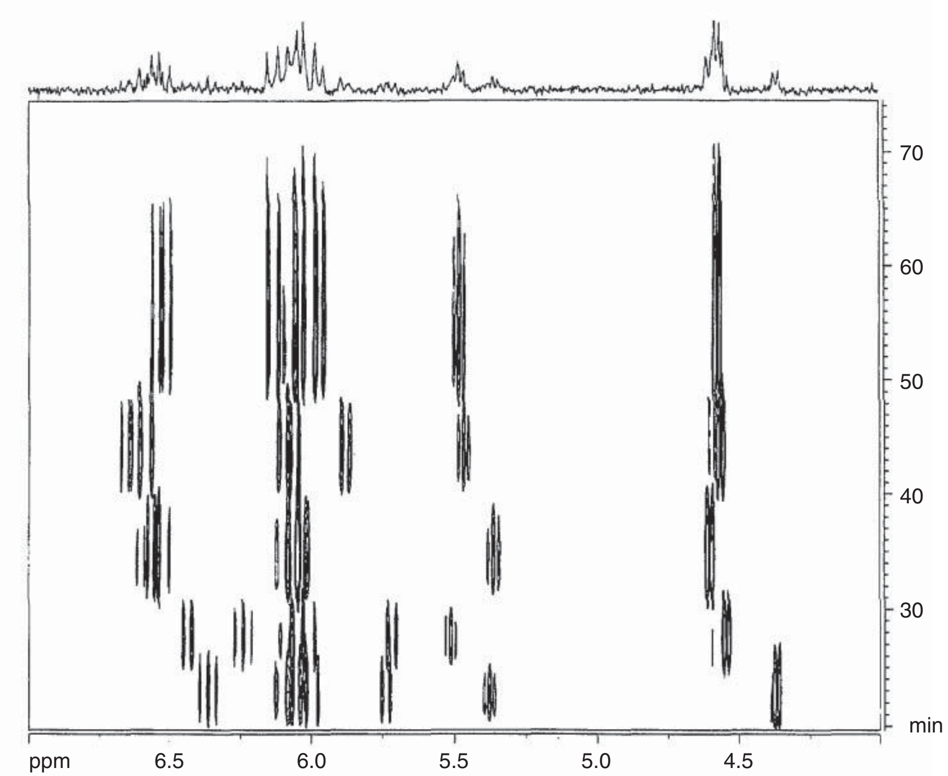

Figure 52.6 ^{1}H NMR chromatogram (contour plot, 400 MHz) of an HPLC separation of five vitamin A acetate isomers reordered in *n*-heptane.

plotted, while the *y* axis (F1 dimension) shows the retention time scale of the separation, resulting in a pseudo-2D NMR contour map.

All isomers of vitamin A acetate can unambiguously be identified. This can especially be noticed at the protons of peak 1 (11,13-di-*cis* vitamin A acetate) and peak 2 (11-*cis* vitamin A acetate).

For a more detailed interpretation of the ^{1}H NMR spectra, the contour plot of the continuous-flow NMR measurement is not useful. Therefore, the extracted proton NMR spectra of the vitamin A acetate isomers at the corresponding peak maxima of the continuous-flow measurement are shown in Figure 52.7. Structure elucidation of all vitamin A acetate isomers can be easily carried out.

In continuous-flow experiments, there is only a short time available for accumulation of transients and therefore for exposure of a ^{1}H NMR spectrum. So, this spectroscopic technique can only be used if there is a high concentration of the sample in the flow cell. Otherwise, the signal-to-noise ratio is too poor. It should be also mentioned that the chemical shifts depend on the solvent composition. Therefore, when utilizing gradient elution programs for chromatographic separation, stopped-flow NMR experiments have to be carried out, too.

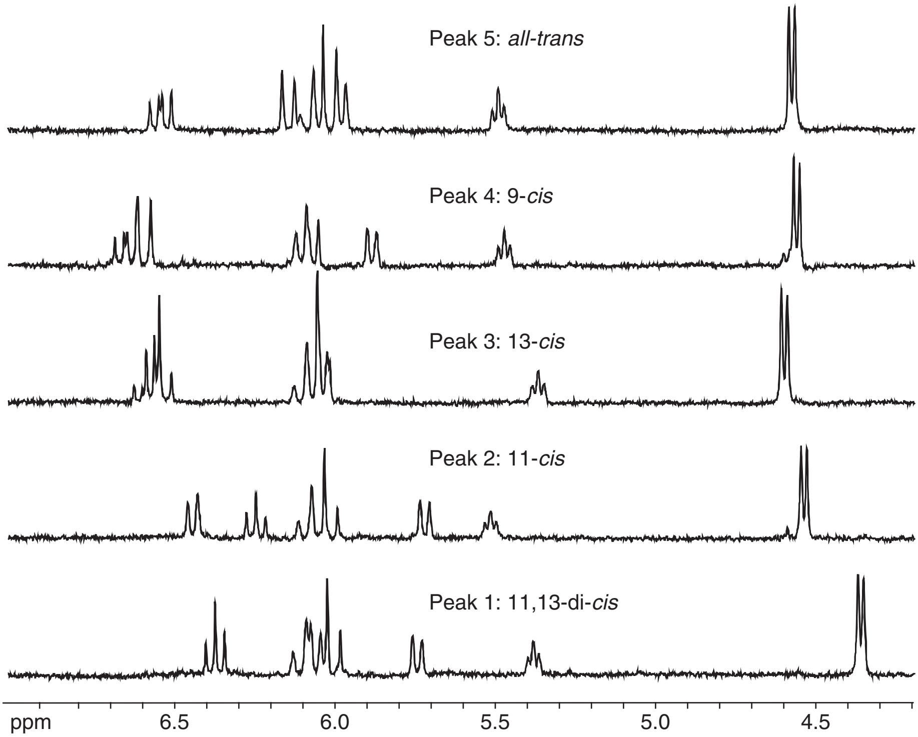

Figure 52.7 Continuous-flow ^{1}H NMR spectra (400 MHz) of the separated vitamin A acetate isomers.

In the stopped-flow mode, the chromatographic run is stopped as soon as the maximum of the peak is in the flow cell (indicated by the UV detector). By switching the valves of the sample or peak parking unit, the exposure of back pressure to the sample in the flow cell is precluded. Conventional NMR experiments can now be performed and, therefore, the NMR experimental time can be adjusted to the sample concentration. Preiss *et al.* [65–67] performed a lot of experiments for the investigation of explosives in environmental analysis employing the stopped-flow mode. Another advantage of the stopped-flow experiment is the acquisition of 2D NMR spectra. Here, SPE has to be performed. Microprobes can also be used for NMR experiments of pure compounds in the flow-injection mode without any loss of spectral information recorded within reasonable acquisition times. Despite the low amount of sample present in the detection coil, these spectra clearly show that all information for structural assignment can be derived. Figure 52.8 depicts one example of a heteronuclear single-quantum correlation (HSQC) 2D-NMR spectrum (^{1}H/^{13}C) of α-tocopherol acetate measured in the flow-injection mode in a solenoidal microcoil probe.

Figure 52.9 shows a homonuclear total correlation spectroscopy (TOCSY) spectrum of α-tocopherol acetate recorded within a saddle-type coil (200 nl detection

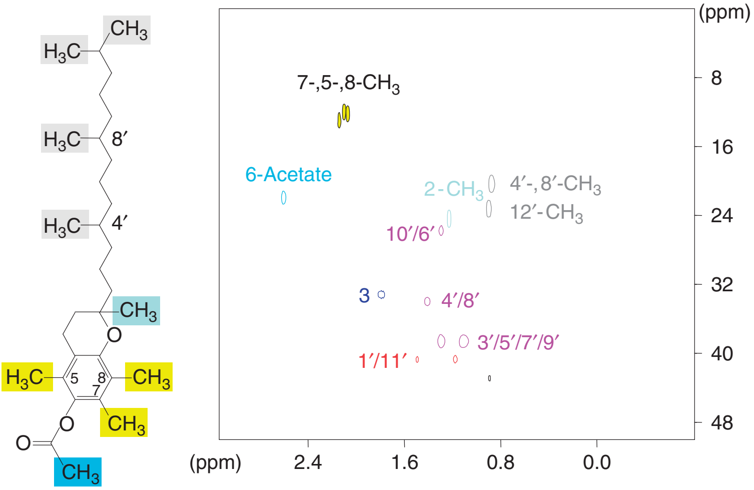

Figure 52.8 HSQC 2D NMR spectrum ($^1H/^{13}C$) of α-tocopherol acetate measured in a solenoidal NMR microcoil probe.

volume) with an acquisition time of 15 h. The projections in the F1 and F2 dimension show conventional ^1H NMR spectra of 0.1% of α-tocopherol acetate in methanol-d_4 directly injected within the capillary. The spectrum was recorded within 7 min with a pulse repetition time of 1.5 s.

52.5
LC-SPE-NMR

Owing to the still low sensitivity of the NMR detection, a modification of the stopped-flow acquisition mode is used. The trick is to trap the different peaks of an HPLC separation on different cartridges (mostly cross-linked polystyrene) and concentrate the peaks by multiple trapping (Figure 52.10).

The aim is to concentrate chromatographic peaks to elution volumes matching the detection volume of the continuous-flow NMR cell (between 30 and 120 μl). After drying the cartridge with nitrogen, the adsorbed analyte is redissolved in a deuterated solvent and pumped to the NMR detection cell. Thus, a narrow elution band is formed. Owing to the use of capillaries between the SPE unit and the NMR flow probe, peak diffusion is minimal. The whole procedure can be fully automated. Care has to be taken to perform a gentle and effective drying of the cartridge. Figure 52.11 shows the effect of multiple trapping ($n = 1$–7) for the ^1H NMR spectra of glyasperin H [68].

HPLC-SPE-NMR is the major technique for the analysis of crude extracts of plant materials. For the investigation of a compound with a molecular weight of about 700 Da, about 2 μg of analyte per 1 μl CD_3CN have to be transferred to the continuous-flow NMR probe. Here, a cryogenic cooled probe with very high

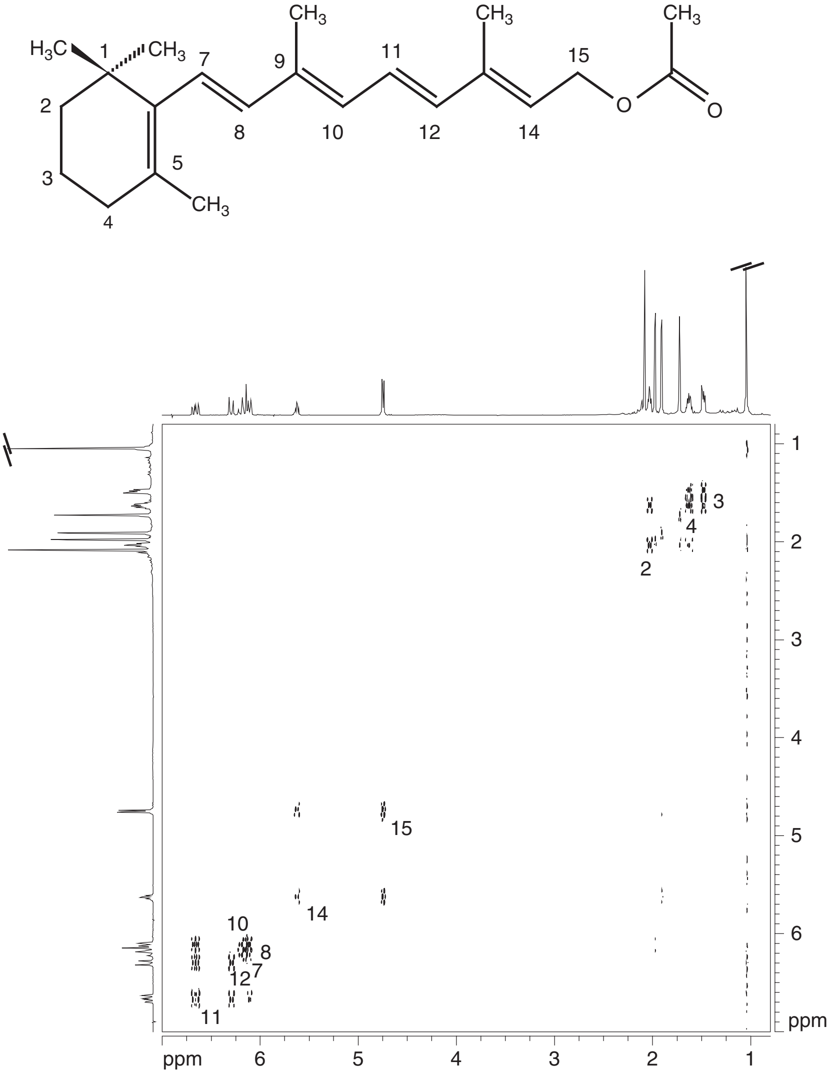

Figure 52.9 Homonuclear TOCSY spectrum of α-tocopherol acetate recorded within a saddle-type coil (200 nl detection volume).

sensitivity is used. A big advantage is the use of the newly introduced "cryo-fit" assembly. Here, a specially designed capillary can be introduced into a conventional cryogenic probe and connected to the SPE apparatus.

The application is pioneered by different groups. Phytopharmaceuticals have been investigated by the groups of Exarchou [45], Jaroszewski and Hansen [69–79], Seger and Sturm [68, 80, 81,], Schneider [82, 83], and Wolfender [84]. Owing to the gain in NMR sensitivity, all two-dimensional structural assignment techniques

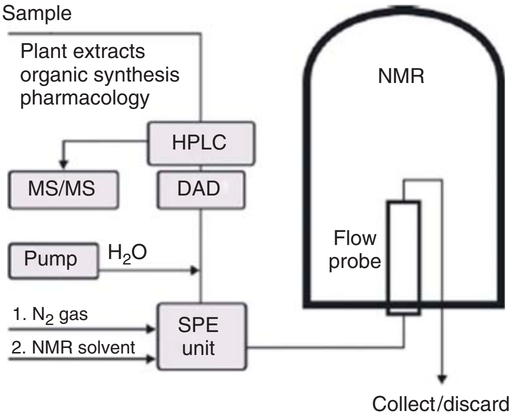

Figure 52.10 Experimental setup for online HPLC-SPE-NMR.

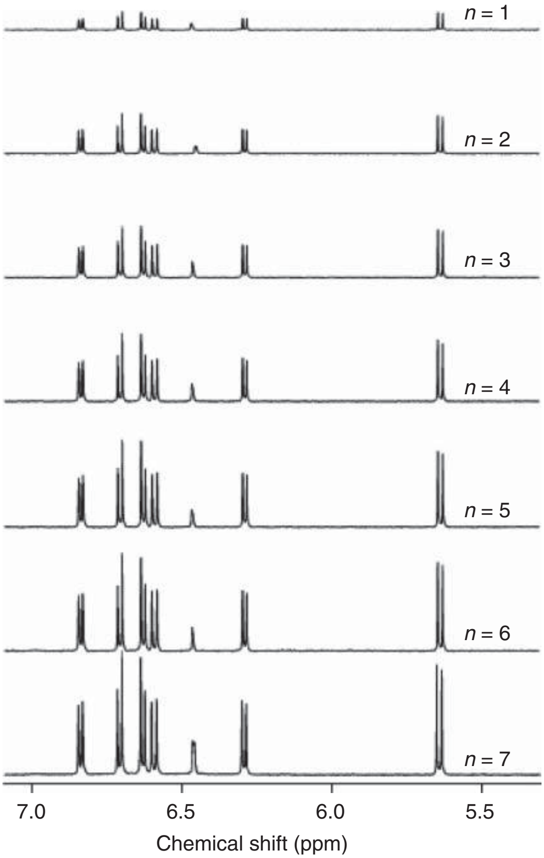

Figure 52.11 Effect of multiple SPE trapping.

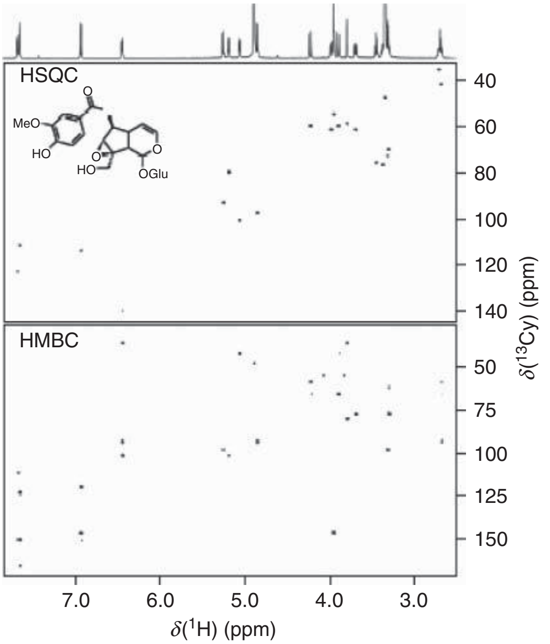

Figure 52.12 HPLC-SPE-NMR-derived HSQC and HMBC spectra of picroside.

can be performed. Figure 52.12 shows the HSQC and heteronuclear multiple bond correlation (HMBC) spectra of picroside [68].

The LC–SPE enrichment approach can be also combined with capillary NMR detection. This work was pioneered by the group of Wolfender and Jaroszewski [84].

52.6
Capillary HPLC-NMR Coupling

The NMR registration of capillary separations employs microcoils with detection volumes between 1.5 and 5.0 μl. The small flow rates used in liquid capillary separations enable the use of deuterated solvents. In capillary GC, NMR spectra are recorded in the gaseous state.

A possible instrumental setup for capillary HPLC-NMR coupling is shown in Figure 52.13.

A feasible experimental setup for online capillary HPLC-NMR (cHPLC-NMR) coupling is outlined in Figure 52.14.

A splitless Waters capillary HPLC pump together with an injection device (100–200 nl) and a separation capillary is connected by fused silica capillaries via a Bischoff UV detector to the NMR microprobe inserted into the room temperature bore of a Bruker 600 MHz cryomagnet. Separations are performed with capillaries (ID 100–250 μm, length 250 mm). Because a nonshielded magnet with a strong

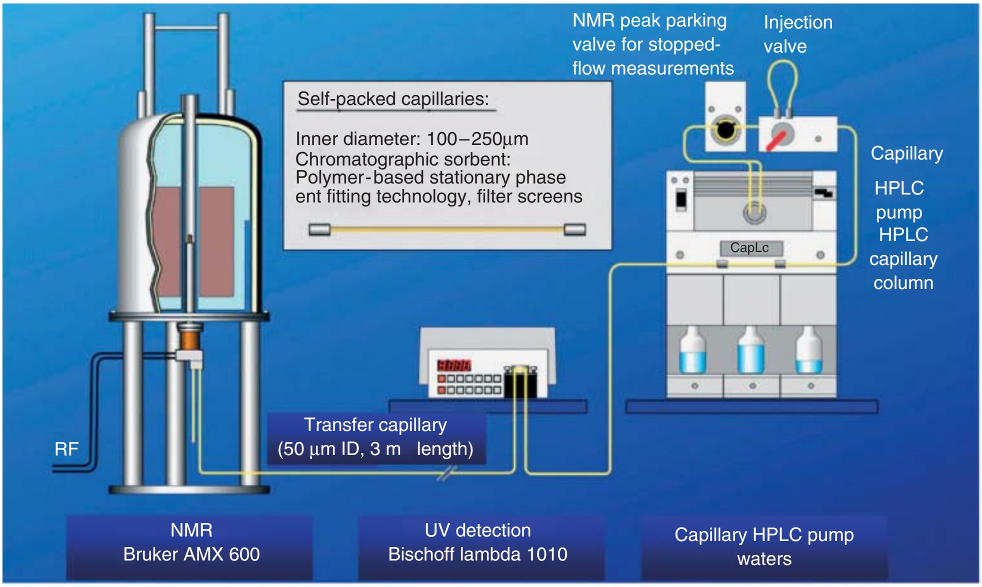

Figure 52.13 Experimental setup for online capillary HPLC-NMR.

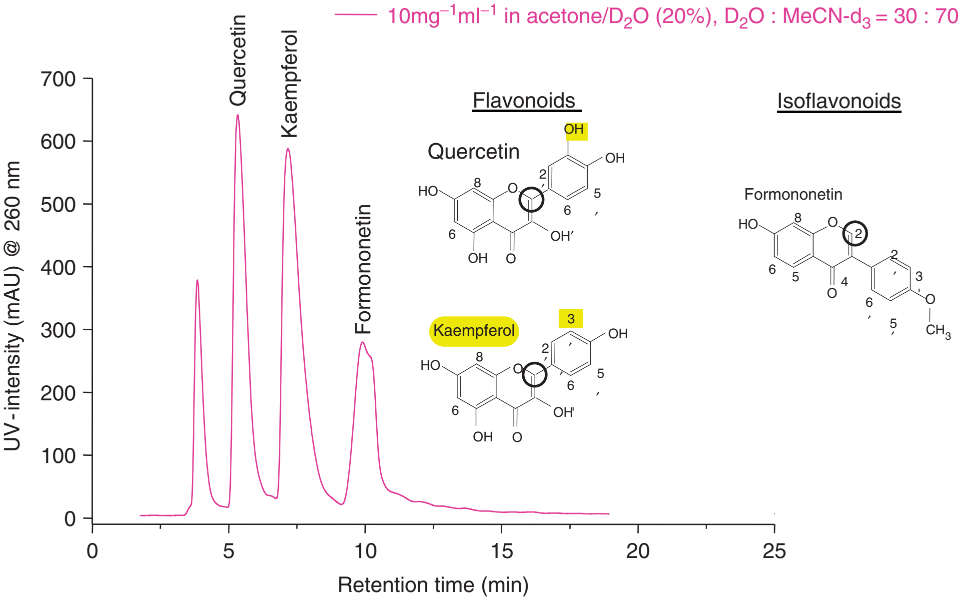

Figure 52.14 HPLC separation of different flavonoids and isoflavonoids.

stray field is used, a transfer capillary with an ID of 50 μm (OD 360 μm) and an overall length of 2.5–3.0 m is employed to connect the HPLC instrument together with the NMR detection cell. Owing to the small diameter of the transfer capillary, a peak broadening of only 1% is observed at flow rates of 5 μl min^{-1}.

Owing to the NMR peak parking valve (Figure 52.13) installed after the separation, capillary measurements either in the continuous-flow mode or the stopped-flow mode are possible.

The approach of coupling capillary compared to conventional separation techniques with NMR [48–62, 84] is promising. The reduced solvent consumption allows the use of deuterated solvents, thus rendering unnecessary the elaborate solvent suppression that minimizes the problems of overlapping analyte and solvent signals by the use of capillary separation techniques.

Real-world applications employing these techniques are possible with stopped-flow NMR detection limits in the 10 ng range [54–62].

Because of the still low sensitivity of the NMR detection, it is favorable to overload the chromatographic separation capillary. For this purpose, new types of C_{18} and C_{30} separation columns show a superior separation behavior. Figure 52.14 shows the HPLC separation of different flavonoids and isoflavonoids performed at a C_{18} capillary column (ProntoSil Eurobond 120 Å, 5 μm, 250 μm × 150 mm) at a flow rate of 5 μl min^{-1}.

At a concentration of 10 mg ml^{-1}, the continuous-flow detection NMR detection is possible. Figure 52.15 shows the contour plot of the ^{1}H chemical shift values versus the chromatographic retention times. Owing to the different chemical shift

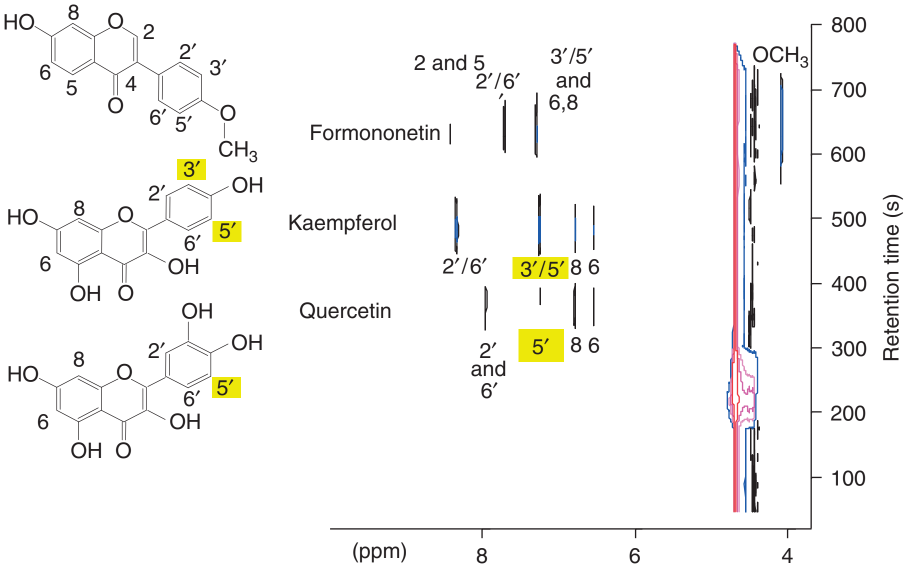

Figure 52.15 Contour plot of the capillary separation of different flavonoids and isoflavonoids.

values, the assignment of the three different compounds — quercetin, kaempferol, and formononetin — is clearly visible. Thus, the different substitution patterns with one or two hydroxyl groups at the phenyl ring of the two flavonoids, quercetin and kaempferol, can be easily recognized.

An example of the stopped-flow acquisition is the identification of the stereoisomers of the Brazilian plant bixin. The cis–trans isomers can be separated with a C_{30} column because of the high shape selectivity (Figure 52.16). The APCI mass spectra of both isomers (Figure 52.17) are identical because MS is unable to differentiate structural and stereoisomers. A clear structural assignment can be achieved by acquiring stopped-flow two-dimensional $^1H-^1H$ correlated spectra [$^1H-^1H$-COSY (correlation spectroscopy)]. Figure 52.18 and Figure 52.19 show the different chemical shift values and correlations for the proton pairs H-7/H-8 and H-7′/H-8′. Owing to the existence of the cis configuration, an isomerization shift of proton 8′ of 0.59–7.94 ppm occurs. The differences between the NMR spectra of the symmetrical *all*-trans and the nonsymmetrical 9′-cis isomer can be immediately recognized in Figure 52.18 and Figure 52.19. The chemical shifts of the protons H-8 and H-8′ of *all-trans*-bixin are the same, but differ for 9′-*cis*-bixin. Thus, unequivocal stereochemical assignment can be readily achieved.

52.7
GPC-NMR Coupling

One big advantage of the use of continuous-flow probes is the enormous gain in efficiency against the conventional recording in NMR tubes. When the amount of sample is not a problem, the application of continuous-flow NMR detection volumes between 40 and 120 µl is favorable [85–90]. Figure 52.20 shows the ^1H NMR spectrum of latex, a copolymer of styrene(S) and *n*-butyl acrylate (A) [86].

The assignment of the proton signals of both constituents is readily available from the ^1H NMR spectrum. With the help of GPC, molecular weight distribution of polymers can be obtained. Here, polymeric compounds with molecular weight elute first. The contour plot of the online GPLC (gel permeation liquid chromatography)-NMR detection is shown in Figure 52.21.

Besides the solvent signal of dichloromethylene, the signals of *n*-butyl acrylate together with styrene can be recognized. The change in the polymer composition can be derived from the changing integration ratio between the aromatic signal of styrene at 7 ppm versus the methyl signal of *n*-butyl acrylate at 0.8 ppm (Figure 52.22).

Thus, the molar concentration of *n*-butyl acrylate varies from row 34 at the beginning of the separation to 29% at row 80 at the end.

The registration of the online GPC-NMR run was accomplished within 1 h. To derive similar data, it would take over 24 h by conventional NMR recording.

The application of GPC-NMR for a detailed characterization of polymers was pioneered by Hiller [88–90]. Especially at the critical point of solvent composition, GPC-NMR experiments reveal valuable data [90].

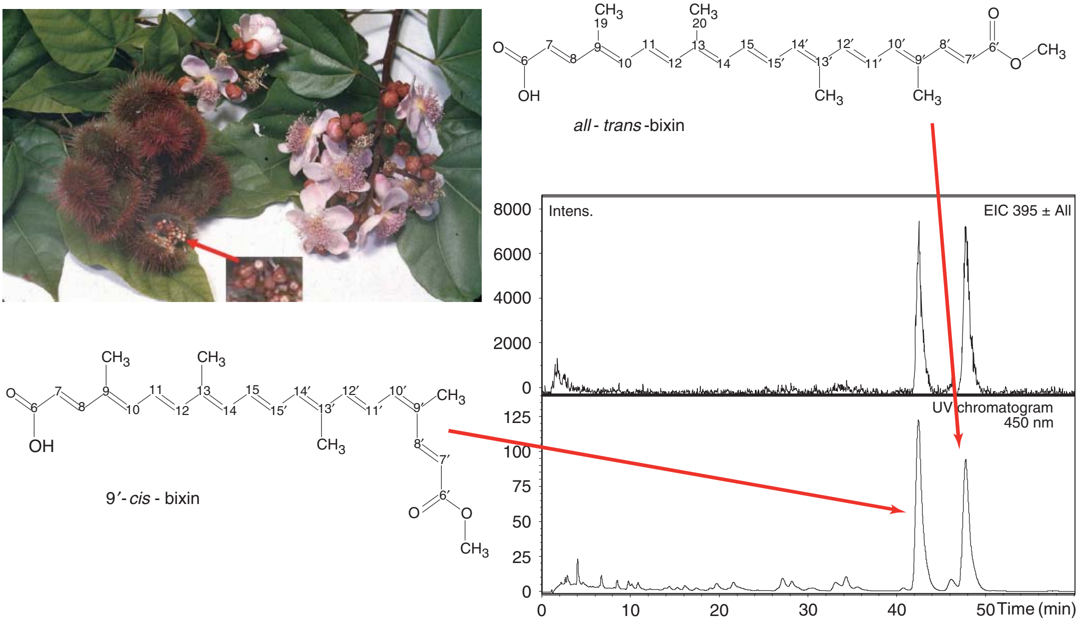

Figure 52.16 Capillary HPLC separation of bixin isomers (9′-*cis*- and *all-trans*-bixin) on a C_{30} phase.

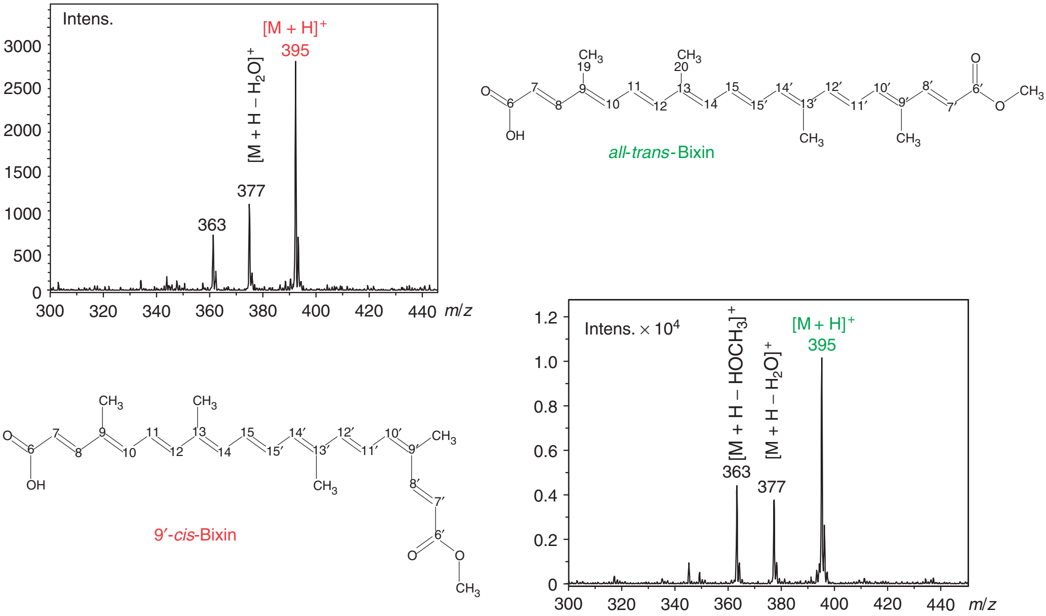

Figure 52.17 APCI mass spectra of bixin isomers (9′-*cis*- and *all-trans*-bixin).

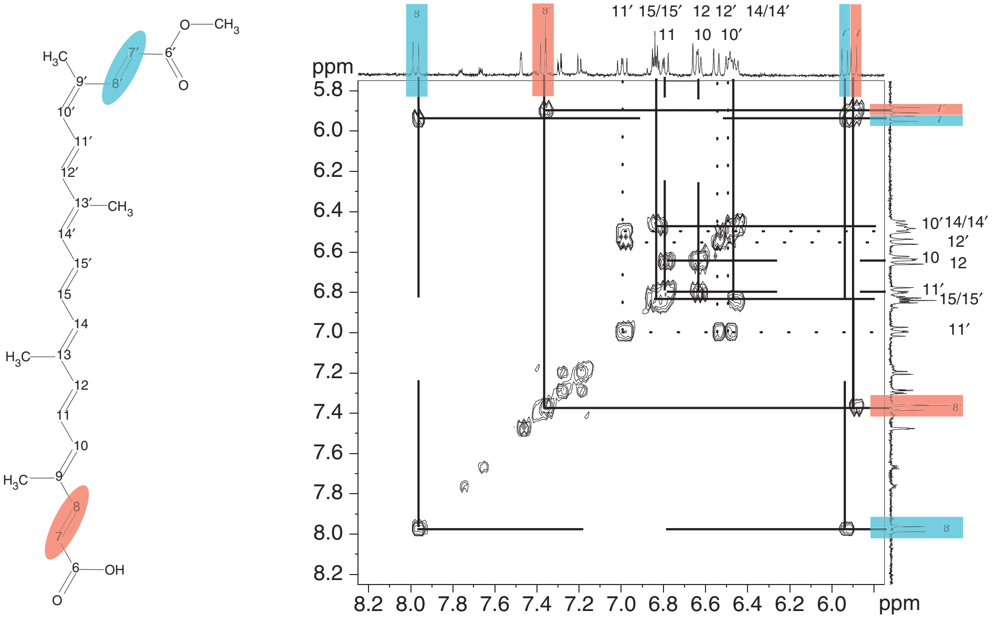

Figure 52.18 Stopped-flow $^1H^1H$ COSY spectrum of 9′-*cis*-bixin.

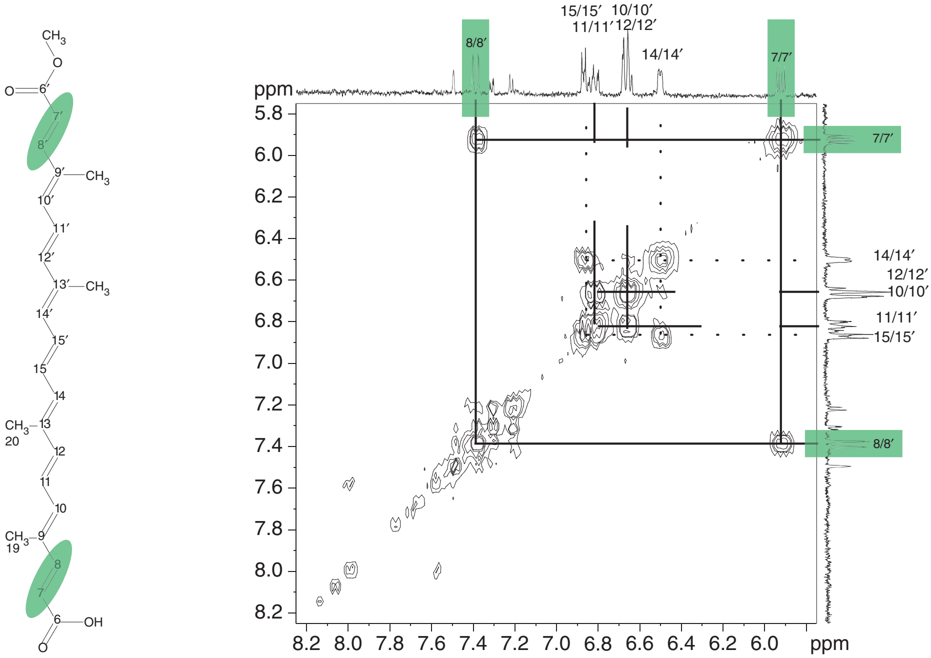

Figure 52.19 Stopped-flow $^1H^1H$ COSY spectrum of *all-trans*-bixin.

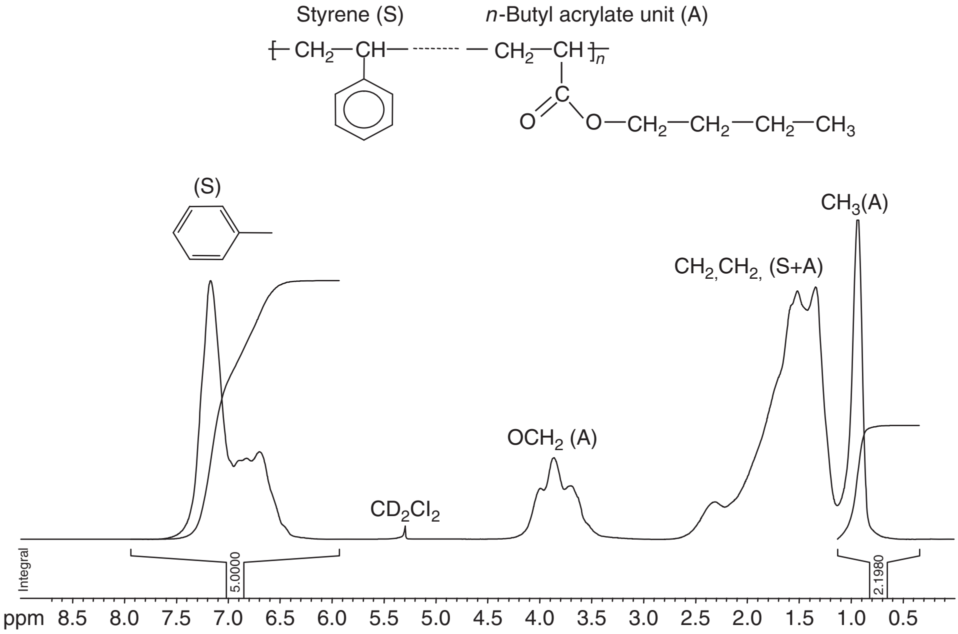

Figure 52.20 ^{1}H NMR spectrum of a latex.

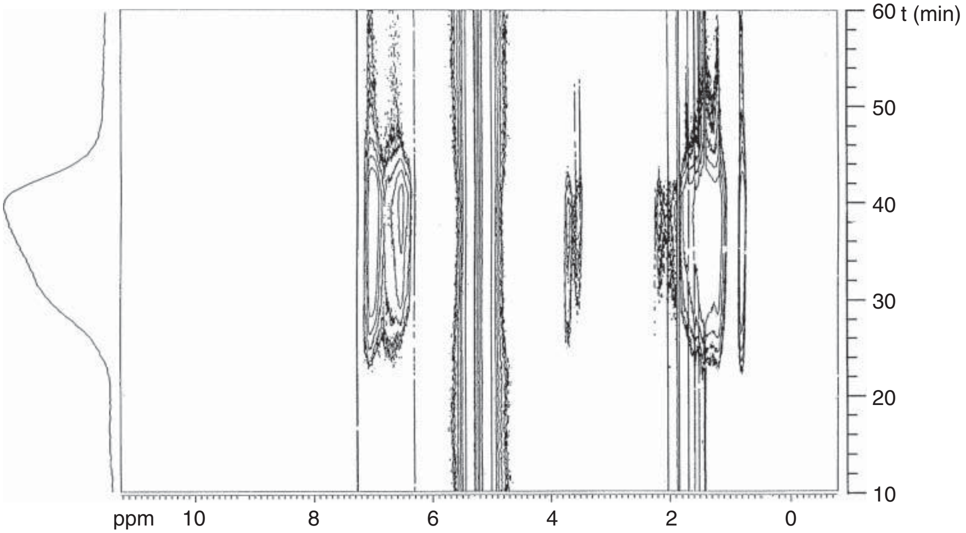

Figure 52.21 Contour plot of the online GPC-^{1}H NMR detection of a latex in CH_2Cl_2 at 300 K.

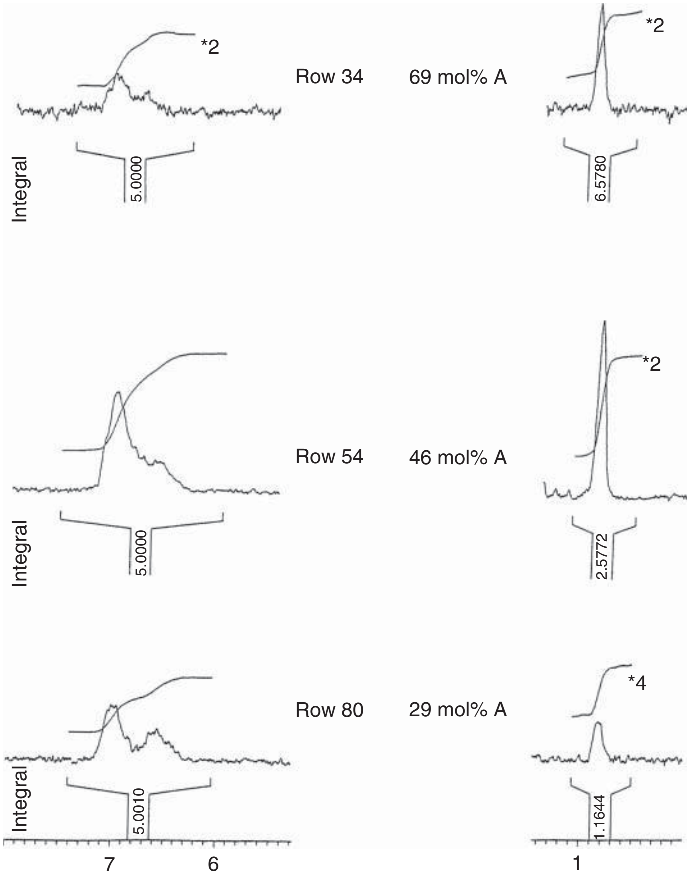

Figure 52.22 Change in the polymer composition of a latex during the GPC-^{1}H NMR on-line separation.

52.8
SFC-NMR

SFC-NMR experiments are performed with a pressure-stable flow cell using a sapphire tube instead of the glass tube. This technique offers a big advantage in that it employs the nonprotonated solvent carbon dioxide. Thus, the whole chemical shift range of the resulting SFC-^{1}H NMR spectra is not obscured from any solvent signal and can be used for structure elucidation purposes [91].

A modified version of this Helmholtz design is also used for coupling of SFC with NMR [92–99]. The inner glass tube of the originating HPLC-NMR probe is substituted with a sapphire tube (detection volume 120 μl), whereas the polyetheretherketone (PEEK) capillaries used in the HPLC-NMR probe are replaced by Titan tubings. A double-tuned proton-deuterium coil is directly fixed to the sapphire flow cell. The whole arrangement is centered in the glass dewar of a conventional probe body, in which a thermocouple is inserted, allowing the execution of well-defined temperature-dependent measurements.

In SFC-NMR experiments, the outlet of the pressure-stable SFC probe is connected to a back pressure regulator to guarantee supercritical conditions in the detection cell (Figure 52.23).

This phenomenon is demonstrated in Figure 52.24, exhibiting the continuous-flow ^{1}H NMR spectra of a separation of five plasticizers [92]. The separation was

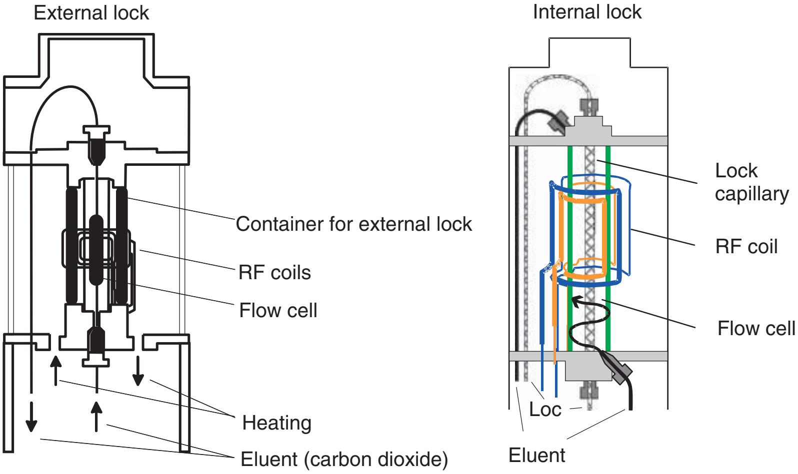

Figure 52.23 SFC-^{1}H NMR probes.

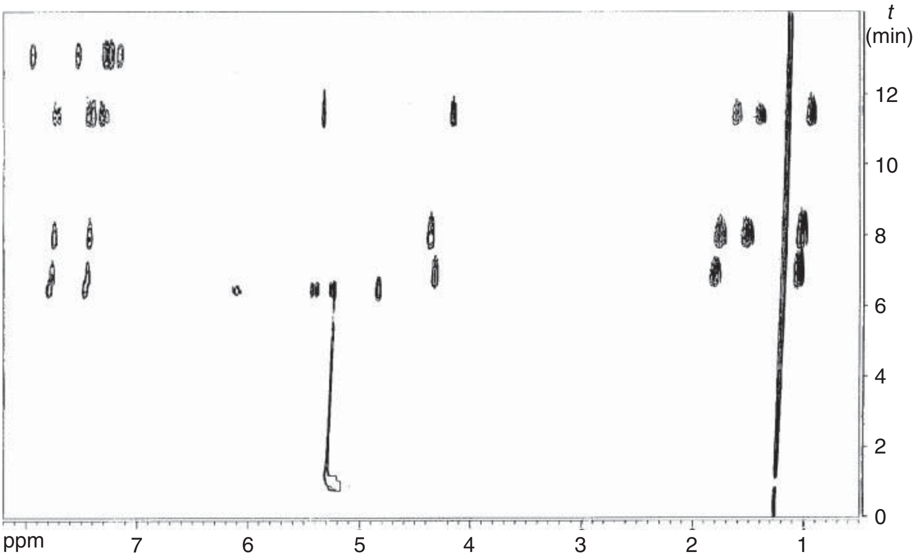

Figure 52.24 SFC-^{1}H NMR separation of five plastifiers.

carried out in supercritical CO_2 with a packed analytical SFC column (C_8 reversed phase, 4.6×250 mm) at a flow rate of 2.0 ml min^{-1}, a linear pressure gradient from 115 to 180 bar in 20 min at a temperature of 353 K. The NMR resolution of all SFC spectra is excellent; even the ^{1}H NMR spectrum of the last eluting compound, diphenylphthalate, does not show any distortion. Supercritical CO_2 is often used for supercritical fluid extraction (SFE) purposes in a lot of processes such as the decaffeination of coffee and the extraction of hops. The direct SFE-^{1}H NMR monitoring of the extraction process of roasted coffee and of black pepper was possible by employing an analytical SFC column as extraction cell. 2D NMR spectra of the extracted compounds could be measured in the stopped-flow mode within registration times of lower than 40 min.

52.9
GC–NMR

Because of the use of capillary detection in LC-NMR coupling in the liquid state, it is also straightforward to implement capillary detection in GC-NMR coupling [100]. Buddrus and Herzog [101, 102] have pioneered GC-NMR with conventional detection. The GC-NMR setup for capillary GC-NMR is shown in Figure 52.25 [63, 64]. The gas chromatograph is connected to a home-built solenoidal microprobe with a detection volume of 3 μl via a transfer capillary (ID 50 μm, length 3 m).

The contour plot of a separation of diethylether, hexane, and tetrahydrofurane (THF) is shown in Figure 52.26. Thirty microliters of the mixture of diethylether,

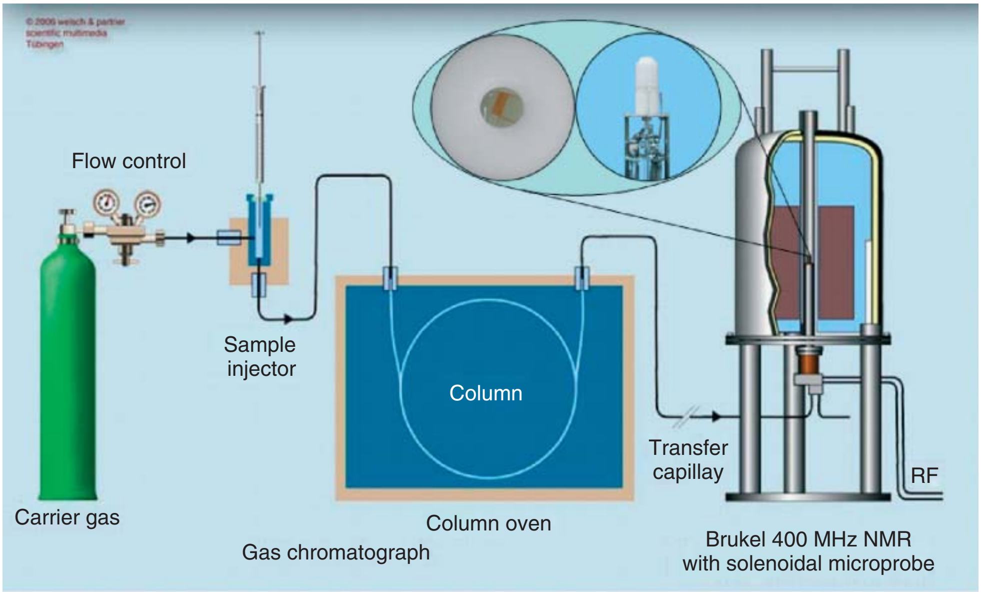

Figure 52.25 Experimental setup for GC-NMR.

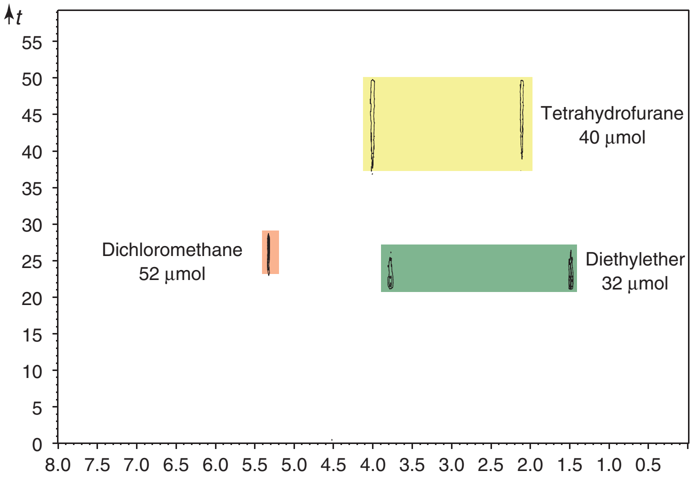

Figure 52.26 Contour plot of the GC-NMR separation of diethylether, hexane, and THF.

hexane, and THF have been injected at a semipreparative GC polysiloxane column. The carrier gas was nitrogen at a pressure of 1–7 bar. The injection temperature was 250 °C and the temperature of the GC oven was 60 °C.

The gas-phase continuous-flow ^{1}H NMR spectrum of diethylether is seen in Figure 52.27. Owing to inherent flow broadening at the employed flow rate of

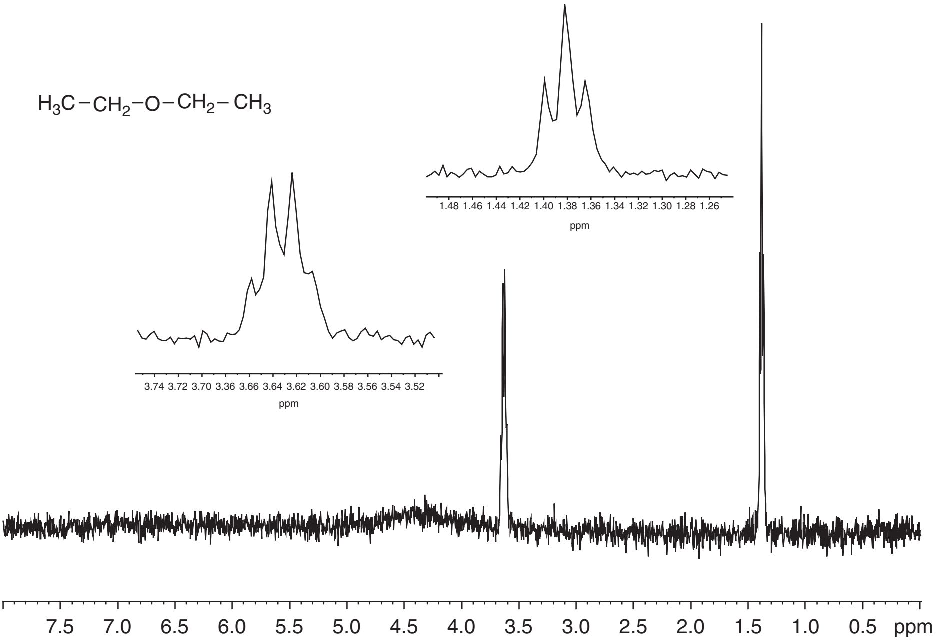

Figure 52.27 Continuous-flow gas-phase ^{1}H NMR spectrum of diethylether.

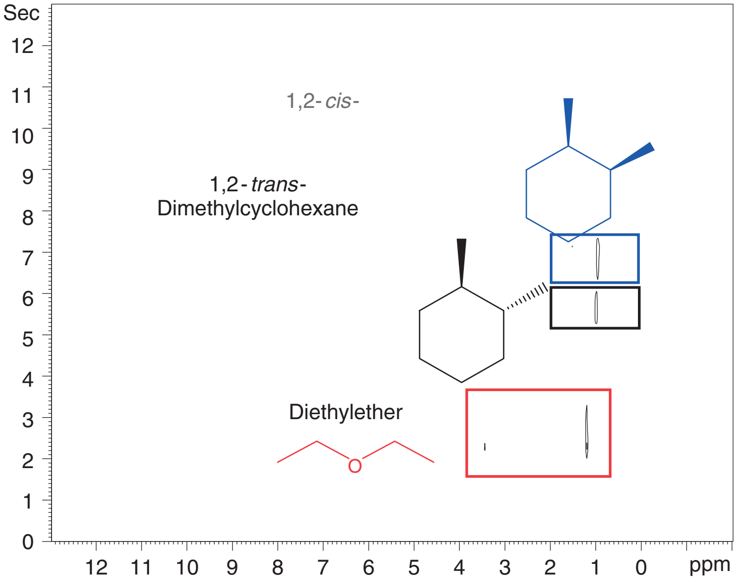

Figure 52.28 Contour plot of the GC-NMR separation of 1,2-*trans*- and 1,2-*cis*-dimethylcylohexane.

5 ml/min, the quartet and the triplet of the diethylether are not base-line resolved, but the stereochemical information of the coupling constant can be easily derived.

Another example is the GC-NMR separation of the stereoisomers of 1,2-*trans*- and 1,2-*cis*-dimethylcyclohexane. The separation shown in Figure 52.28 was performed on a chirasil-β-dex column (ID 250 μm, length 25 m, film thickness 0.25 μm), employing nitrogen as carrier gas at 1 bar pressure at an oven temperature of 60 °C. A further separation of 2-*trans*/*cis* pentene/hexene under similar conditions is shown in Figure 52.29.

The current further development of GC-NMR deals with the implementation of a heatable transfer capillary and the development of a solenoidal NMR probe for high-temperature NMR detection up to 200 °C.

52.10
CE-NMR and CEC-NMR

Electrodriven separations such as capillary electrophoresis (CE) and pressurized capillary electrophoresis (pCEC) have an application potential in separation science [103–114]. Because of the plug flow in electrodriven separations, very high number of plate rates can be obtained. Owing to the additional magnetic field introduced by the high current (up to 20 000 A) of the electroosmotic separation, the application of vertically oriented flow cell is favorable (Figure 52.30).

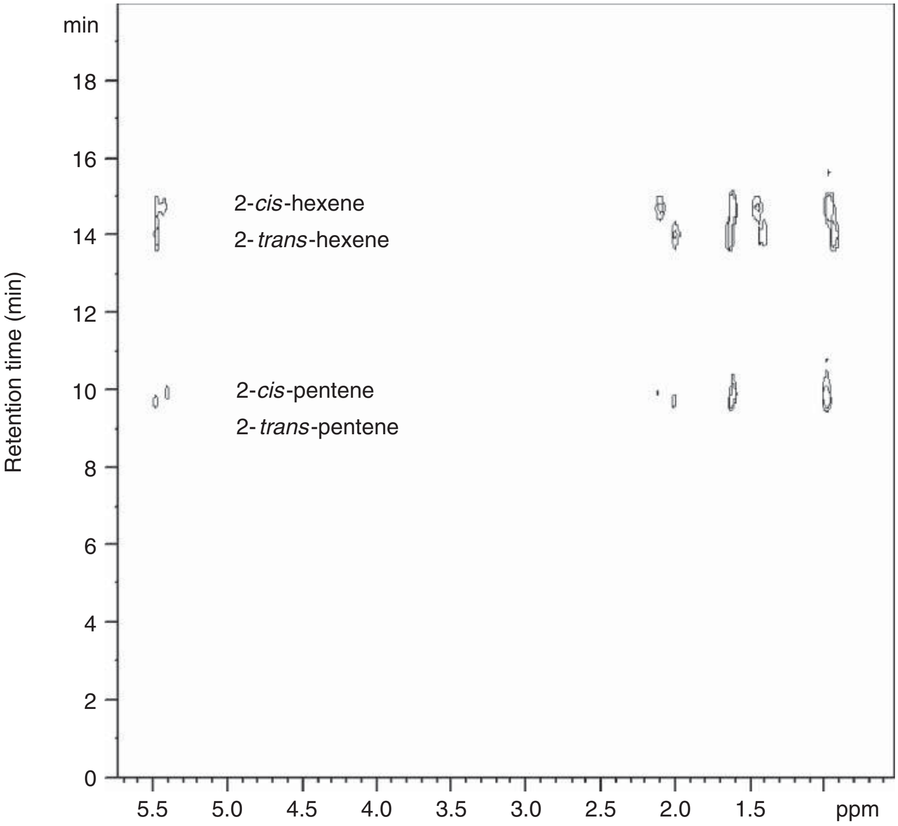

Figure 52.29 Contour plot of the GC-NMR separation of 2-*trans*/*cis* pentene/hexene.

Figure 52.31 and Figure 52.32 show the CE and pCEC separation of fatty esters. A further extension of the NMR registration of electrodriven separation is the use of isotachophoresis for peak focusing. This work was pioneered by Larive [111–114].

52.11
Current Developments

Modern NMR assignment techniques for the structure elucidation of unknown organic compounds employ the combined use of ^{1}H and ^{13}C NMR spectroscopy. This is outlined in Section 52.5 where the employed stopped-flow technique is ideal for the application of two-dimensional ^{1}H^{13}C assignment techniques such as HSQC and HMBC.

But similar to the direct online monitoring of a separation by ^{1}H NMR spectroscopy, it would be favorable to perform a continuous-flow registration by ^{13}C NMR spectroscopy. ^{13}C NMR spectroscopy offers the big advantage of direct

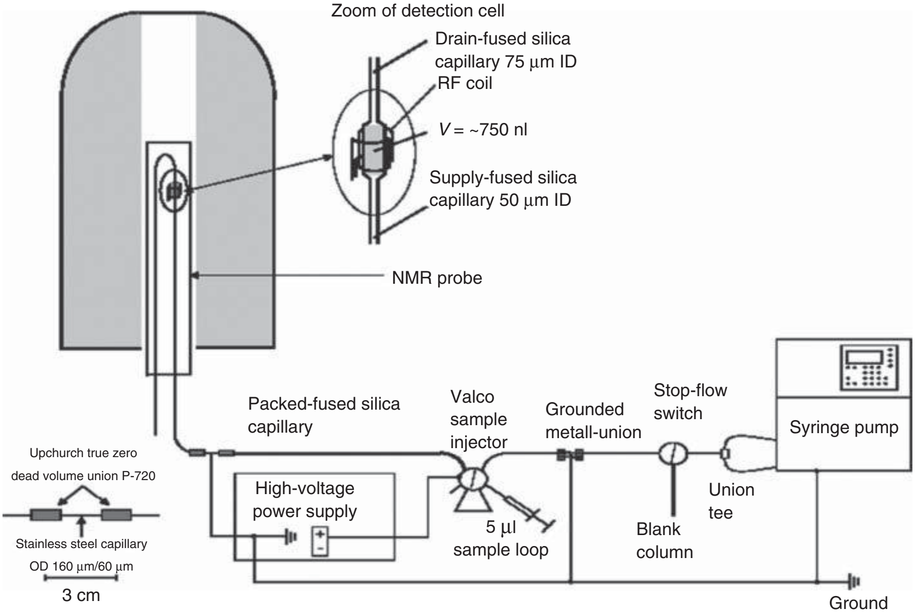

Figure 52.30 Experimental setup for CE-NMR and CEC-NMR.

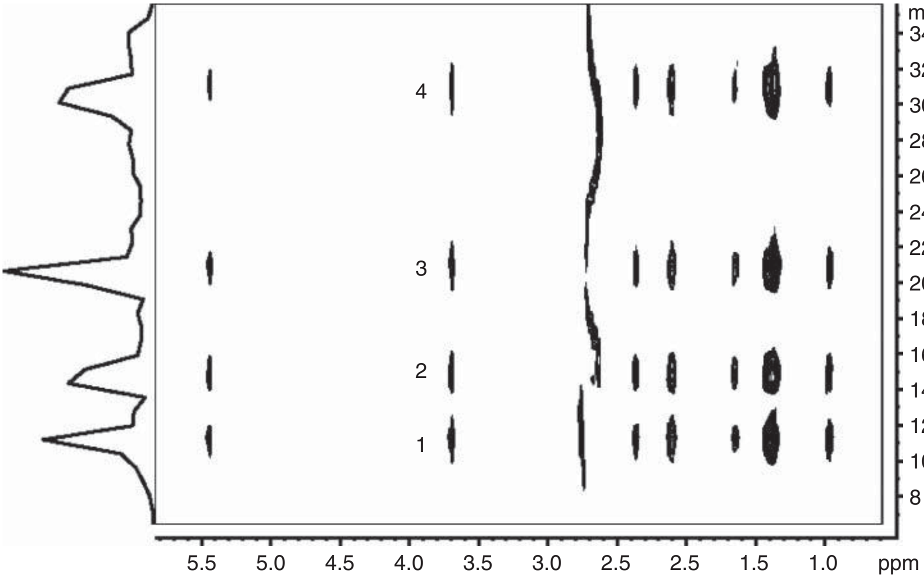

Figure 52.31 Separation of fatty acid methyl esters on a C_{18} phase 1 palmitoleic acid methyl ester (C16:1, *cis*-9), 2 oleic acid methyl ester (C18:1, *cis*-9,3 eicosenoic acid methyl ester (C20:1, *cis*-11), 4 erucic acid methyl ester (C22:1, *cis*-13) CE-^{1}H NMR coupling (flow rate 2 μl min^{-1}, voltage + 17 kV, current + 1.5 μA, back pressure 30 psi).

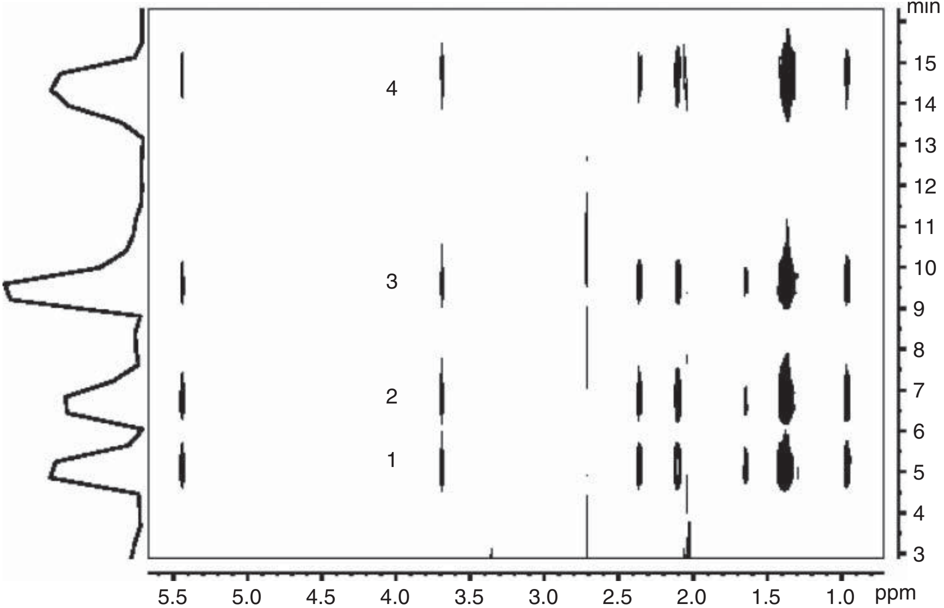

Figure 52.32 Separation of fatty acid methyl esters on a C_{18} phase pCEC-^{1}H NMR coupling (flow rate 4 µl min^{-1}, voltage + 17 kV, current + 1.5 µA, back pressure 550 psi).

access to the molecular framework of organic compounds. The high ^{13}C chemical shift range of 200 ppm versus the ^{1}H chemical shift range of only 10 ppm allows for a much easier peak assignment. The disadvantage of ^{13}C NMR spectroscopy is the low natural abundance of only 1.1% of ^{13}C nuclei and the long spin–lattice relaxation times T_1 up to several seconds. ^{1}H nuclei have a natural abundance of 99.9%, and spin–lattice relaxation times are between 0.1 and 1 s. Because spin–lattice relaxation times define the pulse repetition rate in the NMR acquisition (Figure 52.33), they directly define the sensitivity either in a static or continuous-flow NMR experiment.

There is one big advantage of continuous-flow NMR: that nuclei can pick up their magnetization before they enter the NMR detection cell. Thus, full Boltzmann

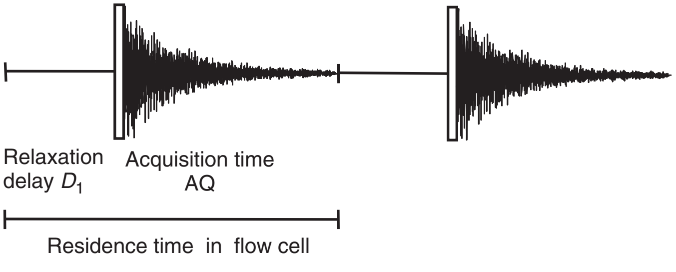

Figure 52.33 NMR acquisition in the continuous-flow mode.

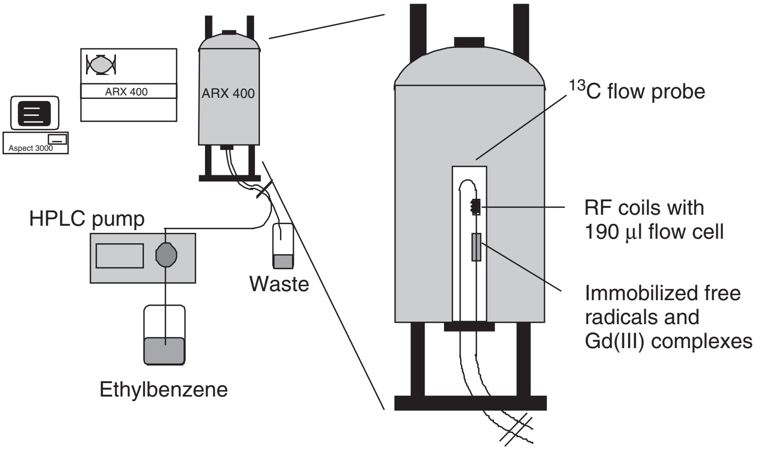

Figure 52.34 Experimental setup for continuous-flow ^{13}C NMR recording.

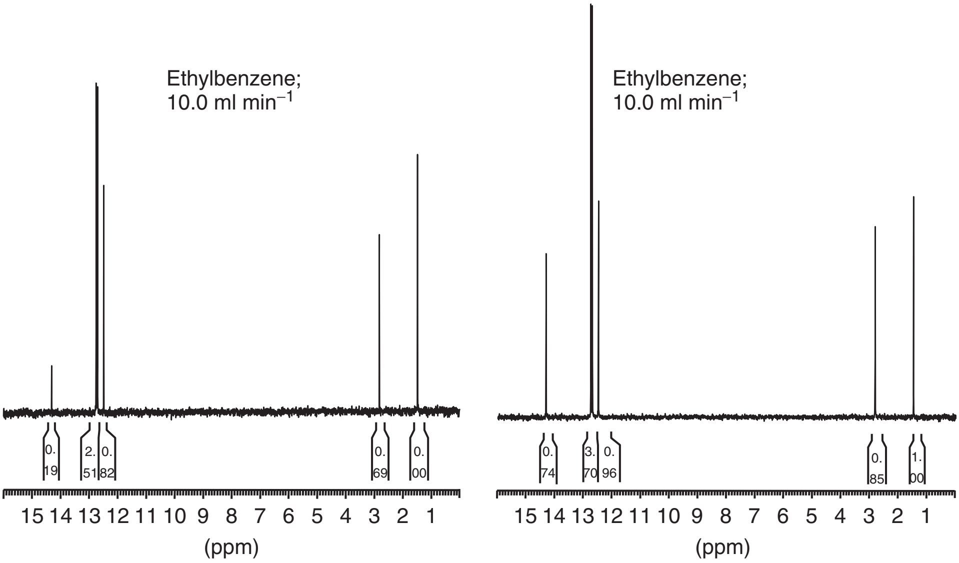

Figure 52.35 Continuous-flow (10 ml min^{-1}) ^{13}C NMR spectra of ethylbenzene without and with Gd-DOTA.

distribution can be obtained by passing the analyte through a premagnetization volume before the NMR detection coil. If this ''premagnetization volume'' is packed with an immobilized free radical, T_1 of the flowing nuclei is reduced and NMR sensitivity can be increased. In NMR imaging, paramagnetic contrast agents such as Gd-DTPA (gadolinium-diethylenetriamine penta-acetic acid) and Gd-DOTA (gadolinium-tetraazacyclododecanetetraacetic acid) are used to reduce the water T_1 in the human body and enable the detection of malignant tissues. The same principle can be used for continuous-flow ^{13}C NMR detection.

A container with immobilized Gd-DTPA can be inserted in the continuous-flow probe before the NMR detection coil (Figure 52.34) [115]. The relaxation effect can be readily seen in Figure 52.35. The signal intensity of the quaternary carbon of ethylbenzene is increased by a factor of 3.9. All ^{13}C signals of ethylbenzene show nearly same intensity ready for quantitation.

The next reach step will be the implementation of the immobilized relaxation agent together with a reversed phase in a special designed probe for ^{13}C NMR detection. This is an ongoing development with Prof. Andrew Webb from Leiden University in The Netherlands.

Because of the small detection volumes necessary for capillary microcoil NMR, it is possible to position several microcoils within one NMR probe. A recent review describes the current status and possible future developments of single and multiple microcoil NMR detection [116].

52.12
Conclusion

The high number of applications dealing with the hyphenation of all existing separation techniques with NMR spectroscopy really proves that NMR spectroscopy can be considered an important chromatography detector. The unambiguous information content derived by NMR spectroscopy justifies the high price of the most expensive chromatography detector.

Currently, two major online coupling strategies with NMR detection are used. One is the application of solid-phase extraction together with separation and NMR detection, for example, LC-SPE-NMR. Here, very sensitive cryprobes are used for NMR detection. The other strategy is the application of microcoils for NMR detection together with capillary separation techniques.

LC-SPE-NMR seems favorable for the investigation of plant extracts, whereas microcoils show some application value for capillary HPLC, GC, SFC; CE and CEC separations. One big advantage of LC-SPE-NMR is that it can be fully automated for screening purposes.

Overall, together with hyphenated MS techniques, online NMR techniques are the methods of choice of an efficient structural peak assignment in chromatography.

Acknowledgment

The author thanks Jan Peter Mayser for his help in preparing the figures.

References

1. Watanabe, N. and Niki, E. (1978) Direct-coupling of FT-NMR to high-performance liquid-chromatography. *Proc. Jpn. Acad. Ser. B*, **54**, 194–199.
2. Bayer, E., Albert, K., Nieder, M., Grom, E., and Keller, T. (1979) On-line coupling of high-performance liquid chromatography and nuclear magnetic

resonance. *J. Chromatogr.*, **186**, 497–507.

3. Haw, F., Glass, T.E., Hausler, D.W., Motell, E., and Dorn, H.C. (1980) Direct coupling of a liquid chromatograph to a continuous flow hydrogen nuclear magnetic resonance detector for analysis of petroleum and synthetic fuels. *Anal. Chem.*, **52**, 1135–1140.
4. Buddrus, J. and Herzog, H. (1980) Coupling of HPLC and NMR. 1. Analysis of flowing liquid-chromatographic fractions by proton magnetic resonance. *Org. Magn. Reson.*, **13**, 153–155.
5. Haw, F., Glass, T.E., and Dorn, H.C. (1981) Continuous flow high field nuclear magnetic resonance detector for liquid chromatographic analysis of fuel samples. *Anal. Chem.*, **53**, 2327–2332.
6. Bayer, E., Albert, K., Nieder, M., Grom, E., Wolff, G., and Rindlisbacher, M. (1982) On-line coupling of liquid chromatography and high-field nuclear magnetic resonance spectrometry. *Anal. Chem.*, **54**, 1747–1750.
7. Dorn, H.C. (1984) Proton-NMR: a new detector. *Anal. Chem.*, **56**, 747A.
8. Laude, D.A. Jr., and Wilkins, C.L. (1984) Direct-linked analytical scale high-performance liquid chromatography/nuclear magnetic resonance spectrometry. *Anal. Chem.*, **56**, 2471–2475.
9. Laude, D.A. Jr., and Wilkins, C.L. (1986) Nuclear magnetic resonance detection for the on-line identification of liquid chromatography eluents. *Trends Anal. Chem.*, **5**, 230–235.
10. Albert, K., Kunst, M., Bayer, E., Spraul, M., and Bermel, W. (1989) Reversed phase high-performance liquid chromatography–nuclear magnetic resonance on-line coupling with solvent non-excitation. *J. Chromatogr.*, **463**, 355–363.
11. Albert, K., Kunst, M., Bayer, E., de Jong, H.J., Genissel, P., Spraul, M., and Bermel, W. (1989) Investigation of a cyclopropyl-containing drug by on-line high-performance liquid chromatography/nuclear magnetic resonance. *Anal. Chem.*, **61**, 772–775.
12. Spraul, M., Hofmann, M., Dvortsak, P., Nicholson, J.K., and Wilson, I.D. (1993) High-performance liquid chromatography coupled to high-field proton nuclear magnetic resonance spectroscopy: application to the urinary metabolites of ibuprofen. *Anal. Chem.*, **65**, 327–330.
13. Wilson, I.D., Nicholson, J.K., Hofmann, M., Spraul, M., and Lindon, J.C. (1993) Investigation of the human metabolism of antipyrine using coupled liquid chromatography and nuclear magnetic resonance spectroscopy of urine. *J. Chromatogr.*, **617**, 324.
14. (a) Albert, K., Schlotterbeck, G., Braumann, U., Händel, H., Spraul, M., and Krack, G. (1995) Strukturbestimmung von vitamin-A-acetat-isomeren mit HPLC-1H-NMR-kopplung. *Angew. Chem.*, **107**, 1102–1104. (b) Albert, K., Schlotterbeck, G., Braumann, U., Händel, H., Spraul, M., and Krack, G. (1995) Structure determination of vitamin A acetate isomers through coupled HPLC and 1H NMR spectroscopy. *Angew. Chem., Int. Ed. Engl.*, **34**, 1014–1016.
15. Höltzel, A., Schlotterbeck, G., Albert, K., and Bayer, E. (1996) Separation and characterisation of hop bitter acids by HPLC-1H NMR coupling. *Chromatographia*, **42**, 499–505.
16. Sudmeier, J., Günther, U., Albert, K., and Bachovchin, W. (1996) Sensitivity optimization in continuous-flow FTNMR. *J. Magn. Reson., Ser. A*, **118**, 145–156.
17. Korhammer, S.A. and Bernreuther, A. (1996) Hyphenation of high-performance liquid chromatography (HPLC) and other chromatographic techniques (SFC, GPC, GC, CE) with nuclear magnetic resonance (NMR): a review. *Fresenius J. Anal. Chem.*, **354**, 131–135.
18. Lindon, J.C., Nicholson, J.K., and Wilson, I.D. (1996) Direct coupling of chromatographic separations to NMR spectroscopy. *Prog. NMR Spectrosc.*, **29**, 1–49.
19. Sidelmann, U.G., Lenz, E.M., Spraul, M., Hofmann, M., Troke, J., Sanderson, P.N., Lindon, J.C., Wilson, I.D., and Nicholson, J.K. (1996) 750 MHz HPLC–NMR spectroscopic

studies on the separation and characterization of the positional isomers of the glucuronides of 6,11-dihydro-11-oxodibenz[b,e]oxepin-2-acetic acid. *Anal. Chem.*, **68**, 106–110.

20. Sidelmann, U.G., Braumann, U., Hoffmann, M., Spraul, M., Lindon, J.C., and Nicholson, J.K. (1997) Directly coupled 800 MHz HPLC-NMR spectroscopy of urine and its application to the identification of the major phase II metabolites of tolfenamic acid. *Anal. Chem.*, **69**, 607–612.
21. Strohschein, S., Pursch, M., Händel, H., and Albert, K. (1997) Structure elucidation of ß-carotene isomers by HPLC-NMR coupling using a C$_3$o bonded phase. *Fresenius J. Anal. Chem.*, **357**, 498–502.
22. Lindon, C., Nicholson, J.K., Sidelmann, U.G., and Wilson, I.D. (1997) Directly coupled HPLC-NMR and its application to drug metabolism. *Drug Metab. Rev.*, **29**, 705–745.
23. Strohschein, S., Schlotterbeck, G., Richter, J., Pursch, M., Tseng, L.-H., Händel, H., and Albert, K. (1997) Comparison of the separation of cis/trans isomers of tretinoin with different stationary phases by liquid chromatography–nuclear magnetic resonance coupling. *J. Chromatogr. A*, **765**, 207–214.
24. Godejohann, M., Preiss, A., and Mügge, C. (1998) Quantitative measurements in continuous-flow HPLC/NMR. *Anal. Chem.*, **70**, 590–595.
25. Dachtler, M., Kohler, K., and Albert, K. (1998) Reversed-phase high-performance liquid chromatographic determination of lutein and zeaxanthin stereoisomers in ox retina using a C30 bonded phase. *J. Chromatogr. B*, **720**, 211–216.
26. de Koning, A., Hogenboom, A.C., Lacker, T., Strohschein, S., Albert, K., and Brinkman, U.A.T. (1998) On-line trace enrichment in hyphenated liquid chromatography–nuclear magnetic resonance spectroscopy. *J. Chromatogr. A*, **813**, 55–61.
27. Albert, K., Dachtler, M., Händel, H., Lacker, T., Schlotterbeck, G., Strohschein, S., Tseng, L.-H., and Braumann, U. (1999) On-line coupling of separation techniques to NMR. *J. High Resolut. Chrom.*, **22**, 135–143.
28. Strohschein, S., Rentel, C., Lacker, T., Bayer, E., and Albert, K. (1999) Separation and identification of tocotrienol isomers by HPLC-MS and HPLC-NMR coupling. *Anal. Chem.*, **71**, 1780–1785.
29. Lacker, T., Strohschein, S., and Albert, K. (1999) Separation and identification of various carotenoids by C30 reversed-phase high-performance liquid chromatography coupled to UV and atmospheric pressure chemical ionization mass spectrometric detection. *J. Chromatogr. A*, **854**, 37–44.
30. Pusecker, K., Albert, K., and Bayer, E. (1999) Investigation of hop and beer bitter acids by coupling of high-performance liquid chromatography to nuclear magnetic resonance spectroscopy. *J. Chromatogr. A*, **836**, 245–252.
31. Strohschein, S., Pursch, M., and Albert, K. (1999) Hyphenation of high performance liquid chromatography with nuclear magnetic resonance spectroscopy for the characterization of β-carotene isomers employing a C30 stationary phase. *J. Pharm. Biomed. Anal.*, **21**, 669–677.
32. Vilegas, W., Vilegas, J.H.Y., Dachtler, M., Glaser, T., and Albert, K. (2000) Application of on-line C30 RP-HPLC-NMR for the analysis of flavonoids from leaf extract of maytenus aquifolium. *Phytochem. Anal.*, **11**, 317–321.
33. Santos, C., Dachtler, M., Andrade, F.D.P., Albert, K., and Vilegas, W. (2000) Application of HPLC-NMR coupling using C30 phase in the separation and identification of flavonoids of taxonomic relevance. *Fresenius J. Anal. Chem.*, **368**, 540–542.
34. Tseng, H., Braumann, U., Godejohann, M., Lee, S.-S., and Albert, K. (2000) Structure identification of aporphine alkaloids by on-line coupling of HPLC-NMR with loop storage. *J. Chin. Chem. Soc.*, **47**, 1231–1236.
35. Santos, C., Piacente, S., Pizza, C., Albert, K., Dachtler, M., and Vilegas,

W. (2001) Planifolin, a new naphthopyranone dimer and flavonoids from paepalanthus planifolius. *J. Nat. Prod.*, **64**, 122–124.

36. Dachtler, M., Glaser, T., Kohler, K., and Albert, K. (2001) Combined HPLC-MS and HPLC-NMR on-line coupling for the separation and determination of lutein and zeaxanthin stereoisomers in spinach and in retina. *Anal. Chem.*, **73**, 667–674.
37. Rühl, R., Thiel, R., Lacker, T.S., Strohschein, S., Albert, K., and Nau, H. (2001) Synthesis, high-performance liquid chromatography–nuclear magnetic resonance characterization and pharmacokinetics in mice of CD271 glucuronide. *J. Chromatogr. B*, **757**, 101–109.
38. Glaser, T. and Albert, K. (2002) Unequivocal structural assignment of steroids in galenic emulsions employing HPLC-NMR coupling. *J. Sep. Sci.*, **25**, 393–398.
39. Andrade, D.P., Santos, L.C., Dachtler, M., Albert, K., and Vilegas, W. (2002) Use of on-line liquid chromatography–nuclear magnetic resonance spectroscopy for the rapid investigation of flavonoids from sorocea bomplandii. *J. Chromatogr. A*, **953**, 287–291.
40. Albert, K. (ed.) (2002) *On-Line LC-NMR and Related Techniques*, John Wiley & Sons, Ltd, Chichester.
41. Lienau, A., Glaser, T., Krucker, M., Zeeb, D., Ley, F., Curro, F., and Albert, K. (2002) Qualitative and quantitative analysis of tocopherols in toothpastes and gingival tissue employing HPLC NMR and HPLC MS coupling. *Anal. Chem.*, **74**, 5192–5198.
42. Glaser, T., Lienau, A., Zeeb, D., Krucker, M., Dachtler, M., and Albert, K. (2003) Qualitative and quantitative determination of carotenoid stereoisomers in various spinach samples using MSPD prior to HPLC-UV, HPLC-APCI-MS and HPLC-NMR on-line coupling. *Chromatographia*, **57**, S-19–S-25.
43. Zöllner, P., Lienau, A., Albert, K., and Lindner, W. (2003) Derivatization reaction of the mycotoxin moniliformin with 1,2-diamino-4,5-dichlorobenzene: structure elucidation of an unexpected reaction product by liquid chromatography / tandem mass spectrometry and liquid chromatography / nuclear magnetic resonance spectroscopy. *J. Mass Spectrom.*, **38**, 709–714.
44. Putzbach, K., Krucker, M., Albert, K., Grusak, M.A., and Dolnikowski, G.D. (2005) Structure determination of partially deuterated (all-E)-α-carotene, (all-E)-β-carotene, and (all-E) lutein from intrinsically labeled spinach. *J. Agric. Food Chem.*, **53**, 671–677.
45. Exarchou, V., Krucker, M., Van Beek, T.A., Vervoort, J., Gerothanassis, I.P., and Albert, K. (2005) LC-NMR coupling technology. recent advancements and applications in natural products analysis. *Magn. Reson. Chem.*, **43**, 681–687.
46. Jaroszewski, J.W. (2005) Hyphenated NMR methods in natural products research, part 1: direct hyphenation. *Planta Med.*, **71**, 691–700.
47. Albert, K., Krucker, M., Grynbaum, M.D., and Putzbach, K. (2006) in *HPLC Made to Measure* (ed. S. Kromidas), Wiley-VCH Verlag GmbH, Weinheim, pp. 551–563.
48. Wu, N., Peck, T.L., Webb, A.G., Magin, R.L., and Sweedler, J.V. (1994) 1H-NMR spectroscopy on the nanoliter scale for static and online measurements. *Anal. Chem.*, **22**, 3849–3857.
49. Olson, T., Peck, T.K., Webb, A.G., Magin, R.L., and Sweedler, J.V. (1995) High resolution microcoil 1H-NMR for mass-limited, nanoliter volume samples. *Science*, **270**, 1967–1970.
50. Behnke, B., Schlotterbeck, G., Tallarek, U., Strohschein, S., Tseng, L.-H., Keller, T., Albert, K., and Bayer, E. (1996) Capillary HPLC-NMR coupling: high-resolution 1H NMR spectroscopy in the nanoliter scale. *Anal. Chem.*, **68**, 1110–1115.
51. Albert, K., Schlotterbeck, G., Tseng, L.-H., and Braumann, U. (1996) Application of on-line capillary high-performance liquid chromatography-nuclear magnetic resonance spectrometry coupling for the analysis of vitamin

A derivatives. *J. Chromatogr. A*, **750**, 303–309.

52. Olson, L., Lacey, M.E., and Sweedler, J.V. (1998) The nanoliter niche: NMR detection for trace analysis and capillary separations. *Anal. Chem.*, **70**, 257A–246A.
53. Li, Y., Wolters, A.M., Malawey, P.V., Sweedler, J.V., and Webb, A.G. (1999) Multiple solenoidal microcoil probes for high-sensitivity, high-throughput nuclear magnetic resonance spectroscopy. *Anal. Chem.*, **71**, 4815–4820.
54. Lacey, E., Tan, Z.J., Webb, A.G., and Sweedler, J.V. (2001) Union of capillary high-performance liquid chromatography and microcoil nuclear magnetic resonance spectroscopy applied to the separation and identification of terpenoids. *J. Chromatogr. A*, **922**, 139–149.
55. Krucker, M., Lienau, A., Putzbach, K., Grynbaum, M.D., Schuler, P., and Albert, K. (2004) Hyphenation of capillary HPLC to mass spectrometry and microcoil 1H NMR spectroscopy for the determination of tocopherol homologues (vitamin E). *Anal. Chem.*, **76**, 2623–2628.
56. Xiao, H.B., Krucker, M., Putzbach, K., and Albert, K. (2005) Capillary liquid chromatography–microcoil 1H nuclear magnetic resonance spectroscopy and liquid chromatography–ion trap mass spectrometry for on-line structure elucidation of isoflavonoids in radix astragali. *J. Chromatogr. A*, **1067**, 135–143.
57. Hentschel, P., Krucker, M., Grynbaum, M.D., Putzbach, K., Bischoff, R., and Albert, K. (2005) Determination of regulatory phosphorylation sites in nanogram amounts of a synthetic fragment of ZAP-70 using cicroprobe NMR and on-line hyphenated capillary HPLC–NMR. *Magn. Reson. Chem.*, **43**, 747–754.
58. Putzbach, K., Krucker, M., Grynbaum, M.D., Hentschel, P., Webb, A.G., and Albert, K. (2005) Hyphenation of capillary high-performance liquid chromatography to microcoil magnetic resonance spectroscopy–determination of various carotenoids in a small-sized spinach sample. *J. Pharm. Biomed. Anal.*, **38**, 910–917.
59. Grynbaum, M.D., Hentschel, P., Putzbach, K., Rehbein, J., Krucker, M., Nicholson, G., and Albert, K. (2005) Unambiguous detection of astaxanthin and astaxanthin fatty acid esters in krill (euphausia superba dana). *J. Sep. Sci.*, **28**, 1685–1693.
60. Hentschel, P., Grynbaum, M.D., Molnar, P., Putzbach, K., Rehbein, J., Deli, J., and Albert, K. (2006) Structure elucidation of deoxylutein-II isomers by on-line capillary high performance liquid chromatography -1H nuclear magnetic resonance spectroscopy. *J. Chromatogr. A*, **1112**, 285–292.
61. Rehbein, J., Dietrich, B., Grynbaum, M.D., Hentschel, P., Holtin, K., Kühnle, M., Schuler, P., Bayer, M., and Albert, K. (2007) Characterization of bixin by LC-MS and LC-NMR. *J. Sep. Sci.*, **30**, 2382–2390.
62. Korir, A. and Larive, C.K. (2007) On-line NMR detection of microgram quantities of heparin-derived oligosaccharides and their structure elucidation by microcoil NMR. *Anal. Bioanal. Chem.*, **388**, 1707–1716.
63. Grynbaum, M.D., Kreidler, D., Rehbein, J., Purea, A., Schuler, P., Schaal, W., Czesla, H., Webb, A., Schurig, V., and Albert, K. (2007) Hyphenation of gas chromatography to microcoil 1H nuclear magnetic resonance spectroscopy. *Anal. Chem.*, **79**, 2708–2713.
64. Kühnle, M., Kreidler, D., Holtin, K., Czesla, H., Schuler, P., Schaal, W., Schurig, V., and Albert, K. (2008) On-line coupling of gas chromatography to nuclear magnetic resonance spectroscopy: method for the analysis of volatile stereoisomers. *Anal. Chem.*, **80**, 5481–5486.
65. Godejohann, M., Mügge, C., Wünsch, G., and Preiss, A. (1997) Application of on-line HPLC 1HNMR to environmental samples: analysis of groundwater near former ammunition plants. *Anal. Chem.*, **69**, 3832–3837.
66. Preiss, A., Elend, M., and Gerling, S. (2007) Identification of highly polar nitroaromatic compounds in leachate and

ground water samples from a TNT-contaminated waste site by LC-MS, LC-NMR and off-line NMR and MS investigations. *Anal. Bioanal. Chem.*, **389**, 1979–1988.

67. Reineke, A., Preiss, A., Elend, M., and Hollender, J. (2008) Detection of methylquinoline transformation products in microcosm experiments and in tar oil contaminated groundwater using LC-NMR. *Chemosphere*, **70**, 2118–2126.

68. Seeger, C. and Sturm, S. (2007) HPLC-SPE-NMR–a novel hyphenation technique. *LC-GC-Eur.*, **20**, 587–597.

69. Lambert, M., Staerk, D., Hansen, S.H., and Jaroszewski, J.W. (2005) HPLC-SPE-NMR-hyphenation in natural products research: optimization of analysis of croton membranaceus extract. *Magn. Reson. Chem.*, **43**, 771–775.

70. Jaroszewski, J.W. (2005) Hyphenated NMR methods in natural products research, part 2: HPLC-SPE-NMR and other new trends in NMR hyphenation. *Planta Med.*, **71**, 795–802.

71. Clarkson, C., Staerk, D., Hansen, S.H., and Jaroszewski, J.W. (2005) Hyphenation of solid-phase extraction with liquid chromatography and nuclear magnetic resonance: application of HPLC-DAD-SPE-NMR to identification of constituents of kanahia ianiflora. *Anal. Chem.*, **77**, 4658–4664.

72. Lambert, M., Staerk, D., Hansen, S.H., Sairafianpour, M., and Jaroszewski, J.W. (2005) Rapid extract dereplication using HPLC-SPE-NMR: analysis of isoflavonoids from sminowia iranica. *J. Nat. Prod.*, **68**, 1500–1509.

73. Clarksom, C., Staerk, D., Hansen, S.H., Smith, P.J., and Jaroszewski, J.W. (2006) Discovering new natural products directly from crude extracts by HPLC-SPE-NMR: chinane diterpenes in harpagophytum procumbens. *J. Nat. Prod.*, **69**, 527–530.

74. Clarkson, C., Staerk, D., Hansen, S.H., Smith, P.J., and Jaroszewski, J.W. (2006) Identification of major and minor constituents of harpagophytum procumbens (devil‘s claw) using HPLC-SPE-NMR and HPLC-ESIMS/APCIMS. *J. Nat. Prod.*, **69**, 1280–1288.

75. Clarkson, C., Madikane, E.V., Hansen, S.H., Smith, P.J., and Jaroszewski, J.W. (2007) HPLC-SPE-NMR characterisation of sesquiterpenes in an antimycobacterial fraction from warburgia salutaris. *Planta Med.*, **73**, 578–584.

76. Clarkson, C., Sibum, M., Mensen, R., and Jaroszewski, J.W. (2007) Evaluation of on-line-solid-phase extraction parameters for hyphenated, high-performance liquid chromatography-solid-phase extraction-nuclear magnetic resonance applications. *J. Chromatogr. A*, **1156**, 1–9.

77. Sprogoe, K., Staerk, D., Jäger, A.J., Adsersen, A., Hansen, S.H., Witt, M., Landbo, A.R., Meyer, A.S., and Jaroszewski, J.W. (2007) Targeted natural product isolation guided by HPLC-SPE-NMT: constituents of hubertia species. *J. Nat. Prod.*, **70**, 1472–1477.

78. Schmidt, B., Jaroszewski, J.W., Bro, R., Witt, M., and Staerk, D. (2008) Combining PARAFAC analysis of HPLC-PDA profiles and structural characterization using HPLC-PDA-SPE-NMR-MS experiments: commercial preparations of st. johns wort. *Anal. Chem.*, **80**, 89–98.

79. Sprogoe, K., Staerk, D., Ziegler, H.L., Jensen, T.H., Holm-Moller, S.B., and Jaroszewski, J.W. (2008) Combining HPLC-PDA-MS-SPE-NMR with circular dichroism for complete natural product characterization in crude extracts: levorotatory gossypol in thespesia danis. *J. Nat. Prod.*, **71**, 516–519.

80. Seger, C., Godejohann, M., Tseng, L.H., Spraul, M., Girtler, A., Sturm, S., and Stuppner, H. (2005) LC-DADFF-MS/SPE-NMR hyphenation. A tool for the analysis of pharmaceutically used plant extracts: identification of isobaric iridoid glycoside regioisomers from Harpagophytum procumbens. *Anal. Chem.*, **77**, 878–885.

81. Seeger, C., Godejohann, M., Spraul, M., Stuppner, H., and Hadadec, F. (2006) Reaction product analysis by high-performance liquid chromatography-solid-phase-nuclear magnetic resonance application to the absolute configuration determination of naturally occurring polyyne alcohols. *J. Chromatogr. A*, **1136**, 82–88.

82. Kuzovkina, I., Alterman, I., and Schneider, B. (2004) Specific accumulation and revised structures of acridone alkaloid glucosides in the tips of transformed roots of ruta graveolens. *Phytochemistry*, **65**, 1095–1100.
83. Schneider, B., Paetz, C., Hölscher, D., and Opitz, S. (2005) HPLC-NMR-for tissue-specific-analysis of phenylphealenone-related compounds in xiphidium caeruleum (haemodoraceae). *Magn. Reson. Chem.*, **43**, 724–728.
84. Lambert, M., Wolfender, J.-L., Staerk, D., Christensen, S.B., Hostettmann, K., and Jaroszewski, J.W. (2007) Identification of natural products using HPLC-SPE combined with capNMR. *Anal. Chem.*, **79**, 727–735.
85. Schlotterbeck, G., Pasch, H., and Albert, K. (1997) On-line HPLC 1H NMR coupling for the analysis of fatty alcohol ethoxylates. *Polym. Bull.*, **38**, 673–679.
86. Händel, H. and Albert, K. (2002) GPC-NMR coupling, in *LC-NMR and Related Techniques* (ed. K. Albert), John Wiley & Sons, Ltd, Chichester, pp. 181–218.
87. Krämer, I., Pasch, H., Händel, H., and Albert, K. (1999) Chemical heterogeneity analysis of high-conversion poly[styrene-co-(ethylacrylate)]s by NMR and on-line coupled SEC-NMR. *Macromol. Chem. Phys.*, **200**, 1734–1744.
88. Krämer, I., Hiller, W., and Pasch, H. (2000) On-line coupling of gradient-HPLC and 1H NMR for the analysis of random poly[(styrene)-co-ethylacrylate]s. *Macromol. Chem. Phys.*, **201**, 1662–1666.
89. Hiller, W., Pasch, H., Macko, T., Ganz, J., Hoffmann, M., Spraul, M., Streck, R., Mason, J., and van Damme, F. (2006) On-line coupling of high temperature GPC and 1H NMR fort he analysis of polymers. *J. Magn. Reson.*, **183**, 309–321.
90. Hiller, W., Sinha, P., and Pasch, H. (2007) On-line HPLC-NMR of PS-b-PMMA and blends of PS and PMMA: LCCC-NMR at critical conditions of PS. *Macromol. Chem. Phys.*, **208**, 19065–1978.
91. Allen, A., Glass, T.E., and Dorn, H.C. (1988) Direct monitoring of supercritical fluids and supercritical chromatographic separations by proton nuclear magnetic resonance. *Anal. Chem.*, **60**, 390–394.
92. Albert, K., Braumann, U., Tseng, L.-H., Nicholson, G., Bayer, E., Spraul, M., Hofmann, M., Dowle, C., and Chippendale, M. (1994) On-line coupling of supercritical fluid chromatography and proton high-field nuclear magnetic resonance spectroscopy. *Anal. Chem.*, **66**, 3042–3046.
93. Braumann, U., Händel, H., Albert, K., Ecker, R., and Spraul, M. (1995) On-line monitoring of the supercritical fluid extraction process with proton nuclear magnetic resonance spectroscopy. *Anal. Chem.*, **67**, 930–935.
94. Albert, K. and Braumann, U. (1995) in *Frontiers in Analytical Spectroscopy* (eds D.L. Andrews and A.M.C. Davies), The Royal Society of Chemistry, Cambridge, pp. 86–93.
95. Albert, K., Braumann, U., Streck, R., Spraul, M., and Ecker, R. (1995) Application of direct on-line coupling of HPLC and SFC with 1H NMR spectroscopy for the investigation of monomeric acrylates. *Fresenius J. Anal. Chem.*, **352**, 521–528.
96. Braumann, U., Händel, H., Strohschein, S., Spraul, M., Krack, G., Ecker, R., and Albert, K. (1997) Separation and identification of vitamin A acetate isomers by supercritical fluid chromatography–1H NMR coupling. *J. Chromatogr. A*, **761**, 336–340.
97. Albert, K. (1997) Supercritical fluid chromatography–proton nuclear magnetic resonance spectroscopy coupling. *J. Chromatogr. A*, **785**, 65–83.
98. Fischer, H., Tseng, L.-H., Raitza, M., and Albert, K. (2000) Application of immobilized free radicals in supercritical fluid chromatography hyphenated with proton nuclear magnetic resonance spectroscopy. *Magn. Reson. Chem.*, **38**, 336–342.

99. Fischer, H., Gyllenhaal, O., Vessman, J., and Albert, K. (2003) Reaction-monitoring of aliphatic amines in supercritical carbon dioxide by proton nuclear magnetic resonance spectroscopy and implications for supercritical fluid chromatography. *Anal. Chem.*, **75**, 622–626.

100. Zuschneid, T., Fischer, H., Handel, T., Albert, K., and Häfelinger, G. (2004) Experimental gas phase 1H NMR spectra and basis set dependence of ab initio GIAO MO calculations of 1H and 13C NMR absolute shieldings and chemical shifts of small hydrocarbons. *Z. Naturforsch.*, **59b**, 1153–1176.

101. Buddrus, J. and Herzog, H. (1981) Coupling of chromatography and NMR. 3. Study of flowing gas-chromatographic fractions by proton magnetic-resonance. *Org. Magn. Reson.*, **15**, 211–213.

102. Herzog, H. and Buddrus, J. (1984) Coupling of chromatography and NMR. Part 5. Analysis of high-boiling gas-chromatographic fractions by online nuclear magnetic-resonance. *Chromatographia*, **18**, 31–33.

103. Wu, N., Peck, T.L., Webb, A.G., Magin, R.L., and Sweedler, J.V. (1994) Nanoliter volume sample cells for 1H NMR: application to online detection in capillary electrophoresis. *J. Am. Chem. Soc.*, **116**, 7929–7930.

104. (a) Albert, K. (1995) Direktkopplung von kapillarelektrophorese und 1H-NMR-spektroskopie. *Angew. Chem.*, **107**, 699–701. (b) Albert, K. (1995) Direct on-line coupling of capillary electrophoresis and 1H NMR spectroscopy. *Angew. Chem., Int. Ed. Engl.*, **34**, 641–642.

105. Pusecker, K., Schewitz, J., Gfrörer, P., Tseng, L.-H., Albert, K., Bayer, E., Wilson, I.D., Bailey, N.J., Scarfe, G.B., Nicholson, J.K., and Lindon, J.C. (1998) On-flow identification of metabolites of paracetamol from human urine using directly coupled CZE-NMR and CEC-NMR Spectroscopy. *Anal. Commun.*, **35**, 213–215.

106. Pusecker, K., Schewitz, J., Gförer, P., Tseng, L.-H., Albert, K., and Bayer, E. (1998) On-line coupling of capillary electrochromatography, capillary electrophoresis, and capillary HPLC with nuclear magnetic resonance spectroscopy. *Anal. Chem.*, **70**, 3280–3285.

107. Gfrörer, P., Schewitz, J., Pusecker, K., Tseng, L.-H., Albert, K., and Bayer, E. (1999) Gradient elution capillary electrochromatography and hyphenation with nuclear magnetic resonance. *Electrophoresis*, **20**, 3–8.

108. Schewitz, J., Pusecker, K., Gförer, P., Götz, U., Tseng, L.-H., Albert, K., and Bayer, E. (1999) Direct coupling of capillary electrophoresis and nuclear magnetic resonance spectroscopy for the identification of a dinucleotide. *Chromatographia*, **50**, 333–337.

109. Gfrörer, P., Tseng, L.-H., Rapp, E., Albert, K., and Bayer, E. (2001) Influence of pressure upon coupling pressurized capillary electrochromatography with nuclear magnetic resonance spectroscopy. *Anal. Chem.*, **73**, 3234–3239.

110. Rapp, E., Jakob, A., Schefer, A.B., Bayer, E., and Albert, K. (2003) Splitless on-line coupling of capillary high-performance liquid chromatography, capillary electrochromatography and pressurized capillary electrochromatography with nuclear magnetic resonance spectroscopy. *Anal. Bioanal. Chem.*, **376**, 1053–1061.

111. Wolters, A.M., Jayawickrama, D.A., Larive, C.K., and Sweedler, J.V. (2002) Capillary isotachophoresis/NMR: extension to trace impurity analysis and improved instrumental coupling. *Anal. Chem.*, **74**, 2306–2313.

112. Wolters, A.M., Jayawickrama, D.A., Larive, C.K., and Sweedler, J.V. (2002) Insights into the cITP process using on-line NMR spectroscopy. *Anal. Chem.*, **74**, 4191–4197.

113. Korir, A.K., Almeida, V.K., and Larive, C.K. (2006) Visualizing ion electromigration during isotachophoretic separation with cITP-NMR. *Anal. Chem.*, **78**, 7078–7087.

114. Eldridge, S.L., Almeida, V.K., Korir, A.K., and Larive, C.K. (2007) Separation

and analysis of trace degradants in a pharmaceutical formulation using on-line cITP-NMR. *Anal. Chem.*, **79**, 8446–8453.

115. Fischer, H., Seiler, M., Ertl, T., Eberhardinger, U., Bertagnolli, H., Schmitt-Willich, H., and Albert, K. (2003) Quantification studies in continuous-flow 13C nuclear magnetic resonance spectroscopy by use of immobilized paramagnetic relaxation agents. *J. Phys. Chem. B*, **107**, 4879–4886.

116. Gökay, O. and Albert, K. (2012) From single to multiple microcoil flow probe NMR and related capillary techniques: a review. *Anal. Bioanal. Chem.*, **402**, 647–669.

Section XV
General Data Treatment: Databases/Spectral Libraries

Handbook of Spectroscopy, Second Edition. Edited by Günter Gauglitz and David S. Moore.

53
Optical Spectroscopy

Steffen Thiele and Reiner Salzer

53.1
Introduction

The spectra measured by any method of optical spectroscopy may be subject to qualitative (what is it?) or quantitative (how much is it?) evaluation. We assume here that the basic rules described in Chapters 1 and 2 for the overall analytical process are obeyed, in particular for sample selection and sample preparation. Errors during sample preparation or simply due to an incorrect positioning of the specimen in the optical beam can never be corrected for in the measured spectra. Restricted quality in the experimental spectra will lead to errors either in qualitative evaluation (e.g., ill-defined results in spectral search) and in quantitative evaluation (e.g., erroneous determination of concentration).

The contrast in spectral images arises from the spectroscopic information behind every pixel (cf. Section 4.7). The spectra behind a spectral image are treated the same way as individual spectra (cf. Section 5.6), that is, the procedures described in the subsequent sections can be applied either to individual spectra or to sets of spectral-like time series or spectral images.

Modern spectrometer software offers a variety of mathematical tools for processing of spectra. These tools provide powerful features to the experienced user but cause serious danger in case of noncritical application. Some types of processing tools do not alter the information content of the spectra (cf. Table 53.1, basic operations), other do (cf. Table 53.1, manipulations). Particular attention has to be paid if the latter have to be used.

The evaluation of spectra will be discussed separately for qualitative and quantitative analysis. Particular emphasis will be laid (i) on state-of-the-art methods for search of spectra in spectral libraries or search for spectroscopic information in data banks and on (ii) procedures for multivariate data analysis [1–3].

Two of the basic operations mentioned in Table 53.1 are of particular importance for the evaluation of spectra, centering, and standardization. They will be considered first.

Handbook of Spectroscopy, Second Edition. Edited by Günter Gauglitz and David S. Moore.

Table 53.1 Types and objectives of spectra processing.

Basic operations	**Prettier display**	**Qualitative evaluation**	**Quantitative evaluation**
Conversion transmission T – absorbance A	X		X
Conversion wavelength λ – wave number k	X	X	X
Background reduction	X	X	X
Centering		X	X
Standardization		X	X
Spectra subtraction			X
Manipulations			
Baseline correction	X	X	
Smoothing	X	X	X !
Derivation	X	X	
Deconvolution		X	
Curve fitting		X	(X)
Band integration			X
Generation of band tables		X	
Spike correction (Raman spectra)	X	X	

53.2
Basic Operations

53.2.1
Centering

Centering is an important step in pretreatment of spectral data before multivariate evaluation both for qualitative as for quantitative analysis. At first, the mean spectrum $\underline{a}_{\mathrm{M}}^{\mathrm{T}}$ is calculated from the set of measured spectra:

$$\underline{a}_{\mathrm{M}}^{\mathrm{T}} = (\overline{a}_1, \overline{a}_2, \ldots, \overline{a}_p) \tag{53.1}$$

$$\text{where } \overline{a}_j = \frac{1}{n}\sum_{i=1}^{n} a_{ij} \quad j = 1, \ldots, p \tag{53.2}$$

The subscript j represents the number p of spectral data points, the subscript i the number n of measured spectra. Subsequently, the mean spectrum is subtracted from each measured spectrum:

$$\underline{a}_{\mathrm{C};i}^{\mathrm{T}} = \underline{a}_i^{\mathrm{T}} - \underline{a}_{\mathrm{M}}^{\mathrm{T}} \quad i = 1, \ldots, n \tag{53.3}$$

As a result of the given data treatment, the mean of the centered spectra $\underline{a}_{\mathrm{C};i}^{\mathrm{T}}$ amounts to zero, that is, the center of the data set of n spectra has been shifted to the origin of the coordinate system (cf. Figure 53.1). All subsequent matrix

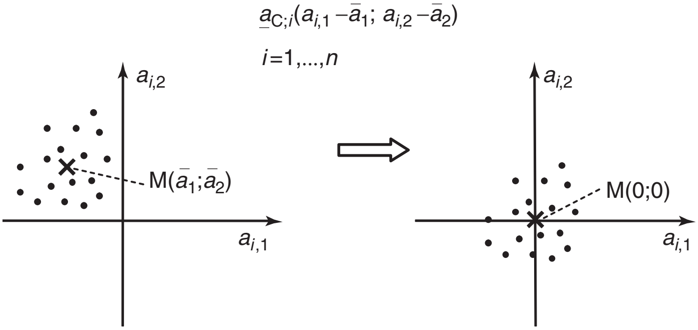

Figure 53.1 Effect of centering the measured absorbance values $a_{i,1}$ and $a_{i,2}$ illustrated for two spectral data points ($p = 2$).

operations in either qualitative or quantitative evaluation benef from the centering because the overlaid offset of the center has been removed and only the significant scattering of the measured spectra around the center is retained.

53.2.2
Standardization (Autoscaling)

Standardization is a method in pretreatment of spectral data before multivariate evaluation both for qualitative as for quantitative analysis, just like centering. In case of standardization, the standard deviation s is calculated at each of the p spectral data points for all n measured spectra:

$$s_j = \sqrt{\frac{\sum_{i=1}^{n}(a_{ij}-\bar{a}_j)^2}{n-1}} \quad j = 1, \dots, p \tag{53.4}$$

The standardized absorbance value of each measured spectrum ($i = 1, \dots, n$) at each spectral wavelength ($j = 1, \dots, p$) is calculated by using

$$a_{S_{ij}} = \frac{a_{ij}-\bar{a}_j}{s_j} \tag{53.5}$$

The standardized set of spectral data shows a mean of 0 and a variance of 1. Standardization may also be useful for gathering and comparing of multicollinearities in later evaluation steps (cf. Section 53.3).

One basic rule should be emphasized here: the set of mathematical operations chosen for the calibration samples has to be applied in an absolutely identical manner to all subsequent test samples. This rule holds as well for the above-mentioned basic operations and for the more advanced operations described later in this chapter.

53.3
Evaluation of Spectra

53.3.1
Introduction

Contemporary spectrometers are enabled to produce huge amounts of data within a very short time. This development continues because of the introduction of array detectors for spectral imaging (cf. Section 4.7). The utilization of as much as possible of the enclosed spectral information can only be attained by chemometric procedures for data analysis. The most commonly used procedures for evaluation of spectra are systematically arranged in Figure 53.2, with the main emphasis on application, that is, the variety of procedures was divided in methods for qualitative analysis and for quantitative analysis. Another distinctive feature refers to the mathematical algorithms on which the procedures are based. The dominance of multivariate over univariate methods is clearly discernible from Figure 53.2.

In case of qualitative analysis, unsupervised learning procedures are employed for explorative data analysis or for empirical investigation of samples with no additional information available. The analyst wants to sense the correlation within the data or the interrelation between the data and particular features or properties of the sample. Such information qualifies for structuring of data with respect to useful data range, property parameters, and arrangement into classes. Excessive data amounts require reduction to a reasonable size by automated procedures

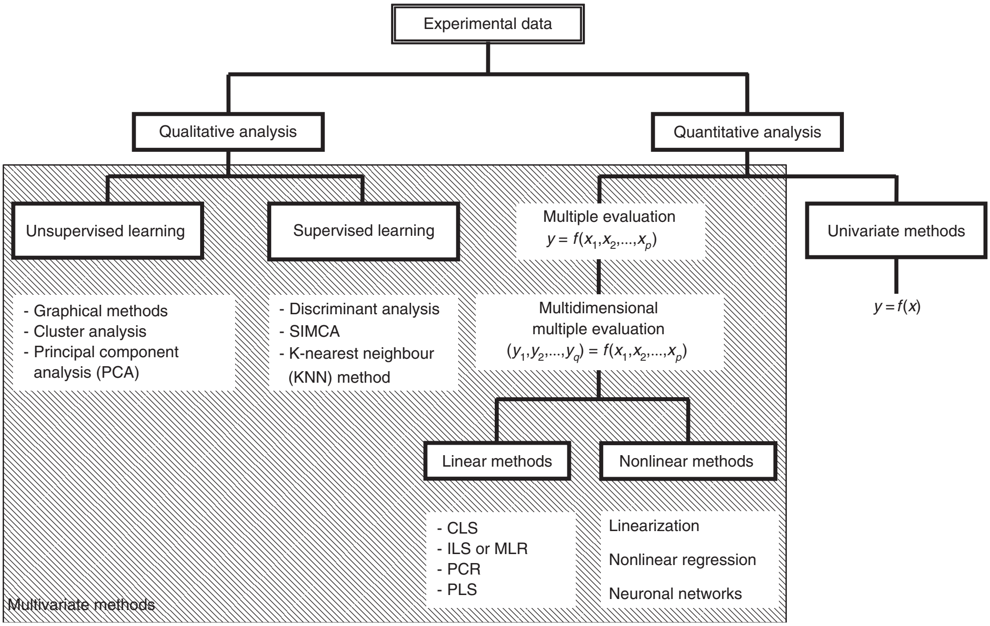

Figure 53.2 Survey of methods for data analysis.

before structuring. Principal component analysis (PCA) is an efficient method for such spectral data reduction. Supervised learning procedures are employed in order to assign new objects to already established classes (available additional knowledge). A simple case is the comparison of features between a new sample and previously characterized samples, for example, during the search for an analyte spectrum in a spectral data base. The aim of this search is the elucidation of the composition or structure, respectively, of an unknown.

In case of quantitative analysis, the amount of – or the exact relation between – the constituents of a compound or a mixture have to be established. The direct relation between the properties of a specimen and the concentration of its constituents could also be the aim of quantitative investigation. In the latter case, so-called calibration models have to be established, the corresponding model parameters have to be estimated, and they have to be confirmed by statistical methods. Calibration models established this way may then be used to determine on a statistically verified basis the concentration of constituents of an analyte within the calibrated range. All multivariate methods for quantitative analysis mentioned in Figure 53.2 are employed for evaluation of spectra.

53.3.2
Qualitative Evaluation of Spectra

53.3.2.1 Spectral Data Banks

Many digital spectral libraries have been transformed from printed spectra collections. Well-known printed collections are the Aldrich spectra collection [4], the Sadtler spectra collection [5–7], the Schrader–Meyer Atlas of IR and Raman spectra [8], the Hummel collection of IR spectra of polymers [9], Merck IR Atlas [10], and the Buback collection of NIR spectra [11]. IR spectra have the largest share of digital optical spectra, followed at a clear distance by Raman spectra. Larger collections of UV/vis spectra have not been established because of their missing fingerprint capability and moreover because of the strong sensitivity of the UV/vis spectra against solvent interactions. A variety of dedicated spectra collections have been created in industrial laboratories without access to the public.

The difference between in-house and online versions of spectral libraries consists mainly in the fee, which depends on conditions of usage. Usually, in-house versions have to be paid for only once on license acquisition and hardware purchase. Afterwards, the actual use is free, regardless of the frequency of usage. In certain cases, an annual license fee has to be paid. Follow-up costs may occur if updates are demanded or if hardware service is needed. In case of in-house systems running on workstations, initial costs as well as upkeep may approach considerable height. In contrast, the costs for online systems solely depend on frequency of usage. Both operativeness and speed of the Internet connection may remarkably influence the size of the expenses. If only occasionally used, the online version is financially certainly more viable than the in-house version. At best, one is able to find free-of-charge Internet offers, sometimes with restricted access to certain features (cf. Table 53.2).

Table 53.2 Optical spectral data bases (according to provider specifications, 1 December 2008).

Data base	Type and amount of spectra (if available)	Availability		Charge
		In-house version	Online version	
Thermo Fisher Scientific Inc. (www.thermo.com)				
FT-IR search (*www.ftirsearch.com*)	IR: 71.000 Raman: 16.000		X	Yes
Spectra online (*www.spectraonline.com*)	IR, Raman		X	No
Examples				
Aldrich condensed phase	FT-IR: 18.500	X		Yes
	FT-Raman: 14.033	X		Yes
Vapor phase	FT-IR: 6.611	X		Yes
Sigma biochemical library	FT-IR: 10.411	X		Yes
Nicolet vapor phase library	FT-IR: 8.654	X		Yes
E.P.A. vapor phase	FT-IR: 3.300	X		Yes
Hummel polymer and additives	FT-IR: 2.011	X		Yes
NIST				
WebBook *(webbook.nist.gov)*	IR: 16.000 UV/VIS: 1600	X	X	No
Bio-Rad (*www.bio-rad.com*)	IR: > 220.000 Raman: > 4465 UV/vis: > 9714	X		Yes
Sadtler condensed phase IR standards	IR: 75.570	X		Yes
Sadtler vapor phase IR standards	IR: 9.190	X		Yes
SDBS				
Organic compounds (riodb01.ibase.aist.go.jp/sdbs)	FT-IR: 51.100 Raman: 3.500		X	No
SpecInfo (*www.specinfo.wiley.com/specsurf.htm*)	IR: 17.073	X	X	Yes
Fiveash Data Manag., Inc. (*www.fdmspectra.com*)				
Examples				
Spectra of drugs/Canadian forensic spectra	FT-IR: 3.750	X		yes
Vapor phase of organic compounds	FT-IR: 5.220	X		yes

Spectral data banks contain all sorts of information about a particular substance in the form of tables. The requested field of a table can be accessed by the user either via abbreviations (e.g., MF for molecular formula) or via input masks, which place the necessary denominations of the field at the user's disposal. Some fields may contain searchable information only as alphanumerical text (e.g., compound names), others may be searched only numerically (e.g., molecular weight). In case of numerical fields, some numerical operators (e.g., <;=;> or – for area allocation) may be applied as well.

It is often possible to search for bands of particular intensity in selected wavelength ranges. During the search, all fields may be interconnected logically (search masks) or by logic operators (and; or; not; proximity operators). A summary of information contained in a spectral data bank for a given compound is given in Table 53.3.

The CAS number (Chemical Abstracts Service Registry Number) is of particular importance. This number went into a wide range of data banks (structural and factual data banks, bibliographic data banks, and substance data banks) and may advantageously be used for fast access to information related to a particular substance. Data banks comprising information about several spectroscopic methods are of high value for structural elucidation if a combination of methods has to be applied (e.g., NIST, SDBS, SpecInfo).

The spectral search itself is based on computation of similarity by comparison of full spectra or of band tables. Necessary means are structural editors and spectral editors, which are usually applied off-line before the spectral search is started. Spectral editors may be used to erase existing bands from or to generate new bands into spectra. Spectral editors may also be used for complete generation

Table 53.3 Searchable information in spectral data banks.

Compound identification	Compound name includes synonyms CAS number Molecular formula Molecular weight Graphical structure representation Additional data possible (e.g., melting point)
Acquisition of spectra	Sample source Sample purity Sample preparation Spectrometer type Spectral resolution Additional data possible (e.g., special sample conditions; file format)
Spectrum	Complete spectrum in numerical and graphical form Band table

of new spectra. Structural editors are used to generate chemical 2D structures or to modify structures, which were previously obtained from chemical drawing programs. These structures can be searched for in the data bank after they have been encoded by the structural editor. Substructure searches are uncommon in IR data banks because IR spectra are rather used for fingerprint identification of compounds than for assembling full structures from subunits.

In case of spectral search by comparison of band tables, the system first computes the necessary band table from the experimental spectrum of the analyte. For the subsequent search, both the position and the intensity of the bands in the spectrum of the unknown and in the spectra on the compounds contained in the data bank are compared. After the search has been completed, the top position in the hit list is assigned to the substance with least differences in band positions and band intensities.

In case of a full spectra search, the complete set of spectral features (absorbance values at p wavelength positions) is compared between the spectrum of the unknown and all spectra contained in the data bank. So-called similarity measures are computed for each individual comparison. In case of the mostly employed similarity measure, the Euclidean distance (cf. Figure 53.6), the spectrum is regarded as p-dimensional spectral vector (data points at p wavelength positions). The comparison between the spectral vector $\underline{u}$ of the unknown and the vector $\underline{b}$ of the data bank spectrum results in a value $d(\underline{u}, \underline{b})$:

$$d(\underline{u}, \underline{b}) = \sqrt{\sum_{j=1}^{p} (u_j - b_j)^2} \tag{53.6}$$

The library spectrum showing the minimal Euclidean distance $d_{\min}$ from the spectrum of the unknown will be assigned the top position in the resulting hit list. In order to ensure comparability of the distances d, each submitted spectrum has to be subjected to a particular normalization (cf. Figure 53.3). At first, the lowest absorbance value across the spectrum is subtracted from all p data points of the spectrum. Afterwards, the spectrum is normalized to the required absorbance

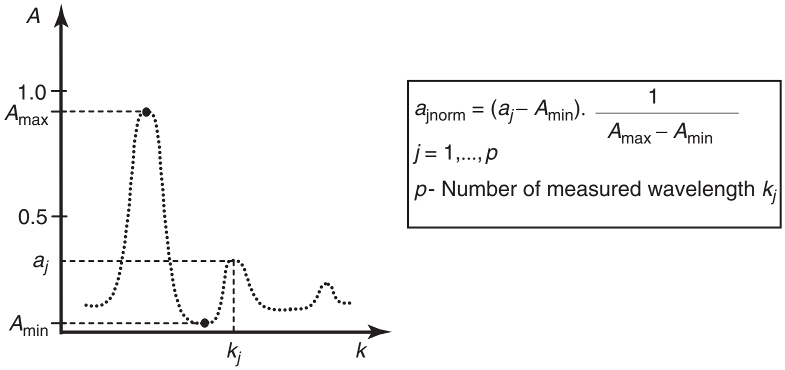

Figure 53.3 Normalization of a spectrum to the absorbance range between 0 and 1.

maximum. The necessity of such a normalization constitutes a serious limitation of the search procedure.

In contemporary search algorithms, each spectral vector is normalized to unit length (unit vector $\underline{x}_{\mathrm{E}}$). The length of a vector $\underline{x}$ (also called *absolute value* or *norm vector*) is given by

$$\|\underline{x}\| = \sqrt{\underline{x}^{\mathrm{T}}\underline{x}} \tag{53.7}$$

and the norm vector $\underline{x}_{\mathrm{E}}$ by

$$\underline{x}_E = \frac{\underline{x}}{\|\underline{x}\|} \tag{53.8}$$

By means of the definition of the scalar product of two vectors $\underline{x}$ and $\underline{y}$

$$\underline{x}^{\mathrm{T}}\underline{y} = \|\underline{x}\|\,\|\underline{y}\| \cdot \cos(\underline{x}, \underline{y}) \tag{53.9}$$

the library search in the p-dimensional Euclidean space (p – number of measured wavelengths) results in the following distance value d_{E}:

$$d_E = 1 - \cos(\underline{u}, \underline{b}) = 1 - \frac{\underline{u}^{\mathrm{T}}\underline{b}}{\sqrt{\underline{u}^{\mathrm{T}}\underline{u}}\sqrt{\underline{b}^{\mathrm{T}}\underline{b}}} \tag{53.10}$$

The calculated results correspond to the cosine of the angle between the spectral vector $\underline{u}$ of the unknown and the vector $\underline{b}$ of the library spectrum. In case of congruency of both vectors $\underline{u}$ and $\underline{b}$, we obtain $\cos(\underline{u}, \underline{b}) = 1$; thus, $d_{\mathrm{E}} = 0$.

A common problem for contemporary search algorithms, caused by varying baseline offsets, can be overcome by centering the spectra (cf. Section 53.2). Centered spectra $\underline{u}_{\mathrm{Z}}$ are obtained by calculating the average $\overline{u}$ of a spectral vector $\underline{u}$ measured at p wavelengths:

$$\overline{u} = \frac{1}{p}\sum_{j=1}^{p} u_j \tag{53.11}$$

The average $\overline{u}$ is subsequently subtracted from all components u_j of the vector $\underline{u}$:

$$\underline{u}_{\mathrm{Z}} = (u_j - \overline{u})^{\mathrm{T}} \quad j = 1, \ldots, p \tag{53.12}$$

These centered vectors $\underline{u}_{\mathrm{Z}}$ are now used for the calculation of a correlated distance d_{C}, as in Eq. (53.10)

$$d_{\mathrm{C}} = 1 - \cos(\underline{u}_{\mathrm{Z}}, \underline{b}_{\mathrm{Z}}) = 1 - \frac{\underline{u}_{\mathrm{Z}}^{\mathrm{T}}\underline{b}_{\mathrm{Z}}}{\sqrt{\underline{u}_{\mathrm{Z}}^{\mathrm{T}}\underline{u}_{\mathrm{Z}}}\sqrt{\underline{b}_{\mathrm{Z}}^{\mathrm{T}}\underline{b}_{\mathrm{Z}}}} \tag{53.13}$$

On the basis of the mathematical definitions, Eq. (53.13) can be reformulated (corr stands for correlation)

$$\operatorname{corr}(\underline{u}, \underline{b}) = \frac{\underline{u}_{\mathrm{Z}}^{\mathrm{T}}\underline{b}_{\mathrm{Z}}}{\|\underline{u}_{\mathrm{Z}}\|\|\underline{b}_{\mathrm{Z}}\|} = \frac{\underline{u}_{\mathrm{S}}^{\mathrm{T}}\underline{b}_{\mathrm{S}}}{p - 1} \tag{53.14}$$

After introduction of the standardized vectors $\underline{u}_{\mathrm{S}}$ and $\underline{b}_{\mathrm{S}}$

$$\underline{u}_{\mathrm{S}} = \frac{\underline{u}_{\mathrm{Z}}}{s(\underline{u})} \text{ and } \underline{b}_{\mathrm{S}} = \frac{\underline{b}_{\mathrm{Z}}}{s(\underline{b})} \tag{53.15}$$

where s denotes the standard deviation of the vectors $\underline{u}$ and $\underline{b}$ (cf. Section 53.2.2):

$$s(\underline{u}) = \frac{\|\underline{u}_Z\|}{\sqrt{p-1}} \text{ and } s(\underline{b}) = \frac{\|\underline{b}_Z\|}{\sqrt{p-1}} \tag{53.16}$$

we obtain

$$\underline{u}_S = \frac{\underline{u}_Z}{\|\underline{u}_Z\|}\cdot\sqrt{p-1} \text{ and } \underline{b}_S = \frac{\underline{b}_Z}{\|\underline{b}_Z\|}\cdot\sqrt{p-1} \tag{53.17}$$

Equation (53.17) corresponds to Eq. (53.8) with the vectors now standardized to the length $\sqrt{p-1}$. In summary, the improvement in the correlated distance value is due to the removal of the baseline offset and to the scale invariance of the pretreated vectors of the unknown and of the library spectrum. The following problems in searching for an unknown in a spectral library persist.

1) The spectrum cannot be satisfactorily normalized because of a nonhorizontal or nonlinear baseline.
2) The composition of the spectral library usually does not cover all necessary groups of chemical compounds.
3) The similarity scores that are used to construct the hit list are not necessarily significant measures for the similarity of structures.

A nonhorizontal baseline may be corrected for by subtracting an angled straight line. In case of a nonlinear baseline, much experience is needed to minimize possible effects of a mathematical correction on the search results. Here, the computation of the second derivative of the spectrum might be the favorable option.

Even if an unknown belongs to a particular class of compounds, which is not represented in the library, the search will always result in a hit list with a number of entries. In general, entries with small scores are not relevant to an identification. In order to gain a feeling for the significance of an entry of its scores, one should experiment with the library, and a sound chemical knowledge is necessary.

53.3.2.2 Data Banks Containing Spectroscopic Information

Fields containing spectroscopic information can specifically be accessed in the data banks Beilstein (organic chemistry) and Gmelin (inorganic chemistry, organometallic chemistry) by means of the on-line system Reaxys. Covered spectral ranges, measured spectral intensity maxima, and references, may be found. Data concerning the state of aggregation of the sample or the solvent may possibly be included as well. Of course, the full text option may be used in any data bank to search for spectroscopic data or experiments, for example, in Chemical Abstracts or in Analytical Abstracts (e.g., Raman spectrum).

If interdisciplinary matters are searched, bibliographic data banks such as Biosis (biosciences and biomedicine), Medline (medicine), Inspec (physics, electroengineering, and engineering) as well as all data banks containing patent information should be considered.

53.3.2.3 Interpretation of Spectra by Means of Group Frequencies and of Characteristic Bands

This topic has already been dealt with in Chapter 6. Currently, there are numerous software products available on the market or under development, which are intended to support the task of spectra interpretation (e.g., AnalyzeIt IR, AnalyzeIt Raman [12], IR-Tutor [13], and SpecTool [14]). Certain tools even permit a spectrum simulation of the structure guessed [15]. Some spectrometer operation systems include tools to aid simple spectra interpretation.

53.3.2.4 PCA (Principal Component Analysis)

PCA is an efficient method for data reduction, in particular, in spectroscopy (cf. Figure 53.4). It has to be performed also before quantitative evaluations by PCR (principal component regression) or PLS (partial least squares).

The mathematical background of PCA consists in the transformation of the initial coordinate system into a new one in order to display the variance of the experimental data optimally. To this aim, the mathematical algorithms provide that

- the principal components (PCs) consist of linear combinations (i.e., weighted sums) of the initial variables (i.e., absorbances at the measured wavelengths);
- the PCs are computed in a way to cover the largest amount of variance (e.g., assuming the variance in spectral data due to the different properties of the measured samples);
- the linear combinations represent new, so-called latent variables (e.g., variables which cannot be assigned to a particular spectral band) with appropriate properties.

Initially, the *n* experimental spectra, each comprising *p* data points, are collected into an *n*,*p*-dimensional data matrix $\underline{A}$. Any row of the matrix $\underline{A}$ comprises all *p* absorbance values of a particular spectrum. Any column consists of all *n* absorbance values at a particular wavelength. As a first step, the data matrix is either centered ($\underline{A}_Z$) or standardized ($\underline{A}_S$) (cf. Section 53.1.2). In order to achieve the above-stated

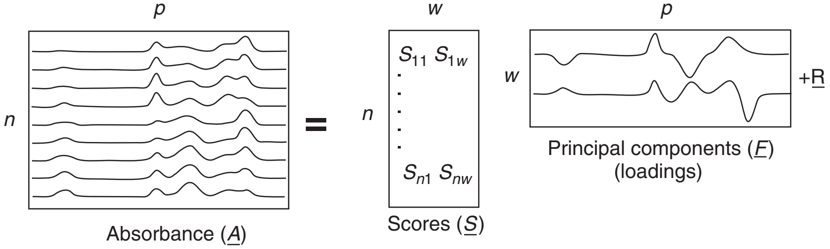

n - Number of spectra
p - Number of measured wavelengths = number of data points
v - Number of neglected principal components
w - Number of retained principal components $w = p - v$

Figure 53.4 Decomposition of the absorbance matrix $\underline{A}$.

aims, this pretreated matrix is afterwards split into two matrices by the chosen algorithm:

$$\begin{array}{lcccc} & \underline{A}_{Z} = & \underline{S}_{n} & \cdot & \underline{F}_{n}^{T} \\ \text{dimensions} & n,p & n,p & & p,p \end{array} \tag{53.18}$$

Matrix $\underline{S}_n$ is called the *score matrix*. The subscript n indicates that no data reduction has been introduced yet. The columns of matrix $\underline{S}_n$ comprise the scaling coefficients. Matrix $\underline{F}_n$ may be called the *loading matrix* or *principal components* or *factors* or *eigenvectors*. Its columns comprise the calculated PCs. The maximum number of components is min(n,p). By multiplication of the matrices $\underline{S}_n$ and $\underline{F}_n$, we are able to reconstruct the centered or the standardized spectra.

As the calculation of the PCs is based on the criterion of covering the largest amount of variance in the experimental data ($\underline{A}_Z$ or $\underline{A}_S$), the first PC features the maximum variance. Subsequent PCs cover less and less variance. Distant PCs may be omitted for data reduction. In that case, Eq. (53.18) may be rewritten as

$$\begin{array}{lcccccc} & \underline{A}_{Z} = & \underline{S} & \cdot & \underline{F}^{T} & + & \underline{R} \\ \text{dimensions} & n,p & n,w & & w,p & & n,p \end{array} \tag{53.19}$$

where w represents the number of retained PCs ($w = p - v$), v is the number of neglected PCs, and $\underline{R}$ is the residual matrix (error matrix) (cf. Figure 53.4). An analysis of the error matrix $\underline{R}$ is necessary in order to choose w. Chemical knowledge has strictly to be applied during interpretation of the PCs, which are computed on pure mathematical considerations. Ideally, $\underline{R}$ merely contains the spectral noise as well as unnecessary information from the experimental spectra.

One method in error analysis is the computation of residual variances. The shares of different PCs in the total variance are sketched in Figure 53.5.

If six PCs are retained for further evaluation, a residual variance in the experimental values remains beyond consideration. Other methods of estimating a reasonable size of w are the eigenvalue-one criterion [16, 17], the Scree-test [16, 17], and cross validation (cf. Section 53.3.3.2).

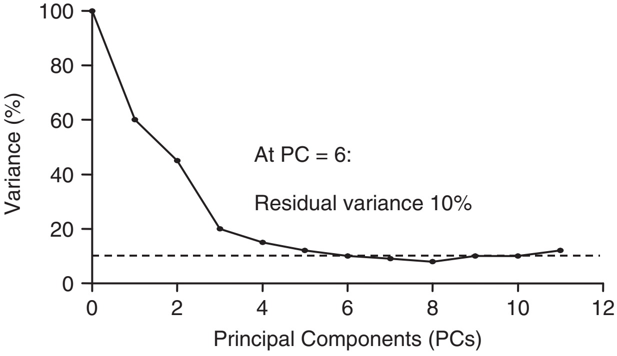

Figure 53.5 Analysis of residual variance in PCA.

53.3.2.5 Cluster Analysis

The aim of cluster analysis is the stepwise merger of objects (spectra) with respect to the similarity of their properties (absorbances at p measured wavelengths). A cluster comprises a group of objects whose similarity is closer than their similarity toward objects outside this group. The similarity of objects is assessed using the same distance measures as described earlier, for example,

- Euclidean distance (cf. Figure 53.6) or
- Mahalanobis distance [18, 19].

The calculation of the Mahalanobis distance is based on the interrelations between absorbance values at various wavelengths using their covariances. For this reason, the Mahalanobis distance is of particular importance for assessing spectroscopic data [16, 17].

Cluster analysis is often the preceding step for discriminant analysis.

53.3.2.6 Discriminant Analysis

In the simplest case, a discriminant analysis is performed in order to check the affiliation (yes/no decision) of an unknown to a particular class, for example, in case of a purity/quality check or a substance identification. A sample may as well be assigned between various classes (e.g., quality levels) if a corresponding series of mathematical models has been established. Models are based on a series of test spectra, which has to completely cover the variations of particular substances in particular chemical classes. From this series of test spectra, classes of similar objects are formed by means of so-called discriminant functions. The model is optimized with respect to the separation among the classes. The evaluation of the assignment of objects to the classes of an established model is performed by statistically backed distance and scattering measures [16, 17].

53.3.2.7 SIMCA (Soft Independent Modeling of Class Analogy)

In soft independent modeling of class analogy (SIMCA), an independent PC model (cf. PCA) is established for each individual class of the test data set. The evaluation

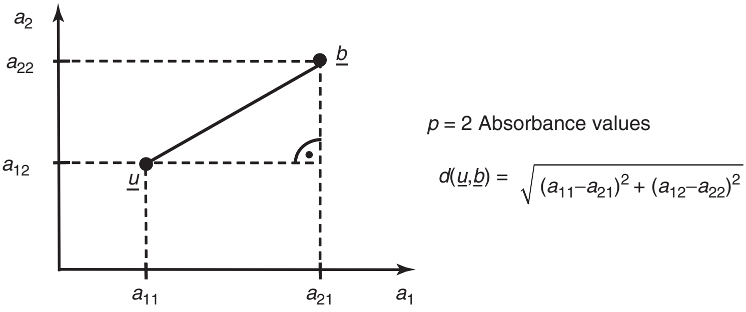

Figure 53.6 Euclidean distance between vector $\underline{u}$ (spectrum of unknown substance) and vector $\underline{b}$ (library spectrum) illustrated for absorbance values at two wavelengths.

of the assignment of objects to these classes of an established model is performed by statistically backed distance measures [16, 17].

53.3.3
Quantitative Evaluation of Spectra

With respect to the applied mathematical algorithms, quantitative evaluation of spectra can be subdivided into univariate and multivariate methods (cf. Figure 53.2). The independent variables x and x_i, respectively, are denoted regressors, whereas the dependent variables y and y_i, respectively, are denoted regressands. The basic sequence of a quantitative evaluation is always the same:

Step 1: Choosing a model.
Step 2: Choosing a training set.
Step 3: Estimation of model parameters.
Step 4: Validation of the model by statistical means.
Step 5: Application of the model for prediction.

In the following paragraphs, the above-mentioned sequence of steps will be discussed for all relevant methods used in evaluating optical spectra quantitatively.

53.3.3.1 Univariate Methods

The only method considered is least squares regression (LSR).

53.3.3.1.1 LSR (Least Squares Regression)

- Step 1: Choosing a model.
  The Beer–Lambert law is expressed

$$A_k = C \cdot K_k \tag{53.20}$$

$$\text{where } K_k = \epsilon_k \cdot l \tag{53.21}$$

  ϵ_k is the absorptivity coefficient at wavelength k and l the thickness of the absorbing medium.
  Within its application range, a linear calibration model can be established already by measuring at a single wavelength position

$$A = bC + a \tag{53.22}$$

  The sample concentration C is calculated from the measured absorbance value A at the sensitivity b and the blank value a.
- Step 2: Choosing a training set.
  Spectra are measured with the analyte at n different concentrations. The absorbance values A_i are determined right at the maximum of a spectral band, which is unambiguously assigned to the analyte.
  The calibration based on band area evaluation instead of a simple height determination might be advantageous. Likewise, ratioing the heights or areas of two bands might be useful to trace a concentration ratio. An initial baseline

correction might be necessary (cf. Sections 53.1 and 53.3.3). Preferably, a straight line should be employed for such corrections (cf. Figure 53.7).

- Step 3: Estimation of model parameters.
  A least squares regression (LSR) is performed in order to estimate $\hat{a}$ and $\hat{b}$:

$$\hat{a} = \frac{1}{n}\left(\sum_{i=1}^{n} A_i - \hat{b}\sum_{i=1}^{n} C_i\right); \quad \hat{b} = \frac{n\sum_{i=1}^{n} C_i A_i - \sum_{i=1}^{n} C_i \cdot \sum_{i=1}^{n} A_i}{n\sum_{i=1}^{n} C_i^2 - \left(\sum_{i=1}^{n} C_i\right)^2} \tag{53.23}$$

- Step 4: Validation of the model by statistical means can be done in two ways:
  a. Analysis of residuals.
  The analysis is performed by calculating

$$r_i = A_i - \hat{A}_i \quad i = 1, \ldots, n \tag{53.24}$$

using the absorbance values $\hat{A}_i$, which were calculated according to the model by

$$\hat{A}_i = \hat{b}C_i + \hat{a} \tag{53.25}$$

and subsequent graphic representation of r_i over C_i (cf. Figure 53.8)

b. Analysis of variance
The variances s_a and s_b of the estimated parameters $\hat{a}$ and $\hat{b}$ are calculated according to

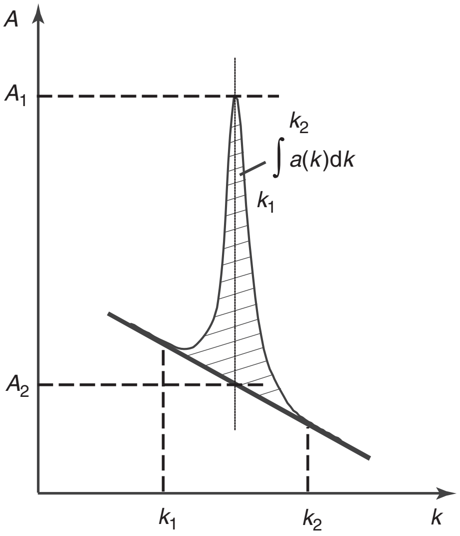

Figure 53.7 Quantitative evaluation of a baseline-corrected spectral band.

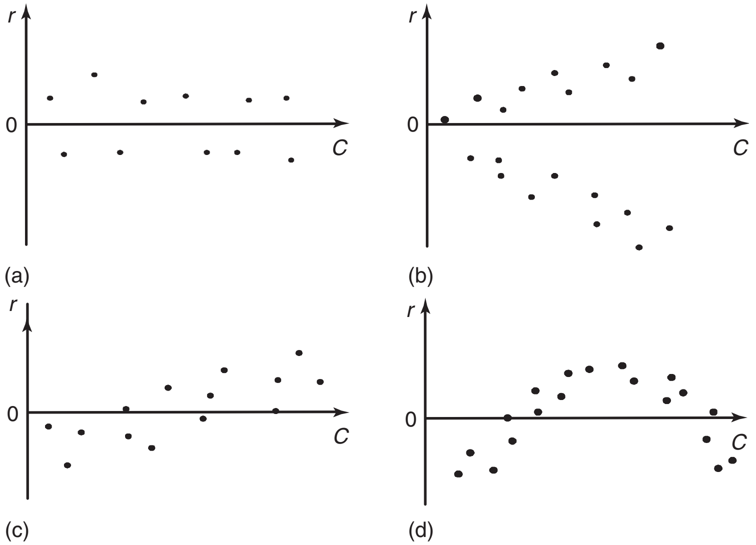

Figure 53.8 Examination of a linear model by analyzing the residuals. The model is validated only for application A. (a) r_i shows normal distribution and uniform variance. (b) r_i shows uneven variance. (c) Erroneous linear model parameter. (d) Nonlinear model.

$$s_a^2 = \frac{s_0^2 \sum_{i=1}^{n} C_i^2}{n \sum_{i=1}^{n} (C_i - \overline{C})^2}; \quad s_b^2 = \frac{s_0^2}{\sum_{i=1}^{n} (C_i - \overline{C})^2} \tag{53.26}$$

$$\text{where } s_0^2 = \frac{\sum_{i=1}^{n} (A_i - \hat{A}_i)^2}{n-2} \text{ and } \overline{C} = \frac{1}{n} \sum_{i=1}^{n} C_i \tag{53.27}$$

The confidence intervals Δa and Δb are calculated according to

$$\Delta a = \pm t(P,f) s_a \text{ and } \Delta b = \pm t(P,f) s_b \tag{53.28}$$

where t indicates a t-distribution, f the degree of freedom ($f = n - 2$), and P the requested probability for the confidence interval.

- Step 5: Application of the model for prediction.
  The predicted concentration C_{pred} may be calculated from measured absorbance values A_{meas} using the developed calibration model according to

$$C_{\text{pred}} = \frac{(A_{\text{meas}} - \hat{a})}{\hat{b}} \tag{53.29}$$

It should be mentioned here that samples used for the estimation of the model parameters in steps 1–4 must not be reused for prediction in step 5.

Advantages and disadvantages of LSR are summarized in Table 53.4.

Table 53.4 Advantages and disadvantages of least squares regression.

	Least squares regression
Advantages	**Disadvantages**
Simple model	Analyte has to have an isolated spectral band
Fast calculation	No application to complex mixtures with overlaid spectral bands

53.3.3.2 **Multivariate Methods**

From a mathematical point of view, applications of multivariate methods [1–3, 16, 17, 20] may be subdivided into the multiple case and the multidimensional multiple case (cf. Figure 53.2). In the former case, several independent variables or features are mapped to merely one dependent variable or target value. In the second case, several independent variables or features are mapped to several dependent variables or target values. As a rule, linear models are used for such problems in optical spectroscopy. In case of nonlinear relations, the calibration range gets restricted, a linearizing data pretreatment is performed in order to get away with linear models, or nonlinear methods (usually neural networks) have to be applied.

All models discussed here belong to the multidimensional multiple case.

53.3.3.2.1 **CLS (Classical Least Squares), K-Matrix**

- Step 1: Choosing a model.

  The generalized form of the Beer–Lambert law for mixtures containing m components may be written in matrix form (cf. Figure 53.9) as

$$\begin{array}{lcccc} & \underline{A} = & \underline{C} & \cdot & \underline{K} \\ \text{dimensions} & n,p & n,m & & m,p \end{array} \tag{53.30}$$

  The measured absorbance values of a spectrum (p data points) are contained in one row of the absorbance matrix $\underline{A}$. The number of rows n in $\underline{A}$ corresponds

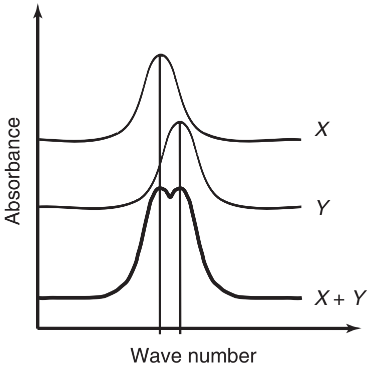

$$A_{k1} = C_X K_{X,K1} + C_Y K_{Y,K1}$$
$$A_{k2} = C_X K_{X,K2} + C_Y K_{Y,K2}$$
$$(A_{k1}\ A_{k2}) = (C_X\ C_Y)\begin{pmatrix} K_{X,K1} & K_{X,K2} \\ K_{Y,K1} & K_{Y,K2} \end{pmatrix}$$

Figure 53.9 Beer–Lambert law for a two-component mixture.

to the number of measured spectra in the training set (cf. Figure 53.4). In the concentration matrix $\underline{C}$, a row contains the concentrations of the individual components of the particular training spectrum. $\underline{K}$ represents the matrix of the absorptivity constants. A row contains these constants of a particular component for all p measured wavelength positions.

- Step 2: Choosing a training set.
  Preparation of n mixtures by variation of the concentration of all m components and subsequent measuring of their absorbance spectra.
- Step 3: Estimation of model parameters.
  Matrices $\underline{A}$ (measured) and $\underline{C}$ (prepared) in Eq. (53.30) are now known. Estimation of the calibration matrix $\underline{\hat{K}}$ is performed by the equation

$$\underline{\hat{K}} = (\underline{C}^{\mathrm{T}}\underline{C})^{-1}\underline{C}^{\mathrm{T}}\underline{A} \tag{53.31}$$

  The condition $n < p$ has to be observed in order to avoid problems with correlating variables and instable matrix inversion. PCR and PLS are more appropriate methods if the above-mentioned condition cannot be met.
- Step 4: Validation of the model by statistical means can be done in several ways, for example,

  a. Analysis of residuals.
  The residual matrix $\underline{R}$ is obtained by calculating the difference

$$\underline{R} = \underline{A} - \underline{\hat{A}} \tag{53.32}$$

$$\text{where } \underline{\hat{A}} = \underline{C}\ \underline{\hat{K}} \tag{53.33}$$

  The n rows of $\underline{R}$ contain difference spectra. Each difference spectrum can be assigned a particular error value

$$\underline{R}_i = \sum_{j=1}^{p} r_{ij}{}^2 \quad i = 1, \ldots, n \tag{53.34}$$

  These error values may be depicted graphically with the number n of the corresponding training spectrum on the abscissa (cf. Figure 53.10). This graph permits an easy detection of outlier spectra.

  b. Cross validation.
  The following sequence has to be completed (leave-one-out strategy):

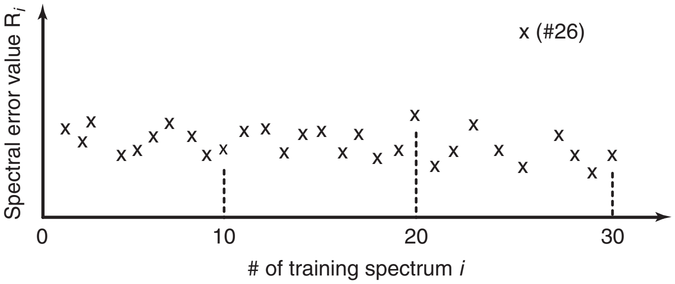

Figure 53.10 Detection of outlier spectra.

  - Selection of a subset of $n-1$ training spectra
  - Estimation of a model
  - Prediction of the concentration of the omitted sample
  - Repetition of the above-mentioned sequence until each of the n training spectra has been omitted and predicted once.

After completion of the above-mentioned cycle, all n experimentally prepared concentration values (C_{exp}) are depicted graphically against the predicted concentration values (C_{pred}) for each of the m components (cf. Figure 53.11). The quality of the calibrated model can be rated from this set of m diagrams.

The data couples (C_{exp}; C_{pred}) in Figure 53.11 may be evaluated by all statistical procedures. Cross-validation is a powerful method for outlier detection and optimization of calibration models. If the predicted concentrations obey the necessary quality standard for all but one training spectrum, the latter can be regarded as outlier. Cross-validation often provides too optimistic results because merely one training spectrum is taken into account. For this reason, the subsequently described set validation may be preferred.

c. Set validation.

The training spectra are randomly separated into two sets. The first set is used for calibration, the second set for validation. Set validation does not demand as much computing power as cross-validation and should be applied only for large data sets. Validation using sets of varying sizes (e.g., 50, 25, 20% of the training data) permits more robust predictions concerning the quality of the model.

- Step 5: Application of the model for predictions.

The calibrated model is finally used to predict the concentrations of the m components (vector $\underline{c}^{\mathrm{T}}$ comprising m concentration values) from the experimental spectrum (vector $\underline{a}^{\mathrm{T}}$ comprising p absorbance values):

$$\underline{c}^{\mathrm{T}} = \underline{a}^{\mathrm{T}} \times (\underline{\hat{K}}^{\mathrm{T}}\underline{\hat{K}})^{-1}\underline{\hat{K}}^{\mathrm{T}} \tag{53.35}$$

Advantages and disadvantages of classical LSR are summarized in Table 53.5.

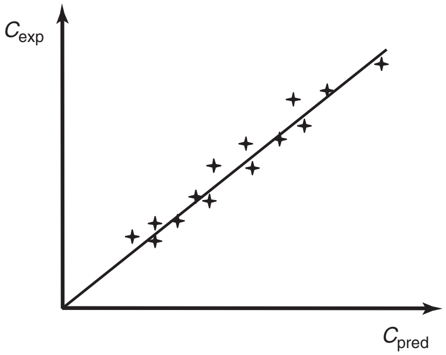

Figure 53.11 Rating of the quality of the calibrated model for one of the m components.

Table 53.5 Advantages and disadvantages of classical least squares regression.

	Classical least squares
Advantages	**Disadvantages**
Relatively fast calculation	The components of the sample have to be known completely, all concentrations have to be varied during calibration
No wavelength selection necessary, complete spectrum applicable	During prediction, all these and only these components have to be present in the sample
Large number of data points per spectrum and large number of calibration spectra ensures low noise	Fails in case of new impurities or components which were not present in the mixture during calibration
	Matrix inversions necessary both during calibration and during prediction

53.3.3.2.2 **ILS (Inverse Least Squares), P-Matrix, or MLR (Multiple Linear Regression (Multidimensional))**

Step 1: Choosing a model.

The generalized form of the Beer–Lambert law (cf. Eq. (53.30)) may be rearranged with respect to the concentration:

$$\begin{array}{lccccc} & \underline{C} & = & \underline{A} & \cdot & \underline{P} \\ \text{dimensions} & n,m & & n,p & & p,m \end{array} \tag{53.36}$$

The structure of matrices $\underline{C}$ and $\underline{A}$ was already described for classical least square (CLS). The elements of the $\underline{P}$ matrix are proportional to the reciprocal absorptivity constants. It is the crucial advantage of inverse least square (ILS) over CLS, that only the concentrations of the components of interest have to be known during calibration.

Step 2: Choosing a training set.

Owing to the mathematical requirement $n > p$ (dimension of the matrix), a very large number of training spectra should be measured. This might evoke the problem of collinearity among the spectra, that is, the spectra are not any more completely independent among each other – as mathematically necessary. Instead, they might be transformed in each other by linear combinations. Linear dependencies occur, for example, if calibration mixtures are simply diluted without changing the concentration ratios between the constituents. Spectra of such diluted samples contain redundant information, which in turn causes mathematical instabilities. In order to keep p small, one should restrict the calibration to spectral areas that comprise distinct contributions by the components of the mixture. Such decisions demand chemical knowledge as well as sure instinct.

Step 3: Estimation of model parameters.

Using the matrices $\underline{A}$ (measured) and $\underline{C}$ (prepared) (cf. Eq. (53.36)), one can now estimate the calibration matrix $\hat{\underline{P}}$:

$$\hat{\underline{P}} = (\underline{A}^{\mathrm{T}}\underline{A})^{-1}\underline{A}^{\mathrm{T}}\underline{C}. \tag{53.37}$$

Step 4: Validation of the model by statistical means.

The validation of the model is performed in the same way as described for CLS.

Step 5: Application of the model for prediction.

On the basis of a measured spectrum of an unknown (vector $\underline{a}^{\mathrm{T}}$ comprising p absorbance values) and on the calibration matrix, the concentrations of the m components can now be predicted (vector $\underline{c}^{\mathrm{T}}$ comprising m concentration values):

$$\underline{c}^{\mathrm{T}} = \underline{a}^{\mathrm{T}} \times (\underline{A}^{\mathrm{T}}\underline{A})^{-1}\underline{A}^{\mathrm{T}}\underline{C} \tag{53.38}$$

Advantages and disadvantages of inverse LSR are summarized in Table 53.6.

53.3.3.2.3 **PCR (Principal Component Regression)**

- Step 1: Choosing a model.
  The main problem in the above-described ILS is caused by possible multicollinearities between regressed spectra. This problem can be overcome by using a PCA (cf. Section 53.3.2.4) not only for data reduction but to combine the data reduction with elimination of multicollinearities as well. The PC scores computed this way are afterwards used as regressors in the ILS scheme.
- Step 2: Choosing a training set.
  - Full spectra or only spectral ranges showing contributions by the components of interest may be selected.
  - Concentrations of the components of interest have to be known.
  - Estimation of the number of PCs with respect to the chemical components to be calibrated (chemical knowledge!). This estimation based on chemical ground ensures the closest relation between the variance represented in the PCs and the change in concentration of the chemical components of interest.

Table 53.6 Advantages and disadvantages of inverse least squares regression.

	Inverse least squares
Advantages	**Disadvantages**
Relatively fast calculation	Difficulties in choosing the right spectral areas
The calibration model may only be based on knowledge about the interesting components, impurities are not important	Often, a larger number of calibration samples necessary ($n > p$ required for mathematical reasons)
Only one matrix inversion during calibration	Multicollinearity may cause problems
Complex mixtures may be analyzed	Time-consuming calibration

- Step 3: Estimation of model parameters.
  At first we introduce into the PCA (Eq. (53.18)) the equation $\underline{F}^{-1} = \underline{F}^{\mathrm{T}}$, which is based on the orthogonality of $\underline{F}$:

  $$\underline{S} = \underline{A}_{\mathrm{Z}}\underline{F} \tag{53.39}$$

  The second step yields in analogy to ILS ($\underline{B}$ corresponds to $\underline{P}$)

  $$\begin{array}{lcccccc} & \underline{C} = & \underline{S} \cdot & \underline{B} = & \underline{A}_{\mathrm{Z}} \cdot & \underline{F} \cdot & \underline{B} \\ \text{dimensions} & n,m & n,w & w,m & n,p & p,w & w,m \end{array} \tag{53.40}$$

  $\underline{B}$ represents the matrix of coefficients of the regression of the PCA scores (regressors) versus the concentrations of the chemical components (regressands). All other symbols are identical to those already described earlier or in Section 53.3.2.4.
  The estimation of the calibration matrix $\hat{\underline{B}}$ yields

  $$\hat{\underline{B}} = (\underline{S}^{\mathrm{T}}\underline{S})^{-1}\underline{S}^{\mathrm{T}}\underline{C} \tag{53.41}$$

- Step 4: Validation of the model by statistical means.
  The selection of the number of PCs was already described for PCA (Section 53.3.2.4). The validation of the model is effected in analogy to CLS.
- Step 5: Application of the model for prediction.
  The concentrations of all m components of interest (vector $\underline{c}^{\mathrm{T}}$ containing m concentration values) can be predicted on the basis of the measured spectrum of an unknown mixture (vector $\underline{a}^{\mathrm{T}}$ containing p absorbance values), the PC matrix $\underline{F}$, and the calibration matrix $\hat{\underline{B}}$:

  $$\underline{c}^{\mathrm{T}} = \underline{a}^{\mathrm{T}} \cdot \underline{F}\ \hat{\underline{B}} \tag{53.42}$$

  Advantages and disadvantages of PCR are summarized in Table 53.7. During the first step of a PCR, the absorbance matrix $\underline{A}$ is separated into its PCs. The regression of the resulting score matrix $\underline{S}$ on the actual target, the concentration matrix $\underline{C}$, is performed subsequently. The first step may involve a data reduction, which could cause a truncation of information. Truncated information cannot be included anymore in regression on the target. The PLS method described in Section 53.3.3.2.4 avoids this restriction during regression.

53.3.3.2.4 **PLS (Partial Least Squares)**

Step 1: Choosing a model.

The starting point is a model analogous to inverse calibration (ILS)

$$\begin{array}{lccc} & \underline{C} = & \underline{A} \cdot & \underline{B} \\ \text{dimensions} & n,m & n,p & p,m \end{array} \tag{53.43}$$

In real applications, the PLS algorithm may result in a better regression of the absorbance matrix $\underline{A}$ on the concentration matrix $\underline{C}$ because of the approach in Eq. (53.43) and the simultaneous separation of the matrices $\underline{C}$

Table 53.7 Advantages and disadvantages of principal component regression.

	Principal component regression
Advantages	**Disadvantages**
Full spectrum or larger parts of a spectrum may be used	PCA demands much chemical knowledge and sure instinct
Large number of spectral data points leads to noise reduction	Large number of calibration samples necessary
Only information about the components of interest necessary	Large calibration effort necessary
Rather complex mixtures may be analyzed	Selection of nonsignificant principal components or neglect of important principal component possible
Data reduction by PCA	

and $\underline{A}$ (while the criterion of maximal covariance is applied). As in PCA, both the concentration matrix $\underline{C}$ and the absorbance matrix $\underline{A}$ are decomposed into score and loading matrices $\underline{S}_\mathrm{C}$ and $\underline{F}_\mathrm{C}$ or $\underline{S}_\mathrm{A}$ and $\underline{F}_\mathrm{A}$, respectively:

$$\underline{C} = \underline{S}_\mathrm{C} \cdot \underline{F}_\mathrm{C}^\mathrm{T}; \underline{A} = \underline{S}_\mathrm{A} \cdot \underline{F}_\mathrm{A}^\mathrm{T} \tag{53.44}$$

The matrices $\underline{C}$ and $\underline{A}$ are decomposed interdependently with regard to their score matrices $\underline{S}_\mathrm{C}$ and $\underline{S}_\mathrm{A}$, which maintains the close coherence between spectral information ($\underline{A}$) and the component concentration ($\underline{C}$) in the best possible manner.

Step 2: Choosing a training set.

Measurement of a large number n of training spectra, covering as much of the concentration range as possible. The concentrations of the different components have to be varied independently.

Step 3: Estimation of model parameters.

The estimation of the calibration matrix $\hat{\underline{B}}$ yields

$$\hat{\underline{B}} = \hat{\underline{W}}(\underline{F}_\mathrm{A}^\mathrm{T} \hat{\underline{W}})^{-1} \underline{F}_\mathrm{C}^\mathrm{T} \tag{53.45}$$

where $\underline{W}$ represents the weight matrix, which is valued during the decomposition.

Step 4: Validation of the model by statistical means.

The selection of an optimal number of factors (loadings) is a central point in PCR and PLS. In both methods, the so-called prediction residual error sum of squares (PRESS) is calculated.

$$\mathrm{PRESS} = \sum_{i=1}^{n} \sum_{j=1}^{m} (C_{ij} - \hat{C}_{ij})^2 \tag{53.46}$$

where n is the number of training spectra, m the number of components in the mixture, C_{ij} are the prepared and $\hat{C}_{ij}$ the predicted concentrations. After a cross-validation is performed, the prediction error (PRESS) can be depicted versus the number of employed factor in order to select an optimized number of factors.

In Figure 53.12, the minimum for the prediction error is found at six factors by cross-validation. The following factors render the most noise, and their retention would deteriorate the quality of the model. Other validations are performed analogous to CLS.

Step 5: Application of the model for prediction.

The concentrations of all m components of interest (vector $\underline{c}^{\mathrm{T}}$ containing m concentration values) can be predicted on the basis of the measured spectrum of an unknown mixture (vector $\underline{a}^{\mathrm{T}}$ containing p absorbance values) and the calibration matrix $\underline{\hat{B}}$:

$$\underline{c}^{\mathrm{T}} = \underline{a}^{\mathrm{T}}\underline{\hat{B}} \tag{53.47}$$

Advantages and disadvantages of PLS regression are summarized in Table 53.8. A survey of presently available software products for data analysis is given in Table 53.9.

53.3.4
Spectral Imaging

Spectral images are constructed from 3D data sets (x and y are spatial dimensions, z the spectral intensities). These data sets are processed using the same algorithms as described in Section 53.3.2 for qualitative evaluation of spectra and in Section 53.3.3 for quantitative evaluation.

The subsequent discussion of data analysis in spectral imaging will be based on Figure 53.2 as the mathematical algorithms are the same for a small number or for a large number of spectra in the evaluation set. For this reason, the same software products as mentioned in Table 53.9 can be applied to calculate spectral images. This section will focus on qualitative analysis of spectral images. A crucial step

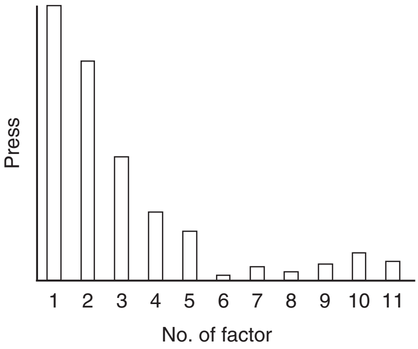

Figure 53.12 Estimation of the number of significant factors by means of the prediction residual error sum of squares (PRESS).

Table 53.8 Advantages and disadvantages of partial least squares regression.

Partial least squares	
Advantages	**Disadvantages**
Full spectra may be used	Abstract model
Most robust calibration	Large number of training spectra necessary
Only information about components of interest necessary	Extended computing time
Very complex mixtures may be analyzed	Determination of the optimal number of factors difficult
Computation of factors and regression in a single step, projection of the features of interest (concentrations) onto the factors superior to PCR	

Table 53.9 Software products for data analysis.

Product	**Manufacturer**	**Methods covered**
GRAMS	Thermo Fisher Scientific Inc.	LSR, PCA, PCR, PLS
PLSplus/IQ Add-on		
MATLAB	MathWorks Inc.	CLS, ILS, PCA, PCR, PLS
Chemometrics Toolbox	Applied Chemometrics Inc.	
PLS_Toolbox	Eigenvector Research Inc.	
Statgraphics	StatPoint Technologies Inc.	Cluster analysis, discriminant analysis, PCA, linear, and nonlinear regression
Statistica	Stat Soft	Cluster analysis, discriminant analysis, PCA, linear, and nonlinear regression
Unscrambler	Camo Software AS	PCA, PCR, PLS

in multivariate data analysis is the preprocessing of the raw spectra. It includes exclusion of nonlinearities of the detector (dead pixels, nonlinear response), elimination of outliers, noise reduction, baseline, and background correction, even a reduction of the data volume without significant loss of information. Details are discussed in Section 5.6.1.

53.3.4.1 Graphical Techniques

Graphical techniques may be regarded as simplest techniques of unsupervised learning. Figure 53.13 shows a false color image of a mixture of polystyrene and polyethene. A thin section of the mixture was measured in transmission. The lateral distribution of polystyrene was evaluated by plotting the height of the characteristic band of the aromatic stretching vibration of polystyrene at 1600 cm^{-1}. The color coding clearly reveals the lateral distribution of polystyrene across the sample. Blue areas indicate low proportions of polystyrene (here, 0.2 absorbance units), red areas high proportions of polystyrene (here, 1.2 absorbance units). The evaluation permits qualitative conclusions – presence or absence of a component, or even semiquantitative conclusions according to the color code. It has to be emphasized that the color code is usually assigned by the software, and the scale mostly differs between images even of the same sample. Cross-comparisons may lead to severe misinterpretations.

Intensity plots as in Figure 53.13 are constructed without much computational effort. Simple evaluation routines do not compensate for particular optical problems within the sample; sometimes they even highlight them. The main origin of these optical problems is the heterogeneity of all samples to be imaged; homogeneous samples need not be imaged. Heterogeneous samples usually exhibit different

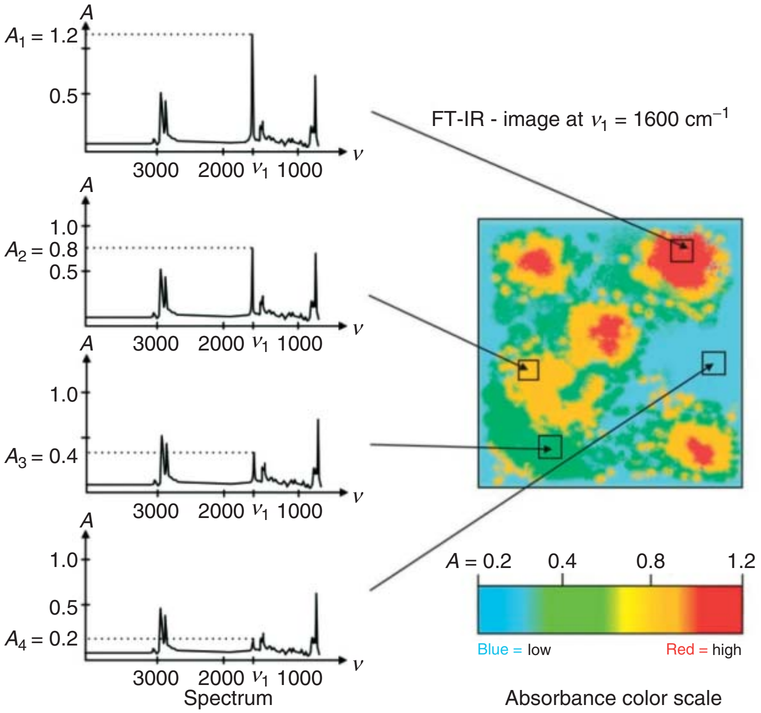

Figure 53.13 Color-coded FT-IR intensity image of a mixture of polystyrene and polyethene calculated from the height of the characteristic band at 1600 cm^{-1} wave numbers.

refractive indices according to the changes in their composition, or the sample thickness may change differently between regions of varying properties. The impact of varying sample thickness may be reduced by calculating intensity ratios instead of simple band heights as in Figure 53.13. Different refractive indices across the sample area require much more elaborated techniques to be dealt with.

53.3.4.2 Chemometric Techniques

In the past, the segmentation of spectroscopic images into regions of different properties was restricted both by the limited availability of dedicated chemometric software packages and by the amount of RAM installed in computer clusters. Both restrictions were significantly lifted during the past decade. Nowadays, large RAMs permit the joint evaluation of huge data sets. New algorithms become available or are adopted from other areas of science. This chapter can only refer to the most important of the algorithms listed in Table 53.2. More details are found in [21]. Application areas for qualitative data analysis for spectral imaging are summarized in Table 53.10 for the techniques of unsupervised learning, and in Table 53.11 for the techniques of supervised learning.

Table 53.10 Application areas for techniques of unsupervised learning.

Technique	Application area
Graphical techniques	Simple and clear Always applicable for structuring and reduction of data sets Particularly suited for explorative data analysis
Cluster analysis	Clusters within the images well visualized Hierarchical cluster analysis Well suited for explorative data analysis Nonhierarchical cluster analyze (e.g., k-means clustering) Distribution of spectral features between independent clusters Problem: distinction between local and global optima
Principal component analysis (PCA)	One of the most powerful techniques for explorative data analysis Can be used for data preprocessing, in particular for reduction and structuring of the data set Can be used in case of complex data sets with correlated variables Provides information about the distribution of variance within spectral features Applied after preceding mean-centering or standardization of the spectra (Section 53.2) Various visualization tools available

Table 53.11 Application areas for techniques of supervised learning.

Technique	Application area
Discriminant analysis	Algorithms of linear discriminant analysis (LDA) used to describe classes Variance between objects in the same class is minimized while variance between class centers is maximized Classification in case of larger deviation from the required statistical equality of the covariance matrices between classes; for this reason not capable for complex data structures
SIMCA	Modeling of complex and heterogeneous data structures possible A separate PC model developed for every class of objects, hence optimal reduction of dimensionality Good adaptation to enlarged data sets
k-nearest neighbor (KNN technnique)	Simple classification technique Optimum number of neighbors k mostly detectable by estimation of the minimum total number of misclassifications using resubstitution and leave-one-out approaches Particularly fast for two-class systems

PCA (Section 53.3.2.4) is one of the most powerful techniques to analyze spectral imaging data. The subsequent example illustrates how the distribution of a minor inorganic component in a polypropylene matrix can be determined and, moreover, how the chemical nature of the minor component can be identified. The size of the scanned area is 270 μm × 270 μm. The diffraction limited lateral resolution depends partly on the quality of the optical system of the spectrometer. A resolution of about 10 μm is considered reasonable for investigations at 1000 cm^{-1} (wavelength 10 μm). Typical technical details for FT-IR imaging (pixel numbers, measurement times, computation) are given in Section 5.6. Seven PCs were calculated, they cover 97% of the total variance in the data set. The first two PCs can be assigned to the polymer matrix. The discussion here shall be focused on the minor inorganic component. Figure 53.14 shows the score map and the loadings for the third PC, which comprises 11% of the total variance. The loading map provides information about the chemical nature of this constituent, while the score map illustrates its local distribution. As PCs are based on variance considerations and not on chemical analysis, a constituent according to PCA may comprise more than one chemical compound. The loadings of the third PC in Figure 53.14a reveal a feature around 1000 cm^{-1}, which can clearly be assigned to the antisymmetric stretching of the silicate group. High-score values (red to yellow in Figure 53.14b) reveal the location of the silicate in the polymer matrix.

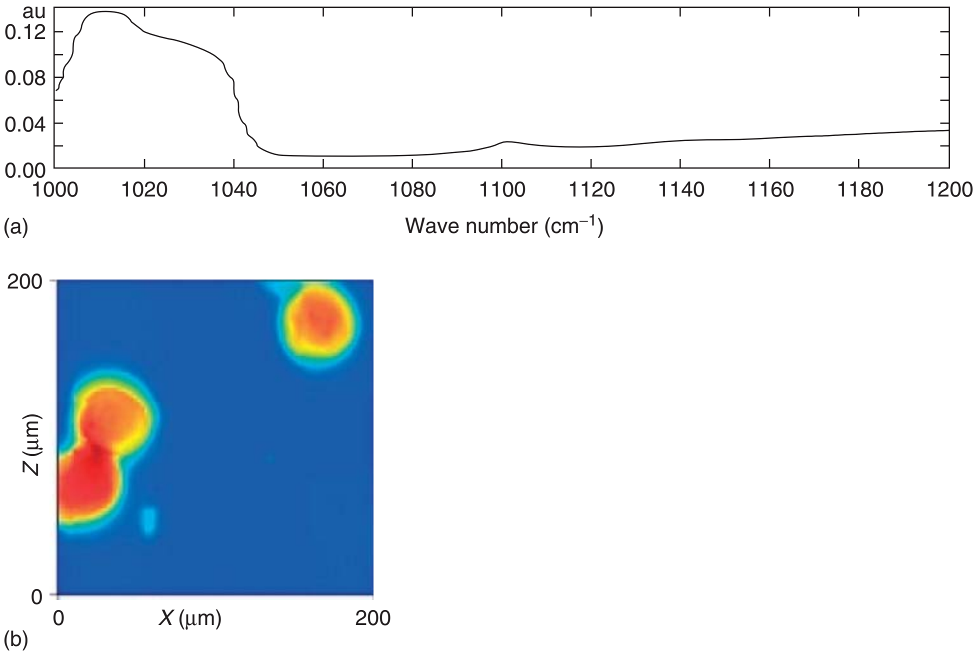

Figure 53.14 PCA of a polymer sample containing an inorganic powder. (a) The loadings of the third PC indicate silicate. (b) The score map reveals the location of the silicate in the matrix (red to yellow: high scores indicate silicate spots, blue: low scores indicate no silicate).

References

1. Brereton, R. (2009) *Chemometrics for Pattern Recognition*, John Wiley & Sons Ltd., Chichester.
2. Naes, T., Isaksson, T., Fearn, T., and Davis, T. (2002) *Multivariate Calibration and Classification*, NIR Publications.
3. Varmuza, K. and Filzmoser, P. (2009) *Introduction to Multivariate Statistical Analysis in Chemometrics*, CRC Press, Boca Raton, FL.
4. Pouchert, C.J. (1981) *The Aldrich Library of Infrared Spectra*, Aldrich Chem. Co., Milwaukee.
5. Simons, W.W. (1978) *The Sadtler Handbook of Infrared Spectra*, Sadtler Research Laboratories Inc., Philadelphia, PA.
6. Simons, W.W. (1979) *Sadtler Handbook of Ultraviolet Spectra*, Sadtler Research Laboratories Inc, Philadelphia, PA.
7. Ferraro, J.R. (1982) *The Sadtler Infrared Spectra Handbook of Minerals and Clays*, Sadtler Research Laboratories Inc., Philadelphia, PA.
8. Schrader, B. (1989) *Raman/Infrared Atlas of Organic Compounds*, Wiley-VCH Verlag GmbH, Weinheim.
9. Hummel, D.O. (1991) *Atlas of Polymer and Plastic Analysis*, Wiley-VCH Verlag GmbH, Weinheim.
10. Pachler, K.G.R., Matlok, F., and Gremlich, H.U. (1988) *Merck FT-IR Atlas*, Wiley-VCH Verlag GmbH, Weinheim.
11. Buback, M. and Vögele, H.P. (1993) *FT-NIR Atlas*, Wiley-VCH Verlag GmbH, Weinheim.
12. Bio-Rad Laboratories Ltd Informatics Division, *http://www.knowitall.com/literature/95115_Spectroscopy_Edition_Brochure.pdf* (accessed 19 August 2013).

13. Abrams, C. *IR-Tutor*, John Wiley & Sons, Inc. (1998) *www.irtutor.com* (accessed 19 August 2013).
14. US Stream Solutions *SpecTool*, John Wiley & Sons, Inc. (1997) *http://www.upstream.ch/products/spt.html* (accessed 19 August 2013).
15. TeleSpec *www2.chemie.uni-erlangen.de/services/telespec* (accessed 19 August 2013).
16. Otto, M. (1999) *Chemometrics*, Wiley-VCH Verlag GmbH, Weinheim.
17. Henrion, R. and Henrion, G. (1995) *Multivariate Datenanalyse*, Springer-Verlag, Berlin.
18. Mahalanobis, P.C. (1936) On the generalised distance in statistics. *Proc. Natl. Inst. Sci. India*, **2**, 49 (original reference).
19. De Maesschalck, R., Jouan-Rimbaud, D., and Massart, D.L. (2000) The Mahalanobis distance. *Chemom. Intell. Lab. Syst.*, **50** (1), 1–18.
20. Martens, H. and Naes, T. (1991) *Multivariate Calibration*, John Wiley & Sons Ltd., Chichester.
21. Salzer, R. and Siesler, H.W. (2009) *Infrared and Raman Spectroscopic Imaging*, Wiley-VCH Verlag GmbH, Weinheim.

54
Nuclear Magnetic Resonance Spectroscopy

Wolfgang Robien

54.1
Introduction

Structure elucidation of organic compounds is mainly based on different types of spectroscopic techniques. Among the methods available, NMR spectroscopy contributes a large amount of information; in many cases, the obtained spectral data are often so rich in structural information content that the constitution, configuration, and the conformation of the unknown can be derived exclusively by the interpretation of such spectra. NMR spectroscopy is, in comparison to other techniques, an insensitive method, leading to a low signal-to-noise ratio of the obtained spectra. This disadvantage has been circumvented by the introduction of the principle of Fourier transformation, leading to much shorter data acquisition times and the possibility of observing more insensitive nuclei than protons and therefore getting more detailed information about the sample under investigation. During the past three decades, a great number of sophisticated pulse techniques have been developed, which allow – together with the use of high-field instrumentation – the investigation of extremely small amounts of samples and, in addition, to get more complete information about them. Especially the tremendous improvement based on two(three)-dimensional methods opened up a new horizon in structure elucidation [1]. For all these reasons, the earlier bottleneck of data acquisition as the most time-consuming step has been dramatically shifted to data interpretation – especially with the background of combinatorial chemistry and LC (liquid chromatography)-NMR coupling.

Structure elucidation of a complex molecule from its spectral data without software support is a challenging and time-consuming procedure, which can only be done by an expert in this field. In order to supply the expert with the necessary information during the spectrum interpretation and structure generation procedure, a large number of computer programs [2–4] and data collections have been developed. A good entry point, collecting links to many chemical shift tables, research groups, software vendors, and database producers in the field of NMR spectroscopy, is the web site spectroscopyNOW.com [5].

Handbook of Spectroscopy, Second Edition. Edited by Günter Gauglitz and David S. Moore.

54.2
Comparison of NMR Spectroscopy with IR and MS

In order to understand the range of possibilities in computer-assisted structure elucidation methods, it is essential to compare the different spectroscopic techniques with respect to their information content and their suitability for computer-assisted handling of their data. High-resolution mass spectral data can lead to the molecular formula, which is a necessary parameter for most interpretation and isomer generation programs. MS is also well suited to detect certain functional groups, which is also true for IR. The main disadvantage of MS is the extremely high dependence of the spectral pattern on the ionization technique applied; this effect can be used to get more specific information about the unknown sample. Another reason that MS gives usually only supporting information during the structure elucidation process is the complex, and yet only partially understandable, correlation between spectral data and structural properties resulting in the absence of reliable methods to predict MS spectra for a given structure. Some work about this topic has been published [6], but the techniques developed were never routinely applied. From IR spectra, a large variety of functional groups and substitution patterns can be derived, but the correlation between spectral behavior and structural property is not as well defined as in NMR spectroscopy. For all these reasons, MS and IR are not well suited to rank a few hundreds of structural proposals as created by an isomer generation program, which is the usual case during computer-assisted structure elucidation, especially when dealing with molecules having a few noncarbon atoms that are only indirectly visible via the chemical shift values of the attached carbons.

NMR spectroscopy is an insensitive method compared to IR and MS, but it has been dramatically improved since its beginning. In organic chemistry, usually ^{1}H- and ^{13}C-NMR spectroscopy is routinely applied for the purpose of structure elucidation. The total shift range for protons spans roughly 12 ppm in typical organic compounds compared to 250 ppm for carbon. Solvent effects on protons are usually more pronounced, an effect (ASIS – aromatic solvent-induced shift) which is also systematically used in structure elucidation, leading to the disadvantage that spectrum prediction by computer programs becomes more complicated. The comparison of a query spectrum against spectra in a reference library is also a more complex task for ^{1}H-NMR spectra than for ^{13}C-NMR spectra because of the field dependence of the spectral patterns. In carbon NMR spectroscopy, the couplings between carbons at natural abundance are usually invisible and the couplings to protons are artificially suppressed by decoupling techniques, leading to simplified spectral patterns. Furthermore, carbon NMR spectroscopy allows direct insight into the skeleton of an organic sample. From all these above-discussed reasons, it can be concluded that ^{13}C-NMR spectroscopy is the method of choice for computer-assisted structure elucidation having the disadvantage of dealing with an insensitive nucleus, which is by a factor 5760 less sensitive than protons are.

54.3
Methods in NMR Spectroscopy

The advantage of NMR spectroscopy is the large number of experimental techniques that allow one to derive a very specific piece of information about the unknown chemical structure. The parameters usually extracted from an NMR spectrum are as follows:

- Chemical shift values
- Signal intensities
- Coupling constants.

The chemical shift value reflects the electron density and therefore gives information about hybridization and the environment of the corresponding nucleus. The signal intensity is proportional to the number of nuclei and therefore gives information about symmetry. The coupling constants give information about spin systems and, therefore, insight into the relationship between different nuclei. Application of additional techniques allows determination of the signal multiplicities in ^{13}C-NMR spectra (e.g., APT = attached proton test; DEPT = distortionless enhancement by polarization transfer) and getting more insight into the coupling network. The most prominent two-dimensional techniques used are as follows:

- *H–H correlation*: COSY (correlated spectroscopy)
- *C–H correlation over one bond*: HMQC (heteronuclear multiple quantum coherence), HSQC (heteronuclear single quantum coherence)
- *C–H correlation over multiple bonds*: HMBC (heteronuclear multiple bond correlation), COLOCs (correlation by long-range couplings)
- *C–C correlation*: INADEQUATE (incredible natural abundance double quantum transfer experiment).

Chemical shift values are the main information source for spectral similarity searches, whereas the correlation between spectral lines and the corresponding structural environment is the basis for spectrum prediction programs. The information derived from the correlation techniques is used by interpretation programs to prove the presence of certain structural fragments from a given set of correlation signals. These correlation signals are also used as distance constraints – in terms of the number of bonds between two coupled nuclei – in the case of ambiguity, which occurs in HMBC-type spectra frequently, and later on during the structure generation process.

54.4
Spectral Similarity Search Techniques

One well-established method used in computer-assisted structure elucidation is the comparison of the spectrum of the unknown against a reference data collection. The largest databases available hold, at the moment, some 500 000 spectra of the same method corresponding to roughly 1% of the known chemical structures. The consequence for the design of the algorithms is that the procedure used for comparison must be able not only to detect the identical spectral pattern in any case but it must also be able to retrieve similar patterns, which usually gives a lot of information about partial structures and typical skeletons contained in the unknown.

The basic algorithms for spectral comparison use the Euclidian distance between corresponding data points when comparing curves or a given deviation when comparing peak lists in order to select compounds having similar resonances. The procedure for comparing peak lists can only be applied sequentially in some computer programs, leading to the unwanted effect that similar structures can be excluded when starting with an uncommon chemical shift value. The better approach handles the complete peak list of the unknown at the same time and allows afterwards the selection of lines that must be present in the reference spectrum. Different implementations of this basic algorithm allow the user to control the number of lines present in the reference spectrum compared to the number of lines available in the query spectrum, allowing to analyze the reference structure with respect to structural fragments present in the unknown or to derive components within a mixture.

The disadvantage of such a type of similarity search based on the comparison of a peak list against the reference data collection on a line-by-line basis is that regions without any lines are completely neglected. Another approach is the SAHO (spectral appearance in hierarchical order) search method, which also takes into account regions without lines [7]. The typical range of the chemical shift values is divided into smaller ranges (typically 10–15 ppm for carbon) and the number of signals within such a region is counted. In order to achieve a higher selectivity, different multiplicities (either odd/even or singlet, doublet, triplet, and quartet) can be counted separately, leading to an array of numbers describing the spectral pattern very well. The same procedure is applied to the reference data collection and the resulting arrays are stored. The comparison of the pattern of the unknown against the reference patterns is extremely fast because only a small amount of data must be handled (typically 8 bytes per spectrum), leading to a speed of 10^6–10^7 comparisons per second. This algorithm is an ideal tool to deduce at least the compound class of the unknown under the assumption that the reference data collection contains examples of similar structures. In any case, it should be mentioned that the results from the similarity search based on line-by-line comparison and the SAHO method are usually complementary and the user is strongly advised to apply both methods when available. These spectral similarity search techniques are extremely fast and should therefore be applied first during the structure elucidation process in order to avoid more time-consuming techniques for solving trivial problems. Such a system based on the predicted ^{13}C-NMR spectra for the approximately 16 million structures available from PUBCHEM has been built recently [8, 9].

54.5
Spectrum Estimation Techniques

From the reasons given in the introduction, ^{13}C-NMR spectrum prediction is more popular than ^{1}H-NMR spectrum prediction; besides, some programs are known to perform at a reasonable level of precision [10–12]. The early work of collecting chemical shift values was severely influenced by the idea of predicting spectra for a given structure. The first very simple, but still useful approach of increment rules has been implemented into a large variety of computer programs. The central concept of this method is to use a parent structure (e.g., benzene [13]) and to start with this chemical shift value in the calculation. Increments are derived from the difference between the chemical shift value of the parent compound and the corresponding chemical shift value of the monosubstituted derivatives. Polysubstituted compounds are treated as ‘‘overlapping’’ monosubstituted derivatives and the tabulated increments are simply added to the base value of the parent compound, neglecting therefore any substituent interaction. More sophisticated systems allow for additional correction parameters, leading to improved results [14, 15]. The advantages of this method are the simple principle behind and the good results for certain compound classes, where other methods tend to fail (e.g., polysubstituted benzenes). One main disadvantage is that only a limited number of increment tables for a limited range of parent compounds are available in the literature.

A more elegant method has been developed to make use of all compounds in a large reference data collection. The increment table for a certain query structure is generated on the fly and therefore all reference spectra contribute to the solution of a particular problem. This method automatically includes substituent interactions if this information is available within the reference data. Furthermore, a polysubstituted compound can be generated by formally overlapping only monosubstituted derivatives (as with the basic increment method), but also by selecting, for example, di- or trisubstituted derivatives allowing different calculation pathways, leading to an expectation range for the signals of the query structure. The disadvantage of this method is the long computing time and the complex algorithms behind using partial structure search technologies [16].

A different approach is called HOSE code [17] (hierarchically ordered spherical description of environments) and is based on the extremely well-pronounced correlation between a ^{13}C chemical shift value and the corresponding carbon-centered substructural unit. The HOSE-code starts at a carbon atom (focus atom) and describes its hybridization and multiplicity. The neighbored atoms are described in the same manner, taking into account their atom type, hybridizations, number of directly bound hydrogens, and the type of bonds between them. This scheme is applied to the first neighbors of the focus atom, then to the second neighbors, and so on, leading to a spherical description of the structural environment. The atoms within each sphere of this carbon-centered fragment are sorted in a canonical way, giving a structure descriptor that is correlated to the known chemical shift value of its focus atom. This procedure is repeated for any carbon of any reference structure available and stored on a file during database creation. The query structure is analyzed in the same way and the fragments generated are compared against the corresponding file of the database. Chemical shift values of coincident structure descriptors are taken for the calculation of the mean value, the total shift range, and the standard deviation. The number of coincident spheres between the reference structures and the query structure determines the precision of the obtained result. For sp^3-carbons, at least three spheres (γ-effects) are necessary; in the case of conjugated systems, four spheres usually give reliable results (effects of para-substituents). This basic principle has been implemented in a very similar way into several computer programs. In addition, solvent-induced effects can be added, leading to an improved spectrum prediction capability. The HOSE-code was designed to handle a two-dimensional structure representation; therefore, stereochemical effects were ignored. Consequently, it was necessary to introduce a further extension that is able to describe steric interactions, leading to an extreme improvement of the precision of the spectral prediction [18, 19]. A further approach for introducing stereochemical information is the CAST-code [20]; in commercially available prediction programs, stereochemical information can be handled by NMRPredict [19] and in a newer release by ACD-CNMR-Predictor [21].

A totally different approach is the utilization of neural network technologies as proposed by several authors [22–24]. The intellectual challenge of designing a neural network is the selection of the structure descriptors in order to reflect the correlation between structural and spectral properties in an optimal manner. Network optimization is a time-consuming task that must be done only once. The application of the trained network to a given structure is extremely fast and the prediction of the chemical shift values to be expected is performed within milliseconds, thereby having an excellent tool for spectrum simulation and subsequent ranking of a large list of candidate structures.

54.6
Spectrum Prediction – Quality Consideration

There is a strong relationship between the quality of the database, the level of sophistication of the algorithms used, and the results obtained. General databases are usually built from literature data; despite most of the assignments given in the public domain literature being correct, a large number of either wrong structures and/or misassignments are known [25]. Even some very common functional groups (e.g., tosylate) are known to be systematically assigned in two different ways. The assignment simply depends on the literature used for reference purpose, thus propagating the wrong assignment when using the wrong reference without checking. These data may appear later in some databases and will be used for further prediction, leading to unreliable results. This type of error can be easily detected by analyzing a large reference collection by means of statistical methods and should be frequently applied by a database administrator. A detailed analysis of the quality of the reference data within the NMRShiftDB collection has been published [26], leading to an intense effort to correct these errors, which has been described shortly afterwards [27].

As stated, spectrum prediction is based on the correlation between structural environments and their corresponding chemical shift values. In order to simulate spectra by the methods described, adequate reference material is necessary, which is not given in some journals – in frequent cases, instead of assignments only peak lists (even without multiplicity information) as given by the spectrometer software have been published, diluting the basis for spectrum prediction of new classes of compounds. During the ongoing efforts of correcting data within the CSEARCH and SPECINFO collections, a list of literature references that needed massive reassignments and/or correction of chemical structures has been published [28].

In order to cover the enormous structural diversity, it is necessary to have the most diverse database available. On the other hand, it is necessary to fill gaps within the area of interest with own data. Usually a very small, but specifically dedicated database is much more powerful for solving a limited range of problems than a general database.

It is absolutely essential to have access to all parameters influencing the spectral simulation process; furthermore, the typical parameters obtained as results (mean value, range, deviation) are not sufficient to evaluate the results, because in many cases a visual inspection of the distribution might be necessary in order to detect outliers or to understand stereochemical effects. The access to the original data contributing to a specific result must be possible in order to clarify any ambiguity.

Spectrum prediction is a frequently used technique during the structure elucidation process, but a detailed inspection of the results is necessary. Some programs offer the possibility of using different algorithms for spectrum prediction (usually HOSE-code technology and neural networks) – in such a situation, both methods should be applied and the obtained results should be carefully compared [18]. At least in the case of different predictions, a further critical evaluation of the result should be an obligation.

54.7
Spectrum Prediction and Quality Control – Examples

Spectrum prediction is an extremely decisive tool for verification of structural proposals and therefore the implementation of the algorithms and the quality of the reference database used cannot be discussed independently, because the obtained results are strongly connected to both parameters. The most severe limitation of the HOSE-code is the availability of sufficient and correct reference material within the database, because a description of the query structure at a lower number of spheres dramatically influences the predicted chemical shift values. In Figure 54.1, an assignment error on carbons 11 and 12 has been *artificially introduced* into the correct assignment as given in the literature in order to demonstrate the effect of accessing wrong entries within the reference database. The predicted spectrum, as given in Figure 54.2 using HOSE-code technology with five coincident spheres (= all neighbors up to five bonds), estimates 93.7 and 94.3 ppm, respectively, for

12-Hydroxychiloscypha- 2, 7–Dione;compound– #4

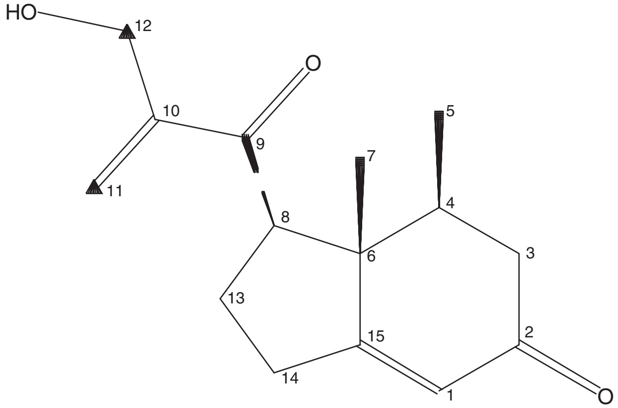

J.NAT.Prod.,60,1281(1997)
$C_{15}H_{20}O_3$ MWT = 248.3
$CDCL_3$

C – 1: 121. 50D
C – 2: 199.00S
C – 3: 41.20T
C – 4: 33.40D
C – 5: 16.80Q
C – 6: 51.20S
C – 7: 18.30Q
C – 8: 52.20D
C – 9: 205.10S
C – 10: 147.40S
▶ C – 11: 62.50T
▶ C – 12: 125.60T
C – 13: 26.70T
C – 14: 29.90T
C – 15: 177.60S

Figure 54.1 An entry from the reference database [18, 29] with an *artificially introduced* assignment error at carbons 11 and 12.

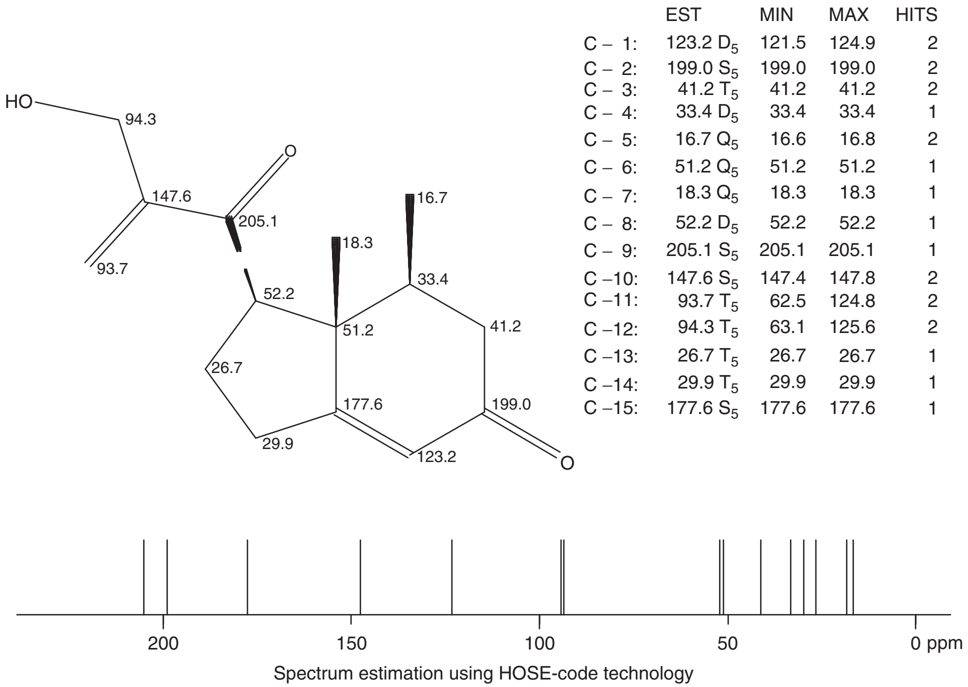

	EST	MIN	MAX	HITS
C – 1:	123.2 D$_5$	121.5	124.9	2
C – 2:	199.0 S$_5$	199.0	199.0	2
C – 3:	41.2 T$_5$	41.2	41.2	2
C – 4:	33.4 D$_5$	33.4	33.4	1
C – 5:	16.7 Q$_5$	16.6	16.8	2
C – 6:	51.2 Q$_5$	51.2	51.2	1
C – 7:	18.3 Q$_5$	18.3	18.3	1
C – 8:	52.2 D$_5$	52.2	52.2	1
C – 9:	205.1 S$_5$	205.1	205.1	1
C –10:	147.6 S$_5$	147.4	147.8	2
C –11:	93.7 T$_5$	62.5	124.8	2
C –12:	94.3 T$_5$	63.1	125.6	2
C –13:	26.7 T$_5$	26.7	26.7	1
C –14:	29.9 T$_5$	29.9	29.9	1
C –15:	177.6 S$_5$	177.6	177.6	1

Figure 54.2 Spectrum estimation using five coincident spheres generating wrong predictions for carbons 11 and 12 at 93.7 and 94.3 ppm, respectively, because of wrong reference material.

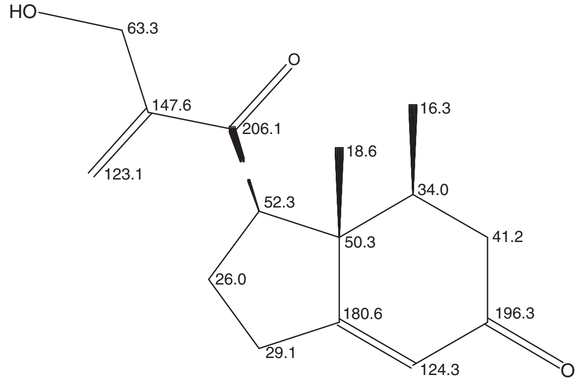

	EST		MIN	MAX	HITS
C – 1 :	124.3	D_2	121.5	137.7	13
C – 2 :	196.3	S_2	177.2	201.0	115
C – 3 :	41.2	T_2	33.2	43.1	38
C – 4 :	34.0	D_2	33.4	35.2	3
C – 5 :	16.3	Q_2	7.6	38.8	1480
C – 6 :	50.3	S_2	49.0	51.2	6
C – 7 :	18.6	Q_2	9.7	36.5	340
C – 8 :	52.3	D_2	51.8	52.8	3
C – 9 :	206.1	S_2	205.1	207.2	2
C – 10 :	147.6	S_2	147.4	147.8	2
C – 11 :	123.1	T_2	62.5	141.1	163
C – 12 :	63.3	T_2	54.9	125.6	37
C – 13 :	26.0	T_2	21.0	28.5	17
C – 14 :	29.1	T_2	27.1	31.3	9
C – 15 :	180.6	S_2	177.6	186.3	3

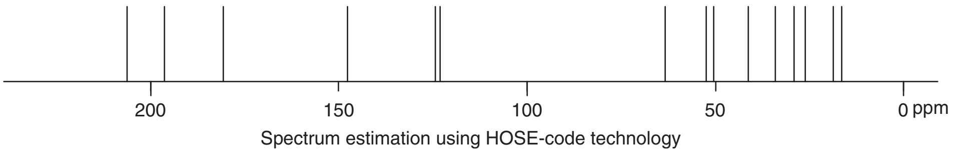

Figure 54.3 Spectrum estimation using two coincident spheres generating better predictions (123.1 ppm for C_{11} and 63.3 ppm for C_{12} respectively) than with five coincident spheres (see Figure 54.4).

carbons 11 and 12 together with an expectation range of some 60 ppm, which is totally useless for the spectroscopist. Estimation with two coincident spheres gives, in this case, the better mean values for carbon 11 and 12, again with extremely large expectation ranges as shown in Figure 54.3. A comparison of the estimated values at 1–5 coincident spheres, as given in Figure 54.4, demonstrates that there is only a small change in the mean values when increasing the number of coincident spheres, except for carbons 11 and 12 for which wrong reference material contributes heavily to the mean values. From this example, it can be concluded that the HOSE-code method is very sensitive to wrong assignments, leading to low-quality spectrum predictions in case of wrong reference material. Neural network technology is far less sensitive to assignment errors – despite the fact that the wrong data set was used during training – reasonable chemical shift values are predicted, as given in Figure 54.5.

Another important feature of spectrum prediction is the utilization of stereochemical information. Stereochemical effects may induce effects of up to about 30 ppm in typical organic compounds. The four isomeric tricyclo-octane derivatives, as given in Figure 54.6, demonstrate this clearly, especially at C_8 with a chemical shift range starting at 23 ppm in the exo, exo-derivative and going up to 53 ppm in the endo,endo-configurated isomer. The comparison of the corresponding carbon NMR spectra in Figure 54.7 shows these large increments were caused by steric interaction.

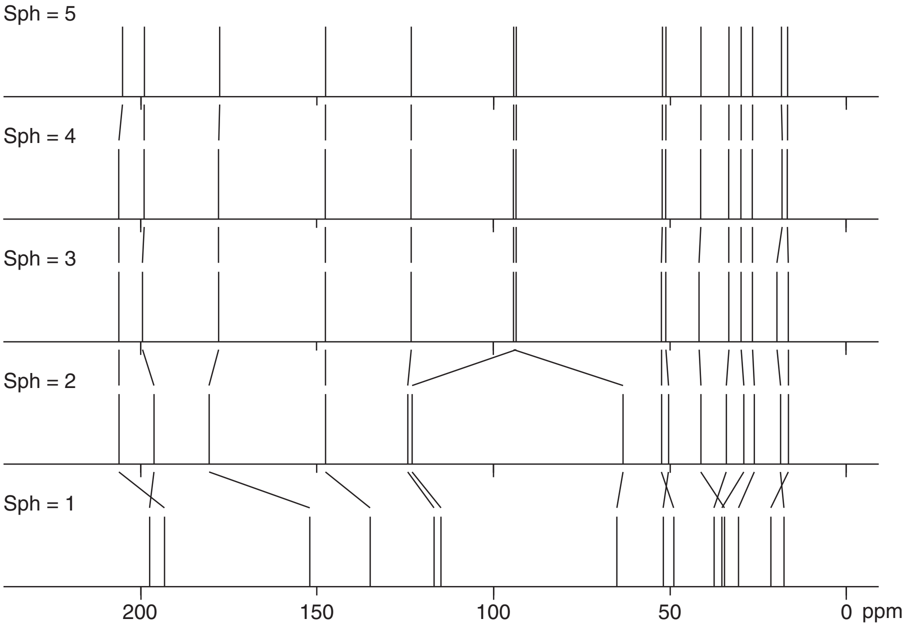

Figure 54.4 Dependence of the predicted chemical shift values from the number of coincident spheres given on the left-hand side. The large change when increasing the number of coincident spheres from two to three is worth a more detailed investigation of the reference material used.

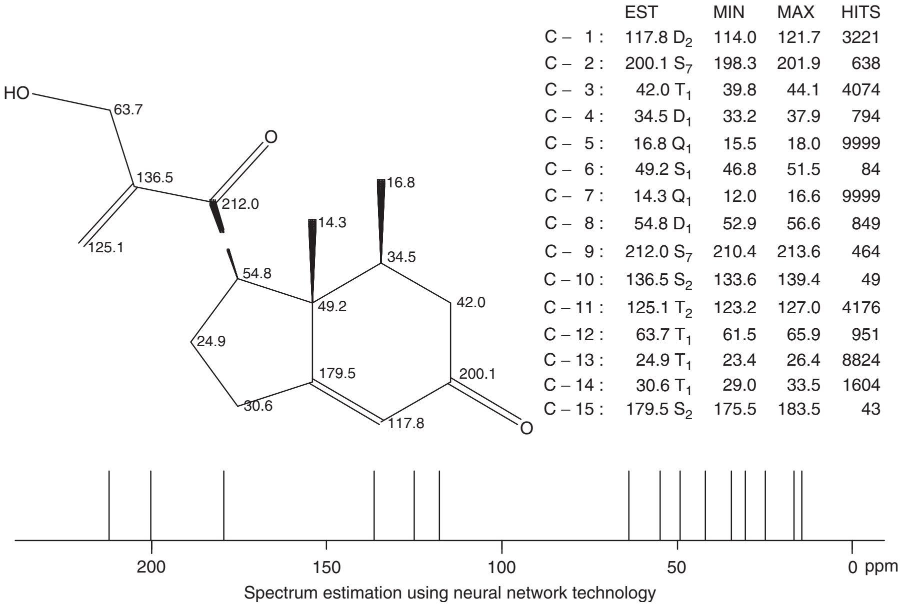

	EST	MIN	MAX	HITS
C – 1 :	117.8 D_2	114.0	121.7	3221
C – 2 :	200.1 S_7	198.3	201.9	638
C – 3 :	42.0 T_1	39.8	44.1	4074
C – 4 :	34.5 D_1	33.2	37.9	794
C – 5 :	16.8 Q_1	15.5	18.0	9999
C – 6 :	49.2 S_1	46.8	51.5	84
C – 7 :	14.3 Q_1	12.0	16.6	9999
C – 8 :	54.8 D_1	52.9	56.6	849
C – 9 :	212.0 S_7	210.4	213.6	464
C – 10 :	136.5 S_2	133.6	139.4	49
C – 11 :	125.1 T_2	123.2	127.0	4176
C – 12 :	63.7 T_1	61.5	65.9	951
C – 13 :	24.9 T_1	23.4	26.4	8824
C – 14 :	30.6 T_1	29.0	33.5	1604
C – 15 :	179.5 S_2	175.5	183.5	43

Figure 54.5 Predicted chemical shift values using neural network technology giving 125.1 ppm for C_{11} and 63.7 ppm for C_{12}, respectively.

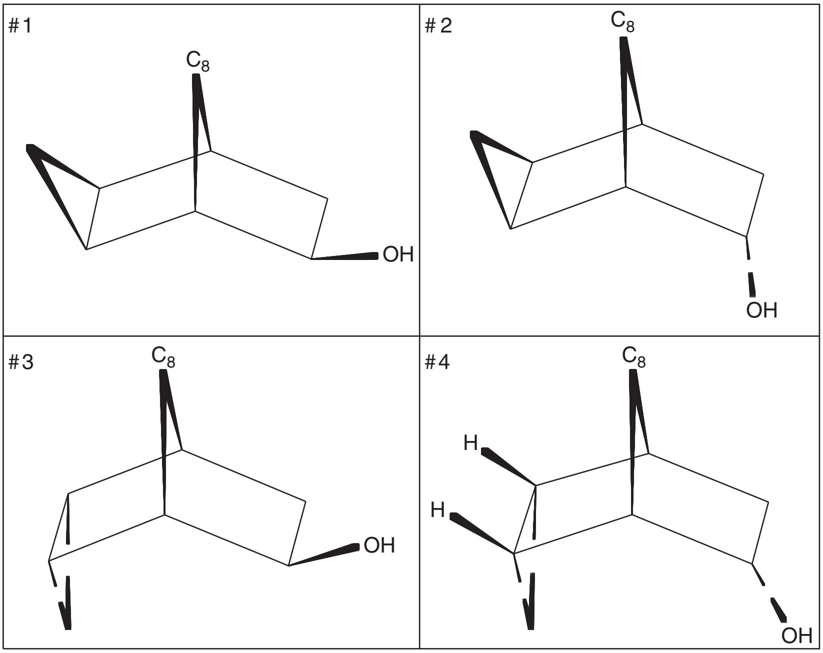

Figure 54.6 Four isomeric tricyclo-octane derivatives showing extremely pronounced effects of stereochemistry on chemical shift values (see Figure 54.7).

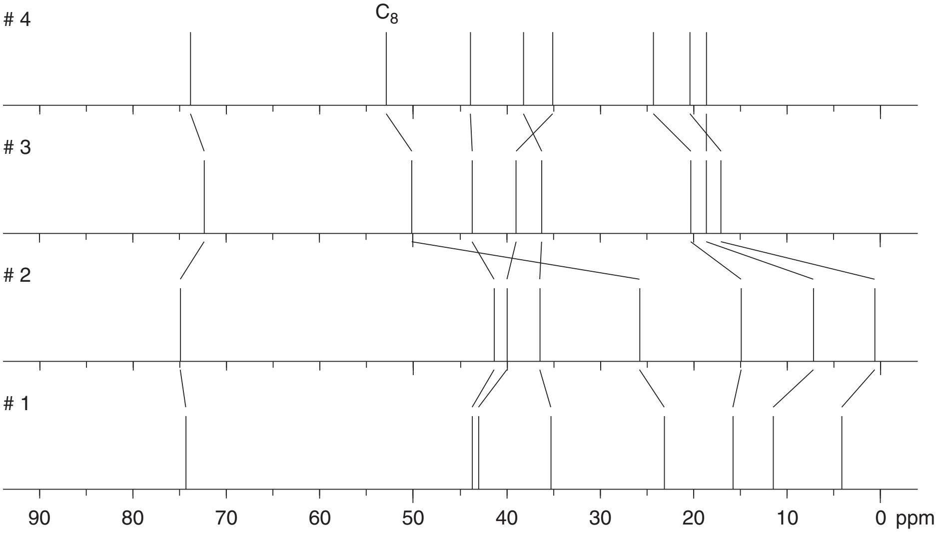

Figure 54.7 The ^{13}C-NMR spectra of the four compounds given in Figure 54.6 showing the effect of steric interactions on the chemical shift values.

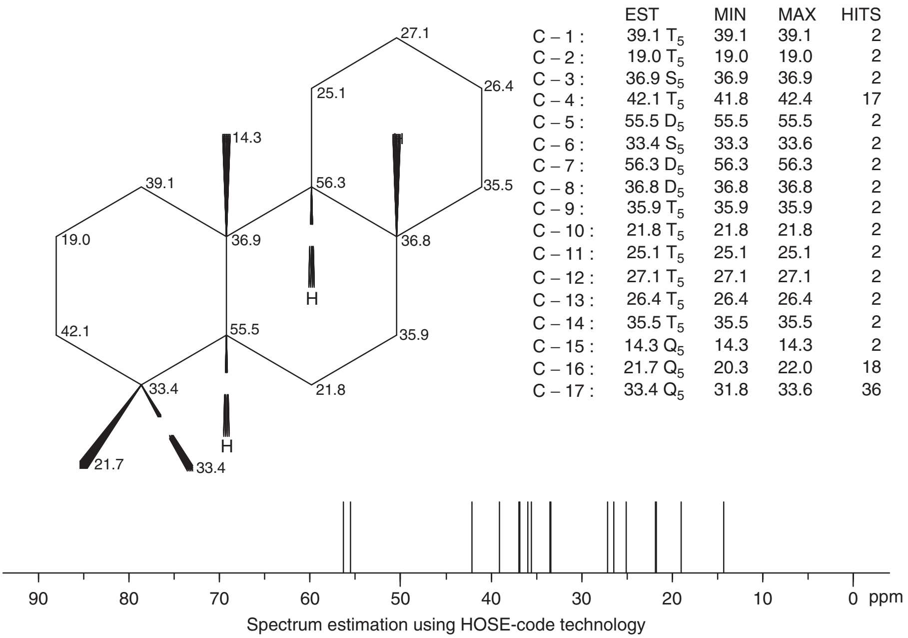

	EST	MIN	MAX	HITS
C – 1 :	39.1 T_5	39.1	39.1	2
C – 2 :	19.0 T_5	19.0	19.0	2
C – 3 :	36.9 S_5	36.9	36.9	2
C – 4 :	42.1 T_5	41.8	42.4	17
C – 5 :	55.5 D_5	55.5	55.5	2
C – 6 :	33.4 S_5	33.3	33.6	2
C – 7 :	56.3 D_5	56.3	56.3	2
C – 8 :	36.8 D_5	36.8	36.8	2
C – 9 :	35.9 T_5	35.9	35.9	2
C – 10 :	21.8 T_5	21.8	21.8	2
C – 11 :	25.1 T_5	25.1	25.1	2
C – 12 :	27.1 T_5	27.1	27.1	2
C – 13 :	26.4 T_5	26.4	26.4	2
C – 14 :	35.5 T_5	35.5	35.5	2
C – 15 :	14.3 Q_5	14.3	14.3	2
C – 16 :	21.7 Q_5	20.3	22.0	18
C – 17 :	33.4 Q_5	31.8	33.6	36

Figure 54.8 Spectrum prediction of podocarpane using HOSE-code technology with stereochemical information [18]. The chemical shift values of the methyl groups located at position 4 are predicted in good agreement with the literature data.

Implementation of steric interactions into the HOSE-code and into neural networks improves spectrum prediction dramatically, as can be seen from the podocarpane example in Figure 54.8. The diastereotopic methyl groups located at C_4 can be well predicted – 21.7 ppm for the axial and 33.4 ppm for the equatorial methyl group – which is in excellent agreement with the values found in the literature. The separation can be easily understood when inspecting the distribution of the entries contributing to the predicted values as given in Figure 54.9. A total number of 34

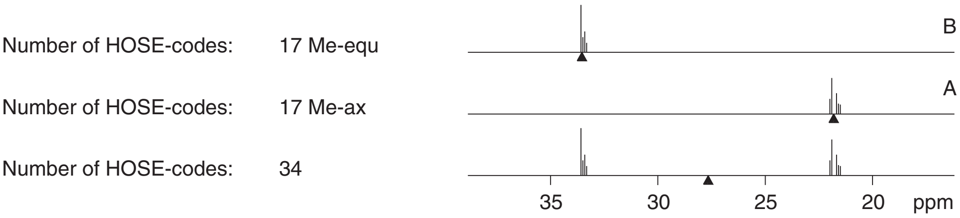

Figure 54.9 Distribution analysis of the entries contributing to the estimation of the methyl groups at position 4 of podocarpane. Bottom trace: stereochemical effects are ignored leading to a useless mean value around 28 ppm (small triangle); a total number of 34 reference data contribute to this mean value. Trace A and B: utilization of stereochemical interactions separates the 34 reference data into two distinct sets of chemical shift values leading to a correct prediction for the axial and equatorial methyl group.

entries selected from the reference database predict a useless mean value at 28 ppm for *both methyl groups* when using the structural descriptors from the original HOSE-code disregarding the stereochemical effects. The introduction of the number of 1,3-diaxial interactions divides these 34 reference data into two groups of shift values, estimating a chemical shift value of 21.7 ppm for the axial methyl group and 33.4 ppm for the equatorial one, which is shown in traces A and B of Figure 54.9.

54.8
Spectrum Interpretation and Isomer Generation

Isomer generation is the well-defined task to generate, exhaustively, and without redundancy, all possible chemical structures that are consistent with a given set of constraints [30–32]. This combinatorial problem itself is optimally suited for computer application and this definition seems to be ready for easy implementation into a piece of computer software. A more detailed look into the background of isomer generation shows immediately the problems associated with this task. The enormous number of possible candidate structures when starting from only the molecular formula can be seen in Table 54.1.

Table 54.1 Number of possible isomers (without stereochemistry) depending on the molecular formula and constraints derived from NMR experiments.

Molecular formula	Additional information	Number of possible isomers [33]
$C_{10}H_{22}$	—	75
$C_{15}H_{32}$	—	4 347
$C_{20}H_{42}$	—	366 319
$C_{10}H_{22}$	—	75
$C_{10}H_{20}$	—	852
$C_{10}H_{18}$	—	5 568
$C_{10}H_{16}$	—	24 938
$C_{10}H_{14}$	—	81 909
$C_{10}H_{12}$	—	201 578
$C_{10}H_{10}$	—	369 067
$C_{10}H_{10}$	—	369 067
$C_{10}H_{10}O$	—	7 288 733
$C_{10}H_{10}O_2$	—	79 402 190
$C_{10}H_{10}O_2$	—	79 402 190
$C_{10}H_{10}O_2$	Signal multiplicity (4S, 3D, 2T, 1Q)	10 370 392
$C_{10}H_{10}O_2$	Carbon hybridization ($3sp^3$, $5sp^2$, 2sp)	240 751
$C_{10}H_{10}O_2$	Signal multiplicity and hybridization as stated	38 353

Even a small molecular formula around C_{10} produces a large number of possible chemical structures. The introduction of one heteroatom and/or a degree of unsaturation increases the size of the problem dramatically. The molecular formulae chosen in Table 54.1 represent comparably small compounds, far away from typical applications in modern organic chemistry. The main problem in making structure generation programs a common routine tool is the necessity to implement all available pieces of information from the most important spectroscopic techniques at the earliest possible step in order to avoid the ''combinatorial explosion'' and therefore long computing times during the structure generation process itself and during the necessary postprocessing of the list of candidate structures. From Table 54.1 it can be seen that a powerful spectrum interpretation step is necessary even for a small molecular formula. The example $C_{10}H_{10}$ gives 369 067 isomers when using only the molecular formula without further constraints. The introduction of one oxygen increases the size of the problem by a factor of 20, a further oxygen leads to roughly 80 millions of possible isomers. The utilization of multiplicity information, which can be easily derived from DEPT spectra, reduces the size of this particular problem by nearly one order of magnitude. In addition, the use of hybridization information, as selected in Table 54.1 [34], reduces the number of possible isomers to 38 353 candidate structures. The determination of the multiplicity can be done by experimental techniques (usually DEPT) and is therefore a piece of information that is very secure. On the other hand, the determination of the hybridization is based on the interpretation of chemical shift value together with further supporting information (e.g., $^1J_{CH}$ couplings); therefore, some ambiguity might remain, especially in the region around 100 ppm where sp^3, sp^2, and sp-carbon atoms have resonance lines.

The process of structure generation is a well-defined task based on graph theory, whereas spectrum interpretation – the translation from the spectral information into structural constraints – is based on heuristics. Even the selection of the hybridization state of a carbon atom cannot be performed with absolute security from its chemical shift value and some further information. A much more complex situation is encountered when deriving substructural fragments from spectral data – the interpretation of the data leads to a large amount of alternative possibilities for substructural units. This feature must be taken into account during the isomer generation process, making the programs more complex and their speed slower.

There are two possible extreme situations that should be analyzed in further detail: the first approach uses a very detailed interpretation process based on a library of larger fragments as done, for example, by SPECSOLV [35], which makes structure generation working fast with the disadvantage that only a part of the possible candidate structure compatible with the given constraints will be obtained – a situation that is less useful for natural product chemistry dealing with new classes of compounds. The other extreme approach is to take into account only absolutely safe pieces of information, for example, signal multiplicities which can be determined experimentally. This situation uses only a very limited set of constraints for the structure generation process, leading to an incredible number of candidates for further processing. In any case, ambiguity (e.g., with valencies and hybridizations) must be handled by the isomer generator, which makes this tool much more complex. Usually, there is a tight connection between the interpretation and the isomer generation part of such systems.

54.8.1
Utilization of 2D-NMR Data

A new horizon was introduced with the popularity of two-dimensional NMR methods giving information about coupled-spin systems, and, therefore, distance information (in terms of intervening bonds between coupled nuclei). The most useful experiments for organic structure elucidation are the methods for H–H-, C–H-, and C–C-correlation, the detailed experimental conditions (e.g., gradient-enhanced, normal-reverse detection) do not change the basic principle of these methods for computer application. The general information is always that correlation signals are translated into distance information between two atoms, which will be used either by the interpretation process directly leading to substructural units or in case of ambiguity (distance over 2 to n bonds) as a constraint during the structure generation process in order to exclude certain combinations of the substructural fragments. The COSY-type spectra give information about H–H correlations over two (geminal), three (vicinal), and four (allylic, W-coupling) bonds, but in many systems long-range couplings over more than four bonds are known, leading again to some ambiguity. The case of a $^2J_{HH}$ coupling can be easily excluded by a heteronuclear correlation experiment. C–H-correlation experiments over one bond (HMQC, HSQC) are able to detect exclusively this type of connections because $^1J_{CH}$-couplings are much larger than any $^nJ_{CH}$-coupling. Long-range correlation techniques have to deal with two problems. The first one is the detection of artifacts from $^1J_{CH}$-correlations, which can be easily excluded from HMQC-type spectra. The second problem is a much more severe one based on the fact that long-range J_{CH} couplings are of similar size, especially $^2J_{CH}$ and $^3J_{CH}$ cannot be distinguished in many cases, prohibiting the differentiation between these two distances and leading to an increased computing time during the structure generation process and in many cases to a larger set of candidate structures produced. Frequently, signals corresponding to correlations over four to six bonds have also been observed, adding a further order of magnitude to the complexity of structure generation, whereas ignoring this possibility leads to wrong structure proposals. In addition, severe signal overlap may also increase the difficulties during the spectrum interpretation process [36]. C–C correlation techniques are well suited for computer-assisted structure elucidation but they have the disadvantage of low sensitivity. Another well-known concept to restrict the number of generated candidate structures is to use a list of forbidden substructures within the candidates. This option should also be used with extreme care, because exotic structures – such as highly strained or unexpected heterocyclic systems – will always be excluded [37].

54.8.2
Examples of Isomer Generator Programs

From the scope of the problem of structure generation it can be seen that there is a demand for spectrum interpretation programs that work in a very carefully designed way, allowing the user access to all constraints and therefore selecting the correct set of constraints from the given experimental data. The basic idea of spectrum interpretation of NMR data is to correlate a certain chemical shift value with a set of functional groups used as building blocks for subsequent structure generation. In order to improve this basic idea of using a single line, a complete subspectrum can be correlated with a set of larger substructural fragments, leading to higher selectivity during the interpretation process and therefore faster post-processing. The approaches known are working either with rule-based correlation tables (e.g., CHEMICS [38], DENDRAL [39], DARC [40]), or HOSE-code technology (SPECSOLV [35]); ACFs (atom-centered fragments) are used in SESAMI [41, 42] and EPIOS [43], three-atom fragments are selected in CSEARCH [44, 45]. The basic principle behind these technologies remains always the efficient correlation between spectral and structural property; in any case, these methods become slower when using smaller fragments or they generate only partial solutions when starting from a too specific set of fragments. The latter effect depends also extremely on the database used for the generation of the subspectra–substructure correlation tables. In any case, a high structural diversity within the reference database is obligatory.

54.9
Ranking of Candidate Structures

The usual case when applying an interpretation/isomer generation program to a real-world structure elucidation problem is not to obtain a single structural proposal to a specific set of constraints. Frequently, a list of possible candidate structures will be generated consisting either of only a few proposals or maybe a few thousands of proposals depending on the number of constraints given. Therefore, a ranking process based on spectrum prediction [45] is necessary to select proposals of higher probability. For ^{1}H- and ^{13}C-NMR spectra, well-established methods are available, which allow to select a set of most probable candidate structures. It is strongly recommended not only to use a single best solution but also useful alternatives should be included for further investigation. Isomer generator programs produce also very uncommon structures, which are not well represented by databases used for spectrum prediction purposes, leading to a biased evaluation of the hit list and to the effect that more common structures might be ranked better than uncommon ones. Spectrum prediction based on a database having a high degree of structural diversity is a fast and reliable method that can be applied to a hit list of a few thousands of chemical structures within a reasonable time. In the case that more structures have been generated, the set of constraints should be refined and/or additional experimental data should be collected.

54.10
NMR Data Collections on the Internet

The incredible development of Web-applications during the past decade has led to an enormous amount of spectroscopic information available on the Internet. A few examples are mentioned here – knowing that every list of such applications might be outdated soon. One of the first examples was the SDBS system [46] holding approximately 108 000 spectra coming from approximately 33 000 compounds, with the advantage of summarizing data for different methods (NMR, MS, IR, Raman, ESR) but having the disadvantage that spectrum prediction is not possible. Another approach based on the ''Open Source – Open Data'' idea was ''NMRShiftDB'' [47], where the community was invited to contribute to the system or, in other words, ''to build their own system.'' At the moment, approximately 25 000 CNMR spectra are available, the greatest part coming from the DKFZ collection and from the in-house database of the University of Mainz; the contribution of the community consists only of a few thousands of spectra. A similar approach has been started on CHEMSPIDER [48], leading to a few hundreds of spectra. The advantage of the aforementioned systems is clearly their availability free-of-charge. Commercial systems such as KnowItAll U [49] and NMRPredict [50, 51] hold up to approximately half a million of NMR data, which leads to an improved structural diversity.

54.11
Conclusions

For the synthetic organic chemist, spectrum simulation in order to verify a structural proposal is the most decisive task; in natural product chemistry, the starting point is usually a spectral similarity search using the experimental spectrum of the unknown. Both methods are extremely fast and can be done automatically immediately after the measurement of the one-dimensional routine spectra. When these basic methods give no solution, usually further spectroscopic experiments are performed giving more detailed information about the unknown sample. Spectrum interpretation and the subsequent isomer generation are mainly successful when a large amount of additional information is available. The most important pieces of information are the presence/absence of certain functional groups and the efficient use of distance constraints as derived from two-dimensional correlation spectroscopy. This information usually allows one to deduce the constitution of an organic compound; in order to determine the configuration and conformation, a more specialized set of tools is available. Many of these techniques – either experimental or computational methods – have been developed to deal with specific classes of compounds, especially with biopolymers [52]. The typical application field of the computer techniques described in this chapter is structure elucidation of organic compounds up to C_{50}. Many steps during the structure elucidation process can be done – or at least simplified and accelerated – by appropriate computational technologies, but the results must be critically evaluated by the expert. A large variety of algorithms and more or less integrated systems have been described in the literature and the field of computer-assisted structure elucidation is dynamically evolving. Also, numerous tools are commercially available and can support the chemist during the structure elucidation process – a critical evaluation of these tools with specific examples from the own field of application is strongly advised.

References

1. (a) Kessler, H., Gehrke, M., and Griesinger, C. (1988) *Angew. Chem., Int. Ed. Engl.*, **27**, 490–536. (b) Parella, T. (1998) *Magn. Reson. Chem.*, **36**, 467–495.
2. Gray, N.A.B. (1986) *Computer-Assisted Structure Elucidation*, John Wiley & Sons, Inc., New York.
3. Munk, M.E. (1998) *J. Chem. Inf. Comput. Sci.*, **38**, 997–1009, and references cited therein.
4. Jaspars, M. (1999) *Nat. Prod. Rep.*, **16**, 241–248, and references cited therein.
5. SpectroscopyNOW.com *http://www.spectroscopyNOW.com/nmr* (accessed 19 August 2013).
6. Gasteiger, J., Hanebeck, W., and Schulz, K.P. (1992) *J. Chem. Inf. Comput. Sci.*, **32**, 264–271.
7. Bremser, W., Wagner, H., and Franke, B. (1981) *Org. Magn. Reson.*, **15**, 178–187.
8. NMRPREDICT *http://nmrpredict.orc.univie.ac.at/identify* (accessed 19 August 2013)
9. NMRPREDICT *http://nmrpredict.orc.univie.ac.at/case/propose.php* (accessed 19 August 2013)
10. Bio-Rad *http://www.knowitall.com* (accessed 19 August 2013).
11. Chemical Concepts GmbH *http://specinfo.wiley-vch.de* (accessed 19 August 2013).
12. ACD/Labs *http://www.acdlabs.com* (accessed 19 August 2013).
13. Ewing, D.F. (1979) *Org. Magn. Reson.*, **12**, 499–524.
14. Hönig, H. (1996) *Magn. Reson. Chem.*, **34**, 395–406.
15. Thomas, S., Ströhl, D., and Kleinpeter, E. (1994) *J. Chem. Inf. Comput. Sci.*, **34**, 725–729, *http://www.science-and-fun.de/tools/* (accessed 19 August 2013).
16. Chen, L. and Robien, W. (1993) *Anal. Chem.*, **65**, 2282–2287.
17. Bremser, W. (1978) *Anal. Chim. Acta*, **103**, 355–363.
18. Robien, W., Purtuc, V., Schütz, V., and Felsinger, S. (1998) Lecture at 13th CIC-Workshop, Bad Dürkheim, Germany, November 15–17, 1998.
19. Modgraph Stereochemistry *http://www.modgraph.co.uk/product_nmr_stereo.htm* (accessed 19 August 2013).
20. Satoh, H., Koshino, H., Uzawa, J., and Nakata, T. (2003) *Tetrahedron*, **59**, 4539–4547.
21. ACD/Labs *http://acdlabs.com/appnotes/technotes/nmr.html* (accessed 19 August 2013).
22. Modgraph Neural Network Prediction, *http://www.modgraph.co.uk/product_nmr_network.htm* (accessed 19 August 2013).
23. Klamt, A., Hoever, P., Bärmann, F., and Wesener, J. (1993) in *Software-Development in Chemistry*, Vol. 7 (ed. D. Ziessow), Gesellschaft Deutscher Chemiker, Frankfurt am Main, pp. 39–44, ISBN: 3-924763-42-9.
24. Meiler, J., Meusinger, R., and Will, M. (1999) *Monatsh. Chem.*, **130**, 1089–1095.
25. Badertscher, M., Bischofberger, K., and Pretsch, E. (1980) *Trends Anal. Chem.*, **16**, 234–241.
26. Robien W. 2007 Quality Check of Nmrshiftdb-Data Using CSEARCH-Algorithms, *http://nmrpredict.orc.*

univie.ac.at/csearchlite/enjoy_its_free.html (accessed 19 August 2013).

27. Blinov, K.A., Smurnyy, Y.D., Elyashberg, M.E., Churanova, T.S., Kvasha, M., Steinbeck, C., Lefebvre, B.A., and Williams, A.J. (2008) *J. Chem. Inf. Model.*, **48**, 550–555.
28. Robien, W. (2008) Basic Misinterpretations, Typos and Other Sad Events in NMR-Spectroscopy, *http://nmrpredict.orc.univie.ac.at/csearchlite/NMR_misinterpretation.html* (accessed 19 August 2013).
29. All Figures have been generated using the CSEARCH-NMR-database system Kalchhauser, H. and Robien, W. (1985) *J. Chem. Inf. Comput. Sci.*, **25**, 103–108.
30. Shelley, C.A., Hays, T.R., Munk, M.E., and Roman, R.V. (1978) *Anal. Chim. Acta*, **103**, 121–132.
31. Masinter, L.M., Sridharan, N.S., Lederberg, J., and Smith, D.H. (1974) *J. Am. Chem. Soc.*, **96**, 7702–7714.
32. Elyashberg, M.E., Williams, A.J., and Martin, G.E. (2008) *Prog. Nucl. Magn. Reson. Spectrosc.*, **53**, 1–104.
33. All calculations have been performed using MOLGEN-3.1Benecke, C., Grund, R., Hohberger, R., Kerber, A., Laue, R., and Wieland, T. (1995) *Anal. Chim. Acta*, **314**, 141–147.
34. Rivera, A.P., Arancibia, L., and Castillo, M. (1989) *J. Nat. Prod.*, **52**, 433–435.
35. Will, M., Fachinger, W., and Richert, J.R. (1996) *J. Chem. Inf. Comput. Sci.*, **36**, 221–227.
36. Mukhopadhyay, T., Nadkarni, S.R., Bhat, R.G., Gupte, S.V., Ganguli, B.N., Petry, S., and Kogler, H. (1999) *J. Nat. Prod.*, **62**, 889–890.
37. Varmuza, K., Jordis, U., and Wolf, G. (1996) ECHET96 – Electronic Conference on Heterocyclic Chemistry, June 24–July 22, 1996.
38. Funatsu, K. and Sasaki, S.I. (1996) *J. Chem. Inf. Comput. Sci.*, **36**, 190–204.
39. Mitchell, T.M. and Schwenzer, G.M. (1978) *Org. Magn. Reson.*, **11**, 378–384.
40. Dubois, J.E., Carabedian, M., and Ancian, B. (1980) *C.R. Acad. Sci. (Paris)*, **290**, 369–372, 383–386.
41. Razinger, M., Balasubramanian, K., Perdih, M., and Munk, M.E. (1993) *J. Chem. Inf. Comput. Sci.*, **33**, 812–825.
42. Munk, M.E., Madison, M.S., Schulz, K.P., and Korytko A. (1998) Lecture at 13th CIC-Workshop, Bad Dürkheim, Germany, November 15–17, 1998.
43. Carabedian, M., Dagane, I., and Dubois, J.E. (1988) *Anal. Chem.*, **60**, 2186–2192.
44. Robien, W. (1986) *Mikrochim. Acta (Wien)*, **II**, 271–279.
45. Seger, C., Jandl, B., Brader, G., Robien, W., Hofer, O., and Greger, H. (1997) *Fresenius J. Anal. Chem.*, **359**, 42–45.
46. AIST *http://riodb01.ibase.aist.go.jp/sdbs/cgi-bin/cre_index.cgi?lang=eng* (accessed 19 August 2013).
47. NMR ShiftDB *http://nmrshiftdb.org* (accessed 19 August 2013).
48. Chem Spider *http://www.chemspider.com* (accessed 19 August 2013).
49. Bio Rad *http://www.knowitallu.com* (accessed 19 August 2013).
50. ModGraph C13 NMR and X-Nuclei Reference Database, *http://www.modgraph.co.uk/product_nmr_database.htm* (accessed 19 August 2013).
51. Mestrelab Research Chemistry Software Solutions *http://mestrec.com/index.php?idp=3* (accessed 19 August 2013).
52. Zhu, F.Q., Donne, D.G., Gozansky, E.K., Luxon, B.A., and Gorenstein, D.G. (1996) *Magn. Reson. Chem.*, **34**, S125–S135.

55
Mass Spectrometry

Wolfgang Werther

55.1
Introduction

Computational data treatment plays an essential role in the world of mass spectrometry (MS). Mass spectrometers have been connected to computers very early, enabling an efficient data acquisition and instrument control. The complex data conversion of measured ion currents behind the user-friendly representations of mass spectra is not fully known to the current users of MS.

However, the main focus of this contribution is the software and database assistance in the interpretation of mass spectra, especially the search for chemical structure information in mass spectral data. Because of the high amounts of measured data, interpretation is often the bottleneck in present day analytical processes.

Complexity of tasks and the requirements for algorithms and computing power have increased since the time of measuring only singly charged nominal mass spectra created by electron impact (EI) ionization in a mass range up to 1000 Da. Electrospray ionization (ESI) produces ions with multiple charges, especially for biomolecules such as proteins and nucleic acids. The mass range has been extremely extended to about a million Dalton. High-resolution MS and tandem MS require for all applications (e.g., databases, library searches, or isotope pattern calculations) new or at least adapted conceptions.

The aim of this chapter is to describe the most important fields of data treatment in MS, where computer-assisted approaches are applied. Principles, strategies, and outcomes of these approaches will be briefly explained.

Some interesting topics cannot be covered, for example, the computer treatment of multiple charged peaks from electrospray mass spectra. Furthermore, the wide field of computer applications for mass spectral data in bio-science is not fully addressed, but the description of the methods used in protein MS should be a first entry.

Handbook of Spectroscopy, Second Edition. Edited by Günter Gauglitz and David S. Moore.

55.2
Databases

Three different types of databases used for evaluation of mass spectral data are discussed:

- *Mass spectral databases*: containing mass spectra of compounds.
- *Fragmentation databases*: containing mass spectral fragmentation reactions described in literature.
- *Structure databases*: containing chemical structure descriptions of compounds (e.g., protein sequence databases) – the mass spectral information is derived mathematically from the structures.

The beginning of mass spectra collection of organic compounds in computerized databases was in the early 1960s [1]. In this period EI ionization of gas-phase molecules was dominating in MS and powerful ionization methods for liquid and solid phases were far from being realized. Therefore, the first large mass spectral databases contained only EI mass spectra. Up to now, collections of EI mass spectra dominate the field of large and commercially available databases; the reasons are discussed later.

The typical data structure of a mass spectral database entry is as follows: of course, a database entry must contain the mass spectrum, which is a list of pairs of numbers: mass/charge (m/z) and peak intensity. In EI databases, m/z information is mostly stored as an integer value. For compounds with a molecular weight above 400 Da real numbers for the m/z values would be desirable, for storage of accurate masses this is a necessity. Molecular weights above 400 Da are important in liquid- or solid-phase MS, especially of biological and pharmaceutical molecules.

For chemical identification, a database entry must contain the name of the molecule, for example, the systematic name supplied by the International Union of Pure and Applied Chemistry (IUPAC). Some databases offer access to an additional list of further common names (especially ‘‘trivial names’’ and ‘‘trade names’’). Chemical Abstracts Service (CAS) numbers as unique identifiers are available in many, but not all mass spectral databases. Molecular formula and molecular weight complement this block of information.

As chemists are familiar with the images of chemical structure drawings, this kind of structure representation is very informative and more intuitive than chemical names alone. The number of mass spectra entries containing structural information has strongly increased during the past years. Chemical structures are stored either only as drawings or as the so-called connection tables. The latter are graph theoretical descriptions of all atoms and bonds and enable computer treatment of the structural information. Thus, substructure retrieval of database entries, structure similarity searches, and the evaluation of spectra structure correlations become possible.

Some databases contain chromatographic retention data (mostly GC retention indices), which are important as a second dimension for compound identification. Information about sources of mass spectra, instrument type, and measurement conditions may be valuable particularly for soft-ionization mass spectra as later discussed.

55.2.1
Databases of Electron Impact (EI) Mass Spectra

An important issue for the storage of mass spectra in databases is the need, that the measurement of the spectra must be reproducible enough to enable comparison for identification purposes. EI mass spectra fulfill this requirement to a high degree. Almost all EI ionization sources use an electron energy of 70 eV. At this energy level, the fragmentation patterns of molecular ions are very stable against small energy fluctuations and highly independent of the instrument.

Even different types of mass spectral analyzers produce very similar EI mass spectra from the same compound. Mass spectra from magnetic sector-field instruments – the dominating analyzer type in the beginning – are comparable to present day quadrupole mass spectra – only the peak intensities in the upper mass range can be higher in sector-field instruments than in quadrupole instruments.

The very first ion trap mass analyzers showed different mass spectra for some chemical compound types (e.g., nitrogen compounds) because of ''self-chemical-ionization.'' These problems have been solved by controlling the sample load of the ion trap. Time-of-flight (TOF) analyzer mass spectra do not show significant differences from mass spectra measured by a quadrupole or a sector-field instrument.

Only labile structures can sometimes give different mass spectra with different instruments or measuring conditions. Labile compounds can be decomposed at active spots before ionization, thus producing partly or totally the mass spectrum of the decomposition product.

Existing databases can be classified in two groups:

- *General collections* of EI mass spectra containing compounds with a widespread chemical diversity. These databases are mostly large or middle sized.
- *Specialized collections* containing only a group of chemical compounds such as drugs, pesticides, essential oils, and so on. These libraries are mostly smaller than the general ones.

Most databases are commercially available as in-house versions and often offered by mass spectrometer suppliers. Some (mostly smaller) libraries are freely available. There exist also Internet databases free of charge or with costs.

55.2.1.1 Wiley Registry and NIST/EPA/NIH Mass Spectral Databases

Two large general collections dominate the field: (i) the ''Wiley Registry of Mass Spectral Data'' [2] – its ninth edition (2009) contains mass spectra of 590 000 chemical compounds. (ii) The NIST/EPA/NIH Mass Spectral Library [3] from 2011 (''NIST 11'') contains mass spectra of 213 000 chemical structures. In addition, there exist 100 000 duplicate spectra within the Wiley registry and 31 000 duplicates within the NIST library.

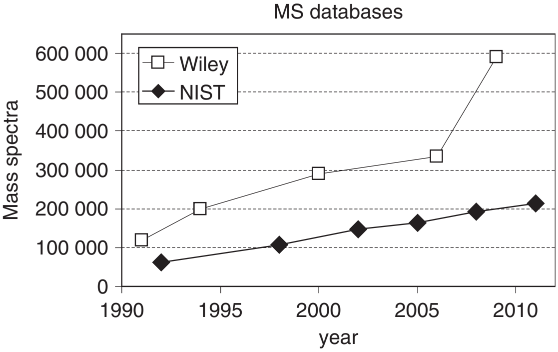

Figure 55.1 Growth of the NIST and Wiley mass spectral databases in the past two decades (total number of unique compounds).

The Wiley database had its origin in the Mass Spectrometry Registry by Stenhagen and Abrahamsson and its enormous growth is connected with the work of McLafferty and his group.

The roots of the NIST/EPA/NIH Mass Spectral Library – now under the auspices of the US National Institute of Standards and Technology (NIST) – go back to the Atomic Weapons Research Establishment (AWRE) in Aldermaston, UK. This database was extended by incorporating collections of the US agencies NBS (National Bureau of Standards), EPA (Environmental Protection Agency), and NIH (National Institutes of Health).

Figure 55.1 shows the growth of the NIST and Wiley libraries during the past years. In spite of all efforts in collecting mass spectra, the enormous numerical gap to total number of documented chemical compounds remains high: CAS registry contains 67 mio. compounds in 2012 [4]. About 10–20% of these compounds are volatile enough for measurement by EI-MS.

Moreover, the theoretically possible number of chemical structures generated by exhaustive structure generation is unimaginable higher. To get an impression about this fact, Table 55.1 shows a comparison of these numbers for three selected molecular formulae.

Nevertheless, both databases supply a considerable benefit, as many "unknowns" of daily routine work are contained. The costs for these databases (~2 cent/spectrum) are low in comparison to infrared or NMR spectra or to some "specialized" mass spectral collections.

55.2.1.2 **Quality of Mass Spectra in Databases**

In the first decades of building mass spectral data collections, the number of entries was the most important criterion for a good database. Scarcely checked, mass spectra were seldom discarded because of measurement deficiencies such as incorrect mass calibration, limited mass range (starting mass too high), electron multiplier saturation (several peaks show 100% base intensity), poor dynamic range, peaks from contaminations, and lacking isotope peaks. Even mass spectra

Table 55.1 Comparison of the number of isomers for three molecular formulae (not considering cis/trans and optical stereoisomers).

Brutto formula	Molecular weight	MS library	Commercially available	CAS registry	Isomer generation
$C_4H_8O_1$	72	17	20	25	26
$C_9H_{18}O_1$	142	78	96	1 682	4 745
$C_{14}H_{18}O_1$	212	25	37	779	839 823

The numbers are given for a mass spectral database (NIST 05), commercially available compounds, registered compounds in the Chemical Abstracts Service (CAS), and exhaustive isomer generation by software MOLGEN [5].

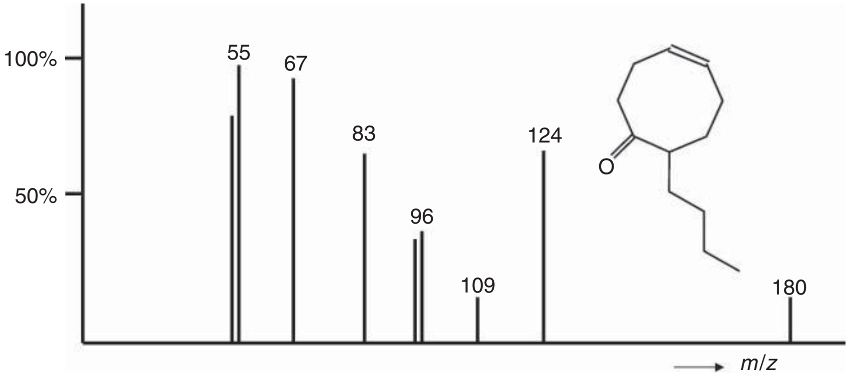

Figure 55.2 Example of a low-quality database mass spectrum: only a few peaks, usually extracted from literature.

reduced to only 8–10 peaks were extracted from scientific literature and have been included in databases (Figure 55.2).

In the meantime, the need for high-quality spectra has been recognized and some attempts were made to evaluate the quality of the existing databases and to eliminate the incorrect and low-quality mass spectra. Quality indices for mass spectra were created [6] and computer algorithms assisted to check automatically for typical errors, quality deficiencies, and inconsistence between structure and mass spectrum.

All these efforts have improved the quality of mass spectral databases. In particular, NIST library editions since 1998 show a high-quality standard, as all mass spectra have been visually evaluated and selected by mass spectroscopic experts [7]. The strategy of the Wiley registry seems to be different: collecting a high number of mass spectra to remain the world's largest database seems to be to still the major driving force. A typical example may illustrate the situation: 29% of the mass spectra of compounds with a molecular weight of 400 Da in the Wiley registry (seventh edition) contain less than 10 peaks – often a hint for lower quality mass spectra. For the NIST'05 database, this value is only 1.4%.

Both strategies have their merits. Sometimes a reduced mass spectrum is better than no mass spectrum and supplies ideas for the identity of an unknown. However, for reliable identifications, good quality library spectra are mandatory.

55.2.1.3 **Other General EI Databases**

The organic compound mass spectra collection of Yarkov [8] (37 000 mass spectra) is a middle-sized database originating partly from combinatorial synthesis.

Two databases can be accessed free of charge via the Internet: the NIST Chemical Webbook [9] presents a selected part of the NIST mass spectra (more than 15 000) and other physical and spectroscopic data. The integrated spectral database system (SDBS) for organic compounds [10] is a Japanese initiative containing 24 700 mass spectra together with NMR and IR spectra.

A huge multispectral organic spectroscopy Internet database (NMR, IR, MS) with user fees is SpecInfo [11]. It is accessible by the web client SpecSurf [12].

55.2.1.4 **Specialized Mass Spectral Databases**

Some analytical areas have a particular need for reliable identification of analytes based on GC–MS data. Typical areas are medicine and toxicology (drugs), regulated compounds (e.g., pesticides), aroma analysis, and metabolomics.

Special requirements are a maximum coverage of the relevant area including possible metabolites, high quality of the mass spectra, and often the availability of GC retention indices. Mass spectra and retention data of silylated, acylated, and otherwise derivatized compounds are of specific interest, as polar analytes are often derivatized to increase their volatility for the gas chromatographic analysis.

Table 55.2 shows a selection of specialized databases. Prices for these databases are higher, usually about $1 per mass spectrum must be assumed.

In a few cases, user initiatives collect mass spectra to make them available to the public or to the contributors, for instance, in forensics [25], in metabolomics [26], and by museum analysts [27].

55.2.1.5 **GC Retention Indices in Mass Spectral Databases**

Retention indices normalize gas chromatographic retention times to *n*-alkane GC peak series [28]. Most GC retention indices in mass spectral databases originate from unpolar stationary phases such as DB-1 (polydimethylsiloxane) and DB-5 (polydimethylsiloxane with 5% phenyl instead of methyl). However, retention index data from GC phases of middle or strong polarity such as OV-1701 (cyanopropyl modified polysiloxane) and WAX (polyethylene glycol) are important too and are contained in some databases, for example, for flavor chemicals [29].

Retention indices are influenced to a certain degree by other GC parameters such as flow rate, phase ratio, and the temperature program, which have all to be standardized for high-quality identifications. Therefore, retention indices extracted from literature can be used only as a rough ‘‘filter.’’

Table 55.2 A selection of specialized collections of EI mass spectra.

Compound classes	No. of compounds	Authors	References
Drugs, pollutants, pesticides, and metabolites	8 800	Maurer *et al.*	[13]
Designer drugs, medicinal drugs, warfare agents, explosives	13 420	Rösner	[14]
Steroid hormones, endocrine disrupters, drugs	4 182	Parr *et al.*	[15]
Volatile compounds in food	1 620	TNO	[16]
Flavors and fragrances of natural and synthetic compounds	3 000	Mondello	[17]
Essential oil components	2 205	Adams	[18]
Terpenoids in essential oils	1 982	König *et al.*	[19]
Pesticides	1 238	Kühnle	[20]
Pharmaceuticals and agrochemicals	4 563	Kühnle	[21]
Pesticides, PAHs, VOCs (“EPA”-compounds)	1 450	Ehrenstorfer	[22]
Geochemicals/petrochemicals and biomarkers	1 100	DeLeeuw	[23]
Gibberellins and related compounds	2 000	Gaskin	[24]

VOC, volatile organic compounds.

55.2.2
Databases for Mass Spectra from LC–MS

55.2.2.1 Soft Ionization versus Electron Impact

Since the late 1980s, powerful “atmospheric pressure” ionization methods exist to measure mass spectra from molecules in the effluent of liquid chromatographs: APCI (atmospheric pressure chemical ionization) and ESI have become established since in routine analysis.

APCI and ESI mass spectra are different from EI mass spectra. Therefore, the existing large EI-MS databases cannot be used for comparison and library searches.

APCI and ESI are both “soft-ionization” methods. As less energy is transferred to the ions than by EI ionization, less or no fragment ions are produced and the mass spectrum is dominated by “quasi-molecular” ions. For a higher information content of the mass spectra, additional fragmentation has to be induced, for example, by “collision-induced dissociation” (CID).

In a single-stage mass spectrometer, fragmentation can be obtained or enhanced by applying appropriate voltages to the orifice of the ion source (“source-CID”).

In true tandem mass spectrometers (“MS/MS”), a “precursor ion” – mostly the quasi-molecular ion – is selected and collides with gas atoms in a collision cell. The produced fragments (“product ions”) are mass analyzed in a second step. These

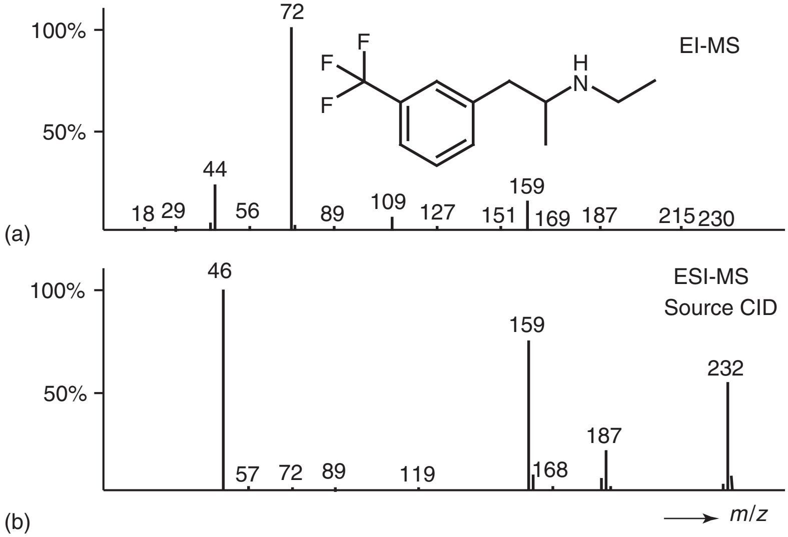

Figure 55.3 Comparison of (a) the EI mass spectrum (70 eV) and (b) the ESI "source-CID" mass spectrum (cone voltage 40 V) of fenfluramine (molecular weight 231).

processes occur either in a separate collision cell and in a second mass analyzer (MS/MS in space, e.g., by triple quadrupoles) or completely in the same mass analyzer (MS/MS in time, e.g., in quadrupolar ion traps).

EI molecular ions are radical cations and have an odd number of electrons. Quasi-molecular adduct ions common in soft ionization as $[M + H]^+$, $[M + NH_4]^+$, $[M + Na]^+$, $[M - H]^-$, and so on, have an even number of electrons. Fragmentation reactions of "even-electron" ions are completely different from those of "odd-electron" ions (Figure 55.3).

55.2.2.2 **Reproducibility of CID Mass Spectra**

Contrary to EI and unfortunately for data collection and comparison issues, CID mass spectra of the same compound are not similar in any case. Large differences in mass spectral appearance stem (i) from different instrument types and (ii) from sensitivity to measurement parameters.

A large diversity of mass spectrometers for ESI-MS and APCI-MS exists: single-stage instruments with source-CID, different collision cell types for low-energy CID (eV range), and high-energy CID (keV range). The energy regime in the collision cell is responsible for the product ions appearing.

Source-CID mass spectra are instrument dependent because ion source geometries play an important role [30].

Low-energy CID in triple quadrupoles and quadrupole/time-of-flight hybrid instruments (QqTOF): consecutive fragmentations are possible

Low-energy CID in quadrupolar ion traps: only unimolecular decays take place, rearrangements can be enhanced because of longer residence time.

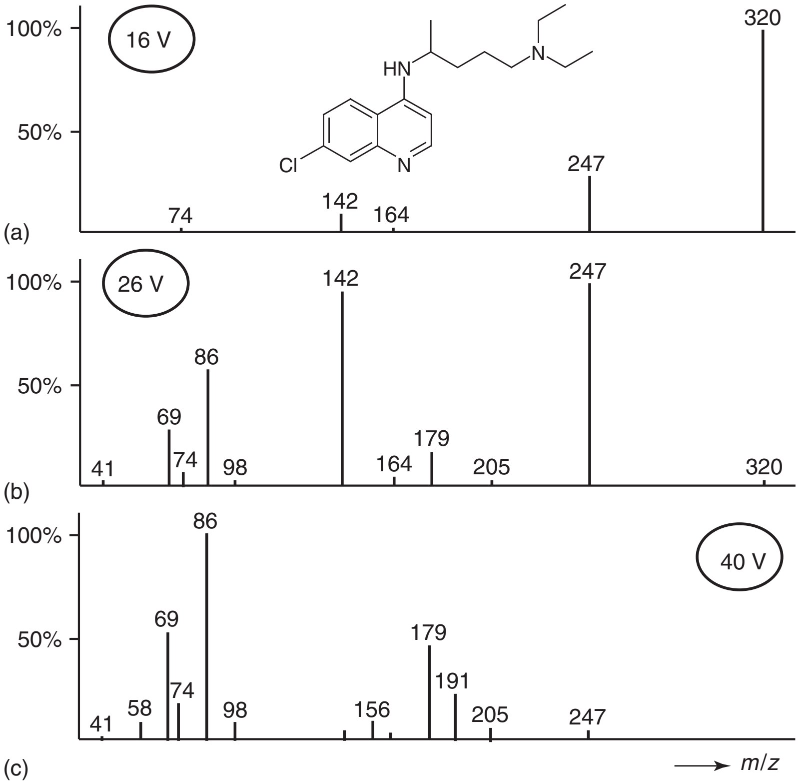

Figure 55.4 Comparison of ESI triplequad CID mass spectra of chloroquine: precursor ion m/z 320 ($[M+H]^+$), collision energies (a) 16 V, (b) 26 V, and (c) 40 V.

High-energy CID in sector-field and TOF–TOF instruments generates considerably more fragments than low-energy CID. As these instruments are not so widespread, we focus on low-energy CID spectra.

Source-CID mass spectra and true tandem MS/MS spectra are both very sensitive to slight changes in instrumental properties and parameters (applied voltages, collision gas pressure, etc.) and therefore of little reproducibility (Figure 55.4). Unlike in EI ionization with its standardized 70 eV electron energy regime, there exist no robust instrumental parameters. Particularly, instrumental parameters for an informative fragmentation with many peaks depend on the measured compound.

55.2.2.3 **Databases of CID Mass Spectra**

For reasons discussed, no large databases of source-CID or MS/MS spectra (comparable in size to Wiley or NIST EI databases) have been collected up to now. Only smaller collections exist for compounds of special interest such as drugs and pesticides (Table 55.3).

Table 55.3 Examples of source-CID and true MS/MS libraries.

Compound classes	No. of unique compounds	CID type	Author	References
Drugs/toxicants	1100	Source-CID	Marquet *et al.*	[31]
Miscellaneous	559	Source-CID	Little	[32]
β-Blocking drugs	400	Triplequad	Gergov *et al.*	[33]
Drugs/toxicants	800	Triplequad	Dresen *et al.*	[34]
Miscellaneous	1200	Ion trap	Baumann *et al.*	[35]
Human/veterinary drugs, natural compounds	1041 pos. 524 neg.	Ion trap (MS^n "trees")	HighChem	[36]
Drugs/toxicants	1200	QqTOF	Oberacher	[37]
Drugs/toxicants	2500	QqTOF	Broecker *et al.*	[38]
Drugs/toxicants	780	Ion trap	Liu *et al.*	[39]
Drugs/toxicants	1253	QqLIT	Dresen *et al.*	[40]
Drugs/toxicants	1000 pos. 250 neg.	QqLIT	Sauvage *et al.*	[41]

QqLIT, quadrupole linear ion trap.

Different strategies have been attempted to overcome the problem of instrument and parameter dependence of CID mass spectra:

1) Collecting 3–10 CID mass spectra varying the relevant instrumental parameter (cone voltage for source-CID, collision energy for tandem MS) [34]. The mass spectra can be stored separately or merged to one composite mass spectrum per compound. Alternatively, one "information-rich" mass spectrum per compound can also be obtained by voltage ramping during measurement [39].
2) Observing a result-oriented measurement protocol in CID analysis, for example, increasing the collision energy until the precursor ion intensity is reduced to 10%: ion trap MS^2 and MS^3 spectra of pharmaceuticals and pesticides have been acquired with this protocol to build a quality spectra database. CID mass spectra from ion traps of different suppliers looked very similar, even independent from ionization mode (ESI, matrix-assisted laser desorption ionization (MALDI)) [42];
3) Collecting as many mass spectra as possible from all available sources. This strategy tries to copy the success story of EI databases. NIST seems to make first attempts in this direction. Their MS/MS library [43] now contains collision-cell CID spectra (triplequad, QqTOF) of 9232 different precursor ions and ion trap CID spectra of 12 047 different precursor ions from overall 6999 compounds (metabolites, drugs, phospholipids, surfactants, sugars, peptides, etc.). Approximately 90% of the spectra have been analyzed in the positive ion mode.

As there is an urgent need for applicable MS/MS databases and powerful search options, there are many different ongoing efforts and it will be highly interesting to see how the situation will consolidate. It will be a laborious way to establish a general MS/MS database comparable to the standard in EI-MS. It must contain a multiple of entries: mass spectra from different instruments, varying voltages, positive and negative ionization.

Standardizations in acquisition techniques will be necessary and some types of mass spectrometers will become specialized ''identification machines'' in the future – the ion trap or the QqTOF seem to have good chances for this task. In ''closed'' areas such as pesticide regulations or toxicological analyses, instrument-specific high-quality databases will further play their role. In each case, it is advisable for users to build their own MS/MS libraries containing the spectra of their research area measured with their own instruments.

A special emphasis has to be spent on MS^n, as ion trap CID spectra can be measured not only from the quasi-molecular ion but also from the resulting product ions. The complete data structure is a tree of mass spectra [44]. All relations should be conserved in the database.

Two MS/MS databases can be accessed free of charge via the Internet: MassBank is a distributed public repository for sharing mass spectral data for life sciences [45]. The MS/MS spectra of 2337 metabolites and 679 synthetic drugs stem from different research groups using various types of mass spectrometers. The METLIN metabolite database is a repository of metabolite information [46] containing also high-resolution MS/MS data for 10 125 of its chemical structures, analyzed with a QqTOF mass spectrometer.

55.2.3
Fragmentation Databases

Mass spectral fragmentation is the result of gas-phase reactions of ions in high vacuum. These reactions have been investigated intensely since the beginning of organic MS. Generalized fragmentation rules are condensed in many textbooks and used nowadays in fragmentation prediction software. However, a limited set of common rules usually cannot explain all fragment ions appearing in a mass spectrum of a chemical structure.

On the other hand, many detailed fragmentation pathways for single compounds or compound groups are documented in the scientific literature. One part of these pathways is thoroughly verified by mass spectrometric means such as isotopic labeling, metastable ion experiments, and high-resolution techniques, supported by theoretical considerations and calculations. Other published pathways rely only on the comparison of mass spectra of differently substituted compounds.

Only one large database with fragmentation reactions from MS is currently available. Nineteen thousand individual fragmentation reactions have been extracted from literature [47] and serve as a knowledge base for the prediction of fragmentation pathways in the software ''Mass Frontier.''

All fragmentation reactions have been manually evaluated for accuracy, plausibility, and consistency of fragment masses with mass spectral peaks. Automatic evaluation algorithms have checked for charge and radical consistency and other electron-related issues.

55.2.4
Protein Databases

Most databases for the interpretation of protein mass spectral analysis contain protein sequences and no measured mass spectra. Mass information is calculated from the amino acid sequences. Protein databases are very large. The sequence information is often derived by translating the protein coding genes from DNA databases, because sequencing techniques for nucleic acids have a higher throughput.

Real proteins show some differences from the sequence information coded in nucleotide databases: after translation of the genetic code, proteins are often modified, for example, starting peptides are cut off, disulfide links are created, and posttranslational modifications such as glycosylation, phosphorylation, and sulfatization can take place. These modifications are annotated only for a part of the protein sequences in the databases.

Protein database entries are characterized by the biological species and the protein name and contain additional information, for example, about biological functions, secondary structures, and bibliographic references.

A number of huge protein sequence databases exist, often freely accessible via the Internet (Table 55.4). The number of entries was growing very fast during the past years.

As information about the same protein sequence can be found in different databases, an urgent need for cross-referencing was given. ‘‘UniParc’’ [55] is the most comprehensive, nonredundant protein sequence archive containing only

Table 55.4 A selection of sequence databases (database sizes from July 2012).

Database	Sequences	Description	References
PIR-PSD	—	The world’s first database of classified and functionally annotated protein sequences, 2004 incorporated in UniProtKB	[48]
UniProtKB/Swiss-Prot	536 789	Manually annotated protein sequences	[49]
UniProtKB/TrEMBL	23 165 610	Protein sequences automatically translated from nucleotide sequences	[49]
EMBL/DDBJ/ GenBank	247 335 689	Nucleotide sequences	[50]
NCBI RefSeq	16 393 342	Explicitly linked protein and nucleotide sequences	[51]
PRF/SEQDB (Osaka)	1 365 912	Peptide and protein sequences from literature and from nucleotide databases	[52]
MSDB	3 239 079	Collection of nonredundant protein sequences from different databases	[53]
NCBI Entrez protein	—	Collection of protein sequences from a variety of sources (SwissProt, PIR, PRF, PDB, GenBank, RefSeq)	[54]

the protein sequences and their cross-references to the source databases. The sequences are stored with a unique protein identifier (''UPI'' and 10 hexadecimal numbers, e.g., UPI000014B174 for horse myoglobin).

55.3
Library Search/Database Retrieval

In a library search, mass spectra of unknowns are compared with all mass spectra of a database. If a mass spectrum of the unknown is present in the database, it should be found and thus the unknown is identified. Library search is the most successful and broadly used method among all computer-based mass spectral interpretation and identification attempts.

Library search is looking for the most similar mass spectrum in a database. That seems to be a simple task, but a library search algorithm has to deal with some obstacles: measurement uncertainties, differences between instruments, low-quality spectra (measured or database spectra), background (air, column bleeding), overlapping chromatographic peaks, and skewing effects on peak intensities within chromatographic peaks.

Typically, the result of a library search is not a single reference compound. The most similar mass spectra are sorted by a similarity measure and form a ''hitlist'' of candidates.

55.3.1
Search Algorithms for EI Mass Spectra

A typical algorithm for library search in large mass spectral databases can be described in four steps:

1) *Transformation of mass spectra*: different types of intensity transformations are applied to change the influence of the peaks, for example, higher weight for significant mass values or transformation to binary (yes/no) values. Examples of more complex transformations are modulo-14 features (''ion series'') or neutral loss spectra.
2) *Data reduction*: the number of variables (original mass values or derived features) is reduced by some heuristics (influenced either only by statistics or also by mass spectrometric ideas) to save computer time in the presearch and the main search.
3) *Presearch (''filter'')*: applying a computationally efficient simple method, the number of candidate mass spectra from the database is strongly reduced to about 100–500 reference spectra;
4) *Main search*: a more or less sophisticated similarity measure between two spectra is calculated for all reference mass spectra surviving the presearch. The most similar reference mass spectra are sorted by this criterion to produce the hitlist.

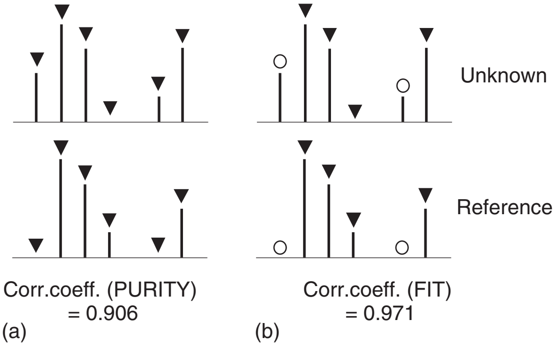

Figure 55.5 Two variants for calculating similarity measures: (a) PURITY (or "forward search") matches all peaks; (b) FIT (or "reverse search") considers only peaks present in the reference and is less affected by contaminations, background and coeluting compounds. Filled triangles designate peaks used in calculating the similarity measure, while unfilled cycles designate peaks that are not considered for calculation.

A widely used similarity measure for spectra comparison is the normalized scalar product (dot product) S_{UR} (Eq. (57.1)) of the two mass spectra (unknown and reference). More complex algorithms have been built by heuristics or by "trial and error."

$$S_{\mathrm{UR}} = \frac{\sum_m x_{\mathrm{U},m} x_{\mathrm{R},m}}{\sqrt{\sum_m x_{\mathrm{U},m}^2 \sum_m x_{\mathrm{R},m}^2}} \tag{55.1}$$

$x_{\mathrm{U},m} =$ Peak intensity at $m/z = m$ of the mass spectrum of the unknown
$x_{\mathrm{R},m} =$ Peak intensity at $m/z = m$ of the reference mass spectrum.

The similarity measures can be calculated in different variants (Figure 55.5) leading to hitlists differently sorted. For example, the "FIT" value ("reverse" or "mixture search") uses only peaks present in the reference spectrum and is less sensitive to contaminations of the unknown mass spectrum often present in real samples.

55.3.1.1 **Library Search Software**

Three widely used library search programs are briefly explained: INCOS (Integrated Control System) [56], PBM (Probability-Based Matching [57], and SISCOM (Search for Identical and Similar Compounds [58]. Some details about the algorithms are shown in Table 55.5.

The algorithm of the INCOS system is simple and robust. Weighting of high mass ions is an important feature emphasizing molecular ions and prominent neutral losses.

The idea behind PBM is that mass values and intensities of mass spectral peaks are not equally distributed. A combination of "uniqueness" (reflecting the different

Table 55.5 INCOS, PBM, and SISCOM algorithms (simplified).

	INCOS	PBM	SISCOM
1. Spectra transformation	Intensity weighting with $\sqrt{m/z}$	A (“abundances”): values corresponding to logarithmic intensity ranges U (“uniqueness”): $^2\log p\ (m/z)$, p = probability of a peak at m/z	1. Original intensities (no transformation) 2. Binary m/z values (yes/no)
2. Data reduction	Iterative selection of most intense peaks in mass windows with decreasing window sizes: approximately 40% of the peaks are selected	Selection of 15–26 peaks with highest significance $(U + A)$ = “condensed” spectrum (base peak, molecular ion, and some neutral losses included!)	Selection of characteristics (char.) = peaks that “exceed” their neighbors in CH_2-homologous modulo-14-series: $I_m > (I_{m-14} + I_{m+14})/2$
3. Presearch (filter)	Match the 16 highest peaks in UNK with the 8 highest in every REF: minimum number of peaks present in both spectra (no intensity match!) About 150 reference spectra survive	Match all significant peaks in the condensed unknown spectrum with the “most significant peak” in every REF (no intensity match!) About 5% of reference spectra survive	1. Only database section of the most dominant modulo-14-ion series in UNK. 2. Preselection by N_C, N_R, and N_U (see below) About 150 reference spectra survive
4. Similarity measure	Normalized *scalar product* (Eq. (57.1))	“Confidence value” K: $K = \Sigma\ (U_i + A_i + W_i)$ for all matching reference peaks i (present within an abundance window in UNK), with “window factor” W (measure matching peak abundances)	“Similarity index” SI combining: N_C: number of matching char. N_R: number of char. only in REF N_U: number of char. only in UNK I_R: intensity of char. only in REF I_U: intensity of char. only in UNK P_C: pattern correlation of char.

UNK, unknown mass spectrum; REF, reference mass spectrum.

frequency of each mass value in the whole library) and ‘‘abundance’’ (categorization to logarithmic peak intensity classes) is the driving force for the selectivity of a fast spectra comparison using only few selected peaks.

INCOS and PBM are implemented in various modifications in the instrument software of mass spectrometers or in standalone library search systems.

The SISCOM algorithm is part of the standalone software MassLib [59]. An interesting feature is the selection of peaks (‘‘characteristics’’) that are locally prominent within their CH_2 homolog peak series. This feature incorporates a kind of ‘‘mass spectral knowledge’’ and is one reason for good ‘‘structural similarity search’’ properties of SISCOM as later explained.

55.3.1.2 **Identity of the First Candidate**

Is the first candidate of the hitlist really the unknown? The best method is visual inspection of the candidates in comparison with the mass spectrum of the ‘‘unknown’’: if significant peaks in the library spectrum are lacking in the unknown mass spectrum, then the library spectrum corresponds certainly not to the ‘‘unknown.’’

To get an unambiguous evidence of the identity of a candidate with the unknown, however, is almost impossible. The absolute value of the similarity measure alone is not a good criterion; therefore, attempts are made to calculate real probabilities for the ‘‘identity’’ of a candidate in a hitlist, for example, by the NIST MS-Search program [60].

Retention indices – if available – can help in the identification in ambiguous situations, especially in cases of very similar mass spectra (e.g., cis/trans isomers or 1-alkenes/1-alkanols). Some library search systems use this ‘‘orthogonal’’ information to filter the hitlist [61].

55.3.1.3 **Structural Similarity Search**

INCOS and PBM search algorithms are optimized to retrieve even database spectra of low quality. The most important requirement for such ‘‘**identity search**’’ programs is that the target compound is in the hitlist and in the best case in rank one. The search criteria look only for significant ‘‘spectral similarity.’’

What is to be done if the unknown is not contained in the library and therefore cannot appear in the hitlist? In this case, a hitlist that contains a multitude of chemical structures similar to the unknown would be helpful. This would supply a first information and a starting point for the interpretation of the unknown’s mass spectrum by comparing it with the mass spectra of obviously related structures. Such a library search is called a ‘‘(**structural**) **similarity search**’’. The algorithm must look for structural similarity features in the mass spectral data.

The SISCOM algorithm is optimized for this purpose: contrary to INCOS and PBM, variable selection in the data reduction step is not only related to intensity and statistics but also respects implicitly mass spectrometric rules. The modulo-14 categories of the presearch and the selection mode for the ‘‘characteristics’’ have a clear correlation to structural properties.

The intensity of mass fragments can be strongly influenced by small structural changes. Thus, in a structural similarity context, the presence of peaks is more important than their intensity. Therefore, SISCOM emphasizes binary variables in addition to the intensity criteria within its similarity measure. The weighting parameters of the algorithm have been heuristically optimized to yield hitlists with a large number of chemical structures similar to the unknown.

It has been shown that using spectral features rather than peak intensities within library search algorithms optimizes structural similarity between the hitlist and the target [62].

Neutral loss searches have "structural similarity search" properties for some classes of compounds. An obstacle to the automatic use of this technique is the necessity to know the molecular ion of the unknown.

The frequency of a distinct substructure in a hitlist of a structural similarity search can be used to predict the presence or absence of this substructure in the unknown. This feature is implemented, for example, in SISCOM search, in the NIST MS Search and in the STIRS (Self-Training Interpretive and Retrieval System) [63].

55.3.2
Search Algorithms for MS/MS Spectra

Up to now, the same algorithms as in EI-MS (especially INCOS derivates such as NIST MS Search) are used for library search in MS/MS databases. Some slight modifications consider increasing mass increments at higher molecular weights by using real m/z values and tolerances instead of nominal masses.

However, there are many differences between MS/MS data and EI mass spectra: MS/MS spectra often show only few peaks and their intensities and intensity pattern can vary to a much higher degree than in EI-MS. Fragment ions can be present or absent dependant on instrument type and collision parameters. While the molecular ion in EI mass spectra may be absent or very small, the precursor ion is always known in MS/MS and can be used as a filter for molecular weight of compounds.

Some new algorithmic developments try to reflect these facts. For instance, a newly presented "matching probability" (mp) uses a high weight for the presence and absence of peaks (raised to the fourth power!) and a low weight for the intensity differences [64]:

$$\mathrm{mp} = \frac{f_{\mathrm{M}}^{4}}{\left(f_{\mathrm{U}} f_{\mathrm{R}} \sum_{m} \left| i_{\mathrm{U},m} - i_{\mathrm{R},m} \right| \right)^{0.25}} \tag{55.2}$$

f_{M} = number of matching peaks
$f_{\mathrm{U}}, f_{\mathrm{R}}$ = number of peaks in the unknown and in the reference, respectively
$i_{\mathrm{U,m}}$ = intensities (%) of matching peaks m in the unknown
$i_{\mathrm{R,m}}$ = intensities (%) of matching peaks m in the reference.

Another algorithm, X-Rank [65], ranks the peaks of the mass spectra by intensity and matches the rank pattern of the reference spectrum with the rank pattern of the unknown. The probability of a correct identification is computed for this match using parameters that have been trained before.

Interpretation of hitlists from searches in MS/MS databases requires a modification: if in EI the first candidate spectrum of a library search does not look like the unknown spectrum, then this candidate is rather sure not identical to the unknown. This conclusion is not valid for MS/MS hitlist candidates, as library spectra can originate from different instruments or measurement conditions producing different spectra with lacking or additional peaks and larger variability in peak intensities.

As accurate mass measurements with high-resolution mass spectrometers play an increasing role, especially in LC–MS/(MS), algorithms should be able to utilize this information by adjusting mass matching limits to instrumental performance.

Special comparison algorithms are needed for library search in databases containing complete tree-structured sets of MS^n experiments [66]. All possible spectral matches should be done and contribute to an overall similarity parameter. The search, however, should also give reasonable results if parts of the MS^n tree have not been measured for the unknown.

A more sophisticated search strategy handles the MS^n tree as a graph with nodes (fragment peaks) and edges (fragmentation reactions) [67]. Thus, concepts from similarity searching for chemical structures can be applied, for example, calculating the Tanimoto coefficient of binary subgraph fingerprints.

55.3.3
Search Strategies for Proteins

Proteolytic digestion of a protein sample and ESI or MALDI MS of the cleavage peptides is the most frequently used strategy for mass spectrometric identification of proteins. The mass spectral data are then compared to large protein sequence databases, available on the Internet or purchased as in-house versions and enlarged by own data.

Digestion of a protein by endopeptidases yields peptides with defined sequences as each enzyme cleaves at distinct amino acids (e.g., trypsin cleaves at arginine or lysine).

Different identification strategies are briefly described here. More detailed overviews can be found, for example, in [68].

55.3.3.1 Peptide Mass Fingerprint (PMF)

The peaks in a MALDI or ESI mass spectrum of the cleavage peptides are matched with the calculated masses from theoretical cleavage of the proteins in a database (Table 55.6). A hitlist of the best matching proteins is generated. Search algorithms have to be robust against missed peptides (some have a low sensitivity in MS), ‘‘missed cleavages’’ (not all theoretically possible cleavages occur), and posttranslational modifications.

Table 55.6 Tryptic peptides of monoisotopic $[M + H]^+$ ions are calculated *in silico* from the database sequence (one-letter amino acid code) of horse myoglobin, the cleavage positions (**K** = lysine, **R** = arginine) are printed in bold.

Sequence of tryptic peptide	Amino acid numbers	*m/z* (calculated)
GLSDGEWQQVLNVWG**K**	2–17	1815.9024
VEADIAGHGQEVLI**R**	18–32	1606.8547
LFTGHPETLE**K**	33–43	1271.6630
FD**K**	44–46	409.2081
……		
……		
YLEFISDAIIHVLHS**K**	104–119	1885.0218
HPGDFGADAQGAMT**K**	120–134	1502.6692
ALELF**R**	135–140	748.4352
NDIAA**K**	141–146	631.3409
Y**K**	147–148	310.1761
ELGFQG	149–154	650.3144

Database sequence of horse myoglobin: MGLSDGEWQQVLNVWG**K**VEADIAGHGQEVLI**R**LFTGHPETLE**K**FD**K**F**K**HL**K**TEAEM**K**ASEDL**KK**HGTVVLTALGGIL**KKK**GHHEAEL**K**PLAQSHAT**K**H**K**IPI**K**YLEFISDAIIHVLHS**K**HPGDFGADAQGAMT**K**ALELF**R**NDIAA**K**Y**K**ELGFQG. The leading methionine is cleaved off at protein synthesis.

Peptide mass fingerprint (PMF) does not need tandem MS. However, high mass accuracy improves the search results.

55.3.3.2 **Peptide Fragment Fingerprint (PFF)**

Low-energy CID fragmentation of peptides results in clearly defined ion series a, b, c, x, y, z (Figure 55.6) [69]. In ESI-MS/MS, mainly b- and y-ions are present, thus simplifying the spectrum interpretation.

Peptide fragment fingerprint (PFF) computes theoretical MS/MS spectra (mostly b- and y-ions) from peptide sequences in the protein databases and compares them with the measured peptide MS/MS spectrum. Currently, PFF is the most

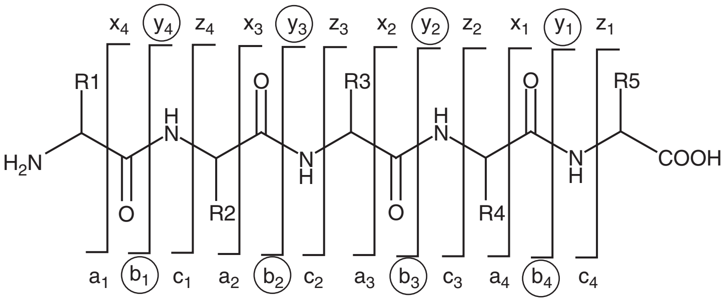

Figure 55.6 CID fragmentation scheme for peptides (nomenclature of Roepstorff and Fohlmann) [69]. In ESI, low-energy CID spectra mainly b- and y-ions are present.

important identification technique for proteins from mass spectral data. A number of commercial and free PFF programs exist; SEQUEST (commercial) and MASCOT (a commercial and a free Internet version) are popular packages. The MASCOT [70] algorithm is probabilistically based, whereas SEQUEST [71] utilizes a cross-correlation approach.

As the size of protein databases is very large, efficient discrimination between correct protein hits and random ‘‘false-positive’’ identifications is a burning issue. According to the importance of MS in proteomics, much effort is undertaken to improve the reliability of protein identification as well as the speed of the searches to enable high-throughput applications.

55.3.3.3 **Sequence Tag**

An alternative strategy for protein identifications by MS/MS spectra matches sequences and not mass spectra. Often, a short part of an amino acid sequence of the peptide can be read directly – either visually or by software – from succeeding peaks of an ion series in the MS/MS spectrum. This information can be used to derive a ‘‘peptide sequence tag’’ [72] with high selectivity (Figure 55.7). Fortunately, this sequence tag can be translated from the amino acid code into the nucleotide

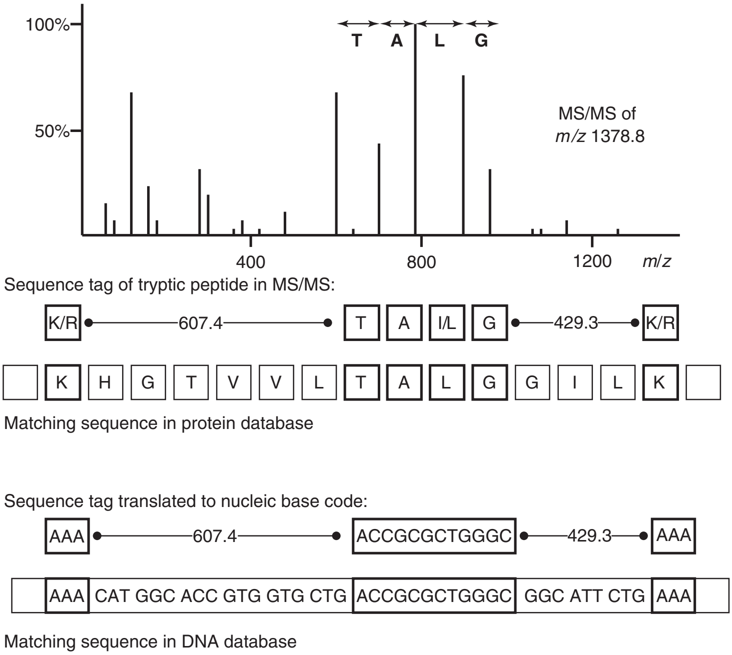

Figure 55.7 A sequence tag is a partial amino acid sequence observed in a peptide MS/MS spectrum (e.g., of b-ions). Its high information content originates from the N-terminal cleavage specificity, the short ‘‘tag’’ of amino acid sequence, the C-terminal cleavage specificity, and the sizes of the two regions between tag and cleavage positions. Amino acid sequence tags can be translated back to the nucleotide base code, enabling searches in the large cDNA databases.

base code. Thus, the search can be performed also on the level of the genome using large nucleotide databases.

55.3.3.4 **Peptide-MS-Search**

Recently, attempts were made to build large databases of measured and reliably identified peptide MS/MS spectra [73]. Searches in those databases yield a higher reliability of identification. Intensities of real database spectra are more similar to the MS/MS spectrum of the unknown peptide than intensities predicted from amino acid sequences by algorithms such as ‘‘SEQUEST.’’ Efforts of spectra collection concentrate to well-characterized proteomes such as the human and yeast proteome.

55.3.3.5 **De novo Sequencing**

The most challenging task in protein identification is the determination of the amino acid sequences from MS/MS spectra of peptides not contained in databases. Excellent mass spectral data are necessary to have a real chance for de novo sequencing, for example, accurate mass measurements from FT-ICR-MS or Orbitrap MS and/or complementary fragmentation methods including high-energy CID (e.g., with a MALDI-TOF/TOF). Several computer programs try to solve this puzzle; however, at best, correct amino acid sequences are derived for only about one-third of the investigated peptide MS/MS spectra [74].

55.4
Fragmentation Pathway Prediction

The knowledge of the chemical structure of fragment ions present in a mass spectrum is often helpful in the interpretation and identification of an unknown. This information can be used to solve problems of different complexity:

- C*orrelate mass spectrum and structure*: explain mass spectral peaks for a known chemical structure.
- *Evaluate structure candidates*: determine ‘‘unexplained peaks’’ in the mass spectrum of the unknown to check the plausibility of the candidates.
- Predict the mass spectrum for a given chemical structure.

Two different approaches have been tried: (i) *Rule-based* methods rely on fragmentation rules (either formulated from experts in textbooks or implicitly contained in fragmentation databases). (ii) *Combinatorial* approaches are based on the connectivities between the atoms and search for all possible fragments or fragmentation paths with a ranking of the results.

For both approaches, the availability of accurate mass measurements of the fragment ions leads to better results and is therefore very valuable.

55.4.1
Rule-Based Approaches

Much scientific efforts have been done in the past to find rules for the fragmentation reactions in EI-MS and later on also for MS/MS fragmentation from soft-ionization precursor ions; the results are condensed in comprehensive textbooks, for example, [75].

These reactions range from simple cleavages and dedicated rearrangements to almost statistically scattering of parts of the molecule and include unexpected wide-range sterical rearrangements. The full complexity of fragmentation rules has reserved this field to the MS experts.

Fragmentation reactions can be implemented in a computer program with benefit for the user: it provides expert knowledge and saves much time by handling logical and calculational issues.

Two prominent commercial software products are (i) Mass Frontier [76] from HighChem and (ii) MS Fragmenter [77] from Advanced Chemistry Development (ACD).

Ionization modes implemented in *Mass Frontier* are EI (nonbonded electron, π bond, σ bond), $[M+H]^+$, and $[M-H]^-$. Fragmentation rules contain alpha cleavage, inductive cleavage, and hydrogen rearrangements. Bond creation (except hydrogen bonds), ring contractions, cyclizations, and non-H-rearrangements are not included. All reactions consider charge localization and the even-electron rule. Only unimolecular reactions are allowed. The number of fragmentation steps can be selected.

The created fragmentations are only formally possible solutions; no checks for stability of ions, thermodynamics or kinetics are performed. The resulting fragmentation paths are presented in a style as chemists and mass spectrometrists are accustomed to seeing them in journals and books (Figure 55.8).

Mass Frontier assists chemists in the explanation of mass spectral peaks for a known structure or at the plausibility evaluation of structural candidates for a

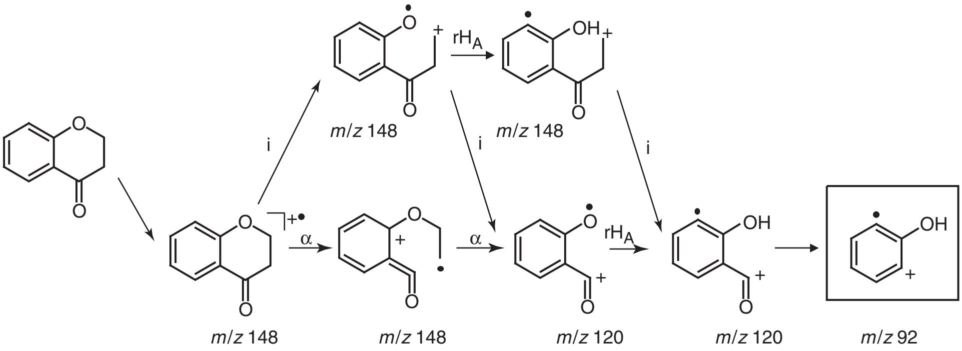

Figure 55.8 Possible fragmentation pathways for the formation of the ion *m*/*z* 92 from 4-chromanone, as evaluated by the software Mass Frontier.

mass spectrum of an unknown. Furthermore, a ''bar code'' mass spectrum without intensities can be predicted from a chemical structure.

Besides the above-introduced set of ''general fragmentation and rearrangement rules'' from textbooks, a database with 19 000 fragmentation reactions extracted from mass spectrometric literature can be used. As no restrictions exist for database fragmentations contrary to the ''general fragmentation and rearrangement rules,'' skeletal and individual rearrangements, ring closures and expansions, and other compound specific mechanisms can also be found in the results.

The *ACD/MS Fragmenter* offers possibilities similar to Mass Frontier, enabling fragmentations of molecules ionized by EI or by APCI or ESI protonation techniques. The number of consecutive fragmentation steps can be selected too. The set of fragmentation rules is partly different from Mass Frontier, for example, ring formations are possible. Other differences concern the logical structure of possible fragmentations and their nomenclature.

The fragmentation reactions predicted for a given chemical structure are represented by a fragmentation tree of ion masses. The corresponding ion structures can be displayed. For comparing mass spectra with structure candidates, an ''assignment quality index'' (AQI) can be calculated.

An important experience has to be noted for all rule-based systems: a small set of rules leads to less ambiguity of the explanations, however, to a not negligible number of unexplained peaks. For structure candidate evaluation, this results in a higher rejection rate of correct structures. Including more rules covering more fragmentations effectuates a higher explanation rate of peaks, but unfortunately also more false-positive candidates.

55.4.2
Combinatorial Approaches

Combinatorial search systems look for all substructures within a given molecule that match the fragment masses in a mass spectrum. The output of the substructures is ranked by varying criteria.

As these algorithms rely only on the connectivity of atoms in a molecule, the description of rearrangements is very limited. Mostly, only rearrangements of one hydrogen are enabled by varying the fragment mass by ±1 Da. Skeletal or steric long-range rearrangements can be hardly realized. Parts of the molecule that are not connected would have to be combined, which would cause a combinatorial explosion of solutions.

Combinatorial approaches have eminent advantages, if the rule base is deficient or does not exist in certain fields of structures and mass spectrometric methods. For the combinatorial explosion of possible fragments, a filtering by accurate mass data is very helpful and more necessary than for methods based on fragmentation rules.

Combinatorial search systems differ in the definition of the substructures, the bonds allowed to break, and the ranking criterion. A very early product was *MASSPEC* [78] working with nonbreakable ''superatoms'' (e.g., benzene ring) and minimizing the number of broken bonds as ranking criterion. New attempts are *EPIC* (differently penalizing broken bonds) [79], *FiD* (ranking by dissociation energies of broken bonds) [80], and the computationally fast *MetFrag* (combining dissociation energies and mass-weighted peak intensities as ranking criterion) [81]. *MassFragment* [82] is a mass spectrometer company's product based on systematic bond disconnection of the precursor structure, earning its power for CID mass spectra evaluation from high accurate mass measurements with switching collision energies.

A less sophisticated tool is *Mass Spec Calculator Pro* [83]. Possible fragment masses for a given molecule can be produced either by manual bond cleavage or by an automatic fragmentation routine. *MS Interpreter* is a software tool of NIST [84] that evaluates bond cleavages by estimating dissociation rates of the precursor ions.

55.5
Determination of the Element Composition

The molecular mass of a compound is determined by the molecular formula. Deriving the molecular formula from a molecular mass, however, is in general not unique because many possible elemental compositions exist for one given nominal mass.

Nevertheless, additional information about the elemental composition is available from (i) the ''accurate'' mass, (ii) the isotope peak pattern, (iii) fragment ions, and (iv) connectivity requirements.

55.5.1
Elemental Composition from Accurate Mass

The monoisotopic masses of elements (relative to carbon-12) show a small and nuclide-dependant difference to the corresponding integer value (Table 55.7). Therefore, the accurate mass of the monoisotopic ion of a molecule also differs from the nominal value by a characteristic increment or decrement.

This information of accurate mass measurements obtained by high-resolution mass spectrometers has been utilized for a very long time. Computer programs

Table 55.7 Accurate relative atom masses of selected nuclides.

Element	Mass	Element	Mass
^{1}H	1.007 825	^{28}Si	27.976 927
^{11}B	11.009 306	^{31}P	30.973 762
^{12}C	12.000 000	^{32}S	31.972 071
^{14}N	14.003 074	^{35}Cl	34.968 853
^{16}O	15.994 915	^{79}Br	78.918 338
^{19}F	18.998 403	—	—

have assisted the generation of possible candidates almost since the beginning, but this strategy was not applied in routine analysis because expensive double-focusing sector-field instruments (or the almost unaffordable FT-ICR mass spectrometers) were necessary to fulfill the accuracy and resolution requirements.

Nowadays, a variety of different high-resolution mass spectrometers is available: TOF instruments, Orbitraps, and FT-ICR in different configuration (with and without MS/MS or MS^n possibility). These instruments produce high to very high resolution data of excellent mass accuracy of both precursor and product ions. These mass spectrometers are still very expensive. However, analytical needs make them a routine instrumentation in some areas of profitable research such as proteomics, metabolite detection, and combinatorial synthesis, but also for regulatory and diagnostic issues in environmental, clinical, and food analysis.

For a given mass accuracy, the number of formula candidates increases with increasing molecular mass and with increasing number of elements allowed to be present. To reduce this ‘‘exploding’’ number, further constraints are helpful: valence considerations, heuristic experiences about element ratios, and the isotope pattern.

Valence constraints for possible molecular formula can be implemented in the form of the *LEWIS* rule (each compound has an even number of electrons and all atoms obey the octet rule) and the *SENIOR* theorem [(i) the sum of valences is an even number; (ii) the sum of valences is greater than or equal to twice the maximum valence; and (iii) the sum of valences is greater than or equal to twice the number of atoms minus 1] [85]. Only a few really existing compounds are undesirably discarded by these rules, for example, radical *N*-pyridinyloxy compounds, because they have an odd number of electrons.

LEWIS and SENIOR checks are preferred because RDBEs (ring and double bond equivalents) rules are too uncomfortable to handle formulae containing atoms of elements with different possible valence states (e.g., nitrogen, phosphorous, and sulfur). Further limits for naturally existing formulae (e.g., for element ratios) can be derived from structure databases of known compounds. This filter can be adapted to the area of research.

55.5.2
Mass Defect Plots and Mass Defect Filtering

Usual mass spectral bar plot representation would be very long and confusing for ultrahigh-resolution mass spectra from complex mixtures. A more appropriate arrangement is a ‘‘mass defect plot’’ of mass defects (to nearest integer mass value) versus mass. Within these plots, compound group membership can be visually detected, as molecular ions of similar compounds are arranged on lines (Figure 55.9). A special kind of this technique is the use of so-called Kendrick masses, which simplifies the peak pattern of hydrocarbon systems [86].

$$\text{Kendrick mass} = \text{IUPAC mass} \times \frac{14.00000}{14.01565} \tag{55.3}$$

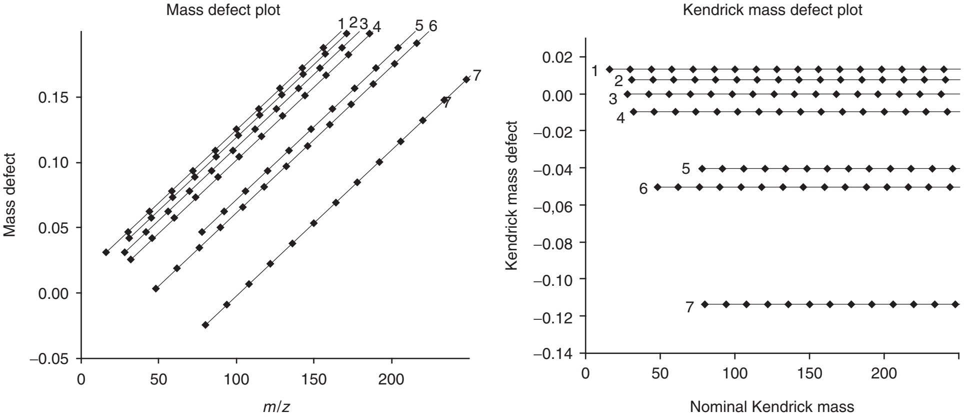

Figure 55.9 CH_2 homolog series are situated on lines in mass defect plots. The Kendrick mass defects for all members of a CH_2 homolog series is constant (1. alkanes, 2. amines, 3. alkenes, 4. aromatic compounds (with one benzene ring), 5. alcohols and ethers, 6. thiols and sulfides, and 7. disulfides).

14.015 65 is the accurate mass of CH_2 group, and IUPAC mass is the measured mass corresponding to $^{12}C = 12.000\,00$.

Mass defect filters can be used for metabolite screening, as the typical metabolizing reactions are connected each to a definite accurate mass shift [87].

55.5.3
Elemental Composition from Isotope Peak Pattern

Chemical elements may be either monoisotopic (e.g., fluorine and phosphorous) or polyisotopic (e.g., Table 55.8). Every mass spectral peak containing polyisotopic elements is accompanied by isotope signals with their natural occurring abundances.

If the formula shows more than one atom from one or from different polyisotopic element species, the observed isotope pattern obeys combinatorial rules. For

Table 55.8 Isotope pattern of selected polyisotopic elements.

A	%	A+1	%	A+2	%
^{12}C	100	^{13}C	1.1	—	—
^{14}N	100	^{15}N	0.37	—	—
^{16}O	100	^{17}O	0.04	^{18}O	0.20
^{28}Si	100	^{29}Si	5.1	^{30}Si	3.35
^{32}S	100	^{33}S	0.8	^{34}S	4.44
^{10}B	24.53	^{11}B	100	—	—
^{35}Cl	100	—	—	^{37}Cl	32.4
^{79}Br	100	—	—	^{81}Br	97.86

Table 55.9 The molecular isotope pattern of Cl_3Br is calculated by expansion of "$(a_0 + a_2)^3 \times (b_0 + b_2)$" derived from Eq. (57.4) and summation of all isobaric contributions using $a_0 = 1$ (^{35}Cl), $a_2 = 0.324$ (^{37}Cl), $b_0 = 1$ (^{79}Br), and $b_2 = 0.979$ (^{81}Br). The resulting isotope pattern is normalized to the most abundant peak.

m/z	Molecular species	Terms of isobaric contributions		Normalized pattern
184	$^{35}Cl_3{}^{79}Br$	$a_0{}^3b_0$	1.000	0.513
186	$^{35}Cl_2{}^{37}Cl^{79}Br$, $^{35}Cl_3{}^{81}Br$	$3a_0{}^2a_2b_0 + a_0{}^3b_2$	0.972 + 0.979	1.000
188	$^{35}Cl^{37}Cl_2{}^{79}Br$, $^{35}Cl_2{}^{37}Cl^{81}Br$	$3a_0a_2{}^2b_0 + 3a_0{}^2a_2b_2$	0.315 + 0.951	0.649
190	$^{37}Cl_3{}^{79}Br$, $^{35}Cl^{37}Cl_2{}^{81}Br$	$a_2{}^3b_0 + 3a_0a_2{}^2b_0$	0.034 + 0.308	0.175
192	$^{37}Cl_3{}^{81}Br$	$a_2{}^3b_2$	0.033	0.017

nominal mass resolution, calculation of the isotope pattern of a small compound with a molecular formula A_mB_n is mostly based on the expansion of the following product of polynomial expressions [88]:

$$(a_0 + a_1 + a_2 + \ldots)^m \cdot (b_0 + b_1 + b_2 + \ldots)^n \tag{55.4}$$

where $a_0, a_1, a_2, \ldots$ and $b_0, b_1, b_2, \ldots$ are the isotopic abundances of the elements A and B. The molecular isotope pattern of A_mB_n then results from adding all terms belonging to isobaric species, as shown for the simple molecule Cl_3Br (bromine trichloride) in Table 55.9.

It is more difficult to build a fast and accurate algorithm for very large compounds such as proteins [89].

The isotope pattern is a kind of information about elemental composition, which is available also on low-cost quadrupole benchtop mass spectrometers with unit mass resolution. This information is utilized in the visual interpretation of mass spectra to recognize elements with remarkable isotope pattern such as chlorine, bromine, or sulfur. There exist numerous software tools (many of them freely available for download or as web calculators), which calculate theoretic isotope patterns for comparison issues [90].

Computer programs have been developed for automatic recognition of specific isotopic patterns, often using variants of correlation coefficients as similarity measures [91]. "Chemometric" detectors (CMDs) have been created applying such algorithms to every mass spectrum of a GC-MS run. The results are selective signal traces for compounds containing selected elements, for example, chlorine or selenium [92].

55.5.4
Combined Algorithms for Element Composition

The discriminative power of algorithms calculating molecular formulae increases if mass accuracy and isotope pattern are concertedly applied. It has been shown

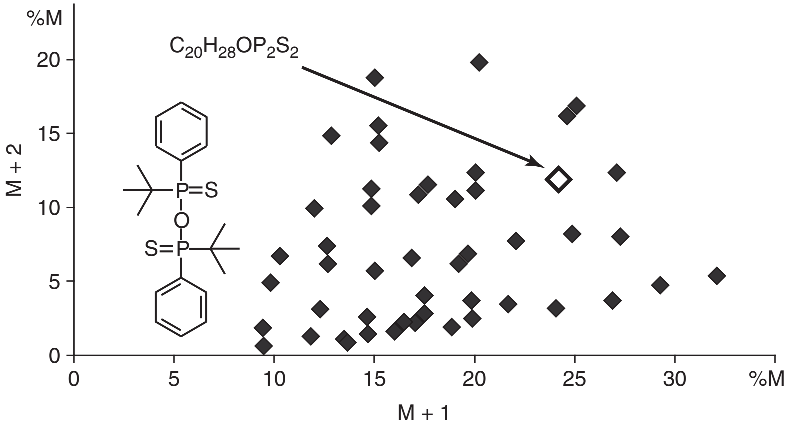

Figure 55.10 The relative isotopic abundances of the M + 1 and M + 2 ions (specified in percentage of the abundance of the monoisotopic molecular ion M) can be used to filter molecular formula candidates. Phenyl-t-butyl-thiophosphinic acid anhydride ($C_{20}H_{28}OP_2S_2$) has an accurate molecular mass of 410.10 568 Da. Forty-nine molecular formulae (C, H, O, N, S, P allowed) are possible within a ±5 ppm range. The correct formula can be found unambiguously by using isotopic abundances of M + 1 and M + 2.

that even 1 ppm mass accuracy (e.g., by Orbitrap or FT-ICR mass spectrometers) is not enough for achieving a moderate number of candidate formulae for molecular masses above 400 Da [93]. Better results are attainable by combining mass accuracy and isotope abundance (Figure 55.10).

For utilizing the full discriminating power of combined accurate mass and isotope pattern information, accurate masses of the M + 1 and M + 2 isotope peaks and their complete mass peak profile should be evaluated, as these peaks are composed of different ion species [94].

Additional information for further narrowing the solution space originates from MS/MS and MS^n experiments. A general rule is that all fragments must have elemental compositions that “fit” into a valid molecular formula. It depends strongly on the instrumental abilities (availability and mass accuracy of MS^1, MS^2, and MS^3 spectra, accuracy of isotope pattern of MS^1, resolution of precursor selection, etc.), which variant of the combined algorithms can be applied.

55.6
Deconvolution and Detection of Components

An important strength of MS is the possibility of being connected to a chromatographic instrument, especially a gas chromatograph or a liquid chromatograph. The resulting data of such hyphenated techniques are time series of mass spectra. Other types of time-resolved MS data are produced by pyrolysis MS and fractionated evaporation MS.

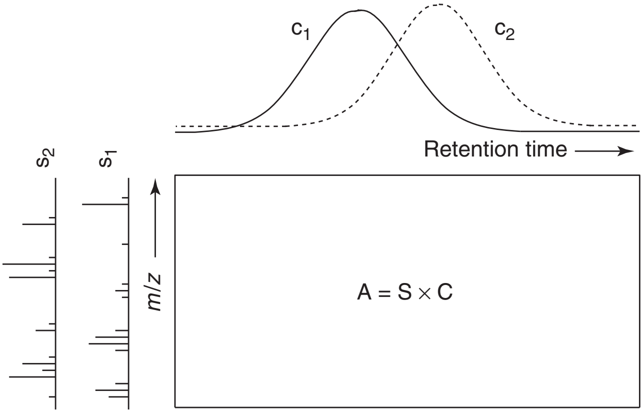

Figure 55.11 Time series of mass spectra form a data matrix A (time axis ×mass axis), which is mathematically a matrix product of the pure compound chromatogram traces (C) times the pure compound mass spectra (S).

Although resolution of chromatography is sometimes extremely high, overlap of chromatographic peaks cannot be excluded. In addition, noisy background from air and column bleeding in GC or from solvents and buffers in LC can hide small peaks from visual detection.

Therefore, computational methods that detect components of a mixture in a chromatogram, also at a high level of background noise and in cases of chromatographic peak overlap, are very valuable.

Time series of mass spectra form a data matrix (time axis × mass axis), which is a matrix product of the pure compound chromatogram traces times the pure compound mass spectra (Figure 55.11). The inverse procedure to this matrix multiplication is called *deconvolution* and should result in the component chromatograms and component mass spectra. Unfortunately, this inverse procedure has mathematically no unique result. Additional information is needed for a solution.

Additional knowledge or assumptions helpful to solve the problem can be ''pure regions'' in the chromatograms, ''unique ions'' representing only one component, knowledge of the typical chromatographic peak shape, number of components in the mixture, or common ''maximizing masses.'' Mass spectrometric time series of different origin need different deconvolution methods for optimal results; for example, components in chromatographic data usually show defined narrow peaks contrary to pyrolysis MS and direct evaporation MS.

55.6.1
GC–MS Deconvolution

The early introduced Biller and Biemann [95] procedure extracts all mass chromatograms that maximize simultaneously. This idea was later improved by considering the time shift between the measurement of high and low masses by scanning mass spectrometers [96].

The ''model peak method'' is a more sophisticated algorithm using also maxima of ion chromatograms to detect components [97]. One maximizing ion forming a ''sharp'' singlet peak is selected as model for the peak shape and those ion profiles that have similar shapes are extracted. Mass spectral intensities of the component are estimated from the extracted mass chromatograms after a local background correction. Components with peak maxima differing only 1.5–2 scan times can be detected and separated.

This very efficient and reliable method was selected for the widely used spectra extraction within the *AMDIS* (Automated Mass Spectral Deconvolution and Identification System) software [98]. Some improvements were made to also extract weak signals. The result of analyzing GC-MS data with AMDIS is a chromatogram with markers for detected mixture components (Figure 55.12). The extracted mass spectrum for each component can be displayed and subjected to library search – either with a built-in algorithm or with an external software.

AMDIS has been developed as a verification tool in the context of the chemical weapons convention. AMDIS is freely available from NIST and has proved to be a widely used and successful software, which can be considered as the present day standard in GC–MS component detection and extraction.

Fast MS of TOF instruments facilitates the deconvolution twofold: no time shift between masses occurs and the peak shape is almost perfectly represented because of the high acquisition rate of up to 500 mass spectra per second. Therefore, deconvolution of *GC-TOF-MS* data exhibits excellent results. Components can be

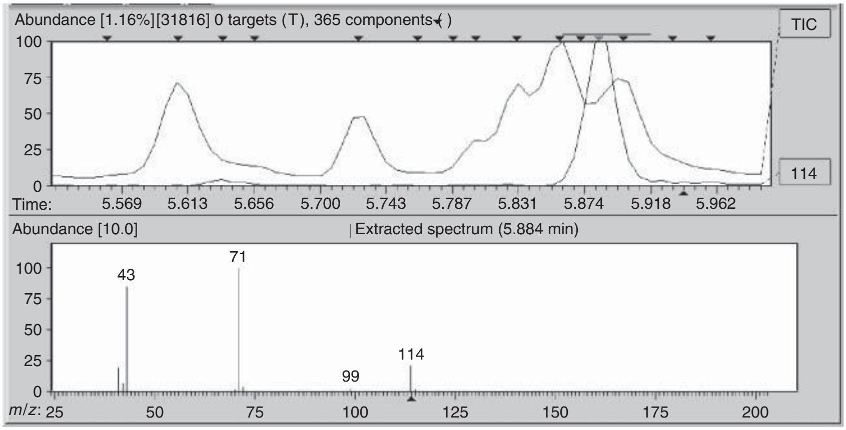

Figure 55.12 All components detected by AMDIS are marked in the GC–MS display as triangles above the chromatogram. Also, minor components can be detected within an overlap of several GC peaks. The extracted spectrum is displayed beneath and can be subjected to library search. The displayed chromatogram section stems from a headspace measurement of a hazelnut paste. The extracted mixture component was identified as one of two isomers: 4-heptanone or 2-methyl-3-hexanone.

detected for very small differences in retention time and small spectral differences of, for example, isomers.

55.6.2
LC–MS Deconvolution

Since LC–MS chromatograms are often dominated by a high level of background and noise, mixture component peaks are often hidden and cannot be visually detected in the total ion current chromatogram. ESI and APCI mass spectra show only one or a very small number of quasi-molecular ion species per component. Therefore, using common maximizing masses is less reasonable.

Two different strategies have been implemented in computer programs for LC–MS deconvolution: (i) considerations about distinguishing noise and meaningful data and (ii) mass spectrometric knowledge about related ion species.

An approach of the first type is *CODA* (component detection algorithm) [99] – the program code is freely available but is also implemented in commercial software. CODA calculates a ‘‘similarity index’’ between each mass chromatogram and its smoothed and mean-subtracted version. Thus, spikes and chemical noise from solvents are removed. Only mass chromatograms with low noise and low background are selected and combined to form a reduced total ion chromatogram.

The software *IntelliXtract* [100] is a more sophisticated LCMS component detector of the second type. After running a modified version of CODA, all ions of a distinct retention time are further analyzed, if they are logical contributors to a chemical component: isotope ions, adduct ions, and usual neutral losses. The real molecular mass is determined within this logical ion cluster and all identified adduct ions are annotated. Comparable strategies of grouping adduct masses, isotopic peaks, and sometimes also different charge states are part of metabolite identification software both of mass spectrometer suppliers and academic research teams.

55.6.3
Factor Analysis Methods

Matrix-based factor analysis approaches making no assumptions about maximizing masses and peak shapes are mainly used in pyrolysis MS and fractionated evaporation MS.

Finding correlations of ions with principal component analysis (PCA) or similar methods is often the first step, but this does not lead to pure component mass spectra [101]. ‘‘Rotation’’ of the factors is necessary – visually or automated. Target factor analysis, VARDIA (‘‘variance diagram’’), SIMPLISMA (‘‘simple-to-use interactive self-modeling mixture analysis’’) [102], and EFA (‘‘evolving factor analysis’’) [103] are examples of algorithmic efforts to solve this task.

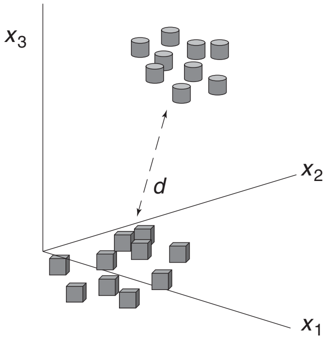

Figure 55.13 Each variable of a multivariate data sample represents a coordinate axis in a data space. Similar objects (samples) are situated close together. This is schematically demonstrated for two categories of samples using three variables.

55.7
Multivariate Data Analysis (MVDA) of Mass Spectra

Mass spectra are multivariate data samples, which means that there exist more than one measured variable for one sample. A multivariate data sample can be seen as a distinct point in a multidimensional data space, each variable representing a coordinate axis of this data space. This can be easily imagined and demonstrated for up to three variables (Figure 55.13). For higher dimensionality, imagination is difficult or impossible, but mathematical algorithms for treatment of such data are analogous to the three-dimensional world. A comprehensive treatment of multivariate data analysis (MVDA) methods in chemistry can be found in a newly published textbook [104].

55.7.1
Distance and Similarity

A basic assumption of MVDA is that similar objects (samples) are situated close together in multivariate data space. Therefore, distances between the samples can be seen as measures of ''dissimilarity.'' Different distance measures (with different properties) can be used, such as Euclidean distance, city-block distance, and Mahalonobis distance. The latter considers the covariance structure of the dataset thus scaling the influence of the different variables.

This distance–similarity concept is also the basis of library search algorithms already discussed in this contribution.

55.7.2
Dimensionality Reduction

There are different reasons for a dimensionality reduction of a high-dimensional data space: (i) Multivariate data often have a lower ''intrinsic'' dimensionality owing to correlations between the variables. (ii) Not all parts of multivariate data may be relevant for the intended data analysis. (iii) High-dimensional data space cannot be imagined well by the human mind.

Linear methods produce new ‘‘latent’’ variables that are linear combinations of the original ones. All significant latent variables can be used as a model for the original dataset or only one- to three-dimensional representative subspaces (lines, planes, 3D spaces) are extracted. In the latter case, two latent variables span a projection plane or a single variable serves for classification of samples.

Nonlinear methods distort the multivariate data space to get lower dimensional representations. Besides different nonlinear ‘‘classical’’ optimization methods, artificial neural networks are often used to deal with nonlinearities. Another new way to import nonlinearities are support-vector-machines (SVMs).

Advantages of linear methods are an easier judgment of the stability of the results and the possibility of estimating the influences of the original variables.

55.7.3
Mass Spectral Features

In principle, mass spectral peak intensities can be used directly as variables in multivariate data. However, structural similarity information is often not directly connected to intensities at distinct m/z values. Mass shifts of characteristic peaks can complicate the relationships between mass spectra and chemical structures.

Therefore, new variables (‘‘spectral features’’) are calculated by mathematical transformations of the original peak list data [105]. Spectral features are often normalized (e.g., to a constant sum) and calculation can be restricted to limited mass ranges. Selected examples of spectral feature calculations from peak intensities I_m are as follows:

- *Modulo-14 features* collect peak intensities of CH_2 homolog series and reflect compound classes ($k = 1$–14 and $n = 0, 1, 2, 3, \ldots$).

$$x_k = \sum_n I_{k+14n} \tag{55.5}$$

- *Autocorrelation features* emphasize periodicities, intense neutral losses, and mass differences (d = mass differences and $m = m/z$).

$$x_d = \sum_m I_m I_{m+d} \tag{55.6}$$

- *Logarithmic intensity ratios* reflect the fact that intensity ratios (especially of neighboring peaks) are more reproducible than absolute mass spectral peak intensities (d = mass differences and $m = m/z$).

$$x_{m,d} = \log\left(\frac{I_m}{I_{m+d}}\right) \tag{55.7}$$

55.7.4
Exploratory Data Analysis

If the used variables contain appropriate chemical (=structural) information, similar chemical compounds should lie close together and form "clusters." Exploratory data analysis tries to find such clusters.

Important methods for exploratory data analysis of mass spectra are mapping methods that extract relevant data to a two-dimensional plane enabling "visual cluster analysis." Linear exploratory methods are the PCA and partial least-squares ("PLS") substructure mapping.

55.7.4.1 Principal Component Analysis (PCA)

PCA produces orthogonal and uncorrelated "latent variables" exhibiting maximum variance [104]. Therefore, it is assumed that interesting information about data structure and similarities between "objects" (samples, spectra) is contained in the first principal components.

Two principal components span a projection plane, allowing visual cluster analysis. As the principal components are linear combinations of the original variables, the coefficients of these linear combinations (called *loadings*) characterize the importance of the original variables for the data structure. Figure 55.14 shows the PCA mapping of an ambiguous library search hitlist containing alkenes and cyclopropane compounds.

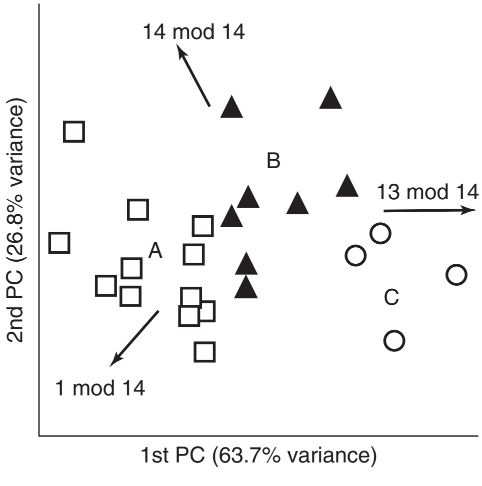

Figure 55.14 PCA mapping of alkenes and cyclopropane compounds using modulo-14 spectral features. Three groups of similar chemical structures ("structural similarity clusters") are observed: (A) 1- and 2-alkenes (squares) (B) cyclopropane compounds (black triangles), and (C) 4- and 5-alkenes (circles). Spectrum-structure relationships can be found by evaluating prominent "loadings" (shown by arrows). An intense peak m/z 43 (→1 mod 14) is characteristic for 1- and 2-alkenes, m/z 56 (→14 mod 14) for cyclopropane compounds, and m/z 55 and 41 (→13 mod 14) for 4- and 5-alkenes.

55.7.4.2 **PLS Substructure Mapping**

Contrary to PCA, the PLS substructure mapping looks not only at mass spectral variables but simultaneously at a set of binary variables describing the presence or absence of substructures in the compounds [106]. The projection plane is spanned by new variables maximizing the covariance between the mass spectral features and the binary structural descriptors. With this method, ''structural similarity clusters'' that are hidden by dominant mass spectral data can be found.

55.7.5
Mass Spectral Classifiers

A mass spectral classifier is a mathematical or logical rule for an assignment of a mass spectrum to a class of chemical compounds. The output of a classifier is a discriminant variable. If the value is above a defined limit, then the answer for class membership is ''yes.'' If the discriminant variable is less than this limit, then the answer is ''no.'' If the complete distribution of the discriminant variable has been estimated, then a probability of class membership can be given (Figure 55.15).

The performance of classifiers can be characterized by two parameters: reliability and recall. The reliability is the probability that the answer to the classifier is correct. It is usually calculated separately for ''yes'' and ''no.'' The recall for a compound class is the probability that a compound belonging to a compound class is actually detected by the classifier. For mass spectral screening procedures, a high recall may be important – all potential candidates for a class membership should be detected. On the other hand, substructure constraints for structure elucidation (e.g., for automatic isomer generation) need a very high reliability – one incorrect substructure constraint makes it impossible to generate the correct chemical

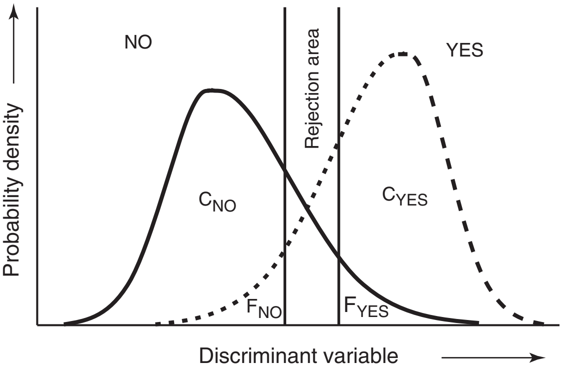

Figure 55.15 Probability densities for answers ''YES'' and ''NO'' (class membership). Selection of the classification limits (vertical lines) and the width of an optional ''rejection area'' influences (i) the probabilities, that a compound of a certain class is classified correctly (''recall'' C_{YES} and C_{NO}) or incorrectly (F_{YES} and F_{NO}), and (ii) the reliabilities $R_{YES} = C_{YES}/(C_{YES} + F_{YES})$ and $R_{NO} = C_{NO}/(C_{NO} + F_{NO})$.

structure. A rejection range can improve the reliability of classifiers, but decreases the recall.

Such classifiers can be built by different methods from multivariate statistics (linear discriminant analysis, PLS discriminant analysis), artificial neural networks, SVMs, and rule-based methods [104].

Chemical classes are often defined by substructures; therefore, classification of the presence or absence of substructures is of great interest for structure elucidation. For example, different types of substructure classifiers have been developed in the past [107]. Application of such classifiers to unknowns does not require a mass spectral database. Database spectra are, however, necessary for the ''training'' of the classifiers.

55.7.5.1 Chemometric Detectors for GC–MS

Mass spectral classifiers can be applied to each mass spectrum of a GC-MS analysis, resulting in selective traces for compound classes. Such CMDs have been developed for different substance categories, for example, for alkanes, PAHs, PCBs, and chlorinated phenols, allowing the fast screening of a complex chromatogram for the target compound class [108]. Figure 55.16 shows the results from a CMD for chloro- and nitrophenols.

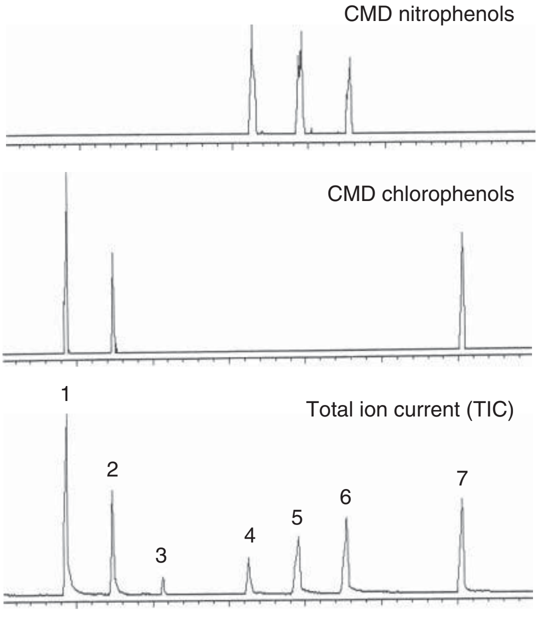

Figure 55.16 A chemometric detector (CMD) produces selective traces for compound categories by classifying every mass spectrum of a GC-MS analysis, as seen in this example of CMDs for nitrophenols and chlorophenols (1. 4-chloro-3-methylphenol, 2. 2,4,6-trichlorophenol, 3. *n*-tetradecane, 4. 2,4-dinitrophenol, 5. 4-nitrophenol, 6. 2-methyl-4,6-dinitrophenol, 7. pentachlorophenol).

55.7.5.2 **Hitlist Substructure Classifiers**

A special type of substructure classifiers is implemented in some library search systems (e.g., NIST, MassLib): the hitlist frequency of a substructure is a measure of the probability of this substructure to appear actually in the target. The relationships between hitlist frequency and probability have been estimated before by extensive ''training searches'' of a high number of known compounds used as unknowns.

A similar approach in the past has been realized in STIRS [63]. Different library search hitlists were produced by using different search criteria (''data classes''), reflecting different aspects of mass spectra – structure – relationships. The result is a list of substructures occurring in the hitlist and showing a high reliability.

55.7.5.3 **Mass Spectral Classifiers Supporting Automatic Structure Elucidation**

A new mass spectrometric approach based on the DENDRAL strategy for systematic structure elucidation [109] has been developed within the software MOLGEN-MS [110]:

1) A molecular formula hitlist is calculated from the combined isotope patterns of the molecular ion and all fragment ions.
2) The presence and absence of substructures (''goodlist'' and ''badlist'') are predicted by mass spectral classifiers.
3) An exhaustive set of isomeric molecular candidate structures obeying these constraints is generated by the mathematical isomer generator MOLGEN.
4) The candidate structures are then evaluated by prediction of the mass spectra and comparison with the measured mass spectrum.

References

1. McLafferty, F.W., Stauffer, D.B., Loh, S.Y., and Wesdesmiotis, C. (1999) Unknown identification using reference mass spectra. Quality evaluation of databases. *J. Am. Soc. Mass Spectrom.*, **10** (12), 1229–1240.
2. W. McLafferty *Wiley Registry of Mass Spectral Data*, 9th edn (2010), John Wiley & Sons, Ltd, Chichester, *http://eu.wiley.com/WileyCDA/WileyTitle/productCd-0470520353.html* (accessed 27 July 2012).
3. NIST Standard Reference Data (2011) NIST/EPA/NIH Mass Spectral Library NIST 11 National Institute of Standards and Technology, Gaithersburg, MD, *http://www.nist.gov/srd/nist1a.cfm* (accessed 27 July 2012).
4. CAS (Chemical Abstracts Service) Columbus, OH, *http://www.cas.org/* (accessed 27 July 2012).
5. Benecke, C., Gruner, T., Kerber, A., Laue, R., Wieland, T. (1997) MOLecular structure GENeration with MOLGEN, new features and future developments. *Fresenius' J. Anal. Chem.* **359** (1), 23–32, *http://www.molgen.de/* (accessed 27 July 2012).
6. Milne, G.W.A., Budde, W.L., Heller, S.R., Martinsen, D.P., and Oldham, R.G. (1982) Quality control and evaluation of mass spectra. *Org. Mass Spectrom.*, **17** (11), 547–552.
7. Ausloos, P., Clifton, C.L., Lias, S.G., Mikaya, A.I., Stein, S.E., Tchekhovskoi, D.V., Sparkman, O.D., Zaikin, V., and Zhu, D. (1999) The critical evaluation

of a comprehensive database. *J. Am. Soc. Mass Spectrom.*, **10** (4), 287–299.

8. Yarkov, A. (2008) Mass Spectra of Organic Compounds, *http://eu.wiley.com/WileyCDA/WileyTitle/productCd-0471667730.html* (accessed 27 July 2012).
9. NIST Chemical Webbook *http://webbook.nist.gov/chemistry* (accessed 27 July 2012).
10. Spectral Database for Organic Compounds (SDBS) *http://riodb01.ibase.aist.go.jp/sdbs/* (accessed 27 July 2012).
11. STMdata Wiley-VCH SpecInfo, *http://www.wiley-vch.de/stmdata/specinfo.php* (accessed 27 July 2012).
12. SpecSurf The Chemical Database Service, *http://cds.dl.ac.uk/cds/help/specsurf.html* (accessed 27 July 2012).
13. Maurer, H. H., Pfleger, K., Weber, A. (2011) *Mass Spectral and GC Data of Drugs, Poisons, Pesticides, Pollutants and Their Metabolites*. Wiley-VCH Verlag GmbH: Weinheim, *http://www.wiley-vch.de/stmdata/ms_mpw2011.php* (accessed 27 July 2012).
14. Rösner, P. (2012) Mass Spectra of Designer Drugs, *http://eu.wiley.com/WileyCDA/WileyTitle/productCd-3527333320.html* (accessed 27 July 2012).
15. Parr, M.K., Opfermann, G., and Schänzer, W. (2011) Mass Spectra of Physiologically Active Substances, *http://www.wiley-vch.de/stmdata/ms_aes.php* (accessed 27 July 2012).
16. Central Institute of Nutrition and Food Research (2003) *Mass Spectra of Volatiles in Food*. Wiley-VCH Verlag GmbH, Weinheim, *http://eu.wiley.com/WileyCDA/WileyTitle/productCd-0471648256.html* (accessed 27 July 2012).
17. Mondello, L. (2011) FFNSC GC/MS Library, *http://www.chromaleont.it/ffnsc.html* (accessed 27 July 2012).
18. Adams, R.P. (2007) *Identification of Essential Oil Components by Gas Chromatography/Mass Spectrometry*, 4th edn, Allured Publishing Corporation, Carol Stream, IL, *http://www.alluredbooks.com/Identification-of-Essential-Oil-Components-by-Gas-Chromatography-Mass-Spectrometry-4th-Edition-p52.html* (accessed 27 July 2012).
19. König, W., Joulain, D., Hochmuth, D. (2001) Terpenoids and Related Constituents of Essential Oils, Terpenoids Library, University of Hamburg, Institute of Organic Chemistry, Hamburg, *http://massfinder.com/wiki/Terpenoids_Library* (accessed 27 July 2012).
20. Kühnle, R. (2009) Mass Spectra of Pesticides, *http://www.wiley-vch.de/stmdata/ms_pest.php* (accessed 27 July 2012).
21. Kühnle, R. (2006) Mass Spectra of Pharmaceuticals and Agrochemicals, *http://www.wiley-vch.de/stmdata/ms_pa.php* (accessed 27 July 2012).
22. Ehrenstorfer, D. (2003) The Library of Mass Spectra, *http://www.ehrenstorfer.com/mslib/e-mslib.htm* (accessed 27 July 2012).
23. DeLeeuw, J.W. (2003) Mass Spectra of Geochemicals, Petrochemicals and Biomarkers, *http://eu.wiley.com/WileyCDA/WileyTitle/productCd-0471647985.html* (accessed 27 July 2012).
24. Gaskin, P. Mass Spectral Library of Gibberellins, *http://www.plant-hormones.info/library.htm* (accessed 27 July 2012).
25. American Academy of Forensic Sciences (2010) Toxicology Section, AAFS-mslib, *http://www.ualberta.ca/~gjones/mslib.htm* (accessed 27 July 2012).
26. GMD@CSB.DB The Golm Metabolome Database Mass Spectral and Retention Time Index Libraries (MSRI), *http://csbdb.mpimp-golm.mpg.de/csbdb/gmd/msri/gmd_msri.html* (accessed 27 July 2012).
27. MaSC Users' Group for Mass Spectrometry and Chromatography (MaSC), *http://www.mascgroup.org/* (accessed 27 July 2012).

28. Van Den Dool, H. and Kratz, P.D. (1963) A generalization of the retention index system including linear temperature programmed gas–liquid partition chromatography. *J. Chromatogr.*, **11**, 463–471.

29. Mondello, L., Dugo, P., Bade, A., Dugo, G., and Bartle, K.D. (1995) Interactive use of linear retention indices, on polar and apolar columns, with a MS-library for reliable identification of complex mixtures. *J. Microcolumn Sep.*, **7** (6), 581–591.

30. Bogusz, M.J., Maier, R.-D., Kruger, K.D., Webb, K.S., Romeril, J., and Miller, M.L. (1999) Poor reproducibility of in-source collisional atmospheric pressure ionization mass spectra of toxicologically relevant drugs. *J. Chromatogr., A*, **844**, 409–418.

31. Marquet, P., Venisse, N., Lacassie, E., and Lachatre, G. (2000) In-source CID mass spectral libraries for the ‘‘general unknown’’ screening of drugs and toxicants. *Analusis*, **28** (10), 925–934.

32. Little, J. *http://littlemsandsailing.files.wordpress.com/2012/12/msms_libraries2.pdf* (accessed 1 July 2013).

33. Gergov, M., Robson, J.N., Duchoslav, E., and Ojanperä, I. (2000) Automated liquid chromatographic/tandem mass spectrometric method for screening β-blocking drugs in urine. *J. Mass Spectrom.*, **35** (7), 912–918.

34. Dresen, S., Kempf, J., and Weinmann, W. (2006) Electrospray-ionization MS/MS library of drugs as database for method development and drug identification. *Forensic Sci. Int.*, **161**, 86–91.

35. Baumann, C., Cintora, M.A., Eichler, M., Lifante, E., Cooke, M., Przyborowska, A., and Halket, J.M. (2000) A library of atmospheric pressure ionization daughter ion mass spectra based on wideband excitation in an ion trap mass spectrometer. *Rapid Commun. Mass Spectrom.*, **14** (5), 349–356.

36. HighChem Spectral Tree Library, HighChem Ltd, Slovakia, *http://www.highchem.com/spectral-tree/highchem-spectral-tree-library.html* (accessed 27 July 2012).

37. Oberacher, H. (2012) MSforID, *http://msforid.com/* (accessed 27 July 2012).

38. Broecker, S., Herre, S., Wüst, B., Zweigenbaum, J., and Pragst, F. (2011) Development and practical application of a library of CID accurate mass spectra of more than 2,500 toxic compounds for systematic toxicological analysis by LC–QTOF-MS with data-dependent acquisition. *Anal. Bioanal. Chem.*, **400** (1), 101–117.

39. Liu, H.-C., Liu, R.H., Lin, D.-L., and Ho, H.-O. (2010) Rapid screening and confirmation of drugs and toxic compounds in biological specimens using liquid chromatography/ion trap tandem mass spectrometry and automated library search. *Rapid Commun. Mass Spectrom.*, **24** (1), 75–84.

40. Dresen, S., Gergov, M., Politi, L., Halter, C., and Weinmann, W. (2009) ESI-MS/MS library of 1,253 compounds for application in forensic and clinical toxicology. *Anal. Bioanal. Chem.*, **395** (8), 2521–2526.

41. Sauvage, F.-L., Saint-Marcoux, F., Duretz, B., Deporte, D., Lachatre, G., and Marquet, P. (2006) Screening of drugs and toxic compounds with liquid chromatography-linear ion trap tandem mass spectrometry. *Clin. Chem.*, **52** (9), 1735–1742.

42. Pittenauer, E., Zehl, M., Belgacem, O., Raptakis, E., Mistrik, R., and Allmaier, G. (2006) Comparison of CID spectra of singly charged polypeptide antibiotic precursor ions obtained by positive-ion vacuum MALDI IT/RTOF and TOF/RTOF, AP-MALDI-IT and ESI-IT mass spectrometry. *J. Mass Spectrom.*, **41** (4), 421–447.

43. NIST 12 MS/MS Database (2012) National Institute of Standards and Technology, Gaithersburg, MD, *http://chemdata.nist.gov/mass-spc/msms-search/* (accessed 20 August 2012).

44. Sheldon, M., Mistrik, R., and Croley, T.R. (2009) Determination of ion structures in structurally related compounds using precursor ion fingerprinting. *J. Am. Soc. Mass Spectrom.*, **20** (3), 370–376.

45. Horai, H. *et al.* (2010) MassBank: a public repository for sharing mass spectral data for life sciences. *J. Mass. Spectrom.*, **45** (7), 703–714.
46. METLIN: Metabolite and Tandem MS Database, Scripps Center for Metabolomics, La Jolla, CA, *http://metlin.scripps.edu/* (accessed 27 July 2012).
47. HighChem Fragmentation Library, HighChem Ltd, Slovakia, *http://www.highchem.com/fragmentation-library/* (accessed 27 July 2012).
48. PIR-PSD *http://pir.georgetown.edu/pirwww/dbinfo/pir_psd.shtml* (accessed 27 July 2012).
49. UniProtKB *http://www.uniprot.org/* (accessed 27 July 2012).
50. EMBL/DDBJ/GenBank *http://www.ebi.ac.uk/embl/* (accessed 27 July 2012).
51. NCBI RefSeq, *http://www.ncbi.nlm.nih.gov/RefSeq/* (accessed 27 July 2012).
52. PRF/SEQDB *http://www.prf.or.jp/seqdb-e.html* (accessed 27 July 2012).
53. MSDB *ftp://ftp.ncbi.nih.gov/repository/MSDB/msdb.nam* (accessed 27 July 2012).
54. NCBI Entrez Protein, *http://www.ncbi.nlm.nih.gov/sites/entrez?db=protein* (accessed 27 July 2012).
55. Leinonen, R., Diez, F.G., Binns, D., Fleischmann, W., Lopez, R., and Apweiler, R. (2004) UniProt archive. *Bioinformatics*, **20** (17), 3236–3237.
56. Sokolow, S., Karnofsky, J., and Gustafson, P. (1978) The Finnigan Library Search Program. Finnigan Application Report No. 2, Finnigan Corporation, San Jose, CA.
57. McLafferty, F.W., Hertel, R.H., and Villwock, R.D. (1974) Probability matching of mass spectra. Rapid identification of specific compounds in mixtures. *Org. Mass Spectrom.*, **9** (7), 690–702.
58. Damen, H., Henneberg, D., and Weimann, B. (1978) SISCOM—a new library search system for mass spectra. *Anal. Chim. Acta*, **103**, 289–302.
59. MassLibTM *http://www.masslib.com/* (accessed 27 July 2012).
60. Stein, S.E. (1994) Estimating probabilities of correct identification from results of mass spectral library searches. *J. Am. Soc. Mass Spectrom.*, **5** (4), 316–323.
61. Mondello, L. Salvatore, A. Tranchida, P.Q., Casilli, A., Dugob, P., Dugoa, G. (2008) Reliable identification of pesticides using linear retention indices as an active tool in gas chromatographic–mass spectrometric analysis. *J. Chromatogr., A*, **1186** (2008) 430–433.
62. Demuth, W., Karlovits, M., and Varmuza, K. (2004) Spectral similarity versus structural similarity: mass spectrometry. *Anal. Chim. Acta*, **516**, 75–85.
63. Haraki, K.S., Venkataraghavan, R., and McLafferty, F. (1981) Prediction of substructures from unknown mass spectra by the self-training interpretive and retrieval system. *Anal. Chem.*, **53** (3), 386–392.
64. Oberacher, H., Pavlic, M., Libiseller, K., Schubert, B., Sulyok, M., Schuhmacher, R., Csaszar, E., and Köfeler, H. (2009) On the inter-instrument and the inter-laboratory transferability of a tandem mass spectral reference library: 2. Optimization and characterization of the search algorithm. *J. Mass Spectrom.*, **44** (4), 494–502.
65. Mylonas, R., Mauron, Y., Masselot, A., Binz, P.-A., Budin, N., Fathi, M., Viette, V., Hochstrasser, D.F., and Lisacek, F. (2009) X-Rank: a robust algorithm for small molecule identification using tandem mass spectrometry. *Anal. Chem.*, **81** (18), 7604–7610.
66. HighChem Spectral Tree Search, HighChem Ltd, Slovakia, *http://www.highchem.com/spectral-tree/spectral-tree-search.html* (accessed 27 July 2012).
67. Rojas-Cherto, M., Peironcely, J.E., Kasper, P.T., van der Hooft, J.J.J., de Vos, R.C.H., Vreeken, R., Hankemeier, T., and Reijmers, T. (2012) Metabolite identification using automated comparison of high-resolution multistage mass spectral trees. *Anal. Chem.*, **84** (13), 5524–5534.

68. McHugh, L. and Arthur, J.W. (2008) Computational methods for protein identification from mass spectrometry data. *PLoS Comput. Biol.*, **4** (2), e12.

69. Roepstorff, P. and Fohlmann, J. (1984) Proposal for a common nomenclature for sequence ions in mass spectra of peptides. *Biomed. Mass Spectrom.*, **11** (11), 601–602.

70. Matrix Science MASCOT Search Overview, Matrix Science Inc., Boston, MA, *http://www.matrixscience.com/search_intro.html* (accessed 27 July 2012).

71. Eng, J.K., McCormack, A.L., and Yates, J.R.III (1994) An approach to correlate tandem mass spectral data of peptides with amino acid sequences in a protein database. *J. Am. Soc. Mass Spectrom.*, **5** (11), 976–989.

72. Mann, M. and Wilm, M. (1994) Error-tolerant identification of peptides in sequence databases by peptide sequence tags. *Anal. Chem.*, **66** (24), 4390–4399.

73. Lam, H., Deutsch, E.W., Eddes, J.S., Eng, J.K., Stein, S.E., and Aebersold, R. (2008) Building consensus spectral libraries for peptide identification in proteomics. *Nat. Methods*, **5** (10), 873–875.

74. Bringans, S., Kendrick, T.S., Lui, J., and Lipscombe, R. (2008) A comparative study of the accuracy of several de novo sequencing software packages for datasets derived by matrix-assisted laser desorption/ionisation and electrospray. *Rapid Commun. Mass Spectrom.*, **22** (21), 3450–3454.

75. McLafferty , Turecek, F., and F. (1993) *Interpretation of Mass Spectra*, 4th edn, University Science Books, Mill Valley, CA.

76. HighChem Mass Frontier, HighChem Ltd, Slovakia, *http://www.highchem.com/massfrontier/mass-frontier.html* (accessed 27 July 2012).

77. ACD/Labs ACD/MS Fragmenter, *http://www.acdlabs.com/products/adh/ms/ms_frag/* (accessed 27 July 2012).

78. Siegel, M.M. and Gill, G. (1990) MASSPEC: a graphics-based data system for correlating a mass spectrum with a proposed structure. *Anal. Chim. Acta*, **237**, 459–472.

79. Hill, A.W. and Mortishire-Smith, R.J. (2005) Automated assignment of high-resolution collisionally activated dissociation mass spectra using a systematic bond disconnection approach. *Rapid Commun. Mass Spectrom.*, **19** (21), 3111–3118.

80. Heinonen, M., Rantanen, A., Mielikäinen, T., Kokkonen, J., Kiuru, J., Ketola, R.A., and Rousu, J. (2008) FiD: a software for ab initio structural identification of product ions from tandem mass spectrometric data. *Rapid Commun. Mass Spectrom.*, **22** (19), 3043–3052.

81. Wolf, S., Schmidt, S., Müller-Hannemann, M., and Neumann, S. (2010) In silico fragmentation for computer assisted identification of metabolite mass spectra. *BMC Bioinformatics*, **11**, 148.

82. Waters MassFragment, *http://www.waters.com/waters/nav.htm?cid=1000943* (accessed 27 July 2012).

83. ChemSW Mass Spec Calculator Professional, *http://www.chemsw.com/Software-and-Solutions/Laboratory-Software/Chromatography-and-Mass-Spec-Tools/Mass-Spec-Calculator-Professional.aspx* (accessed 27 July 2012).

84. NIST MS Interpreter, *http://chemdata.nist.gov/mass-spc/interpreter/* (accessed 27 July 2012).

85. Kind, T. and Fiehn, O. (2007) Seven golden rules for heuristic filtering of molecular formulae obtained by accurate mass spectrometry. *BMC Bioinf.*, **8**, 105.

86. Hughey, C.A., Hendrickson, C.L., Rodgers, R.P., Marshall, A.G., and Qian, K. (2001) Kendrick mass defect spectrum: a compact visual analysis for ultrahigh-resolution broadband mass spectra. *Anal. Chem.*, **73** (19), 4676–4681.

87. Mortishire-Smith, R.J., Castro-Perez, J.-M., Yu, K., Shockcor, J.P., Goshawk, J., Hartshorn, M.J., and Hill, A. (2009) Generic dealkylation: a tool for increasing the hit-rate of metabolite rationalization, and automatic customization of mass defect filters. *Rapid Commun. Mass Spectrom.*, **23** (7), 939–948.

88. Budzekiewicz, H. (1998) *Massenspektrometrie: Eine Einführung*, Wiley-VCH Verlag GmbH, Weinheim.
89. Rockwood, A.L. and Van Orden, S.L. (1996) Ultrahigh-speed calculation of isotope distributions. *Anal. Chem.*, **68** (13), 2027–2030.
90. University of Sheffield ChemPuter: Isotope Patterns Calculator, *http://winter.group.shef.ac.uk/chemputer/isotopes.html* (accessed 27 July 2012).
91. Varmuza, K. (1985) Automatic recognition of isotope peak pattern in mass spectra. *Fresenius' J. Anal. Chem.*, **322** (2), 170–174.
92. Anderegg, R.J. (1985) A selenium-selective chromatographic detector based on isotope clusters. *Anal. Chim. Acta*, **176**, 175–183.
93. Kind, T. and Fiehn, O. (2006) Metabolomic database annotations via query of elemental compositions: mass accuracy is insufficient even at less than 1 ppm. *BMC Bioinf.*, **7**, 234.
94. Grange, A.H., Genicola, F.A., and Sovocool, G.W. (2002) Utility of three types of mass spectrometers for determining elemental compositions of ions formed from chromatographically separated compounds. *Rapid Commun. Mass Spectrom.*, **16** (24), 2356–2369.
95. Biller, J.E. and Biemann, K. (1974) Reconstructed mass spectra, a novel approach for the utilization of gas chromatograph—mass spectrometer data. *Anal. Lett.*, **7** (7), 515–528.
96. Colby, B.N. (1992) Spectral deconvolution for overlapping GC/MS components. *J. Am. Soc. Mass Spectrom.*, **3** (5), 558–562.
97. Dromey, R.G., Stefik, M.J., Rindfleisch, T.C., and Duffield, A.M. (1976) Extraction of mass spectra free of background and neighboring component contributions from gas chromatography/mass spectrometry data. *Anal. Chem.*, **48** (9), 1368–1375.
98. Stein, S.E. (1999) An integrated method for spectrum extraction and compound identification from gas chromatography/mass spectrometry data. *J. Am. Soc. Mass Spectrom.*, **10** (8), 770–781.
99. Windig, W., Phalp, J.M., and Payne, A.W. (1996) A noise and background reduction method for component detection in liquid chromatography/mass spectrometry. *Anal. Chem.*, **68** (20), 3602–3606.
100. ACD/Labs ACD/IntelliXtract, *http://www.acdlabs.com/products/adh/ms/intellixtract/* (accessed 27 July 2012).
101. Windig, W. (1988) Mixture analysis of spectral data by multivariate methods. *Chemom. Intell. Lab. Syst.*, **4** (3), 201–213.
102. Windig, W., Heckler, C.E., Agblevor, F.A., and Evans, R.J. (1992) Self-modeling mixture analysis of categorized pyrolysis mass spectral data with the SIMPLISMA approach. *Chemom. Intell. Lab. Syst.*, **14** (1–3), 195–207.
103. Windig, W. (1992) Self-modeling mixture analysis of spectral data with continuous concentration profiles. *Chemom. Intell. Lab. Syst.*, **16** (1), 1–16.
104. Varmuza, K. and Filzmoser, P. (2009) *Introduction to Multivariate Statistical Analysis in Chemometrics*, CRC Press, Boca Raton, FL.
105. Werther, W., Demuth, W., Krueger, F.R., Kissel, J., Schmid, E.R., and Varmuza, K. (2002) Evaluation of mass spectra from organic compounds assumed to be present in cometary grains. Exploratory data analysis. *J. Chemom.*, **16** (2), 99–110.
106. Werther, W. and Varmuza, K. (1994) in *Software-Development in Chemistry*, Vol. 8 (ed C. Jochum), Gesellschaft Deutscher Chemiker (GDCh), Frankfurt am Main, pp. 129–134.
107. Varmuza, K. and Werther, W. (1996) Mass spectral classifiers for supporting systematic structure elucidation. *J. Chem. Inf. Comput. Sci.*, **36** (2), 323–333.
108. Lohninger, H. and Varmuza, K. (1987) Selective detection of classes of chemical compounds by gas chromatography/mass spectrometry/pattern

recognition: polycyclic aromatic hydrocarbons and alkanes. *Anal. Chem.*, **59** (2), 236–244.

109. Lindsay, R.K.; Bruce G. Buchanan, B.G.; Edward, A. Feigenbaum, E.A. and Joshua Lederberg, J. (1980) *Applications of Artificial Intelligence for Organic Chemistry: The DENDRAL Project*. McGraw-Hill, New York.

110. Schymanski, E.L., Meinert, C., Meringer, M., Brack, W. (2008) The use of MS classifiers and structure generation to assist in the identification of unknowns in effect-directed analysis. *Anal. Chim. Acta* **615**, 136–147, *http://www.mathe2.uni-bayreuth.de/markus/ei-ms/* (accessed 27 July 2012).

56
Raman Spectroscopy Fundamentals

David Moore

This chapter presents the state of the art in Raman fundamentals including theory, laser sources, spectrometers, detectors, Raman microscopy (confocal and micro-Raman), Raman imaging, fiber optic probes, and methods to obtain depth profile information.

Next, the chapter discusses data treatment. Raman spectra should be calibrated both along the abscissa and the ordinate to be universally utilizable. The calibration of the abscissa (Raman shift) is presented using the ASTM-E-1840 (American Society for Testing and Materials) guide. Several methods to calibrate the ordinate (Raman intensity) are discussed. The issue of fluorescence interference will be considered from the perspectives of excitation wavelength selection and post-acquisition data reduction.

Finally, the chapter deals with the concept of Raman spectral databases. There are at present several such databases, including common data format libraries and proprietary libraries. However, such databases and libraries should ultimately satisfy stringent criteria for long-term data archiving, including readability for long times into the future, robustness to changes in computer hardware and operating systems, and use of public domain data formats. The latter criterion implies that the data format should be platform independent and the tools to create the data format should be easily and publicly obtainable or developable. Several examples of attempts at spectral libraries exist, such as the ASTM ANDI format (analytical data interchange), and the joint committee on atomic and molecular physical data exchange (JCAMP-DX) format. On the other hand, proprietary library spectra can be exchanged and manipulated using proprietary tools. As the above-mentioned examples have deficiencies according to the three long-term data archiving criteria, Extensible Markup Language (XML; a product of the World Wide Web Consortium (W3C), an independent standards body) as a new data interchange tool is being investigated and implemented. This chapter presents today's status of this effort.

Handbook of Spectroscopy, Second Edition. Edited by Günter Gauglitz and David S. Moore.

56.1
Theory

Raman scattering is one of a family of scattering processes involving interaction of a primary light quantum with atoms, molecules, or crystals by which a secondary light quantum is produced. Raman involves inelastic scattering, producing secondary light quanta of different energy from the primary light quanta. The energy difference is equal to the vibrational energy of a molecule or crystal and/or the rotational energy of a molecule, and thereby Raman scattering provides a means of measuring vibrational spectra, alternatively to infrared (IR) absorption spectroscopy. These two types of spectroscopy are illustrated schematically in Figure 56.1. If monochromatic radiation is used for the primary light quanta, recording the secondary quanta produces a Raman spectrum. Scattering from molecules or crystals in their ground rotational and/or vibrational states produces a Stokes, or redshifted, Raman spectrum. Scattering from excited vibrational and/or rotational states produces an anti-Stokes, or blueshifted, Raman spectrum. The relative intensity of the Raman lines in the Stokes and anti-Stokes Raman spectra may be used, via the Boltzmann equation, for the determination of the vibrational (or rotational) temperature [1–4].

An electric field incident on a molecule forces the electrons and nuclei to move in opposite directions. A dipole moment is induced, which is proportional to the electric field strength and the molecular polarizability. A molecular vibration described by the normal coordinate q_k can be observed in the Raman spectrum only if it modulates to first order the molecular polarizability. Molecular symmetries that fulfill this condition are allowed, or Raman active; otherwise forbidden, or Raman inactive.

IR absorption, on the other hand, involves direct resonance between the frequency of the IR radiation and the vibrational frequency of a particular mode of vibration, with the absorption strength proportional to the change in dipole moment with

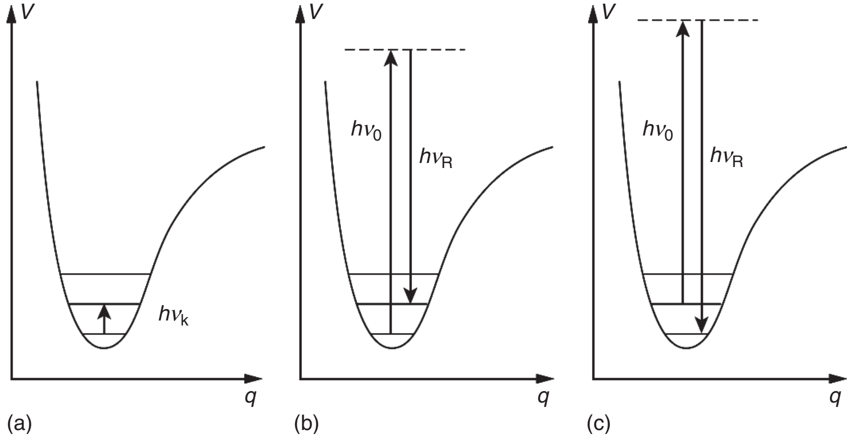

Figure 56.1 (a) Infrared absorption, (b) Stokes Raman scattering, and (c) anti-Stokes Raman scattering.

respect to the particular vibrational motion. The photon incident on the molecule, if it is absorbed, disappears, and leaves the molecule in an excited vibrational state. The molecular symmetries that modulate the dipole moment are IR active. Often, there are symmetries in a given molecule that are Raman active, but IR inactive and vice versa, making IR and Raman complementary vibrational spectroscopic methods. This attribute is illustrated in Figure 56.2 [5]. Figure 56.2 also illustrates the recommended spectrum presentation, that is, linear abscissa scale with increasing wavenumber from right to left for better comparison to standard IR spectra representation; linear ordinate scale increasing from bottom to top (whereas IR spectra are usually represented as percent transmission, increasing from bottom to top) [1].

A normal vibration is described by the normal coordinate q_k and the normal frequency ν_k

$$q_k = q_k^0 \cos(2\pi \nu_k t) \tag{56.1}$$

If a molecule is put into an alternating electric field of frequency ν_0, a dipole moment p with alternating polarity at the frequency ν_0 is induced. The components of the vector of the electric field according to a molecular fixed Cartesian coordinate system are described by E_x, E_y, and E_z. The *induced dipole moment* p_i can be described by its components:

$$\begin{aligned} p_x &= \alpha_{xx} E_x + \alpha_{xy} E_y + \alpha_{xz} E_z \\ p_y &= \alpha_{yx} E_x + \alpha_{yy} E_y + \alpha_{yz} E_z \\ p_z &= \alpha_{zx} E_x + \alpha_{zy} E_y + \alpha_{zz} E_z \end{aligned} \tag{56.2}$$

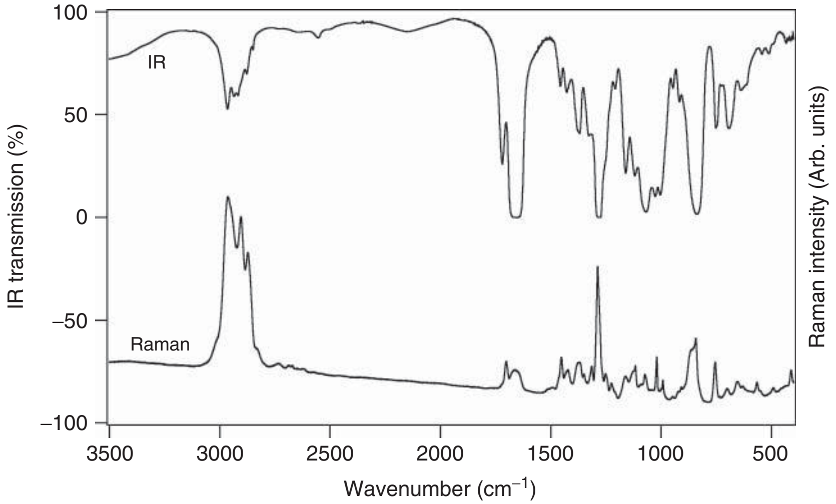

Figure 56.2 Raman and IR transmission spectra of nitrocellulose, illustrating their complementary nature. (From Ref. [5], used with permission.)

where α_{ij} are components of the *polarizability tensor* α:

$$\alpha = \begin{bmatrix} \alpha_{xx} & \alpha_{xy} & \alpha_{xz} \\ \alpha_{yx} & \alpha_{yy} & \alpha_{yz} \\ \alpha_{zx} & \alpha_{zy} & \alpha_{zz} \end{bmatrix}$$

which projects the electric field vector to produce the induced dipole moment vector. This can be written in matrix notation as

$$\mathbf{p} = \alpha \mathbf{E}$$

$$\alpha_k = \alpha_0 + \left[\frac{\partial \alpha}{\partial q_k}\right]_0 q_k^0 \cos 2\pi \upsilon_k t + \cdots \tag{56.3}$$

Equations (56.2) and (56.3) can be combined to give

$$p_k = \alpha_0 E_0 \cos(2\pi\nu_0 t) + \frac{1}{2}\left(\frac{\partial \alpha}{\partial q_k}\right)_0 q_k^0 E_0 \left\{\cos\left[2\pi\left(\nu_0 - \nu_k\right) t\right] + \cos[2\pi(\nu_0 + \nu_k)t]\right\} \tag{56.4}$$

This oscillating *Hertzian dipole* $|\mathbf{p}_k|$ produces electromagnetic radiation. The first term in Eq. (56.4) describes Rayleigh scattering, the second term *Stokes Raman scattering*, and the third *anti-Stokes Raman scattering*. This classical equation, however, does not show the individual intensities of *Stokes* and *anti-Stokes Raman lines*.

Placzek's theory (1934) describes the Raman effect quantitatively on the condition that the exciting frequency differs considerably from the frequencies of electronic as well as of vibrational transitions.

In order to describe the intensity of the Raman lines of liquids or gases, the parameters α'_k and γ'_k are used. They stand for the isotropic and the anisotropic parts of the polarizability change during a normal vibration ν_k, respectively, and are given by (in order to simplify these equations, the subscript k has been omitted):

$$\alpha' = \frac{1}{3}[\alpha'_{xx} + \alpha'_{yy} + \alpha'_{zz}] \tag{56.5}$$

$$\gamma'^2 = \frac{1}{2}\left[\left(\alpha'_{xx} - \alpha'_{yy}\right)^2 + \left(\alpha'_{yy} - \alpha'_{zz}\right)^2 + \left(\alpha'_{zz} - \alpha'_{xx}\right)^2 + 6\left(\alpha'^2_{xy} + \alpha'^2_{xz} + \alpha'^2_{zy}\right)^2\right] \tag{56.6}$$

The terms $\alpha'_{ij} = \left[\frac{\partial \alpha_{ij}}{\partial q}\right]_0$ are the components of the *tensor of the polarizability change* resulting from a normal vibration q.

The polarizability has the dimension $\mathrm{J^{-1}\,C^2\,m^2}$. In older literature, the polarizability has been described as a volume, in analogy with the molecular volume ($1\,\text{Å}^3 = 10{-}24\,\mathrm{cm}^3$). The *polarizability volume* results when the polarizability given in SI units is divided by $4\pi\varepsilon_0$ (in $\mathrm{J^{-1}\,C^2\,m^{-1}}$). The normal coordinates are mass weighted and have the dimension cm $\mathrm{g}^{1/2}$.

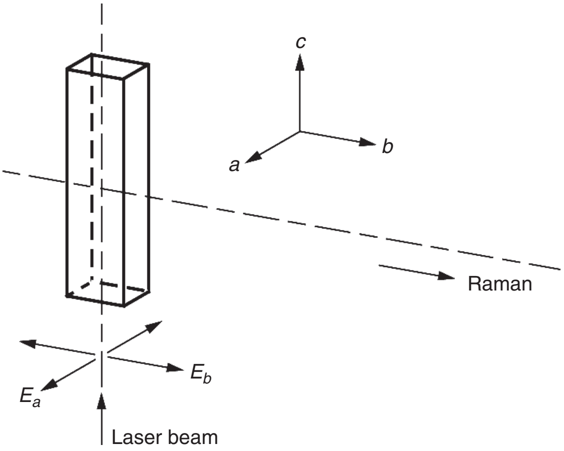

Figure 56.3 Orientation of the electric vector of the exciting laser beam to the Raman observation direction.

Referring to Figure 56.3, when the Raman spectrum of a liquid or a gas is measured by irradiating along the *c*-axis with linearly polarized radiation whose electric vector is oriented in the *a* direction and the Raman spectrum is observed along the *b* axis, then the *c* and *b* axes define the *plane of observation*.

The *integral Raman scattering coefficient* (the *absolute differential Raman scattering cross section* $(\mathrm{d}\sigma/\mathrm{d}\Omega)$ in $\mathrm{cm}^2\,\mathrm{sr}^{-1}$) of the Stokes line (shifted to lower energies) of the *k*th Raman-active vibration of wavenumber, $\tilde{\nu}$ (symbol defined in Ref. [6]), with the electric vector of the exciting radiation oriented perpendicular to the plane of observation, is given by

$$\left(\frac{\mathrm{d}\sigma}{\mathrm{d}\Omega}\right)^{-}_{k\perp} = \frac{\pi^2}{45\varepsilon_0^2}\cdot\frac{b_k^2(\tilde{\nu}_0-\tilde{\nu}_k)^4}{1-\exp(-hc\tilde{\nu}_k/kT)}\cdot g_k(45\alpha_k'^2+7\gamma_k'^2) \tag{56.7}$$

where σ is the scattering cross section, Ω is the solid angle, and g_k is the *degeneracy* of this vibration and the superscript $^-$ indicates Stokes Raman scattering. The expression

$$g_k(45\alpha_k'^2+7\gamma_k'^2) \tag{56.8}$$

is known as the *scattering activity*, and

$$b_k^2 = h/8\pi^2 c\tilde{\nu}_k \tag{56.9}$$

is the square of the *zero point amplitude* of the vibration. Equation (56.7) may be simplified:

$$\left(\frac{\mathrm{d}\sigma}{\mathrm{d}\Omega}\right)^{-}_{k\perp} = \frac{h}{2^3 c\varepsilon_0^2}\cdot\frac{(\tilde{\nu}_0-\tilde{\nu}_k)^4}{\tilde{\nu}_k[1-\exp(-hc\tilde{\nu}_k/kT)]}\cdot g_k\left(\alpha_k'^2+\frac{7}{45}\gamma_k'^2\right) \tag{56.10}$$

This equation is valid for observation without a polarization analyzer. Equations valid for the other polarization conditions and a discussion of depolarization ratio measurements can be found in Refs. [1–3].

The differential Raman scattering cross section is proportional to the fourth power of the emitted frequency, the ν^4 *factor*. Dividing Eq. (56.7) by $(\nu_{\text{ref}} - \nu_k)^4$, gives the *absolute normalized Raman scattering cross section* (Eq. (56.11)) of a Raman line with frequency shift ν_k [3].

$$\left(\frac{\mathrm{d}\sigma}{\mathrm{d}\Omega}\right)^{-}_{k\perp} \cdot (\tilde{\nu}_{\text{ref}} - \tilde{\nu}_k)^{-4} = \frac{h}{2^3 c\nu\varepsilon_0^2} \cdot \frac{g_k}{\tilde{\nu}_k[1 - \exp(-hc\tilde{\nu}_k/kT)]} \cdot \left(\alpha_k'^2 + \frac{7}{45}\gamma_k'^2\right) \tag{56.11}$$

where ν_{ref} is the *reference excitation wavenumber* (Ref. [4]). The right-hand side of Eq. (56.11) represents the microscopic parameters of the sample and has been tabulated for a number of gases and liquids and for several ν_{ref} in Ref. [4]. According to Placzek's theory, this expression should be independent of the frequency of the exciting radiation in the absence of a resonance or a near-resonance Raman effect. The term on the left-hand side normalizes the observed Raman intensity by including the ν^4 factor.

The radiant power of the observed radiation is proportional to the absolute normalized Raman scattering cross section, that is, to the ν^4 factor and to the *number of molecules per unit volume N*. The *Raman scattering coefficient* s_{R} of this line is thus:

$$s_{\text{R}} = \left(\frac{\mathrm{d}\sigma}{\mathrm{d}\Omega}\right)^{-}_{k\perp} \cdot (\tilde{\nu}_{\text{ref}} - \tilde{\nu}_k)^{-4}(\tilde{\nu}_0 - \tilde{\nu}_k)^4 N L_{\text{n}} \tag{56.12}$$

where L_{n} is the internal field factor:

$$L_{\text{n}} = \left(\frac{n_{\text{R}}}{n_0}\right)(n_{\text{R}}^2 + 2)^2 \frac{(n_0^2 + 2)^2}{3^4} \tag{56.13}$$

and n_0 and n_{R} are the refractive indices of the scattering medium at the wavelength of the exciting and the Raman radiation, respectively, which takes into account the increase of the incident and scattered electric field due to the dielectric nature of the scattering medium.

The *radiance of a Raman line* L_{R} (scattered power per unit solid angle per unit area of sample integrated over the Raman line in question) is proportional to the radiant power of the exciting radiation divided by the cross-sectional beam area r^2 π and multiplied by the Raman scattering coefficient:

$$L_{\text{R}} = \frac{\Phi_0}{r^2\pi} d s_{\text{R}} \tag{56.14}$$

where *d* is the *sample thickness* of the observed sample and *r* is the beam radius.

56.2
Qualitative Analysis

Schrader [3] has provided an excellent compilation of typical characteristic vibrational frequencies and Raman and IR intensities for organic compounds. The complete listing is found in his Table 4.1-1. A similar table is available as a PDF download from Horiba Jobin-Yvon [7]. A recent book by Socrates [8] provides an extensive collection of characteristic frequencies. These characteristic frequencies can be divided into typical regions as follows. The X–H stretching vibrations are located in the highest frequency region, between 3700 and 2500 cm^{-1}. The O–H vibrations are weak in the Raman spectrum, so that water is a weak Raman scatterer (making Raman an excellent probe of aqueous samples, in contrast to IR). Most C–H and S–H vibrations are strong (with the exception of acetylenic hydrogens), and N–H medium. The next region, between 2500 and 2000 cm^{-1}, contains stretching vibrations of groups with triple bonds as well as the antisymmetric stretching vibrations of groups with cumulated double bonds, X=Y=Z. The following region, between 2000 and 1500 cm^{-1}, exhibits stretching vibrations of double bonded X=Y groups. X–H deformation vibrations are observed between 1500 and 1000 cm^{-1}. The region between 1300 and 600 cm^{-1} shows stretching vibrations of single bonds of atoms of the second period. The next region contains bending vibrations of these groups and stretching vibrations of groups with heavier atoms. Finally, the region between 200 and 20 cm^{-1} is characterized by lattice vibrations of crystalline molecular materials. Some examples of often-utilized characteristic spectral features are the C=O stretching vibrations (usually strong in the Raman) between 1820 and 1680 cm^{-1} and the C–(NO_2) stretches, with the antisymmetric stretch between 1530 and 1590 cm^{-1} (medium to weak) and the symmetric stretch between 1340 and 1380 cm^{-1} (very strong).

56.3
Experimental Details

The most convenient monochromatic light source for excitation of Raman spectra is the laser. The currently preferred excitation sources are solid-state lasers and their harmonics, or specialty lasers for specific wavelength regions. The most common excitation laser is a 785 nm diode laser, with Si-based charge-coupled device (CCD) for detection. However, the long wavelength responsivity cutoff of Si-based detectors only allows collecting the Raman spectrum with any efficiency to $\sim$2500 cm^{-1}. Figure 56.4 shows efficiency curves of a typical Si-based CCD detector for three different excitation wavelengths, illustrating the restriction on how far into the near-infrared (NIR) the excitation laser can be pushed. Fourier transform Raman instruments using 1064 nm neodymium-doped yttrium aluminum garnet (Nd:YAG) lasers and cooled semiconductor detectors have allowed fluorescence reduction by moving further into the NIR [9]. Other harmonics of solid-state Nd:YAG (or variants) lasers allow excitation at 532, 355, 266, and 212.8 nm. A large number of compact portable Raman spectrometers have appeared recently from commercial suppliers, which allows taking Raman on the road [10]. Deep UV excitation has recently become easier using efficient transversely excited hollow cathode lasers [11].

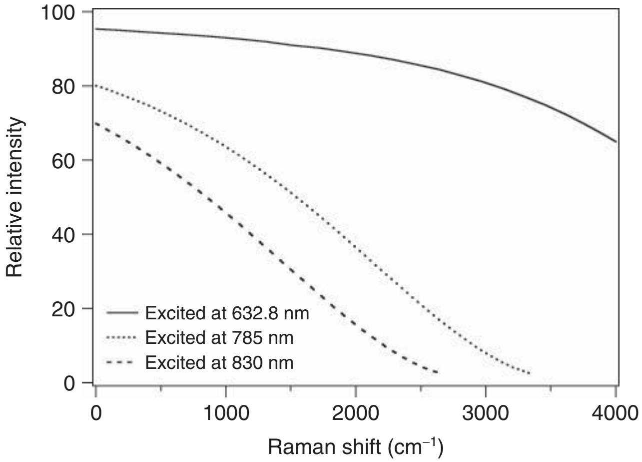

Figure 56.4 Relative Raman intensity of typical Si-based CCD detectors for three different excitation wavelengths, based on a quantum efficiency versus wavelength curve for a thinned, backside-illuminated, visible antireflection coated CCD. (From Ref. [10], used with permission.)

56.3.1
Fluorescence Interference

The principal detriment to Raman spectroscopy is fluorescence, either native to the analyte or from background, matrix, or interferent materials. Several methods have been developed to reduce the effects of fluorescence. Most utilize far-red or NIR excitation sources because of the assumption that there are fewer molecules with strong absorption and fluorescence when excited in the red or NIR. However, such a choice extracts a severe signal penalty because of the ν^4 factor, for example, the ratio of signal strength (all other things being equal) for 785 nm versus 514.5 nm excitation is 0.18. In addition, not all fluorescence is eliminated. Fourier transform Raman was developed to enable excitation with the Nd:YAG fundamental at 1064 nm, reducing fluorescence as well as decomposition issues for biological samples [9].

Another choice is to use UV excitation, with the aim of exciting at energies high enough that most of the vibrational Raman spectrum occurs at wavelengths shorter than fluorescence from the majority of organic molecular species (typically >250 nm). For example, for excitation at 224.3 nm (transversely excited hollow cathode laser) [11], the Stokes Raman spectrum from 0 to 4000 cm^{-1} ends at 246.4 nm, much before the onset of most fluorescence. Second, the ν^4 factor increases the scattering coefficient by a factor of ~25 over that at 532 nm. Finally, a large fraction of molecules have electronic potential energy surfaces near 5 eV above the ground state, resulting in large resonance enhancements of the Raman cross section (up to factors of 10^8). This combination makes deep UV Raman very attractive especially for detection of small amounts of material or micro-Raman imaging. On the other hand, a large fraction of molecules react photochemically when excited in the deep UV, so that the Raman process is no longer generally noninvasive.

Other fluorescence interference removal schemes have been developed, including correlation of spectra obtained using two or more alternating, closely spaced, excitation wavelengths (the two-wavelength version is commonly called *shift excitation Raman difference spectroscopy* or SERDS [12]), time gating methods, which take advantage of the near instantaneous response of Raman scattering and the longer lifetimes of fluorescence [13, 14], and various forms of filtering, such as Fourier-domain filtering and edge detection algorithms [15].

56.3.2
Imaging

Raman microscopy can be performed using point-by-point, linescan, or imaging methods. All methods inject the excitation laser into the microscope via reflection from a dichroic or notch filter and focusing of the excitation light onto the sample and gathering of the Raman scattering using the microscope objective. The Raman scattering then passes through the dichroic or notch filter to be dispersed and detected. For creation of Raman images, the point-by-point method utilizes a programmable sample stage synchronized with the detection electronics so that complete spectra are obtained at each sample voxel, giving at the end a hyperspectral image from which various display options can be explored via software (i.e., concentration maps, species maps, spectra at any spatial location, etc.). If high-axial spatial resolution is needed, a confocal microscope can be used.

Linescan images can be obtained by dithering the laser spot (using a vibrating mirror) and recording the Raman spectrum at each point along the line by image transfer onto the spectrometer slit. Then the complete image only requires coordinated sample stage movement in one (2D image) or two (3D image) orthogonal directions.

Another concept for obtaining Raman images is to illuminate the entire microscope field of view using a defocused laser source, then record CCD images through a tunable filter (acousto-optic or liquid crystal variations have been used), building up the data hypercube by consecutive spectral bands. A confocal version and coordinated z-axis sample movement allows building up a volume spectral hypercube layer by layer.

56.3.3
Fiber Optic Probes

Finally, remote applications of Raman have been accomplished using various optical fiber coupled probes. In most cases, the Raman signals produced through transit of the excitation laser through long distances of optical fiber are removed using a dichroic filter built into the probe housing, and the excitation laser elastically scattered (or reflected) from the sample is removed via a notch or dichroic filter

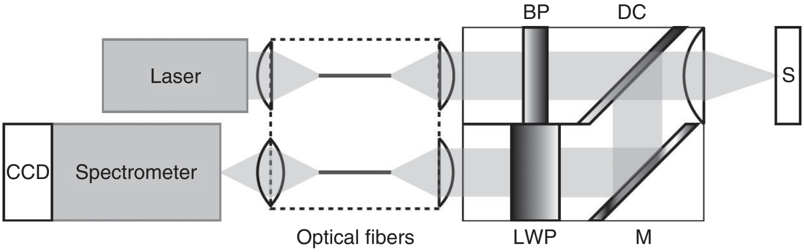

Figure 56.5 The essential elements of a portable Raman system, with optical fiber coupling shown in the dashed block: CCD charge-coupled device detector, BP, bandpass filter; DC, dichroic filter; LWP, long wavelength pass filter; M, mirror; and S, sample.

before the collected Raman light is focused into the return fiber (or fibers). This concept is illustrated schematically in Figure 56.5. The optical conductance trade-offs necessary for optical fiber couple probe Raman are discussed in Ref. [10]. More recently, stand-off Raman has been demonstrated for distances of many tens of meters using pulsed laser excitation and large aperture telescopes to collect the scattered light [16–18].

56.4
Raman Data Treatment and Calibration

Figure 56.6 illustrates schematically the present situation for Raman data calibration in the worldwide Raman spectroscopy community, and presents some of the terminology used.

Figure 56.7 shows three Raman spectra of polystyrene obtained using three different compact Raman systems. The spectra in Figure 56.7 and the concepts

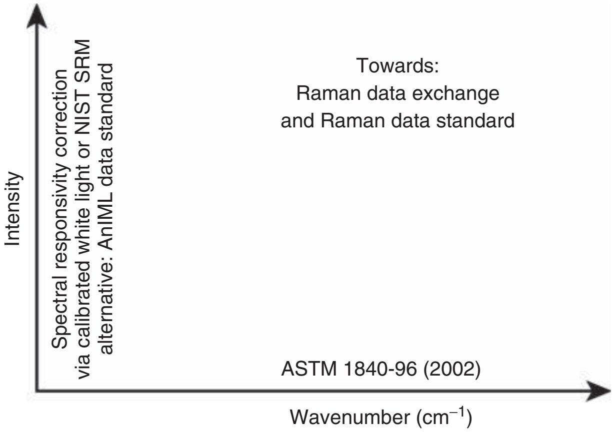

Figure 56.6 Present status of Raman data standard as well as abscissa and ordinate calibrations.

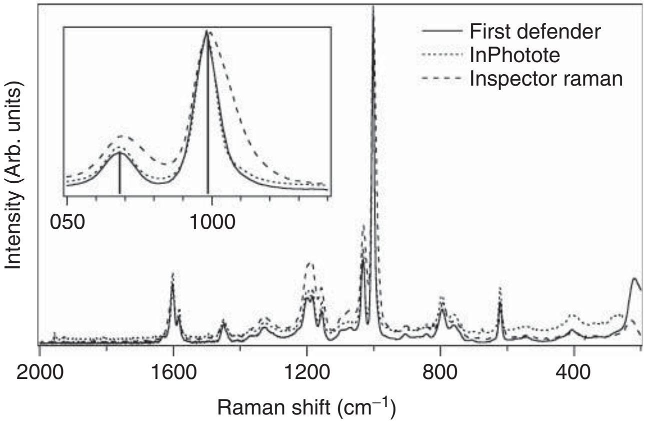

Figure 56.7 Raman spectra of polystyrene obtained using (solid line) First Defender (Ahura Scientific), (dotted line) InPhotote (Inphotonics, Inc.), and (dashed line) Inspector Raman (DeltaNu, LLC). The solid vertical lines in the inset are at the ASTM-E-1840 calibrated wavenumbers and relative intensities.

in Figure 56.6 will be used in the discussion in subsequent text to illustrate the various facets of Raman data calibration.

In order to enable the most accurate comparison of Raman spectra obtained from various instruments, abscissa (wavenumber axis) calibration must be performed, and some method of accounting for the system spectral responsivity should be used to correct the ordinate. For abscissa calibration, the ASTM-E-1840 guide recommends several means [19]. [Note: despite the ASTM guide usage of the term *Raman shift* for the abscissa, it is not a recognized physical quantity [6], and the term *wavenumber* (or *Raman wavenumber*) should instead be used with the unit cm^{-1} [6].] The ASTM utilized a round-robin methodology to determine the peak wavenumbers for eight different readily available materials having no known polymorphs, selected to cover a wide wavenumber range (85–3327 cm^{-1}) for both solids and liquids. The standard error for the peaks is usually <1.0 cm^{-1}. Often, Raman instruments have some kind of calibration routines built in, which involve measurement of the excitation laser wavelength and calibration of the detector pixel versus wavelength using an atomic line source. The results of this type of calibration should be verified using at least one of the approved ASTM-E-1840 guide materials before reporting abscissa wavenumbers for any Raman spectral features.

The spectra in Figure 56.7 were abscissa calibrated according to each instrument vendor's instructions or routines. The inset shows the recommended polystyrene wavenumber values as vertical lines. Two of the instruments produced spectra with calibrations better than 0.4 cm^{-1} compared to ASTM-E-1840, and one was right at $\sim$1 cm^{-1}, the standard error for the ASTM recommendations.

One abscissa parameter not considered by the ASTM-E-1840, which has less to do with wavenumber calibration than with the ultimate ability of library search algorithms to identify materials, is the instrumental spectral resolution. The spectra in Figure 56.7 show that two of the instruments have very similar resolution

($\sim$5 cm^{-1}) but one has much less ($\sim$8 cm^{-1}). The ASTM-E-1840 recommends peak wavenumbers, but some search routines are also influenced by line widths, so that library spectra obtained with instruments of different spectral resolution could result in identification errors.

Correction of ordinate data is more problematic. The ν^4 factor causes changes in Raman signal strength with excitation wavelength. In addition, electronic preresonance and resonance effects can cause changes in the relative intensities of various Raman features depending on their associated chromophore. For a given selected excitation wavelength, however, the ordinate correction process is straightforward. The detected Raman intensities should be multiplied by a relative spectral responsivity correction curve obtained for the entire optical train from sample to detector. Two methods are available to measure the spectral responsivity curve. One is using a calibrated white light irradiance source. More recently, NIST has developed three certified luminous optical glasses (for different excitation wavelengths, 785, 532, and 488/514.5 nm) that emit a broad luminescence spectrum when illuminated with the Raman excitation laser [20]. To perform the correction, either the white light irradiance or the glass luminescence is recorded using the Raman system. Then the spectral irradiance value curve or the relative spectral luminescence curve (I_{SRM}) is used to obtain the spectral intensity correction curve C_{SRM} by dividing I_{SRM} by the spectrum measured by the Raman instrument S_{SRM}. The relative-intensity-corrected Raman spectrum is then obtained by multiplying the measured Raman spectrum by C_{SRM}.

Note the ordinate differences shown in Figure 56.7 for the polystyrene Raman spectrum obtained using three different portable Raman systems, which is indicative of the kinds of ordinate calibration problems that can occur. At low wavenumbers, one of the spectra has too high a baseline compared to the other two. In the middle wavenumber region, another of the instruments produces peaks that are too large compared to the other two, relative to the largest peak at 1001.4 cm^{-1}. The inset shows the relative intensities of two features near 1000 cm^{-1}, for which spectra from two instruments match very well, but the spectrum from the third instrument (the same one that has lower spectral resolution) is quite different. These differences apparently occur because of inadequate (or lack of) ordinate spectral responsivity correction, and could affect library search outcomes (see subsequent text).

56.5
Raman Spectral Databases

There are a number of Raman spectral databases available [21]. For example, Raman spectra for a large number of minerals are available at the Caltech/University of Arizona RRUFF™ Project Web site (allows download of spectra in American Standard Code for Information Interchange (ASCII) text pairs) [22]. Raman spectra of natural and synthetic pigments are available at the University College London Web site [23]. The University of Siena has a Raman database (graphical spectra with listing of selected peaks) for minerals and inorganic materials [24]. A searchable database of molecular spectra (from NMR to IR and Raman) of organic compounds is available from the Advanced Industrial Science and Technology (AIST) in Japan [25]. Some commercial enterprises offer online Raman database searching, such as the Fourier transform infrared spectroscopy (FTIR)/Raman search.com from Thermo Fisher Scientific. It uses the GRAMS/AI methodology and Thermo Scientific spectral databases [26]. In addition, a number of instrument manufacturers offer extensive proprietary Raman spectral databases.

Nevertheless, these databases do not satisfy the stringent criteria for long-term data archiving, which include readability for long times into the future, robustness to changes in computer hardware and operating systems, and use of public domain data formats. The latter criterion implies that data formats should be platform independent and the tools to create the data forms should be easily and publicly obtainable or developable. In the United States, there is regulatory pressure to archive ‘‘accurate and complete’’ copies of electronic records provided to government agencies ((Food and Drug Administration) FDA 21 CFR 11 (Code of Federal Regulations): data formats).

To date, none of the available Raman spectral databases abide by all long-term data archiving criteria, yet there has been some progress. Some open source spectral library formats have been developed. The ASTM E01.25 Subcommittee on Laboratory Analytical Data Interchange Protocols and Information Management develops ANDI protocols to increase laboratory efficiency and productivity by facilitating the integration and use of data from multiple vendors’ instruments. The International Union of Pure and Applied Chemistry (IUPAC) developed the JCAMP-DX data format for spectroscopic data [27]. JCAMP is completely ASCII based for simple transport and readability, and utilizes a fixed dictionary of tags, but suffers from numerical accuracy (translation of binary to decimal). Galactic developed the SPC data format primarily for optical spectroscopy, and has made its structure available in the public domain [28]. The ANDI and SPC protocols suffer from not being human readable. None of the three are easily validated for formatting and content nor extensible for future changes in equipment and analysis methods.

56.6
Database Searching

For identification of unknowns, many Raman practitioners perform some sort of search of the spectrum obtained for the unknown against a library of spectra, with the hit quality index (HQI) being the measurement of the likelihood of identity. The searches utilize a variety of algorithms, from full spectrum methods such as simple Euclidean distance (essentially a normalized dot product of the unknown spectrum with a library spectrum, with HQI as given in one embodiment in Eq. (56.15):

$$\mathrm{HQI} = \sqrt{2}\left[1 - \frac{(\mathrm{Lib}\cdot\mathrm{Unkn})}{\sqrt{(\mathrm{Lib}\cdot\mathrm{Lib})}\sqrt{(\mathrm{Unkn}\cdot\mathrm{Unkn})}}\right] \qquad (56.15)$$

where Lib is the library entry being searched and Unkn is the unknown spectrum; best match gives HQI = 0; no match gives HQI = 1.414), correlation (similar to Euclidean distance, but with both library and unknown spectra centered about their respective means, which makes the HQI independent of the spectral normalization, as given in one embodiment in Eq. (56.16):

$$\mathrm{HQI} = 1 - \frac{(\mathrm{Lib_m} \cdot \mathrm{Unkn_m})^2}{(\mathrm{Lib_m} \cdot \mathrm{Lib_m})(\mathrm{Unkn_m} \cdot \mathrm{Unkn_m})} \tag{56.16}$$

where $\mathrm{Lib_m} = \mathrm{Lib} - \sum_{i=1}^{n} \mathrm{Lib}_i/n$ and similarly for $\mathrm{Unkn_m}$; best match gives HQI = 0; no match gives HQI = 1), to first derivative correlation (FDC, correlation of first derivatives of both unknown and library spectra, which helps remove nonlinear effects of baselines that cannot be removed by baseline preprocessing) [29]. Denton *et al.* [21] found that the first derivative absolute value algorithm produced the best HQI when searching an unknown spectrum against an arbitrary Raman spectral library obtained with a different Raman system. This algorithm has the advantage of removing most of the error from a slowly varying baseline in the unknown, especially when the baseline is not linear (similar to the FDC algorithm). It also appears to be relatively insensitive to spectral resolution effects. Other algorithms used include peak matching, absolute value, and least squares.

An example of the use of these library search routines is given in Figure 56.8, for an unknown spectrum taken from a small amount (1.5%) of TATB (triamino trinitrobenzene) in soil, and searching a spectral library of about 100 different explosives.

Using the correlation algorithm, automatic baseline correction, and involving the entire spectrum (rather than several distinct regions) in the search, the best HQI for the Figure 56.8 sample spectrum was obtained for TATB (0.738), followed by DAAZF (diaminoazofurazan, 0.818) and HNS (hexanitrostilbene, 0.825), and a number of other materials with HQI above 0.84. The library search identified the correct material, but an HQI of 0.738 does not instill a great deal of confidence. In fact, the "HQI" does not provide any absolute measure of the probability that the sample actually is the same as the library sample. The arbitrary scale of the HQI values does not provide a good statistical measure of the similarity of the spectra. This occurs because using only a single training spectrum to represent all possible samples in the future does not give any statistical assurance that the unknown and library spectra are truly the same or different. It only provides a relative measure for all the library samples. Nevertheless, useful criteria for confidence in the identification (for systems where the best HQI is 0 and the worst 1.0) are HQI between 0 and 0.2 indicates a close match, 0.2–0.5 a suggestive match, and above 0.5 one should "be careful" [30]. (For algorithms with other HQI ranges, the criteria are within 20% of the best HQI is a close match, 20–50% a suggestive match, and >50% one should be careful.)

Alternatively, Raman databases and unknown spectra can be analyzed using multivariate analysis or chemometrics methods. These are particularly valuable when a large number of very similar spectra from complex mixtures, such as from

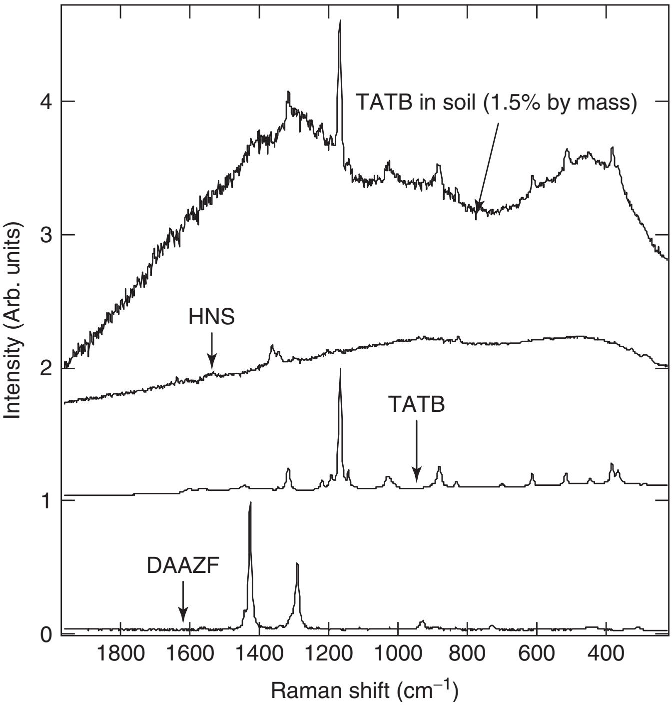

Figure 56.8 Raman spectrum of 1.5% TATB (triamino trinitrobenzene) in Bandelier Tuff soil, with library spectra of the three best matches (not plotted in order – see text) using the correlation algorithm and baseline correction.

biological samples, need to be categorized or the salient important characteristic features identified. This subject is handled in depth in Chapter 27: Principles of Vibrational Spectroscopic Methods and their Application to Bioanalysis.

56.7
Extensible Markup Language (XML) Data Model

XML is not a file format, but rather a universal markup language for exchanging structured documents and data on the Web with its own vocabulary and syntax, constrained by the recently adopted XML Schema Definition (XSD) language. It can be used to represent any data structure. The XML model provides the ability to link to other documents, called *XML Schema*, that describe exactly what each piece of data means and how it is related via XML language descriptions of a particular type of information and its storage. With the appropriate Schema, a software application can parse data from any XML data structure as well as determine that it is well formed. Therefore, XML documents can be externally validated for both content and syntax. XML data is human readable ASCII text, and the XML standard is public domain managed by the W3C.

The latest implemented version of this idea is embodied in the Analytical Information Markup Language, AnIML, *http://animl.sourceforge.net/* [31]. The project is a collaborative effort between many groups and individuals and is sanctioned by the ASTM under subcommittee E13.15. A variety of techniques have Definition Documents, which apply tight constraints to the flexible core and are in turn defined by the Technique Schema. The Open Source development is hosted on SourceForge. As of this writing, there is a Technique Definition Document for IR and UV–visible spectroscopic data, as well as sample parameters, but not yet for Raman spectroscopic data.

References

1. Schrader, B. and Moore, D.S. (1997) *Pure Appl. Chem.*, **69**, 1451–1468.
2. Long, D.A. (2002) *The Raman Effect: A Unified Treatment of the Theory of Raman Scattering by Molecules*, John Wiley & Sons, Ltd, Chichester.
3. Schrader, B. (1995) *Infrared and Raman Spectroscopy*, Wiley-VCH Verlag GmbH, Weinheim.
4. Schrötter, H.W. and Klöckner, H.W. (1979) in *Raman Spectroscopy of Gases and Liquids* (ed A. Weber) Chapter 4, Springer, Berlin.
5. Moore, D.S. and McGrane, S.D. (2003) *J. Mol. Struct.*, **661–662**, 561–566.
6. Mills, I., Cvitas, T. *et al.*, and International Union of Pure and Applied Chemistry (1993) *Quantities, Units and Symbols in Physical Chemistry*, 2nd edn, Blackwell Science, Oxford.
7. *http://www.horiba.com/fileadmin/uploads/Scientific/Documents/Raman/bands.pdf* (accessed 27 June 2013).
8. Socrates, G. (2004) *Infrared and Raman Characteristic Group Frequencies: Tables and Charts*, John Wiley & Sons, Ltd, Chichester.
9. Hirschfeld, T. and Chase, B. (1986) *Appl. Spectrosc.*, **40**, 133–137.
10. Moore, D.S. and Scharff, R.J. (2008) *Anal. Bioanal. Chem.* doi: 10.1007/s00216-008-2499-5
11. Hug, W.F., Reid, R.D., Bhartia, R., and Lane, A.L. (2008) *Proc. SPIE*, **6954**, 69540I.
12. Shreve, A.P., Cherepy, N.J., and Mathies, R.A. (1992) *Appl. Spectrosc.*, **46**, 707–711.
13. Yaney, P.P. (1972) *J. Opt. Soc. Am.*, **62**, 1297–1303.
14. Lieber, C.A. and Mahadevan-Jansen, A. (2003) *Appl. Spectrosc.*, **57**, 1363–1367.
15. Mosier-Boss, S.H., Lieberman, S.H., and Newbery, R. (1995) *Appl. Spectrosc.*, **49**, 630–638.
16. Carter, J.C., Scaffidi, J., Burnett, S., Vasser, B., Sharma, S.K., and Angel, S.M. (2005) *Spectrochim. Acta, Part A*, **61**, 2288–2298.
17. Sharma, S.K., Misra, A.K., Lucey, P.G., Angel, S.M., and McKay, C.P. (2006) *Appl. Spectrosc.*, **60**, 871.
18. Sedlacek, S.J. III,, Ray, M.D., and Wu, M. (2004) *Trends Appl. Spectrosc.*, **5**, 19–38.
19. ASTM International (2002) E1840-96(2002). Standard Guide for Raman Shift Standards for Spectrometer Calibration, ASTM International.
20. Choquette, S.J., Etz, E.S., Hurst, W.S., Blackburn, D.H., and Leigh, S.D. (2007) *Appl. Spectrosc.*, **61**, 117–129.
21. Denton, M.B., Sperline, R.P., Giles, J.H., Gilmore, D.A., Pommier, C.J.S., and Downs, R.T. (2003) *Aust. J. Chem.*, **56**, 117–131.
22. RRUFF *http://rruff.info/* (accessed 23 March 2013).
23. UCL Chemistry *http://www.chem.ucl.ac.uk/resources/raman/index.html* (accessed 23 March 2013).
24. *http://www.dst.unisi.it/geofluids/raman/spectrum_frame.htm* (accessed 27 June 2013).
25. National Institute of Advanced Industrial Science and Technology (AIST) *http://riodb01.ibase.aist.go.jp/sdbs/cgi-bin/*

cre_index.cgi?lang=eng (accessed 23 March 2013).

26. Thermo Fisher Scientific *https://ftirsearch.com/default2.htm* (accessed 23 March 2013).
27. IUPAC *http://www.jcamp-dx.org/* (accessed 23 March 2013).
28. Thermo Scientific *http://www.thermo.com/com/cda/resources/resources_detail/1,,112125,00.html* (accessed 23 March 2013).
29. Thermo Scientific *http://www.thermo.com/com/cda/resources/resources_detail/1,2166,13229,00.html* (accessed 23 March 2013).
30. Smith, B.C. (1996) *Fundamentals of Fourier Transform Infrared Spectroscopy*, CRC Press, Boca Raton, FL.
31. AnIML: Analytical Information Markup Language (2008) *http://animl.sourceforge.net/* (accessed 27 June 2013).

Index

Handbook of Spectroscopy, Second Edition. Edited by Günter Gauglitz and David S. Moore.